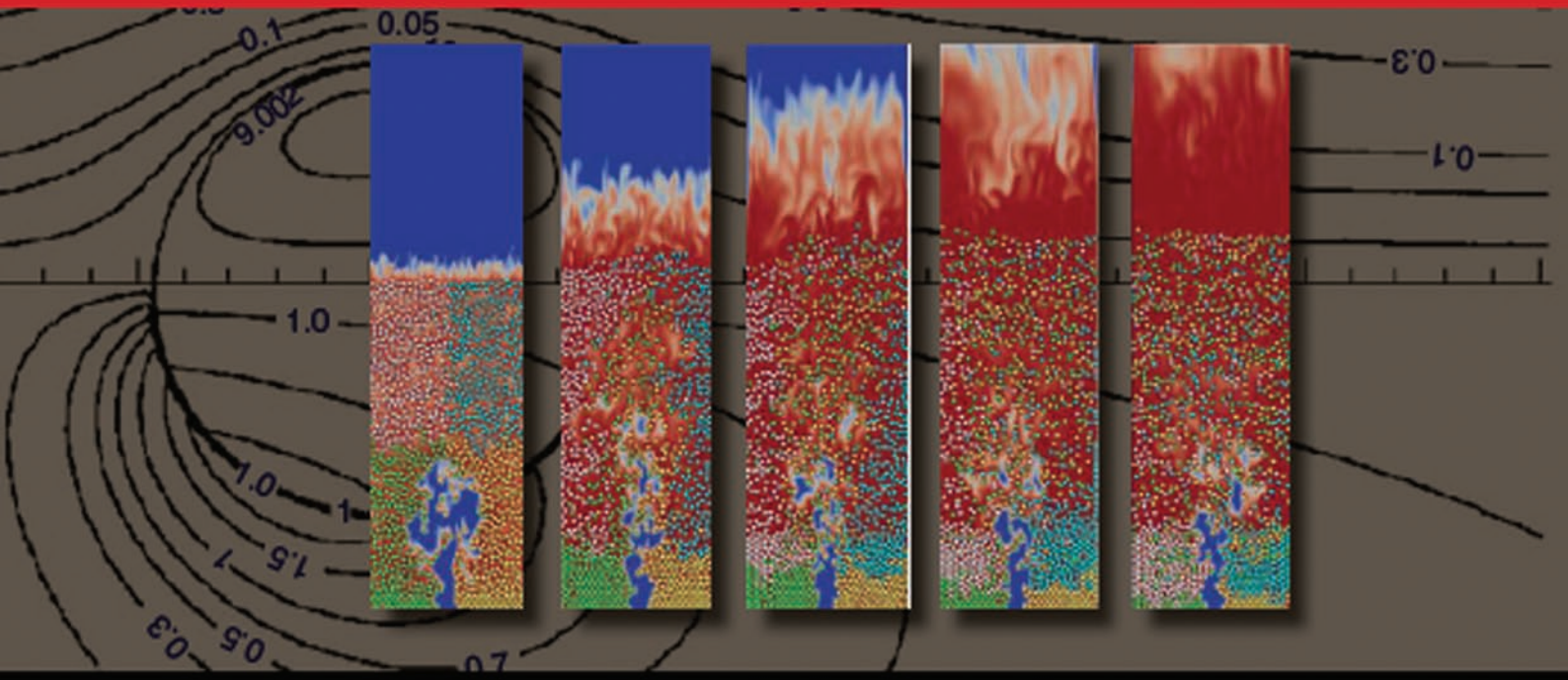
MULTIPHASE FLOW HANDBOOK

SECOND EDITION



EDITED BY

Efstathios E. Michaelides

Clayton T. Crowe

John D. Schwarzkopf

CRC Press

Taylor & Francis Group

MULTIPHASE FLOW HANDBOOK

SECOND EDITION

MECHANICAL and AEROSPACE ENGINEERING

Frank Kreith
Series Editor

RECENTLY PUBLISHED TITLES

Air Distribution in Buildings, *Essam E. Khalil*

Alternative Fuels for Transportation, *Edited by Arumugam S. Ramadhas*

Computer Techniques in Vibration, *Edited by Clarence W. de Silva*

Design and Control of Automotive Propulsion Systems,
Zongxuan Sun and Guoming (George) Zhu

Distributed Generation: The Power Paradigm for the New Millennium,
Edited by Anne-Marie Borbely and Jan F. Kreider

Elastic Waves in Composite Media and Structures: With Applications to Ultrasonic Nondestructive Evaluation, *Subhendu K. Datta and Arvind H. Shah*

Elastoplasticity Theory, *Vlado A. Lubarda*

Energy Audit of Building Systems: An Engineering Approach, *Moncef Krarti*

Energy Conversion, Second Edition, *Edited by D. Yogi Goswami and Frank Kreith*

Energy Efficiency and Renewable Energy Handbook, Second Edition,
Edited by D. Yogi Goswami and Frank Kreith

Energy Efficiency in the Urban Environment, *Heba Allah Essam E. Khalil and Essam E. Khalil*

Energy Management and Conservation Handbook, Second Edition,
Edited by Frank Kreith and D. Yogi Goswami

Essentials of Mechanical Stress Analysis, *Amir Javidinejad*

The Finite Element Method Using MATLAB®, Second Edition, *Young W. Kwon and Hyochoong Bang*

Fluid Power Circuits and Controls: Fundamentals and Applications, *John S. Cundiff*

Fuel Cells: Principles, Design, and Analysis, *Shripad Revankar and Pradip Majumdar*

Fundamentals of Environmental Discharge Modeling, *Lorin R. Davis*

Handbook of Hydrogen Energy, *Edited by S.A. Sherif, D. Yogi Goswami, Elias K. Stefanakos, and Aldo Steinfeld*

Heat Transfer in Single and Multiphase Systems, *Greg F. Naterer*

Heating and Cooling of Buildings: Design for Efficiency, Revised Second Edition,
Jan F. Kreider, Peter S. Curtiss, and Ari Rabl

Intelligent Transportation Systems: Smart and Green Infrastructure Design, Second Edition, *Sumit Ghosh and Tony S. Lee*

Introduction to Biofuels, *David M. Mousdale*

Introduction to Precision Machine Design and Error Assessment, *Edited by Samir Mekid*

Introductory Finite Element Method, *Chandrakant S. Desai and Tribikram Kundu*

Large Energy Storage Systems Handbook, *Edited by Frank S. Barnes and Jonah G. Levine*

Machine Elements: Life and Design, *Boris M. Klebanov, David M. Barlam, and Frederic E. Nystrom*

Mathematical and Physical Modeling of Materials Processing Operations, *Olusegun Johnson Ilegbusi, Manabu Iguchi, and Walter E. Wahnsiedler*

Mechanics of Composite Materials, *Autar K. Kaw*

Mechanics of Fatigue, *Vladimir V. Bolotin*

Mechanism Design: Enumeration of Kinematic Structures According to Function, *Lung-Wen Tsai*

Mechatronic Systems: Devices, Design, Control, Operation and Monitoring, *Edited by Clarence W. de Silva*

The MEMS Handbook, Second Edition (3 volumes), *Edited by Mohamed Gad-el-Hak*

- MEMS: Introduction and Fundamentals
- MEMS: Applications
- MEMS: Design and Fabrication

Multiphase Flow Handbook, *Edited by Clayton T. Crowe*

Nanotechnology: Understanding Small Systems, Third Edition, *Ben Rogers, Jesse Adams, Sumita Pennathur*

Nuclear Engineering Handbook, *Edited by Kenneth D. Kok*

Optomechatronics: Fusion of Optical and Mechatronic Engineering, *Hyungsuck Cho*

Practical Inverse Analysis in Engineering, *David M. Trujillo and Henry R. Busby*

Pressure Vessels: Design and Practice, *Somnath Chattopadhyay*

Principles of Solid Mechanics, *Rowland Richards, Jr.*

Principles of Sustainable Energy Systems, Second Edition, *Edited by Frank Kreith with Susan Krumdieck, Co-Editor*

Thermodynamics for Engineers, *Kau-Fui Vincent Wong*

Vibration and Shock Handbook, *Edited by Clarence W. de Silva*

Vibration Damping, Control, and Design, *Edited by Clarence W. de Silva*

Viscoelastic Solids, *Roderic S. Lakes*

Weatherization and Energy Efficiency Improvement for Existing Homes: An Engineering Approach, *Moncef Krarti*


Taylor & Francis
Taylor & Francis Group
http://taylorandfrancis.com

MULTIPHASE FLOW HANDBOOK

SECOND EDITION

EDITED BY

Efstathios E. Michaelides
Clayton T. Crowe
John D. Schwarzkopf



CRC Press
Taylor & Francis Group
Boca Raton London New York

CRC Press is an imprint of the
Taylor & Francis Group, an **informa** business

CRC Press
Taylor & Francis Group
6000 Broken Sound Parkway NW, Suite 300
Boca Raton, FL 33487-2742

© 2017 by Taylor & Francis Group, LLC
CRC Press is an imprint of Taylor & Francis Group, an Informa business

No claim to original U.S. Government works

Printed on acid-free paper
Version Date: 20160404

International Standard Book Number-13: 978-1-4987-0100-6 (Hardback)

This book contains information obtained from authentic and highly regarded sources. Reasonable efforts have been made to publish reliable data and information, but the author and publisher cannot assume responsibility for the validity of all materials or the consequences of their use. The authors and publishers have attempted to trace the copyright holders of all material reproduced in this publication and apologize to copyright holders if permission to publish in this form has not been obtained. If any copyright material has not been acknowledged please write and let us know so we may rectify in any future reprint.

Except as permitted under U.S. Copyright Law, no part of this book may be reprinted, reproduced, transmitted, or utilized in any form by any electronic, mechanical, or other means, now known or hereafter invented, including photocopying, microfilming, and recording, or in any information storage or retrieval system, without written permission from the publishers.

For permission to photocopy or use material electronically from this work, please access www.copyright.com (http://www.copyright.com/) or contact the Copyright Clearance Center, Inc. (CCC), 222 Rosewood Drive, Danvers, MA 01923, 978-750-8400. CCC is a not-for-profit organization that provides licenses and registration for a variety of users. For organizations that have been granted a photocopy license by the CCC, a separate system of payment has been arranged.

Trademark Notice: Product or corporate names may be trademarks or registered trademarks, and are used only for identification and explanation without intent to infringe.

Library of Congress Cataloging-in-Publication Data

Names: Michaelides, Efstathios, editor. | Crowe, C. T. (Clayton T.), editor. | Schwarzkopf, John D., editor.
Title: Multiphase flow handbook / editors, Efstathios E. Michaelides, Clayton T. Crowe, and John D. Schwarzkopf.
Description: Second edition. | Boca Raton : Taylor & Francis, CRC Press, 2015. | Series: Mechanical and aerospace engineering | Includes
bibliographical references and index.
Identifiers: LCCN 2015048725 | ISBN 9781498701006 (alk. paper)
Subjects: LCSH: Multiphase flow--Handbooks, manuals, etc.
Classification: LCC TA357.5.M84 M85 2015 | DDC 620.1/064--dc23
LC record available at http://lccn.loc.gov/2015048725

Visit the Taylor & Francis Web site at
http://www.taylorandfrancis.com

and the CRC Press Web site at
http://www.crcpress.com

To all the assiduous researchers and students of Multiphase Flow, who contributed to the rapid and significant scientific progress of this field in the last fifty years.


Taylor & Francis
Taylor & Francis Group
http://taylorandfrancis.com

Contents

Preface xiii

Editors xv

Contributors xvii

Nomenclature xxi

1 Fundamentals of Multiphase Flow 1
Efstathios E. Michaelides and Zhi-Gang Feng

2 Computational Methods 79

2.1 Overview of Numerical Approaches....79
Eric Loth

2.2 Direct Numerical Simulations of Gas–Liquid Flows....95
Gretar Tryggvason

2.3 The Lattice Boltzmann Method....108
Cyrus K. Aidun, Dennis E. Oztekin, Yuanzheng Zhu, Tomas Rosén, and Fredrik Lundell

2.4 Immersed Boundary Method....126
Zhi-Gang Feng and Efstathios E. Michaelides

2.5 Pdf Models for Particle Transport Mixing and Collisions in Turbulent Flows....144
Michael W. Reeks, Olivier Simonin, and Pascal Fede

2.6 Euler–Lagrange Methods....202
Martin Sommerfeld and Santiago Lain

2.7 Two-Fluid Model in MFIX....242
Madhava Syamlal, Jordan Musser, and Jean-François Dietiker

2.8 Uncertainty Quantification....275
Madhava Syamlal, Jordan Musser, and Jean-François Dietiker

3 Gas–Liquid Flow in Ducts 287
Afshin J. Ghajar and Swanand M. Bhagwat

4 Fluid–Solid Flow in Ducts 357
4.1 Pneumatic Conveying 357
Shrikant Dhodapkar and Karl Jacob
4.2 Slurry Flows 407
Shenggen Hu

5 Compressible Multiphase Flow 455
John D. Schwarzkopf, S. Balachandar, and William T. Buttler

6 Combustion with Particles and Drops 515
Farzad Mashayek and Farhad A. Jaberi

7 Microgravity Two-Phase Flows 545
Kamiel S. Gabriel

8 Boiling 559
Satish G. Kandlikar

9 Condensation 605
Jacob N. Chung and Tailian Chen

10 Powder and Granular Flow 637
Fu-Ling Yang and Keng-Lin Lee

11 Multiphase Flow in Porous Media 685
John R. Fanchi and John P. Seidle

12 Turbulence Interactions 729
John K. Eaton and Ellen K. Longmire

13 Bubble Dynamics and Cavitation 753
13.1 Bubble Dynamics 753
Yoichiro Matsumoto and Kazuyasu Sugiyama
13.2 Cavitation 774
Steven L. Ceccio

14 Aggregation, Collisions, and Breakup 795
14.1 Particle Interactions and Collisions 795
Yutaka Tsuji
14.2 Droplet Breakup, Coalescence, and Wall Impact 809
Cameron Tropea and Ilia V. Roisman

15 Particle Separation Methods and Systems 829
15.1 Separation Efficiency and Grade Efficiency 829
Chikao Kanaoka
15.2 Classification of Particle Separation Systems 831
Chikao Kanaoka
15.3 Flow-Through-Type Separators 833
Chikao Kanaoka
15.4 Gravitational Collectors 836
Chikao Kanaoka

15.5 Centrifugal Separation: Dry Cyclones....837
Hideto Yoshida and Kunihiro Fukui

15.6 Electrostatic Precipitators....848
Hisao Makino and Naoki Noda

15.7 Obstacle-Type Separators....861
Chikao Kanaoka

15.8 Inertial Dust Collectors....863
Chikao Kanaoka

15.9 Air Filters....864
Chikao Kanaoka

15.10 Scrubbers....870
Chikao Kanaoka

15.11 Barrier-Type Separators....873
Chikao Kanaoka

15.12 Bag Filters....873
Chikao Kanaoka

15.13 Liquid-Phase Particle Separation (Hydrocyclone)....877
Hideto Yoshida

16 Biological Systems and Biomimetics 887

16.1 Airflow and Particle Deposition in the Upper Respiratory Airways....887
Goodarz Ahmadi and Omid Abouali

16.2 Blood Flow....937
Shu Takagi, Kazuyasu Sugiyama, and Satoshi Ii

16.3 Biomimetics and Bioinspiration....948
Yoshimichi Hagiwara

17 Fluidized Bed Reactors 955

17.1 Hydrodynamics of Fluidization....955
John R. Grace

17.2 Heat and Mass Transfer....994
Bo Leckner

17.3 Applications of Fluidized Bed Reactors....1029
Jesse Zhu and Yi Cheng

18 Nanofluids 1059
Efstathios E. Michaelides and Yulong Ding

19 Spray Systems 1091
Udo Fritsching and Xing-gang Li

20 Aerosols 1251
Yannis Drossinos and Christos Housiadas

21 Dispersed Flow in Non-Newtonian Fluids 1321
Raj P. Chhabra

Index 1371


Taylor & Francis
Taylor & Francis Group
http://taylorandfrancis.com

Preface

Multiphase flow is the flow of heterogeneous mixtures of two or more phases, such as gas–liquid, solid–liquid, or gas–solid. Multiphase flow is encountered in numerous industrial and scientific applications, such as boiling and condensation processes, aerosol flows in the environment, gas and petroleum flows, gas–solid and slurry flows in pipelines, particle and fiber flows in airways, fluidized bed reactors, and nanofluids.

The first edition of the *Multiphase Flow Handbook* was published ten years ago with the late professor C.T. Crowe as the editor. The handbook provided a plethora of scientific and practical information to scientists, engineers, researchers, and students and has been useful to many. A great deal of research and development in multiphase flow occurred since the first edition of the handbook, and a lot of additional information is now available, especially in the area of computational modeling. The purpose of this second edition is to provide the reader with the fundamental principles of multiphase flow and useful current information for research, engineering design, and the classroom.

The structure of the second edition is different from that of the first: Several new chapters have been added, primarily on the applications. The material is divided into three sections: (1) fundamentals, (2) descriptions of specific types of multiphase flow and processes, and (3) significant applications. Chapters 1 and 2 pertain to fundamental concepts and numerical methods that are used in all types and applications of multiphase flow. Chapters 3 through 13 describe general types of multiphase flow, such as gas–solid, compressible multiphase flow, flow in porous media, bubble formation and cavitation, etc. Chapters 14 and 15 cover the processes of aggregation and industrial separation of particles, bubbles, and drops. Chapters 16 through 21 examine significant applications of multiphase flow from fluidized bed reactors to nanofluids to multiphase flow with non-Newtonian fluids.

I am grateful to the many distinguished contributors who lent their expertise and spent significant time and effort writing the chapters of this handbook within the time constraints of a publication. Jonathan Plant of Taylor & Francis Group/CRC Press was always there to provide managerial support and advice. Jessica Vakilli put together three of the sections from edited material supplied by the contributors. She and Kyra Lindholm completed all the administrative work such a big undertaking requires. Dr. John Schwarzkopf assisted in the early stages of the project. I am also indebted to Mr. Aranganathan Arunkumar of the production team of this publication, who spent many hours putting together the chapters and sections of this handbook. Last, but not least, I am thankful to my family, Laura, Emmanuel, Dimitri, and Eleni, for their continuous support and encouragement for such ambitious projects.

Efstathios E. Michaelides
Fort Worth, Texas


Taylor & Francis
Taylor & Francis Group
http://taylorandfrancis.com

Editors

Efstathios E. Michaelides holds the Tex Moncrief Chair of Engineering at Texas Christian University (TCU), Fort Worth, Texas. Prior to this, he was chair in the Department of Mechanical Engineering at the University of Texas in San Antonio, where he also held the Robert F. McDermott Chair in engineering and was the founder and director of the NSF-supported Center on Simulation, Visualization and Real Time Computing (SiViRT). He was also the founding chair of the Department of Mechanical and Energy Engineering at the University of North Texas (2006–2007); the Leo S. Weil professor of mechanical engineering at Tulane University (1998–2007); director of the South-Central Center of the National Institute for Global Environmental Change (2002–2007); associate dean for graduate studies and research in the School of Engineering at Tulane University (1992–2003); head of the Mechanical Engineering Department at Tulane University (1990–1992). Between 1980 and 1989, he was on the faculty of the University of Delaware, where he also served as the acting chair of the Mechanical Engineering Department (1985–1987).

Professor Michaelides was awarded an honorary MA from Oxford University (1983); the Casberg and Schillizzi scholarships at St. Johns College, Oxford; the student chapter ASME/Phi, Beta, Tau excellence in teaching award (1991 and 2001); the Lee H. Johnson award for teaching excellence (1995); a senior Fulbright fellowship (1997); the ASME Freeman Scholar award (2002); the Outstanding Researcher award at Tulane (2003); and the ASME Fluids Engineering award (2014).

Professor Michaelides was a member of the executive committee of the Fluids Engineering Division of the ASME (2002–2008) and served as the chair of the Division in 2005–2006. Prior to this, he served as the chair (1996–1998) of the Multiphase Flow Technical Committee. He also served as the president of the ASEE Gulf-South Region (1992–1993 and 2015–2016); he chaired the *Fourth International Conference on Multiphase Flows* (New Orleans, Louisiana, May 27 to June 1, 2001) and was the vice-chair of the *Fifth International Conference on Multiphase Flows* (Yokohama, Japan, May 2004). He has published more than 140 journal papers and has contributed more than 250 papers in national and international conferences. He has also published four books: *Particles, Bubbles and Drops—Their Motion and Heat Transfer* (World Scientific, 2006); *Alternative Energy Sources* (Springer, 2012); *Heat and Mass Transfer in Particulate Suspensions* (Springer, 2013); and *Nanofluidics—Thermodynamic and Transport Properties* (Springer, 2014). Professor Michaelides earned a bachelor's degree (honors) from Oxford University and master's and doctorate degrees from Brown University.

Clayton T. Crowe was a professor of mechanical and materials engineering at Washington State University in Pullman, Pullman, Washington. He is recognized as a leading scholar and author in fluid mechanics, and, in particular, the area of multiphase flows. Among his achievements was the development of the particle-source-in-cell (PSI-Cell) method for the numerical simulation of multiphase flow that has been used extensively in industry and in commercial simulation software. He was the author of numerous technical articles and of *Engineering Fluid Mechanics*, a widely used college textbook now in its eleventh edition. His other publications include *Multiphase Flows with Droplets and Particles, Second Edition* (CRC Press, 2012), and *Multiphase Flow Handbook, First Edition* (CRC Press, 2005). He received many honors for his work, including ASME fellow, the ASME Fluids Engineering Award, and the Senior International Prize for Multiphase Flows. Dr. Crowe passed away in 2012.

John D. Schwarzkopf is a staff scientist within the Theoretical Design Division at Los Alamos National Laboratory, Los Alamos, New Mexico. He has more than 10 years of experience in the application of multiphase flows and computational code development. His work contributed to two patents and several technical articles on the topic of multiphase and multicomponent flow applied to electronics cooling, atomization, and turbulence modeling. He is a coauthor of the book *Multiphase Flows with Droplets and Particles, Second Edition* (CRC Press, 2012).

Contributors

Omid Abouali
Shiraz University
Shiraz, Iran

Goodarz Ahmadi
Clarkson University
Potsdam, New York

Cyrus K. Aidun
G.W. Woodruff School of Mechanical Engineering
Parker H. Petit Institute for Bioengineering and Bioscience
Renewable Bioproducts Institute
Georgia Institute of Technology
Atlanta, Georgia

S. Balachandar
Department of Mechanical and Aerospace Engineering
University of Florida
Gainesville, Florida

Swanand M. Bhagwat
School of Mechanical and Aerospace Engineering
Oklahoma State University
Stillwater, Oklahoma

William T. Buttler
Physics Division
Los Alamos National Laboratory
Los Alamos, New Mexico

Steven L. Ceccio
University of Michigan
Ann Arbor, Michigan

Tailian Chen
Department of Mechanical Engineering
Gonzaga University
Spokane, Washington

Yi Cheng
Department of Chemical Engineering
Tsinghua University
Haidian, Beijing, People's Republic of China

Raj P. Chhabra
Department of Chemical Engineering
Indian Institute of Technology at Kanpur
Kanpur, India

Jacob N. Chung
Department of Mechanical and Aerospace Engineering
University of Florida
Gainesville, Florida

Shrikant Dhodapkar
The Dow Chemical Company
Freeport, Texas

Jean-François Dietiker
West Virginia University Research Corporation
Morgantown, West Virginia

Yulong Ding
School of Chemical Engineering
University of Birmingham
Birmingham, England

Yannis Drossinos
Joint Research Centre
European Commission
Ispra, Italy

John K. Eaton
Department of Mechanical Engineering
Stanford University
Palo Alto, California

John R. Fanchi
Department of Engineering
Texas Christian University
Fort Worth, Texas

Pascal Fede
Université de Toulouse
Toulouse, France

Zhi-Gang Feng
Department of Mechanical Engineering
University of Texas at San Antonio
San Antonio, Texas

Udo Fritsching
Department of Particles and Process Engineering
University of Bremen
Bremen, Germany

Kunihiro Fukui
Department of Chemical Engineering
Hiroshima University
Higashi-Hiroshima, Japan

Kamiel S. Gabriel
University of Ontario Institute of Technology
Oshawa, Ontario, Canada

Afshin J. Ghajar
School of Mechanical and Aerospace Engineering
Oklahoma State University
Stillwater, Oklahoma

John R. Grace
University of British Columbia
Vancouver, British Columbia, Canada

Yoshimichi Hagiwara
Department of Mechanical and System Engineering
Kyoto Institute of Technology
Kyoto, Japan

Christos Housiadas
Institute of Nuclear & Radiological Sciences & Technology, Energy & Safety
"Demokritos" National Centre for Scientific Research
Athens, Greece

Shenggen Hu
Commonwealth Scientific and Industrial Research Organisation
Pullenvale, Queensland, Australia

Satoshi Ii
Department of Mechanical Science and Bioengineering
Osaka University
Osaka, Japan

Farhad A. Jaberi
Department of Mechanical Engineering
Michigan State University
East Lansing, Michigan

Karl Jacob
Solids Processing Laboratory
The Dow Chemical Company
Midland, Michigan

Chikao Kanaoka
Department of Civil Engineering
Kanazawa University
Kanazawa, Japan

Satish G. Kandlikar
Department of Mechanical Engineering
Rochester Institute of Technology
Rochester, New York

Santiago Lain
Department of Mechanical Engineering
Universidad Autónoma de Occidente
Cali, Colombia

Bo Leckner
Department of Energy and Environment
Chalmers University of Technology
Göteborg, Sweden

Keng-Lin Lee
Department of Mechanical Engineering
National Taiwan University
Taipei, Taiwan, Republic of China

Xing-gang Li
Process and Chemical Engineering Division
IWT Foundation Institute of Materials Science
Bremen, Germany

Ellen K. Longmire
Department of Aerospace Engineering and Mechanics
University of Minnesota
Minneapolis, Minnesota

Eric Loth
University of Virginia
Charlottesville, Virginia

Fredrik Lundell
KTH Royal Institute of Technology
Stockholm, Sweden

Hisao Makino
Energy Engineering Research Laboratory
Central Research Institute of Electric Power Industry
Yokosuka, Japan

Farzad Mashayek
Department of Mechanical and Industrial Engineering
University of Illinois at Chicago
Chicago, Illinois

Yoichiro Matsumoto
Department of Mechanical Engineering
The University of Tokyo
Tokyo, Japan

and

RIKEN
Wako, Japan

Efstathios E. Michaelides
Department of Engineering
Texas Christian University
Fort Worth, Texas

Jordan Musser
National Energy Technology Laboratory
U.S. Department of Energy
Morgantown, West Virginia

Naoki Noda
Energy Engineering Research Laboratory
Central Research Institute of Electric Power Industry
Yokosuka, Japan

Dennis E. Oztekin
Georgia Institute of Technology
Atlanta, Georgia

Michael W. Reeks
Newcastle University
Newcastle, England

Ilia V. Roisman
Institute of Fluid Mechanics and Aerodynamics
Technische Universität Darmstadt
Darmstadt, Germany

Tomas Rosén
KTH Royal Institute of Technology
Stockholm, Sweden

John D. Schwarzkopf
Theoretical Design Division
Los Alamos National Laboratory
Los Alamos, New Mexico

John P. Seidle
MHA Petroleum Consultants
Denver, Colorado

Olivier Simonin
Institut National Polytechnique de Toulouse
Toulouse, France

Martin Sommerfeld
Center for Engineering Science
Martin-Luther University Halle-Wittenberg
Halle (Saale), Germany

Kazuyasu Sugiyama
Department of Mechanical Science and Bioengineering
Osaka University
Osaka, Japan

Madhava Syamlal
National Energy Technology Laboratory
U.S. Department of Energy
Morgantown, West Virginia

Shu Takagi
Department of Mechanical Engineering
The University of Tokyo
Tokyo, Japan

Cameron Tropea
Institute of Fluid Mechanics and Aerodynamics
Technische Universität Darmstadt
Darmstadt, Germany

Gretar Tryggvason
Department of Aerospace and Mechanical Engineering
University of Notre Dame
Notre Dame, Indiana

Yutaka Tsuji
Osaka University
Osaka, Japan

Fu-Ling Yang
Department of Mechanical Engineering
National Taiwan University
Taipei, Taiwan, Republic of China

Hideto Yoshida
Department of Chemical Engineering
Hiroshima University
Higashi-Hiroshima, Japan

Jesse Zhu
Particle Technology Research Centre
University of Western Ontario
London, Ontario, Canada

Yuanzheng Zhu
Georgia Institute of Technology
Atlanta, Georgia


Taylor & Francis
Taylor & Francis Group
http://taylorandfrancis.com

Nomenclature

Latin Symbols

a	Acceleration
A	Area
A_{eff}	Hamaker constant
B	Blowing factor
Bo	Bond number
Boi	Boiling number
c	Specific heat capacity
c_A, c_B,…	Mass concentration of species A, B,…
c_l	Speed of sound in liquid
C	Coefficient (dimensionless)
Ca	Capillary number
Co	Convection number
C_A	Added mass coefficient
C_D	Drag coefficient
C_H	History term coefficient
d	Diameter of small-scale features (particles, droplets, bubbles, etc.)
d_{32}	Sauter mean diameter (SMD)
D	Diameter of large-scale features (pipes, bends, etc.)
$\mathfrak{D}_{(\ )}$	Diffusion coefficient
e	Internal energy
E	Young's modulus
$E(\kappa)$	Energy intensity (for spectra)
Eo	Eötvös number
Eu	Euler number
f	Friction factor
$\mathfrak{F}$	Frequency
$F(D)$	Cumulative distribution
F_i	Force vector
Fo	Fourier number
Fr	Froude number
g	Gravitational acceleration
g_I	(i = 1, 2, 3,…) Gibbs free energy (molar)
G	Mass flux
Gr	Grashoff number
h	Enthalpy
h_c	Convective heat transfer coefficient
h_{fg}	Latent heat of evaporation
h_m	Convective mass transfer coefficient

H	Head
He	Hedstrom number
I	Intensity
Ja	Jakob number
$J_A, J_B,\ldots$	Mole fluxes of species A, B,…
k	Thermal conductivity
k_B	Boltzmann constant
k_s	Pipe roughness
k_w	Wave number
K	Turbulent kinetic energy
K_{nu}	Knudsen number
Ki	Kirpichev number
Ku	Kutateladze number
l	Length scale
L	Characteristic length
m	Mass
M	Mass flux
$\mathfrak{M}$	Molecular weight
M_a	Mach number
n	Power-law factor, number or number density
$n_A, n_B,\ldots$	Mole concentration of species A, B,…
n_i	Unit normal vector
N	Total number
N_{av}	Avogadro number
Nu	Nusselt number
Oh	Ohnesorge number
P	Pressure
p	Perimeter
P_{ij}	Collision frequency
Pe	Peclet number
q_e	Electric charge
$\dot{Q}$	Heat rate
q''	Heat flux
r, θ, φ	Spherical coordinates
r, θ, z	Cylindrical coordinates
$\mathfrak{R}_u$	Universal gas constant
Ra	Rayleigh number
Re	Reynolds number
R_{ij}	Turbulence Reynolds stress tensor
$R(\tau)$	Velocity correlation function
S	Surface
S_w	Swirl parameter
Sh	Sherwood number
Sha	Shannon number
St	Stokes number
St_h	Strouhal number
S_{ij}	Stress tensor
S_{mass}	Mass source term
S_{mom}	Momentum source term
t	Time
T	Temperature
$T(\kappa)$	Spectral energy transfer rate
U, u	Continuous phase velocity
u_i, v_i, w_i	Velocity vectors
v	Dispersed phase velocity

v_T	Terminal velocity
V	Volume
$\dot{V}$	Volumetric flow rate
We	Weber number
x, y, z	Cartesian coordinates
X	Lockhart–Martinelli parameter
Y	Mass fraction
Y_{mol}	Mole fraction
Z	Loading
z	Length scale

Greek Symbols

a	Particle radius
α_f	Thermal diffusivity of fluid
α_s	Absorptivity
β	Slip parameter
β_P	Expansion coefficient at constant pressure
β_T	Expansion coefficient at constant temperature
γ	Specific gravity
Γ	Torque
δ	Distance or spacing
δ_{ij}	Kronecker delta
ε	Turbulence energy dissipation rate
ε_0	Electric permeability of vacuum
ε_p	Porosity
ϵ	Emissivity
ζ	Dimensionless parameter
η	Kolmogorov length scale, amplitude
θ	Angle
Θ	Granular temperature, dimensionless temperature, wall scattering function
κ	Wave number, ratio of specific heats
κ_p	Permeability
κ_T	Expansion coefficient
λ_{m}	Molecular mean free path
λ	Factor of ratio
μ	Chemical potential, dynamic viscosity
ν	Kinematic viscosity
ρ	Density
Π	Coupling parameter
σ	Surface tension, standard deviation, Stefan–Boltzmann constant
$\sigma_n, \sigma_1, \sigma_2, \sigma_3$	Normal or principal stresses
τ	Response time, time scale
τ_s	Shear stress
φ	Velocity ratio
ϕ	Porosity
Φ	Two-phase flow multiplier, potential
ϕ_c	Volume fraction of continuous phase, void fraction
ϕ_d	Volume fraction of dispersed phase
χ	Gas mass quality
ψ	Stream function
ψ_s	Surface potential
Ψ	Shape factor
ω	Frequency
ω_i	Chemical source for species "i"
ω_n	Natural frequency
Ω	Angular velocity

Subscripts

,	Derivative
an	Annular
avg	Average
agg	Agglomeration
b	Bubble
B	Bulk
c	Continuous phase
ch	Characteristic
cr	Critical
co	Core
coag	Coagulation
coll	Collision
conv	Convective
d	Dispersed or dense phase
D	Drag
e	Eddy or equilibrium
eff	Effective
eq	Equivalent
f, *F*	Fluid
fg	Latent heat/enthalpy
fr	Friction
gas, *G*	Gas
gs	Superficial gas
GM	Geometric mean
h	Homogeneous
HM	Harmonic mean
i	Indices (1, 2, 3)
in	In or inlet
int	Interface
in	In or inlet
iso	Isolated
j	Indices (1, 2, 3)
k	Indices (1, 2, 3) or particle number
l	Lift
liq, *L*	Liquid
lo	Liquid only
ls	Superficial liquid
m	Mixture or pertains to mass
max	Maximum
min	Minimum
mom	Momentum
mol	Molecular
M	Mean
MD	Median
n	Number
nw	Nonwetting
nuc	Nucleation
NB	Nucleate boiling
o	Oil
opt	Optimum
out	Out or outlet
ONB	Onset of nucleate boiling
p	Particle
PB	Partial boiling region

r	Relative or reduced
rad	Radiation
rot	Rotational
s	Solid
sat	Saturation
sen	Sensor
sl	Slip
sol	Solution
ss	Steady state
str	Stratified
sub	Subcooled
sur	Surface
SM	Surface mean
th	Thermal
tot	Total
tp	Two-phase
tr	Transition
vap	Vapor phase
VM	Volumetric mean
W	Wall
w	Wetting phase or water
∞	Ambient, far away, free stream, undisturbed
0	Initial or incident

Superscripts

*	Dimensionless
0	Undisturbed field, incident or pure component at infinite dilution
′	Temporal fluctuation or spatial deviation
″	Favre fluctuation
·	Rate
g	Gas
I	Image variable
inc	Incident vector
m	Mixture
s	Sensor
S	Solid
sca	Scattered vector

Abbreviations

BL	Boundary layer
CFD	Computational fluid dynamics
CHF	Critical heat flux
DNS	Direct numerical simulations
MD	Molecular dynamics


Taylor & Francis
Taylor & Francis Group
http://taylorandfrancis.com

1

Fundamentals of Multiphase Flow

Efstathios E. Michaelides and Zhi-Gang Feng

1.1 General Features of Multiphase Flows
1.2 Fundamental Definitions
1.3 Size of Particles, Drops, and Bubbles
1.4 Interactions of Fluids with Particles, Drops, and Bubbles

1.1 General Features of Multiphase Flows

Solid, liquid, and vapor are the three natural phases of materials. Gases and ideal gases are parts of the vapor phase where specific constitutive equations, for example, the ideal gas equation, apply. A multiphase system contains materials of two or more phases. Multiphase flow is the flow of a mixture of phases such as gases (bubbles) in a liquid or liquid (droplets) in gases. Liquids of different densities and solids of different crystalline systems are often considered as separate phases. Thus, the flow of oil droplets in water is considered multiphase flow.

1.1.1 Dispersed Phase and Separated Flows

In dispersed phase flows, one phase consists of discrete, noncontinuous elements and the second phase consists of a continuous fluid matrix. Examples of dispersed multiphase flows are the flow of bubbles in a liquid and the flow of particles or droplets in a gaseous matrix. In a separated flow, the two phases are separated by a single surface of contact. For example, the annular flow in a pipe, which includes a liquid layer on the pipe wall and a vapor core, is a separated flow.

1.1.2 Gas–Liquid Flows

The motion of bubbles in liquids and the motion of droplets in gas streams are examples of gas–liquid flows. Bubble columns are commonly used in several process industries including chemical reactions and fluid purification processes. The atomization of a liquid to generate small droplets for combustion is important in power generation and automotive systems. Droplet formation and impaction are important in spray forming for materials processing. Steam–water flows in pipes and heat exchangers are very common in power systems with vapor cycles, such as fossil fuel plants and nuclear reactors. Gas–liquid flows in pipes can assume several geometric configurations ranging from bubbly flow to churn and annular flow.

1.1.3 Gas–Particle Flows

The particles in this case are either solid particles or liquid droplets. This type of multiphase flow includes the pneumatic transport of solids, fluidized beds for solids combustion, and the burning of fuel droplets.

The operation of pollution control devices, such as cyclone separators and electrostatic precipitators, is based on the principles of gas–solid flows. The combustion process of coal in fossil fuel power systems depends on the dispersion and burning of coal particles. The micron-size particles in a solid propellant rocket exhaust affect the performance of the rocket. Another type of a gas–solid flow is the motion of particles down a chute or an inclined plane. These are known as granular flows where particle–particle and particle–wall interactions determine the transport of the solid phase. In the extreme case, where the particulate phase is motionless, the flow becomes flow through a porous medium as, for example, in a pebble-bed heat exchanger or a stationary bed reactor.

1.1.4 Liquid–Solid Flows

Liquid–solid flows are flows where solid particles are carried by the liquid. Oftentimes, such flows are referred to as slurry flows. Slurries cover a wide spectrum of applications ranging from the transport of minerals (including coal) to the flow of toothpaste. Several environmental flows and processes, such as the removal of sediment from water and waterways, involve slurry transport. Typically, the solid particles are discrete and for this reason, slurry flows are classified as dispersed flows. When the solids are stationary, the flow of liquid through the solid is another example of flow in a porous medium.

1.1.5 Three-Phase Flows

Three-phase flows are also encountered in a few engineering systems. For example, gaseous bubbles rising in slurry are three phases flowing together. Three-phase flows are met in specialized systems and have a high degree of complexity. For this reason, not much research work has been reported in the literature on these flows.

1.1.6 Scope of This Handbook

Before the 1980s, the design of multiphase systems was based primarily on empirical observations and correlations of experimental data. Since the early 1980s, the design of more advanced instruments and the application of more scientific measurement techniques have led to the measurement and quantification of fundamental parameters that improved our understanding of multiphase systems and processes. In parallel, the tremendous improvement of computational capacity and numerical techniques has enabled the development of numerical models that are now reliably used to complement engineering design. The improvements of the experimental instruments and the numerical models for multiphase flows are rapidly growing areas of technology, which have far-reaching benefits in upgrading the operation and efficiency of current engineering systems and processes and in supporting the development of new and innovative technologies.

This handbook is designed to provide a background for engineers and scientists and to serve as a source of information on current technology. This chapter introduces fundamental definitions of dispersed multiphase flows, including size distributions and fundamental interactions of particles, bubbles, and drops with fluids. This chapter also addresses the current state of the art and examines commonly used instruments and processes for measuring multiphase flows. Chapter 2 deals with the numerical modeling of multiphase flows. It includes numerical modeling methods such as direct simulation, Lagrangian modeling, two-fluid modeling, and PDF modeling, as well as specific numerical techniques, such as the discrete element, the immersed boundary, and the lattice Boltzmann techniques. Chapters 3 and 4 cover the fundamentals of multiphase flow in ducts and apply to engineering systems for the transport of gas–liquid mixtures, pneumatic transport, and slurry transport. Chapter 5 addresses a more recently researched area, the area of compressible multiphase flow, and includes the interactions of particles, bubbles, and drops in compressible fluids. Chapter 6 addresses the subject of chemical reactions and combustion with drops and particles. The subject of Chapter 7 is multiphase flow and heat transfer under microgravity and zero-gravity conditions. Chapters 8 and 9 address the boiling and condensation processes in multiphase systems and include the local and global heat transfer processes in industrial boiling and condensation equipment. Chapter 10 addresses powder and granular flows, where the forces between the solid particles or between the solid particles and the boundaries are by far greater than the hydrodynamic forces between the particles and the interstitial fluid. The subject of multiphase flow in porous media, such as the flow of oil and gas in rock formations and cracks, is surveyed in Chapter 11. The complex interactions between the dispersed phase (bubbles, particles, and drops) and

the turbulence of the continuous fluid phase are the subject of Chapter 12. Chapter 13 addresses the dynamics of deformable bubbles and the process of bubble cavitation, which is of paramount importance in the shipping industry. Chapter 14 addresses the fundamentals of the collision process, which may result in the aggregation of particles and the formation or breakup of clusters. Chapter 15 addresses the separation processes and equipment, including the removal of dust and droplets from gaseous streams. Chapter 16 covers the flow of particles in biological systems, such as the blood stream and the respiratory tract. Chapter 17 is devoted to the industrial systems known as fluidized bed reactors that are increasingly used for chemical and combustion processes. Chapter 18 is devoted to the new application of multiphase fluids, which are known as nanofluids. Nanofluids exhibit very high heat and mass transfer characteristics. The formation and dynamics of spray systems is addressed in Chapter 19. The flow and processes of aerosols, with particular emphasis on aerosol deposition, are covered in Chapter 20. Finally, Chapter 21 addresses the fundamentals of flow and heat transfer characteristics of a dispersed phase in a non-Newtonian fluid.

1.2 Fundamental Definitions

This section introduces parameters that are fundamental to multiphase flows. For brevity and convenience, the terms *discrete phase* and *dispersed phase* will be used for the particles, drops, or bubbles, while the terms *carrier fluid* and *continuous phase* will be used for the fluid that carries the dispersed phase.

1.2.1 Volume Fraction and Densities

The continuum hypothesis enables one to define material properties at any point (x, y, z) despite the fact that matter is discontinuous at the molecular level. According to the continuum hypothesis, all properties, variables, and derivatives of the variables are defined within a limit volume, V_{lim}, that is big enough and contains a sufficient number of molecules so that all the variables and their derivatives have stationary values. An extension of the continuum hypothesis may be used with dispersed multiphase systems to define their properties (Michaelides, 2014). The extension defines the property of an inhomogeneous mixture at a point (x, y, z) by considering a volume, V, around the point (x, y, z). This volume must be greater than a limit volume, V_0, which is defined so that the calculated or measured values of the properties of the dispersed phase are stationary and independent of the motion of the dispersed phase elements (Michaelides, 2014).

Under this extension of the continuum hypothesis, the volume fraction of the dispersed phase is defined as

$$\alpha_d(x,y,z) = \frac{V_d}{V} \quad \text{with } V > V_0, \tag{1.1}$$

where V_d is the volume of the dispersed phase within the volume V. The volume V_0 is the limit volume that ensures a stationary average of the volume fraction despite the motion of the elements of the dispersed phase (particles, bubbles, or drops).

Similarly, the volume fraction of the continuous phase is

$$\alpha_c(x,y,z) = \frac{V_c}{V} \quad \text{with } V > V_0, \tag{1.2}$$

where V_c is the volume of the continuous phase in the volume under consideration.

In gas–liquid flows, the volume fraction is sometimes referred to as the "void fraction." From the volume conservation principle, the total volume is occupied either by the dispersed or by the continuous phase. This implies that, at any point of the continuum, the sum of the two volume fractions equals 1:

$$\alpha_c(x,y,z) + \alpha_d(x,y,z) \equiv 1. \tag{1.3}$$

The *density* or *apparent density* of the dispersed phase is equal to the mass of the dispersed phase per unit volume of the mixture. Similarly, the apparent density of the continuous phase is equal to the mass of the

continuous phase per unit volume of the mixture. If the dispersed material is composed of a single chemical substance with material density ρ_d and the material density of the continuous phase is ρ_c, the apparent densities of the two phases are

$$\bar{\rho}_d = \rho_d \alpha_d \quad \text{and} \quad \bar{\rho}_c = \rho_c \alpha_c. \tag{1.4}$$

Finally, the *mixture density*, which is defined as the total mass of the mixture divided by the total volume, is equal to the sum of the two apparent densities:

$$\rho_m = \bar{\rho}_c + \bar{\rho}_d. \tag{1.5}$$

1.2.2 Phase Velocities and Superficial Velocities

The *phase velocity* of a phase—u_c and u_d for the continuous and dispersed phases, respectively—is the actual velocity of each phase of a multiphase flow mixture and may be defined and measured at any point of the mixture. The *superficial velocity* of a phase is oftentimes used for calculations in channel flows and is defined as the mass flow rate of the phase divided by the total channel area and the material density of the phase:

$$U_d = \frac{\dot{m}_d}{A\rho_d} \quad \text{and} \quad U_c = \frac{\dot{m}_c}{A\rho_c} \tag{1.6}$$

It is apparent that the superficial velocity is the velocity of the phase if that phase were flowing alone and occupied the entire channel area. The phase velocities and the superficial velocities are related through the following volume fractions:

$$u_d = \frac{U_d}{\alpha_d} \quad \text{and} \quad u_c = \frac{U_c}{\alpha_c} \tag{1.7}$$

1.2.3 Quality, Concentration, and Loading

The quality, which is primarily used in vapor–liquid flows, is the ratio of the mass of the gas to the mass of the mixture. If the gas is the dispersed phase, the quality is defined as follows:

$$x = \frac{m_d}{m_c + m_d} = \frac{\bar{\rho}_d}{\bar{\rho}_m}. \tag{1.8}$$

The *mass concentration* or simply *concentration* of the dispersed phase is used in fluid–solid mixtures. This is a local variable defined at every point and is equal to the ratio of the apparent densities:

$$C = \frac{\bar{\rho}_d}{\bar{\rho}_c}. \tag{1.9}$$

The volume fraction, α_d, is used by some authors as an alternative definition of the concentration. A third variable, the loading, is often used in fluid–solid flows. The loading is the ratio of the two mass flow rates and is defined as follows:

$$Z = \frac{\dot{m}_d}{\dot{m}_c}. \tag{1.10}$$

1.2.4 Response Times

The response times of particles, bubbles, and drops are pertinent to their interactions with fluids and the interfacial transfer of momentum, energy, and mass. Oftentimes, the response times are called characteristic times. The momentum response time, τ_v, is of the order of magnitude of the time required for a sphere

to respond to a change in velocity. A measure of the momentum response time for a sphere may be derived from the equation of motion of a sphere in a fluid, which, in the absence of the transient terms, may be written as

$$\frac{\pi d^3}{6}\rho_d \frac{dv}{dt} = \frac{1}{2} C_D \frac{\pi d^2}{4}\rho_c (u-v)|u-v|, \tag{1.11}$$

where v is the particle velocity in the direction of the carrier fluid velocity u. The drag coefficient C_D is a function of the Reynolds number of the sphere, which is defined in terms of the relative velocity

$$Re_r = \frac{\rho_c d|u-v|}{\mu_c}, \tag{1.12}$$

where μ_c is the viscosity of the continuous phase. Rearranging the terms of Equation 1.11, one obtains

$$\frac{dv}{dt} = \left(\frac{C_D Re_s}{24}\right)\left(\frac{18\mu_c}{\rho_d d^2}\right)(u-v). \tag{1.13}$$

At the limit of vanishingly small Re_r, the so-called Stokes flow, the factor in the first parenthesis, $C_D Re_s/24$, is equal to 1. The factor in the second parenthesis has the dimension of (time)$^{-1}$. The inverse of this variable defines the momentum response time

$$\tau_V = \frac{d^2\rho_d}{18\mu_c}. \tag{1.14}$$

With this definition of the response time, the equation of motion is simplified to

$$\frac{dv}{dt} = \frac{1}{\tau_V}(u-v). \tag{1.15}$$

When the (uniform) fluid velocity undergoes a step from 0 to U, the solution to the last equation is

$$v = U\left[1-\exp\left(-\frac{t}{\tau_V}\right)\right]. \tag{1.16}$$

Therefore, the momentum response time is the time required for a particle released from rest to reach 63% or $(1 - 1/e)$ of the free-stream velocity under Stokes flow conditions.

The thermal response time, τ_T, is defined in a similar way, using a simplified form of the energy equation of a solid sphere at the limit of vanishingly small Peclet numbers:

$$\frac{dT_d}{dt} = \frac{Nu}{2}\left(\frac{12k_c}{\rho_d c_d d^2}\right)(T_c - T_d). \tag{1.17}$$

Since at vanishingly small Peclet numbers $Nu = 2$, the last equation defines the thermal response time

$$\tau_T = \frac{\rho_d c_d d^2}{12k_c}, \tag{1.18}$$

where c_d is the specific heat (at constant pressure) of the dispersed phase. When the fluid temperature undergoes a temperature step, τ_T is the time required for a particle's temperature to reach 63% or $(1 - 1/e)$ of this temperature step.

A third response time may be defined for the mass transfer process from a sphere. Since the mass transfer process is analogous to the heat transfer, the characteristic time for the mass transfer is

$$\tau_M = \frac{d^2}{12D_c}, \tag{1.19}$$

where D_c is the diffusion coefficient of the dispersed phase species inside the continuous phase. The three response times are related as follows:

$$\frac{\tau_V}{\tau_T} = \frac{2}{3}\frac{c_c}{c_d}\frac{1}{Pr}, \quad \frac{\tau_V}{\tau_M} = \frac{12D_c\rho_d}{18\mu_c} = \frac{2\rho_d}{3\rho_c}Sc, \quad \frac{\tau_T}{\tau_M} = \frac{Pr}{Sc}\frac{\rho_d}{\rho_c}\frac{c_d}{c_c}. \tag{1.20}$$

The Prandtl and Schmidt numbers pertain to the properties of the continuous phase. The order of magnitude considerations of the two dimensionless numbers proves that the mass transfer process is by far the slowest of the three transfer processes (Michaelides, 2014).

1.2.5 Dimensionless Numbers

The carrier fluid also has characteristic times and length scales that depend on the process under consideration and the domain geometry. The ratios of the particle to fluid characteristic times and length scales define several dimensionless numbers. These numbers are classified here according to the pertinent effects (Michaelides, 2013a,b, 2014):

1. *Viscosity effects*: Three Reynolds numbers for the particles are defined with respect to the rectilinear velocity, the rotational velocity, and the local fluid shear. In addition, a separate Reynolds number is defined for the carrier fluid. The first three dimensionless groups are based on the particle diameter. The last is defined with respect to the characteristic length scale of the fluid, L, and pertains to the entire suspension. The four Reynolds numbers are defined as follows:

$$Re_r = \frac{d\rho_c|\vec{u}-\vec{v}|}{\mu_c}, \quad Re_\gamma = \frac{d^2\rho_c\gamma}{\mu_c}, \quad Re_{rot} = \frac{d^2\rho_c|\vec{\Omega}|}{\mu_c}, \quad Re_c = \frac{L\rho_c|\vec{u}|}{\mu_c}. \tag{1.21}$$

2. *Heat and mass transfer effects:* Four Peclet numbers that correspond to the four Reynolds numbers ($Pe = Re * Pr$), the Nusselt number, the Biot number, and the Sherwood number of the particles and the suspension are defined as follows:

$$\begin{aligned} &Pe_r = \frac{d\rho_c c_c|\vec{u}-\vec{v}|}{k_c}, \quad Pe_\gamma = \frac{d^2\gamma\rho_c c_c}{k_c}, \quad Pe_M = \frac{d|\vec{u}-\vec{v}|}{D_c}, \\ &Pe_c = \frac{L\rho_c c_c|\vec{u}|}{k_c}, \quad Nu = \frac{2\alpha h_c}{k_c}, \quad Bi = \frac{dh_c}{k_c}, \quad Sh = \frac{dh_M}{D_c}. \end{aligned} \tag{1.22}$$

3. *Surface tension effects*: These are characterized by the Bond number, the capillary number, the Eötvos number, the Morton number, and the Weber number:

$$\begin{aligned} &Bo = \frac{gd^2|\rho_d-\rho_c|}{\sigma}, \quad Ca = \frac{\mu_c|\vec{u}-\vec{v}|}{\sigma} = \frac{We}{Re_r}, \quad Eo = \frac{d^2g\rho_c}{\sigma}, \\ &Mo = \frac{g\mu_c^4}{\rho_c\sigma^3}, \quad We = \frac{d\rho_c|\vec{u}-\vec{v}|^2}{\sigma} = Re_rCa. \end{aligned} \tag{1.23}$$

4. *Dimensionless property numbers*: The Prandtl number, the Lewis number, and the Schmidt number, which are pertinent to the transport properties of the fluid, are defined as follows:

$$Pr = \frac{c_c \mu_c}{k_c}, \quad Le = \frac{k_c}{\rho_c D_c c_c}, \quad Sc = \frac{\mu_c}{\rho_c D_c}. \tag{1.24}$$

5. *Other effects*: Molecular or rarefaction effects are quantified by the Knudsen number, phase-change effects by the Stefan number, and oscillatory and transient effects by the Strouhal number:

$$Kn = \frac{L_{mol}}{d}, \quad Ste = \frac{c_c \Delta T}{h_{fg}}, \quad Sl = \frac{df}{|\vec{u} - \vec{v}|}. \tag{1.25}$$

Of particular significance in the literature of dispersed multiphase flow is the Stokes number, *St*. The Stokes number characterizes the inertia of the particle and is defined as the ratio of the momentum timescale of the sphere to the characteristic timescale of the carrier fluid:

$$St = \frac{\tau_V}{\tau_c}. \tag{1.26}$$

The characteristic time of the fluid, τ_c, related to a spherical particle is defined as the diameter of the particle divided by the pertinent fluid velocity or by the rms of the velocity fluctuations in the case of turbulence. When $St \ll 1$, the particle has ample time to respond to changes in the flow velocity and follows closely the fluid velocity changes. When $St \gg 1$, the particle has no time to respond to the fluid velocity and does not follow the carrier fluid changes or fluctuations. The Stokes number is frequently used in turbulent flows to determine the response of particles, drops, and bubbles to the turbulent velocity fluctuations.

1.3 Size of Particles, Drops, and Bubbles

While drops and bubbles are largely spherical or ellipsoidal, most particles have irregular shapes that may not be described by one or two easily measurable dimensions. Despite this, it is often advantageous to include in calculations the characteristic length or *size* of the elements of the dispersed phase. The *size* of a spherical particle is equal to its diameter. The *size* of a nonspherical particle is subject to interpretation and must be well defined. Following the practice of spherical particles—for which most of the analytical and experimental work has been performed in the past—fan *equivalent diameter* may be defined for nonspherical particles, drops, and bubbles. The practical usefulness of the equivalent diameter is that one may correlate the transport coefficients of irregularly shaped particles, for example, drag coefficients and heat/mass transfer coefficients, with the known transport coefficients for spheres. Several equivalent diameters have been proposed in the past for nonspherical particles including the diameter of a sphere that would have the same volume, *V*; the diameter of a sphere that would have the same area, *A*; and the diameter of a sphere that would have the same perimeter, *P*, projected in the direction of the motion of the nonspherical particle. These three equivalent diameters are defined as follows:

$$d_V = \sqrt[3]{\frac{6V}{\pi}}, \quad d_A = \sqrt{\frac{4A}{\pi}}, \quad \text{and} \quad d_P = \frac{P}{\pi}. \tag{1.27}$$

For a sphere, the three equivalent diameters are the same and equal to the actual diameter, *d*. A fourth equivalent diameter, which is frequently used with irregular particles and aggregates, is the diameter of the minimum sphere, in which the irregular particle will fit in. Typically, this is the longest dimension of the particle, d_L. While d_P depends on the direction of the particle movement and its magnitude may vary in an arbitrary way, for all the other measures of the *size* of a particle, the inequality $d_V \leq d_A \leq d_L$ holds, with the equal sign applying to spheres only. Figure 1.1 shows schematically the last three diameters or *sizes* for a particle that appears as an elongated parallelepiped. It may be seen in this figure that the three equivalent

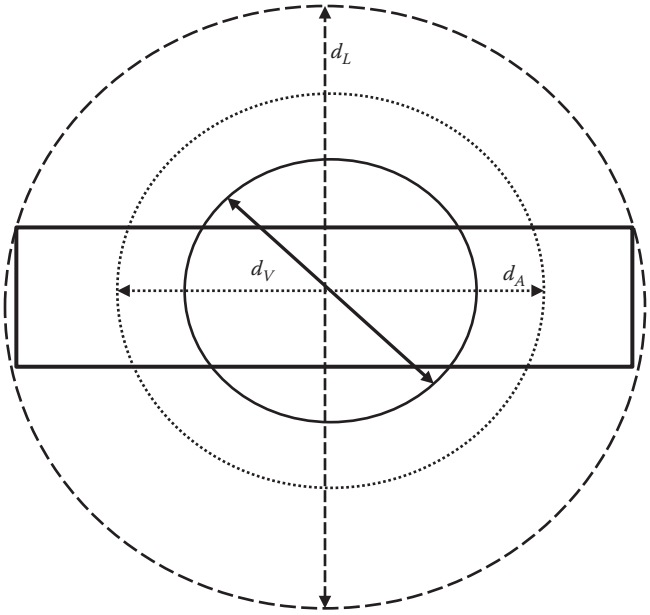


Figure 1.1

A schematic diagram of the three equivalent diameters, d_V, d_A, and d_L, for a particle with the shape of a parallelepiped.

diameters, which are also depicted, vary significantly in magnitude. Because of the significant variability, a precise definition or measurement of the *size* of particles, bubbles, and drops must include how this *size* has been defined or measured (Michaelides, 2014).

Another definition of an equivalent diameter that is extensively used with sediments and sedimentary suspensions of particles is the "sieve diameter." This is obtained from a sieve mesh analysis and is defined as the maximum standard sieve mesh size (or minimum sieve aperture) through which the particles may pass through (Leeder, 1982). Since the standard sieves do not extend to the micrometer and nanometer sizes, this method is not applicable to micro- and nanosize particles.

Regarding shapes, the *Corey shape factor* has been defined as the ratio of the shortest principal axis of the particle to the square root of the product of the longest two principal axes. The Corey factor, although widely used in the past with ellipsoidal particles, is not related to volume or area calculations, which are important in the calculations of the transport coefficients. In addition, it is difficult to apply this factor to irregular particles, where the principal axes are not well defined.

1.3.1 Fractal Dimensions of Particles and Aggregates

Fractal geometry is a recent tool that is often used to analyze the structure of irregular patterns of lines, surfaces, and volumes. The fractal shapes are composed of self-similar parts when viewed or measured by different length scales. For example, if we take photographs of a fractal object at different scales, as the scale changes, we will observe that the shapes in the photographs remain the same. When viewed and measured at the different length scales, the length and area of the fractal shape are different and, actually, increase when the scale of measurement decreases. The classical example of a fractal shape is the coastline of a country (Mandelbrot, 1967): one may measure the length of the coastline using a map, using aerial photographs, using a 1 m ruler on the ground, or using a smaller ruler, whose length is one grain of sand. The length of the coastline increases as the unit of measurement becomes smaller, and more details are revealed and counted. Figure 1.2 illustrates an example of this concept using the so-called Koch curve. The Koch curve is a complex, self-similar curve that evolves from a single straight segment according to the following rule: at each stage of evolution, every straight segment of the curve is substituted by four other straight segments of length 1/3 the length of the old segment. Two of the new segments span the ends of the old segment. The other two segments, which occupy one-third of the old segment's length, form the sides of an equilateral triangle and make up the inner part of the new segment. The process of evolution of the curve may produce an infinite number of stages, three of

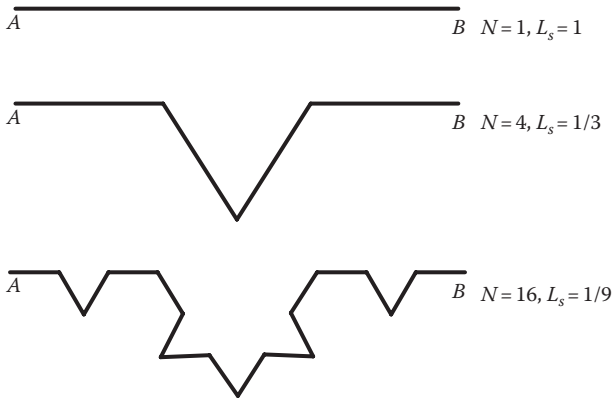


Figure 1.2

The length of a complex, fractal curve increases as the unit of measurement decreases.

which are shown in Figure 1.2. The end points of all the stages, A and B, are at the same distance apart in all the stages of the pattern evolution.

Without loss of generality, we may stipulate that the segment AB is of unit length. The measure of the length in the first stage of the curve is $N = 1$. In the second stage, the length scale is $L_s = 1/3$ and the number of segments $N = 4$. In the third stage, the length scale is $L_s = 1/9$ and the number of segments $N = 16$. In terms of the original units, the total length of the curve is 4/3 units in the second stage, 16/9 in the third stage, and so on. For self-similar objects, such as this curve, there is a fundamental dimension, the *fractal dimension*, L_f, which does not change with the scale of measurement. The fundamental dimension is related to the fundamental equation of self-similar patterns:

$$N = \left(L_s\right)^{-L_f}, \tag{1.28}$$

where N is the number of straight line segments of the scale length, L_s, that spans the entire length of the curve. From the definition of the fractal shapes, N is a strong function of the scale length. The value of L_f for a straight line is 1 and for a sphere 3. All other shapes have fractal dimensions between the two limits.

It must be noted that fractal dimensions describe a shape or a surface in very general terms. They do not define shapes and patterns and they do not contain enough information to construct them. In the case of the Koch curve, which has $L_s = 1.2619$, there are several other complex patterns that have the same fractal dimension but are dramatically different in shape and complexity.

Single particles have irregular but not self-similar shapes. The fractal dimension, L_f, of single particles is meaningless in most cases. Aggregates of primary particles, and especially very large aggregates of spheres, have been observed to have complex shapes, surfaces, and perimeters, which are oftentimes approximated as self-similar surfaces and lengths. In these cases, a fractal dimension of the aggregates, L_f, may be defined using the limit of Equation 1.28 as the length scale, L_s, vanishes (Vicsek, 1999):

$$L_f = -\lim \frac{\ln\left(N\right)}{\ln\left(L_s\right)} \quad \text{as } L_s \to 0. \tag{1.29}$$

For particle aggregates, L_f is typically calculated by taking microscopic images of the aggregates at different scales and using Equation 1.29 with the measuring length scale, L_s, taking several different values. Oftentimes, optical image software performs this task (Lee and Kramer, 2004, Wang and Chau, 2009). A simpler, albeit not as accurate method, is to measure the fractal dimension from light scattering (Bushell et al., 2002).

It must be noted that in the determination process of the fractal dimension of aggregates, the scale L_s cannot attain values that are smaller than the dimension of the largest primary particle of the aggregate. Therefore, the determination of the fractal dimension of particle aggregates is only an approximation to Equation 1.29. Also that for any measurement of L_f to be meaningful, the variation of the measurement length scale, L_s, must span at least two orders of magnitude. This implies that the method may only be used with big aggregates that contain a very large number of primary particles (at least 500).

The fractal dimension of the aggregates is often used to give an estimate of the porosity, ε_p, of the aggregate (Li and Logan, 2001):

$$\varepsilon_p = 1 - \left(\frac{d_a}{d}\right)^{3-L_f}, \tag{1.30}$$

where

d is the diameter of the primary particles

d_a is the *diameter* of the aggregate

The latter is typically assumed to be equal to the longest dimension of the aggregate, that is, $d_a = d_L$.

Several authors have used the fractal dimension to describe the structure and morphology of particles or aggregates of particles. Two conditions must be explicitly satisfied when one uses the fractal dimension in a quantitative manner:

1. The original object must have a self-similar shape to make the fractal dimension, L_f, meaningful.
2. The 2D microscopic images or the light scattering method must be adequate for the determination of the fractal dimension, L_f, of particles that are inherently three dimensional.

Because the second condition is not always satisfied, it has been observed that measurements of L_f by 2D photographic images may be laden with high measurement errors. The measurement error becomes significantly high if the *measured* fractal dimension is close to or greater than 2 (Vicsek, 1999).

1.3.2 Size Distributions

The sizes of particles, drops, and bubbles are important parameters that govern the flow of a dispersed multiphase mixture. In most cases, there is not a single size of these elements of dispersed flows but several sizes, which constitute the size distribution. Because of this, it is important to have a basic knowledge of the statistical parameters of the size distributions. A general characterization of particle size distribution is *monodisperse* and *polydisperse*. In a monodisperse mixture, the particles' sizes are close to a single size and typically, the standard deviation of the sizes is less than 10% of the mean size. In a polydisperse mixture, there is a wide range of particle sizes. Particle, drop, and bubble size distributions can also be classified as discrete or continuous. The continuous size distribution derives from the discrete distribution as the sampling interval approaches zero.

1.3.2.1 Discrete Size Distribution

For the size measurements of particles, one chooses a measuring technique, such as photography or sieve measurements, and also chooses size intervals, Δd, which are not necessarily of equal magnitude. The size intervals are large enough to contain a significant fraction of particles, yet small enough to yield sufficient detail. The representative size of the particles in each interval may be defined as the diameter corresponding to the midpoint of the interval. For the size measurements, the number of particles in each interval is counted, recorded, and divided by the total number of particles in the sample. The results are plotted in the form of a histogram (bar chart) as shown in Figure 1.3. Such histograms are identified as the *discrete number frequency distribution* for the particle size. For large samples of particles, the distribution is also referred to as the "probability density function" or "pdf." The ordinate of the histogram is the number frequency of the particles, $\tilde{f}_n$, within a size interval. The sum of the number frequency over all the size categories is equal to 1.

The number-average particle diameter of this distribution is defined as

$$\bar{d}_n = \sum_{i=1}^{N} d_i \tilde{f}_n(d_i), \tag{1.31}$$

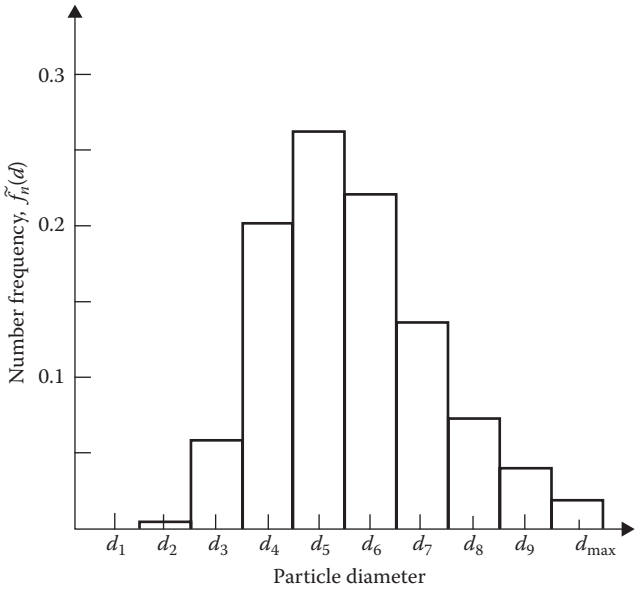


Figure 1.3

Histogram of the number frequency distribution of a sample of particles. The sum of the nine values of the frequency distribution is equal to 1.

where N is the total number of intervals. The number variance is

$$\sigma_n^2 = \frac{N}{N-1}\sum_{i=1}^{N}\left(d_i - \bar{d}_n\right)^2 \tilde{f}_n(d_i) = \frac{N}{N-1}\sum_{i=1}^{N} d_i^2 \tilde{f}_n(d_i) - \bar{d}_n^2 . \tag{1.32}$$

The standard deviation, σ_n, is the square root of the variance of the sizes. Oftentimes, the ratio of the standard deviation to the average diameter is used as a measure of the spread of the distribution. A narrow distribution is characterized by the relationship $\sigma_n / d_n < 0.1$, and the mixture is characterized as monodisperse.

Two other approaches are used to describe the size distribution using the particle mass and volume *in lieu* of the particle number as the dependent variable. Thus, for the mass distribution, the mass of each particle is measured or inferred from measurements, and the fraction of mass associated with each size interval is used to construct the distribution. This is known as the discrete mass frequency distribution, $\tilde{f}_m$. Using this distribution, one may calculate the mass-averaged particle diameter and mass-averaged variance as follows:

$$\bar{d}_m = \sum_{i=1}^{N} d_i \tilde{f}_m(d_i), \tag{1.33}$$

and

$$\sigma_m^2 = \frac{N}{N-1}\sum_{i=1}^{N}\left(d_i - \bar{d}_m\right)^2 \tilde{f}_m(d_i) = \frac{N}{N-1}\sum_{i=1}^{N} d_i^2 \tilde{f}_m(d_i) - \bar{d}_m^2 \tag{1.34}$$

The volume-averaged particle diameter and volume-averaged variance are calculated in a similar manner. If the material density of the particles is constant, the volume- and mass-averaged distributions are identical. It must be noted that in order to achieve a reasonably smooth frequency distribution function, a very large number of particles must be counted. Several modern optical experimental techniques make this task feasible with relatively low effort.

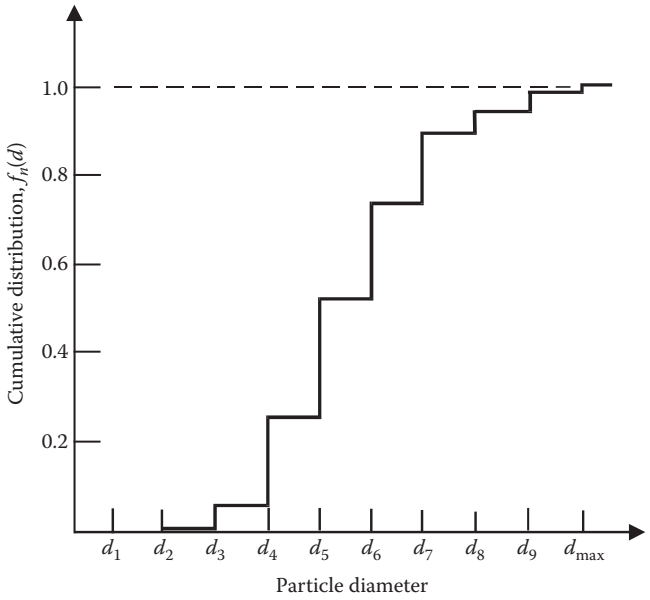


Figure 1.4

The cumulative number distribution that corresponds to the number frequency distribution of Figure 1.3.

Another commonly used method to quantify particle size is using the *cumulative* distribution, which is the sum of the components of the frequency distribution. The cumulative number distribution associated with size d_k is

$$\tilde{F}_n(d_k) = \sum_{i=1}^{k} \tilde{f}_n(d_i). \tag{1.35}$$

The numerical value of $\tilde{F}_n$ is the fraction of particles with sizes less than d_k. It is apparent that the cumulative number distribution is equal to 0 at the very fine sizes and close to 1 at the higher end of the sizes of the particles. The cumulative number distribution that corresponds to the number frequency distribution of Figure 1.3 is shown in Figure 1.4. Both cumulative number and cumulative mass distributions may be determined from the data of the corresponding frequency distribution.

1.3.2.2 Continuous Size Distributions

If the size intervals in a discrete distribution are made progressively smaller, in the limit as Δd approaches very small values, one obtains the continuous number frequency function

$$f_n(d) = \lim_{\Delta d \to 0} \left(\frac{\tilde{f}_n(d)}{\Delta d} \right). \tag{1.36}$$

The number fraction of particles with diameters between d and $d + d(d)$ is given by the differential $f_n(d)\, d(d)$. The function of the continuous frequency distribution is a continuous function of the diameter as shown in Figure 1.5. In a similar manner, one obtains the mass frequency function based on the mass distribution $\tilde{f}_m$. If the continuous distribution is normalized, as in Figure 1.5, then the area under the continuous frequency distribution curve is equal to 1.

The continuous cumulative distribution is obtained from the integral of the continuous frequency distribution as follows:

$$F_n(d) = \int_0^d f_n(\xi) d\xi. \tag{1.37}$$

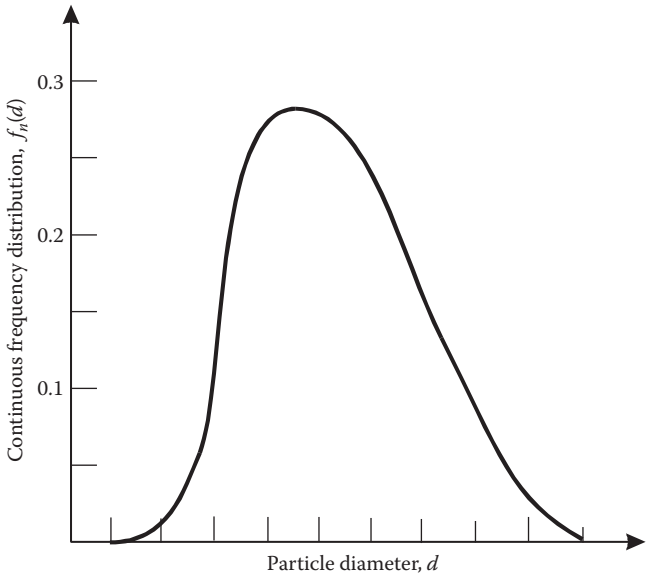


Figure 1.5

Continuous number frequency distribution of a sample of particles.

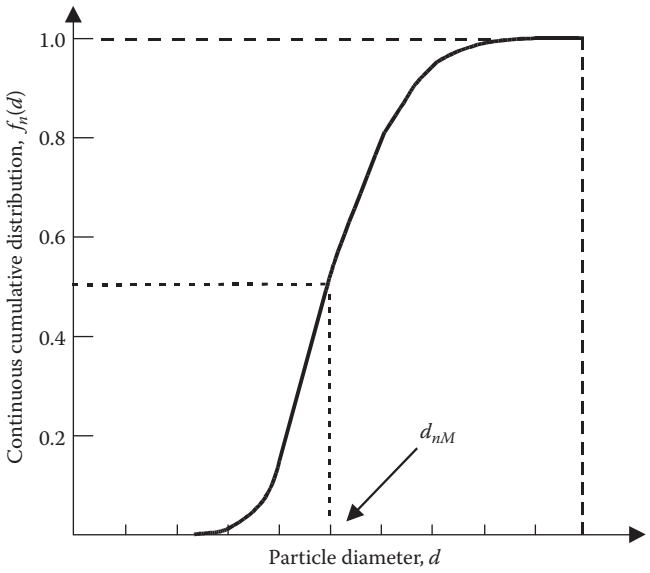


Figure 1.6

The cumulative distribution function that corresponds to the continuous distribution function of Figure 1.5.

The cumulative distribution function associated with the continuous distribution function of Figure 1.5 is an S-shaped curve, which is shown in Figure 1.6. The cumulative distribution of a uniform (constant) continuous distribution is a straight line. All cumulative distribution functions approach the value 1, as the particle size approaches the maximum size.

It must be noted that measurements of size data for particles generate discrete distributions. Continuous distributions may be obtained for convenience by fitting empirical functions to the discrete size data.

1.3.3 Statistical Parameters of the Size Distributions

Several parameters are used with discrete and continuous size distributions. We present here the most commonly used parameters in dispersed multiphase flow. Typically, these parameters have different values for the number, mass, and volume distributions.

1.3.3.1 Mode

The mode is the size that corresponds to the maximum of a continuous frequency function. A distribution that has two local maxima is referred to as a bimodal distribution and it has two modes. Similarly, trimodal and multimodal distributions may be defined, but they are seldom met in dispersed multiphase flows. The corresponding mode for a discrete size distribution is the size that corresponds to the highest value in the frequency histogram. For example, d_5 is the mode of the discrete distribution depicted in Figure 1.3.

1.3.3.2 Mean

For a discrete distribution, the mean is equal to the average and is given by Equations 1.31 and 1.33. The mean of a continuous distribution is obtained from the integral of the size, d, multiplied by the pertinent frequency distribution. For the continuous number distribution function, the corresponding mean is

$$\mu_n = \int_0^{d_{\max}} d\tilde{f}_n d(d). \tag{1.38}$$

A similar expression applies to the continuous mass distribution mean, μ_m. Sometimes, this mean is called the arithmetic mean diameter d_{AM}. Other mean diameters that are used in dispersed multiphase flows are the surface mean diameter

$$d_{SM} = \left[\int_0^{d_{\max}} d^2 \tilde{f}_n d(d) \right]^{1/2} \tag{1.39}$$

and the volume mean diameter

$$d_{VM} = \left[\int_0^{d_{\max}} d^3 \tilde{f}_n d(d) \right]^{1/3}. \tag{1.40}$$

1.3.3.3 Sauter Mean Diameter

The Sauter mean diameter (SMD) is encountered frequently in the spray and atomization literature and is defined as follows:

$$d_{32} = \frac{\int_0^{d_{\max}} d^3 f_n(d) d(d)}{\int_0^{d_{\max}} d^2 f_n(d) d(d)}. \tag{1.41}$$

The SMD is a measure of the volume-to-surface area ratio for particles, bubbles, and drops.

1.3.3.4 Variance

The variance of the continuous distribution with mean μ is calculated from the expression

$$\sigma^2 = \int_0^{d_{\max}} (d-\mu)^2 f(d) d(d) = \int_0^{d_{\max}} d^2 f(d) d(d) - \mu^2. \tag{1.42}$$

As with the mean, a variance may be defined to the number, the mass, or the volume distributions of particle sizes. As with the discrete distributions, the variance is a measure of the spread of the distribution and the square root of the variance is the standard deviation. A continuous distribution may be classified as monodisperse if $\sigma/\mu < 0.1$.

1.3.3.5 Median

The median diameter, d_M, corresponds to the diameter for which the cumulative distribution has the value 0.5. The number median diameter, d_{nM}, is shown in the cumulative distribution of Figure 1.6. A corresponding value for the mass median diameter, d_{mM}, may be determined from the cumulative mass distribution function.

1.3.4 Size Distributions

While there is a multitude of distributions in the literature of statistics, this section presents the statistical distributions that are most often used in the literature of dispersed multiphase flow.

1.3.4.1 Log-Normal Distribution

The number frequency function of the log-normal distribution is (Marshall, 1954)

$$f_n(d) = \frac{1}{\sqrt{2\pi} d\sigma_G} \exp\left[-\frac{1}{2}\left(\frac{\ln(d) - \ln(d_{nM})}{\sigma_G} \right)^2 \right], \tag{1.43}$$

where

d_{nM} is the median diameter of the number distribution
σ_G is the geometric standard deviation

The corresponding expression for the mass frequency distribution is

$$f_m(d) = \frac{1}{\sqrt{2\pi} d\sigma_G} \exp\left[-\frac{1}{2}\left(\frac{\ln(d) - \ln(d_{mM})}{\sigma_G} \right)^2 \right], \tag{1.44}$$

where d_{mM} is the mass median diameter. The geometric standard deviation is determined by plotting the cumulative distribution on logarithmic coordinates. The plot is a straight line with a positive slope, and the value for σ_G may be determined from the relationship

$$\sigma_G = \ln \frac{d_{84}}{d_M}, \tag{1.45}$$

where

d_{84} is the diameter corresponding to the 84th percentile on the logarithmic plot
d_M is the median diameter, which is the diameter corresponding to the 50th percentile

The same value for σ_G is used for the mass and number distributions. For the calculation of the several statistical parameters in this distribution, a useful mathematical relationship is

$$d_M^k \exp\left(\frac{k^2 \sigma_G^2}{2} \right) = \frac{1}{\sqrt{2\pi}\sigma_G} \int_0^\infty \left[d^k \exp\left[-\frac{1}{2}\left(\frac{\ln(d) - \ln(d_{mM})}{\sigma_G} \right)^2 \right] \right] \frac{d(d)}{d}, \tag{1.46}$$

or

$$d_M^k \exp\left(\frac{k^2 \sigma_G^2}{2} \right) = \int_0^\infty d^k f(d) d(d). \tag{1.47}$$

These relationships may be readily used to calculate the various statistical parameters of the distribution.

1.3.4.2 Upper-Limit Log-Normal Distribution

A derivative of the log-normal distribution is the upper-limit log-normal distribution (Mugele and Evans, 1951), which is frequently used to model droplet data from spray nozzles. The distribution makes use of a maximum particle size as the upper limit of the distribution and its number frequency function is defined as

$$f_n(d) = \frac{1}{\sqrt{2\pi} d \sigma_G} \exp\left[-\frac{1}{2} \left(\frac{\ln(\alpha d) - \ln\left(d_{\max} - d_{nM}\right)}{\sigma_G} \right)^2 \right], \tag{1.48}$$

where

$d_{\max}$ is the maximum diameter in the distribution
a is a constant equal to

$$\alpha = \frac{d_{\max}}{d_M} - 1. \tag{1.49}$$

As with the log-normal distribution, the standard deviation may be calculated from the slope of the logarithmic plot of the data.

1.3.4.3 Square-Root Normal Distribution

The number frequency function for the square-root normal distribution is given by the expression (Tate and Marshall, 1953)

$$f_n(d) = \frac{1}{2\sqrt{2\pi\sigma} d} \exp\left[-\left(\frac{\left(\sqrt{d} - \sqrt{\bar{d}}\right)}{2\sigma} \right)^2 \right], \tag{1.50}$$

where σ is the variance of the square-root normal distribution. This distribution appears to fit well empirical data from vane-type atomizers and does not have the end "tails" of a normal distribution. When using this distribution, one must be cognizant that several relationships that were derived for the other types of normal distributions are not applicable to the square-root normal distribution.

1.3.4.4 Rosin–Rammler Distribution

The Rosin–Rammler distribution (Mugele and Evans, 1951) is frequently used to model droplet size distributions in sprays. It is expressed in terms of the cumulative mass distribution

$$F_m(d) = 1 - \exp\left[-\left(\frac{d}{\delta} \right)^n \right]. \tag{1.51}$$

where δ and n are two empirical constants, which are determined by plotting the cumulative distribution on logarithmic coordinates. By taking twice the logarithm of Equation 1.51, one obtains

$$\ln\left[-\ln\left(1 - F_m(d)\right) \right] = n\left(\ln(d) - \ln(\delta)\right). \tag{1.52}$$

Therefore, n is the slope of this line and δ can be obtained from the expression

$$\delta = \frac{d_{mM}}{0.693^{1/n}}. \tag{1.53}$$

The mass frequency function of this distribution may be obtained by taking the derivative of the cumulative distribution of Equation 1.51:

$$f_m(d) = \frac{dF_m(d)}{d(d)} = \frac{n}{\delta}\left(\frac{d}{\delta}\right)^{n-1} \exp\left(\left[-\left(\frac{d}{\delta}\right)^n\right]\right). \tag{1.54}$$

When using the Rosin–Rammler distribution, the gamma function,

$$\Gamma(x) = \int_0^\infty \lambda^{x-1} \exp(-\lambda) d\lambda, \tag{1.55}$$

is a useful tool to calculate the moments of the distribution because

$$\int_0^\infty n d^\alpha \left(\frac{d}{\delta}\right)^{n-1} \exp\left[-\left(\frac{d}{\delta}\right)^n\right] d\left(\frac{d}{\delta}\right) = \delta^\alpha \Gamma\left(\frac{\alpha}{n}+1\right), \tag{1.56}$$

which leads to the relationship for the statistical parameters of this distribution

$$\int_0^\infty d^\alpha f_m(d) d(d) = \delta^\alpha \Gamma\left(\frac{\alpha}{n}+1\right). \tag{1.57}$$

1.3.4.5 Nukiyama–Tanasawa Distribution

The Nukiyama–Tanasawa distribution is a more general distribution from which the Rosin–Rammler distribution is a special case. The frequency function of this distribution is

$$f_n(d) = Bd^2 \exp\left(-Cd^q\right), \tag{1.58}$$

where B, C, and q are empirical parameters. For spray distributions, q typically varies from 1/6 to 2 with the higher values corresponding to narrower distributions.

1.3.4.6 Log-Hyperbolic Distribution

Some empirical studies on sprays showed that neither the log-normal nor the Rosin–Rammler distribution fits the data sufficiently well. Two droplet size distributions fitted with a Rosin–Rammler distribution may have the same parameters, but the actual distribution may be quite different. This happens because one of the shortcomings of both the log-normal and Rosin–Rammler distributions is the representation of the tails of the distribution—the values of the frequency function for very large and very small values of the sizes. A better fit for the tails of the distributions is the log-hyperbolic distribution proposed by Barndorff-Nielsen (1977). The form of the number frequency function for this distribution is

$$f_n(d) = A \exp\left[-\alpha\sqrt{\delta^2 - \left(\ln(d)-\mu\right)^2} + \beta\left(d-\mu\right)\right], \tag{1.59}$$

where α, β, δ, and μ are empirical parameters. It is apparent that the random variable of this distribution is the logarithm of the particle diameter. The coefficient A is a normalization factor related to the other parameters by the expression

$$A = \frac{\sqrt{\left(\alpha^2-\beta^2\right)}}{2\alpha\delta K_1\left(\delta\sqrt{\left(\alpha^2-\beta^2\right)}\right)}, \tag{1.60}$$

where K_1 is the third-order Bessel function of the third kind. The logarithm of the frequency function yields the equation of a hyperbola:

$$\ln(f_n) = \ln(A) - \alpha\sqrt{\delta^2 - (\ln(d) - \mu)^2} + \beta(d - \mu). \tag{1.61}$$

For $[\ln(d) - \mu]/\delta < 0$, the slope of the asymptote is $\alpha + \beta$, while for $[\ln(d) - \mu]/\delta > 0$, the slope of the asymptote is $-\alpha + \beta$. Thus, when the logarithm of the frequency data is plotted versus $\ln(d)$, the slopes of the two asymptotes may be measured to determine the parameters α and β. It may be proven that the parameter μ is the mode of the distribution. The value of this parameter may be determined from data fitting. A practical problem of the log-hyperbolic distribution for particle or drop size distributions is that if the tails are not long enough to generate accurate values of the slopes, there is a great deal of inaccuracy in the determination of the parameters α and β. A three-parameter log-hyperbolic distribution may be used in such cases to alleviate this problem.

1.4 Interactions of Fluids with Particles, Drops, and Bubbles

1.4.1 Introduction

Because the sphere is the simplest, 3D shape, mass, momentum, and heat transport problems pertaining to spheres have been the subjects of the first analytical methods as well as of the intellectual curiosity of scientists. These problems belong to the class of the most fundamental problems in fluid dynamics, heat transfer, and mass transfer and have attracted the attention of many mathematicians, physicists, and engineers. They are also subjects that have numerous practical applications including combustion and propulsion, chemical reactions and catalysis, mixing and separation, boiling and condensation, environmental sedimentation and resuspension, and biological flows. The transport of momentum, heat, and mass is of primary interest in all of these processes, which are often expressed in terms of *transport coefficients* or in terms of dimensionless parameters that are pertinent to these coefficients. For example, the instantaneous loss or gain of mass of a sphere during any process may be expressed in terms of the mass transfer coefficient, h_M, or its dimensionless representation, the Sherwood number, Sh, and the material properties of the sphere and the carrier fluid:

$$\dot{m}_s = \frac{dm_s}{dt} = -\pi h_M d^2 \rho_c (Y_s - Y_\infty) = -\pi (Sh) d D_c \rho_f (Y_s - Y_\infty), \tag{1.62}$$

where D_c is the diffusivity of the material of the sphere inside the carrier fluid. Similarly, the instantaneous temperature change of the sphere, in the case of convective heating (when radiation is negligible), may be expressed in terms of the heat transfer coefficient, h, or its dimensionless representation, the Nusselt number:

$$m_s c_{ps} \frac{dT_s}{dt} = \dot{Q} = -\pi h d^2 (T_s - T_\infty) = -\pi d Nu k_c d (T_s - T_\infty). \tag{1.63}$$

Finally, the equation of motion of a sphere may be expressed by Newton's second law in terms of all the instantaneous forces that act on the sphere. These forces are the hydrodynamic force on the sphere, F_H (which is composed of two parts, the drag and lift, F_D, and, F_L), and the body or volume force, F_B. The latter is normally the gravity/buoyancy force, and the former may be written in terms of two dimensionless factors: the drag coefficient, C_D, and the lift coefficient, C_L:

$$\begin{aligned} m_s \frac{dv_i}{dt} = F_{Di} + F_{Li} + F_{Bi} + F_{AMi} + F_{Hi} &= \frac{1}{8}\pi d^2 \rho_c C_D (u_i - v_i)\left|u_m - v_m\right| \\ &+ \frac{1}{8}\pi d^2 \rho_c C_L \left|u_m - v_m\right| \frac{e_{ijk}(u_k - v_k)\Omega_j}{\sqrt{\Omega_l \Omega_l}} + \frac{1}{6}\pi(\rho_s - \rho_c) d^3 g_i + F_{AM} + F_H, \end{aligned} \tag{1.64}$$

where e_{ijk} is the permutation symbol. The added mass force, F_{AM}, and the history term, F_H, emanate from the transient response of the particle and the surrounding fluid. Functional forms for the two terms are given in

Section 1.4.3.6. For the performance of any calculations on the motion of the sphere, one would need accurate information for the *transport coefficients*: drag coefficient, lift coefficient, heat transfer coefficient, and mass transfer coefficient. The numerical values of these coefficients emanate from analytical or numerical results and from experimental data.

This section intends to be a succinct presentation of analytical, experimental, and numerical results that pertain to the transport processes involving a carrier fluid and bubbles, drops, or particles and are useful for the performance of engineering calculations. In particular, mass transfer, momentum transfer, and heat transfer from a particle, bubble, or drop with the carrier fluid will be examined. For a historical background and a more extensive description of the development of these subjects, one may consult the review article by Michaelides (2003). Of the other recent studies, the main results on the momentum transfer from a sphere to a fluid as well as the energy and mass transfer at wide ranges of Reynolds and Peclet numbers may be found in several treatises and monographs, such as those by Leal (1992), Kim and Karila (1991), Crowe et al. (1998), Sirignano (1999), Michaelides (2006), and Michaelides (2014).

1.4.2 Mass Transfer

1.4.2.1 Thermodynamic Relations of Evaporation, Sublimation, and Condensation

In this section, we seek to determine the thermodynamic equilibrium relations between the carrier fluid and a sphere that undergoes phase change. For this reason, the thermodynamic properties are assumed to be equilibrium properties and this implies no (or very weak) heat and mass transfer within the system. Consider a sphere of radius a, inside a carrier gas of density ρ_f, in a spherical system of coordinates that follow the center of the sphere. The carrier gas and the sphere have different chemical composition, and their species will be denoted by c and l, respectively. Mass is allowed to cross the boundary of the sphere due to one of the processes of sublimation, evaporation, or condensation. Because of this, the gaseous phase is composed of both the species l and c, while the sphere, which may be either solid or liquid, is composed solely of the species l. Figure 1.7 is a schematic diagram of such a process. The directions and numerical signs of the pressure and temperature gradients in this figure are such that they correspond to the case of condensation. The total pressure in the gaseous mixture is constant and equal to p_T. The total pressure comprises two parts: the partial pressure, or vapor pressure, of the species l, p_l, and the partial pressure of the carrier gaseous species c, p_c. In all the transport processes that are pertinent to mass transfer, both the partial pressures are functions of the radial direction, r:

$$p_T = p_c(r) + p_l(r). \tag{1.65}$$

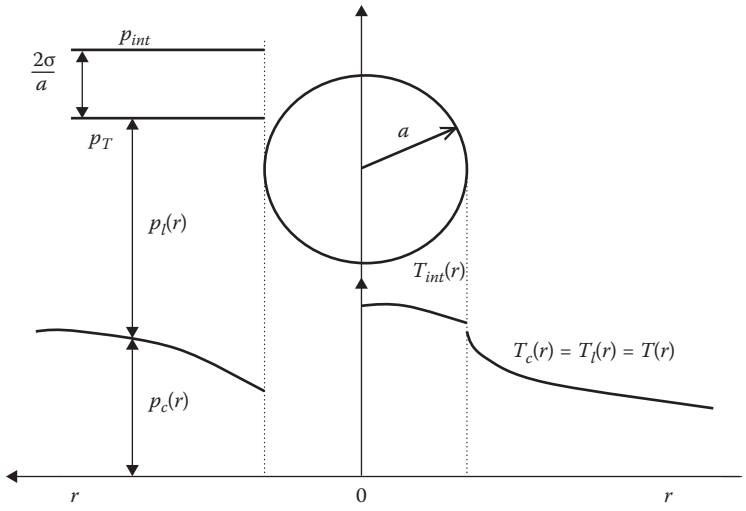


Figure 1.7

Pressure and temperature fields developed in the vicinity of a drop carried by the fluid of different compositions.

If the carrier phase is composed of a number of species, $c1$, $c2$, $c3$, … as, for example, in the case of air, then the total pressure is the sum of all the partial pressures of these species:

$$p_T = \sum_i p_{ci}(r) + p_l(r). \tag{1.66}$$

When the sphere is a liquid drop, the pressure in the interior of the drop would be higher than p_T by the amount contributed by the surface tension:

$$p_{int} = p_T + \frac{2\sigma}{a}. \tag{1.67}$$

In most practical applications, the radius of the sphere, a, is large enough to satisfy the condition $p_T \gg 2\sigma/a$. Hence, the internal pressure, p_{int}, is approximately equal to the total pressure in the gas phase, p_T. Thermodynamic equilibrium implies that the temperatures of the species l and c at the surface anywhere in the gaseous mixture are equal, that is, $T_c(r) = T_l(r) = T(r)$, where $r > a$. The temperature inside the sphere may be nonuniform and hence a function of the radial distance. This temperature will be denoted as $T_{int}(r)$, where $r < a$.

At the surface of the sphere, there is a phase transition, for example, liquid–vapor or solid–vapor, that normally occurs within a very short layer of molecular dimensions. The phase of the matter in this film layer is not well defined. Hence, the material and thermodynamic properties within this molecular layer are not well defined too. For this reason, they are depicted by the dashed lines in Figure 1.7. It is known that the specific properties of matter exhibit a jump discontinuity within this layer, for example, from liquid-specific enthalpy to vapor-specific enthalpy. The intensive properties of matter, temperature, and pressure exhibit a discontinuity of lower magnitude. The discontinuity of the intensive properties is not noticeable unless the Knudsen number of the flow is higher than 0.01 (see Section 1.4.3.5. for more details) where the molecular effects play an important role in the behavior of the sphere.

With the exception of very fast combustion processes, in most of the practical applications involving drops and particles that undergo mass, momentum, and heat transfer with a carrier fluid, the thermodynamic relaxation time is much shorter than all the response times of the sphere. For this reason, thermodynamic equilibrium is normally established fast at the interface and does not affect significantly the transport processes. When the interface may be considered sufficiently flat for the surface tension to have negligible impact, the partial pressure of the vapor and the temperature of the vapor at the interface are related via the Clausius–Clapeyron equation

$$\frac{dp_l}{dT}\Big|_a = \frac{h_{fg}}{T(a)\left[\dfrac{1}{\rho_v(a)} - \dfrac{1}{\rho_s(a)}\right]}, \tag{1.68}$$

where the symbols in parentheses denote arguments of functions and the derivative must be evaluated at the conditions of the interface $r = a$. Thus, $T(a)$ is the temperature at the interface, $\rho_v(a)$ is the density of the species l in its vapor phase at the interfacial pressure and temperature, and $\rho_s(a)$ is the density of the material in the sphere, evaluated also at the interfacial pressure and temperature. Therefore, the temperature and vapor pressure at the interface of the sphere are related by the so-called saturation relation, $p_l = p_{sat}(T)$. The function $p_{sat}(T)$ for any of the commonly used materials may be obtained in tabular form from thermodynamics texts or in tables of properties. It must be emphasized that this thermodynamic relationship between the prevailing pressure and temperature applies only at the surface of the sphere $r = a$. In general, $p_l(r)$ and $T_l(r)$ are two independent functions that are only related at $r = a$.

As in the case of the pressure (Equation 1.67), the surface tension may have an influence on the saturation relation. In this case, the value for the partial pressure of the vapor at the interface must be corrected as follows:

$$p_l(a) = p_{sat}(T(a))\exp\left[\frac{2\sigma(T(a))}{a\rho_s(a)R_vT(a)}\right]. \tag{1.69}$$

where the parentheses denote arguments of functions and R_v is the specific gas constant for the material species of the vapor, l, that is, $R_v = R/\mathcal{M}_l$ and $R = 8.314$ kJ/kg > K. The term in the square brackets is sometimes called the "Kelvin number," *Ke*, and in most practical applications its value is very low ($Ke \ll 1$). Hence, in most practical applications, $p_l(a) \approx p_{sat}(T(a))$. A glance at Equation 1.69 proves that the Kelvin number and hence the effects of surface tension become significant when $a \to 0$, a condition that is met at the last stages of combustion, evaporation, or sublimation of a sphere.

Within the gaseous phase that comprises the vapor of the sphere and the carrier fluid, the mole fraction of the vapor and the mole fraction of the components of the carrier fluid at any distance $r > a$ are defined in terms of their partial pressures as follows:

$$X_v(r) = \frac{p_l(r)}{p_T} \quad \text{and} \quad X_{ci}(r) = \frac{p_{ci}(r)}{p_T}. \tag{1.70}$$

Obviously, at any point, the condition applies that the sum of all the mole fractions in the gaseous mixture is equal to one. At the surface of the sphere, the pressure $p_l(a)$ is equal to the saturation pressure at the prevailing temperature, $T(a)$. Hence, the mole fraction of the vapor at the interface is determined from the knowledge of the total pressure and the temperature of the sphere.

The mole fraction of any species, denoted by the letter X_j, and the mass fraction of this species, Y_j, are related via the molecular weights, M_i, of the species that are present in the gaseous mixture:

$$Y_j = \frac{X_j M_j}{\sum_i X_i M_i} \quad \text{and} \quad X_j = \frac{Y_j/M_j}{\sum_i Y_j/M_j}, \tag{1.71}$$

where the sum in the denominator is over all the species that are present in the gaseous phase, namely, the carrier gas and the vapor. As in the case of the mole fractions, at any point outside the sphere, the sum of all the mass fractions is equal to one.

In the cases of sublimation and evaporation, the variation of the intensive vapor properties $T_v(r)$ and $p_v(r)$ is in the opposite direction from the one shown in Figure 1.7. In such processes, any mass flow rate from the sphere to the gas results in a radial velocity w from the surface of the sphere to the gas, which is described by the following mass conservation equation:

$$d^2 \frac{d\rho_f}{dt} + \frac{d(\rho_f d^2 w)}{dr} = 0. \tag{1.72}$$

where d, when it is not part of a differential operator such as d/dt or d/dr, is the diameter of the sphere and r is the radial coordinate. In a quasi-steady case, where the density of the carrier fluid may be considered to be constant, the aforementioned equation may be integrated on the surface of the sphere to yield the mass flow rate from the sphere to the fluid:

$$\frac{dm}{dt} = -\pi d^2 \rho_f w\big|_s. \tag{1.73}$$

The velocity w is evaluated with respect to the surface of the sphere at the gas side. Since the radial velocity w is an outward velocity with respect to a control volume that encloses the sphere, the negative sign signifies that mass is transferred from the sphere to the fluid when w is positive.

Evaporation, condensation, sublimation, and chemical reactions are the basic processes for the mass transfer to or from a sphere. Processes without chemical reactions will be examined in this section, while processes with chemical reactions, such as combustion, will be mentioned briefly in the next section and will be examined in more detail in Chapter 6. It must be recalled that when mass transfer occurs without chemical reactions, the driving force for the process is the difference of the concentration of the species the sphere is composed of (evaluated at the surface of the sphere) and the concentration of the same species in the carrier fluid (evaluated far from the sphere). For example, in the case of an evaporating water droplet in air, the driving force is the difference of the specific humidity at the surface of the sphere and

the specific humidity of the carrier fluid, far from the sphere. The former is a function of the temperature and pressure at the surface of the sphere, while the latter is a property of the carrier fluid. If the carrier fluid becomes completely saturated with water vapor, there is no such difference, and hence, no evaporation takes place.

The mass flux at the surface of an evaporating or condensing droplet in a binary mixture is given by Fick's law:

$$\rho_f w = -\rho_f D_c \frac{\partial Y_s}{\partial r}\Big|_s, \tag{1.74}$$

where D_c is the diffusion coefficient of the species the drop is composed of in the carrier fluid.

At the surface, we also require the following condition:

$$D_c \frac{\partial Y_s}{\partial r} = h_M (Y_s - Y_c), \tag{1.75}$$

where h_M is the convective mass transfer coefficient, which is analogous to the convective heat transfer coefficient. For a droplet of diameter $d = 2a$, the gradient of the mass fraction of any species at the droplet surface is proportional to the difference between the mass fraction at the surface and in the free stream and inversely proportional to the droplet diameter. Therefore,

$$\frac{\partial Y_s}{\partial r}\Big|_s \sim \frac{Y_s - Y_\infty}{d}, \tag{1.76}$$

where Y_∞ is the mass faction of the species in the free stream far from the droplet. A combination of the last two equations yields

$$\frac{dm}{dt} \sim \pi \rho_f D d (Y_\infty - Y_s). \tag{1.77}$$

The parameter that makes this expression an equation is the Sherwood number, *Sh*, which is often determined by experiment. Thus, the following expression may be derived for the rate of mass transfer from a sphere:

$$\frac{dm}{dt} = Sh \pi \rho_f D_c d (Y_\infty - Y_s). \tag{1.78}$$

Without mass advection caused by forced or free convection processes, the pure molecular diffusion dominates the mass transfer process, and hence, $Sh = 2$. The effect of fluid advection and relative velocity between the droplet and the carrier fluid is frequently represented by the so-called "Ranz–Marshall relation" (Ranz and Marshall, 1952):

$$Sh = 2 + 0.6 Re_r^{1/2} Sc^{1/3}, \tag{1.79}$$

where

Re_r is the Reynolds number based on the relative velocity
Sc is the Schmidt number

Since the mass transfer process from a sphere is closely related to the heat transfer process via the well-known heat/mass transfer analogy, one may also use alternative expressions for the Sherwood number, which are given as expressions for the Nusselt number in Section 1.4.4. In particular, one may use the *Sh*–*Nu* analogy and obtain expressions for the Sherwood number based on the numerical correlations of Section 1.4.4.2 for the heat and mass transfer from viscous spheres at finite Reynolds numbers.

1.4.2.2 Chemical Reactions

When chemical reactions take place, the mass transfer from the sphere is related to the reaction rate of the fuel, ξ. This is expressed in units of the reaction per unit time, which are sometimes referred to as DeDonder/second. If we assume that the spherical symmetry of the drop is retained during the processes of mass transfer and chemical reaction, the mass conservation equation for the fuel, the oxidant, and an inert component, such as nitrogen, which may be present in the reaction, may be written as follows:

1. For the fuel, whose mass fraction is denoted by the subscript *F*:

$$\frac{\partial}{\partial t}(\rho d^2 Y_F) + \frac{\partial}{\partial r}(\rho u d^2 Y_F) - \frac{\partial}{\partial r}\left(\rho d^2 D_F \frac{\partial Y_F}{\partial r}\right) = \rho d^2 \xi. \tag{1.80}$$

   The last term in this equation is a measure of the mass of the fuel that is consumed by the reaction.
2. For an oxidant, whose mass fraction is denoted by the subscript *O*:

$$\frac{\partial}{\partial t}(\rho d^2 Y_O) + \frac{\partial}{\partial r}(\rho u d^2 Y_O) - \frac{\partial}{\partial r}\left(\rho d^2 D_O \frac{\partial Y_O}{\partial r}\right) = \rho d^2 F_{OF} \xi, \tag{1.81}$$

   where FOF is the stoichiometric ratio of oxidant to the fuel that is consumed by the reaction.
3. For an inert component, such as nitrogen, the total mass is conserved and the right-hand side of the corresponding equation is equal to zero:

$$\frac{\partial}{\partial t}(\rho d^2 Y_N) + \frac{\partial}{\partial r}(\rho u d^2 Y_N) - \frac{\partial}{\partial r}\left(\rho d^2 D_N \frac{\partial Y_N}{\partial r}\right) = 0. \tag{1.82}$$

4. The mass conservation equation for any product, denoted by the subscript *P*, which appears as a result of the reaction, is

$$\frac{\partial}{\partial t}(\rho d^2 Y_P) + \frac{\partial}{\partial r}(\rho u d^2 Y_P) - \frac{\partial}{\partial r}\left(\rho d^2 D_P \frac{\partial Y_P}{\partial r}\right) = -\rho d^2 (F_{OF} + 1)\xi. \tag{1.83}$$

From the definition of the mass fractions for all the components of the reaction, one may also derive the following identity, which is useful as a closure equation:

$$Y_F + Y_O + Y_N + Y_P = 1. \tag{1.84}$$

The mass balance for any species at the surface of an evaporating or reacting droplet may be imposed on all the species that are present in the droplet and the gas. Because of the loss of liquid mass, there is a radial convection at the surface that is often called "Stefan convection." The rate of mass convection on the side of the gas is equal to the rate of mass convection on the liquid side:

$$\dot{M} Y_{is} - \rho \pi d^2 D_c \frac{\partial Y_i}{\partial r}\Big|_s = \dot{M} \delta_{iF} \quad i = O, F, N, P, \tag{1.85}$$

where

the left-hand side represents the advection and diffusion at the gas side
$\dot{M}$ is the rate of mass vaporization or reaction of the droplet
the subscript *i* extends over the species of fuel, oxidant, inert, and products
δ_{iF} is the Kronecker delta

More details on the combustion processes and methods for calculating the mass transfer from a burning drop are presented in Chapter 6. Since the subject of mass transfer from a sphere is closely connected to the processes of evaporation and sublimation and since the corresponding mass transfer or *blowing effect*

influences significantly the momentum transfer and the hydrodynamic forces exerted on the droplet, the relevant correlations and useful information on engineering computations will be presented in Sections 1.4.3.4 and 1.4.4.4.

1.4.3 Momentum Transfer

The functional form and expressions for the steady and transient hydrodynamic force exerted by a fluid on a sphere will be presented in this section. The hydrodynamic force is a surface force. The body forces (gravity, magnetic, electric, etc.) that may act on the sphere will not be included in the analysis for brevity. These forces are added to the hydrodynamic force and all the other forces acting on the sphere to generate the Lagrangian equation of motion.

We consider the rectilinear flow of a viscous fluid around a sphere of radius $a(d = 2a)$. The fluid velocity field is nonuniform and given by the function $u_i(x_i, t)$ outside the volume occupied by the sphere. If the sphere is solid that does not rotate,* its velocity is only a function of the time, $v_i(t)$. If the sphere is composed of a viscous fluid (as in bubbles and drops), its velocity is $v_i(x_i, t)$, which signifies that there is fluid motion inside the fluid sphere. In both cases, the governing equations for the process of mass and momentum exchange are the continuity, or mass conservation, equation

$$\frac{\partial \rho_f}{\partial t} + \rho_f \vec{\nabla} \cdot \vec{u} = 0, \tag{1.86}$$

and the momentum conservation equation

$$-\vec{\nabla} p + \mu_f \nabla^2 \vec{u} = \rho_f \left(\frac{\partial \vec{u}}{\partial t} + \vec{U} \cdot \vec{\nabla} \vec{u} \right), \tag{1.87}$$

where U is the fluid velocity at the surface of the sphere. The last equation may be rendered dimensionless by using the diameter, $2a$, as the characteristic dimension of the problem and the characteristic time $\tau_s = 4\alpha^2 \rho_f / \mu_f$. This yields the following dimensionless expression:

$$-\vec{\nabla}^\star p^\star + \nabla^{\star 2} \vec{u}^\star = \frac{\partial \vec{u}^\star}{\partial t^\star} + Re\left(\vec{U}^\star \cdot \vec{\nabla}^\star \vec{u}^\star \right). \tag{1.88}$$

Depending on the details of the process, the characteristic velocity for the definition of $u^\star$ is either the characteristic velocity of the fluid itself or the relative velocity of the sphere with respect to the fluid. This defines two Reynolds numbers for the flow, Re and Re_r:

$$Re = \frac{2a\rho_f |\vec{u}|}{\mu_f} \quad \text{and} \quad Re_r = \frac{2a\rho_f |\vec{u} - \vec{v}|}{\mu_f} \tag{1.89}$$

When applied to particulate flows, Equations 1.87 and 1.88 are sometimes referred to as the "Oseen equations." They contain the velocity at the surface of the sphere and the nonlinear advection term of the fluid flow, which is the last term in the two equations (Oseen, 1913). When $Re \ll 1$, the nonlinear advection term may be neglected in comparison to the viscous term. Then the momentum equation becomes linear and reads as follows:

$$\rho_f \frac{\partial \vec{u}}{\partial t} = -\vec{\nabla} p + \mu_f \nabla^2 \vec{u} \tag{1.90}$$

or in dimensionless form

$$-\vec{\nabla}^\star p^\star + \nabla^{\star 2} \vec{u}^\star = \frac{\partial \vec{u}^\star}{\partial t^\star}. \tag{1.91}$$

* If the solid sphere rotates, its interior points move according to the solid body rotation principles.

This flow is often called "Stokes flow" or "creeping flow" (Stokes, 1851) and the last two equations *Stokes equations*. Creeping or Stokes flow basically implies that the relative Reynolds number of the flow, Re_r, is very small, the viscous effects dominate the hydrodynamic force on the sphere, and the inertia effects, which are represented by the nonlinear term of the governing equation, may be neglected. Micron-size and nanoparticles satisfy this condition as well as larger particles in fluids of high viscosity and low relative velocity.

1.4.3.1 Stokes or Creeping Flow

The steady-state solution of Equation 1.90 yields the *Stokes drag* for the hydrodynamic force ($F_D = 6\pi a v \mu_f$). The full, transient solution of the equation is the so-called Boussinesq–Basset expression (Maxey and Riley, 1983, Boussinesq, 1885, Basset, 1888a, Michaelides, 2003), which is elucidated in Section 1.4.3.6. Although the Stokes drag is obtained for $Re_r \ll 1$, the expression for it is accurate up to $Re_r = 0.5$ (see Table 1.1). Because many industrial applications with small particles and drops in viscous fluids occur at $Re_r < 1$, this type of flow is of immense interest to engineers and scientists.

Consider the motion of a viscous fluid sphere inside the fluid of different viscosities at $Re_r \ll 1$. The fluid velocity is uniform and equal to U, far from the sphere and the no-slip condition applied on the surface of the sphere. The center of coordinates is coincident with the center of the sphere, and the flow domain is much larger than the diameter of the sphere. This is referred to sometimes as an "infinite domain." The viscous sphere problem in a fluid was solved independently by Hadamard (1911) and Rybczynski (1911) who obtained the following analytical expressions for the stream functions inside and outside the sphere:

$$\psi_i = \frac{Ur^2(a^2 - r^2)\sin^2\theta}{4(\lambda+1)a^2} \tag{1.92}$$

and

$$\psi_o = \frac{Ur^2\sin^2\theta}{2}\left[1 - \frac{(3\lambda+2)a}{2(\lambda+1)r} + \frac{\lambda a^3}{2(\lambda+1)r^3}\right], \tag{1.93}$$

where λ is the ratio of the dynamic viscosities, μ_s/μ_c. The case of a solid sphere is given at the limit $\lambda \to \infty$, and the case of an inviscid sphere (a bubble) is given at the limit $\lambda \to 0$. It is apparent that even at this very low relative velocity, the presence of the sphere in a flow field creates a disturbance in the velocity field of the fluid, which is determined in the radial and transverse directions from the following last two equations:

$$u_r = U\cos\theta\left[1 - \frac{(3\lambda+2)a}{2(\lambda+1)r} + \frac{\lambda a^3}{2(\lambda+1)r^3}\right] \tag{1.94}$$

and

$$u_\theta = -U\sin\theta\left[1 - \frac{(3\lambda+2)a}{4(\lambda+1)r} - \frac{\lambda a^3}{4(\lambda+1)r^3}\right]. \tag{1.95}$$

Table 1.1 Drag Coefficients of Spherical Particles Calculated by Four Different Expressions

Re_r	Stokes	Equation 1.103	Equation 1.104	Equation 1.105
0.05	480.0	484.5	484.3	489.2
0.1	240.0	244.5	244.1	247.4
0.2	120.0	124.5	123.9	126.0
0.5	48.0	52.5	51.6	52.5
0.8	30.0	34.5	33.5	33.9
1.0	24.0	28.5	27.6	27.6
1.2	20.0	24.5	23.7	23.4
1.5	16.0	20.5	19.9	19.2
1.8	13.3	17.8	17.6	16.3
2.0	12.0	16.5	16.5	14.9

It is evident that the velocity field described by these equations yields $u_r = 0$ on the surface of the sphere and $u = U$ far away from the sphere. These velocity solutions can be used to determine the pressure field and the fluid stress tensor.

Integration of the normal and shear stresses on the surface of the fluid sphere yields the total hydrodynamic force exerted by the fluid on the viscous sphere as follows:

$$F_D = 2\pi a U \mu_c \frac{3\lambda + 2}{\lambda + 1}. \tag{1.96}$$

The corresponding drag coefficient for the viscous sphere in Stokes flow becomes

$$C_D = \frac{2F_D}{\pi \rho U^2 a^2} = \frac{8(3\lambda + 2)}{Re_r(\lambda + 1)}. \tag{1.97}$$

The last expression yields the so-called Stokes drag for a solid sphere $C_D = 24/Re_r$ and for an inviscid bubble $C_D = 16/Re_r$. The corresponding expressions for the drag force are $F_D = 6\pi a U \mu_c$ for the solid sphere and $F_D = 4\pi a U \mu_c$ for the inviscid bubble. The latter is sometimes referred to as the "form drag," while the difference of the two expressions, which is equal to $2\pi a U \mu_c$, is referred to as the "friction drag." The form drag or pressure drag is due to pressure distribution over the surface of the sphere, while the friction drag results from the viscous stress at the surface of the sphere. While several authors make this distinction between the two parts of the drag force, it must be noted that the drag force is a single entity that arises from the interactions between the fluid and the sphere and not two different forces.

Spheres settling or rising under gravity at Stokes flow conditions are subjected to the gravity and buoyancy force and the hydrodynamic/drag force. At steady flow, the two opposing forces are equal in magnitude and the spheres move at constant velocity. Depending on the actual application, this velocity is known as the "terminal, rising, or settling velocity" of the sphere. An expression for the terminal velocity of a viscous sphere in Stokesian flow is

$$V_t = \frac{2}{3} \frac{g a^2 (\rho_c - \rho_s)}{\mu_c} \frac{\lambda + 1}{3\lambda + 2}. \tag{1.98}$$

In some industrial applications, bubbles and drops do not follow the predictions of the Hadamard–Rybczynski analysis, because of the presence of impurities that act as surfactants in the fluid. The surfactants, in general, dampen the internal velocity field, thus increasing the effective viscosity of the internal fluid. In this case, the viscous sphere behaves as a solid sphere. When the bubble or drop is in motion, the surfactants are swept to the aft, leaving the forward surface relatively uncontaminated. This establishes a concentration gradient on the surface of the sphere, which results in a surface tension gradient and, subsequently, in a tangential stress that opposes the motion of the surface. The net result of this phenomenon is an increase in the total drag force, which is manifested in the retardation of the terminal velocity of the viscous sphere (Levitch, 1962). In practical cases of bubble and droplet flows, one must consider the drag given by Equation 1.96 as the lower limit of the hydrodynamic force, which is reached under conditions of exceptional carrier fluid purity. Similarly, the terminal velocity given by Equation 1.98 is the upper limit of the velocity that can be attained by a bubble or drop under Stokes flow (or creeping flow) conditions.

The work by Bond and Newton (1928) and similar more recent studies suggest that as long as the flow may be characterized as Stokes flow and $Re_r \ll 1$, the viscous spheres behave as solid spheres in the range $Eo < 4$. This Eötvos number is based on the density difference between the two fluids:

$$Eo = \frac{(\rho_c - \rho_s) g d^2}{\sigma}. \tag{1.99}$$

In the range $Eo > 4$, the spheres follow more closely the Hadamard–Rybczynski analysis and Equations 1.97 through 1.99. It must be noted that in the Stokes flow regime ($Re_r \ll 1$), all viscous spheres (bubbles and drops) remain spherical, regardless of the value of the Eötvos number (for more details see Section 1.4.3.8).

1.4.3.2 Reynolds Number Effects

1.4.3.2.1 Solid Spheres At finite Re_r, the fore-aft symmetry of the flow around the sphere, which is implied by the Stokes flow conditions, breaks down and the equations of the last section do not apply. Experimental observations have proven that, even at low Re_r, a wake is formed behind the sphere. This is a steady wake that becomes stronger as the Reynolds number increases and the inertia of the flow around the sphere overcomes the viscosity effects on the surface of the sphere. Experimental observations (Taneda, 1956, Achenbach, 1974, Seeley et al., 1975), as well as numerical computations, give sufficient evidence that the following flow descriptions or *regimes*, related to the presence and behavior of the wake, are observed around a sphere:

1. *Attached flow*: In the range $0 < Re_r < 20$, the flow is attached to the sphere and there is no visible recirculation behind it. There is a *velocity defect* region behind the sphere, which is the characteristic of a weak wake. The fore-aft asymmetry of the flow becomes progressively more pronounced as Re_r increases.
2. *Steady wake*: The onset of wake separation occurs at approximately $Re_r = 20$ and a very weak recirculating wake becomes visible. The wake is very small in volume and is attached to the aft of the sphere. As the Re_r increases, the wake becomes wider and longer and its point of attachment on the sphere moves forward. The wake is steady up to approximately $Re_r = 150$. With the steady wake, the separation angle is a monotonically decreasing function of Re_r, while the wake length and volume increase with Re_r. An approximate correlation for the length of the wake in this flow regime is

$$L_W = 2a\left[0.0203\left(Re_r - 20\right) + 0.00012\left(Re_r - 20\right)^2\right]. \tag{1.100}$$

3. *Unsteady wake regime in laminar flow*: The onset of the wake instability occurs in the range $130 < Re_r < 150$, where a weak, long-period, laminar oscillation appears at the tip of the wake and its amplitude increases with Re_r. Pockets of vorticity begin to shed from the tip of the sphere and influence the flow field downstream. The unsteady wake regime has been observed in experiments in the range $(130–150) < Re_r < 270$.
4. *High subcritical range*: This regime covers the range $270 < Re_r < 3 * 10^5$. As Re_r increases, vortices are shed regularly from alternate sides of the sphere. At the lower end of this regime, the Strouhal number, *Sl*, of the vortices is a monotonic function of Re_r and ranges from 0.1 at $Re_r = 400$ to approximately 2 at $Re_r = 6000$. The following relationship between the *Sl* and Re_r shows the best fit with the data in the range $400 < Re_r < 4000$:

$$Sl = 1.89 * 10^{-5} Re_r^{1.43}. \tag{1.101}$$

   In the range $4000 < Re_r < 6000$, there is too much scatter in the experimental data, with *Sl* appearing to level at the value 0.21. In the range $Re_r > 6000$, separation occurs at a point that rotates around the sphere with frequency equal to the shedding frequency. The result of the wake separation above $Re_r = 6000$ is the drastic reduction of *Sl* to 0.125. In the range $6000 < Re_r < 3 * 10^4$, *Sl* rises from 0.125 to 0.18, while in the range $3 * 10^4 < Re_r < 2 * 10^5$ *Sl* only rises to 0.19 (Achenbach, 1974). All the studies indicate that in this flow regime, the wake is periodic but not turbulent. The observations by Seeley et al. (1975) have shown that at values of Re_r above 1300 small jets and eddies appeared, signifying 3D rotation of the flow. The observations confirm that, in the subcritical range, the separation point moves forward and the angle where separation occurs is

$$\theta_S = 83 + 660 Re_r^{-0.5}. \tag{1.102}$$

5. *Supercritical flow*: The onset of the transition to a turbulent wake occurs at $Re_r = 2 * 10^5$, and the transition is completed at $Re_r = 3.7 * 10^5$. In this range, changes in the flow pattern occur that are referred to as "critical transition." At $Re_r > 3.7 * 10^5$, the separation begins to move downstream and fluctuations in the position of the separation point become evident. The free shear layer becomes turbulent and attaches to the surface of the sphere. The most evident result of the transition is a

sharp drop of the drag coefficient from approximately 0.44 to approximately 0.07. It must be noted that the transition to a turbulent boundary layer is sensitive to the intensity of the free-stream turbulence and it may be accelerated by "tripping" the flow with a thin wire, a devise that has often been used in experimental studies of turbulent boundary layers (Maxworthy, 1969). The effects of the free turbulence on the flow field and other transient effects are presented in Sections 1.4.3.3 and 1.4.3.6, respectively.

The first accurate determination of the hydrodynamic force on a sphere at finite Reynolds numbers is attributed to Oseen (1913). He used a simple perturbation method to calculate a first-order correction for the steady drag coefficient. His expression

$$C_D = \frac{24}{Re_r}\left(1+\frac{3}{16}Re_r\right) \tag{1.103}$$

is valid for finite but small values of Re_r. Maxworthy (1975) verified experimentally that the Oseen correction is accurate up to $Re_r = 0.45$. This range covers many practical applications in the chemical industry, where particles are very small and the fluids have high viscosity.

At finite values of Re_r, the nonlinear advection term in the governing momentum equation (1.87) or (1.88) is retained in the solution of the equations. This implies that the vorticity and vorticity gradients around the sphere are transported by the advection of the fluid as well as by the molecular diffusion processes. An analysis of the governing equations reveals that the diffusion part of the process is dominant in an inner region surrounding the sphere with radius aRe_r^{-1}, while the advection process is dominant at distances far from this region. At the overlap of the two regions, $r \sim aRe_r^{-1}$, the two processes, advection and diffusion, are of the same order of magnitude, and their effects must be calculated simultaneously. In this case, the characteristic time of the advection process is a/U, while that of the diffusion process is equal to a^2/ν_f. Because the characteristic times are of different orders of magnitude, an analytic solution for the problems of the transport of momentum and energy at finite Reynolds and Peclet numbers may be solved asymptotically, usually by a singular perturbation method.

Proudman and Pearson (1956) used an asymptotic method to calculate the velocity field around a solid sphere and around a cylinder at steady flow. This approximation enabled them to extend the Oseen result and to calculate the steady drag coefficient to $O(Re_r^2 \ln Re_r)$. Their expression for the drag coefficient is

$$C_D = \frac{24}{Re_r}\left[1+\frac{3}{16}Re_r+\frac{9}{160}Re_r^2\ln\left(\frac{Re_r}{2}\right)+O\left(Re_r^2\right)\right]. \tag{1.104}$$

Expressions such as this may be used with accuracy in applications of finite but small Re_r in the range from 0 to 1.5. At higher values of Re_r it is advisable to use one of the empirical or semiempirical expressions for the steady drag coefficient that abound in the literature. One of them is the Schiller and Nauman (1933) correlation, which is relatively simple and accurate:

$$C_D = \frac{24\left(1+0.15Re_r^{0.687}\right)}{Re_r}. \tag{1.105}$$

This expression is recommended in the range $1 < Re_r < 800$. The similar and simpler expression

$$C_D = \frac{24}{Re_r}\left(1+\frac{1}{6}Re_r^{2/3}\right) \tag{1.106}$$

is easier to integrate analytically and is also recommended in the same range $1 < Re_r < 800$.

Of interest to several engineering applications is the range $Re_r < 2$, and Table 1.1 gives the numerical values of the drag coefficients calculated by the Stokes equation, the Oseen equation (Equation 1.103), the Proudman and Pearson equation (1.104), and the Schiller and Nauman correlation (Equation 1.105).

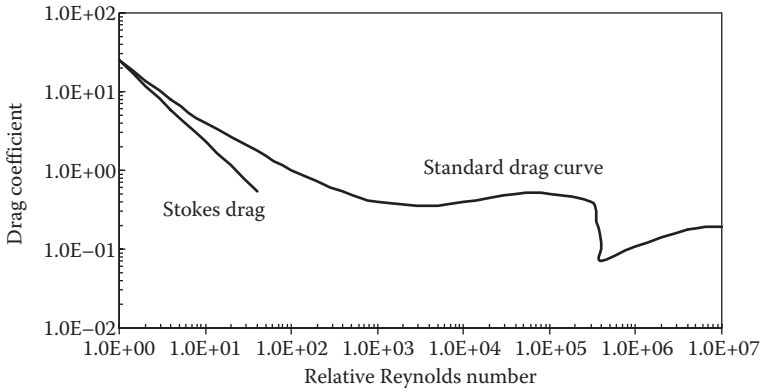


Figure 1.8

The standard drag coefficient curve for a solid sphere in steady flow.

It is observed in Table 1.1 that the Stokes drag agrees within 10% with the values of the other expressions up to $Re_r = 0.5$ and that the other three expressions agree within 10% up to $Re_r = 2$ despite the fact that the analytical equations were derived under the condition $Re_r < 1$.

The empirical equations give rise to the *standard*, *steady drag coefficient curve*, which is depicted in Figure 1.8 and extends to $Re_r = 10^7$. It is apparent in this figure that the steady drag coefficient of a sphere becomes constant and approximately equal to 0.44 in the range $10^3 < Re_r < 3 * 10^5$. In this range, the friction part of the drag force is insignificant and all the contribution comes from the form drag.

A key determinant of the magnitude of the drag coefficient is the type of the boundary layer that is formed outside the sphere and the separation point of the flow field behind the sphere. At $Re_r = 3 * 10^5$, this boundary layer becomes turbulent and the separation point of the flow moves downstream. The result is a sharp reduction of the form drag and hence a drastic reduction of the drag coefficient from 0.42 to 0.07, which is typical of laminar-to-turbulent transitions. At these high values of Re_r, the flow becomes inherently unsteady because vortices are shed regularly behind the sphere. In this case, as well as in all transient flows, the standard hydrodynamic drag on a sphere may be used (instead of the transient expressions that are presented in Section 1.4.3.6) only if the timescale of the sphere ($\tau_s = 4\alpha^2\rho_f/\mu_f$) is much smaller than the timescale of the transients in the carrier fluid, $\tau_s \ll \tau_f$. This condition implies that $St \ll 1$.

1.4.3.2.2 Viscous Spheres At higher Re_r, internal circulation creates a flow field inside the viscous spheres. This modifies the external flow field and hence the drag coefficient. Figure 1.9 (from Feng and Michaelides, 2001a) shows the streamlines (a) and vorticity (b) of these flow fields for $\lambda = 7$ and $Re_r = 10$, 100, and 500. At first, it is evident from the streamlines that there is a fore-aft asymmetry, which is also seen in the case of rigid spheres. Even though at $Re_r = 10$ the recirculation region behind the sphere has not been formed, there is an obvious velocity defect region. At $Re_r = 100$, there is a well-defined recirculation region, and at $Re_r = 500$, this region expands considerably and extends to a distance more than one diameter downstream. Second, at $Re_r = 500$, there are sharp gradients of vorticity in the outer field of the sphere, which indicate the formation of a boundary layer. This boundary layer is characteristic of flows with $Re_r > 400$, and its thickness is of the order of $Re_r^{-1/2}$. Third, there are two counterrotating vortices inside the sphere (sometimes referred to as "Hill's vortices") whose strength increases with Re_r. An internal recirculation region at the aft end of the sphere may also be formed at higher values of Re_r or at lower values of λ. The formation of the internal flow in viscous spheres modifies the whole velocity field and results in the lower drag on the spheres.

LeClair and Hamielec (1972), Rivkind et al. (1976), and Oliver and Chung (1987) used analytical and numerical studies to derive expressions for the drag coefficients of viscous spheres (bubbles and drops) at relatively low Re_r. Feng and Michaelides (2001a) used a two-layer concept for the computational grid and were able to perform more accurate computations that extend to higher values of Re_r, where the boundary layer is well formed on the outside of the viscous sphere. They used their computational results to derive simple engineering correlations for the drag coefficients in terms of the viscosity ratio up to $Re_r = 1000$. Figure 1.10 depicts these results for several values of the viscosity ratio, λ. The standard drag coefficient

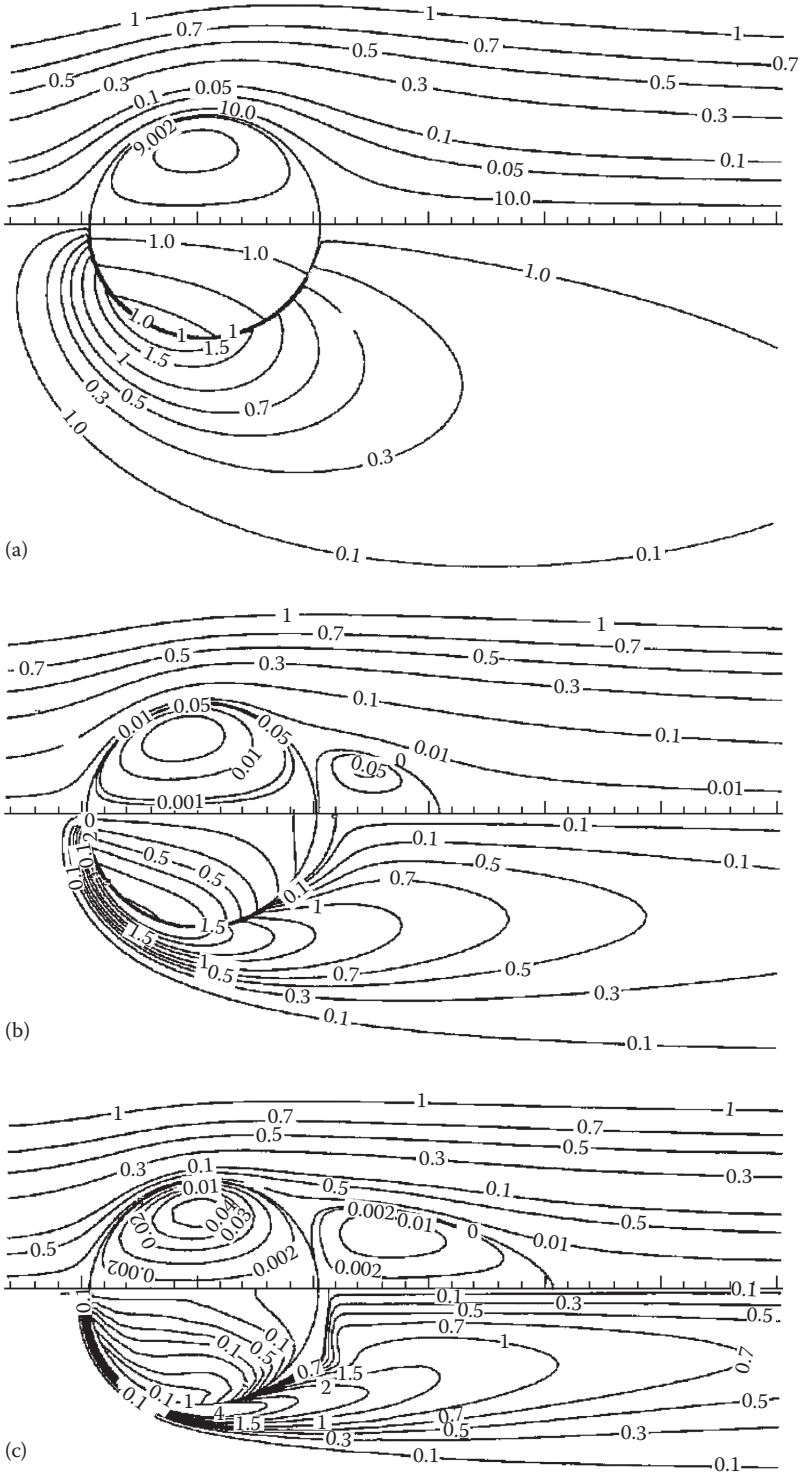


Figure 1.9

Streamlines and vorticity around a viscous sphere with viscosity ratio 7 at *Re* = 10 (a), 100 (b), and 500 (c).

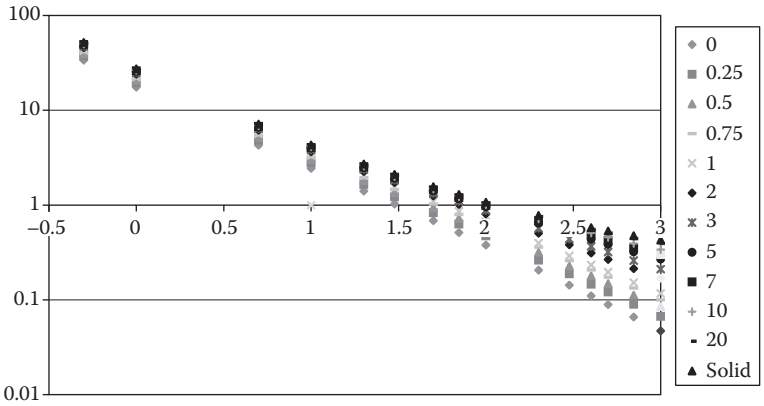


Figure 1.10

Drag coefficients for viscous spheres at different values of λ.

curve for solid spheres in this figure corresponds to the limit $\lambda \to \infty$. When expressed in terms of Re_r, the correlations derived by Feng and Michaelides (2001a) may be written as follows:

$$C_D\left(Re_r,\lambda\right)=\frac{2-\lambda}{2}C_D\left(Re_r,0\right)+\frac{4\lambda}{6+\lambda}C_D\left(Re_r,2\right) \quad \text{for } 0\le\lambda\le 2 \quad \text{and} \quad 5<Re_r\le 1000 \tag{1.107}$$

and

$$C_D\left(Re_r,\lambda\right)=\frac{4}{\lambda+2}C_D\left(Re_r,2\right)+\frac{\lambda-2}{\lambda+2}C_D\left(Re_r,\infty\right) \quad \text{for } 2\le\lambda\le\infty \quad \text{and} \quad 5<Re_r\le 1000 \tag{1.108}$$

The functions $C_D(Re_r, 0)$, $C_D(Re_r, 2)$, and $C_D(Re_r, \infty)$ are the drag coefficient for inviscid bubbles, for viscous drops with $\lambda = 2$, and for solid spheres, respectively. The following functions are recommended to be used with the two aforementioned correlations:

$$C_D\left(Re_r,0\right)=\frac{48}{Re_r}\left(1+\frac{2.21}{\sqrt{Re_r}}-\frac{2.14}{Re_r}\right), \tag{1.109}$$

$$C_D\left(Re_r,2\right)=17.0Re_r^{-2/3}, \tag{1.110}$$

and

$$C_D\left(Re_r,\infty\right)=\frac{24}{Re_r}\left(1+\frac{1}{6}Re_r^{2/3}\right). \tag{1.111}$$

In the lower range of Re_r, which is not covered by these equations, the following expression is recommended:

$$C_D=\frac{8}{Re_r}\frac{3\lambda+2}{\lambda+1}\left(1+0.05\frac{3\lambda+2}{\lambda+1}Re_r\right)-0.01\frac{3\lambda+2}{\lambda+1}Re_r\ln\left(Re_r\right) \quad 0\le Re_r\le 5. \tag{1.112}$$

The last expression has been derived from the results of the numerical computations in a way that it reduces asymptotically to the Hadamard–Rybczynski solution at $Re_r = 0$ and to the Oliver and Chung expression for very small Re_r.

The density ratio ρ_f/ρ_s does not influence significantly the drag coefficient of viscous spheres. Feng and Michaelides (2001a) observed that the variation of the density ratio by two orders of magnitude had an effect of less than 2% on the values of the drag coefficients. The maximum fractional difference of the correlations from the pertinent computational results is 4.6%, and the standard deviation of all the fractional differences is 2.1%. It must be noted that at the high range of Re_r the wake behind the spheres is unsteady and a transient expression for the total drag force should be used, if one is known. In such cases, the aforementioned expressions may be used for the steady part of the total hydrodynamic force.

It is well known that viscous spheres at higher Re_r become elongated. The drag coefficient of elongated viscous spheres is a function of the variables that appear in the aforementioned correlations as well as of the amount of deformation, which is characterized by the elongation or eccentricity. Correction functions must be used with these correlations, such as the ones presented in Sections 1.4.3.7 and 1.4.3.8. Experimental results by Winnikow and Chao (1966) and others on the free fall or rise of drops in liquids show that a liquid drop will remain spherical when the dimensionless Bond number, *Bo*, is less than or equal to 0.2, that is, when

$$Bo = \frac{We}{Fr} = \frac{gd^2|\rho_s - \rho_f|}{\sigma} \leq 0.2. \tag{1.113}$$

Accordingly, water droplets in air will maintain their spherical shape at values of Re_r up to 470. In the case of substances with high surface tension (liquid metals), the corresponding Re_r is much larger (up to $Re_r = 1150$ for mercury droplets in air).

1.4.3.2.3 Effect of Interfacial Velocity Slip All the aforementioned results and expressions for the drag force and the drag coefficient pertain to applications where the no-slip boundary condition applies at the interface of the carrier fluid and the bubble, particle, or drop. It has been observed that when the size of the elements of the dispersed phase is very small, of the order of 1000 nm and lower, there is velocity slip at the interface that modifies significantly the drag coefficient. This modification of the drag is of immense interest in flows of nanoparticles and nanodroplets. Several authors, starting with Basset (1888b), derived expressions for the drag modification due to interfacial slip. Basset (1888b) stipulated that the shear stress on the sphere is proportional to the tangential slip: $\tau = \beta \Delta u_t$. The coefficient β is often referred to as the "slip parameter" and the dimensionless ratio $\mu_c/a\beta$ as the "slip ratio." Feng et al. (2012) derived a comprehensive correction to the steady drag force with slip, which applies to viscous as well as inviscid spheres:

$$\frac{F_D}{6\pi\alpha\mu_c U} = \frac{1}{3}\frac{2\beta\alpha + 3\lambda\beta\alpha + 6\lambda\mu_c}{\beta\alpha + \lambda\beta\alpha + 3\lambda\mu_c} + \frac{1}{24}\left(\frac{2\beta\alpha + 3\lambda\beta\alpha + 6\lambda\mu_c}{\beta\alpha + \lambda\beta\alpha + 3\lambda\mu_c}\right)^2 \frac{Re_r}{2} + \frac{1}{120}\left(\frac{2\beta\alpha + 3\lambda\beta\alpha + 6\lambda\mu_c}{\beta\alpha + \lambda\beta\alpha + 3\lambda\mu_c}\right)^3 \frac{Re_r^2}{4}\ln\left(\frac{Re_r}{2}\right) + O\left(Re_r^2\right). \tag{1.114}$$

For a solid sphere, $\lambda \to \infty$, the last equation yields

$$\frac{F_D}{6\pi\alpha\mu_c U} = \frac{\beta\alpha + 2\mu_c}{\beta\alpha + 3\mu_c} + \frac{3}{8}\left(\frac{\beta\alpha + 2\mu_c}{\beta\alpha + 3\mu_c}\right)^2 \frac{Re_r}{2} + \frac{9}{40}\left(\frac{\beta\alpha + 2\mu_c}{\beta\alpha + 3\mu_c}\right)^3 \frac{Re_r^2}{4}\ln\left(\frac{Re_r}{2}\right) + O\left(Re_r^2\right). \tag{1.115}$$

By using dimensionless slip ratio $S = \mu_c/a\beta$, this equation can be expressed as the drag coefficient of the solid sphere:

$$C_D = \left(\frac{1+2S}{1+3S}\right)\frac{24}{Re_r}\left(1 + \frac{3}{16}\left(\frac{1+2S}{1+3S}\right)Re_r + \frac{9}{160}\left(\frac{1+2S}{1+3S}\right)^2 Re_r^2 \ln\left(\frac{Re_r}{2}\right) + O\left(Re_r^2\right)\right). \tag{1.116}$$

The last equation reduces to the expression (Equation 1.104) derived by Proudman and Pierson (1956) when there is no slip at the interface ($S \to 0$).

Under rarefied conditions, interfacial slip may occur at higher values of the Re_r. Feng et al. (2012) performed extensive numerical simulations at higher Re_r and derived a correlation for the drag coefficient with slip flow, for S between 0 and ∞, at Reynolds number up to 150:

$$C_D = \frac{1+2S}{1+3S}\frac{24}{Re_r}\left(1+0.1509\sqrt{\frac{1+2S}{1+3S}}Re_r^{0.678} - 0.0254\frac{S}{1+3S}Re_r^{1.104}\right). \tag{1.117}$$

1.4.3.3 Effects of Flow Turbulence

Turbulence in the carrier fluid (free-stream turbulence) implies an unsteady flow field and unsteady motion of particles, bubbles, and drops. For this reason, the effects of the free-stream turbulence are transient flow effects. Numerous experiments on the drag for solid spheres proved that the free-stream turbulence modifies the drag coefficient of particles, sometimes significantly. Typical results of such experiments are reproduced in Figure 1.11 from Clift et al. (1978). It is observed in this figure that when the relative Reynolds number is in the range $10 < Re_r < 500$, the drag coefficient of solid spheres in a turbulent flow is almost always higher than the values of the standard curve. The influence of the free-stream turbulence on the boundary layer around the sphere and the wake behind the sphere is manifested by the sharp changes observed at approximately $Re_r = 50$ and the leveling of the drag coefficient curves at values that are 2–4 times higher than the corresponding values of the standard drag curve. In the range $500 < Re_r < 20{,}000$, the drag coefficient of a sphere is first reduced dramatically in a short range of Reynolds numbers, often reaching a value 50% lower than the value of the standard curve (Clamen and Gauvin, 1969). Then, C_D increases gradually and may reach a maximum, which is two to five times higher than the values predicted by the standard curve. Thereafter, C_D decreases to the values of the standard curve. The sudden dip of the drag coefficients is often attributed to the formation of a turbulent boundary on the surface of the particle. Apparently, the transition, which in the standard drag curve occurs at $Re_r = 3 * 10^5$, is accelerated and occurs earlier when the free stream is turbulent. Clift and Gauvin (1970) introduced the critical Reynolds number for the gaseous boundary layer. This is the relative Reynolds number at which the turbulent transition happens and is given by the following expressions:

$$\begin{aligned} Re_{cr} &= 10^{5.477-15.8I_r} \quad \text{for } I_r \le 0.15 \\ Re_{cr} &= 10^{3.371-1.75I_r} \quad \text{for } I_r > 0.15 \end{aligned}, \tag{1.118}$$

where I_r is the turbulence intensity based on the relative velocity of the sphere. As with all the correlations that involve exponential expressions, the results of the two aforementioned equations must be strictly used within the range of the experimental conditions (Re_r and I_r) for which they were derived.

It must be noted that the experimental uncertainty associated with the results of Figure 1.11 and Equation 1.118 is significant and that there is a considerable discrepancy with the data emanating from the different experimental studies. Part of this uncertainty is inherent in the measurements of unsteady turbulent flows.

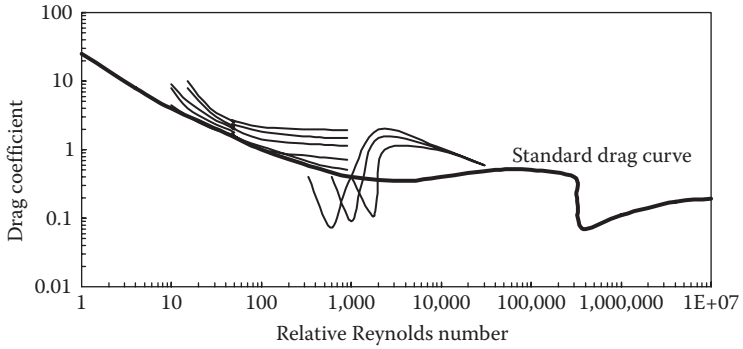


Figure 1.11

The effect of the free-stream turbulence on the standard drag coefficient for a solid sphere.

Another part of the uncertainty stems from the fact that the response of particles in a turbulent flow has been implicitly treated as steady and not as transient process, while it is evident that the response of particles to the turbulent eddies depends strongly on the frequency of the eddies and that the particle movement is transient.

The presence of particles, bubbles, and drops in turbulent flows also has an effect on the intensity and characteristics of the carrier fluid turbulence. This was observed in many relatively recent experimental studies and is called "modulation" or "modification" of the turbulence, regardless of any transition in the boundary layer of the particles. A great deal of work was devoted in the last 30 years on this subject, which is treated extensively in Chapter 12.

1.4.3.4 Blowing Effects

The mass transfer from the surface of a sublimating particle or an evaporating droplet causes an outward radial flow and hence a drastic change in the gaseous boundary layer around the sphere. This flow modification reduces the drag coefficient from the steady value as it is given by the standard curve. The exchange of mass from the particle or droplet to the surrounding fluid causes two significant effects:

1. The change in the viscosity of the surrounding fluid, because of temperature and composition changes
2. A regression of the surface of the droplet, which is associated with the flow of the vapor from the surface to the carrier fluid (Stefan convection)

Yuen and Chen (1976) conducted experiments on the drag force of evaporating drops and on the effect of the change of the transport properties of the carrier fluid as a result of the transfer of mass from the surface of the droplet. They concluded that their results are well represented when a reference viscosity for the carrier fluid is used, the *film viscosity*, which is defined as follows:

$$\mu_m = \mu_s + \frac{1}{3}(\mu_\infty - \mu_s), \tag{1.119}$$

where

μ_∞ is the viscosity of the fluid far from the sphere
μ_s is the gas viscosity on the surface of the sphere

This equation is sometimes referred to as the 1/3 *rule* for the film properties. The experimental data and analysis on the density and viscosity averages by Lerner et al. (1980) confirmed this relationship. The data also suggested that the standard drag curve with the aforementioned correction for the viscosity may be applied to slightly ellipsoidal drops if the equivalent diameter of the ellipsoid, d_V, is used and the two axes of the ellipsoid are within 10% of each other.

Eisenklam et al. (1967) and later Renksizbulut and Yuen (1983) examined the effects of the radial flow and Stefan convection process away from the surface of an evaporating droplet. They recommend that the following correction for the effect of the Stefan convection on the drag coefficient be used in calculations:

$$C_D = \frac{C_{D,0}}{1 + B_M}, \tag{1.120}$$

where $C_{D,0}$ is the value of the drag coefficient in the absence of mass transfer, which is calculated from the correlations presented in Section 1.4.3.2.

The coefficient B_M is the *blowing coefficient* and is based on the mass transfer from the surface of the sphere.

It is defined in terms of the mass fractions of the vapor on the surface and far away from the sphere:

$$B_M = \frac{Y_s - Y_\infty}{1 - Y_s}. \tag{1.121}$$

Chiang et al. (1992) conducted a numerical study of evaporating droplets with variable transport properties and derived a correlation for their drag coefficients, which is valid in the range $30 < Re_r < 200$:

$$C_D = \frac{24.432}{\left(1+B_H\right)^{0.27}\left(Re_m/2\right)^{0.721}}. \tag{1.122}$$

The relative Reynolds number in this case, Re_m, is defined in terms of the gas-film viscosity (Equation 1.119) and the free-stream gas density, $\rho_{f\infty}$. In the last equation, B_H is another blowing coefficient, which is based on the thermodynamic enthalpy of the evaporating fluid:

$$B_H = \frac{h_\infty - h_s}{h_{fg}^{eff}}. \tag{1.123}$$

The effective latent heat of vaporization, in the denominator of the last expression, is the sum of the latent heat of the vapor at the drop surface and the sensible heat conducted to the interior of the drop.

When the radial velocity of blowing, V_n, is known or may be calculated from mass flow rate data, Clift and Lever (1985) used a numerical analysis and derived the following relationship for the drag coefficient:

$$C_D = \frac{24}{Re_r}\frac{1+0.545Re_r+0.1Re_r^{0.5}\left(1-0.03Re_r\right)}{1+ARe_n^B}, \tag{1.124}$$

where Re_n is the blowing Reynolds number based on the radial (normal to the surface) velocity, $Re_n = \rho d V_n/\mu$, and the functions A and B are correlated to Re_r:

$$A = 0.09 + 0.077\exp\left(-0.4Re_r\right) \quad \text{and} \quad B = 0.4 + 0.77\exp\left(-0.04Re_r\right). \tag{1.125}$$

The last two expressions are valid in the ranges $10 < Re_r < 200$ and $1 < Re_n < 20$. At lower values of the Reynolds numbers, $Re_r < 10$ and $Re_n < 1$, the following modification in the function $A(Re_r)$ has been recommended:

$$A = 0.06 + 0.077\exp(-0.4Re_r). \tag{1.126}$$

These correlations and the pertinent studies suggest that the drag coefficient of burning and evaporating droplets departs only slightly from the corresponding values without mass transfer. The blowing effects may be perceived as corrections to the standard drag curve for spheres, caused by the different composition of the gaseous boundary layer and by mass convection from the sphere.

1.4.3.5 Compressibility and Rarefaction Effects

When the carrier gas is rarefied, for example, under conditions that are prevalent in the upper atmosphere, the length of the molecular free path, L_m, is comparable or even greater than the size of the particles or drops. Therefore, the medium surrounding the particle/drop may not be considered to be a continuum, and hence, the hydrodynamic force is not the same as in the case of continuum flows. The Knudsen number,

$$Kn = \frac{L_m}{d}, \tag{1.127}$$

is a dimensionless measure of the relative magnitude of the two length scales. Continuum flows imply that $Kn \ll 1$. Since the molecular free path of a gas is proportional to the ratio of the viscosity divided by the

product of the speed of sound and the gas density ($L_m \sim \mu/c\rho$), it follows that Kn is proportional to the ratio of the Mach number and the Reynolds number ($Kn \sim M/Re$). Schaaf and Chambre (1958) identified four flow regimes to characterize rarefaction flows, and Crowe et al. (1969) showed that, in the case of rocket nozzles, a burning particle or droplet is subjected to all four flow regimes:

1. The *free molecule flow*, where there are no interactions among the molecules and individual molecules collide with the particles exchanging momentum ($Kn > 10$ and $M > 3Re_r$). In this regime, the drag coefficient of a sphere is equal to 2, regardless of the value of the Reynolds number.
2. The *transitional flow*, where the size of the particles is comparable to the size of the mean free path. Since molecules interact by collisions, the collisions between the particles and the molecules create a distinct flow field around the particles. The effect of this flow field and the collisions is manifested on the force exerted by the gas on the particles ($0.25 < Kn < 10$, $0.1\, Re_r^{1/2} < M < 3Re_r$).
3. In the *slip flow* regime, there is a distinct flow field around the particles. The temperature and velocity at the surface of the particle are different from the temperature and velocity on the side of the gas close to the surface ($0.001 < Kn < 0.25$ and $0.01\, Re_r^{1/2} < M < 0.1\, Re_r^{1/2}$). This gives rise to a velocity difference (slip) between the gas and particle velocities at the particle surface. When $Kn < 0.01$, the flow field around the particles may be obtained from the solution of the Navier–Stokes equations with the stipulation of a suitable closure equation for the slip. Equations 1.114 and 1.115 were obtained using the stipulation for the slip velocity $\tau = \beta \Delta u_t$.
4. The *continuum flow* is characterized by the absence of velocity slip on the surface of the particles ($Kn < 0.01$, $M < 0.1\, Re_r^{1/2}$). The no-slip boundary condition applies to the surface of the particles, and the flow field is obtained by the analytical or numerical solution of the Navier–Stokes equations.

It is intuitive that an evaporating droplet or a sublimating particle will pass sequentially through all these flow regimes, starting in continuum flow and ending in the free molecular flow regime. However, under ambient conditions, when $Kn > 0.001$, there is very small mass remaining in the particle or droplet. Under these conditions and typical rates of evaporation, sublimation, and burning, the process passes rapidly through the first three regimes. When treating these processes by a numerical scheme, one has to be cognizant of this fact and to use the timescales and time steps that are appropriate to the processes.

At high Reynolds numbers, the effects of the Mach number on the drag coefficient become significant when $M > 0.6$. This is sometimes called the critical Mach number, and the flow around the particle is characterized by the formation of a shock wave, which increases significantly the form drag of the particle. Hence, the drag coefficient, which does not vary with the Mach number in the range $0 < M < 0.6$, increases rapidly beyond $M = 0.6$; reaches a maximum, which depends on the value of Re but is always greater than 2; and, thereafter, decreases gradually and approaches asymptotically the theoretically predicted value of 2 for free molecular flows (Schaaf and Chambre, 1958). At low Reynolds numbers, an increased Mach number signifies that the flow is rarefied. In this case, there is a shock wave associated with the presence of the particle and the drag coefficient decreases monotonically with M.

In general, the effect of the Knudsen number and the Mach number on the drag coefficient is given by correction factors $f(M)$ and $f(Kn)$. The classic experiment by Millikan (1923) yields the following correction factor for drops in rarefied flows, which is valid in the Stokesian flow regime:

$$f\left(Kn\right) = \frac{24C_D}{Re_r} = \left[1 + Kn\left[1.209 + 0.406\exp\left(-\frac{0.447}{Kn}\right)\right]\right]^{-1}. \tag{1.128}$$

The coefficients in the last equation appear with the corrections made for the more accurate knowledge of the molecular free path for air by Kim et al. (2005). The latter suggests that the three coefficients in the square bracket be 1.165, 0.483, and 0.449, respectively. An assessment of several studies on the subject reveals that these coefficients are approximately 1.15, 0.5, and 0.5 (Michaelides, 2014).

An equation for the drag coefficient, proposed by Crowe et al. (1973) and later simplified by Hermsen (1979), has been applied successfully to burning particles in solid propellant rocket nozzles:

$$C_D = 2 + \left(C_{D,0} - 2\right)\exp\left[-\frac{3.07\sqrt{k}\,g\left(Re_r\right)M}{Re_r}\right] + \frac{h\left(M\right)}{M\sqrt{k}}\exp\left(-\frac{Re_r}{2M}\right), \tag{1.129}$$

where

k is the ratio of the specific heats of the gas

$g(Re)$ and $h(M)$ are the empirical functions

$$g\left(Re\right) = \frac{1 + Re_r\left(12.278 + 0.548Re_r\right)}{1 + 11.278Re_r} \quad \text{and} \quad h\left(M\right) = \frac{5.6}{1+M} + 1.7\sqrt{\frac{T_p}{T_c}}. \tag{1.130}$$

In the last expressions

T_c is the mean temperature of the carrier gas far from the particle

T_p is the temperature of the particle

Alternatively, Carlson and Hoglund (1964) derived the following empirical relationship for the function $f(M)$, which is used in some computations pertaining to particles in shock waves and other compressible flow fields:

$$f\left(M\right) = \frac{1 + \exp\left(-\dfrac{0.427}{M^{4.63}} - \dfrac{3}{Re_r^{0.88}}\right)}{1 + \dfrac{M}{Re_r}\left[3.82 + 1.28\exp\left(-1.25\dfrac{Re_r}{M}\right)\right]}. \tag{1.131}$$

It must be noted that the last three equations are correlations of experimental data and must be used within the range of the independent variables for which the original data have been derived.

1.4.3.6 Transient Flow Effects

Most of the practical applications of dispersed multiphase flows involve time-dependent flows. When the characteristic time of the flow transients is of the same order of magnitude as the response time of bubbles, drops, or particles, a transient equation should be used for the exchange of momentum between the carrier fluid and the dispersed phase. Exact analytical expressions for transient flows have been derived for creeping flow (Stokes flow) conditions ($Re \ll 1$), and asymptotic expressions have been derived for finite but small Reynolds numbers ($Re_r < 1$). Semiempirical expressions, which emanate from a combination of experimental data and analyses, have also been developed and frequently used at high Re_r.

1.4.3.6.1 Creeping Flow ($Re \ll 1$) The so-called Boussinesq–Basset equation,

$$F_i(t) = -6\pi\alpha\mu_c(v_i - u_i) - \frac{1}{2}m_c\frac{d}{dt}(v_i - u_i) - 6\alpha^2\sqrt{\pi\mu_c\rho_c}\int_0^t \frac{d/d\tau(v_i - u_i)}{\sqrt{t-\tau}}d\tau, \tag{1.132}$$

which was independently derived by Boussinesq (1885) and Basset (1888a), is the first equation for the transient hydrodynamic force acting on a solid sphere. The expression applies to creeping flow conditions ($Re \ll 1$), where the inertia terms in the momentum equation of the fluid may be neglected in

comparison to the viscous effects. Maxey and Riley (1983) performed a more detailed analysis for a rigid sphere in an arbitrary nonuniform flow field, whose velocity is given by the functional relationship $u_i(x_i, t)$. The latter is not an arbitrary function, since it must be a solution of the Navier–Stokes equations. Maxey and Riley (1983) obtained the following expression for the equation of motion of a sphere:

$$m_s\frac{dv_i}{dt} = -\frac{1}{2}m_c\frac{d}{dt}\left(v_i - u_i - \frac{a^2}{10}u_{i,jj}\right) - 6\pi a\mu_c\left(v_i - u_i - \frac{a^2}{6}u_{i,jj}\right)$$
$$-\frac{6\pi a^2\mu_c}{\sqrt{\pi\nu_f}}\int_0^t \frac{d/d\tau\left(v_i - u_i - \frac{a^2}{6}u_{i,jj}\right)}{\sqrt{t-\tau}}d\tau + (m_s - m_c)g_i + m_c\frac{Du_i}{Dt}. \tag{1.133}$$

In the last equation

m_s is the mass of the sphere

m_c is the mass of the carrier fluid that occupies the same volume as that of the sphere

The repeated index with comma ($,jj$) denotes the Laplacian operator and the derivative D/Dt is the total Lagrangian derivative following the center of the sphere

All the spatial derivatives are evaluated at the center of the sphere. The left-hand side in this equation represents the acceleration of the sphere. Of the terms on the right-hand side, the first is the steady drag, the second is the added mass (or virtual mass) of the fluid, and third term is the history term. The remaining terms on the right-hand side are the net gravitational or body force and the Lagrangian acceleration term of the fluid. The Laplacian terms in all the parentheses account for the nonuniformity of the fluid velocity field. They are second-order corrections for the curvature of the flow field and are called sometimes the "Faxen terms." These derivatives become zero when the fluid velocity field is uniform. The Faxen terms scale as a^2/L^2, where L is the macroscopic characteristic length of the fluid velocity field, and in most applications of dispersed multiphase flows, where $a/L \ll 1$, they are small enough to be neglected.

It must be noted that the derivation of the last equation is based on the following assumptions:

- Spherical shape
- Infinite fluid domain initially undisturbed
- No rotation
- Rigid sphere ($\mu_f/\mu_s \ll 1$)
- Zero initial relative velocity
- Negligible inertia effects ($Re_r \ll 1$)

If the initial relative velocity is different than zero, the following expression/correction replaces the history term (Michaelides, 2003, 2006):

$$\frac{6\pi a^2\mu_c}{\sqrt{\pi\nu_c}}\int_0^t \frac{d/d\tau\left[v_i - u_i - \frac{a^2}{6}u_{i,jj}\right]}{\sqrt{t-\tau}}d\tau + \frac{6\pi a^2\mu_c[v_i(0) - u_i(0)]}{\sqrt{\pi\nu_c t}}, \tag{1.134}$$

where the quantity $v_i(0) - u_i(0)$ represents the initial relative velocity at time $t = 0$.

Integrodifferential equations, such as (1.133), do not have an explicit analytical solution for the dependent variable (v_i). Since they are implicit in their dependent variable, they must be solved numerically by an iteration method and this requires a great deal of computational resources in both memory and CPU time with repetitive calculations, such as the Lagrangian computations of a large group of particle trajectories. Michaelides (1992) and later Vojir and Michaelides (1994) devised an analytical method to convert such first-order implicit integrodifferential equations to second-order integrodifferential equations, which are explicit in the dependent variables v_i (or T_s in the case of temperature).

For viscous spheres (drops and bubbles) in a carrier fluid, there are two timescales for the motion of the fluid inside the sphere and the motion of the external fluid. For this reason, an analytical expression for the equation of motion, similar to Equation 1.133, is impossible to be derived in the time domain. Galindo and Gerbeth (1993) derived an expression for the hydrodynamic force on a viscous sphere under creeping flow conditions in the Laplace domain, which is as follows:

$$\overline{F_i} = -6\pi a \mu_c \left[\overline{v_i} - \overline{u_i}\right] \left\{ \frac{\chi_c^2}{9} + (\chi_c + 1) - \frac{(\chi_c + 1)^2 f(\chi_s)}{[\chi_s^3 - \chi_s^2 \tanh(\chi_s) - 2f(\chi_s)]\lambda + (\chi_c + 3) f(\chi_s)} \right\}. \tag{1.135}$$

The overbar in the last expression denotes functions in the Laplace domain; χ represents the two dimensionless timescales, also in the Laplace domain,

$$\chi_c = \sqrt{\frac{s\alpha^2}{\nu_f}} \quad \text{and} \quad \chi_s = \sqrt{\frac{s\alpha^2}{\nu_s}} \tag{1.136}$$

and the function $f(\chi)$ is defined as follows:

$$f(\chi) = (\chi^2 + 3)\tanh(\chi) - 3\chi. \tag{1.137}$$

Transient flow with tangential slip at the interface occurs with nanoparticles, submicron-sized drops, and colloidal particles, as well as larger drops and particles in rarefied gases. Michaelides and Feng (1995) performed a study that included the effect of the viscosity ratio, λ, and also allowed for the existence of a finite tangential velocity slip at the interface. The analysis proved that an expression for the complete hydrodynamic force may only be obtained Laplace domain:

$$\begin{aligned} \overline{F^i} = &-6\pi a \mu_c \left[\overline{v_i}(s) - \overline{u_i}(\vec{Y}(t), s)\right] \\ &\times \left\{ \frac{\chi_c^2}{9} + \chi_c + 1 - \frac{(\chi_c + 1)^2 < [\chi_s^3 - \chi_s^2 \tanh(\chi_s) - 2f(\chi_s)]\lambda(\mu/\alpha\beta) + f(\chi_s) >}{[1 + (\mu/\alpha\beta)(\chi_c + 3)][\chi_s^3 - \chi_s^2 \tanh(\chi_s) - 2f(\chi_s)]\lambda + (\chi_c + 3) f(\chi_s)} \right\}, \end{aligned} \tag{1.138}$$

where the variables χ_c and χ_s are the same as in expression (1.134) and β is the same slip parameter that was defined earlier in Equation 1.114 for the steady drag coefficients.

When there is no slip on the surface of the sphere, that is, $\beta \to \infty$, Equation 1.136 reduces to the Galindo and Gerbeth equation (1.133). Remarkably, the case of a sphere with perfect slip, $\beta = 0$, and the case of an inviscid sphere, $\lambda = 0$, are equivalent and result in the same equation of motion. This equation was first derived for an inviscid bubble by Morrison and Stewart (1976) in an implicit integrodifferential form. Therefore, if extremely small particles and drops in the last stages of vaporization/combustion are to be modeled by a continuum approach with finite velocity slip at their interface, then the values of their drag coefficients would be between the theoretical values for the drag coefficients of bubbles and the drag coefficients of rigid particles.

Parmar et al. (2011) examined the effects of fluid compressibility on the transient motion of a solid sphere in a compressible flow. They performed an analytical study at $Re_r \ll 1$ and expressed the effects of the fluid compressibility by a correction function, which depends on Kn and the ratio of the bulk to the dynamic viscosities. In a companion study, Ling et al. (2011a,b) determined the effects of the unsteady terms on the dispersion of small particles in shock waves. The results of the two studies show that the transient term contributions to the hydrodynamic force and heat transfer coefficients of the particles are significant. At the early stages of the blast wave, when particles are traveling in the expansion fan, the gas density surrounding the particles is larger. This makes the transient components of the hydrodynamic force and the rate of heat transfer to be of the same order of magnitude as the steady terms. Consequently, the error from neglecting the transient terms in such applications may become significant.

1.4.3.6.2 Finite but Small Reynolds Numbers Sano (1981) used an asymptotic analysis to derive an expression for the transient hydrodynamic force acting on a rigid sphere at small but finite values of Re_r, when the sphere undergoes a step change in its velocity, from 0 to v_i:

$$F_i(t)=3\pi d\mu_f v_i\left\{H(t^\star)+\frac{1}{3}\delta(t^\star)+\frac{1}{2\sqrt{\pi t^\star}}+\frac{3}{16}Re_r\left[\left(1+\frac{16}{Re_r^4 t^{\star 2}}\right)\operatorname{erf}\left(0.5Re_r t^{\star 1/2}\right)\right.\right.$$
$$\left.\left.+\frac{2}{(\pi t^\star)^{1/2}Re_r}\left(1-\frac{2}{Re_r^2 t^\star}\right)\exp\left(-\frac{1}{4}Re_r^2 t^\star\right)-\frac{8}{3(\pi t^\star)^{1/2}Re_r}\right]+\frac{9}{160}Re_r^2\ln\left(\frac{1}{2}Re_r\right)\right\}+O\left(Re_r^2\right). \quad (1.139)$$

The time variable in this equation is made dimensionless by dividing with a characteristic time based on the properties of the viscous fluid, $\tau_f = a^2\rho_f/\mu_f$. The expression in the square brackets results from the contribution of the outer velocity field and is a consequence of the advective terms in the Oseen equations. For this reason, it has been referred to as the "Oseen contribution." It appears that the most important effect of the higher Re_r on the hydrodynamic force is on the history term. The last term of the Oseen contribution cancels the third term in the right-hand side, $(\pi t)^{-1/2}$. The remaining transient history terms decay exponentially. This rate of decay is faster than the decay of the transient terms of the creeping flow equation. From the physical point of view, this occurs because the finite velocity difference allows for the faster advection and evolution of the vorticity field around the sphere. While in the creeping flow case the vorticity field around the sphere was transported by viscous diffusion alone, which is a slower molecular process, in the case of advection, the finite velocity "carries" the vorticity field far from the sphere with the characteristic velocity of advection. With the faster decay of the transient terms, a spherical particle does not retain any "memory" of its initial velocity, which is characteristic of the $t^{-1/2}$ rate of decay.

Mei et al. (1991) conducted such a numerical study on the motion of a rigid spherical particle in the range $0 < Re_r < 50$ when the free-stream velocity fluctuates with a small amplitude. The results of this study show that, in the low-frequency limit, the history term of the hydrodynamic force decays faster than the conventional $t^{-1/2}$ rate. Subsequently, Mei and Adrian (1992) obtained an analytical solution for the motion of a solid sphere, which is valid at very low frequencies ($Sl \ll Re_r < 1$). Their results revealed a different history term for the hydrodynamic force acting on the particle, which may be written as follows:

$$\int_0^t \frac{(dv_i/d\tau)-(du_i/d\tau)}{\left[\left(\frac{\pi\nu_c}{a^2}(t-\tau)\right)^{1/4}+\left(\frac{\pi}{2a\nu_c}\left(\frac{|u_i(\tau)|}{f_H}\right)^3(t-\tau)^2\right)^{1/2}\right]^2}d\tau, \quad (1.140)$$

where f_H is a function, which has been correlated from the numerical data

$$f_H = 0.75 + 0.105Re_r. \quad (1.141)$$

It is evident that, at short times, this history term matches the asymptotic behavior of the typical history term at creeping flow, $t^{-1/2}$, while at long times the term decays asymptotically as t^{-2}. With this functional form of long-term decay, the sphere does not retain any memory of its initial velocity. Lovalenti and Brady (1993) confirmed this in a more general study on the transient flow of particles.

1.4.3.6.3 High Reynolds Numbers: The Semiempirical Equations While all the known analytical expressions for the transient hydrodynamic force on particles, bubbles, or drops apply to low Re_r, many engineering applications occur at higher ranges of this parameter: slurry transport and practical pneumatic conveying systems operate in the range $10^1 < Re_r < 10^3$; drops in combustion processes may reach Re_r up to 10^3; bubble columns in chemical processes operate in a range of Re_r from 0 to 10^3, depending on the properties of the

carrier fluid; and particulate flows in the environment may reach relative, Re_r, up to 10^4. Since there is no applicable theory, other than some asymptotic studies that only lead to approximate analytical expressions for the hydrodynamic force at $Re_r > 1$, experimental data and empirical correlations have been used for the calculation of the steady as well as for the transient hydrodynamic force and the corresponding drag coefficient.

The steady flow empirical relations for the drag coefficients of a solid or a viscous sphere have been presented in Section 1.4.3.2 and are summarized in the standard drag curve of Figure 1.8. Following the practice used for the steady term, Odar and Hamilton (1964) proposed modifications and correlation functions that extend to the transient terms of the hydrodynamic force. They essentially treated the three terms of the Boussinesq–Basset expression as separate forces and associated each one of them with a correction factor or function that accounts for the higher Re_r. Their equation is

$$F_i = C_1 6\pi a \mu_f (v_i - u_i) + \Delta_A \frac{1}{2} m_f \frac{d(v_i - u_i)}{dt} + \Delta_H a^2 \sqrt{\pi \rho_f \mu_f} \int_0^t \frac{\frac{d(v_i - u_i)}{d\tau}}{\sqrt{t - \tau}} d\tau, \tag{1.142}$$

where the functions C_1, Δ_A, and Δ_H are the empirical functions determined by experiments. Odar and Hamilton used the Schiller and Nauman (1933) correlation for the coefficient C_1 (Equation 1.104) and reduced their experimental data to derive the following expressions for the added mass and history term coefficients:

$$\Delta_A = 1.05 - \frac{0.066}{0.12 + Ac^2} \quad \text{and} \quad \Delta_H = 2.88 + \frac{3.12}{(1 + Ac)^3}, \tag{1.143}$$

where Ac is the dimensionless acceleration number

$$Ac = \frac{|u_i - v_i|^2}{2a\left|\frac{dv_i}{dt}\right|}. \tag{1.144}$$

Bataille et al. (1990) measured independently the added mass coefficient for bubbles and concluded that, within the experimental error of the measurements, the added mass coefficient Δ_A is consistently equal to 1 up to $Re_r = 1000$, even when some of the bubbles are not exactly spherical. Also Auton et al. (1988) and Mei et al. (1991) confirmed analytically that the potential flow solution, which yields the value $\Delta_A = 1$ for the added mass coefficient, is correct and that neither the Reynolds number nor the acceleration number has a significant impact on this term. Based on these analytical and experimental observations, Michaelides and Roig (2011) reinterpreted and recorrelated the original data by Odar and Hamilton (1964) and determined that for $\Delta_A = 1$, the correct expression for the history coefficient is

$$\Delta_{HNEW} = 6.00 - 3.16\left[1 - \exp\left(-0.14 Re_r Sl^{0.82}\right)^{2.5}\right]. \tag{1.145}$$

A more thorough discussion on the use of the semiempirical expressions as well as the results of several other analytical, computational, and experimental studies is that by Michaelides (2003, 2006).

1.4.3.7 Deformable and Irregular Particles

Simple experiments based on sedimentation have shown that the drag coefficients for nonspherical particles are significantly different from those of spheres. Shape factors have been proposed for the quantification of the effect of nonsphericity of particles, bubbles, and drops. Wadell (1933) suggested that the volume-equivalent diameter of a sphere, d_V, or the area-equivalent diameter be used as the characteristic length of

the particles for the determination of the drag coefficient. These two diameters may be given in terms of the volume and the projected area of the irregular particle as follows:

$$d_V = \sqrt[3]{6V/\pi} \quad \text{and} \quad d_p = \sqrt{4A_p/\pi} \tag{1.146}$$

where

V is the total volume of the particle

A_p is the projected area of the particle in the direction of the flow

For the determination of d_p, one must have information on the orientation of the particle during the flow. Wadell (1933) suggested that a shape factor, Ψ, may be defined as a dimensionless measure of the irregularity of the particle:

$$\Psi = \frac{d_V^2}{d_p^2} = \frac{\pi^{1/3}(6V)^{2/3}}{A_p}. \tag{1.147}$$

Since the drag coefficient is defined in terms of the projected area of the particle, the shape factor may be used to correct for the irregular shape of particles according to the following expression:

$$\Psi C_D A = (C_D A)_s. \tag{1.148}$$

The quantity in the parenthesis in the last expression pertains to the characteristics of a sphere, defined in terms of the volume-equivalent diameter, d_V.

While Equation 1.148 may be used as a first approximation for a correction to the steady drag coefficient for particles that are nearly spherical, several other researchers (Haider and Levenspiel, 1989, Hartman and Yates, 1993) determined that when particles are very elongated and the correction factors are very large, this equation introduces significant errors in the determination of the drag coefficient. For this reason, another quantity, the circularity, which is also called surface sphericity, c, was introduced:

$$c = \frac{\pi d_A}{P_p}, \tag{1.149}$$

where P_p is the projected perimeter of the particle in its direction of motion, which is an easier parameter to measure in particles than the projected area. The circularity suffers from the drawback that it yields the same value for some 3D and 2D objects. For example, spheres and disks that fall on their flat sides have the same circularity, while their drag coefficients differ significantly.

Expressions for the drag coefficients of irregular particles have been derived by several researchers for different types and shapes of particles, including Pettyjohn and Christiansen (1948), Masliyah and Epstein (1970), Lasso and Weidman (1986), Haider and Levenspiel (1989), and Hartman and Yates (1993). Each one of these correlations applies to a specific type of particles (e.g., disks, pyramids, prisms) or to a group of shapes. Chhabra et al. (1995) conducted an experimental study and determined the drag coefficients of chains of agglomerates of spheres in viscous fluids at relatively low Reynolds numbers ($Re_r < 2.5$). They concluded that in all cases the drag of the irregular agglomerate is higher (up to 50%) than the drag of a sphere with diameter d_V. Madhav and Chhabra (1995) presented experimental data for the terminal velocity and the drag coefficients of spheres, cylinders, needles, and prisms in the range $1 < Re_r < 400$.

More recently, Tran Cong et al. (2003) performed an experimental study that included several types of irregular particles: spheroids; prisms; star-shaped; H-shaped; elongated bars and cylinders; X-shaped; and cross-shaped. They correlated their data using several suitable functional forms and concluded that the following expression not only correlates the data best but also agrees very well with the correlations of the others:

$$C_D = \frac{24}{Re_r}\frac{d_A}{d_V}\left[1 + \frac{0.15}{\sqrt{c}}\left(\frac{d_A}{d_V}Re_r\right)^{0.687}\right] + \frac{0.42}{\sqrt{c}\left[1 + 4.25\times10^4\left(\frac{d_A}{d_V}Re_r\right)^{-1.16}\right]}. \tag{1.150}$$

This is valid in the ranges $0.15 < Re_r < 1500$, $0.80 < d_A/d_V < 1.50$, and $0.4 < c < 1.0$. These ranges cover most of the irregularly shaped particles in engineering applications.

1.4.3.8 Deformable Bubbles and Drops

Oftentimes, bubbles and drops become spheroidal. Lawrence and Weinbaum (1986, 1988) conducted an analytical study on the transient motion of a rigid spheroid of revolution with small eccentricity, under creeping flow conditions. The results of this study are applicable to bubbles and drops if the internal circulation has negligible effect. The study used essentially the method employed by Maxey and Riley (1983) with the added complexity of domain decomposition to account for the eccentricity and extended to the second-order expansion in terms of ε. The resulting expression for the transient hydrodynamic force on the spheroid is

$$F_i = -6\pi\mu_f a\left[\left(v_i-u_i\right)\left(1-\frac{\varepsilon}{5}+\frac{37\varepsilon^2}{175}\right)+\frac{a}{\sqrt{\nu\pi}}\left(1-\frac{2\varepsilon}{5}+\frac{81\varepsilon^2}{175}\right)\int_0^t \frac{d\left(v_i-u_i\right)/d\tau}{\sqrt{t-\tau}}d\tau\right.$$
$$\left.+\frac{a^2}{9\nu}\left(1+\frac{\varepsilon}{5}-\frac{26\varepsilon^2}{175}\right)\frac{d\left(v_i-u_i\right)}{dt}+\frac{8a\varepsilon^2}{175\sqrt{\pi\nu}}\int_0^t \frac{d\left(v_i-u_i\right)}{d\tau}G\left(t-\tau\right)d\tau\right] \tag{1.151}$$

The function G of the last term is a frequency-dependent term:

$$G\left(t\right) = Im\left[\sqrt{\frac{\pi\phi}{3}}e^{\phi t}erfc\sqrt{\phi t}\right],\ \text{with}\ \phi=\frac{3}{2}\left(1+i\sqrt{3}\right). \tag{1.152}$$

The first three terms of (1.149) are similar to the steady drag, the history, and the added mass term of the Boussinesq–Basset equation. Their form is the same as the form of the corresponding terms of Equations 1.132 and 1.133 with the correction terms due to the eccentricity of the spheroid. However, the last term of Equation 1.151 does not have a counterpart in the Boussinesq–Basset expression. The term depends on the eccentricity as well as the frequency of variation of the velocity of the fluid and vanishes asymptotically as ε^2. This is a new history integral term, which emanates from the elongated shape of the immersed object. The presence of such terms in an equation derived under the creeping flow assumption is another indication that the transient Boussinesq–Basset and Maxey–Riley expressions are significantly modified when there are departures from the assumptions these equations were derived from and which were listed in Section 1.4.3.6. Given that the modifications are on the functional form of these expressions, simple empirical corrections of the three terms of the hydrodynamic force would not be sufficient for the development of the correct transient expressions.

The motion of bubbles and drops in viscous fluids at finite Re_r creates surface stresses that deform the spherical symmetry of these objects. This has a very important effect on the transport coefficients, because the shape of an object is one of the primary determinants of the hydrodynamic force, the heat, and the mass transfer coefficient. The physical properties of the bubbles/drops and the carrier fluid, such as surface tension and viscosity, play an important role in the deformation of the bubbles and drops as well as in the determination of their shapes. For bubbles freely rising in a column of water under the action of gravity, Haberman and Morton (1953) concluded that the following variables determine their shape:

1. The terminal velocity, v
2. The characteristic length, defined as the diameter of the volume-equivalent sphere, d_V
3. The density of the carrier fluid, ρ_f
4. The viscosity of the carrier fluid, μ
5. The surface tension, σ
6. The gravitational acceleration, g

Three independent dimensionless groups may be derived from these six variables:

1. The Reynolds number, $Re = \rho_f d_V v/\mu$, or, equivalently, the relative Reynolds number, Re_r
2. The Eötvös number, $Eo = g\rho_f d_V^2/\sigma$
3. The Morton number, $Mo = g\mu_f^4/\rho_f\sigma^{\,3}$

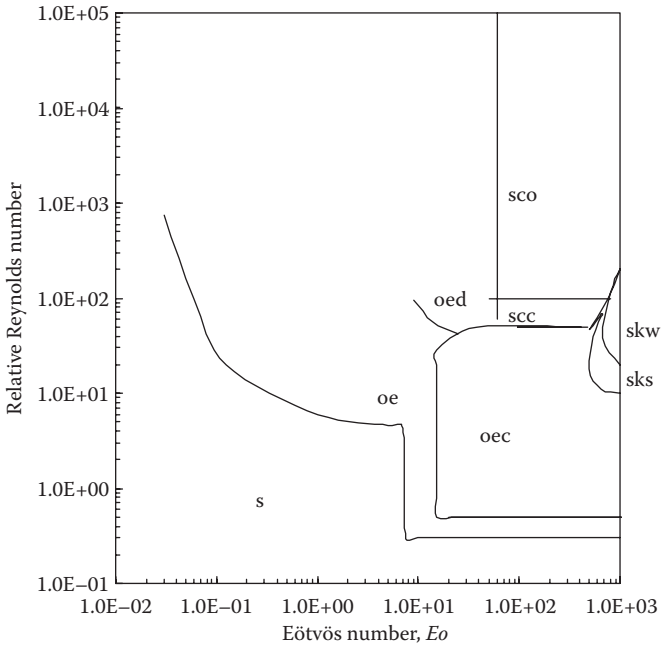


Figure 1.12

The shape map of the deformed bubbles. (Reproduced from the data of Bhaga, D. and Weber, M.E., *J. Fluid Mech.*, 105, 61, 1981.)

Another dimensionless group that appears often in the literature, the Weber number, is defined by the relationship $We = \rho_f v^2 d_V/\sigma$, or $We = Re^2(Mo/Eo)^{-1/2}$.

When experiments are carried in a constant gravitational field, such as laboratories on the Earth's surface, the list of the important variables is reduced to five. This leaves only 2D groups that would determine the shape of bubbles. This pair may be one of the combinations (*Re*, *Eo*), (*Re*, *Mo*), or (*Eo*, *Mo*).

It is standard practice to reduce experimental observations on the shape of bubbles and drops in the so-called shape maps with two of the aforementioned dimensionless groups as coordinates. Such a shape-map has been constructed from the data by Bhaga and Weber (1981) and is reproduced in Figure 1.12. The acronyms on the map are

- s: spherical
- scc: spherical cap with steady, closed wake
- sco: spherical cap with open unsteady wake
- oe: oblate ellipsoidal
- oed: oblate ellipsoidal disk (very elongated and wobbling in motion)
- oec: oblate ellipsoidal with cap in the bottom
- sks: skirted with steady skirt
- skw: skirted with wavy unsteady skirt

It is apparent in this figure that while there is a complexity with the conditions on the shapes of bubbles, in general, bubbles assume the spherical shape at low Reynolds numbers, regardless of the value of the Eötvös number. Also, bubbles are spherical at intermediate values of Re_r, when $Eo < 1$. Bubbles become ellipsoidal at intermediate values of Eötvös numbers and high Re_r. Finally, bubbles assume the shape of a spherical cap at high *Eo* and at relatively high Re_r.

While a shape map, such as that given earlier, which represents static or steady conditions, is useful in determining the shape of flowing bubbles, recent experimental studies on the subject suggest that the method of the creation and release of bubbles also affects their shape, their drag coefficients, and their trajectories. Tomiyama (2001) observed that when bubbles are released with small initial deformation, their shape remains very close to spherical, their drag coefficient is higher than expected, and their motion is rectilinear or zigzag on a plane. However, when the bubbles are released with high initial deformations as ellipsoids,

their shape continues to be ellipsoidal, their drag coefficient is higher, and their motion is helical or rectilinear. In a similar study, Wu and Gharib (2002) also concluded that the initial method of the release of bubbles (whether they are released from a narrow or from a wide tube) plays a role in the eventual shape, the rise velocity, and the drag coefficient. Apparently, the shape oscillations that occur after a bubble is detached from the nozzle are strong enough to disperse the contaminants and to render the bubble surface clean, at least in the initial stage of the bubble trajectory. In most practical cases, the surrounding water contains a sufficient concentration of contaminants for the bubble surface to become immediately contaminated. However, in the case of very pure systems such as the ones used in the study by Wu and Gharib (2002), the recontamination process of the surface was very slow, the bubbles' surface remained clean for the duration of the experiment, and the bubbles remained spherical at significantly higher values of Re_r.

The drag coefficient of inviscid spheres (bubbles) is of importance in practical applications, such as boiling, aeration, and water purification. In this case, the surfactants and contaminants in the water that finally line up on the interface of the bubble and the carrier fluid also play an important role in the determination of the drag coefficient of bubbles. Among the various studies on the drag coefficients, Tomiyama et al. (1998) studied the rise of bubbles in a wide range of Reynolds and Eötvös numbers and derived the following expression for the drag coefficients of clean uncontaminated bubbles:

$$C_D = \max\left\{\min\left(\frac{16}{Re_r}\left(1+0.15Re_r^{0.687}\right), \frac{48}{Re_r}\right), \frac{8Eo}{3Eo+12}\right\}. \tag{1.153}$$

This expression is consistent with the correlations of the numerical data that were given in Section 1.4.3.2, Equations 1.107 through 1.112. It must be noted that when the bubbles become bigger, their shape becomes ellipsoidal. Consequently, the drag coefficient of bubbles depends strongly on the surface tension, which is a determinant of their shape. In the case of elongated bubbles, their drag coefficient is independent of Re_r and is given by the last expression in Equation 1.153, which is a simple function of the Eötvös number. This expression is valid for fairly large hemispherical bubbles, up to 3 cm in diameter.

Because the surfactants in the gas–fluid interface play a major role in the friction part of the drag force and contaminants/surfactants accumulate on this interface, the degree of contamination of the liquid is an important factor in the determination of the drag coefficient of bubbles. The data by Sridhar and Katz (1995) suggest that small bubbles in filtered water, which may be characterized as *contaminated*, behave as solid spheres, and their drag coefficients are very well correlated by the Schiller and Nauman (1933) expression (Equation 1.104) up to $Re_r = 85$. In the case of *grossly contaminated* bubbles, such as those involving tap or industrial water, Loth (2000) recommends the Oseen expression (Equation 1.102) for $Re_r < 1$ and the following expressions, which are based on data from Clift et al. (1978):

$$C_D = \frac{24}{Re_r}\left(1+0.1935Re_r^{0.6305}\right), \quad 1 < Re_r < 78 \quad \text{and} \quad C_D = \frac{24}{Re_r}\left(1+0.03875Re_r\right), \quad 78 < Re_r < 300. \tag{1.154}$$

Beyond this range of Re_r, it is very likely that the bubbles are not spherical, and hence, their shape is the major factor that influences the drag coefficient. It must be noted that the drag coefficient expressions for *clean* and *grossly contaminated* conditions may be considered as the lower and the upper limits for the drag coefficients of bubbles. The actual value of the drag coefficient of bubbles is expected to be between these two limits.

1.4.3.9 Lift Effects and Transverse Forces

The drag force is always acting in the direction of the motion of the particle, and its magnitude is monotonically increasing with the relative velocity of the sphere. Particle rotation combined with finite relative velocity or fluid velocity gradients (shear) induces a transverse component in the hydrodynamic force on the sphere, which is often called the "lift force."

When the rigid, spherical particle travels in an inviscid fluid with a relative velocity and also rotates with respect to the far field of the flow, the velocity asymmetry around the particle induces a transverse pressure difference on the surface of the sphere, which generates the *Magnus force* (Magnus, 1861):

$$F_{LMi} = \pi\alpha^3\rho_f[e_{ijk}\Omega_j(u_k - v_k)], \tag{1.155}$$

where Ω_j is the relative rotation of the particle with respect to the inviscid fluid. The term in the square brackets represents the vector product of the relative rotation and the relative velocity vectors. It is apparent that the direction of the Magnus force is perpendicular to the plane of the relative velocity and the axis of rotation.

The functional form of the lift force in a viscous fluid is influenced by the Reynolds number. In this case, the magnitude of the lift force is often expressed as a function of a dimensionless *lift coefficient*, C_{LM}, which is correlated with experimental data. While many expressions have appeared in the past, the investigation by Oesterle and Bui-Dinh (1998) appears to be based on accurate data and is recommended to be used for the lift coefficient of a sphere rotating in an infinite fluid:

$$C_{LM} = \frac{\left|\vec{F}_{LM}\right|}{\pi\alpha^3\rho_c\left|\vec{\Omega}\right|\left|\vec{u}-\vec{v}\right|} = 0.45 + \left(\frac{Re_R}{Re_r} - 0.45\right)\exp\left(-0.05684 Re_R^{0.4} Re_r^{0.3}\right) \quad \text{for } Re_R < 140, \tag{1.156}$$

where Re_R is the Reynolds number based on the relative rotational speed of the sphere

$$Re_R = \frac{\rho_f d^2\left|\vec{\Omega}\right|}{\mu_c}. \tag{1.157}$$

The lift coefficient is, in general, a monotonically decreasing function of Re_R and increases with the dimensionless *rotation parameter*, $(|\vec{\Omega}|d)/(|\vec{u}-\vec{v}|)$. This is a dimensionless measure of the rotational speed of the particle. Experiments at low values of the rotation parameter suggest that C_{LM} may become negative (Tanaka et al., 1990). This is most likely due to a higher relative velocity on one side of the sphere and a premature transition to turbulence of the boundary layer on that side. As a consequence, the wake behind the sphere deflects in a direction that is opposite to what is expected in rotating flow. This reverses the direction of the lift force.

Saffman (1965, 1968) considered the case of a very small sphere in a shear flow at the limit of vanishing Reynolds numbers (creeping flow). He derived an expression for the lift force due to shear, which is

$$\vec{F}_{LS} = \frac{6.46\alpha^2\sqrt{\rho_c\mu_c}}{\sqrt{|\vec{\gamma}|}}\left(\vec{u}-\vec{v}\right)\times\vec{\gamma}, \tag{1.158}$$

where $\vec{\gamma}$ is the fluid velocity shear evaluated at the center of the sphere. The direction of this force is the perpendicular direction to the plane defined by the relative velocity vector and the shear vector. Sufficient conditions for the validity of the aforementioned expression are very low Re_r as well as:

$$\left|\vec{v}-\vec{u}\right| \ll (\gamma\nu)^{1/2}, \quad \gamma a^2/\nu \gg 1 \quad \text{and} \quad a^2\left|\vec{\Omega}\right|/\nu \ll 1. \tag{1.159}$$

The last three conditions imply one of the following alternatives:

- **a.** Either very low particle velocity, shear, and angular rotation for the particle
- **b.** Extremely high kinematic viscosity for the fluid if the particle has finite velocity, shear, or angular rotation

The first alternative is compatible with the assumptions implied in the derivation of the transient Basset–Boussinesq equation. The second alternative implies very high viscosity in combination with finite shear or rotation and is not strictly compatible with the implied conditions of the transient equation. It must be noted that although Saffman's result (Equation 1.158) is occasionally referred to as the "Saffman force," it is not a separate force from the *Magnus force* but a special case of the latter at the limit $Re_r \to 0$. For this reason, the lift force must be only accounted once in computations of particle dynamics.

The lift force developed on a sphere is very much weaker than the longitudinal drag force. However, the transverse lift plays a dominant role in the lateral migration of bubbles, drops, and particles toward the walls

of cylindrical pipes as well as in dispersion processes. This occurs because in most engineering systems particles, bubbles, and drops have to travel relatively very short distances in order to approach the walls of a pipe or a channel and, hence, a weak force would be sufficient to induce a lateral motion that covers such short distances. These weak transverse forces contribute significantly to radial diffusion and dispersion, wall deposition, mixing, and separation processes.

Tsuji et al. (1985) measured experimentally the shear-induced lift on bubbles and concluded that the expression by Saffman yields satisfactory results for the magnitude of the force. McLaughlin (1991) extended the theoretical analysis by Saffman to higher Re_r and derived a correction to the expression by Saffman, which shows that the magnitude of F_{LS} decreases with the increase of Re_r. McLaughlin's expression for the lift force is as follows:

$$F_{LS} = \frac{9}{\pi}\mu_f a^2 |\vec{v} - \vec{u}| \sqrt{\frac{\gamma \rho_f}{\mu_f}} J(\varepsilon), \tag{1.160}$$

where ε is the dimensionless velocity ratio $\varepsilon = \sqrt{\gamma \mu_f / \rho_f} / |\vec{v} - \vec{u}|$ and the function $J(\varepsilon)$ is given in tabular form by McLaughlin (1991). Two approximate asymptotic expressions for this function are $J(\varepsilon) = 2.255 - 0.6463/\varepsilon^2$ for $\varepsilon \gg 1$ and $J(\varepsilon) = 32\pi^2\varepsilon^5 \ln(\varepsilon^{-2})$ for $\varepsilon \ll 1$.

The numerical results for the shear lift force exerted on a sphere obtained by Dandy and Dwyer (1990) were reduced to a useful correlation by Mei (1992):

$$\begin{aligned} &C_{LS} = \frac{F_L}{6.44\rho_f a^2 \gamma^{1/2} \nu^{-1/2}} = \left(1 - 0.3314\sqrt{\beta}\right)\exp\left(-\frac{Re_r}{10}\right) + 0.3314\sqrt{\beta} \quad \text{for } Re_r \le 40 \\ &C_{LS} = 0.0524\sqrt{\beta Re_r} \quad \text{for } Re_r > 40, \\ &\text{where} \quad \beta = \frac{d|\nabla \times \vec{u}|}{2|\vec{u} - \vec{v}|}. \end{aligned} \tag{1.161}$$

The parameter β in the last equation is a dimensionless measure of the shear. The recommended range of this correlation is $0.005 < \beta < 0.4$, and Mei (1992) showed that this empirical equation fits well McLaughlin's results.

There is no widespread agreement on the magnitude of the lift coefficients. The experimental results by Sridhar and Katz (1995) suggest that at least for bubbles, the magnitude of the lift component of the hydrodynamic force is higher than the values predicted by the two aforementioned expressions. Another experimental study by Tomiyama et al. (1999) for bubbles in shear flows concluded that the lift coefficient of larger bubbles depends on the surface tension too and included the Eötvös number in the correlation. Tomiyama et al. (1999) also concluded that rising bubbles tend to accumulate close to the walls if their radii are less than 6 mm, while bigger bubbles with $a > 6$ mm migrate toward the center of the apparatus.

The lift of growing or receding bubbles and drops close to a wall is very important in the boiling, condensation, and evaporation processes, because the global rate of the heat transfer greatly depends on the amount of vapor in contact with the wall or in the immediate vicinity of the wall. In convective boiling systems, such as heated pipes, the lift due to shear facilitates the detachment of small spherical bubbles from the wall and subsequently the nucleation and the commencement of the growth process of other bubbles. Thorncroft et al. (2001) studied the growth and detachment of bubbles from a surface and concluded that the growth of a bubble, whose radius is a function of time, $a(t)$, close to a wall enhances the lift force exerted by the shear. In their analytical and computational study, Thorncroft et al. (2001) derived the following expression for the lift, due to the shear:

$$F_{SLi} = \frac{1}{2}|\vec{u} - \vec{v}|(u_i - v_i)\pi\rho_f a^2(t)\gamma^{1/2}\left\{\left[\frac{1.46J}{Re_r^{1/2}}\right]^2 + \left[\frac{3}{4}\gamma^{1/2}\right]^2\right\}^{1/2}, \tag{1.162}$$

where J is a scalar function of the dimensionless shear rate and Re_r. The augmented lift force in this case facilitates the detachment of the bubble from the wall, reduces the amount of vapor close to this wall, and thus contributes to the enhancement of the heat transfer from the wall to the bulk fluid.

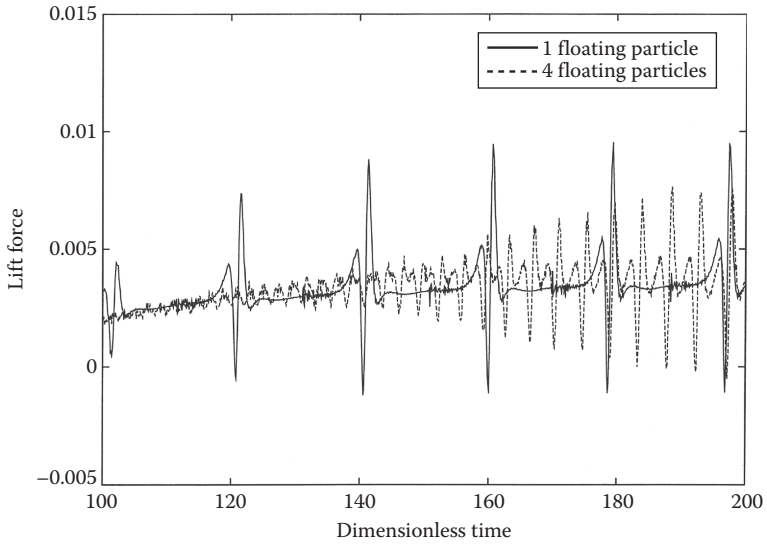


Figure 1.13

The effect of the flow of suspended particles on the lift and drag on a stationary particle.

The transverse force on particles is also influenced by the advection of other particles in the flow. The shear-induced lift on solid spheres attached or deposited on a boundary, in the presence of other spheres in the flow field, known as suspension flow, was studied numerically by Feng and Michaelides (2002a). Their results show that the instantaneous hydrodynamic force exerted by the suspension flow on a solid particle attached to a wall is increased by a factor of 2–4 by the presence of similar particles, which are carried by the fluid. This effect is depicted in Figure 1.13, which shows the instantaneous lift on an embedded sphere, when other spheres in the suspension pass by it. This augmentation includes both the lift and the drag components of the hydrodynamic force and is caused by the interactions of the suspended spherical particles with the stationary particle when they are in the range of 0–5 diameters. As a result of this type of hydrodynamic interaction, a particle that lies on a horizontal plane may be lifted and become part of the suspension flow without any physical collisions with other particles.

Regardless of the method of evaluation of the lift component, the ratio of the transverse component to the longitudinal component of the hydrodynamic force, F_L/F_D, is of the order of $d(\gamma/\nu)^{1/2}$, which is typically a very small number. Despite this, the transverse component of the hydrodynamic force is important in engineering because it causes the lateral migration and dispersion of spheres and plays an important role in several applications, such as bubble detachment from the pipe walls during boiling, particle sedimentation, and resuspension in water as well as particulate and aerosol dispersion in the atmosphere. The accurate knowledge of the transverse component of the transient hydrodynamic force is of importance in calculations that pertain to such processes, even though the method of the determination of the drag component is not fully compatible with the assumptions used for the determination of the lift. It is common practice in such calculations to superpose an expression for the transverse or lift component, such as Equation 1.153 or Equation 1.158 with an expression for the transient hydrodynamic force in the longitudinal direction, such as Equation 1.133, and compute the longitudinal and transverse motion of particles, bubbles, and drops. The result of such a superposition is that the transient hydrodynamic force on a sphere appears to have a lateral, albeit steady, component in addition to the longitudinal component. Although the superposition is not justified on analytical grounds, it is very convenient to use and the results obtained appear to be accurate. When one uses this superposition, it is important to ensure that the necessary conditions for the validity of the expressions used for the several components of the hydrodynamic force are not violated. This implies that there is very low relative velocity and that the local shear is low.

The influence of mass transfer from the sphere (evaporation or sublimation) on the lift has been investigated experimentally and numerically. A numerical study by Kurose et al. (2003) determined that in linear shear flow, the outflow from a sphere acts in a way to push the sphere toward the lower flow velocity side. Thus, a negative lift is developed at high Reynolds numbers. This counteracts the positive lift on the sphere, which is directed toward the higher velocity side. According to Kurose et al. (2003), the diffusion

and reaction rates are strongly affected by the outflow velocity and the fluid shear because of the deformation of the vortices that appear behind the evaporating sphere. This suggests that surface evaporation and/or reaction influences significantly the lateral motion of drops and hence the concentration field of the drops.

1.4.3.10 Effects of the Boundaries

The effect of a wall, in general, is to retard the motion of particles in both the parallel and the perpendicular direction to the wall, thus reducing the rate of mass transport. In addition, the presence of particles and bubbles in boundary layers and mixing layers significantly modifies the stability and transport properties of these layers. The motion of particles, bubbles, and drops in the vicinity of a boundary is important in many practical applications especially those related to boiling of liquids and the transport of particulates and slurries. In particulate transport processes, particle collisions with the walls cause pipeline erosion and particle adhesion to the walls, scale buildup, and oftentimes pipeline clogging.

Faxen (1922) was the first to consider the motion of a particle in rectilinear motion parallel to a wall and to derive an expression for the hydrodynamic force on a spherical particle. He used the method of reflections for the movement of the sphere under creeping flow conditions and obtained an asymptotic solution for the total force acting on a sphere, which settles along the centerline of an orthogonal cylinder. The ratio, Ξ, of the particle diameter, d, to the diameter of the cylinder, D, ($\Xi = d/D$) is the most important parameter that affects the hydrodynamic force. Faxen's expression for the hydrodynamic force is given in terms of a wall drag multiplier, K_{wall}. This is the ratio of the steady hydrodynamic force to the Stokesian force the same sphere experiences in an unbounded flow. By using the same method, Bohlin (1960) obtained a higher-order approximation for the wall drag multiplier, which may be written as follows:

$$K_{wall} = \frac{1}{1 - 2.01443\Xi + 2.088777\Xi^3 - 6.94813\Xi^5 - 1.372\Xi^6 + 3.87\Xi^8 - 4.19\Xi^{10} + \cdots}. \tag{1.163}$$

Haberman and Sayre (1958) developed a theoretical method to compute the wall correction factor, K_{wall}, for spheres settling in cylinders up to very high values of Ξ, and later Paine and Scherr (1975) computed the values for K_{wall}. Their results are tabulated in the range $0 \leq \Xi \leq 0.9$. A comparison between the expression by Bohlin (Equation 1.160) and the exact theory by Haberman and Sayre (1958) shows that the last equation yields accurate results only up to $\Xi = 0.6$. There are also several experimental studies pertaining to the settling of a sphere along the centerlines of orthogonal circular cylinders or plane walls. Among them, the experimental studies by Iwaoka and Ishii (1979) and Miyamura et al. (1981) demonstrate good agreement with the theoretical predictions by Faxen (1922), Bohlin (1960), and Paine and Scherr (1975).

Happel and Brenner (1986) considered creeping as well as inertia flows for the settling of a sphere in a cylinder and stipulated that the total effect on the hydrodynamic force is a simple linear combination of the separate effects of proximity to the outside boundary and inertia:

$$K = K_{wall} + K_{inertia} - 1, \tag{1.164}$$

where

K_{wall} is the effect of the wall at creeping flow conditions as calculated by an expression similar to (1.160)
$K_{inertia}$ is the additional correction factor due to inertia at higher Re_r

The last equation simply implies that the drag on a sphere is composed of two additive terms: one term is due to the effect of the cylindrical boundary and the other to flow inertia. The latter is usually obtained from one of the empirical correlations for the drag coefficient at higher Re_r, such as the one by Schiller and Nauman (1933). Equation 1.164 is a conjecture, partly based on the experimental data by Fayon and Happel (1960). The data set pertains to a diameter ratio, Ξ, in the range of 0.1250–0.3125 and the Reynolds numbers in the range 0.1–40.

Feng and Michaelides (2002b) conducted a more general numerical study in the ranges $0.1 < \Xi < 0.8$ and $0 < Re_r < 35$ for cylindrical as well as for prismatic enclosures. They concluded that the two effects of inertia and of flow confinement are not additive and may not be linearly combined as Equation 1.164 implies. Because of this, in calculating the hydrodynamic force on a sphere, it is more accurate to use computational and experimental results, which are not restricted by the conjecture (1.161). One of the significant results by Feng and

Table 1.2 Wall Correction Factors for Various Orthogonal Rectangular Prisms

$L/W = 1.0$								
$\Xi(=d/W)$	0.2	0.3	0.4	0.5	0.6	0.7	0.8	0.9
K	1.72	2.30	3.18	5.01	8.03	13.98	27.9	61.8
$L/W = 1.5$								
$\Xi(=d/W)$	0.3	0.4	0.5	0.6	0.7	0.8		
K	1.90	2.47	3.32	4.46	6.11	9.24		
$L/W = 2.0$								
$\Xi(=d/W)$	0.3	0.4	0.5	0.6	0.7	0.8		
K	1.73	2.12	2.67	3.33	4.37	5.76		
$L/W = 5.0$								
$\Xi(=d/W)$	0.3	0.4	0.5	0.6	0.7	0.8		
K	1.53	1.75	2.11	2.48	3.06	3.78		

Michaelides (2002b) is that at the higher values of the parameter, $\Xi > 0.5$, the effect of inertia is less than 10% of the total correction factor, K. Table 1.2, which is reproduced from this study, shows the total correction factor, K, for a sphere of diameter, d, when it falls in a rectangular prismatic enclosure whose cross section has length, L, and width, W. The results shown are for $Re_r \ll 1$.

It must be noted that the effect of boundaries on settling spheres is different in the case of prismatic enclosures than in circular cylinders, because secondary flows are induced in the corners of the prisms. Even though the secondary flows are relatively weak, they affect considerably the hydrodynamic force on the spheres.

The asymmetrical velocity and pressure fields due to walls cause the radial migration of particles in pressure-driven flows in pipes and small capillaries away from the wall. Cox and Brenner (1967) expressed the effect of a vertical wall on a particle using the concept of a *migration velocity* of a sphere that is falling freely close to a wall. An analytical expression for the migration velocity is as follows:

$$V_r = \frac{6\pi V_t^2}{\nu} I_h, \tag{1.165}$$

where

V_t is the terminal velocity of the sphere in a stagnant, unbounded fluid

I_h is an integral of Green's function for the point force representing the sphere

The last expression is valid under the conditions $Re_r \ll a/l_w \ll 1$, where l_w is the distance of the center of the sphere from the wall. The implications of this condition are that the sphere is relatively far from the wall and the flow field is Stokesian (creeping flow). Later, Cox and Hsu (1977) calculated analytically the integral, I_h, for spheres and derived the following expression for the migration velocity:

$$V_r = \frac{3}{64} Re_r V_t, \tag{1.166}$$

which is also valid under the condition $Re_r \ll a/l_w \ll 1$. A close look at the last expression reveals that the migration velocity of the sphere is independent from its distance from the wall. This does not constitute a paradox, because the expression is valid only at distances sufficiently far from the wall as required by the condition $a/l_w \ll 1$.

Vasseur and Cox (1976) derived analytically another expression for the lateral migration velocity of a sphere:

$$V_r = \frac{3}{8}\frac{\alpha v_s^2}{\nu}\left[\left(\frac{\nu}{l_w V_t}\right)^2 + 2.219\left(\frac{\nu}{l_w V_t}\right)^{5/2}\right]. \tag{1.167}$$

The terms in the two parentheses are obviously the inverse of a Reynolds number, which is based on the distance of the center of the sphere from the wall. The last expression was later confirmed by the experimental data of Cherukat and McLaughlin (1990) to be valid up to $Re_r = 3.0$.

The repulsive effect of the wall on particles is very important in the distribution of phases in dispersed flows in pipes as well as in sedimentation–resuspension processes with particles. The effect has been demonstrated in a number of experimental and numerical studies, such as the one by Segre and Silberberg (1962) with neutrally buoyant spheres. They concluded that neutrally buoyant particles in a pressure-driven Poiseuille flow (pipe flow) experience a radial force and tend to align at 0.6 pipe radii away from the centerline. This shows that there exists an equilibrium position, where the radial force is zero and where particles tend to accumulate. Two-dimensional numerical studies have also concluded that there is an equilibrium position for cylinders at a distance of 0.4234 half-channel width away from the centerline. Inamuro et al. (2000) concluded that this distance is the same for both a single cylinder and a group of naturally buoyant cylinders in pressure-driven channel flows. Mortazavi and Tryggvason (2000) also studied the lateral migration of 2D drops in Poiseuille flows and determined that drops either move halfway between the pipe centerline and the wall, as Segre and Silberberg (1962) also observed, or they oscillate around an off-center equilibrium position. In a study involving the resuspension of particles in simple shear flow over a flat plate, Feng and Michaelides (2003) concluded that particles, which are slightly heavier than the fluid, do not settle down on a flat surface, but reach an equilibrium position at a certain height from the plane and then drift with the main flow at this vertical position without settling. Their numerical results are shown in Figure 1.14, where the lower facing triangles denote particles that settled under gravity and the upper facing triangles denote particles that drifted at a vertical equilibrium distance. The dividing line separates the settled particles from the particle that reach the equilibrium position, which is usually at a height less than a single diameter from the flat surface. Feng and Michaelides (2003) derived the following expression for the line that separates the settled from the suspended particles:

$$Re_\gamma = \frac{\rho_f \gamma d^2}{\mu_f} = 58\left[\frac{\rho_s}{\rho_f} - 1\right]^{0.59}. \tag{1.168}$$

At a given shear Reynolds number heavier particles settle, while lighter particles move to an equilibrium position and stay suspended in the flow, even though they may be heavier than the fluid. Patankar et al. (2001) also examined the behavior of particles close to the wall in a Poiseuille flow and observed a similar

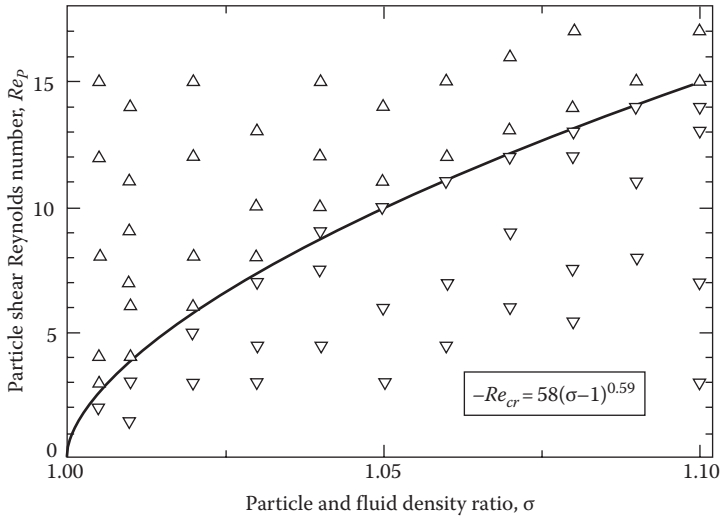


Figure 1.14

Settling or suspended particles with the density ratio and Reynolds number as parameters. The symbol Δ is for suspended and ∇ is for settled particles.

behavior for the particles. They developed a corresponding expression for Re_γ and the density ratio, which may be written as follows:

$$\frac{\rho_s}{\rho_f} - 1 = 2.3648 \frac{\mu_f^2}{d^3 \rho_f^2 g} Re_\gamma^{1.3904}. \tag{1.169}$$

Equation 1.168 applies to shear flows over flat plates, while (1.167) applies to pipes and channels, where Poiseuille flows are more likely to occur. It must be noted that neither of the last two equations takes into account turbulence in the flow nor turbulent bursts that result in the advection of particles and the resuspension of groups of particles.

Walls also retard the movement of spheres that travel perpendicular to them. Regarding these flows, Brenner (1961) obtained asymptotically a first-order correction for the drag coefficient of a small rigid sphere moving toward the wall and concluded that the Stokes drag coefficient, f, increased by a factor:

$$f = \frac{C_D}{24/Re_r} = 0.625 \left(\frac{d}{l_w} \right)^{-1}, \tag{1.170}$$

where l_w is the distance from the center of the sphere to the wall. Brenner's results indicate that the hydrodynamic force on the particle increases dramatically when the particle approaches very closely the wall. This is related to the thin fluid layer that develops between the particle and the wall. Draining such thin layers, where viscous effects dominate, is a very slow process. In this case, the hydrodynamic force opposing the motion of the sphere becomes very large and the particle velocity drops significantly. The study by Kalio (1993) indicates that the influence of the wall on the drag of the particles is important when the particle is within 20 diameters from the wall. The experimental and computational study by ten Cate et al. (2002) confirmed this rapid and significant increase in the drag coefficient of settling spheres, which are within one diameter from a horizontal wall.

It must be pointed out that the analytical expressions of all transverse components of the hydrodynamic force and of the effect of the walls on the motion of a sphere are not based on a rigorous derivation of the transient equation of motion, but on specific analytical, experimental, and numerical studies, most of which were performed at steady flow conditions. One has to be aware that the rectilinear transient equations of motion mentioned in Section 1.4.3.6 implicitly assume that there is no rotation of the sphere, no significant shear in the flow, and the sphere is in an unbounded fluid, which essentially means far from any wall or other boundary. The addition of the lift or of any wall effect on a rigorously derived transient equation for the rectilinear motion of a particle must be viewed as an *ad hoc* assumption. Such assumptions are frequently used, because practice has shown that they produce reliable results on the average movement of particles. It must be remembered, however, that such assumptions, even though justified by validation with experiments or other means, have practical limitations.

1.4.3.11 Thermophoresis and Turbophoresis

When particles, bubbles, or drops are present in a fluid where a temperature gradient is applied, they experience molecular impulses that are stronger on the side of higher temperatures. This induces stronger Brownian motion in the hotter regions of the flow domain than in the colder ones. As a result, the particles, on the average, migrate to the colder regions of the flow domain, as was first observed by Tyndal (1870). A constant temperature gradient creates the steady average movement of an ensemble of particles, bubbles, and drops to the colder regions of the flow domain, a phenomenon called "thermophoresis." The latter is expressed quantitatively in terms of a thermophoretic velocity, v_{tp}, or of a thermophoretic force, F_{tp} (Epstein, 1929, Brock, 1962, Talbot et al., 1980). The directions of the thermophoretic force and thermophoretic velocity are opposite to the temperature gradient, and their magnitudes are

$$v_{tp} = -K_{tp} \frac{\mu_f}{\rho_f} \frac{\nabla T}{T_\infty} \quad \text{and} \quad F_{tp} = -6\pi\mu_f^2 \alpha K_{tp} \frac{\nabla T}{\rho_f T_\infty}. \tag{1.171}$$

The function K_{tp} depends on the Knudsen number, $K_{tp}(Kn)$, and on the properties of the fluid and the solid particles. By considering the velocity slip as well as a temperature slip of particles in gases, the

following expression for K_{tp}, in terms of the thermal conductivities, and the Knudsen number, Kn, was derived by Brock (1962):

$$K_{tp} = \frac{2C_s\left(k_f + 2k_s Kn\right)}{(1+6C_m Kn)(2k_f + k_s + 4k_s C_t Kn)}. \tag{1.172}$$

The parameters C_s, C_m, and C_t are determined empirically from the flow field around the particles and the discontinuities on the fluid–particle interface. Talbot et al. (1980) used the velocity slip expression that was recommended by Millikan (1923) and derived empirical correlations for these parameters. Experimental data and engineering practice have shown that reasonable results may be obtained by treating these parameters as constants with the numerical values for gases $C_s = 1.17$, $C_m = 1.14$, and $C_t = 2.18$ in the range $Kn < 0.1$. For liquids, McNabb and Meisen (1973) showed that the magnitude of the thermophoretic force is much lower, approximately 17% of the values predicted by Equations 1.171 and 1.172.

However, a disadvantage of the last two equations becomes obvious: when the equations are used for liquids with highly conducting particles (nanofluids), the thermophoretic velocity becomes vanishingly small, because $K_n \ll 1$ and $k_f \ll k_s$ for typical nanofluids. Since thermophoresis is a consequence of the Brownian movement, its effects are significant in very small particles, bubbles, and drops in the submicron range and becomes insignificant for larger particles of mm sizes. Michaelides (2015) used a stochastic Lagrangian method to derive the functional relationship for the dimensionless thermophoretic coefficient of spherical particles K_{tp} that appears in the last two equations:

$$K_{tp} = A\left(\frac{\alpha}{\alpha_0}\right)^{-B} \Rightarrow v_{tp} = -A\left(\frac{\alpha}{\alpha_0}\right)^{-B} \frac{\mu_f}{\rho_f T_\infty}\nabla T, \tag{1.173}$$

where $\alpha_0 = 1$ nm appears to correlate well all the combinations of particle types and base fluids. One of the advantages of the last expression is that it has been derived specifically for liquids, where typically $K_n \ll 1$ and applies to all types of spheres including the highly conducting spheres of nanofluids. The pairs of coefficients (A, B) for 20 common combinations of particles and fluids used in nanofluids are given in Table 1.3.

It must be noted that an implicit assumption of Equation 1.171 and all similar expressions of thermophoresis is that the effect of a temperature gradient on the motion of the particle is decoupled from all the other forces that act on the particle, such as lift forces and effects of boundaries. Also, although the thermophoretic force is a weak force and has a vanishing effect on larger particles, it may become the dominant force for very small nanoparticles, where gravity—as well as all other volume/body forces—is very weak. A glance at Equation 1.171 proves that the ratio of the thermophoretic to the force of gravity varies as α^{-2} and that the thermophoretic force would be dominant on nanoparticles in a gravitational field with a strong temperature gradient. Because of this, thermophoresis has often been used for the collection of nanoparticles on collection surfaces (Leung and Crowe, 1993). Nevertheless, the thermophoretic force is weak and this collection method takes very long time. It also requires precise equipment and suppression of any flow instabilities. Artificial centrifuging is a more effective method to concentrate and collect nanoparticles (Michaelides, 2014).

It must be emphasized that the thermophoretic force is a consequence of the molecular collisions, which also cause the Brownian motion. The thermophoretic and Brownian forces are not independent forces to be accounted separately in the Lagrangian simulations of particle motion. The simple inclusion of the Brownian

Table 1.3 Pairs of Coefficients (A,B) for the Correlation of Equation 1.173 for Several Spherical Particles in Common Fluids

	Water	Engine Oil	Ethyl Glycol	R-134a
Aluminum	(1264, 1.417)	(3.0920, 1.242)	(14.615, 1.869)	(4401, 1.774)
Aluminum oxide	(1227, 1.434)	(7.1026, 1.579)	(5.1095, 1.621)	(6270, 1.819)
CNT	(945.5, 1.263)	(5.8044, 1.445)	(3.6765,1.406)	(8580, 1.894)
Copper	(2039, 1.870)	(7.1391, 1.724)	(2.3558, 1.587)	(4191, 1.659)
Gold	(3155, 1.799)	(6.6483, 1.917)	(4.2431, 1.672)	(2721, 1.603)

force in the Lagrangian simulations of particle motion in fluids with temperature gradients will reproduce the thermophoretic velocity as the steady *drift velocity* of the particles toward the colder regions of the system.

Turbophoresis is a phenomenon similar to thermophoresis and results from the gradients of turbulence intensity, which develop in boundary and shear layers. In this case, the particle is subjected to a higher force on the side where turbulence is higher. Thus, the net turbophoretic force acts in the direction opposite to $\nabla\overline{u'^2}$. Analysis and experiments have shown that in a wall boundary layer, the process of turbophoresis tends to bring the particles closer to the wall, where the turbulent fluctuations are weaker. However, when the particle concentration at the wall becomes high, the accumulation of particles and the more frequent interparticle collisions cause a *drift velocity* away from the high particle concentrations. The balance of the two driving forces, turbulence and concentration, leads to an equilibrium condition. Portela et al. (2002) concluded that the local equilibrium predict well the particulate concentration, except when very close to the wall ($y^+ < 20$) where the turbulent fluctuations are very weak and turbophoresis cannot even be defined in a physically meaningful way.

1.4.4 Heat Transfer

While the development of the equation of motion for a sphere was based predominantly on analytical work followed by corrections derived from experiments, most of the analyses on the subject of heat transfer are based on Fourier's work (Fourier, 1822). His treatise, which was preceded by his seven shorter articles on heat conduction, has been subsequently supplemented by numerous experimental studies that have provided semiempirical correlations for the rate of heat transfer or, equivalently, for the Nusselt number. For this reason, the subject of heat transfer from spheres is based primarily on correlations that stem from experiments or, in the recent past, from numerical studies.

The governing equations for the heat transfer and for the mass transfer are strictly similar. For this reason, the solution of one equation also yields the solution of the other equation by simple substitution of the corresponding dimensionless numbers. Therefore, all the results, analytical, experimental, or computational, for the heat transfer coefficients are also applicable to the pertinent mass transfer coefficients.

An important parameter in the study of convective heat and mass transfer from spheres is the Peclet number (for heat or mass transfer), which accounts for the heat or mass advected by the fluid. The Peclet number is analogous to the Reynolds number in the equation of motion and is defined as follows for the cases of heat transfer and mass transfer, respectively:

$$Pe = d\rho_f c_{pf} U/k_f \left(\text{or } Pe = Re^* Pr\right) \quad \text{and} \quad Pe_M = \frac{dU}{D}, \tag{1.174}$$

where

U is the characteristic velocity of the fluid
c_{pf} is the specific heat capacity of the fluid
k_f is the conductivity of the fluid
D is the diffusivity of the fluid

The Prandtl number, Pr, is the dimensionless group of the fluid properties, $Pr = \mu_f c_{pf}/k_f$. When there is relative motion between the sphere and the fluid, which is characteristic of most advection processes, the magnitude of the relative velocity is used as the characteristic velocity U in the expressions for the Peclet number as in Equation 1.22. The Nusselt number, the Sherwood number, and the Biot number, which are also given in Equation 1.22, are other dimensionless groups frequently used in heat transfer from particles, bubbles, and drops.

1.4.4.1 Creeping or Stokes Flow

As in the case of momentum transfer, creeping flow or Stokes flow implies $Re_r \ll 1$. Since $Pe_r = Re_r{}^* Pr$, unless Pr for the sphere is very large, as is the case of some organic oils, this condition also implies that $Pe_r \ll 1$, or at least that $Pe_r < 1$. Heat convection comprises two parts, conduction and advection. Since in creeping flows the advection is negligible, the conduction part dominates in the convection process. Therefore, studies that implicitly or explicitly assume that $Pe_r \ll 1$ or $Re_r \ll 1$ essentially neglect the effects of the advection part of the process and are treating the conduction part of the process alone.

The solution of the conduction equation (or $Pe_r \ll 1$) yields the following expression for the steady flow Nusselt number:

$$Nu = 2. \tag{1.175}$$

Acrivos and Taylor (1962) conducted a study on the heat transfer from a solid sphere, analogous to the study by Proudman and Pierson (1956) for the equation of motion. They implicitly assumed a Stokesian flow around a sphere and derived an asymptotic heat transfer solution, which is valid at higher order of Pe_r. With the corrections in the coefficients (Acrivos, 1980), their expression for the steady Nu, which is applicable in the ranges $Re_r \ll 1$ and $Pe_r < 1$, is

$$Nu = 2 + \frac{Pe_r}{2} + \frac{1}{4} Pe_r^2 \ln \frac{Pe_r}{2} + 0.2073 Pe_r^2 + \frac{1}{16} Pe_r^3 \ln \frac{Pe_r}{2}. \tag{1.176}$$

Acrivos and Taylor (1962) also proved that the functional relationship $Nu(Pe_r)$ obtained for creeping flow is less sensitive to an increase of Re_r than the corresponding functional relation for the drag coefficient, $C_D(Re_r)$, of solid spheres. Therefore, it is generally accepted that the last equation is valid not only under creeping flow conditions but also when Re_r is finite but small.

Acrivos and Goddard (1965) also derived an asymptotic solution for high Pe_r assuming a Stokesian velocity distribution. Their expression, which is valid for $Pe_r > 5$, is

$$Nu = 1.249 \left(\frac{Pe_r}{2} \right)^{1/3} + 0.922 \tag{1.177}$$

In the case of viscous spheres, with viscosity ratio, λ, Levich (1962) derived an asymptotic first-order solution for a liquid sphere at very large Pe_r and $Re_r \ll 1$:

$$Nu = \sqrt{\frac{4 Pe_r}{3\pi(1+\lambda)}}. \tag{1.178}$$

Feng and Michaelides (2000b) under the assumption of a Stokesian velocity profile around a viscous sphere (drop or bubble) solved numerically the energy equation and derived the following correlation for the heat transfer coefficients:

$$Nu = 1.49 Pe_r^{0.322 + \frac{0.113}{0.361\lambda + 1}}. \tag{1.179}$$

It must also be pointed out that the implicit conditions for the use of the last three expressions are as follows: $Re_r < 1$ and $Pe_r \gg 1$. These conditions are satisfied for spheres with $Pr \gg 1$. Several organic liquids, including gasoline and engine oil, satisfy these conditions.

More recently, Feng (2014) used a combined regular and singular perturbation method to solve the heat and mass transfer from a slightly deformed sphere at low but finite Peclet numbers in Stokes flow. The deformed sphere was assumed to be axisymmetric, and its shape is described in the spherical coordinates (r, θ, ϕ) by a power series of a small parameter ε ($|\varepsilon| \ll 1$) as follows:

$$r = 1 + \varepsilon \sum_{n=0}^{\infty} b_n P_n(\cos\theta) + O(\varepsilon^2). \tag{1.180}$$

Here, the origin of the spherical coordinate system is at the center of the undeformed sphere, $P_n(\cos\theta)$ is the Legendre polynomial of nth order, and b_n are constants of order $O(1)$. The correction to the Nusselt number due to the deformation of the sphere was obtained through a regular perturbation method, while the correction to Nu number due to the small Peclet number was obtained through a singular perturbation method.

The analytical solution for the averaged Nusselt number in terms of the Peclet number and the deformation parameter is

$$Nu = 2 + \frac{1}{2}Pe_r + \frac{1}{4}Pe_r^2 \ln Pe_r + 0.03404Pe_r^2 + \frac{1}{16}Pe_r^3 \ln Pe_r + \varepsilon\Delta(Pe_r) + O(\varepsilon^2) + O(Pe_r^3), \tag{1.181}$$

where

$$\Delta(Pe_r) = 2b_0 + b_0 Pe_r + \left(\frac{3}{4}b_0 - \frac{1}{20}b_2\right)Pe_r^2 \ln Pe_r + \left[\left(\frac{1721}{2400}b_0 + \frac{1}{16}b_1 + \frac{611}{8400}b_2\right) - \left(\frac{3}{16}b_0 - \frac{1}{80}b_2\right)\ln 2\right]Pe_r^2$$
$$+ \left(\frac{3}{16}b_0 - \frac{1}{80}b_2\right)Pe_r^3 \ln Pe_r. \tag{1.182}$$

In the case of a spheroid with its surface described in Cartesian coordinates by,

$$\frac{x^2 + y^2}{[(1+\varepsilon)c]^2} + \frac{z^2}{c^2} = 1. \tag{1.183}$$

If we choose the semiaxis c as the reference length ($c = 1$), the surface points of the spheroid are described by the equation

$$r = 1 + \varepsilon\left[\frac{2}{3}P_0(\cos\theta) - \frac{2}{3}P_2(\cos\theta)\right] + O(\varepsilon^2). \tag{1.184}$$

If $\varepsilon > 0$, the spheroid is an oblate; if $\varepsilon < 0$, it is a prolate; if $\varepsilon = 0$, it reduces to a sphere. By letting $b_0 = 2/3$ and $b_2 = -2/3$, the Nusselt number becomes

$$Nu = 2 + \frac{1}{2}Pe + \frac{1}{4}Pe^2 \ln Pe + 0.03404Pe^2 + \frac{1}{16}Pe^3 \ln Pe$$
$$+ \varepsilon\left[\frac{4}{3} + \frac{2}{3}Pe + \frac{8}{15}Pe^2 \ln Pe + 0.33714Pe^2 + \frac{3}{15}Pe^3 \ln Pe\right] + O(\varepsilon^2) + O(Pe^3). \tag{1.185}$$

1.4.4.2 Reynolds Number Effects

1.4.4.2.1 Solid Spheres Among the correlations of experimental data that have been used for the steady heat transfer from a solid sphere due to forced convection without mass transfer on the surface, for example, in the absence of evaporation, sublimation, or chemical reactions, are the expressions derived by Ranz and Marshal (1952) and Whitacker (1972), which may be written, respectively, as follows:

$$Nu = 2 + 0.6Re_r^{0.5}Pr^{0.33} \tag{1.186}$$

and

$$Nu = 2 + (0.4Re_r^{1/2} + 0.06Re_r^{2/3})Pr^{0.4}. \tag{1.187}$$

These correlations are valid for solid spheres only and may be used up to $Re_r = 10^4$.

In many heating and cooling applications involving dispersed flows, the convective heat transfer is of a mixed type, with the free convection part induced by the different temperature of particles. Since the free convection takes place in the direction of gravity and the forced convection is arbitrary, the directions of the free and forced convection are not necessarily the same. The overall heat transfer of a sphere resulting from the mixed flow is significantly influenced by the direction of the forced flow. Musong and Feng (2014) examined numerically the mixed convection from a heated sphere at an arbitrary incident flow angle in laminar

flows at moderate Reynolds numbers ($1 \le Re_r \le 100$) and Richardson numbers ($1 \le Ri \le 5$). Based on the simulation results, they developed a correlation for the mixed convection with incident angles in the range $0 \le \theta < \pi/2$:

$$Nu = aRe^{b}Ri^{0.5b}\theta^{2} + cRe^{d}Ri^{0.5d}\theta + nRe^{f}Ri^{0.5f} - gRe^{1+h}Ri^{0.5} - kRe^{m}, \tag{1.188}$$

where $a = -0.0208$, $b = 0.4851$, $c = 0.0250$, $d = 0.05$, $n = 1.436$, $f = 0.3642$, $g = 0.2534$, $h = -0.722$, $k = -0.2602$, and $m = 0.2412$. The units of the incident angle θ are radians.

1.4.4.2.2 Viscous Spheres Feng and Michaelides (2000a, 2001b) conducted two numerical studies on the subject of heat transfer from viscous spheres without mass transfer at the interface and derived useful and accurate correlations, with Re_r and Pe_r as independent variables. The first study pertains to high Re_r and any Pe_r and the second to any values of Re_r and Pe_r. Their results in correlation form are summarized in the following equations:

1. At small but finite values of Re_r ($0 < Re_r < 1$) and $Pe_r > 10$, the expression for the Nusselt number is

$$Nu(\lambda, Pe_r, Re_r) = \left(\frac{0.651}{1+0.95\lambda}Pe_r^{1/2} + \frac{0.991\lambda}{1+\lambda}Pe_r^{1/3}\right)\left(1+\alpha(Re_r)\right) + \left(\frac{1.65\left(1-f(Re_r)\right)}{1+0.95\lambda} + \frac{\lambda}{1+\lambda}\right), \tag{1.189}$$

where the function $f(Re_r)$ is defined as

$$f(Re_r) = \frac{0.61Re_r}{Re_r + 21} + 0.032. \tag{1.190}$$

2. As with the drag coefficient in Section 1.4.3.2, for higher Re_r and Pe_r, the analysis of numerical data revealed that the most accurate correlations of the numerical data are obtained when the general expression for Nu is given in terms of the following three functions, which pertain to specific values of the viscosity ratio λ:

a. The correlation for an inviscid sphere ($\lambda = 0$), which is given by the following expression:

$$Nu(0, Pe_r, Re_r) = 0.651Pe_r^{1/2}\left(1.032 + \frac{0.61Re_r}{Re_r + 21}\right) + \left(1.60 - \frac{0.61Re_r}{Re_r + 21}\right). \tag{1.191}$$

b. The Nusselt number expression for a solid sphere ($\lambda = \infty$):

$$Nu(\infty, Pe_r, Re_r) = 0.852Pe_r^{1/3}\left(1 + 0.233Re_r^{0.287}\right) + 1.3 - 0.182Re_r^{0.355}. \tag{1.192}$$

c. The corresponding function for a sphere with $\lambda = 2$, which was derived from the numerical results:

$$Nu(2, Pe_r, Re_r) = 0.64Pe_r^{0.43}\left(1 + 0.233Re_r^{0.287}\right) + 1.41 - 0.15Re_r^{0.287}. \tag{1.193}$$

Accordingly, the final correlations for the heat transfer coefficients are given by the following expressions in the two ranges of the viscosity ratio, $0 \le \lambda < 2$ and $2 < \lambda \le \infty$:

$$Nu(Pe_r, Re_r, \lambda) = \frac{2-\lambda}{2}Nu(Pe_r, Re_r, 0) + \frac{4\lambda}{6+\lambda}Nu(Pe_r, Re_r, 2)$$
$$\text{for } 0 \le \lambda \le 2 \quad \text{and} \quad 10 \le Pe_r \le 1000 \tag{1.194}$$

and

$$Nu\left(Pe_r,Re_r,\lambda\right)=\frac{4}{\lambda+2}Nu\left(Pe_r,Re_r,2\right)+\frac{\lambda-2}{\lambda+2}Nu\left(Pe_r,Re_r,\infty\right)$$
$$\text{for } 2\le\lambda\le\infty \quad \text{and} \quad 10\le Pe_r\le 1000. \tag{1.195}$$

For smaller values of $Pe_r < 10$, it was not possible to obtain a simple correlation of the numerical results, $Nu(Pe_r, Re_r, \lambda)$, with any satisfactory degree of accuracy. For this reason, for applications in the range $0 < Pe_r < 10$, it is recommended that one uses the numerical results in the original publication (Feng and Michaelides, 2001b), which are given in tabular form and their accuracy is only limited by the numerical accuracy of the method.

As in the case of the hydrodynamic force on a viscous sphere, it was determined that for a fixed value of Re_r and viscosity ratio, λ, the variations of the density ratio, ρ_s/ρ_f, have only a minimal effect on the external flow field. When one considers the governing equation for the heat or mass transfer processes and the pertinent boundary conditions, one will conclude that the density ratio (as well as the internal Reynolds number, Re_i) does not affect appreciably the corresponding transport coefficients, h and h_M, and, consequently, the Nusselt and Sherwood numbers. This was verified numerically by Feng and Michaelides (2001a,b) for both the hydrodynamic force and the rate of heat transfer: the influence of the density ratio on the heat transfer coefficient is less than 0.1%. This is of the same order of magnitude as the numerical uncertainty of the computations and much lower than the required accuracy for engineering calculations.

1.4.4.2.3 Interfacial Velocity Slip and Temperature Difference All the aforementioned expressions for Nu are based on the no-slip velocity condition at the interface as well as on the assumption that the temperatures of the sphere and the fluid at their interface are equal. It has been experimentally observed that when the size of particles is comparable to the mean free path of the base fluid, there is a significant discontinuity of both the velocity and the temperature at the solid–fluid interface. The effect of the two discontinuities is to decrease the magnitude of the convective heat transfer. The velocity discontinuity at the interface is modeled as in Equations 1.114 and 1.115. The discontinuity at the solid–liquid interface is usually modeled in terms of an *accommodation coefficient*, $\zeta = f(T)$, defined in terms of the molecular collisions on the surface of the sphere. Accordingly, the temperature discontinuity at the solid–liquid interface is expressed by the following boundary condition:

$$T_f-T_s\big|_{r=\alpha}=\left(\frac{c_p}{c_v}\right)\frac{2\left(2-\zeta\right)L_{mol}}{\left(\frac{c_p}{c_v}+1\right)\zeta Pr}\frac{\partial T_f}{\partial r}. \tag{1.196}$$

In most cases with liquids, the ratio of the specific heats of the fluid, c_p/c_v, is approximately equal to 1. When the mean free path is expressed in terms of the Knudsen number, the last equation becomes

$$T_f-T_s\big|_{r=\alpha}=\frac{2\left(2-\zeta\right)aKn}{\zeta Pr}\frac{\partial T_f}{\partial r}. \tag{1.197}$$

Brun (1982) also derived an expression for the heat transfer from a sphere using this thermal boundary condition and verified his solution with experimental data and other analytical results. Feng and Michaelides (2012) used an asymptotic method and derived a solution to the more general problem of heat transfer from solid spheres with velocity and thermal slip at the interface. Their expression agrees with the expression by Brun (1982) for a solid sphere with thermal slip only and with the experimental data by Mikami et al. (1966) in the range $0.01 < Kn < 2$. This general expression for the viscous spheres is

$$Nu=\frac{2}{1+\lambda_t}+\frac{1}{2\left(1+\lambda_t\right)^2}Pe_r+\frac{f_s}{4\left(1+\lambda_t\right)^2}Pe_r^2\ln\left(Pe_r\right)+\frac{1}{2\left(1+\lambda_t\right)^2}$$
$$\times\left[\frac{-156+148f_s-152\lambda+341\lambda f_s+129f_s^2+528\lambda f_s^2}{960\left(1+2\lambda_t\right)}-0.06+0.58\lambda_t\right]Pe_r^2+\frac{1}{16\left(1+\lambda_t\right)^3}Pe_r^3\ln\left(Pe_r\right)+O\left(Pe_r^3\right), \tag{1.198}$$

where f_s is a dimensionless parameter related to the dimensionless velocity slip, $S = 2\mu_c/\beta\alpha$:

$$f_s = \frac{\beta\alpha + 2\mu_c}{\beta\alpha + 3\mu_c} = \frac{1+2S}{1+3S}. \tag{1.199}$$

This parameter is evident in the expression for the drag force on a solid sphere with slip, Equation 1.114. λ_t is another dimensionless parameter that characterizes the thermal slip as modeled by Equation 1.197:

$$\lambda_t = \frac{2(2-\zeta)}{\zeta}\frac{Kn}{Pr}. \tag{1.200}$$

Because λ_t is always positive, the effect of the thermal slip is to reduce *Nu* and by extent the convective heat transfer coefficient of the solid sphere. Equation 1.198 reveals that the velocity slip affects the heat transfer process only at the higher values of Pe_r. Since velocity and temperature discontinuities are observed only with very small spheres of submicron dimensions, where the internal circulation effects are restricted, Equation 1.200 is also a good approximation to the heat (and mass) transfer from viscous spheres as well.

1.4.4.3 Effects of Rotational Motion

The problem of convection heat (or mass) transfer over a heated rotating sphere in a fluid is a classical problem that has been studied extensively in the past. There are several studies found in the literature focusing on the development of experimental techniques to measure the mean heat transfer rate or the average Nusselt number. Kreith et al. (1965) studied the cooling and heating of a solid sphere in several fluids including oil, water, and air. They correlated their measurements for the forced convection heat transfer with the following equation:

$$Nu = 0.43 Pr^{0.4} Re_{rot}^{0.5}. \tag{1.201}$$

Tieng and Yan (1993) studied the mixed convection of a rotating sphere in air. They considered the mixed convection as a resultant effect composed of both free and forced convections. Their results for forced convection at large Reynolds numbers also supported this correlation. However, for smaller Re they suggested a new correlation:

$$Nu = 2 + 0.175 Re_{rot}^{0.583}, \quad Re_{rot} < 33{,}320, \quad Pr = 0.71. \tag{1.202}$$

This is a similar expression as the one initially proposed by Farouk (1985) for the Nusselt number of forced convective heat transfer of a rotating sphere in air. Dorfman and Serazetdinov (1973) used boundary layer theory and derived analytically a similar relation to Equation 1.201, but with a smaller coefficient of 0.33.

The correlations in Equations 1.201 and 1.202 were obtained for flows of Reynolds number above 1000, where a boundary layer is formed at the surface of the sphere. These correlations show that the Nusselt number is proportional to $Re_{rot}^{1/2}$, a characteristic arising from laminar boundary layer theory. For flows of small to moderate Reynolds numbers where the boundary layer theory may not be valid, these correlations are not applicable.

Feng (2014) employed a direct numerical simulation approach combined with immersed boundary method (IBM) to study the convective heat transfer of a heated rotating sphere in otherwise stationary air at low to moderate Reynolds numbers. The sphere is assumed to have a constant temperature; the Prandtl number of air is chosen to be 0.72; the flow Reynolds numbers in study range from 0 to 1000. Figure 1.15 shows the relationship between the mean Nusselt numbers and Reynolds numbers. The correlations by Kreith et al. (1965), by Tieng and Yan (1993), and by Dorfman and Serazetdinov (1973) are also plotted in the figure. It can be seen that these correlations fail to predict the mean Nusselt numbers correctly at $Re < 500$. At Reynolds number between $0 \le Re \le 500$, the simulation data are best fit by the following correlation, as seen in Figure 1.15:

$$Nu = 2 + 0.00051 Re_{rot}^{1.5}, \quad Pr = 0.72, \quad 0 \le Re_{rot} \le 500. \tag{1.203}$$

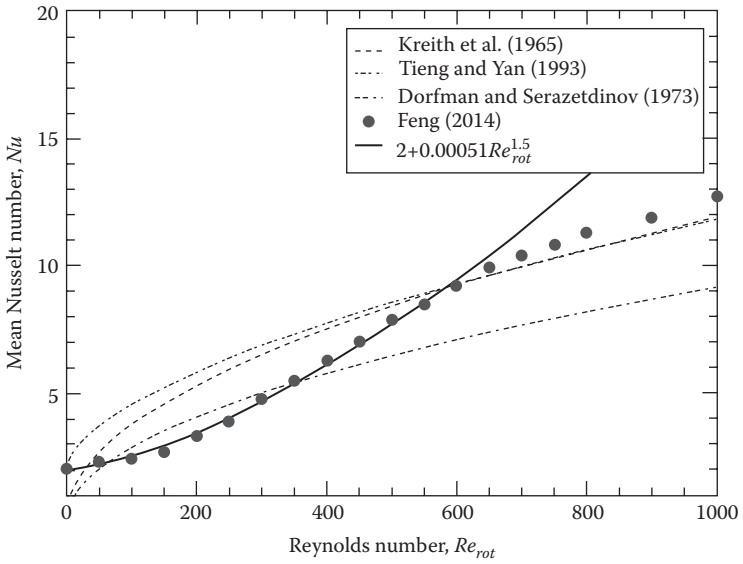


Figure 1.15

Mean Nusselt number versus Reynolds number of rotation for $0 \le Re_{rot} \le 1000$.

1.4.4.4 Effects of Flow Turbulence

As in the case the drag coefficient of particles, free-stream turbulence causes an increase in the heat transfer coefficients. Early experimental studies by Raithby and Eckert (1968) in grid-generated turbulence show that Nu increases rapidly with the turbulence intensity up to $I_r = 1\%$ when Re_r is of the order of 10^3. The Nusselt number subsequently increases, but only linearly with I_r. When Re_r is of the order of 10^4, Nu is proportional to I_r in the whole range of the investigations. Based on several sets of available experimental data, Clift et al. (1978) suggest the following correlation for the increase in the heat transfer coefficient:

$$\frac{Nu}{Nu_0} = 1.0 + 4.8 * 10^{-4} \frac{I_r}{I_{rc}} Re_r^{0.57}, \tag{1.204}$$

where

Nu_0 is the Nusselt number in the absence of free-stream turbulence
I_r is the turbulence intensity
I_{rc} is the critical turbulence intensity

The latter is defined in a way that it makes the Reynolds number of the particle, Re_r, equal to the critical Reynolds number, which was defined in Equation 1.118. From that expression, one may derive the following expression for the critical turbulence intensity, I_{rc}:

$$\begin{aligned} I_{rc} &= \left[5.477 - \log_{10}\left(Re_r\right)\right]/15.8 \quad \text{for } I_r \le 0.15 \\ \text{and} \quad I_{rc} &= \left[3.71 - \log_{10}\left(Re_r\right)\right]/1.75 \quad \text{for } I_r > 0.15. \end{aligned} \tag{1.205}$$

A more recent study on the effect of free-stream turbulence by Yearling and Gould (1995) conducted with evaporating droplets of water, ethanol, and methanol yields the following dependence of Nu on the intensity of turbulence:

$$\frac{Nu}{Nu_0} = 1 + 3.4 I_r^{0.843}. \tag{1.206}$$

Since Yearling and Gould (1995) considered evaporating droplets, Nu_0 is the Nusselt number with the blowing effects, which is given by Equation 1.210. The film properties must be used for all the properties of the materials in the last equation.

1.4.4.5 Blowing Effects

Blowing effects are important for burning droplets when the timescale of burning (mass transfer from the droplet) is of equal or lesser order of magnitude than the timescale for energy transfer. As in the case of momentum transfer, corrections to the heat transfer coefficient have been developed. These corrections take into account the change of the properties of the gaseous boundary layer and the phase change on the surface of the sphere. The two dimensionless numbers, *blowing factors or transfer numbers*, B_H and B_M, which were defined in Equations 1.121 and 1.123, account for the heat and mass transfer effects on the surface of the sphere. These factors are used in corrections for the empirical and analytical correlations on heat and mass transfer from the surface of a constant volume sphere.

Since the origin of the two blowing factors is the radial mass transfer from the surface of the sphere to the carrier fluid, it is evident that the two are not independent. Abramzon and Sirignano (1989) conducted an analytical study on the evaporation of drops and derived expressions for these blowing factors to be used in engineering calculations. In the case of a fuel droplet that burns in air, they derived the following relationship between the two blowing factors:

$$B_H = (1 + B_M)^n - 1. \tag{1.207}$$

The exponent n represents the ratio

$$n = \frac{c_{pF}}{c_{pf}} \frac{1}{Le} \frac{1 + \frac{k}{2} \frac{\sqrt{Re_r/2}}{F(B_M)}}{1 + \frac{k}{2} \frac{\sqrt{Re_r/2}}{F(B_H)}}. \tag{1.208}$$

In the last equation

c_{pF} is the specific heat of the fuel vapor
c_{pf} is the specific heat of the carrier gas
Le is the dimensionless Lewis number
k is an empirical coefficient equal to 0.848
F is a function of the corresponding blowing factor

$$F(B) = (1 + B)^{0.7} \frac{\log(1 + B)}{B}. \tag{1.209}$$

When there is thermodynamic equilibrium and the properties of the material satisfy the conditions $Pr = Sc = 1$, the two transfer coefficients are equal: $B_H = B_M$ (Sirignano, 1999).

Abramzon and Sirignano (1989) obtained semianalytical expressions for the Nusselt and Sherwood numbers for a drop with mass transfer on its surface. Chiang et al. (1992) improved on that study by relaxing some of the most restrictive assumptions and conducting numerical computations on the vaporization of drops. They derived a more general and, very likely, more accurate correlations for the heat and mass transfer coefficients:

$$Nu = 1.275\left(1 + B_H\right)^{-0.678} Re_m^{0.438} Pr_m^{0.619} \tag{1.210}$$

and

$$Sh = 1.224\left(1 + B_M\right)^{-0.568} Re_m^{0.385} Sc_m^{0.492}. \tag{1.211}$$

Both the Reynolds and Schmidt numbers, Re_m and Sc_m, must be calculated using the film transport coefficients, defined by Equation 1.119 and, in the case of Re_m, the free-stream gas density, $\rho_{f\infty}$, far from the droplet. One may use the aforementioned correlations with the heat and mass transport equations to derive the following expressions for the rate of heat and mass transfer of vapor from the surface of a spherical drop:

$$\begin{aligned} \dot{Q} &= 1.275\pi k_f d\left(T_s - T_\infty\right)\left(1 + B_H\right)^{-0.678} Re_m^{0.438} Pr_m^{0.619} \\ \dot{m} &= 1.224\pi d\rho_f D\left(Y_s - Y_\infty\right) B_M \left(1 + B_M\right)^{-0.568} Re_m^{0.385} Sc_m^{0.492}. \end{aligned} \tag{1.212}$$

An alternative method to calculate the heat and mass transfer from a drop is to use another empirical relationship, which is derived from the experimental results by Renksizbulut and Yuen (1983). They correlated their experimental data on the heat transfer from a sphere with mass transfer at its surface by the expression

$$Nu = \frac{2 + 0.584 Re_m^{0.5} Pr^{0.33}}{\left(1 + B_M\right)^{0.7}}. \tag{1.213}$$

This yields the following expressions for the rates of heat and mass transfer from the surface of the spherical drop:

$$\dot{Q} = \pi k_f d\left(T_s - T_\infty\right) \frac{2 + 0.584 Re_m^{0.5} Pr^{0.33}}{\left(1 + B_M\right)^{0.7}} \tag{1.214}$$

and

$$\dot{m} = \pi d \rho_f D (Y_s - Y_\infty) \frac{2 + 0.584 Pe_m^{0.5} Sc^{0.33}}{(1 + B_M)^{0.7}}. \tag{1.215}$$

All the fluid properties in the last four equations that define the Nusselt, Prandtl, and Schmidt numbers are the film properties defined by Equation 1.119. In addition, the relative Reynolds and Peclet numbers Re_m and Pe_m are defined in terms of the gas-film viscosity as in Equation 1.119 and the free-stream gas density, $\rho_{f\infty}$, which is far from the droplet. It is evident from an inspection of these equations that their functional form and coefficients are very similar. It has been confirmed (Sirignano, 1999) that the results of the two expressions do not differ substantially.

1.4.4.6 Transient Effects

Michaelides and Feng (1994) conducted a study on the transient energy equation for spheres, which is analogous to the one by Maxey and Riley (1983) for the equation of motion. The implicit and explicit assumptions for this study are similar to the assumptions for the derivation of the equation of motion and may be summarized as follows:

- **a.** Spherical shape
- **b.** Infinite fluid domain
- **c.** No rotation
- **d.** Highly conducting ($Bi \ll 1$ or $k_f/k_s \ll 1$)
- **e.** Zero initial relative temperature
- **f.** Negligible advection ($Pe_r \ll 1$)

For a rigid, isothermal sphere in a time-variable, nonuniform fluid temperature field $T_f(x_i, t)$, the final form of the transient Lagrangian energy equation is

$$m_s c_{ps} \frac{dT_s}{dt} = -m_f c_{pf} \frac{DT_f}{Dt} - 4\pi a k_f \left[T_s - T_f - \frac{1}{6} a^2 T_{f,jj} \right] - 4\pi a^2 k_f \int_0^t \frac{d/d\tau \left[T_s - T_f - \frac{1}{6} \alpha^2 T_{f,jj} \right]}{\left[\pi \alpha_f (t - \tau) \right]^{1/2}} d\tau, \tag{1.216}$$

where

c_{pf} and c_{ps} are the specific heat capacities of the fluid and the sphere, respectively

α_f in the denominator of the last term is the thermal diffusivity of the fluid, which is equal to $k_f/\rho_f c_{pf}$

The differential operator D/Dt represents the Lagrangian derivative with a reference system of coordinates at the center of the sphere

The temperature T_f is the temperature function of the fluid far from the sphere

The left-hand side of the aforementioned equation denotes the change in the temperature of the sphere due to the heat transfer

The first term in the right-hand side is analogous to the inertia term in the momentum equation and accounts for the (Lagrangian) change in temperature of the mass of displaced fluid. The second term is the usual conduction term from the sphere to the fluid and is analogous to the steady drag term of the equation of motion. This term represents the rate of heat transfer due to the bulk temperature difference between the fluid and the sphere. It is similar to the well-known conduction term that appears in texts, with the inclusion of the Laplacian derivative, which accounts for any nonuniformities of the temperature field. The Laplacian terms are analogous to the Faxen terms of the equation of motion and scale as a^2/L^2. In most of the practical applications where the particle radius is significantly smaller than the characteristic dimension of the fluid and $a^2/L^2 \ll 1$, these corrections are insignificant and may be neglected. The last term in the energy equation is a history integral, which results from the diffusion of the temperature gradients in the fluid temperature field and is also corrected for the nonuniformity (curvature) of the temperature field. It is apparent that this history term depends on the temporal as well as the spatial variation of the temperature field and is exactly analogous to the history term of the equation of motion. This history term may account for a significant part of the transient heat transfer to a sphere, as it may be seen in Figure 1.16.

It must be pointed out that the added mass term in the equation of motion derives from the pressure gradient term in the momentum equation. Since the governing equation for the energy transfer does not have a term equivalent to ∇p, there is no term corresponding to the added mass term in the transient energy equation. The absence of the added mass term is the main difference in the functional forms of the equations of motion and temperature variation under creeping flow conditions as well as at finite Reynolds numbers. It is apparent that there is not a mathematical similarity between the transient equations of motion and energy for particles, drops, or bubbles. However, there are several analogous results in the momentum and heat exchange processes for viscous and solid spheres.

As with the equation of motion, the assumption of equal temperatures at the interface may be relaxed. In this case, the history term is substituted by the expression

$$4\pi a^2 k_f \int_0^t \frac{d/d\tau\left[T_s - T_f - \frac{1}{6}a^2 T_{f,jj}\right]}{\left[\pi\alpha_f (t-\tau)\right]^{1/2}} d\tau + 4\pi a^2 k_f \frac{T_s(0) - T_f(0)}{\sqrt{\pi a_f t}}. \tag{1.217}$$

Gay and Michaelides (2003) conducted a numerical study to compute the effect of the history term on the heat transferred to a sphere at creeping flow conditions by considering three types of variation of the carrier fluid temperature: (1) a step change, (2) a ramp change, and (3) a sinusoidal variation. The main parameters for this

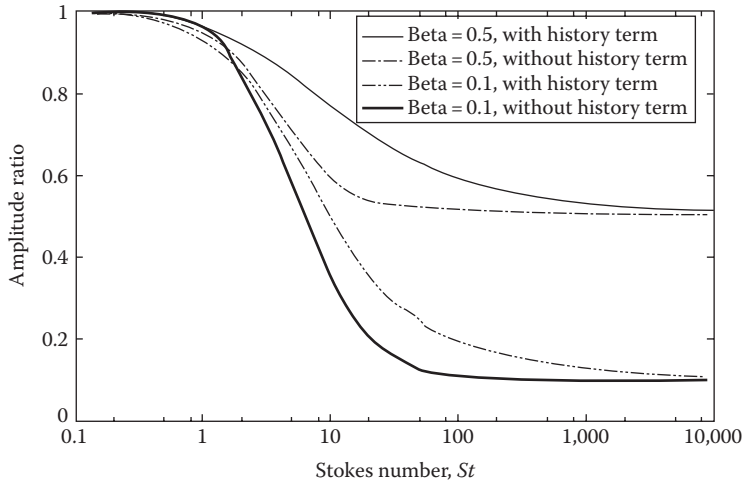


Figure 1.16

The effect of the thermal Stokes number on the heat transfer from rigid particles with and without the history term.

study are the volumetric heat capacity ratio $\beta = \rho_f c_{pf}/\rho_s c_{ps}$ and a thermal Stokes number, St_t, which is defined as the ratio of the thermal timescale of the particle $\tau_s = a^2\rho_f c_f/k_f$ to the characteristic timescale of the fluid:

$$St_t = \frac{a^2 \rho_f c_f \omega}{k_f}. \tag{1.218}$$

The history term is of importance in the computations of the heat flux when the ratio of the volumetric heat capacities, β, is between 0.002 and 0.5. This is the range of liquid–solid flows and droplet flows in heavier gases. The study found almost no effect of the history term on the heat transfer for bubbles, which are in the range $\beta > 10$. Typical result of these computations for a sinusoidal oscillation of the fluid temperature field with frequency ω is depicted in Figure 1.16 (from Gay and Michaelides, 2003). This figure demonstrates that neglecting the history term in the energy equation may lead to an underestimation of the instantaneous rate of heat transfer by as much as 35%, a significant fraction for most engineering computations.

Feng and Michaelides (1997) performed a study on the transient energy equation for a spheroid of eccentricity ε, which is analogous to the study by Lawrence and Weinbaum (1986) for the drag on a spheroid. They derived the following equation for the heat transfer from a spheroid:

$$Q(t^\star) = -4\pi\left\{\left(1+\frac{2}{3}\varepsilon-\frac{1}{45}\varepsilon^2\right)(T_s^\star - T_\infty^\star)+\left(1+\frac{4}{3}\varepsilon-\frac{2}{3}\varepsilon^2\right)\int_0^t \frac{d/d\tau^\star (T_s^\star - T_\infty^\star)}{\sqrt{\pi(t^\star-\tau^\star)}}d\tau^\star + \right.$$
$$\left. +\frac{1}{3}\left(1+\frac{2}{9}\varepsilon+\varepsilon^2\right)\frac{DT_\infty^\star}{Dt^\star}+\varepsilon^2\frac{4}{45}\sqrt{\frac{\pi}{3}}\int_0^t\left[\frac{d}{dt^\star}(T_s^\star - T_\infty^\star)\right]G'(t^\star-\tau^\star)d\tau^\star\right\}, \tag{1.219}$$

where all the variables are in dimensionless form and the function $G'(t)$ depends on the frequency of variation of the fluid temperature field

$$G'(t) = Im\left[\sqrt{\pi\Phi}e^{\Phi t^\star}erfc\left(\sqrt{\Phi t^\star}\right)\right] \quad \text{and} \quad \Phi = 3e^{i\frac{\pi}{3}}. \tag{1.220}$$

The last term in Equation 1.219 depends entirely on the eccentricity and the frequency of variation of the external temperature field. The kernel of this term does not necessarily follow the $t^{-1/2}$ decay of the typical history term in creeping flows and depends on the frequency of the variation of the velocity of temperature fields. Feng and Michaelides (1997) showed that when the frequency of variation of the velocity and temperature fields is not high, the contribution of this new history term to the total heat flux is much smaller than the contributions of the other transient terms.

Feng and Michaelides (1998a) also performed a study on the energy equation of a particle with arbitrary motion and in an arbitrary temperature field with finite but small inertia. This study is analogous to the one performed by Lovalenti and Brady (1993) for the equation of motion, and its results are expressed in terms of Pe_r and *Sl*. Details of the transient hydrodynamic force and heat transfer of particles, bubbles, and drops at finite Re_r and Pe_r may be found in Michaelides (2006).

1.4.4.7 Radiation Effects

Thermal radiation is the mode of heat transfer through which electromagnetic energy is continuously emitted and absorbed by a system. This energy exchange applies to the system under observation as well as all the other systems in its surroundings. For a sphere whose surface temperature is T_s, the emitted radiation energy is equal to

$$\dot{Q}_{rad}^{em} = \sigma\varepsilon\pi d^2 T_s^4, \tag{1.221}$$

where

σ is the Stefan–Boltzmann constant, $5.669 * 10^{-8}$ W/m^2 K^4

ε is the emissivity of the sphere

The emissivity of a blackbody is equal to one. Similarly, the sphere absorbs heat from all the objects in its surroundings. In the simple case where the sphere is enclosed by a single medium of temperature T_∞, the sphere absorbs thermal radiation equal to

$$\dot{Q}_{rad}^{ab} = \sigma\alpha\pi d^2 T_\infty^4, \tag{1.222}$$

where α is the absorptivity of the sphere. In general, the absorptivity and the emissivity of a material are functions of its temperature and are equal in magnitude: $\alpha(T_s) = \varepsilon(T_s)$.

The net rate of energy that enters the sphere as a result of thermal radiation is equal to the difference of the two aforementioned equations and, in analogy with the convection mode of heat transfer, may be given in terms of a radiation coefficient, h_{rad}:

$$\dot{Q}_{rad}^{ab} - \dot{Q}_{rad}^{em} = \sigma\varepsilon\pi d^2 (T_\infty^4 - T_s^4) = \pi d^2 h_{rad} (T_\infty - T_s). \tag{1.223}$$

The radiation coefficient is a strong function of temperature. It is obvious that when the temperature difference of the sphere and its surroundings is sufficiently high, the net energy exchanged by radiation is significant and may actually surpass the energy exchange due to the other two modes of heat transfer, conduction and convection. The total rate of heat entering the sphere is the sum of the convection and radiation:

$$\dot{Q}_T = \pi d^2 (h_{rad} + h)(T_\infty - T_s). \tag{1.224}$$

It must be pointed out that in the case of radiation one has to account not only for the carrier gas but also for all the boundaries and other objects in the vicinity of the sphere. The sphere exchanges radiation with any other object or surface that it "sees." In the general case, when this body is surrounded by many objects, including other similar bodies in the same carrier fluid, the determination of the net thermal radiation or the thermal radiation coefficient must be carried out by carefully evaluating the effects of all the surfaces in the surroundings and the shape factors of these surfaces. This may become a challenging task. A more extensive description of the processes and the methods used for the determination of radiative heat transfer may be found in a specialized treatise on the subject, such as the one by Siegel and Howel (1981).

An interesting consequence of radiation heat transfer with particles is that radiation may cause a significant deviation of the temperature of the particle from that of the surrounding fluid and in extreme cases natural convection from a particle. Let us consider a spherical particle in a fluid stream of temperature T_f and velocity u, inside a long channel whose walls are at a different temperature T_w. The particle reaches an equilibrium temperature, which is defined by a zero net heat gain at its surface and is characterized by equal and opposite magnitudes of the convection and radiation. In the simplest case of blackbody radiation and a nonabsorbing gas, this equilibrium yields the following expression for the temperature of the particle:

$$h_c (T_f - T_s) = h_{rad} (T_{th} - T_w) \Rightarrow T_s = \frac{h_c T_f + h_{rad} T_w}{h_c + h_{rad}}. \tag{1.225}$$

This analysis implies that the particle temperature will be close to the temperature of the gas, T_f, only when $h_c \gg h_{rad}$. On the contrary, the particle temperature will be close to that of the surrounding boundaries, T_w, when $h_c \ll h_{rad}$. In all cases, the particle will reach an intermediate temperature, which is not equal to the temperature of the fluid, T_f, that surrounds it. Several interesting effects may occur if the temperature difference between fluid and particles, $T_s - T_f$, becomes significant: natural convection and buoyancy effects will develop around the particles and the particles will experience an upward draft. The draft affects both the particle motion and the heat transfer from it. If this natural convection is strong enough, the particles may even be carried upward with the locally buoyant fluid (Feng and Michaelides, 2008, 2009).

1.4.5 Effects of Concentration

Most of the analytical, experimental, and numerical results presented in the previous sections were derived for single particles, bubbles, and drops. However, the majority of practical applications involve the flow of groups of interacting particles, bubbles, or drops. Interactions of these objects and the formation of clusters

and aggregates with correlated motions play an important role on the value of the hydrodynamic force and heat transfer. It is accepted, in general, that one may use the results and apply the theory of single particles, bubbles, and drops in a flowing mixture if the mixture is *dilute*, that is, if the concentration of the mixture is less than 6.5%. In dispersed mixtures like this, spheres are separated on the average by one diameter. Intermediate concentrations are in the range $6.5\% < C < 30\%$. In this range, particle-to-particle interactions are as important in the determination of all the transport coefficients as particle-to-fluid interactions. In applications with very dense concentrations, $C > 30\%$, particle interactions are the main mechanism for the transport processes and particle–fluid interactions are of lesser importance. Therefore, the effect of concentration on the transport coefficients is of paramount importance in engineering processes.

Regarding the steady hydrodynamic force, Richardson and Zaki (1954) carried one of the earlier series of experiments on the sedimentation of particles in a quiescent fluid, which is bounded by a channel of diameter D. By correlating the settling velocity of the particles to the concentration of the mixture, they concluded that the drag coefficient of a single sphere must be multiplied by a correction factor equal to

$$(1 - C)^{-K}, \tag{1.226}$$

where

C is the concentration of solids

exponent K is a weak function of the Reynolds number

K was correlated as follows:

$$\begin{array}{ll} Re_r \le 0.2 & K = 4.65 + 19.5 d/D \\ 0.2 < Re_r \le 1 & K = (4.35 + 17.5 d/D) Re_r^{-0.03} \\ 1 < Re_r \le 200 & K = (4.45 + 18 d/D) Re_r^{-0.1} \\ 200 < Re_r \le 500 & K = 4.45 Re_r^{-0.1} \\ Re_r > 500 & K = 2.39. \end{array} \tag{1.227}$$

It is apparent that the exponent K may attain any value in the range 2.4–5.7. Later experimental data by Rowe (1961) with arrays of solid spheres in water and air determined that the drag coefficients are better correlated with the single constant $K = 3$.

Another correlation, which is widely used in fluidization systems, is the one by Wen and Wu (1966). They included the effects of Re_r on the terminal velocity of a single particle and derived a correlation for the effect of concentration that is independent of the Reynolds number:

$$C_D = C_{D0}(1-C)^{-K} \quad \text{with } K = 3.7\,. \tag{1.228}$$

Wen and Wu (1966) recommend the Schiller and Nauman expression for the drag coefficient at zero concentration, $C_{D0} = 24(1 + 0.15 Re_r^{0.687})/Re_r$.

Di Felice (1994) used several sets of data available in the literature, including those by Richardson and Zaki (1954) and Wen and Wu (1966), to develop a more general and probably more accurate expression for the drag coefficient. He derived the following correlation, which is applicable in the range $10^{-2} < Re_r < 10^4$:

$$C_D = C_{D0}\left(1-C\right)^{-K} \quad \text{with } K = 3.7 - 0.65 \exp\left[-\frac{\left(1.5 - \log Re_r\right)^2}{2}\right]. \tag{1.229}$$

The subject of interacting particles, bubbles, and drops is rather difficult to investigate experimentally, but ideally suited for computational simulations, where different initial conditions may be examined and statistical results are relatively easy to derive. Modern computational techniques and more powerful computers have allowed the accurate modeling of groups of spheres with the flow properties of solid particles, bubbles, or drops to be studied in numerical experiments. Finite element methods and the lattice

Boltzmann method (LBM) have enabled scientists and engineers to perform *thought experiments* of groups of interacting spheres and, thus, to obtain the effect of interactions on the hydrodynamic force exerted on individual spheres under specific and well-defined conditions. In particular, the LBM and its derivative, the IBM (Feng and Michaelides, 2004b, 2005), are ideally suited methods for the determination of the interaction of groups of particles, drops, and bubbles of any shape and material properties. These recently developed methods have enabled the simulation of processes involving very large groups of particles, of the order of tens of thousands.

Kaneda (1986) used an asymptotic method to derive the steady component of the hydrodynamic force on an array of solid spheres at small but not vanishing Re_r and very low concentrations. He developed the following relationship for the average drag coefficient, C_D:

$$C_D = 1 + (\sqrt{2}/3)C^{1/2} + (\sqrt{2}/40)C^{-1/2}Re_r^2, \tag{1.230}$$

which is valid at distances where the inertia of the sphere is important. In the case of flows with several interacting objects, inertia becomes important at distances far from the *Brinkman screening length*. In the case of an array of spheres, the Brinkman screening length is equal to $C^{1/2}$, and hence, the range of applicability of this expression is $C^{1/2} \gg Re_r$. Kaneda (1986) also concluded that in the opposite limit, ($C^{1/2} \ll Re_r$), the Oseen correction to the Stokes drag ($1 + 3/16Re_r$) should be used for the average drag coefficient of the spheres. Working with arrays of two-dimensional particles in flows at small but finite Re_r and using the LBM, Koch and Ladd (1997) and Rojas and Koplik (1998) also confirmed that the Oseen relationship for the steady component of the hydrodynamic force applies to particles at small but finite Re_r.

Koch and Sangani (1999) used the LBM for a packed bed of particles and performed calculations on the rectilinear drag coefficients with fixed arrays of spheres. Their system is essentially a well-organized porous medium. They found out that the steady drag component may be scaled as Re_r^2 in high-concentration suspensions and depends on the concentration. Koch and Sangani (1999) obtained the following relationship for the steady hydrodynamic force in dense concentrations, $C > 40\%$, applicable to finite but small values of Re_r:

$$C_D = C_{D0}(C) + C_{D1}(C)Re_r^2. \tag{1.231}$$

The first function of this expression, which is the equivalent of the dimensionless Stokes drag force, is

$$C_{D0}(C) = \frac{1 + 3(C/2)^{1/2} + 2.11C\ln C + 16.14C}{1 + 0.681C - 8.48C^2 + 8.16C^3}. \tag{1.232}$$

The ratio of the functions C_{D1}/C_{D0} in this study diminishes with the increasing concentration of the solid particles. Hence, the second term in Equation 1.231 is very small in comparison to the first term at sufficiently high values of C. Because of this, Koch and Sangani (1999) claimed that the nonlinear behavior of the steady part of the average hydrodynamic force for close-packed arrays is difficult to be observed with the currently available experimental means.

Koch and Hill (2001) also performed computational studies using the LBM at higher Reynolds numbers and concluded that the steady component of the hydrodynamic force increases linearly with Re_r according to the following correlation:

$$C_D = C_{D0}(C) + \left[0.0673 + 0.212C + 0.0232(1 - C)^{-5}\right]Re_r, \tag{1.233}$$

where the function $C_{D0}(C)$ is the same as in Equation 1.231. Koch and Hill (2001) concluded that this expression agrees very well with experimental results and empirical relations derived in the past for packed beds of particles.

Bubbles are modeled as inviscid and weightless spheres moving in a medium, which is often idealized as an inviscid fluid. Because in the case of bubbles the added mass term is by far greater than the other components of the hydrodynamic force, such spheres accelerate as if their masses were equal to the mass of the

fluid occupying half of their volume, that is, fluid of mass $m_s = 2/3\pi\rho_f a^3$. For swarms of bubbles moving in a fluid with concentration C, the added mass coefficient, Δ_A, is a function of the concentration of the bubbles. Zuber (1964) used the simple theory of a bubble in a cell model for the flow of groups of bubbles to obtain analytically the following correction to the added mass coefficient:

$$\Delta_A = \frac{1+2C}{1-C}. \tag{1.234}$$

This expression is very simple to use in repetitive computations, and according to Sangani et al. (1991), it is sufficiently accurate and applies to a wide variety of conditions. Van Wijngaarten (1976) performed an asymptotic analytical study in the case of a swarm of bubbles that are impulsively accelerated and concluded that, with accuracy of the order of C^2, the added mass coefficient of a group with concentration C is equal to

$$\Delta_A = 1 + 2.76C + O(C^2). \tag{1.235}$$

A great deal of knowledge on the behavior of interacting bubbles has been recently developed as a result of computer simulations. Spelt and Sangani (1998) performed such a simulation to determine the influence of the fluid pseudo-turbulence—the velocity fluctuations in the carrier fluid, due to the motion of particles and bubbles—on the hydrodynamic force and the drag coefficient of a swarm of bubbles. They concluded that there is a weak dependence of the added mass coefficient on the fluid velocity fluctuations, but a significant dependence of the added mass on the bubble concentration. Their final expression, valid for $C < 0.3$, is

$$\Delta_A = \frac{1+2C+0.225CJ_A}{1-C}, \tag{1.236}$$

where J_A is a dimensionless measure of the temporal velocity fluctuations of the fluid. With a similar analysis, Spelt and Sangani (1998) obtained the following expression for the steady viscous drag coefficient for a swarm of bubbles in a viscous fluid:

$$C_D = \frac{1+0.15CJ_A}{(1-C)^2}. \tag{1.237}$$

1.4.5.1 Porous Particles

Large groups of interacting particles, clusters, and aggregates in dense flows may be approximated and treated as porous media. The permeability and porosity of such a porous media depend on the concentration. Similarly, clouds or large groups of smaller spheres may be approximated as larger porous spheres that are transported in a fluid medium. Jones (1973) obtained an expression for the steady hydrodynamic force on a porous sphere at creeping flow conditions:

$$F_i = 6\pi a\mu_f(u_i - v_i)\frac{2\zeta^2(1+2\eta\zeta^{-1})}{2\zeta^2+3+6\eta\zeta+6\eta\zeta^{-1}}, \tag{1.238}$$

where

ζ is the inverse of the dimensionless permeability of the sphere ($\zeta = a/\kappa^{1/2}$, with κ being the permeability of the sphere)

η is a dimensionless constant that depends on the properties of the porous medium

The permeability, κ, of a group of particles that form a porous medium is related to the porosity and, by extent, to the concentration, C, by the so-called Carman–Kozeny equation:

$$\kappa = \frac{(1-C)^3}{180C^2}d^2. \tag{1.239}$$

Feng and Michaelides (1998b) used an asymptotic expansion and extended this result to finite Reynolds numbers, Re_r, by developing corrections for Re_r up to the order Re_r^2. Their final expression for the drag force of such porous spheres is

$$F_i = 6\pi a\mu_f\left(u_i - v_i\right)\frac{2\left(1+\frac{\eta}{\zeta}\right)\zeta^2}{4\eta\zeta+2\zeta^2+3\frac{\eta}{\zeta}+1}\left[1+Re_r\frac{3\left(1+\frac{\eta}{\zeta}\right)\zeta^2}{4\left(4\eta\zeta+2\zeta^2+3\frac{\eta}{\zeta}+1\right)}+Re_r^2\ln\left(Re_r\right)\frac{9\left(1+\frac{\eta}{\zeta}\right)^2\zeta^4}{10\left(4\eta\zeta+2\zeta^2+3\frac{\eta}{\zeta}+1\right)^2}\right]. \tag{1.240}$$

$$C_D = \frac{24}{Re_r}\frac{2\left(1+\frac{\eta}{\zeta}\right)\zeta^2}{4\eta\zeta+2\zeta^2+3\frac{\eta}{\zeta}+1}\left[1+Re_r\frac{3\left(1+\frac{\eta}{\zeta}\right)\zeta^2}{4\left(4\eta\zeta+2\zeta^2+3\frac{\eta}{\zeta}+1\right)}+Re_r^2\ln\left(Re_r\right)\frac{9\left(1+\frac{\eta}{\zeta}\right)^2\zeta^4}{10\left(4\eta\zeta+2\zeta^2+3\frac{\eta}{\zeta}+1\right)^2}+O\left(Re_r^2\right)\right]$$

Re_r is based on the diameter of the whole cloud of small spheres and on the average relative velocity of the cloud. The last equation yields the correct behavior in the extreme cases of zero and infinite permeability: for a solid sphere ($\kappa \to 0$), this expression yields the hydrodynamic force expression obtained by Proudman and Pearson (1956) (Equation 1.103), while at low permeability ($\kappa \to 0$), it yields the result by Joseph and Tao (1964). At creeping flow, it yields the expression for the drag force that was first predicted by the study of Saffman (1971).

Looker and Carnie (2004) studied the transient hydrodynamic force of an oscillating porous sphere with velocity slip at its interface (a condition that was also studied by Saffman, 1971). They derived an asymptotic expression for the transient hydrodynamic force on the porous sphere with slip, valid up to the order of $\kappa^{1/2}$. Most of the results of this study may also be derived from the fundamental equation of a sphere with slip at its interface, Equation 1.138.

Nomenclature

Latin

a	Particle, droplet radius (m)
A	Area (m^2)
B_H	Blowing factor
B_M	Blowing parameter
c	Specific heat
c_p	Specific heat at constant pressure (J/kg·K)
c_v	Specific heat at constant volume (J/kg·K)
C	Concentration
C_D	Drag coefficient
C_L	Lift coefficient
d	Particle, droplet diameter (m)
d_A	Area-equivalent diameter (m)
d_V	Volume-equivalent diameter (m)
D	Diffusion coefficient (m^2/s)
D	Pipe/channel diameter (m)
f	Frequency distribution (continuous)
$f,$	Frequency distribution (discrete)
$F,$	Cumulative distribution
F	Force (N)
F_D,$F_{D,i}$	Drag force vector (N)
F_L,$F_{L,i}$	Lift force vector (N)
g,g_i	Gravity vector (m/s^2)
h	Specific enthalpy (J/kg), heat transfer coefficient (J/m^2-K)
h_{fg}	Latent heat of evaporation (J/kg)

h_M	Mass transfer coefficient
ΔH	Heat of combustion
I	Turbulence intensity
k	Thermal conductivity (J/m-K)
k	Ratio specific heats
l_m	Molecular mean free path
l_w	Distance to wall
L	Characteristic length (m)
m	Mass (kg)
$\dot{m}$	Mass flow rate (kg/s)
M	Molecular weight (kmol/kg)
n	Number density ($1/m^3$)
p	Pressure (Pa)
$\dot{Q}$	Heat transfer rate (W)
r, r_i	Radius vector
R	Gas constant (kJ/kg·K)
R_u	Universal gas constant (kJ/kmol K)
S	Dimensionless slip
T	Temperature (K)
t	Time (s)
u	Phase velocity of fluid (m/s)
U_a	Superficial velocity of phase "a" (m/s)
u	Velocity component in x-direction (m/s)
u_i,u	Velocity vector, continuous phase (m/s)
U	Characteristic velocity (m/s)
v_i,v	Velocity vector, dispersed phase (m/s)
V	Volume (m^3)
V_r	Migration velocity (m/s)
V_s	Settling velocity (m/s)
V_t	Terminal velocity (m/s)
w	Relative velocity (m/s)
w_i	Relative velocity vector (m/s)
x_i	Coordinate vector (m)
x	Quality, coordinate direction (m)
X	Mole fraction
y	Coordinate direction (m)
Y	Mass fraction
z	Vertical coordinate direction (m)
Z	Loading

Greek

α	Absorptivity
α_a	Volume fraction of phase "a"
β	Density ratio
β	Slip parameter
γ	Shear, rate of strain
Δ	Additional term of the Nusselt number
Δ_A	Added mass coefficient
Δ_H	History term coefficient
ε	Emissivity
ζ	Inverse of the dimensionless permeability
η	Dimensionless constant
θ	Angle, azimuthal angle (°)
κ	Permeability
λ	Viscosity ratio
μ	Dynamic viscosity (N/m-s), mean value

ν	Kinematic viscosity (m^2/s)
Ξ	Particle–cylinder diameter ratio
ρ	Density (kg/m^3)
ρ_m	Mixture density (kg/m^3)
σ	Surface tension (N/m)
σ	Standard deviation
σ	Stefan–Boltzmann constant
τ_V	Velocity response time (s)
τ_T	Thermal response time (s)
τ_c	Collision time (s)
ϕ	Velocity ratio
ψ	Stream function
Ψ	Shape factor for particles
Ω	Angular velocity (1/s)

Subscripts

c	Continuous phase, cluster
cr	Critical
d	Dispersed phase
f	Fluid
GM	Geometric mean
HM	Harmonic mean
m	Maximum, mass
M	Magnus, median
n	Number
p	Particle
r	Relative
s	Solid
S	Dimensionless slip ratio
*S*M	Surface mean
T, t	Thermal
VM	Volumetric mean
w	Wall
θ	Circumferential, tangential direction
∞	Free stream

Dimensionless Numbers

Ac	Acceleration number
Bo	Bond number
Eo	Eötvös number
Kn	Knudsen number
Le	Lewis number
Ma	Mach number
Mo	Morton number
Nu	Nusselt number
Pe	Peclet number
Pr	Prandtl number
Re	Reynolds number
Re_γ	Shear Reynolds number
Re_r	Relative Reynolds number
Re_R	Rotation Reynolds number
Sc	Schmidt number
Sh	Sherwood number
Sl	Strouhal number
St	Stokes number
We	Weber number

References

Abramzon, B. and Sirignano, W.A., Droplet vaporization for spray combustion calculations, *Int. J. Heat Mass Transfer*, 32, 1605–1618, 1989.

Achenbach, E., Vortex shedding from spheres, *J. Fluid Mech.*, 62, 209–221, 1974.

Acrivos, A., A note on the rate of heat or mass transfer from a small particle freely suspended in linear shear field, *J. Fluid Mech.*, 98, 299–304, 1980.

Acrivos, A. and Goddard, J.D., Asymptotic expansions for laminar convection heat and mass transfer, *J. Fluid Mech.*, 23, 273–291, 1965.

Acrivos, A. and Taylor, T.E., Heat and mass transfer from single spheres in stokes flow, *Phys. Fluids*, 5, 387–394, 1962.

Auton, T.R., Hunt, J.R.C., and Prud'homme, M., The force exerted on a body in inviscid unsteady non-uniform rotational flow, *J. Fluid Mech.*, 197, 241–257, 1988.

Barndorff-Nielsen, O., Exponentially decreasing distributions of the logarithm of particle size, *Proc. Res. Soc. Lond. A*, 353, 401, 1977.

Basset, A.B., *Treatise on Hydrodynamics*, Bell, London, U.K., 1888a.

Basset, A.B., On the motion of a sphere in a viscous liquid, *Philos. Trans. R. Soc. Lond.*, 179, 43–63, 1888b.

Bataille, J., Lance, M., and Marie, J.L., Bubbly turbulent shear flows, in J. Kim, U. Rohatgi, and M. Hashemi (Eds.), *ASME-FED*, *99*, New York, 1990, pp. 1–7.

Bhaga, D. and Weber, M.E., Bubbles in viscous liquids: Shapes, wakes and velocities, *J. Fluid Mech.*, 105, 61–85, 1981.

Bohlin, T., *Terminal Velocities of Solid Spheres in Cylindrical Enclosures*, Report # 155, Transactions of the Royal Institute of Technology, Stockholm, Sweden, 1960.

Bond, W.N. and Newton, D.A., Bubbles, drops and Stokes law, *Philos. Mag.*, 5, 794–800, 1928.

Boussinesq, V.J., Sur la Resistance qu' Oppose un Liquide Indéfini en Repos…, *Comptes Rendu*, *Acad. Sci. Paris*, 100, 935–937, 1885.

Brenner, H., The slow motion of a sphere through a viscous fluid toward a plane surface, *Chem. Eng. Sci.*, 16, 242–251, 1961.

Brock, J.R., On the theory of thermal forces acting on aerosol particles, *J. Colloid Interface Sci.*, 17, 768–780, 1962.

Brun, P.O., Heat or mass transfer from single spheres in a low Reynolds number flow, *Int. J. Eng. Sci.*, 20, 817–822, 1982.

Bushell, G.C., Yan, Y.D., Woodfield, D., Raper, J., and Amal, R., On techniques for the measurement of the mass fractal dimension of aggregates, *Adv. Colloid Interface Sci.*, 95(1), 1–50, 2002.

Carlson, D.J. and Hoglund, R.F., Particle drag and heat transfer in rocket nozzles, *AIAA J.*, 2, 1980–1984, 1964.

Cherukat, P. and McLaughlin, J.B., Wall-induced lift on a sphere, *Int. J. Multiphase Flow*, 16, 899–907, 1990.

Chhabra, R.P., Singh, T., and Nandrajog, S., Drag on chains and agglomerates of spheres in viscous Newtonian and power law fluids, *Can. J. Chem. Eng.*, 73, 566–571, 1995.

Chiang, C.H., Raju, M.S., and Sirignano, W.A., Numerical analysis of a convecting, vaporizing fuel droplet with variable properties, *Int. J. Heat Mass Transfer*, 35, 1307–1327, 1992.

Clamen, A. and Gauvin, W.H., Effects of turbulence on the drag coefficients of spheres in a supercritical flow regime, *AIChE J.*, 15, 184–189, 1969.

Clift, K.A. and Lever, D.A., Isothermal flow past a blowing sphere, *Int. J. Numer. Methods Fluids*, 5, 709–715, 1985.

Clift, R. and Gauvin, W.H., The motion of particles in turbulent gas streams, *Proc. Chem. ECA*, 1, 14–24, 1970.

Clift, R., Grace, J.R., and Weber, M.E., *Bubbles*, *Drops and Particles*, Academic Press, New York, 1978.

Cox, R.G. and Brenner, H., The slow motion of a sphere through a viscous fluid towards a plane surface, *Chem. Eng. Sci.*, 22, 1753–1777, 1967.

Cox, R.G. and Hsu, S.K., The lateral migration of solid spheres in a laminar flow near a plane, *Int. J. Multiphase Flow*, 3, 201–222, 1977.

Crowe, C.T., Babcock, W.R., and Willoughby, P.G., Drag coefficient for particles in rarefied low Mach number flows, *Prog. Heat Mass Transfer*, 6, 419–428, 1973.

Crowe, C.T., Babcock, W.R., Willoughby, P.G., and Carlson, R.L., Measurement of particle drag coefficients in flow regimes encountered by particles in a rocket nozzle, United Technology Centre Report, 2296-FR, Sunnyvale, CA, 1969.

Crowe, C.T., Sommerfeld, M., and Tsuji, Y., *Multiphase Flows with Droplets and Particles*, CRC Press, Boca Raton, FL, 1998.
Dandy, D.S. and Dwyer, H.A., A sphere in shear flow at finite Reynolds number: Effect of particle lift, drag and heat transfer, *J. Fluid Mech*., 226, 381–398, 1990.
Di Felice, R., The voidage function for fluid–particle interaction systems, *Int. J. Multiphase Flow*, 20, 153–162, 1994.
Dorfman, L.A. and Serazetdinov, A.Z., Laminar flow and heat transfer near rotating axisymmetric surface, *Int. J. Heat Mass Transfer*, 8, 317–327, 1973.
Eisenklam, P., Arunachalam, S.A., and Weston, J.A., Evaporation rates and drag resistance of burning drops, in *Proceedings of the 11th International Symposium on Combustion*, Pittsburgh, PA, 1967, pp. 715–721.
Epstein, P., Zur theorie des radiometers, *Z. Physik*, 54, 537–563, 1929.
Farouk, B., Mixed convective flow around a slowly rotating isothermal sphere, *Trans. ASME*, *J. Heat Transfer*, 107, 431–438, 1985.
Faxen, H., Der Widerstand gegen die Bewegung einer starren Kugel in einer zum den Flussigkeit, die zwischen zwei parallelen Ebenen Winden eingeschlossen ist, *Ann. Phys*., 68, 89–119, 1922.
Fayon, A.M. and Happel, J., Effect of a cylindrical boundary on a fixed rigid sphere in a moving viscous fluid, *AIChE J*., 6, 55–58, 1960.
Feng, Z.G., A correlation of the drag force coefficient on a sphere with interface slip at low and intermediate Reynolds numbers, *J. Dispersion Sci. Technol*., 31, 968–974, 2010.
Feng, Z.G., Forced heat and mass transfer from a slightly deformed sphere at small but finite Peclet numbers in Stokes flow, *J. Heat Transfer*, 135, 081702, 2013.
Feng, Z.G., Direct numerical simulation of forced convective heat transfer from a heated rotating sphere in laminar flows, *J. Heat Transfer*, 136, 041707, 2014.
Feng, Z.-G. and Michaelides, E.E., Transient heat and mass transfer from a spheroid, *AIChE J*., 43, 609–616, 1997.
Feng, Z.-G. and Michaelides, E.E., Transient heat transfer from a particle with arbitrary shape and motion, *J. Heat Transfer*, 120, 674–681, 1998a.
Feng, Z.-G. and Michaelides, E.E., Motion of a permeable sphere at finite but small Reynolds numbers, *Phys. Fluids*, 10, 1375–1383, 1998b.
Feng, Z.-G. and Michaelides, E.E., A numerical study on the transient heat transfer from a sphere at high Reynolds and Peclet numbers, *Int. J. Heat Mass Transfer*, 43, 219–229, 2000a.
Feng, Z.-G. and Michaelides, E.E., Mass and heat transfer from fluid spheres at low Reynolds numbers, *Powder Technol*., 112, 63–69, 2000b.
Feng, Z.-G. and Michaelides, E.E., Drag coefficients of viscous spheres at intermediate and high Reynolds numbers, *J. Fluids Eng*., 123, 841–849, 2001a.
Feng, Z.-G. and Michaelides, E.E., Heat and mass transfer coefficients of viscous spheres, *Int. J. Heat Mass Transfer*, 44, 4445–4454, 2001b.
Feng, Z.-G. and Michaelides, E.E., Inter-particle forces and lift on a particle attached to a solid boundary in suspension flow, *Phys. Fluids*, 14, 49–60, 2002a.
Feng, Z.-G. and Michaelides, E.E., Hydrodynamic force on spheres in cylindrical and prismatic enclosures, *Int. J. Multiphase Flow*, 28, 479–496, 2002b.
Feng, Z.-G. and Michaelides, E.E., Equilibrium position for a particle in a horizontal shear flow, *Int. J. Multiphase Flow*, 29, 943–957, 2003.
Feng, Z.-G. and Michaelides, E.E., An immersed boundary method combined with lattice Boltzmann method for solving fluid and particles interaction problems, *J. Comput. Phys*., 195, 457–472, 2004b.
Feng, Z.-G. and Michaelides, E.E., Proteus: A direct forcing method in the simulations of particulate flow, *J. Comput. Phys*., 202, 20–51, 2005.
Feng, Z.G. and Michaelides, E.E., Inclusion of heat transfer computations for particle laden flows, *Phys. Fluids*, 20, 1–10, 2008.
Feng, Z.G. and Michaelides, E.E., Heat transfer in particulate flows with Direct Numerical Simulation (DNS), *Int. J. Heat Mass Transfer*, 52, 777–786, 2009.
Feng, Z.G. and Michaelides, E.E., Heat transfer from a nano-sphere with temperature and velocity discontinuities at the interface, *Int. J. Heat Mass Transfer*, 55, 6491–6498, 2012.
Feng, Z.G., Michaelides, E.E., and Mao, S.L., On the drag force of a viscous sphere with interfacial slip at small but finite Reynolds numbers, *Fluid Dyn. Res*., 44, 025502, 1–16, 2012.
Fourier, J., *Theorie Analytique de la Chaleur*, Acad. de Paris, Paris, France, 1822.
Galindo, V. and Gerbeth, G., A note on the force on an accelerating spherical drop at low Reynolds numbers, *Phys. Fluids*, 5, 3290–3292, 1993.
Gay, M. and Michaelides, E.E., Effect of the history term on the transient energy equation of a sphere, *Int. J. Heat Mass Transfer*, 46, 1575–1586, 2003.

Haberman, W.L. and Morton, R.K., *An Experimental Investigation of the Drag and Shape of Air Bubbles Rising in Various Liquids*, D.W. Taylor Model Basin Report, Vol. 802, Department of the Navy, Washington, DC, 1953.
Haberman, W.L. and Sayre, R.M., *Motion of Rigid and Fluid Spheres in Stationary and Moving Liquids Inside Cylindrical Tubes*, Report No. 1143, David Taylor Model Basin, U.S. Navy, Washington, DC, 1958.
Hadamard, J.S., *Mouvement Permanent Lent d' une Sphere Liquide et Visqueuse dans un Liquide Visqueux*, Compte-Rendus de' l' Acad. des Sci., Paris, France, Vol. 152, 1911, pp. 1735–1738.
Haider, A.M. and Levenspiel, O., Drag coefficient and terminal velocity of spherical and nonspherical particles, *Powder Technol.*, 58, 63–70, 1989.
Happel, J. and Brenner, H., *Low Reynolds Number Hydrodynamics*, Martinus Nijhoff, Washington, DC (reprint, orig. publ. 1963), 1986.
Hartman, M. and Yates, J.G., Free-fall of solid particles through fluids, *Collect. Czech. Chem. Commun.*, 58, 961–974, 1993.
Hermsen, R.W., Review of particle drag models, *JANAF Performance Standardization Subcommittee 12th Meeting*, Vol. CPIA 113, Washington, DC, 1979.
Inamuro, T., Maeba, K., and Ogino, F., Flow between parallel walls containing the lines of neutrally buoyant circular cylinders, *Int. J. Multiphase Flow*, 26, 1981–2004, 2000.
Iwaoka, M. and Ishii, T., Experimental wall correction factors of single solid spheres in circular cylinders, *J. Chem. Eng. Jpn.*, 12, 239–242, 1979.
Jones, I.P., Low Reynolds number flow past a porous spherical shell, *Proc. Camb. Philos. Soc.*, 73, 231–238, 1973.
Joseph, D.D. and Tao, L.N., The effect of permeability on the slow motion of a porous sphere in a viscous liquid, *Z. Angew. Math. Mech.*, 44, 361–367, 1964.
Kalio, G.A., Random walk modeling of particle deposition, in D.E. Stock et al. (Eds.), *Gas–Solid Flows—1993*, ASME FED, New York, 166, 1993, pp. 161–167.
Kaneda, Y., The drag on a sparse random array of fixed spheres in flow at small but finite Reynolds number, *J. Fluid Mech.*, 167, 455–463, 1986.
Kim, J.H., Mulholland, G.W., Pui, D.Y.H., and Kukuck, S.R., Slip correction measurements of certified psl nanoparticles using a nanometer Differential Mobility Analyzer (nano-DMA) for Knudsen number from 0.5 to 83, *J. Res. Natl. Inst. Stand. Technol.*, 110, 31–54, 2005.
Kim, S. and Karila, S.J., *Microhydrodynamics: Principles and Selected Applications*, Butterworth-Heineman, Boston, MA, 1991.
Koch, D.L. and Hill, R.J., Inertial effects in suspension and porous media flows, *Annu. Rev. Fluid Mech.*, 33, 619–647, 2001.
Koch, D.L. and Ladd, A.J.C., Moderate Reynolds number flows through periodic and random arrays of aligned cylinders, *J. Fluid Mech.*, 349, 31–66, 1997.
Koch, D.L. and Sangani, A.S., Particle pressure and marginal stability limits for a homogeneous monodisperse gas fluidized bed: Kinetic theory and numerical calculations, *J. Fluid Mech.*, 400, 229–263, 1999.
Kreith, F., Roberts, L.G., Sullivan, J.A., and Sinha, S.N., Convection heat transfer flow phenomena of rotating sphere, *Int. J. Heat Mass Transfer*, 6, 881–895, 1965.
Kurose, R., Makino, H., Komori, S., Nakamura, M., Akamatsu, F., and Katsuki, M., Effects of outflow from surface of sphere on drag, shear lift and scalar diffusion, *Phys. Fluids*, 15, 2338–2351, 2003.
Lasso, I.A. and Weidman, P.D., Stokes drag on hollow cylinders and conglomerates, *Phys. Fluids*, 29, 3921–3934, 1986.
Lawrence, C.J. and Weinbaum, S., The force on an axisymmetric body in linearized time-dependent motion: A new memory term, *J. Fluid Mech.*, 171, 209–218, 1986.
Lawrence, C.J. and Weinbaum, S., The unsteady force on a body at low Reynolds number: The axisymmetric motion of a spheroid, *J. Fluid Mech.*, 189, 463–498, 1988.
Le Clair, B.P. and Hamielec, A.E., A theoretical and experimental study of the internal circulation in water drops falling at terminal velocity in air, *J. Atmos. Sci.*, 29, 728–740, 1972.
Leal, L.G., *Laminar Flow and Convective Transport Processes*, Butterworth-Heinemann, Boston, MA, 1992.
Lee, C. and Kramer, T.A., Prediction of three-dimensional fractal dimensions using the two-dimensional properties of fractal aggregates, *Adv. Colloid Interface Sci.*, 112(1–3), 49–57, 2004.
Leeder, M.R., *Sedimentology, Process and Product*, Allen and Unwin, London, U.K., 1982.
Lerner, S.L., Homan, H.S., and Sirignano, W.A., Multicomponent droplet vaporization at high Reynolds numbers-size, composition and trajectory histories, *AIChE Annual Meeting*, Chicago, IL, 1980.
Leung, A.L. and Crowe, C.T., Collection of nanoclusters by thermophoresis, in D.E. Stock et al. (Eds.), *Gas–Solid Flows—1993*, ASME, New York, 1993.
Levich, V.G., *Physicochemical Hydrodynamics*, Prentice-Hall, Englewood Cliffs, NJ, 1962.
Li, X.-Y. and Logan, B.E., Permeability of fractal aggregates, *Water Res.*, 35(14), 3373–3380, 2001.

Lien, F.S., Chen, C.K., and Cleaver, J.W., Mixed and free convection over a rotating sphere with blowing and suction, *ASME J. Heat Transfer*, 108, 398–404, 1986.
Ling, Y., Haselbacher, A., and Balachandar, S., Importance of unsteady contributions to force and heating for particles in compressible flows: Part 1: Modeling and analysis for shock–particle interaction, *Int. J. Multiphase Flow*, 37, 1026–1044, 2011a.
Ling, Y., Haselbacher, A., and Balachandar, S., Importance of unsteady contributions to force and heating for particles in compressible flows: Part 2: Application to particle dispersal by blast waves, *Int. J. Multiphase Flow*, 37, 1013–1025, 2011b.
Looker, J.R. and Carnie S.L., The hydrodynamics of an oscillating porous sphere, *Phys. Fluids*, 16, 62–72, 2004.
Loth, E., Numerical approaches for the motion of dispersed particles, droplets, or bubbles, *Prog. Energy Combust. Sci.*, 26, 161–223, 2000.
Lovalenti, P.M. and Brady, J.F., The hydrodynamic force on a rigid particle undergoing arbitrary time-dependent motion at small Reynolds numbers, *J. Fluid Mech.*, 256, 561–601, 1993.
Madhav, G.V. and Chhabra, R.P., Drag on non-spherical particles in viscous fluids, *Int. J. Miner. Process.*, 43, 15–29, 1995.
Magnus, G., A note on the rotary motion of the liquid jet, *Ann. Phys. Chem.*, 63, 363–365, 1861.
Mandelbrot, B.B., How long is the coast of Britain? *Science*, 156, 636–638, 1967.
Marshall, W.R., Atomization and spray drying, *Chem. Eng. Prog. Monogr. Ser.*, 50(2), AIChE, New York, 1954.
Masliyah, J.H. and Epstein, N., Numerical study of steady flow past spheroids, *J. Fluid Mech.*, 44, 493–512, 1970.
Maxey, M.R. and Riley, J.J., Equation of motion of a small rigid sphere in a non-uniform flow, *Phys. Fluids*, 26, 883–889, 1983.
Maxworthy, T., Experiments on the flow around a sphere at high Reynolds numbers, *J. Appl. Mech.*, 91, 598–607, 1969.
Maxworthy, T., Accurate measurements of a sphere drag at low Reynolds numbers, *J. Fluid Mech.*, 23, 369–372, 1975.
McLaughlin, J.B., Inertial migration of a small sphere in linear shear flows, *J. Fluid Mech.*, 224, 261–274, 1991.
McNabb, G.S. and Meisen, A., Thermophoresis in liquids, *J. Colloidal Interface Sci.*, 44, 339–346, 1973.
Mei, R., An approximate expression of the shear lift on a spherical particle at finite Reynolds numbers, *Int. J. Multiphase Flow*, 18, 145–160, 1992.
Mei, R. and Adrian, R.J., Flow past a sphere with an oscillation in the free-stream and unsteady drag at finite Reynolds number, *J. Fluid Mech.*, 237, 323–341, 1992.
Mei, R., Lawrence, C.J., and Adrian, R.J., Unsteady drag on a sphere at finite Reynolds number with small fluctuations in the free-stream velocity, *J. Fluid Mech.*, 233, 613–631, 1991.
Michaelides, E.E., A novel way of computing the Basset term in unsteady multiphase flow comput., *Phys. Fluids A*, 4, 1579–1582, 1992.
Michaelides, E.E., Hydrodynamic force and heat/mass transfer from particles, bubbles and drops—The Freeman Scholar Lecture, *J. Fluids Eng.*, 125, 209–238, 2003.
Michaelides, E.E., *Particles, Bubbles and Drops—Their Motion, Heat and Mass Transfer*, World Scientific Publishers, Singapore, in print, 2006.
Michaelides, E.E., Transport properties of nanofluids—A critical review, *J. Non-Equilib. Thermodyn.*, 38, 1–79, 2013a.
Michaelides, E.E., *Heat and Mass Transfer in Particulate Suspensions*, Springer, New York, 2013b.
Michaelides, E.E., *Nanofluidics—Thermodynamic and Transport Properties*, Springer, New York, 2014.
Michaelides, E.E., Brownian movement and thermophoresis of nanoparticles in liquids, *Int. J. Heat Mass Transfer*, 81, 179–187, 2015.
Michaelides, E.E. and Feng, Z.-G., Heat transfer from a rigid sphere in a non-uniform flow and temperature field, *Int. J. Heat Mass Transfer*, 37, 2069–2076, 1994.
Michaelides, E.E. and Feng, Z.-G., The equation of motion of a small viscous sphere in an unsteady flow with interface slip, *Int. J. Multiphase Flow*, 21, 315–321, 1995.
Michaelides, E.E. and Roig, A., A reinterpretation of the Odar and Hamilton data on the unsteady equation of motion of particles, *AIChE J.*, 57(11), 2997–3002, 2011.
Mikami, H., Endo, Y., and Takashima, Y., Heat transfer from a sphere to rarefied gas mixtures, *Int. J. Heat Mass Transfer*, 9, 1435–1448, 1966.
Millikan, R.A., The general law of fall of a small spherical body through a gas and its bearing upon the nature of molecular reflection from surfaces, *Phys. Rev.*, 22, 1–23, 1923.

Miyamura, A., Iwasaki, S., and Ishii, T., Experimental wall correction factors of single solid spheres in triangular and square cylinders, and parallel plates, *Int. J. Multiphase Flow*, 7, 41–46, 1981.
Morrison, F.A. and Stewart, M.B., Small bubble motion in an accelerating fluid, *J. Appl. Mech.*, 97, 399–402, 1976.
Mortazavi, S. and Tryggvason, G., A numerical study of the motion of drops in Poiseuille flow. Part 1: Lateral migration of one drop, *J. Fluid Mech.*, 411, 325–350, 2000.
Mugele, R.A. and Evans, H.D., Droplet size distribution in sprays, *Ind. Eng. Chem.*, 43, 1317–1324, 1951.
Musong, S. and Feng, Z.G., Mixed convective heat transfer from a heated sphere at an arbitrary incident flow angle in laminar flows, *Int. J. Heat Mass Transfer*, 78, 34–44, 2014.
Odar, F. and Hamilton, W.S., Forces on a sphere accelerating in a viscous fluid, *J. Fluid Mech.*, 18, 302–303, 1964.
Oesterle, B. and Bui-Dihn, T., Experiments on the lift of a spinning sphere in the range of intermediate Reynolds numbers, *Exp. Fluids*, 25, 16–22, 1998.
Oliver, D.L. and Chung, J.N., Flow about a fluid sphere at low to moderate Reynolds numbers, *J. Fluid Mech.*, 177, 1–18, 1987.
Oseen, C.W., Uber den Goltigkeitsbereich der Stokesschen Widerstandsformel, *Ark. Mat. Astron. Fysik*, 9(19), 1–15, 1913.
Paine, P.L. and Scherr, P., Drag coefficients for the movement of rigid spheres through liquid-filled cylindrical pores, *Biophys. J.*, 15, 1087–1091, 1975.
Parmar, M., Haselbacher, A., and Balachandar, S., Generalized Basset-Boussinesq-Oseen equation for unsteady forces on a sphere in a compressible flow, *Phys. Rev. Lett.*, 106, 084501, 2011.
Patankar, N., Ko, T., Choi, H.G., and Joseph, D.D., A correlation for the lift-off of many particles in plane Poiseuille flows of Newtonian fluids, *J. Fluid Mech.*, 445, 55–76, 2001.
Pettyjohn, E.S. and Christiansen, E.R., Effect of particle shape on free-settling rates of isometric particles, *Chem. Eng. Prog.*, 44, 157–172, 1948.
Portela, L.M., Cota, P., and Oliemans, R.V.A., Numerical study of the near-wall behaviour of particles in turbulent pipe flows, *Powder Technol.*, 125, 149–157, 2002.
Proudman, I. and Pearson, J.R.A., Expansions at small Reynolds numbers for the flow past a sphere and a circular cylinder, *J. Fluid Mech.*, 2, 237–262, 1956.
Raithby, G.D. and Eckert, E.R.G., The effect of turbulence parameters and support position on the heat transfer from spheres, *Int. J. Heat Mass Transfer*, 11, 1233–1246, 1968.
Ranz, W.E. and Marshall, W.R., Evaporation from drops, *Chem. Eng. Prog.*, 48, 141–146, 1952.
Renksizbulut, M. and Yuen, M.C., Experimental study of droplet evaporation in high temperature air stream, *J. Heat Transfer*, 105, 364–388, 1983.
Richardson, J.F. and Zaki, W.N., The fall velocities of spheres in viscous fluids, *Trans. Inst. Chem. Eng.*, 32, 35–41, 1954.
Rivkind, V.Y., Ryskin, G.M., and Fishbein, G.A., Flow around a spherical drop in a fluid medium at intermediate Reynolds numbers, *Appl. Math. Mech.*, 40, 687–691, 1976.
Rojas, S. and Koplik, J., Non-linear flow in porous media, *Phys. Rev.*, E58, 4776–4782, 1998.
Rowe, P.N., The drag coefficient of a sphere, *Trans. Inst. Chem. Eng.*, 39, 175–181, 1961.
Rybczynski, W., On the translatory motion of a fluid sphere in a viscous medium, *Bull. Acad. Sci., Krakow, Ser. A*, 40, 40–46, 1911.
Saffman, P.G., The lift on a small sphere in a slow shear flow, *J. Fluid Mech.*, 22, 385–398, 1965.
Saffman, P.G., The lift on a small sphere in a slow shear flow-corrigendum, *J. Fluid Mech.*, 31, 624–625, 1968.
Saffman, P.G., On the boundary condition at the surface of a porous medium, *Stud. Appl. Math.*, 50, 93–101, 1971.
Sangani, A.S., Zhang, D.Z., and Prosperetti, A., The added mass, Basset and viscous drag coefficients in nondilute bubbly liquids undergoing small-amplitude oscillatory motion, *Phys. Fluids*, A3, 2955–2970, 1991.
Sano, T., Unsteady flow past a sphere at low Reynolds number, *J. Fluid Mech.*, 112, 433–441, 1981.
Schaaf, S.A. and Chambre, P.L., Fundamentals of gas dynamics, in H.W. Emmons (Ed.), *High Speed Aerodynamics and Jet Propulsion*, Vol. 3, Princeton University Press, Princeton, NJ, 1958, pp. 689–793.
Schiller, L. and Nauman, A., Uber die grundlegende Berechnung bei der Schwekraftaufbereitung, *Ver. Deutch Ing.*, 44, 318–320, 1933.

Seeley, L.E., Hummel, R.L., and Smith, J.W., Experimental velocity profiles in laminar flow around spheres at intermediate Reynolds numbers, *J. Fluid Mech*., 68, 591–608, 1975.
Segre, G. and Silberberg, A., Behavior of macroscopic rigid spheres in Poiseuille flow, *J. Fluid Mech*., 14, 115–157, 1962.
Siegel, R. and Howel, J.R., *Thermal Radiation Heat Transfer*, McGraw-Hill, New York, 1981.
Sirignano, W.A., Fluid dynamics of sprays, *ASME J. Fluids Eng.*, 115, 345–378, 1993.
Sirignano, W.A., *Fluid Dynamics and Transport of Droplets and Sprays*, Cambridge University Press, Cambridge, U.K., 1999.
Spelt, P.D.M. and Sangani, A.S., Properties and averaged equations for flows of bubbly liquids, in A. Biesheuvel and G.F. van Heijst (Eds.), *Fascination of Fluid Dynamics*, Kluwer Academic, Dordrecht, the Netherlands, 1998, pp. 337–386.
Sridhar, G. and Katz, J., Drag and lift forces on microscopic bubbles entrained by a vortex, *Phys. Fluids*, 7, 389–399, 1995.
Stokes, G.G., On the effect of the internal friction of fluids on the motion of a pendulum, *Trans. Camb. Philos. Soc*., 9, 8–106, 1851.
Talbot, L., Cheng, R.K., Schefer, R.W., and Willis, D.R., Thermophoresis of particles in a heated boundary layer, *J. Fluid Mech*., 101, 737–758, 1980.
Tanaka, T., Yamagata, K., and Tsuji, Y., Experiment on fluid forces on a rotating sphere and a spheroid, in *Proceedings of the Second KSME-JSME Fluids Engineering Conference*, Seoul, Korea, Vol. 1, 1990, pp. 266–378.
Taneda, S., Experimental investigation of the wake behind a sphere at low Reynolds numbers, *J. Phys. Soc. Jpn*., 11, 1104–1108, 1956.
Tate, R.W. and Marshall, Jr., W.R., Atomization by centrifugal pressure nozzles (Part II), *Ind. Eng. Prog*., 49, 226–234, 1953.
ten Cate, A., Nieuwstad, C.H., Derksen, J.J., and Van den Akker, H.E.A., Particle imaging velocimetry experiments and lattice-Boltzmann simulations on a single sphere settling under gravity, *Phys. Fluids*, 14, 4012–4025, 2002.
Tieng, S.M. and Yan, A.C., Experimental investigation on convective heat transfer of heated rotating sphere, *Int. J. Heat Mass Transfer*, 36, 599–610, 1993.
Thorncroft, G.E., Klausner, J.F., and Mei, R., Bubble forces and detachment models, *Multiphase Sci. Technol.*, 13, 35–76, 2001.
Tomiyama, A., Reconsideration of three fundamental problems in modeling bubbly flows, in *39th European Two-Phase Flow Group Meeting*, Aveiro, Portugal, 2001.
Tomiyama, A., Kataoka, I., Zun, I., and Sakaguchi, T., Drag coefficients of single bubbles under normal and micro gravity conditions, *JSME Int. J., Ser. B*, 41, 472–479, 1998.
Tomiyama, A., Tamai, H., Zun, I., and Hosokawa, S., Transverse migration of single bubbles in simple shear flows, in *Proceedings of Second International Symposium on Two-Phase Flow Modeling and Experimentation*, Pisa, Italy, Vol. 2, 1999, pp. 941–948.
Tran Cong, S., Gay, M., and Michaelides, E.E., Drag coefficients of irregularly shaped particles, *Powder Technol.*, 139, 21–32, 2004.
Tsuji, Y., Morikawa, Y., and Mizuno, O., Experimental measurements of the magnus force on a rotating sphere at low Reynolds numbers bubble in an axisymmetric shear flow, *J. Fluids Eng.*, 107, 484–498, 1985.
Tyndall, J., On haze and dust, *Proc. R. Inst*., 6, 1–6, 1870.
van Wijngaarden, L., Hydrodynamic interaction between bubbles in a liquid, *J. Fluid Mech*., 77, 27–44, 1976.
Vasseur, P. and Cox, R.G., The lateral migration of spherical particles in two-dimensional shear flow, *J. Fluid Mech*., 78, 385–413, 1976.
Vicsek, T., *Fractal Growth Phenomena*, 2nd edn., World Scientific, Singapore, 1999.
Vojir, D.J. and Michaelides, E.E., The effect of the history term on the motion of rigid spheres in a viscous fluid, *Int. J. Multiphase Flow*, 20, 547–556, 1994.
Wadell, H., Sphericity and roundness of rock particles, *J. Geol*., 41, 310–331, 1933.
Wang, W. and Chau, Y., Self-assembled peptide nanorods as building blocks of fractal patterns, *Soft Matter*, 5(24), 4893–4898, 2009.
Wen, C.Y. and Wu, Y.H., Mechanics of fluidization, *Chem. Eng. Prog. Symp. Ser.*, 62, 100–125, 1966.

Whitaker, S., Forced convection heat transfer correlations for flow in pipes past flat plates, single cylinders, single spheres, and for flow in packed beds and tubes bundles, *AIChE J.*, 18, 361–371, 1972.
Winnikow, S. and Chao, B.T., Droplet motion in purified systems, *Phys. Fluids*, 9, 50–61, 1966.
Wu, M. and Gharib, M., Experimental studies on the shape and path of small air bubbles rising in clean water, *Phys. Fluids*, 14, L49–L52, 2002.
Yearling, P.R. and Gould, R.D., Convective heat and mass transfer from a single evaporating water, ethanol and methanol droplet, *Proc. ASME-FED*, 233, 33–39, 1995.
Yuen, M.C. and Chen, L.W., On drag of evaporating droplets, *Combust. Sci. Technol.*, 14, 147–154, 1976.
Zuber, N., On the dispersed two-phase flow in the laminar flow regime, *Chem. Eng. Sci.*, 19, 897–917, 1964.

2

Computational Methods

2.1 Overview of Numerical Approaches
2.2 Direct Numerical Simulations of Gas–Liquid Flows
2.3 The Lattice Boltzmann Method
2.4 Immersed Boundary Method
2.5 Pdf Models for Particle Transport Mixing and Collisions in Turbulent Flows
2.6 Euler–Lagrange Methods
2.7 Two-Fluid Model in MFIX
2.8 Uncertainty Quantification

2.1 Overview of Numerical Approaches

Eric Loth

2.1.1 Classification by Particle Reference Frame

While continuous-flow computational fluid dynamics (CFD) formulations are generally considered in an Eulerian reference, the dispersed-phase characteristics (velocity, concentration, diameter, etc.) can be treated with either Lagrangian or Eulerian representations. This difference of the reference frame for dispersed phase is the key division between the different multiphase numerical methods. The Lagrangian representation for particles is a natural approach since the particle positions are declared and updated along the particle paths. These paths are defined by the center of mass of the particle (or center of mass for a cloud of particles) as shown in Figure 2.1a. This approach can include wall collisions and other trajectory information in a straightforward manner. In contrast, the Eulerian approach for the particles considers cell-averaged particle characteristics based on the continuous-phase grid nodes (Figure 2.1b). This approach is efficient in terms of predicting particle concentration.

The two different approaches (Lagrangian and Eulerian) lead to significantly different formulations and numerical constraints. The Lagrangian approach leads to ordinary differential equations (ODEs) along the particle path but requires interpolation of the continuous-phase properties to the particle centroids. In contrast, the Eulerian approach leads to partial differential equations (PDEs) for the particle characteristics on an Eulerian grid but requires a continuum assumption for the particle characteristics. These two approaches are, respectively, discussed in the following two sections.

2.1.1.1 Lagrangian Approach for the Dispersed Phase

2.1.1.1.1 Lagrangian Particle Equation of Motion Since the dispersed phase is treated in terms of individual particle paths (or a group of particles), the Lagrangian method is also sometimes referred to as the "discrete" approach. When coupled with an Eulerian representation of the continuous phase, this combined treatment is termed the "Eulerian–Lagrangian" approach.

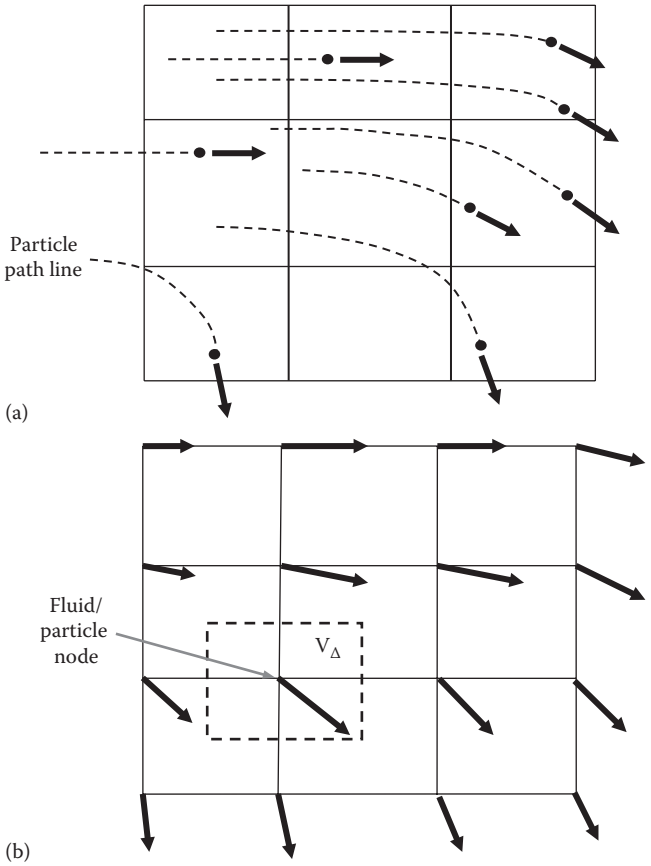


Figure 2.1

Particle velocity vectors in different reference frames in the context of an Eulerian continuous-phase grid: (a) Lagrangian vectors based on particle positions and (b) Eulerian particle velocity vectors based on average over a control volume centered at a discrete grid node used to store fluid properties and particle properties.

In the Lagrangian methodology, ODEs for the particle properties are based on particle path derivatives. The differential equations for particle position ($\mathbf{x}_p$), velocity ($\mathbf{v}$), mass (m_p), and internal energy (e_p) are summarized as follows:

$$\frac{d\mathbf{x}_p}{dt} \equiv \mathbf{v} \tag{2.1}$$

$$m_p \frac{d\mathbf{v}}{dt} = \mathbf{F}_{body} + \mathbf{F}_{sur} + \mathbf{F}_{coll} \tag{2.2}$$

$$\frac{dm_p}{dt} \equiv \dot{m}_p \tag{2.3}$$

$$m_p \frac{de_p}{dt} = \dot{Q}_p + \dot{m}_p h_{phase} \tag{2.4}$$

The RHS of Equation 2.2 contains the body force ($\mathbf{F}_{body}$), the fluid dynamic surface force ($\mathbf{F}_{sur}$), and the collision force with other particles or walls ($\mathbf{F}_{coll}$). The RHS of Equation 2.3 contains the mass transfer rate to the particle ($\dot{m}_p$, which is positive when the particle mass is increasing). The RHS of Equation 2.4 contains the heat transfer to the particle ($\dot{Q}_p$, which is positive when the particle temperature is increasing) and enthalpy for phase change (h_{phase}). The particle specific energy is equal to the product of the particle specific heat at constant pressure and particle temperature ($e_p = c_{p,p}T_p$). If there is negligible mass

or heat transfer (e.g., if temperature variations are small), the last two ODEs are not needed. The models for these RHS terms are listed as follows.

For a steady uniform continuum surrounding fluid moving past a single solid spherical particle at finite Reynolds numbers, the momentum RHS term (of Equation 2.2) neglecting collision effects can be modeled as

$$\mathbf{F}_{\text{body}} + \mathbf{F}_{\text{sur}} = -3\pi d\mu_f f \mathbf{w} + \rho_f \forall_p \left[\left(\frac{\rho_p}{\rho_f} - 1 \right) \mathbf{g} + \frac{3}{2} \frac{\mathcal{D}\mathbf{u}_{@p}}{\mathcal{D}t} - \frac{1}{2} \frac{d\mathbf{v}}{dt} \right] \tag{2.5}$$

$$\mathbf{w}(t) \equiv \mathbf{v}(t) - \mathbf{u}_{@p}(t) \tag{2.6}$$

$$f = 1 + \frac{Re_p/4}{1 + \sqrt{Re_p}} + \frac{Re_p}{60} \tag{2.7}$$

$$Re_p = \frac{\rho_f w d}{\mu_f} \tag{2.8}$$

In these expressions,

- d is the particle diameter
- μ_f is the fluid viscosity
- $\mathbf{w}$ is the particle relative velocity
- ρ_f is the fluid density
- $\forall_p$ is the particle volume
- ρ_p is the particle density
- $\mathbf{g}$ is the gravitational acceleration
- $\mathbf{u}_{@p}$ is the undisturbed fluid velocity (seen by the particle and interpolated to the particle centroid)
- Re_p is the particle Reynolds number

The RHS terms for mass and energy transfer (of Equations 2.3 and 2.4) can be modeled as

$$\dot{m}_p = -\pi d \rho_f Sp \Theta_{p@f} Sh \tag{2.9}$$

$$Sh = \left(2 + 0.6 \cdot Re_p^{1/2} \cdot Sc_f^{1/3} \right) \frac{\ln(1+Sp)}{Sp} \tag{2.10}$$

$$\dot{Q}_p = \pi d \kappa_f \left(T_{f@p} - T_p \right) Nu \tag{2.11}$$

$$Nu = \left(2 + 0.6 \cdot Re_p^{1/2} \cdot Pr_f^{1/3} \right) \frac{\ln(1+Sp)}{Sp} \tag{2.12}$$

In these expressions,

- Sp is the Spalding number
- $\Theta_{p@f}$ is the mass diffusivity of the particle matter into the surrounding fluid
- Sh is the Sherwood number
- Sc_f is the Schmidt number
- κ_f is the fluid thermal diffusivity
- $T_{f@p}$ is the fluid temperature extrapolated to the particle centroid
- Nu is the Nusselt number

These RHS terms neglect effects of lift, history force, collisions, internal recirculation, turbulence, and three-way coupling. Additions and corrections for these effects are described by Crowe et al. (1998, 2012), Loth (2000), and Michaelidis (2006, 2014).

2.1.1.1.2 Numerical Interpolation from Eulerian Grid To numerically integrate the particle ODEs, one must obtain the fluid properties interpolated to the particle centroid, for example, $\mathbf{u}_{@p}$ and $T_{f@p}$. These properties can be interpolated numerically from the Eulerian nodes of the continuous phase. For example, if the continuous-phase discretization is based on grid shape functions Φ, then the "unhindered" fluid velocity extrapolated to the particle centroid is given by

$$\mathbf{u}_{@p}(\mathbf{x}_p, t) = \sum_{j=1}^{N_\Phi} \mathbf{u}_j(t)\Phi_j(\mathbf{x}_p) \tag{2.13}$$

In this equation, N_Φ is all the number of computational cells associated with a particle location. The use of the shape function allows the velocity of all surrounding nodes to be included in the evaluation of $\mathbf{u}_{@p}$. This is shown schematically in Figure 2.2a for a 2D grid.

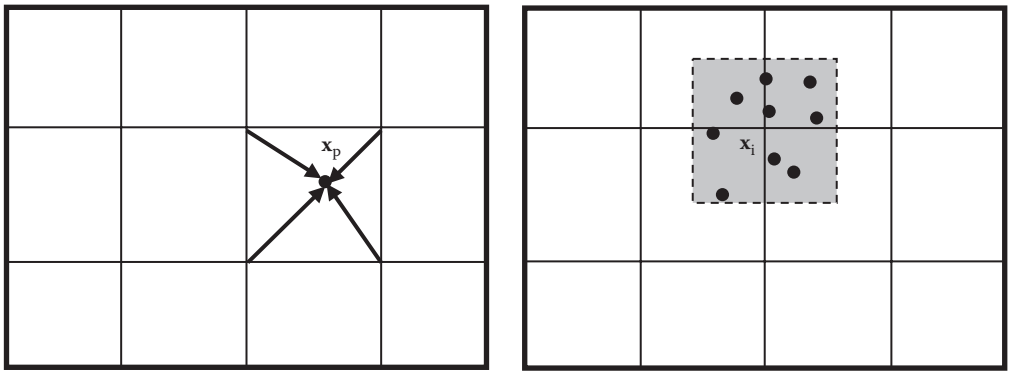
To predict particle concentration with a Lagrangian particle approach, the distribution of discrete particle positions must be translated into discrete volume averages. This can be accomplished by averaging all the respective particle volumes ($V_{p,j}$) whose centroids are within a discrete cell volume (V_Δ). Denoting this sum of particles in a cell as $N_{p\Delta}$, the particle number density (n_p) and particle volumetric fraction (ϕ_d) can be given as

$$n_p = \frac{N_{p\Delta}}{V_\Delta} \tag{2.14}$$

$$\phi_d = \frac{1}{V_\Delta}\sum_{j=1}^{N_{pD}} \forall_{p,j} = \frac{N_{p\Delta}\langle V_p \rangle}{V_\Delta} \tag{2.15}$$

The RHS of Equation 2.15 uses angled brackets, that is, <..>, to indicate a cell-based ensemble average. This cell-based ensemble averaging is illustrated in Figure 2.2b, and similar equations can convert Lagrangian particle velocities and temperatures to cell-averaged Eulerian particle velocities and temperatures. To ensure that ϕ_d can vary spatially as a continuum, the mixed-fluid volume should encompass many particles so that the concentration is continuously differentiable in space, that is,

$$N_{p,\Delta} \gg 1 \quad \text{for a well-posed continuum particle concentration} \tag{2.16}$$



(a) Interpolate $\mathbf{u}_{@p}$ at particle location (b) Collect ϕ_d for cell volume associated with a node

Figure 2.2

Schematic of Lagrangian point-force particles in a 2D Eulerian continuous-phase grid showing (a) interpolation of fluid velocity of the surrounding nodes to the particle position at $\mathbf{x}_p$ and (b) summation of particle volumes in a computational volume to compute volume fraction associated with a node $\mathbf{x}_i$.

If a continuum of particle concentration is not required, a more relaxed discrete concentration requirement can be imposed specifying that $\phi_d < 1$. Using the particle diameter (d) and assuming an isotropic grid ($\Delta x = \Delta y = \Delta z$), this inequality can be roughly expressed as

$$d < \Delta x \quad \text{for a well-posed discrete particle concentration} \tag{2.17}$$

If the grid is anisotropic, the RHS of this inequality can be replaced with grid length scale, for example, $(\Delta x \Delta y \Delta z)^{1/3}$ or the minimum of the three grid scales. This criterion ensures that the interpolation used in Equation 2.13 is reasonable assuming that the flow gradients within a given computational cell are small. Thus, the particle size is limited for a given discretization of the continuous phase. Approaches not bound by this constraint will be discussed in Section 2.1.3.

If the number of physical particles is very high (e.g., hundreds of particles per computation cell), it may be impossible or inconvenient to track all of the particles with individual Lagrangian ODEs. An alternative approach is to use representative Lagrangian particles called "parcels." These representative particle groups are essentially a small cloud of particles that are all modeled with the same Lagrangian trajectory and are also sometimes called "computational particles" or "superparticles." If we denote N_{pP} as the number of physical particles in a parcel and $N_{P\Delta}$ as the number of parcels in a cell, the particle concentration can be evaluated as

$$\phi_d = \frac{1}{V_\Delta}\sum_{j=1}^{N_{P\Delta}} N_{pP,j} V_{p,j} = \frac{N_{P\Delta}\left\langle N_{pP} V_p \right\rangle}{V_\Delta} \tag{2.18}$$

Further denoting $\mathbf{v}_P$ as the velocity of the parcel, the corresponding ODEs for the trajectory and momentum are given as

$$N_{pP}\left(\frac{d\mathbf{x}_P}{dt}\right) = N_{pP}\mathbf{v}_P \tag{2.19}$$

$$N_{pP} m_p \left(\frac{d\mathbf{v}_P}{dt}\right) = N_{pP}\left(\mathbf{F}_{body} + \mathbf{F}_{sur} + \mathbf{F}_{coll}\right) \tag{2.20}$$

$$\frac{N_{pP} dm_p}{dt} = N_{pP}\dot{m}_p \tag{2.21}$$

In this expression, all the particles in a parcel are assumed to have the same properties (i.e., diameter, temperature, and mass). If there is no mass transfer, breakup, or coalescence, the number of particles per parcel will be constant along its trajectory. In this case, the aforementioned trajectory and momentum equations for a single parcel are the same as those for a single particle (i.e., Equations 2.19 through 2.21 normalized by N_{pP} is the same as Equations 2.1 through 2.4). Thus, the parcel approach is much more computationally efficient as the number of equations reduces as the number of particles per parcel increases, for example, $N_{pP} = 100$ allows the number of computed trajectories to be reduced 100-fold. This is the key benefit of the parcel approach. However, there is an upper limit to how many particles per parcel can be used. In particular, if the parcel cloud is too large, there can be a substantial variation of continuous-phase flow variables across its length so that Equations 2.13 and 2.18 are not reasonable.

The parcel cloud volume (V_p) is the mixed-fluid volume occupied by the particles and the surrounding fluid. If the particle and surrounding fluid are both incompressible and there is no loss of particles (N_{pP} remains constant), the parcel "cloud" volume will stay fixed along its trajectory and be initialized based on the initial particle concentration prescription ($\phi_{d,inj}$)

$$V_P \equiv \text{volume occupied by particles and fluid for a parcel} = \frac{V_p N_{pP}}{\phi_{d,inj}} \tag{2.22}$$

To ensure that particles associated with a parcel will, on average, be physically within the computational cell (to be consistent with Equation 2.18), the parcel cloud volume should be smaller than the host computational cell volume, that is,

$$V_P < V_\Delta \quad \text{for a well-posed continuum particle concentration} \tag{2.23}$$

If particle concentration is needed, this criterion (combined Equation 2.22) places an upper bound on the number of particles per parcel (N_{pP}) at the point of injection as well as anywhere the parcel will travel.

2.1.1.2 Eulerian Approach for the Dispersed Phase

2.1.1.2.1 Eulerian Dispersed-Phase Equations of Motion In the Eulerian approach, the particle concentration and momentum are solved with transport equations in a manner similar to the density and momentum for the continuous phase. To allow this, we assume that the particle concentration (n_p or ϕ_d) can be described as a continuum (the requirements for this will be discussed later). Based on this assumption, the conservation equations for the Eulerian dispersed-phase mass, momentum, and energy can be derived. For continuity, the rate of mass change in a control volume is equal to the mass flux through its boundaries and any mass source term within the control volume. Written in PDE form and ignoring particle collisions, the governing equations for particle mass, momentum, and energy (per unit volume of the mixed-volume fluid) can be obtained in conservative form (Crowe et al., 1998) as

$$\frac{\partial\left(m_p n_p\right)}{\partial t} + \nabla\left(m_p n_p \mathbf{v}\right) = n_p \dot{m}_p \tag{2.24}$$

$$\frac{\partial\left(m_p n_p \mathbf{v}\right)}{\partial t} + \nabla\cdot\left(m_p n_p \mathbf{v}\mathbf{v}\right) = n_p\left(\mathbf{F}_{body} + \mathbf{F}_{sur} + \dot{m}_p \mathbf{v}\right) \tag{2.25}$$

$$\frac{\partial\left(m_p n_p e_p\right)}{\partial t} + \nabla\left(m_p n_p e_p \mathbf{v}\right) = n_p\left[\dot{Q}_p + \dot{m}_p h_{phase} + \dot{m}_p e_p\right] \tag{2.26}$$

Note the conservative form results in a RHS mass transfer term for the momentum and energy equations. These Eulerian equations can be rewritten in terms of particle volume fraction as

$$\frac{\partial\left(\phi_d \rho_p\right)}{\partial t} + \nabla\left(\phi_d \rho_p \mathbf{v}\right) = \frac{\phi_d}{V_p}\dot{m}_p \tag{2.27}$$

$$\frac{\partial\left(\phi_d \rho_p \mathbf{v}\right)}{\partial t} + \nabla\cdot\left(\phi_d \rho_p \mathbf{v}\mathbf{v}\right) = \frac{\phi_d}{V_p}\left(\mathbf{F}_{body} + \mathbf{F}_{sur} + \dot{m}_p \mathbf{v}\right) \tag{2.28}$$

$$\frac{\partial\left(\phi_d \rho_p e_p\right)}{\partial t} + \nabla\left(\phi_d \rho_p e_p \mathbf{v}\right) = \frac{\phi_d}{V_p}\left[\dot{Q}_p + \dot{m}_p\left(h_{phase} + e_p\right)\right] \tag{2.29}$$

The RHS values for these equations are given by Equations 2.5 through 2.8.

Once the Eulerian conservation equations are discretized, each (cell-averaged) node in the computational domain will include cell-averaged particle-phase variables. When coupled with an Eulerian representation of the continuous phase, this overall multiphase treatment is termed the "Eulerian–Eulerian" or "two-fluid" approach. Importantly, this approach allows the dispersed-phase PDEs to be treated with the same discretization techniques as used for the continuous-phase PDEs. It also conveniently allows the same grid for both phases so that the grid resolution is equivalent ($\Delta x_f = \Delta x_p$). Because of this, the average interphase coupling terms are treated in the same manner for both phases so that Eulerian–Eulerian approaches are especially efficient and accurate when two-way coupling effects are present (to be discussed in Section 2.1.1.2.2).

2.1.1.2.2 Dispersed-Phase Continuum Approximation A formal derivation of the Eulerian dispersed-phase equations requires careful consideration of the spatial and temporal averaging limits and the assumption of small but finite particle size. As such, the reader is particularly referred to details given by Drew (1983), Zhang and Prosperetti (1994), Crowe et al. (1998), and Prosperetti (2007). There are subtle differences among these derivations in these sources that are particular to different assumptions. However, a key tenant for the Eulerian description of the dispersed phase is that the particle properties (such as concentration, velocity, or temperature) can be approximated as a continuum at the grid scale. This is generally known as the "particle-phase continuum" assumption (Drew and Passman, 1999) and requires that changes in grid cell position or further refinements in grid cell do not fundamentally alter the predicted particle concentration distribution.

The particle-phase continuum assumption is related to the number of physical particles per computational cell ($N_{p\Delta}$). To demonstrate this, consider two neighboring control volumes with a particle concentration defined as $n_{p,i}$ and $n_{p,i+1}$ as shown in Figure 2.3a. In this case, one may apply a Taylor series expansion to express the number concentration at node i + 1 in terms of the value and gradients at node i + 1/2 using a forward shift ($\Delta x/2$) as

$$n_{p,i+1} = n_{p,i+1/2} + \frac{\Delta x}{2}\left(\frac{\partial n_p}{\partial x}\right)_{i+1/2} + \frac{1}{2!}\left(\frac{\Delta x}{2}\right)^2\left(\frac{\partial^2 n_p}{\partial x^2}\right)_{i+1/2} + O(\Delta x)^3 \ldots \tag{2.30}$$

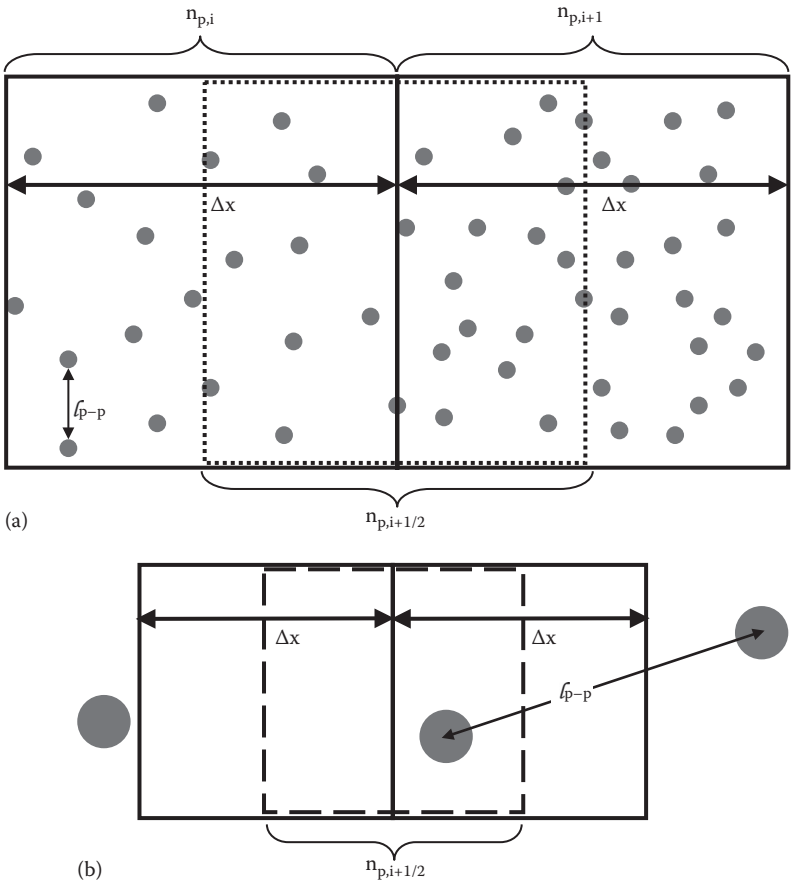


Figure 2.3

Two-dimensional Eulerian grid that contains discrete particles in adjoining computational control volumes: (a) $N_{p,\Delta} \gg 1$ allowing a continuum approximation and (b) $N_{p,\Delta} \sim 1$ so that a continuum approximation is *not* appropriate.

The last term on the RHS term corresponds to all terms of Δx^2 or higher. Comparing this result to a similar expansion for $n_{p,i}$ but with a backward shift ($-\Delta x/2$) yields

$$\left(\frac{\partial n_p}{\partial x}\right)_{i+1/2} = \frac{n_{p,i+1} - n_{p,i}}{\Delta x} + O\left(\Delta x\right)^2 \tag{2.31}$$

By dropping the second RHS term (which corresponds to terms of order Δx^2 or higher), we obtain a second-order finite difference expression. Such expressions can be used to discretize the spatial gradients for the Eulerian approach, for example, Equations 2.24 through 2.26. If the computational cell volume contains many particles as shown in Figure 2.3a, the number density will vary smoothly between cells and will not depend significantly on the exact volume position, that is, it will be continuously differentiable. A much different result arises if $N_{p\Delta}$ is no longer large. In this case, the grid resolution is on the order of the local interparticle spacing ($\Delta x \sim \ell_{p-p}$), which leads to discontinuities in particle concentration depending on where the grid cell is taken. For example, $n_{pi+1} = 1$ while $n_{p,i} = 0$ as in Figure 2.3b. This leads to uncertainty with respect to the spatial gradient of particle concentration. This uncertainty can be quantified for uniformly or randomly space particle positions. If the particles are uniformly spaced, the error of number density ($\mathcal{U}n_p$) is proportional to the number of particles

$$\frac{\mathcal{U}n_p}{n_p} \sim \frac{1}{N_{p\Delta}} \tag{2.32}$$

Thus, 10 particles are needed to achieve 10% accuracy. For a random Gaussian distribution of particle positions, the error is proportional to the square root of the sample size

$$\frac{\mathcal{U}n_p}{n_p} \sim \frac{1}{\sqrt{N_{p\Delta}}} \tag{2.33}$$

Thus, 100 particles per cell are needed for an uncertainty of 10%. In either case, if $N_{p\Delta}$ is order unity, the error in n_p will be on the order of 100% as shown in Figure 2.3b.

Therefore, a large number of particles per cell are needed for an accurate instantaneous Eulerian representation of n_p or ϕ_d, that is,

$$N_{p\Delta} \gg 1 \quad \text{for approximate Eulerian particle concentration “continuum”} \tag{2.34}$$

Thus, 10 or more particles in a cell are a practical lower bound for this approximation. Concentration continuum can be more rigorously specified by stating that the grid spacing should be much larger than the particle–particle spacing, that is,

$$\Delta x \gg \ell_{p-p} \quad \text{for an Eulerian particle concentration “continuum”} \tag{2.35}$$

This requirement reflects a lower bound for the computational grid size for which the concentration and its gradients are well defined.

In a sense, the requirement of Equation 2.35 is similar to the continuum assumption for a single-phase flow that requires a large number of molecules within a fluid control volume, that is,

$$\Delta x \gg \ell_{f-f} \quad \text{for a fluid “continuum” on an Eulerian grid} \tag{2.36}$$

Since the mean free path for most fluids is extremely small (e.g., on the order of nanometers), the requirement of Equation 2.36 is readily met for most CFD grids while that of Equation 2.35 is more conservative and more likely to be constraining.

It should be noted that the continuum approximation constraint for instantaneous concentration (Equation 2.35) may be relaxed if just the *mean* or properties are of interest. For example, consider the time-averaged number density obtained from an unsteady simulation over a number of time steps ($N_{\Delta t}$) as

$$\bar{n}_p = \frac{\bar{N}_{p\Delta}}{V_\Delta} = \frac{1}{V_\Delta N_{\Delta t}} \sum_{k=0}^{N_{\Delta t}} N_{p\Delta}(t_o + k\Delta t) \tag{2.37}$$

If the total number of particles considered all times (the summation on the RHS) is large, then $\bar{n}_p$ can be considered as a continuum in the mean sense, even if $N_{p\Delta}$ at a given instant is small or even zero. For example, a mean can be based on 0.1 particles in a cell (equivalent to a 10% probability that one particle is in the cell at any given time). Similar reasoning can be used if a time-averaged Reynolds-averaged Navier–Stokes approach is employed. As such, the uncertainty of Equation 2.33 only arises if one wishes to convert this probability into an instantaneous realization. Using a time average such as this allows the constraints of Equations 2.18 and 2.34 to be relaxed, but the continuum approximation still requires that the cell volume be well posed (Equation 2.17) so that

$$d < \Delta x \quad \text{for a mean particle concentration "continuum"} \tag{2.38}$$

This more relaxed criterion allows a smaller computational grid size as compared to Equation 2.35.

2.1.1.3 Eulerian Approach for the Continuous Phase

For two-way and three-way coupling, the continuous-phase mass, momentum, and energy must incorporate interphase transfer of mass, momentum, and energy interphase to the particles as sinks into the single-phase equations. In particular, these conservation equations must also take into account that the continuous-phase mass only occupies part of the mixed-fluid volume, for example, the continuous-phase fluid mass per mixed-fluid volume is $(1 - \phi_d)\rho_f$. Application of the Reynolds transport theorem to this quantity yields the continuous-phase continuity equation, where the interphase mass transfer is included as a sink term

$$\frac{\partial\left[(1-\phi_d)\rho_f\right]}{\partial t} + \nabla\left[(1-\phi_d)\rho_f \mathbf{u}\right] = -\frac{\phi_d}{V_p}\dot{m}_p \tag{2.39}$$

The RHS is thus equal and opposite to the source term used for the particle-phase Eulerian transport of Equations 2.27 through 2.29.

2.1.1.3.1 Continuous-Phase Momentum Conservation with Two-Way Coupling The same principle applied to mass conservation for Equation 2.39 can be applied to the continuous-phase momentum by defining the interphase force ($\mathbf{F}_{int}$) as the interphase momentum transfer from the continuous fluid to a single particle. This force is equal but opposite to the force that a particle exerts on the fluid ($-\mathbf{F}_{int}$), which is the sink term for continuous-phase equation. However, the fluid stress acts on a volume regardless of whether the volume is occupied by a particle or by fluid element. As such, it is not part of the interphase force, which can then be written as

$$\mathbf{F}_{int} = \mathbf{F}_{surf} - V_p\left(-\nabla p + \nabla \cdot \tau_{ij}\right) \tag{2.40}$$

$$\tau_{ij} = \mu_f\left(\frac{\partial u_i}{\partial x_j} + \frac{\partial u_j}{\partial x_i} - \frac{2}{3}\delta_{ij}\nabla \cdot \mathbf{u}\right) \tag{2.41}$$

The fluid stress term on the RHS of Equation 2.30 is the sum of the pressure gradient and that of the viscous stress. A rigorous derivation and discussion of the term is given by Prosperetti (2007).

Applying the Reynolds transport theorem to describe the change in continuous-phase momentum per unit volume yields

$$\frac{\partial\left[(1-\phi_d)\rho_f \mathbf{u}\right]}{\partial t} + \nabla \cdot \left[(1-\phi_d)\rho_f \mathbf{u}\mathbf{u}\right] = (1-\phi_d)\rho_f \mathbf{g} + (1-\phi_d)\left[\nabla \cdot \tau_{ij} - \nabla p\right] - \frac{\phi_d}{V_p}\left(\mathbf{F}_{int} + \dot{m}_p \mathbf{v}\right) \tag{2.42}$$

The first and second terms on the RHS are the body and fluid stress forces applied to the continuous-phase mass per unit volume, while the third term stems from Equations 2.40 and 2.41.

A coupled continuous-phase energy equation can be similarly obtained by employing the same assumptions used for particle energy transport (Equations 2.9 through 2.12) and by neglecting effects associated with particle volume or shape changes

$$\frac{\partial\left[(1-\phi_d)\rho_f e_{tot}\right]}{\partial t}+\nabla\left[(1-\phi_d)\rho_f e_{tot}\mathbf{u}\right]=(1-\phi_d)\rho_f\mathbf{u}\cdot\mathbf{g}-\frac{\phi_d}{V_p}\left(\mathbf{F}_{int}\cdot\mathbf{v}\right)$$
$$+\frac{\partial\left[(1-\phi_d)\tau_{ij}u_i\right]}{\partial x_j}-\nabla\cdot\left[(1-\phi_d)p\mathbf{u}\right]+\tau_{ij}\frac{\partial\left(\phi_d v_i\right)}{\partial x_j}-p\nabla\cdot\left(\phi_d\mathbf{v}\right)$$
$$-\frac{\phi_d}{V_p}\left[\dot{Q}_p+\dot{m}_p\left(h_{phase}+e_p\right)+\left(\dot{m}_p\mathbf{v}\cdot\mathbf{v}\right)\right]+\nabla\cdot\left[k_{eff}\nabla T\right] \tag{2.43}$$

The LHS terms on the first line include the Eulerian and convective changes in the total fluid energy, while the RHS terms on this first line include the work associated with moving the fluid against the body force and against the particle interphase force. The RHS terms on the second line include work against the fluid stress forces, while those on the third line arise from heat and mass transfer as well as the thermal diffusion within the continuous-phase volume. The thermal diffusion is based on an effective conductivity (k_{eff}), typically taken to be the mixed-fluid conductivity (k_m). This mixed-fluid conductivity is based on the volume fraction weighted values from the particles and from the continuous phase:

$$k_{eff}\approx k_m\equiv\phi_d k_p+(1-\phi_d)k_f \tag{2.44}$$

This approximation is appropriate if the particles have a small thermal response time compared to the timescale of temperature changes in the fluid. On the other hand, a very long particle thermal response time will limit the thermal diffusivity to only that conducted through the continuous phase, that is, $k_{eff}\rightarrow(1-\phi_d)k_f$. Since the differences in thermal conductivities for most substances do not vary widely, the difference between these two limits is small for most dispersed flows ($\phi_d < 10\%$). As such, Equation 2.44 is both common and generally reasonable (Crowe et al., 1998, Elghobashi, 2006).

Finally, the terms in the third line include interphase energy coupling due to heat and mass transfer, the kinetic energy losses due to generation of particle mass, and the work required to move the particles based on interphase force and fluid stress force. A more detailed derivation and accounting of these terms is given by Crowe et al. (1998).

2.1.1.3.2 Influence of Dispersed-Phase Reference Frame The Eulerian transport equation given earlier for the continuous phase can be paired with dispersed-phase equations in the form of either the Lagrangian ODEs or Eulerian PDEs. In both cases, the key is determining the cell-averaged volume fraction at the continuous-phase nodes. If the particles are treated with an Eulerian approach, the interphase coupling terms can be obtained directly via the particle concentration predicted from Equations 2.27 through 2.29. For example, the interphase force per unit volume evaluated at the fluid node i is simply

$$\left(\frac{\phi_d}{V_p}\mathbf{F}_{int}\right)_i=\frac{\phi_d\left(\mathbf{x}_i,t\right)\mathbf{F}_{int}\left(\mathbf{x}_i,t\right)}{V_{p,i}} \tag{2.45}$$

This Eulerian–Eulerian formulation is numerically convenient since communication of data between the phases occurs at coincident node locations so that there is no interpolation error.

For Lagrangian particles, the coupling to a continuous-phase node can be computed based on the computational volumes associated with the nodes as shown in Figure 2.2b. For example, the interphase force coupling term for particle and parcel approaches can be given as

$$\left(\frac{\phi_d}{V_p}\mathbf{F}_{int}\right)_i=\frac{1}{V_{\Delta,i}}\sum_{j=1}^{N_{p\Delta}}\mathbf{F}_{int,j}=\frac{1}{V_{\Delta,i}}\sum_{j=1}^{N_{p\Delta}}N_{pP,j}\mathbf{F}_{int,j} \tag{2.46}$$

In this expression, $V_{\Delta,i}$ is the volume associated with node $\mathbf{x}_i$ that contains $N_{p\Delta}$ number of particles per cell if individual trajectories are followed or (as given by the RHS) contains $N_{p\Delta}$ parcels per cell with N_{pP} particles per parcel. To ensure that the coupling to the continuous phase can be described as a continuum, the constraint of Equation 5.14 must be placed on the number of Lagrangian particles or a similar constraint based on the number of parcels as

$$N_{p\Delta} \gg 1 \quad \text{for Lagrangian parcels with two-way or three-way coupling} \tag{2.47}$$

For example, four or more particles or parcels per element are typically needed for accurate two-way coupling. As a result, the Eulerian–Lagrangian approach can be an order of magnitude less efficient for two-way coupling as compared to the Eulerian–Eulerian approach (Druzhinin and Elghobashi, 1998, 1999).

2.1.2 Classification by Relative Velocity Magnitude

There is a second type of classification that is based on increasing particle relative velocity and includes mixed-fluid, weakly separated, and separated-fluid treatments. The separated-fluid treatment generally assumes that the continuous phase and dispersed phase have distinct transport equations and is described earlier for the Eulerian–Lagrangian approach and the Eulerian–Eulerian approach. The separated-fluid approach places no restriction on the magnitude of the relative velocity but can require significant computation to compute the associated surface forces. In contrast, the mixed-fluid approach assumes that the relative velocity be negligible compared to the fluid velocity ($w/u \to 0$). Finally, the weakly separated approach is intermediate to the other two approaches as it assumes a small but finite relative velocity ($w/u \ll 1$). These mixed-fluid and weakly separated approaches are discussed later and are advantageous to use when the test conditions are appropriate because they generally only require one momentum PDE for both phases.

2.1.2.1 Mixed-Fluid Approach

The mixed-fluid approximation assumes that the dispersed phase and the continuous phase are in local kinetic and thermal equilibrium, that is, the relative velocities and temperatures between the two phases are negligible in comparison to variations of the overall flow field

$$\frac{w}{u} \to 0 \tag{2.48}$$

for kinetic and thermal equilibrium assumption

$$\frac{(T_p - T)}{T_p} \to 0 \tag{2.49}$$

Using these assumptions, the mixed-fluid values are set equal to the respective continuous phase and particle values at the centroid locations for the mixed-fluid approach, that is,

$$\mathbf{u}_m(\mathbf{x},t) \equiv \left[\mathbf{u}_{@p}(\mathbf{x},t) = \mathbf{v}(\mathbf{x},t)\right] \tag{2.50}$$

mixed-fluid treatment

$$T_m(\mathbf{x},t) \equiv \left[T(\mathbf{x},t) = T_p(\mathbf{x},t)\right] \tag{2.51}$$

This is equivalent to assuming negligible momentum and thermal inertias (zero response times), which is consistent with particles for which all the relevant Stokes numbers are much less than unity, for example, $St_D \ll 1$ for the macroscopic flow or $St_\lambda \ll 1$ for turbulent flow. Therefore, the mixed-fluid approach is only reasonable for very small particles (equivalent to an *immiscible* mixture distributed throughout a domain). Since the velocities and temperatures of both phases are now assumed to be represented by single values, this mixed-fluid approach has also been termed the *locally homogeneous flow* approach (Faeth, 1987), the *single-fluid scalar transport* approach, and the *modified-density* approach.

Since both phases move at the same velocity, the overall mixture can be described to have a mixed-fluid density that is simply the mass of all phases per unit volume and can be related to the volume fraction as

$$\rho_m \equiv \rho_p \phi_d + \rho_f (1 - \phi_d) \tag{2.52}$$

As a result, the mixed-fluid approximation results in a single set of conservation equations for the flow mixture (as opposed to one set for the continuous phase and one set of the dispersed phase). In particular, the transport of mass, momentum, and energy can be obtained by applying Equations 2.50 and 2.51 to both the Eulerian dispersed-phase and continuous-phase equations and then summing the two sets of equations together

$$\frac{\partial \rho_m}{\partial t} + \nabla\left(\rho_m \mathbf{u}_m\right) = 0 \tag{2.53}$$

$$\frac{\partial\left(\rho_m \mathbf{u}_m\right)}{\partial t} + \nabla \cdot \left(\rho_m \mathbf{u}\mathbf{u}\right) = \rho_m \mathbf{g} - \nabla p + \nabla \cdot \tau_{m,ij} \tag{2.54}$$

$$\frac{\partial\left(\rho_m e_m\right)}{\partial t} + \nabla\left(\rho_m e_m \mathbf{u}\right) = \left(\tau_{m,ij} - p\delta_{ij}\right)\frac{\partial u_{m,i}}{\partial x_j} + \nabla \cdot \left(k_m \nabla T_m\right) \tag{2.55}$$

The second and third equations include a mixed-fluid viscous stress tensor ($\tau_{m,ij}$) that can be written in terms of a mixed-fluid viscosity

$$\tau_{m,ij} = \mu_m\left(\frac{\partial u_{m,i}}{\partial x_j} + \frac{\partial u_{m,j}}{\partial x_i} - \frac{2}{3}\delta_{ij}\nabla \cdot \mathbf{u}_m\right) \tag{2.56}$$

A key benefit for this approach is that the relative velocity and momentum ODE need not be employed (the same is true for the relative particle temperature and energy transfer ODE). Thus, the presence of the particle is only realized through the modification of the mixture density (ρ_m).

These aspect differences between the mixed-fluid and separated-fluid approaches are illustrated in Figure 2.4. Some key aspects of the mixed-fluid approach are especially relevant. First, the mixed-fluid set of equations is inherently a two-way coupled system since all phases act in concert and collision effects are ignored since **u** = **v**. Second, a single set of equations (without interphase momentum and energy transfer formulations) allows significant numerical simplicity, which should be used whenever appropriate (Equations 2.48 and 2.49). Third, the mixed-fluid approach generally uses the Eulerian reference frame for both phases, that is, an Eulerian–Eulerian approach. Figure 2.4 shows that the mixed-fluid method and the separated-fluid method are quite different. However, there is an intermediate method, as described later, which retains some of the features of each of these two distinct approaches.

2.1.2.2 Weakly Separated Approach

A hybrid approach between that of separated flow and mixed-fluid flow is the weakly separated approach or also called the "partially mixed" method. This approach is useful to describe motion of small particles whose dynamics are primarily controlled by the surrounding flow but which have a small but significant settling velocity. The simplest and most common version of the weakly separated method assumes that the particle relative acceleration is negligible in comparison to the fluid acceleration. This assumption allows a finite relative velocity that can be approximated by the terminal velocity

$$\mathbf{v}(\mathbf{x},t) = \mathbf{u}_{@p}(\mathbf{x},t) + \mathbf{w}_{term} \tag{2.57}$$

This is also called the "terminal velocity" approach and can be used for flows with slow sedimentation or rise. If the particle is considered to be in thermal equilibrium $T_p = T$, the dispersed phase only requires a mass transport equation given by either the Eulerian particle concentration PDE or a Lagrangian position ODE

$$\frac{\partial\left(\phi_d \rho_p\right)}{\partial t} + \nabla\left[\phi_d \rho_p\left(\mathbf{u}_{@p} + \mathbf{w}_{term}\right)\right] = \frac{\phi_d}{V_p}\dot{m}_p \tag{2.58}$$

$$\frac{d\left(\mathbf{x}_p\right)}{dt} = \mathbf{u}_{@p} + \mathbf{w}_{term} \tag{2.59}$$

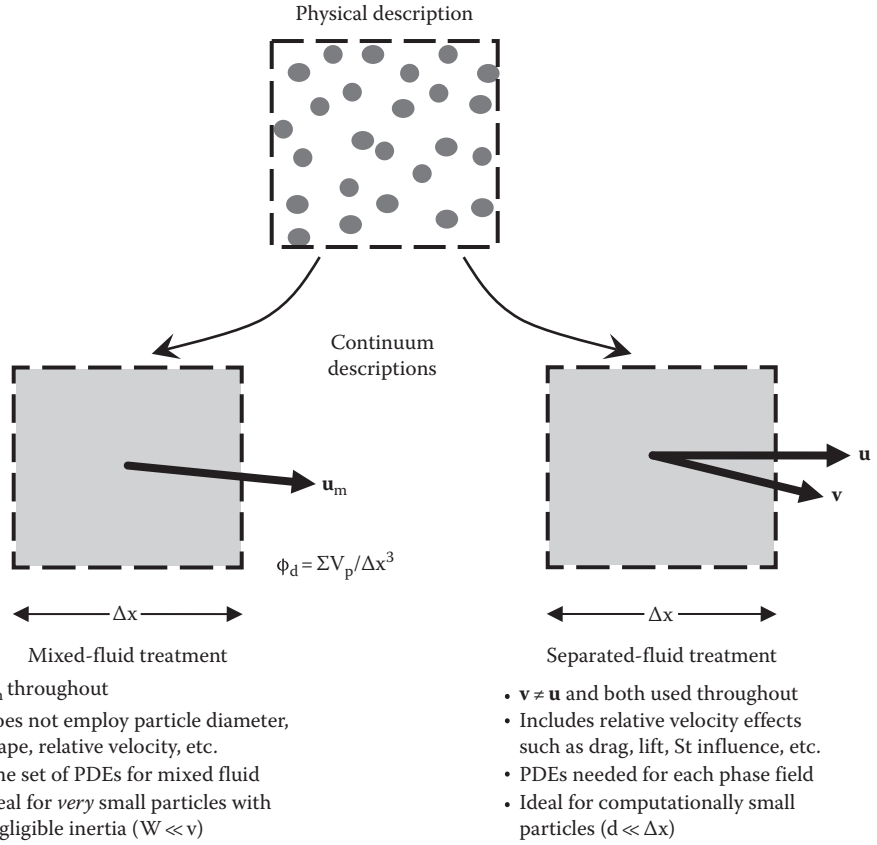


Figure 2.4

Comparison of mixed-fluid and separated-fluid treatments for a computational cell based on an Eulerian–Eulerian approach.

Thus, Equation 2.57 effectively serves as the momentum equation for the particles. This method is thus nearly as efficient as the mixed-fluid method but captures mean relative velocity effects. However, this approach cannot capture any effects associated with an initial particle velocity or due to a collision with a wall or another particle.

2.1.3 Classification by Particle Size Relative to Grid Size

As discussed earlier, there are three main approaches for multiphase numerical treatments based on particle size: point force, distributed force, and resolved surface. The choice is related to the capability in predicting the surface forces acting on the particle ($\mathbf{F}_{surf}$), which is needed for the separated-fluid treatment as discussed earlier. These forces are also needed if two-way and three-way coupling effects are to be included for the continuous-phase fluid solution. In determining $\mathbf{F}_{surf}$, there are three primary approaches: the "point-force" representation for particles smaller than the grid scale ($d < \Delta x$), the "distributed-force" representation for particles on the order of the grid scale ($d \sim \Delta x$), and the "resolved-surface" representation for particles much larger than the grid scale ($d \gg \Delta x$). These are discussed in the following three subsections.

2.1.3.1 Point-Force Approach

The point force (also referred to as the "point mass" or "point volume") has the advantage of eliminating the need to simulate the detailed flow around the particle. For an Eulerian treatment of the dispersed phase, the relative velocity is defined at the grid nodes

$$\mathbf{w}(\mathbf{x}_i, t) = \mathbf{v}(\mathbf{x}_i, t) - \mathbf{u}(\mathbf{x}_i, t) \tag{2.60}$$

Once the unhindered flow characteristics are known, a point-force equation can be used to describe the surface forces based on a linear combination of drag, lift, added mass, history, fluid stress, and so on. The fluid dynamic forces on the particle can be obtained with empirical or theoretical treatments.

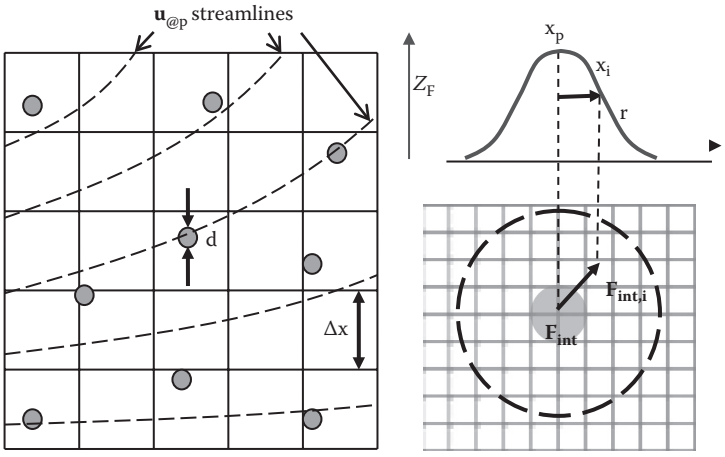


Figure 2.5

Different representations for particle treatment based on particle size in relation to continuous-fluid grid resolution for (a) a point-force representation and (b) a distributed-force representation.

The continuous-phase characteristics in either case do not include the fluid disturbances associated with individual particles. This indicates that the particle should be smaller than the length scales associated with continuous-phase gradients. Since this is also true for the discretization of the continuous phase, it yields a size criterion based on computational resolution

$$d < \Delta x \quad \text{for point force with one-way coupling} \tag{2.61}$$

A more rigorous criterion would be $d \ll \Delta x$ (Figure 2.5a) such that the particle will see only very weak continuous-fluid gradients over the length scale associated with its diameter. Since the continuous-phase computational resolution must be small enough to provide grid-independent results, the point-force technique is limited to particles that are smaller than any spatial features to be resolved in the computational domain. For example, a direct numerical simaultion (DNS) description of turbulent flow requires that the particle diameter be smaller than the friction length scale if in the laminar sublayer ($d^+ < 1$) or less than the Kolmogorov turbulent microscale ($d < \lambda$) if in the outer portion or above the boundary layer.

2.1.3.2 Distributed-Force Approach

The distributed-force technique is employed when the particle diameter is on the order of the spatial resolution of the continuous phase, that is,

$$d \sim \Delta x \quad \text{for distributed-force treatment} \tag{2.62}$$

In this case, the variations in the flow properties in the region of the particle should be considered since the fluid interactions between the two phases occur over distances extending several particle diameters. As such, the coupling should extend over a region larger than a single grid cell (Figure 2.5b). To include the surface force on the particle, there are two distributed-force methods: "spatially averaged" and "semiresolved." The spatially averaged approach approximates the unhindered conditions (e.g., $\mathbf{u}_{@p}$) by surface and volume averages in the vicinity of the particle as opposed to using a single interpolated point at the centroid. This approach is generally limited to $d < 3\Delta x$ without two-way coupling but $d < \Delta x$ with two-way coupling.

In contrast, the semiresolved approach directly integrates two-way coupling effects and thus allows for larger particles (or finer resolutions) based on $3\Delta x < d < 10\Delta x$. Note that both techniques share a similar approach for distributing the interphase force on the fluid.

For two-way coupling, there are many variants of the distributed-force technique. To impart $\mathbf{F}_{int}$ over a region (instead of at a point), a force distribution function ($\mathcal{Z}_F$) can be used about the vicinity of the particle as illustrated in Figure 2.5b. Similar distributions can be applied for mass and heat transfer. The distributed-force technique is thus a hybrid between the point-force approach and the resolved-surface approach, the latter of which is discussed later.

2.1.3.3 Resolved-Surface Approach

For very large particles, the resolved-surface approach can be used if the detailed local flow over the particle surface is numerically discretized and computed. This approach resolves the fluid surface stresses so that they may be computationally integrated to compute the resulting fluid dynamic forces on the particle. This method is also called the "full DNS" approach and requires the computational resolution to sufficiently describe the detailed stress distribution over the particle surface, for example,

$$d \gg \Delta x \quad \text{for resolved-surface treatment} \tag{2.63}$$

This criterion requires many fluid nodes per individual particle, for example, hundreds or thousands depending on the particle geometry, Reynolds number, and so on. As such, this technique is only reasonable when there are few particles in the computational domain. However, this technique has the advantage of allowing complex particle geometries and incorporating detailed nonlinear flow fields around the particles (Figure 2.6).

Since the surface force is obtained from the surrounding flow, it does not require any force decomposition in terms of lift, drag, added mass, history, fluid stress, and so on since all these effects are directly incorporated by the discrete surface integration. In particular, no assumptions of particle shape, particle Reynolds number, particle or flow acceleration, surface conditions, flow gradients, and so on are required for the use of this formulation. Thus, there is no need to determine $\mathbf{u}_{@p}$, and no empirical or analytical force expressions for $\mathbf{F}_{sur}$ are required. Furthermore, in the case of a fluid particle (e.g., drop or bubble), the internal fluid dynamics may also be directly simulated using internal discretization (this can be important since the recirculation can affect the surface stresses). Also note that two-way coupling, three-way coupling, and four-way coupling are automatically included in the resolved-surface approach since the interstitial fluid and contact dynamics can be fully resolved as well. As such, the resolved-surface technique is the most desirable in terms of accuracy as it allows the most physically realistic surface force method but is also the most computationally intensive approach.

There are two primary treatments for the resolved-surface method that depend on how the interface between the particle and the continuous phase is treated: the "gridded interface method" (GIM) and the "immersed interface method" (IIM). These two approaches are illustrated in Figure 2.6 (where the outward normal of the interface is $\mathbf{n}$) and are overviewed in the following sections.

2.1.3.3.1 Gridded Interface Method The GIM approach is typically used when the particle shape is simple (e.g., a sphere or an ellipsoid) so that the grid resolution over the surface is straightforward. In this case, the interface between the particle and the surrounding fluid is discontinuous, that is, infinitely thin (Figure 2.6b). The boundary condition on a solid particle surface is typically specified as *a no slip for continuum conditions*. For an uncontaminated fluid particle with significant recirculation, the particle interior should also be discretized.

Once the flow field around the particle surface is known and described by the resolved velocity and pressure ($\mathbf{U}$ and P), the surface force can be determined by numerically integrating the pressure and the continuous-phase shear stress over the discretized surface elements

$$\mathbf{F}_{sur} = \sum_{k=1}^{N_k} \left(-P\mathbf{n} + \tau_{resolved,ij} n_j \right)_k \Delta A_{p,k} \tag{2.64}$$

$$\tau_{resolved,ij} = \mu_f \left(\frac{\partial U_i}{\partial x_j} + \frac{\partial U_j}{\partial x_i} - \frac{2}{3}\delta_{ij} \nabla \cdot \mathbf{U} \right) \tag{2.65}$$

In this equation, ΔA_p is a discrete particle surface area element, while $\mathbf{U}$ and P are the resolved velocity and pressure, that is, the values on the particle surface that take into account the particle's volume and impact

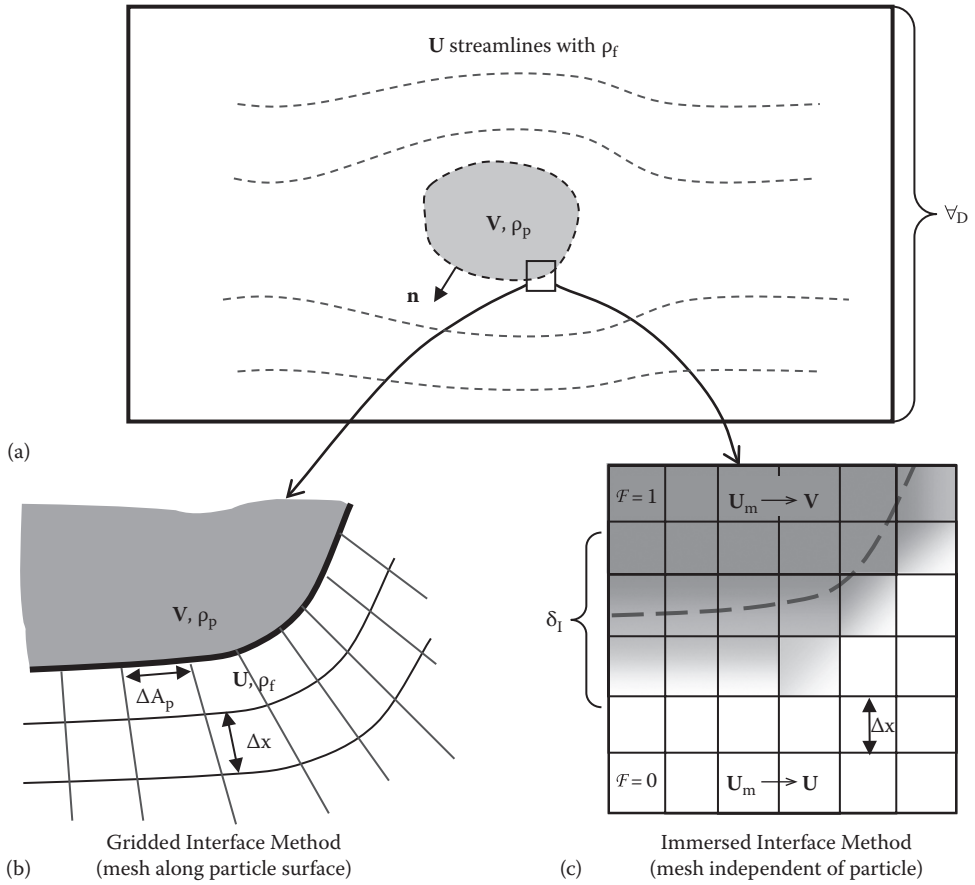


Figure 2.6

Resolved-surface approaches showing (a) schematic of particle in a computational domain along with (b) near-surface close-ups of a GIM mesh, and (c) that of an IIM mesh superimposed on the marker function distribution.

on the flow. This resolved-surface force can be combined with Equation 2.1 to move the particle to the next position with a new velocity and acceleration.

2.1.3.3.2 Immersed Interface Method The IIM is fundamentally based on a structured Eulerian grid for the computational domain that does not need to coincide with the particle surface. This allows the flow PDEs to be solved efficiently on simple Cartesian grids. A popular IIM category is the continuous interface methods that can be applied if the particle is a fluid. The approach introduces a nonphysical interface thickness (δ_I) as shown in Figure 2.6c. Instead of letting the flow properties between the particle and the surrounding fluid jump discontinuously (as is physically appropriate) across the molecularly thin interface, the CIM smoothly distribute these flow properties of velocity, density, and viscosity across a finite thickness interface that is several grid cell thick. This smooth distribution is accomplished with a "marker function" ($\mathcal{F}$) that is defined as the fraction of the computational cell occupied by particle matter. This function $\mathcal{F}$ equals 0 outside of the particle, varies smoothly from 0 to 1 across this interface, and equals 1 inside the particle. This function assumes that a computational cell volume is much smaller than the particle diameter. This function is distinct from the continuum-based volume fraction that assumes a computational volume much larger than the particle diameter. This marker function can then be used to define the "one-fluid" density that tends to the physical values outside the interface as

$$\rho = (1-\mathcal{F})\rho_f + \mathcal{F}\rho_p \tag{2.66}$$

Similarly, the velocity fields of both phases are represented by a one-fluid velocity ($\mathbf{U}_m$) that reverts to the correct physical limits outside of the interface but takes on a nonphysical (numerically convenient) value within the interface

$$\mathcal{F} = 0 \quad \mathbf{U}_m \rightarrow \mathbf{U} \text{ (outside of the particle)} \tag{2.67}$$

$$0 < \mathcal{F} < 1 \quad \mathbf{U}_m \rightarrow \mathbf{V}_I \text{ (within particle interface)} \tag{2.68}$$

$$\mathcal{F} = 1 \quad \mathbf{U}_m \rightarrow \mathbf{V} \text{ (inside of the particle)} \tag{2.69}$$

This formulation provides a single set of continuum PDEs for the entire domain based on $\mathbf{U}_m$ using the one-fluid density and viscosity. This allows for solutions on a simple Cartesian grid (which generally allows the fastest computation for a given number of grid points). Note that the finite interface thickness is nonphysical but is constructed to be as thin as possible while still allowing a stable continuum variation of velocity, density, and viscosity across the grid. This typically results in a prescribed thickness of 2–4 computational cells depending on the magnitude of the density ratio (although specialized sharp interface methods can reduce this thickness to one computational cell). A distinct advantage of the one-fluid approach is that the surface force of Equations 2.64 and 2.65 is satisfied (in contrast to the GIM). As such, this one-fluid approach avoids the ODEs needed to update particle velocity and rotation and complexities associated with gridding along the particle surface.

References

Crowe, C.T., Sommerfeld, M., and Tsuji, Y., *Multiphase Flows with Droplets and Particles*, CRC Press, Boca Raton, FL, 1998.

Crowe, C.T., Schwarzkopf, J.D., Sommerfeld, M., and Tsujii, T., *Multiphase Flow with Droplets and Particles,* CRC Press, 2nd edition, Taylor and Francis group, 2012.

Drew, D.A., Mathematical modeling of two-phase flow, *Ann. Rev. Fluid Mech*., 15, 261–291, 1983.

Drew, D.A. and Passman, S.L., *Theory of Multicomponents Fluids*, Springer, New York, 1999.

Druzhinin, O.A. and Elghobashi, S., Direct numerical simulations of bubble-laden turbulent flows using the two-fluid formulation, *Phys. Fluids*, 10(3), 685–697, 1998.

Druzhinin, O.A. and Elghobashi, S., On the decay rate of isotropic turbulence laden with micro-particles, *Phys. Fluids*, 11(3), 602–610, 1999.

Elghobashi, S., in C. Crowe (Ed.), Direct simulation of turbulent flows laden with dispersed particles, *Multiphase Flow Handbook*, CRC Press, Boca Raton, FL, 2006.

Faeth, G.M., Mixing, transport and combustion in sprays, *Prog. Energy Combust. Sci*., 13, 293–345, 1987.

Loth, E., Numerical approaches for motion of dispersed particles, bubbles, and droplets, *Prog. Energy Combust. Sci.,* 26, 161–223, 2000.

Michaelides, E., *Particles, Bubbles, and Droplets: Their Motion, Heat and Mass Transfer*, World Scientific Publishing, Hackensack, NJ, 2006.

Michaelides, E., *Nanofluidics – Thermodynamic and Transport Properties*, Springer, New York, 2014.

Prosperetti, A., Averaged equations for multiphase flow, in A. Prosperetti and G. Tryggvason (Eds.), *Computational Methods for Multiphase Flow*, Cambridge University Press, Cambridge, U.K., 2007.

Zhang, D.Z. and Prosperetti, A., Averaged equations for inviscid dispersed two-phase flow, *J. Fluid Mech*., 267, 185–219, 1994.

2.2 Direct Numerical Simulations of Gas–Liquid Flows

Gretar Tryggvason

An analytical solution of the equations governing multiphase flows is the ultimate reference to which experimental results and approximate models can be compared to. Unfortunately, analytical solutions for multiphase flows are few and limited to very simple systems. Solutions of the equations using numerical methods have, since the latter part of the last century, come to the rescue, and it is now possible to obtain accurate solution for a wide range of parameters, where analytical solutions, even approximate ones, cannot be found. Numerical solutions have, however, done much more than simply provide solutions where analytical

techniques do not work. It is now possible to solve the governing equations for the unsteady motion of systems that approach the complexity that was only addressable by experiments earlier. The emergence of direct numerical simulations (DNS) has changed multiphase flow research in fundamental ways, and yet, it is clear that so far we have only started to explore the full potentials of this approach. It is useful for the purpose of the present discussion to define DNS as simulations of unsteady complex flow with a large range of scales where every continuum spatial and temporal scale is fully resolved. The early computations of the Rayleigh–Taylor instability, gravity currents, and droplet splatting by the marker-and-cell (MAC) method—impressive as those were—are therefore not DNS by the present definition, since the range of length and timescales was so limited. For single-phase flows, DNS generally require the flow to be turbulent, but for multiphase flows the unsteady motion of different phases can lead to the expected range of scales.

In many industrial and natural processes, multiphase gas–liquid flows consist of one phase in the form of well-defined bubbles or drops dispersed in another continuous phase. Bubbly flows occur in boiling heat transfer, cloud cavitation, aeration and stirring of reactors in water purification and wastewater treatment plants, bubble columns and centrifuges in the chemical industry, cooling circuits of nuclear reactors, the exchange of gases and heat between the oceans and the atmosphere, and explosive volcanic eruptions, just to name a few examples. Similarly, drops are found in sprays used in atomization of liquid fuels, painting and coating, emulsions, and rain. Understanding the evolution and properties of *dispersed* flows is therefore of major technological as well as scientific interest.

For engineering applications involving a large number of bubbles and drops, computational modeling usually relies on equations that describe the average flow field. The two-fluid model, where separate equations are solved for the dispersed and the continuous phase, is the most common approach. Since no attempt is made to resolve the unsteady motion of individual particle, closure relations are necessary for the unresolved motion and the forces between the particle and the continuous phase. Closure relations are usually determined through a combination of dimensional arguments and correlation of experimental data. The situation is analogous to computations of turbulent flows using the Reynolds-averaged Navier–Stokes equations where momentum transfer due to unsteady small-scale motion must be modeled. For details of two-fluid modeling, see Drew (1983), Ishii (1975), Drew and Lahey (1993), and Zhang and Prosperetti (1994). For the turbulent motion of single-phase flows, DNS, where the unsteady Navier–Stokes equations are solved on fine enough grids to fully resolve all flow scales, have had a major impact on closure modeling. The goal of DNS of multiphase flows is similar. In addition to information about how the drift Reynolds number, velocity fluctuations, and bubble dispersion change with the properties of the system, the computations should yield insight into how bubbles and drops interact, both with each other and with the continuous phase. The simulations should show whether there is a predominant microstructure and/or interaction mode, and if the flow forms structures that are much larger than the size of the dispersed particles. Information about the microstructure is essential for the construction of models of multiphase flows and can also help to identify what approximations can be made.

In this section, we first review briefly the various numerical techniques developed for the DNS of multiphase flows and then discuss a few results, focusing mostly on disperse flows of gas bubbles in liquids. Although the focus is on simulations of complex systems with a broad range of scales, most of the methods used are applicable to much simpler systems and, indeed, the methods have been developed and tested for such problems. Thus, some references to computations of simple problems—even if they are not DNS by the definition used here—are unavoidable.

2.2.1 Simple Flows (Re = 0 and Re = ∞)

In the limit of high and low Reynolds numbers, it is sometimes possible to simplify the flow description considerably either by ignoring inertia completely (Stokes flow) or by ignoring viscous effects completely (inviscid, potential flow). Early attempts to understand the collective motion of bubbles, drops, and solid particles therefore focused on these limits. For undeformable spheres, it is, in both these limits, possible to reduce the governing equations to a system of coupled ordinary differential equations for the particle positions. For Stokes flows, several authors have examined the properties of suspensions of solid particles in shear flows (see Brady and Bossis, 1988, for a review of early work), but studies of inviscid systems are more limited. Sangani and Didwania (1993) and Smereka (1993) examined the behavior of many bubbles in periodic domains, specifying the rise velocity to prevent continuing acceleration. They observed that the bubbles tended to form horizontal "rafts," particularly when the variance of the bubble velocities was small. As this "rafting" is generally not observed experimentally, the results cast considerable doubt on the utility of the potential flow approximation for the interactions of many bubbles. This is somewhat unexpected since for single bubble this approximation is rather good (see, however, Harper, 1997) for a discussion of bubbles

rising in-line). Deformable bubbles and drops can be simulated using boundary integral techniques in both the Stokes and the inviscid limits. Several authors have examined suspensions of very viscous drops, including Li and Pozrikidis (2000) and Zhou and Pozrikidis (1993), who followed the dynamics of 2D drops in a channel, and Loewenberg and Hinch (1996) and Zinchenko and Davis (2000) have examined fully 3D drops. The boundary integral method for Stokes flow has been described in detail in the book by Pozrikidis (1992), and Pozrikidis (2001) gives a detailed summary of various applications. Unlike Stokes flow, inviscid models are generally only suitable for a transient short-time evolution since eventually viscous dissipation becomes important (see Chahine and Duraiswami, 1992, for early work). Although studies of flows in the limits of zero and infinite Reynolds number played an important role in early work on multiphase flows, their role is now much diminished, although there are situations where they constitute important limiting cases.

2.2.2 Methods for Finite Reynolds Number Flows

For intermediate Reynolds numbers, it is necessary to solve the full Navier–Stokes equations. The first method to allow computations of multifluid flows was the MAC method developed at Los Alamos by Harlow and collaborators. In Harlow and Welch (1965), the method was introduced and two sample computations of the so-called dam breaking problem shown. Several papers quickly followed: Harlow and Welch (1966) examined the Rayleigh–Taylor problem and Harlow and Shannon (1967) studied the splash when a drop hits a liquid surface. As originally implemented, the MAC method assumed a free surface, so there was only one fluid involved. This required boundary conditions to be applied at this surface and the fluid in the rest of the domain to be completely passive. The Los Alamos group quickly realized, however, that the same methodology could be applied to two-fluid problems. Daly (1969b) computed the evolution of the Rayleigh–Taylor instability for finite density ratios, and Daly and Pracht (1968) examined the initial motion of density currents. Surface tension was then added by Daly (1969a), and the method was again used to examine the Rayleigh–Taylor instability. The MAC method quickly attracted a small group of followers that used it to study several problems: Chan and Street (1970) applied it to free surface waves, Foote (1973) and Foote (1975) simulated the oscillations of an axisymmetric drop and the collision of a drop with a rigid wall, and Chapman and Plesset (1972) and Mitchell and Hammitt (1973) simulated the collapse of a cavitation bubble. Although the MAC method was designed specifically for multifluid problems (hence the M for Markers!), it was also the first method to successfully solve the Navier–Stokes equation using the primitive variables (velocity and pressure). The staggered grid used was a novelty, and today, it is common practice to refer to any method using a projection-based time integration on a staggered grid as a MAC method.

The next generation of methods for multifluid flow evolved gradually from the MAC method. It was already clear in the Harlow and Welch (1965) paper that the marker particles could cause inaccuracies, and among the number of algorithmic ideas explored by the Los Alamos group, the replacement of the particles by a marker function soon became the most popular alternative. Thus, the volume-of-fluid (VOF) method was born. VOF was first discussed in a refereed journal article by Hirt and Nichols (1981), but the method apparently originated a few years earlier. While the results were generally superior to those of the MAC method, early VOF results showed considerable irregularities at the interface between the different fluids. In the 1980s and early 1990s, better advection methods (Youngs, 1982) and new ways to find surface tension (Brackbill et al., 1992) improved the results significantly. Fairly advanced VOF methods are now available, and many commercial CFD codes include the option of simulating free surface or multiphase flows using the VOF method. For a review of VOF methods, see Scardovelli and Zaleski (1999) and Tryggvason et al. (2011). Other methods, based on similar ideas but advecting the marker function in a different way, include the level set method (reviewed by Osher and Fedkiw, 2001, and Sethian, 2001) and the CIP method of Yabe and collaborators (see Yabe et al., 2001).

While the MAC methodology and its successors were being developed, other techniques were also being explored to capture fluid interfaces. Hirt et al. (1970) describe one of the earliest use of structured boundary-fitted Lagrangian grids. This approach is particularly well suited when the interface topology is relatively simple and no unexpected interface configurations develop. In a related approach, a grid line is aligned with the fluid interface, but the grid away from the interface is generated using standard grid generation techniques such as conformal mapping or other more advanced elliptic grid generation schemes. Such a method was used by Ryskin and Leal (1984) to compute the steady rise of buoyant, deformable, axisymmetric bubbles. Ryskin and Leal assumed that the fluid inside the bubble could be neglected, but Dandy and Leal (1989) and Kang and Leal (1987) extended the method to two-fluid problems and unsteady flows. Several authors have used this approach to examine relatively simple problems such as the steady-state motion of single particles or moderate deformation of free surfaces. Fully 3D simulations are relatively rare, and it is probably fair to say that it is unlikely that this approach will be the method of choice for very complex problems such

as the 3D unsteady motion of several particles. Similar comments apply to methods based on resolving the fluid by unstructured grid that are updated to ensure that the interface coincides with a grid line.

Several hybrid methods combine the ideas discussed earlier in a variety of ways. Front tracking, where the interface is marked by connected marker points but a fixed grid is used for the fluid within each phase has been particularly successful. In the method of Tryggvason and collaborators (Unverdi and Tryggvason, 1992, Tryggvason et al., 2001), the tracked front is used to advect a smoothed marker function and to compute the surface tension. The method is therefore very similar to methods that work directly with a grid-marker function, but the advection of the interface is greatly improved. For other implementation of similar ideas, see van Sint Annaland et al. (2006), Hao and Prosperetti (2004), Hua and Lou (2007), and Muradoglu and Kayaalp (2006). Other methods have been designed to capture the interface more accurately. These include the method of Glimm and collaborators (Glimm and McBryan, 1985) where the fixed grid is modified near the front to make a grid line follow the interface, as well as more recent "sharp-interface methods" (such as Fedkiw et al., 1999, Ye et al., 1999, Lee and LeVeque, 2003). The increased accuracy does, however, come at the cost of a considerably increased complexity, and it is not clear at the time of this writing what the impact of these new methods will be on the DNS of finite Reynolds numbers flows.

The most recent addition to the collection of methods capable of simulating finite Reynolds number multiphase flows is the lattice Boltzmann method (LBM). Although there have been some doubts about the accuracy and correctness of the LBM, it seems now clear that they can be used to produce results of accuracy comparable to more conventional methods. It is still not clear whether the LBM is significantly faster or simpler than other methods (as sometimes claimed), but most likely these methods are here to stay. For a discussion see, for example, Shan and Chen (1993).

Although there are many possible ways to solve the Navier–Stokes equations for multiphase flows, the most successful approaches have been based on the so-called one-fluid formulation, where one set of equations are solved for the whole flow field and the phase boundary is treated as an embedded interface by adding the appropriate source terms. These source terms are in the form of delta functions localized at the interface and are selected to provide the correct matching conditions at the phase boundary. Although the integral form is often used as a starting point, here we write the "one-fluid" Navier–Stokes equations for incompressible flows in the following differential form:

$$\frac{\partial \rho \mathbf{u}}{\partial t} + \nabla \rho \mathbf{u}\mathbf{u} = -\nabla p \cdot \rho \mathbf{g} + \nabla \cdot \mu(\nabla \mathbf{u} + \nabla \mathbf{u}^T) + \int_f \sigma \kappa \mathbf{n} \delta(\mathbf{x} - \mathbf{x}_f) ds. \tag{2.70}$$

Here,

u is the velocity
p is the pressure
ρ and μ are the discontinuous density and viscosity fields, respectively
σ is a 3D delta function constructed by repeated multiplication of 1D delta functions
κ is twice the mean curvature
n is a unit vector normal to the front

Formally, the integral is over the entire front, thereby adding the delta functions together to create a force that is concentrated at the interface, but smooth along the front. **x** is the point at which the equation is evaluated and $\mathbf{x}_f$ is the position of the front. In most cases, the flow is assumed to be incompressible, so Equation 2.70 is supplemented by

$$\nabla \cdot \mathbf{u} = 0. \tag{2.71}$$

When combined with the momentum equation, this leads to an elliptic equation for the pressure. The single field formulation naturally incorporates the correct mass, momentum, and energy balances across the interface and integration of the conservation equations across the interface directly yields the standard jump conditions.

Equations 2.70 and 2.71 are usually solved on a regular staggered grid using a projection method for the time integration. The spatial and temporal accuracy are usually of second order, although sometimes higher-order time integration is used and the advection terms are treated by methods that are more robust than centered differences such as QUICK, ENO, or WENO. The elliptic pressure equation is generally solved by a multigrid iteration or Krylov subspace methods.

This solution strategy is, in particular, used in most implementations of VOF, level set, and front-tracking methods. What distinguishes between the various methods is how the marker function identifying the different fluids is updated. For flows where the material properties are constant in each fluid, a marker function is usually used to identify the different fluids. The marker moves with the fluid velocity:

$$\frac{DH}{Dt} = \frac{\partial H}{\partial t} + \mathbf{u} \cdot \nabla H = 0, \tag{2.72}$$

where

$$H(\mathbf{x}) = \begin{cases} 1 \text{ in fluid } 1 \\ 0 \text{ in fluid } 2 \end{cases}. \tag{2.73}$$

The density and viscosity are then set as functions of H, usually by

$$\rho = \rho_2 + (\rho_1 - \rho_2)H(\mathbf{x}) \quad \text{and} \quad \mu = \mu_2 + (\mu_1 - \mu_2)H(\mathbf{x}) \tag{2.74}$$

Other material properties are set similarly, when needed. Sometimes, the density is used as a marker function and other variables set as functions of the density.

In the VOF method, the marker function is advected directly, using specialized techniques to ensure that the interface stays sharp and well defined. In level set methods, a smooth function is advected and the interface identified by the zero contour line. The marker function is then constructed by mapping the smooth function into a function that transitions relatively sharply from one value to the other. To keep the mapping well behaved, the smooth function is readjusted periodically to keep it close to a distance function in the vicinity of the interface. In both VOF and level set methods, surface tension must be computed from the marker function on the fixed grid. In front-tracking methods, the phase boundary is tracked by connected marker points (the "front") that are advected by the flow velocity, interpolated from the fixed grid. The gradient of the marker function becomes a delta function when the change is abrupt across the boundary. To transfer the front singularities to the fixed grid, the delta functions are approximated by smoother functions with a compact support on the fixed grid. At each time step, after the front has been advected, the marker function is reconstructed by integration of the smooth grid-delta function. The surface tension is computed on the front, distributed to the grid, and then added to the nodal values of the discrete Navier–Stokes equations.

Many reviews are available that discuss computational methods for multiphase flows. Early reviews that discuss the many possible approaches include Hyman (1984) and Floryan and Rasmussen (1989), and more specialized treatment can be found in Scardovelli and Zaleski (1999) for VOF methods, Anderson et al. (1998) for phase field methods, and Osher and Fedkiw (2002) who discuss level set methods. The book by Shyy et al. (1996) also covers several aspects of computations of multiphase flows. Several articles about various aspects of computations of multiphase systems and related problems can be found in a special issue of the *Journal of Computational Physics* (volume 169, 2001). More recent coverage, focusing on VOF and front-tracking method, can be found in Tryggvason et al. (2011).

2.2.3 Bubbly Flows

One of the major applications of DNS of multiphase flows has been of bubbly flows. Studies of many interacting bubbles in periodic domains can be found in Esmaeeli and Tryggvason (1998, 1999) who simulated the unsteady motion of several 2D and 3D bubbles and Bunner and Tryggvason (1999, 2002a,b) who examined 3D systems with a much larger number of bubbles. The results of these simulations have helped clarify various aspects of the bubble interactions. One of the fundamental questions was, in particular, if relatively modest number of bubbles in fully periodic domains could be used to model homogeneous bubbly flows. The simulations showed that relatively low-order statistics, such as the average rise velocity of the bubbles and the pair probability distribution, converge rapidly with increasing size of the simulated domain, but other quantities, like the self-diffusion coefficient, converge much more slowly. The results also showed that for nearly spherical buoyant bubbles at modest Reynolds numbers that the dominant interaction mode is the "drafting, kissing, and tumbling" mechanism described by

Fortes et al. (1987). Thus, a bubble behind another bubble is drawn into the wake of the bubble in front, once in the wake it catches up and collides with the one in front and the two bubbles then "tumble" and move apart. This collision mode is inherently a finite Reynolds number effect, since two buoyant bubbles in Stokes flow do not change their orientation unless acted on by the third bubble and bubbles in potential flow repel each other if they are rising in an in-line configuration. The results also helped clarify the very different dynamics of nearly spherical bubbles that tender to line up side by side and more deformable ones that often rose one behind the other.

A number of recent studies have also focused on bubbles in laminar and turbulent flows in channels (Lu et al., 2005, 2006, Lu and Tryggvason, 2006, 2008, 2013). The results show that for clean bubbles in vertical channels, the flow structure is determined by the lift force on the bubbles. Nearly spherical bubbles in upflow are pushed to the walls, resulting in a bubble-rich wall layer and a lower void fraction in the middle, while in downflow the bubbles move away from the wall and the void fraction in the middle increases. For steady-state flow, this results in a very simple model for the void fraction. The removal of bubbles from the core region in upflow decreases the mixture density, and eventually, the weight of the mixture balances the imposed pressure gradient and the transfer stops. For downflow, the addition of bubbles to the core decreases the mixture density and again, the transfer continues until the buoyancy of the mixture matches the weight of the mixture. Thus, in both cases, the void fraction at steady state in the channel core is easily found, and if the average void fraction is known, then the void fraction in the wall layer for upflow and the thickness of the bubble free wall layer for downflow can be computed. The lift on deformable bubbles is generally either small or in a direction opposite to nearly spherical bubbles, so bubble-rich wall layers are not seen, in agreement with experimental studies. Simulations of the transient evolution toward the steady state have shown that while the lateral migration of bubbles occurs relatively fast, the velocity takes longer to adjust to the changes in the void fraction distribution.

As computer power increases, it is possible to examine both larger and more complex systems. In Figure 2.7, one example of a relatively large-scale simulation of bubbles in a turbulent channel flow is shown. The domain size is $2\pi \times 4 \times \pi$ computational units in the streamwise, wall-normal, and spanwise direction, respectively, resolved by about 0.4 billion grid points. The physical parameters are selected such that the Morton number is equal to 5.75×10^{-10} and the void fraction is about 3%. The bubbles come in four sizes, with the smallest bubbles having a diameter of 0.16 in computational units, and the largest one with a diameter of 0.44. The majority of the bubbles are small, and we expect the smallest bubbles to accumulate at the wall. The flow is driven upward by an imposed pressure gradient, giving a friction Reynolds number of $Re^+ = 500$. The bubbles are initially distributed nearly uniformly across the domain but as they start to rise, the smaller bubbles start to migrate toward the walls and form a dense wall layer. In the figure, the bubbles are shown at a relatively early time, where many of the small bubbles have moved to the wall, but there are still several small bubbles in the middle, along with most of the larger bubbles. The bubbles are shown along with the vorticity, visualized using the λ_2 method (Jeong and Hussain, 1995), where dark and light color indicates rotation in the opposite direction. Near the wall, most of the vortices are aligned with the flow and usually come in pairs, where nearby vortices have opposite rotation. Although bubbles moving toward the walls disrupt the vortices there, some have survived, at least at the time plotted here. The figure also shows that the vorticity shed by the large bubbles is responsible for the majority of the vorticity in the interior of the channel. Figure 2.8 shows a close-up of the bubbles and the vortices near the right wall, where we have selected a different value for the isocontour of λ_2.

For other simulations of various aspects of bubbly flows, see, for example, the LBM studies by Takada et al. (2000, 2001) and Sankaranarayanan et al. (2002); VOF simulations by Rabha and Buwa (2010); and computations using a front-tracking method similar to the one used for the results in Figure 2.7 by Dijkhuizen et al. (2010a,b). Large-scale simulations using a finite element flow solver coupled with a level set method to advect the phase boundary can be found in Bolotnov et al. (2011) and Bolotnov (2013).

Although bubbly flows have received considerable attention, the interface topology is often much more complex, particularly if the void fraction is high. Not only can the interface topology be very complex, but the interfaces may undergo repeated coalescence and breakup. Modeling such flows is still very primitive, but DNS should be able to provide considerable light on the various processes governing the flow. Topology changes in multiphase flows occur through two primary mechanisms: films that rupture and threads that break. Methods that track the indicator function identifying the different fluids directly on an Eulerian grid (such as VOF or level set methods) lead to coalescence or breakup whenever the film or the thread is underresolved, but front-tracking methods will generally not allow a change in topology. If the interface is tracked, it is possible to either prevent or allow topology changes. Generally, threads that

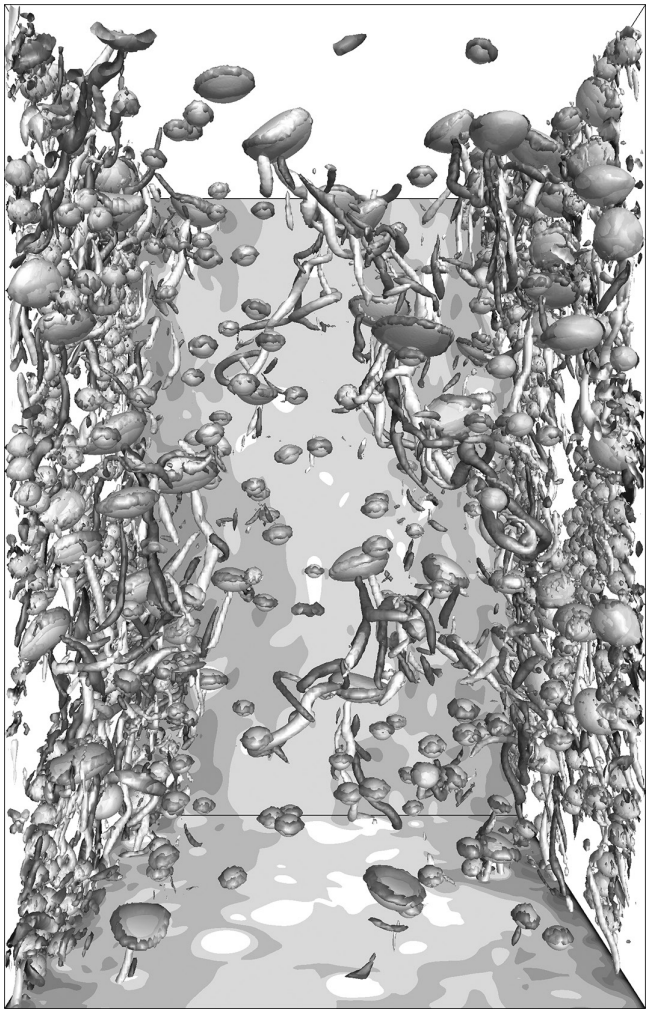


Figure 2.7

One frame from a simulation of many bubbles of different sizes in a turbulent channel flow. The bubbles and the vortical structures, visualized by $\lambda_2 = -2$, along with contours of the vertical velocity in the bottom horizontal plane and the back vertical plane. (Courtesy of Dr. Jiacai Lu, University of Notre Dame, Notre Dame, IN.)

break are by far the easier to deal with than the rupture of thin films. The diameter of threads goes to zero in a finite time, and the evolution is governed by the Navier–Stokes equations so that no additional physical modeling needs to be included. In addition, the breakup is very fast, so even if the final stage is not well resolved, that often does not have a significant effect on the overall flow dynamics. Thus, thread breakup is generally handled easily by most methods. Film draining and rupture are more complex, since the topology change takes place due to short-range attractive forces that are usually not included in the simulations. The attractive forces lead to an instability that results in holes that are then enlarged either by the formation of other holes that merge with the first one or by the enlargement of the original hole by rim breakup involving the formation of very small drops that are difficult to resolve. While methods that track the indicator function directly often produce ruptures that look plausible, the rupture is an artifact of the finite resolution, and in some cases, it is found that refining the grid postpones the rupture and prevents the solution from converging. It is possible that in some cases it does not make a big difference whether the rupture is physical or due to the resolution, but, in general, the importance of capturing the rupture accurately is not well understood. When the interface is tracked by connected marker points, it is necessary to explicitly add a strategy to rupture the interfaces when they are close enough, but at least it is possible to control when rupture takes place and when it does not. Thus, it should be possible to examine how sensitive the overall evolution of the flow is to how the rupture takes place, even if a complete rupture model is not included.

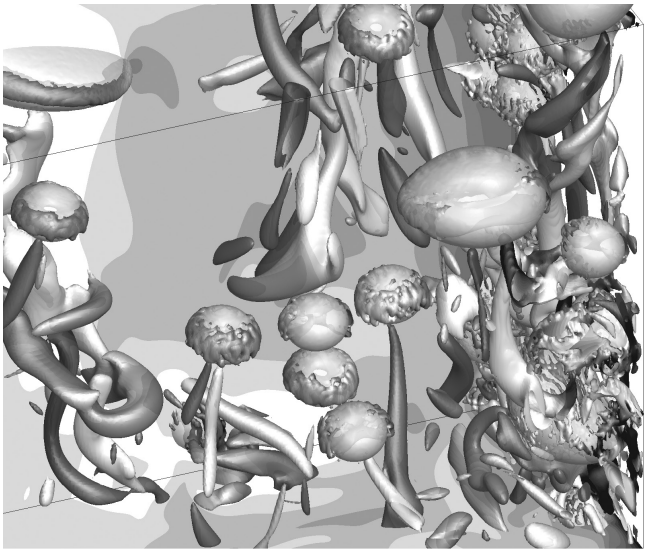


Figure 2.8

A close-up for the results shown in Figure 2.7, showing bubbles and vortical structures near the right wall. Here, $\lambda_2 = -1$. (Courtesy of Dr. Jiacai Lu, University of Notre Dame, Notre Dame, IN.)

Figure 2.9 shows results from two simulations of 40 bubbles in a channel flow. The bubbles are initially placed in a rectangular channel of size $\pi \times 2 \times \pi/2$ computational units in the streamwise, wall-normal, and spanwise direction, respectively, resolved by a $192 \times 128 \times 96$ grid. The bubble diameter is selected such that the void fraction is 13.6%. The flow is initially turbulent, with a friction Reynolds number of 128. All parameters except the surface tension are the same for both runs, giving a Morton number of 2.41×10^{-12} for the high surface tension case and 1.54×10^{-7} for the low surface tension case. The initial Eötvös

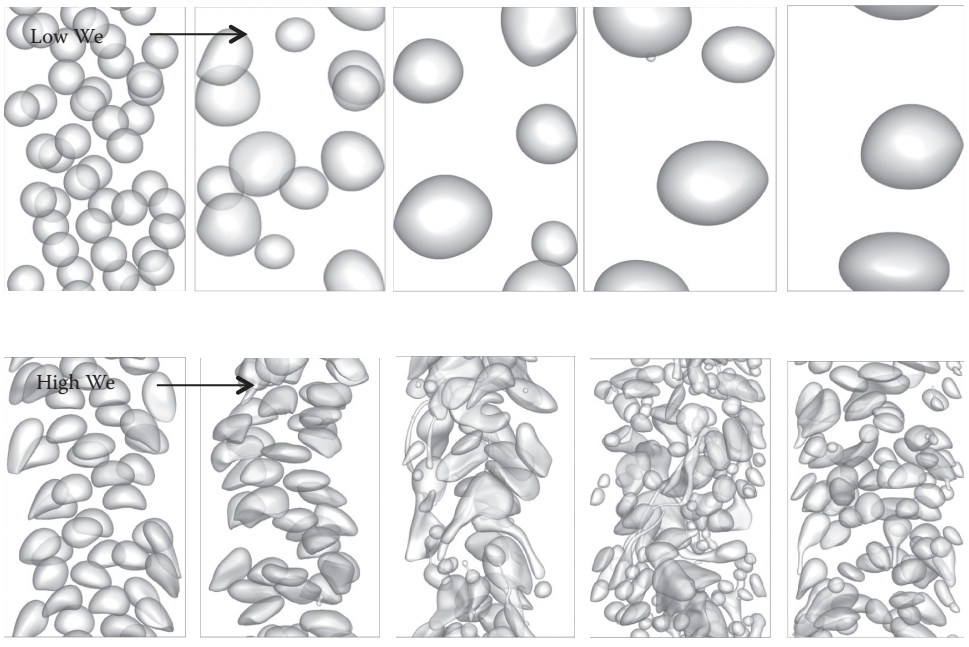


Figure 2.9

A few frames from two simulations of the evolution of several bubbles placed in an initially turbulent channel flow, when the bubbles are allowed to coalesce. In the top frames the surface tension is high and in the bottom frames the surface tension is low, so the bubbles break up after the initial coalescence. (Courtesy of Dr. Jiacai Lu, University of Notre Dame, Notre Dame, IN.)

number is 0.2 for the first case and 8.0 for the second case. As the bubbles rise, they collide and coalesce if the liquid film between them becomes sufficiently thin. For the high surface tension case, the bubbles keep coalescing until there is only one large bubble left (the two bubbles in the last frame will eventually become one), but for the high Weber number the bubbles first coalesce and then breakup again, eventually leading to a mixture of bubble sizes. Here, the thin films are ruptured if they become thinner than a third of a grid spacing, thus making the results similar to what we would expect from a VOF or level set computation.

While simulations of bubbles undergoing topology changes are just starting, many authors have examined the atomization of liquid jets, where the topology changes are critical for the formation of drops. Such studies include air-assisted breakup due to the coinjection of air as well as the breakup due to cross flow (Ménard et al., 2007, Desjardins et al., 2008, Gorokhovski and Herrmann, 2008, Lebas et al., 2009, Desjardins and Pitsch, 2010, Herrmann, 2011). The breakup remains the main challenge in these simulations and in spite of very large grids (Shinjo and Umemura, 2010, 2011) or the use of locally refined grids (Fuster et al., 2009), the breakup is generally dependent on the grid resolution and the smallest drops are underresolved. Thus, several authors have proposed hybrid approaches, where very small drops are modeled as point particles whose motion is modeled by empirical correlations for the drag force and ordinary differential equations are solved for the velocity and location (Herrmann, 2010, Tomara et al., 2010). The challenge is when to convert a fluid blob resolved on a grid to a point particle, and sometimes back again, in such a way that all conservation principles are satisfied.

2.2.4 Outlook

DNSs of multiphase flows have come a long way during the last decade. It is now possible to follow the motion of hundreds of bubbles, drops, and particles at finite Reynolds numbers in simple geometries for sufficiently long time so that meaningful averages can be computed. Much remains to be done, however. At higher Reynolds numbers, the number of grid points required to resolve each bubble and the flow around them increases and the cost of doing simulations with many bubbles increases. With larger computers, such simulations will become increasingly more feasible. The formation of bubbles and drops, as well as coalescence, must also be addressed and except for a few simulations of the breakup of drops in well-defined flows, little has been done. These problems are, nevertheless, well within reach.

As DNS of multiphase flows become more common, the need for advances in the development of the theoretical framework for modeling such flows is also becoming more urgent. Current models have mostly been developed in an environment where relatively little has been known about the details of the flow, and for the most part, these models are far behind what is available for single-phase turbulent flows. While our abilities to simulate directly more and more complex multiphase systems will certainly increase dramatically in the next few years, it is important to realize that our desire to compute will always be ahead of what we can do by DNS. Thus, the condensation of knowledge obtained by DNSs into reduced or averaged models that allow faster predictions will remain at the core of multiphase flow research for a long time to come. Given the experience from modeling turbulent single-phase flows, it is likely that many such models will involve resolving the large-scale motion but modeling the smallest scales. Efforts to develop such large eddy simulation–like model have just started (Labourasse et al., 2007, Toutant et al., 2008, 2009, Vincent et al., 2008).

Although much more can be done for two-fluid disperse systems, it is the longer-term development of the ability to compute the coupled motion of complex systems that will bring about the full impact of DNS. Most engineering fluid systems include a large number of physical phenomena such as fluid flow, evaporation, solidification, and chemical reactions, and simulations of the full systems will allow unprecedented insight. Real bubbles are, for example, rarely clean, and it is well known that surfactants change the behavior of a single bubble significantly. Extensions of various of methods to include surfactants can be found in James and Lowengrub (2004), Muradoglu and Tryggvason (2008), Booty and Siegel (2010), and Muradoglu and Tryggvason (2014), and results for a single bubble show significant effects, including changes in the lift force. However, DNS studies of the collective dynamics of many contaminated bubbles remain to be done. Heat transfer has been examined by Deen and Kuipers (2013), who showed that the passage of a small group of bubbles generally increases the local heat transfer, and by Tanaka (2011) and Dabiri and Tryggvason (2015) examined the motion of many bubbles in turbulent channel flows and showed that the bubbles enhance the overall heat transfer, both for nearly spherical bubbles that form wall layers and for more deformable ones that stay away from the walls. Mass transfer and reactions require us to solve additional advection/diffusion equations that include source terms when there are reactions, but the large range of scales, due to low mass diffusivities and fast reactions, introduce significant challenges. Similarly, several authors have simulating

boiling flows (for early work for relatively simple systems, see Juric and Tryggvason, 1998, Son and Dhir, 1998, Shin and Juric, 2002, and Esmaeeli and Tryggvason, 2003). The main challenge for most of these systems is that the different physical processes take place on very different temporal and spatial scales. While adaptive grid refinement can, in principle, be used for most of those cases, the reality is that that approach will quickly consume all the available grid points. In some cases, the small-scale motion is relatively simple, because surface tension and viscosity are significant, and the dynamics is well described by analytical models. When applicable, it is tempting to couple an analytical model of the small-scale motion with a full simulation of the larger-scale motion. The point particle approximation for small bubbles and drops is perhaps the best example, but a similar approach has also been used for nucleate boiling (Son and Dhir, 1998) and mass transfer (Aboulhasanzadeh et al., 2012). Although we defined DNS as simulations where all continuum length and timescales are fully resolved, and one can argue that we do not really have a DNS if some scales are treated differently, it is likely that as our problems become more complex, our numerical strategies must allow for more flexible approaches. As additional physical processes are incorporated into our mathematical models, we are also likely to be faced with increased uncertainty in the mathematical models used to describe the new physics, rendering traditional DNS less applicable.

References

Aboulhasanzadeh, B., Thomas, S., Taeibi-Rahni, M., and Tryggvason, G., Multiscale computations of mass transfer from buoyant bubbles, *Chem. Eng. Sci.*, 75, 456–467, 2012.

Anderson, D.M., McFadden, G.B., and Wheeler, A.A., Diffuse-interface methods in fluid mechanics, *Ann. Rev. Fluid Mech.*, 30, 139–165, 1998.

Bolotnov, I.A., Influence of bubbles on the turbulence anisotropy, *J. Fluids Eng.*, 135, 051301, 2013.

Bolotnov, I.A., Jansen, K.E., Drew, D.A., Oberai, A.A., Lahey, R.T. Jr., and Podowski, M.Z., Detached direct numerical simulations of turbulent two-phase bubbly channel flow, *Int. J. Multiphase Flow*, 37, 647–659, 2011.

Booty, M.R. and Siegel, M., A hybrid numerical method for interfacial fluid flow with soluble surfactant, *J. Comput. Phys.*, 229, 38643883, 2010.

Brackbill, J.U., Kothe, D.B., and Zemach, C., A continuum method for modeling surface tension, *J. Comput. Phys.*, 100, 335–354, 1992.

Brady, J.F. and Bossis, G., Stokesian dynamics, *Ann. Rev. Fluid Mech.*, 20, 111–157, 1988.

Bunner, B. and Tryggvason, G., Direct numerical simulations of three-dimensional bubbly flows, *Phys. Fluids*, 11, 1967–1969, 1999.

Bunner, B. and Tryggvason, G., Dynamics of homogeneous bubbly flows. Part 1. Rise velocity and microstructure of the bubbles, *J. Fluid Mech.*, 466, 17–52, 2002a.

Bunner, B. and Tryggvason, G., Dynamics of homogeneous bubbly flows. Part 2. Velocity fluctuations, *J. Fluid Mech.*, 466, 53–84, 2002b.

Chahine, G.L. and Duraiswami, R., Dynamic interactions in a multibubble cloud, *ASME J. Fluids Eng.*, 114(4), 680–686, 1992.

Chan, R.K.-C. and Street, R.L., A computer study of finite-amplitude water waves, *J. Comput. Phys.*, 6, 68–94, 1970.

Chapman, R.B. and Plesset, M.S., Nonlinear effects in the collapse of a nearly spherical cavity in a liquid, *Trans. ASME, J. Basic Eng.*, 94, 142, 1972.

Dabiri, S. and Tryggvason, G., Heat transfer in turbulent bubbly flow in vertical channels, *Chem. Eng. Sci.*, 122, 106–113, 2015.

Daly, B.J., A technique for including surface tension effects in hydrodynamic calculations, *J. Comput. Phys.*, 4, 97–117, 1969a.

Daly, B.J., Numerical study of the effect of surface tension on interface instability, *Phys. Fluids*, 12, 1340–1354, 1969b.

Daly, B.J. and Pracht,W.E., Numerical study of density-current surges, *Phys. Fluids*, 11, 15–30, 1968.

Dandy, D.S. and Leal, G.L., Buoyancy-driven motion of a deformable drop through a quiescent liquid at intermediate Reynolds numbers, *J. Fluid Mech.*, 208, 161–192, 1989.

Deen, N.G. and Kuipers, J.A.M., Direct numerical simulation of wall-to liquid heat transfer in dispersed gas–liquid two-phase flow using a volume of fluid approach, *Chem. Eng. Sci.*, 102, 268282, 2013.

Desjardins, O., Moureau, V., and Pitsch, H., An accurate conservative level set/ghost fluid method for simulating turbulent atomization, *J. Comput. Phy.*, 227, 83958416, 2008.
Desjardins, O. and Pitsch, H., Detailed numerical investigation of turbulent atomization of liquid jets, *Atomization Sprays*, 20, 311336, 2010.
Dijkhuizen, W., Roghair, I., Annaland, M.V.S., and Kuipers, J., DNS of gas bubbles behaviour using an improved 3d front tracking model–drag force on isolated bubbles and comparison with experiments, *Chem. Eng. Sci.*, 65, 1415–1426, 2010a.
Dijkhuizen, W., Roghair, I., Annaland, M.V.S., and Kuipers, J., DNS of gas bubbles behaviour using an improved 3d front tracking model–model development, *Chem. Eng. Sci.*, 65, 1427–1437, 2010b.
Drew, D.A., Mathematical modeling of two-phase flow, *Ann. Rev. Fluid Mech.*, 15, 261–291, 1983.
Drew, D.A. and Lahey, R.T. Jr. Analytical modeling of multiphase flow, in *Particulate Two-Phase Flow*, Editor M. C. Roco, Butterworth-Heinemann Series in Chemical Engineering 1993, pp. 509–566.
Esmaeeli, A. and Tryggvason, G., Direct numerical simulations of bubbly flows. Part I. Low Reynolds number arrays, *J. Fluid Mech.*, 377, 313–345, 1998.
Esmaeeli, A. and Tryggvason, G., Direct numerical simulations of bubbly flows. Part II. Moderate Reynolds number arrays, *J. Fluid Mech.*, 385, 325–358, 1999.
Esmaeeli, A. and Tryggvason, G., Computations of explosive boiling in microgravity, *J. Sci. Comput.*, 19, 163–182, 2003.
Fedkiw, R., Aslam, T., Merriman, B., and Osher, S., A non-oscillatory Eulerian approach to interfaces in multimaterial flows (the ghost fluid method), *J. Comput. Phys.*, 152, 457–492, 1999.
Floryan, J.M. and Rasmussen, H., Numerical analysis of viscous flows with free surfaces, *Appl. Mech. Rev.*, 42, 323–341, 1989.
Foote, G.B., A numerical method for studying liquid drop behavior: Simple oscillations, *J. Comput. Phys.*, 11, 507–530, 1973.
Foote, G.B., The water drop rebound problem: Dynamics of collision, *J. Atmos. Sci.*, 32, 390–402, 1975.
Fortes, A., Joseph, D.D., and Lundgren, T., Nonlinear mechanics of fluidization of beds of spherical particles, *J. Fluid Mech.*, 177, 467–483, 1987.
Fuster, D., Bague, A., Boeck, T., Moyne, L., Leboissetier, A., Popinet, S., Ray, P., Scardovelli, R., and Zaleski, S., Simulation of primary atomization with an octree adaptative mesh refinement and vof method, *Int. J. Multiphase Flow*, 35, 550565, 2009.
Glimm, J. and McBryan, O., A computational model for interfaces, *Adv. Appl. Math.*, 6, 422–435, 1985.
Gorokhovski, M. and Herrmann, M., Modeling primary atomization, *Ann. Rev. Fluid Mech.*, 40, 343–366, 2008.
Hao, Y. and Prosperetti, A., A numerical method for three-dimensional gas–liquid flow computations, *J. Comput. Phys.*, 196, 126–144, 2004.
Harlow, F.H. and Shannon, J.P., The splash of a liquid drop, *J. Appl. Phys.*, 38, 3855–3866, 1967.
Harlow, F.H. and Welch, J.E., Numerical calculation of time-dependent viscous incompressible flow of fluid with a free surface, *Phys. Fluid*, 8, 2182–2189, 1965.
Harlow, F.H. and Welch, J.E., Numerical study of large-amplitude free-surface motions, *Phys. Fluid*, 9, 842–851, 1966.
Harper, J.F., Bubbles rising in line: Why is the first approximation so bad? *J. Fluid Mech.*, 351, 289–300, 1997.
Herrmann, M., A parallel eulerian interface tracking/lagrangian point particle multi-scale coupling procedure, *J. Comput. Phys.*, 229, 745759, 2010.
Herrmann, M., On simulating primary atomization using the refined level set grid method, *Atomization Sprays*, 21, 283301, 2011.
Hirt, C.W., Cook, J.L., and Butler, T.D., A Lagrangian method for calculating the dynamics of an incompressible fluid with a free surface, *J. Comput. Phys.*, 5, 103–124, 1970.
Hirt, C.W. and Nichols, B.D., Volume of Fluid (VOF) method for the dynamics of free boundaries, *J. Comput. Phys.*, 39, 201–226, 1981.
Hua, J. and Lou, J., Numerical simulation of bubble rising in viscous liquid, *J. Comput. Phys.*, 222, 769–795, 2007.
Hyman, J.M., Numerical methods for tracking interfaces, *Phys. D*, 12, 396–407, 1984.
Ishii, M., *Thermo-Fluid Dynamic Theory of Two-phase Flows*, Eyrolles, Paris, 1975.
James, A.J. and Lowengrub, J., A surfactant-conserving volume-of-fluid method for interfacial flows with insoluble surfactants, *J. Comput. Phys.*, 201, 685722, 2004.
Jeong, J. and Hussain, F., On the identification of a vortex, *J. Fluid Mech.*, 285, 69–94, 1995.

Juric, D. and Tryggvason, G., Computations of boiling flows, *Int. J. Multiphase Flow*, 24, 387–410, 1998.
Kang, I.S. and Leal, L.G., Numerical solution of axisymmetric, unsteady free-boundary problems at finite Reynolds number. I. Finite-difference scheme and its applications to the deformation of a bubble in a uniaxial straining flow, *Phys. Fluids*, 30, 1929–1940, 1987.
Labourasse, E., Lacanette, D., Toutant, A., Lubin, P., Vincent, S., Lebaigue, O., Caltagirone, J.-P., and Sagaut, P., Towards large eddy simulation of isothermal two-phase flows: Governing equations and a priori tests, *Int. J. Multiphase Flow*, 33, 1–39, 2007.
Lebas, R., Menard, T., Beau, P.A., Berlemont, A., and Demoulin, F.X., Numerical simulation of primary break-up and atomization: Dns and modelling study, *Int. J. Multiphase Flow*, 35, 247260, 2009.
Lee, L. and LeVeque, R.J., An immersed interface method for incompressible Navier–Stokes equations, *SIAM J. Sci. Comput.*, 25, 832–856, 2003.
Li, X. and Pozrikidis, C., Wall-bounded shear flow and channel flow of suspensions of liquid drops, *Int. J. Multiphase Flow*, 26, 1247–1279, 2000.
Loewenberg, M. and Hinch, E.J., Numerical simulation of a concentrated emulsion in shear flow, *J. Fluid Mech.*, 321, 395–419, 1996.
Lu, J., Biswas, S., and Tryggvason, G., A DNS study of laminar bubbly flows in a vertical channel, *Int. J. Multiphase Flow*, 32, 643–660, 2006.
Lu, J., Fernandez, A., and Tryggvason, G., The effect of bubbles on the wall shear in a turbulent channel flow, *Phys. Fluids*, 17, 095102, 2005.
Lu, J. and Tryggvason, G., Numerical study of turbulent bubbly downflows in a vertical channel, *Phys. Fluids*, 18, 103302, 2006.
Lu, J. and Tryggvason, G., Effect of bubble deformability in turbulent bubbly upflow in a vertical channel, *Phys. Fluids*, 20, 040701, 2008.
Lu, J. and Tryggvason, G., Dynamics of nearly spherical bubbles in a turbulent channel upflow, *J. Fluid Mech.*, 732, 166–189, 2013.
Ménard, T., Tanguy, S., and Berlemont, A., Coupling level set/vof/ghost fluid methods: Validation and application to 3d simulation of the primary break-up of a liquid jet, *Int. J. Multiphase Flow*, 33, 510–524, 2007.
Mitchell, T.M. and Hammitt, F.H., Asymmetric cavitation bubble collapse, *Trans. ASME, J. Fluids Eng.*, 95, 29–37, 1973.
Muradoglu, M. and Kayaalp, A.D., An auxiliary grid method for computations of multiphase flows in complex geometries, *J. Comput. Phys.*, 214, 858–877, 2006.
Muradoglu, M. and Tryggvason, G., A front-tracking method for computation of interfacial flows with soluble surfactants, *J. Comput. Phys.*, 227, 2238–2262, 2008.
Muradoglu, M. and Tryggvason, G., Simulations of soluble surfactants in 3d multiphase flow, *J. Comput. Phys.*, 274, 737–757, 2014.
Osher, S. and Fedkiw, R.P., Level set methods: An overview and some recent results, *J. Comput. Phys.*, 169, 463–502, 2001.
Osher, S. and Fedkiw, R.P., *Level Set Methods and Dynamic Implicit Surfaces*, Springer, 2002.
Pozrikidis, C., *Integral and Singularity Methods for Linearized Viscous Flow*, Cambridge University Press, Cambridge, U.K., 1992.
Pozrikidis, C., Interfacial dynamics for Stokes flow, *J. Comput. Phys.*, 169, 250–301, 2001.
Rabha, S.S., and Buwa, V.V., Volume-of-fluid (VOF) simulations of rise of single/multiple bubbles in sheared liquids, *Chem. Eng. Sci.*, 65, 527–537, 2010.
Ryskin, G. and Leal, L.G., Numerical solution of free-boundary problems in fluid mechanics. Part 2. Buoyancy-driven motion of a gas bubble through a quiescent liquid, *J. Fluid Mech.*, 148, 19–35, 1984.
Sangani, A. and Didwania, A.K., Dynamic simulations of flows of bubbly liquids at large Reynolds numbers, *J. Fluid Mech.*, 250, 307–337, 1993.
Sankaranarayanan, K., Shan, X., Kevrekidis, I.G., and Sundaresan, S., Analysis of drag and virtual mass forces in bubbly suspensions using an implicit formulation of the lattice Boltzmann method, *J. Fluid Mech.*, 452, 61–96, 2002.
Scardovelli, R. and Zaleski, S., Direct numerical simulation of free-surface and interfacial flow, *Ann. Rev. Fluid Mech.*, 31, 567–603, 1999.

Sethian, J.A., Evolution, implementation, and application of level set and fast marching methods for advancing fronts, *J. Comput. Phys.*, 169, 503–555, 2001.
Shan, X.W. and Chen, H.D., Lattice Boltzmann model for simulating flows with multiple phases and components, *Phys. Rev. E*, 47, 1815–1819, 1993.
Shin, S. and Juric, D., Modeling three-dimensional multiphase flow using a level contour reconstruction method for front tracking without connectivity, *J. Comput. Phys.*, 180, 427–470, 2002.
Shinjo, J. and Umemura, A., Simulation of liquid jet primary breakup: Dynamics of ligament and droplet formation, *Int. J. Multiphase Flow*, 36, 513532, 2010.
Shinjo, J. and Umemura, A., Detailed simulation of primary atomization mechanisms in diesel jet sprays (isolated identification of liquid jet tip effects), *Proc. Combust. Inst.*, 33, 20892097, 2011.
Shyy, W., Udaykumar, H., Rao, M., and Smith, R., *Computational Fluid Dynamics with Moving Boundaries*, Taylor & Francis, 1996.
Smereka, P., On the motion of bubbles in a periodic box, *J. Fluid Mech.*, 254, 79–112, 1993.
Son, G. and Dhir, V.K., Numerical simulation of film boiling near critical pressures with a level set method, *J. Heat Transfer*, 120, 183–192, 1998.
Tanaka, M., Numerical study on flow structures and heat transfer characteristics of turbulent bubbly upflow in a vertical channel. In: Zhu, J. (Ed.), *Computational Simulations and Applications*. InTech, Rijeka, Croatia, 119–142, 2011.
Takada, N., Misawa, M., Tomiyama, A., and Fujiwara, S., Numerical simulation of two- and three-dimensional. two-phase fluid motion by lattice Boltzmann method, *Comput. Phys. Commun.*, 129, 233–246, 2000.
Takada, N., Misawa, M., Tomiyama, A., and Hosokawai, S., Simulation of bubble motion under gravity by lattice Boltzmann method, *J. Nucl. Sci. Technol.*, 38, 330–341, 2001.
Tomara, G., Fustera, D., Zaleskia, S., and Popine, S., Multiscale simulations of primary atomization, *Comput. Fluids*, 39, 18641874, 2010.
Toutant, A., Chandesris, M., Jamet, D., and Lebaigue, O., Jump conditions for filtered quantities at an under-resolved interface. part 2: A priori tests, *Int. J. Multiphase Flow*, 35, 11191129, 2009.
Toutant, A., Labourasse, E., Lebaigue, O., and Simonin, O., DNS of the interaction between a deformable buoyant bubble and spatially decaying turbulence: A priori tests for LES two-phase flow modelling, *Comput. Fluids*, 37, 877–886, 2008.
Tryggvason, G., Bunner, B., Esmaeeli, A., Juric, D., Al-Rawahi, N., Tauber, W., Han, J., Nas, S., and Jan, Y.-J., A front tracking method for the computations of multiphase flow, *J. Comput. Phys.*, 169, 708–759, 2001.
Tryggvason, G., Scardovelli, R., and Zaleski, S., *Direct Numerical Simulations of Gas-Liquid Multiphase Flows*, Cambridge University Press, Cambridge, U.K., 2011.
Unverdi, S.O. and Tryggvason, G., A front-tracking method for viscous, incompressible, multi-fluid flows, *J. Comput. Phys.*, 100, 25–37, 1992.
van Sint Annaland, M., Dijkhuizen, W., Deen, N., and Kuipers, J., Numerical simulation of gas bubbles behaviour using a 3D front tracking method, *AIChE J.*, 52, 99–110, 2006.
Vincent, S., Larocque, J., Lacanette, D., Toutant, A., Lubin, P., and Sagaut, P., Numerical simulations of phase separation and a priori two-phase les filtering, *Comp. Fluids*, 37, 898–906, 2008.
Yabe, T., Xiao, F., and Utsumi, T., The constrained interpolation profile (CIP) method for multi-phase analysis, *J. Comput. Phys.*, 169, 556–593, 2001.
Ye, T., Mittal, R., Udaykumar, H.S., and Shyy, W., An accurate cartesian grid method for viscous incompressible flows with complex immersed boundaries, *J. Comput. Phys.*, 156, 209–240, 1999.
Youngs, D.L., Time dependent multimaterial flow with large fluid distortion, in K. M. Morton and M.J. Baines (Eds.), *Numerical Methods for Fluid Dynamics*, Academic Press, New York, 1982, pp. 27–39.
Zhang, D.Z. and Prosperetti, A., Ensemble phase-averaged equations for bubbly flows, *Phys. Fluids*, 6, 2956–2970, 1994.
Zhou, H. and Pozrikidis, C., The flow of ordered and random suspensions of two-dimensional drops in a channel, *J. Fluid Mech.*, 255, 103–127, 1993.
Zinchenko, A.Z. and Davis, R.H., An efficient algorithm for hydrodynamical interaction of many deformable drops, *J. Comput. Phys*, 157, 539–587, 2000.

2.3 The Lattice Boltzmann Method

Cyrus K. Aidun, Dennis E. Oztekin, Yuanzheng Zhu, Tomas Rosén, and Fredrik Lundell

2.3.1 Introduction and Basics of Lattice Boltzmann Method

The lattice Boltzmann method (LBM) is a computational tool that has been growing in popularity since its development due to the simplicity with which it is implemented and the ease with which it can be scaled to parallel processing systems. The method was introduced in the late 1980s (Higuera and Jimenez, 1989) and addressed a number of problems with its predecessor, the lattice gas automation method (Frisch et al., 1987). New variations of the method are being developed constantly, extending range of applicable problems for LBM. This constant development creates opportunities for new investigations on a variety of fronts.

This chapter will focus primarily on four areas that have been under intense study recently as fields of research that lend themselves well to newer lattice Boltzmann variants. The first section will focus on fluid–solid interaction. Here, the bounce-back boundary condition will be discussed, along with the newer external boundary force (EBF) method for treating solid interfaces. Following this, there will be a section about the suspension of deformable capsules and then a section about the suspension of deformable fibers. Finally, there will be a section on the methods by which lattice Boltzmann deals with liquid–gas problems.

2.3.1.1 Brief Background

All of lattice Boltzmann research is based on the Boltzmann equation, which states

$$\frac{\partial f}{\partial t} + \boldsymbol{\zeta} \cdot \nabla f + \frac{\boldsymbol{F}}{m_p} \cdot \frac{\partial f}{\partial \boldsymbol{\zeta}} = \left\{ \frac{\partial f}{\partial t} \right\}_{collision} \tag{2.75}$$

In this equation,

$\boldsymbol{F}$ is the term of body forces

m_p is the particle mass

$\boldsymbol{\zeta}$ is the velocity of the particle

f is the density distribution function, that is, for some position and some time, the number of particles per volume, or density ρ, with a velocity between $\boldsymbol{\zeta}$ and $\boldsymbol{\zeta} + d\boldsymbol{\zeta}$. From this definition, we can write

$$\rho = \int f d\boldsymbol{\zeta} \tag{2.76}$$

The moment of this equation can be taken to get a very important relationship in recovering the conservation of momentum:

$$\rho \boldsymbol{u} = \int \boldsymbol{\zeta} f d\boldsymbol{\zeta} \tag{2.77}$$

Here, it is very important to distinguish $\boldsymbol{u}$, the macroscopic fluid velocity, from $\boldsymbol{\zeta}$, the particle velocity. The macroscopic fluid velocity is the property that is commonly utilized in fluid mechanics; as such, this is the property that is typically solved for in the following sections. The particle velocity is only the velocity of a single particle; if it is assumed that the individual particles only move along a discretized grid, this will be reduced to the aptly named lattice velocity, $\boldsymbol{e}_k$. This will be presented later. Before any discretization can occur, the Boltzmann equation needs to be reduced to a usable form. First, the forcing term is dropped. Later in the chapter, more numerically friendly methods of including the force will be discussed. The next term that needs to be addressed is the rate of change of the density distribution due to the collision of particles. This is the right-hand side of the Boltzmann equation displayed earlier. To address this term, the Lattice Bhatnagar-Gross-Krook, LBGK, approximation (Bhatnagar et al., 1954) is applied. This approximation

introduced an equilibrium density distribution function f^{eq}, which is a function of velocity and density, and a relaxation time τ, which is a function of viscosity. The approximation becomes

$$\left\{\frac{\partial f}{\partial t}\right\}_{collision} = \frac{f^{eq} - f}{\tau} \tag{2.78}$$

With this, the Boltzmann equation is put into a usable form and is ready for discretization.

2.3.1.2 Discretization

The most immediate effect of the discretization is allowing the expansion of the derivative term remaining on the left-hand side of the Boltzmann equation. With these simplifications, the Boltzmann equation is reduced to

$$f_k(\boldsymbol{x}+\boldsymbol{e}_k, t+1) - f_k(\boldsymbol{x},t) = -\frac{1}{\tau}\left[f_k(\boldsymbol{x},t) - f_k^{eq}(\boldsymbol{x},t)\right] = \boldsymbol{C}\left(f_k(\boldsymbol{x},t)\right) \tag{2.79}$$

where the subscript k denotes the lattice direction and $\boldsymbol{C}$ is the collision operator. The lattice direction represents which path from the lattice node a given particle might be taking. For reference, the lattice arrangements used in this study are D2Q9 and D3Q19. Where the notation DxQy means there are x dimensions and y lattice arrangements. D2Q9 is commonly used two dimensional arrangement which includes the node itself, the four cardinal direction, and its four diagonals. D3Q19 is a common three dimensional arrangement which includes the node itself, its six cardinal directions, and the twelve diagonals that lie on the three planes normal to the cardinal directions. From this equation, commonly called the evolution equation, the equilibrium density distribution function can be determined in a number of ways; however, the most general way is demonstrated by He and Luo (1997). This derivation starts with a Maxwell–Boltzmann distribution and takes a Taylor expansion about the macroscopic velocity. The result is

$$f_k^{eq}(x,t) = \frac{3\rho}{(2\pi c^2)^{D/2}}\left\{1 + \frac{6\boldsymbol{e}_k\boldsymbol{u}}{c^2} - \frac{3\boldsymbol{e}_k^2}{c^2} + \frac{9\boldsymbol{e}_k\boldsymbol{u}^2}{c^4}\right\} \tag{2.80}$$

Here,

D is the number of dimensions being modeled

c is called the lattice speed, which is the distance between two adjacent nodes divided by the time of a single time step.

2.3.2 Fluid–Solid Interaction

In this section, we will discuss how fluid–solid interaction can be modeled in Lattice Boltzmann, LB, simulations. As an example, we will consider a single solid particle suspended in the fluid domain and describe two methods for coupling the solid and fluid motion.

2.3.2.1 Standard Bounce-Back Method

The standard bounce-back (SBB) method for simulating particles in flows was described by Aidun et al. (1998) and will be summarized in this section.

Consider a particle at a position $\boldsymbol{X}(t)$ with a certain velocity $\boldsymbol{U}(t)$ and angular velocity $\Omega(t)$ at time instance t. The particle has mass m and inertial tensor $\boldsymbol{I}$. The position, orientation, and geometry of the particle determine the location of the particle boundary $\Gamma(t)$. Using the SBB method, the following steps are performed:

1. Each link k is classified according to the boundary $\Gamma(t)$ (see Figure 2.10). The link in the opposite direction of k is denoted k'. The link is
   a. A boundary link (*BL*) if it is crossing the particle boundary
   b. A regular link (*RL*) otherwise

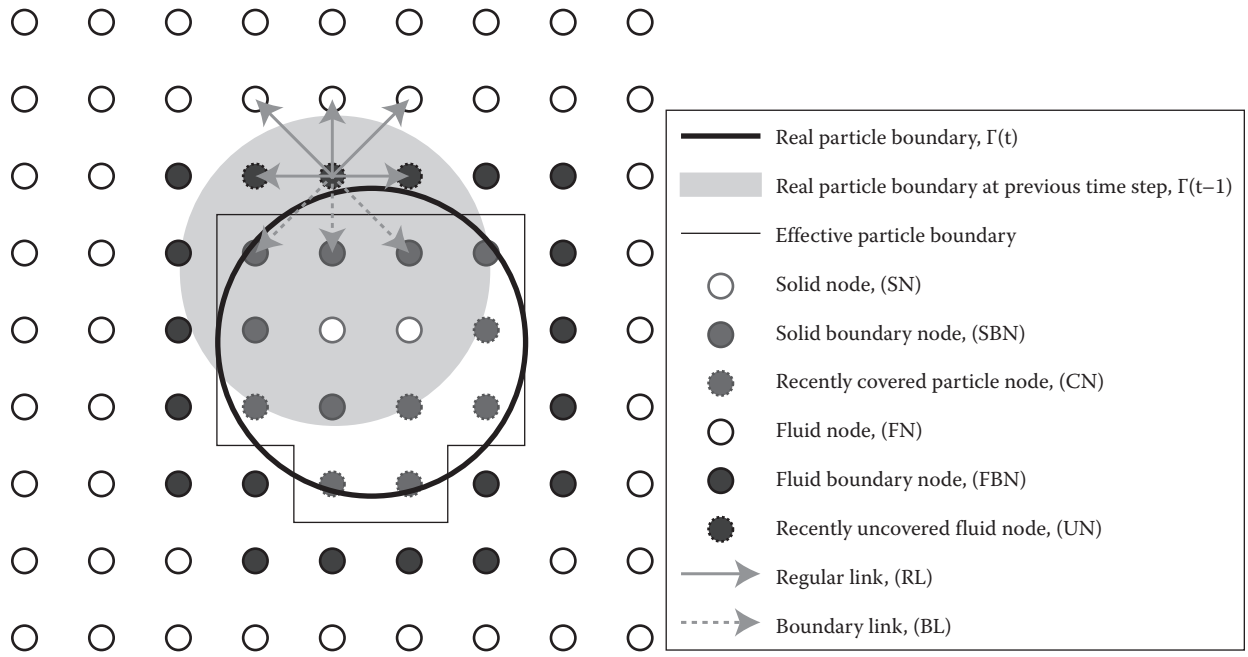


Figure 2.10

Definitions and classifications of the standard bounce-back method for a D2Q9 arrangement.

Note that the effective boundary of the particle is defined by the halfway point of the BLs and thus gets a staircase shape.

2. The lattice nodes are classified according to the boundary $\Gamma(t)$ (see Figure 2.10). The node is
   - **a.** A fluid node (*FN*) if the node is outside $\Gamma(t)$ and all links are RLs
   - **b.** A fluid boundary node (*FBN*) if the node is outside $\Gamma(t)$ and has one or more BLs
   - **c.** A recently uncovered node (*UN*) if the node is outside $\Gamma(t)$ but was inside $\Gamma(t-1)$
   - **d.** A solid node (*SN*) if the node is inside $\Gamma(t)$ and all links are RLs
   - **e.** A solid boundary node (*SBN*) if the node is inside $\Gamma(t)$ and has one or more BLs
   - **f.** A recently covered node (*CN*) if the node is inside $\Gamma(t)$ but was outside $\Gamma(t-1)$.
3. Density and velocity are corrected for UNs:

$$\rho(\boldsymbol{x},t)=\frac{1}{N_b}\sum_{k\in RL}\rho(\boldsymbol{x}+\boldsymbol{e}_k,t) \tag{2.81}$$

$$\boldsymbol{u}(\boldsymbol{x},t)=\boldsymbol{U}(t)+\boldsymbol{\Omega}(t)\times[\boldsymbol{x}-\boldsymbol{X}(t)] \tag{2.82}$$

where N_b is the amount of RLs for the UN and $\boldsymbol{x}\in UN$.

4. Collision step:

$$f_k(\boldsymbol{x},t_+)=\boldsymbol{C}f_k(\boldsymbol{x},t) \tag{2.83}$$

where $\boldsymbol{C}$ is the collision operator described in the previous section.

5. Propagation step:

$$\tilde{f}_k(\boldsymbol{x},t+1)=\begin{cases} f_{k'}(\boldsymbol{x},t_+) & \text{if } k'\in BL \\ f_k(\boldsymbol{x}+\boldsymbol{e}_{k'},t_+) & \text{otherwise} \end{cases} \tag{2.84}$$

6. The correct fluid density is obtained at each node through

$$\rho(\boldsymbol{x},t+1)=\frac{\sum_k \tilde{f}_k(\boldsymbol{x},t+1)}{1-2\sum_{k'\in BL} B_k \boldsymbol{u}_{k'}(t)\cdot \boldsymbol{e}_k} \tag{2.85}$$

where $B_0 = 1/3$, $B_{1-6} = 1/6$, and $B_{7-18} = 1/12$ in the D3Q19 lattice arrangement. The velocity of the wall $\boldsymbol{u}_k$, crossing the BL $k' \in BL$, is obtained through

$$\mathbf{u}_{k'}(t)=\mathbf{U}(t)+\boldsymbol{\Omega}(t)\times\left[\boldsymbol{x}+\frac{1}{2}\boldsymbol{e}_{k'}-\boldsymbol{X}(t)\right] \tag{2.86}$$

7. The modification of the distribution function components is obtained through

$$f_k(\boldsymbol{x},t+1)=\begin{cases}\tilde{f}_k(\boldsymbol{x},t+1)+2\rho(\boldsymbol{x},t+1)B_k\boldsymbol{u}_{k'}(t)\cdot\boldsymbol{e}_k & \text{if } k'\in BL\\ \tilde{f}_k(\boldsymbol{x},t+1) & \text{otherwise}\end{cases} \tag{2.87}$$

8. The force and torque contributions on the particle from the BLs are obtained through

$$\boldsymbol{F}_k^{BL}\left(\boldsymbol{x}+\frac{1}{2}\boldsymbol{e}_{k'},t+\frac{1}{2}\right)=2\boldsymbol{e}_{k'}[f_k(\boldsymbol{x},t+1)+\rho(\boldsymbol{x},t+1)B_k\boldsymbol{u}_{k'}(t)\cdot\boldsymbol{e}_{k'}] \tag{2.88}$$

$$\boldsymbol{T}_k^{BL}\left(\boldsymbol{x}+\frac{1}{2}\boldsymbol{e}_{k'},t+\frac{1}{2}\right)=\left[\boldsymbol{x}+\frac{1}{2}\boldsymbol{e}_{k'}-\boldsymbol{X}(t)\right]\times\boldsymbol{F}_k^{BL}\left(\boldsymbol{x}+\frac{1}{2}\boldsymbol{e}_{k'},t+\frac{1}{2}\right) \tag{2.89}$$

where $k' \in BL$.

9. The force and torque contributions on the particle from the recent CNs are obtained through

$$\boldsymbol{F}^{CN}\left(\boldsymbol{x},t+\frac{1}{2}\right)=\sum_k f_k(\boldsymbol{x},t)\boldsymbol{e}_k \tag{2.90}$$

$$\boldsymbol{T}^{CN}\left(\boldsymbol{x},t+\frac{1}{2}\right)=[\boldsymbol{x}-\boldsymbol{X}(t)]\times\boldsymbol{F}^{CN}\left(\boldsymbol{x},t+\frac{1}{2}\right) \tag{2.91}$$

where $\boldsymbol{x} \in CN$.

10. The force and torque contributions on the particle from the recent UNs are obtained through

$$\boldsymbol{F}^{UN}\left(\boldsymbol{x},t+\frac{1}{2}\right)=-\rho(\boldsymbol{x},t)\boldsymbol{u}(\boldsymbol{x},t) \tag{2.92}$$

$$\boldsymbol{T}^{UN}\left(\boldsymbol{x},t+\frac{1}{2}\right)=[\boldsymbol{x}-\boldsymbol{X}(t)]\times\boldsymbol{F}^{UN}\left(\boldsymbol{x},t+\frac{1}{2}\right) \tag{2.93}$$

where $\boldsymbol{x} \in UN$.

11. The force and torque contributions are summed together according to

$$\boldsymbol{F}\left(t+\frac{1}{2}\right)=\sum_{\boldsymbol{x}\in FBN}\sum_{k'\in BL}\boldsymbol{F}_k^{BL}\left(\boldsymbol{x}+\frac{1}{2}\boldsymbol{e}_{k'},t+\frac{1}{2}\right)+ \\ +\sum_{\boldsymbol{x}\in CN}\boldsymbol{F}^{CN}\left(\boldsymbol{x},t+\frac{1}{2}\right)+\sum_{\boldsymbol{x}\in UN}\boldsymbol{F}^{UN}\left(\boldsymbol{x},t+\frac{1}{2}\right) \tag{2.94}$$

$$\boldsymbol{T}\left(t+\frac{1}{2}\right)=\sum_{\boldsymbol{x}\in FBN}\sum_{k'\in BL}\boldsymbol{T}_k^{BL}\left(\boldsymbol{x}+\frac{1}{2}\boldsymbol{e}_{k'},t+\frac{1}{2}\right)+ \\ +\sum_{\boldsymbol{x}\in CN}\boldsymbol{T}^{CN}\left(\boldsymbol{x},t+\frac{1}{2}\right)+\sum_{\boldsymbol{x}\in UN}\boldsymbol{T}^{UN}\left(\boldsymbol{x},t+\frac{1}{2}\right) \tag{2.95}$$

12. Force $\boldsymbol{F}(t)$ and torque $\boldsymbol{T}(t)$ on the particle are found through averaging with the previous time step:

$$\boldsymbol{F}(t)=\frac{1}{2}\left[\boldsymbol{F}\left(t+\frac{1}{2}\right)+\boldsymbol{F}\left(t-\frac{1}{2}\right)\right] \tag{2.96}$$

$$\boldsymbol{T}(t)=\frac{1}{2}\left[\boldsymbol{T}\left(t+\frac{1}{2}\right)+\boldsymbol{T}\left(t-\frac{1}{2}\right)\right] \tag{2.97}$$

13. The new particle position $\boldsymbol{X}(t+1)$, velocity $\boldsymbol{U}(t+1)$, angular velocity $\boldsymbol{\Omega}(t+1)$, and orientation are found through numerical integration of the particle equations of motion:

$$m\frac{d\boldsymbol{U}(t)}{dt}=\boldsymbol{F}(t) \tag{2.98}$$

$$\boldsymbol{I}\cdot\frac{d\boldsymbol{\Omega}(t)}{dt}+\boldsymbol{\Omega}(t)\times[\boldsymbol{I}\cdot\boldsymbol{\Omega}(t)]=\boldsymbol{T}(t) \tag{2.99}$$

14. The particle boundary $\Gamma(t+1)$ is updated according to the new particle position and orientation.

2.3.2.2 External Boundary Force Method

The EBF method is an improved way of simulating particles in flows using LBM and was described by Wu and Aidun (2010a). Instead of having the particle defined on the fixed Eulerian fluid grid, the particle is defined by an overlapping Lagrangian grid that can move freely in the domain. The nodes in the fluid domain are denoted as $\boldsymbol{x}^e \in \Pi_f$ and the nodes in the particle grid are denoted (for the jth node) $\boldsymbol{x}_j^l \in \Gamma_s$. Each node in the particle grid is associated with an area element of size ΔA_j and gets a characteristic volume $\Delta v_j = \Delta A_j^{3/2}$. The best results are obtained by keeping $\Delta A_j \approx (\Delta x)^2$, with Δx as the node spacing in the fluid grid.

Fluid quantities are mapped onto the particle grid by using a discrete delta function as defined by Peskin (2002):

$$D(\boldsymbol{x})=\begin{cases}\dfrac{1}{64\Delta x^3}\left(\left(1+\cos\left(\dfrac{\pi x}{2\Delta x}\right)\right)\left(1+\cos\left(\dfrac{\pi y}{2\Delta x}\right)\right)\left(1+\cos\left(\dfrac{\pi z}{2\Delta x}\right)\right)\right), & |\boldsymbol{x}|\le 2\Delta x \\ 0, & |\boldsymbol{x}|>2\Delta x.\end{cases} \tag{2.100}$$

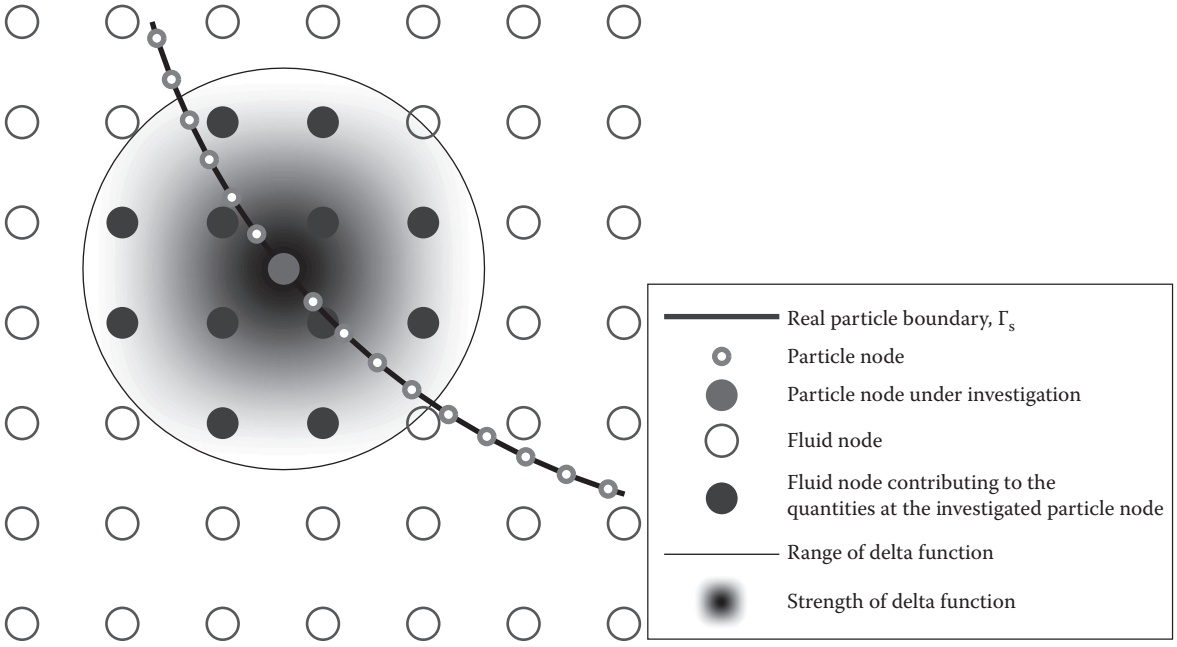


Figure 2.11

Illustration of the principle of the external boundary force method; the mapping of fluid quantities onto a particle node of investigation is done through a discrete delta function.

Again, we consider a particle with mass m, inertial tensor $\boldsymbol{I}$, position $\boldsymbol{X}(t)$, velocity $\boldsymbol{U}(t)$, and angular velocity $\boldsymbol{\Omega}(t)$ at time instance t. The following steps are performed when using the EBF method:

1. Propagation step:

$$\tilde{f}_k(\boldsymbol{x}^e,t) = f_k(\boldsymbol{x}^e + \boldsymbol{e}_{k'}, t-1) \tag{2.101}$$

2. The precollisional distributions $\tilde{f}_k(\boldsymbol{x}^e,t)$ are used to calculate the fluid velocity $\boldsymbol{u}(\boldsymbol{x}^e,t)$, which is then mapped to the particle grid through (see Figure 2.11):

$$\boldsymbol{u}(\boldsymbol{x}_j^l,t) = \sum_{\boldsymbol{x}^e \in \Pi_f} \boldsymbol{u}(\boldsymbol{x}^e,t) D(\boldsymbol{x}^e - \boldsymbol{x}_j^l)(\Delta x)^3. \tag{2.102}$$

3. The force acting on the particle node is calculated through

$$\boldsymbol{F}^{fsi}(\boldsymbol{x}_j^l,t) = \boldsymbol{f}^{fsi}(\boldsymbol{x}_j^l,t)\cdot\Delta v_j = \rho_0[\boldsymbol{u}(\boldsymbol{x}_j^l,t) - \boldsymbol{U}_p(\boldsymbol{x}_j^l,t-1)]\cdot\Delta v_j \tag{2.103}$$

with $\boldsymbol{f}^{fsi}(\boldsymbol{x}_j^l,t)$ as the force density at the jth particle node, ρ_0 as the reference fluid density, and $\boldsymbol{U}_p(\boldsymbol{x}_j^l,t-1)$ as the jth particle node velocity at time $t-1$.

4. The particle force $\boldsymbol{F}(t)$ and torque $\boldsymbol{T}(t)$ are determined by summing the contributions from the nodes:

$$\boldsymbol{F}(t) = \sum_{\boldsymbol{x}_j^l \in \Gamma_s} \boldsymbol{F}^{fsi}(\boldsymbol{x}_j^l,t) \tag{2.104}$$

$$\boldsymbol{T}(t) = \sum_{x_j^l \in \Gamma_s} (\boldsymbol{x}_j^l - \boldsymbol{x}^{lc}) \times \boldsymbol{F}^{fsi}(\boldsymbol{x}_j^l,t) \tag{2.105}$$

where $\boldsymbol{x}^{lc}$ is the center of gravity of the particle.

5. The new particle position $\boldsymbol{X}(t+1)$, velocity $\boldsymbol{U}(t+1)$, angular velocity $\boldsymbol{\Omega}(t+1)$, and orientation are found through numerical integration of the particle equations of motion:

$$m\frac{d\boldsymbol{U}(t)}{dt} = \boldsymbol{F}(t) \tag{2.106}$$

$$\boldsymbol{I}\cdot\frac{d\boldsymbol{\Omega}(t)}{dt} + \boldsymbol{\Omega}(t)\times[\boldsymbol{I}\cdot\boldsymbol{\Omega}(t)] = \boldsymbol{T}(t) \tag{2.107}$$

6. The force acting on the FNs from the particle is determined by

$$\boldsymbol{g}(\boldsymbol{x}^e,t) = -\sum_{\boldsymbol{x}_j^l\in\Gamma_s} \boldsymbol{f}^{fsi}(\boldsymbol{x}_j^l,t)D(\boldsymbol{x}^e-\boldsymbol{x}_j^l)\Delta v_j \tag{2.108}$$

7. Collision step:

$$f_k(\boldsymbol{x},t) = \boldsymbol{C}\tilde{f}_k(\boldsymbol{x},t) + 3w_k\boldsymbol{g}(\boldsymbol{x}^e,t)\cdot\boldsymbol{e}_k \tag{2.109}$$

where $\boldsymbol{C}$ is the collision operator, $w_0 = 1/3$, $w_{1-6} = 1/18$, and $w_{7-18} = 1/36$.

Even though the EBF method has many advantages over the SBB method, one drawback of EBF is that the code gets unstable as the particle density becomes significantly lighter than the density of the surrounding fluid. For simulating a particle with $\rho_p < \rho_f$, the SBB method is a better choice.

2.3.2.3 Example: Single Prolate Spheroid in Linear Shear Flow

One of the several advantages of the SBB and EBF methods is the ability to efficiently study nonspherical particles in flows with inertia. In many industrial applications, for example, in papermaking, the particles of interest are elongated and thus highly nonspherical fibers. The quality of the final product is dependent not only on the spatial distribution but also on the orientation distribution of fibers. This, in turn, is dependent on the orientational dynamics of the fibers due to local velocity gradients in the flow of paper pulp. Consequently, it is important to understand how a single fiber behaves in a linear shear flow. The easiest way of going from a spherical particle to a fiber is to consider a prolate spheroid, which can be seen as a sphere that is elongated along a line. This line is thus an axis of rotational symmetry $\boldsymbol{s} = (s_x, s_y, s_z)$ and also determines the particle orientation. The aspect ratio of the particle is given by $r_p = l/w$, where l is the particle length and w is the equatorial diameter.

Considering a single prolate spheroid in a linear shear flow (illustrated in Figure 2.12a), there are two dimensionless quantities governing the orientational dynamics. The fluid inertia is quantified by the particle Reynolds number $Re_p = \dot{\gamma}l/\nu$ ($\dot{\gamma}$ is the shear rate and ν is the kinematic viscosity), and the particle inertia is quantified by the Stokes number $St = (\rho_s/\rho_f)\,Re_p$ (ρ_s and ρ_f are the solid and fluid densities, respectively).

Without any inertia ($Re_p = St = 0$), Jeffery (1922) found that the prolate spheroid is rotating in one of an infinite amount of periodic orbits determined by the initial orientation (see trajectories of (s_x, s_y) in Figure 2.12b). Using the EBF method, the flow problem was investigated by Rosén et al. (2014, 2015). It was found that there are several dynamical transitions that occur when increasing Re_p, which leads to different stable rotational states as described in Table 2.1 and illustrated in Figure 2.12c. Depending on the choice of Re_p and St, certain rotational states are stable, and it is found that there are 13 distinct regimes in the Re_p/St parameter space according to Figure 2.13. This parameter space furthermore looks qualitatively the same (i.e., the same sequence of transitions with increasing Re_p and/or St, but quantitative values are different) for any prolate spheroid with $r_p = 2$–6 but is believed to be even qualitatively valid for a wider range of r_p.

In regimes II–IV, the planar states (rotating or tumbling) coexist with a nonplanar state (Log-rolling, inclined rolling, inclined kayaking, or kayaking). In these regimes, there is an unstable limit cycle that separates the initial orientations leading to the planar and nonplanar rotation, respectively (see Figure 2.12), for example, a particle initialized at rest with an orientation inside the unstable limit cycle will enter a nonplanar rotation.

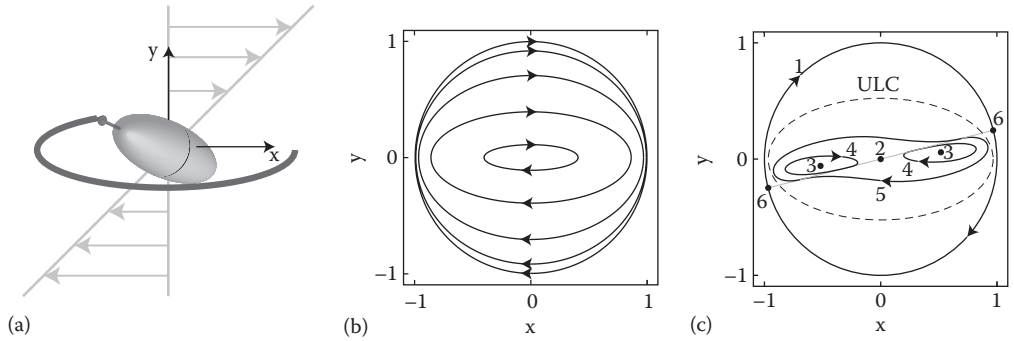


Figure 2.12

(a) A prolate spheroid is placed in a linear shear flow. The particle orientation is given by the direction of its symmetry axis, $\boldsymbol{s}$. (b) Trajectories of (s_x, s_y) at $Re_p = St = 0$ for a particle with $r_p = 4$ given by Jeffery (1922). (c) Schematic trajectories of (s_x, s_y) of stable rotational states at $Re_p > 0$. (1) Tumbling or rotating. (2) Log-rolling. (3) Inclined rolling. (4) Inclined kayaking. (5) Kayaking. (6) Steady state; An unstable limit cycle separates the nonplanar states (2–5) with the coexisting planar state (1).

Table 2.1 Description of the Rotational States of the Prolate Spheroid in Shear Flow

Rotational State	Rotational State (Abbr.)	Definition
Tumbling	T	$s_z = 0, \boldsymbol{s} = \boldsymbol{s}(t), \tau_p > \tau_c$
Rotating	R	$s_z = 0, \boldsymbol{s} = \boldsymbol{s}(t), \tau_p < \tau_c$
Steady state	S	$s_z = 0, \boldsymbol{s} = const.$
Log-rolling	LR	$s_z = 1, \boldsymbol{s} = const.$
Inclined rolling	IR	$0 < s_z < 1, \boldsymbol{s} = const.$
Inclined kayaking	IK	$0 < s_z < 1, \boldsymbol{s} = \boldsymbol{s}(t), \langle s_x \rangle \neq 0$
Kayaking	K	$0 < s_z < 1, \boldsymbol{s} = \boldsymbol{s}(t), \langle s_x \rangle = 0$

τ_p is the period of the rotation and $\tau_c = (\pi/\dot{\gamma}) \cdot (r_p + r_p^{-1} + 2)$.

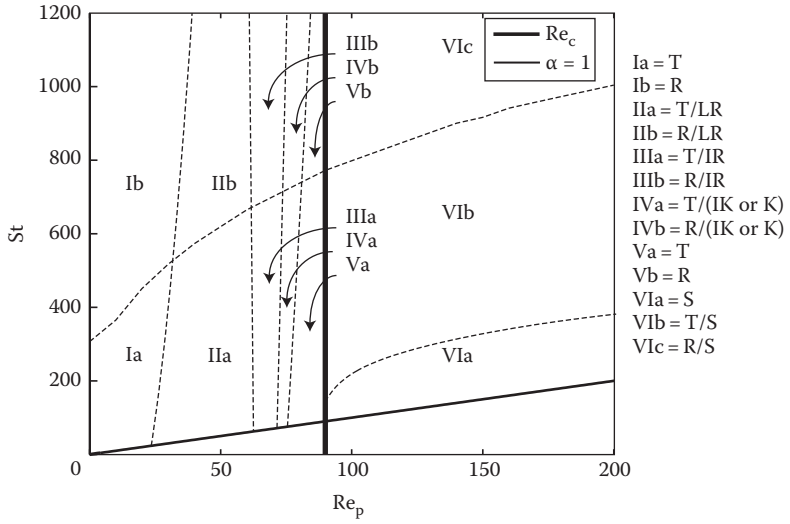


Figure 2.13

Stable rotational states of a prolate spheroid of $r_p = 4$ in a linear shear flow as found by Rosén et al. (2014, 2015); in regions with two stable states, the final state depends on initial conditions; and the steady state is created in a saddle-node bifurcation at $Re_p = Re_c$. The abbreviations of rotational states are found in Table 2.1.

At $Re_p = Re_c$, a steady state is created through a saddle-node bifurcation. This state will exist at all $Re_p > Re_c$. However, if St is high enough, the particle can gain enough angular momentum for a planar rotation to coexist with the steady state.

One of the main difficulties with the presented methods in this section (SBB and EBF) is the fact that there is no local grid refinement close to the particle surface. At higher Re_p, boundary layers need to be resolved around the particle to get quantitative results of critical Reynolds numbers (e.g., Re_c) that are independent of grid resolution. On the other hand, increasing resolution to fulfill the desired accuracy might be computationally unfeasible due to the uniform grid. Fortunately, the qualitative dynamics and the sequence of bifurcations are independent of resolution using the EBF method as long as $w \geq 6\Delta x$ (Rosén et al., 2015). The conclusion is that these methods are excellent tools for exploring unknown qualitative features of non-spherical particles in flows, but methods with local grid refinement are desirable for obtaining quantitative results at higher Re_p.

2.3.3 Suspension of Deformable Particles and Capsules

The dynamics of deformable capsules, vesicles, and soft particles have been of continued interest to the scientific community. Deformable particles exhibit much more complex dynamic behavior than rigid particles. Also, treating them as rigid solids will not properly capture the micro and macroscopic properties.

In suspensions, these complex dynamics affect the rheology of the bulk flow, creating non-Newtonian flow characteristics. For example, one of the most intensely studied deformable capsules, the red blood cell (RBC), is the major constituent of blood. As the local shear increases, so does the deformation of RBC, which results in a decreased suspension viscosity. This effect causes the shear-thinning behavior of blood.

2.3.3.1 Coupling Lattice Boltzmann with Finite Element Method

MacMeccan et al. (2009) introduced a method to simulate both deformable solid particles and deformable fluid-filled membranes, namely, capsules. This method couples the LBM for the fluid phase to a linear-elastic finite element analysis (FEA) describing particle deformation.

For deformable solid particles, the shear elastic number (Goddard Miller, 1967, Pal, 2003), $N_s e = \mu\gamma \cdot /G_S$, governs particle deformation, where μ is the fluid dynamic viscosity, γ is the fluid shear rate, and G_S is the particle shear modulus. For fluid-filled elastic capsules, the capillary number, $Ca_G = \mu\gamma \cdot R/G_M$, governs particle deformation, where R is the particle radius and G_M is the effective membrane shear modulus ($G_M = G_S \cdot t_M$ for membranes with thickness, t_M).

In both cases, deformable solid particle and fluid-filled elastic capsules, the trajectory and deformation of an elastic deformable particle are governed by Cauchy's equation,

$$\frac{D\rho_s \boldsymbol{u}_s}{Dt} = \nabla \cdot \boldsymbol{T} \tag{2.110}$$

in which the left-hand side is the material derivative of solid momentum and $\boldsymbol{T}$ is the elastic stress tensor. A transient FEA is chosen to calculate the time evolution of deformable particles in suspension, which integrates virtual work over the volume of the element:

$$\int tr(\bar{\varepsilon} \otimes \boldsymbol{T}) dV = \int \bar{\boldsymbol{X}} \cdot \boldsymbol{F}^{tr} dA + \int \bar{\boldsymbol{X}} \cdot \boldsymbol{F}^{b} dV \tag{2.111}$$

where

$\bar{\boldsymbol{X}}$ is the elemental virtual displacements
$\bar{\varepsilon}$ is an elemental virtual strain due to virtual displacements
$\boldsymbol{F}^{tr}$ are the traction stresses on the surface
$\boldsymbol{F}^{b}$ is the body stresses
A is the surface area
V is the volume

In this method, linear-elastic solid elements are used to model solid deformable particles such as platelets, and linear-elastic shell elements are used to model deformable fluid-filled membranes such as RBCs. The linear-elastic solid element is shown in Figure 2.14a with four nodes, and the linear-elastic shell element is shown in Figure 2.14b with three nodes.

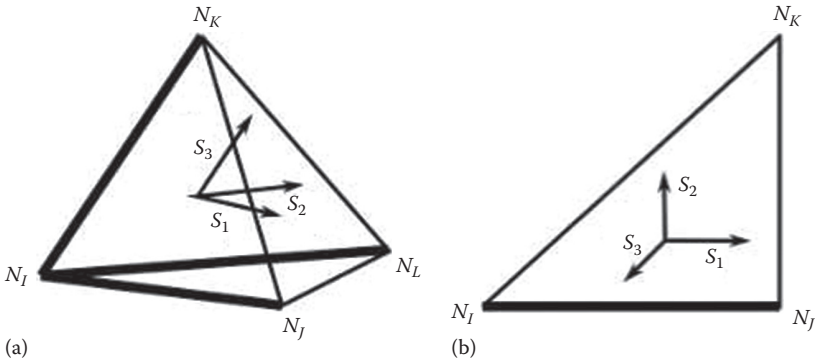


Figure 2.14

(a) Linear-elastic solid element with four nodes (tetrahedron) and (b) linear-elastic shell element with three nodes (triangle). Shell elements have a constant thickness and rotational degrees of freedom along elemental coordinates at each node for bending stiffness.

Through an interpolation or shape function, nodal displacements and positions can be related to elemental displacements and positions (for details, see MacMeccan et al., 2009, and Clausen, 2010). The integrals in 37 are evaluated in terms of nodal virtual displacements; elemental stiffness and mass matrices are constructed from elemental material properties such as density and elasticity. A detailed derivation of this process can be found in Bathe (1996). On summing over all elements in the object, the resulting transient finite element equation is obtained:

$$\boldsymbol{M}\ddot{x} + \boldsymbol{C}\dot{x} + \boldsymbol{K}x = \boldsymbol{F} \tag{2.112}$$

which determines the time evolution of the nodal displacement vector, x, and its time derivatives, $\dot{x}$ and $\ddot{x}$, where the nodal displacement vector is defined as the deformed node location minus the undeformed node location. The global mass, M, and stiffness, K, matrices are constructed from summing the elemental matrices, and the force vector, F, is calculated from traction forces resulting from the fluid–solid coupling. This transient finite element equation, 38, is solved using Newmark's integration method (for details, see MacMeccan et al., 2009, and Clausen, 2010).

In order to simulate large numbers of deformable particles in suspension, it is necessary to improve the efficiency of FEA by making the assumption of small body-fixed deformation. To comply with this assumption, a particle coordinate system is fixed on a particle's center of mass and oriented using the average angular displacement of the finite element nodes. Although elemental corotational procedures are typically used for large rotation problems (Rankin and Brogan, 1986, Campanelli et al., 2000), when averaged, the corotational procedure gives less consistent results than a simple average angular displacement. The use of a body-fixed coordinate system for the solid particles results in invariant linear-elastic stiffness, mass, and damping matrices that may be determined a priori for each type of particle.

Coupling between fluid and solid is based on lattice links crossing the solid boundary. These lattice links lie along lattice direction vectors and have endpoints on lattice nodes on either side of the particle boundary (Aidun et al., 1998). Lattice links are found on the discretized finite element surface using a ray-tracing algorithm commonly used in computer graphics. In this method, rays are projected along the lattice directions and tested for intersection with the triangles comprising the solid surface using a fast and minimum storage algorithm. The intersection is found through direct 3D calculation using barycentric coordinates, which eliminate the need for 2D projections or calculation of the plane equation for the triangle. For more details on this method, see the implementation by Moller and Trumbore (1997).

This LB–FEA hybrid method is capable of simulating $O(10^2)$ particles at high volume fraction (40%) on a desktop workstation. A snapshot from a wall-bounded shear simulation of 2472 RBCs at 40% volume fraction is shown in Figure 2.15 (Aidun and Clausen, 2010).

2.3.3.2 Coupling Lattice Boltzmann with Coarse-Grained Spectrin-Link Method

The spectrin-link (SL) method models the RBC membrane as a surface consisting of a triangular network. High-resolution studies using SL modeling were conducted by Li et al. (Li et al., 2005). This study set the SL

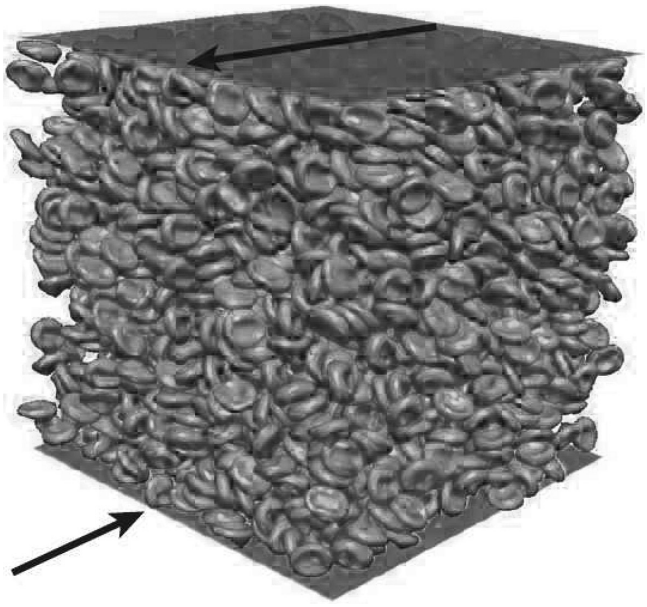


Figure 2.15

Wall-bounded simulation of 2472 deformable RBCs in shear at 40% concentration.

length scale to the same order of magnitude as the lengths of the proteins found in an actual RBC, see Figure 2.16 for a demonstration of this scale. While this method of modeling is incredibly realistic, it required the use of >25,000 vertices per RBC. This level of fidelity is not suitable for simulations of blood flow with realistic hematocrit. The use of a coarse-graining SL approach (Pivkin and Karniadakis, 2008, Fedosov et al., 2009) allows for the extension of the SL method to flows with thousands of deformable RBCs. One such benefit of the coarse-grained SL approach is the ability to resolve RBC deformation in capillary and shear flows (Pivkin and Karniadakis, 2008) where the high-resolution models are too expensive.

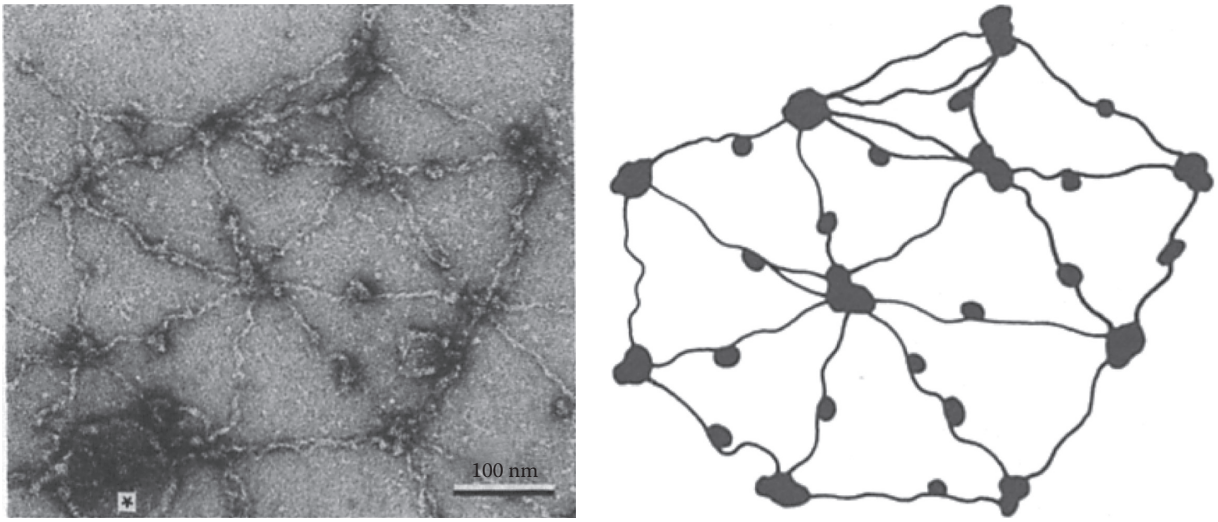
SL models, with the same number of vertices per RBC as linear finite element methods (MacMeccan et al., 2009) use less computer memory and expense but slightly more MPI communication. The SL method also does not require storage of a $(3N)^2$ (where N is the number of surface nodes with 3 degrees of freedom)-sized effective stiffness matrix inverse for updating RBC membrane deformation.

In the SL model, each RBC membrane consists of a network of points $\{\mathbf{x}_n, n \in 1\ldots N\}$, which are the vertices of the RBC surface triangulation. The area of a triangle $\alpha \in 1\ldots\prod$ formed by the vertices (l, m, n) is given by $A_\alpha = 1/2|(\mathbf{x}_m - \mathbf{x}_l) \times (\mathbf{x}_n - \mathbf{x}_l)|$. The total area of the RBC surface is given by, $A_{\text{total}} = \sum_{\alpha\in\prod} A_\alpha$, and the total volume is given as $\Omega_{\text{total}} = \sum_{\alpha\in\prod} (\mathbf{x}_\alpha \cdot \mathbf{n}_\alpha) A_\alpha/3$, where $\mathbf{x}_\alpha = 1/3(\mathbf{x}_m + \mathbf{x}_n + \mathbf{x}_l)$ is the center of triangle α. The length of the link $i \in 1\ldots S$ connecting two vertices m and n is given by $L_i = |\mathbf{x}_m - \mathbf{x}_n|$. The lists of unique links and unique triangle pairs are established prior to simulations. The Helmholtz free energy of the system is given as

$$E\{\mathbf{x}_n\} = E_{\text{in-plane}} + E_{\text{bending}} + E_{\text{volume}} + E_{\text{area}}. \tag{2.113}$$

The in-plane contribution relevant to shear properties is a force–length relationship rooted in DNA mechanics (Marko and Siggia, 1995, Bustamante et al., 2003). The bending contribution takes into account the spontaneous and instantaneous angles between adjacent pairs of triangles (Fedosov et al., 2009). The constraint on volume ensures the volume of the RBC enclosed by the triangulated membrane remains constant, with a similar constraint on the surface area. This conservation of area is essential in a realistic model of blood cells. Each of the vertices combines to form the triangulated RBC membrane surface advances according to Newton's equations of motion:

$$\frac{d\mathbf{x}_n}{dt} = \mathbf{v}_n; \quad M\frac{d\mathbf{v}_n}{dt} = \mathbf{f}_n + \mathbf{f}_n^{\text{LB}} + \mathbf{f}_n^{\text{PP}} \tag{2.114}$$



(a) (b)

Figure 2.16

(a) A highly magnified image of a spread membrane skeleton derived from normal red cell ghosts. Displayed to provide a scale to the order of the proteins in an actual red blood cell. (b) A diagram demonstrating the structure of the proteins in a red blood cell (Liu et al., 1987).

where $\mathbf{v}_n$ is the velocity of vertex n and M is taken to be a fictitious mass at each point chosen to yield the same membrane mass as previous linear finite element studies (MacMeccan et al., 2009). The external forces $\mathbf{f}_n^{\mathrm{LB}}$ are forces on the vertex due to fluid–structure interaction and $\mathbf{f}_n^{\mathrm{PP}}$ are forces due to particle–particle interactions. The forces due to the SL model via Helmholtz free energy contributions are denoted by $\mathbf{f}_n$ and are given as

$$\mathbf{f}_n = -\frac{\partial E\{\mathbf{x}_n\}}{\partial \mathbf{x}_n} \tag{2.115}$$

This method uses analytic forms obtained by using Mathematica's symbolic manipulation capabilities as was the case in Pivkin and Karniadakis (2008). This method aims to minimize the total energy given from Equation 2.113. In the absence of bending energy, the equilibrium shape will be a sphere with the volume specified by a desired RBC volume. When bending energy is present, the equilibrium shape is a biconcave disk representative of a RBC. As a result, spherical membrane meshes can be used as a starting point for RBC simulations. Equation 2.114 are solved using a first-order accurate time integration scheme.

2.3.4 Suspension of Deformable Fibers

Modeling suspensions of deformable fibers are of interest in many material processing applications, for example, papermaking (Lundell et al., 2011). Fibers are characterized by the fact that they have a large aspect ratio: the smallest length scale is very small compared to the fiber length. Thus, the resolution needs to be very high if the flow on the length scale of the fiber diameter is to be resolved and systems much larger than the fiber length cannot be simulated. Furthermore, the deformation of the fibers needs to be modeled.

Wu and Aidun (2010b) used LBM with EBF together with a flexible fiber model and showed that suspensions with deformable fibers could be modeled without totally resolving the flow on the fiber diameter scale and the resolution is approximately one lattice per fiber diameter. The simulation results obtained from the model agree well with available measurements, both in terms of fiber deformation and rheological data. This method has been used to investigate the effect of fiber stiffness on the rheology of sheared fiber suspensions (Wu and Aidun, 2010c).

2.3.4.1 Flexible Fiber Model and Fluid–Solid Interaction

The fibers are assumed to have elastic and shear moduli of E_γ and E_G, respectively, and each fiber is modeled as a chain of rods connected by hinges (see Figure 2.17). A fiber bends and twists at the hinges and changes length by the elasticity of the rods, which remain straight. The resistances to elongation, bending, and twisting are given by E_γ and E_G. The fiber is exposed to forces and the total force on a fiber determines its acceleration whereas the distribution of this force among its hinges determines its deformation.

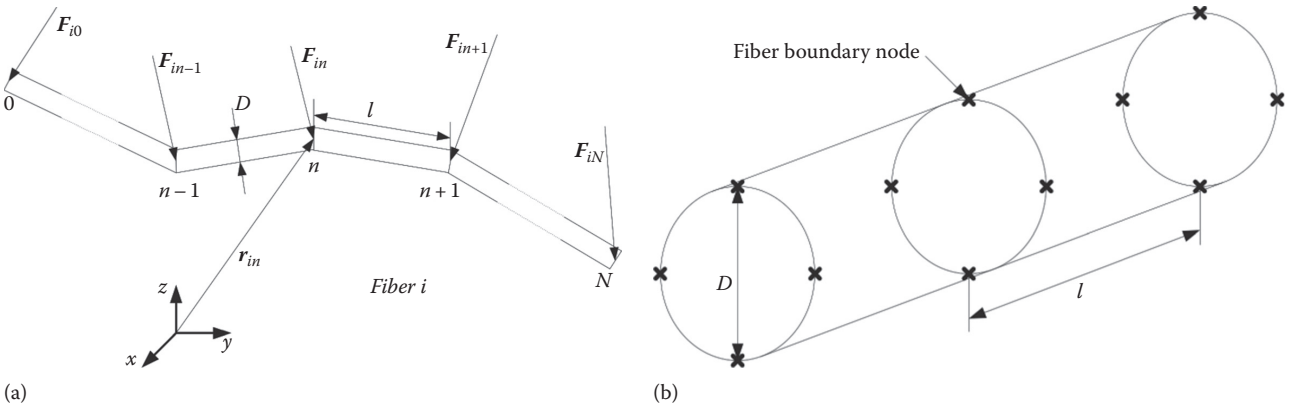


Figure 2.17

(a) Illustration of a fiber consisting of rods and hinges with external forces acting on the hinges. (b) Two rods and three hinges with the fiber boundary nodes are indicated (Wu and Aidun, 2010b).

There are several sources of forces on a fiber. The fluid–structure interaction forces $\mathbf{F}^{fsi}$ can be complemented with gravity $\mathbf{F}^{gra}$ and other forces due to external fields. There are also interparticle forces (electrical $\mathbf{F}^{ele}$, contact $\mathbf{F}^{con}$, or lubrication $\mathbf{F}^{lub}$). The fibers are assumed to be large enough so that Brownian forces can be neglected.

In a model used by previous investigators (Wu and Aidun, 2010b,c), all forces on the fiber are exerted on the hinges. Since buoyant fibers with no external field are only exposed to the fluid–solid interaction forces $\mathbf{F}^{fsi}$, they are calculated according to equation 3 at the four boundary nodes of each hinge. In order to prevent fibers from crossing each other and avoid singularities, a lubrication force (Yamane et al., 1994) proportional to the relative velocity between two hinges is used if the hinges are closer to each other than 0.25D. In order to ensure stability, the hinge velocities are reset to nonapproaching values if the hinges come very close to each other in spite of the lubrication force (which is repelling for approaching hinges).

2.3.4.2 Example Results

A model of suspensions of flexible fibers should be evaluated by its ability to predict both single fiber motion and suspension rheology. In Figure 2.18a, it is shown that the calculated flipping period of a fiber in linear shear flow from the LBM-EBF model agrees with previous results. For the flexible fibers, Figure 2.18b shows that the position of the fiber endpoints agrees well with the experiments of EMBC (2009) who took photographs of a long nylon filament (with an aspect ratio of 170) at short time intervals during rotation in shear.

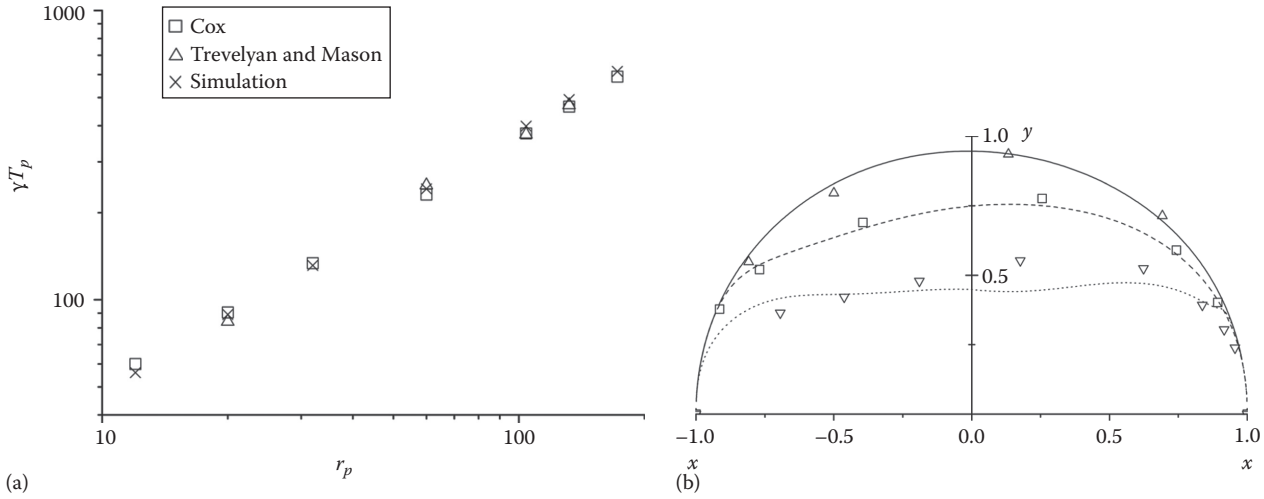


Figure 2.18

(a) Period for one rotation in creeping shear flow as a function of fiber aspect ratio r_p for a stiff fiber compared with theoretical (Cox, 1971) and experimental (Trevelyan and Mason, 1951) results. (b) Trajectory of a fiber endpoint during one flip of elastic fibers; the full, dashed, and dotted lines are present simulations and markers are (EMBC, 2009) at different shear rates. The physical properties of the liquid and fibers are matched. (From Wu, J. and Aidun, C.K., *Int. J. Multiphase Flow*, 36, 202, 2010b.)

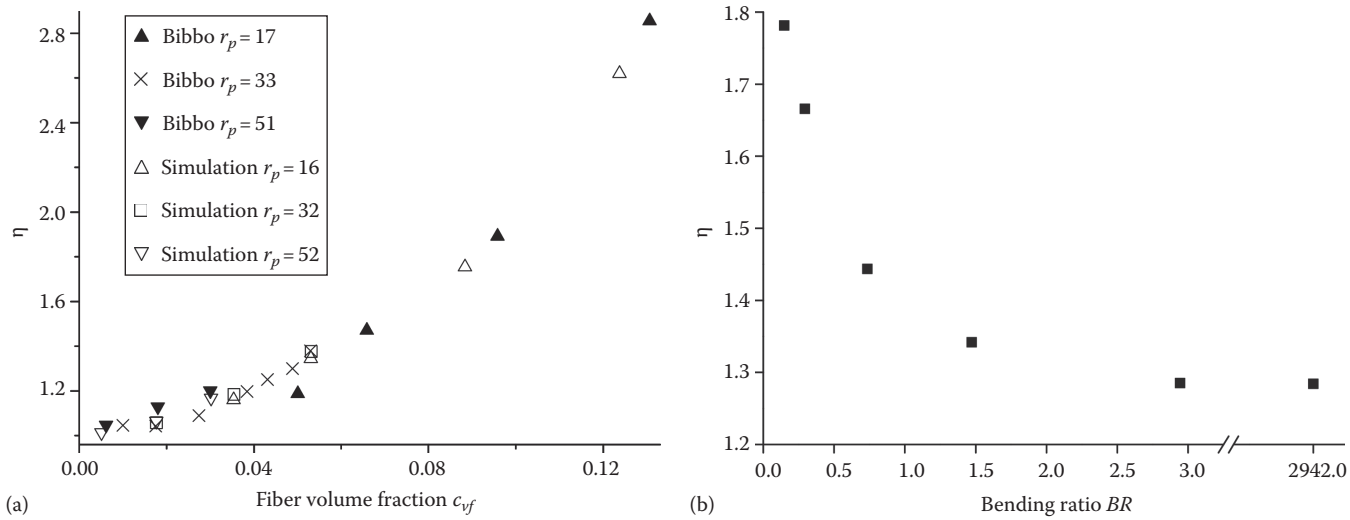


Figure 2.19

(a) Relative shear viscosity as a function of fiber volume fraction from present simulations (open symbols) and previous experiments (Bibbo, 1987). The bending ratios are 2942, 248, and 42 for r_p = 16, 32, and 52, respectively. (b) Relative viscosity as a function of bending ratio for an aspect ratio of r_p = 16 and a fiber volume fraction of c_{vf} = 0.053. (From Wu, J. and Aidun, C.K., *Int. J. Multiphase Flow*, 36, 202, 2010b.)

The stiffness of fibers is often characterized by the nondimensional bending ratio

$$BR = \frac{E_\gamma(\ln 2r_e - 15)}{2\mu\dot{\gamma}r_p^4}$$

where

r_p is the aspect ratio of the cylindrical fiber

$r_e = 1.24r_p/\sqrt{\ln r_p}$ is an equivalent aspect ratio relating results for ellipsoids with results to circular cylinders

μ is the dynamic viscosity of the fluid

$\dot{\gamma}$ is the shear rate

Rheological verification for elastic fibers is demonstrated in Figure 2.19a where the relative shear viscosity obtained from the LBM-EBF method as a function of volume fraction is shown to agree with experiments (Bibbo, 1987) for r_p = 16, 32, and 52 (BR = 2942, 248, and 42). The LBM-EBF simulations can also be used to study the decay of relative shear viscosity as BR is increased; see Figure 2.19.

2.3.5 Liquid–Gas Flow

Since very early into the development of LB models, investigators have been attempting to develop a method of studying multiphase flow problems. At first glance, it would seem that LB lends itself quite naturally to these problems. Because of the way the model works, the fluids in question can be modeled individually with some manner of separating influence acting between them. Building on this idea, the earliest idea in LB multiphase modeling was formed. The R–K model, developed by Rothman and Keller (1988), was later refined into the color fluid model proposed by Gunstensen et al. (1991). This method worked on the idea described earlier. It introduces a distribution function for each fluid and then added a segregation step that forced particles of each fluid into their own regions. Soon after, another idea, following the same premise of modeling the two fluids independently and interacting them, was developed. This was the Shan and Chen method (Shan and Chen, 1993). Rather than interacting the fluids by forcing them apart with a separation step, the S–C method introduced an external force acting on both fluids. This was the interaction force between the two fluids. The S–C model is the most popular LB variant for the modeling of multiphase problems; most likely because of the ease with which it is implemented. However, the S–C model has a number of problems that will be detailed later in this section. In response to these problems a couple of new methods arose: the free energy method and the mean field theory model. These two models operate on completely different theories than the R–K and S–C models. The previous

two models were very intuitive. When there was a single fluid, there would be a density distribution function for it. So, if there are two fluids, then there should be a density distribution for each fluid. Afterward, some manner of interaction is added to ensure that all the fluids involved are affected by one another. However, the next two models operate very differently. They take advantage of the fact that density is not the only property that can be expressed as a distribution function and modeled with an evolution equation. The free energy model, developed by Swift et al. (1995), solves an evolution equation with a distribution function of the total density and another evolution equation with a distribution function of the difference in the densities. Next, the mean field theory model was proposed by He et al. (1999). This model introduces a distribution function for pressure and a distribution function for an index function, which is function of the two densities.

2.3.5.1 The R–K (Rothman and Keller) Model

This model begins by creating a density distribution function for each fluid:

$$f_k^i(\boldsymbol{x}+\boldsymbol{e}_k,t+\delta_t)-f_k^i(\boldsymbol{x},t)=-\frac{1}{\tau^i}\left[f_k^i(\boldsymbol{x},t)-f_k^{i,eq}(\boldsymbol{x},t)\right]+\Omega^i, \tag{2.116}$$

Here, the superscript *i* denotes which fluid is being studied and ranges from 1 to the total number of fluids, α. Also immediately noticeable is the presence of an extra term, Ω^i, added to the LBGK collision term. This extra term in the collision operator has been modified by several investigators in the past; the extension for D2Q9 proposed by Grunau et al. (1993) had it in the form

$$\Omega^i=\frac{A^i\,|\boldsymbol{Co}|}{2}\frac{\boldsymbol{e}_k\cdot\boldsymbol{Co}}{|\boldsymbol{Co}|^2}-\frac{3}{4} \tag{2.117}$$

Here, ***Co*** is an approximation of the gradient of the density difference, written for two fluids as

$$\boldsymbol{Co}(\vec{x})=\sum_{k=1}^{8}\boldsymbol{e}_k(\rho^1(\boldsymbol{x}+\boldsymbol{e}_k)-\rho^2(\vec{x}+\vec{e}_k)) \tag{2.118}$$

One more important change to the collation operator is in the equilibrium density distribution function itself. In order to ensure a stable interface, a modified version of the pressure-corrected equilibrium distribution function proposed by Chen et al. (1991) is used. The details of the modification to this single-phase function can also be found in Grunau et al. (1993).

2.3.5.2 Shan and Chen Model

As mentioned earlier, the S–C model keeps with the theme introduced by the R–K model of simply adding another density distribution function for each fluid and allowing for some interaction. As with R–K, we first introduce an evolution equation for the density distribution of each fluid; in this model, we use

$$f_k^i(\boldsymbol{x}+\boldsymbol{e}_k,t+\delta_t)-f_k^i(\boldsymbol{x},t)=-\frac{1}{\tau^i}\left[f_k^i(\boldsymbol{x},t)-f_k^{i,eq}(\boldsymbol{x},t)\right] \tag{2.119}$$

and as earlier

$$\sum_{k=1}^{8}f_k^i=\rho^i\quad\text{and}\quad\sum_{k=1}^{8}f_k^i\boldsymbol{e}_k=\rho^i\boldsymbol{u}^i \tag{2.120}$$

The S–C model differs from the R–K model in how the fluids in question are allowed to interact. To allow for the interaction, a modified velocity term is included in the calculation of the equilibrium density distribution function. To calculate this modified velocity, first, a common velocity term, $\bar{\boldsymbol{u}}^i$, is needed. This is calculated by what is effectively mass averaging

$$\bar{\boldsymbol{u}}^i=\frac{\sum_{i=1}^{\alpha}\frac{\rho^i\boldsymbol{u}^i}{\tau^i}}{\sum_{i=1}^{\alpha}\frac{\rho^i}{\tau^i}} \tag{2.121}$$

Now, the modified velocity, sometimes called the equilibrium velocity, can be determined by

$$\rho^i \boldsymbol{u}^{ieq} = \rho^i \bar{\boldsymbol{u}}^{ieq} + \tau^i \boldsymbol{F}^i \tag{2.122}$$

Here, the force term, $\boldsymbol{F}^i$, is the sum of the forces acting on the fluid i at the node; this means other forces can be added to the model as well. A good example, demonstrated by Huang et al. (2009), is the inclusion of external forces and adhesion forces. For simplicity, in this demonstration, only the interparticle forces will be considered. The derivation of the interparticle forces, demonstrated in Martys and Chen (1996), is rather simple. Start with the interaction potential

$$V(\boldsymbol{x}, \dot{\boldsymbol{x}}) = G^{i,\dot{l}} \psi^i(\boldsymbol{x}) \psi^{\dot{l}}(\dot{\boldsymbol{x}}) \tag{2.123}$$

This is the equation for the interaction potential between a fluid i at a position $\boldsymbol{x}$ and a fluid l at a position $\dot{x}$. ψ^i is the effective mass of fluid i at position $\boldsymbol{x}$. The effective mass is a function of density derived from the equation of state. It is shown by Yuan and Schaefer (2006) that with pressure as a function of density known, an expression for the effective mass can be derived. Finally, G controls the strength of the interaction between the two points in question. At this point, the model makes a key simplification. It assumes that only the neighboring nodes affect the interaction. This allows the description of the rate of change of momentum to be simplified, which in turn allows for an expression for the interparticle force as

$$F^i_{int}(\boldsymbol{x}) = -\psi^{\dot{l}}(\boldsymbol{x}) \sum_{\dot{x}} \sum_{\dot{l}=1}^{\alpha} G^{i\dot{l}}(\boldsymbol{x}, \dot{\boldsymbol{x}}) \psi^{\dot{l}}(\dot{\boldsymbol{x}}) (\dot{\boldsymbol{x}} - \boldsymbol{x}) \tag{2.124}$$

Again, it should be emphasized that this G is assumed to be 0 for any two nodes, except when they are directly adjacent. With this, it is possible to calculate the equilibrium velocity, and the equilibrium velocity can be used to calculate the equilibrium density distribution function. This part of the method is identical to the process in the single relaxation time lattice Boltzmann.

2.3.5.3 Free Energy Model

The free energy model is immediately different from the previous two models. It introduces three new variables: total density, ρ^t; mean fluid velocity, $\boldsymbol{u}$; and the density difference, $\Delta\rho$. For two fluids

$$\rho^t = \rho^1 + \rho^2 \quad \text{and} \quad \Delta\rho^t = \rho^1 - \rho^2 \tag{2.125}$$

The density distribution function of ρ^t is called f, due to it similarity to the density distribution function in single-fluid lattice Boltzmann. The density distribution function of $\Delta\rho$ is called Δ. These distribution functions can be related to their physical counterparts by

$$\sum_k f_k = \rho, \quad \sum_k f_k \boldsymbol{e}_k = \rho \boldsymbol{u}, \quad \text{and} \quad \sum_k \Delta_k = \Delta\rho \tag{2.126}$$

Now the two evolution equations can be introduced:

$$f^i_k(\boldsymbol{x} + \boldsymbol{e}_k, t + \delta_t) - f^i_k(\boldsymbol{x}, t) = -\frac{1}{\tau_t}\left[f^i_k(\boldsymbol{x}, t) - f^{i,eq}_k(\boldsymbol{x}, t) \right] \tag{2.127}$$

$$\Delta^i_k(\boldsymbol{x} + \boldsymbol{e}_k, t + \delta_t) - \Delta^i_k(\boldsymbol{x}, t) = -\frac{1}{\tau_\Delta}\left[\Delta^i_k(\boldsymbol{x}, t) - \Delta^{i,eq}_k(\boldsymbol{x}, t) \right] \tag{2.128}$$

The equilibrium functions and their derivations can be found in the original paper by Swift et al. (1995).

2.3.5.4 The Mean Field Theory Model

Like the free energy model, the mean field theory model operates with distributions of new variables. The first distribution function is g, where g is related to the density distribution function f by

$$g = fRT + \psi(\rho)\Gamma(\mathbf{0}) \tag{2.129}$$

As earlier, the function, $\Psi(\rho)$, is the effective mass and can be determined from the equation of state. R is the gas constant and T is the temperature. The function, $\Gamma(\boldsymbol{u})$, is dependent on the velocity by

$$\Gamma(\boldsymbol{u}) = \frac{1}{(2\pi RT)^{D/2}} exp^{-\frac{(\boldsymbol{e}_k - \boldsymbol{u})}{2RT}} \tag{2.130}$$

where D is the dimension of the problem. From what is known about the density distribution function and the definition of incompressible fluids, He et al. (1999) derive an evolution equation for g as

$$g_k^i(\boldsymbol{x} + \boldsymbol{e}_k, t + \delta_t) - g_k^i(\boldsymbol{x}, t) = -\frac{1}{\tau_t}\left[g_k^i(\boldsymbol{x}, t) - g_k^{i,eq}(\boldsymbol{x}, t)\right] + (\boldsymbol{e}_k - \boldsymbol{u}) \cdot (\Gamma(\boldsymbol{u})(\boldsymbol{F}_s + \boldsymbol{F}_b) - (\Gamma(\boldsymbol{u}) - \Gamma(\mathbf{0}))\nabla\Psi(\rho)) \tag{2.131}$$

Here,

F_b is an external body force

F_s is a force associated with the surface tension

From g, the total density and total velocity can be recovered by

$$\sum_k g_k = \rho \quad \text{and} \quad \sum_k g_k \boldsymbol{e}_k = \rho RT\boldsymbol{u} \tag{2.132}$$

This alone cannot close the equations in multiphase problems. Another variable is introduced, an index function, ϕ, such as the ones introduced in the level set approaches used by Osher and Sethian (1988). Its distribution function h is defined by

$$\sum_k h_k = \phi \tag{2.133}$$

And the evolution equation for h comes to

$$h_k^i(\boldsymbol{x} + \boldsymbol{e}_k, t + \delta_t) - h_k^i(\boldsymbol{x}, t) = -\frac{1}{\tau_t}\left[h_k^i(\boldsymbol{x}, t) - h_k^{i,eq}(\boldsymbol{x}, t)\right] + \frac{(\boldsymbol{e}_k - \boldsymbol{u}) \cdot \nabla\Psi(\phi)}{RT}\Gamma(\boldsymbol{u}) \tag{2.134}$$

It can be shown that g and h have simple equilibrium equations of the form

$$h^{eq} = \phi\Gamma(\boldsymbol{u}) \tag{2.135}$$

$$g^{eq} = \rho RT\Gamma(\boldsymbol{u}) + \Psi(\rho)\Gamma(0) \tag{2.136}$$

2.3.5.5 Front Tracking in Lattice Boltzmann

There exist a number of problems with each of these methods of treating multiphase problems with lattice Boltzmann. Since the S–C method is the most popular method, its problems have been discussed the most. In particular, the S–C method has difficulty in producing a sharp boundary. The method produces a great deal of unphysical diffusion that blurs the interface between fluids. This problem can be eliminated by switching to another method; the mean field theory method in particular produces a very sharp interface by virtue of how the index function works. However, no other method can match S–C in the ease with which it is implemented. In recent years, research has been done in using front tracking with

the S–C model. The aim is to maintain the simplicity of the S–C method and produce a sharp interface. In the past, Popinet and Zaleski (1999) used the idea of placing a large number of particles on an interface and tracking the movements of these particles to get a more accurate representation of the evolution of the interface. The idea has since also been used by Shin et al. (2005). This method works by placing a dense line of particles over the initial fluid interface. These particles do not interact with one another and they only interact with the fluid. The idea is that the particles should be moving with the fluid flow. Any deviation between the location of the interface and the location of the particles must be a numerical error and needs to be corrected.

References

Aidun, C.K. and Clausen, J.R., Lattice-boltzmann method for complex flows, *Ann. Rev. Fluid Mech.*, 42, 439–472, 2010.

Aidun, C.K., Lu, Y., and Ding, E.-J., Direct analysis of particulate suspensions with inertia using the discrete Boltzmann equation, *J. Fluid Mech.*, 373, 287, 1998.

Bathe, K., *Finite Element Procedures*, Prentice-Hall International Series in, Prentice Hall, Upper Saddle, NJ, 1996.

Bhatnagar, P.L., Gross, E.P., and Krook, M., A model for collision processes in gases. i. small amplitude processes in charged and neutral one-component systems, *Phys. Rev.*, 94, 511–525, May 1954.

Bibbo, M., Rheology of semi-concentrated fiber suspensions, PhD thesis, Massachusetts Institute of Technology, Cambridge, MA, 1987.

Bustamante, C., Bryant, Z., and Smith, S.B., Ten years of tension: Single-molecule DNA mechanics, *Nature*, 421(6921), 423–427, 2003.

Campanelli, M., Berzeri, M., and Shabana, A.A., Performance of the incremental and non-incremental finite element formulations in flexible multibody problems, *J. Mech. Des.*, 122(4), 498–507, 2000.

Chen, S., Doolen, G., Eggert, K., Grunau, D., and Loh, E., Local lattice-gas model for immiscible fluids, *Phys. Rev. A*, 43(12), 7053, 1991.

Clausen, J.R., The effect of particle deformation on the rheology and microstructure of noncolloidal suspensions, 2010.

Cox, R.G., The motion of long slender bodies in a viscous fluid. part 2. shear flow, *J. Fluid Mech.*, 45, 625, 1971.

EMBC 2009. *Annual International Conference of the IEEE*, IEEE, Minneapolis, MN, 2009, pp. 4266–4269.

Fedosov, D.A., Caswell, B., and Karniadakis, G.E., Coarse-grained red blood cell model with accurate mechanical properties, rheology and dynamics, in *Engineering in Medicine and Biology Society, 2009. EMBC 2009. Annual International Conference of the IEEE*, IEEE, 2009, pp. 4266–4269.

Frisch, U., dHumieres, D., Hasslacher, B., Lallemand, P., Pomeau, Y., Rivet, J.-P. et al., Lattice gas hydrodynamics in two and three dimensions, *Complex Syst.*, 1(4), 649–707, 1987.

Goddard, J. and Miller, C., Nonlinear effects in the rheology of dilute suspensions, *J. Fluid Mech.*, 28(4), 657–673, 1967.

Grunau, D., Chen, S., and Eggert, K., A lattice boltzmann model for multiphase fluid flows, *Phys. Fluids A: Fluid Dyn. (1989–1993)*, 5(10), 2557–2562, 1993.

Gunstensen, A.K., Rothman, D.H., Zaleski, S., and Zanetti, G., Lattice boltzmann model of immiscible fluids, *Phys. Rev. A*, 43(8), 4320, 1991.

He, X., Chen, S., and Zhang, R., A lattice boltzmann scheme for incompressible multiphase flow and its application in simulation of rayleigh–taylor instability, *J. Comput. Phys.*, 152(2), 642–663, 1999.

He, X. and Luo, L.-S., Lattice boltzmann model for the incompressible navier–stokes equation, *J. Stat. Phys.*, 88(3–4), 927–944, 1997.

Higuera, F. and Jimenez, J., Boltzmann approach to lattice gas simulations, *EPL*, 9(7), 663, 1989.

Huang, H., Li, Z., Liu, S., and Lu, X.-Y., Shan-and-chen-type multiphase lattice boltzmann study of viscous coupling effects for two-phase flow in porous media, *Int. J. Numer. Methods Fluids*, 61(3), 341–354, 2009.

Jeffery, G.B., The motion of ellipsoidal particles immersed in a viscous fluid, *Proc. R. Soc. Lond. A*, 102, 161, 1922.

Li, J., Dao, M., Lim, C., and Suresh, S., Spectrin-level modeling of the cytoskeleton and optical tweezers stretching of the erythrocyte, *Biophys. J.*, 88(5), 3707–3719, 2005.

Liu, S.-C., Derick, L.H., and Palek, J., Visualization of the hexagonal lattice in the erythrocyte membrane skeleton, *J. Cell Biol.*, 104(3), 527–536, 1987.

Lundell, F., Söderberg, L.D., and Alfredsson, P.H., Fluid mechanics of papermaking, *Ann. Rev. Fluid Mech.*, 43, 195, 2011.

MacMeccan, R.M., Clausen, J., Neitzel, G., and Aidun, C., Simulating deformable particle suspensions using a coupled lattice-boltzmann and finite-element method, *J. Fluid Mech.*, 618, 13–39, 2009.
Marko, J.F. and Siggia, E.D., Stretching DNA, *Macromolecules*, 28(26), 8759–8770, 1995.
Martys, N.S. and Chen, H., Simulation of multicomponent fluids in complex three-dimensional geometries by the lattice boltzmann method, *Phys. Rev. E*, 53(1), 743, 1996.
Möller, T. and Trumbore, B., Fast, minimum storage ray-triangle intersection, *J. Graph. Tools*, 2(1), 21–28, 1997.
Osher, S. and Sethian, J.A., Fronts propagating with curvature-dependent speed: Algorithms based on hamilton-jacobi formulations, *J. Comput. Phys.*, 79(1), 12–49, 1988.
Pal, R., Rheology of concentrated suspensions of deformable elastic particles such as human erythrocytes, *J. Biomech.*, 36(7), 981–989, 2003.
Popinet, S. and Zaleski, S., A front-tracking algorithm for accurate representation of surface tension, *Int. J. Numer. Methods Fluids*, 30(6), 775–793, 1999.
Peskin, C.S., The immersed boundary method, *Acta Numer.*, 11, 479, 2002.
Pivkin, I.V. and Karniadakis, G.E., Accurate coarse-grained modeling of red blood cells, *Phys. Rev. Lett.*, 101(11), 118105, 2008.
Rankin, C. and Brogan, F., An element independent corotational procedure for the treatment of large rotations, *J. Pressure Vessel Technol.*, 108(2), 165–174, 1986.
Rosén, T., Lundell, F., and Aidun, C.K., Effect of fluid inertia on the dynamics and scaling of neutrally buoyant particles in shear flow, *J. Fluid Mech.*, 738, 563–590, 2014.
Rothman, D.H. and Keller, J.M., Immiscible cellular-automaton fluids, *J. Stat. Phys.*, 52(3–4), 1119–1127, 1988.
Shan, X. and Chen, H., Lattice boltzmann model for simulating flows with multiple phases and components, *Phys. Rev. E*, 47(3), 1815, 1993.
Shin, S., Abdel-Khalik, S., Daru, V., and Juric, D., Accurate representation of surface tension using the level contour reconstruction method, *J. Comput. Phys.*, 203(2), 493–516, 2005.
Swift, M.R., Osborn, W., and Yeomans, J., Lattice boltzmann simulation of nonideal fluids, *Phys. Rev. Lett.*, 75(5), 830, 1995.
Trevelyan, B. and Mason, S.G., Particle motions in sheared suspensions. 1. Rotations, *J. Colloid Sci.*, 6, 354, 1951.
Wu, J. and Aidun, C.K., Simulating 3D deformable particle suspensions using lattice Boltzmann method with discrete external boundary force, *Int. J. Numer. Methods Flow*, 62, 765, 2010a.
Wu, J. and Aidun, C.K., A method for direct simulation of flexible fiber suspensions using lattice Boltzmann equation with external boundary force, *Int. J. Multiphase Flow*, 36, 202, 2010b.
Wu, J. and Aidun, C.K., A numerical study of the effect of fibre stiffness on the rheology of sheared flexible fibre suspensions, *J. Fluid Mech.*, 662, 123, 2010c.
Yamane, Y., Kaneda, Y., and Doi, M., Numerical simulation of semi-dilute suspensions of rodlike particles in shear flow, *J. Non-Newton. Fluid Mech.*, 54, 405, 1994.
Yuan, P. and Schaefer, L., Equations of state in a lattice boltzmann model, *Phys. Fluids* (*1994-present*), 18(4), 042101, 2006.

2.4 Immersed Boundary Method

Zhi-Gang Feng and Efstathios E. Michaelides

2.4.1 Introduction

The prescription of the interfacial boundary conditions is a rather peculiar feature within the framework of the governing equations the numerical codes solve. In our Newtonian scientific framework, the governing equations that are solved for the transport of momentum are given in terms of forces (rates of change of momentum), while velocity interfacial conditions need to be prescribed at the interface by a commonly agreed convention or experimental data. A more consistent approach within the Newtonian framework would be to describe the interfaces and other boundaries in terms of interfacial forces. Peskin (1977) used such an approach and developed the immersed boundary method (IBM) in order to model the flow of blood in the heart. The method uses a fixed Cartesian mesh for the fluid, which is composed of Eulerian nodes. For the solid boundaries, which are immersed in the fluid, the IBM uses a set of Lagrangian points that are advected according to the rules of fluid–solid interactions. The boundaries are modeled as continuous force fields acting on the fluid.

Feng and Michaelides (2004) combined the IBM and the lattice Boltzmann method (LBM) for the first time to model the flow and interactions of groups of particles in flow systems. They computed the boundary surface force at the interfaces using a numerical penalty method. The advantage of the IBM is that instead of remeshing the fluid domain to account for the flow of particles, the method uses a fixed mesh to represent the fluid field. The moving boundaries of the particles are represented by a set of Lagrangian boundary points, which are advected by the fluid. Feng and Michaelides (2005) developed the *Proteus* code, using a numerical method that combines direct forcing (DF) scheme (Mohd-Yusof, 1997) and the IBM. *Proteus* makes use of Eulerian lattice nodes for the fluid flow field and Lagrangian boundary nodes to represent particles or moving boundary surfaces. A few months later, Uhlmann (2005) also developed a similar computational method that combines the IBM with a finite-difference-based fluid solver. This section describes in more detail the implementation of the IBM in isothermal particulate flows as well as particulate flows with interfacial heat and mass transfer. A recent extension of the IBM has been developed in combination with the resolved discrete particle model (RDPM) to be used primarily with heat and mass interaction in the particulate flow systems. This numerical scheme has also received significant attention (Gan et al., 2003, Yu and Shao, 2007, Feng and Michaelides 2008, 2009a, Tavassoli et al., 2013, Tenetti et al., 2013) and is briefly described at the end of this section.

2.4.2 Fundamentals of the Immersed Boundary Method

The key characteristic of the IBM is that the existence of a solid body is represented by its effect on the fluid as a force field. This is implemented by introducing a *body force density* term into the fluid momentum equations. Let us consider a particle with a boundary surface, Γ, immersed in a 3D incompressible viscous fluid with a domain, Ω. The particle boundary surface, Γ, is represented by the Lagrangian parametric coordinates, $\boldsymbol{s}$, and the flow domain, Ω, is represented by the Eulerian coordinates $\boldsymbol{x}$. Hence, the positions of the surface may be written as $\boldsymbol{x} = \boldsymbol{X}(\boldsymbol{s},t)$. The no-slip boundary condition at the particle surface is satisfied by enforcing the velocity at all interfaces to be equal to the velocity of the fluid at the same location:

$$\frac{\partial X(s,t)}{\partial t} = \boldsymbol{u}(\boldsymbol{X}(\boldsymbol{s},t),t), \tag{2.137}$$

where $\boldsymbol{u}$ is the fluid velocity. Let $\boldsymbol{F}(\boldsymbol{s},t)$ and $\boldsymbol{f}(\boldsymbol{x},t)$ represent the particle surface force density and the fluid body force density, respectively. In this treatment of the particulate system, the entire domain, Ω, can be regarded to be filled with fluid, and its velocity field is described by

$$\rho\left(\frac{\partial \boldsymbol{u}}{\partial t} + \boldsymbol{u}\cdot\nabla\boldsymbol{u}\right) = \mu\nabla^2\boldsymbol{u} - \nabla p + \boldsymbol{f}. \tag{2.138}$$

$$\nabla\cdot\boldsymbol{u} = 0. \tag{2.139}$$

with

$$\boldsymbol{f}(\boldsymbol{x},t) = \int_{\Gamma} \boldsymbol{F}(\boldsymbol{s},t)\delta\big(\boldsymbol{x} - \boldsymbol{X}(\boldsymbol{s},t)\big)d\boldsymbol{s}, \tag{2.140}$$

and

$$\frac{\partial X}{\partial t} = \int_{\Omega} \boldsymbol{u}(\boldsymbol{x},t)\delta\big(\boldsymbol{x} - \boldsymbol{X}(\boldsymbol{s},t)\big)d\boldsymbol{x}, \tag{2.141}$$

where

$p(\boldsymbol{x},t)$ is the fluid pressure
ρ is the fluid density
μ is the fluid viscosity

Equations 2.138 and 2.139 are the governing equations for viscous, isothermal, incompressible flow, which include the effect of the particle interface as a force density. Equation 2.140 shows how the force density of the fluid, $\boldsymbol{f}(\boldsymbol{x},t)$, may be calculated from the immersed boundary surface force density, $\boldsymbol{F}(\boldsymbol{s},t)$. Equation 2.141 is essentially the no-slip condition at the interface, since the particle moves at the same velocity as the neighboring fluid.

In its original development, the IBM theory was tailored for solving the interaction between elastic fibers and fluid. To model a particle, the density force is only defined on the particle surface, as indicated by Equation 2.140. This force field is set to be zero inside the particle. In the numerical implementation of the IBM, the entire fluid domain, including the parts that are occupied by immersed bodies, is divided into a set of fixed regular nodes. The fixed nodes are not moving with the flow and are simple Eulerian nodes. The immersed fiber is discretized by a set of segments with each segment represented by a boundary point that moves under the action of the fluid. We will call these boundary Lagrangian nodes. It must be noted that the Lagrangian nodes do not necessarily coincide with the Eulerian nodes.

There are several schemes to compute the surface force density associated with the Lagrangian nodes that represent the fluid–particle interface. For example, the penalty method considers the particle boundary as an elastic fiber with high stiffness in the case of modeling solid particles (Feng and Michaelides, 2004). In this case, we define a set of reference nodes and a set of boundary nodes for each particle. We use a template that is undergoing a rigid body motion consisting of the reference nodes. Before the particle deforms, the reference nodes are coincident with the particle boundary nodes. Once the particle has deformed under particle–fluid interaction, the particle boundary nodes are compared to the reference nodes. During one time step, the reference nodes are following the motion of a template that is a rigid particle, while the boundary nodes are following the motion of fluid, thus resulting in a distortion. Such a distortion between the boundary nodes and reference nodes causes an elastic restoration force on the particle boundary node. This method requires the input in the computational scheme for the stiffness of the fiber or particle. A very large value for the stiffness is used for modeling solid particles.

Figure 2.20 is a schematic diagram of the main steps that constitute the IBM. Part (a) shows the boundary of an ellipsoidal particle, which is carried by the fluid, within the Eulerian grid where the fluid computations take place. Part (b) shows the discretization of the fluid–particle interface using a fixed number of points. If the interface is deformable, these interfacial points are connected by springs with finite spring constants (Feng and Michaelides, 2004). If the interface is rigid, the spring constant value is set to be very large. Part (c) depicts the substitution of the ellipsoidal particle surface and its effect on the fluid domain by a system of forces acting on the nodes of the Lagrangian grid. Part (d) is the final step in the interface modeling and shows the spreading of the forces from the Lagrangian points that move with the particle to the nodes of the Eulerian grid, which are stationary and where the flow computations take place.

In modeling the interactions between a rigid body and a fluid, the IBM can be extended by replacing the surface force $\boldsymbol{F}$ with a body force $\boldsymbol{f}$ that acts only in the region occupied by the solid. The body force in the region of the particles is determined in a way to enforce that this region moves exactly like a solid.

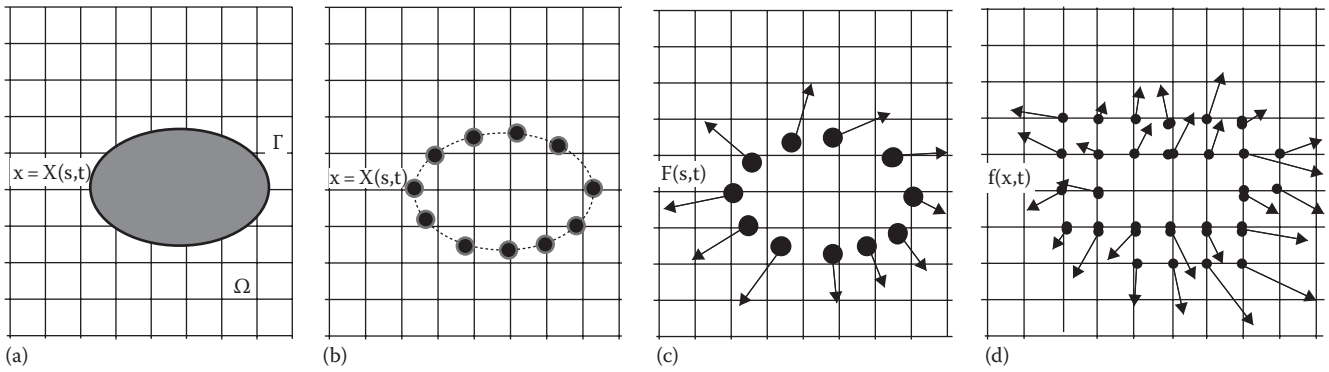


Figure 2.20

The four main steps in the implementation of the IBM. From left to right: (a) The Eulerian grid and the (ellipsoidal) particle whose surface is described by the parameter s, $\boldsymbol{X}(\boldsymbol{s},t)$, (b) discretization of the particle surface into Lagrangian points, (c) substitution of the particle surface with a system of forces at the Lagrangian points that enforce the no-slip velocity condition, and (d) spreading of the forces in the Eulerian grids in the form of force density.

This method is called DF scheme and provides a very good way to compute the velocity field. Unlike the penalty method, this method does not require another artificial input. If we consider the entire geometric domain as being occupied by fluid, with the body density force acting in regions that are known to be occupied by a solid particle, the fluid motion can be described by Equations 2.138 and 2.139.

Let us assume that the velocity in the regions occupied by a solid particle represents/mimics the motion of a solid particle is $\boldsymbol{u}$. Then the force density must satisfy the following equation:

$$\boldsymbol{f} = \rho\left(\frac{\partial \boldsymbol{u}}{\partial t} + \boldsymbol{u}\cdot\nabla\boldsymbol{u}\right) - \mu\nabla^2\boldsymbol{u} + \nabla p. \tag{2.142}$$

Therefore, the body force at a point $\boldsymbol{X}_\mathrm{P}$ can be computed by replacing the fluid velocity $\boldsymbol{u}$ in Equation 2.142 with the expected velocity of that point attached to the particle, $\boldsymbol{U}_\mathrm{P}$. With known velocity and pressure fields at the time step $t = t_n$, we then have an explicit scheme to determine the force term at the Lagrangian boundary point L at time $t = t_{n+1}$:

$$\boldsymbol{f}_P^{(n+1)} = \rho\left(\frac{\boldsymbol{U}_P^{(n+1)} - \boldsymbol{u}_P^{(n)}}{\Delta t} + \boldsymbol{u}_P^{(n)}\cdot\nabla\boldsymbol{u}_P^{(n)}\right) - \mu\nabla\cdot\nabla\boldsymbol{u}_P^{(n)} + \nabla p_P^{(n)}. \tag{2.143}$$

For a rigid particle, some of the terms in this Equation 2.143 can be further simplified. For example, the viscous force can be dropped because of the zero strain rate when the fluid is within the solid boundary and undergoes a rigid body motion. However, in order to reduce computational complexity, the force density is typically set to zero inside the boundaries of particles and the inside fluid is not strictly in rigid body motion.

Mohd-Yusof (1997) proposed this scheme to compute the body force directly at the Eulerian nodes with interpolation. In the case of particulate flows, where the particle interfaces are constantly moving, the task to directly compute these forces at the Eulerian nodes becomes formidable, and for this reason, Feng and Michaelides (2005) computed the force density at a Lagrangian point, *P,* using Equation 2.143. The velocity at *P* can be obtained using Equation 2.141 with a delta function. Alternatively, one may employ a bilinear interpolation using the velocity values of four neighboring grid points for 2D flows or eight neighboring grid points for 3D flows. This scheme was adopted in the *Proteus* code and is obtained through interpolations based on their values at the surrounding Eulerian nodes. The calculated force density is then spread from the Lagrangian points to the neighboring Eulerian points, where the computations take place. Goldstein et al. (1993) explained this spreading as the smoothing of the boundary surface and used a Gaussian function to smoothen the boundary within one grid spacing. In the *Proteus* code, a delta function was used to spread the force density to the nearby Eulerian nodes.

When the fractional step method is used in a Navier–Stokes solver, let $\boldsymbol{u}^\star$ be the intermediate velocity without including the body force:

$$\rho\frac{\partial \boldsymbol{u}}{\partial t} = \rho\left(\frac{\boldsymbol{u}^\star - \boldsymbol{u}^{(n)}}{\Delta t}\right) = -RHS(\boldsymbol{u}^\star). \tag{2.144}$$

$-RHS\,(\boldsymbol{u}^\star)$ is the sum of all the terms in Equation 2.138 other than $\rho\dfrac{\partial \boldsymbol{u}}{\partial t}$ and the body force f after they are moved to the right hand side of the equation.

When the force term is included, we use the expression

$$\rho\left(\frac{\boldsymbol{U}_P^{(n+1)} - \boldsymbol{u}^{(n)}}{\Delta t}\right) = -RHS\left(\boldsymbol{u}^\star\right) + \boldsymbol{f}^{(n+1)}. \tag{2.145}$$

From these two equations and by replacing the flow velocity at $t = t_{n+1}$ with the particle velocity, the density force can be easily computed as follows:

$$\boldsymbol{f}^{(n+1)} = \rho\left(\frac{\boldsymbol{U}_P^{(n+1)} - \boldsymbol{u}^\star}{\Delta t}\right). \tag{2.146}$$

When the DF scheme is used, the force acting on the particle can be obtained by integrating the fluid stress over the particle surface:

$$\boldsymbol{F} = \oint_{\Gamma} \boldsymbol{\sigma} \cdot \boldsymbol{n} dS = -\int_{\Omega} \boldsymbol{f} dV + \rho \frac{d}{dt} \int_{\Omega} \boldsymbol{u} dV = -\int_{\Omega} \boldsymbol{f} dV + \rho_f V_s \frac{d\boldsymbol{U}_s}{dt}. \tag{2.147}$$

where

ρ_f is the fluid density
$\boldsymbol{V}_s$ is the volume of the particle
$\boldsymbol{U}_s$ is the particle velocity
$\boldsymbol{\sigma}$ is the fluid stress tensor at the particle–fluid interface
$\boldsymbol{n}$ is the outward normal unit vector

When the particle is fixed, one can calculate the particle drag from first principles as follows:

$$\boldsymbol{F}_D = -\int_{\Omega} \boldsymbol{f} dV. \tag{2.148}$$

The volume integral is taken only over the external layer where the force density is nonzero.

When the Lagrangian nodes of the external layer or the boundary nodes are placed exactly at the particle–fluid interface, the use of a delta function to spread the body force field results the distributed forces cover a volume that is larger than the volume of the particle. Consequently, the size of the particle that influences the flow field is larger, and this may introduce errors in the interfacial transport of mass, momentum, and energy. To achieve better accuracy, each boundary node has to be placed at the centroid of the small volume associated with the body force (typically, it is beneath the particle surface by about 0.5 grid steps when a very fine grid is used) rather than on the particle surface (Feng and Michaelides, 2009b).

2.4.3 Numerical Implementation of the IBM in 3D Isothermal Flows

This section contains details of the numerical implementation of the IBM in 3D isothermal flows when the DF scheme is used to determine the density force. Consider solid particles suspended in a Newtonian flow. The entire flow domain is discretized with a fixed regular grid or Eulerian grid. At time step t_n a solid particle whose mass center is at point C and has a translational velocity $\boldsymbol{U}_s^{(n)}$ at C and angular velocity $\boldsymbol{\omega}_s^{(n)}$. In order to obtain the particle drag, determine the particle motion, and solve the flow velocity at the next time step t_{n+1}, we need to compute the force density due to the momentum interactions between the particle and fluid.

The first issue arising in the implementation of the IBM is how to set up the Lagrangian boundary nodes in order to accurately represent the particle surface. For a spherical particle in three dimensions, it is impossible to find evenly distributed boundary nodes that represent the surface of the sphere. Feng and Michaelides (2005, 2009b) used a number of strips, with the width of a strip being comparable to the grid spacing. Each strip is composed of a number of evenly distributed points. The number of the points in each strip is chosen in a way that the spacing between two neighboring points is approximately equal to the width of the strips. The boundary nodes are placed slightly beneath the actual particle–fluid interface, as discussed at the end of the previous subsection.

After outlining the particle with a set of boundary nodes, the velocity at a boundary node $\boldsymbol{X}_P$ can be determined by the expression

$$\boldsymbol{U}_P^{(n+1)} = \boldsymbol{U}_s^{(n+1)} + \boldsymbol{\omega}_s \times (\boldsymbol{X}_P - \boldsymbol{X}_C). \tag{2.149}$$

To force the fluid velocity at the next time step t_{n+1} to be equal to the predicted particle velocity at the Lagrangian boundary node, $\boldsymbol{U}_P^{(n+1)}$, the force can be computed at each Lagrangian boundary node using the

DF scheme, Equation 2.143 or 2.146. These forces are then spread in the Eulerian nodes, where the computations for the fluid motion take place.

The force corresponding to each Lagrangian boundary node is spread into all its neighboring Eulerian nodes. The choice of the spreading function must meet certain criteria, which were discussed by Peskin (2002). For the 3D simulations on a regular Eulerian grid of grid spacing h, the following expressions can be used:

$$\delta(r)=\begin{cases}\dfrac{1}{4}\left[1+\cos\left(\dfrac{\pi r}{2h}\right)\right], & |r|\le 2h\\ 0, & |r|>2h\end{cases}, \tag{2.150}$$

and

$$D(\boldsymbol{x}-\boldsymbol{x}_{mn})=\delta(x-x_{mn})\delta(y-y_{mn})\delta(z-z_{mn}). \tag{2.151}$$

With the use of these expressions, the spreading occurs within a distance of two units of the Eulerian grid spacing from each Lagrangian node. The spreading process is performed for each Lagrangian boundary node. The force on each Eulerian node is the summation of all the contributions from the surrounding Lagrangian boundary nodes. The spreading process can be stated succinctly as follows: For a system of N number of particles, with M Lagrangian boundary nodes used to represent each particle, and the force density at these Lagrangian boundary nodes $f(x_{mn}(t),t)$, the flow force density at an Eulerian node $\boldsymbol{x}_i$ is computed as follows:

$$\boldsymbol{f}(\boldsymbol{x}_i,t)=\sum_{n=1}^{N}\sum_{m=1}^{M}\boldsymbol{f}(\boldsymbol{x}_{mn}(t),t)(\delta V)_{mn}D(\boldsymbol{x}_i-\boldsymbol{x}_{mn}(t))\frac{1}{h^3}, \tag{2.152}$$

where

$\boldsymbol{x}_{mn}$ is the position of the mth Lagrangian boundary point for the nth particle at the time t

δV_{mn} is the volume represented by boundary point, $\boldsymbol{x}_{mn}$; and the function $D(\mathbf{r})$ is given by Equation 2.151

It must be pointed out that in the original concept of IBM proposed by Peskin (1977), the surface force is used for mimicking a solid boundary. In this case, the volume associated with Lagrangian point, δV_{mn}, should be replaced by the surface area associated with the boundary point, δA_{mn}. This applies to the case when the penalty method is used. However, when DF scheme is used, the surface force can be converted to volume force based on the Cauchy theorem, which will be seen in Equation 2.158.

In general, the spreading of forces from the Lagrangian nodes to Eulerian nodes may deteriorate the accuracy of the results, especially when flow Reynolds number becomes high. Several authors proposed schemes such as sharp immersed boundary to improve the accuracy (Cristallo et al., 2006) in the case of fixed boundary. However, some of these methods are cumbersome to be used for particles in motion.

Once the force is transferred onto Eulerian nodes as a body force, the fluid velocity can then be determined. This is done by either solving the Navier–Stokes equation with an added body force or using other fluid solvers, such as the LBM. In the original implementation of the IBM (Feng and Michaelides, 2004, 2005), the fluid velocity was solved using the LBM. The latter originates from the Boltzmann equation, which describes the statistical behavior of a very large number of particles moving in a space:

$$\frac{\partial f}{\partial t}+\boldsymbol{\xi}\cdot\nabla_{\mathbf{x}}f+\boldsymbol{F}\cdot\nabla_{\boldsymbol{\xi}}f=\left(\frac{\partial f}{\partial t}\right)_{col}, \tag{2.153}$$

where

f is the particle probability density function

$\boldsymbol{\xi}$ is the particle's velocity

$\boldsymbol{F}$ is the external force exerted on a particle

$\nabla_{\mathbf{x}}$ and $\nabla_{\boldsymbol{\xi}}$ are gradient operators with respect to the position space $\boldsymbol{x}$ and the velocity space $\boldsymbol{\xi}$, respectively

The term on the right side accounts for the particle collision effect. The Boltzmann equation can be discretized in time, position space, as well as velocity space. Therefore, there are various schemes to solve Equation 2.153 based on the ways of discretization and the number of relaxation times. The most commonly used scheme is the explicit scheme that is commonly called the LBM.

In LBM, the fluid motion is modeled by the transport of imaginary fluid particles on the lattice sites of a Cartesian grid. These fluid particles move from one lattice site to another site along a limited number of specified directions to a neighboring site at discrete velocity per time step in two steps: first streaming to the neighboring sites and then colliding with imaginary fluid particles at the local site. A discretized distribution function, $f_i(\boldsymbol{x},t)$, is used to represent the populations of the particles residing at the node $\boldsymbol{x}$ and moving in the ith direction. The evolution of the imaginary fluid particle distributions resulting from the collision and streaming processes is modeled using the single-relaxation time (SRT) *Bhatnagar–Gross–Krook* model (BGK),

$$f_i\left(\boldsymbol{x}+\boldsymbol{c}_i\delta t,t+\delta t\right)=f_i\left(\boldsymbol{x},t\right)-\frac{1}{\tau}\left[f_i\left(\boldsymbol{x},t\right)-f_i^{(eq)}\left(\boldsymbol{x},t\right)\right]+\frac{3}{2}w_i\boldsymbol{f}\cdot\boldsymbol{c}_i. \tag{2.154}$$

where

$\boldsymbol{c}_i$ is the fluid particle velocity along ith direction
τ is a relaxation time, which can be related to the fluid viscosity
w_i is the weighting factor
the vector $\boldsymbol{f}$ is the body force term

When the IBM is used for enforcing the no-slip boundary condition on particle surface, the force density can be treated as a body force term and added on the right side to account for the effect of the presence of the particle. The fluid density, ρ, and velocity field, $\boldsymbol{u}$, are obtained from $f_i(\boldsymbol{x},t)$ as follows:

$$\rho\left(\boldsymbol{x},t\right)=\sum_i f_i\left(\boldsymbol{x},t\right), \tag{2.155}$$

and

$$\rho\left(\boldsymbol{x},t\right)\boldsymbol{u}\left(\boldsymbol{x},t\right)=\sum_i f\left(\boldsymbol{x},t\right)\boldsymbol{c}_i. \tag{2.156}$$

There are other numerical schemes in the literature for adding a body force term in Equation 2.154. Mohamad and Kuzmin (2010) reported that there are no significant differences in the results obtained from these schemes in most applications.

During the simulations of the particle motion, it is necessary to compute the total force and torque acting on each particle. The force on a particle includes the gravity; the buoyancy; the particle collision forces, $\boldsymbol{F}^{\text{col}}$; as well as the hydrodynamic force exerted by the fluid. Hence, the total force exerted on the ith particle is

$$\boldsymbol{F}=\left(1-\frac{\rho_f}{\rho_s}\right)\rho_s V_s\boldsymbol{g}+\oint_\Gamma\boldsymbol{\sigma}\cdot\boldsymbol{n}dS+\boldsymbol{F}^{col}, \tag{2.157}$$

where

V_s is the volume of the particle
ρ_f is the fluid density
ρ_s is the particle density

When the DF scheme is used, it is more convenient to replace the surface integral with a volume integral of the body force within the particle. Utilizing the Gauss integral and the Cauchy theorem, we have

$$\oint_\Gamma\boldsymbol{\sigma}\cdot\boldsymbol{n}dS=-\int_\Omega\boldsymbol{f}dV+\rho\frac{d}{dt}\int_\Omega\boldsymbol{u}dV=-\int_\Omega\boldsymbol{f}dV+\rho_f V_s\frac{d\boldsymbol{U}_s}{dt}. \tag{2.158}$$

Thus, the conservation of linear momentum, $\boldsymbol{P} = \rho_s V_s \boldsymbol{U}_s$, follows

$$\frac{d\boldsymbol{P}}{dt} = \rho_s V_s \frac{d\boldsymbol{U}_s}{dt} = \left(1 - \frac{\rho_f}{\rho_s}\right)\rho_s \boldsymbol{V}_s \boldsymbol{g} - \int_V \boldsymbol{f} dV + \rho_f V_s \frac{d\boldsymbol{U}_s}{dt} + \boldsymbol{F}^{col}. \tag{2.159}$$

When a first-order forward finite difference numerical scheme is used to solve the earlier ODE, the term $\rho_f V_s (d\boldsymbol{U}_s/dt)$ is evaluated at the current time step t_n. Without combining $\rho_f V_s (d\boldsymbol{U}_s/dt)$ with $\rho_s V_s (d\boldsymbol{U}_s/dt)$, this scheme is able to resolve the instability issue for low particle-fluid density ratio, as demonstrated by Feng and Michaelides (2009b).

The torque on a particle is computed using the following expression:

$$\boldsymbol{T} = \oint_\Gamma \left(\boldsymbol{x} - \boldsymbol{X}_C\right) \times (\boldsymbol{\sigma} \cdot \boldsymbol{n}) dS. \tag{2.160}$$

In the case of a spherical particle, its rotational motion can be described by the following equation:

$$\frac{d\boldsymbol{L}}{dt} = \frac{d\left(\boldsymbol{I}_s \cdot \boldsymbol{\omega}_s\right)}{dt} = -\int_\Omega (\boldsymbol{x} - \boldsymbol{X}_C) \times \boldsymbol{f} dV + \frac{d(\boldsymbol{I}_f \cdot \boldsymbol{\omega}_s)}{dt} + \boldsymbol{T}^{col}, \tag{2.161}$$

where

$\boldsymbol{L}$ is the angular momentum

$\boldsymbol{I}_s$ and $\boldsymbol{I}_f$ are the moment of inertia matrices of the solid particle and fluid particle, respectively

We add a $\boldsymbol{T}^{\text{col}}$ to include additional torques that may arise, such as the torque due to the tangential collision force component when the soft-sphere collision model is used.

In order to minimize the skewing effect (drift) due to the accumulation of the numerical error when one uses the rotational matrix of the particle, a unit quaternion is used to represent the rotation of the particles. In the 3D implementation of the method, the following set of differential equations are solved to get the equation of motion of a particle:

$$\frac{d}{dt}\begin{bmatrix} \boldsymbol{x}(t) \\ \boldsymbol{q}(t) \\ \boldsymbol{P}(t) \\ \boldsymbol{L}(t) \end{bmatrix} = \begin{bmatrix} \boldsymbol{U}_s(t) \\ \frac{1}{2}\Xi\left[\boldsymbol{\omega}_s(t)\right] \cdot \boldsymbol{q}(t) \\ \boldsymbol{F}(t) \\ \boldsymbol{T}(t) \end{bmatrix}. \tag{2.162}$$

with the prescribed initial conditions. Here, $\boldsymbol{q}(t)$ is the unit quaternion form for the rotation matrix of the particle with its initial value determined from the initial rotation matrix, $\Xi(\omega_s(t))$ is the rotational tensor associated with $\boldsymbol{\omega}_s(t)$, which can be expressed as

$$\Xi_{ij} = -\epsilon_{ijk}\omega_k \tag{2.163}$$

where ϵ_{ijk} is the permutation tensor.

At any given time, the translational and rotational velocities of particles are computed by the following expressions:

$$\dot{\boldsymbol{U}}_s(t) = \frac{\boldsymbol{P}(t)}{m_s}, \tag{2.164}$$

and

$$\dot{\boldsymbol{\omega}}(t) = \boldsymbol{I}_s^{-1}(t)\boldsymbol{L}(t), \tag{2.165}$$

where $m_s = P_s V_s$ is the mass of the particle, $\boldsymbol{I}_s(t)$ is the moment of inertia matrix of the particle in the current coordinate system. This is related to the moment of inertia matrix I_{s0} at the initial coordinate system and the rotation matrix of the particle, $\boldsymbol{R}_s(t)$, by the expression

$$\boldsymbol{I}_s(t) = \boldsymbol{R}(t)\boldsymbol{I}_{s,0}\boldsymbol{R}(t)^T. \tag{2.166}$$

This numerical scheme is capable of simulating the motion and rotation not only of spherical particles but also of particles with irregular shapes. In the special case of spherical particles, $\boldsymbol{I}_i(t)$ is a constant diagonal matrix:

$$I_s = \begin{bmatrix} \frac{2}{5}m_s a^2 & & \\ & \frac{2}{5}m_s a^2 & \\ & & \frac{2}{5}m_s a^2 \end{bmatrix}. \tag{2.167}$$

where a is the radius of the particle.

It must be noted that many times the rigid body motion inside the particle is not enforced *a priori*. Therefore, the problem that is actually solved with these techniques is the interaction between a fluid and a solid shell filled with the same fluid. The solid shell has the same boundary as the particle and carries the total mass of the particle. The contribution of the interior fluid mass is typically ignored. In general, the contribution from the internal flow to the resulting motion of the particle is not significant for low-frequency flows.

One may enforce the rigid body motion for the internal fluid by setting up a few internal Lagrangian points in order to remedy this deficiency. The velocity at these points is determined by the rigid body motion of the particle. With this addition to the numerical scheme, an advantage of the DF scheme is that it enforces the rigid body motion in the interior of the particles in a straightforward way.

There are a few recent developments in improving the accuracy and stability of the original implementation of the SRT-LBM-based explicit IBM. For example, Wu and Shu (2009) pointed out that the explicit IBM method can only approximately satisfy the no-slip boundary condition at the Lagrangian nodes. They proposed an implicit velocity correction-based IBM that provides better accuracy. Lu et al. (2012) applied the IBM with a multirelaxation time scheme LBM. Seta et al. (2014) developed a two-relaxation-times (TRT)-based IBM and compared the simulation results between the SRT-LBM, the TRT-LBM, and the MRT-LBM.

2.4.4 Implementation of the IBM with Heat Transfer

In the case of nonisothermal flow due to the presence of hotter or colder particles suspended in a viscous fluid or of particulate flow with heat transfer, a similar IB-based method can be proposed. Kim and Choi (2004) proposed a method based on the IBM for the solution of 2D heat flow problems with complex geometries. Pacheco et al. (2005) presented a finite volume IBM to study the heat transfer between a fixed solid and a fluid.

A glance at the implementation of the IBM proves that the method is ideally suited for the solution of applications involving simultaneous multiphase flow with mass and energy transfer. While for the momentum exchange the boundaries of particles are substituted with a system of forces, for the energy interactions the boundaries of particles may be substituted by a system of heat sources or heat sinks. Feng and Michaelides (2008, 2009a) recognized this analogy and extended the IBM from isothermal systems of particulate flows to systems that included heat transfer. They used a DF scheme for the computations.

Similar to the momentum interaction equations, the temperature field in the Eulerian domain of the fluid is governed by the following modified energy equation:

$$\rho_f c_f \left(\frac{\partial T}{\partial t} + \boldsymbol{u} \cdot \nabla \mathrm{T} \right) = k_\mathrm{f} \nabla^2 T + \lambda, \tag{2.168}$$

where c_f and k_f are the specific heat and thermal conductivity of the fluid, respectively. The additional term, λ, is an energy density term that is added to enforce the temperature field in the region occupied by

the particles. As in the case of the momentum balance equations, this term is equal to zero in the field occupied by the fluid. In the solid region, this term is computed by the following equation:

$$\lambda = \rho_f c_f \left(\frac{\partial T}{\partial t} + \boldsymbol{u} \cdot \nabla T \right) - k_f \nabla^2 T, \tag{2.169}$$

In the original publications, the temperature of each particle was assumed to be uniform, that is, $T = T_s(t)$, which essentially implies that the Biot number vanishes ($Bi \ll 1$). This assumption may be relaxed by solving the energy equation inside the particles to obtain the temperature field, $T_s(\boldsymbol{x},t)$, though the computational cost could be prohibitive for a large number of particles.

The transient temperature of the particles, $T_s(t)$, is determined by solving the following differential equation, which is obtained from the energy balance for each particle:

$$\rho_s V_s C_s \frac{dT_s}{dt} = \oint_\Gamma k_f \nabla T_f \cdot \boldsymbol{n} ds = -\int_\Omega \lambda dV + \rho_f V_s C_f \frac{dT_f}{dt} dV. \tag{2.170}$$

The last term in the last equation is the rate of heat that would have entered the control volume occupied by the sphere in the absence of the latter (Michaelides and Feng, 1994). In the case of constant particle temperature, the heat transfer rate between the particle and its surrounding fluid may be calculated by the volume integral of energy density λ instead of a surface integral.

Whenever particles have different temperatures than the fluid, the term λ creates a temperature gradient within the fluid, which would modify the fluid properties. This effect may be computed in a conceptually easy manner by using empirical equations for the properties of the fluid at every point of the Eulerian grid. For relatively small temperature differences between the particles and the fluid, the Boussinesq approximation is typically used successfully for the coupling of the energy and momentum equations. Hence, the momentum equation of the fluid is written as follows:

$$\rho_{f0} \left(\frac{\partial \boldsymbol{u}}{\partial t} + \boldsymbol{u} \cdot \nabla \boldsymbol{u} \right) = -\nabla p + \mu_f \nabla^2 \boldsymbol{u} + \beta_f \left(T - T_{f0} \right) \boldsymbol{g} + \boldsymbol{f}, \quad x \in \boldsymbol{\Omega}. \tag{2.171}$$

where

the subscript 0 denotes values far from the particles

β_f is the thermal expansion coefficient of the fluid

The fluid velocity and temperature fields can also be solved using the LBM (Kang et al., 2011). More recently, a variation of this method, the IBM-based resolved discrete particle method (IBM-RDPM), has been used to study the convective heat transfer of particulate flows. An example of the application of this method is given in the last part of this section.

2.4.5 Particle–Particle and Particle–Wall Interactions

When a Lagrangian–Eulerian method such as the RDPM is used in modeling particulate flows of large groups of particles, interparticle collisions and collisions between particles and flow boundaries are unavoidable and need to be modeled appropriately. In general, even at low Reynolds numbers, the Eulerian grid used in a RDPM study is not fine enough to handle the lubrication force that develops between the particles or between particles and a solid boundary, when the boundaries almost touch. Therefore, a mechanism is necessary to be introduced in the IBM numerical scheme in order to account for the repulsive forces that develop before and during the collision processes. In the absence of such a mechanism, the motion of the particles will result in the partial penetration of the particle surfaces. When significant boundary penetrations occur, the computational results may become meaningless. Therefore, the prescription of a definitive collision scheme is necessary for any discrete particle method. This becomes even more important when the particle phase is dense.

There are several collision schemes that have been reported in the literature. We will introduce three of the most commonly used schemes: the soft-sphere scheme, the repulsive force scheme, and the lubrication scheme. Notwithstanding, it must be pointed out that the general consensus is that the use of a particular collision model will not significantly alter the simulation results for dilute particulate flows (Abdelsamie et al., 2014).

2.4.5.1 Soft-Sphere Collision Scheme

The soft-sphere scheme is the most common collision model used in Eulerian–Lagrangian particulate flow simulations. It allows particles to deform during a contact. However, the deformation is only used to determine collision force and particles remain geometrically rigid. This model is suitable for fixed time step simulations since it allows multiple collisions within one time step. It is composed of a spring-dashpot system. The spring provides the elastic rebound while the dashpot dissipates energy. The collision force when two spheres are in contact is composed of normal and tangential force components, which are calculated from the overlapping displacement and their relative velocities. However, the spring can be a linear spring, Hertzian spring, or other nonlinear spring. For small length and timescale simulations such as nanoparticles suspended in a fluid, the Hertzian spring model can be applied (Sloan et al., 2012). For most other engineering applications, a linear spring model is sufficient to produce satisfactory results.

In the linear spring-dashpot model, the normal contact force between two particles, i (located at $\boldsymbol{X}_i$) and j (located at $\boldsymbol{X}_j$), can be computed by the following expression:

$$f_{ij}^n = -k_n \delta_{ij}^n - \eta_n u_{ij}^n, \tag{2.172}$$

with

$$\delta_{ij}^n = R_i + R_j - \left|\boldsymbol{X}_i - \boldsymbol{X}_j\right|, \tag{2.173}$$

and

$$u_{ij}^n = \boldsymbol{u}_{ij} \cdot \frac{\boldsymbol{X}_i - \boldsymbol{X}_j}{\left|\boldsymbol{X}_i - \boldsymbol{X}_j\right|}, \tag{2.174}$$

where

δ_{ij}^n is the normal overlapping displacement
k_n and η_n are the normal spring stiffness and damping coefficient
u_{ij} is the relative velocity of particle j with respect to particle i

Here,

$$\boldsymbol{u}_{ij} = \boldsymbol{U}_j - \boldsymbol{U}_i \tag{2.175}$$

where u_{ij}^n is the relative normal velocity component of particle j with respect to particle i.

When one considers the friction at contact, the tangential contact force can be calculated from the following equation:

$$f_{ij}^t = \begin{cases} -k_t \delta_{ij}^t - \eta_t u_{ij}^t & \text{if } \left|f_{ij}^t\right| \le \mu_s \left|f_{ij}^n\right| \\ \mu_k \left|f_{ij}^n\right| \dfrac{\delta_{ij}^t}{\left|\delta_{ij}^t\right|} & \text{if } \left|f_{ij}^t\right| > \mu_s \left|f_{ij}^n\right| \end{cases}. \tag{2.176}$$

where

μ_s and μ_k are the coefficients of static and dynamic friction, respectively
δ_{ij}^t is the tangential overlapping displacement
$\mathbf{k}_t$ and η_t are the tangential spring stiffness and damping coefficients, respectively

The relative tangential velocity component at the contact point is given as

$$\boldsymbol{u}_{ij}^t = \boldsymbol{u}_{ij} - \boldsymbol{u}_{ij}^n. \tag{2.177}$$

The slider distance or tangential displacement can be computed by integrating the relative tangential velocity within the contact time.

However, most studies do not differentiate between μ_k and μ_s and use a single coefficient of friction, μ. The following damping coefficient is obtained based on the following dry collision assumption (Tsuji et al., 1998):

$$\eta_n = \begin{cases} \dfrac{-2\ln(e_n)\sqrt{m_{ij}k_n}}{\sqrt{\pi^2+\ln^2(e_n)}} & \text{if } e_n \neq 0 \\ 2\sqrt{m_{ij}k_n} & \text{if } e_n = 0 \end{cases}. \tag{2.178}$$

The particle–wall collision may be considered as a special case of the interparticle collision when the radius of one of the particles becomes approaches infinity, thus applying also the method described earlier. In the case of particle collisions in a viscous flow, the collision parameters must be modified to account for the flow viscous effects as noted in the study by Feng et al. (2010).

2.4.5.2 Repulsive Force Scheme

Glowinski et al. (2003) suggested an artificial collision technique by introducing a repulsive force when the gap between two particles is lower than a given threshold, the so-called safe zone. This artificial short-range repulsive force is added as an external force in the IBM. Thus, when two particles with radii R_i and R_j approach very closely, the collision force exerted on each particle is

$$\boldsymbol{F}_{ij}^{P} = \begin{cases} 0, & \|\boldsymbol{x}_i - \boldsymbol{x}_j\| > R_i + R_j + \xi \\ \dfrac{c_{ij}}{\epsilon_P}\left[\dfrac{\|\boldsymbol{x}_i - \boldsymbol{x}_j\| - R_i - R_j - \xi}{\xi}\right]^2 \left(\dfrac{\boldsymbol{x}_i - \boldsymbol{x}_j}{\|\boldsymbol{x}_i - \boldsymbol{x}_j\|}\right), & \|\boldsymbol{x}_i - \boldsymbol{x}\|_j \leq R_i + R_j + \xi \end{cases} \tag{2.179}$$

where

$\boldsymbol{x}_i$ is the position of the particle i

ε_P is the stiffness parameter for collisions

ζ is the threshold or safe zone, which is specified in advance and typically chosen to be one or two units of grid spacing

c_{ij} is the force scale in the problem that is studied, for example, a good choice for this scale in sedimentation problems is the net gravity force on a single particle

Similarly, the repulsive force between a particle and a wall is given by the reflection method assuming that an identical, fictitious particle approaches the wall from the other side with a normal velocity that is equal and opposite to that of the particle under consideration. Glowinski et al. (2001) provide an extensive discussion on the choice of the stiffness parameters.

This collision technique allows particles to interpenetrate when the stiffness parameter ε_P is very large. In this case, it is said that the particles undergo soft collisions. Depending on the type of flow and the particle density, the partial overlapping of particles may be significant. This phenomenon is accentuated when a large number of particles undergo a packing process: the particles at the bottom, which have to bear the load of the particles above, overlap significantly. To counteract this overlapping, one has to choose a higher value for the repulsive force when the collision scheme of Equation 2.179 is used. Feng and Michaelides (2005) employed a novel collision scheme with the *Proteus* code: before the contact of the two particles, a repulsive force given by Equation 2.179 is used. If the particles start overlapping, a higher spring force is applied. The spring force is proportional to the overlapping distance of the two particles and typically is much larger than the repulsive force before the overlapping process. Thus, the functional form of this collision force scheme is

$$\boldsymbol{F}_{ij}^{P} = \begin{cases} 0, & \|\boldsymbol{x}_i - \boldsymbol{x}_j\| > R_i + R_j + \xi \\ \dfrac{c_{ij}}{\epsilon_P}\left[\dfrac{\|\boldsymbol{x}_i - \boldsymbol{x}_j\| - R_i - R_j - \xi}{\xi}\right]^2 \left(\dfrac{\boldsymbol{x}_i - \boldsymbol{x}_j}{\|\boldsymbol{x}_i - \boldsymbol{x}_j\|}\right), & R_i + R_j \leq \|\boldsymbol{x}_i - \boldsymbol{x}_j\| \leq R_i + R_j + \xi, \\ \dfrac{c_{ij}}{\epsilon_P}\left\{\left[\dfrac{\|\boldsymbol{x}_i - \boldsymbol{x}_j\| - R_i - R_j - \xi}{\xi}\right]^2 + \dfrac{c_{ij}}{E_p}\dfrac{\left(R_i + R_j - \|\boldsymbol{x}_i - \boldsymbol{x}_j\|\right)}{\xi}\right\}\left(\dfrac{\boldsymbol{x}_i - \boldsymbol{x}_j}{\|\boldsymbol{x}_i - \boldsymbol{x}_j\|}\right), & \|\boldsymbol{x}_i - \boldsymbol{x}_j\| \leq R_i + \boldsymbol{R}_j \end{cases} \tag{2.180}$$

where E_P is a smaller parameter than ε_P to ensure that the spring force after the overlapping is significantly larger. It was observed that when this type of force was applied, the overlapping of two particles and the overlapping of particles and walls become very low and do not affect significantly the computational results. It must be noted that the first term of the last function of Equation 2.180 is present so that the collision force is continuous before and after penetration. The implementation of this collision scheme enables one to use smaller repulsive forces that keep the particles from overlapping under normal flow conditions. The additional spring force is added that separates the particles quickly when overlapping occurs.

2.4.5.3 Hybrid Lubrication Force Scheme

An early lubrication force model was developed by Ladd (1994) to be applied to low Reynolds and Stokes numbers. The model can be extended to higher Reynolds numbers by permitting a possible overlap between the colliding particles, after the particles contact. In a similar manner as the modified repulsive force scheme, we consider two particles approaching each other along their line of centers (Musong and Feng, 2012). The drag force and buoyancy of the particles then become characteristics of this lubrication model. The gap width between the surfaces of the two spheres at the tangents normal to the line of their centers has a threshold value $\xi_0 = \delta$, where δ can be the Eulerian grid spacing. The normal lubrication force exerted when the viscous fluid is squeezed or compressed by the two approaching particles before contact and when they start to overlap is given by

$$f_{ij}^{n} = \begin{cases} 0 & \xi > \delta \\ -F_d\left(\dfrac{\delta}{\max(\xi,\delta_s)} - 1\right) & 0 \le \xi < \delta \\ -F_d\left(\dfrac{\delta}{\max(\xi,\delta_s)} - 1\right) - k_n(-\xi) & \xi < 0 \end{cases}. \tag{2.181}$$

In the last equation, F_d is the effective drag force that can be calculated by several drag force models and δ_s is a small positive gap (e.g., $\delta_s = (1/10)\delta$) to prevent singular value at $\xi = 0$. If the particles continue to approach and overlap, a force proportional to the overlapping distance is applied on top of the modified lubrication force with a spring stiffness k_n.

2.4.6 Examples on the Application of IBM

In this subsection, we provide two examples on two types of problems to demonstrate that the IBM-based method may be used to obtain needed data for engineering and scientific applications. The first application pertains to the fundamental problem of calculating the drag and heat transfer for a pair of particles and the second to an engineering application of heat transfer in a smaller-scale fluidized bed.

2.4.6.1 Drag and Heat Transfer Rate of a Pair of Heated Spheres

The drag and heat transfer rate of a spherical particle is significantly changed by the presence of neighboring particles. We consider a uniform flow over a pair of spheres aligned along the flow direction and separated by a distance δ, ranging from 1 to 6 sphere diameters, at different Reynolds numbers. The Prandtl number is chosen to be Pr = 7 (approximately that of water). Periodic boundary conditions are applied at the two directions other than the flow direction. The size of simulation domain is $6D \times 6D \times 20D$, where D is the diameter of the sphere. One sphere is outlined by a number of grid points ranging from 13 to 27 depending on the chosen Reynolds numbers.

Table 2.2 shows the computed drag coefficients of a pair of spheres at different Reynolds numbers and different separation distances. It also lists the drag coefficients of a single sphere in uniform flow obtained from the numerical simulations by Feng and Michaelides (2001a) and from the following correlation (Clift et al., 1978):

$$C_D = \frac{24}{Re}(1 + 0.15Re^{0.687}) \tag{2.182}$$

It is observed in this table that the present simulation results for a single sphere case agree very well with those found in the literature at Re = 10 and 100, with an overall difference of a few percentages. However, more

Table 2.2 Drag Coefficient of Spheres

		Re = 10		Re = 100		Re = 400	
Single sphere	Clift et al. (1978)	4.15		1.092		0.612	
	Feng and Michaelides (2001a)	4.30		1.103		0.579	
	Present	4.50		1.124		0.711	
A pair of spheres at δ/D		Sphere 1	Sphere 2	Sphere 1	Sphere 2	Sphere 1	Sphere 2
1		3.81	2.23	1.061	0.247	0.734	−0.064
2		4.19	2.94	1.054	0.430	0.710	0.028
3		4.28	3.34	1.081	0.548	0.690	0.190
4		4.45	3.51	1.105	0.620	0.679	0.331
5		4.47	3.71	1.117	0.671	0.702	0.382
6		4.49	4.00	1.121	0.709	0.710	0.421

than 15% difference is observed at Re = 400. Two factors contribute to this deviation. The first is that the current simulation domain is much smaller compared to those used in the literature where the sphere is isolated. The second is that the grid used for Re = 400 is not sufficiently fine to fully resolve the laminar boundary layer near the surface of the sphere (Feng and Musong, 2014). Nevertheless, the simulation is able to capture the principal flow structures behind spheres.

Table 2.2 clearly shows that the drag of the trailing sphere is considerably reduced. In general, the influence of the second sphere on the drag of the leading sphere is not significant, especially when the separation distance is more than 3D. However, the influence of the leading sphere on the drag of the trailing sphere can be very large and increases as the Reynolds number increases, even when the separation distance remains the same. Thus, at a separation distance of 2D, the drag on the trailing sphere is 70% that of the leading sphere at Re = 10, 41% at Re = 100, and only 4% at Re = 400. At a separation distance of 5D, the drag on the trailing sphere is 83% at Re = 10, 60% at Re = 100, and 54% at Re = 400. At Re = 400, the drag of the leading sphere is largest when it is almost in contact with the trailing sphere, and it gradually decreases as the separation distance increases. However, after the separation distance exceeds 4D, the drag starts to increase again because the trailing sphere is out of the main wake of the leading sphere. This nonmonotonic behavior is also observed in the case of two cylinders placed in tandem at moderate Reynolds numbers between 1 and 40 in a recent study by Vakil and Green (2013).

Figure 2.21 shows the temporal behavior of the drag coefficient at Re = 400 for a single sphere and a pair of spheres with a separation distance of 1D, 3D, and 6D. The accompanying vortex structures are shown in Figure 2.22 using the λ_2 method of vortex identification. There are a few interesting observations in these Figures. In the case of a single sphere, periodical vortex loops or hairpin vortices are constantly shed from the surface of the sphere at a period of 0.87 s, with a constant Strouhal number, St = 0.12. This observation agrees very well with the data by Wu and Faeth (1994) who observed Strouhal numbers around 0.13 for $335 \leq \text{Re} \leq 620$.

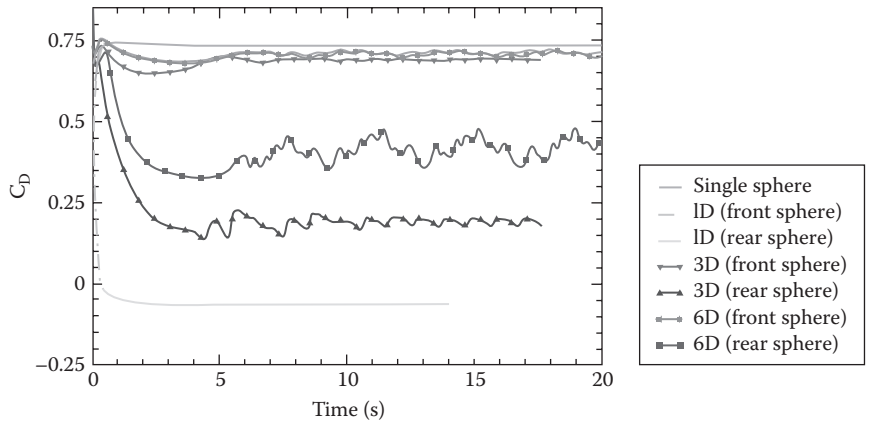


Figure 2.21

Drag coefficients of spheres versus time.

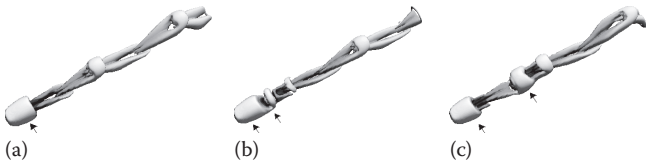


Figure 2.22

Vortex structures behind spheres at Re = 400 identified by $\lambda_2 = -0.002$: (a) a single sphere, (b) two spheres separated by 3D, (c) two spheres separated by 6D. Arrows indicate the position of a sphere; gray scale indicates fluid velocity magnitude.

In the case of two spheres placed along the flow direction, a slight increase in the drag coefficient of the leading sphere and a negative drag coefficient on the trailing sphere are observed when they are in contact (separation distance $\delta = D$). The negative drag coefficient on the trailing sphere implies a "push" effect on the leading sphere. It is due to the recirculation or wake behind the leading sphere that explains the higher drag coefficient of the leading sphere. It is also observed that the trailing sphere stabilizes the flow when placed closely with a gap of one or two diameters. In these cases, no hairpin vortex shedding was observed. However, as the gap increases to 3D or more, the vortex shedding occurs again. At $\delta = 3D$, the wake of the leading sphere induces vortex hairpins, which are interrupted by the presence of the trailing sphere. At $\delta = 6D$, the wake of the leading sphere is almost fully developed before it is interrupted by the trailing sphere. In this case, in addition to the Strouhal number of 0.12 that is due to the leading sphere vortex shedding, an additional higher Strouhal number of 0.5 is also observed, which is most likely due to the flow instability of the trailing sphere.

Table 2.3 shows the Nusselt numbers for a single sphere and a pair of spheres at different separation distances. In the case of forced convection of an isolated sphere in a large flow domain, Ranz and Marshall (1952) developed the following correlation experimentally:

$$Nu = 2 + 0.6Re^{0.5}\,\mathrm{Pr}^{0.33} \tag{2.183}$$

Feng and Michaelides (2001b) also proposed the following correlation based on their numerical results:

$$Nu = 0.852\left(PrRe\right)^{0.333}\left(1 + 0.233Re^{0.287}\right) + 1.3 - 0.182Re^{0.355} \tag{2.184}$$

The results of Table 2.3 show that the momentum and thermal wakes created by the leading sphere also have a significant effect on the heat transfer rate of the trailing sphere. Even at $\delta = 6D$ away from the leading sphere, the Nusselt number of the trailing sphere is only 60% compared to the leading sphere. However, it is seen that the trailing sphere has an insignificant effect on the heat transfer rate of the leading sphere. In the conduct of these calculations, the simulation results were significantly improved using the centroid of a control volume associated with the body force as the boundary node.

Table 2.3 Nusselt Number of Spheres

		Re = 10		Re = 100		Re = 400	
Single sphere	Ranzand Marshal (1952)	5.61		13.40		24.8	
	Feng and Michaelides (2001b)	5.98		14.54		27.4	
	Present	5.43		12.70		29.8	
A pair of spheres at δ/D		Sphere 1	Sphere 2	Sphere 1	Sphere 2	Sphere 1	Sphere 2
1		4.97	3.00	12.04	4.98	29.3	5.2
2		5.31	3.52	12.34	6.26	29.3	9.9
3		5.39	3.83	12.56	6.85	29.3	13.8
4		5.41	4.04	12.63	7.22	29.4	17.4
5		5.42	4.16	12.67	7.51	29.7	18.1
6		5.42	4.30	12.69	7.75	29.8	18.6

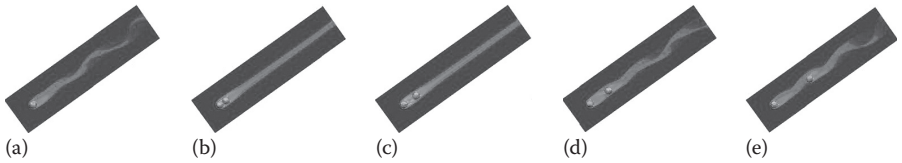


Figure 2.23

Temperature contours at Re = 400. (a) A single sphere, (b) δ = 1D, (c) δ = 2D, (d) δ = 3D, (e) δ = 6D.

The temperature contours for the cases of a single sphere and of a pair of spheres with separation distances 1D, 2D, 3D, and 6D are plotted in Figure 2.23. The vortex shedding for a single sphere and of a pair of spheres at δ = 3D and 6D causes nonsymmetric temperature distributions behind both spheres. However, at a separation distance of 1D and 2D, the flows remain stable and symmetric even after a long period of time.

In summary, the results presented in this subsection show that the drag and heat transfer rate of a sphere is significantly affected by its neighboring spheres. A simple influencing factor that depends only on the solid fraction may not be sufficient to account for the effect from the neighboring particles. In order to obtain accurate representations of drag and heat transfer rate in a complex flow filled with many neighboring particles, the RDPM or DNS must be applied as elucidated further in the next subsection.

2.4.6.2 Fluidization of 1204 Spheres by a Jet Flow Using a RDPM

In this example, we study the fluidization of 1204 spheres by a jet flow using an IBM-based RDPM. The bed setup and fluid and particle properties are the same as the one used by Pan et al. (2002) who studied the particle fluidization by a uniform flow in a slit bed using a fictitious domain method. The bed geometry is 20.3 cm × 0.6858 cm × 70.22 cm, the sphere diameter is 0.635 cm, the particle density is 1.14 g/cm^3, the fluid density is 1 g/cm^3, the viscosity is 0.01 g/(cm·s), and the Prandtl number is 7.

The high-velocity jet is placed at the center of the inlet. The jet orifice has a width of 2.03 cm and a depth of 0.6858 cm. The jet velocity is 40 cm/s, resulting in the same mass flow rate as that of a uniform flow across the entire bed at V = 4 cm/s. A time step Δt = 0.0002 s is used in the simulation because of the much higher maximum flow velocity in a jet flow fluidized bed.

Figure 2.24 shows the distribution of 1204 spherical particles at five different time instants: 1, 3, 5, 7, and 10 s. For better visualization, the particles are colored with four different colors based on their initial locations. From these snapshots, it is clearly seen that the particles are well mixed during the fluidization. The bottom region, where the particles are dense (the so-called dead zone), accounts for roughly a quarter of the entire bed. It is observed that the particles inside the "dead zone" are not stationary. During the

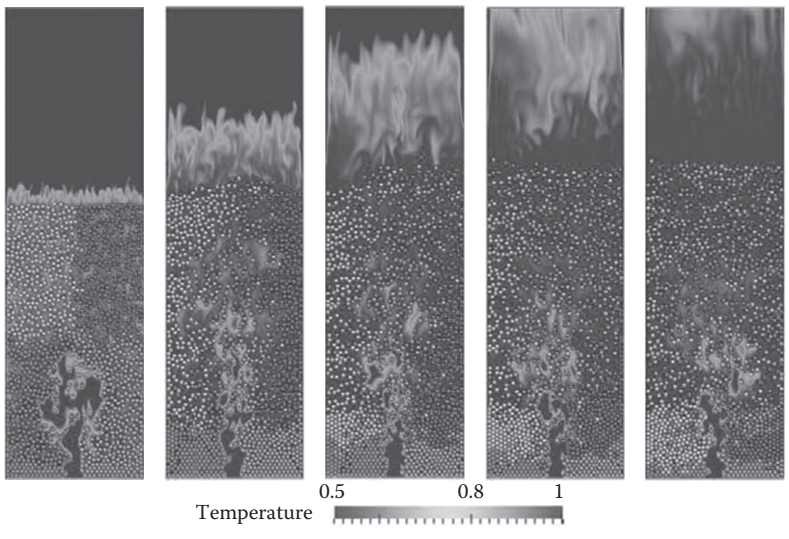


Figure 2.24

Snapshots of particle positions and flow temperature contours in a jet flow fluidized bed. From left to right, t = 1, 3, 5, 7, and 10 s.

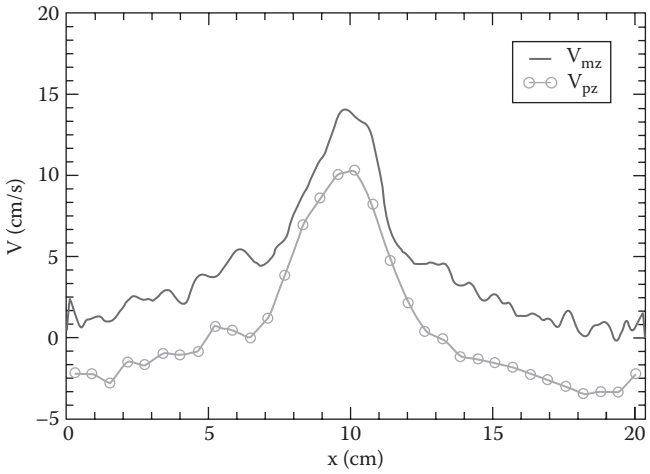


Figure 2.25

Time- and space (z-direction)-averaged particle velocity V_{pz} and fluid–particle composite velocity V_{mz} for a jet flow fluidized bed.

fluidization, some of the particles originally trapped in the dead zone are being fluidized, while "fresh" particles fall down and are entrained into the dead zone.

The time- and space-averaged particle velocity (in the z-direction) and fluid–particle composite velocity when the bed reaches a quasi-steady condition are computed, and their results are shown in Figure 2.25. The space averaging in the z-direction is achieved by averaging all the vertical velocity components of each node or each particle within a vertical column (Feng et al., 2014). As expected, the particles in the middle of the bed are entrained into the jet and move upward. However, as the jet's momentum is dissipated, the entrained particles start to fall downward near the left and right walls of the bed. With the particles rising in the central region and falling at the sides, the x-averaged particle velocity approaches zero, while the x-averaged mixture velocity approaches V = 4 cm/s as the bed becomes quasi-stable.

We also studied the fluidization by a uniform flow and compared its results with those from jet flow fluidization (Feng and Musing, 2014). There are a few interesting findings that are worth mentioning: The simulation results show that the bed is slightly higher when uniform flow is used for fluidization. However, the wall pressure gradient, which is an indication of wall friction, is much lower in the jet flow fluidized bed. This can be explained by the much smaller velocity gradient of the mixture in the jet flow fluidized bed compared to a higher velocity gradient of mixture in the uniform flow fluidized bed near the wall. As a result, the pressure drop over the jet flow fluidized bed is much lower than that of the uniform flow fluidized bed. Another observation is that the particle-averaged Nusselt number in the jet fluidized bed is significantly higher than that of the uniform flow fluidized bed. One plausible explanation is that the fluid warms up quickly as it moves upward in the case of the uniform flow fluidized bed. This reduces the temperature differences and the heat transfer rate of particles. However, in the case of the jet flow fluidized bed, the high jet stream forces cold fluid to penetrate deeper into the bed, resulting in a higher heat transfer rate when it interacts with particles along its path.

Acknowledgments

This work was partly supported by a grant from the U.S. Department of Energy (award number DE-FE0011453) with Mr. Steven Seachman as the project administrator and by the Tex Moncrief Chair of Engineering at TCU.

References

Abdelsamie, A., Fard, A.E., Oster, T., and Thevenin, D., Impact of the collision model for fully resolved particles interacting in a fluid, in *ASME Fourth Joint US-European Fluids Engineering Division Summer Meeting*, paper FEDSM2014–21447, Chicago, IL, August 3–7, 2014.

Clift, R., Grace, J.R., and Weber, M.E., *Bubbles, Drops, and Particles*, Academic Press, New York, 1978.

Cristallo, A. and Verzicco, R., Combined immersed boundary/large-eddy-simulations of incompressible three dimensional complex flows. *Flow, Turbulence and Combustion*, 77(1–4), 3–26, 2006.
Feng, Z.-G. and Michaelides, E.E., Drag coefficients of viscous spheres at intermediate and high Reynolds numbers, *ASME J. Fluids Eng.*, 123, 841–849, 2001a.
Feng, Z.-G. and Michaelides, E.E., Heat and mass transfer coefficients of viscous spheres, *Int. J. Heat Mass Transfer*, 44, 4445–4454, 2001b.
Feng, Z.-G. and Michaelides, E.E., An immersed boundary method combined with Lattice Boltzmann Method for solving fluid and particles interaction problems, *J. Comput. Phys.*, 195, 602–628, 2004.
Feng, Z.-G. and Michaelides, E.E., *Proteus*-A direct forcing method in the simulation of particulate flows, *J. Comput. Phys.*, 202, 20–51, 2005.
Feng, Z.G. and Michaelides, E.E., Inclusion of heat transfer computations for particle laden flows. *Physics of Fluids*, 20(4), 040604, 2008.
Feng, Z.-G. and Michaelides, E.E., Heat transfer in particulate flows with direct numerical simulation (DNS), *Int. J. Heat Mass Transfer*, 52, 777–787, 2009a.
Feng, Z.-G. and Michaelides, E.E., Robust treatment of no-slip boundary condition and velocity updating for the Lattice-Boltzmann simulation of particulate flows, *Comput. Fluids*, 38, 370–381, 2009b.
Feng, Z.-G., Michaelides, E.E., and Mao, S.-L., Numerical simulation of particle-wall collision in a viscous fluid using a resolved discrete particle method with the soft-sphere collision model, *ASME J. Fluids Eng.*, 132, #091302, 2010.
Feng, Z.-G. and Musong, S.G., Direct numerical simulation of heat and mass transfer of spheres in a fluidized bed, *Powder Technol.*, 262, 62–70, 2014.
Feng, Z.-G., Ponton, M.E., Michaelides, E.E., and Mao, S.-L., Using the direct numerical simulation to compute the slip boundary condition of the solid phase in two-fluid model simulations, *Powder Technol.* http:/dx.doi.org/10.1016/j.powtec.2014.01.020, 2014.
Fogelson, A.L. and Peskin, C.S., A fast numerical method for solving the three-dimensional stokes equation in the presence of suspended particles, *J. Comput. Phys.*, 79, 50–69, 1988.
Gan, H., Chang, J.Z., and Howard, H.H., Direct numerical simulation of the sedimentation of solid particles with thermal convection, *J. Fluid Mech.*, 481, 385–411, 2003.
Goldstein, D., Handler, R., and Sirovich, L., Modeling a no-slip flow boundary with an external force field, *J. Comput. Phys.*, 105, 354–366, 1993.
Kang, S.K. and Hassan, Y.A., A direct-forcing immersed boundary method for the thermal lattice Boltzmann method, *Comput. Fluids*, 49.1, 36–45, 2011.
Kim, J. and Choi, H., An immersed-boundary finite-volume method for simulations of heat transfer in complex geometries, *Korean Soc. Mech. Eng. Int. J.*, 18, 1026–1035, 2004.
Ladd, A.J.C., Numerical simulations of particulate suspensions via a discretized Boltzmann equation. Part I. Theoretical foundation, *J. Fluid Mech.*, 271, 285–310, 1994.
Lu, J., Han, H., Shi, B., and Guo, Z., Immersed boundary lattice Boltzmann model based on multiple relaxation times, *Phys. Rev. E*, 85, 016711, 2012.
Michaelides, E.E., *Particles*, *Bubbles and Drops*, World Scientific Publishing, Hackensack, NJ, 2006.
Michaelides, E.E. and Feng, Z.-G., Heat transfer from a rigid sphere in a non-uniform flow and temperature field. *Int. J. Heat Mass Transfer*, 37.14, 2069–2076, 1994.
Mohamad, A.A. and Kuzmin, A., A critical evaluation of force term in lattice Boltzmann convection problem, *Int. J. Heat Mass Transfer*, 53, 990–996, 2010.
Mohd-Yusof, J., Combined immersed boundaries/B-splines methods for simulations of flows in complex geometries, Annual Research Briefs, Center for Turbulence Research, Stanford University, Stanford, CA, 1997.
Musong, S. and Feng, Z.-G., The effect of model parameters of the soft-sphere scheme on particle-particle collisions, in *DOE/NETL Conference on Multiphase Flow Science*, Morgantown, WV, May 22–24, 2012.
Pacheco, J.R., Pacheco-Vega, A., Rodic, T., and Peck, R.E., Numerical simulations of heat transfer and fluid problems using an immersed-boundary finite-volume method on non-staggered grids, *Numer. Heat Transfer B*, 48, 1–24, 2005.
Pan, T.W., Joseph, D.D., Bai, R., Glowinski, R., and Sarin, V., Fluidization of 1204 spheres: Simulation and experiment, *J. Fluid Mech.*, 451, 169–192, 2002.
Peskin, C.S., Numerical analysis of blood flow in the heart, *J. Comput. Phys.*, 25, 220–252 1977.
Peskin, C.S., The immersed boundary method, *ActaNumer.*, 11, 479–517, 2002.
Ranz, W. and Marshall, W., Evaporation fromdrops, *Chem. Eng. Prog.*, 48, 141–146, 1952.
Seta T., Rojas, R., Hayashi, K., and Tomiyama, A., Implicit-correction-based immersed boundary-lattice Boltzmann method with two relaxation times, *Phys. Rev. E*, 89, 023307, 2014.

Sloan, G., Feng, Z.-G., Bhaganagar, K., and Banerjee, D., Coupled direct numerical simulation and experimental approach to develop framework for nanofluids, in *Proceedings of the ASME 2012 International Mechanical Engineering Congress & Exposition*, paper IMECE2012–89271, Houston, TX, November 9–15, 2012.

Tavassoli, H., Kriebitzsch, S., van der Hoef, M., Peters, E., and Kuipers, J., Direct numerical simulation of particulate flow with heat transfer, *Int. J. Multiphase Flow*, 57, 29–37, 2013.

Tenneti, S., Sun, B., Garg, R., and Subramaniam, S., Role of fluid heating in dense gas-solid flow as revealed by particle-resolved direct numerical simulation, *Int. J. Heat Mass Transfer*, 58, 471–479, 2013.

Tsuji, Y., Tanaka, T., and Yonemura, S., Cluster patterns in circulating fluidized beds predicted by numerical simulation (discrete particle model versus two-fluid model), *Powder Technol.*, 95, 254–264, 1998.

Uhlmann, M., 2005. An immersed boundary method with direct forcing for the simulation of particulate flows. *Journal of Computational Physics*, 209(2), pp. 448–476.

Wu, J. and Shu, C., Implicit velocity correction-based immersed boundary-lattice Boltzmann method and its applications, *J. Comput. Phys.*, 228, 1963–1979, 2009.

Wu, J.-S. and Faeth, G.M., Sphere wakes at moderate Reynolds numbers in a turbulent environment, *AIAA J.*, 32.3, 535–541, 1994.

Vakil, A. and Green, S.I., Numerical study of two-dimensional circular cylinders in tandem at moderate Reynolds numbers, *ASME J. Fluids Eng.*, 135, 071204, 2013.

Yu, Z. and Shao, X., A direct-forcing fictitious domain method for particulate flows, *J. Comput. Phys.*, 227, 292–314, 2007.

2.5 Pdf Models for Particle Transport Mixing and Collisions in Turbulent Flows

Michael W. Reeks, Olivier Simonin, and Pascal Fede

2.5.1 Introduction

Probability density function (pdf) equations have proved very useful in studying the behavior of stochastic systems. Obvious examples of their usage occur in the study of Brownian motion (Chandrasekhar, 1943) and in the kinetic theory of gases (Chapman and Cowling, 1952). In more recent times, they have been used extensively by Pope and others to model both turbulence (Pope, 1985) and turbulence-related phenomena such as combustion (Pope, 1991) and atmospheric dispersion (MacInnes and Bracco, 1992). In this section, we review how this approach has been used to model the behavior of a particle-laden turbulent gas: in particular how in a two-fluid model it has been used to derive the continuum equations and constitutive relations of the dispersed particle phase and deal with the near-wall behavior when the natural boundary conditions (bc's) and strong inhomogeneity lead to a breakdown of the traditional form of the two-fluid model equations.

As in other approaches, the independent variables that describe the system are the phase space variables and the pdf equation describes the transport of the average phase space density in terms of those variables in phase space: the solution of the equation is the pdf that the system will be in any particular state as it evolves randomly in time. In the particular case of gas–particle flows, the phase space variables are taken to be the particle velocity and position.

The approach we consider here has much in keeping with the kinetic theory of gases: that is, the pdf equation is an analogue of the Maxwell–Boltzmann equation and can be used in precisely the same way to generate the continuum equations and constitutive relations from known solutions under the so-called equilibrium conditions. Likewise, the pdf equation may be regarded as a more exact description of the behavior of a gas–particle flow than that given by the continuum equations (with constitutive relations, especially, as we have said, near the wall when the inhomogeneity and natural boundary cause significant departures from the so-called equilibrium solutions upon which the constitutive relations are based). To emphasize its similarity to the kinetic theory, we have in the past referred to this approach as the pdf–kinetic approach. Like the kinetic theory, it can be regarded as a rational approach to two-fluid modeling; by this we mean that the equation and in particular the terms it contains can be traced back in a rational manner to the underlying equations of motion of the individual particles themselves. In the case of certain simple but generic flows, the solutions of the pdf equations are exact solutions and can be made the basis of approximate solutions of more complex flows in a formal and precise way.

This is different from what has gone before. In the past, for instance, it has been traditional to assume that the particle phase behaves as a simple Newtonian fluid (e.g., Elghobashi and Abou-Arab, 1983): that is, the particle Reynolds stresses are proportional to the mean symmetric rate of strain of the particle flow via

some particle eddy viscosity that is related to that of the carrier flow in some empirical way. Now, we can examine the validity of these assumptions within the context of a more reliable and complete framework using techniques that are well tested and understood and ultimately replace them with more legitimate relationships that do not rely on intuition and empiricism. Perhaps more importantly, we have an approach that is crucial to the formulation of particle–wall interactions (which is referred to as the natural boundary conditions (bc's) of a gas–particle flow).

In this section, we will show how the pdf–kinetic approach deals with both aspects of a two-fluid model; how it generates the equations for mass, momentum, and energy (so-called continuum equations) and constitutive relations for the dispersed phase (which would be appropriate for the far-wall solution of a gas–particle flow); and how it generates near-wall solutions that take account of the inhomogeneity of the flow and the natural bc's. Throughout the chapter, we will concentrate on dilute gas–particle flow where interparticle collisions can be safely ignored. For the application of the pdf approach to dense flows, see the recent work of Boëlle et al. (1995). Though we will consider the form of the momentum coupling between phases, specific examples will be taken from situations where that coupling is sufficiently small to not influence the underlying carrier gas flow itself.

In Section 2.5.1, we will present the pdf equation itself and discuss about how it is derived from the underlying particle equations of motion. In Section 2.5.2, we will consider analytic solutions of the equation for simple flow in which the turbulence is homogeneous and stationary and the mean flow is uniform or is a simple shear or a rotational flow. These solutions have important implications for the behavior of the particle phase as a simple Newtonian flow. In Section 2.5.3, we will present the continuum equations as derived from the pdf equation and the constitutive relations for the particle Reynolds stress flux as derived using the Chapman–Enskog (C–E) approximation and show some predictions using these equations compared with those of a random walk simulation. Section 2.5.4 is concerned with the application of the pdf approach to the prediction of near-wall behavior. In particular, we will consider natural bc's involving partial absorption and both specular and diffuse reflection, and finally, we will consider solutions for the well-known problem of particle deposition in a turbulent boundary layer with perfectly absorbing walls (this is a much–studied system both theoretically and experimentally) and highlight the breakdown of the so-called gradient transport due to both the strong inhomogeneity of the flow near the wall and the strong departure of the velocity distribution at the wall compared with that in the far wall (bulk flow). In the final section, we will draw some comparison between the pdf approach used by Simonin (1991), for which there are strong similarities, and a practical point of view identical as far as dilute gas–particle flows).

2.5.2 Formulations of pdf Equations

There are currently two forms of the pdf equation in use. In the first form, the pdf, as in the kinetic theory, refers to the probability density that a particle has a certain velocity and position at a given time. We will refer to this pdf approach as the kinetic method (KM). This approach was originated by Buyevich (1971, 1972a,b) and developed since then by a number of workers most notably Reeks (1980, 1983, 1991, 1992), Swailes and Darbyshire (1997), Derevich and Zaichik (1988), Zaichik (1991), Pozorski and Minier (1998), and more recently Li and Zhou (1996). In all these developments, the pdf approach was restricted to inert nonreactive particles. More recently, Pandya and Mashayek (2001) extended the approach to reactive condensing or evaporating particles in a turbulent gas. In contrast, the second form of pdf equation, first proposed by Simonin et al. (1993), is for a more general pdf that includes the velocity of the carrier flow local to the particle as a phase space variable as well as the particle position and velocity. As an example of how pdfs and pdf equations are obtained, consider the motion of evaporating/condensing particles (droplets) in a dilute suspension in which there are no interparticle collisions. Let $\mathbf{X}(t)$ be the phase space vector at time t of a single particle as it moves through phase space. So, in this case,

$$\mathbf{X} = \left[m, T, \boldsymbol{v}, \boldsymbol{x}\right] \tag{2.185}$$

where

m is the mass of the particle
T is its temperature
$\boldsymbol{v}$ is its velocity
$\boldsymbol{x}$ is the position of its center of mass at time t

The n number of independent variables that defines the phase space dimension is thus $n = 8$. For a single realization of the underlying carrier flow velocity field $\boldsymbol{u}(\boldsymbol{x}, t)$ and temperature field $T(\boldsymbol{x}, t)$, the number of

particles in an elemental volume $d^n\mathbf{X}$ of phase space located at $\mathbf{X}$ is given by $W(\mathbf{X}, t)d^n\mathbf{X}$, where $W(\mathbf{X}, t)$ is the phase space density, that is, the number of particles per unit volume in phase space. So, if we consider conservation of particle number within that elemental volume at $\mathbf{X}$, then with respect to P, we have

$$\frac{\partial W}{\partial t}+\frac{\partial}{\partial \mathbf{X}}\cdot\left[W\dot{\mathbf{X}}\right]=0 \tag{2.186}$$

So, for the case of the evaporating droplet, we have explicitly

$$\dot{\mathbf{X}}=\left[\dot{m},\dot{T},\dot{\boldsymbol{v}},\dot{\boldsymbol{x}}\right] \tag{2.187}$$

where the equations for components of $\dot{\mathbf{X}}$ represent the *particle equations of motion* in the most general sense and are derived from the mass, momentum, and energy conservation equations for an individual particle/droplet (see, e.g., Crowe et al., 2012). However, because the underlying carrier flow field is turbulent, $\dot{\mathbf{X}}$ has a random component, so we can only usefully refer to the pdf that a particle has a set of values $\mathbf{X}$ at any given time. This is represented by the ensemble average of W over all realizations of the system, symbolically $\langle W\rangle$. The equation for $\langle W\rangle$ (the pdf equation) can be found by ensemble averaging the conservation equation for W (the Liouville equation). For convenience, we use Reynolds decomposition, whereby the instantaneous components of $\dot{\mathbf{X}}$ are decomposed into their mean components $\langle\dot{\mathbf{X}}\rangle$ and fluctuating (zero mean) components $\dot{\mathbf{X}}'$, noting that $\dot{\boldsymbol{x}}=\boldsymbol{v}$, so that explicitly the pdf equation for the evaporating/condensing particle is

$$\begin{aligned}&\frac{\partial\langle W\rangle}{\partial t}+\left(\frac{\partial}{\partial m}\langle\dot{m}\rangle+\frac{\partial}{\partial T}\langle\dot{T}\rangle+\boldsymbol{v}\cdot\frac{\partial}{\partial\boldsymbol{x}}+\frac{\partial}{\partial\boldsymbol{v}}\cdot\langle\dot{\boldsymbol{v}}\rangle\right)\langle W\rangle\\&\quad=-\frac{\partial}{\partial m}\langle\dot{m}'W\rangle-\frac{\partial}{\partial T}\langle\dot{T}'W\rangle-\frac{\partial}{\partial\boldsymbol{v}}\cdot\langle\dot{\boldsymbol{v}}'W\rangle\end{aligned} \tag{2.188}$$

where on the left-hand side (LHS) we have the convective part (the transport in the absence of the turbulence) and on the right-hand side (RHS) the dispersive part involving the gradients of the net fluxes due to the turbulence. To close the equation, we need to relate the turbulent fluxes in some way, directly or indirectly, to $\langle W\rangle$ and its derivatives. That is, we have a closure problem to resolve, which is the most important element of the pdf approach.

To illustrate the way in which the values of $\dot{\mathbf{X}}$ depend upon the properties of the particle and the underlying carrier flow, let us consider the case of the evaporating droplet in more detail. From mass conservation of a spherical droplet of diameter d_p evaporating in a gas of mass density ρ_g, we have the general relationship

$$\dot{m}=\pi\rho_g d_p D_g Sh(Re_p,S_c)\ln\left[\frac{1-\alpha_v}{1-\alpha_{vs}}\right] \tag{2.189}$$

where

α_v is the mass fraction of vapor emitted by the particle in the locally undisturbed gas flow

α_{vs} is the (saturated) vapor mass fraction at the droplet/particle–surface assumed to be in equilibrium with the particle (so it depends directly on the temperature T of the particle)

D_g is the molecular diffusion coefficient of the vapor

Sh is the droplet Sherwood number for the mass transfer of vapor to or from the droplet that is a function of the vapor Schmidt number S_c and the local particle Reynolds number Re_p given by

$$Re_p=\frac{d_p|\boldsymbol{v}-\boldsymbol{u}|}{\nu_g};\quad Sc=\frac{D_v}{\nu_g} \tag{2.190}$$

where

$\boldsymbol{u}(\boldsymbol{x}, t)$ is the gas flow velocity local to the droplet at $\boldsymbol{x}$ at time t

ν_g is the kinematic viscosity of the gas

From momentum conservation (Crowe et al., 2012), we have

$$m\dot{\boldsymbol{v}} = mg - V\frac{\partial \cdot \underline{\sigma}}{\partial x} + \mathbf{F}_A + (\boldsymbol{u} - \boldsymbol{v})\dot{m} \tag{2.191}$$

The first term on the RHS of this equation is the gravitational force. The second and third terms represent the force exerted by the surrounding gas flow from the external stresses $\underline{\sigma}$ and the aerodynamic force $\mathbf{F}_A$ that has both lift and drag components $\mathbf{F}_L$ and $\mathbf{F}_D$ arising from the locally disturbed gas flow field due to the presence of the particle that has a volume V. For a spherical particle, this is well represented by the drag force in most cases so that

$$\mathbf{F}_A \cong \mathbf{F}_D = -\frac{1}{2}\rho_g A C_D(Re_p)\left|\boldsymbol{v} - \boldsymbol{u}\right|(\boldsymbol{v} - \boldsymbol{u}) \tag{2.192}$$

where

C_D is the drag coefficient

A is the projected area of the particle normal to the flow

From energy conservation, we would have an equation of the form

$$mC_p\dot{T} = S_r - \pi k_f d_p Nu(Re_p, Pr) + \Delta H\dot{m} \tag{2.193}$$

where C_p is the specific heat of the particle/droplet and, on the RHS of the equation, the first term S_r is the heat source due to the external field (radiation), the second term is the particle to surrounding gas heat transfer rate where Nu is the Nusselt number (depending upon the local particle Reynolds number and the Prandtl number of the gas/vapor mixture), and the third term is energy exchange during the evaporation/condensation that depends upon ΔH (the difference in enthalpy between the droplet and the vapor mass flux).

The point to note here is that the equations of motion are all coupled and all depend upon the instantaneous particle Reynolds number based upon the relative velocity between particle and locally undisturbed gas.

2.5.2.1 Pdf Equation for Inertial Particles

As we have said earlier, there are currently two pdf approaches in use that we refer to as the kinetic method (KM) and the generalized Langevin method (GLM), respectively. To illustrate the differences and similarities between these approaches, we consider here the simplest case of transport of inertial nonreacting solid particles in a turbulent gas flow that we will assume all to be identical to one another. To simplify the situation still further, we will linearize the drag acting on the particle with respect to the relative velocity, that is,

$$\mathbf{F}_A \cong \eta\left(\boldsymbol{u} - \boldsymbol{v}\right) \tag{2.194}$$

where η is the net friction coefficient and is given by

$$\eta = \frac{1}{2}\rho_g A C_D(\overline{Re}_p)\left|\bar{\boldsymbol{u}} - \bar{\boldsymbol{v}}\right| \tag{2.195}$$

where

$\bar{\boldsymbol{v}}$ is the net particle velocity

$\overline{Re}_p$ is the value of the particle Reynolds number based on the net relative velocity between particle and local carrier flow

The equations of motion for an identical particle are thus

$$\frac{d\boldsymbol{x}}{dt} = \boldsymbol{v} \tag{2.196}$$

$$\frac{d\boldsymbol{v}}{dt} = \beta\left(\boldsymbol{u} - \boldsymbol{v}\right) \tag{2.197}$$

where β is the inverse particle response time and is given by $m^{-1}\eta$ for a particle of mass m: in the case $Re_p \ll 1$ corresponding to Stokes drag, β is a constant of the motion. To the particle equations of motion, we add an equation of motion of the carrier flow velocity **u** along a particle trajectory, namely,

$$\frac{du_i}{dt} = F_i\left(\boldsymbol{v}, \boldsymbol{u}, \boldsymbol{x}, t\right) \tag{2.198}$$

In the KM approach, we consider continuum equations derived from an equation for the phase space density $W(\mathbf{v}, \mathbf{x}, t)$ in which $\mathbf{u}(\mathbf{x}, t)$ is a random function of **x** and t and **v** and **x** are independent random variables. In the GLM approach, the continuum equations are derived from a conservation equation for the phase space density $P(\boldsymbol{v}, \boldsymbol{u}, \boldsymbol{x}, t)$ where $\boldsymbol{v}, \boldsymbol{u}, \boldsymbol{x}$ form a set of independent variables. The transport/conservation equations for $W(\boldsymbol{v}, \boldsymbol{x}, t)$ and $P(\boldsymbol{v}, \boldsymbol{u}, \boldsymbol{x}, t)$ are, respectively,

$$\left\{\frac{\partial}{\partial t} + \frac{\partial}{\partial x_i}v_i + \frac{\partial}{\partial v_i}\beta\left(u_i(\boldsymbol{x}, t) - v_i\right)\right\}W\left(\boldsymbol{v}, \boldsymbol{x}, t\right) = 0 \tag{2.199}$$

$$\left\{\frac{\partial}{\partial t} + \frac{\partial}{\partial x_i}v_i + \frac{\partial}{\partial v_i}\beta_i\left(u_i - v_i\right) + \frac{\partial}{\partial u_i}F_i\left(\boldsymbol{v}, \boldsymbol{u}, \boldsymbol{x}, t\right)\right\}P\left(\boldsymbol{v}, \boldsymbol{u}, \boldsymbol{x}, t\right) = 0 \tag{2.200}$$

Note that integrating the equation for P over all $\boldsymbol{u}$ gives the equation for W. We resolve $u_i(\boldsymbol{x}, t)$ and $F_i(\boldsymbol{v}, \boldsymbol{u}, \boldsymbol{x}, t)$ into mean and fluctuating parts:

$$u_i = \langle u_i \rangle + u_i''; \quad F_i = \left\langle F_i \right\rangle + F_i'' \tag{2.201}$$

where $\langle \ldots. \rangle$ represents an ensemble average. Then the transport equations for mean values of W and P, namely, $\langle W \rangle$ and $\langle P \rangle$, are

$$\left\{\frac{\partial}{\partial t} + \frac{\partial}{\partial x_i}v_i + \frac{\partial}{\partial v_i}\beta\left(\left\langle u_i \right\rangle - v_i\right)\right\}\left\langle W \right\rangle = -\frac{\partial}{\partial v_i}\beta\left\langle u_i'' W \right\rangle \tag{2.202}$$

$$\left\{\frac{\partial}{\partial t} + \frac{\partial}{\partial x_i}v_i + \frac{\partial}{\partial v_i}\beta\left(u_i - v_i\right) + \frac{\partial}{\partial u_i}\left\langle F_i \right\rangle\right\}\left\langle P \right\rangle = -\frac{\partial}{\partial u_i}\left\langle F_i'' P \right\rangle \tag{2.203}$$

when suitably normalized $\langle W \rangle$ and $\langle P \rangle$ represent the probability density at time t that a particle has $(\boldsymbol{v}, \boldsymbol{x})$ and $(\boldsymbol{v}, \boldsymbol{x}, \boldsymbol{u})$, respectively. To solve these equations, closure relations for $\left\langle u_i'' W \right\rangle$ and $\left\langle F_i'' P \right\rangle$ are required. For simplicity, we will just deal with the case where $\beta_{ij} = \beta\delta_{ij}$.

2.5.2.2 Closure Approximation for a Nonreactive Gas–Particle Flows

2.5.2.2.1 Kinetic Model A range of strategies for closing the turbulent flux can be found in the literature. The methodologies underpinning these approaches can be divided into three distinct categories: (1) Furutsu–Novikov-based (EN) methods (Furutsu, 1963, Novikov, 1965, Derevich and Zaichik, 1990, Swailes and Darbyshire, 1997, Zaichik, 1997, Hyland et al., 1999a, Zaichik, 1999, Derevich, 2000, Zaichik et al., 2004), (2) Lagrangian history direct interaction (LHDI) methods (Reeks, 1992), and (3) Van Kampen (VK) operator representation methods (Pozorski and Minier, 1998, Pandya and Mashayek, 2001). These different approaches have been reviewed and analyzed recently by Bragg et al. (2012a). Recent work has suggested that the corresponding kinetic equations are essentially equivalent (Pandya and Mashayek, 2001). However, while the three closure expressions exhibit superficial similarities, Bragg et al. have shown that there are fundamental differences that have an important bearing on their validity in inhomogeneous turbulence. What all three

methods do have in common is that they represent the net force due to the turbulence $\langle \beta u' W \rangle$ by gradient diffusion contributions both in velocity and position and in body force (per unit mass) dependent on the statistical inhomogeneity of the turbulence, that is, it is zero in statistically stationary homogeneous turbulence. Thus, in general,

$$\langle f_i W \rangle = -\left(\frac{\partial}{\partial x_j} \langle W \rangle \lambda_{ji} + \frac{\partial}{\partial v_j} \langle W \rangle \mu_{ji} - \kappa_i \langle W \rangle \right) \tag{2.204}$$

where for convenience we have written f_i for $\beta u_i'$. Note that dispersion coefficients appear on the other side of the gradients in velocity and position than is normal. So, in this context, they are more appropriately the components of stress tensors $\boldsymbol{\lambda}$ and $\boldsymbol{\mu}$ (per unit particle mass) rather than diffusion coefficients. Reeks (1991) has shown that this form is a general requirement of random Galilean transformation invariance. Taking the forms for $\boldsymbol{\lambda}$ and $\boldsymbol{\mu}$ and $\boldsymbol{\kappa}$ given by the Furutsu–Novikov (FN) method,

$$\begin{aligned}
\lambda_{ji} &= \int_0^t \langle \mathcal{G}_{jk}(t|s) R_{ki}(\boldsymbol{x}^p(t|s), s; \boldsymbol{x}, t) \rangle ds \\
\mu_{ji} &= \int_0^t \langle \dot{\mathcal{G}}_{jk}(t|s) R_{ki}(\boldsymbol{x}^p(t|s), s; \boldsymbol{x}, t) \rangle ds \\
\kappa_i &= \int_0^t \left\langle \mathcal{G}_{jk}(t|s) \frac{\partial}{\partial x_j} R_{ki}\left(\boldsymbol{x}^p(t|s), s; \boldsymbol{x}, t\right) \right\rangle ds
\end{aligned} \tag{2.205}$$

$\boldsymbol{R}$ denotes an Eulerian two-point, two-time correlation tensor of the turbulent force field $\boldsymbol{f}$, that is,

$$R_{ki}(\boldsymbol{y}, s; \boldsymbol{x}, t) = \langle f_k(\boldsymbol{y}, s) f_k(\boldsymbol{x}, t) \rangle \tag{2.206}$$

where $\boldsymbol{x}^p(t|s)$ is the particle position evaluated at time s along all particle trajectories passing through $\boldsymbol{x}$ and v at time t, that is, in Equation 2.206 $\boldsymbol{y} = \boldsymbol{x}^p(t|s)$, with $\boldsymbol{x}^p(t|t) = \boldsymbol{x}$ and $\dot{\boldsymbol{x}}^p(t|t) = \boldsymbol{\upsilon}$. $\mathcal{G}_{jk}(t \mid s)$ are the components of a response tensor $\mathcal{G}$ given formally by the functional derivative

$$\mathcal{G}_{jk}(t|s) = \frac{\delta x_j^p(t|t)}{\delta f_k(\boldsymbol{x}^p(t|s), s) ds} \tag{2.207}$$

That is, they describe the effect of a perturbation in the field $\boldsymbol{f}(\boldsymbol{x}, s)$ applied at the particle position $\boldsymbol{x}^p(t|s)$ at time s upon the position of the particle at time t. This can be obtained by taking the functional derivative with respect to $\boldsymbol{\delta f}(\boldsymbol{x}, s)$ of the particle equation of motion Equation 2.197 so that

$$\ddot{\mathcal{G}}_{jk} + \beta \dot{\mathcal{G}}_{jk} - \beta \left(\frac{\partial \langle u_j \rangle}{\partial x_k} + \frac{\partial u_j''}{\partial x_k} \right) \mathcal{G}_{jk} = 0 \tag{2.208}$$

with the "initial" conditions $\mathcal{G}_{jk}(s|s) = 0$ and $\dot{\mathcal{G}}_{jk}(s|s) = \delta_{jk}$. In Equation 2.208, the spatial derivatives of $\boldsymbol{u}$ and $\boldsymbol{u}'$ are evaluated along the particle trajectories $\boldsymbol{x}^p(t|s)$. The closure term given by Equation 2.204 based on the forms for $\boldsymbol{\lambda}$ and $\boldsymbol{\mu}$ and $\boldsymbol{\kappa}$ given by Equation 2.205 is *exact* if the flow field $\boldsymbol{f}(\boldsymbol{x}, t)$ is Gaussian. We note that in the case of high-inertia particles, $\beta \to \infty$, the velocity gradient term in Equation 2.204 dominates and the kinetic equation reduces to the well-known Fokker–Planck equation. The forms $\boldsymbol{\lambda}$ and $\boldsymbol{\mu}$ and $\boldsymbol{\kappa}$ based on the LHDI approach (Reeks, 1992) are the same as those based on the Furutsu–Novikov method except that the Eulerian correlation R is replaced by $f_k(\boldsymbol{x}^p(s), s) f_i(\boldsymbol{x}, t)$. Thus, it is Lagrangian correlations that are involved rather than Eulerian correlations. In addition, the stochastic response functions $\mathcal{G}_{jk}$ are replaced by its deterministic components $\langle \mathcal{G}_{jk} \rangle$ so that the equation for $\langle \mathcal{G}_{jk} \rangle$ is given by

$$\langle \ddot{\mathcal{G}}_{jk} \rangle + \beta \langle \dot{\mathcal{G}}_{jk} \rangle - \beta \frac{\partial \langle u_j \rangle}{\partial x_k} \langle \mathcal{G}_{jk} \rangle = \delta(t - s) \delta_{jk} \tag{2.209}$$

In the LHDI case, then

$$\lambda_{ji} = \langle \Delta x_j(t) f_i(\boldsymbol{x},t) \rangle \quad \mu_{ji} = \langle \Delta v_j(t) f_i(\boldsymbol{x},t) \rangle \quad \kappa_i = \left\langle \Delta x_j(t) \frac{\partial f_i(\boldsymbol{x},t)}{\partial x_j} \right\rangle \tag{2.210}$$

where explicitly $\Delta x_j(t)$ and $\Delta v_j(t)$ are shorthand for $\Delta x_j(\boldsymbol{x}, \boldsymbol{v}, t|0)$ and $\Delta v_j(\boldsymbol{x}, \boldsymbol{v}, t|0)$ denoting changes in the particle position and velocity for a particle starting somewhere in the particle phase space at some initial time $s = 0$ and arriving at the point $\boldsymbol{x}$, $\boldsymbol{\upsilon}$ at time $s = t$. In terms of the deterministic response functions $\langle \mathcal{G}_{jk} \rangle$, these changes are given by

$$\begin{aligned} \Delta x_j(\boldsymbol{x},\boldsymbol{v},t\,|\,0) &= \int_0^t ds \langle G_{jk} \rangle (t|s) f_k(\boldsymbol{x}^p(t|s),s) \\ \Delta v_j(\boldsymbol{x},\boldsymbol{v},t\,|\,0) &= \int_0^t ds \langle \dot{\mathcal{G}}_{jk} \rangle (t|s) f_k(\boldsymbol{x}^p(t|s),s) \end{aligned} \tag{2.211}$$

It is claimed that the result is exact for a process in which the displacements $\Delta x_j(\boldsymbol{x}, \boldsymbol{v}, t|0)$, $\Delta v_j(\boldsymbol{x}, \boldsymbol{v}, t|0)$ form a Gaussian process. While both LHDI and FN closures would both claim to be exact for Gaussian processes, the Gaussian processes to which they refer are not the same: in the case of LHDI, the Gaussian process refers to the Lagrangian statistics of $\boldsymbol{f}(\boldsymbol{x}^p(s), s)$ along a particle trajectory in phase space, while in the FN case, it refers to the field $\boldsymbol{f}(\boldsymbol{x}, t)$. Given that one process is prescribed as Gaussian, it does not imply that the other is Gaussian. Bragg et al. (2012a) pointed out that in the previous FN formulations, the deterministic response functions $\langle \mathcal{G}_{jk} \rangle (t|s)$ were used in place of $\mathcal{G}_{jk}$ so that the contribution of the fluctuations in the spatial gradient of $\boldsymbol{f}(\boldsymbol{x}, t)$ was omitted. While using this nonrandom form for $\mathcal{G}$ formally closes the equation for $\langle f_i W \rangle$, Bragg et al. (2012b) have shown that the inclusion of this random term ensures the fully mixed criterion for a passive scalar (particle Stokes number $St \to 0$),* that is, the absence of spurious drift. We need to refer to this feature in more detail later on (see Section 2.5.4.1.1). There is good reason, however, to use $\langle \mathcal{G}_{ji} \rangle$ instead of $\mathcal{G}_{ji}$ other than for practicality. Calculations of the value of the dispersion coefficients by Bragg et al. (2012a) in a fully developed KS of a turbulent boundary using both $\langle \mathcal{G}_{ji} \rangle$ and $\mathcal{G}_{ji}$ show little difference for $St = 0.3$, negligible difference at $St = 0.8$, and an imperceptible difference at $St = 3$. Using the deterministic response $\langle \mathcal{G}_{ji} \rangle$ shows a resemblance between the FN and LHDI approaches that is reminiscent of Corrsin's independence hypothesis (Corrsin, 1974) that gives an approximate relationship between Lagrangian and Eulerian timescales. So, the Lagrangian correlation is given as

$$\begin{aligned} \left\langle f_j(\boldsymbol{x},\boldsymbol{v},t\,|\,t') f_i\big(\boldsymbol{x},t\big) \right\rangle &\simeq \int R_{ji}(\boldsymbol{x}',t';\boldsymbol{x},t) \left\langle \delta(\boldsymbol{x}' - \boldsymbol{x}^p(t\,|\,t')) \right\rangle d^3\boldsymbol{x}' \\ &= \int d^3\boldsymbol{x}' R_{ki}(\boldsymbol{x}',t';\boldsymbol{x},t) G(\boldsymbol{x}' - \boldsymbol{x}, t - t') \end{aligned} \tag{2.212}$$

where $G(\boldsymbol{x}' - \boldsymbol{x}, t - t')$ is Green's function solution for an instantaneous point source $\delta(\boldsymbol{x}' - \boldsymbol{x})\delta(t' - t)$. This relationship arises naturally through the comparison between between LHDI and FN approaches without the necessity of invoking Corrsin's hypothesis.

Finally, we mention briefly the operator representation of VK that was used by Pozorski and Minier (1998) to obtain a pdf–kinetic equation. This third form of the kinetic equation is formally consistent with the fully mixed condition but fails to account for a nonzero scalar flux contribution associated with nonuniform scalar distributions in inhomogeneous, incompressible flows. Furthermore, this VK closure is based on an expansion in terms of a small parameter reflecting the magnitude of turbulence intensity relative to a rate scale for the decorrelation of turbulent flow velocities (weak turbulence approximation). Correlations are based on mean trajectories, that is, due to the mean flow, ignoring the influence of the turbulence, and while this affords a significant simplification to the closure problem, removing conditional averages within the dispersion tensors makes the validity of such an approximation in strongly inhomogeneous flows

* For Stokes number St, we mean the ratio of β^{-1}/τ_f where τ_f is the typical timescale of the turbulence encountered by a particle.

highly questionable. In addition, as Bragg et al. (2012a) pointed out, even for the simpler case of dispersion in isotropic turbulence, there seems to be a serious issue with the VK formulation. The VK diffusion coefficients for fluid point dispersion in isotropic turbulence suggest that the dispersion rate should be proportional to the Eulerian integral timescale rather than the Lagrangian integral timescale. This is clearly incorrect and arises precisely because the VK dispersion tensors contain correlations of the fluid velocity field evaluated along mean trajectories. Therefore, the question of the validity of the VK closure relates not only to inhomogeneous flows but also to homogeneous, isotropic flows. This is not as we will see the case with FN and LHDI formulations.

2.5.2.2.2 GLM SDM (Simonin et al., 1993) derived an equation of motion for the fluid velocity along a particle trajectory by starting from the Langevin equation that Pope (Haworth and Pope, 1986) has used as the analogue of the Navier–Stokes equation for fluid point motion. Thus, along a fluid point trajectory,

$$\frac{du_i}{dt} = -\alpha_{ij}(\boldsymbol{x})u_j'' + f_i(\boldsymbol{x}) + f_i''(t) \tag{2.213}$$

where

$f_i(\boldsymbol{x})$ is the net viscous and pressure force per unit mass of fluid
$f_i''(t)$ is a white noise function of time.

Both SDM and Pope consider the equation of motion in differential form because the white noise is assumed nondifferentiable. For convenience, we have assumed that the white noise, like all turbulence-related functions, is differentiable: it has white noise properties simply because it has a timescale much shorter than the timescale over which $\boldsymbol{u}(t)$ varies along a fluid point trajectory $O(\alpha^{-1})$. For future reference, we note that

$$f_i(\boldsymbol{x}) = \frac{D_f \langle u_i \rangle}{Dt} + \frac{\partial \langle u_j'' u_i'' \rangle}{\partial x_j} \tag{2.214}$$

where

$$\frac{D_f}{Dt} = \frac{\partial}{\partial t} + \langle u_j \rangle \frac{\partial}{\partial x_j}. \tag{2.215}$$

SDM use this equation to generate an equation of motion for the fluid velocity along a particle trajectory. That is, if d_p/dt is the time derivative of the fluid velocity along a particle trajectory and similarly d_f/dt along a fluid point trajectory, then we have

$$\begin{aligned}
\frac{d_p u_i}{dt} &= \left(\frac{\partial}{\partial t} + v_j \frac{\partial}{\partial x_j} \right) u_i(\boldsymbol{x},t) \\
&= (v_j - u_j)\frac{\partial u_i(\boldsymbol{x},t)}{\partial x_j} + \frac{d_f u_i}{dt} \\
&= (\boldsymbol{v}_j - u_j)\frac{\partial u_i(\boldsymbol{x},t)}{\partial x_j} \\
&= -\alpha_{ij}u_j'' + f_i(\boldsymbol{x}) + f_i''(t)
\end{aligned} \tag{2.216}$$

SDM consider only the contribution from the gradient of the mean fluid velocity in this equation of motion for the fluid velocity along a particle trajectory. That is, they consider the equation

$$\frac{d_p u_i}{dt} = (v_j - u_j)\frac{\partial \langle u_i(\boldsymbol{x},t) \rangle}{\partial x_j} - \alpha_{ij}u_j'' + f_i(\boldsymbol{x}) + f_i''(t) \tag{2.217}$$

In effect, this is equivalent to assuming that the contribution of the fluctuating fluid velocity gradient is absorbed into the white noise function $f_i''(t)$. In the case of the white noise function, the equation for $\langle P\rangle$ can be closed exactly, namely,*

$$\begin{aligned}\left\langle F_i''(\boldsymbol{x},t)P(\boldsymbol{v},\boldsymbol{u},\boldsymbol{x},t)\right\rangle &= \left\langle f_i''(t)P(\boldsymbol{v},\boldsymbol{u},\boldsymbol{x},t)\right\rangle \\ &= -\int_0^\infty \left\langle f_i''(0)f_j''(s)\right\rangle ds\frac{\partial\langle P\rangle}{\partial \boldsymbol{u}_j}\end{aligned} \tag{2.218}$$

Then from Equation 2.203, the equation for $\langle P\rangle$ used by SDM is

$$\begin{aligned}&\frac{\partial\langle P\rangle}{\partial t}+\frac{\partial}{\partial x_i}v_i\langle P\rangle+\frac{\partial}{\partial v_i}\beta\left(u_j-v_j\right)\langle P\rangle+\frac{\partial}{\partial u_i}\left[-\alpha_{ij}u_j''+f_i(\boldsymbol{x})+(v_j-u_j)\frac{\partial\langle u_i\rangle}{\partial x_j}\right]\langle P\rangle \\ &=\int_0^\infty \left\langle f_i''(0)f_j''(s)\right\rangle ds\frac{\partial^2\langle P\rangle}{\partial u_i u_j}\end{aligned} \tag{2.219}$$

which are spatially independent but varying in time.

2.5.3 Analytic Solutions in Simple Flows

In cases where the turbulence is homogeneous and stationary and the mean carrier flow is a linear flow field, the pdf equations for both KM and GLM have analytic solutions. Moreover, when the fluctuating aerodynamic force is a Gaussian random force, both pdf approaches, given the same form for the carrier flow correlation along a particle trajectory, will give identical results (Reeks, 2005). Furthermore, these solutions can be used as a basis for dealing with more complex flow fields (e.g., in constructing appropriate constitutive relations), can give some insights into the basic diffusion process, and can be used as test cases to check out numerical methods that are appropriate in more general cases. In this section, we will present some results for dispersion of point sources in mean flows that are (1) uniform, (2) simple shear, and (3) rotational. The results are taken from Hyland et al. (1999b), Swailes and Darbyshire (1997), and Reeks (2005). As a preliminary, we note as in the work by Swailes and Darbyshire (1997) that if for convenience we introduce the phase space variable $\wp = (\boldsymbol{x}, \boldsymbol{v})$, then the solution of the pdf equation for an instantaneous point source is a Gaussian $G(\wp, t)$ given by

$$G(\wp,t)=(2\pi)^{-n}\det\left\{\underline{\Theta}\right\}^{-\frac{1}{2}}\exp\left\{-\frac{1}{2}(\wp-\boldsymbol{m})\cdot\underline{\Theta}^{-1}(\wp-\boldsymbol{m})\right\} \tag{2.220}$$

where $\underline{\Theta}$ is the matrix of ensemble covariances of $\wp$ as a function of time t and $\boldsymbol{m}=(\hat{\boldsymbol{x}},\hat{\boldsymbol{v}})$ where $\hat{x}$ and $\hat{\boldsymbol{v}}$ are the solutions of $\boldsymbol{x}(t)$ and $\boldsymbol{v}(t)$, respectively, without the turbulence starting from some initial values $\boldsymbol{x}^0$ and $\boldsymbol{v}^0$ at time zero (the point of release) and $\det\underline{\Theta}(0) = 0$. The solution for the particle spatial concentration at $\boldsymbol{x}^*$ in a frame of reference moving with velocity $\hat{\boldsymbol{v}}(t)$ whose origin coincides with the point of release $\boldsymbol{x}^0$ at time zero satisfies the following simple diffusion equation:

$$\frac{\partial\langle\rho\rangle}{\partial t}=\frac{\partial}{\partial x_i^*}D_{ij}(t)\frac{\partial}{\partial x_j^*}\langle\rho\rangle+\delta(\boldsymbol{x}^*)\delta(t) \tag{2.221}$$

where the diffusion coefficients $D_{ij}(t)$ are the particle ensemble covariances $\langle x_i^*(t)v_j^*(t)\rangle$. The solution is a Gaussian in $\boldsymbol{x}^*$ of the general form

$$G(\boldsymbol{x}^*,t)=(2\pi)^{-3/2}\det\left(\langle\boldsymbol{x}^*\,\boldsymbol{x}^*\rangle\right)^{-1/2}\times\exp\left(-\frac{1}{2}\boldsymbol{x}^*\langle\boldsymbol{x}^*\,\boldsymbol{x}^*\rangle^{-1}\boldsymbol{x}^*\right) \tag{2.222}$$

* Note that the closure is also exact if $f''(t)$ is Gaussian nonwhite but will include gradients of $\langle P\rangle$ in $\boldsymbol{x}$ and $\boldsymbol{v}$ as well.

That is, in the fixed frame of reference, the contours of constant concentration will be concentric ellipses (in 2D) centered at $\hat{\boldsymbol{x}}(t)$. For the mean density-weighted particle velocity, we have

$$\bar{\boldsymbol{v}} = \hat{\boldsymbol{v}} + \langle \boldsymbol{v}^* \boldsymbol{x}^* \rangle \langle \boldsymbol{x}^* \boldsymbol{x}^* \rangle^{-1} \boldsymbol{x}^* \tag{2.223}$$

that is, the mean particle flow field is linear in x, and for the density-weighted particle velocity covariances, we have

$$\overline{\boldsymbol{v}'\boldsymbol{v}'} = \langle \boldsymbol{v}^* \boldsymbol{v}^* \rangle - < \boldsymbol{v}^* \boldsymbol{x}^* \rangle \langle \boldsymbol{x}^* \boldsymbol{x}^* \rangle^{-1} \langle \boldsymbol{x}^* \boldsymbol{x}^* \rangle \tag{2.224}$$

which are spatially independent but varying in time.

2.5.3.1 Uniform Flows

The features of dispersion in this flow have been extensively simulated and measured, particularly the particle diffusion coefficient and particle velocity covariances (see Stock, 1996). Forms for the long-time particle diffusion coefficient $D_p(\infty)$ have been much quoted in isotropic turbulence both with and without gravity (e.g., Reeks, 1977). The pdf equation reproduces the right result, namely, for Stokes drag

$$D_p(\infty) = \frac{1}{3} \int_0^\infty \langle \boldsymbol{u}(0) \boldsymbol{u}(s) ds \tag{2.225}$$

where we have used $\boldsymbol{u}(s)$ as shorthand for $\boldsymbol{u}(\boldsymbol{x}|s)$, that is, the carrier flow velocity along a particle trajectory measured at time s with $\boldsymbol{u}(\boldsymbol{x}|0) = \boldsymbol{u}(0)$. The absence of $\boldsymbol{x}$ in Equation 2.225 is meant to imply an independence on the initial position at $s = 0$. It is a result we will deduce later from the momentum equation, which shows that the particle response time (inertia) dependence is reflected only in the way this quantity determines the timescale of $\boldsymbol{u}(s)$ along a particle trajectory: whether the carrier flow timescales along a particle trajectory are bigger or smaller than those along a fluid element trajectory. In fact, particles with more inertia appear to have a long-time diffusion coefficient that is greater than that for a fluid element or passive tracer. This is shown in Figure 2.26 based on the results obtained by Squires and Eaton (1991) for particle diffusion in a direct numerical simulation (DNS) of statistically stationary isotropic homogeneous turbulence.

The vertical axis is the ratio of the particle diffusion coefficient compared to that of the fluid or passive scalar. The calculations were done for a range of particle Stokes numbers St from 0.06 to 0.35 where Stokes number is the ratio of the particle response time τ_p to integral timescale of the flow T_f. You can see that for all

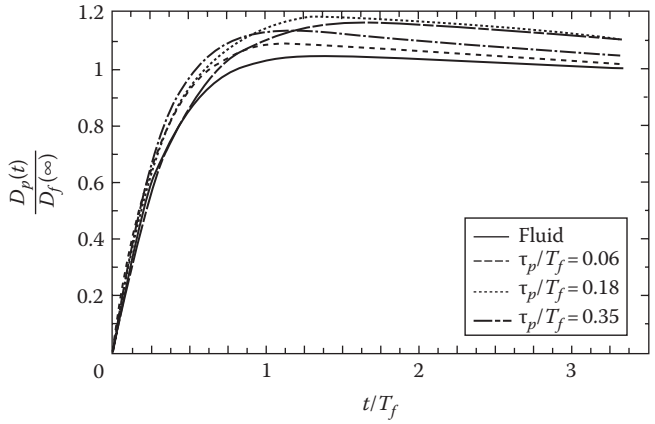


Figure 2.26

Ratio of particle diffusion coefficient to long-term fluid element diffusion coefficient in homogeneous isotropic turbulence: direct numerical simulation and experimental measurements, the influence of inertia (Stokes number St) τ_p/T_f, and settling v_g/u'. (Taken from Squires, K.D. and Eaton, J.K., *J. Fluid Mech.*, 226, 135, 1991.)

the Stokes numbers, the long-time values of the diffusion coefficient are greater than that of the carrier flow, the greatest value being for St =.35 but with little difference between this value and the value for St = 1.09. The formula in Equation 2.225 is also appropriate for particles settling under gravity or in an electric field as with the measurements of Wells and Stock (1983). The timescales of fluid motion along a particle trajectory depend upon the time it takes for a particle to move from one eddy to another in the flow field. The faster the particle moves, the shorter the timescale of the fluid motion it encounters, assuming that the eddy lifetime is much longer than the transit time of the particle. If v_g is the settling velocity and l_e the spatial length scale, then $l_e/v_g \ll \tau_e$, where τ_e is the eddy decay time. Since $\tau_e \sim l_e/u'$, this implies $u'/v_g \ll 1$ in which case

$$D_p(\infty) = \int_0^\infty R_E(0, \boldsymbol{v}_g t)\, dt \tag{2.226}$$

where $R_E(t, \boldsymbol{x})$ is the carrier flow spatial velocity correlation (in a frame moving with the settling velocity $\boldsymbol{v}_g$ with a separation $\boldsymbol{x}$ measured in the direction of gravity). ϵ in this case refers to the diffusion coefficient for diffusion in the direction of gravity. Reeks (1991) shows how the phase space density changes with time as it moves toward its long-term form, in which case the velocity distribution is a Maxwell–Boltzmann distribution with a mean square velocity given by

$$\langle v^2(\infty)\rangle = \beta \int_0^\infty e^{-\beta s} \langle \boldsymbol{u}(0) \cdot \boldsymbol{u}(s)\rangle\, ds \tag{2.227}$$

where $v = |\boldsymbol{v}|$.

2.5.3.2 Simple Shear and Rotational Flows for KM and GLM

While the KM and GLM approaches are compatible with one another for a Gaussian process, there is an important difference between the two approaches, namely, the GLM approach provides a model for particle transport and at the same time a model for the turbulence encountered by the particle, which encompasses in the limit of very small particles, the turbulence of the carrier flow itself. In the KM approach, this information must be prescribed independently, either on the basis of experiment or from a separate model like the GLM.

2.5.3.2.1 Analytic Solutions Based on KM Using the general result in Equations 2.204 and 2.206, Swailes et al. (1995) have evaluated the particle spatial concentration and mean velocity fields in a simple shear and rotational mean carrier flow fields and compared them with results obtained from a random flight simulation in which the turbulence is Gaussian with an exponential decaying autocorrelation. Results were obtained for both Stokes drag and a combination of drag and lift appropriate for low particle Reynolds numbers. In all these cases, the equation of motion of the particle is given by

$$x = \dot{v} = \underline{\beta} \cdot (\boldsymbol{S} \cdot \boldsymbol{x} - \boldsymbol{v} + \boldsymbol{u}''(t))$$

where **S** is the strain rate tensor. Some of their results are reproduced in Figure 2.27 for the case of Stokes drag with the particle response times and shear rates normalized on the fluid integral timescale along a particle trajectory. For the simple shear and rotating flow, we have, respectively,

$$\mathbf{S} = \begin{bmatrix} 0 & S \\ 0 & 0 \end{bmatrix} \quad \mathbf{S} = \begin{pmatrix} 0 & \omega \\ -\omega & 0 \end{pmatrix}$$

For the sake of brevity, we show in Figure 2.27 only analytic solutions for the form of the underlying mean particle flow for both these types of dispersion at some time after releasing the particles from the origin. Normalizing timescales on the integral timescale of the turbulence, the cases shown in Figure 2.27 correspond to t = 1, β = 1, S = 1, and ω = 1. We will consider the results for particle concentration in the simple shear when we consider solutions based on the GLM in the next section for which KM using the same carrier flow autocorrelation along particle trajectories would give identical results. We note that for the simple shear flow the concentration contours are ellipses concentric about the origin of the shear whose principal axes rotate in time as the concentration decays until they align with the carrier mean shear. In contrast to

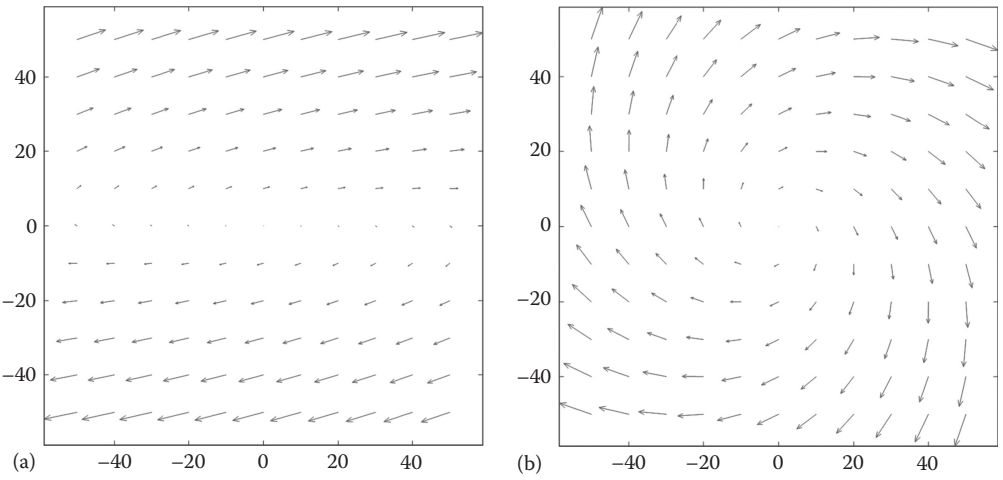


Figure 2.27

Analytic solutions for the mean particle velocity field for an instantaneous point source at the center of a simple shear flow and a rotating flow: β = 1, S = 1, and ω = 1, t = 1. (a) Simple shear flow, (b) rotating flow. (From Swailes, D.C. et al., Analysis of particle dispersion using a pdf equation: Results for simple shear and rotating flows, in *Gas-Particle Flows ASME Summer Meeting*, Hilton Head Island, SC, ASME FED-Vol. 228, August 1995, pp. 257–263.)

the rotating flow, the concentration contours, like those in uniform flow, are all circles centered about the origin. The rate of diffusion outward is greater than that in uniform flow because the mean spatial variation of the flow enhances the diffusion (the spreading of the particles).

2.5.3.2.2 GLM for a Simple Shear In this regard, a more detailed analysis has been performed for particle dispersion in simple shear based on the GLM approach that demonstrates the compatibility of the two approaches while at the same time highlighting the extra information that the GLM approach provides relating to the underlying carrier flow encountered by the particle. In this simple case, Pope's analogue equation is

$$\frac{du_i}{dt} = \alpha\left(S_{ij}x_j - u_i\right) + f_i''(t)$$
$$S_{ij} = S\delta_{i1}\delta_{j2} \tag{2.228}$$

where α in this simple case is assumed constant.

Using a simple model for the Reynolds shear stresses based on Pope's GLM model (Haworth and Pope, 1986), exact solutions have been obtained for the particle kinetic stresses (velocity covariances) and the particle diffusion coefficients associated with an instantaneous point source located at the center of the shear (Reeks, 2005). The results for the particle kinetic stresses are shown in Figure 2.28a as a function of the particle response time suitably normalized on the timescale of the turbulence that is homogeneous and stationary (effectively the particle Stokes number St). x_1 is the streamwise direction and x_2 cross-streamwise direction. What is plotted is the difference between the streamwise and cross-streamwise components for the normal stresses normalized on $S^2\langle u'^2\rangle$, where S is the strain rate normalized on the timescale of the turbulence. What is noticeable is that the difference is positive and increases with the Stokes number. As the particles cross the shear, they extract turbulent energy from the mean flow—it is the work done by shear stresses in the streamwise direction that appears as an increase of turbulent kinetic energy in the streamwise direction. The second graph in Figure 2.28b is even more revealing. A calculation is made of the diffusion coefficients ϵ_{ij}^S that relate the diffusion current j_i to the gradients of the concentration gradient, that is,

$$j_i = \langle u_i\rangle\langle\rho\rangle - \epsilon_{ij}^S\frac{\partial}{\partial x_j}\langle\rho\rangle \tag{2.229}$$

Here, we see the particle current composed of a convective term proportional to the local mean carrier flow and a long-term diffusive current. What is most interesting is the particle diffusion coefficient in the

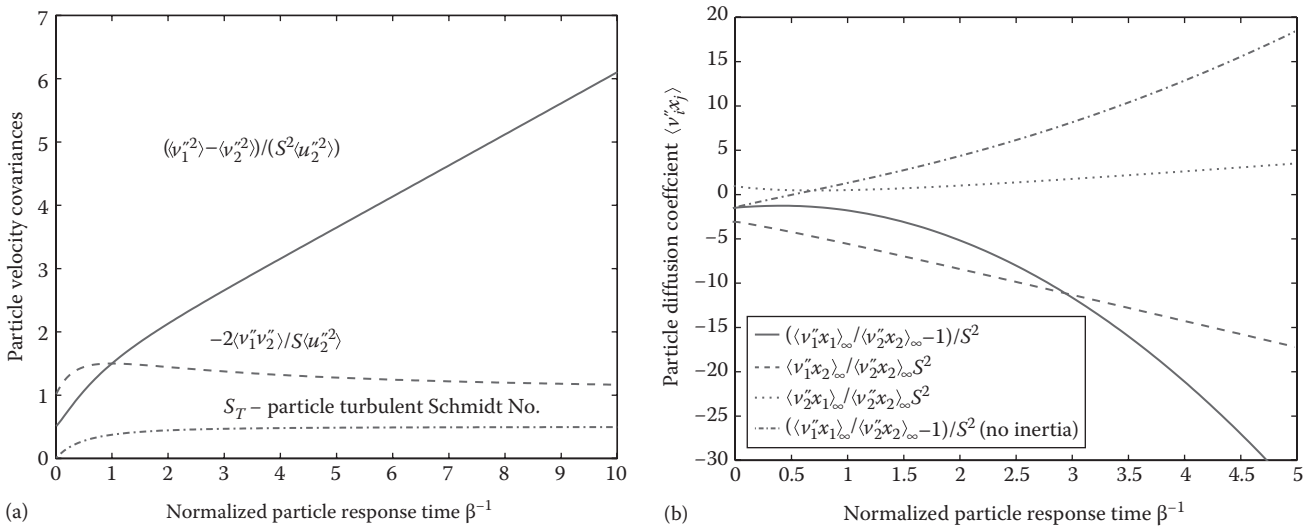


Figure 2.28

Dispersion of particles in a simple shear based on Pope's generalized Langevin method versus Stokes number β^{-1}. S is the strain rate normalized on turbulence integral timescale versus Stokes number β^{-1}. In the graphs $\epsilon_{ij}^S = \langle v_i'' x_j\rangle$. (a) Particle covariance (kinetic stresses) (b) Long-time particle dispersion coefficients ϵ.

streamwise direction compared to that in the cross-streamwise direction. We note that for all Stokes numbers it is *−ve*, which includes that for a passive scalar! This does not imply, however, that contrary to the second law a blob of particles will always contract rather than expand. These diffusion coefficients make a small contribution to the way a blob will diffuse. Particles will diffuse in the streamwise direction because as they move upward or downward, they will experience larger positive or negative velocities according to how far they are away from the origin. And that displacement is randomly positive or negative because it is determined by dispersion in the cross-streamwise direction. So, it is this process that makes the blob stretch in the streamwise direction. The *−ve* diffusion coefficients reduce this process but never reverse it.

Figure 2.29 shows a picture of the concentration contours and the mean particle velocities at a time on an integral timescale after they were released from the center of the shear where the mean velocities are almost

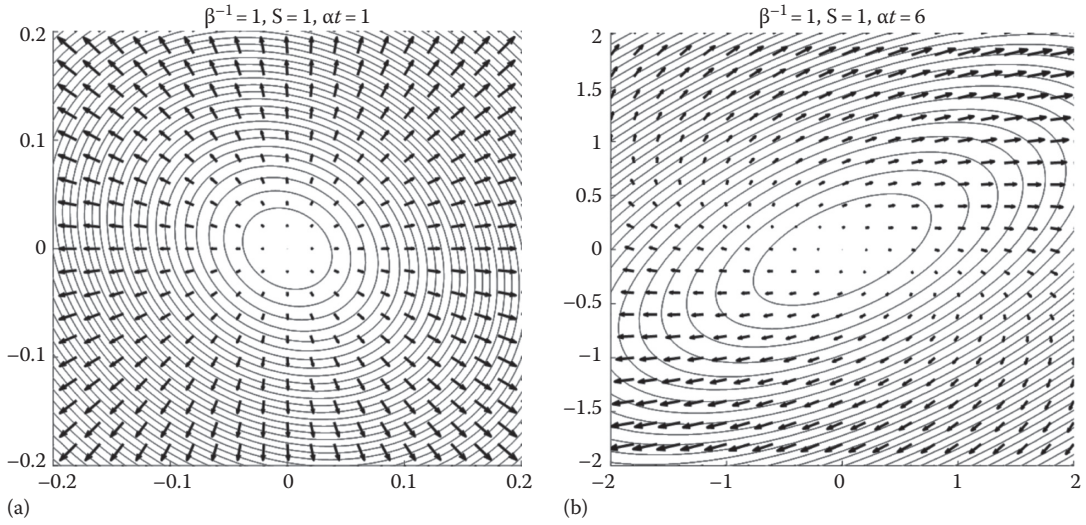


Figure 2.29

Concentration contours and particle mean velocity for St = 1 and normalized strain rate S =1, at (a) t = 1 and (b) t = 6, where t is in units of the integral timescale. Concentration contours represent a constant fraction f of the concentration at the center of the shear, $f = 1 - 0.02n$, $n = 1, 2, \ldots, k$.

radial and later where they have rotated to align with the velocities of the shear during which time the contours have expanded. As noted earlier, the mean concentration contours at any given time are expanding ellipses possessing the same principal axes centered at the origin, which rotate first anticlockwise and then clockwise until the major principal axis aligns with the streamwise direction. The rotational component of the particle mean velocity follows a similar behavior though the changeover from anticlockwise to clockwise is much more gradual. Although one of the principal strain rates of the mean particle velocity field becomes compressional during the approach to equilibrium, the divergence of the mean particle velocity field is always positive, ensuring the mean particle concentration decreases everywhere and for all time consistent with the second law of thermodynamics. See Figure 2.29 for the corresponding concentration and mean velocity vectors during the dispersion.

The possibility of this occurring has been noted earlier for passive scalar diffusion.

2.5.4 Continuum Equations and Constitutive Relations for the Dispersed Phase (without Collisions)

Continuum equations refer to the equations that describe the net transport of mass, momentum, and kinetic stress of the particle phase and can be generated from the pdf equations for $\langle P\rangle$ or $\langle W\rangle$ by multiplying them by an appropriate power of $mv_i'^p v_j'^q v_k'^r \ldots$ and then integrating over all $\boldsymbol{u}$ and $\boldsymbol{v}$ (for $\langle P\rangle$) and over all $\boldsymbol{v}$ (for $\langle W\rangle$), where m is the mass of a particle (assuming that all the particles for the sake of simplicity have the same mass m) and $\boldsymbol{v}'$ is the fluctuating value of $\boldsymbol{v}$ relative to its mean density-weighted value $\bar{\boldsymbol{v}}$. Thus, the following equations are derived:

$$\text{Mass } (\langle\rho\rangle) = m\int \langle P\rangle(\boldsymbol{v},\boldsymbol{u},\boldsymbol{x})d\boldsymbol{v}d\boldsymbol{u} \tag{2.230}$$

$$\text{Momentum } \langle\rho\rangle\bar{v}_i = m\int \langle P\rangle(\boldsymbol{v},\boldsymbol{u},\boldsymbol{x})v_i d\boldsymbol{v}d\boldsymbol{u} \tag{2.231}$$

$$\text{Kinetic stress } \langle\rho\rangle\overline{v_i v_j} = m\int \langle P\rangle(\boldsymbol{v},\boldsymbol{u},\boldsymbol{x})v_i' v_j' d\boldsymbol{v}d\boldsymbol{u} \tag{2.232}$$

So, the quantities $\bar{v}_j$ and $\overline{v_i'v_j'}$ are the particle mass density-weighted mean and covariance* of the particle velocities at $(\boldsymbol{x}, t)$. The continuum equations are from Equation 2.202:

$$\frac{\partial\langle\rho\rangle}{\partial t} + \frac{\partial}{\partial x_i}\langle\rho\rangle\bar{v}_i = 0 \tag{2.233}$$

$$\langle\rho\rangle\frac{D_p}{Dt}\bar{v}_i = -\frac{\partial}{\partial x_j}\langle\rho\rangle\overline{v_i'v_j'} + \langle\rho\rangle\beta(\langle u_i\rangle - \bar{v}_i) + \beta\langle\rho\rangle\overline{u_i''} \tag{2.234}$$

$$\begin{aligned}\langle\rho\rangle\frac{D_p}{Dt}\overline{v_i'v_j'} = &-\frac{\partial}{\partial x_k}\langle\rho_i\rangle + \langle\rho\rangle\overline{v_j'v_k'}\frac{\partial\bar{v}_i}{\partial x_k} + \langle\rho\rangle\overline{v_i'v_k'}\frac{\partial\bar{v}_j}{\partial x_k}\\ &-\langle\rho\rangle\beta\left(2\overline{v_i'v_j'} - \left\{\overline{v_i'u_j'} + \overline{v_j'u_i'}\right\}\right)\end{aligned} \tag{2.235}$$

where D_p/Dt is the particle substantial derivative, that is,

$$\frac{D_p}{Dt} = \frac{\partial}{\partial t} + \bar{v}_j\frac{\partial}{\partial x_j}$$

* Alternatively the particle kinematic kinetic stresses.

So, we require closed expressions for

1. $\overline{\boldsymbol{u}'}$, the average fluid velocity relative to $\langle \boldsymbol{u} \rangle$ encountered by a particle
2. $\overline{u_k' v_j'}$, the carrier–particle velocity covariances
3. $\langle \rho v_k' v_j' v_i' \rangle$, the turbulent kinetic energy flux

Note the distinction here between variables u_i'' and u_i'. Here and throughout, we will use superscripts $''$ and $'$ to refer to random variables relative to $\langle \boldsymbol{u} \rangle$ and particle density-weighted averages, respectively, for example, $\boldsymbol{v}'' = \boldsymbol{v} - \langle \boldsymbol{u} \rangle; \boldsymbol{v}' = \boldsymbol{v} - \bar{\boldsymbol{v}}$.

2.5.4.1 Constitutive Relations Based on Kinetic Model

Using the kinetic Equation 2.202 with Equation 2.204, together with the simpler LHDI forms for the phase space dispersion coefficients given in Equation 2.210 and suitably integrating Equation 2.202 over all particle velocities to form transport equations for the particle phase momentum and particle kinetic stresses and then comparing the resulting equations with Equations 2.234 and 2.235, we obtain the following identities:

$$\overline{u_i''}\langle \rho \rangle = -\frac{\partial}{\partial x_j}\left(\Delta x_j(\boldsymbol{x}, t \,|\, 0) \langle u_i''(\boldsymbol{x}, t) \rangle \langle \rho \rangle \right) - \left\langle \Delta x_j(\boldsymbol{x}, t \,|\, 0) \frac{\partial u_i''}{\partial x_j} \right\rangle \langle \rho \rangle \tag{2.236}$$

$$\overline{u_i' v_j'} = \langle \Delta v_j(\boldsymbol{x}, t \,|\, 0) u_i''(\boldsymbol{x}, t) \rangle - \frac{\partial \overline{v_j}}{\partial x_m} \langle \Delta x_m(\boldsymbol{x}, t \,|\, 0) u_i''(\boldsymbol{x}, t) \rangle \tag{2.237}$$

where

the displacements $\Delta \boldsymbol{v}$ and $\Delta \boldsymbol{x}$ refer to all particle trajectories arriving at $\boldsymbol{x}$ at time t irrespective of their velocity

$\langle u_i''(\boldsymbol{x}, t) \Delta v_j(\boldsymbol{x}, t \,|\, 0) \rangle$ is the fluid–particle velocity diffusion coefficient

$\langle u_i''(\boldsymbol{x}, t) \Delta x_j(\boldsymbol{x}, t \,|\, 0) \rangle$ is the fluid–particle spatial diffusion coefficient

It is noticeable from Equation 2.236 that the turbulent interfacial momentum transfer term $\beta \overline{\boldsymbol{u}''} \langle \rho \rangle$ will contribute an interfacial surface force to the particle phase momentum equation that combines with the particle Reynolds stresses to give a pressure tensor $\boldsymbol{p}$ whose components are expressible in terms of an equation of state, namely, at $\boldsymbol{x}$

$$\frac{p_{ij}}{\langle \rho \rangle} = \langle v_i' v_j' \rangle + \beta \langle \Delta x_j(\boldsymbol{x}, t \,|\, 0) u_i''(\boldsymbol{x}, t) \rangle \tag{2.238}$$

where $\boldsymbol{v}'$ is the particle velocity fluctuation relative to the mean velocity $\bar{\boldsymbol{v}}$ at ($\boldsymbol{x}$, t). Equation 2.238 in turn encapsulates a fundamental relationship between the components of $\boldsymbol{p}$ and a set of coefficients ϵ_{ij}:

$$\frac{p_{ij}}{\langle \rho \rangle} = \beta \epsilon_{ij}^{\dagger} \tag{2.239}$$

$$\epsilon_{ij} = \beta^{-1} \langle v_i' v_j' \rangle + \langle u_i''(\boldsymbol{x}, t) \rangle \Delta x_j(\boldsymbol{x}, t | 0) \tag{2.240}$$

where $\epsilon_{ij}^{\dagger}$ is the transpose of ϵ_{ij}. Expressing the RHS in the way we have done earlier demonstrates a close relationship to the particle diffusion coefficients associated with particle dispersion in generic flows like those considered in Section 3. We note that it is these coefficients that are the analogue of temperature, not the particle kinetic energy. These results have also been derived independently using the Clausius virial theorem of the classical kinetic theory (Reeks, 1991).

2.5.4.1.1 Particle Momentum Equation Interpreted as an Advection–Diffusion Equation It is clear from the momentum equation that when the inertial term $D\bar{v}_i/Dt$ is small compared to the other terms, the transport is described by a simple advection gradient diffusion equation with the components of the particle mass flux $\boldsymbol{j}$:

$$j_i = -\epsilon_{ij} \frac{\partial \langle \rho \rangle}{\partial x_j} + \boldsymbol{v}_D \tag{2.241}$$

in which the diffusion coefficients ϵ_{ij} are identical to those given in Equation 2.239 and the convection velocity is given by

$$\underline{v}_D = \langle \boldsymbol{u} \rangle + \boldsymbol{v}_d \tag{2.242}$$

$$\boldsymbol{v}_d = -\beta^{-1}\left\{\frac{\partial}{\partial \boldsymbol{x}} \cdot \overline{\mathbf{v}'\mathbf{v}'}\right\} - \left\langle \left(\frac{\partial}{\partial \boldsymbol{x}} \cdot \Delta \boldsymbol{x}(\boldsymbol{x}, t \,|\, 0)\right) \boldsymbol{u}''(\boldsymbol{x}, t) \right\rangle \tag{2.243}$$

The first term on the RHS of Equation 2.243 has been referred to as the turbophoretic velocity (Reeks, 1983); the additional contribution from the second term is entirely due to the structure of the flow. It should be zero for inertialess particles that follow the flow (Bragg et al., 2012a). According to this approach, gradient diffusion is always the case for particles that follow the flow: indeed, the set of diffusion coefficients ϵ_{ij} reduce to the local average

$$\epsilon_{ij} = \langle u_i''(\boldsymbol{x}, t) \Delta x_j(\boldsymbol{x}, t|0) \rangle \tag{2.244}$$

In the case of statistical stationary homogeneous turbulence, advection–diffusion applies to the case for inertial particles in the long term for dispersion in an unbounded flow when $\beta t \gg 1$ or when the particles are confined and the system approaches equilibrium, in which case $\partial \rho / \partial \boldsymbol{x} \to 0$. In this case, substituting the formulae $\left\langle v'_i v'_j \right\rangle = \beta \int_0^\infty e^{-\beta s} u_i''(0) u''(s) ds$ and $\Delta x_j(\boldsymbol{x}, t \,|\, 0|) = \int_0^\infty (1 - e^{-\beta s}) u_j''(s) ds$ into the formula for ϵ_{ij} in Equation 2.240, we would obtain the result in 2.225 for statistically stationary isotropic homogeneous turbulence.

It is very interesting to point out that similar arguments were used by Einstein (1905) to evaluate the diffusion coefficient of Brownian particles. Here, we have an almost identical particle equation of motion except that the driving force (due to the turbulence carrier flow) in our case is not limited to white noise as it is in the case of Brownian motion due to molecular bombardment of the suspended particles. What Einstein recognized was that the momentum equation (in his case the balance of the pressure gradient with the weight of the particles) implies a diffusion equation for the suspended particles as they approached their long-term equilibrium state and in particular as the gradient of the average particle concentration $\nabla \langle \rho \rangle \to 0$. So, instead of an isothermal system, what we have is a statistical stationary homogeneous isotropic turbulent flow and we consider an equilibrium state in which there is a balance between the pressure gradient and a body force acting on the particles, the obvious one being the weight of the particles. So in effect we are considering the weight of an elemental volume of particles balanced by the pressure gradient acting across it as Einstein did.

We note, however, that the coefficients ϵ_{ij} defined in general in Equation 2.240 are not the same as the diffusion coefficients ϵ_{ij}^S for particle dispersion in a simple linear shear flow referred to in Equation 2.229 except in the case of inertialess particles that follow the flow $\beta^{-1} = 0$. In general,

$$\epsilon_{ij}^S = \langle v_i'' x_j \rangle \tag{2.245}$$

The reason for the discrepancy between ϵ_{ij} and ϵ_{ij}^S for particles with inertia is that while the process is still diffusive (for particles released from the center of the shear), the inertial acceleration term $D\bar{v}_i/Dt$ in the particle momentum in Equation 2.234 also makes a finite contribution to ϵ_{ij}^S along with normal gradient diffusion term in the momentum equation from which ϵ_{ij} is derived.

2.5.4.1.2 Particle–Carrier Velocity Covariances Referring to the transport equation Equation 2.235 for the particle kinetic stresses (which includes the particles' turbulent kinetic energy), the particle-carrier flow velocity covariances are given in KM by

$$\overline{u'_i v'_j} = \langle u_i''(\boldsymbol{x}, t) \Delta v_j(\boldsymbol{x}, t|0) \rangle - \langle u_i''(\boldsymbol{x}, t) \Delta x_m(\boldsymbol{x}, t|0) \rangle \frac{\partial \overline{v_j}}{\partial x_m} \tag{2.246}$$

where the displacements $\Delta \boldsymbol{v}$ and $\Delta \boldsymbol{x}$ refer to all particle trajectories arriving at $\boldsymbol{x}$ at time t irrespective of their velocity. Substituting these expressions for the carrier flow–particle velocity covariances into the transport equation (2.235) for the particle kinetic stresses gives

$$\langle \rho \rangle \frac{D}{Dt} \overline{v'_m v'_n} = -\frac{\partial}{\partial x_i} \langle \rho v'_i v'_m v'_n \rangle - \langle \rho \rangle \left[\frac{\partial \bar{v}_n}{\partial x_l} p_{lm} + \frac{\partial \bar{v}_m}{\partial x_l} p_{ln} \right] + 2 \langle \rho \rangle \beta \left\{ \mu^S_{mn} - \overline{v'_m v'_n} \right\} \tag{2.247}$$

where μ^S_{mn} refers to the components of the symmetric part of $\mu = \langle \boldsymbol{u}''(\boldsymbol{x}, t) \Delta \boldsymbol{v}(\boldsymbol{x}, t|0) \rangle$.

So, we refer to the terms on the RHS of the aforementioned equation:

1. The first term is a third-order velocity moment of the particle pdf, which can be referred to as the turbulent kinetic stress flux, which for $m = n$ includes the turbulent kinetic energy flux and is a term that requires closure. In this case, one can use the methods developed in kinetic theory to approximate this term. In particular, applying the Chapman–Enskog (C–E) approximation gives the following relationship involving the gradients of the velocity covariance and the particle diffusion coefficients ϵ_{ij}, a result obtained by Swailes et al. (1998), among others:

$$\overline{v'_i v'_j v'_k} = -\epsilon_{li} \frac{\partial}{\partial x_l} \overline{v'_j v'_k} - \epsilon_{lj} \frac{\partial}{\partial x_l} \overline{v'_i v'_k} - \epsilon_{lk} \frac{\partial}{\partial x_l} \overline{v'_i v'_j} \tag{2.248}$$

Compare their result with the form used for third-order moment in single-phase flow by Daly and Harlow (1970). The answers to the questions how accurate it is and how important it is to take it into account are illustrated by the two graphs in Figure 2.30, giving a comparison with the results from tracking many particles in a channel flow and then averaging. Figure 2.30a shows the particle tracking result for the triple moment in the normal streamwise direction by comparing that obtained from the C–E approximation and those based on an approximation derived from a transport equation for the triple moments where fourth-order moments are closed, assuming a Gaussian distribution known as the quasi-normal approximation. The C–E approximation does

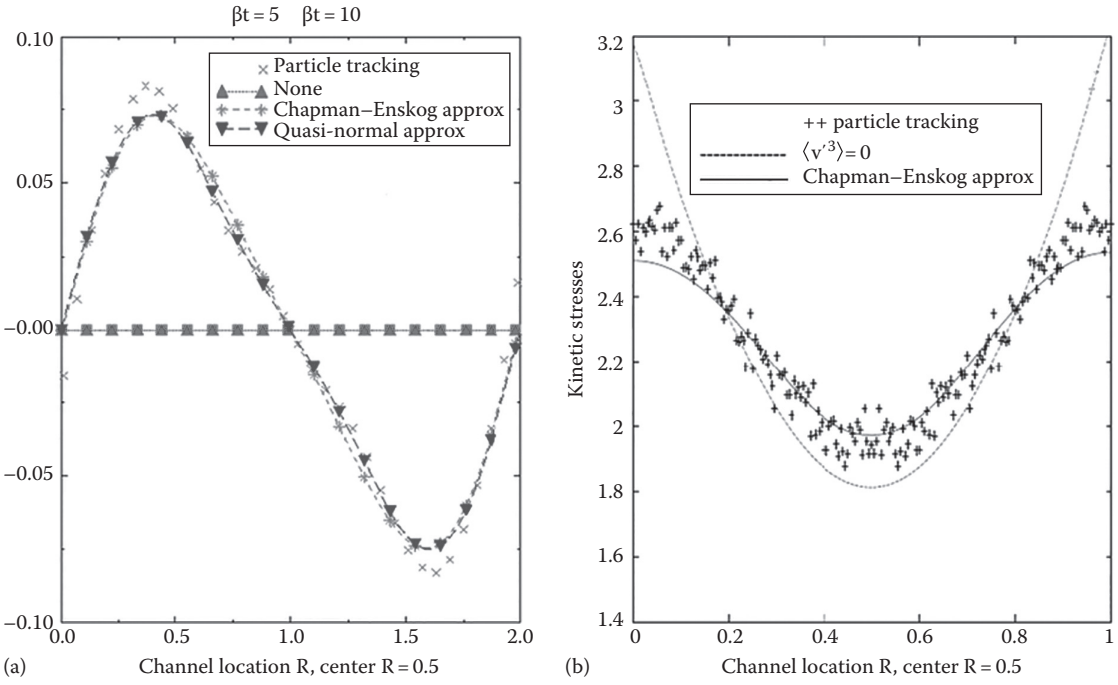


Figure 2.30

Simulation (particle tracking) and kinetic method predictions using Chapman–Enskog approximation in Equation 2.248 for turbulent pipe flow. (a) Particle triple correlation, (b) particle kinetic stresses.

well but underpredicts the maximum. The center of the channel is at R = 1 and the walls at R = 0. Figure 2.30b shows the contribution the triple correlation makes to the particle velocity covariance or kinetic stresses, thus clearly indicating the significant contribution they make near the walls.

2. The second term in brackets represents "viscous"* losses from the action of surface forces p (as defined in Equation 2.239) in changing the shape and size of an elemental volume of the dispersed flow as it moves through the mean shear gradients of that flow. So, this term acts as a source of production of turbulent kinetic energy for the suspended particles. We recall that in the case of particle dispersion in a simple shear flow, the particle rms velocity in the streamwise direction (in the direction of the straining flow) is greater than that in the cross-streamwise direction by an amount that is proportional to the strain rate (see Figure 2.28a).
3. The third and fourth terms are net loss and production terms arising from an internal volume dissipative force $-\beta \boldsymbol{v}'$ and a driving force $\beta \cdot \boldsymbol{u}''(\boldsymbol{x}, t)$, respectively. Here, $v' = |\boldsymbol{v}'|$. We note that at equilibrium in homogeneous turbulence

$$\overline{v'^2} = \langle \boldsymbol{u}''(\boldsymbol{x},t) \cdot \Delta \boldsymbol{v}(\boldsymbol{x},t|0) \rangle$$

with all other terms being zero. Using the appropriate form for $\Delta v_i(\mathbf{x}, t|0)$ gives the correct analytic form of Equation 2.227:

$$\overline{v'^2} = \beta \int_0^\infty e^{-\beta s} \langle u''(0) \cdot \boldsymbol{u}''(s) \rangle ds$$

where *vecu″*(*s*) is the fluctuating carrier flow velocity along a particle trajectory;

2.5.4.1.3 Form for Kinetic Stresses for $\beta^{-1} \ll 1$ The particle kinetic stresses depend explicitly on the shearing of the dispersed phase (the term in square brackets in Equation 2.247) and the shearing of the carrier flow (the terms involving $\langle \boldsymbol{u}_i''(\boldsymbol{x},t) \Delta \boldsymbol{v}_n(\boldsymbol{x},t\,|\,0) \rangle$ in Equation 2.247).

To illustrate this behavior still further, let us refer to $\langle \boldsymbol{u}''(\boldsymbol{x}, t) \Delta \boldsymbol{v}(\boldsymbol{x}, t|0) \rangle$ by $\underline{\zeta}$ composed of a part $\underline{\zeta}^{(0)}$ (as if the flow was uniform and independent of the shearing of the carrier flow) and a deviatoric part $\delta\underline{\zeta}$ that is linear in the local shearing of the carrier flow. Likewise, we divide the particle kinetic stress into similar components. Consider thus the case when β^{-1} is very small (almost fluid point motion). Only a balance of the terms of order β is important in the kinetic stress equation so that we have

$$-2\delta\overline{v_n' v_m'} + \{\delta\zeta_{mn} + \delta\zeta_{nm}\} - \epsilon_{mi} \frac{\partial \bar{v}_n}{\partial x_i} - \epsilon_{ni} \frac{\partial \bar{v}_m}{\partial x_i} = 2\overline{v_n' v_m'}^{(0)} - \{\zeta_{mn}^{(0)} + \zeta_{nm}^{(0)}\}$$

The terms on the LHS contain all the deviatoric terms and the terms on the RHS all the homogeneous terms. The whole equation must express the fact that in this limit, the particle velocity covariances are the same as the carrier flow covariances: this is consistent with the bracketed terms containing all the homogeneous forms and the deviatoric terms being both zero. The implication for the sum of the deviatoric terms being zero is that

$$\delta\overline{v_n' v_m'} = -\epsilon_{mi} \frac{\partial}{\partial x_i}(\bar{v}_n - \bar{u}_n) - \epsilon_{ni} \frac{\partial}{\partial x_i}(\bar{v}_m - \bar{u}_m) \quad \beta^{-1} \to 0 \tag{2.249}$$

That is, the particle deviatoric kinetic stresses in the limit of very small particles are linear in the relative shearing between the carrier and dispersed phases. For the case of very large particles, the contribution from the interfacial momentum transfer term to the deviatoric particle Reynolds stresses drops to zero with no explicit dependence on the shearing of the carrier flow: the contribution is entirely viscous.

* Equivalent to viscous losses; increases the temperature in a flowing gas.

2.5.4.2 Constitutive Relations Based on GLM

The closure expressions in this case are transport equations for $\overline{\boldsymbol{u}''}$ and $\overline{u_k'v_j'}$, which are derived from the GLM pdf equation for $\langle P\rangle$, that is, Equation 2.219. Multiplying Equation 2.219 by u_i and integrating over all $\boldsymbol{v}$ and $\boldsymbol{u}$, we have

$$\frac{\partial}{\partial t}\langle \rho u_i\rangle + \frac{\partial}{\partial x_j}\langle \rho v_j u_i\rangle = \left\{ f_i(\boldsymbol{x}) - \alpha_{ij}\overline{u_j''} + (\bar{v}_k - \bar{u}_k)\frac{\partial \langle u_j\rangle}{\partial x_k}\right\}\langle \rho\rangle$$

Recognizing that we can rewrite the LHS as

$$\frac{\partial}{\partial t}\langle \rho u_i\rangle + \frac{\partial}{\partial x_j}\langle \rho v_j u_i\rangle = \langle \rho\rangle \frac{D_p}{Dt}\langle u_i\rangle + \langle \rho\rangle \frac{D_p}{Dt}\overline{u_i''} + \frac{\partial}{\partial x_j}\overline{v_j'u_i'}\langle \rho\rangle \tag{2.250}$$

and that from Equation 2.215 to 2.201

$$\left(\frac{\partial}{\partial t} + \bar{u}_j\frac{\partial}{\partial x_j}\right)\langle u_i\rangle = \left(\frac{D_f}{Dt} + \overline{u_j''}\frac{\partial}{\partial x_j}\right)\langle u_i\rangle$$

and using the relationship given in Equation 2.214, we finally derive the following transport equation for $\overline{u_i''}$:

$$\langle \rho\rangle \frac{D_p}{Dt}\overline{u_i''} = -\frac{\partial}{\partial x_j}\overline{v_j'u_i'}\langle \rho\rangle + \langle \rho\rangle \frac{\partial}{\partial x_j}\left\langle u_j''u_i''\right\rangle - \left\{\frac{\partial \langle u_i\rangle}{\partial x_j} + \alpha_{ij}\right\}\overline{u_j''}\langle \rho\rangle \tag{2.251}$$

A transport equation can also be obtained for $\overline{u_k'v_j'}$ by transforming the GLM pdf equation into an equation for $P(\boldsymbol{v}', \boldsymbol{u}', \boldsymbol{x}, t)$, multiplying the resulting equation by $u_i'v_j'$, and then integrating over all $\boldsymbol{u}'$ and $\boldsymbol{v}'$. This gives

$$\langle \rho\rangle \frac{D_p}{Dt}\overline{u_i'v_j'} = -\frac{\partial}{\partial x_k}\langle \rho\rangle \overline{u_i'v_j'v_k'} - \langle \rho\rangle \overline{v_j'v_k'}\frac{\partial \overline{u_i''}}{\partial x_k} - \left(\langle \rho\rangle \overline{u_i'v_k'}\frac{\partial \bar{v}_j}{\partial x_k} + \overline{v_j'u_k'}\frac{\partial \overline{u_j}}{\partial x_k}\right) - \langle \rho\rangle \beta\left(\overline{u_i'v_j'} - \overline{u_i'u_j'}\right) + \langle \rho\rangle \alpha_{ik}\overline{u_k'v_j'} \tag{2.252}$$

2.5.4.2.1 Fluid–Particle Velocity Correlation Models The general form of α in Pope's GLM model is assumed to be linear in the local strain rates of the carrier flow, that is,

$$\alpha_{ij} = \alpha_{ij}^{(0)} + \beta_2\frac{\partial \overline{u_i}}{\partial x_j} \tag{2.253}$$

where $\alpha_{ij}^{(0)}$ is the homogeneous (strain rate independent) component and β_2 a constant whose value is obtained from measured values of one-point statistics. In the case of the SDM model, the values of $\alpha_{ij}^{(0)}$ are dependent on the particle itself since they refer to fluid timescales viewed by the particle. In particular, SDM account for the influence of crossing trajectories by choosing the following form for $\alpha_{ij}^{(0)}$:

$$\alpha_{ij}^{(0)} = \frac{\delta_{ij}}{\tau_{pf,\perp}} + \left[\frac{1}{\tau_{pf,\parallel}} - \frac{1}{\tau_{pf,\perp}}\right]n_i n_j$$

where $\tau_{pf,\perp}$ and $\tau_{pf,\parallel}$ are the turbulent characteristic timescales of the fluid velocity fluctuations viewed by the particles in the direction normal and parallel to the mean relative velocity vector $\bar{\mathbf{V}}_r$ between particle and

carrier flow that has direction cosines n_i. Thus, by adopting the same approach as that of Csanady (1963) for gravitational settling, $\tau_{pf,\perp}$ and $\tau_{pf,\parallel}$ are given by

$$\tau_{pf,\parallel} = \tau_f (1 + C\zeta_r^2)^{-1/2} \tau_{pf,\perp} = \tau_f (1 + 4C\zeta_r^2)^{-1/2}$$

where

$$\zeta_r^2 = \frac{3\left|\bar{\mathbf{V}}_r\right|^2}{\langle \boldsymbol{u}' \cdot \boldsymbol{u}' \rangle}$$

and C is a given parameter characterising the Eulerian to Lagrangian integral time scale ratio.

For the closure of the transport equation for the fluid–particle covariances in Equation 2.252, we need finally a closed expression for the fluid–particle velocity $\overline{\rho u_i' v_j' v_k'}$ for the particle fluid covariance flux. In the case of the scalar particle fluid covariance $\langle \mathbf{u}' \cdot \mathbf{v}' \rangle$, Simonin (1996a) has used a Boussinesq approximation

$$\langle \rho \boldsymbol{u}' \cdot \boldsymbol{v}' \boldsymbol{v}_i' \rangle = -\langle \rho \rangle \nu_{pf}^t \frac{\partial}{\partial x_i} \langle \boldsymbol{u}' \cdot \boldsymbol{v}' \rangle$$

where ν_{pf}^t is referred to as the fluid–particle turbulent viscosity written in terms of the timescale of the fluid along a particle trajectory τ_{pf}, namely,

$$\nu_{pf}^t = \frac{1}{3} \langle \boldsymbol{u}' \cdot \boldsymbol{v}' \rangle \tau_{pf}$$

Using this gradient approximation of the particle fluid velocity fluxes and the expressions for α_{ij}, the transport equation can, in principle, be solved for the linear form for α_{ij} in Equation 2.253. Fevrier and Simonin (1998), from a computational point of view, have derived an algebraic model for the off-diagonal particle–fluid covariances, which they then use in conjunction with a transport model for the scalar fluid–particle covariance $\langle \boldsymbol{u}' \cdot \boldsymbol{v}' \rangle$. This algebraic model is derived from Equation 2.252, assuming equilibrium of the fluid–particle turbulent velocity correlation tensor in single-phase flow, namely,

$$\langle u_m' v_m' \rangle \left[\frac{d}{dt} \langle u_i' v_j' \rangle - D_{ij} \right] = \langle u_i' v_j' \rangle \left[\frac{d}{dt} \langle u_m' v_m' \rangle - D_{mm} \right]$$

where D_{ij} refers to the diffusive component (gradient of the fluid–particle velocity flux) in the transport equation for the fluid–particle covariance. Then from the fluid–particle correlation transport (Equation 2.252), one obtains the following models:

2.5.4.2.2 Algebraic Model

$$\begin{aligned} \langle u_i' v_j' \rangle = {} & \frac{1}{3} \langle \boldsymbol{u}' \cdot \boldsymbol{v}' \rangle \delta_{ij} + \frac{\langle \boldsymbol{u}' \cdot \boldsymbol{v}' \rangle}{\langle u'^2 \rangle} \left[\langle u_i' u_j' \rangle - \frac{1}{3} \langle u'^2 \rangle \delta_{ij} \right] - \frac{1}{2\beta \langle u'^2 \rangle} \left[\langle \boldsymbol{u}' \cdot \boldsymbol{v}' \rangle \left\{ \langle u_i' v_k' \rangle \frac{\partial \overline{v_j}}{\partial x_k} + (1 - \beta_2) \langle u_i' v_k' \rangle \frac{\partial \overline{u_j}}{\partial x_k} \right\} \right. \\ & \left. - \langle u_i' v_j' \rangle \left\{ \langle u_m' v_n' \rangle \frac{\partial \overline{v_m}}{\partial x_n} + (1 - \beta_2) \langle v_m' u_n' \rangle \frac{\partial \overline{u_m}}{\partial x_n} \right\} \right] \end{aligned} \tag{2.254}$$

where $\langle u'^2 \rangle = \langle \boldsymbol{u}' \cdot \boldsymbol{u}' \rangle$. For practical application, this algebraic expression may be used with the transport equation of the fluid–particle covariance $\langle \boldsymbol{u}' \cdot \boldsymbol{v}' \rangle$ obtained directly from Equation 2.252. Fevrier and

Simonin (1998) go further and derive an even simpler model than the algebraic model by assuming that the fluid–particle covariance tensor anisotropy is small so that, for instance, certain ratios in the algebraic model equation can be replaced by their local quasi-homogeneous value. Thus,

$$\frac{\langle \boldsymbol{u}' \cdot \boldsymbol{v}' \rangle}{\langle u'^2 \rangle} = \frac{\beta \tau_f}{1+\beta \tau_f}$$

This sort of approximation gives a Boussinesq or eddy viscosity model for the fluid–particle velocity covariance as follows:

2.5.4.2.3 Eddy Viscosity Model

$$\langle u_i' v_j' \rangle = \frac{1}{3}\langle \boldsymbol{u}' \cdot \boldsymbol{v}' \rangle \delta_{ij} + \frac{\beta \tau_f}{1+\beta \tau_f}\left\{ \langle u_i' u_j' \rangle - \frac{1}{3}\langle \boldsymbol{u}' \cdot \boldsymbol{v}' \rangle \right\} - \frac{\nu_{pf}^t}{1+\beta \tau_f}\left\{ \frac{\partial \overline{v_j}}{\partial x_i} - \frac{1}{3} div \bar{\boldsymbol{v}} \right.$$

$$\left. + (1-\beta_2)\left(\frac{\partial \overline{u_i}}{\partial x_j} - \frac{\delta_{ij}}{3} div \bar{\boldsymbol{u}} \right) \right. \tag{2.255}$$

In Section 2.5.4.3, we compare the predictions for the dispersion of particles in a particle-laden jet and a vertical channel flow.

2.5.4.3 Comparison of Predictions with Experimental Results for Nonuniform Unbounded Flows

Here, we briefly consider the application of the pdf approach for predicting the concentration, mean velocity, and velocity covariances of a dilute suspension of particles in nonuniform flows where near-wall behavior is not a feature. In particular, in Figure 2.31, we show the predictions of Simonin and Fevrier (1996a,b) using a particle kinetic stress transport model of the particle mean and rms velocities in a vertical channel flow and in a turbulent round jet in comparison with the experimental measurements of Rogers and Eaton (1963)

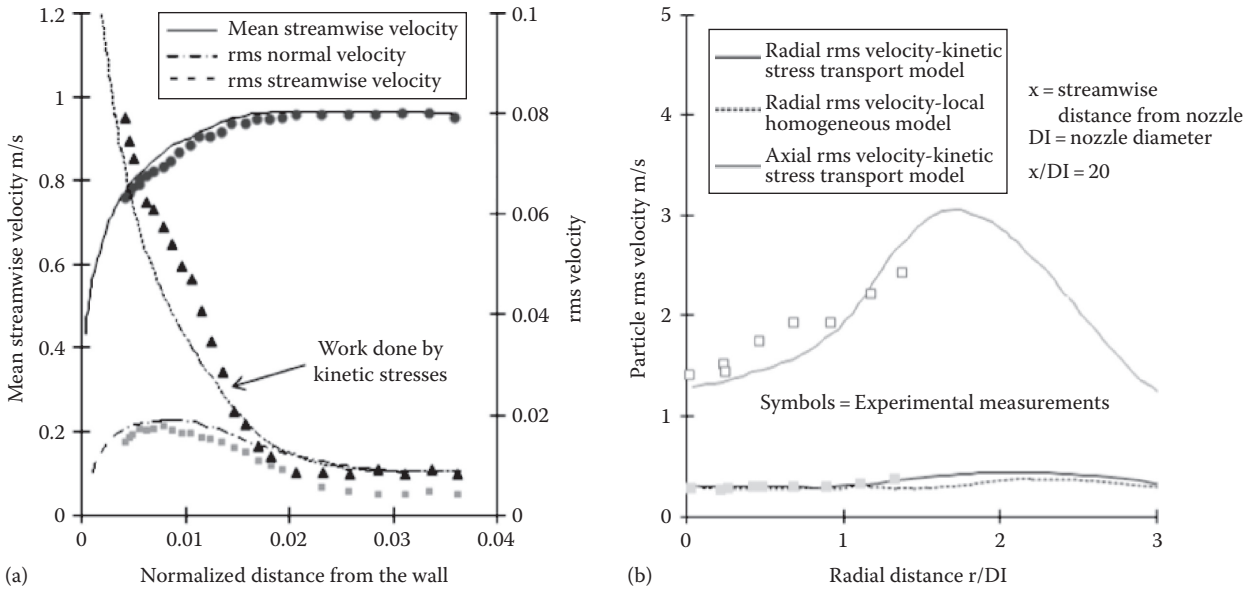


Figure 2.31

(a) Particle rms velocity predictions of Simonin (1996b) using kinetic stress transport compared to experimental measurements in a vertical channel flow. (From Rogers, C.B. and Eaton, J.K., Int. J. Multiphase Flow, 16(5), 819, 1963.) and (b) a turbulent round jet. (From Hishida, K. and Maeda, M., Turbulent characteristics of gas-solid two-phase confined jet: Effect of particle density, in *Fifth Workshop on Two Phase Flow Predictions: Proceedings*, Erlangen, Germany, March 19–22, 1990.)

for the vertical channel flow and that of Hishida and Maeda (1990) for the round jet. The results show the significant difference between the streamwise and normal streamwise rms particle velocities in the case of channel flow and between the axial and radial rms velocities for the round jet. You can see the greatest difference near the walls in the vertical channel flow where the shear stresses are greatest and also near the nozzle in the case of the round jet. In both cases, this is due to the work done by the kinetic stresses as the mean shearing of the particle flow compresses or dilates the particle flow in the streamwise direction or axial direction (see the terms proportional to the mean shearing (Equation 2.235), which are responsible for the difference). Note that in the case of the jet, the kinetic stress transport model gives slightly better predictions for the radial rms velocities than the quasi-homogeneous model due to the contribution of the gradients of the triple correlation. This is one of the many examples where comparison between model predictions and experimental measurements has been made. However, it does provide very good examples of the application of the transport equation for the particle kinetic stresses (Equation 2.232) where the work done by the mean shear of either phase introduces a significant anisotropy into the particle velocity covariance as is also the case of dispersion in a simple shear.

Figure 2.32 shows the axial and radial particle rms velocities for the turbulent round jet as a function of radial location for a range of axial distances from the jet nozzle. While showing the same anisotropy in the axial and radial rms velocities as in Figure 2.32, the figure also indicates the contribution of

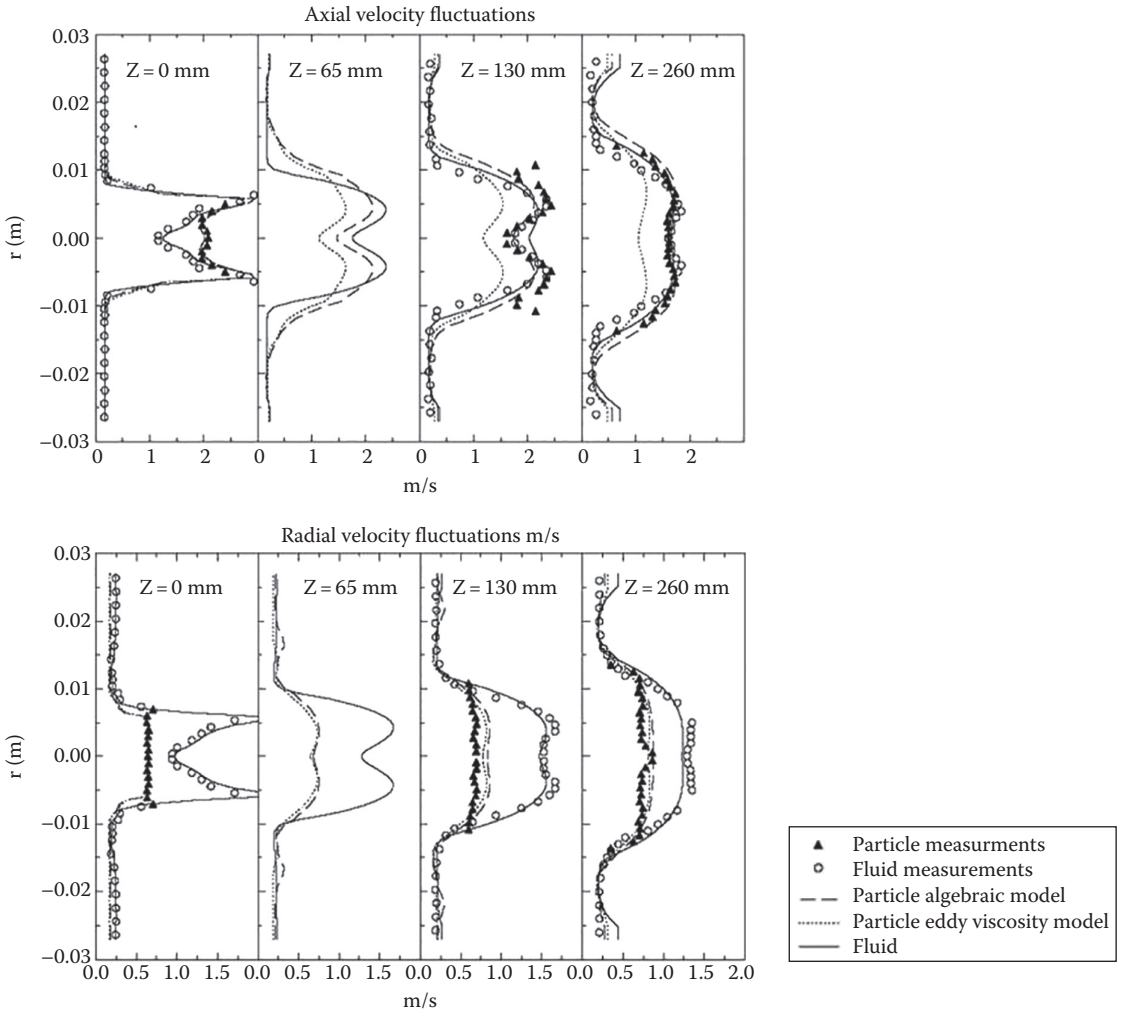


Figure 2.32

Turbulent round jet. Further generalized Langevin method probability density function predictions versus experimental measurements of the radial and axial particle rms velocities as a function of radial location for a range of axial distances (Simonin [1996a]).

the particle fluid covariances based on the algebraic model (Equatin 2.254) and the eddy viscosity model (Equation 2.255). Application of the algebraic model accurately predicts the values in the particle velocity fluctuations in both the axial and radial directions for all measured axial locations. The fluid–particle eddy viscosity model is reasonably accurate in predicting the radial velocity fluctuations but clearly underpredicts the axial values.

2.5.5 Particle–Wall Interactions and Transport in Turbulent Boundary Layers

Not only does the pdf approach provide a formal way of deriving the continuum equations and constitutive relations of the dispersed phase, but it also correctly deals with the near-wall behavior and particle–wall interactions that form the natural bc's of the dispersed phase. Applying bc's to the continuum equations themselves, as is done for the continuous-phase two-fluid modeling, is inappropriate because such bc's imposed are artificial. In reality, the natural bc's have to do with the particles' response to the surface molecular forces that, for an impacting particle at a solid surface, express a relationship between the distribution of particle velocity before and after impact and the possible deposition/absorption and subsequent resuspension of the deposited particles sometime later. So while the velocity distribution at the wall is an important feature of the bc's, it is not known a priori but is an intrinsic part of the calculation.

In this section, we briefly review the work of Swailes et al. (Swailes and Reeks, 1994, Darbyshire and Swailes, 1996, Reeks and Swailes, 1997, Devenish et al., 1999) on the application of the pdf approach to near-wall behavior in a turbulent boundary and the influence of natural bc's. We note that the steep change in the level of turbulence at the wall means that only for very small particles are the two-fluid equations (mass, momentum, and energy) likely to apply, that is, the particle distribution of velocities at any position within the turbulent boundary layer will not be locally related to the turbulence: depending on its size, a particle will retain some memory of its behavior in the far wall or bulk flow. More precisely, this depends on the variation of the turbulence over a particle mean free path, which is defined as the distance a particle travels in a time equal to its correlation time ϵ/v': the same sort of conditions apply in a gas at low pressure when the dimensions of the container are comparable to the molecular mean free path. Under such circumstances, the so-called continuum theory no longer applies. It is to be noted that even without the steep change in turbulence, the bc's at the wall are in themselves likely to cause a lack of validity of two-fluid model equations simply because the particle–wall distribution will be so very much different from the distribution away from the wall (one mean free path away) and far from the assumption that it is close to Gaussian.

However, to begin with, we consider particles whose inertia is sufficiently large that their transport through the turbulent boundary layer is ballistic, that is, they are unaffected by the turbulent boundary layer adjacent to the wall and the effective mean free path of the particles is comparable to the dimensions of the containment. We consider first the interesting case of particles settling out under gravity with partial absorption and diffuse reflection at the wall with inelastic collision for those particles that rebound. All this is a valuable precursor to our consideration of the way the pdf method deals with the most challenging case of transport of particles through a turbulent boundary where the transport through the boundary layer rate limits the particle deposition at the wall. It is a case where inhomogeneity of the flow and the nonlocal nature of the transport and the particle–surface interactions (through impact and absorption followed by resuspension) all play an equally important role.

2.5.5.1 General Boundary Conditions at the Wall

Referring to Figure 2.33, the general bc for a particle impacting at a wall at $\boldsymbol{x}$ with velocity $\boldsymbol{u}$ and rebounding with a range of possible velocities $\boldsymbol{v}$ is the flux condition

$$\boldsymbol{v}P(\boldsymbol{v},\boldsymbol{x},t) = \int_{\boldsymbol{u}\cdot\mathbf{n}\le 0} \boldsymbol{u}P(\boldsymbol{u},\boldsymbol{x},t)\Theta(\boldsymbol{v}\,|\,\boldsymbol{u})d\boldsymbol{u} \tag{2.256}$$

where

$\boldsymbol{n}$ is the direction normal to the wall at $\boldsymbol{x}$

$\Theta(\boldsymbol{v}|\boldsymbol{u})$ is the transition or scattering probability density that a particle will rebound with a velocity $\boldsymbol{v}$ after impacting the surface with velocity $\boldsymbol{u}$

$\boldsymbol{u}$ and $\boldsymbol{v}$ are related deterministically (specular reflection) or stochastically (diffuse scattering as in the case of a microscopically rough surface). Swailes and his coworkers (Swailes and Reeks, 1994, Swailes, 1997,

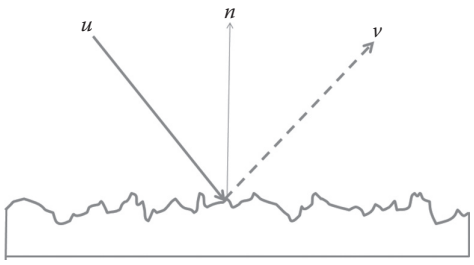


Figure 2.33

Particle impact and rebound velocities at a rough wall.

Reeks and Swailes, 1997, Devenish et al., 1999) have obtained solutions for the pdf equation for simple flows in these cases. Both cases involve duct flow in which the turbulence is regarded as homogeneous with uniform mean velocity in the streamwise direction. In these cases, therefore, the particle's response time is sufficiently large that it does not respond to the spatial variations in the mean flow and the turbulence especially near the wall. In these cases, it is the bc's themselves that determine the near-wall behavior where the continuum equations are inappropriate and the behavior can be well approximated by a simple steady-state solution of the pdf equation in 1D in $\boldsymbol{x}$ and in $\boldsymbol{v}$. The conditions for particle response times are consistent with the spatial gradients flux term in Equation 2.204 being set to zero as well as the body force due to inhomogeneity in the flow. In this case, the pdf equation can be normalized in a universal form under steady conditions as (Reeks and Swailes, 1997)

$$\left(v\frac{\partial}{\partial y}-\frac{\partial}{\partial v}v+g\frac{\partial}{\partial v}+\frac{\partial^2}{\partial v^2}\right)\langle W(y,x,t)\rangle=0 \tag{2.257}$$

where y is the normal distance from the wall ($y = 0$) and positive velocities are directed toward the wall, particles are acted upon by a gravitational force g directed toward the wall, and velocities and distances are normalized on the particle rms velocity at equilibrium (perfectly reflecting walls) and on the particle mean free path ϵ/v'.

In the simple flows considered by Swailes et al., the flow is divided into a far-wall region, which acts as a constant source of particles entering the near-wall region. The interface is set at some distance Υ from the wall in particle mean free paths where the spatial distribution of the particles is uniform. It follows from Equation 2.257 that this distribution will be Gaussian:

$$w(0,v)=(2\pi)^{-1/2}\exp\left(-\frac{1}{2}v^2\right)\quad \text{for } v>0. \tag{2.258}$$

2.5.5.1.1 Method of Solution The pdf equation is solved numerically using a spectral expansion in terms of Hermite polynomials, looking for solutions in the form

$$w(y,v)\approx\sum_{n=0}^{N}\phi_n(y)\psi_n(v) \tag{2.259}$$

where ψ_n are the orthonormal functions based on the Hermite polynomials H_n. They are

$$\psi_n(v)=\left(\frac{b}{2^n n!\sqrt{\pi}}\right)^{1/2}\exp\left(-\frac{1}{2}(bv)^2\right)H_n(bv) \tag{2.260}$$

The inclusion of the scaling factor b allows the placement of a set of collocation points v_j ($j = 0, 1, \ldots, N$) to be optimized. At these collocation points, the approximation in Equation 2.259 is exact. In this problem,

the collocation points are taken to be the zeros of the function ψ_{N+1} which provide discrete orthonormal properties for $\psi_n(v_s)$. Substituting the approximation in Equation 2.259 into 2.257 and making it exact at these collocation points give a system of first-order equations:

$$\frac{\mathrm{d}}{\mathrm{dy}}\mathbf{W} = A\mathbf{W} \tag{2.261}$$

where

W is the column vector whose elements are the values of the pdf at the collocation points

A is a matrix whose elements are functions of ψ_n^s.

The bc's given by Equations 2.256 and 2.258 are discretized at the points v_j. If we define N^* to be the integer such that $v_j < 0$ for $j < N^*$ and $v_j \geq 0$ for $j \geq N^*$, then the bc at the interface $y = \Upsilon$ can be written as

$$\sum_{n=0}^{N} \zeta_{jn} w_n = 1, \quad j \geq N^* \tag{2.262}$$

where $w_n = w(v_n, \Upsilon)$ and

$$\zeta_{jn} = \delta_{jn}(2\pi)^{1/2} \exp\left(\frac{1}{2}v_j^2\right) \quad j \geq N^* \tag{2.263}$$

The bc at the wall $y = 0$ is

$$\sum_{n=0}^{N} \zeta_{jn} w_n = 0, \quad j < N^* \tag{2.264}$$

where

$$\zeta_{jn} = \delta_{jn} v_n + h_n^{-1} \sum_{m=0}^{N} \psi_m^n I_m(v_j) \quad j \geq N^* \tag{2.265}$$

with

$$I_m(v_j) = \int_0^\infty \psi_m(u) u \Theta(v_j|u) du \tag{2.266}$$

The interface and wall bc's represent standard two-point bc's for the solutions of Equation 2.261 and can be solved by a standard numerical method. Figures 2.34 and 2.35 show some of the results obtained by Reeks and Swailes (1997), for particle deposition at a wall with or without gravity for specific examples of the wall scattering function $\Theta(v_j|u)$. In each case, results are compared with those obtained from a random walk simulation that simulates the system precisely. In this case, it was assumed that upon impact there was an energy loss that was conveniently described by defining a critical impact velocity v_c below which a particle adhered upon impact but above which a particle will rebound with a prescribed rebound velocity $\boldsymbol{v} = \Theta(\boldsymbol{u})$. Thus, $\Theta(\boldsymbol{v}|\boldsymbol{u})$ for specular reflection is

$$\Theta = \begin{cases} 0 & \text{for } 0 < v \leq v_c \\ \delta(v - \theta(u) & \text{for } v > v_c \end{cases} \tag{2.267}$$

Modeling the dependence of $v = \theta(u)$ from a constant energy loss upon impact as

$$v = -\sqrt{u^2 - v_c^2} \quad \text{for } u > v_c \tag{2.268}$$

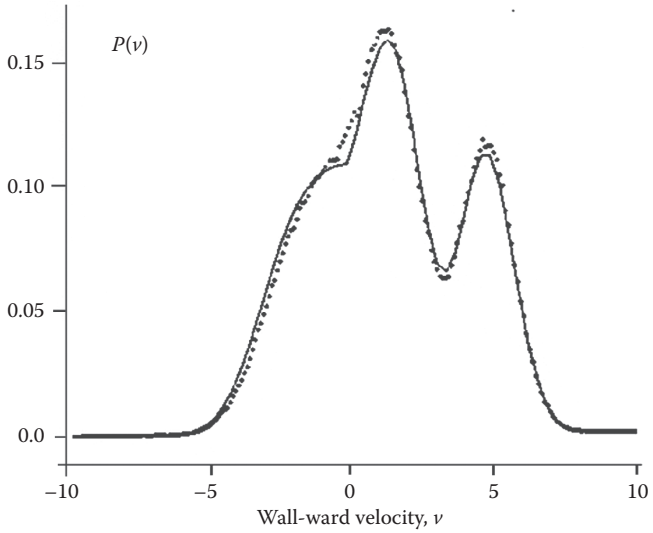


Figure 2.34

Velocity distribution $P(v)$ for particles settling under gravity in a homogeneous turbulent flow, impacting at a wall with partial absorption: $v_c = 5$, $v_g = 5$ (in normalized units). Impact velocities are for $v > 0$.

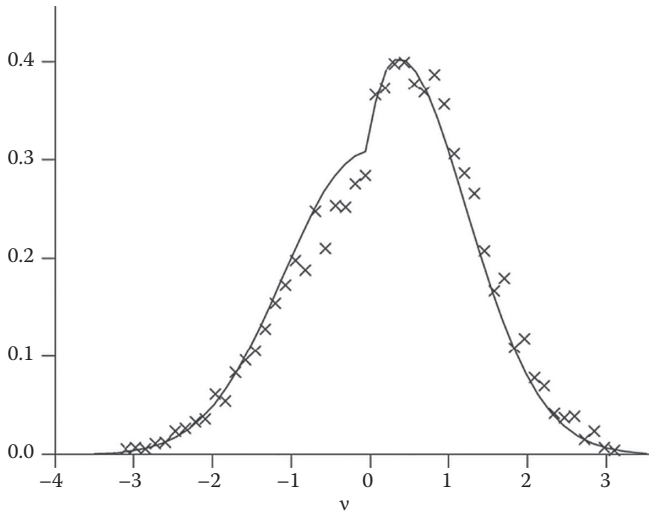


Figure 2.35

Wall distribution for specular reflection: $\gamma = 0°$, $v_c = 1$.

gives the simple form

$$\langle W(v,0)\rangle = \langle W(u,0)\rangle \quad \text{for } u > v_c \tag{2.269}$$

where v and u are related by Equation 2.268.

We note that $v_c = 0$ no absorption and no energy loss give the perfect reflection bc condition $\langle W(v,0)\rangle = \langle W(-v,0)\rangle$, while letting $v_c \to \infty$ gives the perfect absorption case $\langle W(v,0)\rangle = 0$, $v < 0$. Results were obtained for a range of values of the gravitational settling velocity v_g and critical impact velocities v_c. Figure 2.34 shows the results of solving the pdf Equation 2.257 with those obtained from the simulation for the velocity distribution at the wall for the specific case of a partially absorbing wall with $v_c = 5$ and $v_g = 5$ (in normalized units). Note there are two peaks: one centered at $v = v_g$ and the one with its center slightly displaced from the origin. The relative heights of these peaks depend upon the ratio of v_c/v_g: for $v_c/v_g = 0$ (zero absorption), the latter peak has a maximum value $v = 0$, with no contribution from the peak at $v = v_g$. In contrast, the reverse is the case when $v_c/v_g \to \infty$.

2.5.5.1.2 Diffuse Reflection with Deposition As an illustration, we suppose that particles arriving at the surface are still reflected with a deterministic speed, but now the velocity vector is directed at some random angle α to the surface. Since we are concerned only with particle transport in the direction normal to the wall, we may consider the rebound velocity to be $v = -r\cos\alpha$, where, as in Equation 2.268, the deterministic speed is $r = \sqrt{u^2 - v_c^2}$. If $u < v_c$, then the particle is considered to adhere.

A variety of distributions $\Theta(v|u)$ can be constructed depending on the prescribed distribution of α. For the purpose of illustration, Darbyshire and Swailes (1996) considered the simple case where the reflection angle α is uniformly distributed on (−γ, γ) in which case

$$\Theta(v \mid u) = \begin{cases} \gamma^{-1}(u^2 - a^2)^{-1/2} & \text{for } a \le u \le c \\ 0 & \text{otherwise} \end{cases} \tag{2.270}$$

where $a(v) = \sqrt{v_c^2 + v^2}$ and $c(v) = \sqrt{v_c^2 + v^2 \sec^2\gamma}$.

Predictions for the velocity distribution at the wall compared with those obtained from random walk simulations are shown in Figure 2.36 for γ = 75°. Compare this distribution with that for specular reflection with the same critical impact velocity shown in Figure 2.35, which illustrates the essential effect of diffuse reflection, namely, the reduction near the wall of the normal component of the particle rms velocity, the effect becoming more pronounced with increasing γ. These features are accompanied with an increase in particle–wall concentration as γ increases.

2.5.5.2 Transport and Deposition in Turbulent Boundary Layers

There has been intensive research over the last 20 years on the near-wall behavior of particles suspended in a turbulent flow (see, e.g., recent review by Li and Ahmadi, 1992), in particular how particles interact with near-wall structures and how are they transported and deposited at the wall. In this regard, DNS has been particularly useful in simulating the behavior of the fluid motion. Much of our understanding comes from particle tracking in these flows. Of particular note is the work of Soldati (2009) in illuminating the transport mechanisms and in developing models for the particle deposition that has been the major preoccupation from a practical point of view. The problems here have been in formulating an appropriate transport equation to account for the influence of the severe changes in the turbulence intensity in the near-wall region that in general makes the particle transport entirely nonlocal, that is, far from local equilibrium. In this regard, the pdf approach has been particularly successful. While the two-fluid equations are inappropriate near the wall, the solution of the pdf equation itself still provides a valid description. Furthermore, the bc's arising from the particle–wall interactions are only expressible in terms of bc's for a pdf equation since as

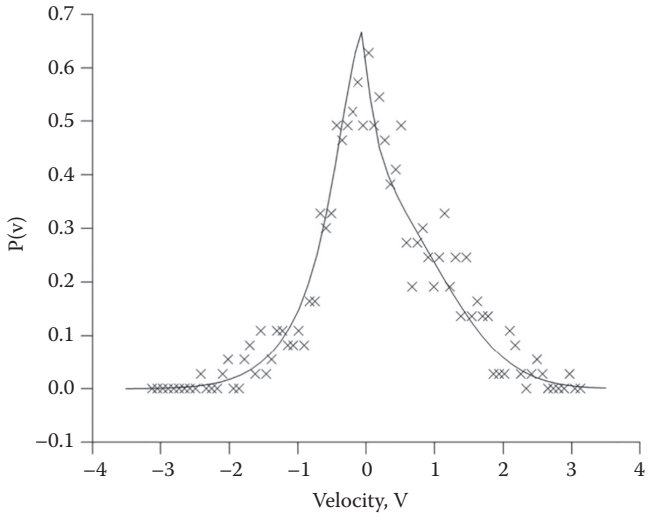


Figure 2.36

Wall distribution for diffuse reflection: γ = 75°, v_c = 1.

we have said they involve changes in the velocity distribution at the wall. Traditional fluid modeling is inappropriate because the bc's imposed are artificial. We note that advection–diffusion models for deposition are implicit in the particle momentum equation derived from the pdf equations where the inertial term is ignored (Reeks, 1993):

$$j = \langle \rho \rangle \boldsymbol{v}_d - \epsilon \cdot \frac{\partial \langle \rho \rangle}{\partial \boldsymbol{x}} \tag{2.271}$$

where

$$v_d = -\tau_p \frac{\partial}{\partial \boldsymbol{x}} \cdot \langle \boldsymbol{v}\boldsymbol{v} \rangle + \boldsymbol{\kappa} - \frac{\partial}{\partial \boldsymbol{x}} \cdot \boldsymbol{\lambda} \tag{2.272}$$

The drift velocity $\boldsymbol{v}_d$ is composed of essentially two terms that are of different origins. The first term arises from the gradients of the kinetic stress and reflects a balance between a drag force and the gradients of a stress, while the remaining terms are derived from body forces that arise directly from spatial inhomogeneous in the flow. The first term has often been referred to as turbophoresis (Reeks, 1983).

2.5.5.3 Particle Deposition in Turbulent Boundary Layers

Deposition of particles in turbulent pipe flow has a huge literature associated with it (see Li and Ahmadi, 1992)—there have been many attempts at predicting the deposition as a function of particle size or response time. The problem as we have seen is the rapid decay of turbulence near the wall and the way the particles respond to that decay and the lack of local equilibrium with the flow. The particles may start out in local equilibrium far away from the wall, but their inability to follow the steep changes in the fluid velocity means that at any point the particles have some memory of their previous history—their velocity has more to do with where they came from than what is happening to the fluid motion locally. The continuum equations break down. Not only that, we have to deal with the problem of bc's if we use continuum equations because perfect absorption at the wall means that the only bc is that there are no particles at the wall with velocities away from the wall. There is no means of fitting that behavior into a traditional no slip at the wall bc. pdf equations are ideally suited for this type of problem—first, they take account of the naturals bc's, and second, they take account of the influence of particle inertia and the steep turbulence gradients. They uniquely handle both effects together which traditional models are incapable of doing. It is useful to show some features of the near-wall behavior before considering what the deposition looks like. The results are taken from the recent analysis of van Dijk and Swailes (2012) based on the solution of the GLM pdf model using a discontinuous Galerkin method of solution. Figure 2.37a shows the concentration ratio as a function of distance $y+$ from the wall (denoted by x_2 in the Figure 2.37) for a range of values of the particle inertia or particle response time in wall units τ^+ equivalent to the Stokes number. You can see a significant peaking of the concentration near the wall as τ^+ reduces from very large values where the motion is basically ballistic (no response at all to the near-wall turbulence). Figure 2.37b shows the ratio of the rms of the particle–wall normal velocities v_2 to the local fluid rms of the fluid u_2 as a function of distance from the wall, indicating that this ratio $\gg 1$ as you approach the wall because of the particles' inertia and the much higher velocities they have attained further away from the wall where the gradients of the turbulence are much less.

Figure 2.37c for the particle pdf $p(v_2, x_2)$ shows that particles enter the domain at $x_2 = 100$ for $v_2 < 0$ and subsequently move toward the wall via, mainly, a diffusive mechanism; the pdf remains close to the local equilibrium state over a large part of the spatial domain. Closer to the wall, at about $x_2 = 20$, the fluid rms velocity decreases rapidly. The effect of this is that the particles are no longer driven by diffusion, but start moving in free flight. Most of the heavy particles ($\tau^+ = 300$, see Figure 2.37) have enough momentum to reach the wall, even those that have a relatively low speed. Only very slowly moving particles get trapped near the wall and slowly drift toward adhesion at $x_2 = X_0$. This results in a small buildup near the wall of particles with low velocity. For lighter particles ($\tau^+ = 10$, Figure 2.37c), only the fast particles reach the wall in free flight, while most will be trapped. Hence, they are only ones that can get to the very sharp peak in the pdf around zero particle velocity. This feature would not be picked up in the particle tracking because of the requirement of a very high resolution. This results in a strong buildup in a concentration that is also clearly visible in Figure 2.37a, where the particle concentration, ρ, in the boundary layer is shown. In fact, recent work suggests that there is threshold velocity of τ^+ below which particles are trapped in the region of almost stagnant fluid near the wall and never get deposited (see the recent analysis of Sikovsky, 2013).

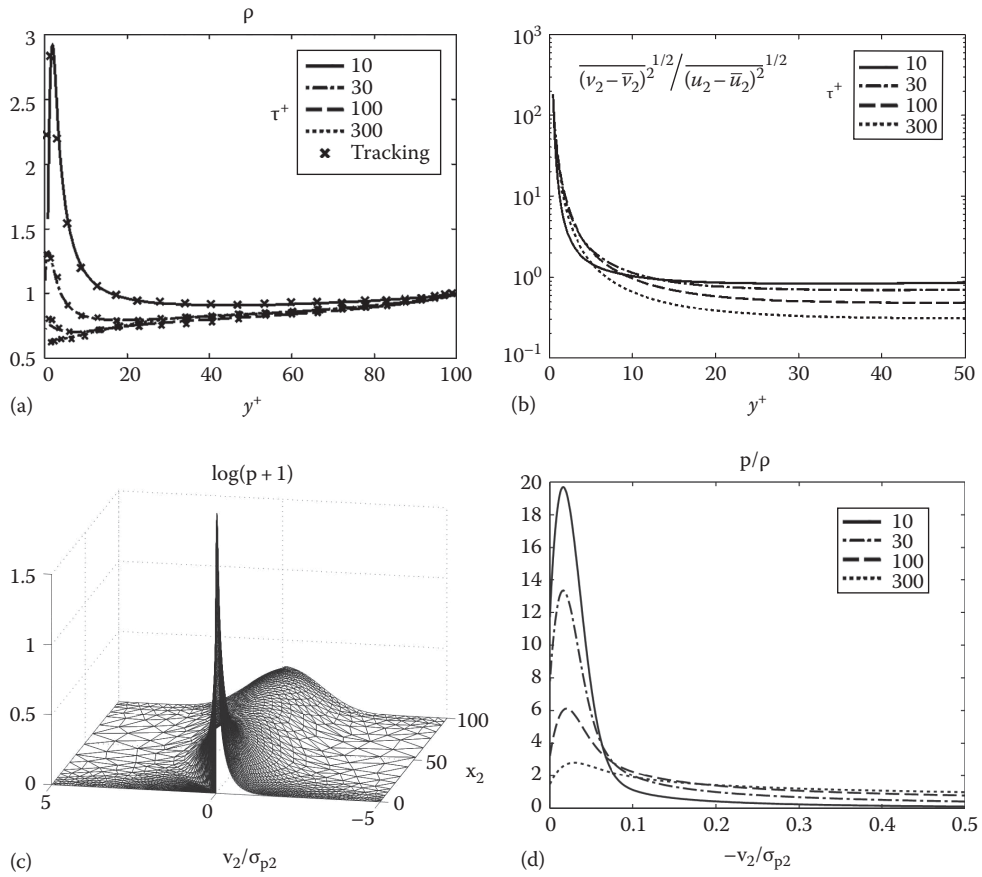


Figure 2.37

Particle near-wall behavior as a function of distance from wall y^+ and particle response time τ^+ (both in wall units) (van Dijk and Swailes, 2012). σ_{p2} is the local particle equilibrium rms velocity in the wall-normal direction. (a) Near-wall particle concentration ρ, (b) near-wall particle normal rms normal velocities, (c) near-wall pdf $\rho(v_2,x_2)$ for $\tau^+ = 10$, (d) particle velocity distribution for $\tau^+ = 10$ at "wall" (one particle radium from wall).

Similar features have been observed in particle pair collisions in homogeneous isotropic turbulence (Wang et al. 2000). The normalized particle velocity distribution, which is presented in Figure 2.37d, illustrates this process as well: the distribution for $\tau^+ = 300$ has a significant tail, while for $\tau^+ = 10$ the distribution is strongly localized near $v_2/\sigma_{p2} = 0$.

Finally, Figure 2.38 shows the predictions of the particle deposition velocity j^+ (in wall units) as a function of particle response time τ^+ obtained by Zaichik et al. (2010) compared to a range of experimental and DNS results. In particular, Zaichik's predictions were obtained by solving a closed set of moment equations derived from the pdf–kinetic equation. The closure is based on a quasi-normal assumption for the fourth-order moments of particle velocity and local equilibrium closure for third-order moments (neglecting their advection). The method of solution has thus much in common with the RANS approach in CFD involving Reynolds stress transport equations. Given the experimental error is very large, the pdf solutions predicts the huge changes in deposition velocity from 10^{-1} to 10^{-5} for a change in τ^+ from 10 to 10^{-1}, which reflects the role of particle inertia on the deposition.

2.5.5.4 Particle Resuspension

Pdf equations and their solutions play an important role in deriving a formula for the rate constant for the removal of particles from a surface by aerodynamic forces. The process is similar to the desorption of molecules from a surface, and the rate constant for removal is very similar to the Arrhenius formula for the molecular desorption rate. Because the near flow is turbulent, it is necessary to take account of the contribution of the fluctuating removal forces as well as the mean forces. This means that the process is stochastic rather than a force balance between the adhesive forces holding the particles onto the surface and the

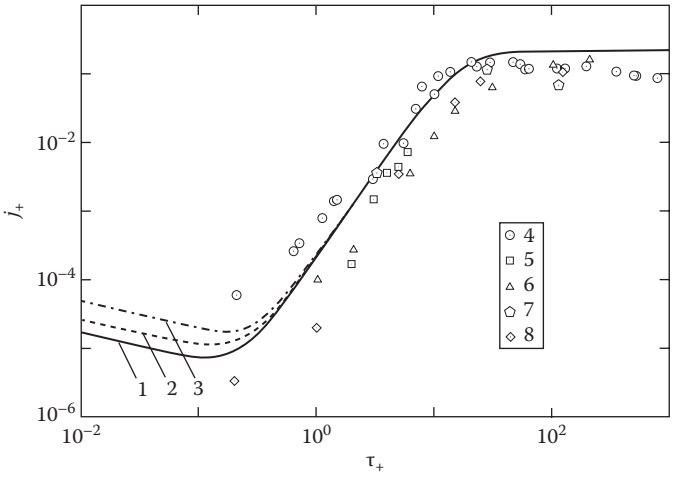


Figure 2.38

Particle deposition in turbulent pipe flow. (From Zaichik, L.I. et al., *Int. J. Heat Mass Transfer*, 53, 154, 2010.)

aerodynamic removal forces. More particularly, the removal process is described by a probability per unit time of a particle being removed from a surface or equivalently a rate constant. So, if the rate constant for removal is p, the fraction of particles $f_R(t)$ remaining on a surface at time t is given by

$$f_R(t) = \exp(-pt) \tag{2.273}$$

Figure 2.39a shows the aerodynamic removal forces acting on a spherical particle on a smooth surface in a turbulent boundary layer together with the van der Waals adhesive force holding the particle onto the surface. It shows the spherical particle to be deformed in the contact area between particle and surface (much exaggerated in Figure 2.39) indicating the presence of elastic restoring forces that balance the adhesive force when the particle is sitting on a surface in static equilibrium (in the absence of external forces). We can represent the dependence of the surface forces (adhesive and elastic forces) and a mean removal lift force upon

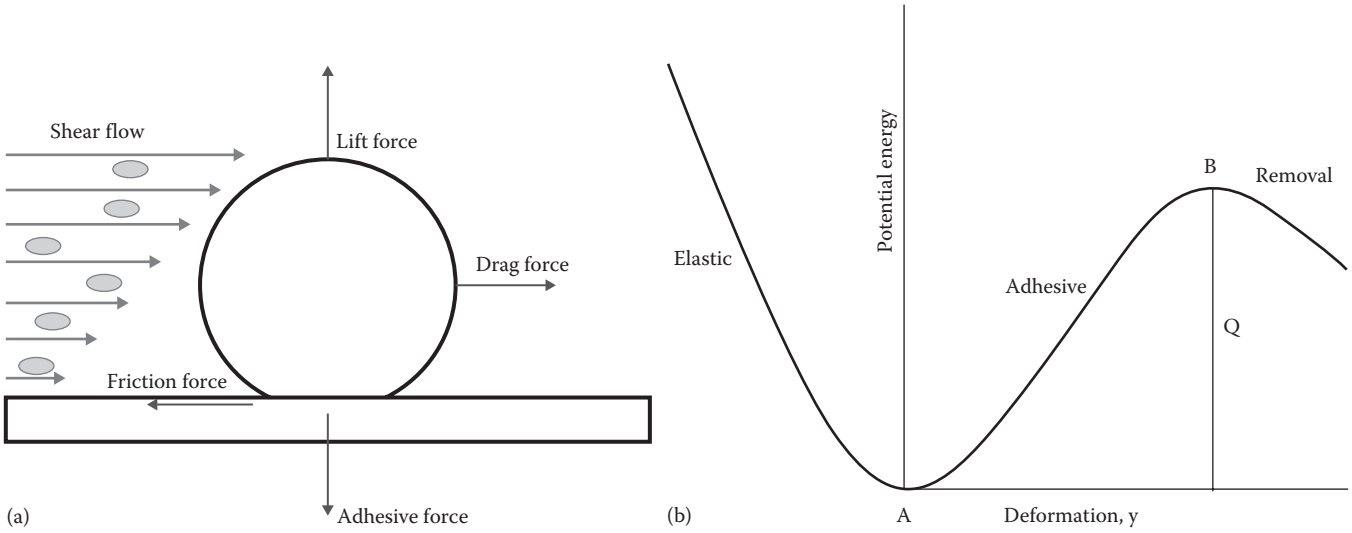


Figure 2.39

Removal of a particle from a surface by aerodynamic forces in a turbulent boundary layer. Note the deformation of the sphere in the region of contact with the surface that is exaggerated in (a). (a) Aerodynamic and surface intermolecular adhesive forces derived from a sphere in smooth contact with a surface, (b) surface adhesive potential well derived from the mean aerodynamic forces and adhesive forces in (a).

surface deformation by a *surface* potential well, a typical profile being shown in Figure 2.39b. This shows a position of stable equilibrium, A, where the adhesive force balances the repulsive elastic restoring force and a constant mean lift force and a position of instability, B, where the attractive adhesive force balances the mean lift force. Increasing the mean lift force reduces both the width of the potential well and the height of the potential barrier of B above A, Q, which a particle has to overcome before it can be detached from the surface. We suppose that the number of particles on the surface is sufficient to form an ensemble of all realizable states of a single particle in a constant potential well. The fluctuating removal force will cause the particle–surface deformation $y(t)$ to oscillate randomly about the point of minimum potential at A until a particle derives enough energy from the fluctuating forces (the turbulence) to escape over the potential barrier at B and detached from the surface. The objective therefore is to use the pdf equation to calculate the flux of particles out of the well at B, and this quantity divided by the number of particles in the well is the probability per unit time of a particle escaping from the well, that is, the resuspension rate constant.

In using the pdf equations to evaluate the rate constant, we recognize that the phase space dispersion coefficients μ and λ are functions of the particle–surface deformation y. In the case of a harmonic potential, the displacement $\Delta y(t)$ in Equation 2.274 determines the dispersion coefficients corresponding to the solution of a very stiff, lightly damped harmonic oscillator. Thus, for a particle of mass m, the deformation displacement $\Delta y(t)$ at time t, about the point of minimum potential, A, is obtained from

$$\ddot{\Delta} y(t) + \beta \dot{\Delta} y(t) + \omega^2 \Delta y(t) = m^{-1} f_L(t) \tag{2.274}$$

where $f_L(t)$ is the random fluctuating component of zero mean associated with the total aerodynamic lift force

$$F_L = \langle F_L \rangle + f_L(t) \tag{2.275}$$

where

$\langle F_L \rangle$ is the mean lift force that in this instance is assumed independent of time
ω is the natural frequency based on the harmonic approximation for small deformations about A
β is the fluid and mechanical damping term

Reeks et al. (1988) show that the rate constant p can be written as

$$p = \frac{\omega_0}{2\pi} \exp\left(\frac{-Q}{\langle PE \rangle} \right) \tag{2.276}$$

where

$\langle PE \rangle$ is the average potential energy of the particles in the potential well
ω_0 is a frequency for particle motion in the well

Both these quantities reflect a process of energy transfer from the turbulence to a particle in the potential well, the particle being resuspended when it has accumulated enough vibrational energy to detach itself from the surface. This is the basis of the kinetic model of RRH (Reeks et al., 1988) that allows for the possibility of resonant energy transfer when the forcing frequency of the lift force fluctuations is not too different from the natural frequency of vibration of the particle–surface deformation. Under such circumstances, a particle is removed much easier from a surface than applying the same lift force quasi-statically (which is the basis of the simple force balance approach). It is a more general model than the so-called force balance model because it admits the possibility of resonant energy transfer. When this transfer is zero, then the formula for the resuspension rate constant reduces to the form appropriate to a force balance. That is, the motion of the particle/surface deformation is approximated by a quasi-static balance between the instantaneous aerodynamic lift force and the adhesive force at each location/deformation in the adhesive surface potential well. This implies a functional relationship between the particle deformation and the removal force at each instant of time. Both resonant energy transfer and quasi-static removal are two extremes in the value of ω_0 and $\langle PE \rangle$ depending on the value n, forcing frequency $\left(\langle \dot{f}^2 \rangle / \langle f^2 \rangle \right)^{1/2}$, so for $n \ll \omega$, $\omega_0 \to n$, $n \to \omega$, and $\omega_0 \to \omega$ with corresponding values for $\langle PE \rangle$ at these limiting frequencies.

The situation of smooth contact of a sphere with a surface represented in Figure 2.39 is somewhat idealized. In reality, microscopic roughness significantly reduces the adhesion between particles and surface even in the case of particle contact with a polished surface. Contact with the surface is made by surface asperities so that the area of contact and hence adhesion are much reduced from that for perfectly smooth contact. In this case, experiments have shown that particles are removed from surfaces by rolling where the drag force plays a much more significant role than the lift force. Even so, the formula in Equation 2.276 still applies if the potential energy is based on the rocking and rolling of particles about surface asperities, and equivalent forces, involving the drag force, are used rather than lift forces normal to the surfaces as in Figure 2.39a. We refer to Reeks et al. (Reeks and Hall, 2001, Zhang et al., 2013a,b) for the way these models have been developed and applied to the resuspension of monolayer and multilayer coverages of particles on a rough surface.

2.5.6 Pdf Approach for Particle Pair Mixing and Dispersion

In this part, we examine and assess the way the pdf approach has been used to describe the motion of particle pairs in turbulent flows and, in particular, how it has been used to quantify interparticle collision rates and the influence they have on the continuum equations and constitutive relations for a particle suspension in a turbulent gas.

We also consider how the pdf approach can be used to quantify the demixing or segregation of particles at the small scales of turbulence through the calculation of the distribution of particle pairs as a function of their separation. The segregation influences the collision rates since it brings particle pairs closer together to begin with, and this in turn causes droplets to coalesce and solid particles to agglomerate. In the case of agglomeration, it is necessary to also consider whether particles stick or bounce upon collision or whether they detach from one another some time later. There is an obvious parallel here with similar processes of deposition and resuspension of particles to surfaces in a turbulent boundary layer.

The calculation of binary collision rates, which interests us here, and the issues that surround it necessitates the use of a two-particle pdf $P_2(\boldsymbol{v}_1, \boldsymbol{x}_1; \boldsymbol{v}_2, \boldsymbol{x}_2, t)$, where subscripts 1 and 2 refer to particles 1 and 2. The net collision rate of an individual particle with surrounding particles depends upon the relative velocities $\boldsymbol{v}_2 - \boldsymbol{v}_1$ between particle pairs and their concentration at their separation $\boldsymbol{x}_2 - \boldsymbol{x}_1$ upon collision. The influence of both on the collision rates is reflected in the value of the collision kernel Γ that we will define and formulate in terms of the two-particle pdf and discuss its dependence on the particle response to the small and large scales of the turbulence.

When considering a suspension of monodisperse particles, there are essentially two mechanisms that influence and control the collision between individual particles. The first is due to the random shearing of the flow and is associated with the small dissipating eddies of the turbulence. This gives rises to a velocity difference for colliding particles arising from the difference in carrier turbulent velocities encountered by particle pairs at the point of collision (the separation of the centers of two colliding spheres being known as the collision radius). This difference in particle velocities will also depend upon the particle response to the shearing itself measured by the particle's Stokes number St_K defined as the ratio of the particle response time τ_p to the typical shear rate $\sim \left(\epsilon/\nu\right)^{1/2}$. The influence of particle inertia defined in terms of St_K is similar to that of particle inertia defined in terms of τ_p^+ for particles deposited at a wall in a turbulent boundary layer where the velocity of depositing particles and local concentration have more to do with the history of their motion than their response to the local fluid motion. So, it is the same in this case with regard to the difference in fluid velocity experienced by a particle pair as a function of separation as the particles approach collision with some memory of the greater separation of velocities from encounters with small scales at earlier times and greater separation. Accompanying this is the process of segregation or clustering observed at the small scales, which leads to an increase in the particle concentration in the neighborhood of individual particles and enhances their collision rate with other particles. We will discuss this process and how the pdf approach can be used to capture and quantify both aspects of this mechanism in more detail later on.

The second mechanism is due to the lack of correlation of the particle motion with the local fluid motion and is entirely dependent upon the particle inertia, in which this time it is defined in terms of the Stokes number as the ratio of the particle response time to the large and inertial range of turbulent scales. For these particles, though they may partially or approximately follow the large scales, they are ballistic on the scale of the small-scale motion and the difference in velocities imposed by the shearing of the large scales is virtually zero. It is due to the influence of these particles with stop distances (spatial correlation) comparable to the integral length scale of the carrier flow that influences the mass, momentum, and energy equations of the dispersed phase, and it is necessary to add an extra term to the pdf equation to account for their collisions. This term is precisely analogous to the Boltzmann collision integral in the Maxwell–Boltzmann equation

but accounting for the correlative motion of particle and fluid. This feature highlights the invalidity of the molecular chaos assumption for particle collisions in turbulent flows except for very inert particles when particles and fluid motion are uncorrelated.

In the following sections, we discuss both these mechanisms in detail but we begin first with the formulation of the collision kernel in terms of the two-particle pdf.

2.5.6.1 Particle Collision Kernel

The particle collision kernel $\Gamma(\boldsymbol{x}_1)$ is the net collision rate $\overline{z}$ of an individual particle at position $\boldsymbol{x}_1$ with surrounding particles normalized by their average number concentration $\overline{n}$ of particles within a control volume where the number of particles remains constant in time (or more correctly the average concentration sufficiently far away from the individual particle at $\boldsymbol{x}_1$ that is constant)*. More precisely, the collision rate is the integrated influx $\boldsymbol{j}^+$ of surrounding particles colliding with an individual particle integrated over the total collision surface formed by the colliding particles. In terms of the particle pair distribution pdf $P_2(\boldsymbol{v}_1, \boldsymbol{x}_1; \boldsymbol{v}_2, \boldsymbol{x}_2, t)$ for arbitrary shaped particles and size, $\overline{z}$ is therefore given by

$$\overline{z} = \int\limits_{d\boldsymbol{S}\cdot(\boldsymbol{v}_2-\boldsymbol{v}_1)\leqslant 1} P_2(\boldsymbol{v}_1,\boldsymbol{x}_1;\boldsymbol{v}_2,\boldsymbol{x}_1+\boldsymbol{r}_c,t)(\boldsymbol{v}_2-\boldsymbol{v}_1)\cdot d\boldsymbol{S}(\boldsymbol{r}_c)d\boldsymbol{v}_1 \tag{2.277}$$

where

$\boldsymbol{r}_c$ defines the point of contact between an individual particle at $\boldsymbol{x}_1$ and a neighboring particle at $\boldsymbol{x}_1 + \boldsymbol{r}_c$,
$d\boldsymbol{S}(\boldsymbol{r}_c)$ is an elemental surface area whose normal is along the line of centers of the colliding particles at the point of contact.

So, $\boldsymbol{r}_c$ defines the location of the collision surface for all possible particle pair collisions. In the case of two small colliding spherical droplets of radii r_1 and r_2, the collision surface is a sphere of radius $r_c = r_1 + r_2$, and for collisions in isotropic homogeneous turbulence, the distribution of relative velocities w_r along the line of centers $\phi_r(w_r)$ is spherically symmetric (independent of ϕ, θ) and independent of $\boldsymbol{v}_1$ and $\boldsymbol{x}_1$. So, if we consider a collision with a single particle,

$$\overline{z} = 4\pi r_c^2 n(r_c)\frac{1}{2}\int |w_r|\,\phi(w_r)dw_r \tag{2.278}$$

where $n(r_c)$ is the number concentration of surrounding particles at r_c. The factor of 1/2 reflects the condition on the velocities for a collision in Equation 2.277 and to account for the fact that half the particles are moving toward a surface as they are moving away, considering that the surface is perfectly reflecting. So, we write explicitly

$$\Gamma = \frac{\overline{z}}{\overline{n}} = 2\pi r_c^2 g(r_c)\langle |w_r| \rangle \tag{2.279}$$

where $g(r_c) = n(r_c)/\overline{n}$ is known as the radial distribution function (Sundaram and Collins, 1997) and accounts for the enhancement of collision rates due to clustering or segregation. $\overline{n}$ may also be interpreted more precisely as the value of $n(r)$ at a sufficiently large distance $r \gg r_c$ from an individual particle that the concentration of surrounding particles is effectively constant and equivalent to the fully mixed concentration. $|w_r|$ is the net velocity toward any individual particle of the neighboring particles at the collision radius along their line of centers.

2.5.6.2 Influence of the Particle–Fluid Velocity Correlation on Particle Collisions

The way particle pairs close together interact with a coherent fluid structure increases the correlation of the velocity of each of the particles with the local fluid velocity and in turn the correlation between them. In so doing, it reduces the relative velocity between particle pairs and the rate of collision over the lifetime of the coherent stricture (see Zhou et al., 1998, for a simple 1D model). This can easily be seen in the expression

* Compare this definition with that of the deposition velocity of particles in a surface exposed to a turbulent flow.

for the mean square relative velocity $\langle v_{12}^2 \rangle$ between particle pairs in terms of the associated velocities of the individual particle pair velocities $\boldsymbol{v}_1$ and $\boldsymbol{v}_2$, namely,

$$\langle v_{12}^2 \rangle = \langle v_1^2 \rangle + \langle v_2^2 \rangle - 2\langle \boldsymbol{v}_1 \cdot \boldsymbol{v}_2 \rangle$$

for which $\boldsymbol{w}_r$ is the resolved component of $\boldsymbol{v}_{12}$ along the line of centers. Following Lavieville et al. (1995, 1997), Simonin et al. (2002) and Zaichik and Alipchenkov (2003), we can see the influence of the fluid–particle velocity correlation on the particle pair pdf, $P_2(\boldsymbol{v}_1, \boldsymbol{x}_1; \boldsymbol{v}_2, \boldsymbol{x}_2, t)$, if we introduce the joint two-point pdf of particle and fluid velocities $\boldsymbol{v}$, $\boldsymbol{u}$, respectively, namely, $P_2(\boldsymbol{v}_1, \boldsymbol{u}_1, \boldsymbol{x}_1; \boldsymbol{v}_2, \boldsymbol{u}_2, \boldsymbol{x}_2)$, given in terms of conditional probabilities, as

$$P_2(\boldsymbol{v}_1, \boldsymbol{u}_1, \boldsymbol{x}_1; \boldsymbol{v}_2, \boldsymbol{u}_2, \boldsymbol{x}_2) = P_1(\boldsymbol{v}_1, \boldsymbol{x}_1 | \boldsymbol{u}_1) P_1(\boldsymbol{v}_2, \boldsymbol{x}_2 | \boldsymbol{u}_2) P_2(\boldsymbol{u}_1, \boldsymbol{u}_2) \tag{2.280}$$

where

$P_1(\boldsymbol{v}_1, \boldsymbol{x}_1 | \boldsymbol{u}_1)$ means the conditional probability density for a particle velocity $\boldsymbol{v}_1$ measured at $\boldsymbol{x}_1$ conditional upon there being a fluid velocity $\boldsymbol{u}_1$ at the same position $\boldsymbol{x}_1$

$P_2(\boldsymbol{u}_1, \boldsymbol{u}_2)$ is the joint probability distribution of carrier flow velocities $\boldsymbol{u}_1$ and $\boldsymbol{u}_2$ encountered by particles 1 and 2 at $\boldsymbol{x}_1$ and $\boldsymbol{x}_2$, respectively

We have

$$P_1(\boldsymbol{v}_1, \boldsymbol{x}_1 | \boldsymbol{u}_1) = \frac{P_1(\boldsymbol{v}_1, \boldsymbol{u}_1, \boldsymbol{x}_1)}{P_1(\boldsymbol{u}_1)}$$

and similarly for $P_1(\boldsymbol{v}_2, \boldsymbol{x}_2 | \boldsymbol{u}_2)$, where $P_1(\boldsymbol{u}_1)$ is the probability distribution of carrier flow velocities observed by particle 1 at $\boldsymbol{x}_1$.

From the two-point particle–fluid velocity distribution $P_2(\boldsymbol{v}_1, \boldsymbol{u}_1, \boldsymbol{x}_1; \boldsymbol{v}_2, \boldsymbol{u}_2, \boldsymbol{x}_2)$, we can calculate $P_2(\boldsymbol{v}_1, \boldsymbol{x}_1; \boldsymbol{v}_2, \boldsymbol{x}_2)$ from

$$P_2(\boldsymbol{v}_1, \boldsymbol{x}_1; \boldsymbol{v}_2, \boldsymbol{x}_2) = \int P_2(\boldsymbol{v}_1, \boldsymbol{u}_1, \boldsymbol{x}_1; \boldsymbol{v}_2, \boldsymbol{u}_2, \boldsymbol{x}_2) d\boldsymbol{u}_1 d\boldsymbol{u}_2 \tag{2.281}$$

using the relationship in Equation 2.280 and assumed formulae for the conditional probabilities. Lavieville et al. (1995), in the case of statistical stationary homogeneous isotropic turbulence, assumed a Gaussian for the conditional probabilities that involve the particle–fluid velocity correlation coefficient ξ at a fixed point in space and at equilibrium, that is, for an isotropic turbulent flow, namely,

$$\xi = \frac{\langle \boldsymbol{u} \cdot \boldsymbol{v} \rangle}{\langle v^2 \rangle^{1/2} \langle u^2 \rangle^{1/2}} \tag{2.282}$$

where, for example, $\langle v^2 \rangle = \langle \boldsymbol{v} \cdot \boldsymbol{v} \rangle$. The implicit assumption is that this correlation is the same as the Lagrangian correlation, which, because of homogeneity, is independent of position, that is,

$$\langle \boldsymbol{v}(\boldsymbol{x}, t) \cdot \boldsymbol{u}(\boldsymbol{x}, t) \rangle = \langle \boldsymbol{v}(\boldsymbol{x}, 0 | t) \cdot \boldsymbol{u}(\boldsymbol{x}, 0 | t) \rangle_{t \to \infty} = \beta^{-1} \mu_\infty$$

For the Stokes drag assuming an exponential autocorrelation for the flow velocity along a particle trajectory,

$$\xi = \left(\langle v^2 \rangle / \langle u^2 \rangle \right)^{1/2} = \frac{1}{(1 + St_L)^{1/2}} \tag{2.283}$$

where St_L is the particles Stokes number $1/\beta T_L$ in which T_L is the Lagrangian integral timescale of the fluid motion (in the case of Lavieville's model (Lavieville et al., 1995, 1997) T_L is associated with the

large-scale motion). The form for $P_2(\boldsymbol{u}_1, \boldsymbol{u}_2)$ in Equation 2.280 used in the evaluation of $P_2(\boldsymbol{v}_1, \boldsymbol{x}_1; \boldsymbol{v}_2, \boldsymbol{x}_2)$ in Equation 2.281 is based on a two-point particle-joint Gaussian distribution for the components of $\boldsymbol{u}_1$ and $\boldsymbol{u}_2$ involving the longitudinal and lateral velocity correlation $F(r)$ and $G(r)$, respectively, where r is the distance between the two points. This gives rise to a Gaussian distribution in the particle velocities $\boldsymbol{v}(\boldsymbol{x}_1)$, $\boldsymbol{v}(\boldsymbol{x}_2)$, which, when transformed to a distribution $P_1(\boldsymbol{w})$ for the relative velocities $\boldsymbol{w}$ between particle pairs, implies a similar Gaussian distribution for the fluid velocities but with values for the radial and normal component velocity correlation $F(r)$ and $G(r)$ scaled by ξ^2. Thus, the radial distribution $P^{(0)}(w_r)$ is given by

$$P_1(w_r) = \left(2\pi\left\langle w_r^2\right\rangle\right)^{-1/2} \exp\left(-w_r^2/2\left\langle w_r^2\right\rangle\right) \tag{2.284}$$

where, at the point of contact between colliding particles,

$$\left\langle w_r^2\right\rangle = 2\left\langle v^2\right\rangle(1-\xi^2 F(r_c)) \tag{2.285}$$

and, that with reference to the collision kernel Γ defined in Equation 2.279,

$$\left\langle\left|w_r\right|\right\rangle = \left(\frac{2}{\pi}\left\langle w_r^2\right\rangle\right)^{1/2} \tag{2.286}$$

So, the formula in Equation 2.285 accounts for both the effects of the induced correlation of particle motion and that of the local fluid for each member of the particle pair and the spatial correlation between particle pair velocities arising from the spatial correlation of fluid velocities themselves. Zaichik et al. (2008) have used these formulae to obtain expressions for Γ in both the large-scale, intermediate inertial subrange and small-scale viscous dissipating (Kolmogorov) range of scales considering both the influence of particle pair separation and fluid–particle correlation and its dependence on particle inertia. In particular, using the formula for $\left\langle w_r^2\right\rangle$ and $\langle|w_r|\rangle$ into Equation 2.279 for Γ and ignoring segregation, that is, we have

$$\Gamma = 4\pi^{1/2} r_c^2 \left\langle v^2\right\rangle^{1/2} (1-\xi^2 F(r_c))^{1/2} \tag{2.287}$$

While the results reproduce the conclusion made by Saffman and Turner (1956) for the collision kernel of inertialess passive scalar particles in the viscous small-scale dissipating range and that of Abrahamson (1992) for the large-scale large inertia $St_L \gg 1$, the approach implicitly assumes a local equilibrium between particles and fluid, which is inappropriate for collision at the small scale. The approach does not take account of the memory and history of the particle pair separation and the relative fluid velocities the particles encounter throughout the entire particle pair history before they collide. It assumes furthermore that particles are fully mixed and that any particles have a uniform concentration of the particles surrounding it. The process we may see is precisely analogous to the way particles are transported through a turbulent boundary layer, where there is a concentration buildup near the wall and nonlocal particle velocities at the wall. A number of deposition models in a turbulent boundary exploit this memory though the concept of free flight to the wall, which is missing from this local equilibrium approach. We will also see that using a solution of the pdf equation for relative particle motion, this feature is accounted for in a way similar to the way the solution of the pdf equation accounts for these features for particle transport in a turbulent boundary layer discussed in Section 2.5.5.3 and in particular the results of van Dijk and Swailes (2012).

2.5.6.3 Contribution of Interparticle Collisions to the Dispersed Phase Continuum Equations

In this section, we consider the transport of particles in a turbulent flow and the influence interparticle collisions have on the continuum equations of the dispersed particle phase. We will approach this in a similar way to the approach we used to obtain the continuum equation due to the turbulence acting alone. That is, we consider the way the collisions affects the pdf–kinetic equation for a single particle as an additional term that represents the rate of change $\partial P/\partial t$ due to particle collisions within and outside an elemental volume in particle phase space. Using the analogy of solid particle collisions with those of gas molecules, following the work of Lavieville et al. (1995), Simonin (1996), Zaichik and Simonin (2003, 2006), Lavieville (1997), we evaluate the Boltzmann collision integral for the collisions of inelastic solid spheres. As in kinetic theory,

we assume that the particle suspension is sufficiently dilute that only binary collisions are significant. We are specifically interested in cases where the particle's response time β^{-1} ~ the integral timescale T_L, $St_L \sim 1$. We note that experiment and numerical simulations have indicated that inert particle collisions have a measurable influence on coarse particle transport properties in gas–solid turbulent flows, even for small values of the dispersed phase volume fraction, $\alpha \sim 10^{-2}$. Neglecting hydrodynamic interaction between colliding particles, hard sphere kinetic theory can be used to account for interparticle inelastic collisions in a pdf approach to particle flows.

Thus, referring to Figure 2.40 for an inelastic collision between two identical spherical particles labeled 1 and 2,

$$\begin{aligned} \boldsymbol{v}_1^* &= \boldsymbol{v}_1 + \frac{1}{2}(1+e_c)(\boldsymbol{v}_{21}\cdot\hat{\boldsymbol{n}})\hat{\boldsymbol{n}} \\ \boldsymbol{v}_2^* &= \boldsymbol{v}_2 - \frac{1}{2}(1+e_c)(\boldsymbol{v}_{21}\cdot\hat{\boldsymbol{n}})\hat{\boldsymbol{n}} \end{aligned} \tag{2.288}$$

where $\boldsymbol{v}_1^*$ and $\boldsymbol{v}_2^*$ are the velocities of particles 1 and 2 after the collision related to the velocities $\boldsymbol{v}_1$ and $\boldsymbol{v}_2$ before the collision, involving the coefficient of restitution e_c, the unit vector $\hat{\boldsymbol{n}}$ directed from the center of the first colliding sphere to the center of the second at impact, and $\boldsymbol{v}_{12}$ is the relative velocity of particle 2 with respect to that of particle 1 at impact. Note that there is no interparticle friction.

While there are certain obvious similarities between molecular collisions and particle collisions in a turbulent flow, there are, as we have pointed out earlier, however fundamental differences, that is, in the kinetic theory of dilute gases, the statistics of binary collisions are derived by assuming that the velocities and positions of any two particles are independent of each other (the molecular chaos assumption), whereas in gas–solid flow, the probable positions and velocities of colliding particles will definitely be correlated through their interaction with the same surrounding turbulent flow. In this section, we describe the original approach due to Simonin (He and Simonin, 1993) that ignores this correlation and then the approach proposed by Lavieville et al. (1995) that attempts to take it into account. The detailed description of the modeling approach can be found in studies by He and Simonin (1993), Lavieville et al. (1995), and more recently Simonin et al. (2002).

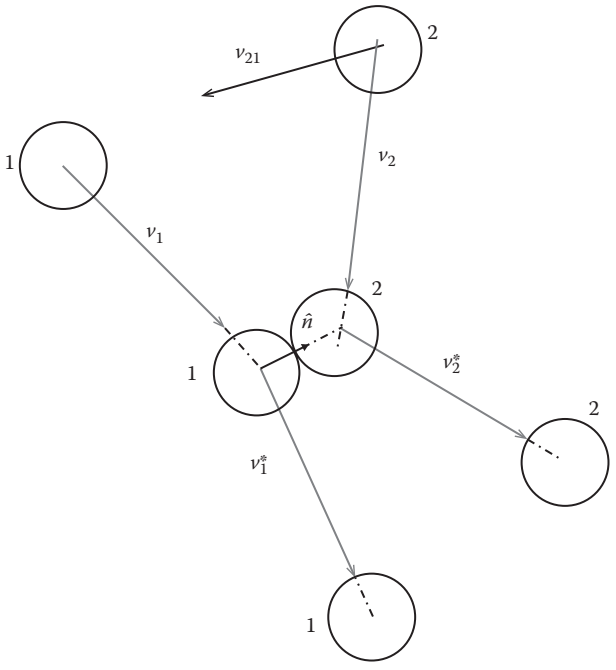


Figure 2.40

The collision of two spherical particles labeled 1 and 2 with velocities $\boldsymbol{v}_1$, $\boldsymbol{v}_2$ before impact and $\boldsymbol{v}_2^*$, $\boldsymbol{v}_2^*$ after impact, respectively.

2.5.6.3.1 Boltzmann Collision Integral for a Suspension of Particles in a Turbulent Flow If particle-to-particle interactions in which more than two particles take place are assumed to be negligible in number and effect, the collisional pdf rate of change may be written in terms of the particle–particle pair probability distribution function $P_2(\boldsymbol{v}_1, \boldsymbol{x}_1; \boldsymbol{v}_2, \boldsymbol{x}_2, t)$ for particle 1 with velocity $\boldsymbol{v}_1$ at position $\boldsymbol{x}_1$ and particle 2 with velocity $\boldsymbol{v}_2$ at position $\boldsymbol{x}_2$ for which special closure assumptions are needed. The net rate of change of the number of particles within an elemental volume of phase space $d\boldsymbol{v}_1 d\boldsymbol{x}_1$ at $\boldsymbol{v}_1$, $\boldsymbol{x}_1$ due to collisions with particles at $\boldsymbol{x}_1 + d_p\hat{\boldsymbol{n}}$ is made up of two contributions: The first contribution is the rate of loss directly due to collisions of particles within the phase space volume $d\boldsymbol{v}_1 d\boldsymbol{x}_1$ with particles at $\boldsymbol{x}_1 + d_p\hat{\boldsymbol{n}}$ over the collision surface for all particles with relative velocities directed toward the collision surface. Referring to Figure 2.40, we can write this explicitly as

$$\partial P^-(\boldsymbol{v}_1,\boldsymbol{x}_1,t)/\partial t = -d_p^2 \int \int_{\boldsymbol{v}_{21}\cdot\hat{\boldsymbol{n}}>0} \hat{\boldsymbol{n}}\cdot\boldsymbol{v}_{12} P_2(\boldsymbol{v}_1,\boldsymbol{x}_1;\boldsymbol{v}_2,\boldsymbol{x}_1+d_p\hat{\boldsymbol{n}},t)\, d\hat{\boldsymbol{n}}\, d\boldsymbol{v}_2 \tag{2.289}$$

The second contribution is a positive increase arising from the collision of particles within the phase space volume $d\boldsymbol{v}_1^+ d\boldsymbol{x}_1$ at $\boldsymbol{v}_1^+, \boldsymbol{x}_1$ with velocities $\boldsymbol{v}_2^+$ at $\boldsymbol{x}_1 + d_p\hat{\boldsymbol{n}}$ and ending up after collision in the elemental phase space volumes $d\boldsymbol{v}_1 d\boldsymbol{x}_1$ at $\boldsymbol{v}_1$, $\boldsymbol{x}_1$ and $d\boldsymbol{v}_2 d\boldsymbol{x}_1$ at $\boldsymbol{x}_1 + d_p\hat{\boldsymbol{n}}$. The total collision rate is then an integration of the collision *arrival* flux over the collision surface and over all $\boldsymbol{v}_2^+$ similar to that in the expression for the rate of loss in Equation 2.289, namely,

$$d\boldsymbol{v}_1^+ d\boldsymbol{x}_1 \partial P^+(\boldsymbol{v}_1^+,\boldsymbol{x}_1,t)/\partial t = d\boldsymbol{v}_1^+ d\boldsymbol{x}_1 d_p^2 \int \int_{\boldsymbol{v}_{21}\cdot\hat{\boldsymbol{n}}>0} \hat{\boldsymbol{n}}\cdot\boldsymbol{v}_{12}^+ P_2(\boldsymbol{v}_1^+,\boldsymbol{x}_1;\boldsymbol{v}_2^+,\boldsymbol{x}_1+\boldsymbol{d}_p\hat{\boldsymbol{n}},t)\, d\hat{\boldsymbol{n}}\, d\boldsymbol{v}_2^+ \tag{2.290}$$

For $\boldsymbol{v}_1^+, \boldsymbol{v}_2^+ \rightarrow \boldsymbol{v}_1\boldsymbol{v}_2$ after collision

$$\boldsymbol{v}_1^+ = \boldsymbol{v}_1 + \frac{1+e_c}{2e_c}\left(\boldsymbol{v}_{21}\cdot\hat{\boldsymbol{n}}\right) \quad \boldsymbol{v}_2^+ = \boldsymbol{v}_2 - \frac{1+e_c}{2e_c}\left(\boldsymbol{v}_{21}\cdot\hat{\boldsymbol{n}}\right) \tag{2.291}$$

which implies that

$$\left|\frac{\partial(\boldsymbol{v}_1^+,\boldsymbol{v}_2^+)}{\partial(\boldsymbol{v}_1,\boldsymbol{v}_2)}\right| = \frac{1}{e_c}; \quad \boldsymbol{v}_{12}^+ = \frac{1}{e_c}\boldsymbol{v}_{12}$$

Using these relations in Equation 2.290, we obtain

$$\begin{aligned}\left(\frac{\partial P(\boldsymbol{v}_1,\boldsymbol{x}_1,t)}{\partial t}\right)_{collisions} &= \partial P^+(\boldsymbol{v}_1^+,\boldsymbol{x}_1,t)/\partial t + \partial P^-(\boldsymbol{v}_1,\boldsymbol{x}_1,t)/\partial t \\ &= d_p^2 \int \int_{\boldsymbol{v}_{21}\cdot\hat{\boldsymbol{n}}>0} d\hat{\boldsymbol{n}}\, d\boldsymbol{v}_2 \cdot \boldsymbol{v}_{12}^+ \Delta P_2\left(\boldsymbol{v}_1,\boldsymbol{x}_1;\boldsymbol{v}_2,\boldsymbol{x}_1+d_p,t\right)\end{aligned} \tag{2.292}$$

where

$$\Delta P_2 = e_c^{-2} P_2(\boldsymbol{v}_1^+,\boldsymbol{x}_1;\boldsymbol{v}_2^+,\boldsymbol{x}_1+d_p\hat{\boldsymbol{n}},t) - P_2(\boldsymbol{v}_1,\boldsymbol{x}_1;\boldsymbol{v}_2,\boldsymbol{x}_1+d_p\hat{\boldsymbol{n}},t)$$

The mean collisional rate of change for some property ψ, for example, kinetic energy, is the integral over all possible binary collisions of the change in ψ in a particular collision multiplied by the probable frequency of such a collision, which can be written as

$$C(\psi) = d_p^2 \int\int \int \int_{\boldsymbol{v}_{21}\cdot\hat{\boldsymbol{n}}>0} (\psi_2^\star - \psi_2) P_2(\boldsymbol{v}_1,\boldsymbol{x};\boldsymbol{v}_2,\underline{x}+d_p\hat{k},t)\boldsymbol{v}_{21}\cdot\hat{\boldsymbol{n}}\, d\hat{\boldsymbol{n}}\, d\boldsymbol{v}_2 d\boldsymbol{v}_1 \tag{2.293}$$

where $\psi_2 = \psi_2(\boldsymbol{v}_1, \boldsymbol{v}_2)$ and $\psi_2^\star = \psi_2(\boldsymbol{v}_1^\star, \boldsymbol{v}_2^\star)$.

2.5.6.3.2 Collision Models Using the molecular chaos approach adopted in kinetic theory, the pair distribution function in the collision integral is simply written in terms of the single distribution function, assuming that colliding particle velocities are completely independent, namely,

$$P_2(\boldsymbol{v}_1,\boldsymbol{x}_1;\boldsymbol{v}_2,\boldsymbol{x}_1+d_p,t)=P_1(\boldsymbol{v}_1,\boldsymbol{x}_1,t)P_1(\boldsymbol{v}_2,\boldsymbol{x}_2+d_p,t)$$

$$\tau_p \gg \tau_e \text{ (eddy lifetime)} \tag{2.294}$$

This has been retained in the derivation of the collision integral used by Simonin (1991) and is referred to as the random collision model. This is also the assumption used implicitly by Oesterle and Petitjean (1993) and Sommerfeld (1995). However, the molecular chaos assumption is valid only when the particle response time is much larger than the eddy–particle interaction time, that is, when the particle motion is ballistic. However, as we have pointed out in Section 2.5.6.2 that when the particle response time is of the same order or smaller than this interaction time, the approaching particle velocities will be correlated through interaction with the same eddy and this needs to be taken account of.

2.5.6.3.2.1 Particle–Fluid-Correlated Collision Model We refer to Equation 2.280 and the particle pair probability density involving the particle position, velocity, and flow velocity encountered by the particle $P_2(\boldsymbol{v}_1, \boldsymbol{u}_1, \boldsymbol{x}_1; \boldsymbol{v}_2, \boldsymbol{u}_2, \boldsymbol{x}_2)$. For two colliding particles, the collision radius is so small compared to the length scale of the energy containing eddies that we may safely assume that both particles encounter the same fluid velocities $\boldsymbol{u}$, so we may write this probability density as

$$P_1(\boldsymbol{v}_1,\boldsymbol{x}_1\,|\,\boldsymbol{u},\boldsymbol{x}_1)P_1(\boldsymbol{v}_2,\boldsymbol{x}_1+d_p\,|\,\boldsymbol{u},\boldsymbol{x})P_1(\boldsymbol{u}_1,\boldsymbol{x}_1)$$

$$=P_1(\boldsymbol{v}_1,\boldsymbol{u},\boldsymbol{x}_1)P_1(\boldsymbol{v}_2,\boldsymbol{u},\boldsymbol{x}_1+d_p)/P_1(\boldsymbol{u},\boldsymbol{x}_1)$$

where we have assumed that since the colliding particles are separated by a distance comparable to the integral length scale and that $P_1(\boldsymbol{u}, \boldsymbol{x}_1) \cong P_1(\boldsymbol{u}, \boldsymbol{x}_{1+}d_p)$,

$$P_2(\boldsymbol{v}_1,\boldsymbol{x}_1;\boldsymbol{v}_2,\boldsymbol{x}_2+d_p)=\int d\boldsymbol{u}P_1(\boldsymbol{v}_1,\boldsymbol{u},\boldsymbol{x}_1)P_1(\boldsymbol{v}_2,\boldsymbol{u},\boldsymbol{x}_1+d_p)/P_1(\boldsymbol{u},\boldsymbol{x}_1) \tag{2.295}$$

2.5.6.3.2.2 Third-Order Moment Expansion (Grad's Theory) Following Grad's theory of rarefied gases (Grad, 1949), the distribution function in the collision term may be approximated by its third-order expansion in Hermite polynomials:

$$P(\boldsymbol{v},\boldsymbol{x},t)=\left[1+\frac{a_{ij}}{2T^2}v_i'v_j'+\frac{a_{ijk}}{6T^3}v_i'v_j'v_k'-\frac{a_{ijj}}{2T^2}v_i'\right]P^0(\underline{v},\underline{x},t) \tag{2.296}$$

where using q^2 to denote the mean particle turbulent kinetic energy per unit particle mass

$$T=\frac{2}{3}q^2;\quad a_{ij}=\overline{v_i'v_{,j}'}-\frac{2}{3}q^2\delta_{ij};\quad a_{ijk}=\overline{v_i'v_j'v_k'}$$

We recall that $\overline{(.....)}$ denotes a particle density-weighted average*.

$P^0(v, x, t)$ is the equilibrium pdf given by a Maxwell (Gaussian) distribution for the particle velocities, that is,

$$P^0(\boldsymbol{v},x,t)=\left(\frac{4\pi q^2}{3}\right)^{-3/2}\exp\left(-\frac{v'^2}{4q^2/3}\right) \tag{2.297}$$

* T is referred to as the granular temperature in granular flows.

Using the hard sphere collision model, Jenkins and Richman (1985) derived the following collisional terms in the transport equations for the particle mass (m), momentum (mv_i), and kinetic stresses $\left(\frac{1}{2}mv'^2\right)$ and kinetic stress flux $\left(mv'_iv'_jv'_k\right)$, respectively,

$$C(m)=0 \tag{2.298}$$

$$C(mv)=0 \tag{2.299}$$

$$C(mv'_iv'_j)=-\alpha_p\rho_p\frac{\sigma_c}{\tau_c}\left(\left\langle v'_iv'_j\right\rangle-\frac{1}{3}\left\{1-\frac{1}{3}(1-e_c^2)\right\}\left\langle v'^2\right\rangle\delta_{ij}\right) \tag{2.300}$$

$$C(mv'_iv'_jv'_k)=-\frac{5}{12}\alpha_p\rho_p\frac{\xi_c}{\tau_c}\left(9a_{ijk}-a_{ill}\delta_{jk}-a_{jll}\delta_{ik}-a_{mll}\delta_{ij}\right) \tag{2.301}$$

where

ρ_p is the particle material density
α_p is the local volume fraction of the dispersed particle phase
τ_c is the time between particle collisions, $\sigma_c=(1+e_c)(3-e_c)/5$, and $\xi_c=(1+e_c)(49-3e_c)/100$

The collisional term in the kinetic stress transport equation is written as a return to isotropy term analogous to the Rotta term in the Reynolds stress transport turbulence modeling approach. Elastic collisions ($e_c=1$) lead to a destruction of the off-diagonal correlations and redistribution of energy among the various normal stresses without modifying the total kinetic energy. The extension to inelastic collisions leads to a linear dissipation rate in the kinetic stress transport equations proportional to the collision frequency and a function of the coefficient of restitution e_c.

Extending the approach of Jenkins and Richman (1985), Lavieville et al. (1997), Simonin et al. (2002), and more recently Zaichik and Alipchenkov (1997), Zaichik et al. (2008), Grad's theoretical approach for particle–fluid-correlated collisions is used by performing a Hermite polynomial expansion on the fluid–particle-joint pdf. This eventually leads to the following generalized form for the collisional source term in the kinetic stress transport equation:

$$C(mv'_iv'_j)=-\rho_p\frac{\sigma_c}{\tau_c}\left(a_{p,ij}+\xi^4a_{f,ij}-\xi^2a_{pf,ij}\right) \tag{2.302}$$

where

$$a_{p,ij}=\overline{v'_iv'_j}-\frac{1}{3}\overline{\boldsymbol{v}'^2}\left\{1-\frac{1}{3}(1-e_c^2)\right\}\delta_{ij}\quad a_{f,ij}=\overline{u'_iu'_j}-\frac{1}{3}\overline{\boldsymbol{u}'^2}\delta_{ij}$$

$$a_{pf,ij}=\overline{u'_iv'_j}^{S}-\frac{1}{3}\xi^2\overline{\boldsymbol{u}'^2}\delta_{ij}$$

ξ is the particle fluid velocity correlation defined in Equation 2.282
τ_c is the interparticle collision time
$\overline{u'_iv'_j}^{S}$ is the symmetric part of $\overline{u'_iv'_j}$

We note that when $\xi=0$, the collision terms reduce to the forms given by Jenkins and Richman.

Following a similar approach, Zaichik et al. (2008) evaluated the collisional terms for the third-order moment C_{ijk} as

$$C_{ijk}=-\frac{3(1-\xi^2)}{\tau_{c2}}\overline{v'_iv'_jv'_k};\quad \tau_{c2}=\frac{180\tau_c}{(1+e_c)(49-33e_c)} \tag{2.303}$$

so that the influence on the C–E approximation for the third-order moment given in Equation 2.248 becomes

$$\overline{v_i' v_j' v_k'} = \frac{\left(1+(1-\xi^2)\tau_p/\tau_{c2}\right)^{-1}}{3}\left(\epsilon_{li}\frac{\partial}{\partial x_l}\overline{v_j' v_k'} - \epsilon_{lj}\frac{\partial}{\partial x_l}\overline{v_i' v_k'} - \epsilon_{lk}\frac{\partial}{\partial x_l}\overline{v_i' v_j'}\right) \tag{2.304}$$

2.5.6.3.2.3 Interparticle Collision Time Referring to the definition of collision rate in terms of the collision kernel and using the form of the collision kernel defined in Equation 2.287 with no segregation and $F(r_c) = 1$, we can write

$$\tau_c = \tau_c^k (1-\xi^2)^{-1/2} \tag{2.305}$$

where τ_c^k is the standard kinetic theory interparticle collision time based on the molecular chaos assumption and given explicitly by

$$\left(\tau_c^k\right)^{-1} = n\pi d_p^2 \sqrt{\frac{32}{12\pi}} \left\langle v^2 \right\rangle^{1/2}$$

where n is the particle number density.

The aforementioned equations show that the effective interparticle collision rate based on the correlated collision model is always smaller than the one given by standard kinetic theory and decreases with respect to the ratio of the eddy–particle interaction time to particle relaxation time as a result of the increase in correlation coefficient ξ_{12}. This behavior was observed by Lavieville et al. (1997) in LES/Lagrangian simulations in homogeneous isotropic turbulent flows showing that neighboring particles have correlated turbulent velocities. The following were also noted: the inclusion of interparticle collisions and the coupling with carrier flow turbulence, its effect on the continuum equations and the constitutive relations, and the influence of collisions on particles kinetic stresses and isotropy.

2.5.6.4 The Effect of Particle Collisions on Turbulent Stresses in a Homogeneous Shear Flow

As an important validation of the correlated collision model, we present the results of Moreau et al. (2003, 2004), who considered perfectly elastic collisions (in the absence of gravity) of spherical particles suspended in an evolving uniform shear flow whose turbulent characteristics were obtained by Lagrangian simulation of individual particle trajectories based on a Langevin equation for the carrier phase using data obtained from an LES. The initial flow conditions corresponded to isotropic turbulence and the particle volume fraction ~1.25×10^{-2}. Figure 2.41 shows the time evolution of normal turbulent stresses in the dispersed phase

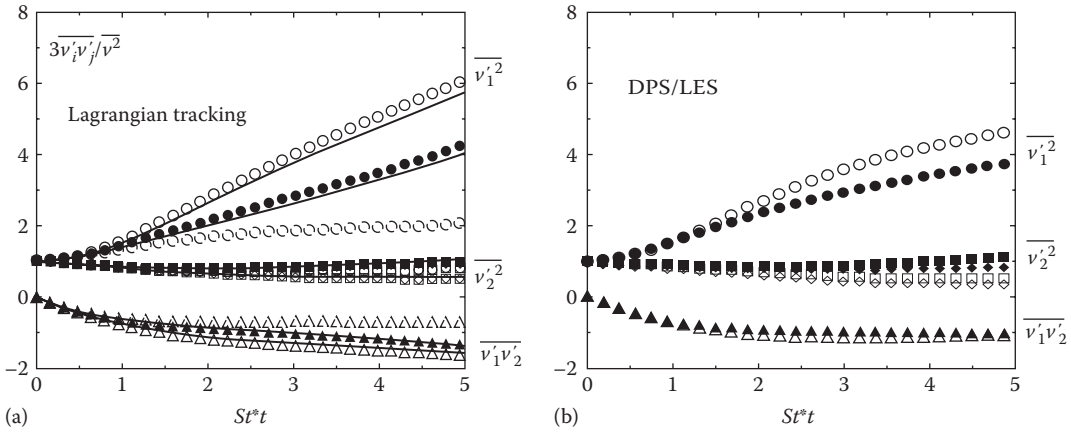


Figure 2.41

Time development of particle kinetic stresses in a developing simple turbulent shear flow showing the influence of particle collisions. (a) Comparison of model predictions against Lagrangian tracking with correlated collisions (filled symbols), without collisions (open symbols), and decorrelated collisions (dashed symbols). (b) Results based on direct particle simulation (DPS) with an LES of the shear flow symbols as in (a).

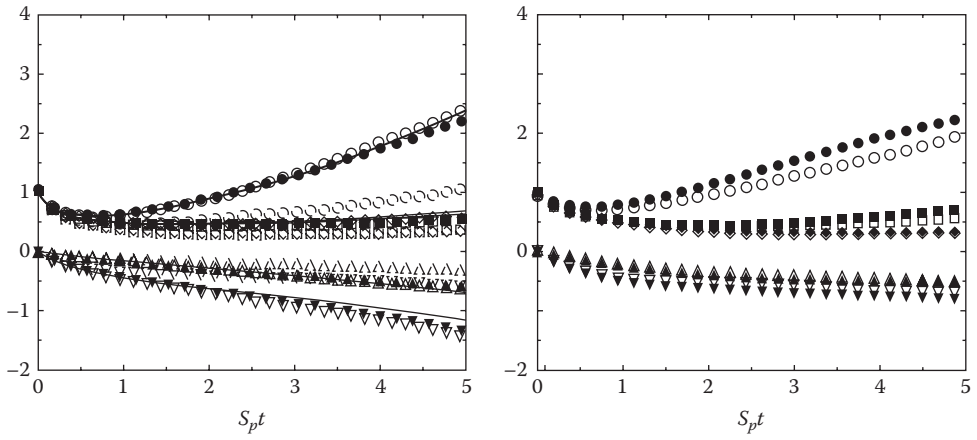


Figure 2.42

Time development of the fluid-particle velocity correlation. Comparison between Monte Carlo simulation results and model predictions based on the moment method GLM model without collisions (empty symbols), with decorrelated collisions (dashed symbols), and with correlated collisions (filled symbols). (a) DPS/LES results (on the right) without collision effect (empty symbols) and with collision effect (filled symbols). *Note:* streamwise components $\overline{u_1'v_1'}$: circles; transverse components: $\overline{u_2'v_2'}$: squares and $\overline{u_3'v_3'}$: diamonds; shear stress components: $\overline{u_2'v_1'}$: triangles up and $\overline{u_2'v_2'}$: triangles down). (Taken from Moreau, M. et al., Stochastic Lagrangian modelling and Monte Carlo simulation of collisions in gas-solid homogeneous shear turbulent flows, in *Fifth International Conference on Multiphase Flow* (*ICMF2004*), Paper no. 426, Yokohama, Japan, May 30–June 4, 2004.)

under the action of the rate of shear, the carrier and dispersed phases evolving from an isotropic the equilibrium state. The results obtained by solving the momentum and kinetic stress equations with and without the collision terms given in Equations 2.302 and 2.303 are given in Figure 2.41. The data obtained by DPS in the presence and in the absence of particle collisions are depicted by solid and open symbols, respectively. Turbulent kinetic stresses of the dispersed phase are normalized by the initial kinetic energy of particles and the correlations of velocity of the continuous and dispersed phases by the initial kinetic energy of these correlations.

Figure 2.41 reveals a strong anisotropy of particle velocity fluctuations in the absence of collisions. This anisotropy manifests in a significantly higher intensity of the longitudinal component as compared to the transverse components. Here, there are two mechanisms responsible for the generation of the longitudinal component of velocity of the dispersed phase: via the average velocity gradient and via the interaction of particles with the turbulent eddies of the continuum. On the other hand, fluctuations in the transverse direction are generated only via the interaction of particles with the turbulent fluid. Collisions tend to equalize the intensities of particle fluctuations in different directions, decreasing the intensity of the longitudinal component of velocity fluctuations and increasing the intensities of the transverse components; in other words, the net effect of collisions is the isotropization of the turbulent characteristics of the dispersed phase. As one can see from Figure 2.42, the theoretical model with collisions based on particle-fluid velocity correlations concurs with the numerical simulation data predicting an increase in $\overline{u_1'v_1'}$ due to collisions. The effect of collisions on $\overline{u_1'v_1'}$ manifests through the dependence of the duration of particle interactions with the turbulence on the time interval τ_c. A comparison of model predictions with the data obtained by Moreau et al. (2004) shows that this model reproduces all the essential features of the dependence of the character of dispersed phases velocity fluctuations as well as correlations of velocity between the two phases on particle collisions between particle collisions.

Figure 2.43 shows the model predictions for the collision times based on Equation 2.305 and the computation of the particle fluid velocity correlation £ from the moment equations. Also shown for comparison are the average particle relaxation time and the Stokes relaxation time together with the eddy particle interaction time.

2.5.6.5 Particle Segregation and Demixing

It is by now well known that turbulence, contrary to traditionally held views, can demix a suspension of particles (see, e.g., Fessler et al., 1994). The process of demixing often referred to as particle segregation,

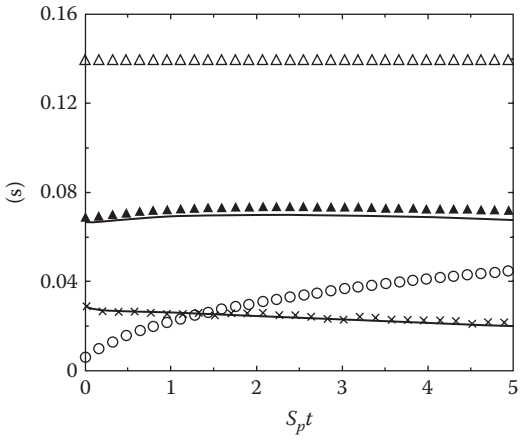


Figure 2.43

Time development of the particle relaxation time and the collision time in homogeneous turbulent shear flow with particle–particle collision influence. Symbols are the stochastic simulation results: mean particle relaxation time τ_{pf}^F (filled triangles), collision time (cross), eddy particle interaction time τ_{pf}^F (circle), Stokes relaxation time (empty triangles) and the lines are predictions from the moment method. (Taken from Moreau, M. et al., Monte Carlo simulation of colliding particles suspended in gas-solid homogeneous turbulent shear flows, in *Proceedings of FEDSM034TH ASME-JSME Joint Fluids Engineering Conference*, Honolulu, HI, Paper FEDSM2003-45736, July 6–10, 2003.)

clustering, or preferential concentration depends upon the ratio of the particle response time to the timescale of the turbulent structures in the flow (i.e., the Stokes number, *St*). Early experiments and simulations (e.g., Crowe et al., 1993) have shown that the demixing reaches a maximum when the particle response time is approximately equal to the timescale of the turbulent structures (i.e., $St \sim 1$) and in particular those associated with the highest strain rate in the flow, the suspended particles being observed to segregate into regions of high strain rate in between the regions of high vorticity. This feature is best illustrated graphically in Figure 2.44, which shows the segregation patterns arising from an initially fully mixed suspension of particles diffusing in a 2D random array of counterrotating vortices. The figure shows the segregation pattern at a given value of time $t = 20$ (in units of the integral timescale) from the initial fully mixed state for three values of the particle Stokes number $St = 0.05$, 0.5, and 5. It is clear that maximum segregation occurs for the case of $St = 1$. What this figure does not show however is the fact that the segregation evolves continuously in time, the patterns becoming more and more filamental as time progresses. Whatever their Stokes number that all particles will segregate, it is just that the greater the Stokes number, the longer the process it takes to achieve a given level of segregation. This is contrary to what many have thought that the segregation reaches an equilibrium state. Particles will continue to segregate until they touch. In fact, what happens is that the segregation forms a network of filamental *caustics* similar to the patterns of light obtained at the bottom of swimming pools as shown in Figure 2.44d, where within these filamental networks it is observed that the light beams cross one another. Similarly, in the case of particle segregation in a turbulent flow within the filamental caustics, particle trajectories are also observed to cross. The formation of caustics in particle demixing processes was first recognized by Wilkinson and Mehlig (2007), and this crossing of trajectories within a caustic is intimately related to the occurrence of random-uncorrelated motion (RUM) in flow fields that are spatially random but smoothly varying (Falkovich et al., 2002, Fevrier et al., 2005).

In recent years, the process of segregation of inertial particles has been studied from different viewpoints when the Stokes number is relatively small. On the one hand, Chen et al. (2006) demonstrated a strong correlation between the positions of small inertial particles and the locations of zero-acceleration points in the carrier flow. On the other hand, Balkovsky et al. (2001) carried out a theoretical analysis based on the assumption that the velocity of inertial particles can be directly related to the carrier flow velocity. By doing so, they were able to show that the segregation of particles continues indefinitely in the course of time, and they showed that the concentration of inertial particles in a turbulent flow is highly intermittent, so the particles are distributed uniformly over space. A similar approach was chosen by Chun et al. (2005) who demonstrated that the time-converged solution of the radial distribution function is of the form $g(r) \sim r^{-\chi}$, where χ is proportional to St_K^2 in which St_K is measured in terms of the particle response to the small dissipating scales of

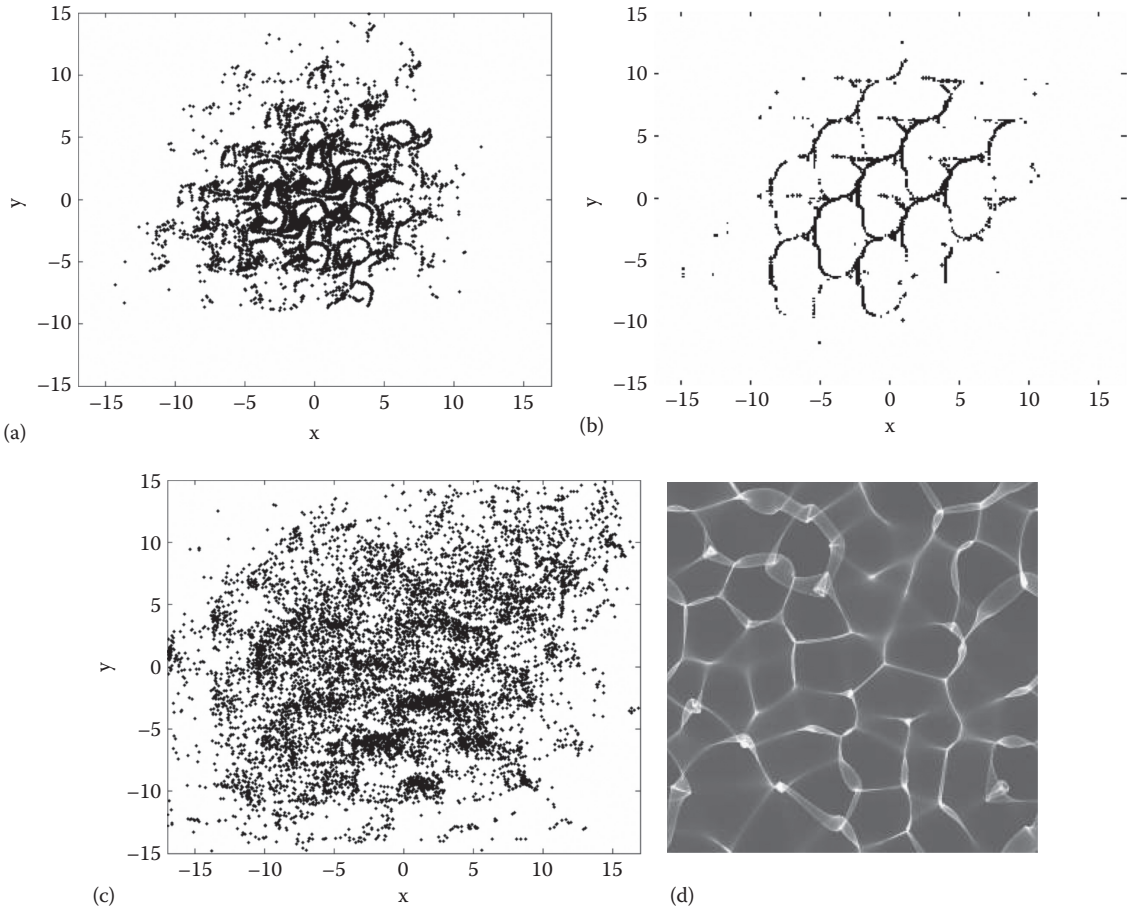


Figure 2.44

(a–c) Positions of 10^4 particles after time $t = 20$ in a nonisotropic random straining flow, for $St = 0.05$ (a), $St = 0.5$ (b), and $St = 5$ (c). (d) Caustic patterns observed at the bottom of a swimming pool.

the turbulence. In addition, they confirmed this by showing results from the DNS of statistically stationary homogeneous isotropic turbulence. Most importantly, the pdf–kinetic approach has been used by Zaichik (Zaichik and Alipchenkov, 2003, 2007) to obtain a similar result. We will discuss these features in more detail in Section 2.5.6.7 on segregation when we will consider the application of two-particle pdfs for calculating segregation using the pdf–kinetic equation for particle pair dispersion derived by Zaichik and his coworkers.

However, before doing so, we will first consider in more detail the mesoscopic and RUM components associated with the particle velocity field and how these components depend upon the particle Stokes number.

2.5.6.6 Formulation of RUM and Mesoscopic Eulerian Particle Velocity Fields

Segregation and RUM are related to the occurrence of interparticle collisions as follows from the seminal work of Sundaram and Collins (1997) and Zhou et al. (1998) in which they demonstrate the following: (1) segregation enhances the particle concentration of certain regions of the flow and (2) RUM, that is, the decorrelation of velocity between particles, causes two nearby particles to collide and possibly to agglomerate. Segregation is well known to manifest itself especially for particle with $St \sim 1$, whereas the effect of RUM is almost invisible for small particles and becomes increasingly important for larger St. Since the interplay between these two effects determines the collision rate in a turbulent flow, it is essential to quantify segregation and RUM as accurately as possible as a function of the Stokes number and some typical flow properties in order to correctly predict the rate of interparticle collisions.

Fevrier et al. (2005) observed that the velocity of suspended particles subject to Stokes drag in the DNS of homogeneous isotropic turbulence consisted of two components: a passive scalar component resulting from transport in a smoothly and continuously varying carrier flow velocity field that accounts for all

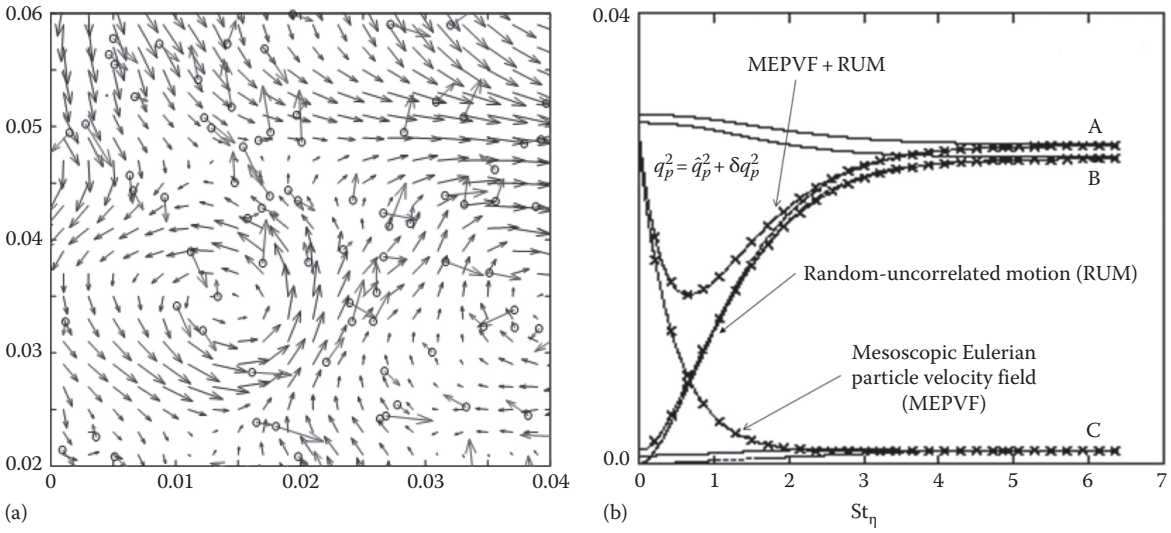


Figure 2.45

Random-uncorrelated motion (RUM): (a) Instantaneous fluid and particle velocity vectors from a single plane of a direct numerical simulation of forced isotropic turbulence with Lagrangian particle tracking. (b) RUM and mesoscopic Eulerian particle velocity field contribution to the particle kinetic energy as functions of Stokes number, St_K.

particle–particle and fluid–particle two-point spatial correlations, which they referred to as the mesoscopic Eulerian particle velocity field (MEPVF), and a spatially uncorrelated component, which we have referred to as RUM, the contribution of which to the particle kinetic energy increases as the particle inertia also increases. FSS attribute this feature to the ability of the particles with inertia to retain the memory of their interaction with very distant and statistically independent eddies in the flow field. This feature had also been observed by Falkovich et al. (2002), which they referred to as the "sling effect."

The presence of RUM in a particle-laden turbulent flow is illustrated in Figure 2.45a taken from FSS (Fevrier et al., 2005), which shows the instantaneous velocity vectors of particles and carrier flow suspended in an isotropic turbulent flow. You can see that a majority of the particle velocity vectors are correlated with a smooth vortex pattern associated with the underlying carrier flow field at that instant of time. But you will notice there are a number of particles whose vectors are randomly oriented and not part of this vortex pattern. It is the motion of these particles that constitutes RUM.

More precisely, Fevrier et al. (2005) quantified the contribution of MEPVF and RUM to the velocity $\boldsymbol{v}_p^m(t)$ of a single particle m by partitioning it into a mesoscopic component derived from the MEPVF $(\boldsymbol{x},t,\mathcal{H}_f)$ (where $\boldsymbol{x}$ is the position in the flow field) and a residual velocity component $\delta\boldsymbol{v}_p^m(t)$ by

$$\boldsymbol{v}_p^m(t) = (\boldsymbol{x}^m(t),t,\mathcal{H}_f) + \delta\boldsymbol{v}_p^m(t) \tag{2.306}$$

where $\mathcal{H}_f$ refers to a single realization of the continuously varying carrier flow velocity field. They pointed out that the MEPVF is defined in an Eulerian frame of reference and therefore may be considered as a velocity field shared by all particles of the dispersed system. In contrast, the total particle velocity $\boldsymbol{v}_p(t)$ and the residual component $\delta\boldsymbol{v}_p(t)$ are Lagrangian quantities defined along trajectories of individual particles $\boldsymbol{x}_p(t)$. The decomposition of the particle velocity given by Equation 6.29 is unique, decomposing the particle velocity into contributions that take into account the spatial structure of the particle velocity field in the first MEPVF term and the spatially uncorrelated motion in the second RUM term (FSS referred to this originally as the quasi-Brownian velocity distribution).

Figure 2.45b shows the contribution of the MEPVF and RUM to the turbulent particle kinetic energy k_p as a function of St_η, the particle Stokes number defined in terms of the Kolmogorov length scale η_K associated with the viscous dissipating length scales of the turbulence for the DNS isotropic homogeneous turbulent flow from which the particle and fluid velocity vectors, as shown in Figure 2.45a, have been extracted. Thus,

$$k_p = \tilde{k}_p + \delta k_p \tag{2.307}$$

where $\tilde{k}_p$ and δk_p are the MEPVF and RUM components of the particle turbulent kinetic energy k_p. Figure 2.45 shows the RUM part starting at zero for zero Stokes number St_η and reaching 100% for $St_\eta \gg 1$, when the particle motion is ballistic (with random velocities in any small volume of the particles). The reverse is the case for the mesoscopic part as a function of St_η.

FSS used the statistics of the particle velocity distribution to evaluate both the Lagrangian temporal correlation and the Eulerian two-point (spatial) correlation, which in this case involves contributions from the MEPVF and RUM. The Lagrangian velocity correlations are defined classically along particle trajectories as

$$R_L^p(\tau) = 1/3\left\langle v_{p,i}(t)v_{p,i}(t+\tau)\right\rangle \tag{2.308}$$

and obtained by averaging over all realizations of the flow for any given particle. This is shown in Figure 2.46a as a function of time t normalized on the fluid Lagrangian integral timescale T_L (along a particle trajectory) for a range of values of the particle Stokes numbers τ_p/T_L. It shows the well-known effect of particles becoming less correlated with their initial velocity with increasing time but becoming more persistent with increasing particle inertia.

The two-point velocity correlation of any two (separate) particles labeled m and n of the system is defined in terms of the two-particle pdf and expressed as

$$R_{ij}^{pp}(\boldsymbol{x},\boldsymbol{x}+\boldsymbol{r},t) = \left\langle v_{p,i}^{(m)}(t)v_{p,j}^{(n)}(t)\middle|\boldsymbol{x}=\boldsymbol{x}_p^{(m)}(t);\boldsymbol{x}+\boldsymbol{r}=\boldsymbol{x}_p^{(n)}(t)\right\rangle \tag{2.309}$$

The dependence on the separation r normalized on the longitudinal integral length scale L_F^f of the carrier flow turbulence is shown in Figure 2.46b for the same values of the particle inertia as in Figure 2.46a. An important result revealed in these spatial correlations is that in the limit $r/L_F^f \to 0$ this correlation does not $\to 1$, indicating that there is a portion of the particle velocity distribution that is not correlated in time or space, that is, the RUM component and analogous to the molecular distribution in kinetic theory of dilute gases. FSS note that if particle motion was completely analogous to molecular motion in a dilute system, the particle positions (in addition to the velocities) would be uncorrelated and the velocity distribution would be Gaussian. For a dilute particle-laden turbulent flow, this component satisfies the molecular chaos assumption.

In the seminal paper of FSS and in the subsequent work of Masi et al. (2010, 2011), a mesoscopic Eulerian formalism (MEF) involving contributions from the MEPVF and RUM has been developed and applied to

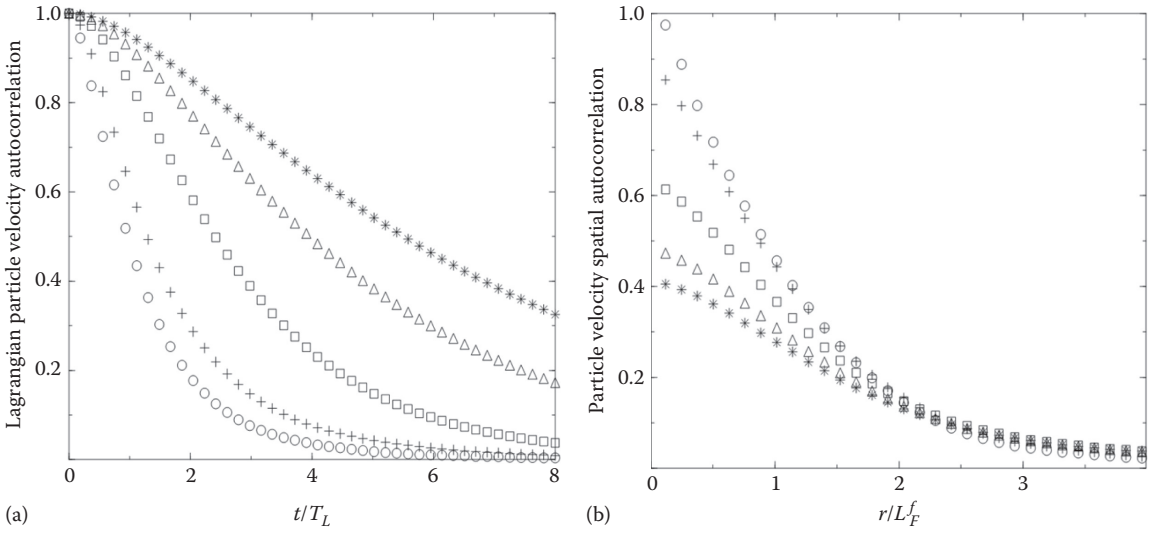


Figure 2.46

Influence of particle inertia on (a) Lagrangian particle velocity correlations and (b) the particle longitudinal spatial correlation function of particles suspended in isotropic turbulence. o, $\tau_p/T_L = 0.05$; +, $\tau_p/T_L = 0.3$; □, $\tau_p/T_L = 1.47$; Δ, $\tau_p/T_L = 3.4$; *, $\tau_p/T_L = 4.83$.

dispersed flows in more complex turbulent shear flows with heat transfer. In particular, the transport equations that describe the evolution of the MEPVF and RUM components have been derived and used to shed light on the properties of the particle velocity and temperature fields. In this regard, MEF has much in keeping with LES where the filtered equations for the large-scale and residual small-scale turbulent motion in LES are analogous to the MPVF and RUM components in MEF. So, for instance, the momentum equations for the MEPVF contain a contribution from the RUM component of the kinetic stress tensor. This tensor represents diffusion and pressure corresponding to the important physical characteristic that within any volume (with dimensions comparable to or smaller than the smallest length scales of the turbulence), separate particles will possess different velocities because of the separate fluid interaction histories. This is the case shown in Figure 2.46a.

2.5.6.7 Pdf Equation and solutions for particle pair dispersion

In this section, we show the way the pdf approach for two-particle dispersion quantifies segregation and RUM and provides a method for calculating particle collision kernel of colliding particles, reflecting the contribution of both processes to the collision rate. We recall the formula in Equation 2.287 that provides an analytic expression for the collision kernel, which, in principle, can be used over the entire range of the scales of turbulence from the large-scale to the small-scale Kolmogorov dissipating scales. We recall, however, recall that it assumes the particles are fully mixed (zero segregation) and that particle velocities are dependent on particle fluid velocity correlations based on a local equilibrium between particle and fluid at the same location. So while this approach is quite valid for the large scales of the turbulence where there is an absence of shear, in the small scales where the shearing of the flow is greatest, the memory of encounters with fluid elements at higher separation and hence higher relative velocities makes a significant contribution to the collision rate. It is of course encounters of this sort for particles transported in a turbulent boundary layer that gives rise to the buildup of particle concentration near the wall and higher wall impact velocities, the combination of both having a profound influence on particle–wall collision rates.

So, we consider a kinetic equation for the particle pairs $P(\boldsymbol{r}, \boldsymbol{w}, t)$, where $\boldsymbol{w}$ is the relative velocity between identical particle pairs a distance $\boldsymbol{r}$ apart for which the corresponding relative fluid velocity experienced by the particle pair is $\Delta\boldsymbol{u}(\boldsymbol{r}, t)$. The statistical properties of $\Delta\boldsymbol{u}(\boldsymbol{r}, t)$ are expressed in terms of its statistical moments that for the small scales of turbulence have spherical symmetry (independent of (θ, ϕ)) dependent only on the distance of separation r. These, therefore, are the structure functions of which the most relevant here are the second-order structure functions $\left\langle \Delta u_r^2(r) \right\rangle, \left\langle \Delta u_\theta^2(r) \right\rangle \sim \left(r/\eta_K\right)^2$ for $r/\eta_k \ll 1$. The equation of motion for $\boldsymbol{w}$ for identical particle pairs is exactly the same as that for the individual particles, so the pdf equation is identical to Equation 2.204 with $\boldsymbol{w}, \boldsymbol{r}, \Delta\boldsymbol{u}$ replacing $\boldsymbol{v}, \boldsymbol{x}, \boldsymbol{u}$. Thus,

$$\left(\frac{\partial}{\partial t} + \boldsymbol{w}\cdot\frac{\partial}{\partial \boldsymbol{r}} - \beta\frac{\partial}{\partial \boldsymbol{w}}\cdot\boldsymbol{w}\right)P(\boldsymbol{w},\boldsymbol{r},t) = -\beta\frac{\partial}{\partial \boldsymbol{w}}\cdot\overline{\Delta\boldsymbol{u}}P \tag{2.310}$$

Using the LHDI or Furutsu–Novikov-based closures, similar to Equations 2.204 and 2.210, we have

$$\beta\overline{\Delta\boldsymbol{u}}P(\boldsymbol{r},\boldsymbol{w},t) = -\left(\frac{\partial}{\partial \boldsymbol{r}}\boldsymbol{\lambda} + \frac{\partial}{\partial \boldsymbol{w}}\cdot\boldsymbol{\mu} - \boldsymbol{\kappa}\right)P(\boldsymbol{r},\boldsymbol{w},t) \tag{2.311}$$

with similar expressions for $\boldsymbol{\lambda}$, $\boldsymbol{\mu}$, and $\boldsymbol{\kappa}$ as those given in Equation 2.205 (Furutsu–Novikov closure) or Equation 2.210 (LHDI) (with velocities and displacements replaced by relative velocities and displacements and the fluctuating force $\boldsymbol{f}$ replaced by $\beta\Delta\boldsymbol{u}(\boldsymbol{r}, t)$, noting that for the small-scale turbulence $\langle\Delta\boldsymbol{u}(\boldsymbol{r}, t)\rangle = 0$. To consider the kinetic equation used by Zaichik and Alipchenkov (2003), we can write Equation 6.311 alternatively as

$$\beta\overline{\Delta\boldsymbol{u}}P(\boldsymbol{r},\boldsymbol{w},t) = \left(-\boldsymbol{\lambda}^T\cdot\frac{\partial}{\partial \boldsymbol{r}} - \boldsymbol{\mu}^T\cdot\frac{\partial}{\partial \boldsymbol{w}}\cdot + \boldsymbol{\kappa} - \nabla\cdot\boldsymbol{\lambda}\right)P(\boldsymbol{r},\boldsymbol{w},t)$$

Zaichik and Alipchenkov (2003, 2007, 2009) assume that

$$\boldsymbol{\kappa} - \nabla\cdot\boldsymbol{\lambda} = 0 \tag{2.312}$$

which is only true in homogeneous turbulence without body forces. It ignores therefore the extra drift that arises because of particle segregation in inhomogeneous flows. However, bearing this in mind, we will consider the results Zaichik obtained from the specific solutions of the moment equations obtained from Equation 2.310 using 2.311 with the drift term set equal to zero and using specific forms for $\left\langle \Delta u_r^2(r) \right\rangle, \left\langle \Delta u_\theta^2(r) \right\rangle$. The momentum equations are similar to those in the 1D case (appropriate for the boundary layer) except that now with spherical symmetry (θ, ϕ) independence, there is a contribution from centrifugal forces. Thus, at equilibrium and for an isotropic stationary flow, using Equation 2.312,

$$-(\boldsymbol{S}_2^p + \boldsymbol{\lambda}^T) \cdot \nabla \langle \rho \rangle - \langle \rho \rangle \nabla \cdot \boldsymbol{S}_2^p = 0 \tag{2.313}$$

where $\boldsymbol{S}_2^p(\boldsymbol{r})$ is shorthand for $\langle \boldsymbol{w}(\boldsymbol{r}, t)\boldsymbol{w}(\boldsymbol{r}, t) \rangle$. Again, if we multiply this equation by β^{-1}, this can be interpreted as an equation representing a balance between diffusion and what we have called turbophoresis.

Referring to Equation 2.247, we have the transport equation for $\boldsymbol{S}_2^p$ as

$$\boldsymbol{S}_2^p = \frac{1}{\beta} \boldsymbol{\mu}^S - \nabla \cdot \langle \rho \rangle \boldsymbol{S}_3^p \tag{2.314}$$

where $\boldsymbol{S}_3^p = \left\langle \boldsymbol{w}(\boldsymbol{r},t)\boldsymbol{w}(\boldsymbol{r},t)\boldsymbol{w}(\boldsymbol{r},t) \right\rangle$. We note, however, that in this case we have spherical symmetry (independent of orientation) and consider only variation along the particle pair separation r, in which the turbophoretic drift, termed in Equation 2.313, along the line of centers of the particle pairs contains an effective component arising from the centrifugal force. Thus, using the same notation as that of Zaichik and denoting $\overline{w_r^2(r)}$ by $S_{2,ll}^p(r)$ and $\overline{w_\theta^2(r)}$ by $S_{2,nn}^p(r)$, the longitudinal component of the turbophoretic velocity (along the line of centers $\overline{w}_r$) is given by

$$\overline{w}_r = \beta^{-1} \left(\frac{2(S_{2,nn}^p - S_{2,ll}^p)}{r} - \frac{dS_{ll}^p}{dr} \right)$$

which then gives the following equation upon combining this term with the radial component of the first term in Equation 2.313:

$$\frac{2(S_{2,nn}^p - S_{2,ll}^p)}{r} - \frac{dS_{ll}^p}{dr} - (\lambda_{ll} + S_{2,ll}^p) \frac{d \ln \langle \rho \rangle}{dr} = 0 \tag{2.315}$$

If we define $\langle \rho \rangle = 1$ for $r \to \infty$, then $\langle \rho \rangle$ becomes the radial distribution $g(r)$. A separate equation for $S_{2,ll}^p$ and $S_{2,nn}^p$ based on Equation 2.314 using the C–E approximation for $\boldsymbol{S}_3^p$ (see Equation 2.248), together with the longitudinal momentum balance Equation 2.315, gives a final set of closed equations for $g(r)$, $S_{ll}^p(r)$, S_{nn}^p (see Zaichik and Alipchenkov, 2003, 2009) that can be solved with appropriate boundary conditions using measured forms for the longitudinal and transverse structure functions for turbulence and integral timescales. These equations in principle, encompass both the large and small scales of the turbulence. The empirical forms used by Zaichik cover both the dissipating range and subinertial range with pair separation scaling as the Kolmogorov length scale η_K and the Kolmogorov timescales τ_K. β^{-1} then becomes the Stokes number $St_K = (\beta\tau_k)^{-1}$. Interestingly, Bragg and Collins (2014a,b) show that ignoring the influence of the divergence terms in Equation 6.314 with $\boldsymbol{S}_2^p = \frac{1}{\beta} \boldsymbol{\mu}^S$ gives a +ve value for $\overline{w_r}$ indicating that the inward –ve drift responsible for clustering arises entirely from the divergence term associated with the third-order moment in Equation 2.314. Furthermore, a *+ve* drift would suggest that the net outward–inward radial pressure gradient is outweighed by the centrifugal force.

Figure 2.47 illustrates the influence of particle inertia measured by the value of Stokes number St_K (associated with the small-scale turbulence) on the mean absolute relative velocity $\langle |w_r| \rangle$ over a wide range of Stokes numbers St_K, $\langle |w_r| \rangle$ being defined in terms of the particle longitudinal structure function using the formula

$$\left\langle |w_r| \right\rangle = \left(\frac{2}{\pi} \langle w_r'^2 \rangle \right)^{1/2} = \left(\frac{2}{\pi} S_{ll}^p \right)^{1/2}$$

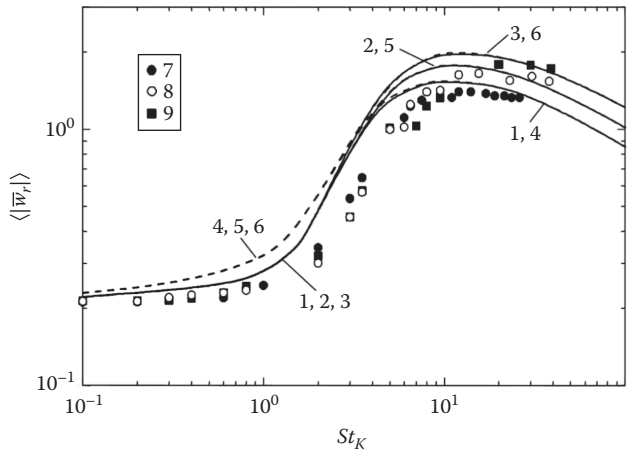


Figure 2.47

Influence of particle inertia St_K on the mean relative velocity magnitude $\langle|w_r|\rangle$ in units of $(\nu\varepsilon)^{1/4}$ for $r/\eta_K = 1$: 1–3, predictions with $r_C/\eta = 0$; 4–6, predictions with $r_C/\eta = 1$; 7–9, direct numerical simulation (Wang et al., 2000); 1, 4, 7, $Re_\lambda = 45$; 2, 5, 8, $Re_\lambda = 58$; 3, 6, 9, $Re_\lambda = 75$.

which assumes a Gaussian distribution for w_r. As is clear, both the predictions and the numerical simulations follow the same trend and indicate a pronounced maximum of $\langle|w_r|\rangle$ as a function of St_K. The initial rise in $\langle|w_r|\rangle$ is attributable to a decrease in the correlation of particle velocities with St_K manifested as RUM. The subsequent decay of $\langle|w_r|\rangle$ beyond the maximum results from a decrease in the particle fluctuating velocities, since the particles become more sluggish and less responsive to the fluid turbulence. Note the similarity to the deposition velocities k^+ as a function of τ^+ for particle deposition in turbulent pipe flow (see Figure 2.38). From Figure 2.47, it is also seen that the predictions with $rc/\eta_K = 1$ overestimate the DNS data at small Stokes numbers. The predictions that correspond to *ghost* particles lead to slightly smaller values of mean relative velocities at small St_K. However, a difference in the mean relative velocities of zero-size and finite-size particles takes place only for relatively small Stokes numbers and vanishes at large St_K.

Figure 2.48a shows the influence of Stokes number St_K on the radial distribution function (RDF) $g(r)$ for the separation $\overline{r} = r/\eta_K$ and Reynolds numbers Re_λ, corresponding to the DNS measurements of Wang et al. (2000). As expected, in the limiting cases of zero-inertia and high-inertia particles, the concentration field is statistically uniform, and so $g(r) = 1$. In accord with the computations, the predicted RDF passes through a peak as St_K increases. Thus, there exists a critical St_K that results in a maximum preferential concentration as simulations demonstrate (see Figure 2.44). Figure 2.48a shows a qualitative agreement between the predicted and simulated RDFs at particle contact, although the predicted effect

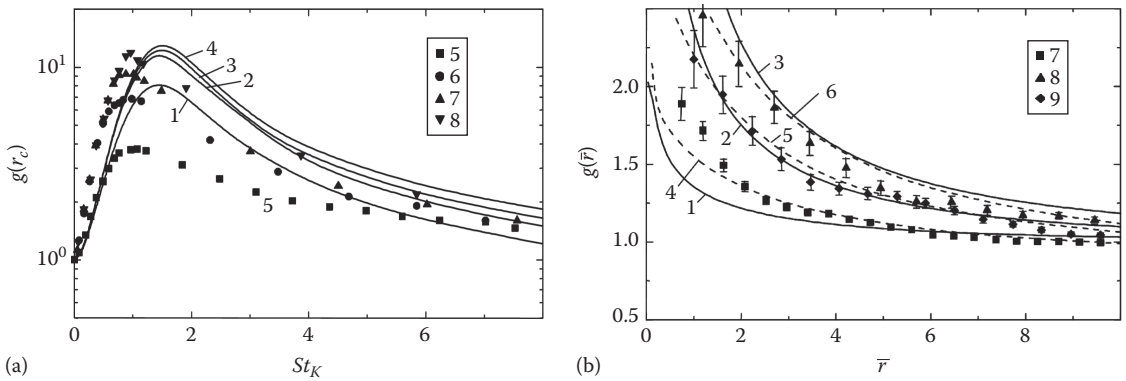


Figure 2.48

(a) RDF as a function of St_K for $r_c/\eta_K = 1$: 1–4, predictions; 5–8, direct numerical simulation (Wang et al., 2000); 1, 5, $Re_\lambda = 24$; 2, 6, $Re_\lambda = 45$; 3, 7, $Re_\lambda = 58$; 4, 8, $Re_\lambda = 75$. (b) RDF $g(r)$ as a function of particle pair separation $\overline{r} = r/\eta_K$: 1–3, predictions; 4–6, DNS (Salazar et al., 2008); 7–9, experiments (Salazar et al., 2008); 1, 4, 7, $St_K = 0.21$, $Re_\lambda = 108$; 2, 5, 8, $St_K = 0.4$, $Re_\lambda = 134$; 1, 4, 9, $St_K = 0.6$, $Re_\lambda = 147$.

of Re_λ is not as strong as it was in simulations and the maxima of $g(r)$ with St_K are slightly shifted toward particles with larger inertia.

2.5.6.8 Analytic Forms for S_2^p and RDF for Inertial Particles

Figure 2.48b shows good agreement of Zaichik and Alipchenkovs' (2009) (Z&A) predictions for the RDF of finite-size particles with low-inertia particles $St_K \lesssim 1$, with both the experimental measurements and DNS calculations of Salazar et al. (2008). In addition, Zaichik and Alipchenkov (2009) have obtained analytic expressions for the particle second-order structure functions $S^p_{2,ll}(r)$, $S^p_{2,nn}(r)$ and the RDF $g(r)$ as a function of St_K for low-inertia particles $St_K \lesssim 1$ with $r_c/\eta_K \ll 1$ as solutions of their closed set of equations for the momentum and kinetic stresses for the relative motion of particle pairs. In this case, the set of equations for ghost particles (overlapping spherical particle pairs) in the vicinity of the origin $\bar{r} = 0$ are solved without regard for bc's and the solutions are expressed in the form

$$S^p_{2,ll} = \alpha_l \bar{r}; \quad S^p_{2,nn} = \alpha_n \bar{r}; \quad g(\bar{r}) = C_g \bar{r}^{\chi} \tag{2.316}$$

in which the $S^p_{2,ll}$,S^p_{nn} coefficients α_l and α_n as well as the RDF exponent χ are functions St_K and Re_λ.

Figure 2.49* compares the exponent χ with DNS data for Re_λ = 47 and for Re_λ = 83, as well as with experimental and numerical data obtained in the range of Re_λ from 108 to 149. As is seen in Figure 2.49, the α_l coefficient and χ are well approximated if $St_K < 0.6$ and $Re_\lambda > 30$ by

$$\begin{aligned} \alpha_l &= \frac{1}{15} + 0.16St_K - 0.21St_K^2 + 0.18St_K^3 \\ \chi &= -6St^2 + 9.8St^3 - 6.2St^4 \\ C_g &= 1 + 12St_K^2 \end{aligned} \tag{2.317}$$

The predicted values of χ are in excellent agreement with DNS results (Chun et al., 2005), but they markedly overestimate those obtained by Salazar et al. (2008) and underestimate those given in Falkovich and Pumir (2007) for relatively large Stokes number.

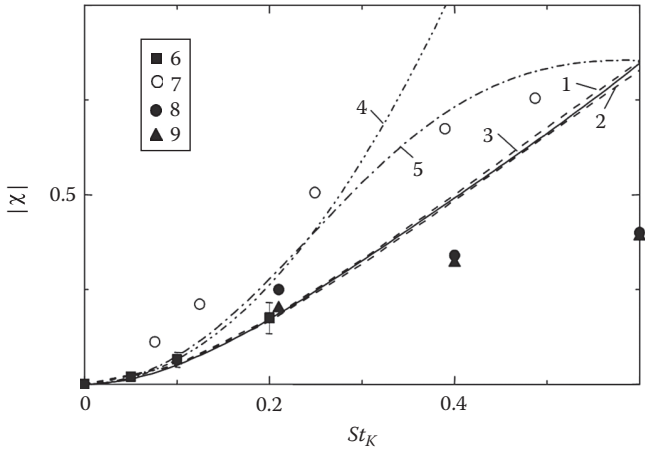


Figure 2.49

Effect of the Stokes number St_K on the power-law exponent of the RDF: 1 and 2, solutions to momentum and kinetic stresses (Equation 2.315) (for Re_λ = 30 and ∞); 3, 4, and 5, approximation equations (Zaichik and Aliphenkov, 2009; Chun et al., 2005) and (Derevyanko et al., 2008); 6, direct numerical simulation (DNS) (Chun et al., 2005); 7, DNS (Falkovich and Pumir, 2007); 8, experiment (Salazar et al., 2008); 9, DNS (Salazar et al., 2008).

* As Z&A point out, of great interest is the derivation of analytic solutions to the problem of preferential concentration of low-inertia particles at large Reynolds numbers as these exist in atmospheric conditions, because to date it is not possible to reach the atmospheric Reynolds number using DNS. Furthermore, the values of St_k and the particle size related to the Kolmogorov length scale for typical atmospheric aerosols and rain droplets are less than those realizable in both direct simulations and laboratory experiments.

Shown in Figure 2.49 is the theoretical dependence derived by Chun et al. (2005) for $St_K \ll 1$, namely,

$$\chi = -6.56St_K^2 \tag{2.318}$$

and the approximation obtained by Derevyanko et al. (2008) using the DNS data of Falkovich and Pumir (2004, 2007), namely,

$$\chi = -0.75St_K^2/(0.1 + St_K^3) \tag{2.319}$$

As can be observed, the dependences in Equations 2.316 and 2.317 correlate quite well with those given by Equations 2.316 at $St_K < 0.1$ are significantly greater when $St_K > 0.1$.

It is worth commenting on the agreement between the model predictions of Chun et al. (2005) in Equation 2.317 and that of Z&A's pdf results based on Equation 2.316, since the two approaches are seemingly very different and in the past have been the source of some controversy (Bragg and Collins, 2014a, Devenish et al., 2012). Only until recently has this agreement and lack of similarity in approach been properly explained [Bragg and Collins 2104a,b]. The probabilistic approach of Chun et al. (2005) is strictly limited to $St \ll 1$, which in essence treats the particles as passive scalars transported by their own velocity field $\boldsymbol{v}(\boldsymbol{r}, t)$ (in the case of two-particle dispersion, it is the relative particle velocity field between particles a distance r apart). The collision flux is modeled as the sum of two parts, namely, a *shear* diffusion flux $\boldsymbol{q}_D$, which depends on the mean concentration gradient of the satellite particles surrounding a target primary particle and a drift flux $\boldsymbol{q}_d$ that depends upon the local mean concentration of satellite particles and the compressibility of the relative particle velocity field. Explicitly for small Stokes numbers, where the concentration gradient is a small perturbation on the uniform concentration for passive tracers,

$$\boldsymbol{q}_i^D = -D_{ij}\frac{\partial\langle\rho\rangle}{\partial r_j}; \quad D_{ij}\int_{-\infty}^{t}\langle v_i(\boldsymbol{r},t)v_j(\boldsymbol{r},t|t')dt'$$

where

$v_j(\boldsymbol{r}, t|t')$ is the velocity of a particle at time t' that arrives at $\boldsymbol{r}$ at time t

D_{ij} is the dispersion coefficient for relative dispersion

and

$$\boldsymbol{q}^d = -\int_{-\infty}^{t}\langle \boldsymbol{v}(\boldsymbol{r},t)\nabla\cdot\boldsymbol{v}(\boldsymbol{r}^p(\boldsymbol{r},t|t'),t')dt'\langle\rho\rangle \tag{2.320}$$

which explicitly involves the divergence $\nabla\cdot\boldsymbol{v}(\boldsymbol{r}^p(\boldsymbol{r}, t)$ of the relative particle velocity field along a particle trajectory $\boldsymbol{r}^p(\boldsymbol{r}, t|t')$ that arrives at $\boldsymbol{r}$ at time t. We note that the form for the drift flux is the same as the form proposed by Maxey (1987) for the enhancement of drift due to gravity and the form derived by Reeks (2012) for particle dispersion in an inhomogeneous compressible flow field. In cases when $St_K \ll 1$, the particle pair equation of motion may be used to approximate $\boldsymbol{w}$ by

$$\boldsymbol{w} = \Delta\boldsymbol{u} - St_K\tau_K\boldsymbol{w}\cdot\nabla\boldsymbol{w} \tag{2.321}$$

Then substituting this in Equation 2.319, we obtain

$$\boldsymbol{w}_T = -\frac{1}{3}St_K\tau_K\boldsymbol{r}\left\langle S^2(\boldsymbol{x}^p(t),t) - R^2(\boldsymbol{x}^p(t),t)\right\rangle \tag{2.322}$$

where S^2 is shorthand for $\boldsymbol{S}$: $\boldsymbol{S}$,$\boldsymbol{S}(\boldsymbol{x}, t)$ being the local symmetric strain rate tensor and similar R^2 for $\boldsymbol{R}$: $\boldsymbol{R}$ $\boldsymbol{R}$ being the rotation tensor. From the force balance equation of Zaichik, we have:

$$\boldsymbol{w}_T = -St_\eta\tau_\eta\langle\rho\rangle\nabla\cdot\boldsymbol{S}_2^p$$

Bragg and Collins (2014a) have shown that using the energy equation for $\boldsymbol{S}_2^p$ and associated closure for $\boldsymbol{S}_3^p$ as Zaichik and Alipchenkov (2009) have done leads to the same expression as in Equation 2.321.

2.5.6.9 Collision Kernel Predictions

We recall the formula for the collision kernel given in Equation 2.279 that indicates the dependence upon two multiplicative factors, the RDF $g(r)$ (due to segregation/preferential concentration) and the collision speed $\langle|w_r|\rangle$, both of which are enhanced by the dependence on particle Stokes number St_K from their fluid tracer values, that is, $g(r)$ due to segregation and $\langle|w_r|\rangle$ due to inertial impaction at the collision surface, both peaking around $St_K \sim 1$. Assuming a Gaussian distribution of velocities w_r at the collision radius r_c and substituting the formulae given in Equations 2.315 for S_{ll}^p and $g(r_c)$, we obtain

$$\Gamma = \overline{r}\left(8\pi\alpha_l\right)^{1/2} C_g\left(\overline{r}_c\right)^{-\chi+3}\left(\frac{\eta_K^3}{\tau_K}\right) = \frac{r}{\eta_k} \tag{2.323}$$

Figure 2.50 shows the behavior of the collision rate predicted by the formula for Γ in Equation 2.322 as a function of the Stokes number $St_K < 0.6$ and collision radius r_c/η_K; in each case, $\Gamma(St_K)$ rises monotonically from the Stuart and Turner value at $St = 0$ for a passive scalar. The Z&A predictions compare favorably with the DNS results of Wang et al. (2001) for low-inertia particles. Figure 2.50 also shows the collision rate of Derevyanko et al. (2008), which accounts for segregation and singularities in the particle concentration (referred to as sling effects). In (60), the RDF exponent is specified by (43).

2.5.6.10 Particle Pair Dispersion RUM and Caustics

In this section, we examine in more detail the relationship between caustics and RUM and the way they have been quantified. In this regard, we refer specifically to the recent work of Bragg and Collins (2014b) who compared the pdf model of Zaichik and a more recent pdf model of Gustavsson and Mehlig (G&M) (Gustavsson and Mehlig, 2011) with DNS results in a Stokes number regime where the formation of caustics and the presence of RUM made a significant contribution to the particle pair structure function $S_{ll}^p(\overline{r})$. In Section 2.5.6.6, we described the observation first made by Fevrier et al. (2005) that the particle velocity field associated with a suspension of inertial particles in a turbulent flow could be split into two parts: a smoothly varying component (the mesoscopic particle velocity field, MEVPM) that was responsible for the finite spatial and temporal correlations of the particle motion and a totally RUM component. The extent to which these components contributed to the overall particle motion and in particular to the particles' kinetic energy that depended upon the particles Stokes number: for $St = 0$ the particle velocity was all derived from the MEPVF and for St

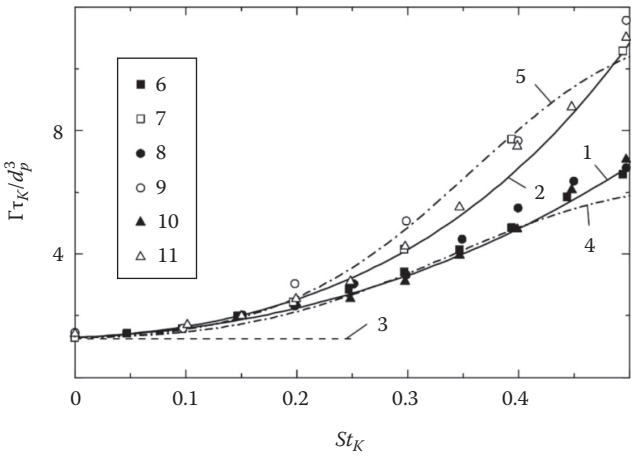


Figure 2.50

Effect of the Stokes number on the collision kernel Γ of low-inertia particles: 1 and 2, Equation 2.322; 3 (Saffman and Turner, 1956); 4 and 5 (Derevyanko et al., 2008); 1, 4, 6, 8, and 10, $r_c/\eta_k = 1$; 2, 5, 7, 9, and 11, $r_c/\eta_K = 0.5$; 6–11, direct numerical simulation (Zhou et al., 1998); 6, 7, $\mathrm{Re}_\lambda = 45$; 8 and 9, $\mathrm{Re}_\lambda = 59$; 10 and 11, $\mathrm{Re}_\lambda = 75$. Particle diameter $d_p = r_c$.

$\to \infty$ it was all RUM. It meant that the particle velocity at any one point in the field was not single valued, and particle trajectories could cross. Simonin et al. (2006) recognized that these features could be explained quite easily by a two-point statistical pdf approach. Thus, in the frame of reference of a moving particle, the RUM component represented the distribution of velocities that existed at point ignoring the fact that particles have a finite radius and could overlap (such particles being referred to as ghost particles). It is this RUM component that is responsible for particle collisions. Thus, according to this formalism, the total kinetic energy of the particulate phase is represented as the sum of the relevant contributions

$$k_p = \tilde{k}_p + \delta k_p$$

where $k_p = \tilde{k}_p + \delta k_p$ and δk_p are the mesoscopic-correlated and random-uncorrelated energy components. These two parts of the particle kinetic energy are expressed in terms of the second-order particle structure function S_{ll}^p as

$$\tilde{k}_p = \frac{S_{ii}^p(0) - S_{ii}^p(\infty)}{4} \quad k_p = \frac{S_{ii}^p(0) - S_{ii}^p(\infty)}{4} \tag{2.324}$$

Figure 2.51 shows the influence of St_K on the correlated (MEPVF) and uncorrelated (RUM) energy components as fractions of the total particle kinetic energy. As is clear, the model predictions obtained from the formulae in Equation 2.323 are in good agreement with the results of numerical simulations and follow the predicted asymptotic behavior with St_K. Compare these results with those shown earlier in Figure 2.45. We recall that RUM and the formation of caustics are intimately related. As an illustration we refer back specifically to the filamental network of caustics shown in Figure 2.44, where we remarked that within a caustic envelope particle trajectories cross one another. It happens because in any caustic there is a folding over of the particle phase space $\boldsymbol{v}, \boldsymbol{x}$ manifold so that particle trajectories double back on themselves, retracing their paths but in opposite directions similar to the motion of many particles distributed uniformly in a simple harmonic potential where at any one point there exists at least two velocities arising from particles traveling in opposite directions along the same trajectory. This feature is illustrated explicitly in Figure 2.52b showing a 2D caustic within which the particle velocities at any one point are multivalued. Outside of the caustic, the particle flow field is single valued corresponding to the smoothly varying mesoscopic velocity field (MEPVF) of FSS (Fevrier et al., 2005). The boundary between the single and multivalued flow fields defines the caustic envelope. The particle velocities within any one particular caustic are not random but are related to one another. It is only because the caustics themselves are randomly distributed in space and time that the particle motion associated with the caustics becomes random and uncorrelated at any one point fixed in space, that is, RUM. The RHS of Figure 2.52 shows the corresponding concentration of particles within the caustic where in the vicinity of the caustic envelope it is significantly enhanced.

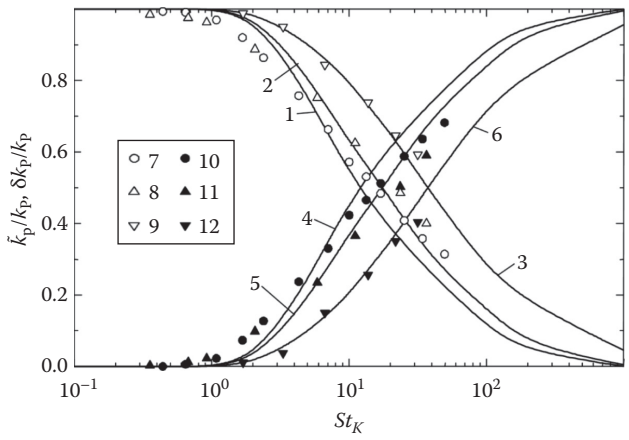


Figure 2.51

Effect of particle inertia on the mesoscopic Eulerian particle velocity field (1–3, 7–9) and random-uncorrelated (4–6, 10–12) components of the particle kinetic energy: 1–6, predictions; 7–12, direct numerical simulation (Fevrier et al., 2005); 1, 4, 7, and 10, $Re_\lambda = 52$; 2, 5, 8, and 11, $Re_\lambda = 67$; 3, 6, 9, and 12, $Re_\lambda = 134$.

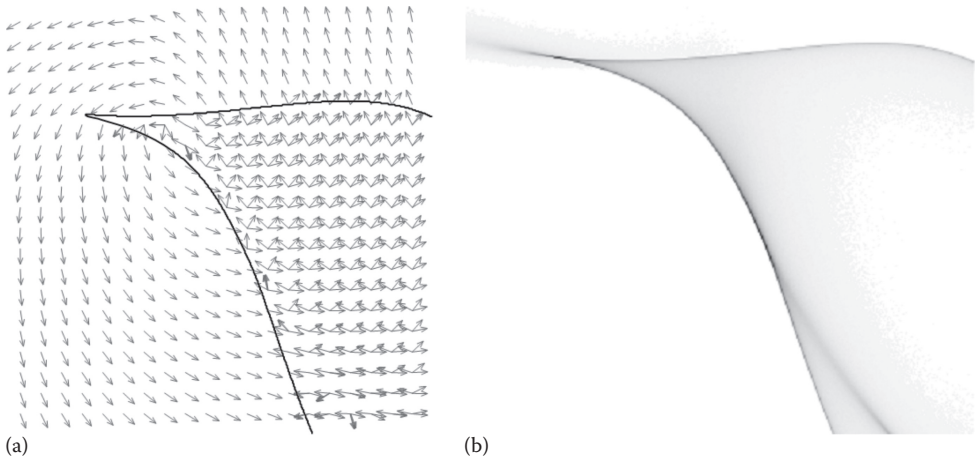


Figure 2.52

(a) Multivalued velocities of particles suspended in a 2D random flow with finite St_K. The orientation of the velocity is that of the arrow. All arrows have the same length (the magnitudes of the velocities are not shown). The blue line delineates the position of the caustics in the x–y-plane. The region of multivalued velocities ends in a cusp that is only approximately resolved. (b) Corresponding particle density in the *x*–*y*-plane, showing significantly enhanced particle number density in the vicinity of the caustic line. Black corresponds to high density and white to low density.

Indeed, the caustic envelope is a line of singularities in the particle concentration being the points at which the particle trajectories are at their extremities and turn back on themselves. The particle trajectories in these circumstances are nonlocal, with the particles possessing a memory of their history of the previous encounters with turbulent eddies. Bragg and Collins (2014b) refer to this as "scale breaking," the particle motion being more associated with the scaling of the inertial subrange and to dependence on Re_λ rather than the dissipating scales in the vicinity of the collision surface. It is this feature that greatly enhances the possibility of particles colliding with one another.

Further insights into the occurrence of caustics on the way they scale and depend on St_K can be inferred from the form of the particle structure function $S_{ll}^p(r)$ as a function of separation based on the predictions by Bragg and Collins (2014b) using Zaichik's pdf model shown in Figure 2.53 for three different Stokes

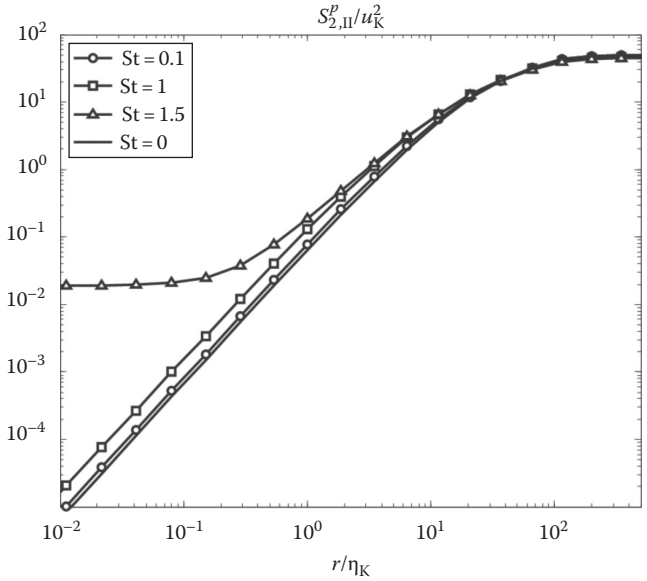


Figure 2.53

The predictions of Bragg and Collins (2014b) on Zaichik's probability density function model predictions of the particle velocity structure function.

numbers St_k. We note that for each value of St_K, $S^p_{2,ll} \geq S^f_{2,ll}$ (the fluid structure functions corresponding to $St_K = 0$) for $r/\eta_k \lesssim 10$, which must be entirely due to nonlocal effects of the particle pair relative motion arising from the contribution of the gradient of the third-order energy flux moment in Equation 2.314. In the case of $St_K = 1.5$, there are clearly two distinct regions for $S^p_{2,ll}$, a power-law region for $r/\eta_K > 0.3$ and a plateau region at smaller separations that follows, resulting in a nonzero intercept for $S^p_{2,ll}$ in the limit $r \to 0$. This is similar to the behavior of depositing particles in a turbulent boundary layer where we recall that particles may start out in local equilibrium far away from the wall but their inability to follow the steep changes in the fluid velocity means that at any point the particles have some memory of their previous history—their velocity has more to do with where they came from than what is happening to the fluid motion locally. The region over which $S^p_{2,ll}(r)$ is roughly constant and significantly different from its local is roughly constant is known as the free flight to the wall region in the particle–wall deposition models. At larger separations, $S^p_{2,ll} \leq S^f_{2,ll}$, implying that the particle's relative motion is growing increasingly local with increasing separation, the form of Δu becomes statistically independent of separation at the integral scales of the turbulence. Moreover, at large separations, the particles become independent of each other, causing the structure function to approach twice the kinetic energy of the particles, a decreasing function of the particle Stokes number due to the filtering effect of particle inertia (Fevrier and Simonin, 1998, Fevrier et al., 2005). Note that all of these trends qualitatively match those found in the DNS study of Salazar and Collins (2012).

Bragg and Collins (2014b) have compared their DNS results based on Zaichik's kinetic equation–based model predictions with that of the theory of G&M (Gustavsson and Mehlig, 2011), which focuses on the existence of caustics and the link they have between RUM and the smoothly varying mesoscopic component and the particle structure function. They use a pdf equation for the particle pair separation and relative velocity; however, Δu is approximated so that the pdf equation they derive is a classical Fokker–Planck equation ($\lambda = 0$, in the kinetic equation of Zaichik) and is therefore only strictly valid for $S_K \ggg 1$. From this, they construct approximate analytical expressions for the moments of the pdf in the dissipation range of the form

$$m_N = f_N \left(\frac{r}{\eta_K} \right)^{N+D_2-1} + g_N \left(\frac{r}{\eta_K} \right)^{d-1} \tag{2.325}$$

where

the subscript N refers to the order of the moment
D_2 is the phase space correlation dimension
d is the physical space dimension (i.e., $d = 3$ for a 3D flow)

The first term on the rhs of Equation 2.325 describes the smooth part of the relative velocity moment and the second term describes the caustic (RUM) contribution, that is, that associated with the nonlocal particle dynamics. The theory is unclosed since $f_N(St_K)$ and $g(St_K)$ are unknown functions (as in D2), although they state that their numerical results imply that $g_N(St_K)$ is of an activated form (i.e., modeled using an Arrhenius rate expression, in which the Stokes number plays the role of temperature in the classical expression). The influence of Re_λ in the G&M theory would be contained in its effect upon the unspecified variables f_N, g_N, and D_2. The particle second-order structure function is found from Equation 2.325 by $S^p_{2,ll} = m_2/m_0$ and for small r/η_K $m_0(r) \propto r^{d_2}$, where $d_2 = min,[D_2,d]$ is the configuration space correlation dimension, which then gives

$$S^p_{2,ll} = \frac{f_2}{f_0} \left(\frac{r}{\eta_K} \right)^2 + \frac{g_2}{f_2} \left(\frac{r}{\eta_K} \right)^{d-d_2} \tag{2.326}$$

In comparing the two theories for caustics and clustering, the case for $St = 1$ is revealing. The results in Bec et al. (2011) (for $d = 3$) show that $d_2(St_K = 1) \approx 2.3$, which implies that for $St = 1$ both contributions in (2.325) tend to zero as $r \to 0$. In other words, this does not allow for the simultaneous existence of small-scale clustering (i.e., $d < d$) and finite relative velocities at $r/nK = 0$. This is in contrast to Zaichik's model predictions and the DNS results (Salazar and Collins, 2012) (Figure 2.50).

In light of this, Zaichik's pdf kinetic equation can be considered to describe S2p $S^p_{2,ll}(r/\eta_K)$ in three regions, which depend upon St_K). The first two regions are qualitatively similar to those in the G&M model: a region of large separation where the effect of inertia is perturbative and locally dependent on $\Delta u(r/\eta_K)$ so that $S^p_{2,ll}/S^f_{2,ll}$ is independent of r and then at smaller separations a smooth transition to a nonsmooth region with $S^p_{2,ll}(r/\eta_K) \propto (r/\eta_K)^{-2}$. However, Zaichik's pdf model, unlike the G&M model, predicts that at sufficiently small r/η_K a third region exists in which the particle motions are entirely ballistic and $S^p_{2ll} \approx$ constant (this is the region that gives rise to the scale break). Bragg and Collins suggest that a possible explanation for this difference between the theories is that in the derivation of the G&M model equation, G&M make an a priori assumption that the clustering is always fractal, thus ruling out the possibility of a scale break at small r/η_K by definition. In fact, it is possible to show that Zaichik's model gives the same scaling predictions as that of the G&M model under the a priori assumption that $g(r) \propto r^{d_2-d}$ (Bragg and Collins, 2014b).

References

Abrahamson, J., Collision rates of small particles in a vigorously turbulent fluid, *J. Chem. Eng. Sci.,* 30, 1371–1379, 1992.

Balkovsky, E., Falkovich, G., and Fouxon, A., Intermittent distribution of inertial particles in turbulent flows, *Phys. Rev. Lett.,* 86, 2790–2793, 2001.

Bec, J., Biferale, J.L., Cencini, M., Lanotte, A.S., and Toschi, F., Spatial and velocity statistics of inertial particles in turbulent flows, *Phys. Conf. Ser.*, 333–345, 2011.

Boelle, A., Balzar, G., and Simonin, O., Second-order prediction of the particle-phase stress tensor of inelastic spheres in simple shear dense suspensions, *Proc. 6th Int. Symp. on Gas-Solid Flows, ASME FED,* Vol. 228, pp. 9–18, 1995.

Bragg, A., Swailes, D.C., and Skartlien, R., Particle transport in a turbulent boundary layer: Non-local closures for particle dispersion tensors accounting for particle-wall interactions, *Phys. Fluids,* 24, 103304, 2012a.

Bragg, A., Swailes, D.C., and Skartlien, R., Drift-free kinetic equations for turbulent dispersion, *Phys. Rev. E,* 86, 056306, 2012b.

Bragg, A.D. and Collins, L.R., New insights from comparing statistical theories for inertial particles in turbulence: II. relative velocities, *New J. Phys.,* 16, 055014, 2014a.

Bragg, A.D. and Collins, L.R., New insights from comparing statistical theories- for inertial particles in turbulence: I spatial distribution of particles, *New J. Phys.*, 16, 055013, 2014b.

Buyevich, Y., Statistical hydromechanics of disperse systems. part 1. physical background and general equations, *J. Fluid Mech.,* 49, 489–507, 1971.

Buyevich, Y., Statistical hydromechanics of disperse systems. part 2. solution of the kinetic equation for suspended particles, *J. Fluid Mech.,* 52, 345–355, 1972a.

Buyevich, Y., Statistical hydromechanics of disperse systems. part 3. pseudo-turbulent structure of homogeneous suspensions, *J. Fluid Mech.,* 56, 313–336, 1972b.

Chen, L., Goto, S., and Vassilicos, J.C., Turbulent clustering of stagnation points and inertial particles, *J. Fluid Mech.*, 553, 143–154, 2006.

Chun, J., Koch, D.L., Rani, S., Ahluwalia, S., and Collins, L.R., Clustering of aerosol particles in isotropic turbulence, *J. Fluid Mech.,* 536, 219–251, 2005.

Corrsin, S., Limitations of gradient transport models limitations of gradient transport models in random walks and in turbulence, *Adv. Geophys.*, 18(A), 25–60, 1974.

Crowe, C.T., Chung, J.N., and Troutt, T.R., Particle dispersion by organized structures, Chapter 18, in M.C. Roco (Ed.), *Particulate Two-Phase Flow,* Heinemann, Oxford, U.K., Vol. 626, 1993, pp. 1–1.

Crowe, C.T., Schwarzkopf, J.D., Sommerfeld, M., and Tsujii, T., *Multiphase Flow with Droplets and Particles*, CRC Press, 2nd edition, Taylor and Francis group, 2012.

Csanady, G.T., Turbulent diffusion of heavy particles in the atmosphere, *J. Atmos. Sci.,* 2, 201–208, 1963.

Daly, B.J. and Harlow, F.H., Transport equations in turbulence, *Phys. Fluids,* 13, 2634, 1970.

Darbyshire, K.F.F. and Swailes, D.C., A pdf model for particle dispersion with stochastic particle-surface interactions, fed-236, gas-solid flows, in *FED-236, Gas-Solid Flows, ASME*, Hilton Head S. Carolina, USA, 1996, pp. 51–56.

Derevich, I. and Zaichik, L., Particle deposition from a turbulent flow, *Fluid Dynamics*, 23(5), 722–729, 1988.

Derevich, I.V., Statistical modelling of mass transfer in turbulent two-phase dispersed flows 1. model development, *Int. J. Heat Mass Transfer,* 43, 3709–3723, 2000.
Derevich, I.V. and Zaichik, L.I., An equation of probability density of velocity and temperature of particles in a turbulent flow modeled by a random gaussian field, *Appl. Math. Mech.,* 54, 631–637, 1990.
Derevyanko, S., Falkovich, G., and Turitsyn, S., Sling effect in collisions of water droplets in clouds, *New J. Phys.,* 10, 075019, 2008.
Devenish, B.J., Bartello, P., Brenguier, J.-L., Collins, L.R., Grabowski, W.W., Ijz-ermans, R.H.A., Malinowski, S.P. et al., Droplet growth in warm turbulent clouds. *Quart. J. R. Meteorol. Soc.,* 138(667), 1401–1429, 2012.
Devenish, B.J., Swailes, D.C., and Sergeev, Y.A., A pdf model for dispersed particles with inelastic particle-wall collisions, *Phys Fluids,* 11(7), 1858–1868, 1999.
Einstein, A., On the theory of brownian motion, *Ann, d. Physik,* IV, 549, 1905.
Falkovich, G., Fouxon, A.S., and Stepanov, M.G., Acceleration of rain initiation by cloud turbulence, *Nature,* 419, 151–154, 2002.
Falkovich, G. and Pumir, A., Intermittent distribution of heavy particles in a turbulent flow, *Phys. Fluids,* 16(7), L47–L50, 2004.
Falkovich, G. and Pumir, A., Sling effect in collisions of water droplets in turbulent clouds, *J. Atmos. Sci.,* 64, 4497–4505, 2007.
Fessler, J.R., Kulick, J.D., and Eaton, J.K., Preferential concentration of heavy particles in a turbulent channel flow, *Phys. Fluids,* 6(11), 3742–3749, 1994.
Fevrier, P. and Simonin, O., Constitutive relations for fluid-particle velocity correlations in gas-solid turbulent flows, in *Third International Conference on Multiphase Flows, ICMF'98, Lyon, France, June 8–12,* 1998.
Fevrier, P. and Simonin, O., Statistical and continuum modelling of turbulent reactive particulate flows. Part 2: Application of a two-phase second-moment transport model for prediction of turbulent gas-particle flows, in *Theoretical and Experimental Modeling of Particulate Flows*, Lecture Series 2000-06, von Karman Institute for Fluid Dynamics, Rhode Saint Genèse (Belgium), 2000.
Fevrier, P., Simonin, O., and Squires, K.D., Partitioning of particle velocities in gas-solid turbulent flows into a continuous field and a spatially uncorrelated random distribution; theoretical formalism and numerical study, *J. Fluid Mech.,* 533, 1–46, 2005.
Furutsu, K., On the theory of radio wave propagation over inhomogeneous earth, *J. Res. Natl. Bur. Stand., Sect. D,* 67, 39–62, 1963.
Grad, H., On the kinetic theory of rarefied gases, *Commun. Pure Appl. Math.,* 2(4), 331–407, 1949.
Gustavsson, K. and Mehlig, B., Distribution of relative velocities in turbulent aerosols, *Phys. Rev. E,* 83, 045304, 2011.
Haworth, D.C. and Pope, S.B., A generalized langevin model for turbulent flow, *Phys Fluids,* 29, 387–405, 1986.
He, J. and Simonin, O., Non-Equilibrium prediction of the particle-phase stress tensor in vertical pneumatic conveying, in *Gas-Solid Flows-1993, ASME FED*, Vol. 166, pp. 253–263, 1993.
Hishida, K. and Maeda, M., Turbulent characteristics of gas-solid two-phase confined jet: Effect of particle density, in *Fifth Workshop on Two Phase Flow predictions: Proceedings*, *Erlangen*, Germany, *March 19–22*, 1990.
Hyland, K.E., Reeks, M.W., and McKee, S., Derivations of a pdf kinetic equation for the transport of particles in turbulent flow, *J. Phys: Math Gen.,* 32, 6169–6190, 1999a.
Hyland, K.E., Reeks, M.W., and McKee, S., Exact analytic solutions to turbulent particle flow equations, *Phys. Fluids,* 11, 1240–1261, 1999b.
Jenkins, J.T. and Richman, M.W., Grad's 13-moment system for a dense gas of inelastic spheres, *Arch. Ration. Mech. Anal.,* 87, 355–377, 1985.
Lavieville, J., Numerical simulations and modelling of interactions of turbulence dragging and inter-particle collisions applied to gas-solid two phase flows, *These de Doctorat de l'Universite de Rouen,* Rouen, France, 1997.
Lavieville, J., Deutsch, E., and Simonin, O., Large eddy-simulation of interaction between colliding particles and a homogeneous isotropic turbulence field, in *Proceedings of the Sixth International Symposium on Gas-Particle Flows, ASME FED,* San Francisco, USA, Vol. 8, pp. 347–357, 1995.
Lavieville, J., Simonin, O., Berlemont, A., and Chang, Z., Validation of inter-particle collision models based on large-eddy simulation in gas-solid turbulent homogeneous shear, in *Proceedings of the Seventh International Symposium on Gas-Particle Flows, ASME Fluids Engineering Division Summer Meeting, FEDSM97,* Vancouver, Canada, 1997, pp. 3623–3627.

Li, A. and Ahmadi, G., Dispersion and deposition of spherical particles from point sources in turbulent channel flow, *Aerosol Sci. Tech.,* 16(4), 209–226, 1992.

Li, Y. *and Zhou*, Z.X., *A k-e model for simulating gas-particle flows*, i*n* M. Sommerfeld (Ed.), *Sixth Erlangen-Merseburg Workshop on Two-Phase Flow Predictions,* Merseburg, Germany, May 1996.

Masi, E., Theoretical and numerical study of the modeling of unsteady non-isothermal particle-laden turbulent flows by an eulerian-eulerian approach, *PhD thesis, Institut National Polytechnique de Toulouse (2010). http://ethesis.inp-toulouse.fr/archive/00001256/01/masi.pdf,* 2010.

Masi, E., Riber, R., Sierra, P., Simonin, O., and Gicquel, L.Y.M., Modeling of the random uncorrelated velocity stress tensor for unsteady eulerian simulation in turbulent flows, *Proceedings of the 7th International Conference on Multiphase Flow (ICMF).* Tampa, FL, May 2010.

Masi, E., Simonin, O., and Bedat, B., The mesoscopic eulerian approach for evaporating droplets interacting with turbulent flows, *Flow Turbul. Combust*., 86, 563–583, 2011.

Maxey, M.R., The gravitational settling of aerosol particles in homogeneous turbulence and random flow fields, *J. Fluid Mech.,* 174, 441–465, 1987.

Moreau, M., Fede, P., Simonin, O., and Villedieu, P., Monte carlo simulation of colliding particles suspended in gas-solid homogeneous turbulent shear flows. *Proceedings of FEDSM034TH ASME-JSME Joint Fluids Engineering Conference*, Honolulu, HI, July 6-10,2003, paper FEDSM2003-45736, 2003.

Moreau, M., Fede, P., Simonin, O., and Villedieu, P., Stochastic lagrangian modelling and monte carlo simulation of collisions in gas-solid homogeneous shear turbulent flows. *5th International Conference on Multiohase Flow*, Paper no 426, ICMF2004 Yokohma, Japan, May 30–June 4, 2004.

Novikov, E.A., Functional and the random-force method in turbulence theory, *Soviet Phys. JETP,* 20, 1290–1294, 1965.

Oesterle, B. and Petitjean, A., Simulation of particle-to-particle interactions in gas-solid flows, *Int. J. Multiphase Flow,* 19, 199–211, 1993.

Pandya, R.V.R and Mashayek, F., Probability density functions modeling of evaporating droplets dispersed in isotropic turbulence, *AIAA J.,* 29(1), 561–568, 2001.

Pozorski, J. and Minier, J.-P., Probability density function modelling of dispersed two-phase turbulent flows, *Phys. Rev. E,* 59(1), 855–863, 1998.

Reeks, M.W., On the dispersion of small particles in an isotropic turbulent flow, *J. Fluid Mech.,* 83, 529–546, 1977.

Reeks, M.W., Eulerian direct interaction applied to the statistical motion of particle, *J. Fluid Mech.,* 83, 529–546, 1980.

Reeks, M.W., The transport of discrete particles in inhomogeneous turbulence, *J. Aerosol Sci.,* 14(6), 729–739, 1983.

Reeks, M.W., On a kinetic equation for the transport of particles in turbulent flows, *Phys. Fluids,* 15, 446–456, 1991.

Reeks, M.W., On the continuum equations for dispersed particles in non uniform flows, *Phys. Fluids,* 446, 1290–1303, 1992.

Reeks, M.W., On the constitutive relations for dispersed particles in nonuniform flows. i: Dispersion in a simple shear flow, *Phys. Fluids,* 5(3), 750–761, 1993.

Reeks, M.W., On probability density function equations for particle dispersion in a uniform shear flow, *J. Fluid Mech.,* 522, 263–302, 2005.

Reeks, M.W., Particle drift in turbulent flows: The influence of local structure and inhomogeneity, *arXiv: 1205.2731v3,* 2012.

Reeks, M.W., The transport of discrete particles in inhomogeneous turbulence, *J. Aerosol Sci*., 14(6), 729–739, 1983.

Reeks, M.W. and Hall, D., Kinetic models for particle resuspension in turbulent flows: theory and measurement, *J. Aerosol Sci*., 32, 31–39, 2001.

Reeks, M.W., Reed, J., and Hall, D., On the resuspension of small particles by a turbulent flow, *J. Phys D: App. Phys.,* 21, 574–589, 1988.

Reeks, M.W. and Swailes, D.C., The near wall behaviour of particles in a simple turbulent flow with gravitational settling and partially absorbing wall, *J. Fluid Mech. Res*., 22(2), 31–39, 1997.

Rogers, C.B. and Eaton, J.K., The behavior of solid particles in a vertical turbulent boundary layer in air, *Int. J. Multiphase Flow,* 16(5), 819–834, 1963.

Saffman, P.G., and Turner, J.S., On the collision of drops in turbulent clouds, *J. Fluid Mech.,* 1(1), 16–30, 1956.

Salazar, J.P.L.C. and Collins, L.R., Inertial particle acceleration statistics in turbulence: effects of filtering, biased sampling and flow topology, *Phys. Fluids,* 24, 083302, 2012.

Salazar, J.P.L.C., de Jong, J., Woodward, S.H., Meng, H., and Collins, L.R., Dissipation rate estimation from piv in zero-mean isotropic turbulence, *J. Fluid Mech.,* 600, 245–256, 2008.

Sikovsky, D.P., Singularity of inertial particle concentration in the viscous sublayer of wall-bounded turbulent flows, in *International Conference on Turbulence Heat and Mass Transfer 2012, Palermo, Italy,* 2013, pp. 51–56.
Simonin, O., Prediction of the dispersed phase turbulence in particle-laden jets, in *Gas-Solid Flows-1991*, ASME FED, Vol. 121, pp. 197–206, 1991.
Simonin, O., Statistical and continuum modelling of turbulent reactive particulate flows part I: Theoretical derivation of dispersed phase eulerian modelling from probability density function kinetic equation, in *Combustion and Turbulence in Two- Phase Flows, 1995–1996 Lecture Series Programme, von Karman Institute for Fluid Dynamics, Belgium*, Europe, 1996a.
Simonin, O., Statistical and continuum modelling of turbulent reactive particulate flows part II: Application of a two-phase second-moment transport model, in *Combustion and Turbulence in Two-Phase Flows, 1995–1996 Lecture Series Programme, von Karman Institute for Fluid Dynamics, Belgium*, Europe, 1996b.
Simonin, O., Deutch, E., and Minier, J.-P., Eulerian prediction of the fluid/particle correlated motion in turbulent two-phase flows, *Appl. Sci. Res.,* 51, 275–283, 1993.
Simonin, O., Février, P., and Laviéville, J., On the spatial distribution of heavy-particle velocities in turbulent flow: From continuous field to particulate chaos, *J. Turbulence*, 3(40), 2002.
Simonin, O., Zaichik, L.I., Alipchenkov, V.M., and Fevrier, P., Connection between two statistical approaches for the modelling of particle velocity and concentration distributions in turbulent flows: The Mesoscopic Eulerian Formalism and the two-point PDF method, *Phys. Fluids,* 18, 125107 (9 pages), 2006.
Soldati, A., Physics and modelling of turbulent particle deposition and entrainment: Review of a systematic study, *Int. J. Multiphase Flow*, 35(9), 827–839, 2009.
Sommerfeld, M., The importance of inter-particle collisions in horizontal gas-solid channel flows, in *Procedings of the Sixrh International Symposium on Gas-Solid Flows, ASME FED,* Vol. 228, 1995, pp. 335–345.
Squires, K.D. and Eaton, J.K., Measurements of particle dispersion obtained from direct numerical simulations of isotropic turbulence, *J. Fluid Mech.,* 226, 135, 1991.
Stock, D.E., Particle dispersion in flowing gases-1994 freeman scholar lecture, *J. Fluids Eng.*, 30, 4–17, 1996.
Sundaram, S. and Collins, L.R., Collision statistics in an isotropic particle-laden turbulent suspension. part 1. direct numerical simulations, *J. Fluid Mech.,* 335, 75–109, 1997.
Swailes, D.C. and Darbyshire, K.F.F., A generalised fokker-planck equation for particle transport in random media physica, *Phys. A*, 242, 38–48, 1997.
Swailes, D.C., Derbyshire, K.F.F., and Reeks, M.W., Analysis of particle dispersion using a pdf equation; results for simple shear and rotating flows, in *Gas-Particle Flows ASME Summer Meeting,* ASME FED-Vol. 228, Hilton Head Island, SC, August 1995, pp. 257–263.
Swailes, D.C. and Reeks, M.W., Particle deposition from a turbulent flow: A steady-state model for high inertia particles, *Phys. Fluids*, 6, 3392, 1994.
Swailes, D.C., Sergeev, Y.A., and Parker, A., Chapman–enskog closure approximation in the kinetic theory of dilute turbulent gas-particulate suspensions, *Phys. A: Stat. Mech. Appl.,* 254(3–4), 517–547, 1998.
van Dijk, P. and Swailes, D.C., Hermite-dg methods for pdf equations modelling particle transport and deposition in turbulent boundary layers, *J. Comp. Phys.,* 231(14), 4094–4920, 2012.
Wang, L.P., Wexler, A.S., and Zhou, Y., Statistical mechanical description and modelling of turbulent collision of inertial particles, *J. Fluid Mech.,* 415, 117–153, 2000.
Wang, L.P., Wexler, A.S., and Zhou, Y., Modelling turbulent collision of bidisperse inertial particles, *J. Fluid Mech.,* 433, 77–104, 2001.
Wells, M.R. and Stock, D.E., The effects of crossing trajectories on the dispersion of particles in a turbulent flow, *J. Fluid Mech.,* 136, 31–62, 1983.
Wilkinson, M., Mehlig, B., Östlund, S., and Duncan, K.P., Unmixing in random flows, *Phys. Fluids,* 19, 113303, 2007.
Zaichik, L.I., Simulation of particle diffusion, segregation, and intermittency in turbulent flows, in *Eighth International Symposium on Turbulent Shear Flows, Technical University of Munich,* Munich, Germany, 1991, pp. 10-2-1–10-2-6.
Zaichik, L.I., Modelling the motion of particles in non-uniform turbulent flow using the equation for its probability function, *Appl. Math. Mech.,* 61, 127–133, 1997.
Zaichik, L.I., A statistical model of particle transport and heat transfer in turbulent shear flows, *Phys. Fluids,* 11, 1521–1543, 1999.
Zaichik, L.I. and Alipchenkov, V.M., Simulation of transport of colliding particles suspended in turbulent shear flows, in *Proceedings of the Second International Symposium on Turbulence, Heat and Mass Transfer*, 1997, pp. 823–832.

Zaichik, L.I. and Alipchenkov, V.M., Pair dispersion and preferential concentration of particles in isotropic turbulence, *Phys. Fluids,* 15(6), 1776–1787, 2003.
Zaichik, L.I. and Alipchenkov, V.M., Refinement of the probability density function model for preferential concentration of aerosol particles in isotropic turbulence, *Phys. Fluids,* 19, 113308, 2007.
Zaichik, L.I. and Alipchenkov, V.M., Statistical models for predicting pair dispersion and particle clustering in isotropic turbulence and their applications, *New J. Phys.*, 11, 103018, 2009.
Zaichik, L.I., Drobyshevsky, N.I., Filippov, A.S., Mukin, R.V., and Strizhov, V.F., A diffusion-inertia model for predicting dispersion and deposition of low-inertia particles in turbulent flows, *Int. J. Heat Mass Transfer,* 53, 154–162, 2010.
Zaichik, L.I., Oesterle, B., and Alipchenkov, V.M., On the probability density function model for the transport of particles in anisotropic turbulent flow, *Phys. Fluids,* 16, 1956–1964, 2004.
Zaichik, L.I. and Simonin, O., Connection between two statistical approaches for modelling of particle velocity and concentrations distributions in turbulent flow: The mesoscopic eulerian formalism and the two-point probability density function method, *Phys. Fluids,* 18, 125107, 2006.
Zaichik, L.I., Simonin, O., and Alipchenkov, V.M., Two statistical models for predicting collision rates of inertial particles in homogeneous isotropic turbulence, *Phys. Fluids,* 15(10), 2995–3005, 2003.
Zaichik, L.I., Simonin, O., and Alipchenkov, V.M., Collision rates of bidisperse inertial particles in isotropic turbulence, *Phys. Fluids*, 18, 035110 (13 pages), 2006.
Zaichik, L.I., Sinaiski, E.G., and Alipchenkov, V.M., Collisions of particles in turbulent flow, Chapter 4, in *Particles in Turbulent Flows*, Wiley-VCH, 2008.
Zhang, F., Reeks, M., and Kissane, M., Particle resuspension in turbulent boundary layers and the influence of non-gaussian removal forces, *J. Aerosol Sci.,* 58, 103–128, 2013.
Zhang, F., Reeks, M.W., Kissane, M., and Perkins, R.J., Resuspension of small particles from multilayer deposits in turbulent boundary layers, *J. Aerosol Sci.,* 66, 31–61, 2013.
Zhou, Y., Wexler, A.S., and Wang, L.P., On the collision rate of small particles in isotropic turbulence, ii. finite inertia case, *Phys. Fluids,* 10(10), 1206–1216, 1998.

2.6 Euler–Lagrange Methods

Martin Sommerfeld and Santiago Lain

2.6.1 Introduction

Particle-laden confined two-phase flows are widely found in the processing industries; typical examples are pneumatic conveying, pneumatic mixing devices, fluidized beds, and particle separation equipment, such as gas cyclones. Pneumatic conveying is widely used in these areas for transporting fine powders within a production process over large distances and to convey pulverized coal in power plants. Depending on the application, different conveying regimes are used, such as dense- and dilute-phase conveying. Essential for the design of such systems is the pressure drop as a function of superficial gas velocity. This pressure drop is composed of the gas-phase pressure drop, which is quite well known already for different pipe elements, and the additional pressure drop due to particle transport. The single-phase pressure loss depends on the wall friction coefficient and hence on the flow Reynolds number and the wall roughness. For an entire pipe system, the contributions of the different elements (e.g., straight pipes, pipe bends, and/or constrictions) have to be added. For the additional pressure loss of the particles also, different contributions may be identified, namely, pressure loss caused by particle–wall friction (i.e., resulting from the momentum loss due to particle–wall collisions), pressure loss due to particle lifting in vertical conveying, and pressure loss due to particle acceleration upon injection or after a bend; hence, the particle contribution is strongly governed by the pipe geometry considered. In addition, the particle-phase pressure drop remarkably depends on pipe material and diameter, particle size, shape and material, wall roughness (since it is strongly correlated with the particle–wall collision frequency, see Sommerfeld, 2003), as well as particle-phase mass loading η, defined as the ratio between the particle mass flow rate and the gas mass flow rate. As a result of this complexity, universal correlations for the pressure drop as a function of conveying velocity are not available and normally experiments are required to develop such correlations as emphasized by Siegel (1991) resulting in an empirical design of pneumatic conveying systems. Quite often, phase diagrams are used to correlate the pressure drop with the superficial gas velocity and the particle mass loading as a parameter. Such experimental phase diagrams unfortunately depend on parameters such as pipe diameter, particle size, or size distribution, which implies that conveying of another type of particles requires conducting new measurements.

Another important design issue for dilute-phase pneumatic conveying systems is the temporal and spatial homogeneous delivery of gas particle mixtures, for example, to the burners of a coal-fired power plant. From the bunker to the burner, however, numerous pipe systems such as bends and branches have to be used, which yield a strong segregation of the mixture due to inertial effects. Consequently, in front of the burner, pipe inserts may be used to homogenize the mixture again, which of course is associated with additional pressure drop. Also, this issue has been experimentally assessed for many years.

Consequently, an experimental design and layout of pneumatic conveying systems is rather tedious and costly. Therefore, during the past two decades, numerical methods based on computational fluid dynamics (CFD) were developed for facilitating the understanding and design of pneumatic conveying systems. The continuous phase computations were mainly based on Reynolds-averaged conservation equations (mostly termed Reynolds-averaged Navier–Stokes [RANS] equations) in connection with an appropriate turbulence model (e.g., k–ε turbulence model or Reynolds stress models). For describing such a particle-laden confined flow, both the two-fluid approach, often termed as Euler–Euler method and the Euler–Lagrange method, were commonly used. For dense gas–solid flows, for example, in a vertical riser, the two-fluid approach was preferred (e.g., Dasgupta et al., 1998, Hidayat and Rasmuson, 2005) although not all details occurring on the particle scale can be described and modeled. The Euler–Lagrange approach, on the other hand, allows a very detailed description of the discrete particle behavior, including all relevant fluid dynamic forces acting on the particles, the rotation of particles mainly induced by wall collisions, interparticle collisions, and collisions of particles with rough walls. This, however, makes computations of large pneumatic conveying systems quite time consuming. The largest benefit in the application of the Euler–Lagrange method is that a particle size distribution, which is normally present in all applications, can be considered with marginal computational effort. The treatment of a particle size distribution in the two-fluid approach requires the solution of a number of conservation equation sets, one for each discretized particle size class. Therefore, this method also becomes computationally expensive.

As a result, dilute-phase pneumatic conveying was in the past mainly computed using the Euler–Lagrange approach with more or less sophisticated modeling. A big challenge for many years was the computation of powder rope formation in a bend and its disintegration in a downstream located vertical pipe (Bilirgen and Levy, 2001, Yilmaz and Levy, 2001, Kuan et al., 2007, Tian et al., 2008, Lain and Sommerfeld, 2012a,b, 2013, Sommerfeld and Lain, 2015).

2.6.2 Euler–Lagrange-Approach

The numerical scheme adopted to calculate the considered particle-laden two-phase flows was the fully coupled Euler–Lagrange approach as described in detail by Lain and Sommerfeld (2008). The fluid flow was calculated based on the Euler approach using a fixed grid by solving the Reynolds-averaged conservation equations (RANS) in connection with the standard k–ε turbulence model. All conservation equations were extended in order to account for the effects of the dispersed phase, that is, two-way coupling through momentum exchange and turbulence. The time-dependent 3D conservation equations for the fluid may be written in the general form (using tensorial notation) as

$$(\rho\phi)_{,t} + (\rho U_i \phi)_{,i} = (\Gamma_{ik}\phi_{,k})_{,i} + S_\phi + S_{\phi p} \tag{2.327}$$

where

ρ is the gas density

U_i are the Reynolds-averaged velocity components

Γ_{ik} is an effective transport tensor

The usual source terms within the continuous phase equations are summarized in S_ϕ, while $S_{\phi p}$ represents the additional source term due to phase interaction, that is, the influence of the particles on the fluid flow (see Lain and Sommerfeld, 2008). In the present study, the computations have been done for a stationary flow situation.

The simulation of the particle phase by the Lagrangian approach is based on tracking a large number of particles through the beforehand computed flow field. Particles are treated as point masses, and their shape is assumed to be spherical, which was also the case in the experiments considered for validation. In order to account for the correct particle mass flow rate, the considered computational particles represent a certain number of real particles with the same properties, which yields a computationally treatable number of parcels.

Tracking requires the solution of the equations of motion for each computational particle or parcels. The forces that were considered include particle inertia, drag, gravity/buoyancy, slip–shear lift force F_{ls}, and slip-rotational lift force F_{lr} (Sommerfeld et al., 2008). The Basset history term, the added mass, and the fluid inertia are negligible for the considered high ratio of particle to gas densities. The change in the angular velocity along the particle trajectory due to the viscous interaction with the fluid (i.e., the torque T_i) requires the solution of additional partial differential equations. Hence, the complete equations of motion for the particles are given by

$$\frac{dx_{pi}}{dt} = u_{pi} \tag{2.328}$$

$$m_p \frac{du_{pi}}{dt} = \frac{3}{4}\frac{\rho}{D_p} m_p c_D (u_i - u_{pi})\left|\vec{u} - \vec{u_p}\right| + m_p g_i \left(1 - \frac{\rho}{\rho_p}\right) + F_{lsi} + F_{lri} \tag{2.329}$$

$$I_p \frac{d\omega_{pi}}{dt} = T_i \tag{2.330}$$

where

x_{pi}, u_{pi}, and u_i are the components of the particle location vector and the instantaneous particle and fluid velocities, respectively
m_p is the particle mass
I_p is the moment of inertia
D_p is the particle diameter
g_i is the gravity vector
ρ and ρ_p are the fluid and particle material densities

The relevant different forces acting on the particles and the respective resistance coefficients allowing the extension of the equation of motion to higher particle Reynolds numbers have been used according to Sommerfeld et al. (2008) as well as Sommerfeld (2010). The drag coefficient is obtained using the following standard correlation:

$$c_D = \begin{cases} 24\,\mathrm{Re}_p^{-1}(1 + 0.15\,\mathrm{Re}_p^{0.687}) & \mathrm{Re}_p \le 1000 \\ 0.44 & \mathrm{Re}_p > 1000 \end{cases} \tag{2.331}$$

with $\mathrm{Re}_p = \rho D_p \left|\vec{u} - \vec{u_p}\right| / \mu$ as the particle Reynolds number.

The slip–shear force is based on the analytical result of Saffman (1965) and extended for higher particle Reynolds numbers according to Mei (1992):

$$\vec{F_{ls}} = 1.615 D_p \mu \mathrm{Re}_s^{1/2} c_{ls}\left[(\vec{u} - \vec{u_p}) \times \vec{\omega}\right] \tag{2.332}$$

where

$\vec{\omega} = \nabla \times \vec{u}$ is the fluid rotation
$\mathrm{Re}_s = \rho D_p^2 \left|\vec{\omega}\right| / \mu$ is the particle Reynolds number of the shear flow
$c_{ls} = F_{ls}/F_{ls,Saff}$ represents the ratio of the extended lift force to the Saffman (1965) force:

$$c_{ls} = \begin{cases} (1 - 0.331\sqrt{\beta})e^{-\mathrm{Re}_p/10} + 0.331\sqrt{\beta} & \mathrm{Re}_p \le 40 \\ 0.0524\sqrt{\beta\,\mathrm{Re}_p} & \mathrm{Re}_p > 40 \end{cases} \tag{2.333}$$

where β is a parameter given by $\beta = 0.5\ \mathrm{Re}_s/\mathrm{Re}_p$.

The applied slip-rotational lift force is based on the relation given by Rubinow and Keller (1961), which was extended to account for the relative motion between particle and fluid. Moreover, several authors allowed an extension of this lift force to higher particle Reynolds numbers. Hence, the following form of the slip-rotation lift force has been used:

$$\vec{F_{lr}} = \frac{\pi}{8} D_p^3 \rho \frac{\mathrm{Re}_p}{\mathrm{Re}_r} c_{lr}\left[\vec{\Omega} \times (\vec{u} - \vec{u_p})\right] \tag{2.334}$$

with $\vec{\Omega} = 0.5\nabla \times \vec{u} - \vec{\omega_p}$ and the Reynolds number of particle rotation is given by $\mathrm{Re}_R = \rho D_P^2 \left|\vec{\omega}\right| / \mu$. The lift coefficient according to Oesterlé and Bui Dinh (1998) is given for $\mathrm{Re}_p < 2000$ by

$$c_{lr} = 0.45 + \left(\frac{\mathrm{Re}_r}{\mathrm{Re}_p} - 0.45 \right) e^{-0.05684\, \mathrm{Re}_R^{0.4}\, \mathrm{Re}_p^{0.3}} \tag{2.335}$$

For the torque acting on a rotating particle, the expression of Rubinow and Keller (1961) was extended to account for the relative motion between fluid and particle and higher Reynolds numbers:

$$\vec{T} = \frac{\rho}{2} \left(\frac{D_p}{2} \right)^5 c_R \left|\vec{\Omega}\right| \vec{\Omega} \tag{2.336}$$

where the coefficient of rotation is obtained from Rubinow and Keller (1961) and direct numerical simulations of Dennis et al. (1980) in the following way:

$$c_R = \begin{cases} \dfrac{64\pi}{\mathrm{Re}_R} & \mathrm{Re}_R \le 32 \\ \dfrac{12.9}{\sqrt{\mathrm{Re}_R}} + \dfrac{128.4}{\mathrm{Re}_R} & 32 < \mathrm{Re}_R < 1000 \end{cases} \tag{2.337}$$

The equations to calculate the particle motion are solved by integration of the differential equations (Equations 2.326 through 2.328). For sufficiently small time steps and assuming that the forces remain constant during this time step, the new particle location, the linear and angular velocities are calculated. The time step for the particle tracking, Δt_L, was chosen to be 50% of the smallest of all local relevant time scales, such as the particle relaxation time, the integral timescale of turbulence, and the mean interparticle collision time. This choice guarantees the stability of the numerical integration scheme (Göz et al., 2004).

2.6.2.1 Modeling of Elementary Processes

In order to account for turbulence effects on particle motion, the instantaneous fluid velocity components along the particle trajectory are determined from the local mean fluid velocity interpolated from the neighboring grid points and a fluctuating component generated by a single-step isotropic Langevin model described by Sommerfeld et al. (1993). In this model, the fluctuation velocity is composed of a correlated part from the previous time step and a random component drawn from a Gaussian distribution function. The degree of correlation depends on the turbulent particle Stokes number St_T and is calculated using appropriate time and length scales of turbulence estimated from the k–ε turbulence model.

Especially in wall-bounded flows, as considered here, the modeling of particle–wall collisions needs special consideration (Sommerfeld, 1992). The applied wall collision model, accounting for wall roughness, is described and validated in Sommerfeld and Huber (1999). The wall roughness seen by a particle is simulated assuming that the instantaneous impact angle is composed of the particle trajectory angle plus a stochastic contribution due to wall roughness, drawn from a normal distribution with a standard deviation $\Delta\gamma$ that depends on the structure of wall roughness and particle size (Sommerfeld and Huber, 1999). Corresponding correlations for the restitution coefficient, the friction coefficient, and the roughness angle are presented by Lain et al. (2002), which are depending on the particle impact angle (Sommerfeld and Lain, 2009). Regardless of particle size, the standard deviation of the roughness angle was assumed to be $\Delta\gamma = 10°$ for all cases considered here, except for one case with low roughness demonstrating this important effect.

Interparticle collisions are modeled by the stochastic approach described in detail by Sommerfeld (2001). This model relies on the generation of a fictitious collision partner at each time step of tracking a real particle and accounts for a possible correlation of the translational velocities of colliding particles in turbulent flows. As model parameters for particle–particle collisions, the restitution coefficient has been taken to be constant with 0.9 and the static and dynamic friction coefficients were chosen to be 0.4. The convergence behavior for pneumatic conveying was demonstrated by Lain and Sommerfeld (2012a).

2.6.2.2 Two-Way Coupling Procedure

The source terms for the momentum equations resulting from the exchange between particles and fluid are obtained on the basis of the Particle-Source-In-Cell concept proposed by Crowe et al. (1977). Hence, the momentum exchange is calculated by averaging over all parcels traversing a given control volume during

one Lagrangian calculation. Instead of summing up all fluid dynamic forces acting on the particles, which is quite cumbersome, the momentum exchange is calculated from the velocity change of the parcels when traversing the control volume. In this procedure however, the external forces have to be subtracted, yielding the momentum source in the following form:

$$\overline{S_{U_I p}} = -\frac{1}{V_{cv}} \sum_k m_k N_k \sum_n \left\{ \left(\left[u_{pi} \right]_k^{n+1} - \left[u_{pi} \right]_k^n \right) - g_i \left(1 - \frac{\rho}{\rho_P} \right) \Delta t_L \right\} \tag{2.338}$$

where the sum over n indicates averaging along the particle trajectory (time averaging) and the sum over k is related to the number of computational particles passing the considered control volume with the volume V_{cv}. The mass of an individual particle is m_k and N_k is the number of real particles in one computational particle. Δt_L is the Lagrangian time step that is used in the solution of 2.326 through 2.328.

The source term in the conservation equation of the turbulent kinetic energy, k, is expressed in the Reynolds average procedure as

$$S_{kp} = \overline{u_i S_{U_i p}} - U_i \overline{S_{U_i p}} \tag{2.339}$$

while the source term in the ε-equation is modeled in the following standard way:

$$S_{\varepsilon p} = c_{\varepsilon 3} \frac{\varepsilon}{k} S_{kp} \tag{2.340}$$

with $C_{\varepsilon 3} = 1.8$ and the sum is implicit in the repeated subindex i.

A converged solution of the coupled two-phase flow system is obtained by successive solution of the Eulerian and Lagrangian part, respectively. Initially, the flow field is calculated without particle-phase source terms until a converged solution is achieved. Thereafter, a large number of parcels are tracked through the flow field (up to 10^6 computational particles) and the source terms are sampled for each control volume. In this first Lagrangian calculation interparticle collisions are not considered, since the required cell-based particle-phase properties are not yet available. Hence, for each control volume, the particle concentration, the local particle size distribution, and the size–velocity correlations for the mean velocities and the rms values are sampled. These properties are updated in each Lagrangian iteration in order to allow correct calculation of interparticle collisions. Additional particle-phase properties and profiles may be sampled for each transverse cell when the computational particles cross a predefined location. From the second Eulerian calculation, the source terms of the dispersed phase are introduced using an underrelaxation procedure in order to facilitate convergence (Kohnen et al., 1994). For the present calculations, typically about 25 to 35 coupling iterations with an underrelaxation factor between 0.5 and 0.1 were necessary in order to yield convergence of the Euler–Lagrange coupling.

2.6.2.3 Conveying Pipe Configuration

The considered configuration of the horizontal to vertical pipe with a 90° bend has an inlet horizontal pipe and an outlet vertical pipe, both 5 m in length. According to the configuration described in Huber and Sommerfeld (1994, 1998), the pipe diameters are D = 0.08 and 0.15 m and the elbow radius is 2.54 times the pipe diameter (i.e., R_{bend} = 0.203 and 0.381 m). The mean conveying velocity is different for each of the cases (Table 2.4). These conditions yield the nondimensional parameters summarized in Table 2.4, where the pipe Reynolds number and the Dean number of the bend flow are determined from

$$\mathrm{Re}_{pipe} = \frac{\rho D_{pipe} U_{av}}{\mu} \quad \mathrm{De}_{bend} = \frac{\mathrm{Re}_{pipe}}{\sqrt{R_{bend}/R_{pipe}}} \tag{2.341}$$

Table 2.4 Parameters and Nondimensional Properties of Pipe System (5 m Horizontal, Bend, and 5 m Vertical) for the Three Standard Experimental Conditions

Pipe Diameter	0.08 m	0.08 m	0.15 m
Bulk velocity	14 m/s	21 m/s	27 m/s
Mass loading	0.5	0.5	0.3
Re_{pipe}	74,667	112,000	270,000
De_{bend}	33,144	49,716	63,890

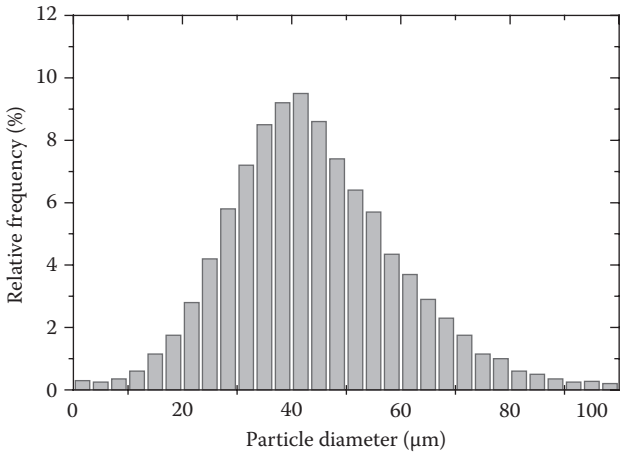


Figure 2.54

Size distribution of spherical glass beads (relative number frequency) used in the experiments of Huber and Sommerfeld (1998).

The considered fluid properties are $\rho = 1.2$ kg/m^3 and $\mu = 18.0\ 10^{-6}$ N s/m^2 (air at room temperature). The multiblock structured O-type grid is composed of 25 blocks with a total of 568,000 hexahedral control volumes to discretize the entire pipe system (i.e., 5 m horizontal pipe, a bend, and 5 m vertical pipe). This resolution was found to be sufficient for producing grid-independent results.

The particles considered in the numerical calculations for all standard cases summarized in Table 2.4 were spherical glass beads ($\rho_p = 2500$ kg/m^3) with the size distribution shown in Figure 2.54. These particles were also used in the experiments. The size distribution has a number mean diameter of 40 μm and is rather wide ranging from about 15 to 85 μm, which was discretized by 7 diameter classes of 10 μm width. It should be noted that the size of injected particles was sampled from a continuous cumulative distribution, yielding also a variation of particle size in a given size class.

The particle mass loading (mass flow rate of particles/mass flow rate of air) for the standard cases was selected according to the experiments (Huber and Sommerfeld, 1994, 1998); see Table 2.4. Besides that, mono-sized particle with 20, 40, 80, and 135 μm diameter and a binary mixture were considered (see Table 2.5), all being spherical glass beads with $\rho_p = 2500$ kg/m^3.

The boundary conditions used for the numerical calculations are as follows. At the inlet of the pipe, the fluid is injected with a uniform velocity profile (i.e., mean conveying velocity provided in Table 2.4) and a fluctuating velocity of around 3% of the bulk flow velocity for each component. At the pipe exit, an outlet condition (i.e., no gradients of the properties in streamwise direction) is applied, while at the pipe walls, no-slip conditions are adopted. The particle injection velocities are sampled from a normal distribution with fixed mean and rms velocities. The mean particle velocity is the bulk gas velocity in the streamwise direction (see Table 2.4), and the mean transverse components are assumed to be zero.

Table 2.5 Summary of Particle Response Characteristics for the Particle Size Distribution, Different Mono-Sized Particle, and a Binary Mixture

Diameter (μm)	Turbulent Stokes[a] (–)	Response Distance (mm)	Bend Stokes[b] (–)
❶ 15–85 (40)	0.169–5.412	0.03–30.49	0.078–2.515
❷ 20	0.300	0.093	0.139
❸ 40	1.199	1.5	0.557
❹ 80	4.794	23.9	2.228
❺ 135	13.653	194.0	6.344
❻ 30 + 60 (40)[c]	0.674 + 2.697	0.47 + 7.57	0.313 + 1.253

[a] Integral timescale of turbulence in the pipe core $T_L = 10.3$ ms.

[b] Calculated according to Equation 2.331 with $R_{bend} = 0.381$ m and $U_0 = 27$ m/s.

[c] Binary mixture with equal number of parcels and mass fractions of $w_{30} = 20\%$ (30 μm) and $w_{60} = 80\%$ (60 μm) and a number mean diameter of 40 μm (calculations were done for those with D = 150 mm and $U_0 = 27$ m/s).

The rms values are 3% of the bulk gas velocity for all three velocity components. These values were randomly drawn from normal distributions. Regarding the three components of the particle angular velocities, a mean of zero and a standard deviation of 10^3 1/s were assumed. For all the particle sizes considered, the two-phase flow was developed after a conveying distance of 5 m through the horizontal pipe. Hence, there is no effect of the specified inlet conditions on the pneumatic conveying through the bend and the connected vertical pipe.

All the numerical computations were done on a quad-core workstation, where the fluid flow was calculated on one processor and the Lagrangian tracking was done on two processors. With these resources, a four-way coupled converged result for the 5 m horizontal pipe, the pipe bend, and the 5 m vertical pipe was obtained after about two weeks with the in-house code FASTEST/Lag3D.

2.6.3 Results Horizontal to Vertical Pipe System

The particle motion in a horizontal straight pipe is determined by the balance between gravitational settling and turbulent dispersion. Hence, with increasing particle size (or response time), turbulence is not sufficiently strong to keep the particles in suspension and hence gravitational settling increases, yielding high particle concentration near the pipe bottom. On the contrary, small particles will be dominantly transported by turbulence whereby they will be more homogeneously distributed in the pipe cross section. The particle response to turbulence is characterized by the turbulent Stokes number given by $St_T = \tau_p/T_L$, where T_L is the integral timescale of turbulence. For the considered monosized particles, St_T ranges from 0.3 to 14, that is, from responsive to inertial particles (see Table 2.5). The particle response distance may be used for identifying the importance of particle–wall collisions. It is defined as $\lambda_p = \tau_p \cdot V_s$, where V_s is the terminal velocity of particles (Sommerfeld et al., 2008). In the case $\lambda_p \geq D$ (pipe diameter), the particles are not able to follow the gas flow after a wall rebound and hence will collide again with the opposite wall of the pipe (see, e.g., Sommerfeld, 2003). For the considered particle sizes, the 135 μm particles are dominantly affected by wall collisions (Table 2.5).

A particle-laden flow through a bend is characterized by strong segregation of the mixture due to inertial effects and secondary flow, whereby the particles accumulate at the outer wall of the elbow forming a relatively dense rope, that is, high-concentration region of particles. This rope will be again disintegrated in the connecting vertical pipe due to interparticle collisions, wall collisions, secondary flow, and turbulence. The redirection of the two-phase flow from horizontal to vertical also leads, as a result of particles inertia, to enhanced wall collisions with the outer bend wall followed by a rebound toward the core of the pipe. The particle response behavior regarding the mean motion through the bend is characterized by the bend Stokes number being the ratio of the particle response time (here the Stokesian response time is used) to the particle residence time along the centerline of the bend:

$$St_B = \frac{\tau_P}{\tau_{bend}} = \frac{\rho_P d_P^2}{18\mu} \frac{U_{av}}{C_{bend,90^o}} = \frac{\rho_P d_P^2}{18\mu} \frac{2U_{av}}{\pi R_{bend}} \tag{2.342}$$

Here,

$C_{bend,\,90^o}$ is the arc of the 90° bend radius measured along the centerline
R_{bend} is the bend radius (2.54 times pipe diameter)
U_{av} is the average conveying velocity

This definition of the bend particle Stokes number is more physical than using the bend timescale obtained as the ratio of pipe radius to the average gas conveying velocity as done in most deposition studies (see, e.g., Crane and Evans, 1977). The bend Stokes number for the different particle systems is also summarized in Table 2.5. Expectedly, an increase in this Stokes number is coupled with an increasing wall collision frequency, especially within the bend, and ultimately a growing pressure drop. The rebound characteristics of the particles are evidently affected by wall roughness and the involved shadow effect (Sommerfeld and Huber, 1999).

The high particle concentration region developing within a bend is of course altering the probability of interparticle collisions with the result that the distribution of the particles throughout the bend is strongly manipulated. In addition, the distribution of the particle phase within the bend will determine the local degree of two-way coupling. As the appearance of the particle concentration distribution within the bend (i.e., degree of segregation) is depending on the bend Stokes number, also the interparticle collision frequency is somehow coupled to this characteristic nondimensional number (i.e., particle inertia) and of course determined by the overall mass loading ratio. In case particles with a wide size distribution are conveyed the so-called impact efficiency also becomes of importance. This means that once a small and large

particle are on a collision trajectory, the small particle still might move around the larger collector particle with the relative velocity field and hence no collision occurs (Ho and Sommerfeld, 2002, Sommerfeld and Lain, 2009). In average, this phenomenon reduces the effective frequency of interparticle collisions as shown by Ho and Sommerfeld (2005) for particle separation in a gas cyclone. However, in the present computations with particle size distribution, impact efficiency is not considered.

In the following sections, the influence of the particle-phase properties and the elementary processes described earlier on the pneumatic conveying characteristics, the particle concentration distribution, and the resulting pressure drop will be discussed.

2.6.3.1 Validation of the Computations

The modeling approach summarized earlier has been thoroughly validated for different pneumatic conveying systems, that is, for a horizontal channel by Lain and Sommerfeld (2008, 2012a) and for a pipe system along the vertical pipe (Lain and Sommerfeld, 2010, 2011, 2013, Sommerfeld and Lain, 2012). In the following, the validation is based on results for the 80 mm pipe system, obtained at several cross sections in the vertical pipe by applying phase-Doppler anemometry (Huber and Sommerfeld, 1994). The average conveying velocity is 14 m/s and the particle mass loading is 0.5 (Table 2.4). Computational results are shown for both two- and four-way couplings in order to emphasize the importance of interparticle collisions.

A comparison between measured and calculated profiles for particle concentration and particle number mean diameter development downstream of the bend exit is shown in Figure 2.55 (please consider 4-way way results). The first two profiles exhibit a very good agreement, both in curve progression and in magnitude. Further downstream however, the predictions still show a higher concentration near the outer wall (right-hand side) than the measurements. Hence, in the experiments, the rope was faster dispersed in the vertical pipe that is most probably the result of the observed unsteady fluctuating motion of the rope downstream of the bend exit. The profiles of the calculated particle number mean diameter show a remarkable good agreement with the measurements, particularly since this property is the result of the size segregation within the bend and requires a good prediction of the size-dependent particle behavior and hence the local particle size distributions. Only the first profile shows some larger deviations, indicating a somewhat stronger rebound of the larger particles in the predictions.

The predicted particle mean velocities (vertical component) and the associated particle rms values are compared in Figure 2.56. The mean velocities in the first two cross sections are in reasonable good agreement; however, some larger deviations are found in the last profile, which is again associated with the differences in predicting the disintegration of the particle rope (Figure 2.55), being most likely due to the rope fluctuations observed in the experiments. The predicted particle-phase rms values of the vertical velocity component are in surprisingly good agreement with the measurements, as this property is affected by all relevant transport processes, especially the description of turbulence seen by the particles.

As to be expected, when neglecting interparticle collisions (two-way coupling), the rope behavior in the vertical pipe cannot be predicted properly (see Figures 2.55 and 2.56), and consequently, all the other particle-phase properties are also not correctly predicted. Here, the particles may be reflected unhindered from the bend outer wall toward the pipe core yielding the highest particle concentrations near the core of the pipe after some distance from the bend exit (Figure 2.55a, y = 0.6 and 1.1 m). Hence, interparticle collisions yield a more concentrated dust rope in a bend. As a consequence of the higher inertia of large particles, the particle number mean diameter left of the pipe axis is remarkably overpredicted when not considering interparticle collisions (Figure 2.55b). The particle velocity profiles (mean and rms) are naturally coupled with the particle concentration distribution and deviate in a two-way coupled calculation from those considering also interparticle collisions (Figure 2.56). Consequently, even at this relatively low overall particle mass loading, correct predictions cannot be expected when neglecting interparticle collisions.

2.6.3.2 Wall Roughness Effects

In order to decouple the problem, first calculations are considered where only the effect of wall roughness is analyzed by neglecting interparticle collisions, that is, conducting two-way coupled calculations, for the case with particle size distribution from 15 to 85 μm. For this case (D = 150 mm, U_{av} = 27 m/s, η = 0.3) *a short inlet pipe of 1 m* is used, which results in an almost homogeneous particle concentration distribution at the bend inlet (Lain and Sommerfeld, 2009, Sommerfeld and Lain, 2012). The degree of accumulation of particles at the bend outer wall depends strongly on wall roughness describing the rebound characteristics of the particles. Two degrees of roughness are considered, namely, Δγ = 1.5° and 10°, and

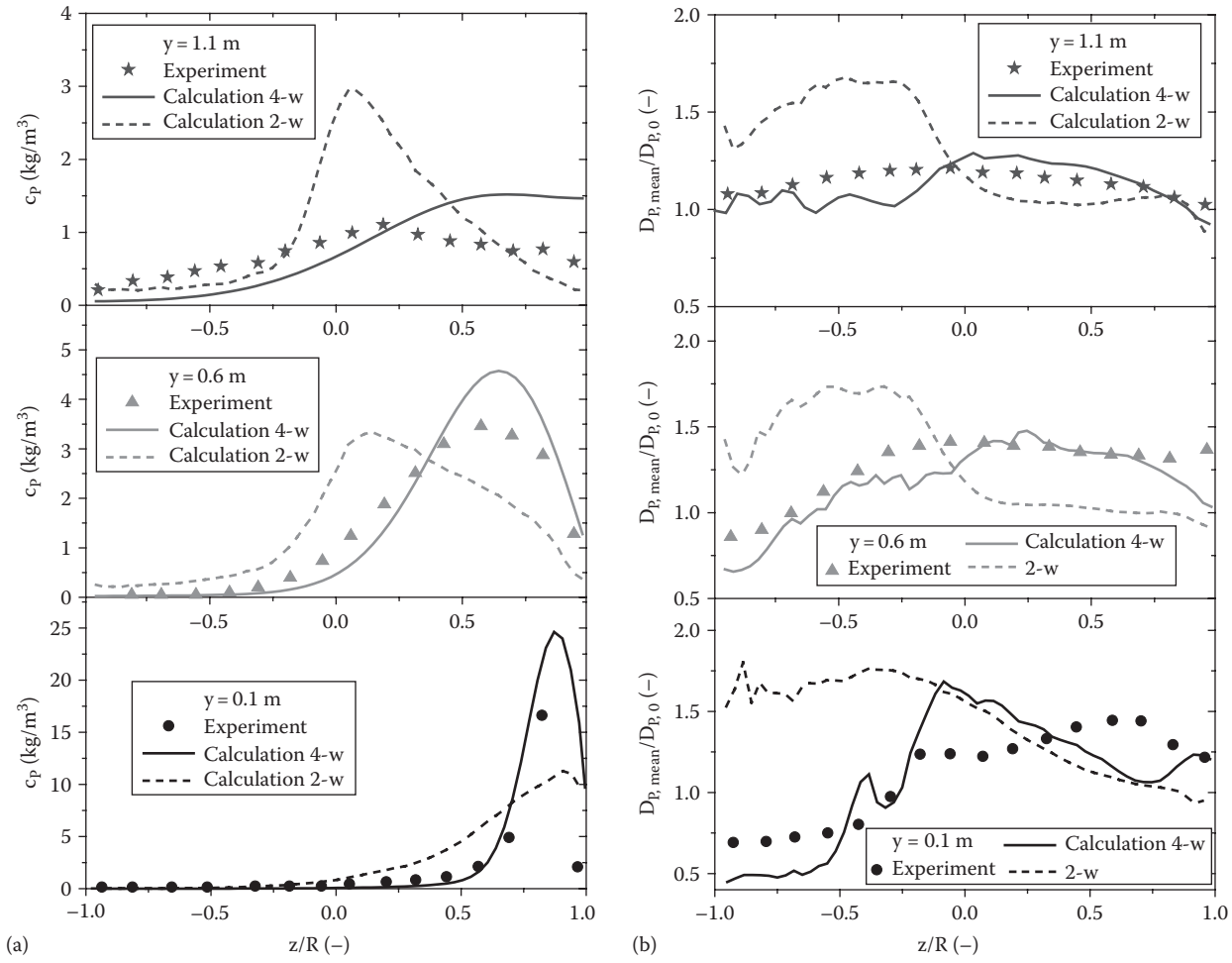


Figure 2.55

Profiles of particle concentration (a) and particle mean number diameter (b) downstream of the bend exit; comparison of calculations with experiments (D = 80 mm, R_{bend} = 0.203 m, U_0 = 14 m/s, η = 0.5, Δγ = 10°, four-way coupling, particle size distribution 15–85 μm, St_g = 0.076–2.445).

the resulting computational results are compared with respect to the particle concentration distribution along bend and vertical pipe (Figure 2.57a). When entering the bend, particles are first driven toward the bend outer wall mainly due to inertia and to a small extent by the secondary flow. For small roughness, Δγ = 1.5°, the particle rebound is not very strong (less pronounced shadow effect), and consequently, a quite dense rope is formed until to the bend exit. In the third cross section within the bend (θ = 60°), a small nose in the concentration distribution is visible caused by the focusing effect, that is, particles coming almost straight into the bend are reflected at a curved bend outer wall and bounced back toward the core of the pipe (Lain and Sommerfeld, 2009). Finally, at the end of the bend, particles are only present near the outer wall of the pipe bend leaving the bend inner region and the core almost without solids (Figure 2.57 upper block). Near the exit of the bend particles are again rebound from the outer (right-hand side) wall toward the core of the pipe (focusing), yielding a strip of high concentration (see magnified section between bend exit and 1 m downstream), which reaches the pipe core after about 1 m. Further downstream (i.e., at 2 and 3 m), a kind of mushroom-shaped concentration pattern is developed within the pipe cross section. This phenomenon is mainly the result of particle transport by secondary flow. This developing high-concentration region is barely dispersed until the exit of the vertical pipe.

The secondary flow structure developing in the bend and the vertical pipe is also shown in Figure 2.57 (upper block, right) for the low roughness case without interparticle collisions. As a result of the particle rebound from the outer bend wall, the particles are reflected back toward the pipe center. The associated momentum transferred to the fluid by this focusing (Lain and Sommerfeld, 2009) produces two new counter-rotating vortices, clearly visible at bend angles θ of 30° and 60°, which push the two secondary flow vortices

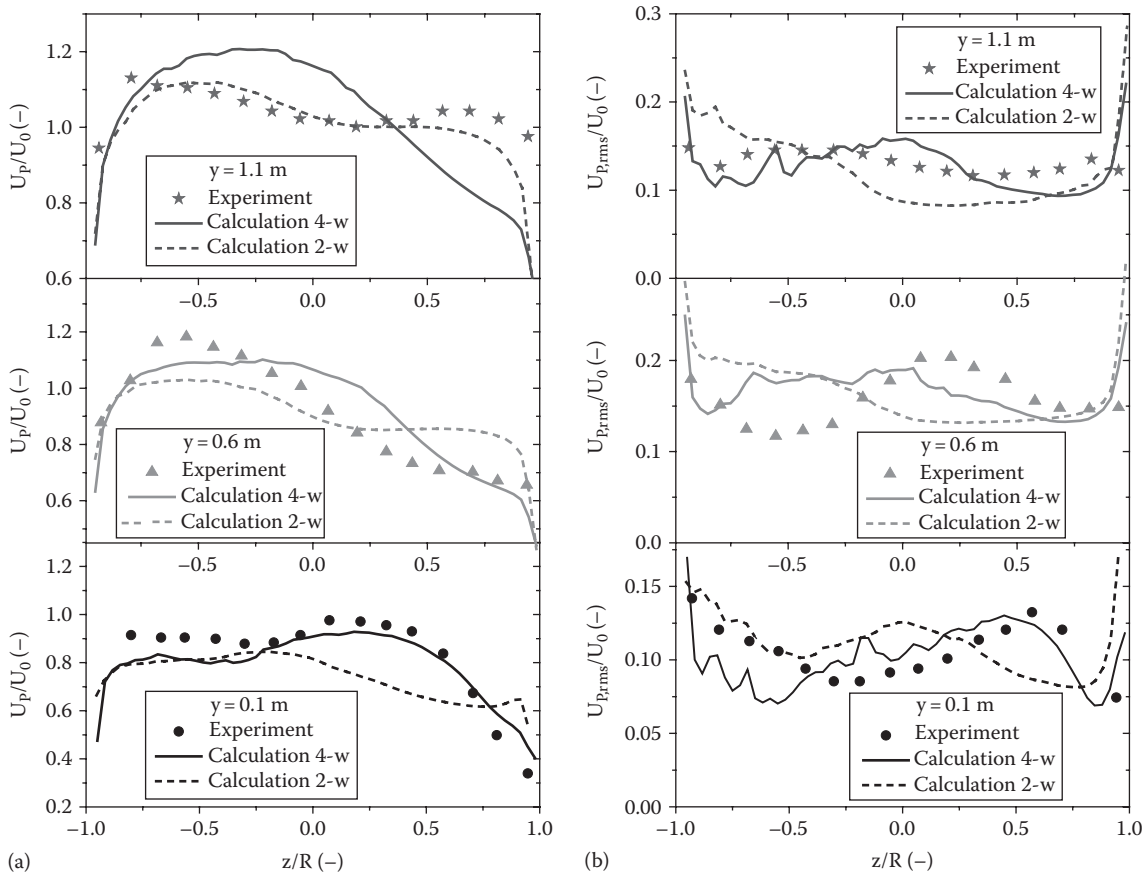


Figure 2.56

Profiles of vertical particle velocity (a) and the associated rms value (b) downstream of the bend exit; comparison of the calculations with experiments (D = 80 mm, R_{bend} = 0.203 m, U_0 = 14 m/s, η = 0.5, Δγ = 10°, four-way coupling, particle size distribution 15–85 μm, St_B = 0.076–2.445).

produced as a result of the bend flow toward the inner part of the pipe cross section. Until the exit of the bend the particle-induced vortices have disappeared again, but the typical single-phase secondary flow structure is completely destroyed. Particle rebound near the end of the bend again introduces momentum to the fluid so that the two-particle-induced counter-rotating vortices again appear a bit downstream the bend exit. Eventually, four vortex structures of roughly equal size develop in the pipe cross section that is preserved until the end of the vertical pipe. Through the associated particle transport, a stem-like and later on mushroom-shaped region of high particle concentration is developing in the vertical pipe (Figure 2.57 upper block, left). Until the end of the vertical pipe element, the regions of high particle concentration have barely disappeared.

In the case of higher roughness, that is, Δγ = 10°, particles rebound from the bend outer wall are farther reflected back into the core region of the bend flow (Figure 2.57 lower block). This behavior is due to the shadow effect of wall roughness (Sommerfeld, 2003, Lain and Sommerfeld, 2008) implying that the rebound angle may become larger than the impact angle if this is relatively shallow (i.e., resulting in an averaged transfer of wall parallel particle momentum toward the transverse components). Hence, although a more or less dense rope is formed at the outer wall near the bend exit, the particles are distributed over a larger portion of the cross section compared to the low roughness case (compare Figure 2.57 left, upper and lower part). Only near the inner wall there are almost no particles (i.e., this region corresponds to about one-third of the cross section). The hat-like shape of the region with high particle concentration developing in the bend is again resulting from the focusing effect, whereby the particles are reflected from the curved bend outer wall toward the pipe core. Therefore, eventually also momentum is transferred to the gas phase affecting the secondary flow. The T-shaped regions of high particle concentration at 1 and 2 m downstream the bend exit are again associated with the focusing effect pushing the particles toward the pipe core in combination with the developing secondary flow structure. Within the bend, already strong counterrotating vortices develop

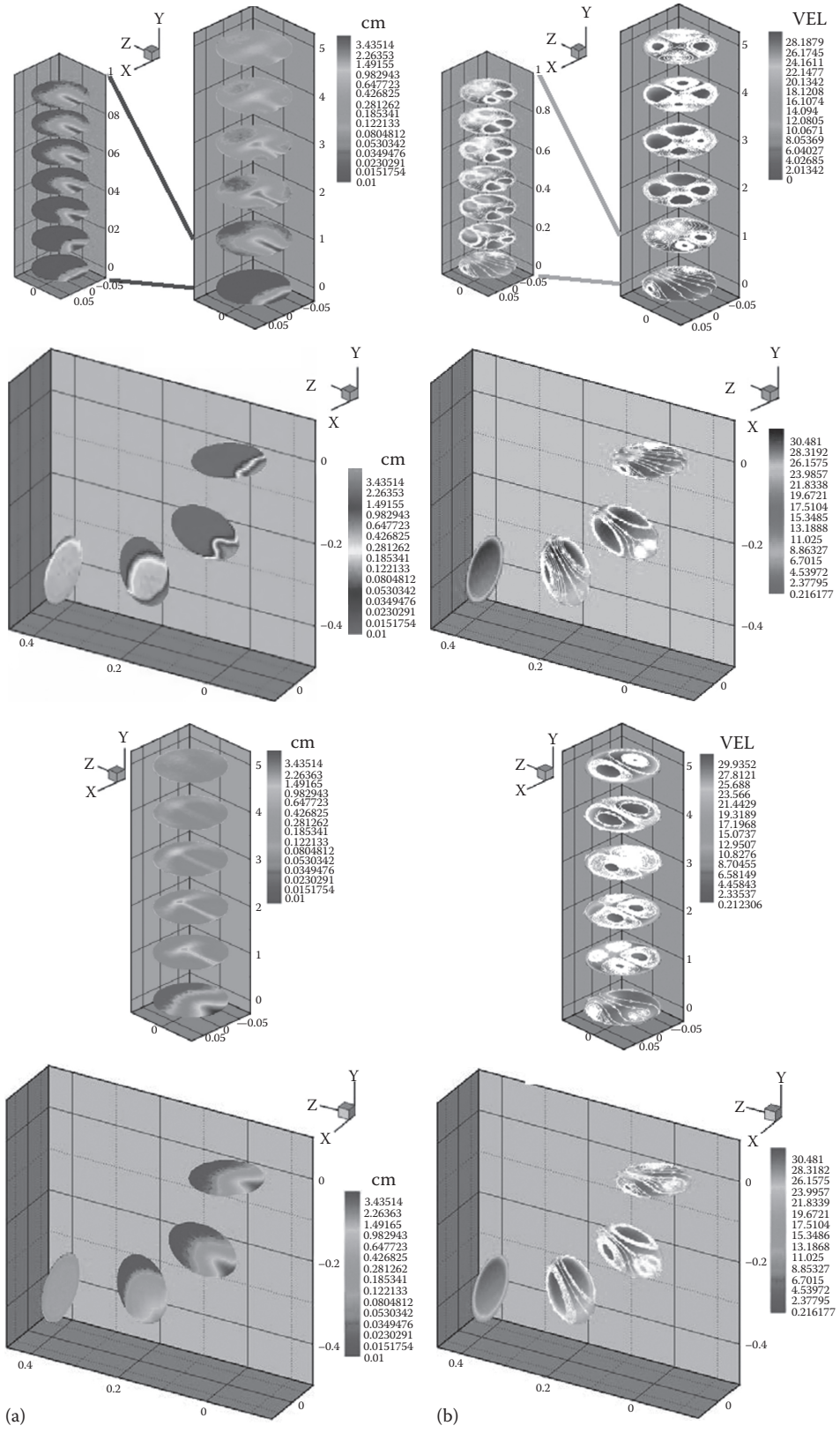


Figure 2.57

Development of cross-sectional distributions of particle concentration cm (kg/m³) (a) and absolute flow velocity *VEL* (m/s) (color) as well as streamlines of the cross-sectional flow (white lines) (b) for a particle-laden flow through the bend and vertical pipe; upper block, $\Delta\gamma = 1.5°$; lower block, $\Delta\gamma = 10°$ ($D = 150$ mm, $U_0 = 27$ m/s, $\eta = 0.3$, particle size distribution 15–85 μm, two-way coupling, 1 m horizontal inlet pipe).

due to the particle focusing, yielding in the initial part of the vertical pipe four circulation cells in the pipe cross section (Figure 2.57 lower block right). As the strength of the particle-induced circulation cells is quite high, the original circulation cells produced in the bend by the centrifuging effect are eventually completely entrapped (i.e., from about 3 m). Hence, at the end of the vertical pipe, two circulation cells are only present with a rotation opposite to that produced initially by the bend flow (i.e., bend angle of 30°).

2.6.3.3 *Influence of Interparticle Collisions*

For the following results, the standard case with a 5 m horizontal pipe, a bend, and a 5 m vertical pipe (pipe diameter 150 mm) is considered and the particles have a size distribution (Figure 2.54, Table 2.5, case ❶). This implies that the particle-laden flow entering the bend shows already a remarkable gravitational settling whereby the particle concentration at the inlet becomes nonsymmetric. The result obtained for solely two-way coupled calculations is shown in Figure 2.58a. Compared to the short inlet pipe with the same wall roughness (Figure 2.57 lower block left), the concentration distribution throughout the bend and in the connecting vertical pipe is remarkably modified. With a long inlet pipe, gravitational settling has altered the particle concentration distribution at the bend inlet cross section, that is, the maximum of particle concentration is shifted to the lower half of the pipe cross section (Figure 2.58a). This implies that most of the particles

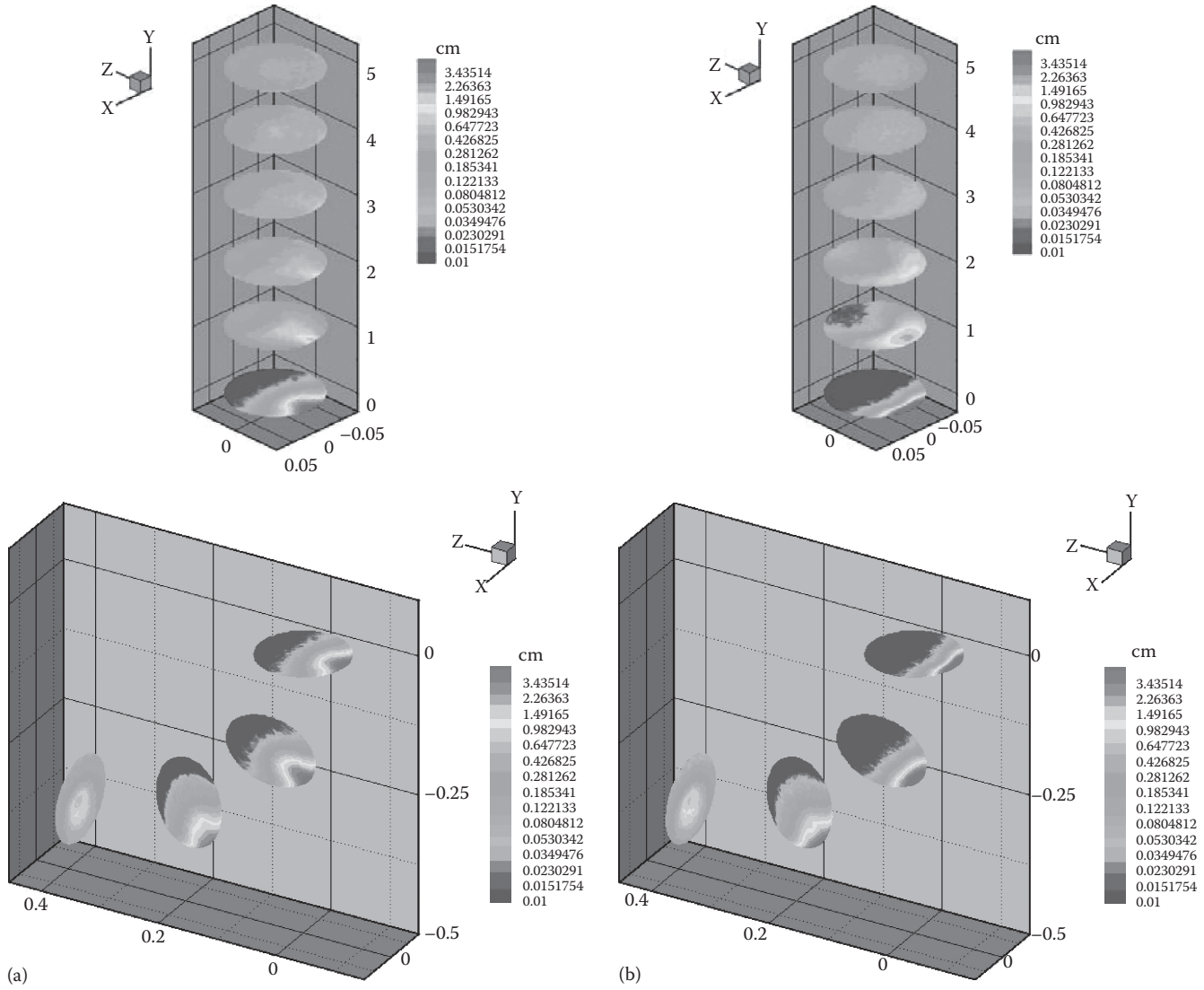


Figure 2.58

Cross-sectional distribution of particle concentration cm (kg/m^3) along bend and connecting vertical pipe demonstrating the effect of interparticle collisions: (a) two-way coupling and (b) four-way coupling (5 m horizontal pipe, bend, 5 m vertical pipe, D = 150 mm, bend radius 2.54 pipe diameters, U_{av} = 27 m/s, η = 0.3, $\Delta\gamma$ = 10°, particle size distribution 15–85 μm).

experience a more gradual redirection, whereby the rebound of particles from the bend outer wall is less strong. This has the consequence that the pipe cross section within the bend is somewhat less filled with the particles compared to a homogeneous distribution at the bend inlet (Figure 2.57 lower block left). The shape of the high-concentration region, however, still indicates the presence of the focusing effect, although it is not as pronounced than in the case with homogeneous inlet distribution. In this case, only weak counterrotating vortices are developed in the bend but do not persist for a long distance in the vertical pipe (not shown here). This is also the reason that the rope formed in the bend is dispersed much quicker in the vertical pipe.

When interparticle collisions are taken into account (i.e., four-way coupling), the particle rope developing in the bend is forced to be more concentrated and the particles are distributed in a smaller part of the cross section near the outer wall of the bend compared to the result with only two-way coupling (compare Figure 2.58a and b). This is caused by collisions of particles moving into the bend with those rebounding from the bend outer wall, which may be called "compression" effect and strongly depends on particle inertia and the overall mass loading. Hence, the rebound particles are "pushed" back toward the bend outer wall and will again collide with it (i.e., the resulting enhancement of wall collision rate will be discussed later). After rebound, they will again collide with other particles within the rope. Consequently, the particles are "trapped" in the rope due to interparticle collisions and the mean free path between particle collisions is rather small. Also, the redispersion of the particles in the vertical pipe section is hindered by interparticle collisions. Instead, a kind of detached closed rope develops near the bend outer wall (i.e., 1 m downstream the bend exit), which moves upward and is only dispersed 3 m downstream the bend exit (Figure 2.58). The trapping of the particles in the dust rope also reduces the focusing effect and the associated development of particle-induced counterrotating vortices (not shown here).

2.6.3.4 Influence of Particle Size

In order to demonstrate the effect of particle size on the conveying through the standard pipe configuration (5 m horizontal pipe, bend, and 5 m vertical pipe), monosized glass beads of 20, 40, 80, and 135 μm are considered. The particle behavior in the different pipe elements may be first analyzed by considering the different relevant transport mechanisms. In the horizontal pipe, particle motion is governed by gravitational settling and response to turbulence, that is, gravitational settling may be balanced by turbulence if the particles are small enough (i.e., their turbulent Stokes number is smaller than one). From the numerical calculations, the integral timescale of turbulence is estimated to be $T_L = 0.16\ k/\varepsilon = 10.3$ ms on the center line of the pipe. With the Stokesian response time of the particles (see Equation 2.332), turbulent Stokes numbers of 0.3, 1.2, 4.8, and 13.7 are found for the four particle sizes (Table 2.5). This shows that only the smallest particle size may be considerably affected by turbulence. The other elementary processes strongly affecting the particle behavior in the horizontal pipe are wall collisions, especially for rough walls and the involved shadow effect (Sommerfeld and Huber, 1999). Particle–wall collisions become of importance if their response distance (i.e., product of particle response time and terminal velocity) becomes larger than the dimension of the confinement (Sommerfeld et al., 2008), here the pipe diameter D:

$$D < \lambda_P = \tau_P V_S = \frac{\rho_P D_P^2}{18\mu} V_S \tag{2.343}$$

The particle response distances for the four particle diameters are as follows: 0.093, 1.5, 23.9, and 194.0 mm, respectively. This clearly demonstrates that the small particles are marginally influenced by wall collisions including roughness, as they, after rebound, quickly follow the flow again and forget about the wall collision event. Therefore, the resulting particle concentration distributions in the pipe cross section after the considered conveying distance of 5 m is the result of three competing effects: gravitational settling, turbulence, and wall collisions. Comparing the vertical profiles of the normalized particle concentration at the bend entrance (Figure 2.59) and later in this section the respective color-coded concentration fields in Figures 2.61 through 2.64, all obtained with four-way coupling, the following conclusions may be drawn:

1. The smallest particles (20 μm) are unaffected by wall collision phenomena, and gravitational settling is almost entirely balanced by turbulence, yielding virtually constant concentration in the pipe cross section, except for a small region near the upper wall.
2. For the 40 μm particle, gravitational settling becomes more dominant and cannot be balanced by turbulence, while wall collisions are still not very important (distinctive concentration maximum near the bottom at about y/D = 0.15, see Figure 2.59).

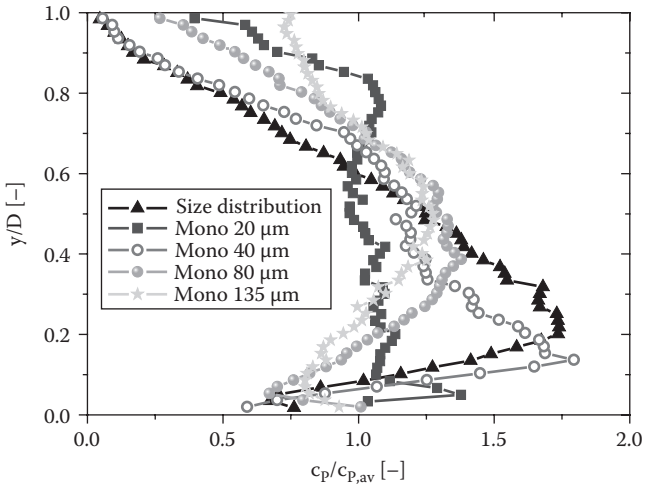


Figure 2.59

Vertical profiles of normalized particle concentration at the bend inlet after a conveying distance of 5 m, comparison for different particle sizes (size distribution according to Figure 2.54 and monosized cases according to Table 2.5); (D = 150 mm, U_{av} = 27 m/s, η = 0.3, $\Delta\gamma$ = 10°, four-way coupling).

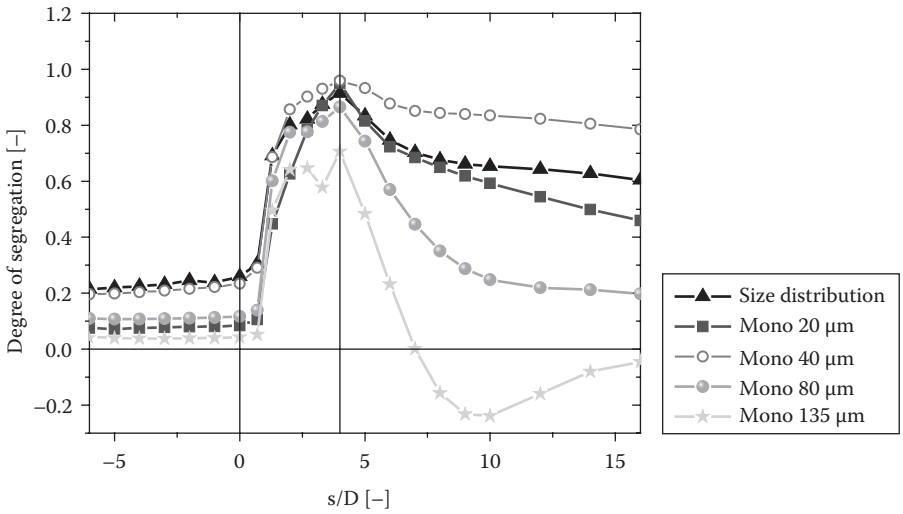


Figure 2.60

Nondimensional segregation parameter (Equation 2.333) along the pipe system for cases ❶ to ❺ in Table 2.5 (D = 150 mm, U_{av} = 27 m/s, η = 0.3, $\Delta\gamma$ = 10°, bend radius 2.54 pipe diameters, four-way coupling); vertical lines indicate bend inlet and outlet.

3. The larger particles (80 and 135 µm) are hardly affected by turbulence, and gravitational settling is more or less balanced by wall collision phenomena (i.e., the shadow effect). Consequently, the concentration maximum is found near the pipe core. Due to the large response distance of the 135 µm particles (i.e., λ_p = 194 mm), they are most likely bouncing from wall to wall (Sommerfeld, 2003).
4. With particle size distribution (Figure 2.54, dp, mean = 40 µm), the concentration profile is quite close to the result for the monosized 40 µm particles; however, due to the presence of smaller and larger particles in the size spectrum, they are slightly better dispersed (Figure 2.59).

The development of the particle concentration distribution along the pipe system may also be characterized in summary through a nondimensional segregation parameter that is a weighted average of the

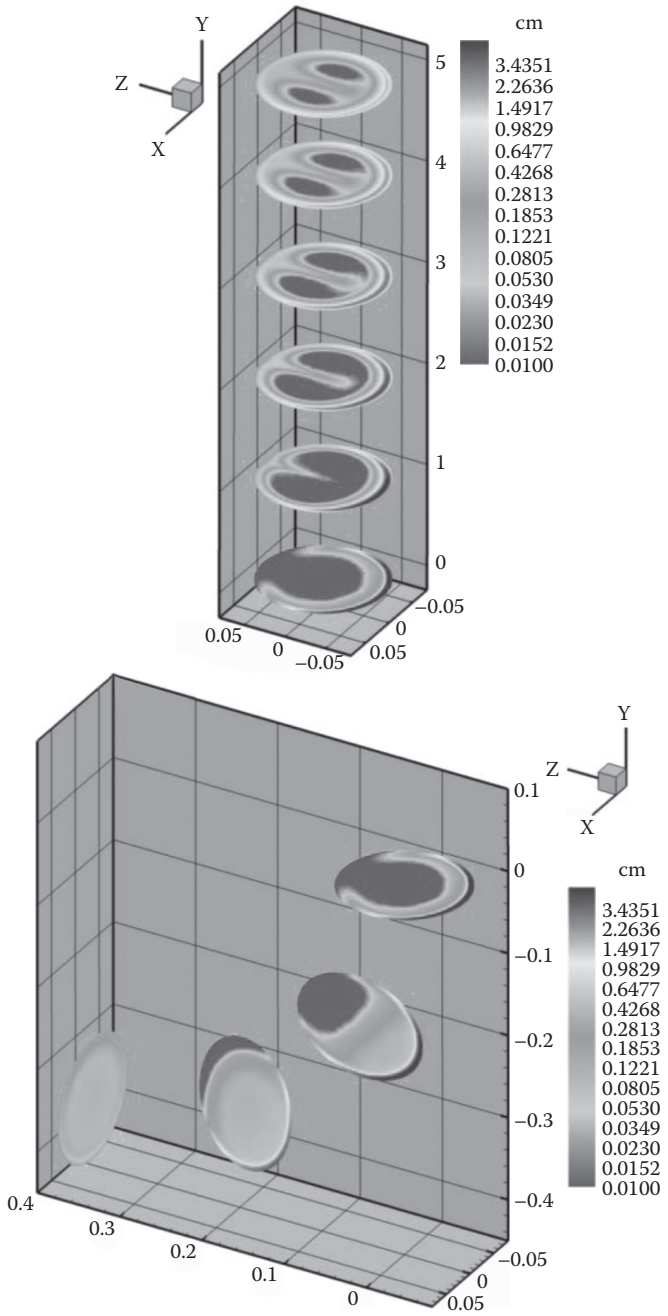


Figure 2.61

Cross-sectional distribution of particle concentration cm (kg/m^3) along bend and vertical pipe (5 m horizontal pipe, bend, 5 m vertical pipe, bend radius 2.54·D, D = 150 mm, U_0 = 27 m/s, η = 0.3, $\Delta\gamma$ = 10°, four-way coupling, monosized 20 μm).

local particle concentration with respect to the radial displacement of the control volume from the pipe center within each cross section:

$$R_{c,max} = \frac{1}{c_{av} R_o V_{cross}} \sum_{1}^{N_i} c_i r_i V_i \tag{2.344}$$

where

c_i is the particle concentration (kg/m^3) in the computational cell
r_i is the vector indicating the center of the cell
V_i is its volume

The product of these three quantities is summarized over all control volumes in one cross section and divided by the average concentration, c_{av}; the pipe radius R_o; and the total volume of the cross-sectional slice V_{cross}. In the present work, r_i is defined to be positive if the control volume is located below (horizontal pipe) or to the right (vertical pipe) of the center line. Hence, the segregation parameter varies in the range $-1 < R_{c,max} < 1$. Therefore, it is possible to identify the location of the maximum particle concentration within the pipe cross section. A value of $R_{c,max} = 0$ corresponds to a completely homogeneous particle distribution or an exactly symmetric distribution with respect to the center plane, which in the present case is not very likely to occur.

This segregation parameter is plotted versus the nondimensional distance along the pipe centerline s/D in Figure 2.60, where D is the pipe diameter. In the horizontal pipe (s/D < 0), gravitational settling can be clearly identified since $R_{c,max}$ is larger than zero. In the horizontal pipe, the strongest gravitational settling is found for the monosized particles with 40 μm and those with the size distribution (i.e., $R_{c,max} \approx 0.2$). The largest particles (135 μm) are clearly very well dispersed due to wall bouncing effects, and the smallest particles (20 μm) are dispersed by turbulence as described earlier.

Within the bend, the behavior of the particles is governed by their response to the mean flow deflection (characterized by the bend Stokes number), secondary flow structure developing throughout the bend, particle–wall collisions, and finally also interparticle collisions as already demonstrated in Figure 2.58. Although for the 20 μm particles the bend Stokes number is quite small, they are not able to completely follow the flow deflection since they are obviously strongly influenced by the secondary flow (Figure 2.61). Already at a bend angle of 30°, a thin layer of high particle concentration develops at the bend outer wall, and eventually, all particles are transported out of the pipe core region. They are carried along the lateral walls of the bend by the secondary flow toward the inner side of the bend, forming at the bend exit a horseshoe-shaped concentration field. Along the vertical pipe, these small particles are further transported by the secondary flow, fully mapping the secondary flow structure at the end of the vertical segment. Within the core of the two counterrotating vortices, almost no particles are present.

For larger particles (i.e., 40 μm), the development of the concentration pattern throughout bend and vertical pipe is completely different (Figure 2.62). Inertial segregation of the particles through the bend is rather strong, and a quite dense rope is formed at the bend exit, which is supported by the fact, that the bend Stokes number approaches unity; that is, ($St_B = 0.557$). The dip in the concentration distribution visible at a bend angle of 60° and at the bend outlet is a result of the particle transport by the secondary flow. More clearly, the transport of the 40 μm particles by the secondary flow becomes visible 1 m downstream of the bend exit where the particles start to be carried along the lateral side walls toward the inner side. At the end of the vertical pipe, the particle distribution in the cross section is still inhomogeneous leaving a core region with almost no particles. For the 40 μm particles, the degree of segregation is largest throughout the entire pipe system showing an almost complete segregation at the bend exit (Figure 2.60).

When the particle size is further increased (Figures 2.63 and 2.64), wall collision and inertial effects become more and more dominating over the developing particle concentration distribution in the pipe system. Consequently, the region with particles being present in the bend is increasing, which is the result of a farther rebound of the particles after a collision with the bend outer wall. The 80 μm particles fill about half the pipe cross section at the end of the bend and the 135 μm particles already more than about 90%. Consequently, the segregation parameter is lower for the 135 μm particles than for the 80 μm particles (Figure 2.60). For both particle sizes, the focusing effect is visible at the bend angle of 60°. In the case of the 80 μm particles, the dust rope is being disintegrated rather slowly. Particle transport happens mainly through secondary flow (Figure 2.63; 1 and 2 m downstream the bend exit). In contrary, the heavy particles (135 μm) are bounced back from the bend outer wall near the exit and move toward the inner side. Consequently, the high-concentration region appears left of the vertical center plane (Figure 2.64; 1 m downstream the bend exit). This results in negative values for the segregation parameter (Figure 2.60).

The evolution of particle concentration throughout the bend and the initial part of the vertical pipe (i.e., up to s/D = 17, corresponding to 1.8 m) may also be characterized by considering the maximum value within a cross section normalized with the average concentration (Figure 2.65). From the beginning toward the end of the bend, the concentration maximum increases rapidly for all particles sizes considered. In the case of the small 20 μm particles ($St_B = 0.139$) where inertial effects are weak, the maximum concentration ratio reaches only a value of about 30. Then increasing particle size and approaching a Stokes number of the order one, the maximum value rapidly increases to about 200 for the 40 μm particles ($St_B = 0.557$), which show the strongest segregation (see Figure 2.62). Beyond $St_B = 1$ (no results available for this case) particle inertia becomes more and more important (i.e., particles begin to bounce from wall to wall), whereby the maximum concentration ratio again drops down and reaches eventually a rather low value for the 135 μm

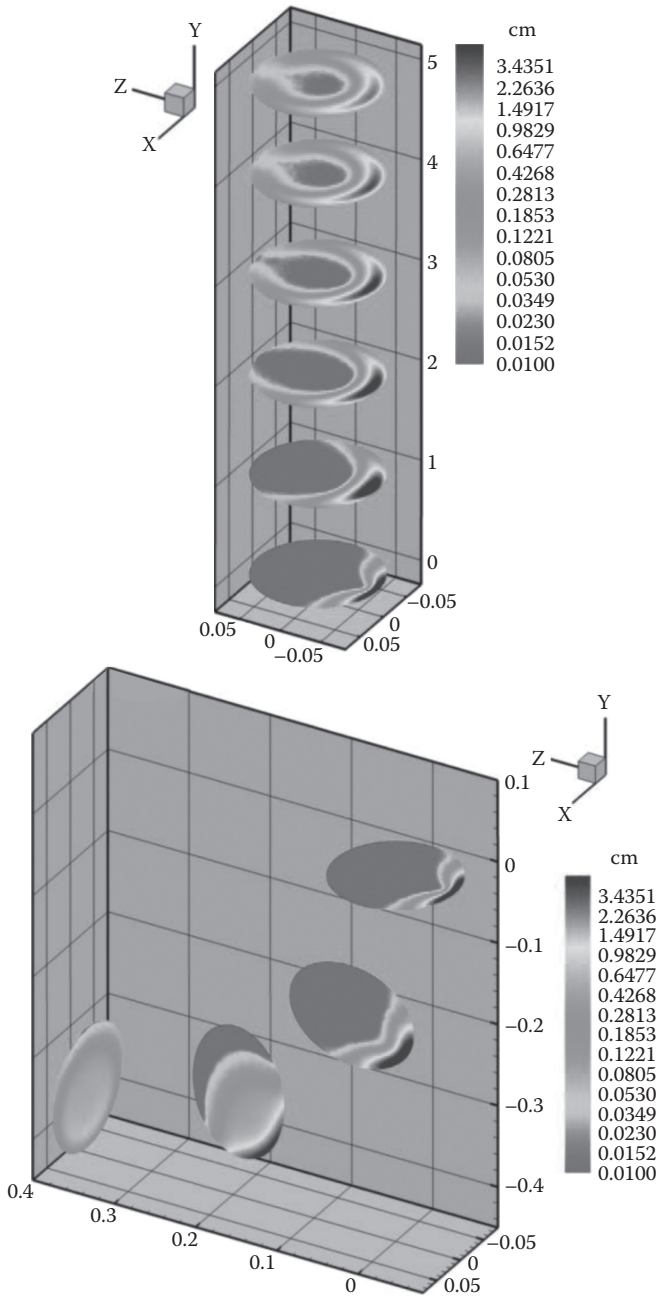


Figure 2.62

Cross-sectional distribution of particle concentration cm (kg/m³) along bend and vertical pipe (5 m horizontal pipe, bend, 5 m vertical pipe, bend radius 2.54·D, D = 150 mm, U_0 = 27 m/s, η = 0.3, Δγ = 10°, four-way coupling, monosized 40 μm).

particles (i.e., St_B = 6.344). From the end of the bend, the concentration ratio continuously decreases for all size cases indicating the dispersion of the dust rope. However, the 40 μm particles still show a high value, indicating a remaining strong segregation (see Figure 2.62).

2.6.3.5 *Influence of Mass Loading*

The influence of particle mass loading on the particle concentration distribution throughout the standard pipe system is analyzed for the case with particle size distribution (case ❶ in Table 2.5). The result for a mass loading of 0.3 with consideration of interparticle collisions is shown in Figure 2.58b. Here, a rather dense rope is formed within the bend filling a segment region of about 40% within the pipe cross section.

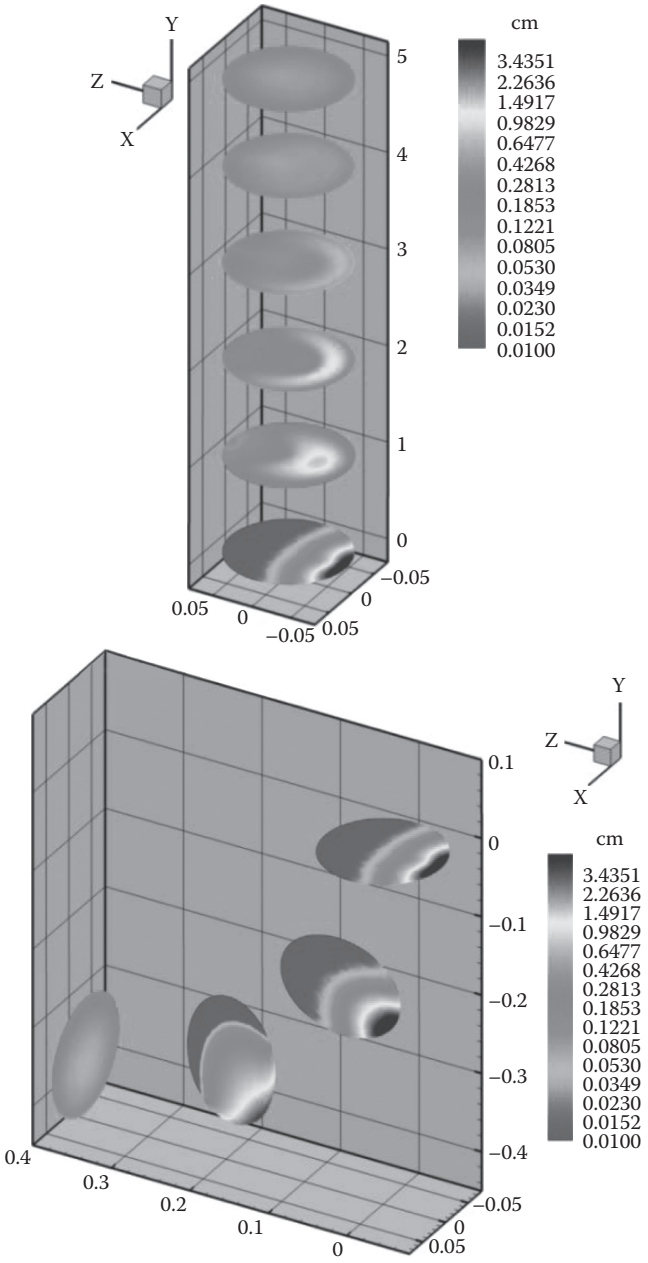


Figure 2.63

Cross-sectional distribution of particle concentration cm (kg/m³) along bend and vertical pipe (5 m horizontal pipe, bend, 5 m vertical pipe, bend radius 2.54·D, D = 150 mm, U_0 = 27 m/s, η = 0.3, Δγ = 10°, four-way coupling, monosized 80 μm).

In the vertical pipe, this dense particle region is rather quickly dispersed yielding an almost homogeneous particle distribution about 3 m downstream of the bend exit. In the case with a mass loading of 1.0, several phenomena may be observed. First, the gravitational settling of the particles in the horizontal pipe is more pronounced (Figure 2.66a). The particle rope formed within the bend is more concentrated for higher mass loading, and at the bend exit, the particles fill only about 30% of the cross section. Of course, the magnitude of particle concentration at the bend outer wall is much higher compared to the low loading case (see Figure 2.58). For the high mass loading, the concentrated rope formed within the bend is not disintegrating very well within the vertical pipe, even after 5 m conveying; however, the rope is expanding laterally along the side walls, being caused by the secondary flow in the pipe cross section. This transport of mainly the smaller particles by the secondary flow is clearly visible in the cross-sectional concentration field 2 m

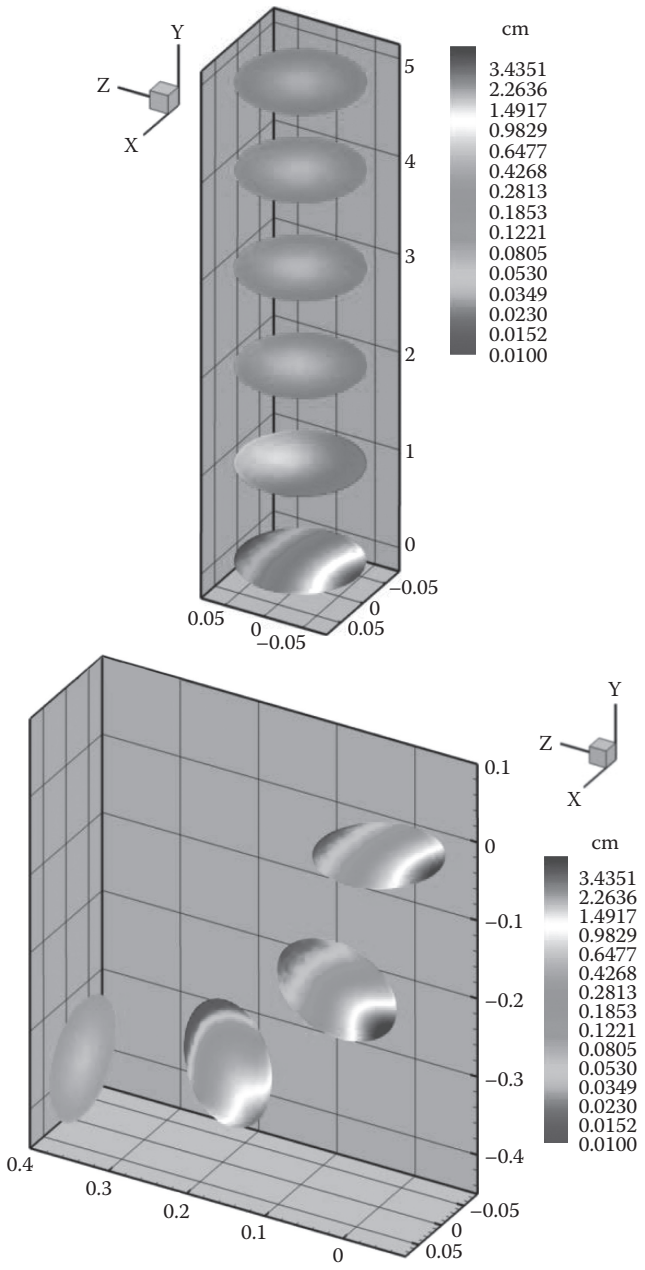


Figure 2.64

Cross-sectional distribution of particle concentration cm (kg/m³) along bend and vertical pipe (5 m horizontal pipe, bend, 5 m vertical pipe, bend radius 2.54·D, D = 150 mm, U_0 = 27 m/s, η = 0.3, Δγ = 10°, four-way coupling, monosized 135 μm).

downstream the bend exit (Figure 2.66a). Here, the particles are transported by the secondary flow from the inner side (left) to the outer side of the cross section, just in the middle between the counterrotating two main secondary vortices. As a result of the strong coupling between the phases and the focusing effect, the secondary flow is remarkably altered within the bend and in the first part of the vertical pipe (Figure 2.66b). Counterrotating particle-induced vortices are already visible at a bend angle of 60° and are preserved in the vertical pipe up to about 1 m downstream of the bend exit. Then they are again entrapped by the two main vortices and eventually disappear. The fact, that the particle rope is not disintegrated even after 5 m conveying in the vertical pipe, is mainly caused by the entrapment of the particles within the high-concentration region as a consequence of interparticle collision. Due to the high particle concentration, the mean free path between particle collisions is remarkably reduced so that the particles are not able to move out of the rope;

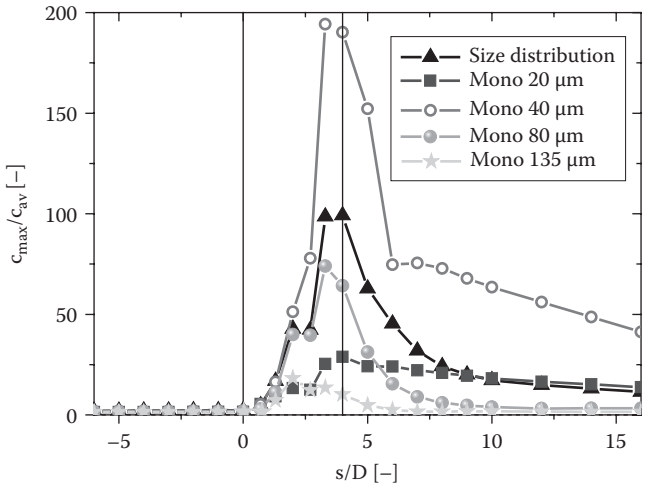


Figure 2.65

Maximum values of particle concentration (in kg/m³) within a cross section normalized with the average concentration along the bend with inlet and outlet sections in the straight pipes for cases ❶ to ❺ in Table 2.5 (D = 150 mm, U_{av} = 27 m/s, η = 0.3, Δγ = 10°, bend radius 2.54 pipe diameters, four-way coupling); vertical lines indicate bend inlet and outlet.

instead, they collide with particles within the rope and bounce back. The cross sections of the streamwise gas velocity being perpendicular to the planes (color coded) reveal that the air velocity within the particle rope is remarkably reduced resulting from two-way coupling (Figure 2.66b).

2.6.3.6 *Effect of Particles on Flow Structure*

In the following section, the secondary flow modification or secondary flow intensity (SFI) that is affected by two-way coupling and will also be influenced by interparticle collisions is analyzed in some more detail. First, the cross-sectional distributions of air velocity and secondary flow structure along bend and vertical pipe are considered for the 40 µm monosized particles comparing two- and four-way coupling (see Figure 2.67). As emphasized earlier, the particle rope formed within the bend is much wider when neglecting interparticle collisions (see Figure 2.58 for the case with size distribution). Accounting for interparticle collisions, the particle moving into the bend will collide with particles being rebound from the bend outer wall and hence the region of high particle concentration is "compressed"; that is, the particles are eventually "trapped" in the powder rope that is much more concentrated in this case. This is reflected in the distribution of the streamwise air velocity along the pipe system originating from two-way coupling. With two-way coupling, relatively wide regions near the bend and vertical pipe outer wall exhibit low gas velocities (Figure 2.67a), being about 75%–80% of the bulk gas velocity. These regions coincide with those of the dust rope where the particles have to be reaccelerated and lifted up against gravity, extracting the required momentum from the gas phase. With interparticle collisions, the dust rope is much more narrow (compare Figure 2.58), and hence, the regions with low gas velocity near the outer wall (right-hand side) are considerably smaller than without collisions (compare Figure 2.67a and b).

The white lines in Figure 2.67 show the cross-sectional air velocity streamlines. In the case of two-way coupling only, two counterrotating vortices develop in the region of high particle concentration between the second and third cross section of the bend and extend into the vertical pipe (Figure 2.67a). These vortices result from the rebound of particles from the bend outer wall toward the pipe core, whereby momentum is transferred to the fluid inducing these vortices. This phenomenon was called focusing effect in Lain and Sommerfeld (2013). The particle-induced vortices extend into the vertical pipe up to about 2 m from the bend exit. Further downstream, the particle-induced counterrotating vortices again decay, but the overall structure of the secondary flow is nevertheless strongly altered compared to the single-phase flow. With interparticle collisions (Figure 2.67b), the dust rope is much more narrow (i.e., particles are trapped within the rope due to collisions between them) and hence also the region with reduced gas velocity. Therefore, strong counterrotating vortices do not develop for this condition and can be only identified within the third cross section of the bend. In conclusion, the flow modification by the particles is much lower in four-way coupling than in two-way coupling.

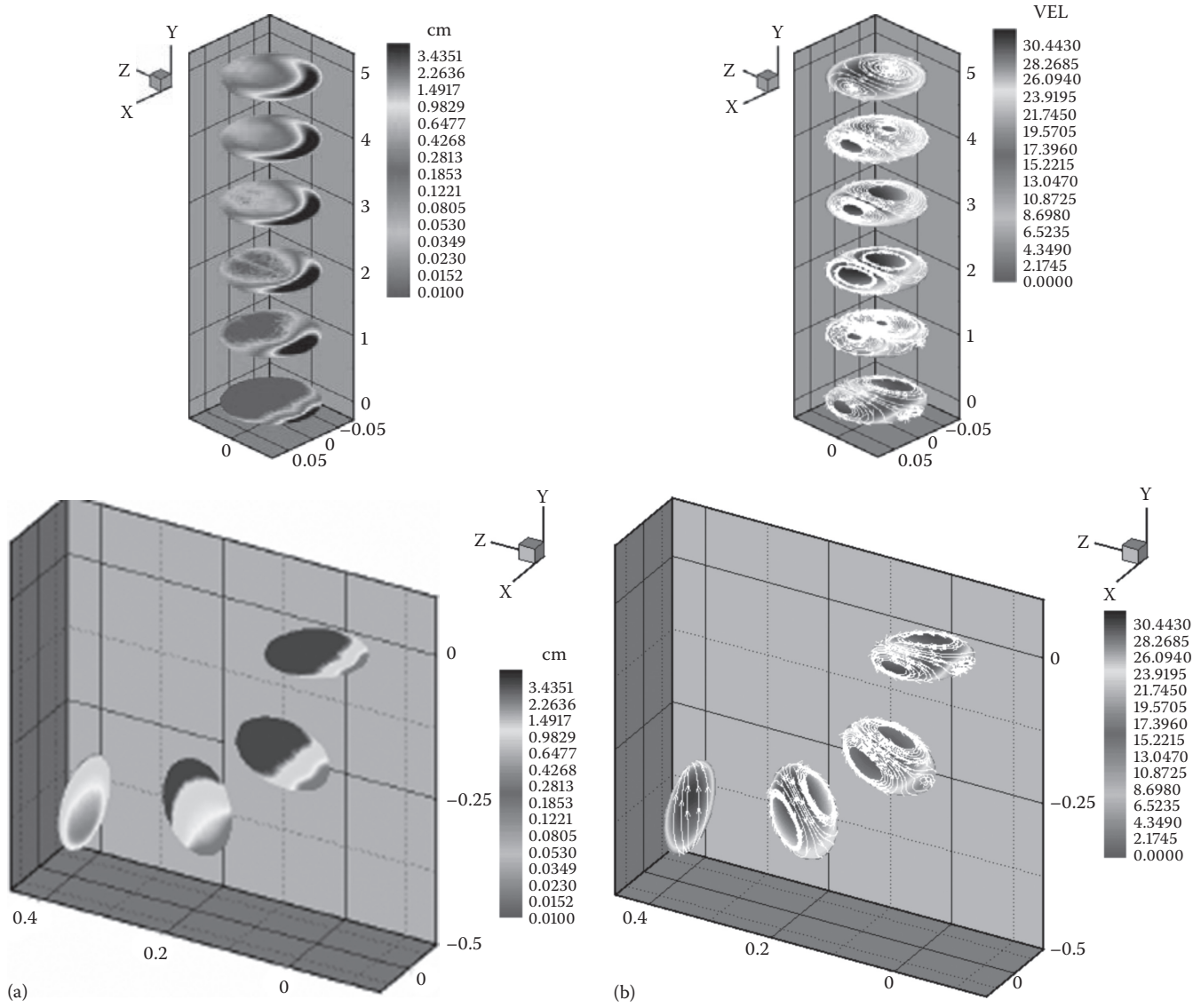


Figure 2.66

Cross-sectional distribution of particle concentration cm (kg/m³) (a) and streamwise air mean velocity *VEL* (m/s) (color) as well as secondary flow stream lines; white lines (b) both along bend and vertical pipe (5 m horizontal pipe, bend, 5 m vertical pipe, bend radius 2.54 · D, D = 150 mm, U_{av} = 27 m/s, η = 1.0, Δγ = 10°, particle size distribution 15–85 μm, four-way coupling).

Also, the other four-way coupled calculations for monosized particles did not show a distinctive development of counterrotating vortices induced through the particles by the focusing effect within bend or connecting vertical pipe. Of course, the secondary flow structure was nevertheless modified by the particles also in four-way coupling. In order to characterize the influence of the particle phase on the secondary flow, the SFI is used, which is obtained for one cross section from:

$$\mathrm{SFI} = \frac{1}{V_{cross}} \sum_{i=N} V_i \frac{U_{1,i}^2 + U_{2,i}^2}{U_{av}^2} \tag{2.345}$$

where

V_i is the volume of a computational cell

V_{cross} is the volume of the cross-sectional slice in the bend or the connecting vertical pipe

$U_{1,i}$ and $U_{2,i}$ are the gas velocity components in each cell lying in the cross-sectional planes

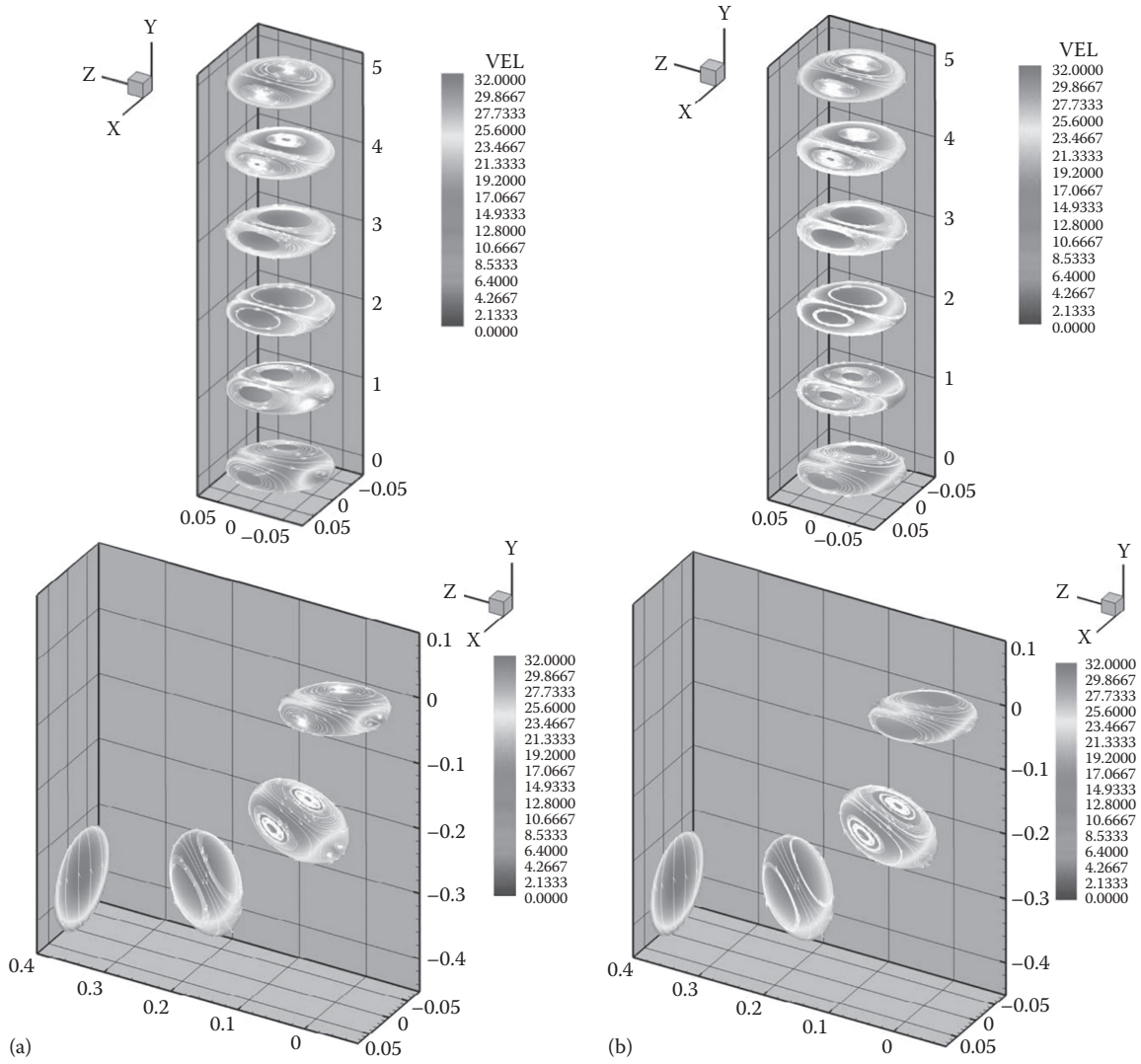


Figure 2.67

Cross-sectional distribution of streamwise air mean velocity *VEL* (m/s) (color) as well as secondary flow stream lines (white lines) both along bend and vertical pipe comparing (a) two-way coupling and (b) four-way coupling (5 m horizontal pipe, bend, 5 m vertical pipe, bend radius 2.54 · D, D = 150 mm, U_{av} = 27 m/s, η = 0.3, Δγ = 10°, particle size 40 μm).

As shown in Figure 2.68 for the development of SFI along the extended bend in the case of four-way coupling, the strongest reduction of the SFI within the first part of the bend (i.e., up to about 70° bend angle) is observed for the larger particles due to their relatively strong rebound and the involved more pronounced focusing effect (see Figures 2.63 and 2.64). Toward the end of the bend and along the vertical pipe, however, the smallest particles (i.e., 20 μm) yield the strongest decay of the SFI as they are closely interacting with the secondary flow and occupy a relatively large region of the pipe cross section; see Figure 2.61 (note there is however still slip between the phases). The lowest SFI modification is observed for the case with particle size distribution.

As shown earlier, also interparticle collisions have an influence on SFI (Figure 2.69), as the particle concentration distribution is modified (i.e., the extent of the dust rope in the bend is mostly reduced), mainly in the bend and the vertical pipe, which is summarized in Figure 2.69 for the overall values of SFI in the pipe bend and the vertical pipe separately in dependence of particle size. Naturally, the influence of particles on fluid flow yields a reduction of SFI compared to single-phase flow. With increasing particle size, the SFI for two-way coupling is continuously reduced in the bend with growing particle diameter. In the vertical pipe, SFI is almost independent of particle size and shows only a slight maximum for the 40 μm particles. When accounting for interparticle collisions, the SFI is mostly increasing again for the particle size cases considered;

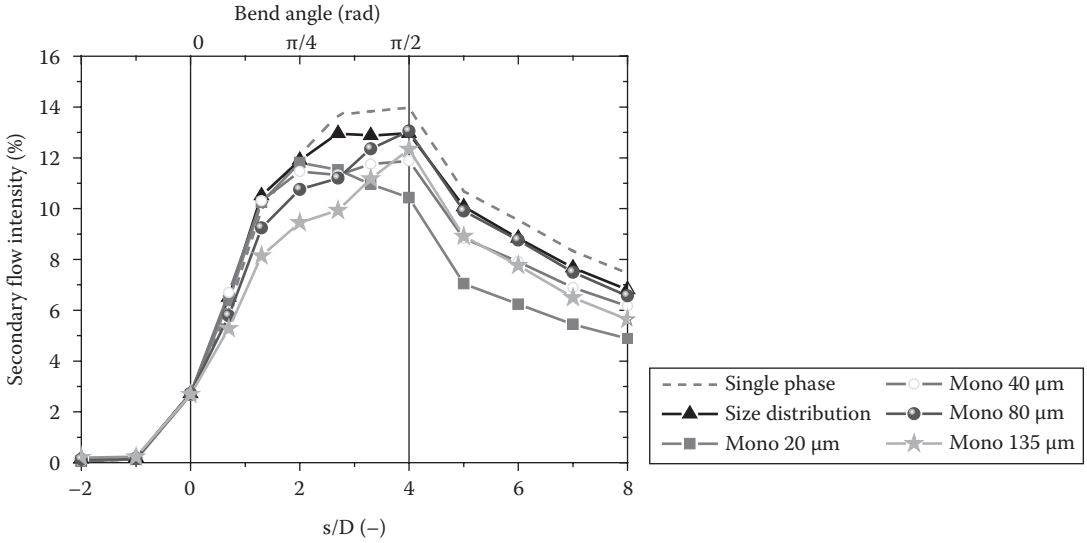


Figure 2.68

SFI (Equation 2.334) along the bend with inlet and outlet sections in the straight pipes for cases ❶ to ❺ in Table 2.5 (5 m horizontal pipe, bend, 5 m vertical pipe, bend radius 2.54 · D, D = 150 mm, U_{av} = 27 m/s, η = 0.3, Δγ = 10°, bend radius 2.54 · D, four-way coupling); vertical lines indicate the bend inlet and outlet.

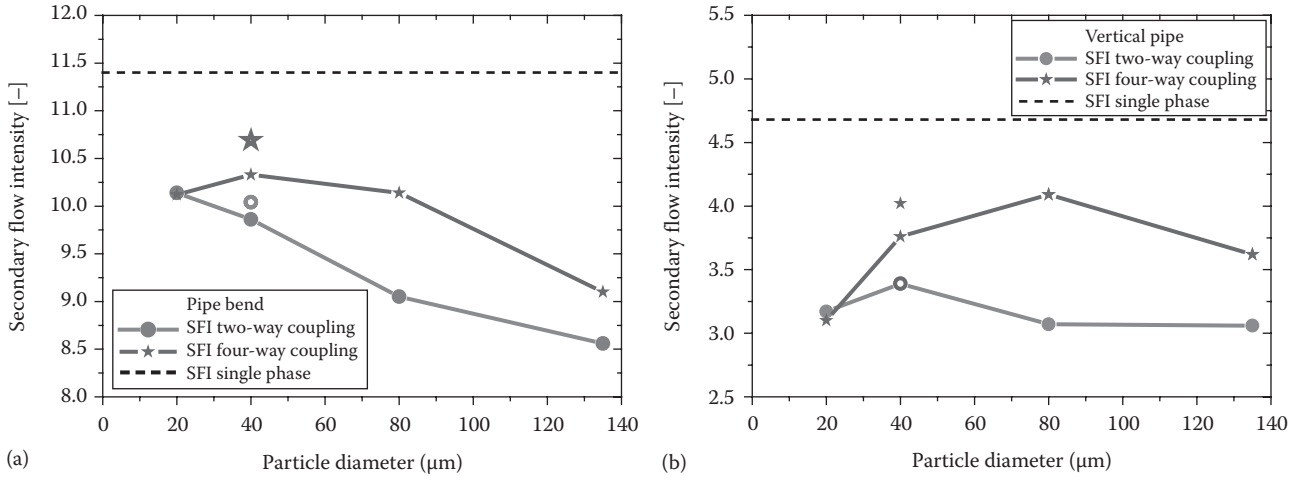


Figure 2.69

Averaged value of SFI along the bend (a) and the vertical pipe (b) for cases ❶ through ❺ in Table 2.5 in dependence of particle size; comparison of two- and four-way coupling; the open circle and star indicate the result for the size distribution (case ❶ in Table 2.5) with a number mean diameter of 40 µm (5 m horizontal pipe, bend, 5 m vertical pipe, bend radius 2.54 · D, D = 150 mm, U_{av} = 27 m/s, η = 0.3, Δγ = 10°).

however, this increase depends on particle inertia and hence the bend Stokes number. This implies that the flow modification by the particles is again reduced. There is almost no difference between two- and four-way coupling for the 20 µm particles with a small St_B = 0.139 (bend and vertical pipe). Then the difference increases, reaching a maximum for the 80 µm particles having a Stokes number of around unity (i.e., St_B = 2.228) for both bend and vertical pipe. For further growing particle size and bend Stokes number, the difference of SFI obtained for two- and four-way coupling is again reduced. For such large particles, the SFI within the bend has the lowest value (i.e., the strongest SFI modification by the particles) since the particles are dispersed over a wide region of the bend. Within the vertical pipe, the strongest flow alteration by the particles is found for the 20 µm particles. Also, the SFI for the case with particle size distribution is indicated in Figure 2.69 as open symbols. With two-way coupling, the SFI is almost identical with the value of the 40 µm monosized particles. However, with four-way coupling, the secondary flow modification by the particles is lower.

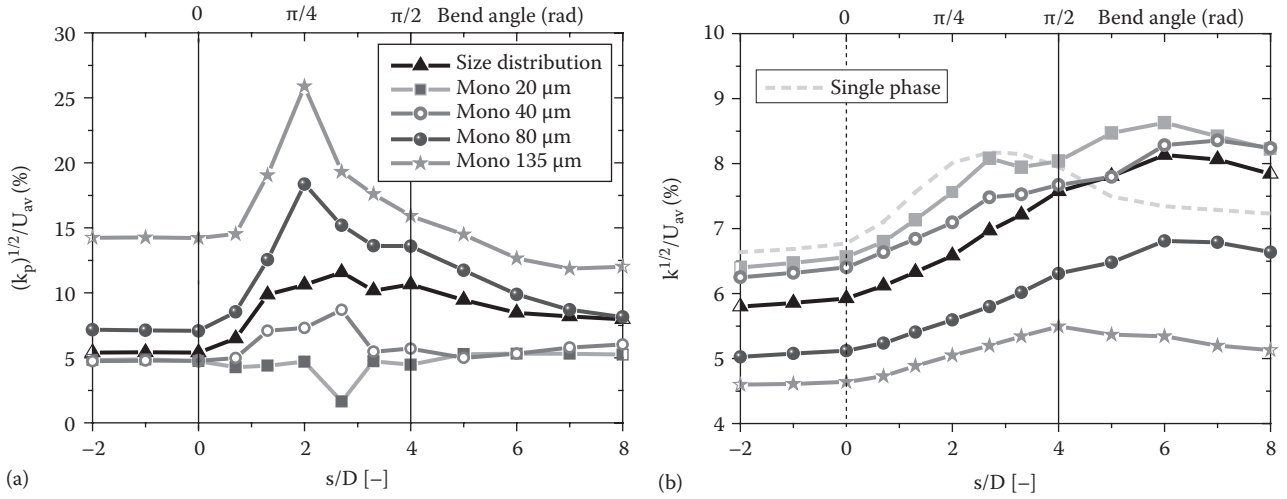


Figure 2.70

Fluctuating energy along the extended pipe bend configuration: (a) particle phase and (b) gas phase (5 m horizontal pipe, bend, 5 m vertical pipe, bend radius 2.54·D, D = 150 mm, U_{av} = 27 m/s, η = 0.3, Δγ = 10°, four-way coupling, different particle sizes).

In the following, cross-sectional averages of the normalized fluctuating velocities of both phases along an extended bend section (i.e., –2 < s/D < 8) are discussed, which are obtained as $k^{1/2}/U_{av}$ and $k_P^{1/2}/U_{av}$, respectively. Generally, the average fluctuating velocity of the particles increases with particle size in the entire considered pipe element (Figure 2.70a). This is associated with the growing particle inertia and the involved increasing importance of particle–wall collisions. Consequently, at the end of the horizontal pipe, the largest particles have the highest averaged fluctuating velocity. Note that these large particles may be expected to bounce from wall to wall (Sommerfeld, 2003). When the particles enter the bend, the wall collision frequency is increasing since the particles cannot follow the flow deflection completely. This of course is depending on the particle size and hence the bend Stokes number. As shown earlier, the wall rebound distance increases with particle size whereby particles with higher inertia are being further bounced back from the bend outer wall toward the pipe core (see Figures 2.61 through 2.64). Consequently, larger particles show a more random motion while smaller particles rather quickly follow the flow deflection. Thus, the particle mean fluctuating velocity drastically increases with particle size. Ultimately, the deflection of the particle stream in the first part of the bend yields growing particle fluctuating velocities, that is, up to about 45° bend angle for the largest particles and up to about 60° for the 40 µm particles. Further downstream, the deflection of the particle stream is largely completed and a more or less dense rope is formed at the bend outer wall. Therefore, the wall collision frequency is reduced, and additionally, the particles are trapped in the rope by interparticle collisions resulting in the damping of the fluctuating motion. Therefore, the particle velocity fluctuations are continuously reduced throughout the bend outlet section and the connecting vertical pipe approaching a new equilibrium value (Figure 2.70a). An exception is the development of the average fluctuating velocity for the smallest particles (20 µm) along the pipe segment. Due to the rapid response of these small particles to the flow deflection and the secondary flow structure, they begin quickly to slide along the bend outer wall and mainly remain in the low-flow-velocity region (see Figure 2.61). The particle velocity fluctuations for the case with size distribution are lying between those of the 80 and 40 µm monosized particles; however, rise beyond their values in the vertical pipe as a consequence of the different response of particles in a wide size spectrum, which was demonstrated by Sommerfeld (1990) for a vertical channel flow.

Cross-sectional averages of gas-phase fluctuation velocity along the bend with inlet and outlet sections are shown in Figure 2.70b. With increasing particle size, the gas-phase fluctuating velocity is remarkably reduced by the particles compared to the single-phase flow in the considered pipe segment. This continuously increasing turbulence dissipation with growing particle size is a consequence of indirect coupling through the momentum source terms (e.g., reduction of SFI and streamwise mean velocity within the dust rope) and direct coupling through the source terms in the k- and ε-equation. The single-phase turbulent kinetic energy increases continuously in the first part of the bend (i.e., up to about 70° bend angle) and then reduces again to approach a new equilibrium value in the vertical pipe, which is of course higher as in the horizontal pipe (Figure 2.70b). The increase of $k^{1/2}/U_{av}$ is associated with the deformation of the streamwise

mean velocity distribution and the development of the secondary flow that first increases up to the bend exit and then decreases in intensity along the vertical pipe section (Figure 2.68).

For most of the different particle size cases, the gas-phase fluctuating velocity continuously increases throughout the bend and also within the first part of the vertical pipe (i.e., up to about s/D = 6), except for the 135 µm particles (Figure 2.70b). As said earlier, this is a consequence of the modification of the streamwise mean gas velocity distribution and the secondary flow structure by the particles. Therefore, also the gas-phase fluctuating velocity becomes larger than the values for the single-phase flow at the beginning of the vertical pipe in the case of the small particles (i.e., 20 and 40 µm) and that with particle size distribution. This implies that turbulence is enhanced through the particles as an outcome of the strong particle segregation and the resulting introduction of additional shear to the gas flow at the edge of the high-concentration region. In more detail, within the narrow dust rope, the streamwise gas velocity is lowest as a result of momentum coupling. At the inner edge of the dust rope, the streamwise gas velocity increases toward the maximum value near the core (see also Figure 2.56), yielding high shear rates whereby turbulence is generated.

For larger particles (i.e., 80 and 135 µm), turbulence is distinctively lower throughout the entire pipe system compared to the single-phase flow and the small particle cases (Figure 2.70b). This is motivated by two effects. First, as a consequence of their inertia and wall rebound, the larger particles are distributed over a bigger region of the pipe cross section within bend and vertical pipe (compare Figures 2.61 through 2.64). Therefore, the particles also affect a larger region of the flow through two-way coupling and reduce turbulence. Second, the slip velocity between gas and particles increases with particle size, whereby the momentum source terms are also growing and consequently reduce turbulence more intensely. It should be mentioned that turbulence generation by the particles through their wakes is not occurring for the present cases (Gore and Crowe, 1989, Hetsroni, 1989, Crowe, 2000, Lain and Sommerfeld, 2003), as the particle Reynolds number is much lower than 200–400 even for the largest particles.

2.6.3.7 Analysis of Pressure Drop

For all the cases discussed earlier, the pressure drop in the entire pipe system, as well as that in the individual pipe elements, was determined from the calculations (Table 2.6). In pneumatic conveying, the pressure drop is composed of the single-phase pressure drop and the additional pressure drop due to the presence of the particles (Lain and Sommerfeld, 2013). This additional pressure drop, of course, depends on conveying velocity, mass loading, particle properties, and pipe geometry and material. In the following, the different effects responsible for the additional pressure drop are summarized and values are calculated with the correlations used for engineering design (Siegel, 1991), exemplarily for case ❶ in Table 2.6:

- Momentum loss due to particle–wall collisions (i.e., often termed particle–wall friction) is relevant for all pipe elements and depends on the wall collision frequency. With an assumed particle friction λ_{Part} according to Sommerfeld and Kussin (2003), one obtains for the different pipe elements with Equation 2.345 the following values:

$$\Delta p_{pwc} = \eta \lambda_{Part} \frac{L}{D} \frac{\rho}{2} U_{av}^2 \tag{2.346}$$

Table 2.6 Calculated Pressure Drop across the Different Pipe Elements for the Various Conditions Considered (D = 150 mm, U_{av} = 27 m/s, η = 0.3 [Except for the Case with η = 1.0], Δγ = 10° (Except for the Case with Δγ=1.5°), 5 m Horizontal Pipe, Bend, and 5 m Vertical Pipe, Bend Radius 2.54 Pipe Diameters, Four-Way Coupling)

Case	Δp Total (Pa)	Δp Hor. (Pa)	Δp Bend (Pa)	Δp Vertical (Pa)
Single phase	556	231	92	233
❶ η= 0.3	770	280	145	345
❶ η = 1.0	902	361	139	402
❶ Δγ=1.5°	757	265	130	362
❷20 µm	744	254	158	332
❸ 40 µm	740	265	126	349
❹ 80 µm	833	309	154	370
❺ 135 µm	1129	449	167	513
❻ 30 + 60 µm	748	276	142	330

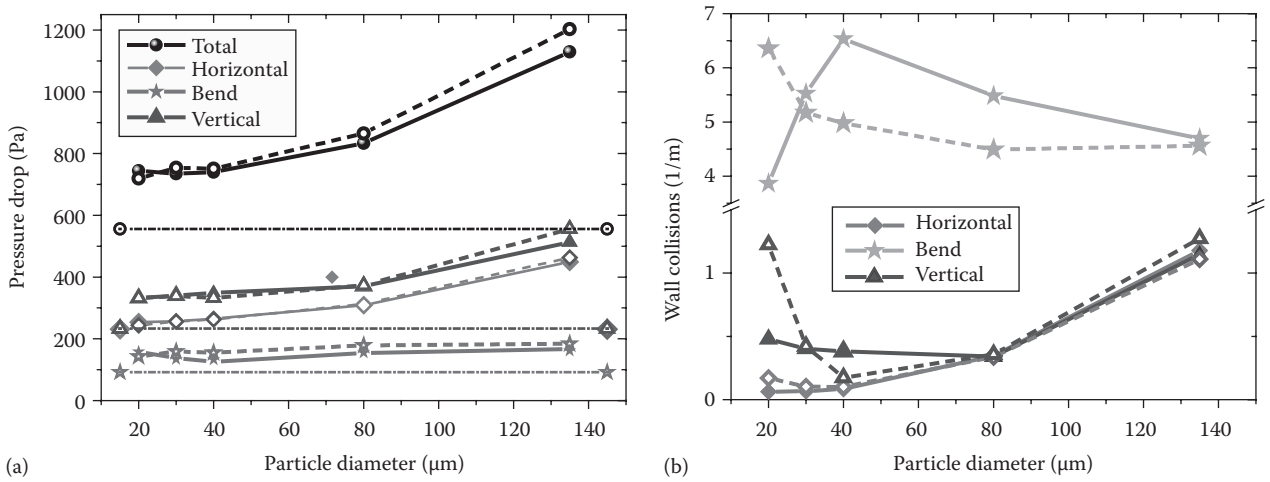


Figure 2.71

Dependence of pressure drop (a) and wall collision frequency (b) on particle size showing the influence of interparticle collisions (i.e., two- versus four-way coupling): closed lines and closed symbols, four-way coupling; dashed lines and open symbols, two-way coupling; and horizontal dash–dot lines with open symbols, single-phase flow pressure drop (5 m horizontal pipe, bend, 5 m vertical pipe, bend radius 2.54·D, D = 150 mm, U_{av} = 27 m/s, η = 0.3, Δγ = 10°).

Horizontal pipe (λ_{Part} = 0.01), 44 Pa
Pipe bend (λ_{Part} = 0.02), 10 Pa
Vertical pipe (λ_{Part} = 0.02), 88 Pa

(Due to the higher wall collision frequency in bend and vertical pipe here, a value of λ_{Part} = 0.02 was assumed; see Figure 2.71b.)

- Particle reacceleration after frequent wall collisions in the bend. Typically, the averaged particle velocity within the bend is reduced by about 20% of the average conveying velocity; this effect is relevant for the bend and partly also for the vertical pipe. According to Equation 2.346 and with $\Delta U_{p,acc}/U_{av}$ = 0.2, one obtains Δp_{pacc} = 52 Pa using the following equation:

$$\Delta p_{pacc} = 2\eta \frac{\Delta U_{p,acc}}{U_{av}} \frac{\rho}{2} U_{av}^2 \tag{2.347}$$

- Particle lifting in the 5 m long vertical pipe against gravity (since the particles are relatively small, it is assumed that $U_{av}/U_{p,av}$ = 1 and one obtains Δp_{plift} = 18 Pa):

$$\Delta p_{plift} = \eta \rho L g \frac{U_{av}}{U_{p,av}} \tag{2.348}$$

- Modification of the SFI in bend and vertical pipe has a minor effect due to the rather small modifications by the particles as shown in Figures 2.68 and 2.69.

In this estimate, the high number of particle–wall collisions occurring in the bend and vertical pipe (see Figure 2.71b) is considered by doubling the wall friction coefficient and the secondary flow modification is not accounted for. The total additional pressure drop for the particle phase is then obtained as 212 Pa (Δp_{hor} = 44 Pa, Δp_{bend} = 62 Pa, Δp_{vert} = 106 Pa). According to Table 2.6, the numerically calculated additional pressure associated with the particles in case of four-way coupling is 214 Pa, indicating that the estimate (Equations 2.344 to 2.346) is already very good, also for the individual pipe elements. It should, however, be kept in mind that the wall friction coefficient was estimated accounting for wall roughness and particle size (Sommerfeld and Kussin, 2003) and that it was assumed that the particle velocity in the bend is reduced by 20%. Moreover, it was presumed that the wall friction in bend and vertical pipe has twice the value assumed for the horizontal pipe, as the wall collision frequency is higher in these pipe segments (see Figure 2.71b) giving of course higher wall friction coefficients.

The calculated gas- and particle-phase pressure drop summarized in Table 2.6 for the different pipe elements allows for the following conclusions:

- Increasing wall roughness enhances wall collisions (through the shadow effect) and hence particle-phase pressure drop due to the required reacceleration of the particles by the fluid.
- Naturally, the pressure drop is increased with the mass loading of the particles since the absolute number of wall collisions increases.
- When increasing the size of monodispersed particles in the range considered here (i.e., from 20 to 135 μm), the particle response to turbulence goes from partly responsive to very inertial (see Table 2.5); thus, the overall wall collision frequency and the pressure drop increase (see Figure 2.71).
- The total pressure drop is the lowest in the bend followed by the horizontal pipe and then the vertical part (see Figure 2.71a). The high pressure drop in the vertical pipe results from particle–wall collisions induced by the bend flow and the required lifting of the particles.
- In the horizontal and vertical pipes, the pressure drop increases distinctively with particle size due to the increase in inertia and wall collision frequency.

The total pressure drop (i.e., gas and particle phase) for the different pipe elements in dependence of particle size is also summarized in Figure 2.71a comparing two- and four-way coupled calculations. The lowest pressure drop is found in the bend due to its size and the highest in the vertical pipe due to the additional effect of particle lifting. In all pipe elements, the pressure drop increases with the particle diameter due to growing particle inertia and wall collision rate, except for the bend region that does not show such strong variations of pressure drop. Interparticle collisions do not have a direct effect on the pressure drop, but only through the alteration of the wall collision rate and the modification of the flow structure (i.e., due to interparticle collisions the dust rope in the bend is compressed and it becomes more concentrated). For all pipe elements, the pressure drop is generally slightly reduced by considering interparticle collisions (Figure 2.71a). However, this trend is changing when going to the very small particles. The smallest impact of collisions between particles on the pressure drop is observed for the horizontal pipe.

In order to explain the main factors by which the pressure drop is modified through interparticle collisions, also the wall collision rate in dependence of particle size (i.e., wall collisions per meter pipe length) was extracted from the simulations for the different pipe elements (Figure 2.71b). For the horizontal and vertical pipe elements, the wall collision rate is increasing with particle size coupled with growing particle inertia; that is, particles increasingly bounce from wall to wall. The wall collision rate is only marginally altered through collisions between particles in the horizontal pipe similar to the pressure drop. The trends for the pipe bend and the vertical pipe are very similar. For the 20 μm particles (i.e., $St_B < 1$), the wall collision rate reduces through interparticle collisions; however, the pressure drop is slightly increased (see Figure 2.71a). In case of particles with $D_P \geq 40$ μm, the wall collision rate within the bend is remarkably higher accounting for interparticle collisions. This is evident, as the particles are trapped in the concentrated rope, bouncing with other particles and also more frequently with the wall. This implies that the decrease in pressure drop through interparticle collisions within the bend (Figure 2.71a) is dominantly the result of flow and pressure gradient modifications (i.e., streamwise velocity field and cross-sectional flow structure) as the dust rope is becoming more concentrated. The effect of growing pressure drop due to increasing wall collision rate is of lower importance in the bend (Figure 2.71b) since the particle reacceleration is the dominant contribution.

In the vertical pipe, the trends regarding the influence of interparticle collisions on the pressure drop closely follow those in the wall collision rate; decreasing wall collision rate also yields decreasing pressure drop (40 μm particles) and vice versa (135 μm particles). Consequently, the particle-phase pressure drop is mainly determined by wall collisions in addition to particle lifting.

As indicated earlier, particle–wall collisions are essentially responsible for the particle-phase additional pressure drop. Therefore, a further analysis of color maps for the wall collision rate (i.e., wall collisions/m^2) throughout the bend is performed for the different particle size cases. Since the small low inertia particles (i.e., 20 μm; $St_B = 0.139$) follow reasonably well the flow deflection through the bend, they also have the lowest wall collision rate as indicated in Figure 2.71b. The majority of wall collisions are observed to occur with the outer wall region of the bend and at large bend angles (i.e., bend angle > 45°), as shown in Figure 2.72a. In accordance with the particle concentration distribution (Figure 2.61), the wall collision rate is also high over a relative wide angular range. When particle size and hence inertia

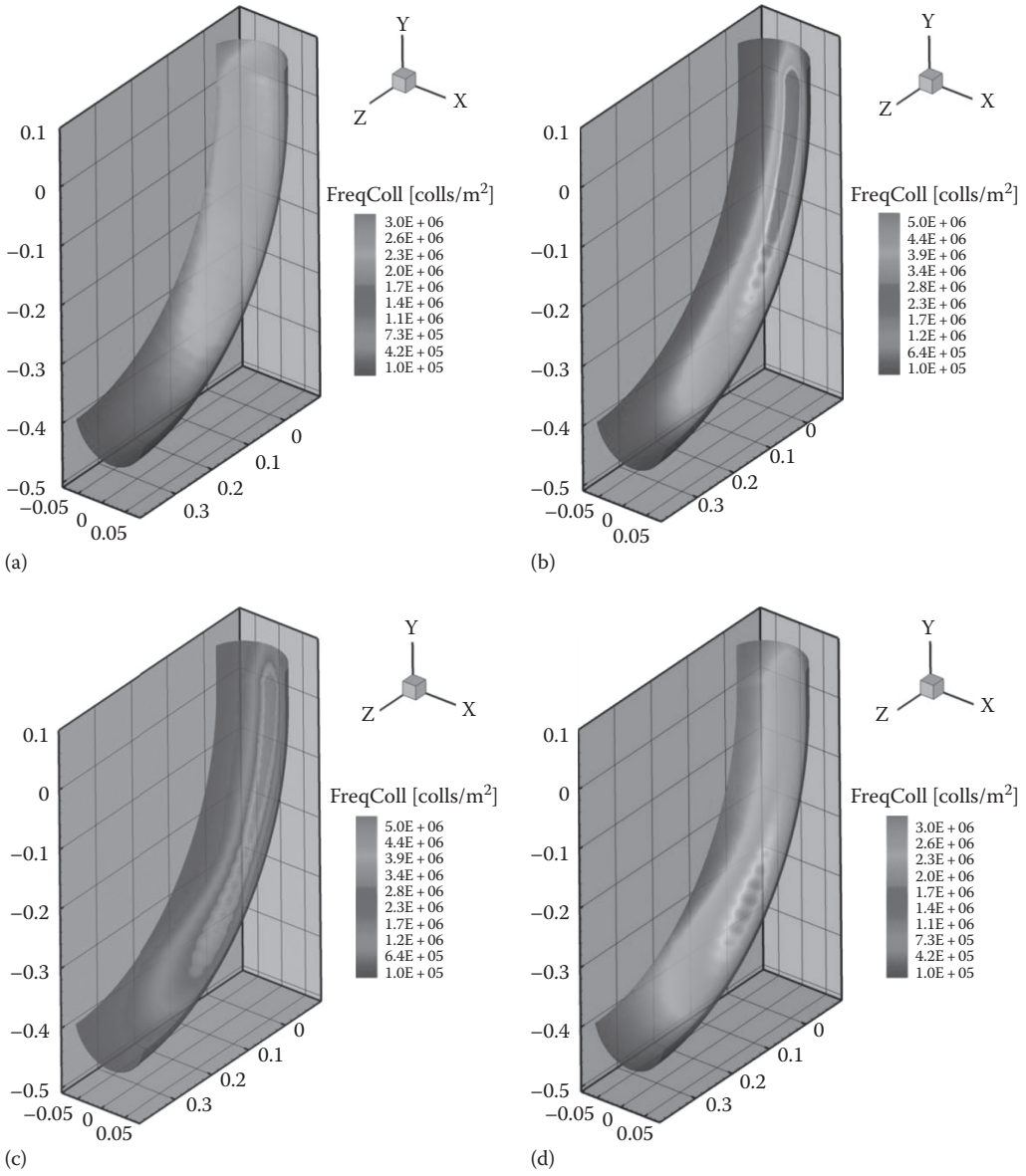


Figure 2.72

Maps of the particle–wall collision rate (collisions/m²) on the outer wall of the bend for different monosized particles: (a) D_P = 20 µm, (b) D_P = 40 µm, (c) D_P = 80 µm, and (d) D_P = 135 µm (5 m horizontal pipe, bend [radius 2.54 pipe diameters], 5 m vertical pipe, D = 150 mm, U_{av} = 27 m/s, η = 0.3, Δγ = 10°, four-way coupling inflow to the bend from the left; note that in graphs (a) and (d), a reduced color scale was used to improve clarity).

are increasing, the wall collision rate is growing (Figure 2.71b) and the pattern at the bend outer wall is shifted toward lower bend angles (i.e., higher wall collision rates are found for θ > 20°) and becomes more narrow (Figure 2.72b). Hence, very high wall collision rates are found in a narrow strip from θ > 40° up to the bend outlet. With a further increase in particle size, the strip of very high wall collision rates is shifted further to the bend entrance and becomes a bit more narrow (Figure 2.72c). These effects are associated with growing particle inertia whereby they are following less and less the flow defection through the bend and the gravitational settling in the horizontal pipe entering the bend that yields a shift of the high-concentration region toward the pipe bottom. The ripple structure in the wall collision pattern observed most pronounced for the 40 and 80 µm particles is a result of the particles' saltation motion along the bend outer wall. The map of wall collision rate is completely changed when considering the very inertial particles (i.e., D_P = 135 µm, St_B = 6.344), which are bouncing from wall to wall when moving through a pipe (Figure 2.72d). First of all, the total wall collision rate is lower due to the reduced number density at

the same mass loading. Second, the region of highest wall impact rates is further shifted toward the bend entrance where the pattern also shows a ripple structure due to saltation motion. Toward the end of the bend, a strip of higher wall collision rate is visible.

2.6.4 Erosion in Pipe Bend

The erosion of wall material in particle-laden confined flows is a severe problem in many areas of process engineering where the process is running for a long time period such as pneumatic conveying, particle separation, especially in cyclones, or fluidized beds. For predicting the erosion rate, mainly Lagrangian models for the particle phase are being used (see, e.g., Pereira et al., 2014). However, also a few studies were done using the two-fluid approach in connection with erosion modeling (see Weickert et al., 2011 and references therein).

As a result of the complexity of single particle erosion and the involved huge number of parameters, generally, erosion experiments are being done to provide input data for the models. Particle erosion is first affected by the involved materials, namely, the wall material and wall surface structure (e.g., wall roughness) and the material of the particles, their shape, and surface structure. This implies that the flow temperature, which influences material properties, also has to be considered. Second, the kinematic parameters of particle motion are of importance, namely, particle velocity (translational and rotation) and particle impact angle. It is generally accepted that the two physical mechanisms that are also coupled with the wall material are relevant for erosion:

- Cutting erosion wear mainly occurring at shallow particle impact angles where swarfs of metal are removed from the wall (Finnie, 1960). This type of erosion is mainly found for ductile material.
- Deformation erosion wear is primarily observed for close to normal particle impact and the material is removed as a result of plastic and elastic surface deformation, mostly after multiple particle impacts. Such kind of erosion is preferably occurring for brittle wall material.

Generally, both erosion phenomena occur at the same time and it is obvious to combine them into one model, as suggested already by Bitter (1963). Following these early research works, numerous erosion models were developed mainly due to the large number of influencing parameters as listed earlier. Consequently, many of the models are very specific to the case considered. For more details on erosion models, the reader is referred to Lyczkowski (2006) and Parsi et al. (2014) for detailed reviews.

This contribution is aimed at highlighting the influence of wall roughness and interparticle collisions (i.e., four-way coupling) as well as mass loading on predicted erosion rates. It should be emphasized that at present wall roughness is not considered directly in a modified erosion rate (which should be realistically also accounted for) but only in an altered wall collision frequency through the shadow effect (Sommerfeld and Lain, 2015) whereby naturally erosion rate is altered.

For describing the combined effect of cutting and deformation erosion, the recently proposed model of Oka et al. (2005) is used. It should be mentioned that the purpose of the Oka et al. (2005) paper was "to propose predictive equations for erosion damage caused by solid particle impact that can be applied to many types of metallic materials under various conditions involving impact angle, velocity, size and the properties of the particles." Therefore, the Oka model has been adopted in this work, which is briefly described as follows.

The predictive equation for erosion damage proposed by Oka et al. (2005) can be expressed as

$$E(\alpha) = g(\alpha) E_{90} \tag{2.349}$$

$E(\alpha)$ and E_{90} denote the volume of eroded material per mass of particles (mm^3/kg), where E_{90} is the erosion damage at normal impact angle

$g(\alpha)$ is the impact angle dependence expressed by two trigonometric functions that also depend on the material Vickers hardness number (Hv) in unit of GPa:

$$g(\alpha) = (\sin\alpha)^{n_1} \left[1 + Hv(1 - \sin\alpha)\right]^{n_2} \tag{2.350}$$

where n_1 and n_2 are the exponents determined by the eroded material hardness and other impact conditions such as particle material properties and shapes. These exponents show the effects of repeated plastic deformation and cutting action, and they are expressed by

$$n_1 = s_1(Hv)^{q_1}; \quad n_2 = s_2(Hv)^{q_2} \tag{2.351}$$

The first factor in Equation 2.349 is associated with repeated plastic deformation or the brittle characteristics and with the vertical component of particle impact energy. It is maximal at normal impact angle. The second term corresponds to the cutting action, which is more effective at shallower impact angles (Oka et al., 2005). The relative cutting action at an arbitrary angle to that at normal angle takes a maximum at 0°. The function $g(\alpha)$ is expressed as the product of the two factors in terms of mutual actions and is a continuous function of the particle–wall impact angle.

The reference erosion ratio E_{90} (erosion damage at normal impact angle) is related to the impact velocity, particle diameter, and eroded material hardness and can be expanded as follows:

$$E_{90} = K\left(aHv\right)^{k_1 b}\left(\frac{u_p}{u_{ref}}\right)^{k_2}\left(\frac{D_p}{D_{ref}}\right)^{k_3} \tag{2.352}$$

where

- u_p and D_p are the impact velocity (in m/s) and the particle diameter (in μm), respectively
- u_{ref} and D_{ref} are, respectively, the reference impact velocity and the particle diameter used in the experiments by Oka et al. (2005)
- The parameters a and b characterize the load relaxation ratio of the wall material
- K denotes a particle property factor, in arbitrary units, that involves particle shape (angularity) and particle hardness
- The exponents k_1 and k_3 are determined by the properties of the particle, although k_3 is found to be roughly constant by Oka et al. (2005)

The exponent k_2 can be determined by the Vickers hardness of eroded material and by particle properties and is given by

$$k_2 = r\left(Hv\right)^p \tag{2.353}$$

According to Oka et al. (2005), the term $K\left(aHv\right)^{k_1 b}$ is highly dependent on the type of the particle and eroded material Vickers hardness, which are not correlated with the impact conditions and other factors. Therefore, for the moment a and b were taken to be unity. The present work used the experimental data from Oka and Yoshida (2005) to obtain the relationship between eroded material Vickers hardness and E_{90} at the reference impact velocity for the materials investigated.

The main strength of the Oka model is that the coefficients for a particular combination of eroded material and eroding material (i.e., the particle) can be derived from more fundamental coefficients, which are specific to either the eroded material or the eroding material. The fundamental coefficients for the eroding material, in turn, are shown to be derivable from measurable properties of the eroding material such as its Vickers hardness.

The vast majority of CFD-based erosion modeling has been applied under conditions of very low particle mass loading. This approximation facilitates the measurements, on one side and on the other hand the computations are much faster because the coupling between the Euler and Lagrange modules is avoided (i.e., one-way coupling only). Moreover, the validation of CFD-based erosion models in complex geometries such as bends, tees, and valves has as target variable an erosion measure (i.e., erosion rate and penetration ratio) along the experimental specimen, but rarely the flow field has been validated.

Validation of the erosion model in this work has been performed by comparing the numerical results with the experiments on a vertical to horizontal bend flow considered by Mazumder et al. (2008) as sketched in Figure 2.73. Aluminum (6061-T6) elbow specimens (density $\rho_w = 2700$ kg/m^3, $Hv = 1.049$ GPa) were used in these studies. By applying CFD-based models, erosion predictions were performed for the same geometry. The continuum phase consists of air with a bulk velocity of 34.1 m/s ($\rho = 1.2$ kg/m^3 and $\mu = 18 \cdot 10^{-6}$ N · s/m^2). Almost monosized angular sand particles (density 2600 kg/m^3) having a mean number diameter of 182 μm

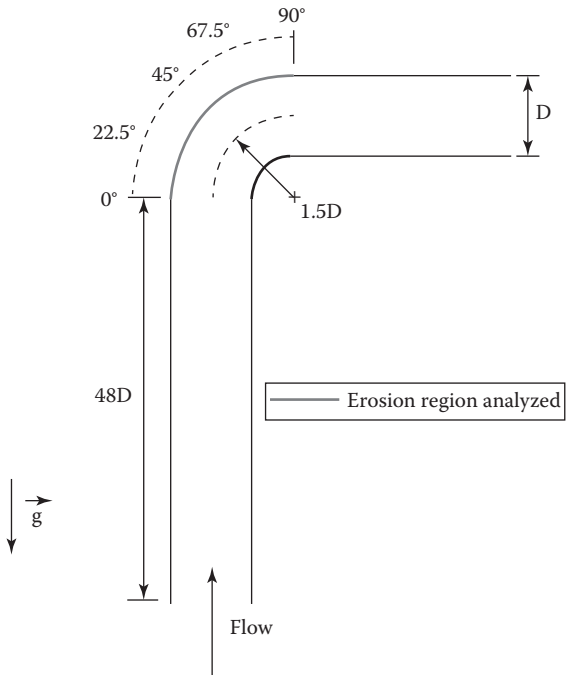


Figure 2.73

Sketch of the experimental pipe configuration of Mazumder et al. (2008), including vertical pipe, bend, and horizontal segment (pipe diameter D = 25.4 mm, bend radius R_{bend} = 1.5·D).

and a mass loading of 0.013 (kg particles/kg air) were injected vertically at about 1.22 m below the test piece. The bend Stokes number in this case is extremely large (St_B = 151) due to the small bend curvature and high conveying velocity. The test piece was a 90° elbow with a diameter of D = 25.4 mm and a curvature radius of R_{bend} = 38.1 mm, as shown in Figure 2.73, which gives a bend radius of 1.5 · D. Hence, the flow deflection is much stronger than in the previous considered cases (see chapter Conveying Pipe Configuration). In order to represent more realistic particle behavior at the specimen location, the whole domain was included in the calculation. After the elbow, a horizontal pipe with 10 pipe diameters was considered. This configuration attempts to reproduce the experimental conditions much better.

Since the geometry is simple, only hexahedra were used in the mesh construction, which generate less numerical diffusion than elements such as tetrahedra and pyramid. Gradual refinement is necessary in the near-wall region, where high-velocity gradients and the boundary layer exist. Hexahedra also allow the generation of higher quality meshes, with fewer distorted elements than one would obtain with tetrahedral, for example. The mesh resolution used in all simulations is approximately 1,000,000 elements, which yielded mesh-independent results. At the inlet 48 · D downstream of the bend, a fully developed pipe flow is imposed. Particles are introduced with the mean streamwise fluid velocity of 34.1 m/s, and a fluctuating velocity for all components of around 4.5% of the bulk flow velocity was specified. As the experiments were performed with very low mass loading of 0.013, interparticle collisions and flow modification by the solids are disregarded in these computations.

At first, the duct walls were considered perfectly smooth. In the simulations, the restitution model of Grant and Tabakoff (1975) was chosen because this model was originally obtained from experiments with sand particles hitting against an aluminum surface, the same materials that were used in the Mazumder et al. (2008) experiments. The normal restitution coefficient $e(\alpha)$ together with the standard deviation σ_e is given by (note the particle impact angle α is given in radians)

$$e(\alpha) = 0.993 - 1.76\alpha + 1.56\alpha^2 - 0.49\alpha^3$$
$$\sigma_e = 2.15\alpha - 5.02\alpha^2 + 4.05\alpha^3 - 1.085\alpha^4 \tag{2.354}$$

The employed friction coefficient, depending on the particle–wall angle of impact, is the same as in the Lain and Sommerfeld (2008, 2012) works. It is written as μ = max(0.15, 0.5–0.0175α), where α is again the particle

impact angle, but this time in degrees. In the present steady-state computations, 10^6 particles are tracked through the computational domain using the fluid forces and time step restrictions described earlier.

The Oka et al. (2005) model provides the erosion damage in mm³/kg (see Equation 2.348), which is converted in erosion ratio *ER* (kg eroded material/kg erodent agent) by

$$ER = 10^{-9}\rho_w E(\alpha) \tag{2.355}$$

where the constant 10^{-9} has the dimension (m^3/mm^3). Finally, the penetration ratio PR_S (m/kg) at each surface element of area A_S is obtained as (the index *S* marks the surface area)

$$PR_S = \frac{ER_S}{\rho_w A_S} = 10^{-9}\frac{E_S(\alpha)}{A_S} \tag{2.356}$$

where ER_s is the erosion ratio in the surface element. It is computed as the sum of erosion ratio caused by N_S particle–wall collisions in the surface area A_S (Parsi et al., 2014) divided by the total injected mass of erodent agent m_T:

$$ER_S = \frac{\sum_{i=1}^{N_f}(m_{pi}ER_i)}{m_{T,S}} \tag{2.357}$$

where m_{pi} represents the mass of particle i colliding with the wall.

The parameters of the model by Oka et al. (2005) for the SiO_2 angular particles colliding with an aluminum wall are listed in Table 2.7. The resulting function $g(\alpha)$ according to Equation 2.349 is shown in Figure 2.74 for the Mazumder et al. (2008) case. Due to the rather soft wall material this function rapidly increases, reaching a maximum around 25° wall impact angle and finally approaches for 90° a value of unity.

In Figure 2.75a, the penetration rate map on the outer wall of the bend geometry of Mazumder et al. (2008) is presented. Particle flow enters from the lower part, following the direction of the arrow. Hence,

Table 2.7 Parameters Used in the Oka Model for the SiO_2 Angular Particles and Aluminum Wall (Hv = 1.049 GPa)

K	k_1	k_2	k_3	u_{ref} (m/s)	D_{ref} (μm)	n_1	n_2
65	−0.12	$2.3Hv^{0.038}$	0.19	104	326	$0.71\ Hv^{0.14}$	$2.4\ Hv^{-0.94}$

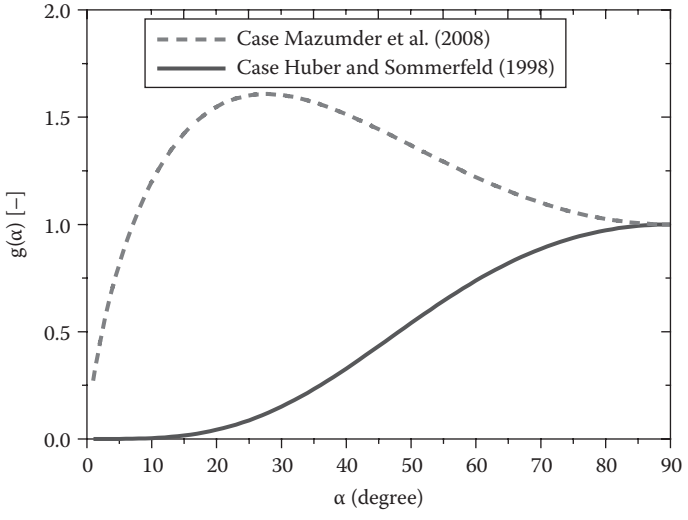


Figure 2.74

Dependence of the function g(α) on the particle–wall impact angle for different wall hardness and particles types: the case of Mazumder et al. (2008) and the case of Huber and Sommerfeld (1998).

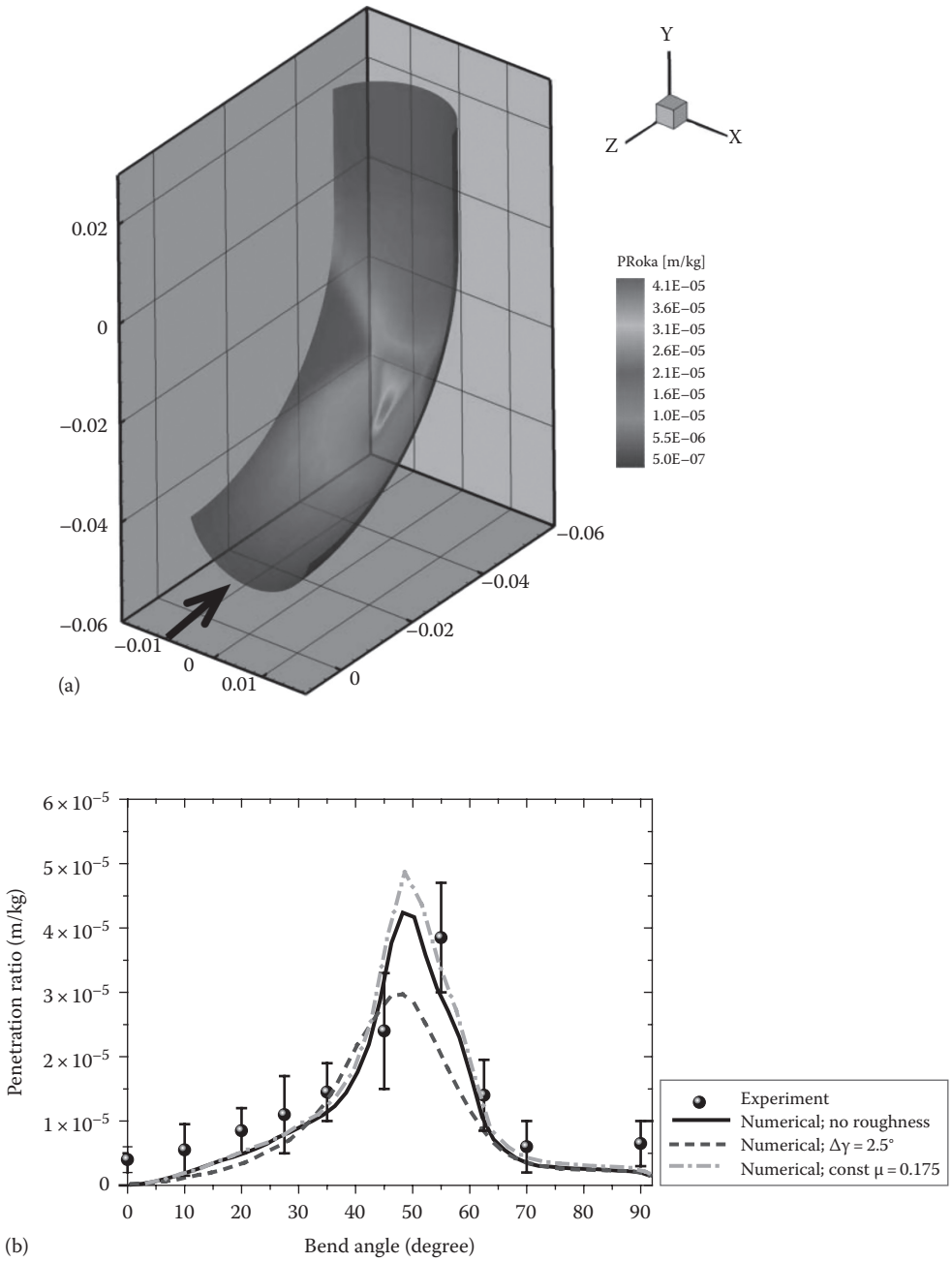


Figure 2.75

Numerical results obtained for the Mazumder et al. (2008) configuration: (a) Predicted erosion map on the bend outer wall. (b) Comparison of penetration ratio obtained for different assumptions in the numerical calculations with the experimental data (pipe diameter D = 25.4 mm, bend radius R_{bend} = 1.5·D).

gravity is acting against the inflow velocity in this illustration. The obtained erosion pattern is very similar to that obtained by other authors using CFD-based erosion models in bends (e.g., Chen et al., 2006, Parsi et al., 2014; Pereira et al., 2014). It consists of a narrow elongated spot of high penetration rate, due to the primary, high-velocity, particle–wall impacts, surrounded by a wider area of moderate erosion. Downstream of the spot of the highest PR, the particle erosion pattern shows a V-shaped structure. This area is mainly produced by secondary particle–wall collisions in the elbow (Pereira et al., 2014).

A quantitative comparison of the numerical results with the measured penetration ratio (including error bars) for a strip of roughly 5 mm width along the center of the bend outer wall is presented in Figure 2.75b. Here, the origin (θ = 0°) is set at the elbow inlet, and θ = 90° corresponds to the elbow outlet. It is obvious

that the simulation results without wall roughness (solid line) are lying within the lower part of the experimental uncertainty (vertical bars indicating the standard deviation of the measurement), and hence, a reasonable agreement with the experiments is obtained.

The presented computations are carried out considering a smooth wall. However, it is known that wall roughness plays a very important role in the particle motion along ducts (Lain and Sommerfeld, 2012a), Sommerfeld and Lain 2015). Therefore, an additional case with moderate roughness ($\Delta\gamma = 2.5°$ in notation of Lain and Sommerfeld, 2012a) was simulated to illustrate the effect of wall roughness in erosion computations. The obtained results are represented by the dashed line in Figure 2.75b. In short, wall roughness in a bend redisperses inertial particles remarkably and the dust rope becomes much wider (see Figure 2.57), which reduces the near-wall particle concentration and eventually results in a reduction of wall collision frequency; the maximum penetration rate is diminished, regarding the case without roughness, and also the location of the erosion peak is slightly displaced toward lower elbow angles.

Finally, the importance of the friction coefficient μ is emphasized by the dot–dashed line in Figure 2.75b. When assuming a constant value for the friction coefficient, that is, $\mu = 0.175$ in this particular case, the maximum of erosion rate increases slightly regarding the basic case (solid line), which has an average value around of 0.25. Although not shown, the results for penetration ratio decrease by a factor of two when friction coefficient is doubled to a value of 0.5, suggesting a nonnegligible sensitivity to this wall collision parameter. Such trends can be understood as follows: higher friction implies a decrease in particle velocity regarding the cases with lower friction; moreover, as the erosion ratio varies with particle impact velocity to a power larger than two, higher friction yields lower penetration ratio and vice versa.

It should be pointed out that in the publication of Mazumder et al. (2008) no information is provided regarding the two-phase flow field developing throughout the bend. Consequently, the gas- and particle-phase properties cannot be validated for this case.

Therefore, a further analysis of bend erosion is conducted for the configuration of a 5 m horizontal pipe, a bend, and a 5 m vertical pipe with a pipe diameter of D = 150 mm as considered earlier (case 3 in Table 2.4). For this case, the numerical calculations of the two-phase flow were thoroughly validated in previous studies (Lain and Sommerfeld, 2013, Sommerfeld and Lain 2015). In this configuration however, the bend radius is larger than in the Mazumder et al. (2008) configuration, namely, $R_{bend} = 2.54$ D and the conveying velocity is lower so that bend erosion is expected to be much smaller. The erosion calculations were conducted for the case with particle size distribution (case ❶ in Table 2.5) and for the monosized particles with 40 and 135 μm (cases ❷ and ❺ in Table 2.5), all with a mass loading of $\eta = 0.3$. The main objective for considering these test cases, although so far no erosion studies were conducted, is related to analyzing the effect of interparticle collisions on bend erosion. For making this effect stronger, a higher mass loading of $\eta = 0.6$ was also simulated for the case with size distribution. The numerical realization of this test case is summarized in detail in the earlier chapter "Conveying Pipe Configuration."

For this test case, the dependence of the normal restitution coefficient on impact angle was modeled for spherical particles as follows: $e(\alpha) = \max(0.7, 1.0–0.0136\ \alpha)$ according to Lain and Sommerfeld (2012). Regarding erosion modeling for this case, the Vickers hardness of the stainless steel wall has been taken as $Hv = 1.96$ GPa (Nguyen et al., 2014) with a density $\rho_w = 7929$ kg/m^3. The parameters of the Oka et al. (2005) model for spherical glass beads and stainless steel wall are listed in Table 2.8. The resulting function $g(\alpha)$ according to Equation 2.349 is also shown in Figure 2.74, yielding lower values than the Mazumder et al. (2008) case due to the higher wall hardness and the consideration of spherical particles. Moreover, here the function continuously increases from zero to one at the wall impact of 90°.

Another difference of this test case compared to the Mazumder et al. (2008) configuration is the direction of gravity being perpendicular to the horizontal pipe, whereby gravitational settling produces a nonsymmetric particle concentration distribution at the bend inlet. This will of course yield a modified erosion pattern at the bend outer wall. Moreover, in the Huber and Sommerfeld (1998) case, particle sizes and conveying velocity are smaller, yielding of course also lower erosion rates.

Interparticle collisions cause a "compression" of the powder rope formed in the bend as discussed earlier and illustrated in Figure 2.58. This phenomenon yields for the considered configuration (Huber and

Table 2.8 Parameters Used in the Model by Oka et al. (2005) for the Glass Beads and Stainless Steel Wall (Hv = 1.96 GPa)

K	k_1	k_2	k_3	u_{ref} (m/s)	D_{ref} (μm)	n_1	n_2
27	−0.16	2.1	0.19	100	200	$2.8\ Hv^{0.41}$	$2.6\ Hv^{-1.46}$

Sommerfeld, 1998) and the particle size distribution an enhancement of particle–wall collision frequency as obvious from Figure 2.71b. For illustrating the effect of interparticle collisions, the penetration ratio obtained with the Oka et al. (2005) model is shown in Figure 2.76 using color contours. Note that for these simulations a wall roughness parameter of $\Delta\gamma = 10°$ has been considered. Without particle–particle collisions, the area of maximum erosion has an elongated tear-like shape whose peak is located at a bend angle of around 35° from the inlet. It is interesting to note that the V-shaped region appearing in Figure 2.75a for the narrow bend is not present. Beyond $\theta = 50°$ the erosion is rather weak. When interparticle collisions are considered, the peak value of penetration ratio decreases by about 50%, the location of maximum erosion is displaced toward smaller bend angles (i.e., $\theta \sim 30°$), and at higher bend angles only a strip of moderate erosion is observed. The extent of the maximum erosion region in the streamwise direction is slightly reduced and broadened sideways. This observation for the erosion pattern is strongly linked with the compression of the dust rope by interparticle collisions and a slight lateral widening (see Figure 2.58). The reduction of penetration rate in the four-way coupling case is not explained readily, since the particle–wall collision rate is slightly increased due to interparticle collisions, that is, from 5.0 to 5.3 1/m, which will in the first instance enhance penetration rate. Therefore, a decrease in erosion can only result from reduced particle impact velocities or modified impact angles, which are both included in the erosion model, and hence, their influence will be further discussed in the following by looking at the profiles of the PR along a small strip (i.e., 5 mm width) of the bend outer wall.

The effect of interparticle collisions on erosion may be more clearly studied by considering monosized particles. Therefore, the PR along the bend outer wall is compared in Figure 2.77a for the case with size distribution (case ❶ in Table 2.5) and 40 μm monosized particles (case ❷ in Table 2.5). As already obvious from Figure 2.76 (color contours of PR), the penetration ratio is remarkably reduced due to interparticle collisions for particles with size distribution (mean number diameter 40 μm), which is quantitatively seen in Figure 2.77a. This reduction of PR is also found in the case of monosized particles although the wall collision rate clearly increases (see Figure 2.71b). Moreover, the PR for the size distribution is larger than for

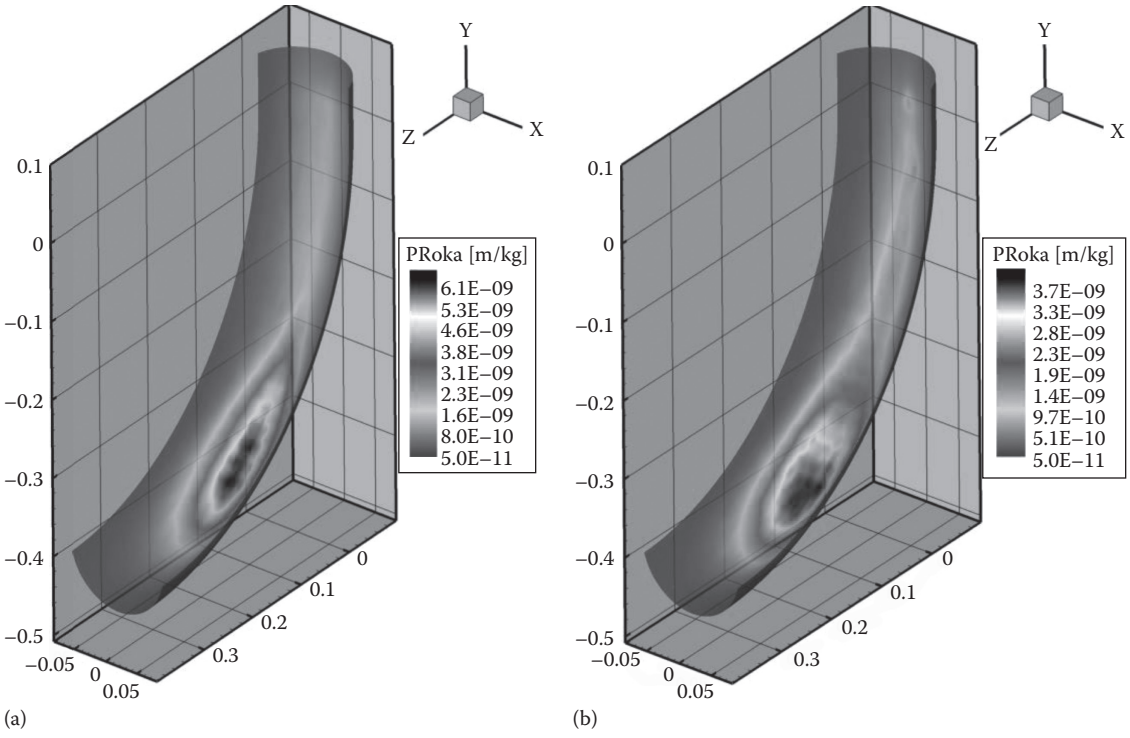


Figure 2.76

Penetration ratio in (m/kg) on the bend outer wall: (a) two-way coupling, (b) four-way coupling (5 m horizontal pipe, bend, 5 m vertical pipe, D = 150 mm, bend radius 2.54 pipe diameters, U_{av} = 27 m/s, μ = 0.3, $\Delta\gamma$ = 10°, particle size distribution 15–85 μm).

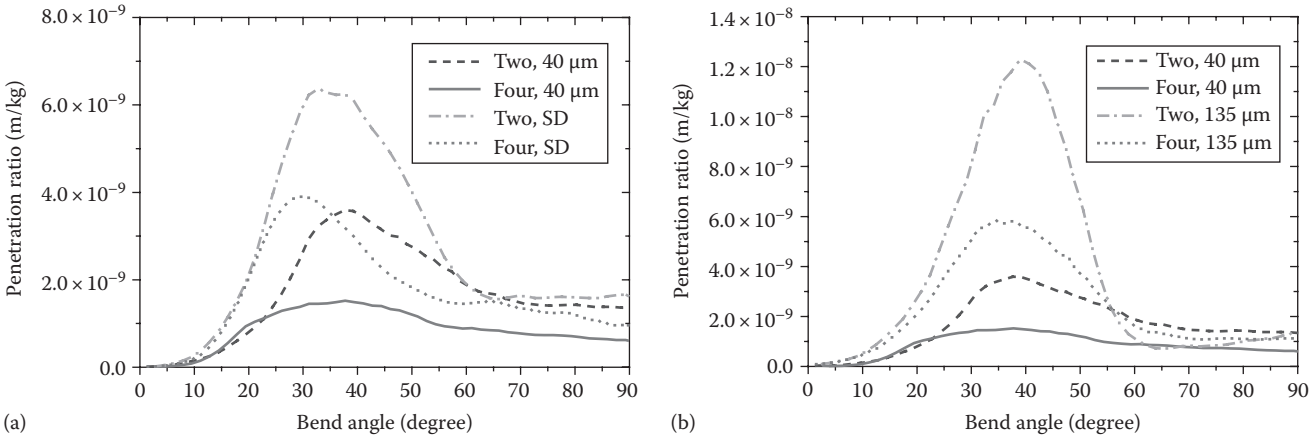


Figure 2.77

Penetration ratio in m/kg for a small strip along in the bend outer wall for spherical glass beads comparing two- and four-way coupling for different particle size distributions: (a) Monosized of 40 µm particles and SD with number mean diameter 40 µm. (b) Monosized 40 and 135 µm particles (5 m horizontal pipe, bend, and 5 m vertical pipe, D = 150 mm, bend radius 2.54·D, U_{av} = 27 m/s, η = 0.3, $\Delta\gamma$ = 10°).

the comparable monosized particles in two- and four-way coupling, respectively. This results from bigger particles being included in the SD, which of course yield higher erosion (i.e., larger impact energy). For the same reason, erosion also begins at smaller bend angles, as these large particles have higher inertia and do not easily follow the flow deflection. This is made clearer comparing the PR for 40 and 135 µm monosized particles (Figure 2.77b). As a consequence of that, the erosion pattern for the larger particles is narrower in the streamwise direction.

The reduction of the PR due to interparticle collisions is mainly caused by the associated decrease in particle–wall impact velocity, since the particles are trapped in the powder rope and experience numerous interparticle collisions and wall collisions reducing the average particle velocity in the near-wall region (see Figure 2.56) as shown in Figure 2.78a for the wall impact velocity of two monosized particles. The impact velocity initially rapidly increase with the bend angle and then continuously decrease toward the bend exit due to continuous loss of particle momentum. Expectedly, the wall impact velocity is larger for the more inertial particles, that is, 135 µm. It should be noted that the PR increases with an exponent larger than the square of the wall impact velocity (see Equation 2.351). The decrease in wall impact velocity begins after the first wall collisions with the bend and is therefore this location is coupled with particle inertia.

The particle–wall impact angle determines the way and the amount of erosion by a single particle and is included in the erosion model of Oka et al. (2005) in the nonlinear term g(α) given by Equation 2.349 and shown in Figure 2.74. Also, the averaged impact angle first continuously increases with growing bend angle and then decreases toward the bend exit again; except for the inertial particles, where the average wall impact angle again increases for two-way coupling from $\theta \approx 65°$ onward since the particles can freely rebound at the bend outer wall (Figure 2.78b). For larger and more inertial particles, the average wall impact angle is higher than for smaller particles throughout the bend. The averaged particle–wall impact angle is remarkably reduced due to interparticle collisions beginning from a bend angle larger than about 25°. The resulting function g(α) given in Equation 2.349 runs very similar than the average wall impact angle (Figure 2.78c); yielding a reduction in erosion due to interparticle collisions.

In conclusion, although the particle–wall collision frequency is increased due to interparticle collisions for monosized particles lager than about 30 µm (see Figure 2.71) the erosion damage is however reduced, mainly due to the distinct reduction of particle–wall impact velocity and average wall impact angle.

Finally, the effect of particle mass loading on bend erosion is analyzed. Due to the increasing particle number density for higher mass loading, one would naturally expect an increase in erosion and PR. The penetration ratio pattern in the bend for a higher particle mass loading of η = 0.6 is shown in Figure 2.79a for the condition when interparticle collisions are considered. In comparison with Figure 2.76b for the case with η = 0.3, it can be readily seen that the maximum penetration ratio decreases and that this region is also displaced toward lower values of the bend angle. The pattern of the highest PR has a V-like shape

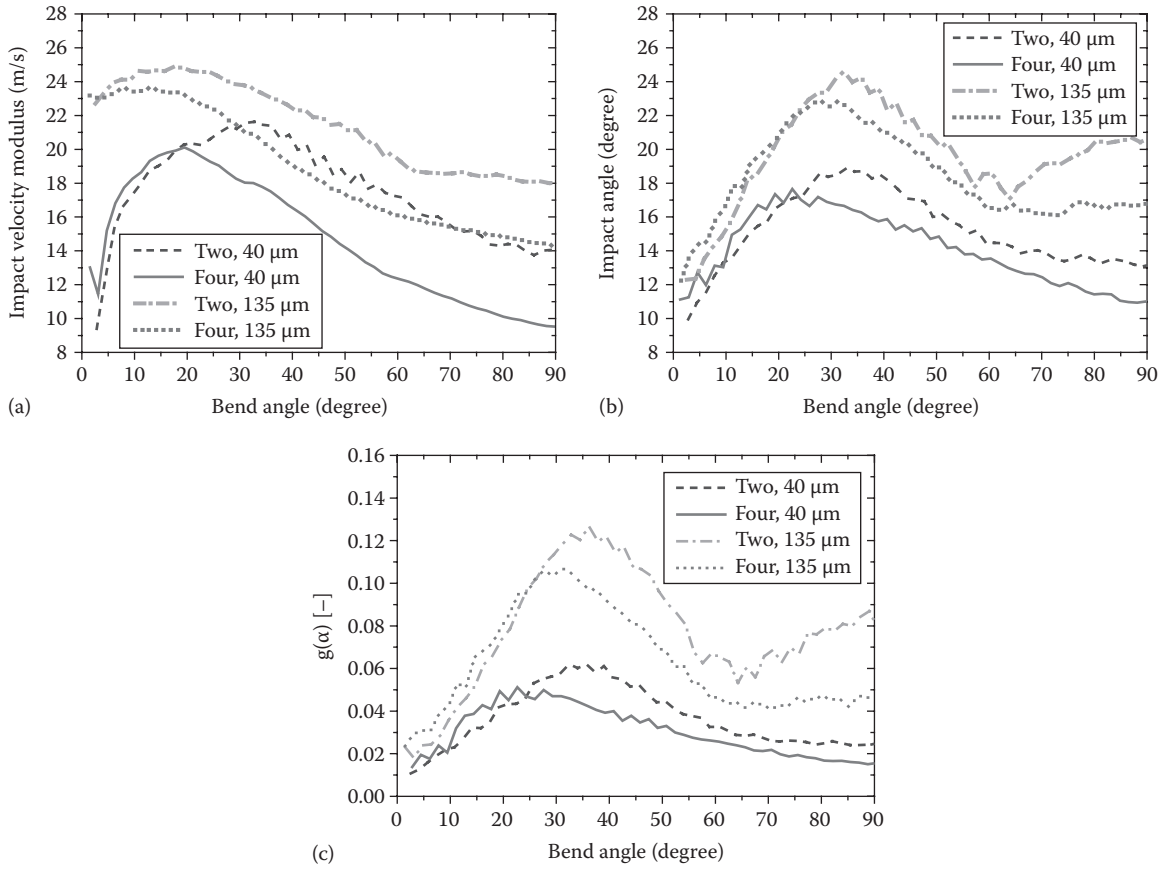


Figure 2.78

Averaged modulus of particle–wall impact velocity (a), averaged wall impact angle (b), and function g(α) given by Equation 2.349 (c) for a 5 mm strip along the bend outer wall for different monosized particles (40 and 135 µm) (5 m horizontal pipe, bend, and 5 m vertical pipe, D = 150 mm, bend radius 2.54·D, U_{av} = 27 m/s, η = 0.3, Δγ = 10°).

and is surrounded by a tear-like shaped region of lower PR values. Toward the end of the bend, a narrow strip of higher PR with two maxima is observed, indicating a multiple impact of particle clouds. Just at the elbow exit, a small spot of rather high PR is identified.

The penetration ratio for a strip along the bend outer wall again allows for a quantitative comparison (Figure 2.79b). The reduction of the erosion damage due to interparticle collisions has been thoroughly explained earlier. Now, the question is why an increased mass loading reduces PR for major parts of the bend outer wall considering both two- and four-way couplings. When interparticle collisions are neglected, a slight decrease in PR with increasing mass loading is observed only between $20° < \theta < 45°$ and above $\theta = 55°$. In the four-way coupling case, however, PR is remarkably reduced with increasing loading between $20° < \theta < 55°$. Beyond this bend angle, however, erosion increases with mass loading reflecting the PR pattern shown in Figure 2.79b, resulting from multiple particle–wall collisions. By comparing Figures 2.58b and 2.67a, it is obvious that the dust rope at higher mass loading appears to become more concentrated occupying as smaller region of the bend cross section. This means that at higher loading, particles moving into the bend will collide more probably with particles in the concentrated dust rope and not with the bend outer wall. This phenomenon may be called "shielding" effect, which however is only relevant for the initial part of the bend (Bikbaev et al., 1979). The extent of this region is correlated with particle inertia.

The main reason for the reduction of erosion with increasing mass loading (at least for the considered values) is related to the trapping of the particles in the rather dense dust rope moving along the bend outer wall, which increases first the wall collision frequency and thereby also reduces particle velocity due to wall collision momentum loss. Moreover, the particles are held in the low-velocity region of the gas flow induced by two-way coupling. This naturally involves a reduced average particle–wall collision velocity as summarized in Figure 2.79c. A remarkable reduction of the impact velocity with growing mass loading is found from

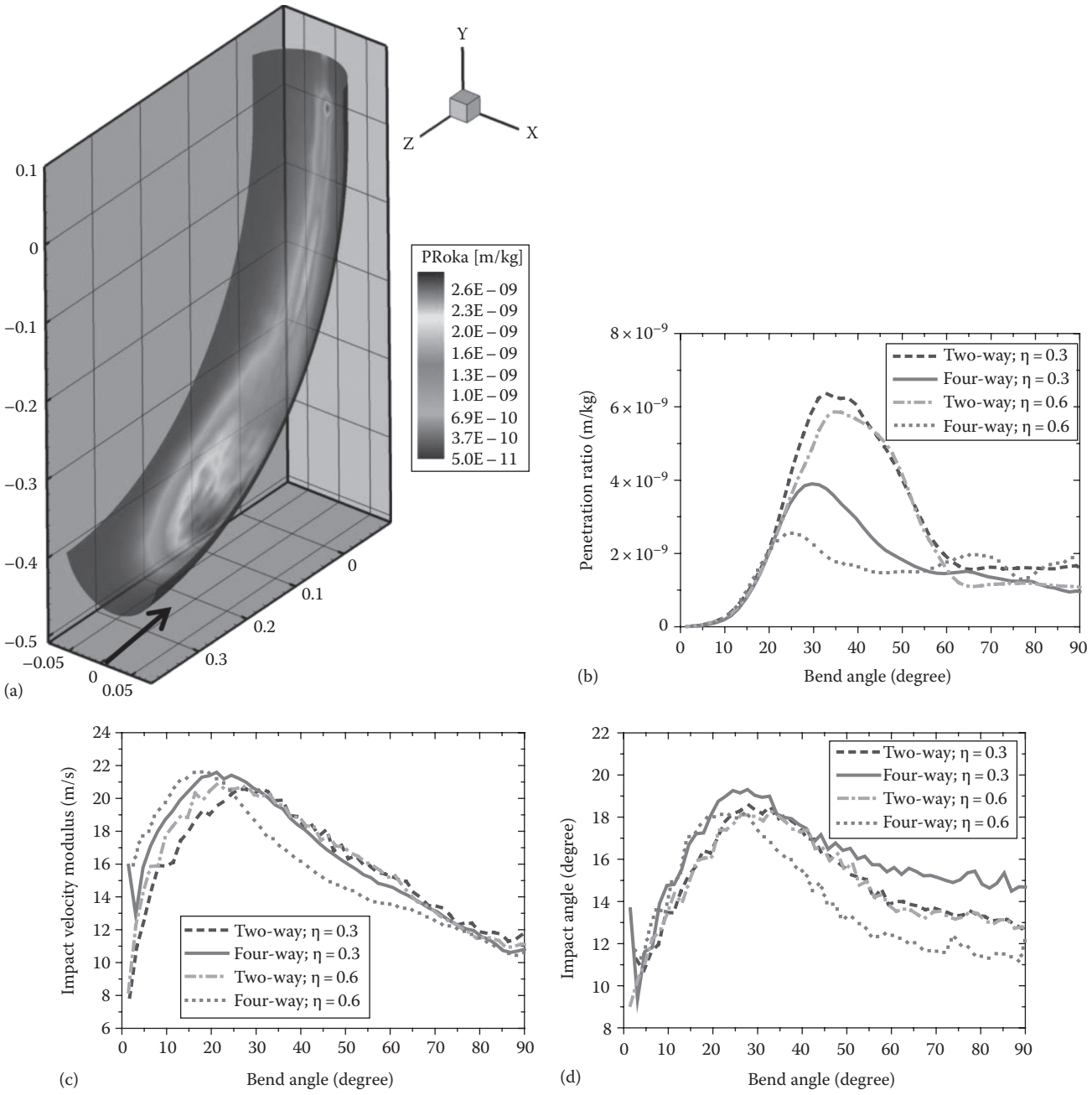


Figure 2.79

Effect of particle mass loading on bend erosion: (a) Color map of penetration ratio in (m/kg) within the bend outer wall for glass beads using four-way coupling (η = 0.6; compared with Figure 2.75b for η = 0.3). (b) Penetration ratio along the bend outer wall for a 5 mm strip. (c) Average particle–wall impact velocity along the bend outer wall for a 5 mm strip. (d) Average wall impact angle along the bend outer wall for a 5 mm strip; comparison of two- and four-way coupled simulations and two mass loadings of η = 0.3 and 0.6 (5 m horizontal pipe, bend, and 5 m vertical pipe, D = 150 mm, bend radius 2.54·D, U_{av} = 27 m/s, Δγ = 10°, particle size distribution 15–85 μm).

bend angles larger than 20° when comparing the four-way coupled calculations. These arguments are also supported by the fact that the two-way coupled calculations show almost no difference for the considered mass loadings. As a result of the compression of the dust rope and the resulting particle trapping, also the average impact angle is reduced when considering four-way coupling (Figure 2.79d). In the dilute conveying regime reduced erosion may be observed with increasing mass loading for a horizontal to vertical bend due to interparticle collisions damping particle motion within the compressed rope.

References

Bikbaev, F.A., Krasnov, V.I., Berezin, V.L., Zhilinski, I.B., and Otroshko, N.T., Main factors affecting gas abrasive wear of elbows in pneumatic conveying pipes, *Chem. Petr. Eng.*, 9, 35–36, 1979.

Bilirgen, H. and Levy, E.K., Mixing and dispersion of particle ropes in lean phase pneumatic conveying, *Powder Technol.*, 119, 134–152, 2001.

Bitter, J., A study of erosion phenomena, part I, *Wear*, 6, 5–21, 1963.

Chen, X., McLaury, B.S., and Shirazi S., Numerical and experimental investigation of the relative erosion severity between plugged tees and elbows in dilute gas/solid two-phase flow, *Wear*, 261, 715–729, 2006.

Crane, R.I. and Evans, R.L., Inertial deposition of particles in a pipe bend, *J. Aerosol Sci.*, 8, 161–170, 1977.

Crowe, C.T., On models for turbulence modulation in fluid-particle flows, *Int. J. Multiphase Flow*, 26, 719–727, 2000.

Crowe, C.T., Sharma, M.P., and Stock, D.E., The particle-source-in-cell (PSI-cell) model for gas-droplet flows, *J. Fluids Eng.*, 99, 325–332, 1977.

Dasgupta, S., Jackson, R., and Sundaresan, S., Gas-particle flow in vertical pipes with high mass loading of particles, *Powder Technol.*, 96, 6–23, 1998.

Dennis, S.C.R., Singh, S.N., and Ingham, D.B., The steady flow due to a rotating sphere at low and moderate Reynolds numbers, *J. Fluid Mech.*, 101, 257–279, 1980.

Finnie, I., Erosion of surfaces by solid particles, *Wear*, 3, 87–103, 1960.

Gore, R.A. and Crowe, C.T., Effect of particle size on modulating turbulent intensity, *Int. J. Multiphase Flow*, 15, 279–285, 1989.

Göz, M.F., Lain, S., and Sommerfeld, M., Study of the numerical instabilities in Lagrangian tracking of bubbles and particles in two-phase flow, *Comput. Chem. Eng.*, 28, 2727–2733, 2004.

Grant, G. and Tabakoff, W., Erosion prediction in turbomachinery resulting from environmental solid particles, *J. Aircraft*, 12, 471–478, 1975.

Hetsroni, G., Particles-turbulence interaction, *Int. J. Multiphase Flow*, 15, 735, 1989.

Hidayat, M. and Rasmuson, A., Some aspects on gas-solid flow in a U-bend: Numerical investigation, *Powder Technol.*, 153, 1–12, 2005.

Ho, C.A. and Sommerfeld, M., Modelling of micro-particle agglomeration in turbulent flow, *Chem. Eng. Sci.*, 57, 3073–3084, 2002.

Ho, C.A. and Sommerfeld, M., Numerische Berechnung der Staubabscheidung im Gaszyklon unter Berücksichtigung der Partikelagglomeration, *Chemie Ingenieur Technik*, 77, 282–290, 2005.

Huber, N. and Sommerfeld, M., Characterization of the cross-sectional particle concentration distribution in pneumatic conveying systems, *Powder Technol.*, 79, 191–210, 1994.

Huber, N. and Sommerfeld, M., Modelling and numerical calculation of dilute-phase pneumatic conveying in pipe systems, *Powder Technol.*, 99, 90–101, 1998.

Kohnen, G., Rüger, M., and Sommerfeld, M., Convergence behaviour for numerical calculations by the Euler/Lagrange method for strongly coupled phases, in C.T. Crowe (Eds.), *Numerical Methods in Multiphase Flows,* ASME Fluids Engineering Division Summer Meeting, Lake Tahoe, Nevada, FED-Vol. 185, 1994, pp. 191–202.

Kuan, B., Yang, W., and Schwarz, M.P., Dilute gas-solid two-phase flows in a curved 90° duct bend: CFD Simulation with experimental validation, *Chem. Eng. Sci.*, 62, 2068–2088, 2007.

Lain, S. and Sommerfeld, M., Turbulence modulation in dispersed two-phase flow laden with solids from a Lagrangian perspective, *Int. J. Heat Fluid Flow*, 24, 616–625, 2003.

Lain, S. and Sommerfeld, M., Euler/ Lagrange computations of pneumatic conveying in a horizontal channel with different wall roughness, *Powder Technol.*, 184, 76–88, 2008.

Lain, S. and Sommerfeld, M., Structure and pressure drop in particle-laden gas flow through a pipe bend: A numerical analysis by the Euler/Lagrange approach, in *Proceedings of the ASME Fluids Engineering Division Summer Meeting*, Vail, CO, Paper No. FEDSM2009–78090, 2009 .

Lain, S. and Sommerfeld, M., Euler/Lagrange computations of particle-laden gas flow in pneumatic conveying systems, in *CD-ROM Proceedings Seventh International Conference on Multiphase Flow, ICMF 2010*, Tampa, FL, May 30–June 4, 2010.

Lain, S. and Sommerfeld, M., Numerical analysis of a pneumatic conveying system consisting of a horizontal pipe, 90°-bend and vertical pipe, in *12th International Conference on Multiphase Flow in Industrial Plants*, Ischia, Italy, Paper No. 141, September 21–23, 2011.

Lain, S. and Sommerfeld, M., Numerical calculation of pneumatic conveying in horizontal channels and pipes: Detailed analysis of conveying behaviour, *Int. J. Multiphase Flow*, 39, 105–120, 2012a.

Lain, S. and Sommerfeld, M., Influence of geometrical and operational conditions on the performance of pneumatic conveying systems: A numerical study by the Euler-Lagrange approach, in *Ninth International ERCOFTAC Symposium ETMM9*, Thessaloniki, Greece, June 6–8, 2012b.
Lain, S. and Sommerfeld, M., Characterisation of pneumatic conveying systems using the Euler/Lagrange approach, *Powder Technol*., 235, 764–782, 2013.
Lain, S., Sommerfeld, M., and Kussin, J., Experimental studies and modelling of four-way coupling in particle-laden horizontal channel flow, *Int. J. Heat Fluid Flow*, 23, 647–656, 2002.
Lyczkowski, R.W., Erosion. In *Multiphase Flow Handbook* (Ed. C.T. Crowe), Chapter 12.4.3, CRC Press, Taylor & Francis Group, Boca Raton, FL, 2006.
Mazumder, Q.H., Shirazi, S.A., and McLaury, B., Experimental investigation of the location of maximum erosive wear damage in elbows, *J. Pressure Vessel Technol*., 130, 1–7, 2008.
Mei, R., An approximate expression for the shear lift force on a spherical particle at finite Reynolds number, *Int. J. Multiphase Flow*, 18, 145–147, 1992.
Nguyen, V.B., Nguyen, Q.B., Liu, Z.G., Wan, S., Lim, C.Y.H., and Zhang, Y., A combined numerical-experimental study on the effect on the water-sand multiphase flow characteristics and the material erosion behavior, *Wear*, 319, 96–109, 2014.
Oka, Y., Okamura, K., and Yoshida, T., Practical estimation of erosion damage caused by solid particle impact: Part 1: Effects of impact parameters on a predictive equation, *Wear*, 259, 95–101, 2005.
Oka, Y. and Yoshida, T., Practical estimation of erosion damage caused by solid particle impact: Part 2: Mechanical properties of materials directly associated with erosion damage, *Wear*, 259, 102–109, 2005.
Oesterle, B. and Bui Dinh, T., Experiments on the lift of a spinning sphere in a range of intermediate Reynolds numbers, *Exp. Fluids*, 25, 16–22, 1998.
Parsi, M., Najmi, K., Najafifard, F., Hassani, S., McLaury, B.S., and Shirazi, S.A., A comprehensive review of solid particle erosion modeling for oil and gas wells and pipelines applications, *J. Nat. Gas Sci. Eng*., 21, 850–873, 2014.
Pereira, G.C., de Souza, F.J., and Martins, D.A., Numerical prediction of the erosion rate due to particles in elbows, *Powder Technol*., 261, 105–117, 2014.
Rubinow, S.I. and Keller, J.B., The transverse force on spinning sphere moving in a viscous fluid, *J. Fluid Mech*., 11, 447–459, 1961.
Saffman, P.G., The lift on a small sphere in a slow shear flow, *J. Fluid Mech*., 22, 385–400, 1965.
Siegel, W., *Pneumatische Förderung: Grundlagen, Auslegung, Anlagenbau, Betrieb*, Vogel Verlag, Würzburg, Germany, 1991.
Sommerfeld, M., Particle dispersion in turbulent flow: The effect of particle size distribution. Part. and Part, *Syst. Charact*., 7, 209–220, 1990.
Sommerfeld, M., Modelling of particle/wall collisions in confined gas-particle flows, *Int. J. Multiphase Flow*, 18, 905–926, 1992.
Sommerfeld, M., Validation of a stochastic Lagrangian modelling approach for inter-particle collisions in homogeneous isotropic turbulence, *Int. J. Multiphase Flows*, 27, 1828–1858, 2001.
Sommerfeld, M., Analysis of collision effects for turbulent gas-particle flow in a horizontal channel: Part I. Particle transport, *Int. J. Multiphase Flow*, 29, 675–699, 2003.
Sommerfeld, M., *Particle Motion in Fluids*, VDI-Buch: VDI Heat Atlas, Springer Verlag, Berlin, Germany, Part 11, 2010, pp. 1181–1196.
Sommerfeld, M. and Huber, N., Experimental analysis and modelling of particle-wall collisions, *Int. J. Multiphase Flow*, 25, 1457–1489, 1999.
Sommerfeld, M., Kohnen, G., and Rüger, M., Some open questions and inconsistencies of Lagrangian dispersion models, in *Proceedings of the Ninth Symposium on Turbulent Shear Flows*, Kyoto, Japan, paper 15-1, 1993.
Sommerfeld, M. and Kussin, J., Analysis of collision effects for turbulent gas-particle flow in a horizontal channel: Part II. Integral properties and validation, *Int. J. Multiphase Flow*, 29, 701–718, 2003.
Sommerfeld, M. and Lain, S., From elementary processes to the numerical prediction of industrial particle-laden flows, *Multiphase Sci. Technol*., 21, 123–140, 2009.
Sommerfeld, M. and Lain, S., Analysis of dilute phase pneumatic conveying through pipe systems by the Euler/Lagrange approach, in *Ninth International Conference on CFD in the Minerals and Process Industries*, CSIRO, Melbourne, Victoria, Australia, December 10–12, 2012.
Sommerfeld, M. and Lain, S., Parameters influencing dilute-phase pneumatic conveying through pipe systems: A computational study by the Euler/Lagrange approach, *Can. J. Chem. Eng*., 93, 1–17, 2015.
Sommerfeld, M., van Wachem, B., and Oliemans, R., *Best Practice Guidelines for Computational Fluid Dynamics of Dispersed Multiphase Flows*, ERCOFTAC, Brussels, Belgium, 2008.

Tian, Z.F., Inthavong, K., Tu, J.Y., and Yeoh, G.H., Numerical investigation into the effects of wall roughness on a gas-particle flow in a 90° bend, *Int. J. Heat Mass Transfer*, 51, 1238–1250, 2008.
Weickert, M., Sommerfeld, M., Teike, G., and Iben, U., Experimental and numerical investigation of the hydroerosive grinding, *Powder Technol.*, 214, 1–13, 2011.
Yilmaz, A. and Levy, E.K., Formation and dispersion of ropes in pneumatic conveying, *Powder Technol.*, 114, 168–185, 2001.

2.7 Two-Fluid Model in MFIX

Madhava Syamlal, Jordan Musser, and Jean-François Dietiker

2.7.1 Introduction to MFIX

Multiphase Flow with Interphase eXchanges (MFIX) is a multiphase computational fluid dynamics (CFD) code written in Fortran for describing the hydrodynamics, heat transfer, and chemical reactions in dense or dilute gas–solid flows. The MFIX team's objective is to create a tool to aid in the understanding, design, optimization, and scale-up of multiphase systems such as gasifiers, carbon capture devices, and chemical looping reactors. The development of MFIX started at the U.S. Department of Energy's (DOE) National Energy Technology Laboratory (NETL) in 1991 as a continuation of a multiparticle (Syamlal, 1985) version of the Eulerian–Eulerian code of Gidaspow and Ettehadieh (1983). Initially developed as a two-fluid model (TFM) for fossil energy applications at NETL, MFIX is now capable of discrete element model (DEM), hybrid TFM-DEM, and particle in cell (PIC) simulations. It is distributed as open-source software and used for solving various multiphase flow problems by numerous institutions around the world. This chapter is on MFIX-TFM and describes the theory, numerical techniques, and example applications.

The first MFIX-TFM version was completed in 1993. The two-fluid modeling technique uses averaging to construct mathematical models describing gases and solids as interpenetrating continua. Public distribution of the code was made through the Energy Science and Technology Software Center starting in 1995. Afterward, the code underwent several revisions whereby high-resolution discretization methods were added, the source code was migrated from Fortran 77 to Fortran 90, and it was parallelized to run on shared memory (e.g., OpenMP) and distributed memory (e.g., MPI) systems (Syamlal et al., 2008). More recent advancements include the development of a $k-\epsilon$ turbulence model (Benyahia et al., 2005), Cartesian cut cells for complex geometries (Dietiker et al., 2013), a stiff chemistry solver, variable solid density (Xue et al., 2011), and a number of kinetic theories for granular flows (Garzo and Dufty, 1999, Iddir and Arastoopour, 2005, Garzo et al., 2007a,b, 2012).

A Lagrangian solid model was implemented in 2004 whereby the position and trajectory of each solid particle are tracked through resolving all particle collisions via a soft-sphere spring-dashpot model (Boyalakuntla, 2003, Garg et al., 2012a). The DEM, MFIX-DEM, is capable of pure granular simulations in addition to being executed alongside the Eulerian gas-phase model for coupled gas–solid simulations. This gas–solid modeling technique uses fewer and less complex closures than the TFM and is therefore considered to contain more certainty overall. However, the computational intensity of tracking particles limits its application to small-scale devices. Recent efforts have included comprehensive verification and validation studies (Garg et al., 2012b, Li et al., 2012a), dynamic solids inventory capabilities, and the inclusion of species and energy conservation equations (Musser, 2011). Moderate-sized investigations containing tens of millions of particles have also been made possible because of recent distributed (Gopalakrishnan and Tafti, 2013) and shared memory (Liu et al., 2014) parallelization efforts.

A second Lagrangian solid model, MFIX-PIC, was implemented in 2013 (Garg and Dietiker, 2013). The multiphase PIC technique uses parcels, also referred to as notional particles, for the solids where a parcel may represent a fraction of one particle or thousands of individual particles. This approach is more computationally efficient than other Lagrangian solid models because collisions are not resolved, but rather approximated using frictional stress models and averaged field quantities. Uncertainty in PIC models arises from the closure needed for the solids, interaction terms as well as the need for accurate interpolation between the Eulerian and Lagrangian frames of reference. However, this approach offers the potential to shorten the time to solution making it ideal for initial design investigations.

The MFIX development activities have been preserved through a concurrent versioning system (CVS) since 1999 to track source code changes. The CVS database has recently been transferred to a Git repository, which accommodates a more flexible development environment between the core MFIX development team and external collaborators. The new repository allows greater transparency with respect to code development

activities because users are permitted to access the archival history of MFIX. This supports efforts to extend the reach of MFIX by encouraging greater community involvement in development and maintenance activities.

The integrity of the source code was originally maintained through nightly regression tests where a subset of tutorial and test cases were executed and the results compared to a fixed solution set (Syamlal et al., 2008). This approach was replaced by a continuous integration (CI) server (www.jenkins-ci.org) to expand the testing capabilities by running all tests and tutorials anytime modifications are committed to the source code repository. Nightly snapshots from the CI server are uploaded to the MFIX website and archived in the code repository.

As of 2014, the MFIX community contains over 3200 registered members and reaches professionals in academia (68%), industry (18%), national laboratories (4%), and other institutions (10%) across the globe. The number of MFIX citations per year has increased in the open literature with 100, 110, 138, and 120 citations in 2010–2013, respectively (https://mfix.netl.doe.gov/citatons.php). MFIX theory and some of the recent developments and applications have been documented in a recently edited book (Pannala et al., 2011). The state-of-the-art technical significance and uniqueness of MFIX has been recognized with several awards including an R&D 100 award in 2007 and a Federal Laboratories Consortium Mid-Atlantic Region Technology Transfer award in 2006.

As the code capabilities are improved, emphasis is being placed on uncertainty quantification, acceleration of time to solution, and realistic geometry representation. This will allow predictive simulations to become an integral part of device scale-up engineering processes and accelerate the introduction of new technologies to market. Current and future code development will continue to appeal to academia for fundamental multiphase flow modeling research and to increase the number and quality of industrial applications.

MFIX is now an active player in the development of computational tools that will enable the deployment of new technologies for clean and efficient utilization of fossil energy. As part of the carbon capture simulation initiative, MFIX is being exercised in a validation, calibration, and scale-up prediction study of sorbent-based CO_2 capture units, and an uncertainty quantification framework tailored to multiphase flow simulations is being developed (Lai et al., 2014a,b).

The open-source nature of the code distribution is essential in the development of new constitutive laws or new models. Large amount of data required to postulate new models can be generated by the original MFIX source code. New models are postulated and coded within the MFIX framework for further testing and refinement. Once finalized, the new models are made available to the MFIX community. This cycle can be repeated to improve or expand the current implementations. This type of model development motivated the open-source distribution strategy of MFIX. Members of the multiphase community can download the code, implement new models, and contribute to the tool's improvement and versatility. The recent migration of the MFIX repository to GitLab will facilitate collaborations among users and shorten the time to make a new model available to the MFIX community.

With the development of high-performance computing, MFIX continues to evolve and follow the trend of hardware development to accelerate computations. Current efforts include porting key sections of the code to GPU and many-core chips. This highlights another benefit of the open-source distribution of MFIX, as there is no limit to the amount of cores the code can be run on.

It is an exciting time to be involved in multiphase flow simulations. The level of maturity of various models and speed of execution are now such that simulations are becoming a vital complement to experiments in the scale-up and optimization of various energy systems such as the next-generation gasification and carbon capture units. Multiphase flow simulations will play a major role in finding solutions to global energy and environmental problems, and MFIX is at the forefront of this momentous challenge.

The following section outlines the conservation equations in MFIX-TFM with details concerning their theoretical development. Subsequent sections describe the numerical technique used to discretize and solve the governing equations as well as some advanced approaches used to extend modeling capabilities. Finally, details concerning MFIX-TFM access and usage are presented along with a few interesting MFIX-TFM applications found in the literature.

2.7.2 Two-Fluid Model Equations

MFIX-TFM (TFM or gas–solid continuum model or Euler–Euler model) describes the motion of a mixture of gas and solids as two or more interpenetrating continuum phases, one gas phase and one or more solid phases. Although referred to as "gas" in this chapter, the continuous phase could also be a liquid. The collective motion of particles is described by the motion of a continuum, referred to herein as a solid phase. The particles may be differentiated by their size, density, or composition and assigned to separate solid phases (Figure 2.80).

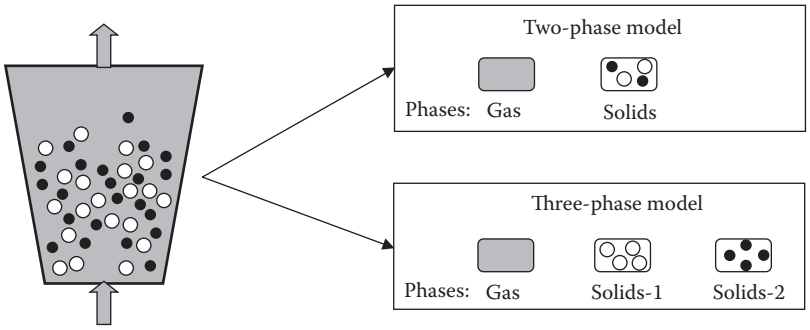


Figure 2.80

A fluidized bed containing two types of particles (black and white) could be described by a two-phase or a three-phase model depending upon the objectives of the modeling study.

By representing the particles as a solid phase, the motion of individual particles or the gas flow around each particle is not calculated. This approach considerably reduces the computational cost. To compensate for the model's reduced resolution, constitutive equations need to be included in the continuum model (e.g., gas–solid drag, solid stress).

The conservation equations governing the multiphase continua are either postulated (mixture theory) or derived by averaging the particle-scale equations. In the mixture theory approach, the multiphase flow equations are postulated, and restrictions on the constitutive relations are derived from general principles of continuum mechanics (Atkin and Craine, 1976, Bowen, 1976, Bedford and Drumheller, 1983). In the averaging approach, the equations are derived by space, time, or ensemble averaging of the local, instantaneous balances for each of the phases (Anderson and Jackson, 1967, Drew, 1983, Ishii and Mishima, 1984, Joseph et al., 1990, Zhang and Prosperetti, 1994a,b, Jackson, 1997, 2000, Prosperetti, 2007). Both approaches yield a set of balance equations for mass, momentum, and energy that need to be closed by specifying constitutive equations. Because of the limited space, only a subset of the equations used in the MFIX code is presented here. For complete details of the equations, see Syamlal et al. (1993), Syamlal and Pannala (2011), Benyahia et al. (2012), and other references mentioned in the following sections.

2.7.2.1 Conservation of Mass

The conservation of mass (or continuity equation) for the gas phase is

$$\frac{\partial}{\partial t}\left(\varepsilon_g \rho_g\right) + \frac{\partial}{\partial x_j}\left(\varepsilon_g \rho_g U_{gj}\right) = \sum_{n=1}^{N_g} R_{gn} \tag{2.358}$$

The first term on the left-hand side accounts for the rate of mass accumulation per unit volume, and the second term is the net rate of convective mass flux. The term on the right accounts for interphase mass transfer because of chemical reactions or physical processes, such as evaporation.

There are M solid-phase continuity equations, one for each solid phase. Subscript m going from 1 to M represents different solid phases.

$$\frac{\partial}{\partial t}\left(\varepsilon_m \rho_m\right) + \frac{\partial}{\partial x_j}\left(\varepsilon_m \rho_m U_{mj}\right) = \sum_{n=1}^{N_m} R_{mn} \tag{2.359}$$

2.7.2.1.1 Equation of State The gas phase is either incompressible or obeys the ideal gas law

$$\rho_g = \frac{P_g M_w}{R T_g} \tag{2.360}$$

The solid-phase densities can be a constant or they can change because of chemical reactions (see Section 2.7.4.2).

2.7.2.2 Conservation of Momentum

The gas-phase momentum balance is

$$\frac{\partial}{\partial t}\left(\varepsilon_g \rho_g U_{gi}\right) + \frac{\partial}{\partial x_j}\left(\varepsilon_g \rho_g U_{gj} U_{gi}\right) = -\varepsilon_g \frac{\partial P_g}{\partial x_i} + \frac{\partial \tau_{gij}}{\partial x_j} + \sum_{m=1}^{M}\left[\mathcal{R}_{mg} U_{mi} - \mathcal{R}_{gm} U_{gi} - I_{gmi}\right] + f_{gi} + \varepsilon_g \rho_g g_i \tag{2.361}$$

where the $\mathcal{R}$ terms represent momentum transfer caused by the mass transfer from the gas phase to the mth solid phase and I_{gmi} is the momentum transfer between the gas phase and the mth solid phase due to interphase forces such as drag force.

The mth solid-phase momentum balance is

$$\frac{\partial}{\partial t}\left(\varepsilon_m \rho_m U_{mi}\right) + \frac{\partial}{\partial x_j}\left(\varepsilon_m \rho_m U_{mj} U_{mi}\right) = -\varepsilon_m \frac{\partial P_g}{\partial x_i} - \varepsilon_m \frac{\partial P_c}{\partial x_i} + \frac{\partial \tau_{mij}}{\partial x_j} + \sum_{l=0}^{M}\left[\mathcal{R}_{lm} U_{li} - \mathcal{R}_{ml} U_{mi} - I_{mli}\right] + \varepsilon_m \rho_m g_i \tag{2.362}$$

where the $\mathcal{R}$ terms represent momentum transfer caused by the mass transfer from the mth phase to the lth phase, and I_{mli} is the momentum transfer between the mth and lth phases ($l = 0$ being the gas phase) due to interphase forces such as drag force. There could be other forces caused by mass transfer that cannot be accounted for in a TFM—caused, for example, by jets of volatile gases issuing from heated coal particles (Syamlal and Pannala, 2011).

In the equations given earlier, $\mathcal{R}_{ml}$ is the rate of mass transfer from the mth phase to the lth phase and $\mathcal{R}_{lm}$ is the rate of mass transfer from the lth phase to the mth phase (m or l set to g or 0 being the gas phase). By definition, both $\mathcal{R}_{ml}$ and $\mathcal{R}_{lm}$ are greater than or equal to zero. They could be equal in magnitude, but usually they are not. For example, in the case of carbon particles burning in air ($C + O_2 \rightarrow CO_2$), $\mathcal{R}_{gm}$ is the mass flux of O_2 from the gas phase to the particle surface and $\mathcal{R}_{mg}$ is the mass flux of CO_2 from the particle surface to the gas phase. Furthermore, the net rate of mass transfer to the mth phase is equal to the total rate of generation of the species mass in that phase:

$$\sum_{l=0}^{M}\left(\mathcal{R}_{lm} - \mathcal{R}_{ml}\right) = \sum_{n=1}^{N_m} R_{mn} \tag{2.363}$$

By default, MFIX accounts for the buoyancy through a shared gas pressure formulation (i.e., $\varepsilon_m(\partial P_g/\partial x_i)$), which Bouillard et al. (1989) call Model A. Although widely used in open-source and commercial computer codes, Model A in the inviscid limit leads to ill-posed initial value problems. This problem could be overcome by explicitly including a buoyancy force term in the momentum equations, which is called Model B option in MFIX, using the terminology of Bouillard et al. (1989). However, Model B accounts for the buoyancy resulting only from the gravitational force and cannot account for a general buoyant force. Syamlal (2011) showed that Model A with a newly proposed buoyant force term (resulting from the relative velocity between gas and solid phases) leads to well-posed initial value problems. The magnitude of the new buoyant force term is likely to be small and, hence, Model A is a good approximation of the well-posed model.

2.7.2.3 Gas–Solid Momentum Transfer

The mechanisms and formulation of momentum transfer have been reviewed in detail by Johnson et al. (1990) and Massoudi (2003). From the studies of the motion of a single particle in a fluid (e.g., Maxey and Riley, 1983), several different mechanisms for momentum transfer have been identified: drag force caused by velocity differences between the phases; buoyancy caused by the fluid pressure gradient; virtual mass effect caused by relative acceleration between phases; Saffman lift force caused by fluid-velocity gradients; Magnus force caused by particle spin; Basset force, originating from the history of the particle's motion through the fluid; Faxen force, a correction applied to the virtual mass effect; and forces caused by temperature and density gradients.

Drag force is the most significant interphase momentum transfer mechanism. Several well-known formulas accurately represent the drag force on a single sphere as a function of the Reynolds number (e.g., Khan et al., 1987). In a multiparticle system, the nearness of other particles makes the drag force on each particle significantly

greater than that given by the single-particle drag formula. Thus, the formula for multiparticle drag force must include the gas volume fraction as an additional parameter to account for the effect of neighboring particles.

To ensure that the aforementioned requirements are satisfied, a multiparticle drag coefficient is defined as follows:

$$I_{gmi} = \frac{3}{4}\frac{C_{Dm}\varepsilon_g\varepsilon_m\rho_g}{d_{pm}}\left|U_g - U_m\right|\left(U_{gi} - U_{mi}\right) \tag{2.364}$$

where C_{Dm} is a function of the Reynolds number and gas volume fraction ε_g.

The drag coefficients are usually obtained from correlations developed from two types of experimental data. One type, valid for high values of the solids volume fraction, is the packed-bed pressure drop correlation, such as the Ergun equation (Ergun, 1952). Because the Ergun equation does not have the correct dependence on the Reynolds number in the limit of $\varepsilon_g \to 1$ (single-particle limit), it is often supplemented with a drag correlation, such as the Wen and Yu equation, applicable in that limit (Gidaspow, 1986). The combined form is sometimes called the Gidaspow drag model (Gidaspow, 1994):

$$C_{Dm} = \begin{cases} \dfrac{200\left(1-\varepsilon_g\right)}{\varepsilon_g^2\,\mathrm{Re}_m} + \dfrac{7}{3\varepsilon_g} & \varepsilon_g \le 0.8 \\ \dfrac{24}{\varepsilon_g\,\mathrm{Re}_m}\left(1+0.15\left(\varepsilon_g\,\mathrm{Re}_m\right)^{0.687}\right)\varepsilon_g^{-2.65} & \varepsilon_g > 0.8, \left(\varepsilon_g\,\mathrm{Re}_m\right) < 1000 \\ 0.44\varepsilon_g^{-2.65} & \varepsilon_g > 0.8, \left(\varepsilon_g\,\mathrm{Re}_m\right) \ge 1000 \end{cases} \tag{2.365}$$

The other type of experimental data is the terminal velocity measured in fluidized or settling beds, given as correlations for the ratio of the terminal velocity of a multiparticle system to that of a single particle. Richardson and Zaki (1954) correlation, for example, is a well-known formula of this type. Syamlal and O'Brien (1987) showed that a formula for the multiparticle drag coefficient can be derived from such terminal velocity correlations as follows:

$$C_{Dm} = \frac{C_{Ds}\left(\dfrac{\mathrm{Re}_m}{V_{rm}}\right)}{V_{rm}^2} \tag{2.366}$$

where

$C_{Ds}(\mathrm{Re}_m/V_{rm})$ is a single-particle drag formula expressed as a function of Re_m/V_{rm} (rather than as a function ofc Re_m)

V_{rm} is the ratio of the terminal velocity of a multiparticle system to that of a single particle given by a Richardson–Zaki-type correlation

An explicit formula for drag can be derived from such a correlation reported by Garside and Aldibouni (1977):

$$V_{rm} = 0.5\left[A - 0.06\,\mathrm{Re}_m + \sqrt{\left(0.06\,\mathrm{Re}_m\right)^2 + 0.12\,\mathrm{Re}_m\left(2B - A\right) + A^2}\right] \tag{2.367}$$

where

$$A = \varepsilon_g^{4.14} \tag{2.368}$$

$$B = \begin{cases} 0.8\varepsilon_g^{1.28} & \varepsilon_g \le 0.85 \\ \varepsilon_g^{2.65} & \varepsilon_g > 0.85 \end{cases} \tag{2.369}$$

and the Reynolds number of the mth solid phase is given by

$$\mathrm{Re}_m = \frac{d_{pm}\left|U_g - U_m\right|\rho_g}{\mu_g} \tag{2.370}$$

Numerous formulas are available for C_{Ds} (e.g., Khan et al., 1987), including the following simple formula proposed by Dalla Valle (1948):

$$C_{Ds} = \left(0.63 + \frac{4.8}{\sqrt{\mathrm{Re}}}\right)^2 \tag{2.371}$$

The parameter Re in Equation 2.370 must be replaced with Re/V_{rm} when this formula is used in Equation 2.365.

The drag coefficients have an irreducible uncertainty, which could be reduced by calibrating them with the minimum fluidization velocity (Syamlal and O'Brien, 2003, Syamlal and Pannala, 2011).

Drag coefficients can also be derived from accurate numerical experiments, some of which are included in MFIX-TFM. For example, Hill et al. (2001a,b) derived a set of drag correlations from their Lattice–Boltzmann simulations. Benyahia et al. (2006) combined those drag correlations with known limiting forms of the drag formula to derive a formula applicable to the full range of void fractions and Reynolds numbers encountered in fluidized beds. MFIX-TFM also includes drag coefficients for polydispersed systems proposed by Beetstra et al. (2007a,b), Yin and Sundaresan (2009a,b), and Holloway et al. (2010). Several other closure equations for the drag force on particles and drops are included in Chapter 1.

2.7.2.4 Solid–Solid Momentum Transfer

As in the case of gas–solid drag, the drag between solid phases arises due to velocity differences. Formulas for the drag have been derived or suggested by several researchers: Soo (1967), Nakamura and Capes (1976), Syamlal (1985, 1987), and Srinivasan and Doss (1985).

In MFIX-TFM, the solid–solid momentum transfer, I_{mli}, is represented as

$$I_{mli} = F_{ml}\left(U_{mi} - U_{li}\right) \tag{2.372}$$

Syamlal (1987) used a simplified version of kinetic theory to derive an expression for the drag coefficient F_{ml}

$$F_{ml} = 3\left(1+e_{ml}\right)\left(\frac{\pi}{2} + C_{fml}\frac{\pi^2}{8}\right)\frac{\left(d_{pm}+d_{pl}\right)^2}{2\pi\left(\rho_m d_{pm}^3 + \rho_l d_{pl}^3\right)}\rho_m\rho_l g_{0ml}\left|U_m - U_l\right| + S_{coef}P_c \tag{2.373}$$

where the last term accounting for a "hindrance effect" caused by particles in enduring contact was later added by Gera et al. (2004) and S_{coef} is an adjustable parameter. The radial distribution function at contact for a mixture of hard spheres is given by Lebowitz (1964):

$$g_{0ml} = \frac{1}{\varepsilon_g} + \frac{3\left(\sum_{\ell=1}^{M}\frac{\varepsilon_\ell}{d_{p\ell}}\right)d_{pl}d_{pm}}{\varepsilon_g^2\left(d_{pl}+d_{pm}\right)} \tag{2.374}$$

MFIX also has polydisperse kinetic theory models with their own inherent solid–solid drag due to relative velocity (e.g., Iddir and Arastoopour, 2005). If one of those theories is invoked, the formula given earlier will be changed to the appropriate one.

2.7.2.5 Gas-Phase Stress Tensor

The total gas-phase stress is given by the formula $-P_g\delta_{ij} + \tau_{gij}$. But the addition of the buoyant force term gives rise to the term $-\varepsilon_g(\partial P_g/\partial x_i)$ in the Model A version of gas-phase momentum equation (see Section 2.7.2.2.)

MFIX-TFM uses modified k–ϵ theories to model gas-phase turbulence:

$$\varepsilon_g\rho_g\left[\frac{\partial k_g}{\partial t} + U_{gj}\frac{\partial k_g}{\partial x_j}\right] = \frac{\partial}{\partial x_j}\left(\varepsilon_g\frac{\mu_g^t}{\sigma_k}\frac{\partial k_g}{\partial x_j}\right) + \varepsilon_g\tau_{gij}\frac{\partial U_{gi}}{\partial x_j} + \Pi_{k_g} - \varepsilon_g\rho_g\epsilon_g \tag{2.375}$$

$$\varepsilon_g \rho_g \left[\frac{\partial \epsilon_g}{\partial t} + U_{gj} \frac{\partial \epsilon_g}{\partial x_j} \right] = \frac{\partial}{\partial x_j} \left(\varepsilon_g \frac{\mu_g^t}{\sigma_\epsilon} \frac{\partial \epsilon_g}{\partial x_j} \right) + \varepsilon_g \frac{\epsilon_g}{k_g} \left(C_{1\epsilon} \tau_{gij} \frac{\partial U_{gi}}{\partial x_j} - \rho_g C_{2\epsilon} \epsilon_g \right) + \Pi_{\epsilon_g} \tag{2.376}$$

The stress tensor τ_{gij} is given by

$$\tau_{gij} = 2(\mu_g + \mu_g^t) D_{gij} - \frac{2}{3} \delta_{ij} \left(\rho_g k_g + (\mu_g + \mu_g^t) D_{gkk} \right) \tag{2.377}$$

where D_{gij} is the strain rate tensor for the gas phase

$$D_{gij} = \frac{1}{2} \left(\frac{\partial U_{gi}}{\partial x_j} + \frac{\partial U_{gj}}{\partial x_i} \right) \tag{2.378}$$

The eddy viscosity μ_g^t is

$$\mu_g^t = \rho_g C_{1\mu} \frac{k_g^2}{\epsilon_g} \tag{2.379}$$

See Benyahia et al. (2005) for the definition of the other functions and constants in the modified $k - \epsilon$ equations: σ_k, σ_ϵ, Π_{k_g}, Π_{ϵ_g}, $C_{1\epsilon}$, $C_{2\epsilon}$, and $C_{1\mu}$.

For dense gas–solid flows without any high-velocity gas jets, the turbulence model could be turned off as the collisional stresses dominate when $\varepsilon_g < 0.99$ (Benyahia et al., 2005). By default, MFIX-TFM does not solve the turbulence equations, and only the molecular viscosity terms remain in Equation 2.376.

2.7.2.6 Solid-Phase Stress Tensor

The development of constitutive equations for particle–particle interactions over the entire range of dilute to dense granular flows must consider the fundamentally different modes for particle–particle force transmission in different flow regimes. A general formulation for solid stresses can be written as

$$\tau_{mij} = \begin{cases} \left(1 - \phi(\varepsilon_g)\right) \tau_{mpij} + \phi(\varepsilon_g) \tau_{mvij} & \varepsilon_g < \varepsilon^* \\ \tau_{mvij} & \varepsilon_g \geq \varepsilon^* \end{cases} \tag{2.380}$$

where the quasi-static and plastic stresses are represented by τ_{mpij} and the viscous stresses are represented by τ_{mvij}. The function $\phi(\varepsilon_g)$ is a blending function that has a smooth but rapid variation across the transition point, the void fraction at close packing ε^* (Pannala et al., 2009, Syamlal and Pannala, 2011). For uniformly sized particles ε^* is a specified constant. For a mixture of particles of different sizes, ε^* can be calculated from the Fedors and Landel (1979) or the Yu and Standish (1987) correlations available in MFIX-TFM.

2.7.2.6.1 Plastic Regime Syamlal et al. (1993) developed constitutive equations for the plastic regime using the frictional theory of Schaeffer (1987):

$$\tau_{mpij} = 2\mu_{mp} D_{mij} \tag{2.381}$$

The shear viscosity is adapted from Schaeffer (1987):

$$\mu_{mp} = \begin{cases} \min \left\{ \dfrac{P_c \sin(\phi)}{\sqrt{4 I_{m2D}}} \dfrac{\varepsilon_m}{\sum_{l=1}^{M} \varepsilon_l}, \mu_s^{\max} \right\} & \varepsilon_g < \varepsilon^* \\ 0 & \varepsilon_g \geq \varepsilon^* \end{cases} \tag{2.382}$$

where

ϕ is the angle of internal friction

$\mu_s^{\max}$ is a specified maximum granular viscosity

The solid pressure in the close-packed regions is related to the void fraction (Jenike, 1987):

$$P_c = \begin{cases} 10^{24}\left(\varepsilon^* - \varepsilon_g\right)^{10} & \varepsilon_g < \varepsilon^* \\ 0 & \varepsilon_g \geq \varepsilon^* \end{cases} \tag{2.383}$$

The second invariant of the rate of strain tensor is

$$I_{m2D} = \frac{1}{6}\left[\left(D_{m11} - D_{m22}\right)^2 + \left(D_{m22} - D_{m33}\right)^2 + \left(D_{m33} - D_{m11}\right)^2\right] + D_{m12}^2 + D_{m23}^2 + D_{m31}^2 \tag{2.384}$$

Another option available in MFX-TFM is the Srivastava and Sundaresan (2003) stress model. Benyahia (2008a) has compared the earlier two plastic regime stress models. Also see Oger and Savage (2013) who modified the Srivastava and Sundaresan model in MFIX-TFM to model the development of higher concentration flows in airslides, which are used to transport granular materials over long distances.

2.7.2.6.2 Viscous Regime The closure relationships for the solid-phase stresses for $\varepsilon_g \geq \varepsilon^*$ are derived from the kinetic theory of granular gases. The kinetic theory equations typically are derived for a monodisperse granular media without considering the gas phase (e.g., Jenkins and Savage, 1983, Lun et al., 1984, Campbell, 1990, Gidaspow, 1994). These equations are combined with two-fluid equations to develop closure relations for the solid-phase stresses (Johnson and Jackson, 1987, Sinclair and Jackson, 1989, Syamlal et al., 1993, Gidaspow, 1994, Peirano and Leckner, 1998, Jackson, 2000, Agrawal et al., 2001). Two things happen when the equations are combined: (1) The solid stress τ_{mv} in TFM is taken as the granular stress in the kinetic theory of granular gases; (2) a granular energy equation is added to the TFM. An example of the kinetic theory stresses implemented in MFIX-TFM is summarized later. Explanations for the equations can be found in Syamlal et al. (1993) and Agrawal et al. (2001). Although a subscript *m* is used, the following equations are valid only for a single solid phase.

The collisional stress tensor from the kinetic theory can be represented by the following equations:

$$\tau_{mvij} = \left(-P_m + \eta\mu_b \frac{\partial U_{mi}}{\partial x_i}\right)\delta_{ij} + 2\mu_m S_{mij} \tag{2.385}$$

where the deviator of the strain rate tensor is

$$S_{mij} = \frac{1}{2}\left(\frac{\partial U_{mi}}{\partial x_j} + \frac{\partial U_{mj}}{\partial x_i}\right) - \frac{1}{3}\frac{\partial U_{mk}}{\partial x_k}\delta_{ij} \tag{2.386}$$

and the normal solid pressure is

$$P_m = \varepsilon_m \rho_m \Theta_m \left[1 + 4\eta \sum_{l=1}^{M} \varepsilon_l g_{0ml}\right] \tag{2.387}$$

The solids, viscosity is

$$\mu_m = \left(\frac{2+\alpha}{3}\right)\left[\frac{\mu_m^*}{g_{0mm}\eta(2-\eta)}\left(1 + \frac{8}{5}\eta\sum_{l=1}^{M}\varepsilon_l g_{0ml}\right)\left(1 + \frac{8}{5}\eta(3\eta-2)\sum_{l=1}^{M}\varepsilon_l g_{0ml}\right) + \frac{3}{5}\eta\mu_b\right] \tag{2.388}$$

where

$$\mu_m^* = \frac{\rho_m \varepsilon_m g_{0mm} \Theta_m \mu}{\rho_m \sum_{l=1}^{M} \varepsilon_l g_{0ml} \Theta_m + \left(\frac{2\beta\mu}{\rho_m \varepsilon_m}\right)} \tag{2.389}$$

$$\mu = \frac{5}{96}\rho_m d_{pm}\sqrt{\pi\Theta_m} \tag{2.390}$$

$$\mu_b = \frac{256}{5\pi}\mu\varepsilon_m \sum_{l=1}^{M}\varepsilon_l g_{0ml} \tag{2.391}$$

$$\eta = \frac{1+e_{mm}}{2} \tag{2.392}$$

Here, Θ_m is the granular temperature or pseudo-thermal energy. The granular temperature is a measure of the kinetic energy of the fluctuating motion of particles, just as thermal temperature is a measure of the kinetic energy of the fluctuating motion of molecules. The granular temperature is calculated from the following granular energy balance equation:

$$\frac{3}{2}\varepsilon_m\rho_m\left[\frac{\partial\Theta_m}{\partial t}+U_{mj}\frac{\partial\Theta_m}{\partial x_j}\right]=\frac{\partial}{\partial x_j}\left(\kappa_m\frac{\partial\Theta_m}{\partial x_j}\right)+\tau_{mvij}\frac{\partial U_{mi}}{\partial x_j}+\Pi_m-\varepsilon_m\rho_m J_m \tag{2.393}$$

The first term on the right-hand side stands for the granular temperature diffusion or conduction, the second term represents the production, the third term includes viscous dissipation and the effect of gas-particle slip, and the final term stands for the collisional dissipation. The granular conductivity, associated with the conduction of granular temperature, is

$$\kappa_m=\left(\frac{\kappa_m^*}{g_{0mm}}\right)\left[\left(1+\frac{12}{5}\eta\sum_{l=1}^{M}\varepsilon_l g_{0ml}\right)\left(1+\frac{12}{5}\eta^2(4\eta-3)\sum_{l=1}^{M}\varepsilon_l g_{0ml}\right)+\frac{64}{25\pi}(41-33\eta)\eta^2\left(\sum_{l=1}^{M}\varepsilon_l g_{0ml}\right)^2\right] \tag{2.394}$$

where

$$\kappa_m^* = \frac{\rho_m\varepsilon_m g_{0,mm}\Theta_m\kappa_m^{**}}{\rho_m\sum_{l=1}^{M}\varepsilon_l g_{0ml}\Theta_m+\left(\frac{6\beta\kappa_m^{**}}{5\rho_m\varepsilon_m}\right)} \tag{2.395}$$

$$\kappa_m^{**} = \frac{75\rho_m d_{pm}\sqrt{\pi\Theta_m}}{48\eta(41-33\eta)} \tag{2.396}$$

The collisional dissipation term and the exchange terms are

$$J_m = \frac{48}{\sqrt{\pi}d_{pm}}\eta(1-\eta)\sum_{l=1}^{M}\varepsilon_l g_{0ml}\Theta_m^{3/2} \tag{2.397}$$

$$\Pi_m = -3\beta\Theta_m + \frac{81\varepsilon_m\mu_g^2\left|U_g-U_m\right|^2}{g_{0mm}d_{pm}^3\rho_m\sqrt{\pi\Theta_m}} \tag{2.398}$$

If the transport of the granular energy is not important (e.g., in bubbling beds the granular energy produced could be mostly dissipated locally), one can construct the algebraic form by equating the rate of production to the rate of dissipation and derive the following algebraic equation:

$$\Theta_m=\left\{\frac{-K_{1m}\varepsilon_m D_{mii}+\sqrt{K_{1m}^2(D_{mii})^2\varepsilon_m^2+4K_{4m}\varepsilon_m\left[K_{2m}(D_{mii})^2+2K_{3m}(D_{mij}D_{mij})\right]}}{2\varepsilon_m K_{4m}}\right\}^2 \tag{2.399}$$

$$K_{1m} = 2\left(1+e_{mm}\right)\rho_m g_{0mm} \tag{2.400}$$

$$K_{2m} = \frac{4d_{pm}\rho_m\left(1+e_{mm}\right)\varepsilon_m g_{0,mm}}{3\sqrt{\pi}} - \frac{2}{3}K_{3m} \tag{2.401}$$

$$K_{3m} = \frac{d_{pm}\rho_m}{2}\left\{\frac{\sqrt{\pi}}{3\left(3-e_{mm}\right)}\left[0.5\left(3e_{mm}+1\right)+0.4\left(1+e_{mm}\right)\left(3e_{mm}-1\right)\varepsilon_m g_{0,mm}\right]+\frac{8\varepsilon_m g_{0,mm}\left(1+e_{mm}\right)}{5\sqrt{\pi}}\right\} \tag{2.402}$$

$$K_{4m} = \frac{12\left(1-e_{mm}^2\right)\rho_m g_{0,mm}}{d_{pm}\sqrt{\pi}} \tag{2.403}$$

The algebraic form may reduce the computational cost of simulations (Van Wachem et al., 2001).

There are several other kinetic theory options available in MFIX-TFM. One option is the Garzó and Dufty (1999) theory, derived from the Enskog kinetic equation, which assumes molecular chaos (i.e., that the velocities of colliding particles are uncorrelated) and is applicable to flows up to moderate concentrations. With the help of that theory, for example, Mitrano et al. (2014) demonstrated that kinetic-theory-based continuum models are surprisingly accurate even at large Knudsen numbers. Benyahia et al. (2007) evaluated MFIX-TFM implementation of the theories of Simonin (1996) and Balzer et al. (1996) and Cao and Ahmadi (1995), which include kinetic theory stresses as well as gas-phase turbulence models that account for the exchange of turbulence energy between the gas and solid phases. Several kinetic theories for describing polydispersed systems have been implemented in MFIX (Garzo et al., 2007a,b, 2012). See Hrenya (2011) for a critical comparison of kinetic theories for polydispersed systems. Benyahia (2008b) compared four different kinetic theories for polydispersed systems and found the most accurate one to be Iddir and Arastoopour (2005) theory, which was implemented in MFIX-TFM by Galvin (2007).

2.7.2.7 Conservation of Species Mass

The gas and solid phases may contain an arbitrary number of chemical species, N_m. The mass conservation equation for the gas-phase species n is

$$\frac{\partial}{\partial t}\left(\varepsilon_g\rho_g X_{gn}\right)+\frac{\partial}{\partial x_j}\left(\varepsilon_g\rho_g U_{gj}X_{gn}\right)=\frac{\partial}{\partial x_j}\left(\mathcal{D}_{gn}\frac{\partial X_{gn}}{\partial x_j}\right)+R_{gn} \tag{2.404}$$

The species conservation equation for solid phase, m, species n, is

$$\frac{\partial}{\partial t}\left(\varepsilon_m\rho_m X_{mn}\right)+\frac{\partial}{\partial x_j}\left(\varepsilon_m\rho_m U_{mj}X_{mn}\right)=R_{mn} \tag{2.405}$$

2.7.2.8 Conservation of Internal Energy

The internal energy balances are implemented in MFIX-TFM in terms of the temperatures. The equation for the gas phase is

$$\varepsilon_g\rho_g C_{pg}\left[\frac{\partial T_g}{\partial t}+U_{gj}\frac{\partial T_g}{\partial x_j}\right]=-\frac{\partial q_{gj}}{\partial x_j}+\sum_{m=1}^{M}\gamma_{gm}\left(T_m-T_g\right)+\gamma_{Rg}\left(T_{Rg}^4-T_g^4\right)-H_g \tag{2.406}$$

where the second term on the right-hand side is the gas–solid interphase heat transfer and the third term is a simplified model for the heat transfer due to radiation. The equation for the mth solid phase is

$$\varepsilon_m\rho_m C_{pm}\left[\frac{\partial T_m}{\partial t}+U_{mj}\frac{\partial T_m}{\partial x_j}\right]=-\frac{\partial q_{mj}}{\partial x_j}-\gamma_{gm}\left(T_m-T_g\right)+\gamma_{Rm}\left(T_{Rm}^4-T_{\boldsymbol{m}}^4\right)-H_m \tag{2.407}$$

where the second term on the right-hand side is the gas–solid interphase heat transfer and the third term is a simplified model for the heat transfer due to radiation. Three simplifying assumptions have been made in the formulation of internal energy Equations 2.404 and 2.405: (1) The irreversible rate of increase in internal energy due to viscous dissipation and interphase momentum transfer has been neglected. Such terms are negligible except in the case of very large relative velocities. (2) The direct heat transfer between different solid phases has been neglected. (3) Interfacial work terms have been neglected.

The total rate of enthalpy change due to chemical reactions and phase changes is given by Syamlal and Pannala (2011) and Musser et al. (2015):

$$H_g = \sum_n^{N_g} h_{gn}\left(T_g\right)\frac{\partial}{\partial x_j}\left(\mathcal{D}_{gn}\frac{\partial X_{gn}}{\partial x_j}\right) + \sum_p^{P}\left(\sum_{m=0}^{M}\left(-\xi_{gmp} + \sum_{n=1}^{N_g} h_{gn}\left(T_g\right)R_{gmnp}\right)\right) \tag{2.408}$$

and

$$H_m = \sum_n^{N_m} h_{mn}\left(T_m\right)\frac{\partial}{\partial x_j}\left(\mathcal{D}_{mn}\frac{\partial X_{mn}}{\partial x_j}\right) + \sum_p^{P}\left(\xi_{gmp} + \sum_{n=1}^{N_m} h_{mn}\left(T_m\right)\left(R_{mgnp} + R_{mmnp}\right)\right) \tag{2.409}$$

The enthalpy change due to species diffusion, although shown in Equations 2.406 and 2.407, is small and has been neglected in MFIX. R_{gmnp} is the rate of formation (or destruction) of the nth gas-phase species attributed to the pth reaction between the gas phase and the mth phase. The case of $m = 0$ represents homogeneous gas-phase reactions. R_{mgnp} is the rate of formation (or destruction) of the mth solid phase's nth species resulting from the pth reaction between the mth phase and the gas phase. R_{mmnp} is the rate of formation in homogeneous mth solid-phase reactions, and any direct solid–solid reactions are not considered. ξ_{gmp} is the enthalpy transfer attributed to mass transfer between the mth solid phase and the gas phase for the pth reaction.

Musser et al. (2015) proposed the following constitutive equation for ξ_{gmp} to account for enthalpy transfer caused by mass transfer:

$$\xi_{gmp} = \sum_{n=1}^{N_g} h_{gn}\left(T_{gm}\right)R_{gmnp} \tag{2.410}$$

The temperature at which the specific enthalpy is evaluated, T_{gm}, is identified explicitly and given by

$$T_{gm} = \begin{cases} T_g & \text{for } R_{gmnp} \le 0 \text{ (i.e., consumption of } n\text{th gas species)} \\ T_m & \text{for } R_{gmnp} > 0 \text{ (i.e., formation of } n\text{th gas species)} \end{cases} \tag{2.411}$$

2.7.2.9 Gas–Solid Heat Transfer

The heat transfer between the gas phase and solid phase m is assumed to be a function of the temperature difference and given by $\gamma_{gm}(T_m - T_g)$, where γ_{gm} is the coefficient of heat transfer between the gas phase and the mth solid phase. γ_{gm} is a corrected heat transfer coefficient, the correction necessitated by the interphase mass transfer (Bird et al., 2006):

$$\gamma_{gm} = \frac{C_{pg}\mathcal{R}_{gm}}{\left[\exp\left(\dfrac{C_{pg}\mathcal{R}_{gm}}{\gamma^0_{gm}}\right) - 1\right]} \tag{2.412}$$

Note that in the limit

$$\lim_{\mathcal{R}_{gm}\to 0}\gamma_{gm} = \gamma^0_{gm}$$

where the intrinsic heat transfer coefficient γ^0_{gm} is calculated from

$$\gamma^0_{gm} = \frac{6\lambda_g \varepsilon_m \mathrm{Nu}_m}{d^2_{pm}} \tag{2.413}$$

where Nu_m is the Nusselt number for the particles constituting the mth solid phase.

The Nusselt number is typically determined from one of the many correlations reported in the literature for calculating the heat transfer between particles and fluid in packed or fluidized beds (e.g., Zabrodsky, 1966, Gelperin et al., 1971, Gunn, 1978). Syamlal and Gidaspow (1985) and Kuipers et al. (1992) used such correlations in their TFMs. MFIX-TFM uses the Gunn (1978) correlation, applicable for a porosity range of 0.35–1.0 and a Reynolds numbers up to 10^5:

$$\mathrm{Nu}_m = \left(7 - 10\varepsilon_g + 5\varepsilon_g^2\right)\left(1 + 0.7\,\mathrm{Re}_m^{0.2}\,\mathrm{Pr}^{1/3}\right) + \left(1.33 - 2.4\varepsilon_g + 1.2\varepsilon_g^2\right)\mathrm{Re}_m^{0.7}\,\mathrm{Pr}^{1/3} \tag{2.414}$$

where the Prandtl number is defined as

$$\mathrm{Pr} = \frac{C_{pg}\mu_g}{\lambda_g} \tag{2.415}$$

2.7.2.10 Conductive Heat Flux in Gas Phase

The conductive heat flux within the gas phase, q_{gj}, is given by Fourier's law

$$q_{gj} = -\lambda_g \frac{\partial T_g}{\partial x_j} \tag{2.416}$$

2.7.2.11 Conductive Heat Flux in Solid Phase

In a simulation of the heat transfer from a fluidized bed to a wall, Syamlal and Gidaspow (1985) found that solid-phase conductive heat flux must be considered in order to accurately calculate bed-to-wall heat transfer coefficients. The conductive heat flux in the solid phase, q_{mj}, is assumed to have a form similar to that in the gas phase:

$$q_{mj} = -\lambda_m \frac{\partial T_m}{\partial x_j} \tag{2.417}$$

MFIX-TFM uses a particle phase conductivity model taken from Syamlal and Gidaspow (1985), who adapted a model proposed by Zehner and Schlunder (Bauer and Schlunder, 1978).

2.7.2.12 Initial and Boundary Conditions

The initial values of all the field variables (ε_g, ε_m, P_g, U_{gi}, U_{mi}, Θ_m, T_g, T_m, X_{gn}, X_{mn}) must be specified for the entire computational domain. Although the initial conditions serve as a starting point for the simulations, the stationary state that is reached after the initial transients subside is the solution that is of interest in most engineering applications. Therefore, the initial conditions chosen are such that the stationary state solution is reached faster. In fluidized beds, for example, the solids, velocity is usually initialized to zero, and the gas velocity is initialized to some uniform unidirectional value.

On the other hand, the accuracy of the stationary state solution critically depends upon the boundary conditions. The different types of boundary conditions available in MFIX-TFM are described as follows:

Inflow boundary: An inflow boundary condition should be specified at a location where uniform flow is expected. All the field variables must be specified at the boundary. Two types of inflow boundary conditions are possible, specified pressure or specified mass flux; the specified mass flux condition is more commonly used inflow boundary condition.

Outflow boundary: Specified constant pressure with zero-gradient velocity at the exit is the most common condition for the gas outflow boundary. For this condition to be valid, the outflow must be spatially uniform with no flow reversal across the boundary. If there is flow reversal at a specified boundary (caused, e.g., by a jet crossing the outflow boundary), the domain must be extended so that the flow is uniform at the outflow boundary.

Cyclic boundary: A cyclic boundary condition may be specified for a pair of boundaries in the x-, y-, or z-direction. The field variable values at one end of the domain in the cyclic direction become the same as those at the other end. There is also the option of fixing the pressure drop so that the gas pressure changes by a specified constant value across the cyclic boundary. Another option is to fix the domain-averaged mass flux of gas instead of the pressure drop.

Walls: Boundary conditions for all the variables must be specified at the walls. Since, in most devices, walls play an important role in the overall performance of the reactor, much attention must be paid to selecting wall boundary conditions. Typically, at the wall, the gas-phase normal component of velocity is set to zero (no-penetration condition) and either the gradient of the tangential component is set to zero (free-slip condition) or the tangential component itself is set to zero (no-slip condition). Benyahia et al. (2005) compared a standard wall function with a wall function modified to include the effect of particles and found only a small effect on the radial profile of gas turbulent kinetic energy.

The boundary conditions for the solids velocities could have a profound effect on the simulation results (e.g., Benyahia et al., 2005). The boundary conditions developed by Johnson and Jackson (1987) are widely used to determine the solutions for solids velocity and granular temperature. These boundary conditions rely on two parameters: the specularity coefficient and the particle–wall coefficient of restitution. Jenkins (1992) has proposed a different form of the boundary condition for frictional particles, which requires parameters related to the frictional properties of the particles and the nature of the wall surfaces. These boundary conditions were further extended for both small and large sliding cases (Jenkins and Louge, 1997). Benyahia et al. (2005) evaluated these boundary conditions by simulating dilute, turbulent gas/solids flows in a pipe and concluded that the experimental data for solids velocity, gas turbulent kinetic energy, and solids turbulent kinetic energy fell between the small-friction/all-sliding and large-friction/no-sliding limits of Jenkins and Louge (1997) boundary condition. The experimental data fell much closer to the small-friction limit. The small-friction limit could be mimicked with a small specularity coefficient in the Johnson and Jackson (1987) boundary condition. The significant effect of the specularity coefficient (and particle–wall restitution coefficient) on the predicted solids, velocity and bubble properties in a bubbling fluidized bed is discussed by Li et al. (2010a). The specularity coefficient is, however, experimentally not measureable, and Li and Benyahia (2012) developed a model for calculating the specularity coefficient as a function of the measurable quantities particle–wall restitution coefficient, the frictional coefficient, and the normalized slip velocity at the wall. Li and Benyahia (2013) evaluated their model by simulating bubbling and circulating fluidized beds. These different boundary condition models for solids velocity and granular temperature are available in MFIX-TFM. Other boundary conditions for MFIX and similar Eulerian models, which are based on DNS simulations, have been studied by Davies et al. (2012) and Feng et al. (2014).

The thermal boundary condition is implemented in MFIX-TFM as

$$\frac{\partial T_m}{\partial n} + h_{wm}(T_m - T_{wm}) = c_m \tag{2.418}$$

where n is the normal pointing from the fluid into the wall. In the limit when the wall heat transfer coefficient $h_{wm} \to 0$, the heat flux at the boundary is a specified value, and in the limit of $h_{wm} \to \infty$, the temperature at the boundary is a specified value.

Similarly, the boundary conditions for the species mass fractions are implemented as

$$\frac{\partial X_{mn}}{\partial n} + h_{wmn}(X_{mn} - X_{wmn}) = c_{mn} \tag{2.419}$$

where n is the normal pointing from the fluid into the wall. In the limit when the wall mass transfer coefficient $h_{wmn} \to 0$, the mass flux at the boundary is a specified value, and in the limit of $h_{wmn} \to \infty$, the species mass fraction at the boundary is a specified value.

2.7.3 Numerical Method

MFIX utilizes the finite volume method to discretize the governing equations over a staggered grid where scalar values are located at the center of a control volume and velocity components are situated along the control volume faces. This approach is desirable because it invokes the physical basis of the conservation equation derivations while ensuring global conservation of mass, momentum, and energy, even on coarse grids (Patankar, 1980). Details on the control volume method are available elsewhere (Patankar, 1980, Versteeg and Malalasekera, 1995, Syamlal, 1998).

MFIX-TFM uses an extension of the SIMPLE algorithm (Patankar, 1980) for solving the discretized conservation equations. As the original algorithm was derived for single-phase flows, Spalding (1980) identified three issues that result from extending it to multiple phases: (1) there are more field variables and therefore more equations to solve, (2) no unique fluid pressure correction equation exists because there are multiple continuity equations, and (3) interphase exchange terms strongly couple momentum equations, which can lead to instability if not adequately addressed.

Two additional concerns arise in granular multiphase flows that determine the success of a numerical scheme (Syamlal, 1998). The first potential problem is managing solids in close-packed regions because it is difficult to constrain the solids, volume fraction to be at or below maximum packing in a numerical algorithm. Overpacking is resisted by the numerical algorithm by using an equation of state for the solid pressure that increases exponentially as the solids, volume fraction approaches the close-packed limit. In monodisperse simulations, MFIX utilizes solids, volume fraction correction equation to account for solid pressure and stabilize computations in close-packed regions.

The second issue encountered with multiphase systems is how to calculate field variables across phase discontinuities where the volume fraction goes to zero. A harmonic mean is used to calculate face values of scalar field variables to ensure that arbitrary values are not used. The linearization of the convection terms in the momentum equations complicates this task because the normal velocity may become very large across a phase discontinuity. The resulting error in momentum conservation is negligible because the product of a near-zero volume fraction and normal velocity remains small. However, the large normal velocities may destabilize calculations (or force the use of very small time steps) and therefore are avoided in MFIX by approximating the normal velocity when the phase volume fraction drops below a threshold value.

MFIX employs automated time step adjustment to account for the inherently transient nature of multiphase flows where the limiting timescales change throughout a simulation. Small upward or downward modifications to the step size are applied to ensure that simulations progress with the highest possible execution speed. This minimizes simulation failure by reducing the time step if divergence is detected or the maximum number of iterations per time step is exceeded. Conversely, the step size is increased when the number of iterations becomes small to reduce the time to solution.

The individual procedures executed during a time step can be summarized as follows:

1. At the start of each iteration, the physical (e.g., specific heat) and exchange coefficients (e.g., convective heat transfer coefficients) are calculated.
2. The gas and solid momentum equations are solved using the pressure fields and volume fractions from the previous time step. The calculated velocities are referred to as the intermediate or starred velocities, $u_m^\star$, $v_m^\star$, and $w_m^\star$. At this time, the coefficients for the fluid pressure correction equation are calculated, but the pressure correction equation is not solved.
3. The solid-phase continuity equations are solved:
   a. Monodisperse simulations solve a solid volume fraction correction equation. The correction is used to update the solid volume fraction and solid velocity components.
   b. Polydisperse simulations solve a solid continuity equation for each phase. No corrections are made to the solid velocities.
4. The gas-phase volume fraction is calculated from the solid volume fractions.
5. The solid pressure is calculated from a state equation, $P_m = P_m(\varepsilon_m)$.
6. The face-centered densities are calculated.
7. The fluid pressure correction equation is solved. The corrections are used to update the gas pressure field and gas velocity components.
8. The material densities and the face-centered mass fluxes are calculated.
9. The scalar equations (e.g., species, energy) are solved.
10. The normalized residuals are calculated and checked for convergence. The time step is advanced if the convergence criteria are satisfied; otherwise, iterations are continued (Step 1).

As noted earlier, details on the control volume method (Patankar, 1980, Versteeg and Malalasekera, 1995, Syamlal, 1998) and SIMPLE algorithm (Patankar, 1980, Spalding 1980) are available elsewhere. Information specific to the numerical methods and implementations of MFIX-TFM, such as the multiphase partial elimination algorithm and solids, volume fraction correction equation, are also available (Syamlal, 1998). The following section presents more advanced methods that have been incorporated to increase modeling capabilities.

2.7.4 Advanced Numerical Methods

This section provides an overview of several advanced numerical techniques used in modeling reacting gas–solid flows as implemented in MFIX-TFM. The stiff chemistry and variable solid density sections discuss how chemical reactions are managed and used to modify the gas and solid phases. The point source and filter model sections discuss coarse grid modeling options to reduce the time to solution. Finally, the Cartesian grid cut-cell technique presents how complex geometries are integrated into staggered grid codes.

2.7.4.1 Stiff Chemistry Solver

As indicated in previous sections, multiphase CFD models solve governing equations for each phase that are tightly coupled through interphase transfer terms. Chemical reactions further couple the continuity, species, and energy equations with the formation and destruction of chemical species, interphase mass transfer, and heats of reaction. Unlike the interphase transfer terms found in the momentum and energy equations, coupling by reactions cannot be separated through "partial elimination" techniques. Therefore, numerical stability of chemically reacting flows is typically achieved through small time steps making the simulations prohibitively time consuming. The objective of a stiff chemistry solver, also referred to as a fractional step method, is to reduce the time to solution. This is accomplished by maintaining stability using time step sizes limited by the hydrodynamic timescales rather than chemical reaction timescales, which may be several orders of magnitude smaller.

The key aspect of a stiff chemistry solver is that transport (convection–diffusion) and chemical reaction effects are treated independently such that different solution methodologies can be used for each problem type. For example, discretized transport equations for nonreacting, cold flow systems result in large, sparse matrices whereby interphase transfer terms binding the phases are decoupled through partial elimination algorithms. The linear systems are solved in succession using iterative techniques that aim to exploit the matrix structure. In contrast, chemical reactions couple mass, species composition, and temperature through highly nonlinear source terms. Locality is such that chemical reactions in a computational cell are independent of reactions occurring in adjacent cells. Therefore, a low-dimensional, nonlinear system of coupled mass, species, and energy equations is solved to account for reactions.

The general approach of a stiff chemistry solver is depicted in Equation 2.419. First, the transport equations are solved without chemical reaction source terms. These intermediate solutions are denoted by a star, $\phi^*(t + \Delta t)$ and provide the initial conditions for the set of differential equations based on the chemical reaction source terms. The set of differential equations is directly integrated for each computational cell, completing the time step:

$$\phi(t) \xrightarrow{transport} \phi^*(t+\Delta t) \xrightarrow{reaction} \phi(t+\Delta t) \tag{2.420}$$

The set of differential equations sent to the stiff solver is dynamically constructed for each computational cell; every time step is constructed to minimize the computational impact of the solver. The form of the chemical reaction conservation equations is given in the following equations:

$$\frac{d}{dt}(\varepsilon_m \rho_m) = \sum_n^{N_g} R_{mn} \tag{2.421}$$

$$\frac{d}{dt} X_{mn} = \frac{1}{\varepsilon_m \rho_m}\left[R_{mn} - X_{mn} \sum_n^{N_g} R_{mn} \right] \tag{2.422}$$

$$\frac{d}{dt} T_m = \frac{-H_m}{\varepsilon_m \rho_m C_{Pm}} \tag{2.423}$$

Following the solution of the transport equations, the stiff solver evaluates the reaction rates for a computational cell, skipping cells where all reaction rates fall below a minimum threshold. If a cell does not contain any reactive solids, the cell is restricted to homogeneous gas-phase reactions to minimize computational overhead. The energy equations for all phases are an important exception and are always included in the set of

differential equations. This allows for an otherwise inert solid phase to act as a solid catalyst, thereby receiving the heat of reaction. Once the set of differential equations is determined, the active variables are mapped into the low-dimensional space and passed to the solver, ODEPACK (Hindmarsh, 1983). After the direct integration is preformed, the results are mapped back to the full dimensional space.

2.7.4.2 Variable Solid Density

A variable solid density model is used to capture the effect of solid particles maintaining a constant size while losing mass due to a chemical reaction or phase change. This is similar to the progressive conversion model of Levenspiel (1972) but adapted for a TFM. The traditional TFM accounts for solids mass sources and sinks by adjusting the solids, volume fraction. If the solids, diameter and density are constant, this leads to the implicit assumption that any loss (or gain) of solids, mass is the result of a decrease or increase in the particle number density.

The variable solid density model, as implemented in MFIX-TFM, requires that each solid phase be defined with a baseline species mass fraction composition, X^B_{mn}, along with the material densities of each species, ρ^B_{mn}. Here, the subscripts m and n indicate the phase and species, respectively. The superscript B indicates that this is a baseline quantity. The baseline apparent solid density for the solid phase is then calculated as

$$\frac{1}{\rho^B_m} = \sum_n^{N_m} \frac{X^B_{mn}}{\rho^B_{mn}} \tag{2.424}$$

where N_m is the total number of species comprising solid phase m.

The term baseline is used to assert that these values are specific to the phase definition and do not restrict the initial conditions or instantaneous composition of the solid phase. For example, consider a solid phase defined to represent coal particles and taken to be composed of the four pseudo-species char, ash, volatiles, and moisture. The baseline composition of the coal would likely reflect the proximate analysis (e.g., 40% char, 15% ash, 35% volatiles, and 10% moisture), whereas the initial conditions for the solid phase might be defined as either a normalized char/ash mixture (73% char and 27% ash) or all ash (100% ash).

The definition of the baseline solid density is only valid with respect to the baseline mass fractions of solids species. The equation employs the assumption that the volume of a particle is equivalent to the mass of a particle divided by the material density; however, as mass is lost or gained, this assumption no longer holds. This is easily demonstrated again by considering a coal particle. If all of the char, volatiles, and moisture are consumed such that only ash remains, then Equation 2.423 indicates that the solid density approaches the material density of ash as the mass fraction of ash goes to one. This is incorrect as the solid density should approach the mass of ash divided by the volume of solids. Xue et al. (2011) noted this phenomenon and suggested that the apparent solid density is related to the baseline density by a porosity, ε_p, such that

$$\rho_m = \rho^B_m \left(1 - \varepsilon_p\right) \tag{2.425}$$

This approach is not desirable in a generalized multiphase CFD code because it requires users to provide an additional closure to account for the evolution of porosity.

The variable solid density model in MFIX-TFM is generalized by having users identify one solid-phase species as inert. This is a reasonable approach given that the solids diameter is considered invariant to mass loss, and therefore, an inert material is needed to provide a rigid matrix to support reactants and/or products. Continuing with the example of a coal particle, the ash species can be marked as inert because it is not consumed or formed by any chemical reactions. The fact that an inert species is neither formed nor destroyed as a result of phase change or chemical reactions can then be exploited to construct a variable density model.

First, observe that an instantaneous solid density can be defined as the sum of the individual species masses, m_{mn}, divided by the volume that the phase occupies, V_m:

$$\rho_m = \sum_n \frac{m_{mn}}{V_m} \tag{2.426}$$

Using the assumption that the inert species mass is constant gives

$$m_m = \frac{m_m^0 X_{mI}^B}{X_{mI}} \tag{2.427}$$

where
the superscript "0" indicates the initial value
the subscript "I" is the index of the inert species

The definition of the initial solids mass, $m_m^0 = \rho_m^0 V_m$, is then used to condense the instantaneous solid density calculation:

$$\rho_m = \sum_n \left(\frac{m_m^0 X_{mI}^B}{X_{mI}} \right) \frac{m_{mn}}{V_m} \rho_m^B V_m = \rho_m^B \frac{X_{mI}^B}{X_{mI}} \tag{2.428}$$

The simplified form of the instantaneous solid density is compact making it ideal for implementation in CFD programs. Additionally, this approach does not require any new information, such as new field variables or additional species data, to calculate the solid density. Finally, the calculation is reasonably safe to perform without risk of floating-point arithmetic errors because the mass fraction of the inert material remains sufficiently large, in most practical cases.

2.7.4.3 Point Sources

As the name implies, point sources provide a way to specify mass sources to the discretized governing equations at either a specific location (point) or a region defined by a plane or volume. They are typically used in place of flow boundary conditions to model features such as injector tubes. Point sources are especially useful when substantial mesh refinement would otherwise be required to model the geometry of these small-scale mass sources as illustrated in Figure 2.81.

In MFIX, point sources are defined by specifying the mass flow rate, species composition, and temperature of incoming material and predominately operate on the scalar field. Unlike a traditional flow boundary condition, which defines the velocity at the face of a computational cell, point sources do not need to contribute directly to the momentum equations. If desired, point sources can be made directional by specifying magnitude and orientation whereby the momentum source is applied to the cell face in the point source's flow direction.

2.7.4.4 Filtered Models

Gas–solid flows in fluidized beds, circulating fluidized beds, and risers typically exhibit fluctuations and instabilities over a wide range of length and timescales. For example, inhomogeneous structures, or clusters,

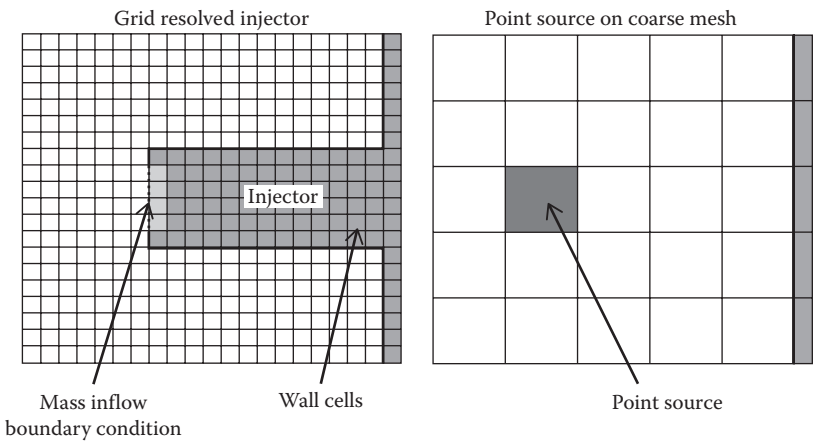


Figure 2.81

Illustrative example of an injector that is modeled either by resolving the grid or by a point source.

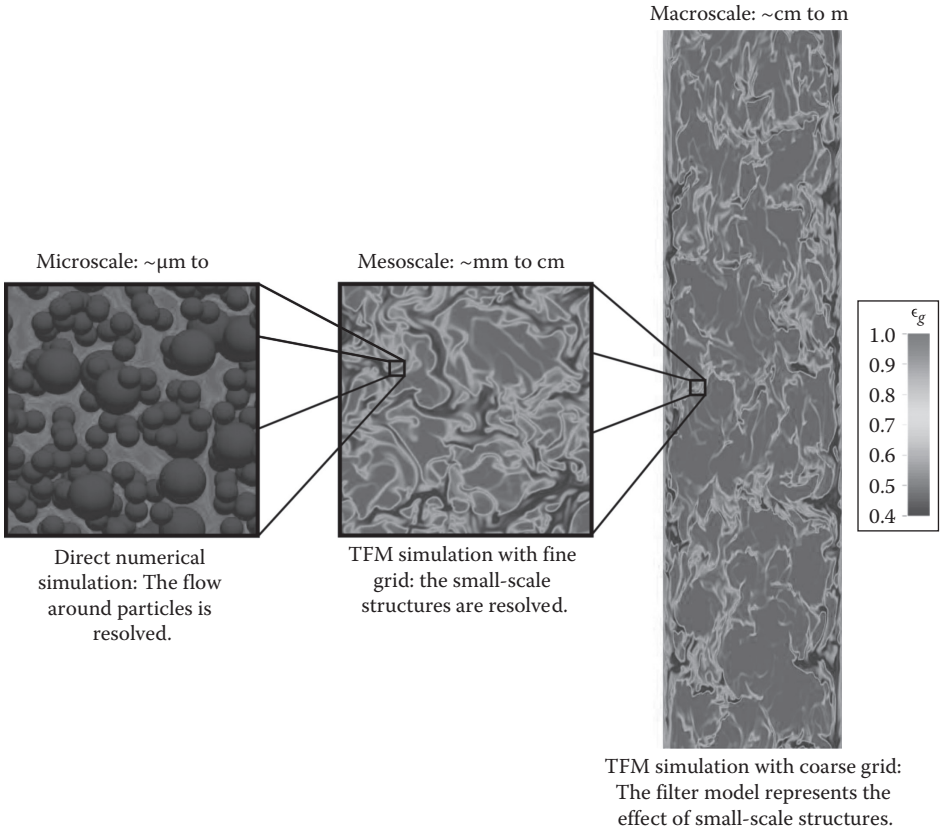


Figure 2.82

Gas–solid flow simulations at various scales. (Adapted from Milioli, C. et al., Constitutive model for the fluid-particle drag coefficient in filtered two-fluid models for gas-particle flows, in *AIChE Annual Meeting*, AIChE, Pittsburgh, PA, 2012.)

can develop within very small scales, on the order of 10 particle sizes (Agrawal et al., 2001), which can affect the flow dynamics. As noted earlier, TFM is based on locally averaged quantities wherein details of the flow at the individual particle level are unresolved, unlike direct numerical simulations (Figure 2.82). This approach requires closures (constitutive relations) to close the system of equations. These closures are typically based on data and/or analysis of homogeneous systems that do not natively take into account the formation of clusters at scales smaller than the computational cell size. When the computational mesh is sufficiently fine to resolve small scales (smaller than the cluster size), no additional modeling effort is required to capture their effects, but the burden is placed on the computational resources to achieve such fine resolution. For example, at the mesoscale level, high-resolution TFM simulations can capture small-scale structures, provided the computational cells are of the order of a few particle diameters. While high-resolution TFM simulations of large-scale devices, like those found in the industry, are theoretically possible, they are practically beyond current computational capabilities. Consequently, coarse mesh simulations are preferred. Coarse grids, however, are insufficient to resolve small-scale structures (i.e., at the subgrid scale level). As a result, the constitutive equations must be modified to account for the effects of the unresolved structures. For example, in the presence of clusters, the drag force needs to be reduced and compared to a homogeneous particle distribution to represent the lower resistance encountered by the air flowing around clusters. Similarly, mass and energy transfer will be reduced due to the tendency of the gas to bypass dense particle regions. The drag law can be corrected through an apparent cluster size (O'Brien and Syamlal, 1993, Heynderickx et al., 2004) or by using an energy minimization multiscale approach (Li and Kwauk, 2003, Yang et al., 2004). The implementation of these correction terms in the constitutive relations is referred to as *filtered models*. Although this is a fairly new development and a rapidly evolving field in the multiphase community, a similar technique is routinely applied to model single-phase turbulent flows and is known as large eddy simulation (Smagorinsky, 1963, Pope, 2000, Sagaut, 2006). The following sections describe two filtered models currently implemented in MFIX for monodisperse systems. For monodisperse systems, the Igci and

Milioli filtered models are currently available in MFIX (Release 2014-1). Details about the formulations can be found in Igci et al. (2008, 2012), Igci and Sundaresan (2011), and Milioli et al. (2012, 2013). A discussion of filtered models for bidispersed system can be found in Holloway and Sunderasan (2014).

2.7.4.5 Cartesian Grid Cut-Cell Technique

MFIX uses a 3D structured Cartesian or cylindrical coordinate system, with staggered grid representation of the velocity components. The advantages of the structured grid are the simple discretization of the governing equations, fairly straightforward programming of the numerical method, and fast mesh generation. However, structured grids have the disadvantage of not being able to accurately represent curved or sloping boundaries, which limits its range of applications. In a structured grid system, a boundary that is not aligned with the grid is typically approximated by a series of steps, referred to as staircase representation. Accuracy can be improved by refining the grid, but this requires additional computational resources, which often proves prohibitive.

For improved flexibility, the Cartesian grid cut-cell technique was implemented to represent complex geometries. This technique has the advantage of keeping the traditional Cartesian grid formulation to discretize the computational domain away from the boundaries, while computational cells near the boundaries are truncated so that they conform to the boundary surface. Therefore, additional treatment is only required for the boundary cells. A description of the Cartesian grid cut-cell method for staggered grid system is given in Kirkpatrick et al. (2003), and the original MFIX implementation can be found in Dietiker et al. (2009). In the latter, improvement over the usual staircase representation of curved or sloped boundary was highlighted through several simple benchmark tests. For a 2D single-phase flow in a skewed channel, the error on the velocity can be reduced by an order of magnitude. Figure 2.83 shows an example of velocity profile across a channel with a coarse grid. The solution with cut cell is smooth and compares well with the exact solution, whereas the solution with staircase boundary exhibits large discrepancies, even far away from the walls.

In the Cartesian grid cut-cell method, once the geometry is defined, the computational cells are truncated to conform to the shape of the boundaries. Current geometry input methods include quadric surfaces for relatively simple shapes (cylinders, cones, etc.), 2D polygons, user-defined functions, or direct input from a CAD file (STL format). Velocity nodes are moved to the center of cut-cell faces, and computation of fluxes through cut-cell faces is modified to account for the new nodes location.

Figure 2.84 shows the computational grid near a curved boundary, where arrows indicate the location of velocity nodes. The wall is represented by a thick solid line. Three types of cells are shown: standard (uncut) cells, cut cells that require special treatment due to the presence of the wall, and blocked cells that are excluded from computations. Figure 2.85 shows an x-momentum cut cell (cell bordering a boundary surface), where u_P refers to the x-velocity in that cell and u_E refers to the x-velocity in the east-neighbor cell. The interpolated velocity, u_e, at a boundary cell surface based on velocity nodes u_P and u_E is not necessarily

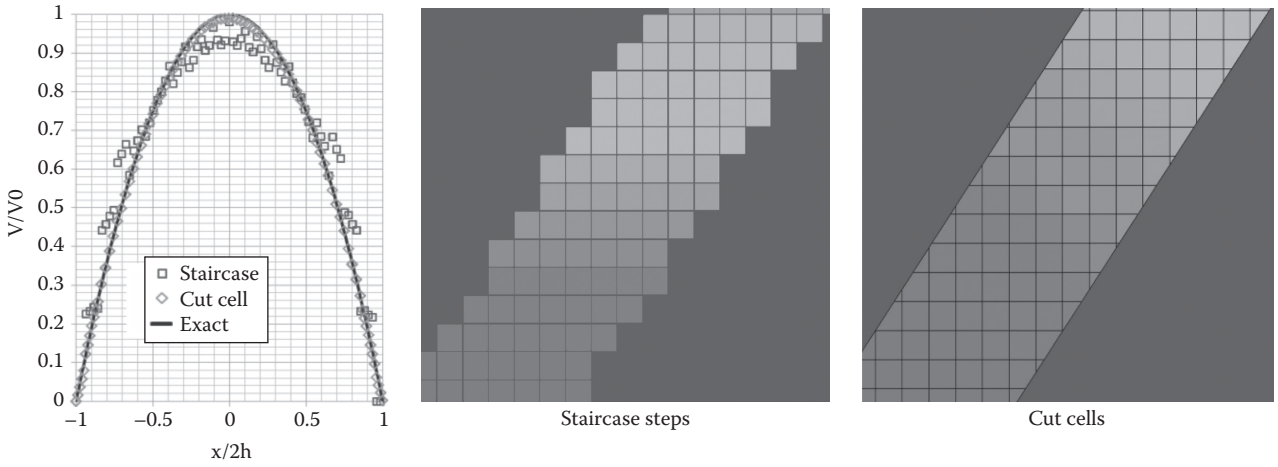


Figure 2.83

Illustration of the benefits of Cartesian grid cut cell. The velocity profile across a skewed channel shows large error with a staircase representation on the boundaries. When cut cells are used, the wall boundary is smooth and the velocity profile matches the exact parabolic solution.

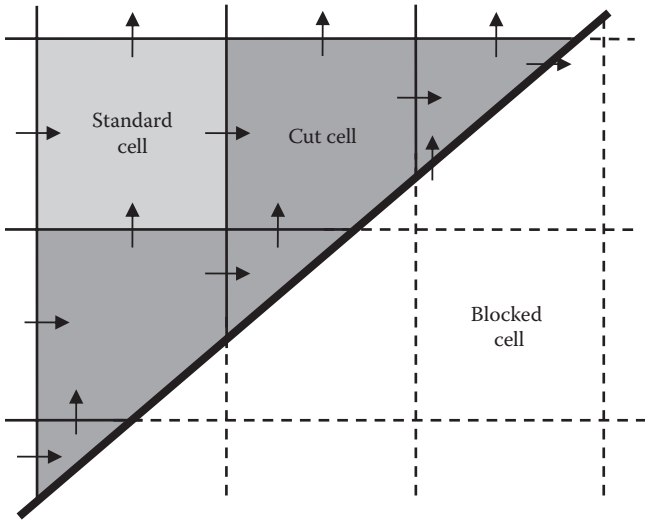


Figure 2.84

Different types of scalar cells and location of velocity nodes with the Cartesian grid cut-cell technique.

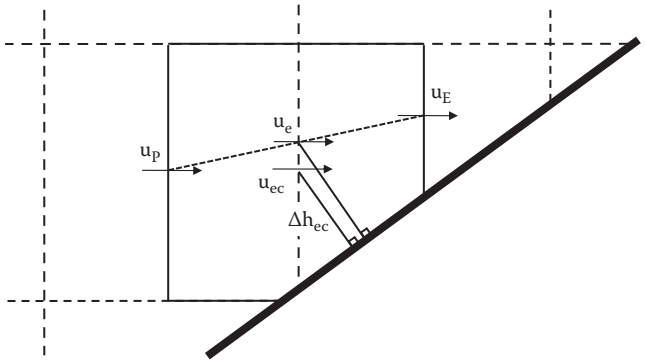


Figure 2.85

Interpolation correction for u_{ec} at the east face of an x-velocity cut cell.

located at the center of the cell face. To calculate the velocity at the cell face center, u_{ec}, a correction is applied. For a no-slip boundary condition, u_{ec} is computed by assuming zero velocity at the wall using the ratio of normal distances to the wall from $u_{ec} = \Delta h_{ec} u_e / \Delta h_e = \alpha_e u_e$. For a free-slip boundary condition, the coefficient α_e is set to one. For partial slip (Johnson–Jackson), the value of α_e is between 0 and 1 and depends on the specularity coefficient. Since the line between u_P and u_E is not aligned with the *x*-axis, nonorthogonality correction terms are included in the computation of velocity gradients.

A wide variety of cut cells are typically generated, and cut cells vary in shape and size. The generation of small pressure cells can lead to stability issues. Due to the staggered grid formulation, velocity cells require pairs of pressure nodes (East/West, North/South, and Top/Bottom) to compute pressure gradients. However, when some pressure cells are removed (blocked cells), the corresponding velocity cells will only have one pressure node and the pressure gradient cannot be computed in that direction. When this situation occurs, the velocity cell is flagged as a "wall cell," and the momentum equation is not solved for this cell. The treatment of single-pressure velocity cells effectively limits their size to half the size of a standard cell in any direction. This criterion automatically avoids problems linked to small velocity cells.

The treatment of cut cells involves additional interpolation and correction terms, which increases the computational cost of the flow solver. However, the geometric parameters are computed during preprocessing and have negligible impact on the overall code efficiency. Cut-cell simulation results are stored in vtk files (Avila, 2010) for visualization. For meshes that contain a large number of unused computational cells (i.e., blocked cells), it is beneficial to reindex the cells in the program memory, such that the flow solver only



Figure 2.86

Example of a simulation using the Cartesian grid cut-cell technique.

loops over fluid and boundary cells. Reindexing is performed after the preprocessing and has been shown to greatly improve the performance of the code. Figure 2.86 shows an example of a chemical looping reactor simulation with a fairly complex geometry. The rendered image shows the void fraction in the unit, where the light gray corresponds to a packed solid phase and the dark gray corresponds to a dilute region. The geometry was created in a CAD software and imported into MFIX at run time. The geometry was defined using an STL file and consists of about 175,000 triangular facets. The total number of cells is about 2.7 million, but due to the large number of blocked cells, only 0.3 million cells are actually active computational cells. In this case, the reindexing method provided a speedup factor of 4.5, which greatly reduces the time to solution. An example of an ongoing industrial application of MFIX-TFM at NETL is shown in Figure 2.87. The entire geometry is defined by quadric surfaces, and the mesh consists of 4 million cells after reindexing.

2.7.5 Accessing and Using MFIX

MFIX is an open-source multiphase flow solver developed and maintained at the NETL. Over the years, many additional researchers from national laboratories or universities have contributed to the code. MFIX can be downloaded for free from the MFIX website (https://mfix.netl.doe.gov/), and a one-time (free) registration is required prior to downloading the source code. Typically, one or two new releases occur per year, and bug fixes are provided on a regular basis.

MFIX is primarily designed to run on Linux operating system; therefore, users should be familiar with basic Linux operating system commands and procedures before attempting to install and use MFIX. A Windows operating system executable file is also available for download, which can run basic models. Advanced models requiring user-defined functions (such as chemical reaction rate specifications) are not available from the Windows executable file. Users that do not have access to a Linux machine can install the Linux emulator Cygwin (https://cygwin.com/) on their machine to have the capability to customize the code. Other options to run MFIX on Windows include MINGW (http://mingw.org/). The code may also be compiled with a Windows Fortran compiler, but the MFIX development team does not support this format.

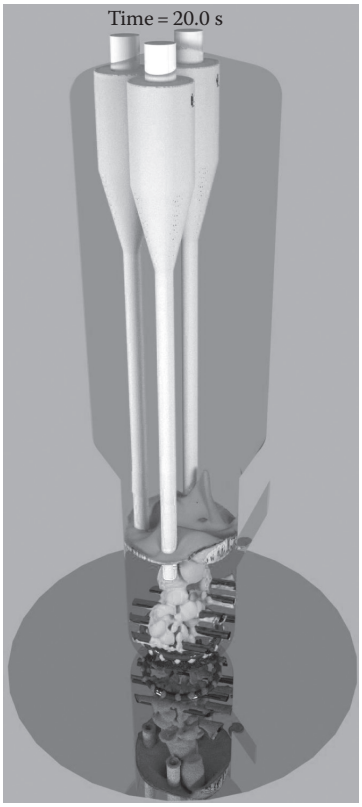


Figure 2.87

Example of an ongoing industrial application of MFIX-TFM at the National Energy Technology Laboratory. The Integrated Waste Treatment Facility Unit, developed to process sodium-bearing waste (acidic radioactive waste resulting primarily from radioactive decontamination of equipment and other components) stored at the Idaho Nuclear Technology and Engineering Treatment Center, will convert the waste into a granular product that can be further processed for disposal with the help of a fluidized bed conversion process similar to coal gasification/combustion. An MFIX-TFM model is providing insights into how the bed operates in the current design and is helping to optimize the bed operation. This figure shows void fraction isosurfaces in the unit, illustrating the bubble pattern in the bed, above the sparge ring and rail distributors.

MFIX is distributed as a single tarball that contains the source code, documentation, and a suite of tutorials. A Fortran 90 compiler is required to compile the code. Typical compilers include GNU (gfortran), Portland Group (pgf90), and Intel (ifort) compilers. For parallel execution in distributed memory parallel (DMP) mode, an MPI library must also be available (mpich or openmpi). Once the tarball is extracted, the code can be installed by invoking a build script. Typically, the compilation is performed in a directory called the run directory, where the input file and user-defined files are located. Invoking the makefile goes through a series of options to select the mode of execution (serial, DMP, SMP, or hybrid mode), the level of optimization (ranging from none for debugging purposes to aggressive for production runs), and the Fortran compiler. Advanced users can customize the compilation flags to use a compiler that is not listed in the makefile or take advantage of their hardware architecture by adding specific compilation flags that will optimize the code. After successful compilation, an executable file called mfix.exe is created.

As with any CFD tool, becoming fully accustomed with the operation of the software requires time, and a careful study of the various tutorials that are distributed along with the source code is recommended. For basic simulations, the entire setup is contained within a single input file, called mfix.dat. This is a text file with a list of keywords/values that can be edited to modify the simulation parameters. A complete description of the keywords is given in the user guide (also called the Readme file). Only keyword values that differ from the default value or do not have a default value need to be specified. Keywords can be entered in any order, but they are usually grouped into logical sections. Typically, new users will study a few tutorials and then select one that is similar to the simulations they want to perform. The input file from the tutorial serves as a starting point, which minimizes the effort required to define the simulation parameters.

Knowledge of Fortran programming language is not required to use MFIX. However, simulations involving chemical reactions require editing a user-defined subroutine to define the chemical reaction rates. Careful study of the tutorials is always recommended to gain experience before attempting to build and run a simulation, especially, a chemically reacting simulation. To implement new models or modify a feature of the code, good knowledge of Fortran is necessary, and time must be invested to understand the code structure and variable names. Both Doxygen (http://www.stack.nl/~dimitri/doxygen/) and STI (https://scitools.com) documentations are available for developers and interested users. These documentations provide in-depth analysis of the code. They allow users to navigate through the code and see how variables, subroutines, and functions are used. Call graphs allow users to get more quickly accustomed with the code structure and reveal where to implement their own models or improve existing ones. Finally, a mailing list system has been set up to provide a mechanism for communication among MFIX users and developers. Users can post technical questions, and members of the development team or other users provide the answers.

MFIX development activities are tracked through a Git repository. Therefore, MFIX users that actively collaborate with the MFIX development team can view the source code changes as they are being made by developers or other users through the Git interface. In addition to downloading the latest release, MFIX users can also retrieve a previous version of the code. Therefore, simulations may be conducted with an older version allowing users to exactly reproduce simulations reported in the literature or compare different versions of the code.

Results can be postprocessed after the simulation is complete, or while the simulation is running, as long as intermediate data are saved regularly. A simple postprocessing tool, called post_mfix, is distributed with MFIX, which allows the flow field to be probed at specified locations. This tool can also be used to extract time or spatial averages. Similar to the flow solver mfix.exe, post_mfix must be compiled prior to its first use. The data can also be visualized by other open-source tools, such as ParaView (www.paraview.org/) and VisIt (wci.llnl.gov/simulation/computer-codes/visit/).

2.7.6 MFIX Applications

The scale and complexity of simulations leveraging the MFIX suite continue to grow as the modeling capabilities are expanded and refined. Although primarily intended to aid in the design and troubleshooting of reacting, multiphase systems, especially with respect to fossil energy technologies such as gasifiers, MFIX has been used in a variety of applications. This section reviews a sample of the interesting MFIX research activities and applications reported in the literature.

2.7.6.1 Kinetic Theory of Gas–Solid Flows

As an open-source project, MFIX is regularly used to test new gas–solid flow theories and modeling techniques. One area of active research is the kinetic theory of gas–solid flows for which MFIX contains several theories (Garzo and Dufty, 1999, Iddir and Arastoopour, 2005, Garzo et al., 2007a,b, Garzo et al., 2012). These types of gas–solid flow theories are derived as pure mathematical models employing different assumptions such as the number of phases, granular or gas solids, and base state of the Enskog expansion (see Garzo et al., 2007b, Hrenya 2011). Verification of the theories is typically restricted to cases that yield analytical solutions for highly idealized conditions (e.g., a homogeneously cooling system). After being implemented into MFIX, these highly sophisticated theories can be evaluated with respect to more complex flow dynamics, compared against existing models, used in validation studies, or used to analyze fundamental flow dynamics (e.g., Mitrano et al., 2014).

2.7.6.2 Subgrid Cylinder Array Model

In industrial-size fluidized beds, heat exchange is often provided by arrays of immersed tubes, such as in a solid sorbent–based CO_2 capture reactor. The tube diameter is much smaller than the vessel size, and it is computationally expensive to model each individual tube. Similar to the filtered drag models discussed in Section 2.7.4.5, Sarkar et al. (2013) developed a subgrid drag model to represent the presence of a horizontal cylinder array in a fluidized bed. A series of highly resolved simulations were conducted to gather the necessary data to construct the closure models. For each simulation, a pressure drop was imposed vertically on a periodic domain with an immersed array of cylinders. The pressure drop controls the average gas and solids velocity in the domain. Figure 2.88 shows an example of a computational domain. The cylinders were represented by the Cartesian grid cut-cell technique described in Section 2.7.4.4. The simulations were conducted with various values of the tube diameters, spacing between tubes, averaged solids, volume fraction in the domain, and pressure drop. Figure 2.89 illustrates the flow structures for various solids, volume fractions.

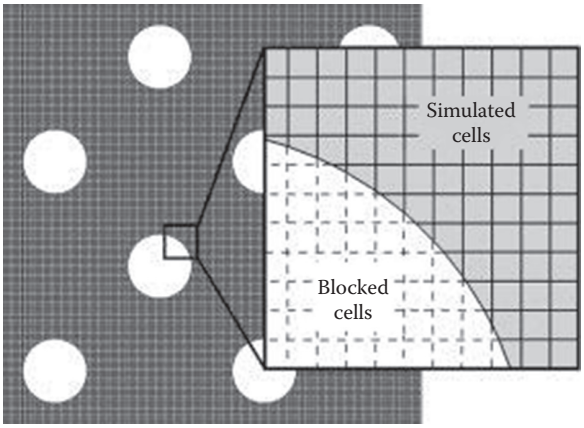


Figure 2.88

Illustration of the computational domain for high-resolution simulations. (From Sarkar, A. et al., *Chem. Eng. Sci.*, 104, 399, December 2013.)

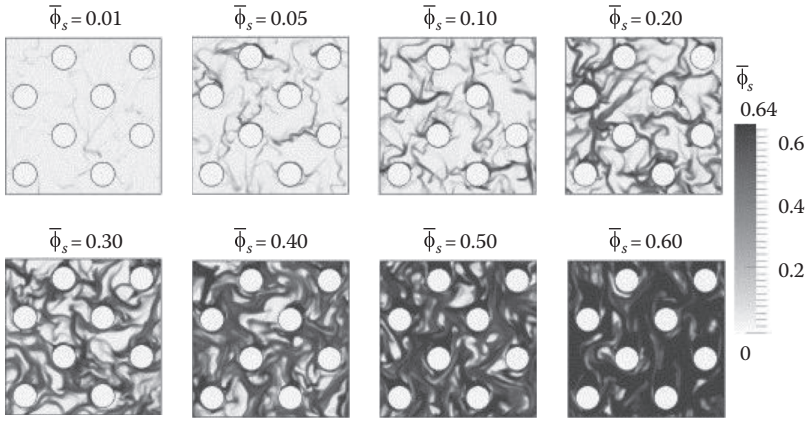


Figure 2.89

Snapshots of the solids, volume fraction distribution for averaged volume fractions ranging from 0.01 to 0.6. (From Sarkar, A. et al., *Chem. Eng. Sci.*, 104, 399, December 2013.)

For small volume fractions, the formation and dissociation of clusters are visible, whereas at larger volume fractions, bubbles develop and break around the tubes.

For coarse grid simulations that cannot resolve the flow around individual cylinders, an additional stationary solid phase is introduced, and a closure is required to model the drag force exerted on the gas–solid suspension by the cylinder array. The filtered drag force was obtained by curve fitting the data obtained from hundreds of simulations and was expressed as a function of averaged volume fractions, velocities, and geometric parameters (cylinder diameter and spacing). The formulation clearly shows a kinetic component and a buoyancy component. Another series of simulations where the pressure drop was imposed horizontally, that is, perpendicular to gravity, showed that the horizontal drag coefficient is smaller than the vertical drag coefficient. The presence of cylinders also modifies the structure of the gas–solid suspension for solids, volume fractions larger than 0.30. For dense suspensions, the cylinders promote the formation of bubbles, and the Igci drag coefficient must be further reduced. Details about the proposed subgrid drag models can be found in Sarkar et al. (2013), and verification of the subgrid models is described in Sarkar et al. (2014).

2.7.6.3 High-Fidelity Gasifier Simulations

First of their kind, high-fidelity gasifier simulations were carried out with MFIX-TFM to demonstrate the use of multiphase CFD as a tool for studying system scalability, performance optimization, and troubleshooting analysis (Gel et al., 2010). As part of this effort, two commercial-scale configurations were simulated with nearly 10 million computational cells each. The nonproprietary, commercial-scale, reactor was 50 m tall with a

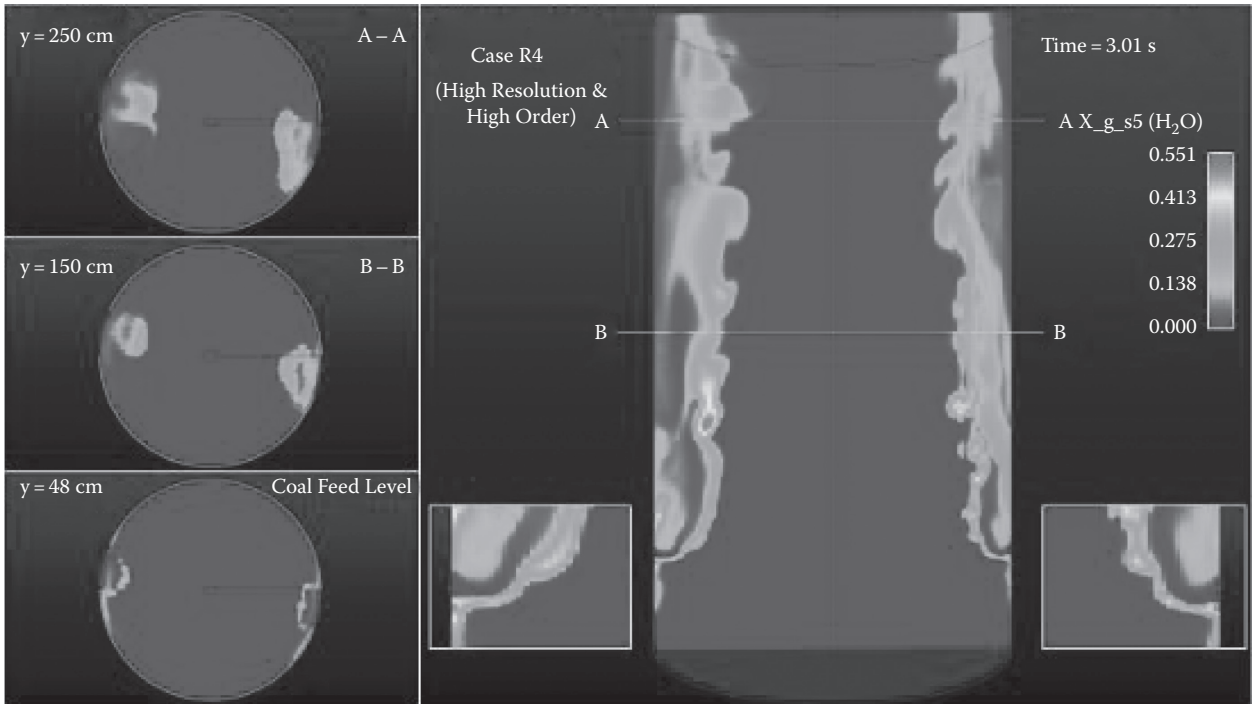


Figure 2.90

Instantaneous gas-phase steam mass fraction predicted in a simulation used for studying jet penetration in a gasifier. (From Li, T. et al., *Ind. Eng. Chem. Res.*, 49, 10767, 2010b.)

1.6 m in diameter, which was represented with a grid at 1 mm resolution in regions of interest. A reduced scale system utilizing 2.4 million computational cells and a high-order discretization scheme was used to investigate coal jet penetration (Li et al., 2010b). Time-averaged data from the full-scale simulations were used to impose the flow boundary conditions for the reduced case. A snapshot of the gas-phase steam mass fraction is shown with a volume rendering in Figure 2.90 for three vertical locations (left) and the centerline (right).

MFIX simulation results of the pilot-scale gasifier at the Power Systems Development Facility in Wilsonville, Alabama, provided insight into the systems operation (Syamlal et al., 2011). Simulations showed that oxygen penetrated into the upper region of the mixing zone, whereas the design called for oxygen to be consumed in the lower mixing zone region. This prediction was later confirmed by measuring the oxygen concentration in the gasifier. Additionally, simulations showed higher concentrations of carbon monoxide in the disengager, which again was later confirmed.

Modifications to the pilot-scale gasifier were simulated in 2 weeks at a cost of around $10 thousand, while the physical changes took 14 weeks and cost approximately $6 million. The simulation predicted a substantial increase in the carbon monoxide concentration in the syngas. Measurements taken on the modified geometry later confirmed these results. Furthermore, it was possible to determine from the simulation results that the increase in the carbon monoxide concentration was caused by the larger concentration of solids along the walls of the modified reactor. Finally, the validated model was employed in the design of a commercial-scale gasifier with a scale-up factor of 50. Simulation results provided guidance in design selection as they indicated that various configurations may lead to hotspots that could impact the gasifier's performance and operability.

2.7.6.4 Wood Gasification

Wood gasification is a promising renewable energy technology that needs to be better understood and optimized. Although experiments are still required to study the complex nature of gasification in fluidized bed reactors, numerical simulation tools provide useful data for quantities that cannot be easily measured in experiments. To gain confidence in those predictions, validation studies are often performed at increasing levels of complexity. For example, Gerber et al. (2010) used the MFIX-TFM to model wood gasification in a bubbling fluidized bed reactor and compared their results with experiment. In this case, they implemented a comprehensive model for wood pyrolysis, char gasification, and homogeneous gas-phase reaction. Three

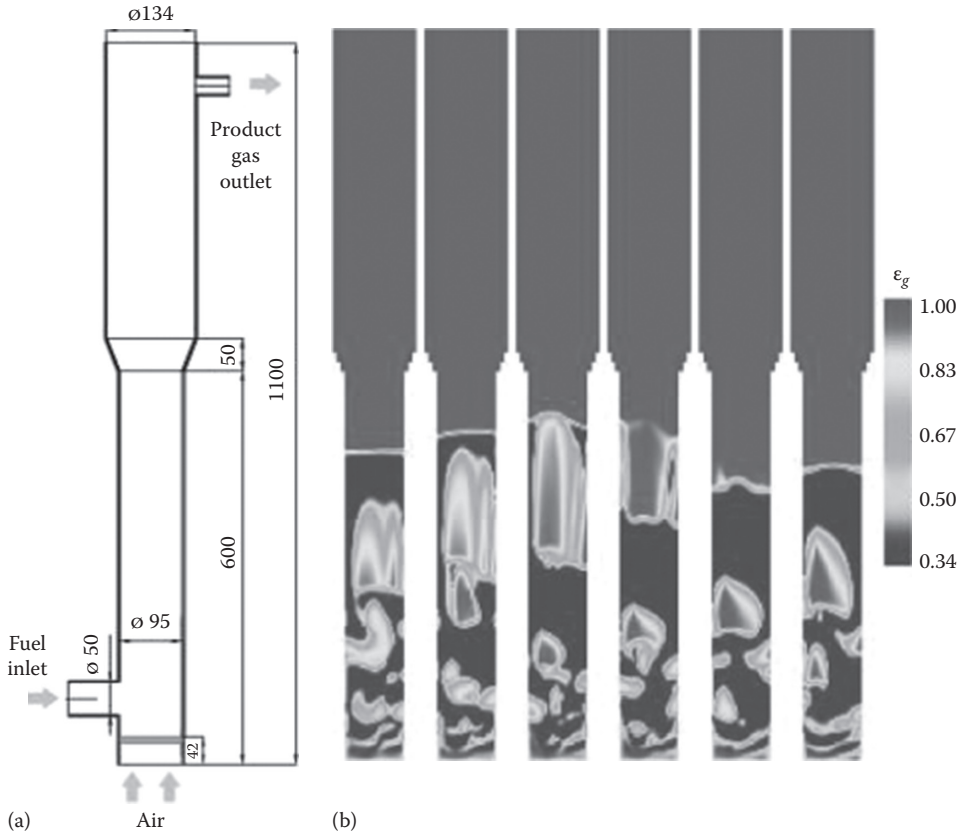


Figure 2.91

(a) Schematic of the wood gasification reactor. (b) Snapshots of the gas-phase volume fraction. (From Gerber, S. et al., *Fuel*, 89, 2903, October 2010.)

solid phases were used, one phase for wood, and two phases of different particle sizes for char. The gas phase consisted of eight species (N_2, O_2, H_2, CH_4, CO, CO_2, H_2O, and tar). A primary pyrolysis model, converting wood into wood gas (CO, CO_2, CH_4, H_2, H_2O), char, and tar was taken from Grønli (1996). For the secondary pyrolysis model, two descriptions (Boroson and Howard, 1989, Rath and Staudiger, 2001) were investigated. Figure 2.91a shows a schematic of the reactor. Wood is fed into the reactor at a rate of 2 kg/h. Preheated air fluidized the bed from the bottom. The products of gasification were analyzed at the outlet, located near the top of the reactor. Figure 2.91b illustrates the gas-phase volume fraction and shows the bubbling pattern in the bed. The steady-state concentrations of some components of the product gas are compared with the experimental data in Table 2.9. The predicted values are all within the experimental range.

2.7.6.5 Spouted-Bed Nuclear Fuel Coater

Pannala et al. (2006, 2007) used MFIX-TFM to model the hydrodynamics of a spouted-bed nuclear fuel coater. The project objective was to model a coating device used for making the tristructural isotropic (TRISO) fuel particle, which is at the heart of the advanced gas reactor concept of U.S. DOE Nuclear Energy (DOE-NE)

Table 2.9 Steady-State Values of Gas Species Concentrations at the Outlet

		Experiments	
Gas Species	MFIX Results	Min	Max
CO	0.139	0.13	0.21
CO_2	0.158	0.13	0.17
H_2	0.076	0.07	0.11
CH_4	0.036	0.02	0.06

(Kinsey, 2014). The TRISO particles consist of a UO_2 kernel coated with buffer carbon (to accommodate fission gases), pyrolytic carbon (to prevent chlorine and other species from attacking SiC), silicon carbide (pressure capsule), and pyrolytic carbon (protect SiC from cracking during fuel assembly). The particles are fabricated in a high-temperature (1300°C–1500°C) spouted-bed reactor operated in a batch mode, cycling them through deposition and annealing zones that affect complex chemical changes in the particles. The particles can be fabricated with very low rates of defect to contain fission products with a high degree of safety. The scaled-up design must maintain optimal temperatures, gas compositions, and residence times in each zone in order to attain the right microstructure of the coating layers at a nanometer scale. Pannala et al. (2006) addressed this scale-up challenge by building an MFIX model and then validating it with lab-scale data. The resulting model was used to conduct simulations and identify important characteristics for evaluating the designs of a production-scale coater.

Pannala et al. (2007) describe 2D and 3D MFIX-TFM simulations of spouted beds and compare the simulation results with experimental data. A key finding of their study was that MFIX-TFM captured the experimentally observed features of the solids, circulation and spout formation. Specifically, MFIX-TFM simulations showed that solids are transported up through the spout and deposited across the bed surfaces. Meanwhile, solids move downward along the walls and accumulate at the spout inlet until sufficient gas pressure builds to push the solid packet up through the bed. This predicted pattern of solids accumulation and discharge at the inlet lead to pulsations in the gas pressure, which were also observed in experiments.

Over 20 discriminating characteristics (DCs) of importance to the coating process (e.g., particle residence time in the coating zone) were determined from the modeling study. Using DCs was necessary because all the nondimensional parameters of the full-scale coater could not be matched in the lab-scale coater. Pannala et al. (2006) evaluated four different designs with the help of the DCs. Cardioid chalice with the multiport design appeared to have the best gas–solid mixing and heat transfer rates (see Figure 2.92). The full-scale coater was built by B&W at Lynchburg, Virginia. After some initial fine tuning, the coater was used to coat nuclear fuel particles for DOE-NE's advanced gas-cooled reactor program. This is an example of reducing the design cycle time from what could be two decades to around 2 years with the help of a validated CFD model (personal communication with S. Pannala, 2009).

2.7.6.6 Pyroclastic Flows from Volcanic Eruptions

A less traditional MFIX application is in the geological and earth sciences field (Dufek and Bergantz, 2006, Dartevelle and Valentine, 2007, Ruprecht et al., 2008, Dartevelle, 2011, Molina et al., 2012). Particularly interesting simulations of the Kos Plateau Tuff volcanic eruption were conducted by Dufek and Bergantz (2007) to investigate the role of bed load and suspended solids as well as the role of topography and overwater/overland effects on the transportation of pyroclastic flows. Specialty boundary conditions were developed to account for flow overwater (leaky) and flow overland (saltation). The simulations were carried out using

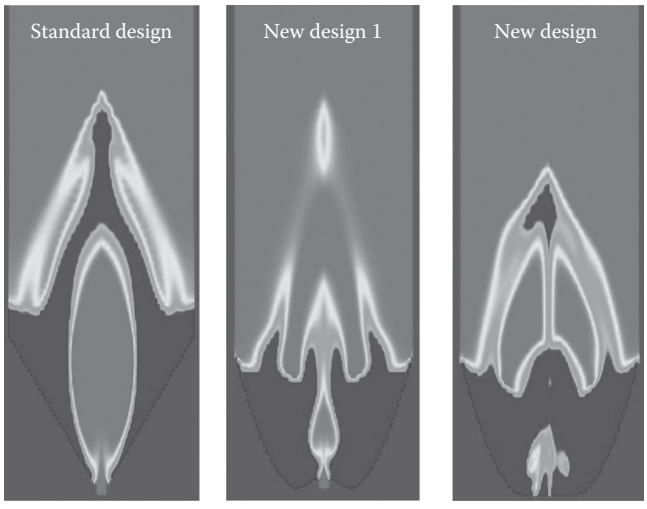


Figure 2.92

Evaluating the design of fluidized bed chemical vapor deposition coater for making nuclear fuel particles. (From Pannala, S., Personal communication, 2009.)

cylindrical coordinates with a vertical resolution of 10 m near the boundary expanding to 100 m in the far field. The horizontal resolution ranged from 20 to 100 m as needed to capture the topography of the model region. Dufek and Bergantz (2006) used simulation results to estimate the ring vent eruptive flux and thereby approximate the eruption duration needed to generate the observed depositional distribution of volcanic solids. Furthermore, simulation results suggested that there was likely a body of water south of Kos at the start of the eruption that could aid in estimating the neotectonic subsidence in the area.

Acknowledgments

This technical effort was performed in support of the NETL's ongoing research in multiphase flows in part under the RDS contract DE-AC26–04NT41817. The authors acknowledge the contributions of the developers of MFIX, the software described in this chapter. The authors thank the following colleagues for reviewing the chapter and pointing out corrections and suggestions for improvement: S. Benyahia (NETL), J. Carney (NETL), T. Li (NETL), and S. Pannala (Oak Ridge National Lab).

Nomenclature

C_{Dm}	Multiparticle drag coefficient
C_{Ds}	Single-particle drag coefficient
C_{fml}	Coefficient of friction between particles constituting the lth and mth solid phases
C_{pm}	Specific heat of the mth phase; J/kg·K
d_{pm}	Diameter of the particles constituting the mth solid phase; m
D_{mij}	Rate of strain tensor for mth phase; s^{-1}
$\mathcal{D}_{mn}$	Diffusion coefficient of nth species in the mth phase; kg/m·s
e_{ml}	Coefficient of restitution for the collisions between particles constituting the lth and mth solid phases
f_{gi}	Fluid flow resistance due to porous media; N/m^3
g_i	Acceleration due to gravity; m/s^2
g_{0ml}	Radial distribution function at contact for a mixture of hard spheres
h_{mn}	Specific enthalpy of the nth species in the mth phase; J/kg
H_m	Total rate of enthalpy change in the mth phase due to chemical reactions and phase changes; $J/m^3 \cdot s$
i,j,k	Subscripts for identifying vector and tensor components; if there are multiple subscripts, these indices appear at the end of the list of subscripts and summation convention is implied only for these indices
I_{mli}	Momentum transfer between the mth and the lth phases due to interphase forces such as drag force; N/m^3
k_g	Gas-phase turbulent kinetic energy; m^2/s^2
m,l	Subscripts for identifying phases: $m = 0$ or g is gas phase; $m = 1$ to M are solid phases
M	Total number of solid phases
M_w	Average molecular weight of gas
n	Subscript for the nth chemical species
N_m	Total number of chemical species in phase m
Nu_m	Nusselt number
p	Subscript for identifying a chemical reaction out of the P chemical reactions in total
p,v	Subscripts for identifying plastic regime (p) and viscous regime (v) stresses in the solid phase
P_g	Gas-phase pressure; Pa
P_c	Solid-phase pressure in close-packed regions; Pa
P_m	Viscous regime pressure in the mth solid phase; Pa
Pr	Prandtl number
q_{mj}	Conductive heat flux in the mth phase; $J/m^2 \cdot s$
R	Universal gas constant; $Pa \cdot m^3/kmol \cdot K$
Re_m	Particle Reynolds number of the mth solid phase
$\mathcal{R}_{lm}$	Rate of transfer of mass from lth phase to mth phase; $kg/m^3 \cdot s$
R_{mn}	Rate of formation (or destruction) of the nth chemical species in the mth phase; $kg/m^3 \cdot s$
R_{mlnp}	Rate of formation (or destruction) of the nth species in mth phase attributed to the pth reaction between the mth and lth phases; $kg/m^3 \cdot s$

S_{mij} Deviator of rate of strain tensor for mth hase; s^{-1}
t Time; s
T_m Thermodynamic temperature of the mth phase; K
T_{Rm} Background temperature in a radiation model; K
u_e Interpolated velocity; m/s
u_{ec} Velocity at the cell face center; m/s
u_E x-velocity in east-neighbor x-momentum cell; m/s
u_P x-velocity in x-momentum cell; m/s
U_{mj} jth component of the mth phase velocity; m/s
v_t Particle terminal velocity; m/s
V_{rm} Ratio of the terminal velocity of a multiparticle system to that of a single particle of the mth solid phase
x_j jth coordinate direction; m
X_{mn} Mass fraction of the nth chemical species in the mth phase

Greek Letters

α_e Ratio of wall distances $\Delta h_{ec}/\Delta h_e$
δ_{ij} Identity tensor
Δh_e Wall distance to the location of interpolated velocity; m
Δh_{ec} Wall distance to cell center; m
γ_{gm} Gas–solid heat transfer coefficient; $J/m^3 \cdot K \cdot s$
γ_{Rm} Radiative heat transfer coefficient for the mth phase; $J/m^3 \cdot K^4 \cdot s$
ε^* Void fraction (or gas volume fraction) of close-packed solids
ε_m Volume fraction of the mth phase
ϵ_g Turbulent energy dissipation rate in the gas phase; m^2/s^3
η Function of the restitution coefficient
Θ_m Granular temperature of the mth solid phase; m^2/s^2
κ_m Granular temperature conductivity of the mth solid phase; $kg/m \cdot s$
λ_g Thermal conductivity of the mth phase; $J/m \cdot K \cdot s$
μ_g Molecular viscosity of the gas phase; $kg/m \cdot s$
μ_g^t Turbulent viscosity of the gas phase; $kg/m \cdot s$
μ_m Granular viscosity of the mth solid phase in plastic or viscous regimes; $kg/m \cdot s$
ρ_m Microscopic (material) density of the mth phase; kg/m^3
ξ_{gmp} Enthalpy transfer attributed to mass transfer between the gas and the mth solid phases for the pth reaction; $J/m^3 \cdot s$
τ_{mij} Stress tensor of the mth phase; Pa
ϕ Angle of internal friction

References

Agrawal, K., Loezos, P.N., Syamlal, M., and Sundaresan, S., The role of meso-scale structures in rapid gas-solid flows, *J. Fluid Mech.*, 445, 151–185, 2001.

Anderson, T.B. and Jackson, R., A fluid mechanical description of fluidized beds, *Ind. Eng. Chem. Fund.*, 6(4), 527–534, 1967.

Atkin, R.J. and Craine, R.E., Continuum theories of mixtures: Basic theory and historical development, *Q. J. Mech. Appl. Math.*, 29(2), 209–244, 1976.

Avila, L.S., *The VTK User's Guide*, 11th edn., Kitware, 2010.

Balzer, G., Simonin, O., Boelle, A., and Lavieville, J., A unifying modelling approach for the numerical prediction of dilute and dense gas–solid two phase flow, CFB5, in *Fifth International Conference on Circulating Fluidized Beds*, Beijing, China, 1996.

Bauer, R. and Schlunder, E.U., Effective radial thermal-conductivity of packings in gas-flow.2. Thermal-conductivity of packing fraction without gas-flow, *Int. Chem. Eng.*, 18(2), 189–204, 1978.

Bedford, A. and Drumheller, D.S., Theories of immiscible and structured mixtures, *Int. J. Eng. Sci.*, 21(8), 863–960, 1983.

Beetstra, R., van der Hoef, M.A., and Kuipers, J.A.M., Drag force of intermediate Reynolds number flow past mono- and bidisperse arrays of spheres, *AIChE J.*, 53, 489–501, 2007a.
Beetstra, R., van der Hoef, M.A., and Kuipers, J.A.M., Erratum., *AIChE J.*, 53, 3020, 2007b.
Benyahia, S., Validation study of two continuum granular frictional flow theories, *Ind. Eng. Chem. Res.*, 47(22), 8926–8932, 2008a.
Benyahia, S., Verification and validation study of some polydisperse kinetic theories, *Chem. Eng. Sci.*, 63(23), 5672–5680, 2008b.
Benyahia, S., Syamlal, M., and O'Brien, T.J., Evaluation of boundary conditions used to model dilute, turbulent gas/solids flows in a pipe, *Powder Technol.*, 156, 62–72, 2005.
Benyahia, S., Syamlal, M., and O'Brien, T.J., Extension of Hill-Koch-Ladd drag correlation over all ranges of Reynolds number and solids volume fraction, *Powder Technol.*, 162(2), 166–174, 2006.
Benyahia, S., Syamlal, M., and O'Brien, T.J., Study of the ability of multiphase continuum models to predict core-annulus flow, *AIChE J.*, 53(10), 2549–2568, 2007.
Benyahia, S., Syamlal, M., and O'Brien, T.J., Summary of MFIX Equations 2012–1, From URL https://mfix.netl.doe.gov/documentation/MFIXEquations2012–1.pdf, January 2012.
Bird, R.B., Stewart, W.E., and Lightfoot, E.N., *Transport Phenomena*, 2nd edn., John Wiley & Sons, New York, 2006.
Boroson, M.J. and Howard, J., Product yields and kinetics from vapor phase cracking of wood pyrolysis, *AIChE J.*, 35, 120, 1989.
Bouillard, J.X., Lyczkowski, R.W., Folga, S., Gidaspow, D., and Berry, G.F., Hydrodynamics of erosion of heat exchanger tubes in fluidized-bed combustors, *Can. J. Chem. Eng.*, 67, 218–229, 1989.
Bowen, R.M., Theory of mixtures, in A.C. Eringen (Ed.), *Continuum Physics*, Vol. 3, Academic Press, New York, 1976.
Boyalakuntla, D.S., Simulation of granular and gas-solid flows using discrete element model (DEM) implemented in MFIX, PhD dissertation, Carnegie Mellon University, Pittsburgh, PA, 2003.
Campbell, C.S., Rapid granular flows, *Ann. Rev. Fluid Mech.*, 22, 57–92, 1990.
Cao, J. and Ahmadi, G., xGas-particle two-phase turbulent flow in a vertical duct, *Int. J. Multiphase Flow*, 21, 1203–1228, 1990.
Dalla Valle, J.M., *Micromeritics*, Pitman, London, U.K., 1948.
Dartevelle, S., Validation approaches to volcanic explosive phenomenology, in S. Pannala, M. Syamlal, and T.J. O'Brien (Eds.), *Computational Gas-Solids Flows and Reacting Systems: Theory, Methods and Practice*, IGI Global, Hershey, PA, 2011.
Dartevelle, S. and Valentine, G.A., Transient multiphase processes during the explosive eruption of basalt through a geothermal borehole (Namafjall, Iceland, 1977) and implications for natural volcanic flows, *Earth Planet. Sci. Lett.*, 10/30/;262(3–4), 363–384, 2007.
Davis, A., Michaelides, E.E., and Feng, Z.-G., Particle velocity near vertical boundaries—A source of uncertainty in two-fluid models, *Powder Technol.*, 220, 15–23, 2012.
Dietiker, J.-F., Guenther, C., and Syamlal, M., A Cartesian cut cell method for gas/solids flows, *AIChE Annual Meeting*, AIChE, Nashville, TN, 2009.
Dietiker, J.F., Li, T., Garg, R., and Shahnam, M., Cartesian grid simulations of gas-solids flow systems with complex geometry, *Powder Technol.*, 235, 696–705, 2013.
Drew, D.A., Mathematical-modeling of 2-phase flow, *Ann. Rev. Fluid Mech.*, 15, 261–291, 1983.
Dufek, J. and Bergantz, G.W., Suspended load and bed-load transport of particle-laden gravity currents: The role of particle-bed interaction, *Theor. Comput. Fluid Dyn.*, 21, 119–145, 2006.
Dufek, J. and Bergantz, G.W., Dynamics and deposits generated by the Kos Plateau Tuff eruption: Controls of basal particle loss on pyroclastic flow transport, *Geochem. Geophys. Geosyst.*, 8, Q12007, 2007.
Ergun, S., Fluid flow through packed columns, *Chem. Eng. Prog.*, 48(6), 89–94, 1952.
Fedors, R.F. and Landel, R.F., An empirical method of estimating the void fraction in mixtures of uniform particles of different size, *Powder Technol.*, 23, 225–231, 1979.
Feng, Z.G. and Michaelides, E.E., Inclusion of heat transfer computations for particle laden flows. *Physics of Fluids*, 20(4), 040604, 2008.
Feng, Z.G., Cortina-Ponton, M.E., Michaelides, E.E., and Mao, S.L., Using the direct numerical simulation to compute the slip boundary condition of the solid phase in two-fluid model simulations, *Powder Technol.*, 265, 88–97, 2014.
Galvin, J.E., On the hydrodynamic description of binary mixtures of rapid granular flows and gas-fluidized beds, PhD thesis, University of Colorado, Denver, CO, 2007.
Garg, R. and Dietiker, J.F., Documentation of open-source MFIX-PIC software for gas-solids flows, From URS https://mfix.netl.doe.gov/documentation/mfix_pic_doc.pdf, 2013.

Garg, R., Galvin, J., Li, T., and Pannala, S., Documentation of open-source MFIX–DEM software for gas-solids flows, From URLhttps://mfix.netl.doe.gov/documentation/dem_doc_2012–1.pdf, 2012a.
Garg, R., Galvin, J., Li, T., and Pannala, S., Open-source MFIX-DEM software for gas–solids flows: Part I—Verification studies, *Powder Technol.*, 220, 122–137, 2012b.
Garside, J. and Aldibouni, M.R., Velocity-Voidage relationships for fluidization and sedimentation in solid-liquid systems, *Ind. Eng. Chem. Process Des. Develop.*, 16(2), 206–214, 1977.
Garzó, V. and Dufty, J.W., Dense fluid transport for inelastic hard spheres, *Phys. Rev. E*, 59, 5895–5911, 1999.
Garzó, V., Dufty, J.W., and Hrenya, C.M., Enskog theory for polydisperse granular mixtures. I. Navier-Stokes order transport, *Phys. Rev. E*, 76, art. no. 031303, 2007a.
Garzó, V., Dufty, J.W., and Hrenya, C.M., Enskog theory for polydisperse granular mixtures. II. Sonine polynomial approximation, *Phys. Rev. E*, 76, art. no. 031304, 2007b.
Garzó, V., Tenneti, S., Subramaniam, S., and Hrenya, C.M., Enskog kinetic theory for monodisperse gas–solid flows, *J. Fluid Mech.*, 712, 129–168, 2012.
Gel, A., Li, T., Guenther, C., and Pannala, S., High resolution numerical simulations of coal gasifiers using high performance computing, in *NETL Multiphase Flow Workshop*, Pittsburgh, PA, May 4–6, 2010.
Gelperin, N.I., Einstein, V.G., and Toskubay, Heat transfer coefficient between a surface and a fluid bed, *Br. Chem. Eng. Process Technol.*, 16(10), 922, 1971.
Gera, D., Syamlal, M., and O'Brien, T.J., Hydrodynamics of particle segregation in fluidized beds, *Int. J. Multiphase Flow*, 30(4), 419–428, 2004.
Gerber, S., Behrendt, F., and Overmann, M., An Eulerian modeling approach of wood gasification in a bubbling fluidized bed reactor using char as bed material, *Fuel*, 89(10), 2903–2917, October 2010.
Gidaspow, D., Hydrodynamics of fluidization and heat transfer: Supercomputer modeling, *Appl. Mech. Rev.*, 39, 23, 1986.
Gidaspow, D., *Multiphase Flow and Fluidization: Continuum and Kinetic Theory Descriptions*, Academic Press, Boston, MA, 1994.
Gidaspow, D. and Ettahadieh, B., Fluidization in two-dimensional beds with a jet; 2. Hydrodynamic modeling. *IEC Fundam.*, 22, 193–201, 1983.
Gopalakrishnan, P. and Tafti, D., Development of parallel DEM for the open source code MFIX, *Powder Technol.*, 235, 33–41, 2013.
Grønli, M.G., A theoretical and experimental study of the thermal degradation of biomass, PhD thesis, NTNU Trondheim, Norway, Europe, 1996.
Gunn, D.J., Transfer of heat or mass to particles in fixed and fluidized-beds, *Int. J. Heat Mass Transfer*, 21(4), 467–476, 1978.
Heynderickx, G.J., Das, A.K., De Wilde, J., and Marin, G.B., Effect of clustering on gas-solid drag in dilute two-phase flow, *Ind. Eng. Chem. Res.*, 43, 4635–4646, 2004.
Hill, R.J., Koch, D.L., and Ladd, J.C., The first effects of fluid inertia on flows in ordered and random arrays of spheres, *J. Fluid Mech.*, 448, 213–241, 2001a.
Hill, R.J., Koch, D.L., and Ladd, J.C., Moderate-Reynolds-number flows inordered and random arrays of spheres, *J. Fluid Mech.*, 448, 243–278, 2001b.
Hindmarsh, A.C., ODEPACK, A systematized collection of ODE solvers, in R.S. Stepleman et al. (Eds.), *Scientific Computing*, North-Holland, Amsterdam, the Netherlands, Vol. 1 of IMACS Transactions on Scientific Computation, 1983, pp. 55–64.
Holloway, W. and Sundaresan, S., Filtered models for bidisperse gas–particle flows, *Chem. Eng. Sci.*, 108, 67–86, 2014.
Holloway, W., Yin, X., and Sundaresan, S., Fluid-particle drag in inertial polydisperse gas–solid suspensions, *AIChE J.*, 56, 1995–2004, 2010.
Hrenya, C., Kinetic theory for granular materials: Polydispersity, in S. Pannala, M. Syamlal and T.J. O'Brien (Eds.), *Computational Gas-Solids Flows and Reacting Systems: Theory, Methods and Practice*, IGI Global, Hershey, PA, 2011.
Iddir, H. and Arastoopour, H., Modeling of multitype particle flow using the kinetic theory approach, *AIChE J.*, 51, 1620–1632, 2005.
Igci, Y., Andrews, A.T., Sundaresan, S., Pannala, S., and O'Brien, T., Filtered two-fluid models for fluidized gas-particle suspensions, *AIChE J.*, 54, 1431–1448, 2005.
Igci, Y., Pannala, S., Benyahia, S., and Sundaresan, S., Validation studies on filtered model equations for gas-particle flows in risers, *Ind. Eng. Chem. Res.*, 51(4), 2094–2103, 2012.
Igci, Y. and Sundaresan, S., Verification of filtered two-fluid models for gas-particle flows in risers, *AIChE J.*, 57, 2691–2707, 2011. doi:10.1002/aic.12486.
Ishii, M. and Mishima, K., 2-fluid model and hydrodynamic constitutive relations, *Nucl. Eng. Des.*, 82(2–3), 107–126, 1984.
Jackson, R., Locally averaged equations of motion for a mixture of identical spherical particles and a Newtonian fluid, *Chem. Eng. Sci.*, 52(15), 2457–2469, 1997.

Jackson, R., *The Dynamics of Fluidized Particles*, Cambridge University Press, Cambridge, U.K., 2000.
Jenike, A.W., A theory of flow of particulate solids in converging and diverging channels based on a conical yield function, *Powder Technol.*, 50(3), 229–236, 1987.
Jenkins, J.T. and Savage, S.B., A theory for the rapid flow of identical, smooth, nearly elastic, spherical particles, *J. Fluid Mech.*, 130, 187–202, 1983.
Jenkins, J.T., Boundary-conditions for rapid granular flow—Flat, frictional walls, *J. Appl. Mech.-Trans. ASME*, 59(1), 120–127, 1992.
Jenkins, J.T. and Louge, M.Y., On the flux of fluctuation energy in a collisional grain flow at a flat, frictional wall, *Phys. Fluids*, 9(10), 2835–2840, 1997.
Johnson, P.C. and Jackson, R., Frictional collisional constitutive relations for granular materials, with application to plane shearing, *J. Fluid Mech.*, 176, 67–93, 1987.
Johnson, P.C., Nott, P., and Jackson, R., Frictional collisional equations of motion for particulate flows and their application to chutes, *J. Fluid Mech.*, 210, 501–535, 1990.
Joseph, D.D., Lundgren, T.S., Jackson, R., and Saville, D.A., Ensemble averaged and mixture theory equations for incompressible fluid particle suspension, *Int. J. Multiphase Flow*, 16(1), 35–42, 1990.
Khan, A.R., Pirie, R.L., and Richardson, J.F., Hydraulic transport of solids in horizontal pipelines—Predictive methods for pressure-gradients, *Chem. Eng. Sci.*, 42(4), 767–778, 1987.
Kinsey, J., Summary of AGR fuel program, presented at the *IAEA Technical Meeting on the Safety of High Temperature Gas Cooled Reactors in Light of the Fukushima Daiichi Accident*, Vienna, Austria, April 8–11, 2014, From http://www.iaea.org/NuclearPower/Downloadable/Meetings/2014/2014–04–08–04–11-TM-NPTDS/17_Kinsey02.pdf.
Kirkpatrick, M.P., Armfield, S.W., and Kent, J.H., A representation of curved boundaries for the solution of the Navier–Stokes equations on a staggered three-dimensional Cartesian grid, *J. Comput. Phys.*, 184, 1–36, 2003.
Kuipers, J.A.M., Prins, W., and Vanswaaij, W.P.M., Numerical-calculation of wall-to-bed heat-transfer coefficients in gas-fluidized beds, *AIChE J.*, 38(7), 1079–1091, 1992.
Lai, K., Xu, Z., Pan, W., Dietiker, J., Li, T., Marcy, P., Storlie, C., Sun, X., and Sundaresan, S., Quantifying CFD predictive confidence on CO_2 capture efficiency of 1MW pilot-scale solid sorbent adsorber with a hierarchical calibration and validation approach, CCSI Milestone Report, 2014b.
Lai, K., Xu, Z., Pan, W., Shadle, L., Storlie, C., Dietiker, J., Li, T., Dartevelle, S., and Sun, X., Hierarchical calibration and validation of high-fidelity CFD models with C2U experiments, CCSI Milestone Report, 2014a.
Lebowitz, J.L., Exact solution of generalized Percus-Yevick equation for a mixture of hard spheres, *Phys. Rev.*, 133(4A), A895, 1964.
Levenspiel, O., *Chemical Reaction Engineering*, John Wiley & Sons, New York, 1972.
Li, J. and Kwauk, M., Exploring complex systems in chemical engineering—The multi-scale methodology, *Chem. Eng. Sci.*, 58, 521–535, 2003.
Li, T. and Benyahia, S., Revisiting Johnson and Jackson boundary conditions for granular flows, *AIChE J.*, 58(7), 2058–2068, 2012.
Li, T. and Benyahia, S., Evaluation of wall boundary condition parameters for gas-solids fluidized bed simulations, *AIChE J.*, 59(10), 3624–3632, 2013.
Li, T., Garg, R., Galvin, J., and Pannala, S., Open-source MFIX-DEM software for gas–solids flows: Part II—Validation studies, *Powder Technol.*, 220, 138–150, 2012a.
Li, T., Gel, A., Syamlal, M., Guenther, C., and Pannala, S., High-resolution simulations of coal injection in a gasifier, *Ind. Eng. Chem. Res.*, 49, 10767–10779, 2010b.
Li, T., Grace, J., and Bi, X., Study of wall boundary condition in numerical simulations of bubbling fluidized beds, *Powder Technol.*, 203(3), 447–457, 2010a.
Liu, H., Tafti, D., and Li, T., Hybrid parallelism in MFIX CFD-DEM using OpenMP, *Powder Technol.*, 259, 22–29, 2014.
Lun, C.K.K., Savage, S.B., Jeffrey, D.J., and Chepurniy, N., Kinetic theories for granular flow—Inelastic particles in Couette-flow and slightly inelastic particles in a general flowfield, *J. Fluid Mech.*, 140(March), 223–256, 1984.
Massoudi, M., Constitutive relations for the interaction force in multicomponent particulate flows, *Int. J. Non-Linear Mech.*, 38(3), 313–336, 2003.
Maxey, M.R. and Riley, J.J., Equation of motion for a small rigid sphere in a nonuniform flow, *Phys. Fluids*, 26(4), 883–889, 1983.
Milioli, C., Milioli, F., Holloway, W., Agrawal, K., and Sundaresan, S., Constitutive model for the fluid-particle drag coefficient in filtered two-fluid models for gas-particle flows, *AIChE Annual Meeting*, AIChE, Pittsburgh, PA, 2012.
Milioli, C.C., Milioli, F.E., Holloway, W., Agrawal, K., and Sundaresan, S., Filtered two-fluid models of fluidized gas-particle flows: New constitutive relations, *AIChE J.*, 59, 3265–3275, 2013. doi:10.1002/aic.14130.

Mitrano, P.P., Zenk, J.R., Benyahia, S., Galvin, J.E., Dahl, S.R., and Hrenya, C.M., Kinetic-theory predictions of clustering instabilities in granular flows: Beyond the small-Knudsen-number regime, *J. Fluid Mech*., 738, R2, 2014. doi:10.1017/jfm.2013.602.

Molina, I., Burgisser, A., and Oppenheimer, C., Numerical simulations of convection in crystal-bearing magmas: A case study of the magmatic system at Erebus, Antarctica, *J. Geophys. Res*., 117, B7209, 2012.

Musser, J., Modeling of heat transfer and reactive chemistry for particles in gas-solid flow utilizing continuum-discrete methodology (CDM), PhD dissertation, West Virginia University, Morgantown, WV, 2011.

Musser, J., Syamlal, M., Shahnam, M., and Huckaby, D.E., Constitutive equation for heat transfer caused by mass transfer, *Chem. Eng. Sci*., 123, 436–443, 2015.

Nakamura, K. and Capes, C.E., Vertical pneumatic conveying of binary particle mixtures, in D.L. Keairns (Ed.), *Fluidization Technology*, Hemisphere Publishing Corporation, Washington, DC, 1976, pp. 159–184.

O'Brien, T.J. and Syamlal, M., Particle cluster effects in the numerical simulation of a circulating fluidized bed, in A. Avidan (Ed.), *Circulating Fluidized Bed Technology. IV. Proceedings of the Fourth International Conference on Circulating Fluidized Beds*, Hidden Valley Conference Center, Somerset, PA, 1993.

Oger, L. and Savage, S.B., Airslide flows. Part 2—Flow modeling and comparison with experiments, *Chem. Eng. Sci*., 91, 22–34, 2013.

Pannala, S., Daw, C.S., Boyalakuntla, D., and Finney, C.E.A., Process modeling phase I summary report for the advanced gas reactor fuel development and qualification program, ORNL/TM-2006/520, March 2006.

Pannala, S., Daw, C.S., Finney, C.E.A., Benyahia, S., Syamlal, M., and O'Brien, T.J., Modeling the collisional-plastic stress transition for bin discharge of granular material, in M. Nakagawa and S. Luding (Ed.), *AIP Conference Proceedings*, *Powders and Grains 2009: Proceedings of the Sixth International Conference on Micromechanics of Granular Media*, Golden, CO, Vol. 1145, July 13–17, 2009.

Pannala, S., Daw, C.S., Finney, C.E.A., Boyalakuntla, D., Syamlal, M., and O'Brien, T.J., Simulating the dynamics of spouted-bed nuclear fuel coaters, *Chem. Vapor Depos*., 13, 481–490, 2007.

Pannala, S., Syamlal, M., and O'Brien, T.J. (Eds.), *Computational Gas-Solids Flows and Reacting Systems: Theory, Methods and Practice*, IGI Global, Hershey, PA, 2011.

Patankar, S.V., *Numerical Heat Transfer and Fluid Flow*, Hemisphere Publishing Corporation, New York, 1980.

Peirano, E. and Leckner, B., Fundamentals of turbulent gas-solid flows applied to circulating fluidized bed combustion, *Prog. Energy Combust. Sci*., 24(4), 259–296, 1998.

Pope, S.B., *Turbulent Flows*, Cambridge University Press, Cambridge, U.K., 2000.

Prosperetti, A., Averaged equations for multiphase flow, In A. Prosperetti and G. Tryggvason (Eds.), *Computational Methods for Multiphase Flow*, Cambridge University Press, Cambridge, U.K., 2007.

Rath, M. and Staudinger, G., Cracking reactions of tar from pyrolysis of spruce wood, *Fuel*, 80, 1379–1389, 2001.

Richardson, J.F. and Zaki, W.N., Sedimentation and fluidization: Part I, *Trans. Inst. Chem. Eng.*, 32, 22, 1954.

Ruprecht, P., Bergantz, G.W., and Dufek, J., Modeling of gas-driven magmatic overturn: Tracking of phenocryst dispersal and gathering during magma mixing, *Geochem. Geophys. Geosyst*., 9, Q07017, 2008.

Sagaut, P., *Large Eddy Simulation for Incompressible Flows*, 3rd edn., Springer, 2006.

Sarkar, A., Sun, X., and Sundaresan, S., Sub-grid drag models for horizontal cylinder arrays immersed in gas-particle multiphase flows, *Chem. Eng. Sci*., 104, 399–412, December 2013.

Sarkar, A., Sun, X., and Sundaresan, S., Verification of sub-grid filtered drag models for gas-particle fluidized beds with immersed cylinder arrays, *Chem. Eng. Sci*., 114(26), 144–154, 2014.

Schaeffer, D.G., Instability in the evolution-equations describing incompressible antigranulocytes flow, *J. Diff. Equat*., 66(1), 19–50, 1987.

Simonin, O., Continuum modeling of dispersed two-phase flows, in *Combustion and Turbulence in Two-Phase Flows*, M. Manna (Ed.), Von Karman Institute of Fluid Dynamics, Belgium, 1996, pp. 1–47.

Sinclair, J.L. and Jackson, R., Gas-particle flow in a vertical pipe with particle-particle interactions, *AIChE J*., 35(9), 1473–1486, 1989.

Smagorinsky, J., General circulation experiments with the primitibe equations, *Mon. Weather Rev*., 91, 99–164, 1963.

Soo, S.L., *Fluid Dynamics of Multiphase Systems*, Blaisdell Publishing Corporation, Waltham, MA, 1967.

Spalding, D.B., Numerical computation of multi-phase fluid flwo and heat transfer, in C. Taylor and K. Morgan (Eds.), *Recent Advances in Numerical Methods in Fluids*, Pineridge Press, Swansea, U.K., Vol. 1, 1980.

Srinivasan, M.G. and Doss, E.D., Momentum-transfer due to particle particle interaction in dilute gas solid flows, *Chem. Eng. Sci*., 40(9), 1791–1792, 1985.

Srivastava, A. and Sundaresan, S., Analysis of a fractional-kinetic model for gas-particle flow, *Powder Technol.*, 129(1–3), 72–85, 2003.
Syamlal, M., Multiphase hydrodynamics of gas-solids flow, PhD dissertation, Illinois Institute of Technology, Chicago, IL, 1985.
Syamlal, M., The particle-particle drag term in a multiparticle model of fluidization, Topical report, DOE/MC 21353 2373, NTIS/DE 87006500, 1987.
Syamlal, M., MFIX documentation: Numerical techniques, DOE/MC-31346–5824. NTIS/DE98002029, 1998.
Syamlal, M., A hyperbolic model for fluid–solids two-phase flow, *Chem. Eng. Sci.*, 66, 4421–4425, 2011.
Syamlal, M. and Gidaspow, D., Hydrodynamics of fluidization—Prediction of wall to bed heat-transfer coefficients, *AIChE J.*, 31(1), 127–135, 1985.
Syamlal, M., Guenther, C., Cugini, A., Ge, W., Wang, W., Yang, N., and Li, J., Computational science: Enabling technology development, *Chem. Eng. Prog.*, 107(1), 23–29, 2011.
Syamlal, M. and O'Brien, T.J., A generalized drag correlation for multiparticle systems, Unpublished Report U.S. Department of Energy, Office of Fossil Energy, Morgantown Energy Technology Center, Morgantown, WV, 1987.
Syamlal, M. and O'Brien, T.J., Fluid dynamic simulation of O_3 decomposition in a bubbling fluidized bed, *AIChE J.*, 49(11), 2793–2801, 2003.
Syamlal, M., O'Brien, T.J., Benyahia, S., Gel, A., and Pannala, S., Open-source software in computational research: A case study, *Model. Simulat. Eng.*, 8, Article ID 937542, 10 pp, 2008. doi:10.1155/2008/937542.
Syamlal, M., Rogers, W., and O'Brien, T.J., MFIX Documentation: Theory Guide (No. DOE/METC-94/1004 (DE94000087)), Morgantown Energy Technology Center, Morgantown, WV, 1993.
Syamlal, M. and Pannala, S., Multiphase continuum formulation for gas-solids reacting flows, in S. Pannala, M. Syamlal and T.J. O'Brien (Eds.), *Computational Gas-Solids Flows and Reacting Systems: Theory, Methods and Practice*, IGI Global, Hershey, PA, 2011.
Uhlmann, M., An immersed boundary method with direct forcing for the simulation of particulate flows. *Journal of Computational Physics*, 209(2), 448–476, 2005.
van Wachem, B.G.M., Schouten, J.C., van den Bleek, C.M., Krishna, R., and Sinclair, J.L., Comparative analysis of CFD models of dense gas–solid systems, *AIChE J.*, 47(5), 1035–1051, 2001.
Versteeg, H.K. and Malalasekera, W., *An Introduction to Computational Fluid Dynamics*, Pearson-Prentice Hall, 1995.
Xue, Q., Heindel, T.J., and Fox, R.O., A CFD model for biomass fast pyrolysis in fluidized-bed reactors, *Chem. Eng. Sci.*, 66, 2440–2452, 2011.
Yang, N., Wang, W., Ge, W., Wang, L., and Li, J., Simulation of heterogeneous structure in a circulating fluidized-bed riser by combining the two-fluid with the EMMS approach, *Ind. Eng. Chem. Res.*, 43, 5548–5561, 2004.
Yin, X. and Sundaresan, S., Drag law for bidisperse gas-solid suspensions containing equally sized spheres, *Ind. Eng. Chem. Res.*, 48, 227–241, 2009a.
Yin, X. and Sundaresan, S., Fluid-particle drag in low-Reynolds-number polydisperse gas-solid suspensions, *AIChE J.*, 55, 1352–1368, 2009b.
Yu, A.B. and Standish, N., Porosity calculation of multicomponent mixtures of spherical particles, *Powder Technol.*, 52, 233–241, 1987.
Zabrodsky, S.S., *Hydrodynamics and Heat Transfer in Fluidized Beds*, The M.I.T. Press, Cambridge, MA, 1966.
Zhang, D.Z. and Prosperetti, A., Averaged equations for inviscid disperse 2-phase flow, *J. Fluid Mech.*, 267, 185–219, 1994a.
Zhang, D.Z. and Prosperetti, A., Ensemble phase-averaged equations for bubbly flows, *Phys. Fluids*, 6(9), 2956–2970, 1994b.

2.8 Uncertainty Quantification

Madhava Syamlal, Jordan Musser, and Jean-François Dietiker

In the current applications of multiphase CFD, some examples of which are discussed in other chapters of this book, predictive calculations are considered deterministic, which seems to be justified by the fact that multiphase CFD is based on a set of deterministic equations. However, various sources of uncertainty can affect predictive simulations, making their results uncertain; quantifying those uncertainties is essential for establishing the degree of confidence in the predictions. If the degree of confidence is known, technology developers will be able to use predictive simulations for making better design decisions, enabling them to take larger steps while scaling up a technology. Thereby, the time and cost of bringing new technologies to

market will be reduced. Quantifying the confidence in multiphase CFD predictions is currently a major research focus at NETL, and some of the methods and recent results are reviewed in this section.

2.8.1 Verification and Validation

A series of steps are required for establishing the degree of confidence in predictive simulations. The first two steps are *verification* and *validation* (V&V): verification is "the process of determining that a model implementation accurately represents the developer's conceptual description of the model and the solution to the model" and validation is "the process of determining the degree to which a model is an accurate representation of the real world from the perspective of the intended uses of the model" (Oberkampf and Trucano, 2002). Typically, CFD code developers ensure that their code solves the model equations correctly by comparing the solution given by their code with benchmark numerical solutions (generated by other highly accurate codes), analytical solutions for simplified problems, or asymptotic solutions (the verification step). Another useful technique is *the method of manufactured solutions*. In that method an analytical solution is picked and the source terms required to generate that solution are determined and added to the governing equations. By numerically solving the modified equations, the discretization error can be determined exactly and the order of reduction of the discretization error can be evaluated. Then by comparing the observed order of accuracy with the formal order of accuracy, coding errors and algorithm inconsistencies can be identified. Choudhary et al. (2014) describe such an approach for verifying MFIX-TFM.

The user of a CFD code ensures that the equations solved by the code accurately describe the real world by comparing the simulation results with data from experiments closely related to their application (the validation step). Usually comparisons with experiments at multiple levels of complexity are necessary for complete model validation because no single lab-scale experiment is sufficient to capture all the complexities of a real-world multiphase reactor and sufficiently detailed data are often not available from the more complex pilot-scale experiments. Such a validation hierarchy is developed and used, for example, by the Carbon Capture Simulation Initiative (CCSI), which is developing multiscale and multiphysics computational tools for enabling the rapid scale-up of carbon capture technologies (Miller et al., 2014). CCSI's validation hierarchy for a solid sorbent-based carbon capture system comprises CFD simulations of experiments ranging from simple fluidized beds to complex CO_2 reactors as shown in Figure 2.93 (Ryan et al., 2012).

2.8.2 Validation Uncertainty Quantification

Traditionally, a *good* agreement between the simulation results and experimental data justifies the use of the model for predictive simulations. This approach has some inherent difficulties, however. The goodness of agreement is a subjective judgment, which could be unreliable and overly optimistic (e.g., Grace and Taghipour, 2004). More importantly, the judgment is solely based on the validation comparison error (E), which by itself may not provide a good estimate of the error in a predicted quantity. E is the mean of an uncertainty distribution, which results from the various sources of uncertainty that unavoidably are introduced in CFD simulations (see Figure 2.94). Unless the *spread* of the uncertainty distribution is known, it is not possible to know whether the error in a predicted quantity will be of the order of E because the error in the predicted quantity will be a realization of the uncertainty distribution and for a wide distribution the probability that the realization falls far away from the mean is high. A solution to this problem is offered by ASME V&V Standard (2009), which requires that the validation uncertainty u_{val}—a measure of the spread of the uncertainty distribution—also be determined to quantify "the degree of accuracy inferred from the comparison of solution and data" (ASME V&V Standard 2009, Coleman and Steele, 2009):

$$u_{val} = \sqrt{u_{num}^2 + u_{input}^2 + u_D^2} \tag{2.429}$$

where three known sources of uncertainties are considered: the numerical solution (u_{num}), the model inputs (u_{input}), and the experimental data (u_D).

If $|E| \gg u_{val}$, the errors other than the model form error (resulting from modeling assumptions and approximations) are very small, and the model form error is approximately equal to E. Then the analyst may decide either that the model form error is acceptably small for the predictive simulations or that the model needs to be improved or calibrated to reduce u_{val}. If $|E| \leq u_{val}$, the other errors are comparable or greater than the model form error, and the analyst cannot judge the acceptability of the model for predictive simulations.

In the earlier discussion we made, the tacit assumption that the model validity established at the validation domain holds good at the prediction domain. That is not necessarily true as the validation and prediction

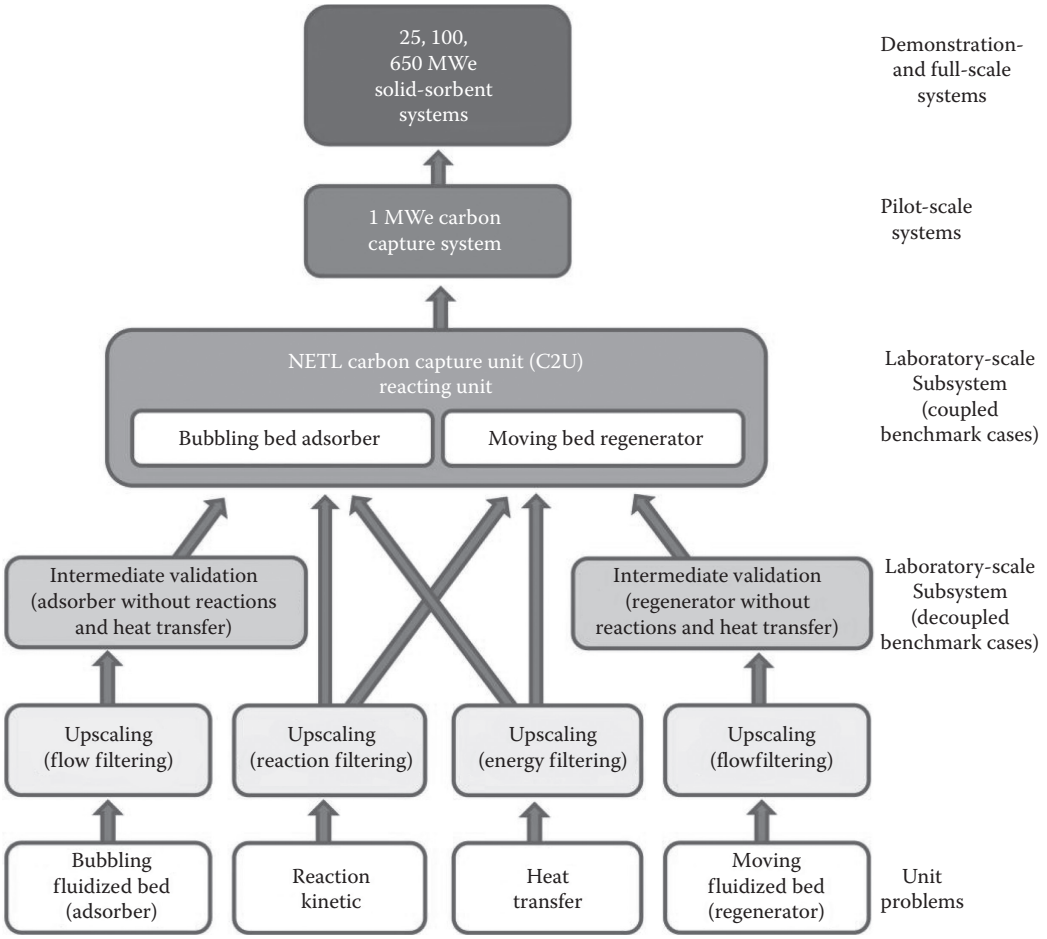


Figure 2.93

A CFD validation hierarchy, illustrating the various unit problems and the levels of validation that lead up to a quantitative confidence on predictions for full-scale devices. (Adapted from Ryan, E.M. et al., CCSI validation and uncertainty quantification hierarchy for CFDmodels, CCSI Technical Report Series, 2012, http://www.acceleratecarboncapture.org/drupal/sites/default/files/elfinder/CCSI_Directory/Deliverables/Sept_30_2012/CCSI_V-UQ%20Hierarchy_FINAL.pdf.)

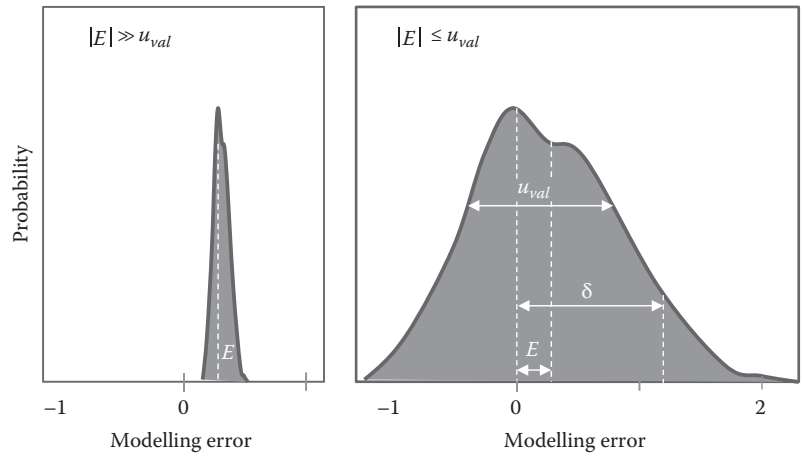


Figure 2.94

The probability distribution of modeling errors. Even when the validation comparison error (E) is small, the error in a predictive simulation (δ) could be large if the error distribution is not narrow ($|E| \leq u_{val}$).

domains can have many different relations: one contained in another, partially overlapping or not overlapping. The prediction domain in a scale-up simulation, for example, is likely not to overlap the validation domain. The first step in quantifying the uncertainty in predictive simulations is the estimation of the model form error from the validation domain as required by ASME V&V Standard (2009). In addition, the model form error must be extrapolated to the prediction domain and other uncertainties in the predictive simulation must be quantified. Such a method was proposed by Roy and Oberkampf (2011), which is discussed in the next section.

2.8.3 Predictive Uncertainty Quantification

Gel et al. (2013a) applies the method of Roy and Oberkampf (2011) to perform a validation assessment of an MFIX-TFM model of a circulating fluidized bed. They use experimental data of Shadle et al. (2011) to validate the model. Their results are discussed later to illustrate the Roy and Oberkampf (2011) method for uncertainty quantification in predictive simulations.

In an uncertainty quantification analysis, first, it is necessary to identify the quantity of interest (QoI), which is an important design parameter that the engineer needs for scaling up a device. Gel et al. (2013a) use the pressure drop (ΔP) across the circulating fluidized bed as their QoI.

Next, all the sources of input uncertainty must be identified and characterized. The input uncertainty could be *aleatory* or *epistemic*, which Roy and Oberkampf (2011) define as follows: "Aleatory uncertainty (also called irreducible uncertainty, stochastic uncertainty, or variability) is uncertainty due to inherent variation or randomness and can occur among members of a population or due to spatial or temporal variations. Aleatory uncertainty is generally characterized by either a probability density function (PDF) or a cumulative distribution function (CDF)." For example, the *inlet gas velocity*, which is an input in the circulating fluidized bed model, is an aleatory uncertainty. The inlet gas velocity can be measured, but its values vary from run to run, making the uncertainty irreducible.

"Epistemic uncertainty (also called reducible uncertainty or ignorance uncertainty) is uncertainty that arises due to a lack of knowledge on the part of the analyst, or team of analysts, conducting the modeling and simulation. Epistemic uncertainty is traditionally represented as either an interval with no associated PDF or a PDF that represents degree of belief of the analyst (as opposed to frequency of occurrence of an event in aleatory uncertainty)." For example, the *particle restitution coefficient* for the glass beads used in the circulating fluidized bed experiment is an epistemic uncertainty. It has a fixed but unknown value because the value is not reported by Shadle et al. (2011). From the physics of particle collisions we can deduce that the restitution coefficient must fall in the interval [0, 1]. The interval can be further narrowed down to [0.8, 0.9] based on the values reported in the literature. Had Shadle et al. (2011) measured the restitution coefficient precisely, the uncertainty would have been reduced or even eliminated.

A list of all the uncertain model input parameters is created by surveying the open literature and polling subject-matter experts. The experts are asked to provide a nominal (or baseline) value and a range for the upper and lower bounds for each of the input parameters. Typically, this list turns out to be long, and considering the entire list is not desirable for two reasons. One, conducting simulations by varying all the input parameters could be prohibitively expensive. Two, the results of the validation study would be less precise (contain higher variability) because the amount of validation data available is often limited. If the subject-matter experts are confident that some input parameters are not important, it is better to eliminate them from the analysis. Therefore, the list is shortened to include only the important input parameters.

The important input parameters could also be determined with the help of a (more expensive) sensitivity analysis. For example, Gel et al. (2013b) use the Sobol' sensitivity indices method to apportion the output uncertainty to the input uncertainty in certain MFIX-TFM simulations. They show that the particle–particle restitution coefficient contributed the most to the variability observed in the QoI *mean bed height*. Therefore, particle–particle restitution coefficient will be the highest ranked input parameter for an uncertainty analysis with the mean bed height as the QoI. A less expensive alternative is to use scatterplots to understand the relationships between the uncertainty in inputs and the uncertainty in the predictions as discussed by Helton et al. (2006).

For the QoI *pressure drop across the circulating fluidized bed*, Gel et al. (2013a) select the gas velocity (U_g) and the solid circulation rate (G_s) as the important input parameters, both of which are aleatory uncertainties. For demonstrating the methodology, Gel et al. (2013a) characterize U_g as a truncated normal distribution with a mean of 7.2 m/s and standard deviation of 0.04 m/s, and G_s as a truncated normal distribution with a mean of 14.0 kg/s and standard deviation of 0.34 kg/s.

The next step is the propagation of the uncertainty in input parameters. This involves running the MFIX-TFM circulating fluidized bed model for multiple realizations of gas velocity and solids circulation rate

sampled from their distributions. This is an impossible task because of the huge number of MFIX-TFM simulations that would be required, each simulation taking 2–4 weeks of computational time. Therefore, the propagation of the input uncertainty is carried out with the help of a *surrogate model*. Gel et al. (2013a) develop a surrogate model by expressing the ΔP predicted by 13 simulations as a polynomial in U_g and G_s. Of the 13, seven are preexisting simulations; six additional simulations are identified through a central composite design sampling method. The optimum form of the surrogate model is determined with the help of an *adjusted* R^2 method. Then the input uncertainty is propagated by drawing 100,000 samples from the distributions of U_g and G_s and conducting a Monte Carlo simulation.

The use of a surrogate model in place of the simulator causes an additional uncertainty, which Gel et al. (2013a) assume to be the maximum difference between MFIX-TFM results and the surrogate model predictions. However, a better estimate of this uncertainty could be obtained by conducting new MFIX-TFM simulations and determining the maximum difference between those simulation results and surrogate model predictions (i.e., cross validated error).

The next step is to determine the *model form uncertainty*, which comes exclusively from the inadequacies of the model. However, model form uncertainty can only be estimated, and the estimates tend to incorporate uncertainties in the validation data and input parameters. Roy and Oberkampf (2011) define model form uncertainty as the minimum area between the CDFs of experimental data and the simulation results. This yields the model form uncertainty at the validation domain.

The model form uncertainty at the prediction domain can be determined through an extrapolation method (Roy and Oberkampf 2011). The total uncertainty in the predictions can be then calculated by combining the model form uncertainty and the uncertainties arising from input, surrogate model, discretization, and time averaging at the prediction domain. See Roy and Oberkampf (2011) for an example of uncertainty quantification for predictive simulations.

Gel et al. (2013a) demonstrate the output of the method by simply combining the uncertainties at the validation domain. The output of the method is the cumulative probability for the QoI ΔP (Figure 2.95). The plot is called a p-box (probability box), which consists of the two S-shaped curves that merge while approaching the cumulative probability values of 0 and 1. The regions within the p-box, identified with different colors in Figure 2.95, are shown only for explaining the contributions from the various sources of uncertainty. The blue curve at the center arises from the (aleatoric) uncertainty in the input parameters U_g and G_s. The other uncertainties (surrogate, model form, discretization, and time averaging) are added to this curve as epistemic uncertainties because we know only their interval values, not their distributions. The addition of these epistemic uncertainties transforms the blue curve into the p-box, which represents all the possible families of CDFs that fit within its bounds. The greatest uncertainty arises from the spatiotemporal discretization

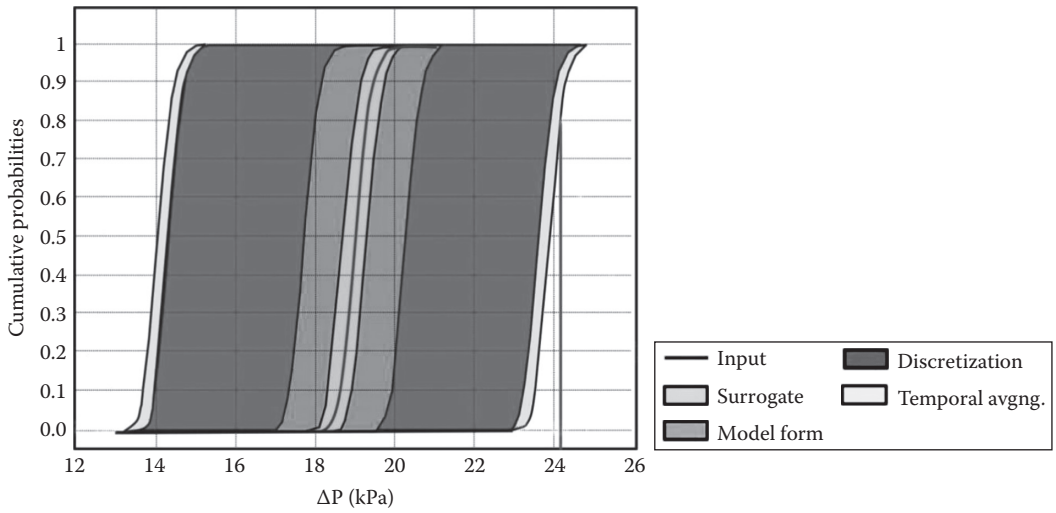


Figure 2.95

The p-box summarizes all the uncertainties considered in a predictive simulation. The box is colored to show the contributions from various sources of uncertainty in a multiphase application. (Adapted from Gel, A. et al., *Ind. Eng. Chem. Res.*, 52(33), 11424, 2013a.)

(17.9%), which Gel et al. (2013a) calculate by applying a mixed-order analysis method proposed by Roy (2003), and the next highest uncertainty is the model form uncertainty (5.2%).

It is instructive to compare the p-box resulting from the uncertainty quantification study with the traditional approach of validation and prediction. In the traditional approach, the calculated ΔP (~19 kPa) would be compared with the experimental value of 20 kPa, to establish the validity of the model. Then it will be assumed that the error in the predictive simulation will be similar to that observed in the validation simulation (~5%). Figure 2.95, which includes all sources of uncertainties, tells an entirely different story. It does not give a unique value for the predicted ΔP or a unique error bar. Rather it gives the upper and lower limits of probabilities for observing different values of ΔP. For example, for $\Delta P = 20$ kPa, the probability range is [0, 1]; that is, no meaningful information can be gained for this value from the p-box. For $\Delta P = 14$ kPa, the probability range is [0, 0.5]; that is, the probability is at most 50% that the ΔP would be less than 14 kPa. For $\Delta P = 24.2$ kPa, the probability range is [0.8, 1.0]; that is, the probability is at least 80% that the ΔP would not exceed 24.2 kPa.

What is the value in making such a nondeterministic prediction of ΔP? Suppose a design specification requires $\Delta P \leq 24.2$ kPa. Then Figure 2.95 predicts that there is [80%–100%] certainty that the specification will be met when the device is built as designed and operated; conservatively, there is 80% certainty. In contrast, the traditional approach would have placed 100% certainty that the design specification will be met. However, that degree of certainty is just an illusion, in light of all the uncertainties involved in making the prediction, especially the epistemic uncertainties arising from the numerical discretization and the model form. Now, an 80% certainty might be sufficient for certain applications, in which case the design engineer would accept the proposed design. For more critical applications, however, the design engineer may need a greater degree of certainty (say 95%) in the predicted quantities. In that case, the engineer can either revise the design or try to reduce the uncertainty in the predictive simulation. The design engineer could choose a higher pressure drop (e.g., 25 kPa) because there is greater certainty (95%) that ΔP would not exceed that value. In that case, the design will need to be revised, for example, by increasing the pressure vessel wall thickness to withstand the higher pressure expected from the predictions. Or the design engineer may try to reduce the uncertainty in the predictions by measuring the important model parameters with greater accuracy or increasing the grid resolution or using higher-fidelity constitutive equations or using a combination of these approaches. The improved predictive simulations could very well increase the certainty in meeting the specification $\Delta P \leq 24.2$ kPa, and the design engineer need not revise the design; however, there is no guarantee that the certainty will increase.

More importantly, Figure 2.95 also tells the design engineer where to put his or her resources in order to reduce the uncertainty. Finer grids and additional experiments for model calibration would be the likely candidates for reducing the uncertainty in the predictions.

2.8.4 Bayesian Calibration

In the approach described earlier, all the uncertainties identified during the validation are attributed to model form uncertainty, and the (epistemic) uncertainties in the model parameters are kept fixed or disregarded. The aforementioned approach cannot handle situations where many parameters are used to describe different physical phenomena in a complex multiphysics problem and a hierarchy of cases is needed to validate the model (e.g., Figure 2.93). The approach does not provide a way to *learn* from each addition of new information and improve the model progressively (or reduce model parameter uncertainty) as the model is hierarchically validated. This limitation can be overcome through the application of Bayes' theorem (Efron, 2013). When new information K (experimental data) becomes available, it can be used to improve our knowledge of the unknown U (model parameters) by applying Bayes' theorem:

$$P(U|K) = P(U)\frac{P(K|U)}{P(K)} \tag{2.430}$$

where

$P(U)$ is the prior distribution of U (our existing knowledge about U)

$P(K|U)$ is the probability of K given U (Little, 2013)

Kennedy and O'Hagan (2001) use this basic idea to propose a method for improving the traditional model calibration by (1) allowing for all sources of uncertainties in predictions and (2) correcting for inadequacies

in the calibrated model by introducing a *discrepancy function*. Higdon et al. (2004) further extend this approach and represent the problem as follows:

$$\boldsymbol{y}(x_i) = \boldsymbol{\eta}(x_i, \theta) + \boldsymbol{\delta}(x_i) + \boldsymbol{e}(x_i) \tag{2.431}$$

where

x_i is the input variables
$\boldsymbol{y}$ is the experimental observations
θ is the model parameters
$\boldsymbol{\delta}$ is the discrepancy between the simulator $\boldsymbol{\eta}$ and reality
$\boldsymbol{e}$ is the experimental observation error

In this approach, θ and $\boldsymbol{\delta}$ are the unknowns (U), although prior knowledge about them may exist. θ are unknown scalars, whose estimate in the Bayesian paradigm is a random variable and the prior information about θ is represented by PDFs (prior distribution). $\boldsymbol{\delta}$ are functions and the prior information is represented by a stochastic process, usually assumed to be a Gaussian process (Kennedy and O'Hagan, 2001). With the new information $\boldsymbol{y}$, the knowledge about θ and $\boldsymbol{\delta}$ is updated to generate their posterior distributions.

The simulator is treated as a *black box*, and computationally expensive simulators are replaced by an *emulator*. An emulator is not just an approximation of the simulator, but rather a statistical approximation. If the simulator (e.g., MFIX) is represented as a function that calculates an output $\mathcal{F}(x)$ for an input x, then a surrogate model (e.g., Section 7.3) is an approximation $f(x)$ that gives a unique value, say $f_0 = f(x_0)$, for each value of the input $x = x_0$. In contrast, an emulator will provide an entire probability distribution for $\mathcal{F}(x = x_0)$ at each value of x, which will be a normal distribution if the emulator is constructed as a Gaussian process (O'Hagan, 2006). At the design points where MFIX simulations were actually run, the variance of the distribution will be equal to zero; the further x_0 is away from those design points, the variance will increase.

As already discussed, four sources of uncertainty must be considered for determining the confidence bands for predicted quantities: (1) model parameters and constitutive models (e.g., friction coefficient, drag model); (2) model form (accounting for the known and unknown approximations in the mathematical model); (3) input parameters (e.g., the solids flux in a circulating fluidized bed); and (4) numerical approximations (e.g., grid resolution, time averaging).

The uncertainties from sources (1) and (2) must be determined during validation simulations. Source (1) includes model parameters that may need to be calibrated because of insufficient measurements (e.g., particle–wall friction coefficient) or the inability to measure certain parameters (e.g., specularity coefficient). From the previously known plausible values of the model parameters (prior distributions) and new experimental observations (e.g., bubble frequencies measured in a fluidized bed), the Bayesian calibration enables the analyst to generate better estimates of the model parameters (posterior distributions). In addition to calibrating scalar parameters, the best categorical parameters also could be identified through Bayesian calibration (e.g., which drag formula explains the new experimental observations the best), as demonstrated perhaps for the first time by Storlie et al. (2014). Source (2) that accounts for the inadequacies in the model is captured by the discrepancy function.

The uncertainties from sources (3) input quantities and (4) numerical approximations are determined during predictive simulations. The analyst may conduct multiple predictive simulations for values sampled from input distributions specified by the design engineer (e.g., solids flux) to quantify the uncertainty in the predicted QoIs (e.g., pressure drop) arising from the input uncertainty. Likewise, the analyst may run longer simulations to reduce and estimate the uncertainty arising from time averaging; the analyst may run simulations with finer grid resolution to reduce and estimate the uncertainty arising from spatial discretization.

This method is demonstrated by Lane et al. (2014) with the help of an MFIX-TFM model developed by Li et al. (2011). The physical system is a bubbling fluidized bed that contains 25 heat transfer tubes. The QoI are chosen as the bubble frequency and bubble-phase fraction around a tube at the center of the tube bank, for which Kim et al. (2003) have reported experimental data. These experimental data are the new information $\boldsymbol{y}$. The bubble frequency and bubble-phase fraction predicted by the MFIX-TFM model or an emulator are $\boldsymbol{\eta}$; the gas velocity and angular location on the tube are the input parameters x_i. The MFIX-TFM model parameters selected are θ (particle–particle and particle–wall restitution coefficients, particle–particle and particle–wall friction angles, packed-bed void fraction, and drag models). There are two discrepancy functions $\boldsymbol{\delta}$, one for the bubble frequency and another for the bubble-phase fraction, each of which is a function of the gas velocity and the angular location. The measurement errors in the bubble frequency and bubble-phase fraction are $\boldsymbol{e}$.

The physical ranges and the most likely values of θ are determined from a literature review and expert advice, and their prior distributions are constructed. Coefficients of restitution and packed-bed void fraction are assigned symmetric distributions: shifted and scaled β-distributions centered at their respective modes. Friction angles are assigned asymmetric distributions: shifted and scaled β-distributions that matched their respective modes. The drag models are treated as three categorical variables weighted equally with a discrete uniform distribution: Gidaspow, Syamlal-O'Brien, and Wen-Yu.

To reduce the computational cost, an emulator is developed. The emulator and discrepancy functions are modeled with Bayesian Smoothing Spline Analysis of Variance (BSS-ANOVA) models (Reich et al., 2009). The BSS-ANOVA model is a form of Gaussian process that increases the ease of handling categorical inputs and correlated outputs. Forty thousand Markov chain Monte Carlo iterations are used to calculate the posterior distributions of the emulator, discrepancy functions, and model parameters. The analysis shows that the posterior distributions of the parameters are similar to the prior distributions in all but two cases. For the parameter particle–particle friction angle, the posterior distribution changes from a wide distribution to a narrow distribution centered at 25° (Figure 2.96); for the categorical variable *drag model*, Wen-Yu is identified as the drag model that best explains the new information. The calibrated model parameters and discrepancy function and the emulator are used to make predictions for a held-out data set (i.e., the data set that was not used for model calibration). For example, Figure 2.96 shows that the experimental data fall well within the 95% confidence bands of the predicted bubble frequency.

2.8.5 Hierarchical Validation and Prediction

Lai et al. (2014a) use the method described in the previous section for the hierarchical validation of an MFIX-TFM model of a CO_2 adsorber. Unit problems with increasing levels of physical complexities are used

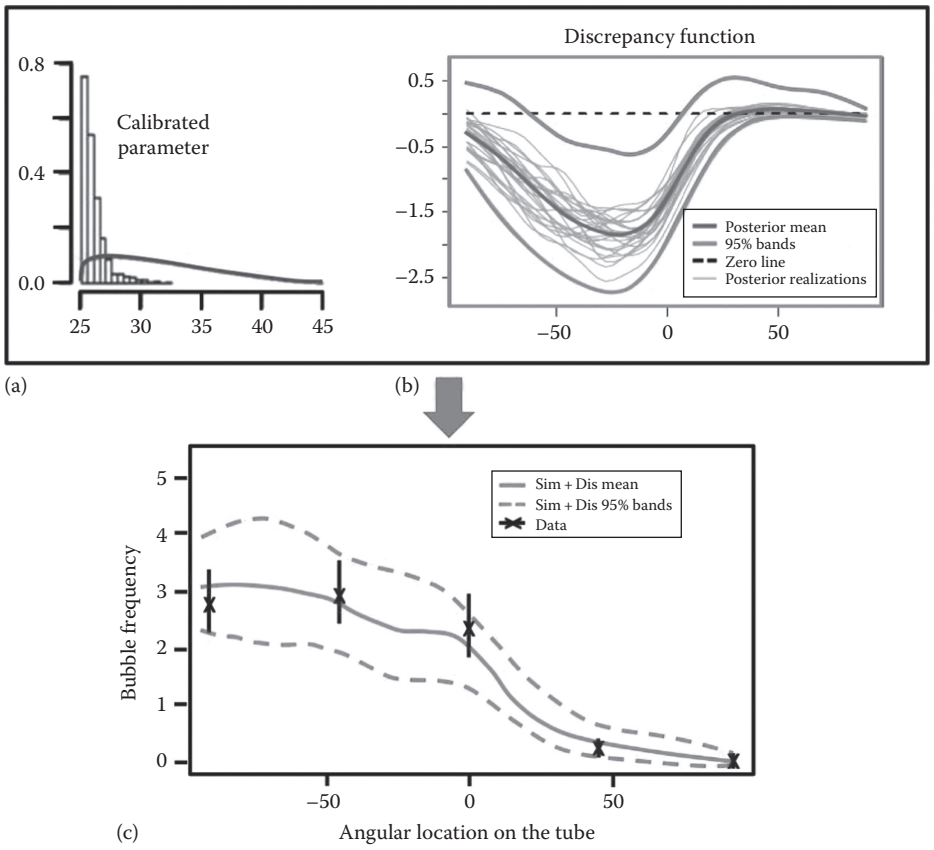


Figure 2.96

Bayesian calibration of a bubbling fluidized bed and the prediction of a held-out data set. (a) The continuous line is the prior distribution and the stacked bar graph is the posterior distribution determined from Bayesian calibration. (b) The mean (dark gray), several realizations (light gray), and the 90% bands (medium gray) of the discrepancy function. (c) Mean (continuous line) and 95% confidence bands (broken lines) given by predictive simulations compared with experimental data. (Adapted from Lane, W.A. et al., *Powder Technol.*, 253, 733, 2014.)

as the building blocks for progressive model parameter calibration (see the hierarchy in Figure 2.93). First, the model is calibrated with data from cold flow experiments where only the hydrodynamics is considered and the pressure drop is the only QoI. Next, heat transfer is considered by simulating a hot, nonreacting bed, where bed temperature (temporal and spatial) is also included as a QoI. Finally, chemical reactions are introduced to simulate the multiphase hydrodynamics coupled with heat transfer and chemical reactions in the adsorber, where CO_2 adsorption capacity and the breakthrough curve are included as QoIs. The posterior distributions from each level of the hierarchy become prior distributions for the simulations for the next higher level in the hierarchy, and the BSS-ANOVA calibration is used to process the simulation data with the corresponding experimental measurements and to determine the new posterior distributions.

The chemical kinetics model developed by Lee et al. (2011) is used to model CO_2 adsorption kinetics. Lee et al. (2011) determined prior distributions of the parameters in the chemical kinetics model with the help of data from thermogravimetric analysis experiments. Fifteen model parameters are calibrated: the sorbent particle size, sorbent capacity, sorbent decay rate, and 12 equilibrium and chemical kinetics parameters for the 3 chemical reactions involved in CO_2 adsorption. The data from NETL's carbon capture unit (C2U) are the new information used for model parameter calibration. Seventy-one experimental data sets for CO_2 breakthrough curves are available from the C2U experiments. Nine of the experimental data sets are not used for the calibration (held out) so that out-of-sample validation predictions could be made for those experimental settings without the benefit of their data influencing the calibration results. These calculations show that "the emulator prediction bands are within observation error in all cases" (Lai et al., 2014a); a typical plot is shown in Figure 2.97.

The posterior distributions of model parameters from the earlier validation study are used by Lai et al. (2014b) to predict the behavior of a conceptual, pilot-scale (1 MW) CO_2 adsorber. They use five flue-gas flow rates and 351 parameter settings sampled from the 15 posterior distributions, to conduct a total of 1755 MFIX-TFM simulations. From the results of the over 1200 successful simulations, they calculate the uncertainty distributions for the QoIs CO_2 *adsorption rate* and *bed height*. At a flue-gas flow rate of 0.72 kg/s, they predict that the conceptual adsorber will capture more than 95% of the CO_2. However, the lower, 95%-confidence bound suggests that the value could be as low as 83% capture. They predict that a flow rate below 0.65 kg/s guarantees that the lower, 95%-confidence bound exceeds the DOE target of 90% capture.

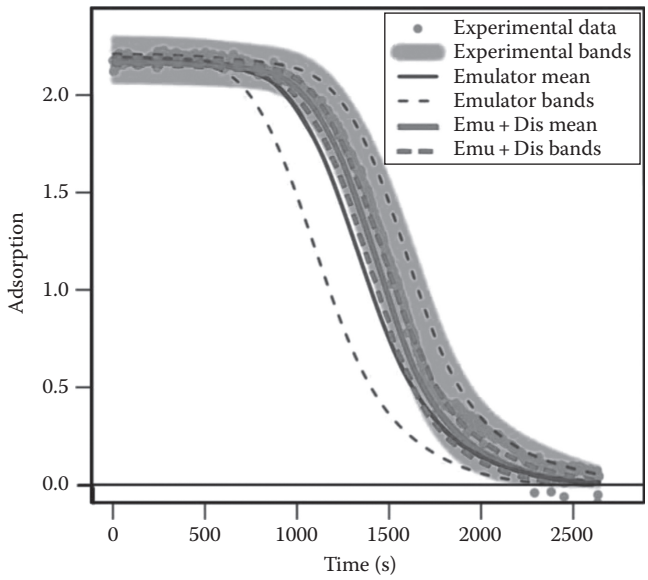


Figure 2.97

The predicted CO_2 breakthrough curves for a held-out data set. The predicted breakthrough curve (continuous red line) and 95% confidence bands (broken red line) are well within observation error (green region). The blue lines are the predictions before the discrepancy function correction is applied. (Adapted from Lai, K. et al., Hierarchical calibration and validation of high-fidelity CFD models with C2U experiments, CCSI Milestone Report, 2014a.)

2.8.6 Comments about the Calibration Process

As mentioned before, treating the computer code as a *black box* is customary in the Bayesian calibration process. Although this process has the great advantage of avoiding custom code development for uncertainty quantification, the process could disregard direct relationships between the input parameters and the output results dictated by the underlying physics. Calibrating the particle diameter with experimental data on pressure drop, for example, is physically reasonable because a direct relationship between the two can be deduced from the multiphase CFD equations. Calibrating the particle diameter with experimental data on the conversion of a gas-phase species, however, need not be physically reasonable. Whereas carbon monoxide (CO) generation from carbon combustion would be affected by the diameter of the carbon particle, CO generation from the (gas phase) water gas shift reaction would not be. The physical connection between CO conversion and particle diameter is then ambiguous, and a deficiency in the reaction kinetics model could corrupt the diameter calibration. Although the reader is cautioned about this possibility, the calibration process need not be so easily fooled: The model form discrepancy should allow for the reaction model deficiency, and the calibration process should (in principle) give the prior distribution for particle size back as the posterior.

The calibration process also must anticipate the design specifications. If, for example, the particle size distribution is one of the design specifications, a calibrated particle diameter would not be useful for conducting predictive simulations. In that case, the predictive simulation needs a method for determining the mean particle diameter from a given particle size distribution (e.g., Sauter mean diameter vs. volume–width diameter). If there is no compelling physical reason for selecting one averaging method over another, the different averaging methods could be included as categorical variables, and a suitable method could be identified through the calibration process.

The discrepancy function accounts for every uncertainty in the CFD model that caused the validation simulation results to differ from the experimental observations and that could not be corrected by calibrating the model parameters. However, the discrepancy function cannot very well compensate for the missing physics or numerical approximations. Suppose a particle-scale, reaction rate model ignores the effects of mass transfer. That deficiency could appear in the discrepancy function developed through the calibration process. The discrepancy function will not be able to account for the missing physics in predictive simulations, however. That is, the discrepancy function may not predict an increased reaction rate in response to an increased relative velocity, although the underlying physics implies an increased reaction rate, caused by an increased mass transfer rate, which, in turn, is caused by an increased relative velocity. Bhat et al. (2016) have proposed a way to correct for the missing physics by putting the discrepancy function directly into the reaction rate and equilibrium expressions. Furthermore, any unquantified uncertainty caused by a poor grid resolution in the validation simulations could appear in the discrepancy function, which may distort the uncertainty arising from the grid resolution used in the predictive simulations.

Acknowledgments

This technical effort was performed in support of the National Energy Technology Laboratory's ongoing research in multiphase flows in part under the RDS contract DE-AC26-04NT41817. The authors would like to thank the following colleagues for reviewing the manuscript and pointing out corrections and suggestions for improvement: C. Roy (Virginia Tech), C. Storlie (Los Alamos National Lab), and X. Sun (Pacific Northwest National Lab).

References

ASME V&V 20-2009, *Standard for Verification and Validation in Computational Fluid Dynamics and Heat Transfer*, ASME, November 2009.

Bhat, K.S., Mebane, D.S., Storlie, C.B., and Mahapatra, P., Upscaling uncertainty with dynamic discrepancy for a multi-scale carbon capture system, *J. Am. Stat. Assoc.*, 2016 (tentatively accepted).

Choudhary, A., Roy, C.J., Dietiker, J.-F., Shahnam, M., and Garg, R., Code verification for multiphase flows using the method of manufactured solutions, FEDSM2014-21608, in *Proceedings of the ASME 2014 Fourth Joint US-European Fluids Engineering Division Summer Meeting*, Chicago, IL, August 3–7, 2014.

Coleman, H.W. and Steele, W.G., *Experimentation, Validation, and Uncertainty Analysis for Engineers*, Wiley, Hoboken, NJ, 2009.

Efron, B., Bayes' theorem in the 21st century, *Science*, 340, 1177–1178, 2013.

Gel, A., Garg, R., Tong, C., Shahnam, M., and Guenther, C., Applying uncertainty quantification to multiphase flow computational fluid dynamics, *Powder Technol.*, 242, 27–39, 2013b.

Gel, A., Li, T., Gopalan, B., Shahnam, M., and Syamlal, M., Validation and uncertainty quantification of a multiphase CFD model, *Ind. Eng. Chem. Res.*, 52(33), 11424–11435, 2013a. Doi: 10.1021/ie303469f.

Grace, J.R. and Taghipour, F., Verification and validation of CFD models and dynamic similarity for fluidized beds, *Powder Technol.*, 139, 99–110, 2004.

Helton, J.C., Johnson, J.D., Sallaberry, C.J., and Storlie, C.B., Survey of sampling-based methods for uncertainty and sensitivity analysis, *Reliab. Eng. Syst. Safety*, 91, 1175–1209, 2006.

Higdon, D., Kennedy, M., Cavendish, J.C., Cafeo, J.A., and Ryne, R.D., Combining field data and computer simulations for calibration and prediction, *SIAM J. Sci. Comput.*, 26, 448–466, 2004.

Kennedy, M.C. and O'Hagan, A., Bayesian calibration of computer models, *J. R. Stat. Soc. Ser. B—Stat. Methodol.*, 63, 425–450, 2001.

Kim, S.W., Ahn, J.Y., Kim, S.D., and Hyun Lee, D., Heat transfer and bubble characteristics in a fluidized bed with immersed horizontal tube bundle, *Int. J. Heat Mass Transfer*, 46(3), 399–409, 2003.

Lai, K., Xu, Z., Pan, W., Dietiker, J., Li, T., Marcy, P., Storlie, C., Sun, X., and Sundaresan, S., Quantifying CFD predictive confidence on CO_2 capture efficiency of 1MW pilot-scale solid sorbent adsorber with a hierarchical calibration and validation approach, CCSI Milestone Report, 2014b.

Lai, K., Xu, Z., Pan, W., Shadle, L., Storlie, C., Dietiker, J., Li, T., Dartevelle, S., and Sun, X., Hierarchical calibration and validation of high-fidelity CFD models with C2U experiments, CCSI Milestone Report, 2014a.

Lane, W.A., Storlie, C.B., Montgomery, C., and Ryan, E.M., Numerical modeling and Bayesian calibration of a bubbling fluidized bed with immersed horizontal tubes, *Powder Technol.*, 253, 733–743, 2014.

Lee, A., Mebane, D., Fauth, D.J., and Miller, D. C., A model for the adsorption kinetics of CO_2 on amine-impregnated mesoporous sorbents in the presence of water, in *Proceedings of the 28th Annual International Pittsburgh Coal Conference (PCC '11)*, pp. 355–365, September 2011.

Li, T., Dietiker, J., Zhang, Y., and Shahnam, M., Cartesian grid simulations of bubbling fluidized bed with a horizontal tube bundle, *Chem. Eng. Sci.*, 8, 6220–6231, 2011.

Little, R.J., In Praise of Simplicity not Mathematistry! Ten simple powerful ideas for the statistical scientist, *J. Am. Stat. Assoc.*, 108(502), 359–369, 2013. Doi: 10.1080/01621459.2013.787932.

Miller, D.C., Syamlal, M., Mebane, D., Storlie, C., Bhattacharyya, D., Sahinidis, N.V., Agarwal, D. et al., Carbon capture simulation initiative: A case study in multi-scale modeling and new challenges, *Annu. Rev. Chem. Biomol. Eng.*, 5, 301–323, 2014. Doi: 10.1146/annurev-chembioeng-060713-040321.

Oberkampf, W.L. and Trucano, T.G., Verification and validation in computational fluid dynamics, Sandia Report SAND2002-0529, Sandia National Laboratories, Albuquerque, NM, March 2002.

O'Hagan, A., Bayesian analysis of computer code outputs: A tutorial, *Reliab. Eng. Syst. Safety*, 91(10–11), 1290–1300, 2006. Doi:10.1016/j.ress.2005.11.025.

Reich, B.B.J., Storlie, C.B., and Bondell, H.D., Variable selection in Bayesian smoothing spline ANOVA models: Application to deterministic computer codes, *Technometrics*, 51, 110–120, 2009.

Roy, C.J., Grid convergence error analysis for mixed-order numerical schemes, *AIAA Journal*, 41(4), 595–604, 2003.

Roy, C.J. and Oberkampf, W.L., A comprehensive framework for verification, validation, and uncertainty quantification in scientific computing, *Comput. Methods Appl. Mech. Eng.*, 200(25–28), 2131–2144, 2011.

Ryan, E.M., Montgomery, C., Storlie, C., and Wendelberger, J., CCSI validation and uncertainty quantification hierarchy for CFD models, CCSI Technical Report Series, 2012. http://www.acceleratecarboncapture.org/drupal/sites/default/files/elfinder/CCSI_Directory/Deliverables/Sept_30_2012/CCSI_V-UQ%20Hierarchy_FINAL.pdf.

Shadle, L., Shahnam, M., Cocco, R., Issangya, A., Guenther, C., Syamlal, M., Spenik, J. et al., Challenge problem III, *CFB X Workshop*, Sun River, OR, 2011.

Storlie, C.B., Lane, W.A., Ryan, E.M., Gattiker, J.R., and Higdon, D.M., Calibration of computational models with categorical parameters and correlated outputs via Bayesian smoothing spline ANOVA, *J. Am. Stat. Assoc.*, 2014 (to appear).


Taylor & Francis
Taylor & Francis Group
http://taylorandfrancis.com

3

Gas–Liquid Flow in Ducts

Afshin J. Ghajar and Swanand M. Bhagwat

3.1 Introduction
3.2 Flow Patterns, Flow Maps, and Transition Theories
3.3 Void Fraction
3.4 Pressure Drop
3.5 Modeling of Stratified Flow
3.6 Modeling of Annular Flow
3.7 Nonboiling Two-Phase Heat Transfer

3.1 Introduction

The phenomenon of gas–liquid two-phase flow embraces several applications pertinent to oil and gas industry, process engineering, heat exchangers (evaporators and condensers), cooling of nuclear reactors, etc. Gas–liquid two-phase flows are classified as one-component and two-component two-phase flow. One-component two-phase flow consists of the two phases of a single chemical species such as steam water and refrigerant vapor–liquid flow used in nuclear and refrigeration applications, whereas two-component two-phase flow consists of the two phases of two chemically different species such as air–water and air–oil. The two-component two-phase flow is often referred to as nonboiling two-phase flow and is usually encountered in industrial applications such as artificial lift systems and simultaneous transportation of oil and natural gas from remote extraction locations to the processing units. Chemical operations requiring flow of two chemical species together for enhanced mass transfer, as in the case of ozone treatment of water, also rely on the two-component two-phase flow phenomenon. For the purpose of flow assurance and designing, sizing, and optimization of industrial processes and equipments handling two-phase flow, the determination of the void fraction, total two-phase pressure drop, and heat transfer is crucial. In particular, for nonboiling two-phase flow applications, the total two-phase pressure drop based on flow patterns, void fraction, and pipe geometry influences the design of a two-phase flow system. Knowledge of nonboiling heat transfer in two-component two-phase flows is equally important to estimate and prevent advent of wax deposition in subsea pipeline carrying hydrocarbons. The two-phase flow literature reports a plethora of correlations for the determination of flow patterns, void fraction, two-phase pressure drop, and nonboiling heat transfer correlations; however, the validity of a majority of these correlations is restricted over a narrow range of two-phase flow conditions. Consequently, it is quite a challenging task for the end user to select an appropriate correlation/model for the type of two-phase flow under consideration. Selection of a correct correlation also requires some fundamental understanding of the two-phase flow physics and the underlying principles/assumptions/limitations associated with these correlations. Thus, it is of significant interest for a design engineer to have knowledge of the flow patterns and their transitions and their influence on two-phase flow variables. To address some of these issues and facilitate selection of appropriate two-phase flow models, this chapter presents a succinct review of the flow patterns, void fraction, pressure drop, and nonboiling heat transfer phenomenon and recommend some of the well-scrutinized modeling techniques. Additionally, this chapter provides three illustrative

Table 3.1 Basic Definitions of Interest to Two-Phase Flow

Parameter	Definition	Description
x	$\frac{\dot{m}_G}{\dot{m}_G+\dot{m}_L}$	Two-phase flow quality
α_G	$\frac{A_G}{A}$ or $1-\frac{A_L}{A}$, $\frac{V_G}{V}$ or $1-\frac{V_L}{V}$	Void fraction
λ	$\frac{U_{SG}}{U_{SG}+U_{SL}}$ or $\left[1+\frac{1-x}{x}\left(\frac{\rho_G}{\rho_L}\right)\right]^{-1}$	Gas volumetric flow fraction
U_{SG}	$\frac{Gx}{\rho_G}$ or $\frac{\dot{m}_G}{A\rho_G}$	Superficial gas velocity (m/s)
U_{SL}	$\frac{G(1-x)}{\rho_L}$ or $\frac{\dot{m}_L}{A\rho_L}$	Superficial liquid velocity (m/s)
U_G	$\frac{U_{SG}}{\alpha_G}$ or $\frac{\dot{m}_G}{A_G\rho_G}$	Actual gas velocity (m/s)
U_L	$\frac{U_{SL}}{1-\alpha_G}$ or $\frac{\dot{m}_L}{A_L\rho_L}$	Actual liquid velocity (m/s)
U_M	$U_{SL}+U_{SG}$ or $U_L(1-\alpha_G)+U_G\alpha_G$	Two-phase mixture velocity (m/s)
S	$\frac{U_G}{U_L}$ or $\left(\frac{x}{1-x}\right)\left(\frac{1-\alpha_G}{\alpha_G}\right)\left(\frac{\rho_L}{\rho_G}\right)$	Slip ratio
Re_{SL}	$\frac{\rho_L U_{SL} D}{\mu_L}$ or $\frac{G(1-x)D}{\mu_L}$	Superficial liquid Reynolds number
Re_{SG}	$\frac{\rho_G U_{SG} D}{\mu_G}$ or $\frac{GxD}{\mu_G}$	Superficial gas Reynolds number

example problems focused on some iterative methods for the determination of void fraction and pressure drop and the use of Reynolds analogy–based and empirical heat transfer correlations for the calculation of nonboiling two-phase heat transfer.

3.1.1 Basic Concepts and Definitions

The gas–liquid two-phase flow is realistically a 3D flow with flow conditions and fluid properties varying with respect to the pipe cross section, length, and time. A valid assumption of 1D two-phase flow to a great extent simplifies several two-phase flow variables and modeling techniques. At the outset, this section introduces some of the primary variables used throughout this chapter and adopted by different two-phase flow models. The parameters listed in Table 3.1 are defined in context to single-phase flow of gas and liquid phase and their simple relationships that represent some two-phase flow variables. The two-phase flow quality (x) is defined using the mass flow rate of the gas ($\dot{m}_G$) and liquid ($\dot{m}_L$) phase and is similar to the thermodynamic quality based on enthalpy balance only when thermodynamic equilibrium exists between the two phases. Based on the measurement technique such as cross-sectional or volumetric method, void fraction (α_G) is defined as the ratio of pipe cross section/volume of pipe occupied by the gas to the total cross section/volume of the pipe. The gas volumetric flow fraction (λ) is essentially the homogeneous void fraction under the assumption of no slippage between the two phases. The phase superficial velocity (U_{SG} or U_{SL}) is defined assuming the phase mass flow rate/mass flux (G) through the entire pipe cross section (A). Actual phase velocity (U_G or U_L) is based on the phase mass flow rate through the pipe cross-sectional area (A_G or A_L) occupied by that phase. The two-phase mixture velocity is simply the summation of the superficial velocity of each phase. The slip ratio (S) is the ratio of actual gas-phase velocity to actual liquid-phase velocity. Finally, the phase superficial Reynolds number (Re_{SL} or Re_{SG}) is based on the phase superficial velocity, phase density (ρ_L or ρ_G), and phase dynamic viscosity (μ_L or μ_G).

3.2 Flow Patterns, Flow Maps, and Transition Theories

The physical structure of two-phase flow known as "flow pattern" is most fundamental among all two-phase flow variables and also forms the basis of two-phase flow modeling methods. Unlike single-phase flow theory, two-phase flow cannot be distinguished as laminar, transitional, or turbulent but rather is classified on the basis

of several user-defined flow patterns. In this section, a brief information about the flow patterns occurring in different pipe orientations, their mapping technique using physically measurable quantities, and mathematical models to estimate their existence is laid out.

3.2.1 Flow Patterns

The flow patterns observed in gas–liquid two-phase flow are quite intriguing in nature and depend on the alignment of one phase with respect to the other across the pipe cross section. The morphological variations in the structure of flow patterns are essentially due to the significantly different physical properties of the two phases such as viscosity and density, compressible nature of the gas phase, and the interaction between gravity, inertia, and buoyant forces. Correct understanding of the physical structure of flow patterns and their transition is instrumental in the general understanding of the mechanism of mass, momentum, and energy transfer in two-phase flow. This preliminary section of this chapter is aimed at describing the physical structure of some key flow patterns illustrated in Figure 3.1 and their physical variations as a function of varying two-phase flow conditions:

Bubbly flow: Bubbly flow often called as dispersed bubbly flow is characterized by the flow of small gas bubbles dispersed in continuous liquid medium. The size (much smaller than the pipe diameter), shape (typically spherical or oblong), and distribution (uniform, center peaked, or wall peaked) of bubble density depend upon the pipe geometry and inclination, fluid properties, and phase flow rates. For nonvertical pipe orientations, bubbly flow appears in the form of small bubbles oriented in the vicinity of pipe upper wall. With increase in liquid-phase flow rates, bubbles tend to get dispersed evenly across the pipe cross section to appear in the form of dispersed bubbly flow. In addition to the dispersed form, bubbly flow may also appear in the form of elongated or agglomerated bubbles during the transition from bubbly to slug or dispersed bubbly to slug/intermittent flows. This physical form of bubbly flow is often identified as bubbly–slug flow.

Slug flow: Slug flow is characterized by the alternate flow of gas and liquid slugs. The size (elongated and comparable to pipe diameter), shape (usually bullet shaped with hemispherical nose and a blunt tail), and frequency of slugs depend upon the pipe geometry, pipe orientation, and fluid properties. For horizontal and nonvertical upward pipe inclinations, gas slug is in the vicinity of the pipe upper wall while it is symmetrically distributed around the pipe axis in vertical flow orientation. The translational velocity of the gas slug along the pipe axis is a function of pipe orientation such that the upward pipe inclinations aid the slug motion, while the downward pipe inclinations oppose the slug motion. The length of the gas slugs reduces, while their frequency increases with increase in the liquid flow rate. The opposite is true for a fixed liquid flow rate and decreasing gas flow rates.

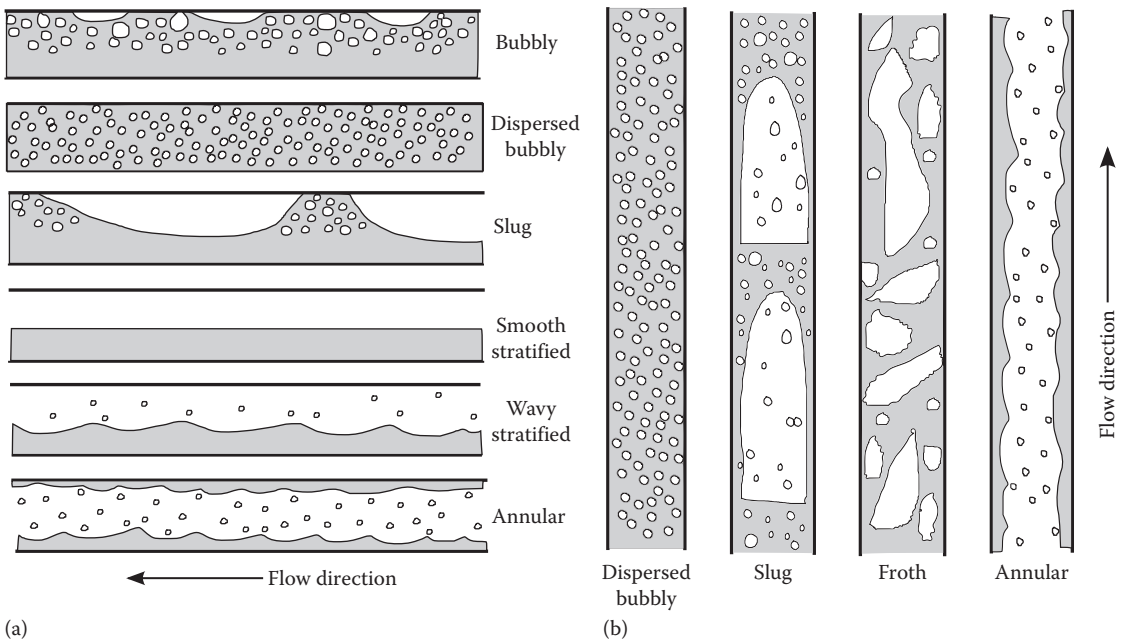


Figure 3.1

Flow patterns in (a) horizontal and (b) vertical upward gas–liquid two-phase flows.

Intermittent flow: The intermittent two-phase flow that typically exists at moderate gas and liquid flow rates is a representation of two-phase flow having chaotic, pulsating, and indefinite phase alignment characteristics. Different subcategories of key flow patterns such as slug wavy, annular wavy, churn, and froth flow exhibit disorderliness, intermittency, and indefinite flow structure, and hence, it is appropriate to club these all different subflow patterns together to call as intermittent flow. This approach of calling certain flow patterns as intermittent flow has been adopted by many researchers to reduce the ambiguity in identifying the transition boundaries between key flow patterns.

Stratified flow: Stratified flow exists in the form of gas and liquid layers flowing parallel to each other such that the pipe bottom wall is in contact with liquid phase, while the upper wall is in contact with the gas phase. Stratified flow in general can be classified as smooth stratified and wavy stratified flow. Smooth stratified flow appears at low liquid and low gas flow rates and is characterized by the complete separation of the two phases sharing a smooth and stable interface, whereas at high gas flow rates, the wavy stratified flow exists and it is characterized by the wavy, dynamic, and rough gas–liquid interface. At relatively high gas and liquid flow rates, the interfacial instability generates disturbance waves at the interface that grow and tend to touch the pipe wall giving an appearance of rolling wave. This type of stratified flow is recognized as rolling wave flow; however, the general flow structure still resembles the stratified flow pattern. A specific case of stratified flow identified as "falling film flow" is observed in vertical downward two-phase flow. The falling film flow is characterized by the downward flow of thin liquid film in contact with the pipe wall. Due to the physical resemblance of this flow pattern with the annular flow, some researchers have classified this flow pattern as a subregion of annular flow. However, there is a significant difference in these two-flow patterns in terms of the intensity of gas core turbulence, interfacial shear, thickness of liquid film, and the amount of liquid entrainment.

Annular flow: Annular flow appears in the form of a turbulent gas core surrounded by the thin/thick (depending upon liquid flow rates) and wavy liquid film. The liquid film distribution in annular flow is affected by the pipe orientation such that for horizontal flow, the asymmetric liquid film is thick at pipe bottom while it is evenly distributed around the circumference in case of vertical two-phase flow. Depending upon the gas and liquid flow rates, the gas–liquid interface may be stable or perturbed by small amplitude waves causing the liquid droplets to detach from liquid film and enter into the turbulent gas core known as the liquid entrainment phenomenon. The amplitude and frequency of interfacial disturbance waves and the amount of liquid entrainment depend on the phase flow rates, fluid properties, pipe geometry, and pipe inclination. A special form of annular flow also known as annular mist flow exists when most of the liquid phase initially flowing in the form of film is entrained into the central gas core by the shearing action of the fast-moving gas core. This type of flow pattern is mostly encountered in applications involving high system pressure and high heat flux conditions.

3.2.2 Flow Maps

The flow pattern maps or flow maps serve as a tool to estimate the span and sequence of appearance of different flow patterns with change in gas and liquid flow rates for a given set of flow conditions. The flow patterns and their transitions are defined qualitatively based on visual observations, and hence, the accurate mapping of the transition between different flow patterns is highly subjective and totally depends upon the observer's perception. Moreover, the transition between different flow patterns is gradual and sensitive to several parameters such as pipe diameter, pipe orientation, and fluid properties making it extremely difficult to have a universal flow pattern map that can correctly predict the existence of different flow patterns covering a wide range of two-phase flow conditions.

Despite the lack of the universal flow pattern map, it is important to consider some of the existing most referred flow pattern maps to get an idea about the sequence, extent, and transitions between different flow patterns. These flow pattern maps may serve as a guideline in understanding the appearance of flow patterns as a function of gas and liquid flow rates. To begin with, let us consider the flow pattern maps of Mandhane et al. (1974) and Taitel and Dukler (1976) for horizontal two-phase flow. The flow map of Mandhane et al. (1974) shown in Figure 3.2 is developed based on the two-phase flow parameters listed as follows:

$12.7 \leq D \leq 165.1$ mm	$0.0003 \leq \mu_L \leq 0.09$ Pa s
$705 \leq \rho_L \leq 1009$ kg/m^3	$10^{-5} \leq \mu_G \leq 2.2 \times 10^{-5}$ Pa s
$0.8 \leq \rho_G \leq 51$ kg/m^3	$0.024 \leq \sigma \leq 0.1$ N/m

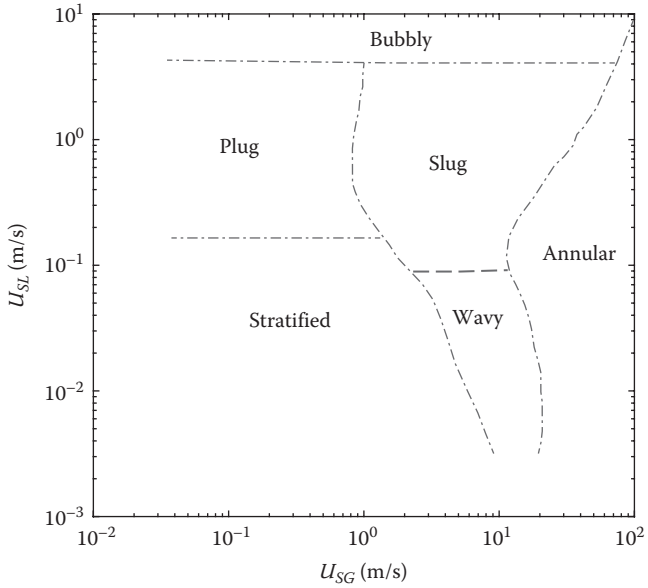


Figure 3.2

Flow pattern map for horizontal flow. (Adapted from Mandhane, J.M. et al., *Int. J. Multiphase Flow*, 1, 537, 1974.)

It is evident that the flow map of Mandhane et al. (1974) considers the existence of bubbly/dispersed bubbly flow to be insensitive to the change in liquid flow rate. Moreover, their flow pattern map shows a common transition boundary between slug and annular flow patterns. Based on the experience, it can be said that the slug flow in the vicinity of annular flow may not exhibit true slug flow characteristics and may appear in the form of agitated two-phase flow without any particular flow structure. Although the flow pattern map of Mandhane et al. (1974) is based on data consisting of a wide range of liquid-phase densities, their flow pattern map is claimed to be more accurate for air–water two-phase flow and is limited to horizontal pipe orientation.

The flow map of Taitel and Dukler (1976) shown in Figure 3.3 is based on mechanistic modeling of two-phase flow patterns and is presented in nondimensional form using the parameter X and parameters F and T of Lockhart and Martinelli (1949) shown in Equations 3.1 through 3.3. The parameter X of Lockhart and

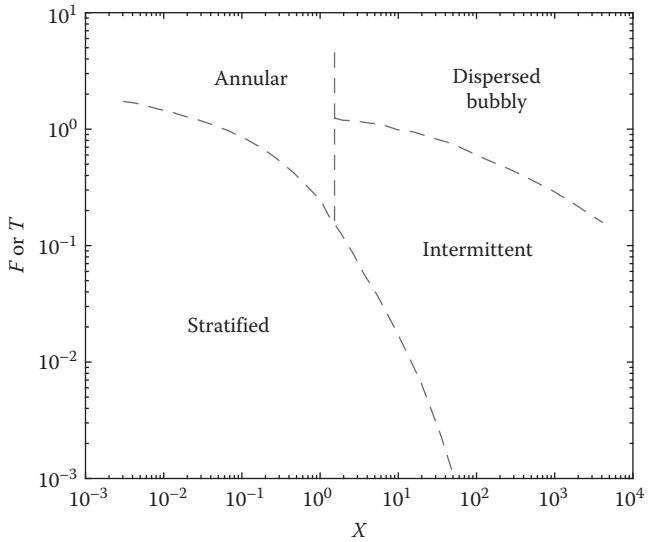


Figure 3.3

Flow pattern map for horizontal flow. (Adapted from Taitel, Y. and Dukler, A.E., *AIChE J.*, 22, 47, 1976.)

Martinelli (1949) is the square root of the ratio of the frictional pressure drop assuming single-phase flow of liquid ($(dp/dz)_L$) and gas ($(dp/dz)_G$) through the pipe, while parameter F is a modified Froude number based on superficial gas velocity (U_{SG}) and accounts for the effect of pipe orientation (θ) and phase densities (ρ_L and ρ_G). For the calculation of single-phase pressure drop, please refer to Section 3.4.7.1. The parameters $F-X$ are used to determine annular, stratified, and intermittent flows, while $T-X$ are used to determine the existence of dispersed bubbly flow. Unlike the flow map of Mandhane et al. (1974), Taitel and Dukler (1976) classify plug/slug/wavy flow patterns as intermittent flow. The flow pattern transition boundaries shown in Figure 3.3 are valid for horizontal two-phase flow. For other pipe orientations, these transition lines could be generated using the transition theories proposed by Taitel and Dukler (1976):

$$X = \sqrt{\frac{(dp/dz)_L}{(dp/dz)_G}} \tag{3.1}$$

$$F = \sqrt{\frac{\rho_G}{\rho_L - \rho_G}} \frac{U_{SG}}{\sqrt{gD}\cos\theta} \tag{3.2}$$

$$T = \sqrt{\frac{(dp/dz)_L}{(\rho_L - \rho_G)g\cos\theta}} \tag{3.3}$$

In case of vertical upward two-phase flow, the flow pattern map of Hewitt and Roberts (1969) developed for air–water two-phase flow and pipe diameters within the range of $10 \leq D \leq 30$ mm provides guidelines on the existence of different flow patterns and transition between them. The flow map of Hewitt and Roberts (1969) shown in Figure 3.4 is plotted using momentum flux of each phase. This flow map is also verified against the high-pressure steam–water data and is found to give satisfactory prediction of the flow patterns. With reference to the horizontal and vertical flow maps, the flow map (in terms of transition boundary between different flow patterns) is systematically affected by the change in upward pipe inclinations. Flow pattern maps for upward pipe inclinations shown in Figure 3.5 are based on the experimental observations and data collected at the Two-Phase Flow Lab, Oklahoma State University (OSU). It is evident from this

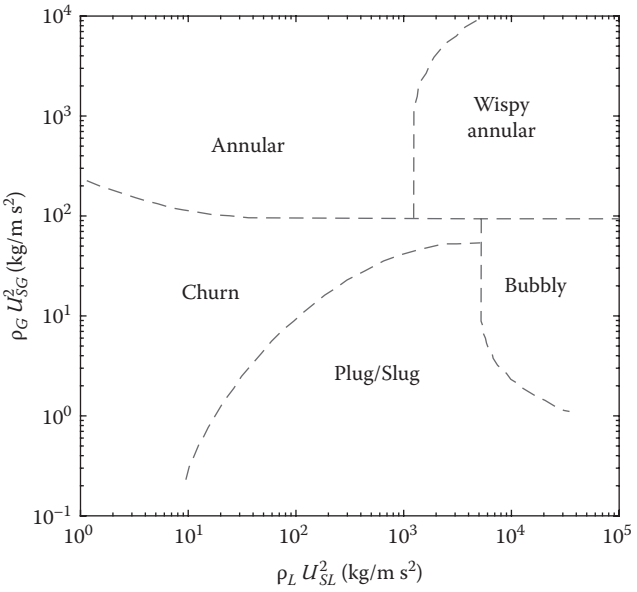


Figure 3.4

Flow pattern map for vertical upward flow. (Adapted from Hewitt, G.F. and Roberts, D.N., Studies of two phase flow patterns by simultaneous x-ray and flash photography, Technical Report AERE-M 2159, Atomic Energy Research Establishment, 1969.)

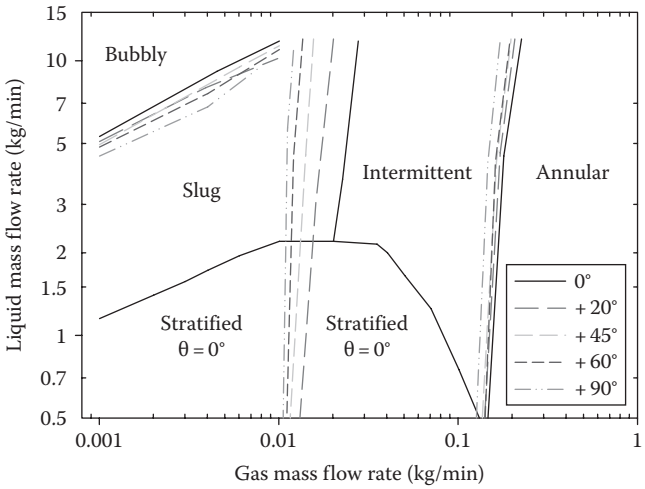


Figure 3.5

Flow pattern map for horizontal and upward inclined two-phase flows. (Based on flow visualization done at the Two-Phase Flow Lab, OSU, Stillwater, OK.)

figure that increase in the pipe orientation from horizontal toward vertical upward direction causes early transition from bubbly to slug flow and shifts the slug/intermittent flow transition line toward lower gas flow rates. The transition boundary between intermittent and annular flow regimes is virtually unaffected by the change in pipe orientation. Note that stratified flow exists in horizontal pipe orientations. For all upward pipe inclinations, this region of stratified flow is replaced by slug and intermittent flow patterns. In comparison to flow map for upward pipe inclinations, the flow pattern map for gas–liquid two-phase flow in downward pipe inclinations is of particular interest due to buoyancy-dominated two-phase flow regions in these orientations. Figure 3.6 shows representative flow pattern maps for different downward pipe inclinations based on flow visualization done at the Two-Phase Flow Lab, OSU. It is found that the effect of change in downward pipe orientation is significant on the transition between stratified–slug and stratified–intermittent flow patterns. The transition from stratified to slug flow regime shifts toward higher liquid flow rates with increase in downward pipe inclinations approximately up to $\theta = -45°$ from horizontal and then again decreases toward lower liquid flow rates thereafter.

It is quite interesting that unlike other pipe inclinations, in steeper downward orientations, two-phase flow pattern that exists inside a pipe for a fixed gas and liquid flow rates may exhibit a transient behavior. This small region where flow patterns tend to change with time is indicated in Figure 3.6. It is also seen that this transient nature of two-phase flow aggravates with increase in downward pipe inclination and propagates toward slightly higher gas flow rates. The transient behavior of flow patterns exists for steeper orientations and is always found to be in the vicinity of bubbly, slug, and stratified flow patterns. The visual observation of this transient nature of flow patterns can also be confirmed by analyzing the two-phase pressure drop signal in time domain as shown in Figure 3.7. A plausible explanation for the transient behavior of flow patterns can be given by considering the two-phase flow physics in downward pipe inclinations. A pressure drop signal in this unsteady region recorded over a period of time shows significant fluctuations. A visual observation of the flow pattern in the transparent test section during the pressure drop data acquisition can confirm the transient nature of two-phase flow that exhibits combined behavior of bubbly, slug, and stratified flows. It is seen that these flow patterns repeat one after another continuously without establishing one fixed flow pattern. For the case of stratified flow with very little gas flow rate, the liquid phase accelerates downstream under the influence of gravity, while the gas phase is believed to either stay virtually stationary or move upstream under the influence of buoyancy. As the liquid phase travels downstream, it further accelerates and creates unstable gas–liquid interface. These instabilities tend to grow at the gas–liquid interface and splash liquid on the pipe upper wall and further try to bridge the entire pipe cross section to trap a gas pocket in the form of slug flow. Slug flow pattern favors dominant buoyancy forces, and consequently, a pseudostationary elongated gas pocket (gas slug) is observed in the pipe. Meanwhile, the liquid phase coming from upstream direction gets accumulated on the top of pseudostationary slug that further slips past the elongated gas bubble and eventually forces the gas bubble to move in the downstream

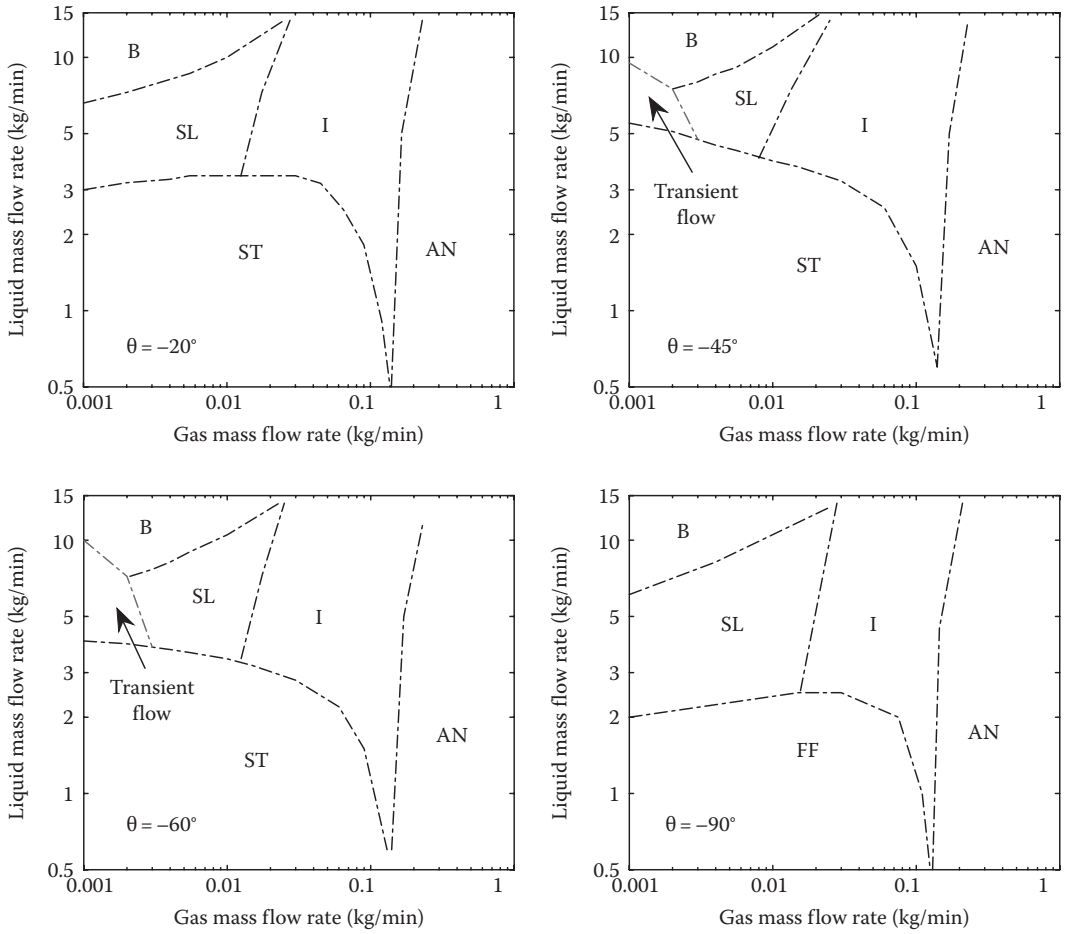


Figure 3.6

Flow pattern map for downward inclined two-phase flow. (Based on flow visualization done at the Two-Phase Flow Lab, OSU, Stillwater, OK.) (B, bubbly; SL, slug; I, intermittent; ST, stratified; FF, falling film; AN, annular.)

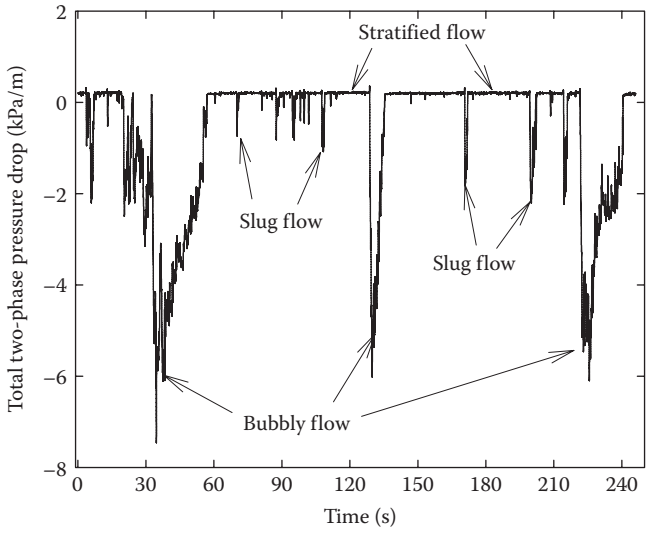


Figure 3.7

Variation in two-phase pressure drop due to transient nature of two-phase flow. (Based on data collected at the Two-Phase Flow Lab, OSU, Stillwater, OK.)

direction. During this process, the liquid phase churns the elongated gas bubbles causing it to disintegrate and move further in the form of small bubbles. After the gas pocket is pushed downstream, the incoming two-phase flow is again in the form of stratified flow pattern, and this process repeats continuously showing stratified, bubbly, and slug flow patterns periodically.

Considering the several forms of flow pattern maps reported earlier, it appears that it is difficult to have an exact agreement between the shape and trends of transition lines between specific flow patterns represented in different flow maps. This is partly because of the different coordinate systems adopted to generate flow maps and variations in the definitions of flow patterns adopted by different researchers. However, in a broad sense these flow pattern maps show agreement between the qualitative range (low, moderate, high) of gas and liquid flow rates that represent certain flow patterns. For instance, the bubbly flow appears at low gas and high liquid flow rates, intermittent and slug flow appears at moderate gas and liquid flow rates, and annular flow exists for low liquid and high gas flow rates. Another important issue that must be brought to the reader's attention is the "gradual" transition between different flow patterns. For the purpose of clarity, the transition boundaries between flow patterns are shown as thin lines; however, in reality, the transition region may be spread over a range of gas and liquid flow rates. In general, keeping in mind the uncertainty, sensitivity, and qualitative identification of flow patterns, following facts and limitations about the flow pattern maps must be perceived:

1. It is difficult to have a universal flow pattern map that can accurately predict the transition of one flow pattern to another for a wide range of two-phase flow conditions.
2. Unlike represented in most flow pattern maps, the transition from one flow pattern to another is always gradual and cannot be presented in the form of a thin continuous line.
3. Correct identification of a flow pattern in the vicinity of the transition line depends on the judgment of an individual.

3.2.3 Flow Pattern Transitions

The two-phase flow literature reports both mechanistic and empirical models to predict transition between different flow patterns. However, these transition models are developed based on the visual observations, limited data bank, and several simplifying assumptions that render uncertainty in their practical applications specifically if the two-phase flow under consideration is on the verge of transition. The following section provides some of the existing flow pattern transition models available in the two-phase flow literature. Considering the vague definition of intermittent flow pattern, the transition models listed here are only for well-defined flow regimes such as bubbly, slug, stratified, and annular flows.

3.2.3.1 Transition between Bubbly and Slug Flows

The transition from bubbly to slug flow occurs when bubbles no longer move independently and tend to coalesce to form a larger bubble usually known as the Taylor bubble. The transition from bubbly to slug flow can be achieved with the decrease in liquid flow rate at a constant gas flow rate or with increase in gas flow rate at a constant liquid flow rate. In general, the two-phase flow literature shows that this transition from bubbly to slug flow occurs for void fraction in the range of 0.25–0.3. The transition from bubbly to slug flow will occur if Equation 3.4 suggested by Taitel et al. (1980) is satisfied. This relationship is obtained by assuming that the maximum void fraction during transition from bubbly to slug flow is approximately 0.25 and that the bubble velocity is equal to the slip velocity ($U_b \cong U_G - U_L$). The bubble velocity at different pipe inclinations represented by Equation 3.5 is the modified form of Haramathy (1960) equation for bubble rise velocity suggested by Taitel et al. (1980) and Barnea (1987):

$$U_{SL} \le 3U_{SG} - 1.32\left(\frac{\sigma g(\rho_L - \rho_G)}{\rho_L^2}\right)^{0.25} \sin\theta \Bigg\} (+60^\circ \le \theta \le +90^\circ) \tag{3.4}$$

$$U_b = 1.53\left[\frac{g\sigma(\rho_L - \rho_G)}{\rho_L^2}\right]^{0.25} \sqrt{1-\alpha_G}\,\sin\theta \tag{3.5}$$

Note that Equation 3.4 is recommended for use for near vertical pipe orientations ($+60^\circ \le \theta \le +90^\circ$) since as per Taitel et al. (1980) and Barnea (1987) it is difficult for bubbly flow to exist in horizontal and near

horizontal pipe orientations. Moreover, Taitel et al. (1980) also reported that the bubbly flow would exist if the pipe diameter of two-phase flow under consideration follows

$$D > 19\left(\frac{(\rho_L - \rho_G)\sigma}{\rho_L^2 g}\right)^{0.5} \tag{3.6}$$

Following a similar concept, Mishima and Ishii (1984) presented a model to predict transition between bubbly and slug flows (valid for vertical upward flow) of the form shown in Equation 3.7. The transition from bubbly to slug flow would occur if Equation 3.7 is satisfied. The parameter C_o is expressed as $C_o = 1.2 - 0.2\sqrt{\rho_G/\rho_L}$ such that for near atmospheric operating conditions $C_o \approx 1.2$. The bubble velocity equation (Equation 3.8) used by Mishima and Ishii (1984) is similar to Equation 3.5, however with different multiplying factors and exponents:

$$U_{SL} \le \left(\frac{3.33}{C_o} - 1\right)U_{SG} - \frac{0.76}{C_o}\left(\frac{\sigma g \Delta\rho}{\rho_L^2}\right)^{0.25}\Bigg\}(\theta = +90°) \tag{3.7}$$

$$U_b = 1.41\left[\frac{g\sigma(\rho_L - \rho_G)}{\rho_L^2}\right]^{0.25}(1-\alpha_G)^{1.75} \tag{3.8}$$

For vertical upward flow, a comparison between Equations 3.4 and 3.7 shows that transition from bubbly to slug flow will occur at relatively lower U_{SL} using the criteria of Mishima and Ishii (1984). This discrepancy is essentially due to their assumption of $\alpha_G \approx 0.3$ during the transition and a slightly different form of bubble velocity (U_b) used by Mishima and Ishii (1984). As mentioned earlier, bubbly flow pattern can be further classified as bubbly–slug and dispersed bubbly flow. Thus, the bubbly flow predicted by Equations 3.4 and 3.7 may contain both bubbly–slug and dispersed bubbly two-phase flow. Unlike bubbly (elongated bubbly/slug bubbly) flow, the dispersed form of bubbly flow is known to exist in the entire range of pipe orientations, and its existence could be determined using the transition model of Barnea (1986). The model of Barnea (1986, 1987) requires calculation of three different diameters, namely, maximum bubble diameter ($d_{\max}$), critical bubble diameter above which bubble is deformed (d_{def}), and critical bubble diameter below which migration of bubbles is prevented (d_{migr}). These different bubble diameters could be determined from Equations 3.9 through 3.11, respectively. Thus, according to Barnea (1986), dispersed bubbly flow would exist if both $d_{\max} < d_{def}$ and $d_{\max} < d_{migr}$ conditions are satisfied. For these conditions typically at high liquid flow rates, dispersed bubbly flow exists since the turbulent fluctuations are capable to break down bubbles to spherical shape and also suppress the bubble coalesce that leads to slug formation.

$$d_{\max} = \left[0.725 + 4.15\left(\frac{U_{SG}}{U_M}\right)^{0.5}\right]\left(\frac{\sigma}{\rho_L}\right)^{0.6}\left(\frac{2f_M U_M^3}{D}\right)^{-0.4} \tag{3.9}$$

$$d_{def} = 2\left[\frac{0.4\sigma}{(\rho_L - \rho_G)g}\right]^{0.5} \tag{3.10}$$

$$d_{migr} = 0.375\left(\frac{f_M U_M^2 \rho_L}{g\cos\theta(\rho_L - \rho_G)}\right) \tag{3.11}$$

In Equation 3.9, f_M is friction factor based on two-phase mixture velocity U_M and can be calculated using any single-phase friction factor correlation. Considering the packing density and packing configuration of bubbles, Barnea (1986) showed that this transition model for dispersed bubbly flow is valid for void fraction in the range of $0 < \alpha_G \le 0.52$. For dispersed bubbly flow, the slippage at gas–liquid interface is quite small and it can be assumed that $\alpha_G \approx \lambda$. Thus, the transition from dispersed bubbly to slug or intermittent flow would occur at $\lambda = U_{SG}/U_M > 0.52$.

3.2.3.2 Transition between Stratified and Nonstratified Flows

The stratified flow pattern exists only in horizontal and downward pipe inclinations, and hence, the transition model for estimating the existence of stratified flow is required to be used for this limited range of pipe orientations. The most referred transition model in the two-phase flow literature to separate out stratified flow from nonstratified flow is that of Taitel and Dukler (1976). Their transition model is based on the momentum balance between the two phases, assumes a smooth and flat gas–liquid interface such that $f_i/f_G \approx 1$, and gives the transition line equation that requires the use of a graphical solution. As per the model of Taitel and Dukler (1976), stratified flow will exist if Equation 3.12 is satisfied where F is defined by Equation 3.2:

$$F^2\left[\frac{1}{(1-\tilde{h}_L)^2}\frac{\tilde{U}_G\sqrt{1-(2\tilde{h}_L-1)^2}}{\tilde{A}_G}\right]<1 \tag{3.12}$$

The nondimensional parameters $\tilde{A}_G$ and $\tilde{U}_G=(\pi/4)/\tilde{A}_G$ are the function of nondimensional liquid height ($\tilde{h}_L=h_L/D$). The nondimensional pipe cross-sectional area occupied by the gas phase is calculated using Equation 3.13. As shown in Figure 3.8, the nondimensional liquid height $\tilde{h}_L$ is obtained through the graphical solution of $\tilde{h}_L$ versus X for different values of Y. The parameters X and Y are obtained from the following equations, respectively:

$$\tilde{A}_G=0.25\left[\cos^{-1}(2\tilde{h}_L-1)-(2\tilde{h}_L-1)\sqrt{1-(2\tilde{h}_L-1)^2}\right] \tag{3.13}$$

$$Y=\frac{(\rho_L-\rho_G)g\sin\theta}{(dp/dz)_G} \tag{3.14}$$

The application of Taitel and Dukler (1976) transition model to predict stratified flow is rather tedious due to the use of a graphical solution to determine nondimensional liquid height $\tilde{h}_L$ and consequently other parameters such as $\tilde{U}_G$ and $\tilde{A}_G$. The use of a graphical solution to determine h_L/D could be circumvented by adopting an iterative solution technique. For more details, refer to Taitel and Dukler (1976).

Taitel and Dukler (1976) further attempted to classify stratified flow as smooth stratified and wavy stratified flows. They suggested that the transition between smooth and wavy stratified flow is associated with the phenomenon of wave generation at the gas–liquid interface and that the smooth stratified flow exists

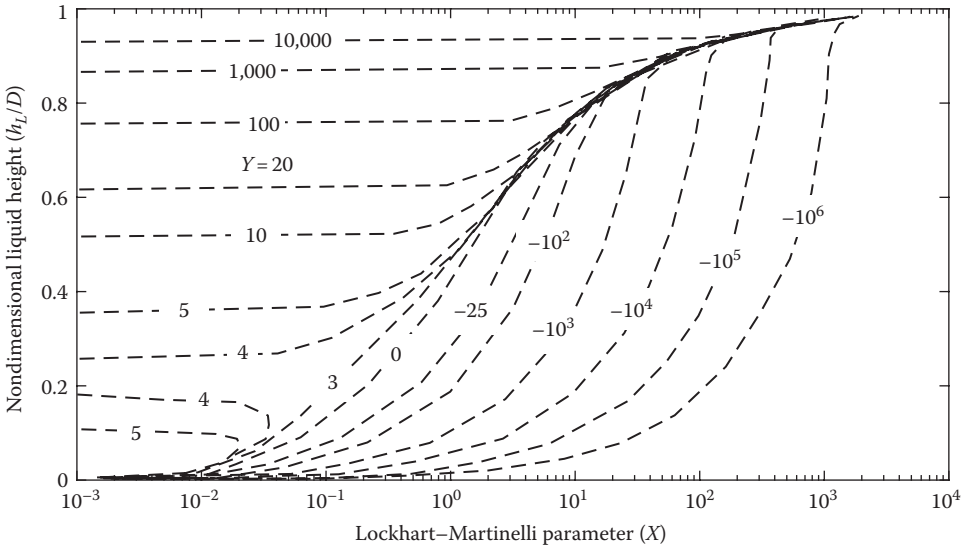


Figure 3.8

Graphical solution to determine the liquid-level height in stratified flow. (Adapted from Taitel, Y. and Dukler, A.E., *AIChE J.*, 22, 47, 1976.)

for superficial gas velocities (U_{SG}) that satisfy Equation 3.15. In practice, smooth stratified flow exists for a very narrow range of two-phase flow conditions and is of less practical significance compared to other flow patterns.

$$U_{SG,t} \geq \left(\frac{4\nu_L g \Delta\rho \cos\theta}{0.01\rho_L U_L} \right)^{0.5} \tag{3.15}$$

A simplifying approximation to the Taitel and Dukler (1976) model has been presented by Cheng et al. (1988). They approximated the trend of Equation 3.12 and presented a criterion given by Equation 3.16 to identify the existence of stratified flow pattern in horizontal pipes in terms of the parameter of Lockhart and Martinelli (1949) applicable for turbulent–turbulent gas–liquid two-phase flow where *Fr* is the modified Froude number given by Equation 3.17:

$$Fr_{SG} \leq \left(\frac{1}{0.65 + 1.11 X_{tt}^{0.6}} \right)^2 \tag{3.16}$$

$$Fr_{SG} = \frac{Gx}{\sqrt{gD\rho_G(\rho_L - \rho_G)}} = \frac{U_{SG}}{\sqrt{gD}} \sqrt{\frac{\rho_G}{\rho_L - \rho_G}} \tag{3.17}$$

Combining these equations gives the criteria for the existence of stratified flow in terms of two-phase mixture mass flux. Equation 3.18 represents the maximum value of two-phase mixture mass flux (for a given quality and fluid properties), below which stratified flow will always exist and is recommended for use only in case of horizontal two-phase flow:

$$G_{\max} = \frac{\sqrt{gD\rho_G(\rho_L - \rho_G)}}{x} \left(\frac{1}{0.65 + 1.11 X_{tt}^{0.6}} \right)^2 \Bigg\} (\theta = 0°) \tag{3.18}$$

Using the concept of growth of disturbance waves on the gas–liquid interface of stratified flow, Mishima and Ishii (1980) presented a criterion to determine the limit of stratified flow in horizontal two-phase flow. Note that the use of this correlation also requires the determination of liquid height that could be obtained using graphical solution given by Figure 3.8.

$$U_G - U_L = 0.487 \sqrt{\frac{g(D_h - h_L)(\rho_L - \rho_G)}{\rho_G}} \Bigg\} (\theta = 0°) \tag{3.19}$$

The recent work of Bhagwat and Ghajar (2015a) expressed by Equation 3.20 provides an empirical correlation to predict the existence of stratified flow in horizontal and downward pipe inclinations. Similar to the approach of Cheng et al. (1988), the correlation of Bhagwat and Ghajar (2015a) attempts to approximate the trends of Taitel and Dukler (1976) in terms of nondimensional parameters of Fr_{SG} and X and is developed based on the experimental data in horizontal and downward pipe inclinations. The Froude number in Equation 3.20 is similar to that given by Cheng et al. (1988) in Equation 3.17. The variables C_1, C_2, C_3, and C_4 required to solve Equation 3.20 are expressed by Equations 3.21 through 3.24. The nondimensional pipe diameter (D^+) is the normalized pipe diameter defined by $D^+ = D/0.0254$:

$$Fr_{SG} \leq (0.6 + C_2) \exp(-C_1 C_2 X^{C_3}) X^{-C_4} \Bigg\} \begin{array}{l} 12 < D < 150 \text{ mm} \\ 750 \leq \rho_L \leq 1420 \text{ kg/m}^3 \\ 1.2 \leq \rho_G \leq 35 \text{ kg/m}^3 \\ 0° \geq \theta > -90° \\ 0.0002 \leq \mu_L \leq 0.08 \text{ Pa s} \end{array} \tag{3.20}$$

$$C_1 = 1.3\ln(D^+) + 2.5 \tag{3.21}$$

$$C_2 = \frac{C_4^{0.65}}{\left[1 + 2\sin(2|\theta|) \times (1 + 10\tanh(1/|\theta|))\right]} \tag{3.22}$$

$$C_3 = \begin{cases} 0.65(D^+)^{-0.15}((\rho_L - \rho_G)/1000) & : \rho_L < 1000\ \text{kg/m}^3 \\ 0.65(D^+)^{-0.15} & : \rho_L \geq 1000\ \text{kg/m}^3 \end{cases} \tag{3.23}$$

$$C_4 = 0.2\sqrt{1/D^+} \tag{3.24}$$

Variables C_1 and C_2 account for the combined effect of pipe diameter and pipe orientation on the shift in transition line. The shift in transition line by including these variables is in accordance with the observations of Nguyen (1975), Barnea et al. (1982), Crawford et al. (1985), and Ghajar and Bhagwat (2014a) that the increase in downward pipe inclination shifts the transition between stratified and nonstratified flow patterns toward higher values of liquid flow rates or alternatively toward higher values of X. Variable C_3 ensures that the transition line between stratified and nonstratified flows is shifted toward higher values of X with a decrease in liquid-phase density. The variables C_1, C_2, C_3, and C_4 are adjusted such that C_1, C_2, and C_3 control the slope of transition line in the buoyancy-driven region (large values of X), while C_4 controls the slope of transition line in inertia-driven region (small values of X).

A graphical comparison between Taitel and Dukler (1976), Cheng et al. (1988), and Bhagwat and Ghajar (2015a) for horizontal two-phase flow is shown in Figure 3.9. Note that Bhagwat and Ghajar (2015a) model given by Equation 3.20 is of empirical form and merely attempts to mimic the trends of Taitel and Dukler (1976) model using $Fr_{SG} - X$ coordinates. Nevertheless, considering the practical difficulty of using a graphical/iterative solution involved in Taitel and Dukler (1976) model, Equation 3.20 may be regarded as a quick method for hand calculations and to get an estimate of the existence of stratified flow in horizontal and downward pipe inclinations.

3.2.3.3 Transition between Annular and Nonannular Flows

Typically, annular flow shares the transition boundary with intermittent (churn/annular wavy) flow patterns. Moreover, in case of horizontal and downward pipe inclinations, the annular flow also shares a transition

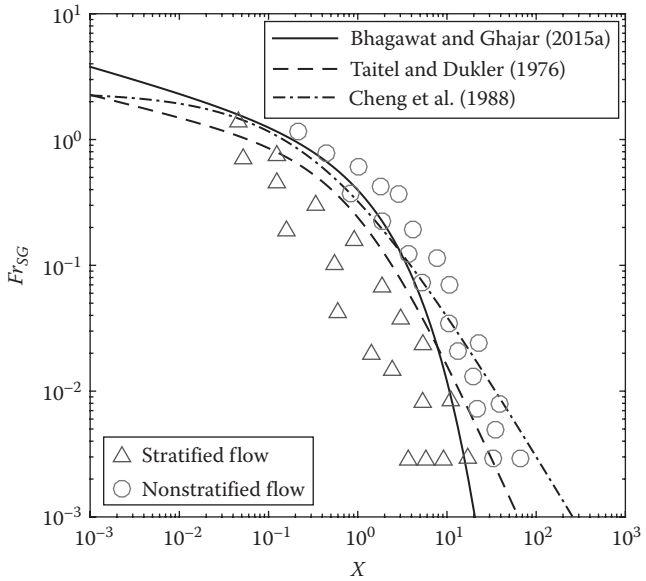


Figure 3.9

Trends of different stratified flow transition models for horizontal flow.

boundary with stratified flow pattern. In annular flow regime, the inertial forces greatly exceed the effect of gravitational forces, and hence, it is usually assumed that the change in pipe orientation will have little effect on the transition between annular and other flow regimes. However, pipe diameter and fluid properties do affect the transition to annular flow regime, and hence, it is desired to have a transition equation for annular flow regime as a function of both pipe diameter and fluid properties. One such transition criterion proposed by Weisman and Kang (1981) is expressed by Equation 3.25 and can be used for all pipe orientations. This criterion, however, at high liquid flow rates is found to incorrectly classify some region of the intermittent flow pattern as annular flow:

$$U_{SL} \geq U_{SG}\left[1.9\left(\frac{gD}{U_{SG}^2}\right)^{0.18}\left(\frac{g\Delta\rho\sigma}{U_{SG}\rho_G^2}\right)^{0.2}\right]^8 \tag{3.25}$$

Another simple yet practical approach to predict the transition to annular flow regime is based on nondimensional gas velocity (Froude number) corresponding to the point of pressure gradient minimum (concept discussed in Section 3.4.6). The two-phase flow literature for vertical upward flow reports that the pressure gradient minimum corresponds to the transition between churn/intermittent and annular flow regimes and the corresponding nondimensional gas velocity satisfies Equation 3.26. Based on the flow visualization and pressure drop measurements carried out at the Two-Phase Flow Lab, OSU, it is found that the criteria given by Equation 3.26 for transition to annular flow regime are a good approximation for the entire range of pipe orientations. The right-hand side of Equation 3.26 gives a range between which the nondimensional gas velocity can vary and for simplicity a value of 1.0 can be used. It also implies that the transition to annular flow regime would be independent of liquid velocity. Based on experience, it is recommended that in conjunction with Equation 3.26, additional simple criteria of $\alpha_G > 0.75$ can be used to confirm the existence of annular flow regime:

$$\frac{U_{SG}}{\sqrt{gD}}\sqrt{\frac{\rho_G}{(\rho_L-\rho_G)}} \geq 0.9-1.1 \tag{3.26}$$

Taitel et al. (1980) present a criterion for transition from dispersed bubbly to annular flow regimes. Their transition criteria based on force balance between the drag on liquid droplet and its weight lead to

$$\frac{U_{SG}\sqrt{\rho_G}}{(g\Delta\rho\sigma)^{0.25}} \geq 3.1 \tag{3.27}$$

A quick comparison between Equations 3.26 and 3.27 shows that the superficial gas velocity (U_{SG}) predicted by Equation 3.27 will always be higher than that predicted by Equation 3.26. This is possibly because Equation 3.26 gives transition to annular flow regime from churn/intermittent flow regimes at lower liquid flow rates, while Equation 3.27 predicts transition from dispersed bubbly flow at high liquid flow rates and hence would need higher gas flow rates for transition to annular flow regime. In addition to the transition theories, here we present in Table 3.2 a thumb rule based on the range of void fraction and qualitative range of gas and liquid flow rates associated with different flow patterns. It must be mentioned that this qualitative and quantitative range of two-phase flow variables is an approximate range based on experience and may give slight deviations compared to the real two-phase flow scenario.

Table 3.2 Thumb Rule for Qualitative Classification of Flow Patterns

	Mass/Volumetric Flow Rate		
Void Fraction (α_G)	Gas Phase	Liquid Phase	Flow Regime
Low ($\alpha_G \leq 0.25$)	Low	Moderate/High	Bubbly
Low to moderate ($0 \leq \alpha_G \leq 0.5$)	Low	High	Dispersed bubbly
Moderate ($0.25 < \alpha_G \leq 0.75$)	Low	Low/Moderate	Slug
Moderate ($0.25 < \alpha_G \leq 0.75$)	Moderate	Low/Moderate	Intermittent
Moderate to high ($0.3 < \alpha_G \leq 0.9$)	Low/Moderate	Low	Stratified
High ($0.75 < \alpha_G < 1$)	High	Low	Annular

3.3 Void Fraction

Void fraction (α_G) also referred to as liquid holdup ($\alpha_L = 1 - \alpha_G$) is defined based on its measurement technique such as local void fraction (using single-point probes), segmental void fraction (using gamma ray absorption method), cross-sectional void fraction (using capacitance probe), and volumetric void fraction (using quick closing valves). It must be noted that irrespective of the measurement technique $\alpha_G + \alpha_L = 1$. Among these different methods, typically the cross-sectional ($\alpha_G = A_G/A$) and volumetric ($\alpha_G = V_G/V$) types of void fraction measurement are most preferred and of practical importance. Under the adiabatic two-phase flow condition over a short pipe length, it can be assumed that the two-phase flow structure remains unaltered throughout the pipe length and cross-sectional void fraction can be equated to volumetric void fraction. The void fraction as a stand-alone physical parameter is typically of no use unless embedded in other constitutive equations to calculate parameters such as actual phase velocity, two-phase mixture density, and hence hydrostatic two-phase pressure drop and heat transfer, liquid height in stratified flow, and liquid film thickness in annular flow regime. Acknowledging the importance of void fraction in practical applications, this section first presents parametric analysis of the void fraction and then provides a quick review of the modeling techniques for the determination of the void fraction.

3.3.1 Effect of Pipe Orientation

The effect of pipe orientation on the void fraction is essentially due to the change in flow patterns and influence of buoyancy force acting on the gas phase. As shown in Figure 3.10, the effect of pipe orientation on void fraction is significant (up to 100%) for low gas and liquid flow rates. These flow rates correspond to slug/intermittent flow in upward pipe inclinations and stratified flow in downward pipe inclinations. At these flow rates, buoyancy acting on the gas phase aids the two-phase flow motion in upward pipe inclinations while resists its flow in downward pipe inclinations increasing its residence time in the pipe and hence the void fraction. For a fixed flow pattern (slug/intermittent) in upward inclined flow, it is seen that the void fraction initially decreases up to $+30° < \theta < +45°$ and then increases again with increase in the pipe orientation. This trend of change in void fraction with change in pipe orientation is due to the similar trend of the translational velocity of the gas slug (as a function of pipe orientation) that decides the residence time of the gas phase in the pipe and hence the void fraction. The effect of pipe orientation on void fraction is found to vanish for the inertia-driven region of intermittent (wavy annular) and annular two-phase flow. Moreover, the void fraction in stratified flow is apparently insensitive to the change in pipe orientation. At moderate

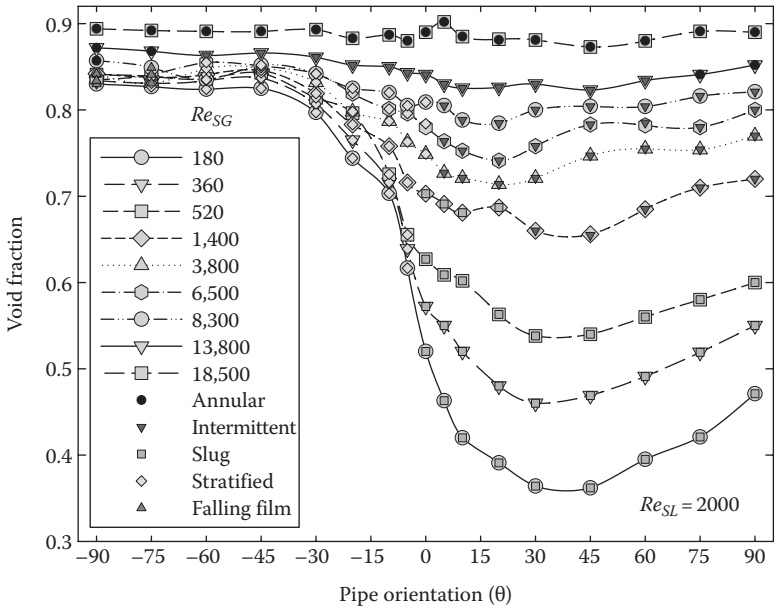


Figure 3.10

Effect of pipe orientation on void fraction at low liquid flow rates. (Data from the Two-Phase Flow Lab, OSU, Stillwater, OK.)

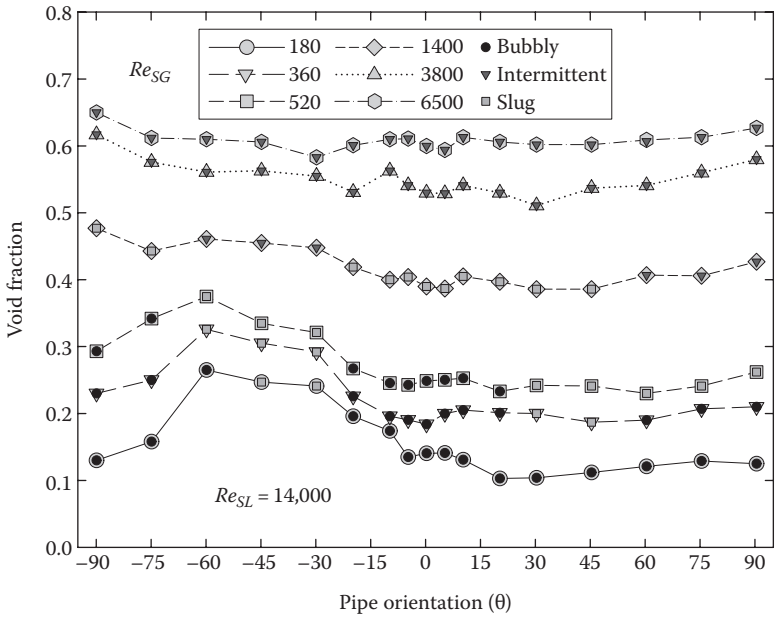


Figure 3.11

Effect of pipe orientation on void fraction at high liquid flow rates. (Data from the Two-Phase Flow Lab, OSU, Stillwater, OK.)

gas and liquid flow rates, void fraction in pipe orientations steeper than −45° drops downs due to the change in flow pattern from stratified to slug/intermittent at similar phase flow rates. As shown in Figure 3.11, at high liquid flow rates, the effect of pipe orientation on void fraction gradually fades away; however, a similar type of flip in void fraction trend as mentioned earlier occurs after −60° of pipe orientations. This change in trend of void fraction is again due to dissimilar flow patterns that may exist for similar phase flow rates but different pipe orientations. It is also clear from these trends that the void fraction in downward pipe inclinations is always greater than that in upward pipe inclinations essentially due to the resistance offered by the buoyancy force to the gas phase.

Considering the overall effect of the pipe orientation on the void fraction, three different relationships between α_G and λ can be deduced such that for buoyancy-driven flows $\alpha_G > \lambda$ and for inertia-driven flows $\alpha_G < \lambda$ hold true. The third relationship would be $\alpha_G = \lambda$ when the change in buoyancy to inertia-driven flow takes place. The relationship $\alpha_G > \lambda$ implies that for buoyancy-driven two-phase flow in downward pipe inclinations, the gas phase travels at a lower velocity than the liquid phase and hence results into higher void fraction values. Note that for all upward pipe inclinations, gas phase moves faster than the liquid phase giving a positive slippage at the gas–liquid interface and hence $\alpha_G < \lambda$ holds true. These three different cases of $\alpha_G - \lambda$ relationship that may exist in downward pipe inclinations are illustrated in Figure 3.12. In general, the flow patterns/pipe orientations that may correspond to these different cases of $\alpha_G - \lambda$ are summarized in Table 3.3.

3.3.2 Effect of Phase Flow Rates and Fluid Properties

The effect of phase flow rate on void fraction is indirectly through the change in flow pattern with change in phase flow rates. Figure 3.13 shows the effect of change in gas and liquid flow rate on void fraction. The void fraction data are plotted against a nondimensional phase velocity ratio (U_{SG}/U_{SL}) to reduce the scatter of the data. Broadly, the void fraction as a function of phase flow rates can be divided into three regions shown in Figure 3.13. In region I occupied by bubbly and slug flow patterns, for a fixed liquid flow rate, void fraction increases rapidly with a small increase in the gas flow rate, whereas in region III occupied by intermittent, stratified, and annular flow patterns, void fraction remains virtually independent of change in gas- and liquid-phase flow rates. Region II is a mixed bag of slug, intermittent, and stratified flow patterns, and its slope merges smoothly with that in regions I and III. Compared to other flow patterns, the void fraction corresponding to stratified flow shows a different behavior in region II. Void fraction in stratified flow regime remains relatively insensitive to the change in phase flow rates for

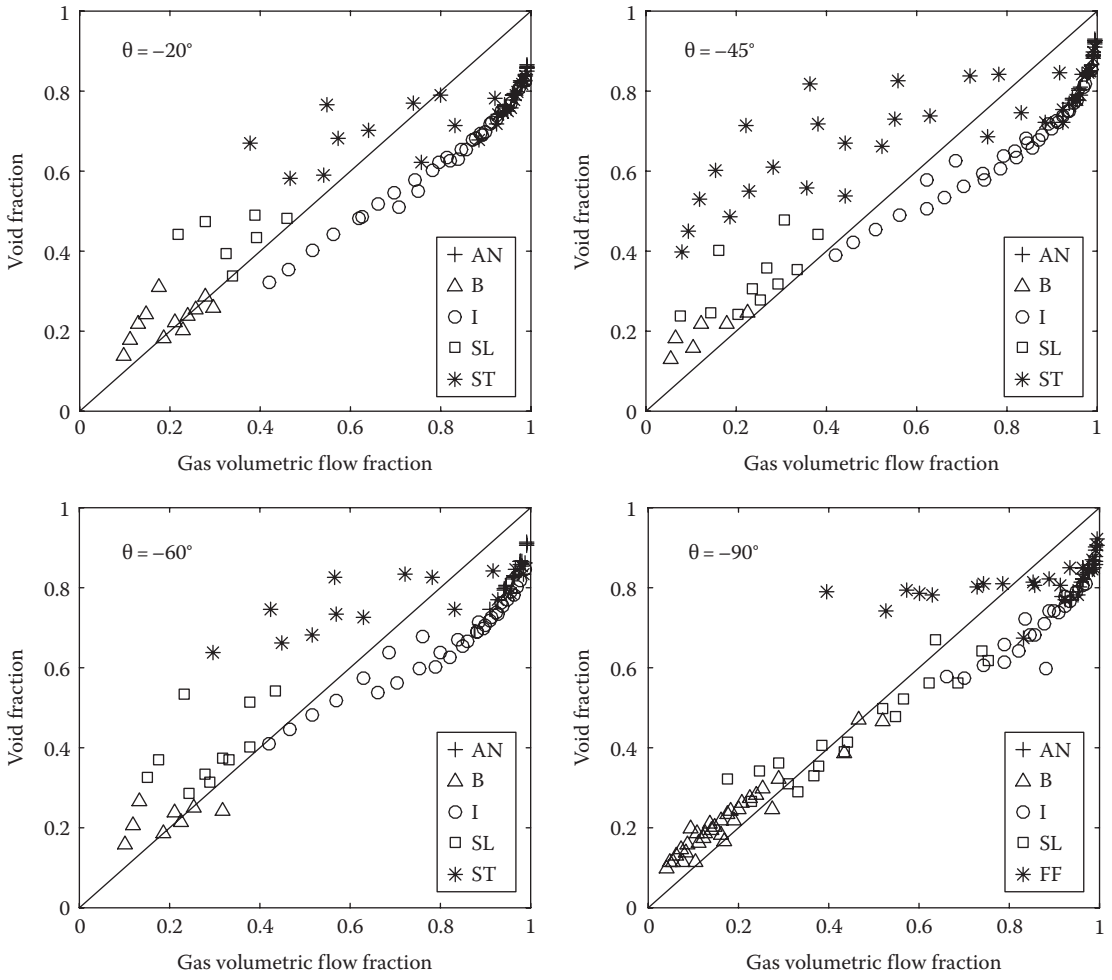


Figure 3.12

Void fraction and gas volumetric flow fraction relationship in downward pipe inclinations. (AN, annular; B, bubbly; FF, falling film; I, intermittent; SL, slug; ST, stratified.)

Table 3.3 Summary of Two-Phase Flow Situations Corresponding to $\alpha_G - \lambda$ Relationships

Condition	Flow Patterns/Pipe Orientation
$\alpha_G < \lambda$ ($U_G > U_L$, $S > 1$)	All flow patterns in upward pipe inclination
$\alpha_G = \lambda$ ($U_G \approx U_L$, $S \approx 1$)	Homogeneous flow (dispersed bubbly, annular mist)
$\alpha_G > \lambda$ ($U_G < U_L$, $S < 1$)	Stratified, slug flow $Fr_{SG} < 0.1$ and $\theta < 0°$

both regions II and III. Similar conclusions could be drawn by plotting the void fraction against two-phase flow quality, a well-adopted presentation style in high system pressure two-phase flows.

The variation of void fraction with change in two-phase flow quality is depicted in Figure 3.14 for (a) constant system pressure and varying slip ratios and (b) constant slip ratio and varying system pressure. For fixed two-phase flow conditions such as system pressure and quality, an increase in slip ratio reduces the void fraction. For these fixed conditions, the maximum void fraction is essentially the homogeneous void fraction obtained for no-slip condition ($S = 1$). In case of fixed slip ratio, an increase in system pressure decreases the specific volume occupied by the gas phase (due to increase in gas-phase density) and hence reduces the void fraction. Intuitively, it can be said that for a limiting case of critical system pressure or ($\rho_G \approx \rho_L$), void fraction varies linearly with change in two-phase flow quality ($\alpha_G = x$). Considering the definition of gas volumetric flow fraction (see Table 3.1), the relationship $\alpha_G = \lambda$ is also true for $\rho_G \approx \rho_L$. In addition to the gas-phase density, void fraction is also known to be affected by the

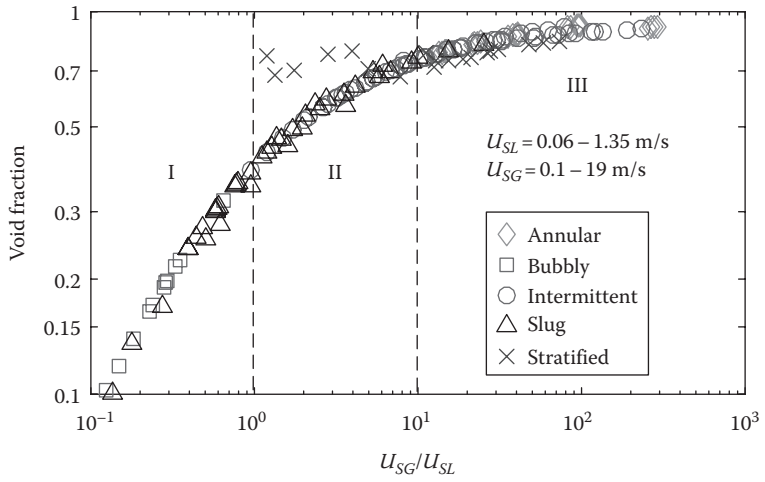


Figure 3.13

Variation of void fraction with change in gas and liquid flow rates.

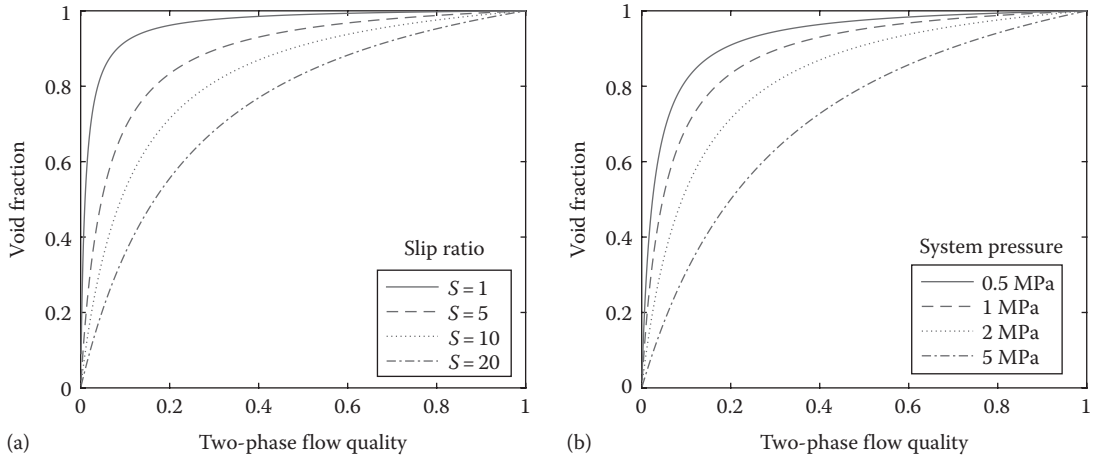


Figure 3.14

Variation of void fraction with change in two-phase flow quality. (a) System pressure = 1 MPa. (b) Slip ratio = 2.

change in liquid dynamic viscosity. Experiments of Oshinowo (1971), Mukherjee (1979), and Gokcal (2008) reveal that the void fraction is inversely proportional to the liquid dynamic viscosity. These studies report that the increase in liquid viscosity increases the viscous drag on liquid phase and reduces its velocity causing it to accumulate in the pipe and hence results in decrease in void fraction due to increase in liquid holdup.

3.3.3 Effect of Pipe Diameter

The effect of pipe diameter on void fraction is reflected in the form of pipe wall–induced drag exerted on the gas phase. In comparison to large pipes, small-diameter pipes offer more resistance to the motion of gas phase increasing its residence time and hence the local and averaged void fraction in pipes. Experimental data of Bowers and Hrnjak (2010) in Figure 3.15 show about 20%–80% increase in measured void fraction for a decrease in pipe diameter from 15 to 7 mm. The void fraction as a function of pipe diameter also depends upon phase flow rates (flow patterns/mass flux/quality) such that the effect of change in pipe diameter on void fraction is most prominent for bubbly/slug/intermittent flows, while it is fairly insensitive to the annular flow regime. Kaji and Azzopardi (2010) have reported negligible effect of change in pipe diameter (5–50 mm) on the void fraction in annular flow regime for similar gas and liquid superficial velocities. This relationship between void fraction and pipe diameter may not be applicable to microscale two-phase flow.

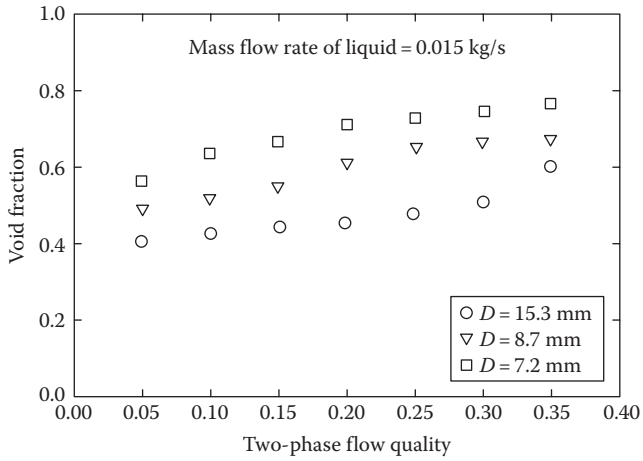


Figure 3.15

Effect of pipe diameter on void fraction. (Adapted from Bowers, C.D. and Hrnjak, P.S., Determination of void fraction in separated two phase flows using optical techniques, *International Refrigeration and Air-Conditioning Conference*, Purdue University, West Lafayette, IN, 2010, pp. 2293–2302.)

The parametric analysis of void fraction reveals that the void fraction must be modeled to consider the effect of flow patterns, pipe orientation, pipe diameters, and fluid properties. What follows is a brief review of some of the void fraction modeling methods available in the two-phase flow literature and recommendation of well-scrutinized void fraction correlations applicable for a wide range of two-phase flow conditions.

3.3.4 Modeling of Void Fraction

The two-phase flow literature reports a plethora of void fraction models/correlations; however, most of these models are confined to certain flow patterns, pipe orientation, and fluid properties. Based on the general physical form of these correlations, they can be broadly classified as those based on separated flow models (SFMs), drift flux model (DFM), $k - \lambda$ models, and empirical models. A comprehensive review of these different types of models is presented by Woldesemayat and Ghajar (2007), Godbole et al. (2011), and Ghajar and Bhagwat (2014b). Among all these models, correlations based on SFM and DFM are more versatile and flexible and are also preferred in several industrial applications. The following is a brief summary of the physical structure of SFM- and DFM-based void fraction correlations.

3.3.4.1 Separated Flow Model

The SFM considers the two phases to flow separately in the form of two streams: each phase is constant but with different velocities sharing a definite interface. The flow patterns such as stratified and annular flow behave as a separated flow and can be effectively modeled using these types of correlations. The SFM-based correlations are mostly preferred in refrigeration industry due to the stratified and annular flow pattern–dominated two-phase flow in evaporators and condensers. The general form of SFM-based void fraction correlations is presented in Equation 3.28. Some of the well-known SFM model-based void fraction correlations are listed in Table 3.4. The multiplying factor "S" is essentially the slip ratio, that is, the ratio of actual gas velocity (U_G) to actual liquid velocity (U_L) (see Table 3.1). The slip ratio (S) for homogeneous flow that assumes no slippage at

Table 3.4 Parameters Used in SFM by Different Correlations

Correlation	S	q	r	s
Homogeneous	1	1	1	0
Lockhart and Martinelli (1949)	0.28	0.64	0.36	0.07
Zivi (1964)	1	1	0.67	0
Chen (1986)	0.18	0.6	0.33	0.07
Smith (1969)	Equation 3.30	1	1	0
Xu and Fang (2014)	Equation 3.31	1	1	0

the gas–liquid interface is equal to unity ($S = U_G/U_L = 1$). Thus, for such a case, the void fraction expressed by Equation 3.28 is essentially equal to the gas volumetric flow fraction (λ) as shown in Equation 3.29:

$$\alpha_G = \left[1 + S\left(\frac{1-x}{x}\right)^q \left(\frac{\rho_G}{\rho_L}\right)^r \left(\frac{\mu_L}{\mu_G}\right)^s\right]^{-1} \tag{3.28}$$

$$\alpha_G = \left[1 + \left(\frac{1-x}{x}\right)\left(\frac{\rho_G}{\rho_L}\right)\right]^{-1} = \frac{U_{SG}}{U_{SG} + U_{SL}} = \lambda \tag{3.29}$$

$$S = 0.4 + 0.6\sqrt{\frac{\rho_L/\rho_G + 0.4(1/x - 1)}{1 + 0.4(1/x - 1)}} \quad \left.\begin{array}{l} 6 < D < 38 \text{ mm} \\ 0.1 \le p_{sys} \le 14.5 \text{ MPa} \\ 50 \le G \le 2050 \text{ kg/m}^2\text{ s} \end{array}\right\} \tag{3.30}$$

Equation 3.30 gives the expression for slip ratio used by Smith (1969). The constant of 0.4 used in Smith (1969) correlation is applicable only for circular pipes and may not guarantee accurate results for other pipe geometries. The correlation of Smith (1969) is valid for all flow patterns and the entire range of two-phase flow quality; however, it is observed that this correlation does not predict void fraction accurately in stratified flow regime. A recent work of Xu and Fang (2014) also provides an expression shown in Equation 3.31 to determine slip ratio to be used in SFM. Their model for slip ratio is mostly based on two-phase flow of refrigerants in small-size pipe ($D < 10$ mm) and is a function of mass flux, gas volumetric flow fraction, pipe diameter, and the liquid-phase density:

$$S = 1 + 2\lambda^{3.5}\left(\frac{G^2}{gD\rho_L^2}\right)^{-0.2} \quad \left.\begin{array}{l} 0.5 \le D \le 10 \text{ mm} \\ 40 \le G \le 1000 \text{ kg/m}^2\text{ s} \\ 6 \le \rho_L/\rho_G \le 250 \end{array}\right\} \tag{3.31}$$

Recently, Cioncolini and Thome (2012a) have developed a void fraction model for annular flow regime consisting of data for both circular and noncircular channels and applicable for both adiabatic and evaporating two-phase flows:

$$\alpha_G = \frac{hx^n}{1 + (h-1)x^n} \quad \left.\begin{array}{l} \text{(annular flow)} \\ 1 < D < 45.5 \text{ mm} \\ 0.1 < p_{sys} < 20 \text{ MPa} \\ 20 \le G \le 3400 \text{ kg/m}^2\text{ s} \end{array}\right\} \tag{3.32}$$

$$h = -2.129 + 3.129\left(\frac{\rho_G}{\rho_L}\right)^{-0.2186} \tag{3.33}$$

$$n = 0.3487 + 0.6513\left(\frac{\rho_G}{\rho_L}\right)^{0.515} \tag{3.34}$$

Figure 3.16 shows the discrepancy between predictions of void fraction by different SFMs typically for $\alpha_G < 0.7$. This difference between the outcomes of different correlations is probably because these correlations

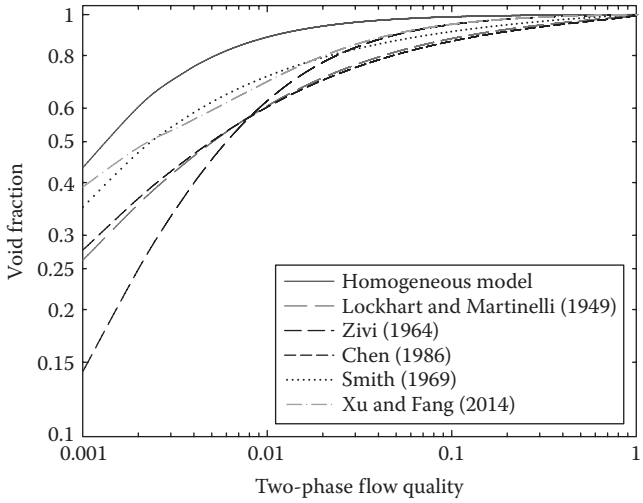


Figure 3.16

Void fraction prediction of separated flow models.

are based on the assumptions and flow physics of annular (separated) flow and are supposed to be used for higher values of void fraction. It is also evident that the homogeneous void fraction (under no-slip assumption) is the highest and sets the theoretical limit of the maximum possible void fraction in two-phase flow systems. This statement is true for all two-phase flow situations with the exception of buoyancy-driven region in downward pipe inclinations identified by $Fr_{SG} < 0.1$. Note that since these correlations based on SFM are essentially developed or valid for annular flow regime and since annular flow is relatively insensitive to the change in pipe orientation, these models can be used independent of pipe orientations provided annular flow pattern exists.

3.3.4.2 Drift Flux Model

The DFM assumes one phase dispersed in other continuous phase and requires the determination of distribution parameter (C_o) and drift velocity (U_{GM}) as variables to calculate the void fraction. The DFM is best applicable for 1D flows and is usually not recommended for flow patterns involving significant interfacial slippage such as stratified and annular flow patterns. The flow patterns such as bubbly flow, slug flow, and mist flow are the preferred flow patterns to be modeled using the concept of drift flux. However, with appropriate formulations that consider the two-phase flow physics, the application of DFM can also be extended to other flow patterns such as annular flow. The general form of DFM to calculate void fraction is presented by

$$\langle \alpha_G \rangle = \frac{\langle U_{SG} \rangle}{C_o \langle U_M \rangle + \langle \langle U_{GM} \rangle \rangle} \tag{3.35}$$

where $U_M = U_{SL} + U_{SG}$.

The terms involving $\langle\rangle$ represent cross-sectional averaged properties, while those involving $\langle\langle\rangle\rangle$ indicate cross-sectional and void fraction weighted averaged properties. The distribution parameter C_o is a representation to account for the distribution of the gas phase across the pipe cross section (concentration profile). It also serves as a correction factor to the homogeneous flow theory (which assumes no local slip between the two phases) to acknowledge the fact that the concentration profile and the two-phase flow velocity profile can vary independently of each other across the pipe cross section. Whereas the physical interpretation of drift velocity (U_{GM}) is the cross-sectional void fraction weighted average of the local relative velocity of the gas phase with respect to the two-phase mixture velocity at the pipe volume center. The local relative motion between the gas- and the two-phase mixtures is considerable and uniform across the pipe cross section when there is a strong coupling between the two phases as in case of the flow of dispersed bubbles in continuous liquid medium, that is, dispersed bubbly flow. As the two-phase flow transits to annular flow regime, the local relative velocity of the gas phase with

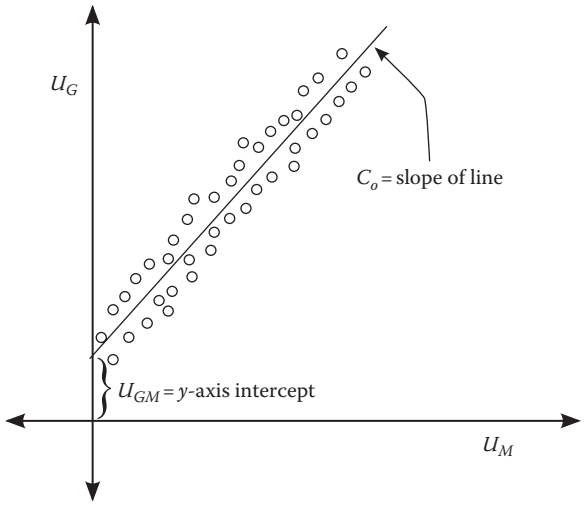


Figure 3.17

Graphical representation of drift flux model.

respect to the two-phase mixture at the pipe volume center becomes negligible and so does the drift velocity. Although the 1D DFM is used in the context of cross-sectional averaged void fraction, there are several DFM-based correlations available in the literature that can be practically implemented for void fraction calculations based on volumetric void fraction experimental data instead of the cross-sectional void fraction. The parity between the cross-sectional and volumetric void fraction holds true in case of nonboiling two-phase flow (two-component two-phase flow) where the cross-sectional distribution of the gas phase with respect to the liquid phase remains virtually unaltered over a short length of pipe. Henceforth, without making any distinction between the cross-sectional and volumetric void fractions, the void fraction is simply expressed as $\langle \alpha_G \rangle = \alpha_G$. Similar justification is applicable for all the cross-sectional averaged quantities involved in Equation 3.35. The physical form of Equation 3.35 resembles the equation of a straight line ($y = mx + c$) shown in Figure 3.17 such that the distribution parameter C_o is analogous to the slope "m" and the drift velocity is analogous to the y-intercept "c." Thus, the distribution parameter and the drift velocity could be obtained by plotting the data with $U_G = U_{SG}/\alpha_G$ and U_M coordinates and then by finding the slope and intercept of the best-fitting line. However, this method is highly impractical since the slope and intercept of line would depend on the scatter of data and cannot be used in case of real-time applications where void fraction information is not known beforehand. Obviously, another approach to determine C_o and U_{GM} is to use empirical correlations (as a function of two-phase flow variables) available in the two-phase flow literature. The following text presents some of the well-scrutinized and validated flow pattern–specific and flow pattern–independent correlations to determine C_o and U_{GM}.

The distribution parameter and drift velocity equations given by Hibiki and Ishii (2003) for vertical upward bubbly flow are given in Equation 3.36. To use these equations, the existence of bubbly flow could be determined by first using flow pattern transition equation given by Equation 3.7.

$$\left.\begin{aligned} C_o &= \left(1.2 - 0.2\sqrt{\frac{\rho_G}{\rho_L}}\right)\left(1 - \exp(-18\alpha_G)\right) \\ U_{GM} &= \sqrt{2}\left(\frac{\sigma g(\rho_L - \rho_G)}{\rho_L^2}\right)^{0.25}(1-\alpha_G)^{1.75} \end{aligned}\right\} \quad \begin{matrix}\text{(bubbly flow)} \\ \theta = +90^\circ\end{matrix} \tag{3.36}$$

Another most referred void fraction model for bubbly flow is that of Gomez et al. (2000) given by Equation 3.37. This model is essentially developed for upward pipe inclinations, and it may not reproduce correct results if used for horizontal two-phase flow since Equation 3.37 would give $U_{GM} = 0$. Moreover, Gomez et al. (2000) have recommended the use of a constant to represent distribution parameter that does not account for the effect of fluid properties, flow properties, and pipe orientation on the

distribution parameter. Although the void fraction model of Gomez et al. (2000) is developed for bubbly flow, our experience shows that this correlation also works well for the slug flow regime. Note that to use Equation 3.37, the existence of bubbly flow can be confirmed by using bubbly–slug flow transition model given by Equation 3.4:

$$\left.\begin{aligned} C_o &= 1.15 \\ U_{GM} &= 1.53\left(\frac{g\sigma(\rho_L-\rho_G)}{\rho_L^2}\right)^{0.25}\sqrt{1-\alpha_G}\sin\theta \end{aligned}\right\} \quad \begin{aligned} &\text{(bubbly, slug flow)} \\ &0° < \theta \le +90° \end{aligned} \tag{3.37}$$

For slug flow regime, Hibiki and Ishii (2003) proposed expressions for distribution parameter and drift velocity given by Equation 3.38. The drift velocity used in their equations is essentially the modified form of proportionality (between pipe diameter and slug translational velocity) proposed by Nicklin et al. (1962). These correlations given by Equations 3.36 and 3.38 are valid for small-diameter pipes ($10 < D_h < 50$ mm). For large-diameter pipes, Kataoka and Ishii (1987) have proposed sets of equations given by Equation 3.39 to account for the effect of pipe diameter and fluid properties on the drift velocity. The nondimensional hydraulic pipe diameter (D_h^+), nondimensional drift velocity (U_{GM}^+), and viscosity number (N_μ) are defined by Equations 3.40 through 3.42, respectively. Their equation is developed based on data of air–water and steam–water vertical upward two-phase flow consisting of data with $20 < D_h < 240$ mm and $0.1 \le p_{sys} \le 18$ MPa. The distribution parameter of Kataoka and Ishii (1987) correlation is the same as that of Equation 3.38. In case of two-phase flow through rectangular ducts, the constants "1.2" and "0.2" in Equation 3.38 are replaced by "1.35" and "0.35," respectively:

$$\left.\begin{aligned} C_o &= \left(1.2-0.2\sqrt{\frac{\rho_G}{\rho_L}}\right) \\ U_{GM} &= 0.35\sqrt{\frac{gD(\rho_L-\rho_G)}{\rho_L}} \end{aligned}\right\} \quad \begin{aligned} &\text{(slug flow)} \\ &\theta = +90° \end{aligned} \tag{3.38}$$

$$U_{GM}^+ = \begin{cases} 0.00019(D_h^+)^{0.809}\left(\dfrac{\rho_G}{\rho_L}\right)^{-0.157} N_\mu^{-0.562} & : N_\mu \le 2.25\times10^{-3}, D_h^+ > 30 \\ 0.030\left(\dfrac{\rho_G}{\rho_L}\right)^{-0.157} N_\mu^{-0.562} & : N_\mu \le 2.25\times10^{-3}, D_h^+ \le 30 \\ 0.92\left(\dfrac{\rho_G}{\rho_L}\right)^{-0.157} & : N_\mu > 2.25\times10^{-3} \end{cases} \tag{3.39}$$

$$D_h^+ = \frac{D_h}{\sqrt{\sigma/(g\Delta\rho)}} \tag{3.40}$$

$$U_{GM}^+ = \frac{U_{GM}}{((\sigma g\Delta\rho)/\rho_L^2)^{0.25}} \tag{3.41}$$

$$N_\mu = \frac{\mu_L}{(\rho_L\sigma\sqrt{\sigma/(g\Delta\rho)})^{0.5}} \tag{3.42}$$

The DFM-based void fraction correlation of Rouhani and Axelsson (1970) given by Equations 3.43 and 3.44 is one of the most preferred correlations used in refrigeration industry to estimate void fraction in

evaporators and condensers. The term $(1 - x)$ ensures decrease in distribution parameter with increase in two-phase flow quality or alternatively shift of flow pattern from bubbly/slug to annular flow.

$$C_o = \begin{cases} 1 + 0.2(1-x)\left(\dfrac{gD\rho_L^2}{G^2}\right)^{0.25} & : \theta = +90°, 0.1 \le p_{sys} \le 14\,\text{MPa} \\ 1 + 0.12(1-x) & : \theta = 0°, 0.1 \le p_{sys} \le 14\,\text{MPa} \end{cases} \tag{3.43}$$

$$U_{GM} = 1.18\left[\frac{g\sigma(\rho_L - \rho_G)}{\rho_L^2}\right]^{0.25} \tag{3.44}$$

To get rid of the flow pattern dependency, Woldesemayat and Ghajar (2007) proposed equations for distribution parameter and drift velocity as a function of fluid properties, pipe diameter, and pipe orientation shown in Equations 3.45 and 3.46. Woldesemayat and Ghajar (2007) correlation is a modification of Dix (1971) correlation for two-phase flow over rod bundles and is independent of flow patterns. The correlation of Woldesemayat and Ghajar (2007) is verified against data for horizontal and the entire range of upward pipe inclinations and pipe diameters in the range of 12–80 mm. In case of unknown flow pattern in horizontal and upward pipe inclinations, Woldesemayat and Ghajar (2007) correlation can be used with a reasonable accuracy (except for stratified flow). Note that the multiplying factor of 2.9 has units of $\text{m}^{-0.25}$.

$$C_o = \lambda\left(1 + \left[\frac{U_{SL}}{U_{SG}}\right]^{(\rho_G/\rho_L)^{0.1}}\right) \tag{3.45}$$

$$U_{GM} = 2.9\left[\frac{gD\sigma(1+\cos\theta)(\rho_L - \rho_G)}{\rho_L^2}\right]^{0.25}(1.22 + 1.22\sin\theta)^{p_{atm}/p_{sys}} \tag{3.46}$$

A recent modeling work of Bhagwat and Ghajar (2014) considers the effect of flow patterns (in the form of phase flow rates), pipe orientation, pipe diameter, and fluid properties on the distribution parameter and drift velocity as shown in Equations 3.47 and 3.50, respectively. The void fraction correlation of Bhagwat and Ghajar (2014) is based on the most comprehensive data bank and is the most robust correlation applicable for a wide range of two-phase flow conditions listed in Table 3.5. The variable $C_{o,1}$ in Equation 3.48 is modeled as a variable such that it may vary between 0.2 and 0 to ensure the variation of distribution parameter for bubbly flow $C_o \approx 1.2$ to annular flow where $C_o \to 1.0$. Note that the two-phase friction factor (f_M) is based on two-phase mixture Reynolds number (Re_M) given by Equation 3.49 and could be calculated using appropriate single-phase friction factor equation for laminar and turbulent flows.

$$C_o = \frac{2 - (\rho_G/\rho_L)^2}{1 + (Re_M/1000)^2} + \frac{\left[\sqrt{(1 + (\rho_G/\rho_L)^2\cos\theta)/(1+\cos\theta)}^{(1-\alpha_G)}\right]^{2/5} + C_{o,1}}{1 + (1000/Re_M)^2} \tag{3.47}$$

Table 3.5 Application Range of Two-Phase Flow Parameters for Bhagwat and Ghajar (2014) Void Fraction Correlation

Parameter	Range
Pipe diameter (mm)	0.5–305
Pipe orientation (θ)	$-90° \le \theta \le +90°$
Density ratio (ρ_L/ρ_G)	6–875
Liquid dynamic viscosity (Pa s)	0.0005–0.6
Mixture mass flux (kg/m^2 s)	10–8450
Two-phase quality (x)	0–1
Two-phase Reynolds number (Re_M)	$10 - 5 \times 10^6$
Pipe geometry	Circular, rectangular, annular
Flow patterns	All (except stratified flow with $Fr_{SG} \le 0.1$ in $\theta < 0°$)

$$C_{o,1} = \left(c_1 - c_1\sqrt{\rho_G/\rho_L}\right)\left[(2.6-\lambda)^{0.15} - \sqrt{f_M}\right](1-x)^{1.5} \tag{3.48}$$

The constant c_1 is 0.2 for circular pipes and 0.4 for rectangular and annular ducts.

$$Re_M = \frac{(U_{SL}+U_{SG})\rho_L D_h}{\mu_L} \tag{3.49}$$

The expression for drift velocity used by Bhagwat and Ghajar (2014) is essentially based on the translational velocity of the gas slug in different pipe inclinations suggested by Bendiksen (1984). However, instead of using the constant of 0.54 as originally proposed by Bendiksen (1984), a proportionality constant of 0.45 is used since it gave a better accuracy in overall prediction of the void fraction. The correction factors c_2 and c_3 used in Equation 3.50 account for the effect of increase in liquid viscosity and pipe diameter on the reduction in drift velocity. These correction factors are expressed by Equations 3.51 and 3.52. More details and justification about the effect of these parameters on drift velocity and hence the use of these correction factors could be obtained from Gokcal et al. (2009), Kataoka and Ishii (1987), and Bhagwat and Ghajar (2014). The pipe diameter beyond which the correction to drift velocity in the form of c_3 is deemed necessary is identified using Laplace number (nondimensional pipe diameter) defined by Equation 3.53:

$$U_{GM} = (0.35\sin\theta + 0.45\cos\theta)\sqrt{\frac{gD_h(\rho_L-\rho_G)}{\rho_L}}(1-\alpha_G)^{0.5}c_2c_3 \tag{3.50}$$

$$c_2 = \begin{cases} \left(\dfrac{0.434}{\log_{10}(\mu_L/0.001)}\right)^{0.15} & : (\mu_L/0.001) > 10 \\ 1 & : (\mu_L/0.001) \le 10 \end{cases} \tag{3.51}$$

$$c_3 = \begin{cases} (La/0.025)^{0.9} & : La < 0.025 \\ 1 & : La \ge 0.025 \end{cases} \tag{3.52}$$

$$La = \sqrt{\frac{\sigma}{g(\rho_L-\rho_G)}}\frac{1}{D_h} \tag{3.53}$$

Note that the correlation of Bhagwat and Ghajar (2014) is not validated against data for microchannels with pipe diameters less than 0.5 mm. For gas–liquid two-phase flow in small-size pipes less than 0.5 mm, the correlation of Xiong and Chung (2006) could be used. Their correlation is based on the experimental data for pipe diameters in the range of 0.1–0.6 mm and consists of bubbly, slug, annular flow, and entire range of gas volumetric flow fraction (λ). The correlation of Xiong and Chung (2006) accounts for the nonlinear relationship between void fraction and gas volumetric flow fraction as a function of hydraulic pipe diameter (D_h) measured in mm:

$$\left.\alpha_G = \frac{a_1\lambda^{0.5}}{1-(1-a_1)\lambda^{0.5}}\right\} \quad \begin{array}{l} 0.1 \le D_h \le 0.6\,\text{mm} \\ 4 \le Re_{SL} \le 1670, 4 \le Re_{SG} \le 1725 \end{array} \tag{3.54}$$

$$a_1 = \frac{0.266}{1+13.8\exp(-6.88D_h)} \tag{3.55}$$

It must be noted that DFM-based void fraction correlations are not suitable to model stratified type of flow. Compared to DFMs, SFMs listed in Table 3.4 work better for stratified flow. However, these models too cannot provide accurate prediction of the void fraction with desired accuracy. In particular for stratified flows, flow pattern–specific models are required, which will be discussed later in Section 3.5.

3.4 Pressure Drop

Similar to single-phase flow, pressure drop in gas–liquid two-phase flow comprises hydrostatic, accelerational, and frictional components as shown in Equation 3.56. However, unlike the single-phase flow, these components of two-phase pressure drop in gas–liquid flows may depend upon several parameters such as void fraction, pipe orientation, flow patterns, and liquid entertainment fraction. The hydrostatic or gravitational component of two-phase pressure drop due to the pipe inclination depends on the two-phase mixture density, which in turn is a function of flow patterns and void fraction. Accelerational pressure drop is due to the change in momentum of the two-phase mixture and can be neglected for adiabatic two-phase flows within a short pipe length. However, for two-phase flow undergoing phase change process or even for adiabatic two-phase flow in long and inclined pipes, depending upon the flow pattern, the accelerational pressure drop can contribute up to 20% of the total two-phase pressure drop. Finally, the frictional component of two-phase pressure drop is a result of the interfacial friction between the two phases and wall friction with both or either phase and depends upon the flow pattern structure, pipe diameter, and fluid properties:

$$-\left(\frac{dp}{dz}\right)_{TP} = -\left(\frac{dp}{dz}\right)_{h} - \left(\frac{dp}{dz}\right)_{f} - \left(\frac{dp}{dz}\right)_{a} \tag{3.56}$$

Before discussing different two-phase pressure drop modeling methods, it is interest to know about the effect of different two-phase flow variables on the two-phase pressure drop. Following text describes the effect of pipe orientation on the total two-phase pressure drop and the effects of phase flow rates and pipe surface roughness on the frictional component of two-phase pressure drop. Following this discussion, different modeling approaches to determine hydrostatic, accelerational, and frictional components of two-phase pressure drop are presented.

3.4.1 Effect of Pipe Orientation

The effect of pipe orientation on two-phase pressure drop is primarily due to the effect of pipe orientation on the hydrostatic component of the two-phase pressure drop. The two-phase literature reports that very few studies focused on the measurement of two-phase pressure drop over the entire range of pipe orientations. Some of these studies include the works of Beggs (1972), Mukherjee (1979), Spedding et al. (1982), and Lips and Meyer (2012). The experimental measurements carried out at the Two-Phase Flow Lab, OSU and that reported in the literature are presented in Figures 3.18 and 3.19.

A comparison between Figures 3.18 and 3.19 shows that the variation of two-phase pressure drop as a function of pipe orientation is similar for both nonboiling and condensing two-phase flows. It is evident that at low gas and liquid flow rates, two-phase pressure drop is relatively insensitive to the change in downward pipe inclination. This is due to the fact that at these flow rates, stratified flow exists and its physical structure and associated void fraction is relatively insensitive to the change in pipe orientation. In upward pipe inclinations, two-phase pressure drop increases rapidly with increase in the pipe orientation, and it is fascinating to see that two-phase pressure drop at lower gas flow rates is greater than that at higher gas flow rates. This is because of the reversal of liquid film that induces decreasing trend of pressure gradient with increase in gas flow rates. Please refer to Section 3.4.6 for more details on this phenomenon. At higher liquid flow rates, negative values of the total two-phase pressure drop in downward pipe inclinations represent partial pressure recovery due to gain in hydrostatic component of two-phase pressure drop.

3.4.2 Effect of Phase Flow Rates

The effect of change in phase flow rates on the two-phase pressure drop is essentially due to the change in physical structure of the flow patterns and is of different nature for the hydrostatic and frictional components of two-phase pressure drop. Since the hydrostatic component of two-phase pressure drop depends only on the void fraction, for a fixed liquid flow rate, increase in gas flow rate decreases the contribution of hydrostatic pressure drop (due to decrease in mixture density), whereas it increases the frictional pressure drop component. The relation between change in phase flow rates and the frictional pressure drop could be construed in a better way by presenting their relationship in different coordinate systems. As shown in Figure 3.20, for low liquid and low gas flow rates, the two-phase frictional pressure drop remains virtually constant and increases drastically only for moderate to high gas flow rates (intermittent and annular flow regimes). For intermittent type of flow, sharp increase in the frictional pressure drop is essentially due to the turbulent and chaotic nature of the two-phase mixture. For annular flow, the pressure gradient increases

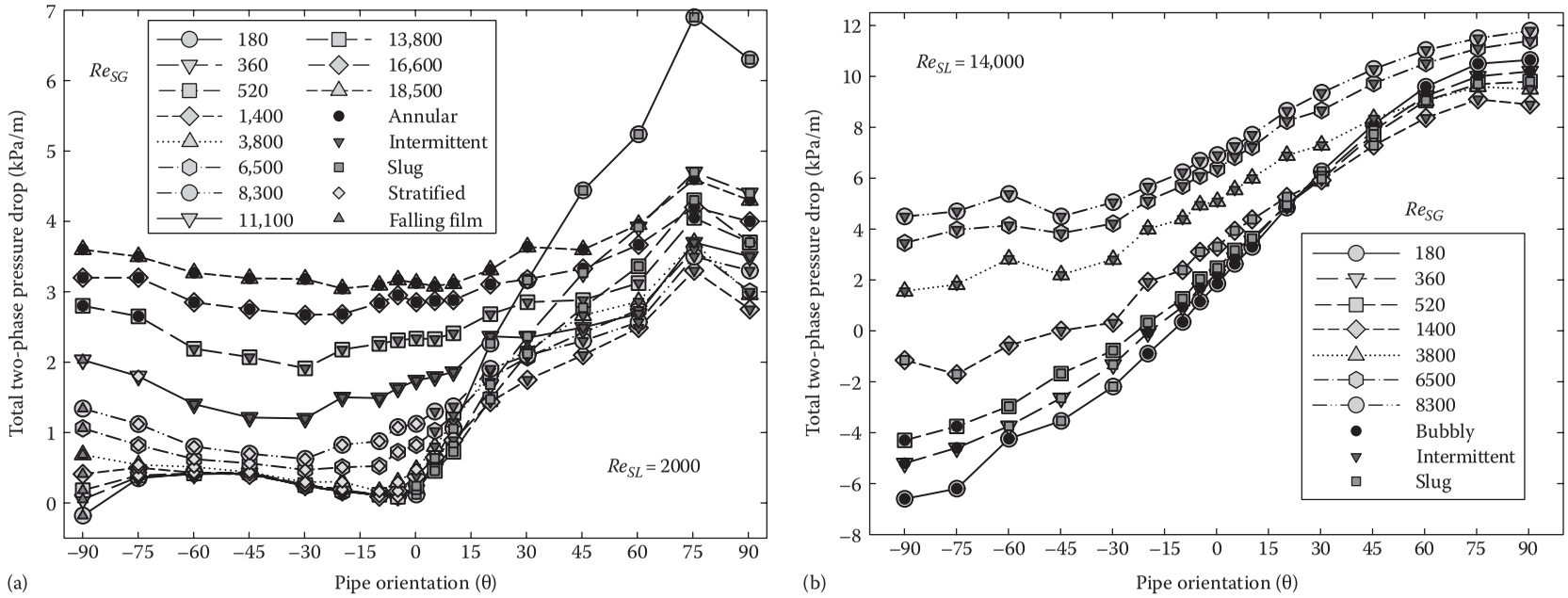


Figure 3.18

Effect of pipe orientation on total two-phase pressure drop. (a) Re_{SL} = 2,000 and Re_{SG} = 180-18,500. (b) Re_{SL} = 14,000 and Re_{SG} = 180-8,300. (Data measured at the Two-Phase Flow Lab, OSU, Stillwater, OK.)

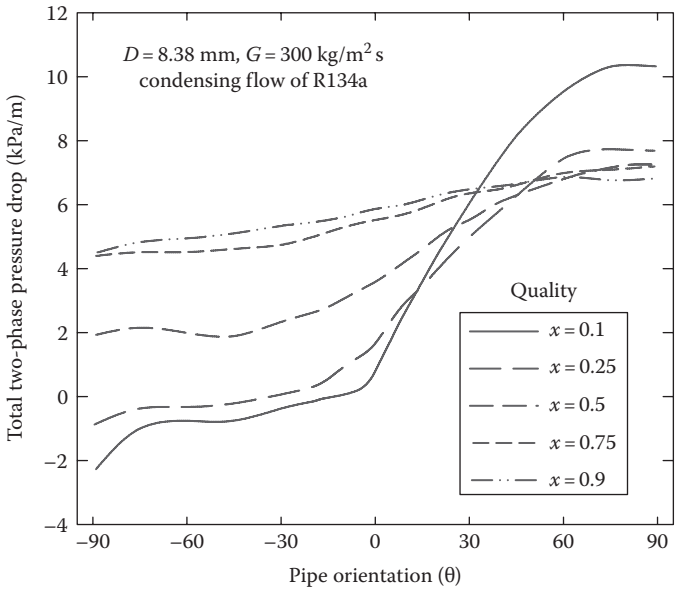


Figure 3.19

Effect of pipe orientation on two-phase pressure drop. (Data of Lips, S. and Meyer, J.P., *Int. J. Heat Mass Transfer*, 55, 405, 2012.)

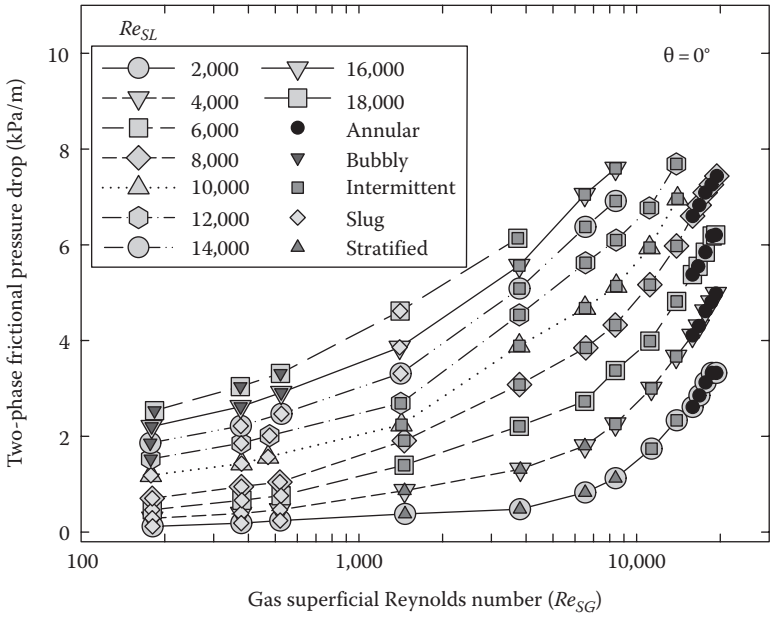


Figure 3.20

Two-phase frictional pressure drop for varying gas and liquid flow rates. (Data measured at the Two-Phase Flow Lab, OSU, Stillwater, OK.)

sharply with increase in the gas and liquid flow rates. At a fixed gas flow rate, increase in the liquid flow rate increases the liquid film thickness and thus reduces the cross-sectional area available for the gas phase. This increases the actual gas velocity and exerts higher shear on the gas–liquid interface to increase the two-phase frictional pressure drop. Additionally, the gas–liquid interface offers a rough surface to the gas flow, and the interface gets roughened progressively with the increase in the liquid film thickness or alternatively the liquid flow rate that augments the frictional pressure drop.

Variation of two-phase pressure drop with change in two-phase flow rates could also be presented in an another perspective using two-phase flow quality. This type of presentation shown in Figure 3.21 is usually

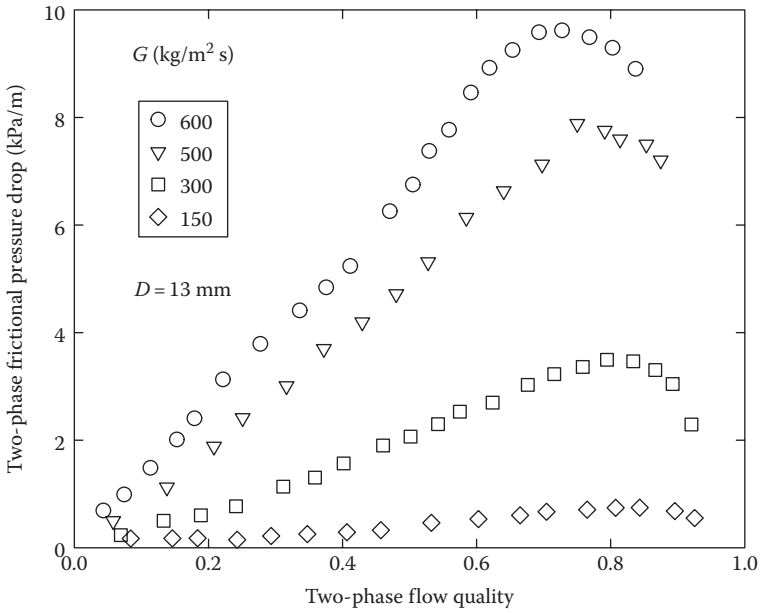


Figure 3.21

Two-phase pressure drop as a function of phase flow rates. (Data of Quiben, J.M. and Thome, J.R., *Int. J. Heat Fluid Flow*, 28, 1049, 2007.)

adopted for high-pressure systems (often encountered in refrigeration and nuclear applications) that tend to occupy the entire range of two-phase flow quality ($0 < x < 1$). It is evident that the two-phase pressure drop increases systematically with increase in the mass flux and quality. An inflection point that flips the trend of increase in two-phase pressure drop with increase in quality is quite noticeable. This change in the trend of two-phase pressure drop could be explained based on the change in structure of the two-phase flow pattern at the inflection point. By the time the two-phase flow system reaches the point of maximum pressure drop (inflection point), the flow pattern attains annular flow structure; however, beyond that point due to severe entrainment process, the liquid phase in contact with the pipe wall is gradually moved to the central gas core reducing the liquid film thickness and consequently reducing the effective viscosity in the near-wall region. This ultimately results into a reduced frictional pressure drop. This type of trend is not evident in Figure 3.20 since the data presented there do not contain two-phase flow with significant entrainment. It is also evident from Figure 3.21 that the quality at the point of maximum pressure drop shifts toward lower qualities with increase in the two-phase mixture mass flux. Additionally, Ducoulombier et al. (2011) reported that the quality associated with maximum frictional pressure drop also depends upon the fluid properties. The combined effect of mass flux and fluid thermophysical properties on the quality at maximum pressure drop is reported in Figure 3.22. It is clear that the two-phase flow quality corresponding to the point of maximum pressure drop may vary approximately between 0.65 and 0.95.

3.4.3 Effect of Pipe Diameter

Similar to the single-phase pressure drop, the effect of decrease in pipe diameter is to increase the two-phase frictional pressure drop. However, this effect of pipe diameter is usually in conjunction with two-phase flow patterns. The two-phase frictional pressure drop in the annular flow regime depends on the pipe diameter to a great extent, whereas it is relatively less sensitive to the pipe diameter in the bubbly flow regime. It is evident from Figure 3.23a that for a fixed mass flux of R134a, the two-phase frictional pressure drop for different pipe diameters deviates significantly for higher values of two-phase flow quality (annular flow pattern), whereas for low values of two-phase flow quality (bubbly flow), the effect of pipe diameter on two-phase frictional pressure drop gradually diminishes. Similar conclusions could be drawn for air–water two-phase flow system from the work of Kaji and Azzopardi (2010) who studied the effect of pipe diameters in the range of 10–50 mm on two-phase pressure drop in the annular flow regime. As shown in Figure 3.23b, for a fixed liquid flow rate, the effect of change in pipe diameter is most significant at higher gas flow rates (i.e., higher two-phase flow qualities). The two-phase frictional pressure

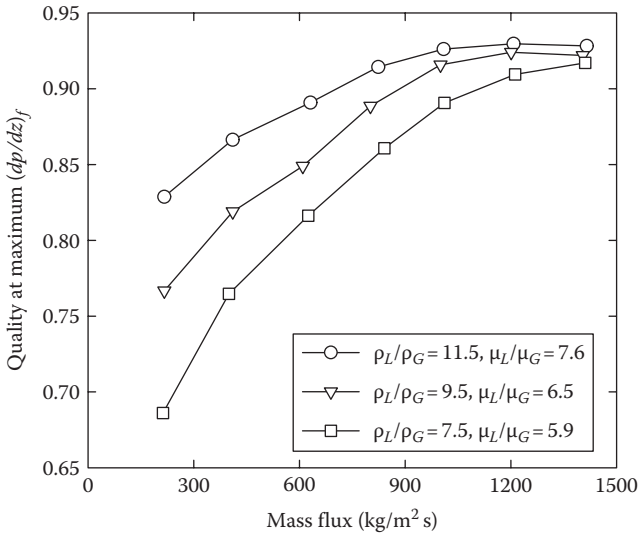


Figure 3.22

Influence of mass flux and fluid properties on quality corresponding to maximum pressure drop. (Adapted from Ducoulombier, M. et al., *Exp. Therm. Fluid Sci.*, 35, 581, 2011.)

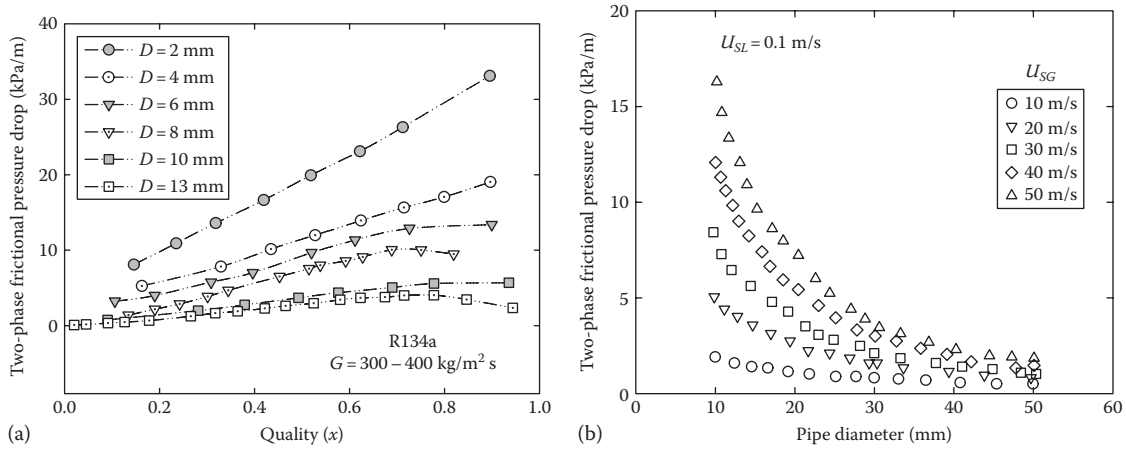


Figure 3.23

Effect of pipe diameter on two-phase frictional pressure drop. (a) Two-phase flow of R134a refrigerant. (b) Two-phase flow of air-water. (Adapted from Kaji, M. and Azzopardi, B.J., *Int. J. Multiphase Flow*, 36, 303, 2010.)

drop is due to the friction at the pipe wall as well as the gas–liquid interface and the gas–liquid interfacial area increases with increase in the pipe diameter, and hence, the nondimensional two-phase pressure drop (Φ^2) may be greater than that for the relatively smaller-diameter pipes. Thus, it is evident that any two-phase frictional pressure drop correlation must definitely account for the pipe diameter effect in the annular flow regime.

3.4.4 Effect of Fluid Properties

The important fluid properties that show a noticeable effect on two-phase frictional pressure drop are the gas-phase density and liquid-phase dynamic viscosity. The increase in gas-phase density decreases the slippage at the gas–liquid interface and hence decreases the frictional component of two-phase pressure drop, whereas the increase in liquid dynamic viscosity increases the shear in the liquid phase in contact with the pipe wall and also the shear at the gas–liquid interface resulting in increase in frictional pressure drop. Intuitively, it can be said that the effect of fluid properties on two-phase frictional pressure drop is more prominent for shear-driven flows than for buoyancy-driven two-phase flow. For more details on the effect

of fluid properties on frictional pressure drop, readers are advised to refer to Oshinowo (1971), Fukano and Furukawa (1998), Abduvayat et al. (2003), Hlaing et al. (2007), and Gokcal (2008).

3.4.5 Effect of Surface Roughness

The effect of pipe surface roughness on two-phase pressure drop is crucial in applications involving two-phase flow through steel or microfinned tubes. The internally ribbed or microfinned tubes are used in air-conditioning and refrigeration applications to improve the tube side heat transfer, however, at the expense of enhanced pressure drop. Most of the two-phase flow research reported in the literature is carried out in a transparent (smooth pipe), while the effect of pipe surface roughness on the frictional two-phase pressure drop is a relatively less investigated issue. The work of Wongs-ngam et al. (2004) and Shannak (2008) reported a considerable effect (20%–60%) of wall roughness on pressure drop especially for the two-phase flow at high mass flux and quality. Figure 3.24 shows that the effect of pipe wall roughness on two-phase pressure drop is considerable at high gas velocities and increases with increase in liquid velocity. Obviously, similar to single-phase flow, the effect of wall roughness on two-phase pressure drop increases with decrease in the pipe diameter. Experiments performed at the Two-Phase Flow Lab, OSU, confirm these observations. Moreover, their work also shows that the effect of pipe roughness on two-phase pressure drop is independent of the pipe orientation. The effect of pipe surface roughness on two-phase frictional pressure drop is maximum for the annular flow (at high gas flow rates) since, in addition to the effect of pipe wall roughness acting on the liquid phase, the structure of this flow pattern also offers a continuous and rough gas–liquid interface responsible for enhanced pressure drop.

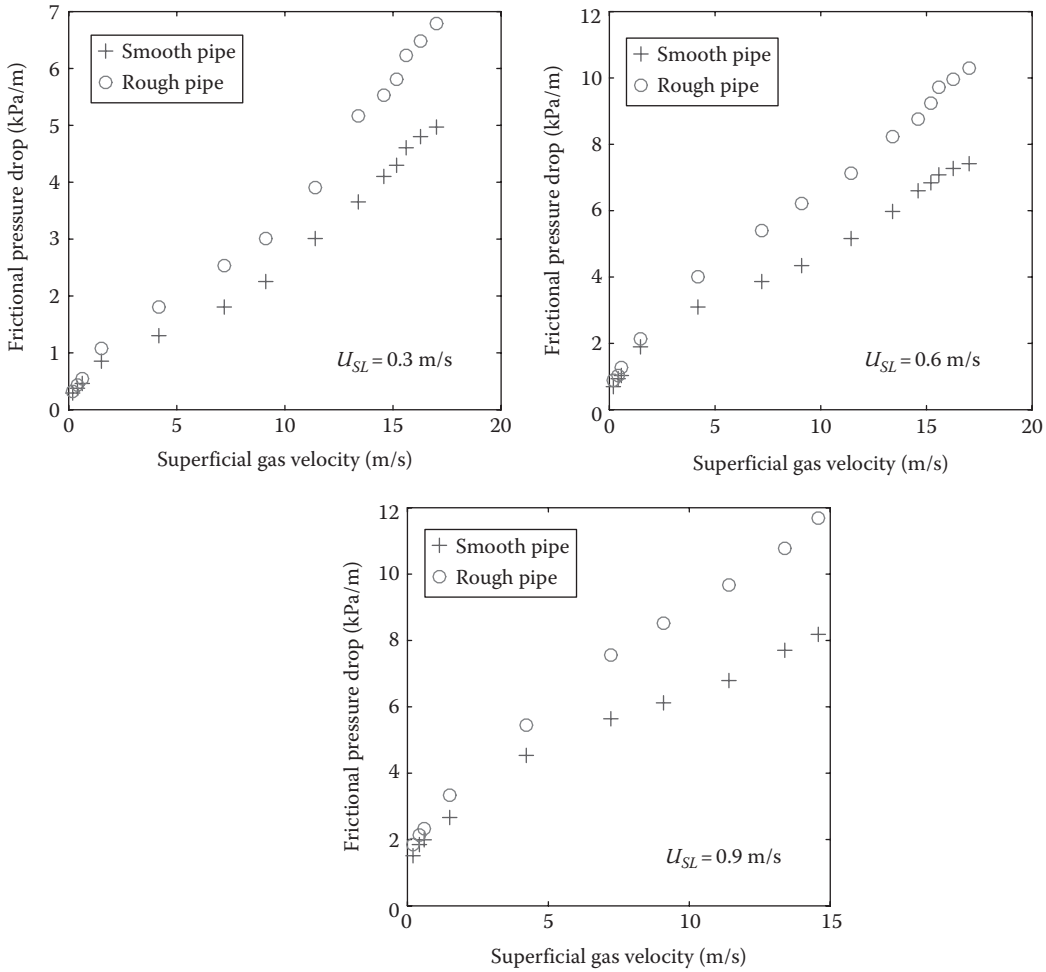


Figure 3.24

Effect of pipe surface roughness on two-phase frictional pressure drop. (Data from the Two-Phase Flow Lab, OSU, Stillwater, OK.) (D = 12.5 mm, ε = 20 μm for rough pipe).

3.4.6 Pressure Gradient Minimum and Flow Reversal in Upward Inclined Flow

In cocurrent gas–liquid upward inclined two-phase flow, at low liquid and moderate gas flow rates, although the net two-phase flow is observed in the upward direction, reversal of liquid film in contact with the pipe wall is observed under the influence of gravity forces. This phenomenon is a consequence of the interaction between the interfacial shear stress (exerted by gas phase on liquid film) and the gravitational forces acting on the liquid film. The liquid film in contact with the pipe wall may undergo a partial reversal (fluctuating wall shear stress) or complete reversal (negative wall shear stress) depending upon the gas and liquid flow rates and exhibit a decreasing trend of two-phase pressure gradient. Assuming churn/annular–annular flow regime with constant phase density, uniform circumferential film thickness, and negligible acceleration of the liquid film, the shear stress distribution in the liquid film in upward inclined flow can be given by Equation 3.57 where d is any given location on the pipe diameter (see Hewitt and Hall-Taylor (1970) and Collier and Thome (1996)):

$$\tau = \tau_i\left(\frac{D-2\delta}{d}\right)+\frac{1}{4}\left(\rho_L g\sin\theta+\frac{dp}{dz}\right)\left(\frac{(D-2\delta)^2-d^2}{d}\right) \tag{3.57}$$

Using the boundary condition of zero wall shear stress at $d = D$ for the case of stationary liquid film in contact with pipe wall, Equation 3.57 can be expressed as

$$\tau_w = \tau_i\left(\frac{D-2\delta}{D}\right)+\frac{1}{4}\left(\rho_L g\sin\theta+\frac{dp}{dz}\right)\left(\frac{(D-2\delta)^2-D^2}{D}\right)=0 \tag{3.58}$$

Assuming negligible acceleration in the gas core and negligible entrainment of liquid drops to the gas core, the interfacial shear stress exerted by the gas phase on the liquid film can be expressed as

$$\tau_i = \frac{D-2\delta}{4}\left(\frac{dp}{dz}+\rho_G g\sin\theta\right) \tag{3.59}$$

After combining Equations 3.58 and 3.59 and considering that $\delta \ll D$, the following relationship given by Equation 3.60 is obtained. Following our assumption of negligible liquid entrainment and uniform film thickness distribution, the void fraction can simply be expressed as that given by Equation 3.61. Using this definition of void fraction, it is evident that the right-hand side of Equation 3.60 is indeed the hydrostatic component of two-phase pressure drop:

$$\left(\frac{dp}{dz}\right)_{\tau_w=0}=\left[\rho_G\left(\frac{(D-2\delta)^2}{D^2}\right)+\rho_L\left(1-\frac{(D-2\delta)^2}{D^2}\right)\right]g\sin\theta \tag{3.60}$$

$$\alpha_G = \frac{A_G}{A}=\frac{(D-2\delta)^2}{D^2}=1-\frac{4\delta}{D}\Bigg\}(\delta \ll D) \tag{3.61}$$

The physical implication of Equation 3.60 is that as long as there is a balance between interfacial shear stress and hydrostatic pressure drop, the liquid film in contact with the pipe wall will either remain stationary or oscillate giving a net zero wall shear stress. Thus, when the interfacial shear stress is large enough to supersede the gravity forces (in the form of hydrostatic pressure drop), the net flow of two-phase mixture will be in upward direction without any reversal of liquid film.

Experimentally, this condition could be determined by analyzing the pressure drop signal as a function of gas and liquid flow rates. At a fixed liquid flow rate and with an increase in the gas flow rate, a point is reached where the gas phase does not have enough potential to carry liquid phase along with it in the downstream direction. At this point, the liquid phase in contact with the pipe wall appears to oscillate or move in the downward direction. The point corresponding to the inception of decreasing pressure gradient trend (in spite of increase in gas flow rate) is regarded as the flow reversal point, while the condition at which the pressure

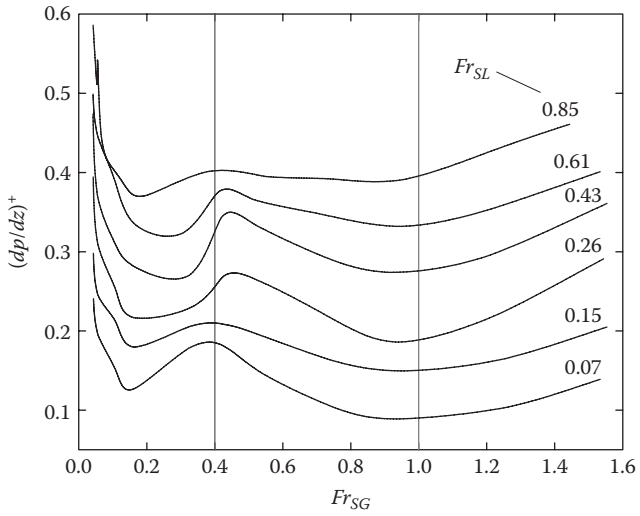


Figure 3.25

Nondimensional pressure drop for varying nondimensional gas and liquid flow rates. (Data measured at the Two-Phase Flow Lab, OSU, Stillwater, OK.)

gradient commence to increase again with increase in gas flow rate is identified as pressure gradient minimum point. The two-phase literature provides several instances of decreasing pressure gradient trends in context to churn–annular transition in vertical upward two-phase flow. As a matter of fact, the decreasing trend of pressure gradient minimum also exists at lower gas flow rates during slug–churn transition in upward inclined pipes. Nevertheless, the flow physics governing these two separate regions of pressure gradient minimum is significantly different. A typical example of decreasing trends of pressure gradient minimum in vertical upward pipe inclination is illustrated in Figure 3.25. The measured two-phase pressure drop and corresponding gas and liquid flow rates are made nondimensional as shown in Equations 3.62 through 3.64, respectively:

$$\left(\frac{dp}{dz}\right)_t^+ = \frac{(dp/dz)_t}{(\rho_L - \rho_G)g} \tag{3.62}$$

$$Fr_{SG} = \frac{U_{SG}}{\sqrt{gD}}\sqrt{\frac{\rho_G}{(\rho_L - \rho_G)}} \tag{3.63}$$

$$Fr_{SL} = \frac{U_{SL}}{\sqrt{gD}}\sqrt{\frac{\rho_L}{(\rho_L - \rho_G)}} \tag{3.64}$$

It is seen that for a fixed liquid flow rate, when the gas flow rate is increased, the two-phase pressure gradient exhibits first a minimum at $Fr_{SG} \approx 0.2 - 0.3$ and a maximum at $Fr_{SG} \approx 0.4$. The first instance of decreasing pressure drop is due to falling film surrounding the gas slug. As the gas slug rises in downstream direction it sheds liquid phase surrounding it to maintain the continuity. The sudden increase in pressure drop between $Fr_{SG} \approx 0.2 - 0.4$ is due to the high level of turbulence caused by disintegration of gas slug during slug to churn/intermittent flow transition. Further this point of maximum pressure gradient at $Fr_{SG} \approx 0.4$, churn/intermittent flow is known to commence and again a decreasing trend of pressure gradient followed by a pressure gradient minimum is observed at $Fr_{SG} \approx 0.9 - 1$. Beyond this point, the annular flow is known to exist. Note that this value of the nondimensional gas flow rate is essentially the criteria given by Equation 3.26.

The second trend of decreasing pressure drop could be explained using Figure 3.26. During churn–annular flow transition, large interfacial disturbance waves are generated that travel in downstream direction (Figure 3.26-sketch b). During the swiping action of disturbance wave, the liquid film travels in downstream direction under the influence of interfacial drag. However, once the disturbance wave passes by a certain pipe cross section, there is no driving potential for the liquid film and it tends to fall back under the influence

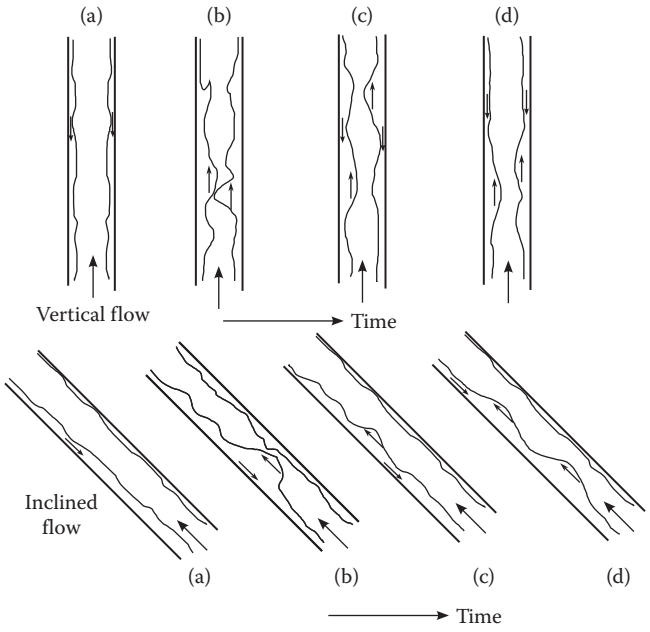


Figure 3.26

Schematics of mechanism governing pressure gradient minimum phenomenon.

of gravity (Figure 3.26 sketch c and d). The direction of travel of liquid film for different cases is depicted by small arrows inside the film. During and just after the encounter of liquid film with the disturbance wave, the portion of liquid film near interface may travel in upward direction, while that away from interface (or near pipe wall) may travel in downward direction leading to severe fluctuations in shear stress and velocity distributions in liquid film. The falling liquid film is again lifted up by upcoming disturbance wave, and the process continues until the frequency of disturbance waves is high enough to prevent the reversal of liquid film. More details about this phenomenon and its dependency on disturbance waves could be found in Hewitt et al. (1965, 1985), Hewitt and Lacey (1965), and Owen (1986).

When it is desirable to operate a two-phase flow system in the region *not affected* by the reversal of liquid film, it is crucial to identify the gas and liquid flow rates that belong to the region *affected* by flow reversal. Compared to first trend of decreasing pressure gradient, its second instance is more important since this region is marked by severe turbulence and instability of the liquid film. The two-phase flow literature reports that the point of second pressure gradient minimum occurs at $Fr_{SG} \approx 1$. However, this criterion does not provide any idea on the range of liquid flow rates for which this trend would exist. Experiments carried out at the Two-Phase Flow Lab, OSU, reveal that the liquid flow rates at which this trend of second pressure gradient minimum would exist depend upon the pipe orientation such that the relationship between nondimensional liquid flow rates and pipe orientation corresponding to second pressure gradient minimum is given by Equation 3.65. Note that this relationship need not be used for pipe orientations less than +10° from horizontal since the effect of pipe orientation on pressure gradient is negligibly small. For a fixed pipe orientation, Equation 3.65 gives a threshold value of nondimensional liquid flow rate (Fr_{SL}) above which decreasing pressure gradient trends or alternatively reversal of liquid film will no longer exist. Independent of pipe orientation and liquid flow rates, the nondimensional gas flow rates (Fr_{SG}) corresponding to this point are in the range of 0.9–1:

$$Fr_{SL} = 0.6575(\sin\theta)^{1.1175}\Big\} + 10° \le \theta \le +90° \tag{3.65}$$

3.4.7 Two-Phase Pressure Drop Modeling

The two-phase flow literature provides different methods for the calculation of two-phase pressure drop that can be broadly classified as methods based on (1) homogeneous flow model, (2) SFM, (3) phenomenological models, and (4) empirical models. The following text provides a brief description of these models and presents some of the top-performing pressure drop correlations.

3.4.7.1 Homogeneous Flow Model

As mentioned earlier, the correlations based on homogeneous flow model assume the two phases to remain well mixed and move with identical velocities (no slippage at the gas–liquid interface). The homogeneous flow model thus considers the two-phase mixture as a pseudo single-phase mixture having two-phase physical properties. Under the consideration of homogeneous flow model, the hydrostatic two-phase pressure drop is calculated using homogeneous two-phase mixture density (ρ_M) as shown in Equation 3.66. The two-phase mixture density can be expressed either in terms of two-phase flow quality (x) or the gas volumetric flow fraction (λ_G). See Table 3.1 for interchangeability between λ and x:

$$-\left(\frac{dp}{dz}\right)_h = \rho_M g \sin\theta \tag{3.66}$$

$$\rho_M = \left(\frac{x}{\rho_G} + \frac{1-x}{\rho_L}\right)^{-1} = \lambda_G \rho_G + (1-\lambda_G)\rho_L \tag{3.67}$$

The pressure drop due to acceleration of the two-phase mixture is calculated from Equation 3.68. For the case of two-component two-phase flow (nonboiling, noncondensing), the two-phase flow quality remains constant for a relatively short length of pipe and the magnitude of pressure drop due to change in specific volume of two-phase mixture is negligible and hence is ignored:

$$-\left(\frac{dp}{dz}\right)_a = G^2 \frac{dv_M}{dz} = G^2\left(v_{LG}\frac{dx}{dz} + x\frac{dv_G}{dp}\frac{dp}{dz}\right) \tag{3.68}$$

Finally, the frictional component of two-phase pressure drop is expressed in terms of the two-phase friction factor. The two-phase friction factor (f_M) is calculated based on two-phase Reynolds number (Re_M), which in turn is the function of two-phase mixture dynamic viscosity (μ_M). The two-phase flow literature provides several models to calculate two-phase dynamic viscosity as a function of two-phase flow quality. Some of these models are listed in Table 3.6:

$$-\left(\frac{dp}{dz}\right)_f = \frac{2 f_M G^2}{D\rho_M} \tag{3.69}$$

$$Re_M = \frac{GD}{\mu_M} \tag{3.70}$$

Table 3.6 Two-Phase Dynamic Viscosity Models

Source	Correlation
McAdams et al. (1942)	$\mu_M = \left(\frac{x}{\mu_G} + \frac{1-x}{\mu_L}\right)^{-1}$
Ciccihitti et al. (1960)	$\mu_M = x\mu_G + (1-x)\mu_L$
Dukler et al. (1964)	$\mu_M = \lambda_G\mu_G + (1-\lambda_G)\mu_L$
Beattie and Whalley (1982)[a]	$\mu_M = \mu_L(1-\lambda_G)(1+2.5\lambda_G) + \lambda_G\mu_G$
Awad and Muzychka (2008) Model 1[b]	$\mu_M = \mu_L\left[\frac{2\mu_L + \mu_G - 2(\mu_L - \mu_G)x}{2\mu_L + \mu_G + 2(\mu_L - \mu_G)x}\right]$
Awad and Muzychka (2008) Model 2[b]	$\mu_M = \mu_G\left[\frac{2\mu_G + \mu_L - 2(\mu_G - \mu_L)(1-x)}{2\mu_G + \mu_L + 2(\mu_G - \mu_L)(1-x)}\right]$
Awad and Muzychka (2008) Model 3[b]	Arithmetic mean of Model 1 and Model 2
Awad and Muzychka (2008) Model 4[b]	$\mu_M = 0.25[(3x-1)\mu_G + [3(1-x)-1]\mu_L] + \sqrt{[(3x-1)\mu_G + [3(1-x)-1]\mu_L]^2 + 8\mu_L\mu_G}$

[a] Use the correlation of Colebrook (1939) to calculate two-phase friction factor.

[b] Use the correlation of Churchill (1977) to calculate two-phase friction factor.

The two-phase friction factor (f_M) is calculated using single-phase fanning friction factor correlations such as Blasius (1913) and Churchill (1977) shown in Equations 3.71 and 3.72, respectively. The Reynolds number (Re_j) is expressed for jth phase that can be gas-, liquid-, or two-phase mixture:

$$f_j = \begin{cases} 16/Re_j & : Re_j \le 2300 \\ 0.079/Re_j^{0.25} & : Re_j > 2300 \end{cases} \tag{3.71}$$

$$f_j = 2\left[\left(\frac{8}{Re_j}\right)^{12} + \frac{1}{(a+b)^{3/2}}\right]^{1/12} \tag{3.72}$$

In Equation 3.72, parameters a and b are expressed as follows:

$$a = \left[2.457 \ln\left(\frac{1}{(7/Re_j)^{0.9} + (0.27\varepsilon/D)}\right)\right]^{16} \quad \text{and} \quad b = \left(\frac{37530}{Re_j}\right)^{16}$$

Thus, the total two-phase pressure drop assuming negligible contribution of the accelerational component is calculated from Equation 3.73. Note that the frictional component of two-phase pressure drop can also be expressed in terms of wall shear stress calculated as $\tau_w = (f_M G^2)/2\rho_M$:

$$-\left(\frac{dp}{dz}\right)_t = \frac{2f_M G^2}{D\rho_M} + (\lambda_G \rho_G + (1-\lambda_G)\rho_L) g \sin\theta \tag{3.73}$$

$$= \tau_w \frac{P}{A} + \rho_M g \sin\theta \tag{3.74}$$

It is interesting to see that the two-phase frictional pressure drop calculation method based on homogeneous flow model can also be expressed in terms of two-phase frictional multiplier (Φ^2) (see Equations 3.85 through 3.88). Consider the two-phase frictional pressure drop equation of homogeneous flow model and divide it with the pressure drop equation for single-phase gas or liquid phase. The resultant equation would be the two-phase frictional multiplier. Assuming turbulent flow of each phase and using the Blasius (1913) correlation for friction factor, this two-phase frictional multiplier using homogeneous flow model approach can be casted as

$$\Phi_{LO}^2 = \frac{(dp/dz)_f}{(dp/dz)_{LO}} = \frac{2f_M G^2/(D\rho_M)}{2f_{LO} G^2/(D\rho_L)} = \frac{\rho_L}{\rho_M}\left(\frac{\mu_L}{\mu_M}\right)^{-0.25} \tag{3.75}$$

Using the definition of homogeneous two-phase mixture density given by Equation 3.67 and two-phase mixture viscosity definition of McAdams et al. (1942) (Table 3.6), Equation 3.75 would become Equation 3.76. Similarly, using the definitions for single-phase pressure drop due to flow of liquid and gas (see Equations 3.86 through 3.88), two-phase frictional multipliers Φ_L^2, Φ_{GO}^2, and Φ_G^2 using homogeneous flow models can be expressed as Equations 3.77 through 3.79, respectively:

$$\Phi_{LO}^2 = \left[(1-x) + x\frac{\mu_L}{\mu_G}\right]^{-0.25}\left[1 + x\left(\frac{\rho_L}{\rho_G} - 1\right)\right] \tag{3.76}$$

$$\Phi_L^2 = (1-x)^{-1.75}\Phi_{LO}^2 \tag{3.77}$$

$$\Phi_{GO}^2 = \left[x + (1-x)\frac{\mu_G}{\mu_L}\right]^{-0.25}\left[x + (1-x)\frac{\rho_G}{\rho_L}\right] \tag{3.78}$$

$$\Phi_G^2 = x^{-1.75}\Phi_{GO}^2 \tag{3.79}$$

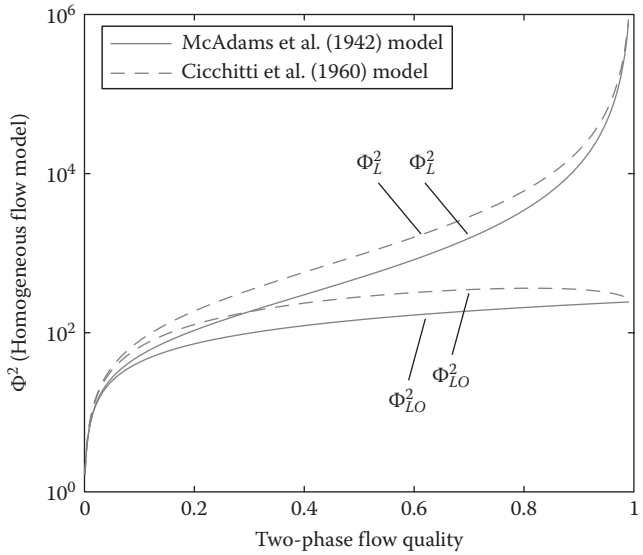


Figure 3.27

Two-phase frictional multiplier based on homogeneous flow model.

It must be mentioned here that the physical form of homogeneous flow model-based two-phase frictional multiplier derived in the aforementioned equations depends on the selection of friction factor and two-phase dynamic viscosity model. For instance, the use of the two-phase dynamic viscosity model of Ciccihitti et al. (1960) would render a different form of two-phase frictional multiplier. The comparison between Φ_{LO}^2 and Φ_L^2 using the dynamic viscosity models of McAdams et al. (1942) and Ciccihitti et al. (1960) is presented in Figure 3.27. Based on the trends of Φ_{LO}^2 and Φ_L^2 using homogeneous flow model, some discrepancies between these theoretical trends and reality can be highlighted. The trend of Φ_{LO}^2 shows a rapid increase with increase in two-phase flow quality up to $x \approx 0.1$ and thereafter increases slowly with increase in quality. Comparatively, Φ_L^2 increases rapidly for both lower and higher values of two-phase flow quality. In reality, Φ_{LO}^2 or Φ_L^2 may not exhibit a continuous increasing trend but rather show an inflection point close to higher values of $x \approx 0.7 - 0.9$ (see Figure 3.21). It must be noted that the two-phase pressure drop calculation based on homogeneous flow model is appropriate for bubbly and annular mist region that to a good extent exhibits homogeneous flow characteristics. The use of these models for intermittent, stratified, and annular flow regimes may result into significant deviations from the actual two-phase flow conditions.

3.4.7.2 Separated Flow Model

As mentioned earlier, SFM assumes two phases to flow separately and share a definite and continuous interface between them, and unlike homogeneous flow model, it considers the slippage at the gas–liquid interface. Thus, using two-phase SFM, the two-phase mixture density and hence the two-phase hydrostatic pressure drop calculation are based on the void fraction as given by Equation 3.80 where the two-phase mixture density is $\rho_M = \alpha_G\rho_G + (1 - \alpha_G)\rho_L$:

$$-\left(\frac{dp}{dz}\right)_h = \rho_M g \sin\theta = (\alpha_G\rho_G + (1-\alpha_G)\rho_L)g\sin\theta \tag{3.80}$$

It is of interest to check the agreement between the calculated values of two-phase mixture density considering the interfacial slippage (SFM approach) and assuming no slip at the gas–liquid interface (HFM approach). It is clear from Figure 3.28 that the agreement between the two methods is valid only for $\lambda < 0.2$ and $\lambda \to 1$. These two conditions approximately correspond to the bubbly and annular mist types of the flow where to some extent two-phase flow may exhibit homogeneous flow characteristics.

The accelerational component of two-phase pressure drop is expressed by Equation 3.81. This expression is valid for all but annular flow pattern with considerable liquid entrainment. In particular, for annular flow,

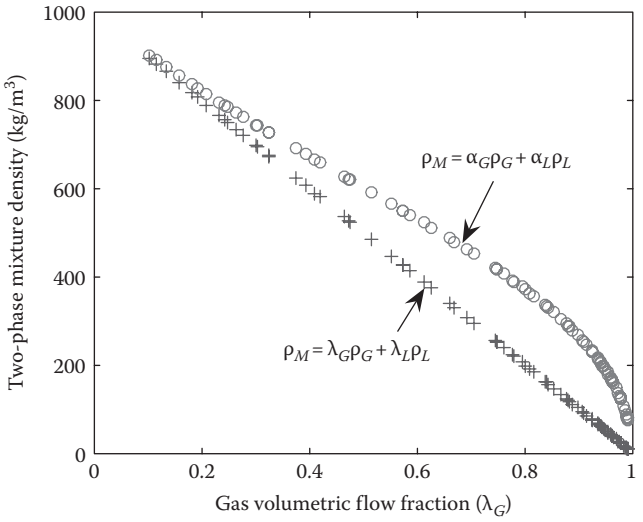


Figure 3.28

Two-phase mixture density calculation using a homogeneous and separated flow model.

when the entrainment of liquid droplets into the central gas core is significant, the error associated with the assumption of negligible accelerational pressure drop can be severe. In case of annular flow with liquid entrainment, the process of entrainment also contributes to the two-phase pressure drop and hence cannot be ignored. For such a specific case (annular flow with liquid entrainment), Equation 3.81 can be expressed in the form of Equation 3.82:

$$-\left(\frac{dp}{dz}\right)_a = G^2 \frac{d}{dz}\left[\frac{x^2}{\alpha_G \rho_G} + \frac{(1-x)^2}{(1-\alpha_G)\rho_L}\right] \tag{3.81}$$

$$-\left(\frac{dp}{dz}\right)_a = G^2 \frac{d}{dz}\left[\frac{x^2}{\alpha_G \rho_G} + \frac{(1-E)^2(1-x)^2}{\beta \rho_L} + \frac{E^2(1-x)^2}{(1-\alpha_G-\beta)\rho_L}\right] \tag{3.82}$$

The volume fraction occupied by the liquid film (β) defined by Equation 3.83 does not consider the fraction of liquid droplets entrained in the gas core and hence may not be confused with liquid holdup (α_L). However, it is evident that under the condition of $E \approx 0$, the volume fraction of liquid film is equal to the liquid holdup, that is, $\beta = \alpha_L$. Equation 3.83 is based on a valid assumption that entrained liquid droplets travel at a velocity same as that of the gas:

$$\beta = 1 - \alpha_G - \frac{\alpha_G E(1-x)}{x(\rho_L/\rho_G)} \tag{3.83}$$

It must be reiterated that this is required only in case of annular flow with considerable liquid entrainment. For the case of annular flow at low system pressures ($E \approx 0$) and at flow patterns other than annular flow ($E = 0$), it is simplified back to Equation 3.81 such that the accelerational pressure drop at a given location can be determined based on void fraction and mass flux of each phase. For the case of adiabatic two-phase flow over a short pipe length, two-phase flow quality and void fraction can be assumed to remain constant and hence $(dp/dz)_a \approx 0$.

Finally, the frictional component of two-phase pressure drop is calculated as

$$\left(\frac{dp}{dz}\right)_f = \Phi_j^2 \left(\frac{dp}{dz}\right)_j \tag{3.84}$$

The two-phase frictional multiplier Φ^2 can be expressed in several different forms depending upon the assumption of flow of either single phase through the pipe. Broadly, four different cases of two-phase

frictional multiplier can be defined as shown in Equations 3.85 through 3.88. In these equations, single-phase pressure drop is the single-phase frictional drop unless otherwise specified and $(dp/dz)_f$ would always represent the frictional component of the two-phase pressure drop:

$$\left(\frac{dp}{dz}\right)_f = \Phi_{LO}^2 \left(\frac{dp}{dz}\right)_{LO} \quad \text{where} \left(\frac{dp}{dz}\right)_{LO} = \frac{2f_L G^2}{D\rho_L} \tag{3.85}$$

$$\left(\frac{dp}{dz}\right)_f = \Phi_{L}^2 \left(\frac{dp}{dz}\right)_{L} \quad \text{where} \left(\frac{dp}{dz}\right)_{L} = \frac{2f_L G^2(1-x)^2}{D\rho_L} \tag{3.86}$$

$$\left(\frac{dp}{dz}\right)_f = \Phi_{GO}^2 \left(\frac{dp}{dz}\right)_{GO} \quad \text{where} \left(\frac{dp}{dz}\right)_{GO} = \frac{2f_G G^2}{D\rho_G} \tag{3.87}$$

$$\left(\frac{dp}{dz}\right)_f = \Phi_{G}^2 \left(\frac{dp}{dz}\right)_{G} \quad \text{where} \left(\frac{dp}{dz}\right)_{G} = \frac{2f_G G^2 x^2}{D\rho_G} \tag{3.88}$$

The two-phase literature provides several frictional pressure drop correlations based on these different two-phase frictional multipliers. One of the first such correlations is proposed by Lockhart and Martinelli (1949). Their correlation expresses two-phase frictional multipliers Φ_L^2 and Φ_G^2 as a function of X parameter and is expressed by Equation 3.89. The parameter (X) of Lockhart and Martinelli (1949) is given by Equation 3.90 where the single-phase friction factors (f_L and f_G) are found using appropriate single-phase friction factors such as Equations 3.71 and 3.72. In these equations, $Re_j = Re_{SG}$ and $Re_j = Re_{SL}$ for gas and liquid phase, respectively:

$$\Phi_L^2 = 1 + C/X + 1/X^2 \quad \text{or} \quad \Phi_G^2 = 1 + CX + X^2 \tag{3.89}$$

$$X = \left[\frac{(dp/dz)_{f,L}}{(dp/dz)_{f,G}}\right]^{0.5} = \frac{1-x}{x}\left[\frac{f_L}{f_G}\frac{\rho_G}{\rho_L}\right]^{0.5} = \frac{U_{SL}}{U_{SG}}\left[\frac{f_L}{f_G}\frac{\rho_L}{\rho_G}\right]^{0.5} \tag{3.90}$$

The value of C used in Equation 3.89 given by Chisholm (1967) is given in Table 3.7, and it depends on the laminar or turbulent nature of the gas and liquid phase, respectively. The graphical form of Equation 3.89 for laminar and turbulent regimes of single-phase flow of gas and liquid phase is illustrated in Figure 3.29. Apart from the correlation of Lockhart and Martinelli (1949), there are several other correlations for two-phase frictional multiplier that could be used to determine the frictional component of the two-phase pressure drop. Some of these correlations valid for a wide range of two-phase flow conditions are listed as follows.

Chisholm (1973) proposed a method to calculate two-phase frictional pressure drop in adiabatic and evaporating flow conditions based on the concept of SFM and applicable for vapor qualities $0 \le x \le 1$. The two-phase friction multiplier is expressed as shown in Equation 3.91, where Y is defined by Equation 3.92:

$$\Phi_{LO}^2 = 1 + (Y^2 - 1)\left(B_s x^{0.875}(1-x)^{0.875} + x^{1.75}\right) \tag{3.91}$$

$$Y = \sqrt{\frac{(dp/dz)_{GO}}{(dp/dz)_{LO}}} \tag{3.92}$$

Table 3.7 Values of Constant C to Be Used in the Correlation of Lockhart and Martinelli (1949) for Different Single-Phase Flow Regimes

Liquid Phase	Gas Phase	C
Turbulent (t)	Turbulent (t)	20
Laminar (l)	Turbulent (t)	12
Turbulent (t)	Laminar (l)	10
Laminar (l)	Laminar (l)	5

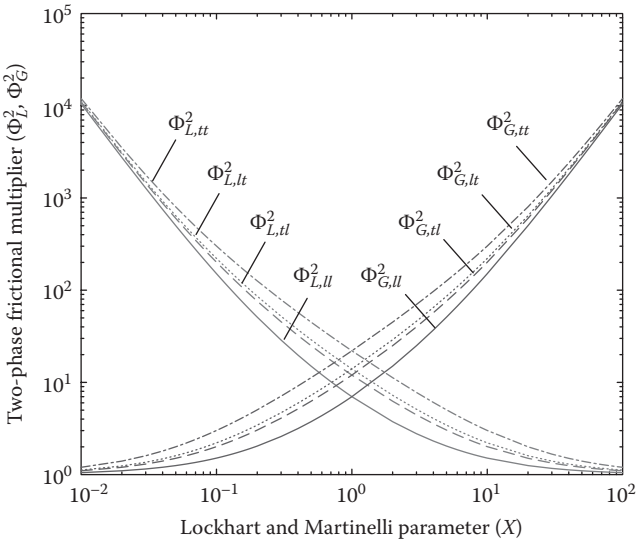


Figure 3.29

Graphical representation of different forms of two-phase frictional multiplier given by Lockhart and Martinelli (1949).

The frictional pressure gradients for single-phase liquid and gas phase are calculated using Equations 3.85 and 3.87, respectively. His correlation is essentially a transformation of graphical solution of Barcozy (1966) to predict the two-phase frictional pressure drop. The correlation is claimed to be applicable for a pressure range of 0.6–4 MPa. Chisholm (1973) proposed a set of different conditional equations to predict parameter B_s for different values of Y and mixture mass flux (G) as shown in Table 3.8.

Muller-Steinhagen and Heck (1986) developed a correlation to extrapolate between single-phase liquid and single-phase gas flow. This correlation can be used for both adiabatic and evaporating two-phase flow conditions (provided the two-phase flow quality distribution across the pipe length is known). The physical form of the correlation is as shown in Equation 3.93. The parameter Y is the same as that defined by Chisholm (1973) in Equation 3.92. The correlation is verified against 9300 measurements including data of air–oil, air–water, and steam–water fluid combinations and pipe diameters ranging from 4 to 39 mm I.D. The application of Equation 3.93 is restricted to $Re_{LO} > 100$ and $Y^2 > 1$. Note that for the determination of single-phase friction factor f_j, their correlation separates single-phase laminar and turbulent regions using a threshold value of $Re_j = 1187$ where "j" can be gas or liquid phase:

$$\Phi_{LO}^2 = Y^2 x^3 + (1-x)^{0.33}(1+2x(Y^2-1)) \tag{3.93}$$

Recently, Xu and Fang (2012) have proposed a two-phase frictional pressure drop correlation for evaporating two-phase flow of refrigerants in horizontal pipe. Their correlation is based on 2622 data points

Table 3.8 Values of Parameter B_s Used in the Correlation of Chisholm (1973)

Y	G (kg/m²s)	Equation for B_s
$0 < Y < 9.5$	$G \geq 1900$	$B_s = 55/\sqrt{G}$
	$500 < G < 1900$	$B_s = 2400/G$
	$500 > G$	$B_s = 4.8$
$9.5 < Y < 28$	$G \leq 600$	$B_s = 520/(Y\sqrt{G})$
	$G \geq 600$	$B_s = 21/Y$
$Y > 28$		$B_s = 15{,}000/(Y^2\sqrt{G})$

of 14 refrigerants (R11, R12, R22, R134a, R32, R407C, R507, R507A, R410A, CO_2, R404A, R32/R125, R123, and ammonia) for $1 < D_h < 19$ mm (circular and rectangular pipe geometries) and $25 < G < 1150$ kg/m^2 s. They found that the pipe hydraulic diameter and gas–liquid interface surface tension affect the two-phase frictional pressure drop significantly than any other two-phase flow parameter, and hence, their correlation accounts for these two variables through the inclusion of nondimensional Laplace number. The physical form of their correlation is as expressed in

$$\Phi_{LO}^2 = \left[Y^2 x^3 + (1-x)^{0.33} \left(1 + 2x(Y^2 - 1)\right) \right] \left(1 + 1.54(1-x)^{0.5} La\right) \tag{3.94}$$

In this equation, Y is calculated from Equation 3.92, while La is the Laplace number defined by Equation 3.53. Their correlation is claimed to predict the two-phase frictional pressure drop data with a mean absolute relative deviation of 25.2%. It should be noted that Xu and Fang (2012) recommend the use of the correlation of Fang et al. (2011) to calculate single-phase Darcy friction factor (4× fanning friction factor), and hence, the single-phase liquid pressure drop required in Equation 3.85 must be changed to $(dp/dz)_f = f_L G^2/(2D\rho_L)$. The correlation of Fang et al. (2011) for single-phase Darcy friction factor is reported in

$$f_{LO} = 0.25 \left[\log\left(\frac{150.39}{Re_{LO}^{0.98865}} - \frac{152.66}{Re_{LO}} \right) \right]^{-2} \tag{3.95}$$

For mini-/microchannels having pipe diameters in the range of 0.1–6 mm, Zhang et al. (2010) proposed a two-phase frictional pressure drop correlation (for adiabatic two-phase flow) based on the experimental data of two-phase flow of refrigerants, air–water and air–ethanol. Their correlation for two-phase frictional multiplier is the same as that of Lockhart and Martinelli (1949) (see Equation 3.89), however with the parameter C as a variable given by

$$C = \begin{cases} 21[1 - \exp(-0.674/La)] \text{ (two-component two-phase flow)} \\ 21[1 - \exp(-0.142/La)] \text{ (one-component two-phase flow)} \end{cases} \tag{3.96}$$

3.4.7.3 Two-Phase Friction Factor Models

In addition to homogeneous and SFMs, the two-phase literature also reports two-phase friction factor models of empirical nature. Although these models provide two-phase friction factor, they are different from two-phase friction factors used in homogeneous flow models. Some of the recent correlations developed for determining two-phase friction factors are that of Shannak (2008) and Cioncolini et al. (2009). The two-phase Darcy friction factor correlation (4× fanning friction factor) of Shannak (2008) is developed based on data for both boiling and nonboiling two-phase flow and accounts for the pipe wall surface roughness. His correlation requires the determination of modified two-phase flow Reynolds number (Re_M) given by Equation 3.97. Based on this two-phase mixture Reynolds number, the two-phase friction factor (f_M) is defined using the correlation of Chen (1979) given by Equation 3.98. The two-phase frictional pressure drop is calculated using the modified form of Equation 3.69 expressed as $(dp/dz)_f = f_M G^2/(2D\rho_M)$ where ρ_M is the homogeneous mixture density defined by Equation 3.67. Equation 3.98 is verified against 16,000 data consisting of the entire range of two-phase flow quality, pipe diameters in the range of 3–150 mm, system pressure in the range of 0.1–17 MPa, and two-phase mixture mass flux in the range of 15–8200 kg/m^2 s:

$$Re_M = \frac{GD\left(x^2 + (1-x)^2 \rho_G/\rho_L\right)}{\mu_G x + \mu_L (1-x)\rho_G/\rho_L} \tag{3.97}$$

$$\frac{1}{\sqrt{f_M}} = -2\log\left[\frac{\varepsilon}{3.7065D} \frac{5.0452}{Re_M} \log\left(\frac{1}{2.2857} \left(\frac{\varepsilon}{D} \right)^{1.1098} + \frac{5.8506}{Re_M^{0.8981}} \right) \right] \tag{3.98}$$

Since Shannak (2008) correlation is based on two-phase mixture Reynolds number and uses Equation 3.67 to find two-phase mixture density, Equation 3.66 based on homogeneous flow model should be used to determine the hydrostatic component of the two-phase pressure drop.

Another two-phase friction factor correlation developed exclusively for the annular flow is given by Cioncolini et al. (2009). The two-phase friction factor (f_M) given by Equation 3.99 is modeled as a function of core Weber number (We_c) and liquid film Reynolds number (Re_{LF}) given by Equations 3.100 and 3.101, respectively. The core mass flux (G_c), core density (ρ_c), and core diameter (D_c) are defined using Equations 3.102 through 3.104, respectively. Appropriate void fraction (see Section 3.3.4) and liquid entrainment fraction E (see Section 3.6.1) correlation developed for the annular flow must be used in the calculation of parameters G_c, ρ_c, and D_c. Note that the expression recommended by Cioncolini et al. (2009) for two-phase frictional pressure drop in the form of Equation 3.105 is based on gas core mass flux (G_c) and core density (ρ_c). Unlike Shannak (2008) correlation, Cioncolini et al. (2009) recommend the use of Equations 3.80 and 3.82 based on SFM to determine the total two-phase pressure drop:

$$f_M = \begin{cases} 0.172 We_c^{-0.372} & : D > 3\,\text{mm} \\ 0.0196 We_c^{-0.372} Re_{LF}^{0.318} & : D \le 3\,\text{mm} \end{cases} \tag{3.99}$$

$$We_c = \frac{G_c^2 D_c}{\rho_c \sigma} \tag{3.100}$$

$$Re_{LF} = \frac{(1-E)(1-x)GD}{\mu_L} \tag{3.101}$$

$$G_c = \frac{4\dot{m}[x + E(1-x)]}{\pi D_c^2} \tag{3.102}$$

$$\rho_c = \frac{x + E(1-x)}{(x/\rho_G) + (E(1-x)/\rho_L)} \tag{3.103}$$

$$D_c = D\alpha_G^2 \sqrt{1 + E\left(\frac{1-x}{x}\right)\frac{\rho_G}{\rho_L}} \tag{3.104}$$

$$-\left(\frac{dp}{dz}\right)_f = \frac{2 f_M G_c^2}{\rho_c D} \tag{3.105}$$

The two-phase pressure drop models listed in this section are some of the relatively good performing correlations validated over a fairly comprehensive range of two-phase flow conditions. The accuracy of these correlations could be up to ±50% compared to actual operating conditions. Considering the difficulty in modeling two-phase pressure drop as a function of several two-phase flow variables, this range of accuracy has received acceptance in the two-phase flow community. All the correlations presented in this section are found to work well for all but stratified flow pattern. In the following section, we will present stratified flow pattern–specific mechanistic and semimechanistic models to estimate void fraction and two-phase pressure drop.

3.5 Modeling of Stratified Flow

As mentioned earlier, stratified flow pattern in horizontal and downward pipe inclinations has a peculiar flow structure, and it is practically difficult to accurately model it with existing flow pattern–independent two-phase flow models. Apparently, the stratified flow pattern needs to be modeled using mechanistic

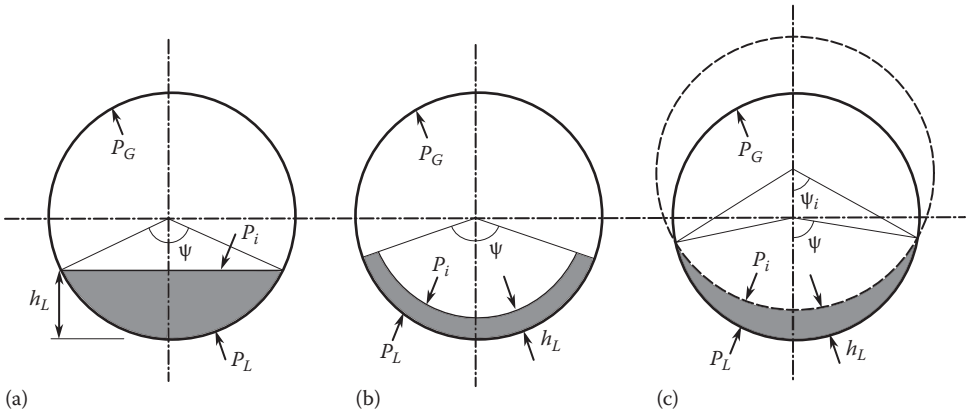


Figure 3.30

Geometry considerations in different types of stratified flow models. (a) Flat surface model. (From Taitel, Y. and Dukler, A.E., *AIChE J.*, 22, 47, 1976.) (b) Apparent rough surface model. (From Hart, J. et al., *Int. J. Multiphase Flow*, 15, 947, 1989.) (c) Double circle model. (From Chen, X.T. et al., *J. Energy Resour. Technol.*, 119, 209, 1997.)

flow model approach introduced by Taitel and Dukler (1976) and its derivatives. In addition to Taitel and Dukler (1976) model, the two-phase literature also reports semimechanistic models such as apparent rough surface (*ARS*) model and "double circle model" to calculate void fraction and two-phase pressure drop in stratified two-phase flow. It must be mentioned that the ARS and double circle models are developed only for stratified flow in horizontal pipe orientation and needs to be scrutinized against stratified flow data in downward pipe inclinations. This section describes step-by-step procedure involved in solving the stratified flow model using these three different methods. The schematics of the type (shape) of gas–liquid interface associated with each of these methods are illustrated in Figure 3.30.

3.5.1 Taitel and Dukler (1976) Model

The Taitel and Dukler (1976) model also known as "flat surface model" is developed for stratified flow at equilibrium, and as its name suggests, it assumes a flat interface between the gas and the liquid phase. It also assumes that the gas–liquid interface is smooth and that the interfacial friction factor is equal to the gas-phase friction factor. Their model considers the stratified flow of the pattern shown in Figure 3.31. The momentum balance equations for each phase (gas and liquid) could be written as shown in Equations 3.106 and 3.107. These equations also show the simplified forms of these momentum balance equations under the assumption of negligible acceleration of each phase and constant liquid level (height) along the pipe length. Considering that the pressure drop in the gas phase is equal to the pressure drop in the liquid phase, the momentum balance equations written for individual phases can be combined together to form Equation 3.108. The individual phase and interfacial shear stress required in Equation 3.108 are calculated using Equation 3.109 where the single-phase friction factor for individual phase ($j = G, L$) is calculated from Equation 3.110:

$$-A_G\left(\frac{dp}{dz}\right) = \tau_{wG}P_G + \tau_i P_i + A_G\rho_G g\left(\sin\theta - \cos\theta\frac{d}{dz}(1-h_L)\right) - A\frac{d}{dz}(GxU_G)$$
$$= \tau_{wG}P_G + \tau_i P_i + A_G\rho_G g\sin\theta \tag{3.106}$$

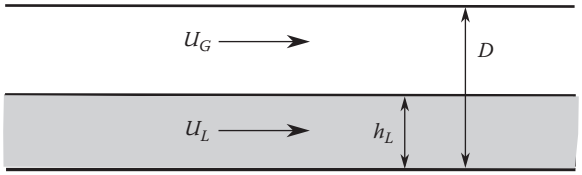


Figure 3.31

Schematic of horizontal stratified flow at equilibrium.

$$-A_L\left(\frac{dp}{dz}\right)=\tau_{wL}P_L-\tau_iP_i+A_L\rho_Lg\left(\sin\theta-\cos\theta\frac{dh_L}{dz}\right)-A\frac{d}{dz}(G(1-x)U_L)$$
$$=\tau_{wL}P_L-\tau_iP_i+A_L\rho_Lg\sin\theta \tag{3.107}$$

$$\tau_{wL}\frac{P_L}{A_L}-\tau_{wG}\frac{P_G}{A_G}-\tau_iP_i\left(\frac{1}{A_L}+\frac{1}{A_G}\right)+(\rho_L-\rho_G)g\sin\theta=0 \tag{3.108}$$

The interfacial friction factor (f_i) is assumed to be equal to the gas-phase friction factor (f_G). The gas- and liquid-phase Reynolds number are based on the actual phase velocity and the hydraulic pipe diameters (based on the area occupied by each phase) expressed as $Re_G = (\rho_G D_G U_G)/\mu_G$ and $Re_L = (\rho_L D_L U_L)/\mu_L$, respectively. The hydraulic diameters are calculated from Equation 3.111 where the area occupied by gas (A_G) and liquid (A_L) phase is defined by Equation 3.112. Considering the flat gas–liquid interface geometry of the Taitel and Dukler (1976) model, the wetted perimeter of pipe occupied by the gas (P_G) and liquid (P_L) phase and the interface (P_i) is expressed by Equation 3.113:

$$\tau_{wG}=\frac{f_G\rho_GU_G^2}{2},\quad \tau_{wL}=\frac{f_L\rho_LU_L^2}{2},\quad \tau_i=\frac{f_i\rho_G(U_G-U_L)^2}{2} \tag{3.109}$$

$$f_j=\begin{cases}16/Re_j & :(Re_j\le 2300)\\ 0.046Re_j^{-0.2} & :(Re_j>2300)\end{cases} \tag{3.110}$$

$$D_G=\frac{4A_G}{P_G+P_i},\quad D_L=\frac{4A_L}{P_L} \tag{3.111}$$

$$A_G=\alpha_G\frac{\pi D^2}{4},\quad A_L=(1-\alpha_G)\frac{\pi D^2}{4} \tag{3.112}$$

$$P_L=\frac{\Psi D}{2},\quad P_G=\pi D-P_L,\quad P_i=\sin\left(\frac{\Psi}{2}\right)D \tag{3.113}$$

$$\alpha_G=1-\frac{\Psi-\sin\Psi}{2\pi} \tag{3.114}$$

$$\Psi=2\arccos\left(1-\frac{2h_L}{D}\right) \tag{3.115}$$

The void fraction, liquid height, and the angle subtended by the flat interface with the pipe centerline are correlated with each other in the form of Equations 3.114 and 3.115. The liquid height (h_L) required in calculation of Ψ can be obtained using graphical solution presented in Figure 3.8. Alternatively, Equations 3.106 through 3.114 are to be solved iteratively until Equation 3.108 is satisfied. The void fraction value that satisfies Equation 3.108 is then used to calculate actual phase velocities, hydraulic diameters, Reynolds number, friction factors, and subsequently the shear stress values. Finally, Equation 3.106 or 3.107 is solved to obtain the frictional pressure gradient.

3.5.2 Apparent Rough Surface Model

The concept of ARS model was first introduced by Hamersma and Hart (1987) and Hart et al. (1989) for wavy stratified two-phase flow in horizontal pipes and is in the form of gas pressure drop equation using

two-phase friction factor. This two-phase friction factor (f_{TP}) is based on the gas (f_G) and interfacial (f_i) friction factors weighted by the fraction of pipe circumference (ϕ) wetted by the liquid phase. The following step-by-step approach needs to be followed to determine the values of α_G, f_G, f_i, ϕ, and f_{TP} and finally the two-phase frictional pressure drop using the ARS model:

1. First, calculate the void fraction using

$$\frac{1-\alpha_G}{\alpha_G} = \frac{U_{SL}}{U_{SG}}\left[1+\left(108 Re_{SL}^{-0.726}\frac{\rho_L}{\rho_G}\right)^{0.5}\right] \tag{3.116}$$

2. Calculate fraction of the pipe circumference (ϕ) wetted by the liquid phase using Equation 3.117. It must be noted that ϕ is the fraction of circumference and not the angle formed by the pipe centerline with the gas–liquid interface (Ψ). The relation between ϕ and Ψ can be expressed as, $\phi = \Psi/2\pi$:

$$\phi = 0.52(1-\alpha_G)^{0.374} + 0.26\left(\frac{\rho_L U_L^2}{(\rho_L-\rho_G)gD}\right)^{0.58} \tag{3.117}$$

3. Calculate interfacial friction factor (f_i) using Equation 3.118, where ε is the interfacial roughness:

$$f_i = \left.\frac{0.0625}{\left[\log\left(\frac{15}{Re_G}+\frac{\varepsilon}{3.715D}\right)\right]^2}\right\} \quad \text{where } \varepsilon = \frac{2.3D(1-\alpha_G)}{4\phi} \tag{3.118}$$

4. From Equation 3.119, calculate the gas-phase friction factor (f_G) based on gas-phase Reynolds number as a function of actual gas velocity ($Re_G = (\rho_G U_G D)/\mu_G$):

$$f_G = \left.\frac{0.07725}{(\log(Re_G/7))^2}\right\} \quad 2100 < Re_G < 10^8 \tag{3.119}$$

5. The two-phase friction factor is then calculated using

$$f_{TP} = f_G(1-\phi) + f_i\phi \tag{3.120}$$

6. Finally, the two-phase pressure drop based on two-phase friction factor is calculated from Equation 3.121. Note that Equation 3.121 uses actual gas-phase velocity (U_G) and not the superficial gas velocity (U_{SG}):

$$-\left(\frac{dp}{dz}\right)_f = \frac{2f_{TP}\rho_G U_G^2}{D} \tag{3.121}$$

3.5.3 Double Circle Model

Double circle model is a mechanistic model proposed by Chen et al. (1997), which considers the concave shape of the gas–liquid interface by using the geometrical intersection of a hypothetical circle with the pipe centerline (see Figure 3.30). Compared to the ARS model, the shape of gas–liquid interface used by double circle model is more realistic and the overall model is based on the mechanistic model of Taitel and Dukler (1976). To begin with, the use of Chen et al. (1997) model requires the determination of Ψ and Ψ_i in radians.

Note that the subtended angle (Ψ) used by Chen et al. (1997) is half of that used by Taitel and Dukler (1976) and ARS models. The following step-by-step procedure is required to solve for void fraction and frictional pressure drop using double circle model:

1. Calculate the angle subtended by the liquid phase with the pipe centerline using the relationship $\Psi = \pi\phi$ where the fraction of pipe circumference wetted by the liquid phase is obtained by Equation 3.117 (same as the ARS model).
2. Once the angle Ψ is known, the angle Ψ_i is calculated from Equation 3.122 using iterative technique. The value of void fraction required in this equation is a guess value obtained by solving for the Taitel and Dukler (1976) flat surface model:

$$\Psi_i = \left(\frac{\sin\Psi_i}{\sin\Psi}\right)^2 \left(\Psi + \frac{\sin^2\Psi}{\tan\Psi_i} - \frac{\sin 2\Psi}{2} - \pi(1-\alpha_G)\right) \tag{3.122}$$

3. Next, the diameter of offset circle (D_i) is determined from

$$D_i = D\frac{\sin\Psi}{\sin\Psi_i} \tag{3.123}$$

4. The perimeter of pipe occupied by the gas and liquid phase and the gas–liquid interface is determined from Equation 3.124. The calculation of the hydraulic diameters (D_G and D_L) and the area occupied by each phase (A_G and A_L) is the same as that given by Equations 3.111 and 3.112:

$$P_G = (\pi - \Psi)D, \quad P_L = \Psi D, \quad P_i = \Psi_i D_i \tag{3.124}$$

5. Interfacial friction factor is calculated using Equation 3.125 where the superficial gas velocity during smooth to wavy stratified flow transition is defined by Equation 3.126. Friction factors for gas (f_G) and liquid (f_L) phase are obtained using the procedure similar to Taitel and Dukler (1976) model, that is, Equation 3.110.

$$\frac{f_i}{f_G} = 1 + 3.75\left(\frac{1-\alpha_G}{\phi}\right)^{0.2}\left(\frac{U_{SG}}{U_{SG,t}} - 1\right)^{0.08} \tag{3.125}$$

$$U_{SG,t} = \sqrt{\frac{4\nu_L(\rho_L - \rho_G)g}{0.06\rho_G U_L}} \tag{3.126}$$

6. Solve for Equation 3.108 by updating the values of void fraction until convergence is obtained.
7. Use converged value of void fraction obtained from step 6 to calculate for two-phase pressure drop using Equation 3.106 or 3.107.

Note that for a quick convergence, the initial guess of void fraction required to calculate actual phase velocities, hydraulic diameters, and Ψ_i is calculated from the Taitel and Dukler (1976) model. It must be mentioned that the double circle method is more complex than the Taitel and Dukler (1976) and ARS models since it involves two iterative solutions for α_G and Ψ_i. The following example problem provides an overview of the procedure required to solve for void fraction and pressure drop in two-phase stratified flow.

Example Problem 3.1

Consider the horizontal two-phase flow of air and water in a 78 mm I.D. smooth polycarbonate pipe. The gas- and liquid-phase superficial velocities are 20 and 0.04 m/s, respectively. Assuming the stratified flow pattern to exist, determine the void fraction and two-phase frictional pressure drop using

(a) Taitel and Dukler (1976) (flat surface), (b) ARS, and (c) double circle models. The physical properties of gas and liquid phase can be taken as follows:

Property	Air	Water
Density	1.2 kg/m^3	998 kg/m^3
Dynamic viscosity	18.5×10^{-6} Pa s	0.001 Pa s

Solution

(a) Calculation of void fraction and pressure drop using Taitel and Dukler (1976) method: First, calculate the Reynolds number based on superficial velocity of gas and liquid phase. The single-phase friction factors for smooth pipe are found using appropriate friction factor correlation such as that of Blasius (1913) (see Equation 3.71):

$$Re_{SG} = \frac{\rho_G U_{SG} D}{\mu_G} = \frac{1.2 \times 20 \times 0.078}{18.5 \times 10^{-6}} = 1.012 \times 10^5 \Rightarrow f_G = 0.00448$$

$$Re_{SL} = \frac{\rho_L U_{SL} D}{\mu_L} = \frac{998 \times 0.04 \times 0.078}{0.001} = 3113.7 \Rightarrow f_L = 0.0107$$

Now calculate single-phase pressure drop (based on superficial phase velocity) for each phase and hence X parameter from Equation 3.90. The single-phase pressure drop calculation for each phase using Equations 3.88 and 3.86 is shown as follows:

$$-\left(\frac{dp}{dz}\right)_G = \frac{2 f_G \rho_G U_{SG}^2}{D} = \frac{2 \times 0.00448 \times 1.2 \times 20^2}{0.078} = 55.14 \text{ Pa/m}$$

$$-\left(\frac{dp}{dz}\right)_L = \frac{2 f_L \rho_L U_{SL}^2}{D} = \frac{2 \times 0.0107 \times 998 \times 0.04^2}{0.078} = 0.438 \text{ Pa/m}$$

$$\therefore X = \sqrt{\frac{(dp/dz)_L}{(dp/dz)_G}} = \sqrt{\frac{0.438}{55.14}} = 0.09$$

For horizontal two-phase flow, Equation 3.14 gives $Y = 0$, and using the graphical solution in Figure 3.8, the nondimensional liquid height is $h_L/D \approx 0.1$. Using this ratio of equilibrium liquid height and pipe diameter, the angle subtended by the liquid phase with pipe centerline and hence the void fraction in stratified flow is calculated using Equations 3.115 and 3.114:

$$\Psi = 2\arccos(1 - 0.2) = 73.74°(1.287^r) \Rightarrow \alpha_G = 1 - \frac{\Psi - \sin\Psi}{2\pi} = 0.948$$

This value of void fraction of 0.948 is an initial estimate of the void fraction obtained using the graphical solution. This void fraction may be further updated to satisfy Equation 3.108. Once the void fraction is determined, the actual phase velocities (see Table 3.1 for U_G and U_L), hydraulic diameters (Equation 3.111), the cross-sectional area occupied by each phase (Equation 3.112), and the wetted perimeter of each phase (Equation 3.113) are calculated as follows:

$$U_G = \frac{U_{SG}}{\alpha_G} = \frac{20}{0.948} = 21.1 \text{ m/s}, \quad U_L = \frac{U_{SL}}{1 - \alpha_G} = \frac{0.04}{1 - 0.948} = 0.77 \text{ m/s}$$

$$A_G = \alpha_G \frac{\pi D^2}{4} = 0.00453 \text{ m}^2, \quad A_L = (1 - \alpha_G)\frac{\pi D^2}{4} = 0.000248 \text{ m}^2$$

$$P_L = 0.0502 \text{ m}, \quad P_G = 0.195 \text{ m}, \quad P_i = 0.0468 \text{ m}, \quad D_G = 0.0749 \text{ m}, \quad D_L = 0.0197 \text{ m}$$

The Reynolds numbers based on actual gas and liquid-phase velocities are found to be

$$Re_G = \frac{1.2 \times (20/0.948) \times 0.0749}{18.5 \times 10^{-6}} = 1.025 \times 10^5$$

$$Re_L = \frac{998 \times (0.04/(1-0.948)) \times 0.0197}{0.001} = 15139$$

The single-phase friction factors for each phase are found using Equation 3.110:

$$f_G = 0.046(1.025 \times 10^5)^{-0.2} = 0.00457$$

$$f_L = 0.046 \times (15139)^{-0.2} = 0.00671$$

Now, the wall and interfacial shear stresses using $f_i = f_G$ are calculated using Equation 3.109:

$$\tau_{wG} = \frac{0.00457 \times 1.2 \times 21.1^2}{2} = 1.232 \text{ N/m}^2$$

$$\tau_{wL} = \frac{0.00671 \times 998 \times 0.77^2}{2} = 1.985 \text{ N/m}^2$$

$$\tau_i = \frac{0.00457 \times 1.2 \times (21.1 - 0.77)^2}{2} = 1.133 \text{ N/m}^2$$

Now solve Equation 3.108 using the known values of shear stress, wetted perimeter, and cross-sectional area occupied by each phase. For these values, Equation 3.108 is not satisfied (residual = –121.1), and hence, the value of h_L/D is updated to find a new value of void fraction and the remaining steps are repeated. Iterate through these calculations until the residual of Equation 3.108 is approximately zero. After a few iterations, it is found that Equation 3.108 is satisfied (residual = 0.008) for $h_L/D \approx 0.1117$ and $\alpha_G = 0.938$ ($\Psi = 78.1° = 1.363^r$). Finally, after the convergence of Equation 3.108, two-phase frictional pressure drop is obtained by solving either Equation 3.106 or Equation 3.107. It should be noted that the use of Equation 3.106 or 3.107 requires calculation of updated values of shear stresses (τ_{wL}, τ_{wG}, τ_i) based on updated friction factors (f_G, f_L, f_i), the cross-sectional area occupied by each phase (A_G, A_L), and wetted perimeters of each phase and the gas–liquid interface (P_G, P_L, P_i). Two-phase pressure drop calculation using Equation 3.107 is shown as follows:

$$-\left(\frac{dp}{dz}\right)_f = \tau_{wL}\frac{P_L}{A_L} - \tau_i\frac{P_i}{A_L} = 1.445\frac{0.0531}{0.000296} - 1.17\frac{0.0491}{0.000296} = 66.1 \text{ Pa/m}$$

(b) *ARS model*: Calculate void fraction using Equation 3.116 where $Re_{SL} = \rho_L U_{SL} D/\mu_L = 3113.7$:

$$\frac{1-\alpha_G}{\alpha_G} = \frac{0.04}{20}\left[1 + \left(108 \times 3113.7^{-0.726} \times \frac{998}{1.2}\right)^{0.5}\right] \Rightarrow \alpha_G = 0.966$$

Now, calculate the actual gas and liquid-phase velocities (see Table 3.1), U_G = 20.7 m/s and U_L = 1.176 m/s. The fractional wetted perimeter is calculated from Equation 3.117:

$$\phi = 0.52(1-0.966)^{0.374} + 0.26\left(\frac{998 \times 1.176^2}{(998-1.2) \times 9.81 \times 0.078}\right)^{0.58} = 0.523$$

Calculate gas Reynolds number based on the actual gas velocity:

$$Re_G = \frac{\rho_G U_G D}{\mu_G} = \frac{1.2 \times 20.7 \times 0.078}{18.5 \times 10^{-6}} = 1.046 \times 10^5$$

Using Equation 3.119, the friction factor for single-phase gas flow (f_G) is calculated as follows:

$$f_G = \frac{0.07725}{(\log(Re_G/7))^2} = \frac{0.07725}{(\log(1.046 \times 10^5)/7)^2} = 0.0044$$

The interfacial friction factor is calculated using Equation 3.118 where the interfacial roughness is $\varepsilon = 2.3D(1-\alpha_G)/4\phi = 0.00291$:

$$f_i = \frac{0.0625}{\left[\log\left(\frac{15}{Re_G} + \frac{\varepsilon}{3.715D}\right)\right]^2} = \frac{0.0625}{\left[\log\left(\frac{15}{1.046 \times 10^5} + \frac{0.00291}{3.715 \times 0.078}\right)\right]^2} = 0.0156$$

Now, from Equation 3.120, the two-phase friction factor is calculated as

$$f_{TP} = (1-\phi) f_G + \phi f_i = (1-0.523) \times 0.0044 + 0.523 \times 0.0156 = 0.01025$$

The two-phase frictional pressure drop is calculated using Equation 3.121:

$$-\left(\frac{dp}{dz}\right)_f = \frac{2 f_{TP} \rho_G U_G^2}{D} = \frac{2 \times 0.01025 \times 1.2 \times 20.7^2}{0.078} = 135.1 \text{ Pa/m}$$

(c) *Double circle model*: Initially, the angle subtended by the liquid layer with the pipe centerline is calculated using the relationship $\Psi = \pi\phi = 1.153^r$ where $\phi = 0.367$ is calculated at a void fraction of $\alpha_G = 0.938$ (converged solution of Taitel and Dukler (1976) model) using Equation 3.117. Next, the angle Ψ_i is calculated using Equation 3.122. It should be noted that the angles (Ψ and Ψ_i) used in Equation 3.122 are expressed in radians:

$$\Psi_i = \left(\frac{\sin \Psi_i}{\sin(1.153)}\right)^2 \left(1.153 + \frac{\sin^2(1.153)}{\tan \Psi_i} - \frac{\sin(2 \times 1.153)}{2} - \pi(1-0.938)\right)$$

The solution to this equation, $\Psi_i = 0.931^r$, is obtained iteratively. Now, the diameter D_i of eccentric circle is found using Equation 3.123:

$$D_i = D \frac{\sin \Psi}{\sin \Psi_i} = 0.078 \times \frac{\sin(1.153)}{\sin(0.931)} = 0.088 \text{ m}$$

The wetted perimeter of gas and liquid phase based on Ψ and that of gas–liquid interface based on Ψ_i is calculated from Equation 3.124. The calculation of hydraulic diameters is similar to that of Taitel and Dukler (1976) given by Equation 3.111:

$$P_L = 0.0899 \text{ m}, \quad P_G = 0.155 \text{ m}, \quad P_i = 0.0827 \text{ m}, \quad D_G = 0.0753 \text{ m}, \quad D_L = 0.0132 \text{ m}$$

The Reynolds number of each phase is based on actual phase velocity and hydraulic pipe diameter, and the single-phase friction factors for each phase using Equation 3.110 are calculated as follows:

$$Re_G = \frac{\rho_G U_G D_G}{\mu_G} = \frac{1.2 \times 21.3 \times 0.0753}{18.5 \times 10^{-6}} = 104{,}036$$

$$Re_L = \frac{\rho_L U_L D_L}{\mu_L} = \frac{998 \times 0.645 \times 0.0132}{0.001} = 8497$$

$$f_G = 0.046(Re_G)^{-0.2} = 0.046(104{,}036)^{-0.2} = 0.00456$$

$$f_L = 0.046(Re_L)^{-0.2} = 0.046 \times (8497)^{-0.2} = 0.00753$$

To find f_i from Equation 3.125, first, determine the superficial gas velocity corresponding to the smooth to wavy stratified flow transition ($U_{SG,t}$) from Equation 3.126:

$$U_{SG,t} = \sqrt{\frac{4 \times (0.001/998)(998 - 1.2) \times 9.81}{0.06 \times 1.2 \times 0.465}} = 0.918$$

$$f_i = 0.00456\left[1 + 3.75\left(\frac{1 - 0.938}{0.367}\right)^{0.2}\left(\frac{20}{0.918} - 1\right)^{0.08}\right] = 0.0198$$

Now, the wall and interfacial shear stresses are calculated using Equation 3.109:

$$\tau_{wG} = \frac{0.00456 \times 1.2 \times 21.3^2}{2} = 1.244 \text{ N/m}^2$$

$$\tau_{wL} = \frac{0.00753 \times 998 \times 0.645^2}{2} = 1.563 \text{ N/m}^2$$

$$\tau_i = \frac{0.0198 \times 1.2 \times (21.3 - 0.645)^2}{2} = 5.087 \text{ N/m}^2$$

Equation 3.108 is not satisfied (residual = 1083), and hence, the void fraction value is updated and all other subsequent steps are repeated. At convergence (residual = 0.002), $\alpha_G = 0.961$, $\Psi = 1.48^r$, and $\Psi_i = 1.407^r$. For the converged value of void fraction, recalculate the gas, liquid, and interfacial shear stress from Equation 3.109 and then calculate two-phase pressure drop using Equation 3.106 or 3.107. Note that these equations require updated values of shear stresses based on the converged values of void fraction. Pressure drop from Equation 3.107 is calculated as follows:

$$-\left(\frac{dp}{dz}\right)_f = \tau_{wL}\frac{P_L}{A_L} - \tau_i\frac{P_i}{A_L} = 4.277\frac{0.1156}{0.0001834} - 4.234\frac{0.1109}{0.0001834} = 135.6 \text{ Pa/m}$$

Discussion: For similar flow conditions, Badie et al. (2000) measured $\alpha_G = 0.956$ and $(dp/dz)_f = 115$ Pa/m. Note that the void fraction and frictional pressure drop obtained by solving for ARS model and double circle model are comparable to the measurements of Badie et al. (2000). The prediction of void fraction using Taitel and Dukler (1976) model is within ±2% of the measured void fraction by Badie et al. (2000). However, the frictional pressure drop calculated using Taitel and Dukler (1976) is significantly less than the experimental value. This is possibly because of the use of $f_i/f_G = 1$ in their model. The use of suitable and more realistic model for f_i/f_G in Taitel and Dukler

(1976) may yield better results. For example, the use of $f_i/f_G = 10$ recommended by Crowley et al. (1992) would give a better prediction of frictional pressure drop as 126.5 Pa/m. Conclusively, the success of these three methods in the prediction of void fraction and pressure drop in stratified two-phase flow is subject to the validity and accuracy of the closure relationships used in these models. Different forms of models for the calculation of f_i/f_G could be obtained from Ottens et al. (2001).

3.6 Modeling of Annular Flow

The annular flow structure exhibits separated flow characteristics and hence could be appropriately modeled using SFM approach. The two-phase flow literature reports several annular flow pattern–specific models to determine two-phase flow parameters such as void fraction, pressure drop, and heat transfer. Section 3.3.4 gives some of the existing correlations in the two-phase flow literature that can satisfactorily predict void fraction in annular flow. This section specifically focuses on some salient features of annular flow such as liquid entrainment fraction, film thickness, film flow rates, interfacial friction, and their interrelationships.

3.6.1 Entrainment

A peculiar phenomenon known as entrainment is observed in the annular flow due to the relative motion between the gas and the liquid phase. The entrainment process is characterized by the flow of tiny liquid droplets into the central fast-moving gas core. The liquid entrainment is a consequence of the significant shear at the gas–liquid interface that causes tearing of the liquid waves crests in the form of ligaments and depends on the phase flow rates, pipe diameter, and orientation and the surface tension at the gas–liquid interface. The liquid entrainment fraction (E) is defined as the ratio of mass flow rate/flux of liquid drops entering into the gas core to the total mass flow rate/flux of the liquid phase. Correct knowledge of the rate of liquid entrainment or alternatively the fraction of liquid entrainment is crucial in analyzing heat and mass transfer processes in annular flows. In case of boiling two-phase flows, accurate estimation of the liquid entrainment fraction is necessary in the determination of critical heat flux and dryout conditions. Ishii and Grolmes (1975) studied the different possible mechanisms responsible for liquid entrainment process. They found that liquid entrainment can happen due to any or all of the wave undercut, wave rolling, wave coalescence, and ripple shearing mechanisms. Additionally, the phenomenon of "bubble burst" due to rupture of liquid-phase crests and "droplet impingement" due to rolling waves may also contribute to the entrainment process.

The different entrainment mechanisms suggested by Ishii and Grolmes (1975) are illustrated in Figure 3.32. As shown in Figure 3.33, critical values of gas and liquid flow rates are associated with the entrainment process and below which no liquid entrainment is expected to occur. Based on the experimental data, two-phase flow literature offers several correlations to determine the nondimensional critical gas

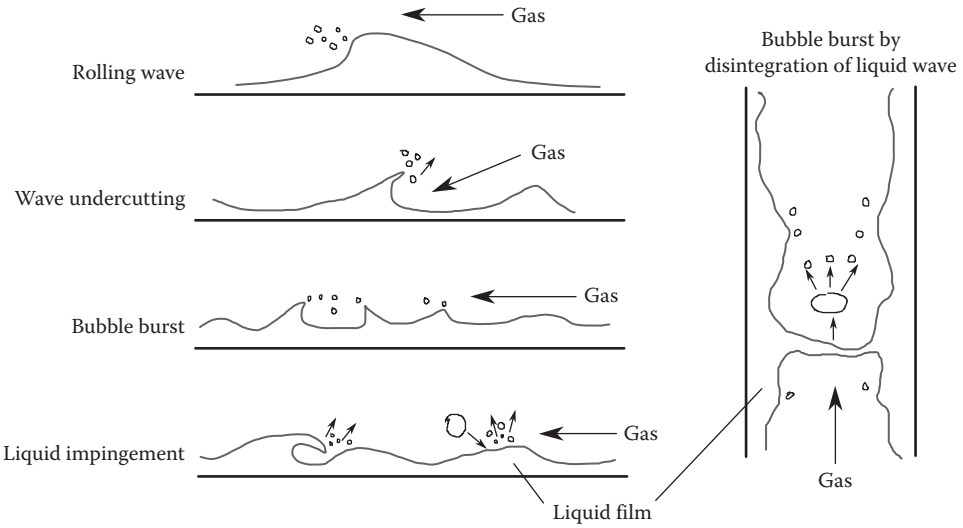


Figure 3.32

Entrainment mechanisms suggested by Ishii and Grolmes (1975).

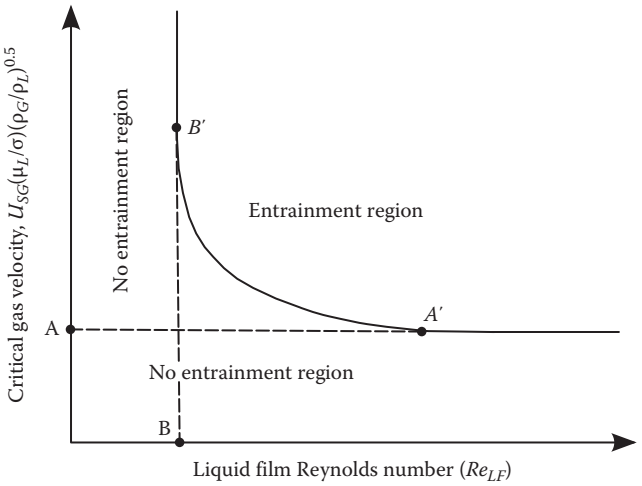


Figure 3.33

Inception criteria for entrainment. (Adapted from Ishii, M. and Grolmes, M.A., *AIChE J.*, 21, 308, 1975.)

velocity and the liquid film Reynolds (Re_{LF}) number below which the entrainment phenomenon is negligible or alternatively above which the amount of liquid entrainment is significant. Note that the Reynolds number based on liquid flowing in the form of film is defined by Ishii and Grolmes (1975) as $Re_{LF} = (4\delta U_L \rho_L)/\mu_L$ and using the concept of equivalent diameter it follows that $Re_{SL} = (\rho_L U_{SL} D)/\mu_L$. Refer to Section 3.6.2, Equation 3.138, for this identity between two forms of Reynolds number ($Re_{LF} = Re_{SL}$).

One such criterion in terms of liquid film Reynolds number proposed by Ishii and Grolmes (1975) is represented by Equation 3.127. Equation 3.127 sets the absolute limit for the inception of entrainment process and represents point *B* in Figure 3.33 below which entrainment cannot take place. Ishii and Grolmes (1975) found that at point *A*′, $Re_{LF} = 1635$ and beyond which the entrainment affected region is insensitive to the increase in liquid flow rates. The critical gas velocity for Re_{LF} greater than that by Equation 3.127 is obtained from Equation 3.128. The critical gas velocity to the left-hand side of this equation is essentially a nondimensional superficial gas velocity normalized using liquid-phase dynamic viscosity and the surface tension. Note that for Re_{LF} greater than $Re_{LF,C}$ but less than 160, critical gas velocity is independent of liquid viscosity number given by Equation 3.129:

$$Re_{LF,C} = 154.7\left(\frac{\rho_L}{\rho_G}\right)^{0.75}\left(\frac{\mu_G}{\mu_L}\right)^{1.5} \tag{3.127}$$

$$\frac{U_{SG}\mu_L}{\sigma}\sqrt{\frac{\rho_G}{\rho_L}} \geq \begin{cases} 1.5Re_{LF}^{-0.5} & : Re_{LF,C} < Re_{LF} < 160 \\ 11.78N_{\mu}^{0.8}Re_{LF}^{-0.33} & : N_{\mu} \leq 0.066, 160 \leq Re_{LF} \leq 1635 \\ 1.35Re_{LF}^{-0.33} & : N_{\mu} > 0.066, 160 \leq Re_{LF} \leq 1635 \\ N_{\mu}^{0.8} & : N_{\mu} \leq 0.066, Re_{LF} > 1635 \\ 0.1146 & : N_{\mu} > 0.066, Re_{LF} > 1635 \end{cases} \tag{3.128}$$

$$N_{\mu} = \frac{\mu_L}{(\rho_L \sigma \sqrt{\sigma/(g\Delta\rho)})^{0.5}} \tag{3.129}$$

Note that Equations 3.127 and 3.128 predict the onset of entrainment and not the magnitude of entrainment fraction. To predict the liquid entrainment fraction, Ishii and Mishima (1989) proposed a correlation applicable to air–water equilibrium annular flow. As shown in Equation 3.130, their correlation is a function of modified Weber number given by Equation 3.131. Although the correlation of Ishii and Mishima (1989) consists of nondimensional numbers as a function of fluid physical

properties, their correlation is primarily based on air–water data and its validity for other fluid combinations must be scrutinized before use:

$$E = \tanh\left(7.25\times10^{-7} We^{1.25} Re_{SL}^{0.25}\right) \left\{ \begin{array}{l} 0.1 \le p_{sys} \le 0.4\,\text{MPa} \\ 9.5 \le D \le 32\,\text{mm} \\ 370 \le Re_{SL} \le 6400 \end{array} \right. \tag{3.130}$$

$$We = \frac{\rho_G U_{SG}^2 D}{\sigma}\left(\frac{\rho_L - \rho_G}{\rho_G}\right)^{0.33} \tag{3.131}$$

Cioncolini and Thome (2012b) proposed a method to predict liquid entrainment fraction in gas–liquid annular flows. In comparison to Ishii and Mishima (1989), their correlation is based on a more comprehensive data set and is claimed to be valid for $5 \le D \le 95$ mm, $0.1 \le p_{sys} \le 20$ MPa, and for both adiabatic and evaporating flows in vertical upward flow. Recently, Bhagwat and Ghajar (2015b) have introduced a correction factor ($\xi + 120\cos^2\theta$) to the Cioncolini and Thome (2012b) correlation to improve its accuracy at high system pressures and horizontal and inclined pipe orientations. This correction factor embedded into the original correlation of Cioncolini and Thome (2012b) is expressed by Equation 3.132 where ξ is calculated from Equation 3.133. The need of a correction factor for the effect of high system pressure on liquid entrainment fraction is explained in the work by Bhagwat and Ghajar (2015b). Note that the use of Equation 3.133 requires system pressure (p_{sys}) with units of MPa. The gas core Weber number and the gas core density are calculated using Equations 3.134 and 3.135, respectively:

$$E = \left(1 + \left(\xi + 120\cos^2\theta\right) We_c^{-0.8395}\right)^{-2.209} \left\{ \begin{array}{l} 0.1 \le p_{sys} \le 20\,\text{MPa} \\ 5 \le D \le 95\,\text{mm} \\ 10 \le We_c \le 10^5 \end{array} \right. \tag{3.132}$$

$$\xi = \begin{cases} 280 & : 0.1 \le p_{sys} < 10\,\text{MPa} \\ 4637.8 \times p_{sys}^{-1.6} & : p_{sys} \ge 10\,\text{MPa} \end{cases} \tag{3.133}$$

$$We_c = \frac{\rho_c U_{SG}^2 D}{\sigma} \tag{3.134}$$

$$\rho_c = \frac{x + E(1-x)}{(x/\rho_G) + (E(1-x)/\rho_L)} \tag{3.135}$$

Equation 3.132 needs to be solved using iterative technique since the core density required in the calculation of the core Weber number depends upon the liquid entrainment fraction. Cioncolini and Thome (2012b) suggested a two-step predictor and corrector method such that the predictor method predicts the liquid entrainment fraction for an initial guess of core density approximately equal to the gas-phase density (i.e., $\rho_c \approx \rho_G$). In the corrector step, the E value from predictor step is used to calculate new value of gas core density and hence the liquid entrainment fraction. The variation of liquid entrainment fraction as a function of system pressure using the proposed modification by Bhagwat and Ghajar (2015b) to the original Cioncolini and Thome (2012b) correlation is illustrated in Figure 3.34. It is evident that at low ($We_c \le 10$) and high ($We_c \ge 10^5$) gas core Weber numbers, the effect of system pressure on liquid entrainment fraction is small. Figure 3.34 is plotted for vertical two-phase flow and can be used as a graphical solution to determine liquid entrainment fraction.

3.6.2 Triangular Relationship in Annular Flow

Triangular relationship in the annular flow in essence is a relationship between three principle dependent system parameters, that is, pressure gradient, liquid film thickness (δ), and the liquid film flow rate ($\dot{m}_{LF}$), such that if any of these two variables are known, the third unknown variable may be calculated. Although the triangular relationship forms a basis for different correlations developed for annular flow, these dependent

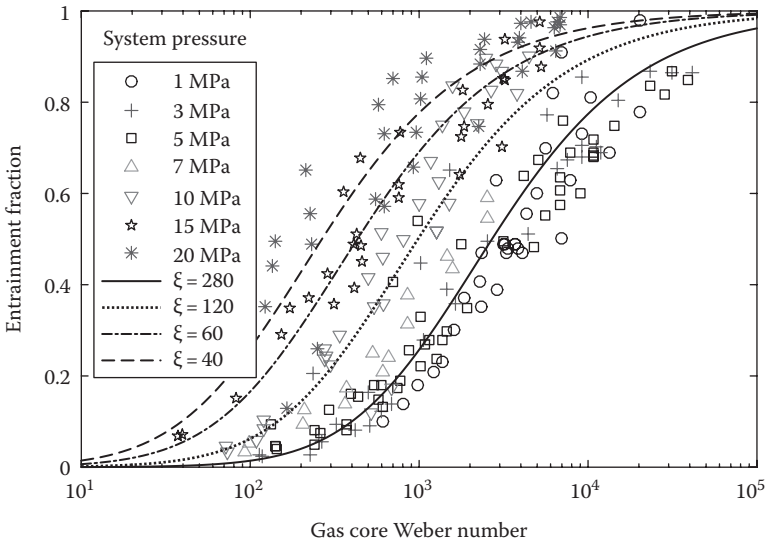


Figure 3.34

Variation of liquid entrainment fraction as a function of system pressure (trends predicted by Equation 3.132).

variables that form a triangular relationship cannot be practically calculated from the independent system parameters such as phase flow rates, fluid properties, and pipe geometry and thus further require closed-form solutions. The closed-form solutions required to form triangular relationship for the annular flow are usually in the form of equations for liquid entrainment fraction (E) and two-phase frictional multiplier (Φ^2) involving two-phase (f_{TP}) or interfacial (f_i) friction factors. This section briefly introduces the concept of triangular relationship and illustrates a step-by-step approach to calculate the system parameters in the annular flow. For more details, refer to works of Hewitt and Hall-Taylor (1970) and Collier and Thome (1996).

In order to solve for the triangular relationship, Hewitt and Hall-Taylor (1970) recommend the use of the following simplifying assumptions:

1. Film thickness is very small with respect to pipe diameter, that is, $\delta \ll D$.
2. Shear stress in liquid film is constant and equal to the wall shear stress.
3. Hydrostatic and accelerational effects on the gas core and liquid film are negligible (compared to frictional pressure drop).

Assuming axis symmetric flow, uniform film thickness, and negligible contribution of hydrostatic and accelerational pressure drops (in comparison to frictional pressure drop), the momentum balance on the liquid film in the annular flow leads to Equation 3.136 for two-phase frictional pressure drop. This two-phase frictional pressure drop is expressed in terms of actual velocity of the liquid flowing in the form of film (in contact with pipe wall) and that the liquid entrainment is negligible. Using the definition of Φ_L^2, Equation 3.86 could also be expressed as Equation 3.137:

$$-\left(\frac{dp}{dz}\right)_f = \frac{4\tau_{wL}}{D} = \frac{2f_{TP}\rho_L U_L^2}{D} \tag{3.136}$$

$$\Phi_L^2 = \frac{(dp/dz)_f}{(dp/dz)_L} = \frac{1}{(1-\alpha_G)^2}\left(\frac{f_{TP}}{f_L}\right) \tag{3.137}$$

Hewitt and Hall-Taylor (1970) have reported that using the concept of equivalent diameter and definition of void fraction under no entrainment, the Reynolds number of liquid flowing in the form of film is identical to the Reynolds number of liquid phase flowing alone through the pipe. This implies that based on identical Reynolds number defined by Equation 3.138, the friction factors of liquid flowing in the form of film and that alone through the pipe must be identical, that is, $f_{TP} = f_L$. Using this relationship,

Equation 3.137 reduces to Equation 3.139. This relationship however does not acknowledge the existence of liquid entrainment fraction that in certain practical cases may not be ignored. To account for the liquid entrainment fraction, Turner and Wallis (1965) have proposed the use of a similar relationship in which the single-phase pressure drop for the total liquid flow is replaced by the single-phase pressure drop for that part of the liquid flow that is in the form of film. The two-phase frictional multiplier suggested by Turner and Wallis (1965) is expressed by Equation 3.140 where the single-phase pressure drop of the liquid film flow is obtained from Equation 3.141:

$$\frac{\rho_L U_L 4\delta}{\mu_L} = \frac{\rho_L U_{SL} D}{\mu_L} \tag{3.138}$$

$$\Phi_L^2 = \frac{1}{(1-\alpha_G)^2} \tag{3.139}$$

$$\Phi_{LF}^2 = \frac{(dp/dz)_f}{(dp/dz)_{LF}} = \frac{1}{(1-\alpha_G)_{LF}^2} \tag{3.140}$$

$$-\left(\frac{dp}{dz}\right)_{LF} = \frac{2f_{LF}\rho_L(U_{SL}(1-E))^2}{D} = \frac{2f_{LF}(G(1-x)(1-E))^2}{D\rho_L} \tag{3.141}$$

Equation 3.140 can be considered as an empirical correlation for the determination of void fraction in the presence of liquid entrainment process; however, its implementation also requires the knowledge of two-phase frictional pressure drop. For a known or measured value of void fraction and liquid entrainment fraction, Equation 3.140 may not predict the correct magnitude of two-phase frictional pressure drop due to lack of information on the interfacial roughness and hence the interfacial shear stress. To address this issue, one more closure relationship is required that links the interfacial friction/roughness to the liquid flow rate or any other previously calculated variables such as void fraction or liquid entrainment fraction. This relationship could be obtained by considering yet another form of two-phase frictional multiplier in the form of Φ_G^2. Using similar assumptions that are used to obtain Equation 3.136, a momentum balance for gas core is used to obtain Equation 3.142. Using Equation 3.142, the two-phase frictional multiplier (Φ_G^2) assuming only gas phase flowing through pipe can be written as Equation 3.143 where the interfacial and gas shear stress are expressed by Equations 3.144 and 3.145, respectively. Thus, Φ_G^2 could be expressed as a function of void fraction, interfacial friction factor, core density, actual gas velocity, and liquid film velocity as expressed by Equation 3.146:

$$-\left(\frac{dp}{dz}\right)_f = \frac{4\tau_i}{(D-2\delta)} \tag{3.142}$$

$$\Phi_G^2 = \frac{(dp/dz)_f}{(dp/dz)_G} = \frac{4\tau_i/(D-2\delta)}{4\tau_G/D} \tag{3.143}$$

$$\tau_i = f_i\left(\frac{\rho_c(U_G - U_{LF})^2}{2}\right) \tag{3.144}$$

$$\tau_G = f_G\left(\frac{\rho_G U_{SG}^2}{2}\right) \tag{3.145}$$

$$\Phi_G^2 = \frac{1}{\sqrt{\alpha_G}}\frac{f_i}{f_G}\frac{\rho_c}{\rho_G}\frac{(U_G - U_{LF})^2}{U_{SG}^2} = \frac{1}{\sqrt{\alpha_G}}\frac{f_i}{f_G}\frac{\rho_c}{\rho_G}\left[\frac{1}{\alpha_G} - \frac{U_L(1-E)}{U_{SG}}\right]^2 \tag{3.146}$$

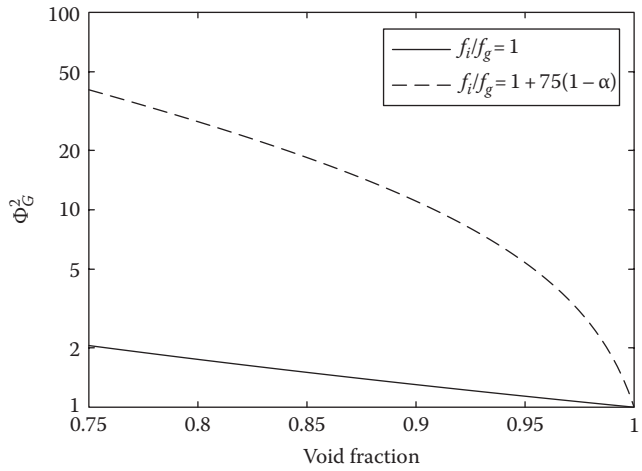


Figure 3.35

Effect of f_i/f_G on two-phase frictional multiplier (Φ_G^2).

Note that for low liquid flow rates, the velocity of liquid flowing in the form of film may be small compared to the fast-moving gas core such that $U_{LF} \ll U_G$. Also for low liquid flow rates, the liquid entrainment fraction may be negligible leading to $\rho_c/\rho_G \approx 1$. Thus, for such a simplified two-phase flow situation, Equation 3.146 reduces to Equation 3.147. Furthermore, for a more simplified assumption of smooth gas–liquid interface, ($f_i \approx f_G$) and Φ_G^2 can be expressed as Equation 3.148:

$$\Phi_G^2 = \frac{1}{\alpha_G^{5/2}} \frac{f_i}{f_G} \tag{3.147}$$

$$\Phi_G^2 = \frac{1}{\alpha_G^{5/2}} \tag{3.148}$$

It must be mentioned that the assumption of smooth gas–liquid interface (f_i/f_G) is an unrealistic assumption for the annular flow and the calculation of two-phase frictional multiplier, and, the two-phase frictional pressure drop may deviate significantly from actual conditions. It is evident from Figure 3.35 that by accounting for the interfacial roughness, the predicted values of Φ_G^2 could be significantly greater than that for the ideal conditions. Going back to Equation 3.146, the ratio f_i/f_G could be replaced with the empirical correlation in the form of Equation 3.149 proposed by Wallis (1962). Note that the two-phase flow literature reports several empirical relationships to model the ratio of f_i/f_G. Some of these correlations are listed in Table 3.9:

$$\frac{f_i}{f_G} = 1 + 300\frac{\delta}{D} = 1 + 75(1-\alpha_G) \tag{3.149}$$

The mass flow rate of liquid phase in the form of film, the actual velocity of the liquid film, and the Reynolds number of the liquid film are defined by Equations 3.150 through 3.152, respectively:

$$\dot{m}_{LF} = \dot{m}_L(1-E) \tag{3.150}$$

$$U_{LF} = U_L(1-E) \tag{3.151}$$

$$Re_{LF} = Re_{SL}(1-E) \tag{3.152}$$

The density of the gas core (ρ_c) is obtained using Equation 3.135 based on liquid entrainment fraction. Note that only for negligible liquid entrainment fraction $\rho_c \approx \rho_G$. Figure 3.36 shows the algorithm to use in

Table 3.9 List of Correlations for Interfacial Friction Factors

Source	Correlation
Moeck (1970)	$f_i = 0.005\left(1+1458\left(\frac{\delta}{D}\right)^{1.42}\right)$
Laurinat et al. (1984)	$f_i = f_G\left(2+2.5\times10^{-5}\frac{Re_{LF}}{D}\right)\alpha_G^{5/2}$
Wallis (1962)	$f_i = 0.005(1 + 75(1 - \alpha_G))$
Wongwises and Kongkiatwanitch (2001)	$f_i = 17.172 Re_{SG}^{-0.768}\left(\frac{\delta}{D}\right)^{-0.253}$
Fore et al. (2000)	$f_i = 0.005\left(1+300\left[\left(1+\frac{17{,}500}{Re_G}\right)\frac{\delta}{D}-0.0015\right]\right)$

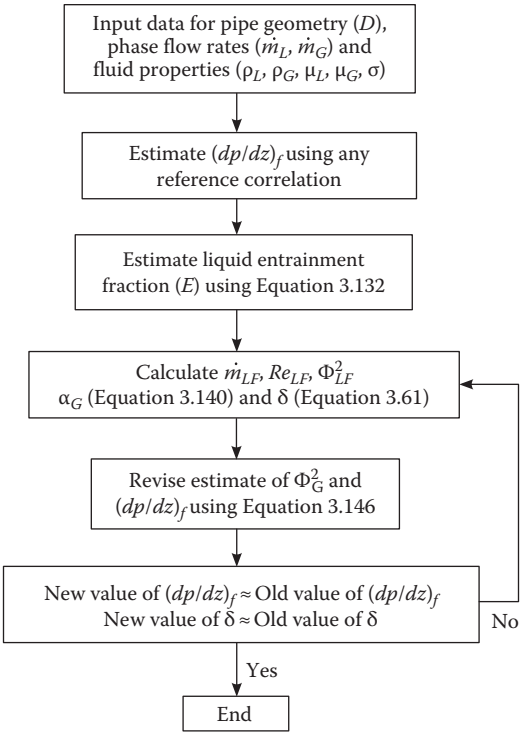


Figure 3.36

Algorithm to solve triangular relationship in annular flow.

triangular relationship for the determination of frictional pressure drop, liquid film thickness, and flow rate of liquid in the form of film.

Example Problem 3.2

Consider the vertical upward two-phase flow of air–water mixture in a 45 mm I.D. smooth pipe. At near atmospheric system pressure, the two-phase mixture flows with a quality (x) and mass flux (G) of 0.25 and 210 kg/m^2, respectively. The physical properties of air and water are as follows: $\rho_G = 1.5$ kg/m^3, $\rho_L = 998$ kg/m^3, $\mu_G = 18.5 \times 10^{-6}$ Pa s, $\mu_L = 0.001$ Pa s, and $\sigma = 0.072$ N/m. Using triangular relationship for annular flow, determine the film thickness (δ), film flow rate ($\dot{m}_{LF}$), and pressure drop $(dp/dz)_f$. Assume that adiabatic annular flow at equilibrium exists in the pipe.

Solution

The solution to this problem follows the calculation algorithm illustrated in Figure 3.36.

(1) *Make initial estimate of two-phase pressure drop*: Calculate gas- and liquid-phase Reynolds numbers (see Table 3.1) and single-phase friction factors from Equation 3.71:

$$Re_{SG} = \frac{GxD}{\mu_G} = \frac{210 \times 0.25 \times 0.045}{18.5 \times 10^{-6}} = 127703 \Rightarrow f_G = 0.00418$$

$$Re_{SL} = \frac{G(1-x)D}{\mu_L} = \frac{210 \times (1-0.25) \times 0.045}{0.001} = 7088 \Rightarrow f_L = 0.0086$$

Calculate the frictional pressure drop for gas and liquid phase assuming each phase flowing alone through the pipe:

$$-\left(\frac{dp}{dz}\right)_G = \frac{2 f_G (Gx)^2}{D\rho_G} = \frac{2 \times 0.00418 (210 \times 0.25)^2}{0.045 \times 1.5} = 341.3 \,(\text{Pa/m})$$

$$-\left(\frac{dp}{dz}\right)_L = \frac{2 f_L (G(1-x))^2}{D\rho_G} = \frac{2 \times 0.0086 (210 \times 0.75)^2}{0.045 \times 998} = 9.5 \,(\text{Pa/m})$$

The parameter (X) of Lockhart and Martinelli (1949) and the two-phase frictional multiplier $\left(\Phi_G^2\right)$ are now obtained from Equations 3.90 and 3.89, respectively. For turbulent–turbulent region of gas and liquid flow $C = 20$ from Table 3.7:

$$X = \sqrt{\frac{(dp/dz)_L}{(dp/dz)_G}} = \sqrt{\frac{9.5}{341.3}} = 0.167$$

$$\Phi_G^2 = 1 + CX + X^2 = 1 + 20 \times 0.167 + 0.167^2 = 4.37$$

Now, the two-phase frictional pressure drop is calculated as

$$\left(\frac{dp}{dz}\right)_f = \Phi_G^2 \times \left(\frac{dp}{dz}\right)_G = 4.37 \times 341.3 = 1491.5 \,(\text{Pa/m})$$

(2) *Estimate liquid entrainment fraction* (E): Liquid entrainment fraction can be estimated using Equation 3.132. First estimate the gas core Weber number using gas-phase density and predict the initial estimate of liquid entrainment fraction. The superficial gas velocity required in the determination of We_c is calculated as $U_{SG} = Gx/\rho_G = 210 \times 0.25/1.5 = 35$ m/s. Then find the gas core density using the initial estimate of E and recalculate Weber number and liquid entrainment fraction in corrector step. For near atmospheric system pressure $\xi = 280$ from Equation 3.133.

$$We_c = \frac{\rho_G U_{SG}^2 D}{\sigma} = \frac{1.5 \times 35^2 \times 0.045}{0.072} = 1148.4$$

$$E = (1 + 280 \times We_c^{-0.8395})^{-2.209} = 0.288$$

$$\rho_c = \frac{x + E(1-x)}{(x/\rho_G) + (E(1-x)/\rho_L)} = \frac{0.25 + 0.288 \times 0.75}{(0.25/1.5) + (0.288 \times 0.75/998)} = 2.8 \,(\text{kg/m}^3)$$

$$We_c = \frac{\rho_c U_{SG}^2 D}{\sigma} = \frac{2.8 \times 35^2 \times 0.045}{0.072} = 2143.7$$

$$E = (1 + 280 \times We_c^{-0.8395})^{-2.209} = 0.44$$

The updated value of core density (ρ_c) based on entrainment in corrector step is $\rho_c = 3.47$ kg/m^3. Based on the predicted entrainment value ($E = 0.44$) and using Equation 3.150, the liquid film flow rate can be calculated as follows. The liquid mass flow rate required in this equation is $\dot{m}_L = G(1-x)\times A = 210(1-0.25)\times \pi/4 \times 0.045^2 = 0.25$ kg/s:

$$\dot{m}_{LF} = (1-E)\dot{m}_L = (1-0.44)\times 0.25\,(\text{kg/s}) = 0.14\,(\text{kg/s})$$

(3) *Estimate liquid film thickness* (δ): To determine the liquid film thickness, first calculate the two-phase frictional multiplier $\left(\Phi_{LF}^2\right)$ based on the liquid film flow rate given by Equation 3.140. To determine Φ_{LF}^2, first calculate the friction factor (f_{LF}) for liquid film flow. The Reynolds number of liquid film is calculated from Equation 3.152 such that $Re_{LF} = Re_{SL} \times (1 - E) = 3969$, and hence, the corresponding friction factor from Equation 3.71 is $f_{LF} = 0.00995$:

$$\left(\frac{dp}{dz}\right)_{LF} = \frac{2f_{LF}(G(1-x)(1-E))^2}{D\rho_L} = \frac{2\times 0.00995\times(210\times 0.75\times 0.56)^2}{0.045\times 998} = 3.45\,(\text{Pa/m})$$

$$\Phi_{LF}^2 = \frac{(dp/dz)_f}{(dp/dz)_{LF}} = \frac{1491.5}{3.45} = 432.3$$

$$\Phi_{LF}^2 = \frac{1}{(1-\alpha_G)^2} = 432.3 \Rightarrow (1-\alpha_G) = \frac{4\delta}{D} = 0.0481$$

$$\therefore \alpha_G = 0.952 \quad \text{and} \quad \delta = 0.541\,\text{mm}$$

(4) *Update the value of two-phase pressure drop*: Use Equation 3.146 along with Equation 3.149 to calculate the new value of two-phase frictional multiplier $\left(\Phi_G^2\right)$ and compare it with the initial calculated value of $\Phi_G^2 = 4.37$. Here, we first find $U_{SL} = G(1 - x)/\rho_L = 210 \times 0.75/998 = 0.158$ m/s and $U_L = U_{SL}/(1 - \alpha_G) = 0.158/0.0481 = 3.28$ m/s:

$$\Phi_G^2 = \frac{1}{\sqrt{\alpha_G}}\frac{f_i}{f_G}\frac{\rho_c}{\rho_G}\left[\frac{1}{\alpha_G} - \frac{U_L(1-E)}{U_{SG}}\right]^2$$

$$\Phi_G^2 = \frac{1}{\sqrt{0.952}}(1+75\times 0.0481)\times\frac{3.47}{1.5}\left(\frac{1}{0.952} - \frac{3.28\times(1-0.44)}{35}\right)^2 = 10.88$$

Now, the updated value of two-phase frictional pressure drop is calculated as

$$\left(\frac{dp}{dz}\right)_f = \Phi_G^2 \times \left(\frac{dp}{dz}\right)_G = 10.88\times 341.3 = 3713.3\,(\text{Pa/m})$$

(5) *Repeat steps (3) and (4) to get consistent values of* δ *and* $(dp/dz)_f$: Since the new value of Φ_G^2 and frictional pressure drop is greater than the initial estimate, recalculate Φ_{LF}^2 value to obtain new estimates of δ and Φ_G^2. After 12 iterations consistent values of liquid film thickness, two-phase frictional multiplier $\left(\Phi_G^2\right)$ and hence the two-phase frictional pressure drop are obtained. The final values of parameters in triangular relationship are

Liquid film thickness (δ) = 0.398 mm.
Liquid film flow rate $\left(\dot{m}_{LF}\right) = 0.14$ kg/s.
Two-phase pressure drop $(dp/dz)_f = 2745$ Pa/m.
In addition, based on the iterated value of Φ_{LF}^2, $\alpha_G = 0.965$.

Discussion: For similar experimental conditions, Nguyen (1975) measured $\alpha_G = 0.951$ and $(dp/dz)_f = 2440$ Pa/m. Note that the converged values of void fraction and pressure drop obtained by solving triangular relationship are comparable with measured data of Nguyen (1975).

Moreover, the film thickness ($\delta = 0.398$ mm) obtained using triangular relationship is comparable to the predicted ($\delta = 0.431$ mm) film thickness by empirical correlation of Henstock and Hanratty (1976). It must be mentioned that the final converged values obtained using triangular relationship depend upon the closure relationships for liquid entrainment fraction (E), interfacial friction factor (f_i), and hence the two-phase frictional multiplier $\left(\Phi_G^2\right)$. There is no unanimity over the use of a particular set of closure equations, and hence, the use of different set of equations may yield slightly different solutions of triangular relationship.

3.7 Nonboiling Two-Phase Heat Transfer

Knowledge about nonboiling two-phase heat transfer is important in several applications in oil and gas and chemical engineering industry. In particular, during the production of two-phase hydrocarbon fluids from oil reservoirs and its transportation to the surface processing facilities, the temperature of hydrocarbons drops drastically and is favorable for hydrates formation and wax deposition. Wax deposition can result in problems including reduction of inner tube diameter causing blockage, increase in surface roughness of tube leading to restricted flow line pressure, and decrease in production and can lead to various mechanical problems. In such situations, the correct knowledge of heat transfer coefficients in two-phase flow is of utmost importance for the purpose of flow assurance in oil and gas industry. The following text provides a brief information on the phenomenon of two-phase flow models for nonboiling two-phase heat transfer. Detailed information on the effect of fluid properties and pipe orientation on two-phase heat transfer coefficient can be obtained from Tang (2011), Ghajar and Tang (2010), and Bhagwat et al. (2012).

3.7.1 Two-Phase Heat Transfer Model

In the two-phase flow literature, majority of the documented nonboiling two-phase heat transfer modeling methods are limited to specific pipe orientations, fluid combinations, and most importantly flow patterns. The subsea and surface pipe lines carrying a mixture of oil and gas together are usually laid in undulated form having near horizontal inclinations, and the existence of a specific flow pattern is uncertain. For such a scenario, the use of flow pattern and pipe orientation-specific two-phase heat transfer correlations may predict significant deviations from the actual conditions. To address this issue, Ghajar and coworkers in a series of papers have extensively studied the phenomenon of nonboiling two-phase heat transfer in pipes at different orientations. Ghajar and Tang (2009) proposed a robust correlation for two-phase heat transfer coefficient (h_{TP}) as presented by Equation 3.153. Their correlation is based on 986 experimental data points for different pipe orientations and fluid combinations:

$$h_{TP} = h_L F_p \left[1 + 0.55 \left(\frac{x}{1-x} \right)^{0.1} \left(\frac{1-F_p}{F_p} \right)^{0.4} \left(\frac{Pr_G}{Pr_L} \right)^{0.25} \left(\frac{\mu_L}{\mu_G} \right)^{0.25} I^{0.25} \right] \tag{3.153}$$

$$F_p = (1-\alpha_G) + \alpha_G F_s^2 \tag{3.154}$$

$$F_s = \frac{2}{\pi} \arctan\left(\sqrt{\frac{\rho_G (U_G - U_L)^2}{gD(\rho_L - \rho_G)}} \right) \tag{3.155}$$

$$I = 1 + Eo\,|\sin\theta| \tag{3.156}$$

The flow pattern factor (F_p) given by Equation 3.154 makes the Ghajar and Tang (2009) correlation independent of the flow patterns and depends on shape factor F_s and void fraction (α_G). The shape factor (F_s) given by Equation 3.155 considers the effect of the shape of gas–liquid interface on two-phase heat transfer, while the void fraction needs to be calculated using the correlations of Woldesemayat and Ghajar (2007) (use Equations 3.45 and 3.46). The variable I given by Equation 3.156 is defined in terms of Eötvös number, and it accounts for the effect of pipe orientation on h_{TP}:

$$Eo = \frac{(\rho_L - \rho_G) g D^2}{\sigma} \tag{3.157}$$

The single-phase heat transfer coefficient required in Equation 3.153 is based on in situ Reynolds number. All thermophysical properties required are calculated at bulk mean temperature except for the μ_w that is calculated at the pipe wall temperature. Note that the in situ liquid phase the Reynolds number used in Equation 3.158 for h_L is defined in terms of the square root of liquid holdup as shown in Equation 3.159:

$$h_L = 0.027 Re_L^{0.8} Pr_L^{0.33} \left(\frac{k_L}{D}\right)\left(\frac{\mu_L}{\mu_w}\right)^{0.14} \tag{3.158}$$

$$Re_L = \frac{4\dot{m}_L}{\pi D \mu_L \sqrt{1-\alpha_G}} = \frac{G(1-x)D}{\mu_L \sqrt{1-\alpha_G}} \tag{3.159}$$

3.7.2 Reynolds Analogy and Two-Phase Heat Transfer

The concept of Reynolds analogy that relates the skin friction factor or the frictional pressure drop with heat transfer in single-phase flow can also be extended to the case of two-phase flow. Using the concept of Reynolds analogy, Tang and Ghajar (2011) have developed a correlation that correlates the two-phase to single-phase heat transfer coefficient ratio to the two-phase frictional multiplier (ratio of two-phase to single-phase pressure drop). The physical form of this correlation is given by Equation 3.160. The two-phase mixture density (ρ_M) is calculated using void fraction, $\rho_M = \rho_L(1 - \alpha_G) + \rho_G\alpha_G$, F_p is calculated from Equation 3.154, h_L is calculated from Equation 3.158 using the Reynolds number (Re_{SL}) based on superficial liquid velocity (see Table 3.1). Note that Φ_L is the square root of the two-phase frictional multiplier calculated using Equation 3.86. In case if the two-phase frictional pressure drop is not known/measured, then suitable correlation valid for given two-phase flow conditions may be used to determine Φ_L. The void fraction required in the calculation of two-phase mixture density (ρ_M) is calculated using Woldesemayat and Ghajar (2007) correlation (Equations 3.45 and 3.46). Tang (2011) suggested that the exponents of F_p and Φ_L could vary between 0.1 and 0.5 depending upon the pipe orientation and fluid properties; however, the general structure of Reynolds analogy–based correlation remains unaltered. In Equation 3.160, the exponent (0.3) of F_p and Φ_L is based on the overall performance of their model for various pipe inclinations and fluid combinations:

$$h_{TP} = h_L F_p^{0.3} \left(\frac{\dot{m}_L}{\dot{m}}\right)\left(\frac{\rho_L}{\rho_M}\right)^{0.5} \Phi_L^{0.3} \tag{3.160}$$

Both the correlations of Ghajar and Tang (2009) (general heat transfer correlation) and Tang and Ghajar (2011) (Reynolds analogy–based heat transfer correlation) are applicable over the following range of parameters: $750 \le Re_{SL} \le 1.27 \times 10^5$, $14 \le Re_{SG} \le 21 \times 10^5$, $0.01 \le Pr_G/Pr_L \le 0.15$, $910 \le \rho_L \le 1210$ kg/m^3, $0.0036 \le \mu_G/\mu_L \le 0.026$, and $0° \le \theta \le +90°$. Within the range of these two-phase flow variables, both correlations are known to predict more than 80% and 90% of data points within ±20% and ±30% error bands, respectively. The physical structure of these correlations is modular and robust, and hence, the application of these correlations can be potentially extended to a wider range of two-phase flow conditions by modifying the empirical multiplying factors and exponents.

Example Problem 3.3

Consider the vertical upward two-phase flow of air and silicone oil in a 12 mm I.D. stainless steel pipe having a surface roughness of 20 μm. The mass flow rates of gas and liquid phase are 0.0015 kg/s and 0.9 kg/s, respectively. The fluid thermophysical properties may be taken as follows: $\rho_G = 1.2$ kg/m^3, $\rho_L = 920$ kg/m^3, $\mu_G = 18.4 \times 10^{-6}$ Pa s, $\mu_L = 0.005$ Pa s, $\mu_w = 0.004$ Pa s, $\sigma = 0.02$ N/m, $k_L = 0.12$ W/mK, $Pr_G = 0.71$, and $Pr_L = 64$. For a measured void fraction of $\alpha_G = 0.5$, determine the two-phase heat transfer coefficient for the flow of air and silicon oil using (1) heat transfer correlation of Ghajar and Tang (2009) given by Equation 3.153 and (2) Reynolds analogy given by Equation 3.160.

Solution

(1) Calculation of h_{TP} using Ghajar and Tang (2009) correlation:
The superficial gas (U_{SG}) and liquid (U_{SL}) velocities and the two-phase flow quality (x) are first calculated as follows:

$$U_{SG} = \frac{4\dot{m}_G}{\pi D^2 \rho_G} = \frac{4 \times 0.0015}{\pi \times 0.012^2 \times 1.2} = 11.05 \text{ m/s}$$

$$U_{SL} = \frac{4\dot{m}_L}{\pi D^2 \rho_L} = \frac{4 \times 0.9}{\pi \times 0.012^2 \times 920} = 8.65 \text{ m/s}$$

$$x = \frac{\dot{m}_G}{\dot{m}_G + \dot{m}_L} = \frac{0.0015}{0.0015 + 0.9} = 0.00166$$

From the given information of void fraction, the actual velocity of each phase is calculated as follows. In case if the void fraction is not known, Woldesemayat and Ghajar (2007) correlation (Equations 3.45 and 3.46) can be used for void fraction calculation. For the given flow conditions, Woldesemayat and Ghajar (2007) correlation gives $\alpha_G = 0.52$ that is within ±5% of the given void fraction value of 0.5:

$$U_G = \frac{U_{SG}}{\alpha_G} = \frac{11.05}{0.5} = 22.1 \text{ m/s}$$

$$U_L = \frac{U_{SL}}{1 - \alpha_G} = \frac{8.65}{1 - 0.5} = 17.3 \text{ m/s}$$

Now, the shape factor is calculated from Equation 3.155:

$$F_s = \left[\frac{2}{\pi} \arctan\left(\sqrt{\frac{\rho_G (U_G - U_L)^2}{gD(\rho_L - \rho_G)}} \right) \right]$$

$$= \left[\frac{2}{\pi} \arctan\left(\sqrt{\frac{1.2 \times (22.1 - 17.3)^2}{9.81 \times 0.012 \times (920 - 1.2)}} \right) \right] = 0.298$$

The flow pattern factor is obtained from Equation 3.154:

$$F_p = (1 - \alpha_G) + \alpha_G F_S^2 = (1 - 0.5) + 0.5 \times 0.298^2 = 0.544$$

The inclination factor for the vertical flow is calculated by Equation 3.156:

$$I = 1 + \frac{(\rho_L - \rho_G) g D^2}{\sigma} |\sin\theta| = 1 + \frac{(920 - 1.2) \times 9.81 \times 0.012^2}{0.02} = 65.9$$

Next, the in situ Reynolds number based on void fraction is calculated from Equation 3.159:

$$Re_L = \frac{4\dot{m}_L}{\pi D \mu_L \sqrt{1 - \alpha_G}} = \frac{4 \times 0.9}{\pi \times 0.012 \times 0.005 \times \sqrt{1 - 0.5}} = 27{,}009.5$$

The single-phase heat transfer coefficient is then calculated using Equation 3.158:

$$h_L = 0.027 Re_L^{0.8} Pr_L^{0.33} \left(\frac{\mu_L}{\mu_w}\right)^{0.14} \left(\frac{k_L}{D}\right)$$

$$= 0.027 \times 27{,}009.5^{0.8} \times 64^{0.33} \times \left(\frac{0.005}{0.004}\right)^{0.14} \left(\frac{0.12}{0.012}\right)$$

$$= 3{,}856 \text{ W/m}^2 \text{ K}$$

Using the two-phase heat transfer correlation of Ghajar and Tang (2009) given by Equation 3.153, h_{TP} is calculated as

$$h_{TP} = h_L F_p \left[1 + 0.55 \left(\frac{x}{1-x}\right)^{0.1} \left(\frac{1-F_p}{F_p}\right)^{0.4} \left(\frac{Pr_G}{Pr_L}\right)^{0.25} \left(\frac{\mu_L}{\mu_G}\right)^{0.25} I^{0.25}\right]$$

$$= 3856 \times 0.544 \left[1 + 0.55 \left(\frac{0.00166}{1-0.00166}\right)^{0.1} \left(\frac{1-0.544}{0.544}\right)^{0.4} \left(\frac{0.71}{64}\right)^{0.25} \left(\frac{0.005}{18.4 \times 10^{-6}}\right)^{0.25} 65.9^{0.25}\right]$$

$$= 4224 \text{ W/m}^2 \text{ K}$$

(2) Calculation of h_{TP} using the concept of Reynolds analogy: To use the concept of Reynolds analogy, we first need to find the two-phase frictional pressure drop and hence the two-phase frictional multiplier $\left(\Phi_L^2\right)$. The following steps calculate the two-phase pressure drop using the method of Lockhart and Martinelli (1949).

The Reynolds number of each phase and associated friction factors are calculated as shown as follows. Since the two-phase flow is through steel pipe having a roughness of 20 μm, we need to use appropriate correlation such as Colebrook (1939) or Churchill (1977) to account for the effect of pipe wall surface roughness on friction factor. Here, we use Colebrook (1939) friction factor correlation:

$$Re_{SG} = \frac{\rho_G U_{SG} D}{\mu_G} = \frac{1.2 \times 11.05 \times 0.012}{18.4 \times 10^{-6}} = 8{,}648 \Rightarrow f_G = 0.0081$$

$$Re_{SL} = \frac{\rho_L U_{SL} D}{\mu_L} = \frac{920 \times 8.65 \times 0.012}{0.005} = 19{,}099 \Rightarrow f_L = 0.0063$$

Now the single-phase pressure drop due to flow of gas and liquid phase is calculated by

$$-\left(\frac{dp}{dz}\right)_G = \frac{2 f_G \rho_G U_{SG}^2}{D} = \frac{2 \times 0.0081 \times 1.2 \times 11.05^2}{0.012} = 197.8 \text{ Pa/m}$$

$$-\left(\frac{dp}{dz}\right)_L = \frac{2 f_L \rho_L U_{SL}^2}{D} = \frac{2 \times 0.0063 \times 920 \times 8.65^2}{0.012} = 72{,}278.5 \text{ Pa/m}$$

The parameter X of Lockhart and Martinelli (1949) is calculated using the single-phase pressure drop as shown here:

$$X = \sqrt{\frac{(dp/dz)_L}{(dp/dz)_G}} = \sqrt{\frac{72{,}278.5}{197.8}} = 19.11$$

Since the single-phase flow of both phases is in turbulent region, we use $C = 20$ from Table 3.7 and the two-phase frictional multiplier using the method of Lockhart and Martinelli (1949) is calculated from Equation 3.89 as shown here:

$$\Phi_L^2 = 1 + \frac{20}{X} + \frac{1}{X^2} = 1 + \frac{20}{19.11} + \frac{1}{19.11^2} = 2.05 \Rightarrow \Phi_L = 1.43$$

Two-phase mixture density based on void fraction is calculated as follows:

$$\rho_M = \alpha_G \rho_G + (1 - \alpha_G)\rho_L = 0.5 \times 1.2 + (1 - 0.5) \times 920 = 460.6 \text{ kg/m}^3$$

Now using Equation 3.160, the two-phase heat transfer coefficient can be found. The value of h_L based on Re_{SL} is calculated from Equation 3.158. The value of $F_p = 0.544$ is found earlier in this problem:

$$h_L = 0.027 Re_{SL}^{0.8} Pr_L^{0.33} \left(\frac{\mu_L}{\mu_w}\right)^{0.14} \left(\frac{k_L}{D}\right)$$

$$= 0.027 \times 19{,}099^{0.8} \times 64^{0.33} \times \left(\frac{0.005}{0.004}\right)^{0.14} \left(\frac{0.12}{0.012}\right) = 2{,}922.6 \text{ W/m}^2 \text{ K}$$

Finally, the two-phase heat transfer coefficient using Reynolds analogy is found using Equation 3.160:

$$h_{TP} = h_L F_p^{0.3} \left(\frac{\dot{m}_L}{\dot{m}}\right) \left(\frac{\rho_L}{\rho_M}\right)^{0.5} \Phi_L^{0.3}$$

$$= 2922.6 \times 0.544^{0.3} \left(\frac{0.9}{0.9015}\right) \left(\frac{920}{460.6}\right)^{0.5} 1.43^{0.3}$$

$$= 3824 \text{ W/m}^2 \text{ K}$$

Discussion: Rezkallah and Sims (1987) made two-phase heat transfer measurements for similar experimental conditions and found that $h_{TP} \approx 3900$ W/m^2 K. The value of h_{TP} predicted by Ghajar and Tang (2009) and that by Reynolds analogy of Tang and Ghajar (2011) is within ±10% and ±2% deviation from their measured values, respectively. The general heat transfer correlation and Reynolds analogy–based heat transfer correlation are sensitive to the void fraction (through F_P and ρ_M). Note that in case if the two-phase frictional pressure drop is not known, the accuracy of the Reynolds analogy concept depends on the choice of two-phase frictional multiplier correlation appropriate to the two-phase flow under consideration.

Nomenclature

Symbols	Description
a_1	Variable in the correlation of Xiong and Chung (2006)
A	Cross-sectional area (m^2)
B_s	Variable in Chisholm (1973)
c_1	Variable in the correlation of Bhagwat and Ghajar (2014)
c_2	Variable in the correlation of Bhagwat and Ghajar (2014)
c_3	Variable in the correlation of Bhagwat and Ghajar (2014)
C	Constant in the parameter of Lockhart and Martinelli (1949)
C_o	Distribution parameter
$C_{o,1}$	Variable used by Bhagwat and Ghajar (2014)
C_1	Variable in the correlation of Bhagwat and Ghajar (2015a)

C_2	Variable in the correlation of Bhagwat and Ghajar (2015a)
C_3	Variable in the correlation of Bhagwat and Ghajar (2015a)
C_4	Variable in the correlation of Bhagwat and Ghajar (2015a)
d	Local distance along the pipe diameter
d_{def}	Bubble diameter above which bubble is deformed
$d_{\max}$	Maximum bubble diameter
d_{migr}	Bubble diameter below which migration of bubbles is prevented
dp/dz	Pressure gradient (Pa/m)
$(dp/dz)^+$	Nondimensional pressure gradient
D	Pipe diameter (m)
D_h	Hydraulic diameter (m)
D^+	Nondimensional pipe diameter used by Bhagwat and Ghajar (2015a)
D_h^+	Nondimensional hydraulic diameter by Kataoka and Ishii (1987)
E	Liquid entrainment fraction
Eo	Eötvös number
f	Fanning friction factor
F, Fr	Froude number
F_p	Flow pattern factor
F_s	Shape factor
g	Acceleration due to gravity (m/s^2)
G	Mass flux (kg/m^2 s)
h	Variable in Cioncolini and Thome (2012a) correlation
h_L	Liquid level in stratified flow (m), single-phase heat transfer coefficient (W/m^2 K)
h_{TP}	Two-phase heat transfer coefficient (W/m^2 K)
I	Inclination factor
k	Thermal conductivity (W/mK)
La	Laplace number
$\dot{m}$	Mass flow rate (kg/s)
n	Variable in the correlation of Cioncolini and Thome (2012a)
N_μ	Viscosity number
p	Pressure (Pa)
P	Perimeter (m)
Pr	Prandtl number
q	Exponent in SFM Equation 3.28
r	Exponent in SFM Equation 3.28
Re	Reynolds number
s	Exponent in SFM Equation 3.28
S	Slip ratio
T	Taitel and Dukler (1976) parameter
U	Phase velocity (m/s)
U_b	Bubble velocity (m/s)
U_{GM}	Drift velocity (m/s)
U_{GM}^+	Nondimensional drift velocity by Kataoka and Ishii (1987)
$U_{SG,t}$	Superficial gas velocity at smooth to wavy stratified flow transition (m/s)
v	Specific volume (m^3/kg)
V	Volume (m^3)
We	Weber number
x	Two-phase flow quality
X	The parameter of Lockhart and Martinelli (1949)
Y	The parameter of Taitel and Dukler (1976), the parameter of Chisholm (1973)

Greek Symbols

α	Void fraction
β	Volume fraction of liquid film
δ	Liquid film thickness in annular flow (m)
Δρ	Density difference (kg/m^3)

ε	Roughness (m)
μ	Dynamic viscosity (Pa s)
ν	Kinematic viscosity (m^2/s)
σ	Surface tension (N/m)
ρ	Density (kg/m^3)
λ	Gas volumetric flow fraction
τ	Shear stress (N/m^2)
θ	Pipe orientation (°)
ϕ	Fraction of pipe circumference occupied by liquid phase
Φ^2	Two-phase frictional multiplier
Ψ	Angle subtended by liquid phase with pipe centerline (radian)
ξ	Correction factor in Equation 3.132

Subscripts

a	Accelerational
atm	Atmospheric
c	Gas core
C	Critical
f	Frictional
G	Gas
GO	Gas only
h	Hydrostatic
i	Interface
j	Phase
L	Liquid
LF	Liquid film
LO	Liquid only
max	Maximum
M	Mixture
S	Superficial
sys	System
t	Total
tt	Turbulent–turbulent
TP	Two phase
w	Wall

Superscripts

~	Nondimensional quantities in the model by Taitel and Dukler (1976)
+	Nondimensional quantities in the model by Kataoka and Ishii (1987)

References

Abduvayat, P., Manabe, R., and Arihara, N., Effects of pressure and pipe diameter on gas-liquid two-phase flow behavior in pipelines, *SPE Annual Technical Conference* SPE 84229, Denver, CO, 2003.

Awad, M.M. and Muzychka, Y.S., Effective property models for homogeneous two-phase flows, *Exp. Therm. Fluid Sci.*, 33, 106–113, 2008.

Badie, S., Hale, C.P., Lawrence, C.J., and Hewitt, G.F., Pressure gradient and holdup in horizontal two phase gas liquid flows with low liquid loading, *Int. J. Multiphase Flow*, 26, 1525–1543, 2000.

Barcozy, C.J., A systematic correlation for two phase pressure drop, *Chem. Eng. Prog.*, 62, 232–249, 1966.

Barnea, D., Transition from annular and from dispersed bubble flow—Unified models for the whole range of pipe inclinations, *Int. J. Multiphase Flow*, 12, 733–744, 1986.

Barnea, D., A unified model for predicting flow pattern transitions for the whole range of pipe inclinations, *Int. J. Multiphase Flow*, 13, 1–12, 1987.

Barnea, D., Shoham, O., and Taitel, Y., Flow pattern transition for downward inclined two phase flow: Horizontal to vertical, *Chem. Eng. Sci.*, 37, 735–740, 1982.

Beattie, D.R.H. and Whalley, P.B., A simple two-phase frictional pressure drop calculation method, *Int. J. Multiphase Flow*, 8, 83–87, 1982.
Beggs, H.D., An experimental study of two phase flow in inclined pipes, PhD thesis, University of Tulsa, Tulsa, OK, 1972.
Bendiksen, K.H., An experimental investigation of the motion of long bubbles in inclined tubes, *Int. J. Multiphase Flow*, 10, 467–483, 1984.
Bhagwat, S.M. and Ghajar, A.J., A flow pattern independent drift flux model based void fraction correlation for a wide range of gas-liquid two phase flow, *Int. J. Multiphase Flow*, 59, 186–205, 2014.
Bhagwat, S.M. and Ghajar, A.J., An empirical model to predict the transition between stratified and non-stratified gas-liquid two phase flow in horizontal and downward inclined pipes, *Heat Transfer Eng.*, 36, 1489–1498, 2015a.
Bhagwat, S.M. and Ghajar, A.J., Modified liquid entrainment fraction correlation for varying pipe orientation and system pressure, *Int. J. Multiphase Flow*, 74, 1–4, 2015b.
Bhagwat, S.M., Mollamahmutoglu, M., and Ghajar, A.J., Experimental investigation and empirical analysis of non-boiling gas-liquid two phase heat transfer in vertical downward pipe orientation, in *Proceedings of ASME 2012 Summer Heat Transfer Conference*, Vol. 2, 2012, pp. 349–359.
Blasius, H., Das Anhlichkeitsgesetz bei Reibungsvorgangen in Flussikeiten, *Gebiete Ingenieurw*, 134, 1913.
Bowers, C.D. and Hrnjak, P.S., Determination of void fraction in separated two phase flows using optical techniques, *International Refrigeration and Air-Conditioning Conference*, Purdue University, West Lafayette, IN, 2010, pp. 2293–2302.
Chen, J.J., A further examination of void fraction in annular two-phase flow, *Int. J. Heat Mass Transfer*, 29, 4269–4272, 1986.
Chen, N.H., An explicit equation for friction factor in pipes, *Ind. Eng. Chem. Fund.*, 18, 296–297, 1979.
Chen, X.T., Cai, X.D., and Brill, J.P., Gas liquid stratified wavy flow in horizontal pipelines, *J. Energy Resour. Technol.*, 119, 209–216, 1997.
Cheng, S.C., Wong, Y.L., and Groeneveld, D.C., CHF prediction for horizontal flow. *International Symposium on Phase Change Heat Transfer*, Chonqing, China, 1988, pp. 211–215.
Chisholm, D., A theoretical basis for the Lockhart-Martinelli correlation for two phase flow, *Int. J. Heat Mass Transfer*, 10, 1767–1778, 1967.
Chisholm, D., Pressure gradients due to the friction during the flow of evaporating two phase mixtures in smooth tubes and channels, *Int. J. Heat Mass Transfer*, 16, 347–358, 1973.
Churchill, S.W., Friction factor equation spans all fluid-flow regimes, *Chem. Eng.*, 7, 91–92, 1977.
Ciccihitti, A., Lombardi, C., Silvestri, M., Soldaini, R., and Zavatarelli, G., Two-phase cooling experiments: Pressure drop, heat transfer and burnout measurements, *Energ. Nucl.*, 7, 407–429, 1960.
Cioncolini, A. and Thome, J.R., Void fraction prediction in annular two phase flow, *Int. J. Multiphase Flow*, 43, 72–84, 2012a.
Cioncolini, A. and Thome, J.R., Entrained liquid fraction prediction in adiabatic and evaporating annular two phase flow, *Nucl. Eng. Des.*, 243, 200–213, 2012b.
Cioncolini, A., Thome, J.R., and Lombardi, C., Unified macro to microscale method to predict two phase frictional pressure drop of annular flows, *Int. J. Multiphase Flow*, 35, 1138–1148, 2009.
Colebrook, C.F., Turbulent flow in pipes, with particular reference to the transition between the smooth and rough pipe laws, *J. Inst. Civil Eng.*, 11, 1938–1939, 1939.
Collier, J.G. and Thome, J.R., *Convective Boiling and Condensation*, 3rd edn., Oxford Science Publications, New Jersey, 1996.
Crawford, T.J., Weinberger, C.B., and Weisman, J., Two phase flow patterns and void fractions in downward flow. Part I: Steady state flow patterns, *Int. J. Multiphase Flow*, 11, 761–782, 1985.
Crowley, C.J., Wallis, G.B., and Barry, J.J., Validation of one-dimensional wave model for the stratified to slug flow regime transition with consequences for wave growth and slug frequency, *Int. J. Multiphase Flow*, 18, 249–271, 1992.
Dix, G.E., Vapor void fractions for forced convection with subcooled boiling at low flow rates. Report NEDO-10491. General Electric Co, 1971.
Ducoulombier, M., Colasson, S., Bonjour, J., and Haberschill, P., Carbon dioxide flow boiling in a single microchannel—Part I: Pressure drops, *Exp. Therm. Fluid Sci.*, 35, 581–596, 2011.
Dukler, A.E., Wicks, M., and Cleveland, R.G., Frictional pressure drop in two phase flow: A comparison of existing correlations for pressure loss and holdup, *AIChE*, 10, 38–43, 1964.
Fang, X.D., Xu, Y., and Zhou, Z.R., New correlations of single phase friction factor for turbulent pipe flow and evaluation of existing single phase friction factor correlations, *Nucl. Eng. Des.*, 241, 897–902, 2011.

Fore, L.B., Beus, S.G., and Bauer, R.C., Interfacial friction in gas-liquid annular flow: Analogies to full and transitional roughness, *Int. J. Multiphase Flow*, 26, 1755–1769, 2000.

Fukano, T. and Furukawa, T., Prediction of the effects of liquid viscosity on interfacial shear stress and frictional pressure drop in vertical upward gas-liquid annular flow, *Int. J. Multiphase Flow*, 24, 587–603, 1998.

Ghajar, A.J. and Bhagwat, S.M., Non-boiling gas-liquid two phase flow phenomenon in near horizontal, upward and downward inclined pipe orientations, *Int. J. Mech. Aerosp. Ind. Mechatron. Eng.*, 8, 1039–1053, 2014a.

Ghajar, A.J. and Bhagwat, S.M., Flow patterns, void fraction and pressure drop in gas-liquid two phase flow at different pipe orientations, *Front. Prog. Multiphase Flow*, 157–212, 2014b (Chapter 4).

Ghajar, A.J. and Tang, C.C., Advances in void fraction, flow pattern maps and non-boiling heat transfer two phase flow in pipes with various inclinations, *Adv. Multiphase Flow Heat Transfer*, 1, 1–52, 2009.

Ghajar, A.J. and Tang, C.C., Importance of non-boiling two phase flow heat transfer in pipes for industrial applications, *Heat Transfer Eng.*, 31, 711–732, 2010.

Godbole, P.V., Tang, C.C., and Ghajar, A.J., Comparison of void fraction correlations for different flow patterns in upward vertical two phase flow, *Heat Transfer Eng.*, 32, 843–860, 2011.

Gokcal, B., An experimental and theoretical investigation of slug flow for high oil viscosity in horizontal pipes, PhD thesis, University of Tulsa, Tulsa, OK, 2008.

Gokcal, B., Al-Sarkhi, A., and Sarica, C., Effects of high oil viscosity on drift velocity for horizontal and upward inclined pipes, *SPE Proj. Fac. Const.*, 4, 32–40, 2009.

Gomez, L., Shoham, O., Schmidt, Z., Choshki, R., and Northug, T., Unified mechanistic model for steady state two phase flow: Horizontal to upward vertical flow, *Soc. Petrol. Eng.*, 5, 339–350, 2000.

Hamersma, P.J. and Hart, J., A pressure drop correlation for gas-liquid pipe flow with a small liquid holdup, *Chem. Eng. Sci.*, 42, 1187–1196, 1987.

Haramathy, T.Z., Velocity of large drops and bubbles in media of infinite or restricted extent, *AIChE J.*, 6, 281–288, 1960.

Hart, J., Hamersma, P.J., and Fortuin, J.M.H., Correlations predicting frictional pressure drop and liquid holdup during horizontal gas-liquid pipe flow with a small liquid holdup, *Int. J. Multiphase Flow*, 15, 947–964, 1989.

Henstock, W.H. and Hanratty, J., The interfacial drag and the height of the wall layer in annular flows, *AIChE J.*, 22, 990–999, 1976.

Hewitt, G., Lacey, P.M.C., and Nicholls, B., Transitions in film flow in vertical tube, in *Proceedings of Two Phase Flow Symposium*, Exeter, U.K., Paper B4 2, 1965.

Hewitt, G.F. and Hall-Taylor, N.S., *Annular Two Phase Flow*, 1st edn., Pergamon Press, Oxford, U.K., 1970.

Hewitt, G.F. and Lacey, P.M.C., The breakdown of the liquid film in annular two phase flow, *Int. J. Heat Mass Transfer*, 8, 781–791, 1965.

Hewitt, G.F., Martin, C.J., and Wilkes, N.S., Experimental and modeling studies of churn-annular flow in the region between flow reversal and the pressure drop minimum, *Physicochem. Hydrodyn.*, 6, 69–86, 1985.

Hewitt, G.F. and Roberts, D.N., Studies of two phase flow patterns by simultaneous x-ray and flash photography, Technical Report AERE-M 2159. Atomic Energy Research Establishment, Harwell, Oxfordshire, England, 1969.

Hibiki, T. and Ishii, M., One-dimensional drift flux model and constitutive equations for relative motion between phases in various two-phase flow regimes, *Int. J. Heat Mass Transfer*, 46, 4935–4948, 2003.

Hlaing, N.D., Sirivat, A., Siemanond, K., and Wilkes, J.O., Vertical two phase flow regimes and pressure gradients: Effect of viscosity, *Exp. Therm. Fluid Sci.*, 31, 567–577, 2007.

Ishii, M. and Grolmes, M.A., Inception criteria for droplet entrainment in two phase cocurrent film flow, *AIChE J.*, 21, 308–318, 1975.

Ishii, M. and Mishima, K., Droplet entrainment correlation in annular two phase flow, *Int. J. Heat Mass Transfer*, 32, 1835–1846, 1989.

Kaji, M. and Azzopardi, B.J., The effect of pipe diameter on the structure of gas-liquid flow in vertical pipes, *Int. J. Multiphase Flow*, 36, 303–313, 2010.

Kataoka, I. and Ishii, M., Drift flux model for large diameter pipe and new correlation for pool void fraction, *Int. J. Heat Mass Transfer*, 30, 1927–1939, 1987.

Laurinat, J.E., Hanratty, T.J., and Dallman, J.C., Pressure drop and film height measurements for annular gas-liquid flow, *Int. J. Multiphase Flow*, 10, 341–356, 1984.

Lips, S. and Meyer, J.P., Experimental study of convective condensation in an inclined smooth tube. Part II: Inclination effect on pressure drop and void fraction, *Int. J. Heat Mass Transfer*, 55, 405–412, 2012.
Lockhart, R.W. and Martinelli, R.C., Proposed correlation of data for isothermal two phase, two component flow in pipes, *Chem. Eng. Prog.*, 45, 39–48, 1949.
Mandhane, J.M., Gregory, G.A., and Aziz, K., A flow pattern map for gas-liquid flow in horizontal pipes, *Int. J. Multiphase Flow*, 1, 537–553, 1974.
McAdams, W.H., Woods, W.K., and Heroman, L.V., Vaporization inside horizontal tubes—II. Benzene oil mixtures, *Trans. ASME*, 64, 193–200, 1942.
Mishima, K. and Ishii, M., Theoretical prediction of onset of horizontal slug flow, *J. Fluids Eng.*, 102, 441–445, 1980.
Mishima, K. and Ishii, M., Flow regime transition criteria for upward two phase flow in vertical tubes, *Int. J. Heat Mass Transfer*, 27, 723–737, 1984.
Moeck, E.O., Annular dispersed two phase flow and critical heat flux, PhD thesis, McGill University, Montreal, Quebec, Canada, 1970.
Mukherjee, H., An experimental study of inclined two phase flow, PhD thesis, University of Tulsa, Tulsa, OK, 1979.
Muller-Steinhagen, H. and Heck, K., A simple friction pressure drop correlation for two-phase flow in pipes, *Chem. Eng. Proc.*, 20, 297–308, 1986.
Nguyen, V.T., Two phase gas-liquid cocurrent flow: An investigation of holdup, pressure drop and flow patterns in a pipe at various inclinations, PhD thesis, University of Auckland, Auckland, New Zealand, 1975.
Nicklin, D.J., Wilkes, J.O., and Davidson, J.F., Two phase flow in vertical tubes, *Inst. Chem. Eng.*, 40, 61–68, 1962.
Oshinowo, O., Two phase flow in a vertical tube coil, PhD thesis, University of Toronto, Toronto, Ontario, Canada, 1971.
Ottens, M., Hoefsloot, H.C.J., and Kamersma, P.J., Correlations predicting liquid holdup and pressure gradient in steady state nearly horizontal cocurrent gas-liquid pipe flow, *Trans. IChemE*, 79, 581–592, 2001.
Owen, D.G., An experimental and theoretical analysis of equilibrium annular flow, PhD thesis, University of Birmingham, Birmingham, U.K., 1986.
Quiben, J.M. and Thome, J.R., Flow pattern based two phase frictional pressure drop model for horizontal tubes. Part I: Diabetic and adiabatic experimental study, *Int. J. Heat Fluid Flow*, 28, 1049–1059, 2007.
Rezkallah, K.S. and Sims, G.E., An examination of correlations of mean heat transfer coefficients in two-phase and two-component flow in vertical tubes, *AIChE Symp. Ser.*, 83, 109–114, 1987.
Rouhani, S.Z. and Axelsson, E., Calculation of void volume fraction in the subcooled and quality boiling regions, *Int. J. Heat Mass Transfer*, 13, 383–393, 1970.
Shannak, B.A., Frictional pressure drop of gas liquid two-phase flow in pipes, *Nucl. Eng. Des.*, 238, 3277–3284, 2008.
Smith, S.L., Void fraction in two phase flow: A correlation based on an equal velocity head model, *Inst. Mech. Eng.*, 184, Part 1, 647–657, 1969.
Spedding, P.L., Che, J.J.J., and Nguyen, N.T., Pressure drop in two phase gas-liquid flow in inclined pipes, *Int. J. Multiphase Flow*, 8, 407–431, 1982.
Taitel, Y., Barnea, D., and Dukler, A.E., Modeling flow pattern transitions for steady upward gas-liquid flow in vertical tubes, *AIChE J.*, 26, 345–354, 1980.
Taitel, Y. and Dukler, A.E., A model for predicting flow regime transitions in horizontal and near horizontal gas-liquid flow, *AIChE J.*, 22, 47–55, 1976.
Tang, C.C., A study of heat transfer in non-boiling two phase gas liquid flow in pipes for horizontal, slightly inclined and vertical orientations, PhD thesis, Oklahoma State University, Stillwater, OK, 2011.
Tang, C.C. and Ghajar, A.J., A mechanistic heat transfer correlation for non-boiling two-phase flow in horizontal, inclined and vertical pipes, in *Proceedings of AJTEC 2011 ASME/JSME Eighth Thermal Engineering Joint Conference*, Paper No. AJTEC2011-44114, Honolulu, Hawaii, 2011.
Turner, J.M. and Wallis, G.B., The separate cylinders model of two phase flow, Technical Report No. NYO-3114-6. Thayer's School of Engineering, Dartmouth College, Hanover, NH, 1965.
Wallis, G.B., The onset of droplet entrainment in annular gas-liquid flow, General Electric Report No. 62GL 127, Schenectady, New York, 1962.
Weisman, J. and Kang, S.Y., Flow pattern transitions in vertical and upward inclined lines, *Int. J. Multiphase Flow*, 7, 271–291, 1981.

Woldesemayat, M.A. and Ghajar, A.J., Comparison of void fraction correlations for different flow patterns in horizontal and upward inclined pipes, *Int. J. Multiphase Flow*, 33, 347–370, 2007.

Wongs-ngam, J., Nualboonrueng, T., and Wongwises, S., Performance of smooth and micro-finned tubes in high mass flux region of R-134a during condensation, *Heat Mass Transfer*, 40, 425–435, 2004.

Wongwises, S. and Kongkiatwanitch, W., Interfacial friction factor in vertical upward gas-liquid annular two phase flow, *Int. Commun. Heat Mass Transfer*, 28, 323–336, 2001.

Xiong, R. and Chung, J.N., Size effect on adiabatic gas-liquid two phase flow map and void fraction in micro-channels, in *Proceedings of International Mechanical Engineering Congress and Exposition*, Chicago, IL, 2006.

Xu, Y. and Fang, X., A new correlation of two phase frictional pressure drop for evaporating two phase flow in pipes, *Int. J. Refrigerat*., 35, 2039–2050, 2012.

Xu, Y. and Fang, X., Correlations of void fraction for two phase refrigerant flow in pipes, *Appl. Therm. Eng.*, 64, 242–251, 2014.

Zhang, W., Hibiki, T., and Mishima, K., Correlations of two phase frictional pressure drop and void fraction in mini-channel, *Heat Mass Transfer*, 53, 433–465, 2010.

Zivi, S.M., Estimation of steady state steam void fraction by means of the principle of minimum entropy production, *Trans. ASME J. Heat Transfer*, 86, 247–252, 1964.

4

Fluid–Solid Flow in Ducts

4.1 Pneumatic Conveying
4.2 Slurry Flows

4.1 Pneumatic Conveying

Shrikant Dhodapkar and Karl Jacob

4.1.1 Background

One of the earliest pieces of documentation, dating back to 1847, of conveying solids for industrial application was an exhaust system for dust removal from grindstones in a Peugeot plant (Molerus, 1996). Later in 1878, applications of pneumatic conveying of agricultural products (grains and wood chips) emerged. While the basic concept matured quickly, advances in the design of air movers, feeders, and dust collectors resulted in a widespread application of this technology. The research in gas-particle dynamics has helped to create a systematic approach for designing pneumatic conveying systems. Presently, pneumatic conveying is the primary means of moving solid products and intermediates between process stages and the transfer of materials to and from silos. Most of the bulk solid unloading operations rely on some kind of pneumatic transfer.

A pneumatic conveying system consists of a gas mover (fan, centrifugal blower, rotary lobe blower, etc.), a product feeder (rotary feeder, screw feeder, blow tank, etc.), conveying line, and a gas–solid separator (cyclone, baghouse, etc.). With a suitable choice of components, the bulk material can be reliably conveyed over considerable distance. The conveying line can be routed to provide maximum flexibility in layout and operation. The material can be picked up from multiple sources and delivered to many destinations easily. Due to the enclosed nature of transfer in pipe, no dust is emitted to the environment. Pneumatic conveying systems are also easy to automate. However, there are some drawbacks to this technology:

1. High specific power consumption
2. Potential particle breakage or degradation
3. High wear rate on components
4. Relatively short distances (typically less than 3000 ft)

It is not uncommon to come across pneumatic conveying systems that do not meet performance expectations. High particle degradation, capacity limitations, and unstable flow are some of the common problems faced by plant personnel. In most cases, these systems have been designed using generalized correlations and procedures

that do not reflect the conveying characteristics of the material at hand. This results in a nonoptimal system design. Lack of clear design guidelines and calculation procedures makes it difficult to optimize these operations.

More accurate design calculations can be made by empirically correlating test data on conveying characteristics. These data can be obtained on a pilot-scale test loop or from a properly instrumented conveying system in the plant. Generally, it is easier to vary conveying conditions and measure the air and solid flow rates along with pressure drops in various sections in a test loop than to adapt conveying systems in the plant. The test data can be condensed into material-specific correlations for solids' friction factor, saltation velocity correlation, and pressure drop correlation for bends and acceleration region. This information can then be used to design new systems and optimize existing systems.

Pneumatic conveying of materials implies the conveying of material in pipelines using gas as a motive fluid. When the fluid is a liquid, it is known as hydraulic conveying. Gas-particle dynamics is the foundation of pneumatic conveying technology and, hence, discussed briefly here.

4.1.1.1 Flow Patterns in Gas–Solid Systems

Consider cocurrent flow of gas and solid particles in a horizontal pipe, where the gas velocity is high enough to keep the particles homogeneously suspended as shown in flow pattern 1 in Figure 4.1. This flow pattern represents ideal dilute phase flow. If the gas velocity were increased from this point, the flow pattern would visually appear to be the same. However, if it were decreased, at some velocity the solids would no longer be homogeneously suspended as shown in flow pattern 2. A moving strand is often observed at the bottom of the pipe. As the gas flow is further reduced, more of the solids fall out of suspension, resulting in a layer of solids on the bottom of the pipe. Further reduction in gas flow results in the formation of dunes (flow patterns 4 and 5) and eventually slugs of solids that completely fill the pipe cross section (flow pattern 7). For most materials, the flow of solids will stop before reaching flow patterns 9 and 10; however, for some materials that aerate easily and have good air retention characteristics, the material can be moved in the form of a fluidized plug. Dilute phase flow is characterized by predominately flow patterns 1 and 2, with some occurrence of flow pattern 3 at or near the point where solids are injected into the conveying line. Dense phase conveying includes all other flow patterns, although stable conveying will most likely not be achieved for any given material in all flow patterns shown.

The range of flow patterns observed during pneumatic conveying of bulk materials depends on the material characteristics (particle size, size distribution, shape, hardness, and density). Broadly speaking, fine powders and coarse materials show characteristically different flow patterns. Fine powders, such as PVC powder,

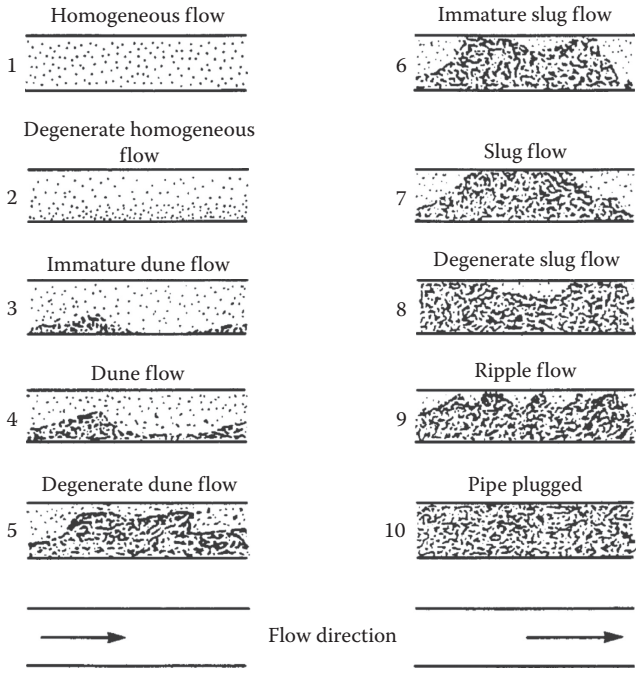


Figure 4.1

Flow patterns in horizontal pneumatic conveying lines. (From Wen, C.Y., US Department of Interior, Bureau of Mines, PA, IC 8314, 1959. With permission.)

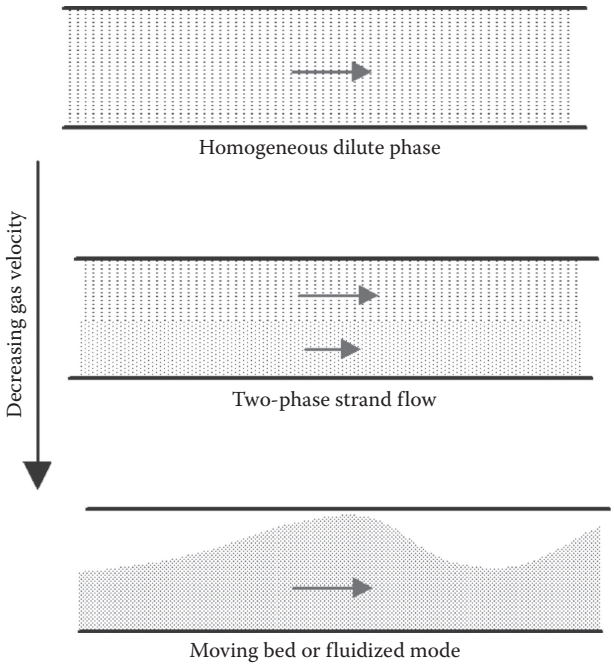


Figure 4.2

Flow patterns for fine powders.

high-density polyethylene powder, fly ash, cement, fine coal, and carbon fines, can be transported in fluidized- or moving-bed mode at low gas velocities. The flow can be turbulent and sometimes appears like a fast-moving bed, waves, or dunes (see Figure 4.2). At higher solids' loadings, the entire cross section of the pipe is filled with a dense mixture of gas and solids. The transition from dilute phase to dense phase is smooth and predictable. Some coarse materials with significant fraction of fines (less than 75 μm) will also exhibit similar behavior. On the other hand, coarse particles, such as plastic pellets, grains, and coffee beans, form slugs naturally when conveyed at low velocity in nonsuspension mode. These slugs show periodic and self-regulating behavior. The transition from dilute to dense flow is marked by an unstable region that corresponds to dune flow (Figure 4.3).

4.1.1.2 Classification of Bulk Solids

Classification or characterization is an essential step in the selection of a suitable conveying mode (dilute or dense) and to optimize the operation of an existing conveying system. Various approaches have been proposed in the literature to predict the expected behavior of a bulk material in a pneumatic conveying system. Unfortunately, due to the complexity of interactions, none of them is definitive but they do provide a good basis for evaluation. It is the authors' experience that a combination of approaches coupled with practical experience must be used. Product classification approaches by Geldart (1973), Dixon (1981), Mainwaring and Reed (1987), Jones and Mills (1990), and Pan (1999) are discussed briefly here. This should provide initial guidance to a process engineer. It is recommended that conveying trials be conducted on new materials to understand the conveying characteristics.

The following properties affect the conveying characteristics of bulk solids:

1. Particle size and size distribution
2. Particle shape
3. Bulk density (loose and tapped)
4. Particle density
5. Permeability
6. Deaeration rate or air retention characteristics
7. Surface characteristics: sticky, wet, cohesive, and electrostatic charging
8. Temperature sensitivity (hardness, modulus, and surface tackiness)

4.1.1.2.1 Geldart or Dixon Classification In his classic paper, Geldart (1973) demarcated regions of different fluidization behaviors based on a 2D plot (Figure 4.4). The *x*-axis is surface volume mean particle size

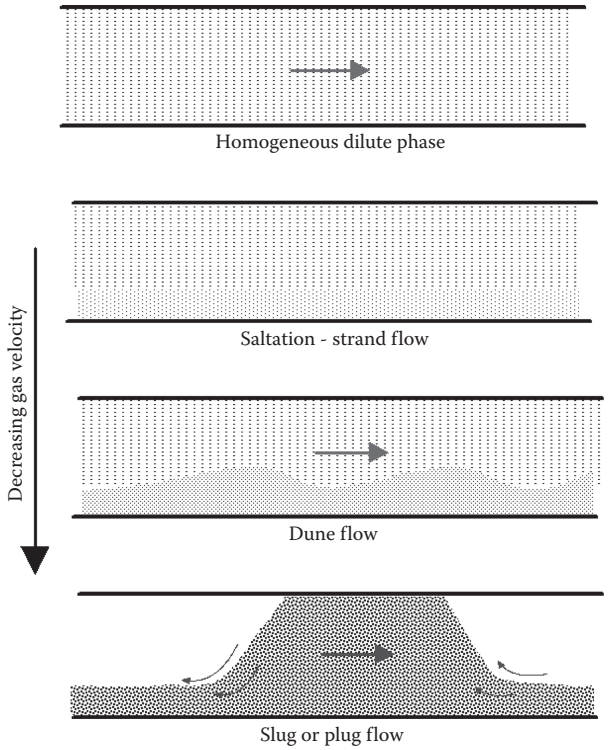


Figure 4.3

Flow patterns for coarse granular materials.

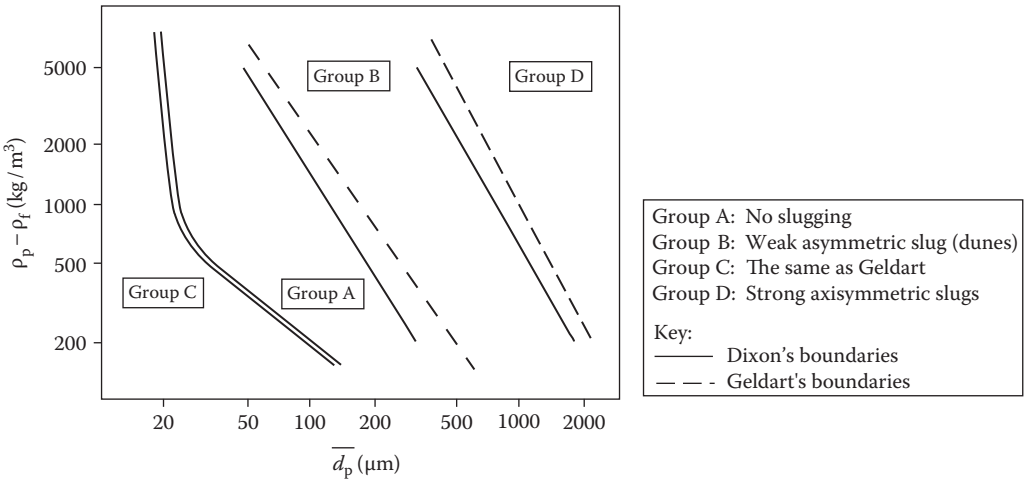


Figure 4.4

Comparison of Geldart and Dixon classification. (From Mason, A., PhD thesis, Thomes Polytechnic, London, U.K., 1991. With permission.)

and the *y*-axis is density difference between the particle and the fluid. This diagram has stood the test of timeand is still used to classify the fluidization behavior of bulk solids. Subsequent work by Dixon (1981) on the classification of slugging behavior in vertical pipes produced a similar diagram. Fluidization, permeability, and deaeration characteristics are closely related to pneumatic conveyability (see Table 4.1).

Wypych (1989) has shown that the use of surface-volume mean diameter overemphasizes the influence of finer fraction on fluidization behavior. He recommended the use of volume median diameter instead. The boundaries in Geldart classification are ambiguous when the particle size distribution is wide or the particle shape is

Table 4.1 Characteristics of Geldart (1973) or Dixon (1981) Classification

Geldart or Dixon Classification	Fluidization Characteristics	Dense Phase Conveying Characteristics
A	Fine powders, good air retention, small bubble size, considerable bed expansion	Can be conveyed in fluidized mode, easy to convey, do not form slugs naturally
B	Coarse granules, poor air retention, low bed expansion, large bubbles, asymmetric slugging	Difficult to convey in "conventional" dense phase, unsteady and unpredictable plug formation, large-pipe vibrations
C	Cohesive, difficult to fluidize, tends to channel, once aerated might retain air for extended periods, adhesion to walls	Very difficult to convey in conventional dense phase, forms impermeable plugs that break up. Special techniques required to convey
D	Highly permeable, negligible bed expansion, high minimum fluidization velocity, large bubbles or slugs can form, axisymmetric slugs	Natural slugging ability and high permeability helps in dense phase conveying. Operationally easiest to convey in dense phase

nonspherical. Wypych (1989) also pointed out that the ratio of particle size to pipe diameter plays a role in the determination of natural slugging behavior. It is recommended that full-scale tests be conducted to ascertain the actual behavior.

4.1.1.2.2 Mainwaring and Reed Classification (1987) Permeability and deaeration have proven to be the two most important properties of bulk material in establishing the conveying behavior. While Geldart (1973) or Dixon (1981) classification is based on a similar concept, this classification relies on the direct measurement of permeability factor and deaeration factor. These measurements are used to determine whether the material can be conveyed in plug-type dense phase conveying, moving-bed-type dense phase conveying, or only in dilute phase mode.

4.1.1.2.2.1 Permeability Factor Permeability is a measure of resistance of gas flow through a packed bed of given bulk material under conditions below minimum fluidization. It can be measured by measuring the pressure gradient across a packed bed at various gas velocities (Figure 4.5a). The permeability factor, p_f, is the ratio A/B. The higher the permeability factor, the lesser the resistance it offers to the gas flow:

$$p_f = \frac{U_g}{(\Delta P/L)_c}$$

The pressure drop curve reaches an asymptotic value at high gas velocities when the drag force on the particles equals the weight of the bed. This critical pressure gradient $(\Delta P/L)_c$ is a property of the bulk material.

The permeability data for various bulk solids were plotted against the critical pressure gradient by Mainwaring and Reed (1987) as shown in Figure 4.5b. A line of constant minimum fluidization can be plotted on the same graph. It has been found from practical experience that a line representing minimum fluidization velocity of 0.05 m/s (50 mm/s) classifies materials that can be conveyed in plug- or slug-type dense phase conveying and those that can be conveyed in moving-bed-type dense phase or dilute phase only. All materials with high permeability (data above the line) can be conveyed in plug or slug conveying mode, whereas materials with low permeability can be conveyed either in moving-bed-type dense phase flow or in dilute phase only. The basic assumption here is that no special air injection or vibration flow aids are being used.

4.1.1.2.2.2 Deaeration Factor Air retention or deaeration characteristics are measured by bringing the bed to a state of minimum fluidization and rapidly turning off the air supply. The bulk density increases and the level falls as the bed deaerates. It would be ideal to monitor the bed height as a function of time. However, most fine powders tend to coat the wall of the column, thereby making the observations difficult. It is reasonable to measure the pressure decay characteristics instead. Research has shown that the pressure gradient in the bed is inversely proportional to the time, as shown in Figure 4.6a:

$$\frac{\Delta P}{L} t = A_f$$

The product of pressure gradient and time is defined as the deaeration constant, A_f. The shape of deaeration curve is sensitive to many parameters. This test needs to be standardized or it must be used for comparative purposes only.

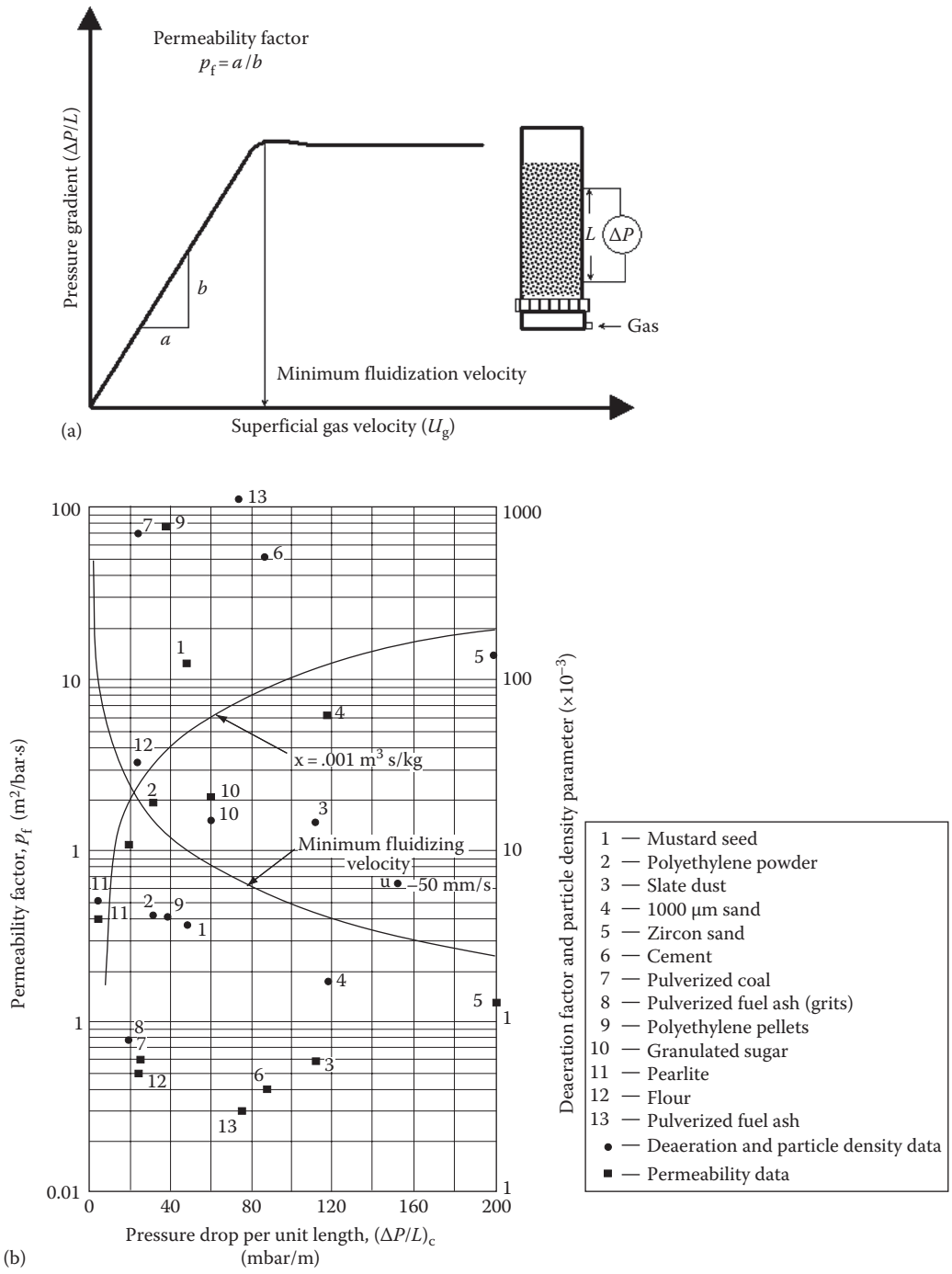


Figure 4.5

(a) Measurement of permeability using a fluidized-bed setup; (b) classification based on permeability. (From Mainwaring, N.J. and Reed, A.R., *Bulk Solids Handling*, 7, 415, 1987. With permission.)

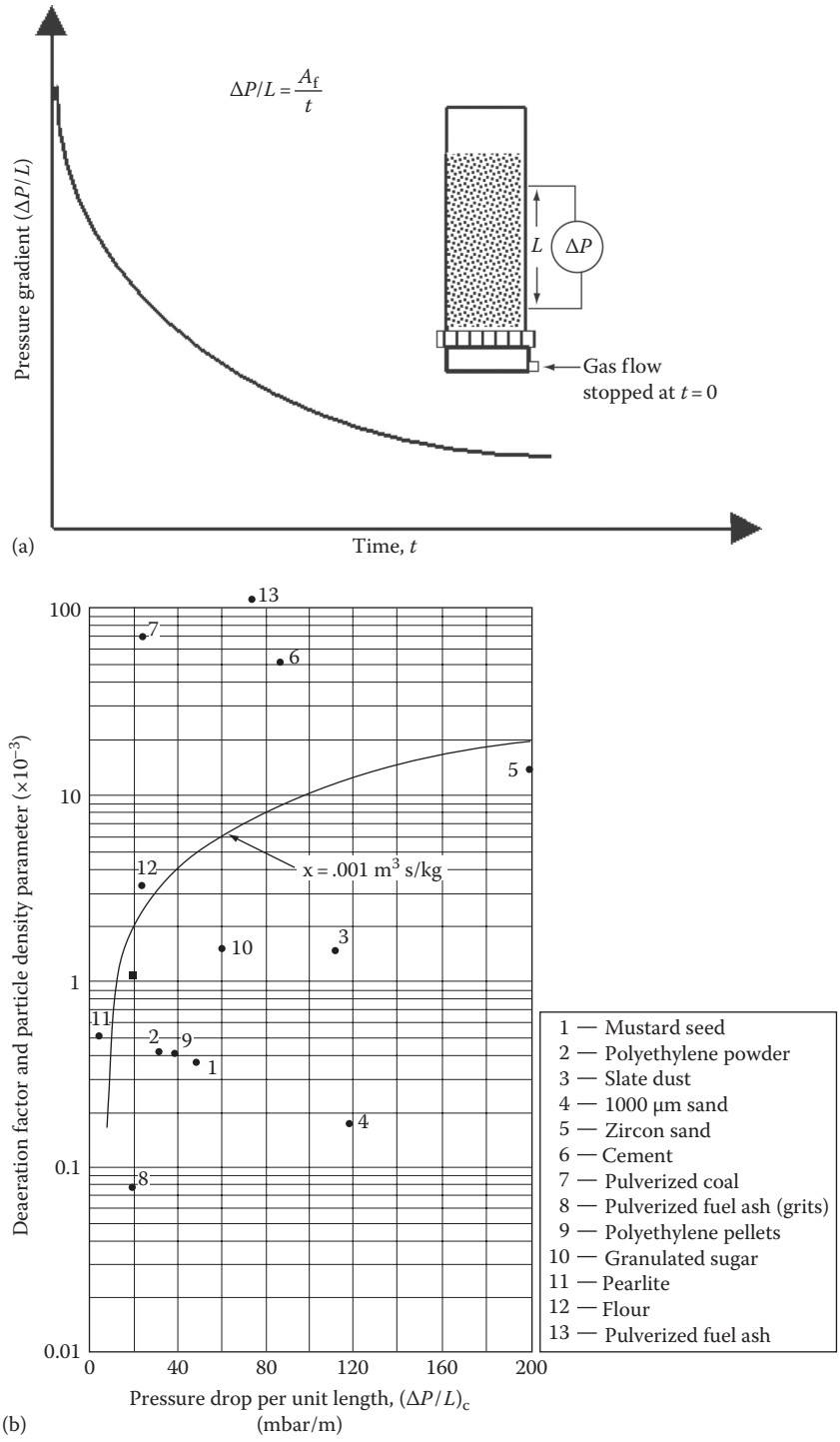


Figure 4.6

(a) Interpretation of deaeration data and proposed test setup; (b) classification based on deaeration factor.

To account for the effect of particle density, it was further proposed that a new factor X (m^3 s/kg) be defined as follows:

$$X = \frac{\left(A_f/\rho\right)}{\left(\Delta P/L\right)}$$

Low values of X imply low air retention and vice versa. As shown in Figure 4.6b, it has been proposed that a curve representing $X = 0.001$ m^3 s/kg classifies materials that can be conveyed in slug- or plug-type dense phase conveying (below the curve) and those suitable for only moving bed or dilute phase (above the curve).

4.1.1.2.3 Jones and Mills (1990) Jones and Mills (1990) have rightly pointed out the limitations of Geldart and Dixon diagram in their failure to account for particle size distribution and shape. Similar to Mainwaring and Reed, they used permeability and deaeration as the two primary factors to determine flow modes. However, the deaeration characteristics were generated in the presence of vibration to assist deaeration of powders, which can take an inordinate amount of time. The proposed product classification is shown in Figure 4.7.

As evident from Jones and Mills classification:

1. Materials with low permeability and high air retention (small deaeration constant) can be conveyed in moving bed or fluidized mode.
2. Materials with high permeability and low air retention can be conveyed in the plug type of dense phase flow.
3. The rest of the materials can be conveyed only in dilute phase mode.

The boundaries between dilute phase (Group 2) and dense phase (Groups 1 and 3), however, are tentative.

4.1.1.2.4 Pan (1999) Pan (1999) proposed a simplified flow mode diagram based on loose, poured bulk density and median particle size. This diagram (Figure 4.8) is based on a database of over 50 materials. The materials are grouped into three categories:

1. Materials in group PC 1 can be transported in dilute phase and dense phase fluidized- or moving-bed mode. Examples are fly ash, pulverized coal, cement, flour, PVC powder, fuel ash, and others.
2. Materials in group PC 2 can be transported in dilute phase and slug- or plug-type dense phase mode. The transition from dilute phase to dense phase is marked by an unstable zone. Examples are plastic pellets, wheat, mustard seeds, granulated sugar, semolina, and others.
3. Materials in group PC 3 can be transported only in dilute phase. Examples are silica sand, alumina, zircon sand, fuel ash grit, and others.

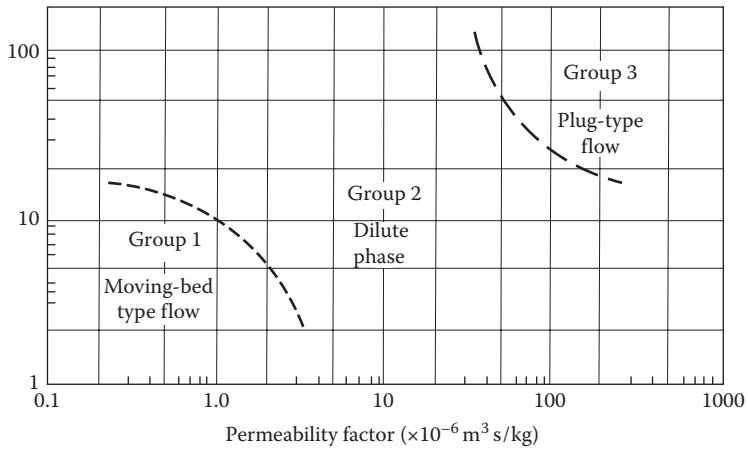


Figure 4.7

Jones and Mills classification. (From Jones, M.G. and Mills, D., *Powder Handling Process.*, 2, 117, 1990. With permission.)

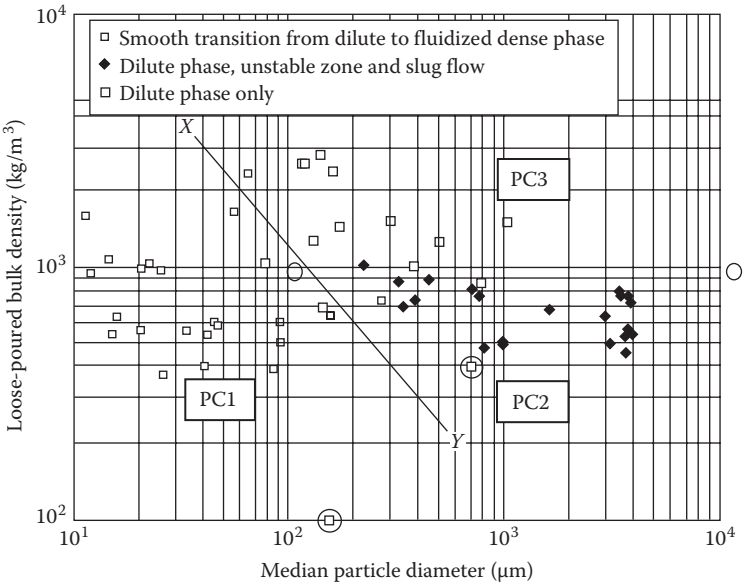


Figure 4.8

Pan classification. (From Pan, R., *Powder Technol.*, 104, 157, 1999. With permission.)

4.1.1.2.5 Limitation of Classification Diagrams Many materials classified as difficult to convey in dense phase can be conveyed by applying special techniques, such as air injection, air bypass, air knife, and pulse piston method. No generalized classification has been developed to predict the effectiveness of these techniques. It is recommended that pilot-scale tests be conducted to determine the feasibility of dense phase conveying for such materials.

4.1.1.3 Phase Diagram

While observing flow patterns is an easy way to differentiate between dilute and dense phase conveying, most conveying systems do not provide this opportunity. Consequently, process measurements such as differential pressure (DP) are used in conjunction with the gas and solids' flow rates to provide a picture of what occurs within the conveying line. An elegant way to represent the performance characteristics of pneumatic conveying systems is to plot the pressure gradient versus gas velocity for different solids' flow rates. This is often known as the "Zenz plot" (see Figure 4.9). The pressure gradient is measured across a test section of known length, pipe diameter, and orientation. Each curve represents system characteristics at constant solids' flow rate. It should be noted that Zenz used logarithmic scales for the two axes. In a log–log plot, the pressure curve due to single-phase gas flow becomes a straight line; however, the curves for gas–solid flow remain nonlinear. It is now common practice to plot the data with linear axes. The saltation transition can be visualized better by using a linear plot.

In the absence of solids, the well-known Darcy's or Fanning's friction factors can be used to quantify the pressure drop in pipes for single-phase flow. The pressure gradient in the conveying line decreases with the gas flow rate and eventually becomes zero under stationary conditions.

4.1.1.3.1 Dilute Phase Conveying Dilute phase pneumatic conveying refers to the transport of solid particles in gas such that all particles are fully entrained in the gas phase. It is possible to achieve dilute phase conveying or fully suspended mode for all materials. The difference in velocity between gas molecules and solid particles, also known as slip velocity, provides necessary drag force to propel them forward. The addition of particles in the gas stream complicates the dynamics. Due to gas–particle interaction, additional energy lost by the gas manifests itself as additional pressure drop. The energy imparted to the particles is used to move them and to overcome the frictional and impact losses at the pipe wall. Unlike the curve for single-phase airflow, a distinct minimum can be observed for two-phase gas–solid flow.

In horizontal orientation, the suspension becomes progressively nonhomogeneous as the gas velocity is reduced (Figure 4.9). The particles start to fall out of the suspension, as the drag and lift forces are no

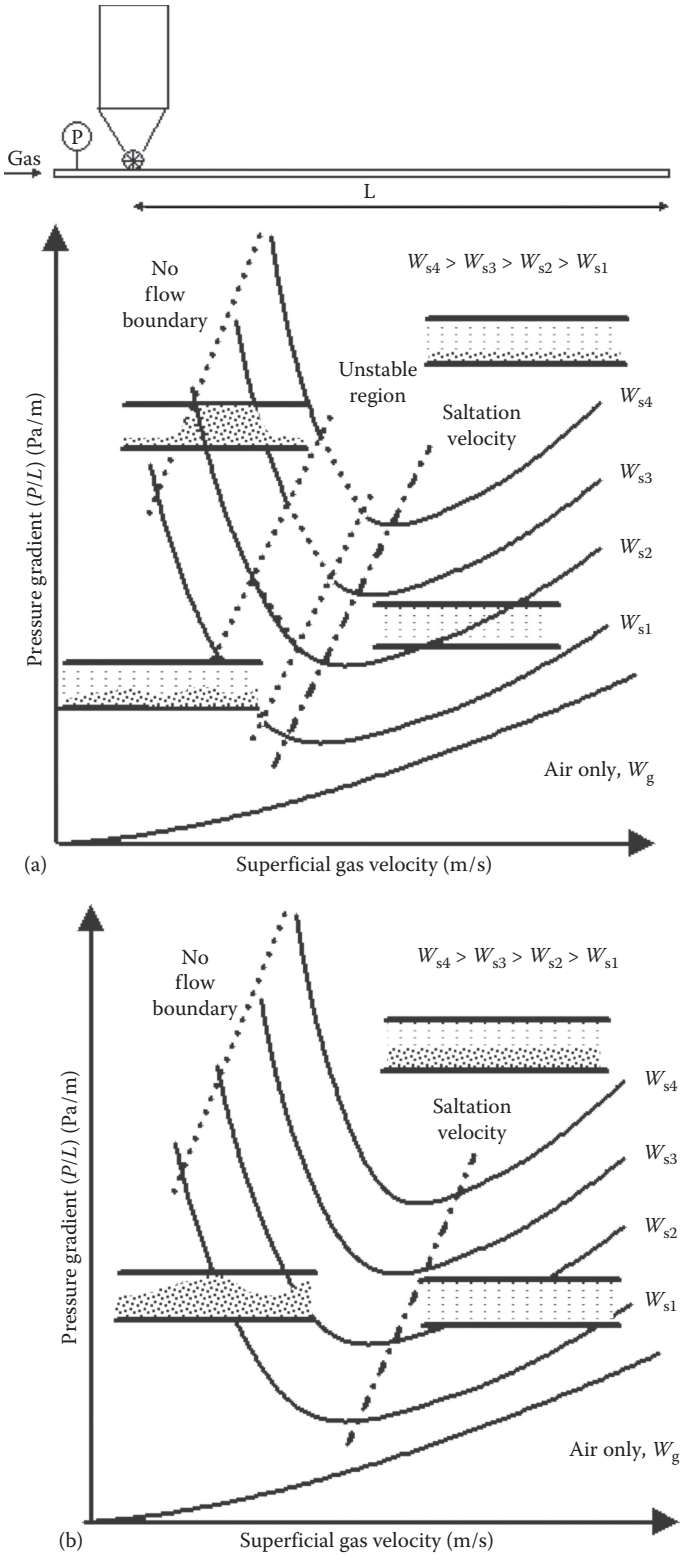


Figure 4.9

Zenz plot with superimposed flow patterns for coarse materials (a) and fine materials (b).

longer able to keep them suspended. The condition when the particles begin to fall out of suspension is called *saltation*. The superficial gas velocity corresponding to this condition is called the saltation velocity. For coarse particles, saltation velocity and the minima in the pressure drop curve are the same, whereas the pressure minima occur at a velocity greater than saltation velocity for fine powders. Since the operating condition at saltation corresponds to minimum pressure drop, it also results in the lowest power consumption. Generally, a safety factor of 10%–20% is added to saltation velocity to account for nonidealities in system configuration.

4.1.1.3.2 Dense Phase Conveying Conveying in nonsuspension flow (slugs, plugs, moving bed, or fluidized bed) is called dense phase conveying. As the gas velocity is reduced below the minimum requirement to maintain the particles in suspension, there are two possibilities:

1. Smooth transition from dilute phase to moving beds or dunes to fluidized mode
2. Transition to dune or degenerate dune flow that eventually transforms into smooth slug flow

The following important observations can be made from this diagram.

1. The pressure gradient curve does not decrease monotonically with gas velocity when conveying solids. This is unlike single-phase gas flow.
2. There is a minimum in the pressure characteristic (at constant solids' conveying rate). This point also corresponds to the lowest power consumption. In dense phase, the pressure gradient increases as the gas velocity is further decreased.
3. At a given pressure gradient and dilute phase flow condition, the conveying rate (capacity) decreases with increase in gas velocity (gas flow rate), as shown by A → B line in Figure 4.10. This can be explained by the fact that more energy is expended in solids' frictional and impact losses at the higher velocity. This observation is extremely important and useful when we are optimizing conveying systems.

In vertical orientation, as the gas velocity reduces at the same solids' mass flow rate, solids' concentration in the pipe increases and the wall frictional loss decreases. Initially, the decrease in wall frictional loss is significantly higher than the increase in gravitational component; therefore, the overall pressure gradient decreases with reduction in gas velocity. However, at sufficiently low gas velocity, the gravitational component due to solids' holdup becomes predominant and the overall pressure gradient starts to increase (Figure 4.11). The flow conditions at and below this gas velocity are classified as dense phase flow.

The mechanism of choking is not clearly understood: Also, not all systems exhibit this behavior. Whether the system will exhibit slugging or nonslugging behavior with internal recirculation of solids depends on the properties of the material and the pipe size. In general, fine particles in large pipes tend toward nonslugging dense phase flow, while choking with slugging is observed with coarse particles in small-diameter pipes. If the transition from dilute or lean phase to dense phase is sharp, then choking corresponds to the pressure minimum. However, if the transition from dilute to dense phase is "fuzzy," then actual choking can occur at a velocity lower than that corresponding to the pressure minimum.

Comparison of saltation velocity and choking velocity data for different materials suggests that

1. For fine particles, saltation velocity is about 3–5 times larger than the choking velocity.
2. For coarse particles, the saltation and choking velocity are almost identical.

Most of the conveying systems are configured such that the material is fed into a horizontal section of the pipe. Therefore, the saltation velocity (with appropriate safety factor) should be used for design calculations; this will result in a conservative design. From a design point of view, it is desirable to choose an operating point that would result in minimum pressure drop, power consumption, erosion, and particle degradation, and yet provide reliable and stable operation. The region immediately to the right (toward higher gas velocity) of the minimum is considered to be the optimal region.

4.1.1.3.3 Saltation Velocity As discussed earlier, the saltation velocity of coarse particles (such as pellets) can be estimated by locating the minimum in the pressure gradient curve in Zenz plot. A nondimensional representation of the saltation velocity data was proposed by Barth (1958) and then successfully extended by Rizk (1976). A straight-line relationship is obtained by plotting solids loading versus Froude number

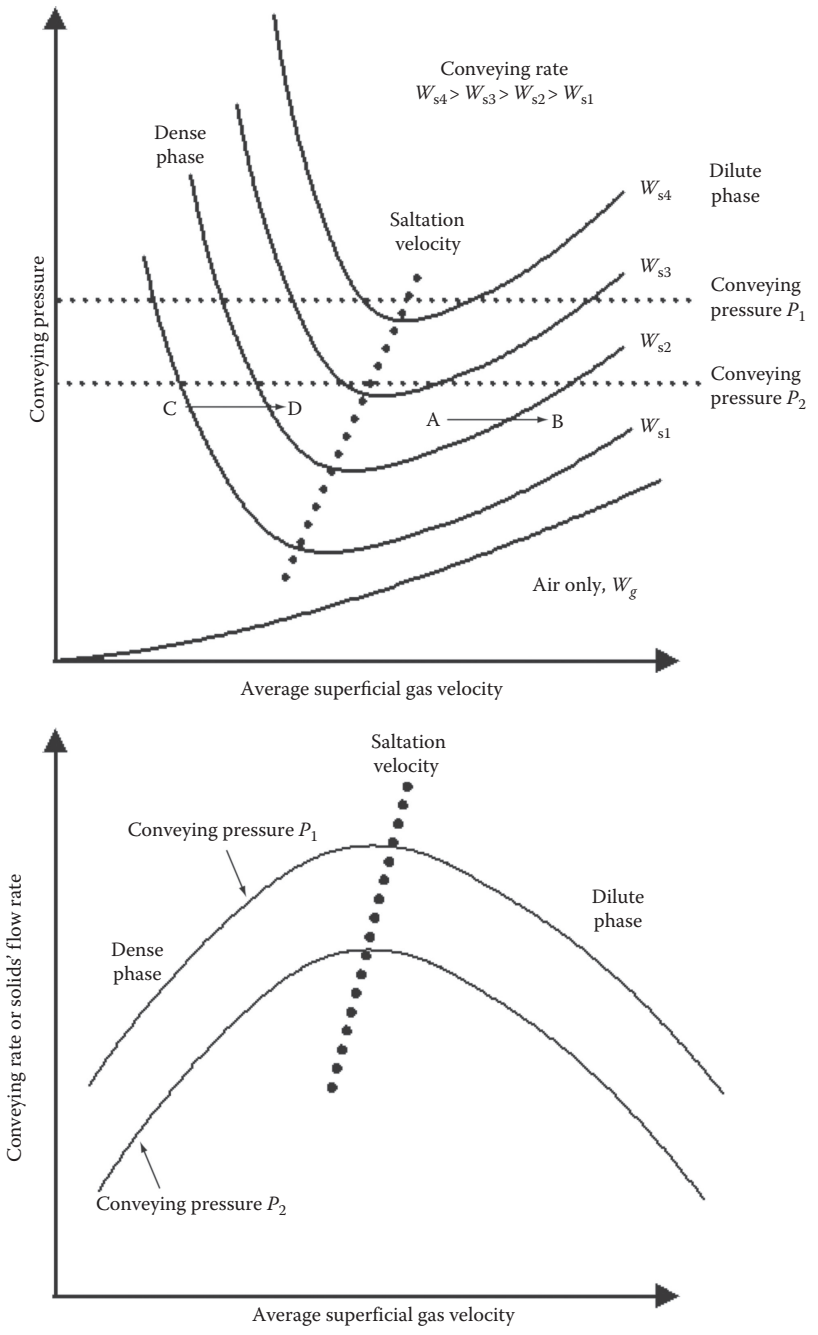


Figure 4.10

Influence of gas velocity on conveying capacity.

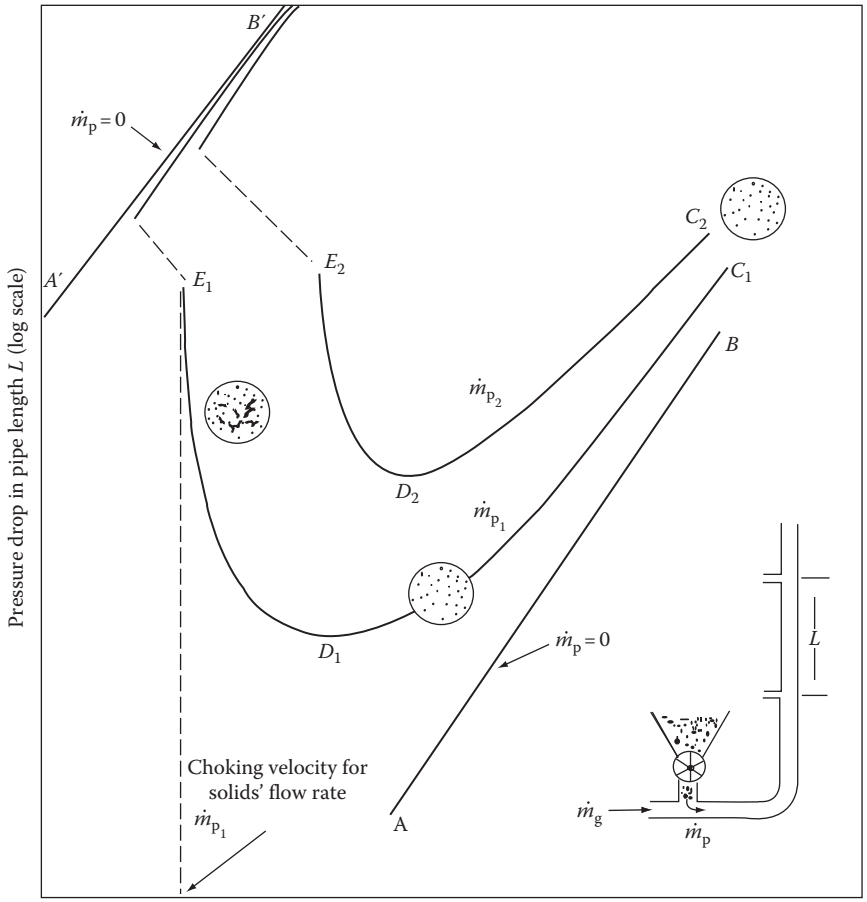


Figure 4.11

Conveying characteristics for vertical pneumatic conveying. (From Zenz, F.A. and Othmer, D.F., *Fluidization and Fluid Particle Systems*, Reinhold, New York. With permission.)

corresponding to each of the pressure minimums (same as saltation) on a log–log scale. This straight line represents a relationship of the form

$$\mu_{\text{saltation}} = \alpha Fr_{\text{saltation}}^{\beta}$$

α and β can be estimated from regression where α and β are dimensionless coefficients.

Barth (1958) suggested that the power-law index β is 4.0. Rizk (1976) proposed the following expressions to estimate the indices:

$$\alpha = \frac{1}{10^{\left(1.4d_p + 1.96\right)}}$$

$$\beta = \left(1.1d_p + 2.5\right)$$

with d_p in millimeters. It should be noted that Rizk's correlation does not include the effect of particle density.

Saltation velocity can be explicitly derived from the earlier expression as follows.

$$U_{gs} = \left[\frac{W_s\left(gD\right)^{\beta}}{A\rho_g\alpha}\right]^{1/(2\beta+1)}$$

Based on an extensive experimental database, Matsumoto et al. (1977) proposed the following correlations. He observed that coarse and fine materials behave differently. The saltation velocity of fine powders decreases with particle size until a critical particle diameter, $d_p^\star$, is reached, and then the saltation velocity increases with particle size.

Critical particle diameter, $d_p^\star$ is defined as

$$\frac{d_p^\star}{D} = 1.39\left(\frac{\rho_p}{\rho_f}\right)^{-0.74}$$

For $d_p \geq d_p^\star$:

$$\mu_s = 0.373\left(\frac{\rho_p}{\rho_f}\right)^{1.06}\left(\frac{Fr_p}{10}\right)^{-3.7}\left(\frac{Fr_{ss}}{10}\right)^{3.61}$$

where

$$Fr_p = \frac{U_t}{\sqrt{gd_p}}$$

$$Fr_{ss} = \frac{U_{gs}}{\sqrt{gD}}$$

$$\mu_s = \frac{W_s}{W_g} \quad \text{(solids loading at saltation condition)}$$

For $d_p < d_p^\star$

$$\mu_s = 55\left(\frac{d_p}{D}\right)^{1.43}\left(\frac{Fr_{ss}}{10}\right)^{4.0}$$

Guidelines for correlation selection

- For coarse particles (d_p > 500 μm) and particle specific gravity less than 3, use the Rizk correlation.
- For coarse particles (d_p > 500 μm) and particle specific gravity greater than 3, use Matsumoto correlation.
- For fine particles (d_p < 500 μm), use Matsumoto correlation.

Example 4.1: Calculate the Saltation Velocity Using the Following Data

- Particle density ρ_p = 950 kg/m^3 = 59.3 lbm/ft^3
- Gas density (ρ_g) = 1.2 kg/m^3 = 0.075 lbm/ft^3
- Average particle diameter (d_p) = 0.003 m = 3 mm
- Inner diameter of the pipe D = 0.161 m = 6.357 in.
- Conveying rate for solids (W_s) = 3.0 kg/s = 23,760 lbm/h

(A) Calculation of Rizk saltation velocity:

$$\mu_s = \frac{1}{10^\delta} Fr_s^x$$

$$\delta = 1.44d_p + 1.96 = 6.28$$

$$\chi = 1.1d_p + 2.5 = 5.8$$

$$Fr_s = \frac{U_{gs}}{\sqrt{gD}}$$

$$\mu_s = \frac{\text{solids' flow rate}}{\text{gas flow rate}} = \frac{W_s}{W_g} = \frac{W_s}{A\rho_f U_{gs}}$$

$$\frac{W_s}{A\rho_f U_{gs}} = \frac{1}{10^{\delta}}\left(\frac{U_{gs}}{\sqrt{gD}}\right)^{x}$$

$$U_{gs} = \left[\frac{W_s 10^{\delta}}{A\rho_f}\left(\sqrt{gD}\right)^{x}\right]^{1/(x+1)}$$

$$U_{gs} = \left[\frac{3\times 10^{6.28}}{0.02\times 1.2}\left(\sqrt{9.81\times 0.161}\right)^{5.8}\right]^{1/6.8}$$

$$U_{gs} = \left(8.938\times 10^{8}\right)^{1/6.8}$$

$$U_{gs} = 20.72 \text{ m/s} = 4077 \text{ ft/min}$$

(B) Calculation of Matsumoto saltation velocity of calculation:

$$\frac{d_p^*}{D} = 1.39\left(\frac{\rho_p}{\rho_f}\right)^{-0.74} = 1.39\left(\frac{950}{1.2}\right)^{-0.74} = 0.00995$$

$$d_p^* = 0.0016 \text{ m}$$

Since $d_p^* < d_p$

$$\frac{W_s}{W_g} = 0.373\left(\frac{\rho_p}{\rho_f}\right)^{1.06}\left(\frac{Fr_p}{10}\right)^{-3.7}\left(\frac{Fr_s}{10}\right)^{3.61}$$

$$Fr_p = \frac{U_t}{\sqrt{gd_p}} = \frac{7.93}{\sqrt{9.81\times 0.003}} = 46.22$$

$$Fr_s = \frac{U_{gs}}{\sqrt{gD}}$$

Rearranging,

$$U_{gs} = \left[\left(\frac{\rho_p}{\rho_f}\right)^{-1.06}\left(\frac{Fr_p}{10}\right)^{3.7}\frac{W_s\times 10^{3.61}\left(\sqrt{gD}\right)^{3.61}}{(0.373)(A\rho_f)}\right]^{1/4.61}$$

$$U_{gs} = \left[(791.66)^{-1.06}(4.622)^{3.7}(3115189.4)\right]^{1/4.61}$$

$$U_{gs} = 18.87 \text{ m/s} = 3713 \text{ ft/min}$$

4.1.1.3.4 Choking Velocity (Yousifi and Gau, 1974) There are numerous correlations available in the literature on choking velocity (Chong and Leung, 1986). The following correlation has been found to be reliable (especially for Geldart A and B class of materials).

$$\frac{U_c}{\sqrt{gd_p}} = 32Re_p^{-0.06}\mu^{0.28}$$

where

$$Re_p = \frac{\rho_f U_t d_p}{\mu_f}$$

$$\mu = \frac{W_s}{W_g}$$

Example 4.2: Calculate the Choking Velocity Using the Following Data

- Particle density $\rho_p = 950$ kg/m^3 = 59.3 lbm/ft^3
- Gas density $\rho_g = 1.2$ kg/m^3 = 0.075 lbm/ft^3
- Average particle diameter $d_p = 0.003$ m = 3 mm
- Inner diameter of the pipe (D) = 0.161 m = 6.357 in.
- Conveying rate for solids $W_s = 3$ kg/s = 23,760 lbm/h
- Gas viscosity $\mu_g = 1.8 \times 10^{25}$ kg/(ms) = 0.018 cP

$$Re_p = \frac{\rho_f U_t d_p}{\mu_f} = \frac{1.2 \times 7.93 \times 0.003}{1.8 \times 10^{-5}} = 1586$$

$$U_c = \left[\sqrt{g d_p} \times 32 Re_p^{-0.06} \left(\frac{W_s}{A \rho_f} \right)^{0.28} \right]^{1/1.28}$$

$$U_c = \left[\sqrt{(9.81 \times 0.003)} \cdot 32 (1586)^{-0.06} \left(\frac{3}{0.02 \times 1.2} \right)^{0.28} \right]^{1/1.28}$$

$$U_c = 7.69 \text{ m/s} = 1514 \text{ ft/min}$$

Note that saltation velocity > choking velocity.

4.1.2 Classification of Pneumatic Conveying Systems

Pneumatic conveying systems can be configured and operated in a number of different ways for a given application. The common classifications and their basis are summarized in Table 4.2. The most fundamental classification from a design and operation perspective is based on flow pattern, that is, dilute phase versus dense phase systems.

Dilute phase conveying: The particles are in a fully suspended state along the entire system. All segments of the system operate at velocities greater than the saltation velocity. Dilute phase conveying systems are typically designed to operate at less than 1 bar gauge with maximum solids' loading less (kg of solids/kg of gas) than 10.

Dense phase conveying: When the material is conveyed in nonsuspension mode (slugs, strand, moving bed, and fluidized mode) for the entire conveying length, the system is classified as a dense phase conveying system. It should be noted that the flow pattern can change from the feed point to the end of the line due to the continual expansion of gas. It is not uncommon to have a well-defined slug flow at the feed point and fully suspended flow at the end of a long transfer system. Therefore, a definition based solely on solids' loading is misleading.

4.1.2.1 Classification of Dilute Phase Conveying Systems

4.1.2.1.1 Pressure Type Any pneumatic conveying system can be operated either at a positive pressure or under vacuum depending on the configuration of its components. Positive pressure or push systems (Figure 4.12) have the air mover positioned upstream of the solids' feed point and the cyclone or dust

Table 4.2 Classification of Pneumatic Conveying Systems

Basis	Type of System
Flow pattern	Dilute phase, strand flow or medium dense phase, dense phase
Loop configuration	Open loop, closed loop
Pressure (type)	Pressure (push), vacuum (pull), combined (pull–push)
Pressure (magnitude)	Low pressure (−0.1 bar to +0.1 bar), medium pressure (−0.5 bar to 1 bar), High pressure (>1 bar)
Feeder type	Air into solids, solids into air
Air mover type	Fan, rotary lobe blower, compressor, other
Solids' loading	Very low (<1), low (0–5), medium (5–15), high (>15), very high (>100)

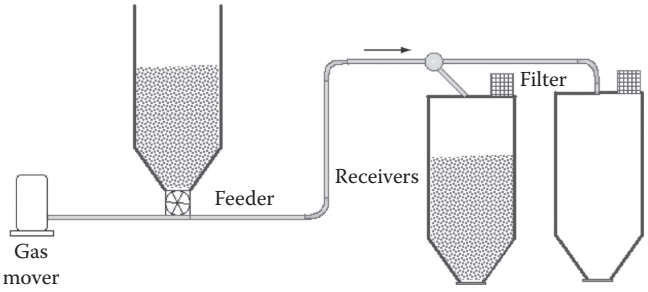


Figure 4.12

Typical positive pressure or push system.

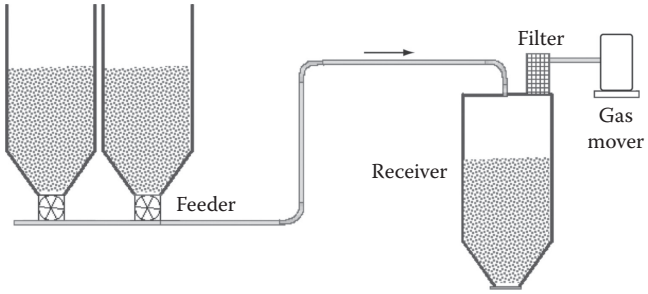


Figure 4.13

Typical vacuum or pull system.

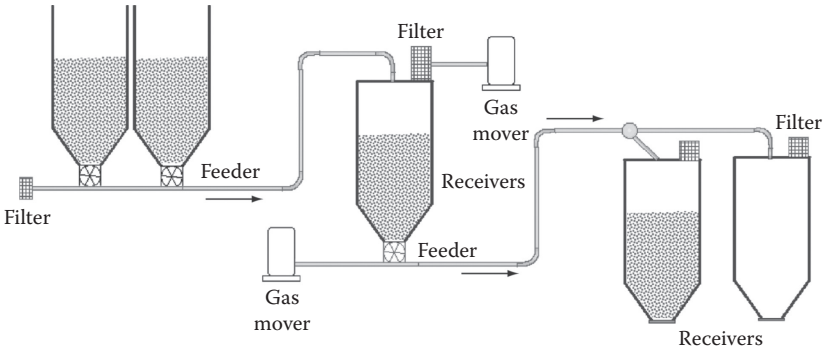


Figure 4.14

Typical combined or pull–push system.

collector operated near atmospheric pressure. The air mover is situated closer to the feed point to provide higher than ambient air pressure, which results in positive pressure in the entire line.

The air mover for a vacuum system or pull system is located downstream of the dust collector and the pressure at the feed point is near the atmospheric pressure (Figure 4.13). A combined system (pull–push) uses a single blower to vacuum convey material from one or more sources to a dust collector and then pressure convey the material using the same gas to one or more destinations (Figure 4.14). A summary of characteristics based on this classification is given in Table 4.3.

4.1.2.1.2 Loop Configuration Most pneumatic conveying systems operate as open-loop systems. An open-loop system is one where the conveying gas is vented (or treated and vented) after a single pass through the conveying line. A closed-loop system recycles the gas to the feed point (Figure 4.15).

Table 4.3 Comparison of Pressure, Vacuum, and Combined Conveying Systems

Process Requirement	Vacuum or Pull System	Pressure or Push System	Combined Vacuum Pressure or Pull–Push System
Multiple source, single destination	Preferred	Expensive to implement	Use when single destination is far
Single source, multiple destinations	Expensive to implement	Preferred	Used if high-pressure feeder cannot be used, for example, railcar unloading system
Handle toxic material (containment)	Preferred	No	No
Explosive material	No	Only with inert gas	No
Long-distance conveying (>500 ft)	Limited capacity	Feasible	Feasible but not necessary
Control	Sluggish	Good	Sluggish

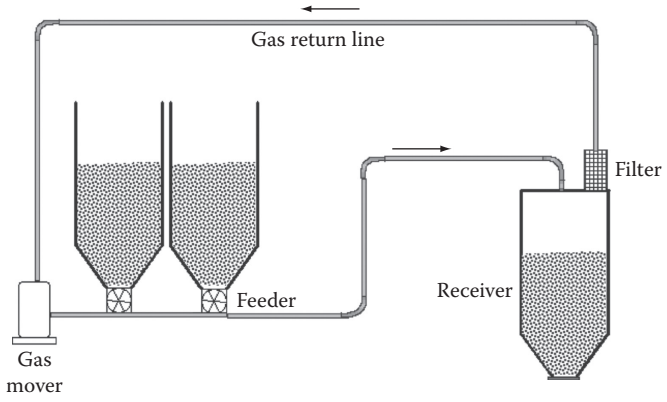


Figure 4.15

Typical closed-loop system.

4.1.2.1.3 Feeder Type or Air–Solids' Mixing Device Conveying gas and solids need to be mixed together to create a gas–solid suspension. This can be accomplished in two ways:

1. Air into material: Using pressure vessel (e.g., blow tank)
2. Material into air: Using mechanical feeders (e.g., screw feeder, rotary feeder, and venturi eductor)

Air-into-material systems are generally batch-type systems that can be operated at very high pressures. It is possible to achieve low velocity, high solids' loading, and long-distance conveying with these systems. Material-into-air systems are continuous systems limited only by pressure rating, leakage rate, wear rate, and feed characteristics of the material.

4.1.2.1.4 Air Mover Type Air movers provide the motive force or energy for conveying. Energy efficiency, system stability, and conveying capacity limitation is largely dictated by the choice of air mover (Table 4.4). Some applications, such as when the material passes through the air mover, require specific types of air movers (e.g., fans).

4.1.2.2 Classification of Dense Phase Conveying Systems

As mentioned earlier, a dense phase pneumatic conveying system operates in a flow regime to the left of saltation velocity (Figure 4.9). The material moves in a nonsuspended mode within the pipe. Unlike dilute phase conveying, where fluid–particle interactions and particle–wall interactions determine the flow behavior, in dense phase conveying the interparticle forces and contact mechanics dominate the flow behavior.

Simple examples of dense phase conveying are conveying of cement and plastic pellets. Once aerated, cement retains air for a long time and remains essentially fluidized. It can be transported through a conveying line at very high solids' loading with nonspecialized hardware over large distances. Similarly, plastic pellets have a natural tendency to slug when fed into a pipe with motive air. This system is self-adjusting and easy to operate.

Table 4.4 Classification Based on Air Movers

Air Mover Type	Typical System Characteristics
Fan or centrifugal blower	Short or lightly loaded systems, low pressure drop, cannot tolerate surging solids' feed, low noise, can tolerate material pass through
Rotary lobe blower	Most common for dilute phase systems, pressure drop up to 1 bar, blower characteristics ideal for varying feed rates
Screw compressors	Common for dense phase system, pressure drop up to 6 bar, blow tanks or high-pressure airlock as feeders

However, there is a broad range of materials that do not possess the high aeration of cement or natural slugging ability of plastic pellets. To convey these materials in smooth dense phase mode, various innovations have been implemented in the industry. The objective of these innovations has been to extend the range of applicability of dense phase system and to make them less sensitive to product characteristics.

Dhodapkar (1990) proposed a broad classification for various dense phase conveying concepts (see Figure 4.16).

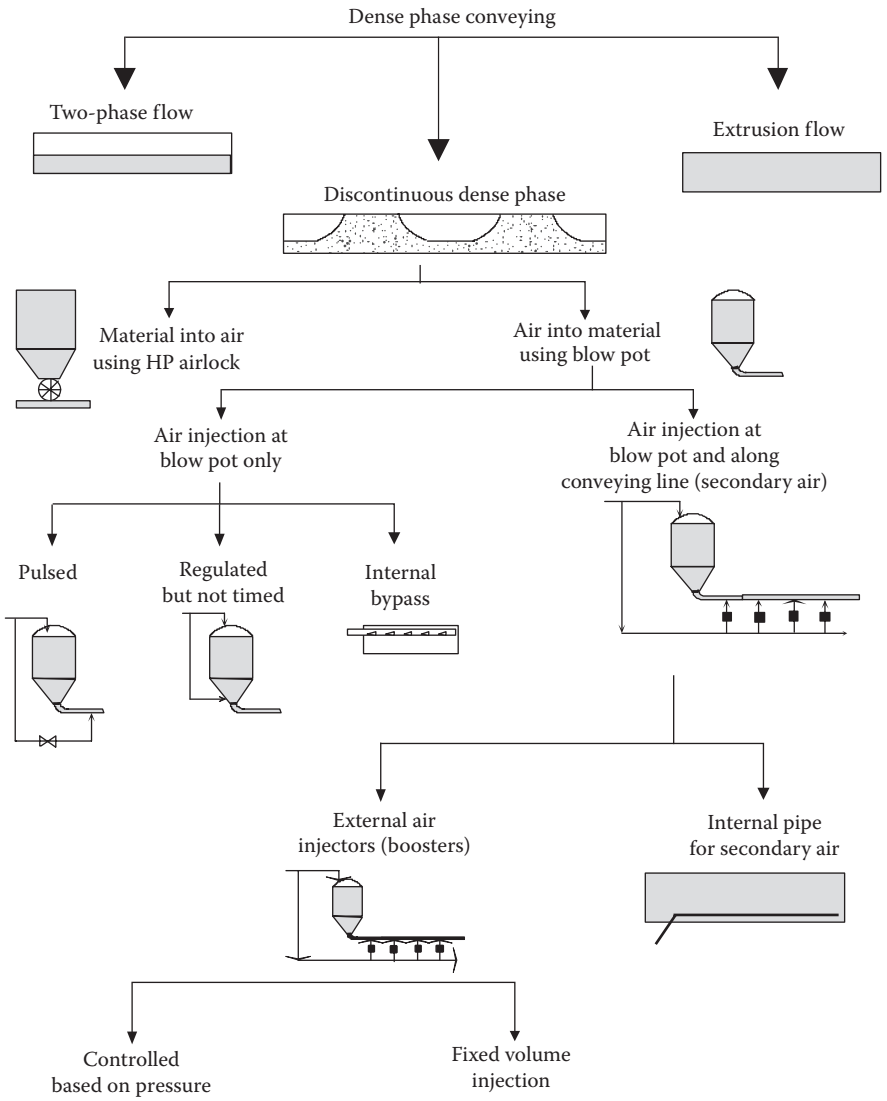


Figure 4.16

Classification of dense phase conveying system.

Two-phase flow: Refers to systems operating just below saltation. The material moves in a strand type flow. The hardware requirements are similar to dilute phase conveying systems, but these systems can operate at much higher pressures (between 1 and 6 bar).

Extrusion flow: A typical example would be dense phase conveying of cement, fine coal, or fly ash. The material is highly aerated, and the gas is homogeneously dispersed with the solids.

Discontinuous dense phase: Refers to plug or slug type of conveying. The conveying gas and material are nonuniformly dispersed to create a variety of flow patterns from slugs and dunes to waves.

Discontinuous dense phase conveying can be achieved either by feeding material into air stream, commonly using a rotary airlock or feeder, or by injecting air into material such as in a blow-tank system.

Material into air: Refers to systems using a high-pressure rotary airlock as a feeder. The construction of these feeders is very similar to conventional rotary airlock with the exception of tight clearances, robust shaft design, and design modifications to minimize gas leakage. It is possible to design continuous dense phase system with high-pressure feeders. The limitations due to abrasive wear and particle degradation can be addressed on a case-by-case basis.

Air into material: Conventional blow tank type of systems fall into this category. The blow tank acts as a high-pressure feeder. These systems typically run in batch mode unless two tanks are operated in tandem. The discharge characteristic of a blow tank is affected by downstream pressure and the nature of air distribution around the blow tank. The main advantage of a blow tank is the lack of moving parts in constant contact with the material. Loss of conveying air due to wearing of valve seat can be a maintenance problem.

Air distribution at the blow tank and along the conveying line can be used as a tool to create and maintain smooth dense phase conveying mode.

4.1.2.2.1 Air Injection Only at Blow Pot or Tank Various methods are possible:

- *Pulsed*. Air injection is used at regular intervals (pulsed) to create air gaps between slugs and plugs and limit their length. The ability to change the length of air gaps between plugs is helpful to run the conveying system at low solids' rate without causing unstable flow. There are several commercial adaptations of this concept.
- *Regulated, not timed*. The conveying air is split between the top and the bottom of the blow tank in a regulated fashion. The top air controls the discharge rate, while the secondary air at the bottom is used to control the solids/air ratio.
- *Internal bypass*. This concept provides a bypass for the conveying air so that it can reach the location of a plug easily. It is assumed that conveying consists of making and breaking of impermeable plugs. No external air is added. The internal bypass line may not be continuous along the conveying length.

4.1.2.2.2 Air Injection at Blow Pot or Tank and Along Conveying Line External air injection can be accomplished by providing either discrete injection points or a perforated tube along the conveying line for continuous air injection.

- *Discrete air injection*. It is commonly known as *Booster Systems*. The air injectors or boosters are installed on the conveying line. Each location has a check valve, which prevents the solids from backing into the air supply header. The majority of systems presently in operation today are based on the concept of fixed volume air injection. Each injector or booster station has a flow control valve that can be set to feed a constant volume of air into the system. The pressure profile or flow conditions in the conveying line generally does not affect the air flow, since these flow control valves act as a critical flow orifice. Some systems are designed with pressure sensors to inject air at locations with high-pressure gradient, which will correspond to a long or stalled plug. The air injection helps to break the plug and maintain smooth conveying conditions.
- *Continuous air injection*. This is accomplished by a pipe in a pipe arrangement. The internal pipe has holes at regular intervals for air injection. Very few of these are commercially available. The clogging of internal pipe is the biggest reason.

4.1.3 Components of Conveying System

A short discussion of the three major components of a conveying system, namely, feeder, air mover, and gas–solid separator, is given here.

4.1.3.1 Feeders

A feeder in a pneumatic conveying system serves the purpose of an airlock between the conveying line and the feed hopper and regulates the feed rate of solids into the line. In vacuum systems, where the feed point is at ambient pressure, the airlock function is not required. Table 4.5 summarizes the operating range and material suitability of various common feeders.

The design of feeder–hopper interface is critical to assure reliable flow out of the hopper. The mass flow pattern in a hopper can be disrupted by a feeder that extracts the material preferentially from one corner of the outlet, which in turn affects the flow into the feeder. Also, the feed shoe or feed box that connects the feeder to the conveying line must be properly designed to provide good mixing and entrainment of solids in gas.

Among these feeders, rotary airlock or feeders and blow tanks are the workhorses of the industry and deserve more attention.

Table 4.5 Summary of Feeders for Pneumatic Conveying Applications

Feeder	Suitable for System Types	Operating Pressure	Suitable Materials	Unsuitable Materials	Conveying Mode	Comments
Suction nozzle	Vacuum	Up to 0.5 bar vacuum	All free flowing	Caking, large chunks, sticky, cohesive	Continuous dilute phase	Feed rate control is difficult
Rotary feeder	Vacuum and pressure	0.5 bar vacuum −3.5 bar pressure (6 bar maximum)	Wide range of materials	Abrasive, caking, sticky, very cohesive	Continuous dilute and dense phases	Most common feeder. Wide variety of design features
Eductor	Pressure	0.25 bar	Free flowing	Abrasive, friable, highly cohesive	Continuous dilute phase	Special design for abrasive materials, high-pressure motive gas may be required
Blow tank–bottom discharge	Pressure	0–10 bar	Wide range of materials, abrasive materials	Very cohesive, sticky or compressible materials	Batch dilute and dense phases	Poorly flowing materials will require air injection in the cone, difficult to control conveying rate
Blow tank–fluidization type, top discharge	Pressure	0–10 bar	Fine fluidizable materials (Geldart class A/C, A)	Geldart class B, B/D, D or material with large chunks	Batch dilute and dense phases	
Double flapper valve	Pressure	0–0.5 bar	Abrasive and free-flowing material	Cohesive	Continuous dilute phase	Pulsing feed. Difficult to obtain; good and consistent seal
Screw feeder	Pressure and vacuum	0.5 bar vacuum to 1 bar pressure	Wide range of materials	Sticky, compressible	Continuous dilute phase	Improper design will result in feed rate control. Rate sensitive to material properties
Fuller–Kinyon Pump	Pressure	2 bar	Fine powders	Coarse materials	Continuous dilute and dense phase	Typically used in cement industry
Slide gate	Vacuum	Up to full vacuum	Coarse materials, preferably free flowing	Cohesive, sticky materials	Continuous dilute phase	Simple, discharge rate depends on material properties
Other specialized feeders: diaphragm pump	Pressure	0–0.5 bar	Materials with high air retention or low deaeration, preferably low bulk density	Sticky, cohesive, low air retention	Continuous dilute and dense phases	

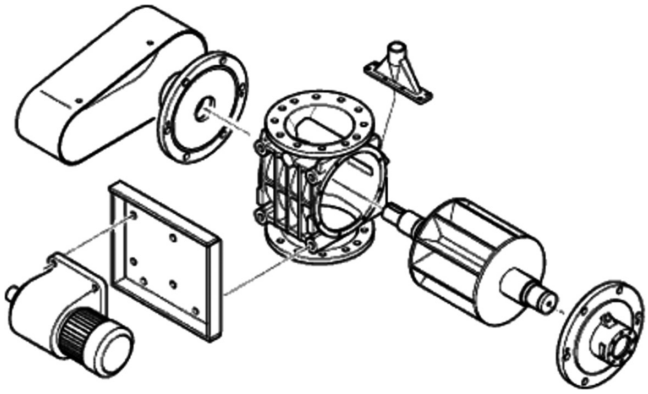


Figure 4.17

Exploded view of a rotary airlock/feeder. (Courtesy of Coperion Waeschle.)

4.1.3.1.1 Rotary Airlock or Feeder This feeder comprises vanes welded on a shaft where the space (pockets) between the vanes fills and empties as the shaft turns (Figure 4.17). The high- and low-pressure sides are isolated by tight clearances between the vanes and the housing. A range of designs are available, and careful selection of features and operating range must be made, based on bulk properties. The critical issues are

- Volumetric capacity of the rotor and its relationship with r/min
- Gas leakage rate at various pressures and r/min
- Particle degradation and wear
- Venting arrangement of gas
- Design of inlet and outlet
- Seal and bearing design

4.1.3.1.2 Blow Tank Blow tanks or blow pots are commonly used as feeders for high-pressure applications. There are two common configurations of blow tanks: bottom discharge and top discharge. The top discharge blow tanks are used for fine powders, whereas bottom discharge blow tanks can be used for powders and coarse materials. The conveying air can be injected at various locations at the blow tank and along the conveying line (as shown in Figure 4.18). Blow tanks operate in batch mode. A complete cycle consists of filling, valve setting, pressurization, conveying, and depressurization (Figure 4.18). The average conveying rate is lower than instantaneous conveying rate due to time lost in nonconveying steps.

The advantages of the blow tank as a feeder are as follows:

1. No moving parts in contact with solids
2. Can operate or feed against high pressures (>3 bar)
3. Good for abrasive materials
4. Low maintenance

However, the disadvantages are as follows:

1. Do not provide good control on discharge rate or solids loading
2. Unsuitable for very cohesive or sticky materials
3. Batch operation, but can be made continuous using two blow tanks

4.1.3.2 Air Movers

Air movers provide the motive energy for pneumatic transfer. Fans, centrifugal blowers, rotary lobe (roots type) blowers, screw compressors, sliding vane compressors, and reciprocating compressors cover the majority of the applications. The suitability of an air mover must be judged based on the operating conditions and requirements of the application.

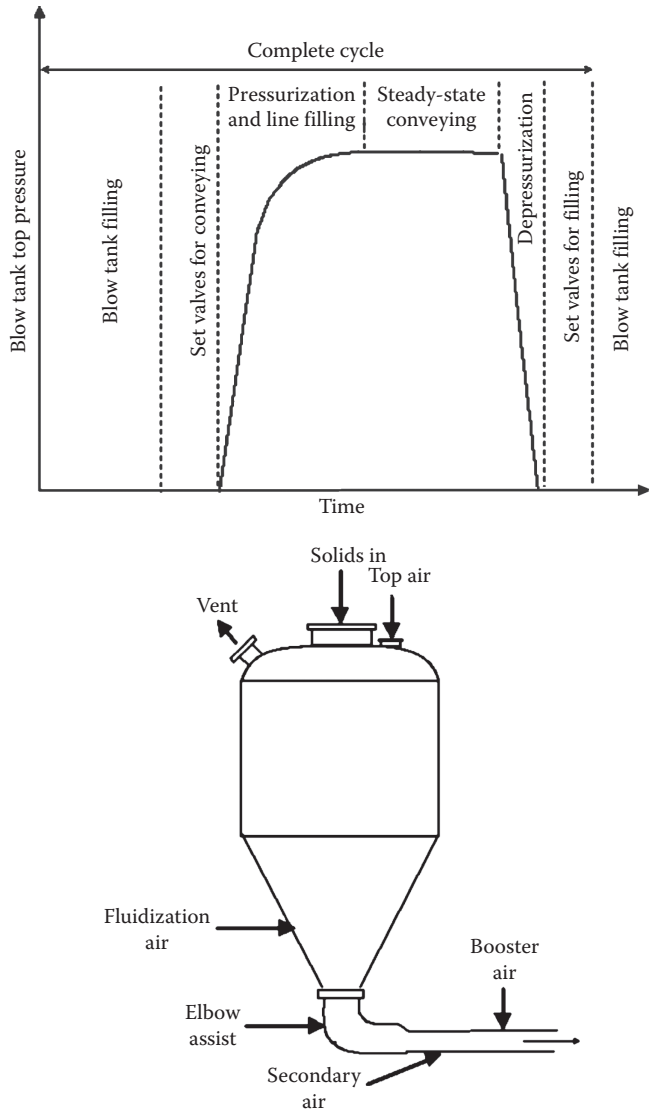


Figure 4.18

Typical bottom discharge blow tank configuration and conveying cycle.

4.1.3.2.1 Fans Fans convert kinetic energy of the gas generated by the rotating impeller into pressure and the volume as a result of displacement of the blades. Depending on the direction of flow through the impeller, fan designs can be broadly classified into four categories, namely, axial flow, radial flow (centrifugal fans), mixed flow (axial and radial), and cross-flow. In pneumatic conveying applications, radial flow or centrifugal fans are primarily used.

There are three primary impeller designs available for centrifugal fans: radial, backward curving, and forward curving. The forward-curved design provides maximum pressure head for a given rotor size and speed, while the backward curved design provides the least. On the other hand, backward-curved impeller design is more energy efficient with lower operating costs. Radial flow fans offer the best compromise. Radial flow design can also tolerate particulate material in the gas stream and tend to be more robust.

Fans are generally driven directly with a motor that limits the speed of rotation. To change the gas flow rate, inlet or outlet throttling valves can be used. Proper balancing of the fans is necessary to minimize the maintenance of the bearings.

The performance of all fans is governed by fan laws that state the following:

1. Air volume varies directly with fan speed.
2. Static pressure varies with square of the speed.

3. Brake horsepower and air horsepower varies with the cube of the speed.
4. For geometrically similar fans, air volume varies with the cube of size.
5. For geometrically similar fans, static pressures vary with the square of the size.
6. For geometrically similar fans, break horsepower varies with the fifth power of size.

These laws can be used to scale up or predict the performance of a machine at different operating conditions. In order to convert the performance curve of a fan from one speed to another, select a number of points on the curve and convert the corresponding data for air volume, static pressure, brake horsepower, and noise using the following equations:

$$\frac{Q_2}{Q_1} = \left(\frac{D_2}{D_1}\right)^3 \frac{\text{rpm}_2}{\text{rpm}_1}$$

$$\frac{P_2}{P_1} = \left(\frac{D_2}{D_1}\right)^2 \left(\frac{\text{rpm}_2}{\text{rpm}_1}\right)^2$$

and

$$\frac{\text{HP}_2}{\text{HP}_1} = \left(\frac{D_2}{D_1}\right)^5 \left(\frac{\text{rpm}_2}{\text{rpm}_1}\right)^3$$

where
Q is the air flow rate
P is the static pressure
D is the impeller diameter of fan
HP is the break horsepower

For detail treatment of fan design, operation, and performance, see Fan Engineering (2003).

4.1.3.2.1.1 Controlling Air Flow Rate The most efficient means of reducing air flow rate from a fan is to change the fan speed. While the efficiency remains unchanged, the noise level and power consumption are significantly reduced. Since the fan curves are shifted, there is no risk of operation in the unstable region. The cost of a variable speed motor can be high if the adjustment needs to be made very often.

Another approach is to install adjustable inlet and outlet vanes. Vane control systems are cheaper to implement but do not provide the same level of power savings as speed control. Inlet vane control is used for large fans since it is cheaper, but the power savings are better than that in the outlet vane control.

4.1.3.2.2 Rotary Lobe Blowers Rotary lobe blowers (roots-type blowers) are ideally suited for pneumatic conveying applications operating at less than 1 bar gauge pressure or 0.5 bar vacuum and require oil-free gas. While most rotary lobe blowers are rated for 1 bar and less, special lobe designs can deliver 1.24 bar differential pressure. These can be considered before opting for a screw compressor as the choice for the air mover. The air mover operates on positive displacement principle where the gas at the inlet is trapped between two counterrotating lobes. As the two lobes rotate, the gas is expelled at the discharge end (see Figure 4.19). There is no gas compression within the lobes, and all the compression occurs as the gas is expelled against the higher

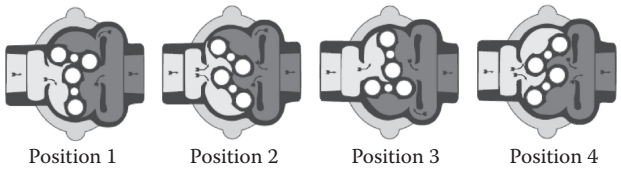


Figure 4.19
Roots blower operating principle. (Courtesy of Roots Dresser Industries.)

pressure at the outlet. Therefore, the horsepower consumption is proportional to discharge pressure and the inlet air volume remains relatively constant with back pressure. The slight decrease in air delivery volume is due to slippage of gas owing to clearances between the lobes. These blowers can be very noisy during the operation, and hence, inlet or outlet silencers are highly recommended. The pulsating nature of the gas flow can be reduced by using a trilobe design. The pulsations also result in the loss of thermodynamic efficiency.

In specifying blower performance, one may use actual cubic feet per minute (ACFM) and inlet cubic feet per minute (ICFM) alternately. These refer to the flow rate at the inlet of blower based on actual conditions of temperature, pressure, and RH% (relative humidity) at the blower inlet. It is essential to distinguish ACFM/ICFM from standard cubic feet per minute (SCFM). SCFM refers to the gas flow rate at a standard reference pressure, temperature, and RH%. According to ASME and CAGI standards, the standard reference is 14.7 psia, 68°F, and 36% relative humidity. Most blower curves are based on ICFM and not SCFM.

4.1.3.2.3 Screw Compressors Screw compressors are required when conveying pressure exceeds 1 bar. The screw compressor is a positive displacement volume reduction machine. In simplest configuration, it consists of a male rotor (driver) and a female rotor (driven). The gas is trapped in the void space between the counterrotating rotors at the inlet. As the screws turn, the volume is reduced and the compression is achieved. Unlike reciprocating compressors, there are no discharge valves in screw compressors. The end of compression automatically occurs at the discharge port. Since the energy is already spent on compressing the gas through the compressor, any changes in system characteristics (reduced load) will not affect the power consumption. The performance of a screw compressor must be controlled independently either through throttling of the inlet valve or the variable speed drive on the rotor.

A comparison of the characteristics of fan, rotary lobe blower, and screw compressor is shown in Figure 4.20 and Table 4.6.

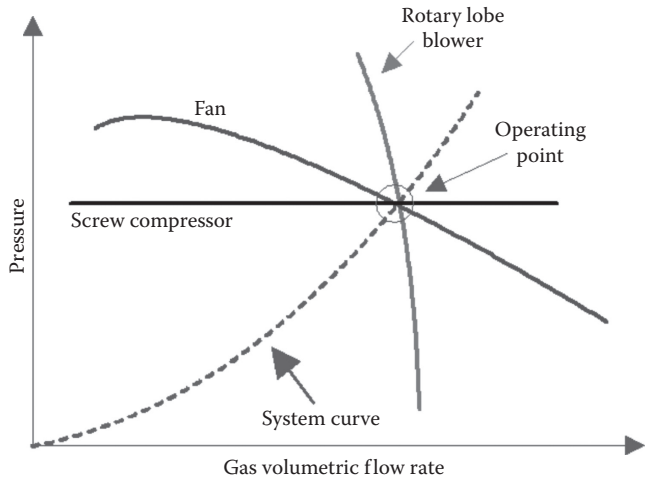


Figure 4.20

Comparison of air mover characteristics and relationship with system characteristics.

Table 4.6 Comparison of Air Movers (Typical Performance Limits)

Type	Maximum Delivery Pressure or Vacuum (bar)	Maximum Flow Rate (m^3/min)
Fans	±0.2	1000
Single-stage centrifugal blowers	−0.5 to +0.5	1000
Rotary lobe blowers	−0.5 to +1	1200
Screw compressors	0–10	1000
Reciprocating compressor	No limit	200
Sliding-vane compressor	1–5	100

4.1.3.3 Gas–Solid Separation Devices

The three common gas–solid separation devices are

1. Inertial separator
2. Cyclone separator
3. Dust collector or baghouse

Selection and specification of suitable gas–solid separation device will depend on process requirements and material properties, namely,

1. Desired efficiency of separation based on particle size distribution of incoming solids
2. Acceptable pressure drop range
3. Operating pressure and temperature
4. Cleanout and contamination requirement
5. Dust explosion potential
6. Acceptable turn down in gas flow rate
7. Compatibility with material (corrosiveness, abrasion, etc.)

A simplified guideline is presented in Table 4.7.

4.1.4 Calculating Pressure Drop in Dilute Phase Systems

The total pressure drop across a conveying system can be assumed to be the sum of pressure drops across various components. The total pressure drop in turn must be overcome by the air mover to satisfy the pressure balance:

$$\Delta P_{\text{air-mover}} = \Delta P_{\text{blower-piping}} + \Delta P_{\text{feed-section}} + \Delta P_{\text{accleration(gas+solids)}} + \Delta P_{\text{straight-sections}} + \Delta P_{\text{bends}} + \Delta P_{\text{filter-receiver}}$$

The equations of pressure drop for the various components are presented as follows.

4.1.4.1 Blower Piping and Feed Section Pressure Drop

The pressure drop in the piping carrying gas from the blower to feed section of the conveying system can be calculated by using the standard calculations for single-phase gas flow in pipes. Additional pressure drop due to inlet or outlet filters and inlet or outlet silencers must be added.

4.1.4.2 Acceleration (Gas–Solids) Pressure Drop

When solids are fed into a gas stream, additional energy is expended to accelerate the solids to their steady-state velocity. This loss occurs at the feed (pickup) point. Similar loss occurs when accelerating the gas phase; however, it is relatively smaller.

For the solid phase,

$$\Delta P_{\text{ACC-solids}} = \frac{U_{\text{p}} W_{\text{s}}}{A}$$

Table 4.7 Comparison of Major Gas–Solid Separation Devices

Type of Gas–Solid	Suitable for	Unsuitable for	Comments Separation Device
Inertial separator	Separating large nonhazardous particles with minimal fines	Fine powders or hazardous materials	Simple, low-pressure drop, no maintenance
Cyclone separator	Most nonfriable and nonabrasive materials	Very hazardous materials where 99.5% collection efficiency must be guaranteed	Typical pressure drop of 10″ WC (25 mbar), proper design and installation is critical, scalability with gas flow rate is limited
Dust collector or baghouse	Efficient solution for most materials	Very few materials	Gives high degree of separation, collection efficiency independent of gas flow rate and particle size, bag replacement is major maintenance issue

For the gas phase,

$$\Delta P_{\text{ACC-gas}} = \frac{\rho_g U_g^2}{2}$$

By adding the components given earlier,

$$\Delta P_{\text{ACC}} = \Delta P_{\text{ACC-solids}} + \Delta P_{\text{ACC-gas}}$$

$$\Delta P_{\text{ACC}} = \frac{U_p W_s}{A} + \frac{\rho_g U_g^2}{2}$$

$$\Delta P_{\text{ACC}} = \frac{\rho_g U_g^2}{2}\left(1 + 2\frac{W_s}{A\rho_g U_g}\left(\frac{U_p}{U_g}\right)\right)$$

$$\Delta P_{\text{ACC}} = \frac{\rho_g U_g^2}{2}\left(1 + 2\mu\left(\frac{U_p}{U_g}\right)\right)$$

The velocity ratio, U_p/U_g, for the horizontal flow can be calculated by the (1953) Hinkle correlation:

$$\frac{U_p}{U_g} = 1 - 0.044 d_p^{0.3} \rho_p^{0.5}$$

or modified Hinkle correlation (IGT correlation):

$$\frac{U_p}{U_g} = 1 - 0.68 d_p^{0.92} D^{-0.54} \rho_p^{0.5} \rho_g^{-0.2}$$

where d_p and D in m and ρ_p and ρ_g in kg/m^3.

For vertical flow, one may simply use slip condition based on single-particle terminal velocity.

$$U_p = U_g - U_t$$

4.1.4.3 Steady-State Pressure Drop in Straight Sections

The overall pressure drop for fully accelerated and steady-state dilute phase conveying in straight pipe can be considered as the sum of static and frictional components:

$$\Delta P_{\text{total}} = \Delta P_{\text{static}} + \Delta P_{\text{frictional}},$$

$$\Delta P_{\text{static}} = \rho_p (1 - \varepsilon) \Delta Z g + \varepsilon \rho_g \Delta Z g$$

where the first term on the right-hand side is the contribution due to solids and the second term is due to gas. ΔZ is the change in elevation or height of the vertical section. The static component is zero for horizontal orientation.

The voidage, ε, can be calculated as

$$\varepsilon = 1 - \frac{W_s}{A\rho_p U_p}, \quad U_p = U_g - U_t$$

where the pressure drop term due to gas–solid friction is customarily split into gas and solids' contributions.

$$\Delta P_{\text{frictional}} = \Delta P_{\text{air}} + \Delta P_{\text{solids}}$$

The first term represents the contribution due to gas friction and the second term due to solids' friction. The pressure drop due to air is calculated by well-established single-phase calculation methods:

$$\Delta P_{\text{air}} = \lambda_{\text{f}} \frac{\rho_{\text{g}} U_{\text{g}}^2 L}{2D}$$

where the friction factor for gas alone can be estimated by the explicit correlation of Swamee and Jain (1976):

$$\lambda_{\text{f}} = \frac{1.325}{\left[\ln\left(k_{\text{s}}/3.7D + 5.74/Re^{0.9}\right)\right]^2}$$

For common pipes, the pipe roughness, k_{s}/D, is typically 0.001.

The expression for pressure drop due to solids is formulated similar to single-phase gas flow with added solids' loading factor:

$$\Delta P_{\text{solids}} = \left(\mu\lambda_{\text{z}}\right)\frac{\rho_{\text{g}} U_{\text{g}}^2 L}{2D}$$

4.1.4.3.1 Estimation of Friction Factor λ_z Several approaches have been proposed in the literature to calculate the solids' friction factor based on material properties and system parameters. Unfortunately, none of them are comprehensive and fundamental enough to cover all factors. Weber (1982, 1991), after analyzing a large set of data, proposed the following expression:

$$\lambda_{\text{z}} = K\mu^a Fr^b Fr_{\text{s}}^c \left(\frac{D}{d_{\text{p}}}\right)^d$$

where

$$\mu = \text{solids loading} = \frac{W_{\text{s}}}{W_{\text{g}}}$$

$$Fr = \frac{U_{\text{g}}^2}{gD}, \quad Fr_{\text{s}} = \frac{U_{\text{t}}^2}{gd_{\text{p}}}$$

In pneumatic conveying literature, two forms of Froude number can be found:

$$Fr_1 = \frac{U_{\text{g}}^2}{gD}, \quad Fr_2 = \frac{U_{\text{g}}}{\sqrt{gD}}$$

The reader is cautioned to verify the definition of Froude number before applying any correlation.

In the absence of any experimental data on a material, the parameters listed in Table 4.8 can be chosen for preliminary calculations. It should be noted that the earlier correlation does not account for the effect of elastic properties of particles and wall, surface characteristics, particle size distribution, and particle shape. The exponent of Froude number is always negative; however, the coefficient of solids loading in the correlation need not be negative.

Table 4.8 Summary of Exponents for Friction Factor Correlation

Investigator/Material	*K*	*a*	*b*	*c*	*d*
Stegmaier, fine powder ($d_{\text{p}} < 0.5$ mm)	2.1	−0.3	−1	0.25	0.1
Weber (Siegel data), coarse material ($d_{\text{p}} > 0.5$ mm)	0.082	−0.3	−0.86	0.25	0.1

Source: Weber, M., *Bulk Solids Handling*, 2(2), 231, 1982. With permission.

In the authors' experience using a constant value of friction factor will usually suffice for preliminary calculations. This value can be backcalculated if operating data from an installed system are available.

From experimental data: If conveying data can be generated on a pilot-scale test rig, a more accurate estimation of material-specific friction factor can be made. It is advisable to install a DP transmitter across a straight horizontal section that is away from the bends at each end. A static gage at the test section is necessary to calculate the local gas velocity:

$$\Delta P_{\text{total}} = \Delta P_{\text{frictional}} = \Delta P_{\text{air}} + \Delta P_{\text{solids}}$$
$$\Delta P_{\text{solids}} = \Delta P_{\text{total}} - \Delta P_{\text{air}}$$

where ΔP_{air} can be estimated by regressing pressure drop data for single-phase air flow in the test section. Solids' friction factor can be calculated from experimental data at each of the test condition by using the following equation:

$$\lambda_z = \frac{\Delta P_{\text{solids}} 2D}{\rho_g U_g^2 \mu \Delta L}$$

These data can be correlated with the generalized format or a simplified expression if the test data are not available for a range of pipe sizes:

$$\lambda_z = K\mu^a Fr^b$$

4.1.4.4 Pressure Drop in Vertical Section

The pressure drop in the vertical section can be calculated as follows:

$$\Delta P_{\text{total}} = \Delta P_{\text{frictional}} + \Delta P_{\text{static}}$$
$$\Delta P_{\text{static}} = \rho_p (1-\varepsilon)\Delta Z g + \varepsilon \rho_g \Delta Z g$$
$$\Delta P_{\text{frictional}} = \Delta P_{\text{total}} - \Delta P_{\text{static}}, \quad \Delta P_{\text{frictional}} = \Delta P_{\text{solids}} + \Delta P_{\text{air}}$$
$$\Delta P_{\text{solids}} = \Delta P_{\text{frictional}} - \Delta P_{\text{air}}, \quad \lambda_z = \frac{\Delta P_{\text{solids}} 2D}{\rho_g U_g^2 \mu L}$$

4.1.4.5 Pressure Drop in Bends

In contrast to straight sections, frictional losses have relatively minor contribution to the pressure drop across a bend. The majority of the pressure drop is due to reacceleration of solids that were slowed down during transit through the bend. Since the particles may continue to reaccelerate even after they exit the bend, the pressure drop due to a bend cannot be measured simply by pressure difference between inlet and outlet of the bend. Also, the pressure drop across a bend depends on its geometry and orientation. No generalized correlation that takes all the factors into account is available in the literature: Bradley (1990), Chambers et al. (1986), Marcus et al. (1990), Morikawa et al. (1978), Park et al. (1980), and Schuchard (1970). The following correlations are sufficiently accurate for practical design:

4.1.4.5.1 Chambers–Marcus Correlation (1986) The Chamber–Marcus correlation is given as follows:

$$\Delta P_B = B(1+\mu)\frac{\rho_g U_g^2}{2}$$

This expression is very similar to the expression proposed by EEuA (1963). The bend loss coefficient B depends on the ratio of bend radius to pipe diameter. In the absence of experimental data, Chambers and Marcus (1986) recommend the use of the values given in Table 4.9.

Table 4.9 Bend Constant B or Various Bends

R_B/D	B
2	1.5
4	0.75
≥6	0.50

Note: R_B is the radius of the bend curve. Bends are often specified by the R_B/D ratio. $R_B/D > 10$ is considered as a long radius bend.

4.1.4.5.2 Correlation (1987) of Westman et al. The correlation of Westman et al. is given as follows

$$\frac{\Delta P_{\text{Bend}}}{0.5\rho_g U_g^2} = \zeta_{\text{Total}} = \zeta_{\text{air}} + \zeta_{\text{solids}}$$

$$\zeta_{\text{air}} = 0.167\left[1 + 17.062\left(\frac{D_B}{D}\right)^{-1.219}\right] Re^{-0.17}\left(\frac{D_B}{D}\right)^{0.84}$$

$$\zeta_{\text{solids}} = \frac{5.4\mu^{1.293}}{Fr^{0.84}\left(D_B/D\right)^{0.39}}$$

4.1.4.6 Pressure Drop in Gas–Solid Separator or Filter Receiver

The pressure drop across gas–solid separators depends on the gas flow rate and solids' loading (see the vendor of the unit for pressure drop estimation). Typically, these units are designed for 5–10 in. WC in the normal operating range.

4.1.4.7 Calculation of Overall Pressure Drop in Dilute Phase Conveying System

The overall pressure drop in a dilute phase conveying system (pressure or vacuum) can be determined by systematically calculating the pressure gradient across various elements (straight horizontal, straight vertical, or bends). It is logical to begin the calculation from a point in the system where the pressure conditions are well defined and then work toward the other end. For pressure systems, the exit conditions are known, whereas feed conditions are known for vacuum systems. The following example outlines the approach for pressure system that can be modified slightly for vacuum system calculations:

Example 4.3: Given

1. Material properties: particle size and particle density
2. Conveying rate
3. Conveying line layout (see Design Tips)
4. Pipe diameter D
5. Pickup or saltation velocity U_{pickup}

find

1. Overall pressure loss
2. Total gas flow rate (SCFM) required

It is assumed that the temperature of the conveying gas is constant along the conveying line. Appropriate corrections to the gas volume must be made if a temperature gradient exists.

Step 1: Draw an isometric layout of the conveying system. Mark all the bends, elbows, and diverter valves.

As mentioned earlier, the gas velocity and gas density continually changes from feed point to destination. The use of an average value leads to inaccurate estimation of the pressure drop. It is recommended

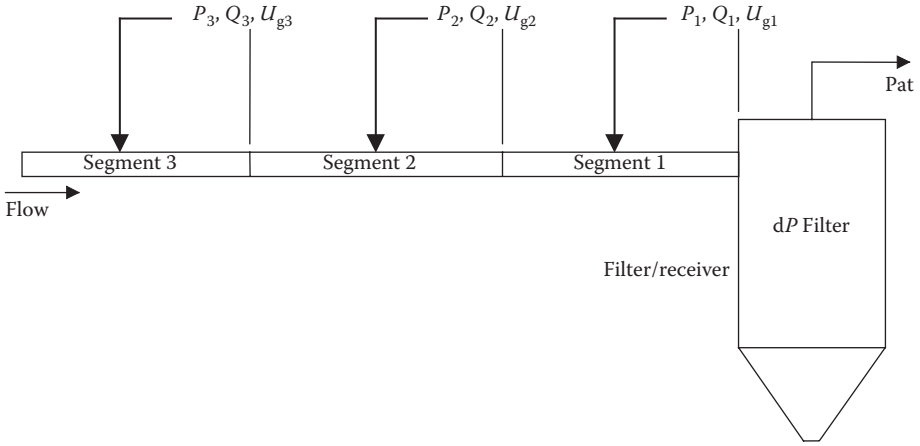


Figure 4.21

Segmentation and flow condition representation.

that the conveying line has to be broken down into smaller segments of 50 ft (15 m) or less. The calculations are performed on an incremental basis by using local values of gas velocity and gas density.

It is assumed that the flow conditions (pressure, velocity, gas density, temperature, etc.) in a segment are represented by the conditions calculated at the exit of the segment (see Figure 4.21). The last segment is the nth segment.

Step 2:

(1) Depending on the total length of the system and material type, select solids to air loading ratio μ from Table 4.10.

(2) Assume the pressure at pickup point (Ppickup, psia). Calculate the saltation velocity. As a first approximation, use saltation velocity as pickup velocity:

$$\mu = \frac{W_s}{W_g} = \frac{W_s}{AU_{\text{gsaltation}}\rho_f}$$

$$D = \sqrt{\frac{4W_s}{\pi U_{\text{gsaltation}}\rho_f}}$$

where ρ_f is the gas density at P_{pickup}.

(3) Calculate the conveying gas flow rate at standard conditions

$$Q_0(\text{scfm}) = U_{\text{gsaltation}}\left(\pi/4 * D^2\right)\left(P_{\text{pickup}}\right)/P_{\text{atm}}$$

Step 3: Estimate the flow conditions at the first segment:

$$P_1 = P_{\text{atm}} = \text{d}P_{\text{filter}}$$
$$Q_1 = Q_0(\text{SCFM})P_{\text{atm}}/P_1$$
$$U_{g1} = Q_1/A$$
$$\rho_{f1} = \left(\rho_{f\text{-atm}}/P_{\text{atm}}\right)P_1$$

Temperature correction for density must be made where temperature gradient exists.

Table 4.10 Selection of Approximate Solids' Loading

System Length (ft)	Coarse Material d_p > 0.5 mm	Fine Material d_p < 0.5 mm
0–500	5	6
500–1000	4	4
1000–1500	2.5	3

Step 4: Estimate the pressure drop across the segment.
If the segment is a straight section,

$$\Delta P_{\text{segment}} = \Delta P_{\text{static}} + \Delta P_{\text{frictional}}$$

$$\Delta P_{\text{static}} = \rho_p (1-\varepsilon)\Delta L \frac{g}{g_c} + \varepsilon \rho_g \Delta L \frac{g}{g_c}$$

where

$$\varepsilon = 1 - \frac{W_s}{A\rho_p U_p}$$

Use IGT correlation to calculate U_p:

$$\frac{U_p}{U_g} = 1 - 0.68 d_p^{0.92} D^{-0.54} \rho_p^{0.5} \rho_g^{-0.2}$$

where
d_p, D are in meters
ρ_p, ρ_g are in kg/m^3

ΔP_{static}, which is the pressure drop due to static head of gas–solid mixture, is zero for horizontal orientation:

$$\Delta P_{\text{frictional}} = \left(\lambda_f + \mu\lambda_z\right)\frac{\rho_g U_g^2 \Delta L}{2Dg_c} = \lambda_f \frac{\rho_g U_g^2 \Delta L}{2Dg_c} + \left(\mu\lambda_z\right)\frac{\rho_g U_g^2 \Delta L}{2Dg_c}$$

Swamee and Jain (1976) correlation for gas friction factor, λ_f, is recommended:

$$\lambda_f = \frac{1.325}{\left[\ln\left(k_s/3.7D + 5.74/Re^{0.9}\right)\right]^2}$$

Use generalized form of solids' friction factor correlation, λ_z:

$$\lambda_z = K\mu^a Fr^b Fr_s^c \left(\frac{D}{d_p}\right)^d$$

$$\mu = \text{solids loading} = \frac{W_s}{W_g}$$

$$Fr = \frac{U_g^2}{gD}$$

$$Fr_s = \frac{U_t^2}{gd_p}$$

In the absence of material-specific data, use Stegmaier's coefficients for fine powders and Weber's coefficient for coarse materials (Table 4.11) as suggested by Chambers and Marcus (1986). The values of K can be adjusted to fit the available plant data and then used for predictive calculations.

Table 4.11 Coefficients for Solids' Friction Factor Correlation

Investigator/Material	K	a	b	c	d
Stegmaier fine powder ($d_p < 0.5$ mm)	2.1	−0.3	−1	0.25	0.1
Weber (Siegel data) coarse material ($d_p > 0.5$ mm)	0.082	−0.3	−0.86	0.25	0.1

If the segment is a bend or an elbow, use Chambers–Marcus bend pressure drop correlation:

$$\Delta P_{\text{segment}} = \Delta P_{\text{B}} = \left(1+\mu\right)\frac{\rho_{\text{g}} U_{\text{g}}^2}{2g_{\text{c}}}$$

where the bend constant B can be experimentally determined or read from Table 4.9 when no data are available.

The flow conditions in the next (upstream) segment (Figure 4.21) can then be established as follows:

$$P_2 = P_1 + \Delta P_{\text{segment}}$$
$$Q_2 = Q_0\left(\text{SCFM}\right)P_{\text{atm}}/P_2$$
$$U_{\text{g}2} = Q_2/A_2$$
$$\rho_{\text{f}2} = \left(\rho_{\text{f-std}}/P_{\text{atm}}\right)P_2$$

Step 5: Repeat Step 4 until the pressure and velocity profile in the entire system is obtained. The last segment corresponds to the feed section.

For remaining segments,

$$P_{i+1} = P_i + \Delta P_{\text{segment}}$$
$$Q_{i+1} = Q_0\frac{P_{\text{atm}}}{P_{i+1}}$$

assuming isothermal conditions.

Step 6: Estimate the pressure at the inlet of the last nth segment (see Figure 4.22). Add acceleration zone pressure drop:

$$P_{\text{pickup}} = \left(P_n + \Delta P_{\text{last segment}}\right) + \Delta P_{\text{ACC}}$$

where

P_{pickup} and P_n are in psia

$\Delta P_{\text{last segment}}$ and ΔP_{ACC} are in psi

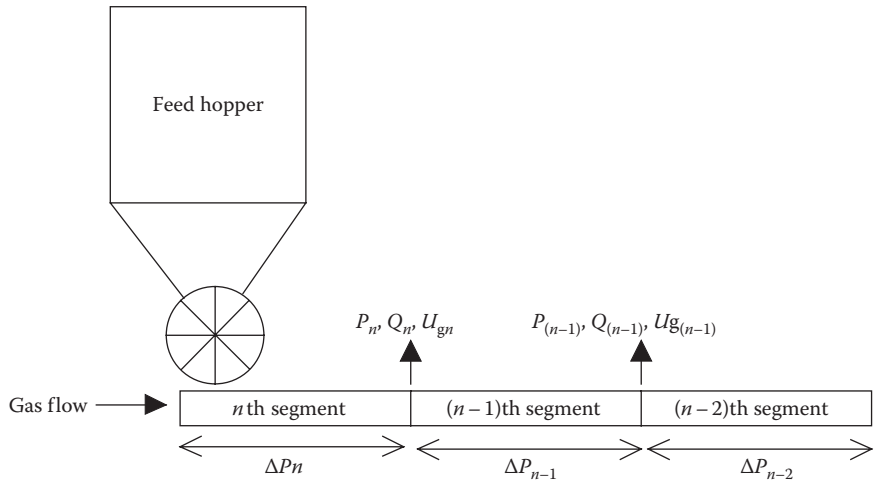


Figure 4.22

Flow conditions at feed point.

$$\Delta P_{ACC} = \frac{\rho_g U_g^2}{2g_c}\left(1 + 2\mu\left(\frac{U_p}{U_g}\right)\right)$$

and ρ_g and U_g are calculated for conditions at the feed point.

Use IGT correlation to calculate U_p/U_g:

$$\frac{U_p}{U_g} = 1 - 0.68 d_p^{0.92} D^{-0.54} \rho_p^{0.5} \rho_g^{-0.2}$$

Step 7: Compare P_{pickup} with the value used in Step 2. Update the estimation of P_{pickup}. Repeat Steps 2 to 6 until convergence is reached.

Step 8: Add the miscellaneous pressure drops due to blower piping and filters or silencer to estimate the blower outlet pressure:

$$\Delta P_{misc} = dP_1 + dP_2 + dP_3$$

(see Figure 4.23 for more details)

$$P_{blower\ outlet} = \Delta P_{misc} + P_{pickup}$$

Step 9: Add the leakage loss through the rotary airlock or feeder to estimate the blower gas delivery rate:

$$Q_{blower\ outlet} = \left(Q_0 + Q_{leakage}\right) P_{atm} / P_{blower\ outlet}$$

$Q_{leakage}$ (scfm) must be estimated from vendor charts and corrected for pressure at the feed point.

Blower inlet cfm can be calculated by using the Gas law:

$$Q_{blower\ inlet} = Q_{blower\ outlet} P_{blower\ outlet} / P_{blower\ inlet}$$

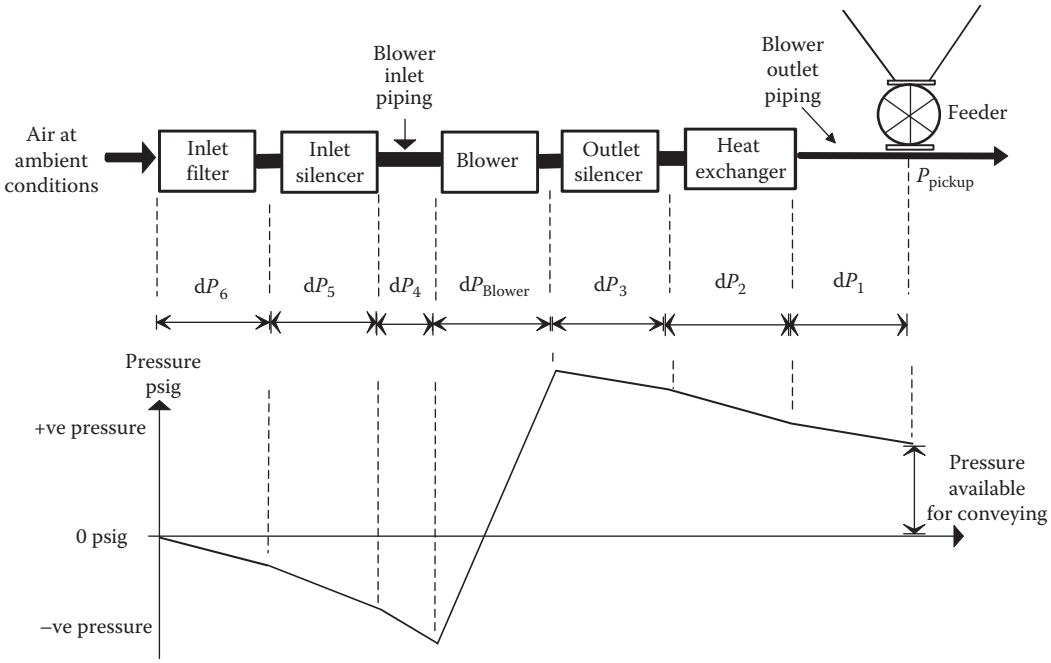


Figure 4.23

Pressure profile at the blower.

where

$$P_{\text{blower inlet}} = P_{\text{atm}} - \left(dP_6 + dP_5 + dP_4\right)$$

From Figure 4.7,

$$P_{\text{blower inlet}} = P_{\text{atm}} - \left(dP_6 + dP_5 + dP_4\right)$$

$P_{\text{blower outlet}}$ and $Q_{\text{blower inlet}}$ define the operating point for the blower.

Example 4.4: Calculate the Pressure Drop Given

Material: Coarse granular material

- Conveying rate W_s = 30,060 lb/h = 8.35 lb/s
- Solids' loading μ = 2.5 lb. solids/lb. gas
- Particle density = 59 lb/ft^3
- Particle size d_p = 4 mm = 0.013 ft
- Pipe diameter D = 10 in. = 0.833 ft
- Pipe roughness k_s/D = 0.0002
- Gas density at standard conditions (14.7 psia, 68°F) = 0.075 lb/ft^3
- Gas viscosity μ_g = 0.018 cP = 1.2 × 10^{-5} lb/(ft s)
- Single particle terminal velocity U_t = 1840 ft/min

Assume

- Pressure drop across cyclone = 0.1 psi
- Gas temperature = 68°F is constant across the system

Conveying line layout is shown in Figure 4.24.

Divide the system into segments starting from the filter or receiver end as shown in Figure 4.21. Start the analysis from segment 1.

Segment 1: System pressure at exit = (14.7 + 0.1) psia = 14.8 psia

$$\rho_g = \left(\frac{14.8}{14.7}\right)0.075 = 0.0755 \text{ lbm/ft}^3$$

$$U_g = \left(\frac{2680}{0.545}\right)\left(\frac{14.7}{14.8}\right) = 4884 \text{ ft/min}$$

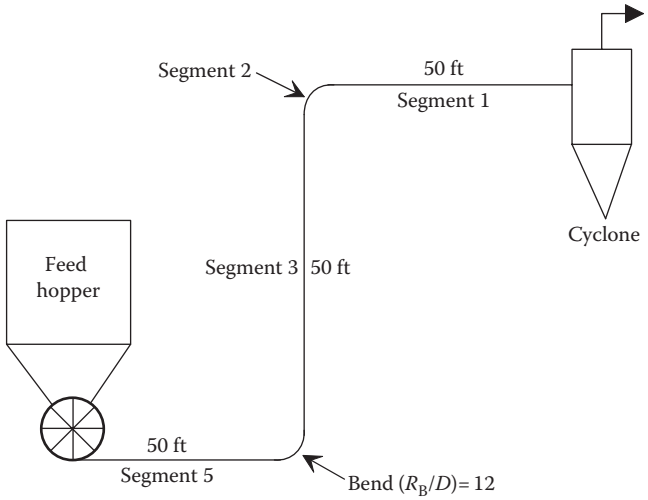


Figure 4.24

Conveying line layout for test problem.

$$Re = \frac{DU_g\rho_g}{\mu_g} = \frac{\left(\frac{10}{12}\right)\left(\frac{4884}{60}\right)(0.0755)}{1.2\times10^{-5}} = 4.268\times10^5$$

$$\lambda_f = \frac{1.325}{\left[\ln\left(k_s/3.7D + 5.74/Re^{0.9}\right)\right]^2} = \frac{1.325}{\left[\ln(0.000054 + 0.000049)\right]^2} = 0.0157$$

$$\Delta P_{air} = \lambda_f \frac{\rho_g U_g^2 L}{2Dg_c} = \frac{0.0157(0.0755)(4884/60)^2 50}{2(10/12)32.2} = 7.31\ \text{lb/ft}^2 = 0.050\ \text{psi}$$

$$\Delta P_{solids} = \mu\lambda_z \frac{\rho_g U_g^2 L}{2Dg_c}$$

For coarse particles,

$$\lambda_z = 0.082\mu^{-0.3} Fr^{-0.86} Fr_s^{0.25}\left(\frac{D}{d_p}\right)^{0.1}$$

$$\mu = 2.5$$

$$Fr = \frac{(4884/60)^2}{32.2(10/12)} = 246.9$$

$$Fr_s = \frac{(1840/60)^2}{(32.2)(0.0131)} = 2229$$

$$\frac{D}{d_p} = 63.6$$

$$\lambda_z = 0.082(2.5)^{-0.3}(246.9)^{-0.86}(2229)^{0.25}(63.6)^{0.1} = 0.00568$$

$$\Delta P_{solids} = 2.5(0.00568)\frac{(0.0755)(4884/60)^2 50}{2(10/12)32.2} = 6.62\ \text{lbf/ft}^2 = 0.046\ \text{psi}$$

$$\Delta P_T = \Delta P_{air} + \Delta P_{solids} = 0.050 + 0.046 = 0.096\ \text{psi}$$

Pressure at the outlet of segment 2 = 14.8 + 0.096 = 14.896 psia.

Segment 2: Segment 2 is a bend:

$$\Delta P_{segment} = \Delta P_B = B(1+\mu)\frac{\rho_g U_g^2}{2g_c}$$

Use $B = 0.5$:

$$\rho_g = \frac{14.896}{14.7}0.075 = 0.076\ \text{lbm/ft}^3$$

$$U_g = \frac{2680}{0.545}\frac{14.7}{14.896} = 4852\ \text{ft/min}$$

$$\mu = 2.5$$

$$\Delta P_{segment} = \Delta P_B = 0.5(1+2.5)\frac{0.076(4852/60)^2}{2.32.2} = 13.5\ \text{lbf/ft}^2 = 0.093\ \text{psi}$$

Therefore, pressure at the outlet of segment 3 = 14.896 + 0.093 = 14.989 psia.

Segment 3: Segment 3 is vertical:

$$\Delta P_{\text{segment}} = \Delta P_{\text{static}} + \Delta P_{\text{frictional}}$$
$$\Delta P_{\text{frictional}} = \Delta P_{\text{air}} + \Delta P_{\text{solids}} = 0.050\,\text{psi} + 0.046\,\text{psi} = 0.096\,\text{psi}$$
$$\Delta P_{\text{static}} = \rho_{\text{p}}(1-\varepsilon)\Delta L\frac{g}{g_{\text{c}}} + \varepsilon\rho_{\text{g}}\Delta L\frac{g}{g_{\text{c}}}$$

where

$$\varepsilon = 1 - \frac{W_{\text{s}}}{A\rho_{\text{p}}U_{\text{p}}}$$

$$\varepsilon = 1 - \frac{8.35}{0.545(59)(0.74)(4822/60)} = 0.995$$

$$\Delta P_{\text{static}} = 59(1-0.995)50\frac{32.2}{32.2} + 0.995(0.0765)50\frac{32.2}{32.2} = 18.55\ \text{lbf/ft}^2 = 0.129\ \text{psi}$$

$$\Delta P_{v} = 0.096 + 0.129 = 0.225\ \text{psi}$$

Pressure at the outlet of segment 4 = 14.989 + 0.225 = 15.214 psia.

Segment 4: Segment 4 is a bend. Calculating similar to segment 2,

$$\Delta P_{\text{B}} = 0.092\ \text{psi}$$

Pressure at the outlet of segment 5 = (15.214 + 0.092) psia = 15.306 psia.

Segment 5: Segment 5 is a straight horizontal section:

$$\Delta P_{\text{frictional}} = \Delta P_{\text{air}} + \Delta P_{\text{solids}} = 0.049\ \text{psi} + 0.047\ \text{psi} = 0.096\ \text{psi}$$

Pressure at segment 5 inlet = (15.306 + 0.096) psia = 15.402 psia.

Add acceleration d*P*:

$$\Delta P_{\text{ACC}} = \frac{\rho_{\text{g}}U_{\text{g}}^2}{2g_{\text{c}}}\left(1 + 2\mu\left(\frac{U_{\text{p}}}{U_{\text{g}}}\right)\right)$$

$$\Delta P_{\text{ACC}} = \frac{(0.078)(4893/60)^2}{2(32.2)}(1 + 2(2.5)(0.74))$$

$$= 34.83\ \text{lb/ft}^2 = 0.242\ \text{psi}$$

Pressure at feed point = (15.402 + 0.242) psia = 15.644 psia.

Assume $\Delta P_{\text{blower piping}}$ = 0.1 psi. Pressure at blower outlet = 15.744 psia = 1.044 psig. Then the overall ΔP = 1.044 psi = 28.9 in WC.

4.1.5 Designing Conveying Systems

The design of a dilute phase conveying system can be subdivided into eight steps, namely:

1. Acquire material properties
2. Establish conveying requirements and performance criterion
3. Selection of system type or conveying mode
4. Identify suitable line layout
5. Select initial pipe diameter based on expected loading
6. Calculate the overall pressure drop and gas flow rate requirement
7. Recheck selection of pipe diameter, consider stepping
8. Select dust collection system, feeder, and air mover

Table 4.12 Material Properties for Conveying System Selection and Specification

Material Property	Required for the Determination of
Particle size distribution and average particle size	Conveying characteristics, feeder selection, filter design
Particle density	Conveying mode, conveying characteristics
Bulk density	Feeder capacity, storage silo capacity, conveying mode
Permeability	Conveying mode, dense phase design
Aeration and deaeration characteristics	Conveying mode, dense phase design
Moisture content, cohesion, and flowability	Storage silo design, feeder selection, dust collector design
Friability	Conveying mode, feeder selection, dust collector selection
Abrasiveness	Feeder selection, dust collector selection, material of construction
Toxicity	Conveying mode, dust collector filter design
Dust explosion potential	Selection of conveying gas, dust collector design, and grounding requirements
Hygroscopic nature	Conditioning of conveying gas, conveying mode
Sensitivity to temperature	Cooling requirement for conveying gas, selection of conveying mode
Corrosiveness	Material of construction
Stickiness or tackiness	Mode of conveying, coating of parts

4.1.5.1 Acquire Material Properties

Characterization of bulk material is the first step in designing conveying system. It is important to acquire a representative sample for analysis and be aware of the variability in properties along with their effect on system performance. Table 4.12 summarizes the relevance of particle properties to selection and specification of a conveying system.

4.1.5.2 Establish Conveying Requirements and Performance Criterion

Many failures in design of dilute phase conveying systems can be traced back to omissions by the designer regarding conveying requirements and performance criteria. Here are some guidelines to avoid costly mistakes.

- Identify the entire range of products (product wheel): It may be impossible to identify a single product as a representative product. For example, the product with least friction factor may be most friable. If one needs to minimize product attrition and maintain conveying rate for all the products, more products need to be tested.
- Establish the correct conveying capacity: If the operation is in batch mode, instantaneous conveying rate will be higher than average conveying rate. Occasionally, even higher rates may be required to catch up after process upsets.
- Identify sources and destinations: All sources and destinations must be identified upfront. Proper thought should be given to future expansions in conveying distance and capacity.
- Identify special requirements for temperature, humidity, inert, containment, toxicity, cross-contamination, and ease of cleanout.
- Establish limits on acceptable product degradation: Pneumatic conveying systems, especially dilute phase systems, result in breakage or degradation of the product. It is important to identify acceptable limits, method of measurement, and sensitivity to operating conditions.
- Wear life of components: When dealing with abrasive materials, it is important to outline expectations on the performance and wear life of components, especially feeder and pipeline.
- Identify the need to have a spare air mover online if the conveying system is a critical link in the process.
- Conveying system can be used for a dual purpose, for example, as a dryer or a cooler. The operational range can be severely limited by combining the two operations and it is important to establish that upfront.

4.1.5.3 Selection of Conveying System Type and Conveying Mode

A fundamental design decision when configuring a new pneumatic conveying system is whether to convey a dilute phase or dense phase mode. Dilute phase conveying can be generally characterized by high velocities, low pressure drops, and low ratios of solids to gas. Conversely, dense phase conveying systems have lower velocities, higher pressure drops, and higher solid to gas ratios (Table 4.13). Due to gas expansion or secondary gas injection along the conveying line, some systems will convey in the dense phase mode near the feed point but will transition into dilute phase near the end of the conveying line.

Table 4.13 Comparison of Dilute Phase and Dense Phase Conveying Modes

Characteristic	Dilute Phase Conveying	Dense Phase Conveying
Degradation or particle attrition	Can be high	Usually low
Change in product properties (particle size distribution, etc.)	Conveying characteristics will change but system can continue to perform at reduced capacity	Conveying characteristics are significantly affected. May result in plugging
Turndown of conveying rate	Easy	Limited turndown
Wear	Can be high for abrasive materials	Slow motion conveying results in minimum wear
Line vibration	None	Significant, special design considerations required
Inert gas conveying	Accomplished by closed-loop system	Low amounts can be once through

The advantages for selecting dilute phase conveying are as follows:

1. Many more materials can be conveyed successfully in dilute phase mode than in dense phase.
2. Dilute phase conveying systems are generally less susceptible to plugging due to changes in material properties or operational upsets such as temporary loss of conveying gas.
3. Dilute phase conveying systems are easier to design. The window of stable operation for dense phase conveying is much smaller than that of dilute phase conveying.
4. Dilute phase systems require less specialized feeders and air movers.

The greatest advantages of dense phase conveying stem from the fact that the conveying velocities are lower. This can impact the amount of particle attrition and the amount of erosion of pipe bends and other system components that can occur. Both these phenomena tend to vary with velocity raised to the third power, although literature values for this exponent range from 2 to 6. For a specific application particle attrition may or may not be a consideration. The definition of particle attrition includes both the breakage or chipping of brittle particles to produce fine fragments and the smearing of polymeric materials along the pipe walls to create fines, floss, and snake skins. Some reasons why particle attrition could be problematic are

1. Attrition can create a real or perceived quality issue.
2. It may adversely affect downstream gravity flow characteristics, such as the minimum hopper outlet size.
3. It may increase specific surface area, which may influence product properties or downstream processing.

Dense phase conveying can be a viable option if

1. Low particle degradation is a requirement.
2. Material is highly abrasive and metal contamination is an issue.
3. Low gas usage (especially inert gases) is desirable.
4. The material does not change significantly from batch to batch.
5. Pressure conveying does not pose problems (toxicity or hygiene).
6. Conveying operation is not from multiple sources to single destination type.
7. The particle size distribution is not very wide.
8. The material tends to coat and plug the conveying line at high velocity.

4.1.5.3.1 Selection of System Type: Open Loop versus Closed Loop Unless there is a compelling reason to do otherwise, a conveying system should be operated in an open-loop manner (Figures 4.12 through 4.14). The advantages for operating this way are

1. *Lower capital cost*. This is due to not needing a gas return line to the feed point, a smaller blower or compressor, less instrumentation, and less extensive conveying gas conditioning.
2. *Simpler operations*. The mass of gas in the conveying system changes during start-up and shutdown. This process is self-regulating in an open-loop system, whereas it needs to be actively managed

for a closed-loop process. Also, unless there is an adequate purge on the closed-loop system or a sophisticated gas conditioning system, moisture or other undesirable condensable materials may accumulate in the recycled gas stream to concentrations where condensation can occur. This can result in restrictions in and possible plugging of the conveying line or blinding of filter media in the dust collector. Also, heat due to compression needs to be removed from the closed-loop system.

Despite the advantages of an open-loop system, there are circumstances where closed-loop systems are preferable and will reduce the overall cost of installing and operating the system. The selection of a closed-loop system (Figure 4.15) should be considered when:

1. The conveying gas is expensive or the supply is limited.
2. Treatment of the gas prior to venting requires more than just gas–solid filtration. If there are either toxic or simply noxious nature of vapors present in the conveying gas stream after the solids have been separated, the gas stream may need to be sent through a carbon bed or incinerated prior to venting to the atmosphere.
3. The solids need to be conveyed in a carefully controlled environment such as very low moisture or oxygen concentrations. The use of a closed-loop system in this case will reduce the size of the gas conditioning equipment required.

4.1.5.3.2 Selection of Pressure Mode: Vacuum, Pressure, or Combined In most situations, it is mechanistically feasible to convey in both pressure and vacuum mode. Therefore, the selection of conveying mode is dictated by process issues. For instance, a pressure system should be used where ambient air leakage into the conveying system cannot be tolerated. This could be due to a quality or product degradation concern by exposure to oxygen or moisture. Another case where a pressure system should be used is if an oxygen lean environment is used as a line of defense for the prevention of a dust or vapor explosion. On the other hand, a pressure system should not be used if material spill cannot be tolerated due to safety or industrial hygiene concerns. A vacuum system should be strongly considered if there are significant consequences in the event of a leak of material from the conveying system, such as cases where the solids are extremely toxic to humans, animals, or plants. While all equipment connections can be made "dust tight," all shaft seals for rotary and diverter valves can be purged, and all high wear areas such as elbows can be monitored for erosion. Experience has shown that considerable preventative maintenance effort is required to keep a pressure conveying system dust tight in all places and at all times.

The final criteria for determining the conveying pressure mode, if not fully dictated by any of the considerations earlier, are based on the number of sources and destination and, to a lesser extent, the source or destination layout:

1. *Single source to single destination (Figure 4.12)*: Either pressure or vacuum system will work for this case. Use a pressure system for long-distance (greater than 300 ft) and high-throughput requirements.
2. *Single source to multiple destinations (Figure 4.12)*: Use a positive pressure (or push) system with diverter valves to direct material to multiple destinations. A vacuum system would require an air mover at each destination and would be expensive to install.
3. *Multiple sources to a single destination (Figure 4.13)*: Use a vacuum (or pull) system. Unless the sources are close together, a blower would be needed for each source if the pressure conveying mode were used. However, if a single conveying line can be routed past the pickup points for each source without significantly altering the number of bends or the overall length of the conveying line, the pressure conveying mode may be a reasonable option as well as vacuum conveying.
4. *Multiple sources to multiple destinations (Figure 4.14)*: Use a combined vacuum–pressure or pull–push system. This recommendation logically follows from the previous two items.

4.1.5.4 Identify Suitable Line Layout

Conveying line layout should never be an afterthought during plant layout. Conveying pipe cannot be routed like other utilities (steam, air, and water) without paying significant penalty on performance. Some effective line layout practices are outlined as follows:

- Layout conveying routes when the plant process equipment is being laid out. This will provide flexibility for the optimization of conveying route.
- Consider creative ways to minimize conveying distance.

- For dilute phase systems, provide sufficient horizontal run after the feed point and before any change in direction (bend) occurs. It is recommended to provide at least 50D of horizontal run. There is no such requirement for dense phase systems.
- For dilute phase systems, avoid inclined lines near the feed point.
- Minimize change in directions (bends, elbows, or 45° bends).
- Avoid placing bends within 50D of one another.
- Minimize the use of flexible hoses.
- For dense phase systems, proper consideration must be given to design line support to handle pipeline vibrations. Current state of knowledge is insufficient to predict the line forces accurately.
- Do not use process equipment or silos to support dense phase lines.
- Components, such as diverter valves, need maintenance. They should be made accessible.

4.1.5.5 Select Initial Pipe Diameter Based on Expected Loading and Velocity at Feed Point

The initial pipe diameter can be calculated by assuming solids loading based on previous experience or general guidelines:

$$\mu = \frac{W_s}{W_g} = \frac{W_s}{A\rho_g U_g}$$

$$A = \frac{W_s}{\mu\rho_g U_g} = \frac{\pi}{4}D^2$$

$$D = \sqrt{\frac{4W_s}{\pi\mu\rho_g U_g}}$$

where

U_g is the gas velocity at feed point
ρ_g the gas density at feed point
μ the assumed solids' loading

4.1.5.6 Calculate Overall Pressure Drop and Gas Flow Rate Requirement

See Section 4.1.4 for details on pressure drop calculations.

4.1.5.7 Recheck Selection of Pipe Diameter

With refined values of conveying pressure at the feed point, the line diameter calculation should be rechecked. The conveying pressure estimation should also be compared with the typical limits of air movers. If the pressure drop is higher than expected, choose a large pipe size. Redo the calculations until convergence is achieved.

4.1.5.8 Select Dust Collection System, Feeder, and Air Mover

4.1.5.8.1 Gas–Solid Separator Selection Factors affecting the selection of gas–solid separation device are

1. Desired efficiency of separation based on particle size distribution of incoming solids
2. Acceptable pressure drop range
3. Operating pressure and temperature
4. Cleanout and contamination requirement
5. Dust explosion potential
6. Acceptable turndown in gas flow rate
7. Compatibility with material (corrosiveness, abrasion, etc.)

4.1.5.8.2 Feeder Selection Factors affecting the selection of feeder are

1. Operating pressure/pressure differential
2. Type of conveying system
3. Material characteristics: bulk density, size, abrasiveness, tackiness, fluidization, and so on

(see Table 4.5 For more details.)

4.1.5.8.3 Air Mover Selection Factors affecting the selection of air mover are

1. Range of pressure or vacuum during operation
2. Volumetric flow rate
3. Stability of solid feed rate and nature of operation
4. Control requirements: turndown and adjustability
5. Special requirements (e.g., material flow through)

4.1.6 Stepping Pneumatic Conveying Lines

The superficial velocity increases as the pressure decreases from feed point to discharge point. From mass balance on the conveying gas, we obtain

$$\left(A\rho_g U_g\right)_{\text{feed_zone}} = \left(A\rho_g U_g\right)_{\text{discharge_zone}}$$

By applying gas laws,

$$\frac{U_{g1}}{U_{g2}} = \frac{P_2}{P_1}$$

where P is the absolute pressure. The superficial gas velocity in a conveying system increases from feed point to destination in all conveying systems. Since higher superficial velocity is related to higher wear and product attrition, it is beneficial to reduce the gas velocity by increasing the line diameter at some point in the system. The same effect is achieved by leaking some gas out of the system.

There are two approaches to stepping (increasing) the line size:

1. To keep the Froude number constant between the feed point and the step location. In other words, maintain a Froude number greater than the minimum required (Fr_{min}) at the stepped location.
2. To keep the superficial velocity at the feed point and at the step location higher than saltation velocity.

Currently, there is no consensus on the best approach for designing stepped lines.

4.1.7 Modeling and Designing Dense Phase Conveying

The mechanisms for dense phase conveying are not as well understood and quantified as dilute phase flow. Significant progress in the modeling of noncohesive granular materials has been made in the last 20 years (Konrad and Harrison, 1980, Legel and Schwedes, 1984, Konard, 1986, Mi and Wypych, 1994). The design equations by Mi and Wypych (1994) are discussed in this section. For fluidized-mode conveying, it is recommended that scale-up approach be used.

4.1.7.1 Modeling of Plug/Slug Flow

Noncohesive coarse granular material (e.g., plastic pellets) exhibits a natural slugging ability. When conveyed in nonsuspension mode, they form slugs or plugs that move in a wave-like fashion. Each slug is constantly picking up material from the stationary layer in the front and dropping off material from the tail end. The material moves a short distance with the passing of each slug.

A force balance on the plug results in the following equation (Figure 4.25):

$$\frac{\Delta P}{l_s} = \frac{4\mu_w \lambda}{D}\sigma_f + 2\rho_b g\mu_w$$

where λ is the stress transmission coefficient or the ratio of radial stress to axial stress. A theoretical estimation of the stress transmission coefficient can be made by assuming active conditions for failure; however, experimental data indicate that the values are between active and passive estimates:

$$\lambda = \frac{1-\sin\phi_s\cos\left(\omega-\phi_w\right)}{1+\sin\phi_s\cos\left(\omega-\phi_w\right)}$$

$$\sin\omega = \frac{\sin\phi_w}{\sin\phi_s}$$

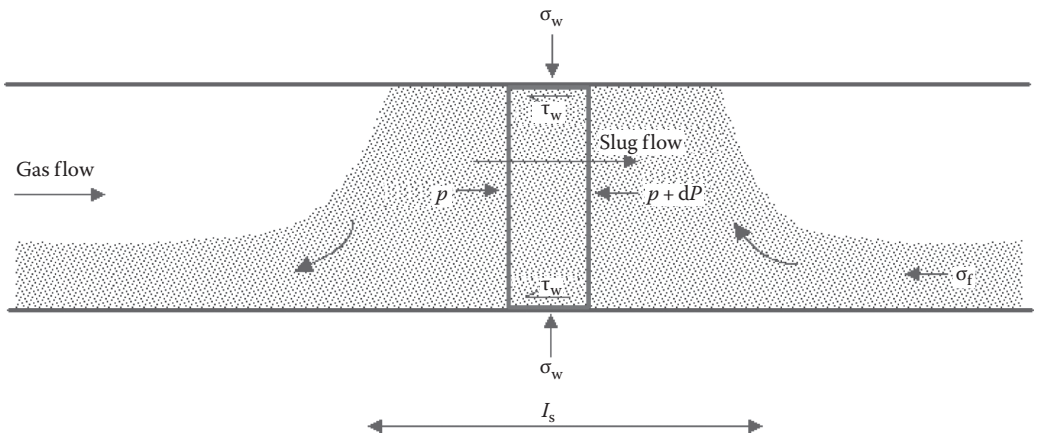


Figure 4.25

Force balance on slug or plug in dense phase conveying.

σ_f represents the frontal stress experienced by the slug due to the stationary layer and uptake of material from the stationary layer. The momentum balance gives the following expression:

$$\sigma_f = \alpha \rho_b U_s^2$$

The existence of stationary layer plays a critical role in the formation, stability, and movement of the slug. The average height of a stationary layer in the line depends on the superficial gas velocity at that location. It decreases with an increase in superficial gas velocity.

The cross-sectional area ratio of stationary bed to pipe, α, is calculated by the following expression:

$$\alpha = \frac{1}{\left(1 + U_s / 0.542\sqrt{gD}\right)}$$

In reality, there are multiple slugs in a transfer system that is separated by air pockets. As the pressure drops and gas expands, the superficial gas velocity increases along the conveying length. Consequently, the slug velocity will also increase. For analysis, if we assume that each slug goes through the same velocity profile, then we can characterize the bulk movement of material through the system by an average slug velocity. Further, if the pressure drop across the air pockets is assumed to be negligible, all the slugs in the system of length L_t can be assumed to be of an equivalent length l_s.

$$l_s = \frac{m_s L_t}{A\left(1-\alpha\right)\rho_b U_s}$$

The overall system pressure drop can be calculated by an appropriate substitution.

$$\Delta P_{system} = \left(1 + 1.084\lambda\sqrt{Fr} + \frac{0.542}{\sqrt{Fr}}\right)\frac{2g\mu_w m_s L_t}{AU_s}$$

where

$$Fr = \frac{U_s^2}{gD}$$

4.1.7.2 Slug or Plug Velocity Estimation

As evident from the previous section, a reliable estimate of slug velocity is critical for design calculations. The slug velocity for impermeable bulk solids is equal to the superficial gas velocity (Figure 4.26). For permeable

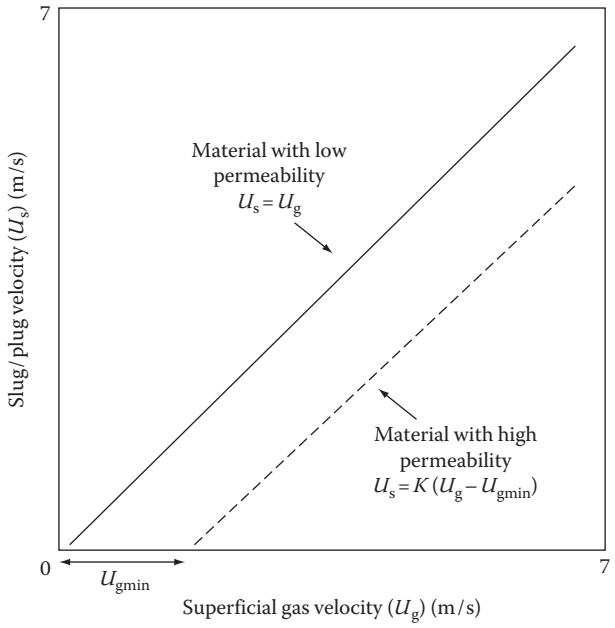


Figure 4.26

Relationship between slug velocity and superficial gas velocity.

Table 4.14 Examples of K and U_{gmin} Values

Test Material	K	U_{gmin} (m/s)
Plastic pellets		
White	0.873	1.02
Black	1.059	1.566
Wheat	1.013	2.19
Barley	1.359	2.77

Source: Mi, B., and Wypych, P.W., *Powder Handling and Processing*, 5(3), 233, 1993. With permission.

materials (e.g., plastic pellets, grains, etc.), a slip between gas and solids has been observed. A minimum gas velocity can also be identified below when the slug velocity is zero, when implies a plugged condition.

Mi and Wypych (1993) have experimentally shown that (see Table 4.14)

$$U_s = K\left(U_g - U_{gmin}\right)$$

The minimum conveying velocity for plugged condition can also be calculated theoretically:

$$U_{gmin} = \frac{\rho_p g \tan\phi_w \varepsilon^3 d_p^2}{180(1-\varepsilon)\eta}$$

The slope of the slug-slip characteristic is empirically calculated as follows:

$$K = C\frac{\varepsilon d}{D}\left(\frac{\tan\phi_w}{\tan\phi_s}\right)^{1/3}$$

where C is a dimensionless constant. Use a value of 100 as an initial estimate.

4.1.7.3 Pressure Drop Calculation in Slug-Type Dense Phase System

According to Mi and Wypych (1994), the following steps are involved:

1. Calculate stress transmission coefficient
2. Assume initial value of total pressure drop. Calculate mean air density and superficial velocity
3. Estimate mean slug velocity and Froude number
4. Calculate pressure drop using the proposed analytical equation
5. Compare the estimate with assumption in step 2. Recalculate until convergence is obtained.

4.1.7.4 Control of Pneumatic Conveying Systems

Production plants are often multiproduct plants where products must be transported from various sources to multiple destinations. The differences in conveying characteristics (friction factor, wear, and attrition) and process constraints (e.g. conveying velocity, temperature, humidity, cleanliness) between various products can pose significant challenges during design phase and subsequent operability of the conveying system. One key process variable, namely, conveying gas velocity, can be adjusted and controlled during operation to broaden the operating window and achieve optimal conveying conditions in a given system (Wilms and Dhodapkar, 2014). Both dilute and dense phase systems can benefit from such an air control system. As shown earlier in Figure 4.10, the system response to change in gas flow rate for dilute and dense phase system is very different.

4.1.7.4.1 Dilute Phase Conveying Dilute phase conveying systems will operate in stable and reliable mode as long as the conveying gas velocities in the pipe at all locations are maintained above saltation velocity, and solids' loading below saturation limit and acceptable design practices regarding line configuration have been followed. The saltation velocity depends on material and gas properties, line diameter, and conveying rates, whereas local gas velocity depends on gas mass flow rate, and pressure, temperature and flow area at a given location.

For a non-stepped system, where the line diameter is constant, the gas velocity is the lowest at the pickup location. Therefore, an air control system that maintains gas velocity at the pickup above saltation for all transfer situations will deliver optimal performance. Three common approaches to hardware configuration for achieving pickup velocity control are shown in Figure 4.27, namely,

a. Gas bleed
b. Control valve or variable orifice Laval nozzle
c. Blower speed control

The gas bleed approach is the simplest to implement; however, system stability and energy efficiency may be compromised. Whether the gas bleeds in or out depends on the type of conveying system (pressure vs. vacuum). Certain conveying systems, for instance vacuum systems or with fan as an air mover, have a sluggish response to changes in air flow rate. They may be difficult to control with the gas bleed approach. Laval (sonic) nozzle offers a stable way to maintain constant pickup velocity in pressure system. The Laval nozzle operates at sonic conditions, so pressure fluctuations in the downstream conveying system do not affect the air mass flow rate. The mass flow rate of air can be varied by changing the upstream pressure or cross section of the throat. They are commonly used in large-scale pneumatic conveying systems. Blower speed control is the most energy efficient approach limited only by the motor and blower specifications.

4.1.7.4.2 Dense Phase Conveying The dense phase region of the classic Zenz plot (Figure 4.9) can be re-plotted with a different set of axes. The overall system pressure drop (instead of pressure gradient) is the *Y*-axis and the conveying gas flow rate at exit conditions (instead of superficial gas velocity) is the *X*-axis. The modified diagram (Figure 4.28), which is unique to a given system configuration and material properties, now serves as a basis for air control system design. The dense phase region is bounded by the plugging zone on the left size (low gas velocity), the unstable zone (high gas velocity) on the right-hand size, and air mover pressure capability as the upper limit. The operating window (Figure 4.28) can be demarcated after allowing for appropriate safety margins. The primary objective of an air control system for dense phase is to maintain the operating point within the stable operating window regardless of the system conveying pressure and conveying rate changes. The system pressure drop can change due to changes in material properties, conveying distance and conveying rate. The air control management strategy requires the knowledge of phase diagram, which is typically obtained through pilot- or full-scale testing. The overall strategy to develop air control

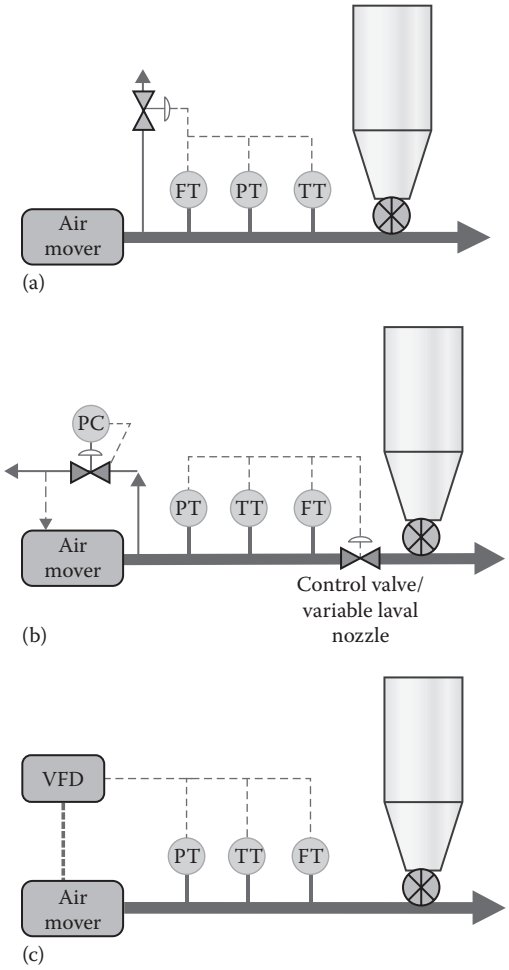


Figure 4.27

General concepts for controlling pickup velocity in pneumatic conveying systems. (a) Gas bleed, (b) control valve or Laval (sonic) nozzle, (c) air-mover speed control. (FT, flow transmitter; PT, pressure transmitter; PC, pressure-control valve; TT, temperature transmitter; VFD, variable-frequency drive.) (From Wilms, H. and Dhodapkar, S., *Chem. Eng.*, 59, October 2014.)

system is shown in Figure 4.29. These systems, which are often implemented in a PLC, can additionally monitor pressure trends and fluctuations and react accordingly. Table 4.15 summarizes typical inputs and corresponding control actions taken by control system. Interesting examples of application of neural networks and self-learning algorithms can be found in the literature. It should be noted that various vendors have developed complex proprietary systems based on their expertise, and the discussion given earlier is meant to be an instructive introduction to the topic.

4.1.8 Practical Design Considerations

4.1.8.1 Common Design Errors

Given the simplicity of the task of moving product from one point to another in a plant, it would appear that the design of pneumatic conveying systems would be relatively straightforward. However, design errors that compromise the system performance are routinely committed. While it would be impossible to list all of the design errors for pneumatic conveying systems, the following section highlights some common ones.

4.1.8.1.1 Selection of Conveying Velocity The optimum conveying for dilute phase system is saltation velocity with an additional 10% factor added for safety. Additional safety factor must be added if the first elbow is within 5 m (15 ft) from feed point. Since saltation velocity depends on the conveying rate, the highest instantaneous rate must be used.

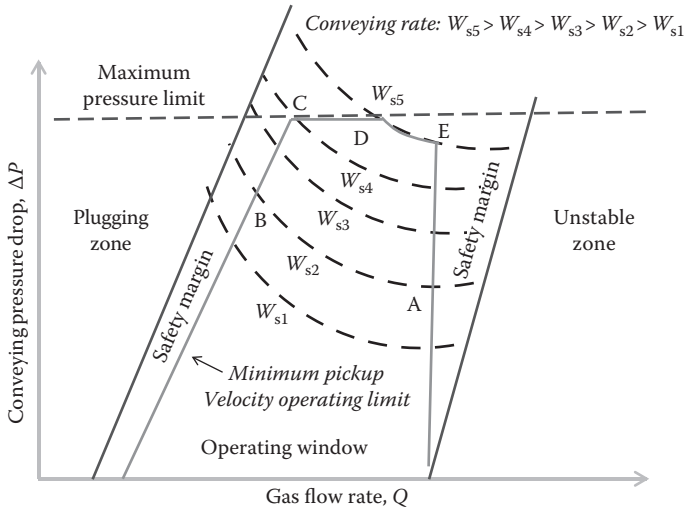


Figure 4.28

Operating window for dense phase conveying. (From Wilms, H. and Dhodapkar, S., *Chem. Eng.*, 59, October 2014.)

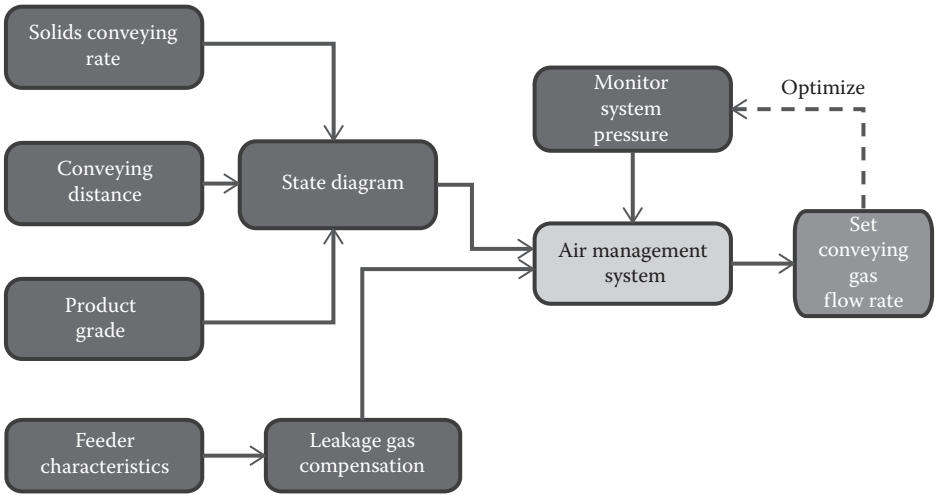


Figure 4.29

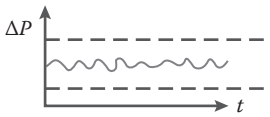
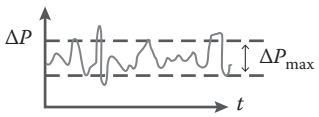
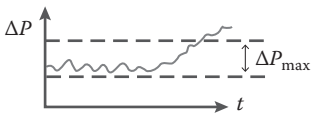
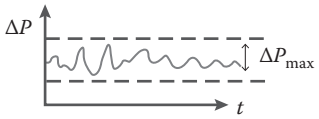
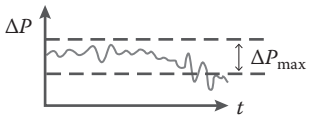
Typical air management control strategy. (From Wilms, H. and Dhodapkar, S., *Chem. Eng.*, 59, October 2014.)

Systems are routinely designed where the design conveying velocity is excessive. In dilute phase conveying systems, this will result in high product degradation or attrition and system wear. Also, the conveying capacity is substantially reduced. The effect of conveying velocity on conveying capacity has been explained in Figure 4.10.

Dense phase conveying systems must be operated within two limits of gas velocity, the lower bound corresponds to fixed bed or nonmoving plugs and the upper bound corresponds to the unstable conveying regime (see Figure 4.9). Excessive gas velocity will result in the system operating in the unstable region and cause severe line vibrations and pressure fluctuations.

4.1.8.1.2 Conveying Line Layout and Use of Elbows and Bends The layout of conveying systems is usually done after the process equipment is laid out and structural steel is designed. A pipe designer adept at configuring process piping will try to route a conveying line in a similar way, with little regard to the negative influence of bends or elbows. In stark contrast to incompressible single-phase fluid flow where the fluid

Table 4.15 Control and Diagnostics Strategy for Dense Phase System Based on Pressure Fluctuations Measurement

Pressure Measurement	Control Strategy
	Pressure fluctuations within acceptable limits, no trend no big spikes • Stable operating conditions • No adjustment of conveying gas flow needed
	Pressure fluctuations exceed permissible range or total pressure exceeds limits, strong fluctuations, no trend: • Close to instable operating conditions • Reduce conveying gas flow rate to leave instable zone
	Pressure fluctuations within acceptable limits, but trend toward higher total pressure (increased flow rate, humidity): • Approaching plugging limit • Incrase conveying gas flowrate
	Pressure fluctuations decrease to acceptable limits, stable operating conditions: • No more adjustments needed • Maintain current conveying gas flowrate
	Pressure fluctuations increase and exceed acceptable limits with trend toward lower total pressure (reduced flow rate, low solids-to-air ratio): • Approaching instable zone • Reduce conveying gas flowrate to return to stable operating window

Source: Wilms, H. and Dhodapkar, S., *Chem. Eng.*, 59, October 2014.
Note: Dashed lines represent acceptable operating limits.

does not slow through a bend, the particles will slow considerably as they proceed through a bend. This problem is further magnified if bends are placed one after another without sufficient distance to permit the solids to reaccelerate. A good conveying layout will minimize the number of bends or elbows and avoid inclined lines.

4.1.8.1.3 Failure to Account for System Gas Leakage It is important to account for gas leakage in and out of the system when estimating conveying velocity and air mover size. For positive pressure systems, the air leakage from the rotary feeder can be significant and can result in plugging at the feed point. If the material is a fine powder, the air leakage will impede material feed and cause reduced capacity. Also, the air leakage can be a significant fraction of the total air flow for dense phase system, and therefore, it must be correctly estimated.

4.1.8.1.4 Multiple Source and Multiple Destination Systems For systems where there are either multiple destinations (when the product is moved from the production process to storage silos) or multiple sources (when the material is moved from the storage silos to a packaging operation), care must be taken to ensure that the conveying capacity is estimated based on the longest pipe run. In many cases, systems are designed for the midpoint of a bank of silos; consequently, these silos that are located further than the midpoint will not deliver the required flow rate. Another extremely important consideration is the potential leakage of conveying gas through multiple rotary, diverter, or flapper valves in multiple source and destination systems. In the vacuum case, gas leakage into the conveying system along its length means that there may be insufficient gas at the pickup point.

4.1.8.1.5 Insufficient Attention to Component Selection Improper selection of air mover, feeder, and dust collector can result in a problematic system. For instance, fans are commonly selected as air movers for low-pressure applications. As discussed earlier, fans typically have a strong relationship between pressure head and volume of gas delivered. If fans are used for systems where the solids' flow is not regulated, it could lead to a plugged condition on account of the fan's inability to deliver the required volume of air for the increased pressure drop. Similarly, if a rotary feeder is chosen for feeding abrasive solids then excessive gas leakage can result in frequent plugging.

4.1.8.1.6 Understand the Limitations of Dual-Purpose Systems There is a tendency when conveying wet material (from a centrifuge or filter to a dryer, e.g.) to use the conveying system to both move the material within the plant and dry at the same time. This will work *only* when the solids' loading is low (0.05–0.25 kg solids/kg of gas).

4.1.8.1.7 Insufficient Support for Dense Phase Conveying Lines Lines forces in dense phase system are orders of magnitude higher than dilute phase systems. It is essential to design the supports and structure to bear these high dynamic loads. A safety factor of 3–5 is often recommended for specifying the structural supports.

4.1.8.2 Performance Measurement in Conveying

Unlike to many pieces of process equipment in plants in which the material is significantly changed either physically or chemically (e.g., composition, particle size, etc.), the conveying system is relatively simple—it is required to move bulk solids from point A to point B. In that sense, the measurement of performance can be distilled into two points: (1) how quickly is the material moved from one point in the plant to another (system throughput) and (2) does the material undergo any attrition (and lose important attributes) during the conveying process. It could be argued that power consumption would be a third important metric. With most conveying systems, it is far more important for the system to deliver the product at the desired rate with little or no attrition as opposed to save a few kW-h of power. This is particularly the case for higher value-added products being manufactured today.

System throughput is important because it is undesirable that the conveying system be the plant bottleneck. In many cases, both dilute and dense phase systems are routinely designed to operate near the maximum pressure that the air mover can deliver in order to maximize system throughput. The speed of the feeding device (quite often a rotary valve with electronic variable speed control) is tied to the air mover discharge or suction pressure to maximize solids' flow through the conveying system.

Another key metric is attrition or degradation. In many cases, product specifications or customer requirements demand that a product be "fines free." As indicated earlier, the creation of fines is a strong function of gas velocity in a conveying system. These fines can have a substantial impact on flowability, dustiness, dissolution rate, to name a few.

Another example is the conveying of polyethylene (PE). Many grades of PE will form angel hair or streamers during conveying. These streamers (they vary in size from short, low centimeter, long threads to large ribbons of several meters long) are formed on the inside of the conveying pipe during the conveying process and subsequently are released from the pipe surface. Often, streamers will aggregate in a silo to form a low-density ball, which in many cases will clog downstream equipment such an extruder. In this case, the product itself shows little or no degradation as a result of the streamer formation process, but it is the streamers that will compromise system performance due to process blockages.

An ancillary metric to attrition is that of wear. Wear can be an important performance metric, especially in cases where extremely abrasive products are handled, such as sand, glass batch, and mineral ores, for example. It is important that the wear situation be addressed such that it is not either a maintenance (and consequently cost) problem or a source of metal contamination in the process.

4.1.8.3 Troubleshooting Basics

Conveying systems will not always perform as designed or the performance may degrade gradually or suddenly. Consequently, there is a need to troubleshoot conveying systems. This should be done in a logical manner with emphasis on finding the root cause of the problem (Dhodapkar and Jacob, 2002), that is, to clearly identify the nature of the problem. For conveying systems, problems fall into three broad categories:

1. Lack of system throughput—the inability for the conveying system to deliver the required throughput. This could mean that the system is operating at less than the desired rate or the instantaneous rate is fine but cycle times are slow (similar to dense phase blow-pot systems) or plugging may be occurring.
2. Material degradation on attrition—on account of the velocities in conveying systems, products may attrite or break as a result of the conveying process.
3. System degradation—with high velocities or particularly abrasive products, both pipe and system components can experience high wear resulting in an inoperable system. Even systems where the product is thought to be relatively benign can experience wear after significant service. For example, aluminum elbows can wear through in conveying service.

Once the nature of the problem is identified, the next logical step in the troubleshooting process is the data gathering phase. A key philosophy in this process is to take the "systems approach" when examining the problem. This means that rather than focusing on the conveying system alone, it is important to look at the process steps both before and after the system as they may be contributing to the problem. For example, if a dryer precedes the conveying system, moisture fluctuations in the product out of the dryer could have a substantial effect on the ability of product to be conveyed.

Initially, it is important to examine the process flow sheet, the original design specifications for the system, if available, and the pneumatic conveying control system as implemented. Equally important is a physical examination of the entire conveying system to check if the system was built as designed and if there have been modifications to the system since start-up. At this point, it is useful to note any abnormalities such as misaligned pipe, worn valves (such as squeaky rotary valves and diverter valves not returning to a fully closed or open position), and so on.

Key process data must be gathered for effective troubleshooting. Key items would be pressure drop across the conveying system, pressure drop across the dust collection device, pipe size, gas velocity (either measured directly or calculated from blower speed, preferably both), system conveying rate. If data are available from a process control system, it can be very useful in troubleshooting a conveying problem, particularly those that are erratic in nature. During the troubleshooting process, it is not uncommon for conflicts in data to occur. For example, a blower curve and a set of measurements made with a Pitot tube or anemometer may not give the same value for gas flow through the system. In these situations, one must experimentally resolve this conflict in data. In this particular case, one can look at the pressure drop across a specific section of pipe in the system for only conveying gas or measure the pressure drop across a cyclone and infer the gas flow rate from that number.

Depending on the nature of the problem, a number of different fixes are possible. The key is to provide the most robust solution at the most economical cost. In many instances, the speed of the blower can be reduced (see prior discussions on the Zenz curve) to increase the capacity. In other cases, where the blower may be operating at or near maximum pressure, it may be logical to step the pipe (see stepping), in order to increase the throughput.

The key to optimization is an understanding of the operating limits (window) of a system and to ensure that the system operating conditions stay within these limits. A detailed discussion on this can be found in Agarwal and Dhodapkar (2004).

4.1.8.4 Start-up of Conveying Systems

Many of the procedures used for the starting up conveying systems are common to that of all process equipment. It makes sense that the plant is built as designed and also ensures that all instrumentation is operating correctly. The following is a list of start-up issues specific to both dense and dilute phase conveying systems:

1. Check that rotary valve rotation is correct in order to minimize the reentrainment of solids into the emptied pockets.
2. Check the valve sequencing is appropriate for blow-tank operation.
3. Check the piping for both alignment (application of self-aligning flange systems is very useful) and the intrusion of welds into the conveying flow.
4. Check that an appropriately designed pipe cushioning system is in place so as to tolerate the dynamic stresses associated with large plugs moving through the conveying system for dense phase systems (especially those > 150 mm pipe diameter).
5. Check that the blower rotation must be correct.
6. Check the clearances on the rotary valves such that the valves not only rotate freely but also are sufficiently close so as to minimize leakage.
7. Check that the relief valves and rupture disks are in place so as to minimize the damage associated with an accidental over or underpressurization. This is particularly important for systems where a dust collector or baghouse is used and the bags have the possibility of being coated over with bulk solid on account of moisture and so on.

4.1.8.5 Wear

Wear issues are pervasive in pneumatic conveying applications. Many studies have been undertaken to quantify the effect of various parameters to predict the wear life of components. While we now understand

the influence of various factors and their relative importance, it is not possible to generalize the conclusions. The solution to one wear problem cannot necessarily be applied to another problem. Further details can be found in Section 12.4.3.

4.2 Slurry Flows

Shenggen Hu

4.2.1 Introduction

Slurry is a suspension of solid particles in a carrier liquid. The transport of slurries through circular pipelines is widespread in the minerals, coal, chemical, food, water, and other industries. Unlike the flow of single-phase liquid, the flow velocity of slurries must be higher than a certain value to maintain solid particles in suspension. The flow of single-phase liquid is homogeneous at all velocities, while slurry flows may behave heterogeneously or exhibit some combination of both. The slurry may also behave rheologically as a Newtonian fluid or may exhibit a variety of non-Newtonian rheological properties.

The large number and range of variables encountered in slurry flows in pipelines cause the flow behavior of these slurry systems to vary over a wide range, and therefore, different approaches have been used to describe their behavior in various flow regimes. The variables influencing the behavior of slurry flows include the orientation of the pipeline, the characteristic dimension of the conduit, flow velocity, particle size, particle size distribution, particle density, particle shape, solids' concentration, and the properties of the fluid–particle interface, which are determined by the compositions of the fluid and the solids. Due to this long list and wide variation ranges of variables, the literature abounds with numerous studies of special cases that cover a limited range of conditions. Consequently, it is impractical to provide a thorough or even an adequate survey of the subject of slurry pipeline flows in a single section of this handbook.

The intent of this section is to summarize what appears to be the most widely accepted and the most comprehensive studies and results in the context of slurry flow, which may apply to various flow regimes. In particular, we will examine the classification of slurry flow regime, the frictional pressure loss estimation for both homogeneous and heterogeneous slurry flows, the prediction of the critical velocity for horizontal pipe flow, design and operation aspects, and measurement techniques.

4.2.2 Basic Concepts of Slurry Flows

4.2.2.1 Basic Definitions

4.2.2.1.1 Slurry Flow Velocity

The mean slurry flow velocity U_m is defined by

$$U_m = \frac{\dot{V}_s + \dot{V}_l}{A} \tag{4.1}$$

where $\dot{V}_s$ and $\dot{V}_l$ are volumetric flow rate of solids and liquid, respectively.

4.2.2.1.2 Solids' Concentration The solids' concentration can be expressed as volume fraction α_s or mass fraction. The volumetric fraction of solids is given by

$$\alpha_s = \frac{\dot{V}_s}{\dot{V}_s + \dot{V}_l} \tag{4.2}$$

and the mass fraction of solids' C_s is defined as

$$C_s = \frac{\rho_s \dot{V}_s}{\rho_s \dot{V}_s + \rho_l \dot{V}_l} \tag{4.3}$$

It can be shown that

$$C_s = \frac{\alpha_s \rho_s}{(\alpha_s \rho_s + (1-\alpha_s)\rho_l)} \tag{4.4}$$

4.2.2.1.3 Slurry Density The density of slurry mixture ρ_m is given by

$$\rho_m = \alpha_s \rho_s + (1-\alpha_s)\rho_l \tag{4.5}$$

4.2.2.1.4 Apparent Viscosity The steady-state rheological behavior of most slurry mixtures can be expressed by the following general form:

$$\tau = \eta \dot{\gamma} \tag{4.6}$$

where
- τ is the shear stress
- $\dot{\gamma}$ is the shear rate
- η is the apparent viscosity

The plot of shear stress τ versus the shear rate $\dot{\gamma}$ is called *rheogram*, which is schematically illustrated in Figure 4.30. If η is a constant and equal to the slope of the straight line from the origin, the slurry rheological behavior is Newtonian. Slurry mixtures that do not behave in this fashion are termed non-Newtonian slurry mixtures, in which η is not a constant and may be expressed as a function of either $\dot{\gamma}$ or τ. In regions in which η decreases with the increasing rate of shear $\dot{\gamma}$ the behavior is termed *pseudo-plastic* or *shear thinning*; in regions in which η increases with the increasing rate of shear $\dot{\gamma}$ the behavior is termed *dilatant* or *shear thickening*. The curve intercepts at zero rate of shear are called *yield stresses*.

4.2.2.2 Slurry Flow Regimes

The slurry flow regime (also referred to as flow pattern) varies with the properties of the solid particles relative to those of the liquid. The flow regime affects the dependence of the pressure drop on the flow rate as well as the magnitude of the pressure drop and it also influences the pipe erosion and other performance characteristics. Because of the complexity of slurry flows and the gradual transitions between flow regimes, only an imperfect classification of the regimes is possible.

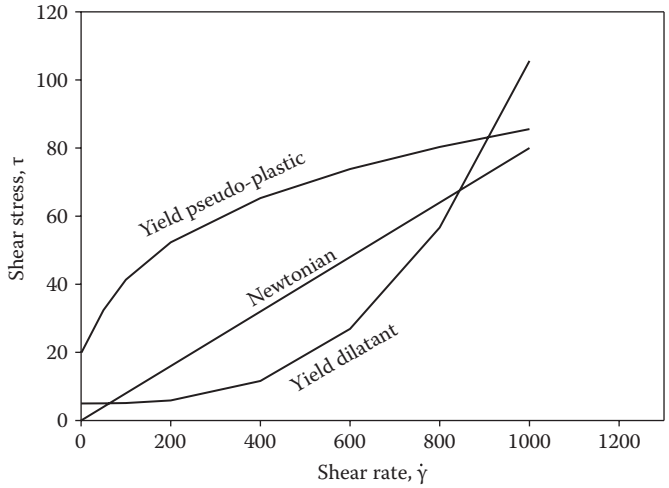


Figure 4.30

Illustrative rheograms.

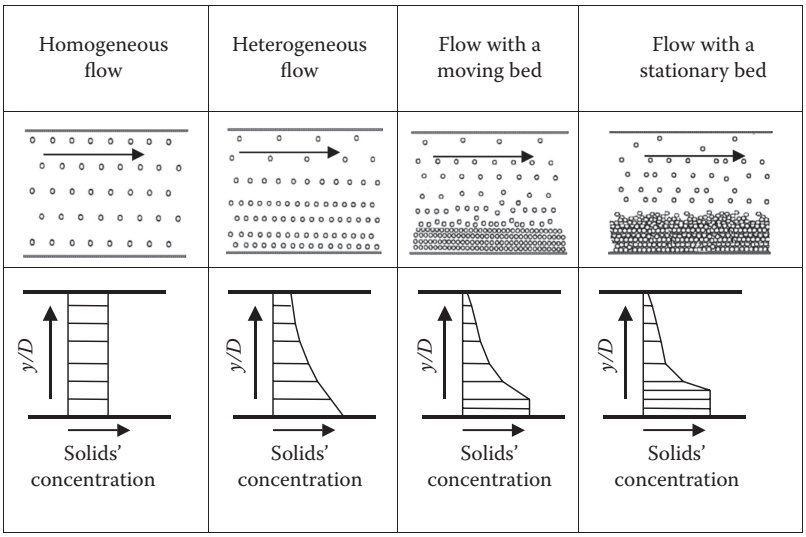


Figure 4.31

Illustration of particle distributions and solids' concentration profiles in a pipe for different slurry flow regimes.

Since Durand and Condolios (1952) proposed the initial classification of slurry flow regimes based on average particle size, a number of refined classifications have been developed over the years (Newitt et al., 1955, Thomas, 1964, Wicks, 1971, Ercolani et al., 1979, Brown, 1991). One of the most common classifications is to broadly categorize slurry flows in pipelines into four regimes: homogeneous, heterogeneous, heterogeneous with a moving bed, and heterogeneous with a stationary bed. The schematic views of particle spatial distributions and solids' concentration profiles in a pipe for different slurry flow regimes are shown in Figure 4.31.

Homogeneous slurry flow is characterized by a uniform distribution of solid particles throughout the carrier liquid and across the pipeline cross section. Typically, this type of slurry has a high solids' concentration of fine solid particles (<40 μm) of low particle density and exhibits viscous behavior. An example of homogeneous flow is the minerals ore slurry after comminution and thickening, in which the particles are very fine and the solids' concentration is high (>40% by weight). Although no slurry is ever truly homogeneous because it consists of distinct phases, there are situations in which the slurry can be described satisfactorily by single-phase models. Therefore, the principle of continuum mechanics may be applied to the analysis of homogeneous slurry flow, and the rheological properties of the slurry are most often non-Newtonian.

In heterogeneous slurry flow, solid particles that are sufficiently large (>40 μm) and sufficiently dense and/or in a sufficiently dilute state will settle to various degrees so that the particles are no longer uniformly distributed in the flow filed, that is, the slurry is heterogeneous, but the majority of the particles are still fully suspended. The different phases retain their properties and the analysis of this flow behavior needs to consider separately the forces on the particles, resulting from interaction with the surrounding suspending medium. Heterogeneous slurries are encountered in many industrial processes, such as minerals' processing. Solids' concentration in these slurries is relatively low, typically less than 35% by weight. Heterogeneous slurry flows are much more complicated than the homogeneous slurry flow, and consequently, most of the experimental studies in the literature have been concerned with these flows. Both critical deposit velocities and pressure losses are of interest.

The terms *nonsettling* and *settling* have often been used synonymously with *homogeneous* and *heterogeneous*.

When a large fraction of particles in a slurry are fine but there remain a sufficient fraction of coarse particles, intermediate regimes may occur, in which the fine particles are homogeneously distributed and the coarse particles are heterogeneously distributed or may deposit as the flow speed is reduced below a minimum value. Intermediate regime flows include tailings from mineral processing plants and a wide range of industrial slurries. Although many of slurry flow cases are clearly homogeneous or heterogeneous, many more are a combination of both. This is because the particle size is the single most important parameter that governs the flow regime. Most of the practical slurry systems contain solid particles having a rather broad

particle size distribution. Such systems are often considered to be in a mixed homogeneous–heterogeneous mode, and their flow behavior must be analyzed accordingly.

Under certain conditions, the flow regime of heterogeneous with moving bed can be observed. In this flow regime, the larger and/or denser particles will accumulate at the bottom of the conduit and form a bed. The particles in the bed will move or slide along the bottom of the conduit because the shear forces due to the moving fluid are sufficiently large. The concentration of this bed corresponds to maximal packing, or nearly so, and the upper part of the pipe cross section is occupied by a heterogeneous mixture.

In the regime of heterogeneous flow with a stationary bed, the slurry flow velocity is too low to enable the motion of all immersed particles, a stationary deposit bed is formed at the bottom of the pipe. On top of this deposit bed particles are transported as a separate moving layer. Although stationary bed type flows can be encountered in practical situations, they should be avoided whenever possible since they tend to result in a highly unsteady type of flow behavior at best and plugging at worst.

The prediction of the flow regime that would exist in the pipe for any given set of operational conditions is very important. One would like to avoid the formation of a stationary deposit, which causes partial blockage of the pipe, thus reducing its efficiency. A moving bed probably enhances pipe wear. Moreover, the pressure drop behavior is different from one flow regime to another. A variety of criteria have been proposed for determining whether a given slurry flow is considered homogeneous or heterogeneous or flows with deposited solids' bed. However, criteria based on a single parameter, such as particle size (Durand and Condolios, 1952), are incomplete, since slurry flow behavior also depend on other parameters. The more reliable approach for the determination of the flow regime is using suitable empirical correlations (Turian and Yuan, 1977, Turian et al., 1987) or mechanistic models, such as two-layer (Wilson, 1970, 1976, Gillies et al., 1991) or three-layer models (Doron and Barnea, 1993). Some of these correlations and models will be examined in Section 4.2.4.

A typical flow regime plot for slurry flow in a pipe is shown in Figure 4.32. This figure was generated using Turian and Yuan's correlations (Turian and Yuan, 1977) for the conditions as given in the figure. According to Figure 4.32, a slurry containing particles of 300 μm would be in the homogeneous regime, if the slurry velocity is higher than 2.3 m/s. A plot such as this is useful to determine the flow regime that applies under a given set of conditions and how much the slurry velocity must change before the flow enters another regime.

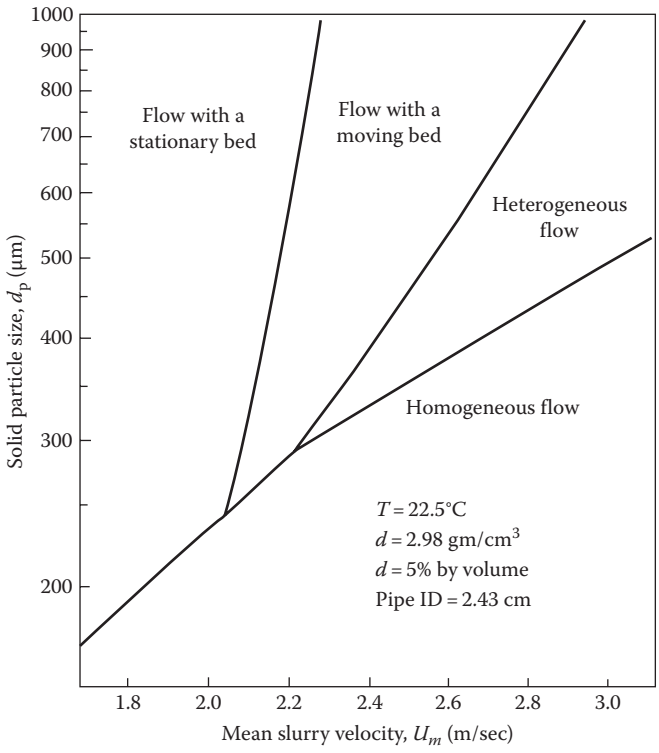


Figure 4.32

Flow regime diagram for slurry flow in 25 mm pipe under the conditions given in the figure. (Adapted from Turian, R.M. and Yuan, T.F., *AIChE J.*, 23, 232–243, 1977. With permission.)

4.2.3 Homogeneous Flow of Nonsettling Slurries

4.2.3.1 Rheological Models

In homogeneous slurry flows, slurries show no segregation or a small but finite tendency to settle when allowed to stand. In this respect, the slurries resemble a single-phase fluid, for which the science of rheology and continuum mechanics are well established. The major technical tasks for assessing homogeneous slurry flows are

1. To determine an appropriate rheological model from a test program and evaluate the specific coefficients for the slurry at the temperature and solids' concentration of interest.
2. To predict the pressure loss for laminar and turbulent flow and the transition point between them.

Rheological property is one of the major factors influencing the homogeneous flow behavior and pressure loss. At the present time, it is not possible to predict slurry rheological properties or the viscosity–concentration–shear rate relationship for most of industrial slurries, except for Newtonian slurries. Experimental characterization of the rheological property is possible and essential, and measurement techniques will be examined in Section 4.2.6.1.

The rheological data may be utilized directly for predicting the flow behavior under certain conditions. However, it is more convenient and more useful if the data can be represented by an appropriate model. It is also desirable to have a model that is as simple mathematically as possible and yet adequately describes the slurry rheological property. A number of models have been proposed for representing the viscosity function of homogeneous slurries. Although there is some degree of logical deduction behind some of the models, they are largely empirical models. The more complex models are capable of representing more complex behavior, although they are also more difficult to evaluate and to apply and often are not necessarily more useful in a practical sense.

4.2.3.1.1 Newtonian Slurries In homogeneous slurry flows, the nonsettling slurries may behave as a Newtonian fluid under certain conditions, such as sufficiently low solids' concentration, low particle densities, and/or high fluid viscosities. Rheological properties of Newtonian slurries are a function of both liquid and solids' characteristics but independent of the magnitude of the shear stress or the shear rate. The viscosity of the Newtonian slurry is often presented as the relative viscosity μ_r, the viscosity of the mixture μ_m normalized with that of the carrier fluid μ_l:

$$\mu_r = \frac{\mu_m}{\mu_l}. \tag{4.7}$$

The relative viscosity μ_r may vary with the volume fraction of solids, particle size and size distribution, particle shape, particle surface properties, fluid electrolyte concentration, and ionic charge and temperature. Some models that relate the relative viscosity μ_r to the volumetric fraction of solids α_s are shown in Table 4.16.

The Einstein's model is only applicable to slurries with the volumetric fraction of solids α_s smaller than 1%. The other models in the table can be used for slurries with a high volumetric fraction of solids. Although a number of other models have also been proposed, one of those shown in Table 4.16 will probably suffice for fitting experimental data. Since solids' concentration is not the only relevant parameter, there is no best model for the relationship between μ_r and α_s. The relative viscosity is also affected by solids' particle size distribution (Probstein and Sengun, 1987) and particle shape (Happel and Brenner, 1965).

Table 4.16 Some Common Relative Viscosity Models for Newtonian Slurries

Model Equation	Model Parameters	Reference
$\mu_r = 1 + 2.5\alpha_s$		Einstein (1906)
$\mu_r = \exp(B\alpha_s)/(1 - \alpha_s/\alpha_{max})$	B and α_{max}	Krieger (1972)
$\mu_r = 1 - \alpha_s/\alpha_{max}$	α_{max}	Krieger (1972)
$\mu_r = \exp[(B - n/\alpha_{max})\,\alpha_s]/(1 - \alpha_s/\alpha_{max})^n$	B, n, and α_{max}	Vocadlo (1976)
$\mu_r = 1 + 2.5\alpha_s + 10.05\alpha_s^2 + 0.00273\exp(16.6\alpha_s)$		Thomas (1965)

4.2.3.1.2 Non-Newtonian Slurries As the solids' concentration increases, the rheological properties of nonsettling slurries will deviate from Newtonian behavior. When this deviation occurs, the apparent viscosity η, as defined in Equation 4.6, is no longer a constant, but is instead dependent upon the magnitude of the shear stress τ or the shear rate $\dot{\gamma}$. Such nonsettling slurries are called non-Newtonian. For the majority of non-Newtonian slurries, η is a decreasing function of shear stress τ or shear rate $\dot{\gamma}$ (pseudo-plastic or shear thinning). However, for some slurries of very fine particles (e.g., starch), η may increase with increasing τ or $\dot{\gamma}$ (dilatant or shear thickening). Certain slurries, such as flocculated slurries encountered in minerals processing plants, may develop an internal structure leading to the time-dependent non-Newtonian behavior (i.e., the thixotropic slurry). Since the dilatant type of behavior is relatively rare and the time-dependent non-Newtonian slurry flows are difficult to model, the examination of rheological models for non-Newtonian slurries in this sections will be limited to the time-independent pseudo-plastic behavior.

Many models have been proposed for representing the viscosity function of non-Newtonian slurries. The model equation that best represents a given slurry depends not only upon the nature of the behavior of that slurry but also upon the quality and range of viscosity data available for that slurry. Hence, a relatively simple equation might be adequate to represent viscosity data over only a limited range of shear rate. However, if a wide range of shear rate is covered, a complex equation might be needed to represent the entire range of data.

Typical models that have been found useful for representing rheological properties of non-Newtonian slurries are shown in Table 4.17. Each model is written in three equivalent equations except the Sisko model. Limitations associated with each model are also indicated in the table.

Both the Bingham plastic and the Casson models contain two parameters: a yield stress (τ_b or τ_c) and a limiting viscosity (η_b or η_c). Both models approach Newtonian behavior with a viscosity of η_b or η_c as shear stress τ or shear rate $\dot{\gamma}$ increases. Although these two models are simple, they exhibit proper limiting behavior at both extremes of shear rate and are consequently useful for representing the viscous properties of slurries that exhibit an apparent yield stress resulting from the interparticle contact resistance in a rest state. The Casson model is a theoretical two-parameter model. Recent work in the prediction of laminar and turbulent pipeline flow of non-Newtonian, nonsettling slurries seems to focus largely on the use of the Casson model rather than the Bingharn plastic and the Herschel–Bulkley models for describing shear-thinning slurry behavior. The Casson model has an advantage over the Bingham plastic model because it can predict the curvature of the rheogram curve at low shear rates. The Casson model has been used to describe the non-Newtonian flow behavior of a wide variety of materials, including printing inks, blood, chocolate, and oil-based drilling mud.

Table 4.17 Typical Rheological Models for Non-Newtonian Slurries

Model Name	Model Equation	Limitations
Bingham plastic (Bird et al., 1960)	$\tau = \tau_b + \eta_b\dot{\gamma}$ for $\tau > \tau_b$ $\dot{\gamma} = 0$ for $\tau < \tau_b$ $\eta = \eta_b + \tau_b/\dot{\gamma}$ or $\eta = \tau\eta_b/(\tau - \tau_b)$	τ_b and η_b depend on solids' concentration α_s and particle size distribution (PSD)
Casson (1959)	$\tau^{1/2} = \tau_c^{1/2} + (\eta_c\dot{\gamma})^{1/2}$ $\eta = [\eta_c^{1/2} + (\tau_c/\dot{\gamma})^{1/2}]$ or $\eta = \tau\eta_c/\left(\tau^{1/2} - \tau_c^{1/2}\right)^2$	τ_c and η_c depend on α_s and PSD
Power-Law (Bird et al., 1960)	$\tau = K_p\dot{\gamma}^n$ $\eta = K_p\dot{\gamma}^{n-1}$ or $\eta = \tau(K_h/\tau)^{1/n}$	Predict $n \to \infty$ for $n < 1$ and $\dot{\gamma} \to 0$; predict $n \to 0$ for $n < 1$ and $\dot{\gamma} \to \infty$; K_p and n depend on solids' concentration and PSD
Herschel–Bulkley (1926)	$\tau = \tau_h + K_h\dot{\gamma}^p$ $\eta = K_p\dot{\gamma}^{p-1} + \tau_h/\dot{\gamma}$ or $\eta = \tau[K_h/\left(\tau - \tau_h\right)]^{1/p}$	Predict $n \to 0$ for $p < 1$ and $\dot{\gamma} \to \infty$; τ_h, K_h, and p depend on α_s and PSD
Sisko (1958)	$\tau = \eta_s\dot{\gamma} + K_s\dot{\gamma}^m$ $\eta = \eta_s + K_s\dot{\gamma}^{m-1}$	η_s, K_s, and m depend on α_s and PSD

The power-law model can represent Newtonian (for $n = 1$), shear thinning (for $n < 1$), or shear thickening (for $n > 1$) behavior. Although most non-Newtonian slurries can exhibit a "power-law" region over a certain range of shear rate, the model will fail at very high and/or low shear rates. For example, the model will predict $\eta \to \infty$ for $n < 1$ and $\dot{\gamma} \to 0$, and $\eta \to 0$ for $n < 1$ and $\dot{\gamma} \to \propto$, both of which are unrealistic for slurries with no yield stress.

The Herschel–Bulkley model (also referred to as the *yield power-law* or *generalized Bingham* model) is basically the power-law model with an added yield stress parameter. Although this model is more flexible than the Bingham model for modeling rheogram data due to the additional model parameter, it suffers the same limitation as the power-law model with regard to unrealistic limiting behavior at high shear rates (or stresses). The estimation of Herschel–Bulkley model parameters from curve fitting often contains a significant degree of uncertainty (Turian et al., 1997), as it is found that different sets of values of the model parameters in the model can provide equivalent fit of the experimental data. This is a fundamental weakness of the Herschel–Bulkley model.

The Sisko model has been found to be a good model for describing the shear stress–shear rate dependence for many non-Newtonian slurries over the range of shear most appropriate to flow in pipes (Turian et al., 1992, 1998a). Unlike other three-parameter empirical models, one of the model parameters, η_s, can be determined independently, as it is given by the high-shear asymptote of the viscosity–shear rate plot. Consequently, the parameter value of η_s is instrument-geometry indifferent and depends upon suspension microstructure. The remaining two model parameters, K_s and m, are then determined through the best curve fitting to the data over the whole range of shear. The rheogram curves for most concentrated non-Newtonian slurries usually possess a power-law region covering the lower and the intermediate shear rate ranges, followed by an asymptotic approach to a high-shear Newtonian limit. The Sisko model not only describes such behavior well but also does so over the entire range of shear rates attainable even in the highest shear rheometer and with a unique set of unambiguously determined model parameter values.

The model parameters in the equations listed in Table 4.17 can be estimated through linear or nonlinear regression. However, extrapolation outside the experimental shear rate range should be done only with caution. Heywood and Cheng (1984) have used two different methods for the curve fitting. One involves nonlinear least-squares regression on weighted data while, in the other method, the data are not weighted. They have shown that while both methods will give best estimates of the three parameters that will then allow prediction of τ to within ±2% over the original viscometric shear rate range, extrapolation well outside this shear rate range leads to very different τ predictions using the two methods.

Bingham plastic, Casson, and Herschel–Bulkley models include a yield-stress parameter, τ_b, τ_c, and τ_h, respectively. However, Turian et al. (1998a) indicated that curve-fitting shear stress/shear rate data to determine these yield-stress parameters will not, and generally does not, insure that a yield stress, as an intrinsic, instrument-geometry indifferent slurry property has been determined or, for that slurry, exists. The yield-stress values obtained from curve fitting should not necessarily be considered as an absolute property of the slurry but rather a constant that arises out of the correlation of shear stress/shear rate data. The true yield stress of a slurry, if it exists, may have a value quite different from the value derived from the curve fitting of experimental data for which the lower limit of the viscometric shear rate range is of the order of tens or even hundreds of reciprocal seconds. A knowledge of the true yield stress facilitates the calculation of the start-up pressure gradient for stagnant fluid in a pipe according to Section 4.2.5.3. A detailed discussion of determination of yield stresses for slurries has been given by Turian el al. (1992).

It should be noted that all model parameters for the models listed in Table 4.17 are influenced by solids' concentration, particle size distribution, and the properties of the interface between solids and liquid. Bird et al. (1982) have summarized various equations from the literature that relate the parameters of the Bingham and Casson models to various properties of slurries, including solids' concentration. In general, the dependence of parameters in Bingham and power-law models on solids' concentration can be modeled using the following equation:

$$\tau_b\,(\text{or}\,\eta_b, K_p, n) = E\exp(F\alpha_s), \tag{4.8}$$

where E and F are constants derived from tests measuring particle size distribution, shape, and the nature of their surface. A number of other empirical models for correlating the parameters in non-Newtonian rheological models with various factors have been reported in the literature (Thomas, 1961, Bird et al., 1982, Turian et al., 1997).

4.2.3.2 Pressure Loss through Straight Circular Pipe

4.2.3.2.1 Friction Factor in Pipe Flows For steady slurry flows in a piping system with straight conduit of uniform cross section, the total pressure change, Δp, in general comprises

$$\Delta p = p_f + p_{ft} + \rho_m g \Delta z \tag{4.9}$$

where

p_f is the frictional pressure loss in the pipe
p_{ft} is the frictional pressure loss arising from flow through fittings
The last term, $\rho_m g \Delta z$, is the pressure loss or gain resulting from elevation changes and is negative for a reduction in static head and positive for an increase in static head
Δz is the net change in pipeline elevation, assuming that the pipeline is full of slurry

The frictional pressure loss over a straight pipe with a length L and an internal diameter D is given by

$$p_f = f\left(4L/D\right)\left(\rho_m U_m^2/2\right) \tag{4.10}$$

where f is the friction factor of pipe flow. This equation shows that the evaluation of f is the major task in the determination of the frictional pressure loss. The friction factor can also be defined in terms of the shear stress at the pipe wall, τ_w:

$$f = \frac{\tau_w}{(\rho_m U_m^2/2)} \tag{4.11}$$

4.2.3.2.2 Laminar Flows For laminar flow, the pipeline pressure loss can be calculated from first principles for any given rheological data or model fitted to the data. The accuracy of pressure drop prediction is limited only by the accuracy of the data and the closeness with which the slurry flow properties fit any chosen model. The rheological models as presented in Section 4.2.3.1 can be used either to obtain analytical expressions for volumetric flow rate as a function of wall shear stress and other relevant variables in the laminar flow regime or for the friction factor as a function of model-specific modified Reynolds number.

The volume flow rate through a pipe with a local slurry velocity $v(r)$ at the radial position r in the pipe is given by

$$\dot{V}_m = \int_0^{D/2} 2\pi v(r) \mathrm{d}r \tag{4.12}$$

The shear stress at a radial position, r, can be related to the frictional pressure loss over the pipe of length, L, by equating the resultant force, $\pi r^2 p_f$, from the pressure drop over a cylinder of radius, r, with the force derived from the shear stress, $2\pi r\tau$

$$\tau = \frac{r}{2}\frac{p_f}{L}. \tag{4.13}$$

After integration by parts and using Equation 4.13, Equation 4.12 becomes

$$\dot{V}_m = \frac{\pi}{8}\left(D/\tau_w\right)^3 \int_0^{\tau_w} \tau^2 \dot{\gamma} \mathrm{d}\tau, \tag{4.14}$$

where the shear stress at the pipe wall, τ_w, is given by

$$\tau_w = \frac{D p_f}{4L}. \tag{4.15}$$

4.2.3.2.2.1 Newtonian Slurries For steady, fully developed, laminar flow of Newtonian slurries in a circular pipe, the apparent viscosity η ($\eta = \mu_m$) is independent of the shear rate or shear stress. Substitution of the Newtonian model (i.e., $\tau = \mu_m\dot{\gamma}$) into Equation 4.14 leads to the well-known Hagen–Poiseuille equation

$$\dot{V}_m = \frac{\pi D^4 p_f}{128\mu_m L} = \frac{\pi D^3 \tau_w}{32\mu_m} \tag{4.16}$$

By using Equation 4.16 to eliminate τ_w in Equation 4.11 and rearranging to solve for f gives

$$f = \frac{16\mu_m}{DU_m\rho_m}. \tag{4.17}$$

This equation can be rewritten in dimensionless form:

$$f = \frac{16}{Re}, \tag{4.18}$$

where $Re = DU_m\rho_m/\mu_m$ is the pipe flow Reynolds number. The upper limit of Newtonian laminar flow regime is defined by the Reynolds number with a value of 2100.

4.2.3.2.2.2 Non-Newtonian Slurries For non-Newtonian slurries, analytical expressions for the volumetric flow rate and the friction factor can be obtained by substituting a non-Newtonian rheology model into Equation 4.14 and then evaluating the integral of the equation. For rheology models with a yield stress (e.g., Bingham plastic), the lower limit of the integral in Equation 4.14 must be replaced by the yield stress. In the evaluation of Equation 4.14, using either data or a model, the range of shear stress from zero (or a yield stress) to $\tau_w = Dp_f/4L$ is involved. Experimental data may not cover this entire range, especially at the lower limit. Consequently, some extrapolation is inevitable. In this situation, the reliability of the results depends upon the degree to which the database covers the range of conditions (i.e., shear stress) of interest.

4.2.3.2.2.2.1 Power-Law Model For the power-law model, $\tau = K_p\dot{\gamma}^n$, the integration of Equation 4.14 gives

$$\dot{V}_m = \frac{\pi D^3}{32}\left(\frac{4n}{3n+1}\right)\left(\frac{\tau_w}{K_p}\right)^{1/n} \tag{4.19}$$

which is the power-law equivalent of the Hagen–Poiseuille equation and reduces to Equation 4.16 for $n = 1$ and $K_p = \mu_m$. Using Equation 4.19 to eliminate τ_w in Equation 4.11 and rearranging to solve for f gives

$$f = \frac{16}{Re_p} \tag{4.20}$$

where Re_p is the equivalent Reynolds number for power-law non-Newtonian slurries and is given by

$$Re_p = \frac{\rho_m U_m D}{K_p}\left(\frac{4n}{3n+1}\right)^n\left(\frac{D}{8U_m}\right)^{n-1}. \tag{4.21}$$

It should be noted that the definition of Re_p does not have any physical meaning, and it is so defined that Equation 4.20 and Equation 4.18 are of identical form.

4.2.3.2.2.2.2 Bingham Plastics Model Due to the yield stress in the Bingham Plastic model (i.e., $\tau = \tau_b + \eta_b\dot{\gamma}$), a region extending from the center of the pipe to $r = R\tau_b/\tau_w = r_0$ will move as a "plug." Therefore,

the total volume flow rate will be the sum of flow rate in the "plug" and that in the deformed region surrounding the plug and is given by

$$\dot{V}_{\mathrm{m}} = \dot{V}_{\mathrm{plug}} + \int_{r_0}^{D/2} 2\pi v(r)\mathrm{d}r \tag{4.22}$$

After integration by parts and substituting the Bingham Plastic model equation, the evaluation of Equation 4.22 yields the Buckingham (1921) equation:

$$\dot{V}_{\mathrm{m}} = \frac{\pi D^3 \tau_{\mathrm{w}}}{32\eta_{\mathrm{b}}}\left[1 - \frac{4}{3}\frac{\tau_{\mathrm{b}}}{\tau_{\mathrm{w}}} + \frac{1}{3}\left(\frac{\tau_{\mathrm{b}}}{\tau_{\mathrm{w}}}\right)^4\right] \tag{4.23}$$

Substituting $\tau_{\mathrm{w}} = f\rho_{\mathrm{m}} U_m/2$ into Equation 4.23 and solving for f give the equivalent dimensionless expression

$$f = \frac{16}{Re_{\mathrm{b}}}\left[1 + \frac{1}{6}\frac{He_{\mathrm{b}}}{Re_{\mathrm{b}}} - \frac{1}{3}\frac{He_{\mathrm{b}}^4}{f^3 Re_{\mathrm{b}}^7}\right] \tag{4.24}$$

where

$$Re_{\mathrm{b}} = DU_{\mathrm{m}}\rho_{\mathrm{m}}/\eta_{\mathrm{b}} \quad \text{and} \quad He_{\mathrm{b}} = D^2\rho_{\mathrm{m}}\tau_{\mathrm{b}}/\eta_{\mathrm{b}}^2 \tag{4.25}$$

in which He_{b} is the Hedstrom number defined for Bingham Plastics model. Since Equation 4.24 is implicit in terms of f, an iterative technique is necessary to obtain f. If the last term in the bracket is small relative to the other terms, a brief iteration using the first two terms as the starting value will converge very rapidly.

4.2.3.2.2.2.3 Herschel–Bulkley or Generalized Bingham Model A procedure analogous to that given earlier can be followed using the Herschel–Bulkley model (i.e., $\tau = \tau_{\mathrm{h}} + K_{\mathrm{h}}\dot{\gamma}^p$) with Equation 4.22 to determine the flow rate and friction factor. The analytical expressions for volume flow rate and the friction factor are

$$\dot{V}_{\mathrm{m}} = \frac{\pi D^3 p}{8(3p+1)}\left(\frac{\tau_{\mathrm{w}} - \tau_{\mathrm{h}}}{K_{\mathrm{h}}}\right)^{1/p}\left[\chi^3 + \frac{2(3p+1)}{2p+1}\frac{\tau_{\mathrm{h}}}{\tau_{\mathrm{w}}}\chi^2 + \frac{(3p+1)}{2p+1}\left(\frac{\tau_{\mathrm{h}}}{\tau_{\mathrm{w}}}\right)^2\chi^2\right] \tag{4.26}$$

where $\chi = (1 - \tau_{\mathrm{h}}/\tau_{\mathrm{w}})$, and

$$f = \frac{2He_{\mathrm{h}}}{Re_{\mathrm{h}}^2} + \frac{16}{Re_{\mathrm{h}}}\left[\chi^3 + \frac{2(3p+1)}{2p+1}\frac{\tau_{\mathrm{h}}}{\tau_{\mathrm{w}}}\chi^2 + \frac{(3p+1)}{2p+1}\left(\frac{\tau_{\mathrm{h}}}{\tau_{\mathrm{w}}}\right)^2\chi^2\right]^{-p} \tag{4.27}$$

where

$$Re_{\mathrm{h}} = \frac{\rho_{\mathrm{m}} U_{\mathrm{m}} D}{K_{\mathrm{h}}}\left(\frac{4p}{3p+1}\right)^p\left(\frac{D}{8U_{\mathrm{m}}}\right)^{p-1} \tag{4.28}$$

and

$$He_{\mathrm{h}} = \left(\frac{\tau_{\mathrm{h}}}{\rho_{\mathrm{m}}}\right)\left(\frac{Re_{\mathrm{h}}}{U_{\mathrm{m}}}\right)^2 \tag{4.29}$$

Due to $\tau_{\mathrm{w}} = f\rho_{\mathrm{m}} U_{\mathrm{m}}/2$, Equation 4.27 requires an iterative procedure to solve for f. Unlike the Bingham model, no simplifying assumption can be made easily to derive an expression from Equation 4.27, which is then explicit in f.

4.2.3.2.2.2.4 Casson Model For Casson model (i.e., $\tau^{1/2} = \tau_c^{1/2} + (\eta_c \dot{\gamma})^{1/2}$), the analytical expressions are

$$\dot{V}_m = \frac{\pi D^3 \tau_w}{32\eta_c}\left[1 + \frac{4}{3}\frac{\tau_c}{\tau_w} - \frac{16}{7}\left(\frac{\tau_c}{\tau_w}\right)^{1/2} - \frac{1}{21}\left(\frac{\tau_c}{\tau_w}\right)^4\right] \tag{4.30}$$

and

$$f = \frac{16}{Re_c}\left[1 - \frac{1}{6}\frac{He_c}{Re_c} + \frac{1}{7}\left(2fHe_c\right)^{1/2} + \frac{1}{21}\frac{He_c^4}{f^3 Re_c^7}\right] \tag{4.31}$$

where

$$Re_c = DU_m\rho_m/\eta_c \quad \text{and} \quad He_c = D^2\rho_m\tau_c/\eta_c^2 \tag{4.32}$$

4.2.3.2.2.2.5 Numerical Integration Method Substituting Equation 4.15 into Equation 4.14 and solving for P_f give

$$P_f = \left(\frac{8\pi L^3}{\dot{V}_m}\int_0^{\tau_w} \tau^2\dot{\gamma}\,d\tau\right)^{1/3} \tag{4.33}$$

This relationship suggests a simplified but rigorous approach to the estimation of the frictional pressure loss for the laminar flow of a slurry having any rheological property. If a rheogram curve (also called flow curve) data for a slurry have been obtained using a smaller (or larger) pipe diameter and there are no *wall-slip* effects, the integral in the equation given earlier can be readily evaluated by plotting $\tau^2\dot{\gamma}$ against τ and calculating the area under the curve. The method is useful for complex rheogram curves that simplified rheological models have a difficulty to represent. It should also be noted that the relationship is valid for any pipe diameter as long as the flow remains in the laminar regime. Thus, this master curve may be used to predict the frictional pressure loss for flows in any other pipe size.

4.2.3.2.3 Turbulent Flows

4.2.3.2.3.1 Newtonian Slurries Unlike in laminar flow, in the turbulent flow of a Newtonian slurry the relative pipe wall roughness can be important and correlations for the friction factor, *f,* can be classified according to whether the pipe wall is essentially smooth or is sufficiently rough to affect frictional losses. These correlations are obtained with or without theoretical guidance. Many different versions of correlations have been developed (e.g., von Karman, 1931, Colebrook, 1939, Moody, 1947, Olujic, 1981). For the turbulent flow of a Newtonian fluid in smooth tubes, the classical mixing length theory of Prandtl was applied by von Karman (1931) to derive the well-known expression

$$\frac{1}{\sqrt{f}} = 4.0\log\left(Re\sqrt{f}\right) - 0.4 \tag{4.34}$$

When the pipe wall is not smooth, an estimate for the relative roughness of the wall, *e*/*D*, is required, as it is an additional variable in equations for the prediction of friction factor (Colebrook, 1939). For rough pipe surfaces, Equation 4.34 was modified by Colebrook (1939) to include the effect of relative roughness, *e*/*D*:

$$\frac{1}{\sqrt{f}} = -4.0\log\left[\frac{e/D}{3.7} + \frac{1.255}{Re\sqrt{f}}\right] \tag{4.35}$$

This equation is the basis for the well-known Moody diagram for pipe friction factors and applies for $Re > 2100$.

However, the equation by Churchill (1977) is probably the most useful for turbulent flows, as it is explicit in f and valid for either smooth or rough pipe surface in both the laminar and turbulent flow regimes:

$$f = 2\left[\left(\frac{8}{Re}\right)^{12} + (A+B)^{-1.5}\right]^{1/12} \tag{4.36}$$

where

$$A = \left[2.457\ln(1/C)\right]^{16}, \quad B = \left(\frac{37530}{Re}\right)^{16}, \quad \text{and} \quad C = \left(\frac{7}{Re}\right)^{0.9} + 0.27\frac{e}{D} \tag{4.37}$$

4.2.3.2.3.2 Non-Newtonian Slurries Turbulence is a natural form of fluid motion that is characterized by random eddy motions both parallel and transverse to the direction of the main flow. Both direction and magnitude of solids and liquid velocities fluctuate on a continuous random basis. The turbulent flow of non-Newtonian slurries is more complex than that for Newtonian slurries, as the turbulent behavior of non-Newtonian slurries appears unrelated to their laminar behavior and yet has been found similar to Newtonian turbulent flow behavior, in spite of the obvious difference in rheology. Many theoretical models have therefore been developed to predict the turbulent flow behavior of non-Newtonian slurries.

Many empirical, semianalytical, and analytical models for turbulent non-Newtonian flow have been developed. Most equations are based on the power-law model or Bingham plastic, for example, those developed by Dodge and Metzner (1959), Tomita (1959), and Szilas et al. (1981), while others have been derived specifically for use with the Herschel–Bulkley flow model, that is, Torrance (1963) and Hanks (1978). Govier and Aziz (1972) give a review of these models.

Dodge and Metzner (1959) developed a semitheoretical equation for the smooth wall fully developed turbulent friction factor for, time independent, purely viscous non-Newtonian fluids. This was based upon Prandtl's mixing length theory with different values for the empirical constants being obtained from experimental data. Tomita (1959) used a similar method to develop equations specifically for Bingham plastic and power-law fluids, respectively. Torrance (1963) extended this work for yield-pseudo-plastics to account for pipe roughness. Wilson and Thomas (1985) developed the work further by including terms for the viscous sublayer due to shear thinning.

Most of the models or methods for turbulent non-Newtonian flow are based on a specific rheological model, while a few of them are generalized models, such as the Wilson and Thomas model (1985). We will proceed in our discussion from a generalized model to those based on a specific rheological model.

4.2.3.2.3.3 The Wilson and Thomas Model Non-Newtonian rheological properties can increase the turbulent micro-eddy size, leading to an increase in the thickness of the viscous sublayer. If other quantities are unaffected the thickened sublayer will, in turn, produce a higher mean velocity for the same wall shear stress, giving a lower friction factor. Based on this consideration, Wilson and Thomas (1985) and Thomas and Wilson (1987) developed a predictive model for non-Newtonian turbulent flow. The model uses the ratio of the integrals under the non-Newtonian and Newtonian rheograms, denoted by α, to estimate the size increase of the micro-eddies, and it was found that the thickness of the sublayer should also be multiplied by a factor equal to α. As shown by Wilson and Thomas (1985), the value of the mean velocity U_m, which results from this thickened viscous sublayer, is given by

$$\frac{U_m}{u^*} = \frac{U_N}{u^*} + 11.6(\alpha - 1) - 2.5\ln\alpha - \Omega \tag{4.38}$$

where

U_m is the mean slurry velocity

u^* is the friction velocity ($u^* = (\tau_w/\rho_m)^{0.5}$)

U_N represents the mean velocity for equivalent Newtonian flow, that is, flow with the same wall shear stress τ_w for Newtonian fluid with the same viscosity corresponding to the non-Newtonian value at $\tau = \tau_w$

The term Ω represents the reduction in mean velocity due to flattening of the central core of the velocity profile when the fluid possesses a yield stress, τ_y

$$\Omega = -2.5\ \ln(1-\xi) - 2.5\,\xi(1+0.5\xi), \quad \xi = \tau_y/\tau_w \tag{4.39}$$

The work by Wilson and Thomas (1985) has some theoretical justification and has been shown to give fairly good agreement with experimental data. It is generally accepted that the model of Wilson and Thomas is the most successful of the Prandtl type of models. For the power-law and some other models, expressions for the area ratio α have been worked out (Thomas and Wilson, 1987).

For a yield power-law fluid (i.e., Herschel–Bulkley fluid, $\tau = \tau_h + K_h\dot{\gamma}^p$, and $\tau_y = \tau_h$,), the area ratio α is

$$\alpha = \frac{2(1+\xi p)}{(1+p)} \tag{4.40}$$

For a power-law fluid ($\tau = K_p\dot{\gamma}^n$ and $\tau_y = 0$), the expression for α is

$$\alpha = \frac{1}{(1+n)} \tag{4.41}$$

For a Bingham fluid ($\tau = \tau_b + \eta_b\dot{\gamma}$ and $\tau_y = \tau_b$), the area ratio α is given by

$$\alpha = 1+\xi \tag{4.42}$$

For a Casson fluid ($\tau^{1/2} = \tau_c^{1/2} + (\eta_c\dot{\gamma})^{1/2}$ and $\tau_y = \tau_c^{1/2}$), the area ratio α is

$$\alpha = 1 + 2\chi^{0.5}/3 + \chi/3 \tag{4.43}$$

Theoretically, the Wilson and Thomas model, that is, Equation 4.38 is applicable to a slurry having any rheological property. If rheogram curve data for a slurry have been obtained, the ratio of the integrals under the non-Newtonian and Newtonian rheograms can be readily evaluated using a numerical technique.

The mean velocity of the equivalent Newtonian flow, U_N, is evaluated using a friction factor determined by using the model-specific Reynolds number: $Re_M = DV_N\rho_m/\eta$. The effective viscosity η is evaluated from the slurry rheogram $(\tau, \dot{\gamma})$ or a rheological model at τ_w. The effective viscosity evaluated at τ_w using typical rheological models is shown in Table 4.18.

The Wilson and Thomas model is not explicit in the friction factor *f*. Equation 4.38 requires the following iterative procedure to solve for *f* for a given slurry mean velocity U_m:

1. Assuming a value of wall shear stress, τ_w
2. Calculating the effective viscosity at τ_w using a suitable rheological model such as those shown in Table 4.18
3. Evaluating the friction velocity using $u^* = (\tau_w/\rho_m)^{0.5}$
4. Assuming a value of the mean velocity of the equivalent Newtonian flow U_N
5. Evaluating the friction factor *f* at the model-specific Reynolds number: $Re_M = DU_N\rho_m/\eta$. The friction factor *f* is calculated using Equation 4.34 for smooth pipe wall or Equation 4.36 for rough pipe wall.

Table 4.18 Effective Viscosity of Typical Rheological Models at τ_w

Model Name	Model Equation
Bingham plastic	$\eta = \tau_w\eta_b/(\tau_w - \tau_b) = \eta_b/(1-\chi), \quad \chi = \tau_b/\tau_w$
Casson	$\eta = \tau_w\eta_c/\left(\tau_w^{1/2} - \tau_c^{1/2}\right)^2 = \eta_c/\left(1-\chi^{1/2}\right)^2, \ \chi = \tau_c/\tau_w$
Power law	$\eta = \tau_w(K_h/\tau_w)^{1/n}$
Herschel–Bulkley	$\eta = \tau_w[K_h/(\tau_w - \tau_h)]^{1/p}$

6. Evaluating U_N using $U_N = (2\tau_w/\rho_m f)^{0.5}$
7. Returning to Step 4 if the difference between the U_N from Step 6 and the one assumed at Step 4 is higher than a specified tolerance
8. Evaluating the U_m using the Wilson and Thomas model
9. Returning to Step 1 if the difference between the U_m from Step 8 and the given value is higher than a specified tolerance

The effect of the pipe wall roughness on the turbulent flow of non-Newtonian slurries can be accommodated in the Wilson and Thomas model by using the appropriate roughness in the determination of U_N, as indicated in the earlier procedure. However, this can only be approximate, since the interaction between the pipe roughness and the laminar sublayer will be different when the thickened laminar sublayer is present.

4.2.3.2.3.4 Models for Power-Law Slurries The equations for the friction factor f, based on the power-law ($\tau = K_p\dot{\gamma}^n$) Reynolds number Re_p defined in Equation 4.21, are given by

1. *Dodge and Metzner (1959).* Dodge and Metzner developed a model of turbulent flow of a power-law fluid in a smooth pipe based on the laminar flow model of Metzner and Reed (1955). The model was developed following the form of the von Karman–Nikuradse equation for Newtonian turbulent flow, and the final relationship is of the same format as Newtonian smooth wall turbulent flow and reverts to the Newtonian form under Newtonian conditions ($K_p = \mu$ and $n = 1$). The model is

$$\frac{1}{\sqrt{f}} = \frac{4.0}{n^{0.75}}\log\left(Re_p f^{1-n/2}\right) - \frac{0.4}{n^{1.2}} \tag{4.44}$$

2. *Tomita (1959).* For power-law fluids, Tomita extended his laminar flow model to turbulent flows in smooth pipes by applying Prandtl's mixing length concept and developed an implicit equation

$$1/\sqrt{f_{T0}} = 4.0\log\left(Re_{T0}\sqrt{f_{T0}}\right) - 0.4 \tag{4.45}$$

where

$$f_{T0} = \left(\frac{1+2n}{1+3n}\right)\frac{4}{3}f \tag{4.46}$$

and

$$Re_{T0} = Re_p 8^{1-n}\left(\frac{1+3n}{4n}\right)^n \frac{6\left[(1+3n)/n\right]^{1-n}}{2n\left[(1+2n)/n\right]} \tag{4.47}$$

3. *Szilas* et al *(1981).* Szilas et al. developed the following equation for power-law oil flow in rough pipes at high Reynolds number

$$\frac{1}{\sqrt{f}} = \frac{4.0}{n}\log\left(Re_p(4f)^{1-n/2}\right) + 1.51^{1/n}\left(4.24 + \frac{1.414}{n}\right) - \frac{8.03}{n} - 2.114 \tag{4.48}$$

4. *Irvine (1988).* Irvine developed a generalized Blasius equation for power-law fluids in smooth pipes

$$f = \frac{F'(n)}{Re_p^{1/(3n+1)}} \tag{4.49}$$

where

$$F'(n) = \frac{2}{8^{n-1}}\left[\frac{8n^n}{7^{7n}(1+3n)^n}\right]^{1/(3n+1)} \tag{4.50}$$

4.2.3.2.3.5 Models for Herschel–Bulkley or Generalized Bingham Slurries The turbulent flow of Herschel–Bulkley or generalized Bingham fluids in circular pipes has been studied by a number of people, including

1. *Torrance (1963).* Torrance developed a theoretical equation for Herschel–Bulkley or generalized Bingham fluids ($\tau = \tau_h + K_h\dot{\gamma}^p$) to include a wall shear stress. For fully turbulent flows in smooth pipes, the Torrance equation is

$$\frac{1}{\sqrt{f}} = \frac{1.966}{n}\ln\left(\left(1-\xi\right)Re_n f^{1-n/2}\right) + \frac{0.682}{n}\left(5n-8\right) + \frac{2.678}{n} - 2.949 \tag{4.51}$$

where $\xi = \tau_h/\tau_w$, and $Re_n = 8^{1-p}D^pU_m^{2-p}\rho_m/K_h$.
For flows in rough pipes with a relative roughness, e/D, the Torrance equation is

$$\frac{1}{\sqrt{f}} = 1.767\log\left(\frac{Re_n}{e}\right) + 6 - \frac{2.65}{n} \tag{4.52}$$

2. *Slatter et al. (1996).* Slatter et al. proposed a new model for describing the turbulent pipe flow of Herschel–Bulkley or generalized Bingham fluids. By analogy with the Newtonian approach, they defined the roughness Reynolds number, Re_r, in terms of friction velocity, Herschel–Bulkley model parameters, and the representative particle diameter d_{85}:

$$Re_r = \frac{8\rho_m\left(u^\star\right)^2}{\tau_h + K_h\left[8u^\star/d_{85}\right]^p} \tag{4.53}$$

If $Re_r < 3.32$ then smooth wall turbulent flow exists and the mean velocity is given by

$$\frac{U_m}{u^\star} = 2.5\ln\left(\frac{D}{2d_{85}}\right) + 2.5\ln\left(Re_r\right) + 1.75 \tag{4.54}$$

If $Re_r > 3.32$ then fully developed rough wall turbulent flow exists and the mean velocity is given by

$$\frac{U_m}{u^\star} = 2.5\ln\left(\frac{D}{2d_{85}}\right) + 4.75 \tag{4.55}$$

and the friction factor is a constant.

Prediction of f for turbulent flow in rough pipes can be also based on the relations for smooth wall pipe. Govier and Aziz (1972) suggested that if the pipe is rough, the pressure loss calculated by the methods for smooth pipes should be multiplied by the ratio of the friction factor for rough pipe to the friction factor for smooth pipe, as determined from the Moody chart for Newtonian materials at the appropriate Reynolds number consistent with the fluid model being used, that is, Re_b, for the Bingham plastic model or Re_p for the power-law models. For pipe flows where friction factors are independent of Reynolds number but are dependent upon relative roughness, e/D, the Torrance equation, that is, Equation 4.52 should be used.

4.2.3.2.3.6 Models for Bingham Plastic Slurries The equations for the friction factor f based on the Bingham plastic ($\tau = \tau_b + \eta_b\dot{\gamma}$) Reynolds number Re_b defined in Equation 4.25 are those given by

1. *Thomas (1963)*: For slurries whose rheograms may be adequately described by Bingham plastic model, Thomas has developed a Blasius-type equation

$$f = B_T Re_b^{-\beta} \tag{4.56}$$

where the parameters B_T and β are related to fluid properties using data in smooth pipes:

$$\left.\begin{aligned} B_T &= 0.079\left[\left(\eta_f/\eta_b\right)^{0.48} + \left(\rho_m \tau_b K_{T1}^2/\eta_f^2\right)^2\right] \\ \beta &= 0.25\left[\left(\eta_f/\eta_b\right)^{0.15} + \left(\rho_m \tau_b K_{T2}^2/\eta_f^2\right)^2\right] \end{aligned}\right\} \tag{4.57}$$

in which K_{T1} = 1.94 μm, K_{T2} = 1.73 μm, and η_f is the Newtonian viscosity of the suspending medium.

2. *Darby and Melson (1981)*: Darby and Melson employed the approach taken by Churchill (1977) to combine the Buckingham equation for f_L for laminar flow (Equation 4.24) with an empirical correlation for f_T for turbulent flow regime to arrive at a single friction factor expression valid for all flow regimes:

$$f = \left(f_L^m + f_T^m\right)^{1/m} \tag{4.58}$$

where the exponent m depends on Bingham Reynolds number according to

$$m = 1.7 + 40{,}000/Re_b \tag{4.59}$$

and the empirical correlation for f_T for turbulent flow regime is

$$\left.\begin{aligned} f_T &= 10^{\beta} Re_b^{-0.193} \\ \beta &= -1.378\left[1 + 0.146\exp\left(-0.29\times10^{-5} Re_b\right)\right] \end{aligned}\right\} \tag{4.60}$$

Equation 4.60 does not apply when the Hedstrom number, defined by Equation 4.25, is less than 1000, but this is not a practical constraint for most slurries with a measurable yield stress.

4.2.3.2.4 Laminar–Turbulent Transition It is important to identify the transition between laminar and turbulent flow for the following reasons:

- The fluid behavior and relevant equations for pressure loss prediction change fundamentally at this point. Once this transition point is defined for a slurry with a particular flow property, it is then possible to decide whether expressions for laminar flow are relevant or whether turbulent flow equations need to be used.
- Overall optimization of slurry pipeline system often suggests that it is most economical to operate the pipeline system in the transition region between the laminar and turbulent regimes.
- It is necessary in some cases to operate into the turbulent flow regime in order to maintain coarse size fraction of the solids in suspension.

For Newtonian slurries, the lower critical Reynolds number for the initial breakdown of laminar flow, Re_1, is 2100 and the upper value of Re_2 for the commencement of fully turbulent flow is approximately 3000. The flow region between these two critical Reynolds numbers is typically referred to as the transitional flow regime. However, for non-Newtonian slurries, the individual values of Re_1 and Re_2 are much more difficult to predict. Various methods have been developed for Re_1 prediction based on different flow models. Cheng (1970) has also developed an approach for predicting both Re_1 and Re_2 valid for both power-law slurries and generalized Bingham slurries. The most economical design often suggests that flow should be in the transitional regime and some pipelines operate just above Re_2. However, Re_2 is difficult to define precisely due to the fact that the fluctuations in pressure gradient prevalent in the transitional regime diminish progressively rather than abruptly as the flow velocity is increased, when the fully turbulent flow regime is reached.

4.2.3.2.4.1 Intersection Method A practical and simple approach toward dealing with the transitional region between laminar and turbulent flow is to assume that the transition, as the flow velocity is progressively increased, occurs completely at a single operating point. In this case, only one critical Reynolds number needs to be predicted and this can be achieved by taking the intersection of the (f, Re) or (f, U_m) relationships for laminar and turbulent flow for the non-Newtonian fluid model under consideration. The degree of success of this method is entirely dependent on the accuracy of the turbulent model used. It should be noted that this approach cannot explain the flow behavior as does the Newtonian Reynolds number approach. This approach also does not work with Newtonian behavior, where the critical point is clearly not the intersection of the laminar and turbulent theoretical lines.

4.2.3.2.4.2 Stability Function Method Ryan and Johnson (1959) defined a stability parameter in terms of the velocity distribution, $v(r)$, in the pipe as follows:

$$Z = -\frac{D}{2\tau_w}\rho_m v(r)\frac{dv}{dr} \tag{4.61}$$

which is the ratio of energy input to energy dissipation within a fluid element. It is clear that Z has the form of a Reynolds number with no reference to a fluid model. It vanishes at both the pipe wall and the centerline, attaining a maximum at some intermediate position. For a Newtonian fluid, the laminar flow solution indicates that Z attains a maximum at the reduced radial position $r/R = 1/\sqrt{3}$, with

$$Z_{max} = 0.3849Re \tag{4.62}$$

Taking the transition Reynolds number for laminar flow as $Re_c = 2100$ gives $Z_{max} = 808$. Since Z is not restricted to any fluid model, Ryan and Johnson (1959) proposed that the laminar–turbulent transition occurs at the same value of the ratio (i.e., $Z_{max} = 808$) for non-Newtonian fluids as it does for Newtonian fluids. For Newtonian fluids, the stability parameter pertaining to this ratio can be expressed in terms of transition Reynolds number. However, since the definition of Reynolds number for non-Newtonian fluids is model dependent, so are the laminar–turbulent transition criteria. Using Equations 4.61 and 4.62 together with the velocity distribution $v(r)$ appropriate to the rheological model, laminar–turbulent transition criteria can be derived.

When applied to the power-law model ($\tau = K_p\dot{\gamma}^n$), Ryan and Johnson (1959) obtained an expression for the lower critical Reynolds number Re_c:

$$Re_c = \frac{6464n(n+2)^{(n+2)/(n+1)}}{(1+3n)^2}, \tag{4.63}$$

or, alternatively, the lower critical friction factor f_c is given by

$$f_c = \frac{(1+3n)^2}{404n}\frac{1}{(n+2)^{(n+2)/(n+1)}}. \tag{4.64}$$

Such results have also been obtained for Bingham plastic slurries by Hanks (1981) and for the Casson and Herschel–Bulkley slurries by Hanks and Ricks (1974).

4.2.3.2.4.3 Metzner–Reed Method Metzner and Reed (1955) developed a generalized Reynolds number for the correlation of non-Newtonian pipe flow data. They define two rheological parameters K' and n':

$$\tau_w = K'\left(\frac{8U_m}{D}\right)^{n'} \tag{4.65}$$

which represents the tangent to the logarithmic plot of $\tau_0 vs 8U_m/D$. The Reynolds number is then defined as

$$Re_{MR} = \frac{8\rho_m U_m^2}{K'(8U_m/D)^{n'}} \tag{4.66}$$

The transition criterion is $Re_{MR} = 2100$.

4.2.3.3 Pressure Losses from Pipe Fittings

Pressure losses arising from flow through pipe fittings are required before the total system head loss estimation can be made. Pipeline fittings may be classified as branching (tees), reducing/expanding (bushes and sudden changes in flow area), or deflecting (elbows and bends).

The literature on Newtonian flow through pipe fittings is extensive and embodies experimental and theoretical studies as well as extensive tabulations of resistance coefficients and empirical correlations. For the turbulent flow of Newtonian nonsettling slurries, much information exists with pressure loss often expressed in terms of the number of equivalent pipe diameters of straight pipe giving the same pressure loss (Perry and Chilton, 1985).

Friction losses for fittings are expressed in terms of the so-called resistance coefficients K_f defined by

$$K_f = \frac{p_f}{(\rho U_m^2/2)} \tag{4.67}$$

Alternatively, the friction loss can be expressed in terms of the equivalent length of straight pipe of the same diameter and having the same friction loss as the fitting. The equivalent length is expressed in numbers of pipe diameters:

$$\frac{L_e}{D} = \frac{K_f}{4f} \tag{4.68}$$

Edwards et al. (1985) reviewed the flow of non-Newtonian slurries in laminar regimes, and they proposed that the model-specific Reynolds numbers (such as Re_b or Re_h) be used to correlate with the resistance coefficients K_f of Newtonian flows in laminar regimes.

For non-Newtonian flows in transition and turbulent regimes, Govier and Aziz (1972) proposed that the method of equivalent length be used, that is, that the equivalent length of pipe fittings for Newtonian liquids be added to computations of total length for pressure loss of the non-Newtonian slurry. Both Cheng (1970) and Turian etal. (1983) have concluded that the pressure losses of non-Newtonian flows through pipe fittings do not depend significantly on the non-Newtonian character of the slurry.

Turian et al. (1998b) carried out an experimental investigation on the friction losses of non-Newtonian slurry flows through pipe fittings and concluded that the resistance coefficients for all tested fittings approached constant asymptotic values that are the same as for the corresponding coefficients for flow of water. This means one can establish the turbulent-flow friction-loss characteristic for any pipe fitting using data with water. Then, one only need to use the density of the suspension to calculate the applicable friction loss.

4.2.4 Heterogeneous Flow of Settling Slurries

4.2.4.1 Transitional Velocities of Horizontal Pipe Flows

Although most of industrial slurries consist of small-size particles (usually up to a few tens of microns), slurries containing coarse and/or high density particles are also widely encountered in various industries. These types of slurries cannot be treated as pseudo-fluids with effective rheological properties, since the solid particles are not uniformly mixed in the horizontal plane and tend to settle at the bottom of the pipe due to the effect of gravity. Hence, they are considered as settling slurries.

Due to the settling tendency of the solids' particles, several flow regimes or patterns may be encountered in a horizontal pipe flow of settling slurries. As illustrated in Figure 4.31, slurry flows of settling slurries can be classified into flow regimes as follows: (1) heterogeneous flow—at high slurry mixture velocities, all the solids' particles are fully suspended by the carrier liquid as a result of high turbulence; (2) flow with a moving bed—at lower slurry mixture velocities, the fluid turbulence is not sufficient to balance the gravity, hence the particles accumulate at the bottom of the pipe, forming a packed bed of moving particles; (3) flow with a stationary bed—when the slurry mixture velocity is too low to move all the immersed particles, and some of them form a stationary deposit bed at the bottom of the pipe.

The flow regimes affect the dependence of the pressure drop on the flow velocity as well as the magnitude of the pressure drop and they also influence pipe erosion and other performance characteristics. Figure 4.33 shows a schematic diagram of pressure gradient dependence on mean slurry mixture velocity for various flow regimes. The straight line in this figure represents the behavior of a carrier fluid, such as water, in a

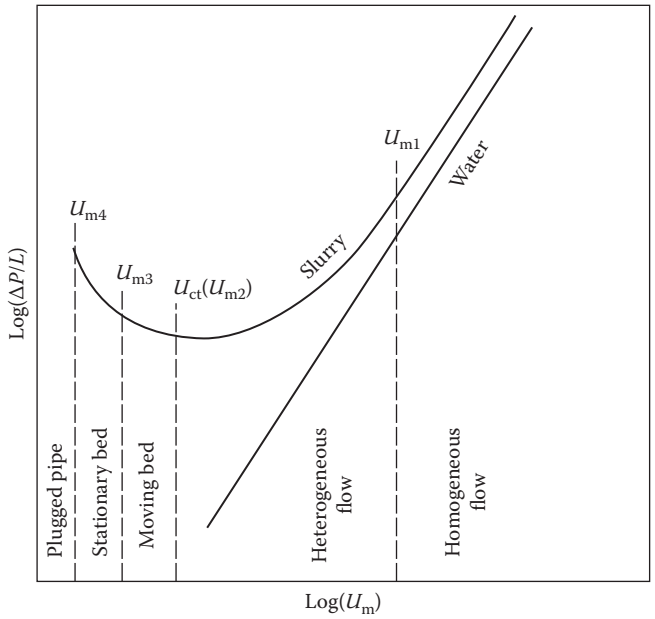


Figure 4.33

Schematic diagram of pressure gradient dependence on mean slurry velocity for various flow regimes.

given pipe size. The pressure gradient for the slurry is always higher than that of the carrier fluid at the same velocity, and the difference increases as the degree of heterogeneity increases. As the velocity decreases, the pressure gradient for slurry will decrease till reaching a minimum after which the pressure gradient will increase with a decrease in the velocity. This was first noticed by Blatch (1906).

There are four transitional velocities (Figure 4.33) between the flow regimes that are usually determined by visual observations. The transitional velocities are defined as

1. U_{m1}: velocity at or above which all solids move as a homogeneous suspension.
2. U_{m2} or U_{ct}: velocity at or above which all particles move as a heterogeneous suspension and below which the solids start to settle and form a moving bed.
3. U_{m3}: velocity at or above which the mixture flows as a heterogeneous mixture with the coarser particles forming a moving bed.
4. U_{m4}: velocity at or above which the bed in the lower half of the pipe is stationary. In the upper half of the pipe, some solids may move by saltation or suspension.

Transitional velocities U_{m3} and U_{m4} are obviously not used for the operation of slurry pipelines, and therefore, the prediction of U_{m3} and U_{m4} will not be discussed here. The transitional velocity U_{m2} or U_{ct} marks the transition to a generally undesirable condition, since deposited particles will greatly enhance erosion problems and a bed of solids promotes unstable operation. Approaches for the prediction of U_{ct} will be presented in the next section.

The determination of the transitional velocity U_{m1} from homogeneous to heterogeneous flow is required in some applications. Newitt et al. (1955) expressed the transitional velocity U_{m1} in terms of particle terminal velocity U_t as

$$U_{m1} = 38.7(gDU_t)^{1/3} \tag{4.69}$$

4.2.4.2 Critical Velocity of Horizontal Pipe Flows

The transition velocity demarcating flows in which the solid particles form a bed at the bottom of the pipe is very difficult to determine experimentally, because the flow becomes unstable near the transition velocity. The definition of transition velocities naturally depends on the definitions of the flow regimes. Therefore, various reports assign different names to the same transition velocity or the same name to different transition

velocities between the flow regimes, leading to quite confusing terminology for the transition velocities. Most of the confusion is associated with the transition from the flows with a stationary bed, since it was claimed by some investigators that it is associated with the velocity at minimal pressure gradient. However, Wasp et al. (1970) claimed that the minimum in the pressure loss versus velocity curve has nothing to do with the transition velocities.

The term *limit deposit velocity* has been employed by a number of investigators, for example, Wilson (1970) for marking the separation between the deposit and nondeposit regimes. This transition velocity is also called the *critical deposit velocity* (Kazanskij, 1979). The *deposition velocity* was used for the same purpose by Parzonka et al. (1981) and Shook and Roco (1991). The term *critical deposit velocity* was defined as the velocity below which there are deposited particles (Oroskar and Turian, 1980, Turian et al., 1987).

In the present contribution, the mean flow velocity required to prevent the accumulation of a layer of stationary or sliding particles on the bottom of a round horizontal pipe is termed as the *critical velocity*, U_{ct}. The prediction of this velocity for any given set of operational conditions is very important, since it is rarely desirable to operate with a partially blocked pipeline. Head losses would be increased by the reduced cross-sectional area and a bed layer would increase pipe wear. In fact, once a deposit forms, fluctuating flow conditions may eventually lead to blockage.

A large number of investigations have been devoted to the prediction of the critical velocity, but most of the more useful results are based primarily on empirical correlations. The approaches used for obtaining empirical correlations or theoretical expressions include the minimum in the pressure loss versus velocity relationship (e.g., Bain and Bonnington, 1970), fluctuating solids' velocity (e.g., Ercolani et al., 1979), balancing the energy required to suspend the particles with that derived from dissipation of an appropriate fraction of turbulent eddies (Oroskar and Turian, 1980), the equilibrium of forces on the first particle layer to form (Hanks and Sloan, 1981), the velocity distribution of solids near the bottom of the pipe (Roco and Shook, 1985), and chord-average solids' concentration close to the bottom of the pipe as a function of bulk velocity (Gillies et al., 2000).

It is important that values of U_{ct} are not excessively conservative (high). Excessively conservative estimates of U_{ct} will result in the high pipeline velocities, high power consumption, and high rates of wear on pipes and pumps. It is always prudent to make the actual pumping velocity some 10% higher than the calculated U_{ct} to cater for uncertainties and possible changes of future pumping conditions. In order to determine the critical velocity U_{ct} accurately, it is necessary to conduct tests with the slurry on a pipeline test rig. As a practical alternative, where this is not possible, the U_{ct} may be estimated by one of the following methods.

4.2.4.2.1 Durand's Correlation The pioneering investigations on critical velocity U_{ct} in horizontal pipelines were carried out by Durand and Condolios (1952) and Durand (1953) using water slurries of sand and gravel with narrow particle size distributions. They developed the following correlation:

$$U_{ct} = F_L\sqrt{2gD(\rho_s/\rho_l - 1)} \tag{4.70}$$

The Durand factor F_L, also known as a modified Froude number, is dependent upon solids' volume fraction α_s and particle diameter d_p. In the correlation, the Durand factor F_L was presented in the graphical form as shown in Figure 4.34.

Subsequent investigations indicated that values of F_L from Figure 4.34 provide conservative (high) values for U_{ct} in respect of

- Slurries containing mixtures of particles of different sizes
- Slurries with a sizing containing significant proportions of particles finer than 100 μm

Although predictions of critical velocities from Durand's original method have been considered conservative, the correlation and nomogram are still in wide use today due to more built-in safety against pipe blockages.

Wilson and Judge (1976) and Judge (1977) developed a sliding bed model for slurries having medium-size particles. The theoretical prediction of the Durand factor F_L can be expressed as a function of particle size d_p, pipe diameter D, and the particle drag coefficient C_D:

$$F_L = 2 + 0.3\log_{10}\left(\frac{d_p}{DC_d}\right) \tag{4.71}$$

This equation was considered to be valid in the range $10^{-5} < d_p/DC_D < 10^{-3}$.

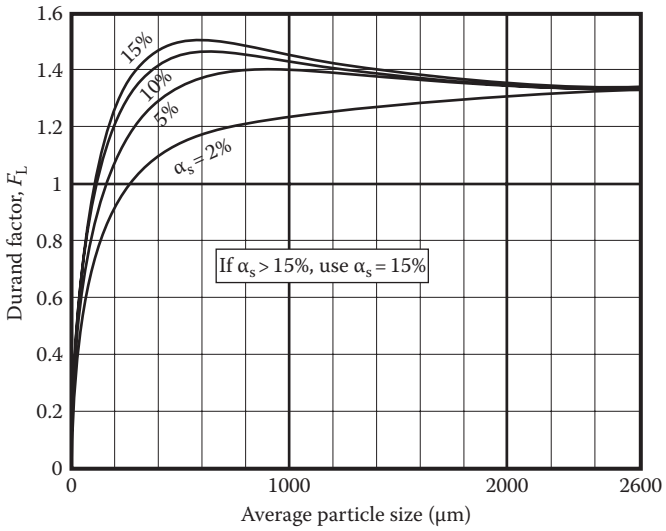


Figure 4.34

Nomogram for estimating the Durand factor F_L as a function of solids' volume fraction α_s and particle diameter d_p. (After Durand, R., Basic relationships of the transportation of solids in pipes—Experimental research, *Proceedings of Fifth Congress of International Association Hydraulic Research*, Minneapolis, MN, 1953.)

Example 4.5

A water slurry of coal (ρ_s = 1600 kg/m^3, d_{50} = 200 μm) is to be pumped in a horizontal pipe with an inner diameter of 0.3 m at the solids' volume fraction of 18%. Using the nomogram and Equation 4.71 to determine the critical velocity U_{ct} if the particle drag coefficient C_D is assumed to be 0.46.

Solution

Nomogram:

From Figure 4.34, for d_{50} = 300 μm and solids' volume fraction α_s = 18%, F_L is 1.25

$$U_{ct} = 1.25 \times \sqrt{2 \times 9.8 \times 0.3 \times (1600/1000 - 1)} = 2.35\,(\text{m/s})$$

Wilson and Judge:

From Equation 4.71, the Durand factor F_L is given by

$$F_L = 2 + 0.3 \log_{10}\left(\frac{0.2}{300 \times 0.46}\right) = 1.15$$

$$U_{ct} = 1.2 \times \sqrt{2 \times 9.8 \times 0.3 \times (1600/1000 - 1)} = 2.16\,(\text{m/s})$$

4.2.4.2.2 Wilson's Nomogram Of the numerous approaches proposed for predicting the critical velocity, Wilson's nomogram (Wilson, 1979) is one of the most notable because the approach incorporates theoretical model of sliding bed and is applicable for a wide range of particle size, pipe diameter, and fluid properties. The critical velocity increases with the delivered solids' concentration till reaching a maximum (denoted U_{cm}) and then decreases with the solids' concentration. The effects of pipe diameter, particle diameter, and relative density on the U_{cm} have been expressed concisely by means of a nomographic chart as shown in Figure 4.35 (Wilson, 1979). This nomogram provides a useful simple method for estimating the conditions where stationary deposition becomes likely.

The left-hand panel in the nomographic chart deals with sand-weight materials (relative density $S = \rho_s/\rho_l$ = 2.65). The pipe diameter appears on the left vertical axis, with U_{cm} on the central vertical axis.

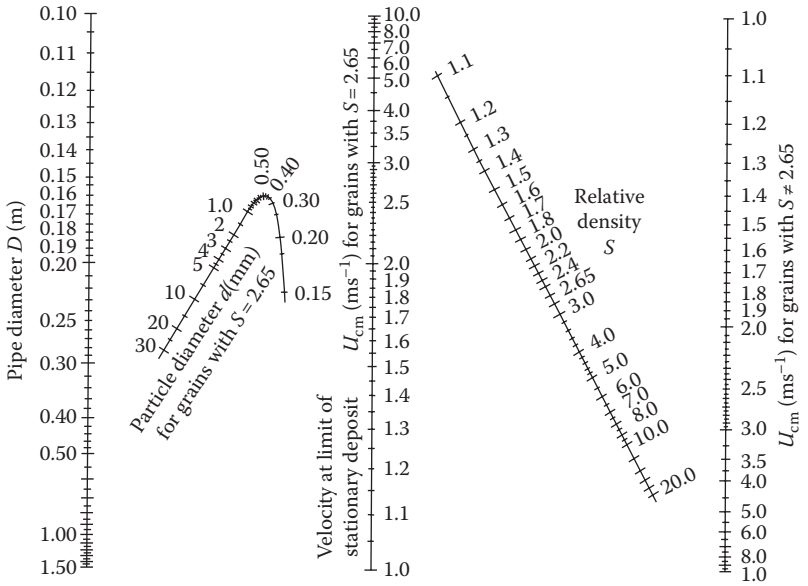


Figure 4.35

Nomogram for estimating the critical velocities. (After Wilson, K.C., Deposition limit nomograms for particles of various densities in pipeline flow, in *Proceedings Hydrotransport 6 Conference*, BHRA, Cranfield, U.K., 1979, pp. 1–12. With permission.)

The particle diameter is plotted on the curved scale. To estimate the critical velocity for particles with a relative density $S = 2.65$ in a given pipe diameter D, a line is drawn from the pipe diameter D-axis through the appropriate particle diameter on the curved scale. The critical velocity U_{cm} is then obtained by projecting to the central vertical scale. For an example, if a slurry flow in a pipe diameter of 0.4 m contains particles with a relative density $S = 2.65$, a particle size d_p of 0.7 mm gives a U_{cm} of about 4.5 m/s. For particles of other relative density values (i.e., $S \neq 2.65$), a point on the central vertical axis ($S = 2.65$) is first determined from a pipe diameter and a particle density, and then this point is joined by a straight line to an appropriate particle relative density on the inclined axis. The extrapolated line intersects with the right-hand vertical axis, giving a value of U_{cm}.

The nomogram summarized the effects of particle size and pipe diameter. According to the nomogram, a maximum critical velocity occurs near a particle diameter of 0.5 mm. However, it has been observed that (Carleton et al., 1978) the decrease in the critical velocity with the particle diameter does not always occur above about 0.5 mm particle diameter. This means that an additional safety allowance is desirable when the nomogram is used for particle sizes larger than 0.5 mm. The nomogram was generated for viscosities near one centipoise and the effect of viscosity is not included in the nomogram so that caution is required when dealing with slurries containing a significant portion of fines.

For applications with limited control of particle size, the conservative estimation of the U_{cm} may be based on the particle size that gives the largest value of U_{cm} for the pipe under consideration. In this case, it should be noted that the values of U_{cm} obtained from the nomogram tend to be conservatively high, especially for large pipe diameters, and hence can be considered to be directly suitable for use as operating velocities.

Example 4.6

Using Wilson's nomogram to determine the critical velocity U_{ct} for the same case as Example 4.5.

Solution

Draw a line from $D = 0.3$ m at D-axis through the $d_p = 0.2$ mm at the curved particle size scale. The critical velocity $U_{cm} = 2.75$ m/s was then obtained by projecting to the central vertical scale for particle density of 2.65 and then this point (i.e., $U_{cm} = 2.75$ m/s) is joined by a straight line to a $\rho_s = 1.6$ kg/m^3 on the inclined axis. The extrapolated line intersects with the right-hand vertical axis, giving a U_{cm} value of 1.55 m/s.

4.2.4.2.3 Turian's Correlations Turian's empirically fitted correlations (Turian et al., 1987) were developed based on a total collection of 864 experimental critical velocity data with pipe diameters up to 0.5 m and particle sizes up to 19 mm, representing a broad variety of solids and pertaining to wide ranges of the important variables involved. The correlations take the following form:

$$\frac{U_{ct}}{\left[2gD(S-1)\right]^{0.5}} = \chi_1 \alpha_s^{\chi_2}(1-\alpha_s)^{\chi_3}\left\{\frac{D\rho_l\left[gD(S-1)\right]^{0.5}}{\mu_l}\right\}^{\chi_4}\left(\frac{d_p}{D}\right)^{\chi_5} \tag{4.72}$$

Five different forms of this equation were developed, and the corresponding values of the adjustable constants in each case are given in Table 4.19. It should be noted that the correlations given earlier do not take in account the effect of the width of particle size distribution.

According to the *SD* and *RMS* values in Table 4.19, the correlations corresponding to all five forms are virtually equally effective in predicting the critical velocity. The parameter values also indicate that the dependence of the U_{ct} on the particle diameter is quite weak and the U_c dependence on pipe diameter is nearly $D^{0.5}$.

4.2.4.2.4 Gillies–Shook Correlation Gillies and Shook (1991) developed a correlation based on data obtained with pipes up to 0.5 m in diameter and aqueous slurries with viscosities between 0.5 and 5 centipoises. The correlation uses an equivalent fluid density defined as

$$\rho_f = \frac{\rho_s\alpha_f + \rho_l(1-\alpha_r)}{1-\alpha_r+\alpha_f} \tag{4.73}$$

where

α_r is the mean in situ total solids' concentration

α_f is defined as $\alpha_r \times$ (volume of less than 74 μm solids/total volume of solids)

The correlation for calculating the critical velocity is given by

$$\frac{U_{ct}}{\left[gD(\rho_s-\rho_f)/\rho_f\right]^{0.5}} = \exp(0.51-0.0073C_D-12.5K_2) \tag{4.74}$$

where C_D is the drag coefficient of the median diameter (d_{50}) of larger than 74 μm fraction, calculating from the density ρ_f and viscosity μ_f. The viscosity μ_f can be measured or estimated from a correlation in Table 4.16 if data are not available. K_2 is calculated by

$$K_2 = \left[\frac{(\mu_l/\rho_l)^{2/3}}{g^{1/3}d_{50}} - 0.14\right]^2 \tag{4.75}$$

4.2.4.2.5 Correlations of Wani et al. Most of the published correlations developed for the critical velocity did not sufficiently account for the breadth of particle size distribution. Wani et al. (1982) believed that the particle

Table 4.19 Parameter Values of Equation 4.72 for Five Different Cases

Case	χ_1	χ_2	χ_3	χ_4	χ_5	*SD*[a]	*RMS*[a]
1	1.7951	0.1087	0.2501	0.00179	0.06623	20.53	0.3416
2	1.08471	0.1126	0.03421	−0.03093	0	21.54	0.3447
3	1.8176	0.1086	0.2525	0	0.06486	20.57	0.3412
4	1.3213	0.1182	0.3293	0	0	21.04	0.3552
5	1.1228	0.07367	0	0	0	21.35	0.3559

[a] SD is the overall absolute average percent deviation and RMS is the root mean square deviation.

size distribution and its width are best represented by the weighted mean diameter d_w and the standard deviation σ of the particle size distribution, and they developed correlations for the critical velocity by including the variables of d_w and σ. Two of the correlations that have been reported to give better predictions are as follows:

$$U_{ct} = \left[2.3\times10^{-4} g d_w (S-1) Re_p^{0.27} \left(\frac{100\sigma}{d_w} \right)^{0.973} \alpha_s^{0.307} \varepsilon_f^{1.67} \right]^{0.5} \tag{4.76}$$

for Re_p in Stokes range (i.e., $Re_p \leq 1$) and

$$U_{ct} = \left[7.7\times10^{-6} g d_w (S-1) Re_p^{0.0014} \left(\frac{100\sigma}{d_w} \right)^{-1.25} \alpha_s^{0.272} \varepsilon_f^{4.77} \right]^{0.5} \tag{4.77}$$

for Re_p in intermediate range (i.e., $1 \leq Re_p \leq 1000$). The particle Reynolds number is given by $Re_p = d_w U_t \rho_l / \mu_l$, where U_t is the free settling velocity of the particle with a diameter of d_w. ε_f is the Hazen–Williams pipe roughness factor.

It has been reported by Wani et al. (1982) that the correlations given earlier give better predictions for slurry mixtures with multisized particles.

4.2.4.3 Pressure Loss of Horizontal Pipe Flows

In addition to the prediction of critical velocity, other important technical problems in the pipe flow of heterogeneous slurries are the determination of the pressure loss—throughput relationship and the prediction of the prevailing flow regimes. The literature contains many correlations and a few mechanistic models for prediction of pressure drop and a number of schemes for delineating slurry flow regimes. Empirical correlations for the determination of the pressure loss include those by Durand and Condolios (1952), Newitt et al (1955), Zandi and Govatos (1967), Turian and Yuen (1977), and Wasp et al. (1977). Mechanistic models are mainly represented by the two-layer model (Wilson, 1970, Gillies et al., 1991) and the three-layer model (Doron and Barnea, 1993).

Most of the correlations make use of the dimensionless excess pressure loss ϕ, which is defined as

$$\phi = \frac{i_m - i_l}{\alpha_s i_l} \quad \text{or} \quad i_m = i_l(1+\varphi\alpha_s), \tag{4.78}$$

where

i_m is slurry frictional pressure loss in terms of meters of fluid per meter of pipe
i_l is the frictional pressure loss for an equivalent volume of carrier fluid
α_s is the volumetric solids' concentration in a homogeneous slurry

For a truly homogeneous slurry flow, ϕ approaches $(S - 1)$ if the friction factor for a slurry is the same as that for a liquid flowing at the same velocity in the same pipe.

4.2.4.3.1 Zandi–Govatos Correlation for Fully Suspended Heterogeneous Flow Based on the first empirical correlation proposed by Durand and Condolios (1952) and more test data, Zandi and Govatos (1967) derived the following correlation:

$$\varphi = K\psi^{-m} \quad \text{and} \quad \psi = \frac{U_m^2 C_D^{0.5}}{gD(S-1)} \tag{4.79}$$

where $m = 0.354$ and $K = 6.3$ for $\psi > 10$ and $m = 1.93$ and $K = 280$ for $\psi < 10$. The drag coefficient C_D is that for settling of the particle at its terminal velocity U_t in the quiescent unbounded liquid. For the equivalent spherical particle of diameter d_p, C_D can be given by the following correlation (Karamanev, 1996)

$$C_D = 432(1+0.047 Ar_c^{2/3})/Ar_c + 0.517/(1+154 Ar_c^{-1/3}) \tag{4.80}$$

where

$$Ar_c = (\rho_s - \rho_l)\rho_l g d_p^3/\mu_l^2 .$$

For particles with a broad size distribution, the weighted mean drag coefficient C_{DM} for the particle mixture is better than using the median particle size (Shook, 1986). The C_{DM} is computed as

$$\frac{1}{C_{DM}} = \sum\left(\frac{\alpha_i}{C_{Di}}\right) \tag{4.81}$$

where

α_i is the volume fraction of ith size fraction with mean diameter d_i and $\sum\alpha_i = 1$
C_{Di} is the drag coefficient of ith size fraction

Although this correlation does not account sufficiently for the effect of solids' concentration, the particle size, and the nonuniform distribution of solids in the flow field, it is still useful for predicting the behavior of slurry flows compatible with these assumptions, that is, narrow particle size distribution and highly turbulent flows. From the analysis of a large number of data points, Zandi and Govatos (1967) concluded that the correlation would apply only if

$$N_I = \frac{U_m^2 C_D^{0.5}}{\alpha_s g D(S-1)} < 40 \tag{4.82}$$

Equation 4.79 does not approach the $(S - 1)$ limit as the flow is near-pseudo-homogeneous, that is, $\psi \to \infty$. Charles (1970) proposed a modified version of the correlation to rectify the deficiency:

$$\varphi = (S-1) + 120\psi^{-1.5} \tag{4.83}$$

For slurries with coarse particles or for slurries in which friction is dominated by the coarse fraction of the mixture, Zandi–Govatos correlation or its modified versions are not recommended.

Example 4.7

A slurry of sand (ρ_s = 2700 kg/m^3, d_{50} = 200 μm) in water (μ_L = 0.00112 Pa · s, ρ_L = 1000 kg/m^3) is to be pumped in a horizontal pipe of D = 0.3 m at 3.5 m/s. The solids' volume fraction is 0.18. The pipe-specific roughness is 1.5 μm. Using Equation 4.79 to determine the slurry frictional pressure loss.

Solution

$$Ar_c = (2700-1000)\times 1000 \times 9.81 \times 0.0002^3/0.00112^2 = 106.4$$

$$C_D = 432(1 + 0.047 \times 106.4^{2/3})/106.4 + 0.517/(1 + 154 \times 106.4^{-1/3}) = 8.36$$

$$\psi = 3.5^2 \times 8.36^{0.5}/(9.81 \times 0.3 \times (2.7-1)) = 7.07 < 10$$

$$\phi = 280 \times 7.07^{-1.93} = 6.4$$

Using Churchill equation (Equation 4.36), the fluid frictional pressure loss in the same pipe at the same flow velocity was found to be 0.02 m water/m pipe

$$i_m = i_l\left(1 + \phi\alpha_s\right) = 0.02 \times \left(1 + 6.4 \times 0.18\right) = 0.043\left(\text{m water/m pipe}\right)$$

4.2.4.3.2 Newitt Correlation In a frequently cited paper, Newitt et al. (1955) developed correlations for a wide range of velocities, solids' loading, and particle size in a 1 in. pipe, which covered homogeneous, fully suspended heterogeneous, and flow with a moving bed. The correlations consist of a set of criteria for defining the flow regime and a regime-specific set of equations.

For homogeneous flow, that is, $U_m > (1800gDU_t)^{1/3}$, they assumed that the friction factor for the slurry is the same as that for carrier fluid so that the difference in density is the only factor causing the difference in pressure loss, leading to

$$\phi = 0.6(S-1) \tag{4.84}$$

where the 0.6 is an empirical constant.

For fully suspended heterogeneous flow, that is, $17U_t < U_m < (1800gDU_t)^{1/3}$, it was assumed that there is no relative velocity between the particles and the fluid and that the extra energy required to transport the particles is proportional to the energy expended when the particles fall at their terminal velocity U_t. The resulting equation can be written as

$$\phi = 1100\frac{gDU_t}{U_m^3}(S-1) \tag{4.85}$$

For flow with a moving bed, that is, $U_m < 17U_t$, they assumed that the work done to overcome sliding friction between the bed and the pipe wall leads to the extra pressure loss due to the solids. The resulting expression is as follows:

$$\phi = 66\frac{gD}{U_m^2}(S-1) \tag{4.86}$$

The transition velocities, $U_H = (1800gDV_s)^{1/3}$ and $U_B = 17V_s$, can be used for delineating the three flow regimes. The boundary between homogeneous and fully suspended heterogeneous flow is obtained by equating Equations 4.84 and 4.85, and the boundary between fully suspended heterogeneous flow and flow with a moving bed is obtained by equating Equations 4.85 and 4.86.

The Newitt correlation applies only to monodispersed systems. For solids with broad size distribution, Newitt suggested a weighted mean particle diameter as

$$d_{pm} = \sum_{i=1}^{n} C_{si}d_{pi} \quad \text{and} \quad \sum_{i=1}^{n} C_{si} = 1 \tag{4.87}$$

where C_{si} is the mass fraction of solids with the particle diameter d_{pi}.

4.2.4.3.3 Model of Wasp et al. Many practical slurries contain both coarse and fine particles. The fines move as a homogeneous mixture while the coarse particles move as a heterogeneous mixture. For the analysis of this kind of compound or heterogeneous–homogeneous mixtures, Wasp et al. (1977) proposed a method based on the assumption that the total pressure loss can be split into two parts: pressure loss due to the vehicle (homogeneously distributed particles) and excess pressure drop due to the bed formation (heterogeneously distributed particles). The method is an iterative procedure, which can be summarized as follows:

1. Dividing the particles into 4–6 size fractions
2. Assuming the slurry mixture to be completely homogeneous and calculating the pressure gradient using the formula:

$$i_{vehicle} = \frac{2fU_m^2}{gD} \tag{4.88}$$

where

$i_{vehicle}$ is the pressure gradient due to homogeneously distributed particles (vehicle)
f is the friction factor evaluated by Wood's equation:

$$f = a + bRe_m^{-c} \tag{4.89}$$

where

$a = 0.026(e/D)^{0.225} + 0.133(e/D)$
$b = 22(e/D)^{0.44}$
$c = 1.62((e/D)^{0.134}$
e/D is the relative pipe roughness
Re_m is the Reynolds number for the slurry and calculated by $Re_m = \rho_m U_m D/\mu_m$

The slurry viscosity μ_m can be calculated using appropriate correlations such as those listed in Table 4.16. For higher flow velocities, the modified Wood's equation (Mukhtar, 1991) should be used for the calculation of the friction factor:

$$f = a + bRe_m^{-c}\left(1 - 0.33C_{wf}\right) \tag{4.90}$$

where C_{wf} is the efflux solids' concentration by weight.

3. For each size fraction, the percentage of solids in the vehicle is calculated as

$$\log\frac{\alpha_j}{\alpha_A} = -1.8\frac{V_s}{\beta\kappa u^*} \tag{4.91}$$

where

α_j/α_A is the ratio of volumetric concentration of jth particle size fraction at $0.08D$ from top to that at pipe axis
κ (=0.4) is vonKarman coefficient
u^* is the friction velocity calculated from the pressure loss obtained in Step 2
V_s is the settling velocity of jth particle size fraction calculated using standard drag relationships
$\beta(\approx 1)$ is the dimensionless particle diffusivity

4. The total percentage of solids in the vehicle is calculated after computing the vehicle portion for each particle size fraction and then calculating the vehicle pressure loss for slurry with this concentration using Equation 4.88.
5. Calculating the pressure loss due to the coarse particles in moving bed in each particle size fraction using Durand type of relationship given as

$$i_{jbed} = 82 i_w C_{vjbed}\left[\frac{gD(S-1)}{U_m^2 C_D^{0.5}}\right]^{1.5} \tag{4.92}$$

where

i_w is the pressure gradient due to the flow of carrier liquid
C_{vjbed} is the volumetric concentration of bed portion of jth size particles
S is the specific gravity of solids

The total pressure drop due to bed is the sum of pressure drop due to each particle size fraction in the bed:

$$i_{bed} = \sum_{j=1}^{n} j_{jbed} \tag{4.93}$$

6. Calculating the total pressure loss, which is the sum of pressure loss due to the vehicle and the total pressure loss due to the moving bed. If the difference in pressure drops in the two successive iterations is greater than 5%, repeat steps 2 to 6.

The critical factors in this model are the determination of the particle size split between the homogeneous vehicle and the heterogeneous phase, and a knowledge of the equivalent homogeneous vehicle properties (i.e., density and viscosity) as a function of particle size fraction and concentration. Experimental data would be required to evaluate these effects. Although Wasp assumed the homogeneous vehicle to behave as a Newtonian fluid, Hanks (1980) has extended this approach to account for non-Newtonian properties of the vehicle.

4.2.4.3.4 Turian–Yuan Correlation Turian and Yuan (1977) developed an extended pressure loss correlation scheme that takes into account the fact that various flow regimes are observed to prevail in slurry transport depending upon flow conditions. Their correlation is given by the following relationship:

$$f - f_L = K\alpha_s^{m1} f_L^{m2} C_D^{m3} \left[\frac{U_m^2}{Dg(S-1)} \right]^{m4} [0,1] \tag{4.94}$$

where K, $m1$, $m2$, $m3$, and $m4$ are regime-specific coefficients given in Table 4.20. In this equation, f and f_L are the friction factors for the slurry and water, respectively, at the same mean velocity. Both f and f_L are defined in terms of the carrier liquid density ρ_l. Thus,

$$f = \frac{1}{2} \frac{D}{\rho_l U_m^2} \left(-\frac{\Delta p_f}{L} \right) \tag{4.95}$$

Turian and Yuan (1977) proposed a regime delineation scheme based on their pressure loss correlation, given by Equations 4.94 and 4.95. In the scheme, maps of the various flow regimes may be drawn using the regime transition number R_{ij}, which pertains to transition between regimes i and j. The flow regime code is defined in Table 4.20. The expression for the regime transition numbers is given by the following equation:

$$R_{ij} = \frac{U_m^2}{K_t \alpha_s^{n1} f_w^{n2} C_D^{n3} gD(S-1)} \tag{4.96}$$

The coefficients in this equation are given in Table 4.21.

The transition point between flow regimes i and j is given by $R_{ij} = 1$. For a given set of conditions, the corresponding flow regime can be determined by evaluating the signs (i.e., "+" or "–") of $(R_{ij} - 1)$ and then

Table 4.20 Coefficients in Turian–Yuan Correlation of Equation 4.94

Flow Regime	Regime Code	K	$m1$	$m2$	$m3$	$m4$
Homogeneous	3	0.8444	0.5024	1.428	0.1516	−0.3531
Heterogeneous	2	0.5513	0.8687	1.200	−0.1677	−0.6938
With moving bed	1	0.9857	1.018	1.046	−0.4213	−1.354
With stationary bed	0	0.4036	0.7389	0.7717	−0.4054	−1.096

Table 4.21 Coefficients for Determining Regime Number (Equation 4.96)

Regime Number	K_t	$n1$	$n2$	$n3$
R_{01}	31.93	1.083	1.064	−0.0616
R_{02}	0.4608	−0.3225	−1.065	−0.5906
R_{03}	0.3703	0.3183	−0.8837	−0.7496
R_{12}	2.411	0.2263	−0.2334	−0.3840
R_{23}	0.2859	1.075	−0.670	−0.9375
R_{13}	1.167	0.5153	−0.3820	−0.5724

Table 4.22 Coefficients for Determining Regime Number (Equation 4.94)

$R_{01}-1$	$R_{12}-1$	$R_{23}-1$	$R_{02}-1$	$R_{03}-1$	$R_{13}-1$	Regime Code
−	−	−				0
+	−	−				1
+	+	−				2
+	+	+				3
−	−	+		−		0
−	−	+		+		3
−	+	+		−		0
−	+	+		+		3
−	+	−	−			0
−	+	−	+			2
+	−	+			−	1
+	−	+			+	3

Adapted from Turian, R.M. and Yuan, T.-F., *AIChE J.*, 23, 232, 1977. With permission.

inspect Table 4.22 to find the regime code. An example of flow regime diagram determined by this delineation procedure is shown in Figure 4.32.

4.2.4.3.5 Two-layer Model It has long been appreciated that the only satisfactory methods for predicting pressure loss for heterogeneous slurry flows in horizontal pipelines are those that take account of the flow mechanisms. In the early 1970s, Wilson (1970) developed a mechanistic model approach by introducing the concept of a two-layer model in which particles were in suspended flow in the upper layer and in which, for at least a proportion of the particles in the lower layer, solids' interaction forces at the pipe wall counterbalanced part of their buoyant weight. After undergoing progressive developments (Shook et al., 1986, Wilson, 1988, Gillies et al., 1991), this two-layer model has been set out in Shook and Roco's book (1991) in a form which is easier to follow.

In the two-layer model, heterogeneous slurry flows in a horizontal or sloping pipe are considered to consist of two layers separated by a hypothetical horizontal interface, as shown schematically in Figure 4.36. The assumptions made in this model are summarized as follows:

- The slurry flowing in a horizontal pipe comprises two hypothetical layers: an upper layer of particles less than 74 μm and a lower layer containing all particle sizes in the slurry.
- Each layer has its own uniform velocity (U_{m1}, U_{m2}) and uniform volumetric solids' concentration (α_{s1}, α_{s2}), and there is no slip between the solids and the liquid within either layer.

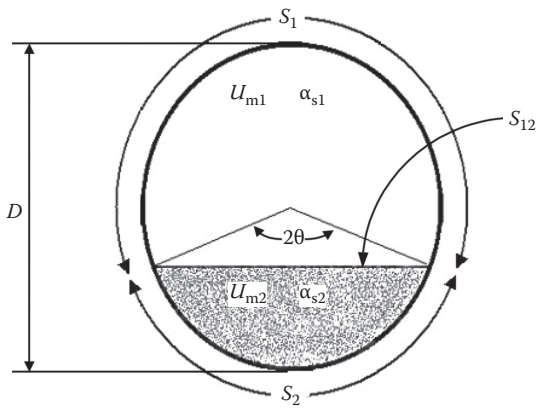


Figure 4.36

Basic concept of the two-layer model.

- The slurry mixture in the upper layer, of volumetric solids' concentration α_{s1}, behaves essentially as a liquid as far as the wall shear stress is concerned, and the wall shear stress in the upper layer is kinematic, that is, velocity dependent.
- The total solids' concentration in the lower layer α_{s2} is that of packed bed and is taken as 0.6. The solids are considered as constituting a suspended load of concentration α_{s1} and solids of concentration $\alpha_{s2} - \alpha_{s1}$ whose buoyant weight is supported at the walls as a result of interparticle contacts. This concentration, averaged over the total cross section of the pipe, is defined as the "contact load" α_c. The "contact load"α_c is given by $\alpha_c = (\alpha_{s2} - \alpha_{s1})A_2/A$.
- The particles in contact with the pipe wall in the lower layer experience a Coulombic friction force.

By referring to Figure 4.36, the total cross-sectional area of flow for the upper layer of fines and the lower layer of coarser particles is $A = A_1 + A_2$, and A_1 and A_2 are given by

$$A_1 = 0.25D^2(\pi - \theta - \sin\theta\cos\theta) \quad \text{and} \quad A_2 = 0.25D^2(\theta - \sin\theta\cos\theta) \tag{4.97}$$

The upper and lower perimeters (S_1 and S_2) and the width of interface (S_{12}) in terms of the half angle θ subtended at the center of the pipe are given by $S_1 = D(\pi - \theta)$, $S_2 = D\theta$ and $S_{12} = D \sin\theta$.

The model employs both mass and force balances. The mass balances in terms of mean delivered concentration α_s are as follows:

For the mixture:

$$U_m A = U_{m1}A_1 + U_{m2}A_2 \tag{4.98}$$

For solids:

$$\alpha_s U_m A = \alpha_{s1}U_{m1}A_1 + \alpha_{s2}U_{m2}A_2 = \alpha_{s1}U_m A + (\alpha_{s2} - \alpha_{s1})U_{m2}A_2 \tag{4.99}$$

For liquid:

$$(1 - \alpha_s)U_m A = (1 - \alpha_{s1})U_{m1}A_1 + (1 - \alpha_{s2})U_{m2}A_2 \tag{4.100}$$

For narrow particle size distribution and $Ar < 3 \times 10^5$ (Ar is the Archimedean number defined by $4gd_p^3(S-1)\rho_l^2/3\mu_l^2$, the "contact load" α_c is calculated using an empirical correlation

$$\frac{\alpha_c}{\alpha_r} = \exp\left[-0.124Ar^{-0.061}\left(\frac{U_m^2}{gd_p}\right)^{0.028}\left(\frac{d_p}{D}\right)^{-0.431}(S-1)^{-0.272}\right] \tag{4.101}$$

where $\alpha_r(=\alpha_{s1} + \alpha_c)$ is the mean in situ concentration.

The two-layer model employs momentum equations for each layer. They are written in terms of the boundary and interfacial stresses. The upper layer is considered to contribute only kinetic friction so that the momentum equation for horizontal flow is

$$i_m = \frac{(\tau_1 S_1 + \tau_{12}S_{12})}{(A_1\rho_1 g)} \tag{4.102}$$

where

i_m is the pressure gradient
τ_1 is the wall stress of upper layer
τ_{12} is the interfacial stress at hypothetical interface
S_1 is the partial perimeter of upper layer
S_{12} is the width of interface

The momentum equation for the lower layer is

$$i_m = \frac{(\tau_2 S_2 - \tau_{12} S_{12} + F_z)}{(A_2 \rho_1 g)} \tag{4.103}$$

where

τ_2 is the kinetic stress at the partial perimeter of lower layer S_2

F_z is the total force per unit length exerted normally to the surface of the pipe by the contact load solids

If the interfacial stress terms are eliminated between Equations 4.102 and 4.103 we have the force balance for the pipe as a whole:

$$i_m = \frac{(\tau_1 S_1 + \tau_2 S_2 + F_z)}{(A \rho_1 g)} \tag{4.104}$$

The boundary stress τ_1 is evaluated using the velocity and density of the upper layer:

$$\tau_1 = \frac{1}{2} f_1 U_{m1}^2 \rho_1 \tag{4.105}$$

where the friction factor f_1 is based on the Reynolds number of the liquid flowing at the mean slurry velocity U_m in the pipe, that is, $DU_m\rho_l/\mu_l$ and on the relative roughness of the pipe e/D. f_1 is calculated using the Churchill equation (Equation 4.36).

At the boundary S_2 of the lower layer, the boundary stress τ_2 is given by

$$\tau_2 = \frac{1}{2} f_1 U_{m2}^2 \rho_2 \tag{4.106}$$

where ρ_2 is the density of (liquid + suspended solids) in the lower layer.

The interface S_{12} is visualized as a boundary with a roughness depending on the diameter of particles. The interfacial stress τ_{12} is calculated from friction factor f_{12} and the difference in velocity between the layers:

$$\tau_{12} = \frac{1}{2} f_{12} (U_{m1} - U_{m2})^2 \rho_1 \tag{4.107}$$

where the interface fraction factor f_{12} is calculated using the following equation suggested by Wilson (1988):

$$f_{12} = \frac{(1 + 2Y)}{\left[4 \log(D/d_p) + 3.36\right]^2} \tag{4.108}$$

where $Y = 4 + 1.42\log(d_p/D)$ for d_p/D greater than 0.0015 and $Y = 0$ otherwise.

The term F_z in Equation 4.103 reflects the balance of forces in the vertical direction in the lower layer for the fluid, the suspended solids, and the contact load particles. The F_z can be calculated using the following equation given by Shook and Roco (1991):

$$F_z = 0.5 f_c D^2 g (\rho_s - \rho_l)(\sin\theta - \theta\cos\theta)\left[\frac{(\alpha_{s2} - \alpha_{s1})(1 - \alpha_{s2})}{1 + \alpha_{s1} - \alpha_{s2})}\right] \tag{4.109}$$

where f_c is the coefficient of Coulombic friction between the particle and the pipe wall. This coefficient depends upon the nature of the two surfaces (the particles and the substrate) and can be experimentally determined using a direct shear cell. The value of f_c is generally between 0.42 and 0.5.

The two-layer model was developed from experimental results of fairly narrow particle size distribution. For industrial slurries with broad particle size distributions, the effects of the fine particles (<74 μm) on

the viscosity and density of the carrier liquid should be taken into account (Shook and Roco, 1991). An appropriate model from Table 4.16 can be used for calculating the viscosity of slurries with fine particles. However, the slurry in the upper layer needs to be represented as a non-Newtonian fluid if the slurry contains sufficient fine particles. Shook and Roco (1991) also indicated that the two-layer model is not suitable for slurry flows with very low contact load concentration. For cases with low contact load concentrations, a homogeneous slurry flow model or correlation should be used.

It must be stressed that the existence of two distinct layers within the pipeline is a concept used simply for modeling purposes and is not of a physical reality, any more than a boundary layer formed during the flow of a fluid over a surface has a distinct identity.

Some models similar to the two-layer model have been proposed since Wilson (1970) reported the original two-layer model. Khan and Richardson (1996) proposed a simplified model that has the major features of the original two-layer model of Wilson (1970). Doron et al. (1987) developed a model with either a stationary or a moving bed at the bottom of the pipe and a heterogeneous suspension in the upper portion.

4.2.4.4 Combined Homogeneous–Heterogeneous Flows in Horizontal Pipes

In many practical systems, the solids are not all of uniform size. The combined heterogeneous–homogeneous slurry system is, therefore, the most important and most common in slurry transportation. It involves coarse and fine particles. The fines move as a homogeneous mixture while the remainder move as a heterogeneous mixture.

Condolios and Chapus (1963) suggested that the particle drag coefficient in correlations, such as Equation 4.79, is replaced by a weighted mean value (Equation 4.81) determined by the relative concentration of each particle size fraction. Newitt et al. (1955) proposed the use of a weighted average particle diameter (Equation 4.87), but Hill et al. (1986) proposed that the particles should be divided. The finer particles would move as a heterogeneous flow, while the coarser particles would move as a bed by saltation. The frictional pressure loss for each size fraction is calculated by correlations, such as Newitt Correlation (Equations 4.84 through 4.86). This approach worked well when applied to pumping water–coal mixtures (Hill et al., 1986, Wasp et al., 1977).

Wasp et al. (1977) employed the concept of a "two-phase vehicle" for the analysis of combined homogeneous–heterogeneous system. The approach is to consider that portion of the suspension existing at the top of the conduit, with its corresponding concentration and size distribution, to comprise the homogeneous vehicle uniformly distributed over the entire conduit, with the remainder of the suspension comprising the heterogeneous phase. The total friction loss is considered to be the sum of that due to the homogeneous vehicle alone, plus that due to the heterogeneous phase carried by the vehicle. Wasp et al. assumed that the vehicle could be described as a Newtonian fluid, although Hanks (1980) has extended this approach to account for non-Newtonian properties of the vehicle, assuming the vehicle behaves as a Bingham plastic. The method proposed by Wasp et al. (1977) has been summarized in Equations 4.88 through 4.93.

4.2.4.5 Vertical Pipe Flows of Slurries

It was suggested that the minimum velocity for vertical pipe flows of slurries should be twice the settling velocity of the largest particles in the flowing mixture (Govier and Aziz, 1972). This suggestion used the settling velocity to estimate the maximum possible slip and included an allowance for the effect of the variation of solids' concentration over the cross section. If the operating velocity falls below the minimum value required to fluidize the solids' high axial stresses are generated that result in a plugged line.

Although it is possible to operate at such low velocities for slurries with narrow particle size distributions, Sellgren's (1982) criterion (a factor of 6 or 7 instead of 2) seems to be a useful practical guide. If the pipeline is to have any horizontal sections, to avoid deposition in these, the velocity will be much greater than a limiting value chosen to accommodate the vertical pipe.

In a steady vertical slurry flow operated at a velocity higher than the minimum velocity, it would not be possible to develop dunes, a bed, or saltation, although redistribution of the particles can occur within the slugs as the coarse, or more dense, material settles through fine, or less dense particles. There is no concentration gradient, and the flow may be treated as pseudo-homogeneous for frictional pressure loss calculations, as discussed in Section 4.2.3.2. At low concentrations of solids (in the region of 2%–5% by volume), the frictional pressure loss at high flow rates is frequently reported to be almost indistinguishable from that of the flow of clear liquid. At higher concentrations, Einstein and Graf (1966) reported that the frictional pressure drop can be approximated by a mixture-density correction to the clear fluid frictional loss.

4.2.4.6 Inclined Slurry Pipe Flows

Inclined slurry pipe flows are important but are not the subject of extensive studies because fairly long inclined pipes are necessary to allow the disturbance produced by a bend to decay before representative measurements are made. One important issue in designing a pipeline is determining the critical slope of the pipe to avoid areas of blockage once the flow is shutdown. Due to lacking predictive approaches, the critical slope has to be experimentally determined. To avoid blockage of the pipeline due to solids' sliding back in the inclined pipeline during shutdown, it is necessary to adopt the design restriction of 10%–16% slope or 5.7°–9° inclined angle when there is no knowledge of the critical slope.

The two-layer model presented in Section 4.2.4.3 has been applied to inclined slurry pipe flows (Shook and Roco, 1991).

4.2.5 Design and Operational Aspects

4.2.5.1 Design Procedure

There are four types of practical slurry pipeline design problems: (1) determination of the net driving force required to move the given slurry through the given pipe at the given flow rate; (2) determination of the flow rate that would result for a slurry with known properties being transported through a given pipe with a specified driving force; (3) determination of the pipe diameter required to transport a slurry with known properties at a specified flow rate with a given driving force; and (4) determination of economic optimum pipe diameter at specified flow rate and slurry properties but being free to select both the driving force (e.g., the pumping power) and the pipe diameter. Only the fourth design problem will be discussed here since it is probably the most frequently used and most practical.

As the flowchart in Figure 4.37 shows, the design of a slurry transport system begins with an identification of the slurry to be conveyed, and relevant information to be collected in this step is solids' density, particle size distribution, solids' concentration, flow rate, and carrier liquid. The next important step is to determine whether the slurry can be considered as settling or nonsettling with regard to pipeline transportation. Typically, nonsettling slurry has a high solids' concentration of fine solid particles (<40 μm) of low particle density and exhibits viscous behavior. Slurries stabilized with additives and those behaving as non-Newtonian fluids are nonsettling. The remaining steps in the design procedure depend on the settling tendency of slurries because the analysis approach for settling slurries is different from those for nonsettling slurries.

4.2.5.1.1 Settling Slurries In the specification of design requirements for settling slurries, a route selection has to be carried out to determine the length of pipe sections of different orientation, the number of pipe fittings of different types, and slopes of inclined pipe sections. The major difference of route selection between no-settling and settling is the requirement that slopes be kept between 10% and 16% for settling slurries. The initial pipe diameter can be selected using Figure 4.35 based on the flow rate and top particle size. Selection of the final pipe diameter will result from an economic balance weighing such factors as initial pipe cost, pipe wear as a function of slurry velocity, solids' abrasivity, slurry corrosiveness, and projected operating costs largely in terms of system horsepower requirements.

After specifying the design requirements, the designer must choose an operating velocity. Pipelines for slurries that settle under conditions of no flow are usually operated without a deposit. The formation of a moving or stationary deposit bed is associated with unstable operating regime. Under these conditions, a small decrease in flow rate can result in increased holdup of solids that may cause a blockage if sufficient pumping capacity is not available to overcome the increase in pressure head. Prediction of the minimum carrying velocity that will sustain transport is an essential starting point from which an operating velocity can be assigned. The critical velocity discussed in Section 4.2.4.2 is the minimum carrying velocity for horizontal pipe slurry flows. This velocity can be determined by predictive models presented in Section 4.2.4.2 or through small-scale experimental tests. The practical operating velocity should be higher than the minimum carrying velocity of pipe sections with different orientations, and the offset must include an allowance for the effect of the variations of solids' concentration and particle size distribution.

The next step is to evaluate the corresponding frictional pressure loss for pipe sections of different orientations as a function of pipe diameter and operating velocity. Estimation of the pressure loss is an essential precursor to pump sizing. For heterogeneous flows of settling slurries, the estimation of the frictional pressure loss of horizontal pipe flow scan follow the predictive models described in Section 4.2.4.3. For the vertical pipe flow of settling slurries, approaches presented in Section 4.2.3.2 can be used for estimating the frictional pressure loss as vertical slurry flows can be treated as homogeneous.

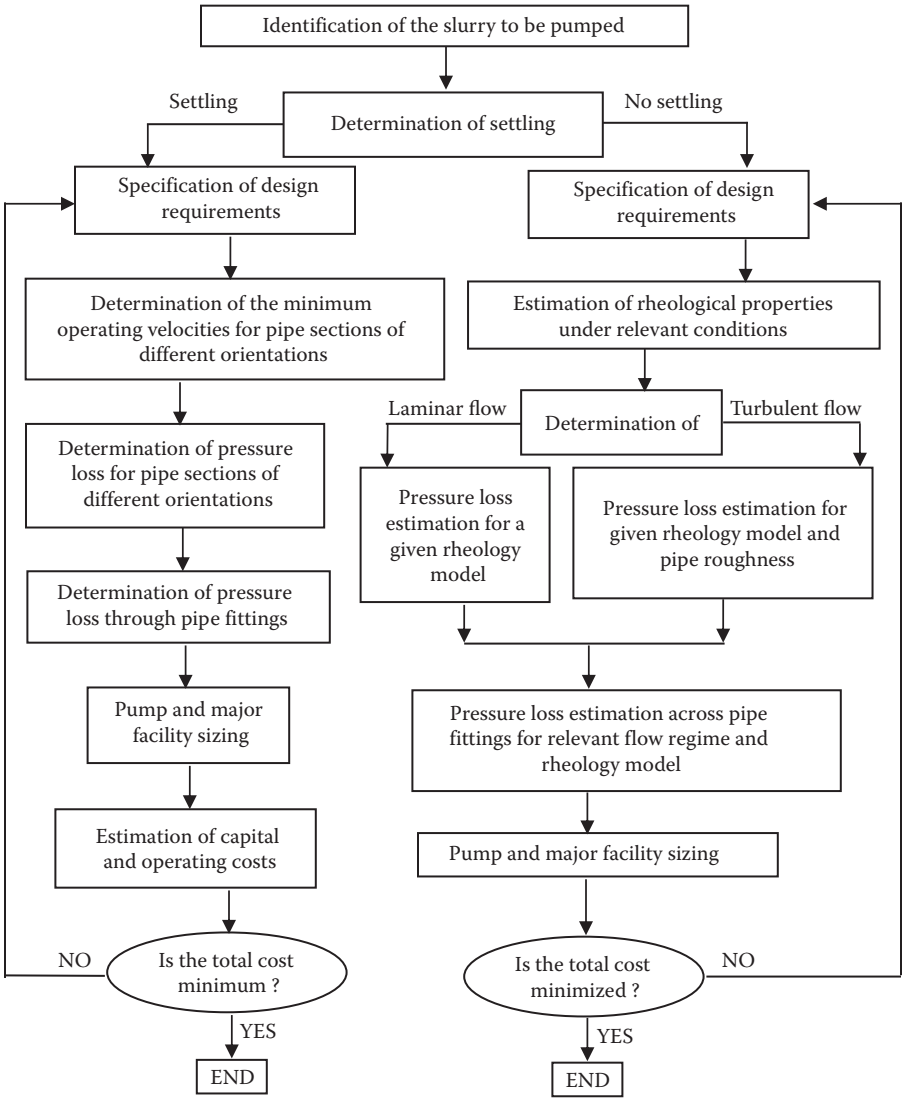


Figure 4.37

Flowchart for slurry pipeline design procedure.

Pressure losses arising from flow through pipe fittings are required before total system head loss estimation can be made. Both the resistance coefficient and the equivalent length methods discussed in Section 4.2.3.3. are suitable for estimating pressure loss from pipe fittings. The total pressure change is the sum of hydrostatic (or potentially recoverable) pressure, frictional (irrecoverable) pressure loss of straight pipe sections, and pressure loss from pipe fittings.

Pumping requirement and other major facilities sizing can then be determined from the design parameters (e.g., pipe diameter, operating flow velocity, total pressure loss, and slurry characteristics). Once proper pump and facility sizing are completed, an economic analysis of the pipeline can be carried out to estimate the capital and operating costs.

To find the design parameters that minimize the total costs of the pipeline system, the design procedure can be repeated for a few times. The optimum values of the design parameters depend on how these parameters affect the capital and running costs for the whole pipeline system and on the effects of likely changes in the operating conditions under normal operation.

4.2.5.1.2 Nonsettling Slurries In the route selection for nonsettling slurries, there is no restriction on the slopes of inclined pipe sections. For nonsettling slurries, the flow can be laminar or turbulent, as the slurry mixture will not segregate under any circumstance, and therefore, the selection of operating flow velocity and hence the pipe diameter are mainly based on the minimum total cost.

Nonsettling slurries may behave as a Newtonian or different types of non-Newtonian fluid. One of the major tasks in the pipeline design for nonsettling slurry flows is to determine an appropriate rheological model from experimental tests, including viscometric and small-scale pipe flow tests. Relevant measurement techniques for characterizing slurry properties can be found in Section 4.2.6.1.

After the determination of slurry rheological property, the next step is to determine whether the flow regime is considered as laminar or turbulent flow with regard to pipeline transportation. The identification of the transition between laminar and turbulent flow is of paramount importance because the fluid behavior and flow equations change fundamentally at this point. As described in Section 4.2.3.2.4, an estimate of the laminar–turbulent transition condition can be obtained. Although most practical operating velocities are in turbulent flow regime, laminar flow can be found in practical slurry pipelines due to high viscosity or other considerations.

Using suitable approaches as discussed in Section 4.2.3.2, the pressure loss under given flow regime, rheology model, and pipe roughness can be evaluated and then pumping requirement and other facilities selected.

The procedures outlined in this section are suitable for both preliminary and detailed design. They also provide a sensible starting point for the design of full-scale tests that are necessary if accurate design data are required. The designer of a slurry pipeline will generally start with a conceptual or preliminary design to generate sufficient data for a budget estimate of capital investment and operating costs. The difficulty in many cases is that a designer will be required to provide a preliminary design before any tests can be performed. In this case, the designer has very few options. He can try to find operating data of systems using similar materials to arrive at approximate figures for operating flow velocity, pressure drop, and pipe diameter. For a detailed design, it is important to perform laboratory tests to establish the actual slurry characteristics to be used for the pipeline under consideration.

4.2.5.2 Limitations of Predictive Models

Many different empirical correlations based on dimensional analysis have been proposed for predicting the critical velocity and pressure loss in the heterogeneous pipe flows of settling slurries, each reportedly providing an improved description of existing and/or new data. While many successful pipelines have been designed using empirical correlations, prediction outside the range of variables for which they were developed would be unsatisfactory because correlations do not consider physical processes that occur within the slurry. It is wise to check the original data. Empirical correlations could be considered as effective tools when correct correlation coefficients are obtained by experimental testing of the slurry system to be pumped.

Considerable success has been achieved in predicting the behavior of settling slurries using mechanistic approaches, such as two-layer and three-layer models. However, these models contain model parameters that require careful calibration that reduces their generality and utility for preliminary design. Therefore, the use of a model validated with similar slurry flows is recommended.

There are a number of assumptions and approximations involved in the development of predictive models for settling slurries, which provide limits to the degree of accuracy of the predictions. One assumption is that the superficial velocity in each layer is uniform in the two-layer or three-layer model. It should be evident that this assumption is adequate for model development but would contribute to the limitation. The error contained in data for the development of empirical correlation is another contribution to the limited accuracy of predictions.

Although predictive models proposed for the turbulent friction factor for non-Newtonian fluids or homogeneous slurries cover a wide range of possible combinations of properties, flow rates, pipe sizes, and so on, there are insufficient data in the literature to provide experimental confirmation of the predictions over a large portion of the range represented by these models. Therefore, caution has to be taken in applying these models to predict turbulent pipe flow behavior, especially for Bingham plastic slurries with high values of the Hedstrom numbers or power-law slurries with low values of the flow index, where the nature of turbulence is much different from that in Newtonian fluids.

The accuracy of the predictions depends not only on the quality of predictive model but also on the validity of a particular rheological model. Predictions of the turbulent friction factor for non-Newtonian fluids from models are generally very sensitive to appropriate determination of parameters of rheological models. However, parameter estimates for various rheological models contain a certain degree of uncertainty due to extrapolation outside the experimental shear rate range. This is because experimental shear rate ranges employed in viscometric measurement are rarely wide enough to cover most of the relevant shear rate range unless adequate resources are available for such work. Thus, it may be worthwhile sometimes to assess different methods of flow model parameter estimation to determine which method gives the least uncertainty in the predictions of shear stress outside the shear rate range used in viscometric tests. The proper selection of a suitable rheological model can

reduce the uncertainty in the model parameter estimation. The Sisko model has been found to be a model for which a unique set of unambiguously determined model parameter values can be obtained (Turian et al., 1992, 1997, 1998).

In lieu of the limitations of predictive models for slurry flows, the design of large-scale slurry pipeline system still demands pipeline trials to insure success, however, and is generally justified because of the costs involved. Data for industrial slurries are highly specific to the slurry mixture for which it has been measured and depends on a large number of variables including relative density of the phases, solids' concentration and particle shape, and size distribution. In addition, the chemical environment of the particles and surface charge can be particularly important to flocculation in fine-particle systems and fluid–particle and particle–wall friction in settling slurry systems.

There is no substitute for good quality experimental data. Testing in flow loops generally requires substantial quantities of slurry and experiments are often costly to execute. Small-scale testing can provide important operating velocities and frictional data. Experimental data are used to validate a predictive model or improve the parameters in the model. The validated model can then be used to scale up the small-scale pipe-flow test data.

4.2.5.3 Transient Pipe Flow Behavior

For non-Newtonian slurries with a yield stress, the start-up pressure developed by the pumping system must be more than adequate to initiate a wall shear stress along the pipeline that exceeds the yield stress. The start-up pressure, p_{st}, for pumping a Bingham plastic expressed in terms of yield stress, τ_0 is given by

$$p_{st} = \frac{4\tau_0 L}{D}. \tag{4.110}$$

It is particularly important to determine if yield stress progressively increases with time as the structure in a slurry builds up at rest. The proposed pumping system must be able to cope with the highest yield stress levels that the slurry could develop. Calculations need to be made to establish the maximum permissible shutdown period beyond which the pumping system would be unable to restart the pipeline flow.

When a velocity change occurs in a flowing slurry, some of the kinetic energy is converted into pressure energy giving an effect called *hydraulic surge*. This can be caused by valve closure or open, pump start-up or shutdown. The hydraulic surge could create pressures significantly above or below those occurring during steady conditions, leading to the risk of mechanical failure. It is prudent for the designer to include hydraulic surge considerations from the earliest stage of the design to remove the risk of failure by modifying either the design or operating conditions.

The pressure rise, Δp, caused by the velocity change, ΔU, is given by

$$\Delta p = -\rho_m \alpha_0 \Delta U, \tag{4.111}$$

where

α_0 is the pressure wave speed
ρ_m is the density of the slurry

If the fluid velocity increases then there is a pressure decrease. The pressure wave speed, α_0, in a slurry is given by (Thorley and Hwang, 1979)

$$\alpha_0 = \sqrt{\frac{1/\rho_m}{\left(\frac{1-\alpha_s}{K_L} + \frac{\alpha_s}{K_s} + \frac{D}{Ee}\right)}}, \tag{4.112}$$

where

E is Young's modulus for the pipe wall
e is the pipe wall thickness
K_L is the bulk modulus of the liquid phase
K_s is the bulk modulus of solid particles

The K_L for water is 2.06 Gpa and K_s for sand 16.0 Gpa (Bechteler and Vogel, 1981).

4.2.6 Measurement Techniques

4.2.6.1 Slurry Viscosity

The experimental determination of slurry viscosity is often required for the analysis of slurry flows. However, many existing standard viscometers for single-phase liquid, such as cone and plate, parallel plate, bob and cup, and capillary tube are not suitable for measuring the viscosity of settling slurries, as they cannot prevent the particles from settling during the measurement. Therefore, there are a number of viscometers that are potentially useful for measuring the viscosity of nonsettling slurries (Dealy, 1984, Heywood, 2000), but only few of the instruments are applicable to settling slurries (Albert et al., 1966, Ferrini et al., 1979, Akroyd and Nguyen, 2003). Basic types of viscometers suitable for measuring slurry viscosity are listed in Table 4.23. Important features of viscometers suitable for slurries include

- Fast response to changes in slurry properties.
- Knowing the shear rate at which viscosity is being measured.
- Being able to operate at different shear rates.
- Maintaining slurry in homogeneous but not promoting turbulence.

Coaxial cylinders are probably the most versatile and hence commonly used viscometers in both laboratory and online applications. The measured quantities are the angular velocity (ω) of the inner cylinder with a radius R_1 and the torque per unit height (T). The expression linking the parameters in a rheological model to the measured quantities is given by

$$\omega = \int_{\tau_2}^{\tau_1} \left(\frac{\dot{\gamma}}{2\tau} \right) d\tau, \tag{4.113}$$

where τ_1 and τ_2 are equal to $T/2\pi R_1^2$ and $T/2\pi R_2^2$, respectively, and R_2 is the radius of outer cylinder. The relationship between $\dot{\gamma}$ and τ for various rheological models can be found in Table 4.17. For a power-law slurry, the integration of Equation 4.113 gives

$$\omega = (n/2)\left(T/2\pi K_p\right)^{1/n}\left(1/R_1^{2/n} - 1/R_2^{2/n}\right). \tag{4.114}$$

By fitting the data (ω, T) to this equation, parameters (n, K_p) can be determined.

The data analysis procedure for other viscometers can be found in the references indicated in Table 4.23. Flow conditions in viscometers must be laminar as it is one of the assumptions that must be met for the calculation of viscosity. The criteria of laminar flow in coaxial cylinders are

$$R_\omega \le 45(R_m/\delta)^{0.5}, \tag{4.115}$$

where

$R_\omega = R_m \omega \delta \rho_m \mu_m$
$R_m = 0.5(R_1 + R_2)$
$\delta = (R_2 - R_1)$

4.2.6.2 Solids' Concentration

Solids' concentration is one of the major process variables in slurry flows. A number of methods have been developed for the online measurement of solids' concentration in the past. Generally, these methods seek to find a specific property that is significantly different for the solids and liquid phases. The value of this property for the mixture will then depend on the solids' concentration m and by measuring this property, one would be able to find the solids' concentration. Examples of the specific property are electrical properties (e.g., conductivity), density, absorption of light, or absorption of radioactive radiation. Measurement techniques suitable for measuring solids' concentration of slurries are listed in Table 4.24.

Table 4.23 Viscometers for Measuring Slurry Viscosity

Viscometer	Operating Principle	Advantages	Limitations
Coaxial cylinder (Shook and Roco, 1991)	Inner cylinder is rotated inside an outer cylinder at a known speed, and the resulting torque on the inner cylinder is measured	Shear rate can be varied, simple procedure for data analysis	Must be mounted vertically, not suitable for settling slurries
Helical flow in coaxial cylinder (Akroyd and Nguyen, 2003)	Rotating inner or outer cylinder with axial slurry flow in the upward or downward direction	Can handle settling slurries, shear rate can be varied	Must be mounted vertically, complex procedure for data analysis
Tube (Shook and Roco, 1991)	Pressure loss required to create the flow is measured across a suitable length of pipe at different flow rate and pipe diameter	Inexpensive, simple procedure for data analysis, shear rate can be varied by changing the diameter	Not suitable for settling slurries
Vibrating sphere (Ferry, 1977)	Immersed sphere oscillates with a controlled amplitude. The viscosity is computed from the force needed to maintain the predetermined amplitude of oscillation	Fast response time, simple installation	Requiring independent density measurement, undefined shear rate
Falling cylinder (Dealy, 1984)	A piston falling in a sample contained in a tube with a closed end. The time of fall is proportional	A wide operating range to viscosity	Not suitable for settling

Table 4.24 Measurement Techniques for Solids' Concentration of Slurries

Measurement	Operating Principle	Advantages	Limitations Technique
Nucleonic gages (Fanger et al., 1978, Brown, 1988)	Gamma rays are attenuated as they pass through matter. The attenuation is an exponential function of the path length and the density	Applicable to a wide range of slurries and large diameter pipes, high precision, and robustness	Sensitive to slurry chemical composition, radioactive nature of the sources
Conductivity (Nasr-El-in et al., 1987)	The conductivity of slurry is a function of volumetric concentration of solids	Inexpensive, simple procedure for data analysis	Sensitive to the change of carrier liquid conductivity
Electrical impedance spectrum (Hu and Firth, 2002, 2003)	The electrical impedance spectrum (EIS) of slurry is a function of volumetric concentration of solids	Applicable to slurry streams where the conductivity of the liquid phase changes with time	A large number of cases required for calibration
DP cell (Clift and Clift, 1981, Shook and Roco, 1991)	The DP over a fixed height of slurry is proportional to the slurry density through a vertical pipe with a constant dynamic head	Simple construction and operation	Not suitable to low solids' concentrations with large particle sizes and wear of the diaphragm face; requires periodic maintenance
Pipe weighing (Kachel, 1986)	Weighing an isolating section of pipe	Direct measurement	Limited pipe diameter and operating pressure
Ultrasonic reflection (Greenwood and Bamberger, 2002)	The amount of ultrasonic beam reflection at the wedge–slurry interface depends on the slurry density	Compact design	The wedge material has to have a low acoustic impedance and subject to wear

Nucleonic gauges are commonly used instrumentation for measuring solids' concentration of industrial slurries due to their high precision and robustness. The basic principle is that if a narrow collimated beam of gamma photons is passed through a slurry, the attenuation of the beam will strictly obey the relationship

$$\frac{I}{I_0} = \exp(-B_\mu \rho_m L), \tag{4.116}$$

where

I is the beam intensity after distance L
I_0 is the initial beam intensity
B_μ is the mass attenuation coefficient of the material
ρ_m is the density of the slurry over distance L

In practice, the predictable logarithmic nature of the gauge response to density means that online calibration can be readily achieved by sampling a minimum of two different densities. Major factors to be considered in their application include the following:

1. Pipes have to be full and free of air as even a small amount of air bubbles will seriously affect the estimation of solids' concentration for low-density solids such as coal.
2. Solids need to be uniformly distributed across the pipe section; hence, it is recommended that installations only be carried out on vertical pipes with upward flows.

Precise and safe measurement of electrical conductivity requires relatively simple instrumentation. Thus, methods based on conductivity have been widely used in practice for measuring solids' concentration. The electrical conductivity of a slurry depends upon the conductivity of the carrier fluid and the volume fraction of solids. For nonconductive solids, the relationship between slurry conductivity and the volume fraction is given by (Maxwell, 1881)

$$\frac{\sigma_m}{\sigma_l} = \frac{2(1-\alpha_s)}{2+\alpha_s}, \tag{4.117}$$

where σ_m and σ_l are conductivities for slurry and the carrier fluid, respectively. MacTaggart et al. (1993) have given a review on other correlations for the relationship between slurry conductivity and the volume fraction.

However, electrical conductivity–based methods are very sensitive to the variations in the electrical conductivity of the aqueous phase of slurry mixtures. When the conductivity of the liquid phase changes with time, the conductivities of both the slurry mixture and the liquid phase are required in order to calculate the solids' content. But the online measurement of the conductivity of the liquid phase in a slurry mixture is generally difficult due to the requirement of separating solids from the liquid phase. Hu and Firth (2002, 2003) developed a new technique for measuring solids' concentrations in slurries. In this technique, the electrical impedance spectrum of slurry mixtures is measured at different excitation signal amplitudes and over a wide frequency range. Changes in the frequency response reflect changes in the slurry composition and the electrical conductivity of the liquid phase. The volumetric fraction of the solids' phase can be determined by analyzing the spectra using an artificial neural network. The technique has been successfully tested for various slurries under different conductivities of liquid phase and temperatures. In contrast with previous techniques based on conductivity, this new technique can be used for the online measurement of solids' concentration in slurry streams even when the conductivity of the liquid phase changes with time.

Another simple technique for measuring solids' concentration is based on the DP over a fixed height of vertical slurry flow in a full and air-free pipe. The DP is then given by

$$\Delta p = \rho_m g h + H_d, \tag{4.118}$$

where

h is the vertical height between the two pressure sensor tappings
H_d is the dynamic head, which is the pressure drop along the pipe due to frictional hydraulic loss

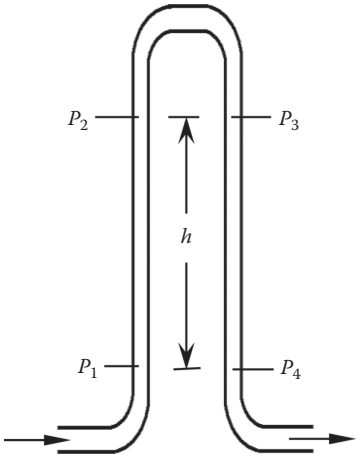


Figure 4.38

U-bend used for solids' concentration measurement.

Hence, by regulation of the flow of slurry through the pipe (such as feeding from a constant head and restricting the outlet through an orifice plate), the dynamic head should be relatively constant. By suitable calibration procedures, the pressure drop can then be related directly to the average density of the slurry.

If a vertical U-bend as shown schematically in Figure 4.38 is used, the pressure drops for the upward and downward flowing sections can be combined on the assumption that the frictional effects are the same in the two limbs of the U bend. The analysis given by Clift and Clift (1981) shows that the averaged slurry density can be obtained from

$$\rho_m = \frac{(p_1 - p_2) + (p_4 - p_3)}{2gh}. \tag{4.119}$$

4.2.6.3 Flow Rate

The measurement of flow rate is another common requirement in processes involving slurry flows. Numerous flowmeter types based on a variety of measurement principles are available. Each type has its own advantages and limitations. Typical flowmeter types for slurry flows are listed in Table 4.25. Except the Coriolis flowmeter, these flowmeters are restricted to fully filled vertical pipe flows where the slurry flow is homogeneous.

Magnetic flowmeters can be used to measure the flow rate or superficial velocity of slurries with conductive carrier liquids. Although their initial purchase price is relatively high, especially for large-diameter pipes, they are highly accurate (typically ±1.0% of full scale) and can be used with confidence without calibration with a wide range of slurries.

There are two types of ultrasonic flowmeters: Doppler and transit-time flowmeters that have been extensively used in slurry flows. Ultrasonic flowmeters have gone through many technological advances, especially in electronic circuitry and with the power of computers crunch numbers faster. Both Doppler and transit time flowmeters may use clamp-on sensors with their associated assemblies and detect flow rate from the outside of the pipe without stopping the process or cutting through the pipe. The clamp-on types of applications have considerably eased the job of the flow survey. Now users are able to ensure that old or new pump is working to its capacity, gather data for flow balancing, check if permanently installed meters are measuring incorrectly or are in need of maintenance, or simply clamp on a flowmeter where there is no flowmeter or where other flowmeter installations are impractical. Doppler ultrasonic flowmeters require the presence of reflectors, such as solids, in the flowstream so that the signal can bounce off them. Hence, they are particularly suitable for slurry flows. Transit time flowmeters send an ultrasonic signal from one side of a pipe to the other. A signal is then sent in the reverse direction. When an ultrasonic signal travels with the flow, it travels faster than when it travels against the flow. The flowmeter measures both transit times. The difference between the two transit times (across the pipe and back again) is proportional to the flow rate. Transit time flowmeters are mainly used for slurries with low solids' concentration.

Table 4.25 Flowmeters for Slurry Flows

Flowmeter	Operating Principle	Advantages	Limitations
Magnetic flowmeter (Heywood and Melita, 1988)	Creates a magnetic field within a pipe, typically using electrical coils. As electrically conductive fluid moves through the pipe, it generates a voltage. Flow rate is proportional to the amount of voltage, which is detected by electrodes	Independent of fluid rheology, density, temperature, and pressure; high accuracy and no pressure drop	Sensitive to magnetic noise from other equipment, not suitable for slurries containing ferrous particles, high initial cost, electrodes subject to coating
Ultrasonic Doppler (Sanderson and Hemp, 1981)	Calculates flow rate based on the shift in frequency observed when ultrasonic waves bounce off particles in the flow stream	Can meter dirty flows, no pressure drop, clamp-on convenience	Sensitive to the velocity profile and air bubble, sensitive to gaps between metal pipe wall and lined materials
Ultrasonic transit time (Sanderson and Hemp, 1981)	The velocity of the acoustic signal is increased when the direction of propagation is with the flow and decreased when it is against. The time difference between the two signals is used to calculate a velocity of the flow	Multiple-path model offers higher accuracy, no pressure loss, clamp-on convenience	Sensitive to variations in concentration and air bubbles, affected by flow profile, some models have high initial cost, attenuation of ultrasound by high solids' concentration.
Cross-correlation (various) (Bech and Plaskowski, 1987)	Flow rate measurement based on measuring the transit time of some kinds of disturbance such as electrical resistance between two points	Simple construction and operation	Not suitable to low solids' concentrations with fine particles
DP (Shook and Roco, 1991)	A flow restriction element (e.g., orifice plate, venturi) in the pipeline causes a pressure loss that is proportional to the density of the medium and the square of the volumetric flow rate	Low initial price, ease of installation, well understood	Creating nonrecoverable pressure loss, flow restriction element subject to wear, requires periodic maintenance, wear of the diaphragm face
Coriolis (Young, 1985)	Slurry is passed through a vibrating tube; this causes the tube to twist. Mass flow is proportional to the amount of twisting by the tube	High accuracy, low maintenance, insensitive to flow profile, pipeline pressure and temperature	High initial costs, units for larger sized pipes are restricted in pressure capability, and bent tubes subject to fouling

Cross-correlation flowmeters are based on measuring the transition time of some kinds of disturbances, such as electrical resistance between two points in a flow system (Beck et al., 1970, 1974). Schematic representation of the cross-correlation flowmeters technique is shown in Figure 4.39. In slurry flows, suspended particles in carrier fluids can lead to fluctuations in the conductivity of slurry flows due to the conductivity difference between solids and water. Two conductance sensors located at X and Y, arranged at an axial distance L in the pipe, detect conductance fluctuations as caused by the random changes of slurry phase composition. $X(t)$ and $Y(t)$ are electrical conductance signals measured at upstream (X) and downstream (Y) sensor locations. The patterns are similar in both signals but time shifted according to the traveling time of disturbances of slurry composition between the two sensor locations. With the assumption of the pipe slurry flow having the constant(bulk) velocity U_m and the fluctuation patterns being "frozen" during the flowing from location X to Y, the signal $X(t)$ detected by the first (upstream) sensor should be equal to the signal $Y(t)$ perceived by the second (downstream) sensor but delayed by the transit time τ^*:

$$X(t) = Y(t + \tau^*). \tag{4.120}$$

However, turbulent pipe flow causes the fluctuation patterns to be convected with velocities dependent on the radial position and Reynolds number and to be dispersed due to turbulent diffusion. As a consequence of these unavoidable processes, the traveling time from location X to Y of individual fluctuation event is a distribution with the transit time τ^* as the norm.

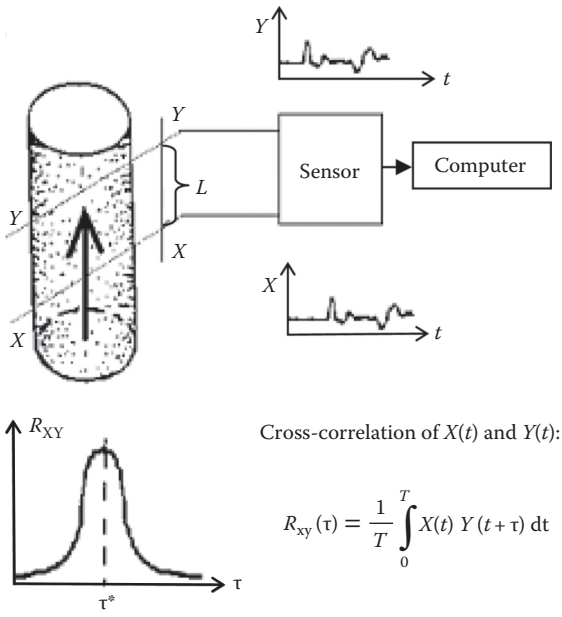


Figure 4.39

Schematic representation of cross-correlation flowmeter.

The distribution of the traveling (or delay) time can be determined from the cross-correlation function of the two signals according to stochastic process theory (Ross, 1996). The cross-correlation function, $R_{xy}(\tau)$ is given by

$$R_{xy}(\tau) = \frac{1}{T}\int_0^T X(t)Y(t+\tau)\mathrm{d}t, \tag{4.121}$$

where

T is the total sampling time

τ is the delay time of similar signal perturbations

The transition time, τ^* is taken here as the delay time τ for which the cross-correlation function has the maximum: $\tau^\star = \tau\,|_{R_{xy}(\tau)=\mathrm{MAX}(R_{xy}(\tau))}$. The mean velocity is therefore given by $U_m = L/\tau^\star$.

DP flowmeter is a less expensive, older technology that measures the flow rate based on the principle of conservation of energy between the liquid static and the velocity head. A flow constriction element (e.g., orifice plate, venturi, nozzle, and pitot) in the pipeline causes a pressure loss that is proportional to the density of the medium and the square of the volumetric flow rate. Two of the advantages of this technology are its consistency and common usage. However, its disadvantage is the permanent pressure loss due to the pipe constriction, potential for fouling, and wear of the constriction element. This type of flowmeter requires regular maintenance to prevent fouling at the constriction point.

Coriolis flowmeters are made up of one or more vibrating tubes. Slurry flows passing through a vibrating tube would cause the tube to twist. The amount of twisting motion is directly proportional to mass flow. Position detectors can sense the positions of the vibrating tubes. Temperature is constantly measured because the oscillatory properties of the tube vary with temperature. This makes it possible to make any necessary adjustments in the measurement.

While these meters are highly accurate, they are limited in terms of the pipe sizes they can efficiently be used on. While they can be used in pipes up to 6 in. in diameter, the flowmeters become expensive. The higher cost of Coriolis flowmeters is offset by normally low maintenance costs.

The selection process of flow measurement device for slurry flows should be based on application (volumetric or mass, pipe size, process temperature and pressure, fluid condition, fluid density and viscosity,

flow profile, range, and Reynolds number constraints), performance (accuracy, reliability, range, and repeatability), cost (purchase price, installation cost, cost of ownership, and maintenance cost), and supplier (flowmeter type, service requirements, training, and responsiveness) criteria in order to select a flowmeter. Reliability and accuracy are the two highest rated performance criteria by flowmeter users. Coriolis meters have the highest accuracy, followed by ultrasonic and magnetic meters. While Coriolis flowmeters typically have a higher purchase price, many users are now distinguishing between initial cost and cost of ownership. A flowmeter that offers reduced maintenance costs may be a better value than one with a lower purchase price that requires significant maintenance.

4.2.6.4 Pressure

Pressure needs to be measured in the majority of slurry handling applications. High-quality pressure transducers are readily available from specializing manufacturers, and the selection of the type of transducer and signal transmitter are not usually of prime importance in slurry flows. However, slurry applications frequently require that the sensing element contained in the transducer is isolated from the slurry in order to reduce wear and corrosion and to prevent fouling with solids. Isolation is usually achieved using an elastomeric sleeves or diaphragm seals.

4.2.6.5 Particle Size

A large number of techniques are available for off-line determination of particle size (Allen, 1981). For samples containing particles above about 1 mm, the choice of techniques is limited to screen analysis. Although wet mechanical screening can be used to analyze samples down to around 5 μm, more sophisticated automated techniques are available that can analyze to smaller particle size. Particle size analyzers based on laser diffraction (e.g., Malvern laser particle size analyzer) are widely used for the laboratory determination. These laboratory systems operate on highly dilute solutions (<5 g solids/L).

Present commercial online slurry particle size analyzers have been based on distance measurement (Miettunen et al., 1993), laser scattering (Sparks and Dobbs, 1993), laser diffraction, and ultrasound. The laser scattering technique is based on a scanning laser microscope technique in which the sample is scanned at constant speed by a high-intensity laser beam and the reflected light is measured. This analyzer has the advantage that dilution of the stream is not necessary. The online version of the Malvern laser particle size analyzer has been available. However, this analyzer has the disadvantages of high cost, sample bylines, high dilution, and sensitivity to window fouling. Particle size analyzers based on ultrasonic techniques (Reibel and Loffler, 1989, McClements, 1991, Pendse and Sharma, 1993, Dukhin and Goetz, 1996) have advantages of operating on undiluted and optically opaque slurries, rapid, precise, robust, compact, and relatively inexpensive.

References

Akroyd, T.J. and Nguyen, Q.D., Continuous rheometry for industrial slurries, *Exp. Therm. Fluid Sci.*, 27, 507–514, 2003.

Albert, C., Dierckes, J.R., and Schowalter, W.R., Helical flow of a non-newtonian polyisobutylene solution, *Ind. Eng. Chem. Fund.*, 5, 263–271, 1966.

Allen, T., 1981, *Particle Size Measurement*, 3rd edn., Chapman and Hall, London, U.K.

Bain, A.G. and Bonnington, S.T., *The Hydraulic Transport of Solids by Pipeline*, Pergamon Press, Oxford, U.K., 1970.

Bech, M.S. and Plaskowski, A., *Cross-Correlation Flowmeters—Their Design and Application*, Adam Hilger, Bristol, U.K., 1987.

Beck, M.S., Gough, J.R., and Mendies, P.J., Flow velocity measurement in a hydraulic conveyor, in *Proceedings of Hydrotransport 1 Conference*, BHRA Fluid Eng., Cranfield, U.K., Paper B3, 1970, pp. 25–53.

Beck, M.S., Mendies, P.J., Walecki, T., and Gatland, H.B., Measurement and control in hydraulic transport systems using cross-correlation measurementsystems and fluidic diverters, in *Proceedings of Hydrotransport 3 Conference*, BHRA Fluid Eng., Cranfield, U.K., paper F5, 1974, pp. 69–80.

Bechteler, W. and Vogel, G., Theoretical considerations and laboratory investigations about water hammer propagation in slurry pipelines, in *Proceedings of Slurry Transport Association 6*, Las Vegas, NV, 1981.

Bird, R.B., Dai, G.C., and Yarusso, B.L., The rheology and flow of viscoelastic materials, *Rev. Chem. Eng.*, 1, 1–70, 1982.

Bird, R.B., Stewart, W.E., and Lightfoot, E.N., *Transport Phenomena*, John Wiley, New York, 1960.

Blatch, N.S., Water filtration at Washington, DC, discussion trans., *Am. Soc. Civ. Eng.*, 57, 400–408, 1906.
Brown, N.P., An instrument to measure chord-averaged concentration profiles in two-phase pipeline flows, *J. Pipelines*, 7, 177–189, 1988.
Brown, N.P., Flow regimes of settling slurries in pipes, in Brown, N.P. and Heywood, N.L. (Eds.), *Slurry Handling Design of Solid-Liquid Systems*, Elsevier, London, U.K., 1991, pp. 41–52.
Buckingham, E., On plastic flow through capillary tubes, *ASTM Proc.*, 21, 1154, 1921.
Carleton, A.J., French, R.J., James, J.G., Broad, B.A., and Streat, M., Hydraulic transport of large particles using conventional and high concentration conveying, in *Proceedings of Hydrotransport 5 Conference*, BHRA Fluid Eng., Cranfield, U.K., paper D2, 1978, pp. 15–28.
Casson, N., A flow equation for Pigment-oil suspension of the printing ink type, in Mill, C.C. (Ed), *Rheology of Dispersed Systems*, Pergamon Press, New York, 1959, pp. 84–104.
Charles, M.E., Transport of solids by pipelines, in *Proceedings of Hydrotransport 1 Conference*, BHRA Fluid Eng., Cranfield, U.K., paper A3, 1970, pp. 25–36.
Cheng, D.C.-H., A design procedure for pipeline flow of non-Newtonian dispersed systems, in *Proceedings of Hydrotransport 1 Conference*, BHRA Fluid Eng., Cranfield, U.K., paper J5, 1970, pp. 77–96.
Churchill, S.W., Friction factor equation spans all fluid-flow regimes, *Chem. Eng.*, 84, 91–92, 1977.
Clift, R. and Clift, D.H.M., Continuous measurement of the density of flowing slurries, *Int. J. Multiphase Flow*, 75, 555–561, 1981.
Coghill, P.J., Millen, M.J., and Sowerby, B.D., On-line measurement of particle size in mineral slurries, *Minerals Eng.*, 15, 83–90, 2002.
Colebrook, C.F., Turbulent flow in pipes with particular reference to the transition region between smooth and rough pipe laws, *J. Inst. Civ. Eng.*, 11, 133–156, 1939.
Condolios, E. and Chapus, E.E., Designing solids-handling pipelines, *Chem. Eng.*, 73, 131–138, 1963.
Darby, R. and Melson, J., How to predict the friction factor for the flow of Bingham plastics, *Chem. Eng.*, 88, 59–61, 1981.
Dealy, J.M., Viscometers for on-line measurement and control, *Chem. Eng.*, 91, 62–70, 1984.
Dodge, D.W. and Metzner, A.B., Turbulent flow of non-Newtonian systems, *AIChE J.*, 5, 189–204, 1959.
Doron, P. and Barnea, D., A three-layer model for solid-liquid flow in horizontal pipes, *Int. J. Multiphase Flow*, 19, 1029–1043, 1993.
Doron, P., Granica, D., and Barnea, D., Slurry flow in horizontal pipes-experimental and modelling, *Int. J. Multiphase Flow*, 13, 535–547, 1987.
Dukhin, A.S. and Goetz, P.J., Acoustic and electroacoustic spectroscopy, *Langmuir*, 12, 4336–4344, 1996.
Durand, R., Basic relationships of the transportation of solids in pipes—Experimental research, *Proceedings of Fifth Congress of International Association Hydraulic Research*, Minneapolis, MN, 1953.
Durand, R. and Condolios, E., Experimental investigation of the transport of solidsin pipes, Paper presented at *Deuxieme Journée de l`hydraulique*, SocietéHydrotechnique de France, Paris, France, 1952.
Edwards, M.F., Jadallah, M.S.M., and Smith, R., Head losses in pipe fittings at low Reynolds numbers, *Chem. Eng. Res. Des.*, 63, 43–50, 1985.
Einstein, A., Zur Theorie der Brownschen Bewegung, *Annalen der Physik*, 19, 248–258, 1906.
Einstein, H.A. and Graf, W.H., Loop systems for measuring sand-water mixtures, *J. Hyd. Div., ASCE*, 92, HY1, paper 4608, 1–12, 1966.
Ercolani, D., Ferrini, F., and Arrigoni, V., Electric and thermic probes for measuring the limit velocity, in *Proceedings of Hydrotransport 6 Conference*, BHRA Fluid Eng., Cranfield, U.K., Paper A3, 1979, pp. 27–42.
Fanger, H.-U., Michaelis, W., Pipelnik, R., and The, H.L., Application of gammaray absorptionmetry in the hydraulic transport of solids, in *Proceedings of Hydrotransport 5 Conference*, BHRA Fluid Eng., Cranfield, U.K., paper G5, 1978, pp. 43–45.
Ferrini, F., Ercolani, D., de Cindio, B., Nicodemo, L., Nicolais, L., and Ranaudo, S., Shear viscosity of settling slurries, *Rheol. Acta*. 18, 289–296, 1979.
Ferry, I.D., Oscillation viscometry—Effects of shear rate and frequency, *Meas. Control*, 11, 89–91, 1977.
Frankel, N.A. and Acrivos, A., On the viscosity of a concentrated suspension of solid spheres, *Chem. Eng. Sci.*, 22, 847–853, 1967.
Gillies, R.G., Schaan, J., Sumner, R.J., McKibben, M.J., and Shook, C.A., Deposition velocities for newtonian slurriesin turbulent flow, *Can. J. Chem. Eng.*, 78, 704–708, 2000.
Gillies, R.G. and Shook, C.A., A deposition velocity correlation for water slurries, *Can. J. Chem. Eng.*, 69, 1225–1227, 1991.

Gillies, R.G., Shook, C.A., and Wilson, K.C., An improved two layer model for horizontal slurrypipeline flow, *Can. J. Chem. Eng.*, 69, 173–178, 1991.
Govier, G.W. and Aziz, K., *The Flow of Complex Mixtures in Pipes*, Van Nostrand Reinhold, New York, 1972.
Greenwood, M.S. and Bamberger, J.A., Ultrasonic sensor to measure the density of a liquid or slurry during pipeline transport, *Ultrasonics*, 40, 413–417, 2002.
Hanks, R.W., Low Reynolds number turbulent pipeline flow of pseudohomogeneous slurries, in *Proceedings of Hydrotransport 5 Conference*, BHRA Fluid Eng., Cranfield, U.K., paper C2, 1978, pp. 23–34.
Hanks, R.W., The influence of non-Newtonian rheology in mixed homogeneous- heterogeneous slurry flow, in *Proceedings of Fifth International Technical Conference on Slurry Transportation*, STA, Lake Tahoe, NV, 1980, p. 251.
Hanks, R.W., Laminar-turbulent transition in pipe flow of Casson model fluids, *J. Energy Resour. Tech., Trans. ASME*, 103, 318–321, 1981.
Hanks, R.W. and Ricks, B.L., Laminar-turbulent transition in flow of pseudoplastic fluids with yield stress, *J. Hydronautics*, 8, 163–166, 1974.
Hanks, R.W. and Sloan, D.G., A rheology-based correlation for minimum deposition velocity, in *Proceedings of Sixth International Conference on Slurry Transportation*, Slurry Transport Assoc., Washington, DC, 1981, pp. 107–112.
Happel, J. and Brenner, H., *Low Reynolds Number Hydrodynamics*, Prentice-Hall, Englewood Cliffs, NJ, 1965.
Herschel, W.H. and Bulkley, R., Measurement of consistency as applied to rubber-benzene solutions, *Proc. ASTM*, 26, 621–633, 1926.
Heywood, N.I., Online monitoring of slurry flows in the process industries, in *Proceedings of 10th Conference on the Transport and Sedimentation of Solid Particles*, Wroclaw, Poland, 2000, pp. 59–83.
Heywood, N.I. and Cheng, D.C-H., Comparison of methods for predicting head loss in turbulent pipeflow of non-Newtonian fluids, *Trans. Inst. Meas. Control*, 6, 33–45, 1984.
Heywood, N.I. and Melita, K., A survey of non-invasive flowmeters for pipeline flow of high concentration settling slurries, in *Proceedings of Hydrotransport 11th Conference*, BHRA, Cranfield, U.K., 1988, pp. 131–156.
Hill, R.A., Snock, P.E., and Gandhi, R.L., Hydraulic transport of solids, in Karassik, I.J., Messina, J.P., Cooper, P., and Heald, C.C. (Eds.), *The Pump Hand Book*, 2nd edn., McGraw-Hill, New York, 1986.
Hu, S. and Firth, B., Smart sensor for on-line monitoring of coal preparation processes, in *Proceedings of Ninth Australian Coal Preparation Conference*, Yeppoon, Queensland, Australia, 2002.
Hu, S. and Firth, B., Intelligent data analysis of electrical impedance spectra for on-line monitoring of industrial processes, *Fifth International Congress of Industrial and Applied Mathematics*, Sydney, New South Wales, Australia, 2003.
Irvine, T.F., A generalised Blasius equation for power fluids, *Chem. Eng. Commun.*, 65, 39–47, 1988.
Jones, M.G. and Mills, D., Product classification for pneumatic conveying, *Powder Handling Process.*, 2, 117–122, 1990.
Kachel, G.C., The slurry monitor, a new development in the precision determination of the density of slurries flowing in pipelines, Paper presented at *Symposium on Slurry Flows and Measurement—Instrumentation*, Anaheim, CA, 1986.
Karamanev, D.G., Equations for calculation of the terminal velocity and drag coefficient of solid spheres and gas bubbles, *Chem. Eng. Commun.*, 147, 75–84, 1996.
Kazanskij, I., Critical velocity of depositions for fine slurries-new results, in *Proceedings of Sixth International Conference on the Hydraulic Transport of Solids in Pipes*, Canterbury, U.K., Paper A4, 1979, pp. 43–56.
Khan, A.R. and Richardson, J.F., Comparison of coarse slurry pipeline models, in *Proceedings of Hydrotransport 13th Conference*, BHR Group, Cranfield, U.K., 1996, pp. 259–281.
Krieger, I.M., Rheology of monodisperse lattices, *Adv. Coll. Interface Sci.*, 3, 111–136, 1972.
MacTaggart, R.S., Nasr-El-Din, H.A., and Masliyah, J.H., A conductivity probe for measuring local solids concentration in a slurry mixing tank, *Sep. Technol.*, 3, 151–160, 1993.
Mainwaring, N.J. and Reed, A.R., Permeability and air retention characteristics of bulk solids material in relation to modes of dense-phase pneumatic conveyor performance. *Bulk Solids Handling*, 7, 415–425, 1987.
Mason, A., PhD thesis, Thomes Polytechnic, London, U.K., 1991.
Maxwell, J.C., *A Treatise on Electricity and Magnetism*, 2nd edn., Clarendon Press, Oxford, U.K., 1881.
McClements, D.J., Ultrasonic characterization of emulsions and suspensions, *Adv. Coll. Interface Sci.*, 37, 33–72, 1991.
Metzner, A.B. and Reed, J.C., Flow of non-Newtonian fluids—Correlation of laminar, transition and turbulent regions, *AIChE J.*, 1, 434–440, 1955.

Miettunen, J., Lahteenmaki, S., and Jamsa-Jounela, S.L., New methods for the control of autogenous grinding circuit, *XVIII International Mineral Processing Congress*, Sydney, New South Wales, Australia, 1993, pp. 301–317.
Moody, L.F., An approximate formula for pipe friction factors, *Trans. ASME*, 69, 1005–1006, 1947.
Mukhtar, A., Investigations of the flow of multisized heterogeneous slurries in straight pipe and pipe bends, PhD thesis, IIT, Delhi, India, 1991.
Nasr-El-Din, H., Shook, C.A., and Colwell, J.A., A conductivity probe for local concentration measurement in slurry flows, *Int. J. Multiphase Flow*, 13, 365–378, 1987.
Newitt, D.M., Richardson, J.F., Abbott, M., and Turtle, R.B., Hydraulic conveying of solids in horizontal pipes, *Trans. Inst. Chem. Eng.*, 33, 93–113, 1955.
Olujic, Z., Compute friction factors fast for flow in pipes, *Chem. Eng.*, 88, 91–93, 1981.
Oroskar, A.R. and Turian, R.M., The critical velocity in pipeline flow of slurries, *AIChE J.*, 26, 550–558, 1980.
Pan, R., Material properties and flow modes in pneumatic conveying, *Powder Technol.*, 104, 157–163, 1999.
Parzonka, W., Kenchington, J.M., and Charles, M.E., Hydrotransport of solids in horizontal pipes: Effects of solids concentration and particle size on the deposit velocity, *Can. J. Chem. Eng.*, 59, 291–296, 1981.
Pendse, H.P. and Sharma, A., Particle size distribution analysis of industrial colloidal slurries using ultrasonic spectroscopy, *Part. Part. Syst. Char.*, 10, 229–233, 1993.
Perry, R.H. and Chilton, C.H. (Eds.), Section 5, *Chemical Engineers' Handbook*, 6th edn., McGraw-Hill, New York, 1985.
Probstein, R.F. and Sengun, M.Z., Dense slurry rheology with application to coal slurries, *Physico-Chem. Hydrodyn. J.*, 8, 299–313, 1987.
Reibel, U. and Loffler, F., The fundamentals of particle size analysis by means of ultrasonic spectroscopy, *Part. Part. Syst. Char.*, 6, 135–143, 1989.
Roco, M.C. and Shook, C.A., Critical deposit velocity in slurry flow, *AIChE J.*, 31, 1401–1404, 1985.
Ross, S.M., *Stochastic Processes*, Wiley, New York, 1996.
Ryan, N.W. and Johnson, M.M., Transition from laminar to turbulent flow in pipes, *AIChE J.*, 5, 433–435, 1959.
Sanderson, M.L. and Hemp, J., Ultrasonic flowmeters—A review of the state of the art, in *International Conference on Advances in Flow Measurement Techniques*, BHRA, Cranfield, U.K., 1981, pp. 157–178.
Sellgren, A., The choice of operating velocity in vertical solid-water pipeline systems, in *Proceedings of Hydrotransport Eighth Conference*, BHRA, Cranfield, U.K., 1982, pp. 211–226.
Sengun, M.Z. and Probstein, R.F., High-shear-limit viscosity and the maximum packing fraction in concentrated monomodal suspensions, *Physico-Chem. Hydrodyn. J.*, 11, 229–241, 1989.
Shook, C.A., Geller, L., Gillies, R.G., Husband, W.H.W., and Small, M., Experiments with coarse particles in 250 mm pipeline, in *Proceedings of Hydrotransport 10 Conference*, BHRA Fluid Eng., Cranfield, U.K., 1986, pp. 219–227.
Shook, C.A. and Roco, M.C., *Slurry Flow: Principles and Practice*, Butterworth-Heinemann, Stoneham, MA, 1991.
Sisko, A.W., The flow of lubricating greases, *Ind. Eng. Chem.*, 50, 1789–1792, 1958.
Slatter, P.T., Thorvaldsen, G.S., and Petersen, F.W., Particle roughness turbulence, in *Proceedings of the 13th International Hydrotransport Symposium on Slurry Handling and Pipeline Transport*, Johannesburg, South Africa; BRH Group, Cranfield, U.K., 1996.
Smith, R.A., Experiments on the flow of sand-water slurries in horizontal pipes, *Trans. Inst. Chem. Eng.*, 33, 85–92, 1955.
Sparks, R.G. and Dobbs, C.L., The use of laser backscatter instrumentation for the on-line measurement of the particle size distribution of emulsions, *Part. Part. Syst. Char.*, 10, 279–289, 1993.
Szilas, A.P., Bobok, E., and Navratil, L., Determination of turbulent pressure loss of non-Newtonian oil flow in rough tubes, *Rheol. Acta*, 20, 487–96, 1981.
Takaoka, T., Hisamitsu, N., Ise, T., and Takeishi, Y., Blockage of slurry pipeline, in *Proceedings of Seventh International Conference on the Hydraulic Transport of Solids in Pipes*, Sendai, Japan, Paper B4, 1980, pp. 71–88.
Thomas, A.D. and Wilson, K.C., New analysis of non-Newtonian turbulent flow, yield power law fluids, *Can. J. Chem. Eng.*, 65, 335–338, 1987.
Thomas, D.G., Transport characteristics of suspensions, Part II, *AIChE J.*, 7, 423–430, 1961.
Thomas, D.G., Non-Newtonian suspensions, Part 2, *Ind. Eng. Chem.*, 55, 27–35, 1963.
Thomas, D.G., Transport characteristics of suspensions, Part IX, *AIChE J.*, 10, 303–308, 1964.
Thomas, D.G., Transport characteristics of suspensions: VIII. A note on the viscosity of Newtonian suspensions of uniform spherical particles, *J. Coll. Sci.*, 20, 267–277, 1965.

Thorley, A.R.D. and Hwang, L.Y., Effects of rapid change in flowrate of solid-liquid mixtures, in *Proceedings of Hydrotransport 6 Conference*, BHRA Fluid Eng., Cranfield, U.K., 1979, pp. 229–242.
Tomita, Y., On the fundamental formula of non-Newtonian flow, *Bull. JSME*, 2, 469–474, 1959.
Torrance, B.M., Friction factors for turbulent fluid flow in circular pipes, *South African Mech. Eng.*, 13, 89–91, 1963.
Turian, R.M., Hsu, F.L., Avramidis, K.S., Sung, D.J., and Allendorfer, R.K., Settling and theology of suspensions of narrow-sized coal particles, *AIChE J.*, 38, 969–987, 1992.
Turian, R.M., Hsu, F.L., and Ma, T.W., Estimation of the critical velocity in pipeline flow of slurries, *Powder Technol.*, 51, 35–47, 1987.
Turian, R.M., Hsu, F.L., and Sami Selim, M., Friction losses for flow of slurries in pipeline bends, fittings and valves, *Particul. Sci. Technol.*, 1, 365–92, 1983.
Turian, R.M., Ma, T.M., Hsu, F.L., and Sung, D.J., Characterization, settling, and rheology of concentrated fine particulate mineral slurries, *Powder Technol.*, 93, 219–233, 1997.
Turian, R.M., Ma, T.M., Hsu, F.L., and Sung, D.J., Flow of concentrated non-Newtonian slurries: 1. Friction losses in laminar, Turbulent and transition flow through straight pipe, *Int. J. Multiphase Flow*, 24, 225–242, 1998a.
Turian, R.M., Ma, T.M., Hsu, F.L., Sung, D.J., and Plackmann, G.W., Flow of concentrated non-Newtonian slurries: 2. Friction losses in bends, fittings, valves and venturi meters, *Int. J. Multiphase Flow*, 24, 243–269, 1998b.
Turian, R.M. and Yuan, T.-F., Flow of slurries in pipelines, *AIChE J.*, 23, 232–243, 1977.
Vocadlo, J.J., Role of some parameters and effective variables in turbulent slurry flow, in *Proceedings of Hydrotransport 4 Conference*, BHRA, Cranfield, U.K., Paper D4, 1976, pp. 49–62.
Von Karman, T., Mechanische Ahnlichkeit and Turbulenz, in *Proceedings of Third International Congress of Applied Mechanics*, Stockholm, Sweden, 1931, p. 85.
Wani, G.A., Sarkar, M.K., and Mani, B.P., Critical-velocity in multisized particle transportation through horizontal pipes, *J. Pipelines*, 2, 57–62, 1982.
Wasp, E.L., Kenny, J.P., and Gandhi, R.L., *Solid Liquid Flow-Slurry Pipeline Transportation*, 1st edn., Trans-Tech Publications, Clausthal, Germany, 1977.
Wasp, E.J., Aude, T.C., Kenny, J.P., Seiter, R.H., and Jacques, R.B., Deposition velocities, transition velocities and spatial distributions of solids in slurry pipelines, in *Proceedings of Hydrotransport 1 Conference*, BHRA, Cranfield, U.K., Paper H4, 1970, pp. 53–76.
Weber, M., Correlation analysis in the design of pneumatic transport plant, *Bulk Solids Handling*, 2(2), 231–233, 1982.
Wen, C.Y., Flow Characteristics in Solids-Gas Transportation Systems, US Dept. of the Interior, Bureau of Mines, PA, IC 8314, pp. 62–72, 1959.
Wicks, M., Transportation of solids of low concentrations in horizontal pipes, in Zandi, I. (Ed.), *Advances Solid-Liquid Flow in Pipes and Its Application*, Pergamon Press, New York, 1971.
Wilms, H. and Dhodapkar, S., Optimal system design, operation and control, *Chem. Eng.*, 59–67, October 2014.
Wilson, K.C., Slip point of beds in solid-liquid pipeline flow, *Proc. ASCE*, *J. Hydrol. Div.*, 96, 1–12, 1970.
Wilson, K.C., A unified physically-based analysis of solid-liquid pipeline flow, in *Proceedings of Fourth International Conference on the Hydraulic Transport of Solids in Pipes*, Banff, Alberta, Canada, Paper A1, 1976, pp. 1–16.
Wilson, K.C., Deposition limit nomograms for particles of various densities in pipeline flow, in *Proceedings Hydrotransport 6 Conference*, BHRA, Cranfield, U.K., 1979, pp. 1–12.
Wilson, K.C., Evaluation of interfacial friction for pipeline transport models, in *Proceedings of Hydrotransport 11 Conference*, BHRA Fluid Eng., Cranfield, U.K., 1988, pp. 107–116.
Wilson, K.C., Addie, G.R., Sellgren A., and Cliff, R., *Slurry Transport Using Centrifugal Pumps*, Springer Science, New York, 2006.
Wilson, K.C. and Judge, D.G., New techniques for the scale-up of pilot plant results to coal slurry pipelines, in *Proceedings of International Symposium on Freight Pipelines*, University of Pennsylvania, Washington, DC, 1976.
Wilson, K.C. and Thomas, A.D., A new analysis of the turbulent flow of non-Newtonian fluids, *Can. J. Chem. Eng.*, 63, 539–547, 1985.
Young, A.M., Coriolis-based mass flow measurement, *Sensors*, 2, 6–10, December 1985.
Zandi, I. and Govatos, G., Heterogeneous flow of solids in pipeline, *Proc. ASCE, J. Hyd. Div.*, 93, 145–159, 1967.
Zenz, F.A. and Othmer, D.F., *Fluidization and Fluid Particle Systems*, Reinhold, New York.


Taylor & Francis
Taylor & Francis Group
http://taylorandfrancis.com

5

Compressible Multiphase Flow

John D. Schwarzkopf, S. Balachandar, and William T. Buttler

5.1 Introduction
5.2 Compressible Multicomponent and Multiphase Continua
5.3 Compressible Dispersed Phase Flows
5.4 Shocked Continua Interfaces

5.1 Introduction

Compressible multiphase flows are found in several applications related to combustion, explosion, or high-speed systems. Examples are solid and liquid propellants such as those used in rocket engines, fragments from explosive devices, energy transformation such as inertial confinement fusion, and supernovae explosions, to name a few. Although the breadth and depth of this topic could produce a book by itself, the purpose of this chapter is to highlight important concepts and aspects of compressible multiphase flows.

In this chapter, we will discuss current modeling practices for multicomponent and multiphase compressible flows. The chapter is divided into three main sections: (1) compressible multicomponent and multiphase continua, (2) compressible dispersed phase flows, and (3) formation of particles from shocked surfaces. The latter section addresses the transition from continua to dispersed flows.

Multiphase compressible flows typically contain a mixing region of one or more materials; therefore, we have included a brief introduction to averaging techniques used to determine mixture properties or statistical quantities. The compressible multicomponent and multiphase continua section will begin with a brief discussion on Lagrangian techniques but will mainly focus on Eulerian techniques. The basic conservation equations for compressible multicomponent single-phase fluid mixtures are introduced, and closure models for turbulence quantities are discussed. Next, the conservation equations for multiphase multicomponent flows, commonly referred to as the two-fluid mechanical and thermal nonequilibrium model, are introduced. The continua section ends with discussions on shock interaction with material interfaces, shock jump conditions, and equations of state. The next section covers compressible dispersed phase flows. Within this section, we discuss dilute and dense particle-laden flows, Reynolds and Mach number effects, particle–shock interaction, and dispersed and carrier phase motion. The chapter is closed with a discussion on particle formation from shocked continua.

We begin this chapter by defining multicomponent, multiphase mixtures, which cover a wide spectrum of flow conditions and applications. A *component* is a chemical species such as oxygen, water, or aluminum. A *phase* refers to the solid, liquid, or vapor state of the component. The Atwood number

Table 5.1 Compressible Single and Multicomponent, Multiphase Flows

	Single Component	Multicomponent
Single phase	Shocked helium gas	Shocked air
Multiphase	Cavitation	Liquid fuel combustion

characterizes the density difference between materials (usually along an interface) and for a binary mixture it is defined as

$$At = \frac{\rho_1 - \rho_2}{\rho_1 + \rho_2}, \tag{5.1}$$

where $-1 < At < 1$ and $At = 0$ for single-phase materials. Examples of compressible single-phase and multicomponent, multiphase flows are provided in Table 5.1.

5.1.1 Averaging Techniques

Much of the current modeling practices involve averaging, which is required if the geometry is large and the mixing scales are small. In order to resolve these large differences in scales, an enormous amount of computational resources would be required. However, many engineering problems involve complex geometries and various levels of scales that should be accounted for using a modest amount of computational resources. This requirement drives the need for averaging.

Near an interface of different phase materials, averages are needed to estimate the property in a mixed region. Mixture averages usually take into account the volume fractions of the materials in the averaging process of the property.

In addition to mixture properties, turbulence may be present and depending on the model may require average properties. Turbulence can be modeled by decomposing an instantaneous property into an average and a fluctuation or deviation. In essence, there are three approaches to averaging turbulence: time, volume, and ensemble averaging. We will limit our discussion to temporal or spatial averaging and its relation to the Favre average.

5.1.1.1 Temporal Averaging

Time average is the result of averaging the flow properties over time at a point in the flow field. A point in this context is the smallest volume that would contain enough atoms to describe a continuum property (such as fluid density). However, the time average cannot distinguish between the different phases that may occupy that continuum point at different times, and therefore, its usefulness is limited to similar phase materials. The time average of some property B of the flow is defined as

$$\overline{\overline{B}} = \frac{1}{T}\int_0^T B dt, \tag{5.2}$$

where T is the total time over which B varies. Time averaging has been used extensively in single-phase flows to treat turbulent fluctuations and develop time-averaged conservation equations with additional terms, such as Reynolds stress, to account for the effects of mixing and turbulence. Obviously, the averaging time, T, must be large compared to the local fluctuation time, t', in order to define a true average value; that is, an average value that is independent of the averaging time. Also, the averaging time must be smaller than a characteristic time associated with the flow system, T', such that $t' \ll T \ll T'$. In some transient flow systems, this condition may not be realizable.

As mentioned earlier, this averaging approach is valid for multicomponent, similar phase fluids where a continuum mixture density can be used, such as air. However, for multiphase fluids, such as rain drops in air, a spatial averaging approach is used to distinguish between the phases.

5.1.1.2 Spatial Averaging

Volume averaging is carried out by averaging properties at an instant in time over a volume. For example, the *volume-averaged* property B would be defined as

$$\overline{B} = \frac{1}{V}\int_{V_A} B dV, \tag{5.3}$$

where

V is the averaging volume
V_A is the volume of fluid A

The bulk average, defined by Equation 5.3, is related to the *phase average*, by the volume fraction,

$$\overline{B} = \alpha_A \langle B \rangle, \quad \text{where } \langle B \rangle \equiv \frac{1}{V_A}\int_{V_A} B dV \tag{5.4}$$

and α_A is the volume fraction of fluid A. If B is the density of the fluid A, then $\langle \rho_A \rangle$ is the average material density of the fluid. If the density is constant, then $\langle \rho_A \rangle = \rho_A$. The constraints on the averaging volume are $\ell^3 \ll V \ll L^3$, where ℓ^3 is the local volume and L^3 is the characteristic volume associated with the flow system. This constraint is essential to approximate the spatial derivatives of $\overline{B}$ in the flow field.

A volume deviation is described as the instantaneous value at a continuum point within the volume average (of the phase of interest) that deviates from the average, such as

$$B = \langle B \rangle + B'. \tag{5.5}$$

Additional details on volume averaging can be found in Crowe et al. (2012).

5.1.1.3 Favre Averaging

Favre averaging is a method of simplifying the equations of fluid motion when variations in density are present, such as found in compressible flows. The Favre average is based on a mass-weighted ensemble average and for property B is defined as

$$\tilde{B} = \frac{\overline{\overline{\rho B}}}{\overline{\overline{\rho}}} \quad \text{or} \quad \frac{\langle \rho B \rangle}{\langle \rho \rangle}, \tag{5.6}$$

which can be formulated from a temporal or spatial decomposition. The instantaneous property B can be defined in terms of a Favre average and a deviation such as (Besnard et al., 1992)

$$B = \tilde{B} + B'' = \frac{\langle \rho B \rangle}{\langle \rho \rangle} + B' - \frac{\langle \rho' B' \rangle}{\langle \rho \rangle} = \langle B \rangle + B', \tag{5.7}$$

which is also equal to the volume average and its deviation.* Although Equation 5.7 is written in terms of a volume average, there is no loss of generality when applying the time average. The Favre deviation is then defined as (Besnard et al., 1992)

$$B'' = B' - \frac{\overline{\overline{\rho' B'}}}{\overline{\overline{\rho}}}, \quad \text{or} \quad B' - \frac{\langle \rho' B' \rangle}{\langle \rho \rangle}. \tag{5.8}$$

* This can be proved by decomposing the instantaneous properties within the Favre average into a volume average and a deviation, such as $\frac{\langle \rho B \rangle}{\langle \rho \rangle} = \frac{\langle \rho \rangle \langle B \rangle}{\langle \rho \rangle} + \frac{\langle \rho' \rangle \langle B \rangle}{\langle \rho \rangle} + \frac{\langle \rho \rangle \langle B' \rangle}{\langle \rho \rangle} + \frac{\langle \rho' B' \rangle}{\langle \rho \rangle}$, where the average of the deviations is zero, for example, $\langle \rho' \rangle = \langle B' \rangle = 0$.

If the property is velocity, then the average of the fluctuations within the Favre deviation (i.e., $\langle B'' \rangle$) can be interpreted as a mass-weighted turbulent velocity, defined as

$$a_i = \frac{\langle \rho' u_i' \rangle}{\langle \rho \rangle}, \tag{5.9}$$

and when multiplied by the average density becomes the turbulence mass flux. The Favre decomposition for velocity is then

$$\tilde{u}_i = \langle u_i \rangle + a_i \quad \text{and} \quad u_i'' = u_i' - a_i \tag{5.10}$$

where
$\langle u_i'' \rangle = -a_i$
$\langle \rho u_i'' \rangle = 0$

5.1.1.4 Mixture Properties

Average properties within a mixture, such as near the interface of different density fluids, are necessary to determine the transition of a property from one fluid to another. Average properties are needed when modeling multiphase flows in Eulerian frames of reference. In a mixed cell, the mixture density is defined as

$$\rho_m = \sum_{k=1}^{K} \alpha_k \rho_k, \tag{5.11}$$

where
α is the volume fraction
k is the material number
K is the total number of materials

This formulation has also been used for various properties such as specific heat and the ratio thereof. The harmonic average can also be used for properties such as specific heat, thermal conductivity, and sound speed. The harmonic average for the ratio of specific heats for a mixture is given as

$$\frac{1}{\gamma_m} = \sum_{k=1}^{K} \frac{\alpha_k}{\gamma_k}, \tag{5.12}$$

but any property could be substituted to obtain the mixture value. Other formulations involving mass concentration have also been used to formulate mixture averages. The mixture speed of sound proposed by Wood (1941) is of the form

$$\frac{1}{\rho c_m^2} = \sum_{k=1}^{K} \frac{\alpha_k}{\rho_k c_k^2}, \tag{5.13}$$

which can produce an average sound speed that is lower than the sound speed in either fluid. The Wood sound speed was derived for a homogeneous mixture of bubbles in a liquid. The effect of the bubbles on compressibility can significantly decrease the overall sound speed of the mixture.

For sound speed, the three averages provided in Equations 5.11 through 5.13 are shown in Figure 5.1 for a mixture of air and helium (multicomponent, single phase) and air and mercury (multicomponent, multiphase). The harmonic and Wood averages are close for moderate Atwood, $|At| \leq 0.75$, but drastically different for very high Atwood, $|At| \geq 0.9998$. Saurel et al. (2007a) also show that the mixture sound speed of water and air is very low over a large range of (air) volume fraction using the Wood model.

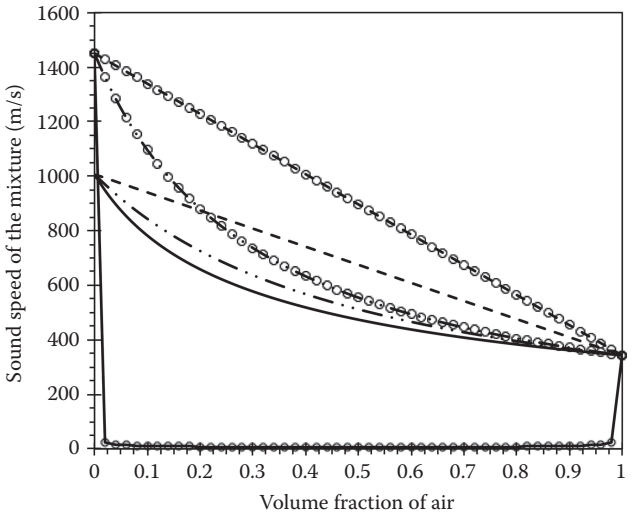


Figure 5.1

Mixture sound speed as a function of volume fraction of air. Dashed lines (Equation 5.11), dashed-double-dot lines (Equation 5.12), and solid lines (Equation 5.13) are shown for air–helium (lines only) and air–liquid mercury (circles). The Wood sound speed underpredicts the sound speed of either fluid. The sound speed of air, helium, and mercury is 343, 1007, and 1450 m/s, respectively, with their corresponding densities 1.21, 0.166, and 13, 600 kg/m^3.

5.2 Compressible Multicomponent and Multiphase Continua

There have been many recent developments in the area of modeling multiphase compressible flows. Two approaches are typically used: Lagrangian and Eulerian, both of which have pros and cons. This section will introduce the Lagrangian approach but mainly focus on the Eulerian approach.

5.2.1 Lagrangian Approach

The Lagrangian approach tracks the change in momentum and energy associated with a fixed mass throughout space and time. This approach minimizes numerical errors associated with advection in an Eulerian reference frame and is typically favored when computational resources are limited and multiphysics processes are numerous. Another benefit of using Lagrangian techniques to model multiphase compressible flows is that the interface of two materials is preserved throughout the dynamic process. Although this assumption is valid for materials containing strength (e.g., solid and gas/liquid interfaces), when the interface loses strength or when the shock is strong enough to overcome strength, instabilities can arise due to perturbations on the surface, which can lead to mixing and/or turbulence. In addition, if molecular diffusion occurs across a material interface or a material changes phase at the interface, a Lagrangian model may overpreserve the interface and constitutive models are needed to accommodate mixing or molecular diffusion at an interface.

Lagrangian codes have proven to capture shock fronts and jumps in material density, pressure, velocity, etc., reasonably well. Additional information on modeling compressible flows in a Lagrangian reference frame can be found in Noh (1987), Sambasivan et al. (2013), Lew et al. (2001), Francois et al. (2013), and for Arbitrary Lagrangian–Eulerian (ALE) methods, Yanilkin et al. (2013), and Waltz et al. (2014) and references therein.

5.2.2 Eulerian Approach

The Eulerian approach tracks mass, momentum, and energy through space and time relative to a fixed grid. With the increase in computational power over the last few decades, this approach has been used extensively to model shocked multicomponent and multiphase flows; however, more computational power is needed to capture viscous/turbulence effects across shocks in industrial applications.

Compressible multiphase and multicomponent flows can be modeled using an Eulerian approach. In the conservation equations, that is, the Euler equations, the viscous terms are neglected in comparison to the pressure terms. The development of the mass, momentum, and energy equations depends on the assumptions

associated with the problem. Because of this, multiphase/multicomponent flows are typically formulated in n-equation models. The basic equations for the instantaneous mass, momentum, and energy are

$$\text{Mass} \quad \frac{\partial}{\partial t}(\rho) + \frac{\partial}{\partial x_j}(\rho u_j) = 0, \tag{5.14}$$

$$\text{Species mass fraction} \quad \frac{\partial}{\partial t}(\rho c^k) + \frac{\partial}{\partial x_j}(\rho c^k u_j) = -\frac{\partial J_j^k}{\partial x_j}, \tag{5.15}$$

$$\text{Momentum} \quad \frac{\partial}{\partial t}(\rho u_i) + \frac{\partial}{\partial x_j}(\rho u_i u_j) = -\frac{\partial p}{\partial x_i} - \frac{\partial \tau_{ij}}{\partial x_j}, \tag{5.16}$$

$$\text{Energy} \quad \frac{\partial}{\partial t}(\rho E) + \frac{\partial}{\partial x_j}(\rho E u_j) = -\frac{\partial q_j^c}{\partial x_j} - \frac{\partial q_j^d}{\partial x_j} - \frac{\partial}{\partial x_j}(p u_j) + \frac{\partial}{\partial x_j}(u_i \tau_{ij}), \tag{5.17}$$

where

- ρ is the material density
- u_i is the velocity
- c^k is the mass fraction of species k,*
- J_j^k is the diffusive flux of mass fraction
- p is the pressure
- τ_{ij} is the viscous stress tensor
- E is the total energy ($e + u^2/2$)
- q^c is the molecular heat conduction
- q^d is the interdiffusion enthalpy flux (Cook, 2009)

In these equations, the potential energy and body forces have been neglected.

Starting with the basic equations, an averaging process can be used to interconnect fluid A and B at a material interface or describe properties across a shock in a mixture. This type of model typically assumes mechanical and thermal equilibrium in the mixture region or across the shock. For instance, if fluid A and B are gases, it is reasonable to assume that the pressure and temperature will rapidly equilibrate relative to the timescales of the shock. However, this assumption may not be valid for a gas next to a solid or liquid interface. Another type of model treats the two fluids as separate materials where the pressure, temperature, and velocity of each species are computed within a mixture region or across the shock. This type of model is typically referred to as a two-fluid model and does not assume mechanical or thermal equilibrium but requires relaxation models. Both types of models will be discussed.

5.2.2.1 Mechanical and Thermal Equilibrium

Starting with the instantaneous equations shown earlier, the instantaneous variables are decomposed into a volume average and a volume deviation to form the Favre average.† The assumption is made that the two fluids in a mixed cell are in mechanical and thermal equilibrium, which is only valid if the mechanical and thermal response times between materials are much smaller than the characteristic timescales of the flow, for example, multicomponent, single-phase flows. The resultant equations for two fluids are

$$\text{Mass} \quad \frac{\partial}{\partial t}\left(\alpha_1 \langle \rho_1 \rangle\right) + \frac{\partial}{\partial x_j}\left(\alpha_1 \langle \rho_1 \rangle \tilde{u}_j\right) = 0, \tag{5.18}$$

* We distinguish the concentration c^k from the sound speed c by the superscript k.

† There is no loss of generality in applying the temporal average instead.

$$\frac{\partial}{\partial t}\left(\alpha_2\langle\rho_2\rangle\right)+\frac{\partial}{\partial x_j}\left(\alpha_2\langle\rho_2\rangle\tilde{u}_j\right)=0, \tag{5.19}$$

$$\text{Species mass fraction}\quad \frac{\partial}{\partial t}\left(\overline{\rho}\tilde{c}^k\right)+\frac{\partial}{\partial x_j}\left(\overline{\rho}\tilde{c}^k\tilde{u}_j\right)=-\frac{\partial}{\partial x_j}\left\langle c''^k\rho u_j''\right\rangle, \tag{5.20}$$

$$\text{Momentum}\quad \frac{\partial}{\partial t}\left(\overline{\rho}\tilde{u}_i\right)+\frac{\partial}{\partial x_j}\left(\overline{\rho}\tilde{u}_i\tilde{u}_j\right)=-\frac{\partial\langle p\rangle}{\partial x_i}-\frac{\partial}{\partial x_j}\left(\overline{\rho}\tilde{R}_{ij}\right), \tag{5.21}$$

$$\text{Energy}\quad \frac{\partial}{\partial t}\left(\overline{\rho}\tilde{E}\right)+\frac{\partial}{\partial x_j}\left(\overline{\rho}\tilde{E}\tilde{u}_j\right)=-\frac{\partial}{\partial x_j}\left(\langle p\rangle\langle u_j\rangle\right)-\frac{\partial}{\partial x_j}\left(\overline{\rho}\tilde{u}_i\tilde{R}_{ij}\right)-\frac{\partial}{\partial x_j}\left\langle p'u_j'\right\rangle-\frac{\partial}{\partial x_j}\left\langle\rho E''u_j''\right\rangle, \tag{5.22}$$

where

k is the species number

$\tilde{R}_{ij}=\left\langle\rho u_i''u_j''\right\rangle/\overline{\rho}$ is the Reynolds stress

$\overline{\rho}$ is the mixture density (or ρ_m defined in Equation 5.11)

The Favre fluctuation terms are related to turbulence transport; the molecular transport and conduction terms were neglected. If we neglect the volume deviation terms, the resultant set of equations are commonly referred to as the four-equation model, where the volume fractions are related due to the saturation constraint

$$\alpha_1+\alpha_2=1. \tag{5.23}$$

Four-equation models are commonly used to model compressible flow, and the results have been compared to a large number of data and exact solutions for shocked flows. When considering the volume fraction, researchers have proposed a transport equation for the volume fraction of the form

$$\frac{\partial\alpha_1}{\partial t}+\tilde{u}_j\frac{\partial\alpha_1}{\partial x_j}=\begin{cases}0 & \text{(Allaire et al. 2002),}\\ \dfrac{\rho_2c_2^2-\rho_1c_1^2}{\dfrac{\rho_2c_2^2}{\alpha_2}+\dfrac{\rho_1c_1^2}{\alpha_1}}\dfrac{\partial\tilde{u}_j}{\partial x_j} & \text{(Saurel et al. 2007a),}\end{cases} \tag{5.24}$$

where c is the sound speed. This model is typically referred to as a five-equation model, where a closure is necessary to relate the volume fraction to pressure and/or internal energy. Allaire et al. (2002) evaluated isobaric and isothermal closure models and concluded that an isobaric model can handle interfaces between fluids without introducing spurious pressure oscillations.

The averages of the fluctuating terms shown in Equations 5.20 through 5.22 are related to turbulence and mixing. Closure models for the Favre fluctuation terms in Equations 5.20 through 5.22 were proposed by Besnard et al. (1987, 1992) and compared to DNS and experimental data for Rayleigh–Taylor (RT) (Rayleigh, 1883, Taylor, 1950), Richtmyer–Meshkov (RM) (Richtmyer, 1960, Meshkov, 1969), and shear-driven instabilities using a single set of coefficients (Schwarzkopf et al., 2011). Other researchers either varied the coefficients from one type of instability to another (Banerjee et al., 2010) or compared a single set of coefficients to a single instability (Grégoire et al., 2005). Closure models for the turbulence parameters are discussed as follows.

5.2.2.1.1 Turbulence Instabilities evolve from a strong acceleration that passes over a change in density with perturbations, such as the surface finish of an interface. Three basic instabilities that evolve into turbulence in compressible flows are as follows: (1) RT, (2) RM, and (3) Kelvin–Helmholtz

(von Helmholtz, 1868, Kelvin, 1871). RT instabilities develop from an acceleration of heavy fluid into a light fluid, such as water or SF_6 into air, with a seeded perturbation at the interface. RM instabilities develop from a shocked interface containing different density fluids on either side and a perturbation seed at the interface. When a strong shock passes across an interface having initial perturbations, the perturbations evolve into instabilities and eventually transition to turbulence. An example is shown in Figure 5.2 where Balasubramanian et al. (2013) set up a heavy gas (SF_6) curtain that is initially created by a series of jets. A Mach 1.2 shock impacts the heavy gas curtain creating RM instabilities that eventually transition to turbulence. Multiple shocks passing through an interface with different density materials

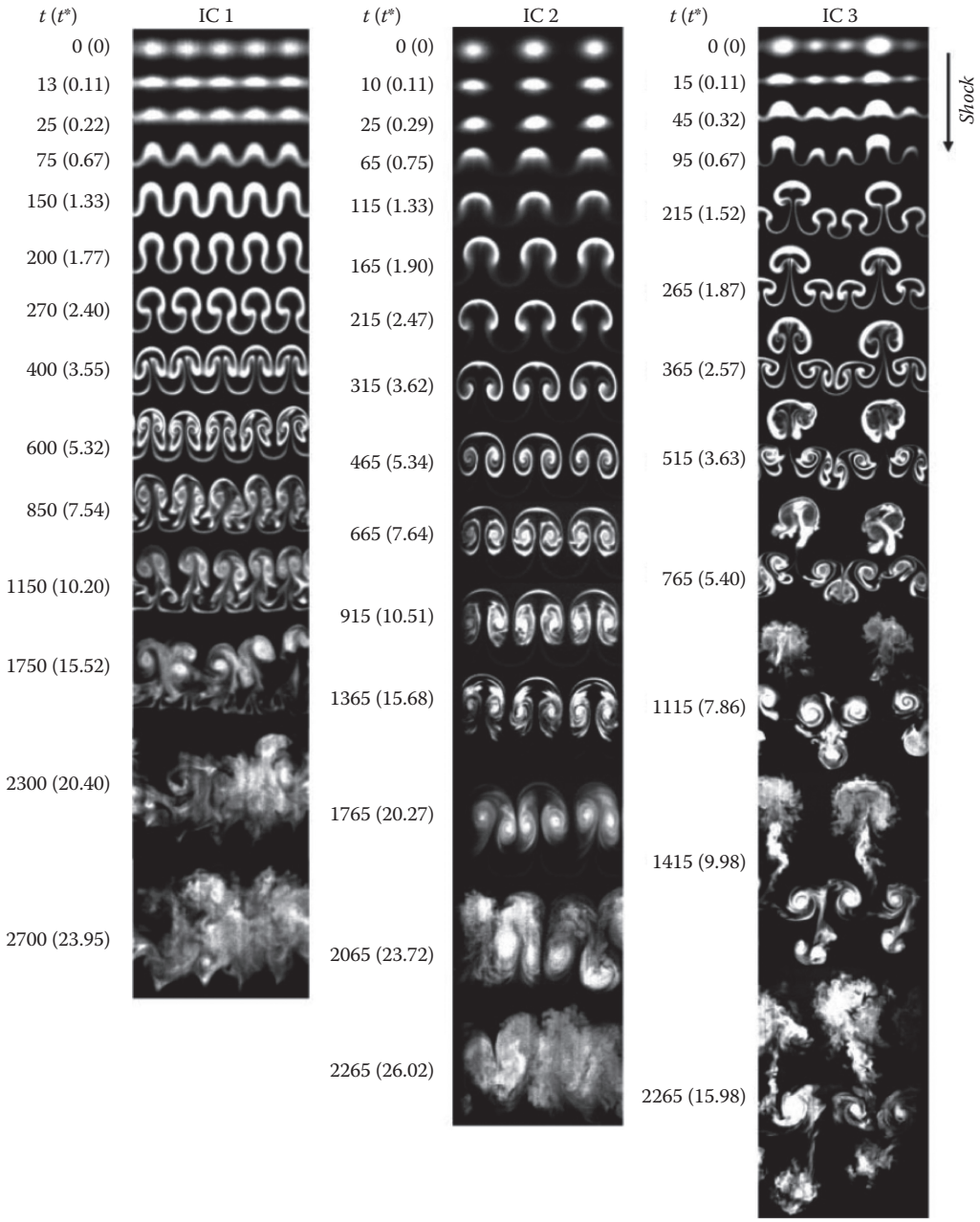


Figure 5.2

Evolution of density fields of a shocked (SF_6 [white] and air [black]) interface (curtain) for three different initial conditions: single mode and short wavelength (IC 1), single mode and long wavelength (IC 2), and multimode (IC 3). Time (t) is in microseconds, and t^* is the normalized time based on the initial linear growth. All modes show transition to turbulence without reshock. (Reprinted from Balasubramanian, B. et al., *J. Turb.*, 14, 170, 2013. With kind permission from Taylor & Francis.)

can also generate turbulence. These reshocked instabilities transition to turbulence much quicker than single shocked interfaces (Balasubramanian et al., 2012).

There are several approaches to modeling turbulence in multicomponent or multiphase compressible flows, some of which are (1) direct numerical simulation (DNS), (2) large eddy simulation (LES), and (3) Reynolds-averaged Navier–Stokes (RANS). Direct numerical and LES are 3D simulations that require large computational resources for complex geometry and multiphysics problems. The main difference between these simulation techniques is that DNS captures the turbulence energy transfer down to the Kolmogorov scale, that is, the scale at which energy is converted to heat through viscosity, whereas LES captures the large-scale effects and models the small-scale effects, which is set by a filter that is related to the grid size. The RANS approach captures the ensemble effects of turbulence without simulating the details related to the energy cascade process. These models are convenient when the 3D problem is complex and/or computational resources are limited.

The average of the Favre fluctuation terms in the species concentration equation is typically modeled as a turbulent diffusion process, such as

$$-\frac{\partial}{\partial x_j}\left\langle c''^k \rho u_j'' \right\rangle \approx C_c \frac{\partial}{\partial x_j}\left(\bar{\rho}\frac{S}{\sqrt{K}}\tilde{R}_{jn}\frac{\partial \tilde{c}^k}{\partial x_n}\right). \tag{5.25}$$

Similarly, the averages of the Favre fluctuation term in the energy equation are combined into a diffusion term

$$-\frac{\partial}{\partial x_j}\left\langle P'u_j'\right\rangle - \frac{\partial}{\partial x_j}\left\langle \rho E''u_j''\right\rangle \approx \frac{\partial}{\partial x_j}\left(\bar{\rho}\frac{S}{\sqrt{K}}\tilde{R}_{jn}\left[C_e\frac{C_v}{\mathrm{Pr_t}}\frac{\partial \tilde{T}}{\partial x_n} + C_k\frac{\partial K}{\partial x_n} + C_c\bar{h}^k\frac{\partial \tilde{c}^k}{\partial x_n}\right]\right), \tag{5.26}$$

where $\bar{h}^k$ is the enthalpy $\left(\tilde{e}^k + \frac{p^k}{\rho^k}\right)$ of species k due to species turbulence diffusion (Cook, 2009) and the sum over k is implied; $Pr_t = C_v\nu_t/k_{eff}$ is the turbulent Prandtl number; $\nu_t = C_\mu S\sqrt{K}$ is the turbulent (kinematic) viscosity;* k_{eff} is the effective thermal conductivity; C_v is the specific heat; and C_e, C_k, and C_c are calibration coefficients. The Reynolds stress is a by-product of the averaging process that results in a velocity covariance that describes the mean momentum flux caused by the fluctuating velocity components (Pope, 2000). RANS models for closing the turbulence quantities are given by Besnard et al. (1992), Grégoire et al. (2005), and Schwarzkopf et al. (2011). A transport equation for the Reynolds stress is given as

$$\begin{aligned}\frac{\partial \bar{\rho}\tilde{R}_{ij}}{\partial t} + \frac{\partial \bar{\rho}\tilde{u}_k\tilde{R}_{ij}}{\partial x_k} &= a_i\frac{\partial\langle p\rangle}{\partial x_j} + a_j\frac{\partial\langle p\rangle}{\partial x_i} - \bar{\rho}\tilde{R}_{ik}\frac{\partial \tilde{u}_j}{\partial x_k} - \bar{\rho}\tilde{R}_{jk}\frac{\partial \tilde{u}_i}{\partial x_k}\\ &+ C_r\frac{\partial}{\partial x_k}\left(\bar{\rho}\frac{S}{\sqrt{K}}\tilde{R}_{kn}\frac{\partial \tilde{R}_{ij}}{\partial x_n}\right) - C_{r3}\bar{\rho}\frac{\sqrt{K}}{S}\left(\tilde{R}_{ij} - \frac{1}{3}\delta_{ij}\tilde{R}_{kk}\right)\\ &- C_{r1}\left(a_i\frac{\partial\langle p\rangle}{\partial x_j} + a_j\frac{\partial\langle p\rangle}{\partial x_i} - \frac{2}{3}\delta_{ij}a_k\frac{\partial\langle p\rangle}{\partial x_k}\right)\\ &+ C_{r2}\bar{\rho}\left(\tilde{R}_{ik}\frac{\partial \tilde{u}_j}{\partial x_k} + \tilde{R}_{jk}\frac{\partial \tilde{u}_i}{\partial x_k} - \frac{2}{3}\delta_{ij}\tilde{R}_{mk}\frac{\partial \tilde{u}_m}{\partial x_k}\right)\\ &- \frac{2}{3}\delta_{ij}\bar{\rho}\frac{K^{3/2}}{S} - Y_{Rij},\end{aligned} \tag{5.27}$$

where

$S = K^{3/2}/\varepsilon$ is the turbulent length scale
$K = \tilde{R}_{ii}/2$ is the turbulence kinetic energy
ε is the turbulence dissipation
$a_i = \overline{\rho' u_i'}/\bar{\rho}$ is the mass-weighted turbulent velocity

* For this model, $C_\mu = 0.28$, but other values, such as 0.09, have been used with a different set of coefficients (Grégoire et al., 2005).

The pressure strain terms were modeled using the *IP* model of Naot et al. (1970) and the return to isotropy model given by Rotta (1951). Banerjee et al. (2009) studied several different pressure strain models (including modern models and the *IP* model) and compared them to experimental results of contraction and expansion flows. Overall, considering the simplicity and robustness of the *IP* model, Banerjee et al. (2009) showed it also compared reasonably well with the experimental data. The turbulent mass flux $\left(\overline{\rho}a_i\right)$ is a result of Favre averaging and the dominant form of advection in an RT instability. The model for the turbulence mass flux $\left(\overline{\rho}a_i\right)$ is

$$\frac{\partial\overline{\rho}a_i}{\partial t}+\frac{\partial\overline{\rho}\tilde{u}_j a_i}{\partial x_j}=b\frac{\partial\langle p\rangle}{\partial x_i}-\tilde{R}_{ij}\frac{\partial\overline{\rho}}{\partial x_j}+\overline{\rho}\frac{\partial a_i a_j}{\partial x_j}-\overline{\rho}a_j\frac{\partial\overline{u}_i}{\partial x_j}+\overline{\rho}C_a\frac{\partial}{\partial x_k}\left(\frac{S}{\sqrt{K}}\tilde{R}_{kn}\frac{\partial a_i}{\partial x_n}\right)-C_{a1}\overline{\rho}\frac{\sqrt{K}}{S}a_i-Y_{ai}, \tag{5.28}$$

where $b=-\overline{\rho'\upsilon'}$ is the density-specific volume covariance, which is a nonnegative measure of how well two fluids mix. For single-component and single-phase fluid and binary fluids, where the two fluids are perfectly mixed (i.e., an azeotropic fluid), $b = 0$. For the immiscible case, $b = \alpha_1\alpha_2(\rho_1 - \rho_2)^2/\rho_1\rho_2$ (Banerjee et al., 2010), and as $At \to |1|$, $b \to \infty$. A model for the density-specific volume covariance is

$$\frac{\partial\overline{\rho}b}{\partial t}+\frac{\partial\overline{\rho}\tilde{u}_j b}{\partial x_j}=-2(b+1)a_j\frac{\partial\overline{\rho}}{\partial x_j}+2\overline{\rho}a_j\frac{\partial b}{\partial x_j}+\overline{\rho}^2C_b\frac{\partial}{\partial x_i}\left(\frac{S}{\overline{\rho}\sqrt{K}}\tilde{R}_{ij}\frac{\partial b}{\partial x_j}\right)-C_{b1}\overline{\rho}\frac{\sqrt{K}}{S}b. \tag{5.29}$$

The final turbulence equation to close is the turbulent length scale. The turbulent length scale is defined as an integral length scale and is derived from combining the turbulence energy and dissipation transport equations.* The turbulent length scale model serves to transfer turbulence energy from this scale to heat. A model for the turbulence length scale is

$$\begin{aligned}\frac{\partial\overline{\rho}S}{\partial t}+\frac{\partial\overline{\rho}\tilde{u}_j S}{\partial x_j}=&-\frac{S}{K}\left(\frac{3}{2}-C_{s1}\right)\overline{\rho}\tilde{R}_{ij}\frac{\partial\tilde{u}_i}{\partial x_j}+\frac{S}{K}\left(\frac{3}{2}-C_{s3}\right)a_j\frac{\partial\langle p\rangle}{\partial x_j}-C_{s4}\overline{\rho}S\frac{\partial\overline{u}_j}{\partial x_j}\\&+C_s\frac{\partial}{\partial x_i}\left(\overline{\rho}\frac{S}{\sqrt{K}}\tilde{R}_{ij}\frac{\partial S}{\partial x_j}\right)-\left(\frac{3}{2}-C_{s2}\right)\overline{\rho}\sqrt{K}-Y_s.\end{aligned} \tag{5.30}$$

The *Y* terms at the end of Equations 5.27 through 5.30 are intended to suppress the turbulence in the presence of material strength. For multiphase problems that contain strength, Denissen and Plohr (2015) developed equations for the suppression parameters shown in the turbulence equations. The model development follows after Youngs (1997), with the idea that the material yield strength acts to suppress turbulence. These models can be applied to two-fluid mixed cells where one material in that cell contains a solid with strength. For such a mixture, the yield strength is given as

$$Y_{mix}=\alpha_1\langle Y_1\rangle+\alpha_2\langle Y_2\rangle. \tag{5.31}$$

The turbulence suppression terms due to material strength are given for binary fluid mixture as

$$Y_{Rij}=4\frac{\overline{\rho}}{|\Delta\rho|}\frac{Y_{mix}}{S}\frac{a_i a_j}{|a|}, \tag{5.32}$$

$$Y_{ai}=C_{a1}\frac{Y_{mix}}{S\sqrt{K}}a_i+2\frac{\overline{\rho}b}{|\Delta\rho|}\frac{Y_{mix}}{S|a|}a_i, \tag{5.33}$$

* Originally developed by Harlow and Steinkamp (unpublished); published details can be found in Schwarzkopf et al. (2011).

Table 5.2 Coefficients for Equations 5.25 through 5.30

C_a	C_{a1}	C_b	C_{b1}	C_c	C_r	C_e	C_k	C_{r1}	C_{r2}	C_{r3}	C_s	C_{s1}	C_{s2}	C_{s3}	C_{s4}
0.3	3.2	0.3	2.0	0.56	0.42	1.0	1.0	0.3	0.6	1.8	4.2	1.2	1.92	1.2	−1.2

$$Y_s = 2\frac{\bar{\rho}}{|\Delta\rho|}\frac{Y_{mix}}{K}|a|, \tag{5.34}$$

where $|a|$ is the magnitude of a_i.* Additional terms were included in Denissen and Plohr's model, but the coefficients were set to zero and therefore omitted in the equations mentioned earlier. For multicomponent, single-phase gas or liquid compressible flows, $Y_{mix} = 0$.

The coefficients for the turbulence model mentioned earlier, Equations 5.25 through 5.30, were tuned using variable density turbulence gas mixing, $|At| \leq 0.5$. A single set of coefficients (given in Table 5.2) were found from turbulence generated by RT and single-phase shear-driven instabilities using DNS and experiments.

Poggi et al. (1998) conducted shock tube experiments and was one of the first few to measure turbulence quantities in a turbulent compressible mixing layer produced by reshocked RM instabilities containing air and SF_6 gases, $|At| = 0.67$. The two gases were initially separated by a thin membrane that also served to seed perturbations. Schwarzkopf et al. (2011) used the previous equations and the coefficients found from RT and shear-driven turbulence (given in Table 5.2) to model Poggi's experiment. The turbulence equations were implemented in a compressible Eulerian hydrocode RAGE (Gittings et al., 2008), which uses a Godunov scheme to solve the mass, momentum, and energy equations, while the turbulence equations were solved using traditional finite volume methods. The experiment of Poggi et al. (1998) was simulated in 1D. The Reynolds stress $\left(\tilde{R}_{ij}\right)$ was initialized as isotropic along the diagonal components ($2K/3$, where K was estimated to be ~1% of the mean kinetic energy) and zero for the off-diagonals, and the length scale (S) initialized to the wavelength of the perturbations (~1 mm). The turbulence mass flux (a_i) was initialized to zero, and the specific volume covariance (b) was initialized as the two-fluid immiscible value, for example, $b = \alpha_1\alpha_2(\rho_1 - \rho_2)^2/(\rho_1\rho_2)$. Overall, considering that the majority of the coefficients were not tuned for this type of compressible flow, reasonable agreement was found for the velocity profile, Reynolds stress components,† and mix widths, shown in Figure 5.3.

This model was also applied to shock impacting an inverse chevron interface with multicomponent fluids. The shape of the chevron and turbulent quantities was compared before and after reshock to ILES simulations and experimental data (Haines et al., 2013). Overall, reasonable agreement was also found.

5.2.2.2 Mechanical and Thermal Nonequilibrium

Next, we consider a system of equations for two-fluid compressible flow where the mechanical and thermal equilibrium assumption is relaxed. Kapila et al. (2001) extended the work of Baer and Nunziato (1986) and developed a seven-equation model with additional terms that are dependent on interfacial effects, and they recognized that the pressure, velocity, and temperature fields can be different for the two fluids. This model was specifically developed around a solid–gas mixture of interacting continua for a porous explosive and includes mass, momentum, and energy transfer effects between the two species. Saurel et al. (2007a) applied a different form of this model to two-phase mixtures. The effects include nonequilibrium interactions between the phases due to interfacial drag, heat transfer, chemical reaction, and compaction. Each of these processes has characteristic length and timescales that can be used to determine if a two-fluid model is necessary, that is, if the velocity of each species rapidly relaxes to a mixture velocity, carrying around two equations for the velocity of each species in a computation is unnecessary.

* A realizability condition such as $0 \leq \bar{\rho}a_i a_j \leq bR_{ij} \leq 1$ should be considered in Equation 5.32. Caution is required to ensure that Equations 5.32 through 5.34 do not become production terms in Equations 5.27 through 5.30.

† The Reynolds-averaged Reynolds stress was compared, and it is related to the Favre average by $\overline{u_i'u_j'} = \tilde{R}_{ij} + a_i a_j - \frac{\overline{\rho' u_i' u_j'}}{\bar{\rho}}$, where the last term is typically negligible compared to the first two terms on the right-hand side.

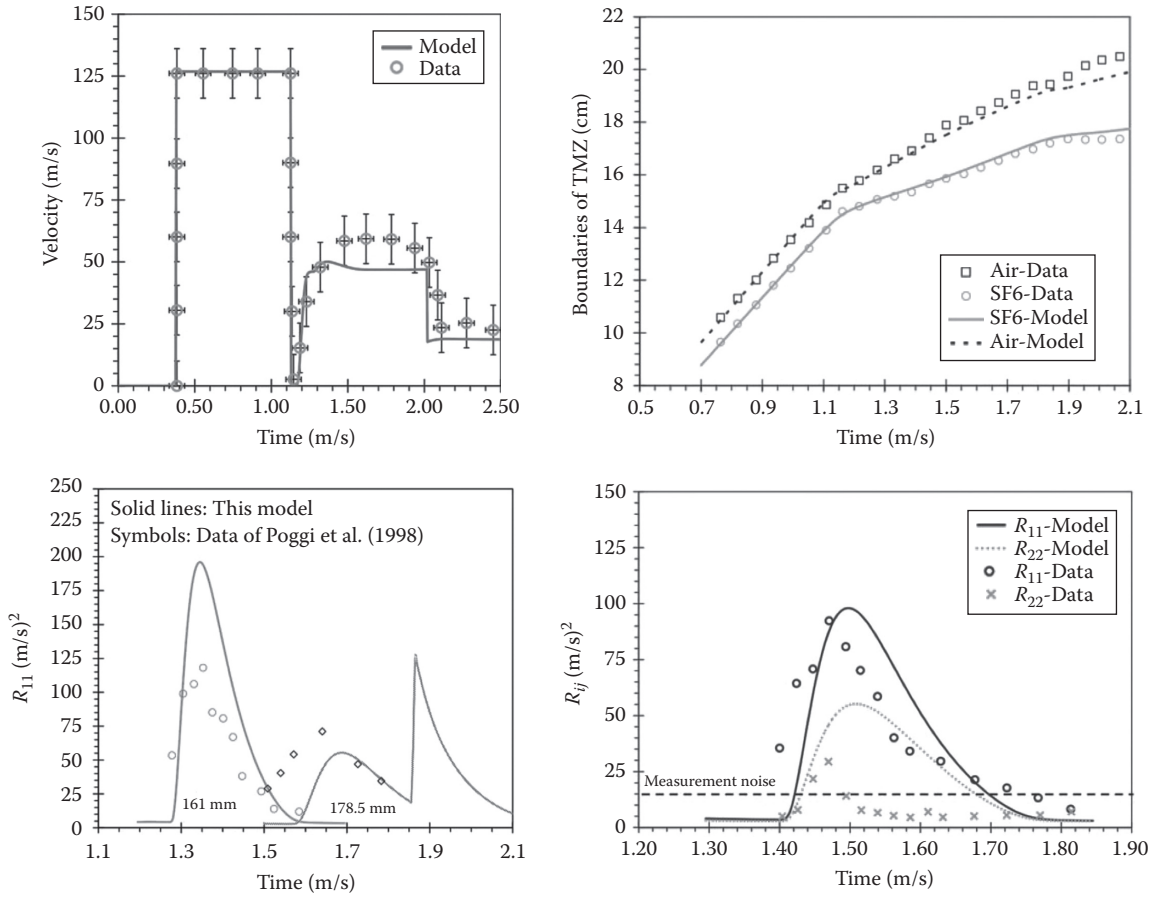


Figure 5.3

Comparison of the velocity, turbulence mixing zone thickness, and Reynolds stresses. Symbols (measurements from shock tube experimental data, Poggi et al. (1998)) and lines (model described by Equations 5.20 through 5.22 and 5.25 through 5.30) show reasonable agreement for 161 mm, 169 mm (shown in the bottom right), and 178.5 mm downstream from the initial interface position. (Reprinted from Schwarzkopf, J.D. et al., *J. Turb.*, 12, 1, 2011. With kind permission from Taylor & Francis.)

The conservation equations are given for

$$\text{Mass} \quad \frac{\partial}{\partial t}\left(\alpha\rho\right)_1 + \frac{\partial}{\partial x_j}\left(\alpha\rho u_j\right)_1 = -\dot{M}, \tag{5.35}$$

$$\frac{\partial}{\partial t}\left(\alpha\rho\right)_2 + \frac{\partial}{\partial x_j}\left(\alpha\rho u_j\right)_2 = \dot{M}, \tag{5.36}$$

$$\text{Momentum} \quad \frac{\partial}{\partial t}\left(\alpha\rho u_i\right)_1 + \frac{\partial}{\partial x_j}\left(\alpha\rho u_i u_j + \delta_{ij}\alpha p\right)_1 = p_I \frac{\partial \alpha_1}{\partial x_i} + \Phi\left(u_{2i} - u_{1i}\right) - \dot{M}u_{1i}, \tag{5.37}$$

$$\frac{\partial}{\partial t}\left(\alpha\rho u_i\right)_2 + \frac{\partial}{\partial x_j}\left(\alpha\rho u_i u_j + \delta_{ij}\alpha p\right)_2 = p_I \frac{\partial \alpha_2}{\partial x_i} - \Phi\left(u_{2i} - u_{1i}\right) + \dot{M}u_{1i}, \tag{5.38}$$

$$\text{Energy} \quad \frac{\partial}{\partial t}\left(\alpha\rho E\right)_1 + \frac{\partial}{\partial x_j}\left(\alpha u_j\left[\rho E + p\right]\right)_1 = p_I U_i \frac{\partial \alpha_1}{\partial x_i} + \Phi U_i^I\left(u_{2i} - u_{1i}\right) - \dot{M}H_1 - \Psi\left(p_1 - p_2\right) + hA_{eff}\left(T_2 - T_1\right), \tag{5.39}$$

$$\frac{\partial}{\partial t}\left(\alpha\rho E\right)_2+\frac{\partial}{\partial x_j}\left(\alpha u_j\left[\rho E+p\right]\right)_2=p_I U_i\frac{\partial\alpha_2}{\partial x_i}-\Phi U_i^I\left(u_{2i}-u_{1i}\right)+\dot{M}H_1+\Psi\left(p_1-p_2\right)-hA_{eff}\left(T_2-T_1\right), \quad (5.40)$$

where

α is the volume fraction (the saturation Equation 5.23 applies)
ρ is the material density
u is the velocity
p is the pressure
E is the total energy ($e + u^2/2$)
$\dot{M}$ is the mass transfer due to burning or phase change (assuming $1 \rightarrow 2$)
Φ and Ψ are coefficients
p_I and U_i are the interfacial pressure and velocity, respectively
U_i^I is the impedance-averaged velocity
H is the enthalpy of the phase transferring mass
h is the heat transfer coefficient
A_{eff} is the effective area over which heat is being transferred from one phase to the other and the subscripts 1 and 2 relate to continua

Saurel et al. (2007a) set $\dot{M}=0$ and neglected the heat transfer coefficient by assuming that the heat transfer was much slower than the mechanical relaxation. The terms containing volume fraction gradients are referred to as the *nozzling* terms, which account for rapid changes in volume or cross-sectional area of the flow due to compression or expansion of one phase relative to the other.

If porous (or solid) materials (assuming subscript 1) are considered, then a compaction equation is necessary to determine the proper density of the material during chemical reactions or after shock release. This process is modeled as (described in Kapila et al. (2001))

$$\frac{\partial\rho_1}{\partial t}+\frac{\partial\rho_1 u_{1j}}{\partial x_j}=-\frac{\rho_1\alpha_2}{\mu_{cp}}\left(p_1-p_2\right), \quad (5.41)$$

where μ_{cp} is the compaction viscosity. Alternatively, the compaction equation can be written in terms of the volume fraction

$$\frac{\partial\alpha_1}{\partial t}+\begin{Bmatrix}u_{1j}\\U_{1j}\end{Bmatrix}\cdot\frac{\partial\alpha_1}{\partial x_j}=\begin{cases}\dfrac{\alpha_1\alpha_2}{\mu_{cp}}\left(p_1-p_2\right)-\dfrac{\dot{M}}{\rho_1} & \text{(Kapila et al. 2001),}\\ \mu_Z\left(p_1-p_2\right) & \text{(Saurel et al. 2007a).}\end{cases} \quad (5.42)$$

In the conservation equations, the parameter, Φ, has units of mass/(length$^3\cdot$time) and represents drag in Kapila's model and is defined as a velocity relaxation coefficient in Saurel's model

$$\Phi=\begin{cases}\mu/L^2-\dot{M}/2 & \text{(Kapila et al. 2001),}\\ \mu_Z\zeta_1\zeta_2 & \text{(Saurel et al. 2007a),}\end{cases} \quad (5.43)$$

where

μ is the dynamic viscosity of the flowing material
L is a characteristic length scale associated with the drag effects
$\zeta = \rho c$ represents the acoustic impedance

The parameter μ_Z is the pressure relaxation coefficient

$$\mu_Z=\frac{A_I}{2\left(\zeta_1+\zeta_2\right)}, \quad (5.44)$$

where A_I is the specific interfacial area (i.e., A_I = (area/vol)). The parameter Ψ is (1) the compaction coefficient in Kapila's model and (2) the pressure relaxation at the two-phase interface in Saurel's model

$$\Psi = \begin{cases} p_2\alpha_1\alpha_2/\mu_{cp} & \text{(Kapila et al. 2001)}, \\ \mu_Z \dfrac{\zeta_2 p_1 + \zeta_1 p_2}{\zeta_2 + \zeta_1} & \text{(Saurel et al. 2007a)}. \end{cases} \tag{5.45}$$

Saurel et al. (2007a) applied the work of Abgrall and Saurel (2003) to close the interface variables U_i and p_I, which are given in terms of the acoustic impedance

$$p_I = \frac{\zeta_2 p_1 + \zeta_1 p_2}{\zeta_2 + \zeta_1} + \text{sgn}\left(\frac{\partial \alpha_1}{\partial x_i}\right)\frac{\zeta_2\zeta_1}{\zeta_2 + \zeta_1}\left(u_{2i} - u_{1i}\right), \tag{5.46}$$

$$U_i = U_i^I + \text{sgn}\left(\frac{\partial \alpha_1}{\partial x_i}\right)\frac{p_2 - p_1}{\zeta_2 + \zeta_1}, \quad \text{where } U_i^I = \frac{\zeta_2 u_{2i} + \zeta_1 u_{1i}}{\zeta_2 + \zeta_1}, \tag{5.47}$$

and Kapila et al. (2001) set the interfacial variables as $p_I = p_2$ and $U_i = U_i^I = u_{1i}$.

The timescale for velocity equilibration between the two materials is estimated as $\tau_{vel} \sim \alpha\rho L^2/\mu$, where L is a characteristic length scale related to the drag and, for porous materials, L^2 is the permeability (Kapila et al., 2001). The timescale for pressure equilibration between two materials is $\tau_{press} \sim \mu/p$, and the timescale for thermal equilibrium is $\tau_{therm} \sim \rho C_v L^2/k$, where k is the thermal conductivity. Kapila et al. (2001) provide estimates for these timescales associated with an explosive material.

According to Saurel et al. (2007a), this nonequilibrium two-fluid model, that is, Equations 5.35 through 5.40, can describe shock propagation in mixtures when solved by an appropriate numerical algorithm.* The model was applied to a test case consisting of periclase and epoxy, $|At| = 0.5$. Overall, excellent agreement is found between the numerical model and the experiments for the shock velocity, material velocity, pressure, and density, shown in Figure 5.4.

In addition to the models mentioned earlier, there are several other two-fluid models in the literature, some of which are tailored to a specific flow type. However, all contain models that capture the general features of interfacial physics such as mass, momentum, and heat transfer and chemical reactions. Llor (2005) describes closure models for the turbulence in two-fluid models and also describes Young's two-fluid turbulence model (Youngs, 1995). Saurel et al. (2007b) and Petitpas et al. (2007) discuss a relaxation method for pressure computation using complex equation of state (EOS) that is capable of problems with interfaces having large density differences and strong shocks. Other approaches to modeling two-fluid nonequilibrium flows can be found in Gallouet et al. (2004), García-Cascales and Paillére (2006), Niu et al. (2008), and Yeom and Chang (2013). These references also provide methods for developing a set of discretized equations and numerical schemes.

5.2.3 Shock Interaction with Material Interfaces

A normal shock (planar wave) impacting an interface with different density materials sends transmitting and reflecting shocks though the materials. If a shock is traveling through a low density material and encounters a high density material, a reflected shock travels back through the lower density material and a transmitted shock propagates through the higher density material, shown in Figure 5.5a. However, if a shock is traveling through a high density material and encounters a drop in density, a rarefaction wave reflects (scatters back) through the high density material and a shock is transmitted through the lower density materials, shown in Figure 5.5b. Harlow and Amsden (1971) note several important observations after a shock has passed across a material discontinuity: (1) if no material passes across the material discontinuity, then the velocity across the interface must be constant, and (2) the pressure across the material discontinuity must be continuous or infinite acceleration would exist. Harlow and Amsden (1971) provide shock relations for the variable density shock tube scenarios shown in Figure 5.5.

Shocks passing over surfaces with perturbations, caused by a manufacturing finish, can lead to the formation of particles, referred to as ejecta. If the shock is strong enough, this process is initiated by the RM instability, which forms sheets, and these sheets transition to ligaments and then break apart to form droplets or particles. Further discussion on the shock interaction with perturbed surfaces is given in Section 5.4.

* The reader is referred to Saurel et al. (2007a) for additional details.

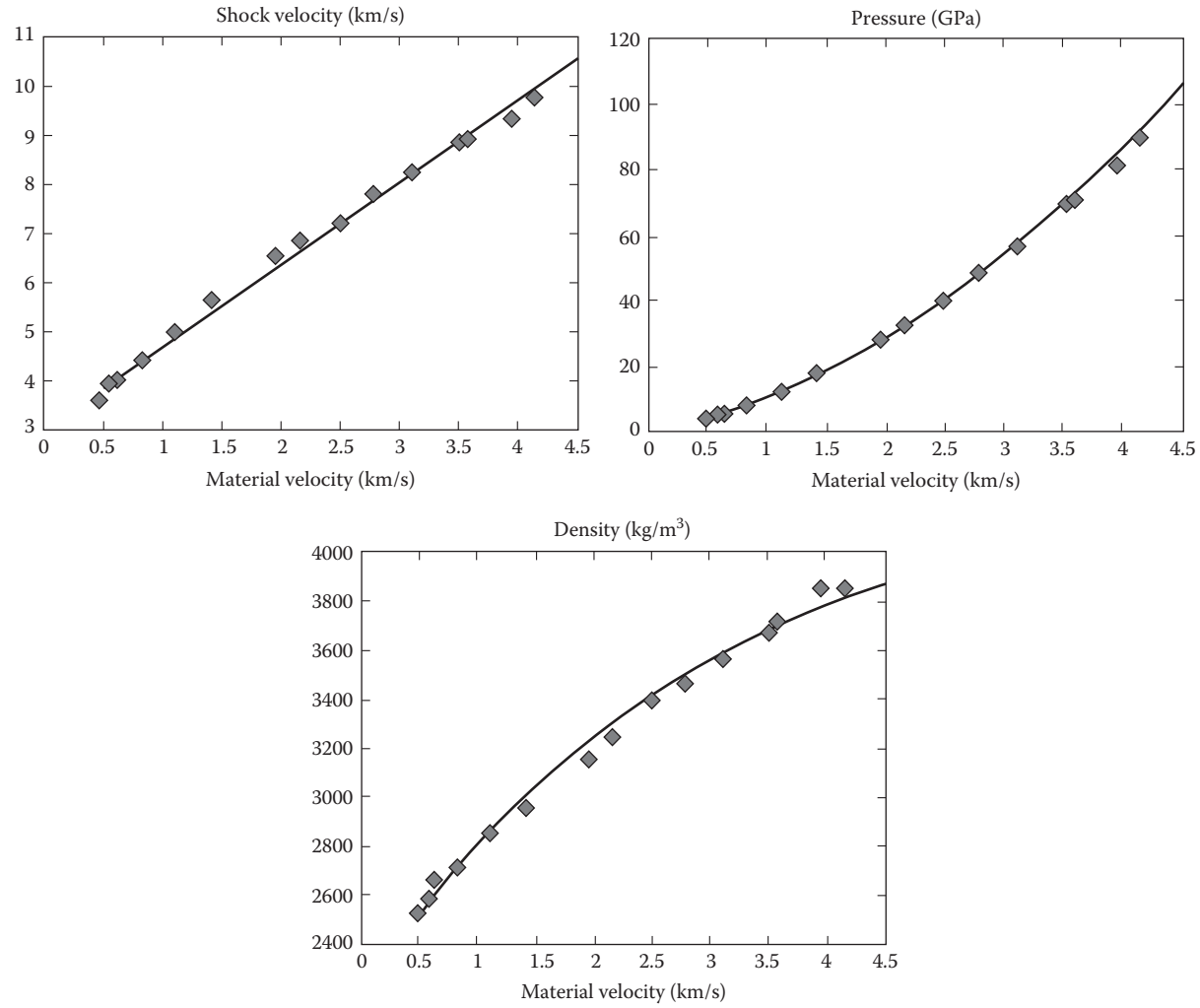


Figure 5.4

Comparison of the numerical results (lines) of Equations 5.35 through 5.40 and the experimental data for a mixture of epoxy and periclase. (With kind permission from Springer Science + Business Media: *Shock Waves*, Shock jump relations for multiphase mixtures with stiff mechanical relaxation, 16, 209, 2007, Saurel, R., Le Métayer, O., Massoni, J., and Gavrilyuk, S.)

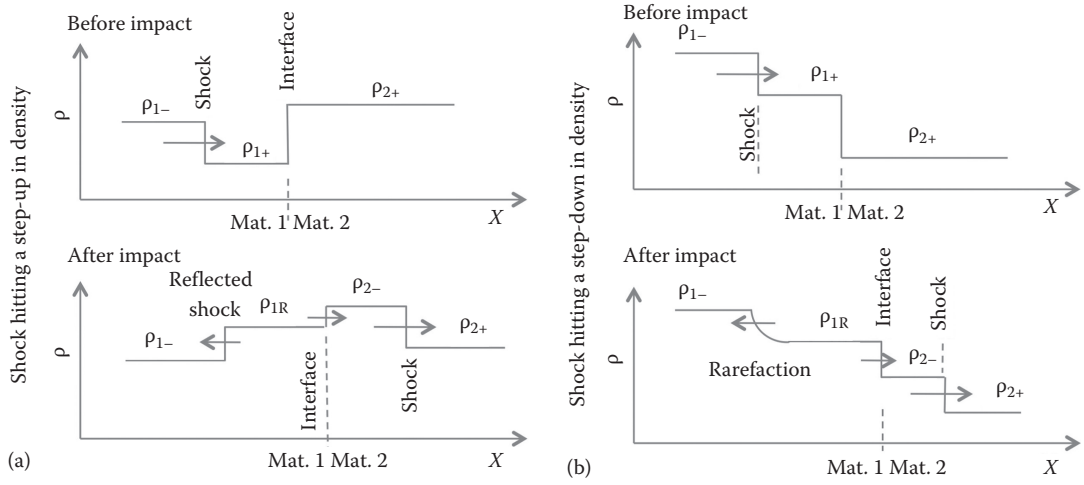


Figure 5.5

Shock impacting a material interface with (a) step-up in density and (b) step-down in density, as depicted by Harlow and Amsden (1971).

5.2.4 Equation of State and Jump Relations

For mechanical and thermal equilibrium and nonequilibrium assumptions, an EOS is needed to relate the average pressure and internal energy. Typical models are the ideal gas, stiff gas, and Mie–Grüneisen (Mie, 1903, Grüneisen, 1912), described as

$$\text{Ideal gas} \quad \langle p\rangle = \left(\langle\gamma\rangle - 1\right)\overline{\rho}\tilde{e}, \tag{5.48}$$

$$\text{Stiff gas} \quad \langle p\rangle = \left(\langle\gamma\rangle - 1\right)\overline{\rho}\tilde{e} + \langle\gamma\rangle\langle p_\infty\rangle, \tag{5.49}$$

$$\text{Mie Grüneisen} \quad \langle p\rangle = \langle\Gamma\rangle\overline{\rho}\left(\tilde{e} - \tilde{e}_H(\rho)\right) + \langle p_H(\rho)\rangle, \tag{5.50}$$

where

$\tilde{e} = \tilde{e}\left(\langle p,\rangle\overline{\rho}\right)$ is the average specific internal energy
$\langle p\rangle$ is the average pressure of the mixture
$\overline{\rho}$ is the mixture density given by Equation 5.11
$\langle\gamma\rangle$ is the ratio of specific heats for the mixture given by Equation 5.12
$\langle\Gamma\rangle = \langle V(dp/de)_V\rangle$ is the average Grüneisen parameter for the mixture

The averages apply only to mixture regions; in regions of pure fluid, the averages are equal to the instantaneous values, for example, $\langle p\rangle = p$. The subscript H in the Mie–Grüneisen equation refers to a reference curve such as a Hugoniot for a specific material. The parameters $\langle\gamma\rangle$ and $\langle p_\infty\rangle$ in the stiff gas equation are fit to a specific material or mixture. For the ideal and stiff gas relations, the temperature is related to the internal energy by the specific heat

$$\tilde{e} = C_v\tilde{T}, \tag{5.51}$$

and for the Mie–Grüneisen

$$\tilde{e} - \tilde{e}_H(\rho) = C_v\left(\tilde{T} - \tilde{T}_H(\rho)\right). \tag{5.52}$$

The Hugoniot curve is approximated by the linear relation

$$u_s = c_+ + su_-, \tag{5.53}$$

where

u_s is the shock speed
c_+ is the speed of sound of the material ahead of the shock
u_- is the postshock velocity of the material behind the shock
the coefficient s is determined by shock compression data for a specific material

In a single material, the averages in the earlier relations are taken as the properties of the material.

Petel and Jetté (2010) note that there are three major categories for determining shock propagation in mixtures: (1) unsteady flow models that attempt to resolve the interactions of mixture components, (2) steady models of mixtures in mechanical equilibrium, and (3) mechanical and thermal equilibrium models. However, the models all assume some sort of mixture properties based on averaging, and therefore, the differences between such models, when comparing to experimental data, are small.

Saurel et al. (2007a) give the general Rankine–Hugoniot jump conditions for a system of conservation laws of the form

$$\frac{\partial B}{\partial t} + \frac{\partial F(B)}{\partial x} = 0, \quad \text{as} \tag{5.54}$$

$$F(B_-) - v_sB_- = F(B_+) - v_sB_+. \tag{5.55}$$

For mechanical and thermal equilibrium conditions, neglecting the turbulence terms, the jump conditions for Equations 5.18 through 5.22 are

$$\alpha_+^k \langle \rho \rangle_+^k \left(\tilde{u}_+ - v_s \right) = \alpha_-^k \langle \rho \rangle_-^k \left(\tilde{u}_- - v_s \right), \quad \text{or} \tag{5.56}$$

$$\bar{\rho}_+ \tilde{c}_+^k \left(\tilde{u}_+ - v_s \right) = \bar{\rho}_- \tilde{c}_-^k \left(\tilde{u}_- - v_s \right), \quad \text{and} \tag{5.57}$$

$$\bar{\rho}_+ \tilde{u}_+ \left(\tilde{u}_+ - v_s \right) + \langle p \rangle_+ = \bar{\rho}_- \tilde{u}_- \left(\tilde{u}_- - v_s \right) + \langle p \rangle_-, \tag{5.58}$$

$$\bar{\rho}_+ \left(\tilde{u}_+ - v_s \right) \tilde{E}_+ + \langle p \rangle_+ \langle u \rangle_+ = \bar{\rho}_- \left(\tilde{u}_- - v_s \right) \tilde{E}_- + \langle p \rangle_- \langle u \rangle_-, \tag{5.59}$$

where subscripts + and − refer to the preshock and postshock conditions, respectively.

However, for mechanical and thermal nonequilibrium models, there arises a complexity in capturing the interaction or relaxation terms. Saurel et al. (2007a) applied the mechanical equilibrium condition to Equations 5.35 through 5.40. This condition eliminates the relaxation parameters, greatly simplifying the equations. Jump conditions were derived with the assumption that the two fluids have different internal energies and are given as

$$\frac{\alpha_+^k \rho_+^k}{\bar{\rho}_+} = \frac{\alpha_-^k \rho_-^k}{\bar{\rho}_-}, \tag{5.60}$$

$$\bar{\rho}_+ \left(\tilde{u}_+ - v_s \right) = \bar{\rho}_- \left(\tilde{u}_- - v_s \right) = m, \tag{5.61}$$

$$p_+ - p_- + m^2 \left(\upsilon_+ - \upsilon_- \right) = 0, \tag{5.62}$$

$$e_+^k - e_-^k + \frac{1}{2} \left(p_+ + p_- \right) \left(\upsilon_+^k - \upsilon_-^k \right) = 0, \tag{5.63}$$

where

v_s is the shock velocity

υ^k is the specific volume of species k

They then applied these jump conditions to a variety of experiments with various Atwood numbers comparing shock velocity, pressure, material velocity, and volume fraction and specific volume where available. Overall, the comparisons are very good for numerous material mixtures. A moderate $At = 0.45$ water and calcite comparison is shown in Figure 5.6.

The earlier discussion on multiphase, multicomponent flows has been central to the assumption that the phases are continuous. Next, we relax this assumption and consider methods to model a discontinuous phase within a continuous phase.

5.3 Compressible Dispersed Phase Flows

Dispersed phase flows contain particles or droplets that are dispersed throughout a continuous phase, such as rain drops in air. This type of flow is typically modeled using an Eulerian frame for the continuous phase and Lagrangian tracking for the particle motion. The boundaries and gradients between the particle (dispersed) and the carrier (continuous) phases require attention. A direct numerical, or fully resolved, simulation for particle-laden flows would simulate the flow near the particle surface, which includes resolving the viscous sublayer and the wake region. For problems involving millions of particles, this is computationally prohibitive. The next best method is to average the carrier phase equations and track the effects of multiple particles.

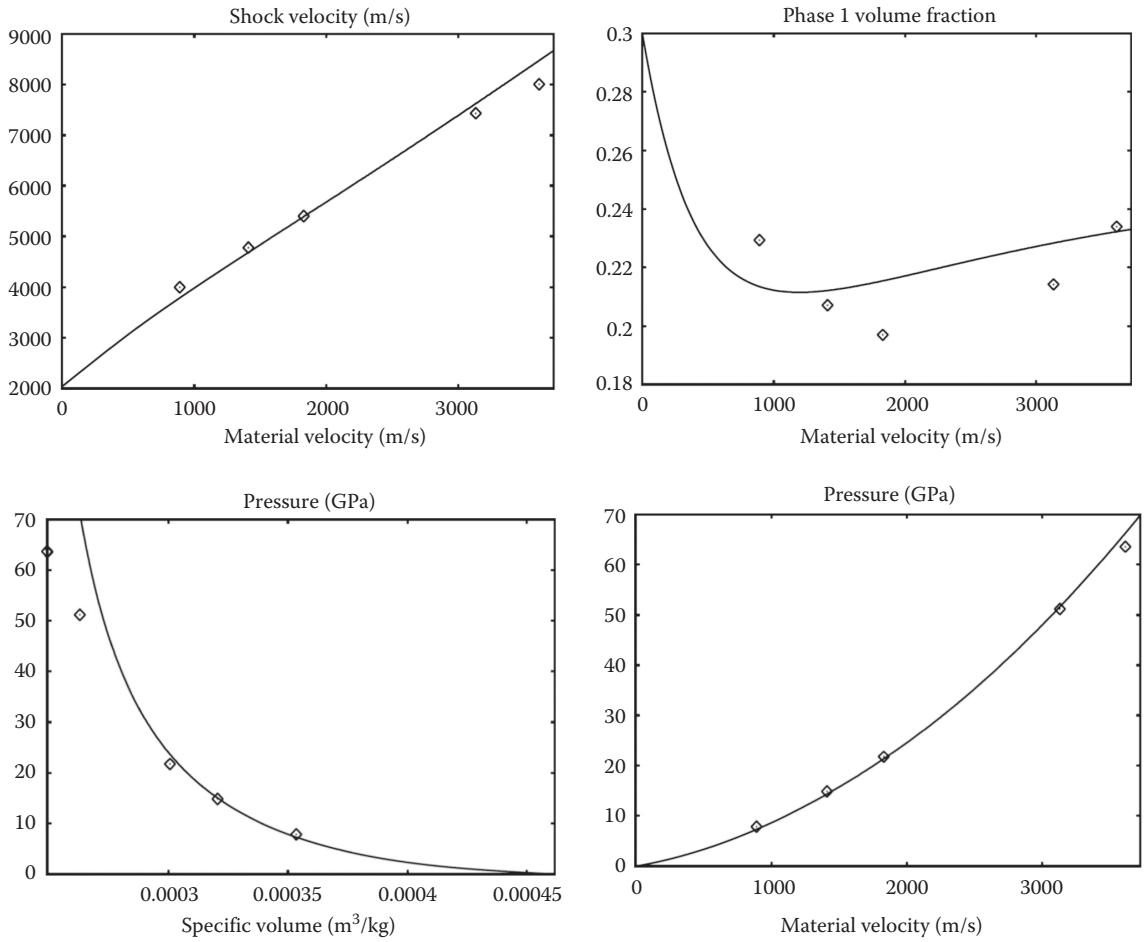


Figure 5.6

Comparison of jump relations with experimental data for a mixture of water and calcite. (With kind permission from Springer Science + Business Media: *Shock Waves*, Shock jump relations for multiphase mixtures with stiff mechanical relaxation, 16, 209, 2007, Saurel, R., Le Métayer, O., Massoni, J., and Gavrilyuk, S.)

The method of volume averaging, introduced by Slattery (1972) and further developed by Crowe et al. (2012) (briefly discussed in Section 5.1.1.2), accounts for the interactions between the dispersed and carrier phases. Models are then applied to determine the hydrodynamic drag force, heat transfer, etc., between the phases. These models are valid for dilute flows, which assume that the particles do not interact and are a sufficient distance apart. Models for tracking multiple particles, such as the particle-source-in-cell method Crowe et al. (2012) or the multiphase particle-in-cell model (Andrews and O'Rourke, 1996), are used to determine the forces acting on several particles that are nominally the same size, velocity, etc.

There are many examples of droplet/particle flows in energy conversion and propulsion systems ranging from coal-fired or oil-fired furnaces to drying systems. Examples of compressible particle-laden flows include fuel injection in a combustion chamber, rocket propulsion, volcanic eruption, explosive debris, supernova explosion, aerodynamic ablation, and shocked liquid or solid surfaces. Previous importance has been placed on explosion in confined areas, such as powder mills, mine shafts, and chemical plants; however, recent importance includes pulsed detonation engines, attenuation or augmentation of detonation waves (Chang and Kailasanath, 2003), and effects of explosive debris.

In this section, we describe some of the physics and present models associated with compressible particle-laden flow, but first we introduce the reader (i.e., new to this field) to some of the nomenclature.

5.3.1 Background and Nomenclature

The dispersed phase is described as particles, droplets, or bubbles that are surrounded and carried by a continuous phase (liquid or gas). An example would be aluminum particles (dispersed phase) transported in air (carrier phase). The terminology used is described as follows.

5.3.1.1 Dilute and Dense Flows

Dilute flows are described as flows with sufficient enough spacing between the particles such that the particle motion is governed by the hydrodynamic forces (i.e., particle contact is absent or minimal). Dense flows are described as collision- or contact-dominated flows, such as granular flows. It is difficult to delineate dense and dilute flows. Typically, if the dispersed phase volume fraction is less than 0.001, the flow is thought to be dilute. Crowe et al. (2012) suggest that dilute flow exists if

$$\frac{\tau_V}{\tau_C} < 1, \tag{5.64}$$

where

τ_V is the particle response time

τ_C is the average time between particle–particle collisions, defined as

$$\tau_C = \frac{1}{f_C} = \frac{1}{4\sqrt{\pi} n D^2 v'}, \tag{5.65}$$

where

n is the particle number density

D is the diameter

v' is the fluctuation velocity (Abrahamson, 1975)

The dilute regime can be further simplified as very dilute when the volume fraction is so low that each particle can be considered dynamically relatively independent of all other particles. When the flow is dilute, but not very dilute, gas-mediated particle–particle interaction must be accounted in terms of volume fraction effect on drag and heat transfer correlations. This indirect influence of the neighboring particles can be substantial in the dilute regime even though direct particle–particle interaction through collisions may be rare and unimportant.

5.3.1.2 Phase Coupling

Depending on the nature of the multiphase flow, phase coupling could be important when considering modeling choices for multiphase flows. Phase coupling describes the interactions between the dispersed and carrier phase flows. One-way coupling accounts for the effects of the carrier phase on the dispersed phase but not vice versa; it assumes that the particle number and size have a negligible effect on the fluid. This typically is the case under very dilute condition. An example of one-way coupling is heat transfer from the carrier phase to a single particle. One-way coupling is sometimes assumed in the derivation of shock jump relations. Two-way coupling considers mass, momentum, and energy transfer between the particle and the carrier phase. Two-way coupling is important in the dilute (but not very dilute) regime. Back coupling is another term (often used in place of two-way coupling) to indicate when the particle influences the carrier phase. When the particle volume fraction increases above the dilute limit then particle–particle interaction becomes important and the flow is in the four-way coupled regime (Elghobashi, 1994, Balachandar and Eaton, 2010).

5.3.2 Compressible Dilute Particle Flows

In this section, we present two-way coupled models for capturing the effect of the dispersed phase on the carrier phase and vice versa and comment on the importance of terms in shocked flows. We begin with a short discussion on particle momentum and thermal response time and how it relates to shock transit times. We then discuss the importance of Mach and Reynolds numbers on the hydrodynamic drag and present recent models developed for compressible flows. We then introduce the carrier phase equations in Eulerian form and the equations for particle motion in Lagrangian form.

5.3.2.1 Response Times

Response times are important characterization parameters in particle-laden flows. The derivations of the response times can be found in Crowe et al. (2012).

The momentum response time is the time required for the velocity of a particle to reach a percentage of the carrier phase velocity due to particle drag and is given as

$$\tau_p = \frac{\rho_d D^2}{18\mu_c}, \tag{5.66}$$

where

ρ_d is the particle density
D is the diameter (assuming spheres)
μ_c is the dynamic viscosity of the carrier phase fluid

The momentum response time of a particle gives an indication of how likely the particle is to accelerate due to a force imposed on it, such as a shock. As a shock passes over nanosized particles with low density, the particles will likely follow closely behind the shock and may produce preferential concentration (Maxey, 1987, Maxey et al., 1997). However, if the particles are large with sufficient mass, their response in motion due to the passage of a shock may be negligible. Likewise, the thermal response time is the time required for a particle to reach a percentage of the carrier phase temperature given as

$$\tau_T = \frac{\rho_d C_d D^2}{12 k_c}, \tag{5.67}$$

where

C_d is the specific heat of the dispersed phase material
k_c is the thermal conductivity of the carrier phase material

The Stokes number is defined as

$$St_V = \frac{\tau_V}{\tau_F}, \tag{5.68}$$

where

τ_F is a characteristic timescale of the carrier phase flow
τ_V is the particle response time and it can be taken to be either τ_p or τ_T

Another important parameter in shocked particle-laden flows is the ratio of the time it takes for a shock to traverse a particle to the response of the particle motion, such as

$$\frac{\tau_s}{\tau_p} = \frac{18\mu_c}{U_s \rho_d}. \tag{5.69}$$

In shocked flows if $\tau_s/\tau_p \geq 1$, the unsteady effects, such as added mass or history terms, are very important, whereas if $\tau_s/\tau_p \ll 1$, the unsteady effects can be neglected. To illustrate this, data were taken from experiments of particles in shocked air, and the ratio of the timescales was plotted as a function of the shock Mach number for various values of particle mass per unit area ($\rho_d D$), shown in Figure 5.7. From the data (for particles in air), if $\tau_s/\tau_p < 10^{-3}$, the acceleration effects can be neglected. For shocked air, particles with large $\rho_d D$ do not respond to the acceleration effects caused by the shock nearly as much as particles with small $\rho_d D$ values. If $\rho_d D > 0.01$ kg/m^2, in air, one can assume that the unsteady terms can be neglected. The previous statements are valid for dilute conditions, such as shock propagation over nearly isolated particles, where the effect of the particles on the gas (back coupling) and gas-mediated particle–particle interaction effects are negligible. When particle volume fraction and the back-coupling effects on the gas flow are substantial, the timescale of the postshock flow can be much longer than the timescale of shock propagation over an individual particle, and correspondingly, the unsteady effects can become important (Ling et al., 2012, 2013).

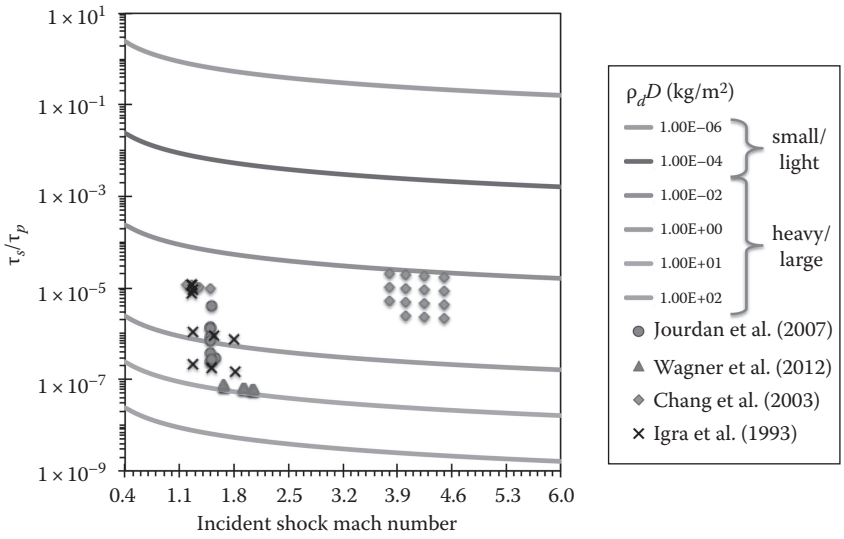


Figure 5.7

Ratio of shock transit time over a particle to the particle response time for various incident shock Mach numbers and $\rho_d D$ values in air.

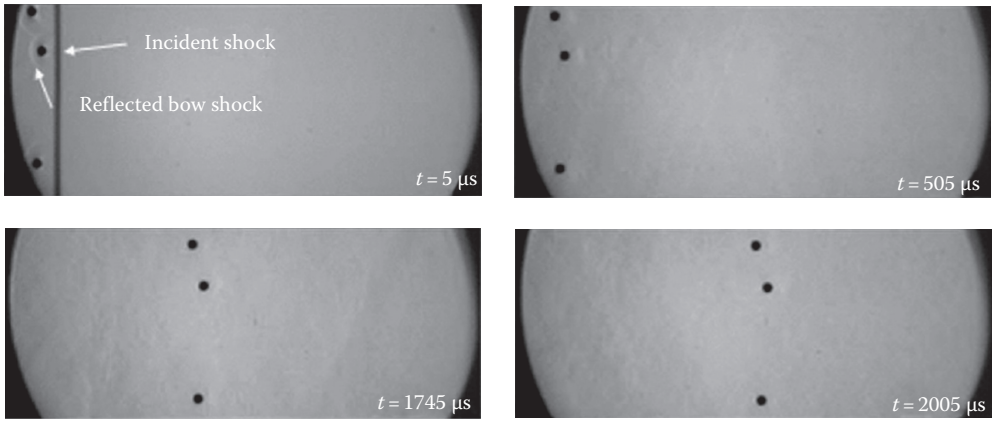


Figure 5.8

Schlieren images, provided by Wagner et al. (2012), showing the lag in particle motion after the passage of a 1.68 Mach shock over stainless steel 1 mm particles. (Reprinted with permission from Wagner, J.L., Beresh, S.J., Kearney, S.P., Pruett, B.O.M., and Wright, E.K., Shock tube investigation of quasi-steady drag in shock-particle interactions, *Phys. Fluids*, 24, 123301. Copyright 2012, American Institute of Physics.)

A Schlieren image of particles with $\rho D \sim 7.6$ kg/m^2 was provided by Wagner et al. (2012), shown in Figure 5.8. At 5 μs, the incident shock has passed over the particles and by 500 μs the shock is out of the image. After the passage of the shock, the pressure and velocity of the gas, outside of the particle wake and reflected shock region, have equilibrated. The particle response time is 23 s and the acceleration of the particle is nearly constant (~10^4 m/s^2) for the first 2 ms, and the gas velocity is constant at 312 m/s. Beyond 5 μs, the particle motion is primarily due to drag effects.

Another indication that the unsteady effects may be negligible is the ratio of the carrier phase density to the particle density. If $\rho_c/\rho_d \ll 0.001$, then the unsteady contribution to the particle motion can be neglected. For the experiment shown in Figure 5.8, $\rho_c/\rho_d \sim 1.5 \cdot 10^{-4}$.

5.3.2.2 Mach and Reynolds Number Effects

Particle Mach and Reynolds number effects are important in compressible particle-laden flows. The particle Reynolds number is defined as

$$Re_p = \frac{\rho_c D|u-v|}{\mu_c}, \tag{5.70}$$

where $|u - v|$ is the relative velocity, which is the magnitude of the velocity difference between the carrier phase velocity (u) and the dispersed phase velocity (v). The particle Mach number is also defined in terms of the relative velocity as

$$M_p = \frac{|u-v|}{c_c}, \tag{5.71}$$

where c_c is the sound speed of the carrier phase. Another important parameter is the particle Knudsen number, which characterizes a rarefied flow and defined as*

$$Kn_p = \frac{\lambda_m}{D}, \tag{5.72}$$

where λ_m is the mean free path of the carrier phase molecules in the vicinity of the particle, defined as

$$\lambda_m = \frac{M_{mol}}{\sigma_c \rho_c A_v}, \tag{5.73}$$

where

σ_c is the collision cross section
M_{mol} is the molar mass
A_v is Avogadro's number

There are several regions described for rarefied flows:

$$\begin{aligned} &Kn_p < 0.01 \quad \text{continuum flow} \\ &0.01 \le Kn_p < 0.1 \quad \text{slip flow} \\ &0.1 \le Kn_p < 10 \quad \text{transition flow} \\ &Kn_p > 10 \quad \text{free molecular flow} \end{aligned}$$

These parameters have an important effect on particle drag in compressible or rarefied flows. The critical M_p is defined as the limit that below the drag coefficient is indistinguishable from incompressible flows. The critical Re_p distinguishes rarefied flow from compressible flow and the critical Kn_p separates continuum from rarefied flow. The established values or ranges are

$$\begin{aligned} &M_{p_c} = 0.6 \quad \text{critical Mach number} \\ &Re_{p_c} = 40 - 45 \quad \text{critical Reynolds number} \\ &Kn_{p_c} = 0.01 \quad \text{critical Knudsen number} \end{aligned}$$

* It can also be shown that $Kn_p \propto M_p/Re_p$ (Loth, 2008, Crowe et al., 2012).

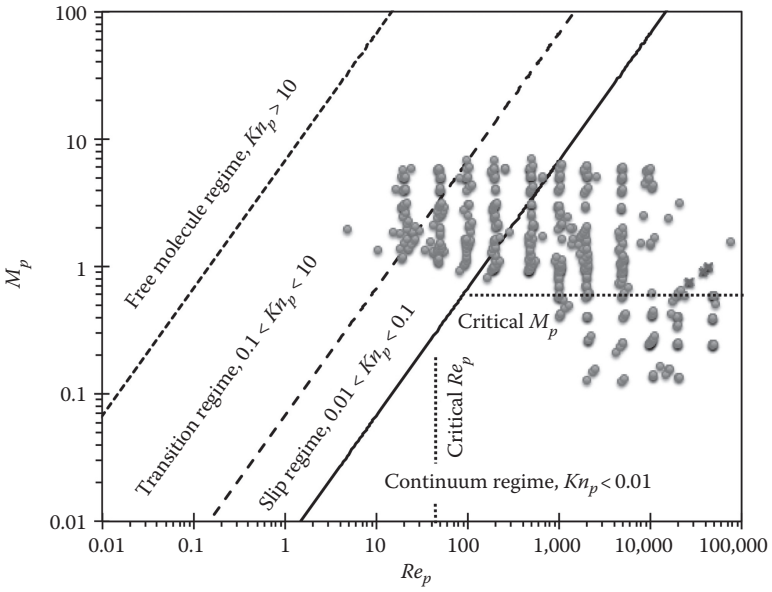


Figure 5.9

Continuum, compressible, transition, and free molecular flow regimes for M_p and Re_p for air (the mean free path was taken at standard pressure and temperature). (Data abstracted from Bailey, A.B. and Hiatt, J., Free-flight measurements of sphere drag at subsonic, transonic, supersonic, and hypersonic speeds for continuum, transition, and near-free-molecular flow conditions, Office of Aerospace Research, Tech. Rep., AEDC-TR-70-291, 1971 (dots); Wagner, J.L. et al., *Phys. Fluids*, 24, 123301, 2012 (x).)

The continuum regime to the free molecular flow regime for air is plotted in M_p and Re_p space and shown in Figure 5.9. The critical M_p and Re_p are identified in this plot along with data from Bailey and Hiatt (1971) and Wagner et al. (2012) spanning the incompressible, compressible, slip, and transition regimes.

5.3.2.3 Drag Coefficient

When a particle travels through a carrier phase (e.g., a gas), the particle experiences a drag force that is caused by the pressure gradient and the viscous shear effects due to the velocity difference between the particle and the surrounding gas. In a Stokes regime, the drag force acting on the particle can be computed analytically; however, outside of the Stokes regime, a Re_p correction to the Stokes drag is required to obtain the measured drag force. In compressible flows, additional corrections for M_p and Kn_p are applied to obtain the measured drag force.

The dependence of the quasi-steady drag coefficient (C_D) on M_p and Re_p is shown in Figure 5.10. The quasi-steady drag is sufficient to compute the total drag force on a particle when unsteady effects are unimportant. These data from Bailey and Hiatt (1971) show that $C_D \to 1$ for large M_p and Re_p and $1 < C_D < 2$ near Re_{pc}. For $Re_p > 1000$, the drag coefficient does not vary much for $1.75 < M_p < 7$. At low Re_p and high M_p, the data by Macrossan (2004) show that $2 < C_D < 3$ and appear to extend into the free molecular regime where the drag coefficient is independent of Re_p (for $M_p > 0.5$) and decreases monotonically toward the transition regime (Crowe, 1967).

In the compressible regime, the quasi-steady drag coefficient is significantly affected by flow compressibility when M_p exceeds a critical value ($M_{p,cr}$). When this happens, the flow, as it accelerates around the particle, becomes locally supersonic resulting in the formation of a shock. With increasing M_p, this shock moves upstream and collapses to a bow shock for $M_p > 1.0$, as shown in Figure 5.8. The presence of a shock increases the quasi-steady drag force, and this effect is distinct from the unsteady effects. Wagner et al. (2012) were careful to reduce the unsteady effects in their shock tube experiment and deduced that the increase in the drag coefficient was due to compressibility effects, for example, increased relative velocity difference and not acceleration/unsteady effects. In order to understand this effect of compressibility, it is convenient to conceptually separate the inviscid and viscous contributions to the drag force on the particle. When $M_p < M_{p,cr}$, the steady inviscid uniform flow around a particle will remain potential (i.e., irrotational) and make zero contribution to the drag force. In this regime, the effect of M_p on the viscous drag is not strong. At postcritical M_p, the appearance of a shock within

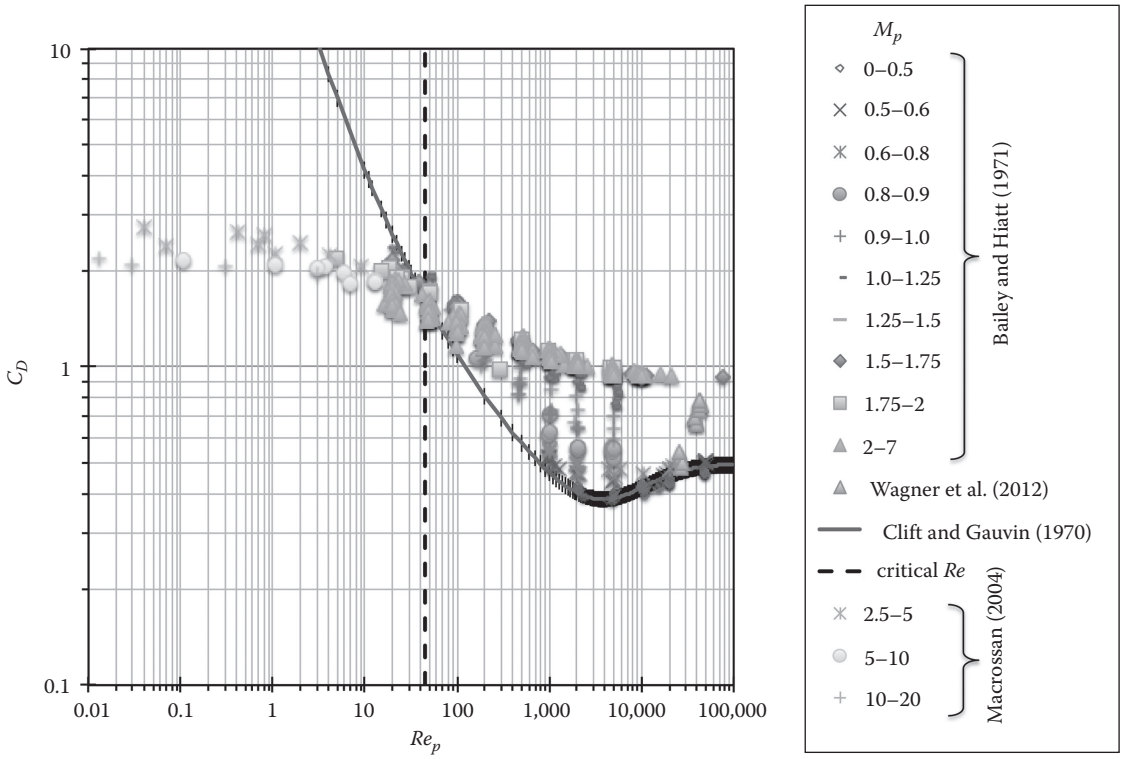


Figure 5.10

Measured drag coefficients for compressible and transitional flow over a wide range of particle Mach and Reynolds numbers. The solid line and the bars represent the uncertainty in the correlation developed by Clift and Gauvin (1970) for the incompressible drag coefficient.

the flow breaks the fore-aft symmetry of even the steady uniform inviscid flow. This results in a nonzero inviscid contribution to the quasi-steady force. Thus, for $M_p > M_{p,cr}$, there is a strong compressibility effect on the quasi-steady drag force.

There are several empirical correlations for the Mach and Knudsen effect on the drag coefficient. Commonly used correlations were developed by Crowe (1967) and Henderson (1976). More recently, Loth (2008) developed a correlation for the compressible and rarefied regimes with transition criteria. Later, Parmar et al. (2010) developed a detailed correlation for the compressible flow region that is valid up to $M_p = 1.75$, $Re_p = 2 \cdot 10^5$, and $Kn_p \leq 0.01$. For the incompressible and compressible regimes, the correlation for the drag coefficient proposed by Parmar et al. (2010) is

$$C_D(M_p) = \begin{cases} C_{D,std} + \left(C_{D,M_{cr}} - C_{D,std}\right)\dfrac{M_p}{M_{cr}} & \text{if } M_p \leq M_{cr}, \\ C_{D,M_{cr}} + \left(C_{D,M=1} - C_{D,M_{cr}}\right)\xi_{sub} & \text{if } M_{p,cr} < M_p \leq 1.0, \\ C_{D,M=1} + \left(C_{D,M=1.75} - C_{D,M=1}\right)\xi_{sup} & \text{if } 1.0 < M_p \leq 1.75. \end{cases} \tag{5.74}$$

The standard equation for the drag coefficient is modeled after Clift and Gauvin (1970) and is of the form

$$C_{D,\chi} = \frac{24}{Re_p}\left(1 + A_1 Re_p^{n1}\right) + A_2\left(1 + \frac{A_3}{Re_p^{n2}}\right)^{-1}, \tag{5.75}$$

where the coefficients A_1 through A_3 and powers $n1$ and $n2$ are given in Table 5.3.

Table 5.3 Coefficients and Exponents for Equation 5.75

χ	A_1	A_2	A_3	$n1$	$n2$
std	0.15	0.42	42,500	0.687	1.16
M_{cr}	0.15	0.513	483	0.684	0.669
$M = 1$	0.118	0.69	3,550	0.813	0.793
$M = 1.75$	0.107	0.646	861	0.867	0.634

Table 5.4 Coefficients a_0–a_5 and C_1–C_3 for $N = sub$ or sup in Equations 5.76 and 5.77

N	f_i	a_0	a_1	a_2	a_3	a_4	a_5	C_1	C_2	C_3
sub	1	−1.884	8.422	−13.7	8.162	0	—			
	2	−2.228	10.35	−16.96	9.84	0	—	6.48	9.28	12.21
	3	4.362	−16.91	19.84	−6.296	0	—			
sup	1	−2.963	4.392	−1.169	−0.027	−0.233	0.011			
	2	−6.617	12.11	6.501	1.182	−0.174	0.010	6.48	8.93	12.21
	3	−5.866	11.57	−6.665	1.312	−0.35	0.012			

The additional factor, ξ, is given by

$$\xi_N = \sum_{i=1}^{3} f_i\left(M_p\right) \prod_{\substack{j=1 \\ j\neq i}}^{3} \frac{\log\left(Re_p\right) - C_j}{C_i - C_j}, \quad \text{where} \tag{5.76}$$

$$f_i\left(M_p\right) = a_0 + a_1 M_p + a_2 M_p^2 + a_3 M_p^3 + a_4 \exp(1 - M_p)/a_5 . \tag{5.77}$$

The coefficients for Equations 5.76 and 5.77 are given in Table 5.4.

The correlation for the drag coefficient given by Parmar et al. (2010) was developed using the data of Bailey and Starr (1976). They applied the correlation to the data of Goin and Lawrence (1968), May and Witt (1953), and Jourdan et al. (2007) for the drag measurement of spheres in a fluid and found excellent agreement.

Wagner et al. (2012) conducted shock tube experiments of particles in a shocked gas to understand if the unsteady terms contributed to the increase in drag coefficient. The drag coefficient of 1 mm stainless steel spheres was measured for three M_p (0.99, 0.91, and 0.75) and shown in Figure 5.11. They also compared recently developed correlations by Parmar et al. (2010) and Loth (2008) to their measured values of C_D and found that Loth's correlation overpredicted the data for high Re_p in the range of $0.75 \leq M_p \leq 0.99$, as shown in Figure 5.11. The correlation of Parmar et al. (2010) provides an excellent match to the data.

The drag coefficient for rarefied flows is given by Loth (2008) as

$$C_D\left(Kn\right) = \frac{\dfrac{24}{Re_p}\left(1 + 0.15\mathrm{Re}_p^{0.687}\right) f_{Kn} + M_p^4 C_{D,fm}}{1 + M_p^4}, \quad \text{for } Re_p \leq 45, \tag{5.78}$$

where the free molecular contribution to the drag coefficient is given as

$$C_{D,fm} = \frac{\Phi(s) + \dfrac{2}{3s}\sqrt{\pi \dfrac{T_p}{T_\infty}}}{1 + \left(\dfrac{\Phi(s)}{1.63} - 1\right)\sqrt{\dfrac{\mathrm{Re}_p}{45}}}, \quad \text{and} \tag{5.79}$$

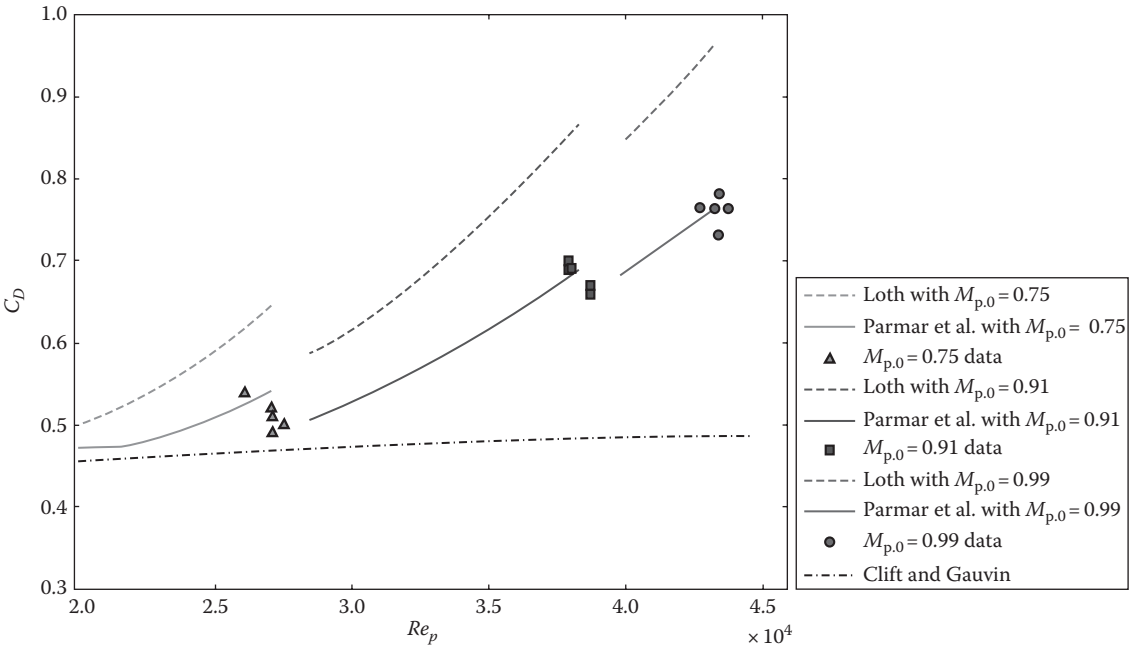


Figure 5.11

A comparison of the compressible drag coefficient correlation by Loth (2008) and Parmar et al. (2010) to the data measured by Wagner et al. (2012). The correlation by Parmar et al. (2010) shows excellent agreement with the measured compressible C_D. (Reprinted with permission from Wagner, J.L., Beresh, S.J., Kearney, S.P., Pruett, B.O.M., and Wright, E.K., Shock tube investigation of quasi-steady drag in shock-particle interactions, *Phys. Fluids*, 24, 123301. Copyright 2012, American Institute of Physics.)

$$\Phi(s) = \frac{\left(1+2s^2\right)\exp\left(-s^2\right)}{s^3\sqrt{\pi}} + \frac{\left(4s^4+4s^2-1\right)\mathrm{erf}\left(s\right)}{2s^4}, \tag{5.80}$$

where $s = M_p\sqrt{\gamma/2}$ is the molecular speed ratio and the parameter f_{Kn} in Equation 5.78 is given as

$$f_{Kn} = \left(1 + Kn_p\left[2.514 + 0.8\exp\left(\frac{-0.55}{Kn_p}\right)\right]\right). \tag{5.81}$$

where Kn_p is given in Equation 5.72.

Comparisons of this drag correlation with those of Crowe (1967), Henderson (1976), and Hermsen (1979) are shown in Loth (2008). Overall, this correlation has been shown to fit the selected data better than prior attempts (Loth, 2008).

The earlier results are all for an isolated particle. When local particle volume fraction exceeds a few percent, then the effect of gas-mediated particle–particle interactions increases C_D. This in turn will influence both the particle motion and the back-coupling effect on the gas (Ling et al., 2013).

5.3.2.4 Nonspherical Effects

Although many experiments use spherical particles for simplicity, in reality, particles are typically irregular. Reviews of the effect of irregular particles on incompressible drag are provided by Clift et al. (1978) and Michaelides (2006) with more recent developments by Tran-Chong et al. (2004) and Hölzer and Sommerfeld (2008). For compressible drag, Boiko and Poplabskii (2005) studied an irregular particle (cube, ~5 mm) and compared it to a sphere of similar size in shocked flows for $M = 0.5 - 1.5$ and $Re_p \sim 10^5$ and concluded that values of the drag were similar, both much higher than the standard drag; however, differentiation between unsteady effects and compressible drag was not discussed. The particles were

made of light wood with a density of 120 kg/m^3 and Schlieren images show slight differences in particle position based on the orientation of the cube normal to the flow. The acceleration of the cube with the flow incident on an edge or apex was lower than when the flow incident on the face.

5.3.2.5 Carrier Phase Equations of Motion

The carrier phase is described as the continuous fluid that transports the dispersed phase. In dilute flows, the volume fraction of the carrier phase α_c is on the order of unity; however, in dense particle-laden flows it can be much less. As Crowe et al. (2012) point out, the carrier phase equations cannot be derived by simply adding representative effects of the dispersed phase (i.e., drag) to the carrier phase equations. The Navier–Stokes equations are valid at a continuum point in the flow; however, the particle drag force is not valid at a continuum point but represents the average force due to the boundary and wake effects of the dispersed on the carrier phase. This region, where the particle affects the surrounding fluid, can span up to a few particle radii away from the particle surface. For this reason, we present the volume average of the carrier equations. The equations describing the mass, momentum, and energy of the carrier phase for a dilute flow are

$$\text{Mass} \quad \frac{\partial}{\partial t}\left(\alpha_c \langle \rho_c \rangle\right) + \frac{\partial}{\partial x_j}\left(\alpha_c \langle \rho_c \rangle \tilde{u}_j\right) = 0, \tag{5.82}$$

$$\text{Momentum} \quad \frac{\partial}{\partial t}\left(\alpha_c \langle \rho_c \rangle \tilde{u}_i\right) + \frac{\partial}{\partial x_j}\left(\alpha_c \langle \rho_c \rangle \tilde{u}_i \tilde{u}_j\right) = -\alpha_c \frac{\partial \langle p \rangle}{\partial x_i} - \frac{\partial}{\partial x_j}\left(\alpha_c \langle \rho_c \rangle \tilde{R}_{ij}\right) - \frac{1}{V}\sum_k F_{k,i}, \tag{5.83}$$

$$\begin{aligned}\text{Energy} \quad & \frac{\partial}{\partial t}\left(\alpha_c \langle \rho_c \rangle \tilde{E}\right) + \frac{\partial}{\partial x_j}\left(\alpha_c \langle \rho_c \rangle \tilde{E}\tilde{u}_j\right) = -\frac{\partial}{\partial x_j}\left(\alpha_c \langle p \rangle \langle u_j \rangle\right) - \frac{\partial}{\partial x_j}\left(\alpha_c \langle \rho_c \rangle \tilde{u}_i \tilde{R}_{ij}\right) - \frac{\partial}{\partial x_j}\left(\alpha_c \langle p' u_j' \rangle\right) \\ & -\frac{1}{2}\frac{\partial}{\partial x_j}\left(\alpha_c \langle \rho u_i'' u_i'' u_j'' \rangle\right) - \frac{\partial}{\partial x_j}\left(\alpha_c \langle \rho e'' u_j'' \rangle\right) + \frac{\partial}{\partial x_j}\left(\alpha_d \langle p \rangle \hat{v}_j\right) + \langle p \rangle \frac{\dot{V}_d}{V} - \frac{1}{V}\sum_k v_{k,j} F_{k,j} - \frac{1}{V}\sum_k \dot{Q}_k,\end{aligned} \tag{5.84}$$

where

$\hat{v}_j$ is the average particle (or parcel) velocity
$v_{k,j}$ is the local particle velocity
$F_{k,i}$ is the force on the particle
$\dot{Q}_k$ is the heat transfer due to the local particle k

In these equations, for simplicity, the effects of mass transfer between particles and the fluid were omitted, and the heat transfer from a severed particle (i.e., the boundary of a numerical cell slicing the particle) and molecular (i.e., conduction and viscous) terms have been neglected.* The force acting on the carrier phase due to the presence of particles is the volume-averaged force, described in Crowe et al. (2012), and includes the effects of quasi-steady drag, lift, rotation, pressure-gradient, added mass, and viscous-unsteady forces (discussed further in Section 5.3.2.6). The average force due to quasi-steady drag is

$$F_{k,i} = 3\pi\mu_c D_k f_k\left(\tilde{u}_i - v_{k,i}\right), \tag{5.85}$$

where

$f = C_D Re_p/24$ is the drag factor
subscript k is the particle number

Ling et al. (2012) and Sun et al. (2005) showed that the pressure-gradient, added mass, and viscous-unsteady forces are of the same order of magnitude and significant while a shock passes over a particle; however, after the shock passes, these forces decay to negligible values on the acoustic timescale, which is typically much shorter than the response time of the particle. Ling et al. (2012), however, point out that the unsteady forces are important for contact dominated, or dense particle flows with high particle

* Further discussion and information on these subjects can be found in Crowe et al. (2012).

volume fractions, for a significant time after the shock passes. The heat transfer $\dot{Q}_k$ can include several effects, such as quasi-steady, undisturbed-unsteady, and diffusive-unsteady contributions (discussed further in Section 5.3.2.8), and can also include radiation and rarefied, compressible and turbulence effects on convection. A simple model for the convective heat transfer between the particle and the carrier phase is given as

$$\dot{Q}_k = Nu\pi Dk_c\left(T_s - \langle T_c \rangle\right) \tag{5.86}$$

where
- Nu is the Nusselt number
- D is the particle diameter
- k_c is the thermal conductivity of the carrier phase
- T_s is the surface temperature of the particle
- $\langle T_c \rangle$ is the average temperature of the surrounding (carrier phase) fluid (formulas for Nu can be found in Crowe et al. (2012), Fox et al. (1978), and Feng and Michaelides (1996))

A simple diffusion model for the covariance terms in the energy Equation 5.84 is

$$-\frac{\partial}{\partial x_j}\left[\alpha_c\langle p'u_j'\rangle + \frac{1}{2}\frac{\partial}{\partial x_j}\alpha_c\langle \rho u_i''u_i''u_j''\rangle + \frac{\partial}{\partial x_j}\alpha_c\langle \rho e''u_j''\rangle\right] \approx \frac{\partial}{\partial x_i}\left(\alpha_c\langle \rho_c\rangle\tilde{R}_{ij}\frac{\varepsilon}{K}\left[C_k\frac{\partial K}{\partial x_j} + C_e k_{eff}\frac{\partial \tilde{T}}{\partial x_j}\right]\right), \tag{5.87}$$

where the pressure–velocity covariance has been neglected and the fluctuation of internal energy is modeled as an effective heat flux.

If the carrier phase is an ideal gas, the average pressure is modeled by the ideal gas EOS

$$\langle p\rangle = \left(\langle \gamma_c\rangle - 1\right)\langle \rho_c\rangle\tilde{e}_c, \tag{5.88}$$

where the internal energy is modeled by the caloric EOS

$$\tilde{e}_c = C_c\tilde{T}_c. \tag{5.89}$$

The carrier phase volume fraction is determined from

$$\alpha_c = 1 - \alpha_d, \tag{5.90}$$

where the particle volume fraction is determined by tallying the number of particles in a computational cell

$$\alpha_d = \frac{1}{V}\sum_k V_k^d, \tag{5.91}$$

where V_k^d is the volume of the dispersed phase particle k.

5.3.2.5.1 Carrier Phase Turbulence Carrier phase turbulence can be augmented or attenuated due to the presence of particles (Schwarzkopf et al., 2009a,b, Balachandar and Eaton, 2010, Crowe et al., 2012). In order to capture the modulation of turbulence due to particles in compressible flow, Horwitz and Schwarzkopf (2015) extended the work of Besnard et al. (1992) and Crowe et al. (2012) to include the effects of particle on the carrier phase compressible turbulence equations. To simplify the equations, dilute flow was assumed and mass transfer was neglected. The viscous stress was assumed to be negligible compared to the pressure gradient. It should be noted that under dilute assumptions $\alpha_d \approx 0$, and several terms were omitted from the

following equations and caution is encouraged when applying these equations to dense flows. The Reynolds stress for the carrier phase fluid is given as

$$\begin{aligned}\frac{\partial \alpha_c \langle \rho_c \rangle \tilde{R}_{ij}}{\partial t} + \frac{\partial \alpha_c \langle \rho_c \rangle \tilde{u}_k \tilde{R}_{ij}}{\partial x_k} &= a_i \frac{\partial \langle p \rangle}{\partial x_j} + a_j \frac{\partial \langle p \rangle}{\partial x_i} - \alpha_c \langle \rho_c \rangle \left(\tilde{R}_{ik} \frac{\partial \tilde{u}_j}{\partial x_k} + \tilde{R}_{jk} \frac{\partial \tilde{u}_i}{\partial x_k} \right) \\ &\quad - C_{r1} \left(a_i \frac{\partial \langle p \rangle}{\partial x_j} + a_j \frac{\partial \langle p \rangle}{\partial x_i} - \frac{2}{3} \delta_{ij} a_k \frac{\partial \langle p \rangle}{\partial x_k} \right) \\ &\quad + C_{r2} \alpha_c \langle \rho_c \rangle \left(\tilde{R}_{ik} \frac{\partial \tilde{u}_j}{\partial x_k} + \tilde{R}_{jk} \frac{\partial \tilde{u}_i}{\partial x_k} - \frac{2}{3} \delta_{ij} \tilde{R}_{mk} \frac{\partial \tilde{u}_m}{\partial x_k} \right) \\ &\quad + C_r \frac{\partial}{\partial x_k} \left(\alpha_c \langle \rho_c \rangle \frac{K}{\varepsilon} \tilde{R}_{kn} \frac{\partial \tilde{R}_{ij}}{\partial x_n} \right) \\ &\quad - C_{r3} \alpha_c \langle \rho_c \rangle \frac{\varepsilon}{K} \left(\tilde{R}_{ij} - \frac{1}{3} \delta_{ij} \tilde{R}_{kk} \right) - \frac{2}{3} \delta_{ij} \alpha_c \langle \rho_c \rangle \varepsilon \\ &\quad + \frac{1}{V} \sum_k 3\pi \mu_c D_k f_k \left(\tilde{u}_i - v_{k,i} \right) \left(u_{k,j} - v_{k,j} \right) \\ &\quad + \frac{1}{V} \sum_k 3\pi \mu_c D_k f_k \left(\tilde{u}_j - v_{k,j} \right) \left(u_{k,i} - v_{k,i} \right), \end{aligned} \tag{5.92}$$

where

$\tilde{R}_{ij} = \langle \rho u_i'' u_j'' \rangle / \langle \rho_c \rangle$ is the Reynolds stress

$a_i = \langle \rho' u_i' \rangle / \langle \rho_c \rangle$ is the mass-weighted turbulent velocity*

The local force acting on the kth particle in the jth direction is $F_{k,j} = 3\pi\mu_c D_k f_k (u_{k,j} - v_{k,j})$, and the particle center-of-mass velocity is $v_{k,j}$. As the flow transitions to single phase, that is, $\alpha_c \to 1$, $F_k \to 0$, and $\langle \rho_c \rangle \to \bar{\rho} = \rho_m$,† the single-phase multicomponent Reynolds stress, Equation 5.27, can be recovered when substituting $\varepsilon = K^{3/2}/S$. The modulation of turbulence is governed by $\frac{1}{V} \sum_k 3\pi\mu_c D_k f_k \left(\tilde{u}_i - v_{k,i} \right) \left(u_{k,j} - v_{k,j} \right)$ and ε. It turns out that for compressible flows, the modulation terms are only slightly different from the incompressible case given in Crowe et al. (2012). The compressible effects come from M_p in the compressible drag coefficient, Equation 5.74, and the mean Favre velocity, $\tilde{u}_i$. In addition, the unsteady and added mass terms were neglected in order to simplify the equation.

In the previous equation, an additional term arises, that is, the mass-weighted turbulence velocity. A model for the carrier phase turbulence mass flux ($\langle \rho_c \rangle a_i$) is

$$\begin{aligned}\frac{\partial \alpha_c \langle \rho_c \rangle a_i}{\partial t} + \frac{\partial \alpha_c \langle \rho_c \rangle \tilde{u}_k a_i}{\partial x_k} &= b \frac{\partial \langle p \rangle}{\partial x_i} - \tilde{R}_{ij} \frac{\partial \alpha_c \langle \rho_c \rangle}{\partial x_j} + \alpha_c \langle \rho_c \rangle \frac{\partial a_i a_j}{\partial x_j} \\ &\quad - \alpha_c \langle \rho_c \rangle a_j \frac{\partial \bar{u}_i}{\partial x_j} + \alpha_c \langle \rho_c \rangle C_a \frac{\partial}{\partial x_k} \left(\frac{K}{\varepsilon} \tilde{R}_{kn} \frac{\partial a_i}{\partial x_n} \right) \\ &\quad - C_{a1} \alpha_c \langle \rho_c \rangle \frac{\varepsilon}{K} a_i + b \frac{1}{V} \sum_k 3\pi \mu_c D_k f_k \left(u_{k,i} - v_{k,i} \right), \end{aligned} \tag{5.93}$$

where $b = -\langle \rho' v' \rangle$ is the density-specific volume covariance (similar to the definition in Section 5.2.2.1). Since $b \geq 0$ (Besnard et al., 1992), the presence of particles can alter the turbulence mass flux based on the sign of $F_{k,i}$. The effects of particles act as a stirring mechanism on the turbulence mass flux. Under the present assumptions, the particle contributions to a_i require that a nonzero b exists in the carrier phase, which can only occur in a multicomponent carrier phase flow or across a shock front. Again, the previous

* These definitions differ slightly when compared to the definitions for mixing continua, given in Section 5.2.2.1.

† For this condition, the transition in density is necessary when going from a single-phase, single-component carrier fluid density to a single-phase multicomponent fluid.

Table 5.5 Coefficient Values for Equation 5.95

C_ε	$C_{\varepsilon 1}$	$C_{\varepsilon 2}$	$C_{\varepsilon 3}$	$C_{\varepsilon 4}$
4.2	1.2	1.92	1.2	−1.2

equation reduces to Equation 5.28 under the conditions mentioned earlier. A model for the density-specific volume covariance is

$$\frac{\partial \alpha_c \langle \rho_c \rangle b}{\partial t} + \frac{\partial \alpha_c \langle \rho_c \rangle \tilde{u}_k b}{\partial x_k} = -2(b+1) a_j \frac{\partial \alpha_c \langle \rho_c \rangle}{\partial x_j} + 2\alpha_c \langle \rho_c \rangle a_j \frac{\partial b}{\partial x_j} + \alpha_c \langle \rho_c \rangle^2 C_b \frac{\partial}{\partial x_i}\left(\frac{K}{\alpha_c \langle \rho_c \rangle \varepsilon} \tilde{R}_{ij} \frac{\partial b}{\partial x_j} \right) - C_{b1} \alpha_c \langle \rho_c \rangle \frac{\varepsilon}{K} b, \tag{5.94}$$

which is similar to Equation 5.29. Although neglected, the effects of particles on b are mainly due to mass transfer from the dispersed to the carrier phase, which could occur due to evaporation, condensation, or mass transfer from chemical reactions. Therefore, this special case shows that b within the carrier phase fluid can only be generated across a shock and by multicomponent carrier phase mixing. A model for the turbulence dissipation, ε, is found by assuming the turbulence dissipation scales with the turbulence energy

$$\frac{\partial \alpha_c \langle \rho \rangle \varepsilon}{\partial t} + \frac{\partial \alpha_c \langle \rho \rangle \tilde{u}_k \varepsilon}{\partial x_k} = -C_{\varepsilon 1} \alpha_c \langle \rho \rangle \frac{\varepsilon}{K} \tilde{R}_{ij} \frac{\partial \tilde{u}_i}{\partial x_j} + C_{\varepsilon 3} \frac{\varepsilon}{K} a_j \frac{\partial \langle p \rangle}{\partial x_j} - C_{\varepsilon 4} \bar{\rho} \varepsilon \frac{\partial \bar{u}_j}{\partial x_j} + C_\varepsilon \frac{\partial}{\partial x_i}\left(\alpha_c \langle \rho \rangle \frac{K}{\varepsilon} \tilde{R}_{ij} \frac{\partial \varepsilon}{\partial x_j} \right) - C_{\varepsilon 2} \alpha_c \langle \rho \rangle \frac{\varepsilon^2}{K} + C_{\varepsilon 5} \frac{\upsilon_c^2}{V} \sum_k f_k \frac{\left| \tilde{u}_i - v_{k,i} \right|^2}{D_k}. \tag{5.95}$$

The last term was derived by Schwarzkopf et al. (2009a) and accounts for the augmentation and attenuation of carrier phase turbulence dissipation due to the dispersed phase. The coefficient $C_{\varepsilon 5}$ is given as a function of the particle Reynolds number*

$$C_{\varepsilon 5} = 0.025 C_{\varepsilon 2} Re_p^{1.524}, \tag{5.96}$$

and there is no understanding of M_p on $C_{\varepsilon 5}$. However, similar to $\tilde{R}_{ij}$, compressibility effects are accounted for in the drag factor (recall $f = C_D Re_p/24$) and in $\tilde{u}_i$. Although not studied, suggested coefficients for Equations 5.92 through 5.94 are given in Table 5.2, and suggested starting coefficients for Equations 5.95 and 5.96 are given in Table 5.5.

5.3.2.6 Dispersed Phase Equations of Motion

Here, we consider a Lagrangian representation of the dispersed phase. For simplicity, we assume the particles to be rigid, nonreacting (no mass exchange with the surround gas), constant heat capacity, and uniform temperature distribution. The governing equations for the dispersed phase (for the kth particles) are given by

$$\frac{d\mathbf{x}_{d,k}}{dt} = \mathbf{u}_{d,k}, \tag{5.97}$$

$$m_{d,k} \frac{d\mathbf{u}_{d,k}}{dt} = \mathbf{F}_{dc,k} + \mathbf{F}_{dd,k}, \tag{5.98}$$

$$m_{d,k} C_{d,k} \frac{dT_{d,k}}{dt} = Q_{dc,k}. \tag{5.99}$$

The position, velocity, temperature, mass, and heat capacity of the kth particle are denoted by $\mathbf{x}_{d,k}$, $\mathbf{u}_{d,k}$ (which is $v_{i,k}$ in the carrier phase equations mentioned earlier), $T_{d,k}$, $m_{d,k}$, and $C_{d,k}$. It should be noted that often the

* The coefficient and exponent for $C_{\varepsilon 5}$ are slightly different from those published in Schwarzkopf et al. (2009b).

number of particles in a real system can far exceed the number of particles used in a simulation. Hence, the term *particle* used in modeling denotes a computational particle, which can account for a collection of physical particles that are located around the location $\mathbf{x}_{d,k}$.

The hydrodynamic force and heat transfer exerted on the kth particle by the surrounding gas is given by $\mathbf{F}_{dc,k}$ and $Q_{dc,k}$. The force and heat transfer appear on the right-hand side of the gas momentum and energy (Equations 5.83 and 8.84, respectively) as the back-coupling effect of the particles on the gas flow. In these equations, $\sum_k$ represents sum over all the particles within a cell. Note that the back-coupling effect of particle force and heat transfer must be appropriately scaled by the local ratio of real to computational particles.

Under dense conditions, the kth particle also experiences a net force due to collisions with its neighbors, which is represented by $\mathbf{F}_{dd,k}$. There can also be associated heat transfer due to such interparticle collisions, whose effects however can be expected to be small, and thus is neglected here.

Following the works of Parmar et al. (2011, 2012) and Ling et al. (2011a, b, 2012), the hydrodynamic force is expressed as the sum of following individual contributions:

$$\mathbf{F}_{dc,k} = \mathbf{F}_{qs,k} + \mathbf{F}_{pg,k} + \mathbf{F}_{iu,k} + \mathbf{F}_{vu,k}, \tag{5.100}$$

where $\mathbf{F}_{qs,k}$, $\mathbf{F}_{pg,k}$, $\mathbf{F}_{am,k}$, and $\mathbf{F}_{vu,k}$ are the quasi-steady, pressure-gradient, inviscid-unsteady, and viscous-unsteady forces, respectively.

5.3.2.6.1 Quasi-Steady Force The expression for quasi-steady force on an isolated particle (limit of zero volume fraction) in a compressible flow with complete Re_p and M_p dependence is presented in Section 5.3.2.3. The corresponding drag coefficient for finite particle volume fraction can be expressed as

$$C_D\left(\mathrm{Re}_p, M_p, \alpha_d\right) = C_{D,0}\left(\mathrm{Re}_p, M_p\right)\xi\left(\alpha_d\right), \tag{5.101}$$

where

$C_{D,0}(Re_p, M_p)$ is the drag coefficient in the limit of zero volume fraction

$\xi(\alpha_d)$ is the particle volume-fraction correction function given by (Sangani et al., 1991)

$$\xi(\alpha_d) = \frac{1+2\alpha_d}{(1-\alpha_d)^3}, \tag{5.102}$$

where α_d is the particle volume fraction given in Equation 5.91. The expression for $\xi(\alpha_d)$ was analytically derived for dilute periodic arrays of spheres in the incompressible regime. However, it has been shown to be a good approximation for random arrays of spheres for $\alpha_d < 0.3$. Here, it is presented in the context of compressible flows and thus requires caution.

5.3.2.6.2 Pressure-Gradient Force The pressure-gradient force arises from the undisturbed flow. Even if the particle was not there (as a result the flow is undisturbed), the volume of fluid at the particle location will experience a force if there is nonzero local stress gradient. This force can be expressed as

$$\mathbf{F}_{pg,k} = V_d(\nabla \cdot \sigma_c)_k, \tag{5.103}$$

where V_d is the volume of the particle. Here, σ_c represents the stress tensor of undisturbed continuous phase (gas). In the case of an inviscid ambient flow, the divergence of the stress tensor becomes the pressure gradient (and hence the term *pressure-gradient force*)

$$\mathbf{F}_{pg,k} = -V_d(\nabla p_c)_k. \tag{5.104}$$

5.3.2.6.3 Inviscid-Unsteady Force In compressible flows, the expression for the added mass force is more complicated than in the incompressible counterpart. The added mass force involves a history integral since the acoustic disturbances resulting from the relative acceleration between the particle and the surrounding gas propagate at a finite speed. In an incompressible flow, these acoustic disturbances travel at sonic speed,

and as a result, the added mass force is directly proportional to the relative acceleration at that instant. This direct proportionality is lost in a compressible flow, and as a result, this force cannot be viewed as an added mass and must be termed inviscid-unsteady force. Due to finite speed of sound, the inviscid-unsteady force at any instance depends on the past history of relative acceleration. As shown in Parmar et al. (2008), the resulting convolution integral can be written as

$$\mathbf{F}_{iu,k} = V_d \int_{-\infty}^{t} K_{iu}(t-\chi)\left[\left(\frac{d}{dt}(\rho_c \mathbf{u}_c)\right)_k - \frac{d}{dt}(\rho_c \mathbf{u}_{d,k})\right]\frac{c_c}{R}d\chi, \tag{5.105}$$

where the density-weighted relative acceleration (the term within the square brackets) is evaluated at χ (an arbitrary time within the impulsive acceleration region) and the inviscid kernel K_{iu} is evaluated at $t-\chi$. Here, $R = D/2$ is the radius of the particle and c_c is the sound speed of the carrier (or continuous) phase. Due to compressibility, the density of the ambient flow cannot be taken as a constant, and thus, flow and particle accelerations must be generalized to their momentum forms. Here, D/Dt is the total derivative following the fluid at the particle location, while d/dt is the rate of change following the particle.

In an incompressible flow, the inviscid-unsteady kernel K_{iu} reduces to a delta function, and thus, the added mass force depends only on instantaneous relative acceleration. In a compressible flow, in the zero Mach number limit, the inviscid kernel takes the following explicit form

$$K_{iu}(t-\chi) = \exp\left[\frac{c_c(t-\chi)}{R}\right]\cos\left[\frac{c_c(t-\chi)}{R}\right], \tag{5.106}$$

where the subscript *iu* stands for inviscid-unsteady force. The inviscid kernel depends only on Mach number. Finite Mach number extensions to the zero Mach number analytic kernel mentioned earlier have been obtained through DNSs (Parmar et al., 2008).

The kernel K_{iu} decays on an acoustic timescale. For example, $K_{iu}(\tau)$ is virtually zero for $\tau > 10R/c_c$, indicating that acceleration history is almost forgotten for times longer than 10 acoustic time units. Such rapid decay allows significant simplification in situations where the acceleration history of the ambient flow and the particle is slow compared to the acoustic timescale. Under nonshock conditions, where the particle is not subjected to rapid flow variation, the relative acceleration in Equation 5.105 can be taken out of the integral and an effective added mass coefficient can be defined as

$$C_M = \int_{-\infty}^{t} K_{iu}(t-\chi)\frac{c_c}{R}d\chi, \tag{5.107}$$

and correspondingly, the inviscid-unsteady force can be expressed as

$$\mathbf{F}_{iu,k} = V_d C_M\left[\left(\frac{d}{dt}(\rho_c \mathbf{u}_c)\right)_k - \frac{d}{dt}(\rho_c \mathbf{u}_{d,k})\right]. \tag{5.108}$$

In the case of shock–particle interaction, this approximation is inappropriate since relative acceleration varies on the acoustic timescale (shock–particle interaction will be discussed in Section 5.3.2.7).

In compressible particle-laden flows of finite particle volume fraction, K_{iu} and C_M will be functions of M_p and α_d. A model for C_M is suggested in Ling et al. (2013) as

$$C_M(M_p, \alpha_d) = 0.5\eta_1(M_p)\eta_2(\alpha_d), \tag{5.109}$$

where 0.5 is the incompressible added mass coefficient for a sphere. Here, η_1 and η_2 are correction functions that take into account the effects of compressibility and particle volume fraction given by

$$\eta_1(M_p) = 1 + 1.8(M_p)^2 + 7.6(M_p)^4, \tag{5.110}$$

$$\eta_2(\alpha_d) = \frac{1+2\alpha_d}{1-\alpha_d}. \tag{5.111}$$

When M_p and α_d approach zero, η_1 and η_2 both reduce to unity and we recover $C_M = 0.5$. When $M_p = 0$ but α_d is finite, Equation 5.109 is identical to the expression of added mass force for a distribution of spheres in incompressible flows given by Sangani et al. (1991). When $\alpha_d = 0$ and $M_p > 0$, Equation 5.109 reduces to the numerical correlation of effective finite Mach number added mass coefficient for a sphere by Parmar et al. (2008). For $M_p > M_{p,cr}$ the increase in quasi-steady force due to the bow shock will be more important than contribution from the added mass force.

5.3.2.6.4 Viscous-Unsteady Force The viscous-unsteady force, also called the Basset history force, can be expressed as

$$\mathbf{F}_{vu,k} = 3\pi\nu_c D \int_{-\infty}^{t} K_{vu}(t-\chi)\left[\left(\frac{d(\rho_c \mathbf{u}_c)}{dt}\right)_k - \frac{d(\rho_c \mathbf{u}_{d,k})}{dt}\right] d\chi, \tag{5.112}$$

where K_{vu} is the viscous-unsteady force kernel, which is a function of Re_p, M_p, and α_d. In the limit of zero Reynolds number incompressible dilute flow, K_{vu} is known as the Basset history kernel. Finite Reynolds number incompressible extension of K_{vu} has been presented by Mei and Adrian (1992) and Kim et al. (1998). The effects of M_p and α_d on viscous-unsteady force are still not fully understood and thus often ignored.

5.3.2.7 Shock–Particle Interaction

Typical shock front thicknesses in gases are on the order of hundred nanometers or less. Thus, even micron size particles will appear to be of finite size compared to the shock wave front. Here, we are concerned with evaluating the time-dependent force on a particle as the shock wave propagates over it. It is important to recognize that not only is the timescale associated with shock propagation rapid but also the length scale over which the flow properties, such as gas velocity, pressure, and temperature, change from preshock to postshock conditions is very thin. For example, consider the expressions for quasi-steady, pressure-gradient, inviscid-unsteady and viscous-unsteady forces given in Equations 5.101, 5.103, 5.105, and 5.112. In these equations, flow quantities such as $\mathbf{u}_c$, ρ_c, and σ_c are the continuous phase velocity, density, and stress tensor as seen by the particle. In the point-particle approach, these are properties of the undisturbed flow that would exist at the particle location in the absence of the particle. Typically, these undisturbed flow quantities are evaluated at the center of the particle. This would be sufficient if the ambient flow variation across the particle is small. In the context of shock–particle interaction, as the shock propagates over the particle, part of the particle sees the preshock flow, while the rest of the particle is subjected to postshock flow. Thus, there is ambiguity in the application of Equations 5.101, 5.103, 5.105, and 5.112 for the calculation of the time-dependent force on a particle during the passage of the shock.

There is a remarkable theorem by Faxén (1923) that generalized the Stokes drag on a spherical particle from a steady uniform flow to an arbitrary spatially varying flow. The key result of Faxén's theorem is to replace in the Stokes drag formula the ambient flow velocity at the particle center with the undisturbed ambient flow velocity averaged over the surface of the sphere. If the ambient flow velocity varies substantially over the size of the particle, then the Faxén's correction to Stokes drag is substantial. The extension of Faxén theorem to unsteady flows has a long history culminating in the works of Maxey and Riley (1983) and Gatignol (1983). The resulting Maxey–Riley–Gatignol (MRG) equation is an exact expression for force on a spherical particle subjected to unsteady spatially varying ambient flow. The MRG equation is rigorous in the limit of zero Reynolds number and assumes the length scale of ambient flow variation to be large compared to particle size.

In the context of shock–particle interaction, clearly, the ambient flow varies on the scale of the particle. Thus, an extension of the Faxén's theorem to the compressible flow regime, in other words a compressible MRG equation, is required in order to accurately model the force on a particle. Parmar et al. (2012) obtained such a compressible extension of the MRG equation for the force on a particle in arbitrary motion in a compressible ambient flow that is varying both in time and in space. This theoretical derivation, as in the MRG equation, is in the limit of zero Reynolds and Mach numbers and for length scales of ambient flow variation much longer than the particle size. For the application of this theory to the case of shock–particle

interaction, the limitation on length scale of ambient flow variation is not appropriate. Recently, this limitation was relaxed, and the force on a particle during the passage of a shock was expressed again as the sum of quasi-steady, pressure-gradient, inviscid-unsteady, and viscous-unsteady forces. As will be seen, each of these forces will depend on either volume or surface averages of the undisturbed ambient flow over the particle, which are well defined even when the ambient flow varies sharply over the scale of the particle. The unsteady forces must again be separated into surface and volume contributions as

$$\mathbf{F}_{iu,k} = \mathbf{F}_{iu,1,k} + \mathbf{F}_{iu,2,k}, \tag{5.113}$$

$$\mathbf{F}_{vu,k} = \mathbf{F}_{vu,1,k} + \mathbf{F}_{vu,2,k} + \mathbf{F}_{vu,3,k}. \tag{5.114}$$

Each of these components can now be expressed as in terms of volume and surface averages of the surrounding gas as

$$\mathbf{F}_{qs,k} = 6\pi\mu R(\overline{\mathbf{u}_c}^S - \mathbf{u}_{d,k}), \tag{5.115}$$

$$\mathbf{F}_{pg,k} = \frac{4}{3}\pi R^3 \overline{\rho_c \frac{D\mathbf{u}_c}{Dt}}^V, \tag{5.116}$$

$$\mathbf{F}_{iu,1,k} = \frac{4}{3}\pi R^3 \int_{\xi=-\infty}^{t} K_{iu}(\tau)\left[\frac{D\overline{(\rho_c \mathbf{u}_c)}^V}{Dt} - \frac{D\overline{(\rho_c \mathbf{u}_{d,k})}^V}{Dt}\right]\frac{c_c}{R}d\xi, \tag{5.117}$$

$$\mathbf{F}_{iu,2,k} = \frac{4}{3}\pi R^3 \int_{\xi=-\infty}^{t} K_{iu}(\tau)\left[\frac{D\overline{(\mathbf{r}\nabla\cdot(\rho_c \mathbf{u}_c))}^V}{Dt} - \frac{D\overline{(\mathbf{r}\nabla\cdot(\rho_c \mathbf{u}_{d,k}))}^V}{Dt}\right]\frac{c_c}{R}d\xi, \tag{5.118}$$

$$\mathbf{F}_{vu,1,k} = 6R^2\sqrt{\pi\nu}\int_{\xi=-\infty}^{t} K_{vu}^V(t-\xi)\left[\frac{D\overline{(\rho_c \mathbf{u}_c)}^V}{Dt} - \frac{D\overline{(\rho_c \mathbf{u}_{d,k})}^V}{Dt}\right]_{t=\xi} d\xi, \tag{5.119}$$

$$\mathbf{F}_{vu,2,k} = 6R^2\sqrt{\pi\nu}\int_{\xi=-\infty}^{t} K_{vu}^V(t-\xi)\left[\frac{D\overline{(\mathbf{r}\nabla\cdot(\rho_c \mathbf{u}_c))}^V}{Dt} - \frac{D\overline{(\mathbf{r}\nabla\cdot(\rho_c \mathbf{u}_{d,k}))}^V}{Dt}\right]_{t=\xi} d\xi, \tag{5.120}$$

$$\mathbf{F}_{vu,3,k} = 6R^2\sqrt{\pi\nu}\int_{\xi=-\infty}^{t} K_{vu}^S(t-\xi)\left[\frac{D\overline{(\rho_c \mathbf{u}_c)}^S}{Dt} - \frac{D\overline{(\rho_c \mathbf{u}_{d,k})}^S}{Dt}\right]_{t=\xi} d\xi. \tag{5.121}$$

In these equations, $\overline{(\,)}^S$ (and $\overline{(\,)}^V$ represent averages over the surface and volume of the spherical particle, respectively. As a consequence of splitting the viscous-unsteady force into surface and volume averages, the viscous-unsteady kernels also split accordingly as

$$K_{vu}^V = C^V(\tau)K_{vu}, \tag{5.122}$$

$$K_{vu}^S = C^S(\tau)K_{vu}, \tag{5.123}$$

where K_{vu} is the incompressible Basset history kernel (Basset, 1888). The effects of compressibility and flow inhomogeneity are built into the correction functions (see Parmar et al., 2012). The previous equation is the generalized version of Faxén's theorem in the time domain.

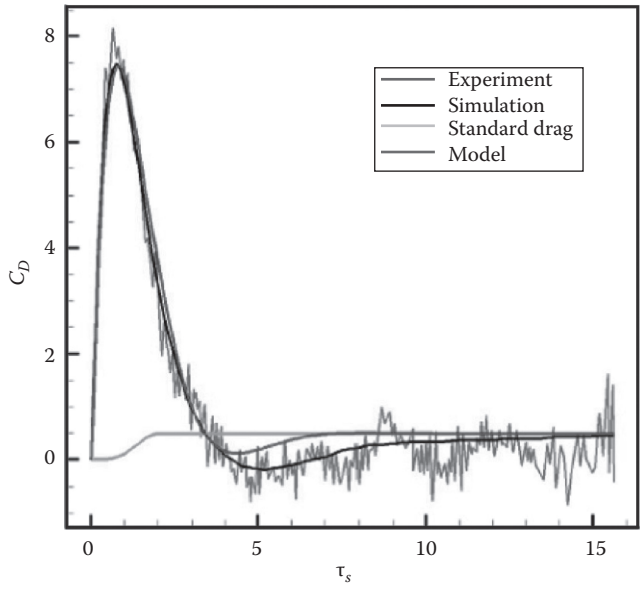


Figure 5.12

Comparison of the experimental measurement of force on an 8 mm spherical particle subjected to shock (in air) of Mach number 1.22 (Sun et al., 2005) against simulation and point-particle model prediction. Shown in the figure are comparisons of time history of the drag coefficient obtained by the experiment, (direct numerical) simulation, standard drag (quasi-steady model), and (improved point-particle) model.

Although the earlier expressions have been rigorously obtained for the limit Re_p, $M_p \to 0$, we now apply the formulation to a particle subjected to a shock wave of Mach number 1.22 propagating over it. This case was experimentally and computationally considered by Sun et al. (2005) for a fixed shock Mach number for a range of particle sizes. Note that the Mach number of the postshock flow is only about 0.3. The experimental results are compared against the model prediction mentioned earlier and shown in Figure 5.12. Also presented is the result from fully resolved DNS. In comparison, the model involves the solution of the force contributions given in Equations 5.115 through 5.121. The model was able to predict the magnitude and time of occurrence ($\tau_s \sim 1$) of the peak force quite well. The deviation in the drag coefficient for $\tau_s > 2.75$ can be attributed to the fact that the model uses zero Reynolds number kernels. Detailed analysis of the different contributions to the total force shows that the viscous-unsteady (Basset) forces, given in Equations 5.119, 5.120, and 5.121, are not significant in predicting the peak force. Therefore, one may obtain a good estimate of the drag force by neglecting the viscous-unsteady forces and computing only the quasi-steady and inviscid-unsteady contributions given in Equations 5.115 through 5.118.

5.3.2.7.1 Particle Deformation Here, we are interested in the problem of a strong shock interacting with a particle, where the shock strength is of sufficient magnitude that the deformation of the particle cannot be ignored. For example, in the context of condensed phase detonation with embedded metal particles, the problem of detonation–particle interaction becomes important. Here, the density of the products of detonation is substantial, and the postshock pressure can be significantly larger than the yield strength of the particle. But experiments of shock interaction with a deforming particle (SIDP) in the context of metal particles subjected to an intense shock in a condensed matter ambience are rare in the literature, due to the complex nature of such experiments. Modeling and simulation are an attractive alternative that can provide time-resolved details of such interaction of a particle with a strong shock wave.

It is of interest to extend the earlier described theoretical model and present an SIDP model that includes the leading order effects of particle deformation and compression heating. To motivate such a model, it is appropriate to first consider the DNS of a deforming particle subjected to a strong shock in condensed matter. The material properties are characterized by appropriate equations of state, for example, Mie–Grüneisen EOS. The DNS results show the interaction details, such as shock reflection, refraction, and evolutions of average properties of particles. Based on the knowledge obtained from the DNS study, one can improve the model by including the effects of particle deformation and compression heating. Note that SIDP occurs in other interesting applications as well. For example, shock interaction with a droplet or a bubble can lead

to significant deformation of the droplet or the bubble. In fact, a sufficiently strong shock can lead to violent breakup and fragmentation of the droplet or bubble, for example, see Niederhaus et al. (2008), Quirk and Karni (1996), and Ranjan et al. (2011). Current modeling and simulation efforts are generally limited to modest deformation, and only limited investigations have addressed more complex scenarios such as breakup and fragmentation (Theofanous and Li, 2008, Theofanous, 2011, Theofanous et al., 2012).

As an example, Figure 5.13 shows the DNS results of Ling et al. (2013) where an aluminum particle is subjected to an intense shock in nitromethane (shock speed is 4800 m/s, the postshock pressure and velocity are 10.7 GPa and 2270 m/s). Details of particle deformation and fully resolved pressure and thermal fields computed at the microscale are shown in frames a–d. The time evolution of particle velocity and average temperature obtained from the DNS are shown in Figure 5.13e and f. A highly resolved axisymmetric grid was used in this simulation; however, it is impossible to resolve the flow around a particle when millions of particles must be considered, so a point-particle approach is often employed at the mesoscale, where all the microscale details must be accurately encapsulated into mass, momentum, and energy coupling models.

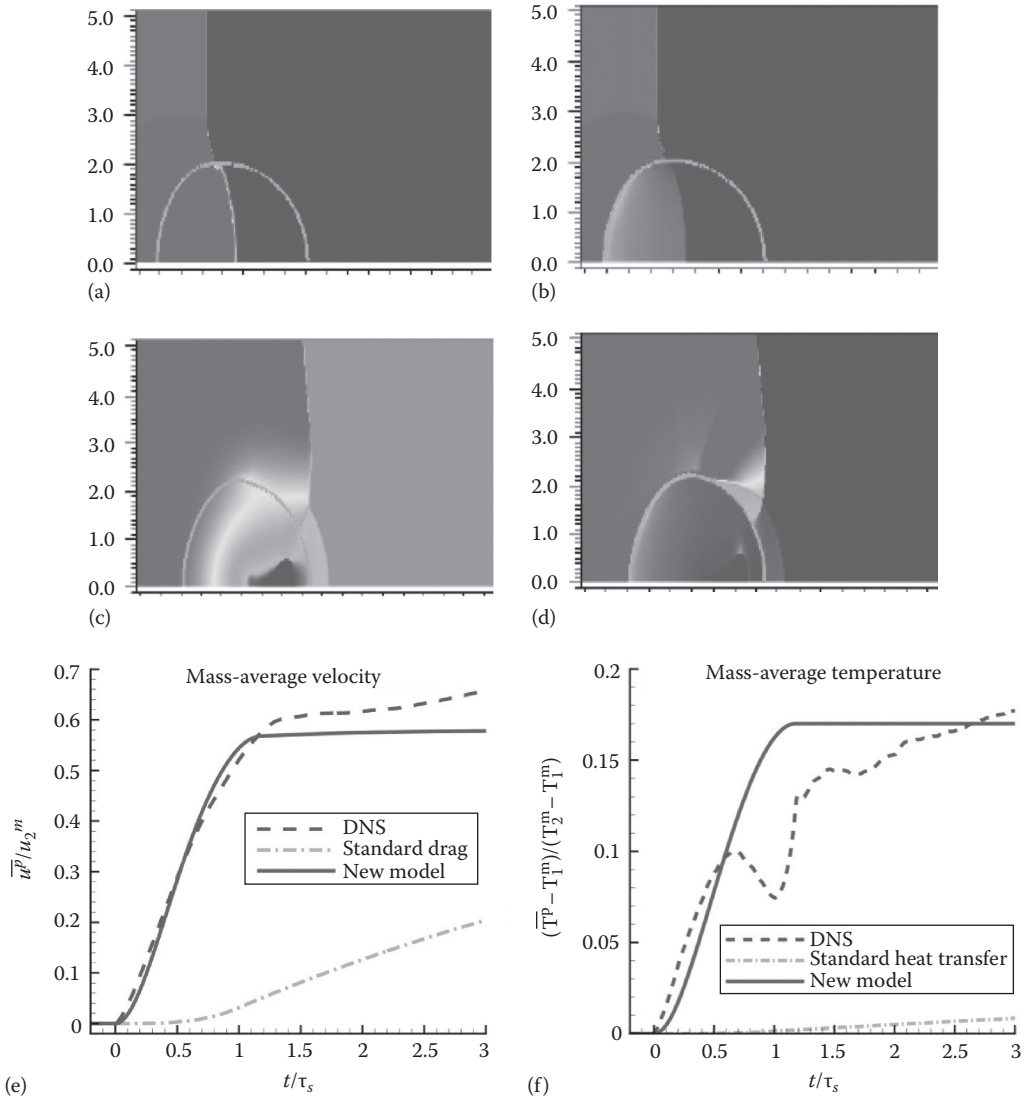


Figure 5.13

ALE3D simulations of intense shock propagation over an aluminum particle embedded in nitromethane (Ling et al., 2013). Frames (a) and (c) are pressures and (b) and (d) are temperature contours at 0.3 and 0.8 ns, respectively. Frames (e) and (f) compare the time evolution of nondimensional particle velocity and volume-averaged temperature against standard and improved physics-based models. (The vertical axis in (a) through (d) shows particle size in μm.)

Also shown in Figure 5.13e and f are the particle velocity and temperature predicted by conventional quasi-steady drag and heat transfer point-particle models. It is quite clear that such standard models result in large errors, since they have not been developed and tested for the intense unsteady pressure and temperature conditions representative of detonation–particle interaction. As a consequence, it can be expected that mesoscale simulations performed with the standard models can result in serious error. In contrast, physics-based coupling models employed in Ling et al. (2013) that include inviscid-unsteady effects can be seen to perform reasonably.

The results of the DNS can be generalized to a broader class of shock–particle interaction conditions. Representative scenarios of flow fields arising from SIDP are shown in Figure 5.14. The two key parameters that characterize the nature of particle deformation and the shock diffraction pattern are the impedance ratio (ζ_d/ζ_c) and the shock speed ratio (U_{st}/U_{si}) (here, ζ_d and ζ_c are the shock impedance in the particle and in the surrounding medium and U_{si} and U_{st} are the incidence and transmission shock propagation speeds in the surrounding medium and in the particle). The former ratio determines the reflected wave to be an expansion fan or a shock wave, while the latter ratio determines the shape of the transmitted shock (see Figure 5.14). In summary, there are four different scenarios: (1) a reflected expansion fan and a convex transmitted shock ($\zeta_d/\zeta_c < 1$ and $U_{st}/U_{si} > 1$), (2) a reflected shock and a concave transmitted shock ($\zeta_d/\zeta_c > 1$ and $U_{st}/U_{si} < 1$), (3) a reflected expansion fan and a concave transmitted shock ($\zeta_d/\zeta_c < 1$ and $U_{st}/U_{si} < 1$), and (4) a reflected shock and a convex transmitted shock ($\zeta_d/\zeta_c > 1$ and $U_{st}/U_{si} > 1$).

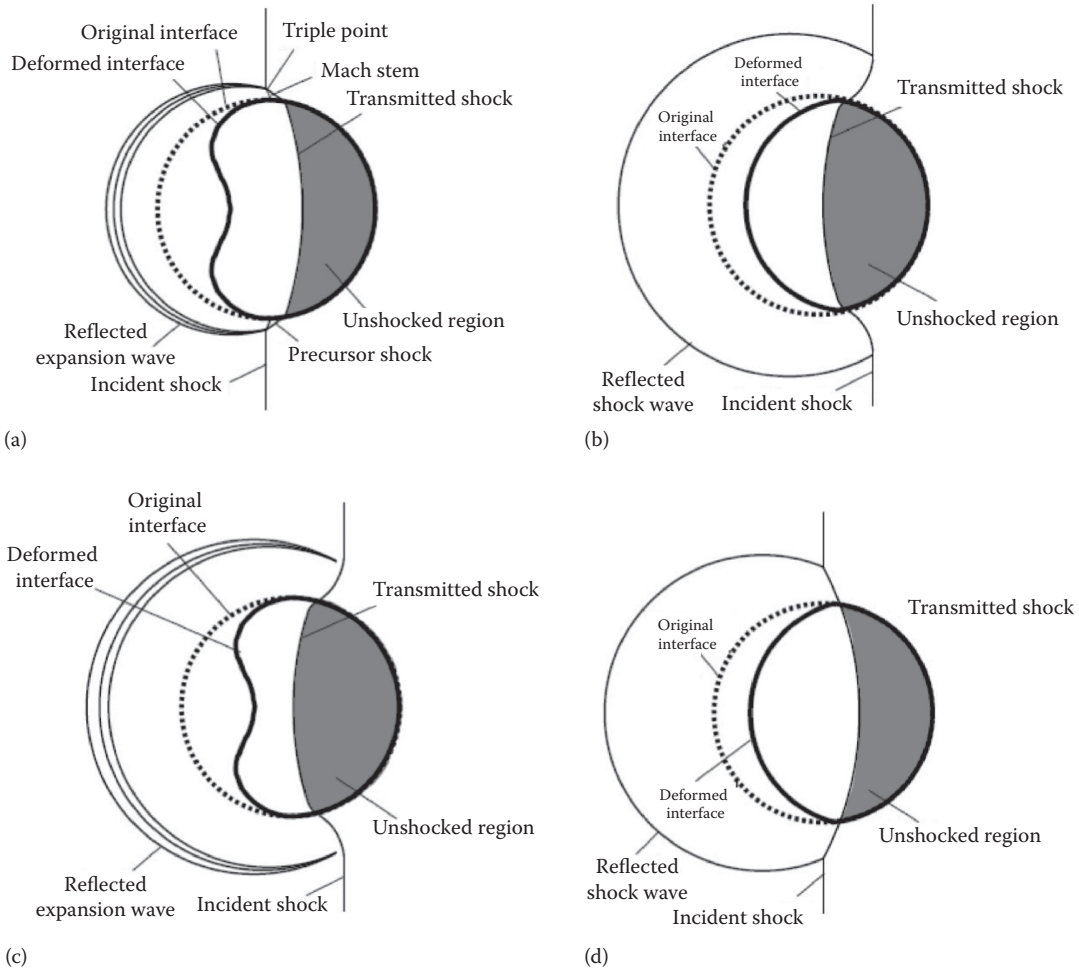


Figure 5.14

Representative scenarios of flow field arising from shock interaction with a deformable particle for different shock impedance and shock speed ratios. (a) $\zeta_d/\zeta_c < 1$, $U_{st}/U_{si} > 1$, (b) $\zeta_d/\zeta_c > 1$, $U_{st}/U_{si} < 1$, (c) $\zeta_d/\zeta_c < 1$, $U_{st}/U_{si} < 1$, and (d) $\zeta_d/\zeta_c > 1$, $U_{st}/U_{si} > 1$.

5.3.2.8 Heat Transfer due to Gas–Particle Interaction

Similar to Equation 5.100, the overall heat transferred to the kth particle $Q_{dc,k}$ is expressed as

$$Q_{dc,k} = Q_{qs,k} + Q_{uu,k} + Q_{du,k}, \tag{5.124}$$

where $Q_{qs,k}$, $Q_{uu,k}$, and $Q_{du,k}$ represent quasi-steady, undisturbed-unsteady, and diffusive-unsteady contributions, which are the thermal analogs of $\mathbf{F}_{qs,k}$, $\mathbf{F}_{pg,k}$, and $\mathbf{F}_{vu,k}$, respectively. Note that there is no thermal analog to the added mass force because the latter is inviscid in nature and arises from the no-penetration boundary condition.

The undisturbed-unsteady contribution accounts for heat conduction and work done by the surface stresses on the volume of gas replaced by the particle (Ling et al., 2011a). For incompressible viscous flows and rigid particles, the expression of $Q_{uu,k}$ is given by Balachandar and Ha (2001). In the present context, gas flow is considered as inviscid, and therefore, $Q_{uu,k}$ reduces to be equivalent to the compression work done by the gas pressure on a particle. When a particle interacts with an intensive shock wave, particles can experience serious compression and deformation and the compression work done by the surrounding gas can contribute significantly in heating the particle (Ruggirello et al., 2010, Ling et al., 2011a,b).

Similar to the analysis for the quasi-steady and viscous-unsteady forces, it can be expected that compressibility and finite particle volume fraction will also influence the quasi-steady and diffusive-unsteady contributions to heat transfer. For lack of detailed information, we can use the expressions of $Q_{qs,k}$ and $Q_{du,k}$ for a single particle given by Fox et al. (1978) and Feng and Michaelides (1996). In the correlation of Fox et al. (1978), the Nusselt number depends on M_p, and therefore, compressibility effect on quasi-steady heat transfer has been taken into account. In the governing equations, heat transfer to particles will influence the gas-phase energy Equation 5.84, which is coupled with the gas momentum Equation 5.83. As a result, the simplification on particle heat transfer model may influence the gas and particle motion. However, the errors caused by the simplified heat transfer model are expected to be of secondary importance.

Another important energy transfer effect in compressible flows is radiation heat transfer. The radiative heat transfer is the net heat transfer due to absorption and emission of radiant energy. If the particle is considered a gray body, then the absorptivity and emissivity are equal and a simple model, which assumes that a particle is within a black body enclosure, is given as (Crowe et al., 2012)

$$\dot{Q}_{rad} = \epsilon \sigma \pi D^2 \left(T_{ec}^4 - T_d^4 \right), \tag{5.125}$$

where

ϵ is the emissivity
σ is the Stefan–Boltzmann constant (5.67×10^{-8} W m^{-2} K^{-4})
D is the particle diameter
T_{ec} is the temperature of the enclosure
T_d is the temperature of the particle

This equation is for a single particle, and it becomes more complex as the volume fraction increases to dense limits primarily due to the modeling of the scattering effects in these regimes. Compressibility and rarefaction effects can play a role by altering the mean free path of the photons in the carrier phase. In addition, particle concentration due to turbulence can also shadow particles within a cloud. There are limited studies on the effect of radiation heat transfer within a cloud of finite size particles; some additional information on this topic can be found in Crowe et al. (2012), Kessel-Deynet and Burkert (2000), Fiveland (1988), Siegel (1981), and Chu and Churchill (1955). There are however many studies on the topic of radiation in aerosols.

5.3.3 Compressible Dense Particle Flows

Dense particle-laden flows (typically between the not-so-dilute and granular limits) are found in applications involving fluidized beds. In these flows, the volume fractions are high 1%–40%, and the effects of neighbor particles and contact forces between particles become important. Shocks in dense particle-laden flows are complex, having multiple reflections, transmissions, and interactions. Because of this, particle wakes and boundary layers are affected and simple models (derived from Stokes flow) to

describe the forces are questioned. Wagner et al. (2012) conducted a set of experiments to address questions related to shocked dense particle flows. Their experiment consisted of a gravity-driven curtain of ~100 μm glass spheres with a volume fraction of ~20%, inside of a shock tube. Three tests were conducted with incident shock Mach numbers in the range of 1.66–2.02, and since the timescales for the falling particles within the curtain were much larger than the timescale of the shock, the particles look stationary relative to the shock. Schlieren images were used to measure the expansion of the curtain (and identify shock locations), and pressure measurements were used to measure the effects of the particles on the downstream shock. Overall, they found that the thickness of the particle curtain expanded ~×10 for Mach 1.62 and nearly × 20 for Mach 2.02. They also concluded that the effect of the particle curtain lowered the momentum and energy fluxes in the gas by 30%–40% far downstream of the curtain relative to experiments without the curtain.

Ling et al. (2012) modeled the experiment of Wagner et al. (2012). In addition to the quasi-steady, pressure-gradient, added mass, and viscous-unsteady forces (further described in Section 5.3.2.6) in dilute particle-laden flows, dense particle-laden flows require an additional force(s) to account for the interparticle interaction, which includes particle–particle contact and the effect of neighbor particles on wake structures. An empirical force ($\mathbf{F}_{dd,k}$, shown in Equation 5.98) to account for these effects was proposed by Harris and Crighton (1994) and used by Andrews and O'Rourke (1996) and is commonly referred to as the gradient of the *solid stress*

$$\mathbf{F}_{dd,k} = -\frac{1}{\alpha_d \rho_d} \nabla \tau, \tag{5.126}$$

where τ is not a stress but a scalar given by (Snider, 2007)*

$$\tau = \frac{P_s \alpha_d^n}{\max\left[\left(\alpha_{d,cp} - \alpha_d\right), \epsilon\left(1 - \alpha_d\right)\right]}, \tag{5.127}$$

where

P_s is an empirical constant with units of pressure

$\alpha_{d,cp}$ is the close-packed particle volume fraction (~68% for spheres in a body-centered cubic configuration (Crowe et al., 2012))

ϵ is a small number ~10^{-7}

($n \sim 3$) the exponent that is an empirical constant (Snider et al., 1998)

This model shows a heavy dependence on the volume fraction and since it is empirical, it may need to be tuned for each set of experiments. When simulating the particle curtain experiments, Ling et al. (2012) found that the results were not all that sensitive to P_s, so long as it had the correct magnitude. They also identified that unsteady forces, volume fraction, compressibility, and interparticle collision were all needed to correctly capture the expansion of the shocked dense particle curtain. The effect of the unsteady forces is very large while the shock transitions over a particle and decays on the acoustic timescale after the passage of the shock to negligible values. Correction functions were applied to the quasi-steady, added mass, and viscous-unsteady forces to account for the effect of volume fraction. In addition, Mach number effects on quasi-steady and added mass forces were accounted for by correction functions. With these corrections, Ling et al. (2012) provided a simulation that agreed rather well with the measured pressure profiles and the time-dependent expansion of the particle curtain. Further discussion on these forces is given in Section 5.3.2.6.

5.3.4 Jump Relations for Dusty Gas Flows

The jump relations for dusty gas flows can be determined by assuming that the shock is steady and planar and that viscous effects are neglected. However, when particles are present within the shock width, complications arise in determining jump conditions. These complexities are due to shock–particle interactions, quasi-steady drag, added mass, unsteady viscous forces, mass transfer, void fractions, contact forces, and turbulence, and differences in properties such as pressure, temperature, internal energy,

* Snider (2007) proposed a modified form of solid stress introduced by Harris and Crighton (1994) to avoid the singularity as $\alpha_d \to \alpha_{d,cp}$.

density, sound speed, and specific heats that can occur in particle-laden flows. For most systems, the momentum and thermal response times are much longer than the shock transit time, and these are important in determining the relaxation behind the shock. Therefore, the assumption of thermal and mechanical equilibrium fails for particle-laden compressible flows containing metal particles in a gas. However, like two-fluid models, simplifications can be made to obtain a set of conservative equations for mass, momentum, and energy. Such simplifications typically require the response times of the particle to be similar to those of the gas. This results in a dusty gas formulation.

Anand (2014) derived such a set of equations for dusty gas conditions. The jump conditions were formulated based on the assumption of mixture properties for the pressure, velocity, mass, sound speed, gamma, and internal energy. In a frame of reference that is moving with the shock wave front, the jump conditions are

$$\text{Mass} \quad \bar{\rho}_{-}\left(v_s-\bar{u}_{-}\right)=\bar{\rho}_{+}v_s, \tag{5.128}$$

$$\text{Momentum} \quad \bar{P}_{-}+\bar{\rho}_{-}\left(v_s-\bar{u}_{-}\right)^2=\bar{P}_{+}+\bar{\rho}_{+}v_s^2, \tag{5.129}$$

$$\text{Energy} \quad \bar{e}_{-}+\frac{\bar{P}_{-}}{\bar{\rho}_{-}}+\frac{\left(v_s-\bar{u}_{-}\right)^2}{2}=\bar{e}_{+}+\frac{\bar{P}_{+}}{\bar{\rho}_{+}}+\frac{v_s^2}{2}, \tag{5.130}$$

where

subscripts + and − refer to the preshock and postshock conditions, respectively
v_s is the velocity of the shock wave front
$\bar{\rho}$, $\bar{u}$, $\bar{P}$, and $\bar{e}$ are the density, velocity, pressure, and internal energy of the mixture, respectively

The EOS for the mixture pressure and temperature is given as

$$\bar{P}=\left(\frac{1-\phi}{1-\alpha_d}\right)\bar{\rho}\Re\bar{T}, \tag{5.131}$$

$$\bar{e}=\left(\phi C_d+\left[1-\phi\right]C_v\right)\bar{T}, \tag{5.132}$$

where

$\phi=\dfrac{\alpha_d\rho_d}{\alpha_c\rho_c}$ is the mass concentration of the dispersed phase
$\Re$ is the gas constant
C_d is the specific heat of the dispersed phase
C_v is the specific heat of the carrier phase

The mixture properties behind the shock relative to those ahead of the shock are formulated in terms of the shock Mach number as

$$\frac{\bar{\rho}_{-}}{\bar{\rho}_{+}}=\frac{\left(\gamma_m+1\right)M_s^2}{M_s^2\left(\gamma_m-1-2\alpha_{d+}\right)+2\left(1-\alpha_{d+}\right)}, \tag{5.133}$$

$$\frac{\bar{P}_{-}}{\bar{P}_{+}}=\frac{2\gamma_m M_s^2-\gamma_m+1}{\gamma_m+1}, \tag{5.134}$$

$$\frac{\bar{T}_{-}}{\bar{T}_{+}}=\frac{\left(\left[2M_s^2-1\right]\gamma_m-1\right)\left(2\left[\left(1-\alpha_{d+}\right)\right]+M_s^2\left[\gamma_m-1+2\alpha_{d+}\right]\right)^2}{M_s^2\left(\gamma_m+1\right)^2\left(M_s^2\left[\gamma_m-1\right]+2\right)}, \tag{5.135}$$

$$\frac{\bar{u}_-}{c_+} = \frac{2\left(1-\alpha_{d+}\right)\left(M_s^2-1\right)}{\left(\gamma_m+1\right)M_s}, \tag{5.136}$$

where

M_s is the Mach number of the incident shock

c_+ is the sound speed of the material ahead of the shock

γ_m is the ratio of the specific heats, defined as

$$\gamma_m = \frac{\gamma_g + \dfrac{\phi}{1-\phi}\gamma_p}{1+\dfrac{\phi}{1-\phi}\gamma_p}, \tag{5.137}$$

where

γ_g is the ratio of specific heats for the gas

γ_p is the ratio of specific heats for the particles (or dispersed phase)

Equations 5.133 through 5.136 reduce to the single-phase shock relations when $\alpha_d \to 0$ and $\gamma_m \to \gamma$.

5.4 Shocked Continua Interfaces

In this section, we discuss the mechanisms that drive the formation of particles from a shocked continua surface, commonly referred to as "ejecta." The term *ejecta* refers to the mass excavated from the rough, back side of a shocked metal sample into the vacuum or atmosphere beyond it. To clarify, metal samples or targets that might be driven with high-pressure shock waves are usually finished with a lathe or milling machine—the metals can of course be cast and then machined, or simply cast. In this context, the tools used to shape the metal leave periodic tooling marks or scratches on the surface that we refer to as (surface) perturbations. These perturbations are usually defined by a periodic wavelength λ and initial amplitude h_0, both of which can be characterized through optical profilometry across the surface. The dominant wavelength scale on the surface is determined as the highest energy mode in a *Fourier* transform of a characteristic set of *xy*-pairs from the profilometry, and the amplitude of the perturbations is related to the average deviation of the amplitude across the surface, R_a:

$$R_a = \int_{x_1}^{x_2} y(x)dx \Big/ \int_{x_1}^{x_2} dx. \tag{5.138}$$

These amplitude variations have finer scale fluctuations $\ll h_0$ along λ, but the dominant amplitude scale R_a is typically half the average perturbation amplitude ($R_a \approx h_0/2$), or about 1/4 the average of the maximum-to-minimum deviation of the perturbation amplitudes, of the dominant λ. The λ typically are set (machined) onto longer scale, slower surface—variations referred to as the *waviness* of the surface, which is typically caused by vibrations in the machining equipment.

If the metal targets/samples are placed in contact with a high explosive (HE) that is otherwise confined, and if the HE is initiated to detonation, then the detonation wave interacting with the metal will form a shock wave that drives through the target's *front side* to its *back side*. When the shock wave reaches the metal–vacuum or metal–gas interface it first releases to zero pressure at the perturbation minima and then reflects back into the metal as a rarefaction wave. A brief time later the shock wave releases to zero pressure at the perturbation maxima, also reflecting back into the metal as a rarefaction wave. Under these conditions, the stresses produced by the shock wave interacting with the perturbations cause the perturbation minima to compress, invert, and then grow in tension as RM instabilities (I), a.k.a. spikes. Because the RMI grow quickly relative to the initial perturbation maxima, the initial maxima invert and form bubbles that grow unstably into the metal causing metal to flow into the spikes to support the spike growth, as illustrated in Figure 5.15. In the RMI picture, bubbles and spikes refer to the peak penetration depth on opposite sides of the free surface, which is nominally defined as the plane through which the

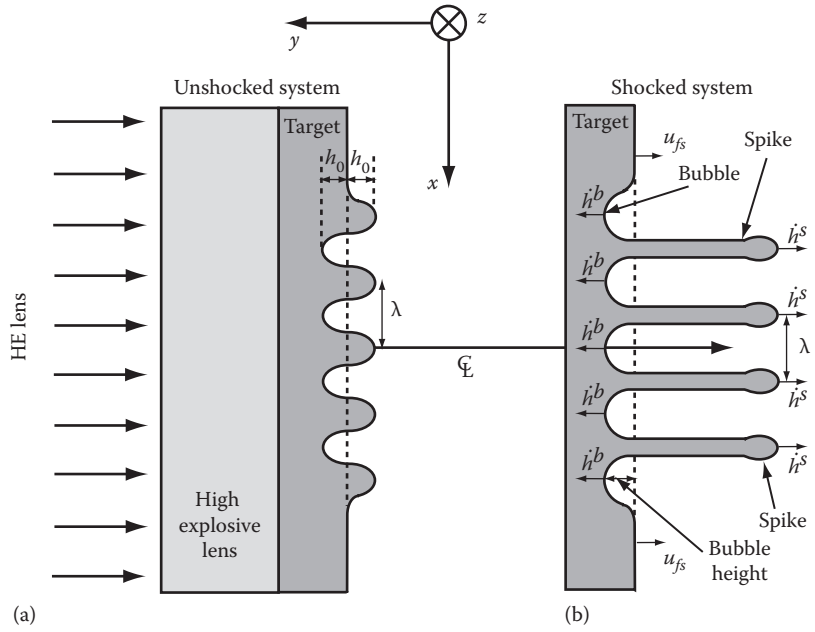


Figure 5.15

The preshocked (a) and postshocked (b) geometries. The preshock geometry includes sinusoidal surface perturbations. Initiation of the high explosive drives a planar shock wave through the target. When the shock wave reaches the metal–vacuum or metal–gas interface, it releases pressure and the free-surface jumps from its initial state to a shock-released state with velocity u_{fs}. During the shock wave loading, leading to release, the perturbations invert and the spikes form (ejecta) and grow beyond the free surface, and the bubbles grow into the free surface and feed mass into the spikes. CL, center line. (A version of this figure appears in Buttler et al. (2012b).)

inflections of the initial 2D surface perturbations center on. Of particular note is that in this geometry ejecta form as a special limiting case of an RMI where the Atwood number $At = -1$, where $\rho_1 \approx 0$ relative to the full density of metals ρ_2.

The formation of the ejecta is referred to as the *source* term. The mass from this source can be ejected into a medium such as a gas, where $0 < \rho_{gas} \Rightarrow \rho_1 \ll \rho_2 \therefore At \approx -1$. During the ejection process, the sheets/ligaments will break up due to Reynold's (hydrodynamic) drag and other potential mechanisms to form particles.

There have been numerous studies of ejecta over the years, most of which have centered on the formation of the source term: mass–velocity distributions $\rho^*(t;z)$ and total ejected areal–mass $\rho_A(t;z)$, where $\rho^*(t;z)$ is a reduced mass density,* and $\rho_A(t;z)$ is the time integral of $\rho^*(t;z)$ from the fastest ejecta down to the free surface—z is a parameter.

Early work in this area was pioneered by Asay (1976, 1977, 1978). In his work, Asay developed a simple prescription for the amount of mass ejected from shocked materials that linked to whether or not the material was shocked, and to the volume of the surface defects, V_{df}, caused by the fabrication of the samples, that is, the surface roughness R_a. In his prescription, Asay postulated that if a material was solid after shock and shock release it would eject about × 1 the target mass that would occupy the perturbations' defect volume V_{df}, $M_{ej} \approx \rho_{metal} V_{df} = \rho_m V_{df}$, and if the shocked metal was liquid it would eject $M_{ej} \approx 10\rho_m V_{df}$. His work was done with flyer plates (guns), and he studied Al, Au, Cu, Pb, and W. To study ejecta, he developed an ejecta diagnostic now known as an Asay foil (Asay, 1976). The Asay foil measurements gave $\rho^*(t;z)$ and $\rho_A(t;z)$ as ejecta mass accumulates with time onto the Asay foil at height z.

Subsequent to Asay's work, mass measurements on Ta, Sn, and CuPb alloys were made by Andriot et al. (1982) and Cheret et al. (1985), concluding that the 2D surface roughness R_a is the source of the ejected mass. Similar to Asay's work, they measured $\rho^*(t;z)$ and $\rho_A(t;z)$ with the Asay foil technique, and they shocked their system with flyer plates. Their gun systems were able to shock some of the materials to a liquid phase on shock release—the Sn and the CuPb alloys. They did observed a sharp increase in $\rho_A(t;z) \Leftrightarrow (M_{ej})$ from

* The density of an individual Sn fragment is the full density of solid or liquid Sn. In this context, $\rho^*(t)$ is the average density of the ejecta cloud arriving at the probes, an average that includes full density particles, as well as vacuum.

liquid metals as predicted by Asay. Shortly afterward, McMillan (1986) measured ejecta particle sizes with a Mie scattering diagnostic (Mie, 1908, Bohren and Huffman, 2004). His work centered on gun experiments on Pb targets with peak shock stresses that liquefied the Pb. McMillan reported ejecta sizes from 1 to 10 μm. Monfared et al. (2015) have reported recent dynamic Mie scattering studies as well.

The body of these early works—mid-1970s to early 1990s—focused on characterizing $\rho^*(t;z)$ and $\rho_A(t;z)$ and the sizes of the ejecta fragments or particles and their size–velocity distribution. Work on improving diagnostic techniques and the precision of mass measurement, and the temporal resolution of the mass–velocity distributions continues. For example, more precise ejecta size measurements on various metals utilizing dynamic holographic techniques have been done (Sorenson et al., 2002a, b), finding size distributions from 1 to 10 μm that nominally follow an r^{-5} percolation model size distribution, which is quite close to a log-normal distribution that is an effective description.

Along these lines, much work on characterizing the mass–velocity distributions on Sn has been done by Vogan et al. (2005), Zellner et al. (2007, 2008b, 2009a,b), Monfared et al. (2014), along with recent work on Pb by Ogorodnikov et al. (2009), Chen et al. (2012a,b), Georgievskaya and Raevsky (2012), and Mikhailov et al. (2014). The goal of the Sn work centered on the development of a physics-based source term model. Other researches have pursued ejecta models as well, for example, Georgievskaya and Raevsky (2012) presented an RMI-based ejecta model, Liu and Grieves (2014) reported on ejecta formation and transport from random and periodic perturbations with DNS, and others have relied extensively on molecular dynamics simulations to inform the understanding of ejecta phenomena as an RMI (Cherne et al., 2012, Durand and Soulard, 2012, 2013, Ren et al., 2014, He et al., 2015). In the Sn experiments, ejecta production was studied with gun and HE techniques, shock-loading techniques that drive the samples with a supported- or triangular-shock wave loading profile.

In one type of ejecta experiment, the perturbation parameters (wavenumber ($k = 2\pi/\lambda$) amplitude products kh_0), and the shock wave breakout pressure P_{SB}, were varied to explore ejecta production from a fixed finish versus P_{SB}. In other Sn experiments, P_{SB} was fixed and kh_0 was varied. Most of the HE Sn results, where P_{SB} was fixed and kh_0 was varied, are reported in Monfared et al. (2014). Zellner et al. (2009a) reported similar Sn experimental results from gun experiments where R_a and λ were fixed (λ, h_0) = (50, 1.6) μm. Some of the HE ejecta data, where P_{SB} was varied and R_a was fixed (λ, h_0) = (50, 1.6) μm, with (λ, h_0) = (25, 0.8) μm, are reported in Zellner et al. (2007). However, we will report later, for the first time, the full collection of the fixed finish HE- and gun-driven experimental ejecta data, where P_{SB} was varied and $R_a \approx 0.8$ μm, with (λ, h_0) = (50, 1.6) μm. The body of the Sn ejecta data was used to develop (Buttler et al., 2012a, b) and implement (Fung et al., 2013) an RMI physics-based ejecta model, which will be discussed later. Any ejecta model must explain the Sn ejecta data set.

5.4.1 Ejecta Experimental Details

To survey the phase space of ejecta variables, we mainly utilized two venues: guns and HE drives. The HE experiments gave unsupported (triangular) or Taylor wave shock waves, and the gun shots supported or square wave shock waves. A supported shock wave is characterized by a steep rise in pressure that is sustained as the shock front traverses the material. Upon reaching the free surface, the shock stress undergoes a steep release to vacuum or low pressure, causing a rarefaction wave to scatter back into the material, releasing the internal pressure. A Taylor shock wave has a similar steep rise in pressure; however, the rise is followed immediately by the propagation of a rarefaction wave from release at the HE backside. Because the HE rarefaction wave propagates into the HE shocked material, that is, into compressed mass at high pressure, it travels at a velocity greater than the shock wave front velocity into the unshocked material with relatively lower pressure. Eventually, the rarefaction wave overtakes the shock wave front and begins to attenuate the peak shock pressure as the shock wave moves through the material. Figure 5.16 schematically presents the different geometries of the two venues. Figure 5.16a shows the Taylor wave geometry and Figure 5.16b the gun geometry. The choice of venue, gun, or HE shock physics was directly tied to the particular ejecta question under investigation.

Figure 5.17 shows the basic HE physics and diagnostics package used to acquire the HE (PBX 9501) Sn ejecta data for all P_{SB}. The Sn sample and standard diagnostics, which included lithium niobate (LN) piezoelectric pins to measure ejecta masses (Figure 5.18), and either an optical heterodyne velocimeter (OHV) (Cummins et al., 1963a,b, Yeh and Cummins, 1964, Forman et al., 1965, Buttler et al., 2004, Strand et al., 2006) or velocity interferometer system for any reflector (VISAR) (Barker and Hollenbach, 1972) probes, that completed the physics package that was usually at 1- to 5-torr pressure for the experiments. The package was always placed inside a test chamber, or "boom box," as shown in Figure 5.16a. The boom box included two replaceable Poly(methyl methacrylate), also known as Plexiglas, Acrylite, Lucite, and Perspex (PMMA) windows—often damaged by debris from the explosion—positioned perpendicular to the target face, allowing for the

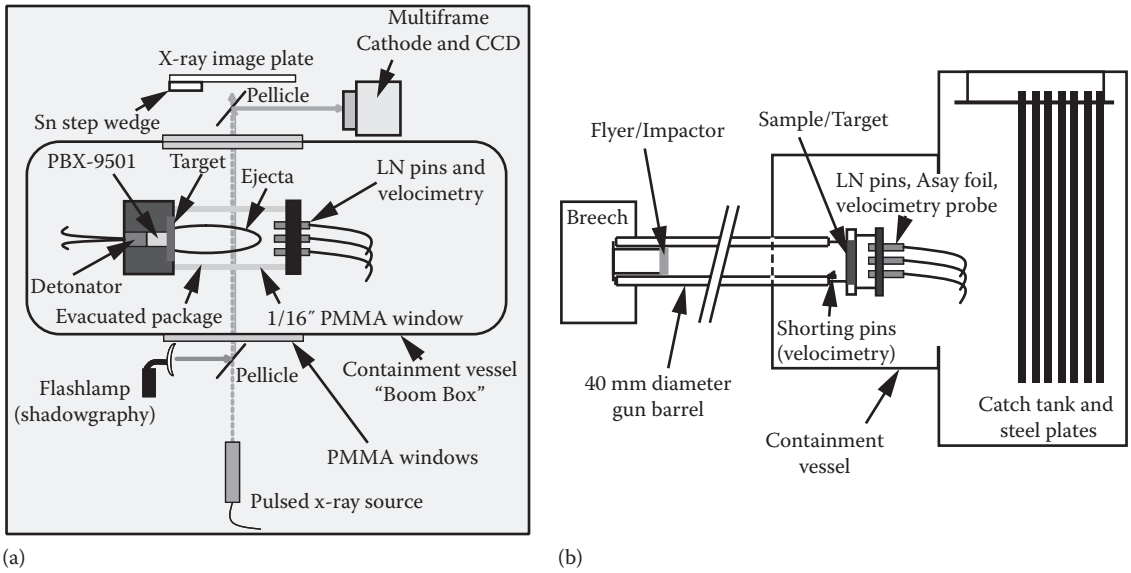


Figure 5.16

These figures illustrate the basic experimental geometries for the high explosive- and gun-driven ejecta experiments, labeled (a) and (b), respectively. Versions of (a) appear in Vogan et al. (2005), Zellner et al. (2007, 2008a,b,c), and Monfared et al. (2014), and a version of (b) appears in Zellner et al. (2009a).

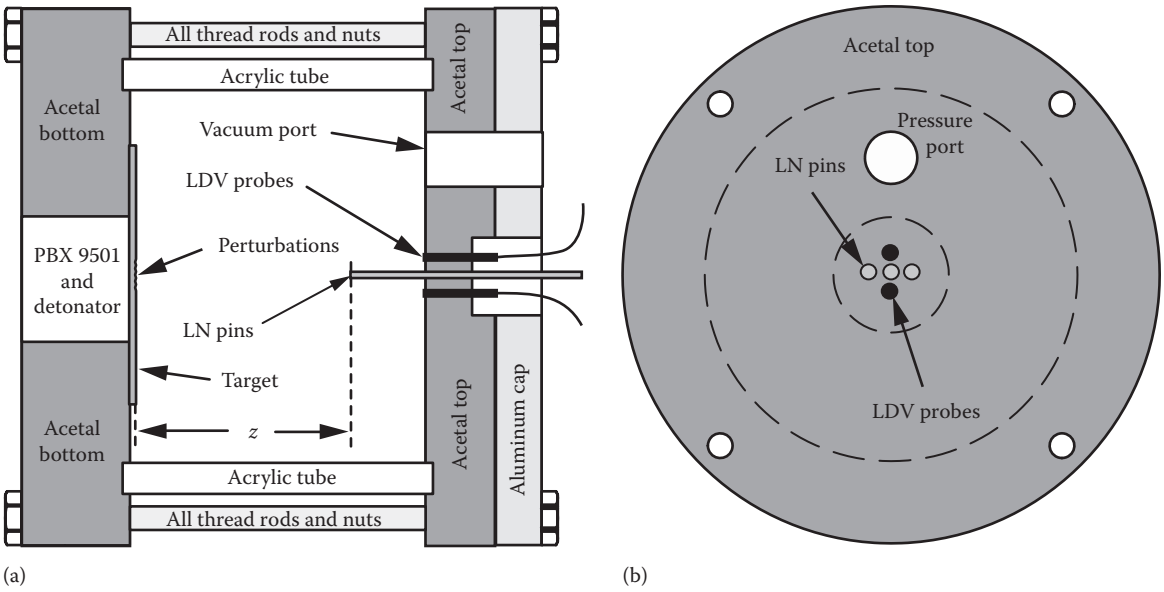


Figure 5.17

(a) A typical ejecta physics package and the all-thread rods out of rotation; otherwise, both schematics are drawn to scale. (b) A common diagnostic arrangement for a typical ejecta experiment, including the frequent locations and orientations of the lithium niobate pins (gray) and the laser Doppler velocimetry probes (black). (A version of this figure appears in Monfared et al. (2014).)

use of both multiframe optical shadowgraphy (usually 9 frames) to observe the ejecta and target evolution, and x-radiography (x-ray) to acquire ejecta density versus distance beyond the shocked target surface at one time, t_{xray}. The LN probes for the HE experiments were distributed above the surface, usually at height 20 μm $\leq z \leq$ 30 μm, and velocimetry probes were adjacent to the LN probes and/or above the target center. The number of LN probes per package was typically determined by the height of the cylindrical Sn sample and by the height and diameter of the HE, variables that were modified as needed to vary P_{SB}. All diagnostics and the HE

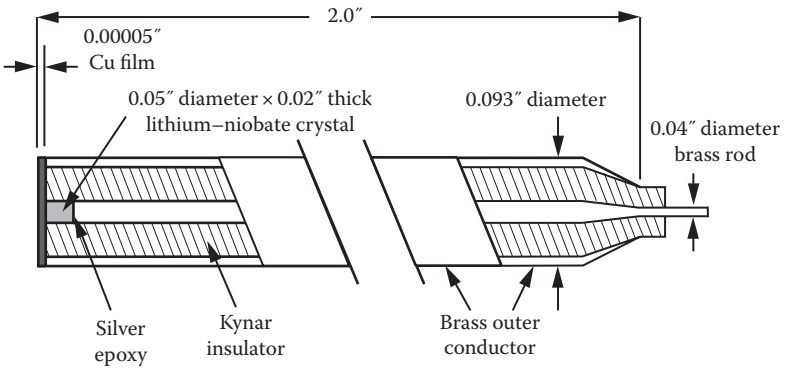


Figure 5.18

The Dynasen piezoelectric probes. (This figure appears in Monfared et al. (2014).)

detonation were initiated from a centrally located high-voltage source (capacitive discharge unit, or CDU), and the diagnostics were *commonly timed* to the CDU voltage pulse for correlated analysis.

The velocimetry provided P_{SB} just prior to shock release; the x-ray diagnostic provided accuracy validation for the piezoelectric measurements; the optical shadowgraphy gave ejecta speeds for comparison with x-ray and LN probe observations, as well as an approximate time of shock wave breakout in the event that the velocimetry diagnostics failed.

The supported shock wave experiments were fielded using the same Sn and machining processes that were used in the HE experiments. The basic gun geometry is depicted in Figure 5.16b. In the gun experiments, the shock wave forms in the target as the gun-fired *sabot*, or flyer, impacts an otherwise stationary Sn target—the sabot moves left to right in this representation. For the gun experiments, the sabots were tipped with either Cu or Ti_{64} cylindrical discs that collided with the stationary target (Ti_{64} is a titanium alloy with 6% vanadium and 4% aluminum).

5.4.2 Ejecta Experimental Results and Analysis Techniques

5.4.2.1 Laser Doppler (Optical Heterodyne) Velocimetry

Figure 5.19 shows two laser Doppler velocimetry (LDV) measurements from a 2012 HE-driven Sn experiment. The two LDV probes were positioned about 50 mm above the target at a radius of 4 mm off the target center. The HE drive was PBX 9501, as described, and the target was 3 mm thick. The perturbations had $(\lambda, h_0) = (50.3, 8.4)$ μm, which gave $kh_0 = 1.05$; this kh_0 product produces ejecta that travel about twice the velocity of the free surface, u_{fs}.

The observed free-surface (release) velocity on both probes was $u_{fs} \approx 1.725$ mm/μs at this radius, about 0.1 mm/μs lower than it would be if the probe was centered above the target. From these data, we also get the shock wave breakout time t_{SB}, which we common time with the LN pins, x-ray data, and the visible imaging to CDU. The release velocity, u_{fs}, is also used to analyze the LN pin data. Essentially, what is needed is the time the shock wave breaks out at (reaches) the free surface, and the time at which the free surface arrives at the LN pins as the ejecta are thought to form quickly and then expand self-similarly beyond the free surface as the shocked system (ejecta and target) approaches the stationary LN pins. Of course, u_{fs} can be integrated to get $z(t)$ as desired.

5.4.2.2 Lithium Niobate Piezoelectric Diagnostic

The LN probes are purchased directly from Dynasen* and are generally used in unmodified form. The probes are compact and have their active piezoelectric material mounted to the ends of copper wires to make "pins." Figure 5.18 presents an engineering diagram of the basic LN probe.

The manufacturer specified sensitivity of the LN piezoelectric crystal is $S = 24.8$ pC/N, and the LN sensitivity is accurately determined by x-ray diffraction from the lattice structure. The LN pin quasi-static failure stress is 6–8 kbar, but we have observed accurate mass measurements up to about 12 kbar. Mears et al. (2010) questioned the accuracy of the value of S used, reporting $S \approx 36$ pC/N, but $S = 24.8$ pC/N is consistent with the x-ray validation data.

* The LN pins are purchased directly from Dynasen, Inc., Goleta, Ca. (www.dynasen.com).

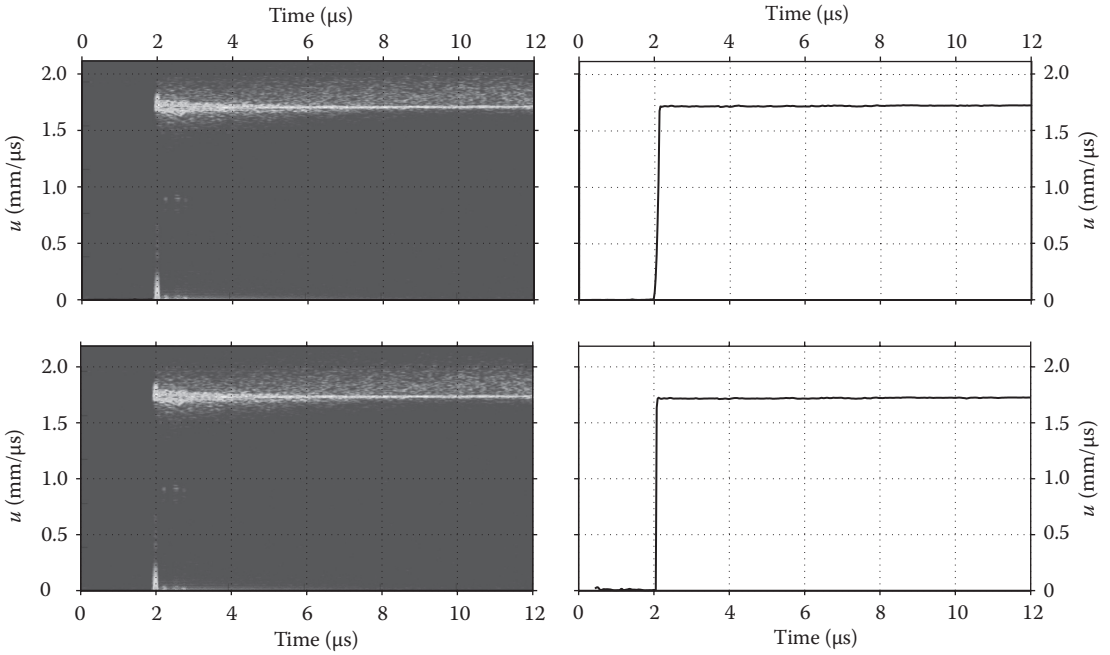


Figure 5.19

Two laser Doppler velocimetry (LDV) measurements, two probes, acquired from a 3 mm thick Sn target. The images on the left follow naturally after *Fourier,* transforming the LDV data from the frequency to time domain, and the plots to the right were extracted from the images. (These LDV data were acquired in June 2012 at STL.)

Extracted quantitative results from the LN pins are based on several assumptions, with the primary assumption being that a probe's response to ejecta is described as

$$\begin{aligned}\frac{d}{dt}(mu) &= u\frac{dm}{dt} + m\frac{du}{dt}\\ &\approx m\frac{\partial u}{\partial z}\frac{\partial z}{\partial t}\\ &= A\rho^{\star}(t;z)u^2(t;z) = AP(t;z),\end{aligned} \tag{5.139}$$

where A is the active area of the piezoelectric probe and the temporally varying quantities are $P(t;z)$, the pressure—linear stress—on the probe; $u(t;z)$, the velocity of a particle or fragment; m, the fragment mass; and $\rho^{\star}(t;z)$, the average density of the fragments sticking to the probes, as caused by the ejecta accreting onto the probe at LN pin height z. It is further assumed that there is no source term for the mass, that is, $dm/dt \equiv 0$.

Equation 5.140 relates the acceleration of the piezoelectric material to the ejecta velocity gradient by the time rate of change of the position z, under the assumptions that (1) the particles inelastically come to rest within an infinitely thin layer on the piezoelectric material ($\delta z \times A \approx V$, the volume), (2) the change in velocity as the particle comes to rest in distance δz is $\delta u \equiv u$, and (3) $\partial z/\partial t \approx u$ is the velocity of the particle. When these conditions are met, the force on the probe is $F(t;z) \approx AP(t;z)$ and the probes respond to the time derivative of the pressure—otherwise, the probes would be an infinite charge source. When the piezoelectric material is abruptly squeezed, it generates charge during the impulse. When it is held at a fixed pressure, that is, the time derivative of the force is zero, it generates no charge. When the pressure is released, the charge flows in the opposite sense.

During usage, the LN probes are connected to a digitizer via coaxial cable terminated into $R = 50\ \Omega$ to measure the $V(t)$, giving a time history of current:

$$\frac{dF}{dt} = \frac{V(t;z)}{RS}. \tag{5.140}$$

The time derivative of the pressure is $dP/dt = A^{-1}dF/dt$. The ejecta cloud pressure is recovered by integrating $A^{-1}dF/dt$:

$$P(t;z) \equiv \rho^{\star}(t;z)u^2(t) = \int dt \frac{V(t;z)}{ARS}. \tag{5.141}$$

Based on our assumption that $P(t;z) \equiv \rho^{\star}(t;z)u^2(t;z)$, the dynamic volume density can be calculated by dividing $P(t;z)$ by $u^2(t;z)$. Because these experiments were executed in vacuum, the arrival of the ejecta is simply characterized as a time-of-flight measurement, that is, $u(t;z) = z/t$ (Buttler et al., 2007, Zellner and Buttler, 2008).

The final quantity we often seek from the data is the cumulative areal mass of material ejected from the shocked surface, which is found after first calculating the dynamic areal density, dm/dA:

$$\rho_A(t;z) = \frac{dm}{dA} = \int dt\, \rho^{\star}(t;z)u(t;z). \tag{5.142}$$

The cumulative areal mass is the value of $\rho_A(t;z)$ at the time of the free surface arrival at the LN probe, $t_{fs} = z/u_{fs}$.

These three quantities ($P(t;z)$, $\rho^{\star}(t;z)$ and $\rho_A(t;z)$) are the main data we seek in our ejecta model development. All three quantities can be expressed versus the velocity ($u(t;z) = z/t(u;z)$), or they can be expressed as a snapshot at time t where the mass is distributed versus z as described in Buttler et al. (2007) and clarified in Zellner and Buttler (2008).

In a presentation of $P(z;t)$, $\rho^{\star}(z;t)$, and $\rho_A(z;t)$, z is the variable and t the parameter, typically chosen as the time at which the free surface arrives at the pin. However, to compare the LN pin data with x-ray data taken at time t', the data can be transformed from the time at which the surface reaches the probe at time t to the earlier time t', again as shown in Buttler et al. (2007) and Zellner and Buttler (2008). In fact, this transformation is used to validate the performance of the LN pin precision and accuracy in Zellner et al. (2008b) and Monfared et al. (2014).

Figure 5.20 shows typical LN pin quantities acquired on Sn ejecta experiments in 2012. We plot $V(t;z)$, $P(u;z)$, $\rho^{\star}(u;t)$, and $\rho_A(u;z)$, where the pin height was $z = 20.4$ mm. In these experiments, our target was cold-rolled Sn of purity 0.9995, which gave Sn grain size diameters on the order of $d \approx \mathcal{O}(100\,\mu\text{m})$. The wavelength and amplitudes were $(\lambda, h_0) = (50\,\mu\text{m}, 8.4\,\mu\text{m})$, which gave $kh_0 = 1.05$. There were three LN pins on the experiment ($z = 20.4$ mm), one above the target center and two at a radius of 4 mm off center. Two Doppler OHV probes were adjacent to the LN pins, also at a radius of 3 mm, to give $u_{fs} = 1.72$ mm/μs. Previous experiments have shown that on center this would be $u_{fs} \approx 1.82$ mm/μs. These velocities imply $P_{SB} \approx 26$ GPa.

In Figure 5.20, $\rho_A(u;z)$, the center pin, integrates up to about 15 mg/cm^2. The other two pins integrated to 10.8- and 11.6-mg/cm^2 so that $\rho_A(u = u_{fs}) = 12.5 \pm 2.2$ mg/cm^2. This variability is higher than normal, but the result is consistent with other data from similar targets presented in Monfared et al. (2014).

5.4.2.3 Accuracy: LN Pin and X-Ray Comparisons

The accuracy of LN pin ejecta mass measurements was validated on numerous STL experiments through a comparison of LN probe with x-ray measurements. The cross-validation is typically achieved by comparing the $\rho^{\star}$ from the LN pin measurement with the $\rho^{\star}$ from the radiography measurement.

Considering x-radiography physics, if an x-ray beam with intensity I_0 passes through material with transverse areal density $\rho_A^{T\star}$ and mass attenuation coefficient κ, then the ratio of the transmitted to incident intensities is

$$\frac{I}{I_0} = e^{-\kappa\rho_A^T}, \tag{5.143}$$

where ρ_A^T is the product of the attenuating material thickness τ with its density $\rho^{\star}$, that is, $\rho_A^T = \rho^{*}\tau$. The determination of ρ_A^T requires a static and a dynamic radiograph of the physics package, which determines I_0 and I,

* The ejecta areal density transverse to the LN pin ρ_A is ρ_A^T, but $\rho_A^T \neq \rho_A^L$. However, the $\rho^{\star}(z;t_{xray})$ calculated from the x-ray and LN pins are quantitatively comparable.

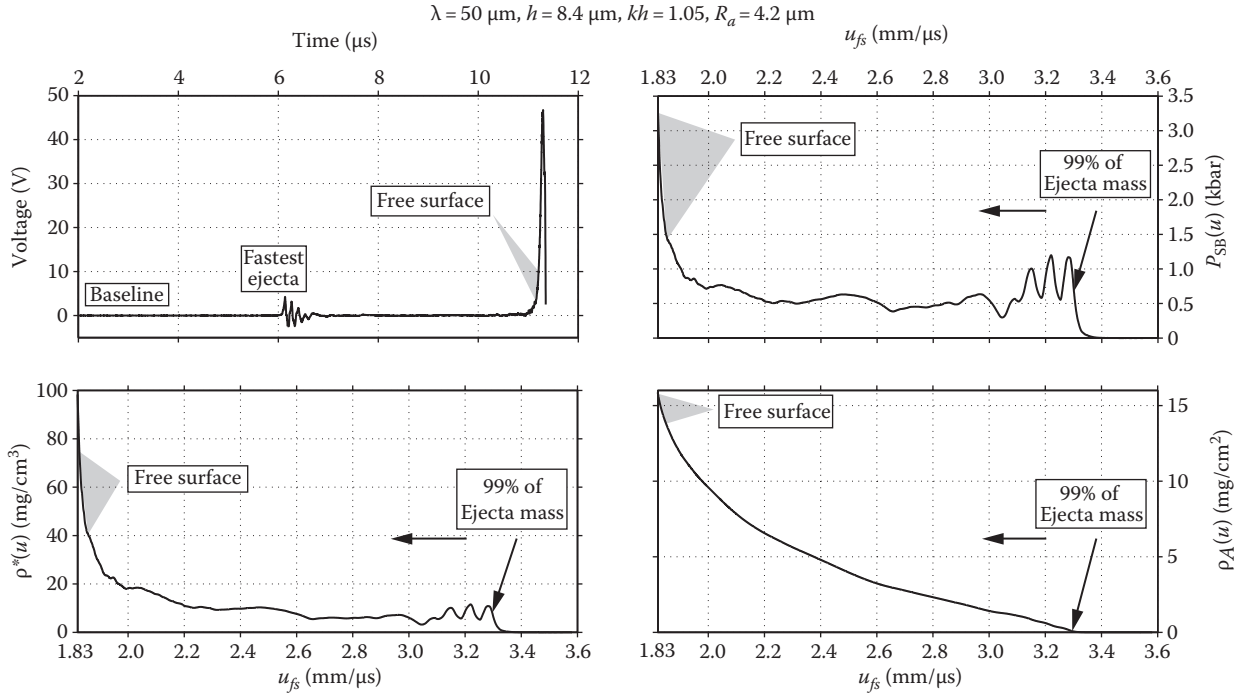


Figure 5.20

The lithium niobate (LN) pin voltage $V(t;z)$ (upper left), $P(u;z)$ (upper right), $\rho^*(u;z)$ (lower left), and $\rho_A(u;z)$ (lower right). The LN pin height is $z = 20.4$ mm, the free-surface velocity on center is $u_{fs} \approx 1.825$ mm/μs, and the finish parameters are quoted above the figures.

respectively. Prior to the dynamic radiograph, however, a Sn step wedge that includes small strips of solid density Sn foils of varying thicknesses (τ_{Sn} = 0.03, 0.05, 0.08, 0.10, 0.13, 0.15, 0.20, 0.46, 0.97, and 1.83 mm) is included in the image area. The static and dynamic images are digitized, and the dynamic image is then divided by the static image to determine I/I_0. Two examples of the x-ray ratios are seen in Figure 5.21, where the x-ray image on the top left is from a 2007 Sn experiment, and the x-ray image on the bottom left is from a 2013 Sn experiment (the x-ray data in Figure 5.21b are discussed extensively in Monfared et al. [2014]).

After the ratio image is computed, the average I/I_0 is fit to the foil (step-wedge) region to compare with the foil's known areal density, $\rho_A^T = \rho^*\tau \equiv \rho_{Sn}\tau_{Sn}$, and the resulting ratio is related as

$$\frac{I}{I_0} = Ae^{-B\rho_A^T}, \tag{5.144}$$

which gives constants A and B. Equation 5.144 is then inverted, and the results are applied to the ratio image pixels to determine ρ_A^T.

Consider the two x-radiographs seen in Figure 5.21; their character is quite different because their HE target geometries were different. In the 2007 experiment, the target was 2 mm thick with a perturbation finish of $(\lambda, h_0) \approx (50, 1.6)$ μm across the entire surface, while the target in the 2013 experiment in the Figure 5.21b x-ray image was 3 mm thick with a perturbation finish of $(\lambda, h_0) = (50, 8.4)$ μm. The latter target, however, had the perturbations embedded in a 4 mm wide strip just below a mirror like finish, a finish that is known to suppress ejecta (see Zellner et al., 2008a). The other differences were the HE. The PBX 9501 on the 2007 Sn experiment was 12.7 mm tall and the HE diameter was d = 12.7 mm, but the HE on the 2013 Sn experiment was 8.9 mm tall with d = 25.4 mm. These geometries gave u_{fs} = 1.9 mm/μs ($P_{SB} \lessapprox 27.7$ GPa) on the 2007 experiment and u_{fs} = 1.74 mm/μs ($P_{SB} \lessapprox 24.6$ GPa) on the 2013 experiment. The dimensionless target parameters were $kh_0 = 0.2$ (2007) and $kh_0 = 1.05$ (2013).

As noted in the discussion, the areal density ρ_A^T extracts simply by the application of Equations 5.143 and 5.144, which requires the ejecta path length τ. The quantity τ is approximated by subtracting twice the Sn height from the diameter of the HE, that is, $\tau_{2007} \approx 12.7 - 4 = 8.7$ mm and $\tau_{2013} \approx 25.4 - 6 = 19.4$ (this analysis follows from simple shock physics release wave rules). An inspection of the 2007 radiograph shows

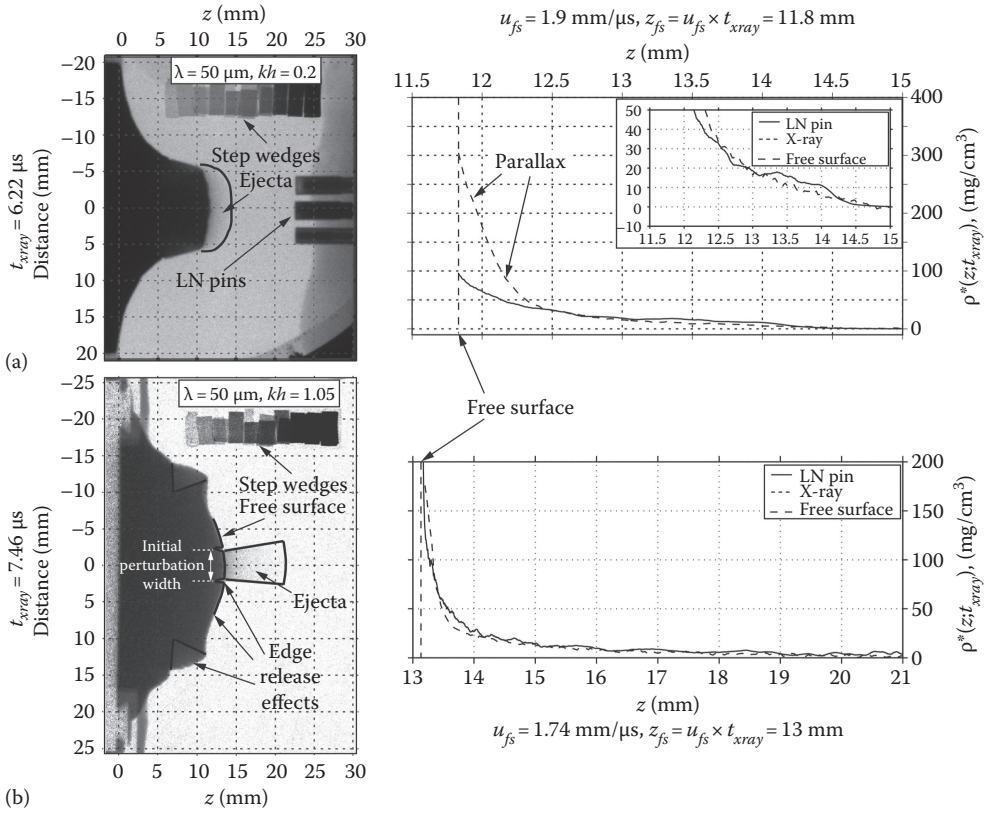


Figure 5.21

Shocked Sn target radiographs (to the left) showing an ejecta cloud (black outline), compared with their lithium niobate (LN) pin and x-ray $\rho_A^*(z;t)$ (to the right). The LN pin data (right) were transformed to the free-surface height (see Zellner et al. (2009a)) at the x-ray time (t_{xray}). The Sn step wedges aid density calibrations. Radiograph (a), t_{xray} = 6.22 μs after breakout. Radiograph (b), t_{xray} = 7.46 μs. (The data in (b) were acquired in 2013 and appear in Monfared et al. (2014).)

that this approximation is supported in the width of the ejecta cloud (vertical dimension), which is $\lessapprox$10 mm wide. Given the target geometry of the 2013 experiment, however, we cannot see the ejecta cloud width. Nevertheless, the curvature of the target in the lower image turns upward when the distance from the center is $\lessapprox$10 mm, or a width of about 20 mm—again consistent with the approximation of 19.4 mm. With this ejecta cloud dimension, $\rho^*(z;t_{xray}) = \rho_A^T(z;t_{xray})/\tau$, with uncertainties of ±10%.

5.4.2.4 Optical Shadowgraphy

Figure 5.22 shows nine *shadowgrams* captured with multiframe optical shadowgraphy. A typical optical shadowgraphy system includes a bright, intense flash lamp that is pulsed orthogonally (transverse) to the dynamic system of interest. Lenses relay the light through the dynamic region onto a photocathode that couples the image onto a fiber-coupled CCD camera. Depending on the number of frames desired, the photocathode directs the images to an appropriate section of the CCD for digitization after the experiment is over. A common CCD includes 4000 by 4000 pixels.

In the Figure 5.22 images, a total of nine "frames" were captured, which means each image is stored in an area of about 1300 by 1300 pixels. A typical pixel size might be 50 μm, and the image might be 30 mm by 30 mm, which relates the optical transfer function of the system, yielding an image resolution of about 3.5 to 4 line pairs per millimeter, about 125 μm.

Important system parameters include the exposure duration and interframe time. For our experiments, we normally used an exposure time of about 150 ns, but shorter times are possible. The minimum interframe time is 300 ns, and we usually chose the interframe times to be 300 ns for the first three frames in an attempt to bracket the time of the shock wave breakout at the surface in the time window of the first three frames. With these first three frames, in the event the velocimetry diagnostic failed, which was frequent with the VISAR diagnostic, then the time of shock wave breakout estimated from the framing camera can be used

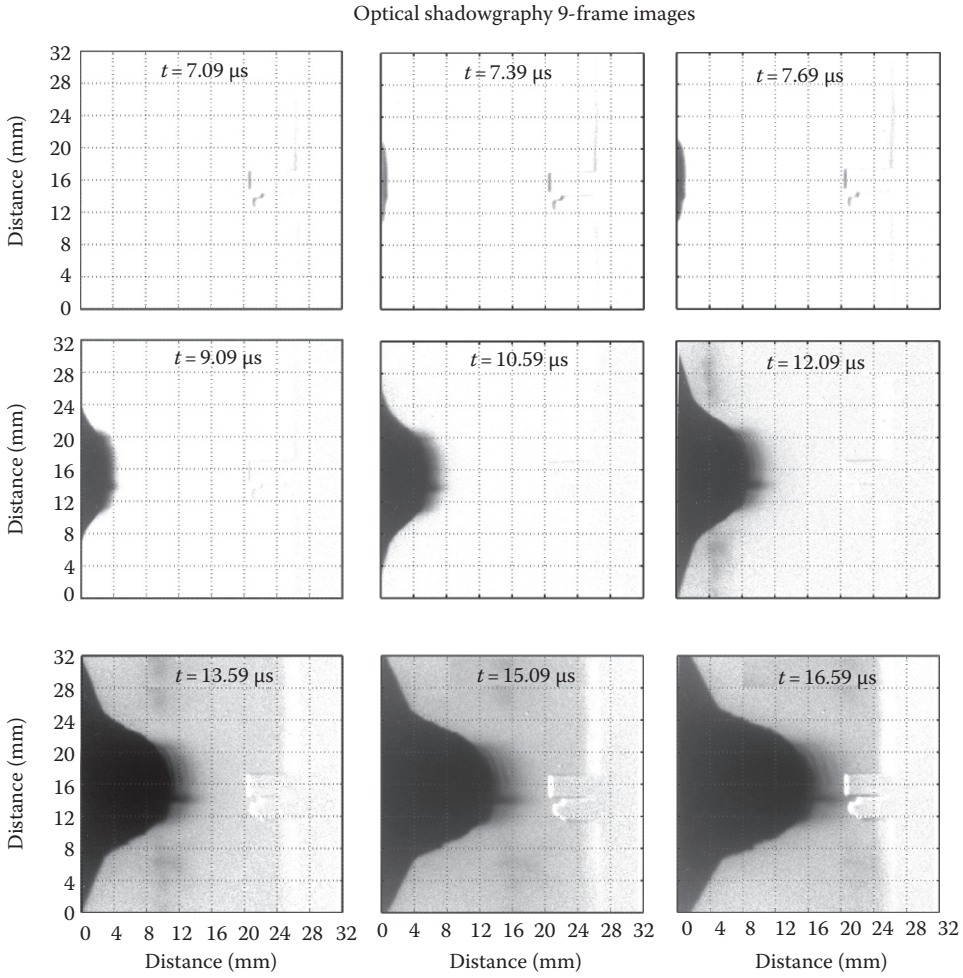


Figure 5.22

Typical optical shadowgraphy data. The first three frames were timed to capture shock breakout and allow an estimate of P_{SB} from the asymptotic pin velocity (the time of shock breakout to pin-failure time—this was vital when VISAR was the velocimetry diagnostic). The ejecta cloud is often optically thick and only reveals the leading ejecta cloud leading edge. Here, however, three ejected layers are seen within the shadowgrams.

with the time of flight of the Sn target to the LN pins to estimate u_{fs} (and P_{SB}).* The final six frames were nominally separated about 2 μs to observe the qualitative hydrodynamics.

Optical shadowgraphy data are useful for validating the qualitative hydrodynamic behavior of the shocked target and ejecta system and the quality of experimental data and results. Quantitative information that can be extracted includes an estimate the shock wave breakout time at the surface, but we also get the speed of the ejecta. In addition, if the ejecta cloud is not optically thick, the structure within the ejecta cloud the x-ray is insensitive to can be observed. The types of structural information that can be observed in the shadowgrams are seen in Figure 5.23a, which is the eighth frame from Figure 5.22. In this image, it is seen that the ejecta are confined between 11 mm and 21 mm in the vertical dimension—about 10 mm as determined in the x-ray image and estimated with the simple shock physics rules. In addition, high- and low-intensity ejecta "waves" are seen in the image—three if one looks closely. There is also an apparent spike traveling faster than the other ejecta around 14 mm in the vertical dimension. Because these are 2D shadows of potentially 3D features we cannot tell where the imaged structures originate, unless the symmetries are observed by the LN pins. As confirmation, consider the x-ray and LN pin $\rho^*(u_{ej}/u_{fs})$ data plotted in Figure 5.23b. The average densities seen by the LN pins and the x-ray agree, but the LN pins see three distinct ejecta waves the low-resolution x-ray data do not resolve. Again, the data confirm the value of the precision and accuracy of the LN pin data.

* Direct LDV (OHV) techniques are the common shock physics velocimetry diagnostic now and that diagnostic is robust.

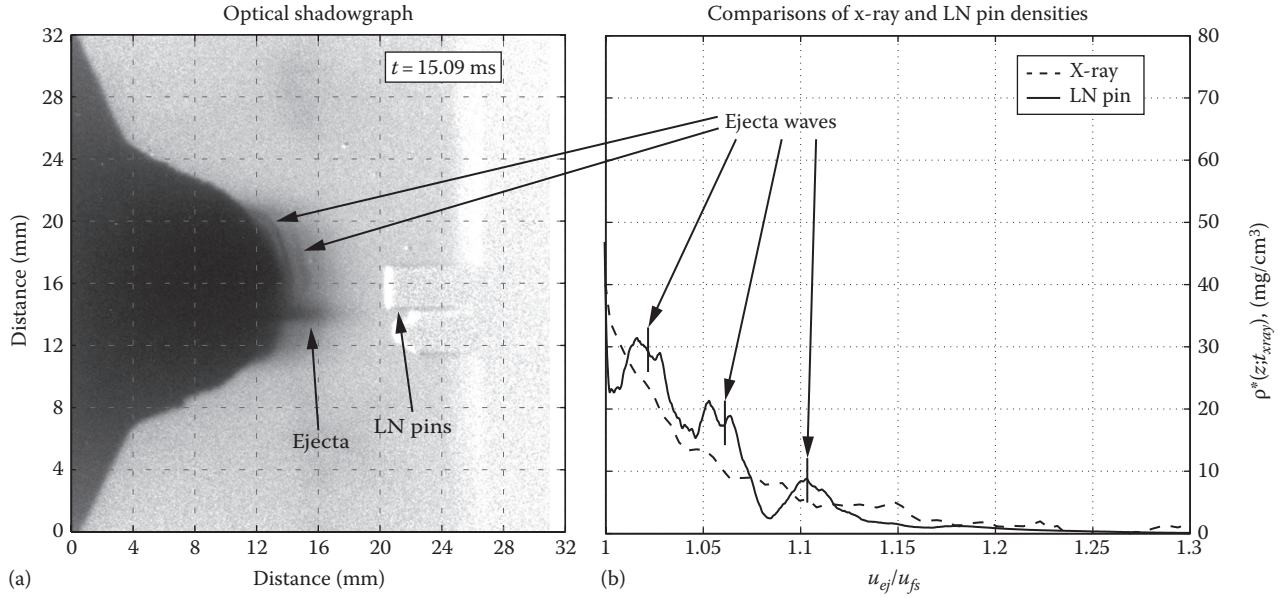


Figure 5.23

Optical shadowgraph (a): the eighth frame from Figure 5.22 (t = 15.09 μs). This image shows ejecta layers not seen in the x-ray $\rho^*_A(u_{ej}/u_{fs};t_{xray})$ in (b). However, $\rho^*_A(u_{ej}/u_{fs})$ from the lithium niobate (LN) pin data shows three ejecta layers, illustrating the better resolution and precision of the LN pin data relative to the x-ray data. This is because the x-ray resolution is only 2–3 line pairs/mm. Also seen in (a) is an asymmetry to the cloud. Because this is a 2D *shadow*, it cannot be determined from where this "jet" originated from the surface. ((a) appears as Figure 5 and the LN data of (b) as Figure 7 in Zellner et al. (2007).)

5.4.3 Richtmyer–Meshkov Instability Model of Ejecta

Studies of the Sn ejecta data set (mentioned earlier) lead to the development of an RM-physics-based ejecta source model (Buttler et al., 2012a,b) and a similar model by Dimonte et al. (2013). The basis of the 2D ejecta-sheet model is conceptually described by the geometry seen in Figure 5.15. There are important solid RMI results in Buttler et al. (2012b), but the key liquid metal RMI results are that the bubble tip velocity versus time is

$$\dot{h}^b(t) = \frac{\dot{h}^b_0}{1+\frac{3}{2}\dot{h}^b_0 kt} \approx \frac{2}{3kt} \equiv \dot{h}^b_t \to 0 \quad \text{as } t \to \infty \tag{5.145}$$

and the spike tip velocity is

$$\dot{h}^s_\infty = \sqrt{3}\,\dot{h}^s_0, \tag{5.146}$$

where superscripts b and s refer to the *bubble* and *spike* and $\dot{h}^{b,s}_0 \equiv \dot{h}^b_0 = -\dot{h}^s_0 = kh_0u_{fs}$ refers to the initial RM impulse for shock wave–driven incompressible linear instability growth, as shown by Richtmyer (1960).* Considering the physics implications of Equation 5.145, it is seen that the bubble velocity decays inversely with time to zero relative to u_{fs}, which is nominally twice the particle velocity u_p that appears naturally in shock physics conservation equations. We also see that for shorter wavelengths ($k \gg 1$) the bubble velocity asymptotes more quickly than for longer wavelengths, which possess more inertia. The spike, on the other hand, obtains a limited ballistic velocity independent of time, and as noted in Mikaelian (2010), this is the *maximum* velocity attainable by 2D spikes, that is, it is more accurate to say

$$\dot{h}^s_\infty \le \sqrt{3}\,\dot{h}^s_0. \tag{5.147}$$

* Equations 5.145 and 5.146 are expressed as Equations 5.16 and 5.17 in Buttler et al. (2012b).

There is an important linear correction to the Richtmyer impulse $\left|\dot{h}_0^{b,s}\right| = kh_0 u_{fs}$ when $At = -1$, namely, because the perturbations must invert through $y(x) = 0$ as they unstably grow they experience a compression different than the case where $At \approx 1$. In the work of Richtmyer, $At \approx 1$, he showed that to account for compressibility, one should use the postshock amplitude $h_0 = (1 - u_{fs}/u_{sh})$ and not the preshock amplitude h_0, where u_{sh} is the shock wave speed in the metal caused by the loading stress P_{SB}. For the opposite case where $At = -1$, however, Meyer and Blewett (1972) found that using the average of the preshock and postshock amplitudes gave better agreement. Therefore, we use

$$F_l = 1 - \frac{u_{fs}}{2u_{sh}} \tag{5.148}$$

as the linear (l) compression factor, which applies to both the bubbles and spikes.

The solutions in Equations 5.145 and 5.146, together with the Richtmyer impulse and the linear correction in Equation 5.148, apply when $kh_0 \ll 1$.* When $kh_0 \gtrsim 1$, nonlinear (subscript nl) corrections to the bubble and spike growth rates become important. The nonlinear corrections to the spikes are informed by simulations found in Velikovich and Dimonte (1996), and Buttler et al. (2012b) did a similar fit to data bound in Dimonte and Ramaprabhu (2010) for the nonlinear bubble correction:

$$F_{nl}^s = \frac{1}{1 + \left(\frac{kh_0}{2}\right)^2} \quad \text{and} \quad F_{nl}^b = \frac{1}{1 + \frac{kh_0}{6}}. \tag{5.149}$$

The product of these nonlinear and linear factors with the Richtmyer impulse and the bubble and spike velocities can be used to bound to the 99% level, ρ^* and ρ_A, where ρ_A is best estimated with an integration of Equation 5.145 to find

$$\begin{aligned} \rho_A(t) &= \frac{\rho_m V_d}{L\lambda} \\ &= \frac{\rho_m}{L\lambda} \int\int\int dt dx dz \cdot \dot{h}^b(t) y(x,t) \\ &= \frac{\rho_m}{L\lambda} \int\int\int dt dx dz \cdot y(x,t) \frac{\dot{h}_0^b}{1 + \frac{3}{2}\dot{h}_0^b kt}, \end{aligned} \tag{5.150}$$

where

$L\lambda$ is the surface area

$y(x, t)$ is the bubble shape function of the unstable RM growth into the surface

The shape function $y(x, t)$ is of great interest in RM unstable ejecta physics. For example, in the event that the surface is shocked again sometime later, and we have developed explosively driven two-shockwave tools to evaluate such mass ejection events (Buttler et al., 2014a,b), then we want to be able to predict the mass ejection source at the second event. In such an event, we postulate the shape and effective height of the bubble at the time of the second shock wave event will lead to an RMI mass ejection as well, meaning our RM models will predict the mass ejection caused by the second shock. The prediction of the second shock mass ejecta requires the effective height of the bubble at the time t' of the second event to know or estimate kh_0', which determines the RM impulse and total mass ejected. It is difficult to measure this height diagnostically in a once shocked metal, but techniques to bound h' are discussed in Buttler et al. (2014b).

So long as there is an infinite well of mass to support spike growth, the Buttler et al. (2012b) RMI model describes a mass ejection that increases with increasing P_{SB}, but that asymptotes with increasing time once the unstable RMI growth has begun. Experimentally, however, we have observed that this is true only for supported shock waves, such as from a flyer plate or gun type of experiment (Zellner et al., 2009a). For explosively

* In Buttler et al. (2012b), the RMI Sn validation data reported in Table I are in excellent agreement when $kh \leq 0.5$, which is typical for finished metals.

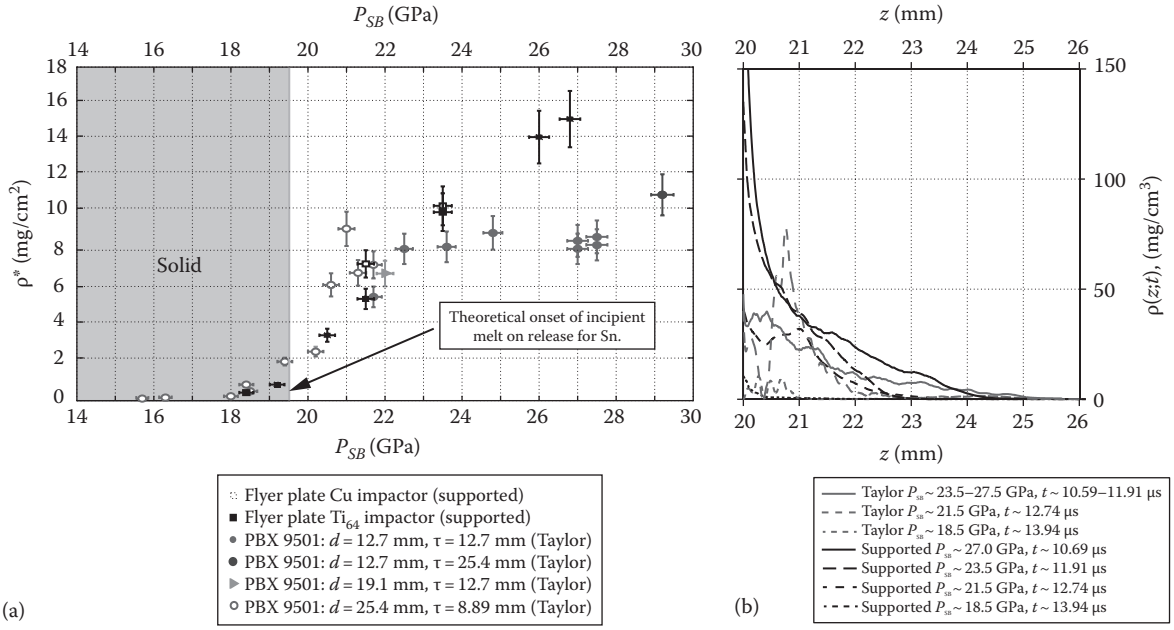


Figure 5.24

Plots in (a) and (b) are ejecta data from gun and HE experiments on Sn targets finished to $R_a \approx 0.8$ μm, $(\lambda, h_0) \approx (50, 1.6)$ μm. The (a) data are $\rho_A(P_{SB})$ and (b) $\rho^*(P_{SB}, z;t)$. In (a) the gray area ($P_{SB} \lesssim 19.5$ GPa) indicates the range of shock pressures below which Sn releases to a solid phase, according to the Sn EOS by Mabire and Hereil (2000) and Greeff et al. (2005); the EOS also says that Sn releases to a mixed solid–liquid phase when $19.5 < P_{SB} < 33$ GPa, and Sn is 100% liquid on release when $P_{SB} > 33$ GPa. The legends in (a) and (b) describe the experimental conditions: HE or flyer plate. P_{SB} was varied on the HE experiments by selecting the HE thickness τ and diameters d or by changing the flyer plate velocity. In (b) t is the time after shock breakout that the flyer reached the lithium niobate pins.

driven experiments, we have observed that the mass feeding into the spikes becomes asymptotic quickly and $\rho_A(P_{SB})$ plateaus (saturates), as seen in Figure 5.24a when $P_{SB} \gtrapprox 22.5$ GPa. This is not to say that the bubble velocity does not asymptote *quickly* in both HE and gun-driven ejecta systems, but in HE systems the asymptotic bubble velocity plateaus so that both ρ_A and ρ^* saturate when $22.5 \lessapprox P_{SB} \lessapprox 28$ GPa. In contrast, on the gun experiments it is seen that ρ_A increases linearly with P_{SB}, and ρ^* presents with higher ejecta densities further beyond the surface with increasing P_{SB}, as seen in Figure 5.24b. This divergence in $\rho_A(z;t)$ and the mass–velocity saturation in $\rho^*(z;t)$ for the HE-driven experiments is surprising. It is simplistic to say that this *plateau* in ρ_A and the different ρ^* distributions is linked to the Taylor wave shape of the shock waves caused by HE drives, as the shocked material will release into tension versus the release to zero pressure of a supported shock—all agree that this is the relevant phenomenon. However, the phenomenon is not well understood as a shutdown caused by spallation or cavitation of the shocked metal as the timescales for those processes appear to be too long. Because of the observed saturation in ρ_A and ρ^* for the HE experiments, our ejecta experiments were focused on HE-driven ejecta phenomena. This realization simplifies the calculation of $\rho_A(t)$ if we can define a $y(x, t)$ to define the mass production versus time. A lower limiting possibility on the total mass ejected assumes that $y(x, t)$ ends as it began, that is, $y(x,t) \mapsto y(x) = h_\infty^b \cos(kx) \mapsto h_0 \cos(kx)$. The opposite limit is that $y(x, t) = 1$. It is more likely that $y(x, t)$ is quadratic, or even some more complex shape, but the lower limit gives

$$\rho_A(t) = \rho(L\lambda)^{-1} \int\int\int dt dx dz \cos(kx) \frac{\dot{h}_0^b}{1 + \frac{3}{2}\dot{h}_0^b kt},$$

$$= \rho \frac{1}{\pi} \int dt \frac{\dot{h}_0^b}{1 + \frac{3}{2}\dot{h}_0^b kt},$$

$$= \frac{1}{\pi} \frac{\lambda\rho}{3\pi} \ln(1 + t/\tau), \tag{5.151}$$

where $\tau = \lambda/(3\pi F_1 F_{nl}^b \dot{h}_0^b) = \lambda^2/(6h\pi^2 u_{fs})$. Our Sn HE experiments indicate that $t/\tau \approx \mathcal{O}(10)$ when $\lambda \approx \mathcal{O}(100\,\mu\text{m})$ and $kh < 1$, which gives a critical time t_c such that $\dot{h}^b(t) = 0$ when $t \geq t_c$. This gives the mass–velocity distributions, which expand self-similarly with the constraint that $\dot{h}^b \mapsto u_{fs}$ when $t/\tau \approx 10$. In the upper limit where $y(x, t) = 1$, we find

$$\rho_A(t) = \rho(L\lambda)^{-1} \int\int\int dt dx dz \cos(kx) \frac{\dot{h}_0^b}{1 + \frac{3}{2}\dot{h}_0^b kt}$$

$$= \rho \int dt \frac{\dot{h}_0^b}{1 + \frac{3}{2}\dot{h}_0^b kt}$$

$$= \frac{\lambda\rho}{3\pi} \ln(1 + t/\tau). \tag{5.152}$$

These results imply an upper and lower bound on the mass ejection, and the mass velocity distribution will be limited less than the spike velocity.

As seen in Figure 5.15, our assumptions in the RMI model development are that the perturbations are described as a sinusoidal perturbation, when in fact a triangular perturbation is the more common surface perturbation geometry caused by machine tooling (see Vogan et al., 2005, Zellner et al., 2008b, Monfared et al., 2014). We assume, and experiments have borne out, that the two are simply related through the ratios of their defect volumes V_{fd}, but work in this area is ongoing, and other shape effect models have been proposed (Mikaelian, 2005, Li et al., 2014).

References

Abgrall, R. and Saurel, R., Discrete equations for physical and numerical compressible multiphase mixtures, *J. Comp. Phys.*, 186, 361, 2003.

Abrahamson, J., Collision rates of small particles in a vigorously turbulent fluid, *Chem. Eng. Sci.*, 30, 1371, 1975.

Allaire, G., Clerc, S., and Kokh, S., A five-equation model for the simulation of interfaces between compressible fluids, *J. Comp. Phys.*, 181, 577, 2002.

Anand, R.K., Shock jump relations for a dusty gas atmosphere, *Astrophys. Space Sci.*, 349, 181, 2014.

Andrews, M.J. and O'Rourke, P.J., The multiphase particle-in-cell method for dense particulate flows, *Int. J. Multiphase Flow*, 22, 379, 1996.

Andriot, P., Chapron, P., and Olive, F., Ejection of material from shocked surfaces of tin, tantalum, and lead alloys, *AIP Conf. Proc.*, 78, 505, 1982.

Asay, J.R., Ejection of material from shocked surfaces, *Appl. Phys. Lett.*, 29, 284, 1976.

Asay, J.R., Effect of shock wave risetime on material ejection from aluminum surfaces, Sandia National Laboratories, Albuquerque, NM, Tech. Rep., SAND-77-0731, 1977.

Asay, J.R., A model for estimating the effects of surface roughness on mass ejection from shocked materials, Sandia National Laboratories, Albuquerque, New Mexico, Tech. Rep., SAND-78-1256, 1978.

Baer, M.R. and Nunziato, J.W., A two-phase mixture theory for the deflagration-to-detonation transition in reactive granular materials, *Int. J. Multiphase Flow*, 12, 861, 1986.

Bailey, A.B. and Hiatt, J., Free-flight measurements of sphere drag at subsonic, transonic, supersonic, and hypersonic speeds for continuum, transition, and near-free-molecular flow conditions, Office of Aerospace Research, Tech. Rep., AEDC-TR-70-291, Arnold Air Force Station, TN, 1971.

Bailey, A.B. and Starr, R.F., Sphere drag at transonic speeds and high Reynolds numbers, *AIAA J.*, 14, 1631, 1976.

Balachandar, S. and Eaton, J.K., Turbulent dispersed phase flow, *Annu. Rev. Fluid Mech.*, 42, 111, 2010.

Balachandar, S. and Ha, M.Y., Unsteady heat transfer from a sphere in a uniform cross-flow, *Phys. Fluids*, 13, 3714, 2001.

Balasubramanian, B., Orlicz, G.C., and Prestridge, K.P., Experimental study of initial condition dependence on turbulent mixing in shock-accelerated Richtmyer-Meshkov fluid layers, *J. Turb.*, 14, 170, 2013.

Balasubramanian, B., Orlicz, G.C., Prestridge, K.P., and Balakumar, B.J., Experimental study of initial condition dependence on Richtmyer-Meshkov instability in the presence of reshock, *Phys. Fluids*, 24, 034103, 2012.

Banerjee, A., Gore, R.A., and Andrews, M.J., Development and validation of a turbulent-mix model for variable-density and compressible flows, *Phys. Rev. E*, 82, 046309, 2010.
Banerjee, S., Ertunç, Ö., Köksoy, Ç., and Durst, F., Pressure strain rate modeling of homogeneous axisymmetric turbulence, *J. Turb.*, 10, 1, 2009.
Barker, L.M. and Hollenbach, R.E., Laser interferometer for measuring high velocities of any reflecting surface, *J. Appl. Phys*., 43, 4669, 1972.
Basset, A.B., *Treatise on Hydrodynamics*, Deighton Bell, London, U.K., 1888.
Besnard, D.C, Harlow, F.H., and Rauenzahn, R.M., Conservation and transport properties of turbulence with large density variations, Los Alamos National Laboratory, Los Alamos, NM, Tech. Rep., LA-10911-MS, 1987.
Besnard, D.C, Harlow, F.H., Rauenzahn, R.M., and Zemach, C., Turbulence transport equations for variable-density turbulence and their relationship to two-field models, Los Alamos National Laboratory, Los Alamos, NM, Tech. Rep., LA-12303-MS, 1992.
Bohren, C.F. and Huffman, D.R., *Absorption and Scattering of Light by Small Particles*, Chapter 13, WILEY-VCH Verlag GmbH and Co. KGaA, New York, 2004.
Boiko, V.M. and Poplavskii, S.V., Drag of nonspherical particles in a flow behind a shock wave, *Combust. Explo. Shock*, 41, 71, 2005.
Buttler, W.T., Lamoreaux, S.K., Omenetto, F.G., and Torgerson, J.R., Optical velocimetry, *arXiv:physics/0409073v1*, 2004.
Buttler, W.T., Routley, N., Hixson, R.S., King, N.S.P., Olson, R.T., Rigg, P.A., Rimmer, A., and Zellner, M.B., Method to separate and determine the amount of ejecta produced in a second material-fragmentation event, *Appl. Phys. Lett.*, 90, 151921, 2007.
Buttler, W.T., Oró, D.M., Mariam, F.G., Saunders, A., Andrews, M.J., Cherne, F.J., Hammerberg, J.E. et al., Explosively driven two-shockwave tools with applications, *J. Phys. Conf. Ser.*, 500, 112014, 2014a.
Buttler, W.T., Oró, D.M., Olson, R.T., Cherne, F.J., Hammerberg, J.E., Hixson, R.S., Monfared, S.K. et al., Second shock ejecta measurements with an explosively driven two-shockwave drive, *J. Appl. Phys.*, 116, 103519, 2014b.
Buttler, W.T., Oró, D.M., Preston, D.L., Mikaelian, K.O., Cherne, F.J., Hixson, R.S., Mariam, F.G. et al., The study of high-speed surface dynamics using a pulsed proton beam, *AIP Conf. Proc.*, 1426, 999, 2012a.
Buttler, W.T., Oró, D.M., Preston, D.L., Mikaelian, K.O., Cherne, F.J., Hixson, R.S., Mariam, F.G. et al., Unstable Richtmyer-Meshkov growth of solid and liquid metals in vacuum, *J. Fluid Mech.*, 703, 60, 2012b.
Chang, E.J. and Kailasanath, K., Shock wave interactions with particles and liquid fuel droplets, *Shock Waves*, 12, 333, 2003.
Chen, Y., Hu, H., Li, Q., Wang, R., and Tang, T., Experimental study of ejecta on lead surface at different loading rates and amplitudes, *AIP Conf. Proc.*, 1426, 1003, 2012a.
Chen, Y., Hu, H., Tang, T., Ren, G., Li, Q., Wang, R., and Buttler, W.T., Experimental study of ejecta from shock melted lead, *J. Appl. Phys.*, 111, 053509, 2012b.
Cheret, R., Chapron, P., Elias, P., and Martineau, J., Mass ejection from the free surface of shock loaded metallic samples, in *The Proceedings of the Fourth American Physical Society Topical Conference on Shock Waves in Condensed Matter*, July 22–25, 1985. Spokane, Washington, 1986.
Cherne, F.J., Dimonte, G., and Germann, T.C., Richtmyer-Meshkov instability examined with large-scale molecular dynamics simulations, *AIP Conf. Proc.*, 1426, 1307, 2012.
Chu, C.M. and Churchhill, S.W., Numerical solution of problems in multiple scattering of electromagnetic radiation, *J. Phys. Chem*., 59, 955, 1955.
Clift, R. and Gauvin, W.H., The motion of particles in turbulent gas streams, *Proc. Chemeca*, 1, 14, 1970.
Clift, R., Grace, J.R., and Weber, M.E., *Bubbles, Drops and Particles*, Academic Press, San Diego, CA, 1978.
Cook, A.W., Enthalpy diffusion in multicomponent flows, *Phys. Fluids*, 21, 055109, 1, 2009.
Crowe, C.T., Drag coefficient for particles in a rocket nozzle, *AIAA J.*, 5, 1021, 1967.
Crowe, C.T., Schwarzkopf, J.D., Sommerfeld, M., and Tsuji, Y., *Multiphase Flows with Droplets and Particles*, CRC Press, Boca Raton, FL, 2012.
Cummins, H., Knable, N., Gampel, L., and Yeh, Y., Frequency shifts in light diffracted by ultrasonic waves in liquid media, *Appl. Phys. Lett.*, 2, 62, 1963a.
Cummins, H.Z., Knable, N., and Yeh, Y., Spurious harmonic generation in optical heterodyning, *Appl. Opt.*, 2, 823, 1963b.

Denissen, N.A. and Plohr, B.J., Youngs-type material strength model in the Besnard-Harlow-Rauenzahn turbulence equations, Los Alamos National Laboratory, Los Alamos, NM, Tech. Rep. LA-UR-15-26480, 2015.

Dimonte, G. and Ramaprabhu, R., Simulations and model of the nonlinear Richtmyer-Meshkov instability, *Phys. Fluids*, 22, 014104, 2010.

Dimonte, G., Terrones, G., Cherne, F.J., and Ramaprabhu, P., Ejecta source model based on the nonlinear Richtmyer-Meshkov instability, *J. Appl. Phys.*, 113, 024905, 2013.

Durand, O. and Soulard, L., Large-scale molecular dynamics study of jet breakup and ejecta production from shock-loaded copper with a hybrid method, *J. Appl. Phys.*, 111, 044901, 2012.

Durand, O. and Soulard, L., Power law and exponential ejecta size distributions from the dynamic fragmentation of shock-loaded Cu and Sn metals under melt conditions, *J. Appl. Phys.*, 114, 194902, 2013.

Elghobashi, S., On predicting particle-laden turbulent flows, *Appl. Sci. Res.*, 52, 309, 1994.

Faxén, H., Die Bewegung einer starren Kugel längs der Achse eines mit zäher Flüssigkeit gefüllten Rohres, *Ark. Mat. Astron. Fys.*, 17, 1, 1923.

Feng, Z.G. and Michaelides, E.E., Unsteady heat transfer from a sphere at small Peclet numbers, *J. Fluid Eng.-T. ASME*, 118, 96, 1996.

Fiveland, W.A., Three-dimensional radiative heat-transfer solutions by discrete-ordinates method, *J. Thermophys.*, 2, 309, 1988.

Forman Jr., J.W., George, E.W., and Lewis, R.D., Measurement of localized fluid flow velocities in gases with a laser Doppler flowmeter, *Appl. Phys. Lett.*, 7, 77, 1965.

Fox, T.W., Rackett, C.W., and Nicholls, J.A., Shock wave ignition of magnesium powders, in *Proceedings of 11th International Symposium on Shock Tubes and Waves*, University of Washington Press, Seattle, WA, 1978, pp. 262–268.

Francois, M.M., Shashkov, M.J., Masser, T.O., and Dendy, E.D., A comparative study of multimaterial Lagrangian and Eulerian methods with pressure relaxation, *Comp. Fluids*, 83, 126, 2013.

Fung, J., Harrison, A.K., Chitanvis, S., and Margulies, J., Ejecta source and transport model in the FLAG hydrocode, *Comput. Fluids*, 83, 177, 2013.

Gallouet, T., Herard, J.M., and Seguin, N., 2004, Numerical modeling of two-phase flows using the two-fluid two-pressure approach, *Math. Mod. Meth. Appl. S.*, 14, 663, 2004.

García-Cascales, J.R. and Paillére, H., Application of AUSM schemes to multi-dimensional compressible two-phase flow problems, *Nucl. Eng. Des.*, 236, 1225, 2006.

Gatignol, R., The Faxén formulae for a rigid particle in an unsteady non-uniform Stokes flow, *J. Mech. Theor. Appl.*, 1, 143, 1983.

Georgievskaya, A.B. and Raevsky, V.A., Estimation of spectral characteristics of particles ejected from the free-surface of metals and liquids under a shock wave effect, *AIP Conf. Proc.*, 1426, 1007, 2012.

Gittings, M., Weaver, R., Clover, M., Betlach, T., Byrne, N., Coker, R., Dendy, E. et al., The RAGE radiation-hydrodynamic code, *Comp. Sci. Disc.*, 1, 015005, 2008.

Goin, K. and Lawrence, W., Subsonic drag of spheres at Reynolds numbers from 200 to 10, 000, *AIAA J.*, 6, 961, 1968.

Greeff, C., Chisolm, E., and George, D., SESAME 2161: An explicit multiphase equation of state for tin, Los Alamos National Laboratory, Los Alamos, NM, Tech. Rep., LA-UR-05-9414, 2005.

Grégoire, O., Souffland, D., and Gauthier, S., A second-order turbulence model for gaseous mixtures induced by Richtmyer-Meshkov instability, *J. Turb.*, 6, 1, 2005.

Grüneisen, E., Theorie des festen Zustandes einatomiger Elemente, *Annalen der Physik*, 344, 306, 1912.

Haines, B., Greinstein, F., and Schwarzkopf, J.D., Reynolds-averaged Navier-Stokes initialization and benchmarking in shock-driven turbulent mixing, *J. Turb.*, 14, 46, 2013.

Harlow, F.H. and Amsden, A.A., Fluid dynamics, Los Alamos National Scientific, Los Alamos, NM, Tech. Rep., LA-4700, 1971.

Harris, S.E. and Crighton, D.G., Solitons, solitary waves, and void disturbances in gas-fluidized beds, *J. Fluid Mech.*, 266, 243, 1994.

He, A.-M., Wang, P., and Shao, J.-L., Molecular dynamics simulations of ejecta size distributions for shock-loaded Cu with a wedged surface groove, *Comp. Mater. Sci.*, 98, 271, 2015.

Henderson, C.B., Drag coefficients of spheres in continuum and rarefied flows, *AIAA J.*, 14, 707, 1976.

Hermsen, R.W., Review of particle drag models, *JANAF Performance Standardization Subcommittee 12th Meeting Minutes*, Chemical Propulsion Information Agency, Columbia, MD, 1979.

Hölzer, A. and Sommerfeld, M., New simple correlation formula for the drag coefficient of non-spherical particles, *Powder Tech.*, 184, 361, 2008.
Horwitz, J. and Schwarzkopf, J.D., BHR equations re-derived with immiscible particle effects, Los Alamos National Laboratory, Los Alamos, NM, Tech. Rep., LA-UR-15-23316, 2015.
Jourdan, G., Houas, L., Igra, O., Estivalezes, J.-L., Devals, C., and Meshkov, E.E., Drag coefficient of a sphere in a non-stationary flow: New results, *Proc. R. Soc. A*, 463, 3323, 2007.
Kapila, A.K., Menikoff, R., Bdzil, J.B., Son, S.F., and Stewart, D.S., Two-phase modeling of deflagration-to-detonation transition in granular materials: Reduced equations, *Phys. Fluids*, 13, 3002, 2001.
Kelvin, L.W.T., Hydrokinetic solutions and observations, *Philos. Mag.*, 42, 362, 1871.
Kessel-Deynet, O. and Burkert, A., Ionizing radiation in smoothed particle hydrodynamics, *Mon. Not. R. Astron. Soc.*, 315, 713, 2000.
Kim, I., Elghobashi, S., and Sirignano, W.A., On the equation for spherical-particle motion: Effect of Reynolds and acceleration numbers, *J. Fluid Mech.*, 367, 221, 1998.
Lew, A., Radovitzky, R., and Ortiz, M., An artificial-viscosity method for the Lagrangian analysis of shocks in solids with strength on unstructured, arbitrary-order tetrahedral meshes, *J. Comput.-Aided. Mater.*, 8, 213, 2001.
Li, B., Zhao, F.P., Wu, H.A., and Luo, S.N., Microstructure effects on shock-induced surface jetting, *J. Appl. Phys.*, 115, 073504, 2014.
Ling, Y., Haselbacher, A., and Balachandar, S., Importance of unsteady contributions to force and heating for particles in compressible flows: Part 1: Modeling and analysis for shock/particle interaction, *Int. J. Multiphase Flow*, 37, 1026, 2011a.
Ling, Y., Haselbacher, A., and Balachandar, S., Importance of unsteady contributions to force and heating for particles in compressible flows. Part 2: Application to particle dispersal by blast waves, *Int. J. Multiphase Flow*, 37, 1013, 2011b.
Ling, Y., Hasselbacher, A., Balachandar, S., Najjar, F.M., and Stewart, D.S., Shock interaction with a deformable particle: Direct numerical simulation and point particle modeling, *J. App. Phys.*, 113, 013504, 2013.
Ling, Y., Wagner, J.L., Beresh, S.J., Kearney, S.P., and Balachandar, S., Interaction of a planar shock wave with a dense particle curtain: Modeling and experiments, *Phys. Fluids*, 24, 113301, 1, 2012.
Liu, Y. and Grieves, B., Ejecta production and transport from a shocked Sn coupon, *J. Fluids Eng.*, 136, 091202, 2014.
Llor, A., *Statistical Hydrodynamic Models for Developed Mixing Instability Flows*, Springer-Verlag, Berlin Heidelberg, Germany, 2005.
Loth, E., Compressibility and rarefaction effects on drag of a spherical particle, *AIAA J.*, 46, 2219, 2008.
Mabire, C. and Hereil, P.L., Shock induced polymorphic transition and melting of tin, *AIP Conf. Proc.*, 505, 93–96, 2000; Shock induced polymorphic transition and melting of tin up to 53 GPa (experimental study and modelling), *J. Phys. IV*, 10, 749, 2000.
Macrossan, M.N., Scaling parameters in rarefied flow and the breakdown of the Navier-Stokes equations, *Dept. Mech. Eng, Tech. Rep.*, 2004/09, Univ. Queensland, 2004.
Maxey, M.R., The gravitational settling of aerosol-particles in homogeneous turbulence and random flow-fields, *J. Fluid Mech.*, 174, 441, 1987.
Maxey, M.R., Patel, B.K., Chang, E.J., and Wang, L.-P., Simulations of dispersed turbulent multiphase flow, *Fluid Dyn. Res.*, 20, 143, 1997.
Maxey, M.R. and Riley, J.J., Equation of motion for a small rigid sphere in a nonuniform flow, *Phys. Fluids*, 26, 883, 1983.
May, A. and Witt, W., Free-flight determinations of the drag coefficients of spheres, *J. Aeronaut. Sci.*, 20, 635, 1953.
McMillan, C.F., Size measurements of high velocity particle distributions, *Proc. SPIE*, 674, 289, 1986.
Mears, A., Routley, N.R., and Kendall, P.A., Impact stress measurement using piezoelectric probes with PZT and lithium niobate elements, *AIP Conf. Proc.*, 1195, 639, 2010.
Mei, R. and Adrian, R.J., Flow past a sphere with an oscillation in the free-stream velocity and unsteady drag at finite Reynolds number, *J. Fluid Mech.*, 237, 323, 1992.
Meshkov, E.E., Instability in shock-accelerated boundary separating two gasses, *Izv. Akad. Nauk SSSR, Mekh. Zhidk. Gasa*, 5, 151, 1969.
Meyer, K.A. and Blewett, P.J., Numerical investigation of the stability of a shock-accelerated interface between two fluids, *Phys. Fluids*, 15, 753, 1972.

Michaelides, E.E., *Particles, Bubbles, and Drops: Their Motion Heat and Mass Transfer*, World Scientific, Singapore, Hackensack, NJ, 2006.
Mie, G., Zur kinetischen Theorie der einatomigen Köper, *Annalen der Physik*, 316, 657, 1903.
Mie, G., Contribution on the optics of turbid media, particularly colloidal metal solutions, *Ann. der Physik*, 25, 377, 1908.
Mikaelian, K.O., Richtmyer-Meshkov instability for arbitrary shapes, *Phys. Fluids*, 17, 034101, 2005.
Mikaelian, K.O., Analytic approach to nonlinear hydrodynamic instabilities driven by time-dependent accelerations, *Phys. Rev. E*, 81, 016325, 2010.
Mikhailov, A.L., Ogorodnikov, V.A., Sasik, V.S., Raevskii, V.A., Lebedev, A.I., Zotov, D.E., Erunov, S.V. et al., Experimental-calculation simulation of the ejection of particles from a shock-loaded surface, *J. Exp. Theor. Phys.*, 118, 785, 2014.
Monfared, S.K., Buttler, W.T., Frayer, D.K., Grover, M., LaLone, B.M., Stevens, G.D., Stone, J.D., Turley, W.D., and Schauer, M.M., Ejected particle size measurement using Mie scattering in high explosive driven shockwave experiments, *J. Appl. Phys.*, 117, 223105, 2015.
Monfared, S.K., Oró, D.M., Grover, M., Hammerberg, J.E., LaLone, B.M., Pack, C.L., Schauer, M.M. et al., Experimental observations on the links between surface perturbation parameters and shock–induced mass ejection, *J. Appl. Phys.*, 116, 063504, 2014.
Naot, D., Shavit, A., and Wolfshtein, M., Interactions between components of the turbulent velocity correlation tensor due to pressure fluctuations, *Israel J. Tech.*, 8, 259, 1970.
Niederhaus, J.H.J., Greenough, J.A., Oakley, J.G, Ranjan, D., Anderson, M.H., and Bonazza, R., A computational parameter study for the three-dimensional shock-bubble interaction, *J. Fluid Mech.*, 594, 85, 2008.
Niu, Y.Y., Lin, Y.C., and Chang, C.H., A further work on multi-phase two-fluid approach for compressible multi-phase flows, *Int. J. Num. Meth. Fluid*, 58, 879, 2008.
Noh, W.F., Errors for calculations of strong shocks using an artificial viscosity and an artificial heat-flux, *J. Comp. Phys.*, 72, 78, 1987.
Ogorodnikov, V.A., Mikhaĭlov, A.L., Burtsev, V.V., Lobastov, S.A., Erunov, S.V., Romanov, A.V., Rudnev, A.V. et al., Detecting the ejection of particles from the free surface of a shock-loaded sample, *J. Exp. Theor. Phys.: Stat. Nonlin. Soft Matter Phys.*, 109, 530, 2009.
Parmar, M., Haselbacher, A., and Balachandar, S., On the unsteady inviscid force on cylinders and spheres in subcritical compressible flow, *Philos. T. Roy. Soc. A*, 366, 2161, 2008.
Parmar, M., Hasselbacher, A., and Balachandar, S., Improved drag correlation for spheres and application to shock-tube experiments, *AIAA J.*, 48, 1273, 2010.
Parmar, M., Haselbacher, A., and Balachandar, S., Generalized Basset-Boussinesq-Oseen equation for unsteady forces on a sphere in a compressible flow, *Phys. Rev. Lett.*, 106, 084501, 2011.
Parmar, M., Haselbacher, A., and Balachandar, S., Equation of motion for a sphere in non-uniform compressible flows, *J. Fluid Mech.*, 699, 352, 2012.
Petel, O.E. and Jetté, F.X., Comparison of methods for calculating the shock hugoniot of mixtures, *Shock Waves*, 20, 73, 2010.
Petitpas, F., Franquet, E., Saurel, R., and Le Métayer, O., A relaxation-projection method for compressible flows. Part II: Artificial heat exchanges for multiphase shocks, *J. Comp. Phys.*, 225, 2214, 2007.
Poggi, F., Thorembey, M.-H., and Rodriguez, G., Velocity measurements in turbulent gaseous mixtures induced by Richtmyer-Meshkov instability. *Phys. Fluids*, 10, 2698, 1998.
Pope, S.B., *Turbulent Flows*, Cambridge University Press, Cambridge, U.K., 2000.
Quirk, J.J. and Karni, S., On the dynamics of a shock-bubble interaction, *J. Fluid Mech.*, 318, 129, 1996.
Ranjan, D., Oakley, J.G., and Bonazza, R., Shock-bubble interactions, *Annu. Rev. Fluid Mech.*, 43, 117–140, 2011.
Rayleigh, L. (John William Strutt), Investigation of the character of the equilibrium of an incompressible heavy fluid of variable density, *Proc. Lond. Math. Soc.*, 14, 170, 1883.
Ren, G., Chen, Y., Tang, T., and Luo, S.N., Ejecta production from shocked Pb surface via molecular dynamics, *J. Appl. Phys.*, 116, 133507, 2014.
Richtmyer, R.D., Taylor instability in shock acceleration of compressible fluids, *Commun. Appl. Math.*, XIII, 297, 1960.
Rotta, J.C., Statistische theorie nichthomogener turbulenz, *Z. Phys.*, 129, 547, 1951 (an English translation can be found in NASA-TT-F-14560, October 1972).

Ruggirello, K.P., DesJardin, P.E., Baer, M.R., and Hertel, E.S., Modeling of particle compressibility and ignition from shock focusing, *Combust. Theor. Model*, 14, 41, 2010.
Sambasivan, S.K., Shashkov, M.J., and Burton, D.E., A finite volume cell-centered Lagrangian hydrodynamics approach for solids in general unstructured grids, *Intl. J. Num. Meth. Fluids*, 72, 770, 2013.
Sangani, A.S., Zhang, D.Z., and Prosperetti, A., The added mass, Basset, and viscous drag coefficients in nondilute bubbly liquids undergoing small-amplitude oscillatory motion, *Phys. Fluids A*, 3, 2955, 1991.
Saurel, R., Franquet, E., Daniel, E., and Le Métayer, O., A relaxation-projection method for compressible flows. Part I: The numerical equation of state for the Euler equations, *J. Comp. Phys*., 223, 822, 2007b.
Saurel, R., Le Métayer, O., Massoni, J., and Gavrilyuk, S., Shock jump relations for multiphase mixtures with stiff mechanical relaxation, *Shock Waves*, 16, 209, 2007a.
Schwarzkopf, J.D., Crowe, C.T., and Dutta, P., A turbulence dissipation model for particle laden flow, *AIChE. J*., 55, 1416, 2009a.
Schwarzkopf, J.D., Crowe, C.T., and Dutta, P., Application of volume-averaged k–ε model to particle-laden turbulent channel flow, *J. Fluids Eng*., 131, 101301, 2009b.
Schwarzkopf, J.D., Livescu, D., Gore, R.A., Rauenzahn, R.M., Gore, R.A., and Ristorcelli, J.R., Application of a second-moment closure model to mixing processes involving multicomponent miscible fluids, *J. Turb*., 12, 1, 2011.
Siegel, R. and Howell, J.R., *Thermal Radiation Heat Transfer*, McGraw Hill, New York, 1981.
Slattery, C., *Momentum, Energy, and Mass Transfer in Continua*, McGraw-Hill, New York, 1972.
Snider, D.M., Three fundamental granular flow experiments and CPFD predictions, *Powder Tech*., 176, 36, 2007.
Snider, D.M., O'Rourke, P.J., and Andrews, M.J., Sediment flow in inclined vessels calculated using a multiphase particle-in-cell model for dense particle flows, *Int. J. Multiphase Flows*, 24, 1359, 1998.
Sorenson, D.S., Minich, R.W., Romero, J.L., Tunnell, T.W., and Malone, R.M., Ejecta particle size distributions for shock-loaded Sn and Al targets, *AIP Conf. Proc*., 620, 531, 2002a.
Sorenson, D.S., Minich, R.W., Romero, J.L., Tunnell, T.W., and Malone, R.M., Ejecta particle size distributions for shock-loaded Sn and Al metals, *J. Appl. Phys*., 92, 5830, 2002b.
Strand, O.T., Goosman, D.R., Martinez, C., and Whitworth, T.L., Compact system for high-speed velocimetry using heterodyne techniques, *Rev. Sci. Instrum*., 77, 083108, 2006.
Sun, M., Saito, T., Takayama, K., and Tanno, H., Unsteady drag on a sphere by shock wave loading, *Shock Waves*, 14, 3, 2005.
Taylor, Sir G.I., The instability of liquid surfaces when accelerated in a direction perpendicular to their planes, *Proc. Roy. Soc. Lond. A Mater*., 201, 192, 1950.
Theofanous, T.G., Aerobreakup of Newtonian and viscoelastic liquids, *Ann. Rev. Fluid Mech*., 43, 661, 2011.
Theofanous, T.G. and Li, G.J., On the physics of aerobreakup, *Phys. Fluids* (1994-present), 20, 052103, 2008.
Theofanous, T.G., Mitkin, V.V., Ng, C.L., Chang, C.H., Deng, X., and Sushchikh, S., The physics of aerobreakup. II. Viscous liquids, *Phys. Fluids* (1994-present), 24, 022104, 2012.
Tran-Chong, S., Gay, M., and Michaelides, E.E., Drag coefficient of irregularly shaped particles, *Powder Tech*., 139, 21, 2004.
Velikovich, A.L. and Dimonte, G., Nonlinear perturbation theory of the incompressible Richtmyer-Meshkov instability, *Phys. Rev. Lett*., 76, 3112, 1996.
Vogan, W.S., Anderson, W.W., Grover, M., Hammerberg, J.E., King, N.S.P., Lamoreaux, S.K., Macrum, G. et al., Piezoelectric characterization of ejecta from shocked tin surfaces, *J. Appl. Phys*., 98, 113508, 2005.
von Helmholtz, H.L.F., On the discontinuous movements of fluids, (*Monthly Reports of the Royal Prussian Academy of Philosophy in Berlin*) *Philos. Mag*., 23, 215, 1868.
Wagner, J.L., Beresh, S.J., Kearney, S.P., Pruett, B.O.M., and Wright, E.K., Shock tube investigation of quasi-steady drag in shock-particle interactions, *Phys. Fluids*, 24, 123301, 2012.
Waltz, J., Morgan, N.R., Canfield, T.R., Charest, M.R.J., Risinger, L.D., and Wohlbier, J.G., A three-dimensional finite element arbitrary Lagrangian-Eulerian method for shock hydrodynamics on unstructured grids, *Comp. Fluids*, 92, 172, 2014.
Wood, A.B., *A Textbook of Sound*, The Macmillan Co., New York, 1941.
Yanilkin, Y.V., Goncharov, E.A., Kolobyanin, V.Y., Sadchikov, V.V., Kamm, J.R., Shashkov, M.J., and Rider, W.J., Multi-material pressure relaxation methods for Lagrangian hydrodynamics, *Comp. Fluids*, 83, 137, 2013.
Yeh, Y. and Cummins, H.Z., Localized fluid flow measurements with an HeNe laser spectrometer, *App. Phys. Lett*., 4, 176, 1964.

Yeom, G.S. and Chang, K.S., A modified HLLC-type Riemann solver for the compressible six-equation two-fluid model, *Comp. Fluids*, 76, 86, 2013.

Youngs, D.L., Representation of the molecular mixing process in a two-phase flow turbulent mixing model, in R. Young, J. Glimm, B. Boston (Eds.), *Proceedings of the Fifth International Workshop on Compressible Turbulent Mixing*, Stony Brook, New York, July 18–21, World Scientific, Singapore, 1995, p. 321.

Youngs, D.L., Inclusion of the effect of material strength in a turbulent mixing model, Atomic Weapons Establishment, Berkshire, U.K., Tech. Report, 96/96, 1997.

Zellner, M.B. and Buttler, W.T., Exploring Richtmyer-Meshkov instability phenomena and ejecta cloud physics, *Appl. Phys. Lett.*, 93, 114102, 2008.

Zellner, M.B., Byers, M., Hammerberg, J.E., Germann, T.C., Dimonte, G., Rigg, P.A., and Buttler, W.T., Influence of shockwave profile on ejection of micron-scale material from shocked Sn surfaces: An experimental study, in *DYMAT 2009—Nineth International Conference on the Mechanical and Physical Behaviour of Materials under Dynamic Loading*, Brussels, Belgium, Vol. 1, 2009a, p. 89.

Zellner, M.B., Dimonte, G., Germann, T.C., Hammerberg, J.E., Rigg, P.A., Stevens, G.D., Turley, W.D., and Buttler, W.T., Influence of shockwave profile on ejecta, *AIP Conf. Proc.*, 1195, 1047, 2009b.

Zellner, M.B., Grover, M., Hammerberg, J.E., Hixson, R.S., Iverson, A.J., Macrum, G.S., Morley, K.B. et al., Effects of shock-breakout pressure on ejection of micron-scale material from shocked tin surfaces, *J. App. Phys.* 102, 013522, 2007.

Zellner, M.B., Grover, M., Hammerberg, J.E., Hixson, R.S., Iverson, A.J., Macrum, G.S., Morley, K.B. et al., Erratum: Effects of shock-breakout pressure on ejection of material from shocked tin surfaces, *J. Appl. Phys.*, 102, 013522, 2007; *J. Appl. Phys.*, 103, 109901, 2008b.

Zellner, M.B., Vogan-McNeil, W., Gray III, G.T., Huerta, D.C., King, N.S.P., Neal, G.E., Valentine, S.J. et al., Surface preparation methods to enhance dynamic surface property measurements of shocked metal surfaces, *J. Appl. Phys.*, 103, 083521, 2008a.

Zellner, M.B., Vogan-McNeil, W., Hammerberg, J.E., Hixson, R.S., Obst, A.W., Olson, R.T., Payton, J.R. et al., Probing the underlying physics of ejecta production from shocked Sn samples, *J. Appl. Phys.*, 103, 123502, 2008c.

6

Combustion with Particles and Drops

Farzad Mashayek and Farhad A. Jaberi

6.1 Introduction
6.2 Overview of Single-Phase (Gaseous) Combustion
6.3 Isolated Drop
6.4 Group of Drops
6.5 Two-Phase Turbulent Combustion

6.1 Introduction

Two-phase flows involving a carrier gas laden with a dispersed phase composed of a large number of solid particles or liquid drops occur in many natural and technological applications. One of the most important applications involves the endothermic chemical reaction of the dispersed phase, as a fuel, with the carrier gas, as an oxidizer. For example, the engines that propel missiles, jets, and many other devices must rely heavily on combustion in a two-phase environment. Within the combustion chamber, the liquid fuel, which is first atomized into small drops, undergoes evaporation and reaction with the oxidizer gas. To enhance the rate of mixing and reaction, these systems are designed to operate in the presence of turbulence. Furthermore, chemical reaction triggers the formation of high-gradient regions in the flow and thus serves as a source for generation and amplification of instabilities that lead to turbulence. As a result, turbulence cannot be ignored in the majority of the situations involving chemically reacting flows. The presence of turbulence significantly adds to the complexity of such flows and to the challenges encountered in their physical understanding, theoretical description, and practical prediction. These challenges are primarily a consequence of the numerous degrees of freedom associated with a turbulent flow, which itself has remained as one of the main unsolved problems in science and engineering. The addition of fuel drops, with the associated phenomena of evaporation and chemical reaction, further introduces new sets of variables, often accompanied by large variations in scales.

The topic of combustion, let alone in the presence of a second phase, is too broad to be covered completely in one chapter. Further, if the solid phase is carbonaceous, both heterogeneous and homogeneous oxidations occur. A thorough description of heterogeneous or homogeneous combustion requires basic knowledge in thermodynamics, fluid mechanics, heat transfer, chemical reaction, two-phase transport, etc. In this section, we deal with drop evaporation and combustion only and refer to the review articles by Annamalai and Ryan (1993), Annamalai et al. (1994), and references therein for detailed discussion of solid particle combustion. We also restrict our discussion to subcritical conditions and refer to the review by Bellan (2000) for supercritical fluid behavior and modeling. As argued earlier, the presence of turbulence cannot be overlooked in a majority of practical situations. Turbulence effects will be discussed in more details in this second edition, but the reader is also referred to several other chapters, in this handbook, which are entirely devoted to interactions of the dispersed phase with turbulence. Regardless of the role of turbulence, the dispersed phase processes could become "interactive" when the distance between the drops is comparable

to a few times the drop radius. In this situation, evaporation and combustion of one drop may significantly be affected by the presence of other drops.

The next section provides a brief overview of single-phase or gaseous combustion. This overview assists the reader with no or little previous knowledge of combustion to follow the main discussions on two-phase combustion. The discussion of drop evaporation and combustion is presented first for an isolated drop. Although in an actual spray, isolated drop burning is somewhat unlikely, the study of isolated drops serves as an important first step toward understanding the physical phenomena and the underlying mechanisms for evaporation and combustion. It should be emphasized that the theoretical study of isolated drops involves several simplifying assumptions, the validity of which may be arguable in real sprays, in particular near the injector where the spray is dense. For example, the isolated drop combustion model results predict increasing temperature as size is reduced, which is contrary to the industrial experience. Therefore, the interactions among the drops must be considered. This is the subject of the second part of this discussion where a group of drops are considered. From a modeling and theoretical point of view, it is noted that the models for group combustion often use the isolated drop results as their starting point, hence another reason for discussing isolated drops. Finally, new to this second edition of the handbook, we provide a general discussion of practical spray modeling, followed by an overview of one of the most advanced modeling approaches currently available for spray combustion simulation.

6.2 Overview of Single-Phase (Gaseous) Combustion

Liquid-fuel combustion systems lead to a chemical reaction between the fuel vapor and the oxidizer gas, thus forming a single-phase, or homogeneous (typically gaseous), combustion process. Therefore, as a necessary prelude to two-phase combustion, in this section we provide a brief overview of the gaseous combustion. Gaseous combustion can be described through continuum transport equations for mass fractions of various species that participate in the chemical reaction. For a system of n chemically reacting species, the mass balance for the mass fraction Y_i of species i yields

$$\rho\frac{\partial Y_i}{\partial t}+\rho\boldsymbol{u}\cdot\nabla Y_i=-\nabla\cdot\boldsymbol{j}_i+\omega_i,\quad i=1,2,\ldots,n \tag{6.1}$$

where $\boldsymbol{j}_i$ and ω_i denote the diffusive flux and the chemical source term, respectively. The molecular transport processes that cause the diffusive flux can be quite complicated (Williams, 1985). For turbulent flows, which occur in many practical applications, this term can be simplified by considering a binary flux approximation, $\boldsymbol{j}_i=-\rho D_i\nabla Y_i$, where D_i is the binary diffusion coefficient, or mass diffusivity, of species i with respect to an abundant species. While this approximation provides a convenient form for describing the governing transport equations in turbulent flows, it should not be used in laminar flame calculations (Peters, 2000).

For a total number of r reactions

$$\sum_{i=1}^{n}\nu'_{ik}X_i\Leftrightarrow\sum_{i=1}^{n}\nu''_{ik}X_i,\quad k=1,2,\ldots,r \tag{6.2}$$

that may be considered in the calculation, the chemical source term ω_i in Equation 6.1 is described as

$$\omega_i=W_i\sum_{k=1}^{r}(\nu''_{ik}-\nu'_{ik})w_k \tag{6.3}$$

where $\sum_{i=1}^{n}\omega_i=0$ and for inert, nonreacting species $\omega_i=0$. In Equation 6.2, ν'_{ik} and ν''_{ik} are the stoichiometric coefficients on the reactants and products sides, respectively, for the ith species in the kth reaction, and X_i represents the chemical formula for species i. In Equation 6.3, W_i is the molecular weight of species i and w_k is the rate of reaction k in a mechanism containing r chemical reactions,

$$w_k=k_{fk}\prod_{i=1}^{n}\left(\frac{\rho Y_i}{W_i}\right)^{\nu'_{ik}}-k_{bk}\prod_{i=1}^{n}\left(\frac{\rho Y_i}{W_i}\right)^{\nu''_{ik}} \tag{6.4}$$

Here, k_{fk} and k_{bk} are the rate coefficients of the forward and backward reactions, respectively, and are in general temperature dependent. They may also depend on pressure in some cases.

To simplify the analysis, a "global" reaction mechanism may be considered. For overall reaction of the fuel F and oxygen O_2, yielding the products P, the global reaction mechanism can be described as

$$\nu_F F + \nu_{O_2} O_2 \rightarrow \nu_P P \tag{6.5}$$

For this single-step reaction, the reaction rate is written as

$$w = A\left(\frac{\rho Y_F}{W_F}\right)^{n_f}\left(\frac{\rho Y_{O_2}}{W_{O_2}}\right)^{n_{O_2}} \exp\left(-\frac{E}{RT}\right) \tag{6.6}$$

where

A is the preexponential factor
E is the activation energy

The exponential expression $A\exp(-E/RT)$ is known as the Arrhenius form and is widely used to describe the temperature dependency of the reaction rate. The exponents n_f and n_{O_2} relate to *reaction order*. According to Equation 6.6, the reaction is of order $n_f + n_{O_2}$ overall. For global reactions, n_f and n_{O_2} are not necessarily integers and are found by curve-fitting experimental data. In general, a particular global expression in the form of Equation 6.6 holds only over a limited range of temperatures and pressures and may depend on the details of the apparatus used to define the rate parameters (Turns, 1996).

In addition to species transport equations (6.1), the overall continuity, momentum, and energy equations of the mixture are needed to fully describe the gaseous combustion system. The continuity and momentum equations are similar to those in nonreacting flows; the energy equation is modified to account for combustion effects. The latter can be derived from the first law of thermodynamics as (Peters, 2000)

$$\rho\frac{\partial h}{\partial t} + \rho \boldsymbol{u}\cdot\nabla h = \frac{\partial p}{\partial t} + \boldsymbol{u}\cdot\nabla p - \nabla\cdot \boldsymbol{j}_q + q_R \tag{6.7}$$

where the frictional heating has been neglected as it has a small contribution for low-speed flows. The last term, q_R, is due to radiation and must be retained in furnace combustion. Here, the enthalpy h of the mixture is defined in terms of the enthalpies h_i of species i,

$$h = \sum_{i=1}^{n} Y_i h_i \tag{6.8}$$

Assuming ideal gas, h_i only depends on temperature T:

$$h_i = h_{ref,i} + \int_{ref}^{T} c_{pg,i}(T)dT \tag{6.9}$$

where

$c_{pg,i}$ is the constant pressure specific heat of species i
T is the temperature in Kelvin

The reference enthalpy $h_{ref,i}$ includes the chemical bond energy and is generally taken to be zero for H_2, O_2, N_2, and solid carbon. The reference enthalpy of combustion products such as CO_2 and H_2O is negative and is tabulated (Burcat, 1984). The specific heat of the mixture is also defined in terms of specific heats of various species:

$$c_{pg} = \sum_{i=1}^{n} Y_i c_{pg,i} \tag{6.10}$$

The heat flux $\boldsymbol{j}_q$ in Equation 6.7 includes the effect of enthalpy transport by the diffusive fluxes $\boldsymbol{j}_j$:

$$\boldsymbol{j}_q = -k\nabla T + \sum_{i=1}^{n} h_i \boldsymbol{j}_i \tag{6.11}$$

To close, the system of continuity, momentum, energy, and species conservation equations is augmented by the equation of state for ideal gas.

6.3 Isolated Drop

Evaporation and combustion of a single drop are among the fundamental processes in liquid-fuel combustion and have been studied extensively since the pioneering works of Spalding (1953) and Godsave (1953). The analysis for a general case involving all important processes such as internal circulation, drop deformation (Haywood et al., 1994a,b, Mashayek, 2001), turbulence (Sornek et al., 2000, Wu et al., 2001), and gravity (Gogos et al., 2003) effects is quite complicated. Under special circumstances, simplifying assumptions can be made to derive an analytical solution. This solution is very useful in providing insights into the physics of drop evaporation and combustion and has produced reasonable predictions in real applications. In this section, we briefly review the derivation of the analytical solution and its underlying physical assumptions.

6.3.1 Evaporation

Consider an isolated drop evaporating in a quiescent and infinitely large medium and assume that the evaporation is quasi-steady, that is, at any instant in time the process can be described as if it were in the steady state. The drop temperature is uniform, typically at the saturation temperature $T_s < T_b$, where T_b is the boiling point of the fuel at the given pressure. Without loss of generality, in the following we assume that the drop is at its boiling temperature. The drop preheat period does not significantly contribute to the overall combustion process and can be neglected. Also, in order to find an analytical solution, all thermophysical properties are assumed constant (Turns, 1996).

With these assumptions, the gas-phase mass conservation for a spherically symmetric drop at quasi-steady state reads

$$\dot{m} = \rho v 4\pi r^2 = \text{constant} \tag{6.12}$$

A relationship for the temperature variation in the gas can be found by considering the gas-phase energy conservation, which states a balance between the conduction and convection heat transfer:

$$4\pi k_g \frac{d}{dr}\left(r^2 \frac{dT}{dr} \right) = \dot{m} c_{pg} \frac{dT}{dr} \tag{6.13}$$

where

T is the gas temperature

subscript g refers to the gas properties

For a unitary Lewis number ($Le = k_g/\rho c_{pg} D$), by defining $\xi = c_{pg}/4\pi k_g = 1/4\pi\rho D$, the following problem can be stated for the gas-phase temperature:

$$\frac{d}{dr}\left(r^2 \frac{dT}{dr} \right) = \xi \dot{m} \frac{dT}{dr} \tag{6.14}$$

with boundary conditions $T(r = a) = T_b$ and $T(r \to \infty) = T_\infty$, where a is the drop radius. The solution of this equation for constant $\dot{m}$ yields

$$T(r) = \frac{(T_\infty - T_b)\exp(-\xi\dot{m}/r) - T_\infty \exp(-\xi\dot{m}/a) + T_b}{1 - \exp(-\xi\dot{m}/a)} \tag{6.15}$$

which indicates a steep temperature gradient near the surface of the drop. This temperature gradient determines the heat conducted into the drop that will be consumed entirely for evaporation since the drop is at its boiling point. Therefore, writing the energy balance at the drop–gas interface gives

$$4\pi k_g a^2 \left.\frac{dT}{dr}\right|_a = \dot{m} h_{fg} \tag{6.16}$$

Differentiating Equation 6.15 and substituting into Equation 6.16 gives the mass flow rate of the vapor

$$\dot{m} = \frac{4\pi k_g a}{c_{pg}} \ln(1 + B_e) \tag{6.17}$$

where

$$B_e = \frac{c_{pg}(T_\infty - T_b)}{h_{fg}} \tag{6.18}$$

is the transfer number, also known as the Spalding number. With the relation for mass in terms of drop diameter and density, a more common form of Equation 6.17 is the so-called d^2-law written as

$$d^2(t) = d_0^2 - Kt, \quad K = \frac{8k_g}{\rho_l c_{pg}} \ln(1 + B_e) \tag{6.19}$$

where

d is the drop diameter with an initial value of d_0

subscript l refers to liquid properties

To account for the temperature dependency of thermophysical properties, following the approach of Law and Williams (1972) for burning drops, c_{pg} and k_g are evaluated at the temperature $\overline{T} = (T_b + T_\infty)/2$:

$$c_{pg} = c_{pF}(\overline{T}), \quad k_g = 0.4k_F(\overline{T}) + 0.6k_\infty(\overline{T}) \tag{6.20}$$

where F refers to fuel vapor. Other approximations are suggested in Hubbard et al. (1975).

Adopting a similar set of assumptions as in the previous analysis, Mashayek (2001) investigated the effect of a deformation in the surface of a drop on its rate of evaporation by conducting finite element simulations of the gas surrounding the drop. The drop was assumed to be at its boiling temperature, and the gas properties were considered constant for a quasi-steady analysis. The surface of the drop was deformed using spherical harmonics:

$$h(\phi) = R_n[1 + \epsilon_n P_n(\cos\phi)] \tag{6.21}$$

where

$P_n(\cos\phi)$ is the Legendre polynomial of degree n

ϵ_n is the amplitude of disturbance (with respect to the spherical shape)

R_n is a correction factor introduced to keep the volume of the drop the same as the amplitude is changed

All lengths were normalized with the radius of the unperturbed (spherical) drop. Figure 6.1 shows the computational domain and the coordinate system used. The angle ϕ is measured from the axis of symmetry toward the equator of the drop.

Figure 6.2 shows the deviation parameter ψ as a function of ϕ for $n = 2$ at various amplitudes. Here, ψ indicates the difference between the evaporation rates of the deformed drop and the spherical drop as normalized by the evaporation rate of the spherical drop. The results indicate that the evaporation rate is larger near the axis of symmetry and lower near the equator, and the deviation from the evaporation rate of a spherical drop increases with the increase in the amplitude. Based on the results of the simulations, the following model was presented for calculating the evaporation rate of a deformed drop:

$$\chi = \left[F_n \left(\mathcal{K} - \frac{2}{\mathcal{R}_s} \right) + \frac{2}{\mathcal{R}_s} \right] \beta \tag{6.22}$$

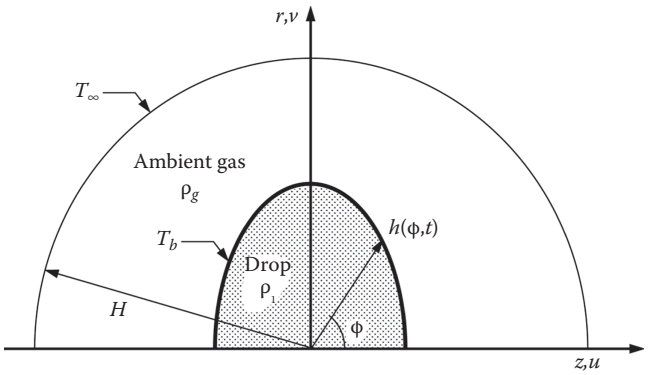


Figure 6.1

Coordinate system and solution domain used in computations of a deformed drop. (From Mashayek, F., *Int. J. Heat Mass Transfer,* 44, 1517, 2001.)

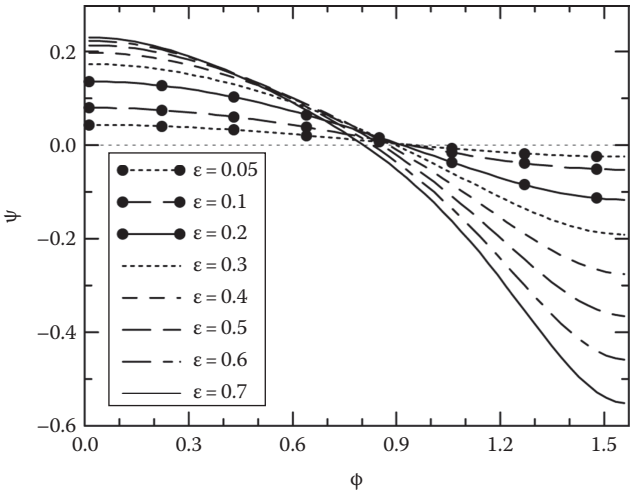


Figure 6.2

Variations of the normalized mass flux with angle ϕ at various amplitudes for a drop deformed with second spherical mode $n = 2$. (From Mashayek, F., *Int. J. Heat Mass Transfer,* 44, 1517, 2001.)

where $\mathcal{K}$ and $\mathcal{R}_s$ are the surface curvature and the nondimensional radius of the equivalent spherical drop, respectively. Also,

$$\chi = \left[\frac{\rho_l \sigma}{r_0}\right]^{(-1/2)} \dot{m} \tag{6.23}$$

is the dimensionless mass flux, and

$$\beta = \frac{1}{2}(\rho_l r_0 \sigma)^{(-1/2)} \left(\frac{k_g}{C_{pg}}\right) \ln(1 + B_e) \tag{6.24}$$

where r_0 and σ are the initial radius of the unperturbed drop and the surface tension coefficient, respectively. The function F_n depends on the mode of the surface disturbance and is defined as

$$F_n = \frac{3n+2}{2[n(n+1)+2]} \tag{6.25}$$

Equation 6.22 is valid for surface amplitudes up to 10% of the initial drop radius and has been tested for $0.1 \leq B_e \leq 2$ and for surface deformation up to $n = 8$. It is noted that Equation 6.22 reduces to Equation 6.17 for a spherical drop for which the surface curvature $\mathcal{K} = 2/\rho$.

6.3.2 Combustion

The analysis of a burning drop is understandably more complicated, but an analytical solution can be found for a simplified case. The diffusion flame requires that fuel and oxidizer react in stoichiometric proportions at the spherical flame that forms around the drop at a radius r_f. The reaction is assumed to be infinitely fast, and the flame is represented by an infinitesimally thin sheet. A single-component fuel is considered with zero solubility for gases, and there is phase equilibrium at the drop surface.

The analysis is also based on a Lewis number equal to 1 ($Le = 1$), where Le represents the relative importance of the thermal conductive transfer and transport by mass diffusion. For $Le > 1$, the mass diffusion transports thermal energy in the direction of increasing concentration. The role of the nonunitary Lewis number has been examined quantitatively in Chiu (2000) using a canonical theory of drop.

Figure 6.3 illustrates the two main regions formed inside and outside the flame. In the first region, between the drop surface and the flame, the fuel vapor concentration decreases monotonically with the radius, whereas the products, concentration shows the opposite variation. Since the products do not dissolve in the liquid, they do not move and remain stagnant in this region. At the flame, the products, concentration reaches the maximum (one) and the fuel concentration is zero. In the region outside the flame, the products, concentration decreases monotonically with increasing radius. The oxidizer concentration decreases from its free stream value of $Y_{Ox,\infty}$ at distances far away from the flame to zero at the flame.

Based on the physical model illustrated in Figure 6.3, the analysis is conducted to determine five parameters: fuel mass flow rate $\dot{m}_F$, fuel mass fraction at the drop surface $Y_{F,s}$, drop surface temperature T_s, flame temperature T_f, and flame radius r_f. The final results can be summarized as follows (Turns, 1996):

$$T_f = \frac{q_{i-l} + h_{fg}}{c_{pg}(Y_{Ox,\infty} + \nu)}[\nu B_c - Y_{Ox,\infty}] + T_s \tag{6.26}$$

$$r_f = a\frac{\ln[1 + B_c]}{\ln[(\nu + Y_{Ox,\infty})/\nu]} \tag{6.27}$$

$$Y_{F,s} = \frac{B_c - Y_{Ox,\infty}/\nu}{1 + B_c} \tag{6.28}$$

$$\dot{m}_F = \frac{4\pi k_g a}{c_{pg}} \ln(1 + B_c) \tag{6.29}$$

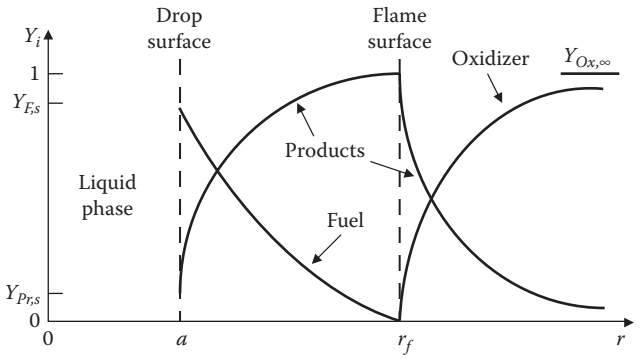


Figure 6.3

Species profiles in spherical drop burning without convection effects.

where

$$B_c = \frac{Y_{Ox,\infty}\Delta h_c/\nu + c_{pg}(T_\infty - T_s)}{q_{i-l} + h_{fg}} \tag{6.30}$$

with Δh_c denoting the lower heating value. One may rewrite Equation 6.29 as

$$\dot{m}_F = \frac{2Sh\pi k_g a}{c_{pg}} \ln(1 + B_c) \tag{6.31}$$

using the Sherwood number $Sh = h_m d/\rho D$ with h_m denoting the mass transfer coefficient. In this form, convective effects can also be included by empirically modifying Sh. For a spherical drop in quiescent atmosphere $Sh = 2$. Empirical correlations are found in the literature for cases with convective effects. It is also noted that Equation 6.29 can be expressed in the form of the d^2-law in Equation 6.19 with B_c replacing B_e.

In Equations 6.26 and 6.30, q_{i-l} is the rate of heat conducted into the interior of the drop per unit mass flow rate of vapor. The expression for q_{i-l} depends on the model used for drop heat up. If the drop rapidly heats up, then one can assume negligible thermal inertia and $q_{i-l} = 0$. The other easily tractable model is the so-called onion skin model for which $q_{i-l} = c_{pl}(T_s - T_0)$, where T_0 is the drop initial temperature.

Equations 6.26 through 6.30 can be evaluated for assumed T_s. For a saturated drop surface, one may alternately use the Clausius–Clapeyron relation to derive an expression for T_s in terms of the gas pressure P:

$$T_s = \frac{-B_c}{\ln\left[\dfrac{-Y_{F,s}PW_{Pr}}{A(Y_{F,s}W_F - Y_{F,s}W_{Pr} - W_F)}\right]} \tag{6.32}$$

where subscript Pr refers to products. This can be used in conjunction with an iterative approach to determine T_s along with the other unknowns. The effects of temperature dependency of the properties can be approximated by following the suggestions in Law and Williams (1972):

$$c_{pg} = c_{pF}(\bar{T}), \quad k_g = 0.4k_F(\bar{T}) + 0.6k_{Ox}(\bar{T}), \quad \rho_l = \rho_l(T_s) \tag{6.33}$$

where $\bar{T} = (T_s + T_f)/2$.

The assumption of quasi-steadiness is convenient for arriving at a closed analytical solution. However, this assumption could break down as a consequence of unsteady diffusion, drop heating, fuel vapor accumulation, compositional change of multicomponent drops, natural and forced convection, and finite-rate chemical kinetics (Chiu, 2000). The effect of this assumption was investigated by Law et al. (1980) for both evaporating and burning drops. The quasi-steadiness assumption implies that the total mass of vapor between the flame and the drop surface remains constant. However, when a drop is suddenly placed in an environment for which the vapor mass fraction is less than the saturation vapor mass fraction, the drop starts to evaporate and the mass of the vapor gradually increases. During these initial times, there is not much fuel vapor available for burning. For a lower flow rate of fuel into the flame, a lower supply of O_2 is required, thus the flame stands closer to the drop surface. As more fuel vapor is produced compared to fuel consumption, fuel vapor accumulates, the flame is pushed away from surface, and the burning rate gradually increases due to larger flame surface area for consumption. At larger times, the drop radius is small, vapor production is low, and hence consumption exceeds supply and as such flame is pushed back toward the surface. This behavior was captured by the analysis in Law et al. (1980) as demonstrated in Figure 6.4 for three different values of $Y_{Ox,\infty}/\nu$. It is observed that for small $Y_{Ox,\infty}/\nu$ the flame may not reach a steady location and instead continue to expand outward. The results in Law et al. (1980) also provided the rate of variation of d^2/d_0^2 and indicated that the d^2-law is adequate in predicting the evaporation rate and the instantaneous drop size. This suggests that despite the variations in flame surface location, the quasi-steady analysis may provide reasonable predictions for the drop burning rate, which is of primary concern in theoretical description of combustion systems.

In the presence of a convective flow, the flame surface could significantly deviate from a spherical shape. Chiu and Huang (1996) formalized the concept of the multistate for a drop, which refers to the existence of more than a single state under a given relative Reynolds number (see below) and ambient temperature. Three

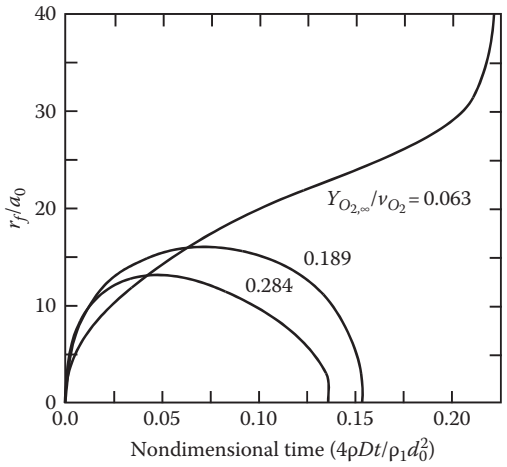


Figure 6.4

Temporal variations of the normalized flame radius for a heptane drop burning in the standard atmosphere. (From Law, C.K. et al., *Combust. Flame*, 38, 173, 1980.)

distinctive flame shapes were recognized, namely, *envelope* flame, *wake* flame, and *boundary layer* flame. The last flame is stabilized in the boundary layer of the liquid sphere. According to Chiu and Huang (1996), there are five distinct regions of Reynolds number bands in which the following multistates are possible: (1) one-state envelope flame, (2) two-state envelope flame vaporization, (3) three-state envelope flame-wake flame vaporization, (4) two-state wake flame vaporization, and (5) one-state vaporization. This multistate behavior also depends on the temperature that affects the transfer number and the Damköhler number *Da*. The Damköhler number is a measure of the relative importance of the flow timescale and combustion timescale. For an infinitely fast reaction $Da \to \infty$.

The effects of convection can be considered in the calculations by introducing a Nusselt number, *Nu*, into Equation 6.29 as

$$\dot{m}_F = \frac{2\pi k_g a Nu}{c_{pg}} \ln(1 + B_c) \tag{6.34}$$

The following empirical relations have been suggested for *Nu* as a function of relative Reynolds number, $Re_r = v_r d\rho_g/\mu_g$, where v_r represents the relative velocity between the drop and the surrounding gas:

1. Ranz and Marshall (1952)

$$Nu = 2 + 0.572 Re_r^{1/2} Pr^{1/3} \quad 1 < Re_r < 2000 \tag{6.35}$$

2. Clift et al. (1978)

$$\begin{aligned} Nu &= 1 + (1 + Re_r)^{1/3} \quad Re_r < 1 \\ Nu &= 1 + (1 + Re_r)^{1/3} Re_r^{0.077} \quad Re_r \geq 1 \end{aligned} \tag{6.36}$$

3. Faeth (1977)

$$Nu = 2 + \frac{0.555 Re_r^{1/2} Pr^{1/3}}{[1 + 1.23/(Re_r Pr^{4/3})]^{1/2}} \tag{6.37}$$

where *Pr* is the Prandtl number. It is noted that for all of these relations *Nu* = 2 in the absence of convection and Equation 6.34 reduces to Equation 6.29. Several other expressions for the heat and mass transfer of particles and drops have been obtained from numerical computations and are included in Sections 1.4.4.1 and 1.4.4.2 of this handbook.

6.4 Group of Drops

The analysis of a single drop is instructive for a basic understanding of evaporation and combustion processes; however, in real applications of liquid-fuel sprays large numbers of drops are present. In these situations, the interactions between neighboring drops become important for high drop number density (Umemura, 1994). These interactions are discussed in this section.

6.4.1 Interactive Evaporation

As the distance between two evaporating drops decreases, the drops compete for heat. Furthermore, the vapor concentration increases while temperature decreases. This combination results in a saturation condition in the spacing between the drops. A criterion for interactive evaporation of two drops is given in Annamalai and Ryan (1992) by considering the temperature profiles, Equation 6.15, around each drop. Based on this criterion, interaction between two drops becomes significant at a distance where the difference between the drop wet-bulb temperature (taken as the drop surface temperature boundary condition) and the local temperature is 90% of the difference between the drop wet-bulb temperature and the ambient temperature. This situation occurs at $r = 10a$; therefore, two evaporating drops begin to interact when the interdrop spacing l is such that $l < 20a$.

Theoretical studies often consider a group of drops confined in a spherical region with radius R_c. The analysis is conducted by considering different timescales, including the individual drop heating time and the time for the penetration of heat from outside to the core of the group of drops (Annamalai and Ryan, 1992). Another important phenomenon is the Stefan flow, which is due to the blowing of vapor from the drops and may drag the drops outwardly in dense sprays (Umemura, 1994). Nevertheless, most studies have neglected the effect of the Stefan flow and, as a result, predict higher evaporation rates. This is also true for an isolated drop, that is, a higher evaporation rate is predicted for an isolated drop when Stefan effects are neglected. However, the ratio of the evaporation rates, termed as the "correction factor" η, remains the same with or without Stefan effects. The correction factor is defined as the ratio of the vapor mass flow rate $\dot{m}_s$ of a single drop in the group to the vapor mass flow rate $\dot{m}_{iso}$ of an isolated drop

$$\eta = \frac{\dot{m}_s}{\dot{m}_{iso}} \tag{6.38}$$

The group evaporation usually results in $\eta < 1$.

In situations like spray combustion, the group of drops is suddenly exposed to a hot ambient gas. In these situations, the drops at the center of the group evaporate rather quickly and create a saturation condition in the spacing between the drops. This case can be analyzed as a confined volume problem with adiabatic condition with respect to the outside gas. A detailed discussion of various studies on group evaporation drop is presented in Annamalai and Ryan (1992); here, we provide a brief summary of the final results from some of these studies.

Zung (1967) presented a "cellular model" in which the inner drops evaporated in an adiabatic impermeable cell. For the drops in the outer cell, it was assumed that only half of the drop (shaded area in Figure 6.5) participated in evaporation and the other half did not evaporate. When the outside layer evaporated then the next layer was considered. Zung's analysis did not consider the energy balance equation and predicted that, for a fixed cloud radius, the cloud evaporation time reduces proportional to the drop radius regardless of the heat transfer from the ambient gas. Improved results were later presented by Tishkoff (1979) by considering a "bubble model" as shown in the inset of Figure 6.5. The spherical shell with radius b, considered around the drop with radius a, was permeable and elastic. Mass, energy, and species conservation equations were solved, and unsteady drop heating was allowed with a quasi-steady analysis for the gas phase. Saturation was reached for small b/a whereas for large b/a the drop fully evaporated. The transition from partial to full evaporation was dependent on temperature and pressure of the gas. The ratio b/a increased with the decrease in the initial gas temperature and/or pressure. Similar studies were also conducted by Bellan and Cuffel (1983) and Bellan and Harstad (1987a, 1988) who also included turbulence effects.

The previous studies were conducted by concentrating on the details of flow around individual drops within a cell, bubble, etc. A different class of studies has been reported in the literature that provides solutions for the global behavior of a cloud of drops by considering continuum transport equations for the entire cloud. These macroscopic equations are derived by averaging over a volume containing the drops of interest and are similar to equations for the gas but with source terms due to drop evaporation (and combustion in case of a reacting system). For example, for quasi-steady evaporation of a cloud of monosized drops,

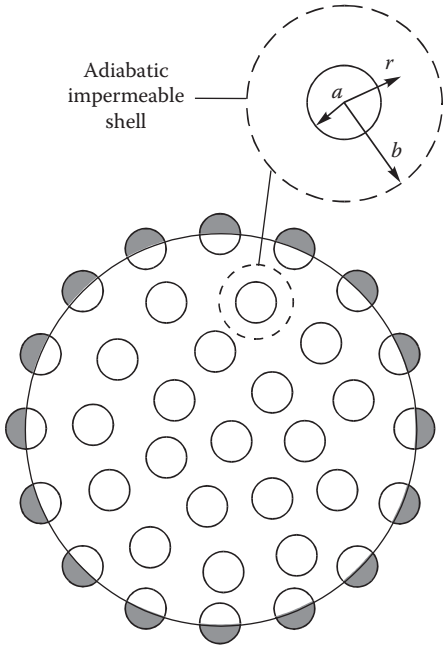


Figure 6.5

Illustration of cell model for group combustion. (From Annamalai, K. and Ryan, W., *Prog. Energy Combust. Sci.*, 18, 221, 1992.)

when the Stefan flow is neglected, the continuum equation for the average vapor mass fraction, $Y(r)$, in a spherical coordinate is described as (Annamalai and Ryan, 1992)

$$\frac{1}{r^2}\frac{d}{dr}\left(\rho D r^2 \frac{dY}{dr}\right) = -\dot{m}''' \quad \text{for } r < R_c$$

$$= 0 \quad \text{for } r > R_c \tag{6.39}$$

The volumetric source term $\dot{m}'''$ is due to evaporation of drops and is obtained by averaging over all the drops present in the volume of interest. The appropriate boundary conditions for this problem are

$$Y(r) = Y_\infty, \quad r \to \infty \tag{6.40}$$

$$\frac{dY}{dr} = 0, \quad r = 0 \tag{6.41}$$

The solution of Equation 6.39 with boundary conditions (6.40) and (6.41) for a monosized and uniform cloud yields the average correction factor as

$$\eta = \frac{3}{G}\left[1 - \frac{\tanh\left\{G^{(1/2)}\right\}}{G^{(1/2)}}\right] \tag{6.42}$$

Here, G is the group evaporation number:

$$G = 2Sh\pi naR_c^2 \tag{6.43}$$

where n is the number density of the drops. It should be noted that the definition of G depends on the geometry and spray distribution parameters in the cloud. Various forms used by researchers were summarized in Table 3 of Annamalai and Ryan (1992).

Annamalai (1985) considered Stefan flow in the quasi-steady analysis of a cloud of drops and showed that

$$\dot{m}_c = \dot{m}_{c,SE}\left[1 - \frac{\tanh\left\{G^{(1/2)}\right\}}{G^{(1/2)}}\right] \tag{6.44}$$

where $\dot{m}_c$ is the cloud evaporation rate for a monosized and uniform (n = constant) cloud and

$$\begin{aligned}\dot{m}_{c,SE} &= 4\pi\rho D\ln(1+B_e)nR_c, \quad \text{Stefan flow included}\\ &= 4\pi\rho DB_e nR_c, \quad \text{Stefan flow neglected}\end{aligned} \tag{6.45}$$

The average evaporation rate per drop is

$$\dot{m}_{s,c} = \frac{\dot{m}_c}{\frac{4}{3}n\pi R_c^3} \tag{6.46}$$

which yields

$$\eta = \frac{\dot{m}_{s,c}}{\dot{m}_{iso}} = \frac{3}{G}\left[1 - \frac{\tanh\left\{G^{(1/2)}\right\}}{G^{(1/2)}}\right] \tag{6.47}$$

for a monosized and uniform cloud. It is interesting to note that Equation 6.47 with Stefan flow included is the same as Equation 6.42, which was obtained by neglecting Stefan flow.

The G number can be used as an indicator for the denseness of a spray. Evaluation of Equation 6.47 shows $\eta \simeq 0.9$ and 0.1 for $G = 0.1$ and 100, respectively. Therefore, for practical purposes, clouds having $G < 0.1$ may be considered dilute enough such that drops can be treated as isolated. Clouds with $G > 100$ should be considered as dense. For very small G values, approaching zero, every drop in the cloud is surrounded by the gas at T_∞ whereas for very large values of G, approaching infinity, every drop in the interior of the cloud is at the same temperature. In the latter case, the vapor mass fraction in the spacing between the drops corresponds to the saturated condition and only drops near the outer region of the cloud evaporate. In this case, the cloud is said to evaporate in the *sheath* evaporation mode. It should also be noted that, in a real spray situation, drops move around with the flow and drop–drop collisions are likely for dense clouds. In this situation, the analysis here may not be applicable.

The effects of size distribution were also considered in Annamalai (1985) by assuming a monotonic distribution for the number density n and drop radius a in the form

$$\frac{na}{(na)_{R_c}} = \left[\frac{r}{R_c}\right]^{-q} \tag{6.48}$$

where $(na)_{R_c}$ is the reference quantity at $r = R_c$. For $q = 0$, Equation 6.48 yields the uniform distribution considered earlier. The correction factor for this case is given as

$$\eta = \left[1 + \frac{G_1}{3-q} + \frac{G_1^{(1/2)}}{3-q}\frac{l_{(5-2q)/(2-q)}[2G_1^{(1/2)}/(2-q)]}{l_{(3-q)/(2-q)}[2G_1^{(1/2)}/(2-q)]}\right]^{-1} \tag{6.49}$$

with G_1 defined as

$$G_1 = (1-q)^{(1/3)}G \tag{6.50}$$

for fixed size and varying number densities and

$$G_1 = (1 - q/3)G \tag{6.51}$$

for fixed number density and varying sizes. In Equation 6.49, $l_{(5-2q)/(2-q)}$ represents the modified Bessel function of order $(5 - 2q)/(2 - q)$.

6.4.2 Interactive Combustion

The analysis in previous sections for an isolated drop assumes that a spherical flame is formed at a radius r_f around the drop. This assumption may be valid as long as there is no other drop in the vicinity of the first drop. When the distance l between two drops is decreased, there is an opportunity for two flames to interact. This interaction is intensified by the fact that the two drops must also compete for oxygen in order to continue their combustion. This intuitive conclusion can also be drawn from Equation 6.27, for the flame radius, in which $Y_{Ox,\infty}$ appears in the denominator. With the decrease of $Y_{Ox,\infty}$, the denominator becomes smaller and the flame radius increases. As the distance between the two drops is further decreased, their flames merge and a common flame is formed around the two drops. According to Williams (1985), a simple criterion for the interaction of two burning drops can be stated as $l < 2r_f$.

Similar interactions occur for a system consisting of a large number of drops, forming a group of drops. In this case, several different "modes" of group combustion can be identified. A large body of literature is devoted to group combustion studies; however, it appears that the studies by Chiu and coworkers (Suzuki and Chiu, 1971, Chiu and Liu, 1977, Chiu et al., 1982) have been more widely recognized. In order to characterize various combustion modes, Suzuki and Chiu (1971) and Chiu et al. (1982) used the group combustion number:

$$G = 3\left[1 + 0.276 Re_r^{(1/2)} Sc^{(1/3)}\right] LeN^{(2/3)}(d/l) \tag{6.52}$$

where

Sc is the Schmidt number

N is the total number of drops in the group

This nondimensional number represents the ratio of the heat transfer in the gas phase and the heat transfer between two phases accounting for the convective effect.

The G number has been used to differentiate between weak and strong drop interactions. According to Chiu et al. (1982), four modes of group combustion are identified as shown in Figure 6.6. For low values of G, the drops are widely separated and individual drop combustion is dominant (Figure 6.6a). As G is

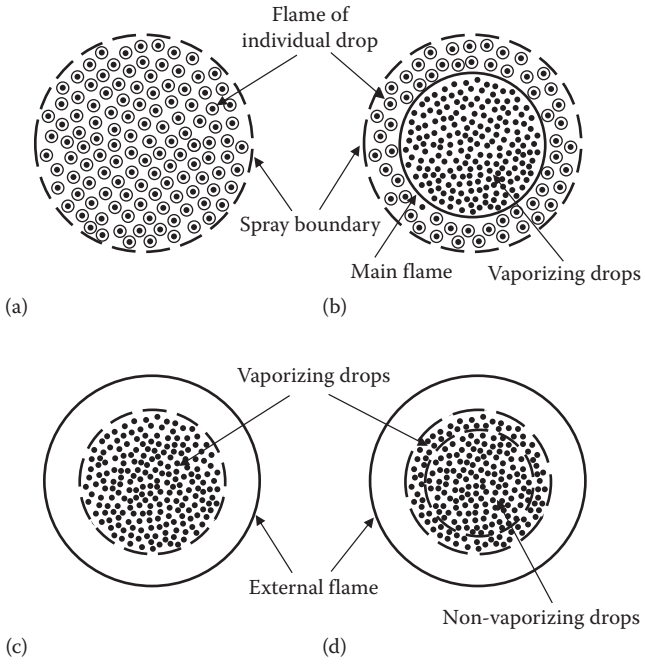


Figure 6.6

Four group combustion modes of a drop cloud. (a) Single drop combustion at low G, (b) internal group combustion, (c) external group combustion with a *standoff* flame, and (d) external group combustion with *sheath vaporization* at high G. (According to Chiu, H.H. et al., Internal group combustion of liquid droplets, in *Proceedings of 19th Symposium* (*International*) *on Combustion*, The Combustion Institute, Pittsburgh, PA, 1982, pp. 971–980.)

increased, the spacing between the drops decreases and the flames from various drops combine. For moderate increases in G, the main flame is located somewhere within the cloud of drops (Figure 6.6b). Between this main flame and the external boundary of the cloud, single drop burning is observed. Further increase in G pushes the flame outside the cloud boundary and forms a *standoff* flame (Figure 6.6c). In this case, all the drops are vaporizing as combustion takes place at the flame. Finally, for very large values of G, while the standoff flame forms outside the cloud, the drops in the core of the flame are saturated and do not evaporate. In this sheath evaporation case, evaporation occurs only for the drops located near the edge of the cloud (Figure 6.6d). As these boundary drops fully evaporate the evaporation front shrinks toward the center of the cloud and the drops in the core begin to evaporate.

The earlier group combustion modes can be applied to spray combustion as shown in Figure 6.7 (Chiu and Croke, 1981). Due to cold temperatures and high drop number density in the spray near the nozzle, the ignition of the spray takes place at a distance from the nozzle exit. Once the spray is ignited, an external flame forms while the core of the spray consists of evaporating drops. Further downstream, the spacing between the drops increases and the flame penetrates into the spray, thus forming multiple group combustion. At the end, combustion continues by consuming the unburnt gaseous fuel.

Annamalai and Ryan (1992) presented a modified form of the spray classification of Chiu and coworkers by considering six modes of combustion as seen in Figure 6.8. This figure maps these various modes on a plot of the total number of drops in the cloud versus the ratio of the drop spacing to drop diameter, l/a, for various values of G in Equation 6.43. Region (I) corresponds to isolated drop combustion for $G < 0.01$, whereas region (II) involves isolated to incipient group combustion for $0.01 < G < 0.1$. The incipient combustion is when the flame radii of the center drops in the cloud just touch each other. Regions (III) through (V) for $0.1 < G < 1$, $1 < G < 10$, and $10 < G < 100$ are termed as partial group combustion, group combustion, and intermediate group combustion, respectively. In partial group combustion, while there is a group flame for the inner drops, the outer drops burn with individual flames but still allow O_2 to penetrate into the flame located within the cloud. Finally, for $G > 100$ combustion is in the sheath mode where the temperature at the cloud surface is at the wet-bulb temperature of the drops and the cloud behaves as an equivalent single drop of radius R_c. Any convective effects will move the lines in Figure 6.8 downward and downward movement will be greater at smaller interdrop spacing.

The model of Chiu and coworkers and their G parameter have been extensively assessed by experimentalists in spray combustion (Chen and Gomez, 1997, Wark et al., 2000). Wark et al. (2000) examined the variation of G in their experiment of an acoustically forced jet. The forcing resulted in the formation of organized structures consisting of core and wings as seen in Figure 6.9. Phase Doppler interferometry was used to obtain drop statistics for the calculation of the group combustion number. It was not possible to experimentally generate the exact conditions to evaluate G using Equation 6.52. Therefore, several assumptions were made, including the neglect of the convective effects and $Le = 1$. The expression of G used by Wark et al. (2000), after applying the simplified assumptions, was

$$G = 2\pi nd(R_c)^2 \tag{6.53}$$

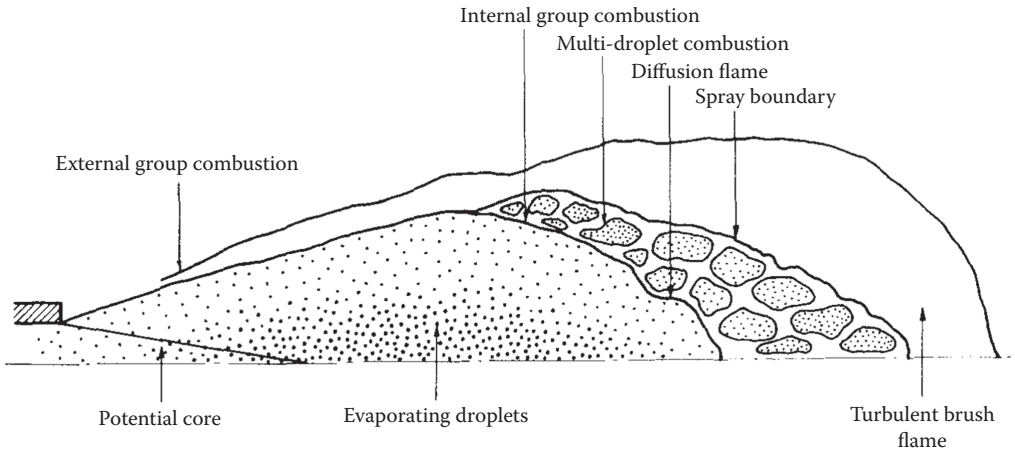


Figure 6.7

Schematic of liquid-fuel spray group combustion. (From Chiu, H.H. and Croke, E.J., Group combustion of liquid fuel sprays, Technical Report 81-2, University of Illinois at Chicago, Energy Technology Lab, Chicago, IL, 1981.)

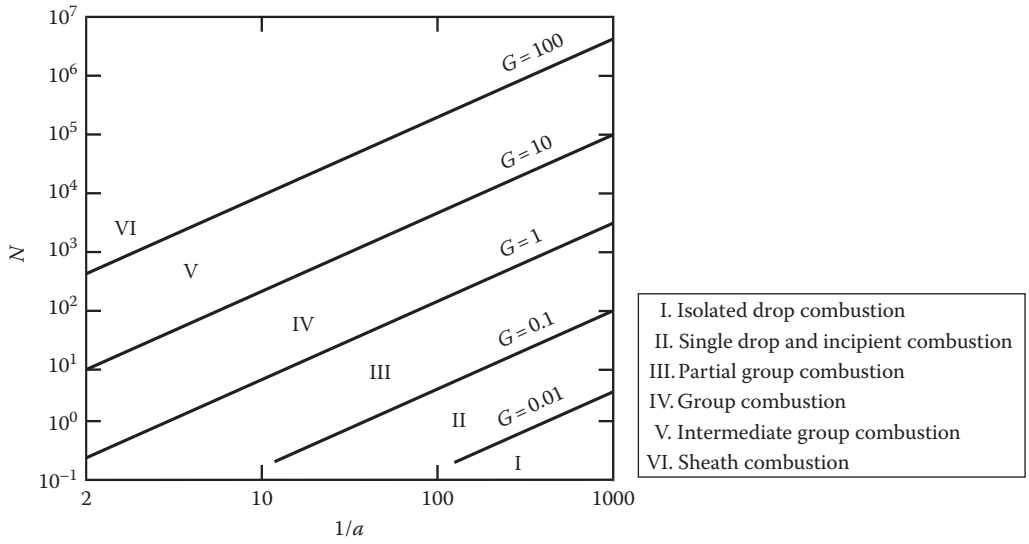


Figure 6.8

Group combustion number as a function of nondimensional spacing *l*/*a* and the total number of drops. (From Annamalai, K. and Ryan, W., *Prog. Energy Combust. Sci.*, 18, 221, 1992.)

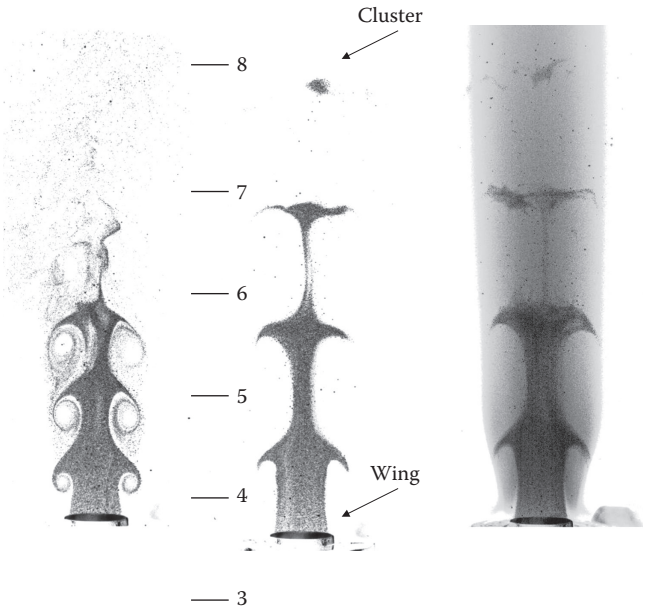


Figure 6.9

Phase-locked images of the drop-laden jet considered in the study of Wark et al. (2000).

which is the same as Equation 6.43 when $Sh = 2$ is used in the absence of convective effects. The drop number density n was obtained directly from the measurements. The mean drop diameter from the measurements was used as a representative diameter for use in Equation 6.53, although the drop size distribution was not uniform. The assessment of G was very sensitive to the choice of R_c as witnessed from Equation 6.53. An appropriate value was chosen for R_c depending on whether the core or the wing region was considered. In the core region, the radius of the drop-laden portion of the jet was considered as a reasonable choice.

Wark et al. (2000) calculated the axial variation of G as shown in Figure 6.10. The results suggested that close to the nozzle the jet was burning in external sheath mode and then changed to internal group burning after $z/D \simeq 2$ where D and z represent the jet diameter and the axial distance, respectively. After the third structure, the value of G dropped significantly, corresponding to individual drop burning.

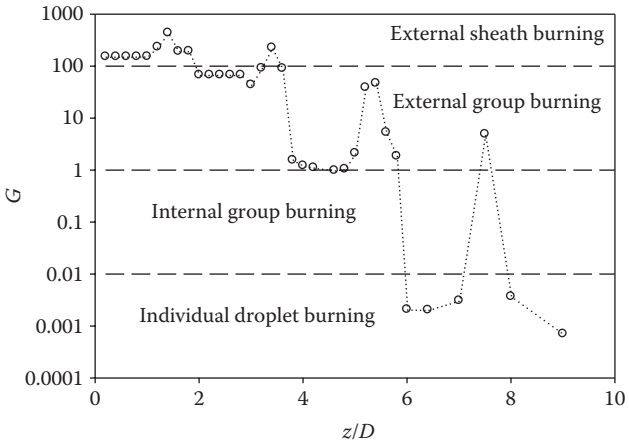


Figure 6.10

Phase-locked (0°) axial development of the group combustion behavior of drops. (From Wark, C. et al., *Combust. Flame*, 120, 539, 2000.)

From the comparison of Figures 6.9 and 6.10, it was not unreasonable to expect external sheath burning early in the flame. However, Wark et al. (2000) questioned whether individual drop burning was taking place between the third and fourth structures, as was predicted by the calculation of *G*. This was in agreement with previous experiments (e.g., McCreath and Chigier, 1973), which did not show any signs of single drop burning in the spray.

Annamalai (1985) provided similar relations to those in Equations 6.44, 6.47, and 6.49 for quasi-steady combustion of a cloud of drops. These relations were provided for both monosized uniform cloud and a cloud with the product of size and number density of the drops given as Equation 6.48. These results gave correction factors that can be used for the calculation of the cloud burning rate in terms of the burning rate of an isolated drop.

6.5 Two-Phase Turbulent Combustion

The theoretical approaches discussed in previous sections are very useful for developing a fundamental understanding of the physical processes involved in two-phase combustion in laminar flows. However, as was also emphasized in the introduction, the practical situations encountered in spray combustion and other multiphase reacting systems often involve turbulence whose effect cannot be fully described by these theories; see Li (1997) for a review of spray combustion in laminar stagnation flows. A thorough description of spray combustion requires modeling of turbulence interactions with drops and its effect on chemical reaction. More specifically, modeling is required for interactive processes involving turbulence and combustion, along with drop dispersion, heat transfer, and evaporation.

The significance of turbulence in multiphase systems and the modeling of turbulence effects on drop dispersion are extensively discussed in Sections 1.4.3.3 and 1.4.4.4 and in Chapter 12 of this handbook. The level of modeling for turbulence varies depending on the nature of the problem and the computational resources available. To this end, the three major simulation strategies, namely, direct numerical simulation (DNS), large eddy simulation (LES), and Reynolds-averaged Navier–Stokes (RANS) simulation, have been widely employed in the computational analysis of multiphase turbulent flows. In addition to these three methods, there are some methods that are labeled as *hybrid* such as hybrid LES/RANS. DNS requires significant computational resources, and its application has been limited to basic research problems involving simple geometries and moderate Reynolds numbers (Mashayek, 2000, Reveillon and Vervisch, 2000). Such simulations make use of high-order computational methods on powerful computer platforms to deal with specific physical issues. They have also been very useful in assessing the performances of many of the closures in RANS and LES. RANS has been the method of choice for practical applications and perhaps this trend will continue for the near future. LES makes use of many of the desirable features of both DNS and RANS and has experienced significant growth in two-phase flow simulations within the past decade or so. However, the predictive capability of LES depends on the success of its subgrid-scale (SGS) closures (Lesieur and Métais, 1996, Meneveau and Katz, 2000) and the numerical solution method.

The numerical methods employed for two-phase turbulent flow simulations are generally based on three different approaches (Brennen, 2005, Crowe, 2006): (1) Eulerian–Eulerian approach (Elperin et al., 1996, Scardovelli and Zaleski, 1999, Shyy and Narayanan, 1999, Lakehal, 2002, Pandya and Mashayek, 2002a,b, Herrmann, 2003, Mashayek and Pandya, 2003, Sethian and Smereka, 2003, Cuenot et al., 2006), (2) Eulerian–Lagrangian approach (Faeth, 1987, Shirolkar et al., 1996, Crowe et al., 1998, Sirignano, 1999, Bellan, 2000, Loth, 2000, Apte et al., 2003, Mahesh et al., 2006, Menon and Patel, 2006, Patel et al., 2007), and (3) Lagrangian–Lagrangian approach (Chen and Doolen, 1998, Mashayek and Pandya, 2003, Salman and Soteriou, 2004). In the first approach, the continuum transport equations for both phases are solved. These equations are somewhat similar for both phases and are often obtained by some form of volume averaging, which is conceptually different from the ensemble averaging in RANS or space averaging in LES. In the second approach, the carrier fluid equations are solved in its instantaneous form in DNS or in its averaged form in RANS and LES over an Eulerian grid system. However, the dispersed phase (particles, drops, etc.) is described by a set of modeled Lagrangian equations that determine the position, velocity, temperature, and other properties of the dispersed phase (Drew, 1983, Zhang and Prosperetti, 1994, Jackson, 1997, Crowe et al., 1998, Sirignano, 1999, Loth, 2000, Pandya and Mashayek, 2003). In the third approach, both phases are described by Lagrangian models.

Most of the practical models for spray have been based on the Eulerian–Lagrangian approach, which is the focus of our attention in this chapter. The Eulerian–Eulerian and Eulerian–Lagrangian models have been employed for RANS, LES, and DNS of a wide range of two-phase or two-fluid turbulent flows including free surface flows or dispersed turbulent flows (Faeth, 1987, Shirolkar et al., 1996, Crowe et al., 1998, Scardovelli and Zaleski, 1999, Shyy and Narayanan, 1999, Sirignano, 1999, Bellan, 2000, Loth, 2000, Menon, 2000, Lakehal, 2002, Mashayek and Pandya, 2003, Sethian and Smereka, 2003, Cressman et al., 2004, Moin, 2004, Madnia et al., 2006). In comparison, there are a limited number of models based on Lagrangian–Lagrangian approach. An example is the two-phase random vortex model of Salman and Soteriou (2004). Neither these types of models are not discussed here nor we discuss RANS models developed based on Eulerian–Eulerian and Eulerian–Lagrangian methods. Detailed descriptions of the numerical methods in multiphase flow are given in Chapter 1.

6.5.1 Modeling in Various Spray Regimes

Multiphase flow systems are often classified by the flow regimes: dilute, moderately dense, and very dense. All of these regimes are present in sprays (Faeth, 1987). In the dilute spray regime, the volume fraction of drops (or particles) to carrier fluid is very small and the drop–drop interactions are rare, making the continuum assumption and Eulerian–Eulerian formulation essentially invalid. In this regime, the drops are often treated as point masses that are affected by the carrier gas through mass, momentum, and energy interactions. The coupling could be two way, allowing the particles to also modify the carrier fluid.

The traditional approach to the spray simulation has been to compute the gas phase by a grid-based Eulerian method and the spray by the particle-based Lagrangian method. For this, the drops are treated as point sources within a given computational cell. The effects of each drop are distributed over the nodes of the cell, with some weights inversely proportional to the distance of the drop from various nodes. This approach is known as particle source in cell (PSIC) method (Crowe et al., 1977). The approximations involved in this approach have prompted some researchers to seek more accurate methods (see, e.g., Maxey et al., 1997); however, due to its simplicity of implementation, PSIC has remained as a method of choice for the simulation of turbulent sprays. In theory, it is possible to simulate the flow domain outside the drop in the boundary layer and wake region. However, these simulations, referred to as "resolved-volume simulations" (Loth, 2000), are very expensive and are usually limited to one or handful number of particles in simple flows and do not seem to be applicable to realistic spray simulations.

In the PSIC and hybrid Eulerian–Lagrangian approach, submodels are required to account for various physical processes taking place at small time and length scales in both Eulerian and Lagrangian fields. Even with an accurate modeling of the gas flow, the accuracy of simulations is still dependent on the models used for the drop transport, liquid evaporation, micromixing, chemical kinetics, and turbulence–combustion interactions (Jiang et al., 2010, Jenny et al., 2012). For the drop transport, a modified nonlinear version of the Lagrangian–Stokes equation is often used (Crowe et al., 1998, Sirignano, 1999, Loth, 2000). The "exact" gas velocity is available in DNS for calculating the drop velocity and for moving the drops. In the most early LES studies of dilute two-phase turbulent flows (Yeh and Lei, 1991), particles were tracked by using only the filtered Eulerian velocity field, and the effects of two-way coupling and SGS velocity on the particles were not taken into account. However, these effects are often considered in later studies (Armenio et al., 1999,

Boivin et al., 2000, Almeida and Jaberi, 2008). Also, with the point mass approximation, the mass and heat transfer between phases are obtained from a set of semiempirical relations. Crowe et al. (1998), Loth (2000), and Sirignano (2010) provide a comprehensive review of the available momentum, heat, and mass transfer models for small particles and droplets, while discussing the effects of turbulence, compressibility, particle spin, particle deformation, virtual mass, Basset history, stress gradient, and wall on the particle forces in details. Chapter 1 of this handbook also provides a comprehensive review of these effects on single drops and particles.

In the dense regime of any particulate turbulent flow, the particle–particle collisions are significant, the particle number density is large, and the volume displaced by the particles often has noticeable influence on the carrier fluid. Normally, a significant portion of the physical activities associated with the fluid–particle and particle–particle interactions takes place at small or SGS. This imposes serious challenges on the LES of dense two-phase turbulent flows. Similarly, in liquid sprays, the primary and secondary breakup regions of the spray are complicated by the presence of complex SGS liquid–gas interfaces that require interface capturing methods. Various grid-based and particle-based Eulerian–Eulerian computational models have been used for the interface simulations (Ashgriz and Poo, 1991, Sethian and Smereka, 2003, Li et al., 2008). Common grid-based methods are volume of fluid (Ashgriz and Poo, 1991) and level set (Sethian and Smereka, 2003) front-capturing methods. Alternatively, in the particle-based front-tracking method (Li et al., 2008), marker particles are used to track the interface. All of these methods have had varying degrees of success in handling interfacial problems in nonturbulent flows but they have also been used for turbulent flows in a limited sense (Shen and Yue, 2001, Herrmann, 2003, Li et al., 2008).

Despite their advantages, Eulerian–Eulerian interface tracking models are not often viable for multiphase turbulent flows that involve preferential concentration of the particles and the simultaneous presence of both dense and dilute regimes, thus they have to be combined with Eulerian–Lagrangian and PSIC models (Som and Aggarwal, 2010). Also, the interface tracking models are not always appropriate for the secondary breakup region of spray, where the volume fraction occupied by liquid is still high and there are considerable collisions between drops and ligaments, which can lead to coalescence, shattering, and bouncing or glancing. For the LES of moderately dense two-phase particulate flows, efficient droplet–droplet or particle–particle collision models can be incorporated in the Lagrangian particle simulations. For example, Apte et al. (2003) developed a mathematical/computational model to incorporate particle collisions and finite particle volume effects in an incompressible suspending fluid. The model has been shown to produce accurate results in relatively simple flows and has been incorporated in an unstructured LES code for simulations of spray in complex flow configurations (Apte et al., 2003).

6.5.2 Modeling of Reacting Flows

The numerical simulation of reacting turbulent sprays is very challenging not only due to multiscale and multitime nature of liquid–gas interactions but also because of the complexity of finite rate evaporation, mixing, and multistep reactions (Aggarwal, 1998, Venugopal and Abraham, 2007, Mastorakos, 2009). In most of spray combustion computational models, the flow is seeded or injected by a large number of drops, which can be followed individually in the Lagrangian frame, using the equations described in Section 1.4 of this handbook. In DNS, no modeling is performed for the gas flow turbulence and all flow time and length scales are resolved exactly by considering small time step and grid sizes. However, for situations involving a large number of drops, it is not possible to resolve the details of the flow in and around each drop. Therefore, physical models are introduced for describing heat, mass, and momentum transfer between the two phases, as elaborated in this section and also reviewed in previous chapters of this handbook.

The other important issue in theoretical description of spray combustion is the interaction between turbulence and chemical reaction. Turbulence modeling for combustion has been the subject of an overwhelming number of studies within the past four decades and cannot be reviewed here in detail. A number of different methods have emerged from these studies with varying levels of success (Pope, 1985, Givi, 1989, Peters, 2000). Nevertheless, the issue of turbulence modeling for combustion still appears far from being fully resolved and is even more complicated by the fact that the chemistry of combustion for most fuels is not yet well understood. Among the more popular models for turbulent combustion simulations are the laminar flamelet models (Williams, 1975, Bray and Peters, 1994), the probability density function (PDF)-based models (Pope, 1985, Givi, 2003), the eddy breakup models (Spalding, 1971), and the eddy dissipation models (Magnussen and Hjertager, 1977), which provide varying levels of accuracy and complexity. Transported PDF methods have proven to be particularly effective in accounting for turbulence–chemistry

interactions (Haworth and Pope, 2011). Filtered mass density function (FMDF) is a single-point SGS PDF model for the LES of turbulent reacting flows (Jaberi et al., 1999). In this approach, the joint statistics of turbulent variables are obtained by solving the transport equation for the FMDF. The main advantage of FMDF is that the single-point statistics like reaction terms appear in a closed form in its formulation. This allows simulations of various types of reactions (slow, fast, premixed, nonpremixed, etc.) with different chemical kinetic models (James and Jaberi, 2000, Sheikhi et al., 2005, Givi, 2006, Raman and Pitsch, 2006, Afshari et al., 2008, Haworth, 2010, Yaldizli et al., 2010). Recently, Li et al. (2014) have developed a two-phase FMDF model for the simulation of two-phase reacting flows. They validated the model by comparison with DNS data in a spatially developing droplet-laden reactive mixing layer.

Depending on the type of spray and flame, the reaction timescales can be very different or comparable to those of the turbulence and the spray. This has led to the development and usage of reaction mechanisms at various levels of details and comprehensiveness (Lu and Law, 2009). For some of the hydrocarbon fuels such as n-heptane (Battin-Leclerc, 2008), *complex* (skeletal or reduced) kinetics models are available beyond simple global mechanisms (Seiser et al., 2000, Liu et al., 2004, Yoo et al., 2011). Complex reaction models are normally needed for high-speed spray combustion simulations. However, the computational cost of performing the chemistry calculations with complex kinetics is often prohibitive and efficient implementation of chemistry is necessary. Several different methods have been proposed for efficient implementation of chemical reaction in computational models such as LES/FMDF. Among them are the storage/retrieval algorithms (Pope and Ren, 2009), including the structured lookup tabulation (Chen et al., 1989), the repro-modeling (Turanyi, 1994), the artificial neural networks (Christo et al., 1996, Blasco et al., 1998), the in situ adaptive tabulation (ISAT) (Pope 1997, Lu and Pope, 2009), the piecewise reusable implementation of solution mapping (Bell et al., 2000), and the high-dimensional model representations (Rabitz and Alis, 1999). ISAT is a storage and retrieval methodology that has been widely adopted especially with PDF methods. The ISAT algorithm has been applied to nonpremixed piloted jet flames (Cao and Pope, 2005) with a speedup factor of 100–1000.

The DNS of high-speed reacting sprays with complex chemistry models is not currently feasible; the latest published DNS work in this area is limited to relatively simple dilute two-phase homogeneous turbulent reacting flows (Borghesi et al., 2013). LES models (Shukla and Mamun, 2002), on the other hand, are applicable to turbulent spray combustion. LES has been widely applied to single-phase reacting flows (Pitsch, 2006, Haworth, 2010, Haworth and Pope, 2011). However, its use for turbulent spray combustion simulations has been somewhat limited (Irannejad and Jaberi, 2014b) mainly because of difficulties in modeling of SGS interactions among droplets, turbulence, and combustion and the computational cost associated with complex chemical kinetic mechanisms (Jenny et al., 2012). The two-phase reacting LES model in Patel et al. (2007) and Sankaran and Menon (2002) is based on the Eulerian–Lagrangian approach. In this model, the carrier gas equations are solved for a fixed 3D grid system. However, the mixing and reaction are implemented in 1D domain using the linear eddy model. The spray is based on a Lagrangian droplet model that includes empirical evaporation and secondary breakup submodel. The reaction is modeled with a global multistep mechanism. The two-phase reacting LES model in Mahesh et al. (2006) is based on a similar hybrid Eulerian–Lagrangian approach. The zero Mach number Navier–Stokes equations are solved on an unstructured grid in the Eulerian part and the spray is modeled with Lagrangian method and some empirical droplet evaporation and breakup submodels. The LES models in Apte et al. (2003), Mahesh et al. (2006), Menon and Patel (2006), and Sankaran and Menon (2002) are applied to realistic (complex) gas turbine combustors. The two-phase reacting LES model of Cuenot et al. (2006) is fundamentally different from the previous models as it solves the Eulerian equations for both phases.

The two-phase reacting LES/FMDF model (Irannejad and Jaberi, 2014b, Li et al., 2014) is different from the models mentioned earlier; it is based on an Eulerian–Lagrangian–Lagrangian methodology. The two-phase FMDF model is recently employed (Irannejad and Jaberi, 2014b) together with complex chemical kinetic mechanisms for simulations of experimentally studied high-speed evaporating and reacting sprays in a closed combustion chamber (Siebers, 1998, Siebers and Higgins, 2001, Siebers et al., 2002, Pickett et al., 2010, Bhattacharjee and Haworth, 2013, Pei et al., 2013). Details of the two-phase FMDF model are given in the following subsection.

6.5.3 LES/FMDF Model

As illustrated in Figure 6.11, the computational method used in two-phase LES/FMDF model has one Eulerian and two Lagrangian solvers. The gas-phase field is computed by a hybrid methodology. The compressible LES equations for velocity and pressure are solved by grid-based Eulerian flow solvers like high-order compact

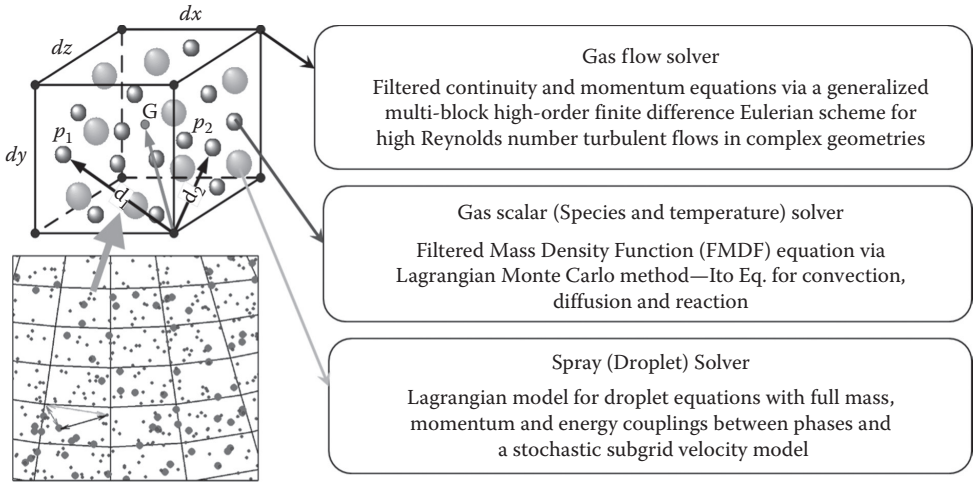


Figure 6.11

A block diagram showing different components of the two-phase LES/FMDF and its Eulerian–Lagrangian–Lagrangian flow solver. Figures on the left show the Eulerian grid together with droplets and Monte Carlo particles. Large particles are droplets, while smaller particles represent Monte Carlo particles.

finite-difference schemes (Afshari et al., 2008, Banaeizadeh et al., 2011, Irannejad and Jaberi, 2014b). The scalar field (i.e., the species mass fractions and enthalpy) is obtained from FMDF by solving the FMDF equation with an efficient Lagrangian stochastic Monte Carlo (MC) method (Jaberi et al., 1999, Li et al., 2014). The spray is simulated with a nonequilibrium Lagrangian particle method together with a stochastic droplet breakup model that allows full two-way mass, momentum, and energy coupling between phases (Irannejad and Jaberi, 2014a). The chemistry is based on finite-rate skeletal kinetics. Consequently, the two-phase LES/FMDF model is composed of three different mathematical components: (1) the filtered gas dynamics equations, (2) the FMDF equations, and (3) the Lagrangian spray/droplet equations.

The gas dynamics field is obtained from the following compressible Favre-filtered continuity, momentum, and energy equations (Irannejad and Jaberi, 2014b):

$$\frac{\partial\langle\rho\rangle_l}{\partial t}+\frac{\partial\langle\rho\rangle_l\langle u_i\rangle_L}{\partial x_i}=\langle\dot{S}^{sp}_{Mass}\rangle_l \tag{6.54}$$

$$\frac{\partial\langle\rho\rangle_l\langle u_i\rangle_L}{\partial t}+\frac{\partial\langle\rho\rangle_l\langle u_i\rangle_L\langle u_j\rangle_L}{\partial x_j}=-\frac{\partial\langle p\rangle_l}{\partial x_i}+\frac{\partial\langle\tau_{ij}\rangle_l}{\partial x_j}-\frac{\partial(\tau^{sgs}_{ij})}{\partial x_j}+\langle\dot{S}^{sp}_{mi}\rangle_l \tag{6.55}$$

$$\frac{\partial\langle\rho\rangle_l\langle E\rangle_L}{\partial t}+\frac{\partial(\langle\rho\rangle_l\langle E\rangle_L+\langle p\rangle_l)\langle u_i\rangle_L}{\partial x_i}=-\frac{\partial(\langle q_i\rangle_l+H^{sgs}_i)}{\partial x_i}+\langle\dot{Q}\rangle_l+\langle\dot{S}^{sp}_E\rangle_l+\frac{\partial[(\langle\tau_{ij}\rangle_l-\tau^{sgs}_{ij})\langle u_j\rangle_L]}{\partial x_i} \tag{6.56}$$

In Equations 6.54 through 6.56, $\langle\cdot\rangle_l$ and $\langle\cdot\rangle_L$ represent the filtering and Favre-filtering operations, respectively. The primary variables are the filtered density $\langle\rho\rangle_l$, the filtered pressure $\langle p\rangle_l$, the Favre-filtered velocity $\langle u_i\rangle_L$, and the Favre-filtered total energy $\langle E\rangle_L=\langle e\rangle_L+\frac{1}{2}\langle u_i\rangle_L\langle u_i\rangle_L$. The filtered viscous stress tensor, $\langle\tau_{ij}\rangle_l$, is assumed to be a linear function of the Favre-filtered strain rate for the simulated Newtonian fluid, and the filtered heat flux vector, $\langle q_i\rangle_l$, is evaluated based on Fourier's law.

The terms involving variable S represent the combustion and droplet/spray source or sink terms (Irannejad and Jaberi, 2014b). The specific internal energy of the mixture is defined as

$$\langle e\rangle_L=\sum_{\alpha=1}^{N_s}\langle\phi_\alpha\rangle_L h_\alpha(\langle T\rangle_L)-\langle R\rangle_L\langle T\rangle_L, \tag{6.57}$$

where h_α is the species sensible enthalpy. The filtered form of ideal gas equation of state is used to close the system of equations. The unclosed SGS terms, which appear in the filtered equations, can be closed by gradient type or other closures (Moin et al., 1991, Ghosal et al., 1995, Irannejad and Jaberi, 2014b).

The scalar FMDF is a joint PDF of the scalars (species mass fractions and energy) at the subgrid level, which was originally developed by Jaberi et al. (1999) for single-phase reacting flows and has proven to be very reliable and accurate for these flows (Jaberi, 1999, James and Jaberi, 2000, Sheikhi et al., 2005, Givi, 2006, Madnia et al., 2006, Afshari et al., 2008, Yaldizli et al., 2010, Ansari et al., 2011, Banaeizadeh et al., 2011, Li et al., 2014). The FMDF is defined as

$$F_L(\boldsymbol{\Psi};\mathbf{x},t)=\int_{-\infty}^{+\infty}\rho(\mathbf{x}',t)\xi\big(\boldsymbol{\Psi},\boldsymbol{\Phi}(\mathbf{x}',t)\big)G(\mathbf{x}'-\mathbf{x})d\mathbf{x}' \tag{6.58}$$

where

t and $\mathbf{x}$ represent time and space vector, respectively

G denotes the filter function

$\boldsymbol{\Phi}$ and $\boldsymbol{\Psi}$ are the scalar vector and scalar vector in the sample space, respectively

ξ is the fine grained density (Colucci et al., 1998), defined based on a series of delta functions

The scalar vector includes species mass fractions ($\alpha = 1, \ldots, N_s$) and specific sensible enthalpy ($\alpha = N_s + 1$).

The FMDF transport equation is obtained by inserting the instantaneous unfiltered scalar equation into the time derivative of the fine grained density and filtering that. For a compressible two-phase reacting system with negligible liquid volume fraction, the FMDF equation can be written in the following form:

$$\begin{aligned}\frac{\partial F_L}{\partial t}+\frac{\partial}{\partial x_i}\Big[\langle u_i(\mathbf{x},t)\rangle_L F_L\Big]&=-\frac{\partial}{\partial x_i}\Big[\big(\langle u_i(\mathbf{x},t)\,|\,\boldsymbol{\Psi}\rangle_l-\langle u_i\rangle_L\big)F_L\Big]\\&+\frac{\partial}{\partial\psi_\alpha}\left[\left\langle\frac{1}{\rho(\boldsymbol{\Phi})}\frac{\partial J_i^\alpha}{\partial x_i}\middle|\boldsymbol{\Psi}\right\rangle_l F_L\right]-\frac{\partial}{\partial\psi_\alpha}(\dot{S}_\alpha(\boldsymbol{\Psi})F_L)-\frac{\partial}{\partial\psi_\alpha}\Big[\langle\dot{S}_\alpha^{comp}\,|\,\boldsymbol{\Psi}\rangle_l F_L\Big]\\&-\frac{\partial}{\partial\psi_\alpha}\left[\frac{\langle\dot{S}_\alpha^{sp}\,|\,\boldsymbol{\Psi}\rangle F_L}{\rho(\boldsymbol{\Psi})}\right]+\frac{\partial}{\partial\psi_\alpha}\left[\frac{\langle\dot{S}_{Mass}^{sp}\,|\,\boldsymbol{\Psi}\rangle\psi_\alpha F_L}{\rho(\boldsymbol{\Psi})}\right]+\frac{\langle\dot{S}_{Mass}^{sp}\,|\,\boldsymbol{\Psi}\rangle F_L}{\rho(\boldsymbol{\Psi})}\end{aligned} \tag{6.59}$$

It is noted here that in the aforementioned FMDF equation, the reaction term (the third term on the right-hand side) is closed but in conventional LES methods it is not closed and requires additional modeling. The first term on the right-hand side of Equation 6.59 represents the SGS convection, which can be modeled with a gradient-type closure as

$$\big(\langle u_i(\mathbf{x},t)\,|\,\boldsymbol{\Psi}\rangle_l-\langle u_i\rangle_L\big)F_L=-\Gamma_t\frac{\partial(F_L/\langle\rho\rangle_l)}{\partial x_i} \tag{6.60}$$

where $\Gamma_t = \mu_t/Pr_t$ or $\Gamma_t = \mu_t/Sc_t$ is the turbulent diffusivity.

The term due to molecular diffusion is decomposed into two parts, the molecular transport and the SGS dissipation. The SGS dissipation can be modeled with the linear mean-square estimation (Dopazo and O'Brien, 1976, O'Brien, 1980) or the interaction by exchange with the mean model (Borghi, 1988)

$$\frac{\partial}{\partial\psi_\alpha}\left[\left\langle\frac{1}{\rho(\boldsymbol{\Phi})}\frac{\partial J_i^\alpha}{\partial x_i}\,|\,\boldsymbol{\Psi}\right\rangle_l F_L\right]=\frac{\partial}{\partial x_i}\left[\Gamma\frac{\partial}{\partial x_i}\left(\frac{F_L}{\langle\rho\rangle_l}\right)\right]+\frac{\partial}{\partial\psi_\alpha}[\Omega_m(\psi_\alpha-\langle\phi_\alpha\rangle_L)F_L] \tag{6.61}$$

where the molecular diffusivity is $\Gamma = \mu/Pr$ or $\Gamma = \mu/Sc$ and the SGS mixing frequency is $\Omega_m=\frac{1}{2}c_\phi(\Gamma+\Gamma_t)/(\overline{\Delta}^2\langle\rho\rangle_l)$.

The source term due to pressure in the scalar FMDF is obtained by taking into account the total derivative of filtered pressure for the mixture enthalpy as (Banaeizadeh et al., 2011)

$$\langle\dot{S}_\alpha^{comp}\,|\,\boldsymbol{\Psi}\rangle_l=\frac{1}{\langle\rho\rangle_l}\left(\frac{\partial\langle p\rangle_l}{\partial t}+\langle u_i\rangle_L\frac{\partial\langle p\rangle_l}{\partial x_i}\right),\quad \alpha=N_s+1 \tag{6.62}$$

For spray combustion, the viscous dissipation term in enthalpy equation is small and neglected. The last three conditionally averaged terms on the RHS of Equation 6.59 represent the spray/droplet effects on FMDF. They involve particle source/sink terms affecting the gas composition and density. For simplicity, the conditionally averaged quantities in spray terms can be replaced by unconditional filtered values of particle source or sink terms (Irannejad and Jaberi, 2014). This approximation is not expected to have a very significant effect on the filtered scalar variables.

The modeled FMDF transport equation is solved to obtain the scalar FMDF and consequently all single-point statistical information concerning reactive species and temperature at various times and locations, including the first moments or filtered variables. The most convenient means of solving the FMDF transport equation is via the Lagrangian MC procedure (Pope, 1985). With the Lagrangian procedure, the FMDF is represented by an ensemble of computational "stochastic elements" or "MC particles." These notional particles evolve through a "stochastic process," described by a set of stochastic differential equations (Gardiner, 1990, Kloeden and Platen, 1995). The stochastic process is described by a Fokker–Planck equation. A comparison between the Fokker–Planck equation and the FMDF equation under consideration identifies the parameters of the stochastic equations (Jaberi et al., 1999). A unique feature of this stochastic procedure is that the large-scale, SGS, and molecular mixing, the chemical reaction and the two-phase effects can be separately incorporated and evaluated, offering a systematic way to compute and interpret these processes in the LES/FMDF calculations. The simplest means of simulating the spatial transport in this equation is via the Euler–Maruyama approximation (Gardiner, 1990). The spray terms in the FMDF equation are weighted averaged from FD grid points to the MC particle locations.

To manage the number of MC particles and to reduce the computational cost, a procedure involving the use of nonuniform weights is considered. The variable weighting for particles allows the particle number density to stay above a certain minimum value regardless of density variations. For the spray simulation, particle weights are modified due to added mass to the carrier gas from the evaporating droplets. The effects of spray heat and mass transfer on the MC particles are implemented by a series of source terms in the particle equations (Irannejad and Jaberi, 2014). Details of SGS mass transfer between droplets and MC particles do not seem to have a very significant effect on the global spray and flame behavior simulated by LES/FMDF (Irannejad and Jaberi, 2014b). However, in some circumstances, when, for example, the individual droplet combustion becomes important, it would be necessary to use a more detailed description of the mass transfer between the liquid and the gas. This issue has been discussed in detail in the context of RANS/PDF spray simulations in Jenny et al. (2012).

The chemical kinetics model plays a crucial role in the LES of reacting spray and is important to the flame ignition, liftoff, and extinction. In a recent study, Irannejad and Jaberi (2014b) used the skeletal mechanism of Liu et al. (2004) for spray combustion simulations using parallel ISAT method (Irannejad and Jaberi, 2014b). This mechanism has 44 species and 185 reactions, counting forward and backward reactions individually. ISAT uses the ordinary differential equation solver DDASAC (Caracotsios and Stewart, 1985) to integrate reaction equations and stores the relevant information in a binary tree, with each termination node (or leaf) representing a record of the tabulation point for a specific composition, the reaction mapping in time step, and the mapping gradient matrix. Using this matrix, for a given query composition close to a tabulated composition point, a linear approximation to the mapping is obtained under a controlled tolerance.

As indicated earlier, the spray can be modeled with a Lagrangian model using drops (Irannejad and Jaberi, 2014a). In this model, the drop motion is simulated using Basset–Boussinesq–Oseen equation (Crowe et al., 1998, Loth, 2000, Sirignano, 2010). Under the assumptions of high liquid-to-gas density ratios, the Lagrangian equations describing the drop motion become

$$\frac{d\mathbf{x}_p}{dt} = \mathbf{u}_p \tag{6.63}$$

$$\frac{d\mathbf{u}_p}{dt} = \frac{\mathbf{u}_{rel}}{\tau_p} \tag{6.64}$$

In Equation 6.64, the relative velocity, $\mathbf{u}_{rel} = \mathbf{u}_g - \mathbf{u}_p$, is calculated based on the gas velocity at the drop location, $\mathbf{u}_g = \langle \mathbf{u} \rangle_L + \mathbf{u}^*$, which is reconstructed using the filtered velocity and the stochastic subgrid velocity $\mathbf{u}^*$

(Pozorski and Apte, 2009). The stochastic subgrid velocity is calculated from the SGS velocity $u_{sgs} = \sqrt{2k_{sgs}/3}$ and characteristic timescale $\tau_L^\star$:

$$du_i^\star = -\frac{u_i^\star}{\tau_L^\star}dt + \sqrt{\frac{2u_{sgs}^2}{\tau_L^\star}}dW_i \tag{6.65}$$

where dW_i is an increment of the Wiener process (Gardiner, 1990). The SGS velocity reconstruction is intended to cover a wide range of drop Stokes numbers (Pozorski and Apte, 2009). Furthermore, the drop relative velocity is reduced by wake interactions of nearby drops in the spray (Irannejad and Jaberi, 2013). This modified relative velocity is then used for drop motion, heat, and mass transfer calculations. The drop response time is defined as

$$\tau_p = \tau_{st}/f_d(Re_{sl})\,, \tag{6.66}$$

in which $\tau_{st} = d_p^2\rho_l/18\mu_g$ is the drop Stokes timescale and $f_d(Re_{sl})$, the drag factor, is the finite Reynolds number ($Re_{sl} = \rho_g d_p u_{rel}/\mu_g$, d_p is the drop diameter) correction to the Stokes drag. The drag factor f_d includes the effects of evaporation through a blowing Reynolds number, Re_{bw} for low Reynolds numbers ($Re_{sl} < 100$) (Bellan and Harstad, 1987b). The drag factor is modified for a distorted drop, using the simple assumption that the drag coefficient of a distorted drop lies between the lower limit of a rigid sphere and the upper limit of a disk where the distortion is computed using Taylor analogy breakup model (Liu et al., 1993).

For high injection pressure evaporating and reacting sprays operating in realistic combustion systems, the initial development of liquid jet is often modeled by a set of round liquid blobs injected from the nozzle with similar mass flow rate (Moin and Apte, 2006, Gorokhovski and Herrmann, 2008, Jiang et al., 2010). These large drops then go through a series of breakup processes mimicking the primary and secondary breakup. This is based on the reasonable assumption that the atomization and fragmentation of liquid jet, blobs, or drops are indistinguishable processes within the dense liquid core region near the injector nozzle exit. Spray atomization is then modeled by a stochastic model in which the characteristic radius of drops is assumed to be a time-dependent stochastic variable with a given initial distribution (Kolmogorov, 1941, Gorokhovski and Saveliev, 2003). The breakup of parent drops into daughter drops is viewed as the temporal and spatial evolution of the distribution function according to the following Fokker–Planck differential equation (Gorokhovski and Saveliev, 2003):

$$\frac{\partial\mathfrak{I}(\chi,t^\star)}{\partial t} = -\frac{\langle\varsigma\rangle}{\tau_{bu}}\frac{\partial\mathfrak{I}(\chi,t^\star)}{\partial\chi} + \frac{1}{2}\frac{\langle\varsigma^2\rangle}{\tau_{bu}}\frac{\partial^2\mathfrak{I}(\chi,t^\star)}{\partial\chi^2} \tag{6.67}$$

where $\langle\varsigma\rangle$ and $\langle\varsigma^2\rangle$ are the first two moments of the breakup intensity spectrum, which is assumed to be Gaussian. The breakup time, τ_{bu} is based on the Lagrangian relative velocity fluctuations for the drop (Irannejad and Jaberi, 2014a).

The following spherically symmetric heat and mass transfer equations inside each individual drop are solved for the liquid density, energy, and species mass fractions (Torres et al., 2003, Srivastava et al., 2013, Irannejad and Jaberi, 2014a):

$$\frac{\partial\rho_l}{\partial t} + \frac{1}{r^2}\frac{\partial}{\partial r}(r^2\rho_l v_l) = 0 \tag{6.68}$$

$$\frac{\partial(\rho_l\phi_{l\alpha})}{\partial t} + \frac{1}{r^2}\frac{\partial}{\partial r}(r^2\rho_l v_l\phi_{l\alpha}) = \frac{1}{r^2}\frac{\partial}{\partial r}\left(r^2\rho_l D_l\frac{\partial\phi_{l\alpha}}{\partial r}\right) \tag{6.69}$$

$$\frac{\partial(\rho_l T_l)}{\partial t} + \frac{1}{r^2}\frac{\partial}{\partial r}(r^2\rho_l v_l T_l) = \frac{1}{c_p r^2}\frac{\partial}{\partial r}\left(r^2\lambda_l\frac{\partial T_l}{\partial r}\right) \tag{6.70}$$

The mass and energy conservation equations provide the necessary drop interface parameters such as radial velocity v_{ls}, and species mass fraction and temperature gradients at the drop surface. Moreover, global drop mass and energy changes such as the total change in the drop internal energy are also obtained by integrating these equations. The internal drop circulation, caused by the relative motion of gas and liquid, and its effect on the drop variables are accounted for by changing the effective mass and thermal liquid diffusivities (Abramzon and Sirignano, 1989). For a multicomponent drop, the mass flux of species α at the drop interface is defined based on the species mass fraction on the liquid side of the drop surface, $\phi_{ls\alpha}$; the drop radius, r_s; the species diffusivity in the gas, $D_{g\alpha}$; the species Sherwood number, Sh_α; and the Spalding mass transfer number, $B_{M\alpha}$ as

$$\dot{m}_\alpha = \phi_{ls\alpha} 2\pi r_s \rho_{gs} D_{g\alpha} Sh_\alpha \ln(1 + B_{M\alpha}) \tag{6.71}$$

The Spalding mass transfer number relates the liquid and gas interface mass fractions ($\phi_{ls\alpha}$ and $\phi_{gs\alpha}$) to the free stream (with respect to drop) mass fraction $\phi_{\infty\alpha}$ as

$$B_{M\alpha} = \frac{\phi_{gs\alpha} - \phi_{\infty\alpha}}{\phi_{ls\alpha} - \phi_{gs\alpha}} \tag{6.72}$$

The Ranz–Marshall correlations for Nusselt and Sherwood numbers may be modified to account for the surface blowing effect (Abramzon and Sirignano, 1989), as explained further in Sections 1.4.3.4 and 1.4.4.5 in this handbook. The surface regression rate can be found by summing the mass flux over all species and by solving the species mass conservation and energy equations at drop interface (Irannejad and Jaberi, 2014a). The effects of drops on the carrier gas are included via a series of source/sink terms in the gas continuity, momentum, energy, and scalar equations and also in the subgrid kinetic energy equations. These source terms are evaluated by volumetric averaging and interpolation of the Lagrangian variables from all drops in each cell (Irannejad and Jaberi, 2014a).

Using isolevel contours of stoichiometric equivalence ratio and background temperature contours, Figure 6.12 illustrates various regions in a reacting n-heptane fuel spray injected in a closed chamber filled with high temperature and pressure air (Irannejad and Jaberi, 2014b). The results in this figure are obtained by the two-phase LES/FMDF model with complex chemical kinetics and ISAT as described in Irannejad and Jaberi (2014b). Figure 6.12 shows that as the spray breaks and drops are formed, dispersed, heated, and evaporated, the combined effects of drop drag and evaporated fuel mass generate a high-speed main gas jet that becomes highly turbulent further downstream. The entrainment and mixing in the turbulent jet are strongly affected by the combustion. The separation of the high temperature and highly turbulent flame from the liquid spray and drops is clearly visible in the simulated reacting spray. The ambient gas temperature is high enough for the drops to evaporate and provide the fuel for the flame without needing the main flame's heat. Yet, the spray is very fast and generates significant gas flow and turbulence that push the flame away from the spray. Consequently, as Figure 6.12 shows, there is a relatively cool evaporated fuel that

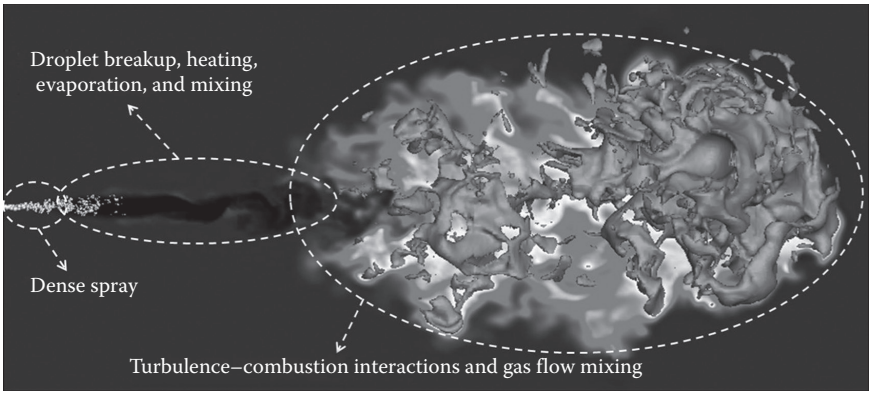


Figure 6.12

Various parts of the reactive high-speed turbulent spray simulated by LES/FMDF model. Isolevels of stoichiometric equivalence ratio are shown on background temperature contours.

separates the main spray from the main flame. The low-temperature, vapor fuel–rich gas jet breaks into smaller turbulent structures with much more effective mixing by the spray-generated gas flow turbulence before disappearing into the complicated flame plume.

The simulation of turbulence, once dominated by RANS models, is now also being conducted using LES models. By offering advantages in highly transient flows, LES is growing as a viable replacement for RANS. Nevertheless, with the current computational resources, RANS still remains as the primary method of choice for very practical multiphase reacting systems.

Acknowledgments

The authors acknowledge the support from the U.S. Office of Secretary of Defense under contract FA8650-12-C-2247. The authors are also grateful to the Air Force Research Laboratory staff for program management support. The supports from the U.S. Department of Energy under agreement DE-FC26-07NT43278 and the U.S. Defense Logistics Agency under agreement DFARS-252232-7010 are also acknowledged. The authors are also grateful to the STAMPEDE supercomputing center at TACC/UT Austin and the High Performance Computing Centers at MSU and UIC for providing computational resources.

References

Abramzon, B. and Sirignano, W.A., Droplet vaporization model for spray combustion calculations, *Int. J. Heat Mass Transfer*, 32, 1605–1618, 1989.

Afshari, A., Jaberi, F.A., and Shih, T.I.P., Large-eddy simulations of turbulent flows in an axisymmetric dump combustor, *AIAA J.*, 46, 1576–1592, 2008.

Aggarwal, S.K., A review of spray ignition phenomena: Present status and future research, *Prog. Energy Combust. Sci.*, 24, 565–600, 1998.

Almeida, T. and Jaberi, F.A., Large eddy simulation of a dispersed particle-laden turbulent round jet, *Int. J. Heat Mass Transfer*, 51, 683–695, 2008.

Annamalai, K., Evaporation and combustion of a cloud of drops, ASME, HTD, Vol. 45, 1985, pp. 27–35.

Annamalai, K. and Ryan, W., Interactive processes in gasification and combustion. Part I: Liquid drop arrays and clouds, *Prog. Energy Combust. Sci.*, 18, 221–295, 1992.

Annamalai, K. and Ryan, W., Interactive processes in gasification and combustion Part II: Isolated carbon, coal and porous char particles, *Prog. Energy Combust. Sci.*, 19, 383–446, 1993.

Annamalai, K., Ryan, W., and Dhanapalan, S., Interactive processes in gasification and combustion. Part III: Coal/char particle arrays, streams and clouds, *Prog. Energy Combust. Sci.*, 20, 487–618, 1994.

Ansari, N., Jaberi, F.A., Sheikhi, M.R.H., and Givi, P., Chapter: Filtered density function as a modern CFD tool, in *Engineering Applications of Computational Fluid Dynamics*, International Energy and Environment Foundation, 2011, pp. 1–22.

Apte, S.V., Gorokhovski, M., and Moin, P., LES of atomizing spray with stochastic modeling of secondary breakup, *Int. J. Multiphase Flow*, 29, 1503–1522, 2003.

Apte, S.V., Mahesh, K., Moin, P., and Oefeleini, J.C., Large-eddy simulation of swirling particle-laden flows in a coaxial-jet combustor, *Int. J. Multiphase Flow*, 29, 1311–1331, 2003.

Armenio, V., Piomelli, U., and Fiorotto, V., Effect of the subgrid scales on particles motion, *Phys. Fluids*, 11, 3030–3042, 1999.

Ashgriz, N. and Poo, J.Y., FLAIR: Flux line-segment model for advection and interface reconstruction, *J. Comp. Phys.*, 93, 449–468, 1991.

Banaeizadeh, A., Li, Z., and Jaberi, F.A., Compressible scalar filtered mass density function model for high-speed turbulent flows, *AIAA J.*, 49, 2130–2143, 2011.

Battin-Leclerc, F., Detailed chemical kinetic models for the low-temperature combustion of hydrocarbons with application to gasoline and diesel fuel surrogates, *Prog. Energy Combust. Sci.*, 34, 440–498, 2008.

Bell, J.B., Brown, N.J., Day, M.S., Frenklach, M., Grcar, J.F., Propp, R.M., and Tonse, S.R., Scaling and efficiency of prism in adaptive simulations of turbulent premixed flames, *Proc. Combust. Inst.*, 28, 107–113, 2000.

Bellan, J., Supercritical (and subcritical) fluid behavior and modeling: Drops, streams, shear and mixing layers, jets and sprays, *Prog. Energy Combust. Sci.*, 26, 329–366, 2000.

Bellan, J. and Cuffel, R., A theory of non-dilute spray evaporation based upon multiple drop interactions, *Combust. Flame*, 51, 55–67, 1983.
Bellan, J. and Harstad, K., Analysis of the convective evaporation of nonlinear cluster of drops, *Int. J. Heat Mass Transfer*, 30, 125–136, 1987a.
Bellan, J. and Harstad, K., The details of the convective evaporation of dense and dilute clusters of drops, *Int. J. Heat Mass Transfer*, 30, 1083–1093, 1987b.
Bellan, J. and Harstad, K., Turbulence effects during evaporation of drops in clusters, *Int. J. Heat Mass Transfer*, 31, 1655–1668, 1988.
Bhattacharjee, S. and Haworth, D.C., Simulations of transient n-heptane and n-dodecane spray flames under engine-relevant conditions using a transported pdf method, *Combust. Flame*, 160, 2083–2102, 2013.
Blasco, J.A., Fueyo, N., Dopazo, C., and Ballester, J., Modelling the temporal evolution of a reduced combustion chemical system with an artificial neural network, *Combust. Flame*, 113, 38–52, 1998.
Boivin, M., Simonin, O., and Squires, K.D., On the prediction of gas-solid flows with two-way coupling using large eddy simulation, *Phys. Fluids*, 12, 2080–2090, 2000.
Borghesi, G., Mastorakos, E., and Cant, R.S., Complex chemistry DNS of n-heptane spray autoignition at high pressure and intermediate temperature conditions. *Combust. Flame*, 160, 1254–1275, 2013.
Borghi, R., Turbulent combustion modelling, *Prog. Energy Combust. Sci*., 14, 245–292, 1988.
Bray, K.N C. and Peters, N., Laminar flamelets in turbulent flames, in P.A. Libby and F.A. Williams (Eds.), *Turbulent Reacting Flows*, Academic Press, London, U.K., 1994, pp. 63–113.
Brennen, C., *Fundamentals of Multiphase Flow*, Lecture Notes in Engineering, Springer-Verlag, 2005.
Burcat, A., Thermophysical data for combustion calculations, in W.C. Gardiner (Ed.), *Combustion Chemistry*, Springer-Verlag, New York, 1984, pp. 455–504.
Cao, R.R. and Pope, S.B., The influence of chemical mechanisms on pdf calculations of nonpremixed piloted jet flames, *Combust. Flame*, 143, 450–470, 2005.
Caracotsios, M. and Stewart, W.E., Sensitivity analysis of initial value problems with mixed odes and algebraic equations, *Comput. Chem. Eng.*, 9, 359–365, 1985.
Chen, G. and Gomez, A., Dilute laminar spray diffusion flames near the transition from group combustion to individual droplet burning, *Combust. Flame*, 110, 392–404, 1997.
Chen, J.Y., Kollmann, W., and Dibble, R.W., Pdf modeling of turbulent nonpremixed methane jet flames, *Combust. Sci. Technol.*, 64, 315–346, 1989.
Chen, S. and Doolen, G.D., Lattice Boltzmann method for fluid flows, *Annu. Rev. Fluid Mech.*, 30, 329–364, 1998.
Chiu, H.H., Advances and challenges in droplet and spray combustion. I. Toward a unified theory of droplet aerothermochemistry, *Prog. Energy Combust. Sci*., 26, 381–416, 2000.
Chiu, H.H. and Croke, E.J., Group combustion of liquid fuel sprays. Technical Report 81-2, University of Illinois at Chicago, Energy Technology Lab, Chicago, IL, 1981.
Chiu, H.H. and Huang, J.S., Multiple-state phenomena and hysteresis of a combusting isolated droplet, *Atomiz. Sprays*, 6, 1–26, 1996.
Chiu, H.H., Kim, H.Y., and Croke, E.J., Internal group combustion of liquid droplets, in *Proceedings of 19th Symposium* (*International*) *on Combustion*, The Combustion Institute, Pittsburgh, PA, 1982, pp. 971–980.
Chiu, H.H. and Liu, T.M., Group combustion of liquid droplets, *Combust. Sci. Technol.*, 17, 127–142, 1977.
Christo, F.C., Masri, A.R., and Nebot, E.M., Artificial neural network implementation of chemistry with pdf simulation of h2/co2 flames, *Combust. Flame*, 106, 406–427, 1996.
Clift, R., Grace, J.R., and Weber, M.E., *Bubbles*, *Drops*, *and Particles*, Academic Press, New York, 1978.
Colucci, P.J., Jaberi, F.A., Givi, P., and Pope, S.B., Filtered density function for large eddy simulation of turbulent reacting flows, *Phys. Fluids*, 10, 499–515, 1998.
Cressman, J.R., Davoudi, J., Goldburg, W.I., and Schumacher, J., Eulerian and Lagrangian studies in surface flow turbulence, *New J. Phys.*, 6, 2004.
Crowe, C., (Ed.) *Multiphase Flow Handbook*, CRC Press, 2006.
Crowe, C., Sommerfeld, M., and Tsuji, Y., *Multiphase Flows with Droplets and Particles*, CRC Press, Boca Raton, FL, 1998.
Crowe, C.T., Sharma, M.P., and Stock, D.E., The particle-source in cell (PSI-Cell) model for gas-droplet flows, *J. Fluids Eng.*, 6, 325–332, 1977.

Cuenot, B., Boileau, M., Pascaud, S., Mossa, J.-B., Riber, E., Poinsot, T., and Bérat, C., Large eddy simulation of two-phase reacting flows, in *Proceedings of European Conference on Computational Fluid Dynamics*, 2006..

Dopazo, C. and O'Brien, E.E., Statistical treatment of non-isothermal chemical reactions in turbulence, *Combust. Sci. Technol.*, 13, 99–122, 1976.

Drew, D.A., Mathematical modeling of two-phase flow, *Annu. Rev. Fluid Mech.*, 15, 261–291, 1983.

Elperin, T., Kleeorin, N., and Rogachevskii, I., Turbulent thermal diffusion of small inertial particles, *Phys. Rev. Lett.*, 76, 224–227, 1996.

Faeth, G.M., Current status of droplet and liquid combustion, *Prog. Energy Combust. Sci.*, 3, 191–224, 1977.

Faeth, G.M., Mixing, transport and combustion in sprays, *Prog. Energy Combust. Sci.*, 13, 293–345, 1987.

Gardiner, C.W., *Handbook of Stochastic Methods*, Springer-Verlag, New York, 1990.

Ghosal, S., Lund, T.S., Moin, P., and Akselvoll, K., Consistent large-eddy simulation of a temporal mixing layer laden with evaporating drops. part 2. a posteriori modelling, *J. Fluid Mech.*, 286, 229–255, 1995.

Givi, P., Model free simulations of turbulent reactive flows, *Prog. Energy Combust. Sci.*, 15, 1–107, 1989.

Givi, P., Subgrid scale modeling in turbulent combustion: A review, AIAA Paper 2003-5081, 2003.

Givi, P., Filtered density function for subgrid scale modeling of turbulent combustion, *AIAA J.*, 44, 16–23, 2006.

Godsave, G.A.E., Studies of the combustion of drops in a fuel spray, in *Proceedings of Fourth Symposium* (*International*) *on Combustion*, The Combustion Institute, Baltimore, MD, 1953, pp. 818–830.

Gogos, G., Soh, S., and Pope, D.N., Effects of gravity and ambient pressure on liquid fuel droplet evaporation, *Int. J. Heat Mass Transfer*, 46, 283–296, 2003.

Gorokhovski, M. and Herrmann, M., Modeling primary atomization, *Annu. Rev. Fluid Mech.*, 40, 343–366, 2008.

Gorokhovski, M.A. and Saveliev, V.L., Analyses of Kolmogorov model of breakup and its application into Lagrangian computation of liquid sprays under air-blast atomization, *Phys. Fluids*, 15, 184–192, 2003.

Haworth, D.C., Progress in probability density function methods for turbulent reacting flows, *Prog. Energy Combust. Sci.*, 36, 168–259, 2010.

Haworth, D.C. and Pope, S.B., Chapter: Transported probability density function methods for Reynolds-averaged and Large-Eddy simulations, in *Turbulent Combustion Modeling: Advances*, *New Trends and Perspectives*, Springer, 2011, pp. 119–142.

Haywood, R.J., Renksizbulut, M., and Raithby, G.D., Numerical solution of deforming evaporating droplets at intermediate Reynolds numbers, *Num. Heat Transfer*, 26, 253–272, 1994a.

Haywood, R.J., Renksizbulut, M., and Raithby, G.D., Transient deformation and evaporation of droplets at intermediate reynolds numbers, *Int. J. Heat Mass Transfer*, 37, 1401–1409, 1994b.

Herrmann, M., Modeling primary breakup: Three-dimensional Eulerian level set/vortex sheet method for two-phase interface dynamics, *Annu. Res. Brief, Center Turbul. Res., Stanford Univ.*, 157, 185–196, 2003.

Hubbard, G.L., Denny, V.E., and Mills, A.F., Droplet evaporation: Effects of transients and variable properties, *Int. J. Heat Mass Transfer*, 18, 1003–1008, 1975.

Irannejad, A. and Jaberi, F., Large eddy simulation of evaporating spray with a stochastic breakup model, SAE 2013-01-1101, 2013.

Irannejad, A. and Jaberi, F., Large eddy simulation of turbulent spray breakup and evaporation, *Int. J. Multiphase Flow*, 61, 108–128, 2014a.

Irannejad, A. and Jaberi, F.A., Large eddy simulation of turbulent spray combustion, *Combust. Flame*, 162, 431–450, 2014b.

Jaberi, F.A., Large eddy simulation of turbulent premixed flames via filtered mass density function, AIAA 99-0199, 1999.

Jaberi, F.A., Colucci, P.J., James, S., Givi, P., and Pope, S.B., Filtered mass density function for large eddy simulation of turbulent reacting flows, *J. Fluid Mech.*, 401, 85–121, 1999.

Jackson, R., Locally averaged equations of motion for a mixture of identical spherical particles and a Newtonian fluid, *Chem. Eng. Sci.*, 52, 2457–2469, 1997.

James, S. and Jaberi, F.A., Large scale simulations of two-dimensional nonpremixed methane jet flames, *Combust. Flame*, 123, 465–487, 2000.

Jenny, P., Roekaerts, D., and Beishuizen, N., Modeling of turbulent dilute spray combustion, *Prog. Energy Combust. Sci.*, 38, 846–887, 2012.

Jiang, X., Siamas, G.A., Jagus, K., and Karayiannis, T.G., Physical modeling and advanced simulations of gas-liquid two-phase jet flows in atomization and sprays, *Prog. Energy Combust. Sci.*, 36, 131–167, 2010.
Kloeden, P.E. and Platen, E., *Numerical Solution of Stochastic Differential Equations*, Springer, 1995.
Kolmogorov, A.N., On the log-normal distribution of particle sizes during breakup process, *Dokl. Akad. Nauk. SSSR*, 31, 99–101, 1941.
Lakehal, D., On the modeling of multiphase turbulent flows for environmental and hydrodynamic applications, *Int. J. Multiphase Flow*, 28, 823–863, 2002.
Law, C.K., Chumg, S.H., and Srinivasan, N., Gas phase quasi-steadiness and fuel vapor accumulation effects on droplet burning, *Combust. Flame*, 38, 173–198, 1980.
Law, C.K. and Williams, F.A., Kinetics and convection in the combustion of alkane droplets, *Combust. Flame*, 19, 393–406, 1972.
Lesieur, M. and Métais, O., New trends in large-eddy simulations of turbulence, *Annu. Rev. Fluid Mech.*, 28, 45–82, 1996.
Li, Z., Banaeizadeh, A., and Jaberi, F.A., Two-phase filtered mass density function for LES of turbulent reacting flows, *J. Fluid Mech.*, 760, 243–277, 2014.
Li, Z., Jaberi, F.A., and Shih, T.I-P., A hybrid Lagrangian-Eulerian particle-level set method for numerical simulations of two-fluid turbulent flows, *Int. J. Num. Methods Fluids*, 56, 2271–2300, 2008.
Li, S.C., Spray stagnation flames, *Prog. Energy Combust. Sci.*, 23, 303–347, 1997.
Liu, A.B., Mather, D., and Reitz, R.D., Modeling the effects of drop drag and breakup on fuel sprays, SAE 930072, 1993.
Liu, S., Hewson, J.C., Chen, J.H., and Pitsch, H., Effects of strain rate on high-pressure nonpremixed n-heptane autoignition in counterflow, *Combust. Flame*, 137, 320–339, 2004.
Loth, E., Numerical approaches for motion of dispersed particles, droplets and bubbles, *Prog. Energy Combust. Sci.*, 26, 161–223, 2000.
Lu, L. and Pope, S.B., An improved algorithm for in situ adaptive tabulation, *J. Comput. Phys.*, 228, 361–386, 2009.
Lu, T. and Law, C.K., Toward accommodating realistic fuel chemistry in large-scale computations, *Prog. Energy Combust. Sci.*, 35, 192–215, 2009.
Madnia, C.K., Jaberi, F.A., and Givi, P., Chapter: Large Eddy simulation of heat and mass transport in turbulent flows, in *Handbook of Numerical Heat Transfer*, John Wiley & Sons Inc., 2006, pp. 167–189.
Magnussen, B.F. and Hjertager, B.H., On mathematical models of turbulent combustion with special emphasis on soot formation and combustion, in *Proceedings of 16th Symposium* (*International*) *on Combustion*, The Combustion Institute, Pittsburgh, PA, 1977, pp. 719–729.
Mahesh, K., Constantinescu, G., Apte, S., Iaccarino, G., Ham, F., and Moin, P., Large-eddy simulation of reacting turbulent flows in complex geometries, *J. Appl. Mech.*, 73, 374–381, 2006.
Mashayek, F., Numerical investigation of reacting droplets in homogeneous shear turbulence, *J. Fluid Mech.*, 405, 1–36, 2000.
Mashayek, F., Dynamics of evaporating drops. Part I: Formulation and evaporation model, *Int. J. Heat Mass Transfer*, 44, 1517–1526, 2001.
Mashayek, F. and Pandya, R.V.R., Analytical description of particle/droplet-laden turbulent flows, *Prog. Energy Combust. Sci.*, 29, 329–378, 2003.
Mastorakos, E., Ignition of turbulent non-premixed flames, *Prog. Energy Combust. Sci.*, 35, 57–97, 2009.
Maxey, M.R., Patel, B.K., Chang, E.J., and Wang, L.P., Simulations of dispersed turbulent multiphase flow, *Fluid Dyn. Res.*, 20, 143–156, 1997.
McCreath, C.G. and Chigier, N.A., Liquid spray burning in the wake of a stabilizer disk, in *Proceedings of 14th Symposium* (*International*) *on Combustion*, The Combustion Institute, 1973, pp. 1355–1363.
Meneveau, C. and Katz, J., Scale-invariance and turbulence models for large-eddy simulation, *Annu. Rev. Fluid Mech.*, 32, 1–32, 2000.
Menon, S., Subgrid combustion modelling for large-eddy simulations, *Int. J. Eng. Res.*, 1, 209–227, 2000.
Menon, S. and Patel, N., Subgrid modeling for simulation of spray combustion in large-scale combustors, *AIAA J.*, 44, 709–723, 2006.
Moin, P., Large eddy simulation of multi-phase turbulent flows in realistic combustors, *Int. J. Prog. Comput. Fluid Dyn.*, 4, 237–240, 2004.
Moin, P. and Apte, S.V., Large-eddy simulation of realistic gas turbine combustors, *AIAA J.*, 44, 698–708, 2006.

Moin, P., Squires, K., Cabot, W., and Lee, S., A dynamic subgrid scale model for compressible turbulence and scalar transport, *Phys. Fluids A*, 3, 2746–2757, 1991.
O'Brien, E.E., Chapter: The probability density function (PDF) approach to reacting turbulent flows, in *Turbulent Reacting Flows*, Springer, 1980, pp. 185–218.
Pandya, R.V.R. and Mashayek, F., Kinetic equation for particle transport and heat transfer in non-isothermal turbulent flows, AIAA Paper Number 2002-0337, 2002a.
Pandya, R.V.R. and Mashayek, F., Turbulent thermal diffusion and barodiffusion of passive scalar and dispersed phase of particles in turbulent flows, *Phys. Rev. Lett.*, 88, 044501–1–044501–4, 2002b.
Pandya, R.V.R. and Mashayek, F., Non-isothermal dispersed phase of particles in turbulent flow, *J. Fluid Mech.*, 475, 205–245, 2003.
Patel, N., Kirtas, M., Sankaran, V., and Menon, S., Simulation of spray combustion in a lean-direct injection combustor, *Proc. Combust. Inst.*, 31, 2327–2334, 2007.
Pei, Y., Hawkes, E.R., and Kook, S., A comprehensive study of effects of mixing and chemical kinetic models on predictions of n-heptane jet ignitions with the pdf method, *Flow, Turbul. Combust.*, 91, 249–280, 2013.
Peters, N., *Turbulent Combustion*, Cambridge University Press, Cambridge, U.K., 2013.
Pickett, L.M., Genzale, C.L., Bruneaux, G., Malbec, L.M., Hermant, L., Christiansen, C., and Schramm, J., Comparison of diesel spray combustion in different high-temperature, high-pressure facilities, SAE 01-2106, 2010.
Pitsch, H., Large-eddy simulation of turbulent combustion, *Annu. Rev. Fluid Mech.*, 38, 453–482, 2006.
Pope, S.B., PDF methods for turbulent reactive flows, *Prog. Energy Combust. Sci.*, 11, 119–192, 1985.
Pope, S.B., Computationally efficient implementation of combustion chemistry using in situ adaptive tabulation, *Combust. Theory Model*, 1, 41–63, 1997.
Pope, S.B. and Ren, Z., Efficient implementation of chemistry in computational combustion, *Flow, Turbul. Combust.*, 82, 437–453, 2009.
Pozorski, J. and Apte, S.V., Filtered particle tracking in isotropic turbulence and stochastic modeling of subgrid-scale dispersion, *Int. J. Multiphase Flow*, 35, 118–128, 2009.
Rabitz, H. and Alis, O.F., General foundations of high dimensional model representations, *J. Math. Chem.*, 25, 197–233, 1999.
Raman, V. and Pitsch, H., A consistent LES/filtered-density function formulation for the simulation of turbulent flames with detailed chemistry, *Proc. Combust. Inst.*, 31, 1711–1719, 2006.
Ranz, W.E. and Marshall, W.R., Evaporation from drops, *Chem. Eng. Prog.*, 48, 141–173, 1952.
Reveillon, J. and Vervisch, L., Spray vaporization in nonpremixed turbulent combustion modeling: A single droplet model, *Combust. Flame*, 121, 75–90, 2000.
Salman, H. and Soteriou, M., Lagrangian simulation of evaporating droplet sprays, *Phys. Fluids*, 16, 4601–4622, 2004.
Sankaran, V. and Menon, S., LES of spray combustion in swirling flows, *J. Turbul.*, 3, 011, 2002.
Scardovelli, R. and Zaleski, S., Direct numerical simulation of free-surface and interfacial flow, *Annu. Rev. Fluid Mech.*, 31, 567–603, 1999.
Seiser, R., Pitsch, H., Seshadri, K., Pitz, W.J., and Gurran, H.J., Extinction and autoignition of n-heptane in counterflow configuration, *Proc. Combust. Inst.*, 28, 2029–2037, 2000.
Sethian, J.A. and Smereka, P., Level set methods for fluid interfaces, *Annu. Rev. Fluid Mech.*, 35, 341–372, 2003.
Sheikhi, M.R.H., Drozda, T.G., Givi, P., Jaberi, F.A., and Pope, S.B., Large eddy simulation of a turbulent nonpremixed piloted methane jet flame, *Proc. Combust. Inst.*, 30, 549–556, 2005.
Shen, L. and Yue, D., Large-eddy simulation of free-surface turbulence, *Combust. Flame*, 440, 75–116, 2001.
Shirolkar, J.S., Coimbra, C.F.M., and McQuay, M.Q., Fundamental aspects of modeling turbulent particle dispersion in dilute flows, *Prog. Energy Combust. Sci.*, 22, 363–399, 1996.
Shukla, P.K. and Mamun, A.A., *Introduction to Dusty Plasma Physics*, Institute of Physics, Philadelphia, PA, 2002.
Shyy, W. and Narayanan, R., *Fluid Dynamics at Interfaces*, Cambridge University Press, Cambridge, U.K., 1999.
Siebers, D.L., Liquid phase fuel penetration in diesel sprays, SAE 980809, 1998.
Siebers, D.L. and Higgins, B.S., Flame lift-off on direct-injection diesel sprays under quiescent conditions, SAE 2001-01-0530, 2001.

Siebers, D.L., Higgins, B.S., and Pickett, L.M., Flame lift-off on direct injection diesel fuel jets: Oxygen concentration effects, SAE 2002-01-0890, 2002.
Sirignano, W.A., *Fluid Dynamics and Transport of Droplets and Sprays*, Cambridge University Press, Cambridge U.K., 1999.
Sirignano, W.A., *Fluid Dynamics and Transport of Droplets and Sprays*, Cambridge University Press, Cambridge, U.K., 2010.
Som, S. and Aggarwal, S.K., Effects of primary breakup modeling on spray and combustion characteristics of compression ignition engines, *Combust. Flame*, 157, 179–193, 2010.
Sornek, R.J., Dobashi, R., and Hirano, T., Effect of turbulence on vaporization, mixing, and combustion of liquid-fuel sprays, *Combust. Flame*, 120, 479–491, 2000.
Spalding, D.B., The combustion of liquid fuels, in *Proceedings of Fourth Symposium* (*International*) *on Combustion*, The Combustion Institute, Baltimore, MD, 1953, pp. 847–864.
Spalding, D.B., Mixing and chemical reaction in steady confined turbulent flames, in *Proceedings of 13th Symposium* (*International*) *on Combustion*, The Combustion Institute, Pittsburgh, PA, 1971, pp. 649–657.
Srivastava, S., Schock, H., and Jaberi, F., Numerical simulations of turbulent sprays with a multicomponent evaporation model, SAE 2013-01-1603, 2013.
Suzuki, T. and Chiu, H.H., Multi-droplet combustion of liquid propellants, in *Proceedings of Ninth Symposium* (*International*) *on Combustion*, The Combustion Institute, Pittsburgh, PA, 1971, pp. 145–154.
Tishkoff, J., A model for the effect of droplet interaction on vaporization, *Int. J. Heat Mass Transfer*, 22, 1407–1415, 1979.
Torres, D.J., OaRourke, P.J., and Amsden, A.A., Efficient multicomponent fuel algorithm, *Combust. Theory Model*, 7, 67–86, 2003.
Turanyi, T., Parameterization of reaction mechanisms using orthonormal polynomials, *J. Comput. Chem.*, 18, 45–54, 1994.
Turns, S.R., *An Introduction to Combustion: Concepts and Applications*, McGraw-Hill Inc., 1996.
Umemura, A., Interactive droplet vaporization and combustion: Approach from asymptotics, *Prog. Energy Combust. Sci.*, 20, 325–372, 1994.
Venugopal, R. and Abraham, J., A review of fundamental studies relevant to flame lift-off in diesel jets, SAE 01-0134, 2007.
Wark, C., Eickmann, K., and Richards, C., The structure of an acoustically forced, reacting two-phase jet, *Combust. Flame*, 120, 539–548, 2000.
Williams, F.A., Recent advances in theoretical description of turbulent diffusion flames, in S.N.B. Murthy (Ed.), *Turbulence in Mixing Operations*, Plenum Press, New York, 1975, pp. 189–208.
Williams, F.A., *Combustion Theory*, 2nd edn., The Benjamin/Cummings Publishing Company, Menlo Park, CA, 1985.
Wu, J.-S., Liu, Y.-J., and Sheen, H.-J., Effects of ambient turbulence and fuel properties on the evaporation rate of single droplets, *Int. J. Heat Mass Transfer*, 44, 4593–4603, 2001.
Yaldizli, M., Mehravaran, K., and Jaberi, F., Large-eddy simulations of turbulent methane jet flames with filtered mass density function, *Int. J. Heat Mass Transfer*, 53, 2551–2562, 2010.
Yeh, F. and Lei, U., On the motion of small particles in a homogeneous isotropic turbulent flow, *Phys. Fluids*, 3, 2571–2586, 1991.
Yoo, C.S., Lu, T., Chen, J.H., and Law, C.K., Direct numerical simulations of ignition of a lean n-heptane/air mixture with temperature inhomogeneities at constant volume: Parametric study, *Combust. Flame*, 158, 1727–1741, 2011.
Zhang, D.Z. and Prosperetti, A., Averaged equations for inviscid disperse two-phase flow, *J. Fluid Mech.*, 267, 185–219, 1994.
Zung, J.T., Evaporation rate and lifetime of clouds and sprays in air—The cellular model, *J. Chem. Phys.*, 46, 2064–2070, 1967.

7

Microgravity Two-Phase Flows

Kamiel S. Gabriel

7.1 Introduction
7.2 Applications of Two-Phase Flows at Microgravity Conditions
7.3 Flow Patterns
7.4 Flow Pattern Transitions
7.5 Flow Pattern Map
7.6 Gas–Liquid Pressure Drop
7.7 Void Fraction
7.8 Heat Transfer in Microgravity
7.9 Interfacial Waves in Microgravity Annular Two-Phase Flow
7.10 Definition of Wave Shape and Wave Characteristic

7.1 Introduction

The majority of analytical and empirical models used for the prediction of hydrodynamics and heat transfer behavior in two-phase gas–liquid flows are based on research data that were collected under terrestrial conditions. Under such conditions, where gravity plays a very important role in *shaping* the flow, empirical correlations used for the prediction of flow regimes, pressure drop, slip velocities, heat transfer rates, etc., may not be adequately suitable for microgravity (or near zero-gravity conditions).

Mainly due to the demand for active heat transport systems in modern communications and earth observation satellites and space stations, two-phase gas–liquid flow loops for space applications emerged in the early 1980s as an active research area in academic institutions as well as space centers in the United States and abroad. When gravity is reduced, buoyancy forces are severely reduced, and secondary forces such as those attributed to surface tension, which are usually very small at terrestrial conditions, play more significant role in establishing the flow conditions. The hydrodynamic characteristics of the flow, as well as the heat transfer mechanism, become different under such conditions in that effects of buoyancy forces on the momentum and heat transfer diminish, while those due to body forces (e.g., surface tension) become more dominant.

Theories and correlations that were derived at terrestrial conditions must be tested and possibly modified (or rejected) before they are used with confidence for conditions of reduced gravity.

For example, at reduced gravity, the slip velocity between the two phases is minimized and in some cases is very small or totally diminished (bubble and slug flows). This allows for better measurements and predictions of actual phase velocity and interfacial areas (since the interface is much more stable in μ-g bubble and slug flows). A better understanding of the actual contribution of each force acting on the flow can then be gained from the analysis of two-phase flow measurements at μ-g.

7.2 Applications of Two-Phase Flows at Microgravity Conditions

One of the major applications of two-phase flows at microgravity conditions is the design and maintenance of active thermal management systems for future space stations and high-power communications satellites. Past thermal management requirements for satellites and orbiting spacecraft have been characterized by low

power (<25 kW) and short lifetime (<3 years). These modest requirements can usually be satisfied by passive devices, such as heat pipes, or by pumped single-phase fluid cooling systems. The performance of passive and single-phase devices is mostly independent of gravity.

In addition, two-phase flow phenomena occur in many life-support systems in space stations and space labs. For example, the environmental conditions inside a space station (e.g., level of O_2 and humidity) have to be maintained at comfortable levels for personnel and living species inside orbiting stations. Water used for personal hygiene or other purposes, in many instances, has to be collected and processed for reuse. Two-phase flows are also prevalent in material processing in space, cryogenic transfer and storage, and several other enabling technologies (mining, water processing, etc.).

Studies of two-phase flows under microgravity conditions are also of great interest to better understand the behavior of terrestrial flows away from the masking effects of earth gravity (9.81 m/s^2). Since earth gravitational force plays an overwhelming role in *shaping* the flow characteristics, microgravity conditions provide an ideal environment to study the influence of other less dominant forces such as those due to surface tension, lift force, and turbulence.

7.3 Flow Patterns

The liquid–gas distribution pattern inside a conduit varies considerably depending on, among other factors, the mass flow rates of both phases, the conduit size, the phase properties, and the gravity vector with respect to the flow direction. Groups with similar phase distribution characteristics are classified into flow patterns (or flow regimes). Extensive efforts have been made to study the flow patterns and their transitions under normal and microgravity conditions. Since the identification of a particular phase distribution is somewhat subjective, the literature contains a host of flow pattern definitions and descriptions. More sophisticated studies aimed at minimizing this subjectivity via statistical analysis of void fraction data were successfully made in the last two decades (e.g., Lowe and Rezkallah, 1999). In those studies, void fraction measurements were taken using helical wound electrodes with electronics operating on a charge/discharge principle. The measurement then represented a true average value of the void fraction at each set point. More details could be found in Gabriel (2007).

Basically, four flow patterns are observed to exist under microgravity conditions. These are as follows: bubbly flow, slug flow, transitional flow, and annular flow. Bubbly flow consists of gas bubbles that are less than or equal to the tube diameter, distributed in a liquid continuum. Figure 7.1a shows a group of spherical medium-sized bubbles with some small dispersed bubbles. The bubbles tend to flow at or near the tube center where the liquid velocity is at maximum.

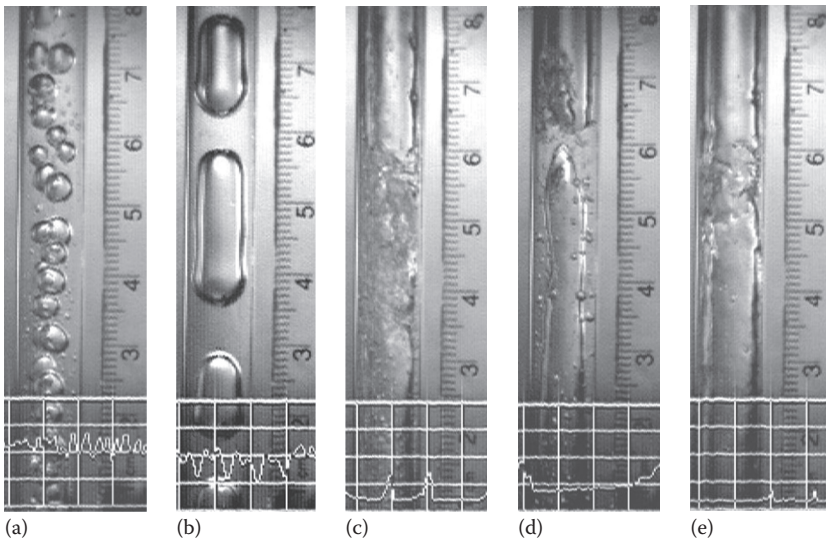


Figure 7.1

Four flow regimes: (a) bubbly flow, (b) slug flow, (c) transitional flow I, (d) transitional flow II, and (e) annular flow.

Slug flow consists of gas bubbles that are longer than the tube diameter but have diameters close to the tube diameter. Figure 7.1b shows a series of rounded, smooth, uniform bubbles of approximately two to three tube diameters.

Transitional or *frothy slug–annular flow* occurs when the liquid flows in the form of a film at the tube wall and the gas phase flows in the center of the tube. Frothy slugs pass frequently and, though it is difficult to discern the details, they likely consist of densely packed fine gas bubbles in a liquid continuum at relatively low gas flow rates or small liquid droplets at relatively high gas flow rates. Figure 7.1c shows transitional flow for a liquid flow rate of 0.16 m/s and a gas flow rate of 5.96 m/s. The figure shows a smooth film interrupted by a frothy slug region. Figure 7.1d shows transitional flow for a liquid flow rate of 0.11 m/s and a gas flow rate of 1.59 m/s. The figure shows a liquid slug that separates two large bubbles. Small bubbles are dispersed in the thick liquid film.

Annular flow occurs when the liquid phase flows at the tube wall and the gas phase flows uninterruptedly at the center of the tube. Figure 7.1e shows the passage of a wave at the center of the image. This flow regime is of special importance as the thermal resistance to heat transfer across the tube wall is minimum under such conditions. It is, therefore, a regime that is usually used by designers to operate at despite the risk of what is known as "dryout" condition where the liquid film is totally wiped out and the transfer of heat is maximized to the point of potential meltdown. We will be addressing this flow regime in some more details in Section 7.10 of this chapter.

7.4 Flow Pattern Transitions

In a two-phase flow system, there are several forces acting on the mixture, each of which has some impact on the overall flow configuration and its characteristics (Figure 7.2). Such forces include those due to inertia, buoyancy, surface tension, and turbulent eddies. The flow pattern is determined by a delicate balance of these forces. The influence of buoyancy force due to gravity can be evaluated using the Froude number:

$$Fr = \frac{V_m^2}{gD} = \frac{\text{inertial force}}{\text{buoyancy force}} \tag{7.1}$$

where

V_m is the sum of the gas and liquid superficial velocities; $V_m = V_{SG} + V_{SL}$

g is the apparent gravity

D is the tube diameter

The influence of surface tension is determined by the Weber number:

$$We = \frac{\rho V^2 D}{\sigma} = \frac{\text{inertial force}}{\text{surface tension}} \tag{7.2}$$

which represents the balance between inertial force and surface tension. This dimensionless group must be an important correlating parameter at microgravity conditions.

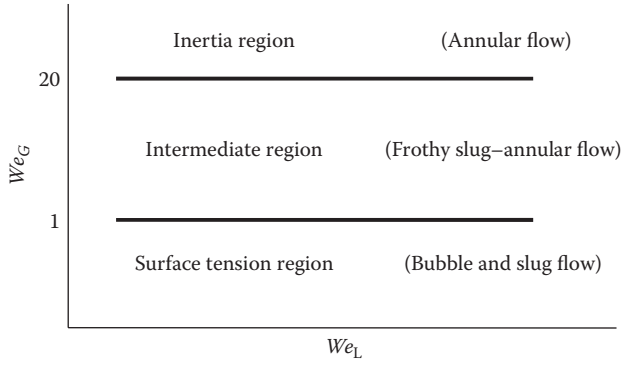


Figure 7.2

Two-phase flow regions at microgravity conditions.

At low gas velocity, and hence for a low We_G, surface tension is dominant. The flow is usually bubbly flow, and the bubble shape is determined by surface tension. Owing to the minimum slip in microgravity bubbly flow, the bubble velocity at microgravity can be reasonably represented by the expression

$$V_G = 1.2\left(V_{SG} + V_{SL}\right) \tag{7.3}$$

When the gas velocity is increased, the inertial force becomes large enough to overcome surface tension. The gas phase breaks through the liquid slug and forms tiny packed gas bubbles. This transition region is called frothy slug–annular due to the continuous appearance of frothy mixtures in the liquid slugs. Based on experimental data, the transition from slug flow to frothy slug–annular flow appears to take place at

$$We_G = \frac{\rho_G V_G^2 D}{\sigma} \approx 1 \tag{7.4}$$

As the gas flow rate further increases, the density of the liquid droplets in the frothy core decreases, and the frothy slugs become thinner until eventually annular flow is reached. In this region, the flow pattern is mainly dominated by forces due to inertia. From the experimental data (Lowe and Rezkallah, 1999), it was found that annular flow occurs at

$$We_G \approx 20 \tag{7.5}$$

7.5 Flow Pattern Map

In general, two-phase gas–liquid flow under microgravity conditions can be divided into three main flow regions.* These are surface tension controlled, intermediate, and inertial force controlled. The first region is where the forces due to surface tension are significantly higher than those due to inertia ($We_G < 1$), which includes bubble and slug flows. The second region is where the two forces are comparable ($1 < We_G < 20$), which is occupied by transitional flows (frothy slug–annular flow). The third region is where the forces due to inertia are dominant ($We_G > 20$). This region is occupied by annular flow. A dimensionless flow pattern map based on these criteria and a very comprehensive dataset was developed (Rite and Rezkallah, 1993) and is shown in Figure 7.3.

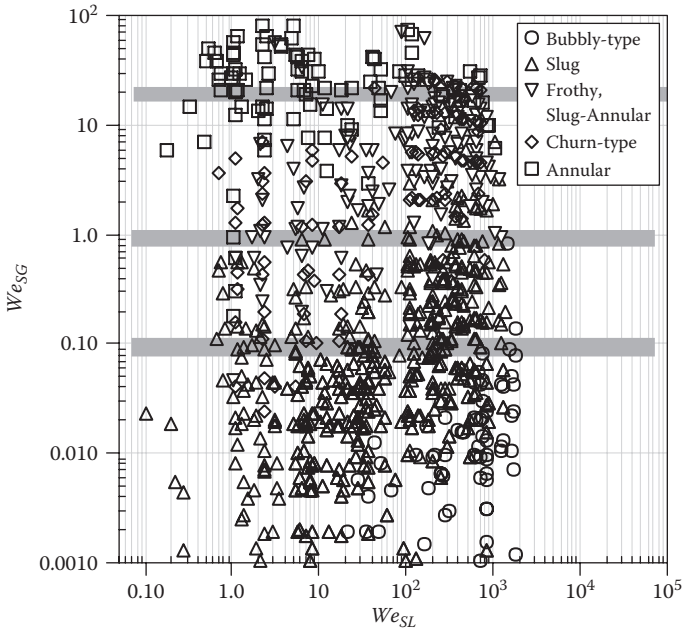


Figure 7.3

Dimensionless flow patterns map and experimental data for microgravity two phase adiabatic flow.

* With kind permission of Springer Science + Business Media.

7.6 Gas–Liquid Pressure Drop

7.6.1 Momentum Equations

The determination of pressure losses in two-phase flow systems is essential to the design of a thermal management system. The pressure loss, dp/dz, in a two-phase flow system includes pressure losses due to friction, f; gravitational force, g; and momentum change, m. The total pressure loss is estimated from

$$\left(\frac{dp}{dz}\right)_{tot} = \left(\frac{dp}{dz}\right)_f + \left(\frac{dp}{dz}\right)_g + \left(\frac{dp}{dz}\right)_m \tag{7.6}$$

The calculations of the last two terms, gravitational and momentum, require the knowledge of the void fraction. The gravitational component can be rewritten as

$$\left(\frac{dp}{dz}\right)_g = \left[\alpha\rho_G + (1-\alpha)\rho_L\right]g \tag{7.7}$$

And for the momentum component, the equation becomes

$$\left(\frac{dp}{dz}\right)_m = G^2\frac{d}{dz}\left[\frac{x^2}{\alpha\rho_G} + \frac{(1-x)^2}{(1-\alpha)\rho_L}\right] \tag{7.8}$$

where G is the total mass flux of both phases. When gravity is changed, the methods to calculate these two terms remain the same, only the numerical value of the void fraction might be different. In this section, only the estimation of the frictional pressure drop component will be discussed in details.

7.6.2 Empirical Methods*

Many empirical or semiempirical correlations are available for the prediction of the frictional pressure drop (e.g., Lockhart and Martinelli, 1949, Dukler et al., 1964a,b, Chisolm, 1967, Friedel, 1979). More details are available in Gabriel (2007). Such correlations were mostly based on experimental data collected at different orientations on ground in different tube diameters and with a wide range of liquid and gas properties. Some of these models are discussed hereafter.

7.6.3 Homogeneous Model

The basic assumption of this model is that the two phases are well mixed and that the velocities of the two phases are equal. These assumptions are closer to what is actually experienced in bubbly and slug flows (short slugs) at microgravity than at 1-g. The mixture density is given in terms of the gas quality, x:

$$\frac{1}{\rho_{mi}} = \frac{x}{\rho_G} + \frac{1-x}{\rho_L} \tag{7.9}$$

The calculation of the mixture viscosity could be done using one of several methods. One of them is to use the liquid viscosity (let $\mu_{mi} = \mu_L$) in the calculation of the Reynolds number. Another is to use a mixture viscosity instead of the liquid viscosity. Several correlations were recommended for μ_{mi}, among which is the correlation suggested by Dukler et al. (1964b):

$$\mu_{mi} = \mu_G\frac{x\rho_{mi}}{\rho_G} + \mu_L\frac{(1-x)\rho_{mi}}{\rho_L} \tag{7.10}$$

The friction factor C_f can be calculated from the *Blasius* equation, in which the Reynolds number is given by

$$\mathrm{Re}_{mi} = \frac{\rho_{mi}V_{mi}D}{\mu_{mi}} \tag{7.11}$$

* With kind permission of Springer Science + Business Media.

The pressure drop can then be obtained from

$$\left(\frac{dp}{dz}\right)_f = \frac{2}{D} C_f \rho_{mi} V_{mi}^2 \tag{7.12}$$

where V_m is the mixture velocity: $V_m = V_{SL} + V_{SG}$.

7.6.4 Lockhart–Martinelli Correlation

Another widely used method for the estimation of two-phase flow pressure drop is the Lockhart–Martinelli correlation. While the original correlation is given in a graphical form (Lockhart and Martinelli, 1949), it could be written using the following expression (Zhao and Rezkallah, 1993a):

$$\left(\frac{dp}{dz}\right)_{TP} = \left(\frac{dp}{dz}\right)_L + C\left(\frac{dp}{dz}\right)_L^{1/2}\left(\frac{dp}{dz}\right)_G^{1/2} + \left(\frac{dp}{dz}\right)_G \tag{7.13}$$

This implies that the two-phase pressure drop equals to the sum of the pressure drop for the liquid phase flowing alone, plus the pressure drop for the gas phase flowing alone, plus a two-phase flow effect. The coefficient "C" represents the importance of the two-phase flow effects. It can be argued that these effects at microgravity conditions are generally high without discriminating between the fluid flow rates. When the velocities of both phases are high, the differences between microgravity and normal gravity conditions are almost negligible. On the other hand, when the flow rates are low, the microgravity pressure drop is higher than that at normal gravity conditions. A constant $C = 20$ fits the experimental data over a wide range of flow rates. In general, the Lockhart–Martinelli correlation underpredicts the pressure drop in microgravity flows.

7.6.5 Dimensional Analysis Model

The μ-g two-phase pressure drop was correlated (deJong and Rezkallah, 2000) in terms of the Euler number. The correlation was based on a dimensional analysis approach and is given by

$$Eu_{SL} = \left[\frac{\left(\partial P/\partial z_f\right)D}{\rho_L V_{SL}^2}\right] = C_L Re_{SL}^{-0.33}\left(\frac{x}{1-x}\right)^{0.80}\left(\frac{\rho_G}{\rho_L}\right)^{0.5}\left(\frac{\mu_G}{\mu_L}\right)^{-0.1} \tag{7.14}$$

The quality ratio term, $(x/1-x)$, has a direct relationship with the superficial liquid Euler number. Modifying Eu_{SL} through dividing it by $(x/1-x)^{0.8}$ enables us to plot the relationship between Eu_{SL} and Re_{SL}; this is shown in Figure 7.4. As Re_{SL} increases, the effect is to reduce the Euler number. The relationship is of a power law type.

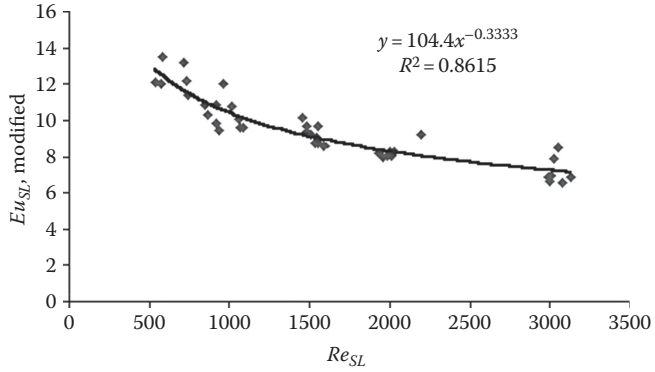


Figure 7.4

Euler number–based correlation. (From deJong, P. and Rezkallah, K.S., A dimensional analysis of microgravity annular flow: Pressure drop and film characteristics, in *Proceedings of Spacebound Conference*, Ottawa, Ontario, Canada, 2000.)

7.7 Void Fraction

Measurement techniques of void fraction in two-phase gas–liquid flow continue to evolve owing to the transient nature of the flow that gives rise to difficulties in relying on traditional instrumentation for accurate measurements. Among the most favorable methods available for measuring void fraction in gas–liquid flow are the nonintrusive techniques. Due to the transient nature of two-phase flows, most analysis techniques involve an ensemble average that is obtained from various data at the same flow conditions or by a time average from a single recording. Some of the common techniques for obtaining void fraction measurements include the following: gamma ray attenuation, conductance probe, quick closing valves, and capacitance methods. The selection of any of these methods depends on its application and whether a volumetric average or a local void fraction measurement is desired.

The volume average void fraction, α, in a two-phase mixture is defined as

$$\alpha = \frac{\text{Volume of gas in mixture}}{\text{Total volume of gas and liquid}} \tag{7.15}$$

In addition to obtaining a void fraction measurement, the statistical analysis of the signal can also be used to determine the flow regimes associated with the flow and their transitions.

Since two-phase flow measurements are strongly flow regime dependent, comparisons between 1-g data and μ-g data were made for each flow regime individually. The main findings from those comparisons are summarized later. For more comprehensive coverage of this topic and actual flow regime photos, see Gabriel (2007)

For a pseudo-void fraction approximately below 0.1, the results in the bubbly flow regime showed a tendency for the μ-g data to be approximately 8%–25% higher than those taken at 1-g. Above $V_{sg}/V_{sl} = 0.1$, the difference is reduced until the trend is reversed with the 1-g data slightly higher than the μ-g counterpart (approximately 7%–16% higher). The higher void fraction at μ-g for $\alpha < 0.2$ can be attributed to the significant reduction in slip between the phases, combined with an increased influence of surface tension under reduced gravity. These changes lead to the bubbles being able to sustain their shape even at high gas content, while the rate of collision and coalescence of the bubbles is significantly reduced.

The slug flow results showed that the void fraction was consistently higher for the μ-g data, with a difference that ranges from 3% to 35%, with an overall average of approximately 10%. This trend seems to be consistent up to a void fraction of approximately 0.70 beyond which the percentage difference in void fraction decreases. This occurs near the transition to slug–annular flow at μ-g and churn flow at 1-g. In the latter, flow reversal due to the pull of gravity is observed and could greatly skew the void fraction readings in that region.

The results for transitional flows (slug–annular flow at μ-g and churn flow at 1-g) showed that the void fractions are comparable in this highly transitional region for both the μ-g and 1-g cases. As mentioned earlier, the slug–annular flow is in a transition where inertia forces become more dominant when compared to surface tension forces. The liquid slug at these conditions contains a highly aerated frothy mixture, which could cause large fluctuations in the void fraction measurements.

Finally, the results for annular flow showed that the μ-g and 1-g data are very similar. This is expected since, under both 1-g and μ-g conditions, the flow is highly turbulent and inertia forces are dominant in both cases. The difference between the 1-g and μ-g void fraction values is within 5% and could be assumed insignificant.

7.8 Heat Transfer in Microgravity

Heat transfer measurements were made during a series of parabolic flights on board NASA's KC-135 zero-gravity aircraft spanning over a number of years and totalling approximately 40 hours. A flight typically consisted of four sets of 10 parabolic maneuvers during which equipment and personnel inside the aircraft experience 20–22 s of near weightlessness followed by a short period of 1.8-g pull-up maneuver. The short duration of the microgravity period during each maneuver gives rise to the question whether the time response of the heated test section and the flow is such that steady-state thermal conditions could have been possibly achieved.

It was determined from extensive analysis (Gabriel, 2007) that *quasi-steady* heat transfer condition existed and that the measured coefficients for two-phase convective flow accurately represented the local heat transfer rates during such periods.

There are two sources of transients during any flight test: one is due to the variation of the gravity field and the other is due to the changing gas and liquid flow rates and the heater power. Changes in these parameters will affect the five basic measured quantities that are of interest in such study: the flow rates of the liquid and gas phases, the heat flux at the surface of the heated test section, the temperatures along the surface, and the bulk fluid temperature.

Since the heat transfer coefficient is based on the difference between the surface temperature and the fluid temperature, the *quasi-steady-state* condition will be determined based on the time when this difference approaches a constant value. Although the absolute values of both of these quantities tended to slowly increase throughout the duration of tests, it was found that the difference between them did in fact reach an approximately constant value. Hence, this difference will be used to define *quasi-steady-state* condition in thermal terms.

To minimize the impact of the set point transient, changes to the set points were always made at the completion of a flight parabola. This allowed a settling time of approximately 60 s before the next data collection window was opened. Therefore, the time constant that the test section must have in order to reach *quasi-steady-state* conditions after a change in set point is on the order of a minute. The transient response of the heated test section to changes in the set point was determined in the laboratory to see if this was indeed feasible. It was found that after 10 s, the difference between the surface and fluid temperatures was within approximately 90% of its *quasi-steady-state* value.

7.8.1 Influence of Flow Patterns

The influence of flow patterns and their transitions on the heat transfer rates in two-phase flows has been recognized for many years. Shortly after the behavior of two-phase flows was first explored in depth for terrestrial applications (such as in the nuclear, petroleum, and process industries), it was discovered that the geometry of the flow was important in determining the local heat transfer values and trends.

Likewise, for microgravity research, the need to account for the influence of the gravitational level as well as the flow regime on the two-phase heat transfer has been well established from early work during the Space lab era in the 1970s. From the results of Rite and Rezkallah (1993), it was shown that, at low liquid velocities and void fractions, 1-g heat transfer data were greater than μ-g data. As the liquid velocity increased, similar trends were observed, but only at very low void fractions in the bubble flow regime. As the void fraction increased, the 1-g and μ-g data points approached one another until the two sets were nearly identical (μ-g was marginally greater than 1-g by 10%–15%). This confirmed that the difference between 1-g and μ-g behavior is flow regime dependent.

It is important to note that the trends in 1-g versus μ-g heat transfer rates that were observed during flights could not be simply correlated with the traditional two-phase heat transfer dimensionless groups of Reynolds number, Prandtl number, and superficial velocity ratio. Other effects due to gravity and surface tension must be included in the analysis, although in some cases their effects may be of secondary importance. The question that needs to be addressed is: What is the mechanism responsible for this effect?

It appears that under 1-g conditions the gas is influencing the local heat transfer by disturbing the liquid flow at the wall of the tube. This agrees with the findings of Vijay et al. (1971), who hypothesized that the effect of buoyancy forces on the gas bubbles caused the gas to have a greater velocity than the surrounding liquid. This *slip* between the phases led to a breakdown in the laminar sublayer near the tube wall, thus leading to a movement away from laminar flow–type behavior. However, under μ-g conditions this would not happen. The reduction of gravity greatly lessens the buoyancy forces and therefore the turbulence-generating ability of the gas bubbles. The bubble dynamics at μ-g do not seem to interfere with the maintenance of the laminar sublayer.

7.8.2 Empirical Correlations*

In order to develop useful empirical correlations to model observed phenomena, the identification of dimensionless groups that describe the phenomena is required. For low-gravity two-phase flow heat transfer, in addition to the most commonly used groups (e.g., Reynolds and Prandtl numbers), the effect of gravitational and surface tension forces on the arrangement of the gas and liquid phases must also be considered in the dimensional analysis.

The flow regime transitions proposed by Zhao and Rezkallah (1993b) were incorporated into the analysis in order to account for the influence of the change in the flow regime due to reduced gravity on the two-phase heat transfer. In their analysis, it was reported that the flow regime transitions were very much dependent on the force balance between inertia forces and surface tension forces. This balance was well

* With kind permission of Springer Science + Business Media.

represented as a function of the gas Weber number such that the annular flow was shown to be present for $We_{SG} > 20$ (inertia-dominated region), slug–annular flow for $1 < We_{SG} < 20$, and slug and bubbly flows for $We_{SG} < 1$ (surface tension–dominated region). In this last range of Weber numbers, another transition has been added at $We_{SG} = 0.1$ to identify the region where true bubbly flow can only exist. The associated heat transfer coefficients for such homogeneously dispersed flows would be different from that of typical Taylor-type slug flows.

From a dimensional analysis, it was determined that for $Re_{SL} < 2300$, the following dimensionless groups are pertinent: Graetz number (Gz_{SL}) based on the liquid superficial velocity and properties, the ratio of the superficial velocities or the pseudo-void fraction α', and a property group known as the liquid Morton number (Mo_L). The Graetz number is defined as

$$Gz_{SL} = Re_{SL} \times Pr_L \times \frac{D}{L} \tag{7.16}$$

where

Pr_L is the Prandtl number of the liquid phase

L is the length of the heated test section

The Morton number is defined by

$$Mo_L = \rho_L \times \frac{\sigma^3}{g} \times \mu L^4 \tag{7.17}$$

where

g is the gravitational acceleration

μ_L is the liquid dynamic viscosity

As seen in the aforementioned equation, Morton number is strictly dependent on fluid properties and gravity. This incorporates the effect of gravitational forces and surface tension forces in the analysis of the heat transfer data.

With liquid superficial Reynolds numbers above 2300, the nondimensional numbers that are important include Re_{SL}, α', the liquid Froude number (Fr_{SL}), and the Morton number (Mo_L).

Froude number, based on the liquid superficial velocity, is defined as

$$Fr_{SL} = \frac{V_{SL}}{\sqrt{gD}} \tag{7.18}$$

For $We_{SG} < 0.1$, the correlation developed for this case is given as

$$\psi^2 = 1 + 0.8 Gz_{SL}^{-0.114} \times \alpha'^{-0.084} \times Mo_L^{0.058} \tag{7.19}$$

where ψ^2 is the normalized two-phase flow heat transfer coefficient with respect to the single-phase liquid heat transfer coefficient; ($\psi = h_{TP}/h_L$).

For the next range of gas Weber numbers, $0.1 < We_{SG} < 1$, the empirical correlation has the following form:

$$\psi^2 = 1 + 2.1 Gz_{SL}^{-0.074} \times \alpha'^{-0.023} \times Mo_L^{0.010} \tag{7.20}$$

For the next range of data, $1 < We_{SG} < 20$, for which the flow regime is predominantly slug, the recommended correlation is given as

$$\psi^2 = 1 + 0.7 Gz_{SL}^{0.106} \times \alpha'^{0.251} \times Mo_L^{-0.010} \tag{7.21}$$

Finally, for $We_{SG} > 20$ (annular flow regime), the correlation is given by

$$\psi^2 = 1 + 37.2 Gz_{SL}^{-0.291} \times \alpha'^{0.194} \times Mo_L^{-0.059} \tag{7.22}$$

Extensive analysis and comparisons with other correlations and actual measured heat transfer data can be found in Gabriel (2007).

7.9 Interfacial Waves in Microgravity Annular Two-Phase Flows

The hydrodynamic and heat transport characteristics of annular two-phase flows are closely connected to the existence of interfacial waves at the gas–liquid interface. Annular flow is of particular interest because of its frequent occurrence in heat transfer systems. Usually, part of the liquid phase flows as droplets entrained in the gas core. In a normal gravity environment, two-phase flow is common in nuclear reactor, power plants, transport of cryogenics, and many petrochemical processing plants. The annular flow is usually the preferred regime of operation for most heat transfer devices due to the high heat transfer rates.

However, if the surface temperature or heat flux is large enough, the film thickness of liquid phase will become thinner and eventually disappear followed by serious deterioration of the heat transfer process. This phenomenon is known as "dryout" in the nuclear industry and could cause catastrophic accidents. Therefore, knowledge of the film thickness characteristic in annular flow is of considerable importance in advancing safety control measures in nuclear industry.

It could be argued that the study on the wave structure is the foundation for further investigations of annular two-phase flows. Most investigators readily admit that the existence of such waves complicates the measurements due to the interfacial shear stress that in turn influences the pressure drop and the liquid film. There are at least two reasons to account for why the interface structure can influence the pressure drop:

1. The existence of the surface waves contributes to increased *surface roughness* at the interface which in turn increases the pressure drop. In fact, not only the increased wave amplitude influences the pressure drop, but also the wave separation affects it. If the waves space sparsely, they should exert different influences compared to when they are densely spaced.
2. The presence of waves enhances the liquid atomization into the gas core and directly changes the mass and momentum transfer between the gas stream and the liquid film. Consequently, the pressure drop is influenced as well.

Microgravity provides an ideal environment to study interfacial waves (small-scale phenomena) without the dominating effects of gravity.

7.10 Definition of Wave Shape and Wave Characteristic

As shown in Figure 7.5, wave spacing equals to the total length of the film thickness time trace divided by the number of peaks that appear in the entire time trace. Starting with as many identified local wave peaks, the local wave shapes were found by extending forward and backward for the length of half-wave spacing. Then a wave band was determined by locating all of the local wave shapes in the film thickness time trace and superimposing them onto one another. The line of average value in the wave band, called the "central trend line", represents the entire local waves in the 4-s window of film thickness time trace.

Referring again to Figure 7.5, the following terms are of significance in terms of the classification and description of the interfacial wave phenomena. The *wave peak height*, H, is defined as the average of observed peaks in the film thickness time trace. The *wave base height*, h, is defined as the average value of the film thickness between the starting and ending points of adjacent waves. The *starting point*, A, in Figure 7.5 represents the first value of the film thickness time trace that exceeded the average film thickness between the starting and ending points by 5% or more. Conversely, the *ending point*, C, is the first value in the film thickness time trace that is 5% greater than the following wave base height.

Generally, the average film thickness between the starting and ending points of the adjacent waves is defined as the wave base height. The ending point also represents the last point in the time trace that is above the wave base height. The *wave roughness height*, (*H-h*), is defined as the difference between the wave

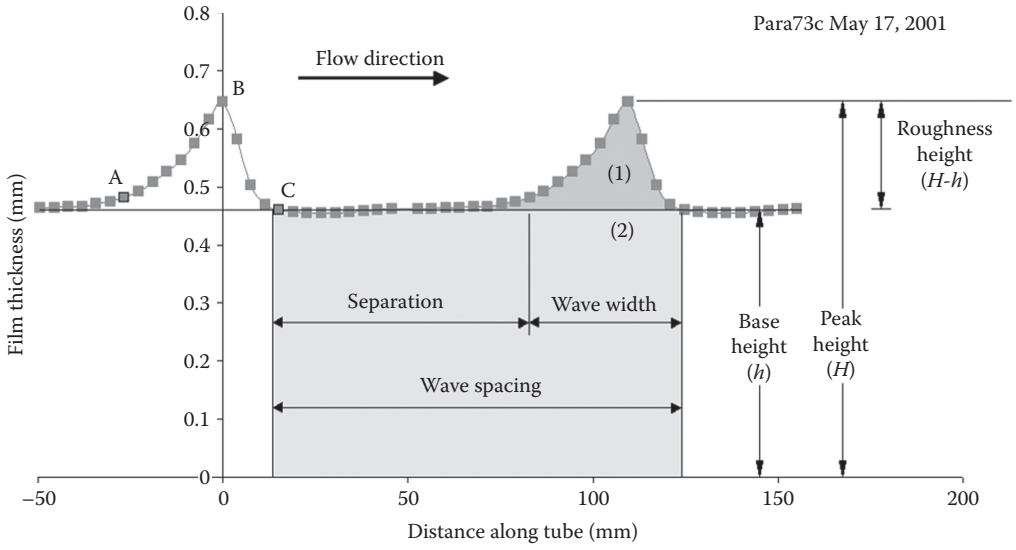


Figure 7.5

A sample wave shape: (1) wavy area and (2) base area.

peak height and the wave base height. The wave structure is separated into two areas, as shown in Figure 7.5. The area below the wave base height is called the "base area," while the region above the wave base height is known as the "wavy area."

The *wave separation* is defined as the distance between the starting point of one wave and the ending point of the previous one. The *wave width* is the distance between the starting point and the ending point of a single wave. It is important to remember that these properties have been determined for a single wave and represent all of the waves in the 4 s window of data acquisition.

In general, an increase in the gas mass flux results in an increase in the interfacial velocity at the liquid–gas interface. More momentum is transferred from the highly energetic gas core to the liquid film, resulting in an increase in the film velocity in the base area. The increase in the interfacial velocity results in an increase in the interfacial shear stress and a subsequent increase in the friction factor; hence, it causes an increase in the pressure drop. The use of an interfacial friction factor to predict the frictional pressure drop has been studied and results could be found in deJong and Rezkallah (2000).

An investigation into the effects of increasing the gas mass flux on the wave characteristics in annular, liquid–gas flows was also carried at 1-g (Wang et al., 2005). A wave shape was obtained for each set point using the recorded film thickness time traces. Two film thickness probes were used in conjunction with the cross-correlation technique to obtain the velocity of the wavy area and the base area. The results from that study can be summarized as follows:

1. At a constant liquid mass flux, the wave spacing increases with decreasing the gas mass flux indicating that the frequency of the disturbance waves in a film thickness decreases. The frequency of the disturbance waves has a direct relationship with the gas mass flux.
2. The wave base height and the average film thickness slightly decrease with an increase in the gas mass flux at a constant liquid mass flux.
3. At a constant liquid mass flux, the wave peak height decreases as the gas mass flux increases.
4. The wave roughness height decreases, and the wave frequency increases with increasing the gas mass flux at a constant liquid mass flux.
5. The wavy area occupies less than 15% of the total liquid volume at a liquid mass flux of 110 kg/m^2 s. The ratio decreases with an increase in the gas mass flux.
6. The liquid velocity in the base area is much less than that in the wavy area (at constant gas and liquid mass fluxes). The ratio is approximately 1:14.
7. The wavy region of the unit wave transports the majority of the liquid mass assuming the wavy region travels at a velocity equal to the velocity of the wave above the base and that the droplet entrainment fraction is so small and could be neglected.

Nomenclature

C_f	friction coefficient
C_L	constant in equation (7.14); $C_L = 1982$
D	tube diameter, m
dp/dz	pressure gradient, Pa/m
Eu	Euler number
Fr	Froude number, $V/(gD)^{1/2}$
G	total mass flux, kg/m^2 s
g	gravitational acceleration, m/s^2
P	pressure, Pa
R	radius, m
Re	Reynolds number, $\rho VD/\mu$
V	velocity, m/s
V_m	sum of gas and liquid superficial velocities, m/s
We	Weber number, $\rho V^2 D/\sigma$
x	gas mass quality

Greek Symbols

α	void fraction
μ	dynamic viscosity, Ns/m^2
ρ	density, kg/m^3
σ	surface tension, N/m

Subscripts

f	friction
G	single-phase gas
L	single-phase liquid
m	momentum change
mi	mixture
SG	superficial gas
SL	superficial liquid
tot	total
TP	two-phase

References

Chisholm, D., A theoretical basis for the Lockhart-Martinelli correlation for two-phase flow, *Int. J. Heat Mass Transfer*, 10, 1767–1778, 1967.

deJong, P. and Rezkallah, K.S., A dimensional analysis of microgravity annular flow: Pressure drop and film characteristics, in *Proceedings of Spacebound Conference*, Ottawa, Ontario, Canada, 2000.

Dukler, A.E., Wicks, M., and Cleveland, R.D., Frictional pressure drops in two-phase flow: A. a comparison of existing correlations for pressure loss and holdup, *AIChE J.*, 10, 38–43, 1964a.

Dukler, A.E., Wicks, M., and Cleveland, R.D., Frictional pressure drops in two-phase flow: B. an approach through similarity analysis, *AIChE J.*, 10, 44–51, 1964b.

Friedel, L., Improved friction pressure drop correlations for horizontal and vertical two-phase pipe flow, in *European Two-Phase Flow Group Meeting*, Ispra, Italy, 1979.

Gabriel, K.S., *Microgravity Two-Phase Flow and Heat Transfer*, Spring-Verlag, Heidelberg, Germany, 2007.

Huckerby, C.S. and Rezkallah, K.S., Flow pattern observations in two phase gas-liquid flow in a straight tube under normal and microgravity conditions, *AIChE Proc.*, 88, 139–147, 1992.

Lockhart, R.W. and Martinelli, R.C., Proposed correlations of data for isothermal two-phase two-component flow in pipes, *Chem. Eng. Prog.*, 45, 39–48, 1949.

Lowe, D.C. and Rezkallah, K.S., Flow regime identification in microgravity two-phase flows using void fraction signals, *Int. J. Multiphase Flow*, 25, 433–457, 1999.

Rite, R.W. and Rezkallah, K.S., An investigation of transient effects on heat transfer measurements in two-phase gas-liquid flows under microgravity conditions, in *ASME Heat Transfer in Microgravity System*, 1993, pp. 49–57.

Vijay, M.M., Savic, P., and Sims, G.E., The Graetz problem for two-phase two-component gas-liquid flow in vertical tubes, in *Proceedings of the Sixth International Heat Transfer Conference*, 1971, pp. 493–497.

Wang, Z., Gabriel, K.S., and Zhu, Z., A study on the effect of gas-liquid flow rate on the wave characteristics in two-phase gas-liquid annular flow, *Microgravity Sci. Technol.*, XVI-1, 259–263, 2005.

Zhao, L. and Rezkallah, K.S., Pressure drop in two-phase annular flow at microgravity conditions, in *31st Aerospace Sciences Meeting & Exhibit*, AIAA-93-0576, 1993a.

Zhao, L. and Rezkallah, K.S., Gas-liquid flow patterns at microgravity conditions, *Int. J. Multiphase Flow*, 19, 751–763, 1993b.


Taylor & Francis
Taylor & Francis Group
http://taylorandfrancis.com

8

Boiling

Satish G. Kandlikar

8.1 Pool Boiling
8.2 Flow Boiling

8.1 Pool Boiling

The change of phase from liquid to vapor across a liquid–vapor interface is called evaporation. Boiling refers to the heat transfer–induced evaporation associated with vapor bubbles nucleating over a heat transfer surface. The nature of the specific liquid–vapor system gives rise to two types of boiling:

1. "Pool boiling" refers to the boiling process in which the liquid is essentially quiescent and vapor bubbles rise as a result of buoyancy forces induced by gravity or other body forces.
2. "Flow boiling" refers to the boiling process in which the liquid and the resulting vapor phase are subjected to a flow field.

In the literature, additional terminology is employed to identify specific configurations; *thin-film evaporation* or *falling-film evaporation* refers to evaporation across the liquid–vapor interface of a thin liquid film that is formed on a heater surface. The term *convective flow boiling* refers to the change of phase from liquid to vapor during internal flow, while *external flow boiling* refers to the change of phase from liquid to vapor during external flow such as flow over tube banks.

Pool boiling is also of interest from the perspective of understanding the boiling phenomenon. Some of its applications include kettle reboilers, batch-type vaporizers, liquid immersed electronic component cooling, and quenching of metals in metallurgical processes. Flow boiling is employed in many applications, such as steam generators and refrigeration evaporators, and is being considered for high-flux cooling of electronic components.

8.1.1 Introduction to Pool Boiling

Although a number of investigators have observed different regions of pool boiling heat transfer, Nukiyama (1934) conducted a systematic study on pool boiling over electrically heated nichrome and platinum wires and presented a boiling curve. Figure 8.1 shows a boiling curve for water at atmospheric pressure. It incorporates a number of additional features that have been identified by later investigators. The heat flux q'' at the heater surface is plotted against the wall superheat ($\Delta T_{Sat} = T_{Heater} - T_{Sat}$). The nature

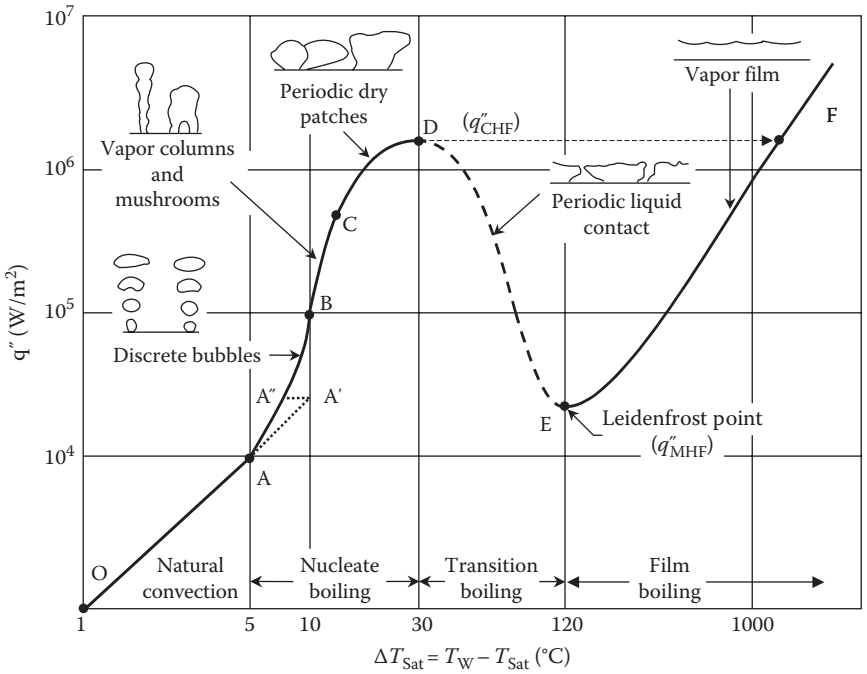


Figure 8.1

Boiling curve showing different regions in pool boiling.

of bubbles or a vapor film surrounding the heater in different regions is also depicted in Figure 8.1. The pool of water is held at its saturation temperature of T_{Sat} corresponding to the system pressure (hence the term *saturated pool boiling*).

In the region O–A in Figure 8.1 with a small ΔT_{Sat}, heat is transferred by *natural convection*. At location A′ corresponding to a certain value of $\Delta T_{Sat} = \Delta T_{Sat,ONB}$, bubble nucleation is initiated on the cavities present on the heater surface. This condition is called *onset of nucleate boiling* (ONB). With the inception of nucleation, the heater surface temperature drops to A″ for a given imposed heat flux. This hysteresis effect shown by the dotted lines AA′A″ disappears during repeated boiling cycles with increasing and decreasing values of heat flux. The slope of the curve beyond the ONB point increases at higher ΔT_{Sat} values as the bubbles grow and depart more rapidly in the partial nucleate boiling region (region A″–B). As heat flux is increased, more nucleation sites become active and *fully developed nucleate boiling* ensues (regions B–C). At higher heat fluxes, the heater surface becomes overcrowded with bubbles at various stages of growth. In addition, the intense evaporation under the bubble leads to periodic dry patches on the heater surface that are rewetted by the surrounding liquid, resulting in a reduction in the slope of the boiling curve (the heat transfer coefficient begins to decrease). As the wall superheat increases further, liquid is unable to rewet the heater surface, causing a sudden formation of a dry patch that eventually covers a large region of the heater surface. A thin film of vapor eventually separates the liquid from the heater surface and leads to a large temperature excursion of the heater surface (drastic reduction in the heat transfer coefficient). The heat flux corresponding to this condition at location D, q''_{CHF}, which represents the maximum heat flux sustained under the nucleate boiling condition, is called the *critical heat flux* (CHF). This is an unstable condition and the heater temperature jumps to point F. The ensuing mode of heat transfer in which the heater is blanketed with a thin vapor film is called film boiling. Through experimental investigation, Nukiyama (1934) observed that the high temperature following the CHF point leads to physical burnout of the nichrome wires, while platinum wires were able to withstand the higher temperatures.

The dotted region D–E in Figure 8.1 following the CHF represents the *transition boiling* region. This region is not accessible with an electrical heater that imposes a constant heat flux boundary condition. It can only be traced under stable conditions by employing a constant temperature boundary condition on the heated wall. In the transition region, the heat transfer is associated with formation followed by rewetting of the dry patches in rapid successions. As the heater surface temperature is increased, eventually the rewetting cannot be sustained at the Leidenfrost condition represented by E, and the heater is surrounded by

a stable vapor film. The heat flux at E is called the *minimum heat flux* (MHF), q''_{MHF}. The region E–F is the film boiling region in which heat is transferred by combined radiative and convective modes across the thin vapor film.

In studying boiling phenomena, the nucleation characteristics and bubble behavior are of great importance as they directly affect the heat transfer. Some of the early investigators, including Moissis and Berenson (1963), Gaertner (1965), and Johnston et al. (1966), employed high-speed photography to reveal the bubble behavior. Gaertner obtained still and video images at 3000 frames/s identifying various boiling regions, such as the discrete bubble region, first transition region (vapor columns are observed), and second transition region (stems of the vapor column become unstable with the formation of local dry patches). Cole (1960) obtained high-speed images and measured bubble frequency, bubble diameter, and contact angles close to CHF condition. The actual CHF mechanism is still a subject of active research, as the Helmholtz instability in the second transition region is used as the basis of some of the CHF models (Zuber, 1959, Haramura and Katto, 1983), while the role of evaporation momentum force and capillary flows is being considered in the recent models (Kandlikar, 2001a, Chu et al., 2013).

8.1.2 Onset of Nucleate Boiling

Bankoff (1958) showed that the presence of nucleating cavities on a heater surface leads to nucleation at lower superheats (heterogeneous nucleation) compared to the homogeneous nucleation in which vapor embryos are formed in a highly superheated liquid. Cavities trap vapor and gases and act as nucleation sites for bubbles on a heater surface. A certain amount of wall superheat is needed to activate the cavities depending on various factors: (1) cavity size and shape; (2) fluid properties, including surface tension and contact angles; and (3) temperature profile in the liquid immediately surrounding the heater surface.

Consider a vapor bubble of radius R_b in a pool of liquid at a temperature T and pressure p_L as shown in Figure 8.2. The pressure inside the bubble is p_G. Taking a diametric section reveals the forces due to pressure difference and surface tension along the circumference. At equilibrium, equating these two forces yields

$$p_G - p_L = \frac{2\sigma}{R_b} \tag{8.1}$$

The liquid and vapor states corresponding to the condition given earlier are shown as L and G, respectively, in Figure 8.2. The liquid state L lies in a metastable condition corresponding to p_L and T. The metastable equilibrium liquid line in the saturation dome represents the equilibrium over a curved interface. The lowest pressure point on this curve corresponds to the homogeneous nucleation condition.

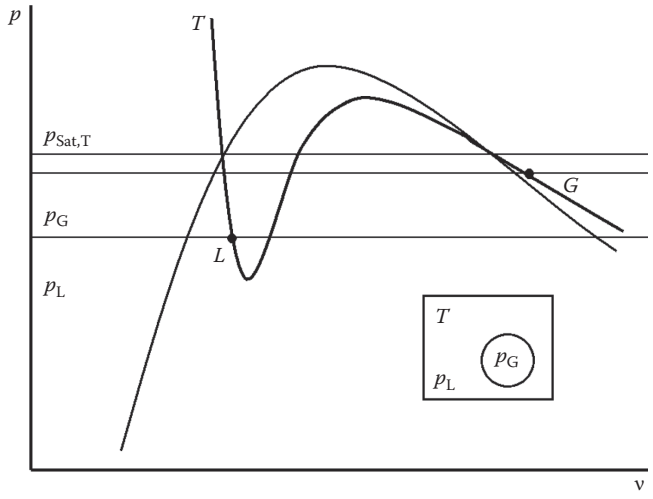


Figure 8.2

Metastable liquid and vapor conditions for a bubble growing in a pool of liquid.

The vapor state G is in the superheated region corresponding to p_G and T. The saturation pressure $p_{Sat,T}$ over a planar interface corresponding to T can be expressed in terms of pressures p_L and p_G by equating the molar Gibbs free energies for the two phases (Fujita, 1999):

$$p_{Sat,T} - p_G = \left(\frac{v_L}{v_{G,Sat,T} - v_L} \right) \frac{2\sigma}{R_b} \tag{8.2}$$

$$p_{Sat,T} - p_L = \left(\frac{v_{G,Sat}}{v_{G,Sat,T} - v_L} \right) \frac{2\sigma}{R_b} \tag{8.3}$$

For low reduced pressures, ($P_r \ll 1$), v_L, $v_{G,Sat}$, and Equations 8.2 and 8.3 are simplified as follows:

$$p_G = p_{Sat,T} \tag{8.4}$$

$$p_L = p_{Sat,T} - \frac{2\sigma}{R_b} \tag{8.5}$$

Figure 8.3 shows the growth of a bubble inside and over a cavity. The residual vapor or gas in the cavity activates the cavity. As the wall temperature rises, the liquid–vapor interface moves out toward the mouth of the cavity, assumed to be circular for the purpose of this analysis. Eventually, the bubble becomes anchored on the cavity's mouth as the contact angle adjusts from the inner cavity surface to the heater surface. The minimum radius of the bubble occurs when the bubble assumes a hemispherical shape with a radius R_b equal to the cavity's mouth radius R_C.

Hsu and Graham (1961) and Hsu (1962) postulated that a vapor bubble will grow, thus initiating nucleate boiling, if the temperature in the liquid at the top of the hemispherical bubble cap exceeds the saturation temperature corresponding to the pressure p_G inside the bubble. Under this condition, Equation 8.1 becomes

$$p_G - p_L = \frac{2\sigma}{R_C} \tag{8.6}$$

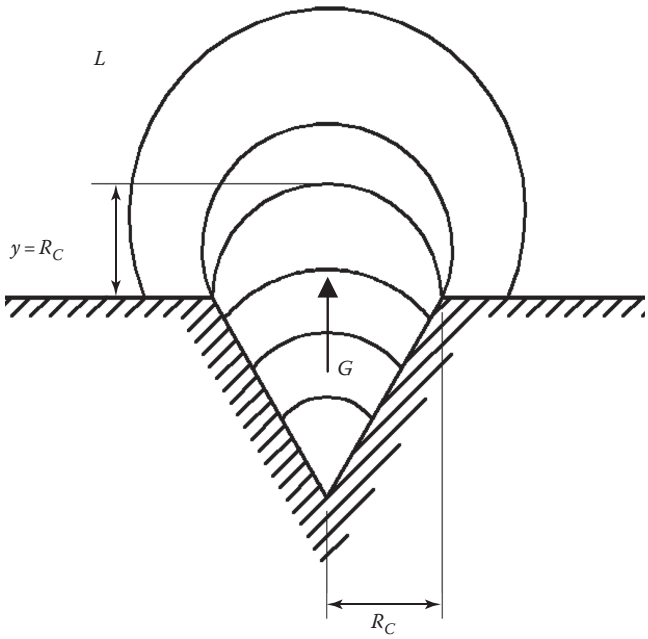


Figure 8.3

Growth of a vapor bubble nucleating from a cavity.

Applying the Clausius–Clapeyron equation, $dp/dT = h_{fg}/(v_{fg}T_{Sat})$, and assuming $v_{fg} \approx v_G$, Equation 8.6 becomes

$$T - T_{L,Sat} = \frac{2\sigma T_{Sat} v_G}{h_{fg} R_C} \tag{8.7}$$

where

T is the temperature of the liquid surrounding the bubble

$T_{L,Sat}$ (=T_{Sat}) is the saturation temperature (in K) corresponding to the liquid pressure p_L

Since there is a temperature gradient in the liquid normal to the heated wall, the minimum liquid temperature adjacent to the bubble interface occurs at $y = R_C$, where y is the distance normal to the heater surface. Using this temperature T in Equation 8.7 as T_G, the equilibrium temperature of the vapor in the hemispherical bubble on the bubble mouth, Equation 8.7, becomes

$$T_G - T_{L,Sat} = \frac{2\sigma T_{Sat} v_G}{h_{fg} R_C} \tag{8.8}$$

The liquid temperature profile in the vicinity of the heater surface can be approximated by applying the heat conduction equation in the liquid:

$$\frac{dT}{dy} = \frac{T_w - T_L}{y} = \frac{q''}{k_L} \tag{8.9}$$

The liquid temperature T_L at $y = R_C$ can be found from Equation 8.9.

Graphically, Figure 8.4 shows the plots of Equations 8.8 and 8.9. The intersection points of these two plots yield the range of the cavity radii, R_{min} and R_{max}, for which $T_L > T_G$ at $y = R_C$. Introducing $\Delta T_{Sat} = T_w - T_{Sat}$ at system pressure p_L, the following range is obtained by solving Equations 8.8 and 8.9:

$$R_{C,\max}, R_{C,\max} = \frac{1}{2}\left\{\frac{\Delta T_{Sat}}{q''} \pm \sqrt{\left(\frac{\Delta T_{Sat}}{q''}\right)^2 - \frac{8\sigma T_{Sat} v_G k_L}{h_{fg} q''}}\right\} \tag{8.10}$$

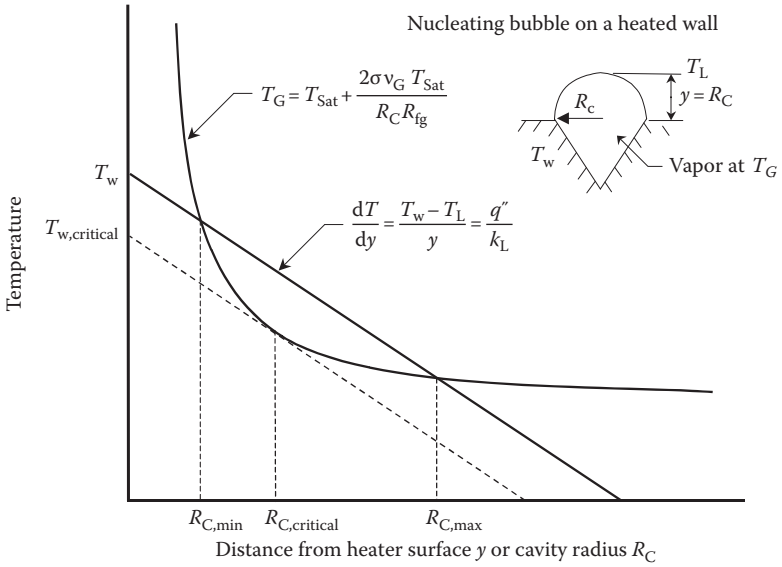


Figure 8.4

Nucleation criterion for the activation of a cavity in pool boiling.

Bubble nucleation further depends on the availability of cavities in the range between $R_{C,min}$ and $R_{C,max}$ over the heater surface. On the other hand, if cavities of all sizes are present, the minimum required heat flux to initiate nucleation and the critical cavity radius, defined as the radius of the first cavity to nucleate under a given heat flux q'', are obtained by drawing a line with a slope given by Equation 8.9 that is tangent to the curve for T_G, resulting in $T_w = T_{w,crit}$ as shown in Figure 8.4. Equating the slope dT_G/dR to the slope given by Equation 8.9, the critical radius R_{crit} at ONB is obtained. Alternatively, the term under the radical can be set to zero to obtain the critical radius:

$$R_{C,crit} = \frac{1}{2}\frac{\Delta T_{Sat}}{q''} \tag{8.11}$$

The wall superheat at the ONB is then obtained by setting the term under the radical in Equation 8.10 to zero:

$$\Delta T_{Sat,crit} = \left[\frac{8\sigma T_{Sat} v_G q''}{h_{fg} k_L}\right]^{1/2} \tag{8.12}$$

The nucleation criterion has been further investigated by researchers to include (1) the effect of cavity shape (Lorentz et al., 1974); (2) the effect of contact angle, resulting in bubbles that are of different shapes when compared with the hemispherical shape at the critical condition (Hsu and Graham, 1961); (3) subcooling; and (4) transient conduction effects due to liquid renewal (Marcus and Dropkin, 1965) and effect of dissolved gases (Murphy and Bergles, 1972). Equations 8.10 through 8.12 provide reasonable estimates of ONB conditions and are used extensively in practical applications.

Cavitation is similar to nucleation in boiling, except that the bubbles are generated as a result of lowering the pressure rather than increasing the temperature. The presence of dissolved gases leads to early nucleation before the local saturation conditions corresponding to a pure liquid are reached. As the liquid temperature increases, the solubility of dissolved gases generally decreases and they begin to come out of the liquid at the nucleation sites on the heater surface. Murphy and Bergles (1972) used the partial pressure of vapor in a gas–vapor mixture inside a vapor bubble for developing the nucleation criterion under these conditions.

8.1.3 Bubble Dynamics in Nucleate Pool Boiling

A bubble on a heater surface goes through an ebullition cycle consisting of the following four stages during nucleate boiling: (1) Bubble nucleation—when the temperatures of the wall and liquid in the vicinity of a cavity reach conditions conducive to nucleation, a bubble forms on the cavity mouth. (2) Growth period—relaxation of liquid superheat around the liquid–vapor interface due to evaporation causes the bubble to grow. (3) Bubble departure—as the bubble grows, eventually the forces tending to push the bubble away from the heater surface become greater than the retaining forces, and the bubble leaves the heater surface. (4) Waiting period—as the cooler liquid from the bulk rushes to take the place of the departed bubble, the temperature of the wall and the liquid adjacent to the cavity begin to rise until the nucleation criterion is met. A bubble is formed again, and the ebullition cycle continues.

8.1.3.1 Bubble Nucleation

Bubble nucleation is closely related to the size and shape of the cavity holding gases or vapors. For a given wall superheat, a range of nucleation cavities are activated. As the wall superheat increases, the active cavity size range increases as the liquid temperature distribution line moves higher in Figure 8.2. The presence of a vapor embryo in the cavity is essential for the activation of a cavity. Reentrant cavities are able to trap the gases or vapor left behind from a previously departed bubble that act as embryos. Bubble nucleation also depends on the availability of cavities, their shape and size ranges, local temperature profile in the liquid near the wall (dependent on the wall superheat and liquid subcooling), presence of dissolved gases, hysteresis effects, liquid properties, and contact angle.

8.1.3.2 Growth Period

The bubble continues to grow due to evaporation occurring at expanding the liquid–vapor interface on the bubble and also from the thin film left behind on the heater surface. The growth period is divided into

inertia-controlled and thermally controlled regions. Inertia-controlled growth occurs in the early stages of bubble growth. Rayleigh (1917) analyzed the growth process and derived the following equation for the bubble growth rate:

$$R(t)=\left\{\frac{2}{3}\left[\frac{T_L-T_{Sat}(P_L)}{T_{Sat}(p_L)}\right]\frac{h_{fg}\rho_g}{\rho_L}\right\}^{1/2} t \tag{8.13}$$

The growth rate is linear in the early stages as seen from Equation 8.13. Superheated liquid provides the thermal energy for rapid evaporation at the interface in this region, but the bubble growth is limited by the inertia of the surrounding liquid.

Subsequent to the initial rapid growth, evaporation is limited by conduction heat transfer from the surrounding liquid to the interface. Thus, bubble growth is thermally controlled. Plesset and Zwik (1954) derived the following equation for bubble growth in this region:

$$R(t)=\frac{2\Delta T_{Sat}k_L}{h_{fg}p_G}\left(\frac{3t}{\pi\alpha_L}\right)^{1/2} \tag{8.14}$$

where α_L is the thermal diffusivity of the liquid.

These equations for bubble growth are derived for the case of uniformly heated liquid over a spherical bubble. Mikic et al. (1970) derived the following equation by incorporating the shape of a bubble growing in the vicinity of a heated surface. The entire growth cycle, including the inertia-controlled and thermally controlled regions, is covered:

$$R^+=\frac{2}{3}\left[\left(t^++1\right)^{3/2}-\left(t^+\right)^{3/2}-1\right] \tag{8.15}$$

where

$$R^+=\frac{R(t)A}{B^2}\quad t^+=\frac{tA^2}{B^2}$$

$$A=\left\{\frac{2\left[T_L-T_{Sat}(p_L)\right]h_{fg}\rho_G}{p_LT_{Sat}(p_L)}\right\}^{1/2}\quad B=\left(\frac{12\alpha_L}{\pi}\right)^{1/2}\left\{\frac{2\left[T_L-T_{Sat}(p_L)\right]c_{p,L}\rho_L}{\rho_Gh_{fg}}\right\}$$

In the limit, this reduces to Equation 8.13 in the inertia-controlled region for small values of t and to Equation 8.14 in the thermally controlled region for large values of t.

8.1.3.3 Bubble Departure Diameter

As the bubble grows, it experiences the following forces: (1) Surface tension force—this holds down the bubble on the heater surface through the contact angle. (2) Inertia force—as the bubble grows, the acceleration and deceleration of the interface introduce inertia forces that push the bubble onto the heater surface during the earlier part of the growth period, while the bubble is pulled away during the later part. (3) Buoyancy force—depending on the orientation and geometry, the buoyancy force helps or opposes the bubble removal. Additionally, there are viscous forces as well as forces due to Marangoni convection in the liquid around the bubble. As a result of all these forces, a bubble departs from the heater surface after attaining a certain size. The bubble shape also undergoes considerable changes. The departure bubble diameter D_b is of great interest in boiling studies and has been extensively studied. Before applying any correlation, it should be realized that D_b depends on a number of additional variables, such as nucleation site interactions and convection currents that are statistical in nature. A wide variation in experimental values of D_b, up to 50%, from the prediction is not uncommon.

The following correlations by Jensen and Memmel (1986) were developed from a data bank of 504 data points for 15 fluids, including water, boiling on mostly horizontal plates and wires over a wide range of pressures. The correlations were compared with 12 other correlations and were found to perform consistently better than the other correlations available in the literature.

For the case when wall superheat is available,

$$\left[g\left(\rho_L-\rho_G\right)D_b^2/\sigma\right]^{1/2}=0.19\left(1.8+10^5K_1\right)^{2/3} \tag{8.16}$$

where

$$K_1=\left(\frac{Ja}{Pr_L}\right)^2\left\{\left[\frac{q\left(\rho_L-\rho_G\right)}{\mu_L^2}\right]\left[\frac{\sigma}{g\left(\rho_L-\rho_G\right)}\right]^{3/2}\right\}^{-1} \tag{8.17}$$

and Ja ($=\rho_L c_{p,L}\Delta T_{Sat}/(\rho_G h_{fg})$) is the Jakob number, Pr ($=\mu_L c_{p,L}/k_L$) is the Prandtl number, and the wall superheat is given by $\Delta T_{Sat} = T_w - T_{Sat}$.

For cases where wall superheat is not available,

$$D_b=2.97\times10^4\left(\frac{p}{p_{cr}}\right)^{-1.09}\left(\frac{KT_{cr}}{p_{cr}M}\right)^{1/3} \tag{8.18}$$

where

K ($=1.38\times10^{-23}$ J/K) is the Boltzmann constant

M is the molecular weight

subscript "*cr*" refers to the critical point for the fluid

The average deviations for Equations 8.16 and 8.18 were 44% and 52%, respectively, when compared with 30 data sources covering 15 different fluids at pressures from about 4.7 to 13,500 kPa.

8.1.3.4 Bubble Frequency

The frequency of bubbles being released from cavities depends on a number of factors, including wall superheat, fluid thermal properties, contact angle, cavity size, and interaction with neighboring bubbles. An empirical correlation by Malenkov (1971) takes into account the interaction between the bubble departure diameter and the bubble departure frequency and is recommended:

$$fD_b=\frac{V_b}{\pi}\left(1-\frac{1}{1+V_b\rho_G h_{fg}/q''}\right) \tag{8.19}$$

where

$$V_b=\left[\frac{D_b g\left(\rho_L-\rho_G\right)}{2\left(\rho_L+\rho_G\right)}+\frac{2\sigma}{D_b\left(\rho_L+\rho_G\right)}\right]^{1/2} \tag{8.20}$$

and D_b is the departure bubble diameter.

8.1.4 Heat Transfer Mechanisms during Nucleate Pool Boiling

Heat transfer in nucleate pool boiling is a result of a number of interacting mechanisms:

1. *Transient conduction*: As the bubble departs, the bulk liquid rushes over the heater surface surrounding the nucleating cavity. The liquid undergoes a transient heat conduction process. The wall thermal properties also play a role during the transient heat conduction process. The superheated

liquid moves away into the bulk during bubble growth and departure. The superheated liquid also contributes to the evaporation at the bubble interface. Mikic and Rohsenow (1969) proposed a model based on transient conduction in which they assumed a liquid layer from a circular region of diameter twice the departure diameter being replaced with the bulk liquid. This liquid experiences transient conduction from the heater surface. Demiray and Kim (2004) modified this model further by accounting for the gradual coverage of the liquid film. Subsequently, Moghaddam and Kiger (2009b) further modified to account for the transient heat transfer after complete rewetting. It is well accepted that the transient conduction plays an important role in heat transfer around a nucleating bubble during the ebullition cycle.

2. *Enhanced convection*: The bubble ebullition cycle introduces convective currents around a nucleating bubble that contribute to the heat transfer during nucleate pool boiling. The microconvection-induced heat transfer is significantly above the natural convection heat transfer. Since it covers a larger area around a bubble, its contribution is higher than from other modes.
3. *Microlayer evaporation*: A thin layer of liquid, called a microlayer, is left below an expanding bubble during the bubble growth period. Evaporation of this liquid film is believed to contribute to heat transfer especially at higher heat fluxes (Judd and Hwang, 1976).
4. *Contact line region heat transfer*: The contact line region separates the bulk liquid from the microlayer, which continues to evaporate until it assumes a thin adsorbed layer and eventual dryout. In this layer, the local curvature introduces a reduction in the saturation temperature of the interface and causes lowering of the heater surface temperature. This is an area of current research interest. The localized heat transfer in the contact line region makes the role of transient substrate conduction an important consideration in the overall heat transfer during nucleate boiling (Kandlikar, 2015).

The periodic nature of liquid flow in the bubble ebullition cycle, development of the superheated liquid layer, release of the liquid sensible energy in the form of evaporation at the bubble interface, and evaporation from the microlayer have all been extensively studied in the literature, for example, Kim (2009) and Moghaddam and Kiger (2009a). These studies provide valuable insight into heat transfer mechanisms and help in identifying pathways for further enhancing the boiling performance.

8.1.5 Models and Correlations for Nucleate Pool Boiling

It has been recognized that the heat transfer during nucleate pool boiling is closely related to the bubble activity over a heater surface. In addition to knowing the contributions from different mechanisms described in the previous section, a detailed knowledge of the nucleation cavity size and distribution on the heater surface is needed for accurately predicting the boiling heat transfer performance of a heated surface. In principle, the heat transfer rate can be predicted by knowing the bubble frequency, active nucleating cavity site density (per unit heater surface area), and heat transferred during each bubble ebullition cycle. Dhir (1999, 2001) numerically solved the conservation equations of mass, momentum, and energy for the two phases while continuously tracking liquid–vapor interfaces at or near a heated surface. These solutions provide detailed information on the underlying physics of the hydrodynamic and thermal processes occurring at the interface. It is now possible to simulate boiling phenomena under a variety of conditions, including nucleate boiling, film boiling, and under microgravity conditions.

The numerical approach often requires detailed information about the nucleation cavity size distribution and density, which is generally not available in practical equipment design. For such cases, semiempirical correlations are available that can predict the heat transfer coefficients generally within ±30% to 50%.

Rohsenow (1952) developed a semiempirical model by using the liquid Reynolds number in the vicinity of a bubble. The influence region was considered to be twice the diameter of the departure bubble diameter. Rohsenow introduced an empirical constant C_{sf} to account for the fluid–surface effect on nucleate boiling and proposed the following correlation:

$$\frac{c_{p,L}\Delta T_{Sat}}{h_{fg}} = C_{sf}\left\{\frac{q''}{\mu_L h_{fg}}\sqrt{\frac{\sigma}{g(\rho_L-\rho_G)}}\right\}^{0.33} Pr_L^n \tag{8.21}$$

The values of C_{sf} and n for different heater materials and surface finishes are given in Table 8.1. These values are derived from Rohsenow (1952) and Vachnon et al. (1968).

Table 8.1 Values of C_{sf} and n in the Rohsenow Correlation (Equation 8.21)

Fluid–Surface Combination	C_{sf}	n
Water–copper		
Scored	0.0068	1.0
Polished	0.0130	1.0
Lapped	0.0147	1.0
Water–brass	0.006	1.0
Water–stainless steel		
Chemically etched	0.0130	1.0
Mechanically polished	0.0130	1.0
Ground and polished	0.0060	1.0
Teflon pitted	0.0058	1.0
Water–platinum	0.013	1.0
Water–nickel	0.006	1.0
Benzene–chromium	0.101	1.7
Carbon tetrachloride–polished copper	0.007	1.7
Ethanol–chromium	0.0027	1.7
Isopropanol–copper	0.0025	1.7
n-Butanol–copper	0.003	1.7
n-Pentane–chromium	0.015	1.7
n-Pentane–copper		
Polished	0.0154	1.7
Emery-rubbed copper	0.0074	1.7
Lapped	0.0049	1.7

In case the constant C_{sf} is not available for a given fluid–surface combination, a value of 0.013 is recommended as an initial guess. Liaw and Dhir (1989) established a clear dependence of the constant C_{sf} and the contact angle during pool boiling of water on copper surfaces. By varying the surface finish, they obtained different contact angles and showed that the contact angle and C_{sf} decreased as the surface was made smoother. This trend is also seen in Table 8.1 for different surface treatments.

Among other empirical correlations, the Stephan and Abdelsalam (1980) correlation is recommended. It is based on 5000 data points derived from 72 published sources. Stephan and Abdelsalam conducted a dimensional analysis and arrived at eight nondimensional groups to represent the nucleate pool boiling phenomenon. By carefully carrying out a regression analysis of the data, the following correlations were developed. The ranges of reduced pressures p/p_{cr} and contact angles θ are listed for different fluids.

Water (mean absolute error = 11.3%):

$$Nu = 2.64\times10^{6} X_1^{0.673} X_4^{-1.58} X_3^{1.26} X_8^{5.22} \quad \text{for } 10^{-4} \le p/p_{cr} \le 0.886, \quad \theta = 45° \tag{8.22}$$

Hydrocarbons (mean absolute error = 12.2%):

$$Nu = 0.0546\left(X_5^{0.5} X_1\right)^{0.67} X_8^{4.33} X_8^{0.248} \quad \text{for } 5.7\times10^{-3} \le p/p_{cr} \le 0.9, \quad \theta = 35° \tag{8.23}$$

Cryogenic liquids (mean absolute error = 14.3%):

$$Nu = 4.82 X_1^{0.624} X_7^{0.117} X_5^{0.257} X_3^{0.374} X_4^{-0.329} \quad \text{for } 4.0\times10^{-3} \le p/p_{cr} \le 0.97, \quad \theta = 1° \tag{8.24}$$

Refrigerants (mean absolute error = 10.6%):

$$Nu = 207 X_1^{0.745} X_5^{0.581} X_6^{0.533} \quad \text{for } 3.0\times10^{-3} \le p/p_{cr} \le 0.78, \quad \theta = 35° \tag{8.25}$$

All fluids (general correlation for all of the aforementioned fluids; mean absolute error = 22.3%):

$$Nu = 0.23X_1^{0.674}X_5^{0.297}X_4^{0.371}X_8^{-1.73}X_4^{0.35} \quad \text{for } 10^{-4} \le p/p_{cr} \le 0.97 \tag{8.26}$$

The definitions of Nusselt number, d, and nondimensional groups X_1 through X_8 are given as follows:

$$Nu = \frac{q''d}{\Delta T_{sat}k_L}, \quad d = 0.145\theta\left[\frac{2\sigma}{g(\rho_L - \rho_G)}\right]^{1/2}$$

$$X_1 = \frac{q''d}{k_L T_{Sat}}, \quad X_5 = \frac{\rho_G}{\rho_L}$$

$$X_2 = \frac{\alpha_L^2\rho_L}{\sigma d}, \quad X_6 = \frac{\mu_L}{\rho_L\alpha_L}$$

$$X_3 = \frac{c_{pL}T_{Sat}d^2}{\alpha_L^2}, \quad X_7 = \frac{(\rho c_P k)_S}{(\rho c_P k)_L}$$

$$X_4 = \frac{h_{fg}d^2}{\alpha_L^2}, \quad X_8 = \frac{\rho_L - \rho_G}{\rho_L}$$

where

$\alpha(=k/(\rho c_p))$ is the thermal diffusivity
d is the equilibrium break-off bubble diameter as defined earlier
θ is the contact angle in degrees (not in rad)
the subscripts S and L refer to the solid surface and liquid, respectively

8.1.6 Effect of Subcooling

Judd et al. (1991) studied the effect of subcooling on pool boiling heat transfer with water on a copper surface. Their results indicate that first, at low subcooling, the wall superheat increases due to changes in the number of active nucleation sites and bubble departure frequency. The subcooling effect is more pronounced at higher heat fluxes. For water with a heat flux of 1.26 MW/m^2, the wall superheat varied from 24 K at the saturation condition to about 32 K at a subcooling of 60 K. For higher values of subcooling, the wall temperature begins to decrease as the natural convection heat transfer is able to accommodate higher heat fluxes.

Subcooling introduces an evaporation condensation mechanism across different regions of a bubble interface. The interface closer to the heater surface continues to evaporate, while vapor condenses at the interface near the cooler bulk liquid. This additional mechanism increases the heat transfer rate over the corresponding saturated boiling condition.

At very high subcooling, a new type of boiling involving microbubble emission was discovered by Inada et al. (1986). The bubbles collapse during the growth and give out multiple microbubbles resulting in high heat flux dissipation (Suzuki et al., 2005).

8.1.7 Effect of Orientation

Orientation affects the bubble removal process at low heat fluxes. A horizontal surface provides the most efficient heat transfer geometry. As the orientation angle changes to a vertical surface and then a downward facing surface, heat transfer deteriorates systematically (Nishikawa et al., 1983). El-Genk (1996) presents an extensive overview of the effect of orientation on the entire pool boiling curve as shown in Figure 8.5. It is important to note that at high heat fluxes all curves tend to merge, but the boiling curve is affected in almost every region.

8.1.8 Nucleate Boiling with Mixtures

Nucleate boiling of mixtures of two liquids with different boiling points results in the preferential evaporation of the more volatile component at the evaporating liquid–vapor interface. The more volatile component is depleted at the interface, and the heat transfer is degraded as the more volatile component diffuses through

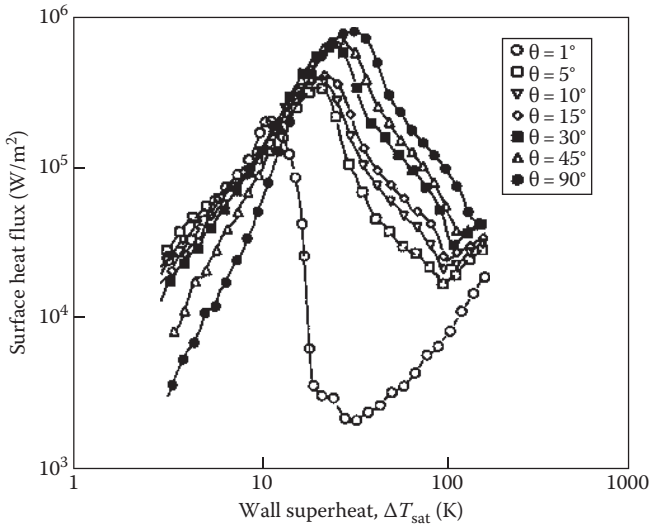


Figure 8.5

Effect of orientation on the pool boiling curve. (Reproduced from El-Genk, M., A review of pool boiling from inclined and downward-facing flat surfaces, in *Second European Thermal-Sciences and 14th UIT National Heat Transfer Conference,* Celta, G.P., Di Marco, P., and Mariani, A., Eds., Edizioni ETS, Pisa, Italy, 1996. With permission.)

the bulk of the liquid toward the interface. The interface temperature therefore rises and heat transfer is degraded. A number of researchers have studied the phenomena and presented detailed models. Kandlikar (1998b) presented a methodology to predict the interface concentration, which can be used in predicting the interface temperature. An extensive survey of the earlier work can be found in Kandlikar (1999). In general, the heat transfer coefficient for the mixture is below the linear-averaged heat transfer coefficient obtained from the respective pure component values.

The interface concentration of a nucleating bubble introduces a mass transport limit. Kandlikar (1998b) analyzed the coupled heat and mass transfer phenomena and presented a methodology to predict the interface concentration, which can be used in predicting the interface temperature. The interface liquid and vapor phase concentrations of more volatile component $x_{1,s}$ and $y_{1,s}$ are related through the equilibrium condition. Further, considering the transient mass transfer through the concentration boundary layer of thickness δ_m,

$$x_{1,s} = x_1 - \frac{2.13}{\pi}\mathrm{Ja}_0\left(\frac{\alpha}{D_{12}}\right)^{1/2}\frac{\rho_G}{\rho_L}\left(y_{1,s} - x_1\right) \tag{8.27}$$

where

x_1 is the bulk liquid–phase concentration
α is the thermal diffusivity
D_{12} is the mass diffusivity of the more volatile component 1 in the mixture
Ja_0 is the modified Jakob number given by

$$\mathrm{Ja}_0 = \frac{(T_W - T_{L,sat})}{\left(\frac{\rho_G}{\rho_L}\right)\left[\frac{h_{fg}}{c_{p,L}} + \left(\frac{\alpha}{D_{12}}\right)^{1/2}\frac{\Delta T_s}{g}\right]} \tag{8.28}$$

where

T_W is the wall temperature
$T_{L,sat}$ is the saturation temperature at the bulk liquid concentration
h_{fg} is the latent heat of vaporization
ΔT_s is the difference between the saturation temperatures corresponding to the interface and the bulk liquid–phase concentrations

An iterative scheme is needed to calculate the interface concentration. The corresponding increase in the interface saturation temperature acts as an additional resistance to heat transfer during pool boiling in a binary system. Kandlikar (1998b) used this concentration and analytically derived an expression for the heat transfer coefficient in a binary system. Readers are referred to this publication for further details.

Fujita et al. (1996) developed an empirical correlation from their own experimental data on methanol/water, ethanol/water, methanol/ethanol, ethanol/*n*-butanol, methanol/benzene, benzene/*n*-heptane, and water/ethylene glycol systems. It incorporates several key features of previous investigators and

$$h_m = \frac{\left(\tilde{x}_1/h_1 + \tilde{x}_2/h_2\right)^{-1}}{1+\left\{1-\exp\left[-2.8\dfrac{\tilde{x}_1\Delta T_1 + \tilde{x}_2\Delta T_2}{T_{Sat,2}\big|_p - T_{Sat,1}\big|_p}\right]\right\}\left\{\dfrac{T_{dp}-T_{bp}}{\tilde{x}_1\Delta T_1 + \tilde{x}_2\Delta T_2}\right\}} \tag{8.29}$$

where

h_1 and h_2 and ΔT_1 and ΔT_2 are the heat transfer coefficients and the wall superheat values with the two pure components

$T_{Sat,1}|_p$ and $T_{Sat,2}|_p$ refer to the saturation temperatures of the pure components at the total system pressure p

Component 1 is the more volatile component with a lower boiling point

T_{dp} and T_{bp} are the dew point and bubble point temperatures, respectively

8.1.9 Critical Heat Flux in Pool Boiling

CHF is defined as the highest heat flux that can be sustained under the nucleate boiling mode. As the heat flux is increased, the bubble activity increases dramatically over a heater surface. Both the number of nucleation sites and bubble frequency increase. The intense vapor–liquid interaction at the heater surface has prevented researchers from gaining clear visual access to the events occurring just prior to CHF.

Early researchers, for example, Kutateladze (1948) and Zuber (1959), formulated their models based on the hydrodynamic instability theory. They assumed the presence of either a stable liquid–vapor interface or stable vapor columns, which are then analyzed for stability conditions based on Helmholtz or Taylor's instability criteria. The hydrodynamic model does not represent the events leading to the CHF, and further, it does not address the interaction between the liquid–vapor interface and the solid-heated surface during frequent rewetting occurring just prior to CHF. The following equation was proposed by Zuber:

$$\frac{q''_{CHF}}{h_{fg}\rho_G^{1/2}\left[\sigma g\left(\rho_L - \rho_G\right)\right]^{1/4}} = K \tag{8.30}$$

where K is a constant equal to 0.13. Another model, developed by Haramura and Katto (1983), considers the depletion of a liquid macrolayer that exists under vapor mushrooms. Estimation of the initial macrolayer thickness and the role of the rewetting phenomenon and contact angles are not adequately addressed by this model.

Kandlikar (2001a) proposed a model based on the rapid evaporation of the liquid–vapor interface near the base of the liquid–vapor contact line at the heater surface. The rapid evaporation occurring in this region introduces a force due to momentum change that causes the interface to retreat, leaving a thin film of vapor underneath. Figure 8.6 depicts the cutback phenomenon, and Figure 8.7 shows a high-speed photographic sequence showing the vapor cutback under a liquid droplet placed on a flat heater surface (Kandlikar and Steinke, 2002).

Figure 8.8 shows the forces acting on a vapor bubble close to CHF condition. Kandlikar (2001a) considered the balance of forces due to evaporation momentum surface tension forces acting on one half of the bubble as shown in Figure 8.8. The balance between the evaporation momentum force F_M and the retaining forces due to surface tension force $F_{s,1}$ and $F_{s,2}$, and the hydrostatic force F_g was used by Kandlikar (2001a) in deriving an expression for CHF. The receding contact angle was introduced in the force balance for retaining surface tension force at the wall. The final expression for CHF is given by

$$q''_{CHF} = h_{fg}\rho_G^{1/2}\left(\frac{1+\cos\theta_r}{16}\right)\left[\frac{2}{\pi} + \frac{\pi}{4}\left(1+\cos\theta_r\right)\cos\phi\right]^{1/2}\left[\sigma g\left(\rho_L - \rho_G\right)\right]^{1/4} \tag{8.31}$$

where

θ_r is the receding contact angle

ϕ is the angle of orientation of the heater surface with respect to the horizontal

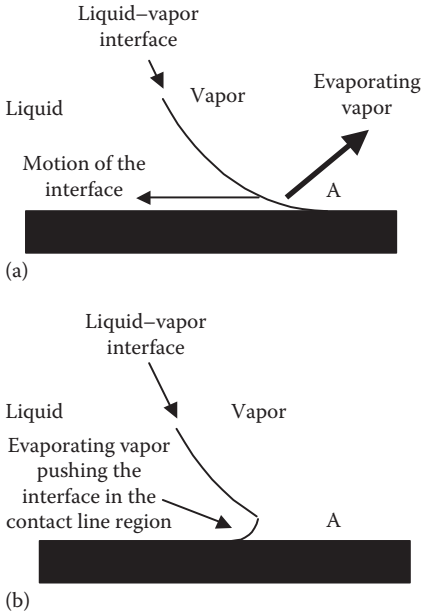


Figure 8.6

Schematic representation of vapor cutback under liquid during rapid evaporation in the contact line region. (Reproduced from Kandlikar, S.G. and Steinke, M.S., *Int. J. Heat Mass Transfer*, 45, 3771, 2002. With permission from Elsevier).

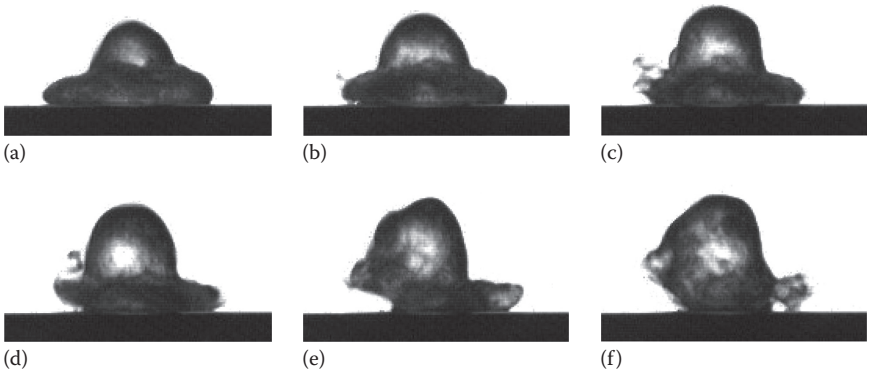


Figure 8.7

High-speed image sequence showing interface movement under a liquid droplet during rapid evaporation, 1 ms interval between successive frames, T_w = 150°C, droplet diameter 2.8 mm. (Reprinted from *Int. J. Heat Mass Transfer*, 45, Kandlikar, S.G. and Steinke, M.S., Contact angles and interface behavior during rapid evaporation of liquid on a heated surface, 3771–3780, Copyright 2002, with permission from Elsevier).

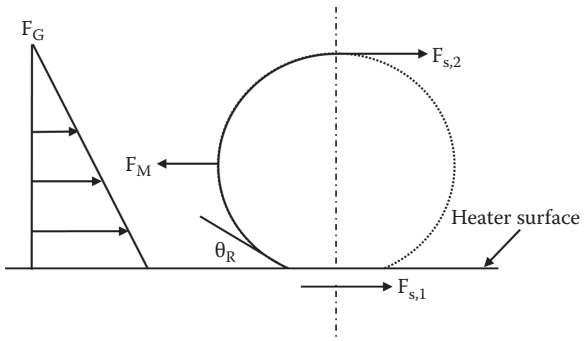


Figure 8.8

Forces acting on a vapor bubble close to CHF condition.

Table 8.2 Variation of Equivalent K Factor (Product of the First Two Bracketed Terms in Equation 8.31)

Receding Contact Angle (deg)	Equivalent K
0	0.186
20	0.178
45	0.150
60	0.126
90	0.0745
120	0.0317
150	0.0072
180	0

Source: Kandlikar, S.G., *J. Heat Transfer*, 123, 1071, 2001a. With permission from Elsevier.

This expression accounts for the contact angle and orientation. Equation 8.31 reduces to the expression given by Kutateladze (1948) with $K = 0.13$ for a horizontal surface with a receding contact angle of 57.5°. Table 8.2 shows the variation of K with contact angle for a horizontal surface as predicted from Equation 8.31.

8.1.10 Enhanced Surfaces

Pool boiling enhancement can be classified into the following types:

- Artificial nucleation cavities
- Fins
- Porous structures
- Microstructures
- Wettability control—nanostructures
- Hybrid microporous structures
- Hybrid micro-/nanostructures
- Other techniques (acoustic, electric field, etc.)

Enhancement in nucleate boiling heat transfer is mainly accomplished by providing more active nucleation sites on the heater surface. A reentrant shape that traps gases or vapors in the cavities is found to be most effective. Figure 8.9 shows a schematic of a reentrant cavity. The reentrant cavities are manufactured by a variety of processes, including rolling of perforated fins protruding from the base, structured surfaces, porous surfaces created through sintering or other techniques, such as machined tunnels with openings of predetermined shapes and sizes. A number of enhanced geometries are commercially available. They are

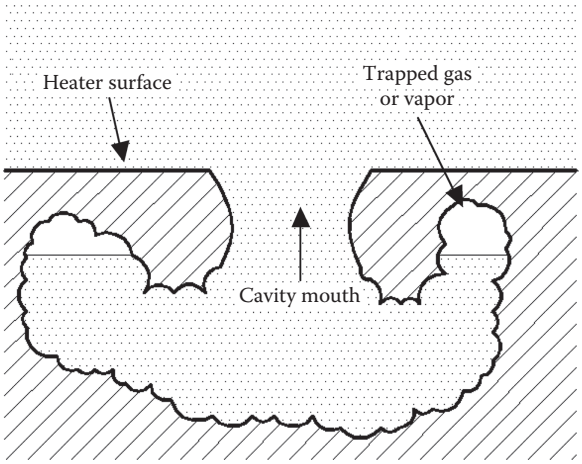


Figure 8.9

Schematic representation of a reentrant cavity trapping gas or vapor.

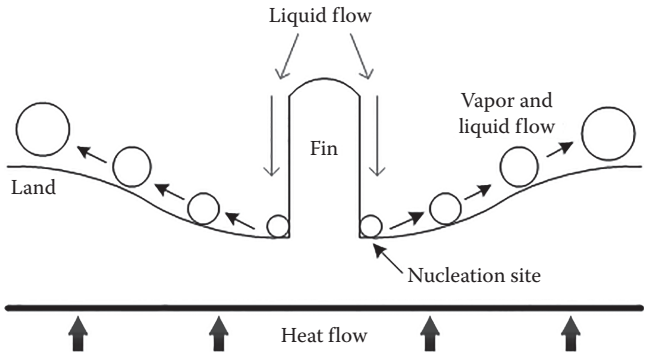


Figure 8.10

Schematic of a microstructure designed by Kandlikar (2013).

routinely employed in cryogenic, air separation, refrigeration, and chemical industries. A good survey of enhancement mechanisms is given by Bergles (1997).

Fins provide additional surface area for heat transfer. They are effective especially when the heat transfer coefficients are relatively low. For pool boiling of water, the high heat transfer coefficient makes short fins, smaller than 0.5 mm attractive. While for refrigerants, since their HTC is relatively low, fins of 1–5 mm are routinely employed.

A new class of enhanced boiling surfaces is being developed to meet the high heat flux dissipation needs in electronics cooling application. Microstructures are specifically designed to provide separate liquid–vapor pathways in an effort to enhance the CHF. Figure 8.10 shows a schematic of a microstructure designed by Kandlikar (2013). It utilizes the evaporation momentum force occurring at the evaporating interface to propel a bubble in a desired direction to create separate liquid–vapor pathways. The departing bubble sweeps over the contoured surfaces, thereby enhancing the HTC as well.

Wettability affects the nucleation as well as heat transfer characteristics. A hydrophobic surface enhances nucleation characteristics, while a hydrophilic surface improves the HTC. Recently, a number of patterned surfaces have been developed with hydrophobic and hydrophilic surface combinations to improve both CHF and HTC (Betz et al., 2010, Yao et al., 2011). Figure 8.11 shows one such patterned surface developed by Betz et al. (2010). Ahn et al. (2010) developed a nano- and microstructure for enhancing boiling on zircaloy-4 surfaces.

Nanostructures are also used to modify the wettability of a surface. Additionally, their ability to retain and wick liquid improves the CHF. Combining the microstructures with nanostructures to create hierarchical surfaces provides the next level of enhancement. Chu et al. (2013), O'Hanley et al. (2013), and Rahman et al. (2012) developed surfaces with microscale posts coated with nanostructures. Cooke and Kandlikar (2013) developed open microchannel surfaces with channels serving as liquid conduits for the nucleating bubble. Yao et al. (2012) coated open microchannels with nanowires on silicon substrates. Patil and Kandlikar (2014) coated fin tops of open microchannels with sintered coatings, while Jaikumar

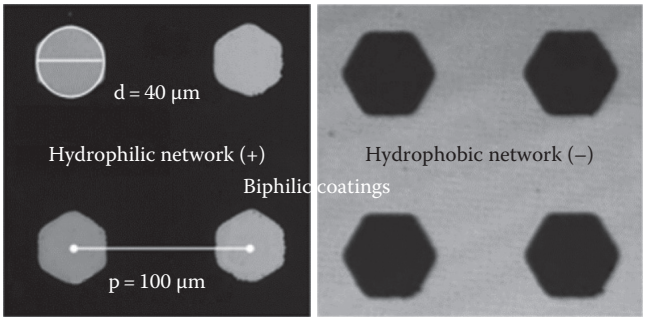


Figure 8.11

Patterned surface developed by Betz et al. (2010).

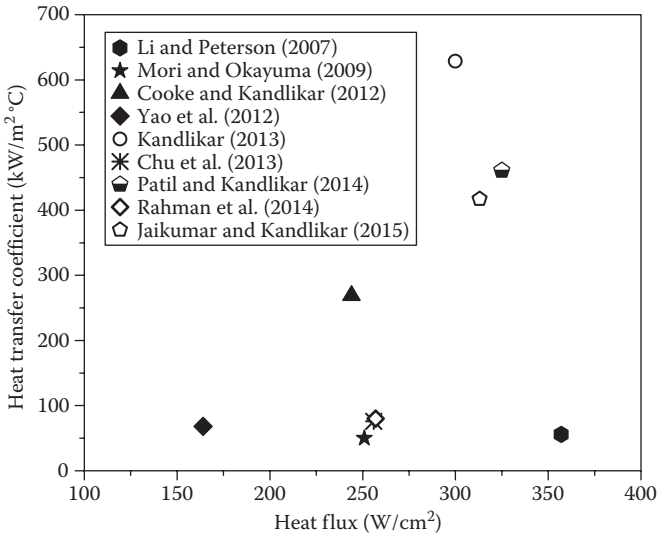


Figure 8.12

Plot of CHF versus HTC for some of the high-performance surfaces in pool boiling.

and Kandlikar (2015) coated all surfaces of open microchannels with a sintered coating. Li and Peterson (2007) developed sintered porous mesh to understand the effect of coating thickness. Mori and Okayuma (2009) used honeycomb plates as porous templates to understand the effect of wicking.

Chu et al. (2013) modified the Kandlikar CHF model (2001a) to incorporate the roughness effect introduced by the hierarchical structures. Their equation for predicting CHF is given as follows:

$$q_c'' = K \times h_{fg} \rho_g^{1/2} \left[\sigma_{lv} g \left(\rho_L - \rho_G \right) \right]^{1/4} \tag{8.32}$$

where

$$K = \left(\frac{1+\cos\beta}{16} \right) \left[\frac{2(1+\alpha)}{\pi(1+\cos\beta)} + \frac{\pi}{4}(1+\cos\beta)\cos\phi \right]^{1/2} \tag{8.33}$$

$$\alpha = r\cos\theta_{rec} \tag{8.34}$$

and r is the modified roughness factor. It is obtained as the ratio of actual surface area divided by the projected area.

Figure 8.12 shows a plot of CHF versus HTC for some of the high-performance surfaces in pool boiling. It is seen that the CHF is enhanced by several folds, and extremely high values of HTC are obtained as compared to the values obtainable with plain polished surfaces.

Other techniques include the application of an electric field and vibrations. The electric field causes enlargement of the bubble base area, thereby exposing more of the thin film underneath a bubble. Mechanical vibrations provide pressure fluctuations that are especially effective under subcooled boiling conditions. These techniques provide marginal improvements, while the techniques employing microstructures and nanostructures are seen as breakthrough technologies in the field of boiling.

8.1.11 Film Boiling and Transition Boiling

The post-CHF region consists of transition boiling (D–E in Figure 8.1), MHF condition in film boiling (point E), and fully developed film boiling (E–F). Heat transfer in the transition region depends on the rewetting characteristics of the heater surface. Some empirical form of averaging techniques is employed between the CHF and MHF locations. The early work by Bromley (1950) provides an excellent insight into the film boiling phenomenon.

The MHF q''_{MHF} is predicted by a correlation developed by Zuber (1959):

$$q''_{MHF} = C\rho_g h_{fg}\left[\frac{g\sigma(\rho_L-\rho_g)}{(\rho_L+\rho_g)^2}\right]^{1/4} \tag{8.35}$$

The value of constant C was determined to be 0.09 by Berenson (1961) based on his data for MHF for a flat plate.

The film boiling heat transfer coefficient h_F consists of the convective and radiative components:

$$h_F = h_{F,C} + h_{F,r} \tag{8.36}$$

The radiative component is approximated by using appropriate radiation correlations between the heater surface and the surrounding vapor film. The emissivity of the liquid surface is generally taken as 1, and an empirical shape factor value of 0.75 is used.

The following correlation by Hsu and Westwater (1960) is recommended for $h_{F,c}$ for a vertical flat plate of length L:

$$h_{F,C} = 0.943\left[\frac{g\sigma(\rho_L-\rho_G)\rho_G k_G^3 h'_{fg}}{L\mu_G(T_w-T_{Sat})}\right]^{1/4} \tag{8.37}$$

where $h'_{fg} = h_{fg}\left[1+0.34c_{p,G}(T_w-T_{sat})\right]$ is the latent heat corrected for the vapor superheating.

For a horizontal flat plate, the correlation by Berenson (1961) is used extensively:

$$h_{F,C} = 0.425\left\{\left[\frac{k_G^3 g\rho_g(\rho_L-\rho_g)h'_{fg}}{\mu_G(T_w-T_{Sat})}\right]\left[\frac{g(\rho_L-\rho_g)}{\sigma}\right]^{1/2}\right\}^{1/4} \tag{8.38}$$

where the corrected latent heat term takes the form $h'_{fg} = h_{fg}\left[1+0.5c_{p,G}(T_w-T_{sat})\right]$.

Transition boiling region occurs as the heater surface temperature is reduced from film boiling condition, and it comes in occasional contact with the liquid. This region is identified by the dotted line DE in Figure 8.1 and is accessible only when the heater surface temperature is independently controlled.

Ramilison and Lienhard (1987) considered the heat transfer in this region as the sum of the heat transfer due to film boiling and during liquid contact. Approaching from the film boiling region, the actual liquid contact with the heater surface is initiated at a heat flux somewhat higher, by 10%–15%, over the MHF given by Equation 8.32. This temperature is identified as T_{dfb} and has been correlated as a function of advancing contact angle by Ramilison and Lienhard (1987). Carey (2007) proposed the following correlation to represent this plot:

$$\frac{T_{dfb}-T_{sat}}{T_{hn}-T_{sat}} = 0.97\exp(-0.000600\theta_a^{1.8}) \tag{8.39}$$

where

θ_a is the advancing contact angle in degrees

T_{hn} is the homogeneous nucleation temperature of the liquid given by the following equation:

$$T_{hn} = \left[0.932+0.077\left(\frac{T_{sat}}{T_c}\right)^9\right]T_c \tag{8.40}$$

where T_c is the critical temperature of the liquid.

The heat flux during the transition boiling is then given by the following equation by Ramilison and Lienhard (1987):

$$Bi^{\star} = 3.74 \times 10^{-6} \left(Ja^{\star} \right)^2 K \tag{8.41}$$

where

$$Bi^{\star} = \frac{\left(q'' - q''_{fb} \right) \sqrt{\alpha_h \tau}}{k_h \left[T_w - T_{sat} \left(P_L \right) \right] K} \tag{8.42}$$

$$Ja^{\star} = \frac{\left(\rho c_p \right) \left(T_{dfb} - T_w \right)}{\rho_v h_{lv}} \tag{8.43}$$

$$\tau = \left[\frac{\sigma}{g^3 \left(\rho_L - \rho_v \right)} \right]^{1/4} \tag{8.44}$$

$$K = \frac{k_L / \alpha_L^{1/2}}{k_L / \alpha_L^{1/2} + k_h / \alpha_h^{1/2}} \tag{8.45}$$

The film boiling heat flux q''_{fb} in Equation 8.42 is the heat flux during film boiling given by the following Klimenko's (1981) correlation for turbulent vapor film:

$$\frac{q''_{fb} \lambda_D}{k_v \left(T_w - T_{sat} \right)} = 0.0086 \sqrt{3} \left[\frac{g \lambda_D}{(3)^{3/2} \nu_v^{2/3}} \left(\frac{\rho_L - \rho_v}{\rho_v} \right) \right]^{1/2} Pr_v^{1/3} \tag{8.46}$$

The most dangerous wavelength λ_D is given by

$$\lambda_D = 2\pi \left[\frac{3\sigma}{\left(\rho_L - \rho_v \right) g} \right]^{1/2} \tag{8.47}$$

Equation 8.46 neglects the radiation effect, which is quite reasonable as the wall temperature is not as high as in the film boiling region.

8.2 Flow Boiling

8.2.1 Introduction to Flow Boiling

The process of flow boiling of a liquid heated in a confined passage is commonly encountered in many applications, such as steam generators in power plants, evaporators in refrigeration and air conditioning equipment, distillation and other processes in chemical and petrochemical industries, and high heat flux removal systems.

Figure 8.13 shows the flow boiling process in a uniformly heated circular tube. Subcooled liquid enters the tube and is heated by single-phase convection. The heat transfer coefficient in the single phase is almost constant except for a small variation due to property changes with increasing liquid temperature along the tube length. Although the wall temperature reaches the saturation temperature, nucleation does not occur immediately because a certain amount of wall superheat is needed to nucleate cavities existing on the wall. The first bubbles appear on the wall at a location identified as the ONB. It may also be associated with a reduction in wall temperature due to improved heat transfer from two-phase flow. The wall temperature begins to level off, as more nucleation sites are activated beyond ONB. Further downstream, as more sites are activated, the contribution to heat transfer from the nucleate boiling continues to rise, while the

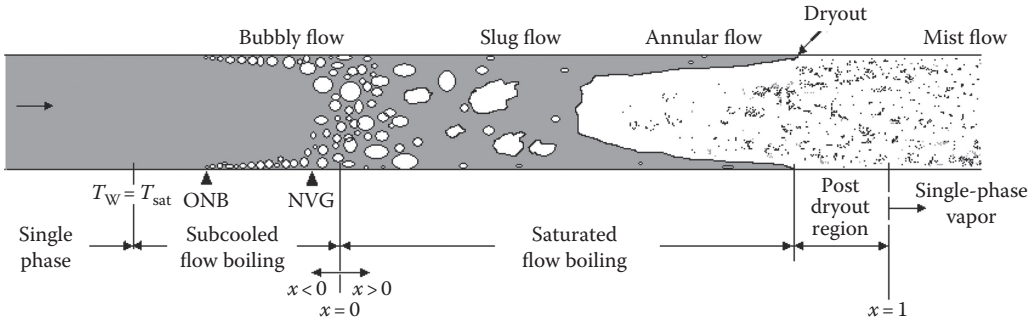


Figure 8.13

Flow boiling in a circular tube.

single-phase convective contribution diminishes. This region is called the "partial boiling region." The convective contribution continues to diminish, and eventually, *fully developed boiling* (FDB) is established. The wall temperature varies depending on the variation of the heat transfer coefficient with quality.

The bubbles generated at the wall immediately following ONB encounter condensation at the bubble surface exposed to the subcooled liquid flow, and their growth is impeded. As a result, a thin layer of stationary bubbles is formed on the wall. As the bulk liquid temperature increases in the flow direction, the layer becomes populated with more bubbles, whose size also increases with decreasing subcooling. At some location, identified as the point of *net vapor generation* (NVG; also called OSV), the bubbles eventually detach from the wall and flow toward the liquid core. Some bubbles condense along the way. The heat transfer following NVG is in the two-phase region.

The vapor present in the subcooled flow following NVG is at the saturation temperature. This gives rise to a thermodynamic nonequilibrium condition with the liquid temperature falling below the equilibrium subcooled liquid temperature dictated by the local enthalpy. As heat addition continues downstream, the saturation condition ($x = 0$) under thermodynamic equilibrium is reached. The flow beyond the location where thermodynamic quality reaches zero falls under the saturated flow boiling region.

The state of the subcooled liquid can be defined in terms of an equilibrium *quality* based on the liquid enthalpy relative to the saturation state:

$$x = \left(h_L - h_{L,Sat}/h_{fg}\right) = -c_p \Delta T_{sub}/h_{fg} \tag{8.48}$$

where ΔT_{Sub} ($=T_{Sat} - T_L$) is the liquid subcooling. This results in a negative quality in the subcooled region. In the single-phase region of the subcooled flow before any boiling is initiated, the heat flux is expressed in terms of the single-phase liquid heat transfer coefficient and the wall-to-liquid temperature difference:

$$q'' = h_L\left(T_W - T_L\right) = h_L\left(\Delta T_{Sat} + \Delta T_{Sub}\right) \tag{8.49}$$

The single-phase heat transfer coefficient h_L is given by the appropriate single-phase heat transfer coefficient in the laminar or turbulent region.

The heat transfer to a liquid flowing inside a tube is by the single-phase mode as long as the liquid and wall are both below the saturation temperature of the liquid at the local pressure. As the wall temperature exceeds the local saturation temperature, boiling can occur depending on the tube surface characteristics and the operating conditions. The bulk liquid may still be in the subcooled region. Boiling under these conditions is called subcooled flow boiling. Saturated flow boiling covers the region when the wall temperature exceeds the local saturation temperature of the liquid, and the equilibrium thermodynamic quality (mass fraction of vapor) is between 0 and 1.

8.2.2 Onset of Nucleate Boiling

The condition for the ONB under flow conditions is obtained as an extension to the pool boiling analysis presented in Section 8.1.2. The liquid temperature profile near the heater surface is obtained from the single-phase heat transfer coefficient prior to nucleation. In the absence of hysteresis effects, the nucleation criterion

suggested by Hsu and Graham (1961) has been confirmed by many later investigators. Bergles and Rohsenow (1964) described the nucleation criterion graphically in terms of the tangency condition and presented an empirical correlation for the ONB condition. Hsu (1962) and Sato and Matsumura (1964) presented equations for $\Delta T_{Sat,ONB}$ and q''_{ONB} considering a hemispherical bubble over a nucleation cavity. This corresponds to a contact angle of 90°:

$$\Delta T_{Sat,ONB} = \frac{4\sigma T_{Sat} v_{1g} h_L}{k_L h_{fg}} \left[1 + \sqrt{1 + \frac{k_L h_{fg} \Delta T_{Sub}}{2\sigma T_{Sat} v_{fg} h_L}} \right] \tag{8.50}$$

and

$$q''_{ONB} = \left[k_L h_{fg} / \left(8\sigma v_{fg} T_{Sat} \right) \right] \left[\Delta T_{Sat,ONB} \right]^2 \tag{8.51}$$

The range of active cavity radii was also presented by Hsu (1962) and Sato and Matsumura (1964). A nondimensionalized form of these equations was presented by Kandlikar and Spiesman (1997) using the following parameters:

$$R_c^* = \frac{R_c}{\delta_t} \tag{8.52}$$

$$\Delta T_{Sat}^* = \frac{\Delta T_{sat} h_{fg} \delta_t}{8\sigma T_{Sat} v_{fg}} \tag{8.53}$$

$$\Delta T_{Sub}^* = \frac{\Delta T_{sub} h_{fg} \delta_t}{8\sigma T_{Sat} v_{fg}} \tag{8.54}$$

where the single-phase thermal boundary layer thickness in the liquid is given by $\delta = k_L/h_L$.

The range of the active cavity radii in nondimensional form is then given by the following equation:

$$R_{\max}^*, R_{\min}^* = \frac{1}{2} \left[\frac{\Delta T_{Sat}^*}{\Delta T_{Sat}^* + \Delta T_{Sub}^*} \pm \sqrt{\left(\frac{\Delta T_{Sat}^*}{\Delta T_{Sat}^* + \Delta T_{Sub}^*} \right)^2 - \frac{1}{\left(\Delta T_{Sat}^* + \Delta T_{Sub}^* \right)}} \right] \tag{8.55}$$

The properties in Equations 8.50 through 8.55 are evaluated at the saturation temperature and h_L is calculated from an appropriate single-phase correlation incorporating a wall temperature correction if necessary.

The nucleation criterion has been further studied, and the effect of contact angle has been incorporated by Davis and Anderson (1966). The effect of flow also modifies the temperature around the bubble surface and affects the onset of nucleation. Kandlikar et al. (1997) considered the stagnation effect of the flow upstream of the bubble and modified the nucleation criterion to include both thermal field and contact angle effects. A detailed presentation of these effects is given by Kandlikar (2014).

8.2.3 Flow Patterns

The distribution of liquid and vapor phases in a flow channel plays an important role in the pressure drop and heat transfer during flow boiling. Figure 8.13 shows the flow patterns observed in a horizontal tube. The major flow patterns are as follows: (1) Bubbly flow—discrete bubbles—exists in the flow field with a continuous liquid phase, generally observed at low vapor qualities. (2) Slug or plug flow—as vapor quality increases, bubbles start to coalesce and fill the entire tube with liquid and vapor flowing alternately in the channel. (3) Annular flow—at higher vapor qualities, the vapor forms a continuous core with liquid flowing around the periphery as a smooth or wavy film. (4) Mist flow—it consists of liquid droplets flowing in a continuous vapor phase; this flow pattern occurs beyond the *dryout* location (see Figure 8.13). There are additional flow patterns, such as a stratified flow pattern, that occur at low flow rates. The transitional flow patterns, such

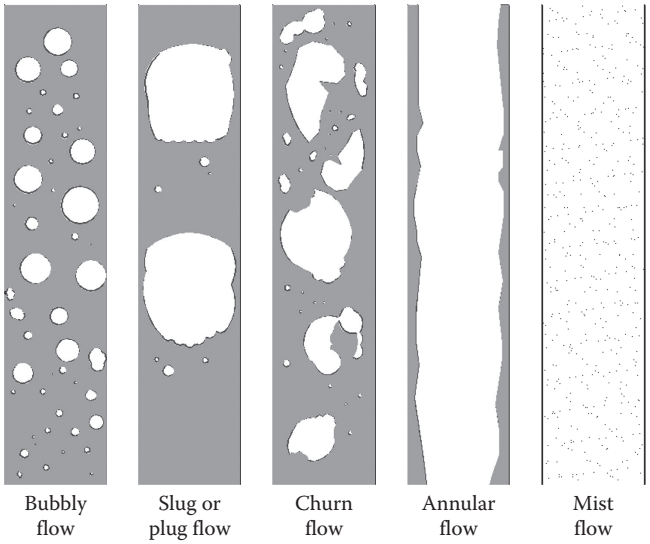


Figure 8.14

Flow patterns during flow boiling in a vertical tube.

as bubbly–slug and annular–mist, also appear as the flow patterns change with increasing quality along the evaporator length. All flow patterns, except for the mist flow and single-phase vapor, can be classified under wetted wall condition, which is desirable from a heat transfer perspective. Heat transfer and pressure drop are closely related to the existing flow patterns.

The flow patterns described in Figure 8.13 refer to flow boiling in a horizontal tube. Figure 8.14 shows the flow patterns in a vertical tube. The major differences are the existence of a churn flow pattern, in which the liquid and vapor flow as an agitated mixture, the distortion of the vapor plugs due to buoyancy forces, and the absence of a stratified flow. Vertical upflow and downflow have some differences, mainly at low flow velocities.

Numerous attempts have been made in the literature to identify flow patterns existing under a given set of operating conditions—liquid- and vapor-phase properties, tube diameter, and mass flux. Flow pattern maps developed for adiabatic flows are generally used for flow boiling, although such an approach introduces significant errors at higher heat fluxes.

The influence of boiling on flow patterns becomes important at higher heat fluxes as the rapidly evaporating liquid–vapor interface of a growing bubble or a vapor plug introduces additional forces. In the studies conducted on the conventional channels (>3 mm hydraulic diameter), the effect of heat flux has been ignored, and researchers have used the adiabatic flow pattern maps for flow boiling as well. As the heat flux increases, the rapid expansion at a nucleating bubble causes major changes in the flow patterns, particularly for small hydraulic diameter channels ($D_h < 3$ mm). This aspect has been extensively discussed by Kandlikar (2004) for flow boiling in microchannels.

8.2.4 Subcooled Flow Boiling Heat Transfer

Kandlikar (1998a) proposed that the nucleate boiling term in the nucleate boiling region of the saturated flow boiling correlation by Kandlikar (1990) (see Equation 8.56) should be able to represent the FDB in a subcooled flow since the convective contribution is negligible. One of the features of this correlation, as reported by Kandlikar (1991a), is its ability to predict the trends in h versus x in the low-quality region, explaining the reasons for increasing or decreasing h for different cases. The heat transfer coefficient h^* in the *FDB* region is thus given by the following equation derived from the nucleate boiling–dominant region of the Kandlikar correlation:

$$h^* = 1058.0 Bo^{0.7} F_{Fl} h_{LO} \tag{8.56}$$

Note that h^* is based on the wall superheat with $q'' = h^* \Delta T_{Sat}$. The boiling number is defined as $Bo = q''/(Gh_{fg})$, with G (kg/m^2 s) being the total mass flux, F_{Fl} the fluid–surface parameter that accounts for the different

nucleation characteristics of different surface–fluid combinations, and h_{LO} the single-phase heat transfer coefficient for all flow in the liquid phase at the saturation temperature obtained from appropriate equations: for the laminar flow, Nu is constant for fully developed laminar flow, or for the turbulent flow (Gnielinski, 1976, Petukhov and Popov, 1963 correlations along with the following property correction factor recommended by Petukhov, 1970)

$$Nu_{LO} = Nu_{LO,cp}\left(\frac{\mu_B}{\mu_w}\right)^{0.11} \tag{8.57}$$

where $Nu_{LO,cp}$ is the Nusselt number with constant properties obtained from the following equations and the subscripts B and w refer to the properties at bulk and wall temperatures, respectively:

Petukhov and Popov (1963), for $0.5 \le Pr \le 2000$ and $10^4 \le Re_{LO} \le 5 \times 10^6$, obtained

$$Nu_{LO,cp} = \frac{Re_{LO}Pr_L(f/2)}{1.07 + 12.7\left(Pr_L^{2/3} - 1\right)(f/2)^{0.5}} \tag{8.58}$$

and Gnielinski (1976), for $0.5 \le Pr \le 2000$ and $2300 \le Re_{LO} \le 10^4$, obtained

$$Nu_{LO,cp} = \frac{\left(Re_{LO} - 1000\right)(f/2)Pr_L}{\left[1 + 12.7\left(Pr_L^{2/3} - 1\right)(f/2)^{0.5}\right]} \tag{8.59}$$

where f is the friction factor given by the following equation:

$$f = \left[1.58\ln\left(Re_{LO}\right) - 3.28\right]^{-2} \tag{8.60}$$

The location of where the FDB begins, corresponding to $q''_{FDB,i}$, is obtained by first locating the heat flux q''_{int} at the intersection of the extended single-phase line and the FDB curve given by

$$1058F_{F1}\left(Gh_{fg}\right)^{-0.7} q''_{int} - q''^{0.3}_{int} - 1058h_{LO}F_{F1}\left(Gh_{fg}\right)^{-0.7}\Delta T_{sub} = 0 \tag{8.61}$$

A model proposed by Bowring (1962) is then used to obtain the location where FDB begins:

$$q''_{FBD,i} = 1.4q''_{int} \tag{8.62}$$

A comparison of the predicted heat flux in the FDB region using Equation 8.56 with experimental data of Bergles and Rohsenow (1964) is shown in Figure 8.15. The other three prediction methods by Shah (1977), Thom et al. (1965), and Mikic and Rohsenow (1969) are also shown in Figure 8.15. It is seen that the present model is able to predict the trend as well as actual values in the FDB region accurately.

The heat transfer in the partial boiling region, from $x = 0$ to the beginning of the FDR, is obtained by interpolation between the two end locations. Further details of the interpolation method are described by Kandlikar (1998a, 1999).

The *partial boiling* region is identified as the region between the ONB and the onset of FDB. The heat transfer in this region is calculated by a procedure outlined by Kandlikar (1998a) as follows.

The heat flux q''_{FDB} at FDB is obtained from Equation 8.62, and q''_{ONB} at ONB is obtained from Equation 8.51. For the heat flux q''_{PB} in the partial boiling region, the following equation is employed:

$$q''_{PB} = a + b\left(T_w - T_{Sat}\right)^m \tag{8.63}$$

The constants a and b are obtained from the known heat fluxes at FDB and ONB as follows:

$$b = \frac{q''_{FBD} - q''_{ONB}}{\left(\Delta T_{Sat,FDB}\right)^m - \left(\Delta T_{Sat,ONB}\right)^m} \tag{8.64}$$

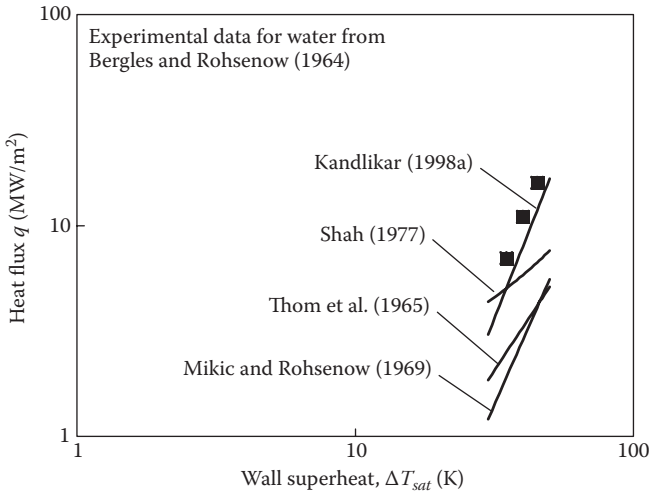


Figure 8.15

Comparison of the predictions from Equation 8.42 in the fully developed boiling with experimental data of Bergles and Rohsenow (1964). (Reproduced from Kandlikar, S.G., *J. Heat Transfer,* 120, 395, 1998a. With permission from ASME.)

and

$$a = q''_{ONB} - b\left(\Delta T_{Sat,ONB}\right)^m \tag{8.65}$$

The exponent m is allowed to vary linearly with heat flux as follows:

$$m = n + pq''_{PB} \tag{8.66}$$

where the constants n and p are obtained by matching the slopes of $m = 1$ at ONB to $m = 1/0.3$ at FDB:

$$p = \frac{\left(1/0.3 - 1\right)}{\left(q''_{FBD} - q''_{ONB}\right)} \tag{8.67}$$

and

$$n = 1 - pq''_{ONB} \tag{8.68}$$

This procedure assures smooth transitions from the single-phase region to the partial boiling region and then to the FDB region. The gradual increase in the exponent m also reflects the fact that more nucleation sites are activated as the wall superheat increases.

A comparison of the present model with the experimental data of McAdams et al. (1949) is shown in Figure 8.16. Equations 8.61 through 8.68 are used in the predictive model. It is seen from this figure that the agreement is quite good in the partial boiling region.

8.2.5 Saturated Flow Boiling Heat Transfer

As liquid flows inside a heated tube surface, nucleate boiling initiates the process of vapor generation during flow boiling. As the bubbles grow and depart, the vapor quality in the flow increases and two-phase flow ensues. The higher specific volume of the vapor causes the flow velocity to increase. The heat transfer in this mode is thus a combination of the nucleation phenomena and enhanced convection, each being influenced by the other mode. The presence of nucleate boiling and convective boiling modes in flow boiling has long been recognized. The heat transfer in saturated flow boiling is thus a combination of the convective heat transfer from the wall to liquid and subsequent film evaporation at the liquid–vapor interface and nucleate boiling at the wall.

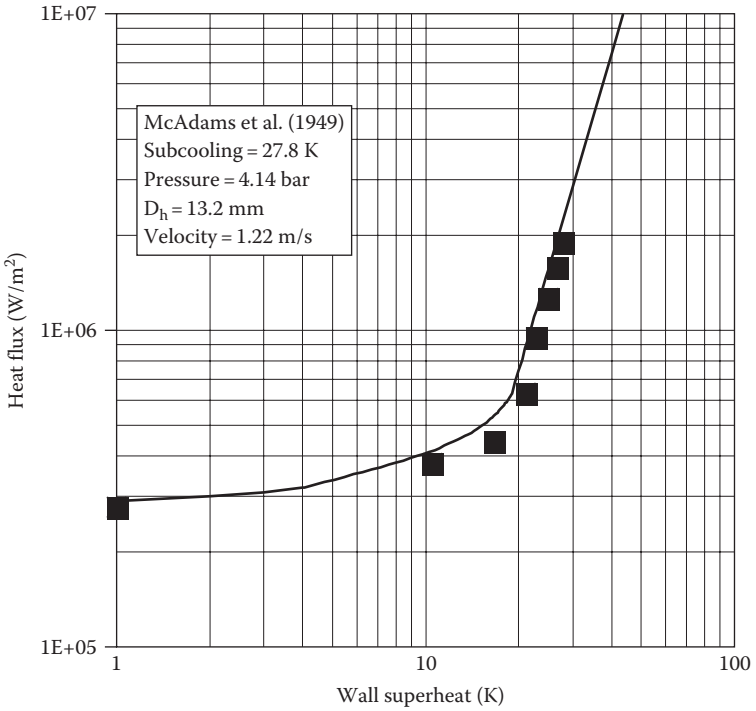


Figure 8.16

Comparison of predictions from Equations 3.47 to 3.54 in the partial boiling region with experimental data of McAdams et al. (1949). (Reproduced from Kandlikar, S.G., *J. Heat Transfer,* 120, 395, 1998a. With permission from ASME.)

There are a large number of correlations available in the literature on the flow boiling of saturated liquids. The Chen (1966) correlation was developed using an additive model with convective enhancement and nucleate boiling suppression due to two-phase flow. It works reasonably well with low-pressure water data but yields significantly higher errors with high-pressure water data and refrigerants. Shah (1982) proposed a correlation in a chart form that worked well with many fluids. Gungor and Winterton (1987) combined the Chen model and the Shah model. Other recent correlations, such as those used by Liu and Winterton (1991) and Steiner and Taborek (1992), employ an asymptotic model in which $h_{\mathrm{TP}}^n = h_{\mathrm{conv}}^n + h_{\mathrm{nucl}}^n$ with $n = 2$ and 3, respectively. The h_{conv} and h_{nucl} are obtained from a combination of earlier models published in the literature. These models work well in some cases; however, because of their highly empirical nature, they do not correctly represent the trends of h_{TP} vs. x. Also, because of their exponentially averaged form, it becomes difficult to identify the role of different mechanisms in studying the parametric effects.

The correlation by Kandlikar (1990, 1991b) is developed from a large data bank consisting of over 10,000 data points and different fluids, including water, refrigerants, and cryogens. It is also able to accurately predict the parametric trends. In particular, it has been shown to predict the variation in h_{TP} well, yielding an increasing trend in h_{TP} with increasing x for fluids with low boiling number, $(=q''/(Gh_{fg}))$, and high liquid-to-vapor density ratio $(=\rho_L/\rho_G)$, representative of the convective boiling–dominant (CBD) region, for example, with water at low pressure and low *Bo*. In contrast, a decreasing trend is predicted for high *Bo* and low density ratio, representative of the nucleate boiling–dominant (NBD) region, for example, with some refrigerants with low density ratios and with high heat fluxes. The flow boiling correlation has been successfully extended to subcooled flow boiling (Kandlikar, 1998a), binary mixtures (Kandlikar, 1998c), and flow boiling in microchannels and minichannels (Kandlikar and Balasubramanian, 2004). In addition, it accounts for nucleation characteristics of a given surface through a fluid–surface parameter F_{Fl}. The Kandlikar (1990, 1991b) correlation is given by

$$h_{TP} = \text{larger of} \begin{cases} h_{TP}\big|_{NBD} \\ h_{TP}\big|_{CBD} \end{cases} \tag{8.69}$$

where h_{TP} in the respective regions are given by the following equations:

$$h_{TP,NBD} = 0.6683 Co^{-0.2} (1-x)^{0.8} f_2(Fr_{LO}) h_{LO} + 1058.0 Bo^{0.7} (1-x)^{0.8} F_{Fl} h_{LO} \tag{8.70}$$

and

$$h_{TP,NBD} = 1.136 Co^{-0.9} (1-x)^{0.8} f_2(Fr_{LO}) h_{LO} + 667.2 Bo^{0.7} (1-x)^{0.8} F_{Fl} h_{LO} \tag{8.71}$$

where

$Co = (\rho_G/\rho_L)^{0.5} [(1-x)/x]^{0.8}$ is the convection number

$Bo = q''/(Gh_{fg})$ is the boiling number

$Fr_{LO}(=G^2/(\rho_L g D))$ is the Froude number with all flow as liquid

The Froude number multiplier $f_2(Fr_{LO})$ is 1 for vertical tubes and for horizontal tubes with $Fr_{LO} \geq 0.04$.

For $Fr_{LO} < 0.04$, $f_2(Fr_{LO})$ is given by the following equation:

$$f_2(Fr_{LO}) = (25 Fr_{LO})^{0.3} \tag{8.72}$$

The single-phase all-liquid heat transfer coefficient h_{LO} is obtained from the Gnielinski (1976) correlation in the range $0.5 \leq Pr_L \leq 2000$ and $2300 < Re_{LO} \leq 10^4$:

$$h_{LO} = \frac{(Re_{LO} - 1000) Pr_L (f/2)(k_L/D)}{\left[1 + 12.7 (Pr^{2/3} - 1)(f/2)^{0.5}\right]} \tag{8.73}$$

The Petukhov and Popov (1963) correlation is employed for $0.5 \leq Pr_L \leq 2000$ and $10^4 < Re_{LO} \leq 5 \times 10^6$:

$$h_{LO} = \frac{Re_{LO} Pr_L (f/2)(k_L/D)}{1.07 + 12.7 (Pr^{2/3} - 1)(f/2)^{0.5}} \tag{8.74}$$

The friction factor f is given by the following equation:

$$f = [1.58 \ln(Re_{LO}) - 3.28]^{-2} \tag{8.75}$$

F_{Fl} is a fluid–surface parameter that depends on the fluid and the heater surface characteristics. Table 8.3 lists the F_{Fl} values for several fluids in copper tubes. These values should be considered as representative for commercial tubing. For stainless steel tubes, F_{Fl} should be taken as 1.0 with all fluids.

Introduction of F_{Fl} in the nucleate boiling term is an important aspect of the Kandlikar correlation. It has been recognized that the nucleation characteristics and associated heat transfer depend on contact angle, surface tension, and available cavity sizes and their distribution on the heater surface. Gaertner (1965) noted that

> …analytical treatments of nucleate boiling that do not consider the nature of the surface cannot accurately predict heat transfer relationships…

The flow boiling model is thus able to account for the different nucleation characteristics of different fluid–surface combinations through the incorporation of F_{Fl}. However, this constant needs to be obtained from the experimental data. Table 8.3 provides the values of F_{Fl} obtained from Kandlikar (1990, 1991b, 1999) and Melin (1996) for different fluids.

Figure 8.17 shows a comparison of the Kandlikar (1990) correlation with the experimental data of Schrock and Grossman (1962). The correlation is able to correctly predict the increasing trend in h_{TP} with x for the low-pressure data (large values of ρ_L/ρ_G) and a decreasing trend for the high-pressure data (low values of ρ_L/ρ_G).

Table 8.3 F_{FI} Values in the Kandlikar Correlation

Fluid	F_{FI}
Water	1.00
R-11	1.30
R-12	1.50
R-13B1	1.31
R-22	2.20
R-32[a]	1.88
R-113	1.30
R-114	1.24
R-125[a]	2.27
R-134a	1.63
R-142b[a]	1.74
R-143a[a]	2.39
R-152a	1.10
R-32/R-132	3.30
60%–40% (by wt)	
Butane[a]	1.50
Kerosene	0.488
Propane[a]	2.15

Note: For stainless steel tubes, use $F_{FI} = 1.0$ for all fluids.

[a] Values obtained by Melin (1996).

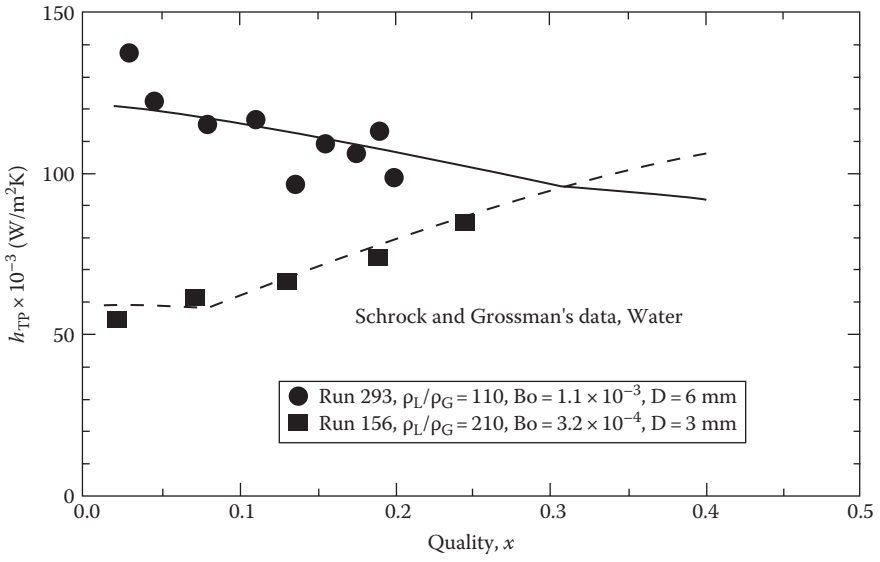


Figure 8.17

Comparison of Schrock and Grossman's (1962) experimental data with the Kandlikar (1990) correlation. (Reprinted from Kandlikar, S.G., Flow boiling in circular tubes, Sections 15.1–15.3, in *Handbook of Phase Change, Boiling and Condensation*, Kandlikar, S.G., Dhir, V.K., and Celata, G.P., Eds., Taylor & Francis, Philadelphia, PA, 1999. With permission from Taylor & Francis.)

The Kandlikar (1990) correlation is recommended in the wetted wall region below a quality of about 0.8. At higher qualities, local dryout may occur with a significant reduction in the heat transfer coefficient.

The Kandlikar (1990, 1991b) correlation was extended to microchannels (10 μm < $D_h \leq$ 200 μm) and minichannels (200 μm < $D_h \leq$ 3 mm) by Kandlikar and Balasubramanian (2004). The final form is given in Kandlikar (2014). As the all-liquid flow Reynolds number enters the laminar region, the use of Nu_{LO} = constant (dependent on geometry and wall boundary conditions) is recommended for calculating h_{LO} instead of the single-phase turbulent flow correlations. Furthermore, for microchannels, it is found that

h_{TP} falls entirely in the NBD region and is given by Equation 8.70 without the Froude number correction (use $f_2(Fr_{LO}) = 1$). The flow boiling heat transfer mechanisms in these geometries are discussed in detail by Kandlikar and Balasubramanian (2004).

8.2.6 Flow Boiling Map

The main parameters governing the flow boiling heat transfer can be represented in terms of the following four nondimensional groups:

1. Nondimensionalized heat transfer coefficient, h_{TP}/h_{LO}
2. Modified boiling number, $Bo^* = Bo(F_{Fl})^{1/0.7} = q''(F_{Fl})^{1/0.7}/(Gh_{fg})$
3. Density ratio, ρ_L/ρ_G
4. Vapor quality, x

The parametric trends of h_{TP} with various operating parameters were represented by Kandlikar (1991a) in terms of a flow boiling map, as shown in Figure 8.18. Density ratio is seen as an important factor governing the role of the convective contribution, which gives rise to an increasing trend in an h_{TP}/h_{LO} versus x plot in the CBD region. The magnitude of Bo^* governs the nucleate boiling contribution, which essentially displays a decreasing trend in an h_{TP}/h_{LO} versus x plot in the NBD region. These parametric trends have been confirmed for a number of fluids, including water and refrigerants.

8.2.7 Flow Boiling of Binary Mixtures

The flow boiling of mixtures is encountered in many practical applications, including chemical, petrochemical, process, and refrigeration industries. The difference in boiling points of the pure components in a mixture causes preferential vaporization of the more volatile component across liquid–vapor interfaces at the nucleating bubbles, near an annular film or around a vapor slug. Depletion of the more volatile component raises the local saturation temperature at the liquid–vapor interface. This also results in the diffusion of the more volatile component in the liquid phase toward the interface. The net result is the lowering of the heat transfer coefficient for the mixture below the average value obtained from the linear mass- or mole-fraction-averaged interpolation between the pure component values.

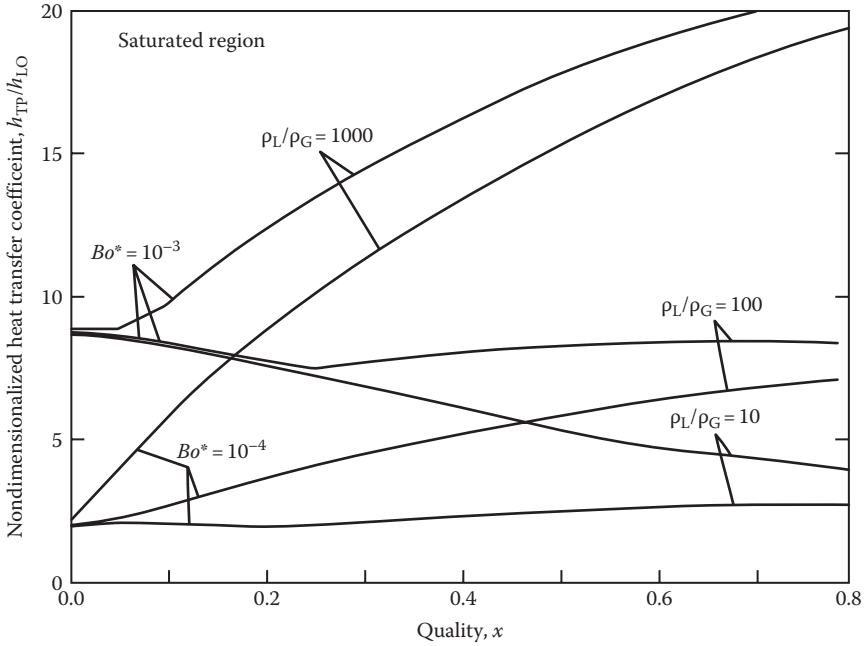


Figure 8.18

Flow boiling map for subcooled and saturated flow boiling. (Reproduced from Kandlikar, S.G., *Trans. ASME, J. Heat Transfer,* 113, 190, 1991a. With permission from ASME.)

A number of researchers have provided useful correlations to predict the heat transfer coefficients in a binary (two components in both liquid and vapor phases) system. Among the more successful ones are Calus et al. (1973), Bennett and Chen (1980), Jung (1988), and Kandlikar (1998c). One of the main difficulties encountered in modeling binary flow boiling is the uncertainty in predicting the interfacial concentration at the nucleating bubble interface. Kandlikar (1998b) used a control volume approach to obtain the interfacial concentration in pool boiling and later extended it to flow boiling.

In the Kandlikar (1998c) model, a volatility parameter V_1 is defined as:

$$V_1 = \left(\frac{c_{p,L}}{h_{fg}}\right)\left(\frac{\alpha}{D_{12}}\right)^{0.5}\left|\frac{dT}{dx_1}\left(y_1 - x_1\right)\right| \tag{8.76}$$

where

α is the thermal diffusivity of the liquid

D_{12} is the mass diffusivity of component 1 in a mixture of components 1 and 2

x_1 and y_1 are the liquid and vapor mass fractions of the more volatile component 1

Three regions in binary flow boiling are identified based on the value of V_1

Region I: Near-azeotropic region, $V_1 < 0.03$:

$$h_{TP} = \text{larger of}\begin{cases} h_{TP}\big|_{NBD} \\ h_{TP}\big|_{CBD} \end{cases} \tag{8.77}$$

Use pure component correlations, Equations 8.70 and 8.71, with mixture properties.

Region II: Moderate diffusion-induced suppression region, $0.03 < V_1 < 0.2$, and $Bo > 1E\text{-}4$:

$$h_{TP} = h_{TP}\big|_{CBD} \tag{8.78}$$

The heat transfer is entirely in the CBD region. Use the pure component correlation in the NBD region, Equation 8.70, with mixture properties.

Region III: Severe diffusion-induced suppression region: (a) for $0.03 < V_1 < 0.2$ and $Bo < 1E\text{-}4$ and (b) $V_1 > 0.2$:

$$h_{TP,CBD} = 1.136Co^{-0.9}\left(1-x\right)^{0.8} f_2\left(Fr_{LO}\right)h_{LO} + 667.2Bo^{0.7}\left(1-x\right)^{0.8} F_{Fl}h_{LO}F_D \tag{8.79}$$

A diffusion-induced suppression factor F_D is introduced in the nucleate boiling term to reflect the reduction in heat transfer coefficient due to the mass diffusion resistance present at the interface. F_D is given by the following equation:

$$F_D = 0.678\left[1 + \left(\frac{c_{p,L}}{h_{fg}}\right)\left(\frac{\alpha}{D_{12}}\right)^{0.5}\left|\frac{dT}{dx_1}\left(y_1 - x_1\right)\right|\right]^{-1} \tag{8.80}$$

The equilibrium phase mass concentrations are calculated at the total system pressure, and dT/dx_1 corresponds to the slope of the bubble point curve at a liquid-phase concentration of x_1. The diffusivity D_{12} is calculated from the following equation:

$$D_{12} = \left(D_{12}^0\right)^{\tilde{x}_2}\left(D_{21}^0\right)^{\tilde{x}_1} \tag{8.81}$$

where

$\tilde{x}_1$ and $\tilde{x}_2$ are the respective molar concentrations of components 1 and 2

D_{12}^0 and D_{21}^0 are the individual component diffusivities at very low concentrations given by the following Wilke–Chang correlation

$$D_{12}^{0} = 1.1782 \times 10^{-16} \frac{(\phi M_2)^{1/2} T}{\mu_{L,2} V_{m,l}} \tag{8.82}$$

where

ϕ is the association factor for the solvent (2.26 for water, 1.9 for methanol, 1.5 for ethanol, 1.9 for ethylene glycol, and 1.0 for unassociated solvents, including benzene, methane, and refrigerants)
M is the molecular weight
μ_L is the liquid viscosity
V_m is the molar volume in m^3/kg mol
T is the temperature in K

Table 8.4 shows the mean deviations between the predicted values using the Kandlikar (1998c) correlation described earlier and the experimental data of Jung et al. (1988), Hihara et al. (1989), Takamatsu et al. (1993), Celata et al. (1993), and Murata and Hashizume (1993). The ranges of parameters are also included in Table 8.4. It is seen that the agreement is quite good in all three regions. Figure 8.19 shows a comparison of a data set obtained by Murata and Hashizume (1993) for R-134a/R-123 mixture in the severe suppressed region, that is, Region III.

Heat transfer coefficients in multicomponent systems are even more difficult to predict. There is no reliable general methodology available to make any recommendation for mixtures of three or more components. It is suggested that the most volatile component be taken as component 1 and the rest of the mixture treated as component 2, and the binary flow boiling correlation scheme applied as a first approximation.

Table 8.4 Comparison of the Binary Flow Boiling Correlation of Kandlikar (1998c) with Experimental Data from the Literature

Data Source	Binary System	*Bo* (×10⁻⁵)	*Co*	V_1	Mean Average Dev. (%)
Jung et al. (1988)	R-12/R-152a	6.1–6.3	0.52–1.8	0.025–0.044	8.3
	R-12/R-152a	8.8–71	0.01–1.45	0.013–0.022	10.4
	R-22/R-114	7.1–77	0.04–1.39	0.1–0.72	13.0
	R-500	7.5–77	0.01–1.83	0.0006–0.002	11.4
Hihara et al. (1989)	R-12/R-22	47–61	0.01–1.91	0.015–0.064	13.3
	R-22/R-114	37–60	0.023–1.64	0.07–0.67	9.0
Takamatsu et al. (1993)	R-22/R-114	19–76	0.018–3.2	0.28–0.54	9.2
Celata et al. (1993)	R-12/R-114	9.4–88	0.52–1.83	0.06–0.15	8.9
Murata and Hashizume (1993)	R-134a/R-123	20–185	0.004–0.05	0.28–0.34	12.1

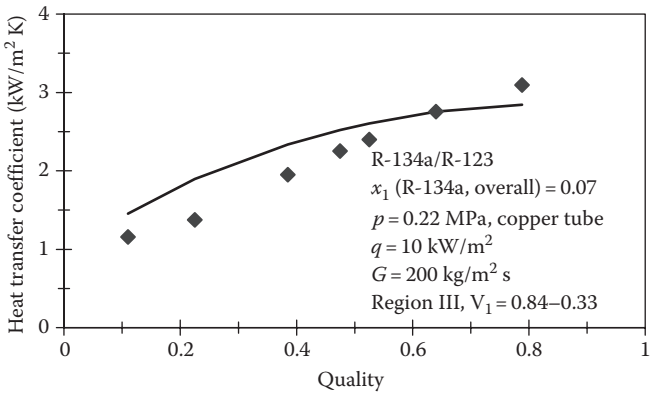


Figure 8.19

Comparison of the Kandlikar (1998c) correlation with R-134a/R-123 flow boiling data of Murata and Hashizume (1993) in the severe diffusion-induced suppression region (Region III). (Reproduced from Kandlikar, S.G., *J. Heat Transfer,* 120, 388, 1998c. With permission from ASME.)

8.2.8 Critical Heat Flux in Flow Boiling

The heat transfer coefficient in flow boiling is dramatically reduced as the liquid ceases to be in contact with the walls of the flow channel. CHF condition represents the upper limit of operation of a boiling system in heat flux–controlled systems. It results in a considerable heat transfer degradation in temperature-controlled systems (Kandlikar, 2001b). *Dryout* condition represents the upper limit of the convective boiling heat transfer. It follows the gradual depletion of liquid due to evaporation and entrainment of the liquid film in the vapor. Knowledge of the conditions leading to CHF and prediction of CHF for a given geometry under a given set of operating conditions are extremely important in the safe operation of flow boiling equipment, such as nuclear reactors, boilers, refrigeration and cryogenic evaporators, and cooling of high heat flux components and devices.

Mitigating the risks associated with a catastrophic failure following the CHF condition have attracted significant research efforts worldwide for over 60 years. Earlier, Lang (1888) recognized the existence of severe heat transfer degradation through his experiments with high-pressure water. Drew and Mueller (1937) provide an excellent summary of historical developments in this area. Extensive experimental and numerical studies have been conducted since the 1960s on the CHF with water in nuclear reactors under safe operating as well as under accident conditions. A better CHF predictive ability allows the operation of a nuclear reactor with lower safety margins, thereby increasing the output capacity of the nuclear power plant. Understanding the mechanisms leading to CHF permit the development of techniques or operating procedures to increase the CHF for a given system configuration.

CHF in subcooled and saturated flow boiling has been studied with water and some other fluids under different conditions: (1) uniform heat flux along a channel length; (2) uniform heat flux along a tube, with a short length of higher heat flux; and (3) circumferentially uniform, but axially nonuniform heat flux.

A brief overview of CHF under subcooled and saturated flow boiling conditions in uniformly heated circular tubes is presented in this section. For more extensive coverage, the reader is referred to the detailed treatise on this topic; see, for example, Tong (1965), Boyd (1983a,b), Tong (1988), Collier and Thome (1994), Hewitt (1998), Celata and Mariani (1999), Kandlikar et al. (1999), and Tong and Tang (1997).

8.2.8.1 CHF in Subcooled Flow Boiling

The CHF in subcooled flow boiling is reached in one of the following three ways (Tong and Hewitt, 1972):

1. A dry patch forms on the heater surface after a bubble has departed. The local temperature in some cases rises to a point where the water fails to rewet the surface, leading to the CHF condition.
2. A thin layer of bubbles is formed on the wall at moderate heat and mass fluxes. The neighboring bubbles then cluster together to form a vapor layer underneath the bulk liquid and restrict liquid access to the heater wall.
3. A slug flow is observed under certain conditions at low mass fluxes. The liquid film surrounding the vapor bubble evaporates and dries out. If the vapor bubble is sufficiently long, the heater wall becomes heated during the passage of the bubble and leads to the CHF condition.

Celata and Mariani (1999) summarize the previous models in the following five categories: (1) boundary layer ejection model, (2) critical enthalpy in the bubble layer model, (3) liquid flow blockage model, (4) vapor removal limit and near-wall bubble crowding model, and (5) liquid sublayer dryout model. A brief description of each of the mechanisms is given as follows (Kandlikar, 2001b).

8.2.8.1.1 Boundary Layer Ejection Model. This model was originally proposed by Kutateladze and Leont'ev (1966). The boiling mechanism is compared with the injection of a gas stream into the liquid flow through a permeable plate. The ejection of bubbles into the mainstream is postulated to be the cause of the boundary layer separation at the heater surface. However, the photographic study conducted by Mattson et al. (1973) does not show any abrupt changes or high-velocity vapor ejection in the macroscopic structure of the flow near the CHF location.

8.2.8.1.2 Critical Enthalpy in the Bubble Layer Model. This model was proposed by Tong et al. (1966). They assumed that a layer of small bubbles flowing adjacent to the heater surface traps the liquid between the bubble layer and the heated surface. This bubble layer separates the trapped superheated liquid layer from the mainstream. They postulated that CHF condition is reached when this superheated liquid layer attains a

certain limiting enthalpy. This model does not provide a clear explanation of the physical events leading to CHF other than stating the existence of a critical liquid enthalpy in the superheated liquid layer.

8.2.8.1.3 Liquid Flow Blockage Model Bergel'son (1980) proposed this model based on the assumption that the flow of liquid toward the heated surface is blocked by the outflow of vapor from the heater surface. This behavior may be feasible under very low mass flux conditions, where the liquid and vapor flow structure is similar to that in the case of pool boiling. However, the vapor flow away from the wall is not seen to be a limiting factor in subcooled flow boiling. Owing to inadequate evidence supporting this mechanism, this model is not being pursued by other researchers.

8.2.8.1.4 Vapor Removal Limit and Near-Wall Bubble Crowding Model This model is based on the limit of turbulent interchange between the bubbly layer and the bulk of the liquid and the crowding of bubbles preventing liquid access to the heated wall (Hebel et al., 1981).

Weisman and Pei (1983) consider the existence of a bubbly layer adjacent to the wall at subcooled or low-quality conditions. It is postulated that the CHF condition occurs when the volume fraction of vapor in the bubbly layer just exceeds the critical volume fraction at which an array of ellipsoidal bubbles can be maintained without significant contact between the bubbles. Weisman and Pei used the homogeneous flow model in the bubbly layer. The resulting model has three adjustable empirical constants that are evaluated from the experimental data. This model includes the two-phase flow considerations that are readily extendable to the saturated flow conditions as well.

8.2.8.1.5 Liquid Sublayer Dryout Model Katto and Yokoya (1968) proposed a preliminary model describing the macrolayer dryout as the mechanism leading to CHF in pool boiling. Later, Haramura and Katto (1983) completed the development of the model by introducing the mechanism for macrolayer formation. This model is extended to flow boiling by considering a liquid film trapped between a bubble and the heater wall. Numerous vapor stems emerge on the heater surface through the liquid film. Under flow conditions, both the liquid sublayer and the vapor film move in the flow direction. Liquid is fed into the film from the upstream end, whereas the film thickness decreases along the flow direction due to evaporation. The CHF condition is reached when the heat supplied by the heater surface provides the necessary latent heat required to completely evaporate the liquid entering the film. Katto (1990a,b) provided a detailed description of the model based on the macrolayer evaporation. His model uses several empirical constants in determining the thickness, liquid film flow rate, and temperature of the liquid entering into the sublayer.

Lee and Mudawar (1988) considered the effect of velocity in the subcooled flow in terms of stretching the large bubble in the Haramura and Katto (1983) model to a vapor blanket of length equal to the critical Helmholtz wavelength. The sublayer mass velocity, its thickness, and the vapor blanket length were calculated with buoyancy and drag forces acting on the vapor blanket. The modeling resulted in a correlation scheme with three empirical constants that were determined from a large set of experimental data.

Celata et al. (1994) eliminated the empirical constants in the Katto (1990a,b) and Lee and Mudawar (1988) models by using the homogeneous flow model and introducing appropriate correlations from available literature to calculate the sublayer thickness, flow rate, enthalpies, and vapor blanket length. However, the basic features of the model are similar to that proposed by Lee and Mudawar (1988).

The recent models discussed in the preceding section present a significant improvement over the earlier models by considering CHF as a local phenomenon. However, further improvements are needed to account for the effect of contact angle on CHF. A major question that remains unanswered in the earlier models is the description of the mechanism that prevents rewetting of the dry patches. The pool boiling model of Kandlikar (2001a) considers the evaporation momentum force experienced by an evaporating interface, and it is postulated that this force is responsible for pushing the liquid front away. Recently, Kandlikar (2004) developed two nondimensional groups that compare the evaporation momentum, surface tension, and inertia forces. The use of these new nondimensional groups in CHF prediction in flow boiling has shown promising results.

8.2.8.2 CHF in Low-Quality Saturated Flow Boiling

CHF at low qualities in saturated flow boiling is similar to CHF in subcooled flow boiling. Bubble crowding and liquid film dryout under a growing bubble or a slug are the two main mechanisms leading to CHF in low-quality subcooled flow boiling. Therefore, the mechanisms and correlations are the same under these conditions.

8.2.8.3 Correlations for CHF in Subcooled Flow Boiling and Low-Quality Saturated Flow Boiling

Numerous correlations specific to certain geometries and operating conditions are available in the literature and are recommended for use if they match the corresponding conditions. An extensive review of CHF correlations for different geometries and operating conditions is given by Tong and Tang (1997).

For general usage, Gunther's (1951) correlation should be used to provide a good approximation:

$$q''_{CHF} = 7198u^{0.5}\Delta T_{Sub.exit} \tag{8.83}$$

(The recommended ranges are p = 0.1 – 1.1 MPa, u = 1.5–12.1 m/s, $q''_{\mathrm{CHF}} = 0.4 - 11.4\ \mathrm{MW/m^2}$, and $\Delta T_{\mathrm{Sub,exit}}$ = 11–39 K.)

Note that this correlation is valid only for water and cannot be extrapolated beyond the quoted ranges of parameters (it does not approach the pool boiling CHF as $u \to 0$).

The correlation of Tong et al. (1968) for CHF with water in uniformly heated tubes is widely accepted:

$$\frac{q''_{CHF}}{Gh_{fg}} = \frac{C}{\mathrm{Re}^{0.6}} \tag{8.84}$$

(recommended ranges are p = 5.5–13.6 MPa; u = 0.68–5.9 m/s; void fraction at CHF, 0.35; D = 3–10 mm; L/D = 5–100; void fraction is evaluated using Thom et al. (1965) model; and $T_{\mathrm{Sub,exit}}$ = 11–39 K) where G is the mass flux, Re the Reynolds number, and

$$C = 1.76 - 7.433x_{exit} + 12.222x_{exit}^2 \tag{8.85}$$

All properties are evaluated at saturation condition. Celata et al. (1994) extended the range of the proposed correlation to lower pressures by replacing C with C' given by the following correlation:

$$C' = \left(1.76 - 7.433x_{exit} + 12.222x_{exit}^2\right)\Psi \tag{8.86}$$

(recommended ranges are p = 5.5 MPa, u = 2.2–40 m/s, $T_{\mathrm{Sub,exit}}$ = 15–190 K, and D = 0.33–15 mm) with Ψ (in MPa) given by the following equation:

$$\Psi = \begin{cases} 1 & \text{for } x_{exit} < -0.1 \\ 0.825 + 0.986x_{exit} & \text{for } 0 > x_{exit} \geq 0.1 \end{cases} \tag{8.87}$$

In evaluating CHF from the previous equations, the heat balance method requiring an iterative procedure is recommended (Celata and Mariani, 1999).

For small-diameter tubes, the experimental data by Vandervort et al. (1994) show the effect of diameter. They performed experiments in tubes having inside diameter ranging from 0.3 to 2.7 mm, mass flux from 5,000 to 40,000 kg/m^2 s, exit subcoolings from 40°C to 135°C, and exit pressures from 0.2 to 2.2 MPa.

8.2.8.4 CHF in Annular Flow due to Liquid Film Dryout in Saturated Flow Boiling

As quality increases, the flow pattern changes to annular flow with its characteristic liquid film around the circumference and a central vapor core. The liquid film dryout depends on the rates of its evaporation, liquid entrainment in the vapor, and deposition of liquid back from the vapor core into the film. The rates of evaporation as well as entrainment to some extent depend on the imposed heat flux. The location of the dryout and the corresponding value of CHF at this location are of interest. It is desirable to extend the dryout location to higher qualities as the heat transfer rate is dramatically reduced following the *dryout*.

Simple correlations are not available to predict the *dryout* location. Elaborate methods are available in the literature to predict the entrainment and deposition rates (e.g., Collier and Thome, 1994). Another method that is widely followed consists of extensive tabulation of CHF data for a standardized circular tube of 8 mm diameter as a function of pressure, mass flux, and quality at CHF. This approach was originally developed by Doroshchuk et al. (1975). The recent updated tables are published by Groeneveld et al. (1996).

Using these tables, the CHF value for various tube diameters under the same pressure, mass flux, and quality conditions is obtained by the following equation:

$$q''_{CHF} = q''_{CHF,8\text{ mm}}\left(\frac{D}{0.008}\right)^{k} \tag{8.88}$$

Groeneveld et al. (1996) recommend a value of $k = -1/2$ based on 22,946 data points for water covering the ranges of pressure from 0.1 to 20 MPa, mass flux up to 8,000 kg/m^2 s, and quality of −0.5 to 1.0 at discrete values covering tube diameters from 3 to 25 mm. Other researchers proposed a value of $k = -1/3$ (Groeneveld et al., 1986, Smith, 1986).

The heat transfer mechanisms were investigated by Kandlikar (2004), who proposed the following two nondimensional numbers. K_1 represents the ratio of evaporation momentum force to inertia force, whereas K_2 represents the ratio of evaporation momentum and surface tension forces:

$$K_1 = \left(\frac{q''}{h_{fg}}\right)^2 \frac{\rho_L}{\rho_G} \tag{8.89}$$

and

$$K_2 = \left(\frac{q''}{h_{fg}}\right)^2 \frac{D}{\rho_G \sigma} \tag{8.90}$$

Kandlikar (2010) considered the scale effects of tube diameter on the evaporation momentum, viscous, inertia, and surface tension forces to propose a CHF model as an extension of the force balance model developed earlier for pool boiling (Kandlikar, 2001a). The forces were nondimensionalized using the following nondimensional numbers, K_2 (ratio of evaporation momentum to surface tension forces); Weber number, We (ratio of inertia to surface tension forces); and capillary number, Ca (ratio of viscous to surface tension forces):

$$K_{2,CHF} = \left(\frac{q''_{CHF}}{h_{fg}}\right)^2 \left(\frac{D_h}{\rho_V \sigma}\right) \tag{8.91}$$

$$We = \frac{G^2 D_h}{\rho_m \sigma} \tag{8.92}$$

$$Ca = \frac{\mu_L G}{\rho_L \sigma} \tag{8.93}$$

The average density ρ_m in Equation 8.92 is given by the following equation:

$$\frac{1}{\rho_m} = \frac{x}{\rho_V} + \frac{1-x}{\rho_L} \tag{8.94}$$

A particular trend was observed with Weber number, and the correlation scheme was distinguished based on the inertia effects as follows:

1. Low-inertia region (LIR): We < 900
2. High-inertia region (HIR): We ≥ 900

Further, the LIR region was found to be split into two CHF subregions. They are classified as follows:

1. Low-inertia region, lower-CHF subregion (LIR-LC)
2. Low-inertia region, higher-CHF subregion (LIR-HC)

The correlating scheme for CHF over the entire range was given by one of the following two equations depending on the specific range of parameters:

$$K_{2,CHF} = a_1\left(1+\cos\theta_R\right) + a_2\,\mathrm{We}(1-x) + a_3\mathrm{Ca}\left(1-x\right) \tag{8.95}$$

or

$$K_{2,CHF} = a_4\left[a_1\left(1+\cos\theta\right) + a_2\,\mathrm{We}(1-x) + a_3\mathrm{Ca}\left(1-x\right)\right] \tag{8.96}$$

where θ_R is the receding contact angle and $a_1 - a_4$ are the constants. The specific equations applicable in different inertia regions and CHF subregions are given as follows:

Low-inertia region (LIR): We < 900
  High-CHF subregion (LIR-HC): $L/D \leq 140$ Equation 8.95
  Low-CHF subregion (LIR-LC): $L/D \geq 230$ Equation 8.96
High-inertia region (HIR): We ≥ 900
  High-CHF subregion (HIR-HC): $L/D < 60$ Equation 8.95
  Low-CHF subregion (HIR-LC): $L/D \geq 100$ Equation 8.96

The values of constants are as follows:

$$\begin{aligned} a_1 &= 1.03\times10^{-4} \\ a_2 &= 5.78\times10^{-5} \\ a_3 &= 0.783 \\ a_4 &= 0.125 \end{aligned} \tag{8.97}$$

The transition criterion between the macroscale and microscale CHF phenomena is obtained by equating the inertia forces with the viscous forces. The following transition criteria are proposed:

$$\frac{\mathrm{We}}{\mathrm{Ca}} = \frac{a_3}{a_2} = \frac{0.783}{5.78\times10^{-5}} = 13{,}547 \tag{8.98}$$

In terms of the diameter and flow Reynolds numbers, the transition criterion may be expressed as follows:

$$D_{h,transition} = 13{,}547\,\frac{\mu_L}{G}\,\frac{\rho_m}{\rho_L} \tag{8.99}$$

$$\mathrm{Re}_{\mathrm{transition}} = \frac{GD_{\mathrm{h,transition}}}{\mu_{\mathrm{L}}} = 13{,}547\,\frac{\rho_{\mathrm{m}}}{\rho_{\mathrm{L}}} \tag{8.100}$$

The microscale effects begin to become important at diameters or Reynolds numbers given by Equations 8.99 and 8.100, respectively. Further details on the scale effects are described by Kandlikar (2010).

The heat transfer in the post-CHF region depends on the extent of droplet deposition on the tube wall. Beyond a certain temperature, the heater surface may exceed the Leidenfrost temperature and the heat transfer rate by convection would reduce significantly. Correlations by Groeneveld (1973) and Nishikawa et al. (1986) are recommended. Since these correlations are developed for specific fluids, geometries, and operating conditions, extreme caution should be exercised while extending their applicability to parameter ranges beyond their parent database.

8.2.9 Flow Boiling in Compact Heat Exchangers

Flow boiling in compact heat exchangers is extensively employed in chemical, process, air liquefaction, and refrigeration applications. The use of plate fin and plate heat exchangers is common in these applications.

A detailed survey on this topic is presented by Kew and Cornwell (1999). They reviewed a number of available correlations for offset-strip fins, perforated fins, and louvered fins. The correlation schemes presented by Feldman et al. (1996), Kandlikar (1991b), and Wieting (1975) are noteworthy. In general, results reveal that, contrary to the common expectation, the role of nucleate boiling becomes more important in narrow channels found in compact heat exchanger passages when compared to conventional channels.

8.2.10 Flow Boiling Augmentation

Although the heat transfer coefficients during flow boiling are relatively high compared to the corresponding single-phase liquid flows, further enhancements are desired in a number of applications. Many augmentation techniques have been proposed in the literature; a comprehensive review of various techniques for accommodating high heat fluxes is given by Bergles (1997). Among the methods employed, microfin tubes, also called grooved tubes in Japanese and Korean literature, have proved to be quite attractive in flow boiling applications. Tubes of different microfin geometries have been studied in the literature (e.g., Khanpara et al., 1986, 1987, Koyama et al., 1995) and are now routinely applied in refrigeration evaporators. The flow boiling performance of these tubes can be predicted by a number of correlation schemes proposed in the literature (e.g., Kandlikar, 1991b, Kandlikar and Raykoff, 1997).

Structured and porous surfaces that promote pool boiling heat transfer have been successfully applied for flow boiling enhancement as well. The use of such surfaces is common especially in the air separation and cryogenic industries, where very small temperature differences are often employed in the evaporation of air constituents during the separation processes.

Microchannels have received significant attention in both single-phase flow and flow boiling because of their higher performance, including higher CHF. The flow instabilities have been identified as one of the major limitations, but these have been overcome with inlet flow restrictors and artificial nucleation sites. Some of the recent developments in this field include open microchannels with taper and vapor venting designs. A detailed analysis of microchannel flow boiling phenomena is presented by Kandlikar (2014), and the new design configurations are discussed in Kandlikar (2015). These designs are able to dissipate heat fluxes over 1,000 W/cm^2 with a heat transfer coefficient in excess of 500,000 W/m^2 °C.

8.2.11 Enhancement of CHF in Flow Boiling

The techniques to enhance the CHF in subcooled and low-quality saturated boiling regions can be divided into passive and active types. Detailed surveys of various enhancement techniques are presented by Celata and Mariani (1999) and Boyd (1985).

The passive devices consist of twisted tapes and swirl flow devices, helically coiled tubes, surface roughness, and extended surfaces. These devices induce secondary radial and circumferential velocity components over the tube wall causing an increase in CHF. These devices result in significantly higher-pressure drop penalties compared with a smooth tube. The CHF enhancement is 1–3 times the corresponding smooth tube values under the same operating conditions, whereas the pressure drop increase is higher, depending on the specific enhancement technique. The Nariai et al. (1992) correlation is recommended for the prediction of CHF enhancement with twisted tapes:

$$\frac{q''_{CHF}}{q''_{CHF,smooth}} = \left\{1 + 10^{-2}\vartheta \exp\left[\left(-10^{-6}p\right)^2\right]\right\}^{1/6} \tag{8.101}$$

where ϑ is the nondimensional centrifugal acceleration given by

$$\vartheta = \frac{\pi^2 u^2}{2gDTTR} \tag{8.102}$$

where

u is the average flow velocity
D is the tube diameter
TTR is the twist ratio

CHF in the high-quality region resulting from *dryout* can be enhanced by effectively replenishing the heated surface with liquid. Liquid retention in grooves and roughness structures effectively delays the dryout location.

Nomenclature

a,b	Constants in Equation 8.63
A,B	Constants in Equation 8.15
Bo	Boiling number, $= q''/(Gh_{fg})$
c_p	Specific heat constant, J/kg °C
Co	Convection number, $= (\rho_G/\rho_L)^{0.5}\,[(1-x)/x]^{0.8}$
$C_{s,f}$	Fluid–surface effect constant, Equation 8.21
d	Equilibrium break-off bubble diameter, m, Equation 8.26
D	Tube diameter, m
D_b	Bubble diameter, m
D_h	Hydraulic diameter, m
D_{12}	Mass diffusion coefficient of species 1 in a mixture of 1 and 2
F_{Fl}	Fluid–surface parameter accounting for nucleation characteristics of different fluid–surface combinations in Kandlikar (1990) correlation
Fo	Fourier number
Fr	Froude number
Fr_{LO}	Froude number with all flow as liquid $= G^2/(\rho_L g D)$
f	Bubble departure frequency, Equation 8.19
f	Friction factor, Equations 8.58 through 8.60
$f_2(Fr_{LO})$	Froude number multiplier in Equations 8.70 and 8.71
F_D	Diffusion-induced suppression parameter, defined by Equation 8.80
F_{Fl}	Fluid–surface parameter, Equations 8.70 and 8.71, Table 8.3
g	Gravitational acceleration, m/s^2
G	Mass flux, kg/m^2 s
H	Heat transfer coefficient, W/m^2 °C
h_{fg}	Latent heat of vaporization, J/kg
h'_{fg}	Latent heat corrected for vapor superheating, Equations 8.37 and 8.38, J/kg
h_L	Heat transfer coefficient for the liquid, W/m^2 °C
h_{LO}	Single-phase heat transfer coefficient for all flow in the liquid phase at saturation temperature, W/m^2 °C
$h_{L,Sat}$	Heat transfer coefficient for the liquid at the saturation point, W/m^2 °C
h_m	Heat transfer coefficient for the mixture, W/m^2 °C
h_{TP}	Two-phase heat transfer coefficient, W/m^2 °C
$h_{TP\|CBD}$	Two-phase heat transfer in the convective boiling–dominant region, W/m^2 °C
$h_{TP\|NBD}$	Two-phase heat transfer in the convective boiling–dominant region, W/m^2 °C
h^*	Heat transfer coefficient using T_{Sat} as the fluid temperature in the subcooled flow boiling, W/m^2 °C
Ja	Jakob number
K	Boltzmann's constant = 1.38×10^{-23} J/K
K_1	Parameter in Equation 8.16
K_1, K_2	New nondimensional groups defined by Equations 8.89 and 8.90
k_L	Thermal conductivity, W/m °C
l	Mixing length
M	Molecular weight
m''	Total mass flux, kg/m^2 s
Nu	Nusselt number
Nu_{LO}	Nusselt number with all flow as liquid
$Nu_{LO,\,cp,\,LO,\,cp}$	Nusselt number with constant properties and all flow as liquid
p	Pressure, N/m^2
p_{cr}	Critical pressure, N/m^2
p_G	Pressure of the gas inside bubble, N/m^2

p_L	Pressure of the liquid, N/m^2
$p_{Sat,T}$	Saturation pressure over a planar interface, N/m^2
Pr	Prandtl number
q	Heat transfer rate, W
q''	Heat flux, W/m^2
q''_{CHF}	CHF, W/m^2
$q''_{FDB,i}$	Heat flux at the initial point of FDB, W/m^2
q''_{int}	Heat flux at the intersection of the extended single-phase line and the FDB curve, W/m^2
q''_{MHF}	MHF, W/m^2
q''_{ONB}	Heat flux at ONB, W/m^2
q''_{PB}	Heat flux in the partial boiling region, W/m^2
R	Radius
R_b	Radius of a bubble, m
R_C	Cavity mouth radius, m
$R_{C,Crit}$	Cavity radius at the ONB
$R_{C,Max}$, $R_{C,Min}$	Minimum and maximum cavity radii available on a surface, m
Re	Reynolds number
$R(t)$	Bubble growth rate function
$R_c^\star$	Nondimensional cavity radius
$R_{min}^\star$, $R_{max}^\star$	Minimum and maximum radii of active cavities
T	Temperature, °C or K
$T_{Sat,1\|p}$,$T_{Sat,2\|p}$	Saturation temperatures of the pure components at the total system pressure, p, °C
t	Time, s
TTR	Tape twist ratio for twisted tapes
u	Velocity, m/s
v	Specific volume, m^3/kg
V	Volatility parameter, defined by Equation 8.76
V_b	Bubble volume, Equation 8.20 m^3
V_m	Molar volume, m^3/kg mol
X_{1-8}	Nondimensional groups defined in Equations 8.22 through 8.26
x	Equilibrium quality
x_1, x_2	Mass fractions of 1 and 2, respectively, in the liquid phase of a mixture of species 1 and 2
$\tilde{x}$	Molar concentration in Equation 8.29
y	The distance normal to the heater surface to the center of the bubble, m
y_1, y_2	Mass fractions of 1 and 2, respectively, in the vapor phase of a mixture of species 1 and 2

Greek Letters

α	Thermal diffusivity, $= k/(\rho c_p)$, m^2/s
Γ	Liquid mass flow rate per unit film width
Γ	Wall superheat ($T_{Wall} - T_{Sat}$), °C
$\Delta T_{Sat,ONB}$	Wall superheat at the ONB, °C
ΔT_{Sub}	Liquid subcooling ($T_{Sat} - T_L$), °C
$\Delta T_{Sat}^\star$	Nondimensional wall superheat
δ_t	Single-phase thermal boundary layer thickness
ε_m	Eddy diffusivity for momentum transport
ε_h	Eddy diffusivity for heat transport
ϕ	Angle of orientation of the heated surface with respect to the horizontal, deg
ϕ	Association factor in Equation 8.82
φ	Spray distribution parameter for skewness
κ	Mixing length constant
μ_B	Viscosity of the bulk liquid, Ns/m^2
μ_L	Viscosity of the liquid, Ns/m^2
μ_W	Viscosity of the fluid at the wall temperature, Ns/m^2
ξ	Spray distribution parameter for uniformity

θ	Contact angle, deg
θ_r	Receding contact angle, deg
ϑ	Nondimensional centrifugal acceleration, Equations 8.101 and 8.102
ρ	Density, kg/m^3
σ	Surface tension, N/m
ψ	Parameter in Equations 8.86 and 8.87

Subscripts

an	Annular flow
1, 2	Species 1 and 2
b	Bubble
bp	Bubble point
c	Critical state
CHF	Critical heat flux
CBD	Convective boiling–dominant region
conv	Convective boiling component
crit, cr	Critical point for the fluid
dp	Dew point
exit	Exit section
f	Stream core
FDB,*i*	Initial point of FDB
F,c	Convective component of film boiling
F,r	Radiative component of film boiling
Fl	Fluid–surface-dependent parameter in Kandlikar (1990) correlation
fl	Fluid
fg	Latent quantity (vapor property–liquid property)
i	At the interface or initial state
int	Intersection of the extended single-phase line and the FDB curve
L	Liquid
LO	All flow as liquid
G	Gas
MHF	Minimum heat flux
max	Maximum
min	Minimum
NBD	Nucleate boiling–dominant region
NVG	Point of net vapor generation
Nu	Nusselt-type solution
nucl	Nucleate boiling component
0	On a flat surface
ONB	Onset of nucleate boiling
PB	Partial boiling region
r	Receding
F,r	Radiative component of film boiling
F,c	Convective component of film boiling
Sat	Saturation point
Smooth	Smooth tube value
str	Stratified flow
Sub	Subcooling
t	Turbulent flow
tr	Transition flow
T	Thermal layer
TP	Two phase
v	Vapor phase
W	Wall
δ	Edge of liquid film

Superscripts

–	Averaged, average over the entire length or dimensionless quantity
+	Dimensionless quantity
m	Exponent in Equation 8.63, given by Equation 8.66
n	Constant in Equation 8.66
p	Constant in Equation 8.66
*	Nondimensional form
0	Pure component value at infinite dilution, Equation 8.81

References

Ahn, H.S., Lee, C., Kim, H., Jo, H., Kang, S., Kim, J., Shin, J., and Kim, M.H., Pool boiling CHF enhancement by micro/nanoscale modification of zircaloy-4 surface, *Nucl. Eng. Des.*, 240(10), 3350–3360, 2010.

Attinger, D., Personal communication, 2015.

Bankoff, S.G., Entrapment of gas in the spreading of liquid over a rough surface, *AIChE J.*, 4, 24–26, 1958.

Bennett, D.L. and Chen, J.C., Forced convective boiling in vertical tubes for saturated pure components and binary mixtures, *AIChE J.*, 26, 454–461, 1980.

Berenson, P.B., Film boiling heat transfer from horizontal surfaces, *J. Heat Transfer*, 83, 351–358, 1961.

Bergel'son, B.R., Burnout under conditions of subcooled boiling and forced convection, *Thermal Eng.*, 27, 48–50, 1980.

Bergles, A.E., Heat transfer enhancement—The encouragement and accommodation of high heat fluxes, *J. Heat Transfer*, 119, 8–19, 1997.

Bergles, A.E. and Rohsenow, W.M., The determination of forced convection surface boiling heat transfer, *Trans. ASME, J. Heat Transfer*, 86, 365–372, 1964.

Betz, A.R., Xu, J., Qiu, H., and Attinger, D., Do surfaces with mixed hydrophilic and hydrophobic areas enhance pool boiling? *Appl. Phys. Lett.*, 97(14), 141909-141909-3, 2010.

Bowring, W.R., Physical model of bubble detachment and void volume in subcooled boiling, OECD Halden Reactor Project Report HPR-10, 1962.

Boyd, R.D., Subcooled flow boiling critical heat flux (CHF) and its application to fusion energy components. Part I. A review of fundamentals of *CHF* and related data base, *Fusion Technol.*, 7, 7–30, 1983a.

Boyd, R.D., Subcooled flow boiling critical heat flux (CHF) and its application to fusion energy components. Part II. A review of microconvective, experimental, and correlational aspects, *Fusion Technol.*, 7, 31–51, 1983b.

Boyd, R.D., Subcooled flow boiling critical heat flux (CHF) and its application to fusion energy components. Part I. A review of fundamentals of CHF and related data base, *Fusion Technol.*, 7, 7–30, 1985.

Bromley, L.A., Heat transfer in stable film boiling, *Chem. Eng. Prog.,* 46, 221–227, 1950.

Calus, W.F., di Montegnacco, A., and Kenning, D.B.R., Heat transfer in a natural circulation single tube reboiler, Part II. Binary liquid mixtures, *Chem. Eng. J.*, 6, 251–264, 1973.

Carey, V.C., *Liquid Vapor Phase Change Phenomena*: *An Introduction to the Thermophysics of Vaporization and Condensation Processes in Heat Transfer Equipment*, 2nd edn., Taylor & Francis, USA, 2007.

Celata, G.P., Cumo, M., and Mariani, A., Assessment of correlations and models for the prediction of CHF in subcooled flow boiling, *Int. J. Heat Mass Transfer*, 37, 237–255, 1994.

Celata, G.P., Cumo, M., and Setaro, T., Forced convective boiling in binary mixtures, *Int. J. Heat Mass Transfer,* 36, 3299–3309, 1993.

Celata, G.P. and Mariani, A., CHF and post-CHF (post-dryout) heat transfer, in S.G. Kandlikar, V.K. Dhir, and M. Shoji (Eds.), *Handbook of Phase Change—Boiling and Condensation*, Taylor & Francis, Philadelphia, PA, Chapter 16, 1999.

Chen, J.C., A correlation for boiling heat transfer to saturated fluids in convective flow, *Ind. Eng. Chem., Process Des. Dev.*, 5, 322–329, 1966.

Chu, K-H., Joung, Y.S., Enright, R., Buie, C.R., and Wang, E.N., Hierarchically structured surfaces for boiling critical heat flux enhancement, *Appl. Phys. Lett.*, 103, 151602, 2013.

Cooke, D. and Kandlikar, S.G., Effect of open microchannel geometry on pool boiling enhancement, *Int. J. Heat Mass Transfer*, 55(4), 1004–1013, 2012.

Cole, R., A photographic study of pool boiling in the region of critical heat flux, *AIChE J.*, 6(4), 533–538, 1960.

Collier, J.G. and Thome, J.R., *Convective Boiling and Condensation*, 3rd edn., McGraw-Oxford University Press, New York, 1994.

Davis, E.J. and Anderson, G.H., The incipience of nucleate boiling in forced flow, *AIChE J.*, 12, 774–780, 1966.
Demiray, F. and Kim, J., Microscale heat transfer measurements during pool boiling of FC-72: Effect of subcooling, *Int. J. Heat Mass Transfer,* 47, 3257–3268, 2004.
Dhir, V.K., Nucleate boiling, Sections 4.1–4.6, in S.G. Kandlikar, V.K. Dhir, and M. Shoji (Eds.), *Handbook of Phase Change, Boiling and Condensation*, Taylor & Francis, Philadelphia, PA, 1999.
Dhir, V.K., Numerical simulations of pool-boiling heat transfer, *AIChE J.*, 47(4), 813–834, 2001.
Doroshchuk, V.E., Levitan, L.L., and Lantzman, F.P., *Investigation into Burnout in Uniformly Heated Tubes*, ASME Publication, New York, 75-WA-HT-22, 1975.
Drew, T.B. and Muller, A.C., Boiling, *Trans*, 33, 449–4715, 1937.
El-Genk, M., A review of pool boiling from inclined and downward-facing flat surfaces, in G.P. Celata, P. Di Marco, and A. Mariani (Eds.), *Second European Thermal-Sciences and 14th UIT National Heat Transfer Conference 1996*, Edizioni ETS, Pisa, Italy, 1996.
Feldman, A., Marvillet, C.H., and Lebouche, M., An experimental study of boiling in plate-fin heat exchangers, in *Second National UK Heat Transfer Conference,* IMechE, London, England, Vol. 2, 1996, pp. 1257–1268.
Fujita, Y., Vapor liquid equilibrium properties, in S.G. Kandlikar, V.K. Dhir, and M. Shoji (Eds.), *Handbook of Phase Change, Boiling and Condensation*, Taylor & Francis, Philadelphia, PA, 1999.
Fujita, Y., Bai, Q., and Tsutsui, M., Heat transfer of binary mixtures in nucleate pool boiling, in G.P. Celata, P. Di Marco, and A. Mariani (Eds.), *Second European Thermal Science and 14th UIT National Heat Transfer Conference*, Rome, Italy, 1996, pp. 1639–1646.
Gaertner, R.F., Photographic study of nucleate pool boiling on a horizontal surface, *J. Heat Transfer, Trans. ASME, Ser. C*, 87, 17–29, 1965.
Gnielinski, V., New equations for heat and mass transfer in turbulent pipe and channel flow, *Int. Chem. Eng.,* 16, 359–368, 1976.
Groeneveld, D.C., Post-dryout heat transfer at reactor operating conditions, National Topical Meeting on Water Reactor Safety, American Nuclear Society, Utah, USA, AECL-4513, 1973.
Groeneveld, D.C., Cheng, S.C., and Doan, S.C., AECL-UO critical heat flux lookup table, *Heat Transfer Eng.*, 7, 46–62, 1986.
Groeneveld, D.C., Leung, L.K.H., Kirillov, P.L., Bobkov, V.P., Smogalev, I.P., Vinogradov, V.N., Huang, X.C., and Royer, E., The 1995 lookup table for critical heat flux in tubes, *Nucl. Eng. Des.*, 163, 1–23, 1996.
Gungor, K.E. and Winterton, R.H.S., Simplified general correlation for saturated flow boiling and comparisons of correlations with data, *Can. J. Chem. Eng.*, 65, 148–156, 1987.
Gunther, F.C., Photographic study of surface-boiling heat transfer to water with forced convection, *Trans. ASME*, 73, 115–123, 1951.
Haramura, Y. and Katto, Y., A new hydrodynamic model of CHF applicable widely to both pool and forced convection boiling on submerged bodies in saturated liquids, *Int. J. Heat Mass Transfer*, 26, 387–399, 1983.
Hebel, W., Detavernier, A., and Decreton, M., A contribution to the hydrodynamics of boiling crisis in a forced flow of water, *Nucl. Eng. Des.*, 64, 433–445, 1981.
Hewitt, G.F., Boiling, in W.M. Rohsenow, J.P. Hartnett, and Y.I. Cho (Eds.), *Handbook of Heat Transfer*, 3rd edn., McGraw-Hill, New York, 1998.
Hihara, E., Tanida, K., and Saito, T., Forced convective boiling experiments of binary mixtures, *JSME Int. J., Ser. II*, 32, 98–106, 1989.
Hsu, Y.Y., On the size range of active nucleation cavities in a heating surface, *Trans. ASME, J. Heat Transfer*, 84, 207–216, 1962.
Hsu, Y.Y. and Graham, R.W., *An Analytical and Experimental Study of the Thermal Boundary Layer and Ebullition Cycle in Nucleate Boiling*, NASA TND-594, NASA Lewis Research Center, Cleveland, OH, 1961.
Hsu, Y.Y. and Westwater, J.W., Approximate theory for film boiling on vertical surfaces, *AIChE Chem. Eng. Prog. Symp. Ser.,* 30, 15–24, 1960.
Inada, S., Miyasaka, Y., Sakamoto, S., and Chandratilleke, G.R., Liquid-solid contact state in subcooled pool transition boiling system, *J. Heat Transfer*, 108, 219–221, 1986.
Jaikumar, A. and Kandlikar, S.G., Enhanced pool boiling heat transfer over selectively sintered open microchannels, *Int. J. Heat Mass Transfer*, 88, 652–661, 2015.
Jensen, M.K. and Memmel, G.J., Evaluation of bubble departure diameter correlations, in *Proceedings of the International Heat Transfer Conference*, San Francisco, CA, 1986, pp. 1907–1912.

Johnston, M.A., Jr., De La Pena, J., and Mesler, R.B., Bubble shapes in nucleate boiling, *AIChE J.*, 12, 334–348, 1966.
Judd, R.L. and Hwang, K.S., A comprehensive model for nucleate boiling heat transfer including microlayer evaporation, *J. Heat Transfer*, 98, 623–629, 1976.
Judd, R.L., Merte, H., and Ulucakli, M.E., Variation of superheat with subcooling in nucleate pool boiling, *J. Heat Transfer*, 113, 201–208, 1991.
Jung, D.S., Horizontal flow boiling heat transfer using refrigerant mixtures, PhD dissertation, University of Maryland, College Park, MD, 1988.
Jung, D.S., McLinden, M., Radermacher, R., and Didion, D., Horizontal flow boiling experiments with a mixture of R-22/R-114, *Int. J. Heat Mass Transfer*, 32, 131–145, 1988.
Kandlikar, S.G., A general correlation for two-phase flow boiling heat transfer coefficient inside horizontal and vertical tubes, *J. Heat Transfer*, 112, 219–228, 1990.
Kandlikar, S.G., Development of a flow boiling map for subcooled and saturated flow boiling of different fluids in circular tubes, *Trans. ASME, J. Heat Transfer*, 113, 190–200, 1991a.
Kandlikar, S.G., A model for predicting the two-phase flow boiling heat transfer coefficient in augmented tube and compact heat exchanger geometries, *J. Heat Transfer*, 113, 966–972, 1991b.
Kandlikar, S.G., Heat transfer and flow characteristics in partial boiling, fully developed boiling, and significant void flow regions of subcooled flow boiling, *J. Heat Transfer*, 120, 395–401, 1998a.
Kandlikar, S.G., Boiling heat transfer in binary systems, Part I—Pool boiling, *J. Heat Transfer,* 120, 380–387, 1998b.
Kandlikar, S.G., Boiling heat transfer with binary mixtures, Part II—Flow boiling, *J. Heat Transfer*, 120, 388–394, 1998c.
Kandlikar, S.G., Flow boiling in circular tubes, Sections 15.1–15.3, in S.G. Kandlikar, V.K. Dhir, and G.P. Celata (Eds.), *Handbook of Phase Change, Boiling and Condensation*, Taylor & Francis, Philadelphia, PA, 1999.
Kandlikar, S.G., A theoretical model to predict pool boiling CHF incorporating effects of contact angle and orientation, *J. Heat Transfer*, 123, 1071–1079, 2001a.
Kandlikar, S.G., Critical heat flux in subcooled flow boiling—An assessment of current understanding and future directions for research, *Multiphase Sci. Technol.*, 13, 207–232, 2001b.
Kandlikar, S.G., Heat transfer mechanisms during flow boiling in microchannels, *J. Heat Transfer*, 125, 8–16, 2004.
Kandlikar, S.G., A scale analysis based theoretical force balance model for critical heat flux (CHF) during saturated flow boiling in microchannels and minichannels, *J. Heat Transfer*, 132, 081501-13, 2010.
Kandlikar, S.G., Controlling bubble motion over heated surface through evaporation momentum force to enhance pool boiling heat transfer, *Appl. Phys. Lett*., 102(5), 051611 (5pp.), 2013.
Kandlikar, S.G., Chapter 5: Flow boiling in minichannels and microchannels, in S.G. Kandlikar, S. Garimella, D. Li, S. Colin, and M.R. King (Eds.), *Heat Transfer and Fluid Flow in Minichannels and Microchannels*, 2nd edn., Elsevier, Oxford, U.K., 2014.
Kandlikar, S.G., Mechanistic considerations for enhancing pool boiling heat transfer, Paper No. InterPACKICNMM2015, in *12th International Conference on Nanochannels, Microchannels and Minichannels*, San Francisco, CA, June 6–10, 2015.
Kandlikar, S.G. and Balasubramanian, P., An extension of the flow boiling correlation to transition, laminar and deep laminar flows in minichannels and microchannels, *Heat Transfer Eng.*, 25(11), 86–93, 2004.
Kandlikar, S.G., Dhir, V.K., and Shoji, M., *Handbook of Phase Change—Boiling and Condensation*, Taylor & Francis, Philadelphia, PA, 1999.
Kandlikar, S.G., Mizo, V.R., Cartwright, M.D., and Ikenze, E., Bubble nucleation and growth characteristics in subcooled flow boiling, HTD-Vol. 342, in *ASME Proceedings of the 32nd National Heat Transfer Conference*, Tianjin, Peoples republic of China, Vol. 4, 1997, pp. 11–18.
Kandlikar, S.G. and Raykoff, T., Predicting flow boiling heat transfer of refrigerants in microfin tubes, *Enhanc. Heat Transfer*, 4, 257–268, 1997.
Kandlikar, S.G. and Spiesman, P.H., Effect of surface characteristics on flow boiling heat transfer, in *Engineering Foundation Conference on Convective and Pool Boiling*, Irsee, Germany, May 18–25, 1997.
Kandlikar, S.G. and Steinke, M.S., Contact angles and interface behavior during rapid evaporation of liquid on a heated surface, *Int. J. Heat Mass Transfer*, 45, 3771–3780, 2002.
Katto, Y., A physical approach to critical heat flux of subcooled flow boiling in round tubes, *Int. J. Heat Mass Transfer*, 33, 611–620, 1990a.

Katto, Y., Prediction of critical heat flux of subcooled flow boiling in round tubes, *Int. J. Heat Mass Transfer*, 33, 1921–1928, 1990b.
Katto, Y. and Yokoya, S., Principal mechanism of boiling crisis in pool boiling, *Int. J. Heat Mass Transfer*, 11, 993–1002, 1968.
Kew, P. and Cornwell, K., Flow boiling in compact heat exchangers, Section. 16.2, in *Handbook of Phase Change, Boiling and Condensation,* Taylor & Francis, Philadelphia, PA, 1999.
Khanpara, A.E., Pate, M.B., and Bergles, A.E., Augmentation of R-113 in-tube evaporation in microfin tubes, *ASHRAE Trans.*, 92, 506–524, 1986.
Khanpara, J.C., Pate, M.B., and Bergles, A.E., Local evaporation heat transfer in a smooth tube and a microfin tube using refrigerants 22 and 113, in *Boiling and Condensation in Heat Transfer Equipment*, ASME HTD, New York, NY, Vol. 68, 1987, pp. 35–46.
Kim, J., Review of nucleate pool boiling heat transfer mechanisms, *Int. J. Multiphase Flow*, 35, 1067–1076, 2009.
Klimenko, V.V., Film boiling on a horizontal plate-new correlation, *Int. J. Heat Mass Transfer*, 24, 69–79, 1981.
Koyama, S., Yu, J., Momoki, S., Fuji, T., and Honda, H., Forced convective flow boiling of pure refrigerants inside a horizontal microfin tube, in *Engineering Foundation Conference on Convective Flow Boiling*, ASME, Banff, Alberta, Canada, April 30–May 5, 1995.
Kutateladze, S.S., On the transition to film boiling under natural convection, *Kotloturbostroenie*, 3, 10–12, 1948.
Kutateladze, S.S. and Leont'ev, A.I., Some applications of the asymptotic theory of the turbulent boundary layer, in *Proceedings of the Third International Heat Transfer Conference*, Chicago, IL, Vol. 6, 1966, pp. 2373–2378.
Lang, C., *Transactions of Institute of Engineers and Shipbuilders*, Scotland, Vol. 32, 1888, pp. 279–295.
Lee, C.H. and Mudawar, I., A mechanistic critical heat flux model for subcooled flow boiling based on local bulk flow conditions, *Int. J. Multiphase Flow*, 14, 711–728, 1988.
Li, C. and Peterson, G.P., Parametric study of pool boiling on horizontal highly conductive microporous coated surfaces, *J. Heat Transfer*, 129(11), 1465, 2007.
Liaw, S.P. and Dhir, V.K., Void fraction measurement during saturated pool boiling of water on partially wetted vertical surfaces, *J. Heat Transfer*, 111, 731–738, 1989.
Liu, Z. and Winterton, R.H.S., A general correlation for saturated and subcooled flow boiling in tubes and annuli based on nucleate pool boiling, *Int. J. Heat Mass Transfer*, 34, 2759–2765, 1991.
Lorentz, J.J., Mikic, B.B., and Rohsenow, W.M., The effect of surface conditions on boiling characteristics, in *Proceedings of Fifth International Conference*, Hemisphere, New York, Vol. 5, 1974.
Malenkov, I.G., Detachment frequency as a function of size of vapor bubbles, *Translated Inzh. Fiz. Zhur.*, 20, 99, 1971.
Marcus, B.D. and Dropkin, D., Measured temperature profiles within the superheated boundary layer above a horizontal surface in saturated nucleate pool boiling of water, *Trans. ASME, J. Heat Transfer*, 87, 333–341, 1965.
Mattson, R.J., Hammitt, F.G., and Tong, L.S., A photographic study of the Subcooled Flow Boiling Crisis in Freon-113, Paper No. HT-39, ASME, 1973, 8pp.
McAdams, W.H., Minden, C.S., Carl, R., Picornell, D.M., and Dew, J.E., Heat transfer at high rates to water with surface boiling, *Ind. Eng. Chem.*, 41, 1945–1963, 1949.
Melin, P., Measurements and modelling of convective vaporization for refrigerants in a horizontal tube, PhD thesis, Department of Heat and Power Technology, Chalmers University of Technology, Göteborg, Sweden, 1996.
Mikic, B.B. and Rohsenow, W.M., New correlation of pool boiling data including the effect of heating surface characteristics, *J. Heat Transfer*, 91, 241–250, 1969.
Mikic, B.B., Rohsenow, W.M., and Griffith, D., On bubble growth rates, *Int. J. Heat Mass Transfer*, 13, 657–666, 1970.
Moghaddam, S. and Kiger, K., Physical mechanisms of heat transfer during single bubble nucleate boiling of FC-72 under saturation conditions-I. Experimental investigation, *Int. J. Heat Mass Transfer*, 52, 1284–1294, 2009a.
Moghaddam, S. and Kiger, K., Physical mechanisms of heat transfer during single bubble nucleate boiling of FC-72 under saturation conditions-II. Theoretical analysis, *Int. J. Heat Mass Transfer*, 52, 1295–1303, 2009b.

Moissis, R. and Berenson, P.J., On the hydrodynamic transitions in nucleate boiling, *J. Heat Transfer, Trans. ASME, Ser. C*, 85, 221–229, 1963.
Mori, S. and Okuyama, K., Enhancement of the critical heat flux in saturated pool boiling using honeycomb porous media, *Int. J. Multiphase Flow*, 35(10), 946–951, 2009.
Murata, K. and Hashizume, K., Forced convection boiling of nonazeotropic refrigerant mixtures inside tubes, *J. Heat Transfer*, 115, 680–689, 1993.
Murphy, R.C. and Bergles, A.E, Subcooled flow boiling of fluorocarbons—Hysteresis and dissolved gas effects on heat transfer, in *Proceedings of Heat Transfer and Fluid Mechanics Institute*, Stanford University Press, Stanford, CA, 1972, pp. 400–416.
Nariai, H., Inasaka, F., Fujisaki, W., and Ishiguro, H., Critical heat flux of subcooled flow boiling in tubes with internal twisted tapes, in *Proceedings of ANS Winter Meeting* (*THD*), San Francisco, CA, November 1992, pp. 38–46.
Nishikawa, K., Fujita, Y., Uchida, S., and Ohta, H., Effect of heating surface orientation on nucleate boiling heat transfer, *ASME-JSME Thermal Eng. J. Conf.*, 1, 129–136, 1983.
Nishikawa, K., Yoshida, S., Mori, H., and Takamatsu, H., Post-dryout heat transfer to Freon in a vertical tube at high subcritical pressures, *Int. J. Heat Mass Transfer*, 29, 1245–1251, 1986.
Nukiyama, S., Maximum and minimum values of heat transmitted from metal to boiling water under atmospheric pressure, *J. Soc. Mech. Eng. J.*, 37, 367, 1934.
O'Hanley, H., Coyle, C., Buongiorno, J., McKrell, T., Hu, L., Rubner, M., and Cohen, R., Separate effects of surface roughness, wettability, and porosity on the boiling critical heat flux, *Appl. Phys. Lett.*, 103(2), 024102 (5pp.), 2013.
Patil, C.M. and Kandlikar, S.G., Pool boiling enhancement through microporous coatings selectively electrodeposited on fin tops of open microchannels, *Int. J. Heat Mass Transfer*, 79, 816–828, 2014.
Petukhov, B.S., Heat transfer and friction in turbulent pipe flow with variable physical properties, *Adv. Heat Transfer*, 6, 503–564, 1970.
Petukhov, B.S. and Popov, V.N., Theoretical calculation of heat exchange in turbulent flow in tubes of an incompressible fluid with variable physical properties, *High Temp.,* 1, 69–83, 1963.
Plesset, M.S. and Zwik, S.A., The growth of vapor bubbles in superheated liquids, *J. Appl. Phys.*, 25, 493–500, 1954.
Rahman, M.M., King, S.M., Olceroglu, E., and McCarthy, M., Nucleate boiling on biotemplated nanostructured surfaces, in *ASME 2012 International Mechanical Engineering Congress and Exposition*, *IMECE 2012*, Houston, TX, American Society of Mechanical Engineers, November 9–15, 2012, pp. 2801–2808.
Ramilison, J.M. and Lienhard, J.H., Transition boiling heat transfer and the film transition regime, *J. Heat Transfer, Trans. ASME,* 109, 746–752, 1987.
Rayleigh, J.W.S., On the pressure developed in a liquid during the collapse of a spherical cavity, *Philos. Mag.*, 34, 94–98, 1917.
Rohsenow, W.M., A method of correlating heat transfer data for surface boiling of liquids, *Trans. ASME*, 74, 969–976, 1952.
Sato, T. and Matsumura, H., On the conditions of incipient subcooled boiling with forced convection, *Bull. JSME*, 7, 392–398, 1964.
Schrock, V.E. and Grossman, L.M., Forced convection boiling in tubes, *Nucl. Sci. Eng.*, 12, 474–481, 1962.
Shah, M.M., A general correlation for heat transfer during subcooled boiling in pipes and annuli, *ASHRAE Trans.*, 83, Part 1, 205–215, 1977.
Shah, M.M., Chart correlation for saturated boiling heat transfer: Equations and further study, *Trans. Am. Soc. Heat., Refrig. Air Cond. Eng.*, 88, Part I, 185–196, 1982.
Smith, R.A., *Boiling Inside Tubes*: *Critical Heat Flux for Upward Flow in Uniformly Heated Tubes*, ESDU Data Item No. 86032, Engineering Science Data Unit International, London, U.K., 1986.
Steiner, D. and Taborek, J., Flow boiling heat transfer in vertical tubes correlated by an asymptotic model, *Heat Transfer Eng.*, 13, 43–69, 1992.
Stephan, K. and Abdelsalam, M., Heat transfer correlation for natural convection boiling, *Int. J. Heat Mass Transfer*, 23, 73–87, 1980.
Takamatsu, H., Momoki, S., and Fujii, T., A correlation for forced convection boiling heat transfer of nonazeotropic refrigerant mixture of HCFC22/CFC114 in a horizontal smooth tube, *Int. J. Heat Mass Transfer*, 36, 3555–3563, 1993.

Thom, J.R.S., Walker, W.M., Fallon, T.A., and Reising, G.F.S., Boiling in subcooled water during flow up heated tubes or annuli, paper presented at the *Symposium on Boiling Heat Transfer in Steam Generating Units and Heat Exchangers*, Manchester, Institute of Mechanical Engineering, London, U.K., September 15–16, 1965.

Tong, L.S., *Boiling Heat Transfer and Two-Phase Flow*, John Wiley, New York, 1965.

Tong L.S., *Principles of Design Improvement for Light Water Reactors*, Hemisphere, New York, 1988.

Tong, L.S., Curin, H.B., and Thorp, A.G., An evaluation of the departure from nucleate boiling in bundles of reactor fuel rods, *Nucl. Sci. Eng.*, 33, 7–15, 1968.

Tong, L.S., Efferding, L.E., and Bishop, A.A., A photographic study of subcooled boiling and DNB of Freon-113 in a vertical channel, ASME Paper 66-WA/HT-39, ASME Winter Annual Meeting, ASME, New York, 1966.

Tong, L.S. and Hewitt, G.F., Overall viewpoint of flow boiling mechanisms, ASME Paper 72-HT-54, 1972.

Tong, L.S. and Tang, Y.S., *Boiling Heat Transfer and Two-Phase Flow*, Taylor & Francis, Washington, DC, 1997.

Vachnon, R.I., Nix, G.H., and Tanger, G.E., Evaluation of constants for the Rohsenow pool-boiling correlation, *J. Heat Transfer*, 90, 239, 1968.

Vandervort, C.L., Bergles, A.E., and Jensen, M.K., An experimental study of critical heat flux in very high heat flux subcooled boiling, *Int. J. Heat Mass Transfer*, 37(Suppl. 1), 161–173, 1994.

Weisman, J. and Pei, B.S., Prediction of critical heat flux in flow boiling at low qualities, *Int. J. Heat Mass Transfer*, 26, 1463–1477, 1983.

Wieting, R.A., Empirical correlations for heat transfer and flow friction characteristics of rectangular offset fin plate heat exchangers, *J. Heat Transfer*, 97, 488–490, 1975.

Yao, Z., Lu, Y.-W., and Kandlikar, S.G., Direct growth of copper nanowires on a substrate for boiling applications, *IET Micro Nano Lett*., 6(7), 563–566, 2011.

Yao, Z., Lu, Y.-W., and Kandlikar, S.G., Pool boiling heat transfer enhancement through nanostructures on silicon microchannels, *J. Nanotechnol. Eng. Med*., 3(3), 031002/1-031002/8, 2012.

Zuber, N., Hydrodynamic aspects of boiling heat transfer, PhD thesis, University of California, Los Angeles, CA, 1959.


Taylor & Francis
Taylor & Francis Group
http://taylorandfrancis.com

9

Condensation

Jacob N. Chung and Tailian Chen

9.1 Fundamentals of Condensation
9.2 Condensation on Flat Surfaces
9.3 Condensation in and on the Tubes
9.4 Condensation in Minichannels and Microchannels
9.5 Effects of Noncondensable Gases and Other Secondary Effects
9.6 Direct Contact Condensation
9.7 Enhanced Condensation

9.1 Fundamentals of Condensation

9.1.1 Homogeneous Nucleation

Thermodynamically, condensation is defined as the change of phase from vapor to liquid with the release of latent heat. The driving force for condensation is a subcooling of the vapor phase under a metastable condition. As shown in Figure 9.1, assume that a droplet embryo is formed with a radius of a that is larger than the mechanical equilibrium radius or the critical radius a^*. The critical radius is defined by the Laplace–Young equation based on the mechanical equilibrium as follows:

$$p_l - p_g = \frac{2\sigma}{a^*} \tag{9.1}$$

where
p_l and p_g are the liquid- and vapor-phase pressures, respectively
σ is the surface tension coefficient

Under the thermal equilibrium condition $T_l = T_g$, for the vapor phase, Thomson (1871) showed that the actual saturation pressure of the vapor, p_g, surrounding the droplet is increased due to surface tension as given by

$$p_g = p_o \exp\left(\frac{2\sigma v_l M}{a^* R_u T_g}\right) \tag{9.2}$$

$$p_g \approx p_o(1 + 2\sigma v_l / a^* p_o v_g) \tag{9.3}$$

where p_o is the saturation pressure corresponding to T_g on a flat surface. The ratio, p_g/p_o, is called the supersaturation ratio. If T_{Sat} is the saturation temperature corresponding to p_g on a flat surface and $p_l > p_g$, as shown

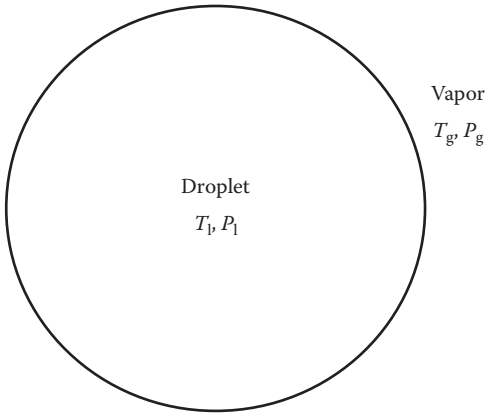


Figure 9.1

Schematic of a droplet embryo in a quiescent vapor environment.

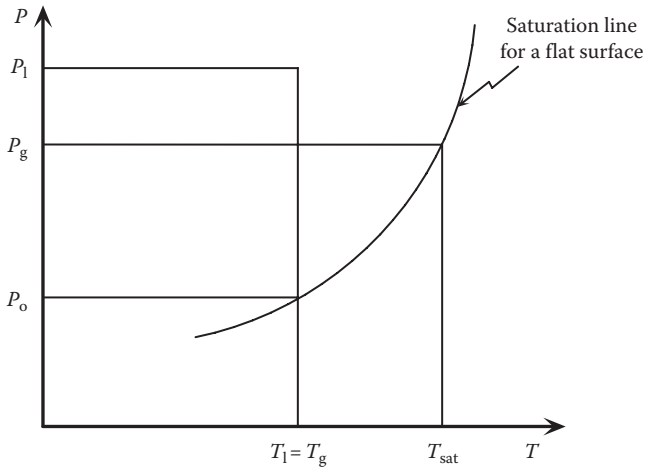


Figure 9.2

Pressure–temperature relationships at saturation.

in Figure 9.2, it is clear that the vapor phase is supersaturated and subcooled because of $p_l > p_g$ and $T_{Sat} > T_g$. With the use of the Clausius–Clapeyron equation, it can be shown that

$$T_{Sat} - T_g \approx \frac{2T_{sat}\sigma v_l}{h_{fg}a^*} \tag{9.4}$$

This provides the degree of subcooling, and it is also called the Gibbs–Thompson condition. As illustrated in Figure 9.3, the initial growth of a droplet embryo is driven by the subcooling condition indicated by Equation 9.4. As the growth continues, the droplet gets larger and the degree of subcooling decreases, which causes the growth rate to decrease.

In an analytical study, Lai (1999) found that the droplet growth is associated with three timescales. The first and second timescales, which are generally small, describe, respectively, the transient temperature distributions of the vapor phase and the droplet phase. The largest timescale controls the droplet growth process. For the case of a large Stefan number, $C_{p,v}(T_{Sat} - T_g)/h_{fg}$, the subcooling effect is dominating, which results in a faster droplet growth. The Gibbs–Thompson effect actually suppresses the droplet growth, and its effectiveness is diminished as time progresses. If the density difference between the liquid and the vapor phases becomes larger, the induced convection effect becomes more relevant.

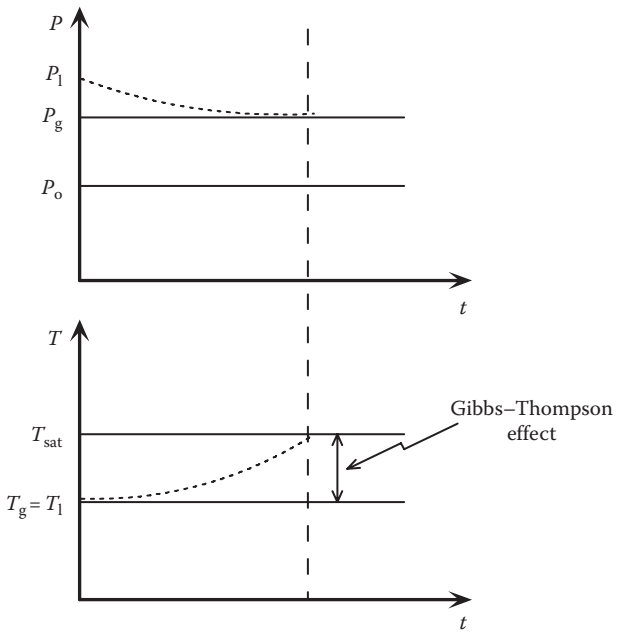


Figure 9.3

Thermodynamics of droplet initial growth.

Oswatitsch (1942) suggested a droplet growth equation for the rate of change of droplet radius with time, which is based on the kinetic theory of gases for droplets smaller than 2 μm:

$$\frac{\mathrm{d}R(t)}{\mathrm{d}t} = \frac{3p_0}{8h_{\mathrm{fg}}\rho_{\mathrm{l}}}\sqrt{\left(\frac{3R_{\mathrm{u}}}{T_{\mathrm{g}}M}\right)\left(T_{\mathrm{Sat}} - T_{\mathrm{g}}\right)} \tag{9.5}$$

For larger droplet growth in the continuum regime, Ford and Lekic (1973) derived an equation for the droplet radius growth rate using conduction and convection heat transfer theories:

$$\frac{\mathrm{d}R(t)}{\mathrm{d}t} = \pi^2 \frac{\alpha\eta}{D_{\mathrm{i}}} \frac{\exp(-\pi^2 Fo)}{[1-\exp(-\pi^2 Fo]^{1/2}} \tag{9.6}$$

where

$$\eta = \left[1 + \frac{C_{\mathrm{p,l}}\left(T_{\mathrm{Sat}} - T_{\mathrm{i}}\right)}{h_{\mathrm{fg}}}\right] - 1 \tag{9.7}$$

and $Fo = 4\alpha_l t/D_{\mathrm{i}}^2$ is the Fourier number, α_{l} the liquid thermal diffusivity, T_{i} the droplet initial temperature, and D_{i} the droplet initial diameter.

9.1.2 Heterogeneous Nucleation

When the nucleation takes place on entrained particulate matter in a vapor environment or on a cold solid surface, the process is called heterogeneous nucleation. There are basically two forms of heterogeneous condensation: dropwise and filmwise condensation. Dropwise condensation usually occurs when the condensate does not wet the surface and, therefore, instead of spreading into a thin film, it takes the shape of droplets. Sometimes, dropwise condensation is just a precursor to film condensation. Filmwise condensation prevails generally on wettable surfaces where a stable condensate removal mechanism is provided. It is well known that dropwise condensation is more efficient in heat transfer than its counterpart of filmwise condensation. According to Rose (2002) in his review of research work on the dropwise condensation,

the detailed mechanism of transition is still not fully understood. Although it is desirable to promote dropwise condensation in order to enhance heat transfer, promoting lasting dropwise condensation under industry conditions remains to be solved despite considerable effort since the early 1990s. More discussions on promoting dropwise condensation are given in Section 9.7.2.

9.2 Condensation on Flat Surfaces

9.2.1 Dropwise Condensation

As stated earlier, dropwise condensation occurs on surfaces that are hard to wet. Usually, this type of surface is associated with high free energy. Droplet embryos first form as a result of nucleation and then these embryos start to grow, which promotes coalescence among small droplets to form larger ones. Then these larger drops are removed by external forces such as gravity or shear. Therefore, from an individual droplet point of view, the process is highly transient and, in general, a cyclic process from one droplet generation to the next. For example, on a cold beer can, when condensed droplets reach sizes that are large enough, gravity force would overcome the surface tension such that droplets would be removed by sweeping down and leave a freshly wiped path for the next generation of droplets to nucleate to start a new cycle.

The transport mechanisms that govern the nucleation, two-phase flow, and heat transfer in dropwise condensation are still in the developmental stage. There are many controversial issues that need to be clarified in the future. Up to this point, there are two basic theoretical models: nucleation theory and film-rupture theory.

The nucleation theory was first introduced by Eucken (1937) and later further developed by Umur and Griffith (1965), Graham and Griffith (1973), Tanaka (1975), and Rose (1988). According to the nucleation theory, the dropwise condensation process starts with very thin liquid film layer and then it breaks up into droplets. These droplets subsequently grow by condensing vapor on their surfaces with the latent heat transported to the surface by conduction. Heat flux is maximum at the vapor–liquid–solid contact line. Following this, droplet–droplet interaction and coalescence produce larger droplets, but the remainder of the surface stays dry.

The film-rupture theory was introduced first by Jakob (1936) and further developed by Welch and Westwater (1961), Silver (1964), and Sugawara and Katsuta (1966). The film-rupture theory claims that vapor condenses on a cold surface and forms microscale thin liquid films. When the film reaches a critical thickness, it would then rupture to form microdroplets.

It is almost impossible to develop a general correlation for the dropwise condensation because of the strong surface property dependence and the condensate removal mechanisms. For the development of a heat transfer correlation, the heat flux is given by

$$q = h\Delta T \tag{9.8}$$

where q is the heat flux in kW/m^2 and ΔT the temperature difference between the vapor and the condenser surface in degrees K. For steam and ethylene glycol, Peterson and Westwater (1966) proposed

$$h = Nu\rho_l h_{fg} k_l (T_{Sat} - T_W)/2\sigma T_{Sat} \tag{9.9}$$

where

$$Nu = 1.46\times 10^{-6} Re_l^{-1.63} \prod_k^{1.16} Pr_l^{0.5} \tag{9.10}$$

in which

$$Re_l = \frac{k_l \left(T_{Sat} - T_w\right)}{\mu_l h_{fg}} \tag{9.11}$$

and

$$\prod_k = -\frac{2\sigma T_{Sat}}{\mu_l^2 h_{fg}} \left(\frac{\partial \sigma}{\partial T}\right) \tag{9.12}$$

with the following limited range:

$$1.75 \le Pr_l \le 23.6$$
$$2\times10^{-4} \le Re_l \le 3\times10^{-2}$$
$$7.8\times10^{-4} \le \Pi_k \le 2.65\times10^{-2}$$

This correlation was recommended only for the fluids with which it was developed. Rose (1999) indicated that because of improvements in experimental quality, recent results from various countries are found to be in reasonably good agreement. For dropwise condensation of pure steam, Rose (1999) suggested the following general correlation that also takes the system pressure into consideration:

$$\dot{q} = T_v^{0.8}\left(5\Delta T + 0.3\left(\Delta T\right)^2\right) \tag{9.13}$$

where

$\dot{q}$ is the heat flux in kW/m^2

T_v is the vapor temperature in Celsius

ΔT is the temperature difference between the vapor and the condenser surface in degrees K

Among the influences on the dropwise condensation heat transfer, there is a controversy in the dependence of the thermal conductivity of the condensing surface. While some studies indicated that thermal conductivity has no influence on the condensation heat transfer (Aksan and Rose, 1973, Rose, 1978), it appears that more studies showed that the dropwise condensation has a strong dependence on the surface thermal conductivity (Tanner et al., 1968, Wilkins and Bromley, 1973, Hannemann and Mikic, 1976). More research in this subject will lead to more fundamental understanding of this important heat transfer process.

9.2.2 Film Condensation

9.2.2.1 Laminar Film

For laminar film condensation on a vertical flat surface, a simplified model was first introduced by Nusselt (1916). The model is based on the following assumptions:

1. The liquid film is laminar and 2D.
2. Thermal properties of the film are constant.
3. Subcooling of the film is negligible.
4. Momentum changes through the film are unimportant.
5. The bulk of the vapor is stagnant, saturated, and free of noncondensables.
6. Interfacial shear is negligible.
7. The heat transfer in the liquid film is dominated by conduction.

The local condensation heat transfer coefficient is defined as follows:

$$h_x = \frac{\dot{q}_x}{\left(T_{sat} - T_w\right)} \tag{9.14}$$

where

$\dot{q}_x$ is the local heat flux

$T_{Sat} - T_w$ is the degree of subcooling. The average condensation heat transfer coefficient over a plate of length L is given as

$$\bar{h}_L = \frac{\bar{\dot{q}}_L}{\left(T_{sat} - T_w\right)} \tag{9.15}$$

where $\bar{q}_L$ is the average heat flux over the entire plate. The local and average heat transfer coefficients for a plate of length L are given by Nusselt (1916) as

$$h_x = \left[\frac{k_l^3 h_{fg} \rho_l (\rho_l - \rho_v) g \sin\theta}{4(T_{Sat} - T_w)\mu_l x} \right]^{1/4} \tag{9.16}$$

$$\bar{h}_L = 0.943 \left[\frac{k_l^3 h_{fg} \rho_l (\rho_l - \rho_v) g \sin\theta}{(T_{Sat} - T_w)\mu_l L} \right]^{1/4} \tag{9.17}$$

Rohsenow (1956) suggested an effective latent heat of condensation to compensate for the liquid subcooling:

$$h'_{fg} = h_{fg} \left[1 + 0.683 \left(\frac{c_{p,l}(T_{Sat} - T_w)}{h_{fg}} \right) \right] \tag{9.18}$$

Sadasivan and Lienhard (1987) introduced a different effective latent heat of condensation that is also a function of the Prandtl number:

$$h'_{fg} = h_{fg} \left[1 + (0.683 - 0.228/Pr_L) \left(\frac{c_{p,l}(T_{Sat} - T_w)}{h_{fg}} \right) \right] \tag{9.19}$$

This is limited for $Pr_L > 0.6$. Many researchers have investigated the validity of the constant thermal property assumption. One acceptable method of including the variation of thermal properties in the liquid film is to use a reference temperature T_r to evaluate the thermal properties. This reference temperature is defined as

$$T_r = T_w + F(T_{Sat} - T_w), \quad 0.25 < F < 0.31 \tag{9.20}$$

One of the assumptions in the Nusselt model allows the neglect of the interfacial shear between the liquid film and the ambient vapor; Koh et al. (1961) investigated this assumption further and found that the interfacial shear is indeed very small for most gases and liquids ($Pr \geq 1$). For condensation of liquid metals, they discovered that the inclusion of the interfacial shear does cause a substantial reduction in heat transfer and suggested the following correction equation:

$$\frac{h}{h_{Nu}} = \left(\frac{1 + 0.68A + 0.02AB}{1 + 0.85B - 0.15AB} \right) \tag{9.21}$$

where

$$\begin{aligned} A &= [c_{p,l}(T_{Sat} - T_w)/h_{fg}] \\ B &= [k_l(T_{Sat} - T_w)/\mu_l h_{fg}] \end{aligned} \tag{9.22}$$

Also, h_{Nu} is the heat transfer coefficient based on the Nusselt model. For laminar film condensation on geometries other than the vertical flat plate, Dhir and Lienhard (1971) introduced the concept of effective gravity for an arbitrary axisymmetric body. Using the coordinates defined in Figure 9.4, Dhir and Lienhard (1971) showed that the local film thickness may be determined by

$$\delta(x) = \left(\frac{4\mu_l k_l (T_{Sat} - T_w) x}{\rho_l (\rho_l - \rho_v) h_{fg} g_{eff}} \right)^{1/4} \tag{9.23}$$

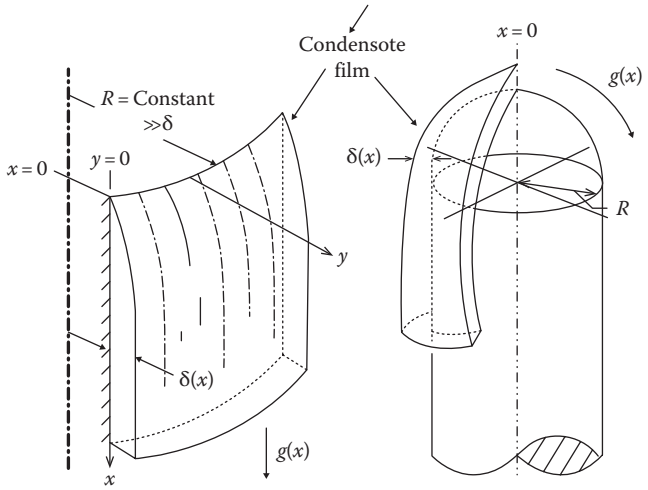


Figure 9.4

Coordinate system for effective gravity model.

where g_{eff} is the effective gravity defined as

$$g_{\text{eff}} = \frac{x\left(gR\right)^{4/3}}{\int_0^x g^{1/3}R^{4/3}\mathrm{d}x} \tag{9.24}$$

The local Nusselt number is therefore given as

$$Nu = \left(\frac{g_{\text{eff}}\rho_1\left(\rho_1-\rho_v\right)h'_{\text{fg}}x^3}{4\mu_1 k_1\left(T_{\text{Sat}}-T_w\right)}\right)^{1/4} \tag{9.25}$$

For example, the average Nusselt number for condensation on a sphere with diameter, D, is equal to

$$\overline{Nu}_D = 0.785\left(\frac{gD^3}{A}\right)^{1/4} \tag{9.26}$$

where

$$A = \frac{\mu_1 k_1\left(T_{\text{Sat}}-T_w\right)}{\rho_1\left(\rho_1-\rho_v\right)h'_{\text{fg}}} \tag{9.27}$$

9.2.2.2 Turbulent Film

As the film thickness increases, the smooth vapor–liquid interface gradually becomes wavy, but the bulk of the liquid film remains laminar. As the thickness increases further, the liquid film eventually becomes turbulent. In order to gage quantitatively the three different regimes, a Reynolds number must be defined first. The local Reynolds number that characterizes the liquid film flow is based on the mean liquid velocity and the hydrodynamic diameter of the 2D liquid film, which is equal to 4δ, where δ is the film thickness. If the liquid film local mass flow rate is represented by the Nusselt model, then the Reynolds number is in the following form:

$$Re_{D_h} = \frac{4g\rho_1\left(\rho_1-\rho_v\right)\delta^3}{3\mu_1^2} \tag{9.28}$$

The three liquid film flow regimes are characterized by the following:

1. $Re_{D_h} \le 30$ (laminar film with smooth interface). In this regime, the Nusselt solution mentioned earlier can be applied.
2. $30 \le Re_{D_h} \le 1800$ (laminar film with wavy interface). Kutateladze (1963) proposed the following equation for this regime:

$$\frac{\bar{h}_L \left(v_l^2/g\right)^{1/3}}{k_l} = \frac{Re_{D_h}}{1.08 Re_{D_h}^{1.22} - 5.2} \tag{9.29}$$

3. $1800 \le Re_{D_h}$ (turbulent liquid film). For the turbulent film, Labuntsov (1957) recommended

$$\frac{\bar{h}_L \left(v_l^2/g\right)^{1/3}}{k_l} = \frac{Re_{D_h}}{58 Pr_l^{-0.5}\left(Re_{D_h}^{0.75} - 263\right) + 8750} \tag{9.30}$$

9.3 Condensation in and on the Tubes

9.3.1 Condensation in a Tube

Condensation in circular tubes is strongly affected by the vapor inlet velocity and the orientation of the tube. For vertical tubes, the flow pattern is in reverse order as that of boiling. As shown in Figure 9.5, the annular flow pattern generally prevails, which is followed by slug flow and then bubbly flow. If the vapor flows upward against the gravity (countercurrent flow), the annular liquid film flowing downward would experience substantial interfacial shear, whereas for cocurrent flows, the interfacial shear is negligible as a result of the large density difference between the vapor and the liquid phases. For horizontal tubes, the annular flow would be maintained if the inlet vapor velocity is relatively high; otherwise, the stratified annular flow would take place because the gravity would tend to drain the liquid condensate in the direction perpendicular to the vapor flow, which would thicken the liquid film along the gravity direction.

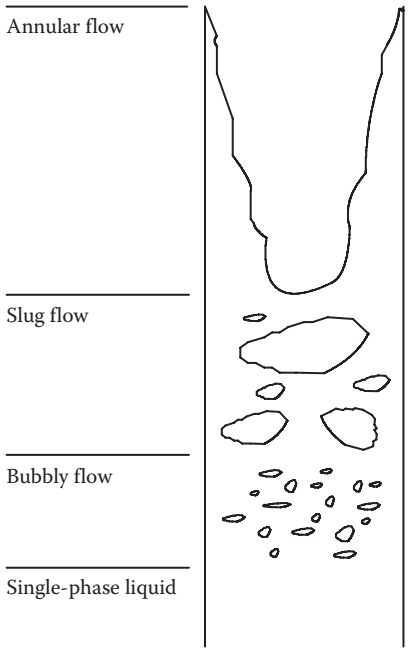


Figure 9.5
Schematic of condensing flow regimes in a vertical tube.

Based on experimental results, Jaster and Kosky (1976) proposed the following criteria for the transition from the initial annular flow to the stratified flow regime:

$$F > 29 \quad \text{annular flow}$$

$$29 > F > 5 \quad \text{transition flow}$$

$$F < 5 \quad \text{stratified flow}$$

The stress ratio, F, is defined as $\tau_w/\rho_l g\delta$, where δ is the liquid film thickness. Jaster and Kosky (1976) also recommended the following for the Nusselt number in the transition flow regime:

$$Nu_{tr} = Nu_{an} + \frac{F-29}{24}\left(Nu_{an} - Nu_{Str}\right) \tag{9.31}$$

The error associated with this equation is of the same order of magnitude as those methods established for annular and stratified flows.

9.3.1.1 Stratified Annular Flow in Horizontal Tubes

For horizontal tubes, when the inlet vapor Reynolds number is <35,000, which corresponds to the mass flow flux of 400 kg/m^2 s for a 1 cm tube, the liquid film is affected by the gravity and the stratified annular flow pattern would be present. Because of the effects of gravity, Chato (1962) proposed a correlation based on the Nusselt film condensation model:

$$h = 0.728K_c\left[\frac{g\rho_l\left(\rho_l-\rho_v\right)k_l^3 h'_{fg}}{\mu_l\left(T_{Sat}-T_w\right)D}\right]^{1/4} \tag{9.32}$$

where h'_{fg} is the effective latent heat of condensation to include the subcooling in the liquid film and is given by

$$h'_{fg} = h_{fg}\left[1+0.68\frac{c_{p,l}\left(T_{Sat}-T_w\right)}{h_{fg}}\right] \tag{9.33}$$

It is noted that Equation 9.32 is identical to the classical Nusselt result for laminar film condensation on a vertical flat plate with height D if K_c is set to 1.295. The physical meaning of K_c is that it is a provision to account for the accumulation of condensate on the bottom of the tube that changes the void fraction. Chato (1962) suggested a value of 0.76 based on the experimental data of R-113.

9.3.1.2 Annular Flow in Horizontal Tubes

As mentioned earlier, when the inlet vapor Reynolds number is >30,000, the annular flow pattern would be maintained along most of the tube length. Near the end of relatively long tubes, the vapor-phase Reynolds number drops substantially such that gravity effects become a factor. Under this situation, the stratified annular flow model mentioned earlier would then describe flow and heat transfer more appropriately.

Heat transfer correlations for condensation in a horizontal tube with an annular flow pattern were first addressed by Ananiev et al. (1961) for single-component pure vapor and smooth tubes. Based on the analogy between the momentum and the heat transport, they proposed that the heat transfer coefficient for the two-phase condensing flow, h, can be correlated with the liquid single-phase forced convection heat transfer coefficient, h_l, as follows:

$$h = h_l\sqrt{\frac{\rho_l}{\rho_m}} \tag{9.34}$$

where the equivalent mixture density, ρ_m, is defined as

$$\frac{1}{\rho_m} = \left(\frac{1}{\rho_l}\right)(1-x) + \left(\frac{1}{\rho_v}\right)x \tag{9.35}$$

and h_l is evaluated based on a correlation for convective-forced convection of single-phase liquid in a circular tube, for example, the Dittus–Boelter-type correlations. Based on the experiments, Boyko and Kruzhilin (1967) found

$$h_l = C\,Re_l^{0.8} Pr_f^{0.43} \left(\frac{Pr_f}{Pr_w}\right)^{0.25} \left(\frac{K_l}{D}\right) \tag{9.36}$$

where $C = 0.024$ and 0.032 for steam condensing on carbon steel tubes and copper tubes, respectively, and Pr_f and Pr_w are the Prandtl numbers evaluated at the stream core and wall temperatures, respectively.

Cavallini and Zecchin (1974) offered the following correlation for saturated vapor inside tubes based on the Reynolds analogy concept and a multiple linear regression analysis:

$$Nu = 0.0344 Re_l^{0.83} \left[1 + x\left(\left(\rho_l/\rho_v\right)^{0.5} - 1\right)\right]^{0.82} Pr_l^{0.35} \tag{9.37}$$

This is suggested for the dimensionless groups and thermal property ratios in the ranges listed as follows:

$$10 < \rho_l/\rho_v < 2{,}000, \quad 0.1 < X < 0.9, \quad 0.01 < \mu_v/\mu_l < 0.1$$

$$15 < Fr = \frac{G\rho_v}{\sqrt{gD}} < 4{,}000, \quad 5{,}000 < Re_f = \frac{GD}{\mu_l} < 5{,}000{,}000$$

$$0.8 < Pr_l < 20, \quad 0.01 < Ja = c_{p,l}\left(T_v - T_W\right)/h_{fg} < 0.2$$

where

G is the total stream mass flux in kg/m^2 s

x is the vapor quality

9.3.1.3 Annular Flow in Vertical Tubes

Chen et al. (1987) divided this problem into two categories: zero shear (cocurrent flow) and high interfacial shear (countercurrent flow) processes. For countercurrent vapor flow, the interfacial shear retards the condensate flow and, therefore, decreases the heat transfer by thickening the liquid film. On the other hand, the cocurrent vapor flow enhances the heat transfer. They suggested the following:

For cocurrent flow,

$$Nu_o = \left[(Nu_{lw})^{n1} + (N\mu_l)^{n1}\right]^{1/n1} \tag{9.38}$$

For countercurrent flow,

$$Nu_x = \left[(Nu_o)^{n2} + (Nu_{hs})^{n2}\right]^{1/n2} \tag{9.39}$$

where all the Nusselt numbers are defined as $(h/k_l)/(v_l^2/g)^{1/3}$. Chen et al. (1987) found that $n1 = 6$ and $n2 = 2$ resulted in the best fit to the reported data. For the laminar wavy flow, Nu_{lw}, Chen et al. (1987) recommended the Chun and Seban (1971) correlation:

$$Nu_{lw} = 0.823 Re_x^{-0.22} \tag{9.40}$$

$$Re_x = \frac{G(1-x)D}{\mu_l} \tag{9.41}$$

For the turbulent film flow, Nu_t, Chen et al. (1987) recommended the following correlation:

$$Nu_t = 0.00402 Re_x^{0.4} Pr_l^{0.65} \tag{9.42}$$

Finally, for the Nusselt numbers for high shear flows, Nu_{hs}, Chen et al. (1987) proposed the Soliman et al. (1968) correlation:

$$Nu_{hs} = 0.036 Pr_l^{0.65} \bar{\tau}_i^{1/2} \tag{9.43}$$

$$\bar{\tau}_i = \frac{\tau_i}{\rho_l (g\nu_l)^{2/3}} \tag{9.44}$$

Chen et al. (1987) proposed the following general equation for the local heat transfer for a vertical cocurrent annular flow:

$$Nu_x = \left[\left(0.31 Re_x^{-1.32} + \frac{Re_x^{2.4} Pr_l^{3.9}}{2.37 \times 10^{14}} \right)^{1/3} + \frac{Pr_l^{1.3} A}{771.6} \left(Re_T - Re_x \right)^{1.4} \right]^{1/2} \tag{9.45}$$

For the case of annular flow in a horizontal tube, this simplifies to

$$Nu_x = 0.036 Pr_l^{0.65} A^{0.5} \left(Re_T - Re_x \right)^{0.7} Re_x^{0.2} \tag{9.46}$$

$$A = \frac{0.252 \mu_l^{1.177} \mu_v^{0.156}}{D^2 g^{2/3} \rho_l^{0.553} \rho_v^{0.78}} \tag{9.47}$$

where Re_T is the film Reynolds number when the total condensation takes place. For the countercurrent flow, the recommended local Nusselt number is

$$Nu_x = \left[\left(0.31 Re_x^{-1.32} + \frac{Re_x^{2.4} Pr_l^{3.9}}{2.37 \times 10^{14}} \right) - \frac{C Pr_l^{1.3}}{771.6} Re_x^{1.8} \right]^{1/2} \tag{9.48}$$

$$C = \frac{0.023 \mu_l^{1.133} \mu_v^{0.2}}{D^2 g^{2/3} \rho_v \rho_l^{0.333}} \tag{9.49}$$

The general correlations by Chen et al. (1987) can be readily incorporated into a condensation model once the interfacial shear is known.

Shah (1989) proposed an alternative formula based on experimental data reported in the literature that includes working fluids of water, refrigerants (R-11, R-12, R-22, and R-113), and organic compounds (methanol, ethanol, benzene, toluene, and trichloroethylene) for vertical, horizontal, and inclined tubes with diameters ranging from 7 to 40 mm:

$$Nu = 0.023 Re_l^{0.8} Pr_l^{0.4} \left[(1-x)^{0.8} + \frac{3.8 x^{0.76} (1-x)^{0.04}}{\left(p_{Sat}/p_c \right)^{0.38}} \right] \tag{9.50}$$

The Shah correlation is valid for the following parameter ranges: $0.002 < p_{Sat}/p_c < 0.44$, $100 < Re_l < 63{,}000$, $1 < Pr_l < 13$, $21°C < T_{Sat} < 310°C$, $3 \text{ m/s} < u_v < 300 \text{ m/s}$, $0 < x < 1$, and $39{,}000 < \dot{m}$ (kg/m^2 h) $< 758{,}000$. The mean deviation of Shah's correlation with 474 data points used in the study is 15.4%.

9.3.2 Mathematical Modeling of Two-Phase Flow and Heat Transfer in Tubes

9.3.2.1 Laminar Film Condensation in a Vertical Tube with Upward Vapor Flow

The goal of the mathematical model is to predict the liquid boundary layer thickness along the tube because it is directly related to the condensation rate. This is accomplished by first addressing the liquid fluid dynamics, then the vapor flow, and finally accounting for the interaction between each along the tube. The following analytical model is based on Seban and Hodgson (1982). All of the Nusselt assumptions, for the vertical flat plate, are applied except that the flow here is an axisymmetric 2D flow that results in an annular flow pattern. Seban and Hodgson (1982) further assumed that the tube radius is relatively large, so the curvature effects were neglected. A schematic representation of the coordinates is shown in Figure 9.6.

9.3.2.1.1 Liquid Layer The momentum equation is

$$\mu_l \frac{d^2u}{dy^2} - \frac{dp}{dx} - \rho_l g = 0 \tag{9.51}$$

After rearrangement,

$$\frac{\mu_l}{\rho_l g}\frac{d^2u}{dy^2} = \left(1 + \frac{1}{\rho_l g}\frac{dp}{dx}\right) = G_p \tag{9.52}$$

It is noted that G_p is a constant. After integration, one obtains the velocity profile as

$$u(y) = \frac{G_p \rho_l g}{\mu_l}\left(\frac{y^2}{2} - \delta(x)y\right) + \frac{\tau_i}{\mu_l}y \tag{9.53}$$

where

τ_i is the interfacial shear stress
δ is the liquid layer thickness

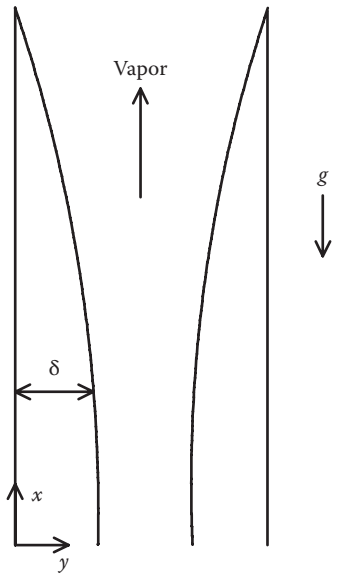


Figure 9.6

Coordinate system for condensation with an upward vapor flow.

This is nondimensionalized as

$$\bar{\delta} = \delta\left(\frac{g}{\nu_l^2}\right)^{1/3}, \quad \bar{y} = y\left(\frac{g}{\nu_l^2}\right)^{1/3}, \quad \bar{u} = \frac{u}{(\nu_l g)^{1/3}} \tag{9.54}$$

The dimensionless velocity profile is therefore given as

$$\bar{u} = G_p\left(\frac{\bar{y}^2}{2} - \bar{\delta}\bar{y}\right) + \frac{\tau_i}{\rho_l g}\left(\frac{g}{\nu_l^2}\right)^{1/3}\bar{y} \tag{9.55}$$

The local Reynolds number is defined by neglecting the pressure drop term, which is $G_p = 1$, as follows:

$$\begin{aligned} Re_l &= \frac{1}{\nu_l}\int_0^{\delta} u\,dy \\ &= N_l\frac{\bar{\delta}^2}{3} - \frac{\bar{\delta}^3}{3} \end{aligned} \tag{9.56}$$

$$N_i = \frac{\tau_i}{\rho_l g}\left(\frac{g}{\nu_l^2}\right)^{1/3} \tag{9.57}$$

The local liquid mass flow rate per unit film width is

$$\Gamma = \rho_l\int_0^{\delta} u\,dy \tag{9.58}$$

The condensation mass flux at a local downstream position, $\dot{m}_c(x)$, is

$$\dot{m}_c = \frac{d(\Gamma)}{dx} \tag{9.59}$$

which is expressed as

$$\dot{m}_c = \mu_l\frac{d(\Gamma/\mu_l)}{dx} = \mu_l\frac{N_2}{\delta} \tag{9.60}$$

for later use. From an energy balance at the vapor–liquid interface, one has

$$\dot{m}_c h_{fg} = \frac{k_l(T_{sat} - T_w)}{\delta} \tag{9.61}$$

Equating Equations 9.60 and 9.61, one has

$$N_2 = \frac{c_{p,l}(T_{Sat} - T_w)}{h_{fg}}\left[\frac{k_l}{\mu_l c_{p,l}}\right] \tag{9.62}$$

9.3.2.1.2 Vapor Layer The detailed velocity profile of the vapor layer is not required to solve the problem if an appropriate friction coefficient is used. First evaluate the friction coefficient of the vapor.

If the vapor were occupying the tube completely in a single-phase flow, the friction coefficient for a fully developed flow would be

$$\frac{c_f}{2} = \begin{cases} \dfrac{8}{Re_V} & \text{for } Re_V < 2000 \quad (9.63) \\ \dfrac{0.04}{(Re_V)^{0.25}} & \text{for } Re_V > 4000 \quad (9.64) \end{cases}$$

Then, with interpolation, one has

$$\frac{c_f}{2} = \frac{(Re_V)0.33}{3050} \quad \text{for } 2000 \le Re_V \le 4000 \tag{9.65}$$

where

$Re_v = (4\dot{M}_V/\pi D\mu_V)$ is the Reynolds number for the single-phase vapor
D is the diameter of the tube
$\dot{M}_V$ is the total vapor mass flow rate

For condensation two-phase flow, the existence of the liquid layer must be accounted for. The vapor Reynolds number is modified as $Re_v = 4\dot{M}_V/\pi D'\mu_V$, where $D' = D - 2\delta$. For the turbulent vapor flow, the single-phase friction factors specified by the previous equations should be multiplied by a quantity that will then produce the effective friction factor $(c_f/2)_E$ to include the liquid layer effects:

$$\left(\frac{c_f}{2}\right)_E = \frac{c_f}{2}(1 + 1400F) \tag{9.66}$$

The value for F is related to F' and is defined as

$$F' = \frac{\sqrt{2}\left(\Gamma/\mu_l\right)^{1/2}}{Re_V^{0.9}}\left(\frac{\nu_V}{\nu_l}\right)\left(\frac{\rho_l}{\rho_V}\right)^{1/2} \tag{9.67}$$

When the liquid flow is laminar, $F = F'$. For low vapor velocities, the factor F must be corrected further since the vapor flow is no longer fully turbulent:

$$\begin{aligned} F &= F'\left[1 - \exp\left(\frac{-\tau_i}{\rho_l g \delta}\right)\right] \\ &= F'\left[1 - \exp\left(\frac{-N_1}{\bar{\delta}}\right)\right] \end{aligned} \tag{9.68}$$

$$F = 0 \quad \text{for } Re_v < 2000 \tag{9.69}$$

The interfacial shear, τ_i, can now be linked to the vapor friction coefficient. The condensation causes a mass flux into the liquid layer, and the interfacial shear stress is affected. The shear stress is

$$\tau_i = \left(\frac{c_f}{2}\right)_E \rho\left(u_V - u_{l\delta}\right)^2 + \dot{m}_c\left(u_V - u_{l\delta}\right) \tag{9.70}$$

where

u_V is the mean vapor velocity based on the total vapor mass flow rate
$u_{l\delta}$ is the liquid velocity at the edge of the liquid film, which can be obtained from Equation 9.55

Equation 9.70 can be nondimensionalized using Equations 9.54, 9.57, and 9.62:

$$N_1 = \left(\frac{c_f}{2}\right)_E \left(\frac{\rho_V}{\rho_l}\right)\left(\bar{u}_V - \bar{u}_{l,\delta}\right)^2 + \frac{N_2}{\bar{\delta}}\left(\bar{u}_V - \bar{u}_{l,\delta}\right) \tag{9.71}$$

If the body force on the vapor flow is neglected ($\rho_V = \rho_l$), Seban and Hodgson (1982) used the integral vapor momentum balance equation, in which the momentum flux term is approximated using u_v as the vapor velocity at the interface instead of $u_v - u_{l,\delta}$ and shows that

$$\frac{1}{\rho_l g}\frac{dp}{dx} = -\frac{4N_1}{\bar{D}'} - \left(\frac{\nu_V}{\nu_l}\right)^2\left(\frac{\rho_V}{\rho_l}\right)\frac{d}{dx}\left(\frac{4\dot{M}_V}{\pi D'\mu_V}\right) \tag{9.72}$$

In general, Seban and Hodgson (1982) concluded that the pressure drop term is negligibly small, which supports the earlier assumption that $G_P = 1$.

For the current case of upward vapor flow in a tube, based on heat and mass transfer coupling and applying Equation 9.60, the liquid layer has the following relationship:

$$\frac{d\left(\Gamma/\mu_l\right)}{d\bar{x}} = \frac{N_2}{\bar{\delta}} \tag{9.73}$$

By differentiating Equation 9.56 with respect to $\bar{\delta}$ and using Equation 9.58, one has

$$\frac{d\left(\Gamma/\mu_l\right)}{d\bar{\delta}} = \left(N_1 + \frac{\bar{\delta}}{2}\frac{dN_1}{d\bar{\delta}} - \bar{\delta}\right)\bar{\delta} \tag{9.74}$$

Combining Equation 9.73 with Equation 9.74, one obtains the governing equation for the liquid film thickness:

$$\frac{d\bar{\delta}}{d\bar{x}} = \frac{N_2}{\left(N_1 + \frac{\bar{\delta}}{2}\frac{dN_1}{d\bar{x}} - \bar{\delta}\right)\bar{\delta}^2} \tag{9.75}$$

The solution procedure is outlined as follows:

1. For a given vapor inlet mass flow rate, $\dot{M}_{V,0}$, at the pipe bottom edge indicated as the starting point of the x coordinate in Figure 9.6, the corresponding condensate flow rate per unit film width, Γ_0, at the same point can be obtained based on an overall mass balance for a steady condition, which means all the vapor is condensed, that is,

$$\Gamma_0 = \frac{\dot{M}_{V,0}}{\pi D} \tag{9.76}$$

   With $\dot{M}_{V,0}$ and Γ_0 known, Equations 9.56 and 9.71 are used to find the corresponding $N_{1,0}$ and $\bar{\delta}_0$ at the bottom edge through an iterative procedure.
2. The next step is to march upward using Equation 9.73. First, choose a small $\Delta\bar{x}$ and then find the condensate flow rate per unit film width, Γ_1, at this new location by using

$$\Gamma_1 = \mu_l\left(\frac{N_2}{\bar{\delta}}\right)\Delta\bar{x} + \Gamma_0 \tag{9.77}$$

3. The corresponding vapor mass flow at this new location is then calculated as

$$\dot{M}_{\mathrm{V},1} = \dot{M}_{\mathrm{V},0} - \pi D\left(\Gamma_0 - \Gamma_1\right) \tag{9.78}$$

Following the same procedure as given in Step 1, one can find $N_{1,1}$ and $\bar{\dot{\delta}}_1$ with known $\dot{M}_{\mathrm{V},1}$ and Γ_1.

4. Repeat Step 2 and march upward to another $\Delta\bar{x}$. Repeating Steps 1 to 3 until $\bar{\delta}$ reaches zero.

Seban and Hodgson (1982) made several sample calculations for specific vapor inlet conditions. They investigated both downward and upward liquid film flow cases. Some of these cases were for an inlet pressure of 900 psia and are related to the operating condition of an industrial steam generating unit. It was reported that for these cases, a complete condensation occurs within a very short height up the tube.

9.3.2.2 Turbulent Film Theory

For annular film flow to take place, the vapor velocity must be high. Therefore, the film is generally in the turbulent or, at least, nonlaminar state. The following is a summary of the theory. The basic assumptions are as follows:

1. The entrainment of vapor by the liquid film is neglected.
2. The film is thin with a smooth interface.
3. The inertia of the liquid film is small.

The schematic representation of the coordinate system is shown in Figure 9.7. From time-averaged turbulence modeling, the shear stress is defined as

$$\tau\left(y\right) = \rho_{\mathrm{l}}\left(\nu_{\mathrm{l}} + \varepsilon_{\mathrm{m}}\right)\frac{\mathrm{d}\bar{u}}{\mathrm{d}y} \tag{9.79}$$

where ε_{m} is the eddy diffusivity for momentum transport. The heat flux is governed by the following equation:

$$\dot{q}\left(y\right) = -\rho_{\mathrm{l}} c_{\mathrm{p,l}}\left(\alpha_l + \varepsilon_{\mathrm{h}}\right)\frac{\mathrm{d}\bar{T}}{\mathrm{d}y} \tag{9.80}$$

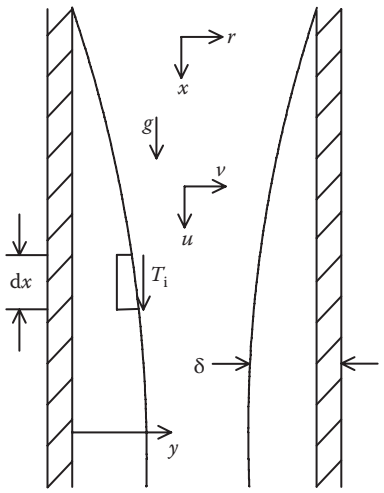


Figure 9.7

Schematic and coordinate system for turbulent film condensation in a tube.

where ε_h is the eddy diffusivity for thermal transport. Using the conventional nondimensional scheme, one has

$$\overline{u}^+ = \frac{u}{\sqrt{\tau_w/\rho_l}}, \quad \overline{u}^+ = \frac{y\sqrt{\tau_w/\rho_l}}{\nu_l}, \quad \overline{y}^+ = \frac{\rho_l c_{p,l}\left(T_w - \overline{T}\right)}{\dot{q}_w}\sqrt{\frac{\tau_w}{\rho_l}}, \tag{9.81}$$

The dimensionless shear stress and heat flux equations become

$$\left(1+\frac{\varepsilon_m}{\nu_l}\right)\frac{d\overline{u}^+}{dy^+} = 1, \quad \frac{\dot{q}}{\dot{q}_w} = \left(\frac{1}{Pr_l}+\frac{\varepsilon_h}{\nu_l}\right)\frac{d\overline{T}^+}{dy^+} \tag{9.82}$$

For the portion where the film is very thin, it is assumed that $\varepsilon_m/\nu_l = 1$, with a no-slip condition at the wall. This leads to the velocity profile of $\overline{u}^+ = y^+$ in the liquid film. On the basis of a mass conservation of the liquid film flow, the following dimensionless equation is obtained as

$$\frac{GD(1-x)}{4\mu_l} = \int_0^{\delta^+} \overline{u}^+ dy^+ \tag{9.83}$$

Using the velocity profile, the dimensionless film thickness is found to be

$$\delta^+ = \sqrt{\frac{1}{2}}Re_{D,l}^{1/2}, dRe_{D,l} = \frac{GD(1-x)}{\mu_l} \tag{9.84}$$

The heat flux is constant across the liquid film, so

$$\frac{\partial}{\partial y}\left[\rho_l c_{p,l}\left(\alpha_l + \varepsilon_h\right)\frac{\partial T}{\partial y}\right] = 0 \tag{9.85}$$

Based on Equation 9.81, the heat flux is therefore constant in the liquid film. After integration and using the boundary conditions, one has

$$\frac{T_{sat} - T_w}{\dot{q}_w/\left(\rho_l c_{p,l}\alpha_l\right)} = \int_0^{\delta} \frac{1}{1 + Pr_l\varepsilon_h/\nu_l} dy \tag{9.86}$$

Following rearrangement, Equation 9.82 becomes

$$\frac{k_l\sqrt{\tau_w/\rho_l}}{h\nu_l} = \int_0^{\delta^+} \frac{1}{1+\left(Pr_l/Pr_t\right)\left(\varepsilon_m/\nu_l\right)} dy^+ \tag{9.87}$$

where $h = \dot{q}_w/\left(T_{sat} - T_w\right)$. Next, the von Karman's mixing length model is adopted for ε_m:

$$\varepsilon_m = l^2\left|\frac{du}{dy}\right|, \quad l = \kappa y \tag{9.88}$$

$$\frac{\varepsilon_m}{\nu_l} = \kappa^2(y^+)^2 \tag{9.89}$$

For the turbulence, the model proposed by Carey (1992) has been used. Carey adopted similar concepts from the general approach for liquid film turbulence:

$$\frac{\varepsilon_m}{\nu_l Pr_t} = \begin{cases} \kappa^2\left(y^+\right)^2/Pr_t & \text{for } 0 \le y^+ \le \delta^+/2 \\ \kappa^2\left(\delta^+ - y^+\right)^2/Pr_t & \text{for } \delta^+/2 \le y^+ \le \delta^+ \end{cases} \tag{9.90}$$

The equation for the $\delta^+/2 \le y^+ \le \delta^+$ region is based on the experimental finding that the eddy diffusivity should approach zero as $(\delta - y)^2$. With the previous information, it may be shown that

$$h = \frac{\kappa k_l \sqrt{\tau_w/\rho_l}}{2\nu_l I}\sqrt{\frac{Pr_l}{Pr_t}} \tag{9.91}$$

where

$$\begin{aligned} I &= \tan^{-1}\left(\sqrt{Pr_l / Pr_t}\,\kappa\delta^+/2\right) \\ &\approx \pi/2 \text{ for large } Pr_l \end{aligned} \tag{9.92}$$

Using the commonly accepted values of $\kappa = 0.4$ and $Pr_t = 0.9$, one has

$$h = 0.134k\sqrt{Pr_l \tau_w/\rho_l/\nu_l} \tag{9.93}$$

The wall shear stress, τ_w, is determined from a force balance:

$$\pi D\tau_w = -\left(\frac{dp}{dx}\right)_f \pi D^2/4 \tag{9.94}$$

The pressure drop due to friction at the wall for two-phase pipe flows is (see Chapter 1)

$$-\left(\frac{dp}{dx}\right)_f = \phi_f^2 \frac{2f_l G^2(1-x)^2}{D\rho_l} \tag{9.95}$$

where

$$\begin{aligned} &\phi_f = \left(1 + \frac{20}{\chi_{tt}} + \frac{1}{\chi_{tt}^2}\right)^{1/2}, \quad \chi_{tt} = \left(\frac{\rho_v}{\rho_l}\right)^{1/2}\left(\frac{\mu_l}{\mu_V}\right)^{0.1}\left(\frac{1-x}{x}\right)^{0.9}, \\ &f_l = 0.05\left(\frac{G(1-x)D}{\mu_l}\right)^{-0.2} \end{aligned} \tag{9.96}$$

With the wall shear stress known, the Nusselt number may be written as

$$\begin{aligned} Nu &= \frac{hD}{k_l} \\ &= 0.134\phi_f\sqrt{f_l}\left[\frac{G(1-x)D}{\mu_l}\right]\sqrt{Pr_l} \end{aligned} \tag{9.97}$$

9.3.3 Condensation on a Plain Tube

As discussed earlier, the laminar condensation on the outside of a horizontal tube can be estimated by the Nusselt theory with the effective gravity modification of Dhir and Lienhard (1971). For a horizontal tube, the average heat transfer coefficient follows Incropera and DeWitt (2002):

$$\bar{h}_D = 0.729\left[\frac{g\rho_l(\rho_l-\rho_V)k_l^3 h'_{fg}}{\mu_l(T_{Sat}-T_w)D}\right] \tag{9.98}$$

This was found to predict the actual heat transfer coefficients on a horizontal single plain round tube quite closely, on the average about 15% lower than the experimental values. The difference is likely attributed to the rippling of the film and early turbulence and drainage instabilities on the bottom side of the tube. In practical industry applications involving condensation on the tube outside surface, the surfaces are typically manufactured with fins to enhance condensation heat transfer, which is discussed in Section 9.7.1.

9.4 Condensation in Minichannels and Microchannels

Aiming to increase the heat transfer performance, reduce the size and weight of components, and reduce the cost of the thermal/fluid systems drives the technology trend of miniaturization over the past decades, with a direct impact now extending into many fields such as electronics cooling, microfluidics, and medical technologies. The increase in the area/volume ratio of the flow passages and the change in the relative importance of different forces create a new class of transport processes that can lead to significant reduction in the device size. In general, according to Kandlikar (2003), the dimensions in the range of 1–3 mm are referred to as minichannels whereas the smaller dimensions in the range of 10–200 μm are said to be microchannels. Kandlikar et al. (2012) gave a review and identified the research needs of heat transfer in microchannels. Condensation heat transfer in microchannels and minichannels has applications in a wide variety of advanced microthermal devices. For example, condensation in microchannels and minichannels is widely used in small devices such as air-cooled condensers for the air conditioning and automotive industry and in heat pipes, thermosyphons, and other applications for system thermal control. Recently, Awad et al. (2014) have provided a comprehensive review of condensation in micro- and minichannels. One can refer to the work by Garimella et al. (2014) for general condensation thermal transport in micro- and minichannels, and also the work by Awad et al. (2014) for condensation in these channels.

9.5 Effects of Noncondensable Gases and Other Secondary Effects

In most of the condensation processes, noncondensables are usually present such as air for those operating in the atmospheric environment. The first comprehensive and detailed study that quantitatively addressed the role of noncondensables was presented by Minkowycz and Sparrow (1966). It is based on the model of Nusselt (1916) except that the environment is a mixture of condensing vapor and noncondensables. Because the vapor–gas phase can no longer be neglected and decoupled from the liquid phase, the coupled boundary layer equations describing continuity, momentum, and energy for both phases were formulated and transformed into similarity variables. The resulting set of coupled nonlinear ordinary equations was solved numerically. To assess exclusively the effects of noncondensable gases, they used the saturated steam–air system with the mixture pressure ranging from 0.5 to 14.7 psia. The results that are based on comparisons with the Nusselt model, where the pure vapor occupies the surroundings, show that the air has a decisive effect in reducing the condensation heat transfer rates. A typical case shows that under 1 atmosphere, when compared with the pure steam condition, a reduction in condensation heat transfer ranging from 35% to 60% for a wall subcooling of 2° to 40° R was found for the air bulk mass fraction as small as 0.5%. In general, when the bulk noncondensable mass fraction increases the condensation heat transfer decreases monotonically. At a given value of noncondensable bulk mass fraction, the heat transfer decreases with increasing wall subcooling except at very small degrees of wall subcooling and large noncondensable bulk mass fractions. The mixture pressure has a strong influence. For a bulk pressure of 0.5 psia, the reduction in heat transfer is from 67% to 83% compared to 35% to 60% for 1 atm.

The physics explains why a small amount of noncondensables have such a detrimental effect on the condensation heat transfer is interesting. The theory is based on the binary convective–diffusive transport in the mixture phase. The net convection flow is moving toward the wall bringing both the vapor and

noncondensables to the liquid surface. Since the noncondensables do not condense, a mechanism must be established to remove them at the same rate as that of arrival during the steady state, thus preventing them from accumulating at the interface. This removal mechanism is basically a diffusion process that sends the noncondensable back to the bulk through a very steep concentration gradient because the diffusion process is much less efficient than the convective process. The requirement for a steep concentration gradient of the noncondensables results in a high noncondensable mass fraction at the liquid–gas interface that drastically reduces the partial pressure of vapor at the interface. The reduction in the vapor pressure at the interface correspondingly decreases the liquid surface temperature, which is the saturation temperature of the condensing vapor. The net consequence is that the temperature difference between the liquid surface and the wall, the condensation driving force, is reduced when compared to the pure vapor case.

The effects of noncondensables discussed earlier are pertinent to a quiescent mixture of vapor and noncondensable gases. Sparrow et al. (1967) investigated the case where a net forced flow field is maintained for the mixture phase, thus resulting in a forced convection laminar boundary layer. Again, a set of coupled nonlinear ordinary different equations was solved numerically and by an integral method. Their results were presented in terms of heat transfer reduction based on the identical system conditions, except that the ambient is composed of pure vapor only. For a mixture pressure of 1 atm, the reduction in condensation heat transfer is only about 2%–5% for the wall subcooling ranging from 2° to 40° R at a noncondensable gas bulk mass fraction of 0.5%. For the low-pressure mixture of 0.5 psia, the reduction in heat transfer is about 3%–10% for the same wall subcooling range and noncondensable gas bulk mass fraction. The reduction becomes substantial at about 40%–55% for the noncondensable gas bulk mass fraction of 10%. The other trends remain similar to those of the quiescent ambient case. Therefore, it is concluded that the forced convection drastically mitigates the noncondensable gas effects on the heat transfer.

Minkowycz and Sparrow (1966) also examined the effects of superheating the mixture phase. In general, for the pure vapor case, the superheating only causes the heat transfer to increase by about 1% at 100° Rankine to 5% at 400° R, whereas for the case of noncondensables, the enhancement in heat transfer due to superheating is more appreciable. For example, with the noncondensable gas bulk mass fraction at 0.5% and a wall subcooling of 10° R, the reductions in heat transfer are 55%, 47%, 43%, and 37% for superheating of 100°, 200°, 300°, and 400° R, respectively. The effect of superheating decreases with decreasing mixture pressure.

Minkowycz and Sparrow (1966) systematically examined the effects of interfacial resistance, diffusion thermo, thermodiffusion, and variable property when noncondensables are present. They concluded that all these effects are of second-order importance.

9.6 Direct Contact Condensation

Direct contact condensation usually refers to vapor condensing on liquid heat sinks that are not attached to a solid surface, for example, condensation on drops, liquid jets, and sheets. For the drop condenser, cold liquid drops are sprayed into the chamber of saturated or superheated vapor. One such design is associated with the emergency cooling system of the nuclear reactor containment. During a main coolant pipe rupture accident, cold water droplets are sprayed into the vapor-filled containment to reduce pressure and temperature by condensing steam.

9.6.1 Condensation on Drops

Lekic and Ford (1980) published a complete study of vapor condensation on a spray of subcooled droplets. They developed a mathematical model that includes the drop size distribution, motion of drop, and heat transfer rate. The model is capable of predicting the average spray temperature as a function of the given spray length. The experimental investigation was also performed where they used three full cone nozzles with different pressure drops. The main results from the experiment are quantified by thermal utilization defined as

$$\varepsilon = \frac{Q_z}{Q_T} \tag{9.99}$$

where

Q_z represents the quantity of heat absorbed per unit time by the spray from nozzle outlet to distance z

Q_T is the maximum amount of heat per unit time that can be absorbed by the spray

The heat transfer Q_z is obtained from

$$Q_z = \frac{\pi}{6}\rho_l h_{fg} \int_0^{D_m} \left(D^3 - D_l^3\right) \mathrm{d}\dot{n} \tag{9.100}$$

where $\dot{n}$ is the number of drops per unit time generated by the nozzle. The following equation provides a relationship between $\dot{n}$ and D_i:

$$\mathrm{d}\dot{n} = \frac{\dot{M}}{\rho_l}\frac{\xi}{\sqrt{\pi}}\frac{D_m}{D_i\left(D_m - D_i\right)}\frac{6}{\pi D_i^3}\exp\left[-\xi^2\left(\ln\frac{\phi D_i}{D_m - D_i}\right)^2\right] dD_i \tag{9.101}$$

where

D is the drop diameter
D_i and D_m are the drop initial diameter and the maximum diameter, respectively
$\dot{M}$ is the mass flow rate of the spray
ξ and ϕ are the spray distribution parameters for uniformity and skewness

Therefore, ε measures the percentage of maximum heat removal capacity. Their experimental results show that the thermal utilization ranges from 0.783 to 0.987 for spray distances of 42 to 356 mm from the nozzle. The model predictions compared well with the experimental results. They concluded that direct condensation is a highly efficient way of condensing pure steam.

Most of the theoretical and analytical investigations were focused on a single droplet. Jacobs and Cook (1978) developed a mathematical model based on pure conduction in the droplet and thin liquid condensate film formed on the droplet surface. The droplet radius history, R_t, is given as

$$\frac{R(t)}{R_i} = \left[1 + \frac{3}{Ja}\int_0^1 \left(\frac{r}{R_i}\right)^2 \frac{\left(T_{r,i} - T_i\right)}{R_i\left(T_{Sat} - T_i\right)}\mathrm{d}r\right] \tag{9.102}$$

where

R_i and T_i are the initial radius and temperature of the drop, respectively
r and $T_{r,i}$ are the radial coordinate and temperature at the radial location r, respectively

Chung et al. (1984a,b) used asymptotic analysis and numerical methods to evaluate the condensation on droplets in the small Reynolds number regime. They included the effects of internal circulation and noncondensable gases. For intermediate and high Reynolds number flows, Sundararajan and Ayyaswamy (1984, 1985a,b) and Huang and Ayyaswamy (1987a,b) have published theoretical and numerical results that address the internal flow field and external boundary layer in addition to the effects of noncondensable gases.

9.6.2 Condensation on Liquid Jets, Liquid Sheets, and Liquid Films

Condensation on jet and sheets has been used in special type condensers. Hasson et al. (1964a) presented a theoretical analysis for vapor condensing on laminar jets. From the same group, Hasson et al. (1964b) experimentally investigated the condensation of steam on laminar water sheets. Later, Taitel and Tamir (1969) extended the study of direct contact condensation by examining the effects of noncondensable gases. For a more complete analysis, Jacobs and Nadig (1987) included the resistance in the condensate that was not addressed in the previous work. They introduced the concept of coolant capacity utilization and produced its relationship with the Graetz number for different noncondensable mass fractions. For example, the percent coolant capacity utilized drops from 100% to 55% for the Graetz number increasing from 0 to 60 at the noncondensable mass fraction of 0.0005. The percent coolant capacity utilized changed from 100% to 30% for the same Graetz number range at the noncondensable mass fraction of 0.1.

9.7 Enhanced Condensation

The enhancement of condensation heat transfer is generally based on the following principles. Because the major heat transfer resistance is associated with the condensate layer, thinning of the condensate film and creating turbulence in the film would accomplish the goal. Increasing the effective condenser surface area such as fluted, finned, corrugated, or wire-wrapped tubes would also enhance the condensation heat transfer. Marto (1988) gave a complete review of the progress made on the enhancement of condensation heat transfer on horizontal integral-fin tubes. It was pointed out that condensate flooding significantly affects the finned tube performance. Heat transfer enhancements are more substantial than the surface area enhancement by adding more fins. Fin spacing has been considered as an important parameter. As the ratio of the surface tension to density of the working fluid is increased, the optimal fin spacing also increases, but the magnitude of the heat transfer enhancement decreases. In cases where the fin shape is important, there is an associated small degree of condensate flooding. When using metals of high thermal conductivities, tall and thin fins are more beneficial. For working fluids of high surface tensions, improvement in the condensate removal may be useful for providing additional heat transfer enhancement. Kedzierski and Webb (1990) proposed a new family of high-performance fin profiles for surface tension–drained condensers that offer improvement over existing commercial fin shapes. They specified each design in terms of the fin tip radius, the fin height, and the fin base thickness. Modern micro-/nanostructured surface fabrication techniques open up new opportunities in innovative engineering surfaces to enhance heat transfer including condensation.

9.7.1 Condensation on an Enhanced Tube

Heat transfer during condensation on the outside surface of a cylindrical tube can be significantly enhanced by using finned tubes due to the increased surface area and thinning of the condensate film by surface tension–driven pressure gradients. Historically, the outside surface enhancement can be loosely categorized into 2D helical ridges and 3D complex surfaces.

9.7.1.1 Condensation on 2D Low Fin Surfaces

Condensation on horizontal low-finned tubes was studied experimentally by Beatty and Katz (1948) who found that the data could be correlated adequately by

$$\overline{h}_{\mathrm{D}} = 0.689\left[\frac{k_{\mathrm{l}}^3\rho_{\mathrm{l}}\left(\rho_{\mathrm{l}}-\rho_{\mathrm{v}}\right)h_{\mathrm{fg}}g}{\mu_{\mathrm{l}}\left(T_{\mathrm{sat}}-T_{\mathrm{w}}\right)}\right]^{1/4}\left(\frac{1}{d_{\mathrm{eq}}}\right)^{1/4} \tag{9.103}$$

where

$$\left(\frac{1}{d_{\mathrm{eq}}}\right)^{1/4} = 1.3\Phi\frac{A_{\mathrm{fin}}}{A_{\mathrm{eq}}}\left(\frac{1}{L}\right)^{1/4} + \frac{A_{\mathrm{root}}}{A_{\mathrm{eq}}}\left(\frac{1}{d_{\mathrm{r}}}\right)^{1/4} \tag{9.104}$$

Also

Φ is the fin efficiency
A_{fin} is the total fin area
A_{eq} is the effective outside area of the finned tube
A_{root} is the plain tube outside heat transfer area based on the root diameter
d_{r} is the root diameter

L is defined by

$$L = \frac{a_{\mathrm{fin}}}{d_{\mathrm{o}}} \tag{9.105}$$

where a_{fin} is the area of one side of one fin:

$$a_{\mathrm{fin}} = \frac{\pi}{4}\left(d_{\mathrm{o}}^2 - d_{\mathrm{r}}^2\right) \tag{9.106}$$

The fin efficiency can be calculated from

$$\Phi = \frac{1}{1 + \frac{m^2}{3}\sqrt{\frac{d_o}{d_r}}} \tag{9.107}$$

where

$$m = H\sqrt{\frac{2}{\left(\frac{1}{h_o} + R_{fo}\right)k_w Y}} \tag{9.108}$$

Also,

$$A_{fin} = \frac{\pi}{2}\left(d_o^2 - d_r^2\right)N_f L \tag{9.109}$$

where

N_f is the number of fins per unit length
L is the finned length of the tube

$$A_{eq} = \Phi A_{fin} + \pi\, d_r L\left(\frac{s}{s+Y}\right) \tag{9.110}$$

And

$$A_{root} = \pi\, d_r L\left(\frac{s}{s+Y}\right). \tag{9.111}$$

It should be noted that these equations, for the calculation of condensation heat transfer on low-finned tubes, are suitable for hydrocarbons, alcohols, and refrigerants with low surface tension as the working fluids, but not suitable for water due to its high surface tension. Water has a high surface tension and the condensate film will bridge the fins with a thick layer of condensate films, significantly reducing the condensation heat transfer.

9.7.1.2 Condensation on 3D Complex Surfaces

The evolution of 2D finned outside surfaces over the last decades to further enhance the condensation heat transfer has led to more complex 3D condensing surfaces, as illustrated in the patents by Withers and Rieger (1974), Chiang et al. (1993), and Thors et al. (1999). These 3D surfaces are formed first by finning a tube outside surface to form 2D fins and followed by notching the extruded fins. With these added secondary or even tertiary fins, the condensation heat transfer is further enhanced not only due to increased surface area but also the thinning of the condensate films and the promoted condensate draining from the condensing surface. Commercially available condenser tubes in the 1990s included the tube Turbo C-II manufactured by Wolverine Tube Inc., which has fins that have been mechanically knurled to produce a saw-tooth fin shape, and the Gewa-SC manufactured by Wieland Metals Inc., which has fins of a Y-shaped cross section. Nowadays, further optimization of the fin structures leads to other variations of 3D condensing surfaces.

Theoretical solutions are problematic owing to the complexity of the condensing surface where the curvature of the fins and the crucial role of the surface tension, which varies in a complicated way over the complicated surfaces, account for major difficulties. Little work has been done on the theoretical analysis of enhancement types other than fins. As a result, invariably the industry resorts to experiments to characterize the heat transfer performance of a condenser tube.

9.7.1.3 Bundle Effect on Condensers

For a vertical tier of N horizontal tubes, Incropera and DeWitt (2002) suggest that the average condensation heat transfer coefficient for the N tubes is $\bar{h}_{D,N} = \bar{h}_D N^{-1/4}$, where N is the number of the tubes in one vertical column of plain tubes. This equation provides a reasonable estimation for N in the range of 20–30. As a result of the more severe inundation for larger bundles, Kern (1958) recommended an exponent of (–1/6) for the plain tube. The decrease in heat transfer is attributed to the increase in the film thickness for the downstream tubes, which is normally called condensate inundation where tubes in the lower portion of the bundle suffer more. For 3D condensing surfaces, which are normally used in practical applications, the effect of inundation varies with different condensing surfaces. Based on the experimentally determined single tube condensation heat transfer where there is zero inundation from tubes above it, Chen (2008) developed a methodology to predict condenser performance by taking into account the condensate inundation over the tubes in the bundle.

Vapor velocity is another factor that affects the overall condensing heat transfer of a bundle. It is well known that the vapor flowing at a high velocity across the tubes can increase the heat transfer coefficient significantly above the theoretical gravity-driven flow model of Nusselt. The general understanding is that the flowing vapor exerts a shear force over the condensate formed on the tube surface, which promotes its removal. The vapor effect on the 3D condensing surfaces is much more complicated. In general, compared with condensation on plain tubes, the vapor effect is smaller for condensation on 3D surfaces. However, very few data actually exist to estimate the significance of the effect, and usually, most of these data are proprietary.

9.7.2 Surface Promoter for Dropwise Condensation

In Section 9.2.1, it was mentioned that dropwise condensation relies on a relatively nonwetting condition between the condensate and the condenser surface for the drops to grow to larger sizes without spreading to liquid films. In most engineering applications, polished metal surfaces that are generally wettable by most liquids are usually used for condensers. Promoters are required to induce the nonwetting condition for dropwise condensation. In general, there are two types of promoters. One is called the additive agent that is sprayed onto the condensing surface or into the vapor phase. The other is coating or plating the condenser surface with the thin layer of materials with high free energy.

9.7.3 Nanostructured Surfaces for Dropwise Condensation

In addition to the additive agent, coating, or plating on the condenser surface to promote dropwise condensation as discussed in 9.7.2, nanostructured surfaces from modern manufacturing technologies have been increasingly studied in recent years to promote dropwise condensation. Examples of these nanostructured surfaces are nanograssed surfaces by Dorrer and Rühe (2008), those with carbon nanotubes by Chen et al. (2007), and those with nanospikes by Narhe and Beysens (2006). Nanostructures on these surfaces convert the surface from wetting to nonwetting, or from superhydrophilic to superhydrophobic, which promotes dropwise condensation and thus enhances condensation heat transfer. Moreover, this interesting phenomenon of wettability switch can be also useful in many compact thermal systems, where the interfacial force plays a more influential role in governing physics. Figure 9.8 shows the dropwise condensation with self-propelled surface by Boreyko and Chen (2009).

Wettability represents an ability of liquid wetting on a solid surface where wetting surface is more favorable to liquid wetting (hydrophilic) and nonwetting surface is unfavorable to liquid wetting (hydrophobic). The wettability can be loosely described by the contact angle at the contact line of a droplet on solid surface as given in Table 9.1. Typically, a surface with $\theta > 150°$ is considered a superhydrophobic surface, where a surface with $\theta < 10°$ is considered a superhydrophilic surface. One droplet deposited on a superhydrophilic surface wets the surface, which is said to exhibit the Wenzel state (Wenzel, 1936). In contrast, one droplet deposited on a superhydrophobic surface curls up with the contact angle $\theta > 150°$, which is said to exhibit the Cassie state (Cassie, 1944).

A stable Cassie state from a superhydrophobic surface is necessary to sustain continuous and rapid removal of condensate from a condenser surface. More studies in engineering superhydrophobic surfaces have been seen in the literature. Chen et al. (2007) achieved continuous dropwise condensation on a biomimetic two-tier texture with short carbon nanotubes deposited on micromachined pillars. Their hexadecanethiol-coated two-tier texture was claimed to surpass lotus leaves in terms of retaining superhydrophobicity. Visualizations of dropwise condensation by Dietz et al. (2010), which showed droplets on a hydrophobic surface, are removed in the form of a number of small droplets with little coalescence.

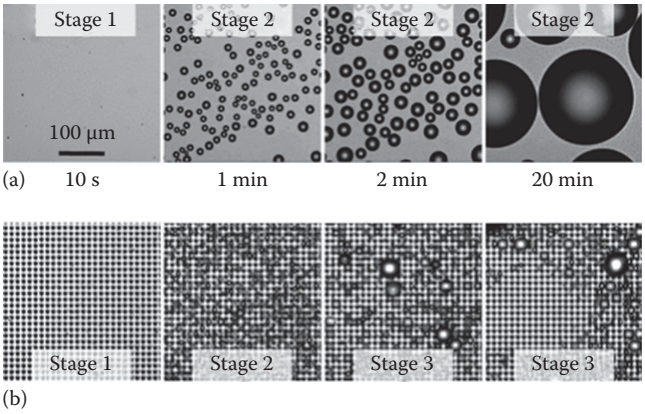


Figure 9.8

Self-propelled dropwise condensation realized by Boreyko and Chen (2009). (a) Dropwise condensation on a smooth hydrophobic substrate and (b) on a rough superhydrophobic substrate where the micropillars are visible.

Table 9.1 Contact Angle and Wettability

		Strength	
Contact Angle	Degree of Wetting	Solid/Liquid	Liquid/Liquid
$\theta = 0°$	Preface wetting	Strong	Weak
$0 < \theta < 90°$	High wettability	Strong	Strong
$90 < \theta < 180°$	Low wettability	Weak	Weak
$\theta = 180°$	Perfect nonwetting	Weak	Strong

Depending on the shape and geometry of nanostructures, a nanostructured surface does not always exhibit superhydrophobicity. Narhe and Beysens (2006) investigated water condensation on a nanostructured surface with nanospikes. Dynamics of water condensate drops was observed to follow three main stages depending on the size of the water drops with respect to the spike feature size. The initial stage is characterized by nucleation of the drops at the bottom (cavities) of the spikes. During the intermediate stage, large drops are surrounded by smaller drops within the neighboring cavities, which persists until coalescence occurs with the central drop. The last stage is characterized by the Wenzel-type drops growing with scaling laws similar to that on a planar surface. Within all stages, condensation on spike surfaces does not exhibit the behavior of superhydrophobicity.

Either a hydrophobic surface or a hydrophobic surface is not sufficient to provide a superior condensing surface. A successful condenser surface necessitates both a wetting surface to facilitate droplet nucleation and a nonwetting surface to promote the removal of condensate drops, which presents a great challenge to design such surfaces. Varanasi et al. (2009) demonstrated the spatial control of heterogeneous nucleation of water drops by manipulating the local nucleation energy barrier and the nucleation rate via the modification of the local intrinsic wettability of a surface. Chen et al. (2011) demonstrated a novel strategy to achieve significant increases in the drop number density from nucleation, drop growth rate, drop departure rate, and surface coverage of small drops, all of which contribute to the enhancement of dropwise condensation heat transfer. The novel strategy includes the use of heterogeneous wettability and hierarchical roughness features in multiscale structures, which enhance both drop nucleation and drop departure on a condensation surface. While promoting dropwise condensation, one issue with nanostructures is the pinning of liquid drops by the nanostructures, which actually is unfavorable for the removal of condensate. To overcome the pinning by the nanostructures, Anand et al. (2012) used an impregnated surface with nanostructures and demonstrated more effective removal of condensate. Whereas much attention has been devoted to dropwise condensation with water, a recent work by Rykaczekski et al. (2014) showed that dropwise condensation can be obtained for low surface tension fluids, such as hydrocarbons, cryogens, and fluorinated refrigerants used in a number of industrial applications, on omniphobic surfaces. More research results in surface engineering are expected to appear in the future.

9.7.4 Electric Field–Enhanced Condensation

Gerstman and Choi (1962) were the first to perform an experiment to demonstrate the enhancement of condensation on a vertical plate by thinning the liquid film with an electrical stress. The idea of using an electric field to enhance the condensation heat transfer was then attempted by Velkoff and Miller (1965). They used Freon-113 vapor condensing on a vertical copper plate. Various electrode geometries and strengths were investigated. It was found that screen electrodes placed parallel to the cold plate generated the largest heat transfer enhancement. Controllable and reproducible increases of 150% were achieved. On the theoretical side, Melcher (1966) was the first to introduce the electrohydrodynamic (EHD) induction pumping based on the electrostatic shear stress at the two-phase interface. Melcher and Taylor (1969) gave a comprehensive review of the EHD-driven convection by a DC or AC field. They also discussed the effects of interfacial instability waves due to the electric field. Jones (1978) further summarized the progress in EHD-enhanced condensation heat transfer. On the basis of the suggestions by Velkoff and Miller (1965), Jones (1978) generalized the following possible mechanisms of EHD-driven condensation:

1. Nucleation sites provided by ions
2. Corona wind to drive ions to heat transfer surfaces
3. Nonuniform electric fields to collect condensate
4. Condensate film surface wave destabilization
5. Electrostatic pumping of condensate
6. Internal mixing of condensate liquid

Miljkovic et al. (2013) recently used an electric field to enhance condensation heat transfer on superhydrophobic nanostructured surfaces. On these superhydrophobic surfaces, after the droplets coalesce, the coalesced droplet experiences a jump as a result of the conversion of excess energy to kinetic energy. The droplet jump results in an increased vapor pressure drop that pulls the droplet back to the condensing surface, thus causing the flooding of the surface. Miljkovic et al. (2013) demonstrated that an externally applied electric field stops coalesced droplets from returning to the original surface that enhances condensation heat transfer on these superhydrophobic surfaces. As more research in this area progresses, innovative technology advancements can be expected, not just limited to new condensing technologies, but also available to other areas such as anti-icing, self-cleaning performance, and thermal diode efficiency.

Nomenclature

c_p	Specific heat constant, J/kg °C
Co	Convection number $(=(\rho_G/\rho_L)^{0.5}\,((1-x)/x)^{0.8})$
D_h	Hydraulic diameter, m
D_{12}	Mass diffusion coefficient of species 1 in a mixture of 1 and 2
D	Tube diameter, m
Fo	Fourier number
Fr	Froude number
Fr_{LO}	Froude number with all flow as liquid $(=G^2/(\rho_L^2 gD))$
G	Gravitational acceleration, m/s^2
G	Mass flux, kg/m^2 s
H	Heat transfer coefficient, W/m^2 °C
h_{fg}	Latent heat of vaporization, J/kg
h_L	Heat transfer coefficient for the liquid, W/m^2 °C
h_{LO}	Single-phase heat transfer coefficient for all flow in the liquid phase at saturation temperature, W/m^2 °C
$h_{L,Sat}$	Heat transfer coefficient for the liquid at the saturation point, W/m^2 °C
h_m	Heat transfer coefficient for the mixture, W/m^2 °C
h_{TP}	Two-phase heat transfer coefficient, W/m^2 °C
h^*	Heat transfer coefficient using T_{Sat} as the fluid temperature in the subcooled flow boiling, W/m^2 °C

Ja	Jakob number
K	Boltzmann constant, k (=1.38 × 10^{-23} J/K)
k_L	Thermal conductivity, W/m °C
l	Mixing length
M	Molecular weight
$\dot{m}$	Total mass flux, kg/m² s
Nu	Nusselt number
Nu_{LO}	Nusselt number with all flow as liquid
$Nu_{LO,cpLO,cp}$	Nusselt number with constant properties and all flow as liquid
$\dot{n}$	Number of drops per unit time
p	Pressure, N/m²
p_{cr}	Critical pressure, N/m²
p_G	Pressure of the gas inside bubble, N/m²
p_L	Pressure of the liquid, N/m²
$p_{Sat,T}$	Saturation pressure over a planar interface, N/m²
Pr	Prandtl number
Pr_L	Prandtl number for liquid
q	Heat transfer rate, W
q''	Heat flux, W/m²
R	Radius
R_b	Radius of a bubble, m
R_C	Cavity mouth radius, m
$R_{C,Crit}$	Cavity radius at the ONB
$R_{C,Max}$, $R_{C,Min}$	Minimum and maximum cavity radii available on a surface, m
Re	Reynolds number
$R(t)$	Bubble growth rate function
R_c^*	Nondimensional cavity radius
R_{min}^*, R_{max}^*	Minimum and maximum radii of active cavities
T	Temperature, °C or K
$T_{Sat,1\|p}, T_{Sat,2\|p}$	Saturation temperatures of the pure components at the total system pressure, p, °C
t	Time, s
TTR	Tape twist ratio for twisted tapes
u	Velocity, m/s
v	Specific volume, m³
V_m	Molar volume, m³/kg mol
x	Equilibrium quality
x_1, x_2	Mass fractions of 1 and 2, respectively, in the liquid phase of a mixture of species 1 and 2
y	The distance normal to the heater surface to the center of the bubble, m
y_1, y_2	Mass fractions of 1 and 2, respectively, in the vapor phase of a mixture of species 1 and 2

Greek Letters

α	Thermal diffusivity (=$k/(\rho c_p)$m²/s)
Γ	Liquid mass flow rate per unit film width
ΔT_{Sub}	Liquid subcooling ($T_{Sat} - T_L$), °C
ΔT_{Sub}^*	Liquid subcooling ($T_{Sat} - T_L$), nondimensional
δ_T	Single-phase thermal boundary layer thickness
ε_m	Eddy diffusivity for momentum transport
ε_h	Eddy diffusivity for heat transport
ϕ	Angle of orientation of the heated surface with respect to the horizontal, deg
φ	Spray distribution parameter for skewness
κ	Mixing length constant
μ_B	Viscosity of the bulk liquid, N s/m²
μ_L	Viscosity of the liquid, N s/m²
μ_W	Viscosity of the fluid at the wall temperature, N s/m²

ξ	Spray distribution parameter for uniformity
θ	Contact angle, deg
θ_r	Receding contact angle, deg
ρ	Density, kg/m^3
σ	Surface tension, N/m^2

Subscripts

An	Annular flow
1, 2	Species 1 and 2
c	Critical state
crit, cr	Critical point for the fluid
dp	Dew point
exit	Exit section
f	Stream core
fl	Fluid
fg	Latent quantity (vapor property–liquid property)
i	At the interface or initial state
L	Liquid
LO	All flow as liquid
G	Gas
MHF	Minimum heat flux
max	Maximum
min	Minimum
NVG	Point of net vapor generation
Nu	Nusselt-type solution
0	On a flat surface
r	Receding
Sat	Saturation point
Smooth	Smooth tube value
str	Stratified flow
Sub	Subcooling
t	Turbulent flow
tr	Transition flow
T	Thermal layer
TP	Two phase
v	Vapor phase
W	Wall
δ	Edge of liquid film

References

Aksan, S.N. and Rose, J.W., Dropwise condensation—The effect of thermal properties of the condenser material, *Int. J. Heat Mass Transfer*, 16, 461–467, 1973.

Anand, S., Paxson, A.T., Dhiman, R., Smith, J.D., and Varanasi, K.K., Enhanced condensation on lubricant-impregnate d nanotextured surfaces, *ACS Nano*, 6, 10122–10129, 2012.

Ananiev, E.P., Boyko, L.D., and Kruzhilin, G.N., Heat transfer in the presence of steam condensation in a horizontal tube, in *Proceedings of First International Heat Transfer Conference*, Part II, Boulder, CO, 1961, p. 290.

Awad, M.M., Dalkiliç, A.S., and Wongwises, S., A critical review on condensation heat transfer in micro-channels and minichannels*, J. Nanotechnol. Eng. Med.,* 5(1), NANO-14–1013, 2014.

Beatty, K.O. and Katz, D.L., Condensation of vapors on outside of finned tubes, *Chem. Eng. Prog.*, 44(1), 55–70, 1948.

Boreyko, J. and Chen, C., Self-propelled dropwise condensate on superhydrophobic surfaces, *Phys. Rev. Lett*., 103, 184501, 2009.

Boyko, L.D. and Kruzhilin, G.N., Heat transfer and hydraulic resistance during condensation of steam in a horizontal tube and in a bundle of tubes, *Int. J. Heat Mass Transfer*, 10, 361, 1967.
Carey, V.P., *Liquid-Vapor Phase-Change Phenomena*, Taylor & Francis, Bristol, PA, 1992.
Cassie, A.B.D. and Baxter, S., Wettability of porous surfaces, *Trans. Faraday Soc*., 40, 546, 1944.
Cavallini, A. and Zecchin, R., A dimensionless correlation for heat transfer in forced convention condensation, in *Proceedings of the Fifth International Heat Transfer Conference*, Tokyo, Japan, Vol. 3, 1974, pp. 309–313.
Chato, J., Laminar condensation inside horizontal and inclined tubes, *ASHRAE J.,* 12, 62, 1962.
Chen, C.H., Cai, Q., Tsai, C., Chen, C.L., Xiong, G., Yu, Y., and Ren, Z., Dropwise condensation on superhydrophobic surfaces with two-tier roughness, *Appl. Phys. Lett.,* 90, 173108, 2007.
Chen, S.L., Gerner, F.M., and Tien, C.L., General film condensation correlation, *Exp. Heat Transfer*, 1, 93, 1987.
Chen, T., Prediction of bundle shell side condensation heat transfer coefficient, in *Proceedings of ASME Summer Heat Transfer Conference 2008* (HT2008–56125), Jacksonville, FL, August 10–14, 2008.
Chen, X, Wu, J., Ma, R., Hua, M., Koratkar, N., Yao, S., and Wang, Z., Nanograssed micropyramidal architectures for continuous dropwise condensation, *Adv. Funct. Mater*., 21, 4617–4623, 2011.
Chiang, R.H.L., Gaffaney, D., and Kallfelz, A.J., 1993, Heat transfer tube, Patent #5203404.
Chun, K.R. and Seban, R.A., Heat transfer to evaporating liquid film, *ASME J. Heat Transf*., 93, 391, 1971.
Chung, J.N., Ayyaswamy, P.S., and Sadhal, S.S., Laminar condensation on a moving drop, Part 1. Singular perturbation technique, *J. Fluid Mech.,* 139, 105, 1984a.
Chung, J.N., Ayyaswamy, P.S., and Sadhal, S.S., Laminar condensation on a moving drop, Part 2. Numerical solutions, *J. Fluid Mech*., 139, 131, 1984b.
Dhir, V. and Lienhard, J.H., Laminar film condensation on plane and axisymmetric bodies in nonuniform gravity, *ASME J. Heat Transfer*, 93, 97, 1971.
Dietz, C., Rykaczewski, K., Fedorov, A.G., and Joshi, Y., Visualization of droplet departure on a superhydrophobic surface and implications to heat transfer enhancement during dropwise condensation. *Appl. Phys. Lett*., 97, 033104, 2010.
Dorrer C. and Rühe, J., Wetting of silicon nanograss: From superhydrophilic to superhydrophobic surfaces, *Adv. Mater*., 20(1), 159–163, 2008.
Eucken, A., Condensation nucleation theory, *Naturwissenschaften*, 25, 209, 1937.
Ford, J.D. and Lekic, A., Rate of growth of drops during condensation, *Int. J. Heat Mass Transfer*, 16, 61, 1973.
Garimella, S., 2014, Chapter 6: Condensation in minichannels and microchannels, in S. Kandlikar, S. Garimella, D. Li, S. Colin, and M.R. King (Eds.), *Heat Transfer and Fluid Flow in Minichannels and Microchannels*, Elsevier Science Ltd., pp. 227–408.
Gerstman, J. and Choi, H.Y., Electrohydrodynamics effects in condensation, Report 62-3*,* Department of Mechanical Engineering, Tufts University, Medford, MA, 1962.
Graham, C. and Griffith, P., Drop size distribution and heat transfer in dropwise condensation, *Int. J. Heat Mass Transfer*, 16, 337, 1973.
Hannemann, R.J. and Mikic, B.B., An analysis of the effect of the surface conductivity on the rate of heat transfer of heat transfer in dropwise condensation, *Int. J. Heat Mass Transfer*, 19, 1299–1307, 1976.
Hasson, D., Luss, D., and Navon, V., An experimental study of steam condensing on a laminar water sheet, *Int. J. Heat Mass Transfer,* 7, 983, 1964b.
Hasson, D., Luss, D., and Peck, R., Theoretical analysis of vapor condensation on laminar jets, *Int. J. Heat Mass Transfer,* 7, 969, 1964a.
Huang, L.J. and Ayyaswamy, P.S., Drag coefficient associated with a moving drop experiencing condensation, *ASME J. Heat Transfer*, 109, 1003, 1987a.
Huang, L.J. and Ayyaswamy, P.S., Heat and mass transfer associated with a spray drop, a fully transient analysis, *Int. J. Heat Mass Transfer*, 30, 881, 1987b.
Incropera, F.P. and DeWitt, D.P., *Fundamental of Heat and Mass Transfer*, Wiley, New York, 2002.
Jacobs, H.R. and Cook, D.S., Direct contact condensation on a non-circulating drop, in *Proceedings of the Sixth International Heat Transfer Conference,* Toronto, Ontario, Canada, Vol. 3, 1978, p. 389.
Jacobs, H.R and Nadig, R., Condensation on coolant jets and sheets including the effects of noncondensible gases, *ASME J. Heat Transfer*, 109, 1013, 1987.
Jakob, M., Film rupture theory of dropwise condensation, *Mech. Eng.,* 58, 729, 1936.
Jaster, H. and Kosky, P.G., Condensation heat transfer in a mixed flow regime, *Int. J. Heat Mass Transfer*, 19, 95, 1976.
Jones, T.B., Electrohydrodynamically enhanced heat transfer in liquids—A review, *Adv. Heat Transfer*, 14, 107, 1978.
Kandlikar, S.G., 2003, Microchannels and minichannels-history, terminology, classification and current research needs, *The First International Conference On Microchannels and Minichannels*, April 24–25, 2003, Rochester, New York.

Kandlikar, S.G., Colin, S., Peles, Y., Garimella, S., Pease, R.F., Brandner, J.J., and Tuckerman, D.B., Heat transfer in microchannels—2012 status and research needs, *J. Heat Transfer,* 135(9), 091001, 2012.
Kedzierski, M.A. and Webb, R.L., Practical fin shapes for surface tension drained condensation, *J. Heat Transfer,* 112, 479–485, 1990.
Kern, D.Q., Mathematical development of loading in horizontal condensers, *AIChE J.*, 4(2), 157–160, 1958.
Koh, J.C.Y., Sparrow, E.M., and Hartnet, J.P., The two-phase boundary in laminar film condensation, *Int. J. Heat Mass Transfer*, 2, 69, 1961.
Kutateladze, S.S., *Fundamental of Heat Transfer,* Academic Press, New York, 1963.
Labuntsov, D.A., Heat transfer in film condensation on vertical surfaces and horizontal tubes, *Teploenergetika*, 4, 72, 1957.
Lai, C.L., Gibbs–Thomson effect on droplet condensation, *ASME J. Heat Transfer*, 121, 632, 1999.
Lekic, A. and Ford, J.D., Direct contact condensation of vapor on a spray of subcooled liquid droplets, *Int. J. Heat Mass Transfer*, 23, 1531, 1980.
Marto, P.J., An evaluation of film condensation on horizontal integral-fin tubes, *J. Heat Transfer*, 110, 1287–1305, 1988.
Melcher, J.R., Traveling wave induced electro-convection, *Phys. Fluids*, 9, 1548, 1966.
Melcher, J.R. and Taylor, G.I., Electrohydrodynamics-a review of role of interfacial shear stress, *Annu. Rev. Fluid Mech.*, 1, 111, 1969.
Miljkovic, N., Preston, D.J., Enright, R., and Wang, E.N., Electric-field-enhanced condensation on superhydrophobic nanostructured surfaces, *ACS Nano* 7(12), 11043–11053, 2013.
Minkowycz, W.J. and Sparrow, E.M., Condensation heat transfer in the presence of noncondensables, interfacial resistance, superheating, variable properties, and diffusion, *Int. J. Heat Mass Transfer*, 9, 1125, 1966.
Narhe, R.D. and Beysens, D.A., Water condensation on a superhydrophobic spike surface, *Europhys. Lett.*, 75(1), 98–104, 2006.
Nusselt, W., Die Oberflachenkondensation des Wasser dampfes, *Z. Vereins deutscher Ininuere*, 60, 541, 1916.
Oswatitsch, K., Rate of droplet growth in condensation, *Z. Angew. Math. U. Mech.,* 22, 1, 1942.
Peterson, A.C. and Westwater, J.W., Dropwise condensation of ethylene glycol, *Chem. Eng. Prog. Symp. Ser.*, 62, 135–142, 1966.
Rohsenow, W.M., Heat transfer and temperature distribution in laminar film condensation, *Trans. ASME*, 79, 1645, 1956.
Rose, J.W., Effect of condenser tube material on heat transfer during dropwise condensation of steam, *Int. J. Heat Mass Transfer*, 21, 835–840, 1978.
Rose, J.W., Some aspects of dropwise condensation theory, *Int. J. Commun. Heat Mass Transfer*, 15, 449, 1988.
Rose, J.W., Condensation heat transfer, *Heat Mass Transfer J.*, 35, 479, 1999.
Rose, J.W., Dropwise condensation theory and experiment: A review, *Proc. Inst. Mech. Eng., Part A—J. Power Energy*, 216, 115, 2002.
Rykaczewski, K., Paxson, A.T., Staymates, M., Walker, M.L., Sun, X., Anand, S., Srinivasan, S. et al., Dropwise condensation of low surface tension fluids on omniphobic surfaces, *Nature,* 4, 4158, 2014. DOI: 10.1038/srep04158.
Sadasivan, P. and Lienhard, J.H., Sensible heat correction in laminar film boiling and condensation, *ASME J. Heat Transfer*, 109, 545, 1987.
Seban, R.A. and Hodgson, J.A., Laminar film condensation in a tube with upward vapor flow, *Int. J. Heat Mass Transfer*, 25, 1291, 1982.
Shah, M.M., A general heat transfer correlation during film condensation inside pipes, *Int. J. Heat Mass Transfer*, 22, 547, 1989.
Silver, R.S., An approach to a general theory of surface condensers, *Proc. Inst. Mech. Eng.*, 179, Part 1, 339, 1964.
Soliman, M., Schuster, J.R., and Berenson, P.J., A general heat transfer correlation for annular flow condensation, *ASME J. Heat Transfer*, 90, 267, 1968.
Sparrow, E.M., Minkowycz, W.J., and Saddy, M., Forced convection condensation in the presence of noncondensables and interfacial resistance, *Int. J. Heat Mass Transfer*, 10, 1829, 1967.
Sugawara, S. and Katsuta, K., Fundamental study on dropwise condensation, in *Proceedings of the Third International Heat Transfer Conference,* Chicago, IL, Vol. 2, 1966, p. 354.
Sundararajan, T. and Ayyaswamy, P.S., Hydrodynamics and heat transfer associated with condensation on a moving drop: Solution for intermediate Reynolds numbers, *J. Fluid Mech.,* 149, 33, 1984.

Sundararajan, T. and Ayyaswamy, P.S., Heat and mass transfer associated with condensation on a moving drop: Solution for intermediate Reynolds numbers by a boundary layer formulation, *ASME J. Heat Transfer*, 107, 409, 1985a.
Sundararajan, T. and Ayyaswamy, P.S., Numerical evaluation of heat and mass to a moving drop experiencing, *Numer. Heat Transfer*, 8, 689, 1985b.
Taitel, Y. and Tamir, A., Condensation in the presence of a noncondensible gas in direct contact, *Int. J. Heat Mass Transfer*, 12, 1157, 1969.
Tanaka, H., A theoretical study on dropwise condensation, *ASME J. Heat Transfer*, 97, 72, 1975.
Tanner, D.W., Pope, D., Potter, C.J., and West, D., Heat transfer in dropwise condensation at low steam pressures in the absence and presence of non-condensable gas, *Int. J. Heat Mass Transfer*, 11, 181–190, 1968.
Thomson, W., On the equilibrium of vapour at a curved surface of liquid, *Philos. Mag.,* 42, 448, 1871.
Thors, P., Clevinger, N.R., Boonie, J.C., and Tyler, J.T., 1999, Heat transfer tubes and methods of fabrication thereof, Patent #5996686.
Umur, A. and Griffith, P., Mechanism of dropwise condensation, *ASME J. Heat Transfer,* 87, 275, 1965.
Varanasi, K.K., Hsu, M., Bhate, N., Yang, W., and Deng, T., Spatial control in the heterogeneous nucleation of water, *Appl. Phys. Lett*., 95, 094101, 2009.
Velkoff, H.R. and Miller, J.H., Condensation of vapor on a vertical plate with a transverse electrostatic field, *ASME J. Heat Transfer*, 87, 197, 1965.
Welch, J.F. and Westwater, J.W., Microscopic study of dropwise condensation, *ASME Int. Dev. Heat Transfer*, Part II, 1961.
Wenzel, R.N., Resistance of solid surfaces to wetting by water, *Ind. Eng. Chem*., 28, 988, 1936.
Wilkins, D.G. and Bromley, L.A., 1973, Dropwise condensation phenomena, *AJChE J*., 19(4), 839–845, 1973.
Withers, J.G. Jr. and Rieger, K.K., Heat transfer tubes having multiple internal ridges, Patent #3847212, 1974.


Taylor & Francis
Taylor & Francis Group
http://taylorandfrancis.com

10

Powder and Granular Flow

Fu-Ling Yang and Keng-Lin Lee

10.1 Background and Stress Models
10.2 Particle-Based Simulations Using the Discrete Element Method
10.3 Granular Flows in a Vertical Vibration Bed
10.4 Discussions: Segregation Phenomenon and Cohesion Effect

10.1 Background and Stress Models

10.1.1 Introduction

Dynamics of grain and power flows has been extensively investigated for their common appearances in industrial processes (gasoline drilling, slurry transportation, surface polishing with fine particles, etc.) and natural events (avalanches, debris flows, sedimentation, etc.). Such flows are, in general, composed of solid constituents of characteristic diameter D greater than 100 nm and within 1–100 nm, respectively. These particles are large enough so that their motion is rather insensitive to disturbances from Brownian motions or thermal energy fluctuations (Rognon et al., 2008, Andreotti et al., 2013) but primarily controlled by the interactions with their neighbors. Grain–grain interactions, in general, are categorized into noncontact near-field cohesion forces and contact forces, including both repulsive collisions and enduring contacts in both elastic recoverable and plastic dissipating modes. Noncontact cohesion force, on the other hand, can result from various mechanisms such as electrostatic force due to frequent surface interaction in humid environment, van der Waals force for materials of high intermolecular potential, and capillary or lubrication force due to thin surface liquid coating.

Unlike conventional fluid or solid continuum at scale several orders of magnitude greater than constituent molecules, separation of flow and grain size scales is not large and particle-level dynamics accumulates to affect grain collective motion at large scale. Based on this understanding, researchers have attempted to develop bulk constitutive models, according to which is the dominating interaction mode in developing continuum governing equations.

Systematic experiments with skillful measuring techniques have been conducted to investigate flow rheology and dynamics with respect to flow conditions so that empirical relations may be formulated. However, such flow information is often limited to averaged properties at flow boundaries due to the discrete and opaque nature of the material. To gain insight from particle-level information, particle-based numerical simulation has become an indispensable research tool that calculates individual grain motions to estimate both rheological properties and transport properties. Along this line, this chapter summarizes some important models and numerical studies for six particular types of steady flows commonly investigated in the literature. The simple linear shear or annular shear flow, inclined flow, and unsteady column collapse are three popular configurations to probe flow rheology and boundary conditions. The other three quasi-steady flows in a rotating drum and on a vertically vibrating bed as well as the discharge from a hopper are commonly studied for

industrial applications. Since extensive reviews and discussions can be found for most flow types except that on a vibrating beds, the rest of this chapter is dedicated to a review for the dynamics of a vibrating bed nearly identical spheres.

10.1.2 Stress Model, Boundary Condition, and Governing Equations

10.1.2.1 Collisional Stress Model

When a granular assembly moves fast at dilute to moderate solid volume concentration, ϕ, most particle–particle interactions are uncorrelated repulsive binary collisions with contact durations much shorter than the timescale associated with bulk shear rate. Such flow is known as a *rapid granular flow* in *collisional regime*. Bulk stress has a collisional part, $\underline{\underline{\sigma}}_c$, and a kinetic part known as the streaming stress, $\underline{\underline{\sigma}}_k = \rho\left\langle\left(\underline{u}_p - \underline{u}\right)\left(\underline{u}_p - \underline{u}\right)\right\rangle$, due to incoherent grain motions (Campbell and Brennen, 1985). Here, $\rho = \rho_p\phi$ is the bulk density depending on the grain intrinsic density ρ_p. Bulk velocity $\underline{u} = \left\langle \underline{u}_p \right\rangle$ is averaged from individual grain velocity $\underline{u}_p$ via a mass- or volume-weighted scheme or a statistical ensemble average, denoted by $\langle\cdot\rangle$, and $\underline{u}_p - \underline{u}$ measures the deviatoric velocity. Except in very dilute flows, $\underline{\underline{\sigma}}_c \gg \underline{\underline{\sigma}}_k$, and the bulk total stress is often approximated by the collisional part in theoretical modeling. Since the dominant micromechanical mechanism resembles how gas molecules interact with each other at a specific thermal state, extensive modeling efforts have been made based on the kinetic theory of dense gas (Ogawa, 1978, Savage and Jeffrey, 1981, Jenkins and Savage, 1983, Jenkins, 1994, Goldhirsch, 2003, etc.). Regardless of the complexity borne in various models, a general form can be expressed as

$$\underline{\underline{\sigma}}_c = \left[C_1 p_T(T) + C_2 \mu_b^\star \nabla \cdot \underline{u} \right] \underline{\underline{I}} + C_3 \mu^\star \underline{\underline{S}}, \tag{10.1}$$

possessing an isotropic normal component and a component that varies with the shear strain rate tensor, $\underline{\underline{S}} = \left[\nabla \underline{u} + \left(\nabla \underline{u}\right)^T \right]/2$, with the superscript T denoting the transpose of a tensor. The coefficients $C_1 \sim C_3$ depend not only on material properties but also on ϕ and other flow properties. The first term in the isotropic component is a *pseudo-thermal* pressure p_T that scales linearly with the *pseudo-thermal* granular temperature $T = 1/3 < (\underline{u}_p - \underline{u})^2 >$ like conventional gases. This similarity in how pressure is related to temperature results from the transport mechanism for momentum flux for both medium is grain collisions and that is why the shear and bulk viscosities $\mu^\star$ and $\mu_b^\star$ also show square root dependence on *T*. By definition, *T* measures the bulk fluctuation energy due to incoherent motion of individual particles from their mean.

One popular collisional stress model is (Lun et al., 1984)

$$\underline{\underline{\sigma}}_c = \left[\rho T\left(1 + 4\eta\phi g_0\right) - \eta\mu_b^\star \nabla \cdot \underline{u} \right] \underline{\underline{I}} - \left(\frac{2+\alpha}{3} \right) \left[\frac{2\mu^\star}{\eta(2-\eta)g_0} \left(1 + \frac{8}{5}\eta\phi g_0 \right) \left[1 + \frac{8}{5}\eta\left(3\eta - 2\right)\phi g_0 \right] + \frac{6}{5}\eta\mu_b^\star \right] \underline{\underline{S}} \tag{10.2}$$

with

$$\mu^\star = \frac{5 m_p \sqrt{T/\pi}}{16 D^2}, \quad \mu_b^\star = \frac{265\phi^2 g_0}{5\pi}\mu^\star \tag{10.3}$$

in which α is a numerical coefficient often assumed to be unity, m_p and *D* are characteristic grain mass and diameter. In Equation 10.2, $\eta = 1/2(1 + e)$ depends on the coefficient of restitution, *e*, for intergrain collisions and $g_0(\phi, \phi_m)$ is the *radial distribution function* that characterizes packing configuration around a single grain and hence depends on both local ϕ and the maximum value ϕ_m at the closest packing.

By this definition, bulk collisional stress is always symmetric and evolves with flow via its dependence on ϕ and *T*. Hence, the momentum conservation equation has to be solved in junction with the conservation equations of mass and pseudo-thermal energy equation as

$$\frac{\partial \rho}{\partial t} + \nabla \cdot \left(\rho \underline{u}\right) = 0 \tag{10.4}$$

$$\rho \frac{D\underline{u}}{\partial t} = \rho \underline{g} - \nabla \cdot \underline{\underline{\sigma}} \tag{10.5}$$

$$\frac{3}{2}\rho\frac{DT}{\partial t} = -\nabla\cdot\underline{q} - \underline{\underline{\sigma}}:\nabla\underline{u} - s \tag{10.6}$$

with $\underline{\underline{\sigma}} \approx \underline{\underline{\sigma}}_c$ and gravity acceleration $\underline{g}$. Additional constitutive relations are needed for the pseudo-thermal flux $\underline{q}$ to account for nonuniform fluctuation energy and rate of dissipation, s, due to inelastic grain interactions in Equation 10.6, and they have been formulated by Lun et al. (1984) as

$$\underline{q} = \frac{\kappa}{g_0}\left\{\left(1+\frac{12}{5}\eta\phi g_0\right)\left[1+\frac{12}{5}\eta^2(4\eta-3)\phi g_0\right]+\frac{64}{25\pi}(41-33\eta)(\eta\phi g_0)^2\right\}\nabla T$$
$$-\frac{\kappa}{g_0}\frac{12}{5}\eta(\eta-1)(2\eta-1)\left(1+\frac{12}{5}\eta\phi g_0\right)\frac{d}{d\phi}(\phi^2 g_0)\frac{T}{\phi}\nabla\phi \tag{10.7}$$

$$s = \frac{48}{\sqrt{\pi}D}\eta(1-\eta)\rho\phi g_0 T^{3/2} \tag{10.8}$$

$$\kappa = \frac{75m\sqrt{T/\pi}}{8\mu^*(41-33\eta)D^2} \tag{10.9}$$

with a pseudo-thermal conductivity κ.

10.1.2.2 Frictional Stress Model

Nonetheless, under the action of gravity, grains tend to rest on their own weight to result in denser flows in which prolonged multiple contacts take place in addition to repulsive binary collisions. Particle elastic deformation, in both normal and tangential directions, and tangential friction with adjacent particles form force chains and cluster-like structures within the bulk. Such internal structures not only provide another micromechanical mechanism for momentum and energy transport but also redistribute and hence sustain external loading to give the bulk plasticity and strength to withstand shear loading. Plugs or basal deposit can further develop within a flow and such phenomenon cannot be captured by the kinetic theory since the modeled predicts a vanishing, instead of diverging, stress model when $\underline{u}$ and hence $\underline{u}'$ and T, μ, and μ_b approach zero.

To address this issue, the deviatoric stress for a slowly deforming dense bulk in the so-called quasi-static regime is often described by the Mohr–Coulomb model as

$$\underline{\underline{\sigma}}_f = P_f\underline{\underline{I}} - \underline{\underline{\tau}}_f = P_f\underline{\underline{I}} - \sin\varsigma P_f\underline{\underline{S}}^\star \tag{10.10}$$

with

$$P_f = tr(\underline{\underline{\sigma}}_f) \quad \text{and} \quad \underline{\underline{S}}^\star = \underline{\underline{S}}/|\underline{\underline{S}}| \tag{10.11}$$

that depends on a quasi-steady friction angle ς. This relation assumes that the stress and strain rate tensor share the same directions of principal axes and the material is incompressible so that $tr(\underline{\underline{S}}) = 0$. The dependence on the *normalized* shear strain rate tensor $\underline{\underline{S}}^\star$ gives a diverging $\underline{\underline{\tau}}_f$ and hence the desired yielding strength when $\underline{\underline{S}}$ approaches zero in slow deformation.

However, the incompressibility assumption inevitably makes $\underline{\underline{\tau}}_f$ independent of changes in ϕ and hence cannot account for the effect of varying ϕ on during deformation—like the Reynolds dilatancy effect upon yielding (Reynolds, 1885). More advanced models have been proposed and one example is the critical-state theory (Wood, 1990, Roux and Radjai, 1998, Radaji and Roux, 2004):

$$\underline{\underline{\tau}}_f = \mu(\psi)P_f\underline{\underline{S}}^{D\star} \tag{10.12}$$

where

$$\underline{\underline{S}}^{D\star} = \underline{\underline{S}}^{D} \Big/ \left|\underline{\underline{S}}^{D}\right| \quad \text{and} \quad \underline{\underline{S}}^{D} = \underline{\underline{S}} - 1/3\, tr\left(\underline{\underline{S}}\right) \tag{10.13}$$

Based on Equations 10.12 and 10.13, the friction coefficient is no longer constant but varies with the *dilatancy angle* ψ. This angle is related to the ratio of the vertical to horizontal relative displacement between two adjacent particle layers and hence depends on local packing configuration and should be positive upon dilation and vice versa. Simple geometric arguments can render a simple relation between ψ and local strain rate tensor as

$$\sin(\psi) = \frac{1}{3} \frac{\mathrm{tr}\left(\underline{\underline{S}}\right)}{\left|\underline{\underline{S}}^{D}\right|} \tag{10.14}$$

where the constant in the denominator should be changed to 2 for a 2D problem. In addition, ψ should further depend on ϕ, and a simple yet feasible linear relation has been proposed (Roux and Radjai, 1998) as

$$\psi = C_4\left(\phi - \phi_c\right) \tag{10.15}$$

with a positive constant C_4 and a critical volume fraction ϕ_c. This critical ϕ_c is the asymptotic value when nearly static packing has undergone sufficient deformation (>1% strain). When $\phi > \phi_c$, $\psi > 0$ and the bulk dilates and vice versa. Equations 10.12 through 10.15 comprise a simple plastic model for granular material under slow deformation, and this model fails when the bulk is under very high confining pressure—often occurs in geophysical events—for which the critical state may change with the bulk quasi-thermal state.

10.1.2.3 Composite Stress Model

With the simplest version of $\underline{\underline{\tau}}_f$ in Equation 10.10, $\underline{\underline{\sigma}}_f$ has been added to $\underline{\underline{\sigma}}_c$ to compose the total stress as the sum: $\underline{\underline{\sigma}} = \underline{\underline{\sigma}}_c + \underline{\underline{\sigma}}_f$ under an *ad hoc* assumption of linear superposition (Savage, 1983b, Johnson and Jackson, 1987). Apart from this, Jenkins modifies the pair interaction model in the kinetic theory to account for long-range interactions through force chains (Jenkins, 1994) so that a transport mechanism faster than that by collisions is added. Some considers the destruction and formation of force chain network as phase transition between mobilized fluid state and arrested solid state to relate the stress tensor to nonlocal functions of velocity field and a structural parameter for the material constituents (Mills et al., 1999, 2000). Another simple yet intriguing model treats force-chain networks as eddies in turbulent flows so that the cluster structure acts like granular eddies to assist transport at a length scale longer than *D* so that $\underline{\underline{\sigma}}$ is modeled by multiplying $\underline{\underline{S}}$ with a flow-dependent viscosity (Ertas and Halsey, 2002). In another work, the bulk is treated as a Herschel–Bulkley type of complex fluid that depends on a hydrostatic normal pressure in the formulation of $\underline{\underline{\sigma}}$ (Balmforth and Kerswell, 2005). The intrinsic biphase behavior inherited in these models promises the success in producing plug flows or a static deposition that is never captured by a model using only the collisional stress.

10.1.2.4 Phenomenological Model Based on μ(I) Rheology Law

Yet, another approach does not distinguish the collision- and friction-induced stress components but employs dimensional analysis to correlate effective friction coefficient, $\mu = |\tau|/P$, to a *dimensionless inertial number I* for incompressible granular flows in uniform shear. Here, μ is the ratio of characteristic tangential to normal stress in the form of the Coulomb-type material due to flow dense nature and *I* is defined as

$$\mathrm{I} = \frac{\left\|\underline{\underline{S}}^{D}\right\| D}{\sqrt{P/\rho}} \tag{10.16}$$

which depends on the second invariant of $\underline{\underline{S}}^{D}$ and mean normal stress *P*. This number represents the ratio of the time for shear-induced streamwise displacement to that for grain transverse movement to adjacent voids under confining *P*. Hence, *I* can be interpreted as a measure of bulk fluidity with respect to settling tendency

so that flows with large I are fast flowing while those with slowly deforming motions are characterized by small I. Empirical $\mu - I$ relation has been sought via laboratory experiments and computer simulations and a conforming trend is discovered for unidirectional steady flows in various simple steady flows (Iordanoff and Khonsari, 2004, MiDi, 2004, Da Cruz et al., 2005, Jop et al., 2006, Forterre and Pouliquen, 2008) as

$$\mu(I) = \mu_s + \frac{\mu_2 - \mu_s}{I_0/I} \tag{10.17}$$

Here, μ_s acts as a bulk static friction coefficient and is associated with the bulk yielding strength as a consequence of lasting frictional contacts and the asymptotic μ_2 characterizes a corresponding value in the collisional regime. Fitted values of $\mu_s = 0.38$ (~tan21°, for the examined glass beads), $\mu_2 = 0.67$(~tan34°), and $I_0 = 0.3$ have been reported to complete the so-called $\mu - I$ rheological relation or frictional law for steady dense granular flows. While μ increases monotonically and nonlinearly with I in Figure 10.1a, the bulk solid volume fraction decreases linearly with I as shown in Figure 10.1b since the flow gets more agitated. A *dilatancy law* has been fitted as

$$\phi = \phi_s - \Delta\phi I \tag{10.18}$$

where ϕ_s is the value for static packing and $\Delta\phi \approx 0.2$ has been fitted for a 3D flow of glass beads. Further details on how these relations are extracted and related to underlying flow physics can be found in Midi (2004), Jop et al. (2006), and Andreotti et al. (2013).

From the algebraic $\mu(I)$ for unidirection flow, a tensorial form for bulk deviatoric stress (with $\underline{\underline{\sigma}} = -p\underline{\underline{I}} + \underline{\underline{\tau}}$) has been proposed as

$$\underline{\underline{\tau}} = \frac{\mu(I)P}{\|\underline{\underline{S}}\|}\underline{\underline{S}} \tag{10.19}$$

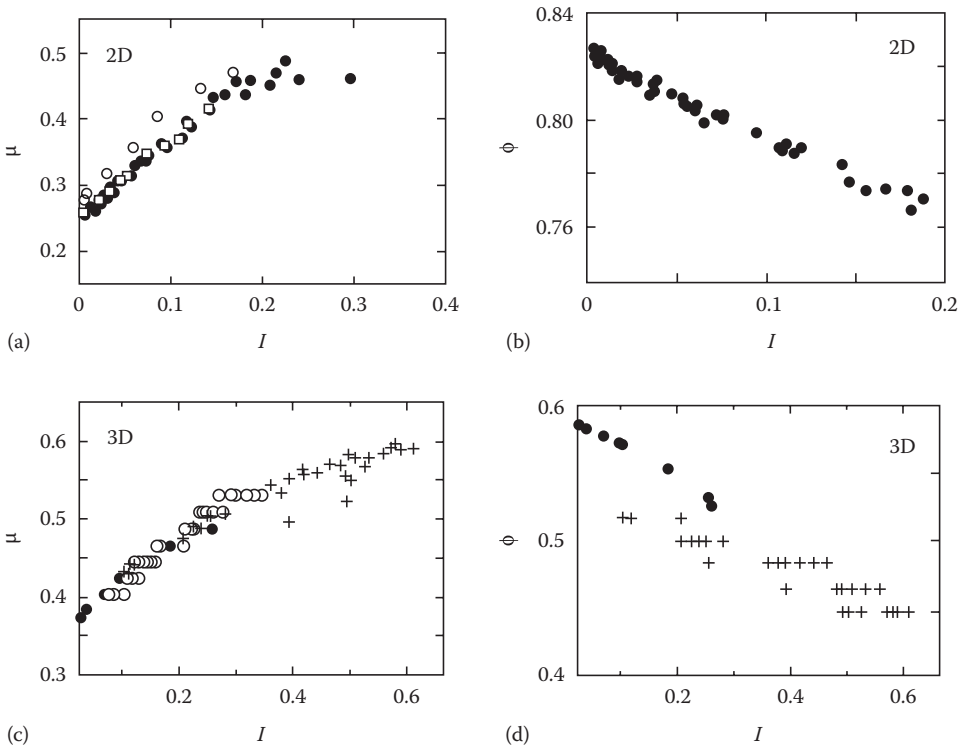


Figure 10.1

The friction law $\mu(I)$ and dilatancy law $\phi(I)$ extracted from 2D (a,b) and 3D systems (c,d). The 3D results in (c) have been fitted into Equation 10.17 for glass beads. (From Andreotti, B. et al., *Granular Media*: *Between Fluid and Solid*, Cambridge University Press, Cambridge, U.K., 2013 and the references therein.)

with

$$\|\underline{\underline{S}}\| = \sqrt{\underline{\underline{S}}\underline{\underline{S}}/2} \tag{10.20}$$

assuming that the principal vectors of $\underline{\underline{\tau}}$ and $\underline{\underline{S}}$ are identical. Both the 2D and 3D rheology laws have been confirmed in flows of various configurations, and researchers have started to investigate how far this simple rheology model can reach when flows are more complex.

The scalar expression in Equation 10.17 is probed in starting and accelerating unidirectional flows over a heap (Jop et al., 2007) and in accelerating and decelerating thin surface flows in a 2D rotating drum (Cortet et al., 2009) and for granular column collapse on a rough plane (Lacaze and Kerswell, 2009). The proposed tensorial form in Equations 10.19 and 10.20 has been incorporated in a 2D incompressible flow solver, and some of the predicted continuum bulk dynamics agree fairly well to either experimental findings or predictions from particle-based simulation methods. For example, the instantaneous surface profile and the final deposit shape from a collapsed column agree to those obtained from a discrete model simulation (Lagrée et al., 2011). The Beverloo law is captured in a rectangular silo and the simulated instantaneous pressure field agrees to the general behavior of a continuum flow (Staron et al., 2014). While these provide supporting evidences for Equation 10.19, it is noted that quantitative comparison on the distribution of bulk velocity is not reported. Further, a recent detailed examination from particle-based simulations reported that unmatched principle stresses for $\underline{\underline{\tau}}$ and $\underline{\underline{S}}$ are slowly creeping bulk in the bed of a 2D rotating drum (Cortet et al., 2009) though the scalar formulation adopting the stress invariants in Equation 10.17 remains valid. Hence, further research on generalizing Equation 10.19 by relaxing the assumptions or by taking into account of nonlocal phenomenon is desired (Kamrin and Bazant, 2007, Pouliquen and Forterre, 2009, Kamrin and Koval, 2012, Shojaaee et al., 2012).

10.1.2.5 Boundary Condition

In addition to these constitutive models, feasible boundary conditions have to be specified so that continuum-like bulk dynamics can be solved via theoretical analysis or numerical simulation. Most common conditions are zero stress at the free surface and vanished velocity (no slip and no penetration) at the solid boundary provided that the flow is sufficiently thick (to validate the continuum-like behavior) or rough (Jop et al., 2005). More complex forms can also be found in the literature for different flow conditions. For example, Johnson and Jackson (1987) consider the transfer of momentum flux between the base and the bulk to propose a more delicate basal condition as

$$\underline{t}\cdot\underline{\underline{\sigma}}\cdot\underline{n} + \frac{\sqrt{3}\pi}{6\phi_m}\Lambda\rho g_0 T^{1/2} u_{SL} = 0 \tag{10.21}$$

with

$\underline{t}$ and $\underline{n}$ denoting the unit vector tangent and normal to the base
u_{SL} is the bulk *basal slip* velocity

The specularity constant factor Λ measures the proportion of the streamwise momentum flux transmitted to the base. The zero stress condition at the free surface has also been modified to account for the normal stress imposed by the overtopping surface particles into the following expression:

$$\underline{\underline{\sigma}}\cdot\underline{n} = \frac{\mathrm{M}\underline{g}}{D^2}\left(\frac{\phi}{\phi_\mathrm{m}}\right)^{2/3} \tag{10.22}$$

in which M is the mass of a layer of grains of unit thickness (a 2D version). As for boundary conditions for the pseudo-thermal energy equation in Equation 10.6, a constant heat influx, $\underline{q}\cdot\underline{n} = q_b$, or constant temperature T is often assigned. Apart from this, there are more advanced models for how basal condition should be related to flow conditions (Artoni et al., 2009a, 2012).

These theoretical models have been applied to describe and explain flow phenomenon, mostly at steady states, and a few are cited in Table 10.1 according to the stress models for six particular types of steady (quasi-steady) flows commonly investigated in the literature. The simple linear shear or annular shear flow, inclined flow, and unsteady column collapse are three popular flow configurations adopted to probe or test flow rheology and boundary conditions. On the other hand, the quasi-steady flows in a rotating drum and

Table 10.1 Selected References for Theoretical Modeling of Six Types of Flows According to the Chosen Stress Models

	Kinetic Theory	Composite	μ(*I*) Rheology Model	Depth-Averaged Model
Simple shear flow	Haff (1983) Savage (1983a) Jenkins and Savage (1983) Lun et al. (1984) Jenkins and Richman (1985) Berzi (2011, 2014)	Johnson and Jackson (1987) Savage (1998)	GDR Midi (2004) Da Cruz et al. (2005) Henann and Kamrin (2013) Tankeo et al. (2013)	
Inclined flow	Hutter et al. (1986) Richman and Marciniec (1990) Jenkins and Askari (1999) Jenkins and Zhang (2002) Jenkins (2006, 2007) Kumaran (2006, 2008, 2014) Berzi (2007)	Johnson et al. (1990) Mills et al. (1999) Ancey (2001) Khakhar et al. (2001) Aranson and Tsimring (2002) Louge (2003) Savage (2008) Chialvo and Sundaresan (2013)	Jop et al. (2005) Jop et al. (2007) de Ryck et al. (2010) Maeno et al. (2013) Chauchat and M´edale (2014) Gray and Edwards (2014) Kamrin and Henann (2015)	Savage and Hutter (1989, 1991) Pouliquen (1999a) Pouliquen (1999b) Douady et al. (1999) Andreotti et al. (2002) Pouliquen and Forterre (2002) Hogg (2007) Razis et al. (2014) Edwards and Gray (2015)
Column collapse			Lagrée et al. (2011)	Balmforth and Kerswell (2005) Kerswell (2005) Larrieu et al. (2006)
Rotating drum flow Hopper flow		Orpe and Khakhar (2007) Srivastava and Sundaresan (2003)	Orpe and Khakhar (2007) Staron et al. (2014)	Gray (2001)
Vibrating bed flow	Haff (1983) Richman and Martin (1992) Hunt et al. (1994) Deng and Wang (2003)	Savage and Lun (1988)		Hutter and Rajagopal (1994)

Simple shear flows include 2D linear flows and quasi-2D annular shear; inclined flows treat both uniform and nonuniform cases; rotating drum flows can be both 2D and 3D; vibrating bed flows are limited to vertical shaking only.

on a vertically vibrating bed as well as the unsteady discharge from a hopper are commonly studied for industrial applications.

10.1.3 Depth-Averaged Shallow Flow Model

Apart from these, it should be noted that a depth-integrated shallow flow theory has been developed for thin surface flows down a slope inclined at θ from the horizontal with no-slip boundary condition. The original 2D model (x–y plane, with z pointing out of the page) developed by Savage and Hutter (1989) is dedicated for landslide problems in which significant shearing, fluidization, and density variation are restricted in a thin basal layer (Melosh, 1986). Hence, the flow is approximated as an incompressible plug flow with *depth-averaged* velocity $\bar{u}$ and density $\bar{\rho}$. Limiting to flows of small depth-to-length aspect ratio, ε, the authors first simplify the transverse momentum equation to obtain a hydrostatic pressure distribution that grows linearly with depth from a surface zero. Further integration of mass and x-momentum conservation equations leads to a set of simplified partial differential equations, accurate to the order of ε, as

$$\frac{\partial h}{\partial \mathrm{t}} + \frac{\partial h\bar{u}}{\partial x} = 0 \tag{10.23}$$

$$\frac{\partial \bar{u}}{\partial \mathrm{t}} + \bar{u}\frac{\partial \bar{u}}{\partial \mathrm{x}} = \sin\theta - \varepsilon\cos\theta K_{a/p}\frac{\partial h}{\partial x} - \mathrm{sgn}\left(\bar{u}\right)\cos\theta f_B \tag{10.24}$$

where h is a varying flow height. The action of bulk stress is converted to zero surface friction and a basal friction in the last term of Equation 10.24 in which $f_B = \tan \varsigma_B$ is the friction coefficient in terms of a

basal friction angle ς_B. The additional constant $K_{a/p}$ is the Coulomb-type active and passive earth pressure coefficient, denoted by the subscripts *a* and *p* as

$$\left.\begin{matrix} K_a \\ K_p \end{matrix}\right\} = \frac{2}{\cos^2\varsigma}\left[1 \mp \sqrt{1-\left(1+\tan^2\varsigma_B\right)\cos^2\varsigma}\right] - 1, \quad \text{for} \quad \begin{matrix} \partial\bar{u}/\partial x > 0 \\ \partial\bar{u}/\partial x < 0 \end{matrix} \tag{10.25}$$

This coefficient is the ratio of bulk lateral to normal stress when the bulk dilates or compresses upon yielding. The authors approximate $\overline{u^2} \approx \bar{u}^2$ when handling the convective acceleration term since the velocity profile is nearly blunt since strong shear is localized in a thin basal layer. The set of partial differential equations can be transformed to an *advection–diffusion equation* governing how $h(x, t)$, equivalently the granular mass, evolve in time and space down the slope. For certain types of flows, a *similarity solution* may be found (Liu and Mei, 1989, Ancey et al., 2009, Pudasaini 2011), and numerical solution can always be sought for more complex cases. This scheme succeeded in capturing the primary mode of bulk dynamics in several surface flow problems and hence is also included in Table 10.1 for interested readers.

Besides of theoretical modeling, systematic experiments with skillful measuring techniques have been conducted to explore how each bulk dynamics vary with flow conditions. However, the information is primarily the averaged properties at flow boundaries due to the discrete and opaque nature of the material. To gain an insight from the particle-level information, a particle-based numerical simulation, which calculates individual grain motion to estimate bulk properties, has become an indispensable research tool, especially with the rapid advance of computation capacity. Hence, the fundamentals of one popular scheme—the discrete element method (DEM)—are described briefly in the following to introduce the basic concepts.

10.2 Particle-Based Simulations Using the Discrete Element Method

10.2.1 Introduction

Ever since the first application to granular systems by Cundal and Strack (1979), the DEM has become a powerful simulation tool for both industrial process design and flow physics investigation (Cundall, 1988, Walton, 1993). The motion of individual grain is computed by the conservation of linear and angular momentum under the action of gravity and grain–grain interaction force. Contact models of varying complexity have been proposed to describe the paired interaction force, and the simplest soft-sphere contact model for identical spherical grains is introduced first for easy comprehension.

10.2.2 Soft-Sphere Contact Model

10.2.2.1 Contact Model and Its Parameters

In an inertial reference frame, let $\underline{\mathrm{p}}_i$ denote the position vector for sphere *i* of diameter *D* and mass m_p. Its contact with an adjacent sphere *j* as sketched in Figure 10.2a is determined when the distance between the centers, $|\underline{\mathrm{p}}_{ij}| = |\underline{\mathrm{p}}_j - \underline{\mathrm{p}}_i|$, falls below *D* and a contact normal for sphere *i* is defined accordingly by $\underline{\mathrm{n}}_i = \underline{\mathrm{p}}_{ij}/|\underline{\mathrm{p}}_{ij}|$. The sphere velocity is decomposed with respect to $\boldsymbol{n}$ into a normal and a tangential component as u_{ni} and u_{ti}. Their relative translational and angular motion result in normal and tangential displacement at the contact point as $\delta_\mathrm{n}(t) = \mathrm{D} - |\underline{\mathrm{p}}_{\mathrm{ij}}(t)|$ and $\delta_\mathrm{t}(t) = \sum_1^N u_{rt}(t)\Delta t$ with instantaneous relative tangential velocity at the contact point $u_{\mathrm{rt}} = u_{\mathrm{ti}} - u_{\mathrm{tj}} + 1/2\underline{\mathrm{p}}_{\mathrm{ij}} \times (\underline{\omega}_\mathrm{i} + \underline{\omega}_\mathrm{j}) \cdot \underline{\mathrm{t}}_\mathrm{i}$. Particle rotation at $\underline{\omega}_\mathrm{I}$ or $\underline{\omega}_\mathrm{j}$ is taken into account, and the unit tangent vector $\boldsymbol{t}_\mathrm{i}$ is perpendicular to $\underline{\mathrm{n}}_\mathrm{i}$ according to the right-hand rule. By this definition, $\delta_\mathrm{t}(t)$ represents the total tangential displacement accumulated over *N* constant DEM steps Δt during one contact. The pair interaction force, $\underline{\mathrm{F}}_{ij}$, is decomposed with respect to $\underline{\mathrm{n}}_\mathrm{i}$ and modeled by an elastic and a dissipating force component (Cundall and Strack, 1979, Campbell and Brennen, 1985, Di Renzo et al., 2004, Kruggel-Emden et al., 2007, Luding, 2008, Yang et al., 2013, etc.). The simplest linear spring–dashpot model describes the normal interaction force by the sum of an elastic spring force, $F_{nS} = -k_n\delta_n$, and a damping force, $F_{nD} = -c_n u_{nr}$, with k_n and c_n denoting the normal spring and damping constant and $u_{nr} = u_{nj} - u_{ni}$ being the normal relative velocity. Tangential force also has a recoverable elastic component $F_{tS} = -k_t\delta_t\,\mathrm{sgn}(u_{rt})$ with a spring constant k_t that acts against the sign of relative tangential velocity at the contact point. This force is switched to a dissipative friction of the Coulomb-type $F_{tF} = -f_c(F_{nS} + F_{nD})\mathrm{sgn}(u_{\mathrm{rt}})$ when gross sliding takes place if $F_{tS} \geq F_{tF}$.

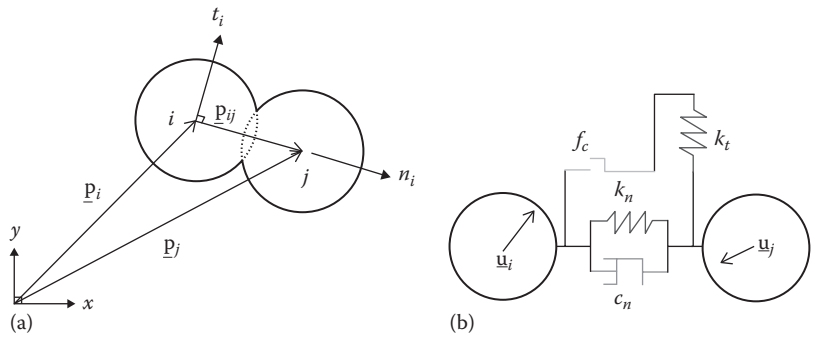


Figure 10.2

(a) Illustration of two contacting spheres at position $\underline{p}_i$ and $\underline{p}_j$ in an inertial reference frame. (b) Illustration of a linear soft-sphere contact model for spheres i and j coming into contact at velocities $\underline{u}_i$ and $\underline{u}_j$: k_n and k_t are the stiffness of the normal and tangential spring, c_n the damping constant, and f_c the sliding friction coefficient.

Here, f_c is the friction coefficient between contacting surfaces. In summary, the normal and tangential force component of $\underline{F}_{ij}$ (with omitted subscript ij) during a contact can be expressed as

$$F_n = F_{nS} + F_{nD} = -\left(k_n \delta_n + c_n u_{nr}\right) \tag{10.26}$$

$$F_t = \begin{cases} F_{tS} = -k_t \delta_t \,\mathrm{sgn}(u_{tr}) & \text{if } F_{ts} < F_{tF} \\ F_{tF} = -f_c F_n \,\mathrm{sgn}(u_{tr}) \end{cases} \tag{10.27}$$

$$\underline{M}_{ij} = 1/2 \underline{p}_{ij} \times \underline{F}_{ij} \tag{10.28}$$

By summing up F_{ij} and M_{ij} from the j concurring contacts, the total force and torque on sphere i are obtained and used to update the sphere's translational and angular velocities as well as displacement.

The next step is to assign the model parameters k_n, k_t, c_n, and f in relation to the grain elastic, plastic, and surface properties so that the simulations give physical bulk quantities. Since the normal displacement in a linear contact model is governed by a second-order differential equation of constant coefficients $m^* d^2\delta_n/dt^2 + c_n d\delta_n/dt + k_n \delta_n = 0$, the analytic solution for $\xi(t)$ can be readily found (Stevens and Hrenya, 2005) as

$$\delta_n(t) = u_{nr}(0) \sqrt{\frac{m^\star}{k_n\left(1-\chi^2\right)}} \exp\left(\frac{-c_n}{2m^\star} t\right) \sin\left(\pi \frac{t}{t_c}\right), \tag{10.29}$$

with the initial conditions upon contact: $\delta_n(0) = 0$ and $d\delta_n/dt(0) = u_{nr}(0)$. In this equation, $m^* = (1/m_i + 1/m_j)^{-1} = m/2$ is the reduced mass, $\chi = c_n/2\sqrt{k_n m^\star}$ is the damping ratio, and the model contact time is specified by the instant when $\delta_n(t)$ returns to zero as

$$t_c = \pi \sqrt{\frac{m^\star}{k_n\left(1-\chi^2\right)}} \tag{10.30}$$

The rebound velocity $d\delta_n/dt(t_c)$ can be used to calculate a coefficient of restitution in relation to the damping ratio as

$$e = -\frac{d\delta_n/dt\big|_{t=t_c}}{u_{nr}(0)} = \exp\left(\frac{-\pi\chi}{\sqrt{1-\chi^2}}\right) \tag{10.31}$$

which characterizes the loss of particle kinetic energy during a contact. By matching e to the experimentally measured value, χ can be specifically determined. A second condition for specifying k_n and hence c_n may

be formulated by matching Equation 10.30 to *Hertzian contact time*, $t_{\text{Hertz}} = 2.86\left(m^*/\sqrt{D^*/2E^*}\right)\left|u_{\text{nr}}(0)\right|^{-1/5}$ (Johnson, 1985), with $D^* = \left(1/D_{\text{i}} + 1/D_{\text{j}}\right)^{-1}$ and $E^{*-1} = (1-\nu_i^2)/E_i + (1-\nu_i^2)/E_j$ depending on the respective radius of curvature, $D_{\text{i}}/2$; Young's modulus, E_i; and Poisson's ratio, ν_{i}, for the contacting surfaces.

As for the tangential spring constant, a popular choice is that derived from elasticity theory (Mindlin, 1949, Mindlin and Deresiewicz, 1953, Cundall and Strack, 1979) by

$$k_t = \frac{2}{2-\nu^*}\left[3G^*(1-\nu^*)a^* F_n\right]^{1/3} \tag{10.32}$$

in terms of averaged Poisson's ratio and shear modulus $\nu^* = \nu_i + \nu_j/2$ and $G^* = G_i + G_j/2$. The friction coefficient f may be assigned to the sliding friction coefficient of the contacting material or according to bulk behavior near yielding. Further discussions will be given shortly in Section 10.2.2.3.

Apart from this possibly the simplest model, different force formulae and components have been adopted in more advanced models (Di Renzo and Di Maio, 2004). For example, a nonlinear Hertzian spring (which scales with $\delta_n^{3/2}$) can replace the linear spring in Equation 10.26 to give more precise description for elastic force–displacement relation during a contact (Stevens and Hrenya, 2005). Additional damping in the tangential direction has also been modeled via a tangential damper and a rolling frictional slider for which tangential damping constant and rolling friction coefficient have to be further assigned.

10.2.2.2 Estimation of Bulk Properties

The bulk local properties can then be estimated from the detailed information of nearby grains by some weighting scheme. For example, an averaging box of volume Δ can be defined at a specific location, and bulk solid volume fraction, velocity field, stress tensor, and granular temperature at the center of the average volume may be calculated as

$$\phi = \frac{\sum_i \Delta_{pi}}{\Delta} \tag{10.33}$$

$$\underline{u} = \frac{\sum_i \Delta_{pi}\underline{u}_{pi}}{\sum_i \Delta_{pi}} \tag{10.34}$$

$$\underline{\underline{\sigma}} = \frac{1}{\Omega}\left[-\sum_i m\Delta_{pi}\underline{u}_{rel}^{ij} \otimes \underline{u}_{rel}^{ij} + \frac{1}{2}\sum_{\substack{i,j \\ i\neq j}} \underline{F}^{ij} \frac{\underline{r}^{ij} \otimes \underline{r}^{ij}}{r^{ij}}\right] \tag{10.35}$$

where

Δ_{pi} is the partial volume of a sphere i included by the averaging box
$\underline{u}_{pi}$ is its instantaneous velocity

The first term on the right-hand side of Equation 10.35 gives the streaming stress due to particle motion in free flights relative to its neighbors, and the second term results from paired contact force, and both are summed over all grains within Δ.

10.2.2.3 Effect of Contact Model and Its Parameters on Bulk Dynamics

A great number of 2D/3D simulations have been conducted to study the constitutive relations for the tangential stress of dry cohesionless grains in a steady simple shear and steady surface flow. Sensitivity tests on the contact model parameters report dynamically similar velocity profiles. Hence, the peak velocity and

the flow transverse length scale have been adopted to scale flow properties bringing merged profiles for dimensionless velocity depth profiles and rheological relations. This leads to the well-known fact that the contact model parameters—as long as they are not vanishingly small or zero—have negligible effects on steady granular flow dynamics (Midi, 2004, Da Cruz et al., 2005).

Nonetheless, when quantitative prediction of flow behavior is desired in addition to its qualitative dynamics, assignment choices of contact model parameters are of concern. A popular remedy is to conduct small-scale experiments to calibrate the parameter constants by examining either properties at the particle size level or the bulk level. Silbert et al. (2001, 2003) assign c_n in a linear contact model by the mean of the measured e and f_c but assigned k_n (with $k_t = 2/7k_n$) to a value 3–5 orders of magnitude smaller than the material true strength to permit larger simulation time step Δt. In reproducing the surface shape and velocity, moving mass, and final deposit of an avalanche-induced 3D granular flow, Teufelsbauer et al. (2009) set k_n and k_t to values of the same order as the material elastic strength, c_n by the measured e, and f_c by the tangent of the interparticle friction. Nonetheless, the authors have to incorporate rolling friction and use a lower solid volume fraction than the measured value to obtain quantitative agreement. When impact force on a rigid downstream wall is examined, the authors report the significance of particle rotation mechanism and refine the switching mechanism between sliding and rolling tangential contact (Teufelsbauer et al., 2011). In another study without rolling friction by Banton et al. (2009), the spring constants and c_n are assigned likewise but f_c is calibrated by bulk static repose angle. Remarkable agreement is reported for the observed and the simulated deposit shapes and satisfying results are obtained for the instantaneous surface geometry (but no quantitative comparison). Also without rolling friction, Valentino et al. (2008) conducted numerical biaxial tests on a unit volume of test sample generated according to the experimental particle properties so that the spring stiffness and f_c are assigned by the simulated bulk stress components.

As commented by many researchers, the friction contact model plays an important role in the governing dynamics of dense flows. Most of the literatures assign f_c either by an intergrain friction coefficient or by a bulk static or nearly yielding property engaging a nearly constant normal load that may exceed the true value if the surfaces are subject to a *time-varying* normal load during a contact. Hence, when tangential interaction alternates between sliding and rolling contact, the mean friction averaged over the contact time can be different from that when pure sliding persists through. Hence, Yang et al. (2013) propose to calibrate f_c by bulk volume discharge rate since this flow property is tight closely to flow dynamics (Pouliquen, 1999b (scaling law.....), Ancey, 2001, Pouliquen and Forterre, 2002) and yet easy to measure in both experiments and simulations upon calibration. Fairly good agreement is obtained for the simulated and the measured motion of individual grains and bulk. More advanced and complex contact models can be found in the literature and the search for a feasible contact model for various applications is still an ongoing research topic (Walton, 1993, Vu-Quoc et al., 2000). In Table 10.2, some references for the six selected flow types are provided to complement the information in Table 10.1, leaving out abundant literature of experimental investigations. The interested readers are always recommended to the comprehensive and informative reviews for the methods and the findings by Hermann and Luding (1998), Yang et al. (2003), GDR Midi (2004), Zhu et al. (2007, 2008), Munjiza et al. (2011), and Paulick et al. (2015). Noticing that updated reviews with in-depth discussions on flow physics can be found for most of the selected flow types except for flows in vibrations beds, the rest of this chapter is prepared to fill in the gap, with a focus on those reported for nearly identical spheres.

10.3 Granular Flows in a Vertical Vibration Bed

10.3.1 Problem Setup

Consider a collection of identical spheres of diameter and density, D and ρ_s, of total mass, M, is packed in a thin box (quasi-2D) of width W to a height of H under the action of gravity g. The box is subject to oscillating vertical displacement of, $z(t) = Z_0F(ft)$, or acceleration at, $A(t) = A_0F(ft)$, with $A_0 = Z_0f^2$ in terms of Z_0 being displacement and acceleration and f being the intrinsic frequency of some periodic function (often sinusoidal) of unit magnitude $F(ft)$. The eight variables (D, ρ_s, W, H, g, M, Z_0, and A_0) involve with three fundamental units (mass, length, and time), and hence, there are five dimensionless parameters pertinent to the dynamic process according to *Buckingham* Π-theory. The commonly used parameters include the *relative acceleration* (or shaking parameter), $A^* = A_0/g$; dimensionless shaking acceleration $\Gamma = Z_0\omega^2/g$ ($\omega = 2\pi f$); aspect ratio of the packed bed, W/H; solid volume fraction,

Table 10.2 Selected References for Six Types of Flows Based on Discrete Element Simulations

Flow Types	Simple Shear Flow	Inclined Flow (Avalanche)	Column Collapse
Ref.	Walton and Braun (1986)	Walton (1993)	Staron and Hinch (2005)
	Schöllmann (1991)	Hanes and Walton (2000)	Zenit (2005)
	Karion and Hunt (2000)	Zhang and Vu-Quoc (2000)	Cleary and Martin (2006)
	Lätzel et al. (2000)	Silbert et al. (2001)	Lacaze et al. (2008)
	Campbell (2002)	Silbert et al. (2003)	Crosta et al. (2009)
	Ciamarra et al. (2005)	GDR Midi (2004)	Lacaze and Kerswell (2009)
	Da Cruz et al. (2005)	Walther and Sbalzarini (2009)	Owen et al. (2009)
	Iordanoff et al. (2005)	Fan et al. (2013)	De Vet et al. (2010)
	Ketterhagen et al. (2005)	Yang et al. (2013)	Reddy and Kumaran (2010)
	Luding et al. (2001)		Girolami et al. (2012)
	Cui and Sullivan (2006)		Kermani et al. (2015)
	Zhang and Thornton (2007)		Tapia-McClung and Zenit (2012)
	Kamrin and Koval (2012)		Brodu et al. (2013)
	Vidyapti et al. (2012)		

Flow Types	Rotating Drum Flow	Hopper Flow	Vibration Bed Flow
Ref.	Cleary et al. (1998)	Langston et al. (1994)	Taguchi (1992, 1994)
	Dury and Ristow (1999)	Langston et al. (1995a)	Lan and Rosato (1995, 1997)
	Cleary (2000)	Langston et al. (1995b)	Asmar et al. (2002)
	Mishra (2003a,b)	Potapov and Campbell (1996)	Fernando and Wassgren (2003)
	GDR Midi (2004)	Lu et al. (1997)	Hsiau and Yang (2003)
	Bertrand et al. (2005)	Cleary and Sawley (2002)	Jung and Lee (2004)
	Renouf et al. (2005)	Wassgren et al. (2002)	Baran and Kondic (2006)
		Zhu and Yu (2004)	
		Anand et al. (2008)	
		Artoni et al. (2009b)	

$\phi = M/\rho_s HW$; and the scaled packing depth, $H^* = H/D$. Other material properties that may come into play in a theoretical model or computer simulation include two elastic modulus—for example, Young's modulus E, Poisson's ratio ν, coefficient of restitution e, and friction coefficient f_c for tangential force upon interparticle sliding.

10.3.2 Dynamics and Flow Physics

10.3.2.1 Transition from Bouncing Bed to Convection Roll

At small excitation amplitudes, the bed moves together with the container as a granular solid and eventually detaches from the base when its inertia balances bulk weight and friction from the container walls. Eshuis et al. (2007) adopt the Rayleigh–Janssen's model (Janssen, 1895, Duran, 2000) to describe the wall friction and determine the detachment acceleration as $\Gamma_\star = 2 - e^{-\Lambda^\star f_{cs} L}$. The exponent represents a decompaction parameter that depends on a coefficient of direction toward the wall, Λ^*; grain static friction coefficient, f_{cs}; and the ratio of material contact area over its projection area, $L = 2(W + W_\perp)H/WW_\perp \approx 2H/W_\perp$. Here, $W_\perp$ denotes the bed transverse width and is much smaller than W for a quasi-2D system. The only fitting parameter $\Lambda^* = 0.15$ is determined. The predicted $\Gamma_\star$ matches well to the measured transition value and grows monotonically with H^* with slight overestimation at smaller shaking amplitude. The free surface of the bouncing bed remains stable and nearly flat.

When Γ is further increased to a threshold value Γ_c slightly above unity ($\Gamma_c = 0.9$–1.2), a thin bouncing bed (roughly $H^* < 3$, Eshuis et al., 2007) is agitated into a dilute cloud of randomly moving particles, showing a transition from *granular solid* to *granular gas*. When the bouncing bed is thick enough, a pair of counterrotating convection roll develops breaking coherent assembly motion and grains are observed to descend at the walls and rise in the center (Faraday, 1831, Laroche et al., 1989). The rising grains near the box center create a central heap with an inclination angle close to, when sufficiently far from the container walls, the material repose angle. Central surface grains then avalanche from the heap apex down the slope and rejoin the descending wall flux to ensure an overall mass conservation. We follow Aoki et al. (1996a) to classify this convection motion as the *downward* mode according to the grain

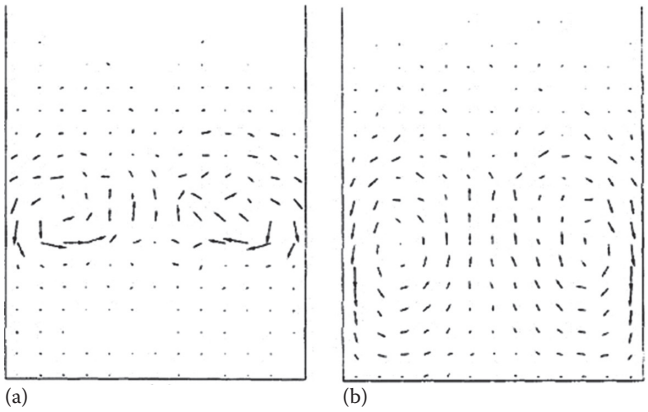


Figure 10.3

Time-averaged velocity vector at $\Gamma = Z_0\omega 2/g = 1.44$ (a) and 2.71 (b) from a 2D particle-based simulation using $e = 0.9$, $Z_0 = 1.1$, $g = 1$, and varying ω. More details regarding the simulation setup can be found in the reference. (From Taguchi, Y.H., *Phys. Rev. Lett.*, 69, 1367, 1992.)

motion next to the wall. This downward convection roll starts to develop beneath the free surface and expands with increasing Γ to fluidize the whole layer as illustrated by the simulated grain velocity vector in Figure 10.3 (2D particle-based simulation, Taguchi, 1992).

Such transition from a coherent bouncing bed has been described by a dynamic model using the analogy to the distinctive response of a single sphere bouncing on a vibrating plate at a critical gravity-scaled acceleration of $\pi(1 - e)/(1 + e)$ (Brennen et al. 1996). Using the same dynamic model, Lan and Rosato (1995) employ an effective bulk restitution coefficient $e_{\text{bulk}} \approx 0.32$ based on the simulated impact and rebound velocity of the assembly and obtain a better agreement to the transition acceleration at $\Gamma_c = \pi(1 - e_{\text{bulk}})/(1 + e_{\text{bulk}}) = 1.66$.

A few mechanisms have been proposed in the literature for the formation of this convection roll. Faraday (1831) has envisioned the effect of interstitial air motion on roll formation almost two centuries ago and wrote: "when the base of the pile loses contact with the plate, it forms a partial vacuum, into which the air round the heap enters with more readiness than the heap itself; as it enters, carries in the powder at the bottom edge with it." When the container decelerates downward from its upper most position (when $A^* < 0$), particles detach from the base into *free flight* creating a small gap at the base that expands and shrinks until the material collides with the base. This basal air gap has lower pressure than the ambient and can entrain air through the comparably loose and thin layer near the lateral walls (packing at a flat boundary is not as dense as internal packing). The grains near the boundary are also more fluidized and collide the base earlier to induce local compaction that in turn squeezes air toward the box center. Condensed stagnant zones hence form at the heap edges on which spheres create an avalanching flow on a bed at the frictional angle as sketched by Laroche et al. (1989) in Figure 10.4. The development of such a local stagnation zone generates successive condensation wave fronts from the container corners at a nearly constant propagation speed (inferred from the base pressure measurement, see Figure 10.5) except very close to the wall. The wave propagation velocity is found to decrease with increasing A^*. This in turn creates horizontal density gradient that drives basal mass fluxes toward the center, as two incoming density waves, which meet and turn up to form the rising central flux under the heap.

Pak et al. (1995) investigated the interstitial air effect on the dynamics of a bed vibrated in concentric cylinders. When the ambient air pressure p decreases below 10–20 torr, the surface elevation decreases monotonically and the heap as well as the convection roll disappears completely when the container wall is made permeable. Similarly, the disappearance of the convection roll was also observed at a lower $p < 10^{-5}$ torr by Laroche et al. (1989) unless the material is agitated in sufficiently narrow containers at high enough frequency that suggests the effect of wall friction and grain–grain interaction.

Besides the induced air stream, grain–grain and grain–wall interaction in response to the external excitation also affect overall bulk dynamics. The base with container pressure measurement suggests that the material does not bounce right after the collision but is brought to a halt by the immense normal impulse upon impact and rise with the container. Bulk kinetic energy is either stored as strain energy or dissipated into

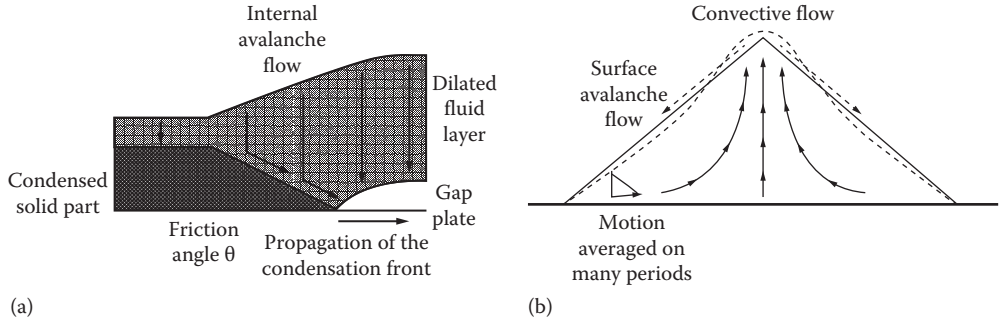


Figure 10.4

(a) Illustration of how the material in free-flight avalanches down an internal slanted stagnant zones at the material friction angle to generate a condensation wave moving toward the container center. (b) The resulting cycle-averaged convection roll (thick arrow) compensated by surface avalanche (dotted arrow) when all the heap material is solidified. (From Laroche, C. et al., *J. de Phys., France,* 50, 699, 1989.)

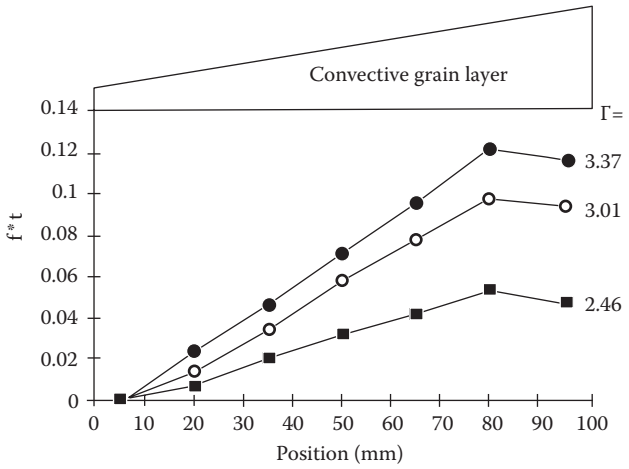


Figure 10.5

Distribution of the collision time of bed material from the container edge toward the convective heap in a bed of $H^* \approx 45$ vibrated at $f = 20$ Hz and different $A^* = 2.46$, 3.01, and 3.37. Note that the authors use the symbol Γ for the relative acceleration but we have changed the plot label to A^* for consistency. (From Laroche, C. et al., *J. de Phys., France,* 50, 699, 1989.)

heat due to inelastic particle interactions. Granulates stay in contact with the container until they resume free flight when the container retrieves from the maximum height at the beginning of next oscillation cycle. Once in free flight, the stress developed upon impact is relaxed but the geometry constraint from the lateral walls restricts the release of horizontal stress. Hence, a higher normal stress is developed at the container walls to induce greater friction that promotes downward granulate motion with the wall (Taguchi, 1992, Wildman et al., 2001). This is why Lan and Rosato (1997) reported from their 3D DEM simulation that the convection velocity grows monotonically with particle-sidewall friction coefficient when the shaking conditions and particle friction coefficient are fixed.

Finally, some authors reported that the central heap configuration is not stable when Γ reaches a certain value above Γ_c and slight asymmetry in the system (container shape, displacement amplitude, packing structure, etc.) can result in transition from a central heap to one that slanted from one wall (Laroche et al., 1989, Wassgren et al., 1996).

10.3.2.2 Reversed Convection and Roll Doubling

10.3.2.2.1 Phenomenon and Mechanism When Γ and A* are further increased above A* = 4.5–5.1 (Aoki et al., 1996a), the layer is not fully condensed before being lifted again so that slight asymmetry in the system can result in unequal wall friction. Knight (1997) reported from experiments the instantaneous profile of the

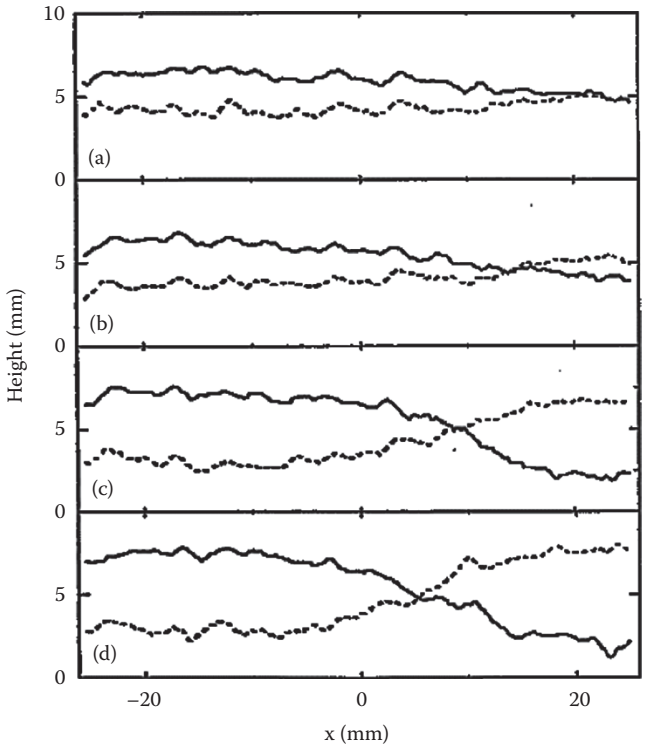


Figure 10.6

Transient development of an internal shear band at the (a) onset of vibration and after (b) 4, (c) 8, and (d) 12 vibration periods for a bed of poppy seeds with $H^* = H/\overline{D} \approx 11.7$, $A^* = 8.7$ and $f = 25$ Hz. The two curves depict the maximum and minimum instantaneous bottom edge of the bed in consecutive vibrations. A mean diameter $\overline{D} \approx 0.85$ mm is estimated here by the mean of the long and short axes of 1 and 0.7 mm of the poppy seeds to scale the bed height. (From Knight, J.B., *Phys. Rev. E*, 55(5), 6016, 1997.)

bottom edge of a bulk at the maximum and minimum elevation during one cycle and the particles exhibited smaller displacement at one wall as shown in Figure 10.6. The intersection of the maximum (thick lines) and the minimum (dashed lines) locates an interface that separates the bed into two adjacent segments in out-of-phase cyclic motions. A shear band develops across the interface and propagates from the right wall toward the container center as the bulk develops into its steady state. The difference between the maximum and minimum bed height at the container center, Δh, grows in time onto a steady plateau (see Figure 10.7a). If lateral boundary effect can be neglected in a large enough container, the steady surface shape across the shear band can be well fitted by $h(x) \sim \tanh(x/x_c)$ where x is the horizontal distance from the shear band and x_c is a length scale of surface curvature (see Figure 10.7b).

Instantaneous particle motions at the shear band can be either positive or negative, but the local cyclic mean is always downward at steady state. At high enough Γ, this internal local flow may reverse the convection roll into the *upward mode* so that particles rise at the container walls but descend in the center, leading to the *DU transition* (defined by Aoki et al. 1996a). The free surface changes accordingly from a central heap to valley as shown by the consecutive experimental images in the left column of Figure 10.8. Unlike the downward mode, convection rolls in the upward mode are stable and can grow with Γ to fluidize more material. When the bed is wide enough or when the shear strength is sufficiently strong, the central shear plane acts as a fictitious wall bisecting the layer and two pairs of convection rolls develop accordingly in each segment as shown in the right column of Figure 10.8. Such roll *doubling bifurcation* (into 2, 4, and 8 pairs) continues with further increment of Γ until a maximum number is reached. The maximum roll number permissible to a granular system is reported to depend on both W^* and H^* and also on particle size and excitation frequency but to a less extent (Aoki et al. 1996a).

Knight (1997) further examines the instantaneous profile of bed bottom edge during the DU transition. The measurements were taken when the container is at its lowest position (dashed line) and at the bed maximum separation from the bed (solid line), and the cycle-averaged bulk velocity distribution within the bed is illustrated. It is interesting to find that when the system goes through the DU transition from

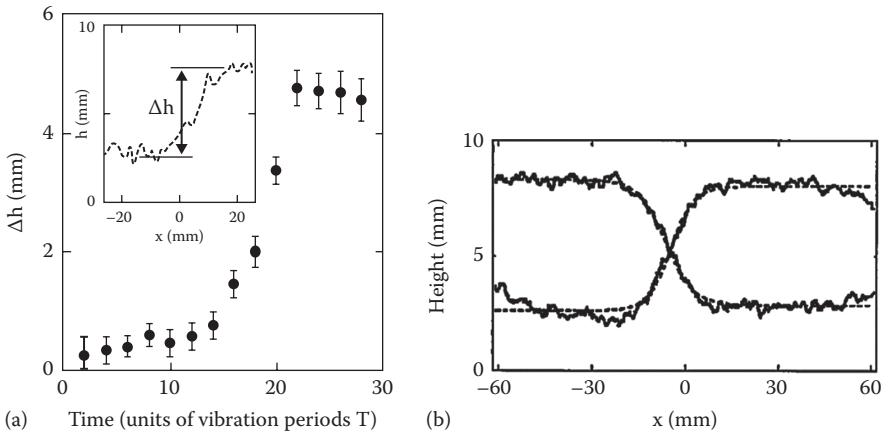


Figure 10.7

(a) Temporal evolution of the deformation amplitude Δh of the bed bottom edge during the shear band development. The inset shows Δh for the dashed curve in Figure 10.6d. (b) Bottom edge of the shaken bed after the development of shear band (following that shown in Figure 10.6). (From Knight, J.B., *Phys. Rev. E*, 55(5), 6016, 1997.)

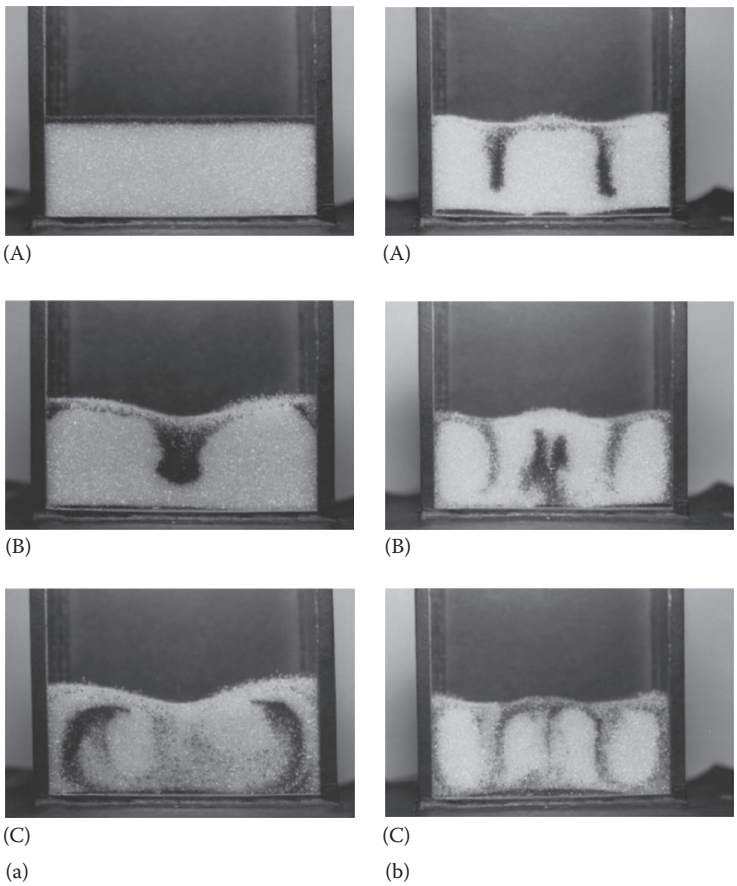


Figure 10.8

Formation of convection rolls of (a) one pair that descends in the center at (A) 0 s, (B) 9 s, and (C) 19 s and (b) two pairs with downward flux in each roll at (A) 9 s, (B) 19 s, and (C) 29 s. Both images are taken for a bed of glass beads of mean diameter $\overline{D} = 0.61$ mm, with initial height $H^* \approx 61$ shaken at $A^* = 5.9$ and $f = 50$ Hz. The glass container has 100 mm width and 30 mm thickness. (From Aoki, K.M. et al., *Phys. Rev. E*, 54(1), 874, 1996.)

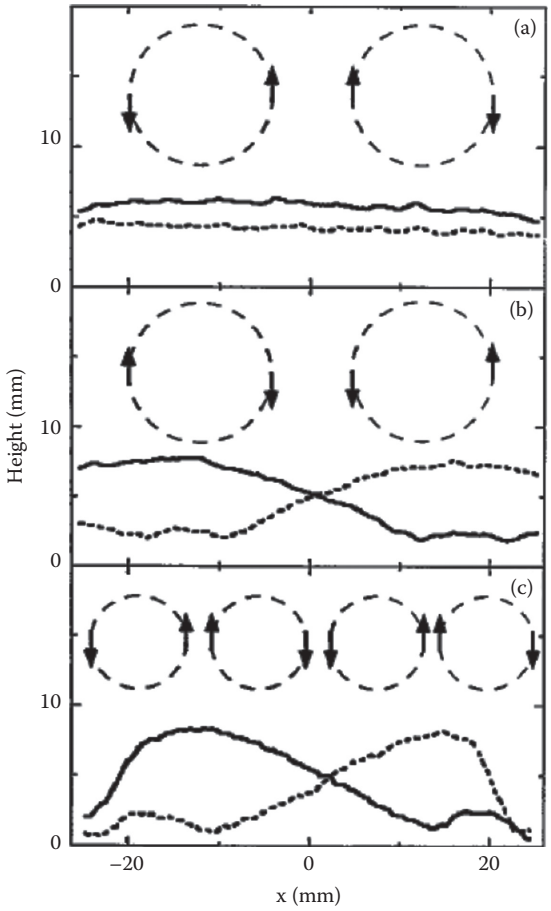


Figure 10.9

(a) Downward convection roll in a bed without internal shear band. (b) The same bed as in (a) but in reverse convection due to the action of an internal shear band. Both (a) and (b) are conducted in the container of smooth walls. (c) Promoted reverse convection in a container with rough walls. The two curves depict the local maximum (—) and minimum (---) bottom edge height when a bed of poppy seeds shaken at $A^* = 8.4$ and $f = 25$ Hz (also used in Figures 10.6 and 10.7). (From Knight, J.B., *Phys. Rev. E*, 55(5), 6016, 1997.)

Figure 10.9a and b, the corresponding changes in the bed profile are from a unified bed motion with a flat boundary to a segment-wise vibration with a step elevation. The incoherent bed segmental motion creates strong shear within the material, and the degree is enhanced in Figure 10.9c when rougher lateral container walls are employed.

Aoki et al. (1996a) also examine how the bed height H^* affects the critical acceleration Γ_{c+} for the DU transition and roll doubling with rising Γ and another critical value Γ_{c-} for the reverse UD transition and the disappearance of convection rolls with decreasing Γ. The results are shown in Figure 10.10a and b for Γ_{c+} and Γ_{c-}, respectively, and deviating Γ_{c+} and Γ_{c-} are observed for roll doubling and cancellation indicating system *hysteresis* at a degree that varies with H^*. For a bed with $H^* > 13$ ($W^* = 128$), DU and UD transition are found at comparable $4.5 < \Gamma < 5.1$ (marked by circles "○"), but deviating Γ_{c+} and Γ_{c-} trends are observed for roll doubling and cancellation indicating strong system hysteresis. This may be attributed to how internal force chains are developed and destroyed in different manners upon acceleration and deceleration. Hysteresis is smaller in the thicker bed, and the multiple rolls (4 and 8 pairs) may disappear abruptly into a single pair (U2) or directly back to downward mode when the bed is too thin due to strong dissipation in the system.

10.3.2.2.2 Surface Pattern and Base Arch In addition to convection rolls, a bulk free surface also develops wavy pattern as a standing wave. When the material collides with the base, an immense normal impulse develops where the bulk exhibits a downward motion so that grains sometimes are observed to bounce from the surface.

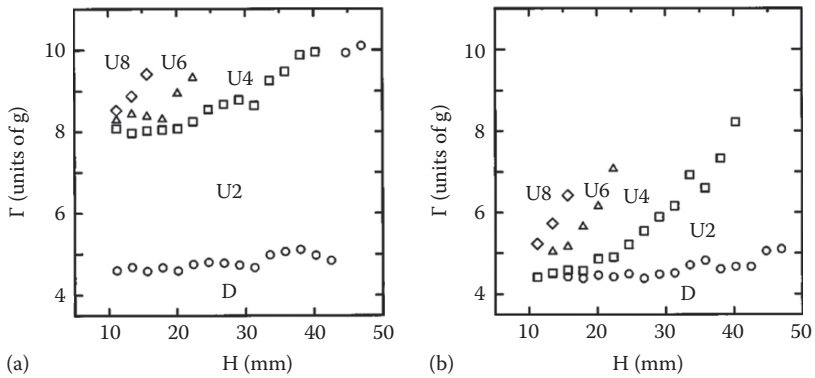


Figure 10.10

Critical Γ for (a) the onset of DU transition and roll doubling and (b) the reverse UD transition and roll reduction as a function of initial bed height H for glass beads of mean diameter $\overline{D} = 0.78$. The acceleration on the y-axis is dimensional, $\Gamma = Z_0(2\pi f)^2$, and can be transformed to the dimensionless shaking acceleration by dividing out the digits by 9.8. The number of rolls is distinguished by different symbols: two (○), four (□), six (△), and eight (◇) with their direction denoted by "D" (downward mode, central heap) and U (upward mode, central valley). (From Aoki, K.M. et al., *Phys. Rev. E*, 54(1), 874, 1996.)

These surface grains fall from the heaps to the valleys during the bed free flight, redistributing the denser regimes so that new heaps form at where the valleys locate in the previous cycle and such alternation continues as demonstrated in Figure 10.11 (3D DEM, Lan and Rosato, 1997). This clearly explains why it takes two vibration cycles for the surface wave pattern to resume its original profile as well-known phenomenon of the *period doubling*. Force chains evolve in the bulk accordingly and form arches near the bed in a wavy pattern similar to that of the free surface as observed in experiments (Wassgren et al., 1996, Lan and Rosato, 1997).

The horizontal distance between adjacent heaps defines half a wavelength, λ/2, which is found to decrease with increasing vibration frequency, f. This is because the lateral distance that grains can relocate during free flight is shortened at higher f. An empirical relation for the nondimensional wavelength has been proposed and confirmed in many systems, following Melo et al. (1994), as

$$\lambda/D = N_\lambda + g_{eff}/Df^2 \tag{10.36}$$

Here, our g_{eff} = 310 cm/s² and N_λ = 11 are reported from a 2D DEM simulation (W* = 200, H^* > 10 from visual inspection, Aoki and Akiyama, 1996b). When a shallow bed of glass beads (H* < 10) are vibrated in a cylinder, standing waves develop as surface stripes or squares and Equation 10.36 has been confirmed in experiments with g_{eff} = 325 cm/s² and N_λ = 5–10 (Metcalf et al., 1997). The dependence of λ on f^{-2} implies that these *surface waves* are gravity waves in nature. When the shaking frequency is further increased to a *crossover frequency* f_X, such wave mode is no longer stable and the trend flattens from $\lambda/D \sim f^{-2}$ to $\lambda/D \sim f^{-1/2}$ as shown in Figure 10.12. Similar bifurcation in surface pattern is also observed in 3D experiments with $f_X \approx 22$ Hz (Metcalf et al., 1997), and the authors attribute it to viscous cutoff effect. The same phenomenon is also reported from a 2D simulation (molecular dynamics) with $f_X \approx$ 30 Hz (Jung and Lee, 2004).

The simulation results are further analyzed to investigate how the wave length of the surface standing wave is correlated to the surface particle lateral displacement, δx, (Jung and Lee, 2004) by examining the distribution function, P(δx). The data averaged over 100 vibration cycles are shown in Figure 10.13a. P(δx) peaks at small δx when $f > f_X \approx 30$ Hz but changes onto a wider spread distribution with a small bump at longer $\delta x \approx \lambda/2$ when $f < f_X$. The probability function is employed to estimate a mean displacement <δx>. The value is normalized by half wavelength, 2 < δx >/λ, and examined with respect to f in Figure 10.13b revealing a sharp change around f_X.

The numerical scheme is also employed to study how the normal component, σ_{xx}, of the collisional and streaming stress vary through the vibration cycle when the bed is shaken below and above f_X. For both excitation, the collisional stress increases sharply at times when the material impacts on the base and then decreases by inelastic and frictional dissipation. At other times, the streaming component exceeds the collisional part for flows at f = 20 Hz since the ballistic surface grains have sufficient time to relax and travel horizontally. In contrast, such horizontal ballistic motion is suppressed when the bed vibrates at a very

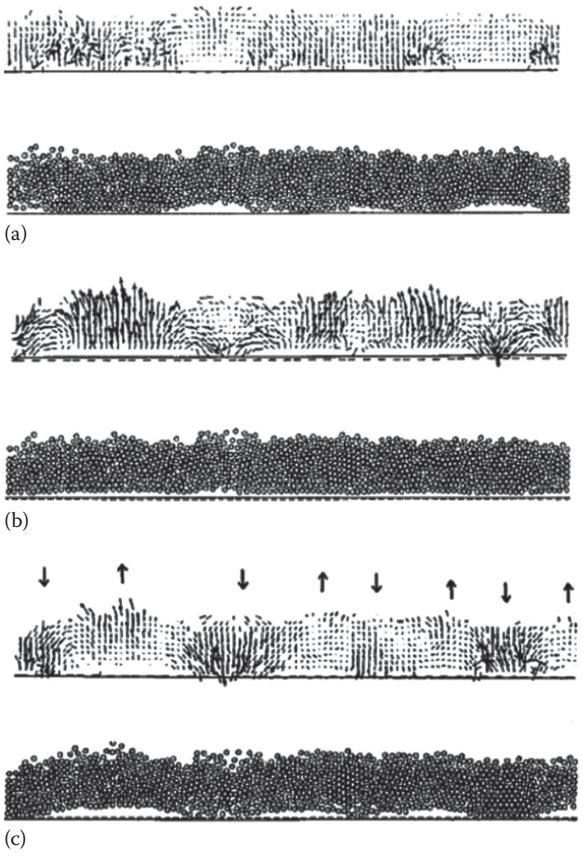


Figure 10.11

Instantaneous velocity vectors and locations of individual spheres shaken at $\Gamma = 10$ ($f = 10$ Hz, $A^* = 0.5$, $W^* = 100$) showing that the bed separates into segments that move out of phase with each other. The time between the snapshot of (a) and (c) is exactly two vibration periods with switched peak and valley locations. Snapshot (b) is taken slightly before the base descends to its equilibrium position (dashed line) in (c) where arch are better formed. (3D DEM, Lan, Y. and Rosato, A.D., *Phys. Fluids*, 9(12), 3615, 1997.)

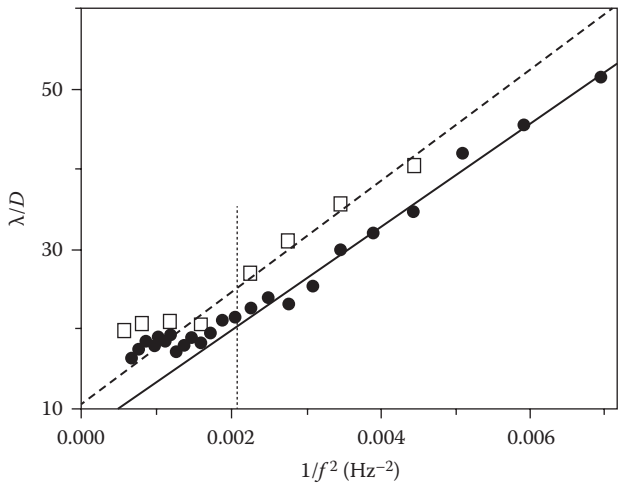


Figure 10.12

Normalized wavelength λ/D examined with respect to $1/f^2$ for system operated at $\Gamma = 3.0$ with $H^* = 8$, $P = 0.04$ Torr (□), and $H^* = 6$, $P = 10$ Torr (●). The crossover frequency for deviating $\lambda/D - 1/f^2$ is determined at 22 Hz as indicated by the dashed line. (From Metcalf, T.H. et al., *Phys. A*, 236, 202, 1997.)

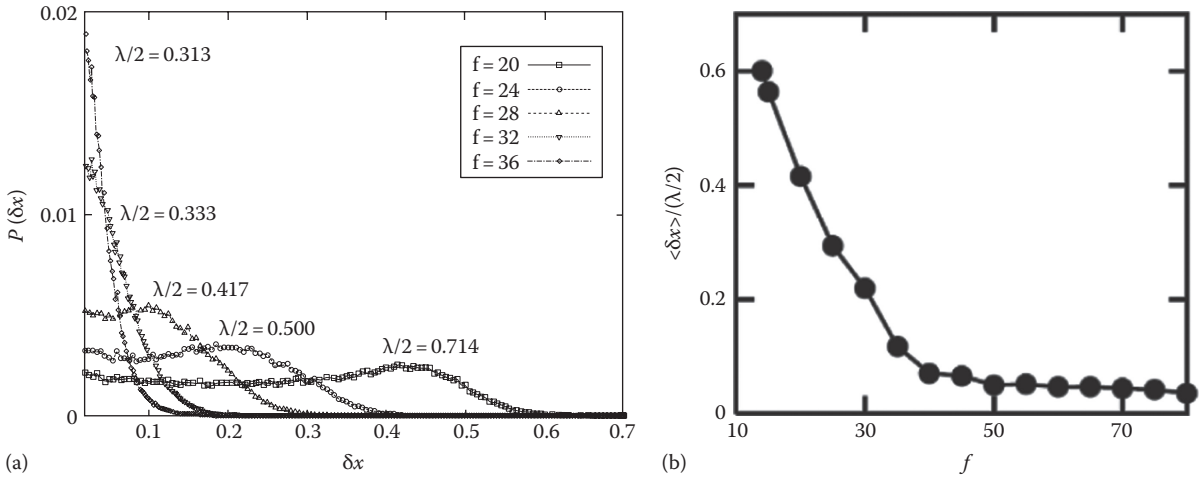


Figure 10.13

(a) The probability distribution function of individual grain horizontal displacement when the bed is shaken at Γ = 2.7. Different distribution profiles are revealed when f is increased beyond the crossover f_X = 30 Hz. Half wavelength of the peak value is indicated. (b) <δx>/(λ/2) increases monotonically when the half wavelength is decreased below f_X = 30 Hz. (From Jung, Y.K. and Lee, J., *Phys. A*, 342, 479, 2004.)

high frequency (>f_X) and the streaming stress is negligible. These observations from detailed grain motions confirm that the changing nature of standing wave when f passes the crossover value should be related to the motion of surface grains.

10.3.2.2.3 Effect of Container Shape Dynamically similar behavior is also observed in a shaking box with outwardly canting side walls at an angle α from the vertical and richer dynamics is reported (Knight, 1997). Since only a portion of the bulk horizontal pressure (with a reduction factor of cos α) acts to induce wall friction during free flight, the net downward friction is reduced. The friction efficacy diminishes with increasing α that combines with the extra room gained next to the walls when approaching the free surface to allow individual grains to exhibit *ratcheting* trajectory. This new type of particle motion dominates at high enough Γ to induce flow reversal as shown by the descended central surface from a cycle-averaged exposure in Figure 10.14a.

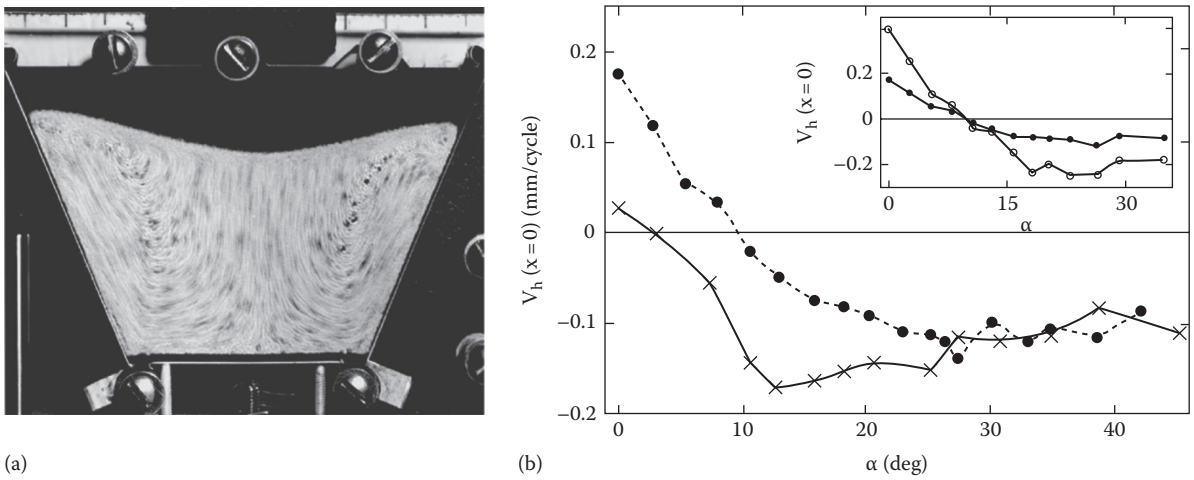


Figure 10.14

(a) Long exposure of flow in a container with walls at Γ = 4.2, 5.6 inclined outward at α = 25° shaken at Γ = 4.2 and *f* = 25 Hz. (b) Cycle-averaged velocity at the center of the convective flow as a function of wall inclination angle with smooth (×) and rough (●) walls, at Γ = 4.2 and *f* = 25 Hz. The inset presents data for rough wall under Γ = 4.2 (●) and 5.6 (○). (From Knight, J.B., *Phys. Rev. E*, 55(5), 6016, 1997.)

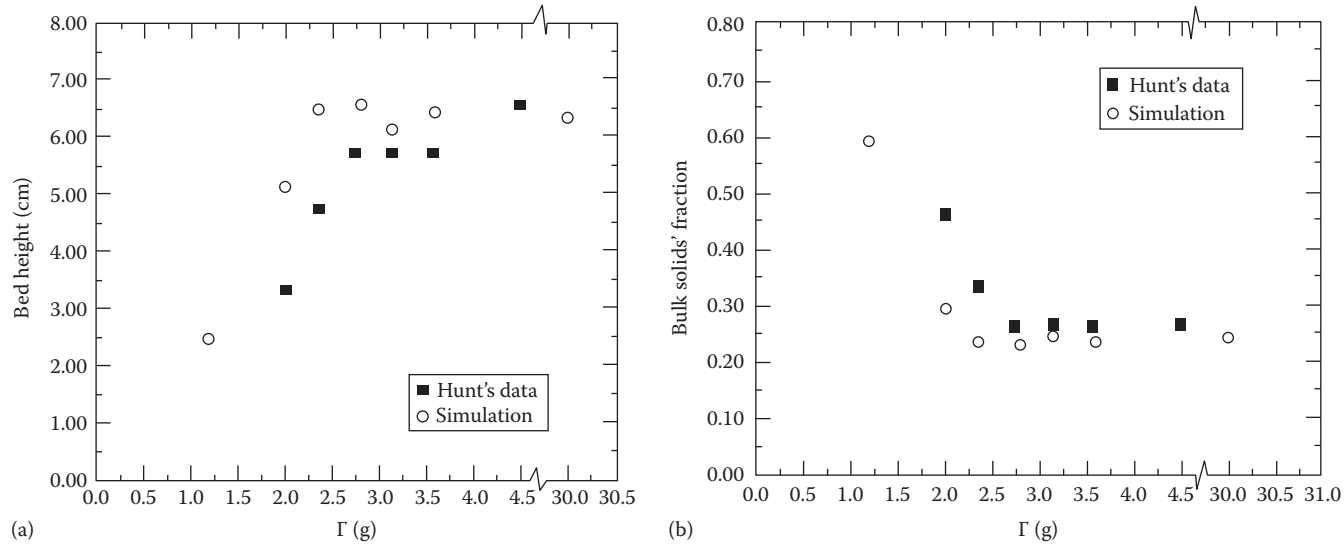


Figure 10.15

Variation of the simulated and the measured (a) system bed height and (b) overall solid volume fraction when G increases from 1.0 to 30. Monotonic rise and drop of T and ϕ is observed when $G > 1$ and both asymptote to constant plateaus when G reaches 3. Note that the authors present the shaking acceleration in units of g and its conversion to the dimensionless value adopted here is straightforward. The simulation results are from 3D DEM using grains of $D = 3$ mm, $\rho_s = 2.49$ g/cm^3, $e = e_w = 0.9$, without surface friction and grain rotation excited at $Z_0 = 5$ mm and $A_0 = 1$–30 g. (From Hunt, M.L. et al., *J. Fluid Eng.*, 116(4), 785, 1994; Lan, Y. and Rosato, A.D., *Phys. Fluids*, 7(8), 1818, 1995.)

Under identical values of Γ, the convective velocity at the container center, V_h, is examined with respect to α in Figure 10.14b and the DU transition angle α_c (zero crossing) is higher in more frictional container, so does the positive V_h in downward mode. Once in upward convection mode, V_h in the more frictional wall becomes smaller owing to degraded ratcheting grain motions. When $\alpha \gg \alpha_c$, the ratcheting mechanism dominates and V_h becomes insensitive to the wall friction as shown by the plateau. The inset of Figure 10.14b shows clearly that increasing Γ does not affect α_c but leads to higher V_h in both downward and upward modes as in the container with vertical walls.

10.3.2.2.4 Overall Dynamics In addition to these detailed observations of surface and bottom shape and individual grain motions, overall flow properties averaged across the bed over a vibration cycle have also been investigated. For example, the bed height is observed to grow abruptly when Γ_c is reached in both simulations (2D DEM [Taguchi, 1992] and 3D DEM [Lan and Rosato, 1995]) and experiments (Hunt et al., 1994) as shown in Figure 10.15a and the corresponding overall ϕ drops accordingly in Figure 10.15b. An overall convection strength in the bed J, as flux across a specific height or velocity at the container center, rises monotonically with Γ (Taguchi, 1992, Lan and Rosato, 1995) and A* (Tai and Hsiau, 2004). These phenomena all indicate that the bulk is better fluidized when Γ exceeds a critical value in which individual grain motion is agitated. Hence, the bulk-averaged granular temperature T shows a sharp rise around $\Gamma = 2 \sim 4$ in both simulation (Lan and Rosato, 1995, Figure 10.16) and experiments (Tai and Hsiau, 2004), and the component in the shaking direction, T_y, is measured to possess greater magnitude than the other component T_x.

10.3.3 Theoretical Modeling

10.3.3.1 Depth Profile of Cycle-Averaged T and ϕ

Apart from systematic experiments and particle-based simulations, theoretical analysis has also been conducted for specific phenomena in vertical vibration bed to consolidate our understanding of the relevant flow physics. For example, Richman and Martin (1992) have developed a model on the kinetic theory framework to describe the depth profiles of cycle-averaged solid volume fraction and granulate temperature in an *infinite* bed of uniform smooth and inelastic spheres. Like most kinetic theory models, the authors assume a Maxwellian velocity distribution function to calculate the ensemble average.

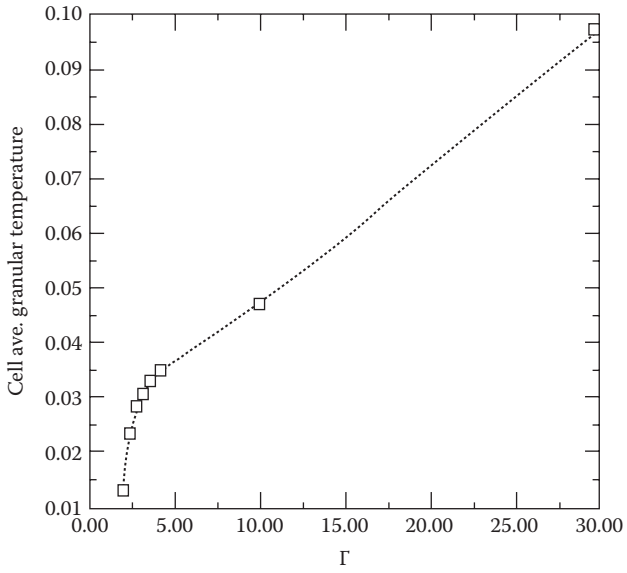


Figure 10.16

Granular temperature increases sharply when Γ increases above 2.0 based on a 3D DEM simulation with details provided in Figure 10.15. (From Lan, Y. and Rosato, A.D., *Phys. Fluids*, 7(8), 1818, 1995.)

The cycle-averaged granulate temperature T decreases monotonically from a maximum bed value onto a minimum plateau near the free surface; a concave depth profile for ϕ is predicted with the midheight maximum occuring at where T approaches its minimum plateau as shown in Figure 10.17. Further, excitation at higher V_b gives higher T (Figure 10.17a vs. c) but lower ϕ (Figure 10.17b vs. d) in dynamically similar depth profiles.

On the same plot, the depth profiles from a 3D DEM simulation with periodic boundary condition under different bed excitation V_b are also presented (Lan and Rosato, 1995). Though it requires much higher A* (>28.3) in the simulation than in real flows to reproduce the analytic T(y) and ϕ(y), it is worth noting that the simulation can capture the critical Γ for bed height expansion and dilatation from the experiment (Hunt et al., 1994). Hence, we infer that the energy dissipation mechanism in the kinetic theory is underestimated, especially when the bulk is not completely fluidized at low acceleration. For example, the effect of enduring frictional contacts and force chain networks on bulk dynamics may be important in denser regimes or when in contact with the vibrating base but is not taken into account in the model.

When the x- and y-components of the deviatoric velocity component, $\underline{u}_p - \underline{u}$, that contributes to total T, namely, T_x and T_y, are examined from simulation data, nearly isotropic Maxwellian (Gaussian with zero mean) is measured when Γ is high enough (A* = 56.5) in Figure 10.18b, confirming the assumption of Maxwellian distribution. Experimental evidences of nearly Maxwellian distribution for the deviatoric velocity when excited above Γc have also been reported (Wildman and Huntley, 2000, Tai and Hsiau, 2004). Nonetheless, asymmetric distribution with a smaller peak at nonzero deviatoric velocity is found at smaller A* = 5.6, in Figure 10.18a, while the other two components show equal and nearly Gaussian profile. This implies non-Maxwellian distribution and the possible failure of the kinetic theory under this flow condition.

10.3.3.2 Upward Convection Roll

In addition to the cycle-averaged quasi-steady depth profiles of T(y) and ϕ(y), the flow during the upward convection has also been modeled, and two different approaches are briefed in the following to shed lights on the underlying physics.

10.3.3.2.1 Acoustic Streaming Model for Averaged Convection Velocity Targeting the phenomenon of upward convection roll velocity, Savage derives an approximate solution on the framework of kinetic theory as the lowest-order asymptotic series solution. Serial assumptions and simplifications have been made

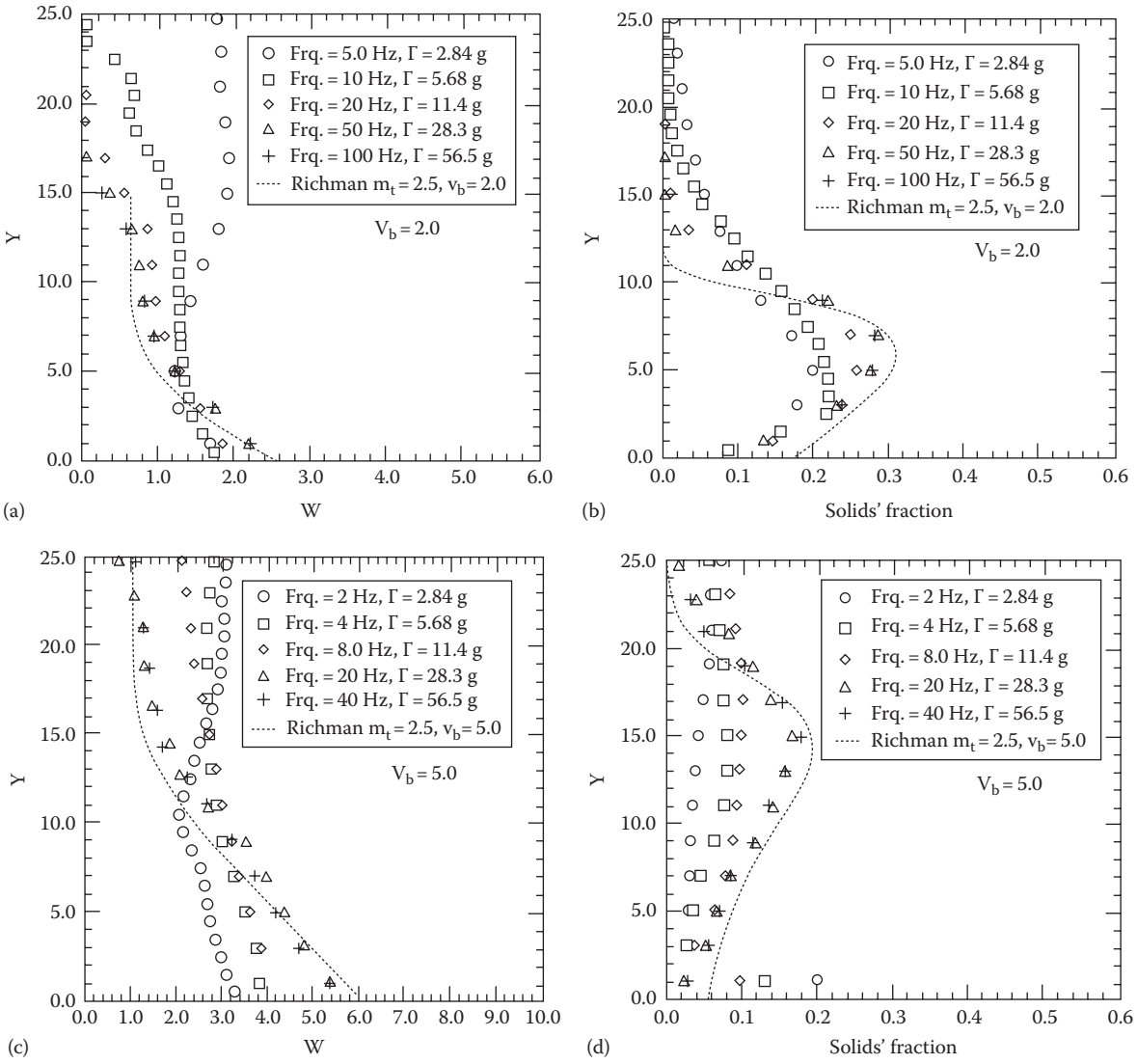


Figure 10.17

Comparison of the predicted and the simulated depth profiles for (a) + (c), granular temperature, and (b) + (d), solid volume fraction using two bed velocities at (a,b) $V_b = 2.0$ and (c,d) $V_b = 5.0$. A range of $\Gamma = 2.84$–56.5 is created in the 3D simulation using grains of $D = 0.1$ cm, $\rho_s = 1.2$ g/cm^3, $e = e_w = 0.9$ without surface friction and grain rotation and a total mass hold up of $m_t = 2.5$. The authors denote granular temperature by W and we have replaced it with T for present symbol consistency. (From Lan, Y. and Rosato, A.D., *Phys. Fluids*, 7(8), 1818, 1995.)

to permit an analytic solution possible. First, simpler constitutive relations are adopted, instead of Equations 10.2, 10.3, 10.7, 10.8, and 10.9, as

$$\underline{\underline{\tau}} = \underline{\underline{\tau}}_c + \underline{\underline{\tau}}_f = \kappa\left[\left(\frac{\sqrt{\pi}\mathrm{T}}{\mathrm{D}} - \frac{2+\alpha}{5}\mathrm{tr}\underline{\underline{\mathrm{D}}}\right)\underline{\underline{\mathrm{I}}} - \frac{2(2+\alpha)}{5}\underline{\underline{\mathrm{D}}}\right] + p_f\left[\underline{\underline{\mathrm{I}}} - \sin\psi\frac{\underline{\underline{\mathrm{D}}}}{\sqrt{1/2\mathrm{tr}(\underline{\underline{\mathrm{D}}}\underline{\underline{\mathrm{D}}})}}\right] \tag{10.37}$$

$$\underline{q} \approx \underline{q}_c = -\kappa\underline{\nabla}T \tag{10.38}$$

$$\kappa = 2\rho_p D(1+e)\phi^2 g_0(\phi)\sqrt{\mathrm{T}/\pi} = \rho DG(\phi,e)\phi g_0(\phi)\sqrt{\mathrm{T}/\pi} \tag{10.39}$$

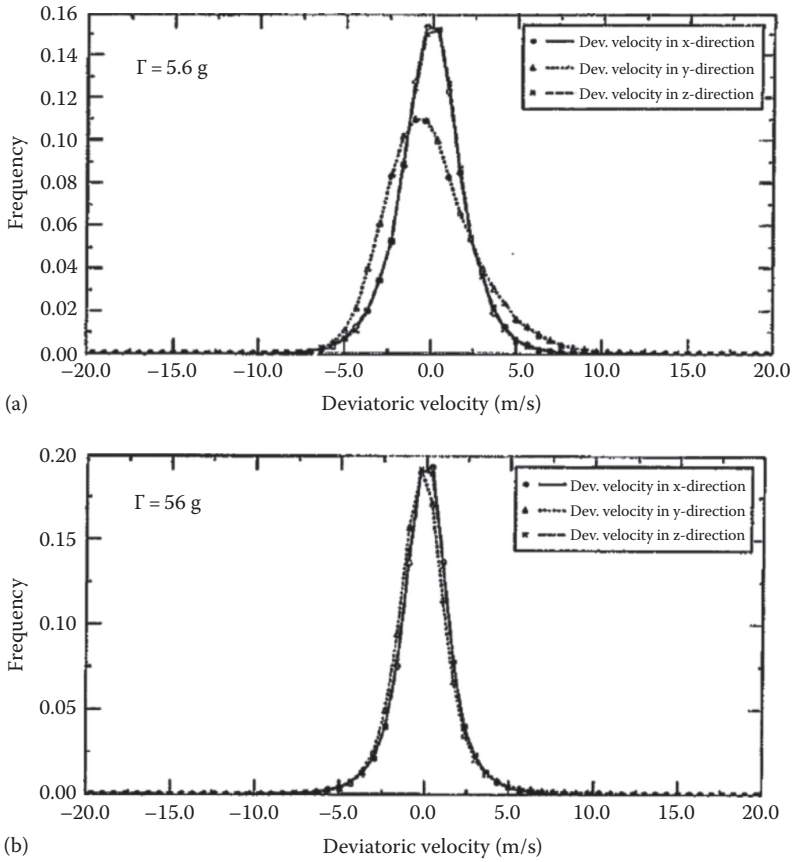


Figure 10.18

Deviatoric velocity distribution at Γ = (a) 5.6 (*f* = 10 Hz) and (b) 56.5 (*f* = 100 Hz) using the same grains of *D* = 0.01 m and $e = e_w = 0.9$ and identical bed velocity $V_b = 2.0$ and total mass holdup $m_t = 2.5$. (From Lan, Y. and Rosato, A.D., *Phys. Fluids*, 7(8), 1818, 1995.)

$$s = \frac{6(1-e)\kappa}{D^2}\left[T - \left(\frac{\pi}{4} + \frac{\alpha}{3}\right)D\sqrt{\frac{T}{\pi}}\,\mathrm{tr}\underline{\underline{D}}\right] \tag{10.40}$$

where $\alpha \approx 1$ and the pseudo-thermal flux due to $\nabla\phi$ is neglected. Savage adopts another radial distribution function, $g_0(\phi) = \left[1 - (\phi/\phi_m)^{1/3}\right]^{-1}$ with $\phi_m = 0.64$ to obtain greater collisional stress that better matches to the experimental results. Note that the streaming stress component is neglected since the bulk concentration is not too low and, likewise, only collision-induced heat flux and dissipation are considered. It is further assumed that there is no static mass under the cyclic base excitation and hence $\psi \to 0$.

Flow variables are then decomposed into a mean and a fluctuating component (denoted by the prime) as

$$\rho = \bar{\rho} + \rho', \quad \underline{u} = \underline{u}_m + \underline{u}', \quad \text{and} \quad T = T_m + T' \tag{10.41}$$

Here, the mean variables with an overhead bar denote a regular average and that with a subscript *m* is from a mass-averaged scheme: $\underline{u}_m = \overline{\rho\underline{u}}/\bar{\rho}$ and $T_m = \overline{\rho T}/\bar{\rho}$. Under the assumption of random fluctuations, $\overline{\rho\underline{u}'} = \overline{\rho T'} = 0$.

Switching to index notation, the mass, momentum, and fluctuation energy conservation equations in Equations 10.4 through 10.6 become

$$\frac{\partial}{\partial t}\left(\bar{\rho} + \rho'\right) + \frac{\partial}{\partial x_j}\left(\overline{\rho u_j} + \overline{\rho u_j'}\right) = 0 \tag{10.42}$$

$$\frac{\partial}{\partial t}\left(\rho u_{mi}+\rho u_j'\right)+\frac{\partial}{\partial x_j}\left(\rho u_{mi}u_{mj}+\rho u_{mi}u_j'+\rho u_i'u_{mj}+\rho u_i'u_j'\right)=\rho g_i-\frac{\partial \tau_{ij}}{\partial x_j} \tag{10.43}$$

$$\frac{3}{2}\frac{\partial}{\partial t}\left(\rho T_m+\rho T'\right)+\frac{\partial}{\partial x_j}\left(\rho T_m u_j+\rho T_m u_j'+\rho T'u_{mj}+\rho T'u_j'\right)=-\tau_{ij}\frac{\partial u_i}{\partial x_j}-\frac{\partial q_j}{\partial x_j}-s \tag{10.44}$$

These *instantaneous* equations are averaged over a vibration cycle to render a set of *mean* governing equations as

$$\frac{\partial}{\partial x_i}\overline{\rho}u_{mi}=0 \tag{10.45}$$

$$\frac{\partial}{\partial t}\overline{\rho}u_{mi}+\frac{\partial}{\partial x_j}\overline{\rho}u_{mi}u_{mj}=\overline{\rho}g_i-\frac{\partial\overline{\tau_{ij}}}{\partial x_j}-\frac{\partial}{\partial x_j}\overline{\rho u_i'u_j'} \tag{10.46}$$

$$\frac{3}{2}\left(\frac{\partial}{\partial t}\overline{\rho}T_m+\frac{\partial}{\partial x_j}\overline{\rho}T_m u_{mj}\right)=-\frac{\partial}{\partial x_j}\overline{\rho T'u_j'}-\overline{\tau_{ij}\frac{\partial u_i}{\partial x_j}}-\frac{\partial\overline{q_i}}{\partial x_j}-s \tag{10.47}$$

Savage reasons that $\partial/\partial x \ll \partial/\partial y$ for flows in a wide bed and assumes, in particular, $u_m \ll u'$ but $\rho \ll \rho'$ and $T' \ll T_m$ for its agitated yet not too dilute state. Based on these flow features, simplification of the instantaneous and mean momentum equation in Equations 10.43 and 10.46 leads to

$$\frac{\partial}{\partial t}\overline{\rho}u_j'+\frac{\partial}{\partial x_j}\left(\overline{\rho}u_i'u_j'\right)=\overline{\rho}g_i-\frac{\partial\tau_{ij}}{\partial x_j} \tag{10.48}$$

$$\frac{\partial}{\partial t}\overline{\rho}u_{mi}+\frac{\partial}{\partial x_j}\overline{\rho}u_{mi}u_{mj}=\overline{\rho}g_i-\frac{\partial\overline{\tau_{ij}}}{\partial x_j}-\frac{\partial}{\partial x_j}\overline{\rho u_j'u_j'} \tag{10.49}$$

where $p_{ij}=\overline{p_{ij}}+p_{ij}'$ and the last term in this equation resembles Reynolds stress in turbulent flows to enhance momentum dissipation. By subtracting Equation 10.48 from Equation 10.49 and further assuming nearly constant mean density $\overline{\rho}\approx\rho_0$ and $\partial/\partial x_j\left[\overline{\rho}\left(u_{mi}u_{mj}-u_i'u_j'\right)\right]$ is much smaller than the rest terms, a linearized equation is obtained for how the fluctuating pressure and velocity are related to each other as

$$\rho_0\frac{\partial u_i'}{\partial t}=-\frac{\partial p_{ij}'}{\partial \mathrm{x_j}} \tag{10.50}$$

Keeping only the dominant terms, the y-component from this equation is

$$\rho_0\frac{\partial \mathrm{v}'}{\partial \mathrm{t}}=-\frac{\partial \mathrm{p}_{yy}'}{\partial \mathrm{y}}=-\frac{\partial \mathrm{p}_T'}{\partial \mathrm{y}}+\frac{9}{5}\frac{\partial}{\partial \mathrm{y}}\left(\kappa\frac{\partial \mathrm{v}'}{\partial \mathrm{y}}\right) \tag{10.51}$$

where p_T' is the fluctuating component of the pseudo-thermal pressure in the first term on the right-hand side of Equation 10.37. Savage then considers the high energy input from the vibrating bed to assume a locally high T and hence negligible transverse variation of κ across most layer thickness (see the definition in Equation 10.39) to write

$$\rho_0\frac{\partial \mathrm{v}'}{\partial \mathrm{t}}=-\mathrm{c}_0^2\frac{\partial \rho'}{\partial \mathrm{y}}+\kappa\frac{9}{5}\frac{\partial^2 \mathrm{v}'}{\partial \mathrm{y}^2} \tag{10.52}$$

Here, $c_0 = \sqrt{\partial p'_T/\partial \rho}$ is a "sound speed" induced by vibration-induced variable fluctuations and Savage has given an estimation as

$$c_0 = \sqrt{\partial p'_T/\partial \rho} = \left[\left(1 + \frac{2}{3}G + \frac{\phi}{G}\frac{dG}{d\phi}\right)GT\right]^{1/2} \tag{10.53}$$

with $G(\phi)$ specified in Equation 10.39. Similarly, the instantaneous mass conservation equation, Equation 10.42, is subtracted from the mean, Equation 10.45, to give

$$\frac{\partial \rho'}{\partial t} = -\rho_0 \frac{\partial v'}{\partial y} \tag{10.54}$$

By eliminating the fluctuating density ρ' in Equations 10.52 and 10.54, a damped wave equation is found for v' as

$$\frac{\partial^2 v'}{\partial t^2} = c_0^2 \frac{\partial^2 v'}{\partial y^2} + \frac{9\kappa}{5\rho_0}\frac{\partial^3 v'}{\partial t \partial y^2} \tag{10.55}$$

When the attenuation is weak, a longitudinal wave solution is found readily as follows:

$$v'(x,y,t) = v_b(x)\cos(\xi y - \omega_{//} t)e^{-\varsigma y} \tag{10.56}$$

with

$$\xi = \omega_{//}/c_0 \quad \text{and} \quad \varsigma = 9\kappa\omega_{//}^2/10\rho_0 c_0 \tag{10.57}$$

In Equations 10.56 and 10.57, $\omega_{//}$ (not to be confused with $\omega = 2\pi f$) and $\xi = \omega_{//}/c_0$ are radian frequency and wave number of the transverse wave going toward the free surface from a bed at a slowly varying velocity distribution $v_b(x)$. It is worth noting that $v_b(x)$ may be interpreted as a way to introduce streamwise non-uniformity to the system to mimic physical property gradient, such as that maintained between coexisting slow denser corner flow and agitated dilute central bulk. Savage prescribes $v_b(x) = V_b\left[1 + \varepsilon N\cos\left(\pi x/W\right)\right]$ with a characteristic V_b, a constant N of order unity, and a small height-to-width ratio, $\varepsilon = H/W$. Further, the approximation of nearly constant density $\overline{\rho} \approx \rho_0$ and κ simplifies the mean continuity equation, the mean stress tensor, and the mean energy equation into the following expressions:

$$\frac{\partial u_{mi}}{\partial x_i} = 0 \tag{10.58}$$

$$\overline{\tau_{ij}} \approx \left[p_{s0} + p_{Tm}\right]\delta_{ij} - \frac{3\kappa}{5}\left(\frac{\partial u_{mi}}{\partial x_j} + \frac{\partial u_{mj}}{\partial x_i}\right) \tag{10.59}$$

$$\frac{dT_m}{dy^2} - \frac{6(1-e)}{D^2}T_m = -\frac{3}{5}\overline{\frac{\partial v'}{\partial y}\frac{\partial v'}{\partial y}} \tag{10.60}$$

where $p_{Tm} = \kappa\sqrt{\pi T_m/D}$ in Equation 10.59 is a pseudo-thermal pressure. The substitution of Equations 10.56 and 10.57 into Equation 10.60 permits a general solution for the mean granular temperature by superposition of the homogeneous solutions, $e^{\pm \beta y}$ with $\beta = 6(1 - e)/D^2$, and the particular solution, $\frac{9}{10}v_b^2\xi^2/(\beta - 4\varsigma^2)e^{-2\varsigma y}$.

Considering that heat flux should go from the constantly agitated bed toward the free surface, the basis solution with positive exponent should vanish, giving the following:

$$T_m(y) = \frac{Ce^{-\sqrt{\beta}y} + \frac{9}{10}\nu_b^2\xi^2}{(\beta - 4\varsigma^2)e^{-2\varsigma y}} \tag{10.61}$$

The unknown constant C is determined later on via stress boundary condition at the bed (see the context following Equation 10.67).

The flow variables are then transformed into dimensionless groups as

$$\begin{aligned} &\mathrm{X} = \frac{x}{W}, \quad \mathrm{Y} = \frac{y}{H}, \quad \mathrm{U} = \frac{u_m}{V_b\varepsilon}, \quad \mathrm{V} = \frac{v_m}{V_b\varepsilon^2}, \\ &\mathrm{P_s} = \frac{p_{s0}}{\rho_0 gH}, \quad \mathrm{T}_\star^{1/2} = \frac{\kappa\sqrt{\pi T_m}}{D\rho_0 gH} \end{aligned} \tag{10.62}$$

so that dimensionless stress components and Reynolds stress are

$$\begin{aligned} &\mathrm{P_{xx}} = \mathrm{P_s} + \mathrm{T}_\star^{1/2} - \mu\varepsilon^3\frac{\partial U}{\partial X}, \quad \mathrm{P_{yy}} = \mathrm{P_s} + \mathrm{T}_\star^{1/2} - \mu\varepsilon^3\frac{\partial V}{\partial Y}, \\ &\mathrm{P_{xy}} = -\frac{1}{2}\mu\varepsilon^3\left(\frac{\partial U}{\partial Y} + \varepsilon^2\frac{\partial V}{\partial X}\right) \end{aligned} \tag{10.63}$$

$$\overline{\rho v' v'} \approx \rho_0\overline{v' v'} = \frac{\rho_0}{2}V_b^2 e^{-2\varsigma Y} \tag{10.64}$$

Solutions are sought in an asymptotic series in expansion with small ε as

$$\begin{aligned} &\mathrm{U} = \mathrm{U}^{(0)} + \varepsilon U^{(1)} + \varepsilon^2 U^{(2)} + \cdots, \quad \mathrm{V} = \mathrm{V}^{(0)} + \varepsilon V^{(1)} + \varepsilon^2 V^{(2)} + \cdots \\ &\left[\mathrm{P_s} + T_\star^{1/2}\right] = \left[\mathrm{P_s} + T_\star^{1/2}\right]^{(0)} + \varepsilon\left[\mathrm{P_s} + T_\star^{1/2}\right]^{(1)} + \cdots \end{aligned} \tag{10.65}$$

The governing equations are then separated into serial sets of equations with increasing order of ε. The zeroth- and first-order governing equations are

$$\begin{cases} \dfrac{\partial \mathrm{U}^{(0)}}{\partial X} + \dfrac{\partial \mathrm{V}^{(0)}}{\partial Y} = 0 \\ \dfrac{\partial}{\partial \mathrm{X}}\left[\mathrm{P_s} + T_\star^{1/2}\right]^{(0)} = 0 \\ \dfrac{\partial}{\partial \mathrm{Y}}\left\{\left[\mathrm{P_s} + T_\star^{1/2}\right]^{(0)} + \dfrac{1}{2}Fe^{-2\varsigma HY}\right\} = -1 \end{cases} \tag{10.66}$$

$$\begin{cases} \dfrac{\partial}{\partial \mathrm{X}}\left[\mathrm{P_s} + T_\star^{1/2}\right]^{(1)} = \dfrac{1}{2}\mu\dfrac{\partial^2 U^{(0)}}{\partial Y^2} \\ \dfrac{\partial}{\partial \mathrm{Y}}\left\{\left[\mathrm{P_s} + T_\star^{1/2}\right]^{(1)} + FN\cos(\pi X)e^{-2\varsigma HY}\right\} = 0 \end{cases} \tag{10.67}$$

where $F = V_b^2/gh$ is a dimensionless number similar to the square of flow Froude number using V_b. Under the stress-free condition at Y = 1, Equation 10.66 can be integrated to yield the following expression:

$$\left[P_s + T_\star^{1/2}\right]^{(0)} = 1 - Y + \frac{1}{2} F e^{-2\varsigma H} \left(1 - e^{-2\varsigma H(Y-1)}\right) \tag{10.68}$$

which is used to determine the only unknown constant C in Equation 10.61 for T_m with the following procedure.

The analysis assumes that, to the first approximation, all the stress at the bed results from particle collisions to obtain $T_\star^{1/2} = 1$ ($P_s = 0$ owing to the earlier assumption of no stagnant layer on the vibrating bed) and hence $T_m = gH/2(1 + e)\phi g_0(\phi)$. Equating this particular value to Equation 10.61 determines C. Likewise, Equation 10.67 can be integrated to give

$$\left[P_s + T_\star^{1/2}\right]^{(1)} = FN \cos(\pi X) e^{-2\varsigma H} \left(1 - e^{-2\varsigma H(Y-1)}\right) \tag{10.69}$$

which is further integrated with Equation 10.67 to give a second-order ordinary differential equation (ODE) for $U^{(0)}$. To specify boundary condition, Savage uses a zero shear stress at the bed, $\partial U^{(0)}/\partial Y|_{Y=0} = 0$, since particles near the bed are well agitated and slide on the smooth bed surface (note that surface friction is not accounted for in this model). A zero total mass flux is further required for the circulating flow as $\int_0^1 U(Y)^{(0)} dY = 0$. The resulting solution is

$$U^{(0)} = \frac{2}{\mu} \pi FN \sin(\pi X) \left\{ \frac{1}{2\varsigma H} \left(Y + \frac{e^{-2\varsigma HY}}{2\delta H} \right) - \frac{1}{2} Y^2 e^{-2\varsigma H} + \frac{1}{6} e^{-2\varsigma H} + \frac{1}{8\varsigma^3 H^3} \left(e^{-2\varsigma H} - 1 \right) - \frac{1}{4\varsigma H} \right\} \tag{10.70}$$

which can be substituted into the continuity equation Equation 10.66 to obtain the leading order vertical velocity profile as

$$\begin{aligned} V^{(0)} = -\frac{2}{\mu} \pi^2 FN \cos(\pi X) \Bigg\{ & \frac{1}{2\varsigma H} \left[\frac{1}{2} Y^2 + \frac{1}{4\varsigma^2 H^2} \left(1 - e^{-2\varsigma HY}\right) \right] \\ & - \frac{1}{6} Y^3 e^{-2\varsigma H} + Y \left[\frac{1}{6} e^{-2\varsigma H} - \frac{1}{4\varsigma H} + \frac{1}{8\varsigma^3 H^3} \left(e^{-2\varsigma H} - 1 \right) \right] \Bigg\} \end{aligned} \tag{10.71}$$

When the coefficient of restitution is set to $e = 0.8$ for typical materials, $\beta^{1/2}$ is of the order of D and much greater than ς^2 so that the second term in Equation 10.61 dominates and $T_m(y)$ decays monotonically but slowly ($\varsigma \ll 1$) from a bed maximum. Savage evaluates a mean value of $D = 1.44$ mm, $\phi = 0.58$, and $\varepsilon N \approx 0.5$ for his experimental materials so that all the coefficients in Equations 10.70 and 10.71 can be evaluated. Figure 10.19 depicts how the predicted velocity components vary across right half of the container and a circulation pattern is clearly captured. Both components grow with the oscillation amplitude but at a rate too fast as compared to real flows. Savage attributes it to the fact that the model does not account for the friction from the container walls (front, back, and side) and internal structure (recall $\psi = 0$) so that frictional stress is underestimated in the model.

10.3.3.2.2 Negative Slip Model for Convection Flow Patterns In a different approach, Bourzutschky and Miller (1995) adopt *compressible* Navier–Stokes equation to approximate the bulk motion and reproduce the downward convection from their numerical solution if a negative apparent wall slip is enforced. Considering that wall friction causes phase delay in local density fluctuations, which relaxes into the bed through inertial transport to cause convection, the authors account for this phenomenon as acoustic wave propagating through the bed. Limiting to small acceleration strength within the parameter space of linear stability

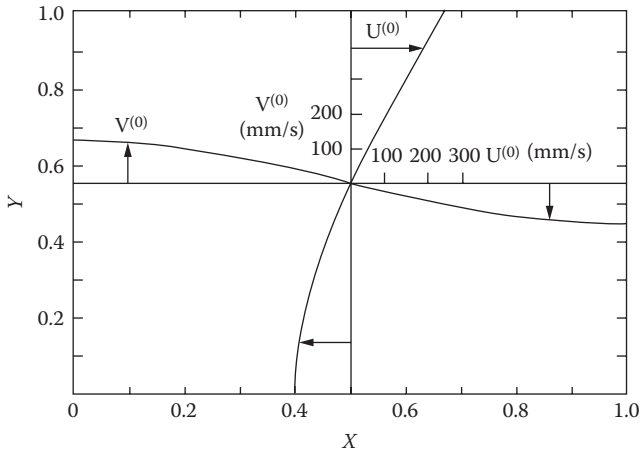


Figure 10.19

Primary mode of the horizontal and vertical velocity components along a vertical and horizontal line, respectively, at the center of the right half of the container by Equations 10.70 and 10.71 using Z_0 = 3 mm, f = 25 Hz, e = 0.85, and H = 62 mm. The velocity variables used in the reference have been changed to current definition. (From Savage, S.B. and Lun, C.K.K., *J. Fluid. Mech.*, 189, 311, 1988.)

without boundary effect (Peyrel and Taylor, 1983), a linear equation of state $p(\rho) = p_0 + c^2\rho$ is integrated to the conservation equations for mass and momentum as

$$\frac{\partial \rho}{\partial t} + \nabla \cdot \left(\rho \vec{u}\right) = 0 \tag{10.72}$$

$$\rho \frac{\partial \vec{u}}{\partial t} + \rho \vec{u} \cdot \nabla \vec{u} = -\nabla p - \mu \nabla^2 \vec{u} + 4\pi^2 Z_0 \sin\left(2\pi t\right) \underline{e}_y \tag{10.73}$$

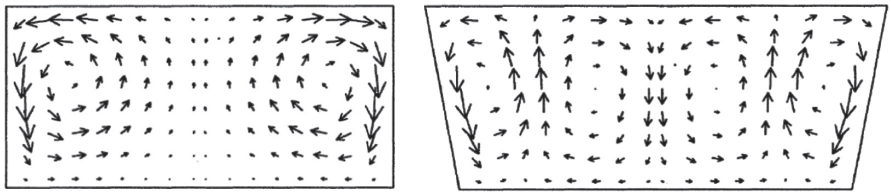
where μ is an equivalent bulk viscosity and the gravity is neglected. The last term on the right-hand side of Equation 10.73 is the bed driving force and $\underline{e}_y$ is the unit normal vector. These partial differential equations are subject to no-through flow and tangential slip at the solid walls as

$$\begin{cases} u_n = 0 \\ u_t + \gamma \partial u_t / \partial n = 0 \end{cases} \tag{10.74}$$

with γ being the wall slip. A positive γ in Equation 10.74 enforces a zero tangential velocity outside of the boundary to give the slip tangential velocity at lateral walls and a negative γ results in zero tangential velocity within the flow. The cycle-averaged bulk velocity with no-slip wall always shows downward convection pattern (see Figure 10.20a). When a *negative slip* is assigned, it creates an internal flow localized to the local flow of strong shear similar to the *shear band* reported by Knight (see Figures 10.7 and 10.9) to induce an internal pair convection roll of opposite direction. The flow pattern in a container with outwardly slanting side walls is shown in Figure 10.20b. When no-slip boundary condition always results in downward flow adjacent to the walls, the critical wall inclination angle for roll reversal grows monotonically with the strength of negative wall slip $|\gamma|$. This finding may serve as another evidence that the development of an internal shear band is essential for the UD transition. We may also interpret such wall boundary condition as a different interaction mode between the bulk and the container wall since the DEM simulations have shown that changing only the dissipation mechanism in particle–wall interaction can lead to flow reversal (Taguchi, 1992).

10.3.3.3 Surface Pattern via Stability Analysis

In addition to the convective bulk flow, Deng and Wang (2003) conducted a linear stability analysis of the motion of a uniform layer under uniform vertical vibrations to explain how surface wave (see Figure 10.11)



(a) (b)

Figure 10.20

Cycle-averaged steady velocity field in a shaking bed using unity shaking frequency, $Z_0 = 0.01$, $c = 1$ in the equation of state, $\mu = 0.05$, and negative wall $\gamma = -0.9$. The two cases differ by (α, u_m) = (a) $(0°, 2.4 \times 10^4)$ and (b) $(8°, 1.1 \times 10^{-4})$. (From Bourzutschky, M. and Miller, J., *Phys. Rev. Lett.*, 74(12), 2216, 1995.)

may develop at high enough agitation. The governing equations in Equations 10.4 through 10.6 are completed by substituting the constitutive relations developed by Lun et al. (1984) in Equations 10.2, 10.3, 10.7 through 10.9. They define dimensionless variables using layer thickness, H; grain density and diameter, ρ_p and D; and gravity as

$$\underline{X} = \underline{x}/H, \quad \underline{U} = \underline{u}/\sqrt{gH}, \quad T^\star = T/gD, \quad t^\star = t/\sqrt{Hg},$$
$$M_t = m_t/\rho_p D, \quad Q_t = Q_0/\rho_p (Dg)^{3/2}, \quad \text{and} \quad H^\star = H/D \tag{10.75}$$

in which m_t is the total mass holdup and Q_0 is the energy flux input at the bed. Unlike most works that adopt acceleration strength (Γ or $A^\star$) and bed height ($H^\star$) as the controlling parameters, the authors used the scaled total mass holdup and heat flux. While M_t is linearly correlated to $H^\star$, there is no explicit correlation between Q_t and Γ, but the two have similar influences on the system dynamics that a more agitated bed is obtained with higher Q_t and acceleration strength. The quasi-steady cycle-averaged *base-state* governing equations become

$$H^\star \int_Y^1 \phi dY = f_1(\phi) T^\star - \frac{\pi}{6}\left(\frac{\phi}{\phi_m}\right)^{2/3} \tag{10.76}$$

$$\underline{U}^\star = 0 \tag{10.77}$$

$$\frac{\partial}{\partial Y}\left[f_3(\phi) T^{\star 1/2} \frac{dT^\star}{dY} + f_4(\phi) T^{\star 3/2} \frac{d\phi}{dY}\right] - H^{\star 2} f_5(\phi) T^{\star 3/2} = 0 \tag{10.78}$$

The dependence on ϕ is incorporated into various functions, $f_i(\phi)$, for brevity, and their explicit forms can be found in Table 10.3. Numerical solutions to these coupled equations are solved via iterations by varying a guessed steady flow height and checking if the computed mass hold up, $H^\star \int_0^1 \phi(Y) dY$, is within a chosen tolerance to the assigned M_t. The boundary conditions at the base and the free surface ($Y = 1$) then become

$$\text{At Y} = 0: f_3(\phi) T^{\star 1/2} \frac{dT^\star}{dY} + f_4(\phi) T^{\star 3/2} \frac{d\phi}{dY} = H^\star \left(1 - e_w^2\right) f_3(\phi) f_6(\phi) T^{\star 3/2} - Q_t \tag{10.79}$$

$$\text{At Y} = 1: f_3(\phi) T^{\star 1/2} \frac{dT^\star}{dY} + f_4(\phi) T^{\star 3/2} \frac{d\phi}{dY} = 0 \tag{10.80}$$

The base-state solution can capture many well-known bulk dynamics including the growing bed height with Q_t, midheight maximum of ϕ(Y), monotonic decrease of T(Y), and the pseudo-thermal energy flux J(Y) toward the free surface as shown in Figure 10.21a through d. The authors also report agreement of their T(Y) with that predicted by Richman and Martin (1992) and attribute the difference found in the surface profile of $\phi(Y)$ to the different boundary conditions adopted at the free surface. Via parameter study, the authors

Table 10.3 Dimensionless Functions, $f_i(\phi)$ for $i = 1 \sim 9$ in Equations 10.76 through 10.80, and 10.82 through 10.89

$$f_1(\phi) = \phi\left[1 + 4\eta\phi g_0(\phi)\right],$$

$$f_2(\phi) = \frac{5\sqrt{\pi}(2+\alpha)}{288\eta(2-\eta)}\left[\frac{1}{g_0(\phi)} + \frac{8}{5}\eta\phi\right]\left[1 + \frac{3}{5}\eta(3\eta-2)\phi g_0(\phi)\right] + \frac{8(2+\alpha)\eta\phi^2 g_0(\phi)}{15\sqrt{\pi}},$$

$$f_3(\phi) = \frac{25\sqrt{\pi}}{16\eta(41-33\eta)}\left\{\left[\frac{1}{g_0(\phi)} + \frac{12}{5}\eta\phi\right]\left[1 + \frac{12}{5}\eta^2(4\eta-3)\phi g_0(\phi)\right] + \frac{64}{25\pi}(41-33\eta)\eta^2\phi^2 g_0(\phi)\right\},$$

$$f_4(\phi) = \frac{25\sqrt{\pi}}{16\eta(41-33\eta)}\left[\frac{1}{\phi g_0(\phi)} + \frac{12}{5}\eta\right]\frac{12}{5}\eta(2\eta-1)(\eta-1)\frac{d}{d\phi}\left[\phi^2 g_0(\phi)\right],$$

$$f_5(\phi) = \frac{48\eta(1-\eta)\phi^2 g_0(\phi)}{\sqrt{\pi}}, \quad f_6(\phi) = \frac{\sqrt{3}\pi\phi g_0(\phi)}{4\phi_m f_3(\phi)}, \quad f_7(\phi) = \frac{\pi\phi g_0(\phi)}{2\sqrt{3}\phi_m f_3(\phi)},$$

$$f_8(\phi) = \frac{\pi\phi g_0(\phi)}{2\sqrt{3}\phi_m f_2(\phi)}, \quad f_9(\phi) = \frac{8\eta\phi^2 g_0(\phi)}{3\sqrt{\pi}}$$

[a] Here, $\eta = (1 + e)/2$ as in Equations 10.2 and 10.3.

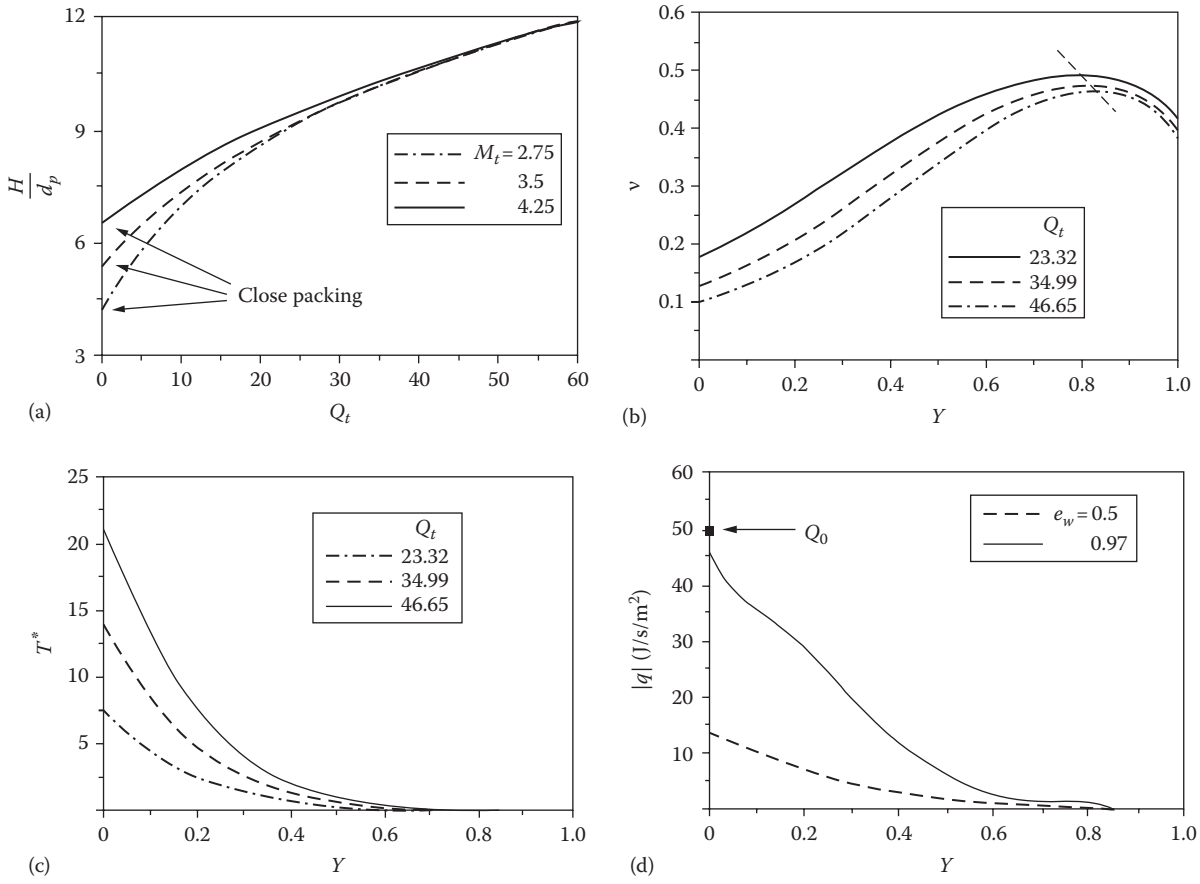


Figure 10.21

(a) Predicted steady-state bed height, H^*, as a function of energy input Q_t; predicted depth profile of (b) solid volume fraction distribution and (c) granular temperature under different Q_t for $M_t = 3.5$. The thin dashed line in (b) locates midheight maximum; (d) depth profile of heat flux using $e_w = 0.5$ and 0.97 for a system operated at (M_t, Q_t) = (4.25, 58.31). (From Deng, R.S. and Wang, C.H., *J. Fluid Mech.*, 492, 381, 2003.)

further conclude that the proportion of dissipated and transported energy depends primarily on the coefficient of restitution between grains (e) and wall (e_w) but not on the operating conditions (M_t and Q_t).

Deng and Wang (2003) then introduce synchronized oscillating perturbations to the base-state solutions—ϕ_0, T_0, and $\underline{U}_0 = 0$ (denoted by a subscript 0)—to describe total variables as

$$\begin{bmatrix} \underline{U} \\ \phi \\ T \end{bmatrix} = \begin{bmatrix} \underline{U}_0 \\ \phi_0 \\ T_0 \end{bmatrix} + \begin{bmatrix} \underline{U}' \\ \phi' \\ T' \end{bmatrix} \quad \text{with} \quad \begin{bmatrix} \underline{U}' \\ \phi' \\ T' \end{bmatrix} = \begin{bmatrix} \underline{U}_e(Y) \\ \phi_e(Y) \\ T_e(Y) \end{bmatrix} \exp(\Omega\tau)\exp(iK_x X)\exp(iK_z Z) \tag{10.81}$$

which is no longer steady and hence subject to Equations 10.4 through 10.6. To conduct the stability analysis, these equations are linearized into

$$\frac{\partial \phi'}{\partial t^\star} + \phi_0 \frac{\partial U'}{\partial X} + \phi_0 \frac{\partial V'}{\partial Y} + \frac{\partial \phi_0}{\partial Y} V' = 0 \tag{10.82}$$

$$\begin{aligned} &-H^\star \phi_0 \frac{\partial U'}{\partial \tau} + H^{\star -1/2} \frac{\partial}{\partial Y}\left[f_2(\phi_0) T_0^{1/2} \right]\left(\frac{\partial U'}{\partial Y} + \frac{\partial V'}{\partial X} \right) - T_0 \left. \frac{\partial f_1}{\partial \phi} \right|_{\phi_0} \frac{\partial \phi'}{\partial X} - f_1(\phi_0) \frac{\partial T'}{\partial X} \\ &+ H^{\star -1/2} T_0^{1/2} \left\{ \left[f_9(\phi_0) + \frac{4}{3} f_2(\phi_0) \right] \frac{\partial^2 U'}{\partial X^2} + f_2(\phi_0) \frac{\partial^2 U'}{\partial Y^2} + \left[f_9(\phi_0) + \frac{1}{3} f_2(\phi_0) \right] \frac{\partial^2 V'}{\partial X \partial Y} \right\} = 0 \end{aligned} \tag{10.83}$$

$$\begin{aligned} &-H^\star \phi_0 \frac{\partial V'}{\partial t^\star} + \left[-H^\star - \frac{\partial}{\partial Y}\left(T_0 \left. \frac{\partial f_1}{\partial \phi} \right|_{\phi_0} \right) \right] \phi' - \left. \frac{\partial f_1}{\partial Y} \right|_{\phi_0} T' - T_0 \left. \frac{\partial f_1}{\partial \phi} \right|_{\phi_0} \frac{\partial \phi'}{\partial Y} - f_1(\phi_0) \frac{\partial T'}{\partial Y} \\ &+ H^{\star -1/2} \left\{ \frac{\partial}{\partial Y}\left[f_9(\phi_0) T_0^{1/2} \right] - \frac{2}{3} \frac{\partial}{\partial Y}\left[f_2(\phi_0) T_0^{1/2} \right] \right\} \frac{\partial U'}{\partial X} \\ &+ H^{\star -1/2} \left\{ \frac{\partial}{\partial Y}\left[f_9(\phi_0) T_0^{1/2} \right] + \frac{4}{3} \frac{\partial}{\partial Y}\left[f_2(\phi_0) T_0^{1/2} \right] \right\} \frac{\partial V'}{\partial Y} \\ &+ H^{\star -1/2} T_0^{1/2} \left\{ f_2(\phi_0) \frac{\partial^2 V'}{\partial X^2} \left[f_9(\phi_0) + \frac{4}{3} f_2(\phi_0) \right] \frac{\partial^2 V'}{\partial Y^2} + \left[f_9(\phi_0) + \frac{1}{3} f_2(\phi_0) \right] \frac{\partial^2 U'}{\partial X \partial Y} \right\} = 0 \end{aligned} \tag{10.84}$$

$$\begin{aligned} &-\frac{3}{2} H^{\star 3/2} \phi_0 \left(\frac{\partial T'}{\partial t^\star} + \frac{\partial T_0}{\partial Y} V' \right) - H^{\star 3/2} f_1(\phi_0) T_0 \left(\frac{\partial U'}{\partial X} + \frac{\partial V'}{\partial Y} \right) \\ &+ \left\{ \frac{\partial}{\partial Y}\left[T_0^{1/2} \left. \frac{\partial f_3}{\partial \phi} \right|_{\phi_0} \frac{\partial T_0}{\partial Y} \right] + \frac{\partial}{\partial Y}\left[T_0^{3/2} \left. \frac{\partial f_4}{\partial \phi} \right|_{\phi_0} \frac{\partial \phi_0}{\partial Y} \right] - H^{\star 2} T_0^{3/2} \left. \frac{\partial f_5}{\partial \phi} \right|_{\phi_0} \right\} \phi' \\ &+ \left\{ \frac{1}{2} \frac{\partial}{\partial Y}\left[f_3(\phi_0) T_0^{-1/2} \frac{\partial T_0}{\partial Y} \right] + \frac{3}{2} \frac{\partial}{\partial Y}\left[f_4(\phi_0) T_0^{1/2} \frac{\partial \phi_0}{\partial Y} \right] - \frac{3}{2} H^2 f_5(\phi_0) T_0^{1/2} \right\} T' \\ &+ \left\{ T_0^{3/2} \left. \frac{\partial f_4}{\partial \phi} \right|_{\phi_0} \frac{\partial \phi_0}{\partial Y} + \frac{\partial}{\partial Y}\left[f_4(\phi_0) T_0^{1/2} \right] + T_0^{1/2} \left. \frac{\partial f_3}{\partial \phi} \right|_{\phi_0} \frac{\partial T_0}{\partial Y} \right\} \frac{\partial \phi'}{\partial Y} \\ &+ \left\{ \frac{1}{2} f_3(\phi_0) T_0^{-1/2} \frac{\partial T_0}{\partial Y} + \frac{3}{2} f_4(\phi_0) T_0^{1/2} \frac{\partial \phi_0}{\partial Y} + \frac{\partial}{\partial Y}\left[f_3(\phi_0) T_0^{1/2} \right] \right\} \frac{\partial T'}{\partial Y} \\ &+ f_4(\phi_0) T_0^{3/2} \left(\frac{\partial^2 \phi'}{\partial X^2} + \frac{\partial^2 \phi'}{\partial Y^2} \right) + f_3(\phi_0) T_0^{1/2} \left(\frac{\partial^2 T'}{\partial X^2} + \frac{\partial^2 T'}{\partial Y^2} \right) = 0 \end{aligned} \tag{10.85}$$

The corresponding boundary conditions become

$$H^{\star} f_8(\phi_0)\phi' U' - \frac{\partial U'}{\partial Y} - \frac{\partial V'}{\partial X} = 0 \tag{10.86}$$

$$V' = 0 \tag{10.87}$$

$$\left\{ \left.\frac{\partial f_3}{\partial \phi}\right|_{\phi_0} \frac{\partial T_0}{\partial Y} + T_0 \left.\frac{\partial f_4}{\partial \phi}\right|_{\phi_0} \frac{\partial \phi_0}{\partial Y} - \left(1 - e_w^2\right) H^{\star} f_3(\phi_0) T_0 \left.\frac{\partial f_6}{\partial \phi}\right|_{\phi_0} - \left(1 - e_w^2\right) H^{\star} f_6(\phi_0) T_0 \left.\frac{\partial f_3}{\partial \phi}\right|_{\phi_0} \right\} \phi'$$

$$+ \left\{ \frac{1}{2} f_3(\phi_0) T_0^{-1} \frac{\partial T_0}{\partial Y} + \frac{3}{2} f_4(\phi_0) \frac{\partial \phi_0}{\partial Y} - \left(1 - e_w^2\right) H^{\star} f_3(\phi_0) f_6(\phi_0) \frac{3}{2} \right\} T' + f_4(\phi_0) T_0 \frac{\partial \phi'}{\partial Y} + f_3(\phi_0) \frac{\partial T'}{\partial Y} = 0 \tag{10.88}$$

$$\left(T_0 \left.\frac{\partial f_1}{\partial \phi}\right|_{\phi_0} - \frac{\pi}{9} \frac{\phi^{-1/3}}{\phi_m^{2/3}} \right) \phi' + f_1(\phi_0) T' + \left[\frac{2}{3} f_2(\phi_0) - f_9(\phi_0) \right] \frac{T_0^{1/2}}{H^{1/2}} \frac{\partial U'}{\partial X}$$

$$- \left[f_9(\phi_0) + \frac{4}{3} f_2(\phi_0) \right] \frac{T_0^{1/2}}{H^{1/2}} \frac{\partial V'}{\partial Y} = 0 \tag{10.89}$$

By extracting the terms involving only the oscillation variables and the variation length scales K_x and K_y, ϕ_e, $\underline{U}_e$, and T_e (also K_x and K_z), a set of ODEs and boundary conditions at the base and the free surface are obtained to form an *eigenvalue problem*. The ODEs are discretized into an equivalent matrix eigenvalue problem and a dispersion relation for the *complex* eigenvalue, $\Omega = \Omega_r + i\Omega_i$, and wave number, K_X (in 2D) and $K_R = \sqrt{K_X^2 + K_Z^2}$ (in 3D), is numerically solved. The result for a 2D flow under the operating condition at $(M_t, Q_t) = (3.0, 19.83)$ and $(4.75, 51.31)$ is shown in Figure 10.22a and b, respectively. The real component Ω_r in the top subplot measures the growth rate of perturbations, and the largest value would dominate the system response. The lower subplot, on the other hand, portrays how the *phase velocity*, $|\Omega_i|/K_X$, of the density wave changes with K_X. At lower excitation (Q_t) in Figure 10.22a, the largest Ω_r (0) occurs in regime I when $K_X = 0$ so that the dominant wave does not vary in the X-direction and the primary bulk motion is in the so-called layer mode as observed in a bouncing bed. When driven at higher Q_t as the results shown in Figure 10.22b, the largest real Ω_r now shifts to regime III with nonzero K_X but zero phase velocity, and hence, a standing wave is obtained and the system is in the so-called stationary mode.

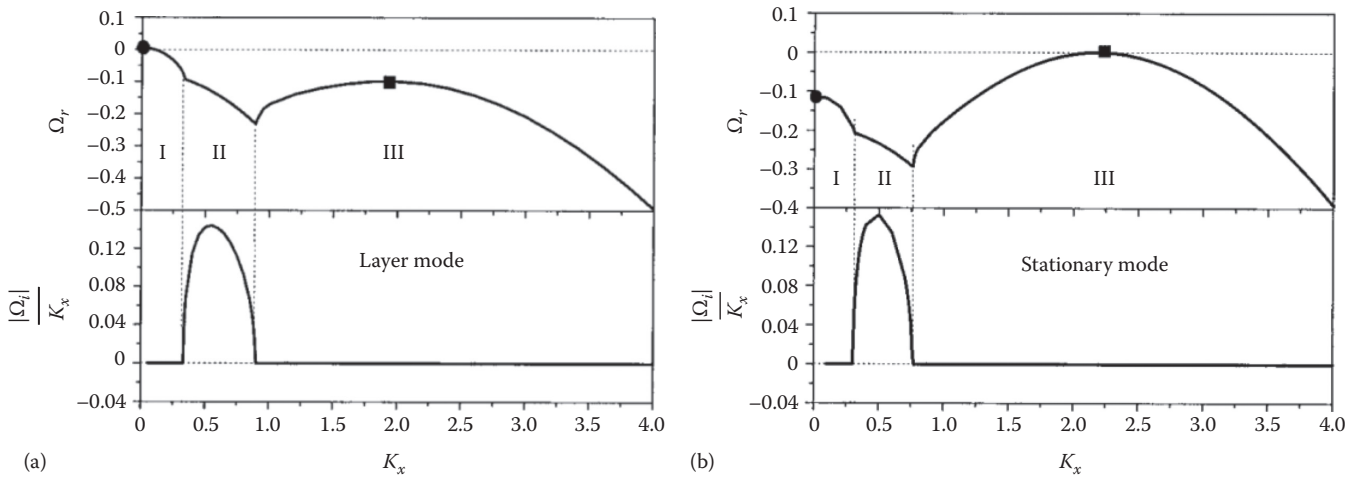


Figure 10.22

Dispersion relation for how the real and the imaginary eigenvalues, Ω_r and Ω_i, change with wave number K_x for a 2D system excited at $(M_t, Q_t) = (a)$ (3.0, 19.83) in the layer mode (largest Ω_r occurs with zero Ω_i) and (b) (4.75, 51.31) in the stationary mode for a standing surface wave with nonzero phase speed Ω_i/K_x. (From Deng, R.S. and Wang, C.H., *J. Fluid Mech.*, 492, 381, 2003.)

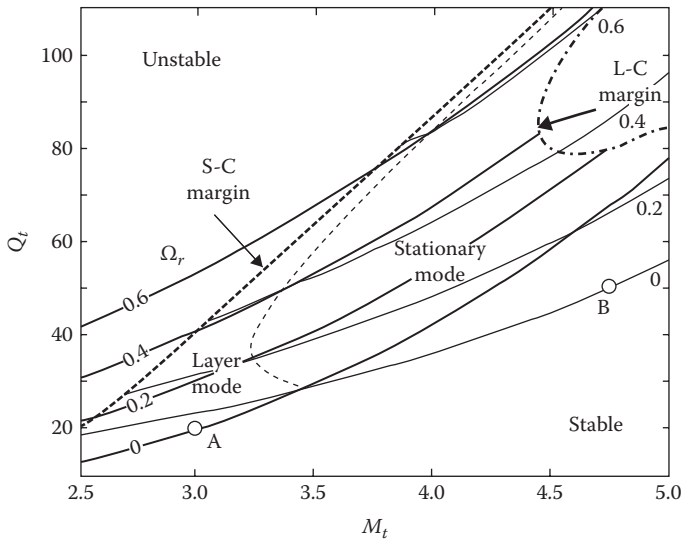


Figure 10.23

Stability diagram by the contours of Ω_r: $\Omega_r < 0$, $\Omega_r = 0$ and $\Omega_r > 0$ correspond to the stable, neutrally stable, and unstable state. The thick solid curve portrays the loci of layer mode with zero Ω_r and phase velocity, as mode in Figure 10.21a, while the thin solid line indicates the standing wave mode with zero Ω_r but positive phase velocity, as the mode in Figure 10.21b. (From Deng, R.S. and Wang, C.H., *J. Fluid Mech.*, 492, 381, 2003.)

By varying Q_t and M_t, the authors locate the contours of constant $\Omega_r = 0$, 0.2, 0.4, and 0.6 for both modes to generate a stability diagram in Figure 10.23. The layer mode (thick solid line) occurs in the left lower corner, while the stationary mode (thin solid line) locates to the right upper corner of the plot. Hence, when subject to identical agitation (Q_t), thin bed (small M_t) develops the coherent layer mode while standing wave structure of incoherent segment motions is found in thicker bed (larger M_t). Further discussions of the stability diagram can be found in the reference.

The dependence of the largest Ω_r in both modes on Q_t and M_t is further investigated in Figure 10.24a, and the system dynamics is always determined by the mode with larger Ω_r. Subject to identical Q_t, the layer mode prevails in thin beds ($M_t < 2.75$) but transits to the stationary mode when the bed is thick

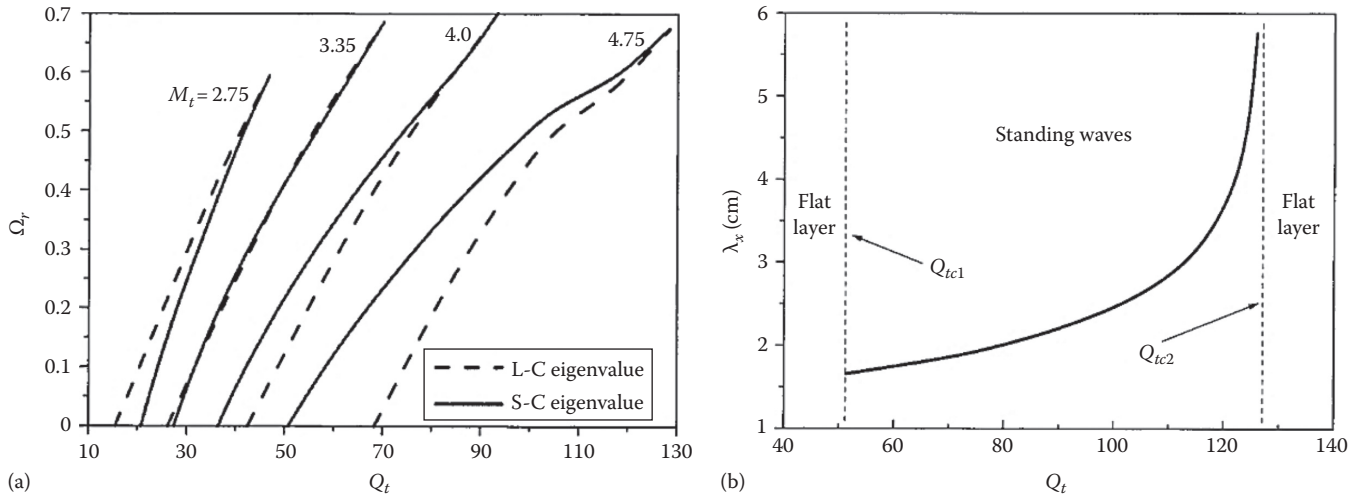


Figure 10.24

(a) Loci of the largest Ω_r in the layer mode (---, L-C) and the stationary mode with standing wave pattern (—, S-C) as a function of energy input Q_t with different M_t. System response is governed by the mode with higher Ω_r under specific Q_t and M_t. (b) Streamwise wave length as a function of Q_t in the standing wave mode. (From Deng, R.S. and Wang, C.H., *J. Fluid Mech.*, 492, 381, 2003.)

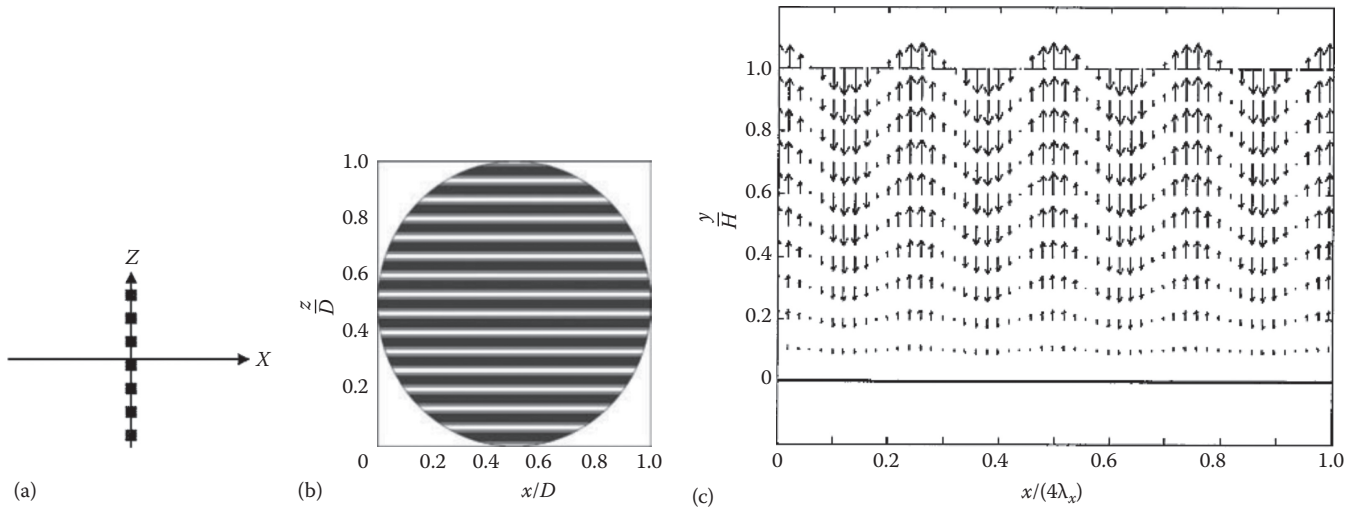


Figure 10.25

Patterns from the 3D stability analysis due to (a) a periodic perturbation along the *Z*-axis and the resulting (b) stripe pattern for $(M_t, \Omega_t) = (4.75, 51.31)$ and $K_x = 2.2$ whose dispersion relation is presented in Figure 10.22b. (c) The corresponding vertical velocity field. (From Deng, R.S. and Wang, C.H., *J. Fluid Mech.*, 492, 381, 2003.)

enough ($M_t > 3$). At a sufficiently large M_t, the stationary mode first appears at a critical Q_{t1} but *disappears* again at a second higher critical Q_{t2} as indicated by the end of the thin solid line marked by the *L-C margin* in the right upper corner of Figure 10.23. When streamwise wavelength λ_X is examined with respect to Q_t in Figure 10.24b, λ_X is found to increase monotonically but slowly when Q_t just exceeds Q_{t1} but the growth rate accelerates when approaching Q_{t2}. When λ_X becomes so large that no wave pattern can be observed in a finite observation window, the flow seems to transit from stationary mode to another mode that will be discussed shortly.

Finally, when perturbations are introduced in both the X- and Z-directions, the authors reveal identical dispersion relations for $\Omega_r - K_X$, $\Omega_r - K_Z$, and $\Omega_r - K$ (with $K^2 = K_X^2 + K_Z^2$), and hence, the system stability response is similar to those revealed from the 2D analysis. The flow response due to small perturbations to the base solution can be constructed from the solution of the eigenvalue problem under specific (M_t, Q_t). For example, when small periodic perturbation in solid volume fraction is introduced along the Z-axis as illustrated in Figure 10.25a, periodic peaks and valleys of $\phi(X, Z)$ form on the surface contour as those horizontal stripes in Figure 10.25b. Meanwhile, the vertical velocity $V_e(Y)$ is found to vary periodically with segments going up and down alternatively as shown in Figure 10.25c, and the magnitude increases monotonically from a basal zero to a surface maximum. When the perturbation is introduced along both axes, a square pattern is found in Figure 10.26a and a hexagon pattern is induced in Figure 10.26b when three perturbations lines of equal included angle are imposed. Note that the principle of superposition of waves has been applied to calculate the net variation at a specific point by linear combination of the local values from each base perturbation. One final remark is that the authors also report that the energy needed to attain the least-stable flow state ($\Omega_r = 0$) increases with decreasing coefficient of restitution (e_w and e) with which the range of the stationary mode is enlarged and the system is stabilized.

10.3.3.4 Phenomenological Model for Granular Leidenfrost Effect

Finally, we would like to relate the transition of the stationary mode to a new mode when $Q_t > Q_{t2}$ to the *granular Leidenfrost effect* experimentally observed by Eshuis et al. (2005, 2007). The authors describe that the highest mode of standing wave becomes unstable when the shaking frequency is beyond a critical level and the bottom layer "evaporates" into a granular gas so that the bulk seems to float atop as shown in Figure 10.27. A phase diagram has been reported by Eshuis et al. (2007) that includes all the dynamics mentioned earlier of a vertically vibrating granular bed with respect to Γ and H^* in Figure 10.28. Special efforts

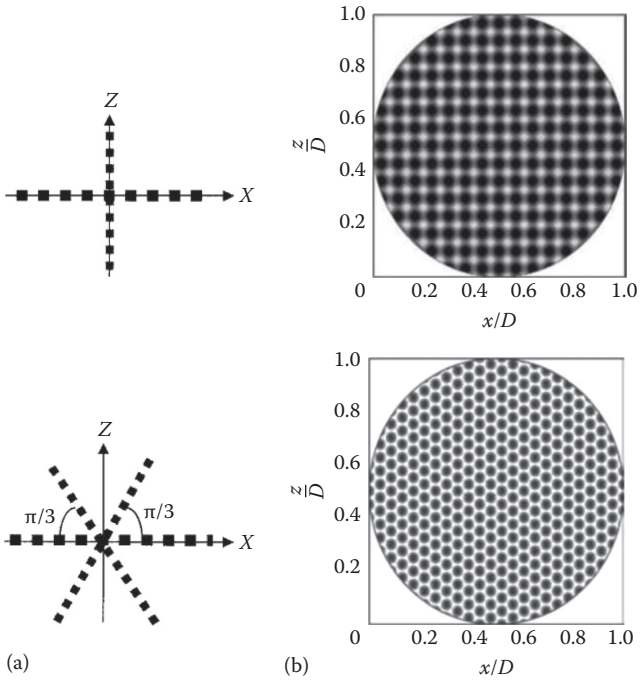


Figure 10.26

Patterns from the 3D stability analysis due to (a) two perpendicular perturbations that result in surface squares and (b) three perturbations with equal included angles that result in surface hexagons. The system is in general identical to that examined in Figure 10.25 and differs only in the how perturbation to base-state solution is applied. (From Deng, R.S. and Wang, C.H., *J. Fluid Mech.*, 492, 381, 2003.)

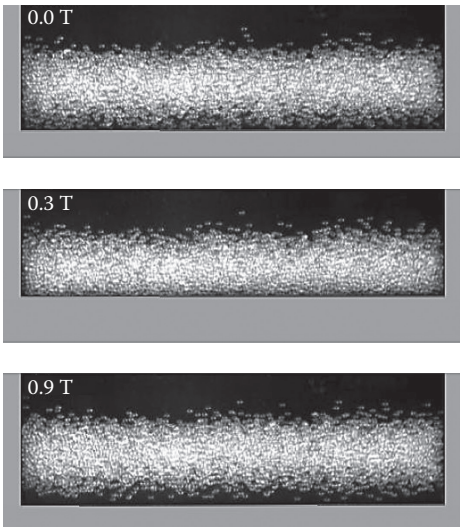


Figure 10.27

Snapshots of the granular Leidenfrost effect for $H^* = H/D = 8.1$ particle layers shaken at $f = 43.0$ Hz and $Z_0 = 3.0$ mm, corresponding to a dimensionless acceleration $\Gamma = 22$. A dense cluster is elevated and supported by a dilute layer of fast particles underneath. The cluster never touches the vibrating bottom, which makes this state distinctively different from the bouncing bed or surface standing wave. (From Eshuis, P. et al., *Phys. Fluids*, 19, 123301, 2007.)

were made to correlate the dimensionless shaking acceleration Γ with the shaking strength $S = \Gamma(A_0/D)$ on the same plot so that the effect of oscillation amplitude relative to the grain diameter may also be evaluated. The phase diagram constructed for the small and large shaking amplitudes, $Z_0 = 2$ and 4 mm (with D = 1 mm), from their experiments shows dynamically similar trends except the disappearance of Leidenfrost regime when larger grains are shaken at milder agitation.

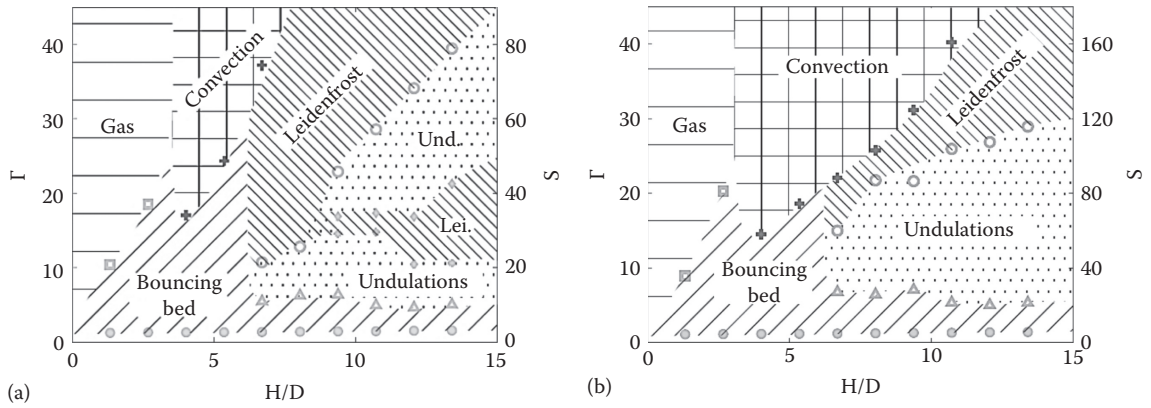


Figure 10.28

Phase diagram of the shallow granular bed ($H^* \approx 8.1$, glass beads of $D = 1$ mm, $\rho_s = 2.6$ g/cm^3, $e \approx 0.95$; thin box of $5D$ thickness and $W^* = 101$) at a shaking amplitude of (a) $a = 2.0$ mm and (b) $a = 4.0$ mm. The "undulation" mode is equivalent to the standing wave mode discussed here. The right axis plots the dimensionless shaking strength $S = \Gamma(Z_0/D)$. (From Eshuis, P. et al., *Phys. Fluids*, 19, 123301, 2007.)

The granular Leidenfrost phenomenon has been successfully captured by a 2D model for a bed that is infinitely long by Eshuis et al. (2005). An equation of state is invoked based on kinetic theory and is incorporated with the balance equations of normal momentum and energy to give

$$p = n\frac{n_c + n}{n_c - n}T \tag{10.90}$$

$$\frac{dp}{dy} = -nm_p g \tag{10.91}$$

$$\frac{d}{dy}\left(\kappa\frac{dT}{dy}\right) = \frac{C_5}{L}\left(1 - e^2\right)nT^{3/2} \tag{10.92}$$

where

n is the number density (number of grains in a control volume)
L is the *mean-free path*
C_5 is a numerical value

These equations are solved numerically with three boundary conditions: constant bed T_0, zero energy flux at the free surface as dT/dy = 0, and conservation of total grain number and the phenomenon is qualitatively captured.

10.4 Discussions: Segregation Phenomenon and Cohesion Effect

All the foregoing contents are for flows of nearly identical grains, the condition of which is rarely met in real flows and grains of dissimilar sizes, densities, geometries, or surface conditions that may separate them and cause segregation. For example, a flow due to landslide often has a surging head primarily composed of large rocks and debris and a thin tail of finer pebbles, soil, and dust. In engineering applications, segregation can assist the separation of different constituent grains in a mixture but, in contrast, can degrade mixing efficiency in other processes. Different segregation mechanisms have been proposed in the literature, and we use this final paragraph to discuss a few and interested readers are referred to the reviews by Bridgewater (1976), Ottino and Khakhar (2000), and Tang and Puri (2004).

When a mixture of large and small grains moves with the presence of gravity, smaller grains fall more easily through the voids to fill the space in deeper layer, the process of which in turn pushes larger grains toward the free surface. The dynamic process can be interpreted as a downward mass flux of small grains

accompanied by an upward flux of large grains so that an overall mass conservation is ensured at each depth. Such a gravity-driven size-induced segregation mechanism is known as the *kinetic sieving* process and the resulting phenomenon can be observed in surface flows down a slope where a layer of coarser grains runs atop and ahead of a basal layer of finer grains (Savage and Lun, 1988, Gray and Thornton, 2005). The same mechanism also explains why larger grains always accumulate at the periphery in a partially filled rotating drum while smaller grains gather near the core (Nityanand et al., 1986, Ottino and Khakhar, 2000, Aranson and Tsimring, 2006). Theoretical models have also been developed for this process by extended kinetic theory of bidisperse mixture (Savage and Lun, 1988, Jenkins and Mancini, 1989, Hsiau and Hunt, 1996), mixture theory (Dolgunin and Ukolov, 1995, Dolgunin et al., 1998, Gray and Thornton, 2005, Gray and Ancey, 2011), statistical theory of cellular automata (Makse et al., 1997, Makse and Einav, 2011), and a depth-averaged model (Boutreux and de Gennes, 1996, Gray and Kokelaar, 2010).

In addition to grain size, other grain properties can come into play to complicate the sieving process and in turn modify the distinct segregation pattern from kinetic sieving (Makse et al., 1997). To name a few, density difference can enhance or counteract size-induced sieving process depending on whether smaller grains possess greater or lower density than larger ones (Drahun and Bridgwater, 1983, Tang and Puri, 2004). Gradient in granular temperature and hence local kinetic stress can create another driving force, especially around regimes of low ϕ, which acts along or against gravity (Ottino and Khakhar, 2000, Berzi et al., 2010). When these mechanisms overcome the sieving process, reverse segregation pattern can even occur such that larger grains are found beneath smaller grains in surface flows or near the core of in rotating drum flows (Nityanand et al., 1986).

Other complication of the segregation process can result from the interplay of different flow processes. For example, while kinetic sieving explains the segregation pattern of surface large grains in vertical vibration beds, a central-rising convection roll may also help to bring large grains to the free surface. After rolling down the heap toward the container walls, these large grains can only remain at the surface since they are too large to be carried by the descending current at the wall (Williams, 1976, Harwood, 1977, Duran et al., 1993, Knight et al., 1993). In addition to bulk convection, segregation may also interfere with local arching effect at the flow boundary (Duran et al., 1994). At times, static deposit may form within a surface flow where local arresting mechanism is crucial to understand the bulk dynamics and hence the segregation pattern, as the case in a heap flow. At high flow rate, the usual deposition process that large grains run faster to the front of an avalanche governs the arresting process, and hence, a typical segregation pattern is developed. Nonetheless, the upslope propagating shock wave may become as effective in bringing the bulk to rest. Hence, large grains may deposit before reaching to the front and the surface over which smaller grains continue to flow downstream to create an alternate inversely graded stripes of large and small grains in a stratification pattern (Makse et al., 1997, Andreotti et al., 2013).

Further, the presence of any near-field noncontact force also modifies grain interactions leading to different bulk dynamics and rheology from that of a dry system. For example, Van der Waal force and electrostatic force are nonnegligible for flows of dry powders for their small sizes (Rietema, 1991, Castellanos, 2005). The presence of a small amount of liquid can result in attracting capillary force between adjacent grains (Mitarai and Nori, 2006) and lubrication force when neighboring solid surfaces are in relative motions (Kim and Karrila, 1991, Pitois et al., 2000, Xu et al., 2007, Simeonov and Calantoni, 2012). Such liquid-induced *cohesion,* in general, helps the grain assembly to resist shear so that a greater angle of repose can develop during heap formation (Albert et al., 1997, Mason et al., 1999, Samandani and Kudrolli, 2001, Tegzes et al., 2002) and in a rotating drum flow (Tegzes et al., 1999, Nase et al., 2001, Bocquet et al., 2002, Chou et al., 2011). Withstanding shear, intergrain cohesion can also result in surface plugs in a surface flow down an incline to destroy the Bagnold profile that explains why the plug size grows with cohesion strength (Brewster et al., 2005). Such phenomenon may further depend on the aggregation of individual grains (Ennis et al., 1991, Yang et al., 2003, Weber et al., 2004, Rognon, 2008), which introduces the bulk to another source of heterogeneity other than the contact-induced force chains. The degree of aggregation depends on the coherence strength as well as local flow conditions (like shear strength and concentration) and hence can interfere with the mixing and segregation process of dissimilar grains (Samandani and Kudrolli, 2000, Samandani and Kudrolli, 2001, Chaudhuri et al., 2006).

Like dry granular materials, the dynamics of cohesive grain assembly has been investigated through particle-based simulation by adding new interaction forces to the contact model (Yang et al., 2003, Zhu et al., 2007, Liu et al., 2011, Marshall and Li, 2014). As for continuum-based theoretical modeling, cohesive collisional flows have been modeled by extended kinetic theory (Kim and Arastoopour, 2002), but it is still an open question of how to incorporate particle-level cohesive interaction to the constitutive models.

For a quasi-static bulk, Nedderman (1992) directly adds a cohesion-induced shear stress c to the Coulomb-type component as $\underline{\underline{\tau}} = (\mu P + c)\underline{\underline{\dot{\gamma}}}/|\underline{\underline{\dot{\gamma}}}|$ in terms of a constant apparent friction coefficient μ and c changes with the particle-level cohesion. Model extension to dense flow regime has also been attempted by de Ryke (2008) using the $\mu(I)$ rheological model of dry flows. Through dimension analysis, Rognon et al. (2008) propose that the bulk frictional coefficient and solid volume fraction should depend on both the inertial number, I, and the cohesion number, η. This new parameter characterizes the ratio of grain-level maximum cohesive force N_c to a typical external load in a particular system. When gravity is the driving force, the cohesion number is equivalent to the Bond number $\eta = Bo = N_c/mg$ (Nase et al., 2001) but changes to $\eta = N_c/PD^{n-1}$ with $n = 2$ or 3 for a 2D or 3D simple shear flow without the presence of gravity. From systematic DEM simulations of plane shear flows, bulk dilatancy law and rheological relation can be expressed as $\phi(\eta,I) = \phi_s(\eta) - a(\eta)I$ and $\mu(\eta, I) = \mu_s(\eta) - b(\eta)I$ in which the fitting coefficients are no longer constant but change with the cohesion intensity η (Rognon, 2008). Such approach dynamically agrees to the findings by Taboada et al. (2006) who attribute cohesive bulk behaviors to different micromechanical mechanisms (the collisional, frictional, and dilational origin) with liquid effects. The variation of $\phi_s(\eta)$, $\mu_s(\eta)$, $a(\eta)$, and $b(\eta)$ with η for flows in different configurations requires further investigations, so does the feasibility of the proposed $\phi(\eta, I)$ and $\mu(\eta, I)$ formulation, which clearly illustrate the research challenges and the richness of powder and grain flows.

References

Albert, R., Albert, I., Hornbaker, D., Schiffer, P., and Barabási, A.-L., Maximum angle of stability in wet and dry spherical granular media, *Phys. Rev. E*, 56(6), R6271, 1997.

Anand, A., Curtis, J.S., Wassgren, C.R., Hancock, B.C., and Ketterhagen, W.R., Predicting discharge dynamics from a rectangular hopper using the discrete element method (DEM), *Chem. Eng. Sci*., 63, 5821–5830, 2008.

Ancey, C., Dry granular flows down an inclined channel: Experimental investigations on the frictional-collisional regime, *Phys. Rev. E*, 65, 011304, 2001.

Ancey, C., Cohard, S., and Andreini, N., The dam-break problem for viscous fluids in the high-capillary-number limit, *J. Fluid. Mech*., 624, 1–24, 2009.

Andreotti, B., Daerr, A., and Douady, S., Scaling laws in granular flows down a rough plane, *Phys. Fluids*, 14, 1, 2004.

Andreotti, B., Forterre, Y., and Pouliquen, O., *Granular Media*: *Between Fluid and Solid*, Cambridge University Press, Cambridge, U.K., 2013.

Aoki, K.M. and Akiyama, T., Spontaneous wave pattern formation in vibrated granular materials, *Phys. Rev. Lett*., 77(20), 4166–4169, 1996b.

Aoki, K.M., Akiyama, T., Maki, Y., and Watanabe, T., Convective roll patterns in vertically vibrated beds of granulates, *Phys. Rev. E*, 54(1), 874, 1996a.

Aranson, I.S. and Tsimring, L.S., Continuum theory of partially fluidized granular flows, *Phys. Rev. E*, 65, 061303, 2002.

Aranson, I.S. and Tsimring L.S., Patterns and collective behavior in granular media: Theoretical concepts, *Rev. Mod. Phys*., 78, 641–692, 2006.

Artoni, R., Santomaso, A., and Canu, P., Effective boundary conditions for dense granular flows, *Phys. Rev. E*, 79, 031304, 2009a.

Artoni, R., Santomaso, A.C., and Canu, P., Simulation of dense granular flows: Dynamics of wall stress in silos, *Chem. Eng. Sci*., 64(18), 4040–4050, 2009b.

Artoni, R., Santomaso, A., Go, M., and Canu, P., Scaling laws for the slip velocity in dense granular flows, *Phys. Rev. Lett*., 108, 238002, 2012.

Asmar, B.N., Langston, P.A., and Matchett, A.J., A generalised mixing index in distinct element method simulation of vibrated particulate beds, *Granul. Matter*, 4, 129–138, 2002.

Azema, E. and Radjai, F., Internal structure of inertial granular flows, *Phys. Rev. Lett*., 112, 078007, 2014.

Balmforth, N.J. and Kerswell, R.R., Granular collapse in two dimensions, *J. Fluid Mech*., 538, 399–428, 2005

Banton, J., Villard, P., Jongmans, D., and Scavia, C., Two-dimensional discrete element models of debris avalanches: Parameterization and the reproducibility of experimental results, *J. Geophys. Res*., 114, F04013, 2009.

Baran, O. and Kondic, L., On velocity profiles and stresses in sheared and vibrated granular systems under variable gravity, *Phys. Fluids*, 18, 121509, 2006.

Bertrand, F., Leclaire, L.-A., and Levecque, G., DEM-based models for the mixing of granular materials, *Chem. Eng. Sci.*, 60, 2517–2531, 2005.
Berzi, D., Analytical solution of collisional sheet flows, *J. Hydraul. Eng.*, 137(10), 1200–1207, 2011.
Berzi, D., Extended kinetic theory applied to dense, granular, simple shear flows, *Acta Mech.*, 225, 2191–2198, 2014.
Berzi, D. and Jenkins, J.T., Surface flows of inelastic spheres, *Phys. Fluids*, 013303, 2011.
Berzi, D., Jenkins, J., and Larcher, M., Debris flows: Recent advances in experiments and modeling, *Adv. Geophys.*, 52, 103–138, 2010.
Bocquet, L., Charlaix, E., and Restagno, F., Physics of humid granular media, *Comptes Rendus Physique*, 3, 207–215, 2002.
Bourzutschky, M. and Miller, J., 'Granular' convection in a vibrating fluid, *Phys. Rev. Lett.*, 74(12), 2216, 1995.
Boutreux, T. and de Gennes, P.G., Surface flows of granular mixtures: I. General principles and minimal model, *J. Phys. I France*, 6, 1295–1304, 1996.
Brennen, C.E., Ghosh, S., and Wassgre, C., Vertical oscillation of a bed of granular material, *J. Appl. Mech.*, 63, 156–161, 1996.
Brewster, R., Grest, G.S., Landry, J.W., and Levine, A.J., Plug flow and the breakdown of Bagnold scaling in cohesive granular flows, *Phys. Rev. E*, 72, 061301, 2005.
Bridgwater, J., Fundamental powder mixing mechanism, *Powder Technol.*, 15, 215–236, 1976.
Brodu, N., Richard, P., and Delannay, R., Shallow granular flows down flat frictional channels: Steady flows and longitudinal vortices, *Phys. Rev. E*, 87, 022202, 2013.
Campbell, C.S., Granular shear flows at the elastic limit, *J. Fluid Mech.*, 465, 261–291, 2002.
Campbell, C.S. and Brennen, C.E., Computer simulation of granular shear flows, *J. Fluid Mech.*, 151, 167, 1985.
Castellanos, A., The relationship between attractive interparticle forces and bulk behavior in dry and uncharged fine powders, *Adv. Phys.*, 54, 263–376, 2005.
Chauchat, J. and Médale, M., A three-dimensional numerical model for dense granular flows based on the rheology, *J. Comput. Phys.*, 256, 696–712, 2014.
Chaudhuri, B., Mehrotra, A., Muzzio, F.J., and Tomassone, M.S. Cohesive effects in powder mixing in a tumbling blender, *Powder Technol.*, 165, 105–114, 2006.
Chialvo, S. and Sundaresan, S., A modified kinetic theory for frictional granular flows in dense and dilute regimes, *Phys. Fluids*, 25, 070603, 2013.
Chou, S.H., Liao, C.C., and Hsiau, S.S., The effect of interstitial fluid viscosity on particle segregation in a slurry rotating drum, *Phys. Fluids*, 23, 083301, 2011.
Ciamarra, M.P., Coniglio, A., and Nicodemi, M., Shear instabilities in granular mixtures, *Phys. Rev. Lett.*, 94, 188001, 2005.
Cleary, P.W., DEM simulation of industrial particle flows, case studies of dragline excavators, mixing in tumblers and centrifugal mills, *Powder Technol.*, 109, 83–104, 2000.
Cleary, P.W. and Martin, F., Three-dimensional discrete element simulation of axi-symmetric collapses of granular columns, http://www.researchgate.net/publication/228530783_Three-Dimensional _Discrete Element_Simulation_of_Axi-symmetric_Collapses_of_Granular_Columns, 2006. Accessed March 9, 2015.
Cleary, P.W., Metcalfe, G., and Liffman, K., How well do discrete element granular flow models capture the essentials of mixing process? *Appl. Math. Model.*, 22(12), 995–1008, 1998.
Cleary, P.W. and Sawley, M.L., DEM modelling of industrial granular flows: 3D case studies and the effect of particle shape on hopper discharge, *Appl. Math. Model.*, 26, 89–111, 2002.
Cortet, P.-P., Bonamy, D., Daviaud, F., Dauchot, D., Dubrulle, B., and Renouf, M., Relevance of visco-plastic theory in a multi-directional inhomogeneous granular flow, *EPL*, 88, 14001, 2009.
Crosta, G.B., Imposimato, S., and Roddeman, D., Numerical modeling of 2-D granular step collapse on erodible and nonerodible surface, *J. Geophys. Res.*, 114, F03020, 2009.
Cui, L. and Sullivan, C.O., Exploring the macro- and micro-scale response of an idealised granular material in the direct shear apparatus, *Géotechnique*, 56, 455–468, 2006.
Cundall, P.A., Computer simulations of dense sphere assemblies, *Micromech. Gran. Mater.*, 113, 113–123 1988.
Cundall, P.A. and Strack, O.D.L., A discrete numerical model for granular assemblies, *Geotechnique*, 29, 47, 1979.
Da Cruz, F., Emam, S., Prochnow, M., Roux, J.N., and Chevoir, F., Rheophysics of dense granular materials: Discrete simulation of plane shear flows, *Phys. Rev. E*, 72, 021309, 2005.

Deng, R.S. and Wang, C.-H., Instabilities of granular material undergoing vertical vibrations: A uniformly driven layer, *J. Fluid Mech*., 492, 381–410, 2003.
De Ryck, A., Granular flows down inclined channels with a strain-rate dependent friction coefficient. Part II: Cohesive materials, *Granul. Matter*, 10, 361–367, 2008.
De Ryck, A., Zhu, H.P., Wu, S.M., Yu, A.B., and Zulli, P., Numerical and theoretical investigation of the surface flows of granular materials on heaps, *Powder Technol*., 203, 125–132, 2010.
De Vet, S.J., Yohannes, B., Hill, K.M., and de Bruyn, J.R., Collapse of a rectangular well in a quasi-two-dimensional granular bed, *Phys. Rev. E*, 82, 041304, 2010.
Di Renzo, A. and Di Maio, F.P., Comparison of contact-force models for the simulation of collisions in DEM-based granular flow codes, *Chem. Eng. Sci*., 59, 525–541, 2004.
Dolgunin, V.N., Kudy, A.N., and Ukolov, A.A., Development of the model of segregation of particles undergoing granular flow down an inclined chute, *Powder Technol*., 96, 211–218, 1998.
Dolgunin, V.N. and Ukolov, A.A., Segregation modelling of particle rapid gravity flow, *Powder Technol*., 83, 95–103, 1995.
Douady, S., Andreotti, B., and Daerr, A., On granular surface flow equations, *Eur. Phys. J. B*, 11, 131, 1999.
Drahun, J.A. and Bridgwater, J., The mechanisms of free surface segregation, *Powder Technol*., 36, 39–53, 1983.
Duran, J., *Sands*, *Powders*, *and Grains: An Introduction to the Physics of Granular Materials*, Springer, New York, 2000.
Duran, J., Mazozi, T., Clément, E., and Rajchenbach, J., Size segregation in a two-dimensional sandpile: Convection and arching effects, *Phys. Rev. E*, 50, 5138, 1994.
Duran, J., Rajchenbach, J., and Clement, E., Arching effect model for particle size segregation, *Phys. Rev. Lett*., 70, 16, 1993.
Dury, C.M. and Ristow, G.H., Competition of mixing and segregation in rotating cylinders, *Phys. Fluids*, 11, 1387–1394, 1999.
Edwards, A.N. and Gray, J.M.N.T., Erosion-deposition waves in shallow granular free-surface flows, *J. Fluid Mech*., 762, 35–67, 2014.
Ennis, B.J., Tardos, J.L.G., and Pfeffer, R., A microlevel-based characterization of granulation phenomena, *Powder Technol*., 65, 257–272, 1991.
Ertas, D. and Halsey, T.C., Granular gravitational collapse and chute flows, *Europhysics Lett*., 60, 931, 2002.
Eshuis, P., van der Weele, K., van der Meer, D., Bos, R., and Lohse, D., Phase diagram of vertically shaken granular matter, *Phys. Fluids*, 19, 123301, 2007.
Eshuis, P., van der Weele, K., van der Meer, D., and Lohse, D., Granular Leidenfrost effect: Experiment and theory of floating particle clusters, *Phys. Rev. Lett*., 95, 258001, 2005.
Fan, Y., Umbanhowar, P.B., Ottino, J.M., and Lueptow, R.M., Kinematics of monodisperse and bidisperse granular flows in quasi-two-dimensional bounded heaps, *Proc. R. Soc. A*, 469, 20130235, 2013.
Faraday, M., On a peculiar class of acoustical figures assumed by groups of particles upon vibrating elastic surfaces, *Phil. Trans. R. Soc. Lond*., 52, 299, 1831.
Fernando, D.N. and Wassgren, C.R., Effects of vibration method and wall boundaries on size segregation in granular beds, *Phys. Fluids*, 15, 3458–3467, 2003.
Forterre, Y. and Pouliquen, O., Flows of dense granular media, *Ann. Rev. Fluid Mech*., 40, 1, 2008.
Gray, J.M.N.T., Granular flow in partially filled slowly rotating drums, *J. Fluid. Mech*., 441, 1–29, 2001.
Gray, J.M.N.T. and Ancey, C., Multi-component particle-size segregation in shallow granular avalanches, *J. Fluid Mech*., 678, 535–588, 2011.
Gray, J.M.N.T. and Edwards, A.N., A depth-averaged μ(I)-rheology for shallow granular free-surface flows, *J. Fluid Mech*., 755, 503–534, 2014.
Gray, J.M.N.T. and Kokelaar, B.P., Large particle segregation, transport and accumulation in granular free-surface flows, *J. Fluid Mech*., 652, 105–137, 2010.
Gray, J.M.N.T. and Thornton, A.R., A theory for particle size segregation in shallow granular free-surface flows, *Proc. R. Soc. A*, 461(2057), 1447–1473, 2005.
Girolami, L., Hergault, V., Vinay, G., and Wachs, A., A three-dimensional discrete-grain model for the simulation of dam-break rectangular collapses: Comparison between numerical results and expreiments, *Granul. Matter*, 14(3), 381–392, 2012.
Goldhirsch, I., Rapid granular flows, *Annu. Rev. Fluid Mech*., 35, 267, 2003.
Haff, P.K., Grain flow as a fluid-mechanical phenomenon, *J. Fluid Mech*., 134, 401–430, 1983.
Hanes, D.M. and Walton, O.R., Simulations and physical measurements of glass spheres flowing down a bumpy incline, *Powder Technol*., 109, 133–144, 2000.

Harwood, C.F., Powder segregation due to vibration, *Powder Technol.*, 16, 51–57, 1977.
Henann, D.L. and Kamrin, K., A predictive, size-dependent continuum model for dense granular flows, *Proc. Natl. Acad. Sci. USA*, 110, 6730, 2013.
Herrmann, H.J. and Luding, S., Modeling granular media on the computer, Continuum MEch, *Thermodynamics*, 10, 189–231, 1998.
Hogg, A.J., Two-dimensional granular slumps down slopes, *Phys. Fluids*, 19, 093301, 2007.
Hsiau, S.S. and Hunt, M.L., Granular thermal diffusion in flows of binary-sized mixtures, *Acta Mech.*, 114, 121–37, 1996.
Hsiau, S.S. and Yang, S.C., Numerical simulation of self-diffusion and mixing in a vibrated granular bed with the cohesive effect of liquid bridges, *Chem. Eng. Sci.*, 58, 339–351, 2003.
Hunt, M.L., Hsiau, S.S., and Hong, K.T., Particle mixing and volumetric expansion in a vibrated granular bed, *J. Fluid Eng.*, 116(4), 785–791, 1994.
Hutter, K. and Rajagopal, K.R., On flows of granular materials, *Continuum Mech. Therm.*, 6, 81–139, 1994.
Hutter, K., Szidarovskiy, F., and Yakowitz, S., Plane steady shear flow of a cohesionless granular material down an inclined plane: A model for flow avalanches, Part I: Theory, *Acta Mech.*, 63, 87–112, 1986.
Iordanoff, I., Fillot, N., and Berthier, Y., Numerical study of a thin layer of cohesive particles under plane shearing, *Powder Technol.*, 159, 46–54, 2005.
Iordanoff, I. and Khonsari, M.M., Granular lubrication, towards an understanding of the transition between kinetic and quasi-fluid regime, *J. Tribol.*, 126(1), 137, 2004.
Jaeger, H.M., Nagel, S.R., and Behringer, R.P., Granular solids, liquids, and gases, *Rev. Mod. Phys.*, 68, 1259–1273, 1996.
Janssen, H.A., Getreidedruck in silozellen, *Z. Oesterr, Ing.-Archit.-Ver.*, 39, 1045, 1895.
Jenkins, J.T., Rapid granular flow down inclines, *Appl. Mech. Rev.*, 47, 240, 1994.
Jenkins, J.T., Dense shearing flows of inelastic disks, *Phys. Fluids*, 18, 103307, 2006.
Jenkins, J.T., Dense inclined flows of inelastic spheres, *Granul. Matter*, 10, 47–52, 2007.
Jenkins, J.T. and Askari, E., Hydraulic theory for a debris flow supported on a collisional shear layer, *Chaos*, 9, 654, 1999.
Jenkins, J.T. and Mancini, F., Kinetic theory for binary mixtures of smooth, nearly elastic spheres, *Phys. Fluids A*, 1, 2050–2057, 1989.
Jenkins, J.T. and Richman, M.W., Grad's 13-moment system for a dense gas of inelastic spheres, *Arch. Rat. Mech. Anal.*, 87, 355–377, 1985.
Jenkins, J.T. and Savage, S.B., A theory for the rapid flow of identical, smooth, nearly elastic, spherical particles, *J. Fluid Mech.*, 130, 187–202, 1983.
Jenkins, J.T. and Zhang, C., Kinetic theory for identical, frictional, nearly elastic spheres, *Phys. Fluids*, 14, 1228–1235, 2002.
Johnson, K.L., *Contact Mechanics*, Cambridge University Press, New York, 1985.
Johnson, P.C. and Jackson, R., Frictional-collisional constitutive relations for granular materials, with application to plane shearing, *J. Fluid Mech.*, 176, 67–93, 1987.
Johnson, P.C., Nott, P., and Jackson, R., Frictional-collisional equations of motion for particulate flows and their application to chutes, *J. Fluid Mech.*, 210, 501–535, 1990.
Jop, P. and Forterre, Y., Pouliquen, Crucial role of sidewalls in granular surface flows: Consequences for the rheology, *J. Fluid Mech.*, 541, 167–192, 2005.
Jop, P., Forterre, Y., and Pouliquen, O., A constitutive law for dense granular flows, *Nature*, 441, 727–730, 2006.
Jop, P., Forterre, Y., and Pouliquen, O., Initiation of granular surface flows in a narrow channel, *Phys. Fluids*, 19(8), 088102, 2007.
Jung, Y.K. and Lee, J., Crossover of the behavior of surface waves in a vibrated granular material, *Phys. A*, 342, 479–490, 2004.
Kamrin, K. and Bazant, M.Z., Stochastic flow rule for granular materials, *Phys. Rev. E*, 75, 041301, 2007.
Kamrin, K. and Henann, D.L., Nonlocal modeling of granular flows down inclines, *Soft Matter*, 11, 179–185, 2015.
Kamrin, K. and Koval, G., Nonlocal constitutive relation for steady granular flow, *Phys. Rev. Lett.*, 108, 178301, 2012.
Karion, A. and Hunt, M.L., Wall stresses in granular Couette flows of mono-sized particles and binary mixtures, *Powder Technol.*, 109, 145–163, 2000.

Kermani, E., Qiu, T., and Li, T., Simulation of collapse of granular columns using the discrete element method, *Int. J. Geomech*., 15, 04015004, 2015.
Kerswell, R.R., Dam break with Coulomb friction: A model for granular slumping? *Phys. Fluids*, 17, 057101, 2005.
Ketterhagen, W.R., Curtis, J.S., and Wassgren, C.R., Stress results from two-dimensional granular shear flow simulations using various collision models, *Phys. Rev. E*, 71, 063307, 2005.
Khakhar, D.V., Orpe, A., Andersen, P., and Ottino, J.M., Surface flow of granular materials: Model and experiments in heap formation, *J. Fluid Mech*., 441, 255–264, 2001.
Kim, H. and Arastoopour, H., Extension of kinetic theory to cohesive particle flow, *Powder Technol*., 122, 83–94, 2002.
Kim, S. and Karrila, S., *Microhydrodynamics*: *Principles and Selected Applications*, Butterworth-Heinemann, 1991. Boston/London.
Knight, J.B., External boundaries and internal shear bands in granular convection, *Phys. Rev. E*, 55(5), 6016, 1997.
Knight, J.B., Jaeger, H.M., and Nagel, S.R., Vibration-induced size separation in granular media: The convection connection, *Phys. Rev. Lett*., 70, 3728, 1993.
Koval, G., Roux, J.-N., Corfdir, A., and Chevoir, F., Annular shear of cohesionless granular materials: From the inertial to quasistatic, *Phys. Rev. E*, 79, 021306, 2009.
Kruggel-Emden, H., Simsek, E., Rickelt, S., Wirtz, S., and Scherer, V., Review and extension of normal force models for the discrete element method, *Powder Technol*., 171, 157–173, 2007.
Kumaran, V., The constitutive relation for the granular flow of rough particles, and its application to the flow down an inclined plane, *J. Fluid Mech*., 561, 1–42, 2006.
Kumaran, V., Dense granular flow down an inclined plane: From kinetic theory to granular dynamics, *J. Fluid Mech*., 599, 121–168, 2008.
Kumaran, V., Dense shallow granular flows, *J. Fluid Mech*., 756, 555–599, 2014.
Lacaze, L. and Kerswell, R.R., Axisymmetric granular collapse: A transient 3D flow test of viscoplasticity, *Phys. Rev. Lett*., 102(10), 108305, 2009.
Lacaze, L., Phillips, J.C., and Kerswell, R.R., Planar collapse of a granular column: Experiments and discrete element simulations, *Phys. Fluids*, 20, 063302, 2008.
Lagrée, P.-Y., Staron, L., and Popinet, S., The granular column collapse as a continuum: Validity of a two-dimensional Navier-Stokes model with a μ(I)-rheology, *J. Fluid Mech*., 686, 378–408, 2011.
Lan, Y. and Rosato, A.D., Macroscopic behavior of vibrating beds of smooth inelastic spheres, *Phys. Fluids*, 7(8), 1818–1831, 1995.
Lan, Y. and Rosato, A.D., Convection related phenomena in granular dynamics simulations of vibrated beds, *Phys. Fluids*, 9(12), 3615–3626, 1997.
Langston, P.A., Tüzün, U., and Heyes, D.M., Continuous potential discrete particle simulations of stress and velocity-fields in hoppers—transition from fluid to granular flow, *Chem. Eng. Sci*., 49, 1259–1275, 1994.
Langston, P.A., Tüzün, U., and Heyes, D.M., Discrete element simulation of granular flow in 2D and 3D hoppers—dependence of discharge rate and wall stress on particle interactions, *Chem. Eng. Sci*., 50, 967–987, 1995a.
Langston, P.A., Tuzun, U., and Heyes, D.M., Discrete element simulation of internal-stress and flow-fields in funnel flow hoppers, *Powder Technol*., 85, 153–169, 1995b.
Laroche, C., Douady, S., and Fauve, S., Convective flow of granular masses under vertical vibrations, *J. de Phys*., *France*, 50, 699–706, 1989.
Larrieu, E., Staron, L., and Hinch, E.J., Raining into shallow water as a description of the collapse of a column of grains, *J. Fluid Mech*., 554, 259–270, 2006.
Lätzel, M., Luding, S., and Herrmann, H., Macroscopic material properties from quasi-static, microscopic simulations of a two-dimensional shear-cell, *Granul. Matter*, 2(3), 123–135, 2000.
Liu, K.F. and Mei, C.C., Slow spreading of a sheet of Bingham fluid on an inclined plane, *J. Fluid. Mech*., 207, 505–529, 1989.
Liu, P.Y., Yang, R.Y., and Yu, A.B., Dynamics of wet particles in rotating drums: Effect of liquid surface tension, *Phys. Fluids*, 23, 013304, 2011.
Lois, G., Lemaitre, A., and Carlson, J., *Phys. Rev. E*, 72, 051303, 2005.
Louge, M.Y., Model for dense granular flows down bumpy inclines, *Phys. Rev. E*, 67, 061303, 2003.
Lu, Z., Negi, S.C., and Jofriet, J.C., A numerical model for flow of granular materials in silos, Part 1, Model development, *J. Agric. Eng. Res*., 68, 223–229, 1997.

Luding, S., Cohesive, frictional powders: Contact models for tension, *Granul. Matter*, 10, 235–246, 2008.
Luding, S., Lätzel, M., Volk, W., Diebels, S., and Herrmann, H.J., From discrete element simulations to a continuum model, *Comput Method Appl. Mech. Eng.*, 191(1), 21–28, 2001.
Lun, C.K.K., Savage, S.B., Jeffrey, D.J., and Chepurniy, N., Kinetic theories for granular flow: Inelastic particles in Couette flow and slightly inelastic particles in a general flow field, *J. Fluid Mech.*, 140, 223–256, 1984.
Maeno, F., Hogg, A.J., Sparks, R.S.J., and Matson, G.P., Unconfined slumping of a granular mass on a slope, *Phys. Fluids*, 25(2), 023302, 2013.
Makse, H.A., Havlin, S., King, P.R., and Stanley, H.E., Spontaneous stratification in granular mixtures, *Nature*, 386, 379–382, 1997.
Marks, B. and Einav, I., A cellular automaton for segregation during granular avalanches, *Granul. Matter*, 13, 211–214, 2011.
Marshall, J.S. and Li, S.Q., *Adhesive Particle Flow: A Discrete Element Approach*, Cambridge University Press, New York, 2014.
Mason, T.G., Levine, A.J., Hertas, D., and Hasley, T.C., The critical angle of wet granular sand piles, *Phys. Rev. E*, 60, R5044, 1999.
Melo, F., Umbanhowar, P., and Swinney, H.L., Transition to parametric wave patterns in a vertically oscillated granular layer, *Phys. Rev. Lett.*, 72, 172, 1994.
Melosh, J., The physics of very large landslides, *Acta Mech.*, 64, 89–99, 1986.
Metcalf, T.H., Knight, J.B., and Jaeger, H.M., Standing wave patterns in shallow beds of vibrated granular material, *Phys. A*, 236, 202–210, 1997.
Midi, G.D.R., On dense granular flows, *Eur. Phys. J. E*, 14(4), 341–365, 2004.
Mills, P., Loggia, D., and Tixier, M., Model for a stationary dense granular flow along an inclined wall, *Europhys. Lett.*, 45, 733, 1999.
Mills, P., Loggia, D., and Tixier, M., Influence of roughness and dilatancy for dense granular flow along an inclined wall, *J. Phys. E*, 1, 5–8, 2000.
Mindlin, R.D., Compliance of elastic bodies in contact, *J. Appl. Mech. Trans. ASME*, 16, 259–268, 1949.
Mindlin, R.D. and Deresiewicz, H., Elastic spheres in contact under varying oblique forces, *J. Appl. Mech.*, 20, 327, 1953.
Mishra, B.K., A review of computer simulation of tumbling mills by the discrete element method, Part I—contact mechanics, *Int. J. Mineral Process.*, 71, 73–93, 2003a.
Mishra, B.K., A review of computer simulation of tumbling mills by the discrete element method, Part II—Practical applications, *Int. J. Mineral Process*, 71, 95–112, 2003b.
Mitarai, N. and Nori, F., Wet granular materials, *Adv. Phys.*, 55, 1–45, 2006.
Munjiza, A.A., Earl, E.K., and Esteban, R., *Computational Mechanics of Discontinua*, John Wiley & Sons, 2011. John Wiley & Sons Ltd, The Atrium, Southern Gate, Chichester, U.K.
Nase, S.T., Vargas, W.L., Abatan, A., and McCarthy, J.J., Discrete characterization tools for cohesive granular material, *Powder Technol.*, 116, 214–223, 2001.
Nedderman, R.M., *Statics and Kinematics of Granular Materials*, Cambridge University Press, Cambridge, U.K., 1992.
Nityanand, N., Manley, B., and Henein, H., An analysis of radial segregation for different sized spherical solids in rotary cylinders, *Metal. Trans. B*, 17, 247–257, 1986.
Ogawa, S., Multitemperature theory of granular materials, in *Proceedings of the U.S.-Japan Symposium on Continuum Mechanics and Statistical Approaches in the Mechanics of Granular Materials*, Gukujutsu Bunken Fukyukai, Tokyo, 1978.
Orpe, A.V. and Khakhar, D.V., Rheology of surface granular flows, *J. Fluid Mech.*, 571, 1, 2007.
Ottino, J.M. and Khakhar, D.V., Mixing and segregation of granular materials. *Annu. Rev. Fluid Mech.*, 32, 55–91, 2000.
Owen, P.J., Cleary, P.W., and Meriaux, C., Quasi-static fall of planar granular columns: Comparison of 2D and 3D discrete element modelling with laboratory experiments, *Geomech. Geoeng. Int. J.*, 4(1), 55–77, 2009.
Pak, H.K., Van Doorn, E., and Behringer, R.P., Effects of ambient gases on granular materials under vertical vibration, *Phys. Rev. Lett.*, 74(23), 4643–4645, 1995.
Paulick, M., Morgeneyer, M., and Kwade, A., Review on the influence of elastic particle properties on DEM simulation results, *Powder Technol.*, 283, 66–76, 2015.
Peyret, R. and Taylor, T.D., *Computational Methods for Fluid Flow*, Springer-Verlag, New York, 1983.
Pitois, O., Moucheront, P., and Chateau, X., Liquid bridge between two moving spheres: An experimental study of viscosity effects, *J. Colloid Interf. Sci.*, 231, 26–31, 2000.
Potapov, A.V. and Campbell, C.S., Computer simulation of hopper flow, *Phys. Fluids*, 8, 2884–2894, 1996.
Pouliquen, O., On the shape of granular fronts down rough inclined planes, *Phys. Fluids*, 11, 1956–1958, 1999a.
Pouliquen, O., Scaling laws in granular flows down rough inclined planes, *Phys. Fluids*, 11, 542–548, 1999b.

Pouliquen, O. and Forterre, Y., Friction law for dense granular flows: Application to the motion of mass down a rough inclined plane, *J. Fluid Mech*., 453, 133–151, 2002.
Pouliquen, O. and Forterre, Y., A non-local rheology for dense granular flows, *Phil. Trans. R. Soc. A*, 26, 5091–5107, 2009.
Pudasaini, S.P., Some exact solutions for debris and avalanche flows, *Phys. Fluids*, 23, 043301, 2011.
Radjai, F. and Roux, S., Contact dynamics study of 2D granular media: Critical states and relevant internal variables, in H. Hinrichsen and D.E. Wolf (Eds.), *The Physics of Granular Media*, Wiley, Berlin, Germany, 2004, pp. 165–187.
Razis, D., Edwards, A.N., Gray, J.M.N.T., and van der Weele, K., Arrested coarsening of granular roll waves, *Phys. Fluids*, 26, 123305, 2014.
Reddy, K.A. and Kumaran, V., Dense granular flow down an inclined plane: A comparison between the hard particle model and soft particle simulations, *Phys. Fluids*, 22(11), 113302, 2010.
Renouf, M., Bonamy, D., Dubois, F., and Alart, P., Numerical simulation of two-dimensional steady granular flows in rotating drum: On surface flow rheology, *Phys. Fluids*, 17, 103303, 2005.
Reynolds, O., On the dilatancy of media composed of rigid particles in contact, *Phil. Mag*., 20, 469–481, 1885.
Richman, M.W. and Marciniec, R.P., Gravity-driven granular flows of smooth, inelastic spheres down bumpy inclines, *J. Appl. Mech*., 57, 1036–1043, 1990.
Richman, M.W. and Martin, R.E., Unconfined granular materials thermalized by fluctuating horizontal surfaces, in L.D. Lutes and J.N. Niezwecki (Eds.), *Proceedings of the Ninth Conference on engineering Mechanics*, ASCE, New York, 1992, pp. 900–903.
Rietema, K., *The Dynamics of Fine Powders*, Elsevier, New York, 1991.
Rognon, P.G., Roux, J.-N.L., Naaim, M., and Chevoir, F., Dense flows of cohesive granular materials, *J. Fluid Mech*., 596, 21–47, 2008.
Rosato, A.D. and Lan, Y., *Discrete Element Modeling of Vibrating Granular Beds*, Powder and Grains 93, Balkema, Roterdam, the Netherlands, 1993, pp. 241–246.
Roux, S. and Radjai, F., Texture-dependent rigid plastic behavior, in H.J. Herrmann, J.-P. Hovi, and S. Luding (Eds.) *Physics of Dry Granular Media*, Springer, the Netherlands, 1998.
Samadani, A. and Kudrolli, A., Segregation transitions in wet granular matter, *Phys. Rev. Lett*., 85, 5102, 2000.
Samadani, A. and Kudrolli, A., Angle of repose and segregation in cohesive granular matter, *Phys. Rev. E*, 64, 051301, 2001.
Savage, S.B., Granular flows at high shear rates, in R.E. Meyer (Ed.) *Theory of Dispersed Multiphase Flow*, Academic Press, 1983a, pp. 339–358.
Savage, S.B., Granular flows down rough inclines: Review and extension, in J.T. Jenkins and M. Satake (Eds.), *Mechanics of Granular Materials*: *New Models and Constitutive Relations*, Elsevier, 1983b, pp. 261–282.
Savage, S.B., Analyses of slow high-concentration flows of granular materials, *J. Fluid Mech*., 377, 1–26, 1998.
Savage, S.B., Free-surface granular flows down heaps, *J. Eng. Math*., 60(2), 221–240, 2008.
Savage, S.B. and Hutter, K., The motion of a finite mass of granular material down a rough incline, *J. Fluid Mech*., 199, 177–215, 1989.
Savage, S.B. and Lun, C.K.K., Particle size segregation in inclined chute flow of dry cohesionless granular solids, *J. Fluid. Mech*., 189, 311–335, 1988.
Schöllmann, S., Simulation of a two-dimensional shear cell, *Phys. Rev. E*, 59, 01, 1991.
Shojaaee, Z., Roux, J.-N., Chevoir, F., and Wolf, D.E., Shear flow of dense granular materials near smooth walls. I. Shear localization and constitutive laws in the boundary region, *Phys. Rev. E*, 86, 011301, 2012.
Silbert, L.E., Granular flow down an inclined plane: Bagnold scaling and rheology, *Phys. Rev. E*, 64, 051302, 2001.
Silbert, L.E., Ertas, D., Grest, G.S., Halsey, T.C., Levine, D., and Plimpton, S.J., Granular flow down an inclined plane, Bagnold scaling and rheology, *Phys. Rev. E*, 64, 051302, 2001.
Silbert, L.E., Landry, J.W., and Grest, G.S., Granular flow down a rough inclined plane, transition between thin and thick piles, *Phys. Fluids*, 15, 1–10, 2003.
Simeonov, J.A. and Calantoni, J., Modeling mechanical contact and lubrication in direct numerical simulations of colliding particles, *Int. J. Multiphase Flow*, 46, 38–53, 2012.
Staron, L. and Hinch, E.J., Study of the collapse of granular columns using DEM numerical simulation, *J. Fluid Mech*., 545(1), 0022–1120, 2005.
Staron, L., Lagrée, P.-Y., and Popinet, S., Continuum simulation of the discharge of the granular silo: A validation test for the mu(I) visco-plastic flow law, *Eur. Phys. J. E*, 37(1), 5, 2014.
Stevens, A.B. and Hrenya, C.M., Comparison of soft-sphere models to measurements of collision properties during normal impacts, *Powder Technol*., 154, 99–109, 2005.

Srivastava, A. and Sundaresan, S., Analysis of a frictional-kinetic model for gas-particle flow, *Powder Technol.*, 129(1–3), 72–85, 2003.
Taboada, A., Estrada, N., and Radjai, F., Additive decomposition of shear strength in cohesive granular media from grain-scale interactions, *Phys. Rev. Lett.*, 97, 098302, 2006.
Taguchi, Y.H., New origin of a convective motion: Elastically induced convection in granular materials, *Phys. Rev. Lett.*, 69, 1367–1370, 1992.
Taguchi, Y.H., Numerical modelling of convective motion in granular-materials, *Adv. Powder Technol.*, 5, 297–303, 1994.
Tai, C.H. and Hsiau, S.S., Dynamic behaviors of powders in a vibrating bed, *Powder Technol.*, 139, 221–232, 2004.
Tang, P. and Puri, V.M., Methods for minimizing segregation: A review, *Particul. Sci. Technol.*, 22, 321–337, 2004.
Tankeo, M., Richard, P., and Édouard, C., Analytical solution of the μ(I)–rheology for fully developed granular flows in simple configurations, *Granul. Matter*, 15, 881–891, 2013.
Tapia-McClung, H. and Zenit, R., Computer simulations of the collapse of columns formed by elongated grains, *Phys. Rev. E*, 85, 061304, 2012.
Teufelsbauer, H., Wang, Y., Chiou, M.-C., and Wu, W., Flow-obstacle interaction in rapid granular avalanches, DEM simulation and comparison with experiment, *Granul. Matter*, 11, 209–220, 2009.
Teufelsbauer, H., Wang, Y., Pudasaini, S., Borja, R., and Wu, W., DEM simulation of impact force exerted by granular flow on rigid structures, *Acta Geotech.*, 6(3), 119–133, 2011.
Tegzes, P., Albert, R., Paskvan, M., Barabasi, A.-L., Vicsek, T., and Schiffer, P., Liquid-induced transitions in granular media, *Phys. Rev. E*, 60, 5823–5826, 1999.
Tegzes, P., Vicsek, T., and Schiffer, P., Avalanche dynamics in wet granular materials, *Phys. Rev. Lett.*, 89(9), 094301, 2002.
Valentino, R., Baria, G., and Montrasio, L., Experimental analysis and micromechanical modeling of dry granular flow and impacts in laboratory flume tests, *Rock Mech. Rock Eng.*, 41(1), 153–177, 2008.
Vidyapti, V., Kheiripour Langroudi, M., Sundaresan, S., Tardos, G.I., and Subramaniam, S., Experimental and computational studies of dense granular flow: Transition from quasi-static to intermediate regime in a Couette shear device, *Powder Technol.*, 220, 7–14, 2012.
Vu-Quoc, L., Zhang, X., and Walton, O.R., A 3-D discrete-element method for dry granular flows of ellipsoidal particles, *Comput. Methods Appl. Mech. Eng.*, 187, 483–528, 2000.
Walther, J.H. and Sbalzarini, I.F., Large-scale parallel discrete element simulations of granular flow, *Eng. Comput.*, 26(6), 688–697, 2009.
Walton, O.R., Chapter 25: Numerical simulation of inelastic, frictional particle-particle interactions, in M.C. Roco (Ed.), *Particulate Two-Phase Flow*, Butterworth-Heinemann, Boston, MA, 1993, pp. 884–911.
Walton, O.R. and Braun R.L., Viscosity, granular temperature, and stress calculations for shearing assemblies of inelastic, frictional disks, *J. Rheol.*, 30, 949–980, 1986.
Wassgren, C.R., Brennen, C.E., and Hunt, M.L., Vertical vibration of a bed of granular material in a container, *J. Appl. Mech.*, 63, 712–719, 1996.
Wassgren, C.R., Hunt, M.L., Freese, P.J., Palamara, J., and Brennen, C.E., Effects of vertical vibration on hopper flows of granular material, *Phys. Fluids*, 14, 3439–3448, 2002.
Weber, M.W., Hoffman, D.K., and Hrenya, C.M., Discrete-particle simulations of cohesive granular flow using a square-well potential, *Granul. Matter*, 6, 239–254, 2004.
Wildman, R.D. and Huntley, J.M., Novel method for measurement of granular temperature distributions in two-dimensional vibro-fluidised beds, *Powder Technol.*, 113, 14–22, 2000.
Wildman, R.D., Huntley, J.M., and Parker, D.J., Convection in highly fluidized three-dimensional granular beds, *PRL*, 86(15), 3304–3307, 2001.
Williams, J.C., The segregation of particulate materials: A review, *Powder Technol.*, 15, 245–251, 1976.
Wood, D.M., *Soil Behaviour and Critical State Soil Mechanics*, Cambridge University Press, Cambridge, U.K., 1990.
Xu, Q., Orpe, A.V., and Kudrolli, A., Lubrication effects on the flow of wet granular materials, *Phys. Rev. E*, 76, 031302, 2007.
Yang, F.-L., Chang, W.T., Huang, Y.T., Hsieh, S.H., and Chen, C.S., Dry granular avalanche down a flume: Choice of discrete element simulation parameters, *Phys. Fluids*, 25, 123303, 2013.
Yang, R.Y., Zou, R.P., and Yu, A.B., A simulation study of the packing of wet particles, *AIChE J.*, 49, 1656–1666, 2003.
Zhang, L. and Thornton, C., A numerical examination of the direct shear test, *Géotechnique*, 57, 343–354, 2007.

Zhang, X. and Vu-Quoc, L., Simulation of chute flow of soybeans using an improved tangential force-displacement model, *Mech. Mater.*, 32, 115–129, 2000.
Zhu, H.P. and Yu, A.B., Steady-state granular flow in a three-dimensional cylindrical hopper with flat bottom, microscopic analysis, *J. Phys. D—Appl. Phys.*, 37, 1497–1508, 2004.
Zhu, H.P., Zhou, Z.Y., Yang, R.Y., and Yu, A.B., Discrete particle simulation of particulate systems: Theoretical developments, *Chem. Eng.*, 62, 3378–3396, 2007.
Zhu, H.P., Zhou, Z.Y., Yang, R.Y., and Yu, A.B., Discrete particle simulation of particulate systems: A review of major applications and findings, *Chem. Eng. Sci.*, 63, 5728–5770, 2008.
Zenit, R., Computer simulations of the collapse of a granular column, *Phys. Fluids*, 17, 031703, 2005.


Taylor & Francis
Taylor & Francis Group
http://taylorandfrancis.com

11

Multiphase Flow in Porous Media

John R. Fanchi and John P. Seidle

11.1 Porosity
11.2 Permeability
11.3 Characterizing Porosity and Permeability
11.4 Directional Permeability
11.5 Rock–Fluid Interaction
11.6 Relative Permeability
11.7 Fractional Flow of Two Immiscible Fluids
11.8 Immiscible Displacement
11.9 Reservoir Flow Model Equations

A porous medium is a medium that contains solid material and pore space. Figure 11.1 is a thin section of a rock displaying grains of sand and pores. The solid part of the material is often referred to as the matrix, skeleton, or frame. Porous media are common in nature, commerce, and daily life. Examples include cement, ceramics, soil, rocks, coal filters, packed columns, sponges, and biological tissues.

The factors that influence the flow of single-phase and multiphase fluids through porous media are considered here. In addition, porous media such as coal and shale contain commercial fluids that are extracted through flow in fractures. We discuss the factors at work in these media by discussing multiphase flow in coal.

11.1 Porosity

The porosity ϕ of a porous medium is the volume fraction of its pore space. Bulk volume is the volume of the solid material and the volume of the pore space. In the case of a rock, bulk volume V_B is the sum of pore volume V_P and grain volume V_G:

$$V_B = V_P + V_G \tag{11.1}$$

Pore volume V_P is the volume remaining when the volume of grains V_G is subtracted from the bulk volume:

$$V_P = V_B - V_G \tag{11.2}$$

The bulk volume of the block in Figure 11.2 is HA.

Porosity is the ratio of pore volume to bulk volume:

$$\phi = \frac{V_P}{V_B} = \frac{V_B - V_G}{V_B} \tag{11.3}$$

Porosity has a value that varies from 0 to 1. It is a factor that determines the volume of fluids that can be contained in the porous material.

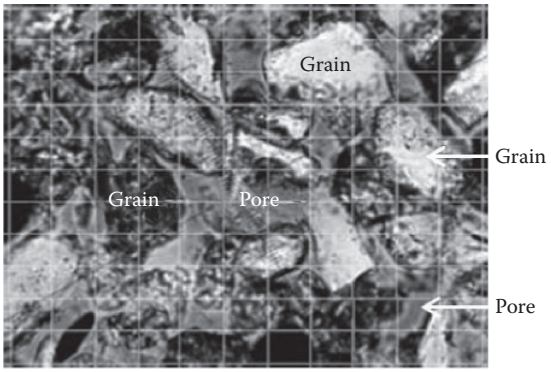


Figure 11.1

Thin section of rock showing pores and grains.

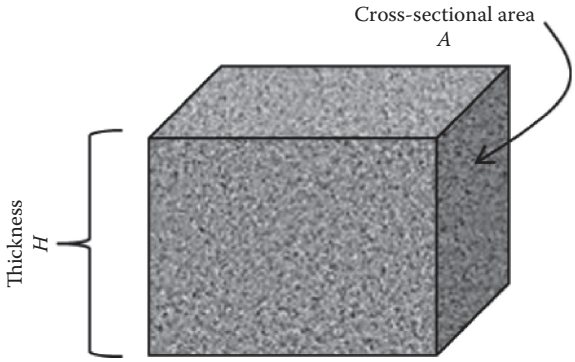


Figure 11.2

Bulk volume of a block or cell.

Pore volume is the product of porosity and bulk volume:

$$V_P = \phi V_B \tag{11.4}$$

11.1.1 Effective Porosity

Two kinds of pores or voids influence flow in porous media: effective pore space and isolated pore space. Effective or open pore space connects enough pores to allow fluid to flow over commercially significant distances such as flow into a wellbore. Effective porosity is the ratio of effective pore volume to bulk volume:

$$\phi_{eff} \equiv \frac{(V_P)_{eff}}{V_B} \tag{11.5}$$

Isolated, "dead," closed, or ineffective pore space consists of pores or voids that are dispersed in the medium and do not allow fluid flow over commercially significant distances. Total porosity is the sum of ineffective porosity and effective (interconnected) porosity. Any further discussion using porosity will assume that porosity is the effective porosity, and the subscript *eff* is omitted.

Fluid flow is possible only in porous media that have connected pore spaces. Porous media that allow fluid flow are called permeable. Permeability is a measure of fluid flow through connected pore spaces and is discussed in greater detail in Section 11.2.

Several porosities are possible in geologic systems. Primary porosity is the original porosity of the medium. The rock porosity changes as a result of the history of the rock. For example, leaching can increase porosity. The resulting porosity is secondary porosity. If breaks or fractures occur in the medium, the pore

space in the fracture is called fracture porosity. The porosity in a relatively large pore space known as a vug is called vuggy porosity.

Porosity can be measured for samples in the laboratory. The porosity of rock can also be measured in the field using well log measurements. Experimental measurements commonly used to determine the porosity of a porous sample include the following:

1. *Imbibition method*: The porous sample is saturated with a preferential wetting fluid by letting the fluid imbibe into the sample under vacuum. The sample is weighed before and after imbibition. The porosity can be calculated from the two weights, the density of the fluid, and the dimensions (bulk volume) of the sample.
2. *Mercury injection method*: A sample is evacuated, and mercury is forced to penetrate into the sample under high pressure. High pressure is needed because mercury will not penetrate the pores of most materials unless pressure is applied. Injection methods that do not rely on mercury have also been developed.
3. *Gas expansion method*: The porous sample is enclosed in a vessel with measured volume V_1 and gas pressure p_1. When the vessel is connected to an evacuated vessel of known volume V_2, the gas expands into this vessel and the gas pressure in the first vessel decreases to a lower value p_2. Applying the ideal gas law to the process mentioned earlier, the effective pore volume V_P of the sample is calculated as

$$V_P = V_B - V_1 - V_2\left(\frac{p_2}{p_2 - p_1}\right) \tag{11.6}$$

   The bulk volume of the sample V_B is determined in a separate measurement.
4. *Density method*: The bulk density of the sample ρ_B and the density of the grains ρ_G in the sample are determined. The total porosity of the sample is calculated as

$$\phi = \frac{V_B - V_G}{V_B} = 1 - \frac{V_G}{V_B} \approx 1 - \frac{\rho_B}{\rho_G} \tag{11.7}$$

11.1.2 Coal Porosity

Coals are characterized by two types of porosity. The first type is associated with the natural fractures (cleats), while the second type, termed *phyteral porosity*, is related to the organic precursors of the coal matrix. Coal cleats (Figures 11.3 and 11.4) are two sets of mutually perpendicular fractures that are, in turn, nominally perpendicular to the coal bedding planes. The first set, termed face cleats, are roughly parallel, thoroughgoing, vertically and laterally extensive, well-developed natural fractures. The butt cleats, perpendicular to the face cleats, are also parallel to one another but are less well developed and shorter, often terminating at a face cleat. Cleat porosity, typical of naturally fractured reservoirs, is on the order of 1% of the bulk volume (Seidle, 2011).

Controls on cleat porosity are poorly understood. Cleating is most pronounced in bituminous coals, but cleat porosity appears to be independent of both coal rank and geologic age. The roles of other parameters such as ash, mineral matter, and maceral population have not been investigated.

The determination of *in situ* coal cleat porosity is difficult. Lab measurements of cleat permeability are often affected by sample size (lab samples are too small to adequately capture the cleat network) and sample preparation (coal rapidly deteriorates when exposed to atmospheric conditions). Laboratory-measured porosities must be reduced due to overburden loads and tectonic stresses to obtain *in situ* values. In practice, cleat porosities are often back calculated from reported water production or reservoir simulation history matches. Cleat porosities determined in this manner typically vary between 0.5% and 2%.

The second type of porosity, phyteral porosity, is relic void space from the original organic material modified during coalification. Phyteral porosity is not linear like cleat porosity nor is it similar to the porosity of conventional sandstone reservoirs formed from nominally spherical sand grains. Pollens, leaves, roots, blossoms, twigs, seeds, and other organic matter in the original swamp are compressed, deformed, and solidified into pores of various sizes, aspect ratios, and connectivity in the coal matrix. A major characteristic of the phyteral porosity seen in coals of all geologic ages and all ranks is the extremely small pore

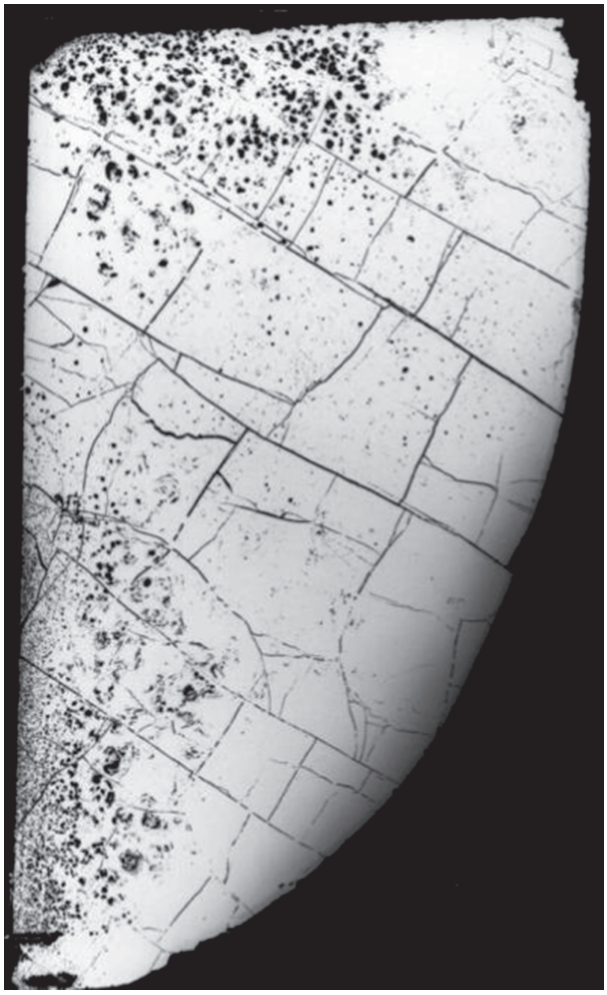


Figure 11.3

Face and butt cleats, Fruitland coal, San Juan Basin, NM. (Courtesy of John Bradley, New Mexico.)

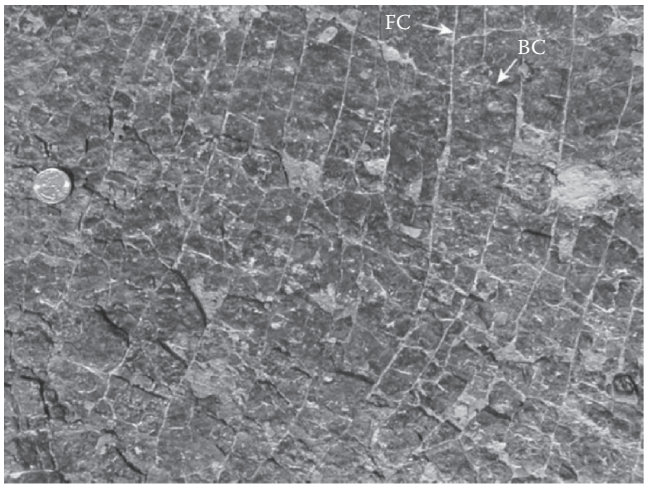


Figure 11.4

Mineral filled face and butt cleats, Warrior Basin, AL. FC, face cleat (systematic joint); BC, butt cleat (cross joint). (Courtesy of George Hampton, Denver, Colorado.)

throats, on the order of 0.5 nm. For comparison, the diameter of a methane molecule is roughly 0.4 nm. Due to these small pore throats, the measurement of coal matrix porosity depends on the method and the material employed.

The imbibition method discussed earlier for porosity measurements in coal is problematic as coal integrity rapidly declines when subjected to a vacuum, yielding erroneously high cleat porosities. Injection pressures required to force mercury into the extremely small pores of a coal often destroy sample integrity, again providing erroneously high matrix porosities. Porosity determined with the gas expansion method depends on the gas employed. Helium gas penetrates the coal matrix more deeply and thoroughly than other molecules, leading to higher porosities, on the order of 7%. In contrast, other gas molecules and injected mercury do not penetrate the matrix so extensively, yielding matrix porosities on the order of a few percent. When the density method is employed, care must be taken to accurately measure coal bulk and grain densities. Assuming a coal with 1% cleat porosity and a bulk density of 1.650 g/cm^3, Equation 11.7 yields a grain density of 1.634 g/cm^3, lower than the bulk density by 0.016 g/cm^3. Clearly, small errors in lab measurements would strongly affect the resulting cleat porosity.

Water transfer between cleat and matrix is minimal at best, leading to the simplified but extremely pragmatic approximation of coals as single porosity reservoirs to water (cleat only) and dual porosity reservoirs to gas (cleat plus matrix). The assumption of an *in situ* coal bed porosity of 1% is often quite adequate for most reservoir engineering calculations.

11.1.3 Porosity Compressibility

Porosity compressibility c_ϕ is a measure of the change in porosity ϕ as a function of fluid pressure p in the pore space. It is defined as

$$c_\phi = \frac{1}{\phi}\frac{d\phi}{dp} \tag{11.8}$$

If porosity compressibility is constant with respect to pressure, porosity ϕ at pressure p can be expressed in terms of porosity ϕ_0 at pressure p_0 as

$$\phi = \phi_0 \exp\left[c_\phi\left(p - p_0\right)\right] \tag{11.9}$$

An approximation to Equation 11.9 is the first-order expansion of the exponential term with respect to pressure difference:

$$\phi \approx \phi_0\left[1 + c_\phi\left(p - p_0\right)\right] \tag{11.10}$$

A typical value of porosity compressibility in sandstone is 3×10^{-6}/psia. It is comparable in magnitude to water compressibility and oil compressibility.

Coal is an organic, reactive, polymeric rock that is highly compressible compared to most reservoir rocks and fluids. The coal matrix is quite rigid, resisting deformation with increasing stress and preventing large changes in the matrix porosity. The high compressibility of a coal is primarily due to narrowing of the cleats with increasing stress. Coal compressibility is difficult to measure in the lab and values reported in the literature range from changes in cleat porosity. As cleating is most pronounced in bituminous coals, cleat compressibility would intuitively peak in these ranks. Available data are insufficient to understand the role of coal rank, geologic age, or composition in coal compressibility. Although not exhaustive, a review of 13 coal cleat compressibilities determined by both laboratory and field methods (Seidle, 2011) showed minimum, median, and maximum values of 3×10^{-4}/psia, 1.3×10^{-3}/psia, and 2.5×10^{-3}/psia, respectively. The eightfold variation in cleat compressibility reflects not only the heterogeneous nature of coals but also the difficulty in measuring this parameter by either laboratory or field methods.

Note the median coal compressibility is more than a hundred times larger than the typical sandstone compressibility reported earlier. In spite of this, the compressibility of a coal deposit is dominated by gas and sorption compressibilities, not cleat compressibility. Dewatering of undersaturated coals is affected by cleat and water compressibilities until reservoir pressure is reduced to the critical desorption pressure and gas is

released off the matrix into the cleats. The estimation of porosity and permeability losses during dewatering of deeply undersaturated coals often requires including at least three terms in the exponential expansion, Equation 11.10.

11.1.4 Saturation and Fluid Volume

The saturation S_ℓ of phase ℓ is the fraction of the volume of pore space occupied by phase ℓ. The sum of the saturations in the pore space must equal one. If the system has N_P phases, the saturation constraint is

$$1 = \sum_{\ell=1}^{N_P} S_\ell \tag{11.11}$$

For an oil–water–gas system, the saturation constraint is $S_o + S_w + S_g = 1$ where the subscripts $\{o, w, g\}$ refer to oil, water, and gas, respectively. The fluid volume of phase ℓ is the product of the saturation S_ℓ of phase ℓ and pore volume:

$$V_\ell = S_\ell V_P = S_\ell \phi V_B \tag{11.12}$$

The volume of fluid in a geologic formation with many contiguous layers depends on gross thickness and net thickness. If we consider the block in Figure 11.2, gross thickness H is the total thickness of the formation and net thickness h is the sum of the thicknesses of the layers in the formation that are permeable. Net thickness is less than or equal to gross thickness. The net-to-gross ratio η_{NTG} is the ratio of net thickness h to gross thickness H:

$$\eta_{NTG} = \frac{h}{H}, \quad 0 \le \eta_{NTG} \le 1 \tag{11.13}$$

The volume V_ℓ of phase ℓ in the permeable intervals is

$$V_\ell = S_\ell \eta_{NTG} HA\phi = S_\ell hA\phi \tag{11.14}$$

for cross-sectional area A.

11.1.5 Tortuosity

The route that a fluid takes through a porous medium can be a straight path or very nonlinear. The property of the rock that measures the length of the path from the entry point to the exit point relative to a straight path is tortuosity. If the path is a straight line, which can occur in a linear fracture, the tortuosity is 1. In most cases, the flow path in a porous medium will be longer than a straight line, so tortuosity is greater than 1. Figure 11.5 illustrates a tortuous path through a porous medium.

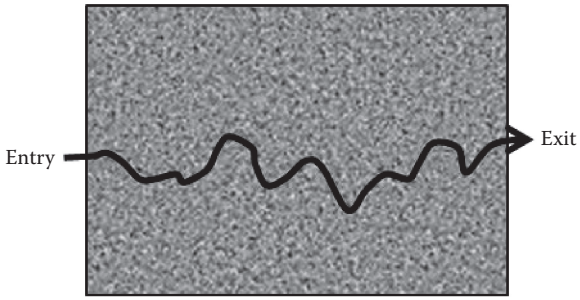


Figure 11.5
Tortuosity.

11.1.6 Specific Surface and Hydraulic Radius

The specific surface S of a porous medium is the pore surface area S_P per unit of bulk volume V_B:

$$S = \frac{S_P}{V_B} \tag{11.15}$$

Pore surface area is the surface area of pores inside the bulk volume. If we assume a medium with porosity ϕ is a packing of spheres with diameter d, the specific surface is (Mavko et al., 2009)

$$S = \frac{3}{2}\frac{(1-\phi)}{d} \tag{11.16}$$

The SI unit of specific surface is 1/m.

Hydraulic radius r_h is the ratio of pore volume V_P to pore surface area S_P (Guéguen and Palciauskas, 1994):

$$r_h = \frac{V_P}{S_P} = \frac{\phi V_B}{S_P} \tag{11.17}$$

Substituting the expression for surface area S_P in Equation 11.15 into 11.17 gives a relationship between hydraulic radius and specific surface S:

$$r_h = \frac{\phi}{S} \tag{11.18}$$

The SI unit of hydraulic radius is m.

11.1.7 Formation Resistivity Factor and Archie's Equation

Processes such as adsorption and desorption, catalysis, and ion exchange depend on specific surface. Formation water, or water in a geologic formation, is brine with a substantial concentration of ionizing molecules, such as sodium chloride and calcium chloride. Mobile ions in a fluid decrease the resistivity of the fluid. Brine usually has more ions in solution than hydrocarbons, so resistivity measurements can be used to indicate the presence of hydrocarbon in a geologic formation. The resistivity R_0 of a porous material saturated with an ionic solution is equal to the resistivity R_w of the ionic solution times the formation resistivity factor F of the porous material:

$$R_0 = FR_w \tag{11.19}$$

Formation resistivity factor F can be estimated using the empirical relationship

$$F(a,m) = a\phi^{-m} \tag{11.20}$$

with two parameters a and m. Parameter a depends on tortuosity and is called the tortuosity factor. Parameter m depends on the degree of consolidation of the rock and is called the cementation exponent. As an example, the cementation exponent m varies from 1.14 to 2.52 and the tortuosity factor a varies from 0.35 to 4.78 (Bassiouni, 1994) for sands.

If a porous medium is partially saturated by an electrically conducting, wetting phase with saturation S_w, the formation resistivity R_t of the partially saturated medium is given by Archie's empirical relationship

$$R_t = R_0 S_w^{-n} \tag{11.21}$$

where n is called the saturation exponent. Note that $R_t = R_0$ when $S_w = 1$. An equation for wetting phase saturation as a function of resistivities and formation resistivity factor is obtained by combining the earlier relationships to obtain Archie's equation:

$$S_w = \left(\frac{FR_w}{R_t} \right)^{1/n} \tag{11.22}$$

Although Archie's equation and its subsequent variations have been widely used to calculate water saturations in sandstone and carbonate reservoirs for over 70 years, it does not give reliable water saturations in coals. Archie's equation is semiempirical and assumes an inert sandstone or carbonate matrix. Coal matrix, which can be considered as a tangle of organic polymers, possesses electrical properties distinct from those of sandstones and carbonates, so it should not be surprising that water saturations and resistivities in coal cannot be described with Archie's equation.

Intentional dewatering of coal beds and recovery of coal gas has been actively pursued for nearly 40 years, yet the determination of water saturation in a coal deposit using wireline logs remains problematic. No logging tool, or combination of tools, can currently assess water saturation of a coal seam. Consequently, water saturations are back calculated from producing gas–water ratios, cumulative produced water and bulk coal porosity, or simulation history matching exercises.

11.2 Permeability

Henri Darcy (1856) found that the flow rate is proportional to the pressure gradient through rock with connected pore space. Permeability quantifies the connectivity of pore spaces. A rock is considered impermeable if there is no connectivity between pore spaces.

Permeability is usually measured using 1D, cylindrically shaped samples. The movement of a single-phase fluid through a cylindrical core of rock is illustrated in Figure 11.6. Fluid flow through the core depends on cross-sectional area A that is normal to the direction of fluid flow, pressure difference Δp across the length Δx of the flow path, and dynamic viscosity μ of the flowing fluid. In the experiment, various flow rates of the fluid are recorded as a function of pressure drop. The permeability is obtained by fitting a straight line to the data points. Theoretically, Darcy's (1856) law for slow (creeping), 1D, horizontal, steady flow of a Newtonian fluid is

$$q = \frac{kA}{\mu} \frac{\Delta p}{L} \tag{11.23}$$

where

q is the volumetric flow rate (cm^3/s)
A is the cross-sectional area of the sample normal to the flow direction (cm^2)
L is the length of the sample in the flow direction (cm)
Δp is the hydrostatic pressure drop (atm)
μ is the viscosity of the fluid (cp)

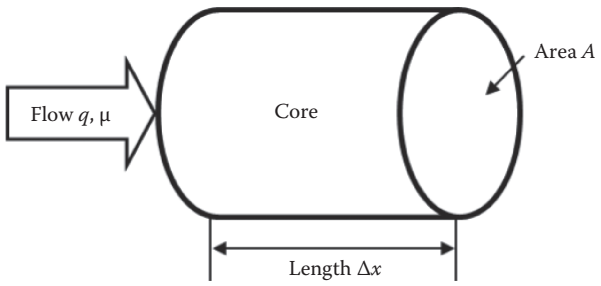


Figure 11.6

Darcy's law for a cylindrical core.

Using these units in Darcy's law gives the practical unit of permeability, darcy (D), with the value

$$1\,\text{darcy} = \frac{(1\,\text{cm}^3/\text{s})(1\,\text{cp})(1\,\text{cm})}{(1\,\text{cm}^2)(1\,\text{atm})} \tag{11.24}$$

The magnitude of permeability typically ranges from 1 millidarcy = 1 md (or 1.0×10^{-15} m^2) to 1 darcy = 1000 md (or 1.0×10^{-12} m^2) for conventional oil and gas reservoirs. Tight gas reservoir permeability is on the order of microdarcies (10^{-3} md) and shale gas reservoir permeability is on the order of nanodarcies (10^{-6} md).

The darcy unit has the dimension of area (L^2) where L is a unit of length. One darcy equals 1000 millidarcies (md). The areal unit (L^2) of permeability can be thought of as a measure of the effective cross-sectional area of a pore throat. A pore throat is the opening that connects two pores. The cross-sectional area of a pore throat tends to increase as grain size increases. Relatively large pore throats imply relatively large values of cross-sectional area transverse to the direction of fluid flow and correspond to relatively large values of permeability.

11.2.1 Darcy's Law

The basic equation describing the fluid flow in porous media is Darcy's law. Darcy's equation for calculating volumetric flow rate q for linear, horizontal, single-phase flow is

$$q = -0.001127\frac{kA}{\mu}\frac{\Delta p}{\Delta x} \tag{11.25}$$

where permeability k is the proportionality constant for the relationship between flow rate and pressure gradient. The minus sign indicates the direction of fluid flow: fluid flows from high pressure to low pressure in a horizontal (gravity-free) system. The constant 0.001127 in Equation 11.23 corresponds to variables expressed in the following oilfield units: volumetric flow rate q (bbl/day), permeability k (md), cross-sectional area A (ft^2), pressure p (psi), fluid viscosity μ (cp), and length Δx (ft). Dynamic viscosity μ is used in Darcy's law. Kinematic viscosity ν is the ratio of dynamic viscosity to fluid density ρ, that is, $\nu = \mu/\rho$.

Departures from the linear relationship between the flow rate and the pressure gradient have been observed. Forchheimer (1901) observed that pressure gradient at high flow rate had the quadratic dependence on the flow rate

$$\frac{\Delta p}{\Delta x} = -\left(\frac{1}{0.001127}\right)\frac{\mu}{k}\left(\frac{q}{A}\right) + \beta\rho\left(\frac{q}{A}\right)^2 \tag{11.26}$$

for fluid with density ρ and turbulence factor β in the non-Darcy q^2 term. The minus sign and conversion factor on the right-hand side (RHS) of Equation 11.26 are inserted to be consistent with the rate convention and units used in Equation 11.25. Equation 11.26 is a special case of the Forchheimer equation.

11.2.2 Superficial Velocity and Interstitial Velocity

Superficial velocity u is the volumetric flow rate q in Darcy's law divided by the cross-sectional area $A_\perp$ normal to flow, as in all other multiphase flow applications (Bear, 1972, Lake, 1989), thus $u = q/A_\perp$ in appropriate units. The actual velocity of fluid moving through tortuous pore space is called interstitial velocity. The interstitial velocity v is the superficial velocity u divided by the porosity ϕ or

$$v = \frac{u}{\phi} = \frac{q}{\phi A_\perp} \tag{11.27}$$

Interstitial velocity is larger than superficial velocity since porosity is a fraction between 0 and 1.

11.2.3 Hydraulic Conductivity

Hydraulic conductivity is used to characterize the ability of water to flow through a porous medium. The relationship between hydraulic conductivity k_H and permeability k is

$$k_H = \frac{k\rho g}{\mu} \tag{11.28}$$

for a fluid with density ρ and viscosity μ. The SI unit of hydraulic conductivity k_H is m/s when permeability k is in m^2, fluid density ρ is in kg/m^3, fluid viscosity μ is in kg/(m · s), and acceleration of gravity g is in m/s^2. Permeability is a property of the porous medium, while hydraulic conductivity depends on the properties of both the porous medium and the fluid.

11.2.4 Darcy's Law for Radial Flow of Liquid

The geometry for radial fluid flow in a porous medium is sketched in Figure 11.7. Darcy's law for steady-state, radial, horizontal, single-phase liquid flow in a homogeneous porous medium with cross-sectional area $A = 2\pi rh$ is

$$q = -\frac{0.00708kh(p_w - p_e)}{\mu B \ln(r_e/r_w)} = -\frac{(0.001127 \times 2\pi)kh(p_w - p_e)}{\mu B \ln(r_e/r_w)} \tag{11.29}$$

where the variables are volumetric flow rate q (stb/day where stb refers to stock tank barrels), inner radius or wellbore radius r_w (ft), outer radius or drainage radius r_e (ft), permeability k (md), thickness h (ft), pressure at inner radius p_w (psi), pressure at outer radius p_e (psi), fluid viscosity μ (cp), and formation volume factor B (rb/stb = reservoir barrel/stock tank barrel). Reservoir barrel is a barrel of volume at reservoir temperature and pressure. Stock tank barrel is a barrel of volume at stock tank temperature and pressure, which is typically surface temperature and pressure. Formation volume factor B is the ratio of volume of fluid at reservoir conditions to volume of fluid at stock tank (surface) conditions. The factor $0.00708 = 2\pi \times 0.001127$ and logarithmic term $\ln(r_e/r_w)$ are due to the change from linear to radial flow. Liquid flow rate q is positive for fluid production $\{p_w < p_e\}$ and negative for fluid injection $\{p_w > p_e\}$.

The outer radius r_e is equated to the drainage radius of a well when analyzing radial flow into a well. The flow rate is less sensitive to an error in the estimate of r_e than a similar error in a parameter like permeability because the radial flow calculation depends on the logarithm of r_e. It is therefore possible to make coarse estimates of the outer radius r_e and still obtain a reasonable value for radial flow rate.

11.2.5 Darcy's Law for Radial Flow of Gas

Darcy's law for the radial flow of gas at reservoir conditions is

$$q_r = -0.006328\frac{2\pi rhk}{\mu_g}\frac{dp_r}{dr} \tag{11.30}$$

where the variables are volumetric flow rate q_r (rcf/day where rcf refers to reservoir cubic feet or cubic feet of volume at reservoir temperature and pressure), radial distance r (ft), permeability k (md), thickness h (ft),

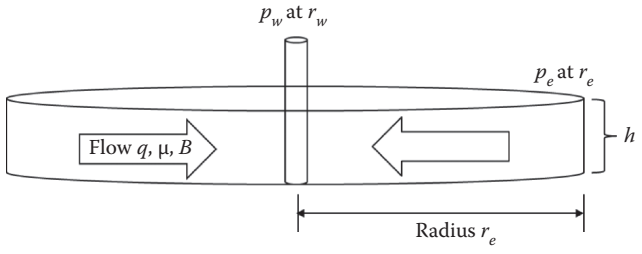


Figure 11.7

Darcy's law for radial flow.

gas viscosity μ_g (cp), and reservoir pressure p_r (psia). Let subscripts r and s denote reservoir and surface conditions, respectively. To convert from reservoir to surface conditions, we divide the gas rate at reservoir conditions by the gas formation volume factor:

$$q_s = \frac{q_r}{B_g} \tag{11.31}$$

where

q_s is the gas rate (scf/day where scf is standard cubic feet or cubic feet of volume at surface conditions)
B_g is the gas formation volume factor (rcf/scf)

Gas formation volume factor B_g is the ratio of the volume of gas at reservoir conditions to the volume of gas at surface conditions. We use the real gas equation of state to express B_g as a function of pressure p, temperature T, and gas compressibility factor Z as

$$B_g = \frac{\text{reservoir volume}}{\text{surface volume}} = \frac{Z_r T_r p_s}{Z_s T_s p_r} \tag{11.32}$$

The flow rate q_s at surface conditions in scf/day is found by combining Equations 11.30 through 11.32 to get

$$q_s = -0.03976 \frac{rhk}{\mu_g} \frac{Z_s T_s p_r}{Z_r T_r p_s} \frac{dp_r}{dr} \tag{11.33}$$

This can be written as

$$q_s = -0.01988 \frac{khT_s Z_s}{p_s T_r \left(\ln \dfrac{r_e}{r_w} \right)} \left[m(p_e) - m(p_w) \right] \tag{11.34}$$

where $m(p)$ is the real gas pseudo-pressure defined by

$$m(p) = 2 \int_{p_{ref}}^{p} \frac{p'}{\mu_g Z} dp' \tag{11.35}$$

where

p_{ref} is a reference pressure
p' is a dummy integration variable

In oilfield units, $m(p)$ has the unit psia^2/cp. Gas viscosity μ_g and gas compressibility factor Z depend on pressure and must be part of the integral. Darcy's law for the radial flow of gas at the standard conditions $Z_s = 1$, $p_s = 14.7$ psia, and $T_s = 60°\text{F} = 520°\text{R}$ is

$$q_s = -0.703 \frac{kh}{T_r \left(\ln \dfrac{r_e}{r_w} \right)} \left[m(p_e) - m(p_w) \right] \tag{11.36}$$

This shows that the flow rate q_s is proportional to the difference in real gas pseudo-pressure.

11.2.6 Permeability Measurements and the Klinkenberg Effect

The permeability of a core can be measured in the laboratory using a permeameter. A core is enclosed in an airtight sleeve, mounted into a steel cell, and a fluid is injected into the cell. The flow rate and pressure drop

across the core are measured and permeability is calculated using Darcy's law. At low flow rates, permeability to gas injection will be larger than permeability to liquid injection due to the slippage of gas molecules along pore walls. The dependence of permeability to gas on the pressure of flowing gas is called the Klinkenberg effect (Klinkenberg, 1941, Satter et al., 2008) and is given by the relationship

$$k_g = k_L\left(1+\frac{b}{\bar{p}}\right) \tag{11.37}$$

where

k_g is the permeability to gas when gas saturation is 100%
k_L is the permeability to liquid when liquid saturation is 100%
$\bar{p}$ is the mean flowing pressure of gas in the flow system
b is the Klinkenberg factor

The Klinkenberg factor b is a positive constant that depends on rock type and type of gas. Consequently, we have the inequality $k_g \geq k_{abs}$ when the factor $\left(1+\frac{b}{\bar{p}}\right) \geq 1$. As $\bar{p}$ increases, the factor $\left(1+\frac{b}{\bar{p}}\right)$ approaches 1 and the permeability to gas k_g approaches the absolute permeability of the rock k_{abs}. The Klinkenberg effect is more significant for gas flow through low-permeability rock than high-permeability rock.

Coals are naturally fractured reservoirs with two sets of mutually perpendicular fractures: face cleats and butt cleats. Both face and butt cleats are perpendicular to the bedding planes. Cleat intensity often varies by bedding plane, but cleat orientation remains nominally constant. Face cleats often cross several bedding planes, while vertical extent of butt cleats is often constrained to a few bedding planes. Face and butt cleat spacing is often on the order of millimeters or centimeters (Figures 11.3 and 11.4).

11.2.7 Coal Permeability

Visualizing coal as a collection of matchsticks with cleat spacing a, in mm, and cleat width b, in mm, lets us express permeability, in md, as (Reiss, 1980)

$$k = \frac{8.444\times10^5 b^3}{a} \tag{11.38}$$

The porosity can be written as (Reiss, 1980)

$$\phi = \frac{2b}{a} \tag{11.39}$$

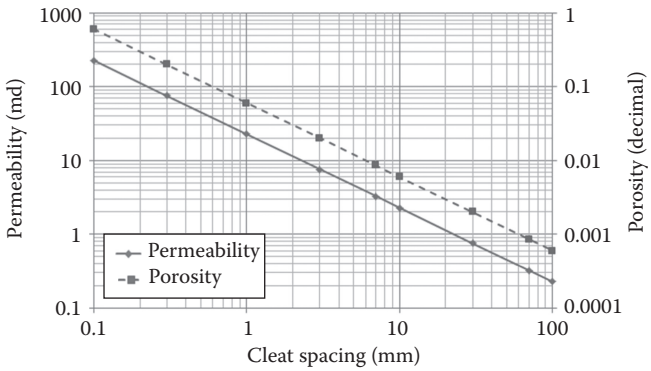


Figure 11.8

Coal permeability and porosity versus cleat spacing.

Assuming a cleat width of 0.050 mm = 50 μm, permeability and porosity are plotted as functions of cleat spacing in Figure 11.8. Cleat spacing on the order of millimeters gives porosities ranging from 0.005 to 0.010 (0.5% to 1%) and permeabilities varying between 2 and 20 md.

11.3 Characterizing Porosity and Permeability

Distributions of porosity and permeability in porous media can be quantified using probability distribution functions (Fanchi, 2000). For example, core plugs are relatively small samples of a geologic formation. Porosity and permeability can be measured in the laboratory using core plugs. Studies of core data have shown that porosity is often normally distributed and permeability is log normally distributed. These distributions are introduced in this section, and some techniques for characterizing porosity and permeability are discussed.

11.3.1 Porosity and Permeability Distributions

The distribution of porosity ϕ can be approximated by the normal, or Gaussian, probability distribution function (pdf) with the form

$$\rho(\phi) = \frac{1}{\sqrt{2\pi}\sigma_\phi} \exp\left[\frac{-(\phi - \phi_{mean})^2}{2\sigma_\phi^2}\right] \tag{11.40}$$

where

$\rho(\phi)$ is the pdf for porosity
ϕ_{mean} is the mean of porosity samples
σ_ϕ is the standard deviation of porosity

The probability P_ϕ that porosity has a value between $\phi - \Delta\phi$ and $\phi + \Delta\phi$ is

$$P_\phi = \int_{\phi-\Delta\phi}^{\phi+\Delta\phi} \rho(\phi')d\phi' \approx \rho(\phi)\Delta\phi \tag{11.41}$$

Figure 11.9 presents a normal probability distribution for a set of cores with average porosity = 0.20 and standard deviation of porosity = 0.05.

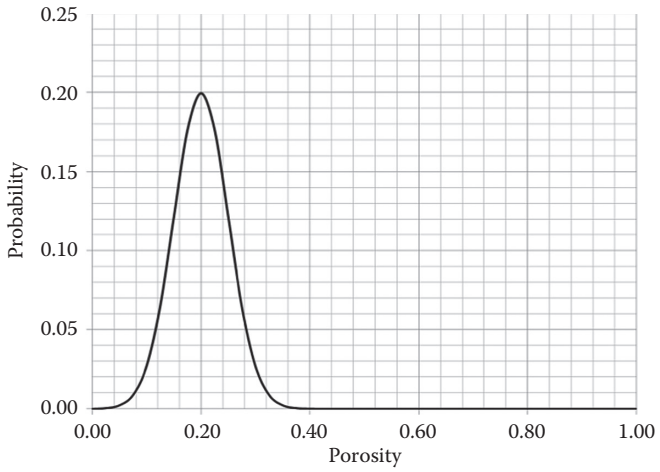


Figure 11.9

Probability distribution for porosity.

The distribution of permeability can be approximated by the normal pdf for the natural logarithm of permeability:

$$\rho(\ln k) = \frac{1}{\sqrt{2\pi}\sigma_k} \exp\left[\frac{-(\ln k - \ln k_G)^2}{2\sigma_k^2}\right] \tag{11.42}$$

where

$\rho(\ln k)$ is the pdf for natural logarithm of permeability
k_G is the geometric mean of permeability samples
σ_k is the standard deviation of permeability

If we have a set of permeability measurements $\{k_1, k_2, \ldots, k_N\}$ for N core samples, the geometric mean k_G of the permeability values is

$$k_G = \left[k_1 k_2 k_3 \ldots k_N\right]^{1/N} \tag{11.43}$$

The standard deviation σ_k is the square root of the variance, which is

$$\sigma_k^2 = \left\langle [(\ln k) - (\ln k_G)]^2 \right\rangle \tag{11.44}$$

where the notation $\langle x \rangle$ denotes the expectation value of variable x.

11.3.2 Permeability Averaging Techniques

Estimates of permeability are needed to make forecasts of fluid flow in porous media. Some practical averaging techniques are presented by Towler (2002), Satter et al. (2008), and Fanchi (2010). For example, the average permeability for flow through a set of parallel beds of differing permeability and thickness (Figure 11.10) can be estimated as a thickness-weighted average

$$k_{ave} = \frac{\sum_{i=1}^{n} k_i h_i}{\sum_{i=1}^{n} h_i} \tag{11.45}$$

where layer i has flow rate q_i, net thickness q_i, and permeability q_i. This is derived from Darcy's law assuming the pressure difference across each layer is the same, and the total flow rate is the sum of the rates in all layers. Equation 11.45 applies to both linear flow and radial flow.

11.3.3 Geostatistics

A fundamental objective of the reservoir characterization process is to distribute rock properties throughout the volume of interest. Geostatistics can be used to characterize a reservoir by determining the statistical distribution of a rock property in space (Hirsche et al., 1997, Kelkar, 2000). Geostatistics, which is also known as spatial statistics, assumes that a spatially distributed property such as porosity is correlated from

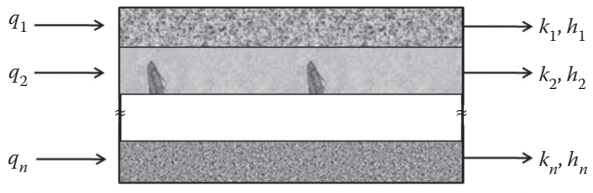


Figure 11.10

Fluid flow through parallel beds.

one point to another in a porous medium. The spatial relationships between data are combined with a geological model to provide a quantitative estimate of a rock property throughout the volume of interest.

The first step in a geostatistical analysis is to gather rock property data. Mathematical algorithms are used to quantify spatial relationships for each rock property. The resulting correlations provide information about the uncertainty associated with the values of rock properties used in different geologic models. Each geologic model is considered a realization, or representation, of the reservoir. A deterministic model of the reservoir is based on a single geologic representation. A stochastic model is a set of realizations obtained from the probability distributions developed during the geostatistical analysis. The first goal of stochastic modeling is to preserve the heterogeneity in a geological system. The second goal is to quantify the uncertainty in the geologic model by generating many possible realizations.

Geostatistics is most successful when data from multiple disciplines are integrated into the reservoir model. The data include thin sections studied under a microscope, laboratory core studies, near-wellbore well log information, and field-scale well test and seismic data. Incorrect reservoir models can occur when basic geostatistical assumptions are violated. For example, geostatistics assumes that rock properties are spatially continuous throughout the region of interest. Inaccuracies can occur if the continuity assumption is invalid by the appearance of a discontinuous change in rock property. Limited well control, biased sampling of well information, and geologic features such as a fault or formation pinch out can disrupt the continuity assumption. Errors may appear in associated maps when the geostatistical assumptions are violated.

11.4 Directional Permeability

Permeability can be a complex function of spatial location and orientation in a gravitational field. The effect of gravity, heterogeneity, and anisotropy on the fluid flow in porous media requires that the simple horizontal, linear form of Darcy's law must be generalized to include gravity and additional spatial dimensions.

11.4.1 Darcy's Law in a Gravitational Field

Fluid flow often occurs in dipping beds and vertical columns of porous media. We modify the 1D form of Darcy's law to include the effect of gravity by writing Darcy's law for single-phase flow in the form

$$q = -\frac{0.001127kA}{\mu}\frac{d\Phi}{dz} \tag{11.46}$$

Pressure is replaced by the potential of phase ℓ

$$\Phi_\ell = p_\ell - \gamma_\ell(\Delta z) \tag{11.47}$$

where

p_ℓ is the pressure of phase ℓ
γ_ℓ is the pressure gradient associated with the gravity term
Δz is the depth relative to a specified datum

The pressure gradient is aligned along the vertical z-axis. Fluid does not flow in the vertical direction when $d\Phi/dz = 0$. Therefore, Equation 11.46 represents the static equilibrium of a fluid column in the presence of a gravitational field and can quantify the movement of fluid when $d\Phi/dz \neq 0$.

The permeability for flow in the direction aligned with the direction of the gravitational field is called vertical permeability. If the fluid flow is in the horizontal plane, permeability is called horizontal permeability. Vertical permeability is usually less than horizontal permeability.

11.4.2 Extension of Darcy's Law to Three Dimensions

Darcy's law in one dimension is extended to three dimensions by writing Darcy's law for single-phase flow as

$$\begin{bmatrix} q_x \\ q_y \\ q_z \end{bmatrix} = -0.001127\frac{A}{\mu}\begin{bmatrix} k_{xx} & k_{xy} & k_{xz} \\ k_{yx} & k_{yy} & k_{yz} \\ k_{zx} & k_{zy} & k_{zz} \end{bmatrix}\begin{bmatrix} \partial\Phi_\ell/\partial x \\ \partial\Phi_\ell/\partial y \\ \partial\Phi_\ell/\partial z \end{bmatrix} \tag{11.48}$$

where the variables are volumetric flow rate q (rb/day), cross-sectional area A (ft^2), fluid viscosity μ (cp), permeability k (md), potential Φ_ℓ of phase ℓ (psi), and Cartesian coordinates x, y, z (ft). Permeability is now treated as a 3 × 3 matrix with nine elements (Fanchi, 2006a). The diagonal permeability elements $\{k_{xx}, k_{yy}, k_{zz}\}$ represent the usual dependence of rate in one direction on pressure differences in the same direction. The off-diagonal permeability elements $\{k_{xy}, k_{xz}, k_{yx}, k_{yz}, k_{zx}, k_{zy}\}$ account for the dependence of rate in one direction on pressure differences in orthogonal directions. The magnitude of the volumetric flow rate is the square root of the sum of the squares of the components q_x, q_y, q_z.

In many cases, it is possible to find a coordinate system $\{x', y', z'\}$ that diagonalizes the permeability tensor. In the diagonal form, the off-diagonal permeability elements $\{k'_{xy}, k'_{xz}, k'_{yx}, k'_{yz}, k'_{zx}, k'_{zy}\}$ are zero and the diagonal permeability elements $\{k'_{xx}, k'_{yy}, k'_{zz}\}$ are nonzero. The diagonal form of the permeability tensor is obtained by a principal axis transformation, and the coordinate axes $\{x', y', z'\}$ are called the principal axes. The flow equations along the principal axes are

$$\begin{aligned} q_{x'} &= -0.001127 \frac{A}{\mu}\left[k_{x'x'}\frac{\partial \Phi}{\partial x'}\right] \\ q_{y'} &= -0.001127 \frac{A}{\mu}\left[k_{y'y'}\frac{\partial \Phi}{\partial y'}\right] \\ q_{z'} &= -0.001127 \frac{A}{\mu}\left[k_{z'z'}\frac{\partial \Phi}{\partial z'}\right] \end{aligned} \tag{11.49}$$

The principal axes in a porous medium can vary from one point to another because of permeability heterogeneity. If the elements of the diagonalized permeability tensor are equal, then

$$k_{x'x'} = k_{y'y'} = k_{z'z'} = k \tag{11.50}$$

and permeability is considered isotropic. If this equation is not true for a particular medium, then flow depends on direction and the medium is anisotropic.

11.4.3 Coal Directional Permeability

Coal deposits should intuitively exhibit directional permeabilities since coal face and butt cleats are visually distinct. Although lab and field studies indicate face and butt cleat permeability contrasts between 2:1 and 17:1, no commercial coal gas development has taken this into account, choosing to space wells based on structure, topography, or culture. Vertical permeabilities of coals are rarely reported but appear to be ten to one hundred times less than horizontal permeabilities. This strong permeability contrast dictates a dominant horizontal flow of gas and water in coal deposits, with minimal vertical flow, primarily through the largest, or "master" cleats, which may extend from floor to roof in thin seams.

11.5 Rock–Fluid Interaction

Multiphase fluid flow in porous media depends on the interaction of the solid material with fluids in the pore space. The focus of this section is on the representation of rock–fluid interactions using physical parameters such as relative permeability and capillary pressure.

11.5.1 Surface Tension and Interfacial Tension

The pressure difference across the interface between two immiscible fluids results in a normal force. The unbalanced force leads to a tension at the interface that is balanced by a force due to the pressure difference when the surface of the interface is curved. The tension between liquids at a liquid–liquid interface is called interfacial tension (IFT), and the tension at a gas–liquid interface is called surface tension. Surface tension may be considered a force per unit length in a surface (dyn/cm, or equivalently, mN/m) or a free energy per unit surface area (erg/cm^2, or equivalently, mJ/m^2).

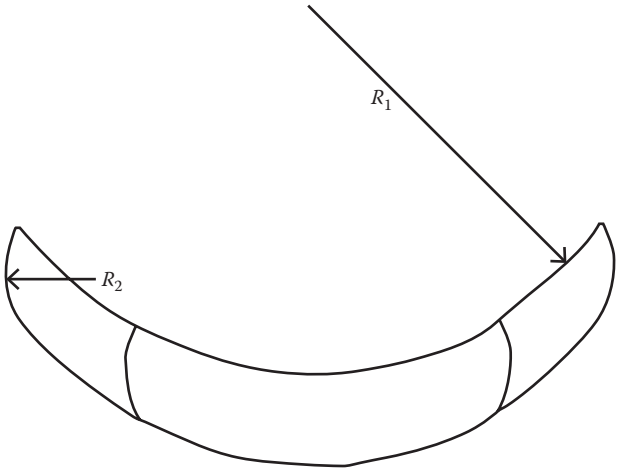


Figure 11.11

Geometry of a curved surface.

In general, two radii of curvature R_1 and R_2 are needed to describe a curved surface (Figure 11.11). The Young–Laplace equation gives the pressure difference Δp across the curved fluid surface or interface:

$$\Delta p = \sigma\left(\frac{1}{R_1} + \frac{1}{R_2}\right) \tag{11.51}$$

where σ is the surface tension. This becomes

$$\Delta p = \frac{2\sigma}{R} \tag{11.52}$$

for a surface where $R_1 = R_2$, such as a sphere. The two radii R_1 and R_2 are infinite for a plane surface, so the pressure difference across a plane surface is zero.

Typical IFT values at an oil–brine interface range from 15 to 40 dyn/cm. Surface tension at a gas–oil interface can vary from 35 to 65 dyn/cm. The surface tension at an air–brine interface can vary from 70 to 100 dyn/cm and tends to be larger than surface tension at a gas–oil interface.

Surface tension and IFT depend on the composition of the two fluids at the interface. The Weinaug–Katz variation of the Macleod–Sugden correlation can be used to estimate surface tension between a liquid and a vapor. The Macleod–Sugden correlation is (Fanchi, 2010)

$$\sigma^{1/4} = \sum_{i=1}^{N_c} P_{chi}\left(x_i\frac{\rho_L}{M_L} - y_i\frac{\rho_V}{M_V}\right) \tag{11.53}$$

where the variables are surface tension σ (dyn/cm), parachor P_{chi} of component i [(dyn/cm)$^{1/4}$/(g/cm^3)], molecular weight of liquid phase M_L, molecular weight of vapor phase M_V, liquid-phase density ρ_L (g/cm^3), vapor-phase density ρ_V (g/cm^3), mole fraction x_i of component i in liquid phase, and mole fraction y_i of component i in vapor phase. The parachor of component i with molecular weight M_i can be estimated using the regression equation (Katz et al., 1943)

$$P_{chi} = 27.0 + 2.75M_i \tag{11.54}$$

for molecular weights up to 100, and the regression equation (Fanchi, 1990)

$$P_{chi} = 10.0 + 2.92M_i \tag{11.55}$$

for molecular weights ranging from 100 to 500.

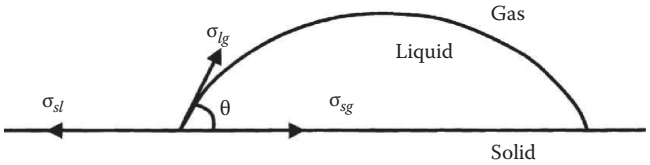


Figure 11.12

Measurement of contact angle.

11.5.2 Wettability

Immiscible fluids compete for space in pores. The configuration of fluids in the pore space is determined by wettability, which is the ability of a fluid phase to be in contact with a solid surface when in the presence of a second immiscible phase. The relative wettability of two fluids in a porous medium is characterized by the contact angle θ and the surface tension (or IFT).

Contact angle θ is defined as the angle between the tangent to the liquid–solid boundary constructed at a point on the three-phase line of contact and the tangent to the gas–liquid boundary constructed at the same point. Figure 11.12 shows a liquid droplet on a solid surface in a gas. The force balance at the point on the three-phase line of contact along the liquid–solid boundary is expressed by Young's equation:

$$\sigma_{sg} - \sigma_{sl} = \sigma_{lg} \cos\theta \tag{11.56}$$

where

σ_{lg} and σ_{sg} are the surface tensions of liquid l and solid s, respectively
σ_{sl} is the IFT between the liquid and the solid

Contact angles are measured on the surface of the denser phase.

The contact angle of a gas–liquid–solid or a liquid–liquid–solid system may have a value between 0° and 180°. It is customary to classify fluids into two categories: wetting fluid and nonwetting fluid. For wetting fluids, $0° \leq \theta \leq 90°$, and for nonwetting fluids, $90° \leq \theta \leq 180°$. Figure 11.13 shows two typical menisci that separate water and gas (or oil) in thin capillaries or pores. The contact angle measured through the water phase in Figure 11.13a is less than 90°, hence the water is the wetting phase and the gas (or oil) is the nonwetting phase. By contrast, the contact angle $\theta > 90°$ in Figure 11.13b, so the water is the nonwetting phase and the gas (or oil) is the wetting phase. The pore surface in Figure 11.13a is a water-wet surface, and the pore surface in Figure 11.13b is as an oil-wet surface.

11.5.3 Capillary Pressure and Capillary Radius

Immiscible fluids in porous media are separated by a curved interface. A pressure difference called capillary pressure p_c exists across the interface. Capillary pressure is the difference in pressure between the wetting and nonwetting phases:

$$p_c = p_{nw} - p_w \tag{11.57}$$

where w and nw represent wetting phase and nonwetting phase, respectively. Capillary pressure is always positive. The pressure difference across the interface is given by Equation 11.51.

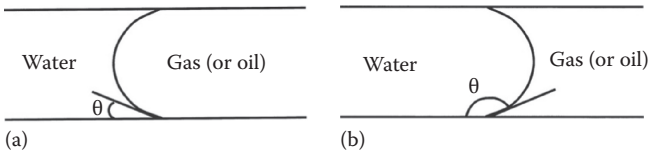


Figure 11.13

Contact angle and wettability. (a) Water wet. (b) Oil wet.

Capillary pressure tends to compress the nonwetting phase relative to the wetting phase. Therefore, pressure in the phase on the concave (curving inward) side of the surface is greater than the pressure in the phase on the convex (curving outward) side. For example, consider the fluid pair consisting of water and gas in Figure 11.13. If water is the wetting phase, the water surface must be concave in shape as shown in Figure 11.13a. By contrast, if water is the nonwetting phase as shown in Figure 11.13b, the water surface is convex in shape and the pressure is higher in the water phase than in the gas phase.

Equation 11.57 is a general form for calculating the pressure difference (or capillary pressure) at any point of a curved interface. The mean radius of curvature r_m of the curved interface with radii of curvature R_1 and R_2 is

$$\frac{1}{r_m} = \frac{1}{2}\left(\frac{1}{R_1} + \frac{1}{R_2}\right) \tag{11.58}$$

The Young–Laplace equation for pressure difference Δp across the curved fluid surface becomes

$$\Delta p = p_c = \sigma\left(\frac{1}{R_1} + \frac{1}{R_2}\right) = \frac{2\sigma}{r_m} \tag{11.59}$$

where σ is the surface tension. If the contact angle of a liquid on the capillary walls is zero, the shape of the interface between two fluids in a cylindrical capillary tube with very small radius is approximately circular. The resulting mean radius of curvature is approximately equal to the radius of the capillary r, and Equation 11.59 simplifies to

$$p_c = \frac{2\sigma}{r} \tag{11.60}$$

In general, the liquid–gas surface or liquid–liquid interface meets the cylindrical capillary wall through contact angle θ, as illustrated in Figure 11.14. If the shape of the interface in a cylindrical capillary tube with radius r is approximately spherical with radius of curvature R, the following geometric relation holds

$$R = \frac{r}{|\cos\theta|} \tag{11.61}$$

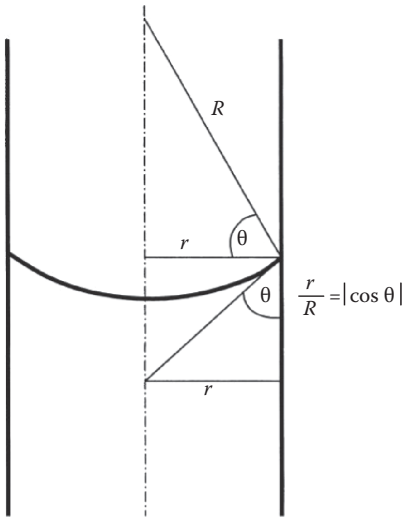


Figure 11.14

Interface between two immiscible fluids in a cylindrical capillary.

and Equation 11.60 becomes

$$p_c = \frac{2\sigma}{r}|\cos\theta| \tag{11.62}$$

This contains the three most important factors in determining the magnitude of the capillary pressure in a porous medium: surface tension σ (or IFT), capillary size *r*, and contact angle θ.

11.5.4 Coal Capillary Pressure

Capillary pressures in coal cleats and matrix differ by one or two orders of magnitude due to the different length scales. Coal cleats are planar with widths ranging from 1 to 100 μm. Coal matrix pores are primarily micropores (diameters less than 2 nm), with some mesopores (diameters between 2 and 50 nm), and a few macropores (diameters greater than 50 nm). Assuming coal cleats are planar and one radius in Equation 11.59 is essentially infinite, cleat capillary pressure can be expressed as

$$p_c = \frac{\sigma}{r}|\cos\theta| \tag{11.63}$$

As the radius is half the cleat width *b*, this expression becomes

$$p_c = \frac{2\sigma}{b}|\cos\theta| \tag{11.64}$$

For bounding calculations, assume water–gas surface tension varies between 70 and 100 dyn/cm and cleat width ranges from 1 to 100 μm. The water–gas interface has a contact angle of zero, making the cosine equal to one. Accounting for dimensions, bounding calculations indicate coal cleat capillary pressures between 0.2 and 29 psi.

Coal matrix pores are formed from organic material but will be considered as spherical pores for bounding calculations. Assuming surface tensions from 70 to 100 dyn/cm, a contact angle of zero, and pore diameters of 2 and 50 nm (radii of 1 and 25 nm), Equation 11.62 gives capillary pressures between 800 and 29,000 psi.

As cleat capillary pressures are on the order of those encountered during coal gas recovery, drainage of the cleats, especially the larger cleats, may be expected. By contrast, coal matrix capillary pressures are so high as to preclude drainage by pressures typically encountered during depletion.

11.5.5 Capillary Pressure and Height of the Interface

The balance of forces between fluid phases in a capillary tube requires that *force up = force down* at the interface between the wetting phase and the nonwetting phase. The upward force is given by

$$\text{Force up} = \sigma|\cos\theta| \times 2\pi r \tag{11.65}$$

where

r is the radius of the capillary tube
θ is the contact angle
σ is the surface tension (or IFT)

Figure 11.15 illustrates the height of the interface between the wetting phase water and the nonwetting phase air in a capillary tube. The downward force due to gravity depends on the difference in density between the wetting fluid with density ρ_w and the nonwetting fluid with density ρ_{nw} in the capillary tube and the height *h* of the interface between the two fluids:

$$\text{Force down} = (\rho_w g - \rho_{nw} g)\pi r^2 h \tag{11.66}$$

where

g is the acceleration of gravity
h is the height of the fluid interface in the capillary tube
πr^2 is the cross-sectional area of the capillary tube

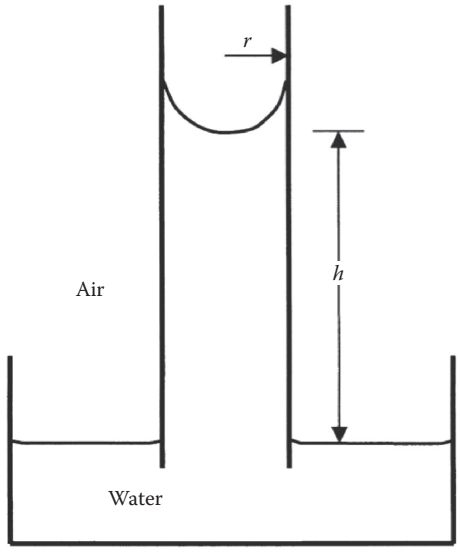


Figure 11.15

Height of the interface in a capillary tube.

The relationship between capillary pressure and height of the interface between the wetting phase and the nonwetting phase can be determined by applying the balance of forces. Capillary pressure P_c can be expressed in terms of force down per unit area as

$$P_c = \frac{\text{force down}}{\pi r^2} = (\rho_w g - \rho_{nw} g)h \tag{11.67}$$

and in terms of force up per unit area as

$$P_c = \frac{\text{force up}}{\pi r^2} = \frac{2\sigma}{r}|\cos\theta| \tag{11.68}$$

Solving Equation 11.67 for h yields the following relationship between capillary pressure P_c and height h of the interface between immiscible wetting and nonwetting phases:

$$h = \frac{P_c}{(\rho_w g - \rho_{nw} g)} \tag{11.69}$$

Equating Equations 11.67 and 11.68 gives a relationship between surface tension (or IFT) and difference in densities between the wetting and nonwetting phases:

$$\sigma = \frac{(\rho_w - \rho_{nw}) rhg}{2|\cos\theta|} \tag{11.70}$$

Equation 11.62 shows that a decrease in capillary radius increases capillary pressure, and Equation 11.69 shows that the increase in capillary pressure increases the height of the interface for a given difference in phase densities. Figure 11.16 illustrates this relationship between capillary radius and interface height.

Using the bounding capillary pressures calculated earlier for coal cleats and matrix gives interface heights in the cleats between 0.5 and 67 ft while interface heights in the matrix 1,800–67,000 ft. Considering that coal seams targeted for coal gas exploitation typically range from a few feet to tens of feet with maybe a few exceptions of 100 ft, seam thickness is often on the order of the cleat interface height. Thus, the thinnest cleats in a seam would be expected to be completely water filled, whereas the widest cleats would have gas–water interfaces present.

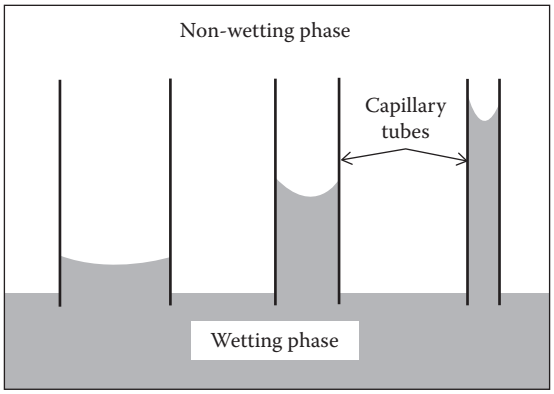


Figure 11.16

Capillary tubes and capillary pressure.

11.5.6 Capillary Pressure Measurement

Laboratory measurements of capillary pressure in reservoir rock can be made using mercury methods, porous-plate methods, and centrifuge methods (Christiansen, 2006). The experiments provide a relationship between capillary pressure P_c and wetting phase saturation S_w. For an oil–water system or an oil–gas system, water is usually the wetting phase.

Figure 11.17 shows several typical features of a capillary pressure P_c versus wetting phase saturation S_w curve:

- The drainage P_c curve starts at $S_w = 100\%$.
- Wetting phase saturation S_w decreases as the nonwetting phase is forced into a porous medium. The threshold or entry pressure is the pressure required to force the first drop of nonwetting phase fluid into the porous medium.
- As pressure increases above entry pressure, more of the nonwetting phase enters the porous medium. Eventually, no further reduction in S_w occurs. The minimum S_w is the irreducible wetting phase saturation, S_{wirr}.
- Capillary pressure increases as the wetting phase saturation decreases during drainage.
- Capillary pressure decreases as the wetting phase saturation increases during imbibition.

The difference in paths between the drainage and imbibition curves is called hysteresis.

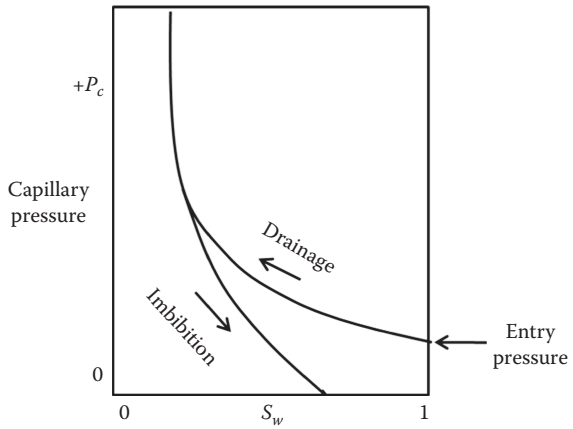


Figure 11.17

Capillary pressure and hysteresis.

Capillary pressure measurements at laboratory conditions should be converted from laboratory conditions to subsurface conditions for fluid flow in geologic formations. The customary correction is

$$P_{c(res)} = P_{c(lab)} \frac{\left(\sigma|\cos\theta|\right)_{res}}{\left(\sigma|\cos\theta|\right)_{lab}} \tag{11.71}$$

where

σ is the surface tension (or IFT)

θ is the contact angle (Amyx et al., 1960, Christiansen, 2006)

Subscripts *lab* and *res* refer to laboratory conditions and reservoir conditions, respectively.

11.6 Relative Permeability

Permeability is a measure of the connectedness of pores in a porous medium. It is necessary to modify permeability when more than one phase is present in the pore space to account for the relative movement of two or more phases in the pore space. Multiphase flow in porous media is simultaneous flow of two or more immiscible fluids, or fluids of limited miscibility, for example, oil and water or air and water. The distribution of the two immiscible fluids flowing simultaneously through a porous sample depends on a number of factors, including saturation, wettability conditions of the pore surface, IFT, fluid viscosities, and pore velocity. Changes in these factors alter the effective permeability of the fluids in the pore space. Relative permeability curves are used to characterize the permeability of a phase as saturation changes during multiphase flow.

11.6.1 Effective Permeability and Relative Permeability

Permeability to single-phase fluid flow through a porous medium depends on the phase and type of fluid flowing through the porous medium. For example, the permeability of air flowing through a core is not the same as water flowing through the same core. We define the permeability of single-phase flow as the effective permeability to that phase. In the case of oil, water, and gas, we have effective permeability to oil k_o, effective permeability to water k_w, and effective permeability to gas k_g.

Two immiscible fluids, such as oil and water or oil and gas, can flow cocurrently through a porous medium. Steady cocurrent flow can be established by injecting both fluids into the porous medium at constant rates and allowing time for the discharge rates to equal the injection rates. Permeability is also affected by the flow of one phase through a porous medium with a residual, immobile second phase. The effect of cocurrent flow of two phases or single-phase flow in the presence of a different phase on the effective permeability is quantified using relative permeability (Ahmed, 2000, Christiansen, 2006, Satter et al., 2008).

Relative permeability is the ratio of effective permeability k_{eff} to reference permeability k_{ref}:

$$k_r = \frac{k_{eff}}{k_{ref}} \tag{11.72}$$

The permeability to air at 100% air saturation is often used as the reference permeability. If we designate the reference permeability as $k = k_{ref}$, the relative permeability of phase ℓ is

$$k_{r\ell} = \frac{k_{\ell eff}}{k} \tag{11.73}$$

where $k_{\ell eff}$ is the effective permeability to flow of phase ℓ.

Relative permeability curves represent the ability of a porous medium to conduct one fluid when other fluid phases are present. The curves are usually plotted as a function of wetting phase saturation as shown in Figure 11.18. The curve labels in the figure depict relative permeability curves for the following conditions: NW-I is the relative permeability of the nonwetting phase during imbibition, NW-D is the relative permeability of the nonwetting phase during drainage, W-I is the relative permeability of the wetting phase during imbibition, and W-D is the relative permeability of the wetting phase during drainage. The arrows in the figure show the direction of wetting phase saturation. Drainage occurs when wetting phase saturation

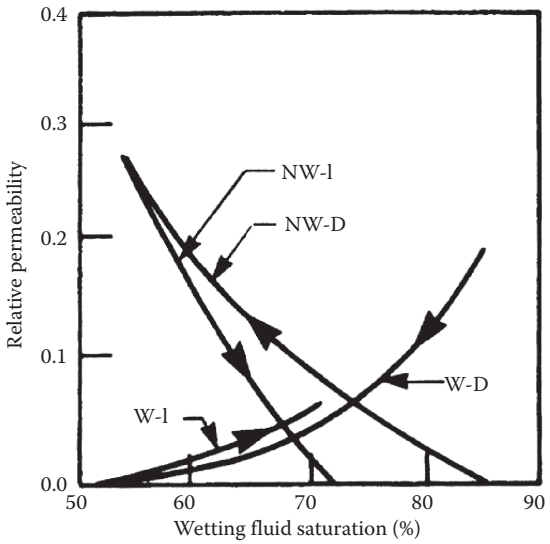


Figure 11.18

Typical relative permeability curves.

decreases, and imbibition occurs when wetting phase saturation increases. The dependence on the history of wetting phase saturation changes is called relative permeability hysteresis.

Relative permeability curves for a porous medium containing two fluid phases are referred to as two-phase relative permeability curves. Relative permeability curves for a porous medium containing three fluid phases are referred to as three-phase relative permeability curves.

The presence of two or more mobile fluid phases reduces the effective permeability, as shown in Figure 11.18. Plots of relative permeability curves for a wetting phase and a nonwetting phase show that the relative permeability of the nonwetting phase (k_{rnw}) goes to 0 before the nonwetting phase saturation S_{nw} reaches 0. This shows that one fluid phase cannot be completely displaced from a porous medium by injecting another phase. The saturation where relative permeability k_r goes to 0 is the end point saturation of the relative permeability curve. The end point saturation for water in an oil–water system is called the irreducible water saturation, S_{wirr} or the connate water saturation S_{wc}. The end point saturation is called residual oil saturation, S_{or} for oil in an oil–water system.

Similar two-phase relative permeability curves can be measured for gas–liquid systems. Gas is the nonwetting phase during two-phase flow of gas and liquid. Critical gas saturation, S_{gc}, is the gas saturation at which gas first begins to flow in a porous medium. Residual or trapped gas saturation (S_{gr} or S_{gt}) is the maximum value of S_g where the relative permeability to gas $k_{rg} = 0$.

11.6.2 Coal Relative Permeability

Gas–water relative permeabilities in coal, as in conventional gas reservoirs, are difficult to predict and are therefore measured experimentally. In addition to the experimental difficulties encountered in measuring relative permeabilities in conventional reservoirs, these measurements in coal are complicated by coal fines shed from the friable, brittle coals, the small cleat porosities, and severe stress and hysteresis effects. Sound and timely collection, preservation, and preparation protocols are critical to obtaining coal samples suitable for gas–water relative permeability measurements.

Coals can hold water chemically bound in the matrix, sorbed to the surface of the coal, and in the cleats. Bound and sorbed water are immobile during depletion of a coal deposit while water drains from the cleats. For engineering purposes, the volume occupied by this cleat water is often characterized as "mobile water" porosity that is defined experimentally as the volume of water that can be displaced by a gas divided by the bulk sample volume. Gas–water relative permeabilities in coals are typically measured across mobile water porosity with a water saturation of one corresponding to fully water filled cleats and a water saturation of zero being associated with fully dewatered cleats. Note that at a mobile water saturation of zero, some immobile water still resides in the smaller coal cleats and matrix. This arbitrarily defined zero water saturation is technically the irreducible water saturation of the coal.

The simplest of the four principal methods of determining gas–water relative permeabilities in coal is to assume they are straight lines that cross, a classic assumption in naturally fractured reservoirs. Second is the laboratory measurement of gas–water relative permeabilities. As seen in Figures 11.19 through 11.21, coal gas water permeabilities vary by coal rank and geologic age (Gash, 1991, Conway et al., 1995, Meaney and Paterson, 1996). Attempts to fit classic Corey curves or other similar equations to gas–water relative data measured on coals have met with limited success. Third, gas–water permeabilities can be calculated from water production data from a well with sufficiently long history. After extrapolating the water rate decline to determine the water estimated ultimate recovery (EUR), division of cumulative water production at any given time by the water EUR yields water saturation. Absolute permeability is estimated from initial water production data, when little, if any gas is present and the water saturation is essentially unity. Effective gas and water perms are calculated from available stabilized gas and water rates and bottomhole or wellhead pressures. Division of effective gas and water permeabilities by the absolute permeability yields the respective gas and water relative permeabilities. Fourth, because of the difficulties encountered in measuring gas–water relative permeabilities in coals and the inaccuracies in estimating them from well performance, many workers choose to regard gas–water relative permeabilities in coal as history match parameters in simulation studies.

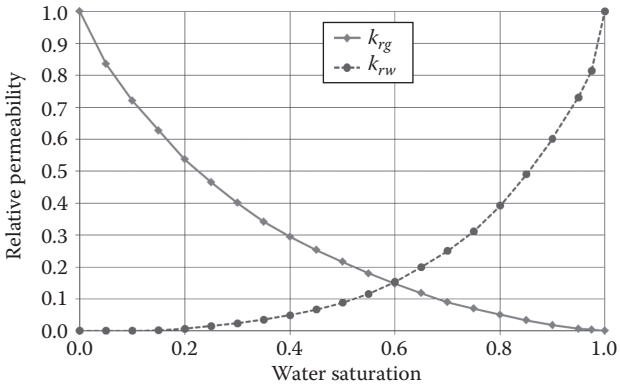


Figure 11.19

San Juan Fruitland gas–water relative permeabilities. (From Gash, B.W., Measurement of "Rock Properties" in coal for coalbed methane production, presented at the *Annual Technical Conference and Exhibition*, SPE 22909, Dallas, TX, October 6–9, 1991.)

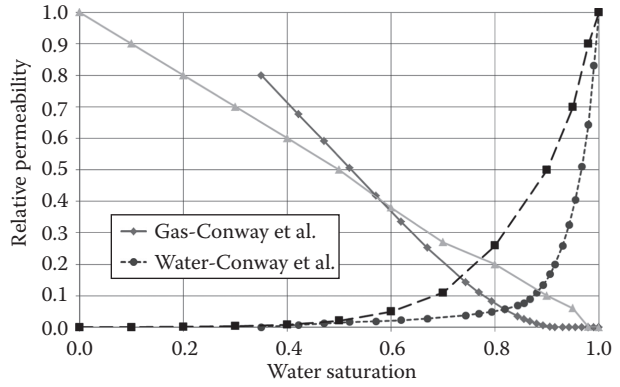


Figure 11.20

Warrior Basin Mary Lee/Blue Creek coal—gas–water relative permeabilities. (From Gash, B.W., Measurement of "Rock Properties" in coal for coalbed methane production, presented at the *Annual Technical Conference and Exhibition*, SPE 22909, Dallas, TX, October 6–9, 1991; Conway, M.W. et al., Multi-phase flow properties for coalbed methane wells: A laboratory and field study, presented at the *Joint Rocky Mountain Regional Meeting and Low-Permeability Reservoirs Symposium*, SPE 29576, Denver, CO, March 20–22, 1995.)

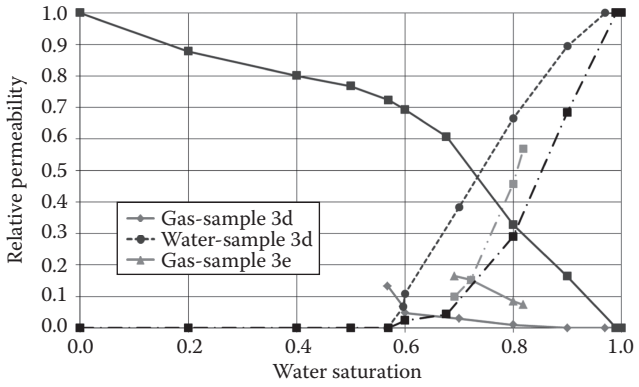


Figure 11.21

Bowen Basin, Australia, German Creek seam—gas–water relative permeabilities. (From Meaney, K. and Paterson, L., *Asia Pacific O&G Conference*, SPE 36986, Adelaide, South Australia, Australia, October 28–31, 1996.)

11.6.3 Darcy's Law for Multiphase Flow

Darcy's law for single-phase flow is given by Equation 11.48 and expresses the flow rate at reservoir conditions. An equation for calculating the flow rate of phase ℓ in the presence of other phases is obtained by replacing permeability in Equation 11.48 with effective permeability of phase ℓ. Darcy's law for flow of phase ℓ in three dimensions at surface conditions must include the formation volume factor B_ℓ of phase ℓ and relative permeability $k_{r\ell}$ of phase ℓ, thus

$$\begin{bmatrix} q_{\ell x} \\ q_{\ell y} \\ q_{\ell z} \end{bmatrix} = -0.001127 \frac{k_{r\ell}}{\mu_\ell B_\ell} A \begin{bmatrix} k_{xx} & k_{xy} & k_{xz} \\ k_{yx} & k_{yy} & k_{yz} \\ k_{zx} & k_{zy} & k_{zz} \end{bmatrix} \begin{bmatrix} \partial\Phi_\ell/\partial x \\ \partial\Phi_\ell/\partial y \\ \partial\Phi_\ell/\partial z \end{bmatrix} \tag{11.74}$$

where the variables are volumetric flow rate q_ℓ of phase ℓ (stb/day) at surface conditions, relative permeability $k_{r\ell}$, cross-sectional area A (ft²), fluid viscosity μ_ℓ of phase ℓ (cp), formation volume factor B_ℓ of phase ℓ (rb/stb), permeability k (md), potential Φ_ℓ of phase ℓ (psi), and Cartesian coordinates x,y,z (ft). Capillary pressure effects are included in the phase potential Φ_ℓ. Darcy's law for the flow of phase ℓ at surface conditions using the diagonal form of the permeability tensor in three dimensions is

$$\begin{aligned} q_{\ell x'} &= -0.001127 \frac{k_{r\ell}}{\mu_\ell B_\ell} A \left[k_{x'x'} \frac{\partial\Phi_\ell}{\partial x'} \right] \\ q_{\ell y'} &= -0.001127 \frac{k_{r\ell}}{\mu_\ell B_\ell} A \left[k_{y'y'} \frac{\partial\Phi_\ell}{\partial y'} \right] \\ q_{\ell z'} &= -0.001127 \frac{k_{r\ell}}{\mu_\ell B_\ell} A \left[k_{z'z'} \frac{\partial\Phi_\ell}{\partial z'} \right] \end{aligned} \tag{11.75}$$

where $\{x', y', z'\}$ are coordinate axes obtained by a principal axis transformation of the permeability tensor.

11.6.4 Mobility and Relative Mobility

The mobility of phase ℓ in multiphase flow is defined as the ratio of the effective permeability of phase ℓ to the viscosity of phase ℓ:

$$\lambda_\ell = \frac{k_\ell}{\mu_\ell} \tag{11.76}$$

where phase permeability is the product of relative permeability and reference permeability. In an oil–water–gas system, gas has a much smaller viscosity than oil or gas and will have a larger mobility. Oil and water often have comparable viscosities, so the ratio of their mobilities depends on the ratio of their relative permeabilities.

Fluid-phase mobilities for oil, water, and gas phases in an oil–water–gas system are

$$\lambda_o = \frac{k_o}{\mu_o}, \quad \lambda_w = \frac{k_w}{\mu_w}, \quad \lambda_g = \frac{k_g}{\mu_g} \tag{11.77}$$

Total mobility for an oil–water–gas system is the sum of individual phase mobilities:

$$\lambda_T = \lambda_o + \lambda_w + \lambda_g \tag{11.78}$$

It is often useful to determine a minimum in total mobility relative to phase saturation by plotting total mobility versus phase saturation.

The relative mobility $\lambda_{r\ell}$ of phase ℓ is the ratio of relative permeability of phase ℓ to the phase viscosity of phase ℓ:

$$\lambda_{r\ell} = \frac{k_{r\ell}}{\mu_\ell} \tag{11.79}$$

Darcy's law for the flow of phase ℓ in three dimensions at surface conditions given by Equation 11.74 can be expressed in terms of relative mobility as

$$\begin{bmatrix} q_{\ell x} \\ q_{\ell y} \\ q_{\ell z} \end{bmatrix} = -0.001127 \frac{\lambda_r}{B_\ell} A \begin{bmatrix} k_{xx} & k_{xy} & k_{xz} \\ k_{yx} & k_{yy} & k_{yz} \\ k_{zx} & k_{zy} & k_{zz} \end{bmatrix} \begin{bmatrix} \partial\Phi_\ell/\partial x \\ \partial\Phi_\ell/\partial y \\ \partial\Phi_\ell/\partial z \end{bmatrix} \tag{11.80}$$

Darcy's law for the flow of phase ℓ at surface conditions along the x-axis is

$$q_{\ell x} = -0.001127 \frac{\lambda_r k_{xx}}{B_\ell} A \frac{\partial p_\ell}{\partial x} \tag{11.81}$$

where p_ℓ is the pressure of phase ℓ.

11.6.5 Effect of Wettability

The effect of wettability on typical water–oil relative permeability curves is presented in Figures 11.22 and 11.23 for water-wet and oil-wet reservoir formation samples, respectively (Craig, 1971). The most noticeable difference in relative permeability characteristics shown in Figures 11.22 and 11.23 is the water saturation at which water and oil relative permeabilities are equal: the relative permeability curves intersect at water saturations greater than 50% for water-wet rock and less than 50% for oil-wet rock. For rocks with neutral wettability, the relative permeabilities are different from the values measured in systems of strongly water wet or strongly oil wet.

11.6.6 Effect of Interfacial Tension

Four possible occupancy patterns of two fluids in cocurrent steady flow are depicted in Figure 11.24. In Figure 11.24a, both fluids flow in separate channels. Fluid 1 wets the solid surface preferentially and tends to occupy the finer pores in the network. There are thick films of the wetting fluid (not shown in the figure) in the pores, where the nonwetting phase (fluid 2) occupies the central part. The contribution by the thick films to the flow of the wetting fluid is negligible. In Figure 11.24b, both fluids flow in the same pores; the wetting fluid is in the form of thick films (the thickness exaggerated in the figure).

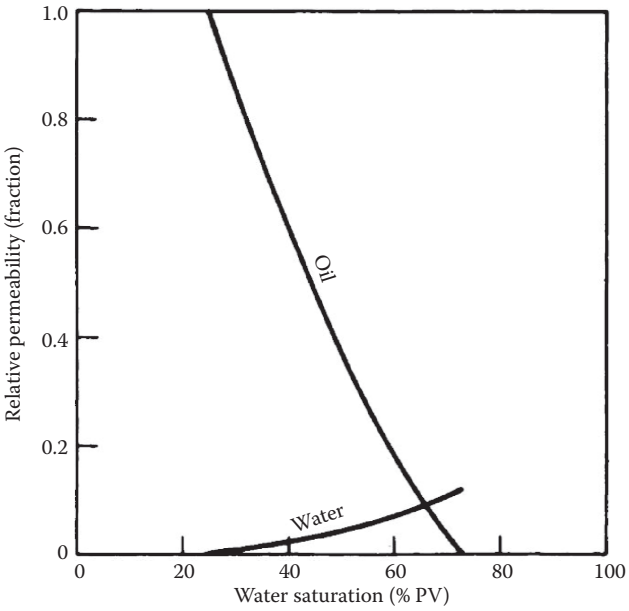


Figure 11.22

Typical water-wet relative permeability curves.

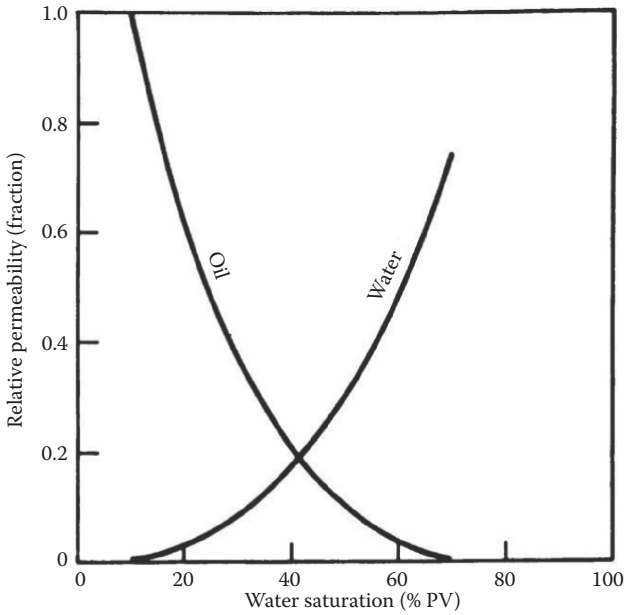


Figure 11.23

Typical oil-wet relative permeability curves.

Such conditions exist at low wetting fluid saturations, where the wetting fluid is no longer continuous in the central parts of the pores.

Figure 11.24c shows the flow pattern in a sample with neutral wettability. There are no thick films of either fluid, and either fluid may fill small as well as large pores. It is conceivable that the two fluids may flow side by side in some pores, as shown in Figure 11.24c. Finally, in Figure 11.24d both fluids flow in the same channel, but one fluid is continuous and the other dispersed. This is the case at low values of the IFT when oil and water form emulsions and it may happen at both low nonwetting phase saturation and high IFTs.

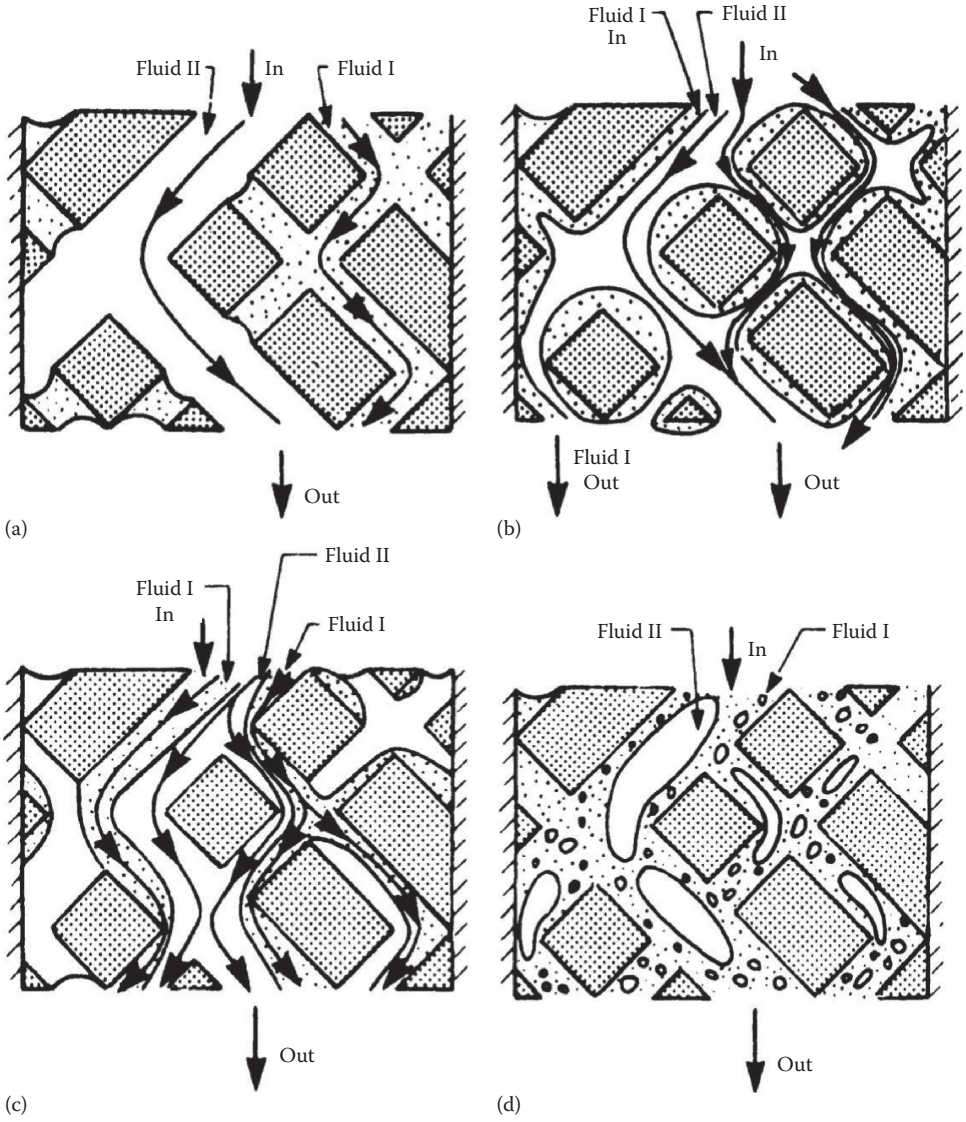


Figure 11.24

Effect of IFT on relative permeability. (a) Fluids flow in separate channels. (b) Fluids flow in same pore space with Fluid I wetting the surface. (c) Fluids flow in same pore space with neutral wettability. (d) Both fluids flow in the same channel with fluid I continuous and fluid II dispersed. (From Dullien, F.A.L., *Chem. Eng. Technol.*, 11, 407, 1988.)

IFTs approximately greater than 1 mN/m usually have a negligible effect on conventional relative permeabilities. For very low IFT systems, however, the networks of the two fluids begin to break up, first in the relatively large pores and then at even lower IFTs and also in the finer pores. Ultimately, an emulsion is formed in the entire pore network (Figure 11.24d) and, at that point, each fluid flows everywhere in proportion to its saturation in the sample. The relative permeability curves become straight diagonal lines for emulsion flows (Figure 11.25).

11.6.7 Effect of Viscosity Ratio

The effect of the viscosity ratio of the two immiscible fluids on the relative permeabilities has been investigated extensively since the work by Leverett (1939). There are two cases to consider. One case is that the relative permeability of a porous medium to a given phase in two-phase flow is dependent only on saturation. A possible explanation is that in cocurrent steady flow under certain conditions each fluid may flow in a separate network of pores, so the two streams do not influence each other (see Figure 11.24a).

The other case is that in low permeability media at low water saturations, when the wetting phase is no longer continuous in the central part of the pores, the lower viscosity of the water may exert a "lubricating effect"

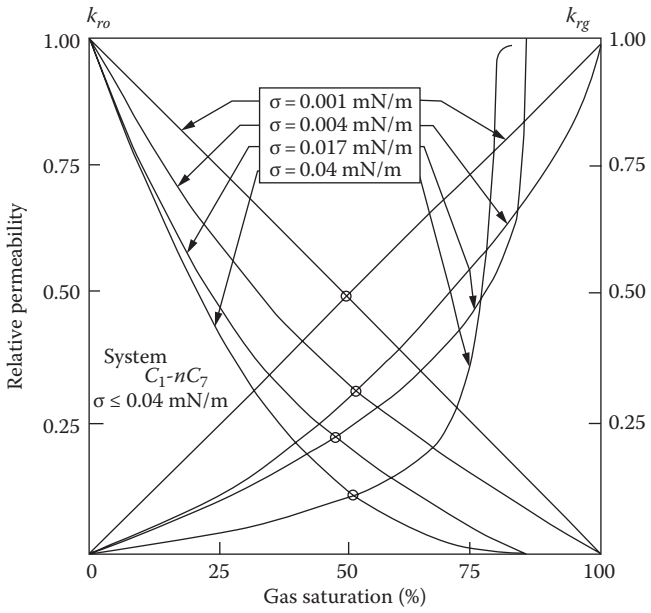


Figure 11.25

Effect of IFT on relative permeability. (From Bardon, C. and Longeron, D., Influence of very low interfacial tensions on relative permeability, Presented at the *53rd Annual Fall Technical Conference and Exhibition*, SPE 7609, SPE of AIME, Houston, TX, 1978.)

on the oil flow under the conditions of steady-state relative permeability measurements. The essence of the lubricating effect is that, as a result of the presence of the lower viscosity fluid (water) near the pore walls, the oil flows at a higher rate than it would if oil instead of water was also present near the wall. Water movement along pore walls provides a moving boundary for oil. Under these conditions, oil relative permeability depends on oil-to-water viscosity ratio, as shown in Figure 11.26 (Odeh, 1959, Danis and Jacquin, 1983).

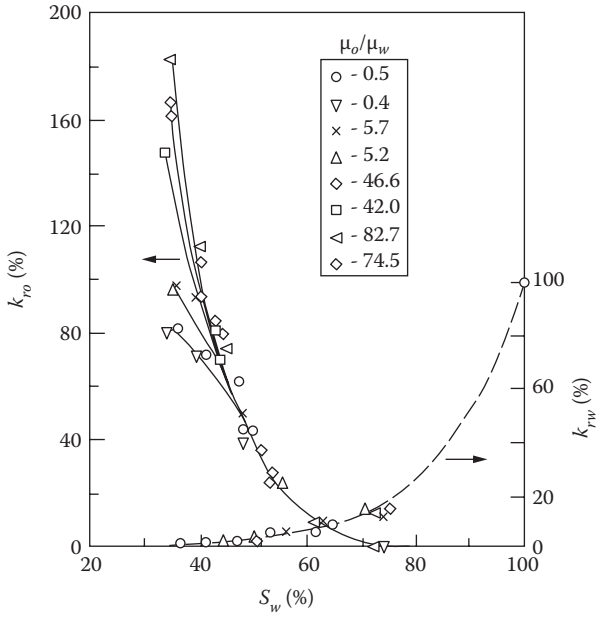


Figure 11.26

Effect of viscosity ratio on relative permeability.

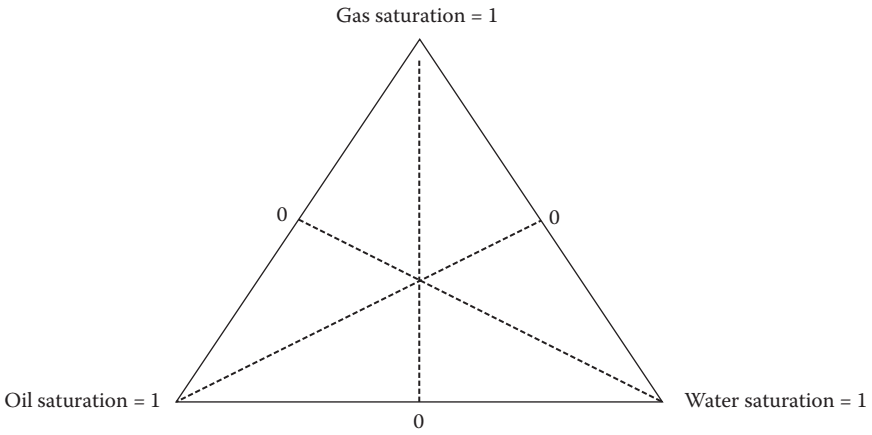


Figure 11.27

Triangle diagram for three-phase relative permeability.

11.6.8 Relative Permeability Correlations

Several correlations exist for two-phase and three-phase relative permeabilities. Correlations are developed from a variety of techniques including empirical correlations based on core flood measurements, statistical models of capillary bundles, and microscopic network models. Correlations should be used in conjunction with laboratory data or when laboratory data are not available.

Three-phase relative permeabilities can be measured in the laboratory using techniques such as steady-state displacement. It is difficult to perform reproducible laboratory measurements over the entire saturation range of interest. Results can be costly and time consuming. Consequently, models of three-phase relative permeability based on two-phase relative permeability curves have been introduced to estimate three-phase relative permeability values. The sensitivity of calculations that depend on three-phase relative permeability is estimated by using different three-phase relative permeability models. Stone (1973) provided two of the most commonly used three-phase relative permeability models. Triangle diagrams are often used to display three-phase relative permeability for an oil–water–gas system. Each axis represents a different phase saturation with a scale ranging from 0 to 1 (Figure 11.27). Three-phase relative permeability is displayed as a set of contours within the triangle diagram.

11.7 Fractional Flow of Two Immiscible Fluids

One of the most important examples of multiphase flow is the flow of a wetting phase and a nonwetting phase through a porous medium. The fractional flow f_w of the wetting phase is

$$f_w = \frac{q_w}{q_T} = \frac{q_w}{q_w + q_{nw}} \tag{11.82}$$

where

q_w is the flow rate of the wetting phase
q_{nw} is the flow rate of the nonwetting phase
$q_T = q_w + q_{nw}$ is the total flow rate

Fractional flow has a value between 0 and 1. A similar equation applies for the fractional flow of the nonwetting phase:

$$f_{nw} = \frac{q_{nw}}{q_T} = \frac{q_{nw}}{q_w + q_{nw}} \tag{11.83}$$

If the only flowing phase is the wetting phase, then $q_{nw} = 0$ and $f_w = 1, f_{nw} = 0$.

An important application of the fractional flow concept is the fractional flow of water f_w in an oil–water system:

$$f_w = \frac{q_w}{q_t} = \frac{q_w}{q_w + q_o} \tag{11.84}$$

where q_w and q_o are water and oil flow rates, respectively. The fractional flow of water is the ratio of water production rate to the total production rate. The fractional flow of oil f_o is related to the fractional flow of water by $f_w = 1 - f_o$.

Fractional flow may be expressed in terms of mobilities. The fractional flow f_w of the wetting phase in a system with a wetting phase and a nonwetting phase is

$$f_w = \frac{q_w}{q_w + q_{nw}} = \frac{1}{1 + \dfrac{q_{nw}}{q_w}} \tag{11.85}$$

The ratio of rates can be determined using Darcy's law. For example, if gravity and capillary pressure are negligible, Darcy's law at the conditions of the porous medium gives

$$\frac{q_{nw}}{q_w} = \frac{-\dfrac{kk_{rnw}A}{\mu_{nw}}\dfrac{\partial p}{\partial x}}{-\dfrac{kk_{rw}A}{\mu_w}\dfrac{\partial p}{\partial x}} = \frac{\dfrac{kk_{rnw}}{\mu_{nw}}}{\dfrac{kk_{rw}}{\mu_w}} = \frac{\lambda_{nw}}{\lambda_w} \tag{11.86}$$

Equation 11.85 becomes

$$f_w = \frac{1}{1 + \dfrac{q_{nw}}{q_w}} = \frac{1}{1 + \dfrac{\lambda_{nw}}{\lambda_w}} \tag{11.87}$$

where λ_w and λ_{nw} are mobilities of the wetting and nonwetting phases, respectively. Equation 11.87 is an expression for wetting phase fractional flow f_w at the conditions of the porous medium. In a geologic reservoir, the fractional flow is calculated using rates and mobilities at reservoir conditions.

11.7.1 Fractional Flow Equation with Capillary Pressure and Gravity

The earlier analysis can be extended to include gravity in the fractional flow equation. The 1D form of Darcy's law with capillary pressure and gravity is

$$\begin{aligned} q_w &= -\frac{kk_{rw}A}{\mu_w}\left(\frac{\partial p_w}{\partial x} + \rho_w g \sin\alpha\right) \\ q_{nw} &= -\frac{kk_{rnw}A}{\mu_{nw}}\left(\frac{\partial p_{nw}}{\partial x} + \rho_{nw} g \sin\alpha\right) \end{aligned} \tag{11.88}$$

where the variables are cross-sectional area A of flow system, reference permeability k, relative permeability to the nonwetting phase k_{rnw}, relative permeability to the wetting phase k_{rw}, capillary pressure $p_c = p_{nw} - p_w$ with nonwetting phase pressure p_{nw} and wetting phase pressure p_w, nonwetting phase density ρ_{nw}, wetting phase density ρ_w, nonwetting phase viscosity μ_{nw}, wetting phase viscosity μ_w, dip angle α of linear flow, and x is the direction of linear flow. We differentiate the capillary pressure function with respect to x

$$\frac{\partial p_c}{\partial x} = \frac{\partial p_{nw}}{\partial x} - \frac{\partial p_w}{\partial x} \tag{11.89}$$

and combine with Equation 11.88 to obtain

$$\frac{\partial p_c}{\partial x} = -\frac{q_{nw}\mu_{nw}}{Akk_{rnw}} - \rho_{nw} g \sin\alpha + \frac{q_w \mu_w}{Akk_w} + \rho_w g \sin\alpha \tag{11.90}$$

Using the total rate $q_t = q_{nw} + q_w$ and density difference $\Delta\rho = \rho_w - \rho_{nw}$ in Equation 11.90 gives, after some rearrangement, the equation

$$\frac{q_w}{Ak}\left(\frac{\mu_{nw}}{k_{rnw}} + \frac{\mu_w}{k_{rw}}\right) = \frac{q_t \mu_{nw}}{Akk_{rnw}} + \frac{\partial p_c}{\partial x} - g\Delta\rho \sin\alpha \tag{11.91}$$

Solving for the fractional flow f_w to the wetting phase gives

$$\begin{aligned} f_w &= \frac{q_w}{q_t} \\ &= \frac{1 + \dfrac{Akk_{rnw}}{\mu_{nw} q_t}\left[\dfrac{\partial p_c}{\partial x} - \left(\rho_w - \rho_{nw}\right) g \sin\alpha\right]}{1 + \dfrac{k_{rnw}}{k_{rw}}\dfrac{\mu_w}{\mu_{nw}}} \end{aligned} \tag{11.92}$$

The general expression for f_w includes the mobility term $(k_{rnw}/k_{rw})(\mu_w/\mu_{nw})$, the capillary pressure derivative $\partial p_c/\partial x$, and the gravity term $(\rho_w - \rho_{nw})g \sin\alpha$. The bracketed term contains capillary pressure and gravity effects. The bracketed term can be neglected if the denominator $\mu_{nw} q_t$ in the term $Akk_{rnw}/\mu_{nw} q_t$ is large enough to make $\dfrac{Akk_{rnw}}{\mu_{nw} q_t}\left[\dfrac{\partial p_c}{\partial x} - \left(\rho_w - \rho_{nw}\right) g \sin\alpha\right] \ll 1$. If the wetting phase is water and the nonwetting phase is oil, the capillary pressure and gravity effects can be negligible when the total flow rate is large. If the wetting phase is water and the nonwetting phase is gas, the capillary pressure and gravity effects may need to be considered at large total flow rate because gas viscosity is small compared to liquid viscosity. Countercurrent flow occurs when the term $1 + \dfrac{Akk_{rnw}}{\mu_{nw} q_t}\left[\dfrac{\partial p_c}{\partial x} - \left(\rho_w - \rho_{nw}\right) g \sin\alpha\right] < 0$ on the RHS of Equation 11.92.

11.8 Immiscible Displacement

The equations for 1D, immiscible flow of a nonwetting phase and a wetting phase in a horizontal, porous medium of constant cross-sectional area A are, respectively,

$$q_{nw} = \frac{k_{rnw} kA}{\mu_{nw}} \frac{\partial p_{nw}}{\partial x} \tag{11.93}$$

and

$$q_w = \frac{k_{rw} kA}{\mu_w} \frac{\partial p_w}{\partial x} \tag{11.94}$$

Total flow q_t is the sum of both flows, that is, Buckley and Leverett (1942) applied this equations and fractional flow concepts to model the advance of a fluid displacement front in an immiscible displacement process.

11.8.1 Buckley–Leverett Theory

The Buckley–Leverett (1942) calculation determines the rate at which an injected wetting phase moves through a porous medium. Flow through a small volume element (Figure 11.28) with length Δx and cross-sectional area A can be expressed in terms of total flow rate q_t given by

$$q_t = q_w + q_{nw} \tag{11.95}$$

The rate of the wetting phase entering the element on the left-hand side (LHS) of the volume element is

$$q_t f_w = \text{entering LHS} \tag{11.96}$$

where f_w is the fractional flow to the wetting phase. The rate of water leaving the volume element on the RHS is

$$q_t \left(f_w + \Delta f_w \right) = \text{leaving RHS} \tag{11.97}$$

The change in wetting phase flow rate Δq_w through the volume element is

$$\begin{aligned} \Delta q_w &= q_t f_w - q_t \left(f_w + \Delta q_t f_w \right) \\ &= -q_t \Delta f_w \end{aligned} \tag{11.98}$$

The change in wetting phase saturation per unit time is Δq_w in Equation 11.98 divided by the pore volume of the element,

$$\frac{\Delta S_w}{\Delta t} = -\frac{q_t}{A\phi} \frac{\Delta f_w}{\Delta x} \tag{11.99}$$

In the limit as $\Delta t \to 0$ and $\Delta x \to 0$, we obtain the differential form

$$\frac{\partial S_w}{\partial t} = -\frac{q_t}{A\phi} \frac{\partial f_w}{\partial x} \tag{11.100}$$

The corresponding equation for the nonwetting phase is

$$\frac{\partial S_{nw}}{\partial t} = -\frac{q_t}{A\phi} \frac{\partial f_{nw}}{\partial x} \tag{11.101}$$

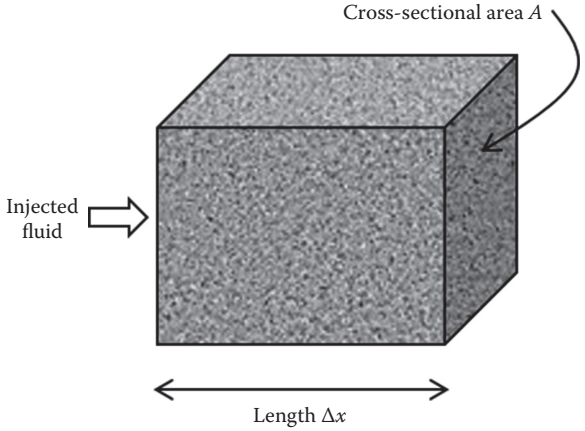


Figure 11.28

Geometry for 1D immiscible displacement.

Assuming fractional flow of the wetting phase f_w depends only on S_w, we obtain the derivative

$$\frac{\partial f_w}{\partial x} = \frac{df_w}{dS_w}\frac{\partial S_w}{\partial x} \tag{11.102}$$

Substituting $\partial f_w/\partial x$ into $\partial S_w/\partial x$ in Equation 11.100 gives

$$\frac{\partial S_w}{\partial t} = -\frac{q_t}{A\phi}\frac{df_w}{dS_w}\frac{\partial S_w}{\partial x} \tag{11.103}$$

Equation 11.103 can be difficult to solve analytically because it is a nonlinear partial differential equation for the general distribution of wetting phase saturation $S_w(x, t)$ in most realistic cases. For example, if water is the wetting phase in rock, water fractional flow is typically a nonlinear function of water saturation.

A simplified approach to solving Equation 11.103 is obtained by tracking the movement of a surface of constant wetting phase saturation. We begin by writing the total differential of $S_w(x, t)$ as

$$\frac{dS_w}{dt} = \frac{\partial S_w}{\partial x}\frac{dx}{dt} + \frac{\partial S_w}{\partial t} \tag{11.104}$$

The derivative $dS_w/dt = 0$ for a surface with constant S_w. If we choose to follow the movement of a surface with constant S_w, we can express Equation 11.104 in the form

$$\left(\frac{dx}{dt}\right)_{S_w} = -\frac{\left(\partial S_w/\partial t\right)}{\left(\partial S_w/\partial x\right)} \tag{11.105}$$

The Buckley–Leverett frontal advance equation is obtained by rearranging Equation 11.103 and substituting the result in Equation 11.105:

$$\left(\frac{dx}{dt}\right)_{S_w} = -\frac{q_t}{A\phi}\left(\frac{df_w}{dS_w}\right)_{S_w} \tag{11.106}$$

The derivative $(df_w/dS_w)_{Sw}$ is the slope of the fractional flow curve. An expression for wetting phase fractional flow f_w as a function of capillary pressure and gravity is given in Equation 11.92. Displacements of one fluid by another in porous media can be analyzed by solving Equations 11.92 and 11.106. This requires the porosity and permeability of the porous medium, fluid viscosities, relative permeability curves, and the capillary pressure curve for the fluids–porous medium system.

11.8.2 Welge's Method

Buckley and Leverett (1942) gave a simplified solution of Equations 11.92 and 11.106 by neglecting the term containing $\partial p_c/\partial x$ in Equation 11.92. Their solution gave multivalued water saturations for the same value of x, which they recognized was physically impossible. Welge (1952) published an approach that is widely used to perform the Buckley–Leverett frontal advance calculation. Welge's approach is best demonstrated using a plot of f_w versus S_w (Figure 11.29).

A line is drawn with its intercept at irreducible wetting phase saturation S_{wirr} and tangent to a point on the f_w curve. The resulting tangent line is illustrated in Figure 11.29 and is called the breakthrough tangent or slope. Wetting phase saturation at the flood front S_{wf} is the point of tangency on the f_w curve. Fractional flow of the wetting phase at the flood front is f_{wf} and occurs at the point of tangency S_{wf} on the f_w curve. Average wetting phase saturation behind the flood front S_{wbt} is the intercept of the main tangent line with the upper limiting line where $f_w = 1.0$. In summary, when the wetting phase exits the volume element, Welge's approach gives the following results:

- The wetting phase saturation at the producing well is S_{wf}.
- The average wetting phase saturation behind the front is S_{wbt}.
- The fractional flow of the wetting phase is f_{wf}.

The Buckley–Leverett procedure is widely available in reservoir engineering software.

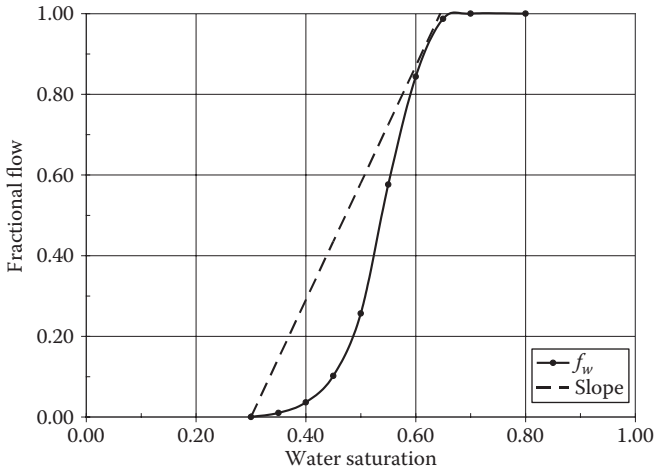


Figure 11.29

Welge's method. (From Fanchi, J.R., *Integrated Reservoir Asset Management*, Elsevier-Gulf Professional Publishing, Burlington, MA, 2010.)

11.8.3 Frontal Advance in a Fracture

Most geologic sediments were deposited in a level plane. Uneven uplift and subsidence over geologic time can break the rock and form natural fractures. Natural fractures affect the fluid flow in a porous medium. Formations with natural fractures are characterized by abrupt changes in porosity and permeability. These changes can result in two physically distinct flow regimes known as the matrix and the fracture. The matrix has a larger porosity and pore volume than the fracture, but a small permeability. Consequently, most of the fluid volume is contained in the matrix while most of the fluid flow occurs in the interconnected fracture volume.

Matrix fluid is usually recovered by flowing into fractures that are open to flow and intersect a production conduit such as a well. The permeability of the fracture when the fracture first formed can be reduced by mineralization. In some cases, there is so much mineralization that the fractures are impermeable are referred to as closed fractures. Open fractures have not undergone mineralization and have the original fracture permeability. Fractures subjected to some mineralization have a permeability that is less than original fracture permeability and are considered partially open. The fluid flow in fractures depends on such factors as fracture permeability, fracture aperture size, orientation of the fracture, net stress on the fracture, and the behavior of the fluids in the fracture.

A model of the displacement of oil by water in a linear, horizontal fracture surrounded by oil saturated matrix rock was given by DeSwaan (1978) as a modification of Buckley–Leverett theory. DeSwaan added a matrix–fracture flow term to Equation 11.101 to get

$$-u\frac{\partial f_{wf}}{\partial x}=\frac{\partial S_{wf}}{\partial t}+\frac{\lambda R_{\infty}}{\phi_f}\int_0^t e^{-\lambda(t-\varepsilon)}\frac{\partial S_{wf}}{\partial \varepsilon}d\varepsilon \tag{11.107}$$

where interstitial velocity $u = q_t/A\phi_f$

f_{wf} is the fractional flow of water in the fracture

S_{wf} is the water saturation in the fracture

ϕ_f is the fracture porosity

ε is a dummy integration variable

The matrix–fracture interaction is represented by the term containing an integral on the RHS of Equation 11.107. The parameters λ and R_∞ are obtained by fitting the equation $R = R_\infty(1 - e^{-\lambda t})$ to a laboratory measurement of oil recovery from a piece of rock surrounded by water. Imbibition of water into the matrix rock does not occur when either λ or R_∞ equal zero. The rate of water imbibition from the fracture

to the matrix increases as λ increases. This increased transfer of water from the fracture to the matrix slows the rate of frontal advance in the fracture. A method for numerically solving Equation 11.107 is presented by Kazemi et al. (1992).

11.9 Reservoir Flow Model Equations

Reservoir flow models play a significant role in designing and assessing the success of a reservoir project. They can be applied to the multiphase flow of fluids in a variety of commercial settings, such as oil and gas reservoirs, coal seams, aquifers, and geothermal reservoirs. The reservoir flow model is an input data set for use in a computer program that simulates the fluid flow based on a set of fluid flow equations. The computer program is often referred to as a reservoir simulator. The set of fluid flow equations is the mathematical representation of the physics incorporated in the reservoir simulator. As an illustration, we consider the multiphase flow of oil and gas in a reservoir. Following Fanchi (2006b), we derive the continuity equation in three dimensions and then develop the equations for a black oil simulator.

A black oil simulator is a computer program that treats the oil and gas phases as two-component systems. The components are a liquid hydrocarbon component and a gaseous hydrocarbon component. The fluid properties (viscosity, density, compressibility, and formation volume factor) are assumed to depend on the two components and pressure. More complex simulators have been developed that include the effects of more components and temperature. The formulation of a black oil simulator illustrates the techniques that are used to develop more sophisticated simulators and has widespread applicability as well. We restrict our attention here to a black oil simulator.

11.9.1 Continuity Equation

Consider the system displayed in Figure 11.30. The block in Figure 11.30 has length Δx, width Δy, and depth Δz. The bulk volume of the block is $\Delta x \Delta y \Delta z$. The symbol J denotes fluid flux. Flux is defined as the rate of flow of mass per unit cross-sectional area normal to the direction of flow. The term *mass* refers to the mass of a component in the fluid. In our case, fluid flows into the block at x with fluid flux J_x and out of the block at $x + \Delta x$ with fluid flux $J_{x+\Delta x}$.

The principle of conservation of mass states that the difference between the mass entering the block and the mass leaving the block is equal to the accumulated mass in the block.

The mass entering the block in a time interval Δt is

$$\left[(J_x)_x \Delta y \Delta z + (J_y)_y \Delta x \Delta z + (J_z)_z \Delta x \Delta y\right] \Delta t = \text{Mass in} \tag{11.108}$$

where the expression includes flux in the x-, y-, and z-directions. The notation $(J_x)_x$ in the first term on the LHS denotes the x-direction flux at location x and $\Delta y \Delta z$ is the cross-sectional area that is perpendicular to the direction of fluid flux. Analogous meanings apply to the remaining terms of Equation 11.108.

The term for mass exiting the block is

$$\left[(J_x)_{x+\Delta x} \Delta y \Delta z + (J_y)_{y+\Delta y} \Delta x \Delta z + (J_z)_{z+\Delta z} \Delta x \Delta y\right] \Delta t + q \Delta x \Delta y \Delta z \Delta t = \text{Mass out} \tag{11.109}$$

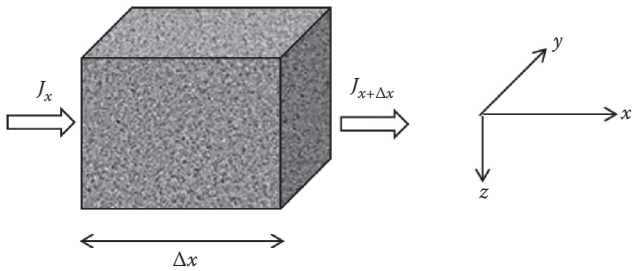


Figure 11.30

Coordinate convention.

A source/sink term q representing the flow of mass into (source) or out of (sink) the block has been added to Equation 11.109. Production is represented by $q > 0$ and injection by $q < 0$. Flow equations may be expressed in terms of volumetric flow rate Q_ℓ for phase ℓ rather than mass flow rate q_ℓ. The flow rates are related by $Q_\ell = q_\ell/\rho_{\ell sc}$ where $\rho_{\ell sc}$ is the density of phase ℓ at standard conditions of pressure and temperature.

The accumulation of mass in the block is the change in concentration of the mass of a component (C) in the block over the time interval Δt. If the concentration C is defined as the total mass of a component in the reservoir block divided by the block volume, then the accumulation term becomes

$$\left[(C)_{t+\Delta t} - (C)_t\right]\Delta x\Delta y\Delta z = \text{Mass accumulation} \tag{11.110}$$

Using Equations 11.108 through 11.110 in the mass balance equation gives

$$\begin{aligned}&\left[(J_x)_x \Delta y\Delta z + (J_y)_y \Delta x\Delta z + (J_z)_z \Delta x\Delta y\right]\Delta t\\ &-\left[(J_x)_{x+\Delta x} \Delta y\Delta z + (J_y)_{y+\Delta y} \Delta x\Delta z + (J_z)_{z+\Delta z} \Delta x\Delta y\right]\Delta t\\ &- q\Delta x\Delta y\Delta z\Delta t = \left[(C)_{t+\Delta t} - (C)_t\right]\Delta x\Delta y\Delta z\end{aligned} \tag{11.111}$$

where

$(C)_t$ denotes the concentration of a component at time t

$(C)_{t+\Delta t}$ is the concentration at time $t + \Delta t$

Dividing Equation 11.111 by $\Delta x\Delta y\Delta z\Delta t$ and rearranging gives

$$\begin{aligned}&-\frac{(J_x)_{x+\Delta x} - (J_x)_x}{\Delta x} - \frac{(J_y)_{y+\Delta y} - (J_y)_y}{\Delta y}\\ &-\frac{(J_z)_{z+\Delta z} - (J_z)_z}{\Delta z} - q = \frac{(C)_{t+\Delta t} - (C)_t}{\Delta t}\end{aligned} \tag{11.112}$$

In the limit as Δx, Δy, Δz, and Δt go to zero, Equation 11.112 becomes the continuity equation for a component in the fluid:

$$-\frac{\partial J_x}{\partial x} - \frac{\partial J_y}{\partial y} - \frac{\partial J_z}{\partial z} - q = \frac{\partial C}{\partial t} \tag{11.113}$$

This is written in vector notation as

$$-\nabla \cdot \vec{J} - q = \frac{\partial C}{\partial t} \tag{11.114}$$

where $\nabla \cdot \vec{J}$ is divergence of flux. A continuity equation for mass is needed for each component of mass in the block.

11.9.2 Black Oil Simulator Equations

Black oil simulators and compositional simulators are the two most common types of computer programs that model fluid flow in reservoirs. Thermal simulators include an energy balance equation that is not considered here. From a physical perspective, black oil and compositional simulators differ in the way they model fluid properties. Compositional simulators use multicomponent equations of state to model fluid properties. Gas and oil properties in a black oil model depend on pressure only. Typical gas and oil properties for a standard black oil model include gas formation volume factor (B_g), gas viscosity (μ_g),

liquid yield (r_s), oil formation volume factor (B_o), oil viscosity (μ_o), and solution gas–oil ratio (R_{so}). We neglect liquid yield in the formulation below later to simplify the presentation. Liquid yield is useful when analyzing condensate reservoirs or reservoirs with hydrocarbon liquid dissolved in the hydrocarbon gas phase. Liquid yield is often included in commercial black oil simulators. Many people prefer to use compositional simulators that provide a more sophisticated model of hydrocarbon fluid properties when modeling condensate reservoirs. Water properties include water formation volume factor (B_w), water viscosity (μ_w), and solution gas–water ratio (R_{sw}).

The flow equations of a black oil simulator are derived from mass conservation and the continuity equation. Fluxes and concentrations are needed for each of the three phases in an oil, water, and gas system. A flux in a given direction can be written as the density of the fluid times its velocity in the given direction. Letting the subscripts *o*, *w*, and *g* denote oil, water, and gas, respectively, the fluxes become

$$\left(\vec{J}\right)_o = \frac{\rho_{osc}}{B_o}\vec{v}_o \tag{11.115}$$

$$\left(\vec{J}\right)_w = \frac{\rho_{wsc}}{B_w}\vec{v}_w \tag{11.116}$$

$$\left(\vec{J}\right)_g = \frac{\rho_{gsc}}{B_g}\vec{v}_g + \frac{R_{so}\rho_{gsc}}{B_o}\vec{v}_o + \frac{R_{sw}\rho_{gsc}}{B_w}\vec{v}_w \tag{11.117}$$

where

R_{so} and R_{sw} are the gas solubilities
B_o, B_w, and B_g are the formation volume factors
sc is the subscript that denotes the standard conditions (usually 60°F and 14.7 psia in oilfield units)
ρ denotes the fluid densities

Liquid hydrocarbon in the form of condensate is not included in this formulation. The velocities in oilfield units are assumed to be Darcy's velocities, and their *x* components are

$$v_{xo} = -k_x\lambda_o\frac{\partial\Phi_o}{\partial x} \tag{11.118}$$

$$v_{xw} = -k_x\lambda_w\frac{\partial\Phi_w}{\partial x} \tag{11.119}$$

$$v_{xg} = -k_x\lambda_g\frac{\partial\Phi_g}{\partial x} \tag{11.120}$$

where

Φ_o, Φ_w, and Φ_g are the oil-, water-, and gas-phase potentials
k_x is permeability in the *x*-direction

Similar expressions can be written for the *y* and *z* components. The relative phase mobility λ_ℓ is defined as the ratio of the relative permeability to the flow of the phase divided by its viscosity:

$$\lambda_\ell = \frac{k_{r\ell}}{\mu_\ell} \tag{11.121}$$

The phase densities are related to formation volume factors and gas solubilities by

$$\rho_o = \frac{1}{B_o}\left[\rho_{osc} + R_{so}\rho_{gsc}\right] \tag{11.122}$$

$$\rho_w = \frac{1}{B_w}\left[\rho_{wsc} + R_{sw}\rho_{gsc}\right] \tag{11.123}$$

$$\rho_g = \frac{\rho_{gsc}}{B_g} \tag{11.124}$$

The concentrations for the oil-, water-, and gas-phase continuity equations are

$$C_o = \frac{\phi\rho_{osc}S_o}{B_o} \tag{11.125}$$

$$C_w = \frac{\phi\rho_{wsc}S_w}{B_w} \tag{11.126}$$

$$C_o = \phi\rho_{gsc}\left[\frac{S_g}{B_g} + R_{so}\frac{S_o}{B_o} + R_{sw}\frac{S_w}{B_w}\right] \tag{11.127}$$

where

ϕ is the porosity

S_ℓ is the saturation of phase ℓ

The gas concentration term in Equation 11.127 accounts for oil (condensate) and water to be dissolved in the gas phase. Saturations satisfy the constraint

$$S_o + S_w + S_g = 1 \tag{11.128}$$

Mass conservation equations for each component in the appropriate phase are given as follows.

Oil component in the oil phase:

$$-\left[\frac{\partial}{\partial x}\left(\frac{v_{xo}}{B_o}\right) + \frac{\partial}{\partial y}\left(\frac{v_{yo}}{B_o}\right) + \frac{\partial}{\partial z}\left(\frac{v_{zo}}{B_o}\right)\right] - \frac{q_o}{\rho_{osc}} = \frac{\partial}{\partial t}\left(\frac{\phi S_o}{B_o}\right) \tag{11.129}$$

Water component in the water phase:

$$-\left[\frac{\partial}{\partial x}\left(\frac{v_{xw}}{B_w}\right) + \frac{\partial}{\partial y}\left(\frac{v_{yw}}{B_w}\right) + \frac{\partial}{\partial z}\left(\frac{v_{zw}}{B_w}\right)\right] - \frac{q_w}{\rho_{wsc}} = \frac{\partial}{\partial t}\left(\frac{\phi S_w}{B_w}\right) \tag{11.130}$$

Gas component in the gas, oil, and water phases:

$$\begin{aligned} &-\frac{\partial}{\partial x}\left(\frac{v_{xg}}{B_g} + \frac{R_{so}}{B_o}v_{xo} + \frac{R_{sw}}{B_w}v_{xw}\right) \\ &-\frac{\partial}{\partial y}\left(\frac{v_{yg}}{B_g} + \frac{R_{so}}{B_o}v_{yo} + \frac{R_{sw}}{B_w}v_{yw}\right) \\ &-\frac{\partial}{\partial z}\left(\frac{v_{zg}}{B_g} + \frac{R_{so}}{B_o}v_{zo} + \frac{R_{sw}}{B_w}v_{zw}\right) - \frac{q_g}{\rho_{gsc}} \\ &= \frac{\partial}{\partial t}\left(\phi\left(\frac{S_g}{B_g} + \frac{R_{so}S_o}{B_o} + \frac{R_{sw}S_w}{B_w}\right)\right) \end{aligned} \tag{11.131}$$

These equations have been simplified by dividing out the constant densities at standard conditions.

Equivalent but more compact forms of the flow equations are presented in terms of vector operators as

$$-\nabla \cdot \frac{\vec{v}_o}{B_o} - \frac{q_o}{\rho_{osc}} = \frac{\partial}{\partial t}\left(\frac{\phi S_o}{B_o}\right) \tag{11.132}$$

$$-\nabla \cdot \frac{\vec{v}_w}{B_w} - \frac{q_w}{\rho_{wsc}} = \frac{\partial}{\partial t}\left(\frac{\phi S_w}{B_w}\right) \tag{11.133}$$

$$-\nabla \cdot \left(\frac{\vec{v}_g}{B_g} + \frac{R_{so}}{B_o}\vec{v}_o + \frac{R_{sw}}{B_w}\vec{v}_w\right) - \frac{q_g}{\rho_{gsc}} = \frac{\partial}{\partial t}\left(\phi\left(\frac{S_g}{B_g} + \frac{R_{so}S_o}{B_o} + \frac{R_{sw}S_w}{B_w}\right)\right) \tag{11.134}$$

The mass conservation equations are nonlinear, partial differential equations that represent the fluid flow in porous media. The equations are discretized using finite difference techniques. The resulting difference equations are solved using matrix solution methods. The mathematical techniques are beyond the scope of this article. They are described in more detail in Batycky et al. (2007) and Gilman and Ozgen (2013).

11.9.3 Reservoir Flow Model Workflows

Reservoir simulators are applied to green fields and brown fields. A green field is an undeveloped field with minimal historical flow data, while a brown field is a developed field. Different flow modeling workflows are used for green fields and brown fields.

Green field and brown field workflows are designed to be systematic procedures for quantifying uncertainty. Green fields have little or no production information to constrain the selection of reservoir realizations or calibrate uncertain model parameters. Each reservoir realization should be a possible representation of reservoir geology. Consequently, it is valuable to have a workflow that can quantify uncertainty. A green field workflow includes gathering data, identifying key parameters and associated uncertainties, generating forecasts of field performance results for a statistically significant distribution of parameters, and generating a probabilistic distribution of field performance results.

Two brown field workflows are currently being used in industry: deterministic reservoir forecasting and probabilistic reservoir forecasting. In deterministic reservoir forecasting, a single reservoir realization is selected and matched to historical performance. Historical performance includes all data about the reservoir, such as seismic data, well log data, well test data, core data, fluid property data, and production data. The uncertainty associated with a deterministic dynamic model can be estimated by evaluating the sensitivity of the model to uncertainties in available data. History match parameters are customarily changed one at a time.

In probabilistic reservoir forecasting, a statistically significant collection, or ensemble, of reservoir realizations is prepared. Reservoir flow models are run for each possible realization, and the results of the model runs are then compared to historical performance of the reservoir. The models that match historical data within a specified set of tolerances are selected as the set of dynamic models that can be used for making predictions. A subset of the ensemble of realizations may be selected for matching to historical data to reduce the number of reservoir flow models that need to be studied. The specific design of a history matching workflow depends on such factors as the objectives of the study, the complexity of reservoir performance, and the availability of history matching technology. More discussion of workflows is presented by Fanchi (2011a,b) and Gilman and Ozgen (2013).

Acknowledgments

The authors thank the publisher for providing material from the corresponding chapter written by M. Dong and FAL Dullien in the first edition (Crowe, 2006).

Nomenclature

Latin Letters

A	Area
a	Tortuosity factor
B	Formation volume factor
b	Klinkenberg factor
Ca	Capillary number
F	Formation resistivity factor
I	Resistivity index
k_H	Hydraulic conductivity
k_r	Relative permeability
k	Permeability
L	Length
M	Molecular weight
m	Cementation exponent, real gas pseudo-pressure
N_p	Number of phases
n	Saturation exponent
P_{ch}	Parachor
p	Pressure
p_c	Capillary pressure
Q	Volumetric flow rate
q_ℓ	Volumetric flow rate of phase ℓ
R_0	Resistivity of porous material
R_t	Formation resistivity of partially saturated medium
R_w	Resistivity of ionic solution
R_1, R_2	Radii of curvature
r	Radius
S	Specific surface
S_ℓ	Saturation of phase ℓ
S_P	Pore surface area or internal surface area of pores
T	Temperature
t	Time
u	Superficial velocity
v	Interstitial velocity
x	Axis, coordinate, distance
y	Axis, coordinate
Z	Gas compressibility factor
z	Axis, coordinate

Greek Letters

β	Turbulence factor
η_{NTG}	Net-to-gross ratio
θ	Contact angle
λ	Mobility
μ	Dynamic viscosity
ν	Kinematic viscosity
ρ	Density
γ	Pressure gradient
σ	Surface tension
ϕ	Porosity

Subscripts

ave	Average
B	Bulk

eff	Effective
f	Fluid
g	Gas
G	Grain
gw	Gas–water
go	Gas–oil
L	Liquid
ℓ	Phase
nw	Nonwetting
o	Oil
ow	Oil–water
P	Pore
r	Reservoir
s	Surface
w	Wetting phase, water, well

Non-SI Units

atm	Atmosphere
bbl	Barrel
cp	Centipoise
d	Day
ft	Feet
md	Millidarcy
psi	Pounds per square inch
psia	Pounds per square inch absolute
rb	Barrels at reservoir conditions
rcf	Cubic feet at reservoir conditions
scf	Cubic feet at surface conditions
stb	Barrels at stock tank conditions

References

Amyx, J.W., Bass, Jr., D.M., and Whiting, R.L., Petroleum Reservoir Engineering: Physical Properties, McGraw-Hill, New York, 1960.

Ahmed, T., *Reservoir Engineering Handbook*, Gulf Publishing, Houston, TX, 2000.

Bardon, C. and Longeron, D., Influence of very low interfacial tensions on relative permeability, presented at the *53rd Annual Fall Technical Conference and Exhibition*, SPE 7609, SPE of AIME, Houston, TX, 1978.

Bassiouni, Z., *Theory, Measurement, and Interpretation of Well Logs*, SPE Textbook Series 4, Society of Petroleum Engineers, Richardson, TX, 1994.

Batycky, R.P., Thiele, M.R., Coats, K.H., Grindheim, A., Ponting, D., Killough, J.E., Settari, T. et al., Chapter 17: Reservoir simulation, in E.D. Holstein and L.W. Lake (Eds.), *Petroleum Engineering Handbook*, Volume 5: Reservoir Engineering and Petrophysics, Society of Petroleum Engineers, Richardson, TX, 2007.

Bear, J., *Dynamics of Fluids in Porous Media*, Elsevier, New York, 1972.

Buckley, S.E. and Leverett, M.C., Mechanism of fluid displacement in sands, *Trans. AIME*, 146, 107–116, 1942.

Christiansen, R.L., Chapter 15: Relative permeability and capillary pressure, in J.R. Fanchi and L.W. Lake (Eds.), *Petroleum Engineering Handbook*, Volume 1: General Engineering, Society of Petroleum Engineers, Richardson, TX, 2006.

Conway, M.W., Mavor, M.J., Saulsberry, J., Barree, R.B., and Schraufnagel, R.A., Multi-phase flow properties for coalbed methane wells: A laboratory and field study, presented at the *Joint Rocky Mountain Regional Meeting and Low-Permeability Reservoirs Symposium*, SPE 29576, Denver, CO, March 20–22, 1995.

Craig, F.F., *The Reservoir Engineering Aspects of Waterflooding*, SPE Monograph Series, Society of Petroleum Engineers, Richardson, TX, 1971.

Crowe, C.T., *Multiphase Flow Handbook*, Taylor & Francis/(CRC), Boca Raton, FL, 2006.
Danis, M. and Jacquin, C., Influence du contraste de viscosité sur les perméabilltés relatives lors du drainage: Experimentation et modélisation, *Rev. d l'IFP*, 38, 723–733, 1983.
Darcy, H., *Les Fontaines Publiques de la Ville de Dijon*, Victor Dalmont, Paris, France, 1856.
DeSwaan, A., Theory of waterflooding in fractured reservoirs, *Soc. Petr. Eng. J.* (April), 117–122; *Trans. AIME*, 265, 1978.
Dullien, F.A.L., Two-phase flow in porous media, *Chem. Eng. Technol.*, 11, 407, 1988.
Fanchi, J.R., Calculation of parachors for compositional simulation: An update, *Soc. Petr. Eng. Reservoir Eng.*, 433–436, 1990.
Fanchi, J.R., *Integrated Flow Modeling*, Elsevier-Gulf Professional Publishing, Burlington, MA, 2000.
Fanchi, J.R., *Principles of Applied Reservoir Simulation*, Elsevier-Gulf Professional Publishing, Burlington, MA, 2006a.
Fanchi, J.R., Chapter 2: Mathematics of fluid flow, in L.W. Lake (Ed.), *Petroleum Engineering Handbook*, Volume 1: General Engineering, Chapter 1. Society of Petroleum Engineers, Richardson, TX, 2006b.
Fanchi, J.R., *Integrated Reservoir Asset Management*, Elsevier-Gulf Professional Publishing, Burlington, MA, 2010.
Fanchi, J.R., Flow modeling workflow: I. Green fields, *J. Petr. Sci. Eng.*, 79, 54–57, 2011a.
Fanchi, J.R., Flow modeling workflow: II. Brown fields, *J. Petr. Sci. Eng.*, 79, 58–63, 2011b.
Forchheimer, P., Wasserbewegung durch Boden, *Z. Ver. Deutsch. Ing.*, 45, 1782–1788, 1901.
Gash, B.W., Measurement of "Rock Properties" in coal for coalbed methane production, presented at the *Annual Technical Conference and Exhibition*, SPE 22909, Dallas, TX, October 6–9, 1991.
Gilman, J.R. and Ozgen, C., *Reservoir Simulation: History Matching and Forecasting*, Society of Petroleum Engineers, Richardson, TX, 2013.
Guéguen, Y. and Palciauskas, V., *Introduction to the Physics of Rocks*, Princeton University Press, Princeton, NJ, 1994.
Hirsche, K., Porter-Hirsche, J., Mewhort, L., and Davis, R., The use and abuse of geostatistics, *The Leading Edge*, March 1997, pp. 253–260.
Katz, D.L., Monroe, R.R., and Trainer, R.P., Surface tension of crude oils containing dissolved gases, *AIME Technical Publication 1624*, American Institute of Mining and Metallurgical Engineers, New York, 1943, pp. 285–294.
Kazemi, H., Gilman, J.R., and Elsharkawy, A.M., Analytical and numerical solution of oil recovery from fractured reservoirs with empirical transfer functions, *SPE Reservoir Eng.*, 7(2), 219–227, May 1992.
Kelkar, M., Application of geostatistics for reservoir characterization—Accomplishments and challenges, *J. Can. Petr. Technol.*, 59, 25–29, 2000.
Klinkenberg, L.J., The permeability of porous media to liquids and gases, in *Drilling and Production Practice*, American Petroleum Institute, Washington, D.C., 1941, pp. 200–213.
Lake, L.W., *Enhanced Oil Recovery*, Prentice Hall, Englewood Cliffs, NJ, 1989.
Leverett, M.C., Flow of oil-water mixtures through unconsolidated sands, *Petr. Trans. AIME*, 132, 149, 1939.
Mavko, G., Mukerji, T., and Dvorkin, J., *The Rock Physics Handbook*, 2nd edn., Cambridge University Press, Cambridge, U.K., 2009.
Meaney and Paterson, *Asia Pacific O&G Conference*, SPE 36986, Adelaide, South Australia, Australia, October 28–31, 1996.
Odeh, A.S., Effect of viscosity ratio on relative permeability, *Petr. Trans. AIME*, 216, 346, 1959.
Reiss, L.H., *The Reservoir Engineering Aspects of Fractured Formations*, Gulf Publishing Company, Paris, France, 1980.
Satter, A., Iqbal, G.M., and Buchwalter, J.L., *Practical Enhanced Reservoir Engineering*, PennWell, Tulsa, OK, 2008.
Seidle, J.P., *Fundamentals of Coalbed Methane Reservoir Engineering*, PennWell, Tulsa, OK, 2011.
Stone, H.L., Estimation of three-phase relative permeability and residual oil data, *J. Can. Petr. Technol.*, 53–61, 1973.
Towler, B.F., *Fundamental Principles of Reservoir Engineering*, SPE Textbook Series Volume 8, Society of Petroleum Engineers, Richardson, TX, 2002.
Welge, H.J., A simplified method for computing oil recovery by gas or water drive, *Trans. AIME*, 195, 91–98, 1952.

12

Turbulence Interactions

John K. Eaton and Ellen K. Longmire

12.1 Introduction
12.2 Particle Motion and Distribution in Turbulent Flow
12.3 Effect of Turbulence on Coupling Forces and Heat Transfer
12.4 Turbulence Modulation

12.1 Introduction

Many of the single- and multiphase flows that we interact with are turbulent. Large-scale flows in nature such as ocean currents, river flows, the atmospheric boundary layer, clouds, and volcanic eruptions are characterized by very large Reynolds numbers and are naturally turbulent with a broad range of eddy length scales. Large fish, birds, and aquatic mammals have turbulent boundary layers and wakes, and flow separation causes turbulence around some smaller animals. In the technological arena, the flows around transport vehicles from motorcycles to airliners are turbulent, as are the flows inside the internal combustion and gas turbine engines powering them. The flows through large-scale industrial equipment such as electric generating plants and chemical processing facilities are almost all turbulent. Considering the built environment, turbulence plays important roles in wind flows through cities, large gas and water pipelines, ventilation ducts, and building interiors.

This chapter discusses the interaction of dispersed particles and droplets with continuous-phase turbulence. Interactions between the particles and the turbulence are almost always important. Some turbulent flows such as dust storms, clouds, particle transport risers, and sediment-laden rivers carry a substantial load of dispersed particles, and the effect of turbulence on particle transport is critical. Turbulence effects on the interphase exchange processes are important in spray combustion and many chemical and food processing systems such as spray dryers. Even in lightly laden flows, particle–turbulence interaction can be important. For example, turbulence may substantially affect the surface deposition of particles such as volcanic ash ingested into jet engines.

There are two important parameters that must be introduced early in any discussion of particle–turbulence interaction. The first is the Stokes number (St) defined as the ratio of the particle aerodynamic time constant to a relevant timescale of the flow. A flow timescale could be based on mean flow parameters. Alternatively, several timescales that characterize the turbulence can be used. For the present discussion, we will use the Kolmogorov timescale, defined as $\tau_k = (\nu/\varepsilon)^{1/2}$. Here, ν is the kinematic viscosity of the fluid and ε is the turbulent dissipation rate. This timescale was chosen because it is unambiguously defined and characterizes the smallest eddies in the flow. We will use the nomenclature St_k to correspond to normalization by

the Kolmogorov timescale, while other normalizations (e.g., a large eddy timescale) would produce different values of the Stokes number. We also introduce a dimensionless particle diameter d_k that normalizes the particle diameter by the Kolmogorov length scale, $\ell_k = (\upsilon^3/\varepsilon)^{1/4}$. This is consistent with the definition of St_k and characterizes the particle size relative to the smallest turbulent eddies.

This chapter covers particle–turbulence interactions for dilute suspensions of particles. Here, the term *particles* can also refer to liquid droplets that are small enough to remain spherical as they interact with the turbulence. Larger droplets that distort and/or break up will have even more complex interactions with the turbulence than are covered here. By dilute we mean that the volume fraction is small enough that the average spacing between particles is many particle diameters. Interparticle collisions may occur, but the particle motion is dominated by interactions with the continuous phase and body forces. Fluidized beds and other dense multiphase flows where the flow dynamics are dominated by collisions will not be discussed, even though some of these flows may be highly turbulent. A particle volume fraction of 0.01 is a rough upper bound for the present regime of interest. Note that the mass loading ratio can be large even at low volume fractions when the continuous phase is a gas. For example, the mass loading ratio for quartz sand particles in air at STP and a volume fraction of 10^{-3} is greater than 2.

We further limit the scope by considering only particle sizes with significant direct particle–turbulence interactions. Very fine particles with Stokes numbers less than around 0.01 are essentially flow tracers, following closely the motion of neighboring fluid elements. Aerosol particles in gas flows and neutrally buoyant dust particles in liquid flows are examples. The turbulent dispersion of such particles can be treated in the same way as turbulent diffusion of heat, contaminant species, or other scalar properties. The particles only affect the turbulence by changing the density or effective viscosity. On the opposite end of the scale, particles with very large St_k and/or d_k are not of interest. If St_k is greater than around 100, the particles move ballistically through the flow and do not respond significantly to the turbulence. Similarly, particles with d_k greater than 10–100 must be treated as moving solid bodies affecting the global flow field. It turns out that many cases of interest both practically and scientifically fall into the range of both St_k and d_k in the range of 0.1–10.

Within our range of interest, there are several different classes of particle–turbulence interactions that may become important. The first class has to do with changes to mass, momentum, and energy coupling between the continuous phase and the particles. These effects are most important when d_k is greater than 1 so that the smallest turbulent eddies are smaller than the particle diameter. For example, heat exchange between particles and fluid usually is calculated using simple correlations for the Nusselt number (hd/k) of a sphere in steady, uniform flow. If the free stream flow around the particle is turbulent with eddy length scales smaller than the particle diameter, the Nusselt number would be considerably higher than indicated by the correlation. For momentum exchange, we must recognize that the particle drag coefficient may be affected by turbulence. Furthermore, local velocity gradients around a particle can create lift so that the composite of aerodynamic lift and drag is not aligned with the instantaneous fluid/particle velocity difference.

The second and broadest class of particle–turbulence interactions involves particle motions induced by the turbulence. Particle dispersion is similar to turbulent scalar transport, in that particle velocities induced by the continuous-phase turbulence act to spread particles away from regions of high mean particle concentration. A related effect is turbophoresis, in which particles move away from regions of high turbulence and accumulate in the regions of low turbulence. This frequently occurs near solid surfaces where fluid turbulence is damped by the wall. Finally, turbulent eddies can induce preferential concentration in which particles are concentrated in clusters with local concentrations much larger than can be accounted for by random particle motions. Similarly, voids in the instantaneous particle concentration field are produced when particles are centrifuged away from vortex cores or local centers of streamline curvature.

The third class of particle–turbulence interactions is turbulence modulation by particles, which is also called the back effect of particles on turbulence. Both increases and decreases in turbulent kinetic energy (TKE) have been observed, and in some cases, the changes are large. Clearly, this effect is strongly coupled to particle dispersion and preferential concentration. For example, if turbulence is strongly attenuated by heavy loading of particles, turbulent dispersion may be substantially reduced.

Finally, the effects of turbulence have to be considered when studying particle collisions. Even in dilute (low volume fraction) flows, particle collisions can be very important. The best example is clouds,

where droplet growth by agglomeration is a critical process leading to precipitation. Turbulence can induce large variations in the velocity of particles within a small region of the flow. This increases the probability of the collisions and also affects the energy of a typical collision. Similarly, preferential concentration can dramatically increase the probability of collisions by concentrating the majority of the particles in a small fraction of the total flow volume.

The following sections cover each of the three types of particle–turbulence interaction discussed earlier. Some areas are better understood than others, and these areas include a more quantitative discussion. Particle–particle collisions including the effects of turbulence are discussed elsewhere in the handbook and are not discussed further in this chapter.

12.2 Particle Motion and Distribution in Turbulent Flow

12.2.1 Overview

To examine the effects of turbulent flow on particles, it is helpful to start from a particle equation of motion. The well-cited equation derived by Maxey and Riley (1983) is

$$\frac{\pi}{6}d_p^3\rho_p\frac{dV_i}{dt}=\frac{\pi}{6}d_p^3\left(\rho_p-\rho_f\right)g_i-3\pi\mu d_p\left(V_i-u_i-\frac{1}{24}d_p^2\nabla^2u_i\right)+\frac{\pi}{6}d_p^3\rho_f\frac{Du_i}{Dt}-\frac{\pi}{12}d_p^3\rho_f\frac{d}{dt}\left[V_i-u_i-\frac{1}{40}d_p^2\nabla^2u_i\right]$$
$$-\frac{3}{2}\pi d_p^2\mu\int_0^t d\tau\left(\frac{d/d\tau\left(V_i-u_i-\frac{1}{24}d_p^2\nabla^2u_i\right)}{[\pi\nu(t-\tau)]^{0.5}}\right),$$

where V indicates the particle velocity, u is the fluid velocity, ρ is the density, g_i is the gravitational acceleration component, and ν is the kinematic viscosity. The subscripts p and f correspond with the particle and fluid phases, respectively. The derivative d/dt represents a time derivative following the particle, while D/Dt denotes the time derivative following a fluid element.

The terms on the right-hand side result from gravitational potential, viscous, pressure gradient, added mass, and Basset history forces on the particle, respectively. It is important to note that, in deriving this equation, Maxey and Riley (1983) assumed an infinite, incompressible fluid (no particle–particle interactions) and that the particle obeyed Stokes drag for a sphere moving through fluid with no disturbances on the order of or smaller than the particle length scale.

If the particle density is much larger than the fluid density as when the continuum phase is a gas, the pressure gradient, added mass, and Basset terms can be neglected leaving a much simpler equation. We can also neglect the third part of the viscous term as typically small compared with the other two parts to get

$$\frac{dV_i}{dt}=g_i+\frac{18\mu}{\rho_p d_p^2}\left(u_i-V_i\right).$$

This equation is linear in V and depends only on viscous and potential (usually gravitational) effects. Also, the equation is still applicable with modified drag coefficients if the particle Reynolds number is not much greater than 1.

In many practical applications, viscous drag is the dominant force acting to accelerate or decelerate particles. The particle inertia is usually assessed based on a time constant τ_p related to the viscous drag. Assuming Stokes flow, this time constant is calculated as the time required for a spherical particle to accelerate from rest to 63% of a constant surrounding velocity. Thus,

$$\tau_p=\frac{d_p^2\left(\rho_f+2\rho_p\right)}{36\mu},$$

where ρ_f is typically negligible in gas flows. The linear equation for particle acceleration and the aerodynamic time constant based on Stokes drag are strictly valid only for particle Reynolds numbers much less than 1, where particle Reynolds number is defined as

$$Re_p = \frac{\rho_f |\boldsymbol{V} - \boldsymbol{u}| d_p}{\mu}.$$

In practice, the simplified equation for particle motion given earlier often is applied for particle Reynolds numbers less than about 10 by applying an empirically derived correction to the drag on the sphere:

$$C_D = \frac{24}{Re_p}\left(1 + 0.15 Re_p^{0.687}\right), \quad \text{with the corresponding corrected } \tau_p = \frac{\rho_p d_p^2}{18\mu}\left(\frac{1}{1 + 0.15 Re_p^{0.687}}\right),$$

where a gas continuum phase is assumed. Various authors define the Stokes number using either the Stokes-derived τ_p mentioned earlier or using a corrected τ_p where the Reynolds number is determined using the average particle slip velocity. There is a misconception in the literature that the use of a Stokes number implies that Stokes drag must be used in evaluating the time constant. However, it is defined that the Stokes number is typically the dominant parameter affecting particle distribution within the fluid. When particle inertia relative to the fluid becomes significant, the particle Reynolds number Re_p also becomes important. First, the drag force is affected by the Reynolds number, and second, when the Reynolds number is sufficiently large, it indicates the presence of individual wakes behind particles that may augment small-scale turbulence (see Section 12.4).

Additional dimensionless parameters of importance can include a Froude number or drift parameter relating gravitational to inertial forces and length scale ratios between the particle diameter and various turbulences or eddy scales. In the following paragraphs, the inertial effects on particle dispersion and preferential concentration are first discussed. Then, the effects of additional forces are discussed in terms of the same phenomena.

Consider a particle with density larger than the surrounding fluid. It will be accelerated or decelerated based on drag interactions. In a turbulent flow, then two effects can result. First, if the local fluid streamlines are curved, fluid elements have an acceleration normal to the flow direction, and particles would tend to take straighter paths than equivalent fluid elements. Second, if the fluid is accelerating linearly, particles will lag the fluid and vice versa. These two components of acceleration have different consequences within the flow, depending on the initial particle distribution and the boundary conditions.

12.2.2 Particle Dispersion

Rigorous studies of mean particle dispersion in the turbulent flow originated with the work of Taylor (1921) and Batchelor (1949), who showed that the dispersion of a single particle in homogeneous, isotropic turbulence is related to the particle's Lagrangian velocity autocorrelation $R_{ij}(t)$ as well as its root-mean-square velocity fluctuations. The Lagrangian velocity autocorrelation, which is measured following a particle trajectory, is defined:

$$R_{ij}(\tau) = \frac{\overline{V_i(t_0) V_j(t_0 + \tau)}}{\overline{v_i' v_j'}},$$

where $\overline{v_i' v_j'}$ represents the particle velocity covariance and the overbar represents an ensemble average based on many particle trajectories. The particle dispersion tensor is then expressed as

$$\overline{X_i X_j(t)} = \overline{v_i' v_j'} \int_0^t \int_0^\tau \left(R_{ij}(\xi) + R_{ji}(\xi)\right) d\xi dt.$$

Since the particle velocity covariance and velocity autocorrelation are typically not known *a priori*, it is unclear from this equation how the mean dispersion varies for different particle time constants and flow geometries.

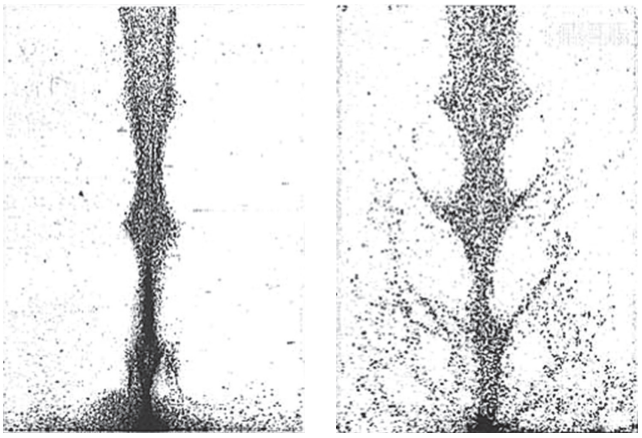

(a) (b)

Figure 12.1

Laser sheet illumination of particle-laden flow in forced impinging air jet. Flow moves top to bottom. Stokes number based on vortex passage frequency is 1.25 (a) and 0.3 (b). (Images reprinted from Anderson, S.L. and Longmire, E.K., *J. Fluid Mech.*, 299, 333, 1995. With permission.)

Early direct numerical simulations by Squires and Eaton (1991a) and Elghobashi and Truesdell (1992) demonstrated that, in the absence of gravity, "heavy" particles with significant inertia dispersed or "diffused" more rapidly than fluid elements. Also, using model spectra and a representation of dispersion in homogeneous, isotropic, stationary turbulence developed by Reeks (1977), Wang and Stock (1993) and Stock (1996) showed that particles disperse more rapidly than fluid elements for any case with $St_k > 0$.

Reeks (1983) derived a term for turbophoretic velocity of particles based on gradients in the fluid velocity covariance (or averaged rms velocity fluctuations):

$$V_{i,turbo} = -\tau_p \frac{\partial(\overline{u_i' u_j'})}{\partial x_j},$$

which corresponded with an earlier one-dimensional derivation by Caporaloni et al. (1975). Here, it can be seen that particles tend to move toward zones of decreasing turbulence intensity. The associated turbophoretic force, which is often discussed in terms of particles approaching walls in boundary layer or pipe flows, clearly increases with both τ_p and the gradient magnitude. References describing the turbophoretic effect include Young and Leeming (1997) and Guha (2008).

In various free shear flows with nonhomogeneous loading of inertial particles, a wealth of experiments and simulations (e.g., Chung and Trout, 1988, Lazaro and Lasheras, 1989, Hishida et al., 1992, Longmire and Eaton, 1992, Tang et al., 1992) demonstrated the importance of coherent eddies to particle dispersion. For example, in free shear layers (Lazaro and Lasheras, 1989) and jets (Longmire and Eaton, 1992) with particles loaded initially in the high-speed stream, particles dragged across the stream by Kelvin–Helmholtz vortices (either 2D or rings) would retain cross-stream inertia longer than fluid elements and thus could be "flung" further into the lower speed stream than the fluid elements. This flinging effect was maximized for Stokes numbers based on large vortex timescales of order 0.3–10. Examples of this phenomenon are shown in Figure 12.1 where the lower Stokes value shown exhibits stronger particle dispersion in the radial direction. At smaller Stokes numbers, particles approximated fluid tracers. By contrast, particles with very large inertia, or larger St, would not couple with the vortices sufficiently and therefore not attain sufficient cross-stream velocity to be "flung," and their cross-stream dispersion would decrease toward zero with increasing St as would occur in the ballistic limit.

12.2.3 Preferential Concentration

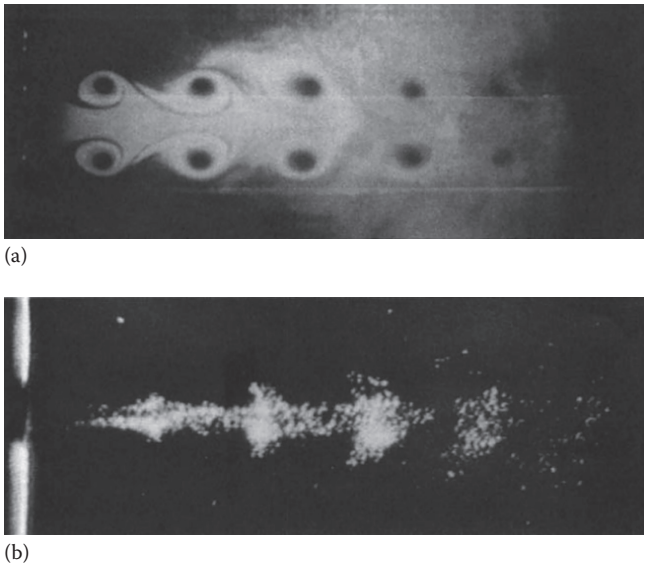
Because of their distinct response to fluid accelerations, particles develop inhomogeneous distributions within turbulent flows such that they become preferentially concentrated in some zones and leave voids in other zones. The preferential concentration of particles or droplets is thought to be of great importance

in both environmental and industrial processes where collisions are important, for example, formation of raindrops in clouds (Shaw, 2003), formation of planets (Cuzzi et al., 2001), and production of powdered materials through aerosol and spray processes (Reade and Collins, 2000). Preferential concentration is also important in reacting flows, for example, combustion of liquid drops or particles, or combustion of fuels containing embedded particles. In reacting flows, local reaction rates can depend strongly (and nonlinearly) on particle concentration. Readers are referred to the reviews of Eaton and Fessler (1994), Balachandar and Eaton (2010), and Monchaux et al. (2012) for detailed descriptions of previous experiments and simulations demonstrating and quantifying the effect of preferential concentration in a range of turbulent flows. Neglecting gravity and assuming $\rho_p \gg \rho_f$, Balachandar and Eaton (2010) derived an equation for divergence of particle velocity with the form

$$\nabla \cdot \boldsymbol{V} = -St\left(1-\beta\right)\left(\left\|\boldsymbol{S}\right\|^2 - \left\|\boldsymbol{\Omega}\right\|^2\right) \quad \text{with } \beta = \frac{3\rho_f}{\rho_f + 2\rho_p},$$

where $\|\boldsymbol{S}\|$ and $\|\boldsymbol{\Omega}\|$ are the local strain-rate and rotation-rate tensors, respectively. This equation shows that when $\rho_p > \rho_f$ $\beta < 1$ so that the divergence is negative, hence particles tend to accumulate in the regions of high strain rate. Conversely, the divergence is positive in the regions of high vorticity, and particles tend to vacate these regions. This is a direct consequence of the particle response to the longitudinal and normal accelerations in the fluid mentioned earlier. Examples of long-lasting negative divergence occur in the zones of linear deceleration such as straining zones between vortices in a shear layer (Martin and Meiburg, 1994), between vortex rings in a round jet (Longmire and Eaton, 1992, 1994), or the stagnation zone of an impinging jet (Anderson and Longmire, 1995). In all of these cases, particles accumulate or cluster in these zones when St based on a vortex timescale is of order 0.5–10. Similarly, the locations of vortex cores in these and other flows, which correspond with zones where the divergence of particle velocity is positive, tend to be void of, or have relatively low concentrations of particles. See Figure 12.2 for an example.

Preferential concentration can also occur in turbulent wall–bounded flows such as boundary layers, channels, and pipes. In the near-wall region, where long streamwise streaky structures are prominent and relatively long lasting, particles tend to concentrate in the slow-moving streaks (see, e.g., Brooke et al., 1992, Marchioli and Soldati, 2002, Kaftori et al., 1995a,b, Nino and Garcia, 1996). By directly visualizing particle distributions, Fessler and Eaton (1999) also demonstrated preferential concentration on the centerplane of a fully developed turbulent channel flow.



(a)

(b)

Figure 12.2

Laser sheet illumination of smoke-laden (a) and particle-laden flow in forced air jet (b). Flow moves left to right. Stokes number based on vortex passage frequency ~6.5. (Images reprinted from Longmire, E.K. and Eaton, J.K., *J. Fluid Mech.*, 236, 217, 1992. With permission.)

Much of the previous work examining particle distribution in homogeneous, isotropic turbulence is numerical and assumes dilute particle concentrations such that particles neither interact nor modify the surrounding turbulence. Squires and Eaton (1991b) and Wang and Maxey (1993) showed how zones of high particle concentration coincided with zones of high strain and low vorticity for a range of Stokes numbers. Bec et al. (2006) plotted a relative concentration of particles within rotating regions over a range of St_k, suggesting that the concentrations were the lowest for $St_k \sim 0.7$ and remained somewhat suppressed beyond $St_k = 3$. They further suggested that differences in concentration distribution for $St_k \sim 3$ were caused less by centrifugation out of small vortices and more by the lack of particle response to the smallest scales of fluid velocity fluctuation. In experiments by Wood et al. (2005) and Saw et al. (2008) and in simulations by Monchaux et al. (2010), preferential concentration was maximized for $St_k \sim 1$. An image of the particle distribution for $St_k \sim 1$ in Wood et al.'s experiment is shown in Figure 12.3. As discussed in the review by Monchaux et al. (2012), many questions remain about the lifetime and persistence of particle clusters forming in turbulence, and research is ongoing in this area.

A number of methods have been employed to quantify and characterize the degree of preferential concentration within a fluid volume (see Monchaux et al., 2012 for a comprehensive review). As explained by Fessler et al. (1994), a random distribution of k particles within a volume satisfies a Poisson distribution:

$$p(k) = \frac{e^{-\lambda}\lambda^{k}}{k!},$$

where λ is the average number of particles in the volume. Methods of characterizing preferential concentration therefore usually attempt to measure a deviation from this distribution. Notable methods include box counting (e.g., Fessler et al., 1994, Aliseda et al., 2002), the radial distribution function (RDF) (see, e.g., Sundaram and Collins, 1997, Balkovsky et al., 2001, Zaichik and Alepchenkov, 2009), the correlation dimension (Tang et al., 1992, Fessler et al., 1994, Bec et al., 2007), and Voronoi diagrams (Monchaux et al., 2010). Box counting methods determine a distribution of particle numbers within boxes of uniform size where the box size can be varied over the range of turbulence length scales. Box sizes that are too small or large to correlate with particle number distribution yield Poisson-like distributions, while sizes corresponding to length scales of either particle clusters or voids will yield deviations from the Poisson distribution. The RDF or pair correlation function examines the probability of finding a particle in each of two volumes

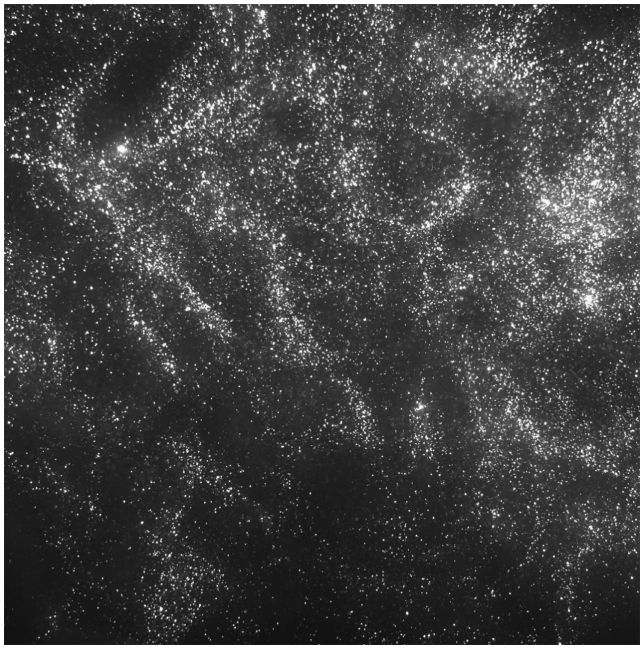


Figure 12.3

Laser sheet illumination of particle-laden homogeneous turbulence with $St_k = 1.5$. (Image reprinted from Wood, A.M. et al., *Int. J. Multiphase Flow*, 31, 1220, 2005. With permission.)

separated by a distance r. Similar to box counting methods, this function provides a method to quantify preferential concentration in terms of a range of specific length scales. The RDF has been used directly in collision models (e.g., Sundaram and Collins, 1997).

The correlation dimension involves counting the number of particles N within a radial distance r of a base particle and comparing the slope of N versus r on a log–log plot (see Fessler et al., 1994 for a detailed explanation). The slope is the correlation dimension. If particles are concentrated preferentially, the slope will be reduced from the value associated with a random distribution. The correlation dimension thus yields a single value to quantify the degree of preferential concentration. As explained by Monchaux et al. (2012), the Voronoi diagram method bins the volumes of void space surrounding each particle into a distribution. This method is similar to the correlation dimension, in that no specific length scale such as box size or separation distance is introduced into the distribution.

12.2.4 Gravitational Effects

Stock (1996) gives an excellent review and explanation of gravitational effects on dispersion in homogeneous, isotropic turbulence. To characterize the importance of gravitational effects, he defined a drift parameter:

$$\gamma = \frac{\tau_p g}{u_{rms}},$$

where $\tau_p g$ is the particle settling or drift velocity for $Re_p \ll 1$, and u_{rms} is the rms velocity in the fluid.

In general, the particle diffusivity or rate of dispersion decreases in all directions as the drift parameter increases. This gravitational effect, originally noted by Yudine (1959), is often called the "crossing trajectory effect." Physically, as particle drift velocity increases, particles tend to cross through, rather than remain within, correlated zones of fluid velocity. The particle velocity autocorrelation decreases, and particles are less likely to be dispersed within these zones.

When gravity is present in homogeneous, isotropic turbulence, multiple investigators, starting with Wang and Maxey (1993), found that the presence of turbulence increases the average particle settling velocity. Again, this effect is most prominent for $St_k \sim 1$. The enhanced settling was explained in the following way: particles settling downward are swept preferentially into the downward moving sides of vortical structures (as opposed to the upward moving sides), hence the increase in average settling velocity. This enhancement must also depend on the relative strength of the vortices versus gravity, which can be characterized by the ratio of particle settling velocity to a characteristic fluid velocity. For example, Yang and Lei (1998), who related the settling velocity to the rms fluid velocity as in the γ mentioned earlier, found the strongest enhancement in settling velocity for $St_k \sim 1$ and $\gamma \sim 0.5$. Even though they were dealing with relatively dilute flows (volume fractions $\leq 7 \times 10^{-5}$), Aliseda et al. (2002) found even greater settling enhancement in their experiments than what was predicted in one-way coupled simulations. They argued that turbulence modification and wake interactions within particle clusters would add to the settling enhancement described by Wang and Maxey. Subsequent simulations of Bosse et al. (2006), which employed two-way coupling, were able to duplicate the trend observed by Aliseda et al. (2002).

12.2.5 Basset, Added Mass, and Pressure Gradient Effects

In simulations of homogeneous, isotropic turbulence, Elghobashi and Truesdell (1992) showed that the Basset force was significant for solid particles in gas, although typically an order of magnitude smaller than the drag force. For their density ratio, the added mass and pressure gradient terms were insignificant. By comparing results with and without the Basset term, they found that the Basset force tended to decrease the Lagrangian integral scales and very slightly decrease particle dispersion. Armenio and Fiorotto (2001) simulated the motion of point particles in a turbulent channel flow for a range of density ratios and Stokes numbers. In addition to viscous drag, the particles were subjected to added mass, pressure gradient, and Basset forces, but not gravity. The simulation results showed that all four of the included forces could be significant in liquid/solid flows. However, the three additional force terms did not appear to have any significant effect on particle dispersion compared against a simulation including only viscous drag. More recently, Olivieri et al. (2014) simulated particles in homogeneous, isotropic turbulence subject to both viscous and Basset forces. They found that the Basset force tended to reduce the clustering or preferential concentration of particles. This suppression effect was strongest for $\rho_p/\rho_f \sim 10$ and $St_k = 1$ but was also

significant for $\rho_p/\rho_f = 1000$. For $\rho_p/\rho_f = 1000$, Basset forces tended to be significant for "extreme events" where particle accelerations were especially large.

12.3 Effect of Turbulence on Coupling Forces and Heat Transfer

The critical multiphase interactions in particle-laden flows are the forces applied on the particles by the flow and the heat transfer at the particle surfaces. Typically, these are represented with simple models often selected for ease of implementation. For example, momentum exchange is represented using Stokes drag for a particle in a uniform steady flow, sometimes with a semiempirical correction for finite Reynolds number as discussed in the previous section. Similarly, heat transfer from particles is represented using empirical correlations for the Nusselt number as a function of the particle Reynolds number (c.f. discussion in Jones et al. 2010). These models assume that the flow is quasi-steady and that the unperturbed flow is uniform. The models generally work well when $d_k \ll 1$, but many interesting particle-laden flows have $d_k = \theta(1)$ or greater. For the latter case, small-scale turbulent eddies can significantly affect both the momentum and energy coupling.

The Maxey/Riley equation described in the previous section is believed to correctly represent the effects of unsteadiness, velocity gradients, and pressure gradient on the force applied to a spherical particle in terms of the undisturbed velocity field. However, a particle with $d_k \geq 1$ disturbs at least the smallest eddies in the flow. Furthermore, flow separation from the particle surface occurs when the particle Reynolds number exceeds about 20 and has a strong effect on the applied forces. The separation behavior is probably very sensitive to turbulent eddies with scales near the particle diameter. The experimental study of turbulence effects on particle forces has been inconclusive (see summary in Balachandar and Eaton, 2009) because it is difficult to discriminate such effects from the effects of trajectory bias (Wang and Maxey, 1993) on particle settling velocity. Definitive evidence of the direct effects of turbulence on momentum coupling for small particles has only recently become available with the advent of particle-resolved direct numerical simulations of particle-laden flows (see review in Tenneti and Subramaniam, 2014).

Bagchi and Balachandar (2003) and Burton and Eaton (2005) performed fully resolved simulations of stationary particles in isotropic turbulence with d_k near 1 and particle Reynolds number in the range of 10–100. Bagchi and Balachandar examined streaming turbulence, while Burton and Eaton examined the case with no mean relative velocity, but their conclusions were similar. The mean particle drag was well represented by standard semiempirical drag correlations, but the predicted instantaneous force yielded large errors and the rms force was underpredicted. The model accuracy was not improved by including the added mass and history integral terms from the Maxey–Riley equation. Similar conclusions were reached by Zeng et al. (2008) for the case of a particle suspended at various locations in a fully developed turbulent channel flow.

The case of $d_k > 1$ clearly violates the assumption in the derivation of the Maxey–Riley equation that the particle diameter is much less than any of the flow scales. Detailed examination of the fully resolved simulations shows that eddies are distorted as they interact with particles, and particle wakes are strongly asymmetric. Most models assume that the force on the particle is parallel to the fluid velocity interpolated to the particle center position in the particle frame of reference. However, the asymmetric wakes caused by the turbulence produce perpendicular forces, that is, there is fluctuating lift, even in the absence of large-scale velocity gradients. As the particle Reynolds number increases, another mechanism becomes important. Kim and Balachandar (2012) showed that vortex shedding and consequently lift oscillations begin at a lower Reynolds number in turbulent flows than in uniform flows. For practical simulations that do not resolve the flow around the particles, the addition of a stochastic force to the conventional semiempirical drag law is recommended to represent these effects. Unfortunately, a universal expression for the dependence of this force on particle and turbulence properties is not available.

There has been even less research on the effects of turbulence on interphase heat transfer. Brian et al. (1969) conducted a series of tests on the melting of spherical ice particles in a stirred bath. The turbulence properties were inferred from the known mechanical power input to the bath. They found that the Nusselt number (hd/k_{fluid}), where h is the convective heat transfer coefficient and k_{fluid} is the fluid thermal conductivity, increases slowly with increasing turbulent dissipation rate. This was tested over a range of scales with d_k generally near 1. Bagchi and Kottam (2008) examined the effect of isotropic turbulence on stationary particle heat transfer for $60 < Re_p < 400$ and d_k ranging from 1 to 8. They included cases in which the flow was

isothermal and others with superimposed temperature fluctuations. The turbulence did not affect the mean heat transfer rate that was well represented by the correlation of Feng and Michaelides (2000):

$$\overline{Nu} = 0.922 + \left[RePr\right]^{1/3} + 0.1Re^{2/3}Pr^{1/3},$$

where

Pr is the Prandtl number

Re is the particle Reynolds number based on the mean fluid velocity relative to the particle

When the turbulent inflow was isothermal, instantaneous heat transfer rate fluctuations of up to 20% of the mean were observed. The fluctuations increased with turbulence intensity but were independent of the turbulent length scale. Much larger fluctuations in *Nu* were observed when the inflow field had turbulent temperature fluctuations. These fluctuations arose due to large fluctuation in the heat transfer near the stagnation point.

Overall, much work remains in refining momentum and energy coupling models to correctly represent flows with $d_k \geq 1$. Widely used correlations for particle drag coefficient and Nusselt number in uniform streams are appropriate only when $d_k \ll 1$. Stochastic models can be used to represent the additional fluctuations in force and heat transfer that arise when the particle diameter is comparable to turbulent length scales. However, there are no models that represent the instantaneous force and heat transfer as a function of the local velocity field structure. Future particle-resolved simulations may provide the insight needed to develop such models.

12.4 Turbulence Modulation

12.4.1 Overview

The main focus in this chapter thus far has been on the effects of continuous-phase turbulence on the particle motion, which is the only significant interaction between the particles and the turbulence when the volume fraction of particles is less than about 10^{-6} and dimensionless particle diameters are small. The motions of particles may be computed assuming that they do not have any global effect on the turbulence, and the turbulence may be represented by any model that is valid for the equivalent single-phase flow. This is the case of one-way coupling, meaning that the turbulence affects the particle motion but the particles do not affect the turbulence.

Flows at higher mass or volume loading are in the two-way coupling regime, where the turbulence is modified by the presence of the particles. The carrier-phase turbulence can be characterized by its statistical properties including the TKE, Reynolds stresses, energy spectra, and two-point correlations. The term *turbulence modulation* means that one or more of those statistical properties is modified by the particles. It is common to find modifications in the high-frequency portion of the energy spectrum. This is observed whenever the Stokes number is large enough ($St > 0.1$) that the particles cannot follow the turbulent fluctuations, or when there is a significant mean velocity difference between the phases. However, turbulence modulation is most important when there is significant modification of the TKE. The kinetic energy may be increased (turbulence augmentation) or decreased (turbulence attenuation) relative to the single-phase flow.

We study turbulence modulation because it can be large enough to change the nature of the particle–turbulence interaction, including dispersion of particles, entrainment from particle beds, particle settling velocity, droplet agglomeration rates, and many other aspects of particle-laden flows. Also, the turbulence has a strong influence on scalar transport, frictional losses, and other aspects of the continuous-phase flow. Substantial turbulence modulation typically is observed in systems where the turbulence production due to continuous-phase mean velocity gradients is weak. Examples are decaying grid turbulence, the centerline region of pipe and channel flows, and the outer regions of turbulent boundary layers. For example, Figure 12.4 shows TKE data from the centerplane of a fully developed turbulent channel flow laden with either 150 μm glass or 70 μm copper particles. At the heaviest mass loading ratio of 0.4, the copper particles reduce the turbulence kinetic energy by a factor of more than 7. Note that this loading corresponds to a volume fraction of only 5.5×10^{-5} and a mean particle separation distance of greater than 20 particle diameters. This is a very dilute flow, but the particles nevertheless have a dominant effect on the turbulence behavior. Such large reductions in the turbulence levels can have major effects on particle dispersion, chemical reaction rates within the fluid or at particle surfaces, and transport in the continuous phase.

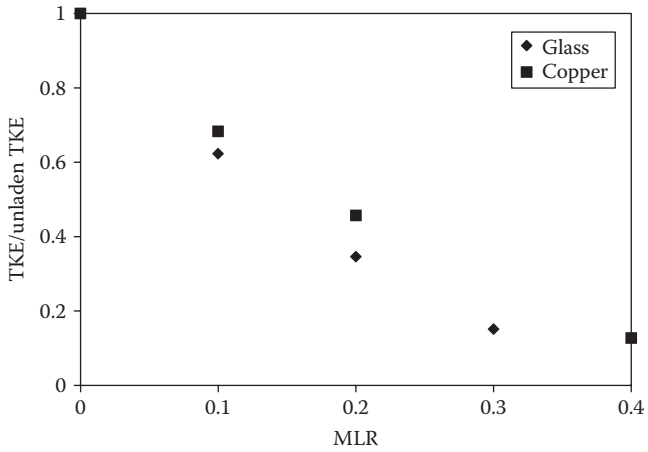


Figure 12.4

Attenuation of TKE as a function of mass loading ratio on the centerplane of fully developed channel flow for 150 μm diameter glass spheres and 70 μm diameter copper spheres. (From Paris, A.D. and Eaton, J.K., Turbulence attenuation in a particle-laden channel flow, Report TSD-137, Department of Mechanical Engineering, Stanford University, Stanford, CA, 2001.)

Turbulence augmentation by particles can be significant when the particle Reynolds numbers are relatively large. Spherical particle wakes become unstable for Reynolds number above about 200 and at even lower Reynolds numbers in turbulent flows (Bagchi and Balachandar, 2003). Regular vortex shedding is observed for Reynolds numbers above about 300 (Sakamoto and Haniu, 1990). The superposition of many unsteady wakes can produce substantial turbulence in the flow. This is most often observed in liquid flows, because particles large enough to have high Reynolds number usually settle out rapidly in gas flows. However, even particles with lower Reynolds number (e.g., $\approx$ 10–100) can generate turbulence by the superposition of randomly positioned and oriented steady wakes. This can be observed in flows where the analogous single-phase flow has very low turbulence intensity, such as particles settling in nominally quiescent fluid.

The degree of turbulence modulation can vary from very small to quite large. Gore and Crowe (1991) reviewed experimental data for the restricted case of particle-laden pipe and jet flows. The percentage change in the streamwise turbulence intensity varied from −90% to +350% over the range of particle and flow parameters examined. While many cases showed substantial modulation, a large fraction of the experiments showed only small changes. The only consistent trend that emerged from the data review was that small particles attenuate turbulence while large particles augment turbulence. They found that the critical particle diameter separating attenuation from augmentation was approximately one-tenth of the scale of the most energetic eddies.

The qualitative rule of thumb developed by Gore and Crowe generally holds, but it does not allow prediction of the degree by which the turbulence will be changed. No general theory or data correlation has emerged that allows reliable prediction of the level or character of turbulence modulation for an arbitrary dispersed multiphase flow. There are several reasons for the lack of progress in this area. First is the difficulty in measuring the carrier-phase turbulence in the presence of a substantial number of particles. Second is the fact that several independent mechanisms may produce turbulence modulation as discussed in the next section. In some flows, two or more of these mechanisms may be active and counteract each other. If the counteracting mechanisms are not recognized, the results may be confusing. Finally, there is the huge parameter space involved. An incompressible, single-phase flow typically is defined by only the geometry and the Reynolds number. The addition of a second phase adds many more parameters, even if the second phase consists of monodisperse round spheres. In that case, additional dimensionless parameters that arise are the particle Stokes number, the dimensionless particle diameter, the particle Reynolds number, and the local particle loading. Of course, even more parameters are important if the particles are polydisperse or nonspherical.

12.4.2 Mechanisms of Turbulence Attenuation and Augmentation

There is no clear consensus on the most important causes of turbulence modulation because different physical mechanisms dominate in different regions of the parameter space. Nevertheless, there are some basic

mechanisms of particle–turbulence interaction that we know play a role in turbulence modulation. All of the known mechanisms require that the particles be large enough that they cannot follow the flow so that there is a substantial instantaneous relative velocity between a particle and the carrier fluid.

One route to turbulence modulation by particles is through the carrier-phase mean velocity. If the mean carrier-phase velocity field is changed by the addition of particles, then the mean strain field and the turbulence production rate also will be changed. For example, if a concentrated stream of high-velocity particles is introduced into a gas flow, a local jet will be formed in the carrier flow due to the drag of the particles applied to the gas. The turbulence production in the jet shear layers is likely to increase the TKE. Presumably, the effects of such large mean flow distortions can be predicted by single-phase turbulence models, so no new understanding of particle–turbulence interaction is needed. On the other hand, this mechanism may be very important in wall-bounded flows where some of the strongest turbulence attenuation has been observed. Turbophoresis tends to concentrate particles near the wall in channel and pipe flows, and particle–fluid mean velocity differences can be large in that region. Therefore, it seems likely that mean velocity changes can occur in the innermost parts of the boundary layer. The region of strongest turbulence production occurs just outside the viscous sublayer due to the steep velocity gradients, so local changes to the mean velocity profile could cause substantial changes in the turbulence. Unfortunately, this is the part of the flow that is most difficult to study either experimentally or by fully resolved simulations, so there is no direct evidence of turbulence modulation due to mean velocity field distortion.

A mechanism for turbulence augmentation when particles are relatively large is unsteady particle wakes. In a uniform carrier stream, the wake of a sphere is asymmetric for Reynolds number above 210 and unsteady for Reynolds numbers greater than 270 (Bagchi and Balachandar, 2002). When there is a mean velocity difference between the particles and the carrier fluid due to gravity or acceleration of the carrier phase, energy is transferred from the particles to small-scale, carrier-phase velocity fluctuations. In most dispersed gas–solid flows, the particle volume fraction is very small and the particle wakes occupy only a small fraction of the flow volume, so the unsteady wake effect creates only minor changes in the turbulence. However, the unsteady wakes are a significant source of turbulence augmentation in some liquid–solid flows where the particle volume fraction is not small and the particle Reynolds number is in the vortex shedding regime. Recent research has shown that these effects can be very complicated. Bellani et al. (2012) studying large particles suspended in the homogeneous turbulence found that spherical particles caused large attenuation of the turbulence while ellipsoidal particles caused far less attenuation. Shao et al. (2012) simulated large particle effects in channel flows and found that the turbulence modification was the largest when particles settled to one wall.

A related mechanism is the superposition of many randomly positioned laminar or "laminar-like" wakes as investigated by Parthasarathy and Faeth (1990) and Chen and Faeth (2001). They investigated turbulence modulation in the absence of shear production, so all the observed turbulence was produced by particle wakes. Chen and Faeth (2001) developed a dimensional correlation that relates the turbulence level to the mean dissipation of energy due to the relative motion of the particles and fluid. For typical multiphase flows, the carrier-phase shear production of turbulence dominates, and laminar wakes are relatively unimportant in setting the level of TKE. However, the superposed effect of the wakes is apparent in several experiments where turbulence spectra were measured. It is common to see a turnup in the spectra at large wave number, which is apparently related to the particle wakes (c.f. Rogers and Eaton, 1991). This effect has also been observed in numerous numerical simulations.

Preferential concentration of particles into specific turbulence structures and preferential sweeping of particles into downflow zones offer two other possible mechanisms of turbulence modulation. A simplified analysis by Eaton and Fessler (1994) showed that particles apply an angular impulse opposing the vortex rotation as they are centrifuged out of a vortex. For Stokes numbers near unity, the ratio of the angular impulse to the initial angular momentum of the vortex is $1.3\phi_m/St_k$, where ϕ_m is the mass loading ratio. This would act to suppress vortices with timescales near the particle time constant. Simulations of homogenous shear flows laden with particles with St_k near unity by Gualtieri et al. (2013) showed that preferential concentration caused the depletion of turbulence in the energy-containing range of the spectrum and augmentation of smaller scales. At high Reynolds numbers, the turbulence has a wide range of time and length scales, so preferential concentration may occur at different length scales depending on the Stokes number. Therefore, the details of turbulence spectrum distortion due to clustering may be Stokes number dependent. Preferential concentration in a gravitational field results in preferential sweeping of particles into downflow zones and a higher than expected average settling velocity (Maxey, 1987). Numerical simulations by Ferrante and Elghobashi (2003) indicate that preferential sweeping at moderate mass loading

creates substantial anisotropy in the turbulence and slows the decay of isotropic turbulence. The preferential concentration causes density variations that lead to buoyancy-induced instability.

The mechanism believed by most to cause turbulence attenuation is the so-called extra dissipation of turbulence by particles. A particle that cannot respond to the turbulent velocity fluctuations exerts a force on the fluid that opposes the relative motion. When the particles are heavy (i.e., have large Stokes numbers) the relative motion is produced mostly by the carrier-phase fluctuations. The cloud of dispersed particles produces a nonuniform force field that instantaneously opposes the carrier-phase velocity fluctuations, thereby extracting energy from the turbulence. Some of the energy taken from the carrier-phase turbulence is transferred to the fluctuating kinetic energy of the particles. However, most goes into producing local flow distortions around each particle. For small particles, the length scales of the flow distortions are small and the corresponding velocity gradients are large, so the local flow distortions are dissipated rapidly by viscosity. Therefore, we see that the particles act as a short circuit of the regular turbulence energy cascade. Energy can be absorbed from the carrier-phase turbulence at any frequency that is too high for the particles to follow. That energy is passed directly to scales comparable to the particle diameter and is dissipated.

An analytical form for the extra dissipation can be derived following Chen and Wood (1985) Berlemont et al. (1990) and Rogers and Eaton (1991). The Navier–Stokes equations for the carrier phase are modified by adding a continuous force field applied onto the fluid by the particles:

$$u_{i,t} + u_j u_{i,j} = -\frac{1}{\rho_f} p_{,i} + \upsilon u_{i,jj} - \frac{1}{\rho_f} F_i \,.$$

Here, indicial notation is used and commas imply derivatives. F_i is the force per unit volume applied by the particles onto the fluid. Assuming a linear drag law and neglecting any other forces, the force field is represented as

$$F_i = \frac{c}{\tau_p}\left(u_i - V_i\right)$$

where

c is the local particle mass concentration
u_i is the continuous-phase velocity
V_i is the particle-phase velocity

A transport equation for the TKE is obtained by applying the Reynolds decomposition, subtracting the mean flow component, squaring the fluctuating component, and averaging. Assuming constant fluid density and particle time constant, the equation is

$$\frac{D}{Dt}\frac{q^2}{2} = P - \varepsilon - \frac{1}{\rho_f \tau_p}\left[\overline{C}\left(\overline{u_i' u_i'} - \overline{u_i' v_i'}\right) + \left(\overline{U}_i + \overline{V}_i\right)\overline{c' u_i'} + \left(\overline{c' u_i' u_i'} - \overline{c' \boldsymbol{u}_i' v_i'}\right)\right].$$

The production term, P, and the dissipation, ε, are identical to their single-phase forms. Also, it is commonly assumed that the second two terms in the square brackets are negligible since they involve correlations of the fluctuating concentration with the fluid and particle velocity fields. The term $\overline{C}/\rho_f \tau_p \left(\overline{u_i' u_i'} - \overline{u_i' v_i'}\right)$ is referred to as the extra dissipation due to particles. There are deficiencies with this analysis, but it gives some idea how turbulence modulation might vary with system parameters. Most obviously, the form of the extra dissipation term suggests that the turbulence attenuation by particles should increase linearly with particle mass loading, a finding that is in rough agreement with experiments. The effect of varying particle time constant is not as obvious, since increases in time constant decrease the leading coefficient but increase the term in parenthesis. The latter is because increasing the Stokes number decreases the particle–fluid velocity correlation $\left(\overline{u_i' v_i'}\right)$. Finally, the equation shows that the extra dissipation term could be negative if the particle velocity fluctuations are large and correlated with the local fluid velocity.

This oversimplified analysis cannot be applied directly because key physical mechanisms have been omitted. In most cases where large turbulence modulation has been observed experimentally, the particles are too large and too widely spaced to be considered as applying a continuous force field onto the turbulence.

An examination of the channel flow case illustrated in Figure 12.4 is instructive. The experiments were performed in air, with a channel half-width of 20 mm, a Taylor microscale of 3000 μm, and a Kolmogorov scale of 170 μm. For the case with the strongest attenuation, the 150 μm particle diameter was comparable to the Kolmogorov length and the 2100 μm average particle spacing was comparable to the Taylor microscale. These values are characteristic of experiments where strong attenuation is observed. In this regime, the particles must be considered as applying local disturbances to the flow rather than a continuous resisting force. Furthermore, the average particle Reynolds numbers in those experiments were 20, which is too high for a linear drag law to be appropriate, but below the range where an unsteady wake or vortex shedding would augment the turbulence.

Experiments have shown that turbulence attenuation can be strong when the dimensionless particle diameter is of order 1 and the particle Reynolds number is below the vortex shedding regime. Generally, models based on the particle analysis earlier strongly underpredict turbulence attenuation in this regime, suggesting that some other mechanism is significantly increasing the turbulence dissipation rate. Simulations that fully resolve all details of the flow around individual particles (Bagchi and Balachandar, 2002, Burton and Eaton, 2005) are casting light on this mechanism. Burton and Eaton simulated a stationary particle with dimensionless diameter of 2 and Re near 20 interacting with homogeneous isotropic turbulence. The dissipation was strongly augmented near the particle surface, and substantial reductions in TKE were observed in a spherical volume roughly five times the particle diameter. Furthermore, snapshots of the turbulence structure showed that eddies with scales up to around 10 times the particle diameter were distorted as they moved around the particle. Highly resolved PIV measurements by Tanaka and Eaton (2010) showed that the dissipation was locally augmented by up to a factor of three near the particles. Unfortunately, widely used large eddy simulation codes augmented by point-force coupling models cannot capture this effect (Segura et al., 2004, Eaton, 2009). While these codes are thought to be accurate for very small particles, modifications such as those under study by Capecelatro and Desjardins (2013) will be needed when the dimensionless particle diameter is comparable to turbulent length scales.

12.4.3 Observations of Turbulence Modulation

Most observations of turbulence modulation have been in simple flows including homogeneous turbulence maintained by external forcing, pipe and channel flows, developing boundary layers, and round jet flows. Generally, the strongest attenuation has been observed in wall-bounded flows where turbulence production is fairly weak except near walls. The brief review in this section concentrates on experiments designed specifically to observe turbulence modulation. In recent years, there has been a proliferation of studies using point-force coupled large eddy or direct numerical simulations to examine homogeneous flows. This technique requires several assumptions that are not strictly valid for typical cases, so the limited sample of results presented here must be used with caution.

12.4.3.1 Homogeneous Gas–Solid Flows

Numerous numerical simulations and a few experiments have examined the case of homogeneous gas phase with dilute loadings of solid particles. Stationary (forced) isotropic turbulence was examined by Squires and Eaton (1990) and Boivin et al. (1998) for particle mass loading ratios ranging from 0.1 to 1.0 and Stokes numbers ranging from 1.3 to 11.4. Both studies indicated substantial turbulence attenuation, with the degree of attenuation increasing with increasing mass loading. The maximum reduction in the TKE was 56%. Squires and Eaton found essentially no effect of varying St_k from about 1.4 to 4.7, while Boivin et al. (1998) found that the attenuation increased monotonically as St_k increased from 1.3 to 11.4 at a mass loading ratio of 0.2. The opposite trend was observed when the mass loading ratio was increased to 1.0. One consistent finding of these studies and many other subsequent works is that the turbulence spectra are distorted, showing attenuation at low frequency and augmentation at higher frequency.

Decaying isotropic turbulence was simulated by Elghobashi and Truesdell (1993), Druzhinin (2001), Druzhinin and Elghobashi (1999), Ferrante and Elghobashi (2003), and Sundaram and Collins (1999). It is difficult to discern any consistent trends from these results. Sundaram and Collins varied the particle diameter and the Stokes number maintaining a constant mass loading ratio of 0.14. They found that the attenuation increased as the Stokes number increased from 1.6 to 6.4. Ferrante and Elghobashi (2003) observed a similar trend for St_k ranging from 0.1 to 5. The overall attenuation levels in the latter case were quite small with a maximum reduction in kinetic energy of 30% at a mass loading ratio of 1.0.

Most of the computations discussed earlier focused on cases without gravity. However, Druzhinin and Elghobashi (1999) and Ferrante and Elghobashi (2003) each ran a case including a body force in the particle equation of motion. In both cases, very substantial turbulence augmentation was observed even though the dimensionless diameters were less than unity.

Some trends can be discerned by combining the results of various homogeneous flow simulations. Figure 12.5 shows the reduction in turbulence kinetic energy as a function of mass loading for selected cases with St_k near 5. Turbulence attenuation was always small (<22%) for mass loadings less than or equal to 20%. Substantial changes to the turbulence were only found for relatively large loadings.

Figure 12.6 shows the turbulence attenuation plotted against St_k for cases in which the mass loading ratio is approximately unity. For the cases of decaying isotropic turbulence, the Stokes number changes with time. A representative value midway through the decay was chosen for the purposes of this plot. There is evidence of a trend of increasing turbulence attenuation with increasing St_k, but the Squires and Eaton (1990) and Boivin et al. (1998) cases for St_k near 1 break with the trend. The differences between these cases

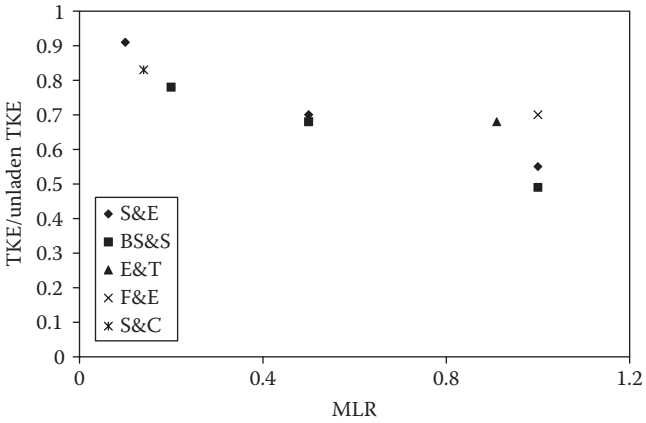


Figure 12.5

Attenuation of TKE in point-force coupled simulations of isotropic turbulence for cases with St_k near 5. (Data from Squires, K.D. and Eaton, J.K., *Phys. Fluids A*, 2, 1191, 1990; Boivin, M. et al., *J. Fluid Mech.*, 375, 235, 1998; Elghobashi, S. and Truesdell, G.C., *J. Fluid Mech.*, 242, 655, 1993; Ferrante, A. and Elghobashi, S., *Phys. Fluids*, 15, 315, 2003; Sundaram, S. and Collins, L.R., *J. Fluid Mech.*, 335, 75, 1999.)

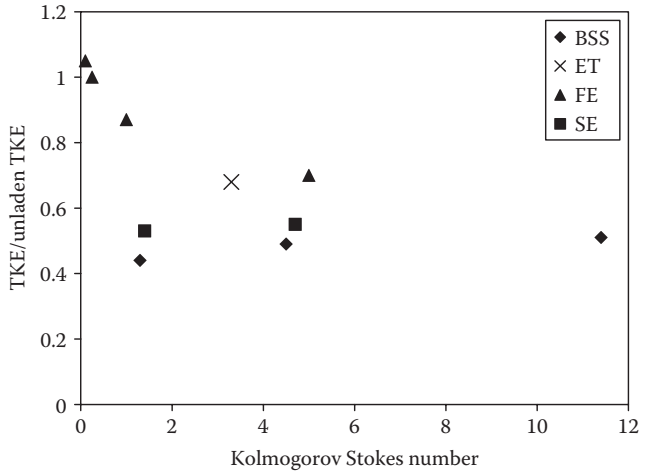


Figure 12.6

Attenuation of TKE as a function of St_k in isotropic turbulence with mass loading ratio near 1. (Data extracted from Boivin, M. et al., *J. Fluid Mech.*, 375, 235, 1998; Elghobashi, S. and Truesdell, G.C., *J. Fluid Mech.*, 242, 655, 1993; Ferrante, A. and Elghobashi, S., *Phys. Fluids*, 15, 315, 2003; Squires, K.D. and Eaton, J.K., *Phys. Fluids A*, 2, 1191, 1990.)

and Ferrante and Elghobashi (2003) are quite large even though the flow and particle parameters are quite similar. This may be due to differences in the implementation of force coupling scheme in the simulation or in the initial conditions for the velocity field. Recent fully resolved simulations by Lucci et al. (2011) on much larger particles found that the Stokes number alone is not adequate to characterize turbulence modification.

Only a few experiments have been reported on modification in particle-laden homogeneous turbulence. Geiss et al. (2001) examined grid turbulence in a downflow wind tunnel. The flow carried a 35% mass loading of 110 μm diameter glass particles. The short paper gives few details on the experiment, but kinetic energy reductions of up to 44% were observed at the most downstream station. Note that this reduction is comparable to the reductions observed in some of the simulations at substantially higher mass loading. Three recent experiments have used specially designed turbulence chambers to examine the effects of particles falling at terminal velocity through homogeneous/isotropic air turbulence. Yang and Shy (2005) used a cruciform apparatus in which turbulence was generated by fans outside the test zone and particles fell through the homogeneous turbulence at their terminal velocity. The volume loading was estimated to be around 5×10^{-6}. Three different particle sizes were used, and all particle diameters were much smaller than the Kolmogorov scale (0.03, 0.06, 0.1). Stokes numbers ranged from 0.36 to 1.9, so preferential concentration was significant in all cases. Terminal velocities ranged from $0.2u_{rms}$ to 0.96 u_{rms}. The particles with the lowest terminal velocity did not significantly change the turbulence, while the large particles produced up to 60% augmentation. There was a clear correlation of increasing augmentation with increasing terminal velocity. Hwang and Eaton (2006) created nearly isotropic turbulence using loudspeaker-driven synthetic jets in the corners of a box. This produced much more energetic turbulence while maintaining small mean velocities. They used glass particles with nondimensional diameters of 1, St_k of 50, terminal velocities at roughly $2u_{rms}$, and estimated mass loadings up to 30%. They observed turbulence attenuation as large as 35%–40%. Tanaka and Eaton (2010) made very high-resolution PIV measurements in the same facility with larger particles (dimensionless d_p = 2.3 and 4.5) at mass loading ratios up to 0.45. Small levels of turbulence modulation were observed, and they concluded that turbulence production in particle wakes was offsetting turbulence attenuation at particle surfaces. Previous measurements had shown reductions in the turbulence dissipation rate in rough proportion to the reduction in TKE. However, the high-resolution measurements by Tanaka and Eaton showed that the overall dissipation rate increases when the high velocity gradients near particle surfaces are resolved. The one consistent feature of all three isotropic turbulence experiments was that the turbulence spectra were augmented at high frequency in agreement with simulations.

12.4.3.2 Wall-Bounded Gas–Solid Flows

The strongest effects of turbulence modification have been observed in wall-bounded flows including pipe flows, channel flows, and boundary layers. Much of the original experimental work on turbulence modulation was done in pipe flows with notable contributions from Lee and Durst (1982), Tsuji and Morikawa (1982), and Tsuji et al. (1984). More recently, considerable effort has been focused on fully developed turbulent channel flows and flat plate boundary layers. Kulick et al. (1994), Paris and Eaton (2001), and Kussin and Sommerfeld (2002) all examined fully developed air channel flows at similar Reynolds numbers. Each experiment covered a reasonably broad range of particle parameters lending new insight into turbulence modulation.

Kulick et al. (1994) conducted experiments in a long vertical downflow air channel flow at a Reynolds number of 13,800 based on the channel half-width and the bulk velocity. Experiments were conducted with 50 and 90 μm diameter glass beads and 70 μm copper beads. The Stokes numbers based on the centerline Kolmogorov timescale were 9, 23, and 50 for the three particle classes. Gas-phase measurements were made using Laser doppler velocimetry with submicron tracer particles that were easily discriminated from the larger dispersed particles. Turbulence modification was small (<10%) for the St_k = 9 particles, substantial for St_k = 23, and very large for St_k = 50. Figure 12.7 reproduced from Kulick et al. (1994) shows the streamwise turbulence intensity profiles for copper beads at various mass loading ratios. The turbulence is attenuated across the entire profile, with the largest attenuation near the centerline.

Paris and Eaton (2001) conducted experiments in the same channel flow facility using phase-discriminated PIV to verify the earlier LDA results for copper beads. They also conducted separate experiments using 150 μm glass beads that had almost the same aerodynamic time constant as the copper. By virtue of their larger diameter, the particle Reynolds numbers were over two times greater for the glass (Re_p = 19 vs. 8). The centerline results, as shown in Figure 12.4, showed similar attenuation levels as observed by Kulick for the copper and larger attenuation levels for the higher Reynolds number glass particles.

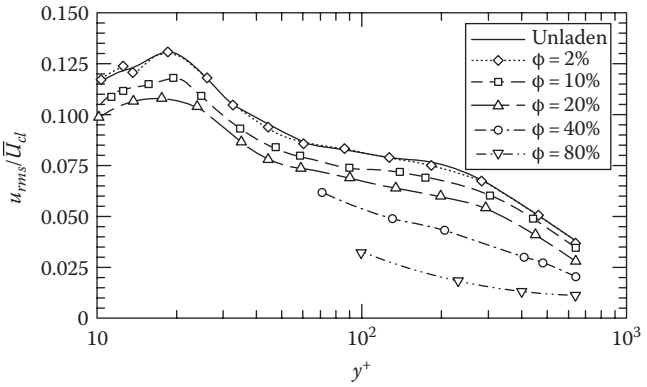


Figure 12.7

Streamwise turbulence intensity in fully developed channel flow laden with 70 micron copper spheres at mass loading ratios from 0 to 0.8. (From Kulick, J.D. et al., *J. Fluid Mech.*, 277, 285, 1994.)

Kussin and Sommerfeld (2002) and Lain et al. (2002) made measurements in a horizontal channel flow for a variety of particle sizes. The half-height Reynolds number was 21,000 and smooth and rough wall cases were examined. Measurements were made using a phase-Doppler anemometer. Unfortunately, the particle size distribution was wide and the flow tracers were large (nominally 4 μm in diameter), so the gas-phase turbulence measurements were contaminated by particle-phase measurements. As a result, the turbulence measurements are quite noisy. Nevertheless, because both the particle size and mass loading ratio were varied over wide ranges, trends were easily observed. Figure 12.8 shows the streamwise turbulence intensity data for Kussin and Sommerfeld's (2002) rough wall cases. The data have been averaged across the channel to reduce noise, normalized by the average value from all cases at zero loading, and squared for comparison to the TKE data presented in other plots. The data are presented for 60, 100, and 195 μm glass beads that have Stokes numbers of 35, 120, and 350 and Reynolds numbers of 7, 23, and 72. All three particle sizes produce substantial attenuation with the degree of attenuation decreasing with increasing particle size. It is interesting to note that the 60 μm particles that produced the largest attenuation in Kussin and Sommerfeld's (2002) experiments have Stokes numbers similar to the 150 μm glass beads that produced the strongest attenuation in the Paris and Eaton experiments.

Kussin and Sommerfeld (2002) also presented measurements with 0.6 and 1 mm diameter glass beads with mass loadings ratios up to 2.0. These cases showed significant turbulence augmentation near the channel centerplane and moderate attenuation near the walls. They concluded that this was a particle Reynolds number effect since the relative velocity between the gas and particles was smaller near the walls than in the channel center region. The particle Reynolds numbers at the centerplane were approximately 350 and 500 for the 0.6 and 1 mm beads, respectively. This indicates that unsteady particle wakes probably played a role

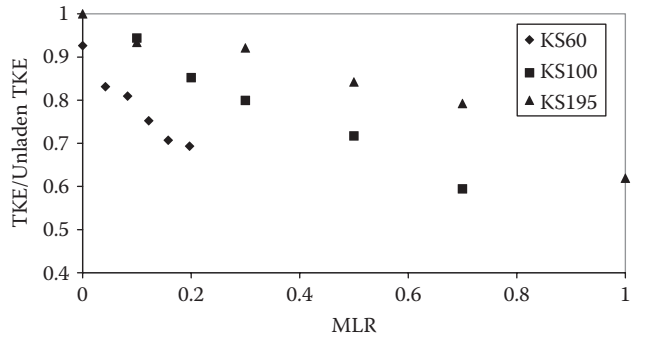


Figure 12.8

Streamwise normal stress ($\overline{u'^2}$) averaged across a fully developed channel and normalized by the averaged stress for an unladen case. Data for three particle sizes are shown. (Data from Kussin, J. and Sommerfeld, M., *Exp. Fluids*, 33, 143–159, 2002.)

in the turbulence augmentation. Hadinoto and Curtis (2009) found a similar behavior in vertical pipe flows laden with relatively large particles at mass loading ratios around 0.5. Large augmentation of the turbulence was observed near the pipe centerline with very little change in the turbulence near the wall.

The channel flow experiments discussed here along with several other wall-bounded flow experiments are beginning to give a fairly consistent picture. Very small particles with St_k less than about 10 do not cause significant changes to the turbulence. As the particle size increases, the particles cannot follow the turbulent fluctuations and turbulence attenuation increases rapidly. Attenuation reaches a maximum around $St_k = 50$. The attenuation can be very large for particles in this size range. As particle size increases further, the effects of superimposed laminar wakes or unsteady wakes begin to have an effect decreasing the overall level of turbulence attenuation, and eventually causing substantial augmentation.

12.4.3.3 Free Shear Flows

The flow geometries and particle parameters for particle-laden jet, mixing layer, and separated flow experiments have varied widely, so it has not been possible to extract trends as was done in the previous two sections. Shuen et al. (1985) and Mostafa et al. (1989) have examined round jets discharging downward into quiescent air. Shuen et al. (1985) examined the far field of a jet discharging from a pipe for a range of particle sizes and mass loading ratios up to 66%. They observed changes in the turbulent stresses of less than 10%. Mostafa et al. (1989) examined the near field of a similar jet at mass loading ratios of 0.2 and 1.0. Detailed comparisons to the unladen turbulence measurements were not presented, but the authors noted a reduction of 40% in the TKE on the jet centerline for a mass loading of 1.0. It is important to note that the jet was supplied from a turbulent pipe flow. Although the jet exit plane was not documented, it is likely that the turbulence level was substantially lower for the particle-laden case than for the single-phase flow.

Free shear flows are subject to the Kelvin–Helmholtz instability that produces large roller vortices. An important issue to understand is how the particles might affect these vortices. A simplified analysis by Yang et al. (1993) showed that particles slow the development of roller vortices. Longmire and Eaton (1992) found little effect of particles on the near-field development of roller vortices for mass loading ratios up to 0.8. This is corroborated by research in backward-facing step flows that have been studied by Maeda et al. (1980), Hishida and Maeda (1991), Hardalupas et al. (1992), and Fessler and Eaton (1999). All of these experiments were conducted in the small particle regime. Some experiments observed almost no change to the turbulence with the others showed either small attenuation or augmentation of the turbulence. Overall, the particle effects on the turbulence are much smaller than in wall-bounded flows probably because the extra dissipation due to particles is overwhelmed by the strong shear production in free shear flows.

Longmire and Anderson (2003) made direct measurements of vortex/particle interaction in an impinging round jet in which the jet was weakly forced to phase lock the dominant vortex ring structures. The jet carried a 4% mass loading of particles with Stokes number of 1.2 based on the vortex ring period. Simultaneous two-phase PIV measurements showed that vortex ring circulation was reduced by around 30% in the impingement zone where the local mean particle loading was elevated by the rapid deceleration of the carrier flow. Also, the velocity difference between the carrier-phase vortices and particles rebounding from the wall was large. This research shows that particles moving with a high relative velocity (hence significant Re_p) can strongly attenuate dominant vortex structures.

12.4.3.4 Liquid–Solid Flows

We consider here cases of solid particles dispersed in liquid flows with relatively low volume fraction so that the flows are not dominated by particle collisions. Typically, liquid–solid material density ratios are between 1 and 5, so the mass loading ratio is very small for dilute volume fractions. Also, the Stokes number is small unless the particles are quite large. The only cases for which turbulence modulation is observed are thus flows in which the particles are large relative to the turbulence scales.

Schreck and Kleis (1993) examined grid turbulence in a downflow water channel laden with particles of $d_k \approx 5$. Volume concentrations were as large as 1.5%. Reductions in the TKE of 20% were observed for the heaviest particles at the largest concentration. Bellani et al. (2012) studied dilute loadings of large ($d_k = 21$) neutrally buoyant particles in homogeneous turbulence produced by opposed arrays of pulsed jets. They found 15% reduction in TKE using spherical particles at a mass loading of 0.0014, but only 3% reduction when the particles were 2:1 ellipsoids. It is apparent from these results that volume fraction rather than mass loading is the critical parameter when considering turbulence attenuation. Lucci et al. (2011) developed fully resolved numerical simulations for spherical particles with the same range of particle size and volume loading

in decaying isotropic turbulence. The five different cases studied all had Stokes number of 61, but particle diameters varying by a factor of 2 and Reynolds numbers around 100. The peak reduction in TKE was only 7.4% while the peak increase in dissipation rate was 16.7% corroborating the air flow experiments of Tanaka and Eaton (2010). Taken together, the five cases showed that no simple parameterization of turbulence attenuation was possible for large particle cases.

Detailed experiments in particle-laden water channel flows have been conducted using PIV in several laboratories. Kiger and Pan (2002) studied a 40 mm wide water channel operated at a Reynolds number of 12,000 and laden with 195 μm diameter glass beads at a mass loading ratio of 0.0006. Relatively small (8%–10%) increases in the turbulence intensity were observed across the channel. Suzuki et al. (2002) used a 40 mm wide, vertical water channel at a very low Reynolds number (Re_h = 2900). The flow was laden with 400 μm ceramic particles at a mass loading ratio of 0.0012. The dimensionless particle diameter was about 2 near the wall, and the particle Reynolds number was on the order of 30. The turbulence was almost unchanged near the wall, but the streamwise turbulence intensity increased by more than a factor of 2 in the channel center.

Sato et al. (2000) examined a similar channel at the same Reynolds number using 190 μm (Re_p = 10) or 400 μm (Re_p = 50) glass beads. The 190 μm particles were smaller than the centerline Kolmogorov scale, while the 400 μm particles were larger. The mass loading ratio was about 0.0004 for the 190 μm particles and 0.00033 and 0.00086 for the 400 μm particles. Data were acquired only near the channel centerline. The smaller particles produced relatively small increases in the kinetic energy, while the larger particles increased the TKE by roughly a factor of 4. Doubling the mass loading for the 400 μm particles had a relatively small effect.

Trends are difficult to discern because of the small number of experiments and resolved simulations examining turbulence modulation in liquid/solid flows. Due to the relatively low density ratio, the particle/turbulence interactions are significant only for relatively large particles that have relatively high Reynolds numbers. Turbulence attenuation can occur due to extra dissipation on the large particle surfaces while turbulence augmentation can occur in particle wakes. The interplay of these effects appears to determine the level (and direction) of turbulence modulation. When attenuation has been observed, the fractional decrease has been substantially less than observed in some air flow experiments.

12.4.4 Simple Parameterization of Turbulence Modulation

There have been several attempts to define a small set of dimensionless parameters that can be used to organize turbulence modulation data and develop predictive correlations. The best known of these is the paper of Gore and Crowe who found that turbulence in simple shear flows is attenuated when the particle diameter is less than 1/10 of the large eddy length scale and augmented for larger particles. This is oversimplistic and does not account for sensitivity to Stokes number, particle density, particle shape, and particle Reynolds number. Even this simple rule of thumb was violated by some experiments performed after the original publication.

Generally, the two-way coupling regime is thought to begin for volume loadings above 10^{-6}. However, the data compilation earlier indicates that turbulence modulation is insignificant for volume loadings less than 10^{-5}. In most experiments where the volume loading has been systematically varied, strong modulation is observed for volume fractions above 10^{-4}. Significant modulation at lower average loadings can occur if the particles are concentrated into specific regions of the flow such as the sublayer in a turbulent boundary layer.

Poelma et al. (2007) proposed a parameter called the Stokes load defined as

$$\Phi_{St} = \frac{\Phi_v \rho_p \eta^3}{3\pi \nu d \tau_k}$$

This is essentially the product of the particle number density and the aerodynamic time constant normalized by the Kolmogorov scales. They found that the decay of isotropic turbulence varied linearly with this parameter. Tanaka and Eaton (2008) nondimensionalized the Reynolds-averaged TKE transport equation and arrived at a parameter they call the particle momentum number:

$$Pa_{St} = StRe_L^2 \left(\frac{\eta}{L} \right)^3$$

where L is an integral scale of the turbulence. Their compilation of pipe and channel flow data showed that attenuation occurs for $3 \times 10^3 < Pa_{St} < 10^5$. Augmentation occurs at both lower and higher particle momentum numbers. The lack of broad success of any of these parameters is probably because there are multiple interacting mechanisms that simultaneously attenuate and augment the turbulence.

References

Aliseda, A., Cartellier, A., Hainaux, F., and Lasheras, J.C., Effect of preferential concentration on the settling velocity of heavy particles in homogeneous isotropic turbulence, *J. Fluid Mech.*, 468, 77–105, 2002.

Anderson, S.L. and Longmire, E.K., Particle motion in the stagnation zone of an impinging air jet, *J. Fluid Mech.*, 299, 333–366, 1995.

Armenio, V. and Fiorotto, V., The importance of the forces acting on particles in turbulent flows, *Phys. Fluids*, 13, 2437, 2001.

Bagchi, P. and Balachandar, S., Shear vs. vortex-induced lift on a rigid sphere at moderate Re, *J. Fluid Mech.*, 473, 379–388, 2002.

Bagchi, P. and Balachandar, S., Effect of turbulence on the drag and lift of a particle, *Phys. Fluids*, 15, 3496–3513, 2003.

Bagchi, P. and Kottam, K., Effect of freestream isotropic turbulence on heat transfer from a sphere, *Phys. Fluids*, 20, 073305-1-17, 2008.

Balachandar, S. and Eaton, J.K., Turbulent dispersed multiphase flow, *Annu. Rev. Fluid Mech.*, 42, 111–133, 2010.

Balkovsky, E., Falkovich, G., and Fouxon, A., Intermittent distribution of inertial particles in turbulent flows, *Phys. Rev. Lett.*, 86, 2790–2793, 2001.

Batchelor, G.K., Diffusion in a field of homogeneous turbulence I. Eulerian analysis, *Aust. J. Sci. Res.*, 2, 437–459, 1949.

Bec, J., Biferale, L., Boffetta, G., Celani, A., Cencini, M., Lanotte, A., Musacchio, S., and Toschi, F., Acceleration statistics of heavy particles in turbulence, *J. Fluid Mech.*, 550, 349–358, 2006.

Bec, J., Biferale, L., Cencini, M., Lanotte, A., Musacchio, S., and Toschi, F., Heavy particle concentration in turbulence at dissipative and inertial scales, *Phys. Rev. Lett.*, 98, 084502, 2007.

Bellani, G., Byron, M.L., Collignon, A.G., Meyer, C.R., and Variano, E.A., Shape effects on turbulent modulation by large nearly neutrally buoyant particles, *J. Fluid Mech.*, 712, 41–60, 2012.

Berlemont, A., Desjonqueres, P., and Gousebet, G., Particle Lagrangian simulation in turbulent flows, *Int. J. Multiphase Flow*, 16 19–34, 1990.

Boivin, M., Simonin, O., and Squires, K.D., Direct numerical simulation of turbulence modulation by particles in isotropic turbulence, *J. Fluid Mech.*, 375, 235–263, 1998.

Bosse, T., Kleiser, L., and Meiburg, E., Small particles in homogeneous turbulence: Settling velocity enhancement by two-way coupling, *Phys. Fluids*, 18, 027102, 2006.

Brian, P.L.T., Hales, H.B., and Sherwood, T.K., Transport of heat an mass between liquids and spherical particles in an agitated tank, *AIChE J.*, 15, 727–733, 1969.

Brooke, J.W., Kontomaris, K., Hanratty, T.J., and McLaughlin, J.B., Turbulent deposition and trapping of aerosols at a wall, *Phys. Fluids A*, 4, 825–834, 1992.

Burton, T.M. and Eaton, J.K., Fully resolved simulations of particle-turbulence interaction, *J. Fluid Mech.*, 545, 67–111, 2005.

Capecelatro, J. and Desjardins, O., An Euler-Lagrange strategy for simulating particle-laden flows, *J. Comput. Phys.,* 238, 1–31, 2013.

Caporaloni, M., Tampieri, F., Trombetti, F., and Vittori, O., Transfer of particles in nonisotropic air turbulence, *J. Atmos. Sci.*, 32, 565–568, 1975.

Chen, C.P. and Wood, P.E., A turbulence closure model for dilute gas-particle flows, *Can. J. Chem. Eng.*, 63, 349–360, 1985.

Chen, J.-H. and Faeth, G.M., Continuous-phase properties of homogeneous particle-laden turbulent flows, *AIAA J.*, 39, 180–183, 2001.

Chung, J. and Troutt, T., Simulation of particle dispersion in an axisymmetric jet, *J. Fluid Mech.*, 186, 199–222, 1988.

Cuzzi, J.N., Hogan, R.C., Paque, J.M., and Dobrovolskis, A.R., Self-selective concentration of chondrules and other small particles in protoplanetary nebula turbulence, *Astrophys. J.*, 546, 496–508, 2001.
Druzhinin, O.A., The influence of particle inertia on the two-way coupling and modification of isotropic turbulence by microparticles, *Phys. Fluids*, 13(12), 3738–3755, 2001.
Druzhinin, O.A. and Elghobashi, S., On the decay rate of isotropic turbulence laden with microparticles, *Phys. Fluids*, 11(3), 602–610, 1999.
Eaton, J.K., Two-way coupled turbulence simulations of gas-particle flows using point-particle tracking, *Int. J. Multiphase Flow*, 35, 792–800, 2009.
Eaton, J.K. and Fessler, J.R., Preferential concentration of particles by turbulence, *Int. J. Multiphase Flow*, 26, 719–727, 1994.
Elghobashi, S. and Truesdell, G.C., Direct simulation of particle dispersion in a decaying isotropic turbulence, *J. Fluid Mech.*, 242, 655–700, 1992.
Elghobashi, S. and Truesdell, G.C., On the two way interaction between homogeneous turbulence and dispersed solid particles I: Turbulence modulation, *Phys. Fluids A*, 5, 1790–180, 1993.
Feng, Z.G. and Michaelides, E.E., A numerical study on the transient heat transfer from a sphere at high Reynolds and Peclet numbers, *Int. J. Heat Mass Transfer*, 43, 219–22, 2000.
Ferrante, A. and Elghobashi, S., On the physical mechanism of two-way coupling in particle-laden isotropic turbulence, *Phys. Fluids*, 15, 315–329, 2003.
Fessler, J.R. and Eaton, J.K., Turbulence modification by particles in a backward-facing step flow, *J. Fluid Mech.*, 394, 97–117, 1999.
Fessler, J.R., Kulick, J.D., and Eaton, J.K., Preferential concentration of heavy particles in a turbulent channel flow, *Phys. Fluids*, 6, 3742–3749, 1994.
Geiss, S., Sadika, A., Maltsev, A., Dreizler, A., and Janicka, J., Investigations of turbulence modulation in turbulent particle laden flows, *Z. Agnew Math. Mech.*, 81, S527–S528, 2001.
Gore, R.A. and Crowe, C.T., Modulation of turbulence by a dispersed phase, *ASME J. Fluids Eng.*, 113, 304–307, 1991.
Gualtieri, P., Picano, F., Sardina, G., and Casciola, C.M., Clustering and turbulence modulation in particle-laden shear flows, *J. Fluid Mech.*, 715, 134–162, 2013.
Guha, A., Transport and deposition of particles in turbulent and laminar flows, *Annu. Rev. Fluid Mech.*, 40, 311–341, 2008.
Hadinoto, K. and Curtis, J.S., Reynolds number dependence of gas-phase turbulence in particle-laden flows: Effects of particle inertia and particle loading, *Powder Technol.*, 195, 119–127, 2009.
Hardalupus, Y., Taylor, A.M.K.P., and Whitelaw, J.H., Particle dispersion in a vertical round sudden expansion flow, *Proc. R. Soc. Lond. A*, 341, 411–442, 1992.
Hishida, K., Ando, A., and Maeda, M., Experiments on particle dispersion in a turbulent mixing layer, *Int. J. Multiphase Flow*, 18, 181–194, 1992.
Hishida, K. and Maeda, M., Turbulence characteristics of particle-laden flow behind a rearward facing step, *ASME FED*, 121, 207–212, 1991.
Hwang, W. and Eaton, J.K., Homogeneous and isotropic turbulence modulation by small heavy (St~50) particles, *J. Fluid Mech.*, 564, 361–393, 2006.
Jones, W.P., Lyra, S., and Marquis, A.J., Large eddy simulation of evaporating kerosene and acetone sprays, *Int. J. Heat Mass Transfer*, 53, 2491–2505, 2010.
Kaftori, D., Hetsroni, G., and Banerjee, S., Particle behavior in the turbulent boundary layer. I. Motion, deposition, and entrainment, *Phys. Fluids*, 7, 1095–1106, 1995a.
Kaftori, D., Hetsroni, G., and Banerjee, S., Particle behavior in the turbulent boundary layer. II. Velocity and distribution profiles, *Phys. Fluids*, 7, 1107–1121, 1995b.
Kiger, K.T. and Pan, C., Suspension and turbulence modification effects of solid particulates on a horizontal turbulent channel flow, *J. Turbulence*, 3, 19, 2002.
Kim, J. and Balachandar, S., Mean and fluctuating components of drag and lift forces on an isolated finite-sized particle in turbulence, *Theor. Comput Fluid Dyn.*, 26, 185–204, 2012.
Kulick, J.D., Fessler, J.R., and Eaton, J.K., Particle response and turbulence modification in fully developed channel flow, *J. Fluid Mech.*, 277, 285–309, 1994.
Kussin, J. and Sommerfeld, M., Experimental studies on particle behavior and turbulence modification in horizontal channel flow with different wall roughness, *Exp. Fluids*, 33, 143–159, 2002.
Lain, S., Sommerfeld, M., and Kussin, J., Experimental studies and modeling of four-way coupling in particle-laden channel flow, *Int. J. Heat Fluid Flow*, 23, 647–656, 2002.

Lee, S.L. and Durst, F., On the motion of particles in turbulent duct flows, *Int. J. Multiphase Flow*, 8, 125–146, 1982.
Lazaro, B.J. and Lasheras, J.C., Particle dispersion in a turbulent plane shear layer, *Phys. Fluids A*, 1, 1035–1044, 1989.
Longmire, E.K. and Anderson, S.L., Particle/vortex interactions in free and impinging air jets, in A. R. Karagozian, L. Cortelezzi, and A. Soldati (Eds.), *Manipulation and Control of Jets in Crossflow*, Springer, Wien, Austria, 2003, pp. 211–222.
Longmire, E.K. and Eaton, J.K., Structure of a particle-laden round jet, *J. Fluid Mech*., 236, 217–257, 1992.
Longmire, E.K. and Eaton, J.K., Active open-loop control of particle dispersion in round jets, *AIAA J*., 32(3), 555–556, 1994.
Lucci, F., Ferrante, A., and Elghobashi, S., Is stokes number an appropriate indicator for turbulence modulation by particles of Taylor-length-scale size, *Phys. Fluids*, 23, 025101, 2011.
Maeda, M., Hishida, K., and Furutani, T., Optical measurements of local gas and particle velocity in an upward flowing dilute gas-solids suspension, in *Proceedings of the Polyphase Flow and Transport Technology*, Century 2-ETC, San Francisco, CA, 1980, pp. 211–216.
Marchioli, C. and Soldati, A., Mechanisms for particle transfer and segregation in a turbulent boundary layer, *J. Fluid Mech*., 468, 283–315, 2002.
Martin, J.E. and Meiburg, E., The accumulation and dispersion of heavy particles in forced two-dimensional mixing layers. I. The fundamental and subharmonic cases, *Phys. Fluids*, 6, 1116, 1994.
Maxey, M.R., The gravitational settling of aerosol particles in homogeneous turbulence and random flow fields, *J. Fluid Mech*., 174, 441–465, 1987.
Maxey, M.R. and Riley, J.J., Equation of motion for a small rigid sphere in a nonuniform flow, *Phys. Fluids*, 26, 883–889, 1983.
Monchaux, R., Bourgoin, M., and Cartellier, A., Preferential concentration of heavy particles: A Voronoi analysis, *Phys. Fluids*, 22, 103304, 2010.
Monchaux, R., Bourgoin, M., and Cartellier, A., Analyzing preferential concentration and clustering of inertial particles in turbulence, *Int. J. Multiphase Flow*, 40, 1–18, 2012.
Mostafa, A.A., Mongia, H.C., McDonell, V.G., and Samuelsen, G.S., Evolution of particle-laden jet flows: A theoretical and experimental study, *AIAA J*., 27, 167–183, 1989.
Nino, Y. and Garcia, M.H., Experiments on particle-turbulence interactions in the near-wall region of an open channel flow: Implications for sediment transport, *J. Fluid Mech*., 326, 285–319, 1996.
Olivieri, S., Picano, F., Sardina, G., Iudicone, D., and Brandt, L., The effect of the Basset history force on particle clustering in homogeneous and isotropic turbulence, *Phys. Fluids*, 26, 041704, 2014.
Paris, A.D. and Eaton, J.K., Turbulence attenuation in a particle-laden channel flow, Report TSD-137, Department of Mechanical Engineering, Stanford University, Stanford, CA, 2001.
Parthasarathy, R.N. and Faeth, G.M., Turbulence modulation in homogeneous dilute particle-laden flows, *J. Fluid Mech*., 220, 485–514, 1990.
Poelma, C., Westerweel, J., and Ooms, G., Particle-fluid interactions in grid generated turbulence, *J. Fluid Mech*., 589, 3315–3351, 2007.
Reade, W.C. and Collins, L.R., Effect of preferential concentration on turbulent collision rates, *Phys. Fluids*, 12, 2530–2540, 2000.
Reeks, M.W., On the dispersion of small particles suspended in an isotropic turbulent field, *J. Fluid Mech*., 83, 529–546, 1977.
Reeks, M.W., The transport of discrete particles in inhomogeneous turbulence, *J. Aerosol Sci*., 14, 729–739, 1983.
Rogers, C.B. and Eaton, J.K., The effect of small particles on fluid turbulence in a flat-plate, turbulent boundary layer in air, *Phys. Fluids A*, 3, 928–937, 1991.
Sakamoto, H. and Haniu, H., A study of vortex shedding from spheres in a uniform flow, *ASME J. Fluids Eng.*, 112, 386–392, 1990.
Sato, Y., Fukuichi, U., and Hishida, K., Effect of inter-particle spacing on turbulence modulation by Lagrangian PIV, *Int. J. Heat Fluid Flow*, 21, 554–561, 2000.
Saw, E.W., Shaw, R.A., Ayyalasomayajula, S., Chuang, P.Y., and Gylfason, Á., Inertial clustering of particles in high-Reynolds-number turbulence, *Phys. Rev. Lett.*, 100, 214501, 2008.
Schreck, S. and Kleis, S.J., Modification of grid-generated turbulence by solid particles, *J. Fluid Mech*., 249, 665–688, 1993.
Segura, J.C., Oefelein, J.C., and Eaton, J.K., Predictive capabilities of particle-laden large eddy simulation, Report TSD-156, Mechanical Engineering Department, Stanford University, Stanford, CA, 2004.

Shao, X., Wu, T., and Yu, Z., Fully resolved numerical simulation of particle-laden turbulent flow in a horizontal channel at a low Reynolds number, *J. Fluid Mech.*, 693, 319–334, 2012.
Shaw, R.A., Particle-turbulence interactions in atmospheric clouds, *Annu. Rev. Fluid Mech.*, 35, 183–227, 2003.
Shuen, J.-S., Solomon, A.S.P., Zhang, Q.-F., and Faeth, G.M., Structure of particle-laden jets: Measurements and predictions, *AIAA J.*, 23, 396–404, 1985.
Squires, K.D. and Eaton, J.K., Particle response and turbulence modulation in isotropic turbulence, *Phys. Fluids A*, 2, 1191–1203, 1990.
Squires, K.D. and Eaton, J.K., Measurements of particle dispersion obtained from direct numerical simulations of isotropic turbulence, *J. Fluid Mech.*, 226, 1–35, 1991a.
Squires, K.D. and Eaton, J.K., Preferential concentration of particles by turbulence, *Phys. Fluids A*, 3, 1169–1178, 1991b.
Stock, D.E., Particle dispersion in flowing gases—1994 Freeman Scholar Lecture, *Trans. ASME, J. Fluids Eng.*, 118, 4–17, 1996.
Sundaram, S. and Collins, L.R., Collision statistics in an isotropic particle-laden turbulent suspension. Part 1. Direct numerical simulations, *J. Fluid Mech.*, 335, 75–109, 1997.
Sundaram, S. and Collins, L.R., A numerical study of the modulation of isotropic turbulence by suspended particles, *J. Fluid Mech.*, 379, 105–143, 1999.
Suzuki, Y., Ikenoya, M., and Kasagi, N., Simultaneous measurement of fluid and dispersed phases in a particle-laden turbulent channel flow with the aid of 3-D PTV, *Exp. Fluids*, 29S, S185–S193, 2002.
Tanaka, T. and Eaton, J.K., Classification of turbulence modification by dispersed spheres using a novel dimensionless number, *Phys. Rev. Lett.*, 101, 114502, 2008.
Tanaka, T. and Eaton, J.K., Sub-Kolmogorov resolution particle image velocimetry measurements of particle-laden forced turbulence, *J. Fluid Mech.*, 643, 177–192, 2010.
Tang, L., Wen, F., Yang, Y., Crowe, C.T., Chung, J.N., and Troutt, T.R., Self organizing particle dispersion mechanism in a plane wake, *Phys. Fluids*, 4, 2244–2251, 1992.
Taylor, G.I., Diffusion by continuous movements, *Proc. Lond. Math. Soc.*, 20, 196–212, 1921.
Tenneti, S. and Subramaniam, S., Particle-resolved direct numerical simulation for gas-solid flow model development, *Ann. Rev. Fluid Mech.*, 46, 199–230, 2014.
Tsuji, Y. and Morikawa, Y., LDV measurements of an air-solid two-phase flow in a horizontal pipe, *J. Fluid Mech.*, 120, 3850409, 1982.
Tsuji, Y., Morikawa, Y., and Shiomi, H., LDV measurements of an air-solid two-phase flow in a vertical pipe, *J. Fluid Mech.*, 139, 417–434, 1984.
Wang, L.-P. and Maxey, M.R., Settling velocity and concentration distribution of heavy particles in homogeneous isotropic turbulence, *J. Fluid Mech.*, 256, 27–68, 1993.
Wang, L.P. and Stock, D.E., Dispersion of heavy particles by turbulent motion, *J. Atmos. Sci.*, 50, 1897–1913, 1993.
Wood, A.M., Hwang, W., and Eaton, J.K., Preferential concentration of particles in homogeneous and isotropic turbulence, *Int. J. Multiphase Flow*, 31, 1220–1230, 2005.
Yang, C.Y. and Lei, U., The role of the turbulent scales in the settling velocity of heavy particles in homogeneous isotropic turbulence, *J. Fluid Mech.*, 371, 179–205, 1998.
Yang, T.S. and Shy, S.S., Two-way interaction between solid particles and homogeneous air turbulence: Particle settling rate and turbulence modification measurements, *J. Fluid Mech.*, 526, 171–216, 2005.
Yang, Y., Chung, J.N., Troutt, T.R., and Crowe, C.T., The effects of particles on the stability of a 2-phase wake flow, *Int. J. Multiphase Flow*, 19, 137–149, 1993.
Young, J. and Leeming, A., A theory of particle deposition in a turbulent pipe flow, *J. Fluid Mech.*, 340, 129–159, 1997.
Yudine, M.I., Physical consideration on heavy-particle dispersion, *Adv. Geophys.*, 6, 185–191, 1959.
Zaichik, L.I. and Alipchenkov, V.M., Statistical models for predicting pair dispersion and particle clustering in isotropic turbulence and their applications, *New J. Phys.*, 11, 103018, 2009.
Zeng, L., Balachandar, S., Fischer, P., and Najjar, F., Interactions of a stationary finite-sized particle with wall turbulence, *J. Fluid Mech.*, 594, 271–305, 2008.


Taylor & Francis
Taylor & Francis Group
http://taylorandfrancis.com

13

Bubble Dynamics and Cavitation

13.1 Bubble Dynamics
13.2 Cavitation

13.1 Bubble Dynamics

Yoichiro Matsumoto and Kazuyasu Sugiyama

13.1.1 Single Spherical Bubble Dynamics

Bubble motion from a surrounding pressure variation is one of the most fundamental gas–liquid two-phase flow problems and is closely related to the macroscale behavior of two-phase flows, the performance of cavitating fluid machinery, and medical ultrasound applications. Of great significance to the analysis of such problems is the prediction of the radial motion of a bubble, namely, its growth and collapse. The bubble motion can be solved exactly by the integration of the conservation equations for mass, momentum, and energy for the gas phase inside the bubble and the liquid phase outside the bubble. Since it is not easy to solve the complete equations in many cases, a polytropic change (isothermal or adiabatic) is assumed for the gas inside the bubble. It is well known that the thermal phenomena inside the bubble can have a significant influence on the bubble motion (Chapman and Plesset, 1971, Nigumatulin et al., 1981, Prosperetti et al., 1988, Kamath and Prosperetti, 1989, Prosperetti, 1991, Takemura and Matsumoto, 1994, Kameda and Matsumoto, 1999). To account for thermal effects, a reduced-order model has been introduced using ordinary differential equations instead of the full conservation equations for mass, momentum, and energy.

13.1.1.1 Direct Numerical Simulation of a Single Bubble

In a single-phase flow, the conservation equations of mass, momentum, and energy are described by partial differential equations (PDEs) if the flow is treated as a continuum. In multiphase flow, these conservation equations are not described by the same set of PDEs, because there are discontinuities between the phases. However, it is possible to describe the governing equations in each phase by PDEs and connect the two phases at the interfaces. The governing equations and boundary conditions at a bubble interface were described by Hsieh (1965). Matsumoto and Takemura (1994) simulated the collapsing bubble motion numerically by using the full equations for mass, momentum, and energy in the gas and liquid phases. Takemura and Matsumoto (1994) calculated the bubble growth caused by an external pressure reduction by taking into account the internal phenomena such as thermal and mass diffusion with mist formation due to homogeneous condensation.

13.1.1.1.1 Governing Equations

A. Gas Phase

1. The mass conservation equations.

– For the gas mixture inside the bubble:

$$\frac{\partial \rho_m}{\partial t} + \frac{1}{r^2}\frac{\partial}{\partial r}\left(r^2 \rho_m u_{mg}\right) = 0, \tag{13.1}$$

where

$\rho_m = \rho_n + \rho_v + \rho_{lg}$

$\rho_m u_{mg} = \rho_n u_n + \rho_v u_v + \rho_{lg} u_{mg}$, the subscript g denotes the gas phase, l the liquid phase, n the noncondensable gas, v the vapor in the gas phase, and m the mixture condition

Also, the subscript lg denotes the mist inside the bubble and gl the noncondensable gas in the liquid phase), ρ is the density, r the coordinate in the radial direction, and u the radial velocity.

– For the vapor:

$$\frac{\partial \rho_v}{\partial t} + \frac{1}{r^2}\frac{\partial}{\partial r}\left\{r^2\left(\rho_v u_{mg} - \rho_{mg} D_{mg}\frac{\partial c_v}{\partial r}\right)\right\} = -\Gamma, \tag{13.2}$$

where

$\rho_{mg} = \rho_n + \rho_v$

$c_v = \rho_v/\rho_{mg}$

D is the diffusion coefficient

c is the concentration

Γ is the mass of vapor, which changes to mist per unit volume and time

– For the number density distribution function of droplets (Frenkel, 1946):

$$\frac{\partial n(a)}{\partial t} + \frac{1}{r^2}\frac{\partial}{\partial r}\left(r^2 n(a) u_{mg}\right) + \frac{\partial (n(a) I_a)}{\partial a} = 0, \tag{13.3}$$

where

$n(a)$ is the number density distribution function versus radius of the droplet

I_a is the growth rate of the droplet radius and is given by

$$I_a = \frac{\alpha(p_v - p_s)}{\left(\rho_l \sqrt{2\pi \Re_v T}\right)}, \tag{13.4}$$

where

α is the accommodation factor whose value is estimated to be 0.4 (Hatamiya and Tanaka, 1986)

p is the pressure and subscript s denotes the saturated condition

$\Re$ is the gas constant

T is the temperature

Critical radius r^* and the nucleation rate J are

$$r^* = 2\sigma/\rho_l \Re_v T \ln(p_v/p_s) \tag{13.5}$$

$$J = \left(\frac{2\sigma m}{\pi}\right)^{1/2} \frac{1}{\rho_l}\left(\frac{p_v}{kT}\right)^2 \exp\left(-\frac{4\pi r^{*2}\sigma}{3kT}\right) \tag{13.6}$$

where
- σ is the surface tension
- m is the molecular unit mass
- k is the Boltzmann constant

Γ in Equation 13.2 is defined as

$$\Gamma = \frac{d}{dt}\int \frac{4}{3}\pi\rho_l a^3 n(a)da. \tag{13.7}$$

2. The momentum conservation equation inside the bubble:

$$\frac{\partial}{\partial t}(\rho_m u_{mg}) + \frac{1}{r^2}\frac{\partial}{\partial r}\left(r^2\rho_m u_{mg}u_{mg}\right)$$
$$= -\frac{\partial p_{mg}}{\partial r} + \frac{4}{3}\frac{\mu_{mg}}{r}\left(\frac{\partial u_{mg}}{\partial r} - \frac{u_{mg}}{r}\right) + \frac{4}{3}\frac{1}{r^2}\frac{\partial}{\partial r}\left\{r^2\mu_{mg}\left(\frac{\partial u_{mg}}{\partial r} - \frac{u_{mg}}{r}\right)\right\}, \tag{13.8}$$

where μ is the viscosity.

3. The energy conservation equation inside the bubble:

$$\frac{\partial}{\partial t}(\rho_n e_n + \rho_v e_v + \rho_{lg} e_{lg}) + \frac{1}{r^2}\frac{\partial}{\partial r}\{r^2(\rho_n e_n u_n + \rho_v e_v u_v + \rho_{lg} e_{lg} u_{mg})\}$$
$$= -\frac{p_{mg}}{r^2}\frac{\partial}{\partial r}\left(r^2 u_{mg}\right) + \frac{1}{r^2}\frac{\partial}{\partial r}\left(r^2\lambda_{mg}\frac{\partial T}{\partial r}\right) + \frac{4}{3}\mu_{mg}\left(\frac{\partial u_{mg}}{\partial r} - \frac{u_{mg}}{r}\right)^2, \tag{13.9}$$

where
- e is the specific internal energy
- λ is the thermal conductivity

4. The equations of state are as follows:

$$p_n = \rho_n \Re_n T, \tag{13.10}$$

$$p_v = \rho_v \Re_v T. \tag{13.11}$$

B. Liquid Phase

1. The mass conservation equations.
- For the mixture of the liquid:

$$\frac{\partial \rho_{ml}}{\partial t} + \frac{1}{r^2}\frac{\partial}{\partial r}\left(r^2\rho_{ml}u_{ml}\right) = 0, \tag{13.12}$$

where $\rho_{ml} = \rho_l + \rho_{gl}$, $\rho_{ml}u_{ml} = \rho_l u_l + \rho_{gl}u_{gl}$.
- For the noncondensable gas in the liquid:

$$\frac{\partial \rho_{gl}}{\partial t} + \frac{1}{r^2}\frac{\partial}{\partial r}\left(r^2\rho_{gl}u_{ml}\right) = \frac{1}{r^2}\frac{\partial}{\partial r}\left(r^2\rho_{ml}D_{gl}\frac{\partial c_{gl}}{\partial r}\right). \tag{13.13}$$

where $c_{gl} = \rho_{gl}/\rho_{ml}$.

2. The momentum conservation equation for the liquid phase is

$$\frac{\partial}{\partial t}(\rho_{ml}u_{ml})+\frac{1}{r^2}\frac{\partial}{\partial r}\left(r^2\rho_{ml}u_{ml}u_{ml}\right)$$
$$=-\frac{\partial p_l}{\partial r}+\frac{4}{3}\frac{\mu_{ml}}{r}\left(\frac{\partial u_{ml}}{\partial r}-\frac{u_{ml}}{r}\right)+\frac{4}{3}\frac{1}{r^2}\frac{\partial}{\partial r}\left\{r^2\mu_{ml}\left(\frac{\partial u_{ml}}{\partial r}-\frac{u_{ml}}{r}\right)\right\}. \tag{13.14}$$

3. The conservation equation of energy for the liquid is

$$\frac{\partial}{\partial t}(\rho_l e_l)+\frac{1}{r^2}\frac{\partial}{\partial r}\left\{r^2\rho_l e_l u_l\right\}$$
$$=-\frac{p_l}{r^2}\frac{\partial}{\partial r}\left(r^2u_l\right)+\frac{1}{r^2}\frac{\partial}{\partial r}\left(r^2\lambda_l\frac{\partial T}{\partial r}\right)+\frac{4}{3}\mu_l\left(\frac{\partial u_l}{\partial r}-\frac{u_l}{r}\right)^2. \tag{13.15}$$

4. The Tait equation is applied with the equations of state in the following form:

$$\frac{p+B}{p_\infty+B}=\left(\frac{\rho}{\rho_\infty}\right)^n, \tag{13.16}$$

where B = 304.9 MPa, n = 7.15 in the case where the liquid is water.

13.1.1.1.2 Boundary Conditions at the Gas–Liquid Interface

1. Boundary conditions for mass conservation
The mass flux due to phase change $\dot{M}_v$ is expressed by the following equation:

$$\dot{M}_v=\frac{\alpha(p_s-p_v)}{\left(\sqrt{2\pi\Re_v T_w}\right)}. \tag{13.17}$$

where the subscript w denotes the bubble wall. The concentrations and gradients of vapor and noncondensable gas in the liquid at the interface are related to $\dot{M}_v$ and $\dot{M}_n$ by the following equations:

$$\dot{M}_v=\frac{D_{mg}\rho_{mgw}\left(\partial c_v/\partial r\right)_w}{1-c_{vw}}+\frac{c_{vw}}{1-c_{vw}}\dot{M}_n, \tag{13.18}$$

$$\dot{M}_n=\frac{D_{gl}\rho_{mlw}\left(\partial c_{gl}/\partial r\right)_w}{1-c_{glw}}+\frac{c_{glw}}{1-c_{glw}}(\dot{M}_v+\dot{M}_{lg}), \tag{13.19}$$

$\dot{M}_{\mathrm{lg}}$ is

$$\dot{M}_{lg}=\begin{cases}0 & (\dot{R}-u_{mg}\geq 0)\\ \rho_{lg}(\dot{R}-u_{mg}) & (\dot{R}-u_{mg}<0)\end{cases}. \tag{13.20}$$

where R is the bubble radius and dot denotes the derivative with respect to time.

2. The boundary condition for the momentum conservation is as follows:

$$-p_{lw}+\frac{4}{3}\mu_l\left(\frac{\partial u_l}{\partial r}-\frac{u_l}{r}\right)_w+\{\rho_{mg}(u_{mg}-\dot{R})(u_{mg}-u_l)\}_w=-p_{mgw}+\frac{2\sigma}{R}+\frac{4}{3}\mu_{mg}\left(\frac{\partial u_{mg}}{\partial r}-\frac{u_{mg}}{r}\right)_w, \tag{13.21}$$

3. The boundary condition for the energy conservation is as follows:

$$\lambda_{ml}\left(\frac{\partial T}{\partial r}\right)_w - \lambda_{mg}\left(\frac{\partial T}{\partial r}\right)_w + \frac{5}{2}(\Re_v - \Re_n)T_w\{(1-c_{vw})\dot{M}_v - c_{vw}\dot{M}_n\}$$
$$= \dot{M}_v\left\{L + \frac{4}{3}\frac{\mu_l}{\rho_{lw}}\left(\frac{\partial u_l}{\partial r} - \frac{u_l}{r}\right)_w - \frac{4}{3}\frac{\mu_{mg}}{\rho_{mg}}\left(\frac{\partial u_{mg}}{\partial r} - \frac{u_{mg}}{r}\right)_w\right\}$$
$$+ \frac{1}{2}\dot{M}_v\left\{(\dot{R}-u_{lw})^2 - (\dot{R}-u_{mgw})^2\right\}, \tag{13.22}$$

where L is the latent heat of the liquid.

The temperature and concentration of the noncondensable gas at the wall in the liquid are

$$T_{lw} = T_{gw}, \tag{13.23}$$

$$c_{glw} = H_n p_{nw}, \tag{13.24}$$

where H_n is Henry's constant.

13.1.1.1.3 Pressure and Temperature Distribution Inside and Outside a Bubble Figures 13.1 and 13.2 show the time histories of the pressure and temperature distribution inside and outside a bubble, and Table 13.1 shows the computational conditions. The pressure surrounding the bubble increases from 10 to 100 kPa stepwise. When the bubble motion starts, the expansion wave propagates outside and the pressure distribution is formed in the liquid phase according to the motion of the bubble interface. At the rebound of the bubble, the pressure peak appears at some distance from the interface and the pressure propagates outward. The pressure inside the bubble is uniform because the speed of sound is much higher than the velocity of the interface. In Figure 13.2, the temperature distribution is uniform in the liquid phase because of the large heat capacity of the liquid. On the other hand, a nonuniform distribution appears in the gas phase, because the temperature rises during the collapse phase as the heat transfers to the liquid at the interface. After rebounding, the temperature inside the bubble decreases to a value less than its initial value. The internal energy of the gas is reduced by thermal diffusion. The heat is trapped and diffuses around the bubble when the gradient of the temperature is negative.

13.1.1.1.4 Effect of Thermal Diffusion on the Bubble Motion Figure 13.3 shows the behavior of the bubbles with different gases inside them under the same conditions as Table 13.1, except for the gas species.

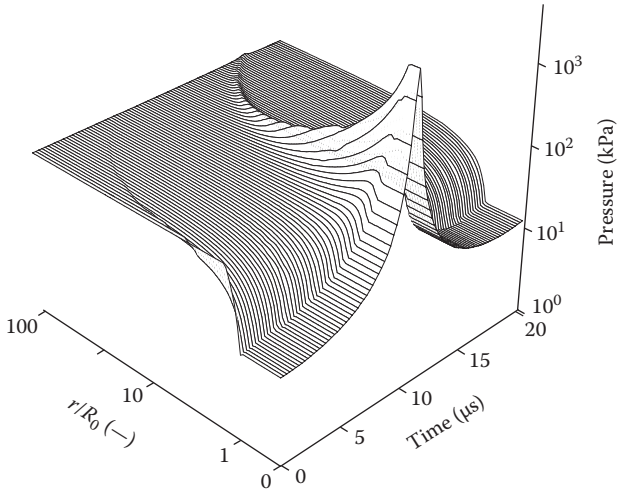


Figure 13.1

Time history of the pressure distribution inside and outside a nitrogen bubble.

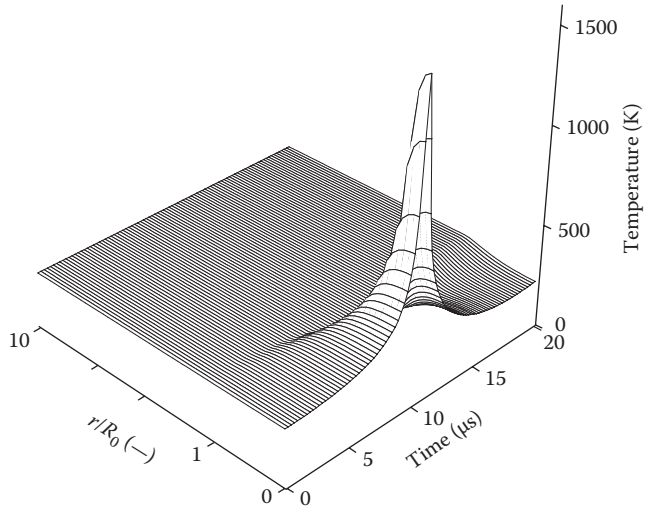


Figure 13.2

Time history of the temperature distribution inside and outside a nitrogen bubble.

Table 13.1 Computational Conditions

Gas phase	Nitrogen
Liquid phase	Water
Initial bubble radius, R_{b0}	100 μm
Initial ambient pressure, p_0	10 kPa
Step increase in ambient pressure	From 10 to 100 kPa
Initial temperature	293 K

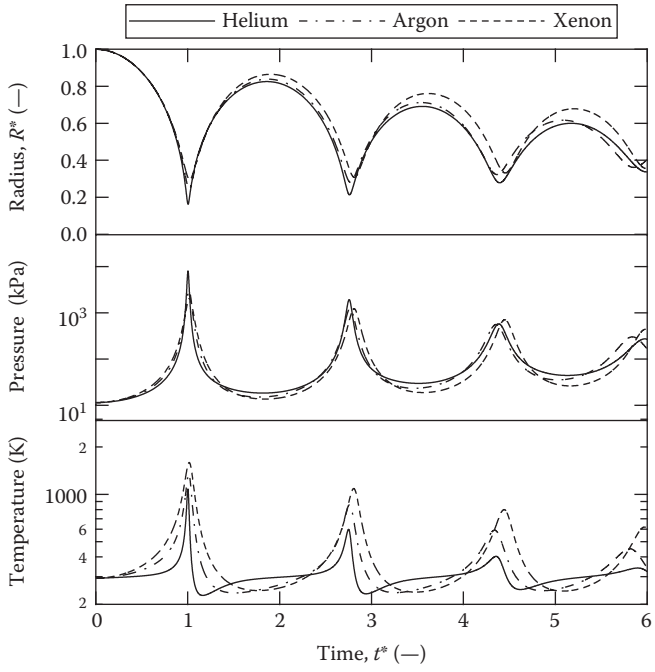


Figure 13.3

Time histories of the bubble radius, pressure at the bubble center, and mean temperature inside the bubble with different gases.

Table 13.2 Properties of the Internal Gas (100 kPa and 293 K)

Gas	Helium	Argon	Xenon
Thermal conductivity (mW/[m·K])	153.5	17.4	5.4
Peclet number, *Pe*	12.3	109.1	347.7

Table 13.2 shows the properties of the internal gas. The Peclet number for the bubbles *Pe* is defined as $Pe = \rho_0 c_{p0} R_0^2 \omega_N / \lambda$, where c_{p0} is the isobaric specific heat and ω_N denotes the natural angular frequency of a bubble, assuming adiabatic changes. Nondimensional length and timescales R^* and t^* are defined as $R^* = R/R_0$, $t^* = t/R_0\sqrt{\rho_{l\infty}/p_{l0}}$, respectively. When the bubble radius takes a maximum or minimum value, the pressure has a minimum or maximum value, respectively. The mean temperature $\left(\text{defined as } T_{mean} = \int_0^R r^2 \rho_g T_g \, dr \Big/ \int_0^R r^2 \rho_g \, dr\right)$ has a maximum at almost the same time as the bubble radius takes a minimum. However, it does not have a minimum when the bubble radius reaches a maximum. This occurs because the heat input has positive or negative values despite the work received from the liquid phase and has a time lag. Therefore, the sum of the work, which the bubble receives per unit time from the liquid phase, and the heat input become zero before the radius attains the minimum or the maximum value. This is the minimum or the maximum point of the temperature.

When the bubble collapses, the work received from the liquid per unit time decreases so rapidly that the temperature takes the maximum at almost the same time as the radius takes the minimum. On the other hand, upon expansion, the bubble supplies work to the liquid phase and the heat flows outward from the gas phase, due to the temperature distribution developed during the collapse phase. Therefore, the temperature decreases rapidly, and the gradient of the temperature at the gas–liquid interface becomes positive. Subsequently, the heat flows inward from the liquid phase and the mean temperature attains the minimum value when the sum of the work received from the liquid per unit time and the heat input become equal to zero.

In the case of a helium bubble (when *Pe* is relatively small), the heat transfers outward through the bubble wall quickly and the bubble shrinks to a smaller size in the collapsing phase. The temperature inside the bubble does not become so high. In the case of xenon (where *Pe* is large), the heat input and output are not large, so the bubble cannot shrink as much and the temperature inside the bubble reaches higher values.

13.1.1.1.5 Bubble Motion and Mist Formation Inside a Bubble Figure 13.4 shows the time histories of the radius, mean temperature, and mean density of mist (a) and the distributions of the temperature, concentration of vapor, and density of mist inside the bubble at several points (b) in the case when the surrounding pressure has a stepwise decrease from 100 to 5 kPa. The other computational conditions are the same as Table 13.1. The bottom figure shows the distributions at the times from A to H indicated in the upper figure. The figures from A to E show the growth period and those from F to H show the collapse period. The abscissa is the nondimensional distance, in which 0 shows the bubble center and 1 shows the bubble wall. As the bubble expands, the temperature inside the bubble decreases at the initial stage and then recovers to the surrounding temperature due to the latent heat released by the formation and growth of mist and the heat penetration from the bubble wall. After that, the temperature is kept almost constant except during the rebounds. The mean density of the mist increases at the beginning of the expansion, and the formation and growth of the mist exert an effect on the bubble motion at that time. After the temperature inside the bubble has become almost constant, the mean density of the mist is also almost constant and the total mass of the mist increases in proportion to the volume of the bubble. The temperature inside the bubble does not become so high at the end of the collapse because energy from the outside is consumed by the mist's evaporation. It is shown that distributions of temperature, vapor concentration, and density of the mist occur and that the distribution of the density of the mist is a rather complicated variable in space due to the slow diffusion process.

13.1.1.2 Reduced-Order Modeling of a Single Bubble

The single bubble motion can be simulated in detail, computing the full equations for the mass, momentum, and energy as outlined in the previous section. However, it is computationally expensive to calculate all equations when many bubbles are treated such as in bubbly flows. Many researchers have developed reduced-order models for the liquid- and gas-phase phenomena.

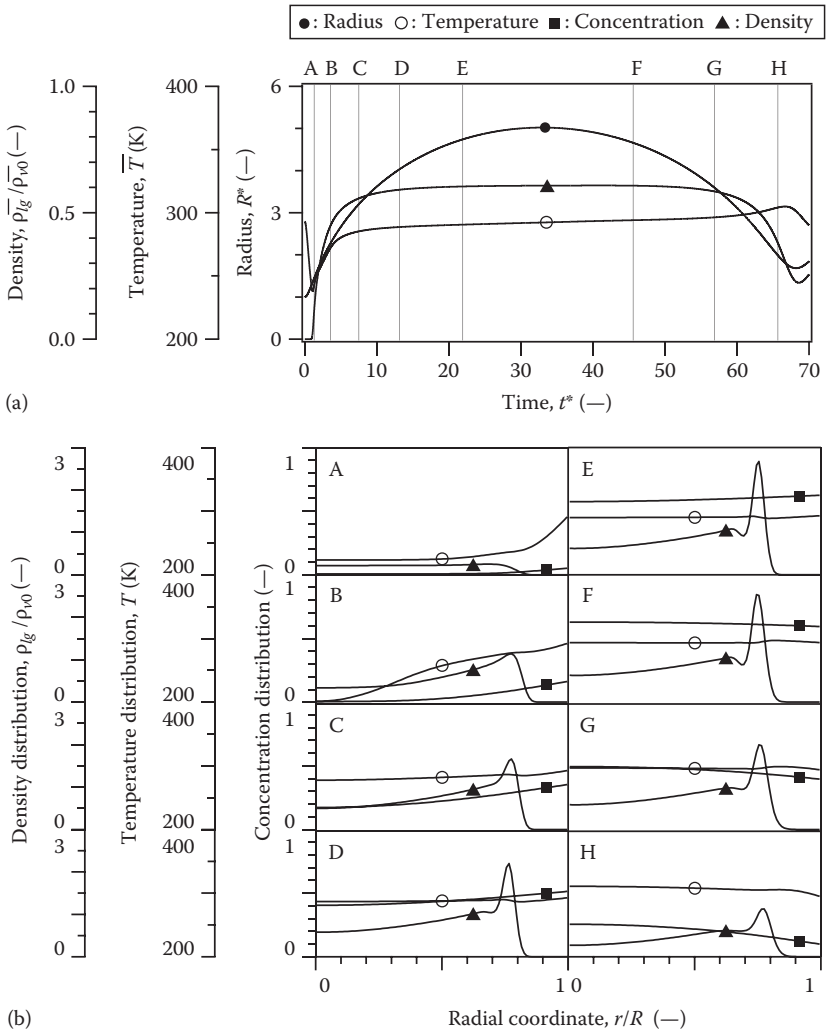


Figure 13.4

Time histories of the bubble radius, mean temperature, and mean density of the mist inside the bubble inside the bubble (a), and the distributions of the temperature, concentration of the vapor, and density of the mist inside the bubble at several points (b) in the case of a nitrogen bubble.

13.1.1.2.1 Effect of Compressibility in the Liquid Phase If the liquid is assumed to be incompressible, the momentum conservation equation can be easily integrated from the bubble wall to infinity and the boundary condition for the pressure can be taken into account. Rayleigh (1917) first considered bubble collapse in a liquid, assuming a vacuum cavity. The effect of the surface tension and viscosity in the liquid was taken into account later, and the Rayleigh–Plesset equation (1949) was defined as shown as follows:

$$R\ddot{R} + \frac{3}{2}\dot{R}^2 = \frac{1}{\rho_l}\left\{p_b - p_\infty - 4\mu_l\frac{\dot{R}}{R} - \frac{2\sigma}{R}\right\}, \tag{13.25}$$

where

p_b is the pressure inside the bubble
p_∞ is the ambient pressure
σ is the surface tension of the liquid

When the velocity of the bubble wall becomes comparable to the speed of the sound in the liquid phase, the compressibility of the liquid has to be considered (Keller and Kolodner, 1956). Thus, the following model with a first-order correction for compressibility is often used:

$$\left(1-\frac{\dot{R}}{c}\right)R\ddot{R}+\frac{3}{2}\left(1-\frac{\dot{R}}{3c}\right)\dot{R}^2=\left(1+\frac{\dot{R}}{c}\right)\frac{1}{\rho_l}\left\{p_b-p_\infty-p_c\left(t+\frac{R}{c}\right)\right\}+\frac{R}{\rho_l c}\dot{p}_b, \tag{13.26}$$

where c is the speed of sound and $p_c(t)$ the variable part of the pressure in the liquid at the location of the bubble center in the absence of the bubble.

A nonequilibrium phase change, such as evaporation and condensation during the collapse phase, is discussed next (Tomita and Shima, 1979, Fujikawa and Akamatsu, 1980). Fujikawa and Akamatsu (1980) derived the equations, which take into account the effects of nonequilibrium behavior at the bubble wall on the bubble motion:

$$\begin{aligned}&R\ddot{R}\left(1-2\frac{\dot{R}}{c}+\frac{\dot{m}}{\rho_l c}\right)+\frac{3}{2}\dot{R}^2\left(1+\frac{4}{3}\frac{\dot{m}}{\rho_l c}-\frac{4}{3}\frac{\dot{R}}{c}\right)\\&-\frac{\ddot{m}R}{\rho_l}\left(1-2\frac{\dot{R}}{c}+\frac{\dot{m}}{\rho_l c}\right)-\frac{\dot{m}}{\rho_l}\left(\dot{R}+\frac{\dot{m}}{2\rho_l}\right)+\frac{p_\infty-p_{l,r=R}}{\rho_l}-\frac{R\dot{p}_{l,r=R}}{\rho_l c}=0,\end{aligned} \tag{13.27}$$

$$p_{l,r=R_b}=p_v+p_g-\frac{\dot{m}^2(\rho_{vi}+\rho_{gi}-\rho_l)}{\rho_l(\rho_{vi}+\rho_{gi})}-2\frac{\sigma}{R}-4\frac{\mu_l}{R}\left(\dot{R}-\frac{\dot{m}}{\rho_l}\right), \tag{13.28}$$

where

$\dot{m}$ is the mass flux caused by the phase change

ρ_{vi} and ρ_{gi} are the density of the vapor and noncondensable gas at the bubble interface, respectively

The nonequilibrium behavior may result in additional cushioning of the bubble collapse.

13.1.1.2.2 Effect of Thermal Phenomena on the Gas Phase The temperature gradient at the bubble wall is used by some researchers instead of calculating the entire temperature distribution inside a bubble. Prosperetti (1991) investigated the thermal diffusive effects and Storey and Szeri (2001) suggested a model in which the bubble interior is assumed to be isothermal when the bubble radius is larger than the equilibrium value and to be adiabatic when the radius is smaller. Shimada et al. (2000) investigated a model, which assumes a homogeneous heat distribution inside a bubble. Toegel et al. (2000) estimated the penetration depth of mass and heat diffusion and calculated the approximated energy flux at the bubble wall. Preston et al. (2007) considered a temperature gradient based on a linear analysis (Prosperetti et al., 1988).

Figure 13.5 shows a comparison of the time history of bubble radii between the isothermal model, the adiabatic model, the reduced-order model, and the direct numerical simulation (DNS). In this case, the reduced-order model of Matsumoto and Beylich (1985) is applied to the governing equations and boundary conditions for the bubble motion, and that developed by Preston et al. (2007) is employed for the temperature gradient at the bubble wall. The gas inside the bubble is air, and the initial bubble radius is 10 μm. The other calculation conditions are the same as Table 13.1. Compared with the DNS, the amplitudes of the bubble motions in the case of isothermal and adiabatic model are too large. In the collapse phase, the bubble radius in the case of the isothermal model is too small because the temperature inside the bubble is assumed to be isothermal and the internal energy of the gas phase does not become high. The bubble in the case of adiabatic model cannot shrink as much as than that of DNS, because the heat inside the bubble does not transfer to the liquid phase. On the other hand, the reduced-order model can capture the DNS-predicted bubble motion well. It is reasonable and efficient to apply such a reduced-order model for the computation of a many-bubble system.

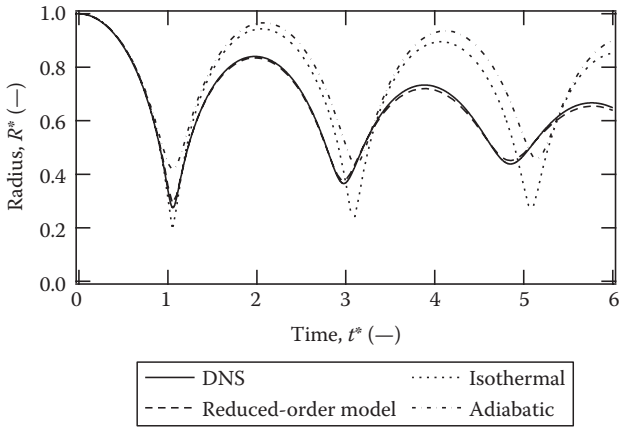


Figure 13.5

Comparison of time histories of radii between DNS and reduced-order model.

13.1.1.3 Nonlinear Behavior and Acoustic Turbulence

13.1.1.3.1 Nonlinear Oscillations of a Microbubble For the dynamics of the bubble in an oscillating field, it is important to take into account the nonlinear phenomena, and many researchers have investigated this topic. Recently, the nonlinear behavior of a microbubble in an ultrasound field has been used for medical ultrasound imaging with microbubble contrast agents. The nonlinear effect was investigated by many researchers (Noltingk and Neppiras, 1950, Neppiras and Noltingk, 1951, Esche, 1952, Borotnikova and Soloukin, 1964, Flynn, 1964, Neppiras, 1969). Lauterborn (1976) simulated the frequency response curve of a bubble (Figure 13.6). This shows the amplitudes of the radial oscillation of a bubble of radius 1.0 μm in water at a mean ambient pressure of 1 bar (100 kPa) plotted as a function of f/f_N for various amplitudes of oscillation. f is a driving frequency, f_N is the natural frequency of the bubble, R_n is a radius at rest, and R_{max} is the maximum radius. The numbers above the peaks indicate the order of the resonance, n/m, and the case $m = 1$, $n = 2, 3, 4$ denotes the higher harmonics and the case $m = 2$, $n = 1$ denotes the subharmonics. The equations that account for the compressibility of the liquid were employed in this calculation. As the amplitude of the ambient pressure grows larger, the superharmonic and subharmonic peak responses become greater. With the increase in the pressure amplitude, these peaks shift to lower frequencies. The influence of the internal phenomena on this nonlinear behavior has also been investigated by Matsumoto and Watanabe (1989).

13.1.1.3.2 Acoustic Turbulence from a Microbubble The bubble motion in an ultrasound field shows chaotic behavior due to the nonlinearity of the oscillation when the sound amplitude is increased. This phenomenon is called "acoustic turbulence" (Lauterborn, 1989). The bifurcation and chaotic behavior of bubble oscillation

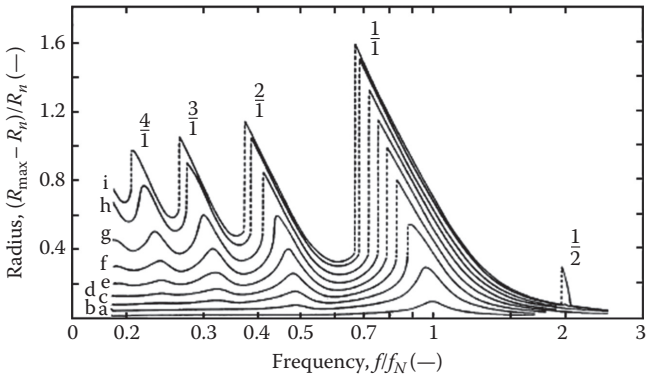


Figure 13.6

Numerically computed amplitudes of radial oscillation of a bubble. (a) 0.1, (b) 0.3, (c) 0.5, (d) 0.7, (e) 0.9, (f) 1.1, (g) 1.3, (h) 1.5, and (i) 1.6 bar. (Adapted from Lauterborn, W., *J. Acoust. Soc. Am.*, 59, 283, 1976.)

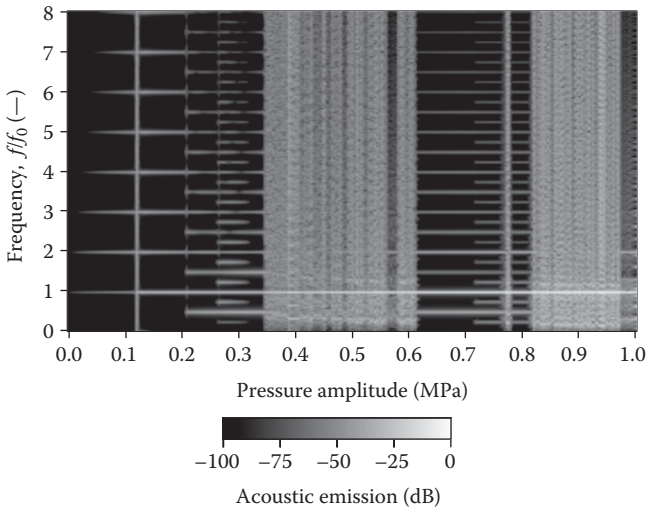


Figure 13.7

Power spectrum of the acoustic pressure from an air microbubble.

have been calculated assuming the interior gas obeys a polytropic relationship, which neglects the thermal dissipation (Lauterborn, 1987).

Figure 13.7 shows the time history of the power spectrum of acoustic pressure from an air microbubble. The bubble motion is simulated for when the ambient ultrasound pressure increases linearly from 0 to 1 MPa in 5000 cycles. The initial bubble radius is 2.0 μm, and the ultrasound frequency is 1 MHz. When the ultrasound driving starts, the bubble begins its oscillation in the fundamental mode. As the ultrasound amplitude increases, the emitted acoustic pressure increases, and it gradually involves nonlinearity with the higher harmonic modes. The bifurcation occurs, and the 1/2 harmonic modes begin to appear in each higher harmonic mode, when the pressure amplitude reaches up to 200 kPa. A further bifurcation appears, and the 1/4 harmonic modes emerge at 250 kPa. After these processes, the bubble oscillation becomes chaotic. When the ambient ultrasound pressure reaches about 600 kPa, nonchaotic oscillations occur for a short time, and then the bubble motion returns to chaotic behavior. In this case, the subharmonic modes are barely visible at this relatively low forcing amplitude.

13.1.2 Bubble Deformation and Fragmentation due to the Collapse

It is well known that the spherical shape of a collapsing bubble is unstable, and it forms a micro-jet that may induce bubble fission. The spherical shape of the bubble is maintained by the surface tension and the viscous force acting on the bubble surface. Deformation will occur when the characteristic anisotropy in the fluid forces overcomes the surface tension and the viscous force. The stability with regard to nonspherical disturbances has been investigated from a hydrodynamic point of view by Birkhoff (1954), Plesset and Mitchell (1956), Brennen (1995, 2002), and Hao and Prosperetti (1999), among others. These analyses essentially examine the spherical equivalent of the Rayleigh–Taylor instability. If the inertia of the gas in the bubble is assumed to be negligible and the viscosity is small enough, then the amplitude, $a_n(t)$, of a spherical harmonic distortion of order n ($n > 1$) will be governed by the equation:

$$\ddot{a}_n + \left[3\frac{\dot{R}}{R} + 2(n+2)(2n+1)\frac{\nu}{R^2}\right]\dot{a}_n + (n-1)\left[-\frac{\ddot{R}}{R} + (n+1)(n+2)\frac{\sigma}{\rho R^3} + 2(n+2)\frac{\nu\dot{R}}{R^3}\right]a_n = 0 \tag{13.29}$$

where ν is the kinematic viscosity.

The coefficients are determined by the dynamic behavior of the bubble radius, $R(t)$. It can be deduced from this equation that the most unstable conditions occur when $\dot{R} < 0$ and $\ddot{R} \geq 0$. These conditions will be

reached just before the rebound of a collapsing bubble. The most stable conditions take place when $\dot{R} > 0$ and $\ddot{R} < 0$, which is the case for growing bubbles as they approach their maximum size.

The fact that the coefficients in Equation 13.29 are not constant in time results in differences from the Rayleigh–Taylor instability for a plane boundary. The coefficient of a is not very different from the case of the plane boundary in the sense that instability is promoted when $\ddot{R} > 0$ while the surface tension and viscosity have stabilizing effects. The primary difference is caused by the $\dot{a}$ term. As the bubble grows, the wavelength on the surface increases, and hence, the growth of the wave amplitude is lessened. The reverse occurs during collapse. It is easily found from Equation 13.29 that the initial acceleration phase of bubble growth in which $\ddot{R} \geq 0$ is unstable with respect to spherical harmonic perturbations of fairly high order, n. However, the remainder of the growth phase during which $\dot{R} > 0$, $\ddot{R} < 0$ is stable with regard to all spherical harmonic perturbations. Therefore, the bubble in the acceleration phase is usually considered to be stable in cavitation experiments. This could be caused either by the briefer acceleration phase or by the greater stabilizing effect of surface tension in smaller bubbles. On the other hand, it is clear from the theory that the bubble may become highly unstable with respect to nonspherical disturbances during stage two because $\ddot{R}$ reaches very large positive values during this rebound phase. The instability appears in several different ways depending on the violence of the collapse and the presence of other boundaries. The instability of the collapsing bubble has been investigated by many researchers (Blake and Gibson, 1987, Tomita and Shima, 1990, Lindau and Lauterborn, 2003). Cavitation bubbles that collapse to a size an order of magnitude smaller than their maximum size inevitably emerge from that collapse as a cloud of smaller bubbles rather than as a single vapor bubble. This fragmentation could be caused by a single micro jet as shown in Figure 13.8 or it could be due to a spherical harmonic disturbance of higher order. The behavior of collapsing bubbles that are filled with a noncondensable gas corresponding with the lower values of $\ddot{R}$ and the instability could be weaker resulting in spherical stability. Thus, acoustically excited cavitation bubbles that contain a substantial amount of gas often remain spherical during their rebound phase. In other instances, the instability is sufficient to cause

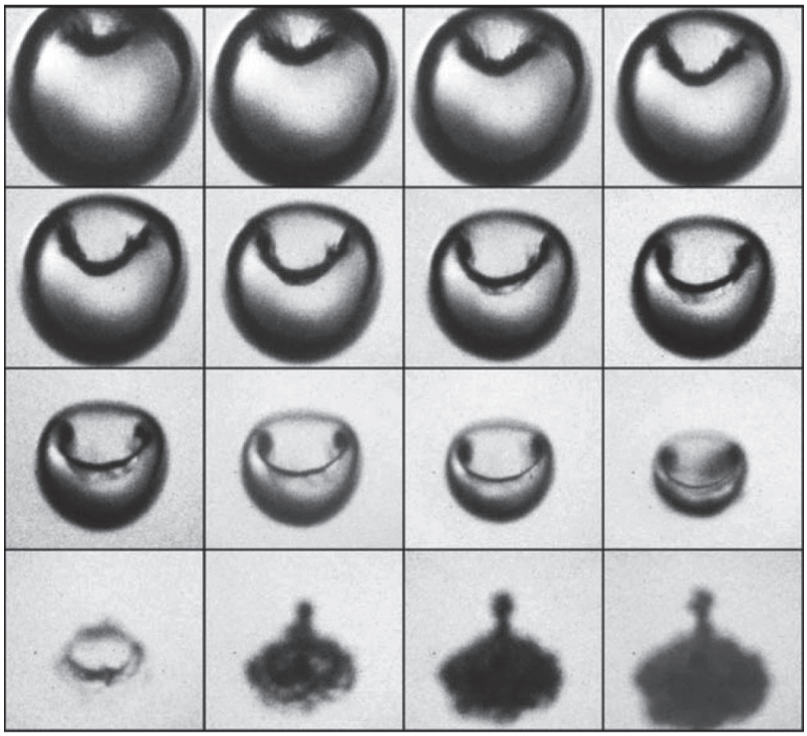


Figure 13.8

Jet and counterjet development at an angle of 45° from above the wall; γ = 2.6 ($\gamma = d/R_{max}$, the distance of the bubble center from the wall at the moment of formation d and the maximum bubble radius R_{max}). Interframe time 1 μs, exposure time 200 ns, R_{max} = 1.5 mm, frame size 1.2 mm × 1.1 mm. (From Lindau, O. and Lauterborn, W., *J. Fluid Mech.*, 479, 327, 2003.)

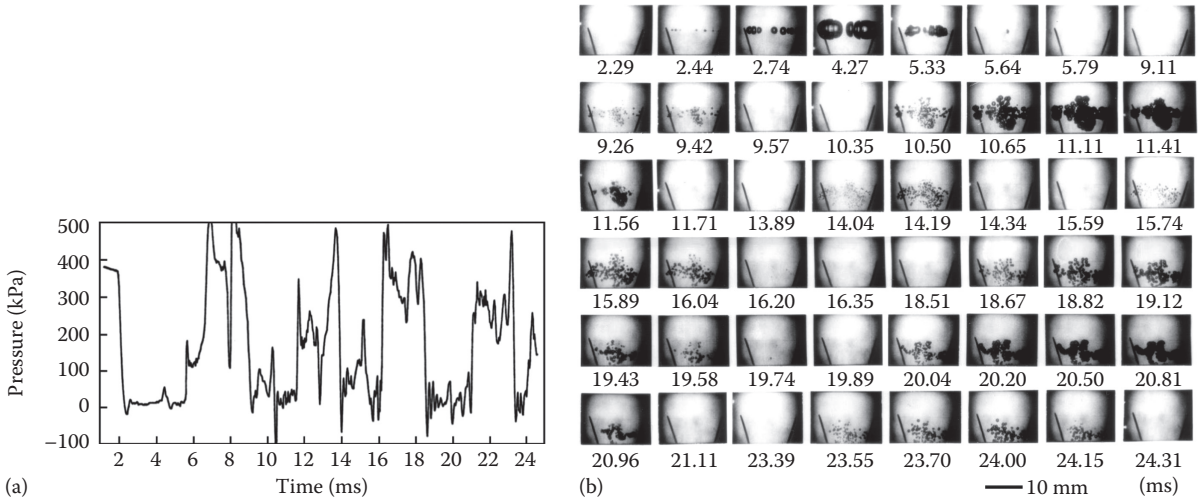


Figure 13.9

Growth and collapse of cavitation bubbles due to decreases and increases in the ambient pressure. The gas content is 2.7 ppm. (a) Pressure in the test section. (b) Snapshots of the cavitation bubbles. (From Matsumoto, Y. and Aoki, M., *Bull. JSME*, 27, 1352–1357, 1984.)

fragmentation. Several examples of fragmented and highly distorted bubbles emerging from the rebound phase are shown in Figure 13.9. The figure shows the dynamic behavior of bubble growth and collapse with the sequential decrease and increase in the surrounding pressure. The first pressure reduction creates cavitation bubbles from a heated thin wire at 2.44 ms, and the bubbles grow under the ambient pressure whose value is almost the same as that of the saturated vapor pressure of the bulk temperature. At 4.27 ms, the pressure increases and the bubbles begin to shrink. Large fluctuations of the pressure are observed due to the interference with the reflected pressure waves from the bubbles and the bottom. Because of nonspherical instability, the bubbles collapse ruggedly into tiny fragments. This creates many small bubbles, and they grow to cavitation bubbles when the ambient pressure decreases at 9.26 ms. With the next intense expansion wave at 10.50 ms, many cavitation bubbles grow from the remaining bubble nuclei, and at 11.11 ms, they are unified into a single bubble whose shape is rugged.

To numerically predict the bubble collapse near a boundary, a boundary integral method based on the potential theory (Blake and Gibson, 1987) has been widely used. This method requires the computational mesh only at the boundary so that the dimension of the problem is reduced. The method has been elaborated to make it possible to predict, for example, the impact due to the formation of the toroidal bubble after jet penetration (Blake et al., 1997) and the role of the heat transfer through the bubble wall (Yuan and Prosperetti, 1997, Yasuda and Takahira, 2003). More recently, owing to the improvement of computational techniques and hardware performance, the finite difference method has also been applied. For instance, Popinet and Zaleski (2002) studied the effect of the viscosity on the jet formation using a front-tracking method, and Johnsen and Colonius (2009) studied the propagation of the shock wave generated at collapse using a shock- and interface-capturing scheme.

13.1.3 Bubble Cloud Dynamics

The cavitating collapse of a bubble cloud generates very high pressure and high temperature. This high pressure reaches 100 MPa–1 GPa in a very short period, and this causes severe erosion, noise, and vibration in hydraulic machines. This high concentration of energy has been utilized recently for biomedical, environmental, and other industrial applications. In particular, the use of microbubbles in high intensity focused ultrasound (HIFU) therapy would enhance the effects of shock wave lithotripsy (Ikeda et al., 2006, Arora et al., 2007) and tissue heating (Coussios and Roy, 2008, Okita et al., 2013).

Many researchers have investigated theoretically and numerically the dynamics of a bubble cloud. There are two approaches: one is to capture the interfacial motion for individual bubble and the other to capture the macroscopic motion of a bubbly mixture using a homogenization technique.

Regarding the former approach, Chahine and Duraiswami (1992) numerically investigated mutual interactions on the dynamics of a multibubble cloud consisting of up to 8 bubbles using a boundary element method (BEM) based on potential theory. They compared their results with analytical results obtained by asymptotic expansions. For the larger systems, Bui et al. (2006) developed a fast algorithm coupled with the BEM, and Wilson et al. (2008) employed a multipole method using surface harmonics. Bremond et al. (2006) described an extended Rayleigh–Plesset equation in consideration of the pressure modification through the surrounding bubbles and made a comparison with the experiments using a patterned surface. Regarding the latter approach, Omta (1987) theoretically and numerically investigated the oscillation and sound emission of a bubble cloud using the averaged equations derived by Biesheuvel and van Wijngaarden (1984). d'Agostino and Brennen (1989) linearized the governing equations for a bubbly mixture together with the Rayleigh–Plesset equation. Shimada et al. (2000) investigated the behavior of cloud cavitation in connection with the cavitation damage using the set of governing equations for the spherical bubble cloud, where the internal phenomena of each bubble and the compressibility of the liquid are taken into account. They concluded that, when the bubble cloud collapses, a very high pressure is emitted from each of the bubbles near the center of the cloud and the variation of the pressure has high frequency.

13.1.3.1 Spherical Bubble Cloud

In this section, the analytical solutions for a spherical bubble cloud are introduced (d'Agostino and Brennen, 1989). The geometry of the spherical cloud is shown in Figure 13.10. The relative motion of the two phases, the mass of the dispersed phase and all the damping mechanisms for the bubble dynamics are neglected, and the liquid is assumed to be inviscid and incompressible. The mass and momentum conservation equations are as follows:

$$\nabla \cdot \mathbf{u} = \frac{\beta}{1+\beta\tau}\frac{D\tau}{Dt} \tag{13.30}$$

$$\rho\frac{D\mathbf{u}}{Dt} = -(1+\beta\tau)\nabla p \tag{13.31}$$

where

β is the number density of bubbles per unit liquid volume
τ is the individual bubble volume
D/Dt indicates the Lagrangian derivative

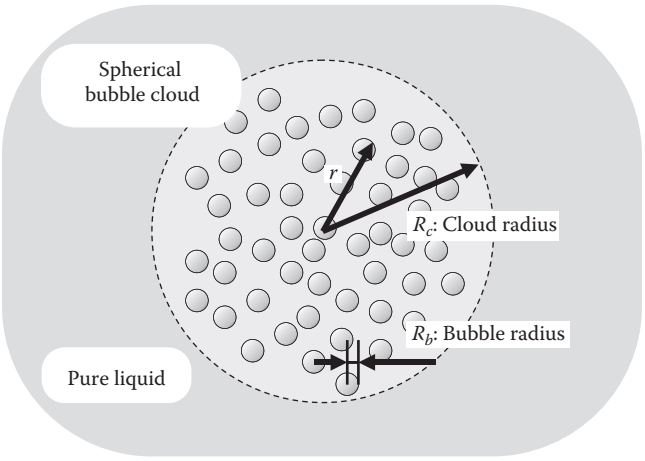


Figure 13.10

Spherical bubble cloud.

The bubble radius, R_b is determined by the Rayleigh–Plesset equation.

$$R_b \frac{D^2 R_b}{Dt^2} + \frac{3}{2}\left(\frac{DR_b}{Dt}\right)^2 = \frac{1}{\rho}\left(p_g + p_v - p - \frac{2\sigma}{R_b}\right) \tag{13.32}$$

where

p_g is the partial pressure of noncondensable gas
p_v is the partial pressure of the vapor
σ is the surface tension

For simplicity, the following assumptions are employed: (1) The bubble cloud is spherical. (2) The mean-flow velocity is purely radial and small. (3) The void fraction is uniform and relatively low inside the cloud. (4) All the bubbles have the same equilibrium radius, R_{b0} (the subscript 0 indicates the unperturbed value). (5) The vapor pressure inside the bubble is constant. (6) The pressure of the noncondensable gas in the bubbles changes isothermally. Let the perturbation of the far-field pressure be defined in the complex plane by the equation: $p_\infty = p_0[1 + \varepsilon \exp(i\omega t)]$ with $\varepsilon \ll 1$. After applying the assumptions and linearizing the Equations 13.30 through 13.32 with the equation $R_b(r,t) = R_{b0}[1 + \varphi(r,t)]$ with $|\varphi(r,t)| \ll 1$, the normalized variation of the bubble radius φ, and the natural frequencies ω_n, are

$$\varphi(r,t) = -\varepsilon \frac{p_0(1-\alpha_0)/\rho R_{b0}^2}{\omega_b^2 - \omega^2}\left(\frac{1}{\cos kR_{c0} - \alpha_0 \sin(kR_{c0})/kR_{c0}}\right)\frac{\sin kr}{kr} e^{i\omega t} \tag{13.33}$$

$$\omega_n^2 = \frac{\omega_b^2}{1 + \left(3\alpha_0(1-\alpha_0)R_{c0}^2/(n-1/2)^2\pi^2 R_{b0}^2\right)} \tag{13.34}$$

$$\omega_b^2 = \frac{3p_{g0}}{\rho R_{b0}^2} - \frac{2\sigma}{\rho R_{b0}^3} \tag{13.35}$$

where,

ω is the frequency of the far-field pressure
ω_b the natural frequency of a single bubble at isothermal conditions
ω_n the natural frequency of the bubble cloud
α the void fraction
R_c the cloud radius
k the wave number in the bubbly flow

The natural frequencies of the spherical bubble cloud will extend to much lower frequencies than that of a single bubble if the initial void fraction, α_0, is much larger than the square of the ratio of bubble size to cloud size $\left(\alpha_0 \gg R_{b0}^2/R_{c0}^2\right)$. Figure 13.11 shows the natural mode shapes of the normalized bubble radius, the pressure, and the bubble concentration per unit liquid volume in the cloud (n = 1–4). The first mode consists of the same phase. Higher modes have n antinodes and $n - 1$ node(s) within the cloud. The envelope is proportional to $1/r$, and the amplitudes at the bubble cloud interface become much smaller in the higher modes.

When the damping effects are included, the attenuation is much greater at the higher frequencies so that the dominant feature of the response is the first mode natural frequency of the cloud. On the other hand, the response at the bubble natural frequency ($n = \infty$) becomes much less significant.

It should be noted that, on the basis of the linearized model (d'Agostino and Brennen, 1989), extended models have been developed. Ando et al. (2011) further developed the model by considering the polydispersity in bubble size and discussed the phase cancellation effect. Grandjean et al. (2012) modelled the void fraction heterogeneities due to the bubble clustering and applied the developed method to predicting the shock wave propagation in bubbly mixture.

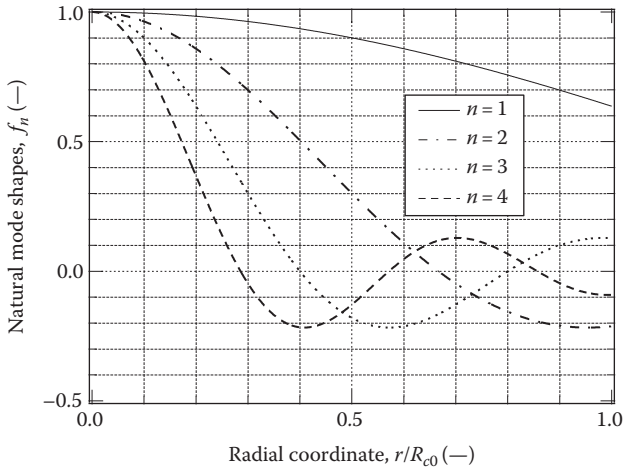


Figure 13.11

Natural mode shapes of the normalized bubble radius, the pressure, and the bubble concentration per unit liquid volume in the cloud (n = 1–4).

13.1.3.2 Spherical Bubble Cloud Model

In the previous section, a theoretical analysis for a spherical bubble cloud was introduced; however, the results are limited to the case in which the volumetric change of the bubbles is very small. In this section, the volumetric change of a spherical bubble cloud is simulated by using the model proposed by Shimada et al. (2000) to illustrate nonlinear response.

13.1.3.2.1 Concept and Assumptions of a Spherical Bubble Cloud Shock waves propagate inside a bubble cloud. Kameda et al. (1996, 1998) clarified that internal phenomena can have a significant influence on shock wave propagation, and in certain cases, the compressibility of the liquid cannot be ignored, depending on the amount of bubble motion. It has been determined that a very high pressure of $O(10^8) \sim O(10^9)$ Pa emerges near the center of the cloud cavitation when it collapses violently. In such a case, the compressibility of the liquid should be taken into account. Therefore, to analyze the collapsing phenomena of a bubble cloud rigorously, the internal phenomena of the individual bubbles and liquid compressibility should be included. Bubbles in the cloud shrink violently so that gases in a bubble cannot be treated as ideal. For simplicity, the ambient temperature rise of the liquid and the mass transfer of noncondensable gases through the bubble wall are not considered. In the numerical simulation, the following assumptions are employed: (1) The bubble cloud and each bubble maintain spherical symmetry as they oscillate. (2) The bubbly liquid inside the cloud is treated as a continuum fluid, whose mass and momentum are assumed to be equal to those of the liquid phase, because the mass in a unit volume of the gas phase is much smaller than that of the liquid phase. (3) Bubbles move with the surrounding liquid. Bubbles are small enough to ignore the slippage between the bubble and the liquid. (4) Coalescence and fragmentation of bubbles in the cloud are ignored. (5) The viscosity of the bubbly mixture is ignored in the cloud because it has little influence on the wave phenomena. (6) The temperature of the liquid in the cloud is constant. (7) The pressure and temperature inside each bubble are uniform except for the thin boundary layer near the bubble wall, compared with the bubble radius. (8) The temperature at the bubble wall is equal to that of the liquid. (9) The mass of the noncondensable gas inside a bubble is constant. (10) Gases inside a bubble obey the van der Waals equation of state. (11) Coalescence and fragmentation of mist inside a bubble are ignored. Then we consider the thermal behavior inside the bubble and the pressure wave phenomena in the bubble cloud, namely, the evaporation and condensation of liquid at the bubble wall, heat transfer through the bubble wall, and the compressibility of the liquid.

The geometry of a spherical bubble cloud is the same as Figure 13.10. A bubble is located at the center of the cloud to avoid a singularity.

13.1.3.2.2 Governing Equations The Keller equation (Keller and Kolodner, 1956) is applied to the equation of motion of the spherical bubble cloud interface (Equation 13.36) to take the compressibility of the surrounding liquid into account.

$$R_c\left(1-\frac{\dot{R}_c}{c}\right)\ddot{R}_c+\frac{3}{2}\left(1-\frac{\dot{R}_c}{3c}\right)\dot{R}_c^2=\frac{1}{\rho_l}\left(1+\frac{\dot{R}_c}{c}+\frac{R_c}{c}\frac{d}{dt}\right)\left(p_w-p_\infty-4\frac{\mu_l}{R_c}\dot{R}_c\right) \tag{13.36}$$

where

R_c is the radius of the bubble cloud
c is the speed of sound in the surrounding liquid
ρ_l is the density of the liquid
p_w is the pressure at the surface of the cloud
p_∞ is the ambient pressure
μ_l is the viscosity of the liquid

In a bubble cloud, the mass and momentum conservation equations of bubbly flow (Equations 13.37 and 13.38) and the conservation equation of the number density of bubbles (Equation 13.39) are also solved. The Tait equation (13.40) is employed as the equation in liquid phase. Thus, the behavior of the bubble cloud is governed by the following set of equations:

$$\frac{\partial(1-\alpha)\rho_l}{\partial t}+\frac{1}{r^2}\frac{\partial}{\partial r}\left\{r^2(1-\alpha)\rho_l u_l\right\}=0 \tag{13.37}$$

$$\frac{\partial(1-\alpha)\rho_l u_l}{\partial t}+\frac{1}{r^2}\frac{\partial}{\partial r}\left\{r^2(1-\alpha)\rho_l {u_l}^2\right\}+\frac{\partial p}{\partial r}=0 \tag{13.38}$$

$$\frac{\partial n_b}{\partial t}+\frac{1}{r^2}\frac{\partial}{\partial r}\left\{r^2 n_b u_b\right\}=0 \tag{13.39}$$

$$\frac{p+B}{p_\infty+B}=\left(\frac{\rho_l}{\rho_{l\infty}}\right)^n \tag{13.40}$$

where

α is the void fraction
u_l is the velocity of the liquid
n_b is the number density of the bubbles

The velocity of a bubble, u_b is assumed to be equal to u_l according to the third assumption. In the Tait equation, B is 304.9 MPa, and n is 7.15 for water.

For each bubble motion, the following phenomena are taken into consideration: the compressibility of the surrounding liquid, the mass and heat transfer through the bubble wall, the evaporation and condensation of the vapor, and mist generation from the vapor inside the bubble (Matsumoto and Beylich, 1985). Equations 13.27 and 13.28 are applied for the dynamic equation for the bubble radius. The energy conservation equation in the gas phase with mist and the nucleation rate equation of mist are also solved.

13.1.3.3 Computational Conditions

In this simulation, the behavior of a spherical bubble cloud, which consists of many microbubbles, is investigated. Such a microbubble cluster may be generated in HIFU applications, which have attracted much attention recently, because they are less invasive than conventional medical treatments. Table 13.3 shows the computational conditions. Acoustic cavitation induced by ultrasound is highly dependent on the ultrasound frequency. In medical applications, a typical frequency of ultrasound is around 0.5–5 MHz. When the ultrasound frequency is 4 MHz, the wavelength is about 0.4 mm in water or tissue. The focal region is considered to be around 2–4 times the wavelength. In this simulation, it is assumed that the region of the bubble cloud

Table 13.3 Computational Conditions

Gas phase	Air
Liquid phase	Water
Initial cloud radius, R_{c0}	0.5 mm
Initial bubble radius, R_{b0}	1 μm
Initial ambient pressure, p_0	101.3 kPa
Initial temperature	293 K
Initial void fraction	0.1%
Amplitude of ambient pressure	10–125 kPa
Frequency of ambient pressure	10 kHz–4 MHz

is 0.5 mm in radius and each bubble radius is 1 μm (the natural frequency is about 4 MHz). The ambient pressure fluctuation is assumed to be a pulse wave, and the frequency of the wave extends from 10 kHz to 4 MHz for amplitudes of 10, 25, 50, 75, 100, and 125 kPa.

13.1.3.4 Frequency Response of a Spherical Bubble Cloud

The bubbles, which are located near the center of the bubble cloud, violently collapse when the bubble cloud oscillates at its resonance frequency. The maximum pressures inside the bubbles and the maximum cloud radii are calculated for various conditions. Figure 13.12 shows the results. The horizontal axis corresponds to the frequency of the ultrasound. The vertical axis corresponds to the maximum pressure inside the bubbles normalized by the amplitude and the maximum cloud radius normalized by the initial radius, respectively.

When the frequency is sufficiently low, around 10 kHz, the normalized maximum pressure is nearly equal to 1. This means that the ultrasound does not focus on the cloud and the attenuation of the bubbly liquid is negligible, corresponding to the long wavelength of the ultrasound. The reason why the normalized maximum pressure inside the bubbles exceeds 1 is the effect of the surface tension. In fact, the normalized maximum pressure in the liquid phase converges to 1 for the same computational conditions. On the other hand, the normalized maximum pressure converges to 0 due to the large attenuation of the bubbly liquid when the frequency is near the natural frequency of a single bubble, which is about 4 MHz. When the frequency range is from approximately 180 to 200 kHz, the bubble cloud resonates and the normalized maximum pressure becomes very high. Furthermore, the normalized pressure becomes higher as the pressure amplitude of the ultrasound becomes greater. The normalized pressure exceeds 2000, which corresponds to 200 MPa, in the case of 100 kPa pressure amplitude at a frequency of 180 kHz. Additionally, in the case of 125 kPa pressure amplitudes, the high pressures appear even for a lower frequency. The maximum pressure exceeds 400 MPa at the frequency range between 50 and 200 kHz. The cloud radius hardly changes in each case. This occurs because the changes of the cloud radius are mainly caused by the volumetric changes of the bubbles in the cloud and the initial void fraction is only 0.1% as shown in Table 13.3.

13.1.3.4.1 Low Pressure Amplitude Cases (Δp = 10 and 25 kPa) The response curves of the maximum pressure in the case of 10 and 25 kPa pressure amplitude are almost the same as those shown in Figure 13.12. Since the cloud shows nearly linear oscillation for these conditions, at first, the ultrasound propagation in these cases is shown. Two different peaks are observed in the response curves of the maximum pressure. One is at 200 kHz and the other is at 600 kHz. Figure 13.13 shows the pressure distributions of the liquid phase over about 0.5 T, at each 0.01 T, where T is the cycle of the ultrasound. The amplitude of the ambient pressure is 10 kPa at a frequency of 200 kHz (left figure) and 600 kHz (right figure). The pressure inside the cloud changes at almost the same phase in the cloud in the 200 kHz case. This is the first resonance mode of a spherical bubble cloud (see Figure 13.11). The first mode frequency is slightly lower than the natural frequency calculated by Equation 13.34 since the damping effects are not considered in that formula. In fact, d'Agostino and Brennen (1989) showed that the natural frequencies become lower when the damping effects are taken into account. In the 600 kHz case, there is one pressure node and the pressure at the center of the cloud is shifted almost π backward from that at the boundary of the cloud. This is the second resonance mode of a spherical bubble cloud (see Figure 13.11). As in the case of the first resonance mode, the frequency is almost the same as the second mode natural frequency (d'Agostino and Brennen, 1989).

13.1.3.4.2 High Pressure Amplitude Cases (Δp = 100 and 125 kPa) When the pressure amplitude becomes greater, the oscillations of the cloud show strong nonlinearity. Figure 13.14 shows the water pressure in the

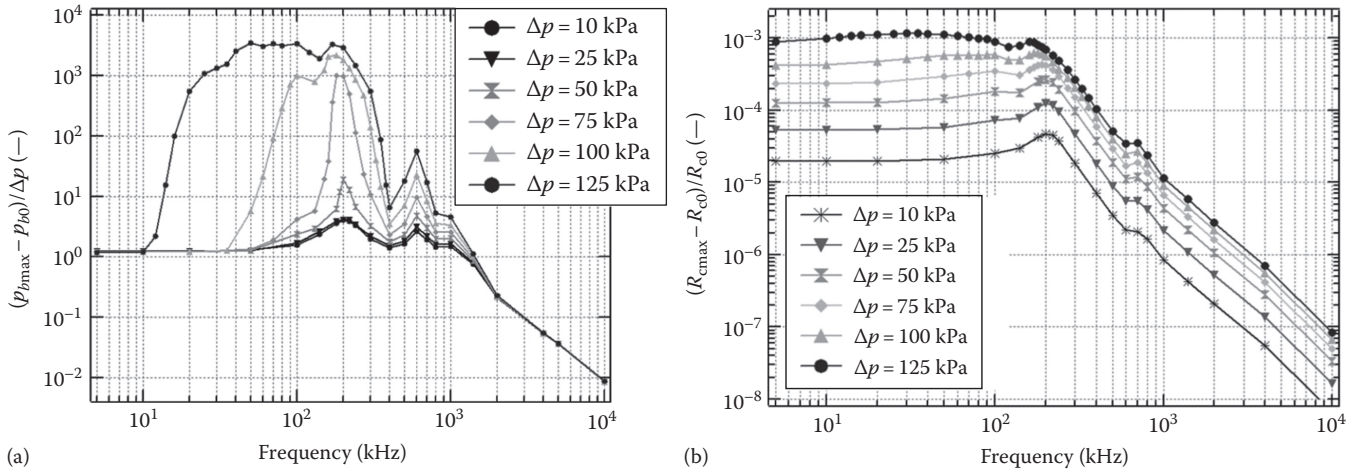


Figure 13.12

Frequency response curves at various amplitudes of the ambient pressure (a: maximum pressure inside the bubbles, b: maximum bubble cloud radius).

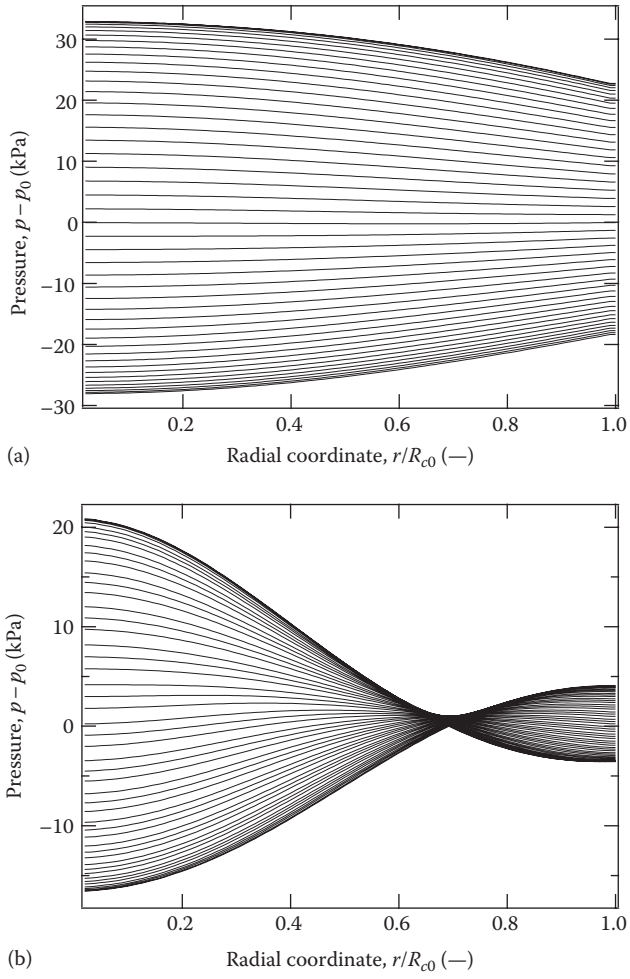


Figure 13.13

Pressure distributions of the liquid phase inside a bubble cloud (a: Δp = 10 kPa, f = 200 kHz, b: Δp = 10 kPa, f = 600 kHz).

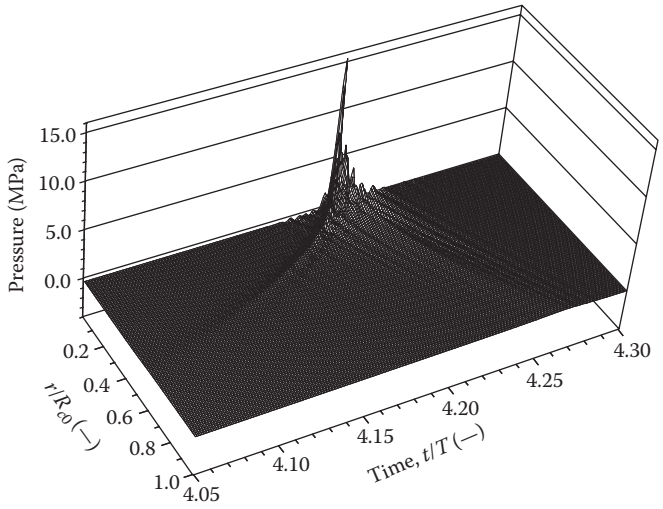


Figure 13.14

Surface plot of the liquid pressure inside a bubble cloud (Δp = 100 kPa, f = 180 kHz).

cloud under the same conditions as the surface plot. The range of the normalized time is from 4.05 T to 4.30 T. In this case, the shock wave is generated inside the cloud by the process of wave focusing. The speed of sound in the bubbly flow strongly depends on the void fraction and is directly dependent on the pressure fluctuations. The sinusoidal pressure wave easily generates the shock wave inside the bubbly liquid. The shock wave in the bubbly liquid causes the collapse of the bubbles so that high energy is concentrated near the center of the cloud. As a result, the normalized pressure becomes much higher when the pressure amplitude becomes significant enough to generate the shock wave. For example, in the case of 100 kPa pressure amplitudes, even when the frequency is much lower, the pressure wave can generate a shock and the high pressures as seen for the 180 kHz case. Additionally, since the high-pressure wave with a high frequency is generated when the bubbles near the center of the cloud collapse, the precursors appear in front of the shock wave before the focusing.

The results indicate that the bubbles inside a bubble cloud violently collapse when the frequency of the irradiated ultrasound is the same or lower than the natural frequency of the cloud for a sufficiently large ultrasound pressure amplitude.

References

Ando, K., Colonius, T., and Brennen, C.E., Numerical simulation of shock propagation in a polydisperse bubbly liquid, *Int. J. Multiphase Flow*, 37, 596–608, 2011.

Arora, M., Ohl, C.D., and Lohse, D., Effect of nuclei concentration on cavitation cluster dynamics, *J. Acoust. Soc. Am.*, 121, 3432–3436, 2007.

Biesheuvel, A. and van Wijngaarden, L., Two phase flow equations for a dilute dispersion of gas bubbles in liquid, *J. Fluid Mech.*, 148, 301–318, 1984.

Birkhoff, G., Note on Taylor instability, *Quart. Appl. Math.*, 12, 306–309, 1954.

Blake, J.R. and Gibson, D.C., Cavitation bubbles near boundaries, *Annu. Rev. Fluid Mech.*, 19, 99–124, 1987.

Blake, J.R., Hooton, M.C., Robinson, P.B., and Tong, R.P., Collapsing cavities, toroidal bubbles and jet impact, *Phil. Trans. R. Soc. Lond. A*, 355, 537–550, 1997.

Borotnikova, M.I. and Soloukin, R.I., A calculation of the pulsations of gas bubbles in an incompressible liquid subject to a periodically varying pressure, *Sov. Phys. Acoust.*, 10, 28–32, 1964.

Bremond, N., Arora, M., Ohl, C.-D., and Lohse, D., Controlled multibubble surface cavitation, *Phys. Rev. Lett.*, 96, 224501, 2006.

Brennen, C.E., *Cavitation and Bubble Dynamics*, Oxford University Press, New York, 1995.

Brennen, C.E., Fission of collapsing cavitation bubbles, *J. Fluid Mech.*, 472, 153–166, 2002.

Bui, T.T., Ong, E.T., Khoo, B.C., Klaseboer, E., and Hung, K.C., A fast algorithm for modeling multiple bubbles dynamics, *J. Comput. Phys.*, 216, 430–453, 2006.

Chahine, G.L. and Duraiswami, R., Dynamical interactions in a multi-bubble cloud, *ASME J. Fluids Eng.*, 114, 680–686, 1992.
Chapman, R.B. and Plesset, M.S., Thermal effects in the free oscillation of gas bubbles, *ASME J. Basic Eng.*, 93, 373–376, 1971.
Coussios, C.C. and Roy, R.A., Applications of acoustics and cavitation to noninvasive therapy and drug delivery, *Annu. Rev. Fluid Mech.*, 40, 395–420, 2008.
d'Agostino, L. and Brennen, C., Linearized dynamics of spherical bubble clouds, *J. Fluid Mech.*, 199, 155–176, 1989.
Esche, R., Untersuchung der schwingungskavitation in Flüssigkeiten, *Acustica*, 2, AB208–AB218, 1952.
Flynn, H.G., Physics of acoustic cavitation in liquids, in Mason, W.P. (Ed.), *Physical Acoustics*, Vol. 1B, Academic Press, New York, 1964.
Frenkel, J., *Kinetic Theory of Liquids*, Oxford University Press, New York, 1946.
Fujikawa, S. and Akamatsu, T., Effect of the non-equilibrium condensation of vapour on the pressure wave produced by the collapse of a bubble in a liquid, *J. Fluid Mech.*, 97, 481–512, 1980.
Grandjean, H., Jacques, N., and Zaleski, S., Shock propagation in liquids containing bubbly clusters: A continuum approach, *J. Fluid Mech.*, 701, 304–332, 2012.
Hao, Y. and Prosperetti, A., The effect of viscosity on the spherical stability of oscillating gas bubbles, *Phys. Fluids*, 11, 1309–1317, 1999.
Hatamiya, S. and Tanaka, H., A study on the mechanism of dropwise condensation, *Trans. Jpn. Soc. Mech. Eng. B* (in Japanese), 52(477), 2214, 1986.
Hsieh, D.-Y., Some analytical aspects of bubble dynamics, *J. Basic Eng.*, 87, 991–1005, 1965.
Ikeda, T., Yoshizawa, S., Tosaki, M., Allen, J.S., Takagi, S., Ohta, N., Kitamura, T., and Matsumoto, Y., Cloud cavitation control for lithotripsy using high intensity focused ultrasound, *Ultrasound Med. Biol.*, 32, 1383–1397, 2006.
Johnsen, E. and Colonius, T., Numerical simulations of non-spherical bubble collapse, *J. Fluid Mech.*, 629, 231–262, 2009.
Kamath, V. and Prosperetti, A., Numerical investigation methods in gas-bubble dynamics, *J. Acoust. Soc. Am.* 85, 1538–1548, 1989.
Kameda, M. and Matsumoto, Y., Shock waves in a liquid containing small gas bubbles, *Phys. Fluids*, 8, 322–335, 1996.
Kameda, M. and Matsumoto, Y., Nonlinear oscillation of a spherical gas bubble in acoustic fields, *J. Acoust. Soc. Am.*, 106, 3156–3166, 1999.
Kameda, M., Shimaura, N., Higashino, F., and Matsumoto, Y., Shock waves in a uniform bubbly flow, *Phys. Fluids*, 10, 2661–2668, 1998.
Keller, J.B. and Kolodner, I.I., Damping of underwater explosion bubble oscillation, *J. Appl. Phys.*, 27, 1152–1161, 1956.
Lauterborn, W., Numerical investigation of nonlinear oscillations of gas bubbles in liquids, *J. Acoust. Soc. Am.*, 59, 283–293, 1976.
Lauterborn, W., On the bifurcation structure of bubble oscillators, in *Proceedings of the 11th International Symposium on Nonlinear Acoustics, Novosibirsk, USSR*, 1987, pp. 71–80.
Lauterborn, W., Acoustic turbulence, Frontiers in physical acoustics, Sette, D. (Ed.), S.I.F.-XCIII, North-Holland, Amsterdam, 1989, pp. 124–144.
Lindau, O. and Lauterborn, W., Cinematographic observation of the collapse and rebound of a laser-produced cavitation bubble near a wall, *J. Fluid Mech.*, 479, 327–348, 2003.
Matsumoto, Y. and Aoki, M., Growth and collapse of cavitation bubbles, *Bull. JSME*, 27, 1352–1357, 1984.
Matsumoto, Y. and Beylich, A.E., Influence of homogeneous condensation inside a small gas bubble on its pressure response, *J. Fluids Eng. ASME*, 107(2), 281–286, 1985.
Matsumoto, Y. and Takemura, F., Influence of internal phenomena on gas bubble motion (Effects of thermal diffusion, phase change on the gas–liquid interface and mass diffusion between vapor and noncondensable gas in the collapsing phase), *JSME Int. J.*, B-37(2), 288–296, 1994.
Matsumoto, Y. and Watanabe, M., Nonlinear oscillation of gas bubble with internal phenomena, *JSME Int. J.*, II-32(2), 157–162, 1989.
Neppiras, E.A., Subharmonic and other low-frequency emission from bubbles in sound-irradiated liquids, *J. Acoust. Soc. Am.*, 46, 587–601, 1969.
Neppiras, E.A. and Noltingk, B.E., Cavitation produced by ultrasonics: Theoretical conditions for the onset of cavitation, *Proc. Phys. Soc. Lond.*, 64B, 1032–1038, 1951.

Nigumatulin, R.I., Khabeev, N.S., and Nagiev, F.B., Heat and mass transfer of vapours–gas bubbles in a liquid, *Int. J. Heat Mass Transfer*, 24(6), 1033–1044, 1981.
Noltingk, B.E. and Neppiras, E.A., Cavitation produced by ultrasonics, *Proc. Phys. Soc. Lond.*, 63B, 674–685, 1950.
Okita, K., Sugiyama, K., Takagi, S., and Matsumoto, Y., Microbubble behavior in ultrasound field for high intensity focused ultrasound therapy enhancement, *J. Acoust. Soc. Am.*, 134, 1576–1585, 2013.
Omta, R., Oscillation of a cloud of bubbles of small and not so small amplitude, *J. Acoust. Soc. Am.*, 82, 1018–1033, 1987.
Plesset, M.S., The dynamics of cavitation bubbles, *ASME J. Appl. Mech.*, 16, 228–231, 1949.
Plesset, M.S. and Mitchell, T.P., On the stability of the spherical shape of a vapor cavity in a liquid, *Quart. Appl. Math.*, 13, 419–430, 1956.
Popinet, S. and Zaleski, S., Bubble collapse near a solid boundary: A numerical study of the influence of viscosity, *J. Fluid Mech.*, 464, 137–163, 2002.
Preston, A.T., Colonius, T., and Brennen, C.E., A reduced-order model of diffusive effects on the dynamics of bubbles, *Phys. Fluids*, 19, 123302, 2007.
Prosperetti, A., The thermal behaviour of oscillating gas bubbles, *J. Fluid Mech.*, 222, 587–616, 1991.
Prosperetti, A., Crum, L.A., and Commander, K.W., Nonlinear bubble dynamics, *J. Acoust. Soc. Am.*, 83, 502–514, 1988.
Rayleigh, Lord. O.M., On the pressure developed in a liquid during the collapse of a spherical cavity, *Philos. Mag.*, 34, 94–98, 1917.
Shimada, M., Matsumoto, Y., and Kobayashi, T., Influence of the nuclei size distribution on the collapsing behavior of the cloud cavitation, *JSME Int. Ser. B*, 43, 380–385, 2000.
Storey, B.D. and Szeri, A.J., A reduced model of cavitation physics for use in sonochemistry, *Proc. R. Soc. Lond. A*, 457, 1685–1700, 2001.
Takemura, F. and Matsumoto, Y., Influence of internal phenomena on gas bubble motion (Effects of transport phenomena and mist formation inside bubble in the expanding Phase), *JSME Int. J.*, B-37(4), 736–745, 1994.
Toegel, R., Gomph, B., Pecha, R., and Lohse, D., Does water vapor prevent upscaling sono-luminescence?, *Phys. Rev. Lett.*, 85(15), 3165–3168, 2000.
Tomita, Y. and Shima, A., The effects of heat transfer on the behavior of a bubble and the impulse pressure in a viscous compressible liquid, *Z. Angew. Math. Mech.*, 59(7), 297, 1979.
Tomita, Y. and Shima, A., High-speed photographic observations of laser-induced cavitation bubbles in water, *Acustica*, 71, 161–171, 1990.
Wilson, M., Blake, J.R., and Haese, P.E., Cloud cavitation dynamics, *ANZIAM J.*, 50, 199–208, 2008.
Yasuda, A. and Takahira, H., Numerical analysis of the dynamics of toroidal bubbles considering the heat transfer of internal gas, *JSME Int. J. Ser. B*, 46, 600–609, 2003.
Yuan, H. and Prosperetti, A., Gas–liquid heat transfer in a bubble collapsing near a wall, *Phys. Fluids*, 9, 127–142, 1997.

13.2 Cavitation

Steven L. Ceccio

Cavitation is the physical phenomenon associated with the inception, growth, and implosion of cavities (vapor-filled voids or bubbles) in the body of a flowing or a quiescent liquid due to changes in the fluid pressure. Cavitation may occur entirely in the bulk of the liquid or close to solid boundaries of the flow. Cavitation is similar to boiling in the inception and growth of bubbles, except that in the latter bubble formation is due to a rise in liquid temperature, while in the former bubble formation is driven by a drop in the liquid static pressure. Pressure variations in the fluid can be achieved hydrodynamically or acoustically. During vaporous (inertial) cavitation, the cavities are filled mostly with fluid vapor. Vaporous cavitation bubbles are often short-lived and produce a high-intensity acoustic pressure upon collapse. Gaseous cavitation bubbles are filled mostly with noncondensable gases, and these gaseous bubbles may persist for longer periods, collapse much less violently, and produce much less noise and damage compared to vaporous bubbles. Pockets of gas and vapor can form and persist on flowing surfaces, and this is referred to as *partial* or *attached* cavitation. Cavitation *inception* occurs when cavitation is first detected in the flow as the mean pressure in the flow is reduced, and *developed* cavitation describes an advanced stage of cavitation, where the size of the cavity is of comparable magnitude

to a characteristic flow dimension. *Desinence* occurs when cavitation is eliminated through an increase in the mean pressure. Cavitation is undesirable in liquid-handling machinery because it may cause damage to solid surfaces, induce noise and vibrations, and lead to reduction in the mechanical efficiency. Conversely, there are useful scientific and engineering applications that employ cavitation. Comprehensive reviews of this subject can be found in Brennen (1995), Young (1989), and Franc and Michel (2006).

13.2.1 Cavitation Nuclei and Bubble Growth

Liquid water can be brought to evaporation at a constant pressure by raising its temperature. This phase change can also be achieved at a constant temperature by reducing the pressure to the corresponding vapor pressure (e.g., water at 1 atm and room temperature, 25°C, can be brought to boiling by heating to 100°C while keeping the pressure fixed, or by reducing the pressure to vapor pressure, 0.03 atm, while keeping the temperature fixed at 25°C). The process of phase change takes place at a phase boundary in the liquid. If such an interface is not present, the bulk of the liquid can sustain pressures below vapor pressure (or remain liquid at temperatures above the saturation temperature) (Carey, 1992). (See Chapter 3 for a discussion on nucleation and boiling.)

Theoretical predictions based on the van der Waals intermolecular forces of attraction indicate that *pure* water (no dissolved gas or impurities) can withstand high levels of tension corresponding to pressures much less than the vapor pressure (several hundred atmospheres of tension). The fracture of the liquid due to the failure of intermolecular forces is called *homogeneous nucleation*. In most practical applications, these high levels of tension are not approached. Instead, voids or bubbles (cavitation) appear in the liquid as the liquid evaporates at the interface of small gas inclusions or *nuclei*. This process is called *heterogeneous nucleation*, and it is the most common form of cavitation initiation. It is often sufficient to bring the operational pressure to or slightly below the evaporation pressure for these bubbles or voids to appear.

Cavitation nuclei can be present in the body of the liquid or on the surfaces of suspended particles or boundaries that come in contact with it as described in Section 3.1. Cavitation nuclei often exist as small bubbles of gas (a few microns to a few hundred microns) that are in equilibrium with the liquid or as gas-filled miniature pockets on the surfaces of solid particles or solid flow boundaries. Nuclei can also form when dissolved gas in the liquid comes out of solution. The amount and properties of nuclei in the fluid can strongly influence the pressure at which inception occurs. The growth of nuclei can often be approximated by the growth of small spherical bubbles in an unbounded liquid.

The Rayleigh–Plesset equation (Brennen, 1995) describes the dynamics of growth and collapse of a spherical bubble nucleus in an otherwise quiescent, infinite fluid medium. It couples the forces acting on the bubble with the motion of the surrounding fluid:

$$\rho_l\left[a_b\frac{d^2a_b}{dt^2}+\frac{3}{2}\left(\frac{da_b}{dt}\right)^2\right]+\frac{4\mu}{a_b}\frac{da_b}{dt}=\left(p_{\infty,0}-p_v+\frac{2\sigma}{a_{b,0}}\right)\left(\frac{a_{b,0}}{a_b}\right)^{3k}-p_\infty+p_v-\frac{2\sigma}{a_b} \tag{13.41}$$

where the subscript 0 refers to the initial conditions of the bubble. The liquid pressure far away from the bubble is p. The bubble contains both vapor and noncondensable gas of partial pressures, p_v and p_g, respectively. The gas obeys the polytropic gas law. The exponent k is the polytropic gas constant and $k = 1$ for isothermal processes and $k = c_p/c_v$ for adiabatic processes. p_g is equal to the first term on the right-hand side of the equation. In this formulation, the liquid compressibility is neglected (see Section 13.1 for further discussion of bubble physics).

With the left-hand side set to zero, Equation 13.41 describes the quasi-static equilibrium of a bubble (temporal dependence of the bubble radius is negligible). Consider a small bubble (cavitation nucleus) that exists in a quasi-static equilibrium in the body of a liquid. The pressure inside the bubble, p_b, is counteracted by the liquid pressure on the bubble surface, p_l, and by the surface tension forces, or

$$p_g+p_v=\frac{2\sigma}{a_b}+p_l \tag{13.42}$$

where $p_b = p_g + p_v$. When this nucleus experiences a drop in the liquid pressure, such as when it passes through a venturi throat, it may grow quasi-statically from its initial equilibrium radius, $a_{b,0}$, to a larger equilibrium radius, provided that the bubble radius does not exceed the *Blake critical radius*. A bubble exposed to tension will grow unboundedly when its radius is above this critical value given by

$$a_{b,c} = \left[\frac{9km_G T_b K_G}{8\pi\sigma}\right]^{1/2} = \left[\frac{3}{2}\frac{ka_{b,e}^3 p_{g,e}}{\sigma}\right]^{1/2} \tag{13.43}$$

The subscript e refers to the equilibrium state of the bubble. Here, m_G and K_G are the gas mass and gas constant, respectively, and T_b the bubble temperature. An equivalent critical liquid pressure is given by

$$p_{l,c} = p_v - \frac{4}{3}\sigma\left[\frac{8\pi\sigma}{9km_G T_b K_G}\right]^{1/2} = p_v - \frac{4}{3}\sigma a_{b,c} \tag{13.44}$$

In the venturi example, if the liquid pressure drops to or below the critical pressure, the bubble radius will grow explosively to a maximum radius that can be of the order of hundred times its initial size, and the nucleus would then be considered to have cavitated. Figure 13.15a and b shows the response of a nucleus, initially in equilibrium, to a sinusoidal variation in the liquid pressure. Figure 13.15a shows the change in bubble radius when the minimum liquid pressure is above the critical pressure: the bubble radius responds quasi-statically. Next, Figure 13.15b, the tension exceeds the critical pressure. Notice the growth rate of the cavitating nucleus, its violent collapse, and the multiple rebounds. Not all nuclei will lead to cavitation (explosive bubble growth). Only the nuclei that reach the critical radius will cavitate, and these are considered the *active nuclei*.

When a bubble cavitates, its radius will grow asymptotically. Thus, the maximum bubble radius, $a_{b,m}$, is related to the total time that the bubble remains in the region of tension, Δt:

$$a_{b,m} \approx \frac{2}{3}\left(\frac{-p_\infty + p_v}{\rho_l}\right)^{1/2} \Delta t \tag{13.45}$$

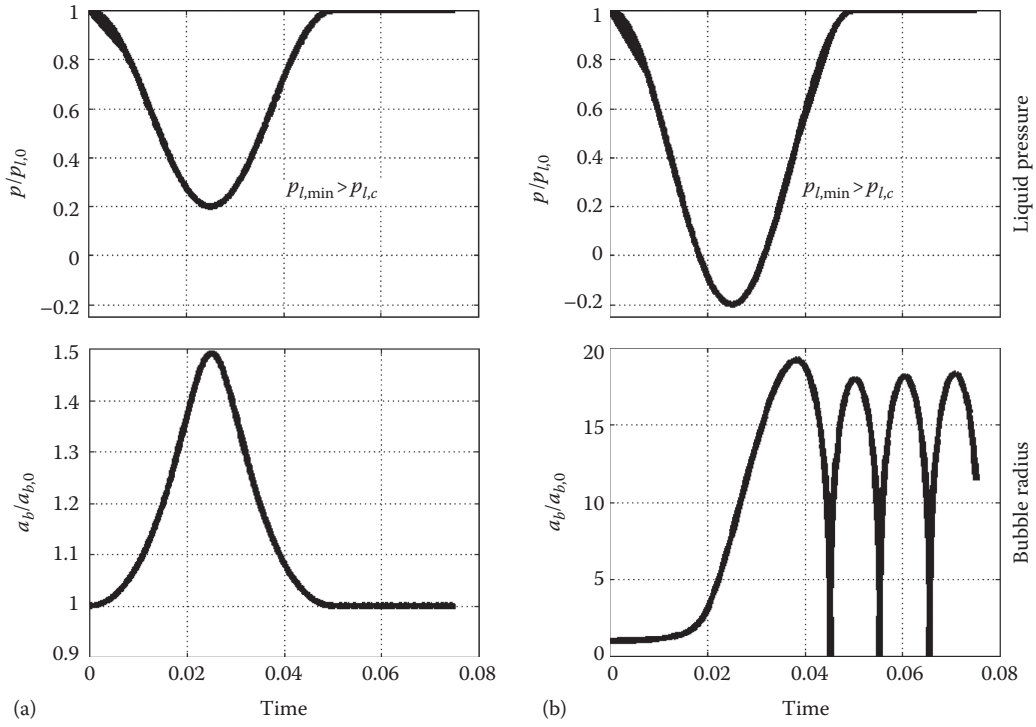


Figure 13.15

Changes in the radius of a bubble as it is exposed to a sinusoidal variation in the surrounding pressure: the minimum pressure is above the critical pressure (a) and below the critical pressure (b).

The nuclei distribution in a flow can be quite variable, depending on the source of the liquid and the upstream flow conditions. Consequently, the characterization of cavitation inception must be accompanied by the measurement of the nuclei content.

Measurement methods for cavitation nuclei can be hydrodynamic, acoustic, or optical (Gindroz and Billet, 1993). Holography and light scattering have been used to detect the presence of cavitation nuclei (Ran and Katz, 1993). In these methods, the optically measured size of detected bubbles is used to infer the critical pressure. The absorption and scattering of acoustic signals is also used to detect and count nuclei (Chahine and Kalumuck, 2003). A direct measurement of the presence of nuclei is achieved when a liquid sample is passed through a region of known low pressure. Nuclei with radii that exceed the critical radius will cavitate. The Blake critical radius is computed from this pressure and presented as the nuclei radius. The event rate of these cavitating bubbles can then be counted by visual observation. Moreover, when a cavitating bubble is convected to a region of higher-pressure downstream, it will collapse producing an acoustic emission. The noise pulses can be detected and counted, giving another independent measurement of the nuclei. Devices that measure nuclei through inducing cavitation events are called *cavitation susceptibility meters* (Ceccio et al., 1991, d'Agostino and Acosta, 1991). The amount of dissolved gas in the liquid will also influence the number of free nuclei and the inception process. Measurements of the total dissolved gas (or of one gas component, such as oxygen) are often reported, but this quantity only indirectly relates to the free gas content.

13.2.2 Collapse of Cavitation Bubbles and Erosion

The collapse of cavitation bubbles is of practical importance because of the associated high potential for damage and noise production. Once a cavitating bubble has reached its maximum radius and encountered a region of higher pressure (either through convection to a high-pressure region or via a change in the mean pressure field), the bubble will start its collapse. During the final stages of bubble implosion, the bubble wall velocity can reach or exceed the liquid speed of sound, and shock waves are produced in the liquid. Liquid compressibility in the vicinity of the bubble cannot be neglected in this instance, and the Rayleigh–Plesset equation (13.41) should be modified to include this effect. One of the existing modifications is the Gilmore equation (Leighton, 1994, Franc et al., 1995) and is given by

$$a_b U \frac{dU}{da_b}\left(1-\frac{U}{c_l}\right)+\frac{3}{2}U^2\left(1-\frac{U}{3c_l}\right)=h\left(1-\frac{U}{c_l}\right)+\frac{a_b U}{c_l}\left(1-\frac{U}{c_l}\right)\frac{dh}{da_b} \tag{13.46}$$

where $U = da_b/dt$, c_l is the liquid speed of sound, and h the enthalpy of the liquid at the bubble wall, with $h = 0$ for the liquid very far away. Whether the bubble wall speed will reach the liquid speed of sound depends on the noncondensable gas mass inside the bubble, which determines the amount of damping of the bubble mechanical energy.

Higher noncondensable gas contents lead to increased damping and result in less violent collapse and reduced possibility for shock pressure production. Experimentally measured values of the pressure levels in the immediate vicinity of spherically collapsing bubbles in water are of the order of hundreds of atmospheres. The intense pressure waves created in the liquid can cause damage to nearby solid surfaces.

A timescale for the bubble collapse is the Rayleigh collapse time, which depicts the time it takes for a vapor-filled spherical bubble to implode from its maximum to its minimum radius, and is given by

$$t_c = 0.915 a_{b,m}\left(\frac{\rho_l}{\Delta p}\right)^{1/2} \tag{13.47}$$

where

$a_{b,m}$ is the maximum bubble radius

Δp is the difference between the liquid static pressure and the vapor pressure

The acoustic emission produced by the collapse of a cavitation bubble is proportional to the mechanical potential energy of the bubble:

$$E_M = \frac{4}{3}\pi a_{b,m}^3 \Delta p \tag{13.48}$$

The collapsing bubble is largely a monopole sound source, with the largest emissions taking place during the rapid volume deceleration and acceleration at the point of minimum bubble volume. The amount of this

energy converted into acoustic energy during bubble collapse is strongly related to the amount of deformation that the bubble undergoes during collapse.

The collapse of the bubble can be influenced by gravity and the presence of free and solid surfaces (Blake and Gibson, 1987). The quantity

$$\gamma = \left(\frac{\rho_l g a_{b,m}}{\Delta p} \right)^{1/2} \tag{13.49}$$

scales the buoyancy force with the force due to the pressure difference across the bubble interface. When $\gamma > 1$, the bubble collapse becomes nonspherical and is characterized by the formation of a jet, where the lower side of the bubble caves inward and upward and penetrates the upper wall of the bubble. A similar jet formation occurs when the bubble collapses near a solid boundary as shown in Figure 13.16. Note that the jet is directed toward the solid surface. Measurements of jet speeds of up to 150 m/s have been observed (Philipp and Lauterborn, 1998, Brujan et al., 2002). The water hammer effect of this jet can induce instantaneous pressures on the surface given by $p_{jet} = \rho_l c_l u_{jet}$, where c_l is the liquid speed of sound and u_{jet} the jet velocity. Jet impact on a nearby solid boundary can lead to very high surface stresses and produce instantaneous pressures on the solid surface exceeding hundreds of bars. These high pressures are capable of inducing surface damage.

Cavitation erosion is caused by the *repetitive* impingement of cavitation-induced pressure pulses on a solid flow boundary and often results from material fatigue. Erosion predictions on metal surfaces have been mostly based on combining the concept of cavitation intensity (frequency of occurrence and levels of peak pressures from collapsing cavities) with one or more representative material properties. Such properties can be the hardness, elastic modulus, tensile strength, or their combinations. An example of such combination is the ultimate resilience, defined as (Hammitt, 1980, Franc, 2009)

$$\text{UR} = \frac{(\text{Tensile strength})^2}{2(\text{Young's modulus})} \tag{13.50}$$

Cavitation intensity depends on the flow conditions and the form of cavitation. Studies on cavitation erosion in metals and alloys often produce scattered results. Erosion measures include mass loss measurements and mean depth of penetration rate (MDPR):

$$\text{MDPR} \sim \rho_l \frac{\eta}{\varepsilon} u^n \tag{13.51}$$

where

η is an energy-transfer efficiency term
ε is related to the material properties
u is the impact speed
n is an exponent

Care should be taken to determine how specific MDPR formulations are derived.

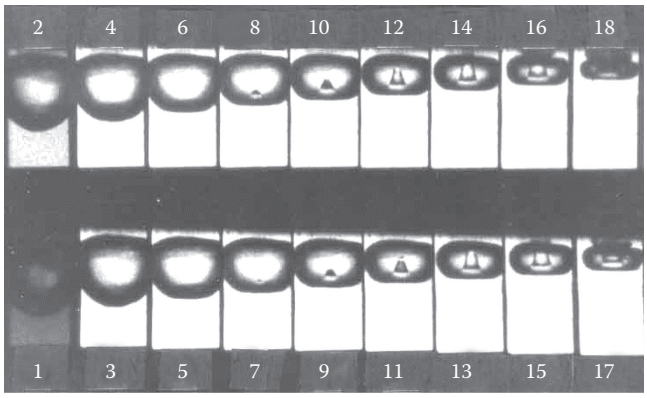


Figure 13.16

A series of images that show the collapse of a cavitation bubble near a solid boundary. The images are with 2 μs time intervals, and each is 1.4 mm wide. Note the formation of the reentrant jet directed toward the wall. (Reproduced from Tomita, Y. and Shima, A., *Acustica*, 71, 161, 1990.)

Despite the scatter in cavitation erosion data, a general trend in erosion behavior can be described as depicted in Figure 13.17 for a ductile metal. There is an *incubation period* (I) before a damage to the surface can be noticed, followed by an *acceleration* of the rate of erosion (II). As the specimen is exposed further to cavitation, the erosion rate will *plateau* (III) for quite some time before it drops, in what is known as the *attenuation phase* (IV). The rate of erosion and the damage properties also depend on the microscopic material structure. For ductile materials that have the potential to store elastically and respond to the

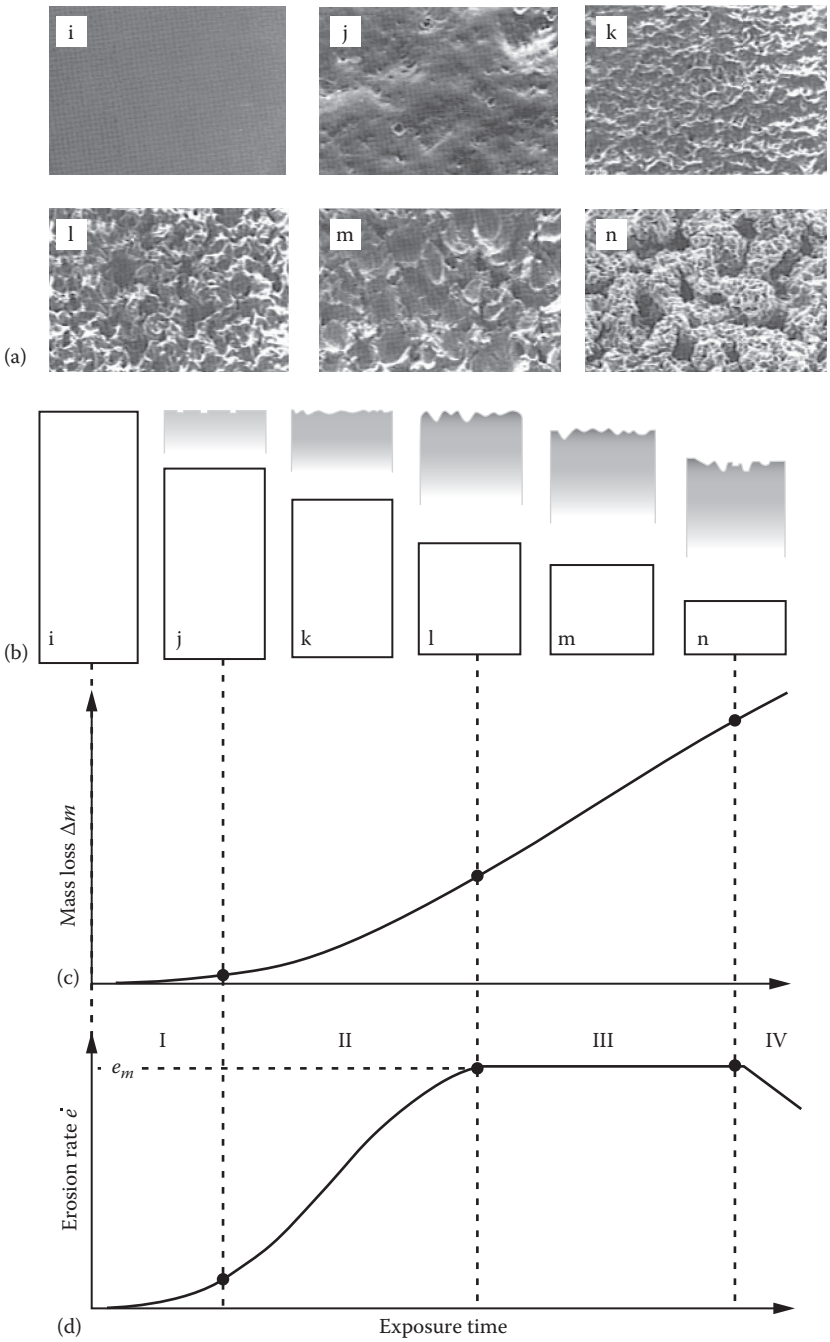


Figure 13.17

Erosion behavior of a ductile alloy with cavitation exposure time: (a) scanning electron microscope images showing the surface appearance; (b) cross-sectional schematics of the pitting behavior; (c) accumulative mass loss; (d) erosion rate showing the four stages of erosion. (From Franc, J.P. et al., *La Cavitation Mecanismes Physiques et Aspects Industriels*, Presses Universitaires de Grenoble, Grenoble, France, 1995. Copyright EDP Sciences, with permission.)

cavitation hammering energy, damage is often due to fragmentation and is in the form of craters. In fragile alloys, erosion often causes cracks and occurs along crystal lines and thus causes more material loss than in ductile metals. And, recent work has extended observations to nonmetallic materials and coatings (Deplancke et al., 2015).

13.2.3 Acoustic Cavitation

Sometimes referred to as vibratory cavitation (low driving frequencies) or ultrasonic cavitation (high driving frequencies), acoustic cavitation describes the growth and collapse of cavitation nuclei due to their exposure to acoustic pressure waves in a liquid (Leighton, 1994). As in many forms of cavitation, the presence of cavitation nuclei is usually required to initiate and sustain the cavitation process. Once the cavitation process is initiated, the collapse of the bubbles and their fragmentation can act as nuclei for new cavitation bubbles. Consider an underwater acoustic horn emitting a sinusoidal pressure signal fluctuating about a mean amplitude. The water will experience compression (high pressure) and rarefaction (low pressure) patterns due to the passage of the wave. If the rarefaction amplitude of the wave drops below the vapor pressure, cavitation can occur. The principle behind the control of acoustic cavitation is the ability to synchronize the acoustic forcing with the dynamics of the bubble in order to achieve the desired effect such as timely bubble growth or collapse. The production of acoustic waves in the liquid can be achieved by magnetostriction type devices or by the more widely used piezoelectric crystal transducers. The electrical input to a piezoelectric element is transformed into displacement of the piezoelectric crystal surface that is then transferred to the liquid in the form of acoustic waves. To achieve acoustic signals of sufficient amplitude for cavitation, acoustic mirrors or acoustic lenses can be used to focus the acoustic energy into a miniature volume. Focusing can also be achieved by using curved emission transducers. The focusing volume is proportional to the emitted acoustic wavelength and inversely proportional to the transducer size.

Pulsed ultrasound refers to the emission of a train of wave packets of fundamental frequency (f_o) and pulse repetition frequency (f). The pulse duration divided by the pulse repetition period ($1/f$) gives the portion of the time that the transducer is actually emitting or the *duty cycle*. Passive acoustic cavitation describes cavitation events induced by the acoustic emissions from other cavitation bubbles.

It can be shown from the Rayleigh–Plesset equation that a bubble acts as spring–damper system. Consider a cavitation nucleus of initial radius (a_o) that is at the focal point of an ultrasonic transducer emitting at a single frequency (f_o) and with peak amplitude P_o. The bubble wall will oscillate under the effect of the forcing acoustic wave, similar to a forced damped oscillator, for *small* bubble oscillation amplitudes. The undamped natural frequency of bubble oscillation in (rad/s) is given by

$$\omega_n = \left(\frac{1}{\rho_l a_{b,e}^2} \left\{ 3k(p_\infty - p_v) + 2(3k-1)\frac{\sigma}{a_{b,e}} \right\} \right)^{1/2} \tag{13.52}$$

The bubble wall motion will be in phase with the forcing pressure if the forcing frequency is less than the bubble natural frequency (resonance). Increasing the forcing frequency above resonance will cause the bubble oscillations to be out of phase with the forcing pressure by 180°. Increasing the driving pressure amplitudes causes the bubble wall motion amplitude to become nonlinear and undergo large volume oscillations, that is, cavitation. The oscillations can be stable (*stable cavitation*) or unstable (*transient cavitation*).

During the growth part of bubble oscillation, the increasing bubble size translates into a drop in the noncondensable gas concentration in the bubble interior below the gas concentration in the liquid. This leads to mass diffusion of the gas from the liquid into the bubble. During the contraction phase of the bubble, the opposite occurs, and gas is diffused from the bubble into the liquid. Due to the larger surface area and thinner concentration boundary layer during the growth phase compared with the contraction phase, there would be a net mass diffusion into the bubble. The overall increase in the gas mass in the bubble interior is called *rectified diffusion* (Blake, 1949, Hsieh and Plesset, 1961). Since the diffusion timescales are usually much larger than the bubble characteristic timescale (Rayleigh time for instance), diffusion can often be neglected. In transient or unstable cavitation, the driving pressure is increased beyond the linear oscillation until the bubble growth becomes unbounded, followed by violent implosion. The bubble may rebound after collapse or it may fragment into multiple fragments. Brennen (2002) suggests that the bubble fission may be due to an instability forming on the bubble wall or due to jet formation. A number of conditions are required for unstable cavitation to occur; one of them satisfies the Blake critical pressure (or radius) threshold.

When the bubble reaches its minimum radius during implosion, the interior pressure and temperature can momentarily reach extremely high levels. Emission of shock waves in the liquid that travel at liquid Mach numbers greater than 1 has been observed (Pecha and Gompf, 2000). Light emission has also been observed from cavitation bubbles collapsing under an ultrasonic pressure field (Holzfuss et al., 1998, Matula et al., 1998, Hilgenfeldt et al., 1999). This phenomenon is known as *sonoluminescence*. Putterman and Weninger (2000) discuss how the high pressures and small minimum bubble volumes during the last stages of collapse result in dramatic increases in the bubble energy density, which is essential for the production of light. The detailed physics of sonoluminescence is still a subject of investigation.

The collapse of cavitation bubbles may cause jet formation and pressure shock waves that have useful noninvasive surgical and lithotriptic effects (Vakil and Everbach, 1993, Coleman et al., 1995, Tran et al., 2003). Ultrasonic cavitation is now commonly used in industrial and electronic component cleaning operations (Niemczewski, 1999, Ferrel and Crum, 2002).

13.2.4 Hydrodynamic Bubble Cavitation

Hydrodynamic cavitation occurs when the flow of a liquid leads to reduction in pressure and cavitation. In these flows, the cavitation number, which is a measure of the level of pressure in the flow, is defined as

$$\sigma = \frac{p_\infty - p_v}{1/2\rho U^2} \tag{13.53}$$

Hydrodynamic bubble cavitation (traveling bubble cavitation) and sheet cavitation (Section 13.2.5) are the two major forms of cavitation that take place on the surface of a hydrofoil or the face of a propeller blade. The operational parameters that give rise to one type or the other can be difficult to predict, and subtle changes in flow conditions (e.g., nuclei content, incident flow angle, boundary layer tripping, or Reynolds number) can lead to the inception or desinence of one or both forms. This underlines the complexity involved in predicting and scaling hydrodynamic cavitation behavior on full-size prototypes from small model tests. The formation of traveling bubble cavitation can lead to significant noise, vibration, and damage if the bubbles collapse on the blade surface.

In traveling bubble cavitation, singly identifiable bubbles can be seen to move in the flow direction while attached to the surface of the blade or hydrofoil. They often have the form of hemispherical caps during the growth phase (Figure 13.18). A closeup examination of traveling bubbles indicates that there is a thin film of liquid separating a bubble from the surface. The dynamics of the boundary layer and its interaction with the bubble have significant impact on cavitation inception, bubble growth, and the consequent cavity collapse (Kuhn de Chizelle et al., 1995).

The growth and collapse of traveling bubbles can be scaled with spherical bubble dynamics for many applications (Ceccio and Brennen, 1991). However, if the bubbles interact with the boundary layer flow, they can be deformed, which reduces the level of noise they emit upon collapse. If many bubbles are present, interaction between the bubbles can become important. These interactions are discussed in Brennen (1995).

13.2.5 Sheet Cavitation

Sheet cavitation occurs when a pocket of gas or vapor forms on a solid surface due to the flow of the liquid (Figure 13.19). Sheet cavitation is often formed when there is wall-flow reversal or boundary layer separation due to an adverse pressure gradient (rising pressure in the flow direction) on the surface. If the cavity

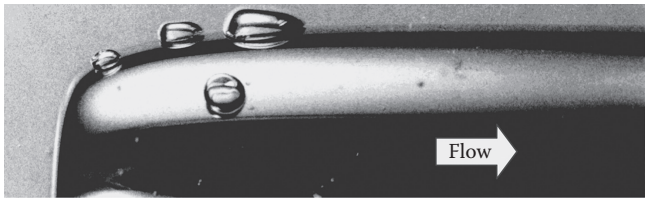


Figure 13.18

Traveling cavitation bubbles over an axisymmetric body of revolution.

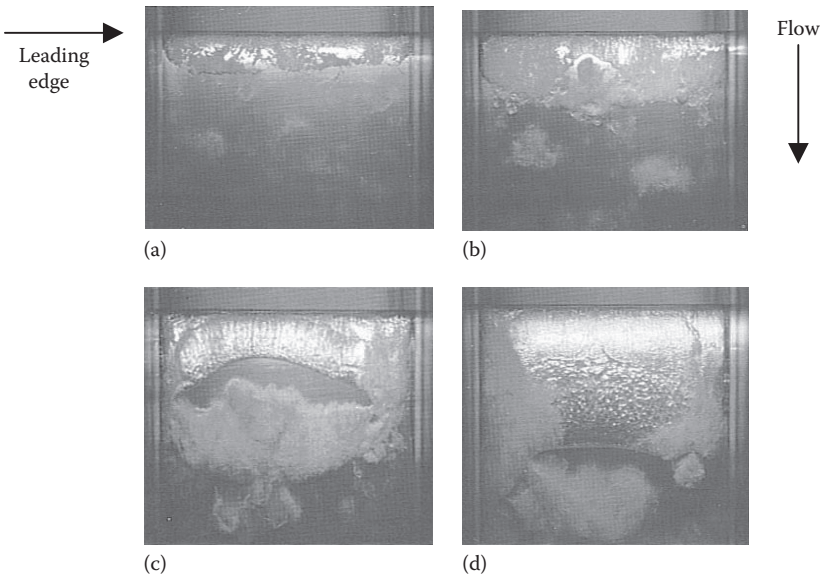


Figure 13.19

Sheet cavitation on a 2D NACA009 hydrofoil: (a) incipient cavitation; (b) developing cavitation; (c) cloud shedding; and (d) cavity refilling.

terminates on the cavitating surface, it is called a *partial cavity*. If the cavity extends beyond the cavitating object into the wake of the flow, it is called a *supercavity*. The shape of the cavity in the detachment region is affected by the type of surface material depending on whether it is hydrophilic or hydrophobic (Leger and Ceccio, 1998). For hydrophilic surfaces, the cavity interface curves downstream forming a forward-facing step, with a recirculation region just upstream. The forward-facing step and the recirculation region are not present on hydrophobic surfaces, and the cavity detachment is close to the boundary layer separation point. Prediction of the cavity detachment point over a given surface can be performed with very good accuracy by invoking the potential flow theory to provide the pressure distribution in the liquid flow. This can then be combined with boundary layer calculations to predict the separation point. Laberteaux and Ceccio (2001a) present such an example.

When a laminar boundary layer separates from the surface, it can become turbulent and reattach to the surface just downstream of the separation point. In this case, the detachment of the sheet cavity is expected to occur in the narrow region between the laminar separation and the turbulent reattachment of the boundary layer, or the "separation bubble". Turbulent boundary layers are more resistant to adverse pressure gradients and separation and can resist the formation of partial cavities. Increased background flow turbulence levels, surface roughness, and surface trips can induce laminar to turbulent boundary layer transition. By artificially tripping the laminar boundary layer on a hydrofoil into turbulence, Arakeri and Acosta (1973) showed that the occurrence of attached cavities could be delayed. Also, if the underlying boundary layer is transitional or turbulent, complex bubble–boundary layer interactions can occur, as shown in Figure 13.20 (Li and Ceccio, 1996).

Franc et al. (1995) map the $\sigma - \alpha$ space of a NACA 16-012 hydrofoil at $Re = 1 \times 10^6$ with relation to the shapes of sheet cavitation occurring on the foil, where α is the angle of attack. For low angles of attack, the laminar boundary layer separation is toward the rear end of the foil, and an attached cavity is formed near the separation point and it extends into the blade wake. Increasing α to a moderate angle of attack leads to the formation of a band of a single hemispherical bubble on the blade surface, which transform with reduction of the cavitation number, σ, into an attached partial cavity terminating on the blade surface. A further reduction in σ forms a supercavity. The interior of partial and supercavities is single-phase vapor (or single-phase gas–vapor mixture). Further increase in the angle of attack α combined with an increase in the cavitation number can cause the attached cavity to become "frothy" or filled with a liquid–vapor mixture, also known as *open* partial cavity. At extreme angles of attack corresponding to stall, the open cavity is not attached to the blade surface anymore except for the leading edge, and cavitation can be noticed in the wake vortices shed in the liquid.

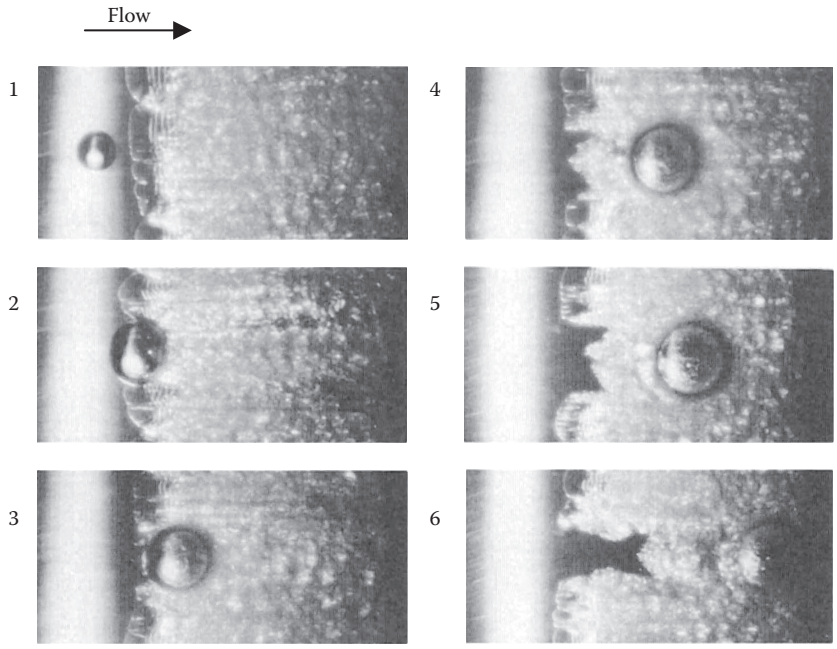


Figure 13.20

Images of several bubbles over a 2D NACA 631A012 hydrofoil. The process of sheet cavity sweeping by the traveling bubble is shown. The bubble does not disturb the cavity, until it has passed downstream, when the sweeping action takes place.

Under certain conditions of Re, σ, and free-stream turbulence levels, a partial cavity can undergo stable or an unstable pulsation. Wade and Acosta (1966) predict that cavities of length, l_c, on a hydrofoil of cord length, c, become unsteady and pulsatile when $(3/4)c < l_c < (4/3)c$. In this pulsatile phenomena, part of the liquid flow that reattaches to the blade surface in the cavity closure region will form a jet that reenters underneath the cavity (jet directed upstream toward the cavity detachment point). When the partial cavity is at its maximum size, the reentrant jet can cause a large portion of the cavity to pinch off and be swept downstream. The bubble cloud will collapse downstream, producing substantial acoustic noise and possible material damage. The small remaining portion of the cavity left attached to the surface will grow smoothly through evaporation and gas diffusion from the liquid to a maximum size, and the cycle repeats. Thick cavities are often unstable and associated with unsteady pulsation. The pulsation phenomena are associated with periodic, strong structural loading, which is undesirable. In stable quasi-steady pulsatile cavities, a Strouhal number (St) can be defined to describe the pulsation:

$$St = \frac{f_p l_c}{U_\infty} \tag{13.54}$$

where

f_p is the pulsation frequency

l_c is the characteristic length

Recent experiments also suggest that the bubbly flows within the sheet cavity can develop condensation shocks that lead to strong cloud shedding (Ganesh et al., 2014).

The Strouhal number for strongly shedding partial cavities is often between 0.2 and 0.4 when l_c is the mean cavity length (George et al., 2000). Laberteaux and Ceccio (2001a,b) studied open partial cavities in detail. They showed that the liquid flow behind the cavity resembled the flow aft of a backward-facing step. The cavities terminated near the point of maximum cavity thickness, and cavitating vortices were shed in the turbulent cavity wake. The collapse of these cavitating vortices is believed to contribute to cavitation damage. The formation of reentrant flow is strongly related to the shape of the cavitating object. Figure 13.21 shows the difference between two cavitating hydrofoils. The first has no spanwise

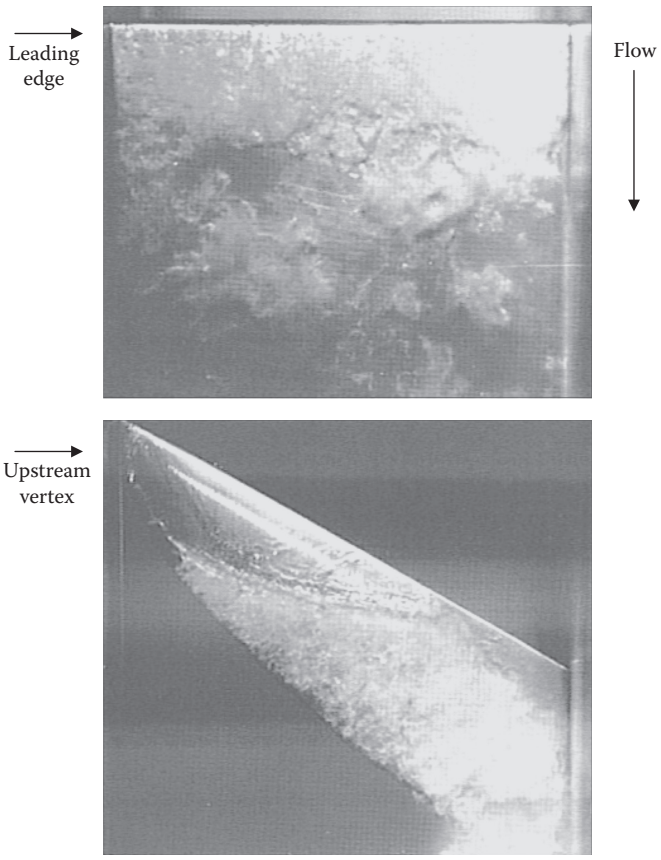


Figure 13.21

Partial cavities on a 2D hydrofoil and on a 3D hydrofoil (swept at 30°). Both hydrofoils have the same section shape.

variation and the second has a swept profile. In the unswept case, the reentrant flow leads to an unstable partial cavity. But the reentrant flow in the swept geometry is deflected in the spanwise direction, producing a stable, closed cavity.

If a partial cavity grows beyond the trailing extent of the cavitating object, it becomes a supercavity. Hydrofoils and propulsors can be designed to form supercavitating on their surface during high-speed operation (Young and Kinnas, 2003). Underwater objects traveling at very high speeds can develop a supercavity that envelope the object, significantly reducing its overall drag (Ceccio, 2010).

13.2.6 Vortex Cavitation

The swirling motion of a vortex requires the presence of a pressure gradient directed away from the center of rotation to counterbalance the centrifugal force. Thus, the pressure in the center of the vortex is lower than the surrounding fluid, and it is possible for the pressure in the core of a liquid vortex to drop below vapor pressure. If nuclei are present in this low-pressure region, they may explosively grow, resulting in *vortex cavitation*. The axial flow inside the vortex core can be slower or faster than the fluid outside the core, which may cause an additional pressure difference. Line vortices often occur near the termination of lifting surfaces, and Figure 13.22 shows developed cavitation occurring in a tip vortex.

The Gaussian vortex, which is a widely used model for concentrated line vortices, is characterized by a zero radial velocity profile and a tangential (azimuthal) velocity profile as a function of radial distance from the vortex center, r, given by

$$u_\theta(r) = \frac{\Gamma_o}{2\pi r}\left(1 - e^{-\eta_l (r/R)^2}\right) \tag{13.55}$$

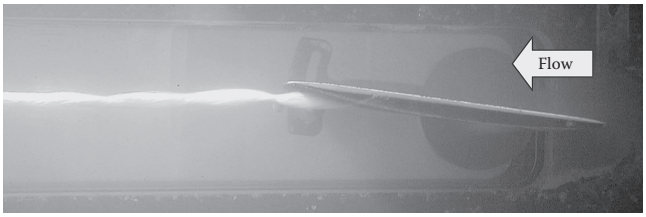


Figure 13.22

Developed tip vortex cavitation from a stationary hydrofoil.

Two parameters are needed to characterize the vortex: its core radius, R, which gives the location of maximum tangential velocity, and its total circulation, Γ_o. The circulation distribution is given by

$$\Gamma(r)=\Gamma_o\left(1-e^{-\eta_l (r/R)^2}\right) \tag{13.56}$$

where $\eta_l = 1.257$ is a constant. The pressure drop at the vortex center is given by

$$p_c = p_\infty - 0.870\rho_1\left(\frac{\Gamma_o}{2\pi R}\right)^2 \tag{13.57}$$

Vortex cavitation is often the first type to appear in hydrodynamic applications. When inception occurs, individual nuclei are captured by the vortex and cavitate. With a further reduction in pressure, the core is filled with a vapor and gas mixture. Based on momentum conservation argument in a Rankine vortex (which has a uniform "top hat" vorticity distribution), Arndt and Keller (1992) predicted the diameter of the vapor-filled region to be 71% of the original liquid vortex core diameter. The inception number is usually *not* equal to the desinence number. This hysteresis pattern is due to the nonlinear bubble dynamics. Vortex cavitation predictions are sensitive to the flow nuclei and dissolved gas content.

The formation of tip vortices results from the pressure difference between the suction side and the pressure side near the tip of a finite-span lifting surface. Prediction of tip vortex cavitation follows the viscous scaling of McCormick (1962). He showed that the tip vortex core radius is scaled with the boundary layer thickness on the blade pressure surface, and this is Reynolds number dependent. In addition, the circulation strength of the tip vortex is related to the lift generated on the lifting surface or the lift coefficient, C_L. Then, the inception cavitation number has the form

$$\sigma_i = KC_L^2 Re^m \tag{13.58}$$

where

K is a scale factor

m is a constant depending on the boundary layer regime (m = 2/5 for a turbulent boundary layer)

In axial pumps and ducted propellers, there is an additional effect due to the confinement gap between the blade tip and the shroud. Other forms of cavitation in concentrated vortices include hub vortex cavitation, which forms on the hub of a propeller or a hydraulic turbine.

Regions of free turbulent shear flow can contain many regions of concentrated vorticity (coherent structures). Shear flow cavitation can form in the high-speed regions of jets, wakes, and separated shear layers. Figure 13.23 shows the cavitating turbulent shear flow associated with a free shear layer. The inception of these flows is often difficult to predict, as it is strongly related to the details of the turbulent flow and nuclei distribution. A recent review of this type of cavitation is found in Arndt (2002).

13.2.7 Cavitation in Hydraulic Machinery

Cavitation can occur in both pumps and turbines. Bubble, sheet, and vortex cavitation have all been observed within these devices, and persistent cavitation can lead to reduction in efficiency, vibration,

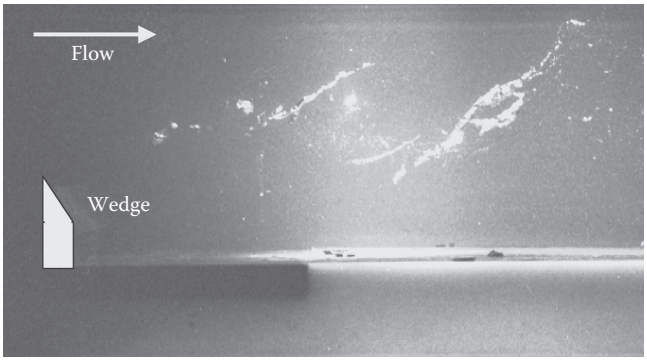


Figure 13.23

Cavitation inception in a turbulent shear flow formed downstream of a wedge.

and erosion damage. The cavitation parameter in hydraulic machinery is usually referred to as the *Sigma Thoma number* and is given by

$$\sigma_T = \frac{H_{sv}}{H} \tag{13.59}$$

where H_{sv} is the net positive suction head (NPSH) and is given by

$$H_{sv} - \frac{1}{g}\left[P_0 - P_v + \frac{1}{2}\rho V_0^2\right] \tag{13.60}$$

with H being the *total head* under which the turbomachinery is operating. If the nondimensional flow rate $Q/2\pi\Omega D^3$ is held constant (analogous to the angle of attack in stationary hydrofoils), then one can write the Thoma number as

$$\sigma_T = \left(\frac{n_s}{S}\right)^{4/3} \tag{13.61}$$

where

$$n_s = \frac{\Omega Q^{1/2}}{(gH)^{3/4}} \tag{13.62}$$

and

$$S = \frac{\Omega Q^{1/2}}{(gH_{sv})^{3/4}} \tag{13.63}$$

where

n_s is the specific speed, while S is the suction specific speed
D is the impeller eye diameter (in m)
Ω is the rotational speed (in rad/s)
Q is the flow rate (in m^3/s)
H and H_{sv} are (in m)

The inlet of a pump or the exit of a turbine are regions of reduced pressure and increased potential for cavitation. Radial flow machines have relatively low specific speeds (high heads and low throughput), and axial machines usually possess high specific speeds (low heads and high throughputs). Knapp et al. (1970) suggest that the flow

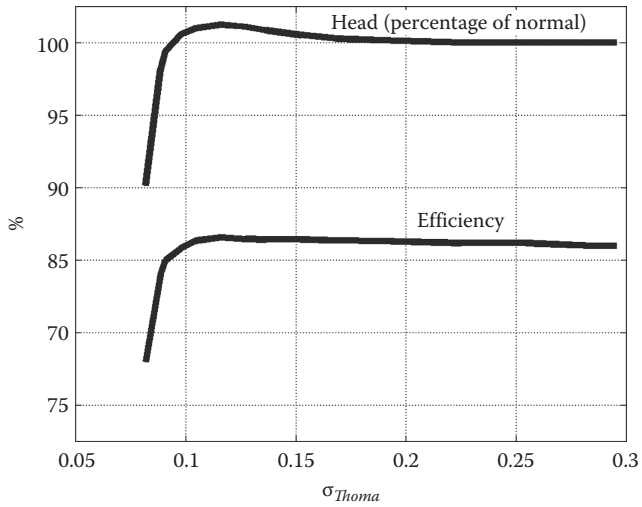


Figure 13.24

Typical pump performance curves at a constant flow rate as a function of the Thoma cavitation number.

in radial machines be treated as flow in passages for cavitation studies, while axial flow machines can be geometrically developed, such that the flow is treated as that over cascade of hydrofoils. They also point out common factors and regions of increased cavitation potential in turbomachinery such as surface discontinuities, junctions between surfaces, gaps, unsteady flows and recirculating regions, and surface roughness effects.

The cavitation performance of turbomachinery is often presented as a plot of specific performance (e.g., specific head rise or specific power output) versus Thoma number. As the Thoma number is decreased to the *inception Thoma number*, cavitation appears, but the performance of the turbomachinery may be only slightly affected. With decreasing Thoma number, cavitation becomes more developed, and the performance of the device will degrade. The *critical Thoma number* is reached when the performance is reduced by a defined fraction from the noncavitating case (e.g., 3%). Further reductions will lead to significant degradation of performance as the *breakdown Thoma number* is reached. Figure 13.24 shows the trends of typical pump performance curves versus the Thoma number.

For marine propellers, the related cavitation number, σ, depends on the advance coefficient $J = U_\infty/(2\pi\Omega D)$ (analogous to the angle of attack in stationary hydrofoils), the thrust coefficient $K_T = T/\rho_l(2\pi\Omega)^2D^4$, and the torque coefficient $K_T = Q/\rho_l(2\pi\Omega)^2D^5$, where T is the thrust and Q the torque.

The degree to which cavitation is developed in turbomachinery can affect various parameters of the device. Incipient cavitation has the possibility of intermittent noise production. In partially developed cavitation, noise, structural vibrations, and damage to surfaces can occur. For fully developed cavitation, where the volume of the cavities becomes significant, mechanical efficiency degradation, head loss, and damage are expected. Figure 13.25 shows vortex, sheet, and cloud cavitation on a model of a marine propeller.

Cavitation is a serious problem in hydraulic systems such as valves because of the potential for damage and vibration (Johnston et al., 1991, Jozsa et al., 1994, Porteiro et al., 1997, Carlson, 2001). Cavitation damage (pitting) has been observed in the liners of diesel engines due to vibratory excitation of nuclei in the liquid (Zhou et al., 1982).

Cavitation can also occur in injector nozzles and fuel pumps in automotive applications. In fuel injection systems, as in diesel engines where the fuel speed is in excess of a 100 m/s, cavitation can occur and cause flow disturbances that can improve the atomization of the injected fuel (Badock et al., 1999, Eisfeld, 2002, Yuan and Schnerr, 2003, Payri et al., 2004).

13.2.8 Cavitation in Biomedical Applications

In contrast with industrial and naval applications where cavitation is most often undesirable because of its erosion potential, the same damaging effects of collapsing bubbles have been implemented as a tool in biomedical applications, namely, surgery and lithotripsy. For example, pulsed ultrasound can be focused with precision on kidney or gall stones. An initial high-intensity pulse is often applied to generate cavitation nuclei and then followed by less intense pulses to drive the bubble nuclei into transient cavitation, that is,

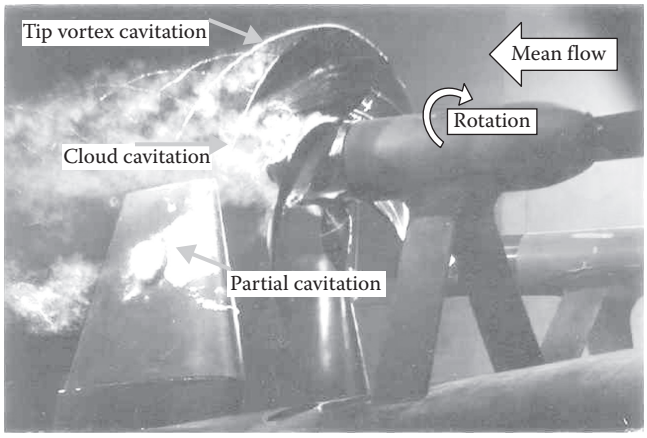


Figure 13.25

Tip vortex cavitation, cloud cavitation, and partial attached cavitation on a model of a marine propeller. (Courtesy of Dr. Y.T. Shen, Naval Surface Warfare Center-Carderock Division, Potomac, MD.)

explosive bubble growth and violent implosion that lead to stone damage. The *in vivo* bubble dynamics are often quite complex. Clouds of bubbles are often created, and the bubble dynamics in these clouds are harder to predict than single bubble dynamics. For instance, the speed of sound in the cloud can be lower than the speed of sound in the liquid alone, and thus, shock wave formation is more likely to occur. The shock can focus in the center of the cloud, leading to an improved lithotriptic effect over single bubble collapse (Brennen, 2003). Ultrasonic focusing can also be used in noninvasive surgery for pulverizing cancer tumors (*necrosis*). Bubble clouds often occur at the focal point. The cloud can backscatter the incoming acoustic pulses, causing increased absorption in the region upstream of the focal point, thus leading to the growth of the lesion (incised tissue) in a direction opposite to the incoming ultrasonic wave. This unintended effect and the resulting pulverization of blood and tissue into a paste have been observed to arrest bleeding in internal organs (*hemostasis*). Jet formation due to cavitation collapse is believed to puncture cell walls and improve drug delivery or allow targeted drug delivery to certain areas such as tumors. Bailey et al. (2003) provide a review of ultrasound in therapy.

Analogous to ultrasound focusing, very short pulses (pico- to nanoseconds) of infrared laser beams from Q-switched YAG (*Yttrium Aluminum Garnet*) or Ruby lasers are focused in laser-eye-surgery procedures into the intended area of the cornea to induce noninvasive, precise surgical effect. A vaporous cavitation bubble grows explosively at the laser focal volume, collapses violently, and generates a shock wave in what is known as optical cavitation, thus producing the surgical effect (Vogel et al., 1986). Additionally, microbubbles are used as contrast agents in ultrasonic imaging. Microbubbles existing in the area under investigation are excited by ultrasonic emissions from an emitting transducer. In response, the bubble volume will oscillate, and the acoustic emissions from the oscillatory motion of the bubble can then be picked by a receiving transducer.

13.2.9 Other Occurrences and Applications of Cavitation

The high pressures and temperatures associated with the collapse of cavitation bubbles have been used to initiate chemical reactions in a process known as *sonochemistry* (Riesz et al., 1990, Suslick, 1997, Beckett and Hua, 2001). These same extreme pressures and temperatures have also been exploited for environmental water purification (*aquasonolysis*) (Madge and Jensen, 2002, Lifka et al., 2003). The formation of radicals upon bubble collapse accelerates the degradation of contaminants through oxidization. Additionally, the shearing effect due to bubble oscillations can break up long-chain molecules. The production of cavitation bubbles near a metal surface can be used to mechanically work the surface in a process known as "shot-less peening." Cavitating jets can be used for this purpose (Soyama and Asahara, 1999).

Last, cavitation can occur in natural processes, for example, when the knuckles are cracked with a popping sound. Head trauma has been associated with cavitation when there is a sudden impact of the cranium (Goldsmith, 2001). *Alpheus heterochaelis* (the "snapping shrimp") uses sound produced by a cavitating jet to stun nearby prey (Versluis et al., 2000). Also, the maximum height of trees may be limited by cavitation during the transpiration of water (Koch et al., 2004).

Nomenclature

Latin

a	Radius
A	Hamaker constant
B	Impact factor
B_e	Transfer number
c_l	Speed of sound in liquid
c_p	Specific heat at constant pressure
Ca	Capillary number
C_D	Drag coefficient
C_L	Lift coefficient
D	Diffusion coefficient
D_j	Jet diameter
e	Specific energy, coefficient of restitution
E	Young's modulus, activation energy
$\dot{E}$	Erosion rate
E_M	Mechanical potential energy
f_p	Pulsation frequency
Fr	Froude number
F	Force vector
g	Acceleration due to gravity
G	Relative velocity vector
h	Enthalpy
h_{fg}	Latent heat of evaporation
H	Total head, hardness
H_{sv}	Net positive suction head
I	Moment of inertia
j_i	Diffusive flux
J	Impulsive force
k	Ratio of specific heats, Boltzmann's constant, spring constant, turbulence energy
k_g	Conductive heat transfer coefficient
K_G	Gas constant
L	Latent heat
m	Molecular unit mass, mass
m_G	Gas mass
M	Mass of abrasive particles
$\dot{M}_V$	Mass flux due to phase change
n	Number density
n	Normal unit vector
N_s	Specific speed
Nu	Nusselt number
Oh	Ohnesorge number
p	Pressure, erosion surface flow stress
q	Charge
q_R	Radiation heat transfer
Q	Volumetric flow rate
r	Radius
$\mathfrak{R}$	Gas constant
R_b	Rayleigh–Plesset bubble radius
R_c	Bubble cloud initial radius
Re	Reynolds number
St	Strouhal number
t	Time
t_c	Collapse time
T	Temperature

u Impact speed
u, v Velocity vector
v_s Solids velocity
W Volume of target material
W_i Molecular weight of species "i"
We Weber number
Y_i Mass fraction of species "i"

Greek Symbols

α Accommodation coefficient, angle of impingement
β Bubble number density
Γ Circulation
δ_n Overlap distance
ε Volume fraction, dissipation rate
ε_o Dielectric constant
λ Viscosity ratio
μ Viscosity
ρ Density
σ Surface tension, cavitation number, Poisson's ratio, charge density
σ_b Flexural strength
σ_y Plastic load limit
σ_T Thoma number
τ Individual bubble volume
ω_i Chemical source term for species "i"
ω_n Natural frequency
Ω Rotational speed
Ω Rotational velocity vector

Subscripts

b Bubble
cr Critical
g Gas
e Equilibrium state
i Species i
iso Isolated
l liquid
m maximum, mixture
n noncondensable gas
r Reduced
s Solids
w Wall
∞ Ambient conditions

References

Arakeri, V.H. and Acosta, A.J., Viscous effects in the inception of cavitation on axisymmetric bodies, *ASME J. Fluids Eng.*, 95, 519, 1973.

Arndt, R.E.A., Cavitation in vortical flows, *Annu. Rev. Fluid Mech.*, 34, 143, 2002.

Arndt, R.E.A. and Keller, A.P., Water quality effects on cavitation inception in a trailing vortex, *ASME J. Fluids Eng.*, 114, 430, 1992.

Badock, C., Wirth, R., Fath, A., and Leipertz, A., Investigation of cavitation in real size diesel injection nozzles, *Int. J. Heat Fluid Flow*, 20(5), 538, 1999.

Bailey, M.R., Khokhlova, V.A., Sapozhinkov, O.A., Kargl, S.G., and Crum, L.A., Physical mechanisms of the therapeutic effects of ultrasound (review), *Acoust. Phys.*, 49, 369, 2003.

Beckett, M.A. and Hua, I., Impact of ultrasonic frequency on aqueous sonoluminescence and sonochemistry, *J. Phys. Chem. A*, 105, 3796, 2001.
Blake, F.G., The onset of cavitation in liquids, Technical Memo, No. 12, Acoustics Research Laboratory, Harvard University, Cambridge, MA, 1949.
Blake, J.R. and Gibson, D.C., Cavitation bubbles near boundaries, *Annu. Rev. Fluid Mech*., 19, 99, 1987.
Brennen, C.E., *Cavitation and Bubble Dynamics*, Oxford University Press, Oxford, U.K., 1995.
Brennen, C.E., Fission of collapsing cavitation bubbles, *J. Fluid Mech*., 472, 153–166, 2002.
Brennen, C.E., Cavitation in biological and engineering contexts, in *Proceedings of the Fifth International Symposium on Cavitation*, Osaka, Japan, 2003.
Brujan, E.A., Keen, G.S., Vogel, A., and Blake, J.R., The final stage of the collapse of a cavitation bubble close to a rigid boundary, *Phys. Fluids*, 14, 85, 2002.
Carey, V.P., *Liquid-Vapor Phase-Change Phenomena: An Introduction to the Thermophysics of Vaporization and Condensation Processes in Heat Transfer Equipment*, Hemisphere, Washington, DC, 1992.
Carlson, B., Avoiding cavitation in control valves, *ASHRAE J*., 43, 58, 2001.
Ceccio, S.L., Friction drag reduction of external flows with bubble and gas injection, *Ann. Rev. Fluid. Mech*., 42, 183–203, 2010.
Ceccio, S.L. and Brennen, C.E., Observations of the dynamics and acoustics of travelling bubble cavitation, *J. Fluid Mech*., 233, 633, 1991.
Ceccio, S.L., Gowing, S., and Gindroz, B., Comparison of CSM bubble detection methods, *ASME Fluids Eng. Div*., FED-226, 43, 1991.
Chahine, G.L. and Kalumuck, K.M., Development of a near real-time instrument for nuclei measurement: The ABS Acoustic Bubble Spectrometer®, in *Proceedings of the Fourth ASME-JSME Joint Fluids Engineering Conference*, Honolulu, HI, 2003.
Coleman, A.J., Kodama, T., Choi, M.J., Adams, T., and Saunders, J.E., Cavitation threshold of human tissue exposed to 0.2-MHz pulsed ultrasound: Preliminary measurements based on a study of clinical lithotripsy, *Ultrasound Med. Biol*., 21, 405, 1995.
d'Agostino, L. and Acosta, A.J., Cavitation susceptibility meter with optical cavitation monitoring. Part Two. Experimental apparatus and results, *ASME J. Fluids Eng*., 113, 270, 1991.
Deplancke, T., Lame, O., Cavaille, J.-Y., Fivel, M., Franc, J.-P., and Riondet, M., Outstanding cavitation erosion resistance of ultra High molecular weight polyethylene (UHMWPE) coatings, *Wear*, 328, 301–308.
Eisfeld, F., Investigation of the penetration, the spreading, and the atomization of a diesel injection jet using high speed cinematography, *Proc. SPIE Int. Soc. Opt. Eng*., 4948, 182, 2002.
Ferrel, G.W. and Crum, L.A., A novel cavitation probe design and some preliminary measurements of its application to megasonic cleaning, *J. Acoust. Soc. Am*., 112, 1196, 2002.
Franc, J.P., Incubation time and cavitation erosion rate of work-hardening materials, *J. Fluids Eng*., 131(2), 021303, 1–14, 2009.
Franc, J.P. and Michel, J.M., *Fundamentals of Cavitation*, Kluwer Academic Press, Dordrecht, the Netherlands, 2006.
Franc, J.P., Avellan, F., Belhadji, B., Billard, J.Y., Briançon-Marjollet, L., Fréchou, D., Fruman, D.H., Karimi, A., Kueny, J.L., and Michel, J.M., *La Cavitation. Mecanismes Physiques et Aspects Industriels*, Presses Universitaires de Grenoble, Grenoble, France, 1995.
Ganesh, H., Makiharju, S., and Ceccio, S.L., Partial cavity shedding due to the propagation of shock waves in bubbly flows, in *Proceedings of the 30th Symposium on Naval Hydrodynamics*, Hobart, Tasmania, Australia, 2014.
George, D.L., Iyer, C.O., and Ceccio, S.L., Measurement of the bubbly flow beneath partial attached cavities using electrical impedance probes, *ASME J. Fluids Eng*., 122, 151, 2000.
Gindroz, B. and Billet, M.L., Influence of the nuclei on the cavitation inception for different types of cavitation on ship propellers, *ASME Fluids Eng. Div*., FED-177, 1, 1993.
Goldsmith, W., The state of head injury biomechanics: Past, present and future: Part 1, *Crit. Rev. Biomed. Eng*., 29, 441, 2001.
Hammitt, F.G., *Cavitation and Multiphase Flow Phenomena*, McGraw-Hill, New York, 1980.
Hilgenfeldt, S., Grossmann, S., and Lohse, D., A simple explanation of light emission in sonoluminescence, *Nature*, 398, 402, 1999.
Holzfuss, J., Ruggeberg, M., and Billo, A., Shock wave emissions of a sonoluminescing bubble, *Phys. Rev. Lett*., 81, 5434, 1998.

Hsieh, D.-Y. and Plesset, M.S., Theory of rectified diffusion of mass into gas bubbles, *J. Acoust. Soc. Am.*, 33, 206, 1961.
Johnston, D.N., Edge, K.A., and Vaughan, N.D., Experimental investigation of flow and force characteristics of hydraulic poppet and disc valves, *Proc. Inst. Mech. Eng. A: Power Process Eng.*, 205, 161, 1991.
Jozsa, I., Sebestyen, G., and Kiss, J., Regulating valve cavitation in the power station, *ASME Fluids Eng. Div. FED*, 194, 89, 1994.
Knapp, R.T., Daily, J.W., and Hammitt, F.G., *Cavitation*, McGraw-Hill, New York, 1970.
Koch, G.W., Sillett, S.C., Jennings, G.M., and Davis, S.D., The limits to tree height, *Lett. Nat.*, 428, 851, 2004.
Kuhn de Chizelle, Y., Ceccio, S.L., and Brennen, C.E., Observations and scaling of travelling bubble cavitation, *J. Fluid Mech.*, 293, 99, 1995.
Laberteaux, K.R. and Ceccio, S.L., Partial cavity flows. Part 1. Cavities forming on models without spanwise variation, *J. Fluid Mech.*, 431, 1, 2001a.
Laberteaux, K.R. and Ceccio, S.L., Partial cavity flows. Part 2. Cavities forming on test objects with spanwise variation, *J. Fluid Mech.*, 431, 43, 2001b.
Leger, A.T. and Ceccio, S.L., Examination of the flow near the leading edge of attached cavitation. Part 1. Detachment of two-dimensional and axisymmetric cavities, *J. Fluid Mech.*, 376, 61, 1998.
Leighton, T.G., *The Acoustic Bubble*, Academic Press, London, U.K., 1994.
Li, C.-Y. and Ceccio, S.L., Interaction of single traveling bubbles with the boundary layer and attached cavitation, *J. Fluid Mech.*, 322, 329, 1996.
Lifka, J., Ondruschka, B., and Hofmann, J., The use of ultrasound for the degradation of pollutants in water: A quasonolysis—A review, *Eng. Life Sci.*, 3, 253–262, 2003.
Madge, B.A. and Jensen, J.N., Disinfection of wastewater using a 20-kHz ultrasound unit, *Water Environ. Res.*, 74, 159, 2002.
Matula, T.J., Hallaj, I., Cleveland, R.O., Crum, L.A., Moss, W.C., and Roy, R.A., The acoustic emissions from single-bubble sonoluminescence, *J. Acoust. Soc. Am.*, 103, 1377, 1998.
Niemczewski, B., Estimation of the suitability of selected organic solvents for ultrasonic cleaning, *Ultrasonics Sonochem.*, 6, 149, 1999.
Payri, F., Bermudez, V., Payri, R., and Salvador, F.J., The influence of cavitation on the internal flow and the spray characteristics in diesel injection nozzles, *Fuel*, 83(4–5), 419–431, 2004.
Pecha, R. and Gompf, B., Microimplosions: Cavitation collapse and shock wave emission on a nanosecond time scale, *Phys. Rev. Lett.*, 84, 1328, 2000.
Philipp, A. and Lauterborn, W., Cavitation erosion by single laser-produced bubbles, *J. Fluid Mech.*, 361, 75, 1998.
Porteiro, J.L., Weber, S.T., and Rahman, M.M., Experimental study of flow induced noise in counterbalance valves, in *ASME Aerospace Division (AD)*, 2, *Proceedings of the Fourth International Symposium on Fluid-Structure Interactions, Aeroelasticity, Flow-Induced Vibration and Noise*, Dallas, TX, Vol. 53, 1997, pp. 557–562.
Putterman, S.J. and Weninger, K.R., Sonoluminescence: How bubbles turn sound into light, *Annu. Rev. Fluid Mech.*, 32, 445, 2000.
Ran, B. and Katz, J., Pressure fluctuations and their effect on cavitation inception within water jets, *ASME Fluids Eng. Div. FED*, 177, 31, 1993.
Riesz, P., Kondo, T., and Krishna, C.M., Sonochemistry of volatile and nonvolatile solutes in aqueous solutions. E.p.r. and spin trapping studies, *Ultrasonics*, 28, 295, 1990.
Soyama, H. and Asahara, M., Improvement of the corrosion resistance of carbon steel surface by a cavitating jet, *J. Mater. Sci. Lett.*, 18, 1953, 1999.
Suslick, K.S., Sonoluminescence and sonochemistry, *Proc. Ultrason. Symp.*, 1, 523, 1997.
Tomita, Y. and Shima, A., High-speed photographic observations of laser-induced cavitation bubbles in water, *Acustica*, 71, 161, 1990.
Tran, B., Seo, J., Hall, T.L., Fowlkes, J.B., and Cain, C.A., Microbubble-enhanced cavitation for noninvasive ultrasound surgery, *IEEE Trans. Ultrason. Ferroelectr. Freq. Control*, 50, 1296, 2003.
Vakil, N. and Everbach, E.C., Transient acoustic cavitation in gallstone fragmentation: A study of gallstones fragmented *in vivo*, *Ultrasound Med. Biol.*, 19, 331, 1993.
Versluis, M., Schmitz, B., von der Heydt, A., and Lohse, D., How snapping shrimp snap: Through cavitating bubbles, *Science*, 289, 2114, 2000.
Vogel, A., Hentschel, W., Holzfuss, J., and Luterborn, W., Cavitation bubble dynamics and acoustic transient generation in ocular surgery with pulsed Neodymium:YAG lasers, *Ophthalmology*, 93, 1259, 1986.

Wade, R.B. and Acosta, A.J., Experimental observation on the flow past a plano-convex hydrofoil, *ASME J. Basic Eng.*, 88, 273, 1966.
Young, F.R., *Cavitation*, McGraw-Hill, London, U.K., 1989.
Young, Y.L. and Kinnas, S.A., Numerical modeling of supercavitating propeller flows, *J. Ship Res.*, 47(1), 48–62, 2003.
Yuan, W. and Schnerr, G.H., Numerical simulation of two-phase flow in injection nozzles: Interaction of cavitation and external jet formation, *ASME J. Fluids Eng.*, 125, 963, 2003.
Zhou, Y.-K., He, J.-G., and Hammitt, F.G., Cavitation erosion of diesel engine wet cylinder liners, *Wear*, 76, 321, 1982.


Taylor & Francis
Taylor & Francis Group
http://taylorandfrancis.com

14

Aggregation, Collisions, and Breakup

14.1 Particle Interactions and Collisions
14.2 Droplet Breakup, Coalescence, and Wall Impact

14.1 Particle Interactions and Collisions

Yutaka Tsuji

With respect to the particle–particle interactions in multiphase flow dynamics, two phenomena are identified: one is collision and the other is contact. From the viewpoint of physics, collision and contact do not differ much. Collision is merely contact with a short-time duration. However, the approach of modeling is different for each. For collision or contact, two models are normally used: the hard particle model and the soft particle model.

The hard particle model is easy to use but applicable only to the binary collision. The relation between the pre- and postcollision velocities is given explicitly using the coefficient of restitution and friction coefficient. When the particulate phase is dispersed, it is sufficient to consider only simple binary collisions and not multiple collisions.

In the soft particle model, the whole process of collision or contact is solved by the numerical integration of the equations of motion. The computation time is much longer in the soft particle model than in the hard particle model, but the applicability of the soft particle model is wider than the hard particle model. Another important issue is the erosion associated with particle–wall contact. Particle impacting a wall can remove material, the amount depending on the impact velocity, the approach angle, and the properties of the material. Particle deposition and erosion is treated in Chapter 19.

14.1.1 Particle–Particle Interaction

In general, particle–particle collisions are negligible in dilute gas–particulate flows. While this is true in most cases, whether particle–particle collision should be considered or not depend not only on the particle concentration but also on the velocity fluctuation or relative velocity between individual particles. If all the particles move at the same velocity, particles do not collide no matter how high the concentration is. On the other hand, studies (Yamamoto et al., 2001) have shown that the particle–particle collision should not be neglected at volume fractions greater than 10^{-4}, which has been regarded to be sufficiently dilute. Dense and dilute flows are discussed in Section 1.4.5.

When particles collide, they lose kinetic energy due to the inelastic property of the particle material. The case of two spheres (1 and 2) shown in Figure 14.1 is considered here. Section 14.1.1.1 describes the hard sphere model, and Section 14.1.1.2 describes the soft sphere model.

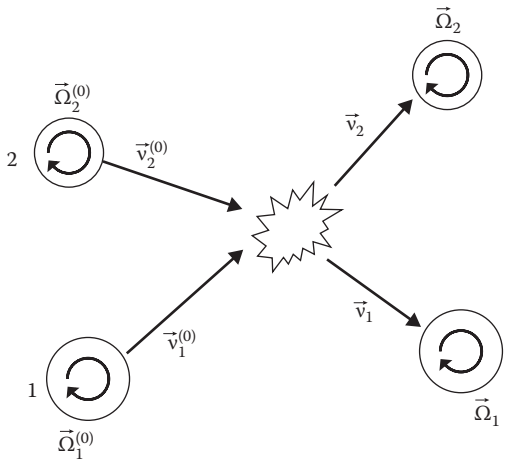


Figure 14.1

Particles colliding.

14.1.1.1 Hard Sphere Model

The hard sphere model is based on the impulsive force, which is defined by integral of the force acting on a particle versus time. If the particles are assumed to be rigid spheres, the impulsive equations are given as follows:

$$m_1\left(\vec{v}_1 - \vec{v}_1^{(0)}\right) = \vec{J} \tag{14.1}$$

$$m_2\left(\vec{v}_2 - \vec{v}_2^{(0)}\right) = -\vec{J} \tag{14.2}$$

$$I_1\left(\vec{\Omega}_1 - \vec{\Omega}_1^{(0)}\right) = a_1\vec{n} \times \vec{J} \tag{14.3}$$

$$I_2\left(\vec{\Omega}_2 - \vec{\Omega}_2^{(0)}\right) = a_2\vec{n} \times \vec{J} \tag{14.4}$$

where

$\vec{n}$ is the normal unit vector directed from particle 1 to particle 2 at the moment of contact
$\vec{J}$ is the impulsive force exerted on particle 1, which acts on particle 2 as the reaction
Subscripts 1 and 2 refer to the two particles
Superscript (0) signifies the values before collision
I is the moment of inertia given by $I = (2/5)ma^2$

In the equations given earlier, the particle mass m, size (radius = a), velocities before collision $\vec{v}^{(0)}$, and positions before collision are given. The unknown variables are the impulsive force $\vec{J}$ and the postcollision velocities $\vec{v}$. The equations given earlier can be solved analytically with some assumptions. The results are shown in Table 14.1. The derivation of the solutions is described by Crowe et al. (2012, pp. 120–124).

14.1.1.2 Soft Sphere Model

14.1.1.2.1 Modeling The basic concept of the soft sphere model is the same as the damping vibration shown in Figure 14.2. The motion of the body with mass m is given by the following differential equation:

$$m\ddot{x} + \eta\dot{x} + kx = 0 \tag{14.5}$$

where

x is the distance from the equilibrium position of the mass
η is the damping coefficient of the dashpot
k is the stiffness of the spring

Table 14.1 Relation between Particle Velocities before and after Collision

	$\frac{\vec{n}\cdot\vec{G}^{(0)}}{\lvert\vec{G}_{ct}^{(0)}\rvert} < \left(\frac{2}{7}\right)\frac{1}{f(1+e)}$	$\frac{\vec{n}\cdot\vec{G}^{(0)}}{\lvert\vec{G}_{ct}^{(0)}\rvert} > \left(\frac{2}{7}\right)\frac{1}{f(1+e)}$
Translation velocity	$\vec{v}_1 = \vec{v}_1^{(0)} - (\vec{n} - f\vec{t})(\vec{n}\cdot\vec{G}^{(0)})(1+e)\frac{m_2}{m_1+m_2}$	$\vec{v}_1 = \vec{v}_1^{(0)} - \left\{(1+e)(\vec{n}\cdot\vec{G}^{(0)})\vec{n} + \frac{2}{7}\lvert\vec{G}_{ct}^{(0)}\rvert\vec{t}\right\}\frac{m_2}{m_1+m_2}$
	$\vec{v}_2 = \vec{v}_2^{(0)} + (\vec{n} - f\vec{t})(\vec{n}\cdot\vec{G}^{(0)})(1+e)\frac{m_1}{m_1+m_2}$	$\vec{v}_2 = \vec{v}_2^{(0)} + \left\{(1+e)(\vec{n}\cdot\vec{G}^{(0)})\vec{n} + \frac{2}{7}\lvert\vec{G}_{ct}^{(0)}\rvert\vec{t}\right\}\frac{m_1}{m_1+m_2}$
Angular velocity	$\vec{\Omega}_1 = \vec{\Omega}_1^{(0)} + \left(\frac{5}{2a_1}\right)\left(\vec{n}\cdot\vec{G}^{(0)}\right)\left(\vec{n}\times\vec{t}\right)f\left(1+e\right)\frac{m_2}{m_1+m_2}$	$\vec{\Omega}_1 = \vec{\Omega}_1^{(0)} - \frac{5}{7a_1}\lvert\vec{G}_{ct}^{(0)}\rvert(\vec{n}\times\vec{t})\frac{m_2}{m_1+m_2}$
	$\vec{\Omega}_2 = \vec{\Omega}_2^{(0)} + \left(\frac{5}{2a_2}\right)\left(\vec{n}\cdot\vec{G}^{(0)}\right)\left(\vec{n}\times\vec{t}\right)f\left(1+e\right)\frac{m_2}{m_1+m_2}$	$\vec{\Omega}_2 = \vec{\Omega}_2^{(0)} - \frac{5}{7a_2}\lvert\vec{G}_{ct}^{(0)}\rvert(\vec{n}\times\vec{t})\frac{m_1}{m_1+m_2}$

e, coefficient of restitution.

f, the Coulomb friction coefficient.

$\vec{G}^{(0)} = \vec{v}_1^{(0)} - \vec{v}_2^{(0)}$, relative velocity of particle centers before collision.

$\vec{G}_c^{(0)} = \vec{G}^{(0)} + a_1\Omega_1^{(0)}\times\vec{n} + a_2\Omega_2^{(0)}\times\vec{n}$, relative velocity of the contact point before collision.

$\vec{t} = \frac{\vec{G}_{ct}^{(0)}}{\lvert\vec{G}_{ct}^{(0)}\rvert}$, unit vector of the tangential direction.

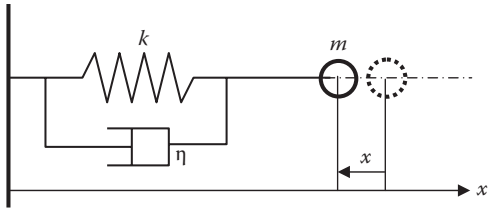


Figure 14.2

Damping vibration.

In the previous equation, the relationship between the force and the displacement is assumed to be linear. The kinetic energy is lost in the dashpot. The work by the dashpot is proportional to the velocity of the mass. There are three modes of motion of the mass depending on the parameters: underdamping, overdamping, and critical damping modes.

In the soft sphere model, the same mechanism is assumed for the particle–particle interaction. Figure 14.3 shows that particle i approaches particle j under the influence of inertia and/or external forces. Particle i at the moment of contact is shown by the dotted line, and the two particles contact at the point C. In the next moment, the contact forces occur between the two particles. Actually, the particles should deform and the

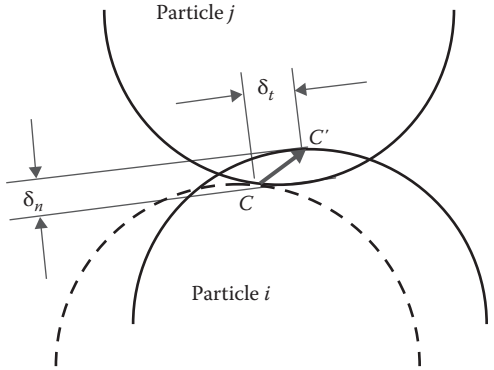


Figure 14.3

Two particles contacting.

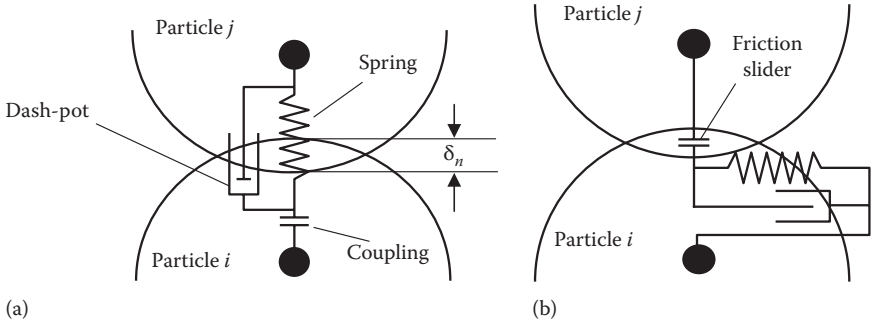


Figure 14.4

Soft sphere model: (a) Normal force. (b) Tangential force.

contact forces could be functions of deformation. In the soft sphere model, the two particles approaching with a relative velocity are made to overlap without changing their shapes. The overlap distance δ is made to correspond to the deformation of the particles. The larger the overlap distance, the larger is the contact force.

A model based on the damping vibration is convenient to express the contact force. Thus, a spring, a dashpot, and other mechanical components are set between particle *i* and particle *j*, as shown in Figure 14.4, where Figure 14.4a corresponds to the case of the normal force and Figure 14.4b to the case of the tangential force. The coupler shown in Figure 14.4a connects the two particles when they are in contact but allows the particles to separate under the influence of repulsive forces. The tangential force is modeled by a spring and dashpot in the same way as the normal force, as shown in Figure 14.4b. If the tangential force exceeds the yield stress, the two particles slide under the application of a normal force and a friction force results. To express this friction force, a friction slider is set in Figure 14.4b. This model for contact forces was proposed by Cundall and Stack (1978). With the soft sphere model, not only can the relationship between pre- and postcollision velocities be obtained but also the forces acting on spheres during contact.

With the hard sphere model, the postcollision velocities are given as functions of precollision velocities and other parameters such as the coefficient of restitution and friction coefficient. The soft sphere model starts with the differential equations. Therefore, variations of momentum and displacement are obtained for arbitrary times as solutions of the differential equations.

The effects of these mechanical components on particle motion appear through the following parameters: stiffness, *k*; damping coefficient, η; and friction coefficient, *f*.

The normal component of the contact force, F_{nij}, acting on particle *i* is given by the sum of the forces due to the spring and the dashpot. If the particles are assumed to be 2D disks, the effect of the spring is linear against the overlap distance and the force F_{nij} is expressed by

$$\vec{F}_{nij} = (-k_n \delta_n - \eta_{nj} \vec{G} \cdot \vec{n}) \vec{n} \tag{14.6}$$

where

δ_n is the overlap distance (displacement of particle caused by the normal force)
$\vec{G}$ is the velocity vector of particle *i* relative to particle *j* ($\vec{G} = \vec{v}_i - \vec{v}_j$)
$\vec{n}$ is the unit vector drawn from the center of particle *i* to that of particle *j*

According to Hertzian contact theory, the normal force varies to the 3/2 power of the displacement in the case of 3D spheres, and therefore, the force F_{nij} acting on particle *i* regarded as a sphere is expressed by

$$\vec{F}_{nij} = (-k_n \delta_n^{3/2} - \eta_{nj} \vec{G} \cdot \vec{n}) \vec{n} \tag{14.7}$$

The tangential component of the contact force, $\vec{F}_{tij}$, is given by

$$\vec{F}_{tij} = -k_t \vec{\delta}_t - \eta_{tj} \vec{G}_{ct} \tag{14.8}$$

where

k_t and η_{tij} are, respectively, the stiffness and damping coefficient in the tangential direction

$\vec{G}_{ct}$ is the slip velocity of the contact point, given by

$$\vec{G}_{ct} = \vec{G} - (\vec{G} \cdot \vec{n})\vec{n} + a_i \vec{\Omega}_i \times \vec{n} + a_j \vec{\Omega}_j \times \vec{n} \tag{14.9}$$

where a_i and a_j are the radii of particle i and particle j, respectively.

Note that the tangential displacement $\vec{\delta}_t$ is a vector and its direction is not equal to the slip velocity vector $\vec{G}_{ct}$ in 3D motion in general. If the following relation

$$\left|\vec{F}_{tij}\right| > f\left|\vec{F}_{nij}\right| \tag{14.10}$$

is satisfied, particle i slides and the tangential force is given by

$$\vec{F}_{tij} = -f\left|\vec{F}_{nij}\right|\vec{t} \tag{14.11}$$

instead of Equation 14.8. Equation 14.11 is the Coulomb-type friction law. The friction coefficient f is measurable and regarded as a parameter that can be given empirically. The vector $\vec{t}$ in Equation 14.11 is the unit vector defined by

$$\vec{t} = \frac{\vec{G}_{ct}}{\left|\vec{G}_{ct}\right|} \tag{14.12}$$

In general, several particles are in contact with particle i at the same time as shown in Figure 14.5. Therefore, the total force and torque acting on particle i are obtained by taking the sum of the forces mentioned earlier with respect to j:

$$\vec{F}_i = \sum_j \left(\vec{F}_{nij} + \vec{F}_{tij}\right) \tag{14.13}$$

$$\vec{T}_i = \sum_j \left(a\vec{n} \times \vec{F}_{tij}\right) \tag{14.14}$$

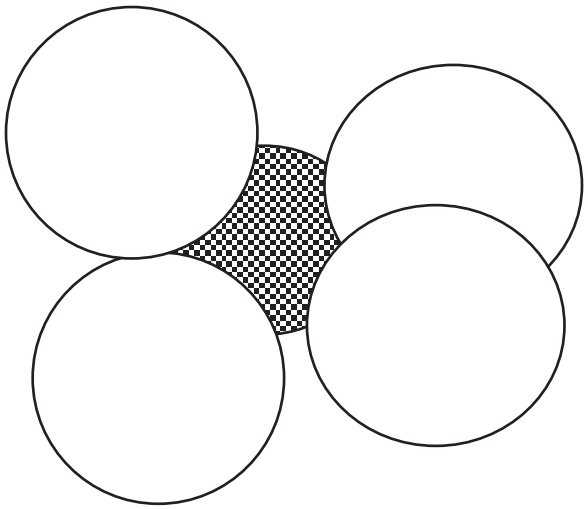


Figure 14.5

Particle with several contact forces.

14.1.1.2.2 Determination of Stiffness k, Damping Coefficient η, *and Friction Coefficient f* The stiffness k_n can be given using the Hertzian contact theory when physical properties such as Young's modulus and Poisson's ratio are known. The stiffness of a sphere is expressed by

$$k_n = \frac{4}{3}\left(\frac{1-\sigma_i^2}{E_i} + \frac{1-\sigma_j^2}{E_j}\right)^{-1}\left(\frac{a_i + a_j}{a_i a_j}\right)^{-(1/2)} \tag{14.15}$$

where

E and σ are Young's modulus and Poisson's ratio, respectively
a is the particle radius
Subscripts i and j denote particle i and particle j, respectively

If particle i and j have the same radius and the same physical properties, the stiffness k_n simplifies to

$$k_n = \frac{\sqrt{2r}E}{3\left(1-\sigma^2\right)} \tag{14.16}$$

The stiffness k_t can be given using the Mindlin theory as

$$k_t = 8\left(\frac{1-\sigma_i^2}{H_i} + \frac{1-\sigma_j^2}{H_j}\right)^{-1}\left(\frac{a_i + a_j}{a_i a_j}\right)^{-(1/2)}\delta_n^{1/2} \tag{14.17}$$

where H_i and H_j are the shear moduli of particle i and particle j, respectively. If both particles have the same properties, the tangential stiffness k_t also simplifies to

$$k_t = \frac{2\sqrt{2r}H}{2-\sigma^2}\delta_n^{1/2} \tag{14.18}$$

where H is related to Young's modulus, E, and Poisson's ratio, σ, as follows:

$$H = \frac{E}{2(1+\sigma)} \tag{14.19}$$

As shown earlier, the stiffness can be determined by material properties. This is the advantage of this model. Unfortunately, it is often difficult in practice to use the stiffness calculated by the Hertzian theory, because the time step Δt for numerical integration is so small that an excessive amount of computational time is needed. It is empirically known that the time step Δt should be <1/10 of the natural oscillation period $2\pi\sqrt{m/k}$ of a mass–spring system. Therefore, in many cases, a small value of stiffness is assumed for convenience of the calculation. In some cases, the results based on a stiffness value much smaller than the actual one are not so different from those based on the precise stiffness value. Fortunately, this is the case for fluid–particle multiphase flows, where fluid forces acting on the particles make the difference in stiffness a minor effect.

14.1.1.2.3 Damping Coefficient Cundall and Strack (1979) proposed the following expressions for the damping coefficients:

$$\eta_n = 2\sqrt{mk_n} \tag{14.20}$$

$$\eta_t = 2\sqrt{mk_t} \tag{14.21}$$

which were derived for the critical damping condition of a single degree-of-freedom system consisting of a mass, spring, and dashpot. The reason for choosing the critical damping condition, as shown in Equations 14.20 and 14.21, can be traced to the requirement that bouncing motion after collision should be damped as soon as possible.

Another method for determining the damping coefficient is based on the idea that the damping coefficient should be related to the coefficient of restitution, which is regarded as a physical property of the particle material. Fortunately, the coefficient of restitution can be measured in a simple experiment.

If the relationship between spring force and displacement is linear, the solution of Equation 14.5 can be used to relate the damping coefficient to the coefficient of restitution (Tsuji et al., 1993). Let us assume that x denotes the distance of particle center from the wall and the particle collides with the wall at time $t = 0$ with the initial velocity $v = v_0$ and initial position of particle center $x = x_0$. The initial velocity is negative. The underdamping solutions are given as follows:

$$\text{Position:} \quad x = \frac{v_0}{q}\sin(qt)\exp(-\gamma\omega t) + x_0 \tag{14.22}$$

$$\text{Velocity:} \quad \dot{x} = \frac{v_0}{q}\exp(-\gamma\omega t)q\cos(qt) - \gamma\omega\sin(qt) \tag{14.23}$$

where

$$\omega = \sqrt{k/m}$$
$$\gamma = \eta/\left(2\sqrt{mk}\right)$$
$$q = \omega\sqrt{1-\gamma^2}$$

The particle position decreases, reaches the minimum value, and recovers to the initial position $x = x_0$ at $t = \pi/q$, which is equal to half of the oscillation period. The particle velocity at $t = \pi/q$ is expressed as

$$v_1 = [\dot{x}]_{t=\pi/q} = -v_0\exp\left(-\frac{\gamma\omega\pi}{q}\right) \tag{14.24}$$

The ratio of v_1 to v_0 corresponds to the coefficient of restitution e:

$$e = \exp\left(-\frac{\gamma\omega\pi}{q}\right) \tag{14.25}$$

From the previous equations,

$$\eta = -\frac{2\ln e}{\sqrt{\pi^2 + \ln e}}\sqrt{mk} \tag{14.26}$$

Tsuji et al. (1992) showed that the damping coefficient η_n for a nonlinear spring is numerically related to the restitution coefficient. According to Tsuji et al. (1992), the damping coefficient η_n is expressed by

$$\eta_n = \alpha\sqrt{mk_n}\delta_n^{1/4} \tag{14.27}$$

where α is a constant related to the coefficient of restitution. The relationship between α and coefficient of restitution e is shown in Figure 14.6. As for the damping coefficient η_t in the tangential direction, the same value as used for η_n is often used for η_t with no firm justification.

14.1.1.3 Cohesive Force

Interparticle forces due to the wetness of particle surfaces, electrostatic charges, and the van der Waals forces are known to cause adhesion of a particle to a wall or to another particle.

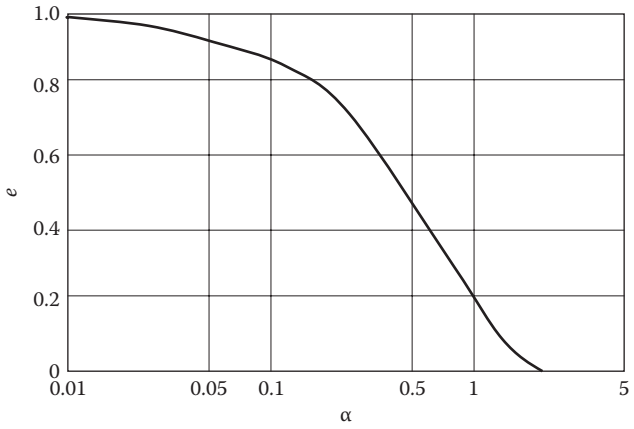


Figure 14.6

Relationship between α and coefficient of restitution *e*.

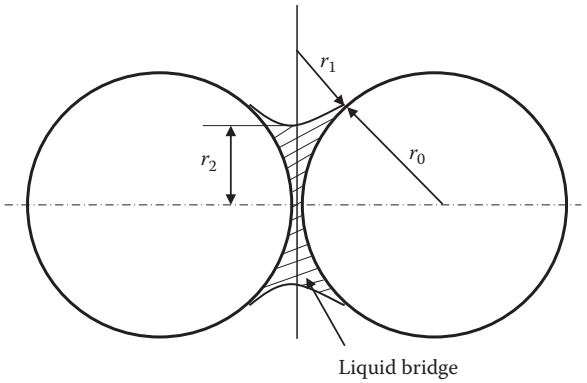


Figure 14.7

Liquid bridge between two spheres.

14.1.1.3.1 Force due to a Liquid Bridge As shown in Figure 14.7, a liquid bridge is formed between particles due to condensation under an environment of high humidity. The liquid surface is concave due to surface tension and the pressure is negative inside the bridge. The force acting on the particle is the sum of the force due to the negative pressure and the cohesive force due to capillarity.

The force due to the liquid bridge F_l is given as follows:

$$F_l = \pi a_2^2 \sigma \left(\frac{1}{a_1} - \frac{1}{a_2} \right) + 2\pi a_2 \sigma \cos\theta \tag{14.28}$$

where

σ is the capillary force (N/m)

θ is the contact angle between liquid and particle surface

The contact angle θ can be assumed to be zero in the case of water. This equation is called the Laplace–Young equation.

14.1.1.3.2 Electrostatic Force Particles in the gas are usually charged and an electrostatic force acts on the particles. Electrostatic force F_e between charged particles is given by the Coulomb formula:

$$F_e = \frac{1}{4\pi\varepsilon_0} \frac{q_1 q_2}{a^2} \tag{14.29}$$

where
q_1 and q_2 are the charges on the particles
ε_0 is the dielectric constant (F/m) in vacuum
a is the distance between particle centers

If the signs of q_1 and q_2 are different, an attractive force acts on the two particles, and if not, the force is repulsive.

The cohesive force acting on the spherical particles in contact with each other is given by

$$F_E = \frac{\pi\sigma_1\sigma_2}{\varepsilon_0} d^2 \tag{14.30}$$

where σ_1 and σ_2 are the charge densities (C/m^2) of the two particles. This equation is derived under the assumption that the particles are charged uniformly and that charging can be regarded as concentrated at the particle centers. The effect of the particle size on the force is larger for the Coulomb cohesive force than for the van der Waals force.

14.1.1.3.3 Van der Waals Forces The van der Waals forces arise from molecular interaction between solid surfaces. This force becomes apparent when very smooth surfaces are brought into contact. To estimate the magnitude of van der Waals forces acting on solid bodies, the contribution of many molecules comprising the surfaces must be considered. Hamaker (1937) carried out calculations for various geometries. The force F between two infinite flat plates with separation is expressed by

$$F = \frac{A_{eff}}{6\pi z^3} \tag{14.31}$$

where
F is the force per unit area
A_{eff} is called the Hamaker constant

The force between the two spheres shown in Figure 14.8 is expressed by

$$F = \frac{A_{eff} d}{12 z^2} \tag{14.32}$$

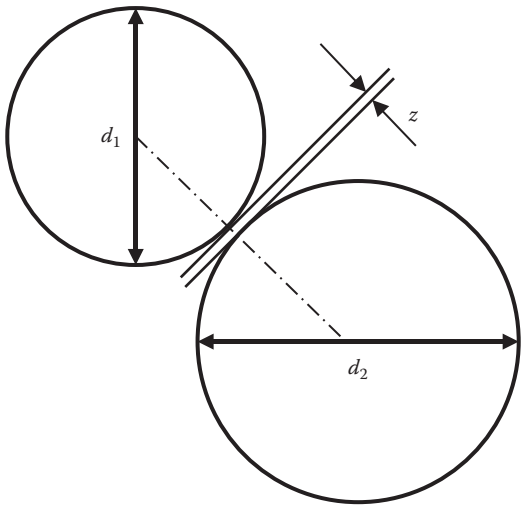


Figure 14.8
Two particles in contact.

Table 14.2 Hamaker Constant

Material	Hamaker Constant [$J \times 10^{20}$]
Water	4.38
Polystyrene	6.15–6.6
Al_2O_3	15.5
Cu	28.4
Au	45.5

where z is the separation distance at the point of contact, which is dependent on the roughness of the sphere and d is

$$d = \frac{d_{p1} \cdot d_{p2}}{d_{p1} + d_{p2}} \tag{14.33}$$

The force between a sphere and a flat plate can be obtained by letting the diameter of one sphere be infinite, that is, $d = d_p$ in Equation 14.33. Table 14.2 shows examples of the Hamaker constant of various materials.

The Hamaker constant between different materials is given by

$$A_{eff\,12} = \sqrt{A_{eff\,11} \cdot A_{eff\,22}} \tag{14.34}$$

where A_{eff11} and A_{eff22} are the Hamaker constants of each material, respectively. This relation is used for *dry* solids. If two solids are separated by a third material between them, the Hamaker constant is expressed by

$$A_{eff\,132} = \left(\sqrt{A_{eff\,11}} - \sqrt{A_{eff\,33}}\right)\left(\sqrt{A_{eff\,22}} - \sqrt{A_{eff\,33}}\right) \tag{14.35}$$

where A_{eff33} is the Hamaker constant of the third material. The Hamaker constant A_{eff33} of air is very small, and thus, Equation 14.35 is reduced to Equation 14.34 in this case. Comparing Equations 14.34 and 14.35, it is found that the attractive force between two solids becomes smaller in water than in air. The equation mentioned earlier means that the sign of the van der Waals force between two solids can be negative, that is, a repulsion force arises if A_{eff33} takes a value between A_{eff11} and A_{eff22}.

14.1.2 Particle–Wall Interaction

The problem of particle–wall interaction is encountered when analyzing gas–particle flows contained within walls such as pipe flows, channel flows, and fluidized beds. The particle–wall interaction falls into two categories: hydrodynamic forces due to proximity of a wall and the purely mechanical interaction in the absence of a fluid. The Saffman lift force due to velocity gradient near the wall is one example of the hydrodynamic interaction. Another example is the fluid force acting on a particle approaching the wall in the normal direction. This interaction is observed when the case of two approaching particles is addressed. Assuming the diameter of one particle to be infinitely large, the particle–particle interaction is reduced to the particle–wall interaction. A hydrodynamic interaction of this type can prevent a particle from making contact with the wall. The postcollisional velocity of the particle is also affected by this interaction. This hydrodynamic interaction can be neglected if the particle inertia force is so large that collision takes place in a time small compared to the hydrodynamic relaxation time of the particle.

The treatment of the mechanical behavior associated with the particle–wall mechanical interaction depends on the inertia of the particle. When a massive particle collides with a wall, it rebounds but loses kinetic energy due to friction and inelasticity. For a very small particle approaching a wall, molecular forces become dominant compared with the inertia force. As a result, the particle is captured by the wall due to cohesion forces (Section 14.1.1.3.3) and neither rebounds nor slides along the wall. Energy loss due to wall collision is considered in Section 14.1.2.1, where the analysis is based on a single spherical particle and a smooth wall. The energy loss at walls is readdressed in Section 14.1.2.2, where the case of a nonspherical particle impacting a rough wall is considered.

14.1.2.1 Momentum and Energy Exchange at Walls

Two models are used to deal with particle–wall collision: the hard sphere model and the soft sphere model, as in the case of particle–particle collisions. The soft sphere model is based on the integration of differential equations. So, variation of velocities from the moment of contact to detachment is calculated step by step in the soft sphere model. Thus, not only the relationship between the pre- and postcollisional velocities is obtained but the instantaneous motion during the whole collision process is obtained as well. The soft sphere model is explained in detail in Section 14.1.1.2.

The hard sphere model is based on the impulsive equations, which are the integrated forms of the equations of motion. Thus, the hard sphere model considers momentum difference between precollision and postcollision. Concerning the hard sphere model, there are a few approaches depending on the definition of the coefficient of restitution, which is described in detail in this section.

The difference in momentum between two instants of time is equal to the impulsive force acting on the particle during that time period:

$$m\left(\vec{v}^{(2)} - \vec{v}^{(1)}\right) = \vec{J} \tag{14.36}$$

where

$\vec{v}^{(1)}$ and $\vec{v}^{(2)}$ are the velocities at time 1 and time 2, respectively

J is the impulsive force acting on the particle during the period between the two times

The difference in angular momentum is expressed as

$$I\left(\vec{\Omega}^{(2)} - \vec{\Omega}^{(1)}\right) = -\vec{r} \times \vec{J} \tag{14.37}$$

where

$\vec{\Omega}^{(1)}$ and $\vec{\Omega}^{(2)}$ are the angular velocities at time 1 and time 2, respectively

I is the moment of inertia of the particle

The impulsive force is defined by integral of the force versus time when the force acts on the body. Equations 14.36 and 14.37 are not sufficient to determine the relationship between the pre- and postcollisional velocities. Auxiliary equations are necessary to close a set of equations. The auxiliary equations originate from the concept of the coefficient of restitution and friction coefficient.

Next, move on to the definition of the coefficient of restitution e. The definition of e is somewhat arbitrary, and there are a few definitions available in the literatures. Consider a particle colliding with a wall as shown in Figure 14.9. The symbol $\vec{v}$ denotes the translation velocity. The velocity vector has two components: longitudinal component (x-component) and the component normal to the wall (y-component). The suffixes (0) and (2) denote the precollision velocity and postcollision velocities, respectively. The following definitions have been used in general:

$$\text{Definition (1)} \quad e = \frac{\left|\vec{v}^{(2)}\right|}{\left|\vec{v}^{(0)}\right|} \tag{14.38}$$

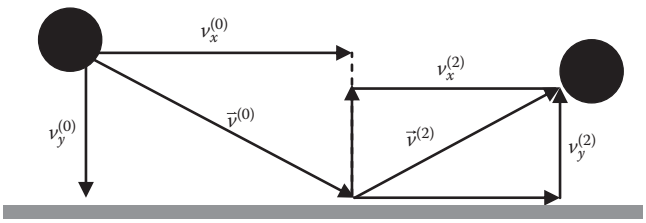


Figure 14.9

Particle colliding a wall.

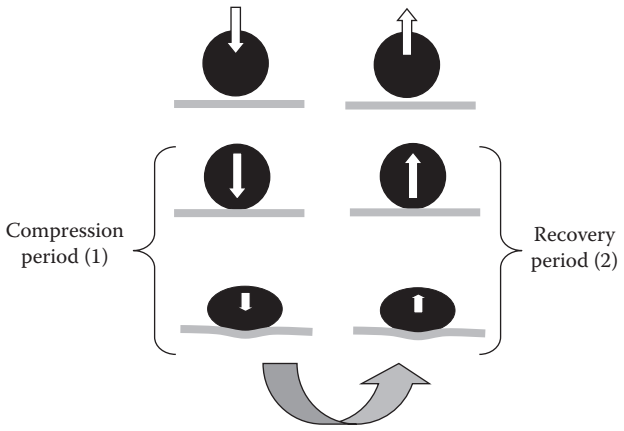


Figure 14.10

Compression and recovery periods in collision process.

$$\text{Definition (2)} \quad e = \frac{v_y^{(2)}}{v_y^{(0)}} \tag{14.39}$$

$$\text{Definition (3)} \quad e_x = v\frac{v_x^{(2)}}{v_x^{(0)}} \cdot e_y = \frac{v_y^{(2)}}{v_y^{(0)}} \tag{14.40}$$

$$\text{Definition (4)} \quad e = \frac{J_y'}{J_y} \tag{14.41}$$

where J_y and J_y' are the normal components of impulses acting on the particle during the collision period. J_y and J_y' are explained as shown in Figure 14.10. The process of collision is divided into two periods, one in which the material is compressed and the other in which the compression is released. J_y and J_y' are the y-components of the impulsive force during the compression and recovery periods, respectively. Among these four definitions, the second definition is used most widely. However, if this definition is adopted, the value of the coefficient for nonspherical particles depends on the location of the contact point between the particle and the wall. If the restitution coefficient is regarded as a property of the material, its value should not depend on the location of the contact point. From this point of view, a reasonable definition for the coefficient of restitution is given by Equation 14.41. If the particle is a sphere, it is found that the impulse ratio J_y'/J_y is equal to the velocity ratio $v_y^{(2)}/v_x^{(0)}$.

Consider a 3D collision of a spherical particle with a smooth flat wall, as shown in Figure 14.11. The velocities $\vec{v}^{(0)}$ and $\vec{\Omega}^{(0)}$ are the precollision translation and angular velocities, respectively. The corresponding postcollision velocities are expressed by $\vec{v}^{(2)}$ and $\vec{\Omega}^{(2)}$. The y-axis is normal to the wall and the x-axis and z-axis are in the plane of the wall. The subscripts x, y, and z signify component directions. If the

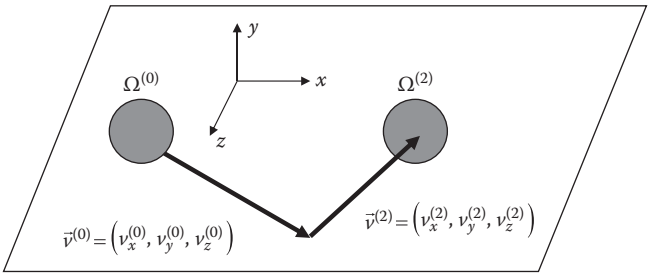


Figure 14.11

Three-dimensional particle–wall collision.

Table 14.3 Relation between Pre- and Postcollisional Velocities

Condition	$\frac{v_y^{(0)}}{\lvert\vec{v}\rvert} < -\frac{2}{7f(e+1)}$	$-\frac{2}{7f(e+1)} < \frac{v_y^{(0)}}{\lvert\vec{v}\rvert} < 0$
Translation velocity	$v_x = \left(\frac{5}{7}\right)\left(v_x^{(0)} - \frac{2a}{5}\Omega_z^{(0)}\right)$	$v_x = v_x^{(0)} + \varepsilon_X f(e+1)v_y^{(0)}$
	$v_y = -ev_y^{(0)}$	$v_y = -ev_y^{(0)}$
	$v_z = \left(\frac{5}{7}\right)\left(v_z^{(0)} + \frac{2a}{5}\Omega_x^{(0)}\right)$	$v_z = v_z^{(0)} + \varepsilon_Z f(e+1)v_y^{(0)}$
Angular velocity	$\Omega_x = \frac{v_z}{a}$	$\Omega_x = \Omega_x^{(0)} - \frac{5}{2a}\varepsilon_Z f(e+1)v_y^{(0)}$
	$\Omega_y = \Omega_y^{(0)}$	$\Omega_y = \Omega_y^{(0)}$
	$\Omega_z = -\frac{v_x}{a}$	$\Omega_z = \Omega_z^{(0)} + \frac{5}{2a}\varepsilon_X f(e+1)v_y^{(0)}$

coefficient of restitution e and kinetic (sliding) friction f are known, the postcollision translation and angular velocities can be obtained by solving the impulsive equations. The results are shown in Table 14.3. In this table, ε_X and ε_Z are factors indicating the proportion of the velocity in each component direction, that is, the direction cosines of the approaching velocity in the x- and z plane. The factors ε_X and ε_Z satisfy the relation:

$$\varepsilon_x^2 + \varepsilon_z^2 = 1 \tag{14.42}$$

In the analysis, the Coulomb friction law is assumed for kinetic (sliding) friction:

$$J_\tau = -f \cdot J_n \tag{14.43}$$

where

J_τ and J_n are the tangential and normal components of the impulsive forces, respectively
f is the friction coefficient

The derivation of the results is described in Crowe et al. (2012, pp. 140–149).

14.1.2.2 Nonspherical Particles and Rough Walls

When the coefficients of restitution e and dynamic friction f are given as physical properties of the particles, the postcollisional velocities can be expressed in terms of the precollisional velocities. The relation between these velocities for the case of a spherical particle and smooth wall is shown in Table 14.3. This relationship is useful for calculating particle trajectories in a field enclosed by walls. However, in some cases, the trajectory calculation in multiphase flows is not as straightforward as it might be. The coefficient of restitution e defined by Equation 14.41 must be less than unity. If trajectory calculations were made for a long horizontal pipe or duct, particles repeatedly colliding with the wall would ultimately lose their vertical velocity component and slide along the wall, as shown in Figure 14.12a. To avoid such an unrealistic result, the irregularity of collisions must be considered. If this irregularity is neglected, large particles cannot be suspended in the carrier fluid. Fluid dynamic forces, such as Magnus or shear lift forces, and fluid turbulence acting on the particles are sufficient to suspend small particles. However, the mechanism responsible for suspending large particles in horizontal pipes is the irregular bouncing of the particles against the wall. In general, the irregularity is caused by particle shape (nonspherical particles) and/or roughness of the wall. In practice, both mechanisms are operative. Several models with regard to the irregular bouncing have been proposed. Those models are classified into two types: one in which the irregularity is attributed to the nonsphericity of the particle (Matsumoto and Saito, 1970a, Tsuji et al., 1989, 1991) and the other to wall roughness (Matsumoto and Saito, 1970b, Tsuji et al., 1987, Sommerfeld and Zivkovis, 1992, Frank et al., 1993, Sommerfeld and Huber, 1999).

In the following paragraphs, the nonspherical model is described first and then the rough wall model. If the problem is two dimensional, the treatment is relatively easy, because the cross-sectional shape of the

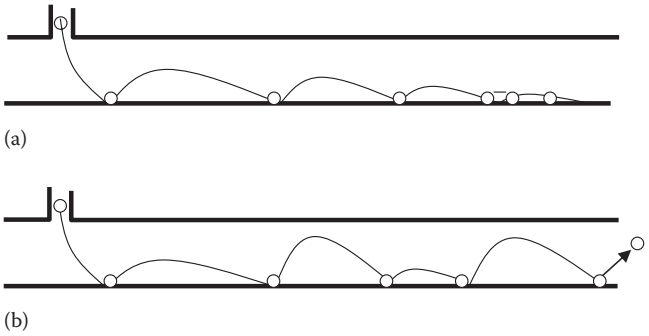


Figure 14.12

Regular and irregular bouncing: (a) Regular bouncing $e > 1$. (b) Irregular bouncing.

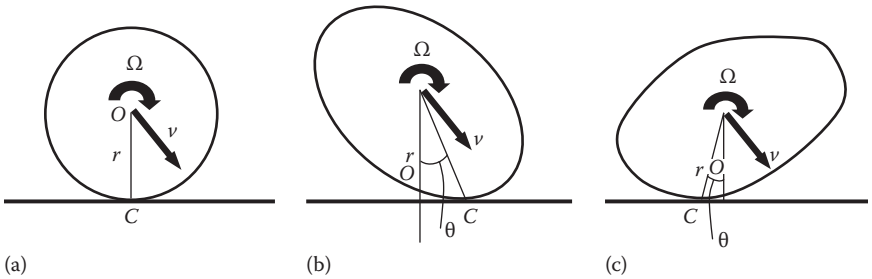


Figure 14.13

Contact point between particle and wall: (a) circular particle, (b) ellipse, and (c) arbitrary shape.

particle is limited to the circle, ellipse, or an arbitrary shape. As shown in Figure 14.13, the distance between the particle center of gravity O and the contact point C depends on the incident attitude of the particle, which does not change in the case of a spherical particle. A set of values for r and θ shown in Figure 14.13b and c describes any particle shape. Impulsive equations are formed for a set of values for r and θ. In the numerical simulation, a pair of values for r and θ is chosen by random numbers. The postcollisional velocities are obtained from solutions of the impulsive equations.

It is difficult to deal, in a rigorous way, with the collision of an arbitrary 3D, nonspherical particle having three components of translational and angular velocities. The complexity of the problem is reduced by using some assumptions. Examples of such assumptions are explained in Tsuji et al. (1991).

The wall roughness model for irregular bouncing is shown in Figure 14.14. The choice of wall roughness is arbitrary. Several configurations could be considered, such as a wavy pattern and a combination of inclined plates. The calculation for a spherical particle bouncing on the rough wall is simpler than that for a nonspherical particle on a flat wall if the pattern of roughness is specified, because the results shown in Table 14.3 can be used with some modifications. In the rough wall model, the point at which the particle collides with the wall is assumed to be on an inclined plane. Each inclined plane has its own coordinate system. The relationship between the coordinates, with and without an inclination angle, is easily described by

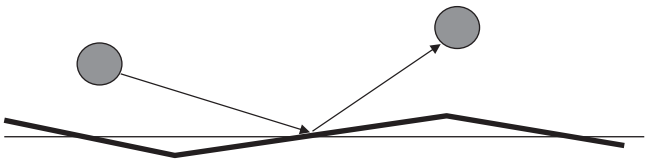


Figure 14.14

Particle collision with a rough wall.

using a matrix. Once particle velocities are transformed by the usual linear transformation technique into the coordinates corresponding to the inclined plane, the results shown in Table 14.3 can be used to obtain the postcollisional velocities. After this, the postcollisional velocities based on the coordinate on the inclined plane are retransformed into the original coordinate system. As with the nonspherical particle model, the rough wall models make it possible for the particles to move along with a bouncing motion in long, horizontal pipes or ducts.

Predicting the impact–rebound relations for particles with sharp edges, such as quartz particles, would be very difficult. Experiments (Tabakoff, 1982) with quartz particles impacting on an aluminum surface show that for a given impact angle, there is a distribution of rebound angles. In this case, it is more pragmatic to use a Monte Carlo method with the measured distribution of rebound angles to model particle-surface impact.

References

Crowe, C., Schwarzkopf, J.D., Sommerfeld, M., and Tsuji, T., *Multiphase Flows with Droplets and Particles*, CRC Press, Boca Raton, FL, 2012, pp. 120–124.

Cundall, P.A. and Strack, O.D., A discrete numerical model for granular assemblies, *Geotechnique*, 29(1), 47–65, 1979.

Frank, Th., Schade, K.P., and Petrak, D., Numerical simulation and experimental investigation of a gas-solid two-phase flow in a horizontal channel, *Int. J. Multiphase Flow*, 19, 187–197, 1993.

Hamaker, H.C., The London-Van der Waals' attraction between spheroid particles, *Physica*, 4, 1058–1072, 1937.

Matsumoto, S. and Saito, S., On the mechanism of suspensions in horizontal pneumatic conveying: Monte Carlo simulation based on the irregular bouncing model, *J. Chem. Eng. Jpn.*, 3(1), 83–92, 1970a.

Matsumoto, S. and Saito, S., Monte Carlo simulation of horizontal pneumatic conveying based on the rough wall model, *J. Chem. Eng. Jpn.*, 3(2), 223–229, 1970b.

Sommerfeld, M. and Huber, N., Experimental analysis and modelling of particle-wall collisions, *Int. J. Multiphase Flow*, 25, 1457–1489, 1999.

Sommerfeld, M. and Zivkovis, G., Recent advances in the numerical simulation of pneumatic conveying through pipe systems, in Hirsch, Ch. (Ed.), *Computational Methods in Applied Sciences*, Elsevier Science Publishers, New York, 1992, p. 201.

Tabakoff, W., Performance deterioration on turbomachinery with the presence of particles, Particulate Laden Flows in Turbomachinery, in *AIAA/ASME Joint Fluids, Plasma, Thermodynamics and Heat Transfer Conference*, St. Louis, MO, Vol. 3, 1982.

Tsuji, Y., Kawaguchi, T., and Tanaka, T., Discrete particle simulation of two-dimensional fluidized bed, *Powder Technol.*, 77, 79–87, 1993.

Tsuji, Y., Morikawa, Y., Tanaka, T., Nakatsukasa, N., and Nakatani, M., Numerical simulation of gas-solid two-phase flow in a two-dimensional horizontal channel, *Int. J. Multiphase Flow*, 13, 671–684, 1987.

Tsuji, Y., Shen, N.-Y., and Morikawa, Y., Numerical simulation of gas-solid flows. I Particle-to-wall collision, *Technol. Rep. Osaka Univ.*, 39, 233–241, 1989.

Tsuji, Y., Shen, N.-Y., and Morikawa, Y., Lagrangian simulation of dilute gas-solid flows in a horizontal pipe, *Adv. Powder Technol.*, 2, 63–81, 1991.

Tsuji, Y., Tanaka, T., and Ishida, T., Lagrangian numerical simulation of plug flow of cohesionless particles in a horizontal pipe, *Powder Technol.*, 71, 239–250, 1992.

Yamamoto, Y., Potthoff, M., Tanaka, T., Kajishima, T., and Tsuji, Y., Large-eddy simulation of turbulent gas-particle flow in a vertical channel: Effect of considering inter-particle collisions, *J. Fluid Mech.*, 442, 303–334, 2001.

14.2 Droplet Breakup, Coalescence, and Wall Impact

Cameron Tropea and Ilia V. Roisman

The usual description of spray transport involves the solution of the mass and the momentum balance equations for the liquid phase (droplets) and of the ambient gas flow as well as the forces associated with the droplet/gas interactions (drag forces). The details and various approaches to such modeling can be found in Chapter 12. The phenomena considered in this chapter include droplet breakup due to the interaction with

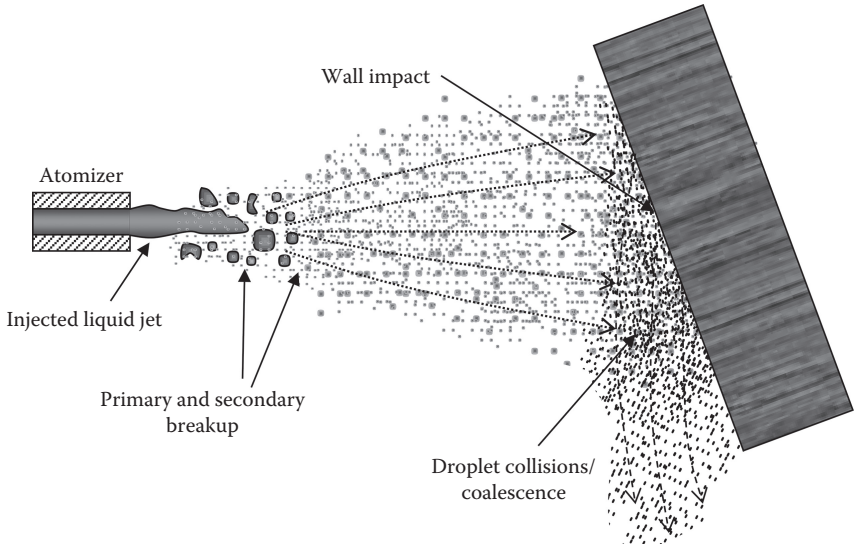


Figure 14.15

Sketch of spray atomization, transport, and wall impact.

the airflow and collisions with another drop or with a wall. In Figure 14.15, the spray atomization, transport, and wall impact are shown schematically, involving these phenomena. They lead to the alterations in the distributions of the drop diameters and velocity in a spray. Accounting for such alterations significantly complicates the modeling of spray transport, considerably extending the numerical simulations, and therefore, in many numerical simulations, the effect of the drop breakup and coalescence is assumed negligibly small and neglected. However, drop fragmentation in the near-atomizer region determines the average drop diameter in the overall spray and therefore cannot be neglected. The secondary breakup of drops can be caused by the interaction of a spray with a high-speed gas jet or by a shock wave. The effect of binary collisions becomes significant in the region of the interaction of two (or more) sprays, in the case of the propagation of very dense spray, or in the near-wall region (where the impacting spray interacts with the spray of the secondary droplets produced by spray/wall impact). When a spray impacts onto a substrate, part of the droplet volume deposits on it and forms a thin fluctuating liquid film. Another part of the spray volume rebounds and creates a flow of secondary droplets. One of the key elements in the creation of such secondary spray is the drop impact onto a wall, also described in this chapter.

The common feature of the phenomena described in this chapter is the significant change of the drop shape due to the impact with another drop (binary drop collisions), its deformation and breakup by ambient airflow, or the impact onto a dry or wetted substrate, as illustrated in Figure 14.16.

The main parameters determining the drop deformation and breakup are the Reynolds number, $Re = DU/\nu$, and the Weber number, $We = DU^2/\sigma$, where D is the drop diameter, U is the characteristic velocity, ν is the kinematic viscosity, and σ is the surface tension. If both these numbers are large ($Re \gg 1$, $We \gg 1$), the droplet deformation is inertia dominated. The drop deformation often leads to the creation of an expanding, relatively thin free liquid sheet (lamella) bounded by a rim, formed due to capillary forces (see Figure 14.17a). In other cases, the drop deformation leads to the appearance of the fingerlike jets ending with a droplet, as shown schematically in Figure 14.17b.

These forms appear due to capillary forces. The rim velocity differs from the velocity of the liquid in the lamella. The motion of the rim is determined by the capillary forces, the internal viscous stresses, the inertia of the liquid entering the rim from the lamella, and the aerodynamic drag force. The simplest case of the motion of the rim bounding a steady uniform liquid sheet was analyzed in Taylor (1959). In this case, the capillary force per unit length, 2σ, is balanced with the inertia of the liquid entering the rim, $\rho w_{rim}^2 \delta$, where δ is the thickness of the lamella. The relative rim velocity w_{rim} is expressed in the form

$$w_{rim} = \sqrt{\frac{2\sigma}{\rho\delta}} \tag{14.44}$$

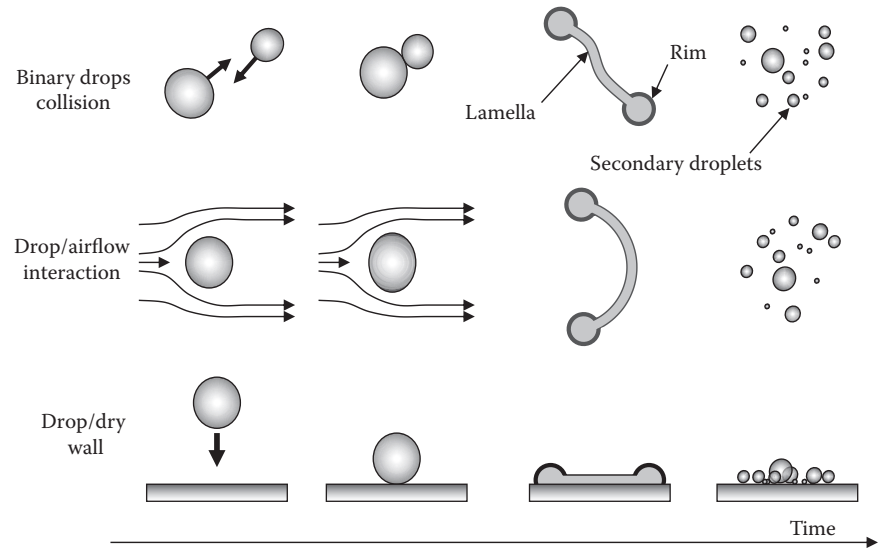


Figure 14.16

Successive stages of drop deformation and breakup due to the binary drop collision, drop/airflow interaction, and drop/wall impact.

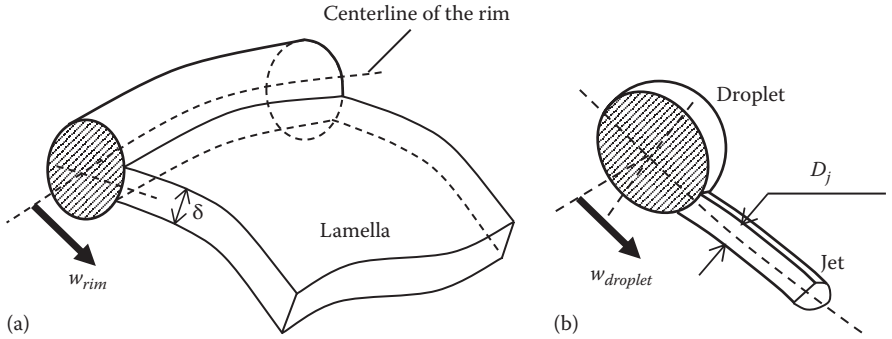


Figure 14.17

Capillary effects at the free boundary: (a) Element of rim bounding a liquid sheet. (b) Droplet appearing at the end of a liquid jet.

The analysis of the droplet appearing at the end of a free liquid jet (Figure 14.17b) is very similar. The momentum equation of this droplet appearing at the end of a steady jet of diameter D_j expresses the balance of the inertia of the liquid entering the droplet from the jet, the capillary forces, and the pressure in the jet due to surface tension. The relative droplet velocity is

$$w_{droplet} = \sqrt{\frac{2\sigma}{\rho D_j}} \tag{44.45}$$

14.2.1 Droplet Breakup Mechanisms

The main topics when studying drop breakup are the regimes of the breakup, the time of breakup, and the outcome: size, number, and velocities of the secondary droplets. We distinguish here two main directions for such studies:

1. Aerodynamic breakup, which is important for the description of sprays, associated with the drop suddenly exposed to a high-speed gas flow or breakup by a shock wave propagating in the ambient gas. The velocity of the drop relative to the velocity of the ambient gas flow and corresponding pressure gradients at the drop surface are the main reason for the breakup.

2. The breakup in a viscous flow, with the application to the rheology of emulsions, when the drop deforms and breaks up mainly due to the shear stresses appearing in the ambient viscous liquid.

In addition, there are many specific cases of drop impact, which will not be described in detail in this chapter, for example, the deformation and breakup involving non-Newtonian drops or flows (Ha and Leal, 2001), in an electric field (Ha and Yang, 1998), in a turbulent fluid flow (Sevik and Park, 1973), and in an acoustic field (Yarin et al., 2002).

14.2.1.1 Regimes of the Aerodynamic Drop Breakup

The typical dimensionless parameters used in the description of the aerodynamic breakup are the Reynolds number, $Re_g = \rho_g w D/\mu_g$, and the Weber number, $We_g = \rho_g w^2 D/\sigma$, based on the properties of the ambient gas, as well as the Ohnesorge number, $Oh = \mu_l/\sqrt{\rho_l D\sigma}$, where w is the relative droplet/gas velocity. These parameters determine the degree of the drop deformation and the mode of the drop breakup.

The first attempt to classify the various regimes of drop breakup using the Weber number, We_g, and Ohnesorge number, Oh, was made by Hinze (1955). A more detailed map of these regimes at various Ohnesorge numbers has since been created on the basis of extensive experimental studies of a drop breakup (Hinze, 1955, Hsiang and Faeth, 1992, 1995). Most of the observations show that the critical We_g numbers, corresponding to the regime thresholds, are almost independent of the Ohnesorge number if it is small ($Oh < 0.1$). Increasing the Weber number leads to an increase in drop deformation. At some critical Weber number, the drop breaks up. Several main regimes of breakup shown schematically in Figure 14.18 can be observed:

Bag breakup, shown in Figure 14.18a, takes place in the range $12 < We_g < 15$ at $Oh < 0.1$. In this regime, the lamella deforms and takes an expanding bag-like shape. At some time instant, the lamella disintegrates. The rim then breaks up due to the Rayleigh capillary instability.

At higher relative velocities, $80 < We_g < 350$ at $Oh < 0.1$, the main drop deformation takes place in the thin boundary layer of the frontal surface of the drop. The flow in the liquid layer leads to *boundary layer stripping* (Hinze, 1955, Ranger and Nicholls, 1969, Delplanque and Siringano, 1994). The resulting thin liquid film then disintegrates in the airflow (Figure 14.18b). This mechanism is also called "shear breakup." An alternative description of the drop breakup mechanism in this range of relative velocities, called "stretching/thinning breakup," is given by Liu and Reitz (1997, 2000). In these studies, the main source of drop deformation is associated with the low-pressure region near the drop equator. The pressure gradient along the drop surface leads to the drop stretching in the plane normal to the direction of the airflow. The edges of the obtained lamella are thin because the inertial forces in the film significantly exceed capillary forces. Such a film is then deflected in the direction of the gas flow (Figure 14.18c).

If the relative velocity is so high such that the gas Weber number exceeds 350 ($We_g > 350$), the droplet deforms very quickly and takes the form of wavy thin sheet. This sheet then breaks up into ligaments and secondary droplets: *catastrophic breakup* shown in Figure 14.18d (Hwang et al., 1996).

Note that the phenomena of drop breakup cannot always be classified by the aforementioned regimes. Some studies are devoted to the investigation of *multimode regimes*, mainly in the range between the bag breakup and shear breakup. In the articles written by Pilch and Erdman (1987) and Joseph et al. (1999), the bag-and-stamen breakup at $50 < We_g < 100$ was mentioned. The description and temporal parameters of bag/plume and plume/shear breakup regimes can be found by Dai and Faeth (2001).

The best fit for the threshold of breakup regimes and the degree of drop deformation by a shock wave based on the experimental data from Hsiang and Faeth (1995) for $Oh < 2 \times 10^{-4}$ is obtained in Schmehl (2003a,b) in the following forms:

$We < 0.6(1 + 0.8Oh^{0.8} + 9 \times 10^{-5}Oh^{2.4})$	Deformation <5%, no breakup	$Oh < 6 \times 10^2$
$We = 1.1(1 + 0.7Oh^{0.85} + 1.5 \times 10^{-4}Oh^{2.4})$	Deformation 10%, no breakup	$Oh < 6 \times 10^2$
$We = 2.3(1 + 0.75Oh^{0.8} + 2.5 \times 10^{-4}Oh^{2.4})$	Deformation 20%, no breakup	$Oh < 6 \times 10^2$
$3(1 + 15Oh^{1.2}) < We < 13(1 + 1.7Oh^{1.4})$	Drop oscillations, no breakup	$Oh < 3 \times 10^{-1}$
$13(1 + 1.7Oh^{1.4}) < We < 35(1 + 0.65Oh^{1.4})$	Bag breakup	$Oh < 4$
$35(1 + 0.65Oh^{1.4}) < We < 80(1 + 0.6Oh^{1.5})$	Multimode breakup	$Oh < 15$
$80(1 + 0.6Oh^{1.5}) < We$	Shear breakup	$Oh < 6$

The increasing drop viscosity slows the rate of drop deformation; however, the maximum drop deformation is virtually not affected by the Ohnesorge number.

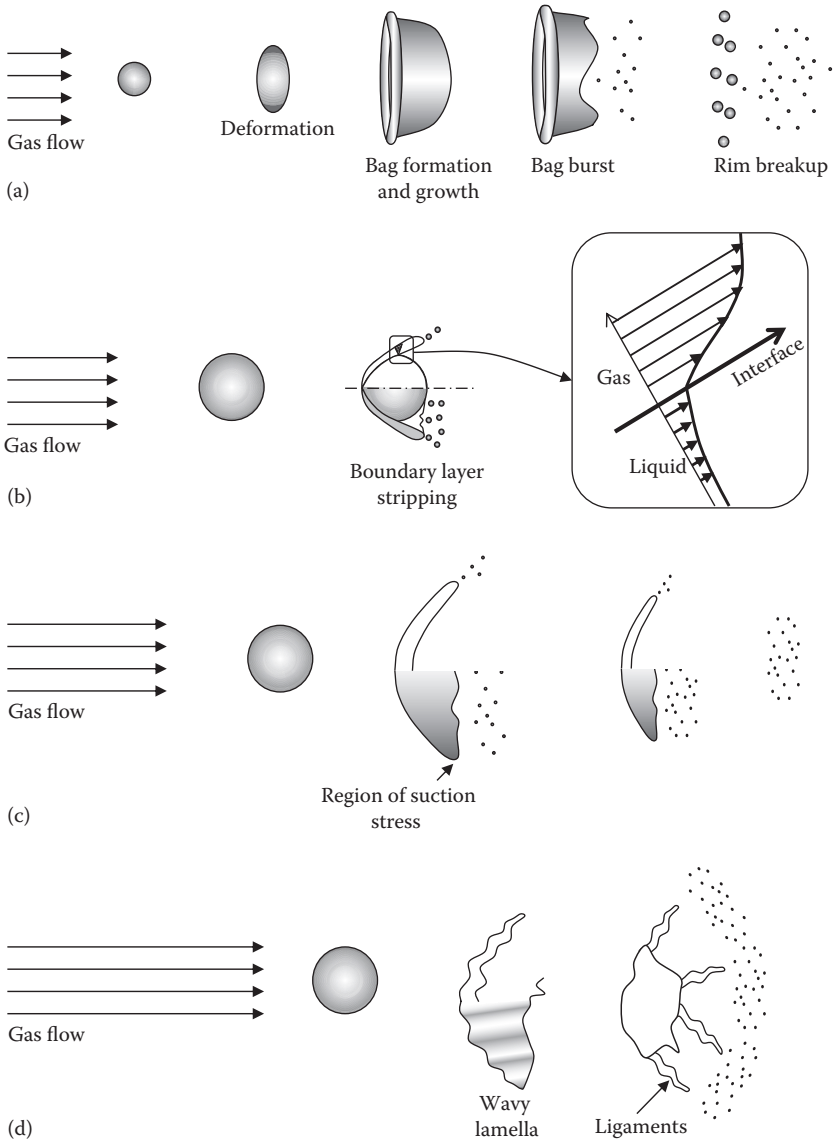


Figure 14.18

Mechanisms of aerodynamic breakup. (a) Bag breakup. (b) Shear breakup. (c) Stretching/thinning breakup. (d) Catastrophic breakup.

The axisymmetric shape of the drop deformed by a shock wave can be approximately described by two dimensions: its length L in the axial direction and its diameter D. The empirical expression for the degree of the maximum drop deformation by a shock wave is given in Hsiang and Faeth (1995):

$$\left(\frac{D}{L}\right)_{\max} = (1 + 0.007We^{1/2})^3 \tag{14.46}$$

The temporal behavior of the drop during the breakup process is illustrated in Figure 14.19 using the characteristic shear breakup time defined by Ranger and Nicholls (1969):

$$t^* = \frac{D_0}{w_0}\sqrt{\frac{\rho_l}{\rho_g}} \tag{14.47}$$

where D_0 and w_0 are the initial drop diameter and the initial relative velocity to the gas, respectively. The gray area corresponds to the time intervals at which a drop breaks up and generates secondary droplets.

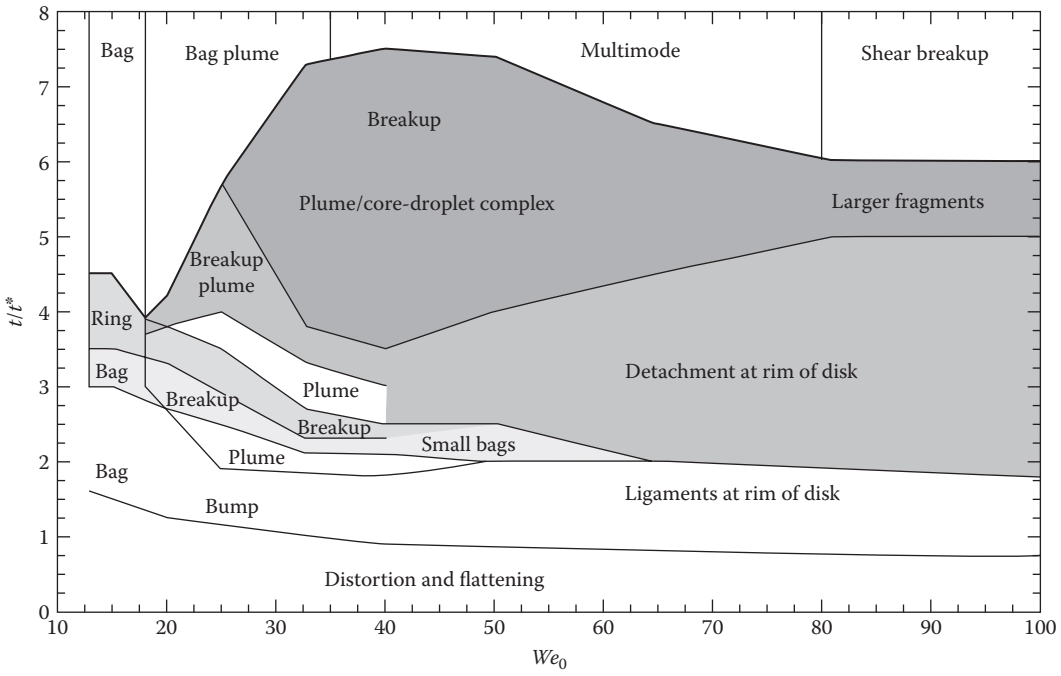


Figure 14.19

Stages of droplet deformation and breakup for various regimes of aerodynamic breakup ($Oh < 0.1$). (Adapted from Schmehl, R., Modeling droplet breakup in complex two-phase flows, in *Proceedings of International Conference on Liquid Atomization and Spray Systems ICLASS-2003*, Italy, July 13–18, 2003b.) (The experimental data are from Dai, Z. and Faeth, G.M., *Int. J. Multiphase Flow*, 27, 217, 2001; Krzeczkowski, S.A., *Int. J. Multiphase Flow*, 6, 227, 1980; Wiezba, A., *Exp. Fluids*, 9, 1329, 1990.)

14.2.1.2 Aerodynamic Breakup Outcomes

The secondary droplets obtained by drop breakup are usually in a relatively wide range of diameters and velocities. The Sauter mean diameter (SMD), D_{32}, is one of the most convenient integral parameters characterizing the drop size. This parameter has been modeled by Hsiang and Faeth (1992) as a function of the size of the viscous boundary layer appearing on the front surface of the drop. The resulting expression for small Ohnesorge number ($Oh < 0.1$) is

$$D_{32} = 6.2 D_0 Oh^{1/2} We_g^{-1/4} \tag{14.48}$$

In an article by Schmehl (2003a), an alternative empirical correlation for the SMD has been proposed, fitting the collected experimental data more precisely:

$$D_{32} = 1.5 D_0 Oh^{0.2} \left(\frac{1 + 1.7 Oh^{1.4}}{We_g} \right)^{0.25} \tag{14.49}$$

Hsiang and Faeth (1992) have found that the diameters of the droplets (excluding the size of the parent drop) can be described well using the universal root normal distribution function with the $D_{0.5}/D_{32} = 1.2$, where $D_{0.5}$ is the mass median diameter. The definitions of various mean diameters can be found in an article by Lefebvre (1989).

For breakup events that occur in the range of $12 < We < 80$ (bag breakup and multimode breakup), the correlation of Wert (1995) can be used:

$$D_{32} = \frac{0.32\sigma}{u_{rel}^2 \rho_g} \left[We (t_{tot} - t_{ini}) \right]^{2/3} \tag{14.50}$$

where

t_{ini} is the dimensionless initiation time after which a drop is deformed beyond an ellipsoidal shape

t_{tot} is the dimensionless total time for the complete breakup process

An empirical correlation for the initiation time has been proposed by Hsiang and Faeth (1992):

$$t_{ini} = \frac{1.6}{1 - Oh/7}, \quad We < 10^3 \; Oh < 3.5 \tag{14.51}$$

For the total breakup time t_{tot}, the correlation is given by Pilch and Erdman (1987):

$$t_{tot} = 6(We - 12)^{-1/4}, \quad 12 < We < 18$$

$$t_{tot} = 2.45(We - 12)^{1/4}, \quad 18 < We < 45$$

$$t_{tot} = 14.1(We - 12)^{-1/4}, \quad 45 < We < 351$$

$$t_{tot} = 0.766(We - 12)^{1/4}, \quad 351 < We < 2670$$

$$t_{tot} = 5.5 \quad 2670 < We < 10^5$$

The next parameter characterizing the breakup outcome is the velocity of the fragments. Their velocity changes during the breakup period due to the drag force applied from the ambient gas flow. The deceleration associated with this drag depends on the fragment's size, yielding a velocity-dependent distribution. The velocity distribution of fragments at the instant when the breakup process is completed is given in Hsiang and Faeth (1993) in the following form:

$$\frac{w_0}{w} = 1 + 2.7\left(\sqrt{\frac{\rho_g}{\rho_l}}\frac{D_0}{D}\right)^{2/4} \tag{14.52}$$

In this empirical correlation, w and D are the relative velocity and the diameter of the fragments, respectively, and w_0 is the initial relative velocity of the drop.

14.2.1.3 Breakup in a Viscous Flow

The interest in the phenomenon of drop breakup in a viscous flow comes from problems of mixing, blending, and dispersion and from the studies of rheology and formation of emulsions. A drop located in the viscous flow deforms, stretches, and then, if the velocity gradient reaches some critical value, breaks up. For the description of the dynamics of the drop deformation and breakup in viscous flows, see the reviews by Stone (1994) and Eggers (1997).

The governing parameters determining the deformation and breakup of drops in a viscous flow are the viscosity ratio, $\lambda = \mu_l/\mu_g$; the density ratio, $\beta = \rho_l/\rho_g$; the capillary and Reynolds numbers, $Ca = G\mu_g D_0/\sigma$; and $Re = \rho_g G^2 D_0/\mu_g$, where G is the magnitude of the velocity-gradient tensor. However, the drop breakup depends not only on the instantaneous flow conditions but also on its history (Grace, 1982, Bently and Leal, 1986). Quick changes in flow conditions enhance drop breakup.

Four mechanisms of drop breakup in a viscous flow are shown schematically in Figure 14.20 (Stone, 1994).

Capillary breakup (Tomotika, 1935, Mikami et al., 1975, Tjahjadi et al., 1992) takes place when the diameter of the threadlike drop is so small that it is broken by a growing capillary waves. The drop can also break near the middle of the thread (Barthes-Biesel and Acrivos, 1973). Such *necking breakup* leads to the formation of two similar droplets. *End pinching* (Taylor, 1934, Grace, 1982, Stone and Leal, 1989a,b, Stone et al., 1989) is the breakup of the threadlike (or fingerlike) drop near the droplet appeared at its end (see also Figure 14.17b). The addition of surfactants to the fluid of a deforming, low-viscosity ratio drop ($\lambda < 0.1$) can lead to the *tip streaming* (de Bruijn, 1993, Ha and Yang, 1998). Tip streaming was also observed in the experiments with the deformation of viscoelastic drops (Milliken and Leal, 1991).

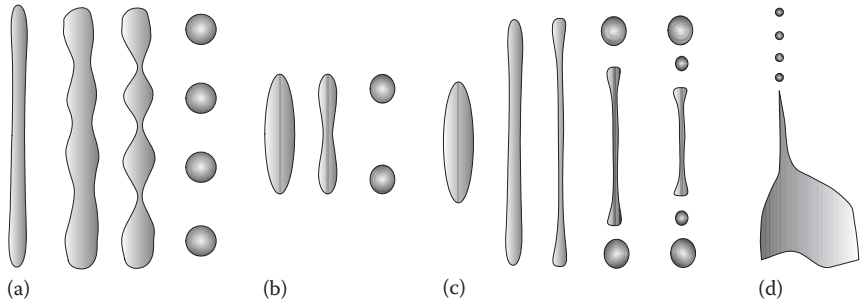


Figure 14.20

Modes of drop breakup in a viscous flow. (a) Capillary breakup. (b) Necking. (c) End pinching. (d) Tip streaming. (Adapted from Stone, H.A., *Annu. Rev. Fluid Mech.*, 26, 65, 1994.)

The shape of the drop deforms under the action of stresses generated by the outer flow. This deformation increases as the capillary number grows. The stable solution for the shape of the deformed drop in an extensional flow has been obtained by Acrivos and Lo (1978) for inviscid drops

$$h(z)=\frac{D_0}{8Ca}\left[1-\left(\frac{z}{10D_0Ca^2}\right)\right] \tag{14.53}$$

and the asymptotic value for the critical capillary number for the viscous drop is

$$Ca_{cr}\lambda^{1/6}=0.148 \tag{14.54}$$

This is valid for the small viscosity ratio ($\lambda \ll 1$).

14.2.2 Binary Drop Collisions

A collision of two drops is shown schematically in Figure 14.21, where also the main geometrical parameters of the collision are determined: the separation distance between the droplet centers χ and the collision angle $\psi = \arcsin[\chi/(R_1 + R_2)]$. The relative velocity is denoted as w. The main dimensionless parameters governing the binary drop collision phenomena include the Weber number, $We = \rho_l w^2(R_1 + R_2)/\sigma_l$; the impact parameter $B = \chi/(R_1 + R_2)$ (see the studies of Ashgriz and Poo, 1990, Jiang et al., 1992, Qian and Law, 1997); the drop diameter ratio, $\Delta = R_1/R_2 < 1$; and the Reynolds number.

The influence of the viscosity of the fluid on the binary collision in vacuum, particularly on the temporal evolution of the drop size, was investigated by Willis and Orme (2003). They found that higher Reynolds number corresponds to higher characteristic times of the drop deformation.

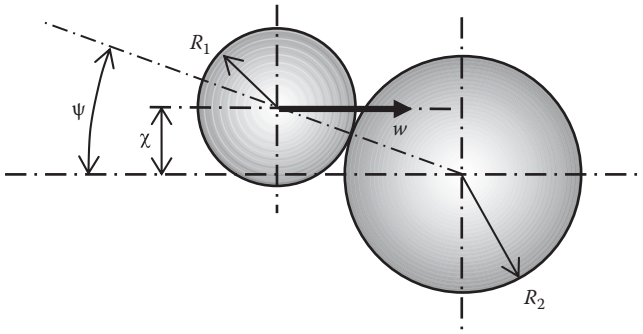


Figure 14.21

Sketch of a binary drop collision.

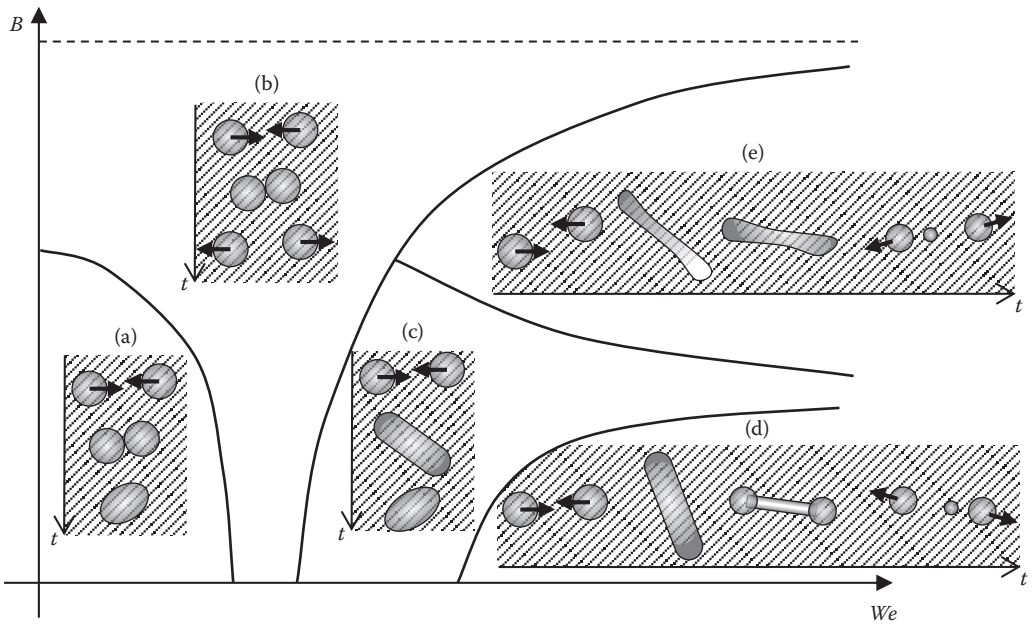


Figure 14.22

Regimes of hydrocarbon droplets: (a) Coalescence. (b) Bouncing. (c) Coalescence. (d) Reflexive separation. (e) Stretching separation. (Adapted from Qian, J. and Law, C.K., *J. Fluid Mech.*, 331, 59, 1997, $\Delta = 1$.)

A detailed study of the collision of drops of the same diameter can be found in an article by Qian and Law (1997). Several regimes of collision are observed in this work: coalescence, bouncing, coalescence, stretching separation, and reflexive separation. These regimes are shown schematically in Figure 14.22.

At relatively high Weber numbers, when the phenomenon is inertia dominated, the near head-on collision (regimes (c) and (d)) can be subdivided into several main stages, similar to the stages of the impact of a drop onto a dry wall (see Section 14.2.3): initial drop deformation leading to the formation of a relatively thin expanding liquid film, bounded by a rim. This rim expands and then recedes. The kinetic energy of the drop is accumulated in the rim at the instant when it merges. This kinetic energy leads to the creation of stretching nearly cylindrical jet bounded by two droplets. The liquid from the jet enters these two droplets. If the time of the jet breakup is smaller than the time of the droplets merging, the collision leads to separation; otherwise, it ends with coalescence.

At relatively small values of the Weber number, the phenomenon is governed by the behavior of the film of the ambient liquid/gas in the gap between the approaching drops. It is known that the expression for the pressure in this film is singular if its thickness approaches zero. The drops will coalesce if the film drains to a thickness comparable with the characteristic distance associated with the van der Waals force (Chesters, 1991).

The stretching separation regime corresponds to nonsymmetric collision of two drops at high Weber number. Such impact produces a stretching filament, which breaks up by *end pinching* (Eggers, 1993, Brenn et al., 2001).

The regimes shown in Figure 14.22 definitely do not reflect all the variety of the considered phenomena. For example, collision of two drops of $\Delta = 1/4$ observed in an article by Podvysotsky and Shraiber (1984) yields the penetration of the smaller drop into the larger, following by the creation of a relatively long jet behind the bigger drop. This jet then breaks up into several secondary droplets.

Among the models describing the critical parameters corresponding to the separation/coalescence threshold are the models of Park (1970), based on the balance of the surface forces in the neighborhood of the contact of two drops and the forces associated with the angular momentum. In an article by Brazier-Smith et al. (1972), the kinetic energy of rotation of the drop obtained by coalescence is accounted for. The energy balance of the collided drops leads to the following expression for the critical impact factor:

$$B_{cr} = \left[\frac{24[1+\Delta^2-(1+\Delta^3)^{2/3}](1+\Delta^3)^{11/3}}{5We\Delta^5(1+\Delta)^2} \right]^{1/2} \tag{14.55}$$

The criterion for the reflexive separation based on the energy balance of the system is obtained by Ashgriz and Poo (1990) in the form

$$We > 3\frac{\Delta(1+\Delta^3)^2}{\Delta^6 C_1 + C_2}\left[7(1+\Delta^3)^{2/3} - 4(1+\Delta^2)\right] \tag{14.56}$$

where

the parameters $C_1 = 2(1-C_3)^2(1-C_3^2)^{1/2} - 1$

$C_2 = 2(\Delta - C_3)^2(\Delta^2 - C_3^2)^{1/2} - \Delta^3$

the parameter C_3 is defined as $C_3 = B(1 + \Delta)/2$

$\Delta < 1$

This expression is obtained by the simplified approximation of the shape of the deformed drop by a disk.

Their model for critical Weber number of the stretching separation is

$$We = \frac{4(1+\Delta^3)^2\left[3(1+\Delta)(1-B)(\Delta^3 C_4 + C_5\right]^{1/2}}{\Delta^2\left[(1+\Delta^3) - (1-B^2)(C_4 + \Delta^3 C_5\right]} \tag{14.57}$$

where

$$C_4 = \begin{cases} 1 - \dfrac{1}{4\Delta^3}(2\Delta - \tau)^2(\Delta + \tau) & \text{for } \tau > \Delta \\ \dfrac{\tau^2}{4\Delta^3(3\Delta - \tau)} & \text{for } \tau < \Delta \end{cases}, \quad C_5 = \begin{cases} 1 - \dfrac{1}{4}(2-\tau)^2(1+\tau) & \text{for } \tau > 1 \\ \dfrac{\tau^2}{4(3-\tau)} & \text{for } \tau < 1 \end{cases}$$

with the parameter τ being $\tau = (1 - B)(1 + \Delta)$.

Qian and Law (1997) have also considered the energy balance of two colliding drops with the same diameter. They have accounted for the energy loss during collision due to viscous dissipation. Their result yields the linear dependence of the critical Weber number corresponding to the separation/coalescence threshold on the Ohnesorge number. Their result for the best fit to the existing experimental data is given in the form

$$We_{cr} = 30Oh + 15 \tag{14.58}$$

with the Ohnesorge number being defined as $Oh = 16\mu_l/\sqrt{\rho_l R \sigma_l}$.

14.2.3 Drop–Wall Impact

Many processes involving drop and sprays also involve their impact onto a surface. Universal relations describing the outcome of drop/wall impact do not exist simply because of the large number of influencing parameters:

- Reynolds number and Weber number of incident drop
- Surface orientation (normal/inclined)
- Surface structure (rough/smooth) and chemical composition (hydrophobic/hydrophilic)
- Dry or wet surface, including the hydrodynamics of the liquid film in the case of a wet surface
- Surface temperature

Obviously, additional properties of the impinging drop may also be of importance, such as boiling point, heat of vaporization, or contact angle with the surface.

Understanding drop–wall impact represents a key technology for some processes, for example, ink jet printing or near net-shape manufacturing, where solidification must also be accounted for (Madejski, 1983, Poulikakos and Waldvogel, 1996, Liu and Orme, 2001). Very-high-speed drop impacts can even lead to

damage or erosion of the solid surfaces, like turbine blades or airplane surfaces. In such ultrahigh-speed drop impacts, compressibility is one important factor, leading to the propagation of shock waves in the drop and in the target material (Lesser and Field, 1983, Korobkin, 1997). However, drop/wall impact is also an elemental part of spray/wall impact, which itself is an essential process in many technologies: spray cooling, spray painting, fuel injection, drop separators, etc.

In the following discussion, the phenomenon of drop impact has been divided into impact onto dry surfaces and onto liquid films. In the former case, the wettability may become important, whereas in the latter case, the hydrodynamics of the liquid film must be considered. A very good collection of papers dealing with various specific aspects influencing drop impact phenomena can be found in an article by Rein (2002).

14.2.3.1 Wetting of a Dry Surface: Static and Dynamic Contact Angles

The stationary shape of a drop on a dry solid surface depends on its volume, density, and surface wettability property, described by a static (or equilibrium) contact angle θ_e, defined in Figure 14.23. In the case of a smooth, homogeneous, rigid surface, this angle depends on the surface (or interface) free energy of the solid–gas interface, σ_{sv}; of solid–liquid interface, σ_{sl}; and of the liquid–gas interface, σ(surface tension). The equilibrium condition at the contact line leads to *Young's relation*:

$$\cos\theta_e = \frac{\gamma_{sv} - \gamma_{sl}}{\gamma} \tag{14.59}$$

The wetting of the substrate is total, $\theta_e = 0$, if the right-hand side of (14.57) is larger than 1. The surface is partially wettable if the absolute value of the RHS of (14.57) is smaller than 1, yielding the value of the equilibrium contact angle in the range $0 < \theta_e < \pi$. Within this range, hydrophobic ($\theta_e > \frac{\pi}{2}$) and hydrophilic ($\theta_e < \frac{\pi}{2}$) surfaces can also be distinguished.

When the liquid spreads on the substrate under action of gravity and capillary forces (spontaneous spreading) or due to inertial forces (forced wetting), the position of the contact line moves and the apparent dynamic contact angle θ_d differs from the static one. The dynamic contact angle depends on the contact line velocity U_c if the capillary number $Ca = U_c\mu/\sigma$ is relatively small. This dependence is shown schematically in Figure 14.24. The sign of U_c is positive if the contact line moves toward the gas phase. Two distinct branches of the curve $\theta_d = \theta_d(U_c)$ are considered in relation to the direction of motion of the contact line: the advancing dynamic contact angle for $U_c > 0$ and receding contact angle for $U_c > 0$.

Next, the static advancing, θ_a, and static receding, θ_r, contact angles can be defined as two different limits of the dynamic contact angle as the velocity U_c approaches zero:

$$\theta_a = \lim_{U_c \to +0} \theta_d(U_c), \quad \theta_r = \lim_{U_c \to -0} \theta_d(U_c)$$

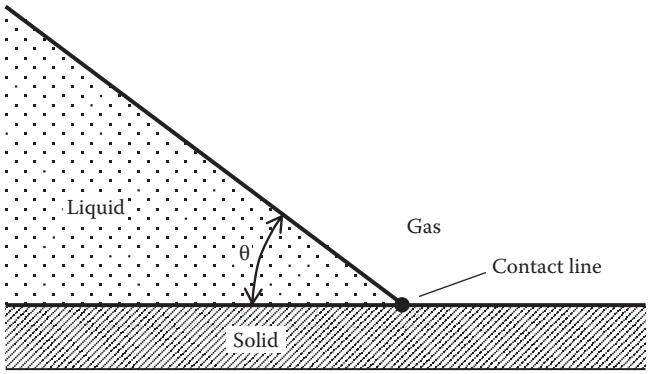


Figure 14.23

Sketch defining the contact angle and the contact (or triple) line.

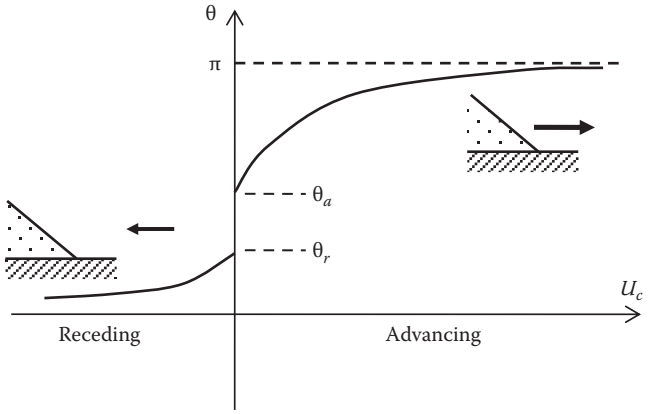


Figure 14.24

Hysteresis of the dynamic contact angle.

The hysteresis in the values of θ_a and θ_r is related to the microstructure of the surface (roughness, chemical nonhomogeneity), the presence of impurities in the liquid, and the substrate. The contact angle of the liquid in the steady state can thus vary in the range $\theta_r < \theta < \theta_a$.

The dynamic contact angle at $\theta_e \approx 0$ and $Ca \ll 1$ depends on the capillary number Ca only (Hoffman, 1975). An empirical correlation for the dynamic contact angle for such cases is given by Voinov (1976) and (Tanner, 1979) in the form

$$\theta_d \sim Ca^{1/3} \tag{14.60}$$

which is known as the "Hoffman–Voinov–Tanner law" (Kistler, 1993).

More generally, the dynamic contact angle may also depend on the hydrodynamics of the liquid behind the contact line and two main approaches to the problem of dynamic contact angle are considered to date: the hydrodynamic approach (with the most general analysis in Cox (1986)) and molecular-kinetic approach (introduced in Blake, 1968, Blake and Haynes, 1969). See the detailed reviews of the wettability phenomena and modeling in Kistler (1993) and Blake (1993). More recent work can be found in Blake et al. (1999).

Some biological or micro- and nanostructured surfaces are extremely hydrophobic. Barthlott and Neinhuis (1997) studied the morphology of lotus plant leaves, revealing a self-cleaning property through rain, fog, or dew (the lotus effect). Considerable effort is presently being spent on producing synthetic water-repellent surfaces with prescribed surface morphologies. Onda et al. (1996) produced a fractal alkylketene dimmer, reaching an apparent contact angle of 174° in their experiments. Bico et al. (1999) and Richard and Quéré (2000) have investigated a single drop impact onto such highly hydrophobic surfaces, observing that the drop can fully bounce after impact on such surfaces.

Spontaneous drop spreading is analyzed in the theoretical works of Hocking and Rivers (1982), Dussan and Chow (1983), Pozdikidis (1990), and Reznik and Yarin (2002). The inertial effects in such low-speed drop impacts are small in comparison with the capillary forces and viscous drag. At higher impact speeds, inertia and viscous forces can no longer be neglected, and this situation is considered in the following section.

14.2.3.2 Drop Impact onto a Dry Substrate

The phenomenon of drop impact onto a dry substrate can be subdivided into several main phases, as shown in Figure 14.25. The first phase is the initial drop deformation during which the drop shape transforms from a nearly spherical shape to a thin liquid film (lamella) expanding on the wall. The duration of this first phase is approximately $t_{init} \sim D_0/U_n$, where D_0 is the initial drop diameter and U_n is the normal component of the impact velocity. During the second phase of drop impact, the spreading lamella is bounded by a rim, formed by capillary forces. The formation of this rim leads to the typical pizza-like shape of a spreading drop. The position of the rim determines the size and the shape of the wetted spot on the substrate. At some time instant, $t = t_{max}$, the size of the wetted spot reaches a maximum. Then, if the substrate is partially hydrophobic, the drop begins to recede, leading to the third phase of drop impact. At some further time

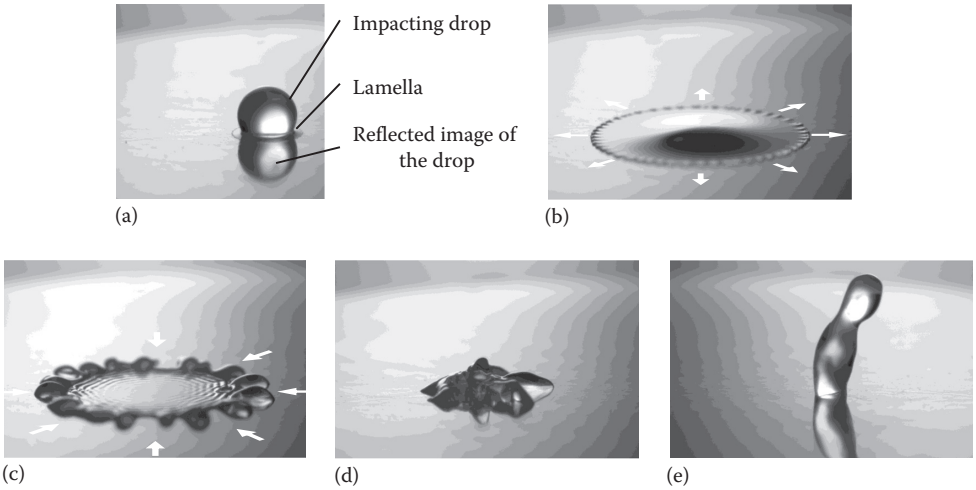


Figure 14.25

Stages of single drop impact onto a dry, partially wettable substrate.

instant $t = t_{merg}$, the rim merges. If the kinetic energy of the rim at the time instant $t = t_{merg}$ is high enough, the rim merging process can lead to the appearance of a fingerlike central jet ejected from the surface.

If the Reynolds and the Weber numbers are high, the first phase of the initial deformation and the spreading of the drop are dominated by inertia. The evolution of drop diameter during these two phases and the value of the maximum spread diameter are almost independent of the static contact angle (Rioboo et al., 2002). The receding of the drop is in contrast caused by forces associated with the wettability.

In each stage of impact, the drop can lose its stability and break up. The experimental studies of drop impact are focused mainly on the determination of various outcomes of the impact event (see Hartley and Brunskill, 1958, Levin and Hobbs, 1971, Stow and Stainer, 1977, Stow and Hadfield, 1981, Mao et al., 1997, Range and Feuillebois, 1998). The influence of the surfactants added to the liquid on the evolution of the diameter of the spreading drop has been studied by Mourougou-Candoni et al. (1999).

A number of different outcomes of drop impact are classified in an article by Rioboo et al. (2001) (see Figure 14.26). A *prompt splash* occurs at high impact velocities onto a rough surface during the first stage of initial drop deformation. A number of jets are formed in the region of the contact line as the result of its perturbations by the wall roughness. These jets then break up into secondary droplets. The mechanism of *corona splash* after a drop impact onto a dry wall is not yet completely clear. It can be caused either by air entrainment into the contact line region or by the bending instability of a lamella spreading radially on the substrate. This type of splash is more typical for the high-speed drop impact onto a wetted wall. At some time instant, this lamella (initially planar) begins to deform and eject a nearly cylindrical, uprising

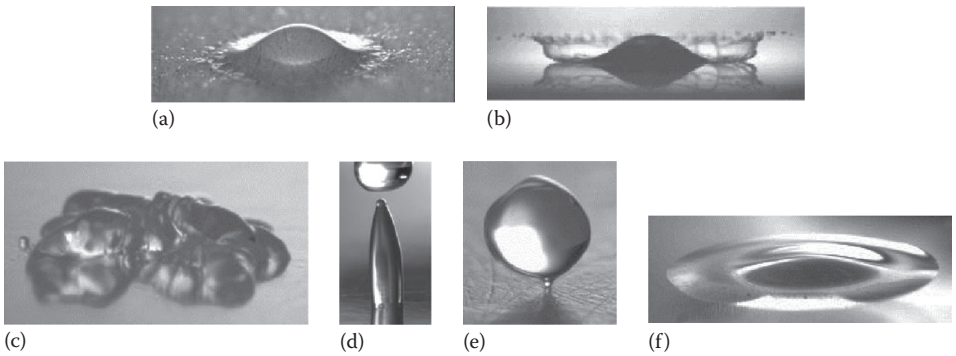


Figure 14.26

Classification of different outcomes of drop impact onto a dry substrate. (The images are from Rioboo, R. et al., *Atomization Sprays,* 11, 155, 2001.)

crown-like sheet. A number of small jets then appear at the edge of this sheet, subsequently breaking up into secondary droplets. The drop can also break up during its receding phase. This *receding breakup* is caused by a disjoining of the contact line due to the local wall microstructure or chemical inhomogeneity. The *partial rebound* occurs when the duration of the central jet stretching is longer than the time required for its capillary breakup. Drop impact onto a highly hydrophobic surface can lead to the complete *rebound*. If the parameters of drop impact are below the splashing threshold, it *deposits* on the surface without breakup.

An empirical relation for the splashing threshold was obtained by Mundo et al. (1998). It was assumed that drop will not splash if

$$K = WeOh^{-0.4} < 657 \tag{14.61}$$

However, more recent parametric studies of drop of variable liquids indicate that the well-known relation (14.59) is not precise and the *K*-number does not describe the splashing threshold well. It is valid probably for relatively narrow range of impact parameters. More generalized expression for the corona splash threshold can be found in Roisman et al. (2015):

$$Ca \geq 0.067 + 0.60Oh^{0.15} \quad \text{at 1 bar} \tag{14.62}$$

is a necessary condition for splash, where the capillary number is based on the drop impact velocity, $Ca = U\mu/\sigma$. Equation 14.62 is recommended for use, since it is based on the analysis of a high number of experiments collected from different sources. The *K*-number is more relevant to the impact of a drop onto a wetted substrate, the case considered in the next section.

The splashing threshold depends also on the ambient pressure. Pressure reduction can lead to a significant increase in the threshold velocity (Xu et al., 2005). Still, no consensus exists on the physical mechanisms leading to the dependence of the splashing threshold on the properties of the ambient gas.

Moreover, it was shown by Roisman et al. (2015) that the prompt splash on rough and porous substrates is determined not on the average roughness but on the characteristic slope of the substrate surface structures. They have introduced an average threshold Weber number for splash

$$We_{\text{average}} = 10.2(Rpk/Rsm)^{-0.83} \tag{14.63}$$

where

Rpk and *Rsm* are the standard parameters characterizing substrate roughness
Rpk is an average height of protruding peaks above the roughness core profile
Rsm is the mean width of a roughness element

14.2.3.3 Drop Impact onto a Wetted Wall

Numerous studies of the drop impact onto a liquid film have led to similar data concerning the splash threshold, drop shape, crown propagation, fingering of the rim, etc. (Levin and Hobbs, 1971, Macklin and Metaxas, 1976, Cossali et al., 1997, 2004).

Depending on the impact parameters and the film thickness, several impingement regimes have been determined. The collision can result in *sticking, rebound, deposition*, and *splash* (Stanton and Rutland, 1996) as shown in Figure 14.27. In an article by Cossali et al. (1997), two types of the splash were observed: *corona splas*h (when the impact results in the creation of a crown-like sheet, which then breaks up) and *prompt splash* (when small secondary droplets are ejected from the region where the drop contacts the free surface of the film). Also, the formation of a central fingerlike jet was observed in the case of high-velocity impact into a deep pool or onto a relatively thick film (Ogũz and Prosperetti, 1990).

The stick regime occurs when the nearly spherical drop adheres to the film. The condition for the stick regime, $We < 5$ in Stanton and Rutland (1996), is based on the experimental results of the studies by Rodrigues and Mesler (1985), Walzel (1980), and Jayaratne and Mason (1964).

The rebound regime occurs in the Weber number range $5 < We < 10$ (Rodrigues and Mesler, 1985).

For the Weber number higher than 10, the deposition of the impinging drop takes place when the parameters of the impact are below the splash threshold.

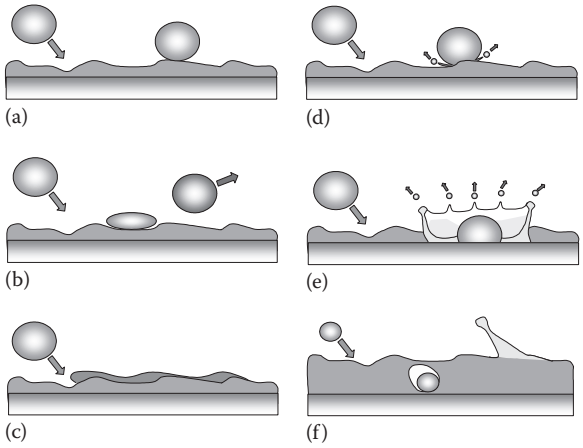


Figure 14.27

Single drop impact onto a wetted surface.

The splash threshold represents the conditions at which secondary droplets are first observed and takes a form similar to Equation 14.59, with empirical modifications for the liquid film (Cossali et al., 1997, Samenfink, 1997, Mundo et al., 1998, Wang and Chen, 2000).

Cossali et al. (1997) have obtained images of a splashing drop, showing the details of the crown formation, and jetting. The following empirical relation for the critical *K*-number depending on the dimensionless film thickness δ (scaled to the drop diameter) has been proposed:

$$K = 2100 + 5800\delta^{1.44} \quad \text{for } 0.1 < d < 1 \quad \text{and} \quad Oh > 7 \times 10^{-3} \tag{14.64}$$

Note that in spite of the fact that the *K*-number is a parameter having "round" powers of *We* and *Oh*, it is completely empirical.

Ogũz and Prosperetti (1990) have studied the impact of a single drop into a deep pool or relatively thick liquid film. The main subjects of this experimental, theoretical, and numerical study were the crater expansion in the liquid pool, bubble entrapment, and the creation of the central jet. The dominant factors influencing the phenomenon are the inertia of the liquid, capillary forces, and gravity. Bubble entrainment takes place in the range of parameters

$$41.3\, Fr^{0.179} < We < 48.3\, Fr^{0.247} \tag{14.65}$$

where

$Fr = U^2/(gD_0)$ is the Froude number

g is the acceleration due to gravity

These upper and lower bounds are obtained by fitting the experimental data.

14.2.3.4 Theoretical Modeling of Drop Impact

Modeling of drop impact phenomena involves description of an unsteady flow governed by inertia, capillary forces, and viscous drag. In the case of the drop impact onto a dry wall also, the forces associated with the wettability are important.

One parameter characterizing drop impact onto a dry wall is the maximum spread diameter. Most of the models are based on the energy balance of the drop: Collins et al. (1990), Chandra and Avedisian (1991), Pasandideh-Fard et al. (1996), Fukai et al. (1995), and Mao et al. (1997). In all of these approaches, the drop shape is assumed to be a disk at the instant when the drop diameter reaches its maximum value. Moreover, the total kinetic energy of the drop at this instant is assumed to vanish.

Other feature of drop impact is the instability of lamella, leading to its breakup, which has been studied by Kim et al. (2000) and Fedorchenko and Chernov (1999).

In the study of normal impact of a drop onto a dry, partially wettable wall (Roisman et al., 2002), the temporal evolution of the drop diameter—its spreading and receding—is determined by the motion of a

torus-like rim, bounding a thin radially expanding film (lamella). The equations of motion of the film are obtained from its mass and momentum balance.

One important result of the studies of drop impact onto a stationary uniform liquid film is the temporal expansion of the radius R_{cr} of the crown. The dependence $R_{cr} \sim \sqrt{t}$ is obtained by Yarin and Weiss (1995) describing the base of the crown as a kinematic discontinuity in the liquid film. In recent work (Trujillo and Lee, 2001), this theory is modified, taking into account the effect of the viscous forces. In Roisman and Tropea (2002), the theory of the formation of the uprising sheet and its shape, valid for the general, nonaxisymmetric case, is developed. All these models are developed for the case of drop impact onto relatively thin films ($\delta < 0.5$).

If the impact Weber and Reynolds numbers are much higher than unity, the evolution of the lamella thickness in time does not depend on viscosity and surface tension (Roisman et al., 2009). An exact solution for the flow generated by drop impact has been obtained by Roisman (2009). Among important results from this solution is an expression for the maximum spreading diameter

$$D_{\max} \approx 0.87 Re^{1/5} - 0.40 Re^{2/5} We^{-1/2} \tag{14.66}$$

and for the minimum (residual) thickness of the lamella

$$h_{res} = 0.79 Re^{-2/5} \tag{14.67}$$

References

Acrivos, A. and Lo, T.S., Deformation and breakup of a single slender drop in an extensional flow, *J. Fluid Mech.*, 86, 641, 1978.

Ashgriz, N. and Poo, J.Y., Coalescence and separation in binary collision of liquid drops, *J. Fluid Mech.*, 221, 183, 1990.

Barthes-Biesel, D. and Acrivos, A., Deformation and burst of a liquid drop freely suspended in a shear field, *J. Fluid Mech.*, 61, 1, 1973.

Barthlot, W. and Neinhuis, C., Purity of the sacred lotus, or escape from contamination in biological surfaces, *Planta*, 202, 1, 1997.

Bently, B.J. and Leal, L.G., An experimental investigation of drop deformation and breakup in steady, two-dimensional linear flows, *J. Fluid Mech.*, 167, 241, 1986.

Bico, J., Marzolin, C., and Quéré, D., Pearl drops, *Europhys. Lett.*, 47, 220, 1999.

Blake, T.D., The contact angle and two-phase flow, PhD thesis, University of Bristol, Bristol, U.K., 1968.

Blake, T.D., Dynamic contact angles and wetting kinetics, in Berg, J.C. (Ed.), *Wettability*, Surfactant Science Series, Marcel Dekker, INC., New York, 1993.

Blake, T.D., Bracke, M., and Shikhmurzaev, Y.D., Experimental evidence of nonlocal hydrodynamic influence on the dynamic contact angle, *Phys. Fluids.*, 11, 1995, 1999.

Blake, T.D. and Haynes, J.M., Kinetics of liquid-liquid displacement, *J. Colloid Interface Sci.*, 30, 421, 1969.

Brazier-Smith, P.R., Jennings, S.G., and Latham, J., The interaction of falling water drops: Coalescence, *Proc. R. Soc. Lond. A*, 326, 393, 1972.

Brenn, G., Valkovska, D., and Danov, K.D., The formation of satellite droplets by unstable binary drop collisions, *Phys. Fluids*, 13, 2463, 2001.

Chandra, S. and Avedisian, C.T., On the collision of a droplet with a solid surface, *Proc. R. Soc. Lond. A*, 432, 13, 1991.

Chesters, A.K., The modeling of coalescence processes in fluid liquid dispersions—A review of current understanding, *Trans. Inst. Chem. Eng.*, 69, 259, 1991.

Collings, E.W., Markworth, J.K., McCoy, J.K., and Saunders, J.H., Splat-quench solidification of freely falling liquid-metal drops by impact on a planar substrate, *J. Mater. Sci.*, 25, 3677, 1990.

Cossali, G.E., Coghe, A., and Marengo, M., The impact of a single drop on a wetted surface, *Exp. Fluids*, 22, 463, 1997.

Cossali, G.E., Marengo, M., Coghe, A., and Zhdanov, S., The role of time in single splash on thin film, *Exp. Fluids*, 36, 888, 2004.

Cox, R.G., The dynamics of the spreading of liquids on a solid surface. Part 1. Viscous flow, *J. Fluid Mech.*, 168, 169, 1986.

Dai, Z. and Faeth, G.M., Temporal properties of secondary drop breakup in the multimode breakup regime, *Int. J. Multiphase Flow*, 27, 217, 2001.
de Bruijn, R.A., Tip streaming of drops in simple shear flows, *Chem. Eng. Sci.*, 48, 277, 1993.
Delplanque, J.-P. and Siringano, W.A., Boundary layer stripping effects on droplet transcritical convecting vaporization, *Atomization Sprays*, 4, 325, 1994.
Dussan, E.B.V. and Chow, R.T., On the ability of drops or bubbles to stick to non-horizontal surfaces or solids, *J. Fluid Mech*., 137, 1, 1983.
Eggers, J., Universal pinching of 3D axisymmetric free-surface flow, *Phys. Rev. Lett*., 71, 3458, 1993.
Eggers, J., Nonlinear dynamics and breakup of free-surface flows, *Rev. Mod. Phys*., 69, 865, 1997.
Fedorchenko, A.I. and Chernov, A.A., Formation of fingers at the front of an axially symmetric film of liquid upon the impact of a drop with a solid surface, *Dokl. Phys*., 44, 570, 1999.
Fukai, J., Shiiba, Y., Yamamoto, T., Miyatake, O., Poulikakos, D., Megaridis, C.M., and Zhao, Z., Wetting effects on the spreading of a liquid droplet colliding with a flat surface: Experiment and modelling, *Phys. Fluids*, 7, 236, 1995.
Grace, H.P., Dispersion phenomena in high viscosity immiscible fluid systems and application of static mixers as dispersion devices in such systems, *Chem. Eng. Commun.*, 14, 225, 1982.
Ha, J.-W. and Leal, L.G., An experimental study of drop deformation and breakup in extensional flow at high capillary number, *Phys. Fluid*s, 13, 1568, 2001.
Ha, J.-W. and Yang, S.-M., Effect of non-ionic surfactant on the deformation and breakup of a drop in an electric filed, *J. Colloid Interface Sci.*, 206, 195, 1998.
Hartley, G.S. and Brunskill, R.T., Reflection of water drop from surfaces, in *Surface Phenomena in Chemistry and Biology*, Vol. 57, Pergamon Press, London, U.K. 1958, pp. 214–223.
Hinze, J.O., Fundamentals of the hydrodynamic mechanism of splitting in dispersion processes, *AIChE J.*, 1, 289, 1955.
Hocking, L.M. and Rivers, A.D., The spreading of a drop by capillary action, *J. Fluid Mech*., 121, 425, 1982.
Hoffman, R.L., A study of the advancing interface. 1. Interface shape in liquid-gas systems, *J. Colloid Interface Sci*., 50, 228, 1975.
Hsiang, L.-P. and Faeth, G.M., Near-limit drop deformation and secondary breakup, *Int. J. Multiphase Flow*, 18, 635, 1992.
Hsiang, L.-P. and Faeth, G.M., Drop properties after secondary breakup, *Int. J. Multiphase Flow*, 19, 721, 1993.
Hsiang, L.-P. and Faeth, G.M., Drop deformation and breakup due to shock wave and steady disturbances, *Int. J. Multiphase Flow*, 21, 545, 1995.
Hwang, S., Liu, S., and Reitz, R.D., Breakup mechanisms and drag coefficients of high speed vaporizing drops, *Atomization Sprays*, 6, 353, 1996.
Jayaratne, O.W. and Mason, B.J., The coalescence and bouncing of water drops at an air/water interface, *Proc. R. Soc. Lond. A*, 280, 545, 1964.
Jiang, Y.J., Umemura, A., and Law, C.K., An experimental investigation on the collision behaviour of hydrocarbon droplets, *J. Fluid Mech*., 234, 171, 1992.
Joseph, D.D., Belanger, J., and Beavers, G.S., Breakup of a liquid drop suddenly exposed to a high-speed airstream, *Int. J. Multiphase Flow*, 25, 1263, 1999.
Kim, H.-Y., Feng, Z.C., and Chun, J.-H., Instability of a liquid jet emerging from a droplet upon collision with a solid surface, *Phys. Fluids*, 12, 531, 2000.
Kistler, S.F., Hydrodynamics of wetting, in Berg, J.C. (Ed.), *Wettability*, Surfactant Science Series, Marcel Dekker, Inc., New York, 1993.
Korobkin, A., Analytic theory of liquid-solid impact, *Phil. Trans. R. Soc. Lond. A*, 355, 507, 1997.
Krzeczkowski, S.A., Measurements of liquid droplet disintegration mechanisms, *Int. J. Multiphase Flow*, 6, 227, 1980.
Lee, C.H. and Reitz, R.D., An experimental study of the effect of gas density on the distortion and breakup mechanism of drops in high speed gas stream, *Int. J. Multiphase Flow*, 26, 229, 2000.
Lefebvre, H., *Atomization and Sprays*, Hemisphere Publishing Corporation, New York, 1989.
Lesser, M. and Field, J., The impact of compressible liquids, *Ann. Rev. Fluid Mech*., 15, 97, 1983.
Levin, Z. and Hobbs, P.V., Splashing of water drops on solid and wetted surfaces: Hydrodynamics and charge separation, *Phil. Trans. R. Soc. Lond. A*, 269, 555, 1971.
Liu, Q. and Orme, M., On precision droplet-based net-form manufacturing technology, *Proc. Inst. Mech. Eng. B, J. Eng. Manuf.*, 215, 1333, 2001.

Liu, Z. and Reitz, R.D., An analysis of the distortion and breakup mechanisms of high speed liquid drops, *Int. J. Multiphase Flow*, 4, 631, 1997.
Macklin, W.C. and Metaxas, G.J., Splashing of drops on liquid layers. *J. Appl. Phys*., 47, 3963, 1976.
Madejski, J., Droplets on impact with a solid surface, *Int. J. Heat Mass Transfer*, 26, 1095, 1983.
Mao, T., Kuhn, D.C.S., and Tran, H., Spread and rebound of liquid droplets upon impact on flat surfaces, *AIChE J*., 43, 2169, 1997.
Mikami, T., Cox, R.G., and Mason, S.G., Breakup of extending liquid threads, *Int. J. Multiphase Flow*, 2, 113, 1975.
Milliken, W.J. and Leal, L.G., Deformation and breakup of viscoelastic drops in planar extensional flows, *J. Non-Newtonian Fluid Mech*., 40, 355, 1991.
Mourougou-Candoni, N., Prunet-Foch, B., Legay, F., and Vignes-Adler, M., Retraction phenomena of surfactant solution drops upon impact on a solid substrate of low surface energy, *Langmuir*, 15, 6563, 1999.
Oguz, H.N. and Prosperetti, A., Bubble entrainment by the impact of drops on liquid surfaces, *J. Fluid Mech*., 219, 143, 1990.
Onda, T., Shibuichi, S., Satoh, N., and Tsujii, K., Super-water-repellent fractal surfaces, *Langmuir*, 12, 2125, 1996.
Park, R.W., Behaviour of water drops colliding in humid nitrogen, PhD thesis, University of Wisconsin, Madison, WI, 1970.
Pasandideh-Fard, M., Qiao, Y.M., Chandra, S., and Mostaghimi, J., Capillary effects during droplet impact on a solid surface, *Phys. Fluids*, 8, 650, 1996.
Pilch, M. and Erdman, C., Use of break-up time data and velocity history data to predict the maximum size of stable fragments for acceleration induced break-up of a liquid drop, *Int. J. Multiphase Flow*, 13, 741, 1987.
Podvysotsky, A.M. and Shraiber, A.A., Coalescence and break-up of drops in two-phase flows, *Int. J. Multiphase Flow*, 10, 195, 1984.
Poulikakos, D. and Waldvogel, J., Heat transfer and Fluid dynamics in the process of spray deposition, *Adv. Heat Transfer*, 28, 1, 1996.
Pozdikidis, C., The deformation of a liquid drop moving normal to a plane wall, *J. Fluid Mech*., 215, 331, 1990.
Qian, J. and Law, C.K., Regimes of coalescence and separation in droplet collision, *J. Fluid Mech.*, 331, 59, 1997.
Range, K. and Feuillebois, F., Influence of surface roughness on liquid drop impact, *J. Colloid Interface Sci*., 203, 16, 1998.
Ranger, A.A. and Nicholls, J.A., The aerodynamic shattering of liquid drops, *AIAA J.*, 7, 285, 1969.
Rein, M. (Ed.), *Drop-Surface Interactions*, Springer-Verlag, Wien, Austria, 2000.
Reznik, S.N. and Yarin, A.L., Spreading of a viscous drop due to gravity and capillarity on a horizontal or an inclined dry wall, *Phys. Fluids*, 14, 118, 2002.
Richard, D. and Quéré, D., Bouncing water drops, *Europhys. Lett*., 50, 769, 2000.
Rioboo, R., Marengo, M., and Tropea, C., Outcomes from a drop impact on solid surfaces, *Atomization Sprays,* 11, 155, 2001.
Rioboo, R., Marengo, M., and Tropea, C., Time evolution of liquid drop impact onto solid, dry surfaces, *Exp. Fluids*, 33, 112, 2002.
Rodrigues, F. and Mesler, R., Some drops don't splash, *J. Colloid Interface Sci.*, 106, 347, 1985.
Roisman, I.V., Inertia dominated drop collisions. II. An analytical solution of the Navier–Stokes equations for a spreading viscous film, *Phys. Fluids*, 21, 052104, 2009.
Roisman, I.V., Berberović, E., and Tropea, C., Inertia dominated drop collisions. I. On the universal flow in the lamella. *Phys. Fluids*, 21, 052103, 2009.
Roisman, I.V., Lembach, A., and Tropea, C., Drop splashing induced by target roughness and porosity: The size plays no role, *Adv. Colloid Interface Sci.*, 2015, http://dx.doi.org/10.1016/j.cis.2015.02.004.
Roisman, I.V., Rioboo, R., and Tropea, C., Normal impact of a liquid drop on a dry surface: Model for spreading and receding, *Proc. R. Soc. Lond. A*, 458, 1411, 2002.
Roisman, I.V. and Tropea, C., Impact of a drop onto a wetted wall: Description of crown formation and propagation, *J. Fluid Mech*., 472, 373, 2002.
Samenfink, W., Grundlegende Untersuchung zur Tropfeninteraktion mit schubspannungsgetriebenen Wandfilmen. PhD thesis, Universität Karlsruhe, Karlsruhe, Germany, 1997.

Schmehl, R., Tropfendeformation und Nachzerfall bei der technischen Gemischaufbereitung, Dissertation, University of Karlsruhe, Karlsruhe, Germany, 2003a.
Schmehl, R., Modeling droplet breakup in complex two-phase flows, in *Proceedings of International Conference on Liquid Atomization and Spray Systems ICLASS-2003*, Sorrento, Italy, July 13–18, 2003b.
Sevik, M. and Park, S.H., The splitting of drops and bubbles by turbulent fluid flow, *J. Fluid Eng.*, 95(1), 53, March 1973.
Stanton, D.W. and Rutland, C.J., Modeling fuel film formation and wall interaction in diesel engines, *SAE Technical Papers Series* 960628, 1996.
Stone, H.A., Dynamics of drop deformation and breakup in viscous fluids, *Annu. Rev. Fluid Mech.*, 26, 65, 1994.
Stone, H.A., Bentley, B.J., and Leal, L.G., An experimental study of transient effects in the breakup of viscous drops, *J. Fluid Mech*., 173, 131, 1989.
Stone, H.A. and Leal, L.G., Relaxation and breakup of an initially extended drop in an otherwise quiescent fluid, *J. Fluid Mech*., 198, 399, 1989a.
Stone, H.A. and Leal, L.G., The influence of initial deformation on drop breakup in subcritical time-dependent flows at low Reynolds numbers, *J. Fluid Mech*., 206, 223, 1989b.
Stow, C.D. and Hadfield, M.G., An experimental investigation of fluid flow resulting from the impact of a water drop with an unyielding dry surface, *Proc. R. Soc. Lond. A*, 373, 419, 1981.
Stow, C.D. and Stainer, R.D., The physical products of a splashing water drop, *J. Met. Soc. Jpn.*, 55, 518, 1977.
Tanner, L.H., The spreading of silicone oil drops on solid surfaces, *J. Phys. D Appl. Phys*., 12, 1473, 1979.
Taylor, G.I., The formation of emulsions in definable fields of flow, *Proc. R. Soc. Lond. A*, 146, 501, 1934.
Taylor, G.I., The dynamics of thin sheets of fluid II. Waves on fluid sheets, *Proc. R. Soc. Lond. A*, 263, 296, 1959.
Tjahjadi, M., Stone, H.A., and Ottino, J.M., Satellite and subsatellite formation in capillary breakup, *J. Fluid Mech*., 243, 297, 1992.
Tomotika, S., On the stability of a cylindrical thread of a viscous liquid surrounded by another viscous fluid, *Proc. R. Soc. Lond. A*, 150, 322, 1935.
Trujillo, M.F. and Lee, C.F., Modeling crown formation due to the splashing of a droplet, *Phys. Fluids*, 13, 2503, 2001.
Voinov, O.V., Hydrodynamics of wetting, (English translation), *Fluid Dyn.*, 11, 714, 1976.
Walzel, P., Zeteilgrenze beim Tropfenprall, *Chem. Ing. Tech.*, 5, 338, 1980.
Wang, A.B. and Chen, C.C., Splashing impact of a single drop onto very thin liquid films, *Phys Fluids*, 12, 2155, 2000.
Wiezba, A., Deformation and breakup of liquid drops in a gas stream at nearly critical Weber number, *Exp. Fluids*, 9, 1329, 1990.
Willis, K. and Orme, M., Binary droplet collisions in a vacuum environment: An experimental investigation of the role of viscosity, *Exp. Fluids*, 34, 28, 2003.
Xu, L., Zhang, W.W., and Nagel, S.R., Drop splashing on dry smooth surface, *Phys. Rev. Lett*., 94, 184505, 2005.
Yarin, A.L. and Weiss, D.A., Impact of drops on solid surfaces: Self-similar capillary waves, and splashing as a new type of kinematic discontinuity, *J. Fluid Mech*., 283, 141, 1995.
Yarin, A.L., Weiss, D.A., Brenn, G., and Rensink, D., Acoustically levitated drops: Drop oscillation and break-up driven by ultrasound modulation, *Int. J. Multiphase Flow*, 28, 887, 2002.


Taylor & Francis
Taylor & Francis Group
http://taylorandfrancis.com

15

Particle Separation Methods and Systems

15.1 Separation Efficiency and Grade Efficiency
15.2 Classification of Particle Separation Systems
15.3 Flow-Through-Type Separators
15.4 Gravitational Collectors
15.5 Centrifugal Separation: Dry Cyclones
15.6 Electrostatic Precipitators
15.7 Obstacle-Type Separators
15.8 Inertial Dust Collectors
15.9 Air Filters
15.10 Scrubbers
15.11 Barrier-Type Separators
15.12 Bag Filters
15.13 Liquid-Phase Particle Separation (Hydrocyclone)

The operation to separate dust from a fluid stream is referred to as particle collection. It has been utilized to recover valuable materials from many chemical processes and to remove air pollutants consisting of particulate matter from exhaust streams before exiting to the atmosphere. In this operation, it is essential to produce a sufficiently large relative velocity between the particles and the fluid. Hence, many types of collectors have been developed and used to accomplish the tasks mentioned. In this chapter, the principles and features of particle separation and typical particle collectors are described. Particle separation in a hydro-cyclone is also described in Section 15.13, because the separation process of particle is similar in both liquid and air.

15.1 Separation Efficiency and Grade Efficiency

Chikao Kanaoka

Separation (overall) efficiency is the ratio of the amount of dust collected to the total amount of dust entering the collector in a given period of time. However, it is difficult, practically, to determine the separation efficiency of an actual dust collector. The efficiency is calculated by one of the following three methods using inlet and outlet dust flow rates, dust concentration, and gas flow rate, as shown in Figure 15.1.

1. Efficiency evaluation using the dust flow rate at the inlet and outlet ducts:

$$\mathfrak{E}\begin{cases} = \dfrac{\dot{m}_{in} - \dot{m}_{p,out}}{\dot{m}_{in}} = 1 - \dfrac{\dot{m}_{out}}{\dot{m}_{in}} \\ = \dfrac{c_{p,in}\dot{V}_{in} - c_{p,out}\dot{V}_{out}}{c_{p,in}\dot{V}_{in}} = 1 - \dfrac{c_{p,out}\dot{V}_{out}}{c_{p,in}\dot{V}_{in}} \\ = \dfrac{c_{p,in,N}\dot{V}_{in,N} - c_{p,out,N}\dot{V}_{out,N}}{c_{p,in}\dot{V}_{in,N}} = 1 - \dfrac{c_{p,out,N}\dot{V}_{out,N}}{c_{p,in}\dot{V}_{in,N}} \end{cases} \tag{15.1}$$

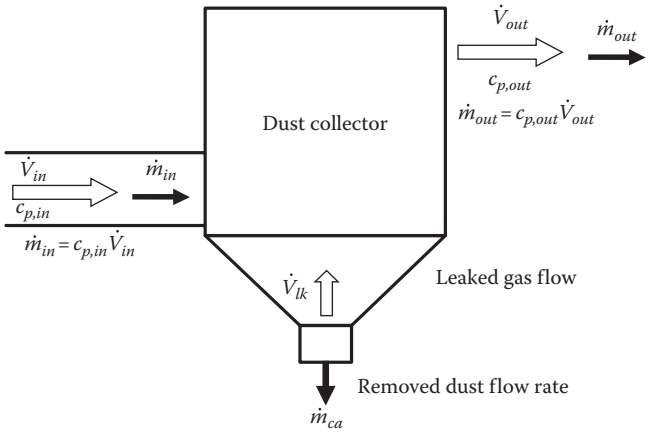


Figure 15.1

Symbols relating the performance of dust collector.

where

$\dot{m}$ is the mass flow rate of dust (kg/s)
c_p is the dust concentration (kg/m^3)
$\dot{V}$ is the volume flow rate of the gas (m^3/s)
The subscripts "in" and "out" refer to the inlet and outlet, respectively
N refers to the standard conditions (dry basis, 0°C, 1 atm)

Without gas leakage and temperature change, the efficiency expression becomes

$$\mathfrak{E} = 1 - \frac{c_{p,out}}{c_{p,in}} = 1 - \frac{c_{p,out,N}}{c_{p,in}} \tag{15.2}$$

2. Efficiency evaluation using the dust flow rate in the inlet duct and the amount of dust removed per unit time in the collector, $\dot{m}_{ca}$:

$$\mathfrak{E} = \frac{\dot{m}_{ca}}{\dot{m}_{in}} \tag{15.3}$$

3. Efficiency evaluation using the dust flow rate at the outlet and the amount of dust removed per unit time in the collector:

$$\mathfrak{E} = \frac{\dot{m}_{cat}}{\dot{m}_{ca} + \dot{m}_{out}} \tag{15.4}$$

Although the separation efficiency can be determined by any of the aforementioned methods, Equations 15.1 and 15.2 are the only methods viable in practice.

Dust particles approaching the collector are polydisperse, and their size distribution depends on the source. The separation efficiency of each individual particle depends on its size, because the particle is separated by a separation mechanism that depends on a physical property related to its inertia and operational conditions. Hence, separation efficiency for a given particle size is called "grade efficiency," "partial separation efficiency," or "fractional efficiency." The separation efficiency for a whole particle size range is a sum of the individual grade efficiencies accounting for the particle size distribution. This is called "overall separation efficiency."

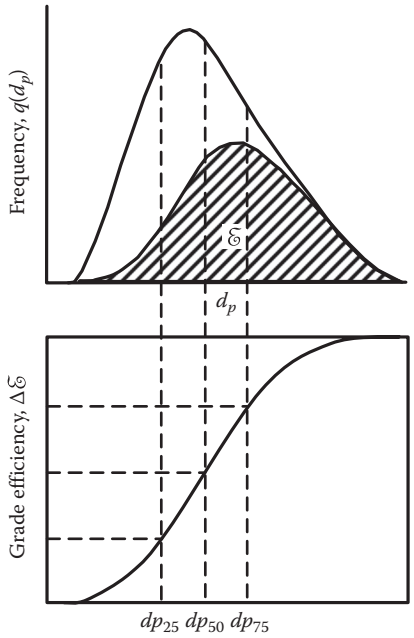


Figure 15.2

Relation between overall separation efficiency and grade efficiency.

The overall separation efficiency $\mathfrak{E}$ is expressed schematically by the hatched area in Figure 15.2 and in terms of grade efficiency $\Delta\mathfrak{E}$ and particle size distribution $q(d_p)$ as

$$\mathfrak{E} = \int_0^{d_p} \Delta\mathfrak{E}\left(d_p\right) q\left(d_p\right) \mathrm{d}d_p \tag{15.5}$$

Since $\Delta\mathfrak{E}(d_p)$ can be calculated for a given dust collector as a function of particle properties and operational conditions, the overall separation efficiency of the dust collector can be estimated without any measurement by knowing the particle size distribution.

The total separation efficiency of dust collectors in series is expressed by

$$\mathfrak{E}_T = 1-(1-\mathfrak{E}_1)\left(1-\mathfrak{E}_2\right)\ldots\left(1-\mathfrak{E}_n\right) \tag{15.6}$$

where

$\mathfrak{E}_T$ is the separation efficiency of the overall system
$\mathfrak{E}_1, \mathfrak{E}_2, \ldots, \mathfrak{E}_n$ are the separation efficiencies of the elemental collectors
n is the number of dust collectors

Hence, when the separation efficiency of each elemental collector is the same, $\mathfrak{E}_T$ is expressed as

$$\mathfrak{E}_T = 1-\left(1-\mathfrak{E}\right)^n \tag{15.7}$$

15.2 Classification of Particle Separation Systems

Chikao Kanaoka

Dust removal equipment can be classified as dry or wet collectors depending on whether the collection medium is liquid or solid. They are also classified according to industrial dust collectors or air filters, depending on inlet dust concentration, which, for industrial collectors, is usually several orders of magnitude higher

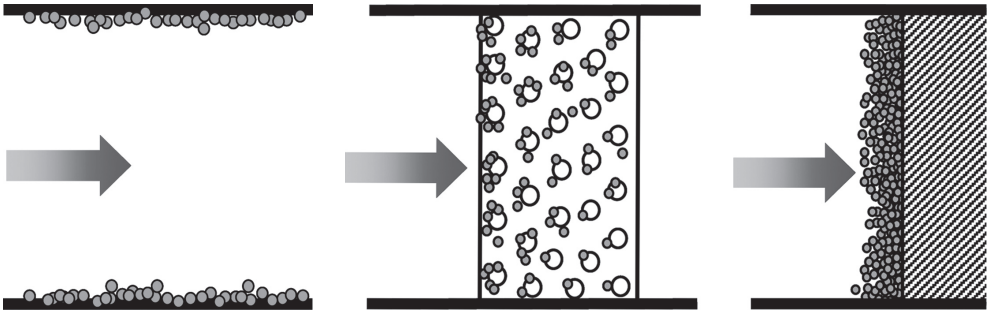


Figure 15.3

Classification of dust collector according to gas flow and collection mechanisms.

than for air filters. When they are classified according to the gas flow and dust collection mechanism, every dust collector belongs to one of the categories shown in Figure 15.3 (Kanaoka et al., 1997):

1. *Flow-through-type dust collectors*: This type of collector utilizes the external force perpendicular to the mean gas flow to remove particles from the flow. Hence, the flow does not change with time and removal performance and pressure drop of the system are always the same. Gravitational dust collector, cyclone, and electrostatic precipitator (ESP) all belong to this collector type.
2. *Obstacle-type dust collectors*: This type of collector captures dust on obstacles inside the equipment. When solid particles are captured by a solid obstacle, the collected particles remain on the obstacle, which results in an increase in both collection performance and flow resistance with time. This also makes the release of captured particles from the obstacles difficult. Therefore, this type of dust collector is normally used as a disposable type of collector. Air filter, granular bed filter, louver-type dust collector, and venturi scrubber belong to this collector type.
3. *Barrier-type dust collectors*: This type of collector uses a permeable medium for the gas but not for the dust, so that the dust is captured and accumulated on the surface. To maintain a continuous operation of this type of dust collector, the accumulated dust has to be removed when the pressure drop becomes too high. Bag and ceramic filters are the typical dust collectors of this type.

Table 15.1 summarizes general features of dust collectors. Compared with the other collectors, the bag filter shows the highest collection performance, but the collector size has to be large, as its lowest filtration

Table 15.1 General Features of Dust Collectors

Type	Removable Particle Size (μm)	Pressure Drop (Pa)	Maximum Temperature (°C)	Inlet Concentration (g/m³)	Initial Capital Cost	Remarks
Flow-through type						
Gravitational collector	>20	50–150	1000	50>	Low	Predust collector
Cyclone	>1	2,000>	1000	500>	Middle	Convenient
ESP	>0.02	300>	400	20>	Highest	Not for explosive material
Obstacle type						
Scrubber	>0.2	10,000>	1000	100>	Middle	Requires waste water treatment
Air filter	>0.01	500>	100	0.01>	Low	For building and house
Air cleaner	>1	1,000>	50	1>	Low	Engine and compressor
Granular bed	>1	10,000>	1000	50>	High	Good for hot gas cleaning
Barrier type						
Bag filter	>0.01	2,000>	250	20>	High	Not good for condensable material
Ceramic filter	>0.01	50,000>	1000	50>	Highest	Good for hot gas cleaning

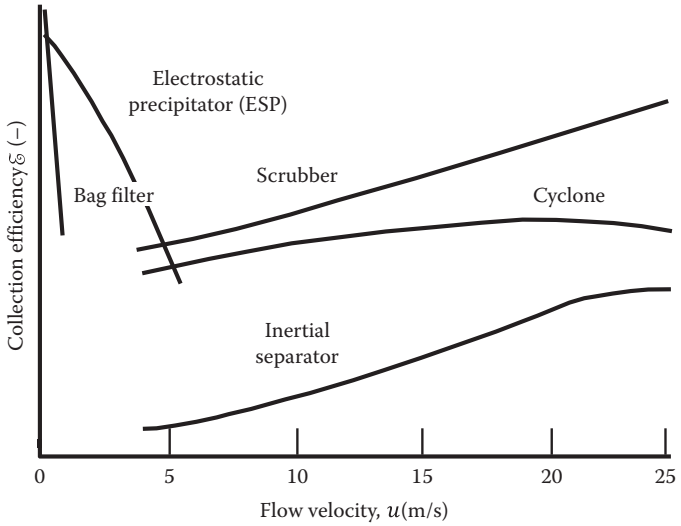


Figure 15.4

A rough sketch of separation performance for various dust collectors.

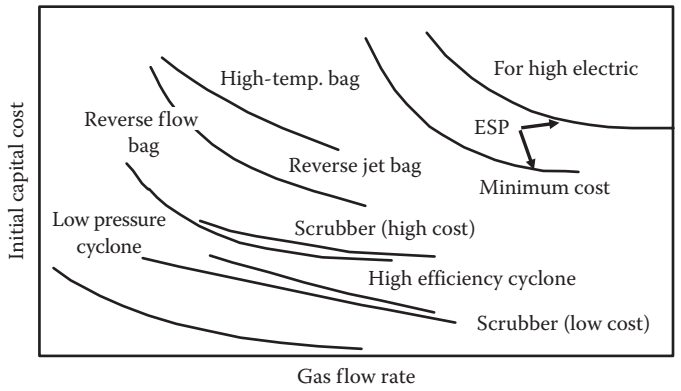


Figure 15.5

Relationship between initial capital cost and dust collector type.

velocity is of the order of 1 m/min. Furthermore, its highest operating temperature is limited to 250°C because of the poor thermal durability of the filter material.

The ESP can treat gases as high as 1 m/s with a very low pressure drop. However, its collection performance depends on the electrical properties of dust particles. Figures 15.4 and 15.5 show the collection efficiency of dust collectors in relation to gas velocity and the initial capital cost of the equipment as a function of the handling gas flow rate. The total annual cost to operate a dust collector is usually the lowest at a gas velocity that differs from the velocity for best performance. Hence, one has to have criteria for the selection of dust collectors.

15.3 Flow-Through-Type Separators

Chikao Kanaoka

This type of collector utilizes the external force perpendicular to the mean gas flow to remove particles from the flow. The flow does not vary with time. Hence, the collection performance and pressure drop of the system are also essentially constant with time.

15.3.1 Separation Efficiency

15.3.1.1 Separation for Laminar Flow

When dust particles collect into a rectangular-shaped dust collector with height H, width W, and length L, as shown in Figure 15.6, the separation efficiency of the collector can be obtained as follows. For simplicity, the gas flow is assumed as laminar and the only force acting on particles is in the direction perpendicular to the gas main flow. Then the particle motion in the collector can be expressed by

$$v_x = \frac{\mathrm{d}x}{\mathrm{d}t} = u(y) \tag{15.8}$$

$$v_y = \frac{\mathrm{d}y}{\mathrm{d}t} = -v_{mig} \tag{15.9}$$

where

v_x and v_y are the particle component velocities in the x and y directions
$u(y)$ is the gas velocity in the flow direction
v_{mig} is the migration velocity of the particle determined from the force balance between the applied external force and fluid drag force

The migration velocities due to different external forces are summarized in Table 15.2.

The particle trajectory can be obtained by integrating

$$v_{mig}\,\mathrm{d}x = -u(y)\mathrm{d}y \tag{15.10}$$

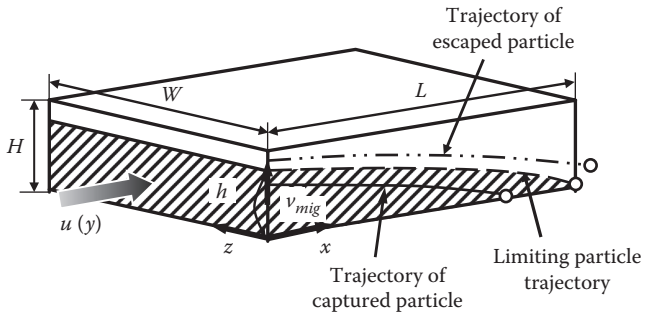


Figure 15.6

Concept of flow-through-type dust collector.

Table 15.2 Migration Velocity by External Force

External Force		Migration Velocity v_{mig}
Gravitational	$\frac{\pi}{6}(\rho_p - \rho_f)d_p{}^3 g$	$\frac{Cc(\rho_p - \rho_f)d_p^2 g}{18\mu}$
Centrifugal	$\frac{\pi}{6}(\rho_p - \rho_f)d_p^3 \frac{u_\theta^2}{r}$	$\frac{Cc(\rho_p - \rho_f)d_p^2}{18\mu}\frac{u_\theta^2}{r}$
Electrostatics	neE	$\frac{CcneE}{3\pi\mu d_p}$

with the initial condition at $y = h$, $x = 0$. Three typical trajectories are illustrated in Figure 15.6. The shapes of these trajectories are the same, but each trajectory shifts horizontally, depending on the inlet height. The lowest trajectory that intersects the bottom plate and the intermediate one reaches at the exit of the collector, while the highest trajectory passes through the collector. In other words, those particles that impact the collector plate and lie below the intermediate trajectory are collected, but those particles higher than the intermediate trajectory are not collected. Hence, the intermediate trajectory is regarded as the "limiting particle trajectory" and the separation efficiency of this dust collector is defined as the ratio of particle flow rate below the limiting particle trajectory (hatched area in the Figure 15.6) to the total particle flow rate entering the collector:

$$\mathfrak{E} = \frac{c_p W \int_h^0 u(y)\mathrm{d}y}{c_p W \int_H^0 u(y)\mathrm{d}y} = \frac{W \int_0^L -v_{mig}\,\mathrm{d}x}{-\dot{V}} = \frac{WLv_{mig}}{\dot{V}} = \frac{A_c v_{mig}}{\dot{V}} \tag{15.11}$$

where

$\dot{V}$ is the flow rate of treated gas

$A_c = WL$ is the area where particles deposit, namely, the total collection area of the collector

Equation 15.11 has been derived based on the assumption that the flow is laminar (without turbulent mixing). Therefore, it is applicable for any flow through the dust collector so long as the flow is laminar.

15.3.1.2 Separation for Turbulent Flow

The situation becomes different when flow inside the collector is turbulent, and it is very difficult to obtain an analytical expression except for the following two extreme cases: (1) complete mixing across the cross section of the collector, that is, uniform concentration throughout the cross section and (2) complete mixing in the whole collector, that is, uniform concentration everywhere in the collector.

For the first case, the concentration change along the mean flow direction can be obtained from the mass balance as follows:

$$c_p uWH - (c_p - \Delta c_p)uWH = c_p v_{mig} W\,\mathrm{d}x \tag{15.12}$$

$$\mathfrak{E} = 1 - \frac{c_{p,out}}{c_{p,in}} = 1 - \exp\left(-\frac{A_c v_{mig}}{\dot{V}}\right) \tag{15.13}$$

In the second case, the particle concentration in the equipment and outlet is the same and the separation efficiency becomes

$$\mathfrak{E} = 1 - \frac{1}{1 + A_c v_{mig}/\dot{V}} = \frac{A_c v_{mig}/\dot{V}}{1 + A_c v_{mig}/\dot{V}} \tag{15.14}$$

The calculated separation efficiency for each case is shown in Figure 15.7. As seen from the figure, the separation efficiency increases with $A_c v_{mig}/\dot{V}$ for any flow condition, but it is the highest for laminar flow. In other words, the presence of turbulence decreases the collection efficiency. Any actual flow is between these two extreme cases, and thus, separation efficiency of each dust collector can be approximated by knowing the turbulent intensity and $A_c v_{mig}/\dot{V}$.

From Figure 15.7, the separation efficiency $\mathfrak{E}$ becomes higher when v_{mig} and A_c become larger and $\dot{V}$ smaller. In practice, the flow rate is usually given so as to enhance the separation efficiency; either v_{mig} has to be increased or A_c made larger, that is, increasing the size of the dust collector.

Furthermore, it is remarkable that Equations 15.11, 15.13, and 15.14 were derived without any restrictions, other than types of gas flow, that is, laminar and turbulent. This suggests that they are applicable for all flow-through-type dust collectors such as gravity, centrifugal force, electrostatic force, and so on. Equation 15.13 is sometimes called the "Deutsch equation" for ESPs.

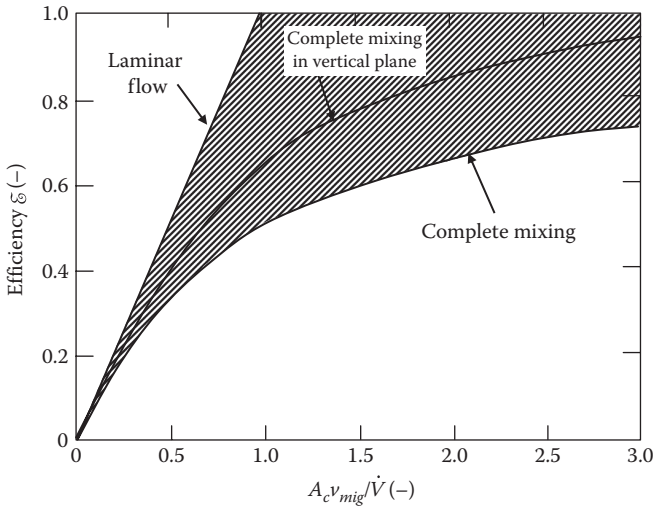


Figure 15.7

Separation efficiency of a flow-through-type dust collector at different flow conditions.

15.4 Gravitational Collectors

Chikao Kanaoka

The gravitational dust collector is the most typical flow-through-type dust collector and separates particles by the difference in the gravitational settling velocity between particles. Figure 15.8 shows some typical dust collectors. Figure 15.8a is the box-type settling chamber and Figure 15.8b is the multiplate-type collector. As indicated earlier, the separation efficiency increases as $A_c v_{mig}/\dot{V}$ becomes large. In the multiplate-type collector, several horizontal trays are installed to shorten the vertical migration distance to separate the particles and thus increase the separation area in keeping with increasing $A_c v_{mig}/\dot{V}$. In both the cases, to improve the gravitational effect, the cross-sectional area of the collector is enlarged to operate at a low gas velocity. Gas velocity in this type of collector is usually 1 m/s, and thus the pressure drop is low (of the order of 100–1000 Pa). However, discharging the separated particles and cleaning the equipment are difficult tasks to perform in practice.

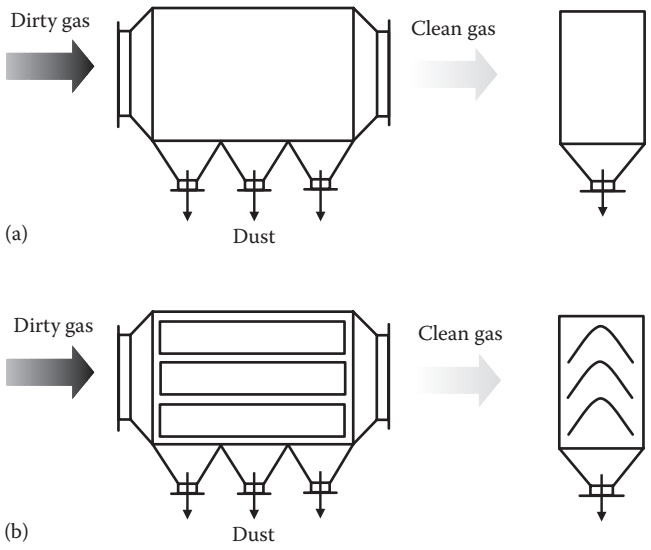


Figure 15.8

Typical gravity dust collector. (a) Gravity settling chamber, (b) multistage settling chamber.

15.5 Centrifugal Separation: Dry Cyclones

Hideto Yoshida and Kunihiro Fukui

Cyclones are widely used for separating powders. Recently, excellent performance with cut size below 0.5 μm has been obtained by Iinoya et al. (1990, 1992, 1993). The optimization of the cyclone dimensions in each part is, however, mainly determined by experiment, because the analyses of fluid flow and particle motions are very complicated. Numerical calculations of fluid flow and particle motions in the cyclone have been conducted by Ayers et al. (1985), Zhou and Soo (1990), Yamamoto et al. (1993), and Yamamoto and Kitamura (1994), but their calculations are conducted by assuming axisymmetrical flow. To model the complicated flow field in the cyclone, it is necessary to do the numerical calculation in three dimensions. Yoshida et al. (1991) have reported such calculations.

Centrifugal acceleration is created either by airflow in cyclone-type classifiers or by the mechanical revolution in air separators. Two types of centrifugal separators are in practical use: the forced vortex type and the free vortex type. For the forced vortex type, a variety of centrifugal classifiers are available. Changing the rotational speed in the separator controls the cut size. On the other hand, the conventional cyclone falls into the free vortex type. Changing the inlet velocity can control the cut size. Compared to the forced vortex type, the range of cut size variation in the conventional free-vortex-type cyclone is small. However, Yoshida et al. (1993) have shown that it is possible to change the cut size over a wide range by using special designs of the conventional cyclone separator.

In this section, recent results using a three-dimensional simulation for the performance of a dry cyclone are presented. The predicted fluid flow pattern and particle trajectories in the cyclone are compared with experimental results. The effects of using blow-down and an apex cone on particle collection efficiency are also shown. Recent results for submicron classification using an improved-type cyclone are also presented.

15.5.1 Classification Theory of Cyclones

Cyclones are widely used in industrial applications. If N is the number of revolutions required for the particle to reach the wall, the particle residence time is

$$\tau_{res,r} = \frac{2\pi RN}{u_{in}} \tag{15.15}$$

In Figure 15.9, R is the cyclone radius and u_{in} is inlet fluid velocity. The radial velocity of the particle toward the wall is represented by

$$v_{rad} = \tau \frac{u_{in}^2}{R} \tag{15.16}$$

The value of τ, the particle velocity response time, defined by

$$\tau = \frac{\left(\rho_p - \rho_f\right) d_p^2}{18\mu} \tag{15.17}$$

is used in the calculation. Assuming that those particles initially at a distance of x from the wall are collected, the time it takes for the particle to reach the wall is

$$\tau_{res,x} = \frac{x}{v_{rad}} = \frac{xR}{\tau u_{in}^2} \tag{15.18}$$

By using Equations 15.15 and 15.18, one has

$$\frac{xR}{\tau u_{in}^2} = \frac{2\pi RN}{u_{in}} \tag{15.19}$$

$$\tau = \frac{x}{2\pi N u_{in}} \tag{15.20}$$

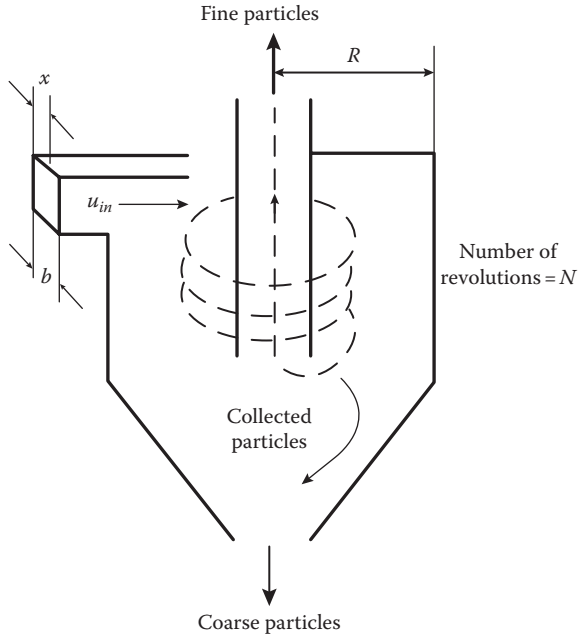


Figure 15.9

Simplified model of cyclone separator.

If the inlet width of the cyclone is b, the fractional separation efficiency is given by

$$\Delta\mathfrak{S} = \frac{x}{b} = \frac{2\pi u_{in}\left(\rho_p - \rho_f\right)d_p^2}{18\mu b} \tag{15.21}$$

Then, the cut size, which is the particle size corresponding to $\Delta\mathfrak{S} = 0.5$, is

$$d_{p,cut} = \sqrt{\frac{9\mu b}{2\pi N u_{in}\left(\rho_p - \rho_f\right)}} \tag{15.22}$$

The value of N can vary from 3 to 8, depending on the cyclone configuration.

Leith and Licht (1972) proposed estimating cut size by using the various dimensions of cyclone separator. A more detailed information regarding cyclone performance is obtained from recent results of numerical simulation.

15.5.2 Numerical Calculations

A 3D numerical simulation of the cyclone separator has been performed by Yoshida et al. (1993, 1994). The flow fields were modeled and particle trajectories calculated according to the methods described in Chapter 2. Two approaches were used in the numerical simulation: In the direct-method approach, a constant (eddy) viscosity was assumed and different values were tried as reflected by using three Reynolds numbers: 3,000, 5,000, and 10,000. The Reynolds numbers are based on the inlet velocity and diameter of the cyclone. The second approach was to use the $\kappa - \varepsilon$ turbulence model.

The component of the fluid velocity in the $r - z$ plane at different circumferential angles is shown in Figure 15.10. The definition of the circumferential angle θ is defined in Figure 15.10. In this figure, the flow Reynolds number in the cyclone is 5000. It is found that the flow field depends on the circumferential angle and the assumption of axial symmetry of the flow in the cyclone is not always correct. For example, the velocity vectors just below the exit tube point toward the central axis in the case of $\theta = 3.8°$, but point in the opposite direction in the case of $\theta = 183.8°$. The downward velocity components near the conical wall (region A) are large and the down-flow (region A) and up-flow (region B) are in close proximity near the entrance of the dust box. It might be thought that a small particle located near the cyclone wall moves downward, but close to the entrance to the dust box, and the particle may be entrained in the up-flow velocity and go out to the exit tube. The calculations also show upward velocity components in the upper part of the dust box.

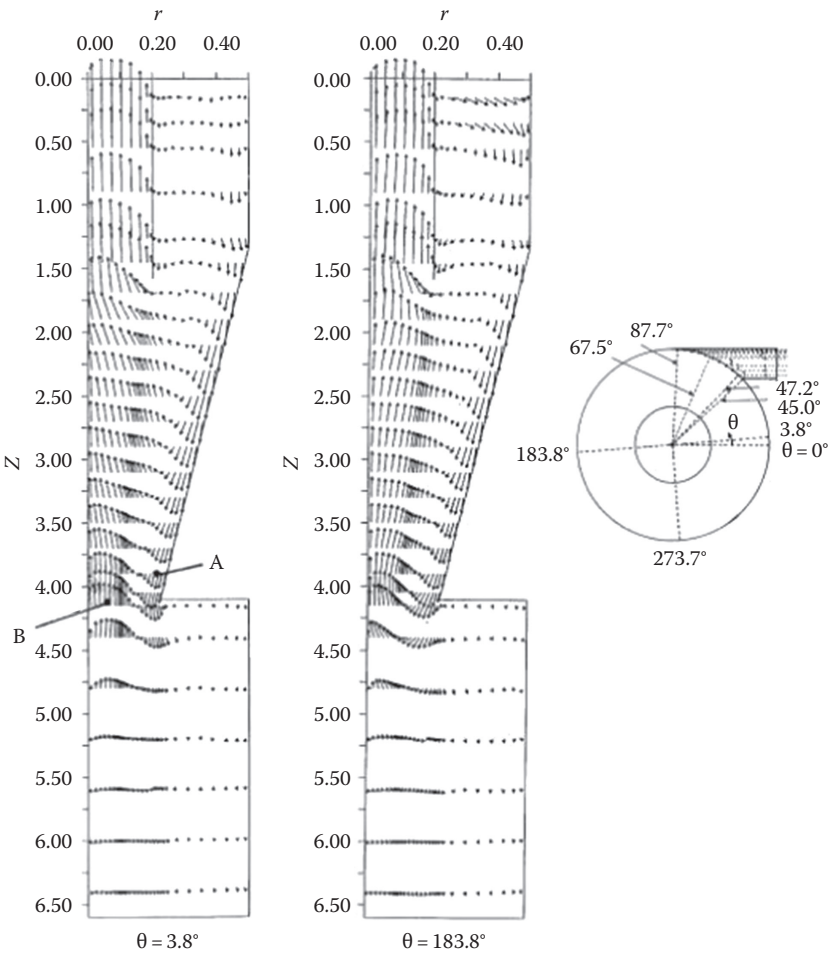


Figure 15.10

Fluid velocity distribution in the *r–z* plane at two circumferential angle (*Re* = 5000).

The predicted particle trajectories for different particle diameters projected on a plane are shown in Figure 15.11. It was assumed that the particles are collected when they contact the wall surface. The large particles (d_p = 2.4 μm) are collected on the conical wall, but some smaller particles (d_p = 2.0 μm) enter into the dust box and then move out of the cyclone because of the upward axial velocity component. If the particles are much smaller (d_p = 0.8 μm), they do not enter the dust box, but move around the vortex finder and exit the cyclone.

The experimental data for partial separation efficiency obtained by Iinoya and Nakai (1969) are shown in Figure 15.12.

The Stokes number *St* is defined in this case as

$$St = \frac{Cc\rho_p d_p^2 u_{in}}{9\mu D} \tag{15.23}$$

where

Cc is Cunningham's slip correction factor
D is the cyclone diameter
u_{in} is the inlet velocity

The test particles were latex, Kanto loam (d_p = 1.8 μm), and stearic acid. The experimental results are compared with the numerical calculations. The solid line indicates calculated results of the direct method and the dotted line is the result when turbulence is included (κ − ε model). The experimental flow Reynolds number is higher than 40,000. The experimental data agree well with the predicted results when the turbulence model is used.

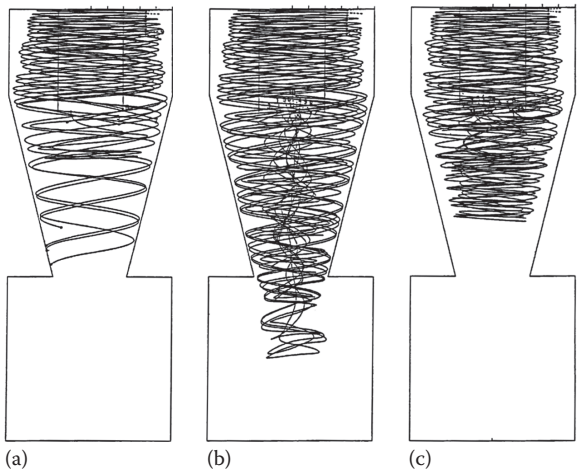


Figure 15.11

Particle trajectories in a cyclone: (a) d_p = 2.4 μm, (b) d_p = 2.0 μm, (c) d_p = 0.8 μm.

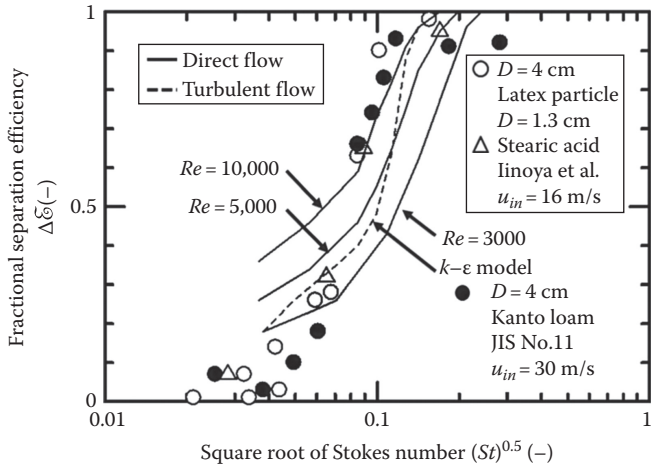


Figure 15.12

Fractional separation efficiency data compared with calculated results.

15.5.3 Effect of Blow-Down

Numerical and experimental studies of fractional separation efficiency under blow-down conditions were carried out by Yoshida et al. (1995). With the blow-down method, a portion of fluid is discharged from the dust box. With the blow-up method, particle-free fluid is introduced into the dust box. The blow-down and blow-up ratios are defined as follows:

$$B_d = \frac{\dot{V}_d}{\dot{V}_{in}} \quad B_u = \frac{\dot{V}_u}{\dot{V}_{in}} \tag{15.24}$$

where

$\dot{V}_{in}$ is the inlet flow rate
$\dot{V}_d$ is the discharge from the dust box
$\dot{V}_u$ is the additional-flow rate into the dust box

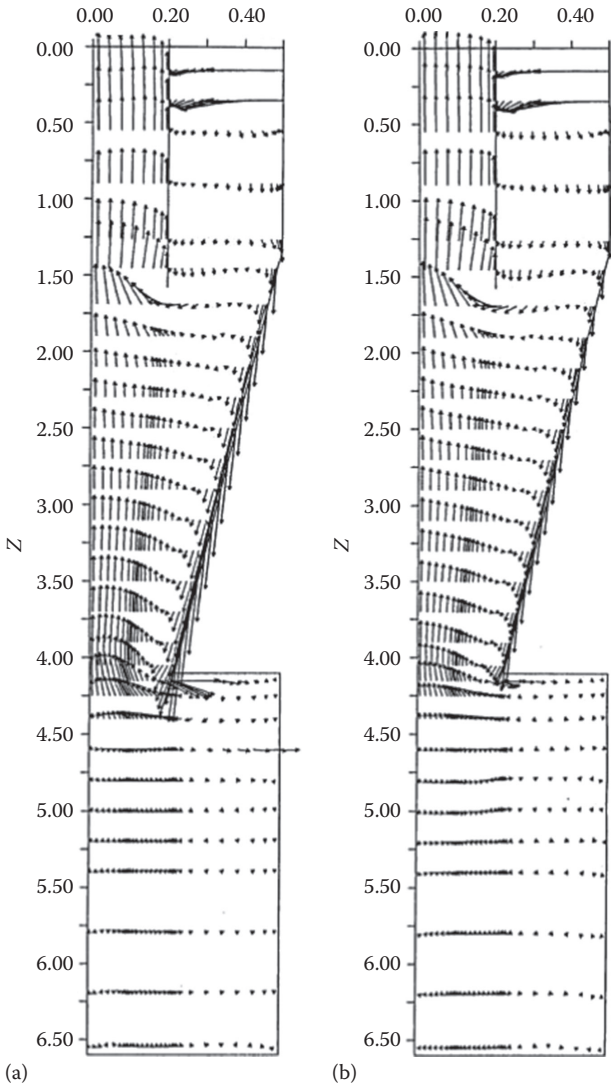


Figure 15.13

Fluid velocity distributions (a) with and (b) without blow-down.

Fluid velocity vectors with and without blow-down are shown in Figure 15.13. The $\kappa - \varepsilon$ turbulence model was used in numerical calculations. The blow-down flow is located at the upper part of the dust box. In this case, the blow-down ratio is 10%. In the case of blow-down, the downward velocity components near the conical wall are larger than without blow-down. With blow-down, small particles collected on the cyclone wall move downward near the conical wall and the particles are more likely to enter the dust box.

The effects of the circumferential angle of the particle starting position on predicted particle trajectories are shown in Figures 15.14 and 15.15. The particle diameter was 0.8 μm, and the three initial circumferential angles were 47°, 65°, and 88°. These circumferential angles correspond to different starting positions for the particles in the inlet duct, as shown in Figure 15.10. The results for blow-down and no blow-down are shown in Figures 15.14 and 15.15, respectively. With blow-down, some of the particles are collected near the blow-down hole in the dust box. On the other hand, nearly no particles are collected without blow-down.

The correlation between fractional separation efficiency and the square root of half value of Stokes number for both blow-down and no blow-down case is shown in Figure 15.16, where it is also observed that the experimental data agree well with the numerical predictions. It is found that the partial separation efficiency with blow-down approaches the value of blow-down ratio as the Stokes number decreases. Iinoya et al. (1993) found that submicron classification is possible by the use of a specially designed cyclone.

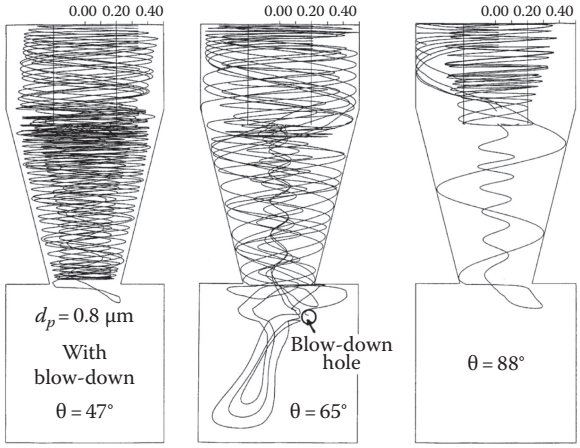


Figure 15.14

Particle trajectories for different initial circumferential angle (with blow-down).

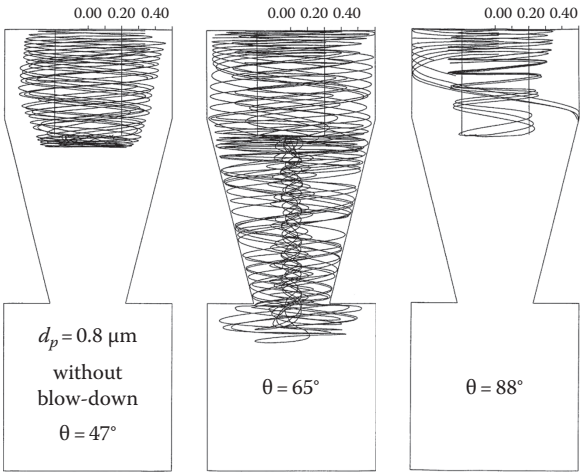


Figure 15.15

Particle trajectories for different initial circumferential angle (without blow-down).

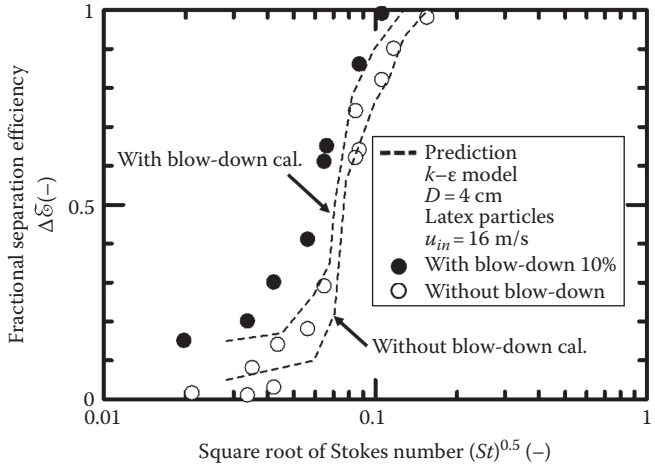


Figure 15.16

Fractional separation efficiency with and without blow-down.

15.5.4 Cut Size Control by Use of a Free-Vortex-Type Classifier

The use of a movable circular slide plate, shown in Figure 15.17, is effective in controlling the cut size in a gas cyclone. Data for classification performance obtained by Yoshida et al. (1993, 1994) are shown in Figure 15.18. Using a movable slide plate and employing the blow-down method, the cut size changes to small size region. Both methods are effective in decreasing the cut size. The effect of an apex cone located at the upper part of the dust box is expected to decrease the cut size and to increase the collection efficiency.

The fluid vectors predicted by Yoshida et al. (2001) are shown in Figure 15.19. The two cases with and without an apex cone are examined. Using the apex cone, it is possible to decrease the magnitude of the fluid velocity component in the upper part of the dust box. As a result, it is possible to reduce re-entrainment of particles from the dust box to the vortex finder.

The predicted particle trajectories with and without the apex cone are shown in Figure 15.20. Particle re-entrainment is not observed with the apex cone. The cut size of cyclones with an apex cone is smaller than that without an apex cone, as demonstrated in Figure 15.21. By using the apex cone, it is possible to move the cut size into fine particle size region.

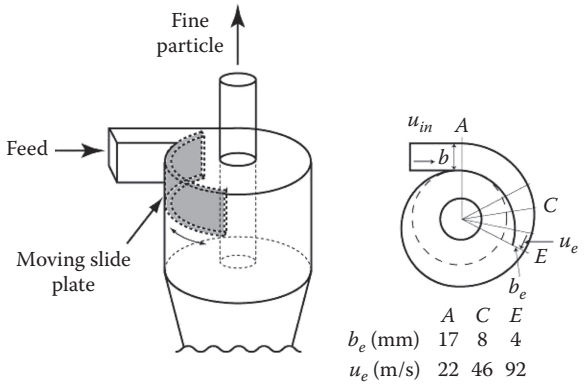


Figure 15.17

Cyclone with movable inlet guide plate.

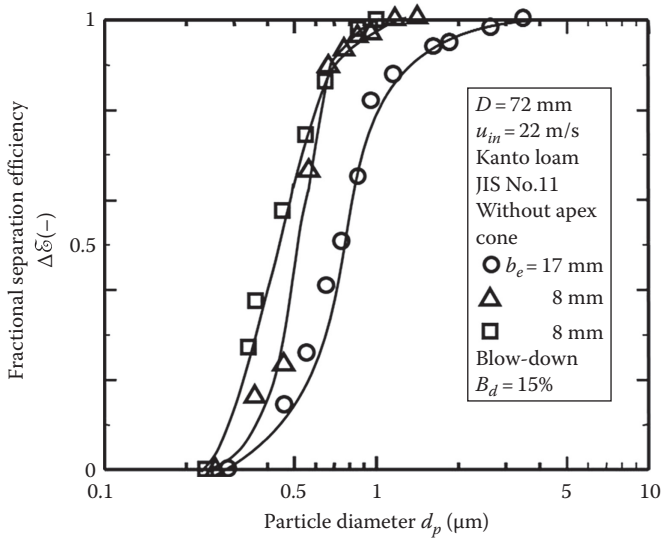


Figure 15.18

Effect of inlet guide plate and blow-down on fractional separation efficiency.

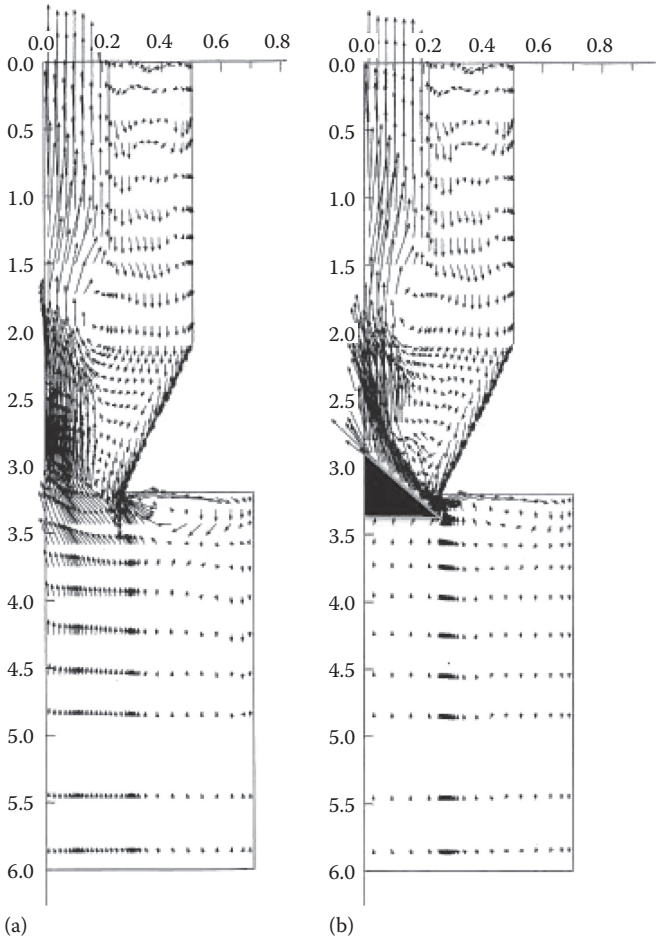


Figure 15.19

Calculated fluid velocity vectors (a) with and (b) without apex cone.

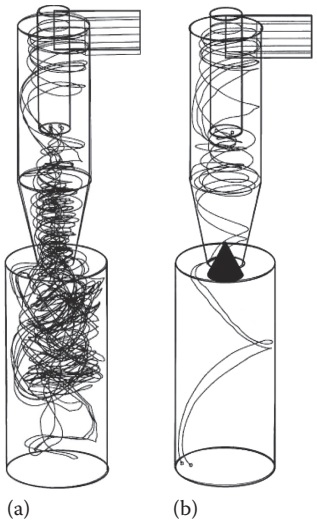


Figure 15.20

Particle trajectories for the two cyclones (d_p = 1.2 μm): (a) Without apex cone and (b) with apex cone.

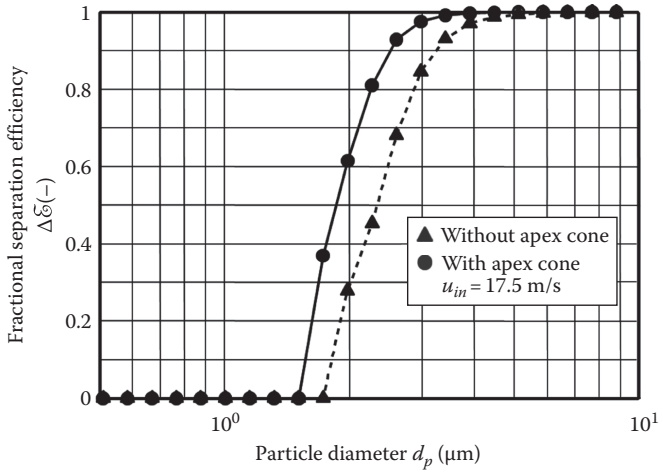


Figure 15.21

Fractional separation efficiency with and without apex cone.

15.5.5 Estimation Method of Pressure Drop and Classification Performance

Many studies have been devoted to the optimization of the overall cyclone design and that of individual components, and as a result, cut sizes have reached the submicron order with improved separation accuracy (Fukui et al., 2011). Figure 15.22 shows the typical flow inlet systems and dimensional ratios of cyclone separators. The cyclone separator can be divided into three types roughly, according to the systems needed to insert the flow into the cyclone. They are the tangential inlet, the scroll inlet, and the axial flow inlet configurations.

The pressure drop of the cyclone mainly consists of three losses: pressure losses at the inlet part, fluid friction losses caused by the vortex flow in the cyclone, and pressure losses at the vortex finder. In many cases, the last term affects the pressure drop most strongly. The pressure drop of the cyclone is usually approximately proportional to the square of the inlet velocity u_{in}. The pressure drop of the cyclone when the dust is not loaded, ΔP_0, can be calculated by the following equation:

$$\Delta P_0 = Eu\frac{\rho_f u_{in}^2}{2} \tag{15.25}$$

Here, the variable Eu, which is called Euler number, can be determined predominantly by the cyclone geometry. It was reported that the variable Eu can be given as follows (Shepherd and Lapple, 1939):

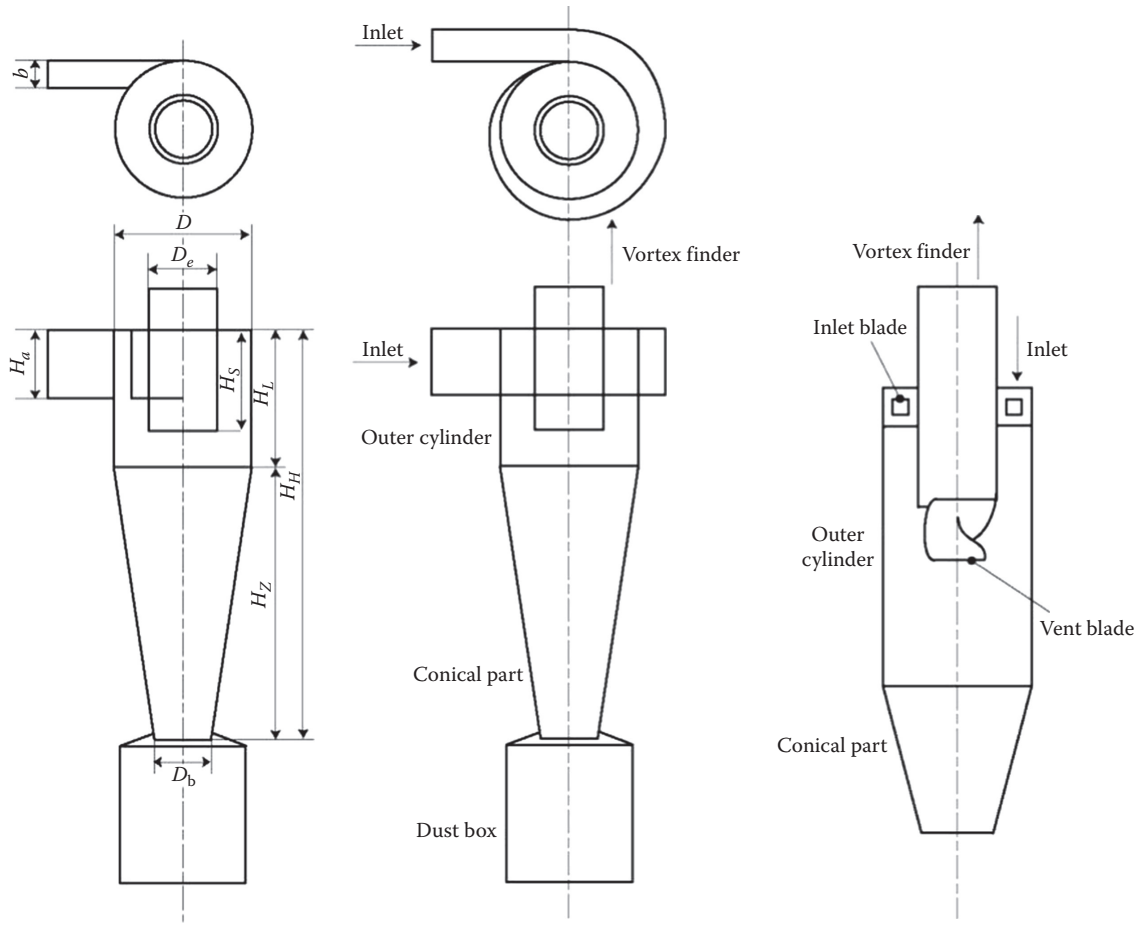
$$Eu = 16\left(\frac{K_a K_b}{K_e^2}\right) \tag{15.26}$$

$$Eu = 11.3\left(\frac{K_a K_b}{K_e^2}\right)^2 + 3.33 \tag{15.27}$$

where K_a, K_b, and K_e are ratios of length to the cyclone diameter D, defined in Figure 15.22, respectively. These equations suggest that the pressure drop depends little on the cyclone size and also on the dimensional ratios.

It is well known that the cyclone pressure drop decreases with increasing concentration of the loaded powder. The following equation was proposed as the empirical formula, which gives the cyclone pressure drop ΔP when the concentration of loaded powder is equal to c_p (Briggs, 1946):

$$\Delta P = \Delta P_0\left(1 - 0.0086\sqrt{c_p}\right) \tag{15.28}$$



	$K_a = H_a/D$	$K_b = b/D$	$K_s = H_S/D$	$K_e = D_e/D$	$K_L = H_L/D$	$K_H = H_H/D$	$K_B = D_b/D$
Yoshida (a)	0.60	0.20	0.85	0.50	1.0	5.0	0.40
Yoshida (b)	0.50	0.24	1.39	0.44	2.08	9.72	0.50
Stairmand	0.50	0.20	0.50	0.50	1.5	4.0	0.38
Lapple	0.50	0.25	0.63	0.50	2.0	4.0	0.25
Barth	0.53	0.13	0.73	0.33	0.69	2.58	0.33

Figure 15.22

Typical inlet systems and configurations for cyclone separator. (a) Tangential inlet, (b) scroll inlet, (c) axial inlet.

Since the actual airflow in the cyclone contains the complicated secondary flow, the turbulent fluctuation, the instability aspect of the vortexes, and so on, it is very difficult to estimate the particle motion and the classification performance of the cyclone exactly. However, many models, which evaluate the classification performance, have been proposed based on the simplified and idealized velocities and forces acting on the particle. Some estimation formulae can successfully give the accurate cut size and fractional separation efficiency.

Most popular formulae for 50% cut size calculation are listed in Table 15.3. Lapple's model (Lapple, 1950) correlates the number of revolutions N with the cyclone configurations in Equation 15.22. On the other hand, regarding Barth's model (Barth, 1956), 50% cut size is calculated by two specified tangential velocities u_{ti} and u_{tw} defined by him. Iozia's model (Iozia and Leith, 1989) also uses the specified maximum tangential velocity $u_{t\max}$.

Table 15.3 Estimation Equations for the 50% Cut Size of Cyclone Separator

Lapple's model	$d_{p,50} = \sqrt{\dfrac{9\mu b}{2\pi N C_c u_{in}(\rho_p - \rho_f)}}$, $N = \dfrac{H_L + (H_H - H_L)/2}{H_a}$
Barth's model	$d_{p,50} = \sqrt{\dfrac{9\mu u_{ti} D_e}{C_c u_{tw}^{\ 2}(\rho_p - \rho_f)}}$
Iozia's model	$d_{p,50} = \dfrac{1}{u_{t,max}} \sqrt{\dfrac{9\mu H_a b u_{in}}{\pi z_c (\rho_p - \rho_f)}}$
	$u_{t,max} = 6.1 u_{in} (K_a K_b)^{0.61} K_e^{-0.74} K_H^{-0.33}$, $d_{cr} = 0.47 D (K_a K_b)^{-0.25} K_e^{1.4}$
	$z_C = H_H - H_S \ (d_{cr} < D_b)$
	$z_C = (H_H - H_S) - \left(\dfrac{H_H - H_S}{K_b - 1}\right)\left(\dfrac{d_{cr}}{D_b} - 1\right) \ (d_{cr} < D_b)$

The fractional separation efficiency $\Delta\mathfrak{E}(d_p)$ of most cyclones can be approximated by the following equation with the 50% cut size $d_{p,50}$ and the slope exponent β:

$$\Delta\mathfrak{E}(d_p) = \frac{1}{1 + (d_{p,50}/d_p)^{\beta}} \tag{15.29}$$

Equation 15.29 is the empirical estimation equation for β reported by Iozia and Leith (1989). The partial separation efficiency curve can be obtained by the 50% cut size calculation in Table 15.3, and Equations 15.29 and 15.30:

$$\ln\beta = -0.62 - 0.87\ln(d_{p,50} \cdot 10^3) + 5.21\ln(K_a K_b) + 1.05\{\ln(K_a K_b)\}^2 \tag{15.30}$$

Further, the formulae for the direct calculation of the fractional separation efficiency have been also proposed, and some of the popular ones are listed in Table 15.4 (Dietz, 1981, Clift et al., 1991).

Figure 15.23 shows the fractional separation efficiency curves estimated by various models for a cyclone separator 72 mm in diameter with the real experimental data. Though the estimated results are not in absolute agreement with the experimental ones, these models can predict them practically with satisfactory accuracy.

As listed in Tables 15.3 and 15.4, the classification performance of the cyclone decreases with the cyclone size. The cut size of the cyclone is usually proportional to the square root of the cyclone size D approximately. In order to collect the particles from large amount of the dust-loaded airflow without reducing the collection efficiency, the multicyclone system where many small size cyclones are contained in parallel is useful. A schematic diagram of the multicyclone is shown in Figure 15.24.

Table 15.4 Formulae for the Partial Separation Efficiency Curve

Clift's model	$\Delta E = 1 - \exp\left[-\dfrac{(\rho_p - \rho_f)}{9\mu}\left(\dfrac{2 d_p u_{in}}{D}\right)^2 t_{res}\right]$
Diez's model	$\Delta E = 1 - \left\{K_0 - \left(K_1^{\ 2} + K_2\right)^{0.5}\right\} \exp\left[-\dfrac{2\pi(2K_S - K_a)}{K_a K_b} St\right]$
	$K_0 = \dfrac{1}{2}\left\{1 + K_2\left(1 + \dfrac{K_a K_b}{\pi K_l St}\right)\right\}$, $K_1 = \dfrac{1}{2}\left\{1 - K_2\left(1 + \dfrac{K_a K_b}{\pi K_l St}\right)\right\}$
	$K_2 = K_e^{\ 2\gamma}$, $K_l = 2.3 D_e (H_a b D)^{-1/3}$
	$\gamma = 1 - (1 - 0.67 D^{0.14})\left(\dfrac{T}{283}\right)^{0.3}$

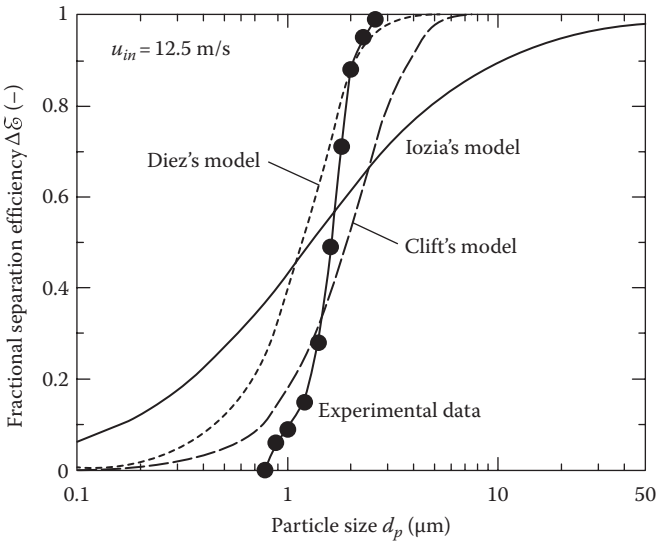


Figure 15.23

Fractional separation efficiency curves estimated by various models.

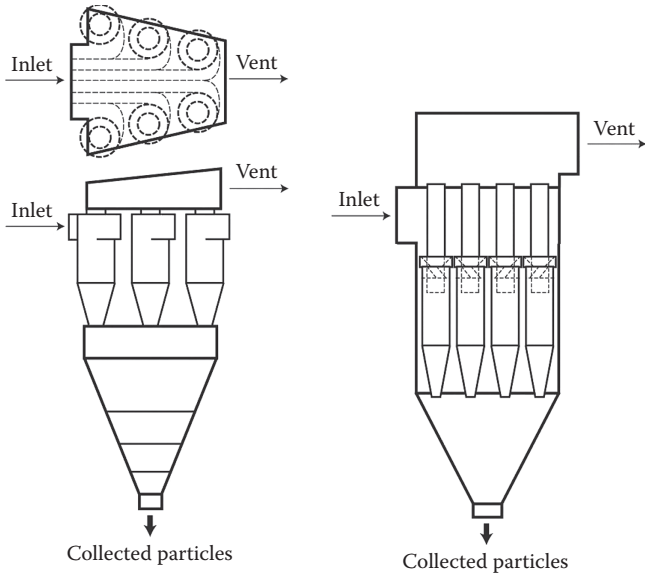


Figure 15.24

Structure of the multicyclone.

15.6 Electrostatic Precipitators

Hisao Makino and Naoki Noda

15.6.1 Principles of Electrostatic Precipitators

The ESP is utilized as a dust collector in large-scale plants, such as thermal power plants, because it has high collection efficiency and is capable of handling large flue gas volume flow rates.

In the EPS, dust particles in the flue gas are charged by a corona current and removed by the electric field. There are two types of ESP: one stage and two stage. In the one-stage ESP, dust charging and separation are performed simultaneously, whereas in the two-stage type, particle charging is performed in the first stage, and collection of the charged particles is performed in the second stage. The one-stage ESP, shown in Figure 15.25, is the most common. This type of ESP with flat-plate collection electrodes is easy

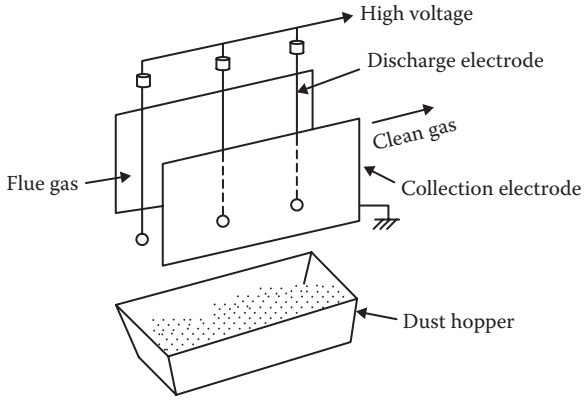


Figure 15.25
Outline of ESP.

to scale up. The wire discharge electrodes are centered between two parallel flat collection electrodes. The pressure drop in the ESP is very low compared to the fabric filter or granular bed. The ESP is suitable for dust collection in large-scale facilities.

A negative high voltage is applied to the discharge electrodes and the collection electrodes are grounded. The negative ions generated by the corona discharge at the electrodes collide with the dust particles in the flue gas to charge the particles. The particles then move toward the collection electrodes by the electric mobility due to the electric field formed between the discharge and collection electrodes. The collected dust particles are released to the hopper under the ESP. The particles adhering to the discharge and collection electrodes are dislodged by tapping the electrodes, which then fall into the hopper.

15.6.1.1 Particle Charging

In the ESP, the dust particles are charged by the ions in the field generated by corona discharge. The amount of charge is determined by particle size, electric field strength, corona current density, and residence time. The mechanisms responsible for particle charging are field and diffusion charging. The particle charge acquired by one of the following two mechanisms may be given by the following expressions:

$$\text{Diffusion:} \quad q_e = \frac{d_p \kappa T}{2e^2} \ln\left(1 + \frac{\pi d_p \overline{G}_i n_i e}{2\kappa T} t\right) \tag{15.31}$$

$$\text{Field:} \quad q_e = \left[1 + \frac{2(\varepsilon_0 - 1)}{\varepsilon_0 + 2}\right] \frac{E d_p^{\,2}}{4e} \cdot \left(\frac{\pi e B_i n_i t}{1 + \pi e B_i n_i t}\right) \tag{15.32}$$

where

$\overline{G}_i$ is the mean thermal mobility of ions (4.5×10^4 cm/s)
n_i is the concentration of ions
ε_0 is the dielectric constant
B_i is the electric mobility of ions (1.4 cm^2/s/V)

The relationship between particle charge and particle size is shown in Figure 15.26. In diffusion charging, the particle charge is not affected by the electric field strength and tends to increase linearly with particle size. In field charging, the particle charge increases with an increase in electric field strength and tends to increase linearly with the square of the particle size. In general, diffusion charging is most effective for fine particles less than 1 μm in diameter, while the field charging is most effective for particles greater than 1 μm.

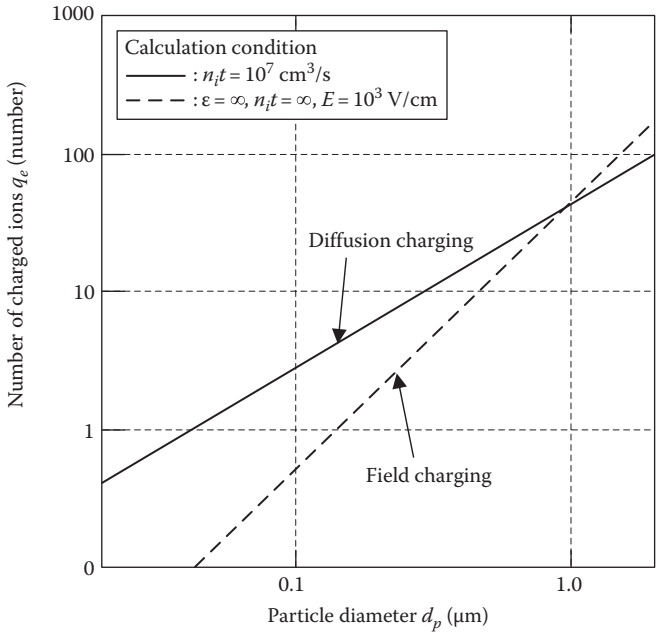


Figure 15.26

Number of charged ions and particle diameter. (From Kanaoka, C. et al., Principle and equipment of dust collectors, *Fundamentals in Aeorsol Science*, Nikkan Kogyo Shinbun, Tokyo, Japan, 1997, pp. 24–99.)

Since it is necessary to charge particles as much as possible in a short period of time, high electric field strength and high current density are required. The charging methods utilized are DC charging, AC charging, and the pulse charging.

1. *DC charging*: The dust particles are charged in a DC electric field. This charging method is the most common. In this method, the ions move in the same direction and the applied voltage is limited to prevent arc discharge, and hence the charging efficiency is reduced for high-resistivity particles.
2. *AC charging*: The dust particles are charged in the AC electric field. The direction of ion movement alternates constantly. In this method, the particles are charged by ion motion from two directions. Thus, it is more effective for the high-resistivity particles than the DC charging method.
3. *Pulse charging*: This type of charging adds the high-voltage pulse to the DC charging type. However, in this type, the DC charging voltage is applied at lower voltage than in the usual simple DC charging method in order to control arc discharge. The maximum voltage in the pulse charging can be higher than in the usual DC charging method, and the voltage increases with a decrease in the pulse period. Using this method, a high and uniform ion density can be achieved, with no restriction on the shape of the discharge electrode or dust adhesion to the electrode. It is suitable for high-resistivity particles.

The most effective charging method depends on the resistivity of dust particles. The electric mobility in the DC charging method is higher than that in pulse charging for particles with electric resistivity less than $10^9\ \Omega \cdot \mathrm{m}$, while the reverse trend is observed for the high-resistivity dust particles.

15.6.1.2 Electric Mobility of Particles

Under the condition of a uniform electric field in the ESP, the electric mobility (velocity) of charged particles toward the collection electrode is expressed by the following equation (Michaelides, 2006):

$$v_e = \frac{Ccq_eE}{3\pi\mu d_p} \tag{15.33}$$

where
q_e is the particle charge
E is the electric field strength
Cc is the Cunningham correction factor (see Section 1.3)

A suitable expression for the later was obtained by Kanaoka et al. (1997), which is derived from the equation given by Takahashi (1978):

$$Cc = 1 + \left\{1.25 + 0.42\exp\left(-\frac{0.435 d_p}{\lambda_m}\right)\right\}\frac{2\lambda_m}{d_p} \tag{15.34}$$

where
d_p is the particle diameter
λ_m is the mean free path of the gas molecules which, in turn, is given by

$$\lambda_m = 0.709\nu_e\left(\frac{\pi\mathfrak{M}}{\mathfrak{R}_u T}\right)^{1/2} \tag{15.35}$$

where
$\mathfrak{M}$ is the molecular mass
ν_e is the kinematic viscosity
T is the gas temperature
$\mathfrak{R}_u$ is the gas constant

Several expressions for Cc, which are suitable for a wide range of particle sizes, may be found in Michaelides (2014).

15.6.1.3 Collection Efficiency

The collection efficiency of ESP is generally expressed by the following equation, called the Deutsch equation:

$$\mathfrak{E} = 1 - \exp\left(-\frac{A_c \nu_e}{\dot{V}}\right) \tag{15.36}$$

where
A_c is the area of the collection electrodes, which is the product of the length and height of the collection electrode
ν_e is the mobility of charged particles
$\dot{V}$ is the volume rate of flue gas

This equation is developed on the basis of assumptions of uniform electric field, monodisperse particle size, and a locally uniform dust concentration. However, in an actual ESP, the situation is quite different and therefore, this equation is useful only as an estimate of the tendency of collection efficiency.

The overall collection efficiency of a practical ESP is approximately 99%, and the fractional collection efficiency, $\Delta\mathfrak{E}$, which is the collection efficiency for the respective particle size, has a minimum value in the range of particle size of 0.1–1.0 μm, as shown in Figure 15.27. In this figure, p represents the penetration efficiency using

$$p = 1 - \Delta\mathfrak{E} \tag{15.37}$$

The reason for the minimum fractional collection efficiency can be explained as follows: According to Equation 15.34, the Cunningham correction factor increases with a decrease in particle size, but the charge

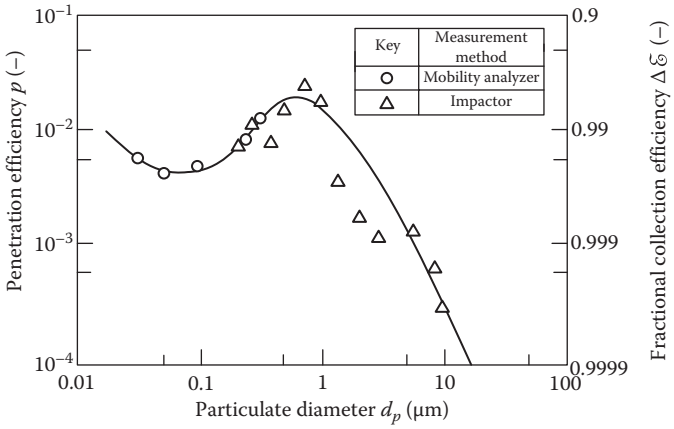


Figure 15.27

Fractional collection efficiency of ESP.

on the particle q increases with an increase in particle size, as shown in Figure 15.26. For particles less than 1 μm, the particle charge accumulation varies linearly with the particle size, but for particles greater than 1 μm, the charge increases with the square of the particle size. Therefore, the fractional collection efficiency shows a minimum value at the particle size in the range of 0.1–1.0 μm.

15.6.2 Characteristics of Electrostatic Precipitators

15.6.2.1 Effect of Collection Conditions

15.6.2.1.1 Influence of Dust Resistivity As the dust particles accumulate at the collection electrodes, they discharge electrons. The performance parameters of the ESP, such as collection efficiency, applied voltage, and corona current, depend on the dust resistivity, ρ_d, as shown in Figure 15.28. In the regions of $\rho_d < 10^2$ $\Omega \cdot$m, and $\rho_d > 5 \times 10^8$ $\Omega \cdot$m, the collection efficiency is low. On the other hand, in the region of 10^2 $\Omega \cdot$m $< \rho_d < 10^8$ $\Omega \cdot$m, the collection efficiency is high. This tendency is explained as follows:

In the case of $\rho_d < 10^2$ $\Omega \cdot$m, when the dust particles accumulate at the collection electrodes, they discharge the electrons immediately and are charged to the same electrostatic potential by the electrostatic conductor. Then the dust particles are re-entrained in the direction of the discharge electrode, and the collection efficiency is decreased. In the case of $\rho_d > 5 \times 10^8$ $\Omega \cdot$m, it is difficult for dust particles to discharge on

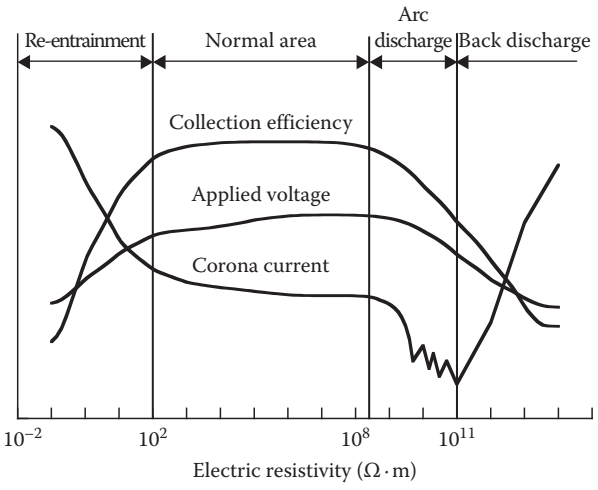


Figure 15.28

Collection characteristics and electric resistivity. (From Kanaoka, C. et al., Principle and equipment of dust collectors, *Fundamentals in Aeorsol Science*, Nikkan Kogyo Shinbun, Tokyo, Japan, 1997, pp. 24–99.)

the collection electrodes and the electrons are stored in the dust layer; hence, the applied voltage is decreased by the dust layer. In addition, as the effective electric field strength becomes lower, the collection efficiency decreases. If ρ_d becomes higher than $10^{11}\ \Omega \cdot m$, back discharge ensues and the collection efficiency is significantly decreased.

In the case of $10^2\ \Omega \cdot m < \rho_d$, $5 \times 10^8\ \Omega \cdot m$, the discharge rate of dust particles is moderate and the collection efficiency remains high.

The resistivity ρ_d is affected by dust properties, temperature, humidity, etc. The relationship between ρ_d of coal ash and the temperature for various humidity conditions is shown in Figure 15.29. The resistivity has a maximum value in the temperature range 100°C–200°C, except under condition of 0% humidity. At the same temperature condition, the resistivity becomes higher with a decrease in humidity, because of the following considerations:

In the low-temperature region, the coal ash particles adsorb moisture from their surroundings and form a water layer on the particle surfaces. Ions can move easily through this water layer, and hence the resistivity is reduced. This layer becomes thicker with a decrease in temperature and an increase in humidity; therefore, the resistivity becomes lower. On the other hand, in the high-temperature region, there is no surface water layer and the electrical conduction must take place through the particles. In this case, the electric resistivity decreases with an increase in temperature. Overall, the resistivity is determined by a combination of these mechanisms, showing maximum values in the temperature range between 120°C and 160°C depending on the humidity.

15.6.2.1.2 Space between Collection Electrodes The space between the collection electrodes is usually set to be 250–300 mm. However, if a sufficient corona current can be achieved, a wider space between collection electrodes can help to maintain or improve the collection efficiency. From Deutsch's equation (Equation 15.36), one notes that to maintain a high collection efficiency, it is necessary to increase the mobility of the particles v_e, because with the wider spacing, the number of electrodes (and collection area) is decreased for space-limited systems.

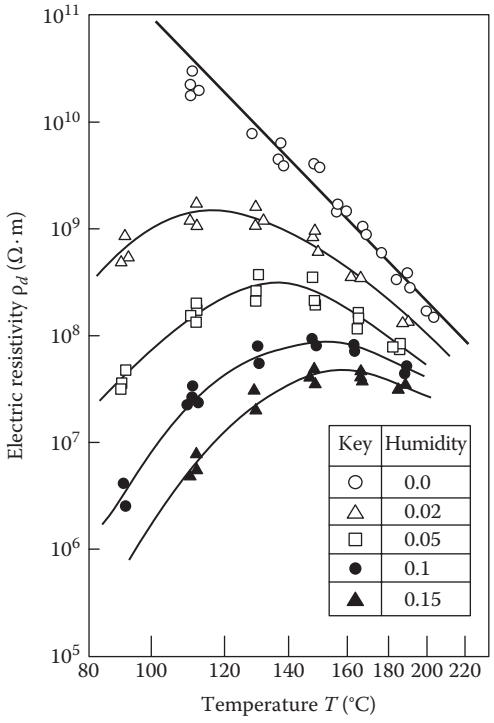


Figure 15.29

Electric resistivity of fly ash. (From Kanaoka, C. et al., Principle and equipment of dust collectors, *Fundamentals in Aeorsol Science,* Nikkan Kogyo Shinbun, Tokyo, Japan, 1997, pp. 24–99.)

15.6.2.2 Dust Collection of Low-Resistivity Particles

An example of low-resistivity dust is the ash from the residual oil combustion, which is in an environment of high humidity. The relationship between applied voltage and collection efficiency for the ash from residual oil combustion is shown in Figure 15.30. The collection efficiency of the ESP increases with an increase in applied voltage, and saturates at 30–40 kV. The collection efficiency is affected by the gas temperature and becomes higher with an increase in gas temperature at the same applied voltage.

The flue gas density decreases with an increase in gas temperature and the corona current increases with a decrease in gas density. On the other hand, as the applied voltage decreases with an increase in gas temperature, the collection efficiency decreases for the same corona current. By these trends, it is evident that collection efficiency is directly related to corona power, which is the product of the applied voltage and corona current, regardless of the gas temperature, as shown in Figure 15.31. This is due to the fact that the properties of the

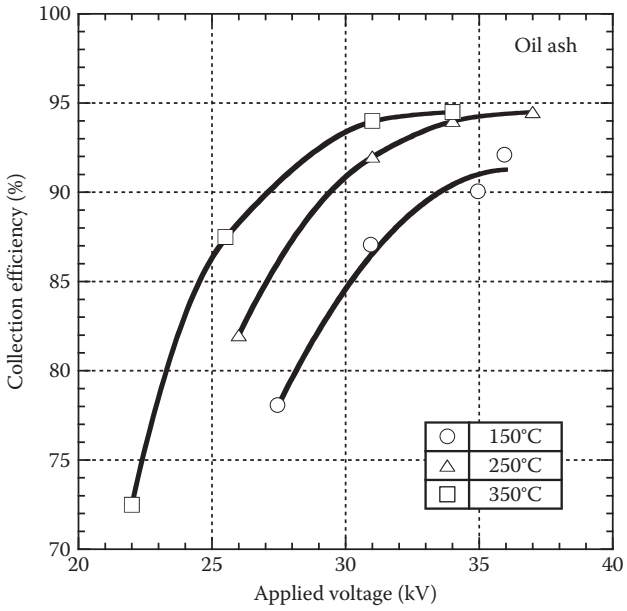


Figure 15.30

Applied voltage and collection efficiency. (From Kanaoka, C. et al., Principle and equipment of dust collectors, *Fundamentals in Aeorsol Science*, Nikkan Kogyo Shinbun, Tokyo, Japan, 1997, pp. 24–99.)

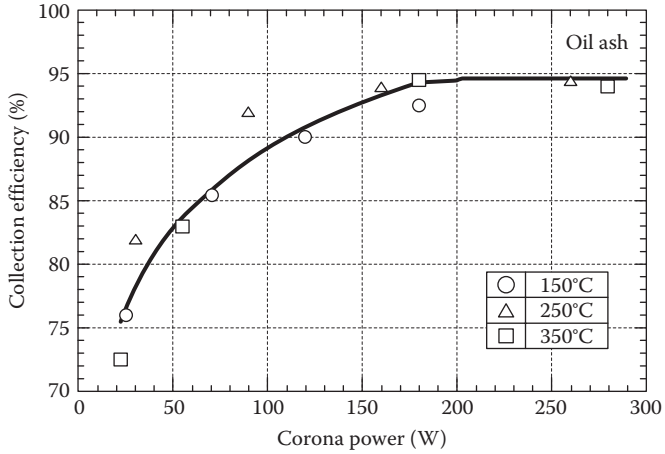


Figure 15.31

Influence of corona power on collection efficiency. (From Kanaoka, C. et al., Principle and equipment of dust collectors, *Fundamentals in Aeorsol Science*, Nikkan Kogyo Shinbun, Tokyo, Japan, 1997, pp. 24–99.)

ash from residual oil combustion remain constant with changes in gas temperature. In other words, if the dust properties are held constant, the collection efficiency of an ESP can be estimated based on corona power.

15.6.2.3 Dust Collection of High-Resistivity Particles

Ash produced by the combustion of pulverized coal is an example of high-resistivity dust. The relationship between corona current density and collection efficiency of an ESP for pulverized coal ash is illustrated in Figure 15.32. The collection efficiency increases with an increase in the current density and saturates at 0.3 mA/m^2, which is the typical operational condition at a coal-fired plant. If the gas velocity is increased, the collection efficiency decreases owing to the lower residence time of the flue gas in the precipitators.

The effect of gas temperature on the collection efficiency is shown in Figure 15.33. For the same corona current density, the collection efficiency decreases with an increase in gas temperature. The reason for this trend is as follows: When the gas temperature decreases, the corona current becomes higher owing to the decrease in gas density and the resistivity of the fly ash. Equivalently, for the same corona current density, the applied voltage becomes lower with an increase in gas temperature and the collection efficiency decreases. The relationship between the applied voltage and the corona current is shown in Figure 15.34, which indicates that at higher gas temperature, the corona current becomes higher at the same applied voltage.

The relationship between corona power, which is the product of the applied voltage and the corona current, and collection efficiency is shown in Figure 15.35. For the same corona power, the collection efficiency decreases with an increase in gas temperature, in contrast to the residual oil combustion ash. This is due to the fact that the resistivity of coal ash decreases with an increase in gas temperature and the applied voltage becomes lower, because of the higher corona current.

In a conventional pulverized coal combustion boiler, the ESP is operated at approximately 150°C. At this temperature, the maximum value of the resistivity of the coal ash is achieved. The collection efficiency for various kinds of coal is shown in Figure 15.36. The collection efficiency depends on coal properties, that is, the collection efficiency for high resistivity ash is lower. Improvements in technology to deal with the decrease in the collection efficiency for high electric resistivity ash are very important to flue gas cleanup.

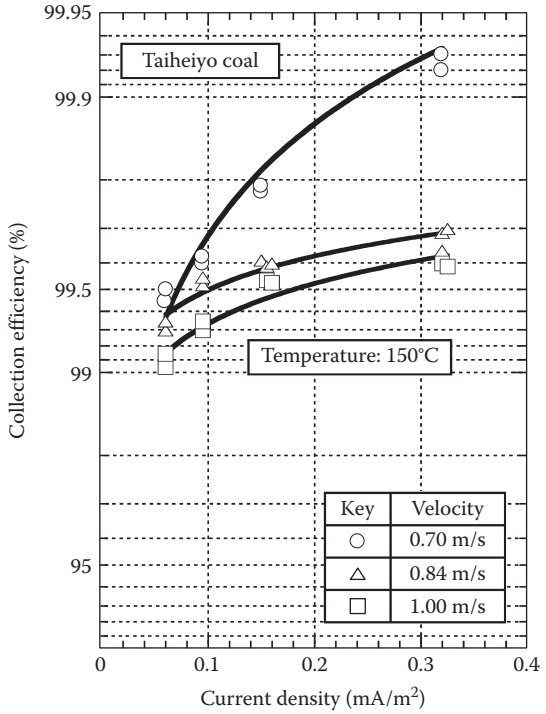


Figure 15.32

Influence of corona current density on collection efficiency. (From Kanaoka, C. et al., Principle and equipment of dust collectors, *Fundamentals in Aeorsol Science*, Nikkan Kogyo Shinbun, Tokyo, Japan, 1997, pp. 24–99.)

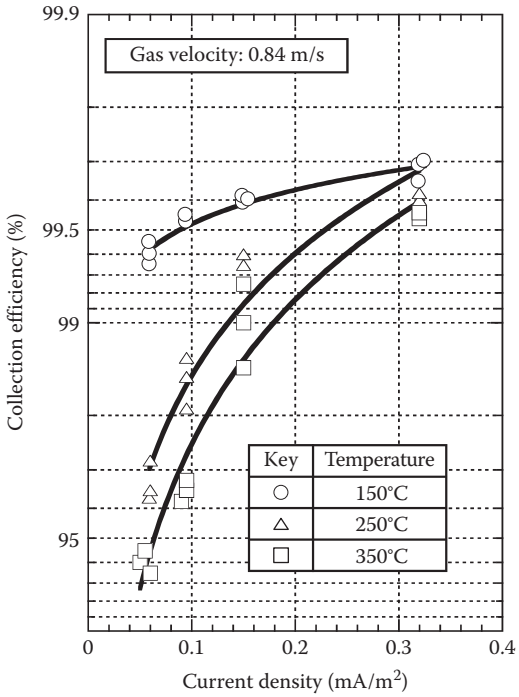


Figure 15.33

Influence of temperature on collection efficiency. (From Kanaoka, C. et al., Principle and equipment of dust collectors, *Fundamentals in Aeorsol Science*, Nikkan Kogyo Shinbun, Tokyo, Japan, 1997, pp. 24–99.)

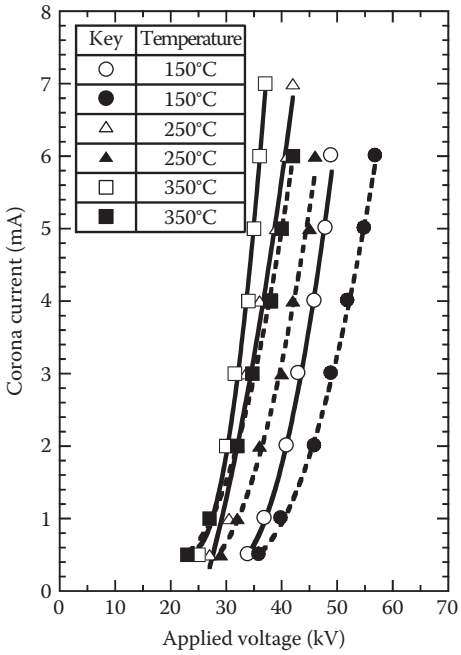


Figure 15.34

Applied voltage and corona current. (From Kanaoka, C. et al., Principle and equipment of dust collectors, *Fundamentals in Aeorsol Science*, Nikkan Kogyo Shinbun, Tokyo, Japan, 1997, pp. 24–99.)

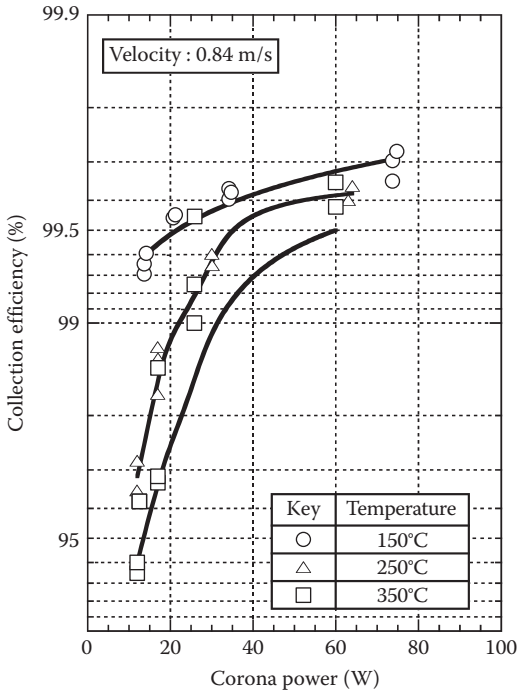


Figure 15.35

Corona power and collection efficiency. (From Kanaoka, C. et al., Principle and equipment of dust collectors, *Fundamentals in Aeorsol Science*, Nikkan Kogyo Shinbun, Tokyo, Japan, 1997, pp. 24–99.)

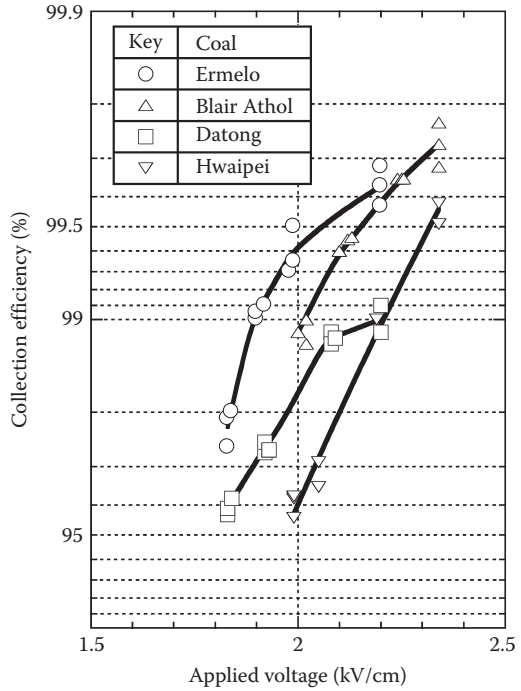


Figure 15.36

Collection efficiency of various kinds of coal.

One such approach is the high-temperature ESP operating at 350°C. This ESP utilizes the fact that the resistivity of coal ash is reduced at higher temperature. Although the gas volume increases with an increase in gas temperature and the corona power increases with an increase in corona current, the high-temperature ESP can use the higher corona power for high electric resistivity ash, because arc discharge is suppressed as shown in Figure 15.37.

Another method to reduce dust resistivity is to inject SO_3. When the SO_3 concentration in flue gas is high, a liquid layer is formed on the surface of the ash particles by the condensation of SO_3, and the collection efficiency is improved due to the decreased resistivity of the ash. The effect of SO_3 concentration on the collection efficiency and the dust concentration at the ESP outlet is shown in Figure 15.38. With increasing SO_3 concentration, the collection efficiency becomes higher and the dust concentration at the ESP outlet decreases.

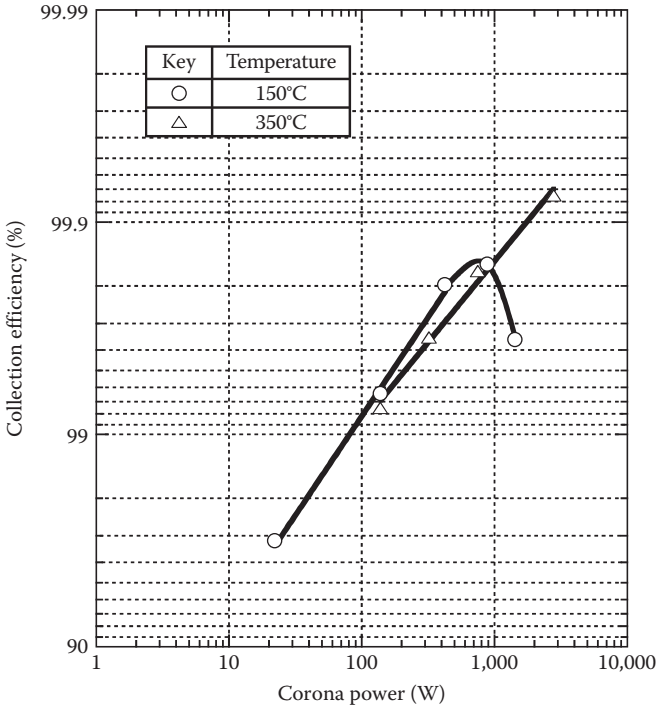


Figure 15.37

Influence of gas temperature on collection efficiency.

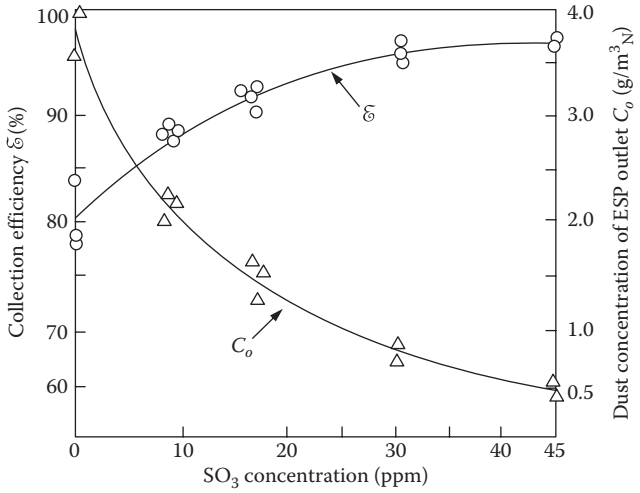


Figure 15.38

Improvement of collection efficiency of ESP by SO_3 injection.

When the operating temperature of the ESP is reduced, the dust resistivity decreases due to the formation of the liquid layer on the surface of the ash particles. The method that utilizes this trend is a new development in advanced low temperature ESPs which operate below 100°C. The relationship between gas temperature and the collection efficiency is shown in Figure 15.39. The collection efficiency is remarkably improved below 120°C. In the future, this type of ESP will be the choice for high-resistivity ash.

On the other hand, since the reduction in collection efficiency for ESPs operating with high-resistivity ash is due to the dust layer adhered on the collection electrodes, methods to minimize this problem are being developed. One of the techniques is a moving collection electrode in which the dust is removed by a brush. Another is the semiwet-type ESP in which the dust layer is removed by washing with water. These two methods offer potential for performance improvement.

The electric resistivity of the ash is affected by the ash composition in addition to operating conditions of ESP including the operation temperature. So, the relationship between collection efficiency and ash composition has been investigated. Bickelhaupt proposed the estimation method of the electric resistivity of ash from the ash composition, particularly Na, K, Ca, and S contents. The relationship between collection efficiency and the content of these elements is shown in Figure 15.40. Although the content of Ca and S in ash does not have a big effect on the collection efficiency of ESP, the content of Na and K in ash has a remarkable correlation with the collection efficiency. Of the two, Na has better correlation than K. Considering these results, the relationship between collection efficiency and the factor of 2Na + K in ash shown in Figure 15.41 has been derived. The collection efficiency of the ESP increased drastically by increasing the value to 2Na + K in ash at 130°C. And the content of Na and K in ash has a small effect on collection efficiency at 90°C in comparison with 130°C. This tendency indicates that the collection efficiency for the particles with high internal electric conduction is affected strongly by the concentration of Na and K in ash at 130°C. On the other hand, collection efficiency at 90°C has been influenced significantly by surface electric conduction more than internal conduction. Therefore, as shown in Figure 15.42, the collection efficiency at 90°C is affected by the moisture concentration and becomes higher, depending on the increase of moisture concentration in flue gas.

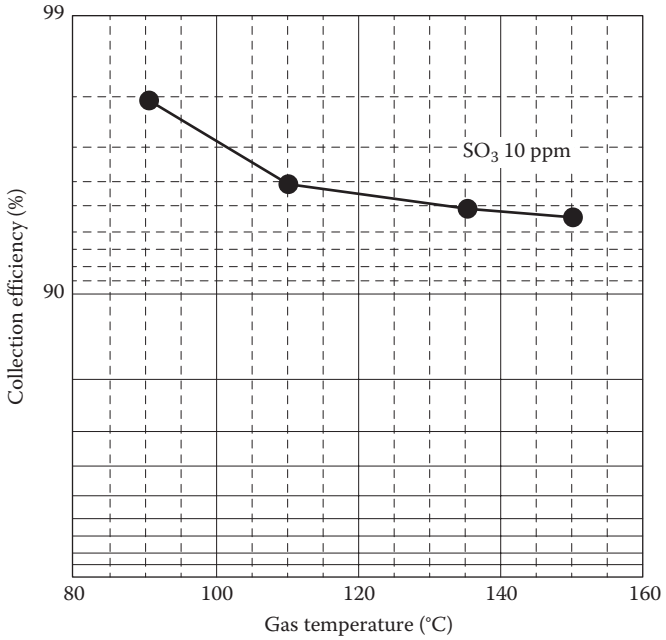


Figure 15.39

Influence of collection efficiency of ESP by low-temperature operation.

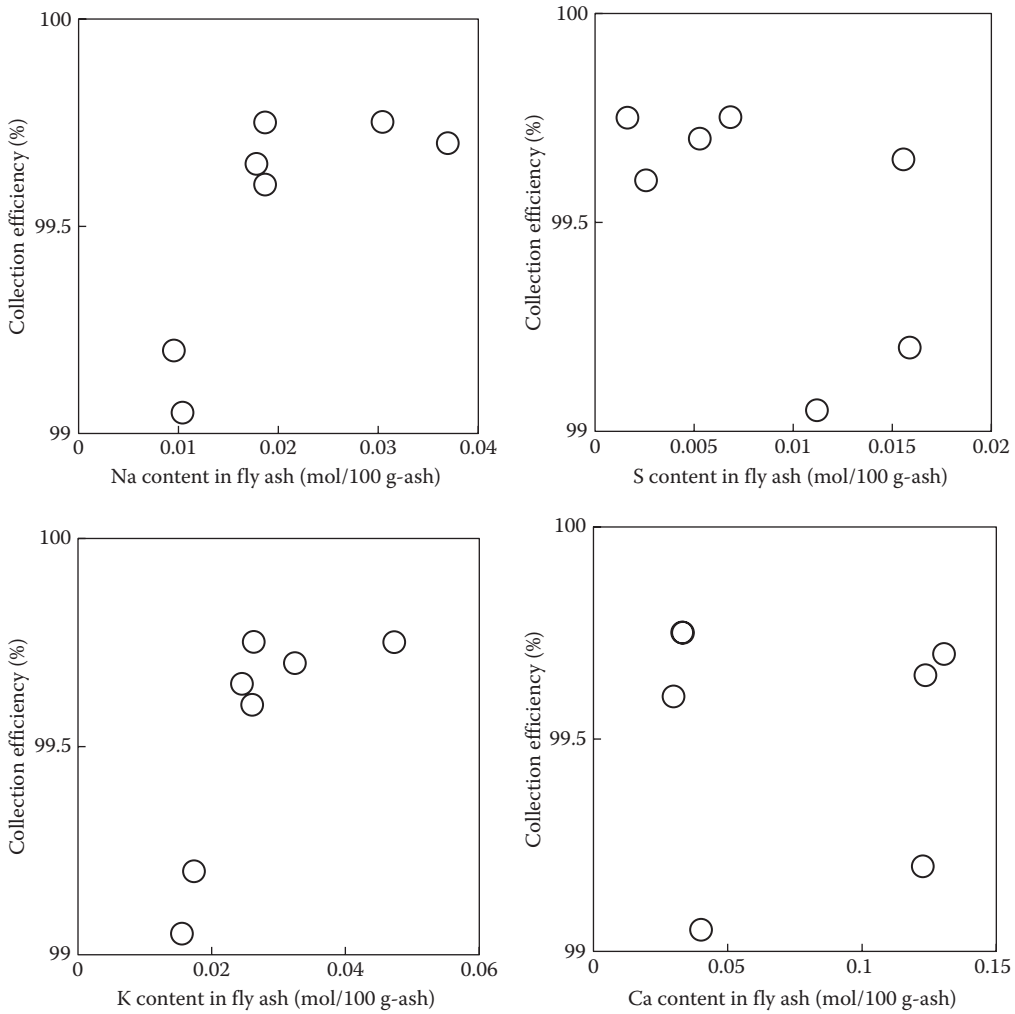


Figure 15.40

Influence of the content of Na, K, Ca and S in fly ash on collection efficiency.

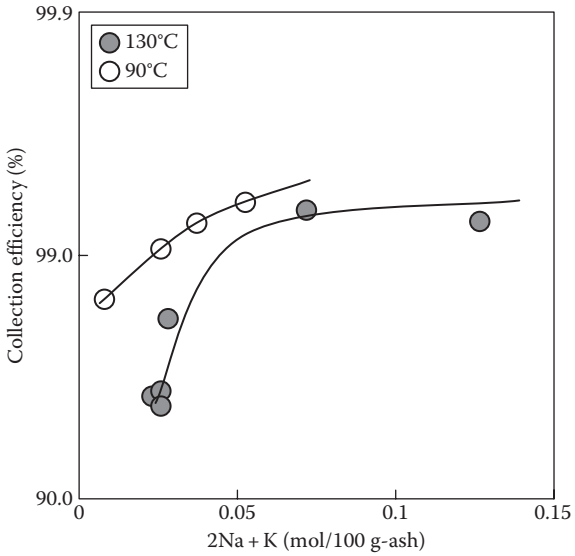


Figure 15.41

Relationship between the value of 2Na + K in fly ash and the collection efficiency.

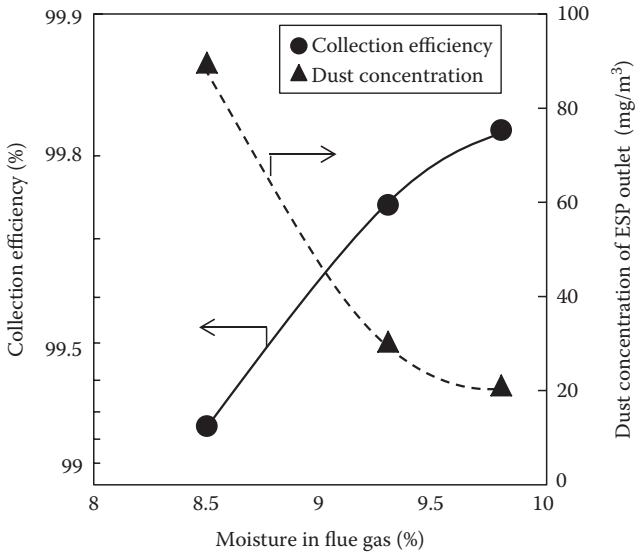


Figure 15.42

Relationship between moisture content in flue gas and the performance of ESP at 90°C.

15.7 Obstacle-Type Separators

Chikao Kanaoka

As described in Section 15.2, this type of collector captures dust particles on each individual obstacle in the system, that is, capturing particles by creating a relative velocity between the gas and particle. Most of the dust collectors belong to this category. Many different shapes and designs to create a relative velocity and enhance particle collection have been developed for this type of equipment.

As shown in Figure 15.43, when a dust-laden gas enters the dust collector with a cross-section A and length L, and obstacles are packed into the collector with a packing density $(1 - \varepsilon)$, the separation efficiency can be derived by considering the mass balance in the differential thickness Δx as follows:

$$uAc_p - uA\left(c_p + \Delta c_p\right) = \eta nA\frac{u}{\varepsilon}c_p\Delta x \tag{15.38}$$

where

n is the number of obstacles in Δx

u is the imposed gas velocity

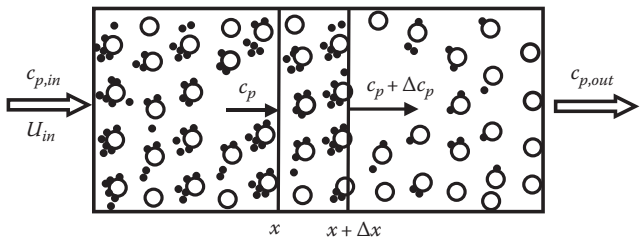


Figure 15.43

A schematic representation of dust collection.

Furthermore, η is the collection efficiency of a single collection obstacle (body) defined by the following equation:

$$\eta = \frac{\dot{m}_c}{\dot{m}_{c,in}} \tag{15.39}$$

where

$\dot{m}_c$ is the rate at which particles are collected on the obstacle

$\dot{m}_{c,in}$ is the flow rate of particles in the area projected by the obstacle

For the case of cylindrical and spherical collectors, the collection efficiency is

$$\eta \begin{cases} = \dfrac{c_{p,in} u 2Y}{c_{p,in} u d_c} = \dfrac{2Y}{d_c} & \text{cylinder} \\ = \dfrac{c_{p,in} u\left(\pi Y^2\right)}{c_{p,in} u\left(\pi d_c^2/4\right)} = \left(\dfrac{Y}{d_c/2}\right)^2 & \text{sphere} \end{cases} \tag{15.40}$$

This is schematically illustrated in Figure 15.44. As may be seen in the figure, the single body efficiency is defined as the ratio of the upstream area of limiting trajectory to the projected area of the collection body. The limiting trajectory is thus the critical particle trajectory that defines collection efficiency. Particles within the limiting trajectory are collected, but particles beyond the limiting trajectory are not collected. The separation efficiency of the collector E is obtained by integrating Equation 15.38 as follows:

$$\mathfrak{E} = 1 - \exp\left(-C\frac{1-\varepsilon}{\varepsilon}\eta L\right) \tag{15.41}$$

where

L is the packed thickness of the filter, that is, length

ε is porosity of the collector

$(1 - \varepsilon)$ is the packing density of the obstacles

The constant C is the constant determined by the shape of obstacle, that is, $C = 4/d_c$ for a cylindrical collector and $3/(2d_c)$ for a sphere. The symbol d_c is the nominal size of the obstacle.

In Equation 15.41, constants other than η are determined from the equipment and shape of single collection obstacle, such that $\mathfrak{E}$ can be estimated if η is specified for a given collector and operational conditions. The collection efficiency for obstacles with different shapes is calculated, as shown in Figure 15.45. In this figure, St is the Stokes number defined by

$$St = \frac{C\rho_p d_p^2 u}{9\mu d_c} \tag{15.42}$$

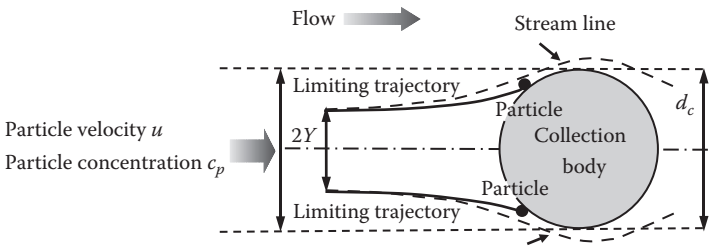


Figure 15.44

Definition of single body collection efficiency.

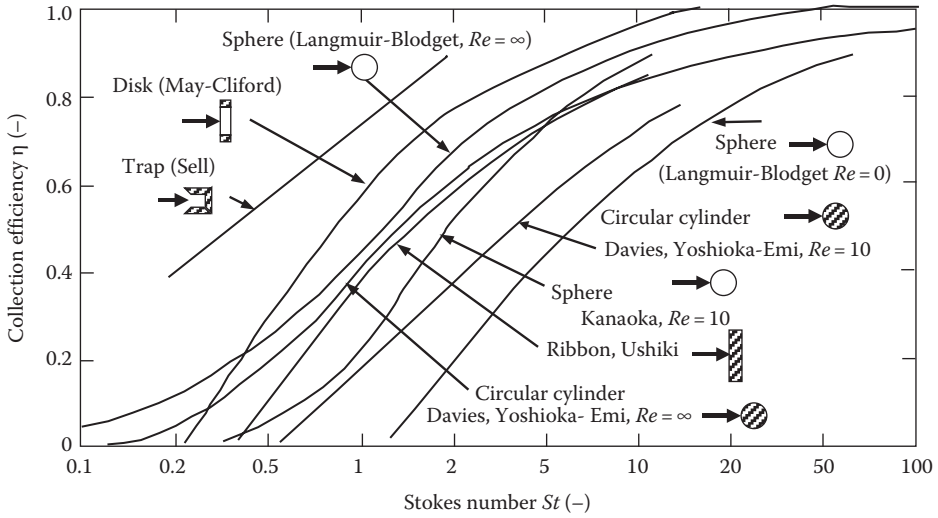


Figure 15.45

Calculated collection efficiencies for single collecting obstacles. (From Kanaoka, 1997.)

where

Cc is the Cunningham's slip correction factor
ρ_p is the particle density
d_p is the particle diameter
d_c is the representative size of the collecting body
u is the gas velocity
μ is the gas viscosity

15.8 Inertial Dust Collectors

Chikao Kanaoka

The inertial dust collector is one of the typical obstacle dust collectors and separates particles based on the difference in the particle trajectory and gas streamlines, as shown in Figure 15.46. Various obstacles are designed to create a relative velocity between particle and gas flow. Typical obstacles are shown in Figure 15.47. The Louver-type dust collector, shown in Figure 15.48, intensifies the inertial effect by a large inclination angle and a small gap between blades.

In practical applications, inertial collectors are used mainly to separate mist rather than solid particles.

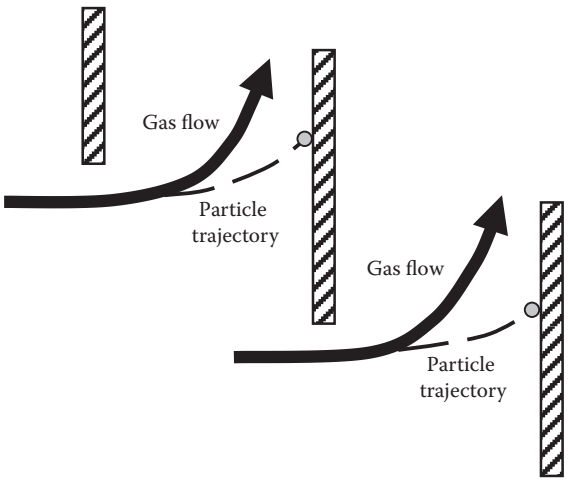


Figure 15.46

Collection mechanism of inertial dust collector.

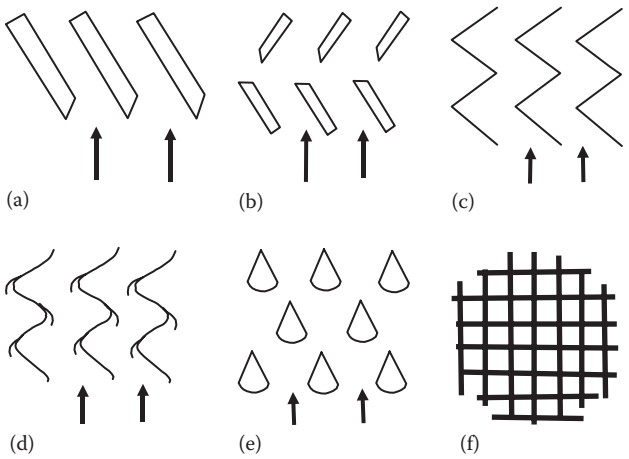


Figure 15.47

Typical types of obstacles. (a) Slope board type, one step. (b) Slope board type, two steps. (c) W type. (d) Wave type. (e) Droplets. (f) Screen type.

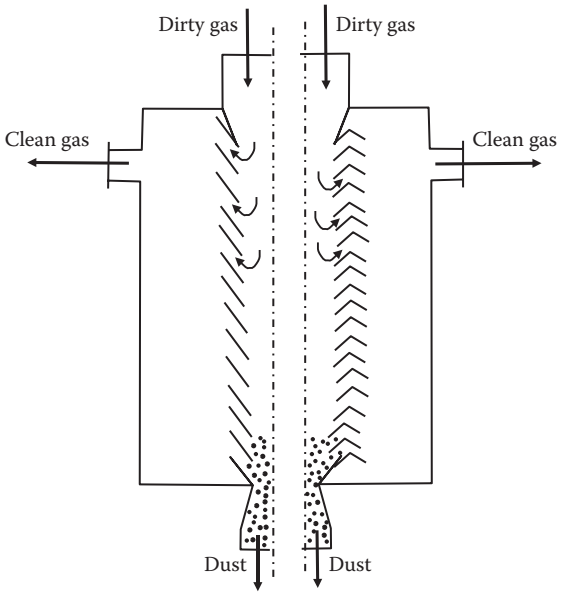


Figure 15.48

Louver-type dust collector.

15.9 Air Filters

Chikao Kanaoka

The air filter is one of the most reliable and efficient methods for dust collection and is mainly used at low dust concentrations. Particles are captured inside the filter, and hence, this type of particle collection system is referred to as depth filtration.

An air filter is mainly used to purify the air in local environments, such as hospitals, manufacturing lines, working spaces, residential and commercial buildings, etc. In these environments, the dust concentration is usually lower than 10 mg/m^3 and the particle size is less than several micrometers. Hence, packed filter materials, especially fibrous mats, are used for this purpose. The porosity of a filter mat is generally

higher than 85%; hence, particles are captured on individual fibers in the filter. The filter efficiency $\mathfrak{E}$ can be calculated from the single fiber collection efficiency for a given filtration condition as follows:

$$\mathfrak{E} = 1 - \exp\left(-\frac{4}{\pi} \frac{1-\varepsilon}{\varepsilon} \frac{L}{d_c} \eta \right) \tag{15.43}$$

where d_c, ε, $(1-\varepsilon)$, and L are the fiber diameter, porosity, fiber packing density, and filter thickness, respectively.

Although particles are collected on a fiber by a combination of effects, the mechanisms of inertia, Brownian diffusion, interception, and gravity are predominant in mechanical filtration. The electrostatic force becomes important when either fibers or particles or both are electrically charged or an external electrical field is applied.

Many theoretical and empirical expressions have been proposed for each collection mechanism. Figures 15.49 through 15.51 show typical single fiber collection efficiencies by different mechanisms and

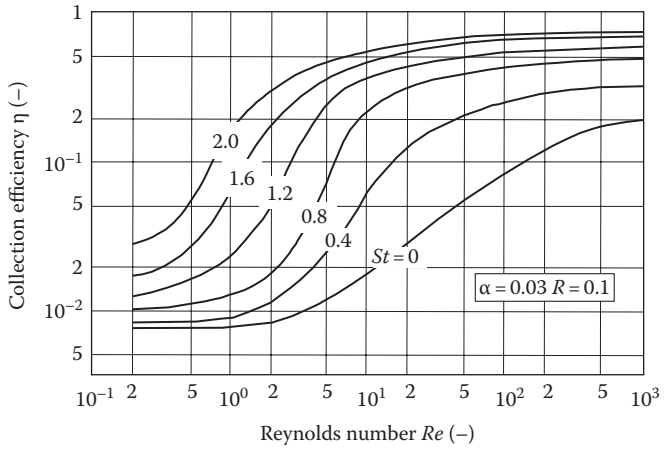


Figure 15.49

Calculated single fiber collection efficiency by inertia and interception effect. (From Emi, H. et al., *J. Chem. Eng. Jpn.*, 10, 148, 1977.)

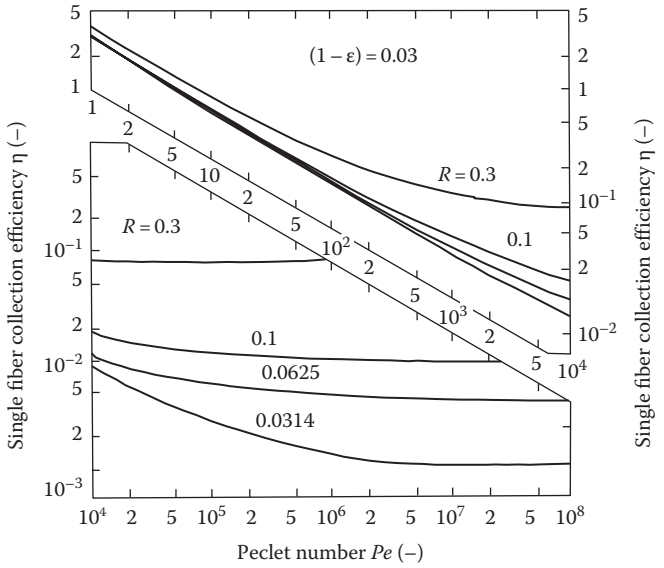


Figure 15.50

Calculated single fiber collection efficiency by diffusion and interception. (From Kanaoka, C., *J. Soc. Powder Technol. Jpn.*, 25, 469, 1988.)

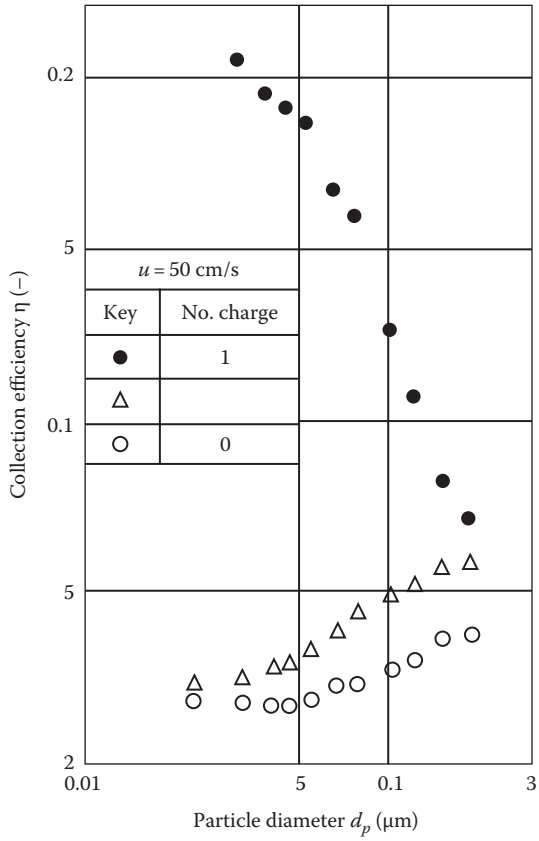


Figure 15.51

Experimental collection efficiency of particles at different charging state by an electret fiber. (From Emi, H. et al., *Particulate Sci. Technol.*, 5, 161, 1987.)

Figure 15.52 provides the efficiency chart obtained by taking inertia, Brownian diffusion, interception, and gravity into the account simultaneously. It is clear from the figure that there exists a particle size or a filtration velocity, which gives minimum efficiency, corresponding to the transition region for different mechanisms.

Filter performance, such as collection efficiency and pressure drop, changes with time and state of particles, as shown in Figures 15.53 and 15.54. These changes are caused by the shadowing effect of already captured particles on the collection of incoming particles, as shown in Figures 15.55 through 15.57. Figure 15.58 summarizes the general morphologies of captured particles by this collection mechanism.

There are two types of air filters: disposable and renewable. For the former type, fiber materials, such as glass, metal, and natural and synthetic fibers, are packed loosely in a frame or are formed into a mat structure. Since captured particles accumulate inside the filter, the pressure drop increases with filtration time, such that a zigzag structure is adopted to increase the filtration area to lengthen its service life. It is finally replaced when the pressure drop reaches a certain level to avoid an increase in the operational cost.

High-efficiency particulate air (HEPA) and ultralow penetration air (ULPA) filters are types of paper filters composed of very fine fibers, less than 1 μm on average. They are defined as the filters that collect 0.3 μm particles at an efficiency higher than 99.7% and 0.1 μm particles at higher than 99.9997%, with a pressure drop that does not exceed 12.7 mm H_2O at their specified flow rate, usually 2.5 cm/s. Therefore, HEPA and ULPA filters are used to create highly purified environments, which are necessary in the semiconductor industry, the precision machine industry, and so on. Penetration curves for HEPA and ULPA filters vary convexly with particle size and the maximum appears around 0.1 μm (i.e., the collection efficiency of the filter is poorest around this particle size at the conventional filtration condition

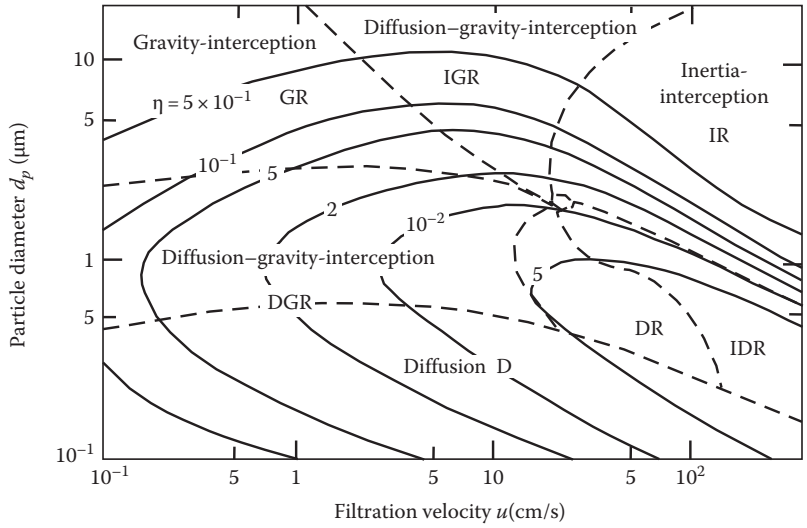


Figure 15.52

Total single fiber collection efficiency (d_c = 10 μm, (1 – ε) = 0. 03). (From Emi, H. et al., *J. Chem. Eng. Jpn.*, 6, 349, 1973.)

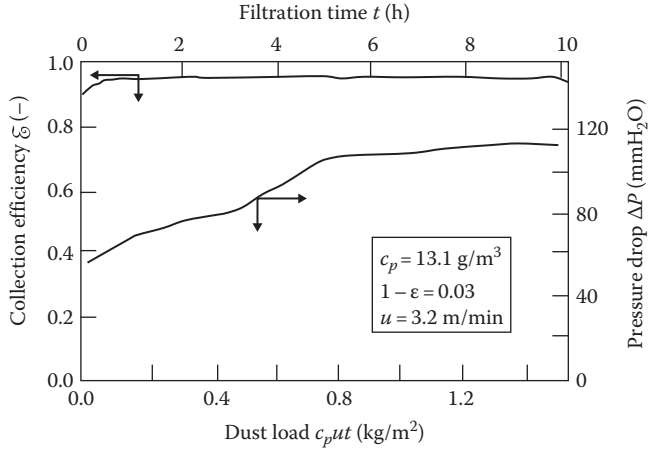


Figure 15.53

Experimental time dependency of performance of an air filter with liquid particles (DOP).

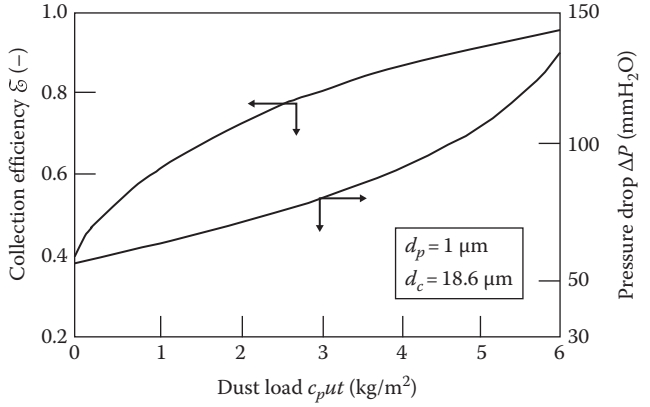


Figure 15.54

Experimental time dependency of performance of air filter with solid particles (stearic acid particles).

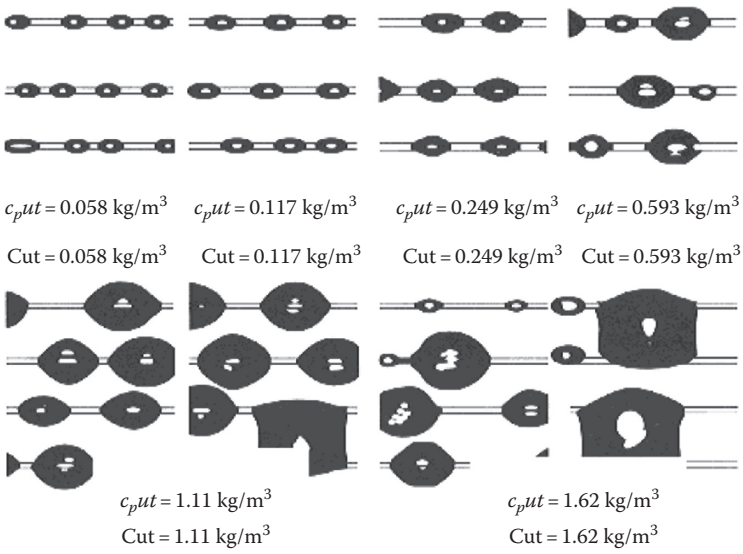


Figure 15.55

Time change in the morphology of captured mist particles on parallel wires. (From Kanaoka, C. and Emi, H., *Kuuki Seijo*, 22, 1, 1985.) Fiber diameter $d_c = 60$ μm, interfiber interval $h_f = 525$ μm, filtration velocity $u = 4$ m/s.

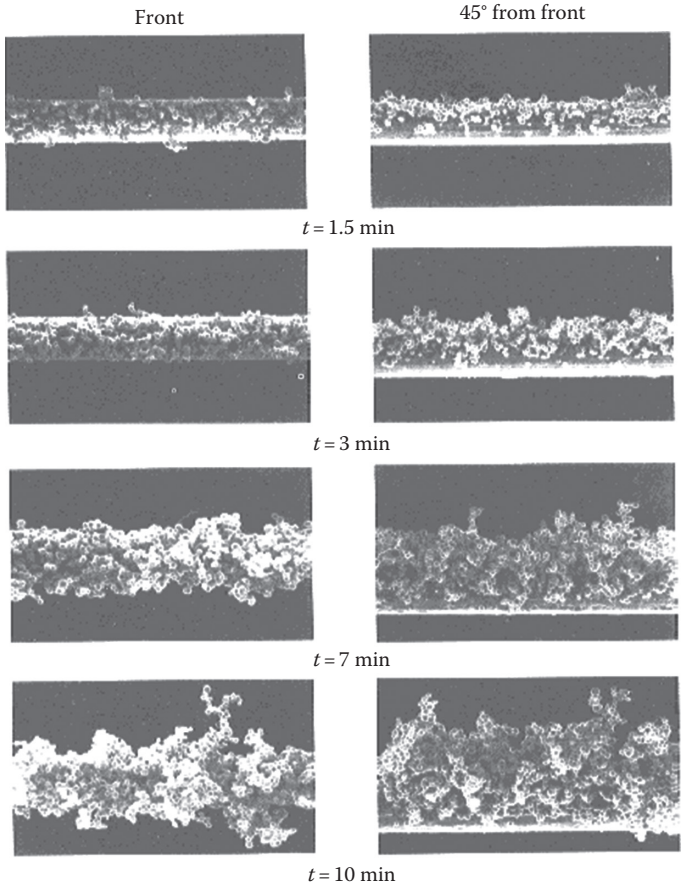


Figure 15.56

Time dependency of morphology of captured solid particles on a wire. (From Kanaoka et al., 1981.) $d_c = 10$ μm, $d_p = 1$ μm, $u = 50$ cm/s, $\rho_p = 11.34$ g/cm^3, $St = 3.5$, $\mathscr{R} = 0.1$.

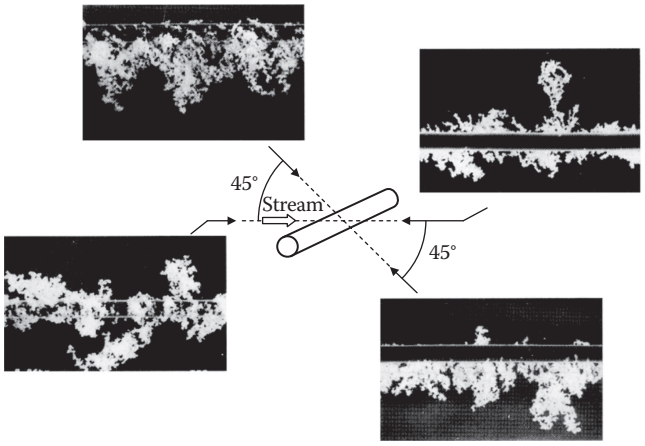


Figure 15.57

Morphology of captured particles on a fiber by inertia and interception effect. (From Kanaoka, 1997.) Fiber diameter d_c = 10 μm, d_p = 0.86 μm, ρ_p = 2.33 g/cm^3, u = 50 cm/s, St = 0.632, $\mathscr{R}$ = 0.086.

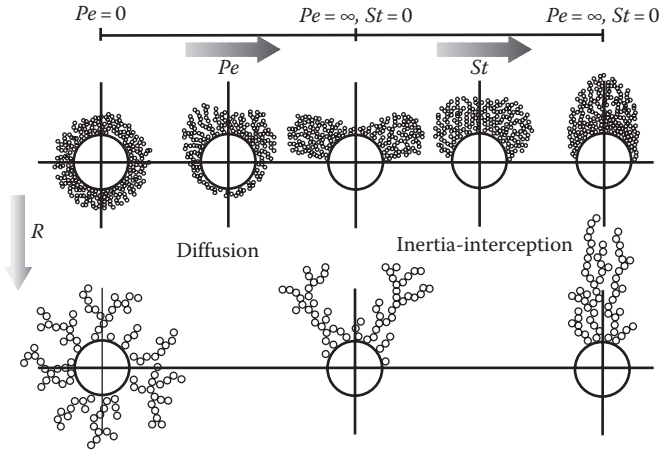


Figure 15.58

General morphology of accumulation on a cylindrical fiber by the change of collection mechanism. (From Kanaoka, C., *Earozoru Kenkyu*, 4, 256, 1989.)

and decreases as the filtration velocity increases), as shown in Figure 15.59. Hence, the filter collection performance can be roughly evaluated by measuring the efficiency around this size range.

An electrostatic fibrous filter is another type of air filter that utilizes electrostatic force to remove particles. An electrostatic attractive force becomes effective when either fiber or particle is charged, but not when both of them are charged with the same polarity. Therefore, several types of electrostatic fibrous filters have been designed, depending on the charging state of fiber and particle. In general, an electrostatic fibrous filter is superior in collection performance to a mechanical fibrous filter but difficult to operate stably. The electret filter is a stable electrostatic fibrous filter, because it is composed of fibers with permanent dipoles and is capable of collecting particles at a high efficiency in the initial filtration stage. However, the efficiency decreases with filtration time owing to dust loading. This drawback has to be eliminated in practical use.

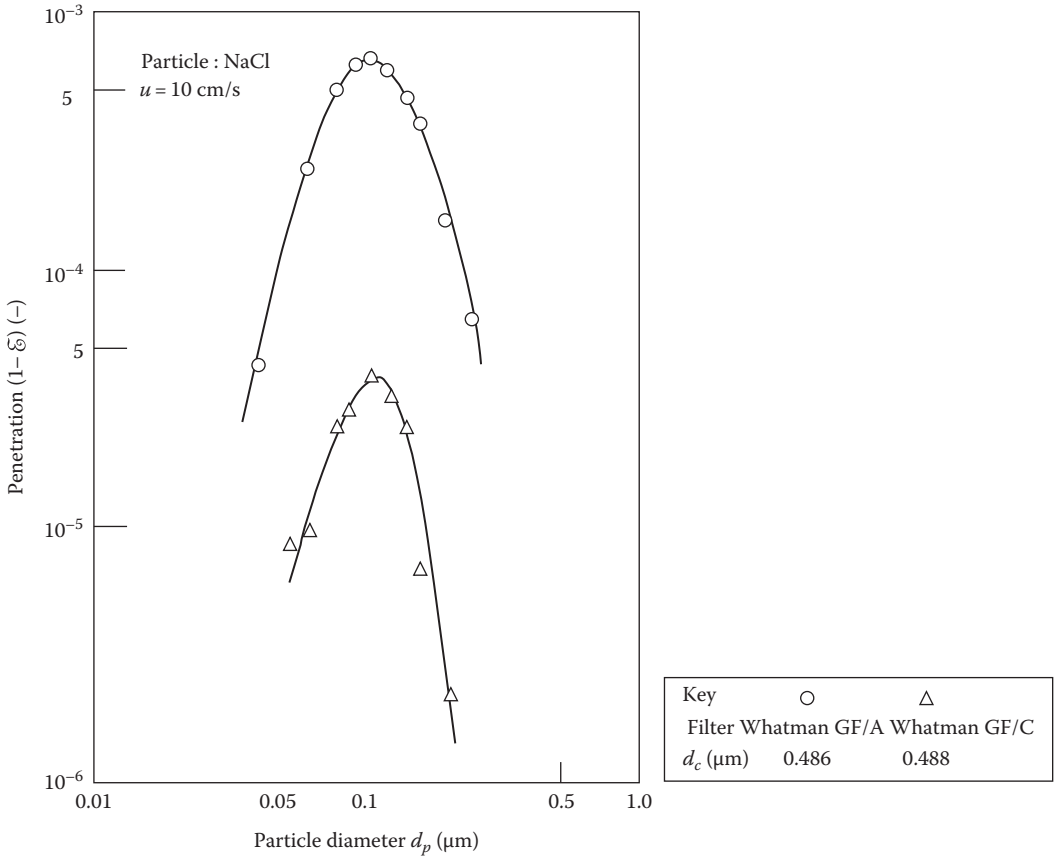


Figure 15.59

Experimental penetration of HEPA filter. (From Emi, H., *Aerosol Engineering*, Yokendo Publisher, Tokyo, Japan, 1984, p. 186.)

15.10 Scrubbers

Chikao Kanaoka

The scrubber is the generic name for a group of dust collectors utilizing liquid droplets or a liquid film as collecting media. Most of them can be classified into obstacle-type dust collectors.

The most important difference between this group and the so-called dry type is that the collection of dust particles is carried out in two operational steps: the capture of the dust by liquid component and then separation from the liquid by some other means. Since a liquid medium is used, this type of collector can be used for the collection of mist particles, even under hot gas conditions. Furthermore, the simultaneous separation of dust and gaseous material is also accomplished. However, the collector consumes a large amount of liquid. Also, secondary treatments of the collected liquid, the resulting sludge, and so on are required. This type of equipment is used only when a cheap and abundant amount of water is available or when a dry-type collector cannot be utilized.

Scrubbers can be classified into four types as shown in Figure 15.60: (a) the water reservoir type, (b) the pressurized water type, (c) the packed tower type, and (d) the forced rotary type. Their performance is summarized in Table 15.5.

As seen from Figure 15.60 and Table 15.5, scrubbers are in general relatively simple in structure. However, their performance is very good. Most scrubbers are capable of removing particles several micrometers in diameter with little difficulty. However, it is rather difficult to separate particles finer than 1 μm, except with a venturi scrubber operating at very high speed.

As described earlier, droplets are often used in the scrubber and their space density is not very high. Therefore, single sphere collection efficiency, shown in Figure 15.45, is directly applicable to the prediction of the separation efficiency of the scrubber. However, both the dust particle and collecting droplet

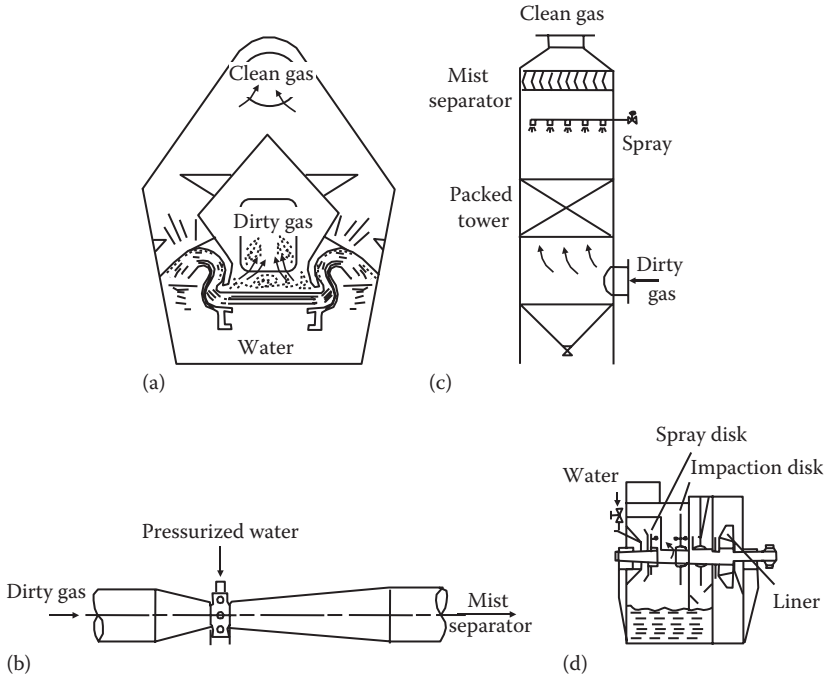


Figure 15.60

Typical scrubbers. (a) Water reservoir type; (b) pressurized water type; (c) packed tower type; (d) forced rotation type.

Table 15.5 Typical Scrubber

	Gas Velocity (m/s)	Gas Volume Flow Rate (m^3/min)	Pressure Drop (Pa)	Liquid–Gas Ratio (L/m^3)	Separation Diameter (μm)
Water reservoir type					
Rotoclone	20–30	1,000	500–1,500	0.1–0.3	0.5
Pressure water type					
Cyclone scrubber	1–2	5,000	500–2,000	0.5–5	1
Venturi scrubber	40–100	10,000	2,000–20,000	0.3–1	0.1
Packed tower type					
Spray scrubber	1–2	1,000	100–500	0.1–1	3
Packed tower	1–2	1,000	1,000–3,000	1–10	1
Forced rotary type					
Theisen washer	1–5	1,000	2,000–4,000	0.5–2	0.2

move in the air and the collection takes place only when there is a relative velocity between them, which does not last very long. Separation efficiency of the collector is expressible by the following equation.

$$\mathfrak{E} = 1 - \exp(-Rem \cdot \mathfrak{L}) \tag{15.44}$$

where

$\mathfrak{L}$ is the liquid–gas ratio

Rem is the dimensionless parameter for the amount of particles captured by a single collecting body (water droplet) defined by

$$Rem = \frac{3\int_0^X \eta \, dx}{2d_w} \tag{15.45}$$

where X is effective collection length of the collector in the water droplet diameter.

Figure 15.61 shows the calculated *Rem* versus collector diameter d_w for a venturi scrubber with a throat velocity of 80 m/s and $X = 1$ m.

As seen from the figure, *Rem* decreases with increasing droplet size for diffusion but displays a maximum for droplet sizes greater than 0.5 μm for inertial collection. The maximum *Rem* for inertial collection can be explained by trends in collection efficiency with the Stokes number and the Reynolds number defined as follows:

$$St = \frac{C\rho_p d_p^2 \Delta u}{9\mu d_w}, \quad Re = \frac{\rho_p d_w \Delta u}{\mu} \tag{15.46}$$

where Δu is the velocity difference between the droplet and the fluid. As the water droplet diameter increases, the velocity difference increases and the Reynolds number and the Stokes number go through maximum values. As seen from Figure 15.45, the collection efficiency will increase and approach an asymptotic value near unity. The value for *Rem* first increases with collection efficiency, reaches a maximum, and decreases as the water droplet diameter becomes larger. The same trend is not observed from the small droplets, because they are in the lower Reynolds number range.

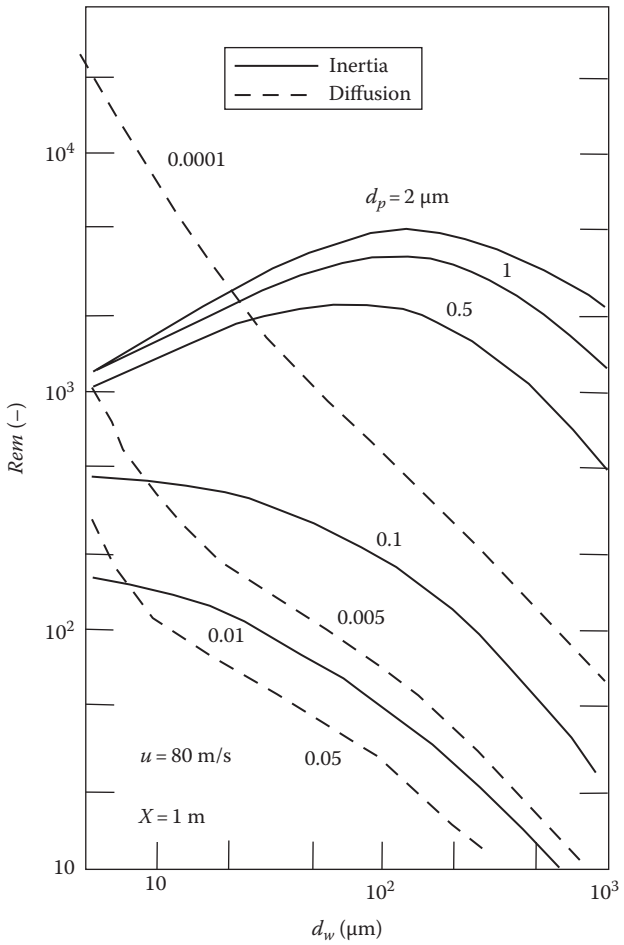


Figure 15.61

Dimensionless amount of particles captured by a droplet in a venturi scrubber. (From Morishima, N., Study on the venturi scrubber, PhD thesis, Osaka City University, Osaka, Japan, 1967.)

15.11 Barrier-Type Separators

Chikao Kanaoka

As described earlier, this type of collector uses a permeable medium for the gas, but not for the dust, and is used to separate dust at high concentrations. Hence, the most pronounced feature of dust collectors of this type is almost perfect particle collection, regardless of size, except just after the dislodgement of accumulated particles on the barrier. This occurs because most of the particles are collected due to the particles captured earlier by a sieving effect. This type of collection is usually referred to as surface or cake filtration. The bag filter is the most common barrier-type dust collector. Recently, the ceramic filter has become popular for high-temperature dust cleaning.

15.12 Bag Filters

Chikao Kanaoka

15.12.1 Collection Mechanism

The bag filter is commonly made of fabric in a cylindrical "bag" shape. Consequently, this type of filter is called a bag filter. The designation "fabric" filter is also popularly used. Figure 15.62 shows the typical shape of the bag filter.

Although any type of fiber with a different weave, such as woven and nonwoven, can be used as a filter material, synthetic fibers such as polyester, polypropylene, nylon, and glass fibers are most often employed owing to their strong resistivity to gas and dust.

The collection of particles by a fabric depends on the weave of the fabric, that is, woven or nonwoven. For a woven fabric, initially (or after cleaning), the particles are captured on fibrils in the texture by inertia, interception, diffusion, and so on. After the texture is filled with captured particles, the capture area expands to the whole fabric surface and forms a very coarse dust layer of porosity ranging between 80% and 85%. At this stage, particles are mainly captured by the sieving effect, because particles have to go through the openings in the layer, the size of which is of the same order as the particles. Hence, the collection performance is not affected by the particle size and is usually very high.

Nonwoven fabric consists of independent fibers, and hence, the porosity is much higher than that of woven fabric with same weight. Therefore, it can operate at higher flow rates than woven fabric and the

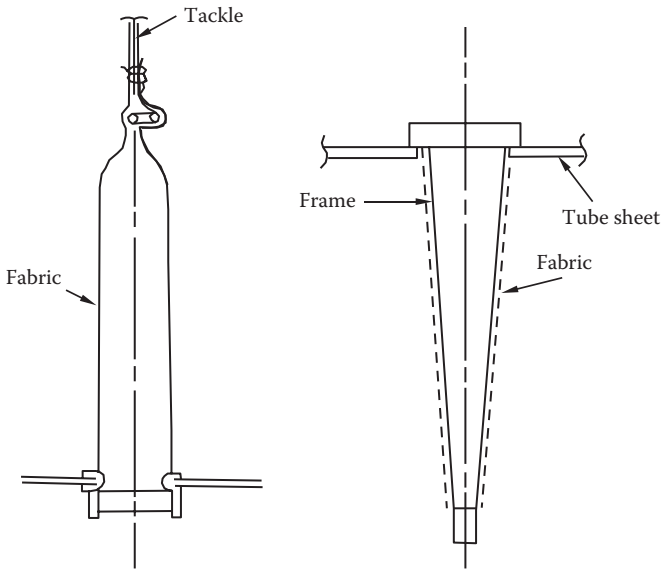


Figure 15.62

Typical shape of bag filter element.

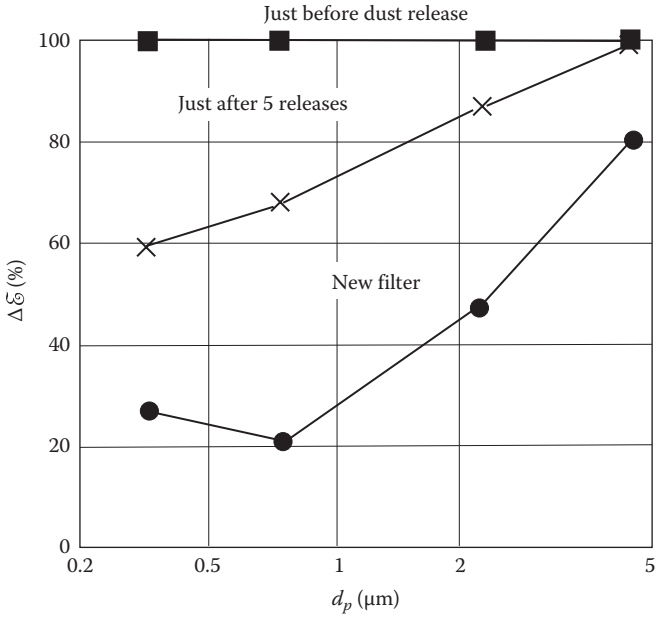


Figure 15.63

Grade efficiency of a singed polyester filter element. (From Kanaoka, C., *Industrial Pollution Control Technologies and Regulations*, Maruzen, Tokyo, Japan, 2003, p. II250.) Fabric: singed polyester nonwoven felt, fiber diameter: 14 μm mass: 600 g/m^2, particle: JIS No.11 test dust (coal flyash, mean diameter 1.5 μm), filtration velocity 3 cm/s, pressure drop of fabric for cleaning: 2 kPa, cleaning air pressure: 100 kPa, duration of air injection: 200 ms.

particle collection behavior is more or less similar to that of an air filter in the initial stage. In this case, the collection behavior after the formation of dust layer is not much different from that of the woven fabric.

As mentioned earlier, the dust release from the fabric is carried out repeatedly either after some prescribed time interval or when the filter pressure drop reaches a predetermined value, above which continuous operation cannot be maintained. However, a small amount of dust remains in the fabric after the release action and forms a primary dust layer, which plays an important role in dust collection in bag filtration. This can be seen from Figure 15.63, which shows the grade efficiency of a flat nonwoven felt just before and after dust release at different cleaning cycles. As seen from the figure, the grade efficiency before dust cleaning is almost 100%, regardless of particle size, but after cleaning it is considerably lower but increases with the number of cleanings, suggesting the formation of the primary dust layer. Once the primary layer is formed, the collection efficiency of the filter does not radically decrease even after cleaning.

Figure 15.64 shows the change measured for outlet dust concentration as a function of dust load. The dust load is the product of the particle concentration, filtration velocity, and time and represents the total incoming particle mass per unit filter area. As seen from the figure, the outlet concentration decreases with time, but the decrease rate is higher for slow filtration velocity and the final stabilized dust concentration is more than two orders of magnitude different, despite the fact that the filtration velocity varied only one order of magnitude. This suggests the possibility of pinhole formation in the dust layer at the faster filtration velocity and thus fairly large penetration of particles from the holes.

15.12.2 Pressure Drop

Pressure drop of a bag filter ΔP is expressed by the sum of the pressure drop in the fabric and the dust accumulated on the fabric as

$$\Delta P = \Delta P_f + \Delta P_d = \left(\zeta_f + \zeta_d m_d\right)\mu u \tag{15.47}$$

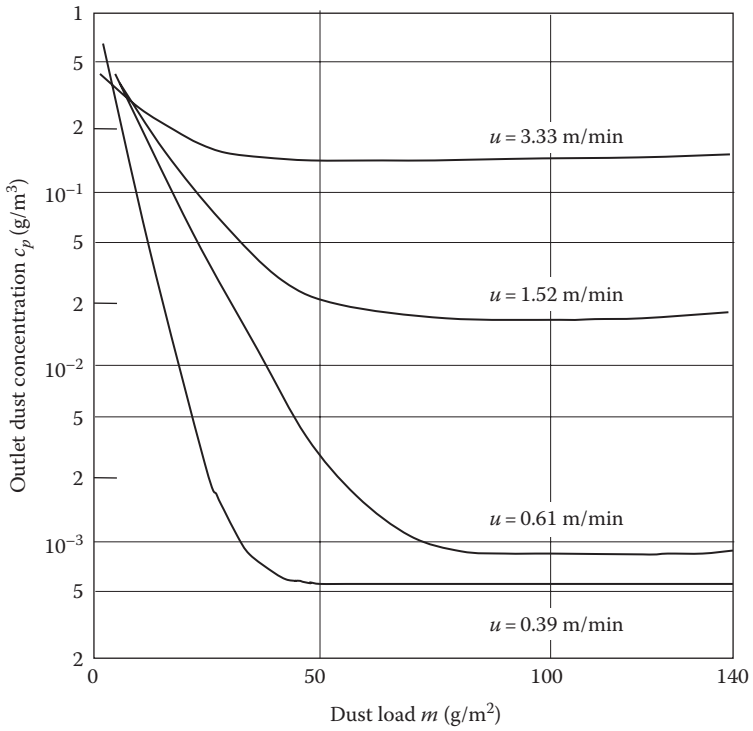


Figure 15.64

Time change of outlet dust concentration at different filtration velocities. (From Chaing, T. and Ostop, R.P., EPA-666/9-82-005C, 1982, p. 261.)

where

ΔP is the pressure drop of a dust loaded fabric (Pa)
ΔP_f and ΔP_d are the pressure drops through the fabric and covering dust layer
ζ_f is the resistance coefficient of the fabric (1/m)
ζ_d is the specific resistance of dust layer (m/kg^2)
m is the dust load (kg/m^2)
μ is the gas viscosity (Pa·s)
u is the filtration velocity (m/s)

At the initial stage of the filtration, ΔP_f of a woven fabric is usually very low and thus negligible. However, it may not be negligible for a very thick nonwoven fabric. Under dust-loaded conditions, the porosity of the fabric decreases so that pressure drop increases as $\Delta P \propto u^n$ where n ranges between 1.5 and 2. The flow through the dust layer is usually laminar, such that the pressure drop ΔP_d is proportional to the filtration velocity and is expressed by the following Kozeny–Carman equation:

$$\Delta P_d = \frac{180(1-\varepsilon)m_d \mu u}{d_{ps}^2 \varepsilon^3 \rho_p} \tag{15.48}$$

where

ε is the porosity
d_{ps} is the specific surface diameter (m^2/m^3)
ρ_p is the particle density (kg/m^3)

15.12.3 Methods of Dislodging the Dust Particles

The collected dust particles accumulate on the fabric surface and increase the pressure drop. Hence, the accumulated dust has to be dislodged to maintain continuous operation. The dislodging categorizes the bag filters into mechanical shaking, reverse flow, and pulse jet types, as shown in Figure 15.65.

The dislodging method can be further categorized as intermittent or continuous dislodging. The mechanical shaking and reverse flow type filters belong to the intermittent category and pulse jet type to the continuous category. With the intermittent type, the gas flow has to be suspended during dislodging; so, the bag house is divided into several compartments so that the entire house does not have to be shut down during cleaning. With the pulse jet type, the cleaning can be performed without ceasing operation, since the injection of intense cleaning air is only needed for a short time. Table 15.6 summarizes the classification of bag filters and their features.

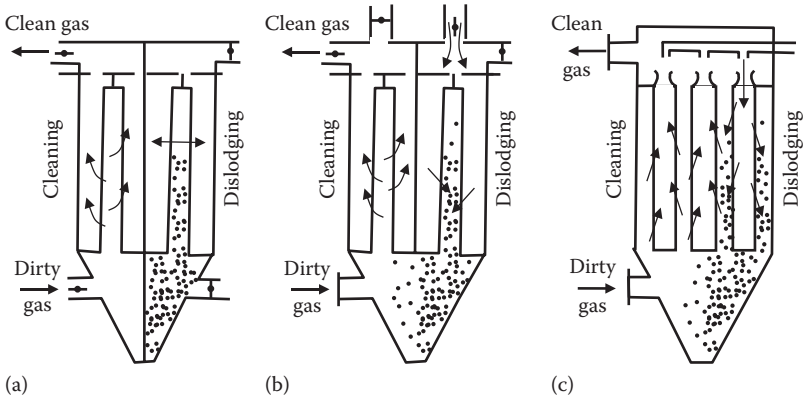


Figure 15.65

Schematics of bag filters. (a) Mechanical shaking type, (b) reverse flow type, (c) pulse jet type.

Table 15.6 Classification of Bag Filter and Feature

Cleaning Mode	Filter			Filtration Side	Filtration Velocity (m/min)	Temperature (°C)	Remarks
	Weave	Shape	Material				
Mechanical shaking		Cylinder		Inside	0.6–1.6	~200	General purpose: Applicable for any gas flow rate and temperature range.
	Woven		Synthetic fiber				Reliable cleaning performance. Suitable for the collection of fume.
Pulse jet	Nonwoven	Envelope	Synthetic	Outside	1~2	~100	Small size collector less than several 10 m^3/min.
		Cylinder	fiber	Outside	1~4	~200	Dust cleaning can be carried out without stopping gas flow.
							Gas flow fluctuation is small. Suitable for small gas flow rate.
							Applicable for high concentration and abrasive dust.
							Applicable for higher filtration velocity.
	Woven	Cylinder	Glass fiber	Outside	0.5~1.5	~250	High resistivity for hot gas. Large filtration area.
	Nonwoven	Cartridge	Synthetic fiber or paper	Outside	0.3~1	~140 ~450	Applicable to low dust concentration, requiring high separation performance like air purification.
	Sintered	Cylinder	Metal fiber Ceramic	Outside	0.5~1.5	~1000	High-temperature gas cleaning.
Reverse flow	Woven or nonwoven	Cylinder	Synthetic fiber	Inside	0.6~1.2	~200	Widely used in cement and iron refining industries.
			Glass fiber		0.3~1	~250	Suitable for high-temperature fume like carbon black, noniron refinery, and so on.
	Nonwoven	Envelope	Synthetic fiber	Outside	1~2	~140	Suitable for large gas flow rates.

15.13 Liquid-Phase Particle Separation (Hydrocyclone)

Hideto Yoshida

The principle of liquid–solid separation is the same as gas–solid separation. Recently, wet separation has been used for producing ceramic particles and in recycling processes. The following should be considered in the wet separation:

1. Particle dispersion control is easy compared to gas–solid separation.
2. A drying or dewatering process is necessary to separate particles from the liquid.
3. The particle inertia is comparable to the fluid inertia.
4. The viscosity of the slurry decreases with increasing temperature, and the particle sedimentation velocity increases as the slurry temperature rises.

15.13.1 Hydrocyclones

Hydrocyclones are widely used in many industrial processes. Experimental studies of the separation efficiency and pressure drop of a hydrocyclone have been reported by Bradley (1958), Yoshioka and Hotta (1955), and Yoshioka (1962). Several flow-controlling methods at the outlet pipe of a hydrocyclone have been proposed by Yamamoto and Jiao (1997) and Chu et al. (2002). Also, a prediction of the flow within a hydrocyclone was made using several turbulence models by Petty and Parks (2001). The performance of axial flow-type hydrocyclone was studied by Sineath and Della Valle (1959). The performance between conical and cylindrical hydrocyclone was examined by Chine and Ferrara (1997).

The characteristics of hydrocyclones are

1. The size of hydrocyclones is small compared to other types of wet classifiers.
2. The cut size decreases with an increase in inlet velocity or with a decrease in the cyclone diameter.
3. The pressure drop is in the range of 0.1–0.5 MPa, depending on the operating conditions.

The general flow pattern in the standard hydrocyclone is shown in Figures 15.16 through 15.66. The coarse particles are collected in the under-flow exit and the fine particles in the over-flow exit. The ratio of inlet volume flow rate to under-flow volume flow rate is referred to as the under-flow ratio, B_d. The normal operating conditions for a hydrocyclone are as follows:

1. Cyclone inlet velocity $u_{in} = 2 \sim 10$ m/s
2. Cyclone diameter $D_c = 1 \sim 30$ cm
3. Pressure drop $\Delta P = 0.1 \sim 0.5$ MPa
4. 50% cut size $d_{p,cut} = 5 \sim 50$ μm
5. Under-flow ratio $B_d = 5\ \% \sim 20\%$

The details of the standard cyclone in Japan (Yoshioka, 1962) with each dimension scaled with the cyclone diameter D_c are also shown in Figure 15.66. The bottom diameter of the conical section is relatively small compared to a gas-cyclone. As the under-flow rate increases, a fluctuating air core is sometimes observed near the axis. In order to improve the sharpness of classification, the air core region should be in a stable state.

Measurements of the tangential velocity distribution for different axial positions obtained by Ohashi and Maeda (1958) are shown in Figure 15.67. The tangential velocity profiles are similar to a gas-cyclone. Solid body rotation occurs near the axial part and a near free vortex profile, represented by the following equation, is created in the outer region:

$$u_\theta r^n = C \tag{15.49}$$

The maximum tangential velocity occurs at about 60% of the vortex finder diameter, and the index n in the aforementioned equation varies from 0.7 to 0.9.

A typical separation efficiency curve obtained using the standard hydrocyclone is shown in Figure 15.68. The fractional separation efficiency approaches the under-flow ratio B_d as the particle diameter decreases.

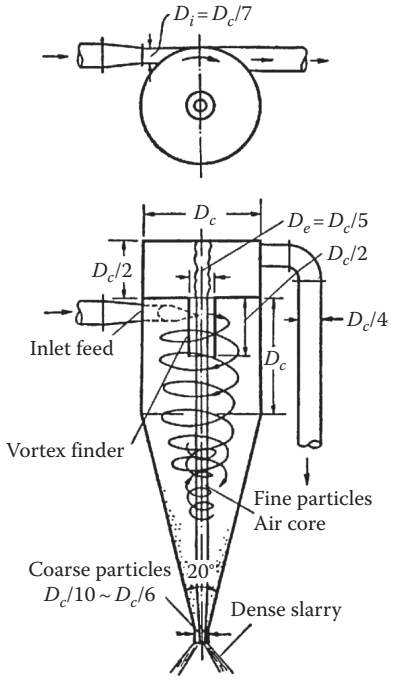


Figure 15.66

Standard hydrocyclone and flow pattern.

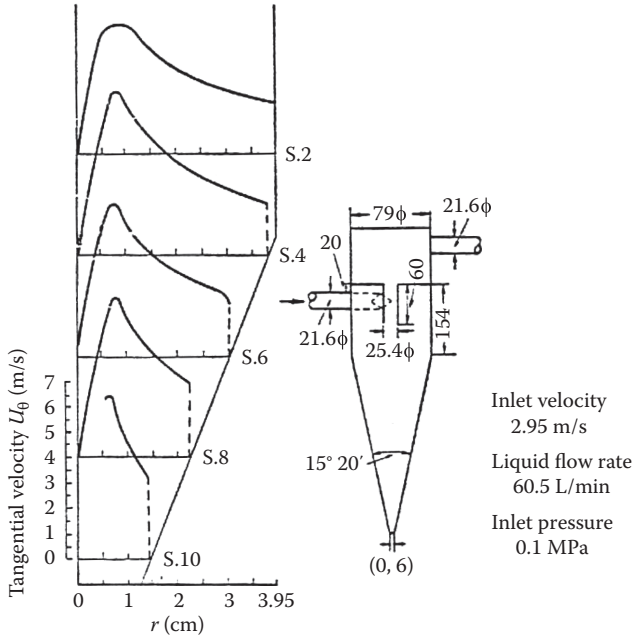


Figure 15.67

Tangential liquid velocity distribution.

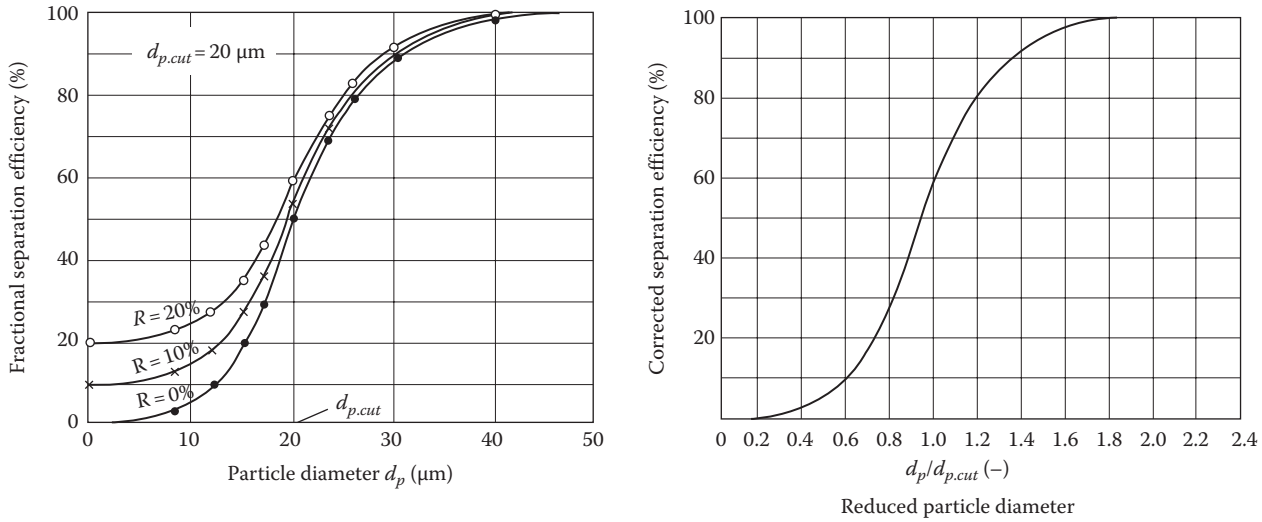


Figure 15.68

Fractional separation efficiency and corrected one.

The experimental data for fractional separation efficiency, $\Delta\mathfrak{E}$, shown in the figure are normalized for different under-flow ratio conditions using

$$\Delta\mathfrak{E}_c = \frac{\Delta\mathfrak{E} - B_d}{1 - B_d} \tag{15.50}$$

where $d_{p,cut}$ denotes a 50% cut size under B_d is zero. The normalized fractional separation efficiency shown in Figure 15.68 can be represented approximately by the following equation:

$$\Delta\mathfrak{E}_c = 1 - \exp\left\{-\left(\frac{d_p}{d_{p,cut}} - 0.115\right)^3\right\} \quad 0.02 \le \Delta\mathfrak{E}_c \le 0.98 \tag{15.51}$$

15.13.2 Control of Cut Size

In order to improve the cut size control easily, the modified hydrocyclone shown in Figure 15.69 has been developed by Isshiki et al. (1997) and Yoshida et al. (2001a). The inlet of the hydrocyclone is fitted with a movable guide plate. The apex cone at the inlet of under-flow side is also attached. Both under-flow and additional-flow methods similar to the gas-cyclone are used to increase classification sharpness in the fine sizes. Using the additional-flow method, pure fluid without particles is introduced in the additional-flow nozzle shown in Figure 15.69. Using the under-flow method, the under-flow is discharged in the under-flow nozzle. In order to decrease the 50% cut size, a movable guide plate, shown in Figure 15.70, was used. Under constant feed rate conditions, the inlet velocity u increases with a decrease in inlet width b_e. The inlet width ratio, G_{eff}, defined by the following equation, is used as a control parameter:

$$G_{eff} = \frac{b_e}{b} \tag{15.52}$$

For the standard case, the value of G_{eff} is unity. Because of increased centrifugal force and the small radial sedimentation distance, small particles are easily collected for the case of a small inlet width. Typical experimental results using the guide plate are shown in Figure 15.71. The 50% cut size decreases from 10 to 7 μm as the inlet width ratio decreases under a constant inlet flow rate. The fractional separation efficiency approaches 0.1 for a particle diameter less than about 5 μm. In order to increase classification sharpness in the small particle diameter region, under-flow and additional-flow methods were used simultaneously.

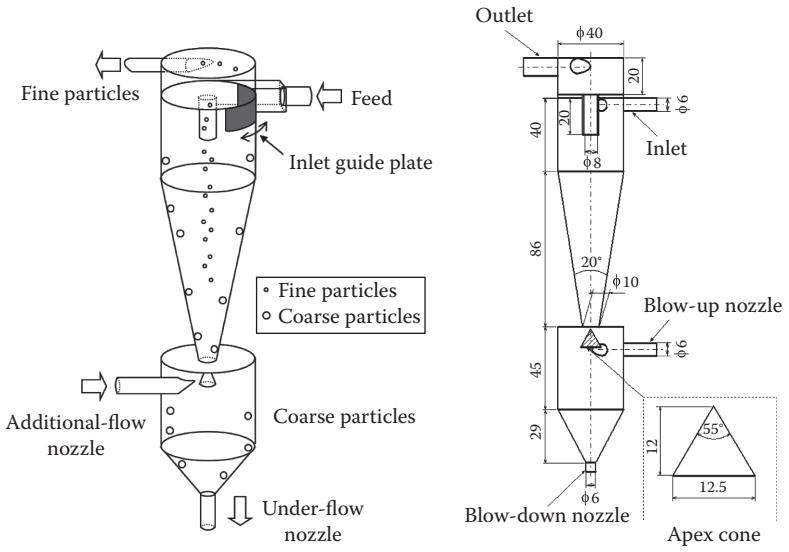
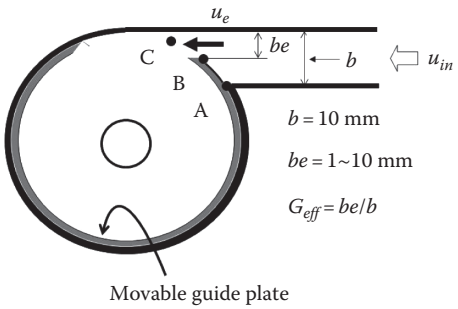


Figure 15.69

Experimental apparatus of a hydrocyclone.



G_{eff} (–)	1.00	0.75	0.50	0.25
u_e (m/s)	1.4	2.1	2.8	3.5

Figure 15.70

Cross section of cyclone with a guide plate.

Some experimental results for the fractional separation efficiency are shown in Figure 15.72. In this case, the under-flow method, additional-flow method, and a movable guide plate were used. The additional-flow ratio was 30%, the under-flow ratio was 10%, and the inlet width ratio was changed from 1 to 0.1. The 50% cut size changes from 35 to 10 μm as the inlet width ratio decreases from 1 to 0.1. The fractional separation efficiency in this case approaches zero as the particle diameter decreases.

15.13.3 Effect of Inlet Slurry Temperature

The viscosity of the slurry decreases with increasing fluid temperature. It would be expected that the cut size would be reduced when the inlet slurry temperature is increased. Yoshida et al. (2004) examined the effect of inlet slurry temperature on cut size change of hydrocyclone. A comparison between the calculated and experimental fractional separation efficiencies for conditions of high slurry temperature is shown in Figure 15.73. For a given value of the fractional separation efficiency, the particle diameter corresponding to the reference temperature of 20°C changes according to the following expression:

$$d_p(T) = d_p(20)\sqrt{\frac{\left(\mu/(\rho_p - \rho_f)\right)_{T°C}}{\mu/(\rho_p - \rho_f)_{20°C}}} \tag{15.53}$$

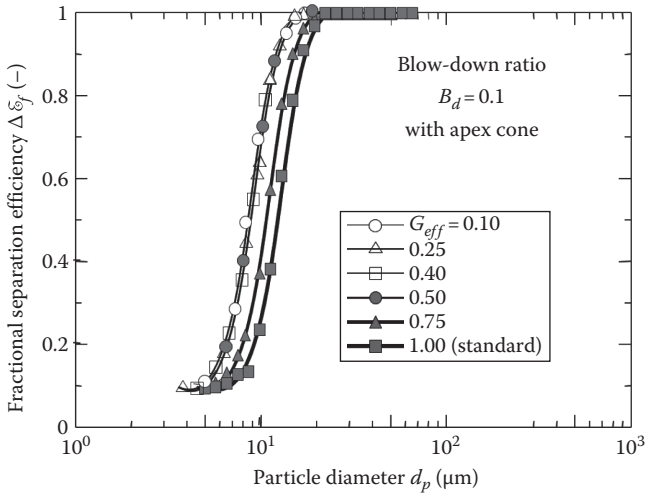


Figure 15.71

Classification performance using inlet guide plate and under-flow method.

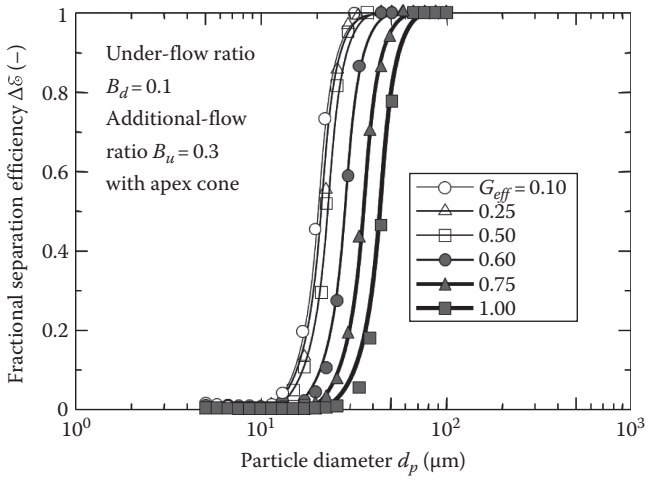


Figure 15.72

Classification performance using inlet guide plate, under-flow, and additional-flow method.

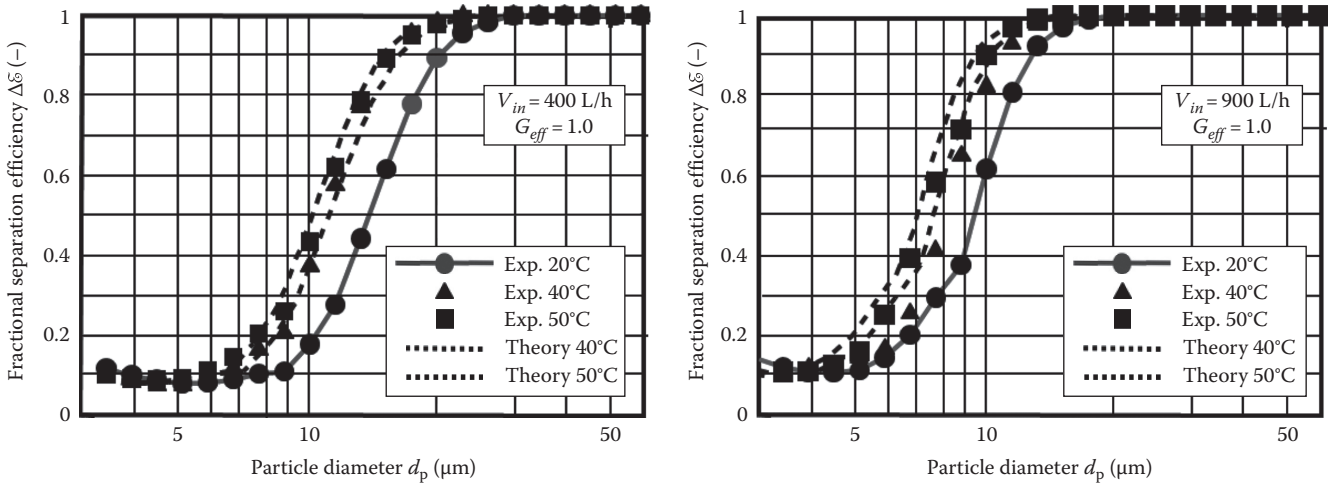


Figure 15.73

Comparison between predicted and experimental fractional separation efficiencies.

Based on the experimental data at 20°C, the fractional separation efficiency for high-temperature conditions can be estimated. The experimental data are in good agreement with the results calculated using this equation. In order to decrease the 50% cut size, the use of an inlet guide plate and an increase in slurry temperature are recommended for practical applications.

Nomenclature

Latin

A	Cross-section area of a dust collector
A_c	Total collection surface area
B_d	Blow-down ratio
B_i	Electric mobility of ions (=1.4 $cm^2/s/V$)
B_u	Blow-up ratio
b	Inlet width of cyclone
b_{eff}	Width of inlet duct
C	Constant with dimension
Cc	Cunningham's slip correction factor
c_p	Particle concentration
$c_{p,in}$	Particle concentration at inlet
$c_{p,out}$	Particle concentration at outlet
D	Cyclone diameter
$\mathfrak{D}$	Diffusion coefficient of particle
D_b	Diameter of discharge duct
D_e	Diameter of vortex finder
d_c	Diameter of a single collector
d_p	Particle size or particle diameter
$d_{p,50}$	50% cut size
$d_{p,cut}$	Cut size
$d_{p,cut}$	Cut size at $R_d = 0$ hydrocyclone
$d_{p,cut}(T)$	Fractional separation efficiency at T°C
d_w	Droplet diameter
E	Electric field strength
$\mathfrak{E}$	Collection efficiency
e	Elementary electric charge
Eu	Euler Number
G_{eff}	Inlet width ratio defined by 15.28
$\overline{G}_i$	Mean thermal mobility of ions (=4.5×10^4 cm/s)
g	Acceleration of gravity
H	Height of the collector
Ha	Inlet height of cyclone
H_H	Total height of cyclone
H_L	Height of cyclone outer cylinder
H_S	Height of vortex finder
H_Z	Height of cyclone cone
h	Inlet height of particle
h_t	Interfiber interval
K	Ratio of length to cyclone diameter defined in Figures 15.16 through 15.22
L	Length of dust collector
$\mathfrak{L}$	Liquid–gas ratio
$\mathfrak{M}$	Molecular mass
$\dot{m}_c$	Mass flow rate collected at dust collector
$\dot{m}_{ca}$	Rate at which particles are collected
m_d	Dust load
m_d	Dust load

$\dot{m}_{in}$	Mass flow rate at inlet
$\dot{m}_{out}$	Mass flow rate at outlet
$\dot{m}_u$	Flow rate of particles in the area projected by obstacle
N	Number of revolution of particle in a cyclone
n	Number of dust collector in series
n	Number of charges on a particle
n	Index for vortex motion
n_i	Ion concentration
ΔP	Pressure drop
ΔP_0	Pressure drop at $c_p = 0$
ΔP_d	Pressure drop due to dust load
ΔP_f	Pressure drop due to fabric
p	Penetration (=1 − ΔE)
Pe	Peclet number (=$d_c u/D$)
$q(d_p)$	Frequency (density) of particle size distribution
q_e	Electric charge on a particle
R	Cyclone radius
$\mathscr{R}$	Interception parameter (=d_p/d_c)
$\mathfrak{R}_u$	Gas constant
r	radius
Rem	Dimensionless parameter defined by 15.44
Re	Reynolds number
S	Total collection surface area
St	Stokes number
T	Gas temperature
u	Fluid velocity
u_{in}	Inlet gas velocity
$\dot{V}$	Gas flow rate
$\dot{V}_b$	Discharge from the dust box
$\dot{V}_{in}$	Inlet flow rate
$\dot{V}_{out}$	Gas flow rate at inlet and outlet
$\dot{V}_u$	Additional-flow rate into the dust box
v_{rad}	Radial velocity of particle to the wall
V_c	Volume of one collection obstacle
v_e	Electric mobility (velocity) of a charged particle
v_{mig}	Migration velocity of particle to the collection wall
v_x, v_y	x-directional particle velocity
v_y	y-directional particle velocity
W	Width
x	Distance from the wall at the entrance of cyclone
X	Effective collection length of a collector
Y	Income height of limiting particle trajectory shown in Figure 15.44

Greek

β	Slope exponent in Equation 15.29
ε_p	Porosity
ε_0	Permittivity
ζ_d	Specific resistance of dust layer
ζ_f	Resistance coefficient of fabric
η	Single body collection efficiency
λ_m	Mean free path of gas molecules
μ	Viscosity
ν	Kinematic viscosity
ρ_p	Particle density

ρ_f	Fluid density
τ	Velocity response time defined by 15.17 relaxation time
τ_{res}	Particle residence time
τ_x	Time to travel from x to reach to collection wall

Subscripts

c	Collector
ca	Captured
d	Dust
f	Fabric
in	Inlet
lk	Leakage
mig	Migration
N	Dry basis at 0°C, 101.3 kPa
out	Outlet
p	Particle
T	Total
t_i	Tangential direction in Table 15.3
t_w	Tangential direction in Table 15.3
θ	Circumferential

References

Ayers, W.H., Boysan, F., Swithenback, J., and Ewan, B.C.R., Theoretical modelling of cyclone performance, *Filtr. Separat.*, 22, 39–43, 1985.

Barth, W., Design and layout of the cyclone separator on the basis of new investigations, *B. W. K.*, 8, 1–9, 1956.

Bickelhaupt, R.E., A Technique for Predicting Fly Ash Resistivity, Interagency Energy/Environment R&D Program Report, EPA-600/7-79-204, 1979.

Bradley, D., Separation efficiency of hydro-cyclone, *Ind. Chem.*, 473–485, 1958.

Briggs, L.W., Effect of dust concentration on cyclone performance, *Trans. Am. Inst. Chem. Eng.*, 42, 511–526, 1946.

Chaing, T. and Ostop, R.P., EPA-666/9-82-005C, 1982, p. 261.

Chine, B. and Ferrara, B., Comparison between flow velocity profile in conical and cylindrical hydrocyclones, *KONA (Powder and Particle)*, 15, 170–179, 1997.

Chu, L.Y., Chen, W.M., and Lee, X.Z., Enhancement of hydro-cyclone performance by controlling the inside turbulence structure, *Chem. Eng. Sci.*, 57, 207–212, 2002.

Clift, R., Ghadiri, M., and Hoffman, A.C., A critique of two models for cyclone performance, *AIChE J.*, 37(2), 285–289, 1991.

Dietz, P.W., Collection efficiency of cyclone separators, *AIChE J.*, 27(6), 888–892, 1981.

Emi, H., *Aerosol Engineering*, Yokendo Publisher, Tokyo, Japan, 1984, p. 186.

Emi, H., Kanaoka, C., Otani, Y., and Ishiguro, T., Collection mechanisms of electret filter, *Particulate Sci. Technol.*, 5, 161, 1987.

Emi, H., Okuyama, K., and Adachi, M., The effect of neighbouring fibers on the single fiber inertia interception efficiency of aerosols, *J. Chem. Eng. Jpn.*, 10, 148, 1977.

Emi, H., Okuyama, K., and Yoshioka, N., Prediction of collection efficiency of aerosols by high-porosity fibrous filter, *J. Chem. Eng. Jpn.*, 6, 349, 1973.

Fukui, K., Yoshida, H., Jikihara, K., and Yamamoto, T., Effects of clean-air injection on particle-separation performance of novel cyclone with sintered metal cone, *Separat. Purif. Technol.*, 80, 356–363, 2011.

Iinoya, K., Fuyuki, T., Yamada, Y., Hisakuni, H., and Sue, H., Dry sub-micron classification by a small blow-down cyclone, *J. Soc. Powder Technol. Jpn.*, 29, 351–355, 1992.

Iinoya, K., Fuyuki, T., Yamada, Y., Hisakuni, H., and Sue, E., Dry sub-micron classification by a small blow-down cyclone, *KONA (Powder and Particle)*, 11, 223–227, 1993.

Iinoya, K., Hisakuni, H., Sue, E., Fuyuki, T., and Yamada, Y., Air cyclone classifier for sub-micron size, in *1990 Proceedings of the Second World Congress on Particle Technology*, Kyoto, Japan, 1990, pp. 120–126.

Iinoya, K. and Nakai, A., Performance of a micro-cyclone, *J. of the Soc. of Material Sci., Jpn,* 18, 189, 523–525, 1969.

Iozia, D.L. and Leith, D., Effect of cyclone dimensions on gas flow pattern and collection efficiency, *Aerosol Sci. Technol.*, 10, 491–500, 1989.
Isshiki, Y., Fukui, K., Yoshida, H., and Kobayashi, A., The control of particle size separation by use of hydrocyclone, *J. Soc. Powder Technol. Jpn.*, 34, 690–696, 1997.
Kanaoka, C., Time dependency of air filter performance, *Earozoru Kenkyu*, 4, 256–264, 1989.
Kanaoka, C., *Industrial Pollution Control Technologies and Regulations*, Maruzen, Tokyo, Japan, 2003, p. II250.
Kanaoka, C. and Emi, H., Collection performance of air filter with dust load, *Kuuki Seijo*, 22, 1–12, 1985.
Kanaoka, C., Emi, H., and Ohta, M., Performances of dust loaded air filters, in *3rd Symposium on the Transfer and Utilization of Particulate Control Technology*, Vol. III, EPA-600/9-82-005c, 1982, 280–289.
Kanaoka, C., Tamori, I., Makino, H., and Yoneda, T., Principle and equipment of dust collectors, in *Fundamentals in Aeorsol Science*, The Association of Powder Process Industry and Engineering, Nikkan Kogyo Shinbun, Tokyo, Japan, 1997, pp. 24–99.
Lapple, C.E., Gravity and centrifugal separation, *Ind. Hyg. Quart.*, 11, 40–47, 1950.
Leith, D. and Licht, W., The collection efficiency of cyclone type particle collectors, new theoretical approach, *AIChE Symp. Ser.*, 126, 196–206, 1972.
Masin, J.G. and Koch, W.H., Cyclone efficiency and pressure drop correlations in oil shale retorts, *Environ. Prog.*, 5(2), 116–122, 1986.
Michaelides, E.E., *Particles, Bubbles and Drops—Their Motion, Heat and Mass Transfer*, World Scientific Publishers, Hackensack, NJ, 2006.
Michaelides, E.E., *Nanofluidics—Thermodynamic and Transport Properties*, Springer, New York, 2014.
Morishima, N., Study on the venturi scrubber, PhD thesis, Osaka City University, Osaka, Japan, 1967.
Noda, N. and Makino, H., Influence of operating temperature on performance of electrostatic precipitator for pulverized coal combustion boiler, *Adv. Powder Technol.*, 21, 495–499, 2009.
Noda, N., Makino, H., Kasai, S., and Nakamura, H., Investigation of improvement methods of dust collection efficiency of advanced low temperature electrostatic precipitator, *J. Soc. Powder Technol. Jpn.*, 51, 349–354, 2014.
Ohashi, H. and Maeda, S., Measurement of velocity distribution in hydro-cyclone, *Chem. Eng. Jpn.*, 22, 200–208, 1958.
Petty, C.A. and Parks, S.M., Flow prediction within hydro-cyclone, *Filtr. Separat.*, 28, 28–34, 2001.
Shepherd, C.B. and Lapple, C.E., Flow pattern and pressure drop in cyclone dust collectors, *Ind. Eng. Chem.*, 31(8), 972–984, 1939.
Sineath, H.H. and Della Valle, J.M., Performance of axial-flow type hydro-cyclone, *Chem. Eng. Prog.*, 55, 59–69, 1959.
Stairmand, C.J., Pressure drop in cyclone separators, *Engineering*, 168, 409–412, 1949.
Takahashi, K., *Kiso Earozoru Kogaku*, Yokendo, Tokyo, Japan, 1978, p. 12.
Yamamoto, K. and Jiao, X., Hydro-cyclone with a perforated inner cylinder, *Trans. Japan Soc. Mech. Eng., Ser. B*, 63, 133–138, 1997.
Yamamoto, M. and Kitamura, O., Computation of turbulent flow in a cyclone chamber with a reynolds stress model, *Trans. Japan. Soc. Mech. Eng.*, 60, 4002–4009, 1994.
Yamamoto, M., Kitamura, O., and Arakawa, C., Computation of turbulent flow in a cyclone chamber with a Reynolds stress turbulence model, *Trans. Jpn. Soc. Mech. Eng.*, 59, 1959–1964, 1993.
Yoshida, H., Akiyama, S., Fukui, K., and Kumagaya, A., Particle classification with improved hydro-cyclone separator, *J. Soc. Powder Technol. Jpn.*, 38, 626–632, 2001a.
Yoshida, H., Akiyama, S., and Taniguchi, S., Fine control of cut size with dry cyclone, *Kagaku Kogaku Ronbunshu*, 27, 574–580, 2001.
Yoshida, H., Fujioka, T., Hashimoto, K., and Nagahashi, K., Effect of blow-down on fluid flow and Particle movement in cyclone classifier, *Kagaku Kogaku Ronbunshu*, 21, 594–602, 1995.
Yoshida, H., Fukui, K., and Iwanaga, T., Effect of inlet shape and slurry temperature on the classification performance of hydro-cyclone, *Powder Technol.*, 140, 1–9, 2004.
Yoshida, H., Ono, K., and Fukui, K., The effect of a new method of fluid flow control on submicron particle classification in gas-cyclones, *Powder Technol.*, 149, 139–147, 2005.
Yoshida, H., Saeki, T., Fujioka, T., and Fuyuki, T., Fine particle separation by revised type air-cyclone classifier, *Kagaku Kogaku Ronbunshu*, 19, 476–482, 1993.
Yoshida, H., Saeki, T., Fujioka, T., and Fuyuki, T., Fine particle separation by revised type air-cyclone classifier, *KONA* (*Powder and Particle*), 12, 178–185, 1994.

Yoshida, H., Saeki, T., Hashimoto, K., and Fujioka, T., Size classification of submicron powder by air cyclone and three-dimensional analysis, *J. Chem. Eng. Jpn.*, 24, 640–647, 1991.
Yoshioka, N., Ekitai-cyclone, *Nikkan Kogyo*, Tokyo, Japan, 1962, pp. 38–41.
Yoshioka, N. and Hotta, Y., Performance of hydro-cyclone, *Chem. Eng. Jpn.*, 19, 632–642, 1955.
Zhou, L.X. and Soo, S.L., Gas–solid flow and collection of solids in a cyclone separator, *Powder Technol.*, 3, 45–53, 1990.

16

Biological Systems and Biomimetics

16.1 Airflow and Particle Deposition in the Upper Respiratory Airways
16.2 Blood Flow
16.3 Biomimetics and Bioinspiration

16.1 Airflow and Particle Deposition in the Upper Respiratory Airways

Goodarz Ahmadi and Omid Abouali

16.1.1 Introduction

The human respiratory system is composed of the upper airways including nasal cavity, throat, larynx, and pharynx and the main body of lung including trachea, main bronchus, and lower bronchial tree, down to the alveolar cavities. This rather complex system provides the supply of oxygen to the blood stream while removing the carbon dioxide. The main role of the upper airways is to condition the inhaled air, including respiration, heating, and humidifying the inhaled air. Another important function of these organs is preventing particles from entering the lungs. The filtering task of the upper airways becomes more important when the breathing of toxic particles through upper airway leads to unhealthy responses (Kreuzer et al., 2000, Balásházy et al., 2003).

16.1.1.1 Anatomy of Human Airway System

The human respiratory system consists of upper airways, including nasal and oral cavity, pharynx, and larynx, and lower airways, including trachea, bronchi, bronchioles, and pulmonary alveoli as shown schematically in Figure 16.1. Air enters from nose or mouth and passes into the pharynx and then flows through the larynx into the trachea and then to the primary bronchi. The bronchioles successively bifurcate about 23 times until they reach the alveoli. In the alveolar cavities, gas exchange with the cardiovascular system occurs.

Figure 16.2 shows a schematic of the nasal cavity that extends from the naris (nostril) to the entrance of nasopharynx. The nostril is the external opening of the nasal passage through which air is inhaled and exhaled. The funnel region following the nostril is the vestibule that extends to the nasal valve region. The nasal passage has its minimum cross-sectional area at the nasal valve region; therefore, the axial component of airflow velocity is the highest in this region. The nasal valve region is connected to the main airway region that has a complex geometry and includes turbinate regions. At the end of the main airway and the beginning of nasopharynx, the left and right nasal cavities merge together and form one passage. Figure 16.2 also shows the inferior, middle, and superior turbinates. One of the functions of the turbinates is to help humidify and thermally condition the inhaled air. In addition, they remove particulate pollutant form the air. The thin wall that is dividing the nose in the center is called the septum. The regions between turbinates and the lateral side of the passage are the inferior meatus, middle meatus, and superior meatus regions.

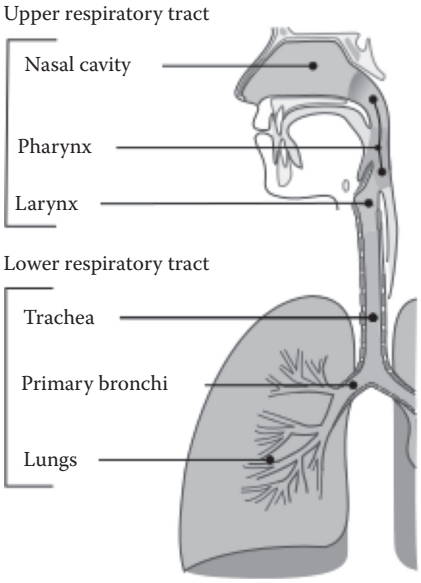


Figure 16.1

Schematic of the human airway system. (From http://en.wikipedia.org/wiki/File:Illu_conducting_passages.svg.)

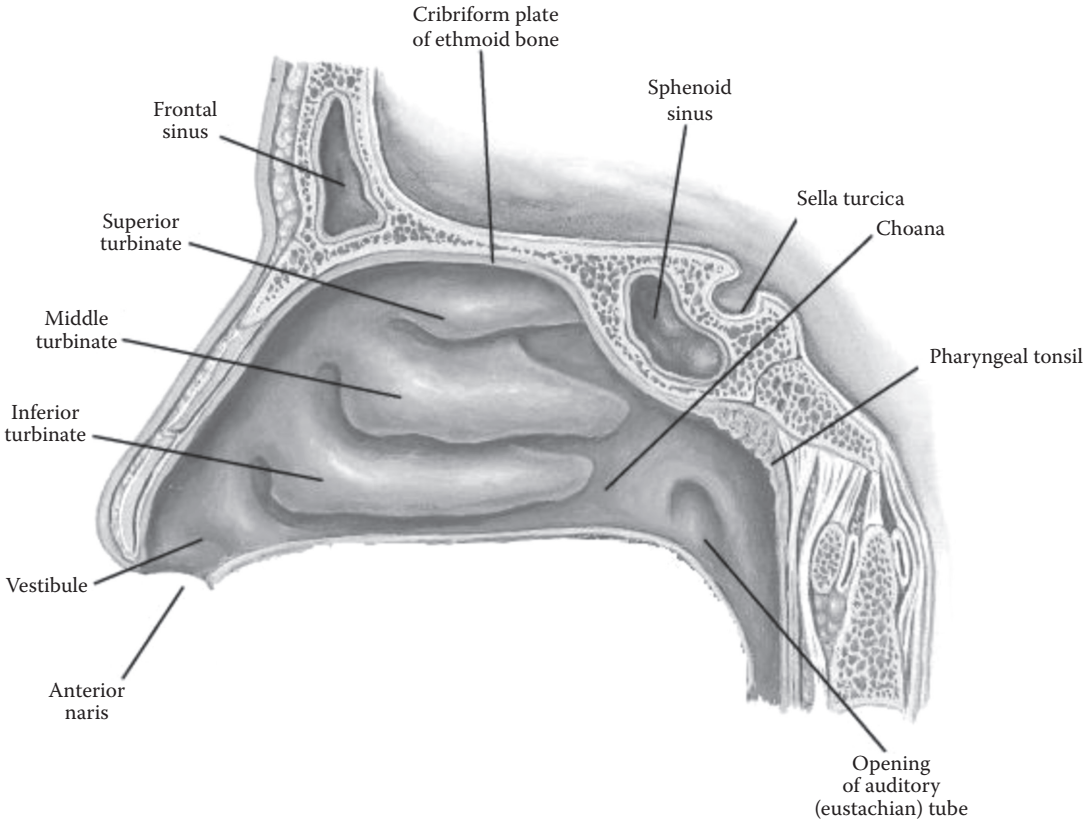


Figure 16.2

Anatomy of a nasal airway. (From http://www.earnosethroatdoctor.net/nose/nose-anatomy2/.)

The sinuses are hollow cavities that are connected in the skull. There are four types of sinuses as shown in Figures 16.3 and 16.4:

1. The maxillary sinuses, which are the largest sinuses of the nasal airway located in the cheekbones
2. The frontal sinuses, which are in the low center of the forehead
3. The ethmoid sinuses, which are between the eyes, at the nasal bridge
4. The sphenoid sinuses, which are located in bones behind the nasal cavity

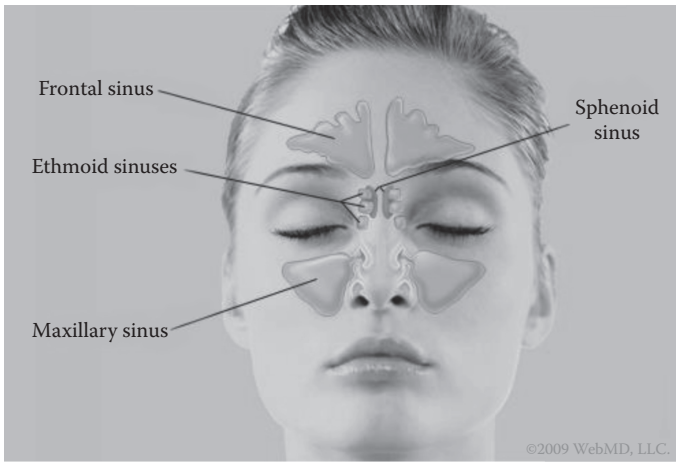


Figure 16.3

Frontal view of a human face showing the locations of the paranasal sinuses: frontal, ethmoid, sphenoid, and maxillary sinuses. (From http://www.webmd.com/allergies/picture-of-the-sinuses.)

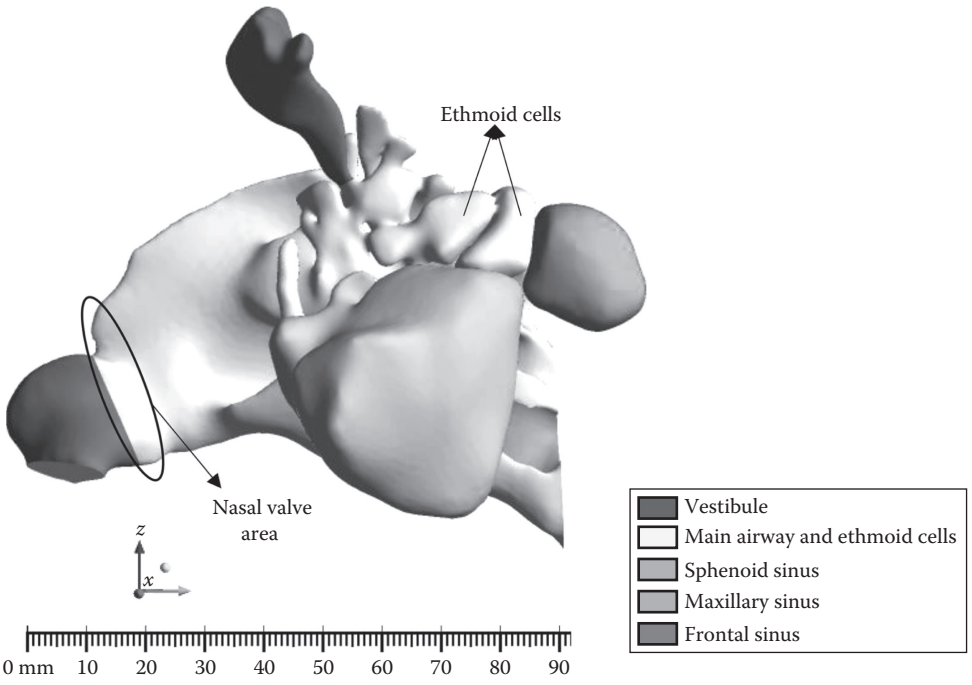


Figure 16.4

A 3-D view of the nasal cavity with all sinuses.

The sinuses walls are lined with mucosa and for a normal person are empty except for a thin layer of mucus. The purpose of the sinuses is not quite clear. It is believed that sinuses have the effect on humidifying the inhaled air and also enhancing the human voices.

16.1.2 Survey of Literature

Understanding the process of inhalation of aerosols has attracted considerable attention because of its significance to human exposure to particulate pollutants and transmission of infectious diseases. Deposition of inhaled particles in the airway passages has been of serious health concerns. These particles include dust, microorganisms, photochemical smog, and other irritants. From the toxicological point of view, all particles that are smaller than 10 μm in diameter can be biologically active and could cause allergic responses and even cancers in susceptible individuals (Cheng, 2003, Heyder, 2004). According to the studies of Frampton (2001), Donaldson et al. (2000), and Oberdorster (2001), fine and especially ultrafine particles are more likely to be harmful and toxic compared to micrometer-sized particles of the same material, and deposition of these ultrafine particles in the lungs can contribute to serious pulmonary diseases such as lung cancer. The sources of these fine aerosols include diesel exhaust 5–500 nm (Kittelson 1998), cigarette smoke (140–500 nm) (Keith, 1982, Bernstein, 2004), and radioactive decay (1–200 nm) (ICRP, 1994). In addition, some of these ultrafine aerosols are biologically active, such as avian flu and SARS, which typically range from 20 to 200 nm (Mandell et al., 2004).

On the other hand, for therapeutic inhalation drug delivery, it is important to make sure particle deposition occurs at targeted areas. Some pharmaceutical aerosols are larger than 20 μm in order to maximize their deposition in nasal cavity and upper airways before entering the lungs. On many other cases, particles smaller than 5 μm (Suman et al., 2006) and sometimes in the submicrometer size range are used in order to make sure of their passage through the upper airways and the delivery of the drug into the lung (Longest and Hindle, 2010). Thus, estimating the fraction of particles of different sizes and physical properties that penetrate into the lung and predicting the distribution of deposited particles in different regions of the human airways are of considerable interest not only to determine what reaches the lung but also to quantify the dose to the upper airways for both health risk and therapeutic effectiveness of inhaled particles. Estimating the regional deposition fraction (DF) of pharmaceutical aerosols is important for treating localized respiratory tract infection. For an acceptable average drug dose, it is still important to be aware of the regional deposition rates since a high local drug dose may cause tissue injuries or initiate a new disease. Thus, understanding the regional particle deposition in human upper airway and the fraction of particles entering the lungs is very important for controlled pulmonary drug delivery.

16.1.2.1 Eulerian and Lagrangian Approaches

Although particles are carried by the breathing air through the respiratory system, their trajectories differ from the airflow streamlines due to their inertia and effects of various forces. The most important forces are gravity, drag, and Brownian motion. Particles are then deposited on the walls of the airway by sedimentation, impaction, and/or diffusion mechanisms (Heyder, 2004). There are two methods for analyzing particle transport and deposition, namely the Lagrangian and the Eulerian methods. The Eulerian approach is more efficient for ultrafine particles when the Brownian excitation is dominant, while the Lagrangian approach is more suitable for dilute suspension of larger particles for which the inertia is important.

All earlier studies suggest that in inertial regime ($d_p \geq 1$ μm), particle deposition increases as particle diameter and airflow rate increases, although there are some differences in the estimated values of DF between different studies even when those estimates are for models constructed from a single set of medical images. This is partly due to the small relative dimension of the airway so that slight differences in the model geometry significantly affect the DF of particles. In addition, variability of the airway of different subjects results in variation of the aerosol deposition under seemingly identical conditions (Wang et al., 2008, Garcia et al., 2009). The differences between evaluated DFs for airway of the same human subject may arise from resolution of magnetic resonance imaging (MRI) or computed tomography (CT) scan images, number of coronal images used for producing the 3-D geometry of the airways, and different techniques of replica cast fabrication.

16.1.2.2 Realistic 3-D Models

Two decades ago, numerical models of the airflow and particle deposition in airway system were limited to simplified and even 2-D models. With improvement of the numerical algorithms and the advances in computer technologies, the numerical solutions for real 3-D geometries of the respiration system have become available. In particular, the computational fluid dynamics (CFD) approach has now matured to the extent that is being widely used to simulate the flow fields in complex configurations and, more recently, the airflow in human airways. In addition, recent advances in developing computer models for complicated geometries provide the opportunity to generate realistic 3-D models for human airways in rather short times. Therefore, the details of airflow and transport of pollutants and aerosols in the respiratory system of individual people can be predicted.

16.1.2.3 Abnormality

CFD models for the airflow dynamic and particle deposition are not limited to healthy human airways; in the past decade, using CFD for studying the respiration systems with different types of abnormalities and performing virtual surgeries and evaluating the outcome of the medical operation in advance have attracted considerable attention. Recent advances in computational modeling allow the creation of models for individual patients with specific abnormalities. In addition, the computational modeling results can be obtained in several days rather than several months that were previously required. Thus, CFD provides the opportunity to predict the details of respiratory airflow and the corresponding transport of gaseous chemicals, aerosols, heat, and water vapor in the airway of an individual patient before and after operations.

Abnormal nasal airways could occur due to the presence of deviation and/or obstruction in the bony or cartilaginous septum of the nasal passage. Deviation in the nasal airways is a common disease that makes septoplasty one of the most frequently performed operations in the nasal airway. The current standard rhinometric measurements provide information on the total nasal airflow rate, pressure drop, and nasal cross-sectional area but cannot reveal changes in the patterns of local airflow. Such general data are inadequate for quantifying the functional impact of nasal obstruction and the effectiveness of the subsequent surgical outcomes. For example, the long-term outcomes of septoplasty are still not quite satisfactory, and a large percent of the patients continue to complain about nasal obstruction following the operation. CFD can be used as a tool for virtual surgery to test various scenarios and for selecting the proper procedure for the optimal outcome of the operation before the surgery (Zachow et al., 2006, Zhao and Dalton, 2007, Ozlugedik et al., 2008, Moghadas et al., 2011). In addition, understanding particle deposition in the human respiratory system is important in connection to odorant delivery rates (Zhao et al., 2004) and therapeutic drug delivery (Inthavong et al., 2008a) of local airflow. Chronic rhinosinusitis (CRS) is another common disease affecting many patients around the globe. When medical management of CRS fails, endoscopic sinus surgery (ESS) is the recommended treatment. Uncinectomy and middle meatal antrostomy (MMA) are fundamental steps in functional ESS (FESS). Uncinectomy involves detachment and removal of the uncinate process, which is a thin, sickle-shaped structure that covers the entrance to the maxillary sinus. MMA means dissection of the medial wall of the maxillary sinus for better exposure of the cavity of this sinus. Uncinectomy and MMA affect the nasal passages' anatomy and may lead to substantial changes in airflow; consequently, the inhaled particle deposition pattern in the nose could also change. From a clinical point of view, it is desirable to perform a virtual surgery in advance of the actual surgery to assess the potential changes in the nasal airflow and the associated aerosol particle deposition pattern and filtration. In addition, the virtual surgery would allow for testing various alternatives and for optimal surgical planning.

Drug delivery devices for airways play an important role in the health issues of human respiratory system. Inthavong et al. (2008) determined critical parameters for the study and design of effective nasal drug delivery devices by taking images of droplet formation from a nasal spray device in an experimental setup. They found that the critical parameters are particle size, diameter of spray cone at a breakup length, and the spray cone angle. They transported the obtained data into initial particle boundary conditions for particle flow simulation within the nasal cavity by using CFD. The results from this qualitative study aim to assist the pharmaceutical industry to improve the design of nasal spray devices. Inthavong et al. (2011) added the nasal spray device in their computational model. They compared the subsequent airflow patterns and its effects on particle deposition, with and without a spray device.

16.1.2.4 Particle Shape

Another concern for particle deposition in the human airway is the shape of the particles. In earlier works, typically the particles are assumed to be spherical, but in reality many natural and man-made particles are nonspherical. For example, although the use of asbestos fibers has been banned, there are still many old buildings that have asbestos-based heat insulation. In addition, new fibrous materials such as vitreous fibers (MMVFs) are currently being manufactured for many applications. It has been shown that some MMVFs may have adverse carcinogenic effects similar to that of asbestos (Cavallo et al., 2004). Therefore, potential risk of lung diseases related to fiber inhalation is still a serious health issue. The adverse effects of particulates also depend on the region of the airway in which the particles/fibers deposit. Thus, the knowledge of regional deposition of fibers in the respiratory tract is of considerable importance. Regional deposition is not likely to be studied in in vivo or even in vitro experimental investigations. In contrast, the computational modeling approaches have the capability to conveniently estimate the regional deposition pattern of aerosols including fibrous particles. In particular, the location of peak deposition in different parts of the respiratory tract can be identified.

16.1.2.5 Upper Respiratory System

In this section, a survey of the earlier work on the upper human respiratory system addressing the noted points is presented. Numerous experimental and numerical studies of the airflow dynamic and the associated particle deposition in the nasal cavity have been reported in the literature. The work of Keyhani et al. (1995), Subramaniam et al. (1998), Zhao et al. (2004), Weinhold and Mlynski (2004), Zachow et al. (2006), and Wen et al. (2008) are some examples of recent numerical studies of the nasal airflows. Computer simulations of particle transport and deposition in the nasal passages were reported by Zamankhan et al. (2006), Shi et al. (2007), Liu et al. (2007, 2010), Xi and Longest (2008), Wang et al. (2009), Se et al. (2010), Moghadas et al. (2011), and Abouali et al. (2012), among others. While most of these numerical studies were restricted to the nasal passages from nostrils to the end of nasopharynx, some others, such as the work of Martonen et al. (2002) and Farhadi Ghalati et al. (2012), included those about the larynx, pharynx, and trachea and/or first bronchial branches. More recently, considerable attention was given to the regional deposition of particles in the respiratory system (Jayaraju et al., 2007, Mylavarapu et al., 2009, Wang et al., 2009, Xi et al., 2011, Abouali et al., 2012, Farhadi Ghalati et al., 2012, Tavakoli et al., 2012, Ghahramani et al., 2014, Dastan et al., 2014).

16.1.2.6 Experimental Studies

Hahn et al. (1993), Schreck et al. (1993), Kelly et al. (2000), and Doorly et al. (2008) performed the experimental investigation of the airflow in the nasal cavity. Experimental results indicated that the nasal airflow was laminar up to a breathing rate of about 24 L/min (Hahn et al., 1993). Later, Kelly et al. (2000) found that for their nasal models the airflow is laminar for airflow rate up to about 15 L/min.

Many experimental studies on particle transport through human nasal passages were also reported in the literature. Strong and Swift (1987), Cheng et al. (1988), and Swift et al. (1992) measured the capture of ultrafine particles in the human nasal passage. Cheng et al. (1993, 1996), Swift and Strong (1996), and Cheng (2003) presented empirical relations for deposition efficiency in the human nasal passage. Kelly et al. (2004a,b) measured the particle deposition in a nasal cavity replica model with different surface qualities. These included a stereolithography (SLA) nasal replica model with greater surface roughness and a Viper nasal replica model (manufactured with a Viper Si2 machine) with a smooth surface. They suggested that the surface quality does not significantly affect the nasal deposition efficiency of nanoparticles. However, the microparticle deposition efficiency strongly depends on the surface roughness. Numerous experimental studies have been performed to measure the total nasal deposition, both in vivo and in vitro using human volunteers. While these provide the most physiologically realistic approach, they are inevitably limited by the number of flow rates and particle sizes that can be used and the data are associated with the intersubject variability. The nasal replica casts, however, offer the opportunity for detailed measurements of the nasal passage and can be studied for a wide range of flow rates and particle sizes. There are, however, limitations on the level of surface finish in the manufacturing process, which affects the airflow and the deposition of micron-sized particles and/or sometimes smaller particles. Schroeter et al. (2011) categorized the sources that cause differences in the estimated DF into *wall roughness* and *surface smoothness*. Accordingly, the term "wall roughness" is used to denote the surface resolution of the rapid prototyping machine used to fabricate the airway replica casts and is normally excluded in numerical approaches, while the term "surface smoothness" is used to describe surface irregularities due to coarse imaging data and poor interpolation between consecutive cross sections in sectional anatomic data. That is, the DF in nasal cavities is strongly affected by the model developing procedure for

both experimental and numerical studies, in addition to the interindividual differences between human subjects. As a result, although it was tried to reduce the data of different cases to a single graph (Wang et al., 2008, Garcia et al., 2009), generally, validation can be done only with the trend of the data.

16.1.2.7 Oral Upper Airway

The airflow structure and particle deposition in oral airway were also studied numerically by many researchers. Most of these studies utilized a simplified model of the oral airway (Zhang et al., 2002, 2005, Kleinstreuer and Zhang, 2003). Jayaraju et al. (2007) and Tavakoli et al. (2012), however, reported the results of their numerical studies for the airflow field and particle deposition in realistic geometries of human oral airway. Cheng et al. (1999) investigated the effects of breathing rate and particle size on the deposition pattern in a human oral airway cast. The airway replica included the oral cavity, pharynx, larynx, trachea, and three generations of bronchi. Except for the oral cavity, all the other airway portions of the cast were made from a cadaver. For micrometer particle sizes, they reported that the deposition efficiency is a function of the Stokes number and concluded that impaction is the dominant deposition mechanism. Grgic et al. (2004) presented regional and total deposition measurements in several realistic mouth and throat geometries and reported the effects of intrasubject and intersubject variations in geometry on both total and regional deposition efficiencies. They showed when the total deposition data from all different geometries are plotted versus Stokes number, all the graphs collapse onto a single curve. They found that the mouth area is the most effective filter for capturing the inhaled aerosols. Verbanck et al. (2011) studied both inspiratory and expiratory deposition efficiencies of microparticles in realistic upper airway geometry both experimentally and numerically. They found that expiratory and inspiratory deposition efficiency curves were almost identical. But the regional deposition efficiency in the upper airway model was different during inspiration and expiration, with preferential deposition, respectively, in oral and pharyngeal regions. Zhang and Kleinstreuer (2011) presented a CFD analysis of airflow and nanoparticle deposition in the combined nasal–oral–tracheobronchial airway model. They found that the change from nasal to oral breathing markedly influenced the regional deposition pattern in the upper airways. Also, the change in breathing route noticeably affects the deposition rates in the regions from pharynx to bronchial airways for nanoparticles less than 5 nm. However, the effect on the regional deposition of larger nanoparticles (>5 nm) beyond the pharynx region is small.

16.1.2.8 Tracheobronchial Airways

The airflow and particle deposition in tracheobronchial airways and lung have also been the subject of a lot of studies in the past three decades. A brief review of some of the pertinent recent work is provided in this section. Zhang et al. (2002) simulated the airflow and particle transport under the 3-D transient laminar flow conditions for a symmetric triple bifurcation lung airway model (i.e., Weibel's generations G3–G6). Three inhalation conditions related to rest, light, and moderate activities were analyzed for ranges of inhaled particles with Stokes numbers, $St < 0.2$. They reported particle deposition patterns in the triple bifurcations. Zhang et al. (2005) presented their numerical simulation results for microparticle and nanoparticle deposition for a simplified human airway model covering the mouth to the planar airway generation G3 under different inspiratory flow conditions. They presented their results in the form of deposition patterns, local concentrations, and segmental averages. Li et al. (2007) studied the particle deposition in the human tracheobronchial airways considering a more realistic computational model under transient condition. Their airway model consisted of trachea to the third bifurcation generation. Adding the trachea rings and accounting for the nonsymmetric behavior of the bifurcations were the new changes to their earlier simple airway model. The results showed that the relation between particle-release positions at the trachea inlet and the particle depositions at specific lung sites are mainly affected by the complex airway geometry and the airflow rate magnitude. Inthavong et al. (2010) studied the micron particle deposition in a tracheobronchial airway model under different breathing conditions. They developed a realistic computational model of a human tracheobronchial airway from CT scans. They found that a deep inhalation with a breathhold of 2 s increases the deposition in the first few airway generations, but it does not necessarily increase the deposition up to the sixth branch generation. Also, their results showed that the breathhold allows the deposition by sedimentation, which could assist in targeted local deposition. Longest et al. (2012) compared the metered dose inhaler (MDI) and dry powder inhaler (DPI) aerosol deposition using in vitro experiments and a new stochastic individual path (sip) model of the conducting airways. Their airway model consisted of the mouth–throat and tracheobronchial trees. They found that the drug delivery to the tracheobronchial region using the MDI is approximately two times more compared with that for the DPI.

16.1.2.9 Nasal Upper Airways

The numerical analysis of the respiratory flow pattern in a realistic nasal human upper airway was presented by Wang et al. (2009). The airway model in their work consisted of the nasal cavity, pharynx, larynx, and trachea fabricated based on the CT images of a healthy volunteer and also the triple bifurcation based on Weibel's model. Mylavarapu et al. (2009) developed an anatomically accurate human upper airway model constructed from multiple MRI axial scans. They used this model to conduct detailed CFD simulations during expiration to investigate the airflow in the airway regions where obstruction could occur. They also measured the pressure and velocity experimentally in a physical model prototype. The airway model in their work consisted of the nasal cavity, pharynx, and larynx and the inlet section of trachea. Xi et al. (2011) evaluated the transport and deposition of respiratory aerosols in a nasal–laryngeal airway model based on MRI head images of a 5-year-old boy. Recently, Farhadi Ghalati et al. (2012) developed a more comprehensive and realistic model, which covered the upper airways from nasal cavity to the end of trachea, and performed a series of numerical analysis of local deposition of micro-/nanoparticles. Knowledge of the localized and subregional particle deposition rates may be helpful in specifying the site of the highest possibility for respiratory lesions. Current risk assessment approach uses the spatially averaged dose overbroad regions of the respiratory tract (G. U.S. General Surgeon report, 2006, Foos et al., 2008). But the concentrations of particulate matter for localized deposition may exceed area-averaged values by several orders of magnitude resulting in the formation of dosage hot spots (Xi and Longest, 2007, 2008). It is important to identify these deposition hot spots for which formation of cancer is more probable. That is, the information of local deposition could be useful for health risk assessment because a high local dose may cause tissue injuries or initiate a disease process (Kim et al., 1996), whereas the average dose could be still negligibly small.

16.1.2.10 Virtual Surgery

There have been a number of papers in literature that studied the effect of pathological conditions in patients. The presence of polyps, swelling, atrophy, or resection of turbinates and enlarged adenoids in the nasal airflow were studied using cadaver models by Tonndorf (1939), Proetz (1951), and Swift and Proctor (1977). Grützenmacher et al. (2006) inspected the presence of compensatory hypertrophy of turbinates. Chung and Kim (2008) applied digital particle image velocimetry procedure to study the consequence of turbinate modification on the airflow patterns during respiration. In addition, they studied the airflow patterns in both nasal cavities of a patient with an asymptomatic deviated nasal septum. Ozlugedik et al. (2008) inspected both the effects of septal deviation and concha bullosa on nasal airflow, as well as the aerodynamic changes induced by virtual septoplasty and partial lateral turbinectomy. Chen et al. (2009) carried out a CFD study to provide information on the aerodynamic consequences of nasal septal deviation on the turbulent airflow patterns and their related physiological functions. Moghadas et al. (2011) investigated numerically the effect of septal deviation on the flow patterns and deposition of micro-/nanoparticles in the realistic human nasal airways before and after septoplasty. Their study showed that CFD provides a suitable tool for predicting the airflow and particle deposition patterns in the nasal passages that specific surgical interventions would produce. Thus, it is expected that CFD could help the medical professional to optimize the selection of surgical interventions for specific patients.

Although in the past decade numerous computational simulations of airflow and particle deposition patterns in the nasal cavity were reported in the literature, in most cases, the sinuses were not included in the numerical model. In fact, the number of papers in the literature discussing the airflow in the nasal airways including the sinuses is very few. Lindemann et al. (2005) simulated the intranasal airflow after radical sinus surgery during inspiration. They performed an aggressive virtual operation on the CT scan model of the nose, which included a bilateral model of the human nose with maxillectomy, ethmoidectomy, and resection of the lateral nasal wall and the turbinates. They concluded that aggressive sinus surgery led to disturbed intranasal airflow patterns and a reduction of the effective surface area in relation to the nasal volume. Zachow et al. (2006) presented their airflow simulations using CFD for a highly detailed anatomy of a nasal airway including the frontal and paranasal sinuses. They showed that a very small part of the airflow entered the sinuses. Using CFD modeling of one volunteer patient's nose pre- and postoperative, Zhao et al. (2006) showed significant improvement in postsurgical ortho- and retronasal airflow and odorant delivery rate to olfactory neuroepithelium (by a factor of 1000 times), which correlated well with olfactory recovery. Ethmoid and sphenoid sinuses were included in their computational model, and it was shown that the airflow velocity within the sinus is quite low, confirming the limited effect of the sinus on the overall nasal airflow field. Xiong et al. (2008) utilized CFD techniques to construct a numerical simulation of nasal

cavity airflow pre- and postvirtual functional endoscopic surgery (FESS). A virtual FESS intervention was performed numerically on the normal nasal model using the Fluent™ software. In the post-FESS model, they found an increase in airflow distribution in the maxillary, ethmoid, and sphenoid sinuses and a 13% increase through the area connecting the middle meatus and the surgically opened ethmoid. Xiong et al. (2011) used CFD to compare nasal airflow after two different surgical interventions, which involved opening the paranasal sinuses, excising the ethmoid sinus, and excising or preserving the uncinate process, in a cadaveric head model. They concluded that the preservation of the uncinate process may significantly reduce the alteration of nasal cavity airflow dynamics after FESS for CRS. Abouali et al. (2012) constructed realistic 3-D computational models of the human nasal passage for pre- and postvirtual uncinectomy and MMA. They showed that after maxillary sinus endoscopic surgery, the maxillary sinus ventilation changes dramatically and the deposition of inhaled nano-/microparticles in the sinus increases. Kim et al. (2013) reviewed methods and challenges for developing patient-specific CFD models of nasal airflow. They described several CFD case studies for deviated nasal septum (decision for surgery), turbinectomy, and maxillary sinus ventilation (simulated and postsurgery) on patient-specific 3-D models of nasal cavity. They concluded that while using CFD for diagnosis and outcomes of nasal surgery has considerable potential, the challenges will be the standardizations of the methodology for creating 3-D airway models and the CFD procedures.

16.1.2.11 Turbulence Effects

Another challenge in the numerical modeling of the airflow and particle transport in human airway system is accounting for the flow turbulence effects. Small particles in a turbulent airflow stream are significantly influenced by the turbulence fluctuating velocities leading to the so-called turbulence dispersion. For a reliable analysis of particle trajectories, these fluctuations should be calculated and the corresponding instantaneous flow velocity should be evaluated. The most accurate approach for evaluating the fluctuation velocity in turbulent flows is the direct numerical simulation (DNS), and that is followed by the large eddy simulation (LES) method. For DNS, the Navier–Stokes equation is solved using sufficiently fine grids that can resolve the Kolmogorov scales (smallest length and time scales of turbulence) to capture the smallest eddies and highest frequencies of turbulence. DNS, however, requires extensive computational resources and so far has been used for very simple geometries such as channels and pipes (Nasr et al., 2009). When the grid size is somewhat larger than the Kolmogorov length scales, the LES method is used, where scales larger than the grid are resolved and the effect of subgrid scale fluctuations are modeled. However, the LES is also computationally expensive and also requires accounting for the effects of turbulence subgrid scale fluctuations. While some investigators (e.g., Liu et al., 2007, 2010, Salmanzadeh et al., 2010, Dehbi, 2011) used LES in their analysis, most researchers used the Reynolds averaged Navier–Stokes (RANS) equations and a turbulence model. In these cases, the effect of turbulence fluctuations on particle dispersion needs to be included. The RANS models were used by many previous investigators. For example, Katz et al. (1999) and Stapleton et al. (2000) used the standard k–ε model and Renotte et al. (2000) used the RNG, k–ε model. Some researchers tried to first validate the models for similar but simpler flow fields and then apply them to more complex flows. For example, Zhang and Kleinstreuer (2003) tested different two-equation turbulence models and recommended the use of the standard k–ω model with low-Reynolds-number (LRN) corrections for LRN flows, which includes laminar to turbulent transition. The application of the standard k–ω model can also be found in the work of Matida et al. (2004), Grgic et al. (2006), Ball et al. (2008), Tavakoli et al. (2009), and Alexopoulos et al. (2010). The SST k–ω is another k–ω-based turbulence model that was used by Liu et al. (2007, 2010) and Jayaraju et al. (2007, 2008). Earlier, Li and Ahmadi (1995) emphasized the importance of anisotropy of turbulence fluctuations near the wall on particle deposition and used an anisotropic nonlinear turbulence model for analyzing particle deposition in the first lung bifurcation. However, in many studies, the isotropic models including the LRN k–ε model that was developed by Launder and Sharma (1974) was used.

As noted before, the RANS models compute the mean flow field, as well as the root mean square (RMS) turbulence fluctuations. To include the turbulence dispersion effects on particle trajectories, the fluctuating velocity field at the location of particles needs to be evaluated. Typically, the discrete random walk (DRW) and the continuous random walk (CRW) models are used. In DRW models, which are also known as the eddy interaction models, it is assumed that each particle has a succession of interactions with turbulent eddies that have limited life and length scales and the fluctuating velocities can be found from turbulent quantities of the eddies. The original form of this model was proposed by Gosman and Ioannides (1983) and was used by a number of researchers such as Katz et al. (1999), Jayaraju et al. (2007, 2008), Kleinstreuer and Zhang (2003), and Liu et al. (2007, 2010) in order to take into account the turbulent fluctuations effect

on particle dispersion in respiratory systems. It should be noted that the use of the original DRW model for inhomogeneous and anisotropic turbulent flows can lead to unrealistic results and the particle deposition would be overestimated since this model shows a tendency for small particles to concentrate near the walls, especially in the diffusion-dominated flows (Mehel et al., 2010). In fact, when this model is combined with turbulent RANS models, it is assumed that the flow is homogenous and isotropic. One major issue with the k-ε and k-ω turbulence models is that they are based on the Boussinesq approximation that assumes that the turbulence fluctuation field is isotropic. Therefore, the use of k–ε or k–ω models in combination with the DRW model leads to unphysical particle dispersion predictions. Tian and Ahmadi (2007) showed that the use of this model even in combination with anisotropic Reynolds stress models (RSMs) can lead to overprediction of particle deposition rate in simple duct flows. However, some investigators tried to use a modified version of this model to take into account turbulence anisotropy (Matida et al., 2004, Zhang et al., 2004, 2005, Inthavong et al., 2006, 2009, Tian and Ahmadi, 2007).

While DRW models describe fluctuating velocities as piecewise constant functions of flow properties, CRW models compute the fluctuation velocities as continuous functions. These models were also extensively used in homogeneous turbulent flows where statistically averaged turbulent properties are position independent. For inhomogeneous flows, Durbin (1983, 1984) and Thompson (1984) suggested the use of the normalized form of the Langevin equation. Dehbi (2008) improved the method and applied it for predicting turbulent dispersion of particles in idealized mouth–throat geometry (Dehbi, 2011).

For modeling the particle transport and deposition in the respiratory systems, the most critical step is the determination of the airflow regime. Like many other flow fields, transition from laminar to turbulent flow regime in the respiratory tract does not occur at a specific flow rate and depends on various factors. In other words, because of the anatomical differences, the flow regime for a given breathing rate may be turbulent in the respiratory tract of a person, while it could be laminar in the airway passages of another person. Jayaraju et al. (2007) studied the flow field in a real mouth–throat model and showed that even for a moderate breathing rate of 15 L/min, the flow is in turbulent regime especially after the glottis. On the other hand, Hahn et al. (1993) concluded that the flow is laminar for a flow rate of less than 12 L/min in a single nasal passage. Also Doorly et al. (2008) reported some instability in the flow field for the flow rate of 12 L/min in a single passage for an inspiratory jet entering the nasal cavity, but they observed a relatively undisturbed laminar flow within most of the cavity. Furthermore, the type of flow may vary with time over a dynamic inhalation/exhalation cycle. While the onset of transition from laminar to turbulent regime depends primarily on Reynolds number, it also varies with the flow geometry (which is somewhat different for different subjects). Nevertheless, it is certain that for flow rates of 30 L/min and more, the transition from laminar to turbulence occurs and the flow field should be simulated using a turbulence model.

16.1.2.12 Surrounding Effects

Another challenge in the study of the inhalation of air and aerosols is the important effects of the surrounding environment including the subject facial feature. In most numerical investigations, a detached airway system with either a uniform pressure or uniform inlet airflow velocity was considered and the external environment to the body was not included in the computational model. It is, however, generally known that many parameters such as air ventilation conditions, ambient airflow speed and temperature, and even people positions affect the inhalation process and particle deposition in the respiratory track. Understanding the effect of external environment and facial features on the human exposure to particulate matter has attracted some attention in the recent years. Kennedy and Hinds (2002) used a full-sized and a torso mannequin and studied particle inhalation through nose and mouth during breathing. Se et al. (2010) studied the effect of human facial feature on particle inhalation and the total deposition in human airways using CFD for a rather crude mannequin model. In their experimental studies, Berry and Froude (1989) and Baldwin and Maynard (1998) paid attention to the air environment calm. They defined the calm air as a condition where the wind speed rarely exceeds 0.3 m/s. Using a mannequin, Hsu and Swift (1999) measured the inhalability of ultra large aerosol in a calm air environment under different breathing conditions. They showed that the breathing condition and age do not significantly affect the aspiration ratio and suggested an empirical correlation for inhalability for the nasal breathing. In their work, torso mannequins of an adult and a child were exposed to nonspherical airborne particles. Several volume flow rates corresponding to human activity condition (rest, moderate, and heavy exercise) were studied. Daia et al. (2006) measured the nasal inhalability of aerosol particles under the calm air condition for ten subjects exposed to different inspiratory flow rates. Comparison of in vivo and mannequin measurements suggested that the natural convection from the human body could affect the particle motions in calm air and cause slightly higher

inhalability for particles smaller than 50 μm. Li et al. (2012) simulated airflow around a simplified mannequin model and investigated effects of facial features on nostril velocity profile. Then, they used the resulted velocity profile as an inlet boundary condition for their nasal cavity flow study. They reported that the facial features affect only a small region in front of the face (10–20 mm) and result in a nonuniform velocity profiles at the inlet of the nostril that may affect the particle inhalation. Inthavong et al. (2012) integrated the human upper airway into a mannequin that was placed inside a room, facing different airflow speeds. Their study provided a better understanding of the air and particle flow patterns near a mannequin exposed to different environmental conditions. In a detailed study, Taylor et al. (2010) investigated the effect of the inflow condition on the numerical simulation of steady nasal inspiration. They compared the cases of (1) uniform velocity profile, (2) a tapered pipe inflow, and (3) a model that fully replicates the external environment and the internal nasal airways. Investigating the airflow inside the nasal airway, they found that a tapered pipe inflow provides a better approximation for the natural inflow than a uniform velocity profile applied to the nares. Recently, Inthavong et al. (2013) investigated the source and trajectories of deposited particles in the upper respiratory system using a computational model that combined the mannequin and respiratory airway in an indoor environment for free stream airflow velocities of 0.05, 0.2, and 0.35 m/s, which is common in an indoor environment. A more recent research in this area was performed by Naseri et al. (2014). They developed a 3-D realistic computational model of the airway system integrated into a standing male mannequin and simulated the external and internal airflows simultaneously. Their results showed when the upper airway is integrated into the mannequin, the airflow focuses the particles toward the central part of the nostril. As a result, the regional deposition of inhaled particles differs markedly from those predicted for detached airways.

16.1.2.13 Fibrous Particle Transport and Deposition

Another issue for the respiratory flow simulations is handling the nonspherical shape of inhaled particles. It should be pointed out that particles in many cases are highly elongated and cannot be approximated as spheres. Suspensions of fibrous particles occur in many industrial applications such as composite material production, paper industry, and chemical and food processing industries. Understanding the motion and transport of fibrous particles with high aspect ratio has attracted the attention of a few researchers in the past. Accordingly, for elongated particles, the orientation and rotation of the fibers need to be included in the analysis. Fan and Ahmadi (1995a,b) studied numerically the effects of shape, aspect ratio, and density of ellipsoidal fibers on their dispersion and deposition in turbulent flow fields. Asgharian and Ahmadi (1998) studied the motion and deposition of fibers in a simplified model of small human airways, while Kvasnak and Ahmadi (1996), Tian et al. (2012), and Zhang et al. (2001) studied fiber transport and deposition in ducts.

Deposition of fibrous particles in nasal cavities, however, has received comparatively less attention, and there is rather limited number of related experimental and numerical studies in the literature. Experimental researchers (Su and Cheng, 2005, Su et al., 2008) investigated the regional fiber deposition in a human airway replica. Wang et al. (2008) conducted an experimental investigation on fibrous particle deposition in several human nasal cavities and studied the effects of particle shape, flow rate, and the nasal geometry on their deposition patterns. For non-Brownian fibers, they showed that the increase in flow rate and fiber length increases the deposition efficiency; therefore, they concluded that the inertial impaction is primarily deposition mechanism. They also noted the dependence of the deposition pattern on the nasal airway geometry. Inthavong et al. (2008) studied numerically the deposition of fibers in both right and left cavities of an adult person. They used the modified drag equation of Haider and Levenspiel (1989) (HL) for the cylindrical fibers. The HL model uses a spherical particle simulation approach with a shape factor for the nonspherical particle. Recently, Dastan et al. (2014) performed simulations of fibrous particle deposition in different realistic human nasal cavities. The coupled translational and rotational equations of motion of ellipsoids were solved and the fiber transport and deposition in the nasal passages were analyzed. They showed that when the DF results and the Stokes-based and pressure-based impaction parameters (IPs) are compared, the results of the different cases for various nose models collapse roughly to a single curve.

16.1.2.14 Targeted Deposition

A new concept that has attracted the attention of researchers is the targeted deposition of particles in the airway using a magnetic field. This idea has the potential for applications to lung cancer treatment. Ally et al. (2006) experimentally studied the factors affecting magnetic retention of particles in the upper airways

using in vitro and ex vivo models. Their results indicated that particle size and aggregation as well as the apparent viscosity of the mucus layer at low shear rates affect the particle retention. Dames et al. (2007) were the first to actually perform targeted aerosol delivery to the lung in mice. They used superparamagnetic iron oxide nanoparticles (nanomagnetosols, i.e., aerosol droplets in addition to a target-directed magnetic gradient field). They also provide a theoretical analysis of the process using computer simulations. They also emphasized that the major challenge for using this technology for humans is the scale-up of the magnetic gradient field for the human lung. Nevertheless, they concluded that targeted inhalation therapy with use of magnetic targeting of nanomagnetosols could be possible in the future. Martin and Finlay (2008) experimentally showed that using magnetic field alignment, deposition of high-aspect-ratio aerosols in small airway bifurcations can be enhanced. The measurements were done in vitro in a physical model of a small bifurcating airway of the lung. In this approach, there is no need for generating a gradient in the magnetic field strength, which decreases the amounts of magnetic material compared to the active drug. The magnetic deposition of aerosols composed of aggregated superparamagnetic nanoparticles was experimentally verified and also simulated with a CFD model by Xie et al. (2010). They showed that the CFD simulations could help design the systems for selective drug delivery in vivo as a function of magnetic properties and aerosol characteristics.

16.1.2.15 Accounting for Unsteady Breathing

The breathing cycle is clearly an unsteady process in which airflow rate increases during the inhalation cycle and decelerates and reverses during the exhalation phase. One major limitation of many of the earlier studies on the respiratory flow modeling and particle deposition is ignoring the effect of unsteadiness of the breathing process. As noted by Doorly et al. (2008), most of the earlier studies have used the mean flow rate averaged over the inhalation breathing cycle. Therefore, the acceleration and deceleration of airflow in the breathing process were not considered. The steady airflow simplification at a constant inhalation rate has also been used for simulation of transport and deposition of particles. Although a given flow rate may occur at certain instant of breathing, the breathing rate is certainly periodic. Therefore, the accuracy of the assumption of steady airflow needs to be understood and verified. Indeed, the time variation of airflow during breathing is known to affect the deposition of microparticles in the nasal cavity that is dominated by inertial impaction. Zhang et al. (2002) reported that the deposition of microparticles in the bronchial airway bifurcation under cyclic airflow was higher compared with the case that the equivalent mean flow was used. This trend was also observed by Grgic et al. (2006) for the human mouth–throat model. Häußermann et al. (2002) observed a reverse trend in total deposition of microparticles in a nasal cavity cast. Their results showed much higher deposition rate for 1.7 and 3 μm particles at constant flow rates compared to that periodic human breathing. Li et al. (2007) studied numerically microparticle deposition in the human tracheobronchial airways due to transient inspiratory breathing patterns. They found that the particle DF is a time varying function following the inhalation waveform. In addition, their numerical results showed that the local deposition efficiencies are higher in the cyclic case compared with those in the steady case. Jiang and Zhao (2010) performed both steady and unsteady CFD simulations for a rat nasal model under realistic breathing and sniffing flow rates. They investigated the transient nature of the airflow, as well as nanoparticle transport and deposition patterns in the nasal cavity and the olfactory region. They found that the total deposition efficiency of nanoparticle during cyclic breathing is lower than that for the steady flow model. While the results of some of the earlier studies are contradictory, they suggest that the use of the steady assumption for analyzing nasal particle transport and deposition during cycling breathing may not be accurate, and for more detailed assessment of the toxicological and therapeutic impact of particle inhalation, an unsteady flow and particle tracking are needed. Detailed CFD studies for the comparison of microparticle deposition in the human nasal cavity for cyclic breathing and the equivalent steady flow are rather scarce.

Zubair et al. (2012) presented a discussion of the limitations of CFD modeling of nasal airflow. Neglecting the mucous layer and other vital anatomical features was noted as some common limitation. They suggested using appropriate CT or MRI data for constructing the CFD models. In addition, the use of the entire upper airway and pull-flow boundary conditions was recommended.

The summary of this section shows there has been increasing interest in computational analysis of airflow and particle transport and in the human respiratory system in the past three decades, and numerous publications have appeared in the literature. Tu et al. (2013) published a book on computational fluid and particle dynamics in the human respiratory system, which is a good reference for researchers as well as graduate students interested in this field.

16.1.3 Computational Methodology

The recent methodology for the computational study of airflow and particle transport in human respiratory airways consists of five main steps: the first step is taking the CT or MRI images of the subject airways. Patient-specific models are obtained in this fashion as needed. The existing medical images taken in routine clinical procedures can also be used when they have sufficient resolution and cover the entire airway of interest. Figure 16.5a shows a sample medical image of a section of the upper airways. For the reconstruction of the airway models, the CT images are preferable, but a complete set of images of sections of the entire airway is needed. The CT and MRI image is usually in Digital Imaging and Communications in Medicine (DICOM) format.

The second step is constructing 3-D computational model of the airway from the CT or MRI medical images. A sample reconstructed volume is shown in Figure 16.5b. In-house codes and/or commercial image processing software such as Mimics (Materialise, Ann Arbor, United States) and Amira (Mercury Computer Systems, Inc., United Kingdom) can be used for this purpose. The commercial Mimics and Amira have

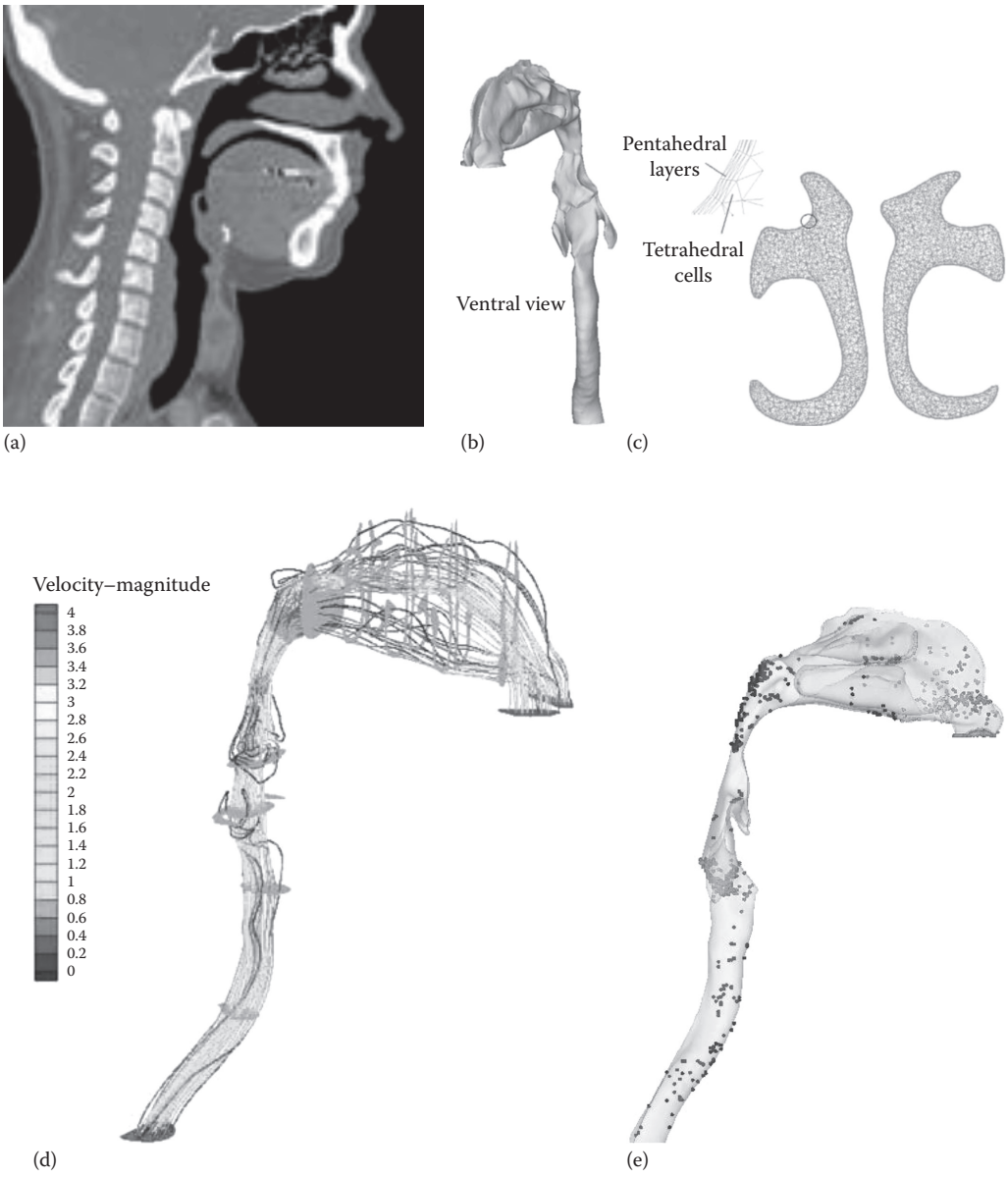


Figure 16.5

Steps for developing a computational fluid dynamics model of human airway system. (a) Medical image. (b) 3D model. (c) Mesh generation. (d) Flow field simulation. (e) Particle deposition analysis.

been widely used for the construction of complicated 3-D anatomical models for medical and biological applications. Alternatively, the CT scan images with DICOM format are processed by MATLAB® software to identify the boundary coordinates of the airway walls. Then, the resulting surface is imported into CAD software (CATIA) or mesh generator tool and the airway surface and volume are created and used for the CFD study. Additional details of these steps may be found in Chapter 3 of the recent book by Tu et al. (2013).

The third step is the grid generation for the created computational volume of the airway. Since most segments of human airways are anatomically complicated, typically unstructured grids have been used in the earlier work. For a better approximation of the velocity gradients and particle deposition, a combination of the pentahedral layers in vicinity of the walls and tetrahedral cells in other regions as shown in Figure 16.5c may be more appropriate. Gambit, ICEM, and ANSYS Workbench are among the software tools that are used for mesh generation. The fourth step is solving the governing equations for the flow dynamics and then the particle motions for evaluating the airflow field and transport and deposition of particles in the airway. ANSYS-Fluent™ has been widely used as flow solver in many of the reported works. ANSYS-CFX™ is also another commercial flow solver that has been used in the earlier numerical studies of the respiratory system. Some researchers have used their own in-house code as solver. The open, source code, OpenFOAM software has also been gaining popularity as a solver and is being used for respiratory applications.

The last step is the postprocessing of the obtained results and their analysis and interpretation. The postprocessing for the flow properties, such as providing contour plots for velocity magnitude, pressure, and turbulence kinetic energy and dissipation rate, as well as path lines, is usually done within the flow solvers (Fluent or CFX) or with use of other software such as Tecplot. Tecplot is a CFD postprocessing tool graphical presentation of the simulation data. Figure 16.5d shows sample particle path lines colored with velocity magnitude. Figure 16.5e shows the particle deposition pattern in the upper airways.

Within these major steps, some additional interesting tasks may be done as needed. For example, a virtual surgery can be performed. That is, under the supervision of a physician, appropriate changes in the image processing software such as Mimics and Amira can be before developing the 3-D surface model of the airway.

16.1.4 Governing Equations

For respiratory deposition, typically the concentration of particles is dilute and the assumption of one-way coupling is used. That is, the fluid flow carries the particles, but the effect of particles on the flow is negligibly small and is neglected. Under this condition, the airflow field is first simulated and the resulting velocity fields are used for analyzing the particle motions. In this case, the interactions of particle are negligible and each particle can be tracked independently. Exhaustive reviews of computational modeling of single-phase fluid flows in laminar and turbulent flow regimes through solving the Navier–Stokes and RANS equations, in conjunction with some turbulence model, are available in the literature (e.g., Tu et al., 2013). Therefore, here only the governing equations for particle motions are outlined.

16.1.4.1 Microparticle Transport Equation

Simulations of the microparticle transport and deposition are usually performed by the Lagrangian trajectory analysis approach. In this method, the individual particles are tracked within the flow field. The primary advantage of this approach is that the effect of forces such as gravity, drag, and inertia are directly considered. In particular, the Lagrangian approach is well suited for microparticles for which the inertia has a noticeable effect on their motion. The second law of Newton governs the dynamic of particle motion:

$$\frac{du_i^p}{dt} = \frac{1}{\tau}\frac{C_D \mathrm{Re}_p}{24}(u_i - u_i^p) + F_i^L + g_i + n_i(t) \tag{16.1}$$

where

u_i^p is the particle velocity
u_i is the fluid velocity
F_i^L is the lift force per unit mass
g_i is the acceleration due to gravity
$n_i(t)$ is the Brownian force per unit mass
τ is the particle relaxation time given by

$$\tau = \frac{Sd^2 C_c}{18\nu} \tag{16.2}$$

where
d is the particle diameter
ν is the gas kinematic viscosity
S is the particle-to-fluid density ratio
C_c is the Cunningham slip correction given as

$$C_c = 1 + \frac{2\lambda}{d}\left(1.257 + 0.4e^{-\frac{1.1d}{2\lambda}}\right) \tag{16.3}$$

where λ is the gas mean free path.

The first term on the right-hand side of Equation 16.1 is the drag force that is typically the dominant force for microparticles. Here, C_D is the drag coefficient, which is given as (Hinds, 1982)

$$C_D = \frac{24}{\mathrm{Re}_p}\left(1 + 0.15\mathrm{Re}_p^{0.687}\right) \quad \text{for } \mathrm{Re}_p < 400 \tag{16.4}$$

where Re_p is the particle Reynolds number given by

$$\mathrm{Re}_p = \frac{\rho^p d\left|u^p - u\right|}{\mu} \tag{16.5}$$

where
d is the particle diameter
μ is the gas dynamic viscosity

While the drag coefficient given by Equation 16.4 is reasonably accurate for applications to aerosol motion, there are a number of expressions with various degree of accuracy in the literature. For example, Clift et al. (1978) suggested the use of

$$C_D = \frac{24}{\mathrm{Re}_p}(1 + 0.1315\mathrm{Re}_p^{\omega}) \quad \text{for } \mathrm{Re} < 20 \tag{16.6}$$

with the exponent given as

$$\omega = 0.82 - 0.05(\log_{10}\mathrm{Re}_p) \tag{16.7}$$

Recently, Barati et al. (2014) suggest a highly accurate expression for the drag force acting on a spherical particle.

The expression for the shear lift force in Equation 16.1 is given as

$$F_i^L = \frac{2K\nu^{1/2}d_{ij}}{Sd(d_{lk}d_{kl})^{1/4}}(u_j - u_j^p) \tag{16.8}$$

where
$K = 2.594$ is the constant coefficient suggest by Saffman (1968)
d_{ij} is the deformation rate tensor expressed as

$$d_{ij} = \frac{1}{2}\left(\frac{\partial u_i}{\partial x_j} + \frac{\partial u_j}{\partial x_i}\right) \tag{16.9}$$

The trajectory of the particle, $x_i(t)$, is obtained by integrating the velocity vector equation. That is,

$$\frac{dx_i}{dt} = v_i \tag{16.10}$$

Equations 16.1 and 16.10 are used to compute the trajectories of individual particles when the flow velocity is known. When the airflow is in the turbulent regime, however, the fluid fluctuating velocities should be estimated and added to the mean flow velocity for the particle trajectory analysis.

For the Lagrangian model, the DF is computed based on the number of deposited particles and the number of particle entering the domain. That is, the DF for a region i is defined as

$$\mathrm{DF}_i = \frac{\text{Number of particles depositing in region } i}{\text{Number of particles entering the geometry inlet}} \tag{16.11}$$

16.1.4.2 Stochastic Fluctuation Velocity Models

As noted before, small particles in a turbulent airflow stream are influenced by the turbulence fluctuating velocities that lead to their turbulence dispersion, which is the key factor in their spreading and deposition. When RANS models are used, for accurate analysis of particle transport in turbulent flow, these fluctuation velocities should be evaluated so that the corresponding instantaneous flow velocity is used in the evaluation of drag and other relevant forces. The RANS models typically provide the mean flow and mean square values fluctuation velocities and/or kinetic energy of turbulence. Some stochastic models are then used to generate the fluctuation velocities using the turbulent kinetic energy and/or Reynolds stresses. Two main models that are commonly used in the literature are outlined here.

16.1.4.2.1 DRW Model The well-known DRW model for describing fluctuation velocities was introduced by Gosman and Ioannides (1983). The DRW also referred to as the eddy lifetime model is used in some commercial codes such as ANSYS-Fluent. In this model, the fluctuating velocities, which are piecewise constant functions, are computed from the following equation:

$$u_i' = \lambda_i \sigma_i \tag{16.12}$$

where

λ_i is a normally distributed random number

σ_i is the RMS velocity fluctuation in ith direction

When an isotropic two-equation turbulence models is used, then this becomes

$$\sigma_i = \sqrt{\tfrac{2}{3}k} \tag{16.13}$$

where k is the kinetic energy of turbulence. In using (16.13), clearly it is assumed that the RMS velocity fluctuations for different directions are equal. This could be an issue for near-wall flows, where the fluctuating velocity in the normal direction is significantly smaller compared with the streamwise direction. The importance of anisotropy of turbulence for estimating particle deposition was noted in the earlier works (Li and Ahmadi, 1992, He and Ahmadi, 1999). While using most researches used the isotropic RAND models, some (Matida et al., 2004, Zhang et al., 2005, Li et al., 2007) used damping functions to correct the anisotropy behavior of normal Reynolds stresses near the walls based on DNS data. He and Ahmadi (1999) and Tian and Ahmadi (2007) used the Reynolds stress turbulence model and captured the anisotropy of the normal Reynolds stresses directly. In these studies, the significance of quadratic variation of wall-normal velocity fluctuation close to the wall for correct evaluation of particle velocity was emphasized.

In the DRW model, the particle is assumed to interact with the eddy over the smaller of the eddy lifetime and the particle-eddy crossing time. When this time is reached, a new value of the fluctuation velocity is obtained by using a new value of random number λ_i in Equation 16.12 (Fluent, 2006). The eddy lifetime is estimated as

$$\tau_e = C_L \frac{k}{\varepsilon} \tag{16.14}$$

where C_L is a constant. Also, the particle-eddy crossing time is expressed as

$$t_{cross} = -\tau \ln\left(1 - \frac{L_e}{\tau\left|u - u^p\right|}\right) \tag{16.15}$$

where

τ is the particle relaxation time defined in Equation 16.2

L_e is the eddy length scale, which is given as

$$L_e = \left(C_\mu\right)^{3/4} \frac{k^{3/2}}{\varepsilon} \tag{16.16}$$

16.1.4.2.2 CRW Model The CRW models are based on solving a Langevin equation to generate a Gaussian random field with appropriate means and variances. The model is also referred to as filtered white nose model and was first introduced by Thompson (1987) and used by others (He and Ahmadi, 1999). Accordingly, the instantaneous flow velocity u_i is evaluated by solving the following Langevin equation:

$$\frac{du_i}{dt} = -\frac{u_i - \overline{u_i}}{T_L} + \left(\frac{2\overline{u_i'^2}}{T_L}\right)^{1/2} \xi_i(t), \tag{16.17}$$

where

$\overline{u_i}$ is the mean flow velocity

$\overline{T_L}$ is the particle Lagrangian integral time scale

$\overline{u_i'^2}$ is the mean square fluctuation velocity in ith direction

$\xi_i(t)$ is a Gaussian white-noise random process

The particle Lagrangian time scale is generally not available, and the Eulerian flow time scale (eddy lifetime) given by Equation 16.14 is typically used. The solution to Equation 16.17 leads to a Gaussian random field with appropriate mean, variance, and time scale. The CRW model given by 16.17 has been implemented in commercial codes such as ANSYS-Fluent.

In order to account for the inhomogeneous turbulence fluctuations, the generalized Langevin equation, including the drift correction term, is used. That is, (Iliopoulos et al., 2003)

$$\frac{du_i}{dt} = -\frac{u_i - \overline{u_i}}{T_L} + \left(\frac{2\overline{u_i'^2}}{T_L}\right)^{1/2} \xi_i(t) + \frac{1}{2(1+Stk)} \frac{\partial \overline{u_i'^2}}{\partial x_i} \delta_{i2}, \tag{16.18}$$

In this equation, the last term is the mean drift correction term for a flow with x_2 being in wall-normal direction. More detail of the upgraded model can be found in the studies by Dehbi (2008) and Ghahramani et al. (2014).

16.1.4.3 Mass Diffusion of Nanoparticles

Nanoparticle transport and deposition are dominated by their Brownian motion. The Lagrangian trajectory analysis approach becomes inefficient for cases that the particle deposition rates very low and/or whenever a very large number of particles need to be traced for accurate estimate of local deposition characteristics. Therefore, the nanoparticle transport and deposition were usually computed by a Eulerian/diffusion approach. This approach treats the particles as a continuum field and neglects the particle inertia effects. The Eulerian/diffusion model is suitable for the sub-100 nm particles because of their very low inertia. The primary advantage of the Eulerian/diffusion model approach is in its simplicity that it can rapidly evaluate the deposition rates. In this method, the steady form of the convective–diffusive equation governing the mass transport of nanoparticles is used. That is, (Friedlander, 2000)

$$\frac{\partial(u_j C)}{\partial x_j} = \frac{\partial}{\partial x_j}\left[(D + D_t)\frac{\partial C}{\partial x_j}\right] \tag{16.19}$$

where

C is the nanoparticle concentration

D is the Stokes–Einstein diffusion coefficient of nanoparticles, which is given as

$$D = \frac{k_B T C_c}{3\pi\mu d_p} \tag{16.20}$$

where

$k_B = 1.38 \times 10^{-23}$ J/K is the Boltzmann constant

T is the absolute temperature of air

C_c is the Cunningham correction factor given in Equation 16.3

In Equation 16.19, D_t is the turbulent diffusion coefficient and needs to be included for turbulent flows in conjunction with a turbulence model.

For the Eulerian model, the DF of nanoparticles in region i of a passage is the ratio of the rate of mass deposition on the walls of the region to the inlet mass flow rate. That is,

$$\left(\mathrm{DF}_i\right)_{nano-particles} = \frac{\dot{m}_{w,i}}{\dot{m}_{in}} \tag{16.21}$$

In a computational model, the total mass deposition can be evaluated using

$$\dot{m}_{w,i} = \sum_{j=1}^{N} -\rho A_j (D + D_t)\frac{\partial C}{\partial n}\Big|_{w,j} \tag{16.22}$$

where

N is the number of cells adjacent to the walls in region i

n is the wall-normal direction

A_j is the area of the each cell face adjacent to the walls in the region

Note that on solid walls D_t is zero.

16.1.4.4 Equations of Motion of Ellipsoidal Fibers

The equations governing the motion of ellipsoidal fiber were described in the literature (Gallily and Eisner, 1979, Fan and Ahmadi, 1995a,b, Dastan and Abouali, 2013). Here, a summary of key equations is presented.

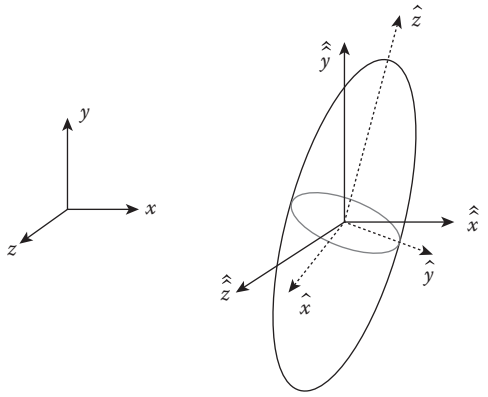


Figure 16.6

Three different coordinate systems used in description of fiber motion.

In comparison to the spherical particles, the equations governing the motion of nonspherical particles are more complex because of the coupling between the translational and rotational motions. Figure 16.6 shows the three different coordinate systems that are typically used to describe the motion of ellipsoidal particles. The inertial coordinate system is given by $\mathbf{x} = [x, y, z]$. The particle coordinate system denoted by $\hat{\mathbf{x}} = [\hat{x}, \hat{y}, \hat{z}]$ is attached to the particle with its origin at the mass center of the particle and its axes along the principal axes of the ellipsoids. Typically, the $\hat{z}$ axis of the particle frame is selected to be along the major axis of the ellipsoid. The third coordinate system $\hat{\hat{x}} = [\hat{\hat{x}}, \hat{\hat{y}}, \hat{\hat{z}}]$ is a comoving coordinate system with its origin at the mass center of the particle (similar to the origin of the particle coordinate) with its axes parallel to the axes of inertial coordinate system. The transformation matrix between these two coordinate systems can be expressed in terms of Euler four parameters $(\varepsilon_1, \varepsilon_2, \varepsilon_3, \eta)$ (Goldestein, 1980). That is,

$$A = \begin{bmatrix} 1-2\left(\varepsilon_2^2+\varepsilon_3^2\right) & 2\left(\varepsilon_1\varepsilon_2+\varepsilon_3\eta\right) & 2\left(\varepsilon_1\varepsilon_3-\varepsilon_2\eta\right) \\ 2\left(\varepsilon_2\varepsilon_1-\varepsilon_3\eta\right) & 1-2\left(\varepsilon_3^2+\varepsilon_1^2\right) & 2\left(\varepsilon_2\varepsilon_3+\varepsilon_1\eta\right) \\ 2\left(\varepsilon_3\varepsilon_1+\varepsilon_2\eta\right) & 2\left(\varepsilon_3\varepsilon_2-\varepsilon_1\eta\right) & 1-2\left(\varepsilon_1^2+\varepsilon_2^2\right) \end{bmatrix} \tag{16.23}$$

The translational and rotational equations of motion of a nonspherical particle in a general flow field are given as

$$m^p \frac{d\mathbf{v}}{dt} = \pi\mu a \hat{\hat{\mathbf{k}}}\left(\mathbf{u}-\mathbf{v}\right) + m^p\mathbf{g} + m^p\mathbf{F}^{\mathbf{L}} \tag{16.24}$$

$$I_{\hat{x}} \frac{d\omega_{\hat{x}}}{dt} - \omega_{\hat{y}}\omega_{\hat{z}}\left(I_{\hat{y}} - I_{\hat{z}}\right) = T_{\hat{x}}^h \tag{16.25}$$

$$I_{\hat{y}} \frac{d\omega_{\hat{y}}}{dt} - \omega_{\hat{z}}\omega_{\hat{x}}\left(I_{\hat{z}} - I_{\hat{x}}\right) = T_{\hat{y}}^h \tag{16.26}$$

$$I_{\hat{z}} \frac{d\omega_{\hat{z}}}{dt} - \omega_{\hat{x}}\omega_{\hat{y}}\left(I_{\hat{x}} - I_{\hat{y}}\right) = T_{\hat{z}}^h \tag{16.27}$$

where m^p, $\mathbf{v}$, $I_{\hat{i}}$, and $\omega_{\hat{i}}$, respectively, are the particle mass, particle mass center velocity vector, particle moment of inertia, and particle angular velocity. Here, μ and a are the fluid viscosity and the ellipsoid

semiminor axis, respectively. The forces included in the translational equation of motion given by (16.24) are the hydrodynamic drag force, the gravitational force, and the lift force. The other forces, such as the added mass and Brownian forces for inertial fibers, are neglected. In Equation 16.24, the flow resistance tensor $\hat{\hat{\mathbf{k}}}$ is given by

$$\hat{\hat{\mathbf{k}}} = \mathbf{A}^{-1}\hat{\mathbf{k}}\mathbf{A} \tag{16.28}$$

where

A is the transformation matrix given by Equation 16.23

$\hat{\mathbf{k}}$ is a diagonal matrix that the diagonal elements are given by

$$k_{\hat{x}\hat{x}} = k_{\hat{y}\hat{y}} = \frac{16\left(\beta^2 - 1\right)}{\left[(2\beta^2 - 3)/(\sqrt{\beta^2 - 1})\ln\left(\beta + \sqrt{\beta^2 - 1}\right) + \beta\right]} \tag{16.29}$$

$$k_{\hat{z}\hat{z}} = \frac{8\left(\beta^2 - 1\right)}{\left[\dfrac{2\beta^2 - 1}{\sqrt{\beta^2 - 1}}\ln\left(\beta + \sqrt{\beta^2 - 1}\right) - \beta\right]} \tag{16.30}$$

Here, β is the fiber aspect ratio (the ratio of semimajor axis to semiminor axis, $\beta = (b/a) > 1$).

The shear-induced lift acting on an arbitrary shaped particle is given by Harper and Change (1968). That is,

$$f^L = \frac{\pi^2 \mu a^2}{\nu^{1/2}} \frac{\dfrac{\partial u_x}{\partial y}}{\left|\dfrac{\partial u_x}{\partial y}\right|^{1/2}} (\hat{\hat{K}} \cdot L \cdot \hat{\hat{K}}) \cdot (u - v) \tag{16.31}$$

where

$$L = \begin{bmatrix} 0.0501 & 0.0329 & 0.00 \\ 0.0182 & 0.0173 & 0.00 \\ 0.00 & 0.00 & 0.0373 \end{bmatrix} \tag{16.32}$$

Here, a simple shear flow is considered.

The components of hydrodynamic torque acting on an ellipsoidal particle under creeping flow condition are given by Jeffery (1922). These are

$$T_{\hat{x}}^h = \frac{16\pi\mu a^3 \beta}{3\left(\beta_o + \beta^2 \gamma_o\right)}\left[\left(1 - \beta^2\right) d_{\hat{z}\hat{y}} + \left(1 + \beta^2\right)\left(w_{\hat{z}\hat{y}} - \omega_{\hat{x}}\right)\right] \tag{16.33}$$

$$T_{\hat{y}}^h = \frac{16\pi\mu a^3 \beta}{3\left(\beta^2 \gamma_o + \alpha_o\right)}\left[\left(\beta^2 - 1\right) d_{\hat{x}\hat{z}} + \left(1 + \beta^2\right)\left(w_{\hat{x}\hat{z}} - \omega_{\hat{y}}\right)\right] \tag{16.34}$$

$$T_{\hat{z}}^h = \frac{32\pi\mu a^3 \beta}{3\left(\alpha_o + \beta_o\right)}\left(w_{\hat{y}\hat{x}} - \omega_{\hat{z}}\right) \tag{16.35}$$

where the nondimensional parameters α_o, β_o, and γ_o are given as

$$\alpha_o = \beta_o = \frac{\beta^2}{\beta^2 - 1} + \frac{\beta}{2\left(\beta^2 - 1\right)^{3/2}} \ln\left[\frac{\beta - \sqrt{\beta^2 - 1}}{\beta + \sqrt{\beta^2 - 1}}\right] \tag{16.36}$$

$$\gamma_o = -\frac{2}{\beta^2 - 1} - \frac{\beta}{\left(\beta^2 - 1\right)^{3/2}} \ln\left[\frac{\beta - \sqrt{\beta^2 - 1}}{\beta + \sqrt{\beta^2 - 1}}\right] \tag{16.37}$$

and $d_{\tilde{i}\tilde{j}}$ and $w_{\tilde{i}\tilde{j}}$ are, respectively, the fluid deformation rate and spin tensors in the particle coordinate system.

The time rate of changes of the Euler parameters is given by

$$\begin{bmatrix} \frac{d\varepsilon_1}{dt} \\ \frac{d\varepsilon_2}{dt} \\ \frac{d\varepsilon_3}{dt} \\ \frac{d\eta}{dt} \end{bmatrix} = \frac{1}{2} \begin{bmatrix} \eta\omega_{\hat{x}} - \varepsilon_3\omega_{\hat{y}} + \varepsilon_2\omega_{\hat{z}} \\ \varepsilon_3\omega_{\hat{x}} + \eta\omega_{\hat{y}} - \varepsilon_1\omega_{\hat{z}} \\ -\varepsilon_2\omega_{\hat{x}} + \varepsilon_1\omega_{\hat{y}} + \eta\omega_{\hat{z}} \\ -\varepsilon_1\omega_{\hat{x}} - \varepsilon_2\omega_{\hat{y}} - \varepsilon_3\omega_{\hat{z}} \end{bmatrix} \tag{16.38}$$

When the mass center velocity is know, the particle position is obtained by integrating Equation 16.10.

The details of the discretization and numerical solution of the fiber equation of motion, as well as the identification of the fiber touch point on the walls, may be found in the earlier works of Fan and Ahmadi (2000), Zhang et al. (2001), Tian and Ahmadi (2012), and Dastan and Abouali (2013).

16.1.4.4.1 HL Model HL (1989) developed an empirical equation for the drag coefficient of nonspherical particles by a curve fitting on the available data from previous researchers. In this approach, the nonspherical particles are treated as spherical particles with an equivalent volume diameter and the use of a shape factor for the drag force. The shape factor (sphericity) is defined as

$$\phi = \frac{s}{S} \tag{16.39}$$

where

s is the surface of a sphere having the same volume as the particle

S is the actual surface of the particle

HL (1989) suggested the following drag coefficient correlation:

$$C_D = \frac{24}{\mathrm{Re}_p}\left(1 + A\,\mathrm{Re}_p^B\right) + \frac{C\,\mathrm{Re}_p}{D + \mathrm{Re}_p} \tag{16.40}$$

where Re_p is the particle Reynolds number based on the relative velocity and volume equivalent diameter and

$$\begin{aligned} A &= \exp(2.3288 - 6.4581\phi + 2.4486\phi^2) \\ B &= 0.0964 + 0.5565\phi \\ C &= \exp(4.905 - 13.8944\phi + 18.4222\phi^2 - 10.2599\phi^3) \\ D &= \exp(1.4681 + 12.2584\phi - 20.7322\phi^2 + 15.8855\phi^3) \end{aligned} \tag{16.41}$$

The drag force acting on the particle then is given as

$$F_D = 3\pi\mu\, d_{eq} C_D \frac{\mathrm{Re}_p}{24}\left(\mathbf{u} - \mathbf{u}^{\mathbf{p}}\right) \tag{16.42}$$

Using this on the right-hand side of Equation 16.24 or Equation 16.1, the translational motion of nonspherical particles can be calculated. It should be pointed out that the HL model ignores the coupling between translational and rotational motions of elongated particles.

16.1.5 Sample CFD Models of Human Upper Airway Systems

In this section, some examples of the recent computational models of upper airway systems are presented.

16.1.5.1 Micro- and Nanoparticle Transport and Deposition in Human Upper Airways

Micro- and nanoparticle transport and deposition in the upper airways were studied by Farhadi Ghalati et al. (2012) using a computational modeling approach. To construct the airway model study, the CT scans of a 24-year-old healthy female subject were used. The scans, which were provided by TABA Medical Imaging Center, are obtained while the person was in a supine position. Imaging was helical and performed using a CTI whole body scanner (GE Medical Systems) with the following parameters: 0.625 mm slice increment, 24.20 cm field of view, 120 kV peak, and 99.00 mA. Under the supervision of a specialist, the boundary between the airway mucosa and air in the upper respiratory tract was defined in the CT scan slices. Figure 16.7 shows some samples of the coronal and sagittal cross sections of the nasal and upper airways. To reconstruct the 3-D model consisting of nasal cavity, pharynx, larynx, and trachea, the boundaries were imported into a CFD preprocessor software tool (GAMBIT). The boundaries are connected to each other to create a smooth surface and form the volume. An unstructured tri-/tetrahedral hybrid volume mesh was generated inside the airway passage. A grid size of approximately 2,600,000 cells was obtained after the grid independency test. The 3-D model for the total volume of the upper airways is shown in Figure 16.8.

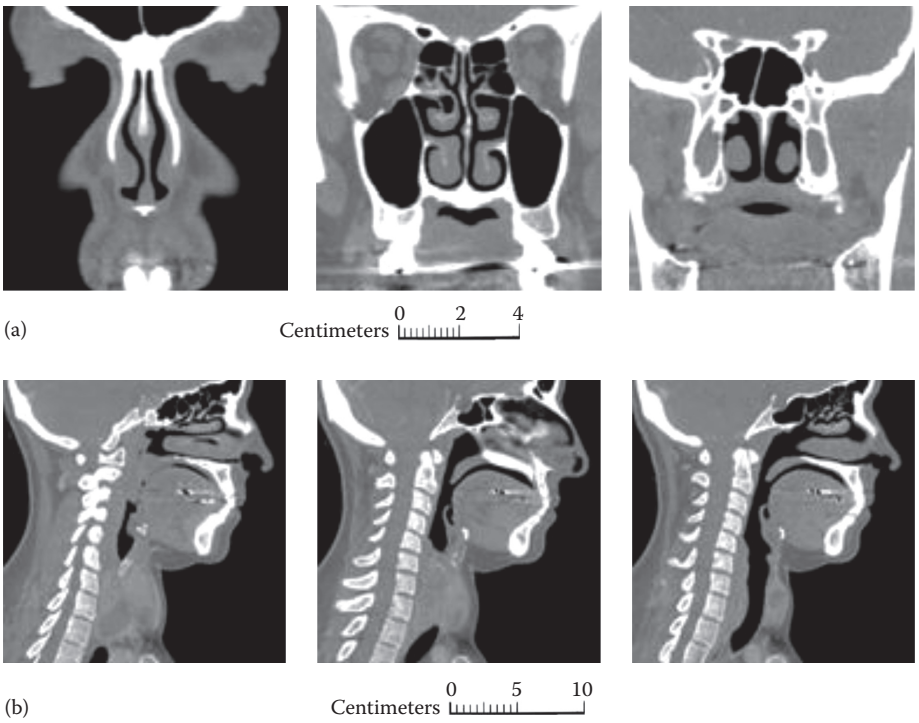


Figure 16.7

Samples of (a) coronal and (b) sagittal cross sections of the nasal and upper airways.

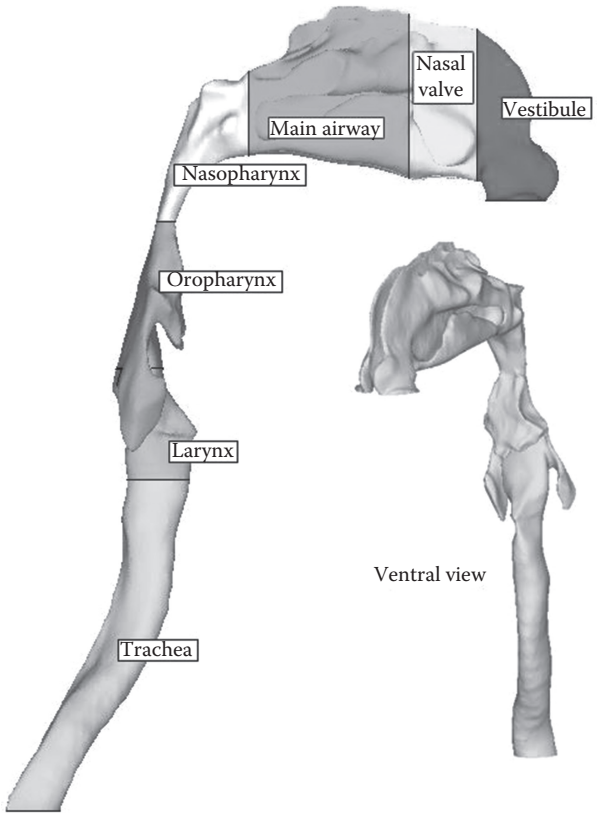


Figure 16.8

The developed 3-D model of the nasal upper airway.

A series of computer simulations was performed for various breathing rates. Sample results for the mean airflow velocity magnitude contours for a breathing rate of 10 L/min are shown in Figure 16.9. It is seen that air enters uniformly from the nostril into the vestibule region and then experiences an almost 90° turn. As a result, due to the centrifugal force effect, the streamlines tend to move toward the upper part of the nasal cavity. This part of the nasal passage, however, has relatively small cross-sectional area; therefore, the air flows mainly in the middle part of this section as seen in Figure 16.9a. After reaching to the nasal valve region shown in Figure 16.9b, the airflow mostly passes through the middle meatus area (Figure 16.9a and b). A small amount of airflow passes through the superior meatus and olfactory region. Additional details of airflow structures in human nasal cavity were described by Doorly et al. (2008).

As the airflow enters the nasopharynx, it turns 90° again to the vertical downward direction and the centrifugal force effect moves the peak airflow toward the upper part of the pharynx as shown in Figure 16.9e. Then, the flow becomes almost fully developed as shown in Figure 16.9f. At the end of the nasopharynx region, the cross-sectional area of the passage reaches to its minimum value and the airflow velocity becomes its maximum value of about 4 m/s as shown in Figure 16.9g. Figure 16.9h clearly shows a high-velocity jet in the pharynx region, which flows along the posterior pharyngeal airway. The velocity distributions in the larynx and trachea shown in Figure 16.9i thorugh k are significantly influenced by the presence of jet flow exiting the pharynx.

Figure 16.10a shows the predicted deposition efficiency versus IP. The IP is defined as

$$\mathrm{IP} = d_p^2 Q \ (\mu\mathrm{m}^2\ \mathrm{cm}^3/\mathrm{s}) \tag{16.43}$$

where Q is the inhaled air volume flow rate in cm^3/s. Figure 16.10a shows that the deposition rate of microparticles increases with the increase in either the particle diameter or inhalation flow rate as the inertial effect is the main mechanism for deposition of these particles. This figure also shows that the curves for various breathing rates nearly coincide with each other, which is as expected for plots

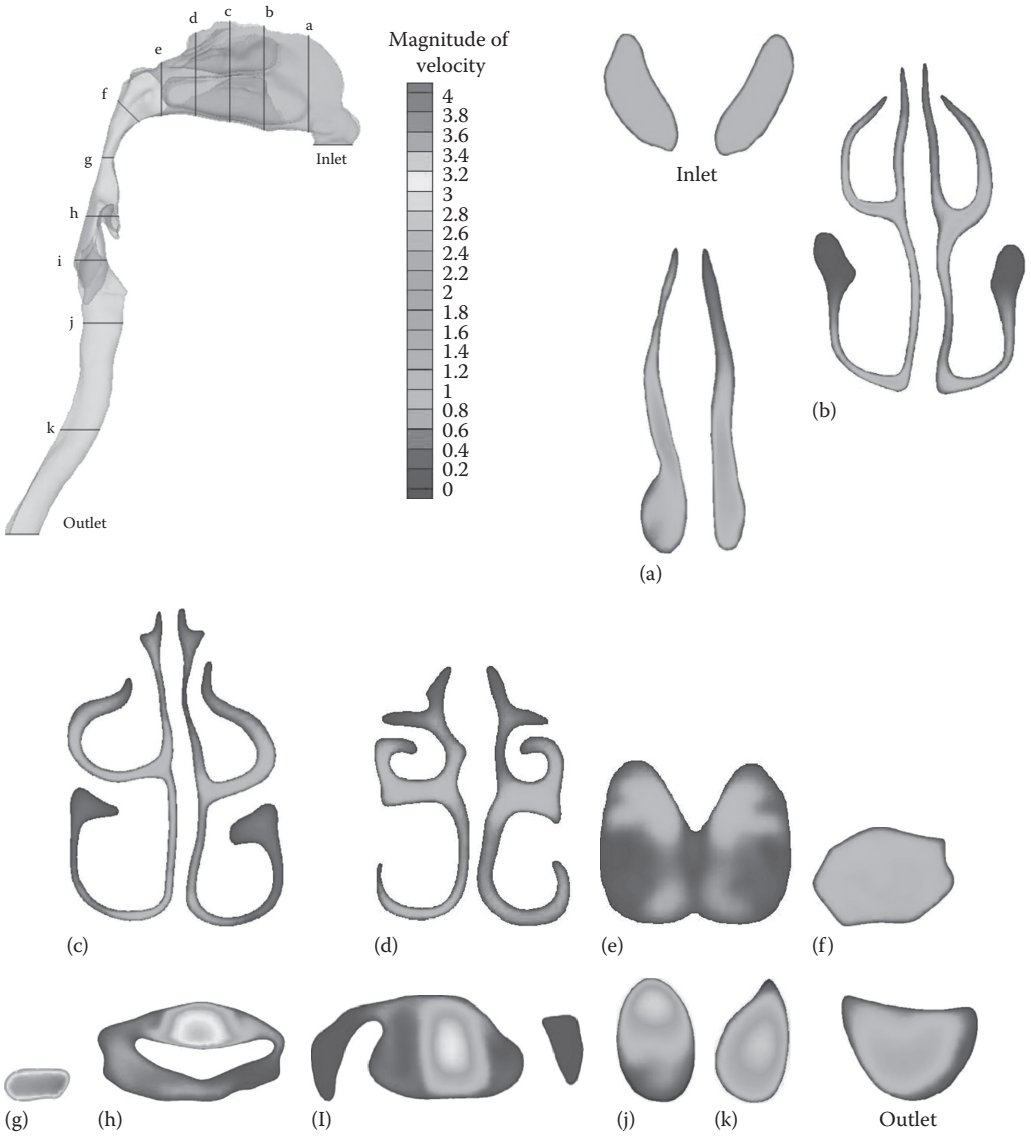


Figure 16.9

Velocity (m/s) contours in different sections for breathing rate of 10 L/min. Cross sections of a–e are in the nasal cavity, f and g are in the nasopharynx, h is in the oral pharynx, i is in the larynx, and j and k are in the trachea.

versus the IP. The experimental data of Kelly et al. (2004a) are also reproduced in Figure 16.10a for comparison. It is seen that while the trend of the predicted deposition curve is similar to that of the experimental data, there are marked differences between the numerical results and the experimental data that were for different subjects. Schroeter et al. (2011) showed that the particle deposition reported by Kelly et al. (2004a) was for a replica model developed from low-resolution MRI images, which led to high deposition rates compared with those for a smooth nasal passage. Golshahi et al. (2011) also found that when the deposition efficiency was reported versus the IP for different anatomical airway passages, there was a wide scatter in the data.

Long ago, Hounam et al. (1971) suggested the use of the deposition parameter that included the pressure drop ΔP across the nasal airways instead to reduce the scatter due to the interpersonal differences, which was confirmed by Golshahi et al. (2011). The disposition parameter (DP) defined as

$$DP = d_p^2 \Delta P \ (\mu m^2\, Pa) \tag{16.44}$$

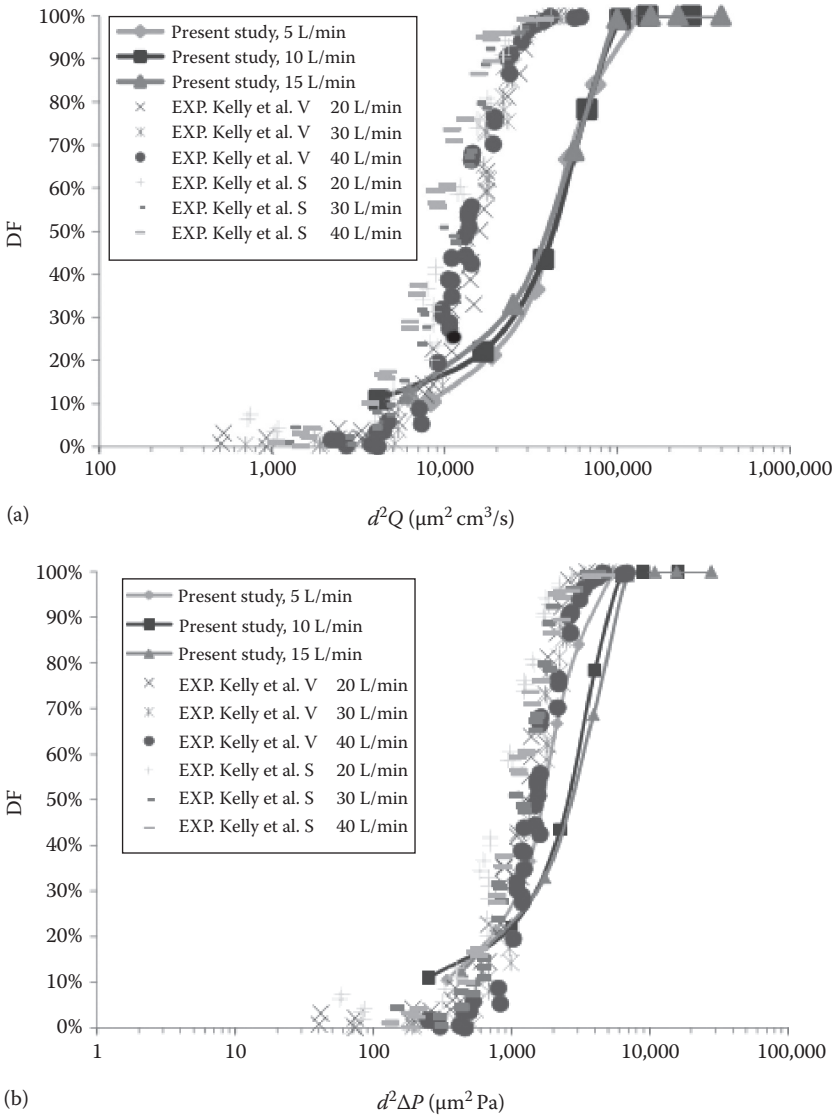


Figure 16.10

Comparison of the computational model predictions with the experimental data of Kelly et al. (2004a), for microparticle deposition in the nasal cavity and nasopharynx at breathing rates of 5, 10, and 15 L/min (a) versus the impaction parameter (b) versus the deposition parameter. Letters S and V refer to the SLA and Viper nasal replica models in their work.

is used for this purpose. Figure 16.10b compares the numerical and experimental DFs when plotted versus the deposition parameter. It is seen that the scatter in the deposition data reduces significantly and the computational model prediction shows a good agreement with the experimental data. The small differences between the simulation results and the experimental data are due to the anatomical and geometrical differences of the nasal passages of different subjects.

Figure 16.11 shows the spatial deposition patterns for particles with aerodynamic diameters of 5, 10, and 20 μm in the realistic geometry of human upper airway system for a breathing rate of 10 L/min. The corresponding total DFs for these particles as extracted from Figure 16.10 are, respectively, 16.6%, 31.4%, and 86.2%. It is clearly seen that the deposition rate increases as the particle diameter increases. This is due to the result of their higher inertia that makes the impaction process more efficient. Figure 16.11 shows that the 5 μm particles, which have low inertia, penetrate deep into the larynx and trachea regions, while the 20 μm particles are mainly trapped in the vestibule and nasal valve with very few reaching the pharynx, the larynx, and the trachea region. The 10 μm particles are also captured mainly in the nasal passage and the larynx area, with some penetrating deeper into the upper airway system. In addition, Figure 16.11 shows there are

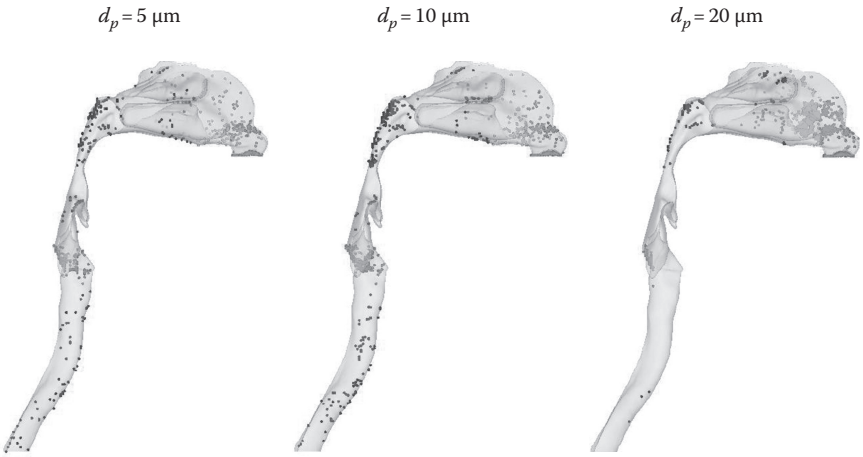


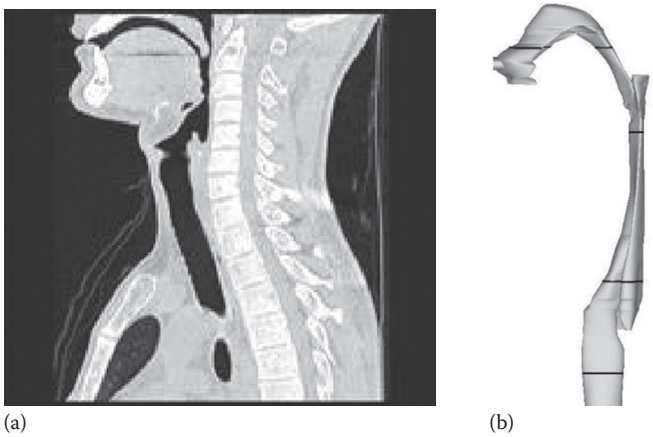
Figure 16.11

Deposition patterns in different passages for 5, 10, and 20 μm particles at a breathing rate of 10 L/min.

regions of the airway that are more susceptible to the accumulation of deposited particles. Here, it seems there are at least four spots. The first is the end of the vestibule region where the flow turns 90° into the nasal valve with sharp variation in the passage size. As mentioned before, the centrifugal force causes the particle to deviate away from the flow streamlines and move toward the upper part of the passage, leading to their deposition on the nasal wall. The second area of concentrated deposition is the top of the middle meatus. In this region, complexity of the geometry is the main reason for particle deposition on the middle meatus wall. The third zone is the nasopharynx wall where there is another 90° bend in the airway passages, and the fourth site is at the beginning of the larynx. There is an abrupt decrease in the cross-sectional area and the air passage becomes narrow, leading to the higher flow velocity. Consequently, the higher inertia of particles prevents them to follow the airflow streamlines, causing the particles to deposit on the larynx wall.

16.1.5.2 Microparticles Transport and Deposition in Realistic Geometry of Human Oral Upper Airways

The transport and deposition of microparticles in human oral airways were studied by Tavakoli et al. (2012), among others. The 3-D geometry of human upper airways is first constructed from CT scan images of a healthy male volunteer subject. Figure 16.12a shows the midsagittal plane of the images of the upper airways of the subject. Reconstructed 3-D geometry of the oral upper airway is shown in Figure 16.12b.



(a) (b)

Figure 16.12

(a) CT scan image of the upper airways (sagittal view). (b) Reconstructed 3-D geometry of the oral upper airway.

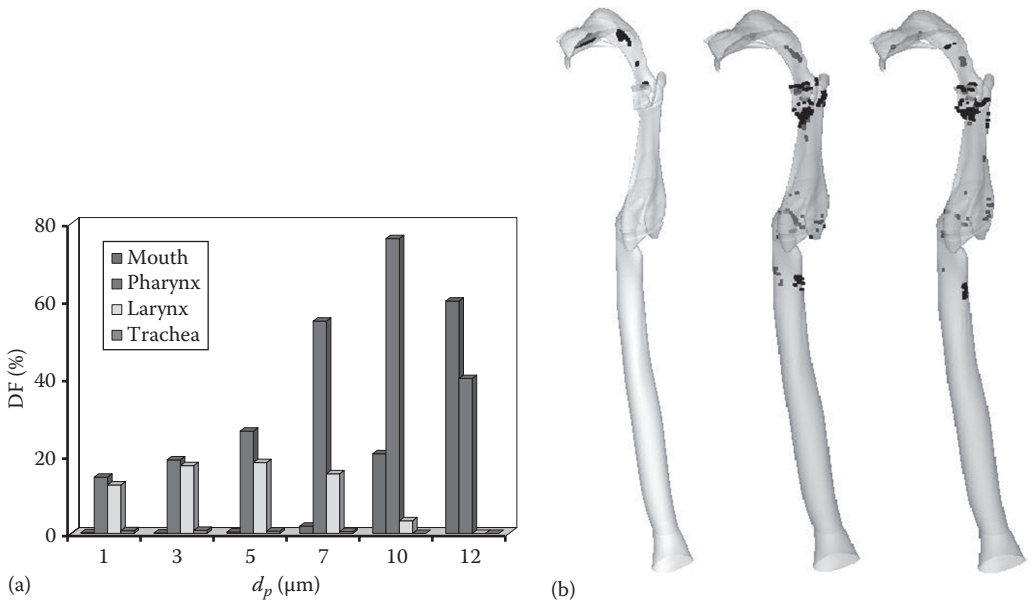


Figure 16.13

(a) Local deposition fraction of microparticles for a breathing rate of 30 L/min. (b) Deposition patterns of 3, 7, and 16 μm particles on the walls of the upper airways during the mouth breathing rate of 30 L/min.

Figure 16.13 shows local DF of microparticles in the mouth, pharynx, larynx, and trachea for the flow rate of 30 L/min. The particles with smaller diameters penetrate deeper into the upper airways and get into the larynx and trachea, while larger particles are captured in the upper parts including the mouth and pharynx. Figure 16.13 shows that large micron-sized particles are predominantly captured in the mouth region. This trend was also reported by Cheng et al. (1999) in their experimental study of mouth breathing. The use of realistic geometry of airway passages is important as the earlier numerical simulations of Zhang et al. (2002) and Tavakoli et al. (2009) using idealized geometry of upper airways for mouth breathing were not able to predict the same trend.

Figure 16.13b shows the spatial deposition patterns of 3, 7, and 16 μm particles in the human upper airways for a breathing rate of 30 L/min. It is seen that most particles are deposited in the pharynx and the inlet of the larynx. This is because of the sufficiently high particle inertia for this relatively high breathing. Figure 16.13b shows that all 16 μm particles are trapped in the mouth region for the 30 L/min flow rate.

16.1.5.3 Computational Modeling of Septal Deviation Effect on Deposition of Nano- and Microparticles in Human Nasal Passage

The effects of surgical correction of septal deviation on particle deposition in human nasal passage were studied by Moghadas et al. (2011) using a computational modeling approach. The adult male subject has actually gone through a real septoplasty surgery. The coronal cross sections of both sides of the nasal cavities obtained by CT scan images of the subject were used to construct smooth airway passages for the pre- and postoperative cases. The coronal cross sections were 2 mm apart and the resolution of the images was 512 × 512 pixels. The postoperative CT scan was taken three months after the septoplasty. The images before the septoplasty were acquired as a part of routine clinical procedure, and the images after the septoplasty were obtained with the approval of ethics and human subject committee.

Figure 16.14 shows the pictures of the axial CT scans of cross sections of the nasal passage. The differences between the left and right cavities for the earlier operation can be clearly seen from this figure. The major deviation is located in the main airway region. Septal deviation started at about 30 mm from the nose tip, in the nasal valve region where the cross-sectional area of the airway begins to decrease. At a distance of 46 mm from the nose tip, the deviation divides the right airway in two separated pathways. This separated segment continues to 50 mm away from the nostril. Deviation decreases the cross-sectional areas and the total volume of the passage, which causes breathing problems for the patient. The two separated pathways reunite at a distance of 72 mm from the nose tip, but the shape of the reconnected pathway is different from the left nasal cavity. The deviation ended at the beginning of the nasopharynx region.

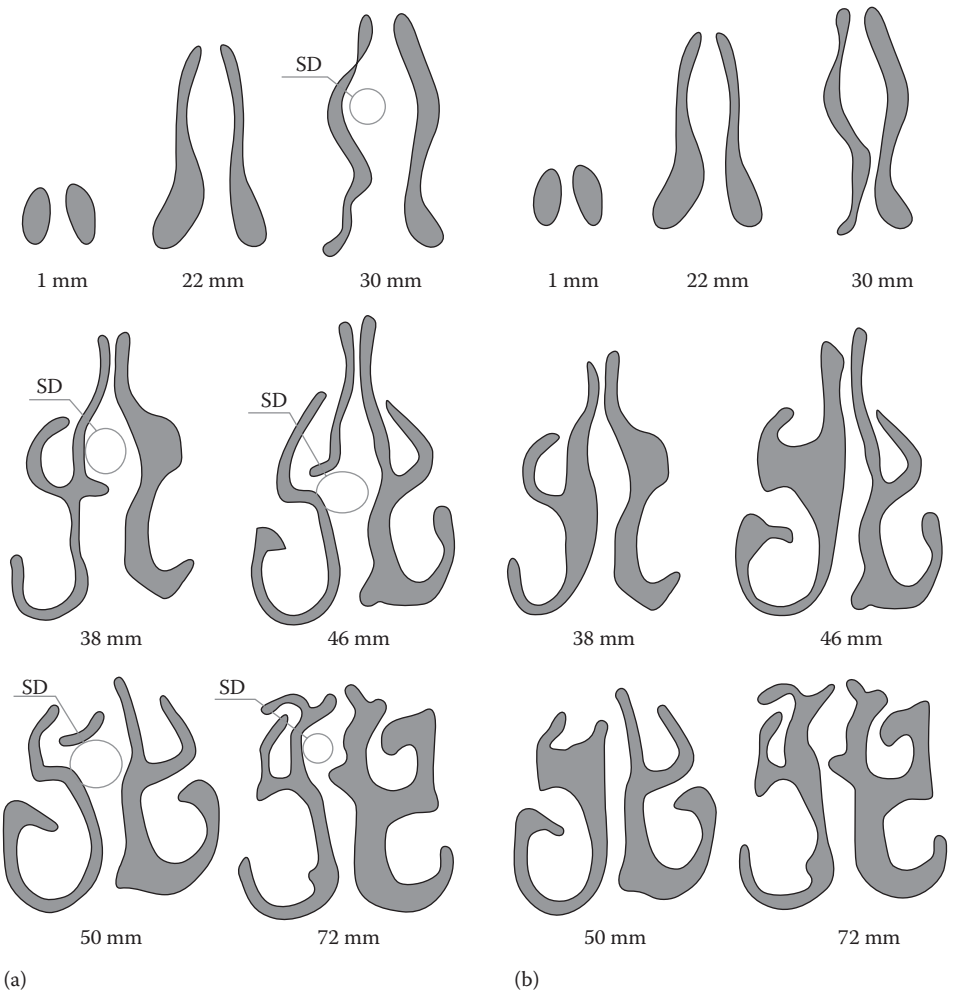


Figure 16.14

Nasal coronal cross sections at various distances from the nostril (a) before and (b) after operation. SD refers to the septal deviation.

Figure 16.14 shows that the two separated pathways of the right-side airway are merged into a single airway after septoplasty and the right cavity looks more like a normal nasal airway postoperatively. It should be pointed out that some parts of the nasal passages might be blocked by the mucus buildup. These can change the shape of the nasal cross sections during different scanning times. The blockage due to the mucus buildup in the scanned pictures can be identified and removed.

The 3-D geometry of human nasal airways can be constructed similar to the procedure described earlier. Here, CT scan images for the subject with septal deviation in the right cavity are processed to form the boundary surfaces of the nasal cavities walls. The 3-D nasal airway volume is exported to the mesh generation software to produce the computational grid. The generated unstructured computational grid includes roughly 800,000 tetrahedral elements for each passage. Several finer computational grids are also used to investigate the effect of grid refinements on the computational results. It is shown that the numerical results are grid independent for a computational grid with about 600,000 cells or more. The initially generated grid typically has high skewness because of the complexity of the nasal passages. Care should be taken to decrease the skewness of the grid, which results in a better convergence of the numerical solutions and decreases the corresponding residual computational errors. For simulation of the airflow and particle transport and deposition, flow solver software (such as ANSYS-Fluent) may be used.

Monodispersed particles in the range of 1–50 μm are injected into the nasal airway, and their transport and deposition for different pressure drops in the range of 10–20 Pa are evaluated. Comparisons of the model predictions for the variation of deposition efficiency with the IP for different nasal passages for a pressure drop of 10 Pa with the experimental data of Kelly et al. (2004a) are shown in Figure 16.15.

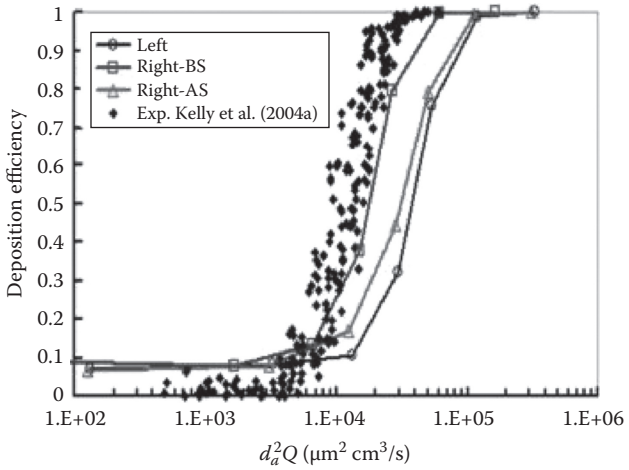


Figure 16.15

Deposition efficiency versus the impaction parameter for different nasal passages for a pressure drop of 10 Pa. (Comparison with the experimental data of Kelly, J.T. et al., *Aerosol Sci. Technol.*, 38, 1063, 2004a.)

The IP as defined in Equation 16.43 has been used extensively to correlate the nasal deposition efficiency of microparticles. The S-shape variation of the deposition efficiency is clearly seen from this figure. The model predictions for the normal left nasal passage and postoperative right cavity, however, are somewhat lower than the experimental data, while the predicted deposition efficiency for the preoperative right passage is in the range of the experimental data. As noted before, differences between the simulation results and the experimental data are due to the anatomical and geometrical differences of the nasal passages.

This study is for a patient with one abnormal nasal passage, while the experimental data are for normal nasal passages. Interestingly, the healthy left passage and the postoperative right cavity exhibit roughly identical trends. This shows that the operation corrected the abnormal passage to behave like the healthy passage. It is also possible that the left nasal passage of the patient may have had anatomically changed to compensate for the right blocked passage. Thus, the left passage may also have some differences with the nasal cavities of typical healthy people. In addition, as noted before, the fabricated experimental models typically have rough surfaces, while the computer model has smooth walls. This could be another reason for the differences seen.

It should also be pointed out that the deposition efficiency reported by Kelly et al. (2004a) is for two nasal chambers, but the presented simulation results are for single nasal passage to clarify the differences between the right nasal passage before and after the septoplasty. For the same pressure drop, Figure 16.15 also shows that the preoperative right cavity has a markedly higher DF compared with the postoperative one. For example, for IP = 26,733 μm² cm³/s, the deposition efficiency is 79% for the right preoperative cavity, 44% for the right postoperative passage, and 35% for the left nasal cavity. That is, there is a difference of 35% between the right preoperative and the normal left cavity, and it decreases to 12% after the septoplasty. The reason for the significant increase in the deposition in the right abnormal nasal cavity is that the septum deviation blocks the airflow and turns the streamlines sharply and thus increases the inertia impaction effect.

16.1.5.4 Micro- and Nanoparticle Deposition in Human Nasal Passage Pre- and Postvirtual Maxillary Sinus Endoscopic Surgery

Use of CFD in conjunction with virtual surgery could provide physicians with an important tool for evaluating the performance of various options before performing actual corrective airway surgery. Abouali et al. (2012) studied the virtual endoscopic surgery of maxillary sinus and the variation of the micro- and nanoparticle deposition in human nasal passage pre- and postoperation. A realistic 3-D model of the nasal cavity including paranasal sinuses was developed. The coronal cross sections for the left side of the nasal cavity and sinuses obtained by CT scan images of an adult male were used for developing a nasal airway model for the pre- and postoperative cases. The resolution of CT scan images was 512 × 512 pixels, and the coronal cross sections were 0.625 mm apart. The images were acquired as a part of routine clinical procedure. Under the supervision of a rhinologist, the boundary between the airway mucosa and air in the upper respiratory tract was defined in the CT scan slices. In addition, the uncinectomy and MMA were performed virtually by the rhinologist by removing the uncinate process and a part of the medial wall of the maxillary sinus on the coronal cross sections.

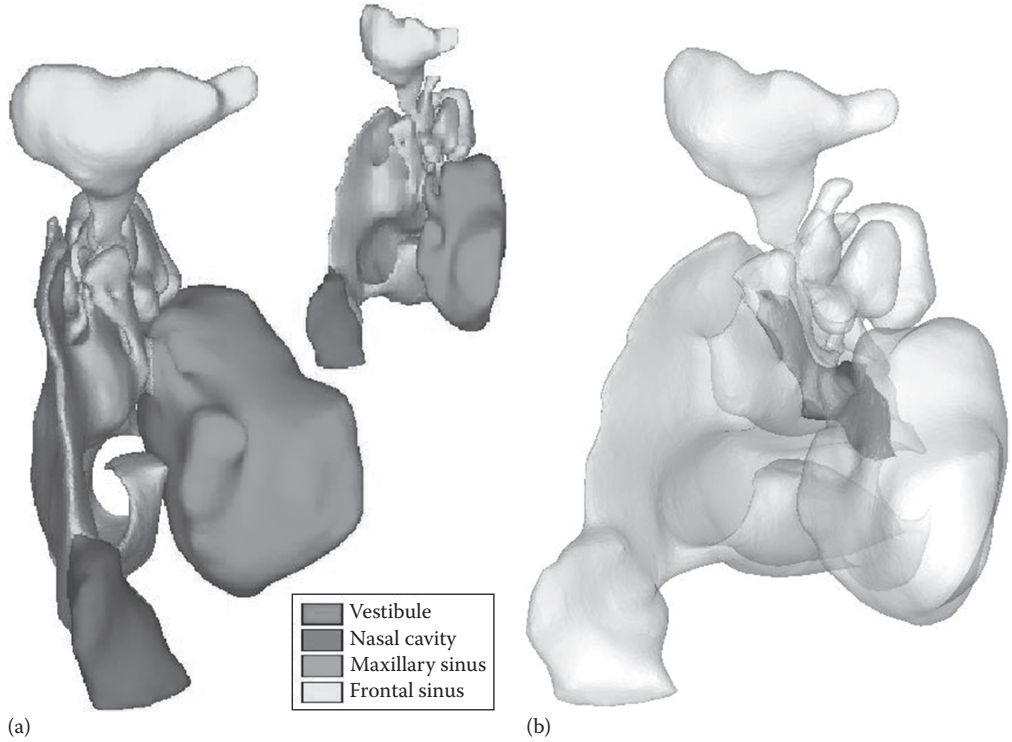


Figure 16.16

(a) Schematic of a constructed model of the left nasal airway and maxillary and frontal sinuses of a male patient. (b) The uncinate process and the removed part of medial wall of the maxillary sinus for the left nasal cavity are highlighted.

To reconstruct the 3-D model consisting of the nasal cavity and maxillary and frontal sinuses, the boundaries were imported into a CFD preprocessor software. The boundaries were connected to create smooth surfaces and form the volume. Figure 16.16a shows the schematic of the constructed model for the left nasal airway and maxillary and frontal sinuses. For clarity, the nasal vestibule, nasal cavity, and maxillary and frontal sinuses are colored differently in this figure. The uncinate process and part of the medial wall of the maxillary sinus that were usually removed in FESS are highlighted in Figure 16.16b. Figure 16.17 shows the streamlines of the inhaled air for a flow rate of 4 L/seen that none of the streamlines that start from the nostril enter the maxillary sinus before the operation. After uncinectomy and MMA, however, the airflow field inside the maxillary sinus changes dramatically, and part of the main airflow through the nasal passage enters the sinus. That is, the maxillary sinus ventilation changes significantly after the operation.

To compare the local deposition of microparticles for pre- and postoperation cases, monodispersed 1, 10, and 20 μm particles are released at the inlet of the nostril, and their trajectories are analyzed. For volume flow rates of 10 L/min, the corresponding deposition patterns are shown in Figure 16.18. This figure shows that practically no particle enters into the maxillary sinuses before the operation. After uncinectomy and MMA, however, some 1 and 10 μm particles enter into the maxillary sinus and deposit on the sinus wall. That is, the uncinate process and medial wall of the maxillary sinus are highly effective in preventing the microparticles to enter the maxillary sinus. It is also seen that almost no 20 μm particles reach the inside wall of the maxillary sinus even after uncinectomy and MMA. This implies that even the increased airflow into the maxillary sinus is not strong enough to move the 20 μm particles into the sinus. It should be noted here that no microparticle enters into the frontal sinus before or after the operation.

A quantitative description on the effect of uncinectomy and MMA on the microparticle deposition in the maxillary sinus is presented in Figure 16.19. DFs of microparticles in the size range of 1–25 μm for breathing rate of 10 L/min are shown in this figure before and after the operation. It is seen that a very small fraction (less than 0.1%) of the entering microparticles into the nasal cavity deposit on the maxillary sinus before ESS. This small fraction of particles also deposits at the opening of the maxillary sinus and none of them deposits on the inside wall of the maxillary sinus as seen in Figure 16.18. Uncinectomy and MMA increase the number of microparticles entering into the maxillary sinus by tenfold. The deposition pattern, however,

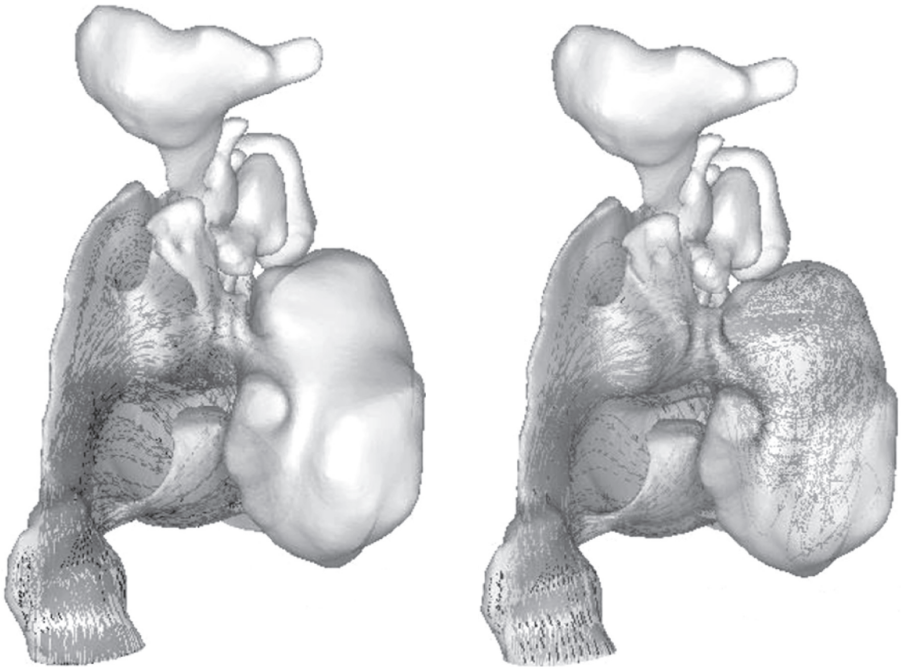


Figure 16.17

Streamlines of airflow (a) before and (b) after surgery for $Q = 4$ L/min.

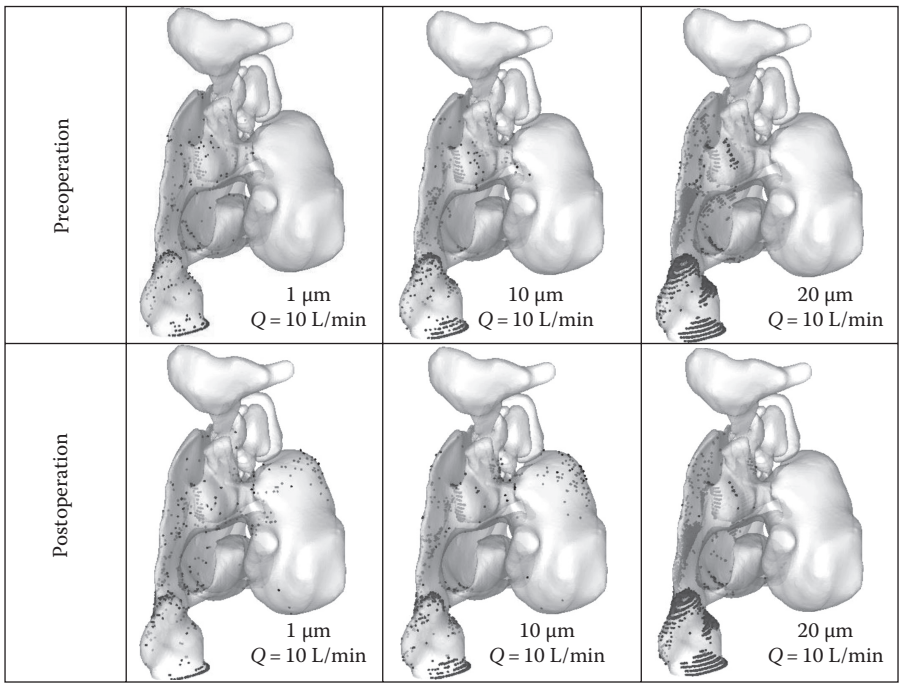


Figure 16.18

Microparticles deposition patterns on the nasal passage and maxillary sinus walls.

varies depending on particle size and breathing rates. For all the studied flow rates (not shown here), the maximum deposition in the maxillary sinus is highest for 10 μm particles.

The presented results provide a better understanding of the consequence of uncinectomy and MMA on therapeutic nasal drug delivery and exposure to inhaled pollutants. In particular, the simulation results show that the therapeutic spray droplets can penetrate the maxillary sinus after the operation. Thus, this treatment can be more

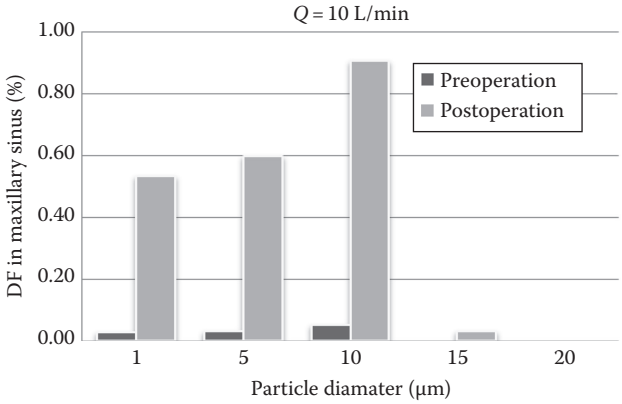


Figure 16.19

Pre- and postoperation deposition fractions in the maxillary sinus for a breathing rate of 10 L/min.

effective in curing allergic sinusitis and similar diseases. At the same time, however, allergens that can trigger the allergic symptoms in sinuses can also reach the sinuses and deposit on their walls. The size of allergens in the form of microparticles that causes most allergic symptoms ranges from 1 to 80 μm, with smaller particles under 50 μm more easily inhaled. Most of pollens that trigger allergic symptoms are in the size range of 15–40 μm, and the present simulations show that the probability of allergens reaching the maxillary sinus increases after uncinectomy and MMA. Thus, the occurrence of persistent maxillary sinus diseases after uncinectomy and MMA may be a consequence of increased deposition of allergens. As noted before, this operation for the presently studied case does not change the transport processes in the nasal valve or the main airway regions.

As mentioned before, a Eulerian diffusion model was used for studying the dispersion and deposition of nanoparticles in the nasal cavity and sinuses. Figure 16.20 shows the nanoparticle deposition flux contours on the walls of the nasal cavity and sinuses in the left passage for 1, 5, 10, and 20 nm particles with a breathing rate of 4 L/min. The particle deposition fluxes are nondimensionalized with respect to the inlet flux. That is, the nondimensional flux is evaluated as $-D(\partial C/\partial n)/U_iC_i$, where U_i and C_i are, respectively, the velocity and concentration at the inlet and n is the normal direction to the passage walls. Figure 16.20 clearly shows that, before the operation, almost no nanoparticles enter the sinuses and/or deposit on the sinus walls. Some nanoparticles, however, penetrate through and deposit on the walls of the maxillary sinus after the uncinectomy/MMA. No deposition of nanoparticles in the frontal sinus occurs before or after the operation. As mentioned before, the uncinate process studied in this work does not include the opening of the frontal sinus. Therefore, no change in the flow filtration and particle deposition in the frontal sinus occurs.

To provide a more detailed insight on the deposition of nanoparticles in the maxillary sinus, the DFs for flow rates of and 10 L/min are shown in Figure 16.21. Here, simulations are performed for particle diameters of 1, 3, 5, 10, and 20 nm. This figure shows that the DF of 1 nm particles increases after the uncinectomy and MMA operation for flow rates of 10 L/min. At a flow rate of 10 L/min, the DF is highest for 1 nm particles. After the uncinectomy and MMA, for 10 nm particles or smaller, the DF is at least 1%. No 20 nm particles enter the maxillary sinus before the operation, but after surgery about 0.5% of 20 nm particles deposit on the sinus wall. Although the DF of nanoparticles in the maxillary sinus is generally small compared with that in the main nasal passage, a comparatively significant increase is observed after the operation.

For a constant breathing rate, Figure 16.21 also shows that the nanoparticle deposition flux increases as the particle size decreases. Furthermore, for a fixed size, the particle deposition decreases as the flow rate increases. These trends are as expected since the Brownian diffusion is the dominant mechanism for nanoparticle deposition.

16.1.5.5 Regional Particle Depositions in the Upper Airway of a Standing Mannequin

There have been concerns on the effect of surrounding conditions including the geometric facial features on respiratory deposition. Recently, Naseri et al. (2014) reported the results of their study on the effect of external environment on the inhalation deposition. In particular, the assumption of uniform velocity and uniform particle concentration that are commonly used for the computer modeling of respiratory systems was examined.

The breathing mannequin used by Naseri et al. (2014) is shown in Figure 16.22. The mannequin resembles a typical male subject (Huston, 2009, Zhuang et al., 2010). The external computational domain is a 4 m side cube with the mannequin standing at its center as shown in Figure 16.23a. This computational

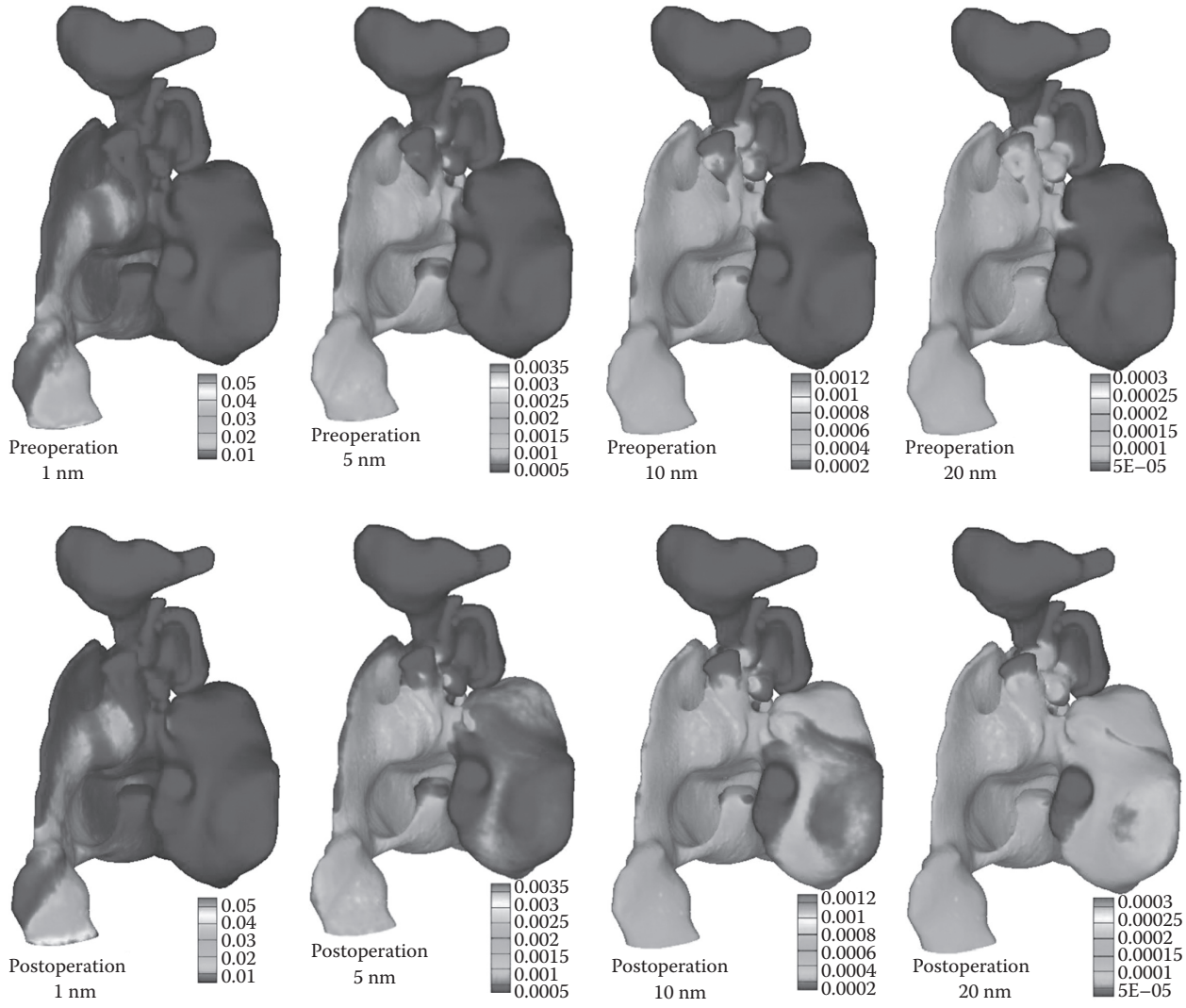


Figure 16.20

Nondimensional deposition flux contours of nanoparticles on the walls of nasal cavity and sinuses for a breathing rate of 4 L/min before and after the uncinectomy and MMA.

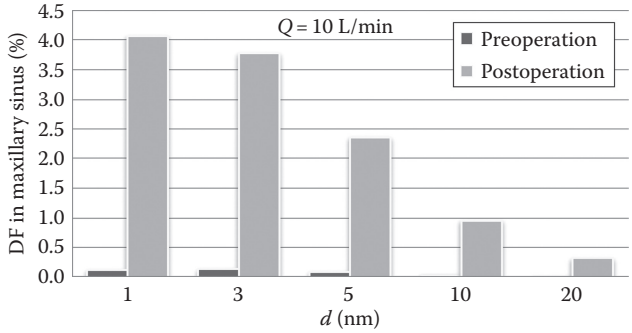


Figure 16.21

Deposition fractions of 1, 3, 5, 10, and 20 nm particles in the maxillary sinus for a breathing rate of 10 L/min before and after uncinectomy and MMA.

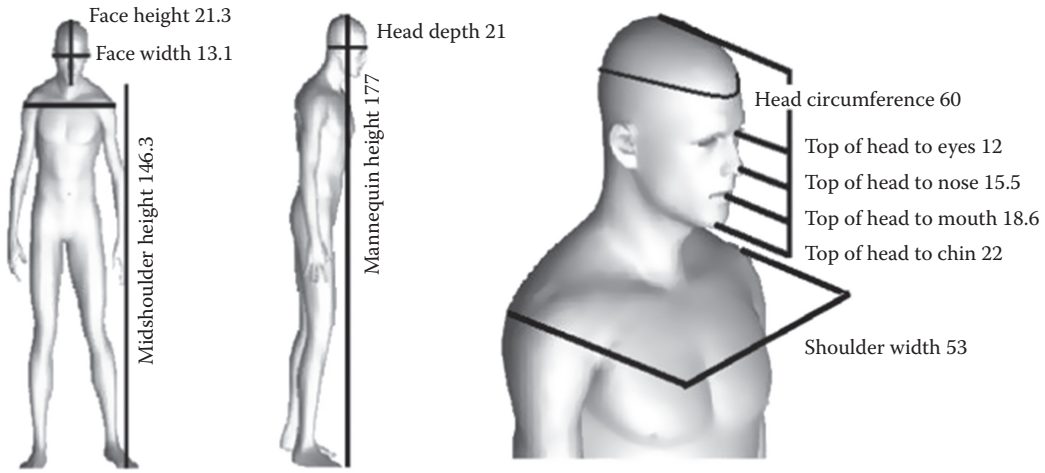


Figure 16.22

Different views of mannequin including the details of its facial features used in the study. All lengths are in centimeters.

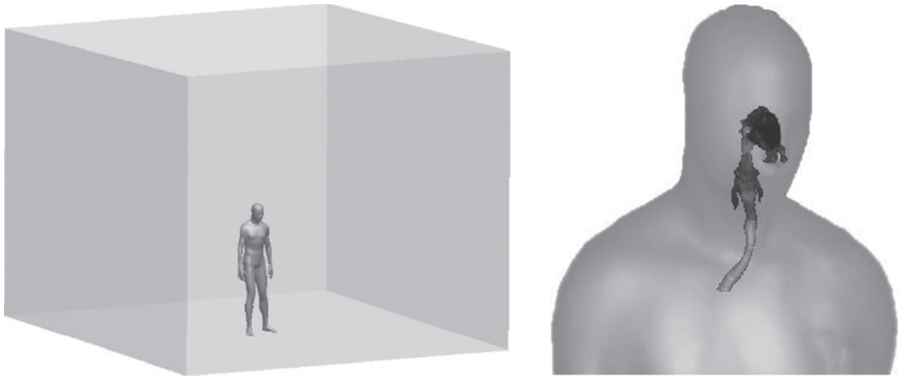


Figure 16.23

(a) Schematic of the computational domain. (b) Model of the mannequin with the attached upper airway.

domain is expected to be sufficiently large to eliminate the boundary effects. Based on the performed grid sensitivity, a grid of about 5.5 million cells was sufficient to achieve mesh-independent solutions. To assess the importance of including the mannequin body and external environment in the computational study of particle deposition in human airways, a 3-D model of the upper airways is connected to the mannequin and included in the computational domain. The airway model is the same as the one used in the example shown in Section 16.5.1. The attachment of the 3-D airway model to the mannequin is shown in Figure 16.23b.

For a breathing rate of 7 L/min, Figure 16.24 shows the path lines of inhaled air from the environment around the mannequin. The path lines are colored by velocity magnitude. It is seen that the peak velocity occurs in the pharynx region where the cross-sectional area is minimum. Sharp changes in the path lines occur in the nasal cavity and in the oropharynx region before the trachea. The detail of the airflow field a detached upper airway can be found in the work of Farhadi Ghalati et al. (2012).

Figure 16.25 shows the total particle deposition in the upper airways from nostril to the trachea, defined as TDF = N_d/N_{total}, where N is the number of particles that is deposited in the airway and N is total number of particles that entered the upper airway at the nostril. This figure compares the simulation results for the case of a separate airway with the case of an airway connected to the mannequin in a calm environment. For the case of separate airway, the particles are injected into the nostril with a uniform distribution. For the case of the airway of a mannequin, the particles are distributed uniformly around the mannequin in the computational domain. The effect of presence of mannequin body and face and external environment depends on both the breathing rate and particle diameter. For a breathing rate of 7 L/min, Figure 16.25

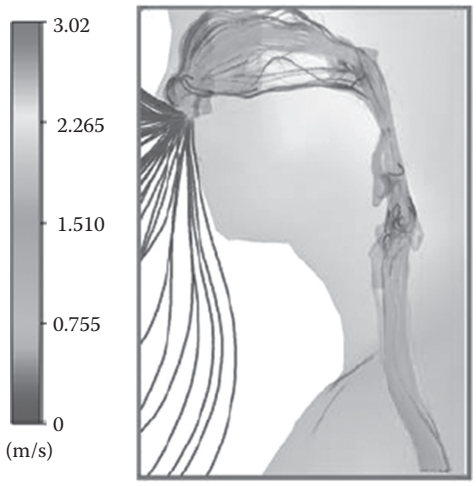


Figure 16.24

Path lines of inhaled air colored with velocity magnitude for the breathing rate of 7 L/min.

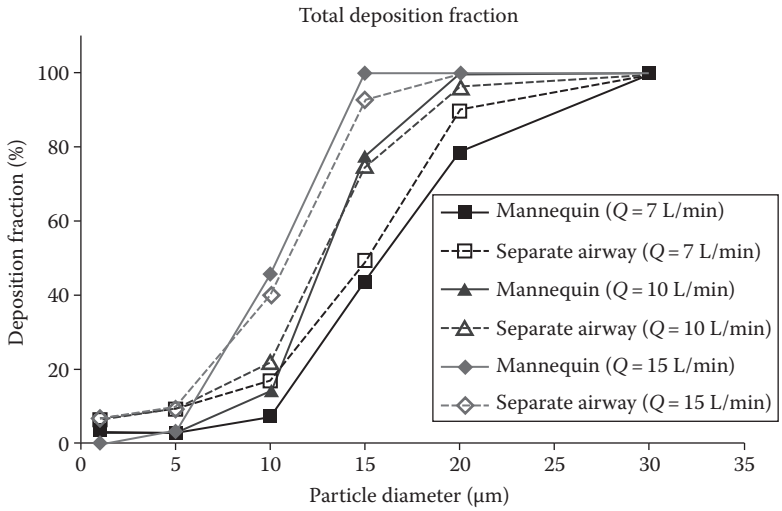


Figure 16.25

Comparison of the total deposition fractions in the detached upper airways with those in the airways attached to the mannequin.

shows that including the body of the mannequin and external environment in the computational model reduces the total deposition in the upper airway compared with that for the separated airway. But for higher breathing rates (10 and 15 L/min) and large particles, the effect reverses and the total DF for some particle size range increases. At a breathing rate of 10 L/min for particles with diameters of 10 μm or smaller, releasing the particles around the mannequin decreases the DF. For higher flow rate of 15 L/min this phenomenon is observed for particles with diameters of 5 μm or smaller.

Figure 16.26 shows the distribution of 2 μm particles at the nostrils when they have a uniform concentration in the surrounding environment. It is seen that particle distributions of inhaled particles at the nostrils are nonuniform. In addition, the particle distributions at the nostrils are different. This is perhaps due to the differences in the left and right nasal passages leading to different flow rates for the two sides of the nose. The simulation results show that the airflow rate through the right nasal passage in this case for a breathing rate of 10 L/min is about 73% of the left passage, and it drops to below 70% for low breathing rate of 7 L/min. It appears that the flow resistance of the left nasal passage for this subject is lower than that for the right one and this leads to a higher flow rate through the left nostril.

Another important observation is that the inhaled particles from the surrounding are concentrated in the high-velocity regions at the nares. In fact due to the presence of mannequin face and body and different

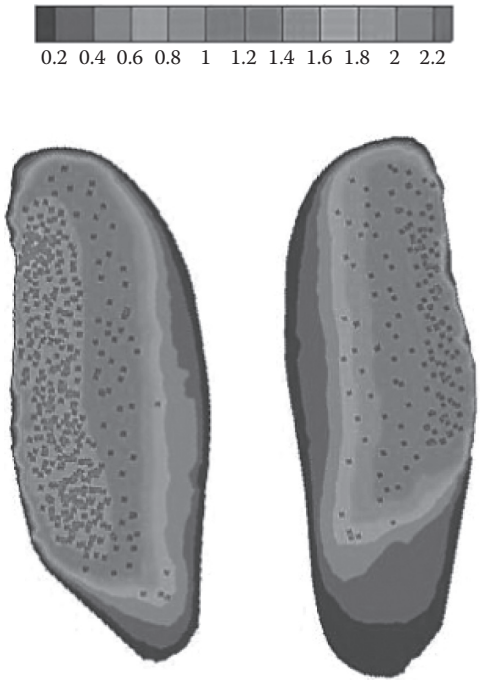


Figure 16.26

Distribution pattern of 2 μm particles released uniformly around the mannequin at the nostrils for a 7 L/min breathing rate. The contours show the velocity magnitude.

resistances of nasal passages, a nonsymmetrical airflow forms at the nostrils. This flow focuses the particles in the regions of high velocity at the nares. For the detached airway model, typically the particles are introduced uniformly at the inlet of the nostril. These different initial distributions lead to the differences in the particle deposition predicted by the two models.

To study the regional deposition, a sample result for the trachea is presented here. Figure 16.27 shows the regional DF for the trachea region, which is generally low. The simulation results of the separated airway model predict the peak DF of the 15 μm particles for the three inhalation rates studied. For the airway model attached to the mannequin, however, the peak deposition occurs for 10 μm particles. For the airway in the integrated mannequin model, the effects of the external environment and geometric features of the mannequin face shift the peak DF in the trachea region toward smaller particles.

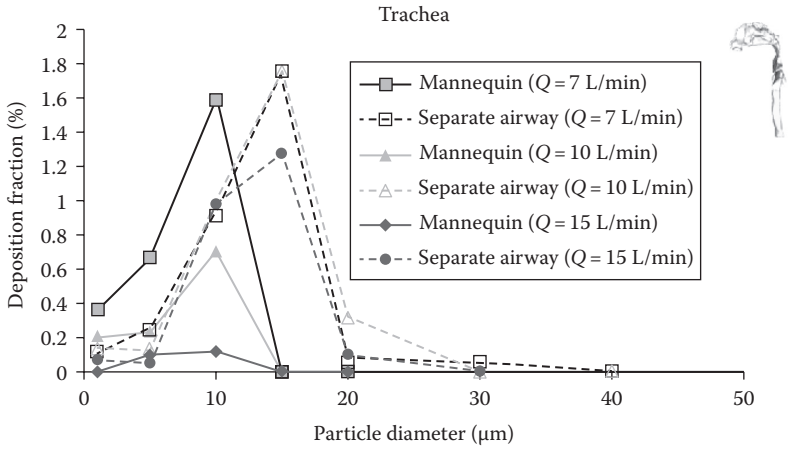


Figure 16.27

Comparison between the regional deposition fractions in the trachea of the separate upper airway and the airway in the mannequin.

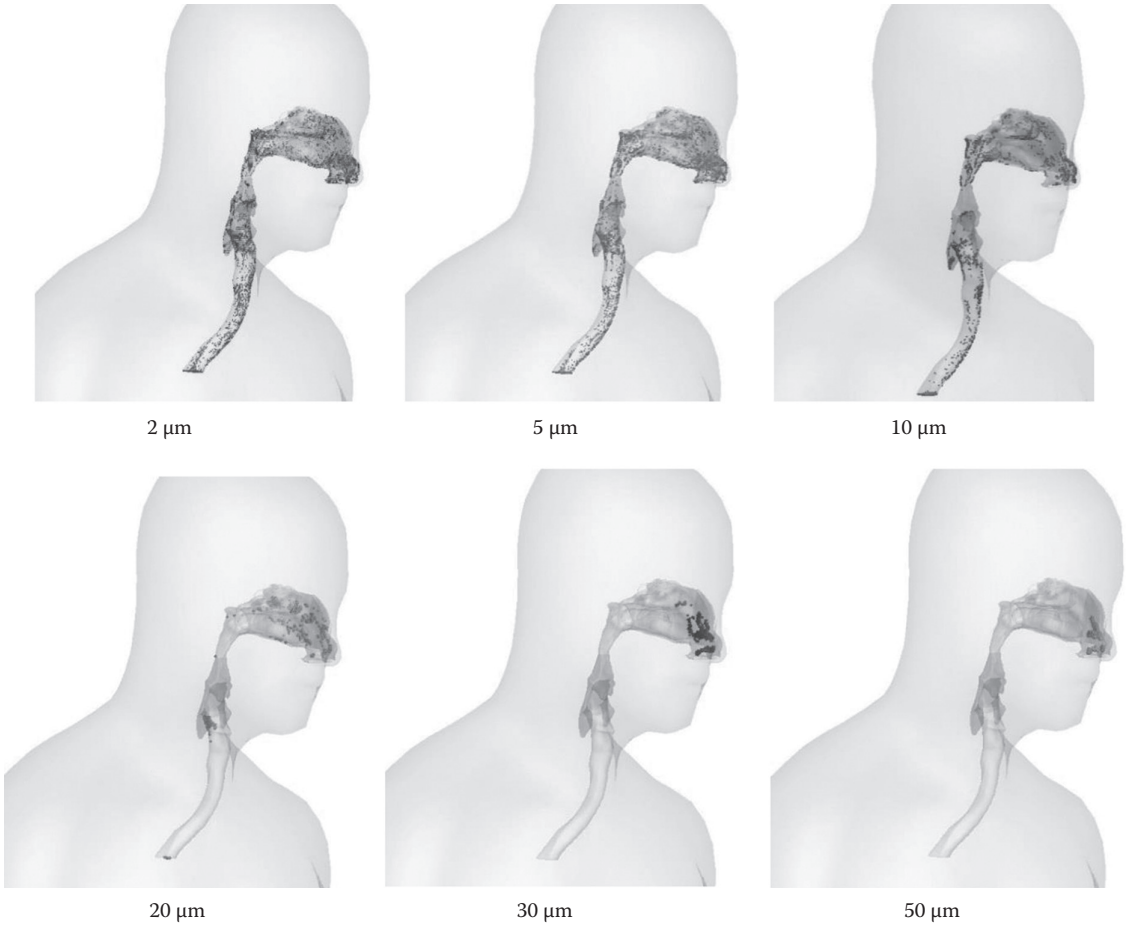


Figure 16.28

Particle deposition patterns in different regions of human upper airways for the breathing rate of 7 L/min.

Figure 16.27 also shows that generally the DF decreases with the increase in the inhalation rate. This might seems counterintuitive as the inertia deposition is the main mechanism for these particle sizes. However, it should be remembered that for higher flow rates the particles are filtered out in earlier sections of the nasal airway and a smaller number of particles have the chance to reach the trachea region. This observation is consistent with the very low DF for large particles in the trachea region.

Figure 16.28 shows the spatial deposition pattern for 5, 10, 20, 30, and 50 μm particles in the human upper airways for a breathing rate of 7 L/min. As expected, smaller particles penetrate deeper into the upper airway and reach the larynx and the trachea regions. All particles with sizes equal or larger than 30 μm are filtered out in the vestibule. Particles with diameters of 10 μm or smaller could reach into the trachea region for low breathing rates. The larynx, because of its rather complex geometry, is a hot spot for the deposition of particles passing through the upper airways.

16.1.5.6 Dispersion of Microparticles in Turbulent Airflows in Upper Airways

Recently, Ghahramani et al. (2014) reported the influence of airflow turbulence on the motion and deposition of microparticles in the upper airways. Accordingly, for a breathing rate of 45 L/min, the airflows in the passages of the upper airways are typically in the state of turbulent motion. The airway model used here is similar to that shown in Section 16.5.1. The velocity magnitude contours of and the turbulence intensity contours at various sections of the airway are shown in Figure 16.29. While the airflow is turbulent, the general pattern of the flow is similar to the laminar flow case at low breathing rate described in Section 16.5.1. The air enters from the nostril into the vestibule region and then turns sharply. The bulk of the airflow passes through the middle part of the passage. Here, however, because of the curvature in the flow passage, turbulence intensity increases significantly as shown in Figure 16.29b. In addition, secondary flows also occur in this part of passage that has

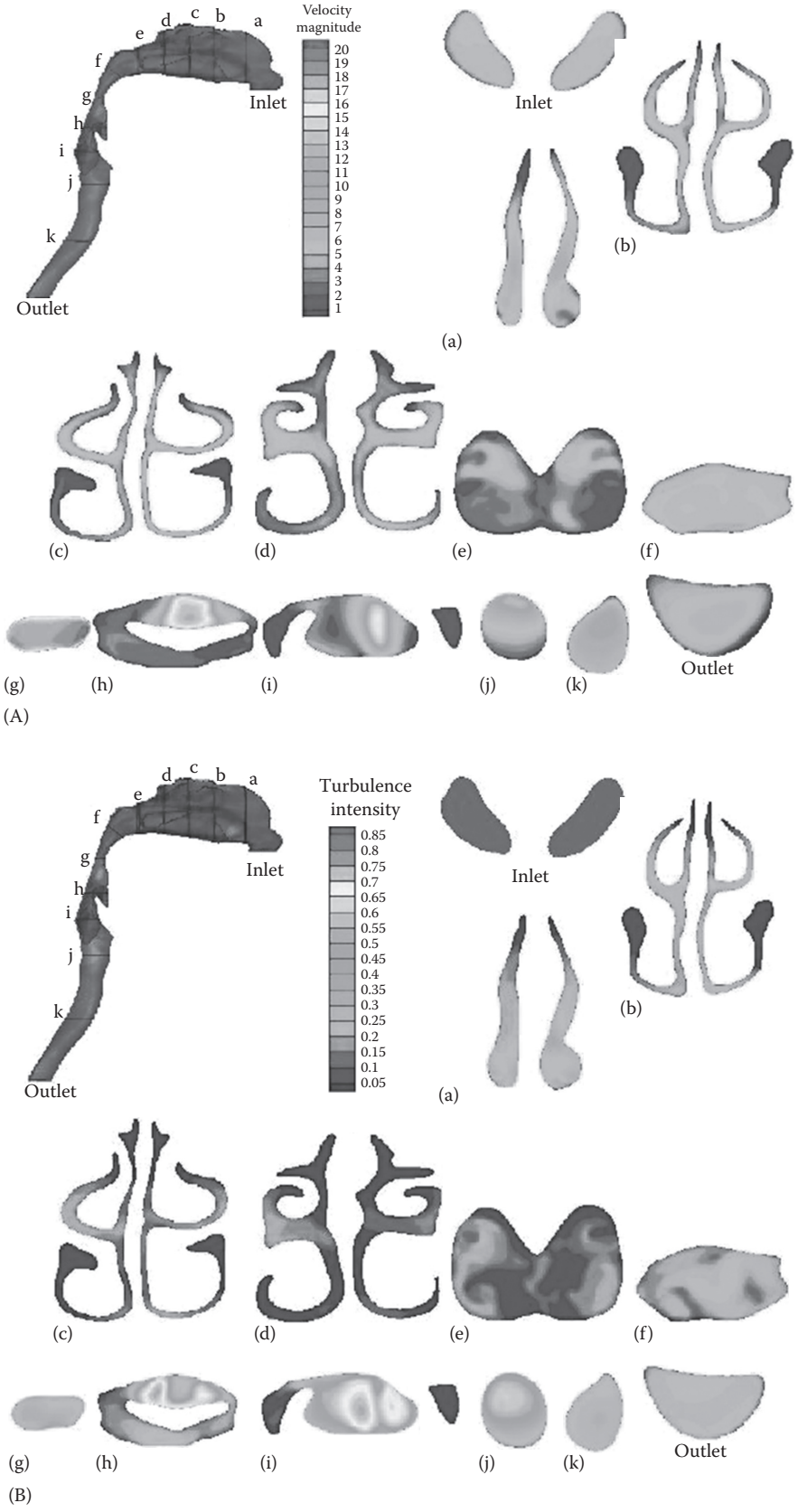


Figure 16.29

Airflow conditions at various sections of airways for a breathing rate of 45 L/min. (A) Velocity magnitude contours. (B) Turbulence intensity contours.

considerable effect on particle deposition. In the nasal valve and the main airway regions, similar to the laminar flow case, the airflow mainly passes through the middle meatus area as can be seen in Figure 16.29b through d. Again only a small fraction of airflow passes through the superior meatus and olfactory regions. In this region, the turbulent intensity decreases and in some parts the flow regime becomes laminar. Thus, while the bulk of the flow is in the turbulent flow regime, there are areas that are in the laminar regime. Therefore, it is important to use a suitable low Reynolds turbulence model, which can predict the relaminarization process appropriately.

In the nasopharynx region, as shown in Figure 16.29e through g, the turbulence intensity and secondary flows increase again. This is because of the presence of a significant curvature and sharp cross-sectional area reduction of the passage. Figure 16.29g shows that the velocity magnitude reaches its highest value at the end of the nasopharynx region. This section has the minimum cross-sectional area, which is about one-third of the area at section f. Therefore, the pressure drop in the nasopharynx region is quite high such that the average pressure at the end of nasopharynx is lower than its corresponding value at the outlet of trachea. In the oropharynx, due to the increase of the flow area, the velocity magnitude decreases, but the turbulent intensity continues to increase because of significant changes of the geometry as seen in Figure 16.29h. The curvature of the flow passage in the larynx causes the turbulent intensity to reach its highest value in this part of the airway (sections i and j, Figure 16.29b). In the trachea, the flow develops gradually, the turbulent intensity decreases, and the velocity magnitude variation diminishes.

For a better understanding of turbulence dispersion effects, particle tracking simulations were performed using the DRW and CRW stochastic models described, respectively, in Sections 16.1.4.2.1 and 16.1.4.2.2, and the results for the particle DF versus IP are presented in Figure 16.30, as well as the Stokes number, and are compared with the available experimental data. In addition, the case that the effect of turbulence fluctuation velocity was neglected and only the mean flow field was used for particle tracking is also plotted in Figure 16.30 for comparison.

This figure shows that the two stochastic methods for simulating the fluctuation velocity lead to roughly the same particle DF for high-inertia particles. In addition, the model predictions with the use of CRW model for low-inertia regime are also reasonable. For particles with low and moderate inertia, the DRW model prediction highly overpredicts the deposition rate. When the effect of turbulent dispersion is ignored and only the mean flow velocity is used, Figure 16.30 shows that the model prediction continuously underpredicts the DF, except perhaps for the very-low-inertia particles for which the DF is quite low. This implies that while turbulence has a significant effect on small particle dispersion, it does not significantly enhance the deposition of low-inertia particles. This figure clearly shows that deposition of particles with midrange inertia is clearly enhanced by turbulence fluctuations. The DRW model, however, markedly overpredicts the DF in this range.

Figure 16.31 shows the deposition pattern for 2.5, 5, and 10 μm particles in the realistic geometry of human upper airway system for a breathing rate of 45 L/min. The total DFs for these cases are, respectively, 17.9%, 66.3%, and 99.3%. It is also seen that particles of different sizes follow different deposition patterns. While a significant fraction of low-inertia particles with $d_p < 5$ μm can penetrate into the larynx and trachea regions, most of the high-inertia particles with $d_p > 10$ μm are captured in the vestibule and nasal valve regions. For these large particles, the inertia is high and the inertial impaction effects are quite effective. Moreover, as can be seen from the figure, some regions are more susceptible for the accumulation of deposited particles. Interestingly, these regions are similar to those described in Section 16.5.1 for the laminar flow analysis model. These accumulation regions are the vestibule, the top of middle meatus, the nasopharynx wall, the entrance to the oropharynx, and the back of the larynx regions.

Figure 16.32 shows the deposition patterns of 10 μm particles for the breathing rates of 30, 45, and 60 L/min. It is seen that the particle DF increases as the breathing rate increases. This trend is as expected since the impaction process dominates the deposition in the upper airways. In fact, the IP, which is the main factor for particle deposition, is directly proportional to the volume flow rate. Another important parameter that is increased by increasing the flow rate is the airflow turbulence, which enhances the turbulent dispersion of particles and consequently their deposition on the walls. However, when compared with the results shown in Figure 16.31, it is seen that the flow rate effect on particle deposition is comparatively less than the particle diameter effect. The stronger effect of particle size is due to the fact that the IP depends on the square of particle diameter compared with the linear dependence on the flow rate.

For the range of the studied inhalation flow rates described in Figures 16.31 and 16.32, the regional DF is highest in the nasal cavity compared with the other parts of the airway. Beyond the nasal cavity, the larynx and pharynx also capture a large number of the particles. Comparing the regional particle deposition patterns shown here to those that were reported by Frahadi Ghalati et al. (2012), who analyzed particle dispersion under strictly laminar flow regime (described in Section 16.5.1), two major differences are noticeable: While

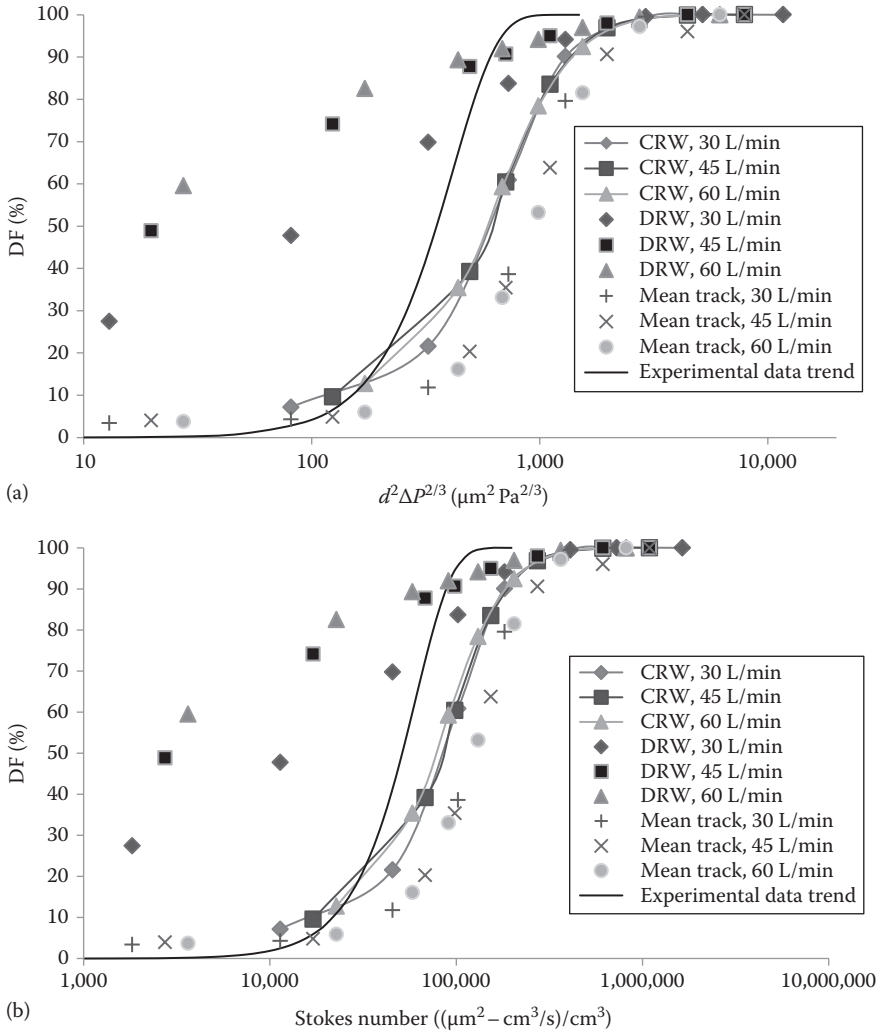


Figure 16.30

Comparison of the predicted results of the CRW model, the DRW model, and the mean track (no stochastic) model as a function of (a) $d_o^2\Delta P^{2/3}$ and (b) Stokes number.

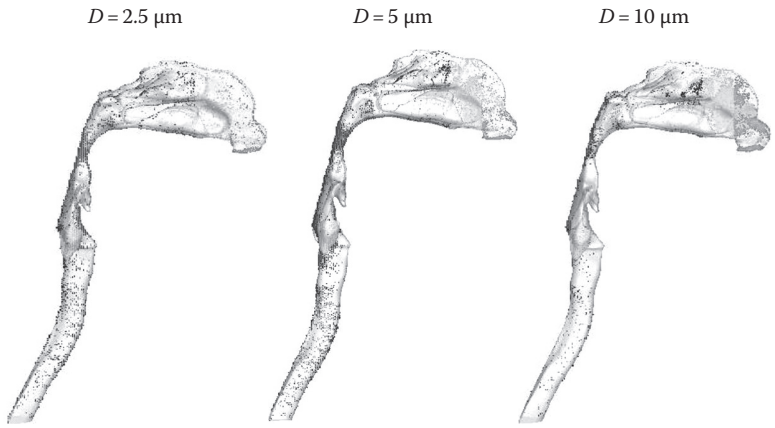


Figure 16.31

Deposition patterns of 2.5, 5, and 10 μm particles in the upper airways for a breathing rate of 45 L/min.

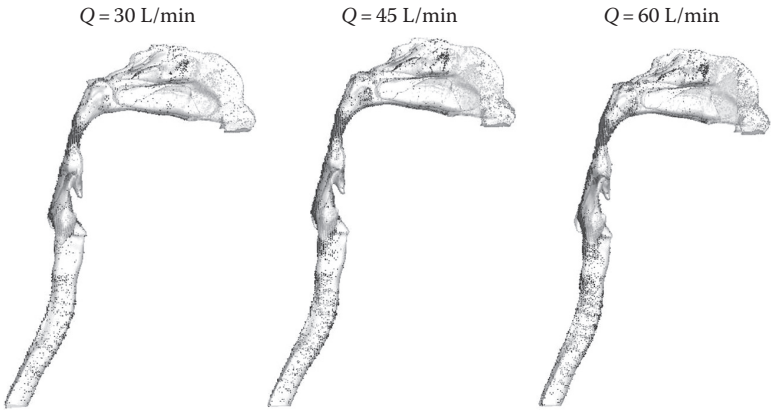


Figure 16.32

Deposition patterns of 10 μm particles in the upper airways for breathing rates of 30, 45, and 60 L/min.

a large fraction of microparticles in the size range of $d_p \sim 10$ μm reach the lung under laminar flow condition, the majority of these particles are filtered out under the turbulent airflow condition. In fact, for high activity breathing rates of $Q \sim 45$ L/min, almost no particles larger than 10 μm enter the lung. Moreover, although a large fraction of small particles pass the nasal cavity, there is moderate chance for their deposition in the pharynx and the larynx in turbulent airflows due to the increased turbulence intensity in the glottis; however, under laminar flow condition, the possibility of small particle deposition in the pharynx and the larynx is not high.

16.1.5.7 CFD Simulation of Total and Regional Fiber Deposition in Human Nasal Cavities

Dastan et al. (2014) presented a recent study on elongated particle deposition in nasal passages. A summary of their work is presented in this section. Three different single-passage nasal cavities are investigated. The first cavity, which will be referred as "case A," is the same as the cavity that was discussed in Section 16.5.4 for which the effects of maxillary sinus surgery were studied (Abouali et al., 2012). Here, only the left nasal cavity with the ethmoidal sinus is considered for the fiber transport and deposition analysis. The second and third nasal cavities considered here are the right and left nasal cavities of an adult healthy female, which is the same as the model that was used in Section 16.5.1 (Farhadi Ghalati et al., 2012). In the earlier section, the upper airway to the end of the trachea was modeled, while in here the main nasal cavity from nostril to the beginning of nasopharynx is used for fiber transport and deposition analysis. These right and left cavities are referred to, respectively, as "case B" and "case C" in the discussion.

16.1.5.7.1 Equivalent Diameter A number of equivalent sphere diameters for fibrous particle deposition in different configurations were introduced by a number of researches in the past (Fan and Ahmadi, 1995b, Balásházy et al., 2003, Inthavong et al., 2008, Tian et al., 2012, Wang et al., 2008). Clearly, the appropriate form of the equivalent diameter depends on the main deposition mechanism, such as inertial impaction, diffusion, or gravitational sedimentation. For relatively large microfibers, in addition to gravity, the inertial impaction is the main mechanism for their deposition in airway passages. Using the point force approximation method, Wang et al. (2008) suggested different expressions for equivalent aerodynamic diameters for fibers moving parallel to the flow, normal to the airflow direction, and with random orientation. These are

$$d_{eq_parallel} = 3a\sqrt{\frac{\rho^p}{\rho^f}[\ln(2\beta) - 0.80685]} \tag{16.45}$$

$$d_{eq_normal} = \frac{3}{2}a\sqrt{2\frac{\rho^p}{\rho^f}[\ln(2\beta) + 0.19375]} \tag{16.46}$$

$$d_{eq_random} = a\sqrt{6\frac{\rho^p}{\rho^f}[\ln(2\beta) - 0.30685]} \tag{16.47}$$

where ρ^p and ρ^f are, respectively, the particle density and the density of water.

Fan and Ahmadi (1995b) suggested the use of Stokes diameter for the presentation of ellipsoidal fiber deposition results. That is,

$$d_{Stk} = 6a\sqrt{\frac{2\beta}{k_{\dot{x}\dot{x}} + k_{\dot{y}\dot{y}} + k_{\dot{z}\dot{z}}}} \tag{16.48}$$

where $k_{\dot{i}\dot{i}}$ are the elements of resistant tensor given in Equations 16.29 and 16.30. For incorporating the effect of particle density, the equivalent aerodynamic diameter corresponding to the Stokes diameter given by (16.48) is given as

$$d_{eq_Stk} = 6a\sqrt{\frac{2\beta\rho^p}{\rho^f\left(k_{\dot{x}\dot{x}} + k_{\dot{y}\dot{y}} + k_{\dot{z}\dot{z}}\right)}} \tag{16.49}$$

The goal of introducing the equivalent diameter and IP is to collapse the data to a narrow curve and make it possible to compare the results of nonspherical particle deposition with those of spherical particles. Figure 16.33 shows the variation of total DF of fibrous and spherical particles versus IP for the nasal passage of case A for a breathing rate of Q = 10 L/min. The IP given by $\text{IP} = d_{eq}^2 Q$ is calculated using different equivalent diameters given by Equations 16.44 through 16.49. It is seen that among the four noted equivalent diameters, the use of the equivalent aerodynamics diameter given by Equation 16.49 collapses the simulation results of fibers on those of spherical particles. Therefore, the equivalent aerodynamic diameter given by Equation 16.49 is used for presentation of data in the rest of the current example.

The total DF of fibrous particles for a range of fiber radii and aspect ratios for different nasal passages are evaluated, and the results are plotted versus the IP with the equivalent diameter given by Equation 16.49 in Figure 16.34. The case of $\beta = 1$ corresponding to spherical particles is also included in these simulations. In the majority of cases, it was assumed that the density of fibers is ρ^p = 1000 kg/m^3 (density of water). However, the results of fiber deposition with density of ρ^p = 2000 kg/m^3 for the case A and breathing rate of Q = 10 L/min are also presented in Figure 16.34 for comparison. It is seen that using the equivalent aerodynamic diameter and presenting the results versus the IP leads to collapsing of the DF results to roughly a

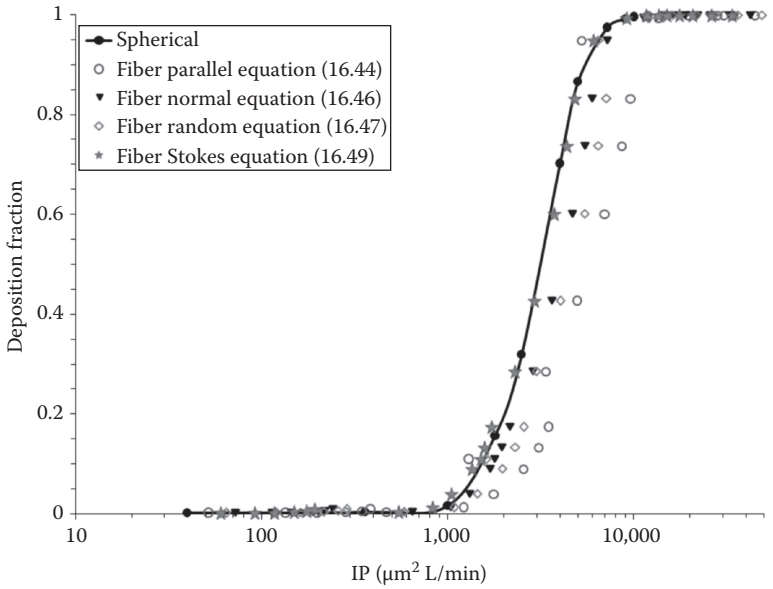


Figure 16.33

Variations of simulated deposition fractions of fibrous and spherical particle versus IP for different equivalent diameters in the nasal cavity of case A for a breathing rate of Q = 10 L/min. (The sizes of particles are in the ranges of $1 \le a \le 15$ μm and $1 \le \beta \le 80$. Particle density is the same as water.)

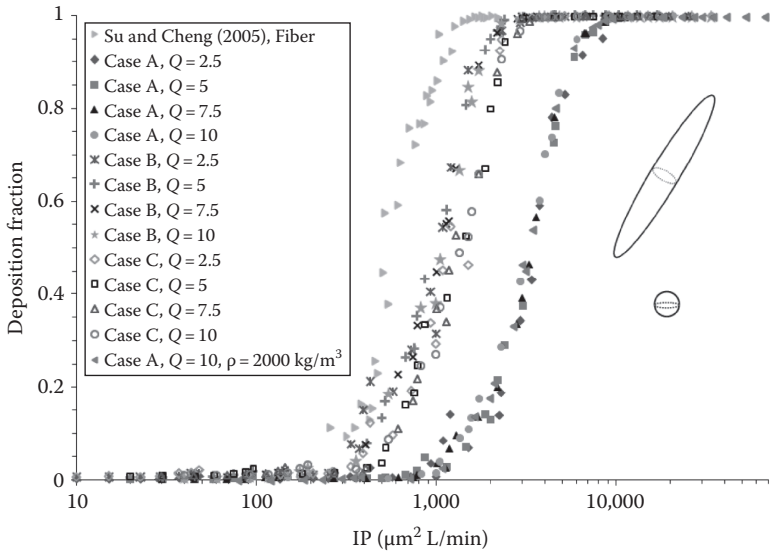


Figure 16.34

Total fibrous particle deposition for the range of $1 \leq a \leq 15$ μm and $1 \leq \beta \leq 80$ and unit density versus impaction parameter for different noses studied. The values of flow rates, Q, are in L/min for single nasal passage. The experimental data of Su and Cheng (2005) for fiber deposition are also reproduced in this figure for comparison.

single graph for each studied nasal passage. However, the intersubject variability between the nasal passages significantly affects the fiber deposition. As expected, the anatomy of the nasal cavity markedly affects the deposition rates of fibers as well as of spherical particles. Variations in the anatomy of the nasal passages are associated with the changes in the pressure drop for a given flow rate. The higher pressure drop in the nasal cavity is due to small effective cross section and leads to an increase in fiber deposition. The experimental data of Su and Cheng (2005) for fiber deposition are also presented in Figure 16.34 for comparison. This figure shows that the experimental DF for the nasal passage used by Su and Cheng is markedly higher than the simulated results. That again shows that the IP cannot reduce the intersubject variations and the differences among the DF values for different nasal cavities still remain.

Figure 16.35 shows the spatial deposition pattern of fibers for case A for a flow rate of $Q = 5$ L/min. It is seen that as the IP increases, the DF increases. This figure also shows that as the IP increases, the regional deposition pattern also changes to an extent. In particular, fibers with high IP deposit heavily in certain region of the nose where sharp changes in flow direction occur.

For nasal passage A, Figure 16.36 compares the DF predicted by the fiber model (solving the coupled translational and rotational equations of motions of ellipsoids) with the HL model described in Section 16.1.4.4.1. It is seen that the HL model follows the trend of the fiber simulation results. The HL model results are, however, somewhat scattered compared with the fiber model and the corresponding simulation results do not collapse onto a single curve. In addition, for the range of the parameter in this figure, the HL model overestimates the DF by factor of about 2. While the HL model is a much simpler model and reduces the computational time, it does not account for the actual physics of the fiber motion in the airflow and does not provide accurate estimates for the fiber DFs.

16.1.6 Conclusions

In this chapter, a review of recent literature on respiratory flow and deposition is presented. Fundamentals of particles and fiber transport and deposition are outlined and particular attention is given to recent advances in computational modeling of nano- and microparticles as well as fiber transport and deposition in human upper airways. Sample results on transport and deposition processes in nasal cavity, throat, larynx, and pharynx, as well as trachea and main left and right bronchus, are presented. Both nasal and oral breathing conditions are discussed. An example of effects of septoplasty surgery on particle deposition in human nasal passage is presented. The particle transport and deposition for pre- and postmaxillary sinus endoscopic surgery are also discussed. The effects of the surrounding environment including the facial features, as well as turbulent airflow

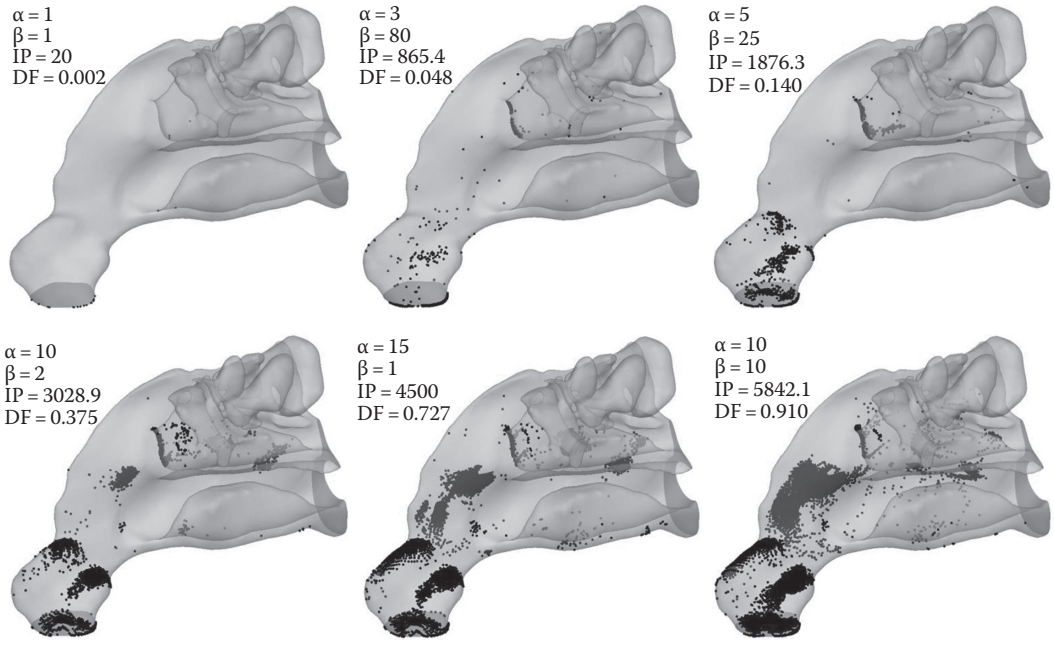


Figure 16.35

Spatial distribution of deposition pattern of fibers in the nasal passage A for a flow rate of $Q = 5$ L/min. Fiber radius, a, is in μm and IP is in μm^2 L/min. DF stands for the total deposition fraction.

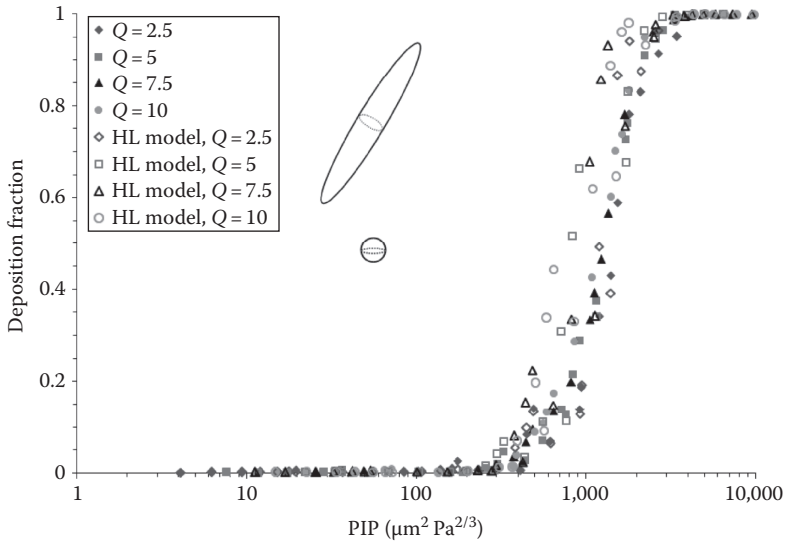


Figure 16.36

Comparison of deposition fractions predicted by the fiber model with those of the HL model for the nasal cavity of case A. The values for flow rate, Q, are in L/min per single passage and the fiber sizes are in the range of $1 \le a \le 15$ μm and $1 \le \beta \le 80$ with unit density.

on the respiratory deposition, are also studied. The motion and deposition of fibrous particle in the upper airways are discussed. The following are the presented results:

- The molecular diffusion and turbulence are dominant for deposition of nanometer size particles and the deposition rate increases as particle diameter decreases.
- For particles larger than a few microns, the impaction is the dominant deposition mechanism and the deposition rate increases with the particle size.

- Computer simulations for spherical and fibrous particles are in good agreement with the available experimental data.
- The computational model could be became a useful tool for performing virtual surgery for testing various options.
- Surrounding environment and facial features markedly affect the regional particle DF in the upper airways.
- The concentration of inhaled aerosol at the nostril is not uniform.

References

Abouali, O., Keshavarzian, E., Farhadi Ghalati, P., Faramarzi, A., Ahmadi, G., and Bagheri, M.H., Micro and nanoparticle deposition in human nasal passage pre and post virtual maxillary sinus endoscopic surgery, *Respir. Physiol. Neurobiol.*, 181, 335–345, 2012.

Alexopoulos, A.H., Karakosta, P., and Kiparissides, C., Particle transfer and deposition using an integrated CFD model of the respiratory system, in *20th European Symposium on Computer Aided Process Engineering*, 2010.

Ally, J., Amirfazli, A., and Roa, W., Factors affecting magnetic retention of particles in the upper airways: An *in vitro* and *ex vivo* study, *J. Aerosol Med.*, 19(4), 491–509, 2006.

Asgharian, B. and Ahmadi, G., Effect of fiber geometry on deposition in small airways of the lung, *Aerosol Sci. Technol.*, 29, 459–474, 1998.

Balásházy, I., Hofmann, W., and Heistracher, T., Local particle deposition patterns may play a key role in the development of lung cancer, *J. Appl. Physiol.*, 94, 1719–1725, 2003.

Baldwin, P.E.L. and Maynard, A.D., A survey of wind speeds in indoor workplaces. *Ann. Occup. Hyg.* 42, 303–313, 1998.

Ball, C.G., Uddin, M., and Pollard, A., High resolution turbulence modeling of airflow in an idealized human extra-thoracic airway, *Comput. Fluids*, 37, 943–964, 2008.

Barati, R., Salehi Neyshabouri, S.A.A., and Ahmadi, G., Development of empirical models with high accuracy for estimation of drag coefficient of flow around a smooth sphere: An evolutionary approach, *Powder Technol.*, 257, 11–19, 2014.

Bernstein, G.M., A review of the influence of particle size, puff volume, and inhalation pattern on the deposition of cigarette smoke particles in the respiratory tract, *Inhal. Toxicol.*, 16, 675–689, 2004.

Berry, R.D. and Froude, S., An investigation of wind conditions in the workplace to assess their effect on the quantity of dust inhaled. HSE Internal Report IR/L/DS/89/3, Health and Safety Executive, London, 1989.

Cavallo, D., Campopiano, A., Cardinali, G., Casciardi, S., Simone, P.D., Kovacs, D. et al., Cytotoxic and oxidative effects induced by man-made vitreous fibers (MMVFs) in a human mesothelial cell line, *Toxicology*, 201, 219–229, 2004.

Chen, X.B., Lee, H.P., Chong, V.H.F., and Wang, D.Y., Assessment of septal deviation effects on nasal airflow: A computational fluid dynamics model, *The Laryngoscope*, 119(9), 1730–1736, 2009.

Cheng, Y.S., Aerosol deposition in the extrathoracic region, *Aerosol Sci. Technol.*, 37, 659–671, 2003.

Cheng, Y.S., Su, Y.F., Yeh, H.C., and Swift, D.L., Deposition of Thoron progeny in human head airways, *Aerosol Sci. Technol.*, 18, 359–375, 1993.

Cheng, Y.S., Yamada, Y., Yeh, H.C., and Swift, D.L., Diffusional deposition of ultrafine aerosols in a human nasal cast, *J. Aerosol Sci.*, 19(6), 741–751, 1988.

Cheng, Y.S., Yeh, H.C., Guilmette, R.A., Simpson, S.Q., Cheng, K.H., and Swift, D.L., Nasal deposition of ultrafine particles in human volunteers and its relationship to airway geometry, *Aerosol Sci. Technol.*, 25, 274–291, 1996.

Cheng, Y.S., Zhou, Y., and Chen, B.T., Particle deposition in a cast of human oral airways, *Aerosol Sci. Technol.*, 31, 286–300, 1999.

Chung, S.K. and Kim, S.K., Digital particle image velocity studies of nasal airflow, *Respir. Physiol. Neurobiol.*, 163, 111–120, 2008.

Clift, R., Grace, J.R., and Weber, M.E., *Bubbles, Drops, and Particles*, Academic Press, London, U.K., 1978.

Dames, P., B. Gleich, A. Flemmer, K. Hajek, N. Seidl, F. Wiekhorst, D. Eberbeck, I. Bittmann, C. Bergemann, T. Weyh, L. Trahms, J. Rosenecker, and C. Rudolph, Targeted delivery of magnetic aerosol droplets to the lung. *Nature Nanotechnology*, 2(8), 495–499, 2007.

Dastan, A. and Abouali, O., Microfiber motion and web formation in a microchannel heat sink: A numerical approach, *Comput. Fluids*, 71, 28–40, 2013.

Dastan, A., Abouali, O., and Ahmadi, G., CFD simulation of total and regional fiber deposition in human nasal cavities, *J. Aerosol Sci.*, 69, 132–149, 2014.
Daia, Y.T., Juang, Y.J., Wu, Y.Y, Breysse, P.N., and Hsu, D.J., In vivo measurements of inhalability of ultra-large aerosol particles in calm air by humans, *J. Aerosol Sci.*, 37, 967–973, 2006.
Dehbi, A., Turbulent particle dispersion in arbitrary wall-bounded geometries: A coupled CFD-Langevin-equation based approach, *Int. J. Multiphase Flow*, 34, 819–828, 2008.
Dehbi, A., Prediction of extrathoracic aerosol deposition using RANS-random walk and LES approaches, *Aerosol Sci. Technol.*, 45, 555–569, 2011.
Donaldson, K., Stone, V., Gilmour, P.S., Brown, D.M., and Macnee, W., Ultrafine particles: Mechanisms of lung injury, *Philos. Trans. Royal Soc.*, 358, 2741–2749, 2000.
Doorly, D.J., Taylor, D.J., and Schroter, R.C., Mechanics of airflow in the human nasal airways, *Respir. Physiol. Neurobiol.*, 163, 100–110, 2008.
Durbin, P.A., Stochastic differential equations and turbulent dispersion. *NASA Reference Publication*, 1103, 1983.
Durbin, P.A., Comments on the papers by Wilson et al. (1981) and Legg and Raupach (1982). *Bound-Layer Meteorol.*, 29, 409–411, 1984.
Fan, F. and Ahmadi, G., Dispersion of ellipsoidal particles in an isotropic pseudo-turbulent flow field, *Fluids Eng.*, 117, 154–161, 1995a.
Fan, F. and Ahmadi, G., A sublayer model for wall deposition of ellipsoidal particles in turbulent stream, *J. Aerosol Sci.*, 26, 813–840, 1995b.
Farhadi Ghalati, P., Keshavarzian, E., Abouali, O., Faramarzi, A., Tu, J., and Shakibafard, A., Numerical analysis of micro- and nano-particle deposition in a realistic human upper airway, *Comput. Biol. Med.*, 42, 39–49, 2012.
Fluent, Fluent 6.3 Users Guide, Lebanon, NH, 2006.
Foos, B., Marty, M., Schwartz, J., Bennett, W., Moya, J., and Jarabek, A.M., Focusing on children's inhalation dosimetry and health effects for risk assessment: An introduction, Part A: Current issues, *J. Toxicol. Environ. Health*, 71(3), 149–165, 2008.
Frampton, M.W., Systemic and cardiovascular effects of airway injury and inflammation: Ultrafine particle exposure in humans, *Environ. Health Perspect.*, 109, 529–532, 2001.
Friedlander, S.K., *Smoke, dust and haze*, *Fundamentals of Aerosol Dynamics*, 2nd edn., Oxford University Press, New York, 2000.
G. U.S. General Surgeon report, The health consequences of involuntary exposure to tobacco smoke: A report of the surgeon general—Executive summary. U.S. department of health and human services, centers for disease control and prevention, coordination center for health promotion national center for chronic disease prevention and health promotion, office on smoking and health, 2006.
Gallily, I. and Eisner, A.D., On the orderly nature of the motion of nonspherical aerosol particle I. Deposition from a Laminar flows. *J. Colloid Interface Sci.*, 68, 320–337, 1979.
Gambit2.3, 2006, Gambit 2006 Users Guide, Gambit 2.3, 2006 by Fluent.
Garcia, G.J.M., Tewksbury, E.W., Wong, B.A., and Kimbell, J.S., Interindividual variability in nasal filtration as a function of nasal cavity geometry, *J. Aerosol Med. Pulmonary Drug Deliv.*, 22(2), 139–155, 2009.
Ghahramani, E., Abouali, O., Emdad, E., and Ahmadi, G., Numerical analysis of stochastic dispersion of micro-particles in turbulent flows in a realistic model of human nasal/upper airway, *J. Aerosol Sci.*, 67, 188–206, 2014.
Goldstein, H., *Classical Mechanics*, 2nd edn., Addison-Wesley Company, Reading, MA, 1980.
Golshahi, L., Noga, M.L., Thompson, R.B., and Finlay, W.H., In vitro deposition measurement of inhaled micrometer-sized particles in extrathoracic airways of children and adolescents during nose breathing, *J. Aerosol Sci.*, 42, 474–488, 2011.
Gosman, A.D. and Ioannides, E., Aspects of computer simulation of liquid fuelled combustors, *J. Energy*, 7, 482–490, 1983.
Grgic, B., Finlay, W.H., Burnell, P.K.P., and Heenan, A.F., In vitro intersubject and intrasubject deposition measurements in realistic mouth-throat geometries, *J. Aerosol Sci.*, 35, 1025–1040, 2004.
Grgic, B., Martin, A.R., and Finlay, W.H., The effect of unsteady flow rate increase on in vitro mouth–throat deposition of inhaled boluses, *J. Aerosol Sci.*, 37, 1222–1233, 2006.
Grützenmacher, S., Robinson, D.M., Grafe, K., Lang, C., and Mlynski, G., First findings concerning airflow in noses with septal deviation and compensatory turbinate hypertrophy—A model study, *J. ORL*, 68, 199–205, 2006.
Hahn, I., Scherer, P.W., and Mozell, M.M., Velocity profiles measured for airflow through a large-scale model of the human nasal cavity, *J. Appl. Physiol.*, 75, 2273–2287, 1993.

Haider, A. and Levenspiel, O., Drag coefficient and terminal velocity of spherical and nonspherical particles, *Powder Technol.*, 58, 63–70, 1989.
Harper, E.Y. and Chang, I.D., Maximum dissipation resulting from lift in a slow viscous shear flow. *J. Fluid Mech.*, 33, 209–225, 1968.
Häußermann, S., Bailey, A., Bailey, M., Etherington, G., and Youngman, M., The influence of breathing patterns on particle deposition in a nasal replicate cast, *J. Aerosol Sci.*, 33, 923–933, 2002.
He, C. and Ahmadi, G. Particle deposition in a nearly developed turbulent duct flow with electrophoresis. *J. Aerosol Sci.*, 30, 739–758, 1999.
Heyder, J., Deposition of inhaled particles in the human respiratory tract and consequences for regional targeting in respiratory drug delivery, *Proc. Am. Thoracic Soc.*, 1, 315–320, 2004.
Hinds, W.C., *Aerosol Technology: Properties, Behavior, and Measurement of Airborne Particles*, 2nd Edition, New York: Wiley, 1999.
Hounam, R.F., Black, A., and Walsh, M., The deposition of aerosol particles in the nasopharyngeal region of the human respiratory tract, *J. Aerosol Sci.*, 2, 47–61, 1971.
Hsu, D.H. and Swift, D.L., The measurements of human inhalability of outrage aerosols in calm air using mannequin, *J. Aerosol Sci.*, 30, 1331–1343, 1999.
Huston, R.L., *Principles of Biomechanics*, Taylor and Francis Group, Boca Raton, FL, 2009.
ICRP, *Human Respiratory Tract Model for Radiological Protection*, Elsevier Science Ltd., New York, 1994.
Iliopoulos, I., Mito, Y., and Hanratty, T.J., A stochastic model for solid particle dispersion in a nonhomogeneous turbulent field, *Int. J. Multiphase Flow*, 29, 375–394, 2003.
Inthavong, K., Choi, L.T., Tu, J.Y., Ding, S., and Thien, F., Micron particle deposition in a tracheobronchial airway model under different breathing conditions, *Med. Eng. Phys.*, 32, 1198–1212, 2010.
Inthavong, K., Ge, Q.J., Li, X.D., and Tu, J.Y., Detailed predictions of particle aspiration affected by respiratory inhalation and airflow, *Atmos. Environ.*, 62, 107–117, 2012.
Inthavong, K., Ge, Q.J., Li, X., and Tu, J.Y., Source and trajectories of inhaled particles from a surrounding environment and its deposition in the respiratory airway, *Inhal. Toxicol.*, 25, 280–291, 2013.
Inthavong, K., Ge, Q., Se, C.M.K., Yang, W., and Tu, J.Y., Simulation of sprayed particle deposition in a human nasal cavity including a nasal spray device, *J. Aerosol Sci.*, 42, 100–113, 2011.
Inthavong, K., Tian, Z.F., Li, H.F., Tu, J.Y., Yang, W., Xue, C.L., and Li, C.G., A Numerical study of spray particle deposition in a human nasal cavity, *Aerosol Sci. Technol.*, 40, 1034–1045, 2006.
Inthavong, K., Tian, Z.F., Tu, J.Y., Yang, W., and Xu, C., Optimising nasal spray parameters for efficient drug delivery using computational fluid dynamics, *Comput. Biol. Med.*, 38, 713–726, 2008a.
Inthavong, K., Tu, J.Y., and Ahmadi G., Computational modelling of gas-particle flows with different particle morphology in the human nasal cavity, *J. Comput. Multiphase Flows*, 1(1), 57–82, 2009.
Inthavong, K., Wen, J., Tian, Z., and Tu, J.Y., Numerical study of fibre deposition in a human nasal cavity, *J. Aerosol Sci.*, 39, 253–265, 2008b.
Jayaraju, S.T., Brouns, M., Verbanck, S., and Lacor, C., Fluid flow and particle deposition analysis in a realistic extrathoracic airway model using unstructured grids, *J. Aerosol Sci.*, 38, 494–508, 2007.
Jayaraju, S.T., Brouns, M., Lacor, C., Belkassem, B., and Verbanck, S., Large eddy and detached eddy simulations of fluid flow and particle deposition in a human mouth–throat, *J. Aerosol Sci.*, 39, 862–875, 2008.
Jeffery, G.B., The motion of ellipsoidal particles immersed in a viscous fluid, *Proc. R. Soc. A*, 102, 161–179, 1922.
Jiang, J. and Zhao, K., Airflow and nanoparticle deposition in rat nose under various breathing and sniffing conditions—A computational evaluation of the unsteady and turbulent effect, *J. Aerosol Sci.*, 41, 1030–1043, 2010.
Katz, I.M., Davis, B.M., and Martonent, T.B., A numerical study of particle motion within the human larynx and trachea, *J. Aerosol Sci.*, 30, 173–183, 1999.
Keith, C.H., Particle size studies on tobacco smoke, *Beitrage zur Tabakforschung Int.*, 11(3), 123–131, 1982.
Kelly, J.T., Asgharian, B., Kimbell, J.S., and Wong, B.A., Particle deposition in human nasal airway replicas manufactured by different methods. Part II. Inertial regime particle. *Aerosol Sci. Technol.*, 38, 1063–1071, 2004a.
Kelly, J.T., Asgharian, B., Kimbell, J.S., and Wong, B.A., Particle deposition in human nasal airway replicas manufactured by different methods. Part II: Ultrafine particles. *Aerosol Sci. Technol.*, 38, 1072–1079, 2004b.
Kelly, J.T., Prasad, A.K., and Wexler, A.S., Detailed flow patterns in the nasal cavity, *J. Appl. Physiol.*, 89, 323–337, 2000.
Kennedy, N.J. and Hinds, W.C., Inhalability of large solid particle, *J. Aerosols Sci.*, 33, 237–255, 2002.

Keyhani, K., Scherer, P.W., and Mozell, M.M., Numerical simulation of airflow in the human nasal cavity, *J. Biomech. Eng.*, 117, 429–441, 1995.
Kim, S.K., Na, Y., Kim, J.I., and Chung, S.K., Patient specific CFD models of nasal airflow: Overview of methods and challenges, *J. Biomech*., 46, 299–306, 2013.
Kim, C.S., Hu, S.C., Dewitt, P., and Gerrity, T.R., Assessment of regional deposition of inhaled particles in human lungs by serial bolus delivery method, *J. Appl. Physiol*., 81, 2203–2213, 1996.
Kittelson, D.B., Engines and nanoparticles: A review, *J. Aerosol Sci*., 29 (5–6), 575–588, 1998.
Kleinstreuer, C. and Zhang, Z., Laminar-to-turbulent fluid-particle flows in a human airway model, *Int. J. Multiphase Flow*, 29, 271–289, 2003.
Kreuzer, M., Muller, M.K., Brachner, A., Gerken, M., Grosche, B., and Wiethege T., Histopathologic findings of lung carcinoma in German uranium miners, *Cancer*, 89, 2613–2621, 2000.
Kvasnak, W. and Ahmadi, G., Deposition of ellipsoidal particles in turbulent duct flows, *Chem. Eng. Sci*., 51, 5137–5148, 1996.
Launder, B.E., and Sharma, B.I., Application of the energy-dissipation model of turbulence to the calculation of flow near a spinning disc. *Letters in Heat and Mass Transfer*, 1, 131–138, 1974.
Li, A. and Ahmadi, G., Dispersion and deposition of spherical particles from point sources in a turbulent channel flow, *Aerosol Science Technology*, Vol. 16, 209–226, 1992.
Li, A. and Ahmadi, G., Computer simulation of particle deposition in the upper tracheobronchial tree, *Aerosol Sci. Technol*., 23, 201–223, 1995.
Li, Z., Kleinstreuer, C., and Zhang, Z., Particle deposition in the human tracheobronchial airways due to transient inspiratory flow patterns, *J. Aerosol Sci*., 38, 625–644, 2007.
Li, X., Inthavong, K., and Tu, J., Particle inhalation and deposition in a human nasal cavity from the external surrounding environment, *Build. Environ*., 47, 32–39, 2012.
Lindemann, J., Brambs, H.J., Keck, T., Wiesmiller, K.M., Rettinger, G., and Pless, D., Numerical simulation of intranasal airflow after radical sinus surgery, *Am. J. Otolaryngol*., 26, 175–180, 2005.
Liu, Y., Matida, E.A., Gu, J., and Johnson, M.R., Numerical simulation of aerosol deposition in a 3-D human nasal cavity using RANS, RANS/EIM, and LES, *J. Aerosol Sci*., 38, 683–700, 2007.
Liu, Y., Matida, E.A., and Johnson, M.R., Experimental measurements and computational modeling of aerosol deposition in the Carleton-Civic standardized human nasal cavity, *J. Aerosol Sci*., 41, 569–586, 2010.
Longest, P.W. and Hindle, M., CFD simulations of enhanced condensational growth (ECG) applied to respiratory drug delivery with comparisons to in vitro data, *J. Aerosol Sci*., 41, 805–820, 2010.
Longest, P.W., Tian, G., Walenga, R.L., and Hindle, M., Comparing MDI and DPI aerosol deposition using in vitro experiments and a new Stochastic individual path (SIP) model of the conducting airways, *Pharmaceut. Res*., 29, 1670–1688, 2012.
Mandell, G.L., Bennett, J.E., and Bolin, R.D., *Principles and Practices of Infectious Diseases*, 6th edn., Churchill Livingstone, New York, 2004.
Martin A.R. and Finlay W.H., Enhanced deposition of high aspect ratio aerosols in small airway bifurcations using magnetic field alignment, *J. Aerosol Sci*., 39, 679–690, 2008.
Martonen, T.B., Zhang, Z., Yue, G., and Musante C.J., 3-D Particle transport within the human upper respiratory tract, *J. Aerosol Sci*., 33, 1095–1110, 2002.
Matida, E.A., Finlay, W.H., Lange, C.F., and Grgic, B., Improved numerical simulation of aerosol deposition in an idealized mouth–throat, *J. Aerosol Sci*., 35, 1–19, 2004.
Mehel, A., Tanie´re, A., Oesterle´, B., and Fontaine, J.R., The influence of an anisotropic Langevin dispersion model on the prediction of micro- and nanoparticle deposition in wall-bounded turbulent flows, *J. Aerosol Sci*., 41, 729–744, 2010.
Moghadas, H., Abouali, H., Faramarzi, A., and Ahmadi, G., Numerical investigation of septal deviation effect on deposition of nano/microparticles in human nasal passage, *Respir. Physiol. Neurobiol*., 177, 9–18, 2011.
Mylavarapu, G., Murugappan, Sh., Mihaescu, M., Kalra, M., Khosla, S., and Gutmark, E., Validation of computational fluid dynamics methodology used for human upper airway flow simulations, *J. Biomech*., 42, 1553–1559, 2009.
Naseri, A., Abouali, O., Farhadi Ghalatii, P., and Ahamdi, G., Numerical investigation of regional particle deposition in an integrated human upper airway in a standing male manikin model and a separated airway model in calm air surroundings, *Comput. Biol. Med*., 52, 73–81, 2014.
Nasr, H., Ahmadi, G., and McLaughlin, J.B., A DNS study of effects of particle–particle collisions and two-way coupling on particle deposition and phasic fluctuations, *J. Fluid Mech*., 640, 507–536, 2009.
Oberdörster, G., Pulmonary effects of inhaled ultrafine particles, *Int. Arch. Occup. Environ. Health*, 74, 1–8, 2001.

Ozlugedik, S., Nakiboglu, G., Sert, C., Elhan, A., Tonuk, E., Akyar, S., and Tekdemir, I., Numerical study of the aerodynamic effects of septoplasty and partial lateral turbinectomy, *Laryngoscope*, 118, 330–334, 2008.
Proetz, A.W., Air currents in the upper respiratory tract and their clinical importance, *Ann. Otol. Rhinol. Laryngol.*, 60, 439–467, 1951.
Renotte, C., BouGoux, V., and Wilquem, F., Numerical 3D analysis of oscillatory flow in the time-varying laryngealchannel. *Journal of Biomechanics*, 33, 1637–1644, 2000.
Saffman, P. G., Corrigendum to: "The lift on a small sphere in a slow shear flow", *J. Fluid Mech*., 31, p. 624, 1968.
Salmanzadeh, M., Rahnama, M., and Ahmadi, G., Effect of sub-grid scales on Large Eddy Simulation of particle deposition in a turbulent channel flow, *Aerosol Sci. Technol.*, 44, 796–806, 2010.
Schreck, S., Sullivan, K.J., Ho, C.M., and Chang, H.K., Correlations between flow resistance and geometry in a model of the human nose, *J. Appl. Physiol.*, 75, 1767–1775, 1993.
Schroeter, J.D., Garcia, G.J.M., and Kimbell, J.S., Effects of surface smoothness on inertial particle deposition in human nasal models, *J. Aerosol Sci.*, 42, 52–63, 2011.
Se, C.M., Inthavong, K., and Tu, J.Y., Inhalability of micron particles through the nose and mouth, *Inhalat. Toxicol.*, 22(4), 287–300, 2010.
Shi, H., Kleinstreuer, C., and Zhang, Z., Laminar airflow and nanoparticle or vapor deposition in a human nasal cavity model, *J. Biomechan. Eng.*, 128, 697–706, 2006.
Shi, H., Kleinstreuer, C., and Zhang, Z., Modeling of inertial particle transport and deposition in human nasal cavities with wall roughness, *J. Aerosol Sci.*, 38, 398–419, 2007.
Stapleton, K.W., Guentsch, E., Hoskinson, M.K., and Finlay, W.H., On the suitability of k-ε turbulence modeling for aerosol deposition in the mouth and throat: A comparison with experiment, *J. Aerosol Sci.*, 31, 739–749, 2000.
Strong, J.C. and Swift, D.L., Deposition of ultrafine particles in a human nasal cast, in *Proceedings of the First Conference of Aerosol Society*, Loughborough University of Technology, Leicestershire, U.K., 1987, pp. 109–112.
Subramaniam, R.P., Richardson, R.B., Morgan, K.T., Kimbell, J.S., and Guilmette, R.A., Computational fluid dynamics simulations of inspiratory airflow in the human nose and nasopharynx, *Inhalat. Toxicol.*, 10, 91–120, 1998.
Swift, D.L., Montassier, N., Hopke, P.H., Karpen-Hayes, K., Cheng, Y.S., Su, Y.F., Yeh, H.C., and Strong, J.C., Inspiratory deposition of ultrafine particles in human nasal replicate cast, *J. Aerosol Sci.*, 23(1), 65–72, 1992.
Swift, D.L. and Proctor, D.F., Access of air to the respiratory tract, in Brain, J.D., Proctor, D.F., Reid, L.M. (Eds.), *Respiratory Defence Mechanisms*. Part 1. Marcel Dekker, New York, 1977, pp. 63–93.
Swift, D.L. and Strong, J.C., Nasal deposition of ultrafine aerosols in human subjects, *J. Aerosol Sci.*, 27(7), 1125–1132, 1996.
Su, W.C. and Cheng, Y.S., Deposition of fiber in the human nasal airway, *Aerosol Sci. Technol.*, 39, 888–901, 2005.
Su, W.C., Wu, J., Marijnissen, J.C.M., and Cheng, Y.S., Deposition of man-made fibers in a human nasal airway, *Aerosol Sci. Technol.*, 42, 173–181, 2008.
Suman, J.D., Laube, B.L., and Dalby, R., Validity of in vitro tests on aqueous spray pumps as surrogates for nasal deposition, absorption, and biologic response, *J. Aerosol Med.*, 19(4), 510–521, 2006.
Tavakoli, B., Abouali, O., Bagheri, M.H., Yazdi, M., and Ahmadi, G., Microparticles transport and deposition in realistic geometry of human upper airways, *Int. J. Eng. Trans. A Basics*, 25(4), 315–322, 2012.
Tavakoli, B., Abouali, O., Yazdi, M., Bagheri, M.H., and Ahmadi, G., Micro/nano-particles transport and deposition in realistic geometry of human upper airways, *ASME 2009 Fluids Engineering Division Summer Meeting*, Vail, CO, August 2–5, 2009.
Taylor, D.J., Doorly, D.J., and Schroter, R.C., Inflow boundary profile prescription for numerical simulation of nasal airflow, *J. Royal Soc. Interface*, 7, 515–527, 2010.
Thompson, D.J., Random walk modeling of dispersion in inhomogeneous turbulence, *Quart. J. Royal Meteorolog. Soc.*, 110, 1107–1120, 1984.
Thompson, D.J., Criteria for the selection of stochastic models of particle trajectories in turbulent flows *J. Fluid Mech*., 180, 529–556, 1987.
Tian, L. and Ahmadi, G., Particle deposition in turbulent duct flow—Comparison of different model predictions, *J. Aerosol Sci.*, 38, 377–397, 2007.
Tian, L., Ahmadi, G., Wang, Z., and Hopke, P.K., Transport and deposition of ellipsoidal fibers in low Reynolds number flows, *J. Aerosol Sci.*, 45, 1–18, 2012.
Tonndorf, J., Der weg der atemluft in der menschlichen nase, *Archiv für Ohren-, Nasen- und Kehlkopfheilkunde*, 146, 41–63, 1939.

Tu, J., Inthavong, K., and Ahmadi, G., *Computational Fluid and Particle Dynamics in the Human Respiratory System*, Springer, 2013.
Verbanck, S., Kalsi, H.S., Biddiscombe, M.F., Agnihotri, V., Belkassem, B., Lacor, C., and O.S. Usmani, Inspiratory and expiratory aerosol deposition in the upper airway, *Inhalat. Toxicol.*, 23(2), 104–111, 2011.
Wang, S.M., Inthavong, K., Wen, J., Tu, J.Y., and Xue, C.L., Comparison of micron- and nanoparticle deposition patterns in a realistic human nasal cavity, *Respir. Physiol. Neurobiol.*, 166, 142–151, 2009.
Wang, Y., Liu, Y., Sun, X., Yu, Sh., and Gao, F., Numerical analysis of respiratory flow patterns within human upper airway, *Acta Mech. Sin.*, 25, 737–746, 2009.
Wang, Z., Hopke, P.K., Ahmadi, G., Cheng, Y.S., and Baronc, P.A., Fibrous particle deposition in human nasal passage: The influence of particle length, flow rate, and geometry of nasal airway, *J. Aerosol Sci.*, 39, 1040–1054, 2008.
Weinhold, I. and Mlynski, G., Numerical simulation of airflow in the human nose, *Eur. Arch. Otorhinolaryngol.*, 261, 452–455, 2004.
Wen, J., Inthavong, k., Tu, T., and Wang, S., Numerical simulations for detailed airflow dynamics in a human nasal cavity, *Respir. Physiol. Neurobiol.*, 161(2), 125–135, 2008.
Xi, J. and Longest, P.W., Transport and deposition of micro-aerosols in realistic and simplified models of the oral airway, *Ann. Biomed. Eng.*, 35(4), 560–581, 2007.
Xi, J. and Longest, P.W., Numerical predictions of submicrometer aerosol deposition in the nasal cavity using a novel drift flux approach, *Int. J. Heat Mass Transfer*, 51, 5562–5577, 2008.
Xi, J., Si, X., Kim, J.W., and Berlinsk, A., Simulation of airflow and aerosol deposition in the nasal cavity of a 5-year-old child, *J. Aerosol Sci.*, 42, 156–173, 2011.
Xie, Y., Zeng, P., Siegel, R.A., Wiedmann, T.S., Hammer, B.E., and Longest, P.W., Magnetic deposition of aerosols composed of aggregated superparamagnetic nanoparticles, *Pharmaceut. Res.*, 27(5), 855–865, 2010.
Xiong, G., Zhan, J., Zuo, K., Li, J., Rong., L., and Xu., G., Numerical flow simulation in the post-endoscopic sinus surgery nasal cavity, *Int. Fed. Med. Biol. Eng.*, 46, 1161–1167, 2008.
Xiong, G.-X., Zhan, J.M. Zuo, K.J., Rong, L.W. Li, J.F., and Xu, G., Use of computational fluid dynamics to study the influence of the uncinate process on nasal airflow, *J. Laryngol. Otol.*, 125(1), 30–37, 2011.
Zachow, S., Steinmann, A., Hildebrandt, T., Weber, R., and Heppt W., CFD simulation of nasal airflow: Towards treatment planning for functional rhinosurgery, *Int. J. Comput. Assist. Radiol. Surg.*, Springer, 165–167, 2006.
Zamankhan, P., Ahmadi, G., Wang, Z., Hopke, P.K., Cheng, Y.S., Su, W.C., and Leonard, D., Airflow and deposition of nano-particle in a human nasal cavity, *Aerosol Sci. Technol.*, 40, 463–476, 2006.
Zhao, K. and Dalton, P., The way the wind blows: Implications of modeling nasal airflow, *Curr. Allergy Asthma Rep.*, 7(2), 117–125, 2007.
Zhao, K., Pribitkin, E.A., Cowart, B.J., Rosen, D., Scherer, P.W., and Dalton, P., Numerical modeling of nasal obstruction and endoscopic surgical intervention: Outcome to airflow and olfaction, *Am. J. Rhinol.*, 20(3), 308–316, 2006.
Zhao, K., Scherer, P.W., Hajiloo, S.A., and Dalton, P., Effect of anatomy on human nasal airflow and odorant transport patterns: Implications for olfaction, *Chem. Senses*, 29(5), 365–379, 2004.
Zhang, H., Ahmadi, G., Fan, F.-G., and McLaughlin, J.B., Ellipsoidal particles transport and deposition in turbulent channel flows, *Int. J. Multiphase Flow*, 27, 971–1009, 2001.
Zhang, Y., Finlay, W.H., and Matida, E.A., Particle deposition measurements and numerical simulation in a highly idealized mouth–throat, *J. Aerosol Sci.*, 35, 789–803, 2004.
Zhang, Z. and Kleinstreuer, C., Modeling of low Reynolds number turbulent flows in locally constricted conduits: A comparison study. *AIAA Journal*, 41, 831–840, 2003.
Zhang, Z. and Kleinstreuer, C., Computational analysis of airflow and nanoparticle deposition in a combined nasal–oral–tracheobronchial airway model, *J. Aerosol Sci.*, 42, 174–194, 2011.
Zhang, Z., Kleinstreuer, C., Donohue, J.F., and Kim, C.S., Comparison of micro- and nano-size particle depositions in a human upper airway model, *J. Aerosol Sci.*, 36, 211–233, 2005.
Zhang, Z., Kleinstreuer, C., and Kim, C.S., Micro-particle transport and deposition in a human oral airway model, *J. Aerosol Sci.*, 33, 1635–1652, 2002a.
Zhang, Z., Kleinstreuer, C., and Kim, C.S., Aerosol deposition efficiencies and upstream release positions for different inhalation modes in an upper bronchial airway model, *Aerosol Sci. Technol.*, 36, 828–844, 2002b.
Zhang, Z., Kleinstreuer, C., and Kim C., Cyclic micron-size particle inhalation and deposition in a triple bifurcation lung airway model, *J. Aerosol Sci.*, 33, 257–281, 2002c.
Li, Z., Kleinstreuer, C., and Zhang, Z., Particle deposition in the human tracheobronchial airways due to transient inspiratory flow patterns, *J. Aerosol Sci*, 38, 625–644, 2007.

Zhuang, Z., Landsittel, D., Benson, S., Roberge, R., and Shaffer, R., Facial anthropometric differences among gender, ethnicity, and age groups, *Ann. Occupat. Hyg.*, 54, 391–402, 2010.
Zubair, M., Abdullah, M.Z., Ismail, R., Shuaib, I.L., Hamid, S.A., and Ahmad, K.A., Review: A critical overview of limitations of CFD modeling in nasal airflow, *J. Med. Biol. Eng.*, 32(2), 77–84, 2012.

16.2 Blood Flow

Shu Takagi, Kazuyasu Sugiyama, and Satoshi Ii

16.2.1 Introduction of Blood Flows as Dispersed Multiphase Flows

Blood flow is a dispersed phase flow, in which red blood cells (RBCs) are the main component of the dispersed phase. RBCs occupied 35%–50% of the total blood volume and there are 10–40 trillion RBCs in a human body. This means that there are approximately 5 million RBCs in 1 mm^3 blood. As is well known, RBC has a biconcave shape and its size is about 8 μm in long axis and 2 μm in short axis. The red color of blood is due to the presence of RBCs and from the aforementioned fact the blood flow can be recognized as a dense dispersed phase flow.

In many situations, blood flow is assumed to be Newtonian fluid that has a larger viscosity than that of pure water. In other situations, they are often assumed to be non-Newtonian. This different approximation highly depends on the vessel diameter. That is, if the vessel diameter is large enough, blood is assumed to be Newtonian since the size of RBCs is negligible compared with the scale of the macroscopic flow structure. Reducing the vessel size down to the O(100 μm) diameter, the size of RBCs becomes more important and the blood flows start showing non-Newtonian behavior. That is, the velocity fluctuations due to the presence of RBCs give the nonlaminar (nonparabolic) velocity profile by the pseudo-turbulence effect even in the laminar flow regime. Furthermore, reducing the vessel size to the scale of capillary vessels, which has less than 10 μm diameter, the vessel diameter becomes comparable with the size of RBCs. In this situation, the blood should not be treated as non-Newtonian fluid of homogeneous media which is expressed by the constitutive equations of the non-Newtonian fluid. In principle, the flows in capillary vessels should be treated as dispersed multiphase flows where the dispersed phase of RBCs is treated individually in blood plasma, since the idea of spatial averaging is not available in this scale. Although the behavior of RBCs is mainly discussed so far, not only the RBCs but also other blood cells, such as white blood cells, platelets, and also drag delivery agents regarded as artificial blood cells, need to be treated in the same manner. Therefore, reducing the vessel size, the characteristics of blood as multiphase flow become more important. Compared with spherical blood cells such as neutrophil, RBCs are highly deformable and can move smoothly into the small vessels. In this chapter, the important characteristics of blood flows in microcirculations are explained in the next section. Then, the modeling of blood cells and the results of numerical simulations for blood flows containing blood cells are also explained.

16.2.2 Apparent Viscosity and Fåhræus–Lindqvist Effect

To express the flow resistance in the vessel, the apparent viscosity is often used as an indicator. The apparent viscosity, which is also known as effective viscosity, gives the pressure drop along the tube. It simply expresses the relative pressure drop to that of blood plasma without RBCs. Due to the dispersed multiphase flow nature of blood with RBCs, the apparent viscosity is always larger than 1.0, since the dispersed phase generates the extra energy dissipation. The apparent viscosity dependence on the vessel diameter is not simple. There is a good review paper by Freund (2014). This figure is shown in Figure 16.37. The horizontal axis is vessel (tube) diameter, and the vertical axis corresponds to apparent (effective) viscosity. It is shown that decreasing the vessel diameter from larger size to about 10 μm, the apparent viscosity gradually decreases. Furthermore, decreasing the diameter, the viscosity rapidly starts increasing. This complicate behavior comes from the relative size of the vessel diameter to the size of RBCs. If a vessel diameter becomes comparable or smaller than the RBC size, the RBCs need to be highly deformed to pass through the vessels and this causes the drastic increase of the apparent viscosity. In the case for the vessel diameter from 10 to 30 μm, the reduction of the apparent viscosity in the smaller diameter is due to the change of RBC positioning. It is easily seen in Figure 16.37. For the smaller diameter less that about 10 μm, RBCs form train-like structure, that is, a single RBC moves at the center for vessel and flows continuously. For the vessel larger than 15 μm, slipper-like shape RBCs flow in the core region of the vessel. It is noted that RBCs are trying to flow in the center of the pipe due to the shear-induced lift effect. Since RBCs are flowing in the center of the pipe, there exists the blood plasma layer close to the vessel walls. This plasma layer ends up with the reduction of average hematocrit value in the smaller vessel.

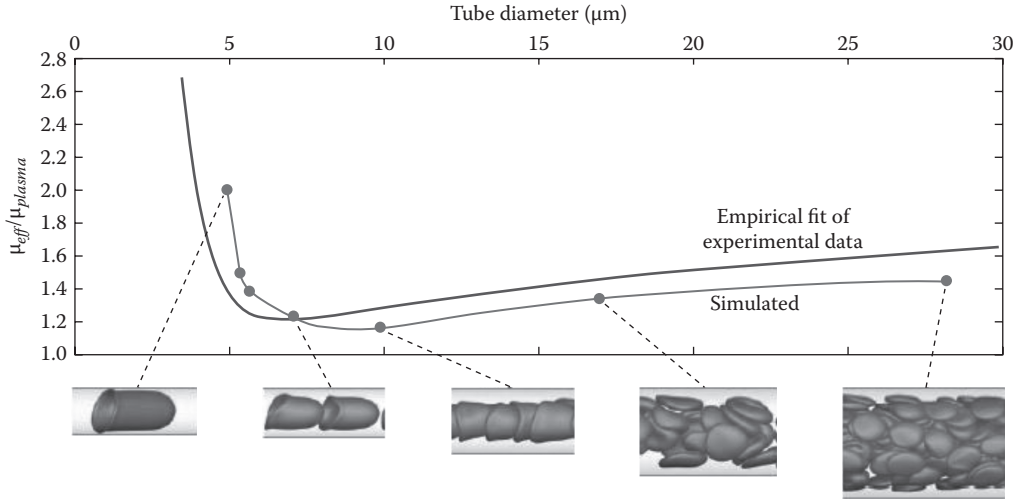


Figure 16.37

Relation between effective viscosity and vessel diameter. (From Freund, J.B., *Annu. Rev. Fluid Mech.*, 46, 72, 2014.)

This is called the Fåhræus effect. And the reduction of hematocrit value gives the reduction of apparent viscosity in the smaller diameter for the vessel of 10–30 μm diameter. This is called the Fåhræus–Lindqvist effect.

16.2.3 Modeling of Blood Cells

Biological cells have lipid bilayer membranes. Since the lipid molecules of the lipid bilayer can easily move around in the membrane, the lipid bilayer membrane is often modeled as 2-D fluid membrane. Furthermore, since the distance between two neighborhood lipid molecules hardly changes, the membrane is assumed to be incompressible. Hence, the lipid bilayer membrane is modeled as a 2-D incompressible fluid deformable in 3-D space. Following this concept, Helfrich (1973) developed the model of lipid bilayer membrane. He considered the effect of bending rigidity and gave the following energy functional E to express the mechanical energy of the membrane:

$$E = \frac{1}{2}k_b \int (c_1 + c_2 - c_0)^2 dA + k_G \int c_1 c_2 \, dA + \lambda \int dA + \Delta P \int dV \tag{16.50}$$

where

k_b is the bending rigidity
c_1 and c_2 are the principal curvatures of the membrane
c_0 is the spontaneous curvature
dA and dV are the microsurface and microvolume elements of the membrane

Under the expression of Equation 16.50, λ and ΔP are the Lagrangian multiplier to impose the constraints of the surface area and the volume constant. The integral $k_G \oint c_1 c_2 \, dA$ term is related to the surface integration of the Gaussian curvature: product of principle curvature. This term keeps constant if there is no breakup or topological changes of the cell shape, through the well-known Gauss–Bonnet theorem in differential geometry. An artificial cell-like structure covered by lipid bilayer membrane is called liposome. A liposome can be used as a drag delivery agent by encapsulating drags inside. The membrane of a liposome is often modeled by this Helfrich model.

Actual living cells including blood cells have not only lipid bilayer membrane but also a protein network structure called cytoskeleton underneath the lipid bilayer. This cytoskeleton structure gives the strength of membrane under the strong shear flow. Due to the presence of cytoskeleton structure, the membrane of blood cells no longer behaves as fluid membrane. It behaves as an elastic material and a hyperelastic membrane model is often introduced to describe the cell membrane. For example, one of the well-known membrane models for RBCs are called the Evans–Skalak (1980) model and the constitutive equation of membrane is given by the following expression:

$$\boldsymbol{\tau}_s = \frac{E_s}{\left(\Lambda_1 + 1\right)^2}\mathbf{B}_s + \left(E_s\Lambda_1 - C_s\frac{\Lambda_2 + 1}{\Lambda_1 + 1}\right)\mathbf{P}_s \tag{16.51}$$

where

$$\Lambda_1 = J_s - 1, \quad \Lambda_2 = \frac{\mathrm{tr}(\mathbf{B}_s)}{2J_s} - 1, \tag{16.52}$$

where

E_s is the shear modulus

C_s is the area dilation modulus

16.2.4 Numerical Method for Solving Blood Flow Containing RBCs

16.2.4.1 Overview of Standard Methods to Simulate Blood Flows

There are several ways to simulate blood flows containing many RBCs. One of the standard methods is using the boundary element method (BEM) for Stokes flow. As mentioned, the presence of blood cells becomes important in the microcirculation, where the flow Reynolds number is very small. So, the Stokes flow assumption is applicable in many situations. The other approach to simulate extra-large number of RBCs is by the lattice Boltzmann method. Both methods and simulated results are explained in detail in the book by Pozrikidis (2010).

In coupled methods for a fluid and elastic membrane typified by the immersed boundary (IB) method (Peskin, 1972, 2002), the Lagrangian description is employed for the membrane motion, whereas the Eulerian description is employed for the fluid. However, there is an open question for the numerical stability in a long time run without any numerical stabilization. For that reason, rather than using the Lagrangian particles, field variables to identify the membrane interface are introduced and utilized for interaction between the fluid and membrane on the Eulerian mesh. Cottet and Maitre (2006) introduced the level-set function to identify the interface; in addition, the membrane stretching or variation of the surface area was obtained from the information of the level-set function. As a result, the membrane force was successfully obtained on the Eulerian mesh without using the interfacial material points. However, since the constitutive law of the membrane elasticity is limited to a model that only involves a variation of the surface area, it has not been applied yet to more general membrane models that depend on the principal strains.

16.2.4.2 Full Eulerian Formulation of the Dispersed Multiphase Blood Flow

In this subsection, the numerical method to solve blood flows containing many blood cells is explained as a fluid–membrane interaction problem. Here, the full Eulerian equation formula is introduced and finite difference approach is introduced to solve the discretized equations.

A novel full Eulerian fluid–membrane interaction method has been proposed by Ii et al. (2012a,b), as an extension of the general idea by Sugiyama et al. (2011). It is assumed that a closed membrane is immersed in a field Ω, where inner and ambient regions Ω_1 and Ω_2 are filled with the incompressible Newtonian fluids ($\Omega = \Omega_1 \cup \Omega_2$). A material phase to describe each fluid is expressed by a smoothed volume fraction volume of fluid (VOF) function ϕ, which extends from 0 to 1 within a few computational meshes. Then a membrane transition region Γ defined as $|\nabla\phi| \leq \varepsilon$, where $|\nabla\phi|$ is regarded as a smoothed delta function (e.g., Brackbill et al., 1992) and ε is an arbitrarily value depending on the mesh size, is introduced as in Figure 16.38.

By making use of a basic theory on the finite deformation (Skalak et al., 1973, Barthés-Biesel and Rallison, 1981), a set of governing equations with a mixture formulation is given as follows in the Eulerian frame:

$$\nabla \cdot \mathbf{v} = 0, \quad \mathbf{x} \in \Omega \tag{16.53}$$

$$\rho\left(\partial_t \mathbf{v} + \mathbf{v} \cdot \nabla \mathbf{v}\right) = -\nabla p + \nabla \cdot (\mu(\nabla \mathbf{v} + \nabla \mathbf{v}^T)) + |\nabla\phi|\,\mathbf{f}_s, \quad \mathbf{x} \in \Omega \tag{16.54}$$

$$\partial_t \phi + \mathbf{v} \cdot \nabla \phi = 0, \quad \mathbf{x} \in \Omega \tag{16.55}$$

$$\partial_t \mathbf{B}_s + \mathbf{v} \cdot \nabla \mathbf{B}_s = \mathbf{B}_s \cdot \nabla_s \mathbf{v} + \nabla_s \mathbf{v}^T \cdot \mathbf{B}_s, \quad \mathrm{x} \in \Gamma \tag{16.56}$$

$$\partial_t J_s + \mathbf{v} \cdot \nabla J_s = J_s \nabla_s \cdot \mathbf{v}, \quad \mathbf{x} \in \Gamma \tag{16.57}$$

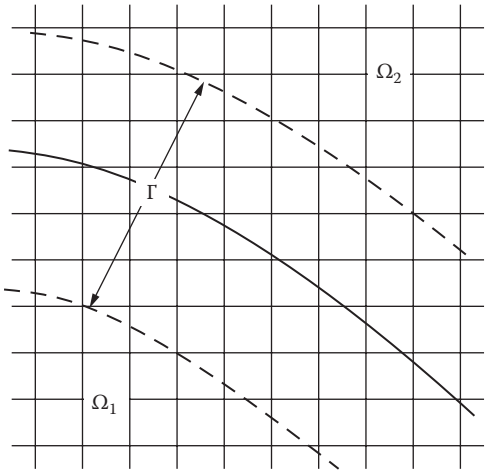


Figure 16.38

The compactly supported or smoothed interface region Γ immersed in the Cartesian mesh.

$$\partial_t \kappa_R + \mathbf{v} \cdot \nabla \kappa_R = 0, \quad \mathbf{x} \in \Gamma \tag{16.58}$$

where

$\nabla_s = \mathbf{P} \cdot \nabla$ is the *surface* gradient operator with a surface projection tensor $\mathbf{P} = \mathbf{I} - \mathbf{nn}$, where $\mathbf{n}$ is a unit normal vector of a membrane surface

$\mathbf{B}_s = \mathbf{P} \cdot \mathbf{B} \cdot \mathbf{P}_R$ the *surface* left Cauchy–Green deformation tensor (subscript R denotes a reference coordinate)

J_s the surface Jacobian (i.e., ratio A/A_0 between an initial surface area A_0 and current area A)

κ_R the reference mean curvature

$\mathbf{f}_s$ the surface singular force (force per area) of the membrane given by the expression

$$\mathbf{f}_s = \nabla_s \cdot \left(\tau_s + \tau_b \right), \tag{16.59}$$

where $\boldsymbol{\tau}_s$ is an in-plane stress tensor, for example, the neo-Hookean material (Barthés-Biesel and Rallison, 1981)

$$\tau_s = \frac{E_s}{3\left(\Lambda_1 + 1\right)} \left(\mathbf{B}_s - \frac{1}{\left(\Lambda_1 + 1\right)^2} \mathbf{P}_s \right) \tag{16.60}$$

and the Evans–Skalak material for RBC given in Equation 16.51

$$\tau_s = \frac{E_s}{\left(\Lambda_1 + 1\right)^2} \mathbf{B}_s + \left(E_s \Lambda_1 - C_s \frac{\Lambda_2 + 1}{\Lambda_1 + 1} \right) \mathbf{P}_s \tag{16.61}$$

Here

$$\Lambda_1 = J_s - 1, \quad \Lambda_2 = \frac{\mathrm{tr}(\mathbf{B}_s)}{2J_s} - 1 \tag{16.62}$$

E_s is the shear modulus

C_s is the area dilation modulus used

$\boldsymbol{\tau}_b$ is a bending stress tensor proposed by Pozrikidis (2001), that is, $\boldsymbol{\tau}_b = \mathbf{q}_s \mathbf{n}$

$$\mathbf{q}_s = \left(\nabla_s \cdot \mathbf{m}_s \right) \cdot \mathbf{P}, \quad \mathbf{m}_s = K_s \left(\boldsymbol{\kappa}_s - \kappa_R \mathbf{P} \right) \tag{16.63}$$

where

K_s is the bending modulus

$\boldsymbol{\kappa}_s = \nabla_s \mathbf{n}$ the Cartesian curvature tensor

The outward unit normal vector defined as $\mathbf{n} = -\nabla\phi/|\nabla\phi|$ and $\boldsymbol{\kappa}_s$ (and also κ_R) are calculated in the Eulerian meshes. A set of PDEs is discretized by the finite difference/volume manner, and the SMAC algorithm (Amsden and Harlow, 1970) is employed to couple with the pressure and velocity fields with the staggered arrangement. For more detailed description on the numerical methods, one may consult Ii et al. (2012a,b).

The updating equation of the VOF function $\phi_s(\mathbf{x}, t)$ is derived from the advection equation (16.52). From a numerical point of view, an accurate treatment is necessary to numerically obtain the flux $\mathbf{v}\phi_s$ in a conservative form without the numerical dissipation and oscillation. In other words, an accurate approximate function $F(\mathbf{x}, t)$ is desirable for the indicator function $I_s(\mathbf{x}, t)$. In the discretization, the approximate function $F(\mathbf{x}, t)$ is piecewisely reconstructed in a single mesh ijk, that is, F_{ijk}. In the present Eulerian FSI method especially for the coupling with the membrane including a diffusive membrane region, a numerical method is required to ensure that the diffusive transition region between respective material phases (fluid and solid regions or inner/outer fluid region of the membrane) is without numerical dissipation over time. In order to satisfy solving such a requirement, a continuous interface capturing method, namely, MTHINC method (Ii et al., 2012c) extended from Xiao et al. (2005), has been proposed. In this method, the (multidimensional) hyperbolic tangent function is utilized for the approximation of the cell-wise indicator function.

16.2.4.3 Results of the Numerical Methods and Discussion

For the sake of validation, a shear-induced deformation problem for a spherical capsule obeying the neo-Hookean law (Equation 16.39) is simulated. A capsule with a diameter of $d = 2$ is located on a computational domain, $[-4, 4] \times [-2, 2] \times [-4, 4]$. An opposing velocity of $\pm V$ that results in a shear rate $\gamma = 2V/H_z$, where $H_z = 8$ is a vertical height of the domain, is imposed on each top/bottom wall in z direction. The periodic boundary conditions are imposed on other x and y directions. The viscosity $\mu(=\mu_1=\mu_2)$ is given by the Reynolds number $\mathrm{Re} = \rho\gamma d^2/(4\mu)$, and the membrane stiffness is given by capillary number $Ca = \gamma d/(2E_s)$. In this test, $\rho = 1$, $\gamma = 1$, and $\mathrm{Re} = 0.001$ are fixed; therefore, the membrane stiffness only depends on the capillary number Ca. Here, the bending force is neglected and the capillary number is varied as 0.0125, 0.025, 0.05, 0.1, and 0.2. Numerical results at steady state with a mesh size $\Delta x = d/32$ are shown in Figure 16.39, where the time increment $\Delta t = 0.0025$ is used. It is confirmed that the deformation becomes larger as the capillary number increases.

The time history of a deformation parameter $D = (l - s)/(l + s)$, where l and s denote the semimajor and semiminor axes of an ellipse fitting to an obtained interface in *shear plane*, that is, x–z cross section passing through $y = 0$, is shown in Figure 16.40. The mesh lengths $\Delta x = d/16$ and $d/32$ are employed, where the time increments $\Delta t = 0.005$ and 0.0025 are used. In this regard, numerical solutions given by the IB method (Eggleton and Popel, 1998) and the BEM (Pozrikidis, 1995) are also shown. As compared with the well-validated results of the IB method and BEM, the present results converge to the reference solutions by increasing the spatial resolution.

16.2.4.4 Suspension of Red Blood Cells and Platelets in a Capillary Tube

Human blood is composed of biological cells (erythrocyte, leukocyte, and thrombocyte, i.e., RBC, white blood cell, and platelet), proteins and plasma. In particular, the deformable RBC highly occupies a blood, where its volume ratio ranges from 30% to 50%; thus, the dynamic motions of the multiple RBCs play an important role in a capillary vessel when its size (or diameter D) is comparable to a RBC size (diameter

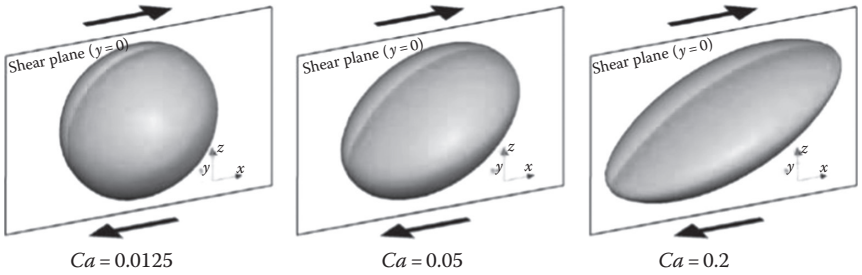


Figure 16.39

The fully developed deformed surface of the neo-Hookean membrane subjected to the linear shear flow for various capillary numbers $Ca = 0.0125$, 0.05, and 0.2. The *shear plane* indicates a plane at $y = 0$, and the arrows indicate a schematic of the imposed shear velocities. (Reproduced from Ii, S. et al., *J. Biomech. Sci. Eng.*, 7, 72, 2012b.)

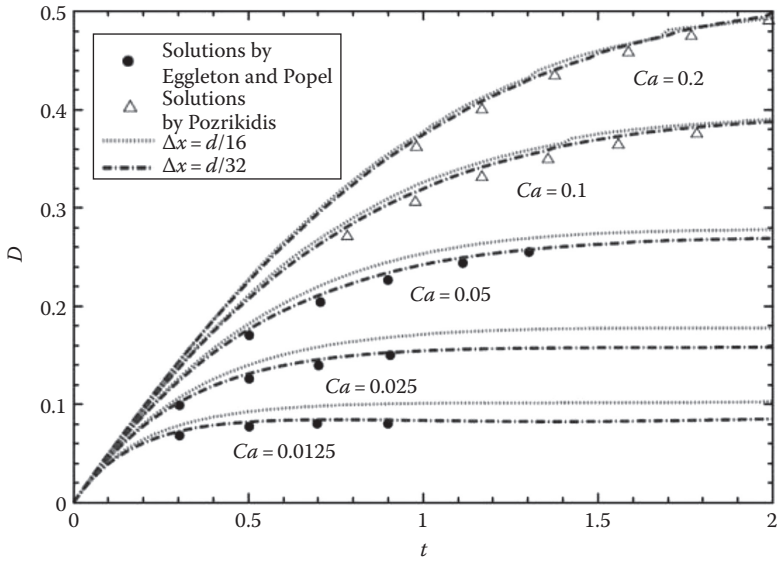


Figure 16.40

Deformation parameter D versus time t for various capillary numbers Ca = 0.0125, 0.025, 0.05, 0.1, and 0.2. The lines are the present solutions with the mesh sizes of $\Delta x = d/16$ and $d/32$, the filled circles indicate the solutions by means of the IB method by Eggleton and Popel (1998), and the open triangles show those of the boundary element method by Pozrikidis (1995). (Reproduced from Ii, S. et al., *J. Biomech. Sci. Eng.*, 7, 72, 2012b.)

$d \sim 8$ μm). In such a small vessel, the blood is no longer a Newtonian fluid due to the presence of the high-density RBCs. When the vessel size D is close to the RBC size d for $D > d$, it has been observed that a flow rate increases even if a same driving pressure is enforced, that is, commonly known as the Fåhræus–Lindqvist effect (Fåhræus and Lindqvist, 1931). Due to a hydrodynamic effect, the deformable RBCs axially aggregate and the RBC-rich core region is created around an axial center, resulting in a cell-free layer (or plasma occupying layer) near the vessel wall. In a primary stage of the thrombus formation (or blood clotting) that stops the bleeding in homeostatic mechanism, the platelets immediately accumulate on an injured vessel wall. Therefore, it is quite important to know how many platelets are confined and drift in the cell-free layer.

A suspension flow of the multiple RBCs and platelets in an elastic capillary vessel is studied using a blood flow analysis based on a full Eulerian approach. To simplify the analysis, the platelet is regarded as an elastic solid with a stiff elastic modulus, whereas the RBC is treated as an elastic membrane obeying an adequate constitutive law with experimentally given parameters (Hochmuth and Waugh, 1987).

A suspension of the RBCs and platelets is enclosed by the elastic vessel tube with a radius of D = 20 μm, obeying the solid material of the neo-Hookean law (Equation 16.17). Here, 30 RBCs are randomly distributed to simulate a pertinent hematocrit H_t of approximately 20%. The Evans–Skalak model (Equation 16.40) and Pozrikidis bending model (Equation 16.42) are employed for the RBC. Meanwhile, 10 platelet-like elastic solids are randomly distributed within a range of $r_c \leq 8$ μm (r_c is a centroid of the platelet in a radial direction) to reveal how the centrally located platelets behave due to the presence of the RBCs. Initial shapes of the RBC and platelets are biconcave discoids (Evans and Fung, 1972) and spheroid, respectively. A flow is induced by a pressure gradient as a body force, and a periodic boundary condition is imposed on a streamwise direction x. Wall boundary conditions are employed for both the spanwise and vertical directions, y and z, respectively. Computational conditions are referred to Table 1 (Ii et al., 2012b).

Snapshots of numerical results at t = 7.5, 30, and 75 ms are shown in Figure 16.41. It is found that the initially distributed RBCs are mixed over time. Each of the RBCs has a different shape such as a parachute shape or slipper one reported in both a numerical simulation (Zhao et al., 2010) and an experiment (Gaehtgens et al., 1980). The deformed RBCs aggregate into large masses around the axial center due to a hydrodynamic effect, causing a plasma phase near the wall, which the so-called cell-free layer.

To clarify the development of the cell-free layer, a spatial occupancy of the RBCs in a streamwise direction x is plotted in Figure 16.42. It is confirmed that the cell-free layer (or nonexisting region of the RBC near the wall) becomes larger and a RBC-rich core region is created around a tube center over time. It has been reported that the RBC-rich core region is sufficiently created at t = 87.5 ms in a 2-D simulation (Zhang et al., 2008), in which the computational conditions are totally different (i.e., 2-D and 3-D, rigid parallel plate and

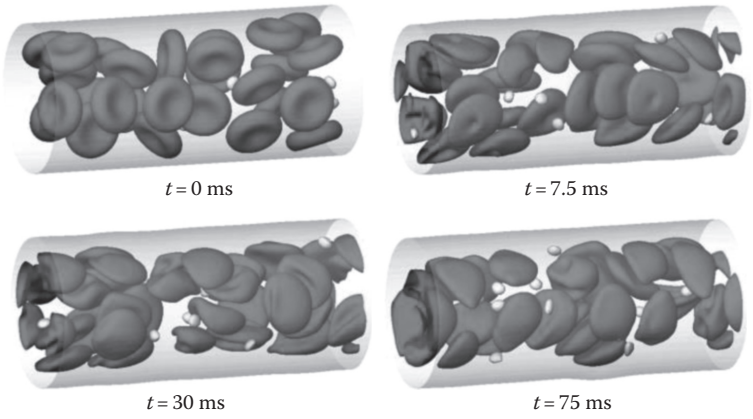


Figure 16.41

Snapshots of the numerical results at t = 0, 7.5, 30, and 75 ms. (Reproduced from Ii, S. et al., *J. Biomech. Sci. Eng.*, 7, 72, 2012b.)

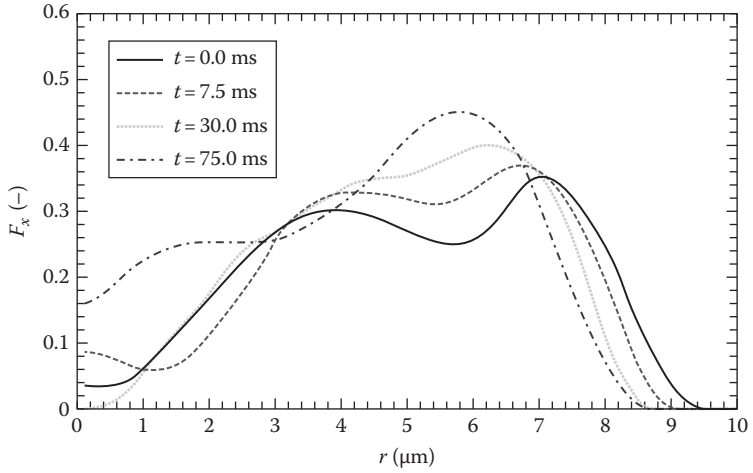


Figure 16.42

Spatial occupancy of the RBC versus axial position at different times. (Reproduced from Ii, S. et al., *J. Biomech. Sci. Eng.*, 7, 72, 2012b.)

elastic tube, $H_t \approx 30\%$ and $H_t \approx 20\%$). Nevertheless, the present result is physically comparable to the result by Zhang et al. (2008) in terms of a time constant for creating the RBC-rich core region. In a bounded flow subjected to a pressure gradient, it is known that a laterally located RBC follows a tank-treading motion due to a strong shear rate near the wall (Zhang et al., 2008, Zhao et al., 2010, Crowl and Fogelson, 2010, 2011). This tendency has been also reported by Doddi and Bagchi (2009) of which simulation employs a parallel plate in 3-D. However, the present result is given by a specific configuration (1 initial distribution); therefore, further discussions for the development of the RBC aggregation will be necessary using various initial distributions.

Trajectories of the respective platelets in a radial direction are plotted in Figure 16.43a. Each platelet moves in a flow undergoing a fluctuation in a radial direction. Such a fluctuation seems to be large around the tube center ($r \leq 4$ μm). It is considered that the axially aggregating RBCs push out the platelets together with the plasma, and the laterally migrated platelets drift with lesser fluctuations. Taking the distribution of the RBCs into account, it is assumed that the RBC-rich core region induces a mixing effect of the flow, which results in a higher fluctuation in respect to the medially located platelets, whereas the cell-free layer restricts the radial motions of the laterally located platelets. Furthermore, a specific separation is observed between the axial center ($r \leq 4$ μm) and near the wall (6 μm $\leq r \leq$ 8 μm) for $t \leq 75$ ms. In the 2-D simulation results (Crowl and Fogelson, 2010, 2011), this separation has relevance to the multiple behaviors of the RBCs playing the tank-treading motions near the wall, and they could perform a kind of barrier to restrict

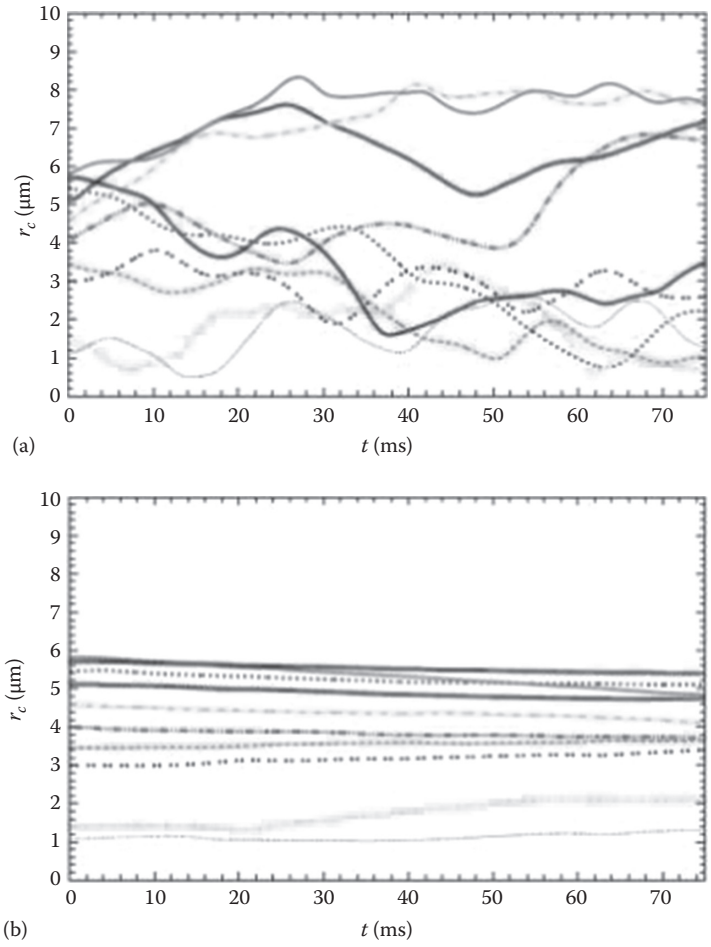


Figure 16.43

Trajectories of the respective 10 platelets in a radial direction. (a) The result with the suspension of the RBCs. (b) The result with the pure plasma. (Reproduced from Ii, S. et al., *J. Biomech. Sci. Eng.*, 7, 72, 2012b.)

the radial drift of the platelet from the sides to the center. In the present simulation, it is not clear by what this separation is triggered because the number of platelets is only 10 and the simulation is run with 1 initial configuration. Nevertheless, it is considered that the radial fluctuation comes from the motions of the RBCs. To clarify it, we carried out a computation without taking account of the RBCs. The platelet trajectories are shown in Figure 16.43b. In a situation without the RBCs, the radial fluctuation of the platelet only comes from the platelet motion itself. Therefore, the platelets straightforwardly drift in the flow with less radial fluctuation for $t \leq 75$ ms. It, therefore, appears that the dynamic motion of the platelets is strongly affected by the motions of the RBCs.

16.2.5 Modeling of Platelet Adhesion at the Initial Stage of Thrombosis

Thrombosis is regarded as one of the most important diseases, which cause the myocardial and cerebral infarctions. It is a very complicated disease affected from molecular-scale protein–protein interaction to continuum scale in blood flow. Initially, platelets start aggregate at the injured wall, where von Willebrand factor (vWF) is attached. The glycoprotein, GPIb-α, on platelet membrane starts showing ligand–receptor-type interaction with this vWF and platelets start aggregating around this spot. From this stage, complicated activation process of platelets and interactions with the blood, vessel walls, RBCs, fibrin, etc. occur and they end up with the blockage of the vessels. The numerical model for conducting the initial stage of thrombus formation is explained here. To analyze this process, we used the full Eulerian fluid–membrane coupling method explained earlier, which is a further extension of the full Eulerian fluid–structure coupling method (Sugiyama, 2011). This method is coupled with the results of a stochastic Monte Carlo simulation on GPIb-α and vWF interactions. The basic concept of this multiscale thrombosis simulator is shown in Figure 16.44.

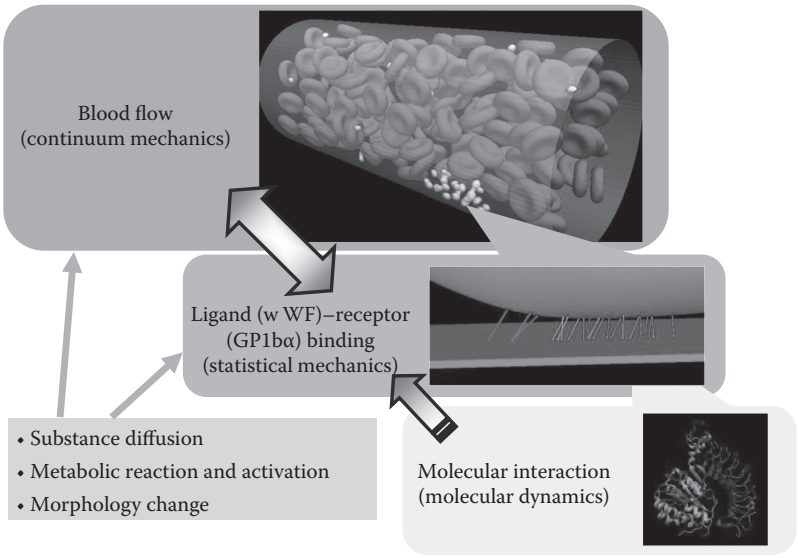


Figure 16.44

Multiscale modeling on the platelet adhesion.

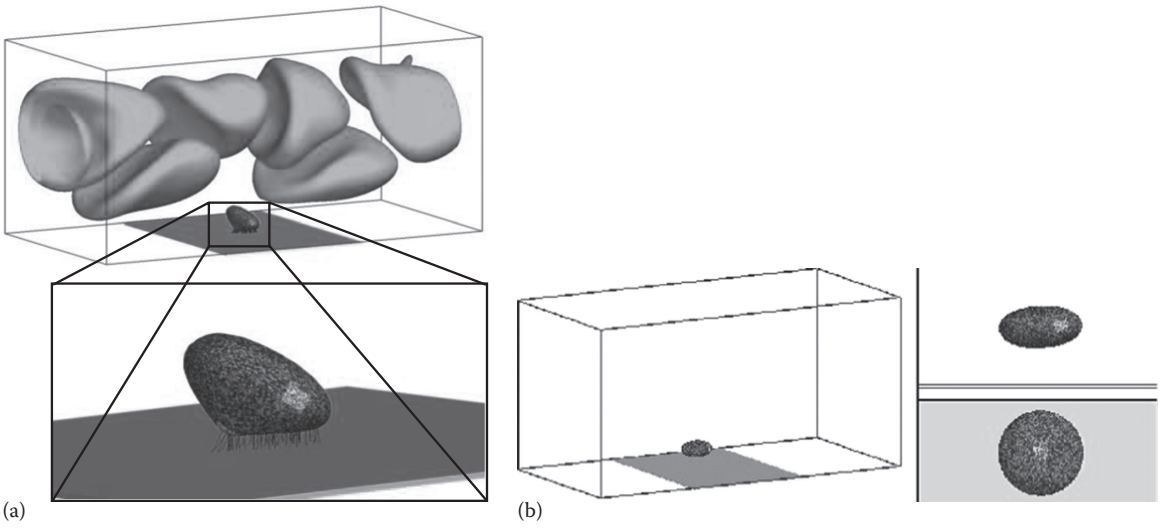


Figure 16.45

Effect of RBCs on platelet adhesion (a) with RBCs and (b) without RBCs (no adhesion).

The pressure-driven flows including the multiple RBCs and platelets in a circular tube were carried out. Figure 16.45 illustrates the time evolution of the shape of RBCs and platelets. It is well known that, in actual blood flows, RBCs tend to flow in the center of the vessels with large deformation constructing the so-called blood plasma layer and that small platelets tend to flow in this plasma layer. It was observed that once the platelets are coming closer to the vessel wall, they stay there. It is rarely observed that they go back to the center region of vessels. Next, the effect of RBCs on the adhesion of platelets is shown in Figure 16.45b. It is very interesting to see that the platelet that is initially located slightly away from the vessel wall does not come to adhere on the wall without RBCs. This is because the platelets flow with the plasma and have a low probability to come close to the vessel wall. On the other hand, in the presence of RBCs, platelets are much easier to adhere on the wall because RBCs produce the velocity fluctuation in the normal direction of the wall. This simulation results support the fact that thrombus does not glow without the presence of RBCs. In summary, in the present simulation, the molecular-scale interaction between platelets and vascular endothelium is taken into account through the molecular dynamics

simulations and the kinetic Monte Carlo simulations. Then, the interacting force obtained from the kinetic Monte Carlo simulation is coupled with the continuum scale simulation. The results illustrate that platelets are much easier to aggregate on the wall in the presence of red blood.

16.2.6 Summary

In this section, blood flows are explained with emphasis on their characteristics as dispersed multiphase flows. From the medical application point of view, microcirculation system is very important since the mass and heat transfer to the cells are given there. The blood flow behavior in microcirculation is no longer assumed to be neither Newtonian Fluid nor non-Newtonian. The behavior of each blood cell needs to be taken into account to understand the essential role of the blood flows in microcirculation systems. Due to an overwhelming number of RBCs, the fluid mechanical characteristics of blood flows in microcirculation systems are dominated by the behavior of RBCs. The several previous studies related to the blood flows in microcirculation concerns mainly about the behavior of RBCs. But from the medical point of view, the behaviors of other cells, white blood cells and platelets, are also very important. Further investigation of coupling effect between fluid mechanics and biochemical reactions inside and outside of these flowing cells is highly expected.

References

Amsden, A.A. and Harlow, F.H., A simplified MAC technique for incompressible fluid flow calculations, *J. Comput. Phys*., 6, 322–325, 1970.

Bagchi, P., Mesoscale simulation of blood flow in small vessels, *Biophys. J*., 92, 1858–1877, 2007.

Barthés-Biesel, D. and Rallison, J.M., The time-dependent deformation of a capsule freely suspended in a linear shear flow, *J. Fluid Mech*., 113, 251–267, 1981.

Brackbill, J.U., Kothe, D.B., and Zemach, C., A continuum method for modeling surface tension, *J. Comput. Phys*., 100, 335–354, 1992.

Belytschko, T., Fluid–structure interaction, *Comput. Struct*., 12, 459–469, 1980.

Cottet, G.H. and Maitre, E., A level set method for fluid–structure interactions with immersed surfaces, *Math. Model. Meth. Appl. Sci*., 16, 415–438, 2006.

Cottet, G.H., Maitre, E., and Milcent, T., Eulerian formulation and level set models for incompressible fluid–structure interaction, *Math. Model. Numer. Anal*., 42, 471–492, 2008.

Crowl, L.M. and Fogelson, A.L., Computational model of whole blood exhibiting lateral platelet motion induced by red blood cells, *Int. J. Numer. Meth. Biomed. Eng*., 26, 471–487, 2010.

Crowl, L.M. and Fogelson, A.L., Analysis of mechanisms for platelet near-wall excess under arterial blood flow conditions, *J. Fluid Mech*., 676, 348–375, 2011.

Doddi, S.K. and Bagchi, P., Three-dimensional computational modeling of multiple deformable cells flowing in microvessels, *Phys. Rev. E*, 79, 046318, 2009.

Dunne, T., An Eulerian approach to fluid–structure interaction and goal-oriented mesh adaptation, *Int. J. Numer. Meth. Fluids*, 51, 1017–1039, 2006.

Eggleton, C.D. and Popel, A.S., Large deformation of red blood cell ghosts in a simple shear flow, *Phys. Fluids*, 10, 1834–1845, 1998.

Evans, E. and Fung, Y., Improved measurement of the erythrocyte geometry, *Microvasc. Res*., 4, 335–347, 1972.

Evans, E.A. and Skalak, R., *Mechanics and Thermodynamics of Biomembranes*, CRC, Boca Raton, FL, 1980.

Fåhræus, R. and Lindqvist, T., The viscosity of blood in narrow capillary tubes, *Am. J. Physiol.*, 96, 562–568, 1931.

Freund, J.B., Numerical simulation of flowing blood cells, *Ann. Rev. Fluid Mech*., 46, 67–95, 2014.

Gaehtgens, P., Duhrssen, C., and Albrecht, K.H., Motion, deformation, and interaction of blood cells and plasma during flow through narrow capillary tubes, *Blood Cells*, 6, 799–817, 1980.

Gao, T. and Hu, H.H., Deformation of elastic particles in viscous shear flow, *J. Comput. Phys*., 228, 2132–2151, 2009.

Glowinski, R., Pan, T.-W., Hesla, T.I., and Joseph, D.D., A distributed lagrange multiplier/fictitious domain method for particulate flows, *Int. J. Multiphase Flow*, 25, 755–794, 1999.

Gong, X., Sugiyama, K., Takagi, S., and Matsumoto, Y., The deformation behavior of multiple red blood cells in a capillary vessel, *J. Biomech. Eng*., 131, 074504, 2009.

Gurtin, M.E. and Guidugli, P.P., The thermodynamics of constrained materials, *Arch. Ration. Mech. Anal.*, 51, 192–208, 1973.
Helfrich, W., Elastic properties of lipid bilayers: Theory and possible experiments, *Z. Naturforsh A*, 28c, 693–703, 1973.
Hochmuth, R. and Waugh, R., Erythrocyte membrane elasticity and viscosity, *Ann. Rev. Physiol.*, 49, 209–219, 1987.
Huang, H., Sugiyama, K., and Takagi, S., An immersed boundary method for restricted diffusion with permeable interfaces, *J. Comput. Phys.*, 228, 5317–5322, 2009.
Ii, S., Gong, X., Sugiyama, K., Wu, J., Huang, H., and Takagi, S., A full Eulerian fluid-membrane coupling method with a smoothed volume-of-fluid approach, *Commun. Comput. Phys.*, 12, 544–576, 2012a.
Ii, S., Sugiyama, K., Takeuchi, S., Takagi, S., and Matsumoto, Y., An implicit full Eulerian method for the fluid-structure interaction problem, *Int. J. Numer. Meth. Fluids*, 65, 150–165, 2011.
Ii, S., Sugiyama, K., Takeuchi, S., Takagi, S., and Matsumoto, Y., A computational blood flow analysis in a capillary vessel including multiple red blood cells and platelets, *J. Biomech. Sci. Eng.*, 7, 72–83, 2012b.
Ii, S., Sugiyama, K., Takeuchi, S., Takagi, S., Matsumoto, Y., and Xiao, F., An interface capturing method with a continuous function: The THINC method with multi-dimensional reconstruction, *J. Comput. Phys.*, 231, 2328–2358, 2012c.
Jiang, G.S. and Shu, C.-W., Efficient implementation of WENO schemes, *J. Comput. Phys.*, 126, 202–228, 1996.
Mooney, M., A theory of large elastic deformation, *J. Appl. Phys.*, 11, 582–592, 1940.
Okazawa, S., Kashiyama, K., and Kaneko, Y., Eulerian formulation using stabilized finite element method for large deformation solid dynamics, *Int. J. Numer. Methods Eng.*, 72, 1544–1559, 2007.
Peskin, C.S., Flow patterns around heart valves: A numerical method, *J. Comput. Phys.*, 10, 252–271, 1972.
Peskin, C.S., The immersed boundary method, *Acta Numer.*, 11, 479–517, 2002.
Pozrikidis, C., Finite deformation of liquid capsules enclosed by elastic membranes in simple shear flow, *J. Fluid. Mech.*, 297, 123–152, 1995.
Pozrikidis, C., Effect of bending stiffness on the deformation of liquid capsules in simple shear flow, *J. Fluid Mech.*, 440, 269–291, 2001.
Pries, A.R., Neuhaus, D., and Gaehtgens, P., Blood viscosity in tube flow: Dependence on diameter and hematocrit, *Am. J. Physiol.*, 263, 1770–1778, 1992.
Rivlin, R.S., Large elastic deformations of isotropic materials IV, further development of general theory, *Phil. Trans. Royal Soc. A*, 241, 379–397, 1948.
Freud, J.B. and Zhao, H. (Chapter 3); Zhang, J., Johnson, P.C., and Popel, A.S. (Chapter 4). *Computational Hydrodynamics of Capsules and Biological Cells*, Pozrikidis, C. (Ed.), Chapman & Hall/CRC, Boca Raton, FL, 2010.
Skalak, R., Tözeren, A., Zarda, P.R., and Chien, S., Strain energy function of red blood cell membranes, *Biophys. J.*, 13, 245–264, 1973.
Sugiyama, K., Ii, S., Takeuchi, S., Takagi, S., and Matsumoto, Y., Full Eulerian simulations of biconcave neo-Hookean particles in a Poiseuille flow, *Comput. Mech.*, 46, 147–157, 2010a.
Sugiyama, K., Ii, S., Takeuchi, S., Takagi, S., and Matsumoto, Y., A full Eulerian finite difference approach for solving fluid-structure coupling problems, *J. Comput. Phys.*, 230, 596–627, 2011.
Sugiyama, K., Nagano, N., Takeuchi, S., Ii, S., Takagi, S., and Matsumoto, Y., Particle-in-cell method for fluid–structure interaction simulations of neo-hookean tube flows. *Theor. Appl. Mech Jpn.*, 59, 245–256, 2010b.
Sui, Y., Chew, Y.T., Roy, P., Cheng, Y.P., and Low, H.T., Dynamic motion of red blood cells in simple shear flow, *Phys. Fluids*, 20, 112106, 2008.
Takagi, S., Sugiyama, K., Ii, S., and Matsumoto, Y., A review of full eulerian methods for fluid structure interaction problems, *J. Appl. Mech.*, 79, 010911, 2012.
Takagi, S., Yamada, T., Gong, X., and Matsumoto, Y., The deformation of a vesicle in a linear shear flow, *J. Appl. Mech.*, 76, 021207, 2009.
Xiao, F., Honma, Y., and Kono, K., A simple algebraic interface capturing scheme using hyperbolic tangent function, *Int. J. Numer. Methods Fluids*, 48, 1023–1040, 2005.
Zhang, J., Johnson, P.C., Popel, A.S., Effects of erythrocyte deformability and aggregation on the cell free layer and apparent viscosity of microscopic blood flows, *Microvasc. Res.* 77, 265–272, 2008.
Zhao, H., Isfahani, A.H.G., Olson, L.N., and Freund, J.B., A spectral boundary integral method for flowing blood cells, *J. Comput. Phys.*, 229, 3726–3744, 2010.

16.3 Biomimetics and Bioinspiration

Yoshimichi Hagiwara

16.3.1 Introduction

Biomimetics, biomimicry, and bioinspired engineering have recently emerged as keywords in engineering. These new technologies have been developed by physicists, chemists, biologists, and engineers. Table 16.1 shows examples of biomimetic or bioinspired products and systems. To date, the origins of these products have been limited to some parts of higher animals, lower animals, and plants under normal temperatures.

16.3.2 Stressors

Creatures do not usually exhibit their special abilities clearly except at times when the environment changes from its normal state. When a creature suffers, due to an external stimulus, it will be in a state of stress. These external stimuli are called stressors. Various stressors have been studied (Murofushi, 2005). The present study classifies these stressors into

1. Physical, chemical, and biological types
2. For each type, a cell level, an immobile level (such as plants and small insects), and a mobile level (such as animals) (Hagiwara, 2008)

Table 16.2 shows typical stressors in each of these categories. The creatures are threatened when the quality or quantity of the stressors exceeds a threshold. The special functions and materials of creatures appear in the defense reactions of these creatures when escaping from such situations. Thus, these functions and materials can be good hints for biomimetics and bioinspired engineering.

Table 16.1 Examples of Biomimetic Products

	Products	Origins
New surfaces	Hook-and-loop fasteners	Seeds of burdock
	Adhesive tapes	Gecko feet
	Oil-stain-free tiles	Snail shells
	Packaging foils	Lotus leaves
New shapes	Automobile body	Boxfish
	Low-noise, high-efficiency blades of wind turbine generators	Chest fins of humpback whales
	Propeller fan of air-conditioner exterior unit	Wings of eagles and albatrosses
	Sirocco fan	Wings of dragonflies
New processes	Shield tunneling method	Motion of shipworm
	Ceramics production	Abalone shells
New systems	Ventilation of office building complexes	Termite mounds
	Front nose of bullet trains	Beaks of kingfisher

Table 16.2 Various Stressors

	Cell or Organ Level	Immobile Level (Plants, Fungi, and Bacteria)	Mobile Level (Fish, Birds, and Mammals)
Physical type	Heating	Heating	Heating
	Freezing	Freezing	Freezing
	Drying	Drying	Drying
	High pressure	Flame	Flame
	Ultraviolet rays	Ultraviolet rays	Sound
			Electric current
Chemical type	High ion concentration	Strong acid or base	Medicine
	Oxygen concentration	Oxygen concentration	Toxins
	Medicine	Oils	Oxygen concentration
		Heavy metals	
Biological type	Bacillus	Bacillus	Bacillus
	Virus	Harmful insects	Virus

In the following sections, we explore research concerning both multiphase flow and biomimetic technologies. We focus on momentum and heat transfer phenomena without strong stressors in the first three subsections, while we focus on the phenomena with the strong stressors (drying and freezing) in the last two subsections.

16.3.3 Capillary Flow

Capillary flow is very efficient for heat and mass transfer in animals. The RBCs are the dispersed phase of the capillary flow. Hassanipour and Lage (2010) carried out heat transfer experiments for water flow with the particles of encapsulating phase-change material, and these experiments were inspired by alveolar capillaries. They obtained heat transfer enhancement due to the mixing of the particles.

16.3.4 Skin Separation

The surfaces of fast-swimming dolphins are affected by the high shear force of water. Thus, small pieces of skin surfaces (submillimeter in dimension) are peeled off continuously. These small pieces of skin affect the small eddies near the skin surfaces. Nagamine et al. (2004) carried out DNS for turbulent water flow near the compliant wall including the separation of pieces of the surface with time. Each piece of skin surface consisted of a cluster model of beads and connecting springs, representing the stratum cornea of dolphin skin (see Figure 16.46). The computational results showed that the compliant wall contributes to drag reduction. When the separation rate of the small pieces of skin surface is high particularly due to the flow acceleration, the separation modifies near-wall turbulence and decreases the shear stress.

16.3.5 Superhydrophobic Surfaces

Some plants have hairy exteriors, which are superhydrophobic. The surfaces of such exteriors are composed of dual micro-/nanoscale features. Neinhuis and Barthlott (1997) showed that the leaf epidermis of many highly water-repellent plants including lotus contain waxy bumps (papillae), approximately 10 μm wide, 10 μm high, and 20 μm apart, covered with nanoscale, waxy tubules. Not only the waxy tubules but also air trapped between the bumps contributes to the water repellency. Since only approximately 5% of the bump surfaces make contact with the droplets surfaces, water droplets on these leaves form near spherical shapes (see Figure 16.47a) that easily roll off, carrying with them foreign particles, such as dust (McHugh, 2010). Thus, the surfaces have self-cleaning effects.

Various methods have been explored to fabricate artificial surfaces that mimic these plant surfaces: separation of multicomponent mixtures (Shirtcliffe et al., 2007), lithography (Dorrer and Rruhe, 2006), crystal growth (Tavana et al., 2006), plasma deposition (Satyaprasad et al., 2007), and electrodeposition (Shirtcliffe et al., 2005). Various materials were used for these studies. The highest values of static contact angles, θ, for water droplets placed on the surfaces in these references were in the range of θ =160°–170°, which is nearly equal to or higher than that in the cases of the surfaces of water-repellent plants including lotuses. In some of these studies, not only the static contact angles but also the advancing contact angle and receding contact

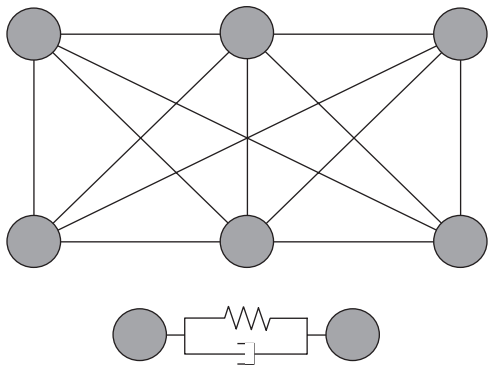


Figure 16.46

A bead–spring–dashpot model representing an aggregated fibrous part of strata corneas: the fibrous parts are replaced by thirteen connecting springs with dashpots and the nodes in the aggregated fibrous parts of corneas are replaced by six beads of the same density as that of the fluid. The bead radius is $0.3\nu/u_\tau$, the shortest spring length is $4.9\nu/u_\tau$, the spring constant is $30\rho\nu u_\tau$, and the dashpot coefficient is $7.4\rho\nu^2/u_\tau$, where ρ is the fluid density, ν is the fluid kinematic viscosity, and u_τ is the friction velocity.

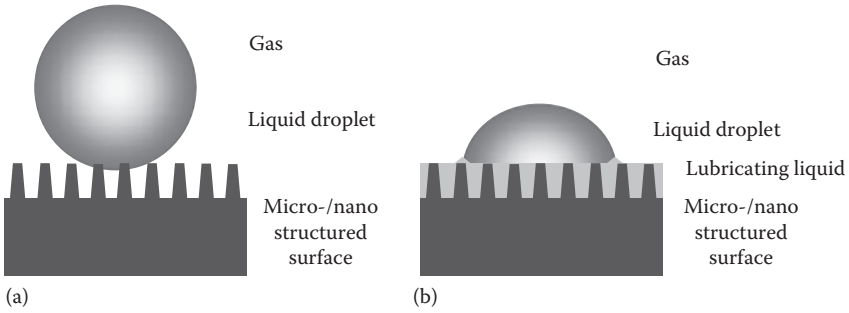


Figure 16.47

Comparison of liquid droplets on micro-/nanostructured surfaces: (a) three-phase system and (b) four-phase system. The gas–liquid–solid three-phase system is seen in lotus leaves, while the gas–liquid–liquid–solid four-phase system is seen in pitcher plants.

angle were discussed (Dorrer and Rühe, 2006, McHugh and Sohal, 2010). The discussion of these angles is useful for the understanding of droplet motion and heat transfer in spray and mist flow.

Recently, another type of superhydrophobic surfaces has been focused on: micro-/nanostructured surfaces with lubricating liquids. Wong et al. (2011) created porous surfaces infiltrated with perfluorinated liquids. These surfaces were inspired by the *Nepenthes* pitcher plants, whose inner surfaces are so slippery that insects cannot crawl up. Wong et al. obtained (1) negligible contact-angle hysteresis for the droplets of low-surface-tension liquids, (2) extreme pressure stability, and (3) optical transparency. Similarly, Solomon et al. (2014) carried out drag measurements for the laminar flow of glycerol aqueous solution over micro-/nanostructured surfaces impregnated with lubricating liquids. The drag reduction was found to depend on the ratio of the solution viscosity to the lubricant viscosity. Anand et al. (2012) conducted experiments on the dropwise condensation on the nanotextured surfaces impregnated with Krytox oils. Novel contact-line morphology of the condensate droplets could be observed due to the four-phase contacting system (Smith et al., 2012, also see Figure 16.47b). It was shown that condensate droplets became highly mobile. This lead to a continuous sweeping effect that cleared the surface for fresh nucleation and resulted in enhanced condensation.

16.3.6 Combination of Surfaces of Different Hydrophobicity

Some insects and plants living in dry areas have special surfaces for collecting water. The tenebrionid beetle living in the Namib Desert collects drinking water from early-morning fog by using its elytra surfaces (Parker and Lawrence, 2001). The peaks of the bumps of the elytra surfaces are smooth and hydrophilic, while the other areas of the surfaces have microstructures coated in wax, and are hydrophobic. The fog water droplets settle on the peaks, forming big droplets, and they are then blown to the hydrophilic peaks. Eventually, the big droplets at the peaks are detached and roll down the tilted surface to the beetle's mouth. Zhai et al. (2006) mimicked the structure by creating a hydrophilic surface with superhydrophobic coatings.

In the heat transfer of spray and mist flow, periods for the liquid contact with the heating surfaces are necessary. When the surface temperature of the horizontal heating wall is low, the deposited droplets form a liquid film. The sensible heat transfer in the liquid film is predominant. Higher heat transfer occurs with thinner films and faster film motion. Thus, the controls of thickness and motion of the liquid film are required. Yamagishi et al. (2010) created a new functional surface that consisted of a nanostructured superhydrophilic area and another hydrophilic area. They observed the liquid film on this surface and measured the temperature on the surface. Figure 16.48 shows the time changes in the temperature of wetted surfaces of a bare glass plate (hydrophilic) (Plate (a)) and a glass plate with the new surface (Plate (b)). The surface temperature reaches the lowest value when the first droplet collides with the surface. In the case of Plate (a), the temperature increases with time, but it drops slightly when the following droplets are added. This shows that the liquid film formed by the droplets is heated regardless of the deposition of successive cool droplets. Thus, the liquid film becomes a form of thermal resistance. On the other hand, the temperature recovers more noticeably until t = 22 s in the case of Plate (b). This is because the droplet moves immediately after the part of it comes into contact with the superhydrophilic part. Even during this period, however, the peak temperature decreases gradually. This suggests that a small amount of liquid still remains after the droplet moves. In the period of t = 22–36 s, the temperature does not change remarkably. This shows that the amount of remaining liquid is still small and that it does not become a form of thermal resistance during

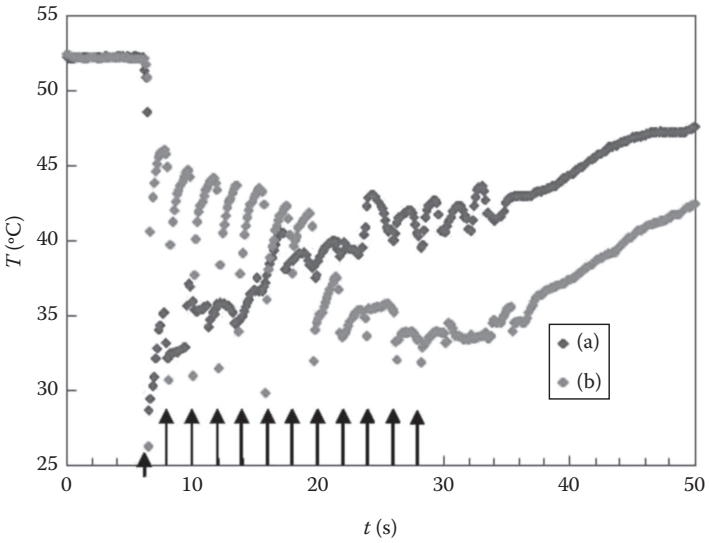


Figure 16.48

Time changes in the temperature of wetted surfaces of a bare glass plate (hydrophilic) (Plate (a)) and a partially modified glass plate (Plate (b)). The chemical-bath deposition method was adopted for the surface modification. Approximately 30% of the surface is covered with numerous pins of nanoorder sizes. This modified part is superhydrophilic. The heat flux was $q_w = 356$ W/m^2. The heat flux from the plate surface to the air was measured by using a heat flux meter. Fifteen droplets of 350 μL in total volume were dropped every 2 s. The arrows in this figure depict the instants of dropping. The surface temperature, *T*, was measured with an infrared camera. A calibration was carried out between the temperature measured with the infrared camera and that measured with a thermocouple attached to the plate surface.

the period. Thus, the local, instantaneous heat transfer coefficient in the case of the new surface was higher than that of the hydrophilic surface after 22 s (Yamagishi et al., 2010).

Betz et al. (2013) and Takata et al. (2013) carried out experiments on pool boiling from the hybrid surfaces of hydrophilic areas and hydrophobic areas. They obtained the pool boiling enhancement and high heat transfer characteristics in specific cases.

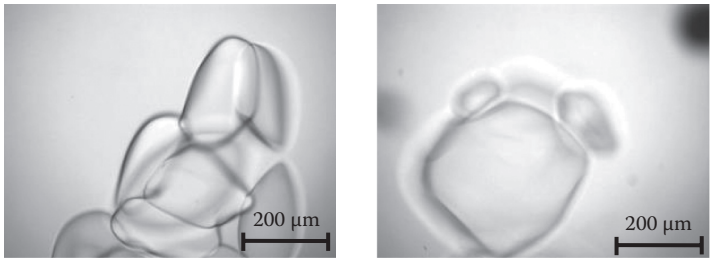
16.3.7 Ice Growth Inhibitors

Some species of fish, insects, plants, fungi, and bacteria have an ice growth inhibitor called antifreeze protein or antifreeze glycoprotein. In the experiments on solutions of these antifreeze substances under thermodynamically quasi-equilibrium states, the freezing point is depressed, while the melting point is retained (Fletcher et al., 1999). Thus, at a temperature between the two points, ice crystals do not grow in a regular way but form peculiar shapes.

Experiments were also carried out for the unidirectional freezing of protein solutions under thermodynamically nonequilibrium states. Furukawa et al. (2005) observed a serrated interface pattern. Hagiwara and Yamamoto (2012) measured the temperature field noninvasively and showed that the balance of heat flux near the bottom edge of the serrated interface was obtained by taking account of heat convection due to high-concentration regions of antifreeze protein, not only protein adsorption to the interface but also the heat conduction/convection contributed to the modification of ice growth.

The antifreeze protein is also effective for the modification of ice particle motion in ice slurry flow. Onishi et al. (2012) measured the motion of ice particles in ice slurry flow in a horizontal minichannel (the cross-sectional area of which was 1×0.7 mm^2). It was found that adding antifreeze protein attenuated the aggregation of ice particles in the flow (see Figure 16.49). A second finding was that the velocity of cluster of ice particles in the saline solution with the protein was lower than that in the saline solution only. This is because a small cluster resulted from the ice/protein interaction being transported near the upper wall of the channel where the mean flow velocity is low.

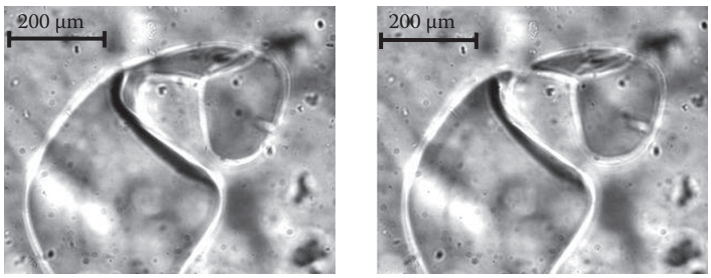
Taira et al. (2014) carried out the observation of the ice slurry in the flow of a mixture of saline solution and preheated protein solution. It was found that cracks appeared on the surface of the ice particles (see Figure 16.50). Furthermore, it was found that the velocity and volume of the ice particle clusters are much higher in the case of the preheated protein solution than those in the case of unheated protein solution.



(a) (b)

Figure 16.49

Typical images of clusters of ice particles in the ice slurry flows: (a) in the case of the saline solution (the concentration is c = 0.90 wt%) and (b) in the case of the equal-volume mixture of saline solution and the antifreeze protein solution (the concentration is c = 0.25 mg/mL). The focus was on the midplane of the horizontal minichannel. When the antifreeze protein solution was added, the ice particles became square and the clusters of ice particles became small. This proves that antifreeze protein inhibits the aggregation of ice particles.



(a) (b)

Figure 16.50

Time change in the shape of a cluster of ice particles in the case of the mixture of saline solution and the heated antifreeze protein solution (heated at 80°C for 3 h): (a) t = 0 s and (b) t = 2.12 s. The cluster, in which the ice particles were adsorbed, broke due to the protein and protein aggregates.

The modification of protein structure and the protein aggregates (submicron in dimension) due to the preheating of the protein solution are thought to be the reasons for these changes (Miyamoto et al., 2016).

16.3.8 Concluding Remarks

We have exposed the readers to several biomimetic or bioinspired pieces of research related to multiphase dispersed flows. In-depth discussion on various aspects of this topic will take place in the near future and will result in significant inventions and products.

References

Anand, S., Paxson, A.T., Dhiman, R., Smith, J.D., and Varanasi, K.K., Enhanced condensation on lubricant-impregnated nanotextured surfaces, *ACS Nano*, 6, 10122–10129, 2012.

Betz, A.R., Jenkins, J., Kim, C.J., and Attinger, D., Boiling heat transfer on superhydrophilic, superhydrophobic, and superbiphilic surfaces, *Int. J. Heat Mass Transfer*, 57, 733–741, 2013.

Dorrer, C. and Rruhe, J., Advancing and receding motion of droplets on ultrahydrophobic post surfaces, *Langmuir*, 22, 7652–7657, 2006.

Fletcher, G.L., Goddard, S.V., and Wu, Y., Antifreeze proteins and their genes: From basic research to business opportunity, *Chemtech*, 29, 17–28, 1999.

Furukawa, Y., Inohara, N., and Yokoyama, E., Growth patterns and interfacial kinetic supercooling at ice/water interfaces at which anti-freeze glycoprotein molecules are adsorbed, *J. Crystal Growth*, 275, 167–174, 2005.

Hagiwara, Y., Some biological hints on the control of heat and mass transfer, *J. Thermal Sci. Technol.*, 3, 381–390, 2008.

Hagiwara, Y. and Yamamoto, D., Temperature distribution and local heat flux in the unidirectional freezing of antifreeze-protein solution, *Int. J. Heat Mass Transfer*, 55, 2384–2393, 2012.

Hassanipour, F. and Lage, J.L., New bio-inspired, multiphase forced convection cooling by ABS plastic or encapsulated paraffin beads, *J. Heat Transfer*, 132, 074501-1–074501-3, 2010.

McHugh, K.M. and Sohal, M.S., Spray-formed tooling with micro-scale features, in *Proceedings of 2010 International Conference on Powder Metallurgy & Particulate Materials*, The Westin Diplomat, Ft. Lauderdale, FL, 2010, pp. 1–11.

Miyamoto, T., Nishi, N., Waku, T., Tanaka, N., and Hagiwara, Y., Effects of preheating on ice growth in anitifreeze polypeptide solutions in a narrow space, in *Proceedings of 7th European Thermal-Science Conference*, Jagiellonian University, Krakow, Poland, 2016 submitted.

Murofushi, K., *Biology of Stresses* (in Japanese) Ohm Publishing Co., Tokyo, Japan, 2005.

Nagamine, H., Yamahata, K., Hagiwara, Y., and Matsubara, R., Turbulence modification by compliant skin and strata-cornea desquamation of a swimming dolphin, *J. Turbulence*, 5, article no. 018, 1–25, 2004.

Neinhuis, C. and Barthlott, W., Characterization and distribution of water-repellent, self-cleaning plant surfaces, *Ann. Botany*, 79, 667–677, 1997.

Onishi, Y., Nakagawa, Y., Kitagawa, A., and Hagiwara, Y., Temperature, flow velocity and protein concentration near ice surfaces in mini-channels, in *Proceedings of 10th IIR Conference on Phase-Change Materials and Slurries for Refrigeration and Air Conditioning*, Kobe University, Kobe, Japan, 2010, pp. 203–210.

Parker, A.R. and Lawrence, C.R., Water capture by a desert beetle, *Nature*, 414(6859), 33–34, 2001.

Quere, D., Wetting and roughness, *Annu. Rev. Mater. Res*., 38, 71–99, 2008.

Satyaprasad, A., Jain, V., and Nena, S.K., Deposition of superhydrophobic nanostructured teflon-like coating using expanding plasma arc, *Appl. Surf. Sci*., 253, 5462–5466, 2007.

Shirtcliffe, N.J., McHale, G., Newton, M.I., Perry, C.C., and Roach, P., Superhydrophobic to superhydrophilic transitions of sol-gel films for temperature, alcohol or surfactant measurement, *Mater. Chem. Phys*., 103, 112–117, 2007.

Smith, J.D., Dhiman, R., Anand, S., Reza-Garduno, E., Cohen, R.E., McKinley, G.H., and Varanasi, K.K., Droplet mobility on lubricant-impregnated surfaces, *Soft Matter*, 9, 1772–1780, 2013.

Solomon, B.R., Khalil, K.S., and Varanasi, K.K., Drag reduction using lubricant-impregnated surfaces in viscous laminar flow, *Langmuir*, 30, 10970–10976, 2014.

Taira, K., Nishi, N., Miyamoto, T., and Hagiwara, Y., Restraint of ice particle cohesion by the association of antifreeze protein and sodium chloride (in Japanese), in *Proceedings of Third Bio-inspired Manufacturing Symposium* (USB memory), Kyoto Institute of Technology, Kyoto, Japan, 2014, pp. 1–3.

Takata, Y., Suroto, B.J., Tashiro, M., Hidaka, S., and Kohno, M., Wettability effects in boiling heat transfer, in *Proceedings of Eight International Conference on Multiphase Flow* (USB memory), International Convention Center, Jeju, Korea, 2013, pp. 1–7.

Tavana, H., Amirfazli, A., and Tsulii, K., Fabrication of superhydrophobic surfaces of n-hexatriacontane, *Langmuir*, 22, 5556–5559, 2006.

Wong, T.-S., Kang, S.H., Tang, S.K.Y., Smythe, E.J., Hatton, B.D., Grinthal, A., and Aizenberg, J., Bioinspired self-repairing slippery surfaces with pressure-stable omniphobicity, *Nature*, 477(7365), 443–447, 2011.

Yamagishi, T., Morita, K., Hagiwara Y., and Kitagawa, A., Effects of droplets impingement on a heated plate composed of hydrophilic surfaces and super-hydrophilic surfaces, in *Proceedings of Seventh International Conference on Multiphase Flow* (USB memory), paper number P2.85, Marriott Tampa Waterside, Tampa, FL, 2010, pp. 1–6.

Zhai, L., Berg, M.C., Cebeci, F.Ç., Kim, Y., Milwid, J.M., Rubner, M.F., and Cohen, R.E., Patterned superhydrophobic surfaces: Toward a synthetic mimic of the Namib Desert beetle, *Nano Letters*, 6, 1213–1217, 2006.


Taylor & Francis
Taylor & Francis Group
http://taylorandfrancis.com

17

Fluidized Bed Reactors

17.1 Hydrodynamics of Fluidization
17.2 Heat and Mass Transfer
17.3 Applications of Fluidized Bed Reactors

17.1 Hydrodynamics of Fluidization

John R. Grace

17.1.1 Key Properties Affecting Fluidization Hydrodynamics

Fluidization occurs when gas or liquid is forced to flow vertically through a bed of particles at such a rate that the buoyed weight of the particles is completely supported by the drag force imposed by the fluid. The particles are then able to move relative to one another. When fluidization occurs, the bed of particles gains the appearance and many properties of a true liquid or fluid. The term "fluidization" reflects this conferring of fluid-like properties onto the solid particles, much as the term liquefaction is used to denote the act of making liquid or conferring liquid properties.

Most applications of fluidized beds are for cases where the fluidizing fluid is a gas rather than a liquid. Hence, except where liquid-fluidized and gas–liquid–solid (three-phase) beds are considered explicitly in the following sections, this chapter is devoted to consideration of fluidized beds where the fluidization is caused by upward flow of a gas.

As detailed in Section 17.3, fluidized beds have many applications. These take advantage of a number of useful features such as low-pressure drops (relative to packed beds), temperature uniformity, excellent surface-to-bed heat transfer, the ability to accommodate a wide range of particle properties, and the capability of handling limited quantities of liquids (e.g., sprayed reactants). Desirable (in some cases necessary) properties of particles and gas for fluidized beds are delineated in Table 17.1. Observing the guidelines with respect to desirable properties will generally lead to good-quality fluidization. It is sometimes possible to extend the range of particle properties, which can be fluidized. For example, the ability to fluidize fine-powders can be enhanced by such means as gentle vibration or stirring, high velocity to cause elementary particles to agglomerate into particles of more favorable sizes, using a tapered bed (larger cross section with increasing height), or some combination of these factors (Deiva et al., 2002).

Geldart (1973) proposed a popular classification scheme for particles fluidized in air under atmospheric conditions. Four powder groups were suggested in order to distinguish broad types of behavior. These four groups (A, B, C, and D) are frequently referred to in the literature. Boundaries between adjacent groups for fluidization by air at room temperature and atmospheric pressure are shown in Figure 17.1. Later, this classification was extended (Grace, 1986a) to cover gases other than air as well as operating temperatures and pressures other than atmospheric. The characteristics of the four groups and criteria to distinguish

Table 17.1 Desirable Properties of Particles and Gases for Gas–Solid Fluidization

Property	Desirable Range	Comments
Particle properties		
Mean diameter[a]	50 μm to 1.6 mm	Finer particles are too cohesive; coarser ones give less desirable fluidization properties.
Size distribution[b]	Neither too narrow nor too broad, e.g., 90th to 10th decile ratio 5–25	Too narrow distribution gives less desirable fluidization properties; too broad a distribution results in particle segregation.
Density	Wide range of values possible, but uniform from particle to particle	Density differences among particles can cause segregation; very low-density materials (e.g., <500 kg/m^3) may be difficult to retain in the bed.
Shape	Rounded and with length-to-thickness ratio no larger than ~3	Avoid extreme shapes like disks and needles, which inhibit fluidization; sharp corners and edges can cause excessive wear of surfaces.
Surface roughness	Smooth	Some roughness is tolerable.
Surface stickiness	Avoid sticky surfaces	Stickiness causes agglomeration and fouling.
Attrition resistance	Usually strong as possible	Particles typically spend hours in the bed; they must withstand the stresses of the bed.
Hardness	Avoid resilience, but also excessive hardness	Compressible particles give excessive interparticle forces; very hard ones tend to cause excessive wear of the equipment components.
Gas properties		
Density	No restriction, but higher value improves properties	High pressure results in improved fluidization characteristics.
Viscosity	No restriction	
Relative humidity	Typically 10%–90%	Below ~10% RH, electrostatics may well be excessive; above ~90%, capillary forces tend to be dominant.

[a] The mean diameter is conventionally defined as $1/\Sigma\,(x_i/d_{pi})$, where x_i is the mass fraction of particles of mean size d_{pi}, usually obtained from the arithmetic average sieve opening in a sieve analysis.

[b] Note that the size distribution in the bed at any point will, in general, differ from the feed or original size distribution due to factors such as attrition, elutriation, and agglomeration.

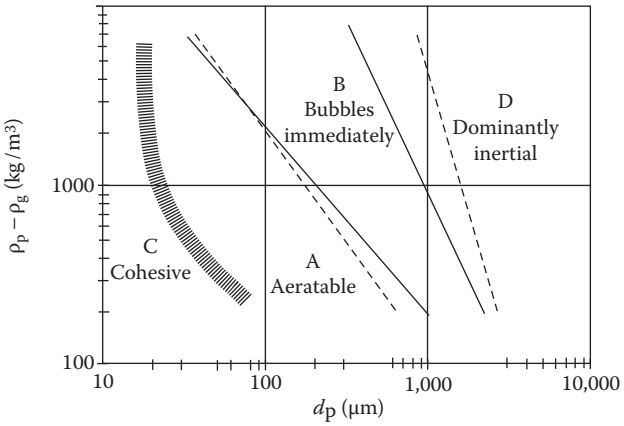


Figure 17.1

Geldart powder groups for fluidization by air at room temperature and atmospheric pressure. CA boundary is typical, but varies with properties such as moisture content of the particles. Solid lines give AB and BD boundaries as suggested originally by Geldart (1973). Dashed lines are AB and BD boundaries from Equations 17.1 and 17.2, respectively.

them are summarized in Table 17.2. Group C particles are usually inappropriate for fluidization due to excessive interparticle forces, whereas groups A, B, and D can be fluidized and used in practical applications. Criteria to distinguish among the powder groups are as follows.

CA boundary. This boundary can be thought of as dividing systems where interparticle forces are so strong that normal fluidization is impossible from those where unaided fluidization is possible, despite significant interparticle forces. It is the most difficult boundary to predict since it depends on a number of nonhydrodynamic factors, such as electrostatic charges and relative humidity, which can affect interparticle forces, primarily caused by van der Waals forces. There is no generally applicable equation. For useful discussion, see Visser (1989). For a review of interparticle forces in fluidized beds, see Seville et al. (2000). In recent

Table 17.2 Powder Groups and Their Key Characteristics

Group	Mnemonic	Example	Key Features	Interparticle Forces Relative to Weight–Buoyancy	Typical Particle Size (μm)
C	Cohesive	Flour	Fluidize poorly due to strong interparticle forces; show channeling	Dominant	<30
A	Aeratable	Fluid cracking catalyst	Excellent fluidization; small bubbles; deaerate slowly when gas flow stopped; high bed expansion, rapid particle mixing	Appreciable	~30–100
B	Bubble readily	Normal sand	Deaerate quickly when gas is shut off; large bubbles; intermediate solids mixing	Negligible	~100–800
D	Dominantly inertial	Peas	Deaerate quickly when gas is shut off; large bubbles; relatively poor solids mixing	Negligible	>800

Sources: Geldart, D., *Powder Technol.*, 7, 285, 1973; Grace, J.R., *Can, J. Chem. Eng.*, 64, 353, 1986a.

years, there has been considerable interest in fluidizing nanoparticles, involving formation of agglomerates, which then act like primary particles (e.g., Zhu et al., 2005, van Ommen et al., 2010).

AB boundary. The AB boundary distinguishes systems where interparticle forces are significant (but not dominant, group A) from those (group B) where interparticle forces do not play a significant role. Data for this boundary for various gases, including air, and for different temperatures and pressures have been correlated (Grace, 1986a) by

$$Ar_{AB} = \left| \frac{g\rho_g(\rho_p - \rho_g)d_p^3}{\mu_g^2} \right|_{AB\ boundary} = 1.0\times10^6\{(\rho_p - \rho_g)/\rho_g\}^{-1.275} \tag{17.1}$$

BD boundary. This boundary separates systems where the flow through the particles is dominated by viscous forces from those where inertial effects are dominant. The boundary between groups B and D can therefore be based on whether the flow through the particulate phase is laminar or turbulent, leading (Grace, 1986a) to

$$Ar_{BD} = \left| \frac{g\rho_g(\rho_p - \rho_g)d_p^3}{\mu_g^2} \right|_{BD\ boundary} = 1.45\times10^5 \tag{17.2}$$

17.1.2 Flow Regimes and Their Transitions

Gas-fluidized beds show a number of distinct flow regimes. The principal ones appear schematically in Figure 17.2 for increasing superficial gas velocity and a column of high height/diameter ratio equipped to return essentially all of the particles entrained from the top. A corresponding flow regime diagram is shown in Figure 17.3 for cases where the column is large enough that the slug flow regime (see Section 17.1.5) is never reached. This form of regime diagram is convenient because the abscissa is simply a dimensionless particle diameter, whereas the ordinate is a dimensionless superficial gas velocity. Approximate boundaries between the powder groups introduced in the previous section are also shown in the figure. Details of the transitions between the flow regimes are considered in the rest of this section.

17.1.2.1 Minimum Fluidization

Consider a bed of solid particles in a cylindrical containing vessel whose bottom is permeable, with gas forced upward through it. The details of the base plate, usually called a "distributor," "distribution plate," or "grid," are considered in Section 17.1.10. As noted earlier, fluidization requires that the pressure drop across the beds matches the buoyed weight of the particles, so that

$$\frac{dP}{dz} = -(\rho_p - \rho_g)(1 - \langle\varepsilon\rangle_A)g \quad \text{or} \quad \Delta P_{bed} = (\rho_p - \rho_g)(1 - \langle\varepsilon\rangle_{av})gH \tag{17.3}$$

where $\langle\varepsilon\rangle_A$ and $\langle\varepsilon\rangle_{av}$ are the volume fraction of gas (usually called "voidage") averaged over the cross-sectional area and the entire bed volume, respectively, while H is the expanded bed depth. If one neglects

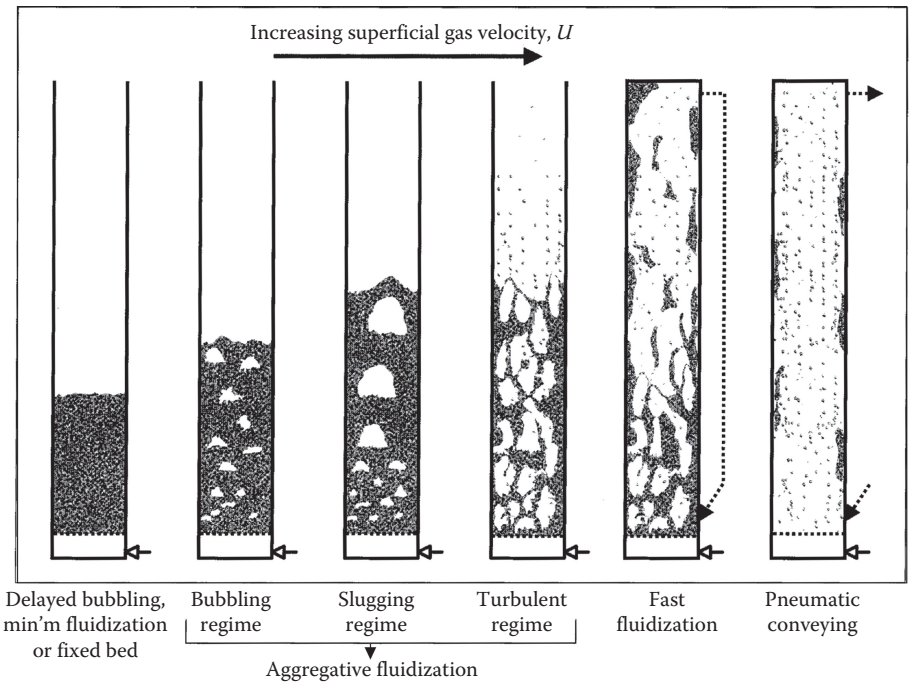


Figure 17.2

Schematic representation showing appearance of flow regimes relevant to gas–solid fluidization.

contributions of wall friction and acceleration to the pressure drop, as it is usually possible to do, this equation should apply no matter what the flow regime. In effect, the time-mean pressure varies as in a static liquid of density $(\rho_p - \rho_g)(1 - \langle\varepsilon\rangle_A)$. In practice, Equation 17.3 is generally accurate for well-fluidized materials in cylindrical columns (with vertical walls). Except in high-density circulating fluidized beds (CFBs) (see Section 17.1.7.2), where wall friction and acceleration terms can be appreciable, deviation by more than approximately ±5% from Equation 17.3 usually indicates "channeling" (i.e., the gas finds fissures or other fixed passages through stationary particles) or other poor gas distribution in the column. Note that Equation 17.3 is also valid for liquid-fluidized beds with the gas density, ρ_g, then replaced by the liquid density, ρ_l.

Pressure drops in fixed beds are commonly predicted by the Ergun equation

$$\Delta P_{\text{fixbed}} = \frac{150\mu_g U(1-\langle\varepsilon\rangle_{av})^2}{\psi^2 d_p^2 \langle\varepsilon\rangle_{av}^3} + \frac{1.75\rho_g U^2(1-\langle\varepsilon\rangle_{av})}{\psi d_p \langle\varepsilon\rangle_{av}^3} \tag{17.4}$$

where

U is the "superficial gas velocity" (total gas volumetric flow rate divided by total column cross-sectional area)

Ψ is a particle shape factor called the sphericity, defined as the surface area of a volume-equivalent sphere divided by the true external surface area of the particle

Transition from a fixed bed to a fluidized bed occurs when the pressure drop across a loosely packed fixed bed reaches the value given by Equation 17.3. Hence, one can estimate the superficial velocity, U_{mf}, at the transition between a fixed and fluidized bed, called the "minimum fluidization velocity," by solving the quadratic equation obtained when the right-hand sides of (17.3) and (17.4) are equated. The result is then an equation of the form

$$Re_{mf} = \frac{\rho_g d_p U_{mf}}{\mu_g} = \sqrt{C_1^2 + C_2 Ar} - C_1 \tag{17.5}$$

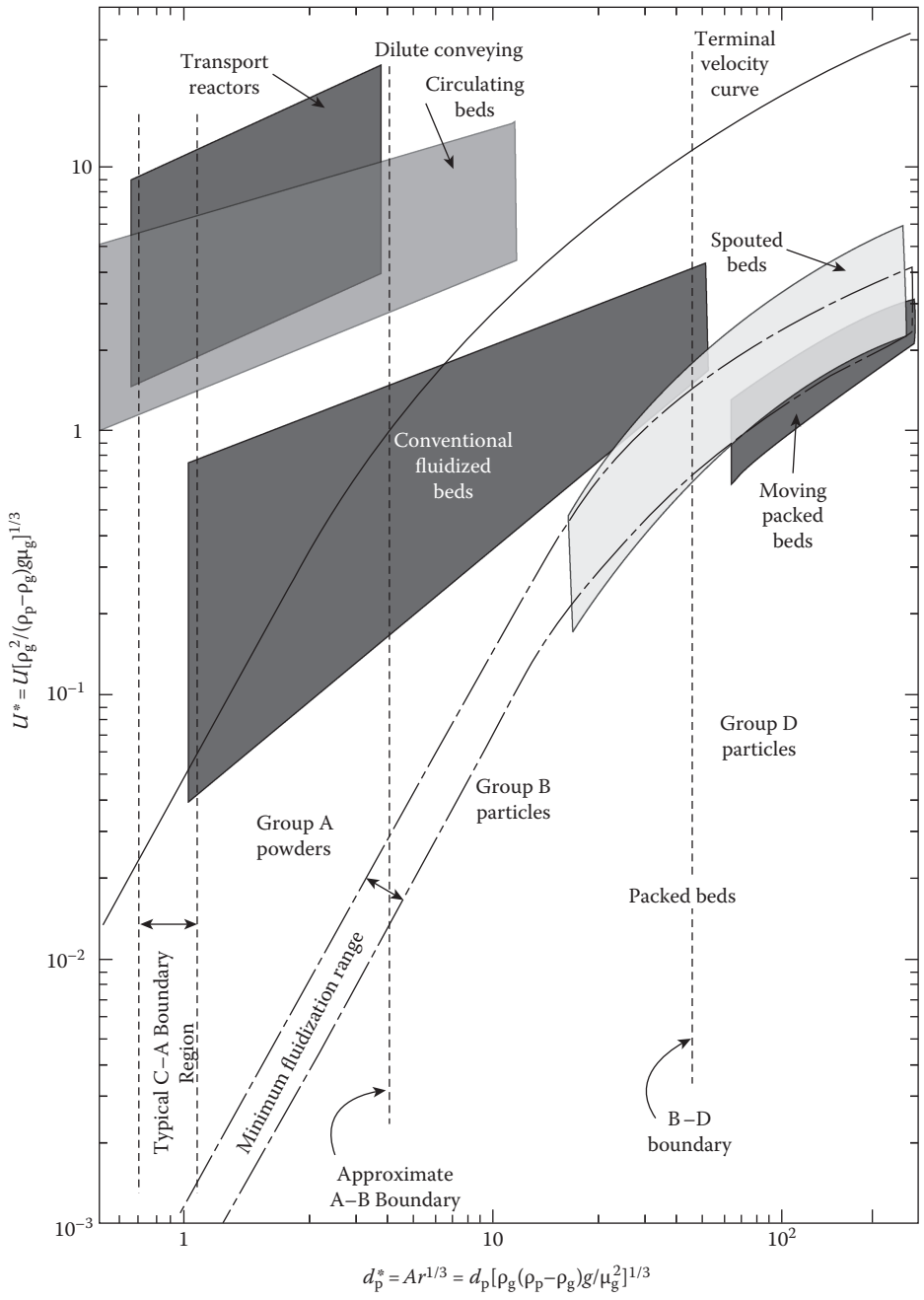


Figure 17.3

Dimensionless flow regime map for upward gas flow through solid particles diagram. Column diameter is assumed to be significantly larger than any bubbles formed, so that slug flow regime is excluded in this diagram. (Adapted from Grace, J.R., *Can. J. Chem. Eng.*, 64, 353, 1986a.)

where

$$Ar = \frac{g\rho_g(\rho_p - \rho_g)d_p^3}{\mu_g^2} \tag{17.6}$$

Different values of the constants, C_1 and C_2, are available in the literature, with the most popular being $C_1 = 33.7$ and $C_2 = 0.0408$, as recommended by Wen and Yu (1966). Typically, this equation predicts the minimum fluidization velocity no better than within approximately ±25%, so it is best to measure it

experimentally whenever possible. The most common method of measurement requires that the pressure drop across the bed be recorded as the superficial velocity is increased stepwise through U_{mf} and beyond; U_{mf} is then taken at the intersection of the straight lines corresponding to the fixed-bed and fluidized-bed portions of the graph obtained when ΔP_{bed} is plotted against U on log–log coordinates. While measuring U_{mf}, it is important to also determine the bed voidage at minimum fluidization, ε_{mf}, requiring that one find the mass, M_p, of the particles, the bed height, H_{mf}, at minimum fluidization, and the particle density, ρ_p, with

$$\varepsilon_{mf} = 1 - M_p/\left(\rho_p A H_{mf}\right) \tag{17.7}$$

Figure 17.4 plots minimum fluidization velocities for particles of different mean diameters and densities fluidized by air at room temperature and atmospheric pressure, based on Equations 17.5 and 17.6 with the C_1 and C_2 values given. As expected, U_{mf} increases with increasing particle diameter and increasing particle density.

Equation 17.5 can be simplified when the particles are either small (low Ar) or large (high Ar). With the C_1 and C_2 values specified earlier, then

$$\text{for } Ar < 10^3: \quad Re_{mf} = 6.1\times10^{-4} Ar \quad \text{or} \quad U_{mf} = 0.00061\frac{g(\rho_p - \rho_g)d_p^{\,2}}{\mu_g} \tag{17.8}$$

$$\text{for } Ar > 10^7: \quad Re_{mf} = 0.202 Ar^{0.5} \quad \text{or} \quad U_{mf} = 0.20\sqrt{\frac{g(\rho_p - \rho_g)d_p}{\rho_g}} \tag{17.9}$$

In all of these expressions, d_p is the mean particle diameter, as defined in the footnote of Table 17.1. Equations 17.5 through 17.9 can also be used for liquid-fluidized beds with ρ_g replaced by ρ_l. Equations 17.8 and 17.9 are important not only because they are useful in their own right for small and large particles, respectively, but also because they show the influence of key variables on U_{mf}. For example, for small particles fluidized by gases, pressure is seen to have virtually no effect, whereas U_{mf} decreases with increasing temperature,

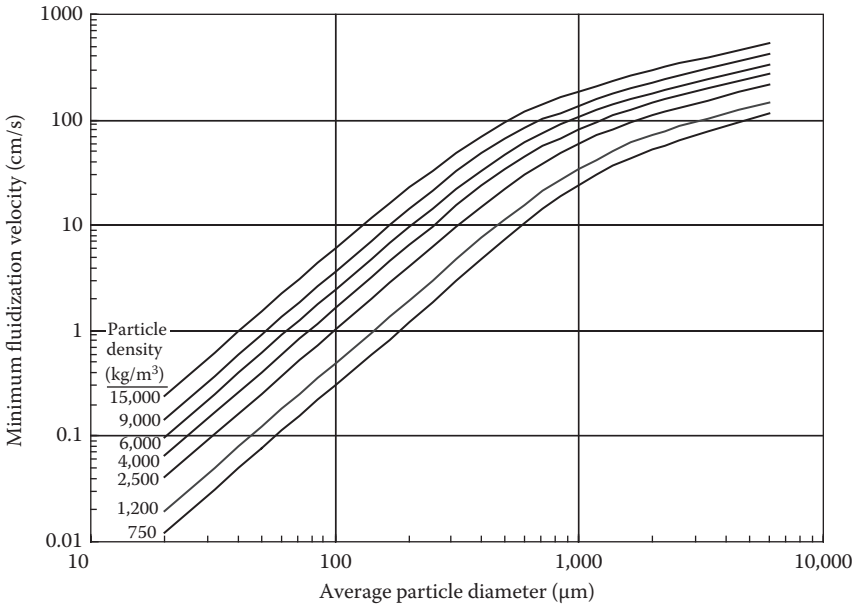


Figure 17.4

Minimum fluidization velocity vs. particle diameter for particles of different densities fluidized by air at atmospheric temperature and pressure.

and it is proportional to the square of the mean particle diameter. On the other hand, for large particles, U_{mf} decreases with an increasing pressure for gas fluidization, increases with increasing temperature, and is proportional to the square root of the mean particle diameter. Equations 17.8 and 17.9 are also notable, because they are identical, except for the coefficients, to expressions for terminal settling velocities of small and large spherical particles of diameter d_p in Newtonian fluids. For small spherical particles ($Ar < 10^3$), Stokes law replaces 6.1×10^{-4} in Equation 17.8 by 1/18, meaning that the terminal settling velocity is approximately 90 times U_{mf}, suggesting a relatively wide range for fluidization before significant entrainment of particles occurs. For large particles ($Ar > 10^7$), where the coefficient in a terminal-velocity equation (Clift et al., 1978) of the form of Equation 17.9 is 1.73, the corresponding V_s/U_{mf} ratio is only 8.6.

17.1.2.2 Overview of Flow Regimes

As the superficial gas velocity, U, is increased stepwise beyond U_{mf} for a bed of solid particles, one encounters a number of different flow regimes. In the most general case, they are in order of increasing U:

- Bubble-free bed expansion (Section 17.1.3)
- Bubbling fluidization (Section 17.1.4)
- Slug flow (Section 17.1.5)
- Turbulent fluidization (Section 17.1.6)
- Fast fluidization and dense suspension upflow (DSU) (Section 17.1.7)

These flow regimes are shown diagrammatically in Figure 17.2, together with dilute pneumatic conveying, reached at even higher gas velocities.

17.1.2.3 Minimum Bubbling Velocity

For particles in groups B and D of the Geldart classification (see Section 17.1.1), bubbling begins as soon as U exceeds U_{mf}. The minimum bubbling velocity, U_{mb}, is then equal to U_{mf}. For group A powders, on the other hand, there is an appreciable gap between these two. Since interparticle forces play a role in determining U_{mb}, correlations in terms of purely hydrodynamic quantities are not very successful. A dimensional correlation due to Abrahamsen and Geldart (1980) gives

$$U_{mb} = 2.07 \exp\{0.176\chi\} \frac{d_p \rho_g^{0.06}}{\mu_g^{0.347}} \tag{17.10}$$

where

χ is the fraction by mass of particles finer than 45 μm (from a sieve analysis)
d_p is again the mean particle diameter defined as in the footnote of Table 17.1

Note that U_{mb} cannot be less than U_{mf}, so that if the value calculated from Equation 17.10 < U_{mf} obtained from Section 17.1.2.1, then set $U_{mb} = U_{mf}$ from Equations 17.5, 17.8, or 17.9.

17.1.2.4 Minimum Slugging Velocity

Slugs are gas bubbles large enough for their volume-equivalent diameters to exceed about 50% of the column diameter. In order for slug flow to occur in fluidized beds, several conditions must be satisfied:

- The ratio of expanded bed depth to column inside diameter (H/D) must be sufficient to give the bubbles enough distance in which to coalesce to voids of a size large enough to be considered slugs. This requires (Darton et al., 1977)

$$\frac{H}{D} \geq 3.5\left(1 - N_{or}^{-0.5}\right) \tag{17.11}$$

- The maximum stable bubble diameter for the particle/gas system (see Section 17.1.4.1) must be of the same order as D or greater.

If both these conditions are met, the superficial gas velocity at minimum slugging is (Stewart and Davidson, 1967)

$$U_{ms} = U_{mf} + 0.07\sqrt{gD} \tag{17.12}$$

For columns of noncircular cross section, D is replaced by the hydraulic diameter, $D_h = 4A/P_c$, where P_c is the column perimeter. This substitution works less well when the width-to-thickness ratio falls outside the range of ~0.4–2.5.

17.1.2.5 Onset of Turbulent Fluidization

Turbulent fluidization occurs when, as U is increased, a point is reached where the bubbles or slugs, instead of continuing to increase in size, begin to break down. The "critical velocity," U_c, which demarcates the onset of the turbulent fluidization flow regime, is usually determined experimentally as the superficial gas velocity at which the standard deviation of pressure fluctuations reaches a maximum. Unfortunately, U_c tends to vary also with level in the bed. Moreover, gage pressure readings lead to different values of U_c than differential pressure measurements. Gage signals register fluctuations from distant locations (including those due to bed surface oscillations and bubble formation), as well as local features, whereas differential signals filter out most information arising from outside the interval between the pair of pressure taps across which the pressure readings are being recorded.

Most correlations of U_c are of the form

$$Re_c = \frac{\rho_g d_p U_c}{\mu_g} = B\,Ar^{\eta} \tag{17.13}$$

Values of $B = 0.565$ and $\eta = 0.461$ are recommended based on a wide range of data for absolute pressure fluctuations (Bi et al., 2000). However, equations of this form fail to include the influence of H/D ratio, which can be significant for relatively shallow beds. A correlation (Ellis et al., 2004) taking this into account and covering columns up to a diameter of 1.6 m is

$$Re_c = \frac{(H/D)^{0.43} Ar^{0.74}}{\sqrt{4.2(H/D)^{0.86} + 3.1Ar^{0.33}}} \tag{17.14}$$

17.1.2.6 Onset of Fast Fluidization Flow Regime

As the superficial gas velocity is increased further, a superficial velocity, called the transport velocity, U_{tr}, is reached where there ceases to be a "bed," that is, there is so much entrainment that there is no distinct upper bed surface. Massive recycling of solids is then required to maintain a large number of particles in suspension. Particles are carried upward in the core of the column and then descend as streamers and clusters along the outer wall. The transition to fast fluidization corresponds to onset of "significant entrainment" and can be predicted (Bi et al., 1995) from

$$Re_{se} = 1.53Ar^{0.5} \quad \text{or} \quad U_{se} = 1.53\sqrt{\frac{g(\rho_p - \rho_g)d_p}{\rho_g}} \tag{17.15}$$

This equation is of the same form as Equation 17.9, which, as noted, is also identical to the expression for terminal settling velocities of large spheres, except for its different constant coefficient. For cases (which only occur for relatively large particles) where the U_{tr} predicted from Equation 17.15 is less than the corresponding terminal settling velocity, V_s, of particles of mean size, U_{tr} should be taken to be equal to V_s.

17.1.2.7 Onset of Dense Suspension Upflow

DSU occurs when, in addition to having a large superficial gas velocity, there is also a high net particle circulation flux, G_s, sufficient to cause the time-mean flux of solids to be upward over the entire column cross

section and the solid's volume fraction is 7% or more (Grace et al., 1999). The transition condition where this occurs is a function of both U and G_s. Kim et al. (2004a) suggest that the onset occurs at

$$\frac{U_{DSU}}{\langle\varepsilon\rangle_A V_s} = 22.8\left\{\frac{G_s}{\rho_p(1-\langle\varepsilon\rangle_A)V_s}\right\}^{0.59} Ar^{-0.20} \tag{17.16}$$

Since the cross-sectional average voidage, $\langle\varepsilon\rangle_A$, varies with height, as discussed in Section 17.1.7.1, regions of fast fluidization and DSU can coexist in the same column.

17.1.2.8 Transition from Fast Fluidization to Dilute Pneumatic Conveying

At high gas velocities and solids holdups $\lesssim$7%, particles are conveyed upward throughout the entire crosssection of a riser column, and the dilute pneumatic conveying flow regime is reached. This condition again demarcates termination of fast fluidization. The transition superficial velocity has been correlated (Kim et al., 2004a) by

$$\frac{U_{DPC}}{\langle\varepsilon\rangle_A V_s} = 1160\left\{\frac{G_s}{\rho_p(1-\langle\varepsilon\rangle_A)V_s}\right\}^{-0.90} Ar^{-0.20} \tag{17.17}$$

As in the previous case, it is seen that this transition is a function of the cross-sectional average voidage, which varies with height in risers, so that transition can again occur within the riser (part way up).

17.1.3 Particulate and Bubble-Free Fluidization

Almost all liquid-fluidized beds expand smoothly without bubbles when the superficial velocity of the fluidizing fluid is increased beyond U_{mf}. This has commonly been called "particulate" or homogeneous fluidization, in contrast to so-called aggregative fluidization (involving division into distinct dilute and dense regions or phases), which occurs for almost all gas-fluidized beds, including all those of practical importance. Particulate beds, gently and homogeneously fluidized by liquids in this manner, are also sometimes referred to as "expanded beds." In practice, the expansion is not perfectly homogeneous, but regions of somewhat increased and decreased voidage propagate slowly enough that beds of practical height can be considered to be homogeneous. An extensive review of liquid fluidization was published by Epstein (2003b). As already noted, the pressure drop, U_{mf}, and ε_{mf} can be predicted by the same relationships as for gas-fluidized beds in Section 17.1.2.1, with the gas density ρ_g replaced by the liquid density ρ_l. The bed expansion can be predicted from the relationship

$$H = H_{mf}\frac{1-\varepsilon_{mf}}{1-\langle\varepsilon\rangle_{av}} \tag{17.18}$$

where the volume-average bed voidage (or liquid fraction) is estimated from an empirical equation suggested by Richardson and Zaki (1954):

$$\langle\varepsilon\rangle_{av} = \left\{\frac{U}{kV_s}\right\}^{1/n} \tag{17.19}$$

with the exponent n and the coefficient k obtained from empirical relationships (Khan and Richardson, 1989)

$$\frac{4.8-n}{n-2.4} = 0.043Ar^{0.57} \quad \text{and} \quad k = 1-1.15\left\{\frac{d_p}{D}\right\}^{0.6} \tag{17.20}$$

These equations are derived from experimental data covering a broad range of conditions, $0.01 < \rho_l d_p V_s/\mu_l < 7000$ and d_p/D up to 0.2. Caution should be exercised for voidages greater than about 0.85 where significant deviations can occur (Epstein, 2003b).

As we have seen in Section 17.1.2.3, gas-fluidized beds of group A particles experience a range of conditions for which $U_{mf} \leq U < U_{mb}$, where the bed expands without bubbles. Since the interstitial gas travels more slowly than bubbles would rise in the same beds, the expansion is greater for given values of U in this range than would be the case if U were to have exceeded U_{mb}. While this range is also often referred to particulate fluidization, there are significant differences between gas-fluidized beds in this range and liquid-fluidized beds (Martin, 1983). The most notable difference is that interparticle forces play a significant role in gas-fluidization case, whereas they are of little or no importance for liquid-fluidized beds.

Bubble-free gas fluidized beds are of little practical importance because of the low gas velocities. However, it is helpful to be able to predict the bed expansion at the minimum bubbling point. Abrahamsen and Geldart (1980) give

$$\frac{H_{mb}}{H_{mf}} = \left(\frac{U_{mb}}{U_{mf}}\right)^{0.22} \tag{17.21}$$

with U_{mf} and U_{mb} obtained from the relationships and procedures described earlier.

17.1.4 Bubbling Fluidization

This section considers the hydrodynamics of the bubbling flow regime, which extends from U_{mb} (Section 17.1.2.3) at the lower limit to either U_{ms} (Section 17.1.2.4) or U_c (Section 17.1.2.5), depending on whether or not slug flow is encountered before reaching the turbulent fluidization flow regime. The bubbles, also often called "voids," form in gas-fluidized beds, because a homogeneous bed is unstable to perturbations once $U \geq U_{mb}$. The bubbles themselves are analogous to spherical-cap bubbles in liquids (Clift et al., 1978). Surrounding the bubbles is a "dense-phase," composed of particles and interstitial gas, acting (Grace, 1970) like a non-Newtonian liquid with an effective viscosity of order 0.1–1 Pa·s, 2–3 orders of magnitude greater than the viscosity of liquid water. As shown in Figure 17.5, the resulting bubbles are well rounded, with total included wake angles (Rowe and Partridge, 1965) of ~200°–260°. The wake approximately completes the base of the sphere, and plays a very important role in determining solids mixing, as discussed in the following. Note that the boundaries of bubbles, unlike those of bubbles in liquids, are permeable. Given the lower pressure at the top of the bubble than at the bottom, an observer riding upward with the bubble on its inside would experience an updraught, often referred to as "throughflow." This plays a vital role in determining mass transfer between the bubbles and surrounding dense phase, while

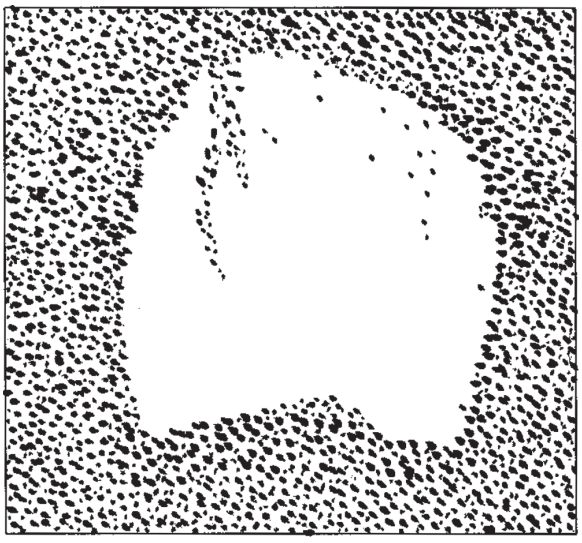


Figure 17.5

Shape of a typical isolated bubble in a three-dimensional fluidized bed. (Based on x-ray photograph of Rowe, P.N. and Partridge, B.A., *Trans. Inst. Chem. Eng.*, 43, 157, 1965.)

stabilizing the roof of the bubble against collapse. Note that there is no load-bearing arch on the bubble roof (Rowe, 1964). In fact, the voidage around the periphery tends to be a little higher than elsewhere in the dense phase (Lockett and Harrison, 1967).

17.1.4.1 Bubble Properties and Bed Expansion in Freely Bubbling Bed without Tubes

The volumetric flow accounted for by the displacement of bubbles or voids rising in the bed can be written as follows:

$$\dot{V}_b = Y(U - U_{mf})A \tag{17.22}$$

Originally, it was assumed that $Y = 1$, and this simple equation, implying that all the gas beyond that required to just fluidize the bed travels as bubbles, is commonly referred to as the "two-phase theory of fluidization." The literature data obtained by many laboratories using various experimental techniques have indicated, however, that Y is usually <1 in practice. Typically, one can assume $Y \approx 0.8$ for group A particles, ~0.7 for group B solids, and ~0.3 for group D particles.

There are a number of empirical and semiempirical equations for predicting the mean bubble size as a function of height in fluidized beds. The approach due to Darton et al. (1977) usually works well for cylindrical columns without any internal tubes or baffles. This considers chains of bubbles rising from the distributor and coalescing pair-wise up the bed. The mean bubble diameter as a function of height, z, is then given (Darton et al., 1977) by

$$D_b(z) = \frac{0.54\left(U - U_{mf}\right)^{0.4}\left(z + 4.0\sqrt{A_c}\right)^{0.8}}{g^{0.2}} \tag{17.23}$$

where A_c is the area of the distributor plate per orifice in the distributor. This equation is intended for cases where bubbles form right at the gas distributor and where the particles are large enough (essentially group B and D solids) that negligible bubble splitting occurs. For group A solids, bubbles commonly reach a "maximum stable diameter," where there is a dynamic equilibrium between bubble coalescence and splitting. This imposes an upper limit on the bubble diameter. The maximum stable bubble diameter can be estimated (see Grace, 1982) by

$$D_{bmax} = 2.0(V_s^e)^2/g \tag{17.24}$$

where V_s^e is the terminal settling velocity of a particle of diameter $2.7d_p$ in the fluidizing gas at the same pressure and temperature as in the bed. An alternative approach, which accounts for bubble splitting as well as coalescence, was suggested by Horio and Nonaka (1987). As suggested by these authors, the height coordinate, z, should be taken from the termination of gas jets in cases where vertical jets form at the distributor (see Section 17.1.10).

Once the mean bubble diameter has been estimated as a function of height from Equation 17.23, subject to the constraint imposed by Equation 17.24, it is then possible to calculate the corresponding bubble rise velocity from

$$U_b(z) = 0.71\sqrt{gD_b(z)} + (U - U_{mf}) \tag{17.25}$$

The first term accounts for the velocity of rise of a spherical-cap bubble with a typical wake angle, whereas the second term corrects, in an approximate manner, for bubble interaction effects inside the bed (Grace and Harrison, 1969).

With the estimates of bubble volumetric flow, that is, $\dot{V}_b$, and rising velocity, that is, U_b, from above, it is now possible to predict the expansion of the bubbling bed, aided by the common assumption that the dense phase retains the same voidage as at minimum fluidization, that is, ε_{mf}. In the next two relationships, it is also assumed that a negligible fraction of the particle inventory is displaced into the freeboard, cyclones, and return system. If this is not the case, then one needs to correct the H_{mf} below to use an effective value, which accounts only for particles in the dense bed (i.e., below the expanded bed surface). An iterative procedure

is then required to estimate the bed expansion: Firstly, guess a value of ε_b, the fraction of dense bed volume occupied by bubbles. Then, calculate a first estimate of the expanded bed depth as

$$H = \frac{H_{mf}}{(1-\varepsilon_b)} \tag{17.26}$$

Next calculate the mean bubble diameter at $z = H/2$ using Equation 17.23 or 17.24, whichever gives the smaller value. Then find the corresponding bubble rise velocity, $U_{b|z=H/2}$, from Equation 17.25. Hence, find a new estimate of ε_b from

$$\varepsilon_b = \dot{V}_b / [A U_{b|z=H/2}] \tag{17.27}$$

If this value is within a chosen tolerance of the original guess, it is accepted; H is then specified as the value calculated previously from Equation 17.26. Otherwise, calculate a new estimate of H from Equation 17.26 using the most recently calculated value of ε_b and proceed as earlier. Generally, three or four iterations should be sufficient to give a good estimate of the bed expansion and other mean bubble properties calculated via this procedure.

Once the bubble properties have been calculated in this manner, it may also be useful to estimate the mean frequency of bubbles passing any level:

$$f_b = \dot{V}_b / V_b \quad \text{with} \quad V_b = \text{bubble volume} = (\pi/6) D_b^3 \tag{17.28}$$

One of the important features, however, of bubbling fluidized beds is that the bubbles are not uniformly distributed across the cross section of the column, even on a time-averaged basis. Instead, as shown both by experimental results and coalescence models show that, the bubbles tend to become depleted near the outer wall, with the maximum frequency and bubble volumetric flow initially occurring about one mean bubble diameter in from the outer wall, and then this position migrates inward toward the axis of the column as bubbles grow and the slug flow regime is approached (Grace and Harrison, 1969, Werther, 1974).

17.1.4.2 Influence of Tubes and Baffles on Bubbling and Bed Expansion

The procedure described earlier for estimating bed expansion and bubble properties applies to cases where there are no internal heat-transfer tubes or other fixed surfaces inside the column. In any section of the column containing an array of horizontal tubes, bubbles can be assumed to grow by coalescence according to Equation 17.23 until they reach either the diameter given by Equation 17.24 or the minimum center-to-center tube separation distance, whichever is smaller. If the array terminates before the top of the bubbling bed, then growth beyond the latter limit will recommence, but of course with the limit imposed by the maximum stable size, Equation 17.24, still in place. In such cases, the expansion is predicted by estimating ε_b separately for each section—that is, below the array of tubes, inside the tube bundles, and above the tubes—and then applying a procedure analogous to that described earlier to balance the total in-bed inventory of solids with the sum of the solids within all of the individual sections.

For vertical tubes or other baffle geometries and configurations, there are no reliable methods for prediction of the evolution of bubble size, and hence the bed expansion. In general, bubbles are smaller when baffles are present as the internal fixed surfaces limit bubble coalescence (Grace and Harrison, 1971), and baffles may also promote bubble splitting. Hence, bed expansion is usually increased by the presence of fixed internal surfaces, with the degree of increase depending strongly on the extent to which the mean bubble size is reduced.

17.1.4.3 Solids Mixing and Motion in a Bubbling Bed

The dominant mechanism by which solids are dispersed in bubbling fluidized beds involves displacement of particles by bubble wakes and due to the "drift" caused by the bubbles. These displacements are illustrated schematically in Figure 17.6. In the case of wake transport, particles are gathered in the wake at the bottom (back) of rising bubbles and transported upward, with occasional shedding of clumps or fragments of particles along the way (Rowe et al., 1965). In the case of drift, particles undergo net displacement outside the wake due to the passage of bubbles. This displacement is upward near the bubble axis, and downward at several bubble radii from

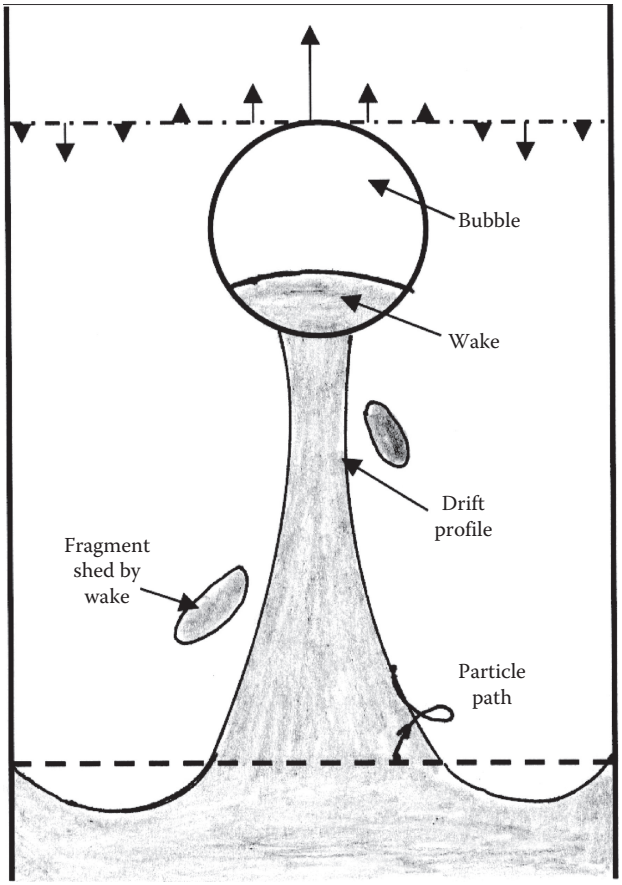


Figure 17.6

Schematic showing particle wake transport and drift due to passage of bubble. Arrows at top indicate relative vertical components of particle velocity across the bed just ahead of the approaching bubble.

the axis, just as in the case of drift net displacement caused by a sphere passing in potential flow through a fluid (Baeyens and Geldart, 1973). Let f_w represent the volume of the wake divided by the volume of the corresponding bubble. Some experimental results for f_w are shown in Figure 17.4 based on x-ray photography of bubbles in fully three-dimensional fluidized beds (Rowe and Partridge, 1965). An effective drift fraction may be defined in a similar manner, with experimental results (Baeyens and Geldart, 1973), suggesting that this is approximately $1.6f_w$. Hence, the upward mass flux of particles due to the rise of bubbles at any level in the bed can be estimated as

$$G_s = 2.6\rho_p(1-\varepsilon_{mf})f_w\dot{V}_b/A \tag{17.29}$$

where

$\dot{V}_b$ is obtained from Equation 17.22

f_w can be estimated based on x-ray photographs of bubbles reported by Rowe and Partridge (1965)

A characteristic mixing time, sometimes called a "turnover time," can then be estimated as the average time for the inventory of particles in the bed to travel through one cycle, from the bottom of the bed to the top and back again to the bottom, leading to

$$t_{mix} = \frac{H_{mf}}{\left\{2.6f_wY\left(U-U_{mf}\right)\right\}} \tag{17.30}$$

Experimental results indicate that homogeneity is effectively achieved in two to three mixing times. For most fluidized beds of practical importance, t_{mix} turns out to be on the order of 10–100 s, whereas particles usually spend much longer times in the bed. Hence, the particles are quickly blended in the vertical direction and perfect axial mixing can commonly be assumed. As long as bubbling is well established, that is, ($U - U_{mb} > \sim 0.1$ m/s), and the distributor has been well designed, height-wise classification by size of particles whose diameters are within an order of magnitude of the mean particle diameter is unlikely to be a problem. Nonuniform particle densities are more likely to give rise to vertical segregation (Rowe and Nienow, 1976). However, vigorous bubbling is usually sufficient to prevent segregation of particles whose densities are within ~30% of each other.

For larger density differences, for example, for biomass particles in beds of sand, the spatial distribution of the two species depends on circulation patterns and is a complex function of the superficial gas velocity, species concentrations, and particle shape (Zhang et al., 2009, Fotovat et al., 2014).

These results refer to vertical mixing (often referred to as axial dispersion). Commonly the literature describes the mixing process in terms of an axial dispersion coefficient, defined by analogy with molecular diffusion, and having the same units (m^2/s) as molecular diffusivity. However, molecular diffusion involves small random steps, clearly differing from the large bubble-generated (and hence deterministic) displacements that dominate the mixing process in bubbling fluidized beds. As a result, axial dispersion coefficients vary widely and are not very useful in practice, except as a gross means of comparing data and seeing trends, as in the review by van Deemter (1980), which provides useful data on mixing in industrial-scale fluidized beds.

Particle transport by bubbles also provides the principal mechanism for horizontal (or radial) solids mixing in bubbling beds. When bubbles that are not perfectly aligned vertically interact and coalesce, gas and particles are displaced horizontally. In addition, particles are displaced horizontally when bubbles erupt at the dense bed surface, resulting in splashing and spraying of particles into the freeboard. Typically, the magnitudes of mixing coefficients are about an order of magnitude less in the horizontal direction than in the vertical direction. Although dispersion models are still strictly inappropriate in this case, as for axial mixing, they are often used (van Deemter, 1980), and the objection to their use for radial (or lateral) dispersion is less than for vertical (axial) dispersion coefficients since the displacement steps are smaller and less ordered.

An issue of considerable importance in bubbling fluidized beds is the establishment of gross overall particle circulation patterns, associated with the bubble coalescence pattern referred to, whereby bubbles initially become more concentrated near the outer wall, and then the region of increased bubbling migrates inward toward the axis of the bed with increasing height. Since bubbles carry particles upward in their wakes and propel particles upward by drift, the nonuniform radial distribution of bubbling leads to nonuniform solid's movement. On a time-mean basis, the patterns then tend to be as indicated in Figure 17.7. As shown, there is a relatively weak cell near the bottom where particle motion is primarily upward near the wall and

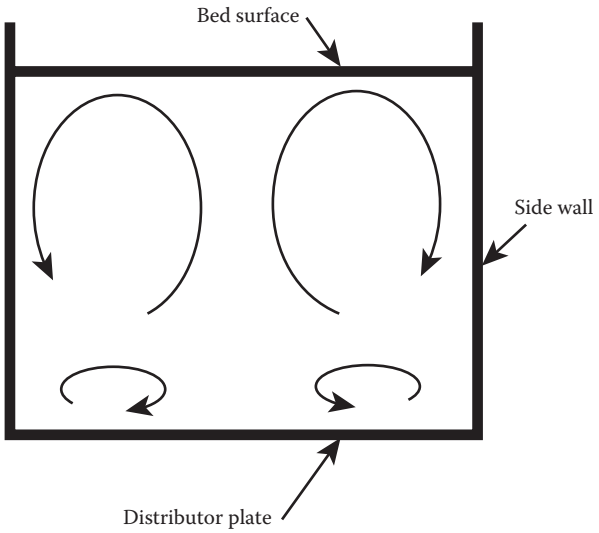


Figure 17.7

Typical time-mean solids motion ("gulf-streaming") in bubbling beds.

downward near the center. In bubbling beds of height/diameter ratio of about 1 or more, this then gives way to a stronger up-the-center, down-the-outside time-mean circulation pattern. These patterns, often referred to as "gulf-streaming," are self-reinforcing, as bubbles tend to be pulled into the upflow regions, where the bubbles are already more abundant, as they rise from the distributor. However, it is important to note that the pattern at any instant may differ significantly from the time-mean patterns.

17.1.4.4 Gas Mixing and Gas–Solid Contacting in a Bubbling Bed

Gas mixing patterns are strongly influenced by solids motion (May, 1959) and also by the two-phase nature of the bed. Since particles are transported upward by bubbles and the bubbles are nonuniformly distributed, as we have seen earlier, particles must travel downward in other parts of the column to maintain the bed of solids in place. Wherever particles descend with a vertical component of velocity larger than the interstitial velocity relative to particles, which is given approximately by U_{mf}/ε_{mf}, the local absolute velocity of gas elements is directed downward toward the distributor plate. Hence, the regions of net downward flow of particles indicated in Figure 17.7 can also be regions where, in a time-mean sense, gas elements are carried downward (Latham et al., 1968, Kunii and Levenspiel, 1991). This is one factor contributing to axial dispersion of gas in bubbling fluidized beds, and it can even lead to true "backmixing," that is, displacement of gas upstream (downward).

Gas dispersion is also affected by the fact that bubbles travel in general with velocities that differ, usually widely, from the interstitial gas velocity. For example, for group A solids, the bubble velocity is typically on the order of 0.6–1.2 m/s, compared with interstitial gas velocities relative to the particles of order 0.01 m/s or less. Hence, even if elements of gas in the dense phase are not descending, they are certainly rising much less quickly than gas elements associated with bubbles. Interphase mass transfer diminishes this effect to some extent, but differences in gas velocities between the two phases contribute in a major way to substantial deviations from plug flow. While gas mixing deviates considerably from plug flow, the residence time distribution is also far from that corresponding to perfect mixing (Gilliland and Mason, 1952, van Deemter, 1980, Kunii and Levenspiel, 1991). The fact that bubbles are widely distributed in size, and hence in rising velocity (see Equation 17.25), further contributes to nonuniform gas residence times of gas elements in the bed. Yet another contributor is that the "throughflow" component of gas velocity, defined earlier, tends to increase as bubbles elongate while bubbles are interacting and coalescing (Levy and Dorfman, 1995, Grace, 2002). Axial mixing can be significantly reduced by the addition of horizontal baffles (Overcashier et al., 1959).

Reactor models for bubbling beds must take into account the difference in gas–solid contacting, axial dispersion, and gas velocity between the dense phase and bubble phase. A simple two-phase bubbling bed model (Grace, 1986b) that covers the major factors assumes stagnant gas in the dense phase and plug flow in the bubble phase. A small proportion of the bubble phase volume, on the order of 0.1%–1%, is assumed to be occupied by particles. Interphase mass transfer is predicted by a semiempirical equation due to Sit and Grace (1981):

$$k_{bd} = \frac{U_{mf}}{3} + \left\{ \frac{4 D_{AB} \varepsilon_{mf} U_b}{\pi D_b} \right\}^{0.5} \tag{17.31}$$

where D_{AB} is the molecular diffusivity of the reacting component. Mole balances are then written for each phase. For example, for a first-order gas-phase reaction, the mole balance for the bubble and dense phases, respectively, is

$$U \frac{dC_{Ab}}{dz} + k_{bd} a_b \varepsilon_b (C_{Ab} - C_{Ad}) + k_r \varphi_b C_{Ab} = 0 \tag{17.32}$$

$$k_{bd} a_b \varepsilon_b \left(C_{Ad} - C_{Ab} \right) + k_r \varphi_d C_{Ad} = 0 \tag{17.33}$$

where

C_{Ab} and C_{Ad} are bulk gas concentrations in the bubble and dense phases at height z
k_r is a first-order kinetic rate constant
$a_b \approx 6/D_b$ is the interphase area per unit volume, whereas φ_b ($\approx 0.001–0.01\varepsilon_b$)
φ_d ($\approx (1 - \varepsilon_b)(1 - \varepsilon_{mf})$) are the fractions of the total dense bed volume occupied by solids associated with the bubble and dense phases, respectively

The bubble diameter, D_b, is usually taken at $z = 0.4H$, that is, at 40% of the expanded bed depth.

With the boundary condition $C_A = C_{A0}$ at $z = 0$, these equations can be integrated to estimate the concentration at the top ($z = H$) of a bubbling bed:

$$C_{AH} = C_{A0} \exp\left\{\frac{-k_r^\star [k_{bd}^\star(\varphi_b + \varphi_d) + k_r^\star \varphi_b \varphi_d]}{k_{bd}^\star + k_r^\star \varphi_d}\right\} \tag{17.34}$$

where $k_{bd}^\star$ and $k_r^\star$ are dimensionless interphase mass transfer and kinetic rate constants defined by

$$k_{bd}^\star = \frac{k_{bd}\alpha_b \varepsilon_b H}{U} \quad \text{and} \quad k_r^\star = \frac{k_r H}{U} \tag{17.35}$$

This simple model illustrates how conversions depend on both interphase mass transfer and chemical kinetics, with the former usually being the rate-determining step. Effectively, some of the gas bypasses the bed by short-circuiting through the bubbles, which, because they are much more dilute and usually travel much faster, are much less effective for reaction than an equal volume of dense phase. Mass transfer resistance within the individual phases is seldom important for gas-phase reactions, but can be important, especially for gas-solid reactions and large (e.g., Geldart group D) particles.

This reactor model can be readily extended to non-first-order kinetics and to multiple reactions; some analytical solutions are available for simple cases (Grace, 1986b). It can also be extended to account for more complex kinetics, axial dispersion in one or both phases, and gas-solid reactions, with numerical solution definitely then being required to solve the resulting set of equations.

17.1.4.5 Entrainment

When bubbles burst at the surface of fluidized beds, clumps of bed particles are ejected into the freeboard region (region between bed surface and top of column). The velocities of the ejected particles are of the same order as the bubble rise velocities. When coalescence is in the process of occurring just as two bubbles reach the bed surface, especially energetic bursts of particles can occur, with the initial vertical component of particle velocity in the freeboard approximately doubled. Most evidence suggests that ejected particles come predominantly from the wake of the bubbles, rather than from the nose. As a result, some particles from deep within the bed can find themselves quickly dispersed in the freeboard, where they may escape altogether with the exit gas stream, or be disengaged and land at some other horizontal position on the bed surface, thereby contributing to lateral mixing. Because small particles experience more drag relative to their weight than larger ones, the finer material is preferentially lost from the bed. This process of preferentially losing finer material from the mixture is often called "elutriation." The overall particle size distribution in the bed is also, of course, influenced by other factors such as agglomeration, attrition, and growth or shrinkage in particle size as a result of chemical reactions occurring in the reactor.

Two quantities are generally used to characterize the entrainment. The "transport disengaging height," usually abbreviated TDH, is the effective freeboard height (measured from the surface of the dense bed below) beyond which there is negligible variation in the entrainment flux. In other words, any ejected particles, which, due to gravity, are able to reverse their direction of motion and return to the dense bed, do so within the TDH. In practice, the TDH is the freeboard height usually provided by fluid bed designers, as any greater height results in a negligible decrease in entrainment, whereas a shorter freeboard increases the carryover from the bed. Experimental evidence shows that the TDH is a strong function of both the gas velocity and the column diameter. A graphical correlation by Zenz and Othmer (1960) is commonly used to provide a conservative estimate of the TDH. This correlation is plotted in SI units in Figure 17.8. Several other approaches are also available to predict the TDH, as summarized by Geldart (1986) and by Werther and Hartge (2003). More recent data by Chen et al. (2010) show fair agreement with the Zenz approach, and these authors provide a new predictive model.

The other quantity of importance with respect to particle carryover is the entrainment flux above the TDH as a function of particle size. This is needed to estimate the efficiency of cyclones or other gas–solid separation devices downstream of the bed, and hence to estimate the overall entrainment from the complete system. There are many empirical correlations, which can be used to predict the specific rate constant, $K_i^\star$

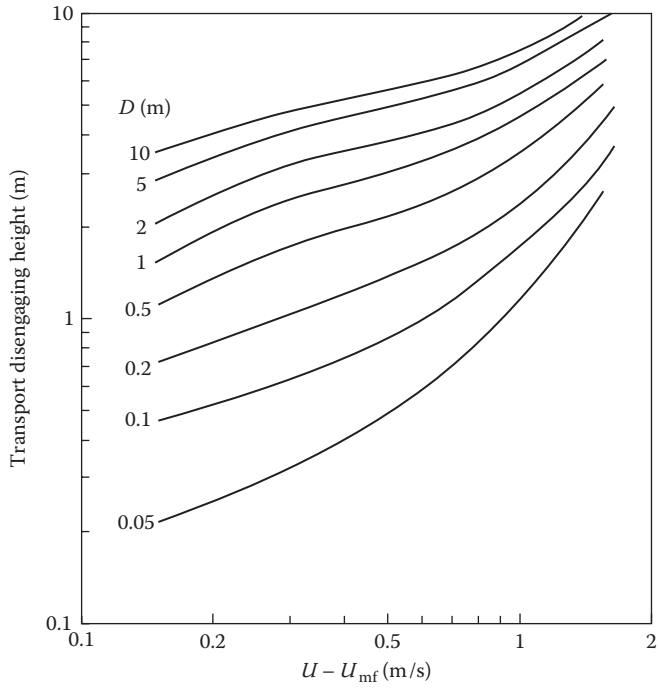


Figure 17.8

Transport disengaging height correlation. (Adapted from Zenz, F.A. and Othmer, D.F., *Fluidization and Fluid—Particle Systems*, Reinhold Publishing Corp., New York, 1960.)

(also called the elutriation constant by some authors). $K_i^\star$ is defined in such a way that the flux of particles in a narrow size range of mean diameter d_{pi} is given by

$$G_{si} = m_i K_i^\star \tag{17.36}$$

where m_i is the mass fraction of particles in the i^{th} size interval. Available approaches and correlations for $K_i^\star$ differ widely, commonly by orders of magnitude, in their predictions (Chew et al., 2015). Summaries of these correlations have been published (Geldart, 1986, Werther and Hartge, 2003). It is important to choose an approach, which was derived for particles and conditions as similar as possible to those of interest. This makes it very difficult to predict entrainment with any degree of accuracy. A correlation based on an extensive range of materials and operating conditions, including data on units up of 1 m in diameter and data obtained at high temperature and pressure (Choi et al., 1999), gives

$$\frac{K_i^\star d_{pi}}{\mu_g} = Ar_i^{0.5} \exp\left\{6.92 - 2.11F_g^{0.303} - \frac{13.1}{F_d^{0.902}}\right\} \tag{17.37}$$

where

$$F_g = g d_{pi}\left(\rho_p - \rho_g\right) \quad \text{and} \quad F_d = C_D \rho_g U^2/2 \tag{17.38}$$

Entrainment at the bed surface itself can be approximated (Wen and Chen, 1982) by

$$G_{so} = 9.6A\left(U - U_{mf}\right)^{2.5} g^{0.5} \rho_g^{3.5} \mu_g^{-2.5} \tag{17.39}$$

Below the TDH, the particle flux decays approximately exponentially with height, with

$$G_{si} = m_i K_i^{\star} + G_{so} \exp\{-\alpha_i z'\} \tag{17.40}$$

where z' is the vertical coordinate measured from the bed surface. The decay constant, α_t, was found (Wen and Chen, 1982) to vary from 3.5 to 6.4 m^{-1}, and can be taken as 4.0 m^{-1} in the absence of specific information.

Solids entrained by the outlet gas are usually passed through at least one stage of cyclones and other separators to remove as many particles as possible. Vertical standpipes are employed to return the captured solids to the bottom of the dense bed. To prevent short-circuiting of gas in the wrong direction up the standpipe, trickle valves are commonly installed at the exit of the standpipe.

17.1.5 Slugging Fluidization

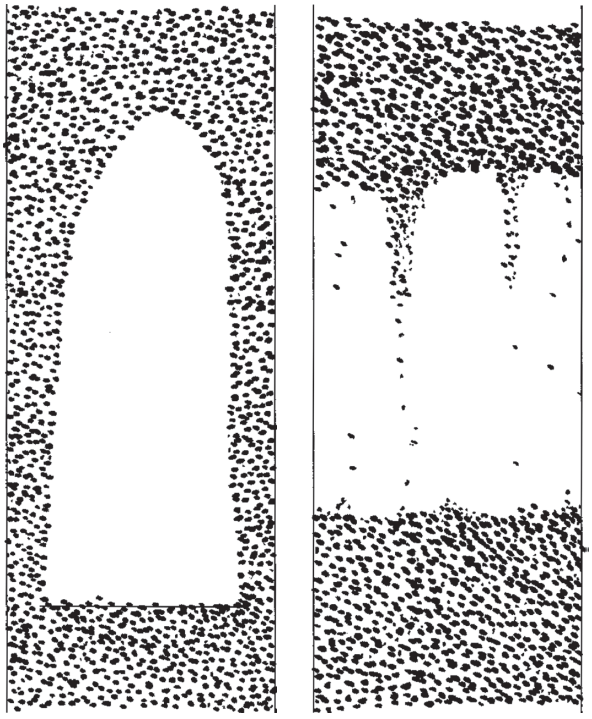
The conditions required for slug flow are summarized in Section 17.1.2.4. These conditions are most likely to apply at high H/D ratios in vessels of relatively small diameter. They are satisfied in many laboratory and pilot units, but are unlikely to be applicable in vessels of commercial scale. A useful review of slugging in fluidized beds was provided by Hovmand and Davidson (1971).

Slugs are bullet-shaped voids, rounded at the top and almost flat at the bottom, as shown in Figure 17.9a. In most cases, they rise nearly symmetrically in the column, though asymmetric slugs clinging to the wall are sometimes observed. Once continuous slugging has become established, the interslug spacing, that is, the separation distance between the bottom of one slug and the nose of the next slug, typically reaches ~ 2D. The flow is then fully developed and the length of slugs, ℓ_s, can be estimated from the quadratic equation

$$\ell_s/D - 0.495\left(\ell_s/D\right)^{0.5}\left(1+\beta\right) + 0.061 - 1.94\beta = 0 \tag{17.41}$$

where

$$\beta = \frac{U - U_{mf}}{U_{si}} \geq 0.2 \quad \text{and} \quad U_{si} = 0.35\sqrt{gD} \tag{17.42}$$



(a) (b)

Figure 17.9

Shapes of slugs: (a) axisymmetric round-nosed slug; (b) square-nosed slug.

The velocity of each slug is approximately given by

$$U_s = U_{si} + \left(U - U_{mf}\right) \tag{17.43}$$

The frequency with which slugs pass a given level and also reach the upper bed surface is then

$$f_s = \frac{U_s}{\left(\ell_s + 2D\right)} \tag{17.44}$$

In slugging beds, the upper surface rises smoothly as the top slug approaches and then falls sharply as each slug breaks the upper surface. The maximum expanded bed height for slugging beds, achieved just as each slug breaks the surface, is approximately

$$H_{max} = H_{mf}\left(1 + \beta\right) \tag{17.45}$$

Like bubbles, slugs have wakes at the bottom, but these are stunted relative to wakes of bubbles of similar volume. As a result, both solids mixing and gas mixing are less for slugging beds than for comparable bubbling beds in which wall effects play a minor role.

These equations provide good estimates of the major hydrodynamic properties of most slugging fluidized beds where $H \gg D$. Results for gas and solids mixing and models for chemical reaction are also available for this flow regime (Hovmand and Davidson, 1971).

Another mode of slug flow, usually called "square-nosed slugging," is also sometimes encountered in columns of small diameter. In this case, the slugs are relatively flat both at top and bottom, as indicated in Figure 17.9b. These slugs rise relatively slowly as particles rain from the top surface (roof) of each slug. Square-nosed slugs are usually attributable to relatively large d_p/D ratios or large, rough, or cohesive particles, coupled with smooth-walled columns. This mode has no useful features, nor can it be scaled up with confidence. Therefore, it should be avoided in practice and is not pursued further here.

17.1.6 Turbulent Fluidization

When the superficial gas velocity reaches U_c (see Section 17.1.2.5), there is a transition to the turbulent fluidization flow regime. The turbulent regime bridges between the bubbling (or slugging) regime, where bubbles (or slugs) are dispersed in a continuous dense phase of particles and interstitial gas, and the fast fluidization regime, where particles streamers and clusters are dispersed in a continuous dilute suspension of particles in gas. While voids appear in the turbulent fluidization flow regime, they are much more transitory in nature, irregular in shape, and generally smaller than the bubbles and slugs encountered in the bubbling or slugging flow regimes. Hence, the distinction between a dense phase and a dilute phase is generally unnecessary for the turbulent flow regime. The turbulent flow regime turns out to be especially favorable for carrying out chemical reactions and certain physical operations. An extensive review of the turbulent flow regime was published by Bi et al. (2000).

17.1.6.1 Hydrodynamics of the Turbulent Fluidization Flow Regime

The overall mean (spatial- and time-average) voidage in the turbulent flow regime is generally in the range 0.65–0.75, intermediate between that in bubbling and fast fluidization. There is little variation in the axial direction until one approaches the bed surface. Because of surging and eruption of voids, the upper surface is indistinct, and hence, the time-mean expanded bed depth is commonly inferred from pressure profiles, ideally involving a series of pressure taps extending from low in the bed to well into the freeboard region. X-rays and γ-rays can also be employed for this purpose. Radial profiles of local time-team voidage show significantly higher values in the core of the column than near the outer wall. A correlation (Wang and Wei, 1997) that accounts for this variation is

$$\varepsilon = 1 - \left(1 - \langle\varepsilon\rangle_A\right)\left\{0.908 + 0.276\left(r/R\right)^4\right\} \tag{17.46}$$

Data on axial and radial voidage variations are summarized by Bi et al. (2000).

The local flow structure within turbulent fluidized beds is complex, as demonstrated by a number of different characterization techniques including spectral analysis, chaos analysis, and wavelet analysis. Whichever of these techniques is used, the character of the profiles for the turbulent regime tends to be quite distinctive (Bai et al., 1999). For cases where the turbulent regime is preceded by slug flow (usually restricted to group B or D solids), there is local intermittency between periods of slug-flow-like behavior and fast-fluidization-like structures. However, when turbulent fluidization is preceded by bubbling (generally encountered with group A solids), the structure is more homogeneous.

Given the relative homogeneity of turbulent fluidized beds and the transient nature of voids, internal baffles are generally not required. When vertical or horizontal heat-transfer tubes are present, they tend to influence the hydrodynamics less than for the bubbling bed flow regime.

17.1.6.2 Gas and Solids Mixing

Since mixing within the turbulent flow regime occurs by much smaller and more random steps than in bubbling fluidized beds, it is more appropriate to apply models based on the analogy with molecular diffusion. The axial dispersion coefficient for the gas, $D_{g,ax}$, has been correlated (Bi et al., 2000), based on data from a number of studies, by

$$Pe_{g,ax} = \frac{UH}{D_{g,ax}} = 3.47 Ar^{0.149} Re^{0.0234} Sc^{-0.231} \left(\frac{H}{D}\right)^{0.285} \tag{17.47}$$

There are relatively few data available with respect to radial gas mixing in the turbulent flow regime. The results, which are available, indicate that radial mixing is again about an order of magnitude smaller than axial mixing. Hence, one can take $D_{g,r} \approx 0.1 D_{g,ax}$ as a first approximation.

Solids mixing in turbulent beds have received only limited attention. Recommended correlations are

1. For group A particles (Lee et al., 1991):

$$D_{s,ax} = 0.365 Re_D^{-0.368} \left[g(U - U_{mf}) D^4 \right]^{1/3} \tag{17.48}$$

2. For group B particles (Lee and Kim, 1990):

$$Pe_{s,ax} = \frac{UH}{D_{s,ax}} = 4.22 \times 10^{-3} Ar \tag{17.49}$$

One may again assume that radial or lateral mixing coefficients are an order of magnitude less than for the corresponding axial dispersion. Overall, solids mixing is generally large enough that temperature gradients are small within turbulent fluidized beds, similar to bubbling beds.

17.1.6.3 Mass Transfer and Chemical Reaction

Given the broad spectrum of local voidages, rapid disintegration and reforming of voids, and the lack of a coherent two-phase structure in the turbulent flow regime, interphase mass transfer is unlikely to provide a significant resistance when considering chemical reactions in turbulent fluidized beds. Hence, single-phase axially dispersed reactor models can be used (e.g., Foka et al., 1996) to predict the conversion and selectivity of gaseous components. The axial dispersion coefficient for the gas can then be estimated from Equation 17.47. Reaction in the freeboard region may be significant, requiring that it also be estimated. Note also that it may be important to make allowance for the radial variation of void fraction when modeling turbulent fluidized-bed reactors.

The simple axially dispersed plug flow approach has been extended (Thompson et al., 1999, Abba et al., 2003) to consider gradual transitions between the flow regimes rather than assuming regime-specific reactor models with step changes at the regime boundaries. In this approach, probabilistic averaging is performed so that, as U increases, the probability of bubbling falls from nearly unity, whereas the probability of turbulent fluidization increases to nearly unity and then falls, and the probability of fast fluidization is initially 0, but ultimately approaches unity.

17.1.6.4 Entrainment

There are many empirical equations in the technical literature, which purport to predict rates of entrainment. However, these can differ by many orders of magnitude in their predictions (Chew et al., 2015), and none of correlations these can be regarded as reliable. This is likely, at least in part, because none of these correlations take electrostatic charging into account, which can alter entrainment rates, as well as downstream separation and flow in the bed itself as the departure of charged particles leaves behind charges of opposite polarity. A correlation that appears to be somewhat more reliable than others for entrainment above the TDH of particles from turbulent fluidized beds (Tasarin and Geldart, 1998) is

$$K_i^* = 14.5\rho_g U^{2.5} \exp\{-5.4 V_{si}/U\} \tag{17.50}$$

The TDH can be predicted using Figure 17.8 or alternatively from correlations in the literature (Wen and Chen, 1982, Baron et al., 1988).

17.1.7 Fast Fluidization and Dense Suspension Upflow

Fast fluidization is usually encountered with group A and B solids at superficial gas velocities >1.5 m/s. To maintain continuous operation, particles must be continuously fed to the bottom of the vertical shaft to replace those carried over from the top. Whereas lower velocity fluidization flow regimes have a relatively dilute freeboard region to disengage particles ejected at the bed surface, there is no bed surface, and hence no "bed," nor is there any freeboard region, in the fast fluidization flow regime. Instead, particles are conveyed upward, individually and as loose clusters, through the entire column height. Efficient gas–solids separators (usually cyclones, but occasionally inertial separators) are relied upon to capture entrained particles and return them via a standpipe or "downer" (Li et al., 2004) to near the bottom of the main column or riser. The overall configuration, including the riser (where the main gas–solid contacting and chemical reaction[s] take place), the gas–solid separator(s), standpipe, and any nonmechanical or mechanical valves in the recirculation line, constitutes the CFB system. A typical CFB configuration is shown schematically in Figure 17.10b. Note that the H/D ratio is usually $\gg 1$, especially for small-scale systems.

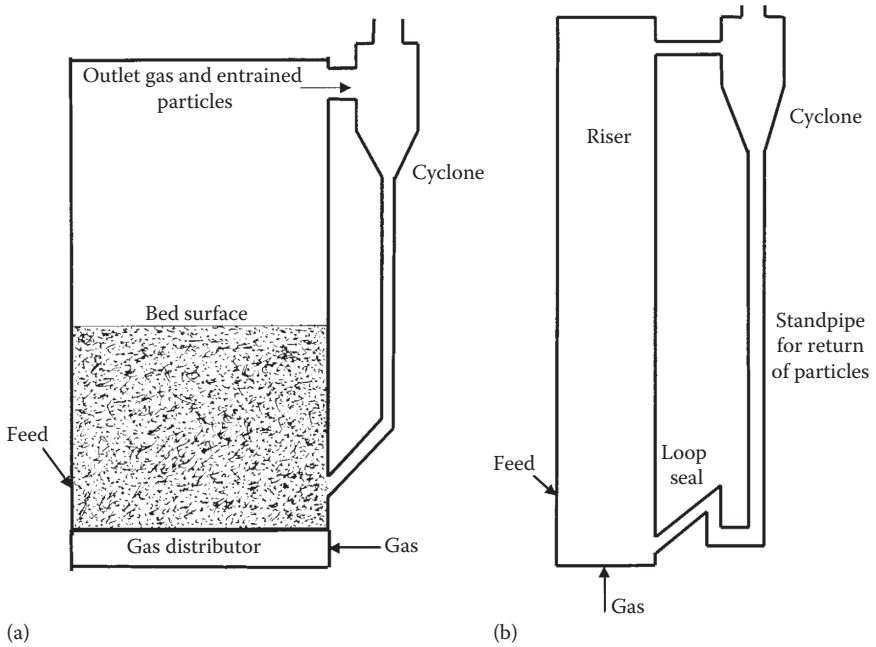


Figure 17.10

Typical equipment configurations of (a) dense (bubbling, slugging, or turbulent) fluidized beds and (b) circulating fluidized beds.

17.1.7.1 Hydrodynamics of the Fast Fluidization Flow Regime

The riser of a CFB system is usually operated in the fast fluidization flow regime. Since, as indicated in Figure 17.10b, the exit at the top of the riser is usually at one side, while the return of solids to the bottom of the riser also involves asymmetric re-entry; flow at the top and bottom of a CFB riser is generally not symmetric about the axis. On the other hand, axisymmetric flow (in risers of circular cross section) or planar symmetry (in risers of rectangular cross section) can commonly be assumed throughout the middle portion of the riser.

To a first approximation, the acceleration and wall friction terms in the momentum equation for flow in CFB risers can be neglected for fast-fluidized beds relative to the gravity terms. It is then possible to derive an approximate profile of axial density from the axial pressure profile since, with $\rho_p \gg \rho_g$,

$$1-\langle\varepsilon\rangle_A \approx -\frac{1}{g\rho_p}\frac{dP}{dz} \tag{17.51}$$

The cross-sectional average voidage within a fast-fluidized bed is generally lowest near the distributor plate, increasing with height, reaching a plateau approximating fully developed conditions at some distance above the bottom, and then varying again toward the top outlet. When the top is constricted (i.e., the area of the exit is less than that of the riser), there tends to be an increase in solids concentration (decrease in voidage) near the exit, whereas a very open or smoothly tapered exit tends to cause an increase in voidage toward the top. The various shapes of axial voidage profile and the influence of various operating variables on them were summarized nicely by Bai et al. (1992). Some typical axial profiles of solids holdup are plotted in Figure 17.11. The main variables, in addition to the exit geometry, are the net solids circulation flux, G_s, and the superficial gas velocity, U. With increasing G_s, U, ρ_p, or d_p, the solids' holdup ($=1 - \langle\varepsilon\rangle_A$) increases, and there is more likely to be an upturn in the axial solids' holdup profile near the top exit. This arises because the top of the column acts as a crude inertial gas–solid separator, in which the particles have more difficulty in negotiating the turn into the exit duct if they are larger, denser, moving more quickly, or present in greater numbers.

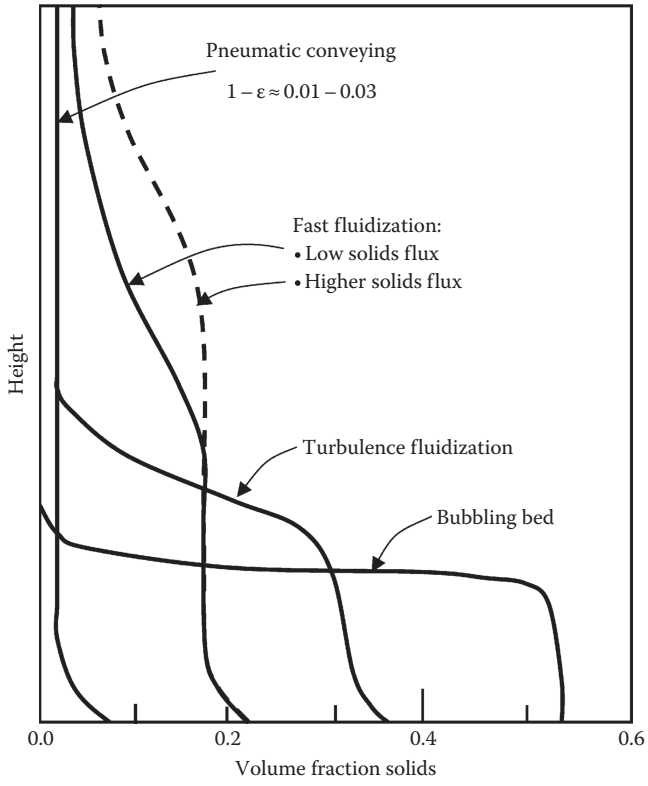


Figure 17.11

Typical solids holdup profiles in bubbling, turbulent, fast fluidization, and dilute pneumatic conveying flow regimes.

Expressions that can be used to estimate the limiting cross-sectional average voidages, ε_d in the lower dense region and ε^* at the top exit, were given by Bai and Kato (1999).

One first calculates the saturation carrying capacity, G_s^{sat}:

$$\frac{G_s^{sat} d_p}{\mu_g} = 0.125 \left(\frac{U}{\sqrt{g d_p}} \right)^{1.85} Ar^{0.63} \left(\frac{\rho_p - \rho_g}{\rho_g} \right)^{-0.44} \tag{17.52}$$

and

$$\varepsilon' = 1 - G_s / \left[\rho_p \left(U - V_s \right) \right] \tag{17.53}$$

For $G_s < G_s^{sat}$ one then calculates

$$\varepsilon_d = 1 - \varepsilon' \left\{ 1 + 6.14 \times 10^{-3} \left(\frac{G_s}{\rho_p U} \right)^{0.23} \left(\frac{\rho_p - \rho_g}{\rho_g} \right)^{1.21} \left(\frac{U}{\sqrt{gD}} \right)^{-0.383} \right\} \tag{17.54}$$

and

$$\varepsilon^* = 1 - 4.04 \left(1 - \varepsilon' \right)^{1.214} \tag{17.55}$$

On the other hand, when $G_s \geq G_s^{sat}$,

$$\varepsilon_d = 1 - \varepsilon' \left\{ 1 + 0.103 \left(\frac{\rho_p U}{G_s} \right)^{1.13} \left(\frac{\rho_p - \rho_g}{\rho_g} \right)^{-0.013} \right\} \tag{17.56}$$

and

$$\varepsilon^* = 1 - \left(1 - \varepsilon' \right) \left\{ 1 + 0.208 \left(\frac{\rho_p U}{G_s} \right)^{0.5} \left(\frac{\rho_p - \rho_g}{\rho_g} \right)^{-0.082} \right\} \tag{17.57}$$

These relationships provide estimates of the voidages in the lower dense region and at the top of the column. Between the bottom region and the top, the voidage varies, asymptotically approaching ε_d when approaching the lower dense zone and ε' as the top exit is approached. Hence, these relationships facilitate estimation of the full axial voidage profiles.

The solids' holdup in fast fluidization is much higher toward the outer wall, where there are descending streamers, than in the core of the riser, where there is upward motion of gas and widely dispersed particles. Except near the solids' entry or re-entry ports and asymmetrically located exit ports, the radial profile of time-mean voidage can then be predicted (Issangya et al., 2001) by

$$\varepsilon = \varepsilon_{mf} + \{ \langle \varepsilon \rangle_A - \varepsilon_{mf} \} \langle \varepsilon \rangle_A^{-1.5 + 2.1 (r/R)^{3.1} + 5.0 (r/R)^{8.8}} \tag{17.58}$$

For columns of rectangular or square cross section, the corners are regions of decreased voidage and more prominent solids' downflow (Zhou et al., 1995).

Solids' velocities are upward throughout most of the cross section of the column, but downward velocities are experienced at the wall, with a time-mean value of approximately (Griffith and Louge, 1998)

$$v_{sw} = -36 \sqrt{g d_p} \tag{17.59}$$

The negative sign in this equation indicates that the solids are traveling downward on average at the wall of the riser when the fast fluidization flow regime is present. This downward velocity corresponds to dense streamers or clusters of elongated lens-shapes, descending jerkily along the outer wall of the riser. The thickness of the wall layer subject to net downward flow of solids has been correlated (Kim et al., 2004b), covering a broad range of conditions by

For $U^{\star}_{slip} < 6.5$,

$$\frac{\delta_w}{D^{0.85}(U^2/g)^{0.15}} = 1.73(U^{\star}_{slip})^{0.21}\left\{\frac{U}{\sqrt{gd_p}}\right\}^{-0.97}\left\{\frac{\rho_p[1-\langle\varepsilon\rangle_A]}{\rho_g\langle\varepsilon\rangle_A}\right\}^{0.16} \tag{17.60}$$

For $U^{\star}_{slip} \geq 6.5$,

$$\frac{\delta_w}{D^{0.85}(U^2/g)^{0.15}} = 0.53(U^{\star}_{slip})^{-0.32}\left\{\frac{G_s}{\rho_p[1-\langle\varepsilon\rangle_A U]}\right\}^{-0.55}\left\{\frac{\rho_p[1-\langle\varepsilon\rangle_A]}{\rho_g\langle\varepsilon\rangle_A}\right\}^{-0.70} \tag{17.61}$$

where

$$U^{\star}_{slip} = \left\{\frac{\rho_g{}^2}{g\mu(\rho_p-\rho_g)}\right\}^{1/3}\left[U - \frac{G_s\langle\varepsilon\rangle_A}{\rho_p[1-\langle\varepsilon\rangle_A]}\right] \tag{17.62}$$

The time-mean particle velocity is upward everywhere, except for this outer wall layer, reaching a maximum at the axis of the column. Radial profiles of solids flux are similar to those of time-mean local particle velocity, positive (upward) and at a maximum at the axis of the column, and negative (downward) at the outer wall. Gas velocity profiles are difficult to measure, but follow similar trends. However, the gas motion is upward relative to the particles.

In some CFB processes such as combustion of solid fuels, secondary gas is fed from the sides of the column through nozzles or orifices at some height well above the principal gas distributor. The resulting gas jets tend to disrupt the downward-moving wall layers. Moreover, the region of lower gas velocity below the secondary nozzles tends to be denser and somewhat isolated from the region above the secondary nozzles. If these secondary jets are introduced tangentially, the resulting swirl tends to cause an increase in solids' holdup near the outer wall due to centrifugal forces.

17.1.7.2 Dense Suspension Upflow

Downward flow of particles in streamers and clusters at the wall, a major feature of the fast fluidization flow regime, no longer occurs when the solids' flux is sufficiently high, typically beyond ~200–300 kg/m^2 s. Instead, the time-mean particle and gas motion is upward throughout the entire cross section, with ~7%–20% or more of the overall cross-sectional area occupied by particles. This flow regime has been called dense suspension upflow or DSU (Grace et al., 1999). It is encountered in fluid catalytic cracking (FCC) and other catalytic processes where there are group A solids combined with high solids throughputs. The transition to the DSU flow regime is covered in Section 17.1.2.7. As noted there, the DSU and fast fluidization flow regimes can coexist, occupying different portions of the same riser.

While there is no net local downflow in the DSU flow regime and the flow is generally more homogeneous, there are still marked radial gradients, with much higher time-average voidages near the axis of the riser than near the wall (Issangya et al., 2000, Liu et al., 2003). The voidage can approach ε_{mf} at the wall. Equation 17.58 can again be used to predict the radial voidage variation as it is based on DSU data, in addition to data from the fast fluidization flow regime. Particle velocities also reach a maximum at the axis of the column, approaching, or even exceeding, 2U. Local solids fluxes are typically 1.5–2.5 G_s at the axis of the column, falling to close to 0 at the wall. Local fluctuations in voidage are strongly correlated with local fluctuations of particle velocity (Liu et al., 2003), so that it is not possible to obtain time-mean solids fluxes from time-mean voidages and particle velocities.

17.1.8 Spouted Beds

Spouted beds provide an alternative to fluidized beds for relatively coarse particles (larger than about 1 mm in diameter). The geometry of a typical spouted bed is shown in Figure 17.12. This generally involves a single

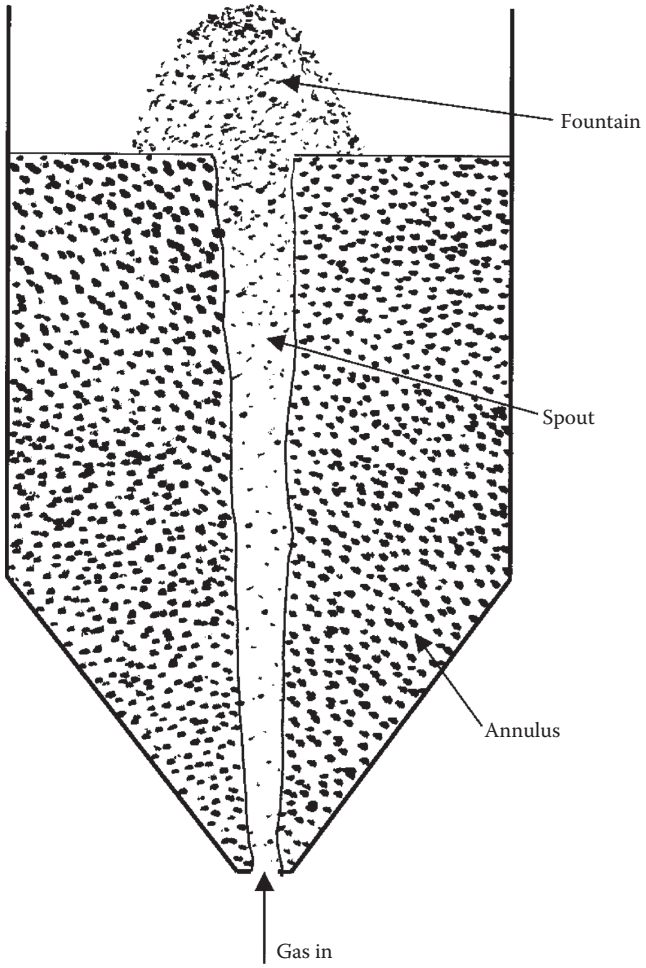


Figure 17.12

Schematic of typical spouted bed.

central orifice at the bottom and a conical section at the base, leading to a vessel of cylindrical cross section at the top. However, there are many variants on this geometry, including flat-bottomed vessels, completely cylindrical and completely conical vessels, columns of rectangular cross section equipped with slot orifices, and reactors equipped with nonporous or porous draught tubes, extending over most of the height of the particles. It is also possible to have multiple orifices (leading to multiple spouts) and a hybrid of spouting and fluidization (called a "spout-fluid bed"). For comprehensive reviews of spouted beds, see Mathur and Epstein (1974) and Epstein and Grace (2011).

A spouted bed is composed of three separate regions: a relatively dilute spout (or jet) region above the orifice extending right up to the bed surface, a surrounding moving-packed-bed annulus region, and a fountain region above the bed surface, where particles travel upward through a certain distance from the top of the spout and then rain back under gravity onto the surface of the annulus. Systematic solids' circulation occurs as particles descend in moving-packed-bed flow through the annulus, are entrained from the spout–annulus interface into the upward jet of gas in the spout where they are accelerated upwards and carried through the top of the spout, and thence return in the fountain to the top surface of the annulus.

Unlike a fluidized bed where all of the particle weight-minus-buoyancy is supported by drag from the fluid, in a spouted bed only part is provided by drag, with the rest of the weight of particles in the annulus borne by particles below. Hence, the pressure drop across a spouted bed is lower, typically by 25%–30%, than in a corresponding fluidized bed. This lower pressure drop results in lower energy costs and therefore constitutes one of the advantages of spouted beds. Other advantages are that the gas and particle motion are more systematic and predictable than in fluidized beds. Disadvantages are that narrower particle size distributions tend to be needed, that scale-up is only possible over a much lower range of column diameters, that particle–particle

contact is more likely to cause agglomeration, and that the range of gas velocities, which can be used, is less broad than for fluidized beds.

Typically, a spouted bed is constrained by certain limits for good operation. In order for a coherent spout to form, the ratio d_{or}/d_p should not exceed about 25, while the ratio D/d_{or} must be greater than ~3 for coarse particles or ~10 for relatively fine materials. The included angle of a conical base should generally be at least 40°.

The minimum spouting velocity is usually predicted by an early correlation proposed by Mathur and Gishler (1955):

$$U_{mS} = \left(\frac{d_p}{D}\right)\left(\frac{d_{or}}{D}\right)^{1/3}\sqrt{\frac{2gH(\rho_p - \rho_g)}{\rho_g}} \tag{17.63}$$

Unlike the minimum fluidization velocity U_{mf} (Equation 17.5), U_{mS} depends on the bed depth, H, and on the equipment used (via the orifice diameter, d_{or}). For relatively large columns where $D > 0.5$ m, the right-hand side of Equation 17.63 should be multiplied by $2D$ (with D in meters) to compensate empirically for systematic underestimation by the original correlation.

The maximum spoutable bed depth, beyond which it is not possible to obtain spouting, can be predicted from the correlation

$$H_m = \frac{D^2}{d_p}\left(\frac{D}{d_{or}}\right)^{2/3}\frac{568b^2}{Ar}\times\left\{\sqrt{1+35.9\times10^{-6}Ar}-1\right\}^2 \tag{17.64}$$

where the empirical constant b can be taken as 1.11 for room temperature conditions and 0.9 for elevated temperatures. It can be shown by differentiation that H_m reaches a maximum at $Ar = 223{,}000$, corresponding typically to $d_p \approx 1$–1.5 mm.

Once spouting has been achieved, the pressure drop across the bed, ΔP_S, is approximately 65%–70% of that across a fluidized bed of the same particles of the same depth, and the axial pressure distribution can be approximated (Lefroy and Davidson, 1969) by

$$\frac{dP}{dz} = \frac{-\Delta P_S}{2H}\pi\sin\left(\frac{\pi z}{2H}\right) \tag{17.65}$$

The flow of gas through the dense annulus at height z can be estimated by a result derived by Mamuro and Hattori (1968):

$$\frac{U_a}{U_{mf}} = 1-\left(1-\frac{z}{H_m}\right)^3 \tag{17.66}$$

This relationship works well, even when $H < H_m$ and for a wide range of particle sizes. The fraction of the total flow that passes through the annulus at any height, z, is then given by $(U_a/U)[1\ 2\ (d_S/D)^2]$, where d_S is the spout diameter, which in turn can be estimated from an empirical dimensional correlation proposed by McNab (1972):

$$d_S = 2.0\left(\rho_g U\right)^{0.49} D^{0.68}\rho_b^{-0.41} \tag{17.67}$$

where ρ_b is the bulk density of the particulate material. In practice, the spout diameter varies with height, with the shape varying, for example, diverging continuously or necking. This equation should therefore be regarded as predicting a longitudinal average spout diameter.

The voidage in the annulus can be approximated as being uniform and equal to the packed-bed value, which for the relatively coarse particles of interest is also nearly equal to ε_{mf}, the voidage at minimum fluidization, with a typical value of 0.41–0.43. The voidage in the spout starts out at 1 at $z = 0$ and then decreases approximately linearly with increasing height, z. The depth of the annulus under operating conditions is

generally very nearly the same as the depth of the same bed of particles without any flow through it. The fountain height can be estimated (Grace and Mathur, 1978) from the semiempirical equation:

$$H_f = \frac{\rho_p \left(\varepsilon_{SH}^{0.93} v_{oSH}\right)^2}{2g(\rho_p - \rho_g)} \tag{17.68}$$

where ε_{SH} is the voidage in the spout at the bed surface, that is, at $z = H$ and v_{oSH} is the particle velocity in the spout on the column axis at the same level. Several models are available for predicting the latter two quantities, and the particle circuit times and trajectories (Mathur and Epstein, 1974, Epstein and Grace, 2011).

When spouted beds are employed as chemical reactors, they have better gas–solid contact in the annulus than in the spout. Hence, two-region models are required to predict gas conversions, with a molar balance at the bed surface to estimate the overall composition of the gas at that level. This approach is analogous to the two-phase models for fluidized-bed reactors discussed in Section 17.1.4.4. Allowance may also be made for additional gas–solid contact in the fountain region. When the particles are reacting (e.g., in spouted-bed combustion or gasification of solid fuels), mole balances for the gas must be coupled with those for the solid phase. The particles can usually be assumed to be perfectly mixed.

Spout-fluid beds are intermediate between spouted beds and fluidized beds. These units, in addition to the spouting gas (or liquid) introduced through a central orifice, a fraction of the total fluid is also introduced around the outer periphery at the bottom, for example, distributed over a lower conical surface. This generally helps to avoid particle agglomeration, improves the distribution of gas between the annulus and spout regions, increases the solids circulation rate, and reduces temperature gradients in the annulus. Various flow regimes exist, depending on geometry, total flow rate, and whether or not the auxiliary gas injected at the bottom is sufficient to fluidize the particles.

17.1.9 Three-Phase Fluidization

Gas–liquid–solid fluidization is practiced in some biochemical reactors and in certain chemical processes where solid particles need to be contacted with both liquid and gas, for example, in hydrotreating of liquid hydrocarbons by gaseous hydrogen in the presence of solid catalyst particles. A thorough review of three-phase fluidized beds (covering their fundamentals as well as their applications) was published by Fan (1989). Many contacting modes and geometries are possible. This brief section only deals with cases where the gas and liquid are both introduced at the bottom and travel cocurrently upward in a cylindrical column without any draught tube or other internal surfaces.

There is considerable extra complexity due to having three distinct phases (gas, liquid, and solid) interacting with each other. Some of the simpler results are presented here. First, the sum of the holdups of the individual phases must be unity, that is,

$$\varepsilon_s + \varepsilon_l + \varepsilon_g = 1 \tag{17.69}$$

Since wall friction and acceleration effects are usually negligible, the hydrostatic pressure gradient in the bed can be written as

$$\frac{dP}{dz} = -\left\{\rho_p \varepsilon_s + \rho_l \varepsilon_l + \rho_g \varepsilon_g\right\} g \tag{17.70}$$

The gas contribution ($\rho_g \varepsilon_g$) term in the brackets can usually be ignored relative to the other terms on the right-hand side. If the pressure gradient is measured experimentally, then a third equation is needed to solve for the three unknown holdups. Frequently, this is obtained as a fair approximation by assuming that all of the particles stay in the bed and that the solids holdup is independent of height, that is,

$$M_p = \rho_p \varepsilon_s AH \tag{17.71}$$

where

M_p is the mass of particles present
H is the expanded bed height

The minimum fluidization condition depends on the flow of both gas and liquid. If the gas flow is fixed at some low value, the liquid minimum fluidization velocity, U_{lmf}, can be predicted by a gas-perturbed liquid model (Zhang et al., 1995), in which the primary role of the gas is assumed to be the occupation of space, causing an increase in the velocity of liquid due to the smaller area available for liquid flow. The best agreement is provided (Lee et al., 2003) when the buoyancy is based on the gas–liquid mixture (rather than the liquid alone) and when allowance is made for a decrease in voidage, observed experimentally, when gas is added to a bed of particles through which liquid is percolating. The resulting equation, analogous to Equation 17.5 for two-phase systems, is

$$Re_{lmf} = \frac{\rho_l d_p U_{lmf}}{\mu_l} = \sqrt{C_1^2 + C_2 Ar'(1-\alpha_{mf})^3} - C_1 \tag{17.72}$$

where

$$Ar' = \frac{\rho_l(\rho_p - [\rho_g \alpha_{mf} + \rho_l(1-\alpha_{mf})]g d_p^3)}{\mu_l^2} \tag{17.73}$$

and α_{mf} is the gas holdup expressed on a solids-free basis at minimum fluidization, which can be predicted from the empirical correlation of Yang et al. (1993):

$$\alpha_{mf} = \frac{0.16 U_g}{\varepsilon_{mf}(U_g + U_l)} \tag{17.74}$$

The observed variation in voidage at minimum fluidization due to gas addition is accounted for by the empirical equation

$$\varepsilon_{mf} = \varepsilon_{mf|U_g=0}\left\{1 - 0.34(1 - U_{lmf}/U''_{lmf}) + 0.22(1 - U_{lmf}/U''_{lmf})^2\right\} \tag{17.75}$$

where U_{lmf} and U''_{lmf} are the liquid superficial velocities at minimum fluidization for three-phase (gas–liquid–solid) and two-phase (liquid–solid) fluidization, respectively. Equations 17.72 through 17.75 are solved simultaneously to yield values of the three unknowns: α_{mf}, ε_{mf}, and U_{lmf}. The Wen and Yu (1966) values of the constants, that is, $C_1 = 33.7$ and $C_2 = 0.0408$, are recommended, as in Section 17.1.2.1. Experimental values of the voidage at minimum fluidization without any gas present are recommended whenever they are available; otherwise, one can employ the correlation of Limas-Ballesteros (1980):

$$\varepsilon_{mf/U_g=0} = \frac{0.42}{\psi^{0.376}} \tag{17.76}$$

where Ψ is the particle sphericity. A similar approach can be used to predict minimum fluidization velocities of inverse fluidization (where the particle density is less than the liquid density) and three-phase systems where the liquid flow is far less than that required to fluidize the solids (Zhang et al., 1998).

When three-phase fluidization has been achieved, it is difficult to obtain accurate predictions of behavior, due to factors such as different flow regimes, the wide range of possible properties and operating conditions, and the role of wettability and surfactants. In practical systems, the liquid phase may be non-Newtonian in nature, further complicating the predictions. Fan (1989) provides a useful summary of the empirical and semiempirical methods available to predict properties such as solids, gas, and liquid holdups, solids holdup in the freeboard region, and bed expansion.

The most successful models for predicting three-phase bed hydrodynamics are heavily based on bubbles and their wakes. Small bubbles are spherical or nearly so. With increasing size, they become ellipsoidal and wobbly, ultimately undergoing a transition to spherical-cap bubbles, whose wakes approximately complete the spheres of which the bubbles form the tops. These wakes (Fan and Tsuchiya, 1990), carried at the back of rising bubbles, are responsible for a number of key behavioral aspects of three-phase systems:

1. They transport liquid and solids rapidly in an upward direction, accounting for much of the rapid axial mixing and transport of both liquid and solids.

2. The rapid transport of liquid in the wake can explain a surprising feature of some three-phase systems, where the introduction of gas bubbles into a liquid–solid system actually causes a decrease in bed expansion. Several criteria are available (Fan, 1989) for when bed contraction, rather than expansion, occurs upon the addition of gas.
3. When the bubbles reach the bed surface, their wakes transport solid particles right into the freeboard region, often leading to significant carryover.

17.1.10 Practical Considerations for Gas–Solid Systems

Important aspects of particle and gas properties are covered in Table 17.1. This section briefly considers some of the important aspects of equipment design and operation. More design tips and details are provided in major texts and information sources on fluidization (Zenz and Othmer, 1960, Hetsroni, 1982, Davidson et al., 1985, Geldart, 1986, Pell, 1990, Kunii and Levenspiel, 1991, Grace et al., 1997, Yang, 2003).

The most important design variable for fluidized beds is the gas distributor (see Figure 17.10a). This should (1) provide a pressure drop across it of approximately 30%, and definitely not less than 10%, of that across the fluidized solids above it; (2) distribute the gas uniformly over the cross section above it, typically requiring that the gas entry points should not be more than 100 mm apart; (3) damp out pressure fluctuations from the blower or compressor; (4) not cause "sand blasting" (erosion) of surfaces or excessive attrition, typically meaning that entry velocity of the gas should not exceed 30–50 m/s and the jet should not impinge directly on fixed surfaces such as vessel walls or heat-transfer tubes; (5) support the dead weight of the bed when the gas is shut off; (6) not cause weeping or dumping of solids into the windbox below (due to pressure fluctuations); and (7) not become blocked by particles or deposits. Many geometries are used in practice including nozzles, tuyeres, downward-facing orifices, and shrouded orifices.

Jet penetration into a zone that does not contain bubbles can be predicted by correlations due to Merry (1971, 1975).

Vertical jets:

$$L_j = 5.2 d_{or} \left(\frac{\rho_g d_{or}}{\rho_p d_p} \right)^{0.3} \left\{ 1.3 \left(\frac{u_{or}^2}{g d_{or}} \right)^{0.2} - 1 \right\} \tag{17.77}$$

Horizontal jets:

$$L_j = d_{or} \left\{ 5.25 \left(\frac{\rho_g u_{or}^2}{(1-\varepsilon_{mf})\rho_p g d_p} \right)^{0.4} \left(\frac{\rho_g d_p}{\rho_p d_{or}} \right)^{0.2} - 4.5 \right\} \tag{17.78}$$

Jet penetration is reduced if the region into which the jet penetrates contains bubbles. In some cases, gas may be introduced in a downward direction, or obliquely downward. Penetration is then considerably reduced, but at the expense of higher particle attrition. It is especially important to assure excellent dispersion and mixing in cases where liquid must be sprayed into the bed or where the particles are wet or sticky. In such cases, high gas velocities coupled with uniform gas distributors and a lack of locations where particles can sit without being immediately set into motion are important to maintain the continuity of fluidization and to prevent defluidization, hot spots, and fouling.

Attrition of particles in fluidized beds may occur due to impact of particles with fixed surfaces or with other particles (e.g., in jets or in cyclones), due to abrasion wearing away surface roughness, due to rapid heating causing thermal stresses, or due to some combination of these factors. Standard tests are available to test the friability of particulate materials. Particle growth may occur as a result of elutriation of fines from the vessel, agglomeration (e.g., due to sintering), deposition, or chemical reaction.

Pressure taps and other orifices installed along the walls of the column should be purged, with gas entering at a linear velocity of not less than 0.5 m/s, to prevent particles from entering. Common instrumentation includes pressure transducers (both gauge and differential) and thermocouples. Both mean values

and fluctuations can be employed to warn about local defluidization and to provide indications of the flow regime and hydrodynamic behavior of the bed (e.g., see van Ommen et al., 2011, Issangya et al., 2013).

When heat-transfer surfaces or other fixed surfaces are immersed in fluidized beds, they should be either vertical or horizontal, not inclined, as oblique surfaces cause short-circuiting of gas up the underside. Fixed surfaces should be separated by at least 20 particle diameters (and preferably $50d_p$) to avoid channeling in the gap, causing defluidization of the region and local bypassing, which reduce gas–solids contacting in the neighborhood. Natural frequencies of bubbles in fluidized beds are usually of order 1 Hz. It is important to design tubes and other surfaces with their natural frequencies well outside this range. Convective heat-transfer coefficients between fixed surfaces and fluidized beds are usually of order 300–500 W/m^2 K for bubbling beds of group A materials, and 200–300 W/m^2 K for group B materials or fast-fluidized beds of group A materials.

Scale-up of fluidized beds is often based on experience rather than first principles. Scaling rules summarized by Glicksman et al. (1994) can sometimes be used to provide hydrodynamic scaling based on geometric and dynamic similarity, with matching of key dimensionless groups between the model and full-scale unit. Dimensionless quantities to be matched include *Ar*, a particle Reynolds number, Froude number, density ratio ρ_p/ρ_g, particle sphericity, and dimensionless particle size distribution. For scale-up of difficult chemical processes in fluidized beds, a common approach is to build a series of units of different scale, beginning with a unit of minimum diameter 100–150 mm and progressing through a substantial pilot plant scale unit to the full-scale unit.

Nomenclature

a_b	Bubble interfacial area per unit volume of bubbles, m^{-1}
A	Cross-sectional area of column, m^2
A_c	Area of distributor per orifice, m^2
Ar	Archimedes number defined by Equation 17.6, dimensionless
Ar'	Modified Archimedes number defined by Equation 17.73, dimensionless
b	Empirical constant in Equation 17.64, dimensionless
B	Empirical constant in Equation 17.13, dimensionless
C_1,C_2	Empirical constants in Equation 17.5 and 17.72, dimensionless
C_{Ab}	Concentration of reactant A in bubble phase, mol/m^3
C_{Ad}	Concentration of reactant A in dense phase, mol/m^3
C_D	Drag coefficient, dimensionless
d_{or}	Orifice diameter, m
d_p	Mean particle diameter, m
d_{pi}	Diameter of *i*th particle size fraction, m
d_S	Spout diameter, m
D	Column diameter, m
D_{AB}	Molecular diffusivity of reacting or tracer gas, m^2/s
D_b	Bubble diameter, m
$D_{g,ax}$	Gas axial dispersion coefficient, m^2/s
D_h	Hydraulic diameter of column, m
$D_{s,ax}$	Solids axial dispersion coefficient, m^2/s
f_b	Bubble frequency, s^{-1}
f_w	Bubble wake fraction (= volume of wake/volume of bubble), dimensionless
F_d	Drag force/unit area defined by Equation 17.38, kg/m s^2
F_g	Gravity force per unit area defined by Equation 17.38, kg/m s^2
g	Acceleration due to gravity, m/s^2
G_s	Net solids flux through column, kg/m s^2
G_{so}	Upwards flux of solids at dense bed surface, kg/m s^2
G_{si}	Entrainment flux of solids of fraction *i* above the TDH, kg/m s^2
H	Expanded bed depth, m
H_f	Fountain height above spouted bed, m
H_m	Maximum spoutable bed depth, m
H_{mf}	Bed depth at minimum fluidization, m

k	Empirical constant in Equation 17.19, dimensionless
k_{bd}	Bubble-to-dense-phase interphase mass transfer coefficient, m/s
$k_{bd}^{\star}$	Dimensionless interphase mass transfer coefficient defined by Equation 17.35, dimensionless
k_r	First-order gas-phase reaction rate constant, s^{-1}
$k_r^{\star}$	Dimensionless first-order rate constant defined by Equation 17.35, dimensionless
L_j	Jet penetration distance into the fluidized bed, m
l_s	Slug vertical length, m
m_i	Mass fraction of particles belonging to the ith size fraction, dimensionless
M_p	Total mass of particles in the bed, kg
n	Empirical constant index, dimensionless
N_{or}	Number of orifices in the gas distributor, dimensionless
Nu	Nusselt number, dimensionless
P	Local pressure, Pa
P_c	Inner perimeter of fluidization column, m
$Pe_{g,ax}$	Peclet number for axial gas dispersion defined by Equation 17.47, dimensionless
$Pe_{s,ax}$	Peclet number for axial solids dispersion, dimensionless
Pr	Prandtl number, dimensionless
r	Radial coordinate, m
R	Radius of column, m
Re	Reynolds number based on particle diameter ($=\rho_g d_p U/\mu_g$), dimensionless
Re_c	Reynolds number corresponding to onset of turbulent regime, Equation 17.13, dimensionless
Re_D	Reynolds number based on column diameter ($=\rho_g DU/\mu_g$), dimensionless
Re_{lmf}	Reynolds number defined in Equation 17.72, dimensionless
Re_{mf}	Reynolds number defined in Equation 17.5, dimensionless
Re_{se}	Reynolds number corresponding to U_{se} ($-\rho_g d_p v_T/\mu_g$), dimensionless
Sc	Schmidt number for gas, dimensionless
Sh	Sherwood number, dimensionless
t_{mix}	Characteristic solids mixing or turnover time, s
u_{or}	Gas velocity through orifice into fluidized bed, m/s
U, U_g	Superficial gas velocity, m/s
U_a	Superficial velocity in annulus of spouted bed, m/s
U_b	Bubble rise velocity, m/s
U_c	Superficial gas velocity at onset of turbulent fluidization, m/s
U_{DSU}	Superficial gas velocity at onset of DSU, m/s
U_l	Superficial liquid velocity, m/s
U_{lmf}	Superficial liquid velocity at minimum fluidization, m/s
U''_{lmf}	Superficial liquid velocity at minimum liquid–solid fluidization, m/s
U_{mf}	Superficial gas velocity at minimum fluidization, m/s
U_{ms}	Superficial gas velocity at minimum slugging, m/s
U_{mS}	Superficial gas velocity at minimum spouting, m/s
U_{se}	Superficial gas velocity at significant entrainment, m/s
U_{si}	Velocity of rise of a single isolated slug, Equation 17.42, m/s
$U_{slip}^{\star}$	Dimensionless slip velocity defined in Equation 17.62, dimensionless
v_{oSH}	Velocity of particles on axis of spouted bed at $z = H$, m/s
v_{sw}	Time-mean particle velocity at wall of riser, m/s
v_T	Particle terminal settling velocity, m/s
V_b	Bubble volume, m^3
V_b	Volumetric flow accounted for by displacement of bubbles, m/s
V_s	Terminal settling velocity of particles, m/s
V_s^e	Terminal settling velocity of particles of diameter d_p in the fluid in question, m/s
V_{si}	Terminal settling velocity of particles in the ith size fraction, m/s
Y	Coefficient modifying two-phase theory of fluidization, Equation 17.22, dimensionless
z	Vertical height coordinate measured from gas distributor, m
z'	Vertical height coordinate measured from surface of dense bed, m

Greek Letters

α_i	Decay constant in Equation 17.40 for entrainment in TDH, m^{-1}
α_{mf}	Gas holdup/(gas + liquid holdup) at minimum fluidization, dimensionless
β	Dimensionless gas velocity for slug flow defined by Equation 17.42, dimensionless
ΔP	Pressure drop, Pa
ΔP_{bed}	Pressure drop across dense fluidized bed, Pa
ΔP_{fixbed}	Pressure drop across fixed bed, Pa
ΔP_{mf}	Pressure drop across fluidized bed at minimum fluidization, Pa
ΔP_S	Pressure drop across spouted bed, Pa
ε	Local time-mean voidage
ε'	Voidage defined by Equation 17.53, dimensionless
ε^*	Voidage at top exit of riser, Equations 17.55 and 17.57, dimensionless
$\langle\varepsilon\rangle_A$	Voidage averaged over cross-sectional area, dimensionless
$\langle\varepsilon\rangle_{av}$	Voidage averaged over entire bed
ε_b	Fraction of bed volume occupied by bubbles, dimensionless
ε_d	Voidage in dense phase region at bottom of riser, dimensionless
ε_g	Gas holdup = fraction of bed volume occupied by gas, dimensionless
ε_l	Liquid holdup = fraction of bed volume occupied by liquid, dimensionless
ε_{mf}	Bed voidage at minimum fluidization, dimensionless
ε_s	Solid holdup = fraction of bed volume occupied by particles, dimensionless
ε_{SH}	Spout voidage at top of spout (i.e., at $z = H$), dimensionless
η	Constant index in Equation 17.13, dimensionless
μ_g	Gas viscosity, kg/m s
μ_l	Liquid viscosity, kg/m s
ρ_b	Bulk density of particulate material, kg/m^3
ρ_g	Gas density, kg/m^3
ρ_l	Liquid density, kg/m^3
ρ_p	Particle density, kg/m^3
φ_b	Fraction of bed volume occupied by particles associated with bubble phase, dimensionless
φ_d	Fraction of bed volume occupied by particles associated with dense phase, dimensionless
χ	Mass fraction of particles, which are finer than 45 μm, dimensionless
Ψ	Particle sphericity, dimensionless

Abbreviations

ATP	Atmospheric-topped bitumen
BGPG	Biomass gasification and power generation
CFB	Circulating fluidized bed
CFBC	Circulating fluidized bed combustor
DSU	Dense suspension upflow
FCC	Fluid catalytic cracking or fluid cracking catalyst
FFB	Fixed fluidized bed
GIEC	Guangzhou Institute of Energy Conversion
GLSFB	Gas–liquid–solid fluidized beds
GLSCFB	Gas–liquid–solid circulating fluidized beds
LSCFB	Liquid–solid circulating fluidized beds
LSFB	Liquid–solid fluidized beds
PCFBC	Pressurized circulating fluidized-bed combustor
PFBC	Pressurized fluidized-bed combustor
QC	Quick contact
RFCC	Residue fluid catalytic cracking
RTD	Residence time distribution
SFB	Stationary fluidized-bed
SFB	Stationary fluidized bed combustor
SINOPEC	Chinese National (Sino) Petroleum Enterprises Corporation

TDH	Transport disengagement height
TCC	Thermofor catalytic cracking
UOP	Universal Oil Products Company
VTP	Vacuum-topped bitumen

Subscripts

AB	Boundary between group A and B solids
BD	Boundary between group B and D solids
b	Bubble
d	Dense phase
g	Gas
l	Liquid
p	Particle
s	Solid particles, slug
S	Spout, spouted bed

References

Abba, I.A., Grace, J.R., Bi, H.T., and Thompson, M.L., Spanning the flow regimes: Generic fluidized-bed reactor model, *AIChE J.*, 49, 1838, 2003.

Abrahamsen, A.R. and Geldart, D., Behaviour of gas fluidized beds of fine powders, *Powder Technol.*, 26, 35, 1980.

Aerov, M.E. and Todes, O.M., *Hydraulic and Thermal Fundamentals on the Operation of Apparatus with Static and Fluidised Particle Bed*, Chimia, Leningrad (in Russian), 1968.

Agarwal, P.K. and La Nauze, R.D., Transfer processes local to the coal particle: A review of drying, devolatilization and mass transfer in fluidized bed combustion, *Chem. Eng. Res. Des.*, 67, 457–480, 1989.

Agarwal, P.K., Mitchell, W.J., La Nauze, R.D., Transport phenomena in multi-particle systems—III. Active particle mass transfer in fluidized beds of inert particles, *Chem. Eng. Sci.*, 43, 2511, 1988.

Aguado, R., Olazar, M., San José, M.J., Gaisán, B., and Bilbao, J., Kinetic study of polyolefin pyrolysis in a conical spouted bed reactor, *Ind. Eng. Chem. Res.*, 41, 4559, 2002.

Andeen, B.R. and Glicksman, L.R., Heat transfer to horizontal tubes in shallow fluidized beds, *ASME-AIChE Heat Transfer Conference*, St Louis, MO, 76-HT-67, 1976.

Andersson, B.-Å. and Leckner, B., Experimental methods of estimating heat transfer in circulating fluidized bed boilers, *Int. J. Heat Mass Transfer*, 35, 3553, 1992.

Andersson, B.-Å. and Leckner, B., Bed-to-wall heat transfer in a 10 m^2 bubbling fluidized bed, in Macías Machín, A. and Winter, G. (Eds.), *Proceedings of Congreso Europeo de Fluidisación*, Universidad de Las Palmas de Gran Canaria, Vol. 1, 1994, pp. 251–260.

Asadullah, M., Ito, S., Kunimori, K., and Tomishige, K., Role of catalyst and its fluidization in the catalytic gasification of biomass to syngas at low temperature, *Ind. Eng. Chem. Res.*, 41, 4567, 2002a.

Asadullah, M., Ito, S.I., Kunimori, K., Yamada, M., and Tomishige, K., Energy efficient production of hydrogen and syngas from biomass: Development of low-temperature catalytic process for cellulose gasification, *Environ. Sci. Technol.*, 36, 4476, 2002b.

Avedesian, M.M. and Davidson, J.F., Combustion of carbon particles in a fluidized bed, *Trans. Inst. Chem. Eng.*, 51, 121–131, 1973.

Avidan, A.A., Fluid catalytic cracking, in Grace, J.R., Avidan, A.A., and Knowlton, T.M. (Eds.), *Circulating Fluidized Beds*, Blackie Academic & Professional, New York, 1997, p. 466, chap. 13.

Avidan, A.A., Edwards, M., and Owen, H., Fluid catalytic cracking. Past and future challenges, *Rev. Chem. Eng.*, 6, 1, 1990.

Avidan, A.A. and Shinnar, R., Development of catalytic cracking technology. A lesson in chemical reactor design, *Ind. Eng. Chem. Res.*, 29, 931, 1990.

Baeyens, J. and Geldart, D., Particle mixing in a gas fluidized bed, in *Fluidization and Its Applications*, Society Chim. Ind., Toulouse, France, 1973, p. 182.

Bai, D., Issangya, A.S., and Grace, J.R., Characteristics of gas fluidized beds in different flow regimes, *Ind. Eng. Chem. Res.*, 38, 260, 1999.
Bai, D., Jin, Y., Yu, Z.-Q., and Zhu, J.X., The axial distribution of the cross-sectionally averaged voidage in fast fluidized beds, *Powder Technol.*, 71, 51, 1992.
Bai, D. and Kato, K., Quantitative estimation of solids holdups at dense and dilute regions of the circulating fluidized bed, *Powder Technol.*, 101, 183, 1999.
Baron, T., Briens, C.L., and Bergougnou, M.A., Study of the transport disengaging height, *Can. J. Chem. Eng.*, 66, 749, 1988.
Baskakov, A.P., The mechanism of heat transfer between a fluidized bed and a surface, *Int. Chem. Eng.*, 4, 320–324, 1964.
Baskakov, A.P., Radiative heat transfer in fluidized beds, in Davidson, J.F. (Ed.), *Fluidization*, Academic Press, London, U.K., 1985, chap. 13B.
Baskakov, A.P., Berg, B.V., Vitt, O.K., Filippovsky, N.F., Kirakosyan, V.A., Goldobin, J.M., and Maskaev, V.K., Heat transfer to objects immersed in fluidized beds, *Powder Technol.*, 8, 273–282, 1973.
Baskakov, A.P. and Filippovsky, N.F, Transfer of heat in fluidized bed, in Einstein, V.G. and Baskakov, A.P. (Eds.), *Fluidization*, Chimia, Moscow, Russia, 1991, chap. 6 (in Russian).
Baskakov, A.P., Filippovsky, N.F., Munts, V.A., and Ashikhmin, A.A., Temperature of particles heated in a fluidized bed of inert material, *J. Eng. Phys.*, 52, 574–578, 1987.
Baskakov, A.P. and Leckner, B., Radiative transfer in CFB furnaces, *Powder Technol.*, 90, 213–218, 1997.
Bassi, A.S., Briens, C.L., and Bergougnou, M.A., Short contact time fluidized reactors (SCTFRs), in Avidan, A.A. (Ed.), *Circulating Fluidized Bed Technology IV*, AIChE, New York, 1994, p. 15.
Basu, P., Heat transfer in fast fluidized beds, *Chem. Eng. Sci.*, 45, 3123–3136, 1990.
Basu, P., Combustion of coal in circulating fluidized-bed boilers: A review, *Chem. Eng. Sci.*, 54, 5547, 1999.
Basu, P. and Nag, P.K., Heat transfer to walls of a circulating fluidized-bed furnace, *Chem. Eng. Sci.*, 51, 1–26, 1996.
Bi, H.T., Ellis, N., Abba, I.A., and Grace, J.R., A state-of-the-art review of gas–solid turbulent fluidization, *Chem. Eng. Sci.*, 55, 4789, 2000.
Bi, H.T., Grace, J.R., and Zhu, J., Regime transitions affecting gas–solids suspensions and fluidized beds, *Trans. Inst. Chem. Eng.*, 73, 154, 1995.
Borodulya, V.A. and Kovensky, V.I., Radiative heat transfer between a fluidized-bed and a surface, *Int. J. Heat Mass Transfer*, 26, 277–289, 1983.
Borodulya, V.A., Teplitsky, Yu.S., Markevich, I.I., Hassan, A.F., and Yeryomenko, T.P., Heat transfer between a surface and a fluidized bed: Consideration of pressure and temperature effects, *Int. J. Heat Mass Transf.*, 34, 47–53, 1991.
Botterill, J.S.M., *Fluid-Bed Heat Transfer*, Academic Press, London, U.K., 1975.
Breitholtz, C. and Leckner, B., Heat transfer in CFB boilers—Do we know sufficiently, *Trends Heat Mass Momentum Transfer*, 3, 85–104, 1997.
Breitholtz, C., Leckner, B., and Baskakov, A.P., Wall heat transfer in CFB boilers, *Powder Technol.*, 120, 14–48, 2001.
Brereton, C.M.H. and Grace, J.R., Microstructural aspects of the behaviour of circulating fluidized bed, *Chem. Eng. Sci.*, 48, 2565–2572, 1993.
Brewster, M.Q., Effective absorbtivity and emissivity of particulate media with application to a fluidized bed, *J. Heat Transfer.*, 108, 710–713, 1986.
Bridgwater, A.V., Renewable fuels and chemicals by thermal processing of biomass, *Chem. Eng. J.*, 91, 87, 2003.
Bridgwater, A.V. and Peacocke, G.V.C., Fast pyrolysis processes for biomass, *Renew. Sustain. Energy Rev.*, 4, 1, 2000.
Choi, J.-H., Chang, I.-Y., Shun, D.-W., Yi, C.-K., Son, J.-E., and Kim, S.-D., Correlation on the particle entrainment rate in gas fluidized beds, *Ind. Eng. Chem. Res.*, 38, 2491, 1999.
Clift, R., Grace, J.R., and Weber, M.E., *Bubbles, Drops and Particles*, Academic Press, New York, 1978.
Collier, A.P., Hayhurst, A.N., Richardson, J.L., and Scott, S.A., The heat transfer coefficient between a particle and a bed (packed or fluidized) of much larger particles, *Chem. Eng. Sci.*, 59, 4613, 2004.
Darton, R.C., LaNauze, R.D., Davidson, J.F., and Harrison, D., Bubble growth due to coalescence in fluidized beds, *Trans. Inst. Chem. Eng.*, 55, 274, 1977.
Davidson, J.F., Clift, R., and Harrison, D., *Fluidization*, 2nd edn., Academic Press, London, U.K., 1985.

Deiva, V., Grmela, R., and Chaouki, J., Improvement of fluidizability of fine powders, in *Proceedings of the World Congress on Particle Technology*, Sydney, New South Wales, Australia, Paper 671, 2002.
Deng, R.S., Wei, F., Jin, Y., Zhang, Q., and Jin, Y., Experimental study of the deep catalytic cracking process in a downer reactor, *Ind. Eng. Chem, Res*., 41, 6015, 2002a.
Deng, R.S., Wei, F., Jin, Y., Zhang, Q., and Jin, Y., Downer catalytic pyrolysis (DCP): A novel process for light olefins production, *Chem. Eng. Technol*., 25, 711, 2002b.
Dewettinck, K. and Huyghebaert, A., Fluidized bed coating in food technology, *Trends Food Sci. Technol*., 10, 163, 1999.
Douglas, W.J.M. and Churchill, S.W., Recorrelation of data for convective heat transfer between gases and single cylinders with large temperature differences, *Chem. Eng. Prog., Symp. Ser.*, 52(18), 23–28, 1956.
Ellis, N., Bi, H.T., Lim, C.J., and Grace, J.R., Hydrodynamics of turbulent fluidized beds of different diameters, *Powder Technol*., 141, 124, 2004.
Epstein, N., Applications of liquid–solid fluidization, *Int. J. Chem. Reactor Eng.*, 1, 1, 2003a.
Epstein, N., Liquid-solids fluidization, in Yang, W.C. (Ed.) *Handbook of Fluidization and Fluid-Particle Systems*, Marcel Dekker, New York, 2003b, chap. 26.
Epstein, N. and Grace, J.R. (Eds.), *Spouted and Spout-Fluid Beds*, Cambridge University Press, Cambridge, U.K., 2011.
Fan, L.-S., *Gas–Liquid–Solid Fluidization Engineering*, Butterworths, Boston, MA, 1989.
Fan, L.-S. and Tsuchiya, K., *Bubble Wake Dynamics in Liquids and Liquid-Solid Suspensions*, Butterworth-Heinemann, Boston, MA, 1990.
Fang, Z.H., Grace, J.R., and Lim, C.J., Radiative heat transfer in circulating fluidized beds, *J. Heat Transf*., 117, 963–968, 1995a.
Fang, Z.H., Grace, J.R., and Lim, C.J., Local particle convective heat transfer along surfaces in circulating fluidized beds, *Int. J. Heat Mass Transfer*, 38, 1217–1224, 1995b.
Farag, I.H. and Tsai, K.Y., Surface-to-suspension heat transfer model in lean gas–solid freeboard flow, *Can. J. Chem. Eng.*, 71, 514–524, 1993.
Foka, M., Chaouki, J., Guy, C., and Klvana, D., Gas phase hydrodynamics of a gas–solid turbulent fluidized bed reactor, *Chem. Eng. Sci*., 51, 713, 1996.
Gartside, R.J., QC—A new reaction system, in Grace, J.R., Shemilt, L.W., and Bergougnou, M.A. (Eds.), *Fluidization VI*, Engineering Foundation, New York, 1989, p. 25.
Geldart, D., Types of gas fluidization, *Powder Technol*., 7, 285, 1973.
Geldart, D. (Ed.), *Gas Fluidization Technology*, Wiley & Sons, Chichester, U.K., 1986.
Gelperin, N.I. and Einstein, V.G., Heat transfer in fluidized beds, in Davidson, J.F., and Harrison, D. (Eds.), *Fluidization*, Academic Press, London, U.K., 1971, chap. 10.
Gibbs, B.F., Kermasha, S., Alli, I., and Mulligan, C.N., Encapsulation in the food industry: A review, *Int. J. Food Sci. Nutr*., 50, 213, 1999.
Gilliland, E.R. and Mason, E.A., Gas mixing in beds of fluidized solids, *Ind. Eng. Chem*., 44, 218, 1952.
Glicksman, L.R., Heat transfer in circulating fluidized beds, in Grace, J.R., Avidan, A.A., and Knowlton, T.M. (Eds.), *Circulating Fluidized Beds*, Blackie, London, U.K., 1997, pp. 261–311.
Glicksman, L.R., Hyre, M., and Farrell, P., Dynamic similarity in fluidization, *Int. J. Multiphase Flow*, 20S, 331, 1994.
Goedicke, F. and Reh, L., Particle induced heat transfer between walls and gas solid fluidized beds, *AIChE Symp. Ser*., 89, 123–136, 1993.
Grace, J.R., The viscosity of fluidized beds, *Can. J. Chem. Eng.*, 48, 30, 1970.
Grace, J.R., Fluidized bed hydrodynamics, in Hetsroni, G. (Ed.), *Handbook of Multiphase Systems*, Hemisphere Press, Washington, DC, 1982, Sect. 8.1.
Grace, J.R., Contacting modes and behaviour classification of gas–solid and other two-phase suspensions, *Can. J. Chem. Eng.*, 64, 353, 1986a.
Grace, J.R., Fluid beds as chemical reactors, in Geldart, D. (Ed.), *Gas Fluidization Technology*, Wiley & Sons, Chichester, U.K., 1986b, Sect 8.1.
Grace, J.R., Interphase mass and heat transfer in gas-fluidized beds, in deKee, D., and Chhabra, R.P. (Eds.), *Transport Processes in Bubbles, Drops and Particles*, 2nd edn., Taylor & Francis, New York, 2002, chap. 7.
Grace, J.R., Avidan, A.A., and Knowlton, T.M. (Eds.), *Circulating Fluidized Beds*, Blackie Academic & Professional, New York, 1997.

Grace, J.R. and Harrison, D., The distribution of bubbles within a gas-fluidized bed, *Inst. Chem. Eng. Symp. Ser.*, 30, 105, 1968.
Grace, J.R. and Harrison, D., The behaviour of freely bubbling fluidized beds, *Chem. Eng. Sci.*, 24, 497, 1969.
Grace, J.R. and Harrison, D., Fluidized beds with internal baffles, in Davidson, J.F. and Harrison, D. (Ed.), *Fluidization*, Academic Press, London, U.K., 1971, chap. 13.
Grace, J.R., Issangya, A.S., Bai, D., Bi, H.T., and Zhu, J.Z., Situating the high-density circulating fluidized bed, *AIChE J.*, 45, 2108, 1999.
Grace, J.R. and Mathur, K.B., Height and structure of the fountain region above spouted beds, *Can. J. Chem. Eng.*, 56, 533, 1978.
Graham, R.G. and Huffman, D.R., Commercial aspects of rapid thermal processing (RTP), in *Proceedings of the Power Production from Biomass II Conference*, Espoo, Finland, April 1995.
Griffith, A.E. and Louge, M.Y., The scaling of cluster velocity at the wall of circulating fluidized bed risers, *Chem. Eng. Sci.*, 53, 2475, 1998.
Gerwal, N.S., Experimental and theoretical investigation of heat transfer between a gas-solid fluidized bed and immersed tubes, Ph.D. thesis, University of Illionois, Chicago, IL, 1979.
Gross, B. and Ramage, M.P., FCC reactor with a downflow reactor riser, U.S., Patent 4,385,985, 1983.
Hayhurst, A.N., Parmar, M.S., Measurement of the mass transfer coefficient and Sherwood number for carbon spheres burning in a bubbling fluidized bed, *Combust. Flame*, 130, 361, 2002.
Hetsroni, G. (Ed.), *Handbook of Multiphase Systems*, Hemisphere, Washington, DC, 1982.
Highley, J. and Kaye, W.G., Fluidized bed industrial boilers and furnaces, in Howard, J.R. (Ed.), *Fluidized Beds Combustion and Applications*, Applied Science Publishers, London, U.K., 1983.
Horio, M. and Nonaka, A., A generalized bubble diameter correlation for gas–solid fluidized beds, *AIChE J.*, 33, 1865, 1987.
Hottel, H.C. and Sarofim, A.F., *Radiative Transfer*, McGraw-Hill, New York, 1967.
Hovmand, S. and Davidson, J.F., Pilot plant and laboratory scale fluidized reactors at high gas velocities; the relevance of slug flow, in Davidson, J.F. and Harrison, D. (Eds.), *Fluidization*, Academic, London, U.K., 1971, chap. 5.
Howard, J.R. (Ed.), *Fluidized Beds Combustion and Applications*, Applied Science Publishers, London, U.K., 1983.
Huff, G.A. and Vasalos, I.A., Oxidative pyrolysis of natural gas in a spouted bed reactor: Reaction-stoichiometry and experimental reactor design, *Catal. Today*, 46, 39, 1998.
Issangya, A.S., Grace, J.R., Bai, D., and Zhu, J., Further measurements of flow dynamics in a high-density circulating fluidized bed riser, *Powder Technol.*, 111, 104, 2000.
Issangya, A.S., Grace, J.R., Bai, D., and Zhu, J., Radial voidage variation in CFB risers, *Can. J. Chem. Eng.*, 79, 279, 2001.
Jacobs, J.P., The future of fluidized-bed combustion, *Chem. Eng. Sci.*, 54, 5559, 1999.
Jahnig, C.E., Campbell, D.L., and Martin, H.A., History of fluidized solids development at EXXON, in Grace, J.R. and Matsen, J.M. (Eds.), *Fluidization*, Plenum Press, New York, 1980, p. 3.
Jin, Y., Yu, Z., and Cai, P., A criterion for transition from bubbling to turbulent fluidizeation, in Ostergaard, K. and Sorensen, A. (Eds.), *Fluidization V*, Engineering Foundation, New York, 1986, p. 289.
Johnsson, F., Zhang, W., Johnsson, H., and Leckner, B., Optical and momentum probe measurements in a CFB furnace, in Kwauk, M. and Li, J. (Eds.), *Circulating Fluidized Bed Technology V*, Science Press, Beijing, China, 1997, pp. 652–657.
Jono, K., Ichikawa, H., Miyamoto, M., and Fukumori, Y., A review of particulate design for pharmaceutical powders and their production by spouted bed coating, *Powder Technol.*, 113, 269, 2000.
Karamanev, D. and Nikolov, L., Bed expansion of liquid–solid inverse fluidization, *AIChE J.*, 38, 1916, 1992.
Kehoe, P.W.K. and Davidson, J.F., Continuously slugging fluidized beds, *Chemeca'70, Inst. Chem. Eng. Symp. Ser.*, 33, 97, 1971.
Khan, A.R. and Richardson, J.F., Fluid-particle interactions and flow characteristics of fluidised beds and settling suspensions of spherical particles, *Chem. Eng. Comm.*, 78, 111, 1989.
Kim, S.W., Kirbas, G., Bi, H.T., Lim, C.J., and Grace, J.R., Flow behaviour and regime transition in a high-density circulating fluidized bed riser, *Chem. Eng. Sci.*, 59, 3955, 2004a.
Kim, S.W., Kirbas, G., Bi, H.T., Lim, C.J., and Grace, J.R., Flow structure and thickness of annular downflow layer in a circulating fluidized bed riser, *Powder Technol.*, 142, 48, 2004b.

Kunii, D. and Levenspiel, O., *Fluidization Engineering*, 2nd edn., Butterworth-Heinemann, Boston, MA, 1991.
Kwauk, M., *Fluidization: Idealized and Bubbleless, with Applications*, Science Press, Beijing, China; Ellis Horwood, New York, 1992.
Lan, Q., Bassi, A.S., Zhu, J.-X., and Margaritis, A., Continuous protein recovery from whey using liquid–solid circulating fluidized bed ion-exchange extraction, *Biotech. Bioeng.*, 78, 157, 2002.
Latham, R., Hamilton, C., and Potter, O.E., Back-mixing and chemical reaction in fluidized beds, *Br. Chem. Eng.*, 13, 666, 1968.
Leckner, B., Fluidized bed combustion: Mixing and pollutant limitation, *Prog. Energy Comb. Sci.*, 24, 31–61, 1998.
Leckner, B., Andersson, B.-Å., and Vijil, J., Operational results from the 16 MW FBB at Chalmers University, *Third International Fluidised Conference*, The Institute of Energy, London, U.K., 1984, Paper Disc/16/134–143.
Leckner, B., Golriz, M.R., Zhang, W., Andersson, B.-Å., and Johnsson, F., Boundary layers–first measurements in the 12 MW CFB research plant at Chalmers University, in Anthony, E.J. (Ed.), *Proceedings of the 11th International Conference on Fluidized Bed Combustion*, ASME, New York, 1991, pp. 771–776.
Lee, D.H., Epstein, N., and Grace, J.R., The variable-voidage effect on modeling the minimum liquid fluidization velocity of gas-liquid fluidized beds, *J. Chem. Eng. Jpn.*, 36, 1111, 2003.
Lee, G.S. and Kim, S.D., Axial mixing of solids in turbulent fluidized beds, *Chem. Eng. J.*, 44, 1, 1990.
Lee, G.S., Kim, S.D., and Baird, M.H.I., Axial mixing of fine particles in fluidized bed, *Chem. Eng. J.*, 47, 47, 1991.
Lefroy, G.A. and Davidson, J.F., The mechanics of spouted beds, *Trans. Inst. Chem. Eng.*, 47, 120, 1969.
Leva, M., Correlations of the dense phase fluidized state and their applications, *Can. J. Chem. Eng.*, 35, 71, 1957.
Levy, Y. and Dorfman, Y., Two-phase flow in the vicinity of elongated bubbles in a fluidized bed, *AIChE J.*, 41, 1113, 1995.
Li, Z.Q., Wu, C.N., Wei, F., and Jin, Y., Experimental study of high-density gas-solids flow in a new coupled circulating fluidized bed, *Powder Technol.*, 139, 214, 2004.
Liang, W.-G. and Zhu, J.-X., Effect of radial flow nonuniformity on the alkylation reaction in a liquid–solid circulating fluidized bed (LSCFB) reactor, *Ind. Eng. Chem. Res.*, 36, 4651, 1997.
Limas-Ballesteros, R., Thèse de doctorat, Institut National Polytechnique, Toulouse, France, 1980.
Lints, M.C. and Glicksman, L.R., Parameters governing particle-to-wall heat transfer in circulating fluidized beds, in Avidan, A.A. (Ed.), *Circulating Fluidized Bed Technology*, AIChE, New York, 1993, pp. 297–304.
Liu, J., Grace, J.R., and Bi, H.T., A novel multi-functional optical fiber probe: II. High-density CFB measurements, *AIChE J.*, 49, 1421, 2003.
Lockett, M.J. and Harrison, D., The distribution of voidage fraction near bubbles rising in gas-fluidized beds, in Drinkenburg, A.A.H. (Ed.), *Proceedings of International Symposium on Fluidization*, Netherlands University Press, Amsterdam, the Netherlands, 1967, p. 257.
Maadhah, A.G., Abul-Hamayel, M., Aitani, A.M., Ino, T., and Okuhara, T., Down-flow FCC reactor, *Oil Gas J.*, 98, 66, 2000.
Mamuro, T. and Hattori, H., Flow pattern of fluid in spouted beds, *J. Chem. Eng. Jpn.*, 1, 1, 1968.
Martin, H., Heat transfer between gas fluidized beds of solid particles and the surfaces of immersed heat exchanger elements, Part I and Part II, *Chem. Eng. Process.*, 18, 157–169 and 199–223, 1984.
Martin, P.D., On the particulate and delayed bubbling regimes of fluidization, *Trans. Inst. Chem. Eng.*, 61, 318, 1983.
Mathur, K.B. and Epstein, N., *Spouted Beds*, Academic Press, New York, 1974.
Mathur, K.B. and Gishler, P.E., A technique for contacting gases with coarse solid particles, *AIChE J.*, 1, 157, 1955.
May, W.G., Fluidized-bed reactor studies, *Chem. Eng. Prog.*, 55(12), 49, 1959.
McNab, G.S., Predictions of spout diameter, *Br. Chem. Eng. Proc. Tech.*, 17, 532, 1972.
Merry, J.M.D., Penetration of a horizontal gas jet into a fluidized bed, *Trans. Inst. Chem. Eng.*, 49, 189, 1971.
Merry, J.M.D., Penetration of vertical jets into fluidized beds, *AIChE J.*, 21, 507, 1975.
Milne, B.J., Berruti, F., Behie, L.A., and de Bruijn, T.J.W., The hydrodynamics of the internally circulating fluidized bed at high temperature, in Avidan, A.A. (Ed.), *Circulating Fluidized Bed Technology VI*, AIChE, New York, 1994, p. 28.
Modest, M.F., *Radiative Heat Transfer*, 2nd edn., Academic Press, Amsterdam, the Netherlands, 2003.
Molerus, O. and Wirth, K.-E., *Heat Transfer in Fluidized Beds*, Chapman & Hall, London, U.K., 1997.

Murphy, J.R., Evolutionary design changes mark FCC process, *Oil Gas J.*, 90, 49, 1992.
Nag, P.K. and Moral, M.N.A., Effect of probe size on heat-transfer in circulating fluidized beds, *Int. J. Energy Res.*, 14, 965–974, 1990.
Nakhla, G., Zhu, J., and Cui, Y., Liquid-solid circulating fluidized bed waste water treatment system for simultaneous carbon, nitrogen and phosphorus removal, U.S. Patent, applied, February, 2004.
Di Natale, F., Nigro, R., and Scala, F., Heat and mass transfer in fluidized bed combustion and gasification systems, in Scala, F. (Ed.), *Chapter 5 in Fluidized Bed Technologies for Near-Zero Emission Combustion and Gasification*, Woodhead Publishing Series in Energy, 2013.
Overcashier, R.H., Todd, D.B., and Olney, R.B., Some effects of baffles in a fluidized system, *AIChE J.*, 5, 54, 1959.
Palchonok, G., Heat and mass transfer in a fluidized bed, PhD thesis, Chalmers University of Technology, 1998.
Palchonok, G.I., Dolidovich, A.F., Andersson, S., and Leckner, B., Calculation of true heat and mass transfer coefficients between particles and a fluidized bed, *Seventh International Conference on Fluidization*, Engineering Foundation, New York, 1992, pp. 913–920.
Palchonok, G.I. and Tamarin, A.I., Study of heat exchange between a model particle and a fluidized bed, *J. Eng. Phys.*, 45, 427–433, 1983a.
Palchonok, G.I. and Tamarin, A.I., Mass transfer to a moving particle in a fluidized bed of coarse material, *J. Eng. Phys.*, 47, 916–923, 1983b.
Palchonok, G.I., Breitholtz, C., Borodulya, V.A., and Leckner, B., Effect of turbulence on heat and mass transfer in the freeboard region of stationary and circulating fluidized beds, in Fan, L.-S. and Knowlton, T.M. (Eds.), *Fluidization IX*, Engineering Foundation, New York, 1998, pp. 413–420.
Pell, M., *Gas Fluidization*, Elsevier, Amsterdam, the Netherlands, 1990.
Prins, W., Fluidized bed combustion of a single particle, Ph.D. thesis, Twente University, Enschede, the Netherlands, 1987.
Reh, L., Fluidized bed processing, *Chem. Eng. Prog.*, 67, 58, 1971.
Reh, L., The circulating fluid bed reactor—A key to efficient gas/solid processing, in Basu, P. (Ed.), *Circulating Fluidized Bed Technology I*, Pergamon, Toronto, 1986, 105.
Reh, L., Challenges of circulating fluid-bed reactors in energy and raw materials industries, *Chem. Eng. Sci.*, 54, 5359, 1999.
Richardson, J.F. and Zaki, Sedimentation and fluidization, Part I, *Trans. I. Chem. Eng.*, 32, 35, 1954.
Rowe, P.N., A note on the motion of a bubble rising through a fluidized bed, *Chem. Eng. Sci.*, 19, 75, 1964.
Rowe, P.N. and Nienow, A.W., Particle mixing and segregation in gas-fluidized beds, a review, *Powder Technol.*, 15, 141, 1976.
Rowe, P.N. and Partridge, B.A., An x-ray study of bubbles in fluidised beds, *Trans. Inst. Chem. Eng.*, 43, 157, 1965.
Rowe, P.N., Partridge, B.A., Cheney, A.G., Henwood, G.A., and Lyall, E., The mechanism of solids mixing in fluidized beds, *Trans. Inst. Chem. Eng.*, 43, 271, 1965.
Royal Dutch Shell Group of Companies, *The Petroleum Handbook*, 6th edn., Elsevier, Amsterdam, the Netherlands, 1983.
Saxena, S.C., Heat transfer between immersed surfaces and gas-fluidized beds, in *Advances in Heat Transfer*, Vol. 19, 1989.
Scala, F., Mass transfer around freely moving active particles in the dense phase of a gas fluidized bed of inert particles, *Chem. Eng. Sci.*, 62, 4159, 2007.
Scott, S.A., Davidson, J.F., Dennis, J.S., and Hayhurst, A.N., Heat transfer to a single sphere immersed in beds of particles supplied by gas at rates above and below minimum fluidization, *Ind. Eng. Chem. Res.*, 43, 5632, 2004.
Schluender, E.-U. et al. (Eds.), *Heat Exchanger Design Handbook*, VDI-Verlag, Duesseldorf, and Heishere Publishing Corporation, Washington, DC, 1987, Part 2, chapter 2.8.4.
Scott, D.S., Majerski, P., Piskorz, J., and Radlein, D., Second look at fast pyrolysis of biomass—The RTI process, *J. Anal. App. Pyrolysis*, 51, 23, 1999.
Scott, D.S., Plskorz, J., and Radlien, D., Liquid products from the continuous flash pyrolysis of biomass, *Ind. Eng. Chem. Process Des. Dev.*, 24, 581, 1985.
Shingles, T. and McDonald, A.F., Commercial experience with synthol CFB reactors, in Basu, P. and Large, J.F. (Eds.), *Circulating Fluidized Bed Technology II*, Pergamon Press, Oxford, U.K., 1988, p. 43.

Silverman, A., Thompson, A.H., Sterynberg, A., Yukawa, Y., and Shingles, T., Development of a dense phase fluidized bed Fischer-Tropsch Reactor, in Ostergaard, K., and Sorensen, A. (Eds.), *Fluidization V*, Engineering Foundation, New York, 1986, p. 441.

Sit, S.P. and Grace, J.R., Effect of bubble interaction on interphase mass transfer in gas fluidized beds, *Chem. Eng. Sci.*, 36, 327, 1981.

Sondreal, E.A., Benson, S.A., Hurley, J.P., Mann, M.D., Pavlish, J.H., Swanson, M.L., Weber, G.F., and Zygarlicke, C.J., Review of advances in combustion technology and biomass cofiring, *Fuel Process. Technol.*, 71, 7, 2001.

Song, Y.-X., *Applying the Principles Learned from the Nature (Tian-Gong-Kai-Wu)*, Shanghai Chinese Book Bureau, Shanghai, China, 1959.

Squires, A.M., Three bold exploiters of coal gasification: Winkler, godel and porta, in Howard, J.R. (Ed.), *Fluidized Beds Combustion and Applications*, Applied Science Publishers, London, U.K., 1983.

Steward, F.R., Couturier, M.F., and Poolpol, S., Analysis for radiative heat transfer in a circulating fluidized bed, in Heinschel, K.J. (Ed.), *Proceedings of the 13th International Conference on Fluid Bed Combustion*, ASME, New York, 1995, pp. 507–513.

Stewart, P.S.B. and Davidson, J.F., Slug flow in fluidized beds, *Powder Technol.*, 1, 61, 1967.

Sundaresan, R. and Kolar, A.K., Core heat transfer studies in circulating fluidized bed, *Powder Technol.*, 124, 138–151, 2002.

Sutton, D., Kelleher, B., and Ross, J.R.H., Review of literature on catalysts for biomass gasification, *Fuel Process. Technol.*, 72, 155, 2001.

Syncrude, Website of Syncrude, www.syncrude.ca, July 2004.

Talman, J.A., Geier, R., and Reh, L., Development of a downer reactor for fluid catalytic cracking, *Chem. Eng. Sci.*, 54, 2123, 1999.

Tasirin, S.M. and Geldart, D., Entrainment of FCC from fluidized beds, *Powder Technol.*, 95, 240, 1998.

Teunou, E. and Poncelet, D., Batch and continuous fluid bed coating—Review and state of the art, *J. Food Eng.*, 53, 325, 2002.

Thompson, M.L., Bi, H.T., and Grace, J.R., A generalized bubbling/turbulent fluidized-bed reactor model, *Chem. Eng. Sci.*, 54, 2175, 1999.

Tsukada, M. and Horio, M., Maximum heat transfer coefficient for an immersed body in a fluidized bed, *Ind. Eng. Chem. Res.*, 31, 1147–1156, 1992.

van Deemter, J.J., Mixing patterns in large-scale fluidized beds, in Grace, J.R. and Matsen, J.M. (Eds.), *Fluidization*, Plenum, New York, 1980, p. 69.

Varygin, N.N. and Martyushin, I.G., Calculation of the heat transfer surface in fluidized bed equipment, *Khim. Mashinostr.*, 5, 6–9, 1959 (in Russian).

Visser, J., Van der Waals and other cohesive forces affecting powder fluidization, *Powder Technol.*, 58, 1, 1989.

Wakao, N. and Kaguei, S., *Heat and Mass Transfer in Packed Beds*, Gordon and Breach Science Publishers, New York, 1982.

Wang, X.S., Gibbs, B.M., Rhodes, M.J., and Geldart, D., Convection wall-to-suspension heat transfer in circulating fluidized bed risers, *AIChE J.*, 42, 2112–2117, 1996.

Wang, Z. and Wei, F., Similarity of the particle concentration distribution between bubbling and turbulent fluidized beds, in *Proceedings of the Symposium of the Chinese Society,* of *Particle Technology*, Beijing, China, 1997, p. 396.

Wen, C.Y. and Chen, L.H., Fluidized bed freeboard phenomena: Entrainment and elutriation, *AIChE J.*, 28, 117, 1982.

Wen, C.Y. and Yu, Y.H., Generalized method for predicting the minimum fluidization velocity, *AIChE J.*, 12, 610, 1966.

Werdermann, C.C. and Werther, J., Heat transfer in large-scale circulating fluidized bed combustors of different sizes, in Avidan, A.A. (Ed.), *Circulating Fluidized Bed Technology*, AIChE, New York, 1994, pp. 428–435.

Werther, J., The influence of the bed diameter on the hydrodynamics of fluidized beds, *AIChE Symp. Ser.*, 70(141), 53, 1974.

Werther, J. and Hartge, E.-U., Elutriation and entrainment, in Yang, W.-C. (Ed.), *Handbook of Fluidization and Fluid Particle Systems*, Marcel Dekker, New York, 2003, chap. 4.

Wirth, K.-E., Heat transfer in circulating fluidized beds, *Chem. Eng. Sci.*, 50, 2137–2151, 1995.

Winkler, F., German Patent, 437,970, 1922.

Vreedenberg, H.A., Heat transfer between a fluidized bed and a horizontal tube, *Chem. Eng. Sci.*, 9, 52, 1958.

Wu, R.L., Grace, J.R., and Lim, C.J., A model for heat transfer in circulating fluidized bed, *Chem. Eng. Sci.*, 45, 3389–3398, 1990.
Wu, R.L., Grace, J.R., Lim, C.J., and Brereton, C.H.M., Suspension-to-surface heat-transfer in a circulating fluidized bed combustor, *AIChE J.*, 35, 1685–1691, 1991a.
Wu, R.L., Lim, C.J., Grace, J.R., and Brereton, C.H.M., Instantaneous local heat transfer and hydrodynamics in a circulating fluidized bed, *Int. J. Heat Mass Transfer*, 34, 2019–2027, 1991b.
Wu, C.Z., Huang, H., Zheng, S.P., and Yin, X.L., An economic analysis of biomass gasification and power generation in China, *Bioresour. Technol.*, 83, 65, 2002.
Yang, W.-C., *Handbook of Fluidization and Fluid-Particle Systems*, Marcel Dekker, New York, 2003.
Yang, X.L., Wild, G., and Euzen, J.P., Study of liquid retention in fixed-bed reactors with upward flow of gas and liquid, *Int. Chem. Eng.*, 33, 72, 1993.
Yerushalmi, J., Applications of fluidized bed, in Hetsroni, G. (Ed.), *Handbook of Multiphase Systems*, Hemisphere Publishing Co., Washington, DC, 1982, chap. 8.3.
Yin, X.L., Wu, C.Z., Zheng, S.P., and Chen, Y., Design and operation of a CFB gasification and power generation system for rice husk, *Biomass Bioenergy*, 23, 181, 2002.
Yu, Z.-Q., Application collocation, *Adv. Chem. Eng.*, 20, 39, 1994.
Zabrodsky, S.S., *Hydrodynamics and Heat Transfer in Fluidized Beds*, MIT Press, Cambridge, MA, 1966.
Zabrodsky, S.S., Choice of design correlations for the estimation of the heat transfer coefficient in a high-temperature fluidized bed to an immersed body, *BSSR Ser. Fiz. Eng. Nauk.*, 4, pp. 193–107, 1974 (in Russian).
Zenz, F.A. and Othmer, D.F., *Fluidization and Fluid-Particle Systems*, Reinhold Publishing Corporation, New York, 1960.
Zhang, J.-P., Epstein, N., and Grace, J.R., Minimum fluidization velocities for gas–liquid–solid three-phase systems, *Powder Technol.*, 100, 113, 1998.
Zhang, J.-P., Epstein, N., Grace, J.R., and Zhu, J.-X., Minimum liquid fluidization velocity of gas–liquid fluidized beds, *Trans. Inst. Chem. Eng.*, 73, 347, 1995.
Zhukauskas, A.A., *Convective Heat Transfer in Heat Exchangers*, Nauka Publishing House, Moscow, Russia, 1990 (in Russian).
Zhou, Z.Y., Yu, A.B., and Zulli, P., Particle scale study of heat transfer in packed and bubbling fluidized beds, *AIChE J.*, 55, 868, 2009.
Zhu, J.-X., Yu, Z.-Q., Jin, Y., Grace, J.R., and Issangya, A., Cocurrent downflow circulating fluidized bed (downer) reactors—A state of the art review, *Can. J. Chem. Eng.*, 73, 662, 1995.
Zhu, J.-X., Zheng, Y., Karamanev, D.G., and Bassi, A.S., (Gas-)liquid-solid circulating fluidized beds and their potential applications to bioreactor engineering, *Can. J. Chem. Eng.*, 78, 82, 2000.

17.2 Heat and Mass Transfer

Bo Leckner

17.2.1 Bed to Surface Heat Transfer

Heat is transferred across various kinds of surfaces:

1. Bed internal heat transfer: fluidization gas ↔ bed material
2. External heat transfer to surfaces in or above the bed: fluidization gas and bed material ↔ heat-receiving surfaces in contact with the bed material

In this section, external heat transfer in dense or dilute particle suspensions will be discussed. Internal heat transfer will be treated in Section 17.2.2.

Heat transfer in fluidized beds has been summarized in several reviews, such as those of Zabrodsky (1966), Gelperin and Einstein (1971), Botterill (1975), Saxena (1989), Kunii and Levenspiel (1991), Baskakov and Filippovsky (1991), and Molerus and Wirth (1997). Heat transfer, especially in CFB, has been treated in the proceedings of the Conference on CFB. Furthermore, reviews related to CFB have been published by Basu and Nag (1996), Breitholtz and Leckner (1997) and Glicksman (1997).

The heat-transfer coefficient h W/m^2, deg for heat exchange between the bed and a heat-transfer surface of area A (m^2) in contact with the bed is defined by the heat flow expression

$$Q = hA\left(T_\mathrm{b} - T_\mathrm{w}\right) \tag{17.79}$$

where T_b and T_w (°C or K) are the bulk bed and wall temperatures. As an approximation, the radiative (index r) and convective (index c) constituents of heat transfer from gas (gc) and particles (pc) are often assumed to be additive. The heat-transfer coefficient then becomes

$$h = h_r + h_{gc} + h_{pc} \tag{17.80}$$

Sometimes, the gas and particle convective constituents are treated together as $h_c = h_{gc} + h_{pc}$. Data on thermal properties are normally taken at the average of surface and bed temperature.

17.2.1.1 Heat Transfer in the Dense, Bubbling Fluidized Bed

17.2.1.1.1 Correlations Related to Maximum Heat Transfer The bed is fluidized between the minimum fluidization velocity, here expressed in terms of a Reynolds number, Re.

$$Re_{mf} = \frac{Ar}{1400 + 5.22Ar^{1/2}} \tag{17.81}$$

and the terminal velocity of a single particle

$$Re_t = \frac{Ar}{\left(18 + 0.61Ar^{1/2}\right)} \tag{17.82}$$

according to empirical correlations (Aerov and Todes, 1968), incorporating Ergun's correlation (Equation 17.5) for minimum fluidization velocity under the assumption that the voidage is $\varepsilon = 0.4$, where *Ar* is the Archimedes number, a relationship between gravity and drag force representing the particle size, and *Re* is the particle Reynolds number related to the superficial velocity.

Figure 17.13 shows the heat-transfer coefficient in beds consisting of monosized particles of various sizes. The beds are fluidized between minimum fluidization and terminal velocities. The particle convective heat transfer to a surface in the bed increases when the velocity rises from the minimum fluidization velocity and reaches a maximum due to the enhancement of heat transfer following an increase in the movement of the bed. Despite further agitation of the bed caused by the increase in velocity toward the terminal velocity, the particle convective heat-transfer coefficient decreases after the maximum due to a simultaneous increase in voidage. Superimposed on the particle convective heat transfer, there is a contribution from the gas flowing through bubbles and particulate phase in the form of a gas convective heat-transfer constituent. The gas convection heat transfer is very small at low velocities (small particle sizes), but for large particles the particle convective heat transfer is small and the gas convective heat transfer is high. The gas convection is often disregarded for small particles (less than a millimeter), but must be considered for large particles (larger than a millimeter).

Figure 17.13 is designed on the basis of a model of Martin (1984). Heat transfer takes place between minimum fluidization velocity, given by Equation 17.81, and terminal velocity given by Equation 17.82. Furthermore, the

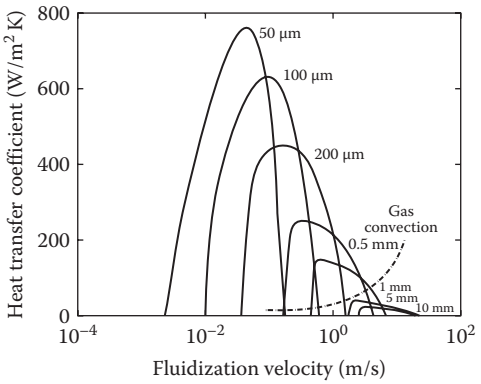


Figure 17.13

Schematic representation of the particle (lines) and gas convective (dashed) heat-transfer coefficients vs. fluidization velocity (log scale) in dense, bubbling fluidized beds of different particle sizes, each bed consisting of monosized particles. (Plotted according to a model for fluidization in air at 25°C and ρ_p = 2500 kg/m³.)

heat-transfer maxima for each particle size follow Equation 17.84. Obviously, the small heat transfer in the fixed bed at lower velocities than that of minimum fluidization is neglected. Likewise, the use of the terminal velocity as an end point is an approximation. The particle suspension in the bed becomes more dilute as the velocity increases (the voidage increases), but there should be some bed left even at the terminal velocity, especially for small particles where clustering makes a suspension endure higher velocities than the terminal velocity of a single particle. The terminal velocity as an end point makes the curves bend more severely at high velocities than what is shown in measurements. However, two aspects should be observed: (1) the scale is logarithmic and that compresses the diagram somewhat, (2) the gas convection should be added to the particle convection, and at higher temperatures also the thermal radiation, to get the resulting total heat-transfer coefficient. These effects would make the curves fall less steeply.

In the surveys on heat transfer in dense, bubbling beds, as mentioned in the reviews quoted above there are many correlations and modeling efforts describing the detailed behavior of heat transfer. The result of one of these models illustrates the general behavior of the heat-transfer coefficient, as shown in Figure 17.13. However, the situation in a fluidized bed is complex and the multitude of efforts has led to a qualitative understanding of the phenomena rather than to a generally valid predictive description. In the following, a simplified approach is preferred and the presentation will focus on the most reliable data, namely, those of the maximum heat-transfer coefficient, for which correlations are available. The maximum heat-transfer coefficient of a rounded fixed object in the interior part of a dense, bubbling fluidized bed, joining the maximum points shown in Figure 17.13, has been determined empirically and expressed as a function of the Archimedes number. One such correlation (Varygin and Martyushin, 1959) is as follows:

$$Nu_{c,max} = 0.86 Ar^{0.2} \left(30 < Ar < 10^5\right) \tag{17.83}$$

where

$Nu_c = h_c d_p / k_{air}$

k_{air} is the thermal conductivity of air

For other gases, h_c should be multiplied by $(k_g/k_{air})^{0.6}$. The location of the maximum can be described according to Aerov and Todes (1968) and Gelperin and Einstein (1971):

$$Re_{opt} = \frac{Ar}{\left(18.0 + 5.22 Ar^{1/2}\right)} \tag{17.84}$$

The optimum fluidization velocity is in the range between the terminal and minimum fluidization velocities, as seen in Figure 17.13 and in a different way in Figure 17.14. The maxima determined empirically are quite wide and the optimum velocity is not as exactly described by experimental data as may be the impression from Figures 17.13 and 17.14.

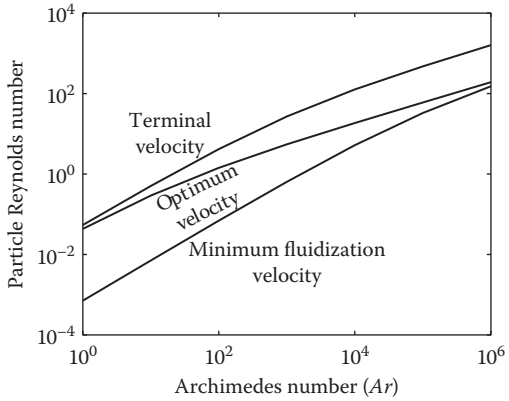


Figure 17.14

The minimum, terminal, and optimum fluidization velocities for different particle sizes (Ar) according to Equations 17.81, 17.82, and 17.84.

Equation 17.83 can be written as

$$h_{c,max} \sim d_p^{-0.4} \rho_p^{0.2} k_g \mu_g \rho_g^{0.2} \tag{17.85}$$

which can be compared with the well-known Zabrodsky (1966) formula, expressed in SI units, valid for objects of sizes between 0.010 and 0.060 m and bed particles between 0.00006 and 0.001 m at room temperature:

$$h_{c,max} = 35.7 d_p^{-0.36} \rho_p^{0.2} k_g^{0.6} \tag{17.86}$$

Both formulae show an approximately equal impact of bed particle size. The thermal conductivity of gas has a different power, which means that the temperature dependence could be different in the two representations. This is not the case, however, as the gas density term in Equation 17.83 provides an additional temperature influence. None of the expressions consider the impact of specific heat of the bed material. As seen from the packet model, Equation 17.98, both density and specific heat of the particles are important, since they account for the transport of heat by particles to the wall. However, the properties of materials reveal that specific heat and density are correlated for most conceivable bed materials. Therefore, in empirical formulae, such as Equations 17.83 and 17.86, the particle density also represents the specific heat.

Similar expressions for vertical and horizontal tube bundles in a fluidized bed have been given by Gelperin and Einstein (1971, Table 10.3, p. 516). The relationship for horizontal in-line tubes is

$$Nu_{d,max} = 0.79 Ar^{0.22} (1 - D/s_h)^{0.25} \tag{17.87}$$

where

D is the tube diameter

s_h is the horizontal distance between the centers of the tubes

In fluidized-bed applications, there is a connection between Re and Ar, as seen from Equations 17.81, 17.82, and 17.84, and these dimensionless numbers can be interchanged in heat-transfer expressions. It is likely that dimensional expressions such as Equation 17.86 also can be transformed into a dimensionless form. For instance, Zabrodsky (1974) tentatively expressed Equation 17.86 in the same form as Equation 17.83 yielding $0.88 Ar^{0.213}$. With Archimedes number, gas density is introduced in Equation 17.83, and therefore, the correlation becomes sensitive to pressure, which was not included in the database used to establish the relationship. Although pressure may have some impact on gas convection and also to some extent on particle convection (Martin, 1984), this impact may be too strong in Equation 17.83 owing to the gas density term, and this form of relationship is therefore applicable only at atmospheric pressure unless supported by heat-transfer measurements at other pressures. However, within its range of applicability, the simpler dimensional relationship, Equation 17.86, could be applied to pressurized situations also, if gas convection is not dominant.

For larger particles, the impact of the gas flow is relatively important, and a gas convective constituent should be added to the particle convection term (Baskakov et al., 1973):

$$Nu_{gc} = 0.009 Ar^{0.5} Pr^{0.33} \tag{17.88}$$

This equation has already been plotted in Figure 17.13.

Figure 17.15 summarizes the details given. The simple relationships, Equations 17.83 and 17.86, include gas convection, but in their range of validity $Ar < 10^6$, gas convection is insignificant. Only at $Ar > 10^7$, gas convection dominates heat transfer.

The total maximum heat transfer can be expressed by a simple Archimedes number relationship over a wide range of particle size, such as proposed by Baskakov (1985)

$$Nu_{max} = 0.85 Ar^{0.19} + 0.006 Ar^{0.5} Pr^{0.33} + h_r d_p / k_g \tag{17.89}$$

valid in the temperature range of 20°C to 1300°C for Ar from 10^2 to 10^9 at atmospheric pressure. More refined expressions of the same kind, also considering pressure, have been presented by Borodulya et al. (1991).

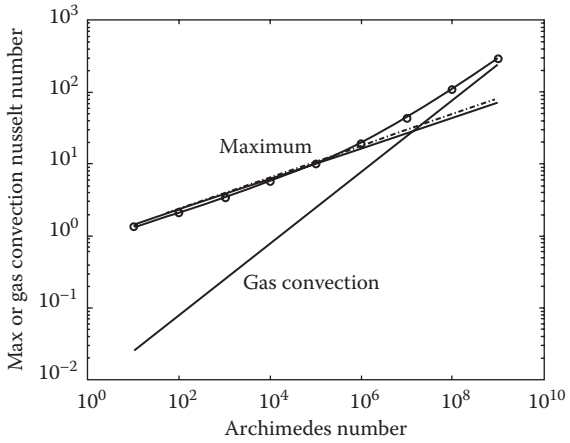


Figure 17.15

Total maximum heat transfer compared to gas convective heat transfer. The straight line, representing maximum heat transfer, is Equation 17.83 and the dashed one is Zabrodsky's formula (Equation 17.86). Gas convection is plotted according to Equation 17.88. The curve denoted by circles is Baskakov's relationship (Equation 17.89) without radiation.

The definition of the additive radiative component of heat transfer between the bed and the surrounding wall is straightforward. Assume a heat-exchanging volume of gas and particles, surrounded by a wall of area A. Then, the radiation heat flow Q_r can be written as

$$Q_r = h_r A\left(T_b - T_w\right) = \varepsilon A\sigma\left(T_b^4 - T_w^4\right) \tag{17.90}$$

where

T_b and T_w are the temperatures of the bulk of the bed and the wall expressed in K
σ is the Stefan–Boltzmann's constant (W/m^2 K^4)
ε is the resulting emissivity

Equation 17.90 yields the definition of the radiative heat-transfer coefficient

$$h_r = \varepsilon\sigma\left(T_b + T_w\right)\left(T_b^2 + T_w^2\right) \tag{17.91}$$

This definition has the consequence that h_r depends on the temperature conditions in each case of application in the range from one extreme ($h_r = 4\varepsilon\sigma T_b^3$ when $T_b = T_w$) to another ($h_r = \sigma\varepsilon T_b^3$ when $T_b \gg T_w$). For an enclosure or a semi-infinite plane-parallel layer, the resulting emissivity can be written as

$$\varepsilon = \frac{1}{1/\varepsilon_b + 1/\varepsilon_w - 1} \tag{17.92}$$

where ε_b and ε_w are the emissivities of bed and wall. The emissivity of the wall can be obtained from handbooks on radiation properties, although it is still an open question if the walls in fluidized beds are more polished by the particles than the materials in general and may have another emissivity for that reason. Owing to the "Hohlraum" effect of the space between the particles, the emissivity of the dense bed, ε_b, is higher than that of the surface of the particles ε_s. According to Borodulya and Kovensky (1983),

$$\varepsilon_b = \varepsilon_s^{0.48} \tag{17.93}$$

which is one of several expressions leading to the same result, as analyzed by Baskakov and Leckner (1997). All data needed for the radiative transfer calculation (T_b, T_w, A, ε_b, and ε_w) are normally available, but still the calculation cannot be carried out since the temperature of the particle layers adjacent to a

heat-transfer surface may differ from the bed temperature, more in the case of small particles than in beds of large particles. Therefore, Equation 17.90 represents the maximum radiative transfer and the actual value is normally lower. Various modeling approaches have tried to describe this reduction of the radiative transfer. For simplified estimates, Baskakov (1985) has suggested maintaining Equation 17.91 as it is and introducing an empirically defined effective emissivity $\varepsilon_{eff} = \varepsilon_b$ to take the variations into account; examples are found in the source quoted. For bed temperatures between 1000 and 1500 K and voidages of $0.3 > \varepsilon_b > 0.6$, and in the absence of more general expressions, an even more simplified relationship has been proposed by Baskakov: $h_r = 7.3\sigma\varepsilon_b\varepsilon_w T_w^3$. The choice of the wall temperature to represent radiative exchange is obviously a considerable approximation and is mostly valid for beds of small particles where the particles close to the wall approach wall temperature. For large particles, on the other hand, the particle temperature is close to the bulk bed temperature, as these particles need more time to cool down after reaching the wall layer. In Schlünder et al. (1987), similar simplifications are found; for instance, it is proposed to use the arithmetic mean between wall and bed temperature as a representative radiation temperature in Equation 17.90.

17.2.1.1.2 Correlations, General The quoted reviews present many correlations describing heat transfer to an element (like a tube) in a fluidized bed. The correlations are not necessarily related to the maximum heat transfer but can cover the rising branch seen in Figure 17.13 or the postmaximum branch or both. Here only one example will be presented: one of the best-known correlations is that of Vreedenberg (1958) related to a horizontal tube. It has been analyzed and criticized by many. For instance, Grewal (1979), observing that the correlation lacked a term ρc_p to express the thermal capacity of the fluidized suspension, proposed an extension of the correlation in addition to an expression for voidage. Andeen and Glicksman (1976) had the opinion that the correlation should consider the influence of voidage instead of just allowing the heat transfer to increase monotonically with velocity, and they suggested the following modification:

$$Nu_D = 900(1-\varepsilon)Pr^{0.3}\left(\frac{uD\rho_s}{\mu}\frac{\mu^2}{d^3\rho_s^2 g}\right)^{0.336} \tag{17.94}$$

Andeen and Glicksman derived an expression for voidage based on a form proposed by Leva (1957)

$$\varepsilon = \frac{1}{2.1}\left(0.4 + \left(\frac{200u\mu}{d^2\rho_s g}\right)^{0.33}\right) \tag{17.95}$$

Grewal used the same starting point (Leva) but fitted the expression to his own extensive measurements:

$$\varepsilon = \frac{1}{2.1}\left[0.4 + \left[4\left(\frac{u\mu}{d^2\rho_s\phi_s^2 g}\right)^{0.43}\right]^{0.33}\right] \tag{17.96}$$

A plot of Equation 17.94 using the voidages of Equations 17.95 and 17.96 is compared with the maximum heat-transfer coefficients according to Gelperin and Einstein's (1971) Equation 17.84 in Figure 17.16.

Figure 17.16 illustrates a few properties of this type of correlations. It is obvious that the original Vreedenberg correlation did not catch the maxima, just as was observed by Andeen and Glicksman (1976) whose improved correlation does reflect the maximum heat transfer. On the other hand, the same correlation (Equation 17.94) employing the voidage correlation of Grewal (Equation 17.96) is more similar to the original Vreedenberg correlation and it does not fall off at high velocities, not even qualitatively describing a maximum. Grewal (1979) himself found that his own correlation (a modified Vreedenberg equation) with his voidage description gives the best fit to available data among the various correlations investigated.

The conclusion is that even though the determination of the velocity at maximum heat transfer can be slightly uncertain, especially at high velocities where there is a substantial contribution of gas convection, correlations describing the maximum heat transfer seem more reliable than the correlations trying to catch

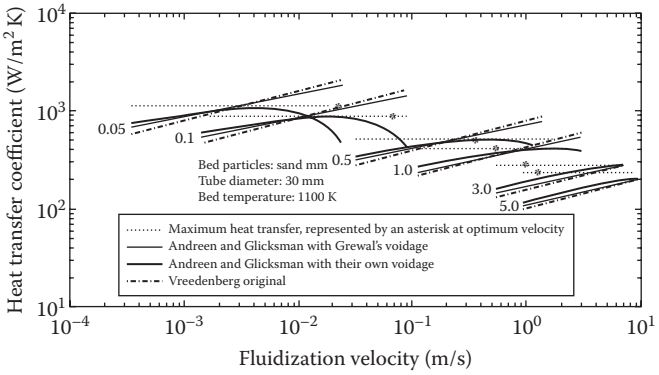


Figure 17.16

Comparison between Vreedenberg's (1958) and Andeen and Glicksman's (1976) correlations of heat transfer to a tube with their own representation of voidage (the thicker curve, showing a maximum) and that of Grewal (1979), and the maximum heat-transfer coefficient from Gelperin and Einstein (1971) for infinite tube distance (s_h) and six bed-particle sizes (from 0.05 to 5 mm). The plot is made considering temperature-dependent gas properties, but it exceeds the range covered by the test data of the correlations. Each set of curves represents the given particle size and ranges from the minimum fluidization velocity to the terminal velocity of a single particle.

the variations with velocity in the rising branch where the development of voidage with velocity, particle size, and geometry play significant roles. The two voidage correlations quoted both use Leva's work as a starting point but nevertheless lead to different results if used as independent expressions. In tube bundles, the voidage conditions may differ even more from available voidage expressions, as reflected by pictures shown on bubbles in a two-dimensional bed containing various tube packings and subject to various velocities, Leckner (1998). This has been little studied and only some correlations on the influence of tube configurations of the kind shown in Equation 17.87 are available in the literature.

17.2.1.1.3 Heat-Transfer Mechanisms The steep rise in heat transfer from the value at minimum fluidization to the maximum value is caused by the increased movement of the bed in the vicinity of the heat-transfer surfaces as a consequence of the stirring action of bubbles. Heat transfer to a surface and the fluid dynamic behavior of the bed are strongly linked. The fluid dynamics change with the position within a bed and depend on several conditions, such as fluidizing velocity, bed material, and size of the containing vessel. This has made it difficult to establish generally valid heat-transfer relationships. The correlations, differ from each other and give different results, showing the complexity of the situation. In Figure 17.17, a striking example is given, illustrating the difficulty involved in the application of heat-transfer correlations, while it also explains the mechanisms of heat transfer. Figure 17.17a shows the resulting heat-transfer coefficients, measured with a heat-transfer probe on a vertical water-cooled wall of a fluidized-bed combustor with a 10 m^2 cross section, operated with sand as bed material at 850°C bed temperature. The heat-transfer coefficient increases from the air-distributor plate, forming the bottom of the bed, to the surface of the bed (which is located above the bed height at rest, given in the figure) during operation at various fluidization velocities. Above the surface of the bed, in the splash zone, the heat-transfer coefficient decreases again with height. Figure 17.17b shows material loss from the heat-transfer steel tubes of the wall owing to erosion by the bed material in the same boiler and on the same wall where the heat-transfer measurements were made.

The similarity between heat transfer and erosion illustrates the mechanism of heat transfer. At the surface of the bed, there is a vigorous movement and the wall is frequently exposed to high-temperature particles. The bed material flows downward along the wall and the agitation declines, although the bed as a whole is vividly fluidized and the air supply nozzles are active. Changes in the fluidization velocity in the range of 1.4–2.2 m/s did not markedly change the conditions. The particle layers close to the wall transfer their heat to the wall and cool, thereby reducing the heat-transfer potential. Heat is transferred by exchange of bed material from the hot core of the bed to the wall. If there is only little or almost no exchange of bed material, the material close to a surface attains the temperature of the surface, and eventually heat transfer takes place only by thermal conduction. The thermal conductivity of stagnant bed material is low, and in this case, when the bed material serves as an insulating agent, heat transfer declines.

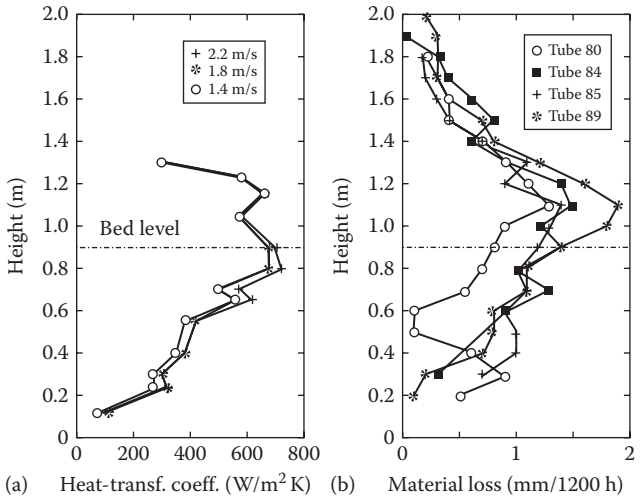


Figure 17.17

Heat transfer to a wall of a stationary fluidized-bed boiler at various fluidization velocities (symbols) (a) compared with erosion on the same membrane tube wall after 1200 h of operation (b). Conditions: bed temperature 850°C; average particle size 0.55 mm. Bed level is the level at rest. (The heat transfer data are from Andersson, B.-Å. and Leckner, B., Bed-to-wall heat transfer in a 10 m² bubbling fluidized bed, in Macías Machín, A. and Winter, G. (Eds.), *Proceedings of Congreso Europeo de Fluidisación*, Universidad de Las Palmas de Gran Canaria, Vol. 1, 1994, pp. 251–260; the erosion data are from Leckner, B. et al., Operational results from the 16 MW FBB at Chalmers University, *Third International Fluidised Conference*, The Institute of Energy, London, U.K., 1984, Paper Disc/16/134–143.)

The heat-transfer correlations presented are for large objects in the central parts of a fluidized bed, a different surrounding compared to a surface element on the sidewall of the bed.

17.2.1.1.4 Models Heat transfer can be modeled together with fluid dynamics and combustion, but here only the classical semiempirical approaches will be summarized. The most general set of semiempirical heat-transfer models describes the exchange of bed material at a heat-transfer surface as a packet of hot bed material, which is brought to the surface by the movements of the bubbles. The packet remains at the surface for a certain contact time, while its temperature approaches that of the heat-transfer wall, and is then replaced by a new packet from the core of the bed. A simplified version of the energy equation describes the thermal behavior of the packet, considered as a semi-infinite continuum with effective thermal properties:

$$\left(\rho c_p\right)_b \partial T/\partial t' = k_{pb}\partial^2 T/\partial x^2 \tag{17.97}$$

where

$\rho_b = \rho_p(1 - \varepsilon)$, ε is the voidage
c_{pb} and k_{pb} are the specific heat and thermal conductivity of the packet
x is a coordinate oriented normal to the surface

The primed values t' and h' denote current time and heat-transfer coefficient, whereas t is the total residence time of a packet at the surface and h is the time-average heat-transfer coefficient. The time-dependent solution of Equation 17.97 for constant wall temperature and with the packet initially at core temperature is

$$h'_{i,c} = \frac{k_{pb}}{x_m}\left(1 + 2\sum_{n=1}^{\infty}\exp\left[-\frac{n^2\pi^2 k_{pb}t'}{x_m^2\left(\rho c_p\right)_b}\right]\right)$$
$$\cdots = \sqrt{\frac{k_{pb}\left(\rho c_p\right)_b}{\pi t'}}\left(1 + 2\sum_{n=1}^{\infty}\exp\left[-\frac{n^2 x_m^2\left(\rho c_p\right)_b}{k_{pb}t'}\right]\right) \tag{17.98}$$

This equation has two equivalent solutions: the first converges fast for long times and the second for short and intermediate times. Truncation gives an approximate expression for short and intermediate times:

$$h'_{i,c} = \frac{\sqrt{k_{pb}(\rho c_p)_b}}{\sqrt{\pi t'}}, \quad \text{i.e., } Nu_{i,c} = 1/(\pi Fo)^{1/2} \tag{17.99}$$

whereas for very long times

$$h'_{i,c} = h_c = k_{pb}/x_m, \quad \text{i.e., } Nu_{i,c} = 1 \tag{17.100}$$

where

$Nu_{i,c} = h'_{i,c}x_m/k_{pb}$ is the Nusselt number of the packet and the dimensionless time

Fo is the Fourier number, defined as $Fo = k_{pb}t'/(c_{pb}\rho_b d_p^2)$

For very short times or large particles, this solution leads to unreasonably high heat transfer, and the heat-transfer resistance $1/h'_{i,c}$ approaches zero. Therefore, a time-independent contact resistance in the form of a gas layer close to the surface is introduced:

$$\frac{1}{h_k} = \frac{\varphi d_p}{k_g}, \quad \text{i.e., } Nu_k = \frac{1}{\varphi} \tag{17.101}$$

where

k_g is the thermal conductivity of the gas adjacent to the surface

φd_p indicates the width of the gas layer in terms of particle diameters

Now, the total particle convective heat-transfer resistance becomes

$$\frac{1}{h'_{pc}} = \frac{1}{h_k} + \frac{1}{h'_{i,c}} \tag{17.102}$$

Baskakov (1964) integrated Equation 17.97 considering the gas gap and obtained the heat-transfer coefficient

$$h'_{pc} = h_k \exp\left[\frac{h_k^2 t'}{k_{pb}(\rho c_p)_b}\right] \operatorname{erf}\left[\sqrt{\frac{h_k^2 t'}{k_{pb}(\rho c_p)_b}}\right] \tag{17.103}$$

Time averaging for the total residence time t of a packet at the wall yields

$$h_{pc} = \frac{1}{t}\int_{t=0}^{t} h'_{pc}\,dt = 2\sqrt{\frac{k_{pb}(\rho c_p)_b}{\pi t}} - \sqrt{\frac{2k_{pb}(\rho c_p)_b}{\pi t h_k}} \ln\left[1 + \sqrt{\frac{\pi t h_k^2}{k_{pb}(\rho c_p)_b}}\right] \tag{17.104}$$

Similar expressions for various boundary conditions have been given by Gelperin and Einstein (1971). This type of expressions is somewhat inconvenient for engineering calculation and a simpler relationship is preferred:

$$h_{pc} = \frac{1}{1/h_k + 1/h_{i,c}} \tag{17.105}$$

where the time-average emulsion heat-transfer coefficient during time t is

$$h_{i,c} = 2h'_{i,c} = 2\frac{\sqrt{k_{pb}(\rho c_p)_b}}{\sqrt{\pi t}} \tag{17.106}$$

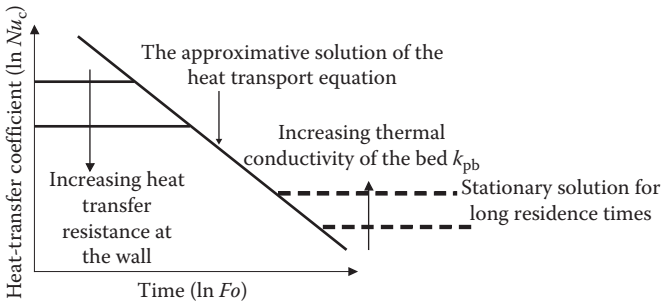


Figure 17.18

The particle convective heat-transfer coefficient as a function of residence time of a packet at the heat-transfer surface.

It has been shown (Fang et al., 1995b) that the deviation between Equation 17.104 and the simplified expression is less than 5%.

Figure 17.18 illustrates the limitations of the simplified solution of the heat-transfer equation, Equation 17.105. At very short times or large particles, the heat-transfer coefficient is limited by the resistance in the gas layer, Equation 17.101, and for hypothetically long residence times, it approaches the limit of pure conduction through a stagnant particle suspension of thickness x_m and thermal conductivity k_{pb}, given by Equation 17.100. The impact of the particles depends on particle size. In the case of very large particles (larger than 1 mm), the resistance of the gas layer becomes more important than that in the emulsion. For smaller particles, the thermal residence time of the emulsion is important, and the coefficient tends to be represented by the sloping part of the relationship shown in Figure 17.18. The packet model explains the particle convective heat-transfer mechanisms at a heat-transfer surface, but the resistance coefficient φ in Equation 17.101, the thermal conductivity of the packet (its density), and its residence time at the surface require further modeling.

If the heat-transfer surface is exposed to bubbles during a fraction of time f_0, the heat-transfer coefficient can be written as

$$h_c = \left(h_{gc,bubbles} + h_{r,bubbles}\right) f_0 + \left(h_{pc} + h_{gc,emulsion} + h_{r,emulsion}\right)\left(1 - f_0\right) \tag{17.107}$$

where the two terms represent the heat-transfer coefficients during the passage of a bubble and during the presence of the particle emulsion. In the common case when gas convection is small and radiation is negligible. Using Equation 17.105, Equation 17.107 can be written as

$$h_c = \frac{\left(1 - f_0\right)}{\left(1/h_k + 1/h_{i,c}\right)} \tag{17.108}$$

The significance of the various terms can be understood from the aforementioned discussion. Here only two extreme cases will be illustrated: those of small and large particles. In the case of small particles, Equation 17.107 results in

$$h_c = h_{r,bubbles} f_0 + h_{i,c}\left(1 - f_0\right). \tag{17.109}$$

In this case only radiation through bubbles and heat conduction through the emulsion (the sloping part of the curve in Figure 17.18) play significant roles as constituents of the heat-transfer coefficient. In the other extreme case, that of large particles, heat conduction through the emulsion is less important than the thermal resistance of the gas gap. Moreover, in this case, the particles at the wall are not essentially cooled and radiation from both emulsion phase and bubbles is important at high temperatures. With radiation and gas convection expressed for the total time, the result for large particles becomes

$$h_c = h_k\left(1 - f_0\right) + h_{gc} + h_r \tag{17.110}$$

The packet model has been the starting point for most fluidized-bed heat-transfer modeling. However, other ways of modeling have also been followed, where the heat exchange between the row of particles adjacent to a wall and the wall is regarded as most important for the heat transfer (Zabrodsky, 1966). An example of such an approach is the model developed by Martin (1984), who regarded the transport of heat by particles moving at an average velocity toward a heat-transfer surface. As in the case of the packet model, particles exchange their heat while remaining for some time at a heat exchange surface, but the thermal conduction in the particle emulsion is disregarded. The principal mechanism of heat transfer is through the gas film between a particle and a wall, and to some extent heat transport within a particle. The unknown parameters in Martin's model are related to the voidage of the bed, and for practical application of the model, a description of bed expansion is needed. A simplified version of this model has been used to illustrate the heat-transfer behavior in Figure 17.13. In the design of this figure, the bed voidage was supposed to vary linearly with the fluidization velocity

$$\varepsilon = \varepsilon_{mf} + (1-\varepsilon_{mf})(u-u_{mf})/(u_t-u_{mf}) \tag{17.111}$$

where $\varepsilon_{mf} \approx 0.4$. The velocities at minimum fluidization u_{mf} and terminal velocity u_t were obtained from Equations 17.81 and 17.82, respectively. The coarse simplification of the description of bed voidage makes the curves more rounded at velocities exceeding the optimum velocity than seen from the measurements. In reality, the curves are flatter, and a heat-transfer coefficient of $0.8h_{max}$ is often recommended for rough calculations over a wide range of velocities above the optimum one. The absence of particles at terminal velocity and, as a result, zero particle convective heat transfer (seen in Figure 17.13) is a consequence of the simplifying assumptions introduced for the present purpose. They are not necessary limitations of the model. A more realistic description of bed expansion in the high-velocity range would improve the result. However, the model assumes that the particles remain in contact with the wall, and it is not intended for the high-velocity modes of fluidization occurring when the bed is being converted into a circulating system.

17.2.1.2 Heat Transfer in the Disperse Suspension of the Circulating Fluidized Bed

17.2.1.2.1 General Conditions The high-velocity fluidized bed, extending in a riser reactor, consists of a dense bottom bed (if there is sufficient bed material in the riser), a transition zone, and a transport zone. The bed material is recirculated from a particle separator (e.g., a cyclone) back to the bottom bed, and hence, the device is called a CFB. Heat transfer in CFB is most common in combustors, and this is the application to be treated here. In a furnace for combustion, heat-transfer surfaces are found on the walls and inside the upper part of the CFB furnace (riser). In some cases, external heat exchangers containing horizontal tube bundles in low-velocity bubbling fluidized beds are connected to the cyclone return. In the CFB riser, the suspension densities are lower and the gas velocities are higher than in a noncirculating, bubbling, bed. Owing to the high velocity, erosion on the heat-transfer surfaces is potentially severe, and there are restrictions, both on the fluidization velocity and on the allocation of heat-transfer surfaces.

The orientation of the surfaces in the CFB riser should be parallel to the principal direction of the particle flow, and the surfaces should be located where the particle density is low, although, then the rate of particle-related convective heat transfer is also low. In the dense bed, often present in the bottom zone of the CFB riser, the conditions are analogous to those in the bubbling bed, but this region is not of interest for heat transfer because erosion makes it impossible to locate heat transfer tubes there; the walls of this zone are refractory lined to protect the tubes. Work on heat transfer in CFB has focused on the transport zone in the upper part of the furnace.

The heat-transfer surfaces of combustors normally consist of membrane tubes (Figure 17.19), exposed for heat transfer from where the bottom refractory ends and up to the top of the riser. In larger furnaces, there are also internal surfaces, such as "wing walls," inside the upper part of the riser, or extending all the way from the bottom to the top of the furnace, again, allocated parallel to the main flow of particles and protected from erosion in critical places. The heat-transfer surface is the entire area exposed to the particle suspension, but for tube walls, it may be expressed as projected surface area if the radiation from a distant suspension of gas and particles or from a flame is important. At a given heat-transfer rate, the coefficient h depends on whether it is related to the projected or to the total surface. The ratio of total and projected area is always less than $\pi/2$ for tube walls, as can be realized from geometrical reasons (see Figure 17.19).

The heat transfer between suspension and wall is affected both by the density of the suspension and by the temperature. Close to the heat-transfer walls, there is a falling film of particles forming particle and thermal boundary layers with higher suspension density and lower temperature than in the core of the riser.

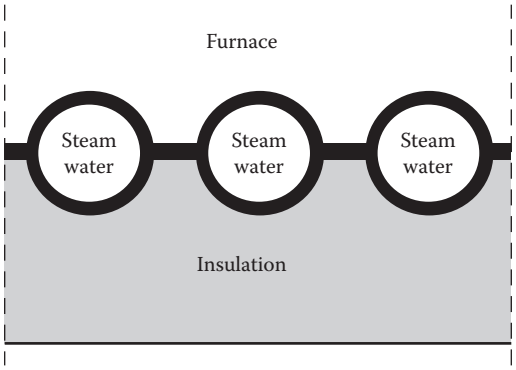


Figure 17.19

Cross section of three tubes of a membrane tube wall.

The boundary layer not only transfers heat by convection, it also participates in the radiative transfer of heat between the bed and the wall. Much of the radiative transfer originates in the hot core, but this radiation is partly absorbed by the particles in the wall layer and reaches the wall only after attenuation (Werdermann and Werther, 1994). The wall layer is colder than the core and its own emission is limited. Heat-transfer correlations are normally related to the average particle density of the cross section ρ_{av}, since this quantity is relatively easy to evaluate from measured pressure drops $\mathrm{d}P/\mathrm{d}z$ along the riser's height z under the assumption that the particles are carried by the gas. Formally, the average density over the cross section is expressed by integration of the local suspension density ρ_b over the cross section A_c of the riser as

$$\rho_{av} = A_c^{-1} \int \rho_b \mathrm{d}A_c = -1/g \; \mathrm{d}P/\mathrm{d}z \tag{17.112}$$

where the suspension density is

$$\rho_b = (1-\varepsilon)\rho_p + \varepsilon\rho_g \tag{17.113}$$

where ρ_p and ρ_g are the densities of particles and gas, respectively. With the exception of the thermal boundary layers, the time-average temperature of the suspension ("the bed temperature"), T_b, is usually constant in the riser. Only in large risers and at part load there may be a small fall of T_b with height and in the corners. An example of a thermal boundary layer is seen in Figure 17.20, where the temperature starts to fall at about 0.1 m from the wall. The measurements were made in a 14 m high CFB furnace with a cross section of about 2.2 m^2. Similar results have been obtained in other CFB furnaces. The shape of the temperature curves is similar at all heights, which reveals that heat is supplied to the boundary layer at almost the same rate as it is removed to the wall. In Figure 17.20, the wall temperature is 200°C, and very close to the wall (<3 mm from the fin), there is obviously a temperature fall from about 500°C to 200°C that can only be explained by the existence of a gas gap, free from particles, close to the wall. The temperature gradient reveals that more than half of the resistance to convective/conductive heat transfer may be found in this gas gap and that the remaining resistance is in the particle suspension of the boundary layer.

The vertical heat-transfer surfaces in a CFB are polished but not severely eroded. Therefore, it can be assumed that the particles touch the walls occasionally, and that the gas gap has at least an average size of the order of a particle diameter (in contrast to the dense bubbling bed where the particles are in closer contact with the walls). The thinnest conceivable dimensionless thickness is that of a gas lens between a particle resting on the wall and the wall $\varphi = 1/6$, where the thickness is $\delta_g = \varphi d_p$ (cf. Equation 17.101). Another geometrically defined limit is that formed by a cubic, expanded, arrangement of particles, assuming that the particle volume fraction at the wall is three times the cross-sectional average volume-fraction:

$$\varphi = \left(\frac{\pi}{\left(18\left(1-\varepsilon_{av}\right)\right)} \right)^{1/3} \tag{17.114}$$

These geometric relationships are compared with various measurements or fits in Figure 17.21.

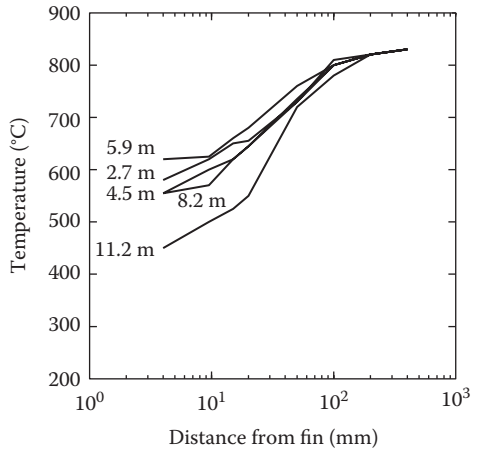


Figure 17.20

Thermal boundary layer measured in a 12 MW CFB boiler at various distances from bottom of the furnace. Conditions: particle size 260 μm; fluidization velocity 4 m/s; bed temperature 850°C. (From Leckner, B. et al., Boundary layers–first measurements in the 12 MW CFB research plant at Chalmers University, in Anthony, E.J. (Ed.), *Proceedings of the 11th International Conference on Fluidized Bed Combustion*, ASME, New York, 1991, pp. 771–776.)

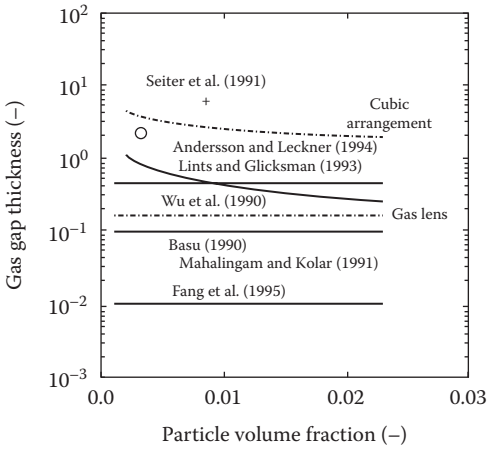


Figure 17.21

Measured and fitted dimensionless gas-gap thickness $\varphi = \delta_g/d_p$ vs. cross-section average solid volume fraction. Theoretical limits set by a gas lens $\varphi = 1/6$ and a cubic packing, Equation 17.114, are marked with dashed lines. (From Breitholtz, C. and Leckner, B., *Trends Heat Mass Momentum Transfer*, 3, 85, 1997. With permission.)

The temperature in the boundary layer varies with time, as illustrated in Figure 17.22. The figure shows simultaneous variations in the boundary layer temperature measured by six thermocouples inserted at various distances from the fin of the membrane tube of a CFB furnace. The variations in temperature are obviously due to high-temperature, streamers of particles, occasionally brought to the wall region from the hot core of the riser, remind on the packets occurring in the dense bubbling bed. These irregularities cause corresponding fluctuations in heat transfer. The temperature in the core is even (at 0.28 m from the wall in Figure 17.22 and further into the core of the suspension), without thermal disturbances. It can be assumed that the temperature variations are accompanied by density variations, as observed visually. The density variations are complex and also contain higher frequencies than the temperature fluctuations shown in Figure 17.22, which are filtered by the thermal inertia of the thermocouples used. Wu et al. (1991) have shown that the fast density variations correspond to variations in the heat transfer to a wall. An intermittency index γ has been defined (Brereton and Grace, 1993) to characterize the density fluctuations at a

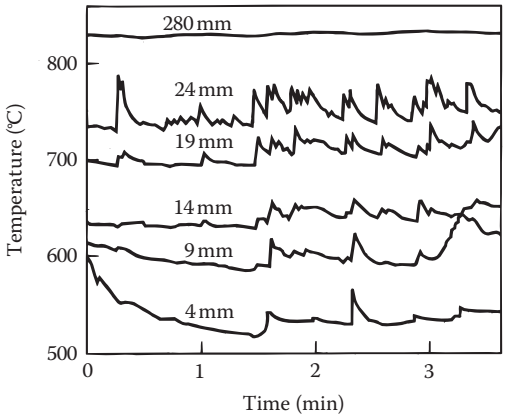


Figure 17.22

Example of simultaneous temperature variations in the boundary layer at various distances from the fin of a membrane tube wall 11.2 m above the bottom in the same case as Figure 17.20. (From Leckner, B. et al., Boundary layers–first measurements in the 12 MW CFB research plant at Chalmers University, in Anthony, E.J. (Ed.), *Proceedings of the 11th International Conference on Fluidized Bed Combustion*, ASME, New York, 1991, pp. 771–776.)

given point, represented by the standard deviation of the density fluctuation σ for two cases with identical time-mean densities

$$\gamma = \frac{\sigma \text{ under the actual conditions}}{\sigma \text{ for a fully segregated flow}} \tag{17.115}$$

This index is zero for a homogeneous flow and unity for a flow consisting of particle swarms of the same volume fraction as a bed at minimum fluidization velocity. In model representations, the particle suspension is often regarded as having a high intermittency index, in the extreme case consisting of a discrete probability of presence of particles, f_c, the coverage factor, indicating how much the wall is covered by particles, and $(1 - f_c)$ is the uncovered part of the wall. In terms of probability distribution, such a fully segregated flow would have a bimodal distribution of particle density and an intermittency index of unity, but measured distributions are continuous around a maximum. They are far from bimodal (Breitholtz and Leckner, 1997, Johnsson et al., 1997), and the intermittency index is below 0.5 (Brereton and Grace, 1993, Johnsson et al., 1997). Hence, although there are density fluctuations in the medium, they are not as distinct as assumed in some models; they are actually gradual variations against a background of a finite concentration of particles.

The description of heat transfer in CFB risers can be roughly separated into four, sometimes combined, approaches:

1. Gas and particle convection are evaluated separately as average values and added to radiation according to Equation 17.80.
2. Particle convection is assumed to take place when a dense streamer is present and gas convection (if not neglected) and radiation are considered during the remaining time.
3. Comprehensive (more or less) modeling, in some cases, allowing the mechanisms to be interrelated.
4. Correlations.

17.2.1.2.2 Addition of Radiative and Convective Heat Transfer (Approaches 1 and 2) It is often assumed that the wall is covered by particles in the form of streamers during a fraction of time f_c, and uncovered during the rest of the time $(1 - f_c)$. The resulting heat-transfer coefficient h is composed of a contribution from convection h_c (or h_{pc}) and radiation $h_{r,w}$ from the boundary layer during coverage f_c, and of radiation from the core of the bed h_r during the particle-free time $(1 - f_c)$. Gas convection may have some minor effect when the wall is uncovered. The heat-transfer coefficient can then be written as

$$hA = f_c\left(h_{pc} + h_{rw}\right)A + \left(1 - f_c\right)\left(h_r A_{proj} + h_{gc} A\right) \tag{17.116}$$

where radiation from distance is received by the projected surface A_{proj} and convective and radiative heat transfer from the streamers, seen from the wall, is received by A, the total surface area. However, the wall coverage f_c is not known. Normally, the terms $h_{r,w}$ and h_{gc} are small and can be neglected. The particle convective coefficient h_c (h_{pc}) consists of two resistances in series

$$\frac{1}{h_c} = \frac{1}{h_k} + \frac{1}{h_l} \tag{17.117}$$

where the resistance in the particle boundary layer is $1/h_l$ and the resistance in the gas film at the wall

$$\frac{1}{h_k} = \frac{\delta_g}{k_g} \tag{17.118}$$

represents the influence of a gas gap between the wall and the suspension (cf. Equation 17.101), with the thickness $\delta_g = \varphi d_p$. The heat transport through the remaining part of the particle wall layer can be expressed as

$$h_l = \frac{k_s}{\delta_s} \tag{17.119}$$

implying that the transfer mechanism is conduction across a particle suspension with the thickness δ_s, promoted by the irregular movement in the bed material having an effective suspension conductivity k_s. Alternatively, heat is transferred by the movements of the particle suspension and the heat-transfer mechanism is assumed to consist of displacement of streamers of particles transferring heat from the core to the wall, similar to the packets of the noncirculating dense bubbling bed (Equation 17.99). Glicksman (1997) and Basu and Nag (1996) have conducted surveys on various approaches of this type. The streamers are parts of the suspension that approach the wall. They are characterized by having higher density than that of the surrounding suspension and are treated like the packets of particles formed by the agitation of bubbles in the dense bed.

In the aforementioned formulation, some factors are known: k_g (thermal conductivity of gas), δ_g (Figure 17.21), the contribution of radiation $(f_c h_{rad,w} A + (1 - f_c) h_{rad} A_{proj})/A \approx 50$ (W/m² deg), (further discussed in connection to Figure 17.25) and δ_s (thermal boundary layer thickness), but essential parameters such as f_c and k_s require additional modeling. Glicksman (1997) has reviewed available information about the various parameters involved.

Radiation in CFB is described by the same expressions as for the noncirculating bed, but at the lower particle concentration of the CFB, radiation attains longer pathlengths. For the calculation of the effective emissivity of the suspension ε_b, two cases can be considered:

1. Combustion gases with low suspension density, for example, in a CFB during low-load operation or in the freeboard of a noncirculating fluidized bed combustor (FBC). In this situation, the influence of boundary layers can be disregarded.
2. Combustion gases with, relatively seen, high suspension density: for example, a CFB boiler under normal load conditions. The boundary layers are important.

Case 1: When the particle concentration is small, scattering of radiation from particles can be neglected, but both combustion gases and suspended particles contribute to the bed emissivity

$$\varepsilon_b = 1 - \left(1 - \varepsilon_g\right)\left(1 - \varepsilon_p\right) = \varepsilon_g + \varepsilon_p - \varepsilon_g \varepsilon_p \tag{17.120}$$

where

ε_g is the emissivity of the combustion gases H_2O and CO_2, which can be evaluated according to standard radiation correlations (Modest, 2003)

ε_p is the emissivity of a particle suspension calculated for the same pathlength L as for the gases, knowing the radiation cross section of particles C_p

$$C_p = \varepsilon_s n \pi d_p^2 / 4 \tag{17.121}$$

and the number of particles

$$n = \frac{\rho_{av}}{\rho_p \pi d_p^3/6} \tag{17.122}$$

where

d_p is the particle diameter
ρ_p is the particle density
ρ_{av} is the bulk bed density along the path considered
ε_s is the emissivity of the surface of the particles

With these relationships, the resulting emissivity of the particle suspension becomes

$$\varepsilon_b = 1 - \exp\left(-C_p L\right) \tag{17.123}$$

For an enclosure with surface A and volume V, the mean pathlength L is calculated according to Hottel and Sarofim (1967) as

$$L = 3.5V/A \tag{17.124}$$

Contributions to the radiative flux from the surface of the bed and from other surfaces also have to be included, according to standard procedures (Modest, 2003).

Case 2: When the particle concentration is high, the gas contribution can be neglected, but scattering in the particle suspension should be considered. The bed emissivity is $\varepsilon_b = \varepsilon_p$, calculated considering scattering (Brewster, 1986):

$$\varepsilon_p = \left[\frac{\varepsilon_s}{(1-\varepsilon_s)B}\left(\frac{\varepsilon_s}{(1-\varepsilon_s)B} + 2\right)\right]^{1/2} - \frac{\varepsilon_s}{(1-\varepsilon_s)B} \tag{17.125}$$

For isotropic scattering ($B = 0.5$) or for diffusely reflecting particles ($B = 0.667$) and a particle surface emissivity ε_s, this formula is represented as in Figure 17.23. Baskakov and Leckner (1997) have shown that several independent derivations of effective emissivity give similar results, among others, Equation 17.93.

At high particle concentration, when the wall layers are substantial, radiation and convection are not simply additive. Radiation from the core of the suspended bed ($\varepsilon_b \sigma T_b^4$) is reduced by the colder, relatively dense, wall layer. One approach has been (Breitholtz and Leckner, 1997) to express radiation from an isothermal medium at bed temperature compared with that affected by a boundary layer, employing the radiation heat transport equation. The result of this operation yields a correction to the maximum radiative heat-transfer coefficient by an empirical coefficient "the radiation efficiency," η, defined in analogy with Steward et al. (1995) and using the definition Equation 17.91

$$h_r = \eta \varepsilon \sigma \left(T_b + T_w\right)\left(T_b^2 + T_w^2\right) \tag{17.126}$$

where the emissivity ε is given by Equation 17.92. The radiation efficiency accounts for absorption of radiation by the wall layer and reduction in emission due to the fall in temperature close to the wall. Figure 17.24 shows the radiation efficiency determined by means of data sets obtained from the literature. Although there might have been inconsistencies in some of the data, it is seen that, at low suspension density, the impact of the wall layer is small (similar to Case 1) and the radiation efficiency is almost equal to unity, but with an increase in suspension density, the wall layers become more important and reduce the contribution of radiation to almost half its value in a suspension without wall layers.

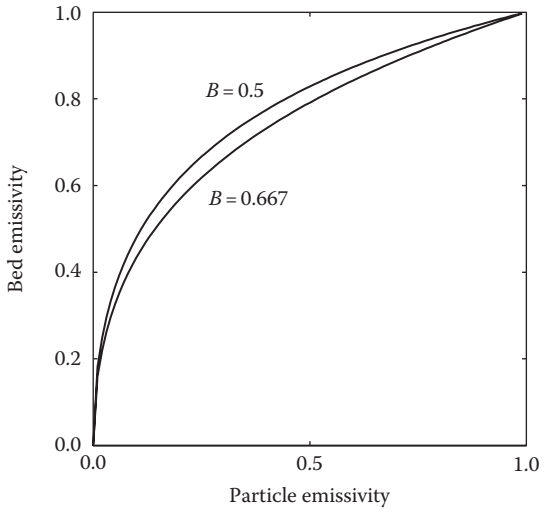


Figure 17.23

Effective bed emissivity vs. particle surface emissivity considering scattering (Equation 17.125).

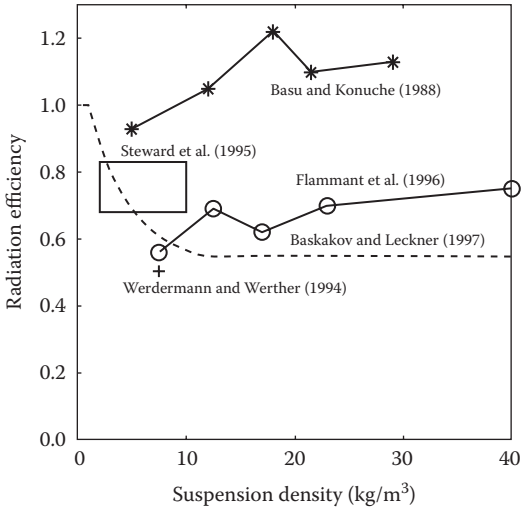


Figure 17.24

Radiation efficiency evaluated for a few experimental results. (From Breitholtz, C. and Leckner, B., *Trends Heat Mass Momentum Transfer*, 3, 85, 1997. With permission.)

The radiation efficiency is presented as a function of suspension density only. Implicitly, this relates to density and thickness of the wall layer. The influence of bed and wall temperatures remains to be further investigated.

17.2.1.2.3 Modeling (Approach 3) Comprehensive modeling involves the energy equation using the flow field from the continuity and momentum equations and considering mass and species balances related to chemical reactions. Although the developments in computer technology opens up new possibilities, most approaches related to heat transfer in fluidized bed have been simplified and are often similar to the models previously developed for bubbling fluidized beds. Assumptions commonly found in the literature can be summarized as follows:

1. Heat transfer between gas and particles is high. This allows the assumption of equal particle and gas-phase temperatures, and an emulsion phase energy equation using lumped thermal properties can be formulated rather than a particle and a gas-phase equation.

2. The main direction of the particle flow is along the wall, and the convective flows in other directions are relatively small and are neglected (but the transport of material to and from the wall layer implies a horizontal component).
3. The temperature gradient is large in the horizontal direction and negligible along the wall (Figure 17.20). Therefore, the conductive, dispersive, and radiative heat flows in the directions along the wall can be omitted from the equations.
4. Despite the obvious coupling of conduction and radiation toward the wall, in many models, these phenomena are treated separately.
5. Because of the low temperature in the wall layer, combustion is slow and heat release from chemical reactions is neglected there.
6. The density of the gas phase is much lower than that of the particle phase and gas convection can be neglected.
7. A thermal conductivity k_{pb} can be defined for the particle suspension.

As a result of these approximations, the energy equation becomes equal to Equation 17.97, and the same solution, Equation 17.98, is obtained, now with strands instead of packets transporting heat to the surface. The problem with high heat-transfer rates at short contact times requires the same solution as for the bubbling bed, and a particle convective heat-transfer coefficient is defined according to Equation 17.102. The fraction of time that the surface is not covered by bubbles $(1 - f_0)$ is now replaced by the wall coverage f_c of strands. To use these relationships, the thickness of the gas gap, the density of the strands, the descending velocity of the particles, or the residence time and length, all have to be known. This requires further modeling or empirical information. Several efforts have been made according to the approach described: for instance, by Wu et al. (1990), Basu (1990), Lints and Glicksman (1993), Fang et al. (1995a), Wang et al. (1996).

There is a striking resemblance between the modeling of the streamers falling along a surface in a CFB and the packets of particles induced by bubbles in a dense, bubbling bed bringing heat to a wall. In both cases, the thermal conduction of the particle suspension has an influence. On the other hand, it was mentioned that Martin's model of heat transfer in a bubbling bed focused attention on the gas gap and on the particles close to the wall, neglecting the transfer in the suspension itself. There are a number of CFB heat-transfer models that follow the same idea and treat single particle behavior at the wall and the influence of the gas gap (e.g., Farag and Tsai, 1993, Goedicke and Reh, 1993, Wirth, 1995).

Breitholtz and Leckner (1997) compared a number of available models of both kinds with two cases represented by average measurement data using similar physical properties: one under ambient conditions and the other was a hot case. The results from the various models showed a scatter of ±75%. In some comparisons, agreement between models was found, but for quite different reasons. Hence, judging available models as a group, it seems that modeling of CFB is not yet a well-established technique and the heat-transfer coefficient can only be reliably modeled in special cases when the importance of the particle boundary layer is small, that is, in the upper part of a CFB and in the freeboard of a noncirculating fluidized bed, where the particle suspension is not dense and absorption of radiation is small; otherwise, at present, empirical correlations have to be used.

17.2.1.2.4 Correlations (Approach 4) The collection of experimental results from various literature sources, presented by Basu and Nag (1996), shows a set of highly scattered data, which gives an impression of experimental difficulties in determining heat transfer in CFB. The variation between data sets is greater than the variation of the parameters studied. In contrast to a noncirculating bed, the CFB is a system, which, in addition to the impact of bed material and gas parameters, is affected by the size of the fluidized-bed vessel (wall effects) and by the operation of the circulating loop. Narrow, hot units have to be heated through the walls (because the wall surface to volume ratio makes heat losses important in small devices), and then the thermal wall layers differ from those of larger units where the walls are cooled; the conditions for thermal radiation heat transfer are different in small and large equipment. Moreover, it has been pointed out (Wu et al., 1989, Nag and Moral, 1990) that the length of the heat-transfer surface is important in research rigs where heat-transfer probes and inserts of limited size are used to measure heat transfer and a thermal boundary layer is formed on the measuring device (on the contrary, in a boiler, thermal boundary layers are already formed). Above a length of a meter or two, this effect is negligible. Hence, it is not a concern in commercial-size equipment, but it has influenced early measurements in research installations. Furthermore, in small research units, radiation from the surrounding walls may contribute unintentionally to the measured heat transfer.

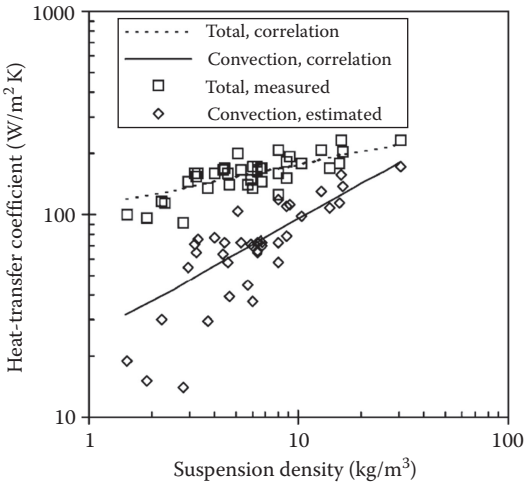


Figure 17.25

Total (convection and radiation) heat-transfer coefficients measured under hot conditions, averaged over the entire heat-receiving wall vs. cross-sectional average suspension density averaged over the corresponding furnace height. The lower curve represents the convective component. (From Breitholtz, C. et al., *Powder Technol.*, 120, 41, 2001.)

To simplify comparison, Breitholtz et al. (2001) classified the available results into two groups: results from boilers operating under hot conditions and results from laboratory-scale units run under ambient conditions. In both cases, long heat-transfer surfaces were used for measurements. This reduced the differences between the results in each of the two groups, but the scatter is still considerable. There are only a few results available from measurements of total heat-transfer coefficients in boilers. (e.g., as shown by Andersson and Leckner (1992), measurement by heat flux meters through holes in a boiler wall is very convenient, but quite unreliable because of the disturbance of the particle wall layer by the hole in the wall and by the variability of heat transfer in the boundary layer; it is difficult to determine a representative measurement value, because it depends on the location of the probe's surface). The data selected from boilers, related to the projected wall surface area (see Figure 17.19), presented as averages over the heat-transfer walls and related to the suspension density averaged over the corresponding furnace volume, have been represented in Figure 17.25 (upper line, "total") by

$$h = 110\rho^{0.21}(\mathrm{W/m^2\,deg}) \tag{17.127}$$

An implicit conclusion from Equation 17.127 is that within the scatter of available data only suspension density was found to be important for CFB heat transfer. This must be interpreted in the context of the evaluation, namely, for the heat-transfer situation in combustors, that is, a bed of sand, limestone, or ashes, operated at a temperature around 850°C and a heat-receiving surface consisting of boiler tubes at a temperature of 200°–500°C and with bed materials with sizes between 200 and 300 μm, in the various cases investigated.

There is a general agreement that the suspension density is a predominant influencing parameter, but often (Basu and Nag, 1996), a power of 0.5 is mentioned instead of 0.2, which was found for the boilers. There are three important aspects in relation to this issue: (1) the value given in Equation 17.127 is a furnace-averaged value and therefore, the slope is low; (2) there is a considerable scatter between various observations (e.g., as seen in Figure 17.25); and (3) radiation is included, which will reduce the power, because radiation is most influential at low suspension densities, and its impact is reduced as particle concentration increases.

In the diagram of Figure 17.25, also the convection constituent h_c is plotted. The convection is obtained from the difference between the measured total heat-transfer coefficient (the upper relationship in Figure 17.25) and the calculated radiative heat-transfer coefficient according to Equation 17.126, using the operational data from the various test cases and assuming that the two heat-transfer constituents are additive.

As a result, the convective heat-transfer coefficient (the lower line in Figure 17.25) becomes

$$h_c = 25\rho^{0.58}(\mathrm{W/m^2\,deg}) \tag{17.128}$$

valid for boiler conditions and $2 < \rho < 40$ kg/m^3). The data points decrease from the trend for $\rho < 10$ and approach a convective heat-transfer coefficient of $h_c \approx 10$ at very low densities, a value that is in the same order as the convective heat-transfer coefficient of gas in an entrance region of a duct (Breitholtz et al., 2001).

If scaled with $Nu_{amb} = Nu_{hot}$, the derived convective heat-transfer coefficients from Figure 17.25 agree with heat-transfer coefficients measured under ambient conditions, Breitholtz et al. (2001) (provided that the thermal conductivity in Nu_{hot} is taken at an average value between bed and wall, which is just a little above the end temperature of the gas gap).

In the upper part of a CFB furnace, the suspension density is low and radiation dominates. Baskakov and Leckner (1997) argued that in such a case the total heat-transfer coefficient should approach the radiative one, which should be around 125 W/m^2 deg at $T_w = 340$°C and $T_b = 850$°C (Equation 17.91), and about 100 W/m^2 deg for the wall temperature $T_w = 200$°C. It was also found that, due to the shielding effect of the colder boundary layer, the radiative contribution declined as accounted for by the radiation efficiency, and at suspension densities of above 25 kg/m^3 the radiation contribution was only about 50 W/m^2 deg (a radiation efficiency of $\eta \approx 0.5$). In investigating several cases, a curve describing the radiation efficiency η, like the one in Figure 17.24, was obtained by Breitholtz et al. (2001).

In summary, the total average heat-transfer coefficient can be obtained from Equations 17.126 and 17.128 as

$$h = h_c + h_r \tag{17.129}$$

by means of data from CFB boilers of thermal sizes between 10 and 300 MW. The expression allows for estimates of the influence of wall and bed temperatures on the heat transfer.

17.2.1.3 Concluding Remarks

Much work on heat transfer in fluidized beds, and in CFB in particular, was motivated by application in combustors. However, it was found during the 1980s that erosion on heat-transfer surfaces prevented the use of surfaces in contact with a dense bed of a combustor. It is still possible, though, to apply heat-transfer surfaces in dense fluidized beds if the velocity is low and erosion is minimized, such as in external heat exchangers of CFB boilers. There is an essential difference between tube bundles in a dense bubbling bed and the vertical surfaces in the transport zone of a CFB: in addition to erosion and the much higher heat-transfer coefficient in the dense bed, there is an obvious influence of particle size, whereas in the riser of the CFB, the contact between wall and suspension is less intensive, and consequently also the influence of particle size is small. In fact, there is no marked influence of particle size observed within the scatter of the experiments (Figure 17.25), except in refined laboratory-scale experiments (Sundaresan and Kolar, 2002). However, the particle size affects the heat transfer indirectly through the particle density ρ_{av}. For similar conditions (a given pressure drop over the furnace and a given fluidization velocity), smaller particles result in higher ρ_{av} in the upper part of the CFB riser than with larger particles, which remain to a larger extent in the bottom region below the heat-transfer surface. In CFB, heat transfer depends on particle size indirectly through the fluid dynamics.

17.2.2 Gas–Particle Heat and Mass Transfer

17.2.2.1 General

This section deals with heat and mass transfer across the surface of the particles in a fluidized bed. As seen from the point of view of the fluidized bed, this is internal heat and mass transfer. Accounts have been given by Gelperin and Einstein (1971), Kunii and Levenspiel (1991), Agarwal and La Nauze (1989), Tsukada and Horio (1992), Prins (1987), Palchonok (1998), and Di Natale et al. (2013).

Following the analogy between heat and mass transfer, the convective part of is these processes is expressed in a similar form:

$$Nu = f\left(Re, Pr\right) \quad \text{for heat transfer} \tag{17.130}$$

$$Sh = f\left(Re, Sc\right) \quad \text{for mass transfer} \tag{17.131}$$

The Sherwood number $Sh = k_m x_0/\mathscr{D}$ for mass transfer is defined similar to the Nusselt number $Nu = hx_0/k_g$ with the mass transfer coefficient k_m and gas diffusivity $\mathscr{D}$ instead of the heat-transfer coefficient h and

thermal conductivity k_g of the surrounding gas. There is an analogy between heat and mass transfer, and the fields of temperature and concentration coincide if the Lewis number $Le = \alpha/\mathscr{D} = Sc/Pr$ is equal to unity, where $\alpha = k_g/(\rho_g c_{pg})$ is the thermal diffusivity. The characteristic dimension x_0 is, except for some cases, the diameter of the particles. Most work presented in the literature concerns spherical particles and this form is also treated here. As will be pointed out, the analogy between heat and mass transfer is not complete. For instance, radiation may affect heat transfer but not mass transfer. Also, in a fluidized bed, the neighboring particles interact in different ways with an active particle for heat and for mass transfer.

In addition to Equations 17.130 and 17.131, there are boundary conditions. For heat transfer at a particle surface (index *w*; *n* is a direction perpendicular to the surface)

$$k_g\left(\partial\left(T - T_o\right)/\partial n\right)_w = h\left(T_w - T_o\right) \tag{17.132}$$

or in dimensionless form

$$\left(\frac{\partial \Theta}{\partial N}\right)_w = Nu \tag{17.133}$$

where

$N = (n/x_0)$ is the dimensionless coordinate

$\Theta = (T - T_o)/(T_w - T_o)$ is the dimensionless temperature, and the Nusselt number is

$$Nu = \frac{hx_0}{k_g} \tag{17.134}$$

Similar boundary conditions can be formulated for mass transfer. In the following, only empirical relationships will be treated.

17.2.2.2 A Spherical Particle in Single-Phase Flow

The conduction heat transfer across a spherical surface of radius r under steady-state conditions in a stagnant medium can be written as illustrated in Figure 17.26:

$$Q = 4\pi r^2 k_g \, \mathrm{d}T/\mathrm{d}r \tag{17.135}$$

Integrated between the temperature $T = T_w$ at $r = R$ (the surface of the sphere) and $T = T_o$ at $r = R_o$, a fictitious surface outside the sphere, and combined with the definition of the heat-transfer coefficient h (Equation 17.79), this becomes

$$Q = \frac{4\pi R k_g}{(1 - R/R_o)}(T_w - T_o) = 4\pi R^2 h (T_w - T_o) \tag{17.136}$$

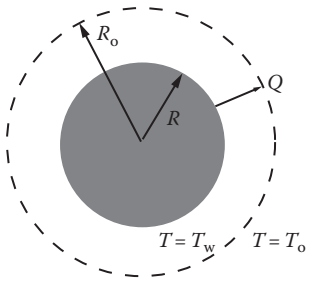


Figure 17.26

The heat flow Q leaving a sphere of radius R and a boundary layer of radius R_o.

When R_o tends to infinity, $hR/k_g = 1$ or $Nu = 2$ if Nu is based on the diameter of the sphere. If the sphere is also exposed to convective heat transfer, the following relationship is obtained:

$$Nu = 2 + f\left(Re, Pr\right) \tag{17.137}$$

A similar derivation yields $Sh = 2$ for mass transfer, and

$$Sh = 2 + f\left(Re, Sc\right) \tag{17.138}$$

These relationships are valid for heat and mass transfer to or from single particles and will be applied here to the special case of particles in fluidized beds. The Frössling–Ranz–Marshall equations are well-known relationships for heat and mass transfer to spheres in single-phase flow

$$Nu = 2 + 0.69\ Re^{0.5} Pr^{0.33} \tag{17.139}$$

$$Sh = 2 + 0.69\ Re^{0.5} Sc^{0.33} \tag{17.140}$$

Two classes of problems to be considered are (1) transfer between an entire bed and the gas flowing through the bed and (2) transfer between the gas and certain, active, particles contained in a bed of passive, inert particles. An example of the latter class is a bed of sand or ash for conversion (pyrolysis, gasification, or combustion) of fuel particles. These active fuel particles usually constitute only a few percent of the total bed.

17.2.2.3 Heat and Mass Transfer to a Bed of Particles

In a fluidized particle bed, one would expect more or less the same relationships for heat and mass transfer as for single particles, but this is apparently not the case as shown by Figure 17.27, where the shaded area (4) is the region of published, measured heat and mass transfer data related to particle beds and (3) represents Equations 17.139 and 17.140 for a single particle in single-phase flow. (The other curves in the figure will be

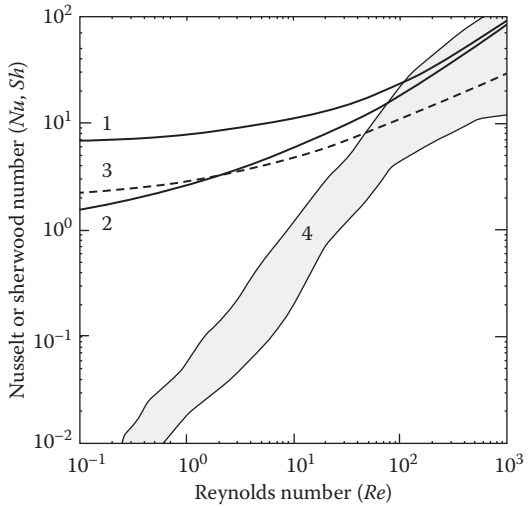


Figure 17.27

Heat and mass transfer coefficients as a function of velocity or particle size: (1) Equation 17.143 for heat transfer and (2) Equation 17.144 for mass transfer are compared with (3) a sphere in single-phase flow (Equations 17.139 and 17.140). The shaded region (4) represents various sets of published data from entire beds. *Ar* in Equations 17.143 and 17.144 has been calculated from Re_{mf} (Equation 17.81), assuming $\varepsilon = 0.4$ and $Pr = Sc = 0.7$. (Adapted from Palchonok, G.I. et al., Effect of turbulence on heat and mass transfer in the freeboard region of stationary and circulating fluidized beds, in Fan, L.-S. and Knowlton, T.M. (Eds.), *Fluidization IX*, Engineering Foundation, New York, 1998b, pp. 413–420.)

further treated below.) Only at higher velocities the coefficients of the various cases are on the same level. For small particles and low velocities the overall coefficients of an active bed appear to be much lower than those of single particles.

This discrepancy is explained by the resistance to gas transfer in fine particle beds (low *Re*), where most of the gas passes the bed through the bubble phase, while the flow through the emulsion phase, where the particles are contained, is much smaller. Thus, the overall resistance at the surface of a particle includes the additional resistance caused by the transfer from the bubble phase to the particulate phase. Furthermore, due to the extremely large specific area of beds of small particles, the gas in the particulate phase reaches saturation (it reaches the state of the particles) already close to the gas distributor, making the transfer potential in the upper part of the bed very small. These two factors result in great deviations of the actual gas property profiles from the log-mean value assumed in the evaluation of most measurements. Consequently, low, measured, overall heat and mass transfer coefficients for an entire fluidized bed are obtained (the shaded region) at the same time as the actual coefficient of a single small particle in the bed is much higher.

For larger particles, the gas flow through the particulate phase is larger and the flow through the entire bed is closer to plug flow (the high *Re* region in Figure 17.27). Therefore, the particles are exposed to the representative gas properties to a greater extent. Furthermore, the flow reaches farther into the bed before saturation. A detailed account of these phenomena is found in Kunii and Levenspiel (1991).

The large surface area encountered by a gas is one explanation for difficulties in interpretation of experimental data. A further explanation related to fixed beds, where the same phenomenon is observed, was given by Wakao and Kaguei (1982) to be due to the neglect of the axial dispersion in the evaluation of experimental results, a transport constituent that becomes increasingly important at low velocities (small particles, low *Re*).

As a consequence of the fast transfer, in most practical applications, the description of heat and mass transfer to the particles in a bed is not important. The problem of design of a bed is converted to what Gelperin and Einstein (1971) called the "thermal balance problem." This means that a heat or mass balance across the bed is sufficient in most design tasks. Only in special cases, for instance, very thin beds, where gas and particle conditions may not have reached equilibrium, the heat and mass transfer in the bed needs to be considered.

17.2.2.4 Heat and Mass Transfer to Active Particles in a Fluidized Bed of Inert Particles

Fuel converted in a fluidized bed forms active fuel particles surrounded by inert bed particles. Usually, the amount of fuel particles in the bed is such that every fuel particle is completely surrounded by inert particles and by gas at the given concentration and temperature, as illustrated in Figure 17.28. The particles are assumed to remain in the particulate phase where the superficial velocity is of the order of minimum fluidization velocity u_{mf}, and hence, there is a direct relation between the Reynolds number (velocity) and the particle size via the Archimedes number according to Equation 17.81. The temperature of the inert particles is practically the same as that of the gas, whereas the temperature of the active particles may differ from that

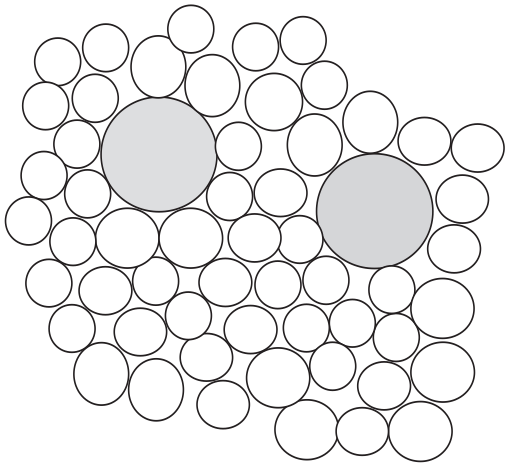


Figure 17.28

Two large, active particles surrounded by smaller, inert particles.

of the surrounding inert bed particles due to release or consumption of heat by some activity, such as chemical reaction in the particle or on its surface.

Depending on the size of the active particle d_a relative to that of the inert particles d_i, two extreme and one intermediate case can be distinguished: $d_a/d_i \gg 1$, $d_a/d_i \approx 1$, and $d_a/d_i \ll 1$. Baskakov et al. (1987) and Palchonok (1998a) established relationships for large active particles and for those of the same size as the inert particles and then proposed to interpolate between these extreme cases to obtain the heat and mass transfer data for active particles of the intermediate size.

Large active particles surrounded by smaller inert particles ($d_a/d_i \gg 1$) can be represented by correlations valid for maximum heat and mass transfer from gas and particle convection to large objects fixed in a fluidized bed (see Equations 17.83, 17.88, and 17.89) based on the size of the inert particles (index i):

$$Nu_{i,large} = 0.85 Ar_i^{0.19} + 0.006 Ar_i^{0.5} Pr^{0.33} \tag{17.141}$$

$$Sh_{i,large} = 0.009 Ar_i^{0.5} Sc^{0.33} \tag{17.142}$$

$Nu_{i,large}$ is the maximum Nusselt number obtained at optimum fluidization velocity according to Equation 17.84. This Nusselt number is assumed to be valid also for higher velocities. Naturally, there is no particle convection that contributes to mass transfer, and the first term of Equation 17.141 is not included in Equation 17.142. The information regarding the gas-convective term is originally gained from mass transfer experiments (Baskakov et al., 1973). (The small, insignificant differences in the coefficients in Equations 17.141 and 17.142 arise from slightly different fits to data at different times of publication.)

For active particles, which are nearly equal in size to the surrounding inert particles ($d_a/d_i \approx 1$), the heat and mass transfer has been represented by (Palchonok et al., 1992)

$$Nu_1 = 6 + 0.117 Ar_i^{0.39} Pr^{0.33} \tag{17.143}$$

$$Sh_1 = 2\varepsilon_{mf} + 0.117 Ar_i^{0.39}\, Sc^{0.33} \tag{17.144}$$

Index 1 is used to indicate that the dimensionless numbers are related to inert or active particles of about the same size. The gas convection term (the second term on the right-hand side) is based on numerous sets of measured data, among others those of Palchonok and Tamarin (1983 and 1985) and the analogy between heat and mass transfer. The first term represents the limiting case at low velocities (for small inert particles, small Ar), where heat and mass transfer are different. The mass transfer is about similar to the single-phase case, approximately corrected for the occlusion caused by the surrounding inert particles through the term ε_{mf}, the voidage at minimum fluidization velocity (Avedesian and Davidson, 1973). In heat transfer, there is no similar occlusion. On the contrary, the surrounding inert particles exchange heat both with the active particle and the gas. In this case, the integration of the heat conduction equation, Equation 17.136, is not carried out to infinity as for single-phase flow, but only to a limit represented by an equivalent spherical space containing the nearby gas. The space is $\varepsilon_{mf} d_p^3$ and part of the gas lenses between the active particle and the six neighboring particles $6(\pi d_p^3/24)$ (the gas lens is that between a cylinder $\pi d_p^3/8$ and a half-sphere, or alternatively, $6\varepsilon d_p^3/6$ can be used) in a cubic arrangement (Palchonok et al., 1992). This yields approximately the number 6, seen in Equation 17.143, a number that agrees with several sets of measurement data. A similar expression was presented by Baskakov et al. (1987):

$$Nu_1 = 10 + 0.23 Ar_i^{0.33} Pr^{0.33} \tag{17.145}$$

where the integration was carried out for a spherical gas shell in a cubic packing of particles, as explained by Zabrodsky (1966) and Gelperin and Einstein (1971). The difference between Equations 17.143 and 17.145 is small in practical applications, which are usually far from the limiting values at low velocities.

Equations 17.143 and 17.144 are compared with the correlation for single-phase heat and mass transfer to a sphere in Figure 17.27, and the limiting expressions for heat and mass transfer (Equations 17.143, 17.141 and 17.144; 17.142) are shown by the thick dashed (heat transfer) and solid (mass transfer) curves in Figure 17.29.

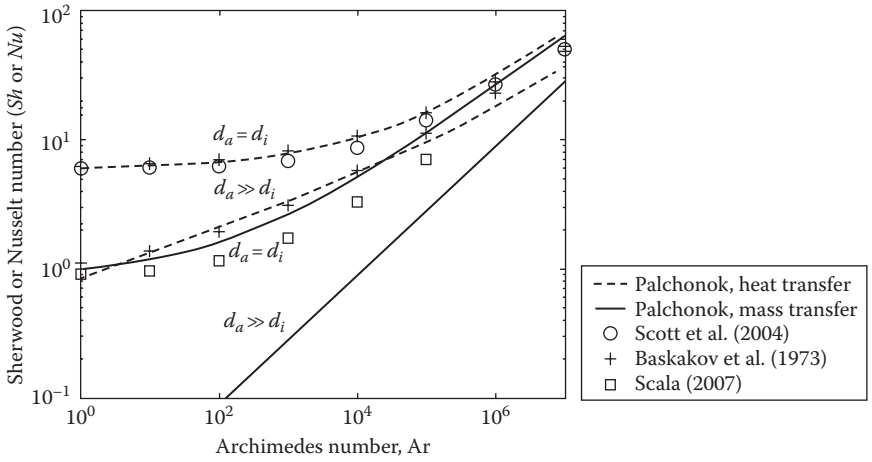


Figure 17.29

Heat and mass transfer in terms of Nusselt and Sherwood numbers at $d_a = d_i$ according to Equations 17.143 and 17.144 compared with some data from literature. The corresponding large active particle limits $d_a \gg d_i$ according to Equations 17.141 and 17.142 are also shown.

Interpolation between $Nu_{i,large}$ or $Sh_{i,large}$ and Nu_1 or Sh_1 yields heat and mass transfer coefficients Nu_i and Sh_i for spherical particles of an intermediate size $d_a/d_i \geq 1$:

$$\left(Nu_i - Nu_{i,large}\right)/\left(Nu_1 - Nu_{i,large}\right) = \left(d_i/d_a\right)^{2/3} \tag{17.146}$$

$$\left(Sh_i - Sh_{i,large}\right)/\left(Sh_1 - Sh_{i,large}\right) = \left(d_i/d_a\right)^{2/3} \tag{17.147}$$

The interpolation is based on available experimental data from literature, which are fitted within a range of ±30% (Palchonok, 1998a). However, there are several data sets that show greater deviation. The reasons for deviation have not yet been explained, and there are matters of discussion, such as the fact that Equation 17.141 describes the conditions at optimum velocity and beyond, whereas some heat transfer tests were carried out at lower velocities. Mass transfer does not seem to be affected by the fluidization velocity.

Scott et al. (2004) and, from the same department, Collier et al. (2004) investigated heat transfer to active particles and came up with the expression (with only some minor differences between the two publications):

$$Nu_a = 2 + 1.0 Re_{mfa}^{0.6} \left(d_a/d_i\right)^{0.26} \tag{17.148}$$

for $100 < Re_{mf,a} < 830$ and $0.2 < d_a/d_i < 2.72$. In this formula, the Prandtl number is not explicitly given and the velocity in Re is u_{mf} instead of u_{mf}/ε_{mf}, the actual interstitial velocity. Moreover, the constant term is 2, compared to 6 or 10 as derived by Palchonok et al. (1992) and Baskakov et al. (1987). Collier et al. (2004) paid particular attention to this matter and extrapolated their data to $Re = 0$ in order to determine the corresponding value. Despite considerable scatter in the data, the authors decided after discussion that the value of 2 was most relevant for the inclusion in Equation 17.148. Subsequently, Zhou et al. (2009) modeled numerically some of the cases investigated by Collier et al., including also $Re = 0$ and differentiating between convection and conduction. For a case of $d_a = d_i$ (Figure 10 in Zhou et al. (2009)), it is possible to derive $Nu(Re = 0) \approx 6$.

Also for mass transfer, alternative expressions have been derived, generally having the form, inspired by Equation 17.140:

$$Sh_a = 2\varepsilon_{mf} + 0.69 Re_{mf,a}^{0.5} Sc^{0.33} \tag{17.149}$$

where

Sh_a is related to d_a

$Re_{mf,a} = u_{mf} d_a/(\varepsilon_{mf}\nu)$

Several variants of this relationship have been proposed. Hayhurst and Parmar (2002) found that their own measurements were close to Equation 17.149 "but only for larger reacting spheres" (i.e., active particles larger than 3 mm). Scala (2007) carried out a comprehensive study in a slugging bed and concluded that Equation 17.149 fitted "excellently" his experimental data. He also concluded that the adequacy of using u_{mf} and ε_{mf} in Re "strongly suggests that the active particles only reside in the dense phase and never in the bubble/slug phase." This statement is not in agreement with Agarwal and co-workers (1988) whose model was based on the idea that the active particles were present both in the bubble and the particle phase. However, there is no doubt that Scala's data fit Equation 17.149 within the range of parameters investigated by him (100 μm $< d_i <$ 1.4 mm; 1.0 mm $< d_a <$ 10.0 mm) with the only uncertainty declared by Scala being the theoretical foundation of the limiting term $2\varepsilon_{mf}$. In the review of Di Natale et al. (2013), a comparison between various representations is made, stating that the results of Equation 17.147 deviate from Equation 17.149.

These correlations have been compared in Figure 17.29 for the special case $d_a = d_i$ at 450°C and $Pr = Sc = 1$. In this comparison, a number 6 has been imposed on the heat-transfer correlations instead of 10 or 2. Moreover, the correlations have been used as formulas beyond the ranges supported by measurement data. The data of Baskakov et al. (1987) (+) coincide rather well with Palchonok's curves, Within the range of data support ($10^2 < Ar < 10^5$), the results of Scala (2007) are lower than those of Palchonok, as stated by Di Natale et al. (2013). When adjusted to 6, Equation 17.148 (o) coincides rather well with Palchonok's data for heat transfer.

In conclusion, there are differences between the various data sets, but agreement is also found, especially if the value of 2 is adjusted to 6 in the heat-transfer correlations. Because of the analogy between heat and mass transfer, the results from heat and mass transfer measurements support each other.

Very small active particles (index a) tend to be carried by the gas through the space between the larger inert particles, constituting the bed. They can be assumed to behave like particles in a single-phase flow (cf. Equations 17.139 and 17.140), exposed to a velocity equal to their terminal velocity:

$$Nu_a = 2 + 0.6 Re_{at}^{0.5} Pr^{0.33} \tag{17.150}$$

$$Sh_a = 2 + 0.6 Re_{at}^{0.5} Sc^{0.33} \tag{17.151}$$

In this case, the terminal velocity of the active particle is equal to or smaller than the gas velocity $u_{mf}/\varepsilon \geq u_{at}$. This yields the Reynolds number in the convective terms of Equations 17.146 and 17.147 according to $Re_{at} = Ar_a/(18 + 0.61 Ar_a^{1/2})$ from Equation 17.82. Normally, these terms are very small, and the limiting Nusselt or Sherwood numbers approach 2 as long as the small particles do not severely interact with the bed particles. The correlations for small particles are related to their dimension d_a.

17.2.2.5 Active Particles above a Dense Bed

The previous account concerns particles in a dense, bubbling fluidized bed. Less information is available about particles in the freeboard or in the disperse phase of a CFB. There are some ways to solve this problem. First, it should be mentioned that in a CFB converter a great deal of the particles remains in the bottom bed and can be handled by the relationships mentioned in the previous section for a dense, bubbling bed. The particles carried away are small, and the surrounding particle loading of inert particles is also small; the voidage ε is almost equal to unity. Hence, the correlations for single-phase flow can be employed. These particles are exposed to a velocity that can be represented by the terminal velocity of a single particle (the velocity of the ascending particle relative to the gas). Refinements, such as accounting for clustering, are not likely to play a key role due to the high bed voidage.

A large, fixed object (a cylinder or a sphere), on the other hand, is subjected to the flow of particles and gas from the bed and particles returning from the space above the dense part of the bed down to the bed. There are some experiences from a CFB and from the splash zone of bubbling noncirculating beds related to heat transfer in this situation, as illustrated in Figure 17.30. The measured heat transfer is higher than the heat transfer to an object in an undisturbed single-phase flow, represented by the solid lines in the figure, and can be written as follows for a sphere ($Nu_{min} = 2$) or for a cylinder ($Nu_{min} = 0$).

$$Nu = Nu_{min} + 0.89 Re^{0.5} Pr^{0.33} \tag{17.152}$$

The additional contribution of radiation, if any, can be described by the relationships presented in the section on heat transfer.

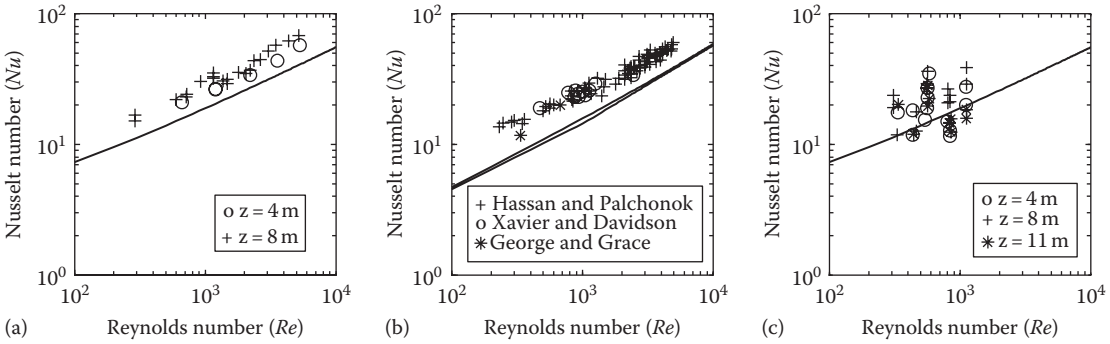


Figure 17.30

Convective heat transfer to a fixed object located at various distances z above the dense, bottom bed (a) in a cold experimental CFB rig, (b) in the splash zone of a bubbling bed, and (c) in a CFB boiler with radiation subtracted. The measurements are compared with the correlations for spheres and cylinders in a single-phase flow (Equation 17.139 in Figure [a] and [c]). The data in (b) are compared with the correlations of Douglas and Churchill (1956) and of Zhukauskas (1990) for a cylinder. (From Palchonok, G.I. et al., Effect of turbulence on heat and mass transfer in the freeboard region of stationary and circulating fluidized beds, in Fan, L.-S. and Knowlton, T.M. (Eds.), *Fluidization IX*, Engineering Foundation, New York, 1998, pp. 413–420.)

Nomenclature

Latin symbols

A	Area, m^2
C	Radiation cross section, 1/m
c_p	Specific heat capacity, J/kg, K
$\mathscr{D}$	Diffusivity, m^2/s
D	Tube diameter, m
d	Particle diameter, m
f_0	Fraction of time, –
f_c	Coverage factor, –
g	Acceleration of gravity, m/s^2
h	Heat-transfer coefficient, W/m^2, deg
h_l	Heat transfer through the particle wall layer, W/m^2, deg
k	Thermal conductivity, W/m, deg
k_m	Mass transfer coefficient, m/s
L	Pathlength, m
n	Number, normal direction
Q	Heat flow, W/m^2
R,r	Radius, m
s_h	Horizontal distance between tube centers, m
P	Pressure, Pa
T	Temperature, K
t	Time, s
u	Velocity, superficial gas velocity, m/s
V	Volume, m^3
z,x	Coordinates, length, m

Greek symbols

α	Thermal diffusivity, m^2/s
δ	Thickness, m
ε	Voidage
ϵ	Emissivity
η	Radiation efficiency
ρ	Density, kg/m^3

σ	Standard deviation, Stefan–Boltzmann's constant, W/m^2, K^4
ν	Kinematic viscosity, m^2/s
μ	Dynamic viscosity, kg/m, s
φ	Fraction of particle size, shape factor

List of Dimensionless Numbers

$Ar = \frac{g d_p^3 (\rho_p - \rho_g)\rho_g}{\mu^2}$	Archimedes number
$Fo = \frac{kt}{c_p \rho d^2}$	Fourier number
$Nu = \frac{hd}{k_g}$	Nusselt number, where d is a dimension
$Pr = \frac{\mu c_{pg}}{k_g}$	Prandtl number
$Re = \frac{ud}{\nu}$	Reynolds number, where d is a dimension
$Sc = \frac{\mu}{\rho_g D}$	Schmidt number
$Sh = \frac{k_d d_p}{D}$	Sherwood number

Indices

a	Active
air	Air
av	Average
at	Active particle at terminal velocity
b	Bed
c	Convective, cross section
eff	Effective
g	Gas
gc	Gas convective
h	Horizontal
i	Instantaneous, inert
k	Contact (resistance)
l	Layer
m	In x_m, thickness of stagnant particle suspension, mass transfer
max	Maximum
mf	Minimum fluidization
mf,a	Active particle at minimum fluidization velocity
opt	Optimum
p	Particle, packet
pc	Particle convective
proj	Projected (surface)
r	Radiative
s	Particle suspension, surface, solids
t	Terminal
w	Wall
∞	Far away, limiting case
1	Index indicating equality in size of active and inert particles
1	Of the same size
0	Characteristic

References

Abba, I.A., Grace, J.R., Bi, H.T., and Thompson, M.L., Spanning the flow regimes: Generic fluidized-bed reactor model, *AIChE J.*, 49, 1838, 2003.

Abrahamsen, A.R. and Geldart, D., Behaviour of gas fluidized beds of fine powders, *Powder Technol.*, 26, 35, 1980.

Aerov, M.E. and Todes, O.M., *Hydraulic and Thermal Fundamentals on the Operation of Apparatus with Static and Fluidised Particle Bed*, Chimia, Leningrad (in Russian), 1968.

Agarwal, P.K. and La Nauze, R.D., Transfer processes local to the coal particle: A review of drying, devolatilization and mass transfer in fluidized bed combustion, *Chem. Eng. Res. Des.*, 67, 457–480, 1989.

Agarwal, P.K., Mitchell, W.J., La Nauze, R.D., Transport phenomena in multi-particle systems—III. Active particle mass transfer in fluidized beds of inert particles, *Chem. Eng. Sci.*, 43, 2511, 1988.

Aguado, R., Olazar, M., San José, M.J., Gaisán, B., and Bilbao, J., Kinetic study of polyolefin pyrolysis in a conical spouted bed reactor, *Ind. Eng. Chem. Res.*, 41, 4559, 2002.

Andeen, B.R. and Glicksman, L.R., Heat transfer to horizontal tubes in shallow fluidized beds, *ASME-AIChE Heat Transfer Conference*, St Louis, MO, 76-HT-67, 1976.

Andersson, B.-Å. and Leckner, B., Experimental methods of estimating heat transfer in circulating fluidized bed boilers, *Int. J. Heat Mass Transfer*, 35, 3553, 1992.

Andersson, B.-Å. and Leckner, B., Bed-to-wall heat transfer in a 10 m^2 bubbling fluidized bed, in Macías Machín, A. and Winter, G. (Eds.), *Proceedings of Congreso Europeo de Fluidisación*, Universidad de Las Palmas de Gran Canaria, Vol. 1, 1994, pp. 251–260.

Asadullah, M., Ito, S., Kunimori, K., and Tomishige, K., Role of catalyst and its fluidization in the catalytic gasification of biomass to syngas at low temperature, *Ind. Eng. Chem. Res.*, 41, 4567, 2002a.

Asadullah, M., Ito, S.I., Kunimori, K., Yamada, M., and Tomishige, K., Energy efficient production of hydrogen and syngas from biomass: Development of low-temperature catalytic process for cellulose gasification, *Environ. Sci. Technol.*, 36, 4476, 2002b.

Avedesian, M.M. and Davidson, J.F., Combustion of carbon particles in a fluidized bed, *Trans. Inst. Chem. Eng.*, 51, 121–131, 1973.

Avidan, A.A., Fluid catalytic cracking, in Grace, J.R., Avidan, A.A., and Knowlton, T.M. (Eds.), *Circulating Fluidized Beds*, Blackie Academic & Professional, New York, 1997, p. 466, chap. 13.

Avidan, A.A., Edwards, M., and Owen, H., Fluid catalytic cracking. Past and future challenges, *Rev. Chem. Eng.*, 6, 1, 1990.

Avidan, A.A. and Shinnar, R., Development of catalytic cracking technology. A lesson in chemical reactor design, *Ind. Eng. Chem. Res.*, 29, 931, 1990.

Baeyens, J. and Geldart, D., Particle mixing in a gas fluidized bed, in *Fluidization and Its Applications*, Society Chim. Ind., Toulouse, France, 1973, p. 182.

Bai, D., Issangya, A.S., and Grace, J.R., Characteristics of gas fluidized beds in different flow regimes, *Ind. Eng. Chem. Res.*, 38, 260, 1999.

Bai, D., Jin, Y., Yu, Z.-Q., and Zhu, J.X., The axial distribution of the cross-sectionally averaged voidage in fast fluidized beds, *Powder Technol.*, 71, 51, 1992.

Bai, D. and Kato, K., Quantitative estimation of solids holdups at dense and dilute regions of the circulating fluidized bed, *Powder Technol.*, 101, 183, 1999.

Baron, T., Briens, C.L., and Bergougnou, M.A., Study of the transport disengaging height, *Can. J. Chem. Eng.*, 66, 749, 1988.

Baskakov, A.P., The mechanism of heat transfer between a fluidized bed and a surface, *Int. Chem. Eng.*, 4, 320–324, 1964.

Baskakov, A.P., Radiative heat transfer in fluidized beds, in Davidson, J.F. (Ed.), *Fluidization*, Academic Press, London, U.K., 1985, chap. 13B.

Baskakov, A.P., Berg, B.V., Vitt, O.K., Filippovsky, N.F., Kirakosyan, V.A., Goldobin, J.M., and Maskaev, V.K., Heat transfer to objects immersed in fluidized beds, *Powder Technol.*, 8, 273–282, 1973.

Baskakov, A.P. and Filippovsky, N.F, Transfer of heat in fluidized bed, in Einstein, V.G. and Baskakov, A.P. (Eds.), *Fluidization*, Chimia, Moscow, Russia, 1991, chap. 6 (in Russian).

Baskakov, A.P., Filippovsky, N.F., Munts, V.A., and Ashikhmin, A.A, Temperature of particles heated in a fluidized bed of inert material, *J. Eng. Phys.*, 52, 574–578, 1987.

Baskakov, A.P. and Leckner, B., Radiative transfer in CFB furnaces, *Powder Technol.*, 90, 213–218, 1997.

Bassi, A.S., Briens, C.L., and Bergougnou, M.A., Short contact time fluidized reactors (SCTFRs), in Avidan, A.A. (Ed.), *Circulating Fluidized Bed Technology IV*, AIChE, New York, 1994, p. 15.

Basu, P., Heat transfer in fast fluidized beds, *Chem. Eng. Sci.*, 45, 3123–3136, 1990.
Basu, P., Combustion of coal in circulating fluidized-bed boilers: A review, *Chem. Eng. Sci.*, 54, 5547, 1999.
Basu, P. and Nag, P.K., Heat transfer to walls of a circulating fluidized-bed furnace, *Chem. Eng. Sci.*, 51, 1–26, 1996.
Bi, H.T., Ellis, N., Abba, I.A., and Grace, J.R., A state-of-the-art review of gas–solid turbulent fluidization, *Chem. Eng. Sci.*, 55, 4789, 2000.
Bi, H.T., Grace, J.R., and Zhu, J., Regime transitions affecting gas–solids suspensions and fluidized beds, *Trans. Inst. Chem. Eng.*, 73, 154, 1995.
Borodulya, V.A. and Kovensky, V.I., Radiative heat transfer between a fluidized-bed and a surface, *Int. J. Heat Mass Transfer*, 26, 277–289, 1983.
Borodulya, V.A., Teplitsky, Yu.S., Markevich, I.I., Hassan, A.F., and Yeryomenko, T.P., Heat transfer between a surface and a fluidized bed: Consideration of pressure and temperature effects, *Int. J. Heat Mass Transf.*, 34, 47–53, 1991.
Botterill, J.S.M., *Fluid-Bed Heat Transfer*, Academic Press, London, U.K., 1975.
Breitholtz, C. and Leckner, B., Heat transfer in CFB boilers—Do we know sufficiently, *Trends Heat Mass Momentum Transfer*, 3, 85–104, 1997.
Breitholtz, C., Leckner, B., and Baskakov, A.P., Wall heat transfer in CFB boilers, *Powder Technol.*, 120, 14–48, 2001.
Brereton, C.M.H. and Grace, J.R., Microstructural aspects of the behaviour of circulating fluidized bed, *Chem. Eng. Sci.*, 48, 2565–2572, 1993.
Brewster, M.Q., Effective absorbtivity and emissivity of particulate media with application to a fluidized bed, *J. Heat Transfer.*, 108, 710–713, 1986.
Bridgwater, A.V., Renewable fuels and chemicals by thermal processing of biomass, *Chem. Eng. J.*, 91, 87, 2003.
Bridgwater, A.V. and Peacocke, G.V.C., Fast pyrolysis processes for biomass, *Renew. Sustain. Energy Rev.*, 4, 1, 2000.
Choi, J.-H., Chang, I.-Y., Shun, D.-W., Yi, C.-K., Son, J.-E., and Kim, S.-D., Correlation on the particle entrainment rate in gas fluidized beds, *Ind. Eng. Chem. Res.*, 38, 2491, 1999.
Clift, R., Grace, J.R., and Weber, M.E., *Bubbles, Drops and Particles*, Academic Press, New York, 1978.
Collier, A.P., Hayhurst, A.N., Richardson, J.L., and Scott, S.A., The heat transfer coefficient between a particle and a bed (packed or fluidized) of much larger particles, *Chem. Eng. Sci.*, 59, 4613, 2004.
Darton, R.C., LaNauze, R.D., Davidson, J.F., and Harrison, D., Bubble growth due to coalescence in fluidized beds, *Trans. Inst. Chem. Eng.*, 55, 274, 1977.
Davidson, J.F., Clift, R., and Harrison, D., *Fluidization*, 2nd edn., Academic Press, London, U.K., 1985.
Deiva, V., Grmela, R., and Chaouki, J., Improvement of fluidizability of fine powders, in *Proceedings of the World Congress on Particle Technology*, Sydney, New South Wales, Australia, Paper 671, 2002.
Deng, R.S., Wei, F., Jin, Y., Zhang, Q., and Jin, Y., Experimental study of the deep catalytic cracking process in a downer reactor, *Ind. Eng. Chem, Res.*, 41, 6015, 2002a.
Deng, R.S., Wei, F., Jin, Y., Zhang, Q., and Jin, Y., Downer catalytic pyrolysis (DCP): a novel process for light olefins production, *Chem. Eng. Technol.*, 25, 711, 2002b.
Dewettinck, K. and Huyghebaert, A., Fluidized bed coating in food technology, *Trends Food Sci. Technol.*, 10, 163, 1999.
Douglas, W.J.M. and Churchill, S.W., Recorrelation of data for convective heat transfer between gases and single cylinders with large temperature differences, *Chem. Eng. Prog., Symp. Ser.*, 52(18), 23–28, 1956.
Ellis, N., Bi, H.T., Lim, C.J., and Grace, J.R., Hydrodynamics of turbulent fluidized beds of different diameters, *Powder Technol.*, 141, 124, 2004.
Epstein, N., Applications of liquid–solid fluidization, *Int. J. Chem. Reactor Eng.*, 1, 1, 2003a.
Epstein, N., Liquid-solids fluidization, in Yang, W.C. (Ed.) *Handbook of Fluidization and Fluid-Particle Systems*, Marcel Dekker, New York, 2003b, chap. 26.
Epstein, N. and Grace, J.R., Spouting of particulate solids, in Fayed, M.E. and Otten, N. (Eds.), *Handbook of Powder Science and Technology*, 2nd edn., Chapman & Hall, New York, 1997, chap. 10.
Fan, L.-S., *Gas–Liquid–Solid Fluidization Engineering*, Butterworths, Boston, MA, 1989.
Fan, L.-S. and Tsuchiya, K., *Bubble Wake Dynamics in Liquids and Liquid-Solid Suspensions*, Butterworth-Heinemann, Boston, MA, 1990.
Fang, Z.H., Grace, J.R., and Lim, C.J., Radiative heat transfer in circulating fluidized beds, *J. Heat Transf.*, 117, 963–968, 1995a.
Fang, Z.H., Grace, J.R., and Lim, C.J., Local particle convective heat transfer along surfaces in circulating fluidized beds, *Int. J. Heat Mass Transfer*, 38, 1217–1224, 1995b.

Farag, I.H. and Tsai, K.Y., Surface-to-suspension heat transfer model in lean gas–solid freeboard flow, *Can. J. Chem. Eng.*, 71, 514–524, 1993.
Foka, M., Chaouki, J., Guy, C., and Klvana, D., Gas phase hydrodynamics of a gas–solid turbulent fluidized bed reactor, *Chem. Eng. Sci.*, 51, 713, 1996.
Gartside, R.J., QC—A new reaction system, in Grace, J.R., Shemilt, L.W., and Bergougnou, M.A. (Eds.), *Fluidization VI*, Engineering Foundation, New York, 1989, p. 25.
Geldart, D., Types of gas fluidization, *Powder Technol.*, 7, 285, 1973.
Geldart, D. (Ed.), *Gas Fluidization Technology*, Wiley & Sons, Chichester, U.K., 1986.
Gelperin, N.I. and Einstein, V.G., Heat transfer in fluidized beds, in Davidson, J.F., and Harrison, D. (Eds.), *Fluidization*, Academic Press, London, U.K., 1971, chap. 10.
Gibbs, B.F., Kermasha, S., Alli, I., and Mulligan, C.N., Encapsulation in the food industry: A review, *Int. J. Food Sci. Nutr.*, 50, 213, 1999.
Gilliland, E.R. and Mason, E.A., Gas mixing in beds of fluidized solids, *Ind. Eng. Chem.*, 44, 218, 1952.
Glicksman, L.R., Heat transfer in circulating fluidized beds, in Grace, J.R., Avidan, A.A., and Knowlton, T.M. (Eds.), *Circulating Fluidized Beds*, Blackie, London, U.K., 1997, pp. 261–311.
Glicksman, L.R., Hyre, M., and Farrell, P., Dynamic similarity in fluidization, *Int. J. Multiphase Flow*, 20S, 331, 1994.
Goedicke, F. and Reh, L., Particle induced heat transfer between walls and gas solid fluidized beds, *AIChE Symp. Ser.*, 89, 123–136, 1993.
Grace, J.R., The viscosity of fluidized beds, *Can. J. Chem. Eng.*, 48, 30, 1970.
Grace, J.R., Fluidized bed hydrodynamics, in Hetsroni, G. (Ed.), *Handbook of Multiphase Systems*, Hemisphere Press, Washington, DC, 1982, Sect. 8.1.
Grace, J.R., Contacting modes and behaviour classification of gas–solid and other two-phase suspensions, *Can. J. Chem. Eng.*, 64, 353, 1986a.
Grace, J.R., Fluid beds as chemical reactors, in Geldart, D. (Ed.), *Gas Fluidization Technology*, Wiley & Sons, Chichester, U.K., 1986b, Sect 8.1.
Grace, J.R., Interphase mass and heat transfer in gas-fluidized beds, in deKee, D., and Chhabra, R.P. (Eds.), *Transport Processes in Bubbles, Drops and Particles*, 2nd edn., Taylor & Francis, New York, 2002, chap. 7.
Grace, J.R., Avidan, A.A., and Knowlton, T.M. (Eds.), *Circulating Fluidized Beds*, Blackie Academic & Professional, New York, 1997.
Grace, J.R. and Harrison, D., The distribution of bubbles within a gas-fluidized bed, *Inst. Chem. Eng. Symp. Ser.*, 30, 105, 1968.
Grace, J.R. and Harrison, D., The behaviour of freely bubbling fluidized beds, *Chem. Eng. Sci.*, 24, 497, 1969.
Grace, J.R. and Harrison, D., Fluidized beds with internal baffles, in Davidson, J.F. and Harrison, D. (Ed.), *Fluidization*, Academic Press, London, U.K., 1971, chap. 13.
Grace, J.R., Issangya, A.S., Bai, D., Bi, H.T., and Zhu, J.Z., Situating the high-density circulating fluidized bed, *AIChE J.*, 45, 2108, 1999.
Grace, J.R. and Mathur, K.B., Height and structure of the fountain region above spouted beds, *Can. J. Chem. Eng.*, 56, 533, 1978.
Graham, R.G. and Huffman, D.R., Commercial aspects of rapid thermal processing (RTP), in *Proceedings of the Power Production from Biomass II Conference*, Espoo, Finland, April 1995.
Griffith, A.E. and Louge, M.Y., The scaling of cluster velocity at the wall of circulating fluidized bed risers, *Chem. Eng. Sci.*, 53, 2475, 1998.
Grewal, N.S., Experimental and theoretical investigation of heat transfer between a gas-solid fluidized bed and immersed tubes, PhD thesis, University of Illionois, Chicago, IL, 1979.
Gross, B. and Ramage, M.P., FCC reactor with a downflow reactor riser, U.S., Patent 4,385,985, 1983.
Hayhurst, A.N., Parmar, M.S., Measurement of the mass transfer coefficient and Sherwood number for carbon spheres burning in a bubbling fluidized bed, *Combust. Flame*, 130, 361, 2002.
Hetsroni, G. (Ed.), *Handbook of Multiphase Systems*, Hemisphere, Washington, DC, 1982.
Highley, J. and Kaye, W.G., Fluidized bed industrial boilers and furnaces, in Howard, J.R. (Ed.), *Fluidized Beds Combustion and Applications*, Applied Science Publishers, London, U.K., 1983.
Horio, M. and Nonaka, A., A generalized bubble diameter correlation for gas–solid fluidized beds, *AIChE J.*, 33, 1865, 1987.
Hottel, H.C. and Sarofim, A.F., *Radiative Transfer*, McGraw-Hill, New York, 1967.
Hovmand, S. and Davidson, J.F., Pilot plant and laboratory scale fluidized reactors at high gas velocities; the relevance of slug flow, in Davidson, J.F. and Harrison, D. (Eds.), *Fluidization*, Academic, London, U.K., 1971, chap. 5.

Howard, J.R. (Ed.), *Fluidized Beds Combustion and Applications*, Applied Science Publishers, London, U.K., 1983.
Huff, G.A. and Vasalos, I.A., Oxidative pyrolysis of natural gas in a spouted bed reactor: Reaction-stoichiometry and experimental reactor design, *Catal. Today*, 46, 39, 1998.
Issangya, A.S., Grace, J.R., Bai, D., and Zhu, J., Further measurements of flow dynamics in a high-density circulating fluidized bed riser, *Powder Technol.*, 111, 104, 2000.
Issangya, A.S., Grace, J.R., Bai, D., and Zhu, J., Radial voidage variation in CFB risers, *Can. J. Chem. Eng.*, 79, 279, 2001.
Jacobs, J.P., The future of fluidized-bed combustion, *Chem. Eng. Sci.*, 54, 5559, 1999.
Jahnig, C.E., Campbell, D.L., and Martin, H.A., History of fluidized solids development at EXXON, in Grace, J.R. and Matsen, J.M. (Eds.), *Fluidization*, Plenum Press, New York, 1980, p. 3.
Jin, Y., Yu, Z., and Cai, P., A criterion for transition from bubbling to turbulent fluidizeation, in Ostergaard, K. and Sorensen, A. (Eds.), *Fluidization V*, Engineering Foundation, New York, 1986, p. 289.
Johnsson, F., Zhang, W., Johnsson, H., and Leckner, B., Optical and momentum probe measurements in a CFB furnace, in Kwauk, M. and Li, J. (Eds.), *Circulating Fluidized Bed Technology V*, Science Press, Beijing, China, 1997, pp. 652–657.
Jono, K., Ichikawa, H., Miyamoto, M., and Fukumori, Y., A review of particulate design for pharmaceutical powders and their production by spouted bed coating, *Powder Technol.*, 113, 269, 2000.
Karamanev, D. and Nikolov, L., Bed expansion of liquid–solid inverse fluidization, *AIChE J.*, 38, 1916, 1992.
Kehoe, P.W.K. and Davidson, J.F., Continuously slugging fluidized beds, *Chemeca'70, Inst. Chem. Eng. Symp. Ser.*, 33, 97, 1971.
Khan, A.R. and Richardson, J.F., Fluid-particle interactions and flow characteristics of fluidised beds and settling suspensions of spherical particles, *Chem. Eng. Comm.*, 78, 111, 1989.
Kim, S.W., Kirbas, G., Bi, H.T., Lim, C.J., and Grace, J.R., Flow behaviour and regime transition in a high-density circulating fluidized bed riser, *Chem. Eng. Sci.*, 59, 3955, 2004a.
Kim, S.W., Kirbas, G., Bi, H.T., Lim, C.J., and Grace, J.R., Flow structure and thickness of annular downflow layer in a circulating fluidized bed riser, *Powder Technol.*, 142, 48, 2004b.
Kunii, D. and Levenspiel, O., *Fluidization Engineering*, 2nd edn., Butterworth-Heinemann, Boston, MA, 1991.
Kwauk, M., *Fluidization: Idealized and Bubbleless, with Applications*, Science Press, Beijing, China; Ellis Horwood, New York, 1992.
Lan, Q., Bassi, A.S., Zhu, J.-X., and Margaritis, A., Continuous protein recovery from whey using liquid–solid circulating fluidized bed ion-exchange extraction, *Biotech. Bioeng.*, 78, 157, 2002.
Latham, R., Hamilton, C., and Potter, O.E., Back-mixing and chemical reaction in fluidized beds, *Br. Chem. Eng.*, 13, 666, 1968.
Leckner, B., Fluidized bed combustion: Mixing and pollutant limitation, *Prog. Energy Comb. Sci.*, 24, 31–61, 1998.
Leckner, B., Andersson, B.-Å., and Vijil, J., Operational results from the 16 MW FBB at Chalmers University, *Third International Fluidised Conference*, The Institute of Energy, London, U.K., 1984, Paper Disc/16/134–143.
Leckner, B., Golriz, M.R., Zhang, W., Andersson, B.-Å., and Johnsson, F., Boundary layers–first measurements in the 12 MW CFB research plant at Chalmers University, in Anthony, E.J. (Ed.), *Proceedings of the 11th International Conference on Fluidized Bed Combustion*, ASME, New York, 1991, pp. 771–776.
Lee, D.H., Epstein, N., and Grace, J.R., The variable-voidage effect on modeling the minimum liquid fluidization velocity of gas-liquid fluidized beds, *J. Chem. Eng. Jpn.*, 36, 1111, 2003.
Lee, G.S. and Kim, S.D., Axial mixing of solids in turbulent fluidized beds, *Chem. Eng. J.*, 44, 1, 1990.
Lee, G.S., Kim, S.D., and Baird, M.H.I., Axial mixing of fine particles in fluidized bed, *Chem. Eng. J.*, 47, 47, 1991.
Lefroy, G.A. and Davidson, J.F., The mechanics of spouted beds, *Trans. Inst. Chem. Eng.*, 47, 120, 1969.
Leva, M., Correlations of the dense phase fluidized state and their applications, *Can. J. Chem. Eng.*, 35, 71, 1957.
Levy, Y. and Dorfman, Y., Two-phase flow in the vicinity of elongated bubbles in a fluidized bed, *AIChE J.*, 41, 1113, 1995.
Li, Z.Q., Wu, C.N., Wei, F., and Jin, Y., Experimental study of high-density gas-solids flow in a new coupled circulating fluidized bed, *Powder Technol.*, 139, 214, 2004.
Liang, W.-G. and Zhu, J.-X., Effect of radial flow nonuniformity on the alkylation reaction in a liquid–solid circulating fluidized bed (LSCFB) reactor, *Ind. Eng. Chem. Res.*, 36, 4651, 1997.
Limas-Ballesteros, R., Thèse de doctorat, Institut National Polytechnique, Toulouse, France, 1980.

Lints, M.C. and Glicksman, L.R., Parameters governing particle-to-wall heat transfer in circulating fluidized beds, in Avidan, A.A. (Ed.), *Circulating Fluidized Bed Technology*, AIChE, New York, 1993, pp. 297–304.
Liu, J., Grace, J.R., and Bi, H.T., A novel multi-functional optical fiber probe: II. High-density CFB measurements, *AIChE J.*, 49, 1421, 2003.
Lockett, M.J. and Harrison, D., The distribution of voidage fraction near bubbles rising in gas-fluidized beds, in Drinkenburg, A.A.H. (Ed.), *Proceedings of International Symposium on Fluidization*, Netherlands University Press, Amsterdam, the Netherlands, 1967, p. 257.
Maadhah, A.G., Abul-Hamayel, M., Aitani, A.M., Ino, T., and Okuhara, T., Down-flow FCC reactor, *Oil Gas J.*, 98, 66, 2000.
Mamuro, T. and Hattori, H., Flow pattern of fluid in spouted beds, *J. Chem. Eng. Jpn.*, 1, 1, 1968.
Martin, H., Heat transfer between gas fluidized beds of solid particles and the surfaces of immersed heat exchanger elements, Part I and Part II, *Chem. Eng. Process.*, 18, 157–169 and 199–223, 1984.
Martin, P.D., On the particulate and delayed bubbling regimes of fluidization, *Trans. Inst. Chem. Eng.*, 61, 318, 1983.
Mathur, K.B. and Epstein, N., *Spouted Beds*, Academic Press, New York, 1974.
Mathur, K.B. and Gishler, P.E., A technique for contacting gases with coarse solid particles, *AIChE J.*, 1, 157, 1955.
May, W.G., Fluidized-bed reactor studies, *Chem. Eng. Prog.*, 55(12), 49, 1959.
McNab, G.S., Predictions of spout diameter, *Br. Chem. Eng. Proc. Tech.*, 17, 532, 1972.
Merry, J.M.D., Penetration of a horizontal gas jet into a fluidized bed, *Trans. Inst. Chem. Eng.*, 49, 189, 1971.
Merry, J.M.D., Penetration of vertical jets into fluidized beds, *AIChE J.*, 21, 507, 1975.
Milne, B.J., Berruti, F., Behie, L.A., and de Bruijn, T.J.W., The hydrodynamics of the internally circulating fluidized bed at high temperature, in Avidan, A.A. (Ed.), *Circulating Fluidized Bed Technology VI*, AIChE, New York, 1994, p. 28.
Modest, M.F., *Radiative Heat Transfer*, 2nd edn., Academic Press, Amsterdam, the Netherlands, 2003.
Molerus, O. and Wirth, K.-E., *Heat Transfer in Fluidized Beds*, Chapman & Hall, London, U.K., 1997.
Murphy, J.R., Evolutionary design changes mark FCC process, *Oil Gas J.*, 90, 49, 1992.
Nag, P.K. and Moral, M.N.A., Effect of probe size on heat-transfer in circulating fluidized beds, *Int. J. Energy Res.*, 14, 965–974, 1990.
Nakhla, G., Zhu, J., and Cui, Y., Liquid-solid circulating fluidized bed waste water treatment system for simultaneous carbon, nitrogen and phosphorus removal, U.S. Patent, applied, February, 2004.
Di Natale, F., Nigro, R., and Scala, F., Heat and mass transfer in fluidized bed combustion and gasification systems, in Scala, F. (Ed.), *Chapter 5 in Fluidized Bed Technologies for Near-Zero Emission Combustion and Gasification*, Woodhead Publishing Series in Energy, 2013.
Overcashier, R.H., Todd, D.B., and Olney, R.B., Some effects of baffles in a fluidized system, *AIChE J.*, 5, 54, 1959.
Palchonok, G., Heat and mass transfer in a fluidized bed, PhD thesis, Chalmers University of Technology, 1998.
Palchonok, G.I., Dolidovich, A.F., Andersson, S., and Leckner, B., Calculation of true heat and mass transfer coefficients between particles and a fluidized bed, *Seventh International Conference on Fluidization*, Engineering Foundation, New York, 1992, pp. 913–920.
Palchonok, G.I. and Tamarin, A.I., Study of heat exchange between a model particle and a fluidized bed, *J. Eng. Phys.*, 45, 427–433, 1983.
Palchonok, G.I. and Tamarin, A.I., Mass transfer to a moving particle in a fluidized bed of coarse material, *J. Eng. Phys.*, 47, 916–923, 1985.
Palchonok, G.I., Breitholtz, C., Borodulya, V.A., and Leckner, B., Effect of turbulence on heat and mass transfer in the freeboard region of stationary and circulating fluidized beds, in Fan, L.-S. and Knowlton, T.M. (Eds.), *Fluidization IX*, Engineering Foundation, New York, 1998, pp. 413–420.
Pell, M., *Gas Fluidization*, Elsevier, Amsterdam, the Netherlands, 1990.
Prins, W., Fluidized bed combustion of a single particle, PhD thesis, Twente University, Enschede, the Netherlands, 1987.
Reh, L., Fluidized bed processing, *Chem. Eng. Prog.*, 67, 58, 1971.
Reh, L., The circulating fluid bed reactor—A key to efficient gas/solid processing, in Basu, P. (Ed.), *Circulating Fluidized Bed Technology I*, Pergamon, Toronto, Ontario, Canada, 1986, p. 105.
Reh, L., Challenges of circulating fluid-bed reactors in energy and raw materials industries, *Chem. Eng. Sci.*, 54, 5359, 1999.

Richardson, J.F. and Zaki, W.N., Sedimentation and fluidization, Part I, *Trans. I. Chem. Eng.*, 32, 35, 1954.
Rowe, P.N., A note on the motion of a bubble rising through a fluidized bed, *Chem. Eng. Sci.*, 19, 75, 1964.
Rowe, P.N. and Nienow, A.W., Particle mixing and segregation in gas-fluidized beds, a review, *Powder Technol.*, 15, 141, 1976.
Rowe, P.N. and Partridge, B.A., An x-ray study of bubbles in fluidised beds, *Trans. Inst. Chem. Eng.*, 43, 157, 1965.
Rowe, P.N., Partridge, B.A., Cheney, A.G., Henwood, G.A., and Lyall, E., The mechanism of solids mixing in fluidized beds, *Trans. Inst. Chem. Eng.*, 43, 271, 1965.
Royal Dutch Shell Group of Companies, *The Petroleum Handbook*, 6th edn., Elsevier, Amsterdam, the Netherlands, 1983.
Saxena, S.C., Heat transfer between immersed surfaces and gas-fluidized beds, in Hartnett, J.H. and Irvine, T.F. (Eds.), *Advances in Heat Transfer*, Vol. 19, Elsevier, Amstrdam, the Netherlands, 1989.
Scala, F., Mass transfer around freely moving active particles in the dense phase of a gas fluidized bed of inert particles, *Chem. Eng. Sci.*, 62, 4159, 2007.
Scott, S.A., Davidson, J.F., Dennis, J.S., and Hayhurst, A.N., Heat transfer to a single sphere immersed in beds of particles supplied by gas at rates above and below minimum fluidization, *Ind. Eng. Chem. Res.*, 43, 5632, 2004.
Schlünder, E.-U. et al. (Eds.), *Heat Exchanger Design Handbook*, VDI-Verlag, Duesseldorf, and Heishere Publishing Corporation, Washington, DC, 1987, Part 2, chap. 2.8.4.
Scott, D.S., Majerski, P., Piskorz, J., and Radlein, D., Second look at fast pyrolysis of biomass—The RTI process, *J. Anal. App. Pyrolysis*, 51, 23, 1999.
Scott, D.S., Plskorz, J., and Radlien, D., Liquid products from the continuous flash pyrolysis of biomass, *Ind. Eng. Chem. Process Des. Dev.*, 24, 581, 1985.
Shingles, T. and McDonald, A.F., Commercial experience with synthol CFB reactors, in Basu, P. and Large, J.F. (Eds.), *Circulating Fluidized Bed Technology II*, Pergamon Press, Oxford, U.K., 1988, p. 43.
Silverman, A., Thompson, A.H., Sterynberg, A., Yukawa, Y., and Shingles, T., Development of a dense phase fluidized bed Fischer-Tropsch Reactor, in Ostergaard, K., and Sorensen, A. (Eds.), *Fluidization V*, Engineering Foundation, New York, 1986, p. 441.
Sit, S.P. and Grace, J.R., Effect of bubble interaction on interphase mass transfer in gas fluidized beds, *Chem. Eng. Sci.*, 36, 327, 1981.
Sondreal, E.A., Benson, S.A., Hurley, J.P., Mann, M.D., Pavlish, J.H., Swanson, M.L., Weber, G.F., and Zygarlicke, C.J., Review of advances in combustion technology and biomass cofiring, *Fuel Process. Technol.*, 71, 7, 2001.
Song, Y.-X., *Applying the Principles Learned from the Nature (Tian-Gong-Kai-Wu)*, Shanghai Chinese Book Bureau, Shanghai, China, 1959.
Squires, A.M., Three bold exploiters of coal gasification: Winkler, godel and porta, in Howard, J.R. (Ed.), *Fluidized Beds Combustion and Applications*, Applied Science Publishers, London, U.K., 1983.
Steward, F.R., Couturier, M.F., and Poolpol, S., Analysis for radiative heat transfer in a circulating fluidized bed, in Heinschel, K.J. (Ed.), *Proceedings of the 13th International Conference on Fluid Bed Combustion*, ASME, New York, 1995, pp. 507–513.
Stewart, P.S.B. and Davidson, J.F., Slug flow in fluidized beds, *Powder Technol.*, 1, 61, 1967.
Sundaresan, R. and Kolar, A.K., Core heat transfer studies in circulating fluidized bed, *Powder Technol.*, 124, 138–151, 2002.
Sutton, D., Kelleher, B., and Ross, J.R.H., Review of literature on catalysts for biomass gasification, *Fuel Process. Technol.*, 72, 155, 2001.
Syncrude, Website of Syncrude, www.syncrude.ca, July 2004.
Talman, J.A., Geier, R., and Reh, L., Development of a downer reactor for fluid catalytic cracking, *Chem. Eng. Sci.*, 54, 2123, 1999.
Tasirin, S.M. and Geldart, D., Entrainment of FCC from fluidized beds, *Powder Technol.*, 95, 240, 1998.
Teunou, E. and Poncelet, D., Batch and continuous fluid bed coating—Review and state of the art, *J. Food Eng.*, 53, 325, 2002.
Thompson, M.L., Bi, H.T., and Grace, J.R., A generalized bubbling/turbulent fluidized-bed reactor model, *Chem. Eng. Sci.*, 54, 2175, 1999.
Tsukada, M. and Horio, M., Maximum heat transfer coefficient for an immersed body in a fluidized bed, *Ind. Eng. Chem. Res.*, 31, 1147–1156, 1992.
van Deemter, J.J., Mixing patterns in large-scale fluidized beds, in Grace, J.R. and Matsen, J.M. (Eds.), *Fluidization*, Plenum, New York, 1980, p. 69.

Varygin, N.N. and Martyushin, I.G., Calculation of the heat transfer surface in fluidized bed equipment, *Khim. Mashinostr.*, 5, 6–9, 1959 (in Russian).
Visser, J., Van der Waals and other cohesive forces affecting powder fluidization, *Powder Technol.*, 58, 1, 1989.
Wakao, N. and Kaguei, S., *Heat and Mass Transfer in Packed Beds*, Gordon and Breach Science Publishers, New York, 1982.
Wang, X.S., Gibbs, B.M., Rhodes, M.J., and Geldart, D., Convection wall-to-suspension heat transfer in circulating fluidized bed risers, *AIChE J.*, 42, 2112–2117, 1996.
Wang, Z. and Wei, F., Similarity of the particle concentration distribution between bubbling and turbulent fluidized beds, in *Proceedings of the Symposium of the Chinese Society,* of *Particle Technology*, Beijing, China, 1997, p. 396.
Wen, C.Y. and Chen, L.H., Fluidized bed freeboard phenomena: Entrainment and elutriation, *AIChE J.*, 28, 117, 1982.
Wen, C.Y. and Yu, Y.H., Generalized method for predicting the minimum fluidization velocity, *AIChE J.*, 12, 610, 1966.
Werdermann, C.C. and Werther, J., Heat transfer in large-scale circulating fluidized bed combustors of different sizes, in Avidan, A.A. (Ed.), *Circulating Fluidized Bed Technology*, AIChE, New York, 1994, pp. 428–435.
Werther, J., The influence of the bed diameter on the hydrodynamics of fluidized beds, *AIChE Symp. Ser.*, 70(141), 53, 1974.
Werther, J. and Hartge, E.-U., Elutriation and entrainment, in Yang, W.-C. (Ed.), *Handbook of Fluidization and Fluid Particle Systems*, Marcel Dekker, New York, 2003, chap. 4.
Wirth, K.-E., Heat transfer in circulating fluidized beds, *Chem. Eng. Sci.*, 50, 2137–2151, 1995.
Winkler, F., German Patent, 437,970, 1922.
Vreedenberg, H.A., Heat transfer between a fluidized bed and a horizontal tube, *Chem. Eng. Sci.*, 9, 52, 1958.
Wu, R.L., Grace, J.R., and Lim, C.J., A model for heat transfer in circulating fluidized bed, *Chem. Eng. Sci.*, 45, 3389–3398, 1990.
Wu, R.L., Grace, J.R., Lim, C.J., and Brereton, C.H.M., Suspension-to-surface heat-transfer in a circulating fluidized bed combustor, *AIChE J.*, 35, 1685–1691, 1989.
Wu, R.L., Lim, C.J., Grace, J.R., and Brereton, C.H.M., Instantaneous local heat transfer and hydrodynamics in a circulating fluidized bed, *Int. J. Heat Mass Transfer*, 34, 2019–2027, 1991.
Wu, C.Z., Huang, H., Zheng, S.P., and Yin, X.L., An economic analysis of biomass gasification and power generation in China, *Bioresour. Technol.*, 83, 65, 2002.
Yang, W.-C., *Handbook of Fluidization and Fluid-Particle Systems*, Marcel Dekker, New York, 2003.
Yang, X.L., Wild, G., and Euzen, J.P., Study of liquid retention in fixed-bed reactors with upward flow of gas and liquid, *Int. Chem. Eng.*, 33, 72, 1993.
Yerushalmi, J., Applications of fluidized bed, in Hetsroni, G. (Ed.), *Handbook of Multiphase Systems*, Hemisphere Publishing Co., Washington, DC, 1982, chap. 8.3.
Yin, X.L., Wu, C.Z., Zheng, S.P., and Chen, Y., Design and operation of a CFB gasification and power generation system for rice husk, *Biomass Bioenergy*, 23, 181, 2002.
Yu, Z.-Q., Application collocation, *Adv. Chem. Eng.*, 20, 39, 1994.
Zabrodsky, S.S., *Hydrodynamics and Heat Transfer in Fluidized Beds*, MIT Press, Cambridge, MA, 1966.
Zabrodsky, S.S., Choice of design correlations for the estimation of the heat transfer coefficient in a high-temperature fluidized bed to an immersed body, *BSSR Ser. Fiz. Eng. Nauk.*, 4, 193–107, 1974 (in Russian).
Zenz, F.A. and Othmer, D.F., *Fluidization and Fluid-Particle Systems*, Reinhold Publishing Corp., New York, 1960.
Zhang, J.-P., Epstein, N., and Grace, J.R., Minimum fluidization velocities for gas–liquid–solid three-phase systems, *Powder Technol.*, 100, 113, 1998.
Zhang, J.-P., Epstein, N., Grace, J.R., and Zhu, J.-X., Minimum liquid fluidization velocity of gas–liquid fluidized beds, *Trans. Inst. Chem. Eng.*, 73, 347, 1995.
Zhukauskas, A.A., *Convective Heat Transfer in Heat Exchangers*, Nauka Publishing House, Moscow, Russia, 1990 (in Russian).
Zhou, Z.Y., Yu, A.B., and Zulli, P., Particle scale study of heat transfer in packed and bubbling fluidized beds, *AIChE J.*, 55, 868, 2009.
Zhu, J.-X., Yu, Z.-Q., Jin, Y., Grace, J.R., and Issangya, A., Cocurrent downflow circulating fluidized bed (downer) reactors—A state of the art review, *Can. J. Chem. Eng.*, 73, 662, 1995.
Zhu, J.-X., Zheng, Y., Karamanev, D.G., and Bassi, A.S., (Gas-)liquid-solid circulating fluidized beds and their potential applications to bioreactor engineering, *Can. J. Chem. Eng.*, 78, 82, 2000.

17.3 Applications of Fluidized Bed Reactors

Jesse Zhu and Yi Cheng

17.3.1 Fluidized Bed Reactors

Fluidized beds as chemical reactors offer many unique advantages such as large interfacial surface area between fluid (gas or liquid) and the particles, high fluid-particle contact efficiency, excellent heat transfer, uniform temperature, and the abilities to handle a wide range of particle properties and a large quantity of particulate materials (Davidson et al., 1985, Geldart, 1986, Kunii and Levenspiel, 1991, Kwauk, 1992, Zhu et al., 2000). Added benefits for the high-velocity circulating fluidized beds include higher gas and solids throughput, more uniform residence time distributions for both gas and solids phases, higher turndown ratio, and the possibility to realize two different reactions in the riser and the solid's downflow return system (Grace et al., 1997). Please also refer to Sections 17.1 and 17.2 for more details.

Fluidized bed reactors include gas–solid, liquid–solid, and gas–liquid–solid fluidized bed reactors, in terms of the fluid-particulate systems. In terms of reactor scheme and operation, there are the so-called stationary fluidized beds (SFBs) or fixed fluidized beds (FFBs), where the particles essentially stay in the fluidized bed, and the so-called CFBs where particles are mostly entrained out of the fluidized beds but at the same time recirculated back to or fresh particles added to the same fluidized beds. SFBs are often called conventional fluidized beds since they were the first realized and used in various industry applications. In gas–solid systems, SFBs include particulate fluidized beds, bubbling fluidized beds, slugging fluidized beds, and turbulent fluidized beds, which are also called fluidization regimes, as detailed in Section 17.1. In liquid–solid systems, the SFBs primarily have one operating regime, the particulate fluidization regime, where the particles are uniformly suspended in the upflowing liquid. In the stationary gas–liquid–solid three-phase fluidized beds, there are three main operating regimes: the dispersed bubble regime, the coalesced bubble regime, and the slug regime (Fan, 1989). Since all CFBs have a dense phase of particulate materials in the bed, they are also referred to as dense phase fluidized beds, in contrast to dilute phase fluidized beds referring to s (CFB).

In CFBs, the fluidizing gas or liquid (or the two combined) velocity is high enough to entrain all particles out of the bed and to retain enough particles in the bed so as to keep a fluidized bed, particles (either recycled or fresh) need to be fed into the bottom of the fluidized beds. In the CFBs, there are also different regimes: the fast fluidization regime and the pneumatic transport regime (Grace et al., 1997), and in terms of the operating conditions, there are low-density (or low-flux) CFB and high-density (or high-flux) CFB, with the latter referring to higher suspension density and high particle flux operations (Zhu and Bi, 1995, Pärssinen and Zhu, 2001, Wang et al., 2004). A new type of fluidized bed reactor, the circulating turbulent fluidized bed (CTFB), was proposed recently, which is shown to have both the benefits of high reaction intensity from the turbulent fluidized bed and suppressed gas and solids dispersion from the CFB (Zhu and Zhu, 2008, Qi et al., 2009, Zhu, 2010). There is also the cocurrent gas–solid downflow operation where both gas and particles are flowing downward in the downer column (Zhu et al., 1995, Cheng et al., 2008).

There are also special types of fluidized bed reactors, such as the spouted bed reactor (Mathur and Epstein, 1974), which has been broadly included in the fluidized bed literature by tradition, although it can also be considered as another multiphase reactor. In a spouted bed, gas (or liquid) is injected from the bottom through a central nozzle into the bottom of a normally cylindrical vessel to form a high-velocity upflow stream of gas (or liquid) and particles in the central region (the spout) and a slow downward moving layer of particles between the central spout and the wall (the annulus). In this pattern, a gross internal particle circulation is created, which gives special features such as the ability to handle larger or sticky particles, making the spouted bed very useful in certain physical operations such as drying and particle coating. Another example is pneumatic transportation, which originated earlier than the concept of fluidized beds. With the development of CFB reactors, however, the distinctions between a CFB reactor and a transport reactor have become less clear (Bi et al., 1995). Associated with pneumatic transportation are particle spray and elutriation, which are normally not separately considered in the fluidized bed literature.

In a broad sense, the application of fluidization technology dates back to the ancient times when peasants winnowed their grains. After the grain particles were swung up, a relative upflow of gas stream was created when the particles fall down. In such a "fluidized" state, the "upflow" gas preferentially segregates the lighter shells from the heavier seeds so as to achieve separation. The first record on application of fluidization technology was perhaps in an ancient Chinese book entitled "Applying the Principles Learned from the Nature" in 1637, where Song (1637) described a process to separate sands out of grain through vibrating winnowing pans in a certain fashion.

Table 17.3 Fluidized Bed Reactors and Their Properties

Type of Fluidized Bed Reactor	Fluidizing Medium	Typical Particle Size	Typical Gas/Liquid Velocity
Bubbling bed	Gas	Medium–large	Low
Slugging bed	Gas	Medium–large	Low
Turbulent bed	Gas	Small–medium	Medium
Circulating turbulent bed	Gas	Small–medium	Medium–high
Circulating riser	Gas	Small	High
Circulating downer	Gas	Small	Medium–high
Spouted bed	Gas	Very large	Low
Liquid–solid bed	Liquid	Medium–large	Low
Gas–liquid–solid bed	Gas and liquid	Medium–large	Low
Liquid–solid circulating bed	Liquid	Small–medium	High
Gas–liquid–solid circulating bed	Gas and liquid	Small–medium	High
Inverse bed	Liquid	Small–medium	Low

The first modern application of a fluidized bed reactor was a stationary, dense-phase gas–solid fluidized bed reactor (Winkler, 1922), operated for coal gasification in Germany to produce synthesis fuel from coal. Over the last 80 years, the concept of such low-velocity "conventional" fluidized bed reactors has been significantly expanded with the development of new types of fluidized bed reactors, including high-velocity circulating or riser fluidized bed reactor by increasing the fluid velocity (Yerushalmi, 1976), to liquid–solid and gas–liquid–solid three-phase fluidized reactors by changing the fluidizing agent (Fan, 1989, Zhu et al., 2000, Epstein, 2003), and to cocurrent downflow downer fluidized bed reactors by changing the direction of the fluid/particle flow (Zhu et al., 1995, Cheng et al., 2008). Experimentally tested but not yet in application is the inverse fluidized bed reactors where lighter particles are fluidized inversely by heavier fluid (Karamanev and Nikolov, 1992, Sang, 2013). The various types of fluidized bed reactors are listed in Table 17.3.

The numerous applications of fluidized bed technology can be classified at least in two manners. The first is by reaction type. For gas–solid systems, they can be divided into four categories:

1. Gas catalytic reaction, where both reactants and products are in gas phase, but the reaction takes place on the surface of a solid catalyst. This is the most frequently encountered application, counting for majority of all fluidized bed applications. Examples of such reactions are the FCC process, and many catalytic synthesis reactions.
2. Gas-phase reaction with solids as heat carriers, where both reactants and products are in gas phase, but the solids are required as heat carriers to either provide the heat for the reaction or carry out the heat produced by the reactions. This is very useful for highly exothermic and endothermic reactions, because solid particles have very high heat capacity.
3. Gas–solid reaction, where both gas and solids are the reactants and the products contain either only gas phase or a combination of both gas and solids. Examples are coal and biomass combustion and gasification.
4. Physical process that involves a gas and particles, where no chemical reaction occurs. A typical example is fluidized bed drying.

A similar classification like the gas–solid systems can also be used for liquid–solid and gas–liquid–solid fluidized beds, but it may not be necessary at this stage given the limited number of applications. Applications of liquid–solid fluidized beds (LSFBs) and three-phase fluidized beds can often be found in hydrocarbon processing and the mineral process industry, and more recently in the biochemical, pharmaceutical, and food industry and the environmental area.

The second manner of classification is to group by the areas of applications in different industrial processes, including

1. Hydrocarbon processing
2. Catalytic synthesis
3. Roasting and calcination
4. Metallurgical processes
5. Materials processing, sprays, and coatings

6. Combustion, gasification, pyrolysis, and incineration
7. Biochemical and environmental processes
8. Pharmaceutical and food processes
9. Physical processes

This section is primarily structured in the first manner, but the type of application for each example in terms of the second classification is clearly referred in the description. Given the limited space, only the most commonly encountered processes and those of special features are included in this section. There are also many potential applications of fluidized beds. A selected few important potential applications, especially those in the late stage of development, are also described.

17.3.2 Catalytic Gas-Phase Reactions

17.3.2.1 Fluid Catalytic Cracking

Fluidized catalytic cracking or fluid catalytic cracking (FCC) for short was the second major application of fluidized bed technology after coal gasification by Winkler in the 1920s and was the largest application of fluidized bed technology for over 60 years, with over 400 units worldwide (Chen, 2011), just surpassed by fluidized bed coal combustion in the last 10 years. The FCC process uses a solid catalyst to crack down the long chain of vaporized heavy oil or residues from the crude and other sources and convert them to light products such as gasoline, kerosene, diesel, and light olefins. Since crude oil on average contains less than 10% gasoline with poor octane value, FCC becomes the critical process in meeting the demands for a higher gasoline fraction (over 50% in North America) plus a higher octane value. FCC is therefore often called the heart of a refinery (Avidan, 1992, Murphy, 1992, Reichle, 1992).

Some numbers provided in a 1997 review (Avidan, 1997) show the enormous economic impact of FCC on petroleum refining and hence on worldwide economy:

1. There are about 350 FCC units operating worldwide. The total worldwide capacity of FCC units is over 2.4 million tonnes/day (16 million barrels/day).
2. The uplift across the FCC unit (difference between the value of products and feed) can be as high as $US10 per barrel.
3. The total inventory of FCC catalyst in the average FCC unit is 300 tonnes. The daily catalyst makeup rate to the typical vacuum gas oil feed FCC unit is 4 tonnes, whereas the daily makeup rate to a residue processing FCC unit can be as high as 30 tonnes.
4. Over 450,000 tonnes of FCC catalyst are manufactured every year, representing a $US600 million business worldwide. The total catalyst manufactured worldwide is approximately 1200 tonnes/day corresponding to a surface area of 380,000 km^2 if laid as single layer particles, the size of Egypt, each year.

Cracking of crude oil to lighter hydrocarbons dated back to the early twentieth century (Royal Dutch Shell, 1983). In 1916, the first catalytic cracking process was carried out in a commercial scale with aluminum chloride as the catalyst. Since the catalyst was too costly, this process did not continue for long. In the 1930s, Houdry obtained an effective catalyst from natural clay and invented the Houdry process. Both were fixed bed processes, which had a long residence time and required cyclic operations for catalyst regeneration. Such processes also required salt bath heat exchangers, which are costly and only partially effective for temperature control. In 1941, the thermofor catalytic cracking (TCC) moving bed process went on operation where the cracking reaction and catalyst regeneration were for the first time realized in two separate vessels with the catalyst particles circulated between the two vessels initially by bucket elevators and later by pneumatic transport.

Because the fixed/moving-bed operation had many limitations in terms of solids handling and transportation, heat addition/removal, gas–solid contact, and process capacity etc., the Standard Oil of New Jersey (now Exxon) began to develop a new FCC process in the late 1930s, with their first commercial unit on line in 1942 (Jahnig et al., 1980). Figure 17.31 sketches the typical early FCC design, the EXXON Model IV, which has two dense phase fluidized beds: one as cracking reactor and one as catalyst regenerator. The reactor runs in the temperature range of 480°C–550°C and the regenerator in the range of 550°C–600°C. The catalyst used was the synthetic amorphous silica-alumina catalyst and the average particle size of FCC is 55–80 μm. The much smaller particle size than that in the fixed bed operation gives much more surface area for the cracking reaction. Figure 17.32 shows an alternative design of the dense phase FCC, the UOP stacked unit.

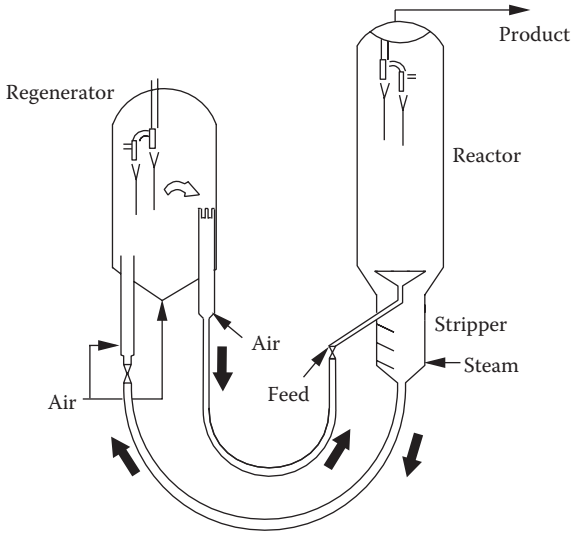


Figure 17.31

Exxon dense-phase fluidized bed FCC, Model IV.

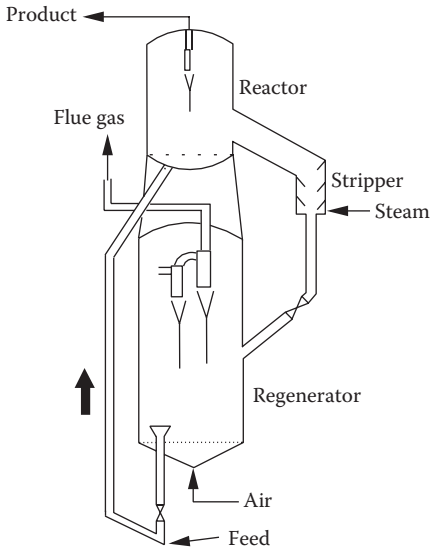


Figure 17.32

UOP stacked dense-phase fluidized bed FCC.

During the operation, the regenerated hot catalyst particles flow into the bottom of the reactor with the feed (crude oil or other heavy residue) injected into the transport line at a position near the bottom entrance to the reactor. The feed vaporizes upon contacting the hot catalyst and the catalytic cracking reaction takes place inside the reactor. Cracking yields lighter products, which leave the reactor in gas phase from the top of the reactor. During the cracking process, rejected carbon deposits onto the catalyst, causing it to deactivate. The deactivated catalyst particles are then circulated to the regenerator, after passing through a steam stripping section below the reactor. The stripping section or the stripper is either a moving bed or a gently fluidized bed with a very low steam rate and its main function is to displace the products adsorbed on the catalyst. The stripper commonly contains baffles to promote staging as significant axial mixing encountered in most SFBs leads to unit inefficiency. The deactivated catalyst is regenerated in the regenerator by burning off the carbon accumulation, before being circulated back to the reactor. During the regeneration, the temperature of catalyst is also increased by this exothermic combustion process, accumulating substantial heat in the catalyst. The hot catalyst then carries the heat

to the reactor, supplying the energy necessary for the endothermic catalytic reaction. Because of fluidization, catalyst particles can be transported easily in the loop between the two units. Both the reactor and the regenerator were reported to operate in the bubbling regimes in the early times. However, it is likely that most of them were operated in the turbulent fluidization regime given the relatively high gas flowrate, although not reported as such since the concept of the turbulent fluidized bed was not proposed until the early 1970s (Kehoe and Davidson, 1971).

The advantages of the FCC process are the excellent gas–solid contact, the much improved heat transfer, the large interfacial area with the reduction of particle size, and the large and controllable solids circulation between the two units. There are also at least two additional key advantages that distinguish the FCC from other fluidized bed processes: The first key advantage is that the reaction and regeneration is completed in one cycle with catalyst particles freely circulated between the two units. This solves the problem of quick catalyst deactivation and allows the process to continue. FCC is classified as a gas-phase catalytic reaction, because the solid particles are the catalyst that does not change its form during the process. The second key advantage is the realization of self-heat sufficiency by using the heat of carbon combustion in the regenerator to supply the heat required for the endothermic cracking reaction. This also gives the feature of a "gas-phase reaction with solids as the heat carrier" as in the first classification. With the second classification by areas of application, FCC clearly belongs to hydrocarbon processing.

While having many advantages, the dense phase FCC process has at least two distinct disadvantages: (1) The residence time of the gas phase in the reactor cannot be controlled precisely, leading to overcracking of the product, and (2) the residence time of the catalyst is also not uniform in the reactor and the presence of deactivated catalyst severely affects the selectivity. With the development of the more active zeolite catalyst by Mobil, the new "riser-cracker" was commercialized in the early 1960s. This new FCC replaces the dense-phase fluidized bed reactor with a transport riser reactor within which the gas velocity is sufficiently high to entrain the particles upward while the cracking reaction takes place. A typical riser FCC unit, the Shell FCC unit, is given in Figure 17.33a. The riser reactor significantly narrows the residence time distributions for both gas and solid phases so that overcracking is reduced and selectivity is increased. The high-velocity operation, in combination with the more active zeolite catalyst, also shortens the reaction time, further enhancing the formation of liquid products and reducing coke formation. The new zeolite catalyst also allows the increase of the regeneration temperature to about 700°C or higher, enhancing the combustion efficiency with more CO burnings and providing a better heat balance. The zeolite catalyst has an average particle size of 50–75 μm and the particles usually have a wide size distribution from 1 to 130 μm (Avidan and Shinnar, 1990), with sufficient fines under 45 μm to ensure excellent fluidity.

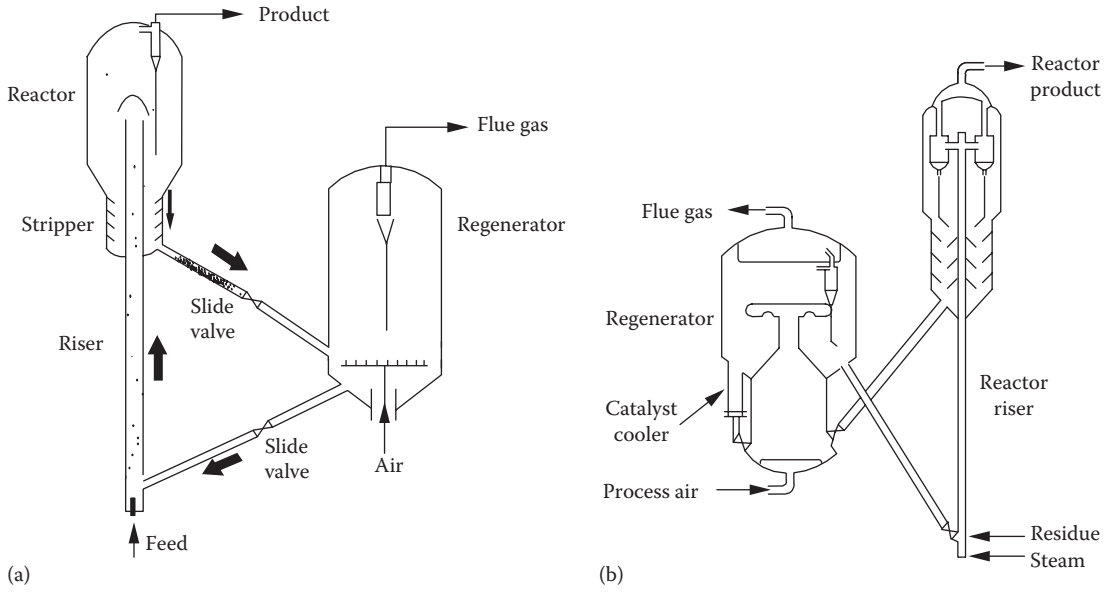


Figure 17.33

(a) Shell riser FCC. (b) SINOPEC riser RFCC.

Typical yields from a modern FCC (Avidan et al., 1990) operated in North America are (all weight %)

Fuel gas	4%
Dry gases $(C_3's + C_4's)$	13%
Gasoline	50%
Light cycle oil	20%
Heavy cycle oil	7%
Coke	6%

The highly endothermic cracking reaction significantly reduces the molecular weight of the feed to yield much more valuable products. The moderate temperature (500°C–550°C) ensures the preference of a more selective catalytic cracking over the less selective thermal cracking. By changing the temperature and other operating conditions, the relative fractions of the different product components can be adjusted to reflect the market requirements. (Avidan et al., 1990).

In recent years, the demand for more light products has led to the cracking of heavier feed. This is sometimes referred to as residue fluid catalytic cracking (RFCC). RFCC requires "deeper" cracking under a higher catalyst/oil ratio. In addition, the heavier feed produces more carbon on the deactivated catalyst, increasing the load of the regenerator. Many new regenerators have been designed to accommodate such a change, featuring two-stage combustion, larger unit, additional catalyst cooler, etc. The catalyst cooler is another external fluidized bed heat exchanger connected to the regenerator, where excess heat from the regenerator can be optionally removed out of the system. This becomes an essential feature for RFCC, since the heat from carbon combustion is normally more than that required for the cracking reaction. It is also used to control the regenerator and the reactor temperatures. The RFCC unit by SINOPEC is shown in Figure 17.33b as an example.

Although the modern FCC coupled by the CFB riser reactor and the turbulent bed regenerator is dominating the world FCC technology, they are not free from some inherent problems. In a typical riser, there is significant radial segregation with higher solids concentration and lower gas and particle velocities near the wall, and, lower solids concentration and higher gas and particle velocities in the center. This reduces the gas–solids contact efficiency, and also causes axial dispersion of the two phases and therefore nonuniform residence time distributions for the gas and solids. The gas dispersion causes overcracking and solids dispersion causes a reduction of selectivity. Solids acceleration at the riser bottom and gas–solids separation at the riser top both also lead to the requirement of longer reaction time.

To overcome this problem, the concept of a cocurrent gas–solid downer was proposed as a quick-contact reactor. In the downer, the radial gas and solids segregation existing in the riser is minimized due to the along-gravity flow directions of both gas and particles. The patent by Texaco appears to be the first to publish this downer concept (Gross, 1983, Gross and Ramage, 1983). Later, Murphy (1992) reviewed the evolutionary design changes of FCC processes and pointed out that the future FCC will involve high temperature, short residence time cracking, and dispersed phase regeneration. He then proposed the use of a downer for cracking reaction and a riser for catalyst regeneration, as shown in Figure 17.34. The Quick Contact (QC) reactor tested by Stone and Webster (Gartside, 1989) and the short contact-time fluidized reactor tested by Bergougnou et al. (1994), though mainly developed for thermal cracking, are both downer reactors that can also be used for FCC. Later on, bench-scale pilot studies by Deng et al. (2002a) show the excellent properties of the downer reactor, which have led to a significant improvement in selectivity, but similar pilot studies by Talman et al. (1999) reveal that the actual conversion in their downer reactor is less than that expected from a pseudo homogeneous reactor. The latter was further confirmed by recent studies of Li et al. (2013) and Wang et al. (2014), which directly compare the performance of a pilot scale pair of riser and downer using ozone decomposition reaction, where the downer is shown to be much more closer to plug flow than the riser but is yet not an ideal plug flow reactor. Associated with hot model studies are many hydrodynamic studies, such as those of Zhang et al. (2001), Luo et al. (2007), Qi et al., (2008), and Wang et al. (2014), as well as those reviewed by Cheng et al. (2008), most showing favorable characteristics of the downer reactor. In the longer run, it is evident that the downer is superior to the riser for the FCC process. Results from a 0.2 b/d demonstration downer unit in Saudi Arabia, operated at a high reaction temperature (above 550°C), short contact time, and with a high C/O ratio, have reported enhanced gasoline and light olefins production, reduced back-mixing, and suppressed thermal-cracking reactions (Maadhah et al., 2000). Based on these results, a 30 b/d demonstration unit was later on built near a Saudi refinery.

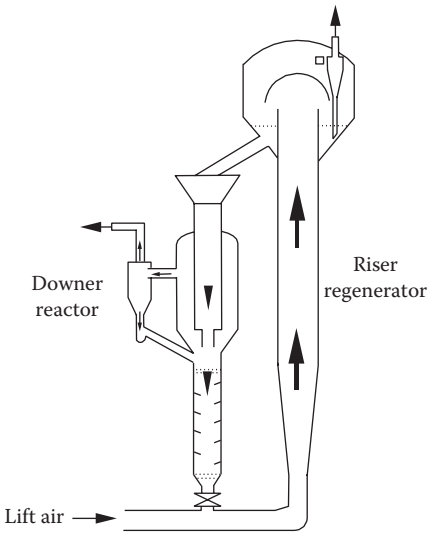


Figure 17.34

Future FCC unit as proposed by Murphy, with downer reactor and riser regenerator.

17.3.2.2 Catalytic Synthesis: Fischer–Tropsch Process

Fischer–Tropsch (F-T) process is the collective name for a group of synthetic reactions that synthesize CO and H_2 to form hydrocarbons of longer chains under high temperature and pressure. This is a strong exothermic reaction. The application of fluidized beds in the F-T process has been an ongoing competition between the SFB and the CFB and important lessons can be learned from the evolution of this process.

The application of fluidized bed in the F-T process started with a sad story regarding the failure of the first such attempt in the United States in the 1950s (Kunii and Levenspiel, 1991). It was the hydrocol process that aimed at the production of high-grade gasoline from cheap natural gas. It was a dense (bubbling) phase fluidized bed (SFB) of iron catalyst with cooling tube banks immersed in the bed to remove the heat (Zenz and Othmer, 1960). Although laboratory experiments were very promising (90% conversion), the 5 m ID commercial unit had much lower conversion. One key reason was attributed to the group C iron catalyst particles, which results in poor fluidization quality including channeling, poor gas–solid contact, and poor mixing. The operation was then abandoned later, with the added consideration of the rising natural gas price.

At the same time, the South African Synthetic Oil Limited (Sasol) was asking Kellogg to develop a new reactor for the same process. At that time, Kellogg has been heavily involved in a consortium of companies to develop the FCC reactors, the first generation of which was a CFB (Shingles and McDonald, 1988). The story was that Kellogg decided to try the CFB approach since they already had the detailed design for FCC, which was then shelved because of the low activity of the amorphous silica-alumina catalyst. The pilot study was a success and CFB was chosen as the Sasol Synthol reactor. The first commercial Sasol reactor, Sasol 1, was in production in 1955 and this was also the first application of CFB in industry, although it turned out later that there is no need to have a CFB, but a more carefully designed SFB would suffice.

The Sasol Synthol reactor is schematically shown in Figure 17.35. It is more like a loop reactor, but has most of the essential features of CFB. The feed is pushed into the bottom of the riser where the F-T reaction takes place. Heat exchangers are located in the middle portion of the riser to remove the heat produced by the reaction. The product is then separated from the recirculating catalyst and the catalyst is returned to the bottom of the standpipe to restart the cycle. The reaction temperature is above 320°C, and the pressure is 10–17 bars. The reactor side gas velocity needs to be above a critical velocity of 1.2 m/s, below which the operation becomes unstable. The voidage on the reactor side is around 0.90 at the bottom to 0.97 at the top (Shingles and McDonald, 1988). A series of scale-ups after the first commercial unit have increased the single unit capacity by several times. Shingles and McDonald (1988) provide a detailed account of the initial startup experience of the first Sasol reactor and the subsequent scale-ups to Sasol 2 and Sasol 3 reactors.

The main reason for using a fluidized bed for the F-T process is the high heat-transfer rate that ensures a nearly uniform reaction temperature. However, because catalyst deactivation is not an issue and there

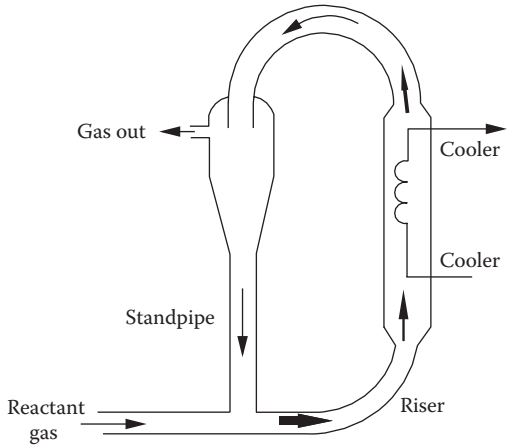


Figure 17.35

Sasol Synthol CFB Fischer–Tropsch reactor.

is no need to remove and return the catalyst continuously, the particles are in complete mixed mode in the Sasol reactors. In this case, a turbulent fluidized bed reactor, an SFB, should suffice and actually is better given the lower cost. While Sasol did make a quick comparison between a CFB and a SFB back in the 1950s, Shingles and McDonald (1988) suggested that the comparison was not made properly, since different particle sizes were used for the two types of reactors. At that time, little was known about the turbulent fluidized bed, so that its positive influence on the F-T process was left to be discovered 30 years later (Silverman et al., 1986).

The competition between the SFB and the CFB on the application of F-T process now finally has a "verdict" with the turbulent bed winning the race. An important lesson is that there is no need to "overkill" and CFB is not necessarily better if not needed. The latter is often mistakenly portrayed to students and young engineers as always being superior when they read the vast literature that describes the benefits of CFB.

17.3.2.3 Other Catalytic Reactions

Besides the F-T process, there are also a number of catalytic gas-phase processes that have been realized in fluidized bed reactors. In most of these cases, the catalyst does not deactivate quickly; that is, there is no need to change the catalyst frequently so that these catalytic reactions take place in SFBs. One key feature for gas-phase catalytic reactions is the large thermal effect of the reactions, and in this regard, fluidized beds are superior to fixed beds, because a uniform temperature can be easily maintained in the fluidized beds. Another key feature for catalytic gas-phase reactions is that the reaction rate is usually very high. As a result, almost all such catalytic reactions employ the turbulent fluidized bed, given the advantages of a smaller particle size that gives a higher gas–solid contact area, the reduction of bubble size, the high gas throughput, and reduced gas backmixing in the turbulent fluidized beds. Some of the reactions may have been reported to operate in the bubbling fluidized beds, due to the fact that the turbulent fluidization regime was not separately defined until the earlier 1970s (Kehoe and Davidson, 1971). Even if some of the earlier catalytic reactors did operate in the lower gas velocity bubbling regime, the operators have learned quickly through online experience that increasing the gas velocity most likely benefits both the yield and the productivity as the bed transfers from the bubbling to the turbulent regime.

Such catalytic gas-phase reactions include the productions of phthalic anhydride, acrylonitrile, aniline, ethylene dichloride, polyethylene, and polypropylene. Some of the processes are illustrated in Figure 17.36. Kunii and Levenspiel (1991) and Yerushalmi (1982) have given a good review for several of these processes with detailed reaction conditions so that an extensive review is not repeated here. Some common key features required for these fluidized bed reactors include good feed nozzle design for liquid feed, uniform gas distribution, efficient heat exchangers, and excellent gas–solid separation. Makeup of the catalyst may also be needed during the process due to catalyst attrition and carryovers.

A point worth mentioning is that the addition of proper internal baffles can enhance these catalytic reaction. Horizontal baffles lead to more staging for the gas flow and can normally increase the conversion and yield. Some more exotic baffles have also been used, which are believed to provide more benefits to certain

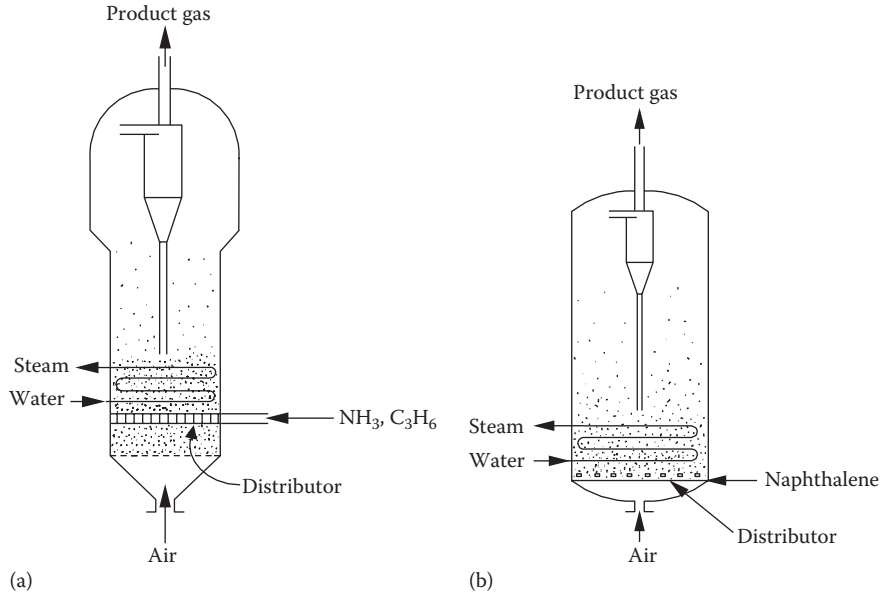


Figure 17.36

(a) Fluidized bed reactor for the production of acrylonitrile. (b) Fluidized bed reactor for the production of phthalic anhydride.

reactions. For example, the installation of pagoda baffles led to a significant increase of both conversion and yield for the production of phthalic anhydride from the oxidation of naphthalene (Yu, 1994). The reason for the success is that the pagoda baffles lead to an earlier transition to the turbulent fluidization regime at lower gas velocities, providing a better fluidization quality (Jin et al., 1986).

17.3.3 Noncatalytic Gas-Phase Reactions

17.3.3.1 Thermal Cracking

The purpose of thermal cracking is to produce light olefins. This is often achieved in a tubular furnace reactor, where the feed is cracked in tubes going through a high-temperature furnace. Currently, most of the world's ethylene is produced in this manner. However, the coke produced in the cracking process deposits on the tube inner wall and blocks up the reactor, so that the feeds to the tubular reactors are limited to light hydrocarbons such as ethane, naphtha, and kerosene, which are much more expensive than the heavier feed such as crude.

A fluidized bed reactor can be used to achieve the same process to crack light hydrocarbons into olefins, with the required heat for the reaction provided by burning additional fuel oil, or burning partially either the feed or the product. Kunii and Levenspiel (1991) described two such processes developed by Luigi and Fujinagata in the 1950s. In these earlier processes, sand particles are used as the heat carrier, and the reaction and heating take place in two different fluidized beds, with the sand circulating in between to transfer the heat generated from a combustion process to the endothermic cracking reactor. The entire concept is similar to the FCC process, but there are no catalyst particles and the reaction temperature is much higher in the range of 700°C–750°C.

The real benefit of using a fluidized bed is the direct cracking of crude oil or heavy oil to lower olefins. This will alleviate the pressure on the use of light hydrocarbons for the ever-increasing demands for light olefins. Such a process, like the FCC process, produces rejected carbon. The carbon deposition, while bad for the tubular reactors, can be turned into a benefit in a fluidized bed process as burning the deposited carbon on the heat carrier particles in a separate fluidized bed can produce the required heat for the endothermic thermal cracking. A similar setup as that of an FCC unit can be envisaged, either with two turbulent fluidized beds or two circulating fluidized beds or a combination of both, for the thermal cracking. In comparison with FCC, this would represent a "deeper" cracking of crude to lighter olefins than the mainly gasoline-kerosene product stream from FCC.

While there have been several encouraging developments on pilot studies for such a deep cracker, there appears to be no commercial application yet. Kunii and Levenspiel (1991) reported two earlier efforts by

BASF (Badische Anilin und Soda-Fabrik) and by MITI (Ministry of International Trade and Industry) in Japan, at 36 and 120 tonnes/day capacity to produce light olefins directly from crude. Both are pilot studies with two dense phase fluidized beds (SFB) with coke particles circulated between the reactor and the combustor. About 25% wt ethylene and 11% wt propylene are produced in both cases at a reaction temperature of 750°C. The lower conversion appears to be the reason that hinders the further development of these fluidized units.

The relatively low conversion may be caused by the backmixing of gas and the long residence time, therefore overcracking in the two pilot reactors mentioned. In response to this problem, Stone and Webster developed a QC reactor, starting from the 1970s (Gartside, 1989). This is a downer reactor with a very short contact time (as low as 200 ms) and very uniform residence time distributions for both gas and solids, permitting "the quick controlled contacting and separation of the fluidizable solids with a feedstock." The process is completed with an entrained bed combustion system to provide the heat required for thermal cracking. Alumina is used as the inert particles. A semicommercial demonstration unit was operated in the early 1980s, with flow capabilities of 34 tonnes/day hydrocarbon feed and 1200 tonnes/day of solids operated at temperatures ranging from 650°C to 1000°C, to show the feasibility of the downer concept. The system comprises a short downer reactor, a rapid mixer, and a quarter turn quick gas–solid separator. The reported reaction residence time from the point of oil-catalyst initial contact to the point of product quench including solids separation can be as low as 200 ms. No conversion rate is given, but it is believed to be higher than that of the SFB units.

Fluidized bed reactors also permit the possibility of adding catalyst into the unit, to further promote the cracking reaction, as initially suggested by Gartside (1989). This route combines the thermal and catalytic cracking and can increase the cracking efficiency. Deng et al. (2002b) have used this concept in a so-called downer catalytic pyrolysis process in a pilot downer reactor, for light olefins production from heavy feeds. Their results show that high olefins yields can be obtained at the temperature of 659°C and a residence time of 0.75 s, with the total yields of ethylene, propylene, and butylenes just over 50%wt. The added benefit to the combined catalytic/thermal cracking is the flexibility to adjust the relative ratio of ethylene, propylene, and butylenes, by switching catalysts that favor either ethylene or propylene/butylenes production. Increasing the temperature boosts the production of ethylene and decreasing the temperature promotes the production of propylene and butylenes. Such flexibility is extremely useful to respond to the changing demands of industry.

17.3.3.2 Coking

Coking is a process that converts heavy residual petroleum stocks into lighter and more valuable products. It is essentially a thermal cracking process at high temperature, but happens at the "higher end" in terms of molecular weight, compared to the thermal cracking discussed in the last section. This is an extremely important process in the petroleum industry, to convert very heavy stocks into lighter fractions. One situation is the need to crack heavy bitumen from oil sand to yield synthetic crude and the other is to crack the heavy residue matters left over from the atmospheric and/or vacuum distillation of crude or other feedstocks. When such cracking occurs, long-chain hydrocarbons break down into smaller molecules by rupture of carbon-to-carbon bond. Because the number of hydrogen atoms present in the parent molecules is insufficient to provide the full complement for each carbon atom, some carbon is rejected to form coke, hence the name "coking." As such, coking is a so-called carbon-rejection process.

There are two such coking processes using fluidized beds: the fluid coking process and the flexi coking process. Among the world's largest fluid cokers are the three in Alberta, Canada, operated by Syncrude, where hot atmospheric topped bitumen (ATB), vacuum topped bitumen (VTB), and residue are cracked or broken down into lighter products (Syncrude, 2012). High temperatures in the coking reactors cause the long-chain molecules to thermally crack in a bubbling fluidized bed of coke. The high temperature comes from the recirculating coke that has been heated in accompanying coker burner. The lighter liquid products, primarily naphtha and gas oils, are sent to hydrotreaters for sulfur and nitrogen removal. The coking reaction also produces sour fuel gas, which is sent to amine treaters for hydrogen sulfide removal. The resulting sweet fuel gas (much like natural gas) is used as an energy source throughout the upgrading and utilities operations. The coking reaction also produces coke, some of which is burned to produce heat for the high temperatures in the reactor. Excess coke is mixed with water and transported to coke cells in the mine area to be stored for potential future use. The two larger fluid cokers were designed to process 72,900 barrels of bitumen a day, but currently are able to process over 110,000 barrels of bitumen/day as a result of continuous improvement efforts (Syncrude, 2012).

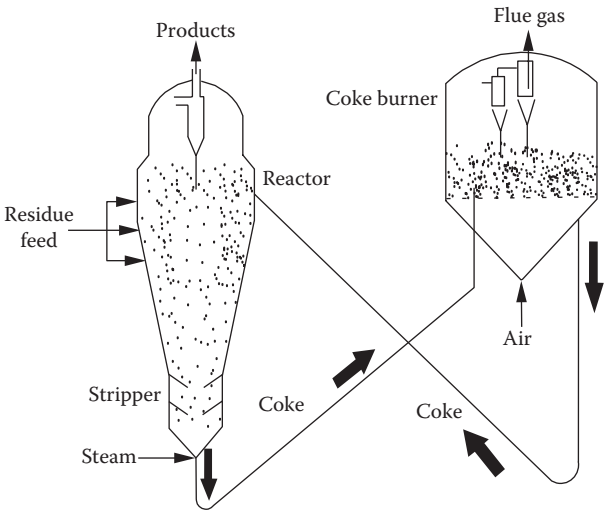


Figure 17.37

A typical fluid coking unit.

A typical fluid coker similar to that operating at Syncrude is shown in Figure 17.37. The reactor (480°C–550°C) operates in the bubbling fluidization regime with large bubbles produced mainly as a result of the formation of lighter products. The residue is fed into the reactor through nozzles from the side and a small amount of steam is injected from the bottom to maintain the fluidization at the bottom and also to displace any product desorbed on the coke particles as they travel down through the stripper at the bottom of the coker, before being transported to the coke burner. Part of the coke particles are combusted in the burner (590°C–700°C) to heat up the coke particles, which are then returned to the reactor to supply the heat required for the coking reaction. The remaining coke is discharged as a by-product. The coke particles are of Geldart type B particles with an average size close to 200 μm, which is maintained by a balance between the growth of particle size due to coke deposition and the reduction of particle size by attrition. Operation with Geldart type B particles leads to a bubbling bed with large bubbles. Cracked products vaporize inside the reactor and escape quickly in the form of large bubbles. Large bubbles are not favorable in most fluidized bed reactors, since they cause by-pass of reactant. In fluid coking, however, large bubbles become desirable, because they can quickly carry the products out of the reactor to minimize the residence time of the vapor products, which in turn avoids overcracking. The large bubbles also ensure vigorous mixing between the wet coke particles covered by the injected liquid and dry coke particles to ensure uniformity in the reaction and also to avoid the wet particles from sticking to each other. All fluid cokers also have a reversed cone shape to accommodate the vapor product formed during the process. Since only a very small amount of steam is supplied from the bottom of the reactor to fluidize the coke particles, the cross section of the reactor needs to be small in the bottom but gradually increases to maintain a relatively constant fluidization velocity as the products vaporize.

Flexi coking, an Exxon technology as shown in Figure 17.38, is similar to fluid coking but with the addition of a coke gasifier at the end of the line to produce boiler fuel, after sulfur removal (Yerushalmi, 1982). In this case, hot coke for the cracking reaction is usually provided by the particles from the gasifier rather than the combustor.

17.3.4 Gas–Solid Reactions

Fluidized bed gas–solid reactions have many applications. Such reactions take place in either a dense-phase SFB or a dilute-phase CFB, making use of the special characteristics of fluidized beds, such as excellent heat and mass transfer, the uniform temperature distribution, and the ability to handle a large quantity of solids and a wide range of solid materials. Coal utilization is a major part of such fluidized bed G-S reactions. The fact that the world's coal reserves are significantly larger than those of oils and natural gas renders them very important both as fuel and as feedstock for chemicals and other materials. Fluidized coal combustion and gasification have been shown to have many advantages. In more recent years, sustainable development and environmental concerns have also led to a large wave of increased utilization and consumption of biomass materials, in incineration and gasification.

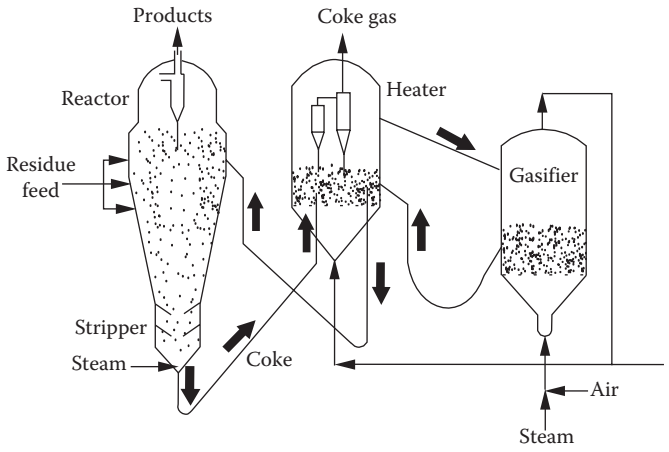


Figure 17.38

Flexi coking unit by Exxon.

17.3.4.1 Coal Combustion

Fluidized bed combustion is now the largest application of fluidized bed technology, both in the number of units and in the scale, with 600 MWe boilers being started recently. In an FBC, coal particles are suspended in an upflowing gas stream (normally air or oxygen enriched air) with a large amount of inert particles that help in stabilizing the combustor temperature and facilitating excellent heat transfer. In an FBC, a coal particle experiences the following process: After a coal particle is fed into the FBC, its temperature rises as the inert particles at higher temperature transfer heat to this colder coal particle. For a short period of time, volatile matters are released and are burned at or beyond the coal particle. Then the remaining solid combustible matters, mainly char, start to be oxidized (burned) with the generation of heat, while the particle is "floating" and move around inside the fluidized bed, leaving behind noncombustible matters such as ash. The char oxidation step takes by far the longest time during the combustion.

The FBC has many advantages, including

- Efficient and large-scale operation
- Very easy to maintain a uniform temperature
- Low-temperature operation, 750°C–900°C
- Very high heat-transfer rate
- Suitable for burning a wide variety of fuels, including low-grade coals and other low-end combustible materials
- No moving parts inside the combustor
- In situ capture of sulfur pollutants
- Lower emission of nitrogen oxides, especially in circulating fluidized bed combustors (CFBCs)

Coal particles contain mainly volatiles, char, and ash, with their relative quantities varying with the type of coal: Anthracite contains the least amount (a few percept) of volatiles and lignite can contain as high as over 50% volatiles. The ash in the coal is a mixture of adventitious ash and inherent ash, which is in the form of very small particles (typically 2 μm size), bound within the coal pieces (Howard, 1983). Most of the adventitious ash is removed in the coal cleaning plant, so that the treated coals have lower sulfur and ash contents and higher calorific values than the untreated coal. In most developed countries, only treated coal is combusted given the tight environmental control.

The following details are given for the volatiles and their combustion properties (Howard, 1983):

1. The volatilization process is not a simple physical vaporization, but the consequence of chemical reactions.
2. The volatiles given off are hydrocarbon gases arising from irreversible chemical reactions, that is, thermal decomposition, which occur when the coal is heated. Condensation and further cooling of these gases will not reconstitute their original chemical and physical form.

3. Volatiles are mostly emitted from the interior of the coal particle from which they seep out to the exposed surface.
4. The chemical reactions may be exothermic.
5. There is no clearly defined temperature at which the volatiles are released, but the higher the surface heat flux into the coal particles, the shorter the time taken for all the volatiles to be given off.
6. The volatiles burn in much the same way as liquid fuel vapors burn, with a flame located a short distance away from the solid surface. The flame provides heat to the particle surface to assist further volatilization until all the volatiles have been evolved.
7. The evolved hydrocarbon gases may not burn completely in the region around the coal particle, but often appear as a smoky yellow flame and deposit shoot on the surfaces downstream.
8. Incompletely burnt volatiles can only be burned to completion if they passed through a high-temperature zone containing excess oxygen.

One key advantage of the fluidized bed coal combustion is that it operates at low temperature, 750°C–900°C, minimizing the volatilization of alkali metals in the fuel and avoids any sintering of the coal ash and sand materials. This partially results from the uniform temperature in a fluidized bed, which is facilitated by the presence of inert particles, mostly sand or ash from coal combustion, plus sorbent particles. The inert particles form the majority of the fluidized bed materials as the coal particles only constitute no more than 10% of the bed materials. The large quantity of inert particles act as a huge heat sink that quickly takes away the heat produced by combustion, transfers a large amount of heat to the heat exchangers, and maintains excellent temperature uniformity. They also act as a heat source to rapidly heat up the cold coal particles fed into the system. Sand particles are usually used as the initial inert materials, which are then gradually replaced by ash from the combustion. Depending on the ash content and the size range of the ash produced, addition of makeup bed materials may be required from time to time. Finer ash leaves the combustor through the cyclone as fly ash and larger sized ash is collected from the bottom drain of the combustor.

Another important advantage of fluidized bed combustion is the ability to capture sulfur within the combustor using low cost sorbent. Sulfur exists in almost all types of coals, varying from less than 1% up to 10%, in the form of pyrites (FeS_2) and organic sulfur compounds. When coal is burned, sulfur is released as sulfur dioxide and, to a smaller extent, as sulfur trioxide, both are air pollutants that form acid rain. The most common way to remove sulfur oxides is to add lime either in the form of limestone (calcium carbonate) or in the form of dolomite (combined calcium and magnesium carbonate) into the FBC where they react with the released sulfur to form calcium sulfate ($CaSO_4$). With this method, sulfur is *fixed* in calcium sulfate, which is then removed with ash. The retention of sulfur by lime in FBCs has the advantage of not requiring a separate gas-scrubbing plant, easier handling and disposal of spent sorbent, and greater overall thermal efficiency. Lime sorbent can be fed into the combustor either with the coal (premixed) or separately.

Another major pollutant of fluidized bed combustion is nitrogen oxides, including nitrogen monoxide and nitrogen dioxide, also collectively called NO_x, plus nitrous oxide. Nitrogen monoxide and dioxide are sources of acid rain, and nitrous oxide induces ozone decomposition in the stratospheric layer. Nitrogen oxides in FBCs come from the nitrogen in the fuel, typically 0.5%–2% by mass. The formation of NO_x is a complex process, but it is clearly known that increasing temperature and the excess air both favor the formation of NO_x due to the increased oxidation rate. Therefore, the low temperature of FBCs helps to limit NO_x formation. However, either low temperature or limited excess air ratio alone is currently not enough for the stationary (bubbling) fluidized bed combustors (SFBCs) to meet the more stringent NO_x emission standard. In this regard, the CFBC is much more advantageous given its ability to create separate reducing and oxidizing zones inside the combustor.

CFBCs emerged as a better alternative to bubbling bed combustors in the late 1970s and early 1980s. A typical CFBC is shown in Figure 17.39. CFBC has a large diameter riser where most combustion occurs. Flue gas and entrained particles are separated in the cyclone on top of the solids return pipe. Collected solids including inert particles, sorbent, and unburnt char are gathered in the return pipe, and then further recirculated to the bottom of the riser combustor. Air is divided into two streams: the primary stream is fed into the riser through the bottom air distributor to fluidize the particles in the bottom region and the secondary air is fed lower midway in the riser to further entrain particles upward and to bring the combustion to completion. Coal and limestone are fed into the bottom region of the riser and so are the returned solids from the return pipe. The splitting of airflow results in a lower gas velocity in the bottom region of the riser.

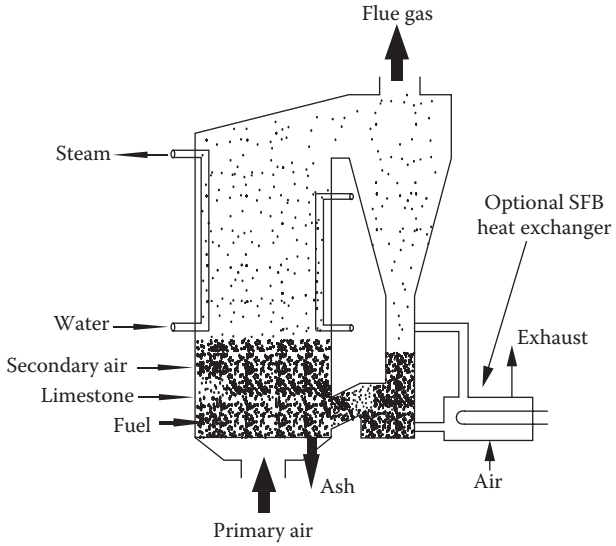


Figure 17.39

A typical circulating fluidized bed combustor.

This creates a bubbling fluidized bed in the bottom, which significantly enhances lateral solids mixing to quickly mix the coal, sorbent, and the returned solids. The bubbling bed also ensures excellent heat transfer to heat up the newly fed coal and sorbent particles. The temperature in the riser is normally 750°C–900°C, and the temperature in the return pipe is 100°C–200°C lower. Major heat transfer is through the membrane wall of the riser and more heat transfer through the fluidized bed heat exchangers in the return pipe, plus possible additional fluidized bed heat exchangers. The bed materials have a size range of 100–300 μm, but the coal and sorbent are usually fed in much larger sizes, in the range of several millimeters. The larger size permits the newly fed and cold coal and sorbent to remain in the bottom bubbling bed region, so that there is sufficient time for them to heat up and to react. As the reactions continue and their temperature rises, the larger particles are broken down into smaller fractions and then entrained into the upper region for continued and higher temperature combustion. The ability to feed larger particles directly is another clear advantage of the fluidized bed, as it eliminates the energy-intensive crashing process upstream, such as those required for pulverized coal combustion.

The partial feeding of the total amount of air required for combustion into the bottom region creates a reducing zone there, which favors the formation of N_2 over the formation of NO_x from the released nitrogen from the fuel. The temperature in the bottom region is also lower, again favoring the reduction of NO_x formation. In addition, the low gas velocity and the larger coal particle size both increase the residence time of the newly fed coal in the bottom bubbling region, to ensure all volatiles, including most of the fuel nitrogen, are released in the bottom reducing region. All of these factors favor the reduction of NO_x emission, making CFBC more preferable than SFBC. Above the point of the secondary air injection, the temperature rises and an oxidizing region forms, to promote fast combustion. However, NO_x emission is not affected, since most fuel nitrogen has been consumed at this time.

Such staging effect also increases the combustion efficiency, by maintaining a higher temperature in the upper region of the riser. Excellent heat transfer is ensured by operating the riser combustor at lower gas velocity (compared to most other CFBs) to promote particle reflux near the wall, creating a dense particle annulus for better bed-to-wall heat transfer. CFBC also provides better gas–solid contact efficiency for the combustion.

Overall, CFBC has several advantages over SFBC:

- High combustion efficiency
- Adjustable primary-to-secondary air flow ratio
- Significantly reduced NO_x emission
- Separate control of air and particle feeds
- Higher turndown ratio

As a result, CFBC has quickly replaced SFBC in the past few decades as the industry standard for fluidized bed combustion. However, SFBC is still used for some small-scale combustors given its low construction cost, and for some special purpose combustors.

Prior to the 1980s, many SFBC of different designs have been commercialized all over the world. For example, China had over 2000 small SFBC in operation in the 1980s. An excellent comprehensive review on the application of SFBC has been provided by Highley and Kaye (1983). Given the rapid replacement of SFBC by CFBC, those design features are not detailed here.

CFB combustion is the fastest growing application of CFB technology and has recently overtaken FCC, to become the largest application of CFB technology. Both capacity and number of CFB boilers in use are increasing drastically in the past 20–30 years. Approximately 600 CFB boilers are either in operation or under construction. The CFB combustor has surpassed the bubbling bed firing system not only by total unit capacity, but also by the number of plants. Now, atmospheric CFB plants stand for about two-thirds of the total installed capacity worldwide. The demand also triggered a fast increase in unit size (Jacobs, 1999). Reh (1999) reported that the boiler companies such as ABB Combustion Engineering, Lurgi and Foster Wheeler Power Systems were pursuing several projects in the 250–400 MWe capacity range at the turn of the century, while Electricité de France (EdF) was planning to scale up its atmospheric CFBC into the 600 MWe capacity range. Yue et al. (2014) reported the world's largest 600 MW CFBC being put into operation in 2013.

A pressurized fluidized bed combustor (PFBC) has the added benefit to also employ the high-pressure flue gas to drive a gas turbine to form the combined cycle power generation, giving higher thermal efficiency. However, operating at higher pressure causes many problems so that PFBC has not been widely used. In connection with the recent development of CFBC, pressurized CFBC may still represent the future direction of fluidized bed combustion, although the current economy does not make PCFBC profitable.

There are also two new trends in the development of FBC. Firstly, in an effort to reduce the emission of greenhouse gas such as CO_2, oxy-fuel combustion has been proposed (Buhre et al., 2005, Kosowska-Golachowska et al., 2011). In an oxy-fuel combustor, coal particles are burnt in the presence of pure or enriched oxygen and recycled flue gas, without nitrogen, so that the flue gas leaving the combustor is highly enriched in CO_2, allowing easy CO_2 sequestration. The second trend is to utilize the supercritical phenomena to improve the water-steam efficiency for supercritical circulating fluidized bed combustion (SCFBC) (Xin et al., 2002, Wu et al., 2004, Yue et al., 2014).

17.3.4.2 Coal Gasification

Coal gasification is the first industrial application of fluidization technology in modern history. The concept was first envisaged by Fritz Winkler (1922) in his German patent in 1922. In 1926, the first Winkler commercial unit began its operation with four additional units added by 1929 (Squires, 1983). In the gasifier, a fluidized bed of coal particles was suspended by a gas mixture of air and steam, or more often a gas mixture of oxygen and steam, to produce raw gas for the chemical industry, such as ammonia synthesis. The temperature is about 800°C–900°C, and the thermal power is up to 100 MW.

As shown in Figure 17.40, the Winkler gasifier is a relatively simple unit, with gas entering from the bottom and product leaving from the top. The coal, crushed to about 10 mm and dried of surface moisture, is fed by a screw feeder into the dense phase. The products are mainly carbon monoxide and hydrogen, sometimes with a minor quantity of methane. When air is used, the products are diluted by nitrogen. The energy required for gasification is supplied by the partial oxidation of coal. There is usually an expanded section above the particle bed to allow the return of ejected particles through bubble eruption and a cyclone is usually there as well to catch and recycle fine carbon particles. In the later models, some additional air or oxygen was injected into the freeboard region, to increase the carbon efficiency by burning off the fine carbon particles there. The resulting temperature rise in the freeboard increases the decomposition of produced methane to the desired CO and H_2. Both primary and secondary gases are injected through nozzles to increase the contact efficiency. Compared to modern technology, the Winkler gas producer is inefficient because of its high oxygen consumption and its large (over 20%) carbon loss through dust carryover. Given the abundance of cheap petroleum and natural gas in the 1950s, most Winkler gasifiers went out of service due to poor economy. Kunii and Levenspiel (1991) reported that all Winkler units were shut down in the 1950s, while Yerushalmi (1982) seemed to suggest that a few Winkler units were still in operation in the 1980s.)

From the 1970s, the oil crises raised the importance of coal, so that a number of companies started to develop new coal gasifiers. There are a number of benefits of coal gasification over straight combustion, including a higher electricity efficiency through the gas-turbine-steam-turbine binary cycle via gasification

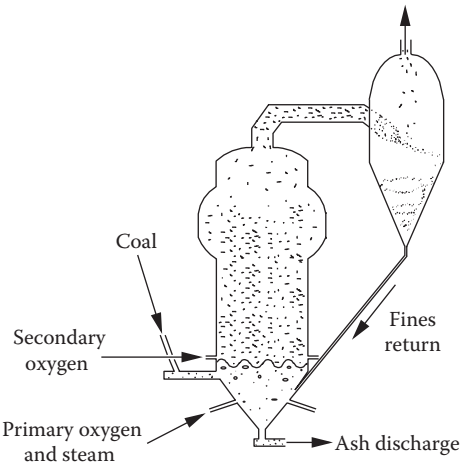


Figure 17.40

A typical Winkler gasifier.

than the conventional steam turbine system via combustion only. Gasification also provides clean gaseous fuels and raw chemicals for synthesis. For example, in the Sasol Synthol process described in Section 17.3.2, the syn-gas for the F-T process was supplied by coal gasification.

However, there are a number of inherent limitations for fluidized bed gasification of coal (Yerushalmi, 1982), including

1. The operating temperature is limited, with the highest temperature limited by the sintering temperature and the lowest by the reactivity of coal.
2. Carbon fines are produced within the fluidized bed, giving rise to problems such as loss of carbon through entrainment.
3. Loss of carbon through purging of ash.

These limitations implied that the complete gasification cannot be achieved in a single-stage fluidized bed operating below the sintering temperature. Therefore, the development of new fluidized bed gasifiers needs to overcome these problems. Many designs include multiple stages to increase the efficiency of carbon use. Unfortunately, there appears to be no commercialization of the fluidized bed gasifier to date, although numerous studies including many pilot studies have been carried out. Kunii and Levenspiel (1991) summarized the various routes and concepts of fluidized bed gasifiers, and pointed out, although the development has been much slower than expected, the fluidized bed route is still beneficial for large-scale production of fuel gas for binary cycle power plants.

17.3.4.3 Incineration of Solids Wastes

Fluidized bed incinerators are mainly used for the elimination of harmful materials and for the utilization of heat value in the wastes. Examples of the subject materials are solids municipal and industrial wastes, saw dust, plastic wastes, dried sewage sludge, and special wastes such as hospital wastes. Electricity generation may be a good use of the energy produced. Fluidized bed incineration is similar to fluidized bed combustion in their structure and in that both fluidized beds are composed of mainly inert particles with the combustible wastes fed into the fluidized bed in the dense phase. However, there are special issues that must be considered for the incineration of wastes:

1. Pretreatment—Some solids waste may contain large objects that need to be crushed or removed, some have high moisture content that need to be at least partially removed, some contain too many noncombustibles such as glass and metal that need to be screened out.
2. Combustibility, flame stability, auxiliary fuel, and cofiring—Not all waste materials have enough heating value, good combustibility, and/or flame stability, so that auxiliary fuel(s) may be needed to cofire the incinerator (Sondreal et al., 2001). Most common cofiring fuels are coal and natural gas.

In most cases, a cofiring facility is normally required although not necessarily always used, because it is needed when switching waste materials and during start-up and the period when the waste supplies are short if a continuous energy supply is required.

3. Variations in waste compositions—Certain solids wastes such as municipal wastes can have their compositions fluctuating. The incinerator must be designed to handle such variations in the change of heating values, ash content, moisture, etc. In this regard, the standby of cofiring is essential to maintain good operation of a fluidized bed incinerator.
4. Feeding—Special attention is needed to feed the different solids wastes. If multiple wastes are to be burned in the same unit, the feeding device must be versatile enough to handle all situations.
5. Secondary air injection—As in coal combustion, secondary air injection may be beneficial for certain cases. This, however, changes with the type of solids wastes and the type of fluidized beds adopted (SFB or CFB).
6. Temperature—Temperature is another key factor. In addition to those issues discussed in Section 17.3.4.1 related to coal combustion, there may be additional factors coming into play. For example, the temperature needs to be high enough to decompose certain harmful constituents.
7. Emission control—Other than the acid rain cursors of SO_2 and NO_x encountered in coal combustion, other harmful gases such as chlorine and bromine might be released during the combustion of, for example, plastic wastes. Dioxins are an even worse issue. Special measures need to be taken to eliminate these harmful gases or trap them in the flue gas.
8. Heavy metals and other toxic solid contents, residue solids disposal—Some wastes contain much higher fractions of heavy metals such as vanadium, lead, and mercury and can cause long-term damages. The containment of those heavy metals must be solved before the incineration of those materials. A related issue is the residue solid's disposal: the presence of heavy metals makes it much harder.

17.3.4.4 Gasification and Pyrolysis of Biomass

Sustainable development requires the use of renewable energy and biomass provides the main renewable energy resource (Bridgwater and Peacocke, 2000, Bridgwater, 2003). Biomass includes grain husk and stalk, sawdust, grass, and wood especially wood from short rotation forestry. There are three methods that can utilize the energy contained in the biomass: combustion, gasification, and pyrolysis. Direct combustion provides heat for use in heating, for steam production and electricity generation; gasification provides fuel gas for combustion for heat or in an engine or turbine for electricity generation, or raw materials for the chemical industry; and pyrolysis provides a liquid fuel that can substitute for fuel oil and that can produce a range of specialty and commodity chemicals. Combustion of biomass using a fluidized bed is currently not competitive, unless the feeds are the wastes, such as that from pulp and paper, and agricultural and forestry industries (Bridgwater, 2003). The nature of biomass combustion is similar to those discussed in the previous sections.

Gasification is the (thermochemical) conversion of biomass to a gaseous fuel by heating in a gasification medium such as air, oxygen, or steam. It is advantageous over combustion because the gaseous fuel is easier and more versatile to use and can also be standardized in its quality. The main reactions are partial/complete combustion and water gas shift reaction, to convert the carbon to CO, CO_2, and H_2, plus some methane. Gasification starts from driving out the moisture, followed by a pyrolysis process to yield gas, vaporized tars or oils, and char residue, and then the much slower process to gasify the solid char, pyrolysis tars, and pyrolysis gases. Alkali metals present in wood ash can act as a catalyst to accelerate the reactions.

Bubbling fluidized bed and CFB both can be used for biomass gasification. Both have good temperature control and high reaction rates, but both have high particulate content in the product gas and high carbon loss with the ash. CFB has the additional advantage of increased process efficiency, more operational flexibility, and better emission control.

The financial assessment of biomass gasification, however, is not always favorable and is very sensitive to many factors. Biomass is of low-energy density and is not produced centrally. In developed countries, the high cost of collecting and transporting the biomass may make the gasification process cost-inhibitive, but the potential of being paid to take biomass wastes should help greatly enhance the economics of power generation. However, biomass gasification can be economically viable in developing countries, where the cost of biomass at feed is much less expensive. Wu et al. (2002) concludes that their 1 MW unit is still profitable if the cost of biomass is less than US$25 per metric ton.

In China, there is an abundance of biomass but a lack of electricity, especially in the rural areas. In the past two decades, the Guangzhou Institute of Energy Conversion has been demonstrating the BGPG (biomass

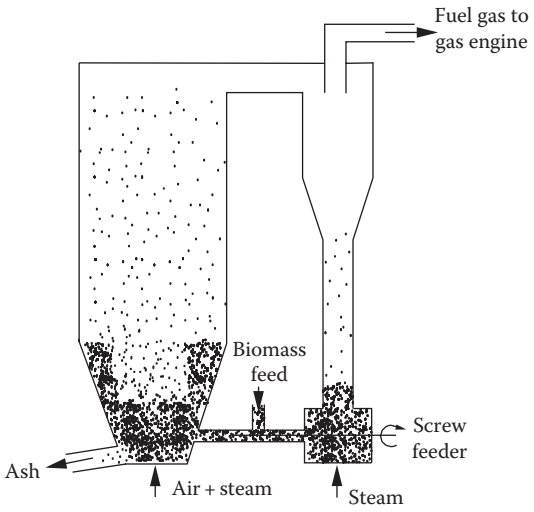


Figure 17.41

CFB biomass gasifier developed by GIEC, for the BGPG process.

gasification and power generation) concept using one 1 MW CFB unit in Fujian Province to gasify rice husk (Yin et al., 2002) and another 1.2 MW CFB unit in Sanya to gasify saw dust (Wu et al., 2002). Taking the 1.2 MW CFB as an example, the unit is a simple CFB gasifier as shown in Figure 17.41, with sawdust fed into the bottom region of the riser through a screw feeder. The solid's recirculation rate is not very high so the riser diameter is significantly larger than the diameter of the return column under the primary cyclone. The product gas passes through a simple scrubber to remove ash and tar, before being burned in four parallel gas engines (Wu, 2010). They (Wu et al., 2002, Yin et al., 2002, Wu, 2010) reached the conclusion that BGPG can reach reasonable efficiency at certain scale and provide a high-quality power supply to the users. It is especially suitable for rural areas in developing countries where such simple and robust technology can assist in the development of rural economies by providing electricity produced from local sources of biomass. Larger units are planned for full commercialization.

The use of a catalyst can further increase the efficiency and therefore the economy of biomass gasification (Sutton et al., 2001). It can also lower the reaction temperature. Asadullah et al. (2002a,b) reported a catalytic gasification process developed for the gasification of wood powder to proceed completely at lower temperature in the presence of a$Rh/CeO_2/SiO_2$ catalyst.

Pyrolysis is a thermal decomposition process in the absence of oxygen. When the reaction is controlled within a short period of time, in the order of milliseconds, more valuable liquid products can be obtained. The liquid products continue to decompose to lighter hydrocarbons of less value, if the reaction continues. Thus, it is very important to control the short reaction time and such a pyrolysis process is therefore called fast pyrolysis. In this process, the critical issues are to bring the reacting biomass particles quickly to the optimum process temperature and minimize its exposure to the intermediate temperatures that favor formation of charcoal and to quickly stop the reaction at the desired time.

Bergougnouet al. (1994) proposed a short contact-time fluidized reactor developed for the ultrapyrolysis of biomass and heavy oil. The design is very similar to the QC concept by Stone and Webster (Gartside, 1989) that the process is realized in a downer reactor. Preheated hot inert solids (sands) and the biomass are injected separately into the top of the downer where vigorous heat transfers quickly bring the biomass to the reaction temperature. While flowing cocurrently downward, pyrolysis proceeds quickly, within about 500 ms. At the bottom of the downer reactor, the products are quickly separated from the sands and quenched.

Based on the aforementioned concept, Ensyn developed a rapid thermal pyrolysis (RTP) process in the 1980s for fast pyrolysis, to produce gaseous and liquid fuels and chemicals of high value (Graham and Huffman, 1995). Instead of a downer, an upflowing riser reactor is used to facilitate rapid and uniform contacts between the biomass and the hot recirculated sand at the riser entrance. Before feeding to the reactor, biomass is comminuted to approximately 6 mm and dried to no more than 10% moisture. At the riser top, the products pass through two cyclones to separate solids and the vapor after the cyclone is rapidly quenched to stop further decomposition of the thermally unstable liquid intermediates of the pyrolysis.

The aforementioned process was commercialized in 1989 to produce food flavorings and additives (Graham and Huffman, 1995). There were later on eight such plants in operation in the 1990s. A variety of feeds including cellulose, wood, lignin, agricultural residues, heavy oils, heavy distillates, asphalt, and bitumen can be processed (Bridgwater and Peacocke, 2000). It may be possible to burn the produced "bio-oil" in an internal combustion engine.

Another technology from the University of Waterloo in Canada uses a SFB for fast pyrolysis instead of a CFB and bench-scale experiments seem to indicate they can achieve the same performance as in CFB (Scott et al., 1985, 1999).

The liquid "bio-oil" contains valuable chemicals and can be easily stored and transported. It can be used as alternative liquid fuel and/or as chemical feedstock because it contains a significant fraction of useful organic chemicals. However, there are still many challenges, such as higher cost, incompatibility with conventional fuels, high viscosity, chemical instability, lack of standards for use and distributions, and the variations in its quality (Bridgwater, 2003).

17.3.4.5 Mineral and Metallurgical Processes: Roasting and Calcination

Another area of application of fluidized bed reactors is in the mineral and metallurgical process. The use of fluidized bed for roasting started in the late 1940s in Ontario Canada for roasting arsenopyrite and to obtain a cinder suitable for gold production by cyanidation (Kunii and Levenspiel, 1991). The roaster is a simple one-stage SFB operated most likely in the bubbling fluidization regime. Air is usually the fluidizing medium, which also supplies the oxygen and the roaster is usually operated at high temperature. The advantages of using fluidized beds for roasting are the excellent mass transfer, uniform temperature, and the ability of continuously adding and withdrawing the particles. Many roasting processes have been realized in fluidized beds, such as the roasting of pyrites, pyrrhotite, zinc sulfide, copper and cobalt concentrates, and other various sulfide and sulfate. Readers are referred to Yerushalmi (1982) for a more comprehensive review on the application fluidized bed roaster, given the limited space here.

Calcination is another important gas–solid reaction. For example, calcination of aluminum hydroxide is an essential step for the production of aluminum, since only completely dehydrated alumina can be fed into the electrolytic cells. Calcination of calcium carbonate is another example. Again, calcination in fluidized bed is to make better use of the special features of the fluidized bed. The added advantages of CFBs can also be utilized. In the late 1960s, Lurgi commercialized the world's CFB calciner, the so-called fast fluidized bed alumina calciner (Reh, 1971, 1986). As shown in Figure 17.42, the CFB calciner has a very similar structure as a CFB combustor. Aluminum hydroxide is fed into the bottom dense region of the riser. Natural gas or fuel oil is fed into the riser to provide the high temperature for calcination. The air is also split into primary

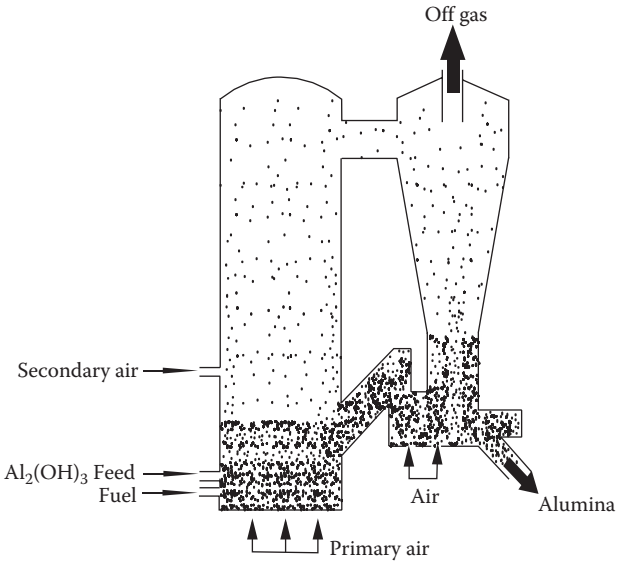


Figure 17.42

Lurgi's CFB calciner.

and secondary streams, with the purpose of creating a dense phase at the bottom to accelerate the heat transfer from the hot bed materials to the newly fed cold $Al_2(OH)_3$ particles and to promote lateral mixing. If not counting the Sasol CFB for F-T process, which could have been better served by a turbulent fluidized bed, the Lurgi CFB alumina calciner would have been the first commercial CFB reactor.

17.3.5 Physical Operations

There are many examples of using fluidized beds for physical operations, where no chemical reaction occurs. These processes use one or more of the special features of the fluidized beds:

- The large interfacial surface area between the fluid and the particles for excellent gas–solid contact, due to the small particle size
- The excellent heat transfer between the gas and particles given the vigorous relative movement between the fluid and the particles
- The excellent heat transfer between the gas–solid suspension and the heat exchanger surfaces
- The uniform temperature from the excellent heat transfer and gross movement of particles
- The ability to handle a large quantity of particulate materials
- The flexibility to fluidize a wide range of particle properties

17.3.5.1 Drying

Fluidized bed dryers have been applied in many industries, such as the food and agriculture industry, the pharmaceutical industry, and the chemical process industry. During a drying process, a significant amount of heat needs to be transferred from air (as in most cases) to the particles and a significant amount of mass (steam) needs to be transferred from the particles back to the air stream. Fluidized beds are very efficient dryers because they have the ability to rapidly provide a large amount of heat and to quickly take away a large amount of vapor. These essential features ensure the excellent use of energy, which is the biggest concern in all nonspecialty drying processes. Aside from excellent heat and mass transfers, fluidized beds also contain the following special features, which make them specially suitable for most drying processes:

1. Fluidized beds have a very uniform and well-controlled temperature. This allows the drying temperature to be raised very close to the maximum allowed temperature for most efficient drying, without worrying about localized overheating. This is particularly useful for drying heat-sensitive particles, such as grains and pharmaceutical products where overheating will permanently damage the materials.
2. Fluidized bed dryers can handle a very large quantity of particulate materials, with easy feeding and product withdrawal. This helps to ensure a continuous and large-scale operation.
3. The vigorous movements of particles inside the fluidized bed promote the uniform drying of all particles and over all surfaces of each particle. This is in favor of more uniform drying products.

The drying process usually has two stages: The first is the constant rate stage when the moisture on the particle surface is being taken away. During this stage, the driving force, the difference between the moisture content in the air stream and that on the particle surface, remains the same, so that the drying rate remains the same. The second drying stage is the reducing rate stage that removes the hard-to-dry moisture contained inside the particles. The first stage is fast and requires a large amount of airflow to provide the heat for evaporation and to remove the steam, while the second stage is slower and requires a longer drying time. Obviously, it is best that the drying process can be designed to suit the needs of both stages.

Figure 17.43 sketches a basic fluidized bed dryer design where hot air passes through the fluidized bed and leaves from the top, and wet particles enter from one side of the fluidized bed and the dry particles leave from the other side. When this is run in a continuous mode, it will not be most efficient, since the particles are well mixed in such a dense-phase fluidized bed. Some wet particles can quickly bypass the dryer, while others may stay in the bed for too long, causing underdried and overdried particles. In order to ensure the drying is complete, the residence time of the particles has to be significantly increased, leading to a much larger unit and the waste of energy through increased airflow. A significant portion of the hot air also tends to pass through the bed as bubbles, bypassing the dryer, leading to a less efficient use of energy.

To increase the uniformity of the solids products in a continuous drying process, it is useful to create some staging effect to prevent the drier particles from remixing (backmixing) with fresh wet particles. Figure 17.44 illustrates several alternative designs of fluidized bed dryers. Figure 17.44a and b show two

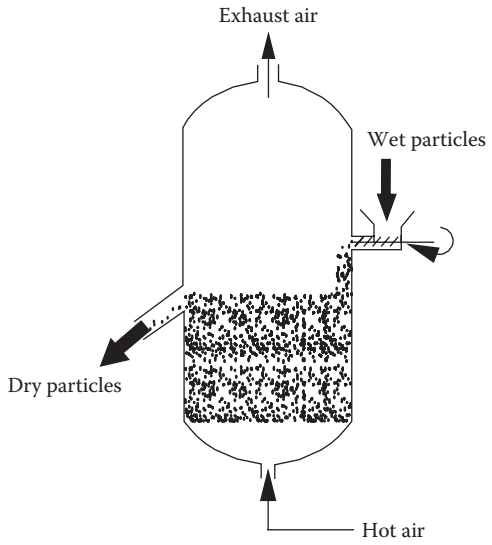


Figure 17.43

A typical fluidized bed drier.

examples of staged drying operations: one with vertical staging and one with horizontal staging. Such staging reduces solids' bypassing and therefore increases drying efficiency. The vertical one with countercurrent flow is more efficiency than the horizontal one with crosscurrent flow for energy use. Figure 17.44c and d are two special designs that accommodate closely the features of the two drying stages. In Figure 17.44c, the two fluidized beds are operated at different hot air velocities: the one on the right at a higher air flowrate to quickly take away the moisture on the particle surface in a relatively short time, the one on the left at much lower air flowrate but with much longer residences of both air and solids, plus staging to remove the moisture inside the particles. A similar method (Figure 17.44d) is to realize the first stage in a riser where the air-particle mass transfer is very high and a very high air velocity can be used to quickly remove the moisture on the particle surface, and then to realize the second stage in a vertically staged fluidized bed at air velocity not much above the minimum fluidization with horizontal baffles to ensure uniform and longer residence time distribution of the particles.

17.3.5.2 Heat Exchangers

Fluidized beds are excellent heat exchangers given the high heat-transfer rate and the huge heat capacity of solid particles. Such a process is usually realized in a set-up similar to a shell-tube heat exchanger where the fluidized particles are usually in the shell side of the exchanger. For example, fluidized bed heat exchangers have been used to take away the large amount of heat generated from chemical reactions. Because of the high heat-transfer rate and large heat capacity, such fluidized bed heat exchangers are highly efficient. Because of higher solids concentration, most fluidized bed heat exchangers are dense-phase SFBs rather than CFBs, given the much higher heat capacity of the solids.

Fluidized beds with inert particulate materials can also be used to maintain a constant temperature for some operations. For instance, it can act as a temperature bath that encases a chemical reactor. It can also be used as a heat sink to provide a well-controlled and uniform temperature source with high heat capacity. Kunii and Levenspiel (1991) mentioned the use of such a fluidized bed to rapidly quench and temper hot metalware to a definite temperature so as to obtain the desired properties of an alloy.

There are also the direct contact heat exchanges inside the fluidized bed. For example, hot flue gas can be used to warm up sand particles that are to be added into the combustor as makeup materials in fluidized bed combustion. This also happens during the start-up of fluidized bed coal combustion when hot air, obtained from the burning of natural gas, for example, is first passed through the FBC to heat up the bed materials to a certain temperature, before coal particles can start to burn on themselves. Similarly, air or other gas can be used to fluidize hot particulate materials in product line to recover the residue heat.

Fluidized bed heat exchangers can also be used as a heat exchanger within a chemical process that already utilizes the fluidized bed. For example, as discussed in Section 17.3.2.1, a catalyst cooler is an essential

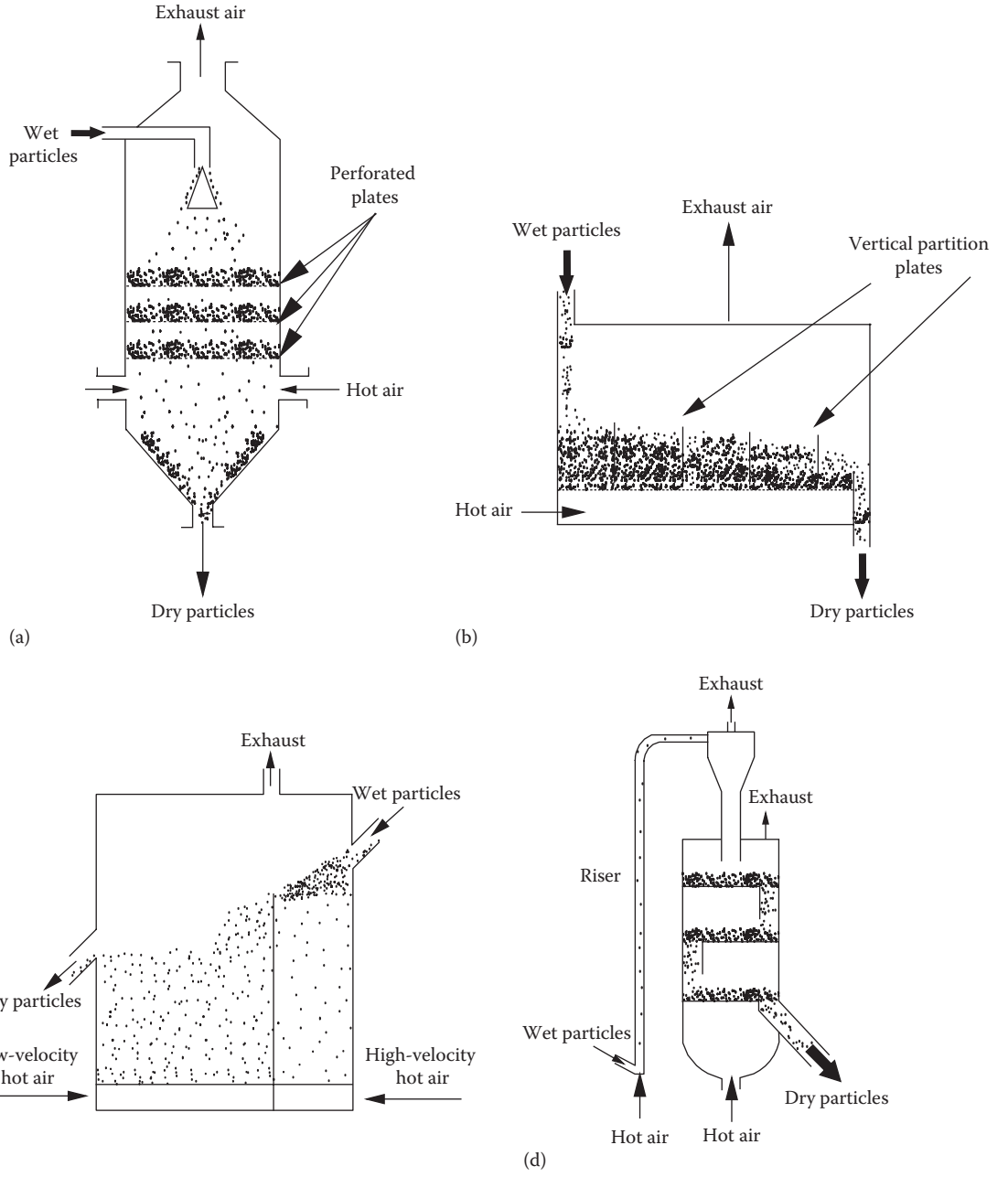


Figure 17.44

(a) Vertically staged fluidized bed drier. (b) Horizontally staged fluidized bed drier. (c) Two-stage SFB fluidized bed drier. (d) Two-stage CFB-SFB fluidized bed drier.

component of modern RFCC , to take away the extra heat from the combustion in order to maintain the heat balance. In combustors, besides the heat exchanger installed inside the fluidized bed combustion chamber, additional dense-phase fluidized bed(s) can also be installed in the solid's return loop to take away extra heat if required.

There are some additional distinct advantages of fluidized bed heat exchangers and two examples are given here.

1. They can be kept at a relatively high temperature, which is difficult to maintain by gas or liquid. For example, to maintain a highly endothermic chemical reaction inside a reactor at 350°C, it is required to have an efficient heat exchanger that can maintain at a constant temperature just slightly higher. This was mostly realized using molten salt since the evaporation temperatures of the most

commonly used gases and liquids are not in this range. However, molten salt causes many problems such as corrosion. Fluidized beds, with sand, for example, are now being used to replace such molten salt heat exchangers.

2. The heat-transfer rate can be easily adjusted in most fluidized bed heat exchangers. Their heat-transfer capacity can be "turned up" or "turned down" almost instantaneously by increasing or decreasing the fluidization gas. As the fluidizing gas velocity increases in a dense-phase fluidized bed, there are more gross movements of solids and therefore higher heat-transfer rates. Such fluidized bed heat exchangers can also be easily "turned off" and "turned on" by shutting off and restarting the fluidization gas, without having to stop any other operations.

17.3.5.3 Fluidized Bed Coating

Coating of particles with a thin layer of film can be realized in a fluidized bed. In such a process, the particles to be coated are first fluidized, with air or with inert gas if needed, and the coating materials, usually in solution, are sprayed into the fluidized bed. Because of the vigorous movement of the particles and the gross flow pattern in the fluidized bed, particles are uniformly coated. Very often, spouted beds are preferentially used for particle coating. Given the gross particle circulation, particles, which get sticky after being sprayed by the coating solution, can still be nicely circulated in the spouted bed. The spouted bed is also a better choice when handling large particles. Figure 17.45 shows three examples of fluidized/spouted bed coaters.

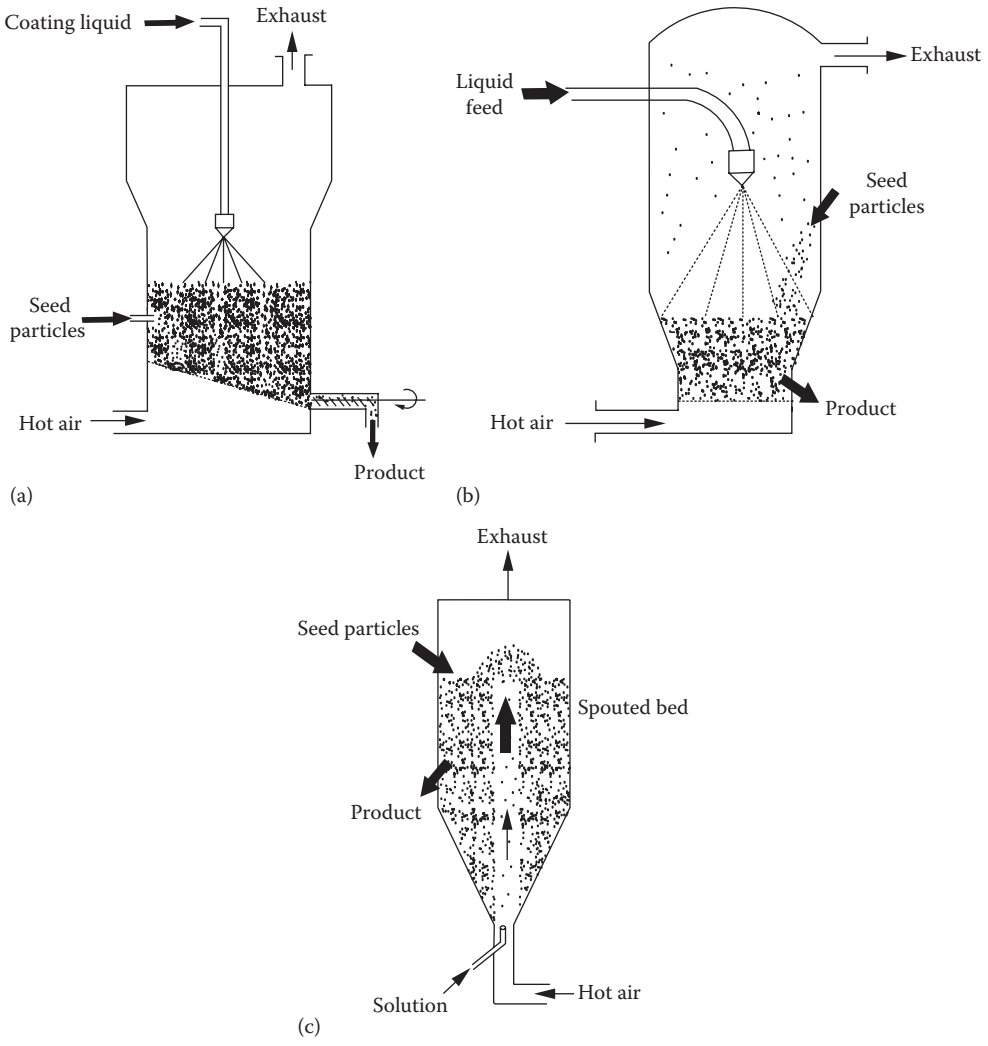


Figure 17.45

(a and b) Fluidized bed coaters. (c) Spouted bed coater.

Particle coating has many industrial applications, including coating the small pellets for pharmaceutical capsules to realize controlled drug release profile.

17.3.5.4 Powder Coating

Powder coating is a process where the materials initially in powder form are coated onto larger objects such as dishwasher racks, filing cabinets, and automotive parts. The powder materials can be thermoplastic or thermosetting. Thermoplastic materials are usually used for simple indoor parts with less stringent requirement. When applying thermoplastic coating, the thermoplastic powder is fluidized with cold or warm air and the heated metal part such as a dishwasher rack is dipped into the bed for a short period of time, normally a few seconds, and then quickly removed. A uniform thermoplastic coating is thus formed onto the dishwasher rack, making it a nice final product.

Thermosetting powder coating is used much more widely and also much more durable than thermoplastic powder coatings. In the thermosetting powder coating process, pigment, resin, and other materials are first dry-mixed together and then put through an extrusion process to homogenize the materials. The solid paint chips from the extrusion are then grinded down to about 30–60 μm to be used as the paint powder.

There are two methods to apply the paint powder onto workpieces, both using electrostatics. The first method is fluidized bed coating, where the air is electrically charged when flowing through the plenum with a high voltage electrode. The parts are then dipped into the fluidized bed of paint powder and the powder forms a thin layer on the parts' surface caused by electrostatic adhesion. The parts are then transported to an oven for curing. This procedure is simple but limited to continuous coating of simple parts of similar size and shape.

The mostly widely used powder coating process, over 90%, is the electrostatic spraying method. A typical powder spray booth with accessories is given in Figure 17.46. Paint powder is first put into the fluidized feed hopper from which the powder is "picked up" by the Venturi effect using a high-velocity airflow in the transport line. At the end of the air transport line is the spray gun, which produces an air and particle flow mixture, projecting toward the parts that are conveyed in the direction perpendicular to the powder flow. The powder, now charged by the high-voltage electrode at the tip of the powder spray gun, preferentially flows onto the earthed metal parts and cling onto them. The coated parts are then conveyed by the continuous conveyor to the oven for solidification (curing). Particles not adhered to the parts are sucked into the solids separation system, typically with cyclones and bag house filters, and the paint particles collected are recycled back to the feeder.

There are many significant advantages of electrostatic spraying powder coating over regular solvent-based coating. First, it eliminates the use of a solvent, which not only eliminates the associated emission problem but also realizes cost savings. The second key advantage is that any unused paint can be recycled and reused. Therefore, dry powder coating has developed very quickly and is replacing solvent coating at an unprecedented rate. However, due to the use of Geldart A powders, the surface quality of powder coating is not very smooth so that powder coating has not been used for high end products such as automobile bodies. While the use of much finer Geldart C paint powder should lead to a much better surface quality, the problem of powder agglomeration makes the results even worse, preventing the use of powder coating

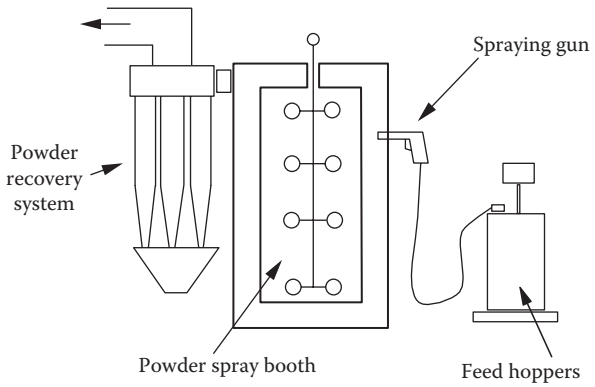


Figure 17.46

The powder coating process.

from being used for high-end products. A new technology has been invented at the authors' university that can essentially eliminate the interparticle forces. Using this new technology, Geldart C particles are made to flow freely, just like Geldart Group A particles. This new technology has now been commercialized in a local company to produce high-end powder coating products.

It is with the use of fine Geldart C particles that this fine powder coating has been extended to coat pharmaceutical tablets (Zhu et al., 2010, 2011). Horizontally rotating coating pans that are currently used for liquid coating are directly adopted for powder coating, so that major change of equipment is not required. Coating powder is made by direct mixing of the ingredient particles, typically including the functional polymer, the pigment, and other additives such as plasticizers. After preheating the tablets in the tumbling coating pan, a thin layer of liquid plasticizer may be first sprayed onto the tablets, to reduce the glass transition temperature as well as to create a moisturized surface for easy adhesion of the coating powder. Then, coating powder was sprayed, followed by curing—this process cycle may be repeated to increase the coating level when required, typically for functional release profiles. This technology has now been fully demonstrated with industry size pilot runs, for all major functional coating profiles, that is, immediate release (Qiao et al., 2010a), sustained release (Qiao et al., 2010b), and enteric release (Qiao et al., 2013). Once commercialized, this will represent the fourth generation of pharmaceutical coating, after sugar coating, organic solvent coating, and aqueous coating, with clear benefits over its predecessors: significantly reduced energy use, environmentally more friendly, and shorter processing time. Additional benefits include reduced coating level to achieve the same functional coating due to the more consolidated film formed by powder coating (Zhu et al., 2010).

17.3.6 Other Fluidized Bed Reactors and Applications

Besides the various gas–solid fluidized bed reactors discussed earlier in this section, there are also other types of fluidized bed reactors, namely, the spouted bed and spout-fluid bed reactors, the LSFB reactors, and the gas–liquid–solid three phase reactors. Given the limited space of this handbook, only the special features are highlighted here, while the readers are directed to key references for more details.

17.3.6.1 Spouted Beds

The spouted bed is essentially a fluidized bed with purposely made "mal-distribution" of gas. All fluidizing gas enters in a central nozzle from the bottom of the bed, which has reversed cone shape, and all the special features of the spouted bed trace back to the central nozzle. As outlined in Section 17.3.1, particles in the spouted bed flow rapidly upward in the spout, reach the top fountain, and then move down slowly in the annulus. Most gases pass through the bed in the central spout and there may be a gas downflow in the annulus as gas is dragged downward by the particles. The gross internal particle circulation inside the spouted bed gives rise to several additional features and it is these features that lead to the application of spouted beds.

First of all, the gross solid's circulation and the more vigorous particle movement allow the spouted bed to handle larger and sticky particles. This makes the spouted bed very useful in certain physical operations such as drying and particle coating, as the gross and vigorous internal circulation prevents the particles from sticking to each other. As a matter of fact, the invention of spouted bed was directly associated with the drying of Canadian wheat (Mathur and Gishler, 1955). Mathur and Epstein (1974) reviewed most of the early applications of spouted beds, including drying and particle coating. There were also a period of time during the 1980s and early 1990s that spouted beds have been studied for coal combustion and gasification, which, however, appears to have not led to commercialization. There were also studies on pyrolysis in spouted beds with and without draft tubes (Huff and Vasalos, 1998, Aguado et al., 2002), and the spouted bed with a more "complete" draft tube is also referred to as an "internal CFB" (Milne et al., 1994).

Spouted beds are also finding applications in new areas such as the food industry (Dewettinck, and Huyghebaert, 1999, Gibbs et al., 1999) and pharmaceutical industry (Jono et al.,, 2000) to coat beads and pellets. In the food industry, encapsulation with thin film of polymers provides specific properties that the natural product does not offer. For example, encapsulation can separate the reactive components within a mixture, mask undesirable flavors, protect unstable ingredients from degradation (due to heat, moisture, air and light), provide controlled and/or delayed release and reduce hygroscopicity, and change the characteristic of the original material (such as flowability, compressibility, dust reduction and density).

17.3.6.2 Liquid–Solid Fluidized Beds

LSFBs have very uniform liquid–solid suspension. Unlike a gas–solid fluidized bed where excess fluidizing gas beyond minimum fluidization forms bubbles, which lead to bypassing of reactant and many other

problems, "excess" liquid in LSFB merely leads to higher bed expansion. Such phenomenon is referred to as particulate fluidization (Kwauk, 1992) and provides many benefits: very uniform contact between the two phases throughout the entire fluidized bed and the ability to adjust the liquid–solid ratio inside the bed by changing the liquid fluidization velocity.

The modern applications of LSFB appear to date back to the 1960s. The more traditional applications of liquid–solid fluidized beds include classification of particles by size and density, backwashing of granular filters, crystal growth, adsorption, ion exchange, and electrolysis with both inert and electrically conducting fluidized particles (Epstein, 2003). Another area of applications is leaching and washing (Kwauk, 1992). More recent applications of the LSFB are in the bioindustry and wastewater treatment industry. A recent review paper by Epstein (2003) provides an excellent collection of applications of LSFBs.

Worth special mentioning is the emergence of the liquid-solid circulating fluidized beds (LSCFBs) as a new liquid–solid reactor, which gives added benefits over the traditional LSFB (Zhu et al., 2000). The added features include more uniform residence time distribution, better mass transfer, the independent control of solid's concentration, the higher turndown ratio, and the possibility of accommodating two reactions/processes in the same LSCFB unit. LSCFB has found potential applications in the chemical industry (Liang and Zhu, 1997), the biotech industry (Lan et al., 2002), and the wastewater treatment industry (Nakhla et al., 2007, Zhu et al., 2010). By early 2015, LSCFB has been successfully demonstrated commercially by Renix at London, Canada, for an ionic exchange process.

17.3.6.3 Gas–Liquid–Solid Three-Phase Fluidized Beds

Gas–liquid–solid fluidized beds (GLSFB) or three-phase fluidized beds may be considered as LSFBs with the additional injection of gas. The GLSFB is generally divided into two phases: the gas or bubble phase and the fluidized dense phase where there are only liquid and solids. In a GLSFB, bubbles form as soon as the gas is injected, since, unlike in the gas–solid fluidized bed, the gas phase is not present in the dense phase. Interaction between the gas phase and particles is mostly indirect through the liquid phase. Generally speaking, a GLSFB is more uniform than a gas–solid fluidized bed but less uniform than an LSFB. In the stationary GLSFB, there are three main operating regimes: the dispersed bubble regime, the coalesced bubble regime, and the slug regime (Fan, 1989). The dispersed bubble regime under higher liquid velocity is more uniform than the coalesced bubble regime under higher gas velocity. This also reflects the point that a "gas-driven" fluidized system is less uniform than a "liquid-driven" fluidized system.

GLSFBs also have many applications. The more traditional applications are in the petrochemical industry for upgrading heavy stocks such as hydrocracking and hydrotreating. Applications in fermentation and pharmaceutical industry also have a long history. More recent applications in the past 20–30 years are seen mostly in the biotech industry and wastewater treatment industry. A very thorough review has been provided by Fan (1989).

Nomenclature

Abbreviations

ATB	Atmospheric topped bitumen
BGPG	Biomass gasification and power generation
CFB	Circulating fluidized bed
CFBC	Circulating fluidized bed combustor
FCC	Fluid catalytic cracking or fluid cracking catalyst
FFB	Fixed fluidized bed
GIEC	Guangzhou Institute of Energy Conversion
GLSFB	Gas–liquid–solid fluidized beds
GLSCFB	Gas–liquid–solid circulating fluidized bed
LSCFB	Liquid–solid circulating fluidized bed
LSFB	Liquid–solid fluidized beds
PCFBC	Pressurized circulating fluidized bed combustor
PFBC	Pressurized fluidized bed combustor
QC	Quick contact
RFCC	Residue fluid catalytic cracking
RTD	Residence time distribution

SFB	Stationary fluidized bed
SFB	Stationary fluidized bed combustor
SINOPEC	Chinese National (Sino) Petroleum Enterprises Corporation
TCC	Thermofor catalytic cracking
UOP	Universal Oil Products Company
VTB	Vacuum topped bitumen

References

Aguado, R., Olazar, M., San José, M.J., Gaisán, B., and Bilbao, J., Kinetic study of polyolefin pyrolysis in a conical spouted bed reactor, *Ind. Eng. Chem. Res.*, 41, 4559, 2002.

Asadullah, M., Ito, S., Kunimori, K., and Tomishige, K., Role of catalyst and its fluidization in the catalytic gasification of biomass to syngas at low temperature, *Ind. Eng. Chem. Res.*, 41, 4567, 2002a.

Asadullah, M., Ito, S.I., Kunimori, K., Yamada, M., and Tomishige, K., Energy efficient production of hydrogen and syngas from biomass: Development of low-temperature catalytic process for cellulose gasification, *Environ. Sci. Technol.*, 36, 4476, 2002b.

Avidan, A.A., FCC is far from being a mature technology, *Oil Gas J.*, 90, 59, 1992.

Avidan, A.A., Fluid catalytic cracking, Grace, J.R., Avidan, A.A., and Knowlton, T.M. (Eds.), Chapter 13 in *Circulating Fluidized Beds*, 1st edn., Blackie Academic & Professional, London, U.K., 1997, p. 466.

Avidan, A.A., Edwards, M., and Owen, H., Fluid catalytic cracking. Past and future challenges, *Rev. Chem. Eng.*, 6, 1, 1990.

Avidan, A.A. and Shinnar, R., Development of catalytic cracking technology. A lesson in chemical reactor design, *Ind. Eng. Chem. Res.*, 29, 931, 1990.

Bergougnou, M.A., Briens, C.L., and Bassi, A.S., Short contact time fluidized reactors (SCTFRs), in Avidan, A.A. (Ed.), *Circulating Fluidized Bed Technology IV*, AIChE, New York, 1994, p. 15.

Bi, H.T., Grace, J.R., and Zhu, J.., Regime transitions affecting gas-solids suspensions and fluidized beds, *Chem. Eng. Des. Dev.*, 73(A2), 154, 1995.

Bridgwater, A.V., Renewable fuels and chemicals by thermal processing of biomass, *Chem. Eng. J.*, 91, 87, 2003.

Bridgwater, A.V. and Peacocke, G.V.C., Fast pyrolysis processes for biomass, renewable and sustainable energy reviews, 4, 1, 2000.

Buhre, B.J.P., Elliott, L.K., Shgn, C.D., Gupta, R.P., and Wall, T.F., Oxy-fuel combustion technology for coal-fired power generation, *Progress Energy Combust. Sci.*, 31, 283, 2005.

Chen, Y.-M., Evolution of FCC—Past present and future–and the challenges of operating a high-temperature CFB system, in *Proceedings of 10th Conference on Fluidized Bed Technology*, Beijing, China, May 2011, p. 68.

Cheng, Y., Wu, C., Zhu, J., Wei, F., and Jin, Y., Downer reactor: From fundamental study to industrial application, *Powder Technol.*, 183, 364–384, 2008.

Davidson, J.F., Clift, R., and Harrison, D., *Fluidization*, 2nd edn., Academic Press, London, U.K., 1985.

Deng, R.S., Wei, F., Jin, Y., Zhang, Q., and Jin, Y., Downer catalytic pyrolysis (DCP): A novel process for light olefins production, *Chem. Eng. Technol.*, 25, 711, 2002b.

Deng, R.S., Wei, F., Jin, Y., Zhang, Q., and Jin, Y., Experimental study of the deep catalytic cracking process in a downer reactor, *Ind. Eng. Chem. Res.*, 41, 6015, 2002a.

Dewettinck, K. and Huyghebaert, A., Fluidized bed coating in food technology, *Trends Food Sci. Technol.*, 10, 163, 1999.

Epstein, N., Applications of liquid-solid fluidization, *Int. J. Chem. Reactor Eng.*, 1, 1, 2003.

Fan, L.S., *Gas-Liquid-Solid Fluidization Engineering*, Butterworths, Boston, MA, 1989.

Gartside, R.J., QC—A new reaction system, in Grace, J.R., Shemilt, L.W., and Bergougnou, M.A. (Eds.), *Fluidization VI*, Engineering Foundation, New York, 1989, p. 25.

Geldart, D., *Gas Fluidization Technology*, Wiley, Chichester, U.K., 1986.

Gibbs, B.F., Kermasha, S., Alli, I., and Mulligan, C.N., Encapsulation in the food industry: A review, *Int. J. Food Sci. Nutr.*, 50, 213, 1999.

Grace, J.R., Avidan, A.A., and Knowlton, T.M., *Circulating Fluidized Beds*, 1st edn., Blackie Academic & Professional, London, U.K., 1997.

Graham, R.G. and Huffman, D.R., Commercial aspects of rapid thermal processing (RTP), in *Proceedings of Power Production from Biomass II Conference*, Espoo, Finland, April 1995.

Gross, B., Heat balance in FCC process and apparatus with downflow reactor riser, U.S. Patent 4,411,773, 1983.
Gross, B. and Ramage, M.P., FCC reactor with a downflow reactor riser, U.S. Patent 4,385,985, 1983.
Highley, J. and Kaye, W.G., Fluidized bed industrial boilers and furnaces, in *Fluidized beds Combustion and Applications*, Howard, J.R. (Ed.), Applied Science Publishers, London, U.K., 1983.
Howard, J.R. (Ed.), *Fluidized Beds Combustion and Applications*, Applied Science Publishers, London, U.K., 1983.
Huff, G.A. and Vasalos, I.A., Oxidative pyrolysis of natural gas in a spouted bed reactor: Reaction stoichiometry and experimental reactor design, *Catal. Today*, 46(2–3), 39, 1998.
Jacobs, J.P., The future of fluidized-bed combustion, *Chem. Eng. Sci.*, 54, 5559, 1999.
Jahnig, C.E., Campbell, D.L., and Martin, H.A., History of fluidized solids development at EXXON, in *Fluidization*, Grace, J.R. and Matsen, J.M. (Eds.), Plenum Press, New York, 1980, p. 3.
Jin, Y., Yu, Z., and Cai, P., A criterion for transition from bubbling to turbulent fluidization, in *Fluidization V*, Østergaard, K., and SØrensen, A. (Eds.), Engineering Foundation, New York, 1986, p. 289.
Jono, K., Ichikawa, H., Miyamoto, M., and Fukumori, Y., A review of particulate design for pharmaceutical powders and their production by spouted bed coating, *Powder Technol.*, 113, 269, 2000.
Karamanev, D. and Nikolov, L., Bed expansion of liquid-solid inverse fluidization, *AIChE J.*, 38, 1916, 1992.
Kehoe, P.W.K. and Davidson, J.F., Continuously slugging fluidized beds, *Chemeca'70, Inst. Chem. Eng. Symp. Ser.*, 33, 97, 1971.
Kosowska-Golachowska, M., Luckos, A., Klos, K., and Musial, T., Oxy-combustion of different coals in a circulating fluidized bed, in *Proceedings of 10th Conference on Fluidized Bed Technology*, Beijing, China, May 2011, p. 481.
Kunii, D. and Levenspiel, O., *Fluidization Engineering*, 2nd edn., Butterworth-Heinemann, Boston, MA, 1991.
Kwauk, M., *Fluidization: Idealized and Bubbleless, with Applications*, Science Press, Beijing, China; Ellis Horwood, New York, 1992.
Lan, Q., Bassi, A.S., Zhu, J.-X., and Margaritis, A., Continuous protein recovery from whey using liquid-solid circulating fluidized bed ion-exchange extraction, *Biotech. Bioeng.*, 78, 157, 2002.
Li, D.-B., Ray, M., Ray, A., and Zhu, J.-X., A comparative study on hydrodynamics of circulating fluidized bed riser and downer, *Powder Technol.*, 247, 235–259, 2013.
Liang, W.-G. and Zhu, J.-X., Effect of radial flow nonuniformity on the alkylation reaction in a liquid-solid circulating Fluidized bed (LSCFB) reactor, *Ind. Eng. Chem. Res.*, 36, 4651, 1997.
Luo, B.-L., Yan, D., Ma, Y.-L., Barghi, S., and Zhu, J.-X., Characteristics of gas-solid mass transfer in a cocurrent downflow circulating fluidized bed reactor, *Chem. Eng. J.*, 132(1–3), 9–15, 2007.
Maadhah, A.G., Abul-Hamayel, M., Aitani, A.M., Ino, T., and Okuhara, T. Down-flow FCC reactor, *Oil Gas J.*, 98, 66, 2000.
Mathur, K.B. and Epstein, N., *Spouted Beds*, Academic Press, New York, 1974.
Mathur, K.B. and P.E. Gishler, A technique for contacting gases with coarse solid particles, *AIChE J.*, 1, 157, 1955.
Milne, B.J., Berruti, F., Behie, L.A., and de Bruijn, T.J.W., The hydrodynamics of the internally circulating fluidized bed at high temperature, in *Circulating Fluidized Bed Technology VI*, Avidan, A.A. (Ed.), AIChE, New York, 1994, p. 28.
Murphy, J.R., Evolutionary design changes mark FCC process, *Oil Gas J.*, 90, 49, 1992.
Nakhla, G., Zhu, J., and Cui, Y., Liquid-solid circulating fluidized bedwaste water treatment system for simultaneous carbon, nitrogen and phosphorus removal, U.S. Patent, 7,261,811, 2007.
Pärssinen, J.H. and Zhu, J., Axial and radial solids distribution in a long and high-flux CFB riser, *AIChE J.*, 47, 2197–2205, 2001.
Qi, X., Zhu, H., and Zhu, J., Demarcation of a new circulating turbulent fluidization regime, *AIChE J.*, 55, 594–611, 2009.
Qi, X.-B., Zhang, H., and Zhu, J.-X., Solids concentration in the fully developed region of circulating fluidized bed downers, *Powder Technol.*, 183, 417–425, April 2008.
Qiao, M., Luo, Y., Zhang, L., Ma, Y., Stephenson, T.S., and Zhu, J., Sustained release coating of tablets with Eudragit RS/RL using a novel electrostatic dry powder coating process, *Int. J. Pharma.*, 399, 37–43, 2010b.
Qiao, M., Zhang, L., Ma, Y., Zhu, J., and Chow, K., A novel electrostatic dry powder coating process for pharmaceutical dosage forms: Immediate release coatings for tablets, *Eur. J. Pharm. Biopharm.*, 76, 304–310, 2010a.

Qiao, M., Zhang, L., Ma, Y., Zhu, J., and Xiao, W., A novel electrostatic dry coating process for enteric coating of tablets with Eudragit(®) L100-55, *Eur. J Pharm. Biopharm*., 83, 293–300, 2013.
Reh, L., Fluidized bed processing, *Chem. Eng. Prog.*, 67, 58, 1971.
Reh, L., The circulating fluid bed reactor—A key to efficient gas/solid processing, in *Circulating Fluidized Bed Technology I*, Basu, P. (Ed.), Pergamon, Toronto, Ontario, Canada, 1986, p. 105.
Reh, L., Challenges of circulating fluid-bed reactors in energy and raw materials industries, *Chem. Eng. Sci*., 54, 5359, 1999.
Reichle, A.D., Fluid catalytic cracking hits 50 year mark on the run, *Oil Gas J*., 90, 41, 1992.
Royal Dutch Shell Group of Companies, *The Petroleum Handbook*, 6th edn., Elsevier, Amsterdam, the Netherlands, 1983.
Sang, L., Ph.D. Dissertation, Particle fluidization in upward and inverse liquid-solid circulating fluidized bed, Supervised by Zhu, J., University of Western Ontario, London, Ontario, Canada, April 2013.
Scott, D.S., Majerski, P., Piskorz, J., and Radlein, D., Second look at fast pyrolysis of biomass—The RTI process, *J. Anal. Appl. Pyrol*., 51, 23, 1999.
Scott, D.S., Plskorz, J., and Radlelnt, D., Liquid products from the continuous flash pyrolysis of biomass, *Ind. Eng. Chem. Process. Des. Dev*., 24, 581, 1985.
Shingles, T. and McDonald, A.F., Commercial experience with synthol CFB reactors, in *Circulating Fluidized Bed Technology II*, Basu, P. and Large, J.F. (Eds.), Pergamon Press, Toronto, Ontario, Canada, 1988, p. 43.
Silverman, A., Thompson, A.H., Sterynberg, A., Yukawa, Y., and Shingles, T., Development of a dense phase fluidized bed Fischer-Tropsch Reactor, in *Fluidization V*, Østergaard, K., and SØrensen, A. (Eds.), Engineering Foundation, New York, 1986, p. 441.
Sondreal, E.A., Benson, S.A., Hurley, J.P., Mann, M.D., Pavlish, J.H., Swanson, M.L., Weber, G.F., and Zygarlicke, C.J., Review of advances in combustion technology and biomass cofiring, *Fuel Process. Technol*., 71, 7, 2001.
Song, Y.-X., *Applying the Principles Learned from the Nature (Tian-Gong-Kai-Wu)*, originally published by Nanchang City Press of the Ming Dynasty, Jiangxi, China, 1637 (first reprinted in modern form by Shanghai Chinese Book Bureau, Shanghai, China, 1959).
Squires, A.M., Three bold exploiters of coal gasification: Winkler, godel and porta, in *Fluidized beds Combustion and Applications*, Howard, J.R. (Ed.), Applied Science Publishers, London, U.K., 1983.
Sutton, D., Kelleher, B., and Ross, J.R.H., Review of literature on catalysts for biomass gasification, *Fuel Process. Technol*., 72, 155, 2001.
Talman, J.A., Geier, R., and Reh, L., Development of a downer reactor for fluid catalytic cracking, *Chem. Eng. Sci*., 54, 2123, 1999.
Teunou, E. and Poncelet, D., Batch and continuous fluid bed coating—Review and state of the art, *J. Food Eng*., 53, 325, 2002.
Wang, C., Zhu, J., Barghi, S., and Li, C., Axial and radial development of solids holdup in a high flux/density gas-solids circulating fluidized bed, *Chem. Eng. Sci*., 108, 233–243, 2014.
Wang, C.-X., Barghi, S., and Zhu, J.-X., Hydrodynamics and reactor performance evaluation of a high flux circulating fluidized bed downer: Experimental study, *AIChE J*., 60, 3412–3423, 2014.
Wang, C.-X., Zhu, J.-X., and Barghi, S., Performance evaluation of high density riser and downer: Experimental study using ozone decomposition, *Chem. Eng. J*., 262, 478–489, 2014.
Winkler, F., German Patent, 437,970, 1922.
Wu, C.Z., Huang, H., Zheng, S.P., and Yin, X.L., An economic analysis of biomass gasification and power generation in China, *Bioresour. Technol*., 83, 65, 2002.
Wu, C.Z., Personal communications, 2010.
Wu, Y., Lu, J., and Zhang, J., Conceptional design of an 800MW supercritical pressure circulating fluidized bed boiler, *Boiler Technol*., 35, 12, 2004.
Syncrude, Website of Syncrude, www.syncrude.ca, February 2012.
Xin, J., Lu, J., and Yue, G., A discussion concerning the development of supercritical circulating fluidized bed combustors, *J. Eng. Therm. Energy Power*, 17, 439, 2002.
Yerushalmi, J., Applications of fluidized bed, Chapter 8.3 in *Handbook of Multiphase Systems*, Hetsroni, G. (Ed.), Hemisphere Publishing Co., Washington, DC, 1982.
Yerushalmi, J., Turner, D.H., and Squires, A.M., The fast fluidized bed, *I&EC, Proc. Des. Dev.*, 15, 47–53, 1976.
Yin, X.L., Wu, C.Z., Zheng, S.P., and Chen, Y., Design and operation of a CFB gasification and power generation system for rice husk, *Biomass Bioenergy*, 23, 181, 2002.

Yu, Z.-Q., Application collocation, *Adv. Chem. Eng.*, 20, 39, 1994.
Yue, G., Lv, J., Yang, H., Su, H., Nie, L., Lei, Xi, Tao, Sl, and Zhang, W., Research on supercritical circulating fluidized bed boiler, in *Proceedings of 11th Conference on Fluidized Bed Technology*, Beijing, China, May 2014, p. 541.
Zenz, F.A. and Othmer, D.F., *Fluidization and Fluid-Particle Systems*, Reinhold Publishing Corporation, New York, 1960.
Zhang, H., Huang, W.-X., and Zhu, J.-X., Gas-solids flow behavior: CFB riser vs. downer, *AIChEJ.*, 47, 2000–2011, 2001.
Zhu, H. and Zhu, J., Gas-solids flow structures in a novel circulating-turbulent fluidized bed, *AIChE J.*, 54, 1213–1223, 2008.
Zhu, J., Circulating turbulent fluidization—A new fluidization regime or just a transitional phenomenon, *Particuology*, 8, 640–644, 2010.
Zhu, J. and Bi, H., Distinctions between low density and high density circulating fluidized beds, *Can. J. Chem. Eng.*, 73, 644–649, 1995.
Zhu, J., Jin, Y., Wang, Z., and Yu, Z.Q., *Fluidization Engineering Principles*, Tsinghua University Press, Beijing, China, 2000.
Zhu, J., Luo, Y., Ma, Y., and Zhang, H., Direct coating solid dosage forms using powdered materials, U.S. Patent 7,862,848, 2011.
Zhu, J., Nakhla, G., and Cui, Y., Liquid-solid fluidized bed waste water treatment system for simultaneous carbon, nitrogen and phosphorus removal, U.S. Patent 7,736,513, 2010.
Zhu, J., Qiao, M., and Ma, Y., A method for electrostatically powder coating tablets, *Tablets Capsules*, 8, 18–23, 2010.
Zhu, J.-X., Yu, Z.-Q., Jin, Y., Grace, J.R., and Issangya, A., Cocurrent downflow circulating fluidized bed (downer) reactors—A state of the art review, *Can. J. Chem. Eng.*, 73, 662, 1995.
Zhu, J.-X., Zheng, Y., Karamanev, D.G., and Bassi, A.S., (Gas-)liquid-solid circulating fluidized beds and their potential applications to bioreactor engineering, *Can. J. Chem. Eng.*, 78, 82, 2000.

18

Nanofluids

Efstathios E. Michaelides and Yulong Ding

18.1 Overview
18.2 Definition of the Effective Transport Properties
18.3 Effective Viscosity
18.4 Effective Thermal conductivity
18.5 Additional Augmentation of the Convective Heat Transfer Coefficients
18.6 Natural Convection
18.7 Boiling with Nanofluids
18.8 Effective Diffusivity
18.9 Specific Heat Capacity
18.10 Conclusions and General Observations

18.1 Overview

Nanofluids are heterogeneous suspensions of nanoparticles in common fluids, which are typically called *base fluids*. Nanofluids exhibit significantly altered heat and mass transfer characteristics and have become the subject of investigations of numerous research projects since 1995. Several sets of experimental data indicate that the addition of very small quantities of nanoparticles in the base fluids has the following effects on the heat and mass transfer characteristics of the mixture:

1. Increases, in many cases, the effective thermal conductivity of the suspensions
2. Increases, in many cases, the convective heat transfer coefficients
3. In general, decreases the pool boiling coefficients, enhances the convective boiling coefficients, and enhances significantly the critical heat flux (CHF)
4. Increases significantly the mass transfer coefficient
5. Increases the viscosity and friction factor
6. Increases the specific heat capacity in some cases

Figure 18.1 depicts the ratio of the thermal conductivities of the nanofluid to that of the base fluid, k_e/k_f, as a function of the volumetric fraction of solids. This ratio is often referred to as the *relative conductivity* of the nanofluid. The figure is a compilation of several sets of experimental data from the literature with the most typical nanoparticles (Eastman et al., 2001, Xie et al., 2002, 2011, Das et al., 2003, Chopkar et al., 2006, 2008, Liu et al., 2006, Turanov and Tolmachev, 2009). The two lines represent typical trends with a metallic nanofluid and an oxide nanofluid.

The following conclusions may be drawn from this figure:

- The percentage conductivity enhancement is significantly higher than the percentage concentration increase of the particles. A very low concentration of particles (less than 1%) may cause more than 20% enhancement of the thermal conductivity.

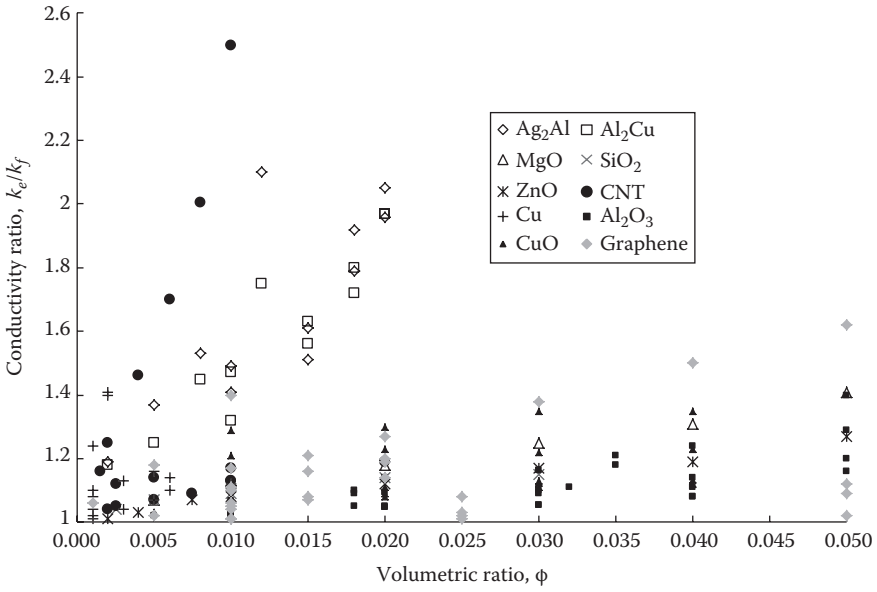


Figure 18.1

Effective thermal conductivity enhancement of several nanofluid systems.

- The thermal conductivity enhancement depends primarily on the type of particles: nanofluids with particles, such as carbon nanotube (CNT), Ag_2Al, and Al_2Cu, exhibit significantly higher effective conductivities, while the effective conductivities of nanofluids with Al_2O_3 nanoparticles are, in general, significantly lower.
- There are diminishing returns to adding more particles beyond a concentration of approximately 1%: the effective conductivity increase is not simply proportional to the volumetric ratio.

Because of their very high relative conductivity, CNT and metallic nanofluids are considered to be excellent heat transfer media. This, and the expectation that nanofluids with desired internal structure and transport properties may be specifically designed by using suitable nanoparticles and surfactants, has sparked a tremendous research interest in these suspensions. It must be noted that this discussion does not take into account the penalty due to viscosity and pressure drop increase, which may outweigh the benefits of the thermal conductivity enhancement. The following sections present a succinct summary of the transport properties of the experimental and analytical results pertaining to nanofluids.

18.2 Definition of the Effective Transport Properties

All the transport properties have been defined in homogeneous fluids as the ratios of a flux and the corresponding conjugate force (Onsager, 1931). For example, the viscosity of a homogeneous, Newtonian fluid has been defined at every point of the fluid in terms of the shear stress and the velocity gradient:

$$\tau = \mu\left(\frac{\partial u}{\partial y}\right) \tag{18.1}$$

Similar expressions yield the thermal conductivity and the diffusivity of homogeneous media. In the case of anisotropic and homogeneous materials, the transport properties are vectorial quantities but are still well defined at every point of the homogeneous medium from the tensors of the fluxes and conjugate forces (Michaelides, 2014).

Nanofluids are heterogeneous media at a scale of the order of magnitude of the nanoparticle size, composed of nanoparticles immersed in the base fluid. As such, there are two geometric domains in a nanofluid: the domain occupied by the solids and the domain occupied by the fluid. It is clear that if Equation 18.1 is to be applied for the viscosity of a nanofluid at two different points, the first inside the base fluid and the

second inside a nanoparticle, one would obtain two different values: the first is close to the viscosity of the pure base fluid and the second is very large (infinite, since the nanoparticle moves as a rigid body and the velocity gradient inside this particle is zero). None of the two values describe accurately the flow behavior of the entire heterogeneous suspension, the nanofluid. Therefore, both values are useless or meaningless to the scientist or the engineer. A more useful property in this case is the *effective viscosity* of the heterogeneous mixture, which includes the effects of the solid particles on the motion of the fluid. The effective viscosity is derived from an extension of the definition of the homogeneous fluid viscosity according to Equation 18.1 and pertains to the velocity gradients that are defined on a scale much larger than the scale of the particles: An average velocity gradient may be defined at any point (x, y, z) in the heterogeneous mixture using a length scale, δy, which is significantly larger than the size of the particles ($\delta y \gg \alpha$) and the velocity difference of the suspension, δu, at the ends of the segment. At this length scale, δy, the fluid–solids suspension may be approximated as a homogeneous fluid and the corresponding velocity difference, δu, as well as the average shear stress, τ, may be measured experimentally. Hence, the effective viscosity of the heterogeneous mixture, μ_e, at the point (x, y, z), which is the midpoint of the segment δy, is defined according to the expression:

$$\gamma \equiv \frac{\delta u}{\delta y} \quad \text{and} \quad \mu_e = \frac{|\tau|}{|\gamma|} \left(\delta y \gg \alpha\right) \tag{18.2}$$

Because of the condition $\delta y \gg \alpha$, Equation 18.2 defines the viscosity property at all points (x, y, z) of the heterogeneous mixture, regardless of whether these points are within the fluid or the solid domains.

This definition of the effective viscosity as a transport property of heterogeneous media is implicit in all the analytical derivations of expressions for the viscosity of heterogeneous mixtures as functions of particle concentration (e.g., Einstein, 1906, 1911, Brinkman, 1952, Batchelor, 1977). In the case of nanofluids, where the size of the particles is very small, this definition is convenient to use locally because the defining length scale, δy, is very short in comparison to the length scales of the pertinent fluids. Experimental and numerical studies prove that the so defined viscosity of the heterogeneous mixtures is uniform in suspensions where the particles are uniformly distributed and is independent of the size of δy, provided that δy is greater than the equivalent of 20 particle radii. Because of this, the effective viscosity of homogeneous suspensions is widely used in engineering flow calculations. If the particles are nonuniformly distributed, for example, in a sedimentation column, the effective viscosity is also nonuniform and, in general, it is a monotonically increasing function of the particle volumetric fraction, ϕ. In nonuniform suspensions, the function $\mu_e(\phi)$ may be also used in engineering calculations to determine the flow behavior of the suspension.

Similar definitions apply to the effective thermal conductivity and the effective diffusivity of heterogeneous materials. As with the effective viscosity, the numerical value of these effective transport properties is relatively easily measured or deduced from other measurements, provided that the measuring instrument does not disturb the particle distribution (Michaelides, 2014). The effective transport properties are routinely used in scientific and engineering calculations.

18.3 Effective Viscosity

18.3.1 Analytical Results

The now famous study by Einstein (1906), with the later correction (Einstein, 1911), was the beginning of the analytical studies on the viscosity of heterogeneous suspensions. He used a molecular model that treats the particles as noninteracting spheres, performed a first-order asymptotic analysis, and, after a correction, derived (Einstein, 1911) the following expression for the effective viscosity:

$$\mu_e = \mu_f (1 + 2.5\phi) \tag{18.3}$$

Brinkman (1952) extended the analysis by Einstein by including the fluid velocity field modification due to the presence of the spheres and derived the expression:

$$\mu_e = \mu_f \frac{1}{(1-\phi)^{2.5}} \tag{18.4}$$

A couple of decades later, Batchelor (1977) extended further this analysis to include the effects of the Brownian motion and the hydrodynamic interactions of pairs of spherical particles. Batchelor's expression is

$$\mu_e = \mu_f(1 + 2.5\phi + 6.5\phi^2) \tag{18.5}$$

It is apparent that the last three expressions yield very similar results for nanofluids that typically have low concentrations, $\phi \leq 5\%$. In cases where aggregation occurs, both the effective particle size and the volumetric concentration are needed for the calculation of the effective suspension viscosity (Chen et al., 2007b).

The only approach that differs significantly from the method used by the Einstein equation is the one by Happel (1957), who accounted for the interactions of particles under creeping flow conditions. He also stipulated that the additional tangential stress due to the presence of the particles vanishes far from the particles. With these modifications to the theory, he derived a higher coefficient for the parameter ϕ:

$$\mu_e = \mu_f(1 + 5.5\phi) \tag{18.6}$$

Among the other analytical studies on fluid–solid suspensions, Krieger and Dougherty (1959), Frenkel and Acrivos (1967), and Lundgren (1972) derived expressions in terms of the maximum allowable packing, which are applicable at higher particle concentrations. The expressions by Krieger and Daugherty (1959) and Lundgren (1972) reduce to the Einstein expression at the very low concentrations that are characteristic of low particle concentration nanofluids. The expression by Frenkel and Acrivos (1967) is only applicable to dense heterogeneous mixtures.

It must be noted that all these studies pertain to spherical particles. Elongated particles, spheroids, and ellipsoids cause a significantly higher enhancement of the effective viscosity (Kuhn and Kuhn, 1945, Michaelides, 2014). For example, spheroidal particles with aspect ratio $E = 20$, which are randomly distributed in a fluid, have an effective viscosity:

$$\mu_e = \mu_f(1 + 39\phi) \tag{18.7}$$

Nanofluids are composed primarily of irregular, elongated particles or long fibers and, for this reason, the experimentally observed effective viscosity of these heterogeneous mixtures is higher than the analytical expressions that are based on the spherical particle model.

18.3.2 Experimental Data and Correlations

The addition of solid particles in a homogeneous fluid, either gas or liquid, has always an enhancing effect on the viscosity of the fluid because of the following two effects:

1. The particles move as rigid bodies with uniform velocity and disrupt locally the velocity profile of the fluid. In order to accommodate the entire fluid velocity gradient, the velocity gradients in the fluid part of the suspension become sharper. The increased strain in the interstitial fluid between the particles causes higher stress at the same overall velocity gradient and this manifests itself as a higher effective viscosity.
2. In a velocity gradient, there is an additional momentum transfer in the direction perpendicular to the gradient, which is due to the solid particles and is similar to the molecular momentum transfer that defines the viscosity at the molecular level (Michaelides, 2014). This momentum transfer always increases the effective viscosity of the suspension.

Pak and Cho (1998) conducted one of the early studies on the effective viscosity and measured the viscosity and thermal conductivity of metal oxide (TiO_2 and Al_2O_3) aqueous nanofluids. Their results show that the coefficient of the volumetric fraction (the intrinsic viscosity) is significantly higher than the Einstein value of 2.5. The experimental data of this study were cast in correlation forms by Buongiorno (2006), who derived the following expression for the alumina–water nanofluids:

$$\mu_e = \mu_f(1 + 39.11\phi + 534\phi^2) \tag{18.8}$$

The viscosity of the titania (TiO_2)–water nanofluids was correlated by the expression

$$\mu_e = \mu_f(1 + 5.45\phi + 108\phi^2) \tag{18.9}$$

Another set of experimental data that determined intrinsic viscosity values significantly higher than 2.5 is that by Wang et al. (1999), with alumina nanoparticles in water and ethylene glycol base fluids. They observed viscosity enhancements in the range 20%–30% at $\phi = 0.03$ and close to 80% at $\phi = 0.07$. They also observed that the measured viscosity values depended on the method of preparation of the nanofluids. A comparison of the data sets by Wang et al. (1999) and by Pak and Cho (1998) shows that the measured viscosity values in the latter study are significantly higher. Wang et al. (1999) attributed this discrepancy to the different methods of preparation of the nanofluids, but there is also a question as to whether or not some of the nanofluids that were used by Pak and Cho (1998) were Newtonian fluids (Michaelides, 2014). The experimental data by Wang et al. (1999) were correlated by Maiga et al. (2005) by the equation

$$\mu_e = \mu_f(1 + 7.3\phi + 123\phi^2) \tag{18.10}$$

Das et al. (2003) also measured the effective viscosity of nanofluids at several temperatures and shear rates. The following conclusions may be derived from this study:

1. The alumina–water nanofluids were Newtonian in the range $0 < \phi < 0.04$.
2. The viscosity of the nanofluids decreased with increasing temperature.
3. The viscosity of the nanofluids increased with increasing volumetric fraction, ϕ.

The magnitude of the viscosity enhancements observed by Das et al. (2003) is close to 50% at $\phi = 0.04$, which implies that their data agree with the Wang et al. (1999) study rather than the Pak and Cho (1998) study.

Another experimental study by Chen et al. (2007a,b) with TiO_2 nanoparticles in ethylene glycol determined a higher value for the coefficient of ϕ, 10.6. The correlation developed in the study is

$$\mu_e = \mu_f(1 + 10.6\phi + 112\phi^2) \tag{18.11}$$

The experiments by Chen et al. (2007a,b) extend to higher volumetric fractions, close to 10%. It is apparent from Equation 18.11 that at the high volumetric ratios, the contributions of the two powers of ϕ are comparable. However, at the volumetric fractions of 1%–2%, which are typical of nanofluids, the term in ϕ contributes significantly higher to the value of the effective viscosity than the term in ϕ^2.

The experimental study by Nguyen et al. (2007) is the only one where the first coefficient agrees with the Einstein expression:

$$\mu_e = \mu_f(1 + 2.5\phi + 150\phi^2) \tag{18.12}$$

The authors of this study observed a hysteresis in the effective viscosity experiments, which is more likely due to particle aggregation and a slightly non-Newtonian behavior of their nanofluids.

A group of authors including Nguyen et al. (2007), Tseng and Chen (2003), and Tseng and Lin (2003) followed the functional form of the viscosity correlation by Mooney (1951), who stipulated that the viscosity of concentrated suspensions is well correlated by an exponential function of the form:

$$\mu_e = A\mu_f \exp(B\phi) \tag{18.13}$$

The values of the coefficients A and B vary significantly in these four studies. For example, the coefficient pairs (A, B) derived by Nguyen et al. (2007) for a water–Al_2O_3 nanofluid are (0.904, 14.8), while coefficient pairs (A, B) derived by Tseng and Lin (2003) for water–TiO_2 nanofluids are (13.47, 35.98).

Numerical calculations show that the last set of coefficients gives very high values for the effective viscosity that may not be realistic for Newtonian suspensions (Michaelides, 2014). In general, the exponential form of the correlation function is not recommended to be used for the following reasons:

1. The form originally has been derived for concentrated suspensions (Mooney, 1951), while all nanofluids are very dilute suspensions.
2. The exponential function $e^{B\phi}$ varies sharply with ϕ. Small errors in the calculation of the volumetric fraction result in high errors of the effective viscosity value. For example, in the expression by Tseng and Lin (2003), a 0.005 error in ϕ, causes a 20% error in the effective viscosity value.
3. The polynomial form is supported by most analytical studies for dilute suspensions and nanofluids are dilute suspensions.

A glance at all the correlations and the viscosity values they generate proves that there is a significant disagreement among the several experimental studies on the functional form as well as on the actual values of the viscosity of nanoparticle suspensions, even when the nanoparticles are of the same type. While each correlation represents fairly well the data it emanates from, correlations that are based on different data sets disagree significantly. The significant disagreement of the experimental data on the viscosity of nanofluids highlights some of the difficulties in designing cooling systems that use nanofluids as coolants.

The results of the experimental investigations suggest that the effective viscosity of nanofluids depends strongly on the shape of solid particles and this is corroborated by the analytical studies. Since most nanoparticles are not spheres, the analytical expressions that were derived for spheres would not be accurate for nanofluids. Some investigators have also suggested that different correlations apply to the same nanoparticle materials that are composed of different particles sizes. Such investigations derived correlations relating the viscosity to the particle *diameter*. This complicates the issue for the determination of the effective viscosity because

1. Aggregation and break-up processes continuously change the apparent *diameter* of the particles in a nanofluid. The aggregation mechanism is associated with interparticle forces, whereas the break-up mechanism is mostly associated with fluid shearing, particle–particle, and particle–wall collisions.
2. Given the size distributions of all nanoparticles, the particle "diameter" is not unique and is very difficult to measure.
3. Most nanoparticles are not spherical for one length scale value to describe their "size" or "diameter." The "size" issue is examined in more detail in Michaelides (2013, 2014) as well as in Chapter 1 of this handbook.
4. In shearing flows, nanofluid experiences different shear rates at different positions of the fluid field. This implies different break-up forces.

18.3.3 Non-Newtonian Behavior

The defining characteristic of non-Newtonian fluids is that their viscosity is not only a function of two independent properties, for example, T and P, but also of the local value of the shear, γ. This implies that the viscosity of non-Newtonian fluids is not an equilibrium material property, but a property that is associated with the local shear. For this reason, it is called the "effective viscosity" even in single-phase non-Newtonian fluids and is denoted by a different symbol, η. In addition to being a function of two thermodynamic properties, η is also a function of the rate of shear: $\eta = \eta(T, P, \gamma)$.*

Krieger and Dougherty (1959) were the first to examine the rheology of fluid–solid suspensions, composed of micro- and nanoparticles in liquids. They analyzed several sets of experimental data and determined that the local strain is best represented by a dimensionless shear Peclet number: $Pe = \mu_f \alpha^3 \gamma / k_B T$, which is a measure of the ratio of the shear force to the Brownian force. Figure 18.2 shows a typical dependence of the effective viscosity of a nanofluid on the rate of shear, γ, at constant T and P. The data in the figure pertain to polystyrene nanoparticles with sizes in the range 108–180 nm in deionized water and were obtained by Krieger (1972).† The effective viscosity of the suspension is typically made dimensionless by the dynamic

* As with the Newtonian fluids and the dynamic viscosity μ, η is also a weak function of the pressure, P.
† At the time of these publications the terms "nanofluid" and "nanoparticles" had not yet been adopted. The experimental data and the conclusions pertain to what are now called "aqueous nanofluids."

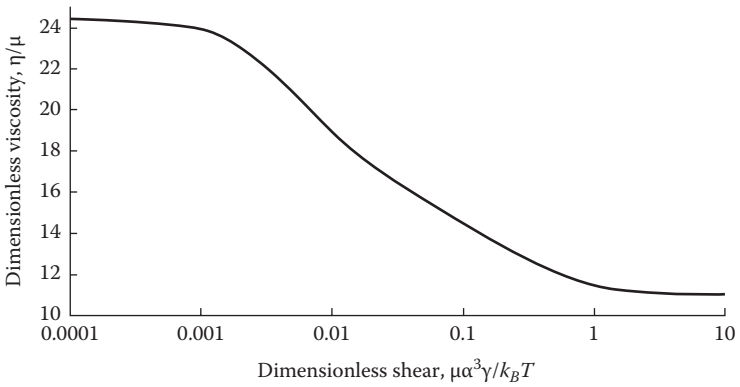


Figure 18.2

Shear dependence of the effective viscosity of a nanofluid. Qualitative behavior using data from Krieger (1972).

viscosity of the base fluid, which is usually a Newtonian fluid, η/μ_f. The following observations may be drawn from this figure about the function η:

1. Since it is known that the viscosity of the base fluid is a function of the temperature and a very weak function of the pressure, $\eta = \eta(\gamma, T)$.
2. The function $\eta(\gamma)$ has two asymptotic limits: one at the low and one at the high values of the shear, η_0 and η_∞.
3. Both asymptotic limits, η_0 and η_∞, are significantly higher than the viscosity of the base fluid, μ_f.
4. The value of the effective viscosity at high shear rates is by orders of magnitude lower than the effective viscosity at the lower shear rates.

The behavior of particulate mixtures to exhibit significantly lower effective viscosities at high shear rates has been called *shear thinning*. The local concentration and configuration of the particles within the base fluid matrix and the particle behavior and interactions during the shearing process are the main parameters that contribute to shear thinning (Russel et al., 1989, Probstein, 1994).

The formation of weak gel structures and the phenomenon of shear thinning have been observed in several experiments with nanofluids: Among these, the experimental study by Kim et al. (2011) on alumina–water nanofluids confirmed that several nanofluids composed of deionized water and alumina nanoparticles exhibit the rheological characteristics of Newtonian fluids at low volume fractions ($\phi \leq 2\%$), but showed a strong non-Newtonian behavior, including shear thinning at slightly higher volume fractions ($3\% \leq \phi \leq 5\%$). Two representative curves from the data of Kim et al. (2011) are shown in Figure 18.3, where it may be seen that the dilute nanofluid with $\phi = 1\%$ exhibits the typical behavior of a Newtonian fluid, since

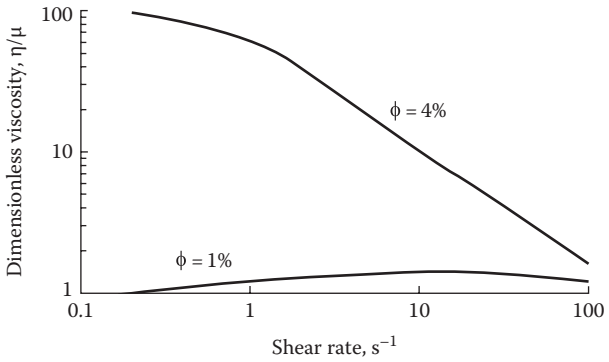


Figure 18.3

Rheological behavior of a water–alumina nanofluid at two different solids concentrations. (Data from Kim, S. et al., *J. Appl. Phys.*, 110, 034316, 2011.)

the ratio η/μ_f remains almost constant and approximately equal to 1 (within the experimental uncertainty of the data) at shear rates that span three decades. On the contrary, the nanofluid composed of the same materials with $\phi = 4\%$ exhibits strong non-Newtonian behavior: the effective viscosity, η, of this nanofluid reaches values close to 100 times higher than the base fluid viscosity, μ_f, at the lower shear rates. The same nanofluid shows very strong shear thinning behavior and its effective viscosity is reduced to approximately $4\mu_f$ at the higher rates of shear. One of the observations in the study by Kim et al. (2011) is that the particles in nanofluids within the range $3\% \leq \phi \leq 5\%$ aggregated, and the entire solutions formed gel-like structures. This explains the very high values of η at the low shear rates.

The study by Kim et al. (2011) also provides a great deal of information and insight on the method of preparation and treatment of the nanofluids that were used in the experiments. It was observed that the preparation process and time-to-settle for the nanofluid played a major role in the values of its effective viscosity. The experiments showed that the milling process of the nanoparticles and the amount of time the solution was left undisturbed had a significant effect on the observed characteristics and the rheological behavior of the nanofluids. For example, an alumina–water nanofluid with $\phi = 4\%$ was milled extensively for 5 h and when tested immediately after, it exhibited Newtonian behavior. When the same nanofluid was left undisturbed for 6 days, it exhibited strong non-Newtonian behavior with $\eta/\mu_f = 80$ at the lower shear rates of the experiments. These observations strongly suggest that, during the time the nanofluid was at rest, the alumina nanoparticles aggregated and the suspension formed a weak gel. The structure of the gel was temporarily broken by the milling process, but was restored when the mixture remained undisturbed for a prolonged time.

The formation of particulate structures and networks that conduct heat and also impede the flow in these experiments is supported by the observation that the effective viscosity of the gels increased significantly when the pH of the solution was modified sufficiently to cause an increase of the electrostatic forces between particles: for example, a change of the pH from 4 to 11 in a mixture of 5% particle concentration caused the dimensionless viscosity, η/μ_f, to increase by three orders of magnitude. Similarly, a dilute nanofluid with $\phi = 1\%$, behaved as a Newtonian fluid at the low pH range, but exhibited gel-like structure and non-Newtonian behavior with $\eta/\mu_f = 6000$ when the pH increased from 4 to 7 (Kim et al., 2011).

18.3.3.1 Viscosity of CNT Nanofluids

The experimental evidence with CNT (either single-walled or multiwalled) nanofluids proves that these suspensions are non-Newtonian, even when the volumetric ratio, ϕ, is very low. Ding et al. (2006) presented some of the early rheological data on aqueous CNT nanofluids and showed that their effective viscosity is a strong function of the rate of shear, γ, and of their volumetric ratio, ϕ. Two sets of data from this study are shown in Figure 18.4. The following observations may be drawn from this figure:

1. The rate of shear alters the viscosity of the nanofluid by five orders of magnitude.
2. The suspension reaches the high shear rate asymptotic value, η_∞, at shear rates between 1,000 and 10,000 s^{-1}.
3. The value of η_∞ is significantly higher than the viscosity of the base fluid (water).

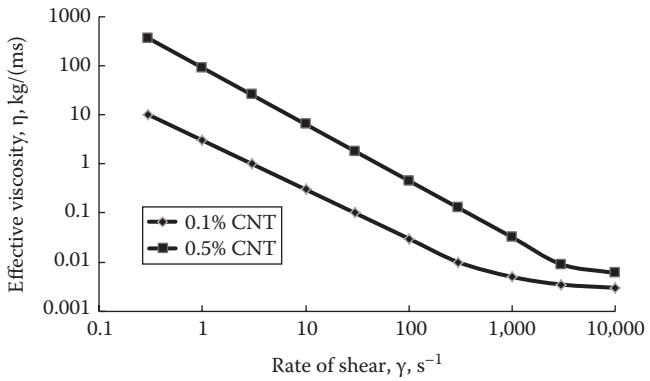


Figure 18.4

Selected aqueous CNT effective viscosity data at 25°C by Ding et al. (2006).

One of the reasons for the non-Newtonian behavior of CNT nanofluids is the addition of surfactants or dispersants, which are typically polymeric materials with long molecular chains. The chemical formula, the relative amount of the surfactants, the pH, and the treatment of the heterogeneous suspensions with ultrasound waves (sonification) influence significantly the effective viscosity of nanofluids that are formed. Yang et al. (2006) made a detailed report on the effect of surfactant concentration as well as on the time and energy of sonification for the effective viscosity of olefin-based CNT nanofluids. Their observations show that, even at the very low values of ϕ (0.12%), the CNT nanofluids exhibited distinct non-Newtonian behavior. One may easily conclude from the data of this study that the concentration of the surfactant affected significantly the effective viscosity of the suspension at the low shear rate, but not at the high shear rate: The effective viscosity of the nanofluid reached a minimum at the surfactant concentration 3% by weight, where the lowest effective viscosity was measured (Yang et al., 2006, Michaelides, 2014). Ding et al. (2006) also allude to the effect of the surfactants in their study of aqueous CNT nanofluids: in the absence of nanoparticles, the surfactant–water solution exhibited non-Newtonian behavior and its effective viscosity depended on the pH of the solution.

It must be noted that there have also been observations on the shear thickening of suspensions of nanoparticles particularly for nonspherical nanoparticles at relatively high concentrations. This is not typical to nanofluids and is therefore not discussed further in this chapter.

18.4 Effective Thermal conductivity

Early experimental work on CNT nanofluids (Choi et al., 2001) reported that the addition of a small fraction of CNTs in engine oil increased the thermal conductivity of the base fluid by a factor of 2–3. Such conductivity enhancements represent significant increases of the convective heat transfer coefficients. Because of this, nanofluids hold the promise to become the heat transfer media of the future. The magnitude of thermal conductivity enhancement was initially characterized as "anomalous" and sparked immense scientific interest during the first decade of the twenty-first century. Several laboratories throughout the globe experimented with different types of base fluids and nanoparticles. Among the most common base fluids that were investigated are water, engine oil and other oils, and ethylene glycol. Among the nanoparticles that were investigated are aluminum oxide (Al_2O_3), copper oxides (both CuO and Cu_2O), single-walled and multiwalled CNTs, copper (Cu), and gold (Au).

18.4.1 Experimental Studies

The more recent experiments show rather convincingly that several other types of nanofluids enhance only moderately the thermal conductivity of the base fluid. Typical enhancements with oxide nanofluids are in the range 5%–50% (Kakaç and Pramuanjaroenkij, 2009, Michaelides, 2013). However, a few studies, conducted typically with metallic and CNT nanoparticles, reported thermal conductivity enhancements close to 100% or above (Chopkar et al., 2006, 2008). The highest increases of thermal conductivity have been observed with suspensions of CNTs—both single-walled and multiwalled—and with metallic nanoparticle suspensions. The lowest enhancements were observed with oxides of nanoparticles, such as TiO_2 and Al_2O_3.

From the several experimental studies, it is apparent that the most important parameters of the conductivity enhancement phenomenon in nanofluids are

1. The type and properties of the nanoparticles
2. The nominal *size* of the nanoparticles
3. The type of the base fluid
4. The volumetric fraction of the nanoparticles
5. The pH and the type of surfactants used to stabilize the nanofluid and prevent aggregation

The thermal conductivity enhancement of the same nanofluid system (same base fluid and particles) is not consistent among all the data sets. This is apparent in the several sets of Al_2O_3 and Cu nanofluids, which differ significantly between different studies. Figure 18.5, which shows the relative conductivity of several CNT nanofluids (Choi et al., 2001, Biercuk et al., 2002, Xie et al., 2003, Liu et al., 2005, Ding et al., 2006), also demonstrates this point. From the discrepancy among different data sets, one may conclude that while the type and concentration of nanoparticles is a major determinant of the thermal conductivity enhancement, variables other than these two also play an important role. The identification and quantification of the effect of such variables is important in engineering studies for the design and optimization of reliable and effective heat transfer media using nanofluids.

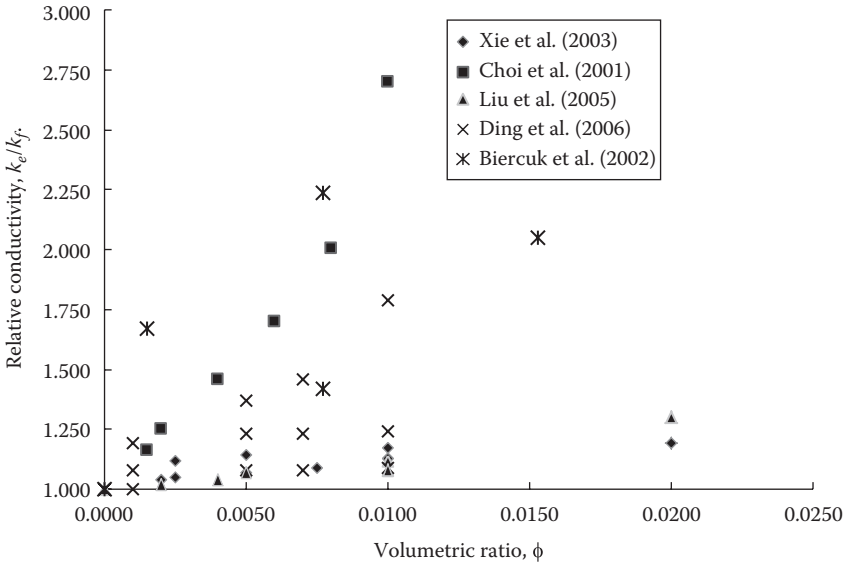


Figure 18.5

Thermal conductivity data for several CNT nanofluid sets.

18.4.2 Analytical Expressions and Correlations

In his study of electricity, Maxwell (1881) derived an expression for the effective electrical conductivity of a heterogeneous mixture with spherical particles. Because of the analogy in the thermal and electrical conduction processes, this expression is also valid for the effective thermal conductivity of heterogeneous mixtures, such as nanofluids. When written in terms of the thermal conductivities of the fluid and solid spheres, the effective thermal conductivity, or Maxwell's equation becomes

$$k_e = k_f\left[1+\frac{3\left(k_s-k_f\right)\phi}{\left(k_s+2k_f\right)-\left(k_s-k_f\right)\phi}\right] \tag{18.14}$$

where

k_f is the conductivity of the base fluid
k_e is the effective conductivity of the suspension
ϕ is the volumetric fraction of the nanoparticles

Later, Bruggeman (1935) and Hamilton and Crosser (1962) extended this expression to short cylinders and irregular particles. It must be noted that at the limit of very high solids conductivity ($k_s \gg k_f$) Equation 18.1 and the similarly obtained analytical expressions yield the following asymptotic expression:

$$k_e = k_f\left[1+\frac{3\phi}{1-\phi}\right] \tag{18.15}$$

It is apparent that the last approximate expression does not include the effect of the very high conductivity of the solid particles ($k_s \gg k_f$). Of particular interest in the study of the thermal conductivity of nanofluids, and especially nanofluids with CNTs, is the analytical study by Nan et al. (1997), who derived an expression for the conductivity of composite materials with high-aspect ratio fibers. They later derived a simplified expression, applicable to nanofluids with high-aspect ratio CNTs, at low solids concentrations ($\phi \ll 1$), which is as follows (Nan et al., 2003):

$$k_e = \frac{3k_f+\phi k_s}{3-2\phi} \approx k_f+\frac{\phi k_s}{3} \tag{18.16}$$

Because $k_s \gg k_f$, it follows that the addition of very small amounts of CNTs—materials that have thermal conductivities that could be as high as 3000 W/m K—may triple the conductivity of the suspension even at volumetric concentrations close to 1%. This largely explains the significant enhancement of the thermal conductivity of CNT nanofluids that was observed by the early researchers and proves that most of the observed thermal conductivity enhancement is not "anomalous."

Several researchers have tried to explain the observed high conductivity of nanofluids using models for the Brownian motion of particles. An analytical study (Xuan et al., 2006) used the mechanism of the stochastic movement of the particles and used the Langevin equation to describe the fluctuations of nanoparticle suspensions. Thus, Xuan et al. (2006) modeled the "heat transfer chain" between nanoparticles and base fluid and, superimposed the effects of the Brownian motion to the effective conductivity expression by Maxwell:

$$k_e = k_f\left[1+\frac{3\left(k_s-k_f\right)\phi}{\left(k_s+2k_f\right)-\left(k_s-k_f\right)\phi}\right]+\frac{9\phi h_c k_B T}{8\pi\rho_s\alpha^4} \tag{18.17}$$

where h_c is the convective heat transfer coefficient between the fluid and the particles that also includes the interfacial resistance to heat transfer. It must be noted that this is a heuristic expression, not supported by detailed analysis.

Among the other expressions, a correlation of several sets of experimental data of aqueous nanofluids resulted in the following expression (Khanafer and Vafai, 2011):

$$\frac{k_e}{k_f} = 1+1.0112\phi+2.4375\phi\frac{47}{d_s}-0.0248\phi\frac{k_s}{k_w} \tag{18.18}$$

where

d_s is the diameter (size) of the particles in nm

k_w is the thermal conductivity of water, $k_w = 0.613$ W/m K.

18.4.3 Mechanisms of Thermal Conductivity Enhancement

The plethora of experimental data on the enhanced conductivity of nanofluids also resulted in several analytical and experimental studies on the mechanisms of the enhanced conductivity. The following chief mechanisms have been suggested for the enhanced conductivity of nanofluids:

1. The significantly higher thermal conductivity of the particles
2. The shape (spheres, fibers, irregular) of the particles
3. The Brownian motion of the particles including the mass of fluid that follows the movement of the particles
4. The development of aggregates and chains that form highly conductive paths in the nanofluid or contribute to the development of such paths
5. Significant changes of the thermodynamic properties of the fluid at the solid–fluid interface and the formation of a "solid layer"
6. The electric charge on the surface of the particles
7. Transient local heat transfer effects
8. Preparation and surfactants

The effects and possible contributions of these mechanisms are summarized in the next sections.

18.4.3.1 Particle Conductivity

The thermal conductivity of the bulk materials of solid nanoparticles is typically higher than the conductivity of the base fluid by three orders of magnitude, as may be seen in Table 18.1. The table lists the thermal conductivities of several materials commonly used as base fluids and solids materials. Although the thermal conductivities of individual nanoparticles are lower than that of the bulk materials when the nanoparticle size is smaller than the mean free path of the energy carriers, the nanoparticles are still expected to have a much higher thermal conductivity than the base liquids. Because of the significantly higher conductivities

Table 18.1 Thermal Conductivities of Several Materials Common in Nanofluids

Solids	k_s (W/m K)	Liquids	k_f (W/m K)
Silver (Ag)	427	Water	0.613
Copper (Cu)	395	Ethylene glycol	0.253
Aluminum (Al)	237	Engine oil	0.145
CNTs	3200–3500	Alcohol	0.115
Brass	120	Glycerol	0.285
Nickel	91		
Quartz (single crystal)	12–7		
Alumina (Al_2O_3)	39		

of the solids, the addition of even a small fraction of particles ($\phi \sim 1\%$) to the base fluid would result in a substantial increase of the thermal conductivity of the liquid–solids mixture.

Because of this mechanism, effective conductivity enhancements have been observed in almost all experimental and analytical studies, regardless of the type, shape, and volume fraction of the particles used. A similar enhancement has also been observed in composite materials where there is no apparent flow.

The very high values of thermal conductivity of nanofluids, which were observed in the early experiments, have led a few authors to characterize the enhancement of the thermal conductivity of nanofluids as "anomalous." The experimentally observed early conductivity enhancements were in the range 100%–180% and were most commonly observed with CNT nanofluids. CNTs have very high aspect ratios (100–1000) and their thermal conductivities are of the order of 2000 times more than the conductivity of water. One of the characteristics of long spheroids and fibers is that the conduction within the heterogeneous mixture is significantly higher in the directions of their long axes and the effective conductivity is more accurately modeled by Equation 18.16. It is rather unfortunate that the results of the earlier studies with fibrous solid particles (CNTs) were compared to analytical models of spheres and short cylinders Equations 18.14 and 18.15, which yield significantly lower values for the thermal conductivity of the heterogeneous suspension. This led to the characterization of the thermal conductivity of nanofluids as "anomalous." A benchmark study led by Buongiorno (2009), which was conducted with the participation of 34 laboratories worldwide, concluded that the observed heat transfer enhancement with nanofluids is not "anomalous," and that 86% of the available experimental data are explained by one of the pertinent equations or their approximations, for example, Equations 18.14 and 18.16.

18.4.3.2 Particle Shape and Orientation

It is apparent from the analytical studies that the shape of the particles plays a significant role in the conductivity of the nanofluid. All the analytical and experimental studies indicate that the effective conductivity of heterogeneous mixtures is significantly higher with elongated rather than with spherical particles (Michaelides, 2013a, 2014). Since elongated particles, such as spheroids and fibers, have a longer dimension, where heat is conducted at a higher rate, the aspect ratio and the orientation of the elongated particles are important parameters in the calculation of the thermal conductivity of these heterogeneous mixtures.

The importance of particle orientation in relation to the direction of heat flow is easily demonstrated by the following example (Michaelides, 2013a, 2014): let us consider the heat transfer between two parallel plates with a liquid–solid heterogeneous mixture and let us assume that all the solid particles are packed together (have fused) in a single layer. The two fluid–particle configurations will yield two extreme orientation cases that correspond to the upper and lower limits of heat conduction:

1. The fused particle layer is parallel to the direction of heat transfer.
2. The fused particle layer is perpendicular to the direction of heat transfer.

The two limit cases are depicted in Figure 18.6, where the "fused" particle layer is portrayed in gray. The heat flux is in the same direction as that of the temperature difference, ΔT. The volumetric fraction of the solids is ϕ. Hence, the dimensionless thickness of the particle layer is ϕ, and that of the liquid layer $1 - \phi$.

In the first case (A) where the orientation of the particle layer is perpendicular to the temperature gradient, the induced heat flux, q, is conducted from one plate to the other and causes temperature differences

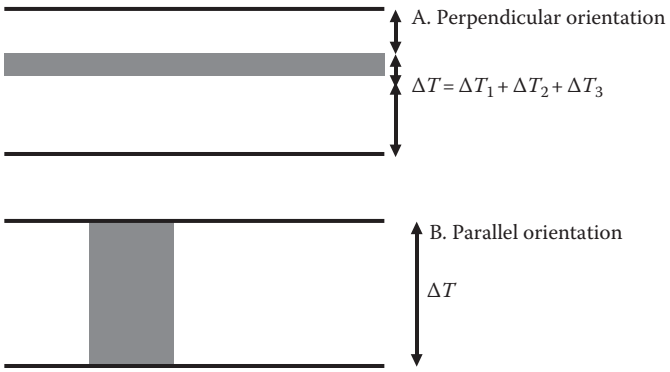


Figure 18.6

The two limiting cases of particle orientation in a liquid.

ΔT_1, ΔT_2, and ΔT_3 in the three layers between the plates, as shown in the figure. From elementary considerations of heat conduction between the two plates, we obtain the following expression for the temperature differences in the case (A):

$$\Delta T_1 + \Delta T_3 = \frac{qL(1-\phi)}{k_f} \quad \text{and} \quad \Delta T_2 = \frac{qL\phi}{k_s} \tag{18.19}$$

The sum of the three temperature differences is equal to the total temperature difference, ΔT, and, hence, we have

$$\Delta T = q\left[\frac{L(1-\phi)}{k_f} + \frac{L\phi}{k_s}\right] \tag{18.20}$$

Given that $q = k_e \Delta T$, Equation 18.20 yields the following expression for the effective conductivity of the medium between the two conducting plates:

$$\frac{1}{k_e} = \frac{1-\phi}{k_f} + \frac{\phi}{k_s} \tag{18.21}$$

Nanofluids typically have very low volumetric fractions of solids ($\phi \ll 1$) and the conductivity of the nanoparticles is much higher than the conductivity of the fluid $k_s \gg k_f$. Under these conditions, the last expression may be approximated as

$$(k_e)_{\phi \ll 1} = k_f(1+\phi) \tag{18.22}$$

In the second case (B), where the orientation of the solid particle layer is parallel to the temperature gradient, the total heat flux is equal to the sum of the heat fluxes in the two layers:

$$q = \left[k_f(1-\phi) + k_s\phi\right]\frac{\Delta T}{L} \tag{18.23}$$

This expression yields the following equivalent conductivity for the heterogeneous mixture:

$$k_e = k_f(1-\phi) + k_s\phi \tag{18.24}$$

For typical nanofluids, where $k_s \gg k_f$, and $\phi \ll 1$, the last equation may be approximated as

$$(k_e)_{\phi \ll 1} = k_f + \varphi k_s \tag{18.25}$$

It is apparent from Equations 18.22 and 18.25 that when particle layers are formed within the fluid, which are perpendicular to the direction of the heat flux, the effective conductivity of the heterogeneous medium does not increase significantly. When the particle layers are formed parallel to the temperature gradient, the effective conductivity of the medium increases linearly with the volumetric fraction and the thermal conductivity of the fibers. The study (Eapen et al., 2010) showed that most of the available experimental data for nanofluids fall within these "classical" limits.

18.4.3.3 Formation of an Interfacial Solid Layer

A few early studies on nanofluids (Keblinski et al., 2002, Yu and Choi, 2003) suggested that a "solidified" liquid layer composed of a few molecular layers of the base fluid is formed on the surface of the solid particles. With this layer, the nanoparticle becomes a composite material and consists of the nanoparticle, which has conductivity k_s, and the solidified layer, whose conductivity is approximately the same as the conductivity of the solid phase of the base fluid k_{sf}. When $k_{sf} > k_f$, the presence of the solidified layer enhances the conductivity of the entire particle. However, for this enhancement to be significant, the ratio of the conductivities of the formed "solid" to the nanoparticle conductivity, k_{sf}/k_s, must be higher than 0.02 and the relative thickness of the interfacial layer, $\delta\alpha/\alpha$, must be less than 0.05 (Michaelides, 2014). In the case of aqueous nanofluids, for which the conductivity of ice is $k_{sf} = 2.2$ W/m K, the first condition is not satisfied with most of the fluid–particle systems listed in Table 18.1. Similar considerations with other nanofluids lead to the conclusion that the formation of the solid layer alone does not explain the vast majority of the experimental observations.

The thickness of the "solid nanolayer," around 43 nm magnetic alumina nanoparticles in water, was measured by an NMR technique to be 1.4 nm (Gerardi et al., 2009). This layer of relatively immobile water molecules is equivalent to five water molecule layers formed on the surface of the nanoparticles. However, the independent measurement of the thermal conductivity of this nanofluid revealed that the formation of this interfacial layer had no effect on the measured effective conductivity of the nanofluid. Molecular dynamics (MD) simulations, which probe into the structure and the properties of interphasial molecular layers, also do not support the theory, especially in the case of the hydrophobic carbon atoms that comprise the CNTs (Din and Michaelides, 1998, Xue et al., 2004).

18.4.3.4 Electric Surface Charge and pH

It is well known that electric charges and the value of the liquid pH do not have an appreciable effect on the transport properties of pure fluids, including the base fluids used with nanofluids. Any effect of these variables on the thermal conductivity of nanofluids could only work for aqueous-based suspensions and must take place through mechanisms that act on the shape and structure of the particles, primarily clustering, aggregation, and the formation of other forms of structures that facilitate the transfer of thermal energy. An extensive experimental investigation by Lee et al. (2006) on the influence of the surface charges of the nanoparticles on the effective thermal conductivity of suspensions concluded that surface charges influence significantly the effective thermal conductivity by altering the structure of the nanofluid. Departures from electric neutrality for the nanoparticles, which appear as high zeta potential measurements, produce higher stability of the suspension overall, and better dispersion of the particles within the base fluid. All of these mechanisms have an enhancing effect on the thermal conductivity of the suspensions.

The structure of the suspension and the zeta potential effect may partly explain the disparities between some sets of experimental data, where researchers used surfactants that alter the electric surface charge of the nanoparticles and the internal structure of the suspensions (Jung and Yoo, 2009, Michaelides, 2014). Two independent studies, which examined the effect of the pH of the base fluid, found significant changes in the effective thermal conductivity of the suspensions. These were attributed to the altered shapes of the nanoparticle aggregates and modifications of the internal structure of the nanofluid (Fan and Wang, 2011, Wamkam et al., 2011).

18.4.3.5 Brownian Movement

The Brownian movement of nanoparticles in the base fluid is the primary mechanism for the "microconvection," which causes agitation in nanofluids—a mechanism that always contributes to higher heat and mass transfer in fluid systems. For this reason, several studies have been undertaken to quantify the effects of the Brownian movement on the thermal conductivity of nanofluids. Since the Brownian movement and the resulting microconvection are difficult to observe experimentally, most of the studies on this mechanism

are analytical and numerical. However, not all of the authors arrive to the same conclusions and several have disagreed significantly on the importance of the Brownian movement on the nanofluid conductivity.

At first, when examining the mechanisms of higher thermal conductivity, one must consider that the two effects of the higher particle conductivity and particle shape account for a large part of the observed higher effective conductivity of nanofluids: 86% of the experimental data in the international benchmark study (Bungiorno, 2009) are explained to within a 15% experimental error by these two effects. Therefore, the Brownian movement and other effects may explain a smaller portion of the data and may help to reduce the uncertainty of the experimental measurements.

Secondly, it is known that the Brownian movement and the associated fluid movement cause "agitation" in the fluid and that all forms of such agitation facilitate the transport of energy and mass. For example, agitation by turbulence and the turbulent motion of larger particles is a major contributor to heat and mass transfer of gas–particle systems (Pfeffer et al., 1966, Michaelides, 1986). The Brownian-induced agitation in the fluid is of lesser magnitude than turbulent agitation and is expected to have a lesser (but not vanishing) effect on the heat transfer coefficient. The benchmark study leaves open the possibility of lesser contributions by other mechanisms, and the Brownian movement is very likely the principal mechanism among them.

Thirdly, the effect of the Brownian movement of particles gives an excellent explanation for the very high dependence of the conductivity of nanofluids on temperature (Das et al., 2003, Li and Peterson, 2006). The increased Brownian movement at higher temperatures and the associated fluid microconvection is touted by most researchers as the main mechanism for the significant temperature effect. The acceptance of the Brownian movement as the primary mechanism for the high dependence of the thermal conductivity on the temperature by the vast majority of researchers is in itself an indication that the Brownian movement is a contributing mechanism to the enhanced effective thermal conductivity of nanofluids, but most likely, a mechanism of lesser importance than particle concentration, shape, and conductivity.

18.4.3.6 Transient Motion of Particles

The transient effects of particulate motion are generated by the Brownian movement and are related to the following (Maxey and Riley, 1983, Michaelides, 2006):

1. The movement of the *virtual* or *added mass* of the base fluid that accompanies the motion of the particles
2. The mass of the fluid that rushes in to replace the volume of the moving particles and the fluid volume of the added mass
3. The contribution of the history term on the heat transfer from the particles

All three effects contribute to the enhancement of the microconvection or fluid "agitation," which leads to higher heat transfer. It must be noted that the Brownian movement of the particles is caused by the motion of the fluid molecules (thermal motion), but manifests itself through the motion of the particles, which have significantly higher inertia than that of the fluid molecules and significantly higher characteristic timescales. It is most likely that the effects of the transient motion would materialize at timescales that span the range of the characteristic timescales of particles. For 10 nm copper nanoparticles in water, the characteristic timescales are approximately 2.0×10^{-10} s, while the timescales of the fluid molecules are of the order of 10^{-14} s. Hence, the Brownian movement of particles and the associated transient particle and fluid movement would not be expected to play a major role in the effective thermal conductivity of the suspension, which is associated with the molecular momentum and energy transfer at the molecular timescales. The Brownian movement and the transient effects are expected to have a more significant influence on the convective heat transfer coefficient of the suspensions, a subject that is treated in Section 18.5.

18.4.3.7 Particle Distribution and Aggregation

Single particles, clusters, and aggregates form structures and layers that may significantly enhance the conductivity of the suspension, even when the volumetric concentration of particles does not change. For example, when two or more spherical particles aggregate, the resulting composite particle is longer. All the theoretical models prove that the formation of longer particles, and especially formation of linear chains of particles, brings the effective thermal conductivity of the suspension closer to that of fibrous nanoparticles, whose contributions to the thermal conductivity of the suspension are given by Equation 18.16 rather than Equation 18.14. This happens because a fraction of the elongated particles is always oriented in the direction of the temperature gradient and, thus, creates conducting paths. Several experimental and numerical

studies on particle aggregation that have observed the formation of highly conducting "paths" or "bridges" support this mechanism of effective conductivity enhancement (Prasher et al., 2006, Timofeva et al., 2007, Philip et al., 2008, Kondaraju et al., 2010).

18.4.3.8 Preparation and Surfactants

The method of preparation of nanofluids and the specific chemicals used as surfactants influence significantly the formation of clusters and aggregates, and the particle distribution within the suspension. Every laboratory, which chemically manufactures nanoparticles, may use their own methods for the stabilization of their respective nanofluids, but the methods are typically not reported in the literature. Some of the methods are even proprietary. Mechanical methods, such as milling and shearing the nanofluid, have been used extensively to produce stable nanofluids. Electromechanical methods, such as the application of ultrasonic waves (sonification or ultrasonification), have also been used extensively to disperse the nanoparticles and prevent them from aggregating and forming a sediment. Chemical methods are routinely used with a variety of surfactants: examples are sodium laurate, sodium dodecyl benzene sulfonate, sodium dodecylsulfate, and gum Arabic acid. A review of the stability and properties of nanofluids (Ghadimi et al., 2011) provides an extensive list of surfactants and stipulates that "…choosing the right surfactant is the most important part of the [preparation] procedure." The choice of chemical surfactants is typically accomplished by a trial and error method.

Oftentimes, the amount or concentration of the surfactants is close or even higher than the concentration of the nanoparticles. This implies that the surfactant must be considered as a component that affects the thermodynamic and transport properties of the mixture. When the actual concentration of the surfactants in the heterogeneous mixture is not high enough to have its own influence, the effect of the surfactants and the method of preparation of nanofluids on the effective conductivity is realized via the size and shape mechanism as in Section 3.3.2.

It must also be noted that surfactants and dispersants often have a lower thermal conductivity than the base liquid. The use of these additives is expected to reduce the effective thermal conductivity of the nanofluid suspension.

18.4.3.9 Other Mechanisms

From the large number of experimental investigations, it follows that a few other mechanisms and parameters have an influence on the transport properties of nanofluids. Among these are

1. Magnetic fields and magnetic nanoparticles, which most likely work via the particle aggregation/distribution mechanism (Philip et al., 2008, Younes et al., 2012)
2. The amount of fluid "trapped" within the volume defined by the boundary of irregular particles (Cherkasova and Shan, 2010, Fantoni et al., 2010)
3. Velocity discontinuity (slip) and thermal discontinuity at the fluid–particle interface (Feng et al., 2012, Feng and Michaelides, 2012)

A purely statistical study (Sergis and Hardalupas, 2011) surveyed the results of 141 nanofluid experimental studies and performed a statistical analysis on the heat transfer enhancement mechanisms. Among the observations of this statistical study are

1. The Brownian movement of the particles—by itself or in combination with other mechanisms—is reported as a significant mechanism for the heat transfer enhancement by approximately 70% of the researchers.
2. Thirty-three percent of the research studies stated that the Brownian motion is the only mechanism for the observed enhancement.
3. The four leading mechanisms or combination of mechanisms promulgated by the researchers were
   - Brownian motion (solely), 33%
   - Interfacial layer formation, 22%
   - Brownian motion with diffusion and aggregation, 11%
   - Brownian motion with thermophoresis, 9%*

* It must be noted, however, that the actual cause of thermophoresis is the Brownian movement of particles in a temperature gradient. Thermophoresis and Brownian movement are not independent phenomena.

18.5 Additional Augmentation of the Convective Heat Transfer Coefficients

Nanofluids as heat transfer media are to be used in channels of all sizes to remove heat by convection from a hotter surface (e.g., from an electronic component). The primary parameter of interest in convection heat transfer applications is the convective heat transfer coefficient, h_c, which is typically given by a closure equation in terms of the Nusselt number:

$$\dot{Q} = h_c A \Delta T \quad \text{with } h_c = Nu \frac{k_e}{L_{ch}} \tag{18.26}$$

where L_{ch} is the characteristic dimension of the heat transfer system. The Nusselt number is typically a function of the Reynolds and Prandl numbers [$Nu = f(Re, Pr)$] and is given by an empirical equation. It is apparent from Equation 18.26 that if the thermal conductivity of a heat transfer medium increases, the convective coefficient increases proportionately.

Several experiments that measured independently the thermal conductivity and the convective coefficients of nanofluids in laminar flows concluded convincingly that the increase of the convective heat transfer coefficient is significantly higher than the simple relationship of Equation 18.26 (Li and Xuan, 2002, Wen and Ding, 2004). These experiments concluded that there is an augmentation* of the convective coefficient, h_c, in addition to the heat transfer enhancement that follows the increased effective thermal conductivity of the nanofluid. Most experimental studies indicate that the additional augmentation increases with the volumetric fraction, ϕ, but the relationship is not linear.

Figure 18.7 shows representative data (Li and Xuan, 2002, Wen and Ding, 2004, Ding et al., 2006, Hojjat et al., 2010) of the convective heat transfer augmentation as the ratio of Nu_{obs}/Nu_e and Re for nanofluids composed of Al_2O_3 nanoparticles in water. Nu_{obs} is the experimentally measured Nusselt number and Nu_e is the Nusselt numbers calculated analytically using the effective conductivity of the nanofluid ($Nu = h_c L_{ch}/k_e$) and the pertinent Reynolds and Prandl numbers. It is observed in this figure that, even though the trend of the ratio Nu_{obs}/Nu_e versus Re is not very clear, the data consistently demonstrate that this ratio is greater than 1, sometimes by as much as 60%. This general observation implies that other than the increased conductivity of the nanofluids, there is an additional increase of h_c, which augments the convective heat transfer and needs to be accounted for in design calculations.

The vast majority of the experimental studies on the convective heat transfer coefficient for laminar flows show that there is such an additional heat transfer augmentation. On the contrary, the

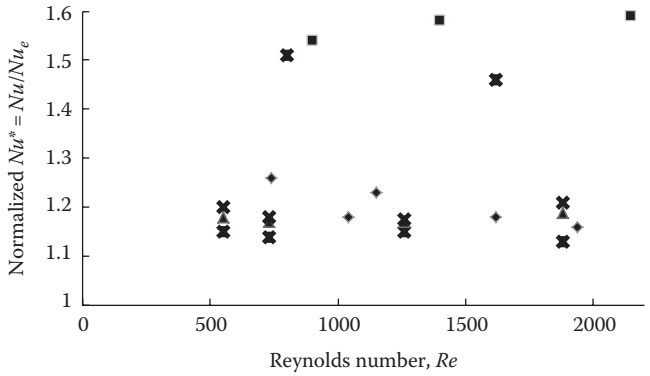


Figure 18.7

Normalized Nusselt numbers for several types of nanofluids. (Data from Li, Q. and Xuan, Y., *Chin. Technol. Sci. Ser. E*, 45, 408, 2002; Wen, D. and Ding, Y., *Int. J. Heat Mass Transfer*, 47, 5181, 2004; Ding, Y. et al., *Int. J. Heat Mass Transfer*, 49, 240, 2006; Hojjat, M. et al., *Korean J. Chem. Eng.*, 27, 1391, 2010.)

* In order to differentiate the two phenomena, the term "augmentation" is used for the observed increase of the heat transfer coefficient and the term "enhancement" for the increase of the thermal conductivity.

experimental evidence with turbulent flow measurements is not clear: a few experimental studies observed some measure of an augmentation in the range 10%–20% (Xuan and Li, 2003, Torri and Young, 2009), while most of the other studies did not observe any augmentation, within the limits of the experimental uncertainty, and concluded that the ratio Nu_{obs}/Nu_e is approximately equal to 1 (Williams et al., 2008, Prabhat et al., 2012).

The most likely explanation for the observed augmentation of the convective heat transfer coefficient, above and beyond the values calculated by the enhanced thermal conductivity of the nanofluid, is the fluid microconvection, which is induced by the Brownian movement of the particles. The microconvection includes the transient effects of the fluid movement due to the added mass and history of the particles (Michaelides, 2006, 2013b), as well as the movement of the masses of fluid that rush in to fill the void left by the particles in their original positions and rush out to allow the particles to move in their final positions (Michaelides, 2013b, 2014). The apparent absence of such augmentation in the turbulent heat transfer regime corroborates this mechanism: the magnitude of turbulent velocity fluctuations and the "agitation" of the fluid caused by turbulence are by far higher than that of the Brownianly induced microconvection process. Therefore, in turbulent flows, the contribution of the microconvection to the value of the convective heat transfer coefficient would be negligible and almost vanishing. On the contrary, any systematic lateral velocity fluctuations in laminar flows contribute significantly to the overall laminar heat transfer coefficient.

18.6 Natural Convection

The addition of nanoparticles in a base fluid has the following effects on the process of natural (free) convection (Michaelides, 2014). Some of the effects promote and some inhibit the flow instabilities that generate and maintain the natural convection process:

1. Increase of the effective fluid viscosity (inhibiting).
2. Local instability damping on the solid surface of the particles (inhibiting).
3. Interactions with the heating surface. Depending on the nature of particles and the interactions, this may have either a promoting or an inhibiting effect.
4. Particle sedimentation. This induces long-range fluid currents and promotes instabilities (promoting).
5. Increase of the effective fluid conductivity (promoting).
6. Chemically active nanoparticles, which are sources or sinks of energy, may cause local thermal and flow instabilities around the particles (promoting).

It appears from these observations that there is not a clear and simple mechanism for the enhancement or reduction of the overall heat transfer coefficients in a natural convection process when nanoparticles are added to the base fluid. This is reflected in the sets of experimental data, which are divided in the overall effect: Some of the experimental data show enhancement and others reduction of the natural convection and the Nusselt numbers associated with it. The picture of the natural convection studies with nanofluids is not clear: on one hand, almost all of the analytical studies (e.g., Shukla and Dhir, 2008, Tsou, 2008) and a few experimental studies (e.g., Okada and Suzuki, 1997) advocate that there is an enhancement of the natural convection heat transfer coefficients, when nanoparticles are added to the base fluid. On the other hand, several experimental studies (e.g., Putra et al., 2003, Wen and Ding, 2005) show that there is a clear and systematic reduction of the natural heat transfer coefficients. More accurate and better documented experiments, where the size and distribution of the nanoparticles are also measured, are needed to improve our understanding of the effect of nanoparticle addition on the natural convection process with nanofluids.

It must be emphasized that a possible earlier onset of natural convection with nanofluids may cause a significant error with the popular (and otherwise accurate in homogeneous systems) method of thermal conductivity measurement using a transient hot wire (THW) instrument. One of the fundamental assumptions of the operation of the THW instrument is that conduction only occurs during the time of the measurements and that the onset of natural convection does not takes place during the effective thermal conductivity measurement. An onset of natural convection earlier than that of the base fluid in a THW instrument results in significantly higher and erroneous value of the "measured" thermal conductivity with nanofluids (Michaelides, 2014).

18.7 Boiling with Nanofluids

18.7.1 Pool Boiling

The addition of nanoparticles in base fluids, which are used for boiling applications, has the following promoting and inhibiting effects (Michaelides, 2014):

1. Nanoparticles provide additional nucleation sites.
2. Nanoparticles—especially at higher concentrations—may deposit, cover, and deactivate a fraction of the nucleation sites on the heated surface.
3. Nanoparticles, left behind during evaporation, deposit on the heating surface and change the characteristics of the surface.
4. The surfactants added for the stability of nanoparticles in suspensions also modify the surface tension of the base fluid. This affects the bubble formation and lift-off.
5. Nanoparticles enhance the microlayer evaporation on the heated surfaces.
6. Nanoparticles alter, sometimes significantly, the thermal and transport properties of the base fluid.

Most of the experimental data on nanofluid nucleate boiling indicate that the presence of nanoparticles decreases the pool boiling heat transfer coefficient of base fluids. Typical pool boiling experimental results with the addition of metal oxide nanoparticles are shown in Figure 18.8. The Nukiyama curve (Nukiyama, 1934), which characterizes the boiling of a homogeneous fluid, is also shown in the figure.

Most of the experimental studies with nanofluids indicate that the addition of metal oxide nanoparticles in a base fluid causes a reduction of the pool boiling heat transfer coefficient (Das et al., 2003, Bang and Chang, 2005, Kim et al., 2007). On the other hand, most of the experimental studies with metallic and CNT nanoparticles indicate an increase of the pool boiling heat transfer coefficient (Witharana, 2003, Park and Jung, 2007). While a more detailed study on the pool boiling coefficients may be needed, a tentative conclusion on the subject, based on the published studies, is that the addition of oxide nanoparticles decreases the pool boiling heat transfer coefficient, while addition of metallic and CNT nanoparticles enhances the pool boiling heat transfer coefficient.

18.7.2 Convective Boiling

Convective or forced boiling occurs in channels, where the nanofluid is forced to flow, usually by a pump. The main differences between pool boiling and convective boiling are

1. The vapor is advected downstream and does not stay close to the nucleation site to be detached slowly by buoyancy.
2. Because the volume and cross-sectional area of the channel are restricted, the liquid and vapor phases arrange themselves in one of the flow regimes that characterize the vapor–liquid (or gas-liquid) two-phase flow.
3. There is frictional pressure drop along the channel that affects the saturation temperature. In most applications though, the pressure drop is very low and has a minimal effect on the heat transfer in the channel.

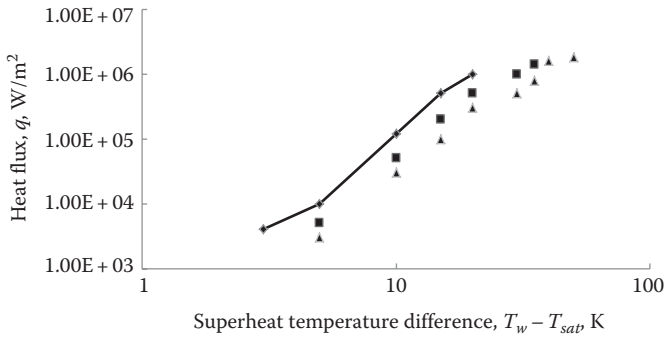


Figure 18.8

Typical experimental data of pool boiling with nanofluids: The pool boiling heat transfer coefficient is the ratio $q/(T_w - T_{sat})$ and is lower than that obtained from the Nukiyama curve. The CHF is enhanced significantly.

The formation of the known vapor–liquid flow regimes—annular, churn, bubbly, etc.—(Bergles et al., 1981) in convective boiling determines the flow and thermal conditions at the boundaries of the channel and, hence, the friction factor and the convective heat transfer coefficient. The mass and volume of the vapor phase increase along the flow direction because of the heat influx, evaporation, and (by a small amount) pressure reduction. There is not a general expression with a high accuracy that is applicable to this type of boiling, but a working and fairly accurate suggestion (Whaley, 1987) is that the heat flux for convective boiling is equal to the sum of the single-phase boiling and the pool boiling heat flux for the liquid:

$$q_{CB} = q_{NB} + q_l \tag{18.27}$$

For most fluids, $q_{NB} \gg q_l$, and, hence, the approximation $q_{NB} \approx q_{CB}$ is often used.

A recent study that was conducted for nanofluids (Chehade at al., 2013) presents several of the more recently developed correlations for the heat transfer coefficients on the convective boiling of liquids in channels. One may conspicuously observe in the data in this study the very high disagreement among the available correlations for liquid flow alone: The uncertainty associated with the experimental correlations for the base fluids is more than 50%. Under the light of this observation, it is reasonable to conclude that the uncertainty for nanofluids would be even higher.

Unlike pool boiling, the preponderance of experimental evidence on the heat transfer coefficients for convective heat transfer points to the enhancement of the convective heat transfer coefficient with the addition of nanoparticles. Of the several experimental studies that were consulted, none observed a reduction of the convective boiling heat transfer coefficient without a clear explanation for the reasons of reduction (Michaelides, 2014). Most of the experimental studies indicate a significant enhancement, or at least no deterioration of the convective boiling heat transfer coefficient (Peng et al., 2009, Rana et al., 2013). A few experimental studies observed significant enhancements of more than 50% (Boudouh et al., 2010). The following mechanisms are responsible for the enhancement of the convective boiling heat transfer coefficients:

1. Channel boundary modification with increased number of nucleation sites.
2. Increase of bubble–surface contact angles
3. Inhibition of the formation of long-lasting dry vapor patches by higher concentrations of deposited particles at the bubble–surface interface
4. Increased frequency of bubble departure from the nucleation sites
5. Formation of larger bubbles

Because of the very high boiling heat transfer coefficients, nanofluids have been touted as the heat transfer media with convective boiling in microchannels. A cause of concern with this application is the long-term reliability of such cooling systems: as the base fluid evaporates, nanoparticles deposit close to the exit of the channel and cause channel blocking, something that has been observed in one of the failed experiments in this area (Faulkner et al., 2003). One may guard against partial or total blocking of the cooling channels by restricting the fraction of base fluid that evaporates.

Since one of the important nanofluid applications is the cooling of miniature electronic components, well-coordinated experiments are needed in the future that will determine under what conditions (types of nanoparticles, base fluid, volumetric fraction, flow conditions, shape of channels, etc.), there is significant enhancement, and what are the optimum conditions for the consistent and reliable removal of heat by nanofluid boiling in micro-channels.

18.7.3 Critical Heat Flux (CHF)

The onset of CHF occurs with the formation and lateral expansion of dry vapor patches on the heated surfaces, including heated microchannels. The process of vapor expansion spreads the vapor patches sideways, joins two or more vapor patches, and creates thin vapor layers over large parts of the heating surface. Because particles do not evaporate with the fluid, they are trapped inside the liquid layer at the heated

surface, a process that creates higher particle concentrations adjacent to the dry patches. The increased concentration of particles has three effects on the vapor phase:

1. Restricts the sideways expansion of the vapor patch, by forming a solid residue that obstructs the spreading of vapor.
2. Maintains, through the interfacial surface tension, thin interstitial liquid layers between the individual particles and between particles and the heating surface.
3. The presence of particles close to the heated surface disturbs the shape of the meniscus at the vapor–liquid interface, thus creating a "structural disjoining pressure," which increases the wettability and inhibits the spreading of the dry patches (Wen, 2008).

All three mechanisms are averse to the spreading of vapor pockets and bubbles. Therefore, one would expect *a priori* that the addition of any small particle, including nanoparticles, to a base fluid would enhance the CHF by modifying the structure of the heated surface and the particle concentration close to this surface. This is corroborated by all the experimental studies on CHF with nanofluids.

All the experimental data of CHF indicate that the addition of nanoparticles—to both pool boiling and convective boiling—increases the CHF of base fluids, sometimes by a factor of 2 or 3 (Milanova and Kumar, 2008, Park et al., 2009). This trend is also illustrated in Figure 18.8, where the CHF increases from approximately 1,000,000 W/m^2 to 1,800,000 W/m^2 (this is not entirely obvious due to the logarithmic scale of the diagram). Significant increases in the CHF have been observed even when the volumetric ratio of the solids is very low, for example, in the range $10^{-6} < \phi < 10^{-5}$. The significant CHF enhancements were observed with all types of nanoparticles (metallic, metal oxides, CNTs, etc.) and with several types of heating surfaces (plates of copper, aluminum, stainless steel; wires of copper, steel, Ni–Cr alloy). General observations from the several experimental studies on CHF are (Michaelides, 2014)

1. CNT nanoparticles cause the highest CHF enhancement, followed by metal nanofluids and oxide nanofluids.
2. CHF enhancement in convective boiling is lower than that of pool boiling.
3. The vapor bubbles departing from the heating surface were significantly larger in the nanofluid experiments than in the pure base fluid experiments. This implies that the nanoparticles or, most likely, the surfactants used for their stabilization modified significantly the surface tension of the water.
4. The heating surfaces were modified by the deposition of a layer of particles, which sometimes formed a thin, solid porous layer.

Surface heat fluxes achieved with boiling fluids (typically of the order of 10^6 W/m^2) are significantly higher than heat fluxes with single-phase fluids. For this reason, boiling heat transfer media, and in particular boiling nanofluids, are touted as the cooling media that may achieve surface fluxes close to 10^7 W/m^2, to be used with the next generations of microelectronic devices (Faulkner et al., 2003). An important consideration in this application is that the surface temperature be kept under 130°C at all times including fast transient processes. The high CHF of nanofluids provides a significant safety margin, which may ensure that the temperature of the heated surface does not exceed the design value.

A glance at Figure 18.8 illustrates this advantage of nanofluids and corroborates the promise of nanofluids as potentially reliable heat transfer media in electronic devices: the base fluid boiling curve (solid line) shows a CHF of 1,000,000 W/m^2 with superheat 20°C. The experimental data (diamonds) extend to a CHF of 1,800,000 W/m^2 with higher superheat, close to 50°C. The difference in the superheat (30°C) is not prohibitively high for a thermal system with higher reliability. One may actually design a cooling system using this nanofluid to operate at a heat flux of 1,400,000 W/m^2 with a superheat 40°C. Such a system would have an adequate safety margin (400,000 W/m^2) before the CHF is exceeded and the electronic components fail.

18.8 Effective Diffusivity

Diffusion is the movement of mass at the molecular level and involves the transfer of a species within a fluid (gas or liquid) and a solid. For nanofluids, let us consider the diffusion of a species, *A*, in a nanofluid composed of a base fluid, *F*, and a single type of nanoparticles, for example, the diffusion of oxygen in an

alumina–water nanofluid. From the beginning, it is recognized that the diffusion process of the species A is much faster in the fluid domain than in the solid. The diffusion process within the solids is very slow and, without any loss of accuracy, the flux of the species A into the solid matrix may be assumed to vanish. This implies that the diffusivity of species A into the solid, D_{AS}, vanishes, while the diffusivity of the species A into the base fluid, D_{AF}, is finite. As with the other transport properties, we introduce an operational definition of the effective diffusivity of the mixture that applies not at a specific point of the nanofluid but at a domain, which is much larger than the characteristic dimension of the nanoparticles:

$$D_{ANe} = \frac{|J_A|}{\left|\frac{\delta n_A}{\delta x}\right|} \left(\delta x \gg \alpha\right) \tag{18.28}$$

where

J_A is the mass flux

n_A is the concentration of the species A

The value obtained from this mathematical operation is the effective diffusivity of species A in the nanofluid, D_{ANe}, defined at the midpoint of the segment δx. Experimental and numerical studies prove that the diffusivity of the heterogeneous mixtures is uniform in nanofluids where the particles are uniformly distributed and is independent of the size of the segment, δx, provided that the latter is greater than the equivalent of 20 nanoparticle radii. If the particles are nonuniformly distributed in the suspension, the effective diffusivity is also nonuniform and, in general, it is a monotonic function of the particle concentration, ϕ.

It must be noted that of interest in the mass transfer applications is the mass transfer coefficient of the nanofluid, h_{AN}, which is defined in terms of the mass transfer equation:

$$\dot{m} = h_{AN} A_c \left(\Delta c\right) \tag{18.29}$$

where

Δc is the difference of the concentration of the species A at the two ends of the instrument

A_c is the cross-sectional area through which the mass is transferred

The mass transfer coefficient is calculated in general through the Sherwood number:

$$Sh = \frac{2\alpha h_{AN}}{D_{ANe}} \tag{18.30}$$

The latter is obtained from empirical correlations, which have been typically obtained from heat transfer experiments using the analogy of heat and mass transfer (Michaelides, 2014).

18.8.1 Analytical Results

The solid particles with vanishing diffusivity are impediments to the diffusion of mass in solid–fluid mixtures. For this reason, it is expected that the effective diffusivity of nanofluids would be lower than the diffusivity of the base fluid. This is corroborated by all the analytical studies on the subject: Joensson et al. (1986) conducted an analysis for the self-diffusion of small molecules in colloidal systems and derived the following expression, for the ratio of the effective diffusivity of the suspension to the diffusivity of the base fluid:

$$\frac{D_{ANe}}{D_{Af}} = \frac{1}{1+0.5\phi} \tag{18.31}$$

Cussler (2009) conducted a more detailed analysis and derived the expression:

$$\frac{D_{ANe}}{D_{Af}} = \frac{1-\phi}{1+0.5\phi} \tag{18.32}$$

The two expressions are expected to be applicable to nanofluids. For nanoparticles, where $\phi \ll 1$, the results from the last two expressions are virtually identical. The same may be said for the expression derived by von Meerwal et al. (1990), who used a model based on the formation of a solid interfacial layer. It is apparent from all the analytical studies that the effective diffusivity of nanofluids—where typically $\phi < 0.05$—is slightly lower than the diffusivity of the base fluid.

18.8.2 Experimental Methods and Results

Several experimental studies on the effective diffusivity of nanofluids produced results markedly different than the analytical solutions: Olle et al. (2006) used a liquid chemical reactor with a small beaker to measure the mass transfer rates of oxygen in aqueous ferric (Fe_3O_4) nanofluids. They observed that the mass transfer coefficients of oxygen, h_{ON}, increased significantly when nanoparticles were added to the water. The mass transfer coefficient, h_{ON}, in these experiments increased up to 60% with the addition of nanoparticles at $\phi = 0.04$. Olle et al. (2006) also used a chemical method for the determination of the mass transfer coefficients, during which the oxygen in the beaker was constantly depleted by a reducing reactant. In the oxygen depletion experiments, they observed h_{ON} enhancements of up to 600%. They also observed that there were diminishing returns with the increase of the volumetric fraction of nanoparticles; that is, the function h_{ON} increases monotonically with ϕ, but the slope of the function progressively decreases.

The data by Krisnamurthy et al. (2006) showed a more dramatic increase of the mass transport coefficient of nanofluids. They used an optical method to observe the diffusion of a fluorescent dye in deionized water with Al_2O_3 nanoparticles, up to volumetric fractions of $\phi = 0.01$. Their results show significant increases of the diffusion coefficients, up to 14 times (1400%) at $\phi = 0.005$.

However, one of the first experimental studies on the mass diffusion with nanoparticles by Wen et al. (2005), which was conducted with an internal loop airlift reactor, reported that the mass transfer coefficient of gases was reduced when TiO_2 nanoparticles were added to the base fluid.

Another study by Kang et al. (2008) used a liquid film absorption process and two aqueous nanofluids with iron (Fe) and CNTs. They observed mass transfer coefficient enhancements in the range 50%–150%. Their results indicate that the CNT nanofluids exhibited significantly higher mass transfer enhancements than the Fe nanofluids.

An increase of the effective diffusivity with the addition of Cu nanoparticles is also indicated by the data obtained in the study by Li et al. (2006). The study was conducted with a refrigerant and Cu nanoparticles. One of the conclusions of this study is that the time of formation of the hydrofluorocarbon-134a hydrates, which is important in energy storage systems, decreased significantly and monotonically with the addition of small amounts of Cu nanoparticles.

Ozturk et al. (2010) conducted an experiment with a fluorescent dye in a microfluidic device that allows two nanofluid streams to flow in parallel. Their observations showed that there was *complexation*—formation of composite particles—of the dye molecules and the nanoparticles along the interface of the two streams and this affected significantly the experimental data. The complexation effect of the Ozturk et al. (2010) study is the same as the *grazing effect* that was observed in slurry flows and was documented by Kars et al. (1979). In the latter study, fine slurry particles adsorbed preferentially a gas solute from a gaseous stream and rapidly transferred it to the suspension, thus showing a very high mass transfer coefficient for the slurry. The grazing effect and the study by Ozturk et al. (2010) for nanofluids raise an important question on the use of optical methods with dyes for the determination of mass transfer coefficients and nanofluid diffusivity: The introduction of a dye in the nanofluid introduces a different type of molecules in the experiment that may not be inert with respect to the species whose diffusion/transfer is to be measured. The dye molecules may react with one or more of the species in the experimental setup, thus giving diffusion results for nanoparticles that are different from those, for which the experiment was designed. In such experiments, the instrument (dye) affects the measurement and this means that the experimental data must be interpreted under a different light.

However, the study by Veilleux and Coulombe (2010), who carefully minimized all dye–nanoparticles interactions, observed a 10 times larger dye diffusion in Al_2O_3 nanofluids than in the base fluid. It is unlikely that complexation has played a role in the last experiments. All the data of this study imply that the addition of the nanoparticles enhances significantly the diffusivity of the nanofluid. A similar study of nanofluids in a refrigerant base fluid by Kim et al. (2006) observed that the addition of very small amounts ($\phi < 0.001\%$) of Cu, CuO, or Al_2O_3 nanoparticles in binary water–ammonia and water–2-ethyl-1-hexanol mixtures increased the mass transfer coefficients of bubble columns by as much as 530%.

In two separate studies by Komati and Suresh (2008, 2009), several types of liquid reactors were used, including a capillary reactor, to measure the mass transfer of CO_2 and O_2 in a variety of reacting and non-reacting liquids laden with magnetic ferrous oxide (Fe_3O_4) nanoparticles. The two studies consistently reported mass transfer enhancements between 200% and 300%. By carefully controlling their experimental setup, they ruled out any complexation or catalytic effects due to the nanoparticles in their experiments. The authors promulgated the hypothesis that a "zone of convective disturbance" (microconvection) is the most likely cause of the observed enhanced mass transfer coefficients.

The study by Turanov and Tolmachev (2009) was conducted with an NMR instrument and measured the self-diffusion coefficient (SDC) of water in colloidal silica (SiO_2) nanofluids. The experiments indicated that the SDC of water actually decreased with the addition of the SiO_2 nanoparticles. The decrease was more than 30% at $\phi = 0.225\%$, a value that is significantly higher than the values predicted by the effective medium theory. Turanov and Tolmachev (2009) attributed the low diffusivities on the formation of solid-like interfacial layers around the nanoparticles.

Another study that did not observe significant changes in the diffusivity of nanofluids is that by Subba-Rao et al. (2011). They used a fluorescence correlation spectroscopy (FCS) method that transforms the signal from the fluorescence process and measures only the random movement of the diffusing species. Nanoparticle–dye interactions and complexation were excluded by the appropriate processing of the data. By this method, they measured the diffusion coefficients, not the mass transfer coefficients. The results of the study show that the diffusion coefficients of both SiO_2 and Al_2O_3 nanofluids do not vary appreciably from the diffusion coefficients of the pure base fluid, up to volumetric fractions close to 2%. The observed slight decrease of the diffusion coefficients in these data agrees with the heterogeneous suspension diffusion models of Equations 18.31 and 18.32, within the range of the experimental uncertainty of the data.

A more recent experimental study where significant mass transfer enhancement was observed is that by Manikandan et al. (2012). They used a stirred-tank cylindrical reactor with oxygen sparged in the tank (sparging is the bubbling of a gas in a liquid or a suspension). Their nanofluids were aquatic suspensions of ferrous oxide, Fe_2O_3. Manikandan et al. (2012) observed mass transfer coefficient enhancements up to 63%, even though the maximum volumetric fraction of the nanoparticles was very low, less than 0.0065%.

An interesting effect of technological importance is the dependence of the diffusivity on the viscosity. The effect was first studied by Perez and Sandall (1974) with colloidal particles: Higher viscosity impedes the diffusion and advection of any species within a fluid and causes lower molecular diffusivities in nanofluids as well as lower mass transfer coefficients. For non-Newtonian nanofluids at low shear rates, whose viscosity may become extremely high, this is a characteristic that impedes significantly the mass transfer of any species within the nanofluid. Park et al. (2006) studied the mass transfer of CO_2 in aqueous SiO_2 nanofluids that exhibited non-Newtonian behavior. Their results show that there was a clear decrease of the mass transfer coefficient, h_{AN}, and this was attributed to the higher viscosity of the nanofluid. The mass transfer coefficient in these experiments improved significantly with the addition of 2% 2-amino-2-methyl-1-propanol (AMP). This compound is a surfactant, which is known to reduce the viscosity of the nanofluid.

The results of the last set of experiments raise the possibility of modifying the mass transfer coefficient and viscosity of nanofluids at will, by increasing or reducing the concentration of the surfactants. This will have significant technological implications in the administration of pharmaceuticals in the blood stream as well as in medical testing processes.

18.8.3 Observations and Conclusion on the Effective Diffusivity

It is apparent that there is a great deal of disagreement resulting from the experimental data on the diffusivity and the transfer of mass: while some studies have observed enhancements by factors as high as 16, other experimental studies indicate no enhancement, and some even indicate a small reduction. It is also apparent that some experiments measured the molecular diffusivity of the species, while others measured the mass transfer coefficients and from these deduced the effective diffusivity. It is rather unfortunate that very few studies make a distinction between the two.

A careful examination of the experimental results reveals that almost all the studies, which have observed significant enhancement, used a liquid reactor or simple optical methods, where the nanofluid flows freely and there is ample evidence of advection (Michaelides, 2014). These studies actually measured the convective mass transfer coefficient, h_{AN}. Most of the studies that concluded there is no enhancement, and actually determined the diffusivity of a species within the nanofluid, D_{AN}, or the self-diffusion coefficient. These studies used techniques such as NMR or permeable membranes, where

advection is restricted, or sophisticated versions of the optical methods such as the FCS, which eliminate the advection effects by the processing of the signal.

A careful examination of the experimental data indicates that the molecular diffusivity of the species remains almost constant and may actually decrease when nanoparticles are added to the base fluid. This is most likely due to obstruction by the particles and the higher viscosity. The data also show that the mass transfer coefficients, which account for both the diffusion and the advection of a species, are invariably increased, when nanoparticles are added to the base fluid and the measuring instrument allows for the unhindered particle motion as well as the microconvection process that follows the Brownian movement. This implies that the addition of nanoparticles primarily causes mass advection and this has a significant impact on the mass transfer within the nanofluid. Almost all the studies, where enhancement of the convective mass transfer coefficients was observed, attribute this enhancement to the Brownian movement of the particles and the associated microconvection.

The molecular diffusion process is a very slow molecular process in comparison to the other transport processes (Michaelides, 2014). Any type of fluid advection, however slow or weak, has the potential to contribute significantly to the mass transfer process. Wherever they are not suppressed, the Brownian movement and the accompanying unsteady microconvection of the base fluid enhance significantly the mass transfer process. In addition, other forms of mass transfer, for example, from catalysis, chemical reactions, or complexation, which may take place with the addition of the nanoparticles, also contribute to the increased mass transport.

The observed low diffusivities in several experiments do not detract from the usefulness of nanofluids as effective mass transfer media. The objective of all pertinent technological applications is the enhancement of the overall mass transfer, not only of the molecular transfer *per se*. For this reason, it is the enhancement of the convective mass transfer coefficient, h_{AN}, of a species that matters in engineering systems and not the effective diffusivity, D_{AN}, of the species. If the overall mass transfer of the base fluid increases by the addition of small amounts of reacting or nonreacting nanoparticles, nanofluids may prove to be very inexpensive media to improve the operation of the microfluidic devices, such as the "lab on a chip" type of systems. An additional advantage may be the possible control of the rate of mass transfer by the addition or removal of surfactants.

18.9 Specific Heat Capacity

The specific heat capacity of a material is an equilibrium thermodynamic property and represents the capability of the material to store heat. It also affects the convective heat transfer coefficient of a fluid. There have been very limited studies on the specific heat capacity of the nanofluid suspensions and the results of these studies are not always in agreement: Zhou and Ni (2008) measured this property for aqueous nanofluids containing alumina nanoparticles and found that the specific heat capacity decreases with increasing nanoparticle concentration. This is in agreement with the conventional model of heterogeneous mixtures, which is based on the thermal equilibrium of the constitutive materials (Gibbs, 1878, Michaelides, 2014). The experimental results are also in agreement with a recent molecular modeling study by Rajabpour (2013).

Shin and Banerjee (2010) measured the specific heat capacity of eutectic salts of $LiCO_3$ and K_2CO_3 containing 1% by weight of silica nanoparticles and observed a specific heat capacity enhancement in the range 19%–24%. The addition of silica nanoparticle to the $BaCl_2$–NaCl–$CaCl_2$–LiCl eutectic mixture also resulted in 14.5% enhancement in the specific heat (Shin and Banerjee, 2011). The authors proposed three mechanisms to explain the observed significant enhancement:

- Nanoparticles have higher surface energy per unit mass than the bulk solid. The surface atoms in the lattice of nanoparticle are less constrained, due to the lesser number of bonds. Because the bonds may be considered as springs, the surface atoms vibrate at a lower natural frequency and higher amplitudes, resulting in higher surface energy.
- The extremely high surface area per unit mass of the nanoparticles causes an increase in the interfacial thermal resistance between the nanoparticles and the surrounding liquid molecules. This higher interfacial thermal resistance may cause the vibrational energy between nanoparticle atoms and the interfacial molecules to store additional energy.
- The existence of a semisolid layer, which depends on the surface energy of the nanoparticles, that has higher heat capacity than the bulk liquid and may thus increase the specific heat capacity of the nanofluid suspension.

Similar mechanisms have also been used to explain the enhanced thermal conductivity of the nanofluids as detailed in Section 18.4, but they have not been validated. Also, the mechanisms do not explain the observed reduction in the specific heat observed by Zhou and Ni (2008). Two preliminary observations/conclusions that may be drawn from the limited experimental and analytical data on the heat capacity are

1. The aqueous nanofluids have reduced specific heat capacity, whereas molten-salt-based nanofluids show heat capacity enhancement.
2. The heat capacity measurements of the aqueous nanofluids were performed at temperatures that are close to the ambient temperature (certainly below the boiling point of water), whereas the molten-salt-based nanofluid measurements were performed at high temperatures (a few hundred degree Celsius).

18.10 Conclusions and General Observations

The addition of nanoparticles in base fluids modifies significantly the transport properties of these fluids. The addition of nanoparticles increases the effective viscosity in almost all cases, and the thermal conductivity of the fluids in most cases, sometimes by a factor of 2 or 3. Higher enhancements were observed for the mass transfer coefficient of some nanofluids—on the order of a factor of 10—even though the effective diffusivity may slightly decrease.

The higher thermal conductivity enhancements were observed with fibrous CNT and metallic nanofluids, which also tend to use the most expensive nanoparticles. Most of the experimental results on oxide nanofluids, which utilize less expensive nanoparticles, indicate that the thermal conductivity enhancement is modest, in the range of 5%–50%. The primary mechanism for the enhancement of the thermal conductivity is the significantly higher conductivity of the solid nanoparticles and in particular of elongated, fibrous nanoparticles. Electric surface charges, particle aggregation, and surfactant choices influence the thermal conductivity of the suspension by affecting the shape and distribution of the nanoparticles. The Brownian movement of the nanoparticles has a rather minor effect on the thermal conductivity. However, the Brownian movement of the particles and the associated microconvection of the fluid have significant effects on the mass transfer process.

In addition to the observed thermal conductivity enhancement, nanofluids also exhibit an augmentation of the convective heat transfer coefficient, above the values that are expected from the observed thermal conductivity enhancement. This augmentation occurs in laminar flows only and is most likely due to the microconvection and the transient effects caused by the Brownian movement of the nanoparticles.

Regarding boiling with nanofluids, the preponderance of experimental evidence is that the pool boiling and convective boiling coefficients are reduced with the addition of all types of nanoparticles. However, the CHF of the suspension increases, often by a factor of 2 or 3. Despite the lower boiling heat transfer coefficients, the CHF enhancement is very significant for the design of thermal systems with boiling nanofluids, because it provides a safety factor that is crucial to the design of electronic cooling systems.

It must be noted that all the reliable experimental observations of the heat and mass transport processes using nanofluids indicate that there is nothing "anomalous" with these suspensions. The high transport coefficients are readily explained with known mechanisms of heterogeneous suspensions, of which the most important are the type, the shape, and the distribution/configuration of nanoparticles. Similarly, the very high mass transfer coefficients are readily explained by the microconvection process. The successful manipulation of the shapes of particle aggregates, the artificial formation of particle structures, the optimized distribution of nanoparticles in base fluids, and the addition or removal or appropriate surfactants may create heat and mass transfer media in the future that are far superior to the base fluids.

Although little attention has been paid to the specific heat capacity of nanofluids, it is a very important property that has significant effect on heat transfer. Limited work so far shows that the specific heat capacity of aqueous-based nanofluids decreases with increasing nanoparticle concentration, while that of molten-salt-based nanofluids increases, sometimes significantly.

Acknowledgments

The research presented in this chapter was partially supported by the Tex Moncrief chair at TCU and by a DOE grant through the National Energy Technology Laboratory to UTSA (DE-FE0011453). The authors are thankful for this support.

References

Bang, I.C. and Chang, S.H., Boiling heat transfer performance and phenomena of Al_2O_3-water nanofluids form a plain surface in a pool, *Int. J. Heat Mass Transfer*, 48, 2407, 2005.

Batchelor, G., The effect of Brownian motion on the bulk stress in a suspension of spherical particles, *J. Fluid Mech.*, 83, 97–117, 1977.

Bergles, A.E., Collier, J.G., Delhaye, J.M., Hewitt, G.F., and Mayinger, F., *Two-phase Flow and Heat Transfer in the Power and Process Industries*, Hemisphere, New York, 1981.

Biercuk, M., Llaguno, M., Radosavljevic, M., Hyun, J., Johnson, A., and Fischer, J., Carbon nanotube composites for thermal management, *Appl. Phys. Lett.*, 80(15), 2767, 2002.

Boudouh, M., Gualous, H.L., and De Labachelerie, M., Local convective boiling heat transfer and pressure drop of nanofluid in narrow rectangular channels, *Appl. Thermal Eng.*, 30(17–18), 2619, 2010.

Brinkman, H., The viscosity of concentrated suspensions in solutions, *J. Chem Phys.*, 20, 571–582, 1952.

Bruggeman, D.A.G., Berehnung vershidener physikalisher Konstanten von heterogenen Substanzen: I, *Anallen der Physik*, 24, 636, 1935.

Buongiorno, J., Convective transport in nanofluids, *J. Heat Transfer*, 128, 240–250, 2006.

Buongiorno, J., Venerus, D.C., Prabhat, N., McKrell, T., Townsend, J., Christianson, R., Tolmachev, Y.V. et al., A benchmark study on the thermal conductivity of nanofluids, *J. Appl. Phys.*, 106, 094312, 2009.

Chehade, A.A., Gualous, H.L., Masson, S.L., Fardoun, F., and Besq, A., Boiling local heat transfer enhancement in microchannels using nanofluids, *Nanoscale Res. Lett.*, 8, 130, 2013.

Chen, H., Ding, Y., He, Y., and Tan, C., Rheological behavior of ethylyne glycol based titania nanofluids, *Chem. Phys. Lett.*, 444, 333–337, 2007a.

Chen, H., Ding, Y., and Tan, C., Rheological behaviour of nanofluids, *New J. Phys.*, 9, 367, 2007b.

Cherkasova, A.S. and Shan, J.W., Particle aspect-ratio and agglomeration-state effects on the effective thermal conductivity of aqueous suspensions of multiwalled carbon nanotubes, *J. Heat Transfer*, 132, 082402, 2010.

Choi, S.U.S., Zhang, Z.G., Yu, W., Lockwood, F.E., and Grulke, E.A., Anomalous thermal conductivity enhancement in nanotube suspensions, *Appl. Phys. Lett.*, 79, 2252, 2001.

Chopkar, M., Das, P.K., and Manna, I., Synthesis and characterization of nanofluid for advanced heat transfer applications, *Scripta Mater.*, 55, 549, 2006.

Chopkar, M., Sudarshan, S., Das, P.K., and Manna, I., Effect of particle size on thermal conductivity of nanofluids, *Metall. Mater. Trans. A*, 39(7), 1535, 2008.

Cussler, E.L., *Diffusion—Mass Transfer in Fluid Systems*, 3rd edn., Cambridge University Press, New York, 2009.

Das, S.K., Nandy, P., Thiesen, P., and Roetzel, W., Temperature dependence of thermal conductivity enhancement for nanofluids, *J. Heat Transfer*, 125, 567, 2003.

Din, X.D. and Michaelides, E.E., Transport processes of water and protons through micropores, *AIChE J.*, 44, 35–46, 1998.

Ding, Y., Alias, H., Wen, D., and Williams, R.A., Heat transfer of aqueous suspensions of carbon nanotubes (CNT nanofluids), *Int. J. Heat Mass Transfer*, 49, 240, 2006.

Eapen, J., Rusconi, R., Piazza, R., and Yip, S., The classical nature of thermal conduction in nanofluids, *J. Heat Transfer*, 132, 102402, 2010.

Eastman, J.A., Choi, S.U.S., Li, S., Yu, W., and Thompson, L.J., Anomalously increased effective thermal conductivities of ethylene glycol-based nanofluids containing copper nanoparticles, *Appl. Phys. Lett.*, 78(6), 718, 2001.

Einstein, A., Eine neue bestimung der molekuldimensionen, *Annalen der Physik*, 19, 289–306, 1906.

Einstein, A., Berichtigung zu meiner Arbeit: "Eine neue bestimung der molekuldimensionen," *Annalen der Physik*, 34, 591–592, 1911.

Fan, J. and Wang, L., Heat conduction in nanofluids: Structure-property correlation, *Int. J. Heat Mass Transfer*, 54, 4349, 2011.

Fantoni, R., Giacometti, A., Sciortino, F., and Pastore, G., Cluster theory of Janus particles, *Roy. Soc. Chem. Soft Matter*, 7, 2419, 2010.

Faulkner, D., Khotan, M., and Shekarriz, R., Practical design of a 1000 W/cm^2 cooling system (high power electronics), in *19th Annual IEEE Semiconductor Thermal Measurement and Management Symposium*, 2003, p. 223.

Feng, Z.G. and Michaelides, E.E., Heat transfer from a nano-sphere with temperature and velocity discontinuities at the interface, *Int. J. Heat Mass Transfer*, 55, 6491, 2012.

Feng, Z.G., Michaelides, E.E., and Mao, S.L., On the drag force of a viscous sphere with interfacial slip at small but finite Reynolds numbers, *Fluid Dyn. Res.*, 44, 025502, 2012.
Frenkel, N. and Acrivos, A., On the viscosity of a concentrated suspension of solid spheres, *Chem. Eng. Sci.*, 6, 847–853, 1967.
Gerardi, C., Cory, D., Buongiorno, J., Hu, L.W., and McKrell, T., Nuclear magnetic resonance-based study of ordered layering on the surface of alumina nanoparticles in water, *Appl. Physics Lett.*, 95, 253104, 2009.
Ghadimi, A., Saidur, R., and Metselaar, H.S.C., A review of nanofluid stability properties and characterization in stationary conditions, *Int. J. Heat Mass Transfer*, 54, 4051, 2011.
Gibbs, J.W., On the equilibrium of heterogeneous substances, in *The Collective Works of J. Willard Gibbs*, Longmans, New York, 1878.
Hamilton, R.L. and Crosser, O.K., Thermal conductivity of heterogeneous component systems, *Ind. Eng. Chem. Fund.*, 1, 187, 1962.
Happel, J., Viscosity of suspensions of uniform spheres, *J. Appl. Phys.*, 28, 1288–1292, 1957.
Hojjat, M., Etemad, S.G., and Bagheri, R., Laminar heat transfer of non-Newtonian nanofluids in a circular tube, *Korean J. Chem. Eng.*, 27, 1391, 2010.
Joennson, B., Wennestroem, H., Nilsson, P.G., and Linse, P., Self-diffusion of small molecules in colloidal systems, *Colloid. Polym. Sci.*, 264, 77–88, 1986.
Jung, J.Y. and Yoo, J.Y., Thermal conductivity enhancement of nanofluids in conjunction with electrical double layer (EDL), *Int. J. Heat Mass Transfer*, 52, 525, 2009.
Kakaç, S. and Pramuanjaroenkij, A., Review of convective heat transfer enhancement with nanofluids, *Int. J. Heat Mass Transfer*, 52, 3187, 2009.
Kang, Y.T., Kim, H.J., and Lee, K.I., Heat and mass transfer enhancement of binary nanofluids for H2O/LiBr falling film absorption process, *Int. J. Refrigerat.*, 31, 850–855, 2008.
Kars, R.L., Best, R.J., and Drinkenburg, A.A.H., The sorption of propane in slurries of active carbon in water, *Chem. Eng. J.*, 17, 201–210, 1979.
Keblinski, P., Phillpot, S.R., Choi, S.U.S., and Eastman J.A., Mechanisms of heat flow in suspensions of nano-sized particles (nanofluids), *Int. J. Heat Mass Transfer*, 45, 855, 2002.
Khanafer, K. and Vafai, K., A critical synthesis of thermophysical characteristics of nanofluids, *Int. J. Heat Mass Transfer*, 54, 4410, 2011.
Kim, J.-K., Jung, J.Y., and Kang, Y.T., The effect of nano-particles on the bubble absorption performance in a binary nanofluid, *Int. J. Refrigerat.*, 29(1), 22–29, 2006.
Kim, S., Kim, C., Lee, W.H., and Park, S.R., Rheological properties of alumina nanofluids and their implication to the heat transfer enhancement mechanism, *J. Appl. Phys.*, 110, 034316–1034316-6, 2011.
Kim, S.J., Bang, I.C., Buongiorno, J., and Hu, L.W., Surface wettability change during pool boiling of nanofluids and its effect on critical heat flux, *Int. J. Heat Mass Transfer*, 50, 4105, 2007.
Komati, S. and Suresh, A.K., CO_2 absorption into amine solutions: A novel strategy for intensification, based on the addition of ferrofluids, *J. Chem. Tech. Biotechnol.*, 86, 1094–1100, 2008.
Komati, S. and Suresh, A.K., Anomalous enhancement of interphase transport rates by nanoparticles: Effect of magnetic iron oxide on gas-liquid mass transfer, *Ind. Eng. Chem. Res.*, 49(1), 390–405, 2009.
Kondaraju, S., Jin, E.K., and Lee, J.S., Direct numerical simulation of thermal conductivity of nanofluids: The effect of temperature two-way coupling and coagulation of particles, *Int. J. Heat Mass Transfer*, 53, 862, 2010.
Krieger, I.M., Rheology of polydisperse lattices, *Adv. Coll. Interface Sci.*, 3, 111–136, 1972.
Krieger, I.M. and Dougherty, T.J., A mechanism for non-Newtonian flow in suspensions of rigid spheres, *Trans. Soc. Rheol.*, 3, 137–152, 1959.
Krishnamurti, S., Bhattacharya, P., Phelan, P.E., and Prasher, R.S., Enhanced mass transport in nanofluids, *Nanoletters*, 6, 419–423, 2006.
Kuhn, W. and Kuhn, H., Bedeutung beschränkt freier Drehbarkeit für die Viskosität und Strömungsdoppelbrechung von Fadenmolekellösungen, *Helvetica Chim. Acta*, 28, 1533–1579, 1945.
Lee, D., Kim, J.W., and Kim, B.G., A new parameter to control heat transport in nanofluids: Surface charge state of the particle in suspension, *J. Phys. Chem. B*, 110, 4323, 2006.
Li, C.H. and Peterson, G.P., Experimental investigation of temperature and volume fraction variations on the effective thermal conductivity of nanoparticle suspensions (nanofluids), *J. Appl. Phys.*, 99, 084314, 2006.
Li, J., Liang, D., Guo, R., Wang, R., and Fan, S., Formation and dissociation of HFC-134a gas hydrate in nano-copper suspension, *Energy Conv. Manage.*, 47, 201–210, 2006.

Li, Q. and Xuan, Y., Convective heat transfer and flow characteristics of Cu-water nanofluid, *Chin. Technol. Sci. Ser. E*, 45, 408, 2002.
Liu, M.S., Lin, M.C.-C., Huang, I.T., and Wang, C.-C., Enhancement of thermal conductivity with carbon nanotube for nanofluids, *Int. Comm. Heat Mass Transfer*, 32, 1202, 2005.
Liu, M.S., Lin, M.C.C., Tsai, C.Y., and Wang, C.C., Enhancement of thermal conductivity with Cu for nanofluids using chemical reduction method, *Int. J. Heat Mass Transfer*, 49, 3028, 2006.
Lundgren, T.S., Slow flow through stationary random beds and suspensions of spheres, *J. Fluid Mech.*, 51, 273–299, 1972.
Maiga, E.S., Palm, J., Nguyen, C.T., Roy, G., and Galanis, N., Heat transfer enhancement by using nanofluids in forced convection flows, *Int. J. Heat Fluid Flow*, 26, 530–546, 2005.
Manikandan, S., Karthikeyan, N., Suganthi, K.S., and Rajan, K.S., Enhancement of volumetric mass transfer coefficient for oxygen transfer using Fe_2O_3-water nanofluids, *Asian J. Sci. Res.*, 5, 271–277, 2012.
Maxey, M.R. and Riley, J.J., Equation of motion of a small rigid sphere in a non-uniform flow, *Phys. Fluids*, 26, 883, 1983.
Maxwel, J.C., *A Treatise on Electricity and Magnetism*, 2nd edn., Clarendon Press, Oxford, U.K., 1881.
Michaelides, E.E., Heat transfer in particulate flows, *Int. J. Heat Mass Transfer*, 29, 265, 1986.
Michaelides, E.E., *Particles, Bubbles and Drops—Their Motion, Heat and Mass Transfer*, World Scientific Publishing, Singapore, 2006.
Michaelides, E.E., *Heat and Mass Transfer in Particulate Suspensions*, Springer, New York, 2013a.
Michaelides, E.E., Transport properties of nanofluids—A critical review, *J. Non-Equil. Thermodyn.*, 38, 1–78, 2013b.
Michaelides, E.E., *Nanofluidics—Thermodynamic and Transport Properties*, Springer, New York, 2014.
Milanova, D. and Kumar, R., Heat transfer behavior of silica nanoparticles in pool boiling experiment, *J. Heat Transfer*, 130, 042401, 2008.
Mooney, M., The viscosity of a concentrated suspension of spherical particles, *J. Coll. Sci.*, 6, 162–170, 1951.
Nan, C.W., Birringer, R., Clarke, D.R., and Gleiter, H., Effective thermal conductivity of particulate composites with interfacial thermal resistance, *J. Appl. Phys.*, 81, 6692, 1997.
Nan, C.W., Shi, Z., and Lin, Y., A simple model for thermal conductivity of carbon nanotube-based composites, *Chem. Phys. Lett.*, 375, 666, 2003.
Nguyen, C.T., Desgranges, F., Roy, G., Galanis, N., Marie, T., Boucher, S., and Mintsa, H.A., Temperature and particle-size dependent viscosity data for water based nanofluids–hysteresis phenomenon, *Int. J. Heat Fluid Flow*, 28, 1492–1506, 2007.
Nukiyama, S., The maximum and minimum values of heat transmitted from metal to boiling water under atmospheric pressure, *J. Japan Soc. Mech. Eng.*, 37, 367, 1934 (English Translation, *Int. J. Heat Mass Transfer*, 9, 1419, 1966).
Okada, M. and Suzuki, T., Natural convection of water-fine particle suspension in a rectangular cell, *Int. J. Heat Mass Transfer*, 40, 3201, 1997.
Olle, B., Bucak, S., Holmes, T.C., Bromberg, L., Hatton, T.L., and Wang, D.I.C., Enhancement of oxygen mass transfer using functionalized magnetic nanoparticles, *Ind. Eng. Chem. Res.*, 45(12), 4355–4363, 2006.
Onsager, L., Reciprocal relations in irreversible processes, I, *Phys. Rev.*, 37, 405–426, 1931.
Ozturk, S., Hassan, Y.A., and Ugaz, V.M., Interfacial complexation explains anoma-lous diffusion in nanofluids, *Nano Letters*, 10, 665–671, 2010.
Pak, B.C. and Cho, Y., Hydrodynamic and heat transfer study of dispersed fluids with submicron metallic oxide particles, *Exp. Heat Transfer*, 11, 151–170, 1998.
Park, K.J. and Jung, D., Enhancement of nucleate boiling heat transfer using carbon nanotubes, *Int. J. Heat Mass Transfer*, 5, 4499, 2007.
Park, K.J., Jung, D., and Shim, S.E., Nucleate boiling heat transfer in aqueous solutions with carbon nanotubes up to critical heat fluxes, *Int. J. Multiphase Flow*, 35, 525, 2009.
Park, S.W., Choi, B.S., and Lee, J.W., Effect of elasticity of aqueous colloidal silica solution on chemical absorption of carbon dioxide with 2-amino-2-methyl-1-propanol, *Korea-Aust. Rheol. J.*, 18, 133–141, 2006.
Peng, H., Ding, G., Jiang, W., Hu, H., and Gao, Y., Heat transfer characteristics of refrigerant-based nanofluid flow boiling inside a horizontal smooth tube, *Int. J. Refrigerat.*, 32(6), 1259, 2009.
Perez, J.F. and Sandall, O.C., Gas absorption by non-Newtonian fluids in an agitated vessel, *AIChE J.*, 20, 770–775, 1974.

Pfeffer, R., Rosetti, S., and Licleinm, S., Analysis and correlation of heat transfer coefficient and friction factor data for dilute gas-solids suspensions, NASA report TN D-3603, Washington, DC, 1966.
Philip, J., Laskar, J.M., and Raj, B., Magnetic field induced extinction of light in a suspension of Fe_3O_4 nanoparticles, *Appl. Phys. Lett.*, 92, 22191, 2008.
Philip, J., Sharma, P.D., and Raj, B., Evidence for enhanced thermal conduction through percolating structures in nanofluids, *Nanotechnology*, 19, 305706, 2008.
Prabhat, N., Buongiorno, J., and Hu, L.W., Convective heat transfer enhancement in nanofluids: Real anomaly or analysis artifact?, *J. Nanofluids*, 1, 55, 2012.
Prasher, R., Evans, W., Meaking, P., Fish, J., Phelan, P., and Keblinski, P., Effects of aggregation on thermal conduction in colloidal nanofluids, *Appl. Phys. Lett*., 89, 143119, 2006.
Probstein, R.F., *Physicochemical Hydrodynamics*, 2nd edn., Elsevier, New York, 1994.
Putra, N., Roetzel, W., and Das, S.K., Natural convection of nano-fluids, *Heat Mass Transfer*, 39, 775, 2003.
Rajabpour, A., Akizi, F.Y., Heyhat, M.M., and Gordiz, K., Molecular dynamics simulation of the specific heat capacity of water-Cu nanofluids, *Int. Nano Lett*., 3, 58, 2013.
Rana, K.B., Rajvanshi, A.K., and Agrawal, G.D., A visualization study of flow boiling heat transfer with nanofluids, *J. Visual*., 16, 133, 2013.
Russel, W.R., Saville, D.A., and Schowalter, W.R., *Colloidal Dispersions*, Cambridge University Press, Cambridge, U.K., 1989.
Sergis, A. and Hardalupas, Y., Anomalous heat transfer modes of nanofluids: A review based on statistical analysis, *Nanoscale Res. Lett*., 6, 391, 2011.
Shin, D.H. and Banerjee, D., Enhanced specific heat of silica nanofluid, *J. Heat Transfer*, 133, 024501, 2010.
Shin, D.H. and Banerjee, D., Enhancement of specific heat capacity of high-temperature silica-nanofluids synthesized in alkali chloride salt eutectics for solar thermal-energy storage applications, *Int. J. Heat Mass Transfer*, 54, 1064–1070, 2011.
Shukla, R. and Dhir, V., Effect of Brownian motion on thermal conductivity of nanofluids, *J. Heat Transfer*, 130, 042406, 2008.
Suba-Rao, V., Hoffman, P.M., and Mukhopadyay, A., Tracer diffusion in nanofluids measured by fluorescence correlation spectroscopy, *J. Nanoparticle Res.*, 13, 6313–6319, 2011.
Timofeeva, E.V., Gavrilov, A.N., McCloskey, J.M., Tolmachev, W.V., Sprunt, S., Lopatina, L.M., and Sellinger, J.V., Thermal conductivity and particle agglomeration in alumina nanofluids: experiment and theory, *Phys. Rev. E*, 76, 061203, 2007.
Torii, S. and Yang, W.J., Heat transfer augmentation of aqueous suspensions of nano-diamonds in turbulent pipe flow, *J. Heat Transfer*, 131, 043203, 2009.
Tseng, W.J. and Chen, C.N., Effect of polymeric dispersant on rheological behavior of nickel–terpinol suspensions, *Mater. Sci. Eng.*, A347, 145–153, 2003.
Tseng, W.J. and Lin, K.C., Rheology and colloidal structure of aqueous TiO_2 nanoparticle suspensions, *Mater. Sci. Eng.*, A355, 186–192, 2003.
Turanov, A. and Tolmachev, Y., Heat- and mass-transport in aqueous silica nanofluids, *Heat Mass Transfer*, 45(12), 1583–588, 2009.
Tzou, D.Y., Thermal instability of nanofluids in natural convection. *J. Heat Transfer*, 130, 072401, 2008.
Veilleux, J. and Coulomb, S., A total internal reflection fluorescence microscopy study of mass diffusion enhancement in water-based alumina nanofluids, *J. Appl. Phys*., 108, 104316–318, 2010.
von Meerwal, E., Mahoney, D., Iannacchione, G., and Skowronski, D., Concentration dependence of solvent diffusion in a colloidal suspension, *J. Coll. Interface Sci*., 139, 437–445, 1990.
Wamkam, C.T., Opoku, M.K., Hong, H., and Smith, P., Effects of pH on heat transfer nanofluids containing ZrO_2 and TiO_2 nanoparticles, *J. Appl. Phys*., 109, 024305, 2011.
Wang, X., Xu, X., and Choi, S.U.S., Thermal conductivity of nanoparticle fluid mixture, *J. Thermophys. Heat Transfer*, 13, 474–480, 1999.
Wen, D., Mechanisms of thermal nanofluids on enhanced critical heat flux (CHF), *Int. J. Heat Mass Transfer*, 51, 4958, 2008.
Wen, D. and Ding, Y., Experimental investigation into convective heat transfer of nanofluids at the entrance region under laminar flow conditions, *Int. J. Heat Mass Transfer*, 47, 5181, 2004.
Wen, D. and Ding, Y., Formulation of nanofluids for natural convective heat transfer applications, *Int. J. Heat Fluid Flow*, 26, 855, 2005.
Wen, J., Jia, X., and Feng, W., Hydrodynamic and mass transfer of gas-liquid-solid three-phase internal loop airlift reactors with nanometer solid particles, *Chem. Eng. Technol*., 28(1), 53–60, 2005.

Whalley, P.B., *Boiling, Condensation and Gas-Liquid Flow*, Clarendon Press, Oxford, U.K., 1987.
Williams, W., Buongiorno, J., and Hu, L.W., Experimental investigation of turbulent convective heat transfer and pressure loss of alumina/water and zirconia/water nanoparticle colloids (nanofluids) in horizontal tubes, *J. Heat Transfer*, 130, 042412, 2008.
Witharana, S., *Boiling of Refrigerants on Enhanced Surfaces and Boiling of Nanofluids*, Lic. thesis, Royal Institute of Technology, Stockholm, Sweden, 2003.
Xie, H., Lee, H., Youn, W., and Choi, M., Nanofluids containing multiwalled carbon nanotubes and their enhanced thermal conductivities, *J. Appl. Phys.*, 94(8), 4967, 2003.
Xie, H., Wang, J., Xi, T., Liu, Y., Ai, F., and Wu, Q., Thermal conductivity enhancement of suspensions containing nanosized alumina particles, *J. Appl. Phys.*, 91(7), 4568, 2002.
Xie, H., Yu, W., Li, Y., and Chen, L., Discussion on the thermal conductivity enhancement of nanofluids, *Nanoscale Res. Lett.*, 6,124, 2011.
Xuan, Y. and Li, Q., Investigation on convective heat transfer and flow features of nanofluids, *J. Heat Transfer*, 125, 151, 2003.
Xuan, Y., Li, Q., Zhang, X., and Fujii, M., Stochastic thermal transport of nanoparticle suspensions, *J. Appl. Phys.*, 100, 043507, 2006.
Xue, Q.Z., Keblinski, P., Philpot, S.R., Choi, S.U.S., and Eastman, J.A., Effect of liquid layering at the liquid–solid interface on thermal transport, *Int. J. Heat Mass Transfer*, 47, 4277, 2004.
Yang, Y., Grulke, E.A., Zhang, Z.G., and Wu, G., Thermal and rheological properties of carbon-nanotube-in-oil dispersions, *J. Appl. Phys.*, 99, 114307, 2006.
Younes, H., Christensen, G., Luan, X., Hong, H.P., and Smith, P., Effects of alignment, pH, surfactant, and solvent on heat transfer nanofluids containing Fe_2O_3 and CuO nanoparticles, *J. Appl. Phys.*, 111, 064308, 2012.
Yu, W. and Choi, S.U.S., The role of interfacial layers in the enhanced thermal conductivity of nanofluids: A renovated Maxwell model, *J. Nanoparticle Res.*, 5, 167, 2003.
Zhou, S.Q. and Ni, R., Measurement of the specific heat capacity of water-based Al_2O_3 nanofluid, *Appl. Phys. Lett.*, 92, 093123, 2008.


Taylor & Francis
Taylor & Francis Group
http://taylorandfrancis.com

19

Spray Systems

Udo Fritsching and Xing-gang Li

19.1 Atomization
19.2 Spray Behavior
19.3 Spray Impact
19.4 Spray Applications

19.1 Atomization

19.1.1 Introduction

Atomization and spraying of liquids (e.g., pure liquids, solutions, suspensions and emulsions, or melts) is a classical process engineering unit operation. The process of liquid atomization has applications in numerous industrial branches, such as in chemical, mechanical, aerospace and civil engineering, as well as in material science and technology and metallurgy, food processing, pharmaceuticals, agriculture and forestry, environmental protection, medicine, and others.

Within atomization, the bulk fluid (continuous liquid phase) is transformed into a spray system (dispersed phase/droplets). The disintegration process itself is caused either by intrinsic (e.g., potential) or extrinsic (e.g., kinetic) energy, where the liquid, which is typically fed into the process in the form of a liquid jet or sheet, is atomized either due to the kinetic energy contained in the liquid itself by the interaction of the liquid sheet or jet with a (high-velocity) gas, or by means of mechanical energy delivered externally, for example, by rotating devices.

The main purpose of technical atomization processes is the generation of a dramatically increased gas/liquid interface in the dispersed multiphase system. All transfer processes across the gas/liquid phase boundary directly depend on the driving potential difference of the exchange property (heat, mass, or momentum) and the size of the exchange surface. This gas/liquid contact area in a dispersed spray system is correlated with the integral sum of the surfaces of all individual droplets within the spray. Increasing the relative interphase area in a dispersed system intensifies momentum, heat, and mass transfer processes between gas and liquid. The total flux of exchange within spray systems thereby is increased by several orders of magnitude.

Applications of atomization techniques in process technology or chemical engineering processes can be divided into

- Impact-related spray processes
- Spray structure–related processes
- Particle (powder) production in spray processes

In impact-related spray processes, the spray typically impinges onto a solid surface or onto a liquid or semi-liquid material deposited by the spray. The spray may be used for coating, preform build-up, or hot surface

cooling applications. In spray structure–related processes, the main aim of the spray process is to produce dispersed spray droplets of a defined size, for example, for powder production or spray combustion.

Some examples for spray process applications in engineering following this subdivision can be given as follows:

- For *impact-related spray applications* within the continuous fine spatial distribution of a liquid continuum, for example, in the field of coating applications:
  - Corrosion protection of (metal) surfaces by spray coating applications
  - Coating applications for technical specimen and parts for use in private or industrial applications including surface protection and color (paint) applications
  - Crop and plant protection by applying agricultural chemicals
  - Protection coatings by thermal spray applications (like plasma- or flame-spraying of particles) for ceramic or metallic coatings in the metal industry
  - Spray granulation or coating of particles (e.g., in pelletizers or in fluidized beds), for example, for pharmaceutical or food industry applications
  - Spray cooling in aluminum and steel manufacturing (e.g., in strip or slab casting) or in heat treatment of metallic specimen
- For utilizing the spray structure and properties of liquids or particulate solids by gas/droplet/particle exchange processes (*spray structure–related spray process*) within
  - Solid particle separation or chemical gas cleaning (e.g., desulphurization) from exhaust gases, for example, in conventional power plants (wet scrubbers, see Section 15.10)
  - Gas conditioning processes, for example, for room air-conditioning (moisture control)
  - Reaction processes within fuel applications for energy conversion in furnaces within pyrolysis process, automotive, airplane or aerospace turbine, or fuel jet applications
- For utilizing the intense heat and mass transfer rates in sprays for solid particle production (particle product–related atomization process)
  - Thermal exchange processes, for example, for rapid cooling and solidification purposes of fluid melts in powder generation
  - Coupled mass and thermal transfer processes, for example, within spray drying of solutions (or spray crystallization) in food or diary industry or chemical mass products production
  - Particle generation for additive manufacturing processes
- In the combination of the aforementioned impact-, spray structure-, and particle product-related spray process applications within
  - Droplet-based manufacturing technologies, for example, for rapid prototyping and 3D printing
  - The generation of specimen and preforms by spray forming of metals

Each technical process couples several subprocesses in a complex away. Therefore, the complete process (in a first analysis approach) is to be subdivided into individual process steps for further analysis. In this context, a common subdivision of a technical atomization and spray process into modular subprocesses is performed. From the viewpoint of multiphase flow analysis, a typical subdivision for the atomization and spray process is illustrated in Figure 19.1. The sketch shows a (relatively rough) subdivision of a general atomization and spray process into four main subprocesses as

- *Media delivery*: The internal liquid flow in the atomizer and delivery (and possible mixing) of atomization media and energy, typically liquid and gas
- *Atomization*: The process of fluid disintegration or fragmentation, from the continuous delivery of the fluid or melt and the necessary supporting materials (like gases or additives), to the primary resulting spray structure and droplet/ligament spectrum from the atomization process
- *Spray*: The establishing and spreading of the spray, to be described as a dispersed multiphase flow process with momentum, heat, and mass transfer, and possible chemical reactions in all phases, and the exchange between the phases, as well as a possible secondary disintegration process of fluid ligaments or coalescence of droplets
- *Impact*: The impact of the spray droplets onto a solid or liquid surface and compaction and possible film formation of the impacting fluid or melt mass as well as the build-up of a remaining layer or preform

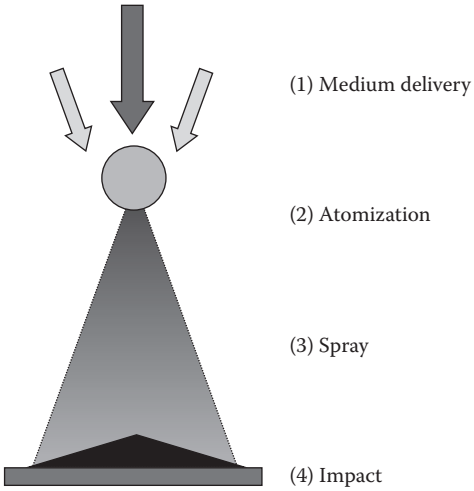


Figure 19.1

Subdivision of atomization and spray process into subprocesses.

A common viewpoint for analysis of all atomization and spray processes is to be seen from multiphase flow analysis with integral heat and mass transfer. Spray processes typically involve two-phase flows of liquid and gas, or even three-phase flow of solid, liquid, and gas (e.g., within atomization of slurries and suspensions or within (solidifying) melt atomization or within composite particle production).

19.1.2 Atomization Principles

The type of atomization principle or atomizer to be used for a specific application depends on the operational parameters to be tackled. Here, the material properties of the liquid to be atomized play an important role. Liquid material properties of importance are (in the order of significance): viscosity, surface tension, and density. These parameters may typically differ by several orders of magnitude. Some typical examples of spray liquid properties are given in Table 19.1. From the overall amount of atomized liquids, fuel and water (or water mixtures) are the most commonly used ones. Metal and ceramic melts are used for powder production and highly viscous liquids are, for example, found in chemical process technology (e.g., paints). The viscosity of these liquids varies up to six orders of magnitude. In addition, material properties typically are not constant within an atomization process. Especially for viscosity, liquids may show non-Newtonian (e.g., shear-dependent) viscosity behavior, for example, for slurries, or temperature-dependent behavior (melts). Therefore, the type of atomizer to be used for a specific application depends on

- The liquid feed material properties
- The targeted liquid throughput
- The spray characteristics to be achieved (e.g., droplet sizes or spray cone shape or spray cone opening angle)

Table 19.1 Material Properties for Atomization Liquids

Liquid	Density ρ (kg/m^3)	Surface Tension σ (kg/s^2)	Dynamic Viscosity μ (kg/ms) × 10^3
Fuel (benzine)	660	0.017	0.27
Water	1000	0.073	1.0
Melt (copper)	7800	1.31	3.12
Melt (iron)	8000	1.83	5.0
Fuel (oil)	830	0.026	20.1
Melt (ceramic)	5000	0.5	1,000
High-viscosity liquid	1000	0.035	20,000

19.1.3 Atomizer Types

Most common for characterization of atomization principles is a subdivision by means of the energy used for the disintegration of the liquid. Here, energy from the liquid itself may be used (pressure), or energy from external media like gas energy (pneumatic), mechanical energy (rotation), or electrical or acoustic energies are used Table 19.2.

19.1.3.1 Pressure Atomizer

The pressure atomizer (single fluid atomizer) is the most common used type of atomizer at all (by number) in technical applications. Main characteristic of this atomizer type is the ejection of a (pressurized) fluid through a small opening at high speeds into a (almost quiescent) gas atmosphere. The energy for atomization is carried by the liquid itself, and the potential energy is transferred into kinetic energy of the liquid. The liquid discharge geometry is either of straight simple type (circular round or flat stream) or swirling type (annular sheet). Pressure atomization typically is used for low viscosity fluids. A principal sketch of a pressure atomizer is illustrated in Figure 19.2a, a pressure swirl atomizer is shown in Figure 19.2b. For the latter, the swirl is generated either by tangential inlet ports and fluid delivery into the atomizer (right part in Figure 19.2b) or by, for example, insert of a vaned swirl generator on top of the atomizer (left part). Due to the swirling liquid flow and the resulting pressure distribution, a hollow air core is produced in the center of the atomizer chamber by suction and the liquid discharges as a swirling annular film from the atomizer. The simplex pressure nozzle produces a full cone or flat sheet spray, the swirl pressure atomizer typically produces a hollow cone spray. Drawbacks in the application of the pressure atomizer are the necessity of pressurizing the liquid (which may be difficult in some cases) and the relatively coarse spray droplet sizes as well as low mass flow rates (Walzel and Musemic, 2013).

19.1.3.2 Pneumatic Atomizer

Pneumatic atomizers (twin-fluid atomizers) typically use the kinetic energy of a pressurized gas that interacts with the liquid surface to disintegrate the liquid. Here, atomizers with external and internal mixture of

Table 19.2 Power Demand of Various Liquid Atomization Principles as per Mass of Liquid

Type of Atomizer	Power Demand (W/kg)
Simple pressure	2–4
Pressure swirl	2–4
Pneumatic twin fluid	50–60
Rotary	15

Source: Bayvel, L. and Orzechowski, Z., *Liquid Atomization*, Taylor & Francis Publishers, Washington, DC, 1993.

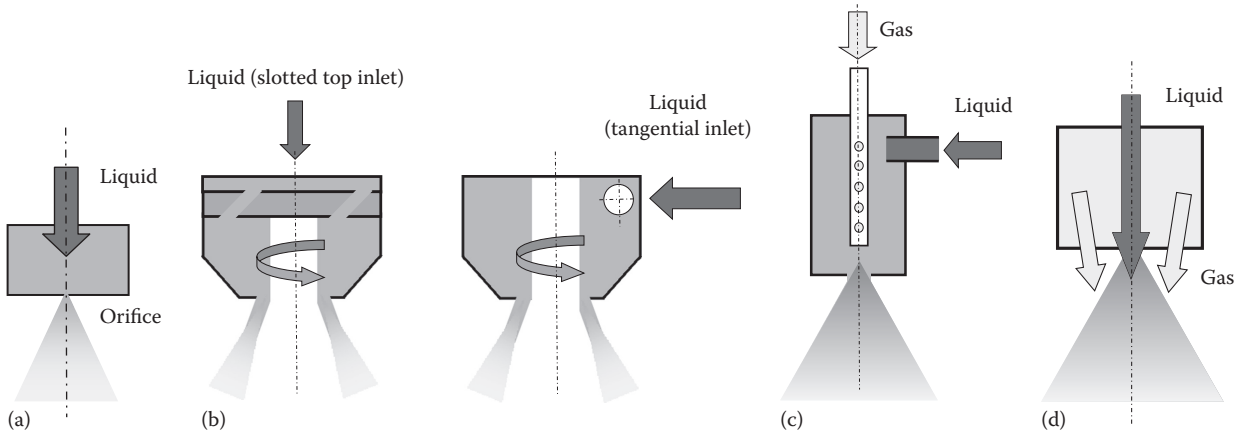


Figure 19.2

(a) Pressure atomizer (full cone or flat sheet spray). (b) Pressure swirl atomizer (hollow cone spray), internal swirl generator (left), tangential inflow (right). (c) Twin-fluid (pneumatic) atomizer with internal mixing. (d) Twin-fluid (pneumatic) atomizer with external mixing.

gas and liquid are to be distinguished. Both principles are shown in Figure 19.2c and d. Within internal mixing atomizers, gas and liquid are mixed in a premixing chamber and the gas/liquid mixture is ejected from the atomizer orifice directly. In twin-fluid atomizers with external mixing, the gas interacts with the liquid outside of the atomizer. Twin-fluid atomizers typically produce a full cylindrical spray cone with relatively small droplets at high liquid mass flow rates.

19.1.3.3 Rotary Atomizer

Within rotary atomization, the liquid typically is fed onto a rotating surface, where it spreads under the action of centrifugal forces. From the rim of the rotating device, for example, a liquid film is ejected at fairly high speeds that disintegrate into droplets. The rotating device as illustrated in Figure 19.3a may be of flat disk, cup, or slotted (vaned) wheel shape. Because the liquid in a rotary atomizer is not flowing through any tiny passages, this kind of atomizer is typically used in process industries where possible nozzle blockage by the fluid (or slurry) may cause major problems. The main drawback of the simple rotary atomizer is the possible slip between liquid and solid surface, thereby limiting the use of this device. This problem is solved in a practical way by using rotating wheels with vanes or channels.

Atomization with narrow drop size distribution width (low span) can be obtained with laminar operated rotary atomizers (so-called LAMROT). In this atomizer concept, the liquid feed is distributed into laminar open channel flows through multiple larger bore holes in the rotating wheel (cup or cylinder). After detachment, the liquid forms thin threads in a very controllable manner, that will be elongated and attenuated by centrifugal acceleration. The bore channels are only partially filled by the flowing liquid, thus exhibiting small hydraulic diameters compared to the bore-hole diameter. Additional attenuation of the threads leads to small drop sizes compared to the detachment diameter. The controlled thread breakup is caused by capillary instability (Rayleigh breakup), leading to narrow distributed droplets. Thereby, small drops are achieved by atomizers with large bores (Schröder and Walzel, 1998, Mescher et al., 2013).

19.1.3.4 Ultrasonic Atomizer

Ultrasonic atomizers either use directly the acoustic energy in a gaseous atmosphere or indirectly the vibrational energy of an ultrasonic excitated surface. Within ultrasonic standing wave atomization, a resonant standing acoustic wave is produced by a system of two opposing ultrasound transducers (or a single transducer and an opposing reflector) that are separated by a distance of a multiple of the half wavelength (typically 1.5–5 λ, i.e., 25–85 mm at a typical frequency of 20 kHz). The acoustic energy in the resulting resonant wave is used to disintegrate the liquid stream that is poured into the center of the standing wave. This principle is illustrated in Figure 19.3b. Main advantage of this atomizer type is the possibility of disintegrating highly viscous liquids (due to its specific disintegration mechanism, see Sections 19.1.5.1.6 and 19.1.8.1); its disadvantage is the limitation to relatively small mass flow rates.

In another type of ultrasonic atomization, vibrating surfaces are used to build fast oscillating capillary waves on the surface of the liquid covering the vibrating solid (see Figure 19.3c). The oscillating liquid ejects

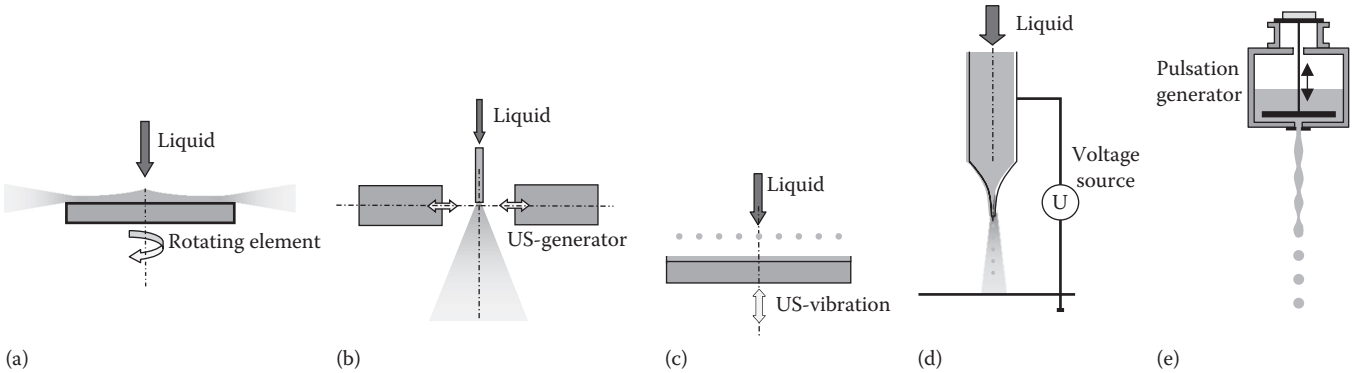


Figure 19.3

(a) Rotary (spinning disk) atomizer. (b) Ultrasonic atomizer (USWA). (c) Ultrasonic capillary wave atomization. (d) Electrostatic atomization. (e) Monosized droplet generation (here: jet excitation by vibrating plunger).

droplets from the wave tips. This device produces especially narrow droplet size distributions at small overall droplet sizes, but is limited to small liquid throughputs.

Ultrasonic gas atomization is a twin-fluid atomization process that uses a resonance cavity in the gas delivery path to generate fluctuating gas flow behavior at the nozzle exit (velocity and pressure fluctuations). The gas fluctuations support the atomization process, especially when their main fluctuating frequency is corresponding to the frequency of the fastest growing instability wave of the liquid stream or jet (e.g., see, Hartmann nozzles in Yule and Dunkley 1994). A direct excitation of the liquid flow may be performed to enhance the natural instability of the liquid jet (see, e.g., Chavez and Obermeier, 2002).

19.1.3.5 Electrostatic Atomizer

Within electrostatic atomization, an electrically charged liquid is accelerated in an electric field, thereby forming an accelerating tiny liquid jet (e.g., Taylor cone) that finally breaks down into fine droplets at the tip, as shown in Figure 19.3d. The achieved yield is relatively low (~1 kg/h). Typical electric potential is in the order <100 kV. Narrow-sized droplets at sizes down to the submicron scale may be produced by electrostatic atomization at very small quantities (Michelson, 1990, Lohmann, 2000).

Within coating applications also, the charging of the droplets in an electric field is used to additionally accelerate the droplets toward a (grounded) target and to spray-coat shadow areas. Thereby, the overspray amount of the process (particles that are deflected around the target, e.g., by aerodynamic effects) is minimized and a sufficient yield of the spray process is achieved. The atomization itself in this case may be performed, for example, by a rotary atomizer.

19.1.3.6 Monosized Droplet Generation

In several applications as in inkjet printing, the need is for droplets or particles of almost identical size (Walzel et al., 2001, Armster et al., 2002). Here, droplet generators that control the disintegration behavior and instability mode of liquid jets or sheets obtain a proper solution. The principal characteristic of a monosize droplet generator is illustrated in Figure 19.3e. An emerging liquid jet is excited (e.g., by mechanical vibration or acoustic excitation) at its most unstable wavelength. The disturbance generates waves of uniform size that leads to continuous breakup of the liquid jet into identical droplets. For increasing the overall mass yield, several individual jets may be combined within a single generator. Another possibility for (almost) monosized drop generation is the controlled breakup of a liquid within rotary atomizer in the ligament formation mode (see the following). Here also, perforated cylindrical elements are used.

19.1.3.7 Prefilming Hybrid Atomizer

The efficiency of an atomization process can be optimized by increasing the specific liquid surface energy before atomization (Lefebvre, 1980). Within twin fluid (gas) atomization, the fragmentation must take place in a region where the velocity difference between the atomization gas and the liquid is highest. Therefore, the liquid must be transformed and transported into an area where the maximum velocity difference occurs. These aspects can be realized in a prefilming hybrid atomizer where the disintegration process can be subdivided into two steps: a prefilming and a gas atomization step. During the prefilming step, a large specific liquid surface area is generated to prepare an efficient secondary disintegration step by gas atomization.

The prefilming hybrid atomizer concept is based on a combination of a single-fluid rotary prefilming concept and an external mixing twin-fluid atomizer, as shown in Figure 19.4a. Within this specific design, the feed material is first spread out by a spinning disk operated in sheet formation mode so that a free-flowing liquid film is formed in the vicinity of the rotary disk. The prefilm is conveyed into the most effective atomization zone by the local gas flow and subsequently atomized by a high-speed gas flow from the external mixing gas atomizer. This configuration allows the generation of a high velocity difference between the atomization gas and the liquid film. The prefilming hybrid atomizer design can be used for disintegrating highly viscous liquids and melts at high throughputs that produce a considerably low droplet size. For atomizing viscous melts, the atomization gas may be heated to prevent fiber-particle formation. See Czisch and Fritsching (2008a) and Fritsching and Uhlenwinkel (2012).

A different hybrid atomization process for particle production was developed to hybridize effectively gas atomization with centrifugal atomization in Liu et al. (2002) and Minagawa et al. (2005). In this hybrid atomizer configuration, the melt spray from an external mixing twin fluid nozzle impinges onto a rotating disk, resulting in a controlled film that finally acts as centrifugal atomizer for fine droplets with narrow particle size distribution within metal particle production.

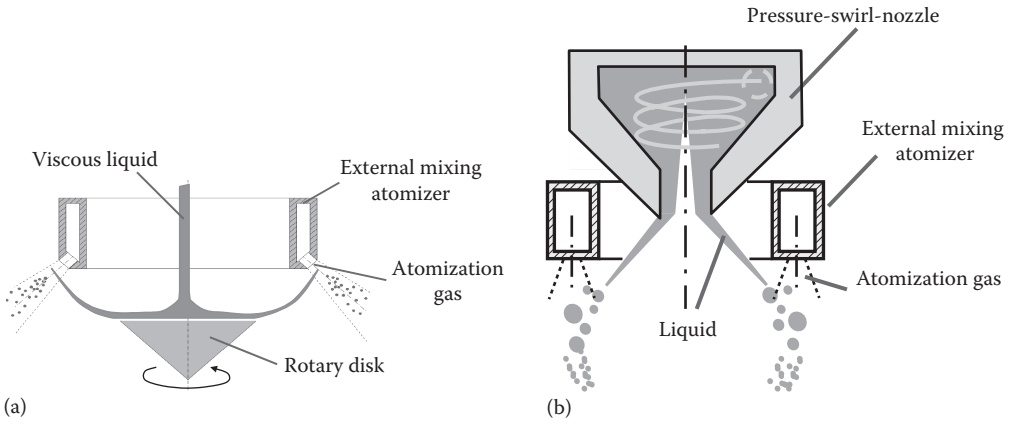


Figure 19.4

(a) Sketch of the prefilming hybrid atomizer: rotary atomizer plus external mixing twin-fluid atomizer. (From Czisch, C. and Fritsching, U., *Mater. Sci. Eng. A*, 477, 21, 2008a. With permission.) (b) Sketch of the pressure gas atomizer: pressure swirl atomizer plus external mixing twin-fluid atomizer. (Adapted from Achelis, L., Drall-Druck-Gas-Zerstäubung von Metallschmelzen, Dissertation, Universität Bremen, Shaker-Verlag, Aachen, Germany, 2009. With permission.)

Pressure gas atomization (PGA) is another prefilming hybrid atomization process that combines pressure swirl atomization as a prefilming step and gas atomization. Within the PGA process, the feed material initially enters a pressure swirl atomizer and leaves the nozzle exit as a conical hollow cone film due to its swirl and centrifugal forces; as the second step, an external mixing gas atomizer is employed to disintegrate the liquid film, ligaments, and any large droplets. The hollow cone film/spray is surrounded by the external mixing gas atomizer. Due to the high velocity gas flow from the external mixing gas atomizer, the hollow cone film/spray from the prefilming process is atomized into small droplets, which are mainly guided to the centerline of the atomizer axis. In Figure 19.4b, the principle of the pressure gas atomizer is illustrated. This atomizer design can be used to produce, for example, fine powders with small median diameters and narrow size distributions. See Uhlenwinkel et al. (2002), Lagutkin et al. (2004), Achelis and Uhlenwinkel (2008), Achelis (2009), Fritsching and Uhlenwinkel (2012), Li et al. (2011), and Li (2014).

19.1.4 Some Global Atomization and Spray Definitions and Characteristics

An initial division of atomization principles has to be done on account of the specific energy input for atomization. The energy supplied to the atomizer is given by

$$E = E_A + E_K + E_L \tag{19.1}$$

where

- E_A is the surface energy of the liquid, that is, the energy used to overcome the resistance or surface-tension forces during disintegration of the liquid into droplets
- E_K is the kinetic energy, that is, the energy used to accelerate the liquid and droplets in the spray
- E_L is the energy loss, that is, due to friction in the atomizer

The efficiency of atomization is given by

$$\eta = \frac{E_A}{E} \tag{19.2}$$

The efficiency of atomization depends mainly on the type of atomizer, the droplet size distribution in the resulting spray, and the physical properties of the liquid. For all conventional atomizers, this efficiency is very small, namely, in the order of less than 0.1%. Pressure atomizers have the relatively best efficiency (e.g., 5% for generation of droplets of 100 μm size, but even much smaller when the mean droplet size in the spray is lower). Even the kinetic energy that is needed to obtain the radial dispersion momentum of a spray,

respectively the droplets (spray cone angle), is at least one order of magnitude higher than the resulting surface energy of the spray.

Another measure for characterization of an atomization process is the approximate energy demand for atomization of a specific liquid amount, as listed in Table 19.2. Here, also pressure atomization is most efficient.

Atomization and spray process analysis is done by means of theoretical, numerical, and experimental approaches. From these results, characterization of atomization and spray processes most successfully is done in terms of nondimensional analysis based on characteristic numbers. For atomization and spray processes, the most important characteristic numbers are

$$\text{The density ratio: } M = \frac{\rho_g}{\rho_l} \tag{19.3}$$

$$\text{The viscosity ratio: } N = \frac{\mu_g}{\mu_l} \tag{19.4}$$

$$\text{The liquid Reynolds number: } \mathrm{Re}_l = \frac{\rho_l u_l d_l}{\mu} \tag{19.5}$$

$$\text{The liquid Weber number: } \mathrm{We}_l = \frac{\rho_l u_l^2 d_l}{\sigma} \tag{19.6}$$

$$\text{The aerodynamic (gas) Weber number: } \mathrm{We}_g = \frac{\rho_g u_{rel}^2 d_l}{\sigma} \tag{19.7}$$

$$\text{The Ohnesorge number Oh (or Laplace number Lp): } \mathrm{Oh} = \frac{\sqrt{\mathrm{We}_l}}{\mathrm{Re}_l} = \frac{\mu_l}{\sqrt{\rho_l \sigma d_l}} = \frac{1}{\sqrt{\mathrm{Lp}}} \tag{19.8}$$

$$\text{The momentum ratio: } I = \frac{\rho_g u_g^2}{\rho_l u_l^2} \tag{19.9}$$

$$\text{The gas (air) to liquid mass flow ratio: } ALR = \frac{\dot{m}_g}{\dot{m}_l} \tag{19.10}$$

Atomization processes yield a spray containing a certain range of droplet sizes. These drop size spectrum is identified by suitable size distribution functions. A general description of particle size distribution functions has been discussed in Section 1.3. Here, in addition, only the most spray relevant size parameters will be given. A spray typically is characterized by

1. A suitable droplet size distribution function
2. The (mean) size parameter
3. The relative width of the distribution (distribution parameter)

For description of the drop size distribution in sprays, either the probability density function (PDF) $q_i(d)$ and/or the cumulative distribution function $Q_i(d)$ are used. Most common is a fit of the drop size distribution by means of (1) the log-normal distribution function, (2) the Rosin–Rammler distribution function, or (3) the Nukiyama–Tanasawa distribution function. A discussion of statistical parameters for classifying size and various size distribution functions are presented in Chapter 1. As typical mean droplet size for these functions, either the arithmetic number mean diameter d_{10} or the arithmetic volume mean diameter d_{30} is used. An important spray characteristic parameter to describe drop size distributions in sprays is the volume to surface area mean diameter d_{32} (Sauter mean diameter [SMD]), that is, the drop diameter with the same total volume to surface area than the entire spray (important for all spray-related atomization processes).

In addition, characteristic spray droplet sizes may be identified as: the modal diameter d_m (corresponding to the most probable drop size in the spray, or peak value of the pdf), and the mass median diameter $d_{0.5}$ (or MMD) that divides the drop size distribution into two identical halves by mass. The width of the drop size distribution may be characterized by the standard deviation (geometric or logarithmic) or by the span value of the distribution:

$$\text{Span} = \frac{d_{0.9} - d_{0.1}}{d_{0.5}} \tag{19.11}$$

19.1.5 Internal Flow in Atomizers

From the viewpoint of multiphase flows in atomization and spray processes, the various kinds of atomization principles that have been illustrated before vary in the type, shape, and form of the gas/liquid interface prior to atomization. The liquid disintegration process is caused by acting forces in or on the liquid. Disintegration is more easily achieved if the liquid is fed into the atomization area in the form of a thin jet or sheet because here the liquid jet already has its highest surface energy and thus greatest instability potential.

19.1.5.1 Liquid Flow

19.1.5.1.1 Pressure Atomizer For simplex pressure atomizers, the overall characteristic of the single-phase (liquid) flow in the atomizer is described by the pressure drop and the state of the liquid at the nozzle exit. The former is described by the discharge coefficient C_D as

$$m_l = C_D A_0 \sqrt{(2\rho_l \Delta p_l)} \tag{19.12}$$

The discharge coefficient depends on the geometry of the atomizer outlet as well as on fluid material properties (Roach et al., 2001, Schneider et al., 2001) and liquid Reynolds number (Lefebvre, 1989). For Reynolds numbers below 10,000, and for a length to diameter ratio l/d_0 between 2 and 120 for the nozzle orifice, the discharge coefficient may be linearly correlated by Lichtarowicz et al. (1965)

$$C_D = 0.827 - 0.0085 \frac{l}{d_0} \tag{19.13}$$

The flow state of the liquid (jet) at the exit of the atomizer depends on the flow field in the atomizer and the orifice. Typically, spray nozzles are of compact size, with short orifices (l/d_0) to minimize the pressure loss. The degree of turbulence in the fluid is determined by the flow state upstream of the orifice and by disturbances generated in the converging region and in the orifice itself. A laminar to turbulent transition within the orifice is unlikely, though the Reynolds number may exceed the typical transition value in tubes (Re = 2300). Though in typical atomizer configurations, maximum Reynolds numbers of up to Re = 10,000 may be achieved, these high values occur only on a very small length scale, where the laminar/turbulent transition of the flow is not realistic. In the investigation on the influence of nozzle geometry on the critical intake length of fluid jets within pressure atomization, van de Sande and Smith (1976) derived a critical Reynolds number Re_{crit} for transition of the flow configuration from the laminar to the turbulent state as follows:

$$Re_{crit} = 12{,}000 \left(\frac{l}{d_0} \right)^{-0.3} \tag{19.14}$$

This critical Reynolds number is typically not reached in atomizer configurations. However, the local distribution and degree of turbulence may strongly influence the atomization process. Based on the description of Giffen and Muraszew (1953), the state of the jet at the atomizer exit may be described as illustrated in Figure 19.5. The jet profile may be either fully developed laminar (Figure 19.5A), or a developing boundary layer profile (Figure 19.5B), or turbulent (Figure 19.5b). Also, the liquid jet may include a turbulent core (Figure 19.5c) or vice versa, and the jet may exhibit a turbulent or disturbed outer shell (e.g., from vortex shedding from edges or cavitation at the wall inside the nozzle (Figure 19.5d). Especially the case of a turbulent outer liquid surface structure of the jet will influence the development of surface instabilities and waves at the liquid/gas interface when the surface wavelength is in the order of the natural instability wavelength. In this case, turbulence may inhibit or promote the disintegration process.

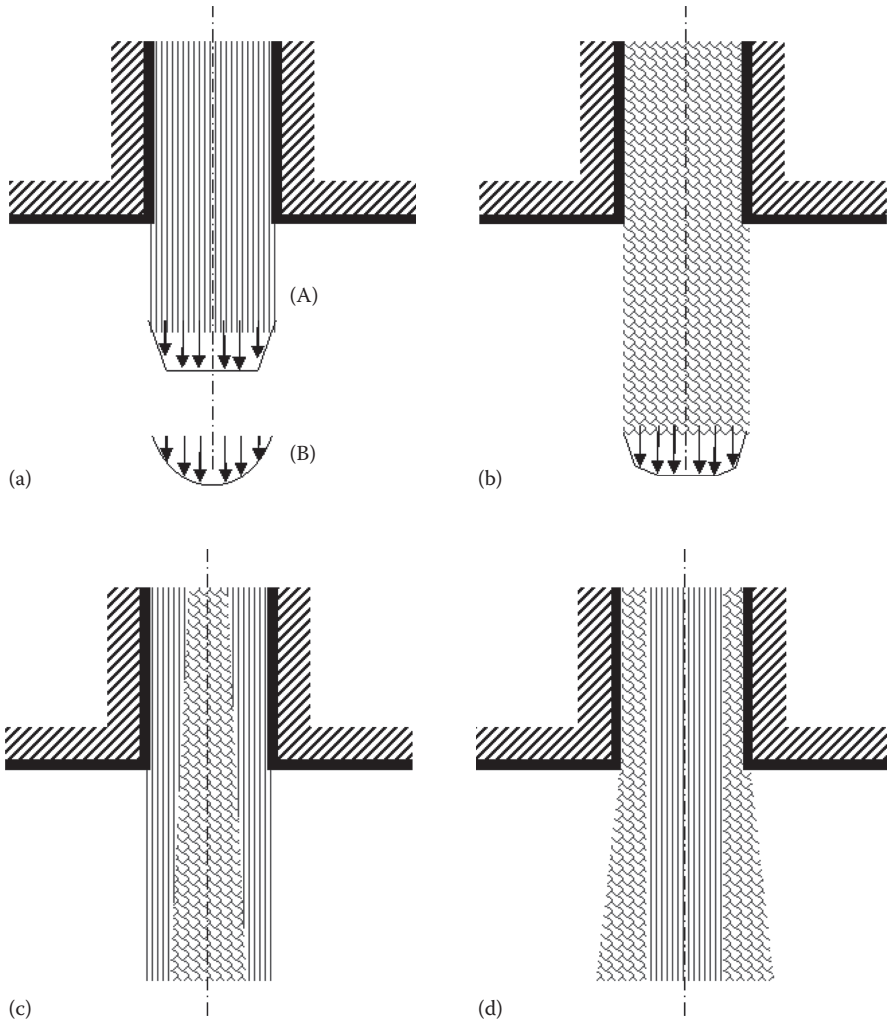


Figure 19.5

Liquid jet condition at the exit of an atomizer: (a) laminar, (b) turbulent, (c) turbulent core, and (d) turbulent shell.

For a pressure film atomizer, Heukelbach and Tropea (2001) have shown that turbulence may have a stabilizing effect on the disintegration of the free film. As long as the velocity fluctuations remain below a certain value (i.e., below 50% in the near-wall region and below 5% in the central flow region), turbulence stabilizes the disintegration process. This result has been explained by the increased vorticity of the turbulent flow, which produces additional shear stresses. These may be interpreted as increased turbulent viscosity, stabilizing the flow. Only if the disturbance level is beyond a certain threshold value, the disruptive forces of the fluctuations seemed to overcome the stabilizing effects, even exceeding the effect of aerodynamic forces. For a cylindrical jet, Mansour and Chigier (1994) found that in the absence of aerodynamic effects, turbulent jets are as stable as laminar jets. Marked differences however were found in the breakup behavior and droplet formation patterns of both laminar and turbulent jets.

19.1.5.1.2 Pneumatic Atomizer Typical atomizer configurations are spraying vertically downward in the direction of gravity. Here, the geometrical shape of the liquid jet in the gravity field and liquid velocity change prior to disintegration is of importance. When neglecting surface tension and frictional effects within and on the liquid jet behavior, the velocity distribution of a cylindrical falling jet is

$$u_l = \sqrt{u_0^2 + 2gx} \tag{19.15}$$

and, therefore, the jet diameter can be calculated as

$$\frac{d}{d_0} = \left(1 + \frac{2gx}{u_0^2}\right)^{-0.25} \tag{19.16}$$

This is independent of the liquid density. By adding surface-tension effects to this one-dimensional analysis (see Anno, 1977, Schröder, 1997, Schneider and Walzel, 1998), a nonlinear relation is achieved, describing the fluid jet contour behavior in a gravity field as a function of the nozzle distance:

$$\frac{d}{d_0} = \left[1 + \frac{2gx}{u_0^2} + \frac{4\sigma(d - d_0)}{\rho u_0^2 d d_0}\right]^{-0.25} \tag{19.17}$$

Numerical evaluation of this correlation is shown in Figure 19.6 for the jet contour of a liquid jet for different values of the surface tension, including $\sigma = 0$ N/m (without surface-tension effects), $\sigma = 0.0725$ N/m (surface tension of water), and $\sigma = 1.83$ N/m (surface tension of a molten steel). Two different Reynolds numbers of the jet are plotted. From this analysis, it is apparent that the effect of surface tension is to slow down the decrease of the liquid jet diameter for small Reynolds numbers. The jet diameter as a function of distance from the nozzle increases with increasing surface tension.

In case of a fully developed parabolic (laminar) velocity profile of the liquid jet at the nozzle exit, Middleman (1999) derived an approximate solution of the decreasing jet diameter (neglecting surface-tension effects) as follows:

$$\frac{d}{d_0} = \left(\frac{4}{3} + \frac{2gx}{u_0^2}\right)^{-0.25} \tag{19.18}$$

A numerical calculation of an exiting fluid jet having a velocity profile, taking into account friction, gravity, and surface tension, has been performed by Duda and Vrentas (1967) for Reynolds numbers Re > 200. Their results indicate that flattening of the developed velocity profile in the jet due to the low tangential stresses on the jet surface is very slow. As shown in Fritsching (2001), a two-dimensional numerical simulation of the liquid jet behavior (taking into account additional frictional effects and velocity profiles in the liquid jet due to the interaction with surrounding gas) produces only small deviations from the analytical solution.

19.1.5.1.3 Pressure Swirl Atomizer *Air core*: Halder et al. (2002) found that below a certain Reynolds number (Re_{l1}) at the inlet of the nozzle the liquid flows full through the nozzle without the formation

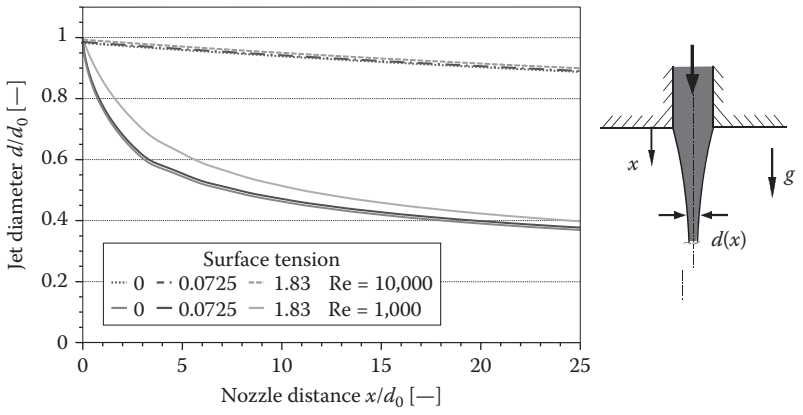


Figure 19.6

Dimensionless jet diameter of a free-falling circular liquid jet in gravity field, effect of density and surface tension.

of an air core, while above a certain Reynolds number (Re_{l2}) the formation of a fully developed central air core of cylindrical shape takes place in the nozzle. The inlet Reynolds number in Halder et al. (2002) takes the form

$$\mathrm{Re}_l = \frac{\rho_l \dot{Q} D_p}{\mu A_p} \tag{19.19}$$

where

$\dot{Q}$ is the total liquid flow rate through the nozzle
A_p is the total area of tangential entry ports

A transition flow with the development of a central air core takes place within the nozzle in between two limiting inlet Reynolds numbers. These two limiting Reynolds numbers are found to be an inverse function of the ratio of orifice to swirl chamber diameter (D_0/D_s) and a direct function of the ratio of tangential entry port to swirl chamber diameter (D_p/D_s). The terms on the nozzle geometry are defined in Figure 19.7. The fully developed central air core is cylindrical in shape with a sudden bulging in diameter at the entrance to the orifice. The air core diameter in both converging and orifice sections of the nozzle increases with an increase in the inlet Reynolds number at its lower range, while it becomes independent of the inlet Reynolds number at its higher range. Halder et al. (2002) gave the empirical correlations between the air core diameter and the pertinent dimensionless controlling parameters as follows:

$$\frac{D_{a1}}{D_0} = 0.42\left(1 - e^{-1.45\times10^{-4}\,\mathrm{Re}_l}\right)\alpha^{0.002}\left(\frac{D_0}{D_s}\right)^{0.735}\left(\frac{D_p}{D_s}\right)^{-0.765}\left(\frac{L_0}{D_s}\right)^{-0.111} \tag{19.20}$$

and

$$\frac{D_{a2}}{D_0} = 0.338\left(1 - e^{-1.45\times10^{-4}\,\mathrm{Re}_l}\right)\alpha^{0.073}\left(\frac{D_0}{D_s}\right)^{0.424}\left(\frac{D_p}{D_s}\right)^{-0.732}\left(\frac{L_0}{D_s}\right)^{-0.252} \tag{19.21}$$

where D_{a1} and D_{a2} are the air core diameters in both converging and orifice sections of the nozzle, respectively. The size of the air core determines the effective flow area at the discharge orifice and thus controls the coefficient of discharge (C_D). If the sheet thickness (h_0) at the orifice is known, the ratio of the air core area at the nozzle exit to the orifice area, X, is given by

$$X = \left(1 - \frac{2h_0}{D_0}\right)^2 \tag{19.22}$$

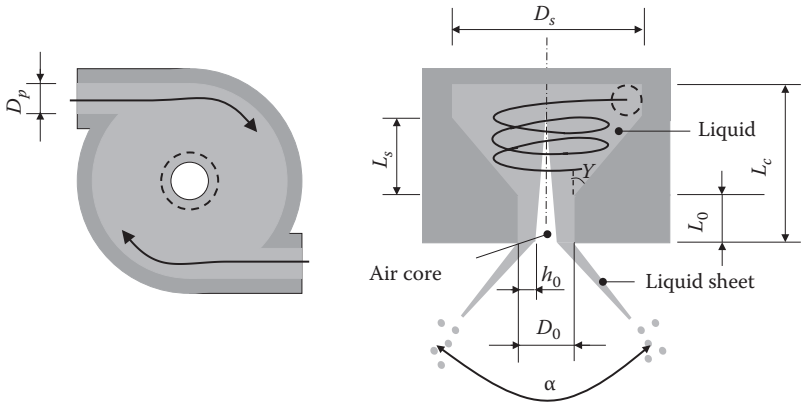


Figure 19.7

Schematic of pressure swirl nozzle together with main geometric parameters. (From Li, X.G., Modeling and simulation of the gas-atomization process of metal melts for metal-matrix-composite production, Dissertation, Universität Bremen, Shaker-Verlag, Aachen, Germany, 2014. With permission.)

Atomizer constant: The atomizer constant (K), which is found to correlate with some performance parameters like discharge coefficient (C_D), liquid film thickness (h), and spray angle (α), is defined as

$$K = \frac{A_p}{D_s D_0} \tag{19.23}$$

where A_p is the total area of tangential entry ports.

Discharge coefficient: The relation of liquid-mass-flow rate ($\dot{M}_l$) and injection pressure differential (Δp_l, i.e., the difference between the driving pressure on the liquid p_l and the ambient in the spray chamber p_a) is correlated by the discharge coefficient (C_D) of the nozzle:

$$C_D = \frac{4\dot{M}_l}{\pi D_0^2 \sqrt{2\rho_l \Delta p_l}} \tag{19.24}$$

where ρ_l is the density of the liquid. Analytical and empirical correlations for the discharge coefficient are summarized in Table 19.3. The correlation in Rizk and Lefebvre (1985) considers only the influence of the nozzle geometry. In Ballester and Dopazo (1994), the injection pressure differential as a factor is taken into account together with the nozzle geometry. In other correlations, the physical properties like liquid viscosity (μ_l) and liquid density (ρ_l) are also involved. The terms on the nozzle geometry are defined in Figure 19.7.

Film thickness: The liquid film inside a swirl nozzle is formed by the centrifugal force of swirling liquid and its thickness is one of the crucial factors governing the film development and atomization process. In fact, the liquid film thickness at the nozzle exit is one of the important input parameters for most of swirl spray atomization models. Suyari and Lefebvre (1986) derived an equation with regard to the effect of the pressure difference (Δp_l), liquid properties, and nozzle diameter (D_0). Badami et al. (2004) suggested an analytical equation, taking into account the nozzle diameter (D_0) and spray angle (α) as main parameters. Kim et al. (2006) modified the correlation in Suyari and Lefebvre (1986) by introducing the effect of the ratio of nozzle length to diameter (L_0/D_0). The experimental results in Moon et al. (2010) indicate that the liquid

Table 19.3 Analytical and Empirical Correlations for the Discharge Coefficient C_D (in SI units)

References	Correlation
Jones (1982)	$C_D = 0.45\left(\frac{L_0}{D_0}\right)^{-0.03}\left(\frac{L_c - L_0 - L_s}{D_s}\right)^{0.05} K^{0.52}\left(\frac{D_s}{D_0}\right)^{0.23} \mathrm{Re}_p^{-0.02}$
Rizk and Lefebvre (1985)	$C_D = 0.35\left(\frac{A_p}{D_s D_0}\right)^{0.5}\left(\frac{D_s}{D_0}\right)^{0.25}$
Richter and Glaser (1987)	$C_D = 1.11\frac{4D_p\mu_l}{\pi D_0^2\sqrt{2\Delta p_l \rho_l}}\left(\frac{D_p}{D_0}\right)^{-0.959}\left(\frac{D_s}{D_0}\right)^{0.049}\left(\frac{D_p}{\mu_l}\sqrt{2\Delta p_l \rho_l}\right)^{0.868}$
Ballester and Dopazo (1994)	$C_D = 1.323\times10^{-3} K^{0.29} D_0^{-0.82} \Delta p_l^{0.03}$
Broll (2006)	For $\frac{L_0}{D_0} < 0.5$, $C_D = C_{D,0}^{1.05} + 9.59 S^{-0.726}\gamma^{-0.591}\left(\frac{D_p}{D_0}\right)^{1.233} \mathrm{Re}_p^{-0.4}$; For $0.5 < \frac{L_0}{D_0} < 1$, $C_D = C_{D,0}^{1.05} + 9.104 S^{-0.798}\gamma^{-0.524}\left(\frac{D_p}{D_0}\right)^{1.079}\left(\frac{L_0}{D_0}\right)^{-0.048} \mathrm{Re}_p^{-0.4}$
Tratnig (2009)	$C_D = 0.9779\left(\frac{D_0}{D_s}\right)^{0.9712}\left(\frac{L_c - L_0 - L_s}{D_s}\right)^{0.3253}\left(\frac{B_p}{D_s}\right)^{0.2783} \Delta p_l^{0.4072}\rho_l^{0.4072} D_s^{1.8144}\mu_l^{0.1856}\frac{4}{\pi D_0^2\sqrt{2\Delta p_l \rho_l}}$
Musemic et al. (2010)	$C_D = C_{D,0}^{1.121} + 0.121 S^{0.352}\gamma^{1.045}\left(\frac{L_c}{D_0}\right)^{1.178} \mathrm{Re}_p^{-0.209}$

Note: $\mathrm{Re}_p = D_0\sqrt{\Delta p_l \rho_l}/\mu_l$; $C_{D,0} \approx \sqrt{(a+bS)^{-3/c}/2 - (a+bS)^{-1/c}}$, $a = 1.016$, $b = 1.135$ and $c = 1.714$; $\gamma(\mathrm{rad}) = \gamma(\mathrm{deg})\pi/180$; $S = \pi(D_s - D_p)D_0/8A_p$; $B_p = D_p$ for circular entry port.

Table 19.4 Analytical and Empirical Correlations for the Liquid Sheet Thickness h at Liquid Nozzle Exit (in SI units)

References	Correlation
Suyari and Lefebvre (1986)	$h = 3.66\left(\frac{D_0 \dot{M}_l \mu_l}{\rho_l \Delta p_l}\right)^{0.25}$
Badami et al. (2004)	$h = \left(\frac{D_0}{2}\right)(1-k)$, where $\alpha = 2\arctan\sqrt{\frac{k^2}{1-k^2}}$, k is cavity factor
Kim et al. (2006)	$h = 1.44 D_0 \left(\frac{\dot{M}_l \mu_l}{\rho_l \Delta p_l D_0^3}\right)^{0.25} \left(\frac{L_0}{D_0}\right)^{0.6}$
Moon et al. (2010)	$h = 0.97 A_p^{0.08} \left(\frac{\mu_l D_0}{\rho_l}\right)^{0.25} \left(\frac{L_0}{D_0}\right)^{0.76} (\tan\gamma)^{-0.12}$, when $\Delta p_l \geq 2$ MPa

film thickness at high injection pressure differential is mainly dependent on the ratio of nozzle length to diameter (L_0/D_0) and independent of the injection pressure differential and the increase in L_0/D_0 ratio causes thicker liquid film thickness. The analytical and empirical correlations for the sheet thickness in terms of flow parameters are summarized in Table 19.4.

Spray angle: The spray cone angle (α) determines the coverage and dispersion of the spray in the surrounding environment. An increase of spray cone angle (α) with the injection pressure differential (Δp_l) is confirmed by most of experimental observations based on types of fluid viscosities and different nozzle geometries (Mulhem et al., 2006a, Achelis, 2009, Musemic et al., 2010). An increase in swirl ratio $S = \pi(D_s - D_p)D_0/(8A_p)$ leads to an increase of the sheet velocity in tangential direction at the nozzle orifice, resulting in a larger spray angle (Musemic et al., 2010). The spray cone angle decreases with increasing atomizer constant (K) (Ballester and Dopazo, 1994). An increase in the orifice length/diameter ratio (L_0/D_0) reduces the spray cone angle (Musemic et al., 2010). An increase in liquid viscosity reduces the spray cone angle (Mulhem et al., 2006a). Analytical and empirical correlations for the spray cone angle in pressure swirl atomization are summarized in Table 19.5.

A way to influence the film formation and the spray and ligament opening angle at the orifice of a pressure swirl atomizer by utilizing the Coanda effect (jet deflection at curved interface) has been illustrated by Kamplade et al. (2013). The liquid film angle deflection and thus the spray by the Coanda orifices mounted to a pressure swirl nozzle has been characterized by geometrical parameters as the Coanda curvature radius R_c/D (versus the orifice diameter) and by the flow or pressure Reynolds number. In general, under proper conditions, it is shown that much higher spray angles than with sharp edged nozzles can be achieved.

Discharge velocity: The discharge velocity, that is, the sheet velocity at the nozzle exit, can be obtained based on the mean flow velocity, which depends on the injection pressure differential Δp_l (Eslamian and Ashgriz, 2011):

$$U = K_v \sqrt{\frac{2\Delta p_l}{\rho_l}} \tag{19.25}$$

Table 19.5 Analytical and Empirical Correlations for the Spray Cone Angle α (in SI units)

References	Correlation
Giffen and Muraszew (1953)	$\sin\left(\frac{\alpha}{2}\right) = \frac{(\pi/2)C_D}{K(1+\sqrt{X})}$
Rizk and Lefebvre (1985)	$\alpha = 6K^{-0.15}\left(\frac{\Delta p_l D_0^2 \rho_l}{\mu_l^2}\right)^{0.11}$
Ballester and Dopazo (1994)	$\alpha = 16.156 K^{-0.39} D_0^{1.13} \mu_l^{-0.9} \Delta p_l^{0.39}$
Rivas et al. (2014)	$\sin\left(\frac{\alpha}{2}\right) = \frac{2\sqrt{2}X}{(1+\sqrt{X})\sqrt{1+X}}$

where K_v is given by the empirical correlation:

$$K_v = \frac{C_D}{(1-X)\cos(\alpha/2)} \tag{19.26}$$

where
C_D is the discharge coefficient
X is the ratio of the air core area at the nozzle exit to the orifice area
α is the spray angle

The axial component of the discharge velocity can be derived by the following equation:

$$U_z = \frac{\dot{M}_l}{\rho_l \cdot \pi h(D_0 - h_0)} \tag{19.27}$$

where
D_0 is the diameter in the nozzle exit area
h_0 is the initial sheet thickness

And then the average swirling velocity at the nozzle exit can be obtained by

$$U_t = \sqrt{U^2 - U_z^2} \tag{19.28}$$

19.1.5.1.4 Rotary Atomizer The film thickness at the rim of a rotating disk has been analyzed using several approaches by solving the equations of motion for the liquid film. Based on the local velocity difference between the angular film and the solid disk velocity, Nikolaev et al. (1967) derived the resulting film thickness. Bruin (1969) analyzed the simplified Navier–Stokes equation using complex functions and Matsumoto et al. (1973) obtained a numerical solution from the Navier–Stokes equations. Their results as well as experimental results (see Lefebvre, 1989) are in principle agreement and may be empirically correlated in terms of the dimensionless film thickness versus the dimensionless liquid flow rate by

$$\frac{t}{(\mu_l/\rho_l\omega)} = -14.5\left(\frac{\dot{Q}}{2\pi R^2(\mu_l\omega/\rho_l)^{0.5}}\right)^2 + 6.72\frac{\dot{Q}}{2\pi R^2(\mu_l\omega/\rho_l)^{0.5}} + 0.2 \tag{19.29}$$

19.1.5.1.5 Internal Mixing (Effervescent) Twin-Fluid Atomizer In the narrowest cross-section (typically in the exit) of an internal mixing, effervescent atomizer for the gas–liquid mixture critical mass flow is observed (Chawla, 1969, 1985, Chawla and Böckh, 1971, Buckner and Sojka, 1991, Whitlow and Lefebvre, 1993, Lund et al., 1993, Sovani et al., 2001). The term critical condition in this context stands for the critical mixture exit velocity (Mach number Ma = 1), the so-called choked nozzle condition. In a gas/liquid two-phase medium, the speed of sound is markedly less than that in either of the individual phase. As an example, Chawla (1985) notes that the minimum speed of sound in an air/water mixture at standard temperature and pressure is 20–30 m/s, as compared to 300 and 1500 m/s in the individual air and water phases, respectively. Since a two-phase flow through a nozzle chokes at a significantly lower velocity than that at which a single-phase flow would choke, a two-phase flow will experience a steep pressure jump at the nozzle exit, even at relatively low flow velocities and low injection pressures. Since atomization quality is greatly enhanced by the sudden pressure drop at the nozzle exit, it is possible to achieve good atomization with two-phase flows even at low flow rates and low injection pressures. Furthermore, due to its low sonic velocity, a two-phase flow can remain choked while flowing through orifices larger than those required for a single-phase flow. As a result, a two-phase flow can provide good atomization even with exceptionally large exit orifices. The lower sonic velocity of a two-phase mixture and the consequent pressure jump at the atomizer exit is an advantage that effervescent atomization shares with other internal-mixing twin-fluid atomization techniques (Sovani et al., 2001).

The total mass flow rate through the nozzle and the loading (mass flow ratio of gas and liquid, GLR) also depends on the actual state of the mixture within the nozzle throat as will be described here. Leaving the nozzle, the gas flow expands and the liquid is dispersed into ligaments and droplets. The atomizer efficiency and temporal and spatial distribution of droplet diameters and droplet velocities depend on the total pressure in front of the nozzle, the volumetric flow rate of liquid and gas, as well as on the spatial and temporal distribution of gas and liquid at the nozzle exit. These distributions are affected by the two-phase flow structure inside the mixing chamber and the nozzle. Chin and Lefebvre (1993) as well as Lörcher (2003), Lörcher et al. (2003), Kim and Lee (2001), Jedelsky and Jicha (2008), and Shepad (2011) and Jedelsky (2013) analyzed experimentally the flow regimes inside of an internal mixing atomizer and in its exit, where bubbly, slug, annular, or dispersed flow regimes with GLR increase are found (see Chapter 3). Their findings for the different flow regimes have been incorporated in the general flow maps, for example, of Oshinowo and Charles (1974). In Jedelsky and Jicha (2008) and Jedelsky (2013), modified Baker's map for vertical downward two-phase flow with transformed coordinates has been used to describe different internal two-phase flow patterns, as shown in Figure 19.8. The coordinates in the map are

$$X = k_x \cdot GLR \cdot \lambda \cdot \psi \quad \text{and} \quad Y = \frac{k_y \dot{m}_g}{\lambda} \tag{19.30}$$

where k_x and k_y are constants needed for conversion from Imperial system to SI system. The other parameters are

$$\lambda = \left(\frac{\rho_g}{\rho_a} \cdot \frac{\rho_l}{\rho_w} \right)^{1/2} \quad \text{and} \quad \psi = \frac{\sigma_w}{\sigma_l} \left(\frac{\mu_l}{\mu_w} \cdot \left(\frac{\rho_w}{\rho_l} \right)^2 \right)^{1/3} \tag{19.31}$$

where ρ, σ, and μ are density, surface tension, and dynamic viscosity, respectively. The subscripts *g*, *l*, *a*, and *w* denote atomizing gas, atomized liquid, air, and water, respectively.

However, as these general flow maps have been derived for a fully developed two-phase flow, the flow regimes inside the internal mixing atomizer do not fit well into these general schemes. Here, the atomizer and mixing chamber lengths are too small to achieve fully developed flow conditions.

Model developments for the different flow regimes in an effervescent atomizer are to be found in Lörcher (2003), Lörcher et al. (2003) and the transition between the modes has been characterized in Kim and Lee (2001), Jedelsky and Jicha (2008), and Shepad (2011). The spray from an effervescent atomizer has been

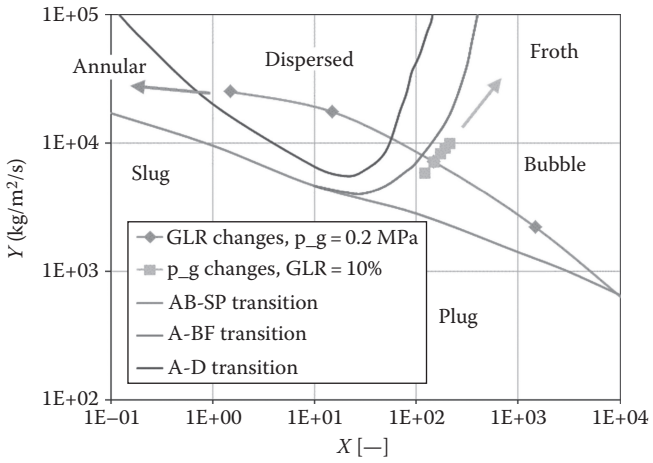


Figure 19.8

Modified Baker's map for vertical downward two-phase flow with transformed coordinates with marked influence of operational conditions on the two-phase flow regimes. Arrows show direction of regime change, while the appropriate values increase. AB-SP: line defining transition between bubble and plug or annular and slug pattern, A-BF: transition between annular and bubble-froth pattern, A-D: transition between annular and dispersed pattern. (Adapted from Jedelsky, J., Some aspects of effervescent atomization: Experimental study, Short version of Habilitation thesis, Brno University of Technology, Brno, Czech Republic, 2013.)

investigated by Whitlow and Lefebvre (1993), Jicha et al. (2002), Luong and Sojka (1999), Jedelsky and Jicha (2008), Liu et al. (2011), and Shepad (2011).

The critical pressure $p_{2,c}$ in the nozzle exit can be correlated by Churchill and Usagi (1972)

$$\left(\frac{p_2}{p_0}\right)_c = \left[\left(\frac{\kappa+1}{2}\right)^{4\kappa/3(\kappa-1)} + \left(\frac{\kappa}{2}\frac{1-\alpha_0}{\alpha_0}\right)^{4\kappa/3(\kappa+1)}\right]^{-3/4} \tag{19.32}$$

The discharge coefficient and the critical mass flow rate at the exit have been empirically correlated, for example, with gas to liquid mass ratio (GLR) by Chen and Lefebvre (1994), Landwehr et al. (1999), Kim and Lee (2001), and Ochowiak et al. (2010). Lörcher (2003) found the best agreement with the simulation results of Richter (1983) and the analytical expression of Leung and Epstein (1990). From the corresponding critical pressure and mass flow rate at the nozzle exit, the void fraction and mean velocities at the exit can be derived.

The comparisons between the two-phase flow structures inside the mixing chamber and the spray structures exiting the nozzle have been performed by Kim and Lee (2001), Jedelsky and Jicha (2008), and Shepad (2011). Figure 19.9 shows how the spray appears under different internal flow regimes. For a relatively small amount of

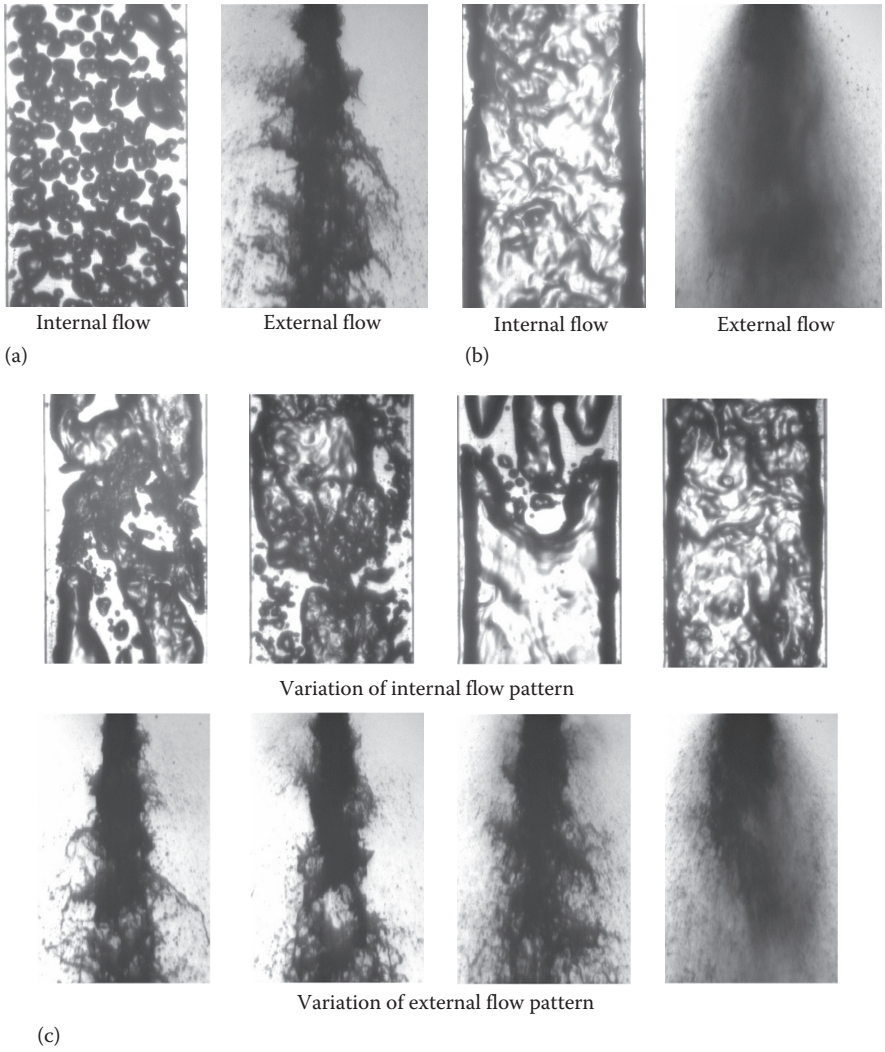


Figure 19.9

Internal vs. external flow characteristics in different regimes, Δp = 0.4 MPa, D_0 = 1.6 mm: (a) bubbly flow, GLR = 0.003; (b) annular flow, GLR = 0.111; (c) intermittent flow, GLR = 0.017. (Adapted from Kim, J.Y. and Lee, S.Y., Dependence of spraying performance on the internal flow pattern in effervescent atomizers, *Atom. Sprays*, 11, 735, 2001. With permission.)

air (GLR = 0.003, Figure 19.9a), the internal flow regime is bubbly and the spray has intermittent disruptions. In the bubbly flow regime, the discharged air/liquid mixture disintegrates into drops through the processes of bubble expansion and ligament breakup. When the internal flow is annular, due to the large amount of gas (GLR = 0.111), the spray breaks up relatively close to the nozzle exit, as evident in Figure 19.9b. In the annular flow regime, the liquid annulus disintegrates into fine drops by aerodynamic interaction due to high relative velocity between the core gas and the liquid film. At GLRs in between the bubbly and annular flow regimes, there is an internally intermittent regime (i.e., slug flow regime) where the unsteadiness of the internal flow structure is observed, and thus, the spray characteristics fluctuate with variation of the internal flow structure. In the slug flow regime, the bubble expansion/ligament disintegration and the annulus disintegration modes appear alternately, and this effectively produces the spectrum of spray characteristics, as shown in Figure 19.9c, demonstrating the unsteadiness of the spray. The spray unsteadiness can be identified by sampling time-dependent droplet velocity and size measurements using phase/Doppler particle analyzer (PDPA) (Hardalupas and Horender, 2001), or based on measurements of pressure fluctuations in the atomizer mixing chamber (Jedelsky and Jicha, 2008), or by analysis of droplet arrival statistics (Edwards and Marx, 1995, Heinlein and Fritsching, 2006, Liu et al., 2011).

19.1.5.1.6 Ultrasonic Standing Wave Atomizer (USWA) Within a typical application of the USWA technique, a cylindrical liquid jet is poured into a node of the standing acoustic wave (Lierke et al., 1988). Here the liquid surface interacts with the acoustic field, resulting in a force on the liquid surface, regarded as sound radiation pressure. The sound radiation pressure is a result of the temporal averaged difference of surface pressure to ambient pressure and, therefore, the local temporal averaged density increases (Langevin sound radiation pressure). Its distribution on a spherical surface was first calculated by King (1934). The sound radiation pressure leads to a deformation of the cylindrical jet into a disk-shaped film (see Figure 19.10). In addition, suction forces act at the rim of the disk. This suction makes the USWA process ideal for disintegration of viscous liquids. The liquid velocity in the disk is increasing when the liquid moves from the center toward the rim of the disk, thereby the sheet thickness decreases. The liquid velocity distribution inside the disk has been derived theoretically by Hansmann (1996) and has been compared to experimental results, as illustrated in Figure 19.10. The liquid disintegrates at the rim of the disk when the film becomes thin and instability occurs.

19.1.5.2 Gas Flow

Analysis of the gas flow field in atomizer configurations is to be done in external mixing twin-fluid atomizers especially to identify the disintegration potential in terms of the operation conditions (gas pressure, nozzle arrangement, etc.). The geometric configuration and arrangement of the gas jet system as well as the

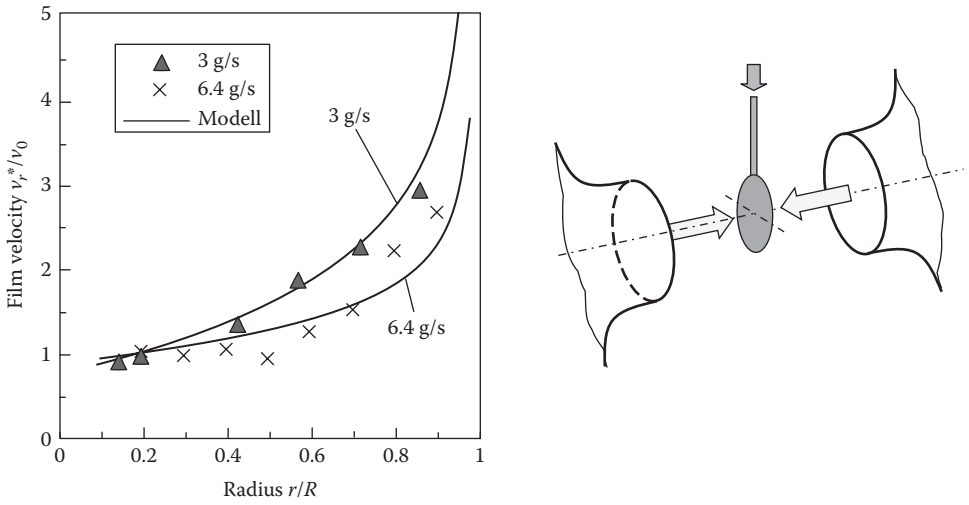


Figure 19.10

Film formation and radial film velocity in ultrasonic standing wave field. (Adapted from Hansmann, S., Einfluss von Stoff- und Betriebsparametern auf die Zerstäubung hochviskoser Flüssigkeiten im Ultraschall-Stehwellenfeld, Dissertation, Universität Bremen, Bremen, Germany, 1996.)

geometry or contour of the individual gas nozzles may be adapted for suitable application of the atomization gas (Espina and Piomelli, 1998a,b, Heck, 1998, Dielewicz et al., 1999, Espina, 1999, Czisch et al., 2003, Zeoli and Gu, 2006, Czisch and Fritsching, 2008b).

The gas flow behavior in front of an external mixing twin-fluid atomizer may have an influence on fundamental atomization parameters like the liquid mass flow rate (yield) or the resulting drop size distribution in the spray. The typical concentric gas flow configuration in an atomizer results in a pressure change in the central liquid feed area that causes variations in the pressure ratio between the liquid feed (or reservoir) and the pressure level in front of the liquid exit. Some possible arrangements of the nozzle tip in an external mixing twin-fluid atomizer are illustrated in Figure 19.11 (Anderson and Figliola, 1988), together with the corresponding measurements of the orifice pressure (also called aspiration pressure) in the gas-only flow field (without liquid atomization). Typical technical atomizers are constructed to give a suction pressure (lower pressure than ambient) at the liquid delivery port rather than overpressure. Also, the arrangement and number of discrete jets or the configuration of the gas nozzle as an annular slit nozzle result in different aspiration pressure behavior (see Lohner et al., 2003). If the spacing between the individual jets is large enough and the interaction between the jets is small, pressure equalization takes place and in between the discrete jets, the aspiration pressure effect is decreased. For a slit nozzle, the aspiration pressure effect tends to a maximum.

Depending on the individual gas jet nozzle contour, underexpansion, overexpansion, or ideal expansion (within a Laval nozzle contour) may be achieved (Sizov, 1999). The gas jet exit condition has a major influence on the jet behavior. In the gas nozzle exit, overexpanded jets in principle contain the highest exit momentum at a constant mass flow rate. This jet configuration is of special interest to achieve a gas kinetic energy maximum in the atomization area (in order to achieve the maximum slip velocity between gas and fluid). The results of a comparison of simulation data for overexpanded, underexpanded, and ideally expanded circular gas jets are illustrated in Figure 19.12. The velocities on the jets centerlines are plotted versus the nozzle distance for constant gas pre-pressure (p_0 = 5.5 bar abs.) and mass flow rate. For the latter, the gas nozzle exit areas of the three jets are different, calculated from isentropic flow conditions. Therefore, the exit area is highest for the overexpanded jet at identical conditions. Because the overexpanded jet also delivers the highest exit gas velocity, the resulting exit momentum in this case is highest (at constant mass flow rates). But downstream of the nozzle exit, the underexpanded jet has the highest velocity values after the first shock cell in the transonic region, especially immediately behind the shock fronts. For analysis of the atomization potential of the three different gas flow configurations, the behavior further downstream in the far field is important. In the subsonic free jet region, the ideally expanded jet shows the highest velocity values on the centerline. For ideally expanded jet behavior without any shock structures, the highest potential for atomization purposes is achieved in the far field.

Figure 19.13a and b shows the simulated gas flow field (velocity contours and vectors) in an external mixing (close-coupled) atomizer configuration (Zeoli and Gu, 2006). The gas exit geometry is an annular slit configuration where the gas emerges from a concentric ring slit nozzle. As the high-pressure gas enters the nozzle, the sharp

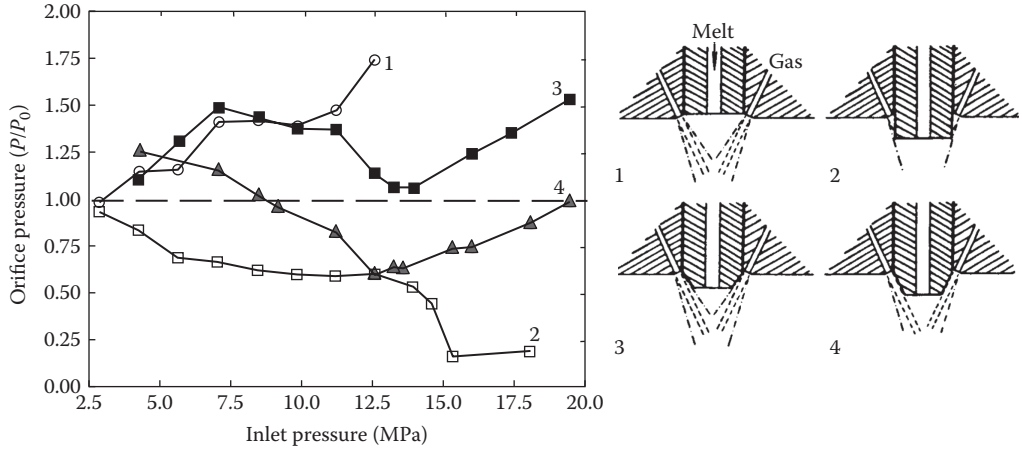


Figure 19.11

Aspiration pressure for different nozzle tip arrangements in close-coupled atomizer. (Adapted from Anderson, I.E. and Figliola, R.S., Observations of gas atomization process dynamics, in P.U. Gummeson and D.A. Gustafson, eds., *Modern Developments in Powder Metallurgy,* Vol. 20, 1988, pp. 205–223.)

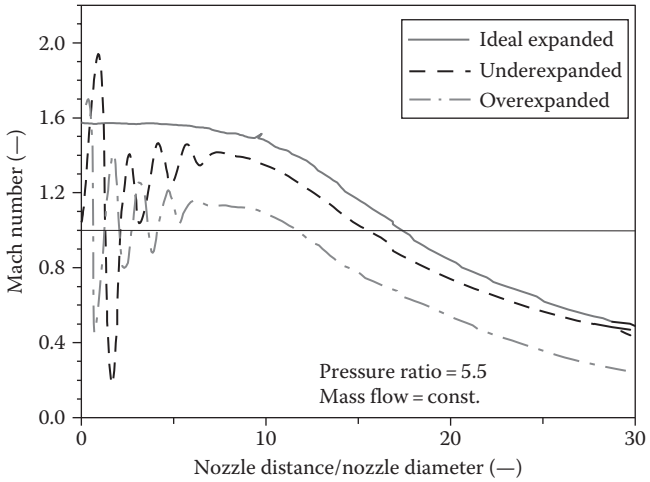


Figure 19.12

Gas jet velocities on the centerline of under-, over- and ideally expanded jets. (From Heck, U., Zur Zerstäubung in Freifalldüsen, PhD thesis, Universität Bremen, Bremen, Germany, 1998. With permission.)

angle with the nozzle causes a detachment of the flow from the wall and a recirculation flow is generated around the corner of the throat. An oblique shock is formed inside the nozzle and reflected by the outer surface of the feeding tube. At the exit, the gas flow expands through a series of Prandtl–Meyer expansion waves and recompression shocks to match the atmospheric pressure inside the atomization chamber and the high-velocity gas continuously overshoots the equilibrium position as the external layer of the jet communicates with the jet core by sound/pressure waves, which is slower than the supersonic flow. The gas flow separation at the corner of the melt tube generates a recirculation vortex under the melt exit hole. The recirculation zone is distinguished from the high velocity gas with the sonic lines. The gas flow in the center of the recirculation zone moves toward the feeding tube and turns outward radially as it moves close to the tip. When the gas flow comes into contact with the sonic boundary, it is pushed inward and flows downstream. Inside the recirculation zone, a turbulent layer separates upstream and downstream flows. At the end of this recirculation zone, there is a stagnation front, where the gas velocity falls to around zero. About 15 mm behind the stagnation point, there is a mach disk (normal shock) and the corresponding velocity drop is more clearly depicted in Figure 19.13c.

Figure 19.14 shows on the left (a) the simulated gas flow field (velocity contours) in an external mixing (free-fall) atomizer configuration for different gas exit boundary conditions. The gas exit geometry is an annular slit configuration where the gas emerges from a concentric ring slit nozzle. The left part of the Figure 19.14a shows an underexpanded gas flow, and the right part shows the result for the ideal expanded case; both cases have been calculated for identical mass flow rates. In the underexpanded case, a shock cell structure in the gas jet is in front of the nozzle. Using ideally expanded gas jets in atomizer jets increases the velocity potential, as seen in Figure 19.14b (right side). Comparison of the gas velocities on the atomizer centerline illustrates that approximately 50–100 mm below the nozzle, where the primary disintegration of the liquid takes place, an increase of the gas velocity of approximately 10%–20% is achieved.

Figure 19.15 shows a sketch of a conventional external mixing free-fall atomizer. This atomizer design combines two separate gas nozzle systems, namely, a primary gas nozzle and a secondary gas nozzle, both concentrically surrounding the central jet (Fritsching and Bauckhage, 1992). The secondary gas nozzle is the main atomization unit, from which the concentric gas jets impinge onto the central liquid jet that is disintegrated due to instabilities from the shearing action of the secondary gas flow and its relative velocity (Markus et al., 2002). The atomization area is located underneath the secondary gas nozzle (Heck, 1998, Lohner et al., 2003).

Depending on the atomizer design and operation conditions, the inclined secondary gas flow jets may lead to the formation of a recirculation gas flow area underneath the secondary gas nozzle. If the intensity of the recirculation flow is reasonably strong, liquid ligaments or droplets may be transported back to the atomizer body. Here, these sticking fragments may clog the gas and/or liquid orifices and negatively influence or even stop the atomization process. Therefore, a primary gas nozzle or a controlled entrainment gas flow may be employed in a free-fall atomizer to suppress the recirculation of the gas. The primary gas flow is coflowing to

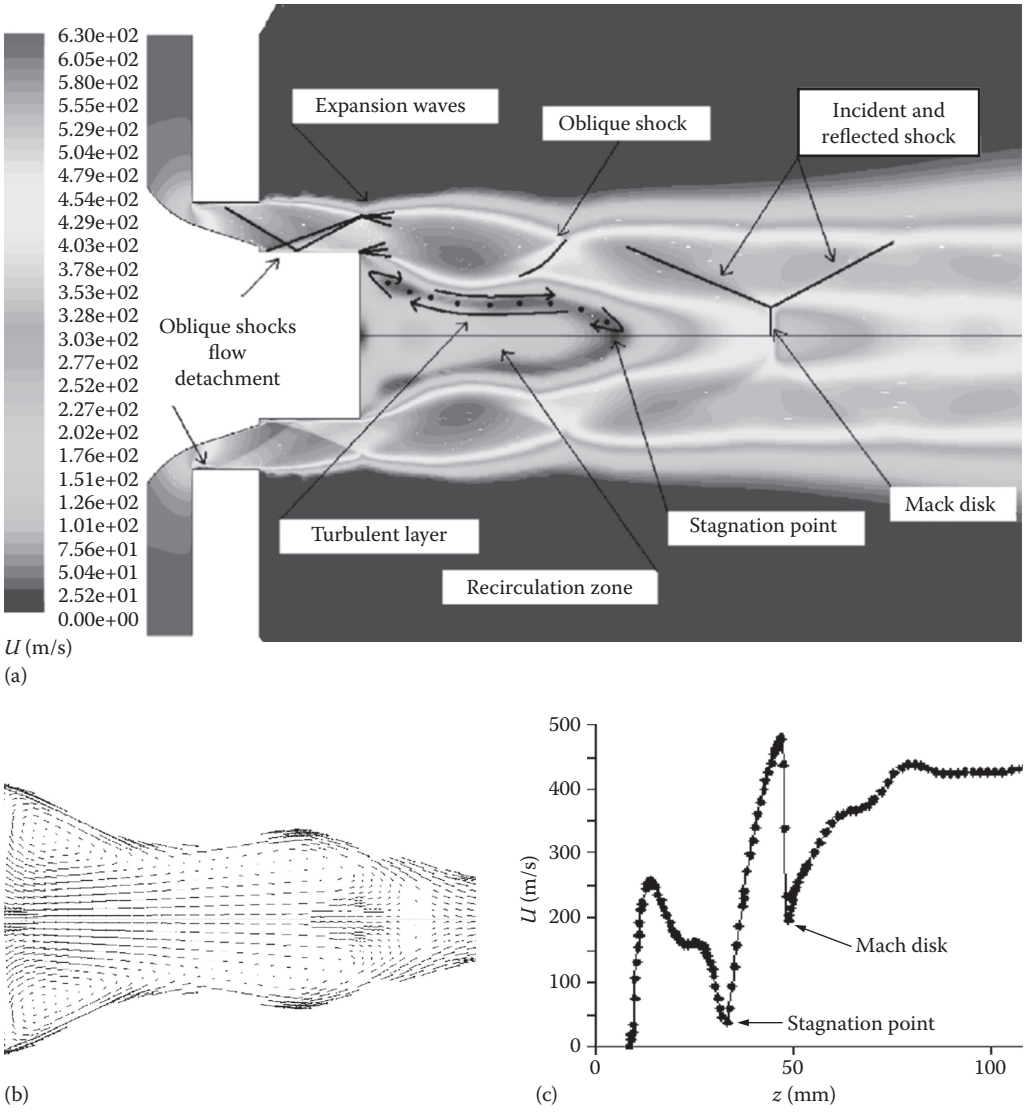


Figure 19.13

Gas flow field simulation for an external mixing (close-coupled) atomizer: (a) velocity contour plot; (b) velocity vector depicting flow recirculation under the melt exit; (c) gas velocity along symmetry axis. (Adapted from Zeoli, N. and Gu, S., *Comput. Mater. Sci.*, 38, 282, 2006. With permission.)

the liquid jet, thereby guiding the liquid into the atomization area. The influence of the primary gas flow on the flow structure in a free-fall atomizer was numerically investigated by Czisch and Fritsching (2008b). In Figure 19.16a, the influence of the primary gas pressure at constant secondary gas pressure (p_0 = 0.5 MPa, rel.) is shown in terms of gas streamlines. Two different operating conditions are to be distinguished, separated by the centerline in the figure. On the left of the figure, the gas flow field is illustrated with primary and secondary gas flow. A reasonable recirculation flow can be seen only close to the primary gas orifice, but no recirculation flow is present underneath the secondary gas nozzle. On the right of the figure, the gas flow field is illustrated when only the secondary flow is applied but no primary gas flow. The shown streamlines illustrate an intense recirculation flow area located from underneath the secondary gas nozzle up to the primary gas nozzle. Figure 19.16b presents the axial gas flow velocity on the centerline of the atomizer at constant secondary gas pressure (p_0 = 0.5 MPa, rel.) for varying primary gas pressures. It can be found that at constant secondary gas pressure the intensity of the gas recirculation underneath the secondary gas nozzle decreases with increasing primary gas pressure, and for primary gas pressures exceeding 0.025 MPa, the recirculation gas flow underneath the secondary gas nozzle is suppressed (no negative velocities in that area). However, the intensity of the recirculation close to the primary gas nozzle increases with increasing primary gas pressure.

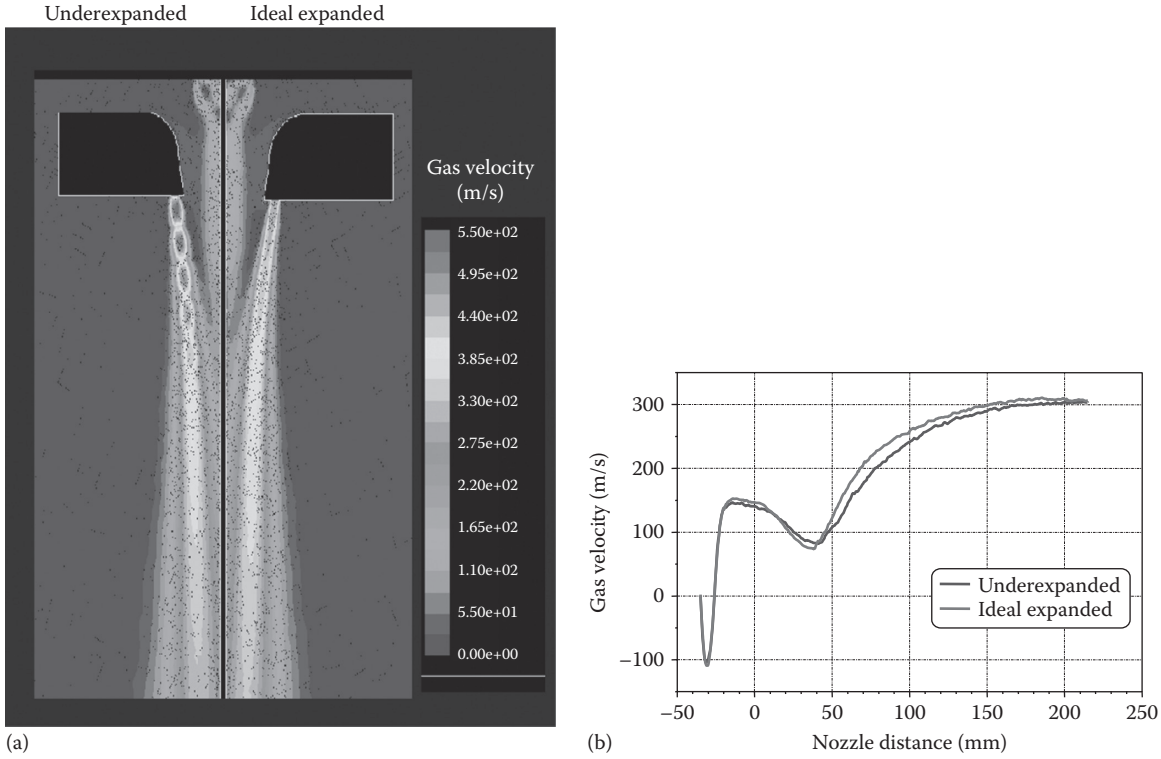


Figure 19.14

Gas flow field simulation for an external mixing (free-fall) atomizer: (a) gas velocity contours: underexpanded exit condition (left), ideal expanded exit condition (right); (b) gas velocity on centerline, comparison of under- and ideally expanded exit conditions. (From Heck, U., Zur Zerstäubung in Freifalldüsen, PhD thesis, Universität Bremen, Bremen, Germany, 1998. With permission.)

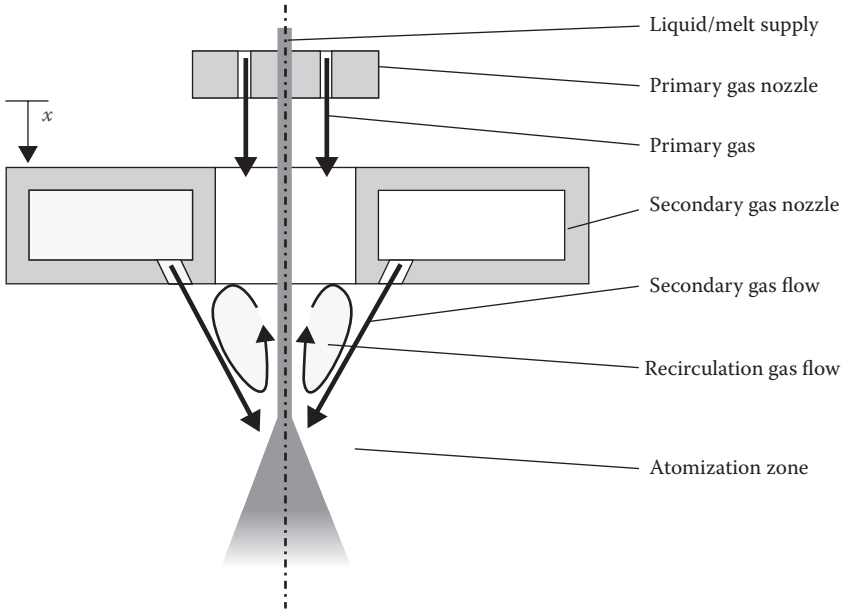


Figure 19.15

Sketch of a conventional free-fall atomizer. (Adapted from Czisch, C. and Fritsching, U., *Atom. Sprays*, 18, 511, 2008b. With permission.)

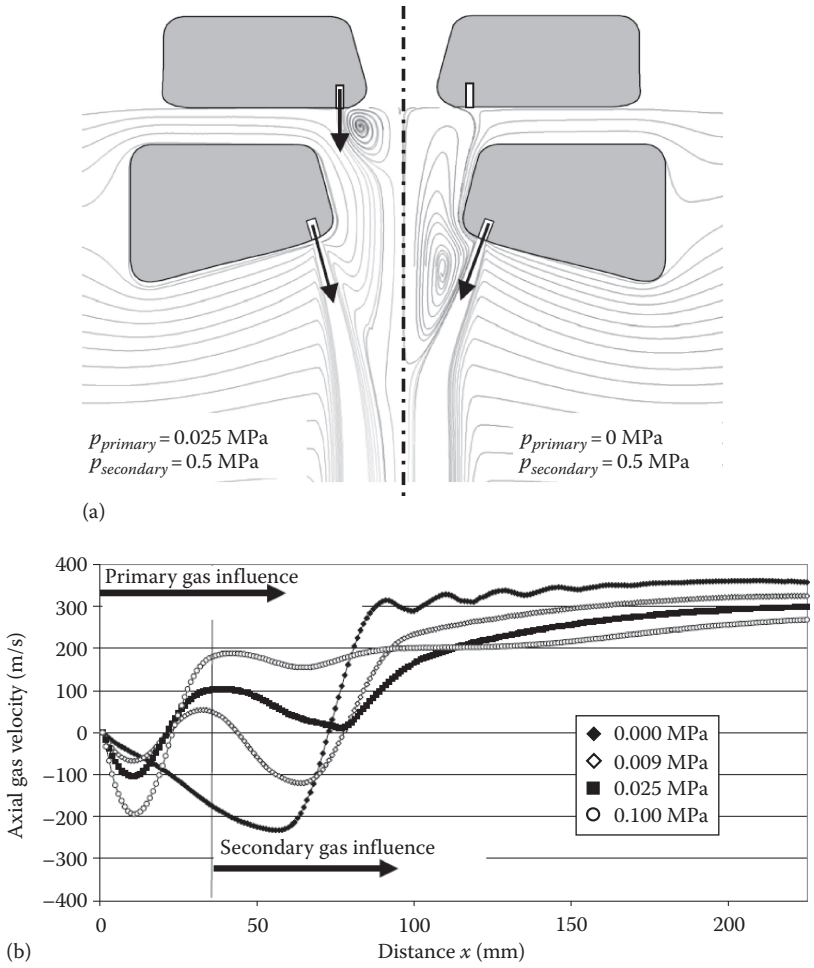


Figure 19.16

(a) Flow field of a conventional free-fall atomizer at different operating conditions. (b) Axial gas velocity on the center-line at varying primary gas pressures (see secondary gas pressure). (From Czisch, C. and Fritsching, U., *Atom. Sprays*, 18, 511, 2008b. With permission.)

During operation of the free-fall atomizer, the gas mass flow rates of both gas nozzle systems are controlled by the primary and secondary gas pressures, respectively. An intense recirculation flow may be generated if the pressure ratio between the primary and the secondary gas nozzle is improperly adjusted. The applicable maximum gas pressure of the primary gas nozzle is limited by initial disturbances that may be generated on the liquid jet before reaching the atomization area. Therefore, the secondary gas pressure is limited also because the secondary gas mass flow rate determines the necessary primary gas mass flow rate for prevention of recirculation. This coupling of the two nozzle systems limits the applicability of the free-fall atomizer (Heck et al., 2000, Bergmann et al., 2001a, Fritsching, 2004).

To improve the operating conditions and to overcome limitations of the free-fall atomizer, a Coanda-flow ring device was developed and installed inside the secondary gas flow (Czisch and Fritsching, 2008b). The applied flow device utilizes the Coanda effect (Wille and Fernholz, 1965) and the injector principle to influence the local atomization gas direction. Within the confined flow device, the secondary gas flow is deflected in the downward direction, the entrainment mass flow is increased, and, therefore, a primary gas nozzle is not necessary for suppression of gas recirculation.

In Figure 19.17a, the flow field of the free-fall atomizer without primary gas application is illustrated as streamline distribution (left) and local static pressure distribution (right) at a secondary pressure of 0.5 MPa (rel.). A recirculation flow field generated underneath the secondary gas nozzle is visible. The area with highest pressure is located where the atomization gas streams impinge onto the centerline. The local static pressure exceeds 50 kPa in this area. Figure 19.17b shows the flow situation of a free-fall atomizer without

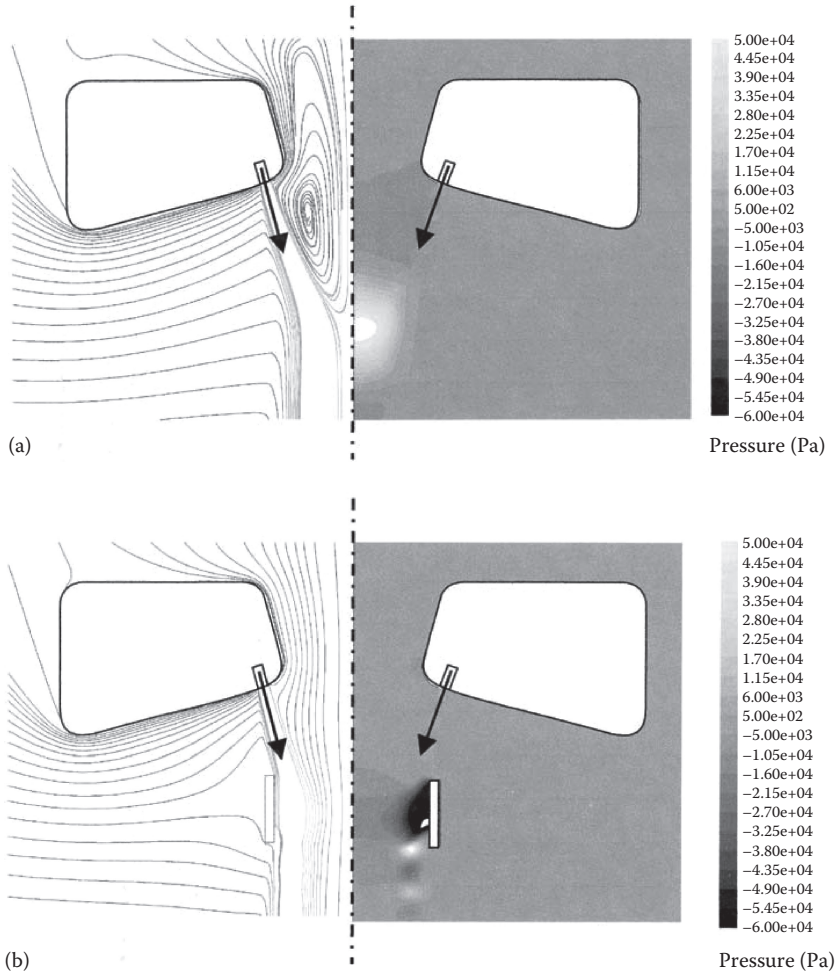


Figure 19.17

(a) Flow field (left) of and pressure distribution (right) of a conventional free-fall atomizer generated only by the secondary gas flow. (b) Flow field (left) of and pressure distribution (right) of a conventional free-fall atomizer generated only by the secondary gas flow but with installed Coanda-flow device. (From Czisch, C. and Fritsching, U., *Atom. Sprays,* 18, 511, 2008b. With permission.)

primary gas application but with the installed Coanda-flow ring device at a secondary gas pressure of 0.5 MPa (rel.). On the left, the flow field is illustrated by its streamline distribution; on the right, the static pressure distribution is displayed. No recirculation flow field is generated in this case. On the right, it can be seen that at the entrance of the installed Coanda-flow device, an underpressure area is generated. Depending on the negative pressure ratio between the underpressure area close to the atomization zone and the environmental gas pressure, the gas flow is deflected downward. Thus, the total gas mass flow rate increases through the liquid passage of the secondary nozzle by suppressing the recirculation completely. The maximum underpressure within the Coanda-flow device exceeds –60 kPa for the given secondary gas pressure.

Figure 19.18 shows the axial velocity on the centerline of the atomizer versus the varying secondary gas pressure without applying primary gas flow but with applying the Coanda-flow ring. There is almost no effect on the axial gas velocity with increasing gas pressure until the gas passed the installed flow device. Up to this point, the flow is completely dominated by the entrained gas flow from outside. After the gas flow passes the Coanda-flow device, the axial gas velocity increases with increasing secondary gas pressure. Thus, it is possible to achieve a recirculation free gas flow in a free-fall atomizer configuration by using the Coanda-flow device.

Figure 19.19a shows a photograph of the atomization area without the Coanda-flow device at secondary gas pressure 0.5 MPa (rel.) and without primary gas application. Obviously, an unstable atomization occurs where droplets are transported from the atomization area upward toward the atomizer body due to the generated

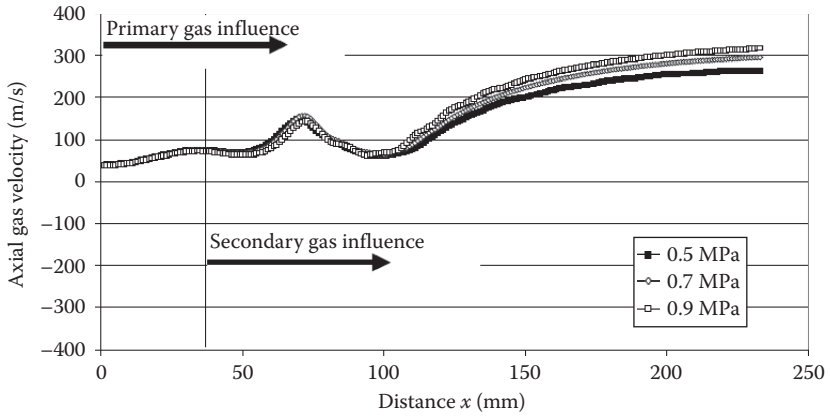


Figure 19.18

Axial gas velocity on the center-line at varying secondary gas pressures with installed Coanda-flow device (no primary gas nozzle). (From Czisch, C. and Fritsching, U., *Atom. Sprays*, 18, 511, 2008b. With permission.)

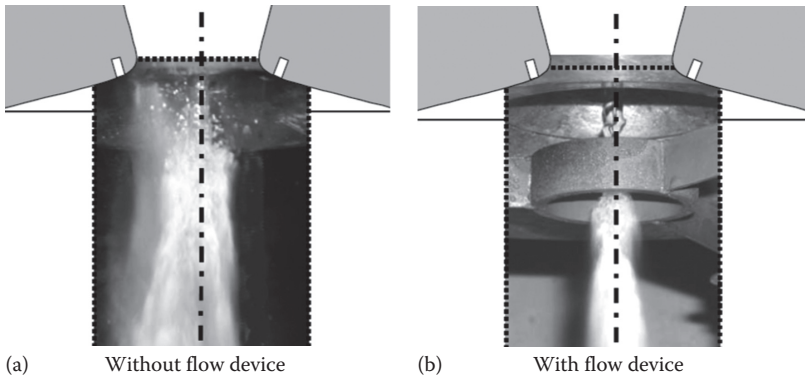


Figure 19.19

(a) Model experiments without Coanda-flow device. (b) Model experiments with Coanda-flow device (p_{sec} = 0.5 MPa, no primary gas, liquid mass flow rate 435 kg/h.) (From Czisch, C. and Fritsching, U., *Atom. Sprays*, 18, 511, 2008b. With permission.)

recirculation flow. The instability of the atomization is visible even as three-dimensional structure (asymmetric). When the Coanda-flow device is installed (Figure 19.19b), the atomization at secondary gas pressure 0.5 MPa (rel.) and without primary gas becomes stable, that is, no major recirculation in the atomization area occurs. Advantages of the flow-adapted atomizer design with Coanda-flow device are a reduction in gas consumption, as well as the potential of generation of small particles (Czisch and Fritsching, 2008b).

19.1.6 Primary Atomization

19.1.6.1 Flow Regimes and Flow Maps

For a first classification of liquid fragmentation in various configurations, the disintegration behavior of a liquid jet or sheet is subdivided into different atomization modes depending on the boundary conditions. As a result of several investigations, the disintegration behavior of a liquid has been globally classified, regimes have been identified, and interfaces between the different regimes have been correlated.

19.1.6.1.1 Single-Fluid (Pressure) Atomization This case holds for a liquid jet emerging into a quiescent gaseous atmosphere. Some examples for water atomization in a pressure nozzle are illustrated in Figure 19.20. Ohnesorge (1936) in an early investigation divided the breakup regimes of a circular liquid jet into three areas, depending on the liquid Reynolds number and a dimensionless number that

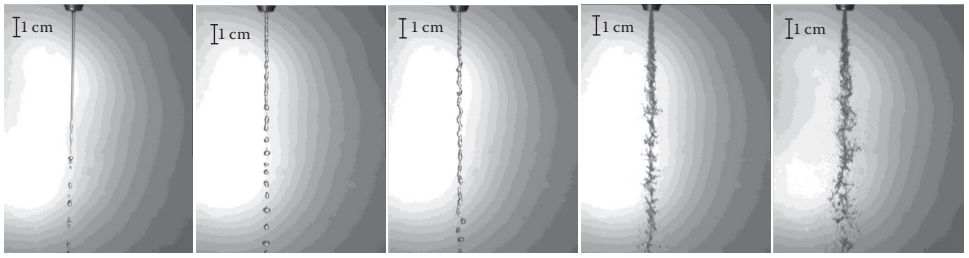


Figure 19.20

Disintegration of a liquid jet in pressure atomization, water, d_l = 1.5 mm.

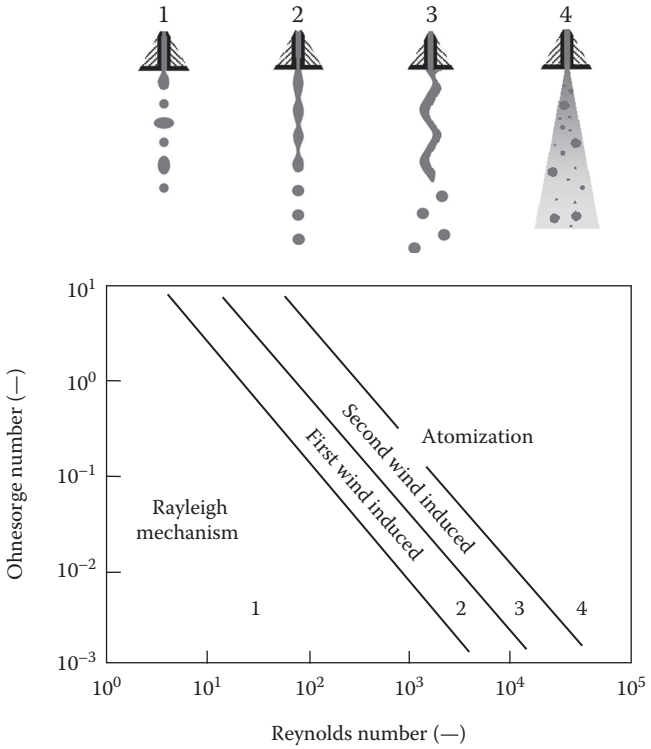


Figure 19.21

Primary fragmentation modes of a liquid jet in pressure atomization. (Adapted from Reitz, R.D., Mechanisms of breakup of round liquid jets, PhD thesis, Princeton University, Princeton, NJ, 1978.)

only contains liquid properties, later referred to as the Ohnesorge number (Oh) (Figure 19.21). These regimes have been further detailed, for example, by Haenlein (1932) and Reitz (1978).

1. At low Reynolds numbers, the jet disintegrates due to surface-tension effects (*Rayleigh regime (a)*, symmetric or varicose instability) into fairly identical droplet sizes.
2. At intermediate Reynolds numbers, drop formation is influenced by aerodynamic forces (non-axisymmetric Rayleigh breakup). These forces cause symmetric (*first wind induced mode (b)*) and asymmetric (*second wind induced mode (c)*, asymmetric or sinusoidal instability) wave growth of the gas/liquid interface that finally leads to jet disintegration.
3. At higher Reynolds number, the jet disintegrates almost spontaneously at the nozzle exit. This mode is called the *atomization regime (d)*.

The transition line from the Rayleigh mode to the aerodynamic mode is identified by

$$\mathrm{We}_l = \frac{1.74\times10^4}{\mathrm{Re}^{0.5}} \tag{19.33}$$

and the transition line between aerodynamic disintegration and the atomization mode is characterized as

$$\mathrm{We}_l = \frac{9.4\times10^5}{\mathrm{Re}^{0.5}} \tag{19.34}$$

19.1.6.1.2 Twin-Fluid Atomizer The first map of breakup regimes for a liquid jet in a coaxial gas flow was introduced by Faragó and Chigier (1992). Hopfinger (1998) introduced the momentum ratio between gas and liquid as an additional parameter (see also Lasheras and Hopfinger, 2000). The main disintegration modes are characterized in Figure 19.22, and some examples are illustrated in Figure 19.23.

1. At small aerodynamic Weber numbers, the jet mainly breaks up due to Rayleigh instabilities (*axisymmetric and nonaxisymmetric Rayleigh mode*).
2. If the Weber number is increased, ligaments are formed. The surface tension acts now at smaller scales. Owing to its smaller radius of curvature, the tip of the ligament recedes and a bulge is formed that may be blown up by the gas to form a membrane. This breakup regime is called the *membrane mode*.
3. At further increasing Weber numbers, the size of the ligaments decreases and the breakup occurs in the form of fibers (*fiber mode*).

Not enough data at present are available to identify the interfaces between the different regimes.

19.1.6.1.3 Pressure Swirl Atomizer In a pressure swirl atomizer, the liquid leaves the nozzle exit as a swirling conical sheet. The sheet disintegration proceeds differently depending on the action of the dominant forces on the sheet. As described in Fraser and Eisenklam (1953), Horvay (1985), Walzel (1982, 2012), Löffler-Mang, 1992, and Broll (2006), four modes of disintegration can be identified (see Figure 19.24), referred to as rim (or edge contraction), perforated, wave, and turbulent sheet disintegration, respectively, corresponding

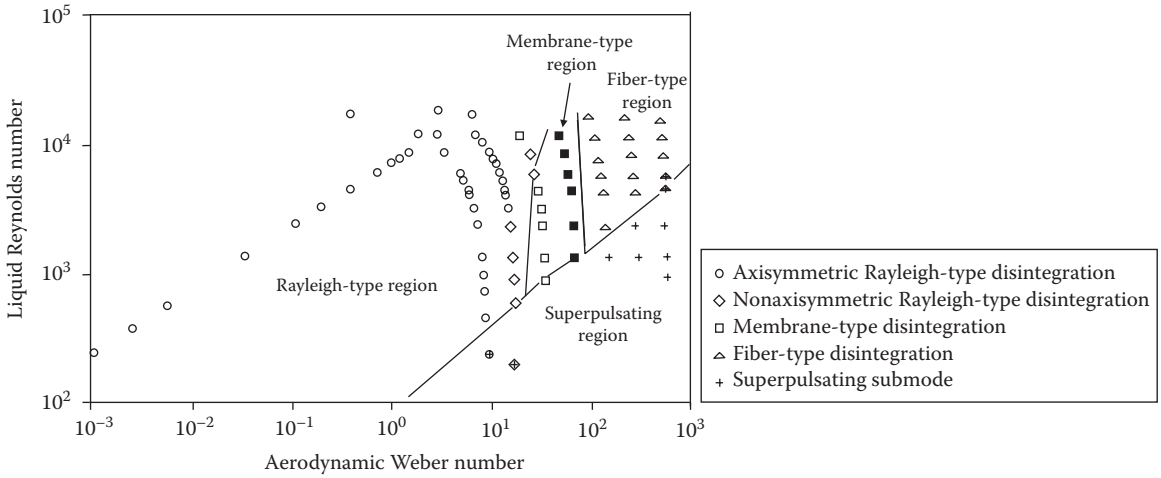
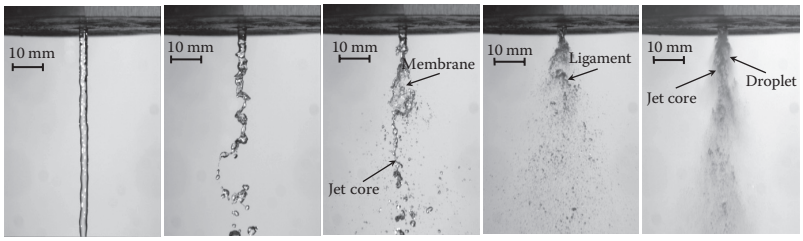


Figure 19.22

Disintegration modes in twin-fluid atomization. (Adapted from Faragó, Z. and Chigier, N., *Atom. Sprays*, 2, 137, 1992.)



$Re_l = 2727$ $We_g = 0$ | $Re_l = 2727$ $We_g = 7.9$ | $Re_l = 2727$ $We_g = 24$ | $Re_l = 2727$ $We_g = 168$ | $Re_l = 2727$ $We_g = 1022$

Figure 19.23

Atomization of a liquid jet in twin-fluid atomization with external mixing: main disintegration modes, $d_l = 3$ mm.

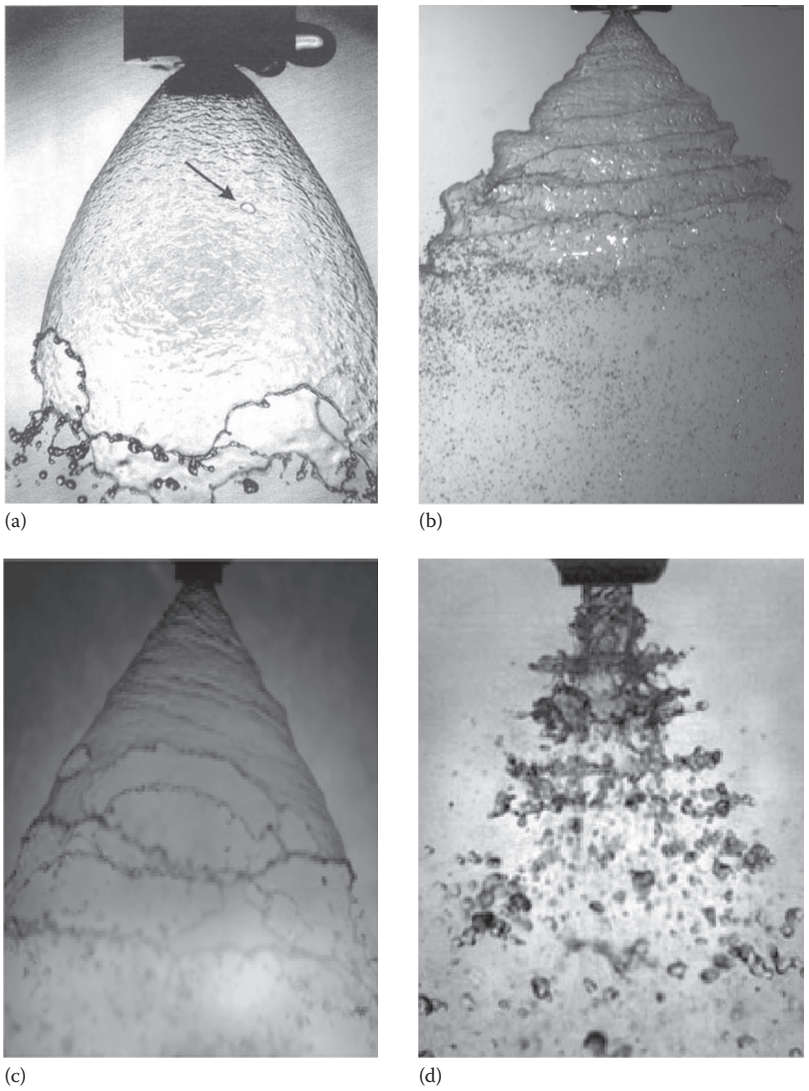


Figure 19.24

Mechanism of conical liquid sheet disintegration. (a) Rim-dominated breakup. (Adapted from Wozniak, G., *Zerstäubungstechnik: Prinzipien, Verfahren, Geräte*, Springer-Verlag, Berlin, Germany, 2003.) (b) Wavy breakup. (Adapted from Mulhem, B. et al., Break-up of hollow cone and flat suspension lamellae of pressure atomizers, in *Proceedings of ICLASS 2006*, Kyoto, Japan, August 27–September 1, 2006a.) (c) Perforation-dominated breakup. (Adapted from Prabhakaran, V.S. et al., Effect of temperature on atomization in gas centered coaxial injection systems, 2009, http://web.nmsu.edu/~sashi/iisc.pdf, date of access: 2013-06-20.) (d) Turbulent breakup. (From Sivakumar, D. and Kulkarni, V., *Exp. Fluids*, 51(3), 587, 2011. With permission.)

to different combinations of liquid inertia, liquid viscosity (μ_l), surface tension (σ), aerodynamic forces, and turbulence of the sheet. Different breakup modes usually coexist.

Walzel (2012) derived an upper limit for rim disintegration as

$$k^{1/2}\mathrm{We}_l < 370 \tag{19.35}$$

where $k = hz/A$ is the sheet number related to the sheet thickness h at some distance z from the nozzle exit and the cross-sectional area A of the nozzle exit. We_l is liquid Weber number based on the diameter at the liquid-nozzle exit (see Equation 19.6). Rim disintegration occurs at the edge of the film, where rims are formed due to the surface-tension-induced contraction and subsequently disintegrate into relatively large droplets. During the whole process, Rayleigh–Plateau (R-P) instability plays a dominating role. Figure 19.24a shows the rim-dominated breakup of a conical water sheet. The edge of the sheet is characterized by a relatively thicker fluid layer and goes through an asymmetric capillary instability (R-P instability). As soon as a drop is pinched off from the rim, the thickness of the rim suddenly drops to the sheet thickness. The sheet is pushed upward by the increased surface-tension forces due to the changed curvature at the rim, reducing the length of the sheet. A small perforation can be found on the intact liquid sheet.

For $k^{1/2}\mathrm{We}_l > 370$, the sheet begins to oscillate. With increasing distance, the quickly growing amplitudes of disturbances cause the sheet disintegration. Liquid ligaments are formed by contraction from the broken sheet and these ligaments subsequently break up into drops, as shown in Figure 19.24b. The majority of the breakup models explain this disintegration process based on aerodynamic sheet stability concepts (see Fraser et al., 1962, Dombrowski and Johns, 1963, Senecal et al., 1999, Nonnenmacher and Piesche, 2000, Mehring and Sirignano, 2004). These models assume the instabilities arising from the aerodynamic stimulation in the ambient gas (Kelvin–Helmholtz instabilities) lead to the sheet disintegration under conditions of low turbulence. However, the oscillations on the air core/liquid interface may also play an important role in the sheet disintegration by affecting the liquid surface inside the nozzle. The existence of helical waves on the surface of the liquid core inside the nozzle has been confirmed in experiments (Cooper and Yule, 2001, Donjat et al., 2003). These disturbances on the air core/liquid interface cause variations in liquid film thickness inside the nozzle. This effect may be in turn transported to the outside conical sheet and manifested by low amplitude three-dimensional waves appearing on the outside conical sheet, giving mechanism of disintegration into droplets. Low-frequency bands of disturbances on the outside conical sheet, which are in the same magnitude as on the air core/liquid interface inside the nozzle, were observed in experiments (Donjat et al., 2003, Landwehr et al., 2006).

Under conditions of low turbulence, experiments also indicate the formation of significant perforations on the sheet as a relevant mechanism of disintegration. The formation of perforations has been ascribed to a variety of cases including suspended solid particles, entrained air bubbles, drop impingement, and wave interactions (Spielbauer and Aidum, 1994). Figure 19.24c shows a typical perforation-dominated breakup of a conical hot-water sheet (82°C) formed by a gas-centered swirl coaxial atomizer. The perforations grow larger as the film extends radially and, finally, the ligaments between the perforations collapse into droplets. The waves on the intact sheet can also be observed as well as the contraction at the edges of perforations.

Turbulent sheet disintegration takes place due to the strong internal turbulence and/or the strong aerodynamic action of the ambient gas. In practice, the term liquid atomization is understood to mean turbulent sheet disintegration. Figure 19.24d shows the turbulent breakup of a conical water sheet from a gas-centered swirl coaxial atomizer. In the rim, wave, and perforated disintegrations, an intact axisymmetric liquid sheet can be observed. Such a feature is absent in the turbulent breakup where the liquid mass is fragmented into ligaments and droplets in the very near region of the orifice exit.

19.1.6.1.4 Rotary Atomizer The flow configuration and liquid condition (and therefore the effective atomization mode) at the rim of a rotating disk, where the fluid is continuously fed to the disk center, depends on the liquid flow rate, the disk rotational speed and size, and the liquid physical properties. A general division may be done based on the liquid feed rate as has been done by Hinze and Milborn (1950). For rotary atomization, the liquid Weber number is expressed as

$$\mathrm{We}_l = \frac{\rho_l \omega^2 d^3}{\sigma} \tag{19.36}$$

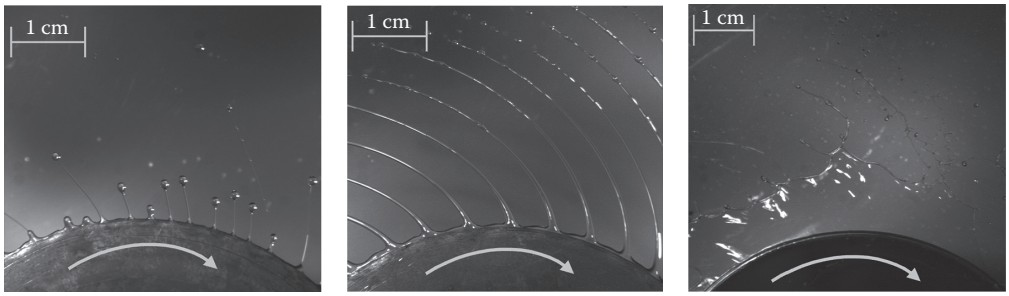


Figure 19.25

Main liquid disintegration modes in rotary atomization.

Main fragmentation modes in rotary atomization are illustrated in Figure 19.25 and may be analyzed as follows:

1. At low liquid flow rates, the liquid spreads out across the disk surface and is centrifuged off in the form of droplets with a narrow size spectrum. This mode is called the direct *drop formation mode (a)*.
2. If the flow rate is increased, ligaments are formed along the periphery that afterward are disintegrated into droplets. This mode is termed the *ligament formation mode (b)*. The number of ligaments increases with increasing flow rate up to a maximum value; beyond this maximum, it remains constant, regardless of flow rate. The thickness of the ligaments increases with flow rate.
3. With continuing increase in flow rate, a condition is finally reached where the ligaments have attained their maximum number and size and can no longer accommodate the flow of liquid. A thick film is produced that extends outward to some distance beyond the cup rim. When this film disintegrates into ligaments, it does so in an irregular manner, which results in a wider droplet size distribution. This disintegration mode is termed the *film formation mode (c)*.

For analysis of a wide range of liquid properties within rotary atomization, Brauer (1971) introduced as additional parameter the fluid number K_F

$$K_F = \frac{\rho_l \sigma^3}{\mu_l^4 g} \tag{19.37}$$

and the volume flow rate number

$$\dot{Q}^\star = \frac{\dot{Q}_l^2 \rho_l}{d^3 \sigma} \tag{19.38}$$

The breakup map for rotary atomization on a spinning disk is illustrated in Figure 19.26. The dimensionless ordinate and abscissa are labeled as

$$\Pi_y = \mathrm{We}^{0.5}\ \mathrm{Oh}^{0.922}\ K_F^{0.491}; \quad \Pi_x = \frac{\dot{Q}^{\star\ 0.5}}{\mathrm{Oh}^{0.47}\ K_F^{0.295}} \tag{19.39}$$

Transition between the individual breakup regimes is characterized in terms of the volume flow rate number, the liquid Weber number, and the Ohnesorge number by

$$\dot{Q}^\star\ \mathrm{We}_l^{0.25}\ \mathrm{Oh}^{0.835} < 2.08 \times 10^{-5} \tag{19.40}$$

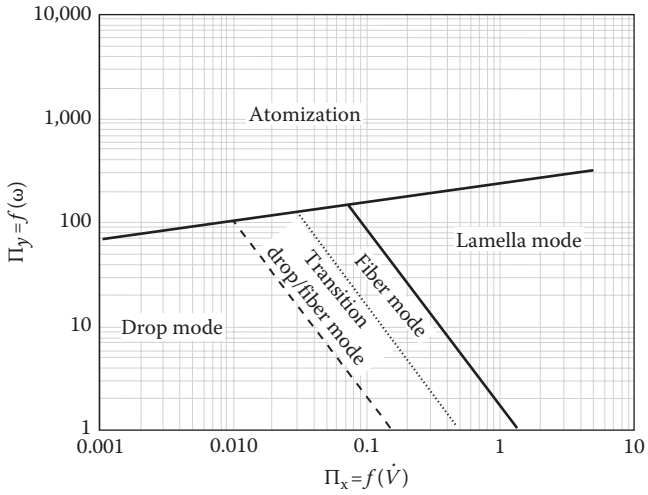


Figure 19.26

Disintegration modes map in rotary atomization. (Adapted from Brauer, H., *Grundlagen der Einphasen-und Mehrphasenströmungen*, Sauerländer Verlag, Frankfurt, Germany, 1971.)

for the transition from drop formation mode to ligament formation mode and

$$\dot{Q}^{*}\,\mathrm{We}_l^{0.6}\,\mathrm{Oh}^{0.835} > 1.77 \tag{19.41}$$

for the transition from fiber formation to film formation mode.

19.1.6.2 Continuous Jet Length

The continuous jet breakup length is an important parameter characterizing the atomization process that determines the region of the liquid jet where the liquid (at least in the center of the jet) remains as a continuous medium. The breakup length is taken as the distance from the nozzle exit to the breakup point. The general behavior of the breakup length versus the liquid jet velocity is illustrated in Figure 19.27. The initial part of the curve is described as the dripping region of the jet. From point A to point B, the laminar

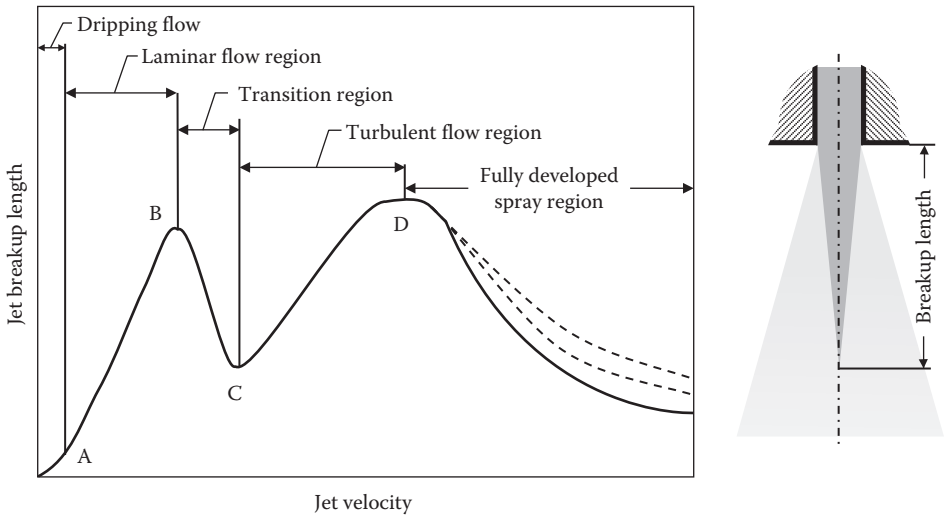


Figure 19.27

Breakup length in different modes.

flow region is located, where symmetric Rayleigh instabilities prevail. Here, the breakup length is linearly increasing and has been empirically determined as (Grant and Middleman, 1966)

$$\frac{L}{d_0} = 19.5\,\mathrm{We}_l^{0.5}(1+3\,\mathrm{Oh})^{0.85} \tag{19.42}$$

The upper point B indicates the transition from varicose to sinusoidal breakup mode. It has been correlated from experiments by Grant and Middleman (1966) for a laminar (fully developed) velocity exit profile of the jet as

$$\mathrm{Re}_{crit} = 3.25\,\mathrm{Oh}^{-0.28} \tag{19.43}$$

In the transition region B to C, the breakup length decreases. When the fluid at the nozzle exit is already in a turbulent flow stage and/or aerodynamic interaction between the liquid jet and the gas dominates the breakup, from point C to D, the jet breakup length increases with increasing velocity (see Walzel, 1980b, 1990, 1999). Here, Grant and Middleman (1966) proposed the empirical relationship

$$\frac{L}{d_0} = 8.51\,\mathrm{We}^{0.32} \tag{19.44}$$

The behavior of the liquid jet breakup length at jet velocities beyond point D is not uniquely defined yet but in general tends to decrease.

19.1.6.3 Stability Analysis

A cylindrical fluid element in a quiescent gaseous atmosphere is inherently unstable. Small perturbations of the surface (at wavelengths $\lambda > \pi d_l$) will always tend to grow. The first stage of the liquid jet disintegration process in atomization is described by an initial perturbation of the liquid/gas interface and next by the growth of surface waves of/on the liquid. Instability itself, for example, is promoted by the formation of the surface tension, leading to a local pressure distribution on the phase boundary depending on the local liquid surface curvature. A first quantitative analytical description of this process has been successfully given by Rayleigh (1878). In his contribution, a derivation of the fundamental system of describing energy conservation equations (by neglecting viscous contributions) and solution of the resulting equation system is performed. Rayleigh's analysis is limited to the case of sinusoidal initial perturbations of small amplitude. The liquid jet that is affected by surface-tension forces will become unstable only in the event of any axisymmetric disturbance whose wavelength satisfies the following equation:

$$\lambda_\delta < \pi d \tag{19.45}$$

For asymmetrical disturbances, the system is always stable. Rayleigh showed that the exponential growth of the fastest growing disturbance is given by

$$q_{\max} = 0.97\left(\frac{\sigma}{\rho_l d^3}\right)^{0.5} \tag{19.46}$$

and the corresponding wavelength of the fastest growing wave is

$$\lambda_{opt} = 4.51d \tag{19.47}$$

A spherical drop forms from the separate ligament (cylinder of length $4.51d$) due to surface-tension force at equal volumes and finally the resulting drop size becomes

$$d_p = 1.89d \tag{19.48}$$

This relation is used, for example, in droplet generators to produce monosized droplets by excitation of the liquid jet at its most unstable wavelength-corresponding frequency (see Figure 19.20).

Weber (1931) investigated in continuation of Rayleigh's work the viscous system. He neglected inertial effects and this solution is also only valid for small initial perturbations. He also found an exponential growth of small perturbations at unstable wavelengths. The ranges of process parameters and liquid properties in real atomization processes afford the inclusion of viscous effects (boundary layer) of the gas flow field. The upper limit for which the inviscid assumption in the instability process can be made with tolerable error in the case of a planar liquid sheet has been derived by Cousin and Dumouchel (1996). The result is summarized in terms of a limiting dimensionless number. The influence of viscous forces on the jet disintegration can be neglected if the dimensionless number M_c is

$$M_c = \frac{\mu_l \rho_g^2 u_{rel}^3 h_f}{\rho_l \sigma^2} < 10^{-3} \tag{19.49}$$

where the properties of the gas (subscript g) and of the liquid (subscript l), the relative velocity between gas and liquid u_{rel}, and the liquid film thickness h_f are used.

Starting from the pioneering works of Rayleigh and Weber, the following analytical stability analyses also are generally limited by one or more basic simplifying assumptions, such as the neglect of viscosity effects of either gas and/or liquid, the partial neglect of inertial effects, or the limitation of small initial perturbation amplitudes.

Investigations of jet instability processes in the area of small perturbation wavelengths (aerodynamic interaction and liquid disintegration), based on the linearized conservation equations and partially neglecting inertial effects and gas viscosity (neglecting the gas boundary layer), were performed for the first time by Taylor (1949, 1959). If, in addition, the liquid viscosity is neglected, this result leads to the classical case of the aerodynamic fluid disintegration based on Kelvin–Helmholtz instability.

A stability analysis that is independent of the ratio of wavelength to jet diameter λ_d/d has been performed by Mayer (1993) based on the contributions of Taylor (1949) and Reitz (1978). The reference system in this analysis moves with the fluid velocity u_l and the results are related to the relative velocity between gas and liquid $u_{rel} = u_g - u_l$. The complex formulation is based on a perturbation of the basic flow in the form of a surface wave with the amplitude

$$\eta_s = \text{real}\left(\eta_0 e^{ikx+im\theta+\omega t}\right) \tag{19.50}$$

where

$k = 2\pi/\lambda_d$ is the wave number

m is the mode of the perturbation

the parameter $\omega = \omega_r + i\omega_i$ is the complex growth rate of the perturbation

The real part of the complex growth rate $\text{Re}(\omega) = \omega_r$ describes the reaction function of the liquid jet by external excitation and the behavior of the perturbation. For negative growth rates $\omega_r < 0$ the perturbation will be damped out, positive growth rates $\omega_r > 0$ will lead to an exponential growth of the initial wave. In this derivation, the linearized flow conservation equations for gas and liquid are solved, based on the introduction of the stream function ψ and the velocity potential ϕ and the related perturbation formulations. Here, the velocity distribution of the gas is neglected, resulting in a velocity jump at the phase boundary between liquid and gas. The solution of the equation system is

$$\omega^2 - 2\frac{\mu_l}{\rho_l}k^2\omega\frac{I_1'(kr_0)}{I_0(kr_0)}\left[1 - \frac{1kl}{k^2+l^2}\frac{I_1(kr_0)}{I_0(kr_0)}\right] = \frac{l^2-k^2}{l^2+k^2}\frac{I_1(kr_0)}{I_0(kr_0)}\left\{\frac{\sigma k}{\rho_l r_0^2}\left[1-(kr_0)^2\right] + \frac{\rho_g}{\rho_l}\left(u_{rel} - \frac{i\omega}{k}\right)\frac{K_0(kr_0)}{K_1(kr_0)}\right\} \tag{19.51}$$

This contains the modified Bessel functions I_n and K_n of nth order and their derivatives I', as well as $l^2 = k^2 + \omega/\nu_l$. From the general solution in Equation 19.50, some specific cases can be derived, which will be discussed in the following.

19.1.6.3.1 Large-Wavelength Area When aerodynamic effects are neglected as well as the fluid viscosity, the gas density and also the relative velocity between fluid jet and gas flow field, the classical solution of Rayleigh (1878) is obtained:

$$\omega^2 - \frac{\sigma}{\rho_l r_0^2} k\left[1-(kr_0)^2\right]\frac{I_1(kr_0)}{I_0(kr_0)} = 0. \tag{19.52}$$

In this equation, I_0 and I_1 are the Bessel functions of zero and first order. As already mentioned, perturbations with wavelengths $\lambda > \pi d_l$ are unstable, resulting always in positive growth rates. If in the total unstable wave spectrum only the particular wavelength with maximum growth rate is considered (the fastest growing wave of all unstable waves, maximum of the instability function), the analysis ultimately leads to the classical case of the Rayleigh disintegration of a liquid jet.

19.1.6.3.2 Small-Wavelength Area In the case of an inviscid flow, the area of small wavelengths is the classical Kelvin–Helmholtz instability as derived by Bradley (1973a,b) for the excitation of the primary disintegration process in the area of small wavelengths within coaxial atomization of liquids.

In the limiting case of very small wavelengths ($\lambda \ll d_l$), the solution of the instability problem leads to

$$\left(\omega + 2\nu_l k^2\right)^2 + \frac{\sigma}{\rho_l}k^3 - 4\nu_l^2 k^2\sqrt{k^2\frac{\omega}{\nu_l}} + \xi_g(\omega + iu_{rel}k)^2\frac{\rho_g}{\rho_l} = 0. \tag{19.53}$$

Introduced in this solution is an assumption for the viscosity influence of the gas flow on jet stability, which has been derived by Sterling and Schleicher (1975). These authors found that accounting for boundary layer effects of the gas flow field stabilizes the wave growth. This can be taken into account as a damping effect of the perturbation pressure on the liquid jet surface. The factor ξ_g is related to this influence where

- $\xi_g = 1$ corresponds to inviscid gas flow
- $\xi_g = 0.8$ accounts for a turbulent boundary layer profile of the gas flow field at the phase boundary between liquid and gas.

In a similar way, Miles (1957, 1958, 1960, 1961) already has taken into account the turbulent boundary layer character of the gas flow field at the phase boundary. By neglecting the gas viscosity, the turbulent logarithmic velocity profile in the fully turbulent region is expressed in terms of a suitable pressure distribution on the wavy liquid surface (see also Bürger et al., 1989, 1992).

Generally from the analyses of aerodynamic disintegration behaviors, the influence of surface tension is found to have a stabilizing effect (shifting of the maximum unstable wavelength towards lower values) and the influence of fluid viscosity is characterized as having a damping effect (lowering of the amplitude of the growth rate while keeping constant the value of the wavelength with maximum growth rate). Increasing the relative velocity between gas and liquid phase always has a destabilizing effect.

The instability of a liquid/gas phase boundary of a jet or sheet is divided into several modes, which are to be described by their specific spatial growth function. Besides the symmetric mode ($m = 0$) of wave growth of phase boundaries, the liquid jet may tend to a long waved oscillatory movement (asymmetric jet oscillations, see Figure 19.28). By neglecting the gas and liquid viscosities and the region of high relative velocities between gas and liquid, a stability analysis of the first asymmetric mode ($m = 1$) of a liquid jet has been given by Levich (1962):

$$\omega^2 + \rho_g k^4 r_0^2 u_{rel}^2\frac{(\ln(kr_0/2))}{2\rho_l} - \frac{\sigma k^2}{2\rho_l r_0}\left(1 - m^2 - k^2 r_0^2\right) = 0. \tag{19.54}$$

In the case of a planar liquid sheet, Hagerty and Shea (1955) have shown that an inviscid fluid shows higher values of the growth rate in the asymmetric mode than in the symmetric mode. Here, the asymmetric mode is always dominant.

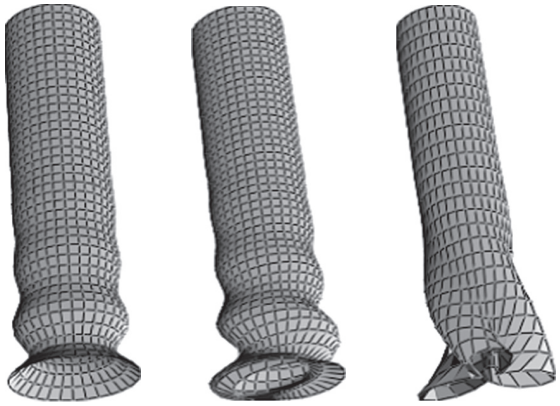


Figure 19.28

Instability modes of a circular liquid jet.

A comparison of the initial stability for laminar and turbulent liquid jet conditions has been made by Mansour and Chigier (1994). The growth rates of initial disturbances have been found to be the same for both laminar and turbulent conditions in agreement with the analysis of Weber (1931). For laminar flow conditions, the optimum wavelength corresponding to the fastest-growing disturbance is $\lambda_{opt} = 4.45 d_0$, which is in agreement with the theoretical value from Weber´s solution of the stability problem. For turbulent flow conditions, $\lambda_{opt} = 9.2 d_0$ has been found, which is approximately twice the optimum wavelength calculated in theory.

Despite the relatively crude assumptions and simplifications, which have to be made to apply linear stability analyses, the use of linear theory has a number of advantages when used as a first step for general analysis of fluid atomization process. First, the linear stability analysis is based on simple assumptions and second, the mathematical efforts for the solution are quite small. This makes the handling of this method easy. Linear stability analyses deliver general stability criteria and trends for the liquid/gas system under investigation and allow calculation of wavelengths and growth rates that mainly cover the disintegration process. An overview of classical solutions for the system of linear ordinary differential equations in the frame of linear stability analyses has been given by Markus et al. (2000). But, as will be described in the following, in comparison to experimental results in technical applications, linear stability analysis typically overpredicts the wavelength by up to one order of magnitude (Markus et al., 2000, Klein et al., 2002).

Nonlinear stability analyses, taking into account some of the simplifications necessary to carry out linear theories, have been reported in the literature for some actual cases and geometrical boundary conditions. The resulting system of conservation equations is solved in the sense of stability analysis using a perturbations approach or by numerical analysis with discrete perturbations (see, e.g., Shokoohi and Elrod, 1987, Dumouchel, 1989, Rangel and Sirignano, 1991, Panchagnula et al., 1998).

For illustration, the results of a linear stability analysis based on these assumptions for a coaxial twin-fluid atomizer with external mixing and the reference system water/air with a liquid jet diameter of $d_l = 2$ mm will be discussed. The results in terms of growth rates for the symmetric mode ($m = 0$, short wave length perturbations) and the asymmetric case ($m = 1$, long wave length perturbations) are shown in Figure 19.29 and 19.30, respectively, for a variation of the relative velocity between coaxial atomizer gas and central liquid. The principal influence of process parameters on the phase boundary excitation can be shown. The relative maximum of each growth rate curve stands for the fastest growing wavelength. Comparing the symmetric mode and the asymmetric mode in this example shows that here the symmetric perturbations always yield higher growth rates than the asymmetric ones. Therefore, the symmetric jet behavior should finally lead to disintegration of the jet in this case. This result cannot be confirmed by experimental studies for these boundary conditions (Faragó and Chigier, 1992, Hardalupas et al., 1997). Hardalupas et al. (1997), experimentally analyzing the spray from a similar type of nozzle, found only a small number of droplets that are immediately sheared from the phase boundary at small wavelengths. These droplets make only a small contribution to the resulting spray; therefore, the results of the stability analysis here need to be scrutinized or extended to more realistic boundary conditions. In addition, the linear evaluation from Figure 19.30 also

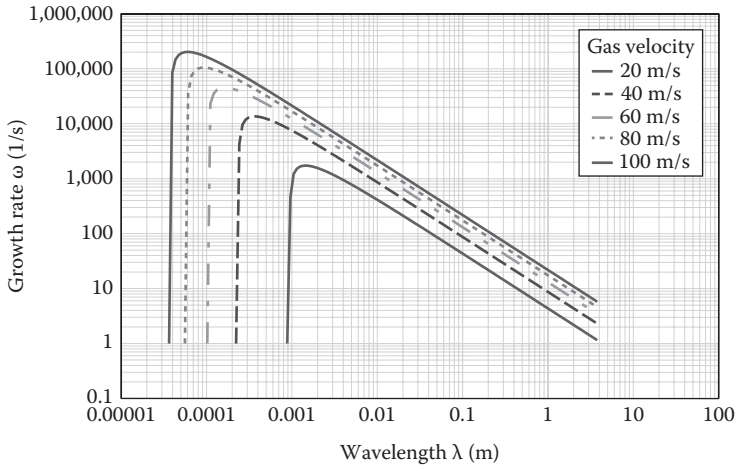


Figure 19.29

Instability growth rates of varicode mode in twin-fluid atomization of circular water jet (d_l = 2 mm, m = 0).

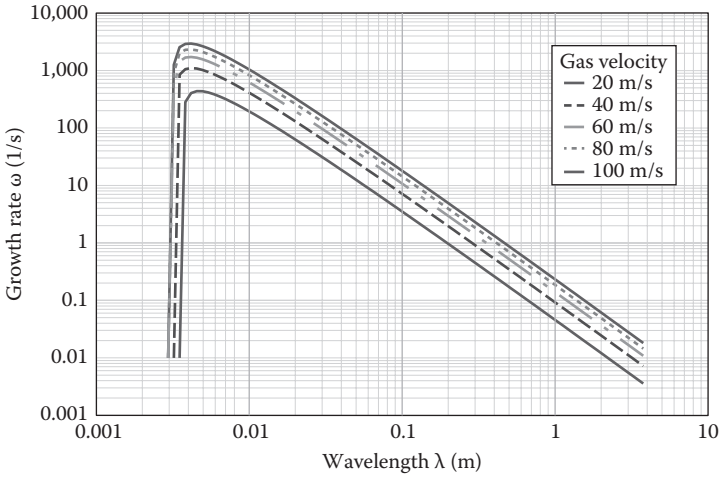


Figure 19.30

Instability growth rates of asymmetric mode in twin-fluid atomization of circular water jet (d_l = 2 mm, m = 1).

indicates that the wavelengths having the maximum growth rate show only a small dependence on the relative velocity between fluid and gas. This result is confirmed by experimental atomization investigations by Hardalupas et al. (1997).

The behavior of the jet changes for varying liquid properties. Here, especially liquid metals show remarkable differences as these have high surface tension at comparably low viscosity. Comparison of different modes of stability for a jet of molten metal in a coaxial gas flow has been discussed by Markus et al. (2000) based on the solution of the stability problem provided by Li (1995). Results for growth rates of different metal melts are shown in Figure 19.31a and results for the three basic modes of instability (m = 0, 1, and 3) for a molten steel jet are illustrated in Figure 19.31b. The results are calculated for a jet diameter of d_l = 4 mm moving at a velocity of u_l = 2 m/s in a coaxial gas flow at a constant velocity of u_g = 100 m/s. The influence of material properties on melt jet stability is observed in the left. Here, mainly the effect of the surface tension, increasing from tin (σ = 0.544 N/m) via copper (σ = 1.31 N/m) to steel (σ = 1.83 N/m), can be observed. Increasing values for surface tension result in decreasing Weber numbers, which finally also result in smaller amplitudes of the growth rate. In the same way, the dominant wavelength of jet disintegration increases. In comparison to water jets, the growth rates for molten metal jets are much lower. Here, somewhat higher energies (relative gas velocities) are needed to achieve atomization characteristics similar to water atomization. At higher relative velocities, the higher instability modes become more significant.

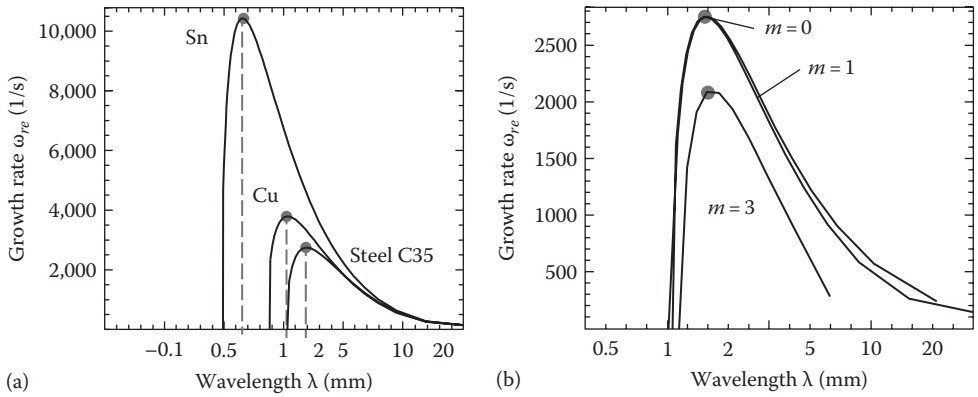


Figure 19.31

Stability curves for liquid metal jets (From Markus et al., 2002. With permission.), (a) Different metal melts and (b) basic instability modes.

Maximum growth rates in this case are observed for the symmetric mode $m = 0$; the asymmetric growth mode $m = 1$ has almost identical growth rates, while higher modes show maximum growth rates at much smaller values (see Figure 19.31b).

A comparison of calculated growth rates and wavelengths with high-speed video pictures for primary perturbation of tin and steel melt jets in Markus et al. (2000) have shown that the theoretical calculated wavelengths are smaller than observed in the experiments by one order of magnitude. This same trend has also been found by comparing experiments and direct numerical simulations (DNSs) and the results from linear theory for atomization of liquid sheets, for example, by Klein et al. (2002). However, a superposition of different modes with adapted growth rates (which do not match those in Figure 19.31) results in a quite good representation of the relevant processes of the primary perturbations of the liquid tin melt jet just in front of the exit of the atomizer nozzle. In Figure 19.32a, a picture of a primary excitation of a tin melt jet within a twin-fluid atomizer is compared to a simulated picture of the superposed three main instability modes in Figure 19.32b.

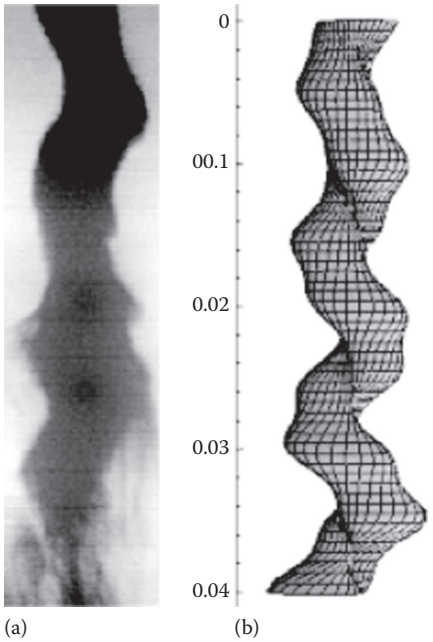


Figure 19.32

Superposition of instability modes (a) and comparison with experiment (b). (From Markus et al., 2002. With permission.)

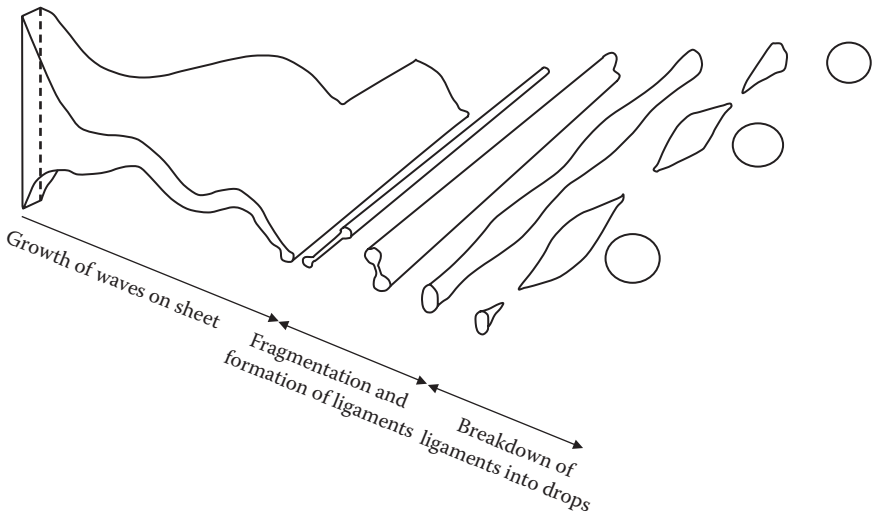


Figure 19.33

Principle of aerodynamic disintegration of a planar liquid jet. (Adapted from Dombrowski, N. and Johns, W.R., *Chem. Eng. Sci.*, 18, 203, 1963.)

In the introduced initial models for gas/liquid interface instability, the focus is on the excitation and initial growth of surface perturbations on/of the liquid jet. In a further step of fragmentation analysis, it needs to be defined when (or where) a growing liquid element is separated from the excited liquid jet (primary droplet or ligament formation). An initial analysis for derivation of the jet disintegration model and a correlation equation for the resulting droplet size distribution have been performed by Dombrowski and Johns (1963). These authors discuss (for the plane liquid jet emerging from a planar slit nozzle) the aerodynamic disintegration behavior, as illustrated in Figure 19.33. Starting from the growth of an instability on the interface, at first in longitudinal direction plane, liquid elements or ligaments are separated from the jet, which are deformed to cylindrical elements further downstream. In the next step, these cylindrical ligaments disintegrate due to capillary instabilities (Rayleigh) into the fragments that form the resulting droplet structure in the initial spray by the action of surface tension.

Additional refinements of such fundamental models for primary disintegration within twin-fluid atomization are based on a more detailed analysis of the liquid stripping mechanism from the liquid surface and the description of the most relevant wavelengths at highest growth rates. Here, the work of Berg et al. (1995) and Bürger et al. (1989, 1992) provide useful and detailed correlations. These authors observed, in agreement with Jeffrey (1924), that the gas flow field interacting with the wave in its critical condition results in a stripping mechanism just on the wave crest and not on the whole wave volume, while the mean height of the wave in its temporal average remains practically unchanged. A principal sketch of this model is shown in Figure 19.34. The turbulent boundary layer character of the gas flow is taken into account using a linear stability analysis of the liquid jet as in the model of Miles (1957). Starting from an energy balance at the wave crest, where the work done by the gas flow on the wave crest

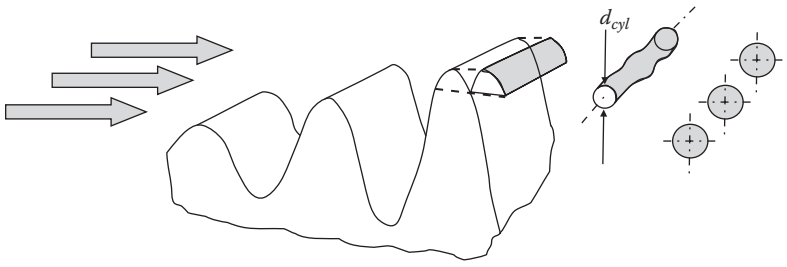


Figure 19.34

Stripping of a liquid fragment from the wave crest of a liquid sheet. (Adapted from Bürger, M. et al., *Powder Metall. Int.*, 21(6), 10, 1989.)

is related to the free surface energy that is created by the newly generated liquid surface, the critical wave height for stripping $\Delta h = \eta_{ab} - \eta_B$ is calculated as follows:

$$\Delta h = \frac{4\sigma}{C_d \rho_g u_{rel}^2} \tag{19.55}$$

In this model, a resistance coefficient C_d is introduced for the gas flow at the wave crest. This coefficient takes either a constant value (Bürger et al., 1984) or, alternatively, is derived from the local pressure distribution at the wave geometry (Bürger et al., 1992). In the latter, the resistance coefficient depends on the local height of the wave. The basic height of the wave η_B is taken as constant with a value of half of the wavelength (length to height ratio of the wave is $l/d = 2$). From this value, the variable diameter of the stripped liquid elements (in the case of a cylindrical element) d_{cyl} is derived.

A two-stage liquid fragmentation model based on stability theory has been introduced by Fritsching (2001) for coaxial twin-fluid atomization (round liquid jet) and a similar model for ring film disintegration by Lund et al. (1993). These models combine a stability analysis in the first stage, resulting in primary fragmentation of the liquid stream with a Rayleigh breakup model to derive the final drop size distribution in the spray. Input parameters of the models have been obtained by experimental and/or numerical flow field studies.

As a refinement of a modeling approach for liquid disintegration, the primary liquid fragmentation process has been coupled directly into a two-phase flow simulation in the disintegration area. Here, the behavior of both phases is simultaneously analyzed based on full conservation equations. In the first step, the stepwise stripping of fluid elements from the central jet is calculated. From this, the resulting decrease of the liquid mass within the remaining liquid jet is obtained. The contribution of the stripped fluid ligament to the successive fragmentation process and the resulting drop size distribution are calculated. In the next step, the development of the now reduced liquid jet diameter is directly related to the local gas flow field at that particular location. The stripped fluid drops and ligaments are introduced as source terms for mass and momentum in the calculation of the multiphase flow field. The continuation of the fragmentation process leads to successive stripping and smaller jet diameter. The coupling and interaction between the phases is treated in this manner. The calculated local drop size contributions of the discrete stripping events are combined to yield the final droplet size distribution in the spray. The initial configuration of the spray after atomization is derived in this way. An ongoing further fragmentation of these droplets due to secondary atomization processes is not taken into account and, therefore, the finest droplets in the calculated droplet size distribution are underrepresented (see Section 19.1.7).

19.1.6.3.3 Liquid Instability Sheet Atomization (LISA) Model A commonly used breakup model for liquid sheet fragmentation in CFD codes is the LISA model proposed by Senecal et al. (1999) and Schmidt et al. (1999). The LISA model was developed based on aerodynamic sheet stability concepts (see Figure 19.33). In the LISA model, the initial film thickness (h_0) and the injection velocity is estimated based on mass conservation, nozzle dimensions, and discharge efficiency. The model takes into account the effects of liquid viscosity, surface tension, and the surrounding gas. The LISA model assumes that wave oscillations on the liquid sheet cause its breakup into ligaments and finally into droplets. The calculated breakup length of the liquid sheet and the size of the resulting drops using a linear instability analysis can be used as a starting point of an integral spray model.

In the LISA model, the sheet is assumed to be broken into ligaments when the wave amplitude (η) reaches the local sheet thickness (h). The breakup length (L) for long waves is given by

$$L = U_{abs}\left(3\ln\left(\frac{\eta_b}{\eta_0}\right)\right)^{2/3}\left(\frac{J\sigma}{(\rho_g/\rho_l)^2 U_{rel}^2 \rho_l}\right)^{1/3} \tag{19.56}$$

and for short waves by

$$L = \frac{U_{abs}}{\omega_{max}}\ln\left(\frac{\eta_b}{\eta_0}\right) \tag{19.57}$$

where η_0 and η_b are the initial disturbance amplitude and the amplitude at the breakup point, respectively, the quantity $\ln(\eta_b/\eta_0)$ is given a value of 12, J is a constant, ω_{max} is the maximum wave growth rate, and U_{abs} and U_{rel} are the absolute sheet velocity and liquid/gas relative velocity, respectively.

For long waves in the limit of ($\rho_g/\rho_l \ll kh/2$), ω_{max} is given by

$$\omega_{max} = \max\left[-2\frac{\mu_l}{\rho_l}k^2 + \sqrt{4\left(\frac{\mu_l}{\rho_l}\right)^2 k^4 + \frac{\rho_g}{\rho_l}\frac{2U_{rel}^2 k}{h} - \frac{2\sigma k^2}{\rho_l h}}\right] \tag{19.58}$$

If short waves are assumed for high-speed sheets and ($\rho_g/\rho_l \ll 1$), ω_{max} is given by

$$\omega_{max} = \max\left[-2\frac{\mu_l}{\rho_l}k^2 + \sqrt{4\left(\frac{\mu_l}{\rho_l}\right)^2 k^4 + \frac{\rho_g}{\rho_l}U_{rel}^2 k^2 - \frac{\sigma k^3}{\rho_l}}\right] \tag{19.59}$$

The wave number k is related to the wavelength by $k = 2\pi/\lambda$. The transition from a long wavelength regime to a short wavelength regime is found to occur at a gas Weber number of $We_g = 27/16$. The gas Weber number is based on the liquid velocity, gas density, and half sheet thickness. Below the critical Weber number, instability due to long waves is dominant, while at higher Weber numbers, short waves occur with a wave rate growth independent of the sheet thickness.

In the LISA model, ligaments are assumed to form from the sheet fragmentation at the point of breakup. For the case of long waves, it is assumed that the ligaments are formed from tears in the sheet twice per wavelength and the resulting diameter is given by

$$d_L = \sqrt{\frac{4h_b}{K_s}} \tag{19.60}$$

where K_s is the most unstable wave number and given by

$$K_s = \frac{\rho_g U_{rel}^2}{2\sigma} \tag{19.61}$$

On the other hand, for short wave growth, it is assumed that the ligaments are formed from tears in the sheet once per wavelength and the resulting diameter is given by

$$d_L = \sqrt{\frac{8h_b}{K_s}} \tag{19.62}$$

where K_s is given by Equation 19.59. The film thickness at the point of breakup (h_b) can be calculated from the breakup length (L), the spray cone angle (α), and the radial distance from the centerline to the midline of the sheet at the nozzle exit (R_0) as

$$h_b = \frac{R_0 h_0}{R_0 + L\sin(\alpha/2)} \tag{19.63}$$

If it is assumed that breakup occurs when the amplitude of the unstable waves is equal to the radius of a ligament, one drop will be formed per wavelength. The drop diameter based on a mass balance is given by

$$d_d = 1.88 d_L (1 + 3\mathrm{Oh})^{1/6}, \quad \text{with } \mathrm{Oh} = \frac{\mu_l}{(\rho_l \sigma d_L)^{1/2}} \tag{19.64}$$

where Oh is the Ohnesorge number.

19.1.6.3.4 Stability of Threads in Cross-Flow Fragmentation of gravity-stretched laminar threads in gas cross-flows at low gas-relative velocities was experimentally investigated by Mescher et al. (2012), where axisymmetric threads emerging from vertically arranged and completely filled circular nozzles are significantly attenuated due to gravity until breakup occurs. The influence of the liquid flow rate, the liquid properties, and the gas cross-flow were chosen close to a typical technical application of stretched threads, that is, at the laminar operated rotary atomization (LAMBOT) process. Viscosity and liquid flow rate were confirmed to be important influences on the breakup process. Intensified gas cross-flows were found to lead to a decreasing breakup length (as shown in Figure 19.35), this is consistent with the theory for cylindrical jets. However, the mean drop size was found to increase at higher gas-relative-velocities, this is in contradiction to the theory for cylindrical jets. The increase of the drop size can be explained by larger breakup diameters of the threads due to shorter breakup lengths at higher gas-relative-velocities. The drop size is a function of both the dominating wave number (representing the breakup wavelength) and the breakup diameter. On the one hand, increased gas-relative-velocities should lead to higher dominating wave numbers and thus, theoretically, to smaller droplets. On the other hand, the breakup length decreases due to the faster growth of perturbations. For almost cylindrical jets, the influence of cross-flow intensities on the breakup wavelength may dominate. In contrast, stretched threads still significantly attenuate close to the breakup point. A distinctly increased breakup diameter occurs for a reduced breakup length. Then, the alteration of the breakup wavelength may be overcompensated and larger drops can be observed. In the range of low gas-relative-velocities, an increasing diameter of the shorter threads could be identified to cause the larger drops. At high cross-flow intensities and especially for thin threads, a fully altered nonaxisymmetric breakup mode (or wind-induced breakup) occurs. The critical gas Weber number ($We_{g,crit}$), characterizing the transition between different breakup modes, is related to the nondimensional volumetric liquid flow rate ($\dot{V}_l^\star$) and the nondimensional viscosity ($\mu^\star$):

$$We_{g,crit} = 1.92\dot{V}_l^{\star 0.15}\mu^{\star -0.39}, \quad \text{with } \dot{V}_l^\star = \dot{V}_l\left(\frac{g^3\rho_l^5}{\sigma^5}\right)^{0.25} \quad \text{and} \quad \mu^\star = \mu\left(\frac{g}{\rho_l\sigma^3}\right)^{0.25} \tag{19.65}$$

where

g is the gravitational acceleration
ρ_l is the liquid density
μ is the liquid viscosity
σ is the surface tension

The span of the DSD (drop size distribution) also increases at higher gas-relative-velocities. Correlations for the breakup length ($L^\star$), the mass-median drop size ($d^\star$), and the span of the DSD were formulated:

$$L_0^\star = 48.24\dot{V}_l^{\star 0.732}(1 + 0.679\mu^\star)^{2.375} \tag{19.66}$$

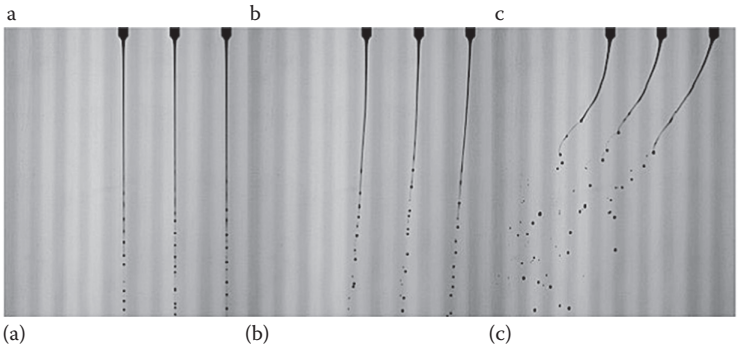


Figure 19.35

Backlight images of thread breakup in gas cross-flow. Experimental parameters: three nozzles of an inner diameter of D = 10 mm were mounted. The impact angle of the gas cross-flow was α = 90°. Glycerol/water mixture, viscosity: μ = 140 mPa s, volume flow rate per nozzle 4.4 L/h, gas Weber numbers: (a) 0, (b) 0.3, and (c) 3.3.

$$L^\star = L_0^\star - 12.56(1+\dot{V}_l^\star)^{0.996}(1+\mu^\star)^{-0.538}\mathrm{We}_g^{0.249(1+\mu^\star)^{1.906}} \tag{19.67}$$

$$d^\star = 1.043\dot{V}_l^{\star 0.259}\mu^{\star 0.038}(1+139.65\mathrm{We}_g)^{0.248(1+4.12\times10^5\mu^\star)^{-0.206}} \tag{19.68}$$

$$\mathrm{span} = (1.616 - \exp(-5.446\mathrm{We}_g - 0.605))\cdot(0.099\mu^{\star 0.364}\mathrm{We}_g + 0.183\mu^{\star -0.128}) \tag{19.69}$$

Here, the nondimensional breakup length ($L^\star$), the nondimensional mass-median drop size ($d^\star$), and the gas Weber number (We_g) are based on the capillary length $L_c = (\sigma/\rho_l g)^{0.5}$.

Kamplade et al. (2014) investigated the breakup of initially nonaxisymmetric laminar threads from open channel flow and from oval nozzles under the influence of gas cross-flows. The results indicate qualitative agreement to the investigation based on axisymmetric laminar threads (Mescher et al., 2012). The comparison to circle nozzles showed that the breakup length is significantly shorter for threads from open channel flow and from oval nozzles, possibly due to the stronger deformation of the nonaxisymmetric threads. Moreover, a lower critical We_g for the transition between the axisymmetric and the wind-induced breakup is observed for the nonaxisymmetric threads.

Gramlich et al. (2011) investigated the perturbations on gravity-stretched threads subject to gas cross-flows by means of linear stability analysis. The dispersion relation is derived as follows:

$$\begin{aligned}&\frac{(\bar{W}K_z-\Omega_T)^2}{K_z}\frac{s^2+K_z^2}{s^2-K_z^2}\frac{I_0(K_z\bar{R}_s)}{I_1(K_z\bar{R}_s)}-\frac{\rho_g}{\rho_l}\frac{K_1(K_z\bar{R}_s)}{K_1'(K_z\bar{R}_s)}\left(\Omega_T+\frac{2}{\bar{R}_s}\bar{U}_{g,rel}-K_z\bar{W}_{g,rel}\right)^2\\&-\frac{2i(\bar{W}K_z-\Omega_T)}{\mathrm{Re}}\left[\frac{-2K_z^2}{s^2-K_z^2}\left(s\frac{I_0(s\bar{R}_s)}{I_1(s\bar{R}_s)}-\frac{1}{\bar{R}_s}\right)+\frac{s^2+K_z^2}{s^2-K_z^2}\left(K_z\frac{I_0(K_z\bar{R}_s)}{I_1(K_z\bar{R}_s)}-\frac{1}{\bar{R}_s}\right)\right]+\frac{1}{\mathrm{We}}\left(\frac{1}{\bar{R}_s^2}-K_z^2\right)=0\end{aligned} \tag{19.70}$$

where

$s^2 = K_z^2 + i\,\mathrm{Re}(\bar{W}K_z - \Omega_T)$ is the dispersion parameter

$I_0(K_z\bar{R}_s)$ and $I_1(K_z\bar{R}_s)$ are the modified Bessel's functions of the first kind

$K_1(K_z\bar{R}_s)$ is the modified Bessel's function of second kind with its derivative $K_1'(K_z\bar{R}_s)$

Dimensionless numbers $\bar{W}$, $\bar{U}_{g,rel}$, and $\bar{W}_{g,rel}$ are time-averaged liquid axial velocity, radial relative velocity, and axial relative velocity, respectively, scaled by the initial liquid axial velocity ω_0; dimensionless numbers $\bar{R}_s$ and Z are the time-averaged jet radius and distance along the jet axis, respectively, scaled by the initial jet radius r_0. Complex quantities $K_z = K_r + iK_i$ and $\Omega_T = \Omega_r + i\Omega_i$ are the spatial and temporal wave functions, respectively. The real parts with their derivatives $K_{r,z} = dK_r/dZ$ and $\Omega_{r,T} = d\Omega_r/dT$ are the wave number and the circular frequency of the oscillation, respectively, whereas the imaginary parts K_i and Ω_i characterize the spatial and the temporal growth or decay of the perturbation, respectively. T is the dimensionless time as $T = t\omega_0/r_0$. The wave with the critical wave number $K_{r,Z,crit}$, resulting in maximum growth of the disturbance $\Omega_{i,\max}$, leads to breakup of the jet into droplets. For the spatial stability analysis, the spatial growth rates $K_{i,Z}$ are determined for fixed values of the angular frequency $\Omega_{r,T}$. The drop size results from the volume-equivalent jet segment with the axial extension λ and the time-averaged cross-sectional area at the breakup point for both temporal and spatial instability:

$$\frac{d}{d_0} = \frac{1}{2}\sqrt[3]{\frac{12\pi}{K_{r,Z,crit}}(\bar{R}_s\big|_{Z=L})^2} \tag{19.71}$$

19.1.6.4 Direct Numerical Simulation

Recent investigations describe the complex behavior of the liquid jet and the gas/liquid interface, including the primary fragmentation process in atomization, using DNS of the multiphase flow system (see, e.g., Mayer, 1993, Lozano et al., 1994, Zaleski et al., 1995, Zaleski and Li, 1997, Lafaurie et al., 1998, Scardovelli and Zaleski, 1999, Klein et al., 2001, 2002, Zaleski and Boeck, 2003, Menard et al., 2007, Desjardins et al., 2008, Desjardins, 2009, Gorokhovski and Herrmann, 2008, Shinjo et al., 2010, Zhu et al., 2013, Zhu, 2014).

The progress in DNS of liquid atomization and liquid fragmentation processes as well as in elementary liquid processes, such as liquid interface coalescence, is tremendous. Appropriate length and time scales are increasingly resolved. The success of fundamental research in this area is mainly driven by tremendously increasing computer power; however, carrier of the progress is the successful cooperation of related disciplines such as physics, chemistry, engineering, and mathematics, respectively.

19.1.6.4.1 Single-Fluid Formulation Direct numerical simulations (DNSs) of liquid atomization and liquid fragmentation processes are based on the continuum approach through integrating the single-fluid Navier–Stokes (NS) equations and identifying the gas/liquid interface at each time. The goal of such a DNS is to resolve all time and length scales, solving the governing equations directly. Because most primary atomization applications occur at low Mach numbers and the two fluids involved are immiscible, the flow is governed by the unsteady Navier–Stokes equations in the variable density, incompressible limit

$$\frac{\partial \rho \vec{U}}{\partial t} + \vec{U} \cdot \nabla \rho \vec{U} = -\nabla p + \nabla \cdot (\mu(\nabla \vec{U} + \nabla^T \vec{U})) + \rho \vec{g} + \vec{F}_s \tag{19.72}$$

$$\nabla \cdot \vec{U} = 0 \tag{19.73}$$

where

U is the velocity
ρ is the density
p is the pressure
μ is the dynamic viscosity
g is the gravitational acceleration
F_s is the surface-tension force, which is a singular force active only at the location of the phase interface Γ

There are three different approaches to model the surface-tension force in this context.

The first approach is the continuum surface force (CSF) method (Brackbill et al., 1992) defined as

$$\vec{F}_s = \sigma \kappa \vec{n}_f \delta(\vec{x} - \vec{x}_f) \tag{19.74}$$

where

κ is the mean curvature of the phase interface
n_f is its normal vector
δ is the delta function concentrated on the phase interface

The second approach is the continuous surface stress (CSS) model (Lafaurie et al., 1994, Gueyffier et al., 1999, Scardovelli and Zaleski, 1999) where the surface-tension force is expressed as the divergence of a surface-tension tensor:

$$\vec{F}_s = -\nabla \cdot ((\mathrm{I} - \vec{n} \otimes \vec{n}) \sigma \delta(\vec{x} - \vec{x}_f)) \tag{19.75}$$

The discretization of the delta function in both CSF and CSS models usually spreads the surface-tension force into a small neighborhood normal to the phase interface. To avoid an interface thickness, an alternative is to use the ghost-fluid method (Kang et al., 2000, Tanguy and Berlemont, 2005, Hong et al., 2007), in which the surface-tension force is acting though the pressure jump condition at the phase interface,

$$[p]_\Gamma = \sigma \kappa + 2[\mu]_\Gamma \vec{n}^T \cdot \nabla \vec{U} \cdot \vec{n} \tag{19.76}$$

and a discretization of the delta function is thus not required.

Interface capturing models (Gorokhovski and Herrmann, 2008, Ashgriz, 2011) are usually applied to obtain the gas/liquid interface evolution and topology by solving an advection equation of an indicator (Φ) that can be attributed to the interface:

$$\frac{\partial \Phi}{\partial t} + \vec{U} \cdot \nabla \Phi = 0 \tag{19.77}$$

The normal vector and curvature are computed from the indicator function using the following formulas:

$$\vec{n}_f = \nabla\Phi, \quad \vec{n} = \frac{\nabla\Phi}{|\nabla\Phi|}, \quad \text{and} \quad \kappa = -\nabla\cdot\vec{n} \tag{19.78}$$

Within interface capturing scheme, two principal methods are the volume of fluid (VOF) method (Hirt and Nichols, 1981, Scardovelli and Zaleski, 1999) and the level set (LS) method (Osher and Sethian, 1988, Sethian, 1996, Osher and Fedkiw, 2002).

19.1.6.4.2 Volume of Fluid (VOF) Method In the VOF method, a volume fraction (f) is defined in each cell as the fraction of the cell containing liquid. If the cell is completely filled with liquid, then $f = 1$, and if it is filled with gas, then its value should be $f = 0$. At the location of the gas/liquid interface, the value of f is between 0 and 1 ($0 < f < 1$). Therefrom, the physical properties in the governing equations can be expressed as

$$\rho = \rho_l f + \rho_g (1-f) \quad \text{and} \quad \mu = \mu_l f + \mu_g (1-f) \tag{19.79}$$

Discontinuity in f propagates according to Equation 19.77, where Φ is replaced with f. In a physical sense, the equation implies mass conservation of one phase in the mixture. The gas/liquid interface needs to be reconstructed in each cell since interface information is lost when the interface is represented by a volume fraction field. Gopala and van Wachem (2008) give a useful comparison between different interface sharpening and reconstruction algorithms in a variety of CFD codes. In general, the geometric piecewise linear interface calculation (PLIC) method (Zaleski et al., 1995, van Wachem and Schouten, 2002) is commonly used because of its accuracy and applicability for complex flows. In the PLIC method, the interface is approximated by a straight line of approximate inclination in each cell. A typical reconstruction of the interface with a straight line in a cell, which yields an unambiguous solution, is perpendicular to an interface normal vector $\boldsymbol{n}_f$ and delimits a fluid volume matching the given volume fraction f for the cell. In the open-source CFD code OpenFOAM, the interface compression scheme of Weller (2008) and Wardle and Weller (2013) has been implemented as interface sharpening methodology, which adds an additional "artificial" compression term to the LHS of the volume fraction transport equation (Equation 19.77 replacing Φ with f).

19.1.6.4.3 Level Set (LS) Method In an LS method, a continuous function F is defined as the signed distance between any point of the domain and the interface. The function F is set to zero at the interface, is positive on one side, and negative on the other. Solving the advection equation (19.77), where Φ is replaced by the LS function F, determines the evolution of the interface. However, as the front propagates, high velocity gradients can produce wide spreading and stretching of the LS, and F will no longer remain a distance function. A reinitialization algorithm is thus applied to keep F as the signed distance to the interface. An iterative procedure is proposed by Sussman et al. (1998) to maintain F as a distance function.

The major drawback of the LS method is that it does not inherently conserve liquid mass. Since liquid volume errors are proportional in size to the employed grid resolution, grid refinement strategies, such as the refined level-set grid (RLSG) method (Herrmann, 2008) and structured adaptive mesh refinement (AMR) (Nourgaliev and Theofanous, 2007), can be employed to reduce their influence. An alternative to grid refinement is to augment and correct the LS function by an additional numerical scheme,, for example, coupling LS and VOF (CLSVOF) (Sussman and Puckett, 2000, van der Pijl et al., 2005). The main concept of the CLSVOF method is to benefit from the advantage of both LS and VOF methods: mass loss is limited through the VOF method and a fine description of interface properties is kept with the LS method.

19.1.6.4.4 DNS of Primary Atomization Such complete three-dimensional, transient, direct numerical analyses, from initial liquid jet deformation to the primary fragmentation of the liquid jet, are based on modeling approaches such as the VOF method (Nichols et al., 1980) in combination with surface reconstruction methods (Brackbill et al., 1992) like the PLIC method (Zaleski et al., 1995). The primary liquid fragmentation and also the simultaneous coalescence of fluid elements are analyzed in this way. Typically, the excited fragmentation of a planar liquid sheet in a parallel gas flow field is observed in a three-dimensional calculation. In Figure 19.36, a sequence of a result from a fragmentation simulation from Zaleski and Li (1997) is shown. The calculation has been performed for a liquid Reynolds number $\mathrm{Re}_l = 200$, a liquid

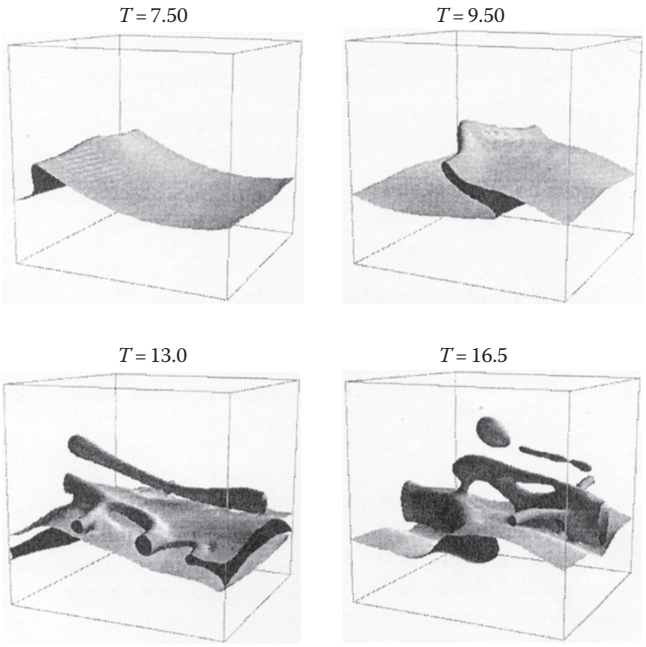


Figure 19.36

DNS of liquid jet fragmentation, $Re_l = 200$, $We_l = 300$, $\rho_l/\rho_g = 10$. (Adapted from Zaleski, S. and Li, J., Direct simulation of spray formation, in *Proceedings of ICLASS-'97*, Seoul, Korea, August 1997, pp. 812–819.)

Weber number of $We_l = 300$ at an artificially low density ratio between liquid and gas of $\rho_l/\rho_g = 10$ (at higher density ratios no stable solutions are achieved). From the tip of the evolving wave, a finger-type ligament is formed, which is stripped off in a later stage from the main liquid jet and is deformed and stretched into the main flow direction to form a cylindrical fluid element. This unstable fluid element is fragmented later on as a result of capillary instabilities. This disintegration results in smaller fragments of different sizes. It is interesting to note that a result of this simulation is that a primary fluid ligament results from initial fragmentation that is orientated in the direction of the main flow (fingering in flow direction). In contrast to this result, the former classical aerodynamic fragmentation models such as Dombrowski and Johns (1963) (see Figure 19.33) used a stripped-of fluid ligament orientated perpendicular to the main flow direction.

A direct numerical calculation (in two dimensions) of the dynamics of phase boundaries of a planar liquid sheet has also been performed based on the VOF method by Lafaurie et al. (1998) and Klein et al. (2002). In their contributions, some major effects of liquid parameters like density ratio, viscosity ratio, and capillary effects on the primary fragmentation mechanism are discussed based on simulation results and comparisons to experimental results.

Zhu et al. (2013) and Zhu (2014) performed DNSs on the primary breakup of inelastic non-Newtonian liquid (PVP solution) jets into stagnant air, with a high liquid/gas density ratio $\rho_l/\rho_g = 871$. The VOF method is employed together with CSS model. The range of the investigated nondimensional quantities covers: Reynolds number (Re_l): 492–1,312, Weber number (We_l): 5,867–41,719, and Ohnesorge number (Oh): 0.1557. The non-Newtonian viscosity is described by modified power law model. Three different destabilizing factors, including inlet velocity profile, inlet Reynolds number, and inflow turbulence, are considered. Compared to Newtonian jets with a similar viscosity, the size of streamwise vortices within the liquid phase is relatively smaller, while the number of vortices is greater. Meanwhile, streamwise contrarotating vortex pair (CVP) and even triple vortex structures are observed in the liquid phase. Two different regimes of ligament formation have been observed. One is caused by the Rayleigh capillary instability, while the other is a result of stretching. A specific shear thinning breakup mechanism, the cavity breakup, is detected, which gives a novel perspective for the analysis of jet disintegration.

Menard et al. (2007), Lebas et al. (2009), and Shinjo et al. (2010) have successfully employed the CLSVOF method in 3D DNS of the primary atomization of a turbulent liquid jet into stagnant air. In Menard et al. (2007) and Lebas et al. (2009), the ghost-fluid method is used to model the surface-tension force, while in Shinjo et al. (2010), the CSF method is applied. These DNSs have been performed with very fine grid

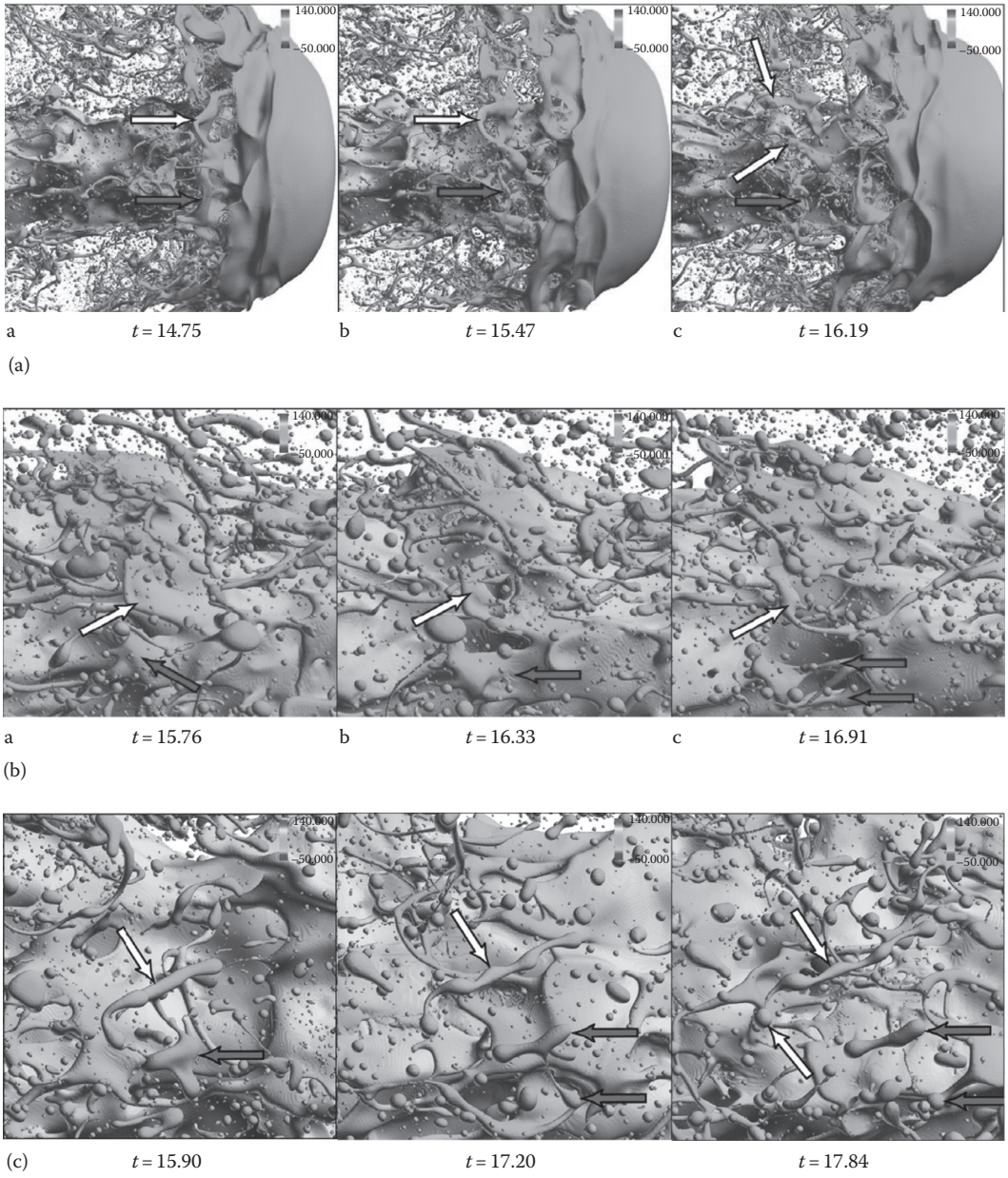


Figure 19.37

(a) Ligament formation from tip edge. (b) Ligament formation from liquid core. (c) Droplet formation from ligament. The greyscale/color indicates the axial velocity in m/s. The flow is from left to right. Bulk liquid Reynolds number $Re_l = 1{,}470$ and bulk liquid Weber number $We_l = 141{,}000$. Nondimensional time $t = t_{real}/(D/U_l)$ with nozzle diameter $D = 0.1$ mm and liquid injection velocity $U_l = 100$ m/s. (Adapted from Shinjo, J. and Umemura, A., *Int. J. Multiphase Flow*, 36, 513, 2010. With permission.)

resolution (grid spacing 0.35–2.36 μm). Therefrom, more detailed information in liquid atomization process can be revealed. Shinjo et al. (2010) found that ligament formation occurs both from the liquid jet tip roll-up (Figure 19.37a) and the liquid core surface (Figure 19.37b). In Figure 19.37a, the mushroom-shape tip is created due to the lateral liquid spread by impingement against the stagnant gas and roll-up by the initial Rayleigh–Taylor (R–T) instability; from the mushroom tip edge, quasi-axisymmetric (or ring-like) ligaments (indicated by the grey arrow) and streamwise ligaments (indicated by the white arrow) are generated alternately. In Figure 19.37b, crests are formed on the liquid core due to surface instability and breakup into ligaments: in the case indicated by the white arrow, the crest breaks up into only one ligament; while in the case indicated by the grey arrow, the central part of the flat crest soon becomes thinner than the rim, and

then a hole is created and grows due to contracting motion by surface tension in the central region of the flat crest, finally resulting in the formation of two ligaments. Shinjo et al. (2010) pointed out that shear from local vortices plays an important role in the ligament formation, and ligaments are created when $We_g \sim O(1)$, where We_g is the local gas Weber number of a ligament based on the baseline radius of the ligament. In Figure 19.37c, droplet formation occurs from the ligament tip mostly by the short-wave mode (as indicated by the grey arrow), and surface capillary wave propagation is clearly observed (as indicated by the white arrow). Recollision of ligaments and droplets often happens and enhances next breakup:

19.1.6.5 Large Eddy Simulation (LES)

In a DNS, the goal is to reduce epistemic uncertainty by resolving all necessary time and length scales inherent in the flow and thus eliminating the need to model the effect of any unresolved scales (Gorokhovski and Herrmann, 2008). In a single-phase turbulent flow, the smallest length scale that must be resolved is the Kolmogorov length scale. Multiphase flows add an additional smallest length scale that requires resolution, the size of the smallest liquid structure. This implies the DNS of primary atomization with a limited domain size, simple geometries, and low turbulent Reynolds numbers.

Reynolds-averaged Navier–Stokes (RANS) formulation can be introduced in industrial solvers. In this case, almost any configuration may be resolved, but much information concerning the liquid properties remains unknown, and the accuracy of the results may be quite low in some situations. Some RANS studies of primary atomization process based on VOF interface capturing can be found in Rivas et al. (2014) and Li and Fritsching (2014a). In Rivas et al. (2014), a 3D numerical simulation of the internal flow in a conical swirl atomizer, as well as the initial water-sheet formation near the nozzle exit, was performed based on the VOF approach and the standard k–ε turbulence model. Because of the low grid resolution, only some macroscopic phenomena such as flow field (velocity and pressure) at the entrance to swirl chamber and the cone angle of the conical sheet after the nozzle exit have been described. In Li and Fritsching (2014a), the formation of a swirling conical sheet and its fragmentation near the nozzle exit were numerically investigated based on the VOF approach, the k–ω SST (shear stress transport) turbulence model, and the AMR technique. The liquid sheet evolution and breakup after the nozzle exit have been described based on a 3D simulation, while more details about spray characteristics such as droplet size and droplet velocity have been extracted from a 2D-axisymmetric simulation. Figure 19.38 exhibits the temporal evolution of a swirling conical sheet of liquid tin (Sn) from the 3D simulation, which indicates two kinds of instabilities existing in the sheet surface: one grows in the longitudinal direction, while the other in the circumferential direction. The latter wavelength (several millimeters) is one order of magnitude larger than the former (hundred micrometers). The ligament formation can be observed. The interconnected ligaments form cellular structures (or perforations), and finally disintegrate into droplets. With the propagation of the liquid sheet, the number of computational cells has increased from ~3.5 million in the base grid to ~12 millions at t = 4.5 ms.

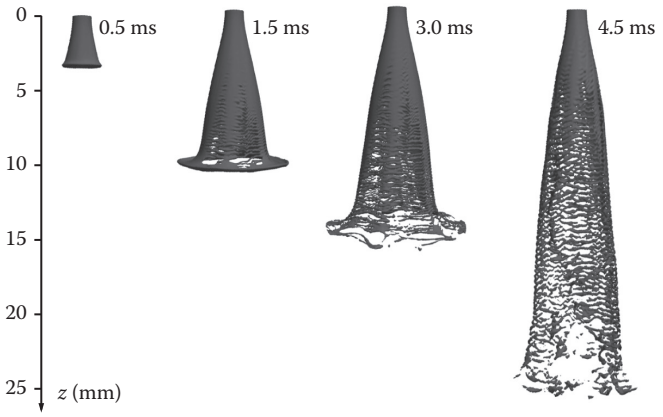


Figure 19.38

3D simulation: temporal evolution of a swirling conical sheet of melt tin (Sn) from a pressure swirl nozzle, Δp_l = 0.6 MPa, D_0 = 1.3 mm. (Adapted from Li, X.G. and Fritsching, U., Multiscale modeling and simulation in spray processing of composite particles, in *Proceedings of Second International Symposium on Multiscale Multiphase Process Engineering*, Hamburg, Germany, September 24–27, 2014b.)

To overcome those difficulties encountered in DNSs and RANS simulations, the current trend in turbulence modeling is the development of LESs. LES is a promising technique between industrial RANS solvers and academic DNS solvers. It solves the largest scales of the flow while the impact of the smallest scales (or the subgrid scales) is modeled. The LES studies of primary atomization process based on interface tracking/capturing schemes can be found in de Villiers et al. (2004), Bianchi et al. (2007), Corbinelli et al. (2010), Desjardins et al. (2013), Xiao et al. (2014), and Tian et al. (2015). In Desjardins et al. (2013), a conservative LS method is used for interface capturing, while in Xiao et al. (2014), a CLSVOF method coupled with ghost fluid method is used. Other studies use VOF interface capturing:

$$\frac{\partial \bar{\Phi}}{\partial t} + \bar{u}_i \cdot \frac{\partial \bar{\Phi}}{\partial x_i} = -\left(\overline{u_i \frac{\partial \Phi}{\partial x_i}} - \bar{u}_i \frac{\partial \bar{\Phi}}{\partial x_i} \right) \tag{19.80}$$

When a usual LES formalism is applied to the interface capturing equation (19.77), an unresolved term appears on the right-hand side of the resulted equation (19.80) and a model is necessary to account for the unresolved subgrid correlation between the velocity and the phase function. However, all the LES studies discussed consider standard subgrid scale (SGS) models for the momentum conservation equation but not for the interface equation. Thus, the impact of the subgrid flow properties on the droplet formation process is neglected and only the large-scale instabilities participate in the spray formation.

Chesnel et al. (2011a) carried out a priori analysis of the subgrid to evaluate the order of magnitude of the contributions of these terms to the flow evolution, where a DNS by use of the CLSVOF method was applied as a reference. The results show that the interface evolution is not mainly controlled by large-scale convection phenomena, and the subgrid contribution results in globally up to 10% of the resolved contribution. Thus, it is necessary to take into account the impact of the small scales on the interface propagation. Furthermore, at the interface level close to the injection, the order of magnitude of the subgrid correlations strongly increases. Therefore, a closure of the interfacial subgrid term has been proposed by Chesnel et al. (2011a,b) based on a scale similarity assumption to close all the subgrid unresolved terms in comparison with a Smagorinsky formulation (Smagorinsky, 1963).

19.1.6.6 Multiscale Simulation Coupling ICM and LPT

The primary atomization of a liquid jet into small droplets is a multiscale phenomenon, in which the size of the smallest droplet is often three orders of magnitude smaller than the diameter of the atomizing liquid jet. DNS with interface tracking/capturing schemes is very useful in understanding fundamental physics of atomization. However, the range of scales that can be covered by DNS with computing ability today is still often much smaller than practical applications. For example, even with a mesh resolution of 0.35 μm (Shinjo and Umemura, 2010), the finest scales of the flow are still not resolved. To optimize the computational cost, some studies use an AMR (Fuster et al., 2009, Agbaglah et al., 2011), but there is still a numerical cut-off scale. To resolve this multiscale challenge in atomization simulation, coupled Eulerian–Lagrangian multiscale models have been proposed by Tomar et al. (2010), Herrmann (2010), Hecht et al. (2013), Osmar et al. (2013), Ling and Zaleski (2014), and Grosshans et al. (2014). In these multiscale models, interface capturing method (ICM) (the Eulerian approach), such as VOF, LS, and CLSVOF methods, describe the large scales of gas/liquid interface during atomization, while the Lagrangian particle tracking (LPT) approach is employed to model the droplets smaller than the Eulerian grid size. The purpose of the coupling procedure is to identify separated regions Ω_d of liquid in gas fulfilling certain criteria, to remove these from the interface capturing representation, and to insert them into a Lagrangian framework, preserving their volume V_d, center of mass x_d, and momentum $\rho_d u_d$:

$$V_d = \int_{\Omega_d} d\vec{x}, \quad \vec{x}_d = \frac{1}{V_d} \int_{\Omega_d} \vec{x}\, d\vec{x}, \quad \text{and} \quad \vec{u}_d = \frac{1}{V_d} \int_{\Omega_d} \vec{u}(\vec{x}) d\vec{x} \tag{19.81}$$

where ρ_d is the constant liquid density. The removal criteria can be based on the derivation assumptions of typical Lagrangian spray models, that is, that individual drops be small and nearly spherical. The size criterion can be expressed in terms of a thresh volume V_{cut} (e.g., the grid volume), in that only those separated liquid structures with volume $V_d < V_{cut}$ are candidates for removal. The shape criterion can be expressed in

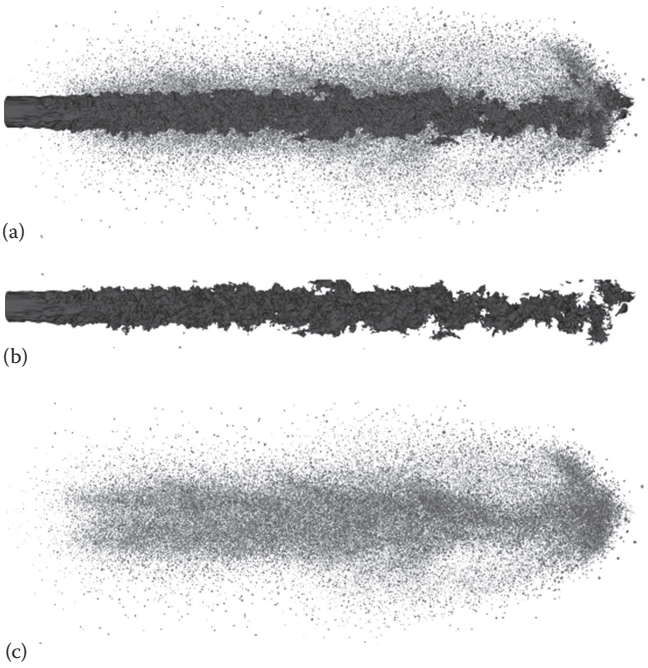


Figure 19.39

Atomization of turbulent liquid jet 20 μs after start of injection. Liquid core and spray (a), tracked phase interface of liquid core (b), and Lagrangian tracked spray (c). Injection Reynolds number $Re_l = 5{,}000$ and Weber number $We_l = 17{,}000$. (Adapted from Herrmann, M., *J. Comput. Phys.*, 229, 745, 2010. With permission.)

terms of an eccentricity measure threshold e_{cut}. Different formulations of eccentricity measure are given by Herrmann (2010) and Hecht et al. (2013), respectively. The Lagrangian to Eulerian transfer has also been considered by Herrmann (2010) in some situations where Lagrangian drops may grow due to drop/drop collisions or move from grid regions of low resolution into that of high resolution so that the drop's size becomes significantly larger than the local grid spacing. The multiscale coupling approach links DNS of the liquid core and the dense spray regime to the LPT simulation of the dilute spray regime. Compared with a full DNS, the computational cost will be reduced by this coupling approach as the unresolved droplets, which are computational expensively tracked in DNS, are only tracked in the LPT frame if these droplets are judged to satisfy Eulerian to Lagrangian transfer criteria. Hecht et al. (2013) pointed out that the transformation between Eulerian droplets and Lagrangian droplets may cause some difficulties to conserve some physical quantities of the system.

Figure 19.39 shows the atomizing liquid jet, the remaining tracked phase interface geometry, and the transferred Lagrangian drops from multiscale simulation of the primary atomization of a turbulent liquid jet at 20 μs after injection into still compressed air under conditions relevant to diesel engine systems (Herrmann, 2010). The injector diameter and the mean injection velocity are $D = 100$ μm and $U = 100$ m/s, respectively. The multiscale simulation has been performed for a liquid Reynolds number $Re_l = 5{,}000$ and a liquid Weber number $We_l = 17{,}000$ at a liquid/gas density ratio $\rho_l/\rho_g = 34$. The RLSG method proposed in Herrmann (2008) has been used to track gas/liquid interface during atomization. In Figure 19.39, roughly 403,000 drops have been transferred into the Lagrangian spray model. Diameters of these transferred drops range from the submicron size up to 10.8 μm. The total computer time per time step needed to identify and remove separated structures is less than 1% of the total computer time of a single time step, which demonstrates the high efficiency of the multiscale atomization model and its applicability to realistic problems.

In Tomar et al. (2010), the multiscale simulation of atomization of a liquid jet by a high-speed coaxial gas flow has been performed based on coupled VOF and LPT approach for a high liquid/gas density ratio of 100 and a high momentum ratio ($M = \rho_g U_g^2/(\rho_l U_l^2)$) of 16. The PDFs of the droplets are derived, which indicates two mechanisms of droplets formation, namely, by primary atomization of the jet and another by breakup of bigger fragments of liquid emerging downstream. The smallest droplets interact with the bigger lumps of liquid downstream, leading to a shift in the droplet size distribution to large droplet sizes.

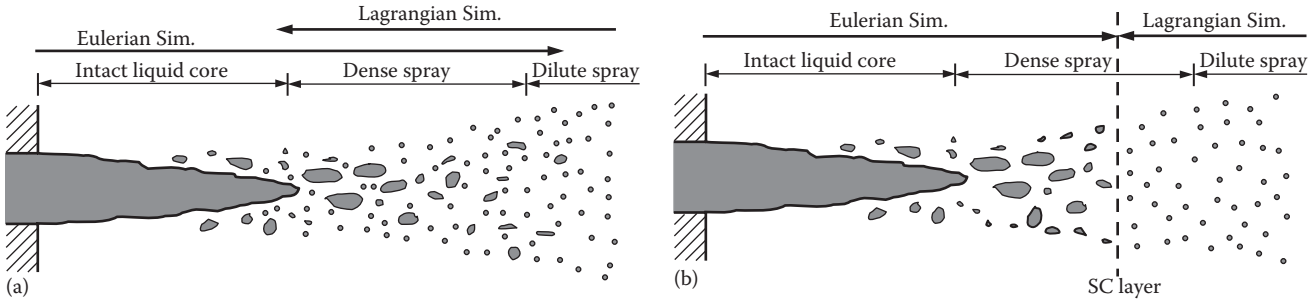


Figure 19.40

Schematic of coupled Eulerian–Lagrangian approaches for liquid atomization: (a) direct coupling approach, DCA; (b) statistical coupling approach, SCA.

Grosshans et al. (2014) categorize coupled Eulerian–Lagrangian approaches into direct coupling approach (DCA) and statistical coupling approach (SCA), as shown in Figure 19.40. In the DCA, each droplet that leaves the Eulerian simulation is injected individually in the LPT simulation, as in Tomar et al. (2010), Herrmann (2010), Hecht et al. (2013), Osmar et al. (2013), and Ling and Zaleski (2014), and both Eulerian and Lagrangian simulations covering the whole spray development are performed in parallel in a same physical domain (or an overlapped physical domain). However, in the SCA, only the statistical distribution of the droplet field properties is transferred from Eulerian to Lagrangian simulation instead of transferring each droplet individually. Compared with the DCA, this leads for two reasons to a computational significantly faster method:

1. In the SCA, the Eulerian simulation has to be run only until statistical convergence of the droplet distributions and not during the whole spray development. A layer, called the statistical coupling (SC) layer, is introduced close to the outlet of the Eulerian simulation (see Figure 19.40b). This layer has to be positioned far enough downstream from the injector, so that the spray is diluted enough to be simulated with the LPT approach. The liquid mass passing through the layer is analyzed. The statistical parameters of the droplet distributions at this layer are extracted from the Eulerian simulation and applied as starting conditions for the LPT simulation. In the SCA, the Eulerian simulation and the LPT simulation can be performed in different physical domains. According to the nature of the numerical methods, the time step and the grid size of the Eulerian simulation by interface capturing schemes are at least one order of magnitude smaller than the ones of LPT simulation. Thus, the computational time of a droplet traveling a certain distance in the Eulerian domain is several orders of magnitude larger than in the LPT domain. In the DCA, the computational time during the whole multiscale atomization simulation is determined by the Eulerian simulation.
2. In the DCA, each droplet in the particle cloud in the LPT simulation is tracked individually. The large number of droplets in a practical spray cannot be handled on individual bases. In the SCA, the droplets can be tracked in the LPT simulation using the stochastic parcel method. Here, a number of droplets are grouped in one parcel. All the droplets within the parcel are assumed to have the same properties, such as same size, position, velocity, temperature, distortion, and composition. Using the stochastic parcel method makes the description of a complete spray process feasible in the SCA.

For statistically stationary sprays, the accuracy of the SCA is only marginally lower than that of the DCA (Grosshans et al., 2014). The drawback of the SCA compared with the DCA is that the coupling layer is fixed in space. Therefore, it cannot be at the ideal position for all liquid structures to be transferred from the Eulerian to the LPT simulation. Another drawback of the SCA is that it cannot deal with transient sprays.

Based on the principle of the SCA, Li and Fritsching (2014a) performed integral process modeling and simulation of PGA of molten metal for powder production. The primary disintegration of swirling conical liquid sheets of the molten metal is described by the VOF approach, while the subsequent droplet spray process is simulated through the LPT approach by taking into account the secondary breakup of produced droplets as well as other in-flight spray phenomena. The characteristics of liquid sheet fragmentation such as breakup length, primary droplet size, and velocity are derived and applied as the

initial conditions for the droplet spray process simulation. The coupled atomization and spray simulation obtained a good prediction of the (MMD) of the metal powder produced by the PGA process.

19.1.6.7 Eulerian–Lagrangian Spray Atomization Model

The Eulerian–Lagrangian spray atomization (ELSA) model, initially proposed by Vallet et al. (2001) and further developed by Blokkeel et al. (2003), Lebas et al. (2005, 2009), Ning et al. (2009), and Chesnel et al. (2011b), is based on an Eulerian approach, which is more suitable for the description of the dense zone of the spray and its atomization. Within the diluted spray region, the ELSA model could switch to the traditional Lagrangian description of the liquid phase. The ELSA model considers the situation of high-speed turbulent sprays where Reynolds and Weber numbers are high, and it proposes a turbulent mixing process between the liquid and surrounding gaseous phases as a single-phase turbulent fluid flow with mean properties. Therefrom an assumption similar to the Kolmogorov hypothesis has been invoked: large-scale features of the flow are supposed to be independent of viscosity and surface tension at high Reynolds and Weber numbers; small-scale features do depend on viscosity and surface tension (Vallet et al., 2001). The separation of the large-scale flow features from the atomization process occurring at smaller scales allows the direct simulation of the large-scale bulk transport of the liquid, while unresolved turbulent transport is modeled using standard closures such as those used in Reynolds-averaged turbulence models (Vallet et al., 2001, Lebas et al., 2009) or LES models (Chesnel et al., 2011b). The small-scale atomization is modeled by solving a transport equation for the evolution of gas/liquid interface density Σ, which is defined as the quantity of gas/liquid interface per unit volume (m^{-1}).

The key formulae in the ELSA model are summarized as follows. Mean liquid volume fraction is denoted ($\overline{Y}$) and mean liquid mass fraction ($\tilde{Y}$) is defined as

$$\tilde{Y} = \frac{\overline{\rho Y}}{\overline{\rho}} \tag{19.82}$$

where $\overline{\rho}$ is the mean density of the mixture, which is obtained as

$$\overline{\rho} = \rho_l \overline{Y} + \rho_g (1 - \overline{Y}) \quad \text{or} \quad \frac{1}{\overline{\rho}} = \frac{\tilde{Y}}{\rho_l} + \frac{1 - \tilde{Y}}{\rho_g} \tag{19.83}$$

with the liquid density (ρ_l) and the gas density (ρ_g). The Favre averaged mean velocity $\tilde{U}$ is expressed in terms of $\tilde{Y}$ as

$$\tilde{U} = \tilde{U}_l \tilde{Y} + \tilde{U}_g (1 - \tilde{Y}) \tag{19.84}$$

and the equation of state

$$\overline{p} = \frac{(1 - \tilde{Y})\overline{\rho} R T_g}{1 - \tilde{Y} \cdot \overline{\rho}/\rho_l} \tag{19.85}$$

Neglecting terms that are related to the viscosity and the surface tension in accordance to the hypothesis of high Reynolds and Weber values, the transport equations for the mean mixture properties are written as

$$\frac{\partial \overline{\rho}}{\partial t} + \frac{\partial \overline{\rho} \tilde{U}_j}{\partial x_j} = S_{EL}^{\tilde{Y}} \tag{19.86}$$

$$\frac{\partial \overline{\rho} \tilde{U}_i}{\partial t} + \frac{\partial \overline{\rho} \tilde{U}_j \tilde{U}_i}{\partial x_j} = -\frac{\partial \overline{p}}{\partial x_i} - \frac{\partial \overline{\rho u_i'' u_j''}}{\partial x_j} + S_{EL}^{\tilde{U}_i} \tag{19.87}$$

To track the dispersion of the liquid phase, this set of equations is completed by Favre averaging the transport equation for the liquid mass fraction

$$\frac{\partial \overline{\rho} \tilde{Y}}{\partial t} + \frac{\partial \overline{\rho} \tilde{U}_j \tilde{Y}}{\partial x_j} = -\frac{\partial \overline{\rho u_j'' Y''}}{\partial x_j} + S_{EL}^{\tilde{Y}} \tag{19.88}$$

where $S_{EL}^{\tilde{Y}}$ and $S_{EL}^{\tilde{U}_i}$ are the sink or source terms due to the droplet generation or absorption when the transition from Eulerian to Lagrangian formulation is activated. The turbulent stress tensor in Equation 19.87 can be closed with a classical or modified k–ε model. Concerning the liquid turbulent diffusion in Equation 19.88, the gradient law approximation (Lebas et al., 2009) can be applied:

$$\overline{\rho u_j'' Y''} = -\overline{\rho}\frac{\nu_t}{\mathrm{Sc}}\frac{\partial \tilde{Y}}{\partial x_j} \tag{19.89}$$

where

ν_t is turbulent kinematic viscosity
Sc is Schmidt number

A transport equation for the gas/liquid interface density ($\tilde{\Omega} = \overline{\Sigma}/\overline{\rho}$) is postulated by analogy with the flame surface density

$$\frac{\partial \overline{\rho}\tilde{\Omega}}{\partial t} + \frac{\partial \overline{\rho}\tilde{U}_j\tilde{\Omega}}{\partial x_j} = \frac{\partial}{\partial x_j}(\overline{\rho}\tilde{\Omega}(\tilde{U}_j - \tilde{U}_{j,\Gamma})) + S_{EL}^{\tilde{Y}} + \overline{\rho}\dot{\tilde{\Omega}}_s \tag{19.90}$$

The first term on the right-hand side of Equation 19.90 represents the turbulent flux of interface, which reflects the difference between the interface velocity and the global mixture velocity. It is often closed using a turbulent diffusion term as follows:

$$\overline{\rho}\tilde{\Omega}(\tilde{U}_j - \tilde{U}_{j,\Gamma}) = \overline{\rho}\frac{\nu_t}{\mathrm{Sc}}\frac{\partial \tilde{\Omega}}{\partial x_j} \tag{19.91}$$

which is similar as that for the closure of the liquid turbulent diffusion term in Equation 19.89. In Chesnel et al. (2011b) where the ELSA model is extended to the LES, the scale similarity assumption has also been proposed to close the turbulent interface flux. The third term on the right-hand side of Equation 19.90 is a source term accounting for the production and/or destruction of the interface area due to the turbulent mixing between liquid and gas, the mean shear stress, breakup, coalescence, and vaporization. The mathematical formulation of the source term is detailed in Lebas et al. (2009).

Together with the mean liquid mass fraction, the gas/liquid interface density can be used to calculate the local SMD (D_{32}) of the spray (Vallet et al., 2001):

$$D_{32} = \frac{6\overline{\rho}\tilde{Y}}{\rho_l\overline{\Sigma}} \tag{19.92}$$

In general, the ELSA model can give an accurate description of the mixing-controlled phenomena such as spray penetration, dispersion, and vaporization processes (Lebas et al., 2009, Ning et al., 2009, Garcia-Oliver et al., 2013), but cannot well describe the droplet-related phenomena, for example, the SMD of the spray (Vallet et al., 2001, Garcia-Oliver et al., 2013).

19.1.7 Secondary Atomization

Secondary breakup in sprays is defined as the disintegration of larger droplets and ligaments into smaller droplets. The breakup of a single droplet in a gas is caused by either relative velocity, turbulence, or shock structure interaction, respectively. The main features of binary droplet collisions are presented in Chapter 14.

19.1.7.1 Droplet Breakup Mechanism

The secondary atomization of drops (drop fragmentation) is a multiphase flow process that is common for a wide variety of spray systems. Since the goal of many atomization processes is to control the final droplet size distribution, one of the most important reasons to study secondary atomization is to determine the conditions that lead to appropriate fragment sizes. Numerous studies of dilute sprays and isolated droplets have been performed in order to increase the understanding of secondary atomization mechanism. In-depth reviews on secondary atomization can be found in Krzeczkowski (1980), Pilch and Erdman (1987), Faeth et al. (1995), Chryssakis and Assanis (2008), and Guildenbecher et al. (2009). Shock tube (Gelfand et al., 1973, Faeth, 1990, 2002, Faeth et al., 1995, Hsiang and Faeth, 1992, 1993, 1995, Ruff et al., 1992, Tseng et al., 1992, Chou et al.,

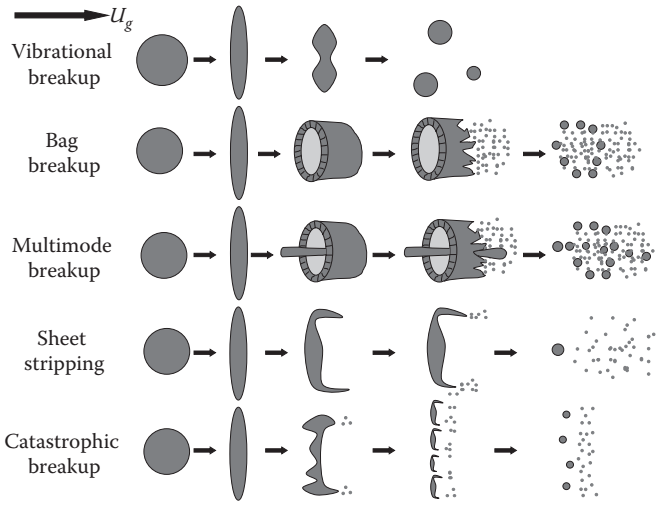


Figure 19.41

Typical modes of drop breakup. (From Li, X.G., Modeling and simulation of the gas-atomization process of metal melts for metal-matrix-composite production, Dissertation, Universität Bremen, Shaker-Verlag, Aachen, Germany, 2014. With permission.)

1997, Chou and Faeth, 1998, Dai and Faeth, 2001, Aalborg et al., 2003) and continuous jet methods (Lane, 1951, Taylor, 1963, Reitz, 1986, Hwang et al., 1996, Lee and Reitz, 2000, Liu and Reitz, 1993, 1997, Schmelz and Walzel, 2003, Cao et al., 2007, Zhao et al., 2010) have been employed to study the secondary breakup process. Both methods attempt to subject droplets to a step change in velocity.

Different flow conditions lead to different breakup modes. Figure 19.41 shows five typical breakup modes for Newtonian drops. From top to bottom, the modes are termed vibrational, bag, multimode (often called bag-and-stamen), sheet stripping (thinning), and catastrophic breakup, respectively.

Vibrational breakup is caused by the amplification of droplet oscillation when surface tension acts to restore the drop to its initial spherical shape. This breakup mode does not always occur and proceeds much more slowly than the other modes. It produces only a few fragments whose sizes are comparable to those of the parent drop.

During bag breakup, separation of the flow around a deformed drop (thin disk) leads to a positive pressure difference between the leading stagnation point and the wake. This tends to blow the center of the drop downstream, resulting in a thin hollow bag. The bag will first break, forming a large number of small droplets; thereafter the rim will break into few larger droplets.

Multimode breakup is a transitional regime, which resembles a combination of bag- and striping-type breakup. Bag formation accompanied by the presence of a core drop results in the formation of a long ligament in the center of the bag, which is referred to as a stamen or plume. Like bag breakup, the bag is the first to break up, followed by the rim and the stamen. Multiple sized fragments are produced.

Joseph et al. (1999) attributed the bag formation during both bag and multimode breakup to RT instability, and suggested that when the diameter of a drop was less than the critical wavelength of RT instability, the drops could not be fragmented by RT instability. Zhao et al. (2010) investigated the effect of RT wave number (k_{RT}) in the region of maximum cross-stream dimension on drop breakup morphology. The RT wave number is defined as the ratio of maximum cross-stream dimension to RT instability wavelength, $k_{RT} = d_{\max}/\lambda_{\max}$. The bag breakup occurred at $k_{RT} = 0.5774$–1, bag-stamen breakup at $k_{RT} = 1$–2, and dual-bag breakup (Cao et al., 2007) at $k_{RT} = 2$–3. Girin (2014) analyzed the role of inertial mass force and drop deformation in drop fragmentation, and raised the temporal and spatial conditions for drop breakup: (1) the period of the steady existence of the inertial force field should be large enough to ensure the proper instability development and (2) the lateral drop deformation exceeds the characteristic length of the fastest growing wave. Depending on the characteristic wavelength, selection mechanism between different breakup modes is built.

In a sheet striping (thinning) regime, the droplet is deformed into a thin disk from which a thin sheet is successively drawn from the periphery of the droplet because of Kelvin–Helmholtz (KH) waves, which is caused by the shear forces in the relative parallel motion at the common interface. The sheet evolves into

ligaments, which disintegrate into small droplets until the droplet is completely fragmented or until it has accelerated to a point where the aerodynamic effect is negligible, leaving a stable diameter of the core droplet.

In a catastrophic breakup regime, both RT and KH instabilities are involved. At first, RT waves due to the normal forces at the gas/liquid interface are grown on the surface of the parent droplet, which causes the droplet fragmentation into large child drops. KH waves are developed on the surface of the child droplets, resulting in a fragmentation mode equal to sheet stripping.

In secondary atomization, the aerodynamic force deforms the drop, causing it to fragment. This deformation is resisted by the surface tension (σ) and drop viscosity (μ). The aerodynamic Weber number We (Equation 19.7) and the Ohnesorge number Oh (Equation 19.8) are employed when describing secondary atomization process. We forms the ratio of the disrupting aerodynamic force to the restorative surface-tension force and Oh represents the ratio of the viscous force to the surface-tension force. A larger We indicates a higher tendency toward fragmentation, while a higher Oh indicates a lower tendency toward fragmentation. Several studies have considered the definitions and conditions for the onset of various deformation and breakup modes of drops in an Oh-We diagram (see Brodkey, 1967, Gelfand et al., 1973, Pilch and Erdmann, 1987, Samenfink et al., 1994, Simpkins and Bales, 1972, Chou et al., 1997, Chou and Faeth, 1998, Dai and Faeth, 2001, Kolev, 2002, Schmehl, 2003). The relation between transitional We and Oh is shown in Figure 19.42. It can be found that for Oh < 0.1, significant drop deformation begins at Weber numbers of roughly unity and the transition We is essentially constant, whereas Oh becomes important for Oh > 0.1 (Gelfand 1996, Nigmatulin, 1990). This can be interpreted by considering that for small Oh, the liquid viscous forces are small and the aerodynamic drag forces can only be balanced by surface-tension effects. However, as the liquid viscosity increases, liquid viscous forces stabilize the gas dynamic forces. At the lowest We region, droplets are not subject to secondary breakup, but they deform and obtain the shape of oblate spheroids, which may significantly affect their aerodynamic drag properties (Triebnigg, 1929, Taylor 1963, Low and List, 1982). With increasing We, three important outcomes appear in sequence: bag breakup, multimode breakup, and sheet thinning breakup. Schmehl (2003) presented the Oh–We functions characterizing the onset of different drop deformation degrees and breakup regimes in Figure 19.42, as

$$\mathrm{We}=\begin{cases}0.6(1+0.8\mathrm{Oh}^{0.8}+9\times10^{-5}\,\mathrm{Oh}^{2.4}),\ \text{defromation 5\%, no breakup, Oh}<600;\\ 1.1(1+0.7\mathrm{Oh}^{0.85}+1.5\times10^{-4}\,\mathrm{Oh}^{2.4}),\ \text{defromation 10\%, no breakup, Oh}<600;\\ 2.3(1+0.75\mathrm{Oh}^{0.8}+2.5\times10^{-4}\,\mathrm{Oh}^{2.4}),\ \text{defromation 20\%, no breakup, Oh}<600;\\ 3(1+15\mathrm{Oh}^{1.2}),\ \text{drop oscillations, no breakup, Oh}<0.3;\\ 13(1+1.7\mathrm{Oh}^{1.4}),\ \text{bag breakup, Oh}<4;\\ 35(1+0.65\mathrm{Oh}^{1.4}),\ \text{multimode breakup, Oh}<15;\\ 80(1+0.6\mathrm{Oh}^{1.5}),\ \text{sheet thinning breakup, Oh}<6.\end{cases}\tag{19.93}$$

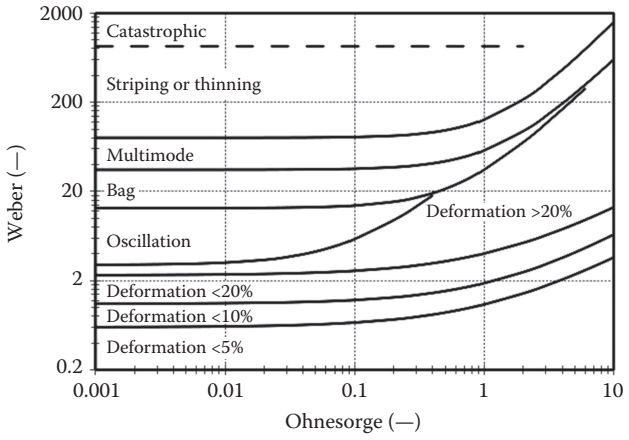


Figure 19.42

Drop deformation and breakup regime map based on Hsiang and Faeth (1995), We = 850 for onset of catastrophic breakup according to Chryssakis and Assanis (2008).

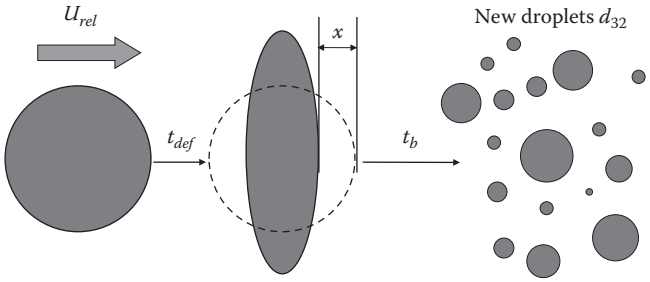


Figure 19.43

Sequential deformation and breakup of a droplet.

At critical conditions, initially the droplet deforms to a disk that finally breaks up into smaller droplets, as illustrated in Figure 19.43. The total breakup time consists of the deformation time t_{def} and the breakup time $t_{breakup}$. The latter describes the time where no further fragmentation occurs.

19.1.7.2 Semiempirical Breakup Models

For computations of the droplet breakup process, models are used that include the following:

- Breakup criteria if the droplet breaks up or not
- An estimation of the deformation time t_{def} and the breakup time $t_{breakup}$
- the resulting droplet size distribution (e.g., in terms of d_{32})
- the spatial distribution of the resulting droplets and their velocities after breakup

In the semiempirical breakup model, the time it takes to deform and disrupt a droplet is described by the characteristic breakup time:

$$t^\star = \frac{d_d}{U_{rel}}\sqrt{\frac{\rho_d}{\rho_g}} \tag{19.94}$$

The initial deformation of a droplet into a disk shape is similar for all breakup modes. The duration of this initial phase is estimated as $t_{def} = 1.6t^\star$ by Hsiang and Faeth (1992). Thereafter, the droplet will fragment depending on the breakup modes. As proposed in Pilch and Erdman (1987), the correlations of $t_{breakup}$ for different intervals of Weber numbers can be formulated as

$$\frac{t_{breakup}}{t^\star} = \begin{cases} 6(\mathrm{We}-12)^{-0.25}, & 12 \le \mathrm{We} < 18 \\ 2.45(\mathrm{We}-12)^{0.25}, & 18 \le \mathrm{We} < 45 \\ 14.1(\mathrm{We}-12)^{-0.25}, & 45 \le \mathrm{We} < 351 \\ 0.766(\mathrm{We}-12)^{0.25}, & 351 \le \mathrm{We} < 2670 \\ 5.5, & \mathrm{We} \ge 2670 \end{cases} \tag{19.95}$$

To account for the viscosity effects observed for Oh > 0.1, a corrected Weber number is used in these relations for the low Oh-number range only (Schmehl, 2000):

$$\mathrm{We}_{corr} = \frac{\mathrm{We}}{1+1.077\mathrm{Oh}^{1.6}} \tag{19.96}$$

When a droplet breaks up, it results in a group of new droplets with a certain size distribution and mean diameter. The SMD d_{32} is computed for bag breakup and multimode breakup from the following relation:

$$\frac{d_{32}}{d_d} = 1.5\mathrm{Oh}^{0.2}\ \mathrm{We}^{-0.25} \tag{19.97}$$

where d_d is the initial droplet diameter. The volume distribution of the child-droplet fragments can be described by a presumed distribution, for example, a root-normal distribution or a log-normal distribution. The MMD $d_{50,3}$ and SMD for the distribution are related by

$$\frac{d_{50,3}}{d_{32}} = 1.2 \tag{19.98}$$

Sheet stripping breakup is characterized by continuous film stripping, leaving a larger core droplet at the end of the breakup process. In the computational model, the maximum stable diameter (d_s) of this droplet is evaluated by

$$d_s = \frac{12\sigma}{\rho_g U_{rel}^2} \tag{19.99}$$

The fine fraction of the droplet fragments is distributed as in bag and multimode breakup regimes based on a reduced SMD $d_{32,red}$, which is derived from the SMD d_{32} given by Equation 19.97 and the maximum stable diameter d_s by Equation 19.99, as follows:

$$d_{32,red} = \frac{4d_{32}d_s}{5d_s - d_{32}} \tag{19.100}$$

Other commonly used droplet breakup models include those based on droplet deformation dynamics and those based on the instability growth on the droplet surface. The former include Taylor analogy breakup (TAB) model, as well as its extensions such as Enhanced TAB (ETAB) and cascade atomization and droplet breakup (CAB) models. The latter include wave breakup model and KH-RT hybrid breakup model.

19.1.7.3 TAB, ETAB, and CAB Model

The TAB model (O'Rourke and Amsden, 1987) treats the oscillation of a distorting droplet with the analogy of a spring-mass system. The external force is represented by aerodynamic force while the restoring force of the spring by the surface tension (σ). The liquid viscosity (μ_l) represents the damping force. Setting $y = 2x/r$, where x is the displacement of the droplet equator from its spherical (undisturbed) position and r is the undisturbed droplet radius (see Figure 19.43), the governing equation of droplet deformation is

$$\ddot{y} = \frac{C_f}{C_b}\frac{\rho_g}{\rho_l}\frac{U_{rel}^2}{r^2} - \frac{C_k\sigma}{\rho_l r^3}y - \frac{C_d\mu_l}{\rho_l r^2}\dot{y} \tag{19.101}$$

where

ρ denotes the density
U_{rel} is the relative droplet-gas velocity
the subscripts g and l denote the gas or liquid properties, respectively

As suggested in O'Rourke and Amsden (1987), the values of the dimensionless constants C_b, C_f, C_k, and C_d are 0.5, 1/3, 8, and 5, respectively. It is argued in the TAB model that a necessary condition for droplet breakup is reached when $We_g > We_{crit}$, where the critical Weber number is experimentally determined as $We_{crit} = 6$. The gas Weber number used in TAB, ETAB, and CAB model is based on the droplet radius, that is, $We_g = \rho_g U_{rel}^2 r/\sigma$. For an inviscid liquid, this condition is met when $y(t) > 1$. The breakup time is taken to be the smallest positive root of the deformation equation $y(t) = 1$. By balancing the deformation energy and surface energy before and after breakup, the expression for the Sauter mean radius (r_{32}) of the child droplets after breakup can be derived as

$$\frac{r}{r_{32}} = 1 + \frac{8K}{20} + \frac{\rho_l r^3}{\sigma}\left(\frac{6K-5}{120}\right)(\dot{y})^2 \tag{19.102}$$

where K is a constant that must be evaluated experimentally by measuring droplet sizes. O'Rourke and Amsden (1987) suggest a value of $K = 10/3$. It is assumed that the product droplets are neither distorted nor

oscillating, that is, $y = \dot{y} = 0$. The TAB model also predicts a velocity of the product droplets normal to the path of the parent droplet, approximately by $U_\perp = \dot{x}$.

The effect of deformation on droplet motion can be significant. For example, at maximum deformation typical at the onset of breakup, drag forces on the droplet are increased by a factor of 4 for steady disturbance and 13 for shock loading due to the droplet-distortion-induced increase in drag coefficient C_d and the cross-sectional area of the droplet (Hsiang and Faeth, 1995). Therefore, when the droplet is deformed into a disk, the drag coefficient needs to be changed accordingly. The distortion parameter y can be used to modify the drag coefficient to account for the droplet deformation by using the relation

$$C_{d,y} = C_{d,sphere}(1 + 2.63y) \tag{19.103}$$

proposed by Liu et al. (1993), where $C_{d,y}$ is the drag coefficient for the deformed droplet and $C_{d,sphere}$ is that of the initially spherical droplet.

The ETAB model developed in Tanner (1997) maintains the droplet deformation dynamics of the TAB model, that is, droplet breakup occurs when the normalized droplet distortion y exceeds the critical value of 1. However, for each breakup event, the ETAB model assumes that the rate of product droplet generation is proportional to the number of the product droplets. From this, the rate of droplet creation, in conjunction with the mass conservation principle, leads to the basic ETAB law

$$\frac{d\bar{m}(t)}{dt} = -3K_{br}\bar{m}(t) \tag{19.104}$$

where $\bar{m}(t)$ denotes the mean mass of the product droplet distribution. The breakup constant K_{br} depends on the breakup regime (bag or stripping breakup) according to the gas Weber number as follows:

$$K_{br} = \begin{cases} k_1\omega, & \mathrm{We}_g \le \mathrm{We}_{trans} \\ k_2\omega\sqrt{\mathrm{We}_g}, & \mathrm{We}_g > \mathrm{We}_{trans} \end{cases} \tag{19.105}$$

with $k_1 = 2/9$, $k_2 = 2/9$ and $\mathrm{We}_{trans} = 80$ (Tanner, 1997). The droplet oscillation frequency ω is given by

$$\omega^2 = C_k\frac{\sigma}{\rho_l r^3} - \left(\frac{C_d\mu_l}{2\rho_l r^2}\right)^2 \tag{19.106}$$

with $C_k = 8$ and $C_d = 5$ (O'Rourke and Amsden, 1987). With an assumption of a uniform product droplet size distribution, Equation 19.104 becomes

$$\frac{r_{new}}{r} = e^{-K_{br}t} \tag{19.107}$$

where r_{new} and r are the radii of the product and parent droplets, respectively. As in the TAB model, after breakup of a parent droplet, the initial deformation parameters of the product droplets are set to $y = \dot{y} = 0$. Also, the product droplets are initially supplied with a velocity component perpendicular to the path of the parent droplet with a value $U_\perp = A\dot{x}$, where A is a constant determined by balancing the deformation energy and surface energy before and after breakup, as follows:

$$A^2 = 3\left[1 - \frac{r}{r_{32}} + \frac{5C_d\mathrm{We}_g}{72}\right]\frac{\omega_0^2}{\dot{y}^2} \tag{19.108}$$

where C_d is the aerodynamic drag coefficient and $\omega_0^2 = 8\sigma/(\rho_l r^3)$. For inviscid, large Weber droplets with initial deformation conditions $y(0) = \dot{y}(0) = 0$, one obtains the relation

$$A^2 = \frac{5C_D}{4} + \frac{18(1 - r/r_{32})}{\mathrm{We}_g} \tag{19.109}$$

For a breakup of a droplet with $We_g = 250$, $C_D = 0.5$, and $r_{32}/r = 0.65$, Equation 19.109 yields $A \approx 0.77$. As in the TAB model where $A = 1$, this radial velocity contributes to the radial expansion of the spray.

The CAB model proposed by Tanner (2004) is a further development of the ETAB model. In the CAB model, the breakup condition is determined by means of the droplet deformation dynamics of the TAB model, and the definition of the rate of droplet creation follows the pattern of the ETAB model (Equation 19.104). However, the individual droplet breakup regions, which, in the ETAB model, were restricted to either bag ($We_{crit} < We_g < We_{b,s}$) or stripping breakup ($We_{b,s} < We_g < We_{s,c}$) have been extended to include the catastrophic breakup regime ($We_{s,c} < We_g$) to accommodate the disintegration of the high-speed droplets. Correspondingly, the breakup constant K_{br} for each breakup regime can be expressed as

$$K_{br} = \begin{cases} k_1\omega, & We_{crit} < We_g < We_{b,s} \\ k_2\omega\sqrt{We_g}, & We_{b,s} < We_g < We_{s,c} \\ k_3\omega(We_g)^{3/4}, & We_{s,c} < We_g \end{cases} \tag{19.110}$$

where the droplet oscillation frequency ω is given by Eq. s-34. In Tanner (2004), the regime-dividing Weber numbers are taken to be $We_{b,s} = 80$ and $We_{s,c} = 350$, and the constant $k_1 = 0.05$ is determined, whereas the values for the constants k_2 and k_3 are chosen such that K_{br} is continuous at the regime-dividing Weber numbers, $We_{b,s}$ and $We_{s,c}$. The way to deal with the velocity of the product droplets in the CAB model is same as that in the ETAB model.

19.1.7.4 Wave and KH-RT Hybrid Breakup Model

The wave breakup model or the Kelvin–Helmholtz (KH) breakup model, developed by Reitz and Diwakar (1987) and further improved by Reitz (1987), assumes that breakup is caused by KH instability on the surface of a cylindrical "blob" of liquid. Under the assumption that the size of the striped-off product droplets is proportional to the length of the fastest growing wave, the wave model postulates that a parent parcel with radius, r, breaks up to form new droplets with radius, r_{new}, as follows:

$$r_{new} = B_0\Lambda_{KH} \tag{19.111}$$

where

Λ_{KH} is the wavelength corresponding to the KH wave with maximum growth rate (Ω_{KH})

B_0 is a constant equal to 0.61

Linear analysis of KH instabilities on a round liquid jet gives the frequency of the fastest-growing wave (Ω_{KH}) and its corresponding wavelength (Λ_{KH}) as follows:

$$\Omega_{KH} = \frac{0.34 + 0.38We_g^{1.5}}{(1+Oh)(1+1.4(Oh\sqrt{We_g})^{0.6})}\sqrt{\frac{\sigma}{\rho_l r^3}} \tag{19.112}$$

$$\Lambda_{KH} = \frac{9.02r(1+0.45\sqrt{Oh})(1+0.4(Oh\sqrt{We_g})^{0.7})}{(1+0.865We_g^{1.67})^{0.6}} \tag{19.113}$$

The definitions of gas Weber number (We_g) and Ohnesorge number (Oh) can be found in Equations 19.7 and 19.8, respectively, but with a substitution of droplet diameter with droplet radius in both equations. During breakup, the parent parcel reduces in diameter due to the loss of mass. The rate of change of the radius of the parent parcel is calculated using

$$\frac{dr}{dt} = \frac{r - r_{new}}{\tau_{KH}} \tag{19.114}$$

where τ_{KH} is the breakup time defined by

$$\tau_{KH} = \frac{3.726B_1 r}{\Omega_{KH}\Lambda_{KH}} \tag{19.115}$$

The constant B_1 has been given a variety of values between 1.73 and 60 (Patterson, 1997, Patterson and Reitz, 1998).

In the KH-RT hybrid atomization model (Patterson, 1997, Patterson and Reitz, 1998, Beale and Reitz. 1999), the wave model is employed to predict the primary breakup of the intact liquid core of a liquid jet. The secondary breakup of individual droplets is modeled with the wave model in conjunction with the RT accelerative instability model. The hybrid model is allowed to grow KH instability and RT instability simultaneously, and the fastest growing instability leads to a droplet breakup event. In the RT model, the frequency of the fastest growing wave is given by

$$\Omega_{RT} = \sqrt{\frac{2}{3\sqrt{3\sigma}} \frac{[-g_t(\rho_l - \rho_g)]^{3/2}}{\rho_l + \rho_g}} \tag{19.116}$$

where g_t is the acceleration in the direction of travel and is defined by $g_t = \mathbf{g} \cdot \mathbf{j} + \mathbf{a} \cdot \mathbf{j}$, where $\mathbf{a}$ is the droplet acceleration, and $\mathbf{j}$ is the unit vector tangent to the droplet trajectory. The corresponding wavelength is

$$\Lambda_{RT} = 2\pi C_{RT} \sqrt{\frac{3\sigma}{-g_t(\rho_l - \rho_g)}} \tag{19.117}$$

where C_{RT} is an adjustable constant set equal to 0.1 (Beale and Reitz, 1999). The RT waves are only allowed to form on the droplet when the diameter of the droplet is larger than the wavelength of the fastest growing disturbances (i.e., $d > \Lambda_{RT}$). The radii of new droplets are given by

$$r_{new} = \frac{\Lambda_{RT}}{2} \tag{19.118}$$

The breakup time in the RT model is calculated using

$$\tau_{RT} = \frac{C_\tau}{\Omega_{RT}} \tag{19.119}$$

where C_τ is a constant usually equal to unity beyond the breakup length, and is equal to 9.0 within the breakup length.

19.1.7.5 Empirical Extension of Droplet Deformation Model

In many application scenarios, the time scale of deformation and breakup is comparable to or larger than the characteristic scales of the gas flow fluctuations, that is, the relative velocity varies significantly during the deformation and breakup process (Schmehl, 2004). In these cases, the deformation and breakup process and the resulting characteristics of secondary fragments do not depend only on instantaneous local flow situations but also on the variation of aerodynamic forces during the disintegration process. As an empirical extension of dynamic droplet deformation model, the breakup model proposed by Bartz et al. (2010) takes into account the temporal evolution of the aerodynamic loading of the droplet. A critical deformation is used as breakup criterion. The actual disintegration process is described empirically.

In Bartz et al. (2010), the subcritical deformation as well as the initial deformation phase during breakup is computed by the nonlinear Taylor analogy breakup (NLTAB) model (Schmehl, 2002). The NLTAB model is a nonlinear variant of the TAB model and is based on the experimental observation that the droplet deformation airflows can be represented by spheroidal (oblate and prolate) shapes. The NLTAB model describes the droplet deformation dynamics in terms of the nondimensional equator coordinate y, which is defined as the ratio of the cross-stream diameter to the spherical diameter $y = D/D_0$. By balancing the kinetic energy of the deformation with the surface energy change, the work performed by the surface pressure and the energy dissipation in the droplet on the time scale $T = t/t^*$ (t^*, the characteristic breakup time, see Equation 19.94), the NLTAB model gives the governing equation of the droplet deformation as

$$\frac{\pi^2 + 16/y^6}{\pi^2 + 16} \frac{d^2y}{dT^2} - \frac{48}{\pi^2 + 16} \frac{1}{y^7} \left(\frac{dy}{dT} \right)^2 + \frac{40}{\mathrm{Re}_{def}} \frac{1}{y^2} \frac{dy}{dT} + \frac{20}{\mathrm{We}_g} \frac{1}{S_0} \frac{dS}{dy} = \frac{2C_2}{y} \tag{19.120}$$

where the Reynolds number Re_{def} is given by

$$\mathrm{Re}_{def} = \frac{U_{rel} D_0}{\mu_l} \sqrt{\rho_g \rho_l} \tag{19.121}$$

and the term relative to the normalized rate of surface change can be expressed by the polynomials of the nondimensional equator coordinate y as follows:

$$\frac{1}{S_0}\frac{dS}{dy} = \begin{cases} 9.98y^3 - 30.34y^2 + 33.94y - 13.58, & 0.5 < y < 1; \\ 0.67y^3 - 4.01y^2 + 9.21y - 5.67, & 1 \le y < 2.3. \end{cases} \tag{19.122}$$

where S_0 is the initial surface of the undeformed droplet and C_2 is an adjustable constant. The aerodynamic drag coefficient C_d of the droplet is determined from a linear interpolation between the drag coefficient of a spherical droplet and a disk shaped droplet, that is,

$$C_d = fC_{d,sphere} + (1-f)C_{d,disc}, \quad \text{with } f = 1 - E^2 \tag{19.123}$$

where E is the droplet aspect ratio defined as $E = 1/y^3$ (Schmehl, 2002).

The linear equation of the TAB model (Equation 19.101) can be reformulated according to the notation of Schmehl (2002, 2004) into

$$\frac{d^2y}{dT^2} + \frac{40}{\mathrm{Re}_{def}}\frac{dy}{dT} + \frac{64}{\mathrm{We}_g}(y-1) = 2C_2 \tag{19.124}$$

The TAB model suggests $C_2 = 2/3$. The critical deformation, $y_c = 1.5$, is reached at a critical Weber number $\mathrm{We}_c = 12$.

Schmehl (2004) performed calculations of the maximum nondimensional equator coordinate for shock-loaded droplets with Oh < 0.1 using the NLTAB model. At the onset of bag breakup for a critical Weber number of $\mathrm{We}_c = 13$, a maximum deformation of

$$y_c \approx 1.8 \tag{19.125}$$

is found. Experimental data from Kim (1977) confirm this critical deformation. Aalburg et al. (2003) performed DNSs of shock-loaded droplets. They concluded that the critical deformation noted in Equation 19.125 is a good estimate of the critical deformation at the onset of breakup for a large range of Ohnesorge numbers.

For higher We_g, the maximum nondimensional coordinate reaches higher amplitudes before breakup. By analyzing experimental data for shock-loading conditions (Dai and Faeth, 2001), it can be concluded that the maximum nondimensional coordinate of disintegrating droplets reaches maximum amplitude

$$y_{\max} \approx 2.1, \quad \text{for } \mathrm{We}_g > 20 \tag{19.126}$$

In Bartz et al. (2010), droplet deformation is modeled by the NLTAB model until a maximum deformation nondimensional coordinate ($1.8 < y_{\max} < 2.1$) is reached. After that, the droplet deformation and breakup process is modeled based on the empirical data from experiments in a shock tube. Therefore, a corresponding shock loading state is calculated when the maximum deformation is reached. The initial gas Weber numbers corresponding to the shock loading state are derived and taken into Equation 19.95 to obtain the total breakup time. Fragment sizes resulting from secondary atomization can be predicted by a global statistical atomization product model as proposed in the semiempirical breakup model or by the detailed atomization product model, which Bartz et al. (2010) obtained by analyzing the experimental data from Chou et al. (1997), Chou and Faeth (1998), and Dai and Faeth (2001). The detailed atomization product model accounts for the volume fraction of the fine droplets produced by the fragmentation of the bag during bag and bag-plume breakup.

Bartz et al. (2011) presented the comparison of droplet trajectories for bag breakup, as illustrated in Figure 19.44. The trajectory of the droplet in the experiment is plotted as a solid line with circles.

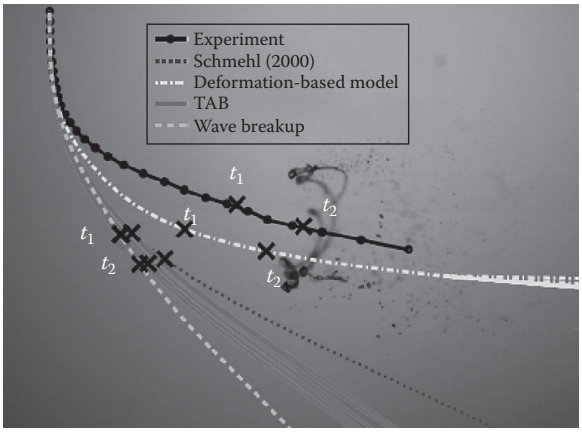


Figure 19.44

Comparison of trajectories for bag breakup, makers denote droplet position at t_1 (fragmentation of the bag) and t_2 (fragmentation of the rim); high-speed-image at t_2 in the background; $We_{max} = 15$. (Adapted from Bartz, F.O. et al., Model comparison for single droplet fragmentation under varying accelerations, in *Proceedings of ILASS-Europe 2011*, Estoril, Portugal, September 5–7, 2011.)

The time when the fragmentation of the bag begins, t_1, and a time t_2 during the fragmentation of the rim are marked. The trajectory predicted with the semiempirical model of Schmehl (2000) is displayed as a dotted line. As stated before, in this model, the characteristic times are calculated based on the instantaneous Weber number at the time step when We_c is first exceeded. The breakup time is overestimated, and fragmentation begins at a location, which is not in the field of view. Trajectories calculated with the TAB model are displayed as solid lines. The droplet exceeded the critical deformation at an early stage and then fragments are released. The trajectories deviate from the experimental trajectory. The calculation using the wave breakup model did not predict fragmentation. As stated earlier, the physics behind this model is only valid for high We. The droplet trajectory as well as the temporal evolution of the trajectory predicted with the deformation-based model showed a better agreement to experimental results than predictions with the other models.

The results based on a semiempirical breakup model (Markus and Fritsching, 2003b) are illustrated in Figure 19.45. Here, atomization in a twin-fluid gas atomizer configuration is studied. In this direct numerical approach, each particle has been tracked throughout the flowfield. Droplet deformation and breakup are considered. If a ligament/droplet breaks up, all daughter droplets created are further tracked. The gas velocity distribution is based on measurements. Figure 19.45 shows a typical cumulative droplet size

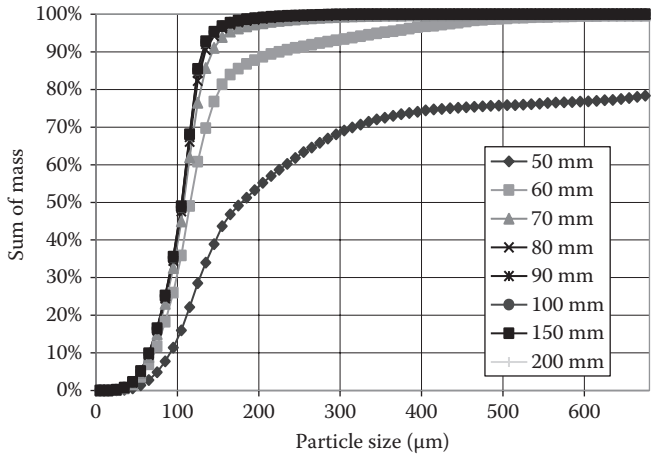


Figure 19.45

Secondary drop fragmentation in liquid spray: evolution of the drop size distribution versus the distance to the atomizer nozzle. (From Markus and Fritsching, 2003b. With permission.)

distribution at increasing distances from the atomizer. Most droplets are created in a short distance behind the region of the primary breakup. Then, the droplets are accelerated and spread out due to turbulence.

19.1.8 Special Liquids

19.1.8.1 Highly Viscous Liquids

Atomization of very viscous liquids (i.e., at dynamic viscosities above 1 Pa s) is a difficult task as these liquids exhibit a certain resistance to the primary deformation process. In this context, prefilming of the liquid stream is a possibility to enhance the size of the gas/liquid interface area prior to the atomization process and therefore contribute to the efficiency of the primary fragmentation mechanism. Prefilming of the liquid stream may be achieved by

- Geometrical arrangement of the liquid feed (in twin-fluid atomization)
- Centrifugal forces (in rotary or pressure-swirl atomization)
- Pressure forces (in ultrasonic standing wave atomization [USWA])

In a variant of the effervescent atomizer (internal mixing), Campanile and Azzopardi (2003) used a mixing chamber that was designed to create annular liquid flow in the nozzle to enhance interaction between gas and liquid (see Figure 19.46). Newtonian liquids at viscosities up to 50 Pa s have been atomized with air. The liquid mass flow rate was approximately 50 kg/h. In Figure 19.47, spray patterns in the fragmentation area are to be seen. For higher viscosities, the liquid is more pronounced to form fibers within primary fragmentation. In Figure 19.47, the MMD achieved at liquid viscosities of 5 and 50 Pa s is illustrated. Typical droplet sizes achieved are in the range of several millimeters. From a model based on the observation that ligaments are formed from the annular film rim acting against surface tension, which tends to form a new liquid surface, the optimum wavelength for lateral instability is

$$\lambda_{opt} = 2\pi\sqrt{\frac{3\sigma}{\rho_l A_c}} \quad \text{where } A_c = \frac{1}{\rho_l}\frac{dp}{dx} + g \tag{19.127}$$

By taking into account the effects of viscosity and compressibility, especially for very viscous liquids at higher air velocities, the model is in good agreement with measured particle sizes.

Effervescent atomization of PVP K30 aqueous solutions was investigated by Schröder et al. (2013). The shear viscosity of PVP K30 solutions increases with increasing mass fraction. The breakup of PVP K30 solutions is changed significantly by their viscosity. With increasing viscosity, the breakup

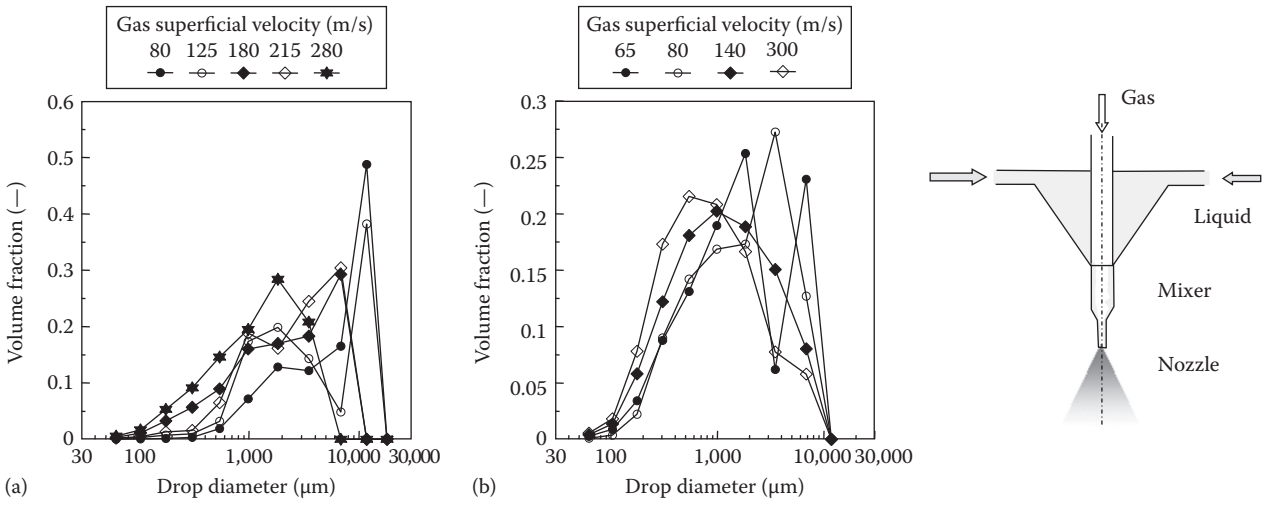


Figure 19.46

MMD for internal mixing twin-fluid atomization of highly viscous liquid; (a) u_l = 0.15 m/s, μ = 50 Pa s, (b) u_l = 0.07 m/s, μ = 5 Pa s. (From Campanile, F. and Azzopardi, B.J., Atomisation of very viscous liquids, in *Proceedings of International Conference on Liquid Atomization and Spray Systems ICLASS 2003*, Sorrento, Italy, 2003. With permission.)

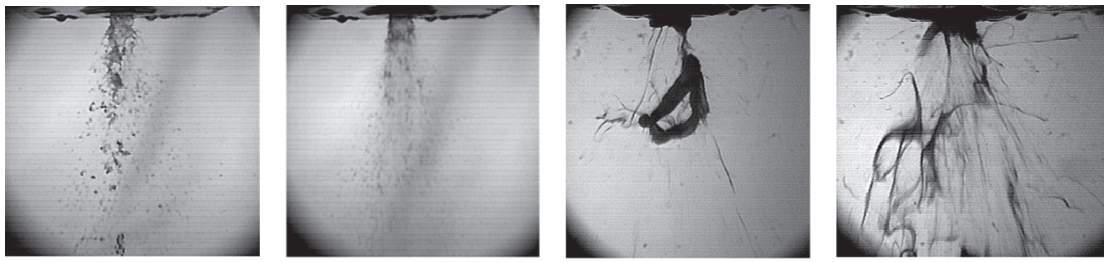


Figure 19.47

Fragmentation process and spray pattern in viscous liquid atomization: for liquid viscosity = 0.001 Pa s and liquid superficial velocity = 0.15 m/s, (a) gas superficial velocity = 51 m/s, (b) gas superficial velocity = 116 m/s; for liquid viscosity = 5 Pa s and liquid superficial velocity = 0.15 m/s, (c) gas superficial velocity = 70 m/s, (d) gas superficial velocity = 256 m/s. (From Campanile, F. and Azzopardi, B.J., Atomisation of very viscous liquids, in *Proceedings of International Conference on Liquid Atomization and Spray Systems ICLASS 2003*, Sorrento, Italy, 2003. With permission.)

changes from complete breakup into drops directly at the nozzle orifice outlet to an incomplete breakup with ligaments present, as shown in Figure 19.48. The corresponding SMD and the standard deviation (representing the width of the drop size distribution) increase with increasing viscosity as well. The air-to-liquid ratio by mass (ALR) has comparably less impact on the breakup at the nozzle orifice outlet, as shown in Figure 19.48. Nevertheless, an increasing ALR results in decreasing SMDs and standard deviations. The atomizer geometry (by changing nozzle orifice length) has a minor impact on the breakup and the resulting drop size distribution.

The application of the atomizing media (gas) from inside of an annular liquid sheet results in a radial droplet size variation in the spray that shows increasing drop size values with increasing radius (Lohner et al., 2003). On the other hand, typical twin-fluid atomizers with external mixing show decreasing droplet sizes at the outer side of the spray with increasing radius. The reason in both cases is as follows: the specific gas velocity distribution and the kinetic energy of the gas are partially absorbed by the dispersed phase. Based on these results, a prefilming atomizer with inner and outer atomization has been proposed for highly viscous liquids, as shown in Figure 19.57 (later in the chapter). This atomizer essentially is a combination of an external mixing atomizer and the internal atomizer. The aim is that by this design the gas/liquid

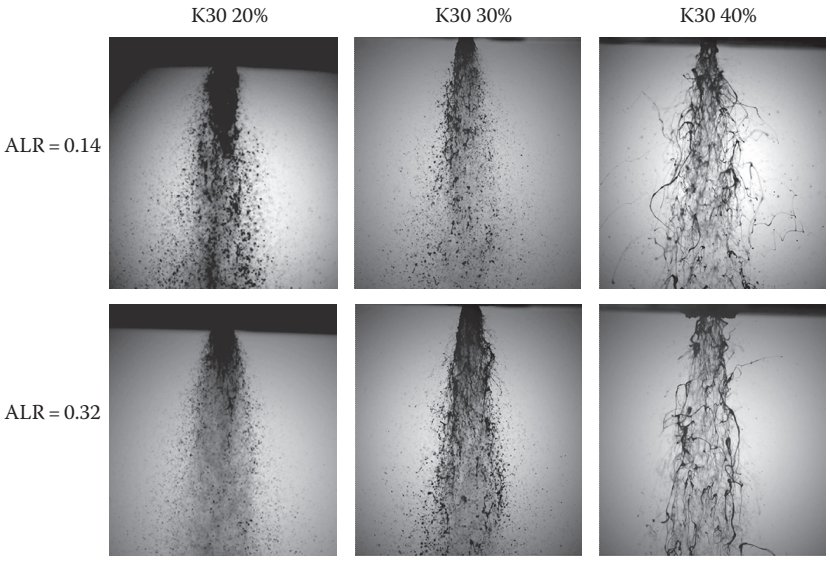


Figure 19.48

Shadowgraphy pictures of liquid breakup acquired at two different ALRs of 0.14 and 0.32 for sprays of PVP K30 solutions at different mass fractions. The diameter of the liquid jet at the nozzle orifice outlet is 1.5 mm. (Adapted from Schröder, J. et al., *Atom. Spray*, 23(1), 1, 2013. With permission.)

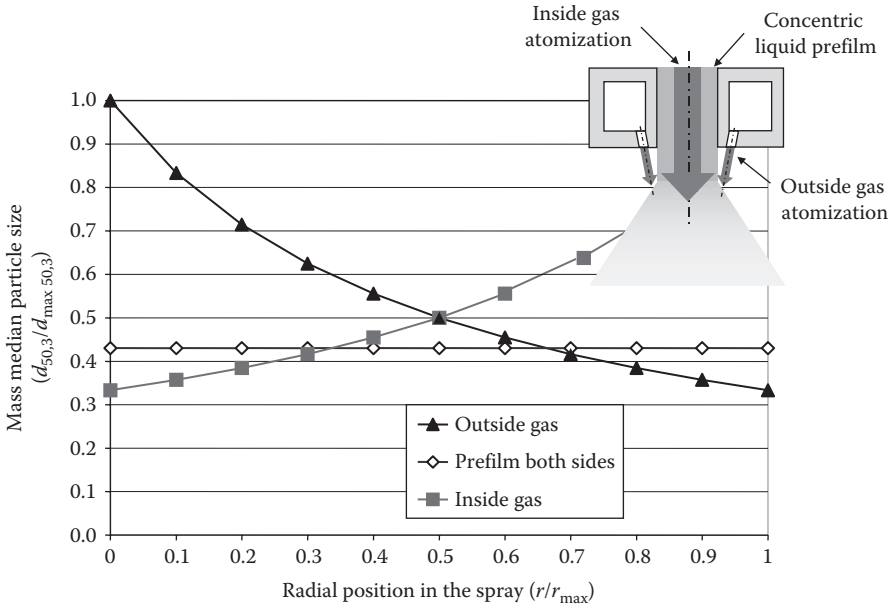


Figure 19.49

Atomizer configuration for viscous liquids and high throughputs, radial droplet size distribution in spray. (From Lohner, H. et al., Impact of gas nozzle arrangement on the flow field of a twin fluid atomizer with external mixing, in *Proceedings of International Conference on Liquid Atomization and Spray Systems ICLASS 2003*, Sorrento, Italy, 2003. With permission.)

contact area is increased for fragmentation of viscous liquids and that a more homogeneous particle size distribution across the spray cross section can be obtained compared to the other two individual atomizers described before. In Figure 19.49, the principal behavior for the radial distribution of the mean droplet sizes in the spray is shown. The mass median particle size is nearly constant when the pressure ratio between the inside and the outside nozzles is unity, as has been verified in experiments (Lohner et al., 2003).

As described in Section 19.1.3, the USWA process is a very suitable method for atomization of highly viscous liquids. The sound radiation pressure within the resonant ultrasound field between two opposing sonotrodes leads to a deformation of the cylindrical feed liquid jet into a disk-shaped film (see Figure 19.10), thereby accelerating the liquid radially outward. At the rim of the disk, additional suction forces are acting. Here, the sheet becomes unstable and disintegrates into droplets/ligaments. The tensile forces in the sheet support the disintegration process at the rim of the disk especially for viscous liquids. In Figure 19.50, a comparison of a liquid atomization photo and a direct simulation of the primary fragmentation process within the USWA process is illustrated (Reipschläger, 2002, Reipschläger et al., 2002). The MMD achieved with USWA atomization of a Newtonian viscous liquid (up to 10 Pa s), as measured by Hansmann (1996), is shown in Figure 19.51 as a function of the liquid throughput.

19.1.8.2 Melts (Polymers, Minerals, or Metals)

Melts of polymers, metals, and glass or ceramic materials are atomized for powder production or coating/preforming applications. In the atomization process of molten materials, in addition to their typically difficult material properties,* the atomization process must ensure that sufficient thermal energy is available in the area close to the atomizer in order to prevent liquid fragments that may get in contact with the atomizer from sticking and freezing. Here, typical process problems in melt atomization arise (Bauckhage et al., 2001). Also, for achieving almost spherical particles, the cooling and solidification of the liquid fragments after atomization needs to be finished after a sufficiently high residence time in the molten stage for the liquid droplets (solidification time < spheroidization time). In addition to the thermal-related freezing problem within the melt nozzle, chemical- or metallurgical-related problems in melt delivery systems are also found frequently in applications. Problems may arise from melt/tundish reactions or melt segregational effects from diffusion.

* Polymer solutions or melts typically are highly viscous and show non-Newtonian flow behaviour, metal melts have high surface tensions, and ceramic melts have high viscosities that drastically change with melt temperature.

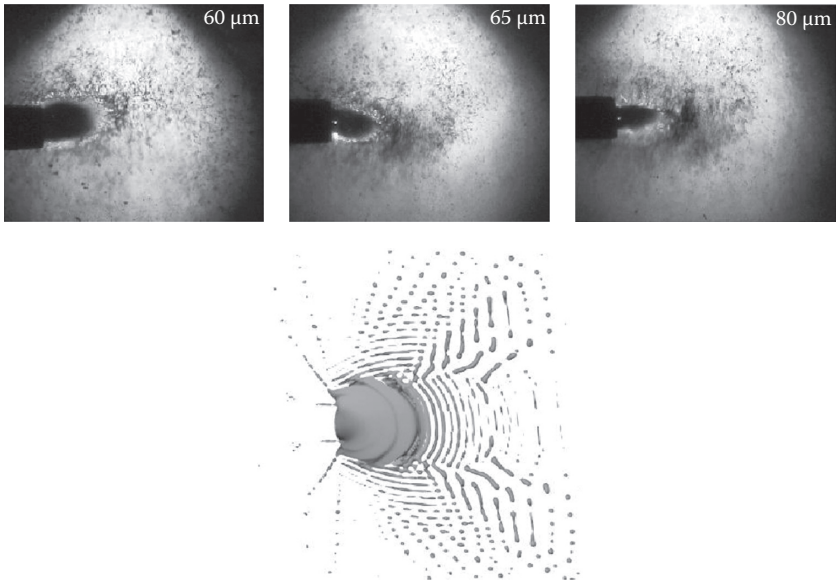


Figure 19.50

Atomization process in USWA, comparison of experiment and simulation. (From Reipschläger, O. et al., Modelling and simulation of the disintegration process in ultrasonic standing wave atomizers, in *Proceedings of 18th Annual Conference on Liquid Atomization and Spray Systems ILASS Europe*, Zaragoza, Spain, 2002. With permission.)

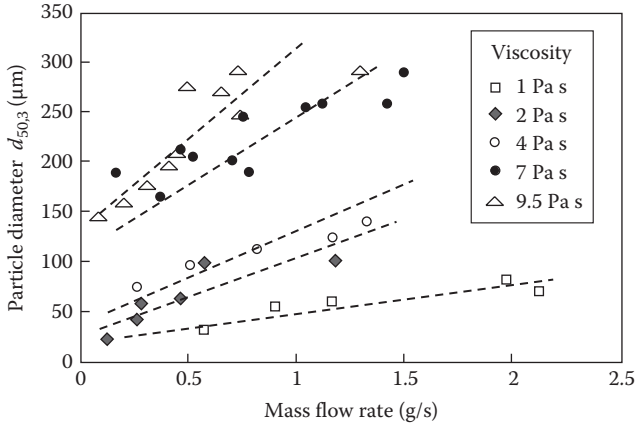


Figure 19.51

MMD within viscous fluid disintegration by USWA. (Adapted from Hansmann, S., Einfluss von Stoff-und Betriebsparametern auf die Zerstäubung hochvoskoser Flüssigkeiten im Ultraschall-Stehwellenfeld, Dissertation, Universität Bremen, Bremen, Germany, 1996.)

Polymer melts may be sufficiently atomized by using the USWA technique (Reipschläger, 2002, Reipschläger et al., 2002) or gas atomization (Watkinson et al., 2001). The energy requirement to overcome the effect of viscosity and surface tension in atomization may be expressed by the ratio of liquid Weber and Reynolds numbers as follows:

$$\frac{E_\mu}{E_\sigma} = \frac{\mu_l u_{rel}}{\omega} = \frac{\mathrm{We}_l}{\mathrm{Re}_l} \tag{19.128}$$

Typically, this ratio is below 1 for a steel melt and above 1000 for polymers.

Mineral melts like glass or slags (e.g., from blast furnace process) have a high viscosity and a low surface tension compared to other melts. When these types of melts are conventionally atomized under cold conditions,

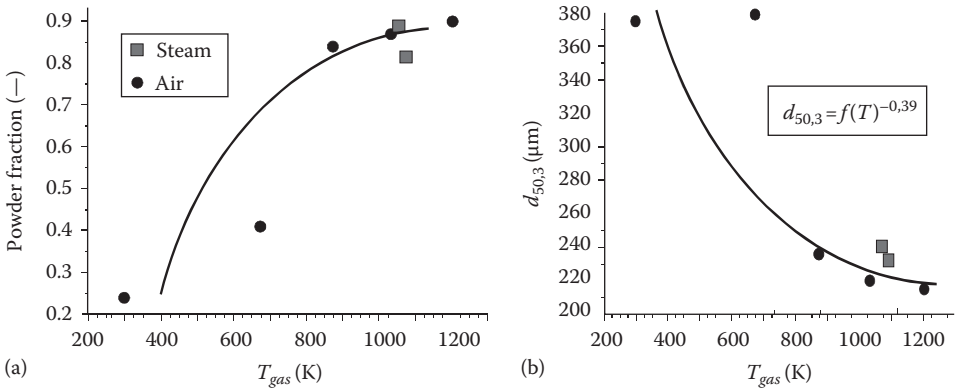


Figure 19.52

(a) Powder fraction and (b) mass median particle size for mineral melt atomization at increased gas temperatures. (From Lohner, H., Zerstäuben von Mineralscmelzen mit Heißgas, Dissertation, Universität Bremen, VDI-Verlag, Düsseldorf, Germany, 2003. With permission.)

the material characteristics lead to a fiber product or at least to a product with a high fiber content instead of a particle product because the viscosity steadily and dramatically increases with decreasing temperature within the atomization process. Thus, it is possible to disintegrate the melt stream into ligaments, because of the high temperature and the low viscosity at the beginning of the atomization process. However, as the temperature of the ligaments decreases and the viscosity increases rapidly, the ligaments cannot be disintegrated further into smaller particles in the secondary atomization step. Therefore, the ligaments remain in a fiber state. To prevent the early termination of the atomization after the first fragmentation step and to allow further disintegration of the ligaments, one possibility is to increase the atomizing gas temperature. The lower temperature difference between the hot atomizer gas and the melt results in a lower heat transfer. Thus, the melt stays longer in a liquid state at low viscosity and the atomization process can finish and finally the fragments spheroidize into globular particles. Figure 19.52a shows as an experimental result the continuous decrease of the fiber content of a gas atomized ceramic melt with increasing gas temperature (Lohner, 2003, Lohner et al., 2005). An external mixing twin-fluid atomizer was used, where a maximum gas temperature of 1000°C could be achieved. In Figure 19.52b, it is evident that in addition to the decrease of the particle size, the efficiency of the atomization process increases with increasing gas temperature (the gas mass flow rate at constant gas pressure is decreasing with increasing gas temperature, see also Strauss, 1997). Here, the MMD of the powder fraction decreases with increasing gas temperature. From an energetic point of view, Strauss and Dunkley (2000) showed that the particle diameter at constant gas pressure and increasing gas temperature should vary as follows:

$$d = KT^{-0.25} \tag{19.129}$$

This correlation has been validated in (molten metal) atomization trials (Strauss and Dunkley, 2000). Experiments for a ceramic melt have shown an exponent that is approximately −0.4 (Czisch et al., 2003).

It has been shown by Lohner (2003) and Lohner et al. (2005), that in the case of hot gas atomization of a viscous ceramic melt, the velocity difference between melt and gas has a primary effect on the atomization process. The kinetic energy of the gas (ρu^2) is constant (for constant gas pressure) with increasing gas temperature. Therefore, assuming a constant surface tension, the aerodynamic Weber number We_g is constant and not a function of the gas temperature:

$$We_g = \frac{\rho_g \cdot \Delta u^2 \cdot D_l}{\sigma} = \text{const.} \tag{19.130}$$

The influence of the increasing shearing action between the melt jet and the gas flow with increasing gas temperature and constant gas pressure is formulated in the gas Reynolds number Re_g formed with the relative velocity Δu between gas flow and melt jet. By rearrangement, the gas Reynolds number may be written as

$$Re_g = \frac{\rho_g \cdot \Delta u \cdot D_l}{\mu} = \frac{\rho_g \cdot \Delta u^2}{\mu(\Delta u / D_l)} \tag{19.131}$$

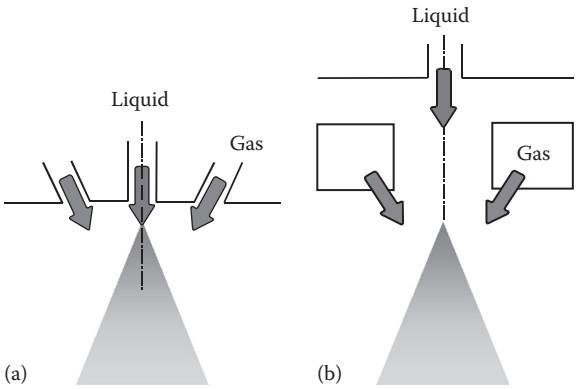


Figure 19.53

Twin-fluid atomizer: (a) close-coupled and (b) free-fall atomizer principles.

Several atomization mechanisms and devices are used for disintegration of *molten metals*, an overview has been given by Lawley (1992), Bauckhage (1992), Yule and Dunkley (1994), Liu (2000b), and Nasr et al. (2002). Especially, twin-fluid atomization by means of (inert) gases or liquids (water) is used because of

- The possibility of high throughputs and disintegration at high mass flow rates
- The high heat transfer rates for rapid cooling of the melt droplets
- The direct delivery of kinetic energy to accelerate the droplets (for compaction purposes)
- The minimization of oxidation by use of inert gases

In most gas atomization cases with external mixing, the central melt jet stream is surrounded by a gas flow from a single (slit) jet configuration or a set of discrete gas jets, which are flowing parallel or inclined toward the melt stream. The coaxial atomizer gas usually exits the atomizer at high pressures with a high kinetic energy. Two main configurations and types of external mixing twin-fluid atomizers need to be distinguished as they result in different fragmentation characteristics. The first one is the confined or close-coupled atomizer and the second is the free-fall atomizer (Figure 19.53). The gas flow in the close-coupled atomizer immediately covers the flowing melt jet. Within the confined atomizer, the distance between gas exit and melt stream is smaller than in the free-fall arrangement, where the melt jet moves a certain distance in the direction of gravity before the gas flow impinges onto the central melt jet; therefore, the close-coupled configuration generally results in higher atomization efficiencies (in terms of smaller particles at identical energy consumption). But the confined atomizer type is more susceptible to freezing problems of the melt at the nozzle tip. This effect can be due to the extensive cooling of the melt by the expanding gas flow, which exits in the close-coupled type near the melt stream and contributes to rapid cooling of the melt at the tip of the melt nozzle. The thermal-related freezing problem is most important directly in the initial phase of the spray process when the melt stream is initiated and exits the nozzle for the first time. At that point, the nozzle tip is still cool and needs to be heated first either externally or by the hot melt flow.

In a close-coupled atomizer, the liquid/melt typically is prefilmed at the nozzle face due to the action of the gas recirculation from the concentric arrangement (see Figure 19.54 adapted from Ünal, 1987, 1989). Modeling the fragmentation process of metal melts within a close-coupled atomizer arrangement has been derived by Antipas et al. (1993) and Liu (1997). Based on experimental observations of fragmentation processes within atomization in close-coupled atomizers (Ünal, 1987, Anderson and Figliola, 1988, Anderson and Terpstra, 2002, Ting et al., 2002), it is assumed that (at least under general conditions) the emerging fluid from the atomizer is moving from the tundish exit as a radial film at the lower side of the nozzle tip toward the gas jets delivery area. The local liquid film thickness τ_f is derived from a Couette flow analogy as follows:

$$\tau_f = \left[\frac{\mu_l}{\mu_g} \frac{\dot{m}_l}{\pi \rho_l r} \left(\frac{du_g}{dz} \right)^{-1} \right]^{0.5} \tag{19.132}$$

At the outer edge of the wetted nozzle tip, the liquid film is influenced by the gas flow field and is reflected into the main gas flow direction. From this point on, the liquid moves as a free concentric ring configuration

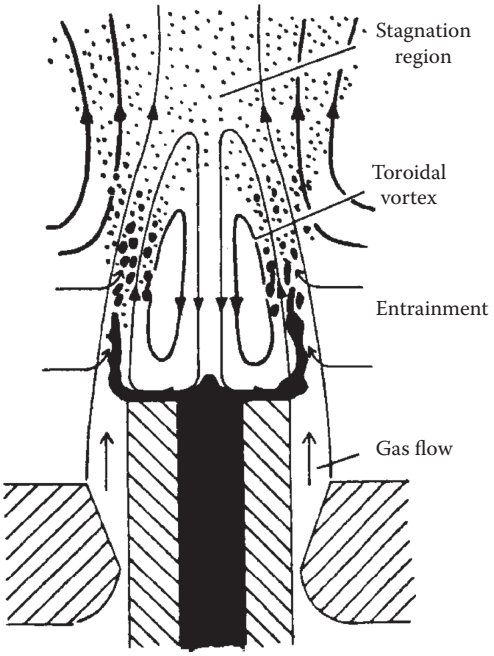


Figure 19.54

Flow field configuration in atomization area of close-coupled atomizer. (Adapted from Ünal, A., *Metall. Trans.*, 20B, 613, 1989.)

in the direction of the gas streamlines. In this area, the liquid film is fragmented after a certain distance in a primary fragmentation process into droplets. The characteristic distance from the atomizer to the fragmentation point is derived from empirical data as

$$L_f = 1.23\,\tau_f^{0.5}\,\mathrm{We}_f^{-0.5}\,\mathrm{Re}_f^{0.6} \tag{19.133}$$

Here, the film Weber number We_f and the film Reynolds number Re_f are derived using the local film thickness τ_f and the relative velocity between gas and liquid u_{rel} respectively the film velocity u_f:

$$\mathrm{We} = \frac{\tau_f \rho_g u_{rel}}{2\sigma}; \quad \mathrm{Re} = \frac{\tau_f \rho_l u_g}{\mu_l} \tag{19.134}$$

Developments for understanding fragmentation of a metal melt in a close-coupled atomizer during atomization have been introduced by Ting et al. (2002). These authors discuss especially the effect of the aspiration pressure on the flow of gas and liquid at gas pressures up to 5.5 MPa. The atomization gas flow field results in a fluctuating pressure distribution at the melt outlet. Based on gas dynamic assumptions for the gas flow field in the nozzle vicinity for increasing gas pressures, these authors finally conclude that for increased gas pressures, an oscillating flow field of the gas may occur. This effect will result in the temporal occurrence of central orthogonal shock structures in front of the nozzle. Based on this observation, a fragmentation process model is developed, which predicts, for gas pressures exceeding a configuration dependent threshold value, a pulsating flow field configuration of the melt flow at the nozzle tip (see Figure 19.55) and therefore highly transient atomization behavior.

19.1.8.3 Solid/Liquid Suspensions

The atomization of solid/liquid suspensions is important in chemical, food, and pharmaceutical industrial applications (e.g., for paints, paper coatings, printing inks, ceramics, cosmetics, detergents) and in energy conversion (coal water slurries). In typical technical suspensions, the solid particle size may range from 1 nm to 1 mm, while the solid concentration may be up to 70 weight/volume %, depending on the specific application. The presence of solid particles in the carrier liquid, which may lead to plugging and/or wear-out of the atomizer material, introduces an additional criterion for the selection of a specific atomizer type (pressure, twin-fluid, or rotary) for suspension atomization.

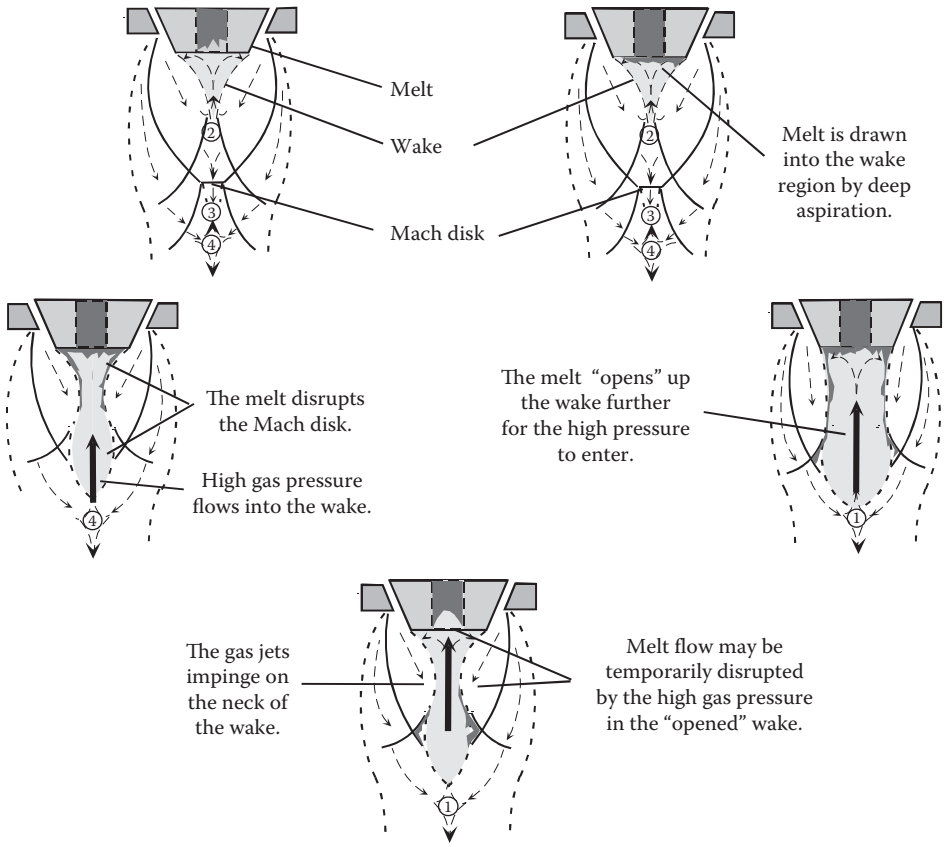


Figure 19.55

Pulsating melt flow in close-coupled atomization. (From Ting, J. et al., *Mater. Sci. Eng. A*, 326(1), 110, 2002. With permission.)

Interactions between the three different phases (solid particles, liquid, and gas) as well as the non-Newtonian rheological properties of the suspension, which strongly depend on the solid particles, play an important role in the disintegration process of suspensions. These parameters make an extension of basic fragmentation theories of pure liquids for analysis of suspension atomization processes difficult. Theoretical work on this subject has been presented by Parthasarathy (1999), who studied the breakup of two-dimensional slurry sheets subjected to gas flow using linear spatial stability analysis for the case of a dilute slurry and a dense slurry. Schütz et al. (2003) used the semi-empirical Carreau–Yasuda model to describe the flow behavior of a suspension in a mathematical–physical model to calculate the resulting mean droplet diameter in suspension spray produced by a hollow-cone nozzle. In the case of suspension disintegration, experimental research dominates the research effort (see, e.g., Dombrowski and Fraser, 1954, Shirley et al., 1987, Glaser, 1989, Kurt et al., 2002, Mulhem et al., 2002, 2003a,b, 2006a,b, Shimizu et al., 2002, Gramlich and Piesche, 2012, Jedelsky, 2013).

The most important parameters controlling the formation process of the droplet in a suspension spray are the atomization energy, the capillary pressure, the cohesion forces between the solid particles, and the suspension viscosity. While the atomization energy depends on the type of the atomizer, the other parameters are strongly influenced by the solid particle size and concentration. The adhesion forces and suspension viscosity increase with decreasing solid particle size and increasing solid particle concentration in the suspension. Therefore, the droplet formation process becomes difficult in the case of a suspension containing small solid particles and/or high solid concentrations.

The influence of the solid particle characteristics and the carrier liquid properties on suspension atomization in film formation atomization processes (e.g., by means of hollow-cone nozzles, flat spray nozzle, or rotary atomization) is reported by Schütz et al. (2003), Glaser (1989), Kurt et al. (2002), and Mulhem et al. (2006a,b). In the film formation process, the breakup length of the suspension sheet is shorter than the breakup length of the comparable pure carrier liquid sheet due to the disturbance of the liquid surface by the particles. The solid particle size and density affect the perforation mechanism in the dilute suspensions.

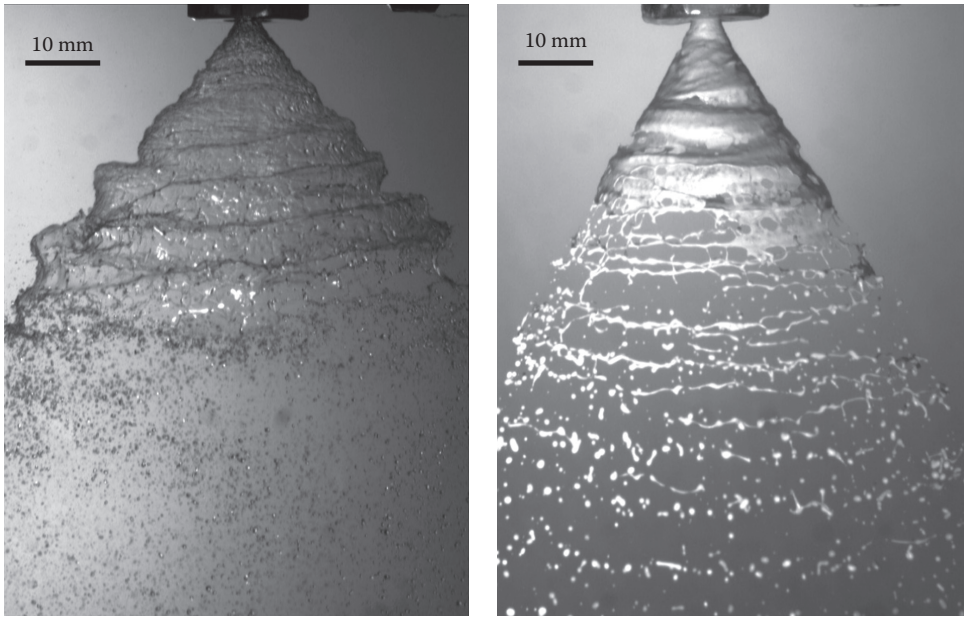


Figure 19.56

Hollow cone lamella for different process fluids: (a) water; (b) clay/water-suspension (30 v.%). (Adapted from Mulhem, B. et al., Break-up of hollow cone and flat suspension lamellae of pressure atomizers, in *Proceedings of ICLASS 2006*, Kyoto, Japan, August 27–September 1, 2006a.)

In this case, solid particles with high relaxation time (large diameter or high density) cannot follow the turbulent fluctuations in the liquid sheet that leads to increase in the velocity difference between the particles and the liquid. Accordingly, the perforation mechanism is promoted by the solid particles. Figure 19.56 shows photographs of the breakup process of the hollow cone sheet of two different process fluids, water and clay/water suspension (30 v.%). By adding solid particles to the basic process fluid, its flow behavior changes, that is, it becomes shear-thinning rather than Newtonian as for the pure carrier liquid. The photographs show that the hollow cone liquid sheets will disintegrate into ligaments and drops according to aerodynamic waves. However, the formation of perforations or cell structures is obvious on the suspension film.

Gramlich and Piesche (2012) investigated the breakup of particle-laden liquid jets or threads in a centrifugal field. Despite an increase in volume concentration of particulate materials from 4.5% to 20%, the variation of the atomization characteristics like drop size is not significant, possibly because of the suspension containing relatively fine particulate materials (particulate materials: 6.55–22.5 μm vs. droplets: 200–2000 μm).

Effervescent atomization of suspension is reported by Jedelsky (2013). Effervescent atomizers have larger orifice than conventional atomizers, and thus can avoid clogging or abrasion during the atomization of suspension, especially for suspension containing large solid particles. The interactions among the three different phases (gas, liquid, solid) occur during the disintegration process.

19.1.9 Drop Size Correlations in Sprays

19.1.9.1 Theoretical Analysis

Approaches for general theoretical descriptions of drop size distributions resulting from atomization processes can be based on statistical approaches and tools, which derive a PDF in relation to the process to be analyzed. The maximum entropy formalism (MEF) is statistical tool that delivers partial information for a specific process (based on a number of compulsatory conditions) by transformation into a suitable distribution function. An MEF is a statistical tool and does not contribute any physical aspects to the analysis of the fragmentation processes. Fundamental model developments in the area of applying MEF to the analysis of fragmentation processes of liquids and the derivation of the resulting droplet size distributions in sprays have been done by Sellens (1989), Sellens and Brzustowski (1985), and Li and Tankin (1987). Their approaches have been further

developed by Ahmadi and Sellens (1993) and Cousin and Dumouchel (1997). The fundamental idea of this modeling is the description of a PDF of the particle size distribution $q_r(d)$ from the Shannon entropy (uncertainty) Sha:

$$\mathrm{Sha} = -k_S \int_0^\infty q_r(d) \ln(q_r(d)) d(d) \tag{19.135}$$

where k_s is a constant, to be determined by the dimensionality of the specific process under investigation.

The MEF allows the prediction of the droplet size PDF, depending on a number of mathematical constraints. These constraints are described based on a number of known conservation properties of the process and their distribution and are equivalent to the moments of different orders of the distribution. Without further limitations, a number of different PDFs fulfill a given set of constraints. The MEF describes the best-fit solution for which entropy reaches a maximum value. Cousin et al. (1996) describe the resulting number density-based particle size distribution of a pressure swirl atomizer from this formalism as

$$q_0(d) = \frac{p^{(p-1)/p}}{\Gamma_S(1/p) d_{p0}} e^{(-d^p/p d_{p0}^p)} \tag{19.136}$$

containing the Gamma function Γ_s. The determination of input parameters like p and d_{p0} in aforementioned derivation is done either based on specific singular measurements (Ahmadi and Sellens, 1993) of moments of a measured spray particle size distribution or by a primary analysis of the fragmentation process based on linear stability analysis (Cousin and Dumouchel, 1997). For an atomization process where the principal mode of the disintegration process is constant (constant fragmentation mode), the resulting particle size distribution in terms of a mean or characteristic particle size and the particle size distribution width can be determined by this method. Applications are described by Malot and Dumouchel (1999), and Prud'homme and Ordonneau (1999). For application within ultrasonic liquid atomization, refer to Dobre and Bolle (1998).

Another model is the approach of Platzer and Sommerfeld (2003). It originates from a structural effects theory based on the work of Naue and Bärwolf (1992) as detailed by Hartmann (1993), and provides functions for drop size and volume distribution. In contrast to conventional MEF models, no mean drop diameter needs to be provided as input parameter. The SMD and the drop size distribution are calculated iteratively using only known geometrical information and operating conditions. This is done assuming a structure formation process that is a function of the critical Weber number. Some varying functions are derived, differing in the number of drops in each class and in the function of the critical Weber number describing the number of classes formed. The complete spray model from internal and primary fragmentation flow to the spray structure simulation is described. The two-fluid model including the prediction of the drop size distribution is used for the first part and the Euler/Lagrange method for the second part.

A two-stage modeling approach of atomization may be based on primary fragmentation in the first step from stability analysis, and ligament fragmentation described as a Rayleigh breakup process in the second step. A model for liquid fragmentation for coaxial twin-fluid atomization (round liquid jet) has been introduced by Fritsching (2001) and a similar model for annular ring film disintegration by Lund et al. (1993). The description of the gas and liquid state prior to atomization within these models has been derived by means of experimental and/or numerical flow field studies. Mean drop size correlations in the initial spray are derived.

19.1.9.2 Empirical Drop Size Correlations

A large number of empirical correlations for drop size distributions in sprays have been derived (Lefebvre, 1989, Bayvel and Orzechowski, 1993, Liu, 2000b, Walzel, 2012, Walzel and Musemic, 2013). These drop size correlations typically fit only a specific atomizer type (respectively atomization principle) and a certain (narrow) range of boundary conditions or disintegration modes. The boundary conditions include the geometric constraints of the atomizer design and operational parameters such as liquid properties, flow rates, pressures, and others. The characteristic droplet size in the spray spectrum (typically given as mean, median or Sauter diameter) is either correlated in terms of dimensionless numbers or in terms of direct material and operational properties. A few of those correlations discussed before with respect to some different atomizer types are given in Table 19.6. The analysis of the drop size distribution width and correlation in a spray is given in few cases only.

Table 19.6 Examples of Empirical Droplet Size Distributions for Various Atomizer Types

Application	Drop Size	Source
Pressure Atomizer	$d_{32} = 47\frac{d_0}{u_0}\left(\frac{\sigma}{\rho_g}\right)^{0.25}\left[1+331\frac{\mu_l}{(\rho_l\sigma d_0)^{0.5}}\right]$	Tanasawa and Toyoda (1955)
Pressure swirl atomizer	$d_{32} = 2.25\sigma^{2.25}\mu_l^{0.25}\dot{m}_l^{0.25}\Delta p_l^{-0.25}\rho_g^{-0.25}$	Lefebvre (1983)
Hybrid atomizer (pressure swirl gas atomizer)	$d_{50,3} = 1.45(1+\dot{M}_l/\dot{M})(360/\alpha)^{0.37}$ $\cdot\left(A\left(\frac{\sigma}{\rho_g U_g^2}\right)^{0.6}\left(\frac{\rho_l}{\rho_g}\right)^{0.1} h_0^{0.4} + B\left(\frac{\mu_l^2 h_0}{\sigma\rho_l}\right)^{0.5}\right)$, $A = 0.07$ and $B = 0.01$	Achelis (2009)
Twin-fluid atomizer (external)	$d_{32} = 0.585\left(\frac{\sigma}{\rho_l u_{rel}^2}\right)^{0.5} + 53\left(\frac{\mu_l^2}{\sigma\rho_l}\right)^{0.225}\left(\frac{\dot{Q}_l}{\dot{Q}_g}\right)^{1.5}$	Nukiyama and Tanasawa (1939)
Twin-fluid atomizer (internal, bubbly flow regime)	$d_{32} = \left[0.023ALR\frac{\rho_l RT_a}{\sigma(\kappa-1)}\left(1-\left(\frac{p_a}{p_c}\right)^{(\kappa-1)/\kappa}\right)+\frac{2.35}{d_0}\right]^{-1}$	Kim and Lee (2001)
Twin-fluid atomizer (internal, annular flow regime)	$d_{32} = 0.14\, d_0\, f\left(\alpha,\frac{\rho_g}{\rho_l}\right)\left(\frac{\rho_g j_g^2 d_0}{\sigma}\right)^{-0.5}$ $f\left(\alpha,\frac{\rho_g}{\rho_l}\right) = \frac{\alpha\sqrt{1-\alpha}}{1-\sqrt{\frac{\rho_g}{\rho_l}\left[\frac{1+75(1-\alpha)}{\sqrt{\alpha}}\right]^{0.5}}}$	Kim and Lee (2001)
Rotary atomizer (drop mode)	$d_{32} = \frac{27}{n_z}\left[\frac{\sigma}{2\rho_l r}\left(1+0.003\frac{\dot{Q}\rho_l}{2r\mu_l}\right)\right]^{0.5}$	Tanasawa et al. (1978)
Rotary atomizer (fiber mode)	$d_{32} = 0.119\frac{\dot{Q}^{0.1}\sigma^{0.5}}{n_z(2r)^{0.5}\rho_l^{0.4}\mu_l^{0.1}}$	Tanasawa et al. (1978)
Rotary atomizer (fiber mode)	$d = (d_0/2)\sqrt[3]{(12\pi/K_{r,Z,crit})(\bar{R}_s\,\vert_{Z=L})^2}$	Gramlich et al. (2011)
Rotary atomizer (film mode)	$d_{32} = 15.6\frac{\dot{Q}^{0.5}}{n_z}\left[\frac{\sigma}{(2r)^2\rho_l}\right]^{0.4}$	Tanasawa et al. (1978)
USWA	$d_{50,3} = 0.53\dot{Q}^{0.27}d_0^{-0.24}\mu^{0.69}\rho_l^{-0.21}p_{max}^{-0.97}\rho_0^{0.48}c_0^{0.97}$	Hansmann (1996)

19.1.9.3 Suspension Atomization

Some correlations for suspension droplet sizes in sprays generated using different atomizer types are summarized in Table 19.7.

The experimental results of Son and Kihm (1998), using laser diffraction particle analysis and assuming a Rosin–Rammler-type droplet size distribution (RRSB) in the spray, showed that the SMD (d_{32}) of coal-water-slurry (CWS) containing smaller coal particles is larger than the SMDs of CWS containing larger coal particles. The separation of the solid particles from each other in the suspension spray has to be controlled by the solid particle characteristics. Mulhem et al. (2003a, 2006b) confirm this assertion experimentally in the case of twin-fluid suspension atomization. Figure 19.57 shows a bimodal droplet size distribution of suspension spray containing large solid particles $d_{50,3}$ = 94 µm (right) and a monomodal droplet size distribution of suspension spray containing small solid particles $d_{50,3}$ = 6 µm (left).

The influence of the solid particle characteristics and the carrier liquid properties on suspension atomization for the case of a twin-fluid suspension atomization process may be summarized as follows. In the case of suspension containing *large solid particles*, the solid particles tend to separate from the carrier liquid (Glaser, 1989, Mulhem et al., 2003a, 2006b). Dry solid particles are being seen in the spray, their characteristic diameter independent of the atomization energy, and pure carrier liquid drops, which disintegrate further with

Table 19.7 Drop Size Correlations for Suspension Atomization

Application	Drop Size	Sources
Internal mixing twin-fluid atomizer	$\frac{d_{50,3}}{d} = \left[\left(A\cdot(\mathrm{We}_g)^{-x} + B\cdot(\mathrm{Oh})^{2x}\right)\right]\left[1+\frac{1}{ALR}\right]^{y}$ $\mathrm{We}_g = \frac{\rho_g u_g^2 d_F}{\sigma}$; $\mathrm{Oh} = \frac{\mu_l}{\sqrt{\rho_l \sigma d}}$; $ALR = \frac{\dot{m}_g}{\dot{m}_l}$ A, B, x, y: parameters depend on coal-slurry coal particles: $d_{50,3} \le 32$ µm, $Cp \le 72$ wt%	Shirley et al. (1987)
External mixing twin-fluid atomizer	$d_{32,susp} = 0.21 d_L (\mathrm{Oh})^{0.0622} (\mathrm{We}_{aero} \times ALR)^{-0.4}$ $\mathrm{We} = \frac{\rho_g u_{rel}^2 d_{susp}}{\sigma}$, $\mathrm{Oh} = \frac{\eta_c}{\sqrt{\rho_{susp}\sigma d_{susp}}}$, $ALR = \frac{\dot{m}_g}{\dot{m}_{susp}}$ for: $70 \le u_{rel}$ (m/s) ≤ 220 solid particles: $d_{50,3} \le 26$ µm, $Cp \le 50$ wt%	Mulhem et al. (2003)
High-pressure injection	$d_{32,susp} = 0.279\ \Delta p^{-0.702}\ \rho_g^{0.285}\ x^{1.521}$ $28 \le \Delta p$ (MPa) ≤ 110; $1.2 \le \rho_g$ $(kg/m^{-3}) \le 25$, $60 \le x$ (mm) ≤ 120 coal particles: $d_{50,3} \le 5$ µm, $Cp \le 50$ wt%	Son and Kihm (1998)
Hollow-cone nozzle	$\frac{d_{32,susp}}{D_E} = 7.8\Delta p^{*-0.651}\left\{\left[\mathrm{Oh}^{0.129}\left(\frac{D_k}{D_E}\right)^{0.027}\left(\frac{D_A}{D_E}\right)^{0.05}\rho^{*-0.268}\right]\right.$ $\left.+\left[38.5(1-C_P)^{-5.862}\left(\frac{\rho_p}{\rho_c}\right)^{-0.295}\left(\frac{d_{32,p}}{D_E}\right)^{0.86}\right]\right\}$ $0.4 \le (1-C_p) \le 1$; $0 \le \frac{\rho_p}{\rho_c} \le 2.43$; $0 \le d_{32,P}$ (mm) ≤ 0.082	Glaser (1989)

Notes: *P*, solid particle; *C*, carrier liquid; *E*, inlet; *K*, chamber; *A*, outlet.

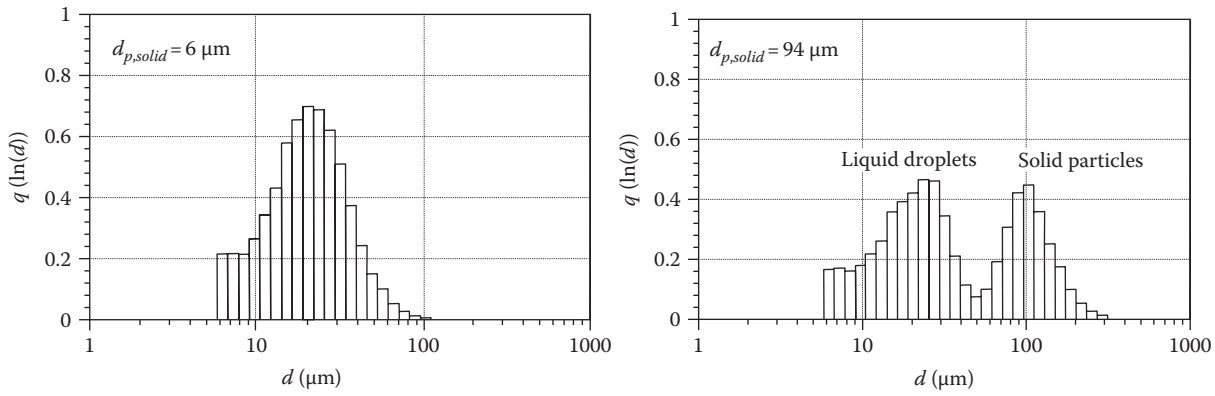


Figure 19.57

Drop size distribution in suspension atomization, monomodal and bimodal distribution. (From Mulhem et al., 2003b. With permission.)

increasing atomization energy, as shown in Figure 19.58. The solid particle size in the suspension influences the resulting diameter of the pure carrier liquid drops, which is explained as a result of reducing the volume of the liquid bridge between the solid particles by decreasing the solid size in the suspension. Investigation of the influence of solid particle concentration on the atomization of suspension containing large solid particles showed only a small influence on the resulting pure liquid diameter. The diameter of the carrier liquid drops in the spray increases with increasing viscosity of the carrier liquid.

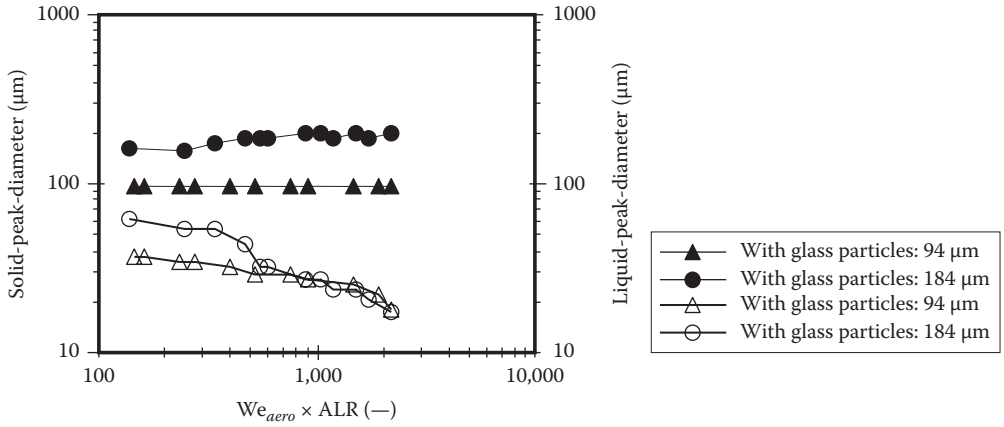


Figure 19.58

Peak of the logarithmic particle size distribution for suspension atomization containing large solid particles. (From Mulhem et al., 2003b. With permission.)

In the case of suspension spray containing relatively *small solid particles*, the large cohesion forces between the particles prevent the liquid/solid separation process. The majority of the droplets in the spray are suspension droplets. The suspension droplets behave like pure liquid droplets, taking into account the change in material properties due to the particles. That means, the suspension droplets may disintegrate into smaller ones with increasing atomization energy. The diameter of the suspension drops in the spray is comparable to the diameter of carrier liquid drops (Isenschmid, 1992). The droplet diameter in the suspension spray increases with increasing solid concentration.

Mulhem et al. (2006b) defined a limit of the separation process within a twin-fluid atomizer (external mixing), assuming that the separation process can take place if the droplet diameter produced by twin-fluid atomization at the given operational parameters equals or is smaller than the solid particle diameter in the suspension. This critical process condition is expressed as

$$0.21 d_l \left(\frac{\mu_l}{\sqrt{\sigma \rho_l d_l}} \right)^{0.0622} \left(\frac{\rho_g d_l}{\sigma} ALR \right)^{-0.4} U_{rel}^{-0.8} \leq \left(\frac{9}{2} \frac{1-\varepsilon_a}{\varepsilon_a} \frac{\sigma}{\rho_g} \right) \frac{1}{U_{rel}^2} \tag{19.137}$$

In this equation, the term on the left represents the mean droplet diameter in the liquid spray, and the term on the right represents the solid particle diameter in the atomized suspension. Other parameters in this equation include liquid viscosity (μ_l), surface tension (σ), liquid density (ρ_l), liquid-nozzle exit diameter (d_l), air density (ρ_g), the air to liquid mass flow rate ratio (ALR), gas-droplet relative velocity (U_{rel}), and the agglomerate porosity of suspension droplet (ε_a). In an approximation, the agglomerate porosity of suspension drops (ε_a) can be calculated as a function of the bulk density (ρ_B) and the particle density (ρ_p) as follows (Rajathurai, 1990):

$$\varepsilon_a = 1 - \frac{\rho_B}{\rho_p} \tag{19.138}$$

19.1.9.4 Melts

In Table 19.8, some empirical correlations for particle sizes within molten metal atomization in free-fall and close-coupled atomization are given. In Lubanska's correlation, a liquid Weber number $We_l = \rho_l u_{max}^2 d_l / \sigma_l$ and the inverse of the mass flow rate ratio (1/GMR; GMR = gas to metal mass flow ratio) are used. The empirical constant K_{lub} reflects different atomizer geometries. Lubanska has given its value to be between 40 and 80, but other investigations have found much larger values. A sample evaluation of particle sizes in molten metal sprays for various metals versus the atomizer gas pressure based on Lubanska's correlation is illustrated in Figure 19.59. Several investigations aimed verification of Lubanska's formula for particle size distributions

Table 19.8 Drop Size Correlations for Molten Metal Atomization

Application	Drop Size	Sources
Free-fall atomizer	$d_{50,3} = d_0 K_{\text{lub}} \left[\frac{\nu_l}{\nu_g} \frac{1}{\text{We}_l} \left(1 + \frac{\dot{m}_l}{\dot{m}_g} \right) \right]^{0.5}$	Lubanska (1970)
Close-coupled atomizer	$d_{3,2} = \frac{12\sigma}{\frac{\rho_l u_{rel}^2}{1 + 1/(\varepsilon(\dot{m}_g/\dot{m}_l))} + 4\frac{\sigma}{\tau_f}}$; $\varepsilon = \frac{1.62}{u_g^{1.3}(\dot{m}_g/\dot{m}_l)^{0.63}\mu_l^{0.3}}$	Liu (1997)

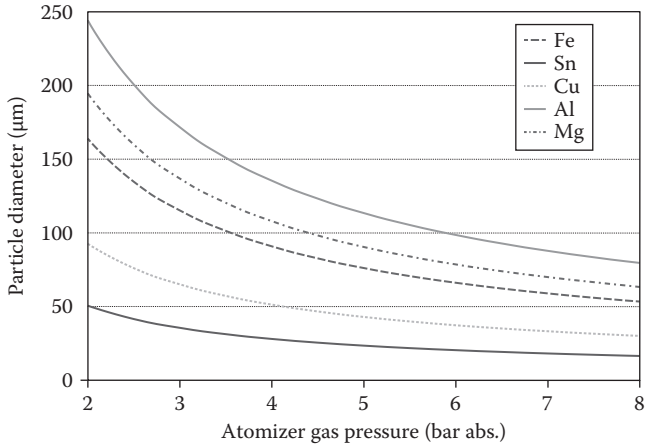


Figure 19.59

Mean particle sizes in molten metal atomization, evaluation of (Lubanska, 1970) correlation.

from melt atomization. The work of Rao and Mehrotra (1980) investigated the influence of nozzle diameter and atomization angle on particle sizes, finding that the mean droplet size decreases with decreasing nozzle diameter and increasing atomization angle. They found a different value of the exponential factor as well as the atomizer constant in Lubanska's correlation. Another modification has been proposed by Rai et al. (1985). These authors studied melt atomization within ultrasonic gas atomizers and also proposed a modification of Lubanska's formula.

A discussion and evaluation of the relevance of Lubanska's formula for the atomization of metal melts in twin-fluid atomization can be found in Bauckhage and Fritsching (2000). A general overview for a number of empirical correlations for mean and median droplet sizes dependent on operational conditions and nozzle types and geometries for melt atomization within different atomizer configurations can be found in Liu (2000b) and Yule and Dunkley (1994).

19.2 Spray Behavior

In terms of a multiphase flow approach to spray analysis, main features of the dispersed spray to be described are

- The overall spray geometry (e.g., spray angle)
- The local fluxes of droplet mass, momentum and enthalpy (where appropriate)
- The equivalent droplet concentrations by number or volume
- The local droplet size and droplet state including velocity and temperature distribution

The analysis of the spray behavior is to be divided into two regions, depending on the relevance of droplet/droplet interactions and the possibility and frequency of droplet/droplet collisions. A rough estimate of the relevance of collisional effects to the overall spray behavior can be done based on the ratio of particle relaxation time τ_p to the time scale between individual particle collisions τ_c. The particle relaxation time is the

time that a droplet takes to be accelerated from velocity u_1 to u_2 that is (in the Stokes flow regime) expressed as (see Chapter 1)

$$\tau_p = \frac{\rho_l d_p^2}{18\mu_g} \tag{19.139}$$

The time constant between collisions for particles is to be derived from the collision frequency as

$$\tau_c = \frac{1}{f_c} \tag{19.140}$$

At low droplet concentrations (dilute flow), the particulate transport mainly is determined by fluid dynamic interactions of the individual particles or droplets with the continuous carrier phase (like drag, lift, etc.). At high particle concentrations (dense flow), the influence of particle collisions affects the movement of the droplets and the droplet size distribution. These two regions may be separated in terms of the ratio of the characteristic time scales as (see also Chapter 1)

$$\text{Dilute: } \frac{\tau_p}{\tau_c} < 1; \quad \text{Dense: } \frac{\tau_p}{\tau_c} > 1 \tag{19.141}$$

In a dense spray, the time between droplet collisions is smaller than the droplet relaxation time. Before reaching another steady slip velocity from the droplet gas interaction, another collision may occur. Therefore, the droplet movement is determined mainly by collisions and fluid dynamic effects are of less importance. In sprays, the area close to the atomizer typically is a dense spray region as here the number concentration of droplets is high, while with increasing distance to the atomizer due to the spreading of the spray cone, droplet collisional effects decrease and transition to dilute flow is achieved.

19.2.1 Dense Spray

19.2.1.1 Collisions and Coalescence

When two liquid droplets are interacting during flight, several events may occur. The colliding droplets may (1) bounce, (2) stably coalesce, (3) temporarily coalesce followed by disruption, or (4) temporarily coalesce followed by fragmentation. The two droplets can be equal or unequal sized from the same liquid, or different miscible liquids, or different immiscible liquids (Brenn, 2011). The merging of the two droplets from different immiscible liquids may result in a complex droplet with core/shell structure. Planchette et al. (2012) describe this phenomenon by use of the term *encapsulation* instead of *coalescence*. Details on binary droplet collision phenomena are discussed in Chapter 14. The following discussion mainly focuses on the collisions of droplets from a same liquid or different miscible liquids.

For relevance in spray processes, experimental works of water/water and hydrocarbon/hydrocarbon droplet collisions have been studied extensively. Orme (1997) reviewed the experimental studies of water and hydrocarbon droplet binary collisions. The basic phenomena of coalescence and separation of droplets during binary collision have been experimentally addressed in some investigations such as by Walzel (1980a), Low and List (1982), Ashgriz and Poo (1990), Rein (1996), Qian and Law (1997) for water and fuel droplets, and Menchaca-Rocha et al. (1997) for mercury droplets.

Brenn et al. (2001b) and Brenn and Kolobaric (2006) have investigated the formation of satellite droplets during unstable binary collisions of equal sized droplets. The satellites are formed by contraction or breakup of a ligament, which is formed from the mass of the two interacting droplets and may eventually pinch off from the remaining portions of the droplets. Stability nomograms of the Weber number (We) and the nondimensional impact parameter (B) have been developed to describe the collision behavior of the droplets by zones with constant numbers of satellite droplets formed only at sufficiently high Weber number due to either reflexive separation (for small impact parameters) or stretching separation (for intermediate and large impact parameters), as illustrated in Figure 19.60. In the reflexive separation regime, the formation of one satellite droplet occurs with highest probability. In the stretching separation regime with moderate values of the impact parameter, the satellite droplets are formed at the ends of the ligament by end-pinching mechanism, and the number of satellite droplets increases with the impact parameter, until a maximum is reached. A further increase of the impact parameter leads to the satellite-droplet formation process dominated by the capillary wave growth and

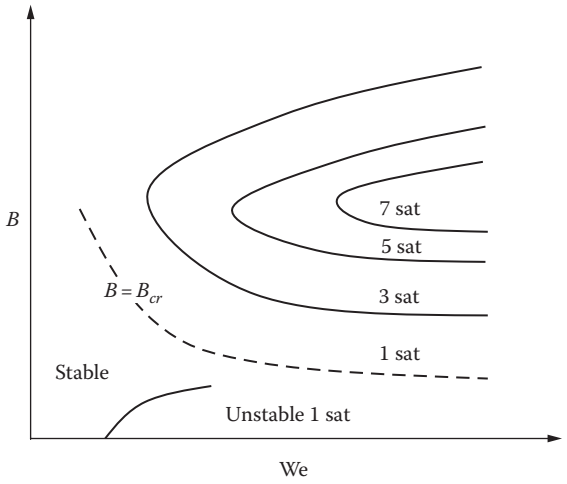


Figure 19.60

Schematic of stability nomogram divided by zones with constant numbers of satellite droplets formed during binary collisions of equal-sized droplets.

thereby a decrease of the number of satellite droplets. An increase of the Weber number generally leads to the formation of more satellite droplets. For example, the collisions of two propanol droplets with a size of 139 μm can produce more than 7 satellites for We > 150. Different satellite-droplet formation mechanisms can be categorized based on the ligament aspect ratio (L_{lig}/d_{lig}, L_{lig} is the ligament length, d_{lig} is the ligament diameter) and the nondimensional ligament diameter (d_{lig}/D, D is the initial droplet diameter): for $L_{lig}/d_{lig} < 10$, the ligament contracts to a single satellite; for $L_{lig}/d_{lig} > 10$ and $d_{lig}/D > 0.17$, the end-pinching mechanism occurs; for $L_{lig}/d_{lig} > 28$ and $d_{lig}/D < 0.17$, the ligament breakup is influenced by capillary waves. Brenn and Kolobaric (2006) have derived the mathematical formulations of the length and volume of the ligaments and the size of the satellite droplets formed after stretching breakup based on the outcomes of binary collisions of propanol droplets.

In most of these experimental studies, only rather low dynamic viscosities, ranging from 1 to 10 mPa s, were considered. Gotaas et al. (2007) investigated different species (i.e., MEG, DEG, and TEG, which is mono-, di-, and triglycol) with viscosities from 21 to 48 mPa s and compared results for the boundary between coalescence and stretching separation as well as reflexive separation. Increasing viscosity results in an upward shift of the boundary between coalescence and stretching separation toward higher impact parameters, and also shifts the onset of reflexive separation to higher Weber numbers.

Binary collisions of solution droplets (i.e., aqueous solutions of saccharose and PVP) have been experimentally investigated by Kuschel and Sommerfeld (2013) and Kuschel (2013), whereby the dynamic viscosities of the aqueous solutions range from 1 up to 73 mPa s by varying the solute contents up to a value, which still allows a production of stable droplet chains. Most of the findings of Gotaas et al. (2007) have also been confirmed by Kuschel and Sommerfeld (2013) and Kuschel (2013). A critical capillary number Ca = 0.577 ($Ca = \mu_l U_{rel}/\sigma$) was suggested by Kuschel and Sommerfeld (2013), below which surface-tension effects govern the collision dynamics, while above which viscous effects govern the collision dynamics. The locations of the triple point (bouncing, coalescence, and stretching separation collapse in one region) and the onset of reflexive separation in a We-B regime map (see Chapter 14) have been formulated by Kuschel (2013), respectively, as

$$\text{Triple point: } \mathrm{Re} = \frac{K^2}{2}\mathrm{Ca}^{-\sqrt{1-(1/e^2)}} \Rightarrow \mathrm{We} \tag{19.142}$$

$$\text{Onset of reflexive separation: } \mathrm{We} = \frac{K^3}{3}\mathrm{Ca} + 2K \tag{19.143}$$

where

Re is the Reynolds number
Ca is the capillary number
We is the Weber number
$K = 6.9451$

The impact parameter (B) corresponding to the triple point can be derived by taking the critical Weber number into the correlations $B = f$ (We) characterizing the onset of stretching separation (as discussed in Chapter 14). As in Brenn et al. (2001b) and Brenn and Kolobaric (2006), the We-B diagram has been employed to describe the formation of satellite droplets. Kuschel and Sommerfeld (2013) found that an increasing of solute content and thereby an increasing of dynamic viscosity lead to a thinner and longer ligament, the breakup of which results in more satellites.

Binary collisions of suspension droplets in off-center collisions (impact parameter $B > 0$) have been experimentally investigated by Kurt et al. (2007, 2008). The formation of satellite droplets during the collisions is correlated by a function based on the basic parameters and dimensionless numbers of the process, for example, the Weber number (We), the particle loading ($\omega = m_{solid}/m_{liquid}$, with m_{solid} the mass of solid particles in a droplet and m_{liquid} the droplet mass), the particle size, and the Reynolds number (Re). The number of satellites produced by stretching separation increases with increasing We and Re values, but decreases with the particle loading.

Binary collisions of equal-sized melt droplets have been experimentally investigated by Gao and Fritsching (2010), where Carnauba wax as a low melting point material has been used. The droplets from two separate droplet-jets are colored differently, one in red and the other in yellow. The results indicate that the molten wax droplet collision shows similar behavior as conventional Newtonian droplets. Figure 19.61 illustrates the process of wax droplet collision in the regime of stretching separation. The right parts of all the figures show the images of the dynamic binary collision process, and the left parts show pictures of the solidified particles collected from that side below the collision zone, in which the yellow droplet is the main droplet color. In the collision regime of the stretching separation, depending on the impact parameter (B), a liquid ligament is formed between the two separating droplets and after

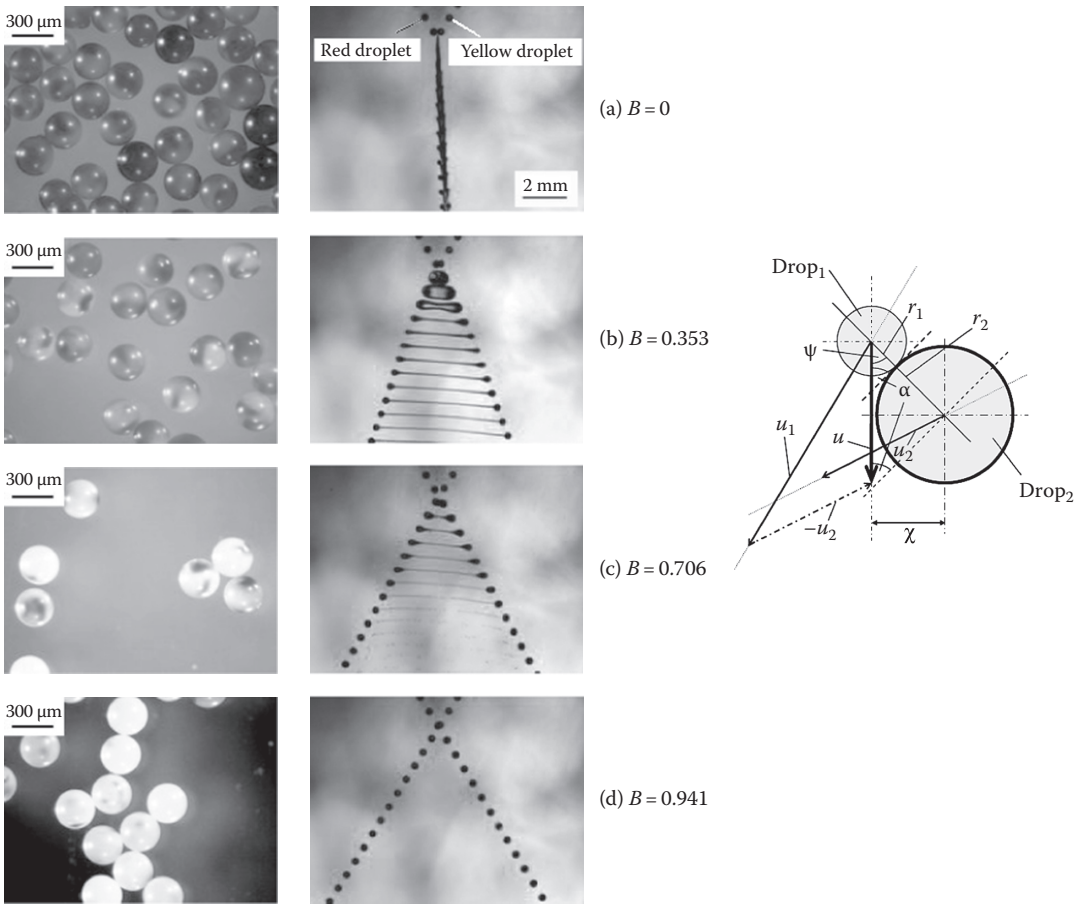


Figure 19.61

Collision process and solidified particles at various impact parameters (We = 570). (Adapted from Gao, S. and Fritsching, U., *Materialwiss. Werkstofftech.*, 41(7), 547, 2010. With permission.)

the ligament breakup, one or more satellite droplets between the two primary drops are formed. The color distribution of the collected particles shows the existence of a certain amount of mass transfer between the two colliding droplets. At smaller values of the impact parameter, this mass transfer is rather large. After the collision, there is a rotation of droplets caused by the angular momentum of the droplets, which plays a role in the process of stretching separation and formation of secondary particles. It should be mentioned that binary droplet collisions in this study have been performed only in the liquid/liquid state of both melt droplets. Fritsching and Gao (2010) have also studied the droplet/droplet and/or droplet/particle collisions in intersecting wax-melt sprays. Thereby, the collisions may lead to coalescence or sticking or aggregation of the particles, depending on the instantaneous solidification states of droplets upon collision.

19.2.1.2 Direct Numerical Simulations of Droplet Collisions

DNSs of the behavior of two droplets during collision have been reported by Nobari and Tryggvason (1996), Nobari et al. (1996), Frohn and Roth (2000), Pan and Suga (2005), Nikolopoulos et al. (2009a,b), Li and Fritsching (2011), Focke and Bothe (2011, 2012), and Kwakkel et al. (2013). Popular methods for DNS are front tracking and front capturing methods. Interface tracking methods are based on the Lagrangian tracking of marker particles that are attached to the interface motion and appear suitable for the interfaces with great regularities and small topological changes. ICMs capture the interface implicitly by a contour of a particular scalar function, for example, the LS function in the LS method and the volume-fraction advection equation in the VOF method. One advantage of the ICMs is its ability to represent topological changes, both in 2D or 3D geometry, quite naturally. Especially, the CLSVOF method combines the sharp interface representation of the LS method with the mass-conserving interface representation of the VOF method. Some principal physical details of drop collisions can be explained by the DNS approach. However, subgrid models are still necessary for an accurate description of the droplet-collision behaviors occurring in different regimes. These subgrid models may not be fully predictive, but nevertheless allow studying more details during the entire collision process.

One example is the modeling of retarded coalescence occurring at low Weber numbers. The reason for this phenomenon is that the air is trapped between the approaching droplets and needs a certain time to leave the gap. This effect is also relevant for the collision result bouncing, where the drops do not merge during the complete time of contact. According to Mackay and Mason (1963) and Bradley and Stow (1978), droplet coalescence may happen when the trapped gas layer thickness reaches a critical value, which is within the range of the molecular interaction, typically in the order of magnitude of 0.01 μm; otherwise, the droplets will bounce. Resolving this scale in a droplet collision simulation would lead to huge computational effort due to a large number of grid cells or levels of adaptive grid refinement, which is currently not feasible in a DNS even with high-performance computing techniques.

To appropriately describe the head-on collision process of retarded coalescence or bouncing during VOF simulation, Li and Fritsching (2011) have introduced an artificial gas layer between the colliding droplets by use of ghost (or dummy) cells adjacent to the symmetry plane. This artificial gas layer prevents the immediate numerical coalescence when two droplets approach each other. At a critical time when the thickness of the gas layer between the droplets reaches a minimum value, the gas layer can be removed, leading to coalescence; otherwise, the two droplets rebound from each other. Figure 19.62 shows collision sequences during retarded coalescence process from the experiment by Qian and Law (1997) and the VOF simulation by Li and Fritsching (2011), respectively.

In Kwakkel et al. (2013), the coalescence is modeled based on a multiple marker CLSVOF method coupled with a computationally efficient film drainage model in Zhang and Law (2011). The film drainage model predicts if and when two colliding droplets will coalesce. If the contact time between the two colliding droplets exceeds the predicted film drainage time, coalescence is numerically accomplished by merging the marker functions of the two separate droplets.

Experiments show that during the extension of the collision complex an extremely thin fluid lamella encircled by the thick rim often appears in case of large Weber numbers. A lamella rupture is not observed in binary collisions at least for Weber numbers up to 2800 in experiments (Focke and Bothe, 2012). In contrast to the physical behavior, simulations often predict the rupture of the lamella because of the unresolved lamella in the vicinity of the rim. If a simulation is continued with the lamella, the restoring forces acting on the rim are significantly reduced, leading to wrong results. According to Focke and Bothe (2011), the droplet collision at a Weber number of 766 can lead to a lamella thickness of 5.5 μm. With a resolution of 4 cells for the lamella thickness to keep the lamella from rupturing, the required resolution

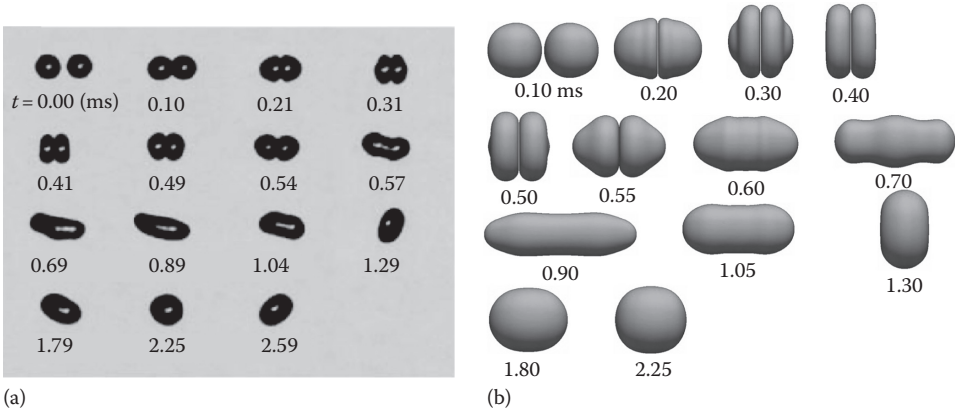


Figure 19.62

Collision sequences during retarded coalescence process: (a) experimental observation, (We, Re, B, D) = (15.2, 139.8, 0.08, 302 μm) (Adapted from Qian, J. and Law, C.K., *J. Fluid Mech.*, 331, 59, 1997.); (b) simulation results, (We, Re, I, D) = (15.2, 139.8, 0, 302 μm). (Adapted from Li, X.G. and Fritsching, U., *J. Comput. Multiphase Flows*, 3(4), 207, 2011.)

is 1.4 μm for the grid cells. Resolving such a lamella thickness in the DNS, even with the AMR technique, will lead to a huge computational cost. To overcome these problems, lamella stabilization schemes have been developed to keep the lamella from rupturing, refer to Focke and Bothe (2011, 2012). The procedure of the stabilization is to guarantee a minimum thickness of the lamella and subsequently compute the surface-tension forces without interactions of the two lamella sides. In the case of a head-on collision of two equal-sized droplets, this can be realized by modifying the volume-fraction (f) field only in the ghost (or dummy) cells adjacent to the symmetry plane. In a general collision, the different sides of a lamella must be firstly distinguished. A minimum thickness of the lamella is guaranteed through the addition of artificial mass. A modified f-field containing interface only on one side of the lamella, which is realized by setting *f*-value to one in all cells which are located on the opposite side of the lamella, is used to compute the surface-tension forces for both lamella sides, respectively. Figure 19.63 shows the shape evolution of the collision complex. The results of the shape using the lamella stabilization show good agreement with the experimental data.

From these droplet collision studies, the outcome of a binary collision can be visualized (see Chapter 14). Typically, droplet collision models are implemented in numerical spray codes such as Sommerfeld (1996), Georjon and Reitz (1999), Aamir and Watkins (1999), and Rüger et al. (2000).

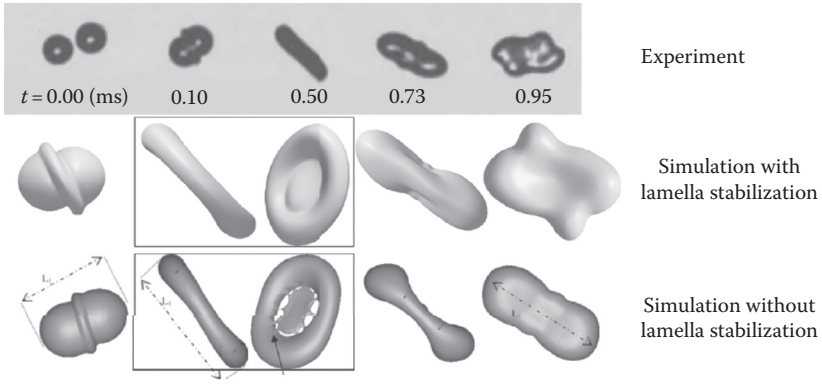


Figure 19.63

Sequences of an off-center collision of water droplets: experimental data (upper row); simulation results with lamella stabilization (middle row) and without lamella stabilization (lower row). (Adapted from Focke, C. and Bothe, D., *Phys. Fluids*, 24, 073105, 1, 2012. With permission.)

19.2.1.3 Numerical Models of Droplet Collisions in Sprays

The most common used water/water collision model is based on O'Rourke (1981). This model considers only grazing collisions (bounce) and permanent coalescence. The decision criterion, whether grazing or coalescence collisions occur, is the critical collision angle:

$$\sin^2 \phi_{crit} = \min\left[2.4\frac{f(\gamma = d_{p,1}/d_{p,2})}{\mathrm{We}}; 1\right] \tag{19.144}$$

In case of a collision angle less than ϕ_{crit}, the droplets coalesce; otherwise, a grazing collision occurs. The function f has been fitted by Amsden et al. (1989) using experimental results as

$$f(\gamma) = \gamma^3 - 2.4\gamma^2 + 2.7\gamma \tag{19.145}$$

Podvysodsky and Shraiber (1994) proposed an empirical formula for liquid droplet collisions in a wide range of material properties. The mathematical expectation $\phi_{1,2}$ of the ratio between a target droplet's mass change and total mass of "projectile" droplets impacting on the target is

$$E\left[\frac{dm_2/dt}{m_1}\right] = \phi_{1,2} = 1 - 0.246\,\mathrm{Re}_{1,2}^{0.407}\,\mathrm{Lp}_2^{-0.096}\cdot\left(\frac{d_2}{d_1}\right)^{-0.278}; \quad \mathrm{Re}_{1,2} = \frac{u_{1,2}d_1\rho_1}{\mu_1}; \quad \mathrm{Lp}_2 = \frac{d_2\rho_2\sigma_2}{\mu_2^2} \tag{19.146}$$

The mass of the droplet after the collision is predicted from

$$m_{2,ac} = m_{2,bc} + \phi_{1,2}\cdot m_{1,bc} \tag{19.147}$$

The subscripts *ac* and *bc* stand for after and before collision, respectively. This empirical formula was obtained within the parameter range $30 \le \mathrm{Re}_{1,2} \le 6{,}000$; $5 \le \mathrm{Lp}_2 \le 300{,}000$ and $1.9 \le d_2/d_1 \le 12$. The parameter $\phi_{1,2}$ should be in the range $-1 \le \phi_{1,2} \le 1$.

Dubrovsky et al. (1992) studied collisions between liquid drops and solid particles. According to their experimental results, collision outcome between a fast moving small drop and a large solid particle was always accompanied by liquid breakup and certain number of fragments. For small solid particle colliding with a large liquid drop target, they reported four types of collision outcomes: (1) projectile capture by target, (2) shooting through, (3) gas bubble formation, and (4) target destruction.

Lagrangian/Eulerian simulation models are most widely used tools to calculate droplet spray behavior. The gas flow is treated as continuum (Eulerian) and discrete parcels of particles (Lagrangian) are injected into the flow field. Each parcel contains many identical droplets. The Lagrangian step may be performed by simultaneous tracking of all parcels in an integral time step, as developed by Amsden et al. (1989), or tracking of each complete trajectory of the parcel in serial manner, as performed by Crowe et al. (1977). Collision models are incorporated into the main gas-spray flow model. Spray collision models reflect the two approaches: (1) simultaneous tracking of all droplet parcels and search for collision partners, as performed by Amsden et al. (1989), or (2) serial tracking of parcel and sampling individual collision partners from statistical information, as performed by Sommerfeld and Zivkovic (1992), Sommerfeld et al. (1993), Sommerfeld (1995), and Osterle and Petijean (1993). The second approach significantly reduces the calculation task. However, as the collision partner is sampled from a statistical value, the postcollision properties have to be treated carefully if the information of both partners is required.

In both models, the collision partners are the uniform particle cloud contained in each parcel. All parcels presented in a control volume are taken into account for determining the collision probability (all real droplets for O'Rourke model and statistical droplets for Sommerfeld model). Therefore, stochastic collision is treated and kinetic theory of gases is applied. Particle collision is assumed to take place within the collision cylinder, as shown in Figure 19.64. The collision cylinder has a cross-section diameter of $(d_{p1} + d_{p2})$ and length of $(U_{rel}\Delta t)$, where Δt is the time step considered.

The model presented by O'Rourke (1981) and implemented in the KIVA computer program (Amsden et al., 1989) tracks all parcels simultaneously and the possibility of collision between each pair of parcels

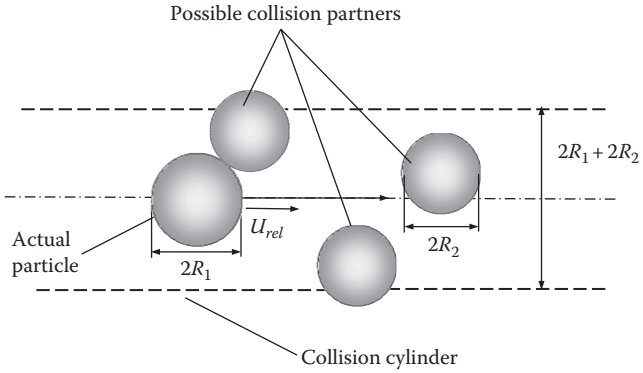


Figure 19.64

Drop collision cylinder from kinetic gas theory.

is evaluated by searching all collisional partners that are present in the computational cell. The criterion whether collision takes place or not is determined by the probability of nil collision:

$$P_{no_collision} = e^{-f\Delta t} \tag{19.148}$$

where f is the collision frequency in a collision cylinder:

$$f = \frac{N_{r_s}}{V}\pi(r_l + r_s)^2\left|\bar{V}_{r_l} + \bar{V}_{r_s}\right| \tag{19.149}$$

N_{r_s} is the number of smaller radius droplets
V is the volume of the computational cell
the subscripts *r_l* and *r_s* describe the properties of larger and smaller droplets, respectively

To decide whether a collision takes place, a random number (RN) is generated from a uniform distribution and compared with $P_{no_collision}$; if RN > $P_{no_collision}$ a collision event is valid. The position of contact point during collision is directly calculated since the collisional partners are both "real" and their trajectories are known. Since the model considers the collision of particles within the same computational cell only, "artifacts" concerning neighboring particles located in an adjacent cell may arise.

Schmidt and Rutland (2000, 2004) developed the no-time-counter (NTC) collision model that predicts how many collisions must occur in a given cell and then randomly samples collision pairs within the cell. In the NTC model, the collision computation is performed on a special collision mesh that is optimized for both sample size and spatial resolution. The mesh is different for every time step to further suppress artifacts.

The proximity collision model has been developed by Bauman (2001) and is designed to improve the previous discrepancy in the KIVA code collision model. To counter the "artifacts" problem, possible collision pairs are chosen based on the proximity of the two particles from each other, irrespective of their placement relative to the computational grid. A user-defined collision radius is introduced to define the maximum distance that two particles can be apart from each other to consider for collision. The equations for determining whether collision occurs, and the outcome of the collision, are nearly identical to the KIVA collision model.

Within the models proposed by Osterle and Petijean (1993) and Sommerfeld and Zivkovic (1992), Sommerfeld et al. (1993), each parcel is tracked in a serial manner and statistical value of particle number density, average and rms velocity size relationship, and other variables are kept and stored in each computational cell. The collision probability assumes a moving droplet while the other droplet (fictitious) is fixed and is calculated within the collision cylinder:

$$P_{collision} = 0.25\frac{N_2}{V}\pi(D_l + D_s)\left|U_r\right|\Delta t \tag{19.150}$$

N_2 is the total particle number density in the computational cell (from the stored particle number in the last Lagrangian step). The particle size of the collision partner (fictitious droplet) is sampled from the local particle size distribution. Rüger et al. (2000) validated this collision model in a spray with experimental results.

The comparison of measurements and predictions showed very good agreement for the profiles of mean properties of both phases and the local droplet size distributions as well as size-velocity correlations. According to the calculation results, the increase of the integral droplet SMD along the spray distance is mainly due to coalescence, while the impact of droplet evaporation on mean diameter decrease is of minor importance.

In a further extension, Sommerfeld (2001) developed an interparticle collision model, taking into account the correlation of the fictitious particle with the velocity of the real particle as a consequence of gas turbulence. The model has been validated with results from LESs in the literature. For all test cases considered, good agreement between model calculations with the results obtained by LES has been found.

Pischke et al. (2012a) developed a hybrid collision algorithm to predict the collision probability: collisions between parcels are described deterministically, that is, by searching for intersecting trajectories between computational parcels, while droplet collisions stochastically. The collision probability formulation eliminates the influence of a gas-phase mesh or a collision mesh by introduction of a parcel diameter, which is a measurement for the volume represented by a specific parcel. Two nonparametric parcel diameter estimators are derived based on the volume-of-influence approach, an isotropic parcel diameter estimator for homogeneous droplet clouds (sphere-of-influence), and an anisotropic parcel diameter estimator for inhomogeneous droplet clouds of reduced dimensionality (ellipsoid-of-influence). During derivation, the exactness for analytical homogeneous dispersions is preserved. The performance of the anisotropic volume-of-influence approach is demonstrated by synthetic validation cases, indicating that the formulation delivers exact predictions in cases where other existing collision algorithms do not even converge. To improve numerical convergence, a velocity decomposition method has been proposed by Pischke et al. (2012b), splitting the relative velocity between the parcels into a velocity gradient (with little influence on collisions, but high numerical sensitivity) and into velocity fluctuations (with high influence on collisions, and little numerical sensitivity). By removing the spurious contribution of the velocity gradient, the convergence of the collision algorithm is increased from first to second order. Based on the anisotropic volume-of-influence approach and the velocity decomposition method, a Lagrangian collision algorithm has been developed by Pischke (2014), which incorporates strategies from Eulerian NTC algorithms. For efficiency reasons, a dedicated collision mesh is introduced, which separates parcels that are improbable to collide. Overlapping control volumes are introduced to avoid mesh artifacts, which typically occur at collision mesh boundaries, while reducing the number of potential collision partners. With the Lagrangian collision algorithm, highly anisotropic sprays with strong velocity gradients appear numerically solvable.

19.2.1.4 Clustering of Droplets

Due to the dynamics of the primary liquid fragmentation process, especially in the dense spray region, a clustering of droplets may occur. Until recently, experimental characterizations of sprays have been limited in most cases to single point statistics of the spray in time or space. Such a description provides as integral information a measure of the mean number density or flux rate of the spray. Progress in measurement techniques like the phase Doppler anemometry (PDA) has made temporal correlated droplet measurements and the particle image velocimetry has made space correlations information available for sprays. Marx et al. (1994) and Edwards and Marx (1995a,b) developed a multipoint statistical description of a spray. Based on this theoretical approach, it is possible to distinguish between steady and unsteady sprays by using the interparticle arrival time τ at a certain position. Steady sprays are defined as those whose interparticle arrival time distribution obeys inhomogeneous Poisson statistics. Unsteady sprays are defined as those whose interparticle arrival time distribution does not obey inhomogeneous Poisson statistics. An example of unsteady spray behavior with droplet clustering is illustrated in Figure 19.65 with a high-speed-video sequence of a disintegrating liquid jet. Areas at higher and lower droplet concentrations in the initial spray have been attributed to the asymmetric instability and primary fragmentation of the liquid jet.

The experimental interparticle time distribution h_{exp} can be determined from a single realization (SR) or multiple short realizations that are ensemble averaged (ER). Edwards and Marx (1995a,b) showed that

$$h_{exp}(\tau_j) = \frac{H(\tau_j)}{N\Delta\tau_j} \tag{19.151}$$

where

τ is the interparticle time gap
$H(\tau_j)$ is the number of events that fall within the jth interparticle time gap
N is the total number of interparticle events
$\Delta\tau_j$ is the width of the jth interparticle time gap

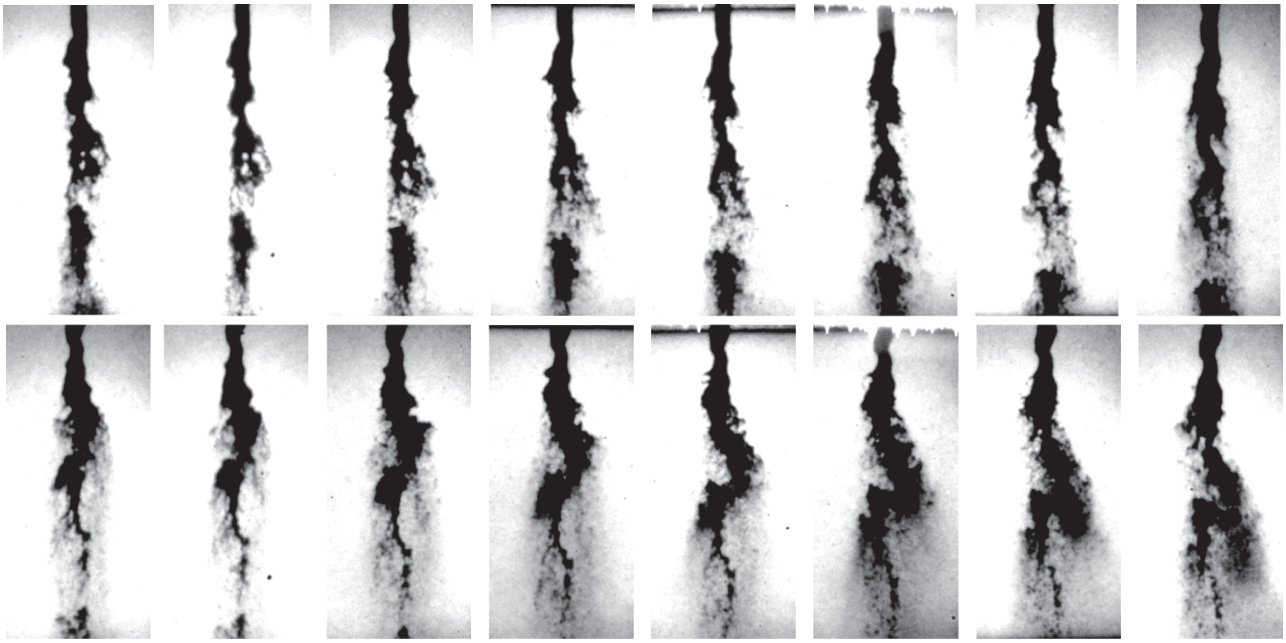


Figure 19.65

Drop clustering in sprays: high-speed photo series of liquid fragmentation process, liquid jet diameter 4 mm, time increment 0.2 ms.

To determine the theoretical interparticle time distribution, the spray is modeled as a marked inhomogeneous Poisson process. The Poisson process is described by the intensity function λ that represents the expected number of particles to be sampled per unit time. The theoretical finite interparticle time distribution is

$$h_{th}(\tau_j) = \frac{\lambda^2 (T-\tau)\exp(-\lambda\tau)}{\lambda T - 1 + \exp(-\lambda T)} \tag{19.152}$$

The theoretical interparticle function is compared with the experimental interparticle distribution function and a decision on spray steadiness or unsteadiness is made based on the statistical analysis using the chi-square tests to get the significance level (Luong and Sojka, 1999).

Figure 19.66 illustrates a sample comparison between experimental data and theoretical steady interparticle time distributions. The data were taken 100 mm downstream of a pressure atomizer (flat sheet cone) on the spray centerline for a liquid mass flow rate of 0.05 kg/min. The bars represent the experimental data in discrete time bins. The solid curve represents the theoretical value, where the error bars show the expected scattering of the theoretical results due to the random nature of a theoretical spray. The experimental interparticle time distribution differs for the first bins from that of the steady theoretical case (e.g. by more than 12 deviations for the first bin). The chi-square value $\chi^2 = 307$ shows the significance and that the two distribution functions are not different due to random fluctuations. For this case, a high probability for having droplets at shorter interparticle arrival times is found, that is, droplet clustering occurs in this spray (unsteady spray). Droplet clustering in spray will lead to significant changes in the main interphase transport mechanisms (momentum, heat and mass, see Chapter 1) because here the local bulk properties vary in between and outside of a droplet cluster.

Heinlein and Fritsching (2006) analyzed the spatial particle distribution in the spray of a pressure and twin-fluid atomizer, respectively, by means of pointwise and time-resolved PDA measurements. Steady and unsteady particle structures are identified by evaluating the interparticle arrival time statistics at a certain position. While for the pressure atomizer clustering takes place mostly within the central area of the spray, this effect is found for the twin-fluid atomizer mostly in the outside spray area. For both atomizers, clustering increases and/or begins only at increasing axial distances. In a droplet cluster, a locally high droplet number density exists, which results in relatively short interarrival times. No significant dependence between the droplet size and the occurrence of droplet clusters has been found; the drop size distribution

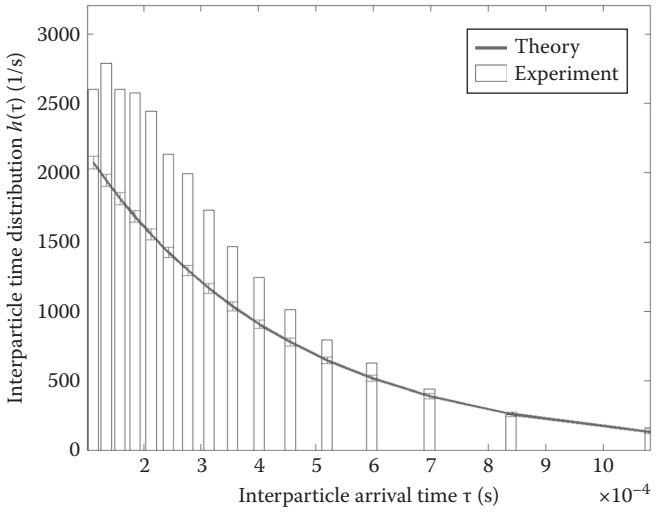


Figure 19.66

Drop clustering: experimental versus theoretical data.

within a cluster corresponds to the drop size distribution of the entire spray. The presence of clusters can be determined, however, primarily in the lower velocity range, which has to be attributed to the fact that collective groups of droplets have different drags than individual droplets.

Lampa and Fritsching (2013) investigated the clustering behavior of droplets in the spray of a twin-fluid atomizer based on different spray chamber geometries. The PIV measurements have captured the large scale vortices located at the edge of the spray cone flow. The LESs indicate that the gas-droplet interaction within the shear layer is the driving force for the formation of droplet clusters.

19.2.2 Dilute Spray

The majority of all spray investigations deal with the dilute spray region where mainly gas/droplet interaction determines the spray behavior. A variety of sophisticated measurement instruments and experimental and numerical techniques are used to investigate details of the gas and droplet behavior in this spray region. These include:

- Nonintrusive laser diagnostic instruments for dispersed multiphase flows, like PDA, diffraction particle sizer, particle image velocimetry and particle-tracking-velocimetry, holography, laser-induced fluorescence, and others (see Hammer et al., 2016)
- Numerical models, based on Euler/Lagrange techniques, Euler/Euler techniques (two-fluid models), direct numerical, or Large–Eddy simulations (Bergström et al., 1999, Bellan, 2000), PDFs, among others (see Chapter 2 on modeling),

These numerical and experimental techniques have contributed to understanding of multiphase transport processes in sprays. Parameters describing the dilute spray structure identify the behavior of the droplets in the spray, the interaction with the gas phase, and the macrostructure of the spray development. These results typically are specific for their spray application under investigation (medium, atomizer type, operational parameters, etc.).

19.2.2.1 Individual Droplet Behavior

The behavior of (individual) droplets in the gaseous atmosphere (Sadhal et al., 1997, Sirignano, 1999) like in a spray is substantially based on aerodynamic and gravitational forces acting on the particles, balanced by the inertia of the droplets (see Chapter 1). Based on a one-dimensional numerical analysis using the droplet trajectory equation (without coupling effects), a principal investigation for the droplet behavior in a spray such as the identification of different atomizer nozzle characteristics is possible:

$$m_p \frac{du_p}{dt} = m_p g - \frac{1}{2}\rho_g (u_p - u_g)\left|u_p - u_g\right| A_p c_d \tag{19.153}$$

Fritsching and Bauckhage (1987) analyzed the interaction of droplets and the surrounding gas phase in a water spray as a function of distance from nozzle for single-fluid (pressure) and twin-fluid (gas) atomizers. Results of measurements of droplet velocities and sizes on the spray centerline measured by PDA have been used for comparison with the one-dimensional model. The two nozzle types and their respective dimensions have been chosen by the criterion of comparable droplet size and velocity spectra in the spray.

For the uncoupled solution of the droplet trajectory, an assumption for a velocity distribution of the gas phase is necessary. This boundary condition has been determined from PDA measurements of droplet velocities of the smallest detected droplets in the spray based on the assumption that these droplets act as tracer particles and the local gas velocity equals the measured droplet velocity (zero slip velocity). The initial droplet (starting) velocity value has been prescribed. For the twin-fluid nozzle, it has been assumed that the starting velocity of the droplets equals the liquid feed velocity from the nozzle. For the pressure atomizer, a constant starting velocity for all droplet size classes has also been assumed. Its value has been obtained by extrapolating the droplet velocities measured for the biggest drop size class detected from the first measurement location in front of the nozzle backward to a common starting location for the droplets in the vicinity of the nozzle.

In Figure 19.67, a comparison between the model results and measurement results (these have been averaged over a certain drop size class) for the pressure atomizer is illustrated. The dash-dotted line in front of the figure indicates the derived distribution of gas velocity as a function of nozzle distance $v_l(z)$. The figure shows that smaller droplets in the spray immediately after fragmentation lose their initial momentum carried from the liquid delivery. This initial momentum is directly transferred to the slow moving (entrained) gas. Further downstream this smaller droplets move at almost the velocity of the gas (the relative velocity between droplet and gas is the constant droplet settling velocity). The bigger droplets are decelerated somewhat more slowly. Therefore, a continuous momentum transfer from the droplets to the slower moving gas occurs. The velocity distribution exhibits strong gradients dependent on droplet size in the nozzle vicinity, while at increased nozzle distances, the velocity distribution for all droplet sizes becomes uniform.

In the spray of the twin-fluid atomizer, a change of the direction of momentum transfer occurs. This can be seen in Figure 19.68. Close to the atomizer, the faster moving atomizer gas accelerates all droplets more or less depending on size. The direction of momentum transfer is always from the gas to the slower particles. Therefore, the gas loses a significant amount of kinetic energy within a small distance from the atomizer. At a certain distance from the atomizer, the direction of momentum transfer is reversed. At greater nozzle distances, all droplets are moving faster than the gas and the direction of momentum transfer is from the droplets to the gas. The droplets in this area accelerate the gas. The point where the

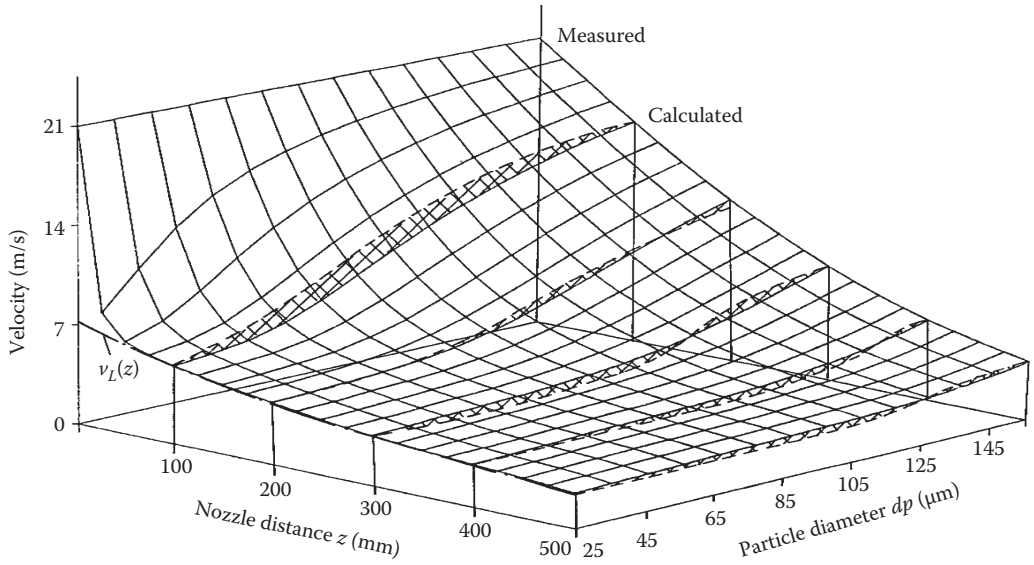


Figure 19.67

Drop velocity on spray centerline: pressure atomization. (From Fritsching, U. and Bauckhage, K., *Chem. Ing. Tech.*, 59(9), 744, 1987. With permission.)

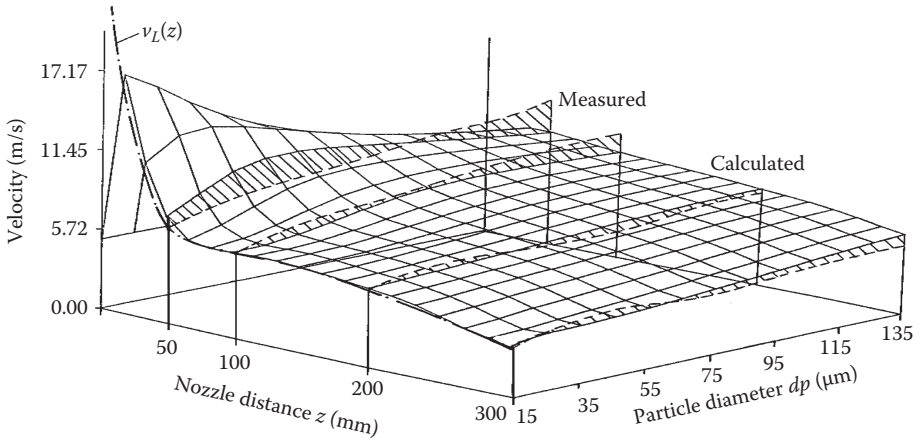


Figure 19.68

Drop velocity on spray centerline: twin-fluid atomization. (From Fritsching, U. and Bauckhage, K., *Chem. Ing. Tech.*, 59(9), 744, 1987. With permission.)

momentum transfer changes direction depends on the droplet size. While the smaller droplets already exhibit this change of momentum transfer closer to the atomizer due to their smaller inertia, the bigger particles change the momentum transfer direction in a somewhat greater nozzle distance.

By comparing the characteristics of these nozzle types, a common characteristic for technical spray processes can be seen. When the aim of the atomizer application is the achievement of almost identical droplet velocities at a specific distance from the atomizer (e.g., for coating application), this behavior is achieved much closer to the atomizer for the twin-fluid atomizer. In addition, the reversal of the momentum transfer direction has to be recognized as an important feature for twin-fluid atomizers.

An important property of a droplet spray is the correlation of drop sizes and velocities. This leads to a two-dimensional distribution of drop properties in sprays. Typical behavior of a drop size/velocity correlation at a single point in the spray of a pressure atomizer is illustrated (from a simultaneous measurement of drop size and velocity by PDA) in Figure 19.69 (Schulte, 1995). In the ground plane of the plot, the measurement result of several ten thousand individual particles is shown (individual droplet size and velocity), while at the two sides of the plot, the integration in terms of number frequencies of drop sizes and velocities respectively is illustrated.

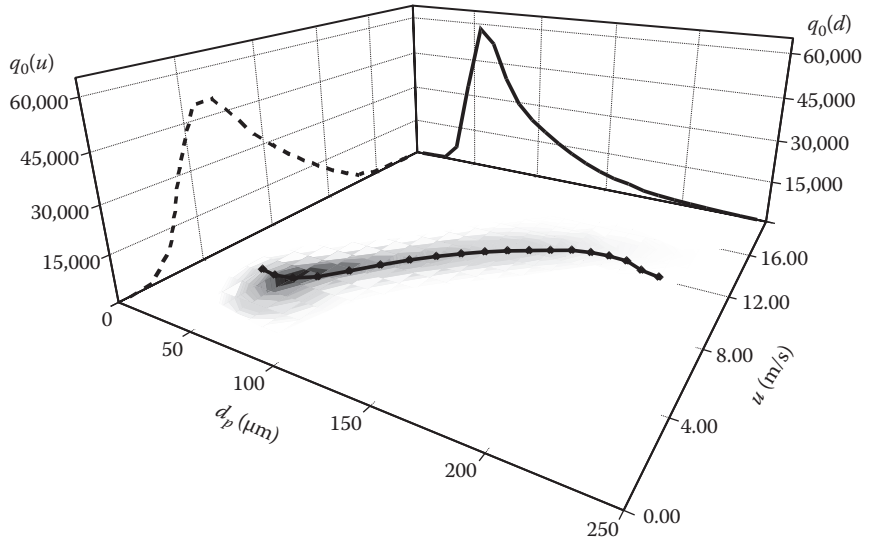


Figure 19.69

Drop size/velocity correlation in spray. (From Schulte, G., *Zweidimensionale Verteilungen von Partikeleigenschaften*, Shaker Verlag, Aachen, Germany, 1995. With permission.)

19.2.2.2 Spray Cone Spreading

The spray cone angle describes the macrogeometry of a spray. Different atomizers yield different spray characteristics, for example, flat, round, or hollow cone. The spray cone angle initially is determined by the liquid exit condition, the main disintegration mode within primary fragmentation (and here the growth rate of asymmetrical disturbances), later on by gas turbulence effects (particle dispersion), interaction with the ambient air (gas entrainment), and finally by gravity.

Within pressure swirl atomization, as already discussed in Section 19.1.5.1, by assuming an inviscid liquid, the spray cone angle is expressed as a function of the nozzle dimensions only. The half cone angle is (Giffen and Muraszew, 1953)

$$\sin\Theta = \frac{(\pi/2)c_D}{K_1(1+\sqrt{X})} \tag{19.154}$$

For a simplex pressure atomizer with a full spray, the work of Reitz and Bracco (1979, 1982) concluded that the spray angle can be determined by combining the radial velocity of the fastest growing of the unstable waves in the primary fragmentation process with the axial injection velocity. This hypothesis results in an expression for the spray angle that has been later on simplified by Bracco et al. (1985) as follows:

$$\tan\Theta = \frac{2\pi}{\sqrt{3}A}\left(\frac{\rho_g}{\rho_l}\right)^{0.5} \tag{19.155}$$

where A is a function of the orifice length to diameter ratio that must be experimentally determined (Lefebvre, 1989).

The distribution of the sprayed liquid mass in the spray cone is described by the mass flux distribution. Adopting the concept of self-similarity from a single-phase jet, the droplet mass flux distribution in a spray may be described. In full cone sprays, this can be expressed in terms of a general empirical formula as follows (Uhlenwinkel, 1992):

$$\frac{\dot{m}}{\dot{m}_{cl}} = e^{-k_1(r/r_{0.5})^{k_2}} \tag{19.156}$$

where

$\dot{m}_{cl}$ is the maximum value of the mass flux distribution function on the spray centerline

$r_{0.5}$ is the half width of the mass flux distribution (see Figure 19.70)

The proposed empirical constants have been given as $k_1 = \ln(2.0)$ and $1.2 < k_2 < 2.0$. The constant k_2 depends on operational process conditions and liquid properties. The spreading behavior of the spray cone may be described either by a function of the mass flux on the centerline or by the distribution of the half width of the mass flux distribution versus nozzle distance, where for a Gaussian type distribution,

$$r_{0.5} = \sqrt{k_2 \frac{\dot{M}_l}{\dot{m}_{cl}}} \tag{19.157}$$

The behavior of the centerline mass flux has been empirically correlated as follows (Uhlenwinkel 1992, Kramer 1997):

$$\dot{m}_{cl} \approx z^{-k_3} \tag{19.158}$$

For water sprays, Uhlenwinkel (1992) has found $k_3 \cong 2$, while for metal melt atomization, Kramer (1997) found $k_3 < 2$. Spray cone spreading (namely the coefficient k_3) depends on atomization parameters. For water atomization, the spreading of the spray increases with higher gas flow rates, while for metal melt, the reverse trend is observed. In this case, the spray cone width narrows when the gas mass flow rate increases with higher pressure (Uhlenwinkel, 1992).

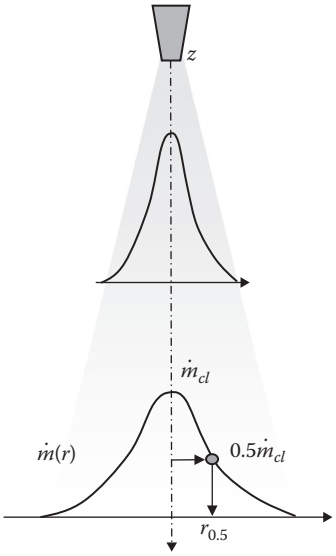


Figure 19.70

Mass flux distribution in sprays (index: centrenline cl; half width 0.5).

19.2.2.3 Spray/Environment Interaction: Entrainment

The spray system interacts with the environmental gas. Like a single-phase jet, it accelerates ambient gas due to friction (entrainment). Thereby, the plume of the dispersed phase (the droplet spray) maintains a narrower width than the complete flowing gas jet (see Section 19.4.2.1).

The spray/gas interaction and gas entrainment may lead in some cases to a change in the spray structure with increasing distance from the atomizer, namely, a drop size segregation. Generally, this effect is pronounced in pressure atomizers, as in this case, the entrainment effect is strongest, and is typically found in pressure swirl atomization. The primary hollow cone structure is changing toward a solid cone with increasing spray distance. Figure 19.71a illustrates the change as a short exposure view onto the spray (instantaneous structure) from outside in comparison to a light-sheet illumination of the central plane of the spray in Figure 19.71b. Here, due to the entrainment of ambient gas into the initially hollow cone spray, droplets are accelerated and transported into the core region of the spray (see sketch in Figure 19.72b). As an example, in Figure 19.72a, PDA data are presented as radial distributions of the arithmetic number mean value of the measured droplet size distribution at several planes below the atomizer. With increased spray distance, the edge of the spray shows increased drop sizes, while in the spray core, the smaller droplets are more prevalent. Because of their smaller inertia, smaller droplets are more easily transported into the spray core than bigger drops. Here, a size segregation effect follows, where the droplet size distribution in the spray is changed, typically as shown in the sketch in Figure 19.72b.

The total spray/gas entrainment rate depends on the atomizer type. With twin-fluid atomization, entrainment can be estimated based on the overall gas flow rate in circular, turbulent jet, and the distance from the nozzle. The ratio of the total gas flow rate to the initial jet flow rate is a linear function:

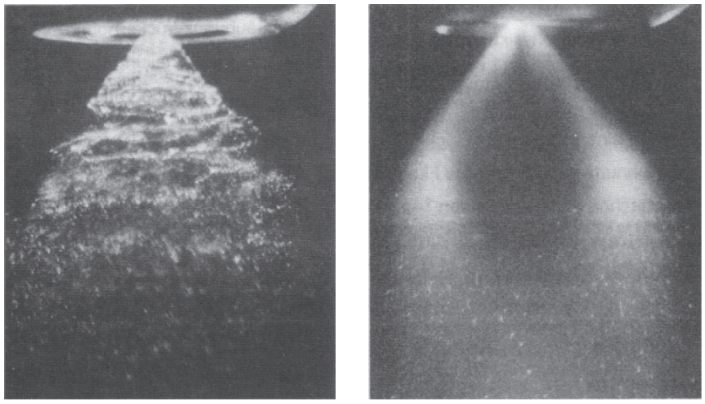
$$\frac{\dot{Q}_{total}}{\dot{Q}_0} = \text{const.}\frac{x}{d_0} \tag{19.159}$$

The constant is 0.4565 from the analytical solution for a turbulent jet and varies from 0.30 to 0.45 in experimental and simulation studies of single- and two-phase jets and spray flows.

19.2.3 Heat and Mass Transfer

Fundamentals of heat and mass transfer from droplets in gases have been derived in Chapter 1). Heat transfer mechanisms are important in melt atomization and spray processes (see Section 19.4.2). Simultaneous heat and mass transfer is important in coating applications (e.g., paint sprays) or spray-drying processes (see Section 19.4.3).

As a liquid droplet spray comes in contact with hot atomization gas, three transfer mechanisms (mass, momentum, and energy) become operative simultaneously. Crowe (1980) and Crowe et al. (1998) described these



(a) (b)

Figure 19.71

Spray from pressure swirl atomizer: (a) short and (b) long time exposure, droplet entrainment in hollow cone spray. (From Lampe, K., Experimentelle Untersuchung und Modellierung der Mehrphasenströmung im düsennahen Bereich einer Öl-Brenner-Düse, Dissertation, Universität Bremen, Bremen, Germany, 1994. With permission.)

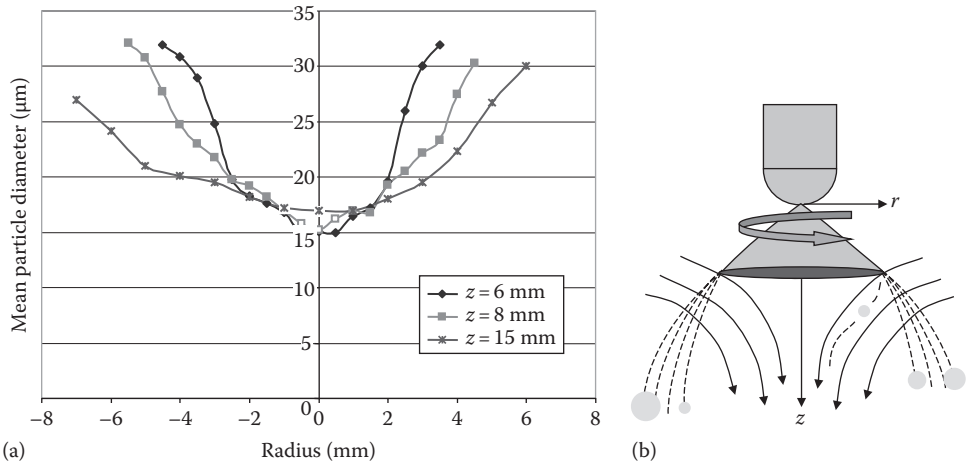


Figure 19.72

Gas and droplet entrainment in hollow cone spray, (a) drop size distribution, (b) spray sketch. (From Lampe, K., Experimentelle Untersuchung und Modellierung der Mehrphasenströmung im düsennahen Bereich einer Öl-Brenner-Düse, Dissertation, Universität Bremen, Bremen, Germany, 1994. With permission.)

transfer mechanisms through spray-drying processes. At the droplet–hot air interface, heat is transmitted into and moisture is transmitted out of the droplet surface. The external transfer of mass or heat can be obtained from

$$\Phi = kA\Delta X \tag{19.160}$$

where

k is the transfer coefficient
A is the particle surface area
ΔX is the driving potential

The transfer is described by the Nusselt number, Nu, for heat transfer and Sherwood number, Sh, for mass transfer that may be obtained from the correlation (Ranz and Marshall, 1952):

$$\mathrm{Nu} = 2 + 0.6\,\mathrm{Re}^{0.5}\,\mathrm{Pr}^{0.33} \tag{19.161}$$

$$\mathrm{Sh} = 2 + 0.6\,\mathrm{Re}^{0.5}\,\mathrm{Sc}^{0.33} \tag{19.162}$$

This correlation has been extended to turbulent effects by Yearling and Gould (1995) (see also Clift et al., 1978). The driving potential ΔX for heat transfer is the temperature difference between droplet and surrounding air, and for mass transfer, the vapor concentration difference between the surrounding air and the vapor film on the droplet surface (Delplanque and Sirignano, 1994).

19.2.3.1 Drying of a Solution/Suspension Droplet

19.2.3.1.1 Drying Mechanism of a Dispersed Droplet Most feed materials in a spray-drying application are dispersed liquids (solution or suspension). Drying of a dispersed liquid droplet may yield a porous-solid shell (or crust) on the droplet skin that significantly changes heat and mass transfer rates compared to those of a pure liquid droplet. When the crust formation begins, the internal mass transfer rate through the porous-solid shell becomes the evaporation-controlling factor for evaporation.

Dolinsky (2001) described the drying mechanism of a dispersed material in high-temperature gas streams ($T_{air} > T_{boil}$). From analysis of experimental data, five successive drying periods have been identified (see Figure 19.73):

1. The period of droplet heating from its initial temperature T_0 up to the temperature of equilibrium evaporation T_{eq}.
2. The period of equilibrium evaporation during which intense removal of moisture from the liquid droplet surface occurs. The period of equilibrium evaporation (t_{cr1}) ends when the solid content on the drop surface is increased to the point that a shell is formed on the surface of the evaporating droplet.
3. The period of crust formation when the droplet temperature increases sharply due to the formation of the dense shell made from dispersed substance.
4. Boiling period: the temperature inside the particle reaches the boiling point and steam is generated.
5. Drying period: the particle temperature sharply increases almost to the temperature of the hot gas. During this period, removal of the bound moisture occurs. Fragmentation may also occur in this period.

Mathematical models permit analysis of the evaporation process at the different stages of a drying droplet. Typically in these models, plug flow of air, no droplet deformation, no droplet–droplet, and droplet–wall

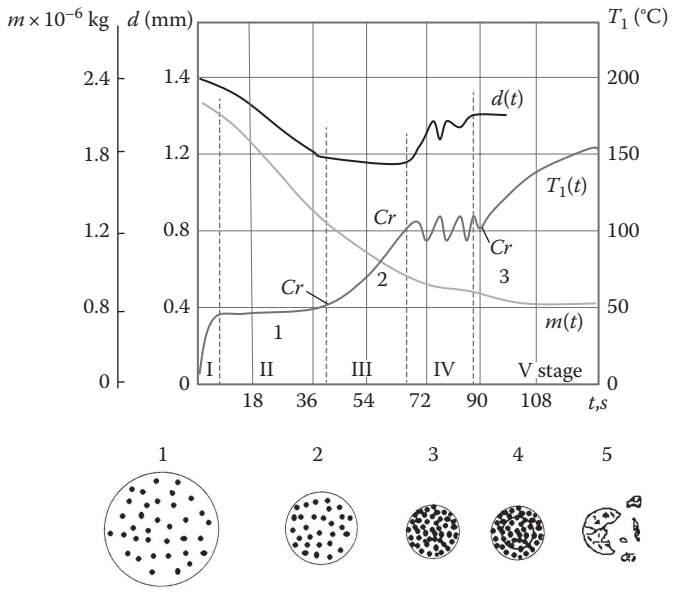


Figure 19.73

Successive drying periods of a suspension droplet, variation of diameter, temperature and mass in a hydration process. (Adapted from Dolinski, 2001.)

collision is assumed. The concentration of average volume at the moment of crust formation, when the equilibrium drying stage ends, is given by

$$C_S = \frac{C_{sat}[C_0 + 3\mathrm{Ki}(C_{sat} - C_0)]}{C_{sat} + 3\mathrm{Ki}(C_{sat} - C_0)} \tag{19.163}$$

where Ki is Kirpichev number

$$\mathrm{Ki} = \frac{D_1 \rho_1}{D_2(\gamma_s - \gamma_\infty)} \tag{19.164}$$

The coefficients C_0 and C_{sat} are the initial and saturation concentration of the solution in an average volume, respectively. D_1 and D_2 are the diffusion coefficients for water in solution and in gas, respectively. This crust concentration is used as a criterion to distinguish constant drying rate period (stage 2) and falling rate period (stage 3). Mass transfer rate during crust formation has to be obtained experimentally.

Elperin and Krasovitov (1995) developed a model that takes into account effects of compressibility and filtration of the gas/vapor mixture within the porous shell. They used the critical volume ratio as crust formation criteria, which could be calculated from a minimum void fraction (ε) attained in packing of spherical particles

$$\delta_c = V_S N_l = \frac{1 - \varepsilon}{\varepsilon} \tag{19.165}$$

The mathematical model—taking into account porosity; permeability; surface tension of solid/gas, solid/liquid, and liquid/gas interface; effective thermal conductivity; and diffusion coefficient—is developed and solved numerically. A pressure balance equation at the liquid interface inside the particle was also included and investigated in this work. Numerical results showed that at the ambient gas temperature above the liquid boiling point, the pressure at the liquid interface increased significantly and thus may cause the fragmentation of the porous shell.

Straatma et al. (1991, 1999) developed numerical drying models for food products, where crust formations are generally found. The drying models take into account both external and internal phenomena. The driving force for mass transfer (from Equation 19.158) is expressed as

$$\Delta X = c_a^\star - c_a \tag{19.166}$$

where $c_a^\star$ is the water vapor concentration that is in equilibrium with the wet surface of droplet. In this work, the GAB equation (Guggenheim, Anderson, and de Boer) was used to calculate $c_a^\star$.

The unstationary diffusion process inside the spherical particles is described by the one-dimensional differential equation

$$\frac{\delta c}{\delta t} = \frac{1}{r^2}\frac{\delta}{\delta r}\left(r^2 D \frac{\delta c}{\delta r}\right) \tag{19.167}$$

The diffusion coefficient (D) depends on the moisture content and the temperature (Ferrari et al., 1989). The differential equation (19.167) is solved numerically in conjunction with external heat and mass transport equations (19.160) through (19.162) using the gas/liquid interface boundary condition and zero gradient boundary condition at the center ($r = 0$). The moisture content at various positions inside droplet can be determined.

A nondimensional differential equation of the concentration field in a solution droplet based on the diffusion equation for mass transfer inside the droplet was proposed by Brenn et al. (2001a). In the nondimensional equation, a characteristic parameter occurs, which is formed from densities and diffusion coefficients in the gaseous and liquid phases and accounts for the Sherwood number of mass transfer and the solvent vapor content in the ambient gaseous medium. The numerical value of this parameter, which separates the regimes leading to the formation of hollow and solid spheres, was calculated using a data set for aqueous sodium chloride solutions from the literature. An experimental verification of the significance of the

threshold value based on measurement results from droplets drying in an acoustic levitator confirmed that drying conditions with values less than the threshold value lead to the formation of hollow spheres, while for larger values, solid spheres are formed.

The solute concentration profiles in a droplet during drying can be obtained by solving the diffusion equation for mass transfer inside the droplet (Brenn, 2005, Eslamian et al., 2006, 2009). The results reveal the formation of large concentration gradients in the droplet at high evaporation rates, and flat concentration profiles for slow drying. If at the onset of the precipitation, which will most likely occur at the droplet surface, the solute concentration everywhere in the droplet is equal to or is above the equilibrium saturation (ES), the solute starts to precipitate everywhere within the droplet. This type of precipitation is called "volumetric precipitation". Therefore, the whole droplet undergoes nucleation, crystallization, and growth of the solute nuclei (Jayanthi et al., 1993). In this case, the final particle is fully filled; otherwise, it is hollow and a crust forms on the surface of the droplet, whose thickness depends on the solute concentration distribution.

19.2.3.1.2 Models of Single-Droplet Drying Kinetics For the prediction of single droplet drying, there are generally four types of approaches to formulate drying models (Mezhericher et al., 2010, Chen and Putranto, 2013):

1. *Empirical models* obtained entirely by regression methods to derive the explicit time-dependent functions.
2. *The concept of characteristic drying curve* (*CDC models*), which recognizes different drying stages, for example, the constant rate period (which may also be called the "unhindered drying period," where the internal transport of the moisture does not affect the surface evaporation) and falling rate ("hindered drying") period (Fyhr and Kemp, 1998, Langrish and Kockel, 2001). In the CDC models, the drying rate can be represented by the following equations:

$$\frac{dX}{dt} = f\frac{Ah}{m_s \Delta H_{evap}}(T_b - T_{wb}) \tag{19.168}$$

$$f = 1, \quad X > X_{cr} \text{ (constant rate period)} \tag{19.169}$$

$$f = \frac{X - X_b}{X_{cr} - X_b}, \quad X \le X_{cr} \text{ (falling rate period)} \tag{19.170}$$

Here

X is the moisture content on a dry basis
A is the droplet surface area
h is the external heat transfer coefficient
m_s is the mass of the solids in one droplet/particle
ΔH_{evap} is the latent heat due to vaporization
T_b and T_{wb} are bulk and wet bulb temperature of the drying air, respectively
X_{cr} is the critical moisture content, which makes the transition from the constant rate period to the falling rate period
X_b is the equilibrium moisture content corresponding to the environmental condition for drying

The constant rate period is identified as the period where the droplet moisture content is above the critical moisture, while the falling rate period below the critical moisture.

Evident in the CDC models, it is assumed that there is a linear drop in drying rate proportional to the moisture in droplet: the constant rate period is simplified analogous to the evaporation of small pure liquid droplet; and the hindering effect of the internal mass transport on the drying rate is simplified by a linear relation relative to the material properties, X_b and X_{cr}. While X_b can be obtained from the isotherms of the material as a function of ambient air humidity and temperature, the X_{cr} is assumed to be constant for the specific material, independent of the drying condition. In reality, this might not be a fair assumption if the droplet experienced extreme contrasting initial

drying rate (Fyhr and Kemp, 1998). In maltodextrin solution, it was observed that a higher initial moisture will result in a higher critical moisture and vice versa (Zbicinski and Li, 2006).

3. *Deterministic drying models*, which describes the comprehensive transport phenomena within a droplet using the continuity, momentum, energy, and species conservation equations (Mezhericher et al., 2007, 2008a,b, Eslamian et al., 2009); deterministic models with distribution of solid component described by population balance are presented by Seydel et al. (2006) and Handscomb et al. (2009a,b).

   The deterministic models take into account and keep track of the detail phenomena within the drying particle (e.g., moisture gradient, diffusion, internal bubble, solid formation) by a set of differential equations with corresponding initial and boundary conditions. Subsequently, the models translate these individual internal phenomena into the internal moisture gradient, which affects the overall drying rate. The solution of this set of equations is complicated by the presence of a moving domain boundary because of the shrinking droplet radius in the constant rate drying stage and the receding interface between the dry crust and wet core regions of the wet particle in the falling rate drying stage. The deterministic models are "physically" realistic, through which the behavior of the main drying characteristics can be predicted for various drying conditions showing a good accuracy and consistency with experimental data. However, solution of the associated partial differential equations in CFD might require high computational effort.

4. *Novel drying models based on reaction engineering approach (REA models)*, which visualizes the drying process as an activation process in which an energy barrier has to be overcome for moisture removal to occur (Chen and Xie, 1997, Chen and Lin, 2005, Patel et al., 2009, Chen and Putranto, 2013). The relation between the drying rate and the apparent activation energy (ΔE_v) can then be expressed as

$$\frac{dm}{dt} = -h_m A\left[\rho_{v,sat}\exp\left(-\frac{\Delta E_v}{RT_d}\right) - \rho_{v,b}\right] \tag{19.171}$$

Here

h_m is the mass transfer coefficient
A is the droplet surface area
$\rho_{v,sat}$ is the saturation vapor concentration
$\rho_{v,b}$ is the bulk vapor concentration
T_d is the droplet temperature
R is the universal gas constant (8.314 J/mol/K)

The first term on the right-hand side of Equation 19.171 is the zero-order drying "reaction," that is, the activation process. The second term on the right is the first-order wetting "reaction." Thus, the rate of moisture removal can be seen as a competitive process between drying and wetting reactions. The apparent activation energy (ΔE_v) reflects the vapor concentration depression or the relative humidity at the droplet surface during drying as

$$\Delta E_v = -RT_d \ln\left(\frac{\rho_{v,s}}{\rho_{v,sat}}\right) \tag{19.172}$$

where $\rho_{v,s}$ is the vapor concentration at the droplet surface.

Based on data sets of different drying temperatures, Chen and coworkers (Chen and Xie, 1997, Chen and Lin, 2005, Patel et al., 2009) suggest that the normalized relation of ΔE_v as a function of average moisture content difference ($X - X_b$) is material specific for each product and is independent of the drying condition. It is assumed that this can be used as the fingerprint of the material to determine ΔE_v at different drying conditions and can be expressed in the following form:

$$\frac{\Delta E_v}{\Delta E_{v,b}} = a\exp(-b(X - X_b)^c) \tag{19.173}$$

where a, b, and c are parameters to be fitted. These parameters can be obtained by back-calculating the ΔE_v value at different moisture contents from experimental data by manipulating Equation 19.171 as

$$\Delta E_v = -RT_d \ln\left(\frac{-(dm/dt)(1/h_m A)+\rho_{v,b}}{\rho_{v,sat}}\right) \tag{19.174}$$

Here, (dm/dt) is obtained from the experimental droplet weight loss curve. At high moisture content, the value of $\Delta E_v/\Delta E_{v,b}$ approaches zero, while at low moisture content, it tends to unity.

Drying models (1), (2), and (4) may be regarded as the "lumped drying models": they do not need solve for the spatially distributed moisture content and temperature within a droplet. These models require solving only algebraic equations, resulting in simpler computational effort, which is desired for CFD modeling. Detailed comparisons between CDC and REA models and their predictions are presented by Chen and Lin (2005), Patel and Chen (2005), and Meng et al. (2008), which indicates that the REA models predict the progressive reduction in drying rate better than the CDC models.

19.2.3.2 Solidification of a Melt Droplet

Solidification of a melt is described by the processes of nucleation and crystal growth. A droplet solidification process model typically is based on equilibrium phase diagrams for slow solidification and time-transfer phase change diagrams and/or experimental solidification investigations for some more realistic (higher) cooling rates. In fact, in spray processes, the cooling rate of droplets especially immediately after atomization might be very high (e.g., max. 10^7 K/s). Therefore, the possibility of undercooling prior to nucleation should be considered. In Figure 19.74b, a typical qualitative temperature/time distribution for a single melt droplet is shown for an equilibrium phase diagram. Here, a low carbon steel droplet (C = 0.3 w%, shown in Figure 19.74a) is considered as an example. Starting with the initial melt temperature (superheat) T_m, the droplet cools down to liquidus temperature T_l. Depending on the actual cooling rate, the droplet may undercool until it reaches the nucleation temperature T_n before solidification starts. Due to the rapid release of latent heat of fusion during recoalescence, the droplet temperature increases until it reaches a local maximum in the cooling curve at T_r. During the following segregated solidification, droplet temperature decreases continuously. At the temperature T_{per} in this specific case, a peritectic transformation takes place at constant droplet temperature. After termination of the peritectic transformation, again segregated solidification occurs until the droplet is completely solidified at T_s. From here on, droplet cooling is in the solid state of the fully solidified particle. The drop cooling behavior in the various stages of solidification is described based on thermal balances (internal and external). For metal droplets, typically no internal temperature gradient is assumed, as the Biot number (Bi) is small for most metal droplets (Bi $\ll$ 1).

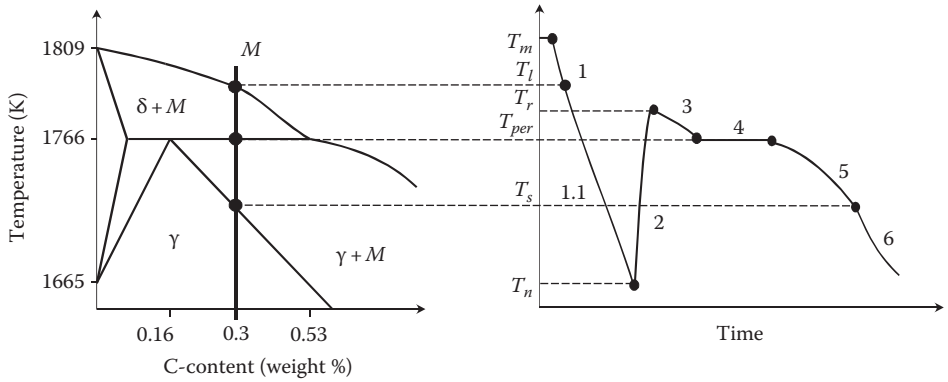


Figure 19.74

Solidification model for melt droplets (here low-carbon steel) (indices: *m* melt; *l* liquidus; *r* recalescence; *per* peritectic; *s* solidus; *n* nucleation).

Depending on cooling rate and droplet size, the temperature T_n where nucleation occurs can be much lower than the liquidus temperature T_l. The nucleation temperature for continuous cooling is defined as the certain temperature, where the number of nuclei N_n in the droplet volume V_d is identical to one:

$$N_n = V_d \int_{T_l}^{T_n} \frac{J(T)}{\dot{T}}\, dT = 1 \approx \frac{0.01 J(T_n) V_d \Delta T_{hom}}{\dot{T}} \tag{19.175}$$

Here

$J(T)$ is the nucleation rate

$\dot{T}$ is the cooling rate (Lavernia, 1996, Lavernia and Wu, 1996, Pryds et al., 1999)

Hirth (1978) has introduced the simplification in the aforementioned equation. ΔT_{hom} is the undercooling temperature difference for homogeneous nucleation. The nucleation rate may be expressed as (Libera et al., 1991)

$$J(T_n) = K \exp\left(-\frac{16\pi\sigma_{sl}^2 V_m^2 T_l^2}{3kT_n \Delta h_{fm}^2 \Delta T_{hom}^2} \right) \tag{19.176}$$

In the work of Turnbull (1950) and Woodruff (1973), a correlation has been given between the solid/liquid interfacial energy σ_{sl}, the latent heat of fusion per atom Δh_{fa}, and the atomic volume V_a. In technical processes, heterogeneous nucleation rather than homogeneous nucleation mechanisms limit the degree of undercooling (Libera et al., 1991). Only in very small droplets does homogeneous nucleation play an important role during solidification. Based on experimental results for different alloys, Mathur et al. (1989b) derived a correlation between the actual undercooling and the amount of undercooling necessary for homogeneous nucleation (Levi and Mehrabian, 1982, Libera et al., 1991). Simulation of molten metal droplet sprays including solidification submodeling has been done by Lee and Ahn (1994), Bergmann (2000), Bergmann et al. (2000, 2001b), Hattel et al. (1999, 2000), and Pedersen et al. (2000) (see also Voller et al., 1991, Wang and Matthys, 1991, 1992, Su and Tsao, 1997).

19.3 Spray Impact

19.3.1 Drop Impingement

Drop impingement is an important process, for example, in coating and surface cooling applications. The different mechanisms for individual drop behavior during wall impact (like deposition, rebounce, or splashing) are introduced in Section 14.2. A main criterion for the different impact regimes is the impact liquid drop Weber number.

19.3.1.1 Spray Deposition

In impact-related spray processes, the deposition rate (or the compaction efficiency) and the deposition mass flux distribution is important. An approach for deposition efficiency is given in Section 19.4.2.2.

19.3.2 Heat Transfer in Impinging Sprays/Spray Quenching

Spray quenching is used extensively in metal casting and welding processes, as well as in heat treatment of metals like aluminum, steel, and other metallic alloys. The combination of large droplet numbers (at small droplet sizes) and large droplet impact momentum is the key attribute to spray cooling, resulting in significant increases in cooling efficiency per flow rate over other cooling techniques. Gas-assisted twin-fluid atomization typically is employed in the cooling of steel, while pressure atomizers are used in aluminum industry (Stewart et al., 1995). Multiphase sprays are more efficient than single-phase sprays because air injected with water increases the droplets momentum and enhances the impaction and heat transfer (Issa, 2009). In gas-atomized spray quenching, heat transfer coefficient of 10,000 W/m^2/K can be achieved within film boiling regime, which is much higher than that of single-phase spray quenching (Alam et al., 2008, Alam, 2011).

During quenching or cooling of a metallic part, the surface experiences successively four different heat transfer regimes (from temperatures above the Leidenfrost temperature to room temperature): film boiling, transition boiling, nucleate boiling, and single-phase liquid cooling. The different heat transfer regimes are identified by the aid of the cooling curve (Nukiyama curve, see Chapter 8). Due to the relatively high initial

temperature, quenching of most metallic surfaces commences in the film boiling regime. Despite the possibility of a momentary contact of the liquid with the surface at the point of drop impact (see Section 14.2), a thermally insulating vapor layer quickly develops on the surface, resulting in a relatively slow cooling process. Better liquid–surface contact is maintained once the surface temperature reaches values below the Leidenfrost temperature (minimum heat flux point). In the transition regime, liquid maintains partial contact with the surface in the region undergoing intense boiling, while other regions remain insulated with vapor. The transition from film to transition boiling occurs not homogeneously across the metal surface, but strongly depends on local surface properties (e.g., geometry, roughness). This significant variation and change in the local heat transfer rate across the specimen causes large stresses on the metallic part that may lead to undesired damage or distortion of the specimen. The intermittent contact in the transitional boiling regime greatly accelerates the cooling. In the nucleate boiling regime, the surface becomes available for liquid–surface contact that accelerates the cooling due to vigorous bubble production and convection. Quenching is concluded in the slow, single-phase liquid cooling regime where the wall superheat becomes too weak to sustain bubble nucleation (Mudawar and Deiters, 1994).

Several investigations have derived correlations for the heat transfer coefficient (HTC, α) in the different boiling regimes, depending on atomizer type, spray conditions, and surface conditions. Among them, for example, Brimacombe et al. (1980), Bolle and Moureau (1982), Mudawar and Valentine (1989), Choi and Yao (1987), Jeschar et al., 1992, Viskanta and Incropera (1992), and Choi and Kang (1993) summarized the results of previous studies for steady-state and transient conditions in liquid and spray jets. Typically, correlations are presented for the heat flux or heat transfer coefficient (HTC, α) in the spray center at different boiling regimes.

In the stable film boiling regime, the heat transfer coefficient of an impinging (dense) spray is independent of the surface temperature. Here, the impinging liquid mass flux (in this context sometimes referred as impingement density or spray density) has the only effect on heat transfer. Other spray parameters such as drop velocities and sizes, as well as spray distance and nozzle type, have only very little effect. Due to the continuous liquid film above the stable vapor film, individual droplets do not impinge directly onto the hot wall. In this region, Müller and Jeschar (1983) derived for the heat transfer coefficient (HTC, α):

$$\alpha = 200 + 109.2\dot{m}_l \tag{19.177}$$

In the transition boiling regime as well as in the single-phase regime, the mean spray droplet size also influences the heat transfer process. In the nucleate boiling regime, the heat transfer coefficient has been found as a function of surface temperature alone, unaffected by variations in any of the spray parameters (Mudawar and Valentine, 1989). As in this contribution, it has been found that the spray boiling curve is insensitive to the type of metallic surface, Müller and Jeschar (1983) found a distinct influence of the metal type on heat transfer at temperatures below the Leidenfrost temperature. This effect has been attributed directly to the coefficient of heat penetration, which is influenced by possible oxide layer formations.

With twin-fluid atomization of water for cooling purposes, when the liquid mass flow rate is decreased by about one order of magnitude to the aforementioned regime, a dilute spray situation results and individual droplets impinge onto the hot liquid surface. Rather than coalescing to a liquid film (with the associated vapor film between liquid and hot solid), the individual droplets either evaporate directly in the liquid/solid contact phase or are blown away by the gas flow field after rebouncing. Therefore, the heat transfer is increased in a range between the conventional spray cooling and a pure evaporative cooling (Choi and Yao, 1987, Puschmann et al., 2001, Puschmann, 2003). The total heat transfer rate in dilute spray cooling is a combined effect of heat transfer during drop contact and heat transfer due to the gas flow field. Also in this dilute spray quenching, the heat transfer is controlled mainly by the liquid mass flux. Drop size and velocity distribution in the spray only play a minor role. Puschmann (2003) correlated his experimental results based on an investigation of liquid/solid contact time for evaporating single droplet impact (Wruck, 1999) by

$$\alpha = \dot{m}_l u^{0.12} d^{-0.29} \tag{19.178}$$

Wendelstorf et al. (2008a) derived an empirical correlation for high surface temperatures and liquid mass fluxes, which correlates the heat transfer coefficient (HTC, α) with spray water mass flux and surface/water temperature difference (ΔT) as

$$\alpha = 190 + \tanh\left(\frac{\dot{m}_l}{8}\right) \times \left(140 \cdot \dot{m}_l \left(1 - \frac{\dot{m}_l \cdot \Delta T}{72{,}000}\right) + 3.26 \cdot \Delta T^2 \left(1 - \tanh\left(\frac{\Delta T}{128}\right)\right)\right) \tag{19.179}$$

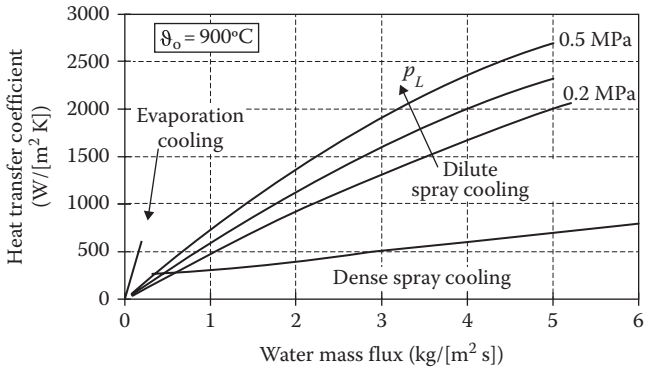


Figure 19.75

Heat transfer coefficient in spray cooling. (From Puschmann, F., Experimentelle Untersuchung der Spraykühlung zur Qualitätsverbesserung durch definierte Einstellung des Wärmeübergangs, Dissertation, University of Magdeburg, Magdeburg, Germany, 2003. With permission.)

Compared to the literature, the correlation is valid for all boiling regimes. The high-temperature values ($\Delta T > 400$ K) are in agreement with the extrapolated data from Equation 19.177.

In Figure 19.75, the result of dilute spray quenching (Puschmann, 2003) is shown. The heat transfer coefficient of dilute spray quenching is higher than for spray quenching but lower than for evaporation quenching. In dilute spray quenching, only single droplets touch the surface, become deformed, and transfer heat. The drops partially evaporate and then move away from the superposed airflow. Thus, the vapor film is avoided as it is the case for other quenching techniques. It is demonstrated that the unintended collapses of the vapor film (Leidenfrost problem) at edges, corners, roughness peaks, etc., are eliminated by this technique (Alam et al., 2008). In this way, mass lumped regions of work pieces can be cooled more intensively than the edges. Consequently, a uniform temperature distribution with reduced thermal stresses can be obtained. For twin-fluid atomization in this dilute spray regime, the heat transfer is also influenced by the atomizer gas flow rate. The dependency of heat transfer on atomizer gas pressure is explained by changing the spray characteristics with respect to drop size and drop velocity (Puschmann, 2003), hence the impact Weber number.

In practical applications, spray cooling is regularly used for the cooling of steel surfaces from high temperatures with an oxide layer. The influence of surface oxidation phenomena on spray water cooling heat transfer has been investigated by Wendelstorf et al. (2008b). Real scale layers on low alloy steels are normally not stable enough to withstand spray cooling. The local (partial) descaling, as well as the formation of vapor gaps at the oxide–metal interface and the movement of scale plates, induces real spatial and temporal fluctuations of the heat transfer, especially in the transition boiling regime, as well as measurement uncertainties. Several general trends have been observed from the measurements: above the Leidenfrost point, the oxide layers normally do not influence the mean HTC but its statistical spatial and temporal fluctuations can reach practically significant values; the oxide layer effect on the HTC decreases with increasing stability and with decreasing thickness of the layer; and the (local) formation of gas gaps between the scale and the hot metal surface can drastically reduce the (local) HTC.

The influences of additives in cooling water on heat transfer in spray quenching process have been investigated by Alam (2011) and Abdalrahman et al. (2014). The addition of salt increases the heat transfer in film boiling, transition boiling, and nucleate boiling regimes. The salt solutions, with increasing cooling ability (or efficiency), are NaCl, $NaHCO_3$, Na_2CO_3, Na_2SO_4, and $MgSO_4$, respectively. With increasing salt concentration (or electrical conductivity (EC) of salt solution in Abdalrahman et al. (2014)), the Leidenfrost point can be shifted to a higher temperature and consequently, the film boiling region is shortened; the total time of quenching is shortened; the critical heat flux is increased; and the wetting front velocity is increased. The cooling ability of a salts mixture is stronger than that of a single salt. Deposition of salts at higher temperature may degrade the surface roughness, which may promote the nucleate boiling heat transfer. Cooling water saturated with CO_2 reduces the cooling rate considerably while that saturated with air causes faster cooling.

19.4 Spray Applications

19.4.1 Energy Conversion/Spray Combustion

Spray combustion is a process to be found in stationary power generation, gas turbines, and internal combustion engines. The combustion of a liquid (or liquid/solid slurry) fuel spray is either a simultaneous or sequential complex process involving fluid dynamics of liquid and gas, heat and mass transfer, and chemical reactions (Williams, 1990, Warnatz et al., 1996). The combustion of individual droplets and groups of droplets is presented in Section 12.7. From atomization, the fuel is present in the form of discrete liquid droplets that have a range of sizes, velocities, and trajectories. This lack of uniformity in the unburnt mixture results in irregularities in the ignition and propagation of the flame through the spray, and thus, the combustion zone is geometrically only poorly defined.

19.4.1.1 Fuel Injection

Direct fuel injection (DI) is applied in diesel and Otto combustion engines (Heywood, 1998). From a first spray analysis, this process is defined as transient high-pressure injection and atomization of a liquid jet. The resulting spray is externally (spark) or self-ignited (Diesel). The principal structure of a *developed* DI diesel flame is depicted in Figure 19.76 as derived by Dec (1997). The sketch shows conceptually how DI diesel combustion develops prior to the end of fuel injection. After the liquid fuel leaves the injector and travels downstream, it atomizes into the droplet spray, entrains hot ambient air, and vaporizes rapidly, forming a sheath-like fuel/air mixture along the sides of the jet. Due to the penetrating nature of the injected liquid jet, macroscopically, a mushroom-like spray structure occurs. The liquid spray penetrates a short distance, during which the vaporized fuel and entrained air form a relatively uniform, rich mixture. The flame fed by the mixture stabilizes at a certain distance from the nozzle as long as the fuel injection continues. Several zones of chemical reaction product formation are found in the spray flame. Soot particles are formed and distributed throughout the cross section of the flame zone and then oxidized in the diffusion flame layer due to the attack of OH and O radicals. NO is formed around the jet periphery on the lean side of the diffusion flame (Tao and Chomiak, 2002). DI diesel combustion is a complex phenomenon in which relevant subprocesses of spray, flow, heat transfer, mass transfer, and chemistry take place over a wide span of time scales. For example, within the sheath near the nozzle at relatively low temperature, the chemical time scale is in the order of 10^0 s, while in the high-temperature zone, chemical reaction time scales span over several orders of magnitude, from about 10^{-6} to 10^0 s.

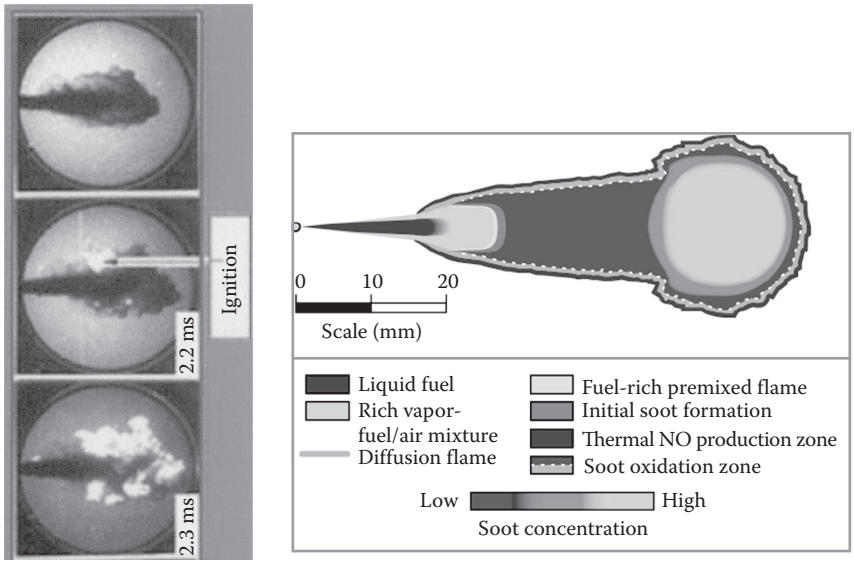


Figure 19.76

Diesel spray flame: photo of injection and ignition, principal stationary flame structure. (From Tao, F., Numerical modeling of soot and NOx formation in non-stationary diesel sprays with complex chemistry, PhD thesis, Chalmers University of Technology, Göteborg, Sweden, 2003. With permission.)

19.4.1.1.1 Diesel Injection (DI) Typical operating parameters of a DI spray in a cylinder are fuel injection pressure up to 200 MPa, injection fuel mass approximately 5–50 mg, injection duration of the order of 1 ms, liquid jet diameter (hole size) about 100 μm, resulting in an SMD droplet sizes of around 10 μm (Spicher, 2001, Tschöke and Leyh, 2003). Two different systems for pressure generation are used: the inline pump system (unit injection system UIS), where each cylinder is connected to and fed by an individual pump, and the common rail system (CRS), where pressure generation and liquid injection are separated as the pressurized fuel is kept at high pressure in a common rail system. An advantage of the CRS is that the injection pressure value, as well as the injection time characteristics (initial time, pre-, main- and postinjection), may be managed electronically depending on the actual engine load. Multihole nozzles are applied at the tip of an injector, as illustrated in Figure 19.77. Two main nozzle configurations are used: valve-covered orifice (VCO) and minisac nozzles. Samples of the injection sprays from these configurations are illustrated in Figure 19.78 (Tsunemoto et al., 2001). These authors deduced that the spray configuration deviations in the VCO nozzle sprays are larger than in the minisac nozzle sprays. Eccentricity of the needle valve as well as slight deviations in hole production deviations may cause asymmetrical spray behavior (from hole to hole and from cylinder to cylinder). The deviation between individual nozzles decreases when the injection pressure increases. These have been identified as sources of emission.

The detailed flame zone structure of a DI diesel spray during combustion may be studied by numerical simulation. It is based on the analysis of transient spray development and drop evaporation (see, e.g., Hohmann (1999)). One key modeling issue in spray combustion is the complex turbulence–chemistry interaction and the formulation of equation closure for mean reaction rates. Typical numerical engine spray combustion studies (Ramos, 1989) use simplified models such as the eddy-breakup model (EBU) (Spalding, 1971), or the eddy-dissipation concept (EDC) (Magnussen and Hjertager, 1977), or models like flamelet models (Kong et al., 1995, Wan et al., 1997, Olguin and Gutheil, 2014) or the "subgrid" partial stirred reactor (PaSR) model (Karlsson, 1995, Tao, 2003). The latter has been used to calculate a diesel flame, as reported by Tao (2003) and Tao and Chomiak (2002). The KIVA-3 code (Amsden et al., 1989, Nordin, 2001) has been modified to include the complex chemical mechanisms based on n-heptane kinetics, where 65 species and 273 elementary chemical reactions are taken into account. Autoignition and lift-off of the flame are calculated in the simulation. The calculated transient diesel spray formation, autoignition, and flame development processes are illustrated in Figure 19.78 as temperature contours in the spray flame between 1 and 4 ms after injection have been started. The fuel jet penetrates deeply into the hot, highly compressed (5 MPa) air before autoignition. The ignition occurs in a fuel-lean premixed region at the side of the jet, downstream from the exit of the nozzle at about 2 ms after injection has started. Following that rapid development of the ignited hot spot leads to a flame propagation toward the axis of the fuel jet, modifying

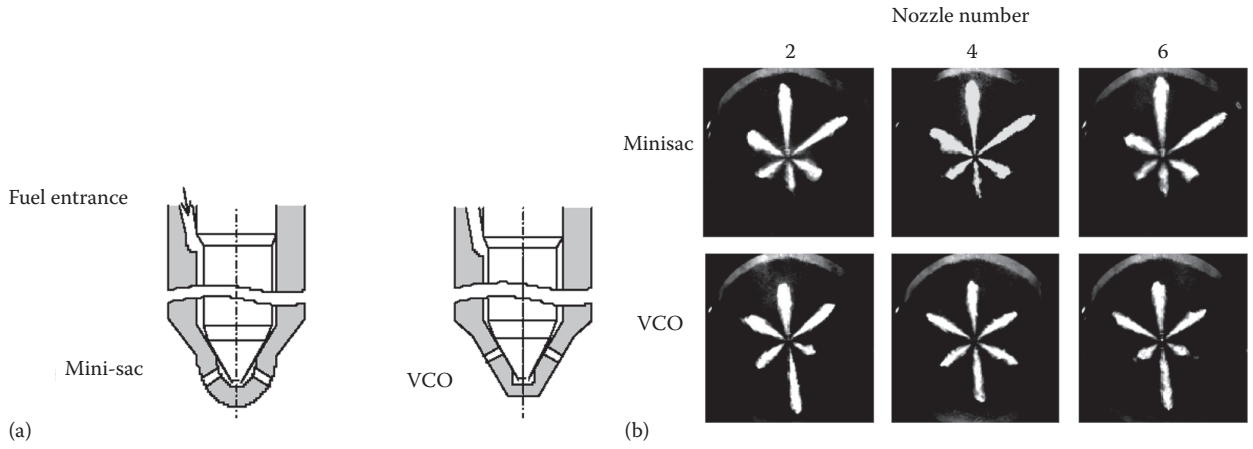


Figure 19.77

Nozzle configurations in high-pressure diesel injection systems: (a) valve-covered-orifice and minisac nozzle; (b) Samples of sprays from high-pressure injection. (Adapted from Tsunemoto, H. et al., Cylinder to cylinder deviations in fuel spray and exhaust emissions at idling in high pressure DI diesel engines, in *Fifth International Symposium Diagnostics and Modeling Internal Combustion Engines*, Nagoja, Japan, 2001.)

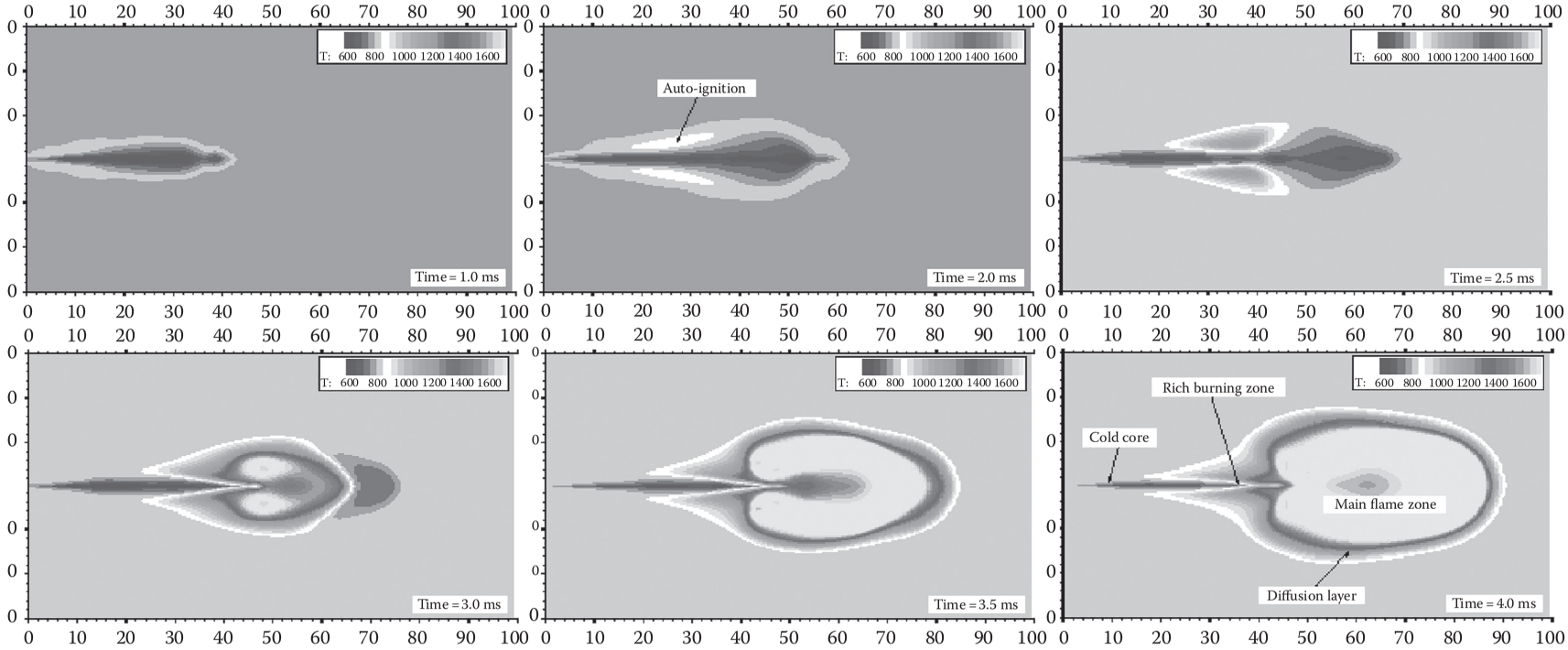


Figure 19.78

Simulation of a DI diesel spray flame, temperature contours. (From Tao, F., Numerical modeling of soot and NOx formation in non-stationary diesel sprays with complex chemistry, PhD thesis, Chalmers University of Technology, Göteborg, Sweden, 2003. With permission.)

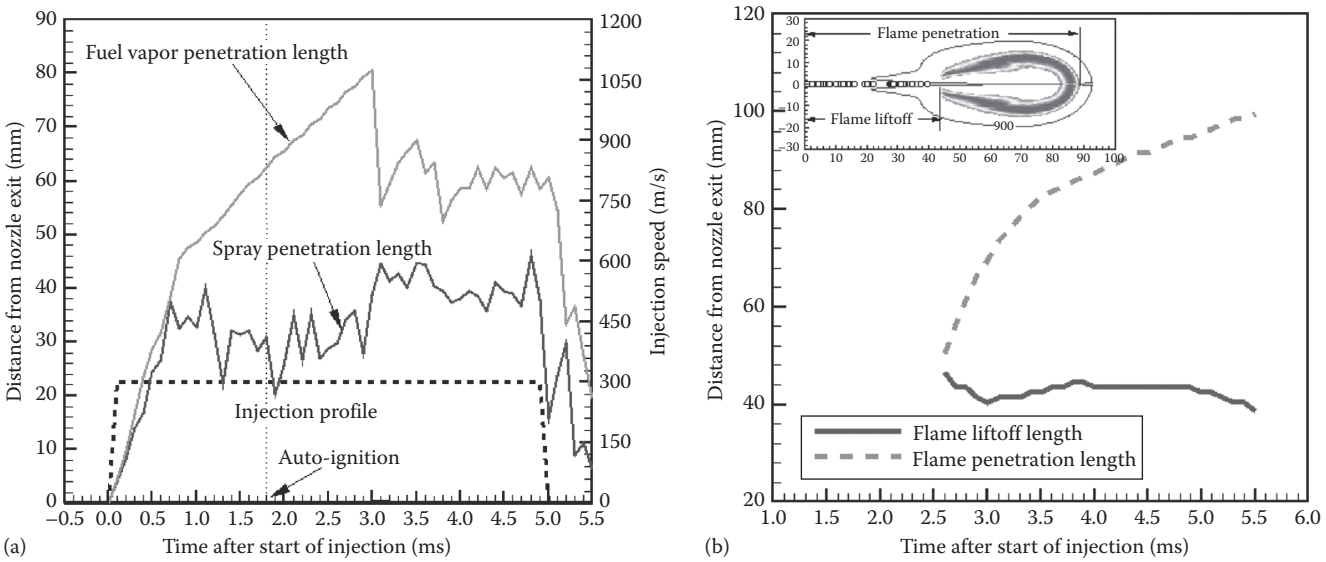


Figure 19.79

Flame structure in DI diesel spray flame: (a) spray and fuel vapor penetrations; (b) flame penetration depth and liftoff length. (From Tao, F., Numerical modeling of soot and NOx formation in non-stationary diesel sprays with complex chemistry, PhD thesis, Chalmers University of Technology, Göteborg, Sweden, 2003. With permission.)

the pattern of the jet penetration. Then, the flame propagates upstream and downstream and finally, its development becomes "quasisteady," stabilizing on the top of the jet. This flame feature is retained until the end of the injection. The spray and fuel vapor penetrations are plotted in Figure 19.79a and b. The plot shows that, even after autoignition, the spray penetration does not vary much and its length remains constant until the end of the fuel injection process. The "quasisteady" flame zone structure may be subdivided into: (1) a cold core zone, (2) a fuel-rich burning zone, (3) a main flame zone, and (4) a lean, thin oxygen diffusion layer. In the cold core region, the combined effect of high velocity gradients and evaporation cooling prevents the flame from propagating upstream to the nozzle exit. The leading edge of the flame, located on the lean side of the stoichiometric surface, stabilizes at a considerable distance downstream from the nozzle. This distance is referred to as the "lift-off" length of the diesel flame, distinguishing the cold zone from the fuel rich burning and main combustion zone. From the transient reaction analysis in these zones, emission formations as soot and NOx in the flame are deduced.

In addition to the model combustion flame configuration discussed before, in car engine applications, the three-dimensional interaction of the injected spray with the cylinder/piston geometry, and the interaction of fuel droplets with the hot walls during impingement plays an important role (Lee and Ryan, 2001).

19.4.2 Spray Aerosol Synthesis

Spray pyrolysis (SP) is widely used in industry to produce fine-grained powders because it is relatively inexpensive and quite versatile. In a conventional spray pyrolysis (CSP) process, submicrometer- and micrometer-sized particles are usually formed through droplet-to-particle route (see Figure 19.80). Here, the liquid precursor is first atomized (usually through twin-fluid atomization or ultrasonic atomization) and sprayed into a heated reactor where the aerosol droplets undergo solvent evaporation (shrinkage stage) and the solute is precipitated on and within the droplets. If the temperature in the reactor (or furnace) is high enough, drying and chemical decomposition of the precipitated precursor particles forms early product particles. The CSP process may produce dense or hollow particles, depending on the operating conditions. Hollow particles form if, at the onset of solute precipitation on the droplet surface, the solute concentration at the droplet center is lower than the ES (Eslamian et al., 2006, Eslamian and Ashgriz, 2007). For an impermeable crust, the substantial pressure build-up on the internal wall of the shell may burst the drying particle into particle flakes or break from the weakest part, resulting in a particle with a small hole. As another scenario,

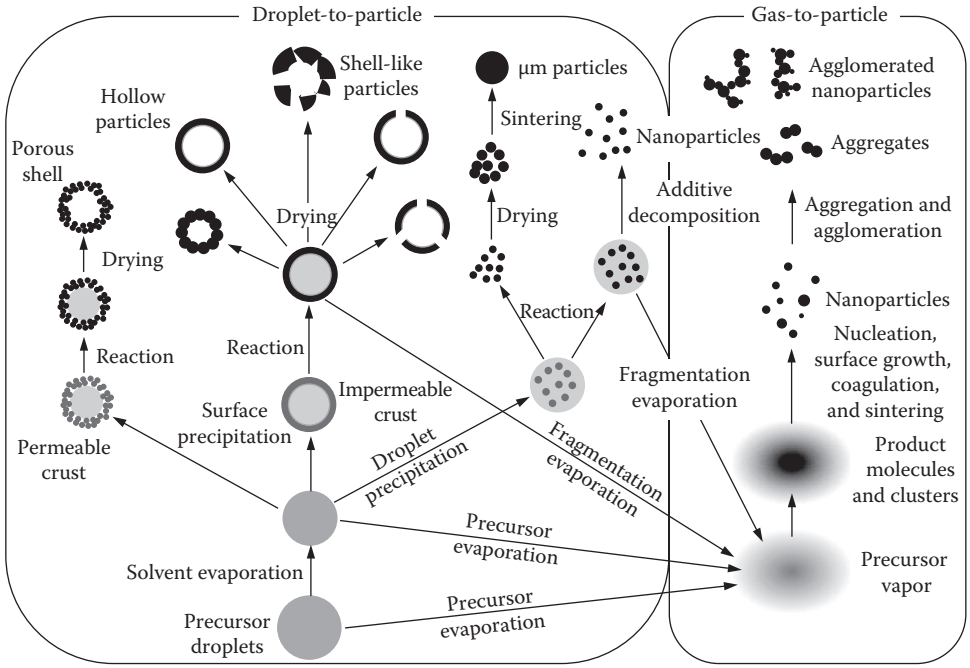


Figure 19.80

Schematic diagram of particle formation mechanisms in spray and flame aerosol synthesis.

if the crust is strong enough to resist the internal pressure, the vapor trapped inside the particle may later condense and the shell may contract due to depression. However, if the shell is fully dried, it is possible that the condensation cannot cause any permanent deformation to the particle, and a hollow smooth-surface particle may form. On the other hand, in the case of a permeable crust, the evaporated solvent leaves the particle, without increasing the internal pressure, and a nondisrupted porous particle forms.

Compared to conventional wet-phase routes with various posttreatment steps, such as filtration, washing, drying, and calcinations, spray aerosol synthesis processes allow one-step preparation of demanding and highly functional products.

Recent advances in combustion engineering, aerosol technology, and materials science now allow scalable spray flame aerosol synthesis (SFAS) of mixed oxides, metal salts, and even pure metals in the form of nanoparticles and films with closely controlled characteristics. In contrast to the CSP processes, spray particle synthesis processes with flames do not require an additional source of energy for precursor convention such as electrically heated walls, making it a rather low capital investment process with proven scalability (Pratsinis, 1998, Maedler, 2004, Teoh et al., 2010, Achelis et al., 2014, Gröhn et al., 2014, Meierhofer et al., 2014). Supplying the energy by a vapor flame allows much higher process temperatures and cooling rates compared to electrically heated hot-wall reactors where temperatures are usually relatively low (<2000°C) and residence time longer (up to a few seconds) (Strobel et al., 2006a). In the SFSA process, the gas-to-particle mechanism (see Figure 19.80) occurs when the metal-organic precursor evaporates soon after it enters the flame, which results in the nanoparticles formation.

Depending on the precursor state (vapor, aqueous-based, solvent-based) fed to the flame and combustion conditions, flame aerosol syntheses are categorized as vapor-fed aerosol flame synthesis (VAFS), flame-assisted spray pyrolysis (FASP), and flame spray pyrolysis (FSP). In the VAFS process, a metal precursor is supplied in the form of vapor into oxygen or air-fuel flames, while both FASP and FSP fall in the regime of liquid-fed aerosol flame synthesis (LAFS) where liquid precursor solution, emulsion, or slurry is atomized into oxygen or air-fuel flames. The core difference between FASP and FSP lies in the origin of majority of combustion enthalpy content of the system. In the FASP process, precursor is supplied in the state of low combustion enthalpy solution (<50% of total combustion energy) usually in aqueous solvent, and an external hydrogen or hydrocarbon flame is thus needed to assist its combustion. In the FSP process, the liquid precursor solution (usually in an organic solvent)

drives the flame process by contributing more than 50% of the combustion energy, and the external flame serves only as an ignition source.

19.4.2.1 VAFS

In the VAFS process, volatile metal precursors (e.g., chlorides) are evaporated and fed into a flame that either supports the process or ignites the process. Metal oxide particles are formed after precursor conversion by nucleation from the gas phase and grow by surface reaction and/or coagulation and subsequent coalescence into larger particles (gas-to-particle route, see Figure 19.80). VAFS is used industrially for synthesis of various ceramic commodities, such as fumed silica, waveguide performs, alumina, and pigmentary titania. However, the need for volatile precursors limits the application of VAFS to products where volatile precursors at reasonable cost are available. The continuous demands for process versatility require the replacement of metal vapor precursor. This prompted the spraying of liquid precursors directly into the flame, that is, LAFS.

19.4.2.2 FASP

In the FASP process, less volatile and economical precursors, especially those of aqueous metal salts (e.g., nitrates and acetates), are used. Many of these precursors, especially aqueous nitrates, have low combustion enthalpy or endothermic in nature and do not form self-sustaining flames. Therefore, an external hydrogen or hydrocarbon flame is employed in the FASP process to support the combustion. The liquid precursor is dispersed into fine droplets (e.g., through ultrasonic or air-assisted nozzle) that are evaporated and pyrolyzed by the external flame. Depending on process conditions, hollow, micron- or nano-sized particles are formed when the precursor reacts in the droplet or gas phase, respectively (see Figure 19.80). In general, complete precursor evaporation leads to solid nanoparticles as in the VAFS process, while incomplete droplet evaporation leads to hollow and shell-like micron-sized particles. The latter usually takes place when operating at low rates of combustion enthalpy (defined as the ratio of combustion rate (kJ/min) to total gas flow (g/min), <4.7 kJ/g), where there is insufficient energy for the formation of metal vapor (Jossen et al., 2005). In such cases, dense particles are formed as a result of drying and solid-state densification, while hollow particles are due to precipitation on surface droplets prior to evaporation of the carrier liquids.

A further step of applying the energy source in closer proximity to the reaction zone is the embedding of the aqueous precursor solution (mainly derived from nitrates) in a combustible droplet environment. This is achieved by preparing an organic solvent–water metal precursor stabilized in an oil (fuel) emulsion phase, which was atomized into micron-sized droplets and subsequently ignited. This self-sustaining spray flame method is called the emulsion combustion method (ECM) (Takatori et al., 1999, Maedler, 2004). This technique has been successfully applied to titania, silica, alumina, zirconia, barium titanate, and zirconia-ceria, as well as electronic, catalytic, and ceramic applications (Tani et al., 1998, 2001, 2003). A major limitation of this method can be the lack of control with respect to product morphology (e.g., hollow particles are often produced) (Maedler, 2004). The presence of incombustible water phase in the ECM precursor not only lowers the combustion enthalpy density, but may also result in poorer gas-phase mixing and reaction as compared to a homogenous solvent-based only precursor, thereby affecting the particles homogeneity (Teoh et al., 2010).

19.4.2.3 FSP

The utilization of the endothermic precursors (mainly metal-nitrates and metal-chlorides dissolved in water) is driven by low cost, availability, and solubility (achievement of high concentration). However, the utilization of these precursors often results in the final product particle formation within the droplet due to insufficient energy, even in the EMC method where very high energy content of the kerosene exists in close proximity to the endothermic-reacting precursor (<1 μm) (Tani et al., 1998). This leads to hollow or fragmented product particles (Maedler, 2004).

The FSP method solves this problem by the use of exothermic liquid precursors. The bulk of flame enthalpy originating from the combustion of liquid precursor maintains a self-sustaining spray flame. This provides direct control over primary particle size by controlling the combustion enthalpy rate and metal concentration of the precursor alone (Maedler et al., 2002). Because of the highly exothermic nature of FSP

liquid precursors, flame temperatures of up to 2600 K (Maedler et al., 2002, Schulz et al., 2005) or 2800 K (Mueller et al., 2004) have been measured. At the same time, the high gas velocities of the FSP induce radial entrainment of surrounding gas. Coupled with the radiation heat loss, this gives rise to extremely short residence times (milliseconds) with high-temperature gradients (170 K/cm) along the flame axis (Schulz et al., 2005). The interplay between high temperature and large temperature gradient is one of the most important features in FSP (Teoh et al., 2010): the high local temperature promotes the formation of homogeneous and highly crystalline materials and also promotes particle growth by sintering and coalescence (Maedler et al., 2002), while the large temperature gradient (and short residence time) preserves the nanoscale feature of the particles. The rapid thermal quenching during FSP may also result in the formation of many metastable materials.

The main particle forming mechanism in the FSP process is through gas-to-particle route (see Figure 19.80), in which particles form in sequential stages: (1) precursor spray evaporation/decomposition forming metal vapor; (2) nucleation as a result of supersaturation; (3) growth by coalescence and sintering; and (4) particles aggregation (forming hard agglomerates by chemical bonds) and agglomeration (forming soft agglomerates by mainly physical bonds).

In the scale-up of nanoparticle production of zirconia by FSP from ~100 to 500 g/h, the product primary particle and agglomerate size as well as the crystallinity are conserved when the precursor and the dispersion flow are increased by keeping the gas-to-liquid mass ratio constant. This is attributed to similar high-temperature particle residence times (PRTs), which is revealed by process simulation with a CFD-based model, employing transport-limited precursor oxidation and monodisperse particle dynamics (Gröhn et al., 2014).

For large-scale nanoparticle production by FSP, a hybrid precursor-atomization concept, as a combination of a liquid pressure swirl nozzle and a swirl dispersion gas nozzle, is presented by Meierhofer et al. (2014). The relevant parameters influencing the atomization process (dispersion gas feed rate, liquid feed rate, nozzle geometry) are investigated (for air, water) in nonburning (cold) spray conditions based on experimental measurements and CFD simulations. Larger gas swirl angles reduce the droplet velocity and furthermore lower the atomization efficiency, leading to larger droplets. Results show that the liquid volume flow rate (and thus the productivity of the process) may be increased significantly while still maintaining an appropriate droplet size compared to the conventional atomization process conditions in FSP reactors.

Within the FSP process for nanoparticle production, the effects of the precursor atomization process and the spray properties on the spray flame structure have been studied by Noriler et al. (2014) using experiments and numerical simulations. The influence of the precursor concentration variations on the spray droplet size distribution was studied for two different FSP nozzles. The resulting spray has been characterized in terms of drop sizes and velocities by means of laser diffraction and particle image velocimetry. A mathematical model was carried out for the spray flame, considering two-way coupling between the gas phase and the droplets. For the combustion model, the eddy dissipation concept model was employed, taking into account the effects of the vaporization of the droplets, chemical reaction mechanisms, and the chemistry–turbulence interaction. Experimental and numerical results are compared to validate the model and to study the potential influence of significant spray parameters on the FSP process. A comparison of the flame height for different nozzle configurations is illustrated in Figure 19.81.

19.4.2.4 Ultrasonic Spray Pyrolysis

In an ultrasonic spray pyrolysis (USP) process, the liquid precursor is atomized through ultrasonic atomization and sprayed into a heated reactor or into a flame under pyrolysis condition, yielding micrometer-, submicrometer-, or nanometer-sized particles through droplet-to-particle or gas-to-particle route. Various principles are applied in ultrasonic atomization (Walzel, 2012, Mwakikunga, 2014), namely,

- Capillary waves (20–100 kHz)
- Cavitation (0.1–5 MHz)
- Stationary ultrasonic waves in a gas
- Exited jet disintegration

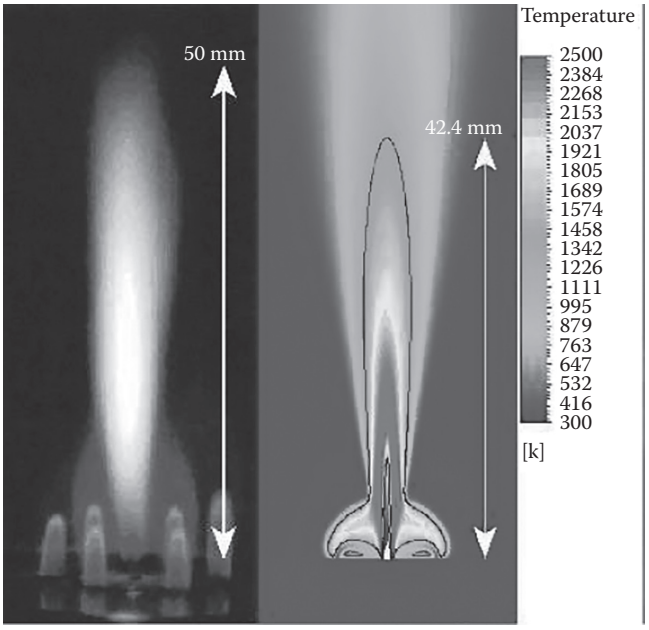


Figure 19.81

Comparison of experimental and numerical simulated spray flame structure (fuel: ethanol) Noriler et al. (2014) in FSP process.

Based on the capillary wave mechanism, Lang (1962) determined the relationship between the wavelength of the capillary waves and the mean size of droplets

$$D = 0.68\left(\frac{\pi\sigma}{\rho f^2}\right)^{1/3} \tag{19.180}$$

without taking into account the dependence of droplet size on liquid viscosity and volumetric flow rate. Here σ is the surface tension, ρ_l the liquid density, and f the frequency of the forcing sound. Since then, the researchers including Davis (1985), Walzel (1993), Rajan and Pandit (2001), and Avvaru et al. (2006) tried to build a universal correlation, which could account for the effects of physical–chemical properties of the liquid (liquid flow rate ($\dot{Q}$), viscosity (μ_l), density, and surface tension) and ultrasonic properties like amplitude (Am), frequency, and the area of vibrating surface. The Avvaru's formula (Avvaru et al., 2006), which suits the so-called Newtonian viscous liquid, is given as

$$D = \left(\frac{\pi\sigma}{\rho f^2}\right)^{1/3} + 0.0013(\mathrm{We})^{0.008}(\mathrm{Oh})^{-0.14/n}(I_N)^{-0.28} \tag{19.181}$$

Here, the symbols We, Oh, and I_N are, respectively, Weber number, Ohnesorge number, and intensity number, defined in the following expressions:

$$\mathrm{We} = \frac{f\dot{Q}\rho}{\sigma};\quad \mathrm{Oh} = \frac{\mu}{fA_m^2\rho};\quad I_N = \frac{f^2A_m^4}{c\dot{Q}} \tag{19.182}$$

Here, the index n in Equation 19.181 can be estimated by fitting the apparent viscosity data to the two-parameter power law model, and c in Equation 19.182 is the speed of sound. Hansmann (1996) also derived a droplet-size expression for USWA (see Table 19.3).

In comparison with twin fluid-atomization (liquid atomization by high-speed gas jets), ultrasonic atomization has the disadvantage of low throughput, but has the advantage of narrow drop size distribution (and therefore narrow particle size distribution) and low momentum associated with ejected droplets (and therefore suitable for coating process).

Besides metal and oxide powders, the USP method can fabricate composite particles with core/shell structure, for example, $Ti_{1-x}Zr_xO_2$ solid solutions (Huang et al., 2006), Ru/Ni nanoparticles (Deng et al., 2008), Cu/Ag submicrometer-sized particles (Jung et al., 2011), and Ru/TiO_2 nanoparticles (Stopic et al., 2010). The core/shell structured particles can be fabricated directly through the gas-to-particle route or the droplet-to-particle route.

In the gas-to-particle route, the kinetic difference of decomposition reaction of the precursor mixture may cause the formation of shell structure on top of a core particle. In the liquid-to-particle route, two hypotheses are proposed to explain the formation of the core-and-shell structure (Deng et al., 2008):

1. The conventional theory believes composite, multicomponent particles are synthesized with precursor solutions consisting of solutes of same or different solubilities (Messing et al., 1993). As the aerosol droplets containing uniform solution of several solutes undergo precipitation, evaporation, drying and coagulation steps, successive precipitation of the solutes occurs; the less soluble components tend to precipitate faster than those with higher solubility and form the core.
2. The second theory is based on melting points of the core and the shell components. The higher melting point element has higher cohesive forces and intermolecular bonding (or lower mobility), leading to the formation of the core (Yang and Kim, 2004, Pingali et al., 2008, Jung et al., 2011).

To achieve phase separation, Stopic et al. (2013) applied multistep USP to synthesize TiO_2 core/RuO_2 shell particles. Here, in contrast to conventional USP, a modified set-up with separated ultrasonic atomizers for each precursor and two horizontal reactors for thermal decomposition was employed. Titania particles are formed in the first pyrolysis zone. The second aerosol stream was then admixed to the stream of solidified titania particles emerging from the first decomposition zone. This mixture was then piped through the second pyrolysis zone, where the desired core/shell particles were formed.

19.4.2.5 Particle Characteristics

The characteristics and the subsequent performance of spray flame-made particles are affected by their synthesis temperature history and concentration that are controlled by burner configuration, precursor composition, and oxidant/fuel flow rates (Pratsinis, 1998). These particles are either aggregates (chemically sinter bonded) of primary particles or agglomerates (physically bonded) of primary single particles and/or aggregates. Short residence times and faster cooling rates decrease primary particle size and extent of aggregation (Strobel and Pratsinis, 2007). Most common flame-made particles are spherically shaped primary particles with different degrees of agglomeration. Other shapes of primary particles depend mainly on crystal structure and related surface energies, as shown in Figure 19.82. Dopants and the related changes in surface energies can be used to alter particle shape.

For synthesis of multicomponent particles, the spatial distribution of individual components is important. Strobel and Pratsinis (2007) and Teoh et al. (2010) summarized five typical configurations of flame-made multicomponent particles, as shown in Figure 19.83: (a) homogeneous mixing between multicomponents; (b) polycrystalline particles with two components forming individual phases within a particle, (c) surface layer of one component coating the other, (d) small clusters supported on the surface of the other component, and (e) an external mixture of separate individual particles of different components.

The distribution of two or more components is strongly affected by their mixing behavior during particle formation in the flame. Similar evaporation, conversion, and nucleation rates favor more homogeneous distribution, whereas a sequential formation of individual particle components favors their segregation. Sequential nucleation/condensation can occur when two materials exhibit large differences in volatility. In some cases, to achieve phase separation, particles can be produced separately by using two flames and mix their plumes downstream by operating two FSP nozzles (Strobel et al., 2006b, Høj et al., 2013, Minnermann et al., 2013, Grossmann et al., 2015), as shown in Figure 19.84. Other factors influencing configuration of multicomponent particles cover composition of precursor and solvent, Strobel and Pratsinis (2011), phase–interface interaction, phase miscibility, oxidant/fuel flow rates, etc. A detailed explanation of formation mechanisms of various particle configurations can be found in Strobel and Pratsinis (2007) and Teoh et al. (2010).

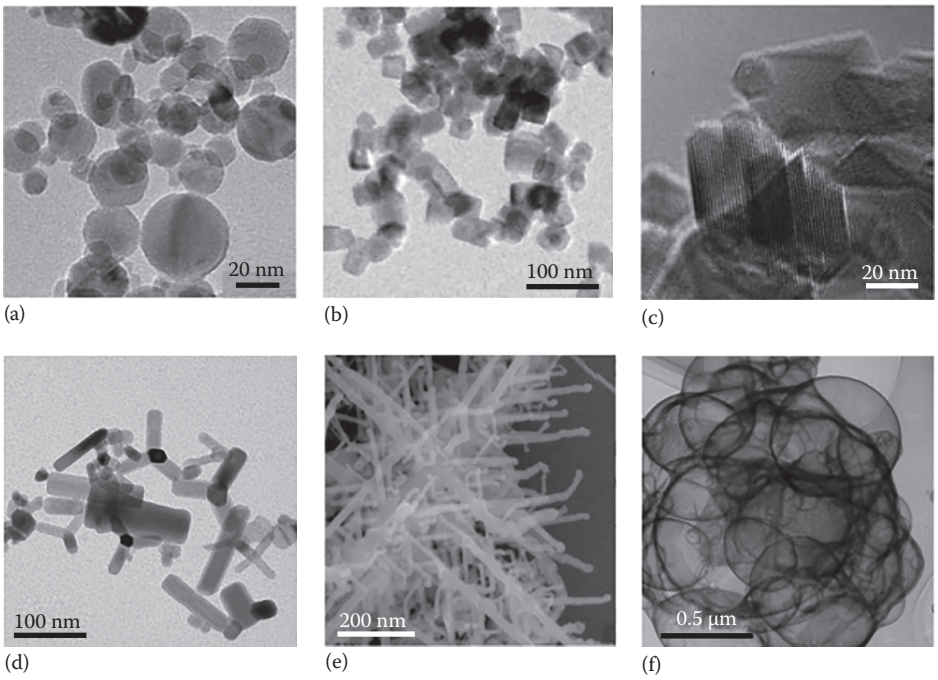


Figure 19.82

Flame-made nanoparticles with different shapes. (a) TiO_2 spheres (Adapted from Teoh, W.Y. et al., *Nanoscale*, 2, 1324, 2010. With permission.); (b) BaF_2 cubes (Adapted from Grass, R.N. and Stark, W.J., *Chem. Commun.*, 2005, 1767, 2005. With permission.); (c) rhomboid-shaped CeO_2 (Adapted from Teoh, W.Y. et al., *Nanoscale*, 2, 1324, 2010. With permission); (d) ZnO rods (Adapted from Hembram, K. et al., *J. Nanopart. Res.*, 15, 1461, 2013. With permission.); (e) SnO_2 nanowires (Adapted from Hou, X. et al., *J. Mater. Chem. A*, 1, 13814, 2013. With permission.); (f) hollow Al_2O_3 spheres. (Adapted from Tani, T. et al., *J. Am. Ceram. Soc.*, 86(6), 898, 2003. With permission.)

19.4.2.6 Spray Flame Deposition Process

Instead of collecting the flame-made powder by filtration, electrostatic precipitation, or in a cyclone, flame aerosol synthesis methods offer the possibility to directly deposit particles on a substrate, resulting in nanostructured films. The structure of films prepared by deposition of flame products strongly depends on the particle formation stage upon arrival at the substrate and on substrate temperature (Liu et al., 2004, Bahlawane, 2006). Figure 19.85 shows a schematic of spray flame deposition processes. Depending on the particle formation stage upon arrival at the substrate, the resulting deposit can be precursor droplets, precursor/product vapor, or product particles with different degrees of agglomeration. This can be controlled, for example, by placing the substrate at an appropriate distance or by altering the precursor/gas flow rates. If unconverted precursor impacts on the substrate, it results in denser films (Bahlawane, 2006), while airborne product particles lead to very porous particle films (Maedler et al., 2006, Pham et al., 2010). Depending on the substrate temperature, this porous film is either preserved or collapses into more compact structures by sintering (Liu et al., 2004). Substrates such as flat plates (Karthikeyan et al., 1997, Sahle-Demessie et al., 1999), tubes (Miki-Yoshida et al., 2002), or foams (Schimmoeller et al., 2006) are used. Sequential deposition of different aerosol materials gives rise to multilayer films, each of which can be in principle designed with controlled thickness and morphologies (Charojrochkul et al., 1999, Sahm et al., 2007, Kemmler et al., 2013).

19.4.3 Metallurgical Processes

19.4.3.1 Metal Powder Production

Powders of different metals and alloys are produced by melt atomization. The amounts produced in industry vary from a few kilograms to a million tonnes per year (for a single facility), for example, in the production of dental amalgams to steel or iron shot (Yule and Dunkley, 1994). Particle sizes vary from micrometer (e.g., for corrosion protection paints) to millimeter (e.g., for shot blasting). Depending on the application, the desired particle shape may also vary from spheres and aggregates to fibers and flakes. These shapes can be achieved by variation in atomizer type, cooling conditions, and atomization liquid.

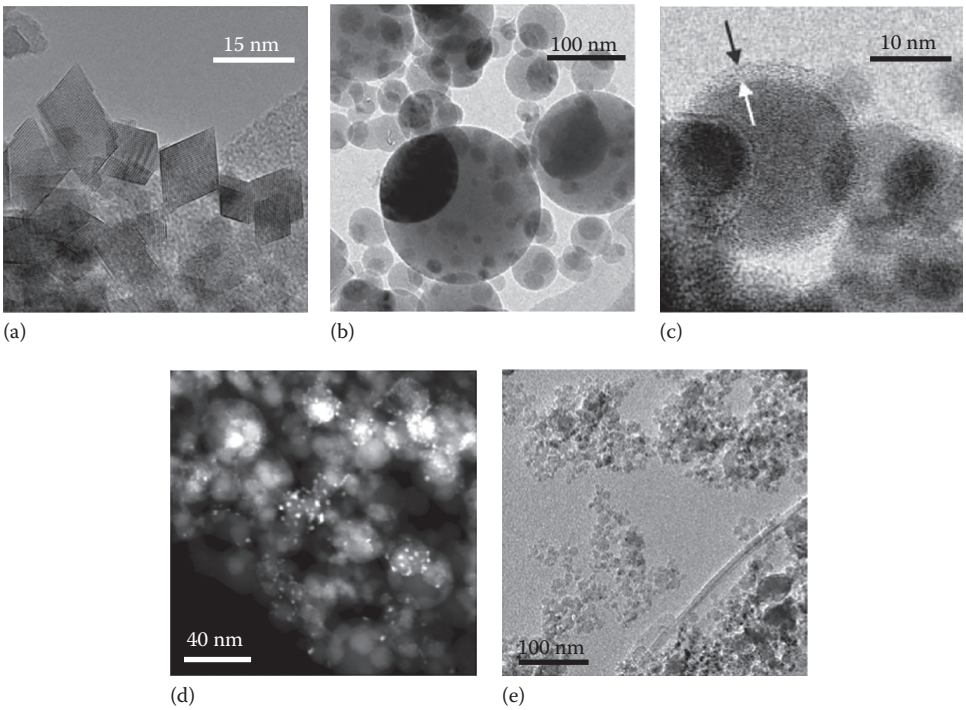


Figure 19.83

Structures of multicomponent flame-made particles. (a) Mixed phase (CeO_2/ZrO_2, Adapted from Stark, W.J. et al., *Chem. Commun.*, 2003, 588, 2003. With permission.); (b) segregated phases in one particle (γ-Fe_2O_3 in SiO_2, Adapted from Li, D. et al., *J. Phys. Chem. C*, 113, 12040, 2009. With permission.); (c) Coated particles ($SiO_2/Ce_{0.5}Zr_{0.5}O_2$, Adapted from Schulz, H. et al., *J. Mater. Chem.*, 13, 2979, 2003. With permission.); (d) Small particles dispersed on a support (Pt/TiO_2, Adapted from Teoh, W.Y. et al., *Chem. Eng. Sci.*, 60(21), 5852, 2005. With permission.); (e) Mixture of individual particles. ($BaCO_3/Al_2O_3$, Adapted from Strobel, R. et al., *Chem. Mater.*, 18(10), 2532, 2006b. With permission.)

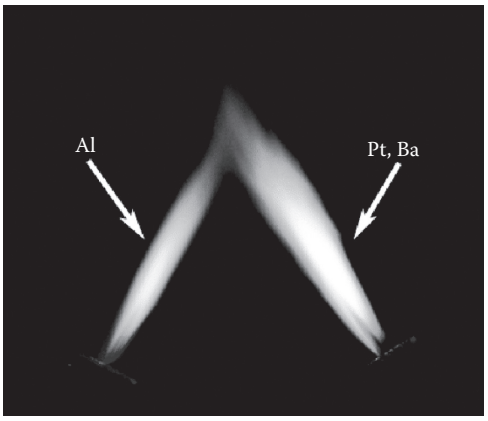


Figure 19.84

Schematic of the FSP setup using two separate nozzles. The image shows two flames producing $Pt/Ba/Al_2O_3$. (Adapted from Strobel, R. et al., *Chem. Mater.*, 18(10), 2532, 2006b. With permission.)

Samples of metal particles produced by atomization are illustrated in Figure 19.86. The width of the particle size distribution ranges from single size particles to large values, as shown in Figure 19.87. Rapidly quenched metal powders (at high cooling rates of 10^4 to 10^7 K/s) from spray processes may exhibit specific material compositions and properties due to fine grain sizes or even amorphous metallographic structure, as shown in Figure 19.88.

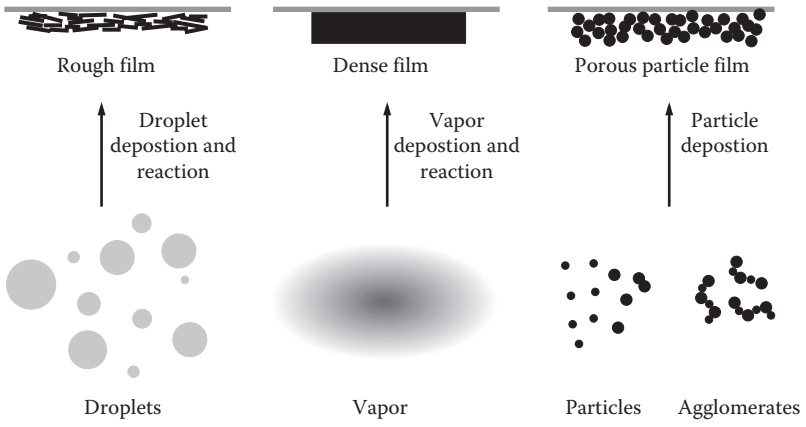


Figure 19.85

Schematic for synthesis of porous or dense films by flame deposition of droplets, vapor, or particles.

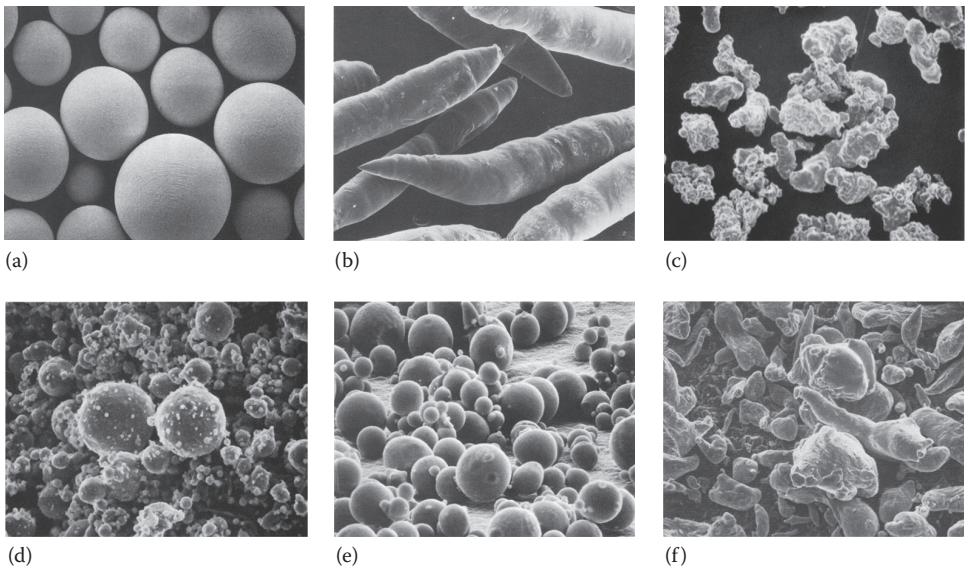
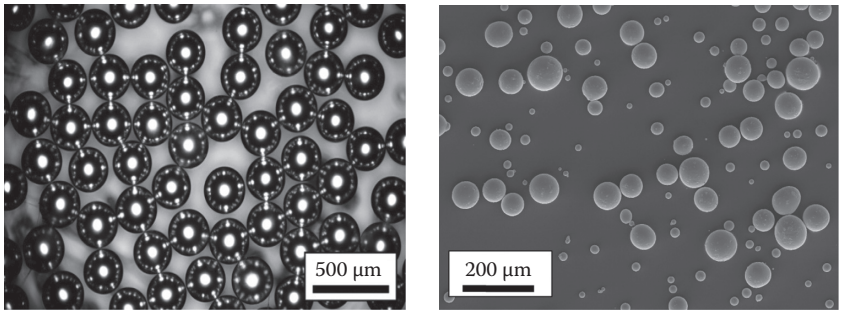


Figure 19.86

Particle shapes in molten metal atomization processes; (a) Rene 95 superalloy powder, produced by the plasma rotating electrode process, (b) aluminum needles produced by rotary atomization with perforated cup, (c) copper particles, produced by twin-fluid atomization with water, (d) aluminum powder, gas atomized with helium, (e) IN-1000 superalloy powder, pressure atomized, and (f) aluminum powder, gas atomized with air. (Adapted from Huppmann, W.J. and Dalal, K., *Metallographic Atlas of Powder Metallurgy*, Schmid, Freiburg, Germany, 1986.)

A major use of metal powders is in manufacturing of complex-shaped mechanical components such as by sintering or (hot or cold) isostatic pressing. In metal injection molding, fine metal powders are blended with a resin or binder to be pressure-injected into a mold, where the resin is removed afterward. Thermal spraying is a coating technique that uses ceramic or metal powders as feed materials. Recently metal powder formulations gained tremendoeus interest due to exploding applications in Additive Manufacturing (AM) techniques where complicated preforms are shaped from powders for instance by selective sintering.

Twin-fluid atomization is by far the most common atomization technique for metal powder production as it gives a high yield. When using oil or water as atomization media, the particle shape is nonspherical, while gas atomized powders show spherical shape. In water atomization, generally higher mass flow rates may be achieved. Gas atomization is typically performed by inert gases for prevention of oxidation



(a) (b)

Figure 19.87

(a) Monosized Sn–Ag particles produced by pulsated orifice ejection method (Adapted from Ellendt, N. et al., Quality of Sn-Ag-powders production by drop-on-demand technique, in *Proceedings of PM 2008*, Washington, DC, June 8–12, 2008.); (b) dispersed Sn-particles produced by PGA. (Adapted from Achelis, L., Drall-Druck-Gas-Zerstäubung von Metallschmelzen, Dissertation, Universität Bremen, Shaker-Verlag, Aachen, Germany, 2009.)

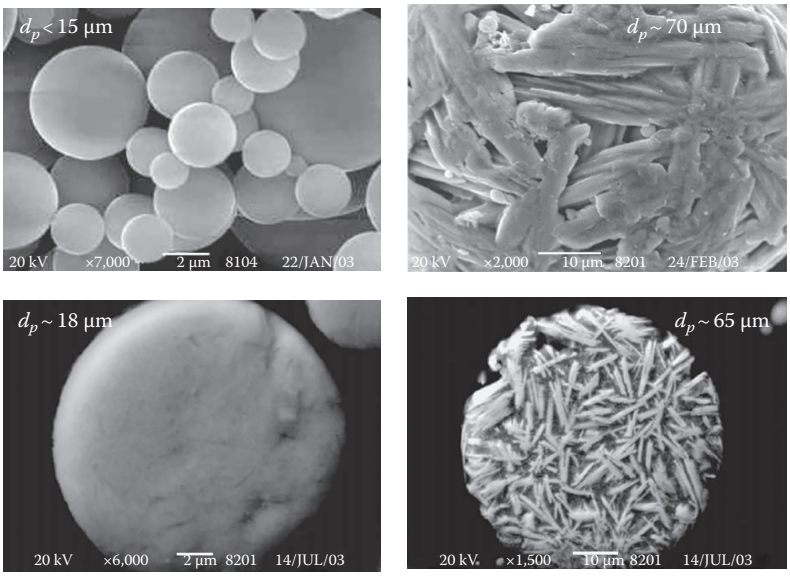


Figure 19.88

SEM observations of surface morphology (upper) and microstructure in cross sections (lower) of the atomized $Al_{82}Ni_{10}Y_8$ powder by Ar gas: (left) amorphous powder; (right) nanocrystalline powder. (Adapted from Liu, Y. et al., *Intermetallics*, 13, 393, 2005. With permission.)

(or sometimes even the other way around, by partial or full oxygen content for controlled oxidation of the material). Twin-fluid atomized powders are in the size range of 10–500 µm at a distribution width (standard variation) of about 2.

For specific applications, metal powder production via atomization also is achieved by rotary or centrifugal atomizers (Halada et al., 1990), metal atomization by means of ultrasound (Bauckhage et al., 1996), in laminar supersonic flows (Gerking, 1993), or by controlled pulses (Henein, 2002) to produce a more narrow width of the size distribution. A general overview on atomization techniques for metal powder production can be found in Klar and Fesko (1984), Yule and Dunkley (1994), Lawley (1992), Bauckhage (1992), Dunkley (1998), Nunez et al. (1999), and Liu (2000b).

In molten metal atomization, the specific atomizer design is typically more complex than that for conventional liquids. Molten metals need to be superheated above liquidus for feeding into the atomizer. Here, these materials become chemically active and chemical reactions and erosions with the containing material in the crucible or tundish may occur. Thermal losses, especially in the combination with cold atomization media like gas, can lower the melt temperature locally below its specific liquidus

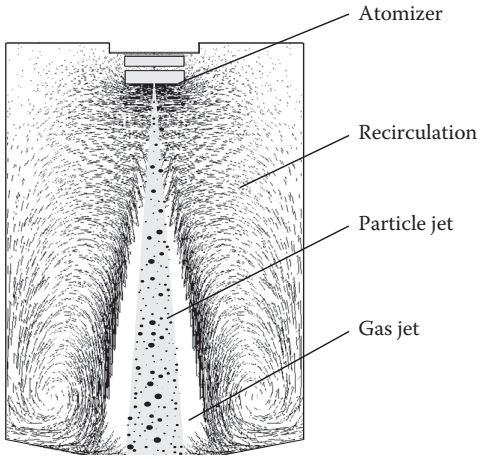


Figure 19.89

Flow field in a spray chamber for powder production, simulation result.

temperature, which may cause solidification and thermal freezing problems of melt atomizer nozzles, influencing the whole process. In this case, local isolation and/or heat sources in combination with suitable materials need to be applied. Molten metals typically have high density, high surface tension, and low viscosity, enabling specific measures to achieve a proper disintegration process. The spray structure in metal atomization is governed by the gas/drop interaction in combination with the high heat transfer between the hot melt and (usually) cold environment.

The principal two-phase flow field in a typical powder production chamber employing gas atomization is illustrated in Figure 19.89 obtained by numerical simulation. The flow is subdivided into three regions (Conelly et al., 1986): (1) the droplet spray in the core, surrounded by (2) the gas jet and (3) a recirculation zone in the outer area of the spray chamber. Typically within the recirculation zone, a large amount of fine particles swirl around in the spray chamber (dust formation). Here, preferably the fine particles can be found due to their small inertia. These particles cool down and solidify in their upward movement and possibly are reentrained into the spray as fine solid particles. As there are a large number of these fines, collisions with spray droplets are likely and result in so-called satellite formation in melt sprayed particles. These satellite formations lower the quality of sprayed powders such as a reduction in free-flow ability. A possibility for satellite formation prevention has been proposed by Dunkley and Telford (2002), Achelis and Uhlenwinkel (2008), and Achelis (2009). Here, part of the exhaust gas (after particle separation) is reinjected from top into the spray chamber (as illustrated in Figure 19.90). The recirculation gas flow rate is controlled by guiding the natural jet entrainment flow (conventionally achieved from recirculating gas inside the chamber) into the spray (see Section 19.2.2.3). As result, dust recirculation and satellite droplet formation is reduced. In Figure 19.91, sprayed particles with and without an antisatellite device are shown, where the number of nonspherical particles is dramatically reduced.

19.4.3.1.1 Metal-Matrix-Composite (MMC) Particles MMC particles can be fabricated through mixing ceramic particles and atomized metallic droplets in a spray atomization and coinjection process (Wu and Lavernia, 1992, Eslamian et al., 2008, Li et al., 2011, Li, 2014). The process is characterized by a three-phase spray flow (gas/droplets/particles). Ceramic particles (usually at least one order of magnitude smaller than atomized droplets), conveyed by the atomization gas or via a separate gas-assisted delivery system, are injected into the metallic droplet spray and likely to be incorporated into the droplets or captured by the droplets surface during frequent impingements, forming MMC droplets that are subsequently solidified as MMC particles. This approach will inherently avoid the extreme thermal excursions, with concomitant degradation in interfacial properties and extensive macrosegregation, normally associated with the MMC production in casting processes. By mixing reinforcements with liquid/semisolid matrix in a spray atomization process, demixing problem associated with the MMC production in powder metallurgy (PM) process can also be eliminated. A maximum incorporation rate (18% vol.%) of ceramic particles in metal matrix was reported by Eslamian et al. (2008), where a prefilming hybrid atomizer was employed for the production of MMC particles.

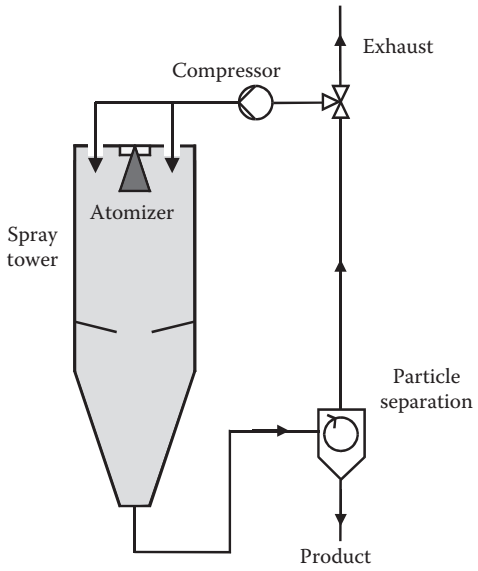


Figure 19.90

Concept for flow configuration in powder production spray process for decreasing of satellite drop formation.

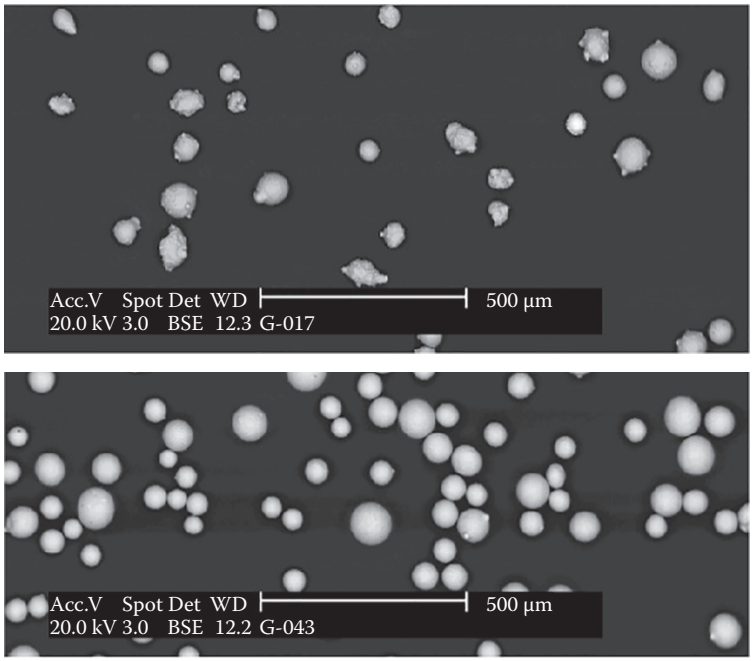


Figure 19.91

Satellite drop formation in melt sprays. (From Dunkley, J.J. and Telford, B., Control of satellite particles in gas atomization, in *Proceedings of World Congress on Powder Metallurgy and Particulate Materials PM²TEC 2002*, Orlando, FL, 2002. With permission.)

For MMC particle production in a spray process, a hybrid gas atomization nozzle configuration ideally fits the requirement of gas/particle/liquid dispersion and mixing in the spray flow field. A typical PGA configuration for MMC particle production is sketched in Figure 19.92a, where solid particles, continuously supplied by a particle pump and conveyed by the atomization gas, are coinjected and impacted by the liquid droplets in the secondary atomization zone. Figure 19.92b shows some spray-processed MMC particles in a PGA process. The fact that the particulate reinforcements are distributed inside or on the surface of the MMC particles

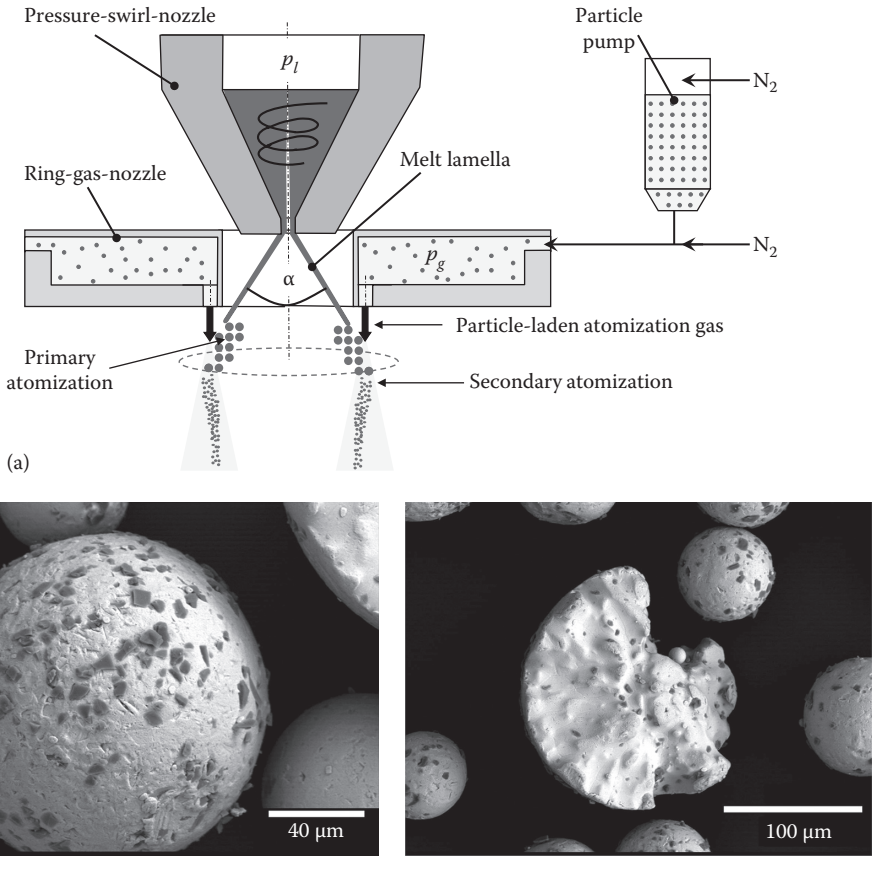


Figure 19.92

(a) Schematic of generation of MMC particles in a PGA process; (b) MMC particles: Sn-matrix + SiC-particulates. (Adapted from Li, X.G. et al., *Atom. Sprays*, 21(11), 933, 2011. With permission.)

proves the concept of MMC particles. MMC particles can be used in powder processes to generate composite parts or for thermal spray coating applications.

Li (2014) and Li and Fritsching (2014b) presented multiscale descriptions of particle–droplet interactions in spray processing of MMC particles based on multiphase computational fluid dynamics (MCFD) models, in which processes such as liquid atomization and particle–droplet mixing spray (macroscale), particle–droplet collision (mesoscale), and particle penetration into droplet (microscale) are taken into account, as shown in Figure 19.93. Thereby, the incorporation efficiency and sticking efficiency of ceramic particles in metal matrix are correlated with the operation conditions and material properties.

On the *macro*scale, the mixing behavior of ceramic particles (SiC) and metallic droplets (Sn) in a PGA configuration is described by an Eulerian–Lagrangian–Lagrangian (ELL) approach. In the PGA process, ceramic particulates conveyed by the atomization gas are coinjected and impacted with the metallic droplets in the secondary atomization zone. The ELL formulation uses Eulerian description for the continuous gas phase; hence, the gas flow through stationary mesh volumes, while the dispersed phases are tracked by the Lagrangian approach. Figure 19.94 shows the particle–droplet mixing configurations at different atomization gas pressures. Here, the TAB model is employed to describe droplet breakup. Increasing atomization gas pressure (i.e., increasing gas-mass-flow rate) causes a spray of tiny droplets, which tend to be involved in the particle-laden gas flow, thus leading to a high particle–droplet mixing degree. However, the fast droplet solidification rate at a high atomization gas flow may reduce the particle–droplet mixing quality. A lower atomization gas pressure results in a more radially expanded droplet spray that tends to intersect the particle-laden gas jets, leading to a poor particle–droplet mixing extent. Therefore, the best particle–droplet mixing configuration is determined at a moderate atomization gas flow.

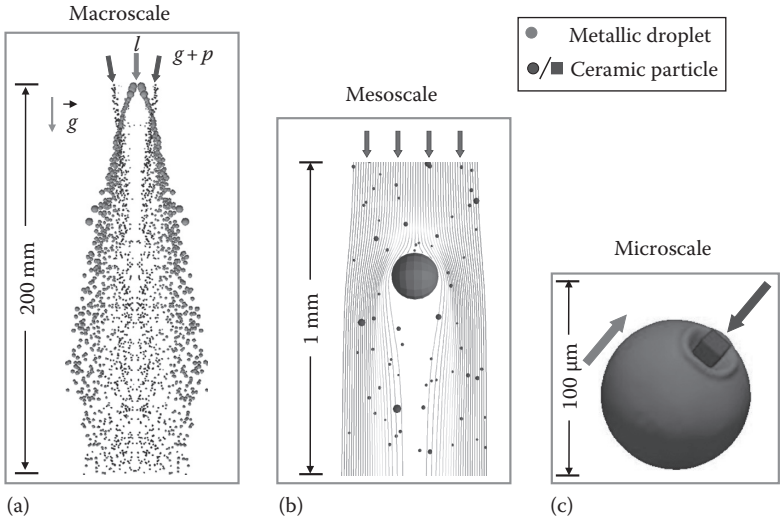


Figure 19.93

Illustration of multiscale modeling of fabrication of MMC particles in spray atomization process: (a) particle–droplet mixing, (b) particle–droplet collision, and (c) particle penetration into droplet. (Adapted from Li, X.G., Modeling and simulation of the gas-atomization process of metal melts for metal-matrix-composite production, Dissertation Universität Bremen, Shaker-Verlag, Aachen, Germany, 2014; Li, X.G. and Fritsching, U., Multiscale modeling and simulation in spray processing of composite particles, in *Proceedings of Second International Symposium on Multiscale Multiphase Process Engineering*, Hamburg, Germany, September 24–27, 2014b. With permission.)

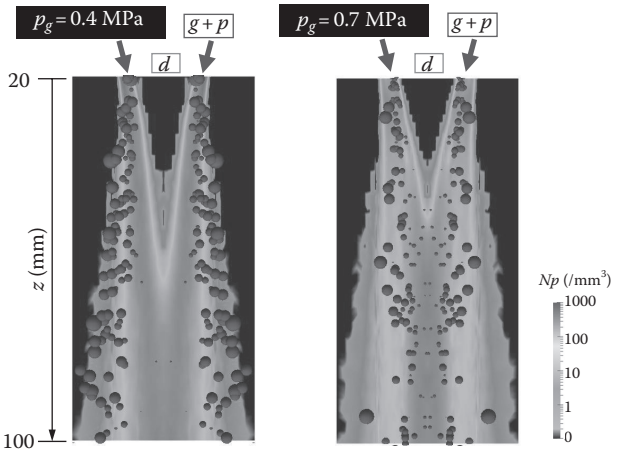


Figure 19.94

Simulation results: mixing configurations of Sn-droplet sprays and SiC-particle jets at different atomization pressures (p_g), melt mass flow rate 180 kg/h, particle mass flow rate 6.4 kg/h, *d*—droplets, *p*—particles, *g*—gas. (Adapted from Li, X.G., Modeling and simulation of the gas-atomization process of metal melts for metal-matrix-composite production, Dissertation Universität Bremen, Shaker-Verlag, Aachen, Germany, 2014; Li, X.G. and Fritsching, U., Multiscale modeling and simulation in spray processing of composite particles, in *Proceedings of Second International Symposium on Multiscale Multiphase Process Engineering*, Hamburg, Germany, September 24–27, 2014b.)

On the *mesoscale*, the collision behavior between a metallic droplet and solid particles along the droplet trajectory is quantitatively described by

$$Q = \int \frac{\pi(d_p + d_d)^2}{4} \cdot \left|\vec{U}_p - \vec{U}_d\right| N_p \cdot \eta \; dt$$
$$\approx \sum \frac{\pi(d_p + d_d)^2}{4} \cdot \left|\vec{U}_p - \vec{U}_d\right| \cdot N_p \cdot \eta \cdot \Delta t \tag{19.183}$$

Here

Q represents the accumulative droplet-particle collision number along the droplet trajectory
d is the diameter
U is the velocity
N_p is the particle number concentration (m^{-3}) in a control volume ΔV
η is the collision efficiency
Δt is the time step for a droplet to move from one position to another
the subscripts p and d denote the physical quantities relative to particle and droplet, respectively

The particle–droplet relative velocity and the particle number concentration along the droplet-moving path can be obtained based on a Lagrangian tracking. The collision efficiency increases with the relative Stokes number. It tends to 0 if St < 0.1 and is close to unity if St > 10 (Schuch and Löffler, 1978, Li et al., 2011). In the PGA process, the relative Stokes number is usually larger than 10, and the collision efficiency can thus take a value of $\eta = 100\%$.

The droplets have different trajectories in the computational domain because of their different inertias. Along the droplet trajectory, the required information in Equation 19.183 such as the particle–droplet relative velocity and the particle number concentration at the droplet location can be extracted from the macroscale simulation to derive the accumulative particle–droplet collision number. Figure 19.95a shows the accumulative particle–droplet collision numbers along the trajectories of different sized droplets in a gas flow field at p_g = 0.4 MPa. The accumulative particle–droplet collision number achieves a maximum value when the droplet flies into a particle-free region or finishes solidification. The collection efficiency of ceramic particles by a metallic droplet is defined as the volume fraction of ceramic particles colliding with the droplet before it achieves a 50% solidification degree (assuming that when the solidification degree in a droplet is over 50%, the particle–droplet collisions will not lead to particle incorporation or sticking in the droplet). The collection efficiency as a function of droplet size and atomization gas pressure is shown in Figure 19.95b. In general, the collection efficiency first increases with increasing droplet size, reaches a maximum value, and then decreases. The particle–droplet mixing quality at a given operation condition can be described by

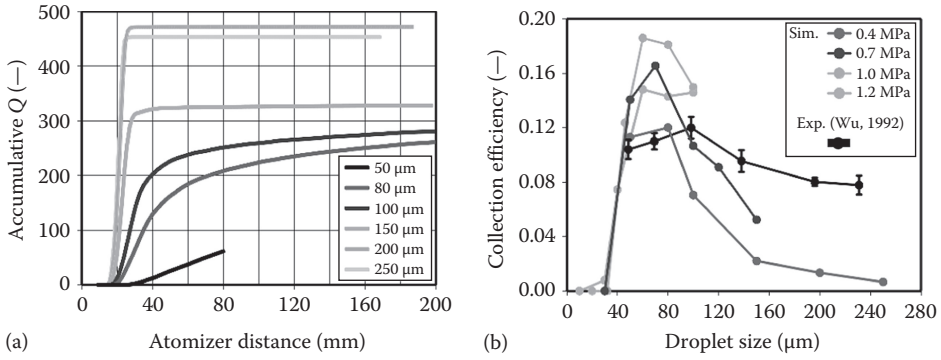


Figure 19.95

(a) Accumulative particle–droplet collision number Q along the droplet flight path vs. droplet size in a gas flow field at p_g = 0.4 MPa. (b) Collection efficiency of SiC-particles by Sn-droplets of different sizes at different atomization-gas pressures. (Adapted from Li, X.G., Modeling and simulation of the gas-atomization process of metal melts for metal-matrix-composite production, Dissertation Universität Bremen, Shaker-Verlag, Aachen, Germany, 2014; Li, X.G. and Fritsching, U., Multiscale modeling and simulation in spray processing of composite particles, in *Proceedings of Second International Symposium on Multiscale Multiphase Process Engineering*, Hamburg, Germany, September 24–27, 2014b.)

a characteristic collection efficiency, for example, the collection efficiency of a droplet with a size of MMD (MMD, $d_{50,3}$) at that operation condition. A maximum characteristic collection efficiency (~16%) is obtained at p_g = 0.7 MPa, which implies a best particle-droplet mixing quality under this operation condition.

On the *microscale*, the numerical simulation of the penetration behavior of a solid particle into a liquid droplet is performed based on a multiphase CFD model, which describes the multiphase flow situation (gas-particle-droplet) by solving incompressible Navier–Stokes (NS) equations coupled with VOF method, six degrees of freedom (6-DoF) method, and dynamic mesh technique (Li and Fritsching, 2014c). Two typical outcomes observed in simulations are (1) the particle partially penetrates into the droplet and (2) the particle completely penetrates into the droplet. The outcomes are categorized with Weber number (We) and Reynolds number (Re) in a regime map, as sketched in Figure 19.96a. The regime boundary is formulated by

$$\ln\left(\frac{\mathrm{We}}{\mathrm{We}_0}\right) = a\left(\ln\left(\frac{\mathrm{Re}}{\mathrm{Re}_0}\right)\right)^b, \quad \text{with } \mathrm{We} = \frac{\rho_l U_{rel,0}^2 d_p}{\sigma}, \mathrm{Re} = \frac{\rho_l U_{rel,0} d_p}{\mu_l} \tag{19.184}$$

Here, We_0, Re_0, a, and b are constants related to solid/liquid contact angle (θ), particle/droplet size ratio (δ), and particle orientation (Li and Fritsching, 2014c). Based on the Re–We regime map, the critical penetration velocity was derived as a function of solid fraction in a droplet by taking into account the variation of viscosity with solid fraction in the solidifying droplet (Li and Fritsching, 2014c). As shown in Figure 19.96b, the critical penetration velocity increases exponentially with increasing solid fraction. An increasing solid/liquid contact angle (θ) leads to an increasing critical penetration velocity, but the increase is not significant when θ ≤ 90°. Based on the discussion, the accumulative collisions derived from the mesoscale modeling and simulation (Figure 19.95) can be thus divided into two groups, as sketched in Figure 19.97:

1. One group of collisions occurring in the penetration regime is the main source for the incorporation of particulate reinforcements in the interior region of MMC particles. The incorporation efficiency can be roughly described by the volume fraction of these particles to the droplet.
2. The other group of collisions will result in particle partial penetration according to the Re-We regime map. Since most of collisions in this regime occur in the downstream spray flow, it is considered reasonable that most of the solid particles are likely to be captured by the droplet surface because of droplet solidification. The sticking efficiency of particulate reinforcements on the surface of MMC particles can be roughly described by the volume fraction of these particles to the droplet.

Suitable process conditions for optimization of the particle sticking/inclusion ratio may be derived from the MCFD simulations. Figure 19.97 shows the calculated characteristic incorporation rate and sticking rate of TiC-particles (θ = 90°) and SiC-particles (θ = 152°) in Tin (Sn)-based MMC particles as a function of atomization gas pressure. It can be found that the incorporation rate as well the sticking rate first increases with increasing atomization gas pressure, reaches a maximum value, and then decreases; a significant portion

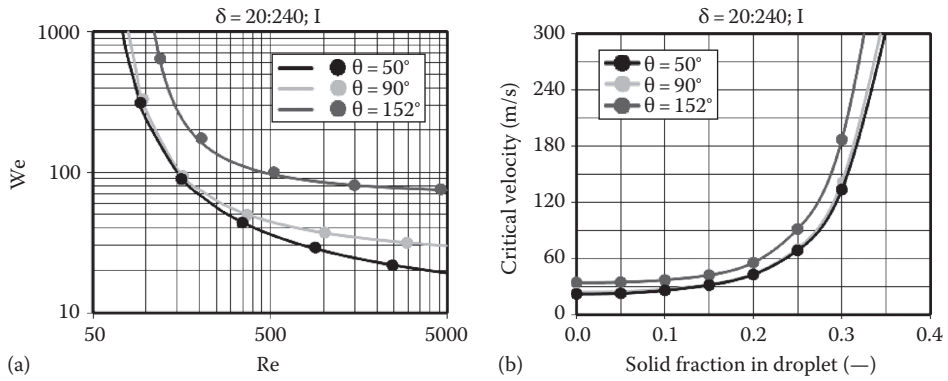


Figure 19.96

Critical penetration condition: (a) shift of regime boundary with variation of solid/liquid contact angle (θ) for head-on particle–droplet collision with particle orientation I; (b) critical penetration velocity vs. solid fraction at different solid/liquid contact angles. (Adapted from Li, X.G. and Fritsching, U., *Materialwiss. Werkstofftech.*, 45(8), 666, 2014c. With permission.)

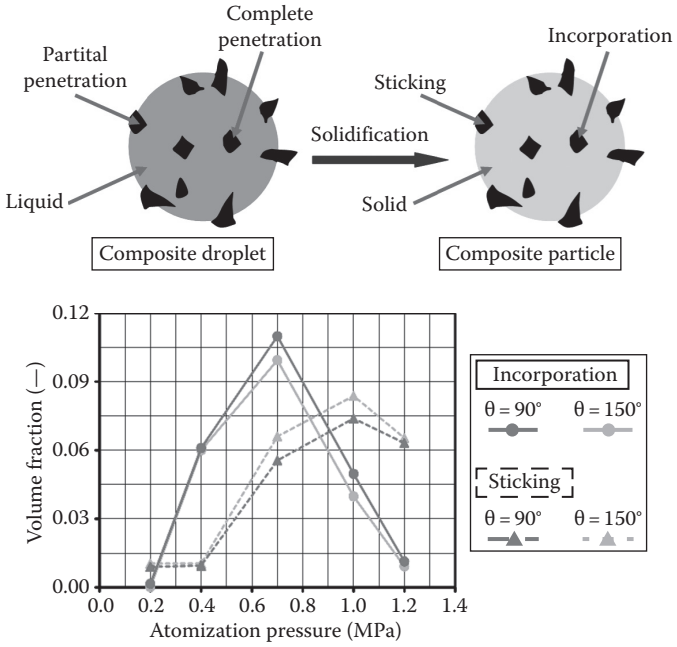


Figure 19.97

Characteristic particle incorporation efficiency in droplet and sticking efficiency on droplet surface at different atomization process operation conditions. (Adapted from Li, X.G., Modeling and simulation of the gas-atomization process of metal melts for metal-matrix-composite production, Dissertation Universität Bremen, Shaker-Verlag, Aachen, Germany, 2014; Li, X.G. and Fritsching, U., Multiscale modeling and simulation in spray processing of composite particles, in *Proceedings of Second International Symposium on Multiscale Multiphase Process Engineering*, Hamburg, Germany, September 24–27, 2014b.)

of collisions is squandered by droplet surface. The maximum incorporation rate occurs at p_g = 0.7 MPa, while the maximum sticking rate occurs at p_g = 1.0 MPa. A larger contact angle results in a smaller particle-incorporation rate but a larger particle-sticking rate.

19.4.3.2 Spray Forming

The spray forming process is a metallurgical manufacturing process that combines the main advantages of the classical processes:

- Metal casting: high-volume production, neat-net shape forming
- Powder metallurgy: near-net shape forming (at small volumes) with homogeneous, fine-grained microstructure

The spray forming process combines the atomization and spraying of a metal melt with the consolidation and compaction of the sprayed mass on a substrate. A typical scheme of the spray forming process is illustrated in Figure 19.98. The metallurgically prepared metal melt is distributed from the melting crucible via a tundish into the atomization area. Typically by means of a twin-fluid atomizer with external mixing, inert gas jets with high kinetic energy impinge onto the metal stream and cause the melt disintegration. In the resulting spray, the droplets are accelerated toward the substrate and thereby cool down and partly solidify by intensive heat transfer to the cold atomization gas. The mixture of liquid droplets and semisolid or solidified particles in the spray impinge onto the substrate consolidating to the desired deposited product. This mixture of droplets in different solidification stages on impingement is an essential feature of the spray forming process. The overall amount of the superheat (above the liquidus temperature) and of the latent heat (solidification) is extracted from the sprayed mass in the spray at high cooling rates (approximately 10^5 K/s). The solidification of the remaining melt in the deposit (typically 10%–40% remaining liquid) is started at an already high (finely distributed) solid content (Annavarapu and Doherty, 1995, Doherty et al., 1997), thereby resulting in extreme fine and equiaxed grain structures. After consolidation, the remaining metal finally solidifies and cools down further at cooling rates that are just comparable to casting processes.

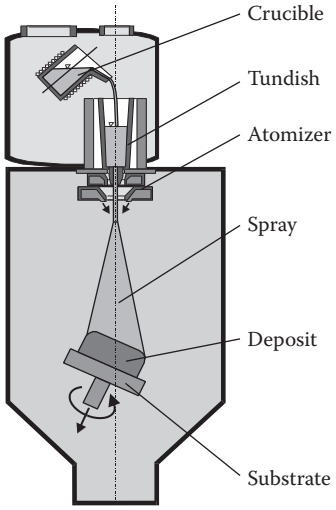


Figure 19.98

Principle of the spray forming process.

An overview of industrial applications and the objectives of spray forming have been given by Lawley et al. (1990), Grant (1995), Lavernia and Wu (1996), Leatham and Lawley (1993), Bauckhage (1997, 2003), Fritsching and Bauckhage (1999), Lawley (2000), Raju et al. (2008), and Antipas (2013). Several materials and alloys are produced with specific advantages via spray forming such as

- Conventional metallic materials and alloys from steel, aluminum, and copper and
- Materials in which alloying components tend to segregate within conventional casting processes, for example, alloys on aluminum, copper and iron bases, super alloys (e.g., on nickel base) for applications in the aircraft and aerospace industries,
- Intermetallic composite materials (IMCs)
- Multilayer composites or gradient materials by cospray forming (Meyer et al., 2009, Cui et al., 2013, Grohmann et al., 2013)
- MMCs, for example, ceramic particle inclusions into a metal matrix (Lavernia, 1996, Schneider, 2005, Raju et al., 2008, Cui et al., 2010)
- Precipitation-controlled alloy composition
- Lightweight materials (e.g., magnesium)
- Metallic glasses (Srivastava et al., 2009, 2013, Cava et al., 2013)

Typical geometries of spray formed preforms in industrial applications are flat products, tubes or rings, and cylindrical billets.

The main advantage of spray formed materials, compared to conventionally produced materials, is related to their outstanding material properties. These are due to the specific cooling and solidification history in the spray process and finally result in

- Absence of macrosegregations
- Homogeneous, globular microstructure
- Increased yield strength
- Decreased oxygen contamination
- Good hot workability and deformability

19.4.3.2.1 Atomization of the Liquid Melt In spray forming, typically twin-fluid atomization with inert gas is used in a free-fall atomizer configuration because

- High mass flow rates of melt can be atomized.
- High heat transfer rates from the droplets can be realized in the spray.
- High momentum transfer rates are achieved to accelerate the droplets.
- Low oxidation rates of the material in the spray process are obtained.

The analysis of the atomization process requires primary knowledge of the gas flowfield of the atomizer gas in the nozzle vicinity. The primary gas flow emerging at low pressure close to the melt exit is responsible for guiding the melt flow into the atomization region below the atomizer, while a secondary gas flow field emerges from the lower gas ring and impinges on the central melt stream, well below the atomizer, and is applied for disintegration of the melt (Uhlenwinkel et al., 1990, Heck et al., 2000, Czisch and Fritsching, 2008).

In Figure 19.99, the results of a numerical simulation of the (subsonic) gas flow in the nozzle vicinity are shown as vector diagrams in comparison to pictures of the atomization of a model fluid (water) in a free-fall atomizer (Fritsching and Bauckhage, 1992). The atomization gas pressure in this case is p_2 = 1.89 bar abs; therefore, the gas exit condition is just critical with an exit velocity equal to the velocity of sound (M = 1). In the first (upper) example, no primary gas flow is applied (p_1 = 0). The secondary atomizer gas flow exits from the gas ring at an inclination angle of 10°, but contracts even more than this angle indicates, and hits the centerline of the atomizer well above the theoretical atomization point, which is the intersection point of the atomizer centerline with the gas jet exit line. By gas entrainment effects, ambient gas is accelerated into the inner flow field. This gas stream flows through the gap between the nozzle main body and the lower atomizer gas ring into the inner area of the flow field. In the middle of the inner area, a recirculating vortex

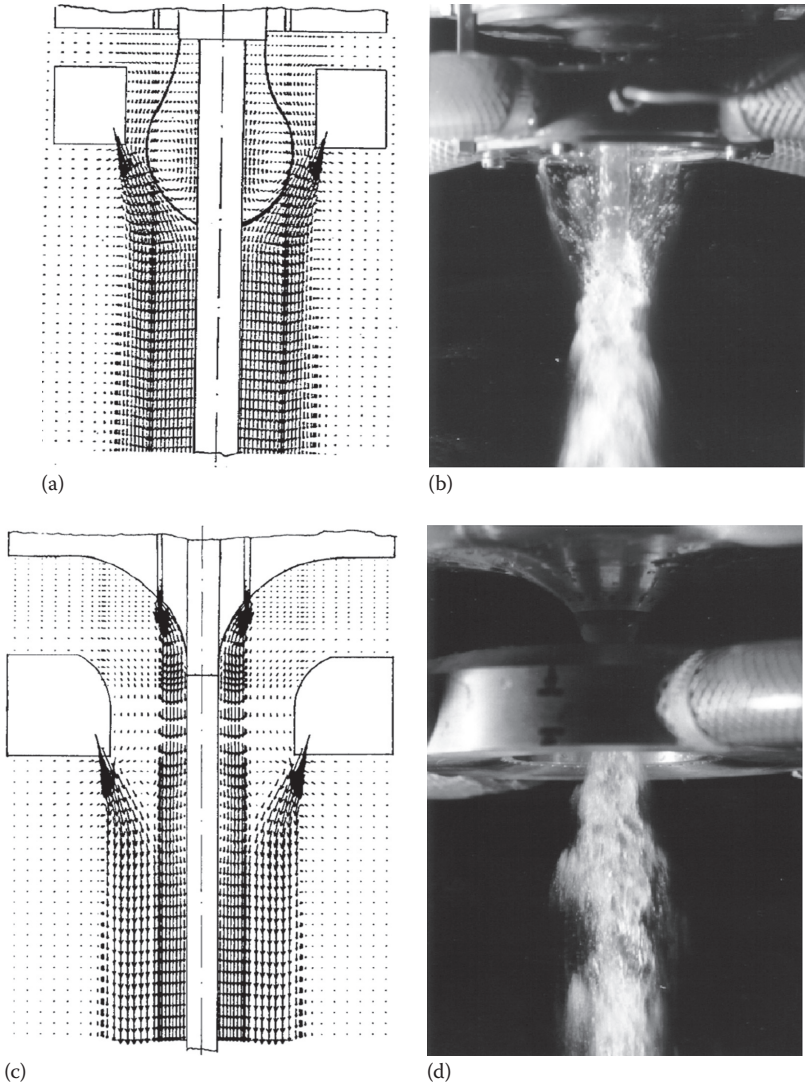


Figure 19.99

Fragmentation process in free-fall atomizer for spray forming application, comparison of gas flow simulation and water atomization; upper: droplet recirculation; p_2 = 0.189 MPa, p_1 = 0; lower: optimized process condition; p_2 = 0.189 MPa, p_1 = 0.14 MPa. (From Fritsching, U. and Bauckhage, K., *PHOENICS J. Comp. Fluid Dyn.*, 5(1), 81, 1992. With permission.)

flow can be seen (indicated by a solid line in the figure). Gas velocities of up to 50 m/s pointing vertically upward are achieved in this area. Individual particles entering this area of upward flowing gas are accelerated toward the nozzle main body and the melt exit. This result can also be observed in some experimental observations of the atomization process, where individual droplets can be seen above the atomization region, which are transported vertically upward. For melt droplets, this effect may cause sticking and even possible blocking of the nozzle. The calculated gas flow field in an optimized free-fall nozzle configuration is shown in the second (lower) example in Figure 19.99 for an atomization gas pressure of p_2 = 1.89 bar abs. and a primary gas pressure of p_1 = 1.4 bar abs (Fritsching and Bauckhage, 1992). Here, a gas flow field without recirculation is seen in the nozzle vicinity. The observation of the atomization model shows the successful prevention of droplet recirculations and illustrates the importance of the primary gas flow for this nozzle.

The interaction of the gas flow and the melt stream has been investigated by Antipas et al. (1993), Markus and Fritsching (2003b, 2006), Liu (1997, 2000a), and Achelis et al. (2010). Here, the primary jet fragmentation and the secondary droplet disintegration have been calculated in a direct way. The principal parameter describing the spray is the droplet size distribution, which in spray forming is typically based on the correlation by Lubanska (1970) (see Table 19.5). In this correlation, a specific liquid Weber number is used as follows:

$$\mathrm{We}_l = \frac{\rho_l u_{g,\max}^2 d_0}{\sigma} \tag{19.185}$$

This needs to be calculated by using the melt properties and the maximum gas velocity of the atomizer gas flow field. The maximum gas velocity in the atomization region has been calculated based on simulations (Fritsching and Bauckhage, 1992) and also measured and correlated for a typical free-fall arrangement (Heck, 1998) as:

$$u_{g,\max} = 645.25 \dot{m}_g^{0.585} \tag{19.186}$$

where the gas mass flowrate is correlated to the absolute atomization gas pressure in the choked flow regime (for nitrogen at pressures above 0.189 MPa) by

$$\dot{m}_g = 0.685 \mathrm{C_d} A_g \frac{p_0}{\sqrt{RT_0}} \tag{19.187}$$

The total gas exit area is A_0 and a typical value for the friction coefficient C_d is 0.84. The result of a sample calculation of the resulting mean droplet sizes for different atomized metals (i.e., aluminum, magnesium, iron, copper, and tin) has been shown in Figure 19.47. The main parameter describing the atomization efficiency (achieving smaller droplets) is the inverse product of dynamic viscosity and surface tension $(\mu\,\sigma)^{-1}$.

19.4.3.2.2 Particle Transport in the Spray In the spray, a complex two-phase flow situation involving gas and particles/droplets occurs. The high-speed gas loses its momentum by accelerating the droplets. Due to the heat transfer from the droplets, the gas undergoes intensive heating in the zone close to the atomizer. The droplets are accelerated and partly solidified during their flight. Modeling the complete dispersed two-phase flow situation including momentum and heat coupling is used to describe and analyze the spray behavior (Grant et al., 1993a,b, Fritsching, 1994c, Fritsching, 1995, Muoio et al., 1995, Bergmann, 2000, Pedersen, 2003, Markus and Fritsching, 2006, Gjesing et al., 2009, Li and Fritsching, 1994c, Fritsching, 2014a). As an example modeling, Figures 19.90 and 19.91 show the behavior of different droplet size classes on the centerline of a spray of molten steel, atomized with nitrogen (Bergmann et al., 1995). The boundary conditions include an atomizer pre-pressure of p_2 = 3 bar abs., a gas to metal flow rate (GMR) of 1.25, and a log-normal droplet size distribution with an MMD of 133 µm. The axial velocity distribution on the spray centerline of gas and particles with different diameters is illustrated in Figure 19.100. The gas velocity upstream of the atomization area is unaffected by the particles. Close to and in the atomization region, the gas velocity decreases due to the momentum transfer associated with acceleration of the droplets. Afterward, the gas velocity further increases because of the heating of the gas and thermal expansion and, also, due to the entrainment of momentum from the edge of the spray cone. The maximum gas velocity is reached at a nozzle distance of ~330 mm. Afterward, the gas velocity decreases due to the spreading of the spray cone. Particles are accelerated in the atomization region and further downstream. In the main region of the spray cone, particle velocities for the bigger particles remain approximately constant.

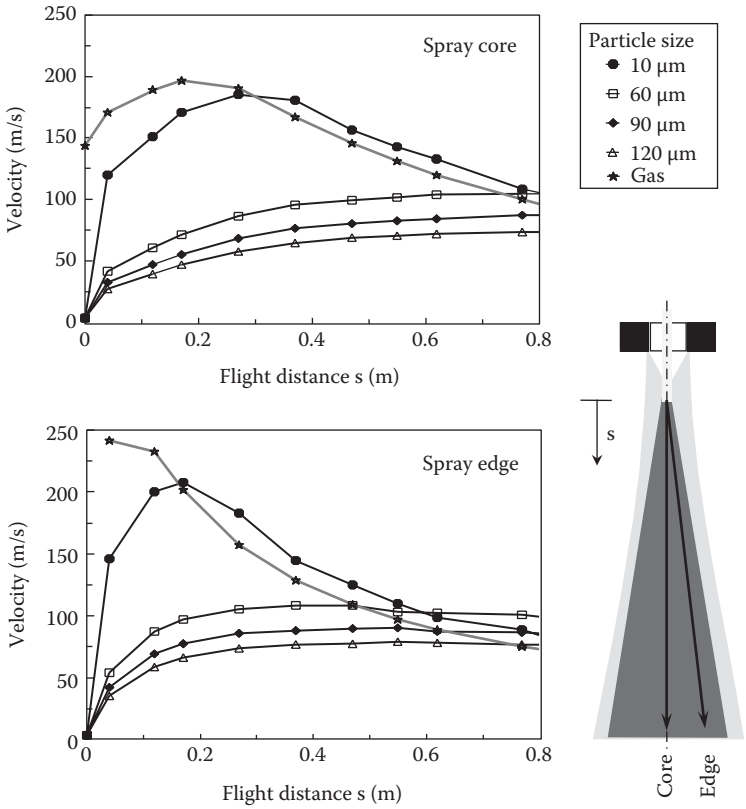


Figure 19.100

Modeling result for gas and particle velocity behavior on spray centerline and edge within spray forming of steel. (From From Bergmann, D. et al., Multiphase flows in the spray forming process, in *Proceedings of the Second International Conference on Multiphase Flow*, Kyoto, Japan, Vol. 1, April 3–7, 1995, pp. SP1–SP8. With permission.)

The gas reaches high temperatures in the atomization region up to 1200 K, as can be seen from Figure 19.101. Further downstream, the local gas temperature on the centerline decreases, but heat transfer from the particles continues, due to the spreading of the spray and mixing with the colder ambient gas. After cooling down to solidification temperature, the phase change occurs inside the particles and the latent heat of the particles is released, whereby the particle temperature remains constant. When the latent heat content of the droplets is removed, the particles further cool down. From these calculations, it can be seen that particles bigger than 210 µm are still in the state of phase change when impacting the substrate/deposit.

Experimental investigations have verified these simulation results. Online measurement techniques have been used to monitor the spray conditions in spray forming. With a modified phase Doppler anemometer (Ziesenis, 2003), local droplet sizes and velocities are measured and used for process control (Bauckhage, 1998). Measurements of individual droplet temperatures (plus droplet sizes and velocities) in metal sprays have been performed by means of a high-speed pyrometer instrument (Krauss et al., 2002, Delshad Khatibi et al., 2011, 2014).

To determine the overall heat and mass fluxes from the spray to the deposit, the droplet data have to be averaged in a suitable manner. Thermal averaging may be performed in two different ways, describing two extreme situations that occur in a molten metal spray (Bergmann et al., 1999). The first averaging method (*the enthalpy method*) describes the thermal status of the particle mass in thermal equilibrium. In this way, the thermal state of a certain particle mass is described after adiabatic equilibration. This means the particle mass has a specific enthalpy, which is directly related to its thermal state (temperature and solid fraction).

In an impinging molten metal spray for forming or coating processes, situations may arise where the particle mass should already be fully solidified depending on its average properties (when calculated by the enthalpy method), although it still contains some liquid. This may occur when the main spray consists of a large proportion of cold, solidified particles, and only a small number of large, fluid, and hot melted particles. These liquid droplets still deliver a certain amount of liquid melt to the mushy layer on the deposit surface, which is not accounted for by the enthalpy method. However, if a *separation averaging method* is used, this difficulty is avoided. Here, the amount of solidified mass or fluid melt mass remaining in the spray is calculated separately.

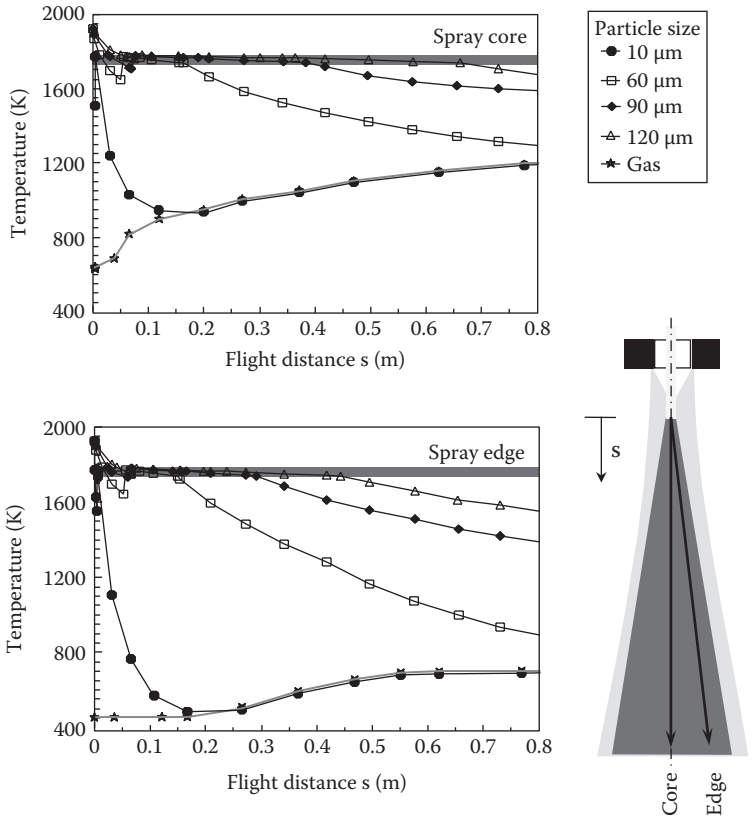


Figure 19.101

Modeling result for gas and particle temperature behavior on spray centerline and edge in spray forming of steel. (From Bergmann, D. et al., Multiphase flows in the spray forming process, in *Proceedings of the Second International Conference on Multiphase Flow*, Kyoto, Japan, Vol. 1, April 3–7, 1995, pp. SP1–SP8. With permission.)

The enthalpy averaging approach yields the thermal equilibrium condition of the total droplet mass (in terms of a discrete number of droplet size classes i):

$$\overline{h_p} = \frac{1}{\sum_i m_{p,i}} \sum_i \{m_{p,i}[(c_{pl}(T_{p,i} - T_s) + \Delta h_f)(1 - f_{s,i}) + c_{ps}((T_{p,i} - T_s)f_{s,i} + T_s)]\} \tag{19.188}$$

Based on the calculated average specific enthalpy $\overline{h_p}$, the mean spray solid fraction $f_{s,h}$ and the mean temperature T_h are calculated according to the solidification state of the droplet mass. In the separation averaging approach, the nonequilibrium situation in the spray process is recognized. The energy exchange within the total particle mass occurs only via the specific heat content and not via the remaining latent heat content of the particles:

$$f_{s,m} = \frac{1}{\sum_i m_{p,i}} \sum_i (m_{p,i} f_{s,i}), \tag{19.189}$$

$$T_m = \frac{1}{(c_{ps} f_{s,m} + c_{pl}(1 - f_{s,m}))\sum_i m_{p,i}} \sum_i (m_{p,i} T_{p,i}(c_{ps} f_{s,m} + c_{pl}(1 - f_{s,m}))). \tag{19.190}$$

Differences in the results obtained using the two averaging methods are shown in Figure 19.102 for the averaged temperatures and solid fractions of the spray along the centerline as a function of the particle flight distance. The results of the enthalpy method represent the thermal equilibrium with respect to the particle mass,

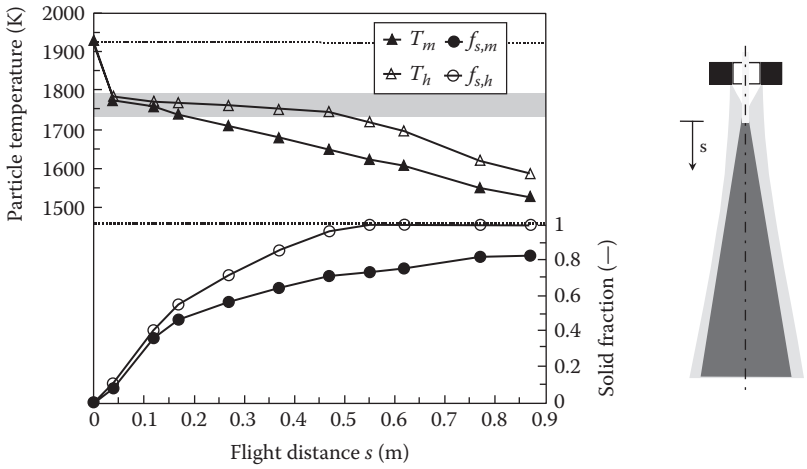


Figure 19.102

Integral temperature and remaining solid fraction in steel melt spray versus the spray distance, two different averaging methods. (From Bergmann, D., Modellierung des Sprühkompaktierprozesses für Kupfer-und Stahlwerkstoffe, Dissertation, Universität Bremen, Bremen, Germany, 2000. With permission.)

considering all particles from a specific location (point of impingement) together and leaving this mass under adiabatic conditions for an inner compensation process (heat conduction and solidification). This compensation process in spray forming immediately occurs when the sprayed particle mass impinges onto the deposit. In the semisolidified mixing layer on top of the deposit, an equilibration process will take place. Therefore, the enthalpy method properly describes the thermal state of the particle mass "in the top mushy layer" after deposition. In contrast, the separation method describes the instantaneous local thermal state (temperature and solid content) of the particle mass *in the spray*. As can be seen in Figure 19.102, the instantaneous mean particle temperatures and mean solidification fractions calculated for the whole particle flight distance by the separation model are lower than the values derived by the equilibrium state (enthalpy) method. With respect to the solidification process after the deposition, this difference means that the overall particle mass is "undercooled" and may be reheated after the deposition (in the mixing layer) by the latent heat released during solidification.

The mass flux distribution in the spray cone is directly connected to the resulting shape of the sprayed deposit. For varying deposit shapes, either the atomizer and/or the substrate can be moved. For a stationary atomizer, the radial profile of the mass flux distribution in the spray cone can be described as an exponential function by Equation 19.154. The maximum mass flux is always found on the spray cone centerline and $r_{0,5}$ is the half width of the mass flux profile (see Figure 19.83). The exponential factor has been correlated as $k_1 = 1.3$ (Uhlenwinkel, 1992) and $k_1 = 1.124$ (Kramer, 1997) for steel atomization. The half width of the mass flux profile is proportional to the maximum mass flux value as

$$\dot{m}(r) = \dot{m}_{\max} e^{(\ln(0.5)|r/r_{0.5}|^{k_2})} \tag{19.191}$$

For calculating the mass flux distribution at each position within the spray cone, a single calibrating measurement on the spray centerline in combination with the mass flux correlations is sufficient.

19.4.3.2.3 Deposition and Consolidation of Droplets The impinging droplets transport mass, momentum, and thermal energy into the top layer of the deposit (Kramer, 1997, Bauckhage et al., 1999, Djuric et al., 1999, Djuric and Grant 2001, Jordan 2003, Markus and Fritsching, 2003a). The compacted mass is not identical to the mass flux in the spray because

- Particles may have a spray trajectory that does not impinge onto the deposition surface.
- Smaller droplets of low inertia will follow the gas streamlines and will be deflected (aerodynamic overspray).
- Droplets may bounce-off or splash (Trapaga et al., 1992, Berg and Ulrich, 1997, Berg, 1999, Bussmann et al., 2000), and secondary droplets may not be incorporated in the deposit.
- Particles with high momentum may tear off parts of the already compacted (soft) mushy top layer.

This particle mass contributes to the overspray. The difference between the mass flux value in the spray cone and the compacted mass is described by the deposition efficiency:

$$k(\vec{x},t)=\frac{\dot{m}_{compac}(\vec{x},t)}{\dot{m}_{spray}(\vec{x})}\leq 1 \tag{19.192}$$

This depends on

- The thermal state of the impingement surface
- The momentum, temperature, and state of solidification of the impinging droplets

The deposition efficiency for spray forming of Gaussian shaped deposits (produced with a stationary atomizer, spraying on a stationary cylindrical substrate) from steel is correlated by (Kramer, 1997)

$$k(T_p,f_l,I_p)=C_4\left[C_1+C_2\left(\frac{T_p}{T_{surf}}\right)^{C_3}\right]f_l^{C_5}I_p^{C_6} \tag{19.193}$$

where the coefficients are: $C_1 = 0.422$; $C_2 = 0.80$; $C_3 = 30.48$; $C_4 = 0.489$; $C_5 = 0.249$ and $C_6 = -0.062$. The main parameter influencing the deposition efficiency is the temperature of the droplets on impact (here, normalized by the liquidus temperature).

During spraying time, the deposit grows continuously and releases its thermal energy by

- Conduction to the substrate
- Convection and radiation to the surrounding gas

To calculate the temperature distribution and history in the deposit and substrate, numerical methods and measurements have been used (Mathur et al., 1989a,b, Fritsching et al., 1993, 1994a,b, Gutierrez-Miravete et al., 1988, Buchholz et al., 2002). The result of a simulation for production of a copper billet is shown in Figure 19.103 (Meyer et al., 2003a,b).

By numerical modeling, a description of the complete material cooling process of metals in the different stages of spray forming, namely, during flight, deposition, and further cooling periods (which are of major importance for the understanding, control, and optimization of the process), can be obtained and analyzed. Integral models

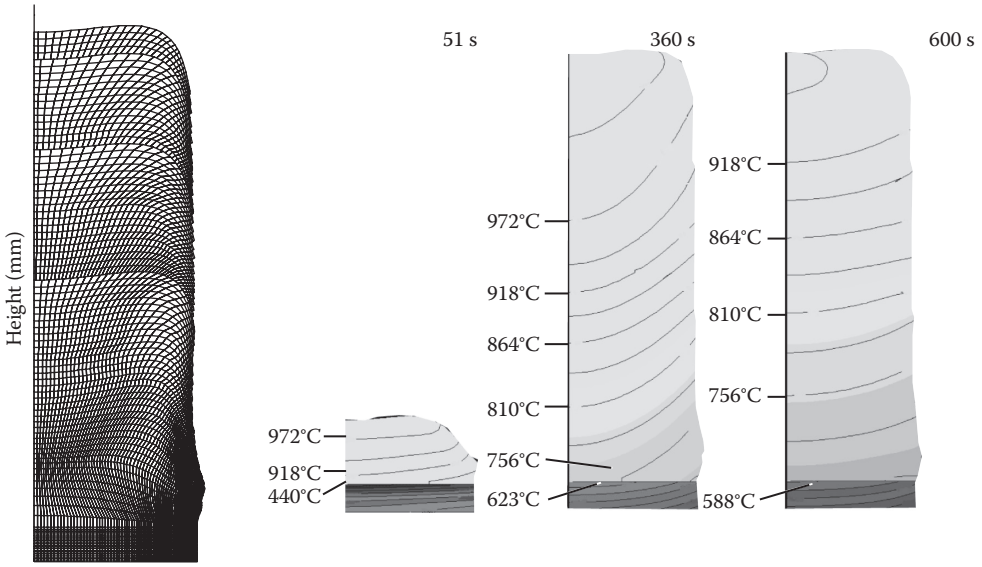


Figure 19.103

Temperature and solid content distribution during spray forming of a copper billet. (From Meyer et al., 2003. With permission.)

of the spray forming process have been dealt with by Lavernia et al. (1988), Mathur et al. (1991), Payne et al. (1993, 1996), Ottosen (1993), Tsao and Grant (1994), Hattel et al. (2000), Pedersen (2003), Pedersen et al. (2000), Bergmann (2000), Markus and Fritsching (2003a), Fritsching (2004), and Gjesing et al. (2009). The quality of spray-formed products in terms of homogeneity and improved material properties is directly controlled by the cooling rate of particles in the spray cone and the further cooling behavior of the resulting preform. The solidification and cooling behavior of the material directly depends on operational parameters. Such temperature simulations based on heat balance in the deposit and substrate show possibilities for thermal homogenization and avoidance of hot spots (Liu et al., 1994, Meyer et al., 2003a).

19.4.4 Spray Drying

In the spray-drying process, the liquid feed material (in form of solution, emulsion or slurry) is atomized into a hot air environment where the moisture is evaporated from the suspended droplets until the dried particles are obtained and collected as a final product. Typical examples are in spray drying of foodstuff (e.g., milk or coffee powders), or in chemical industry (e.g., detergents drying), or in formulation and encapsulation of pharmaceutics. This process is ideal for drying of heat-sensitive feed materials since the droplet–hot air contact time (residence time in the process) is reasonably short. Another advantage of spray drying is the ability to handle highly sticky or corrosive materials (Masters, 1991, 2002, Mujumdar, 2014).

The spray-drying process typically is subdivided into three steps (Crowe, 1980):

1. Atomization: Here, either a (1) rotary, (2) pressure swirl nozzle, or (3) twin-fluid nozzle is used to atomize the liquid and discharge into the spray chamber.
2. Droplets–air contact: the droplet spray is dried by the interaction with hot gases in the spray chamber. The spray-air flow pattern can be categorized into three types: cocurrent flow (Figure 19.104a and b) countercurrent flow (Figure 19.104c) and mixed cocounter current flow (Figure 19.104d). The spray chamber geometry depends on the atomizer used: if a rotary atomizer is used, a "wide-form" (Figure 19.104a) chamber is required. If a pressure nozzle or twin-fluid nozzle is used, "tall-form" dryer (Figure 19.104b through d) is required. The cocurrent flow arrangement is suitable for more heat-sensitive material,

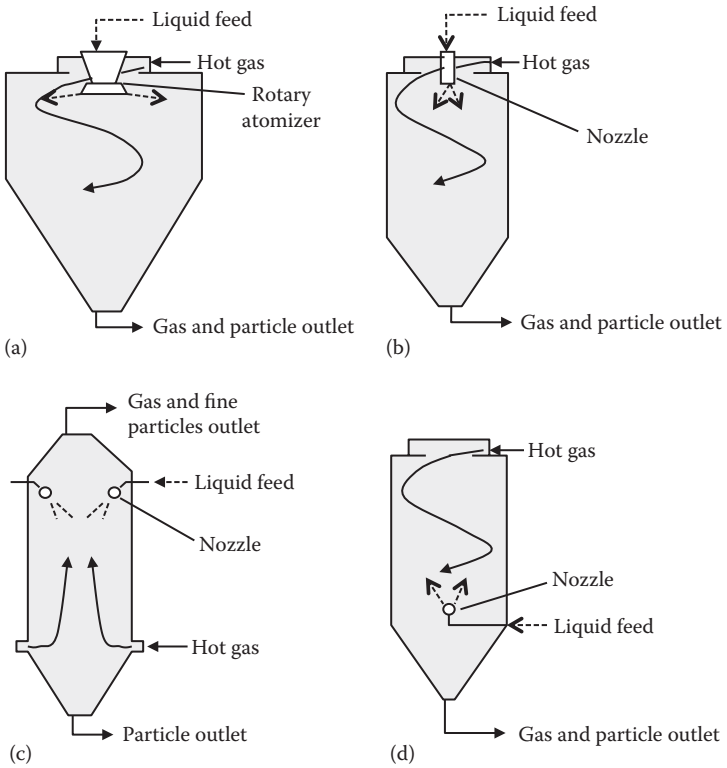


Figure 19.104

Spray dryer configurations: (a) cocurrent with rotary atomizer; (b) cocurrent with pressure nozzle; (c) countercurrent with pressure nozzle; (d) mixed flow with pressure nozzle.

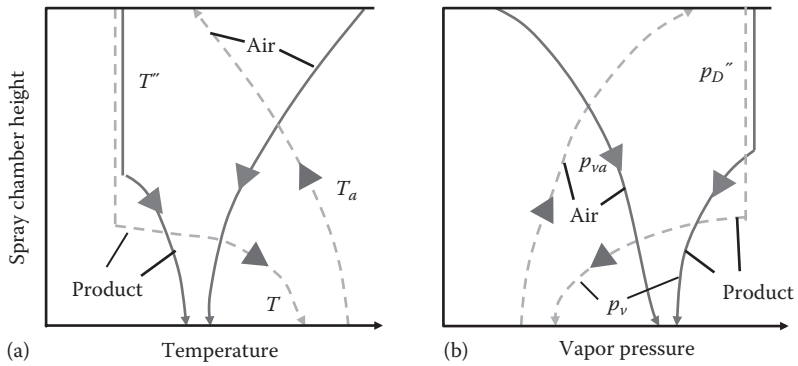


Figure 19.105

(a) Temperature and (b) vapor pressure distribution in cocurrent and countercurrent spray-drying process. (Adapted from Mujumdar, 1987.)

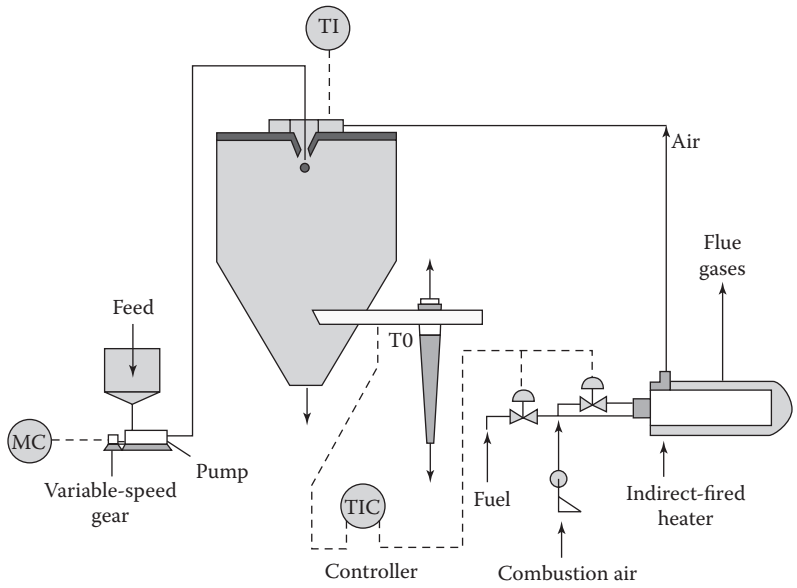


Figure 19.106

Configuration of a spray-drying plant. (Adapted from Oakley, D.E., *Chem. Eng. Progress*, 12, 48, 1997.)

since the air-spray contact time is shorter and the spray is protected from the high inlet air temperature due to evaporative cooling and the dried particles contact with cooler air at the lower section of dryer. Countercurrent flow arrangement is suitable for materials that are not heat sensitive since the dried particles contact with high inlet air temperatures. Although much less common than cocurrent arrangement, the countercurrent arrangement is suitable for some applications. For example, in spray drying of detergent powder, multiple pressure nozzles are used with countercurrent arrangement to attain high bulk density agglomerate form. Typical temperature and vapor pressure profiles (as indicator of moisture content) of cocurrent and countercurrent spray dryers are illustrated in Figure 19.105.

3. Removal of the powder from the drying medium by means of gravity settling and/or cyclone separation.

A typical spray-drying process configuration is illustrated in Figure 19.106.

19.4.4.1 Particle–Gas Interaction

In the droplet spray contact with the drying gas, all three interface transfer mechanisms (mass, momentum and energy) become operative. Crowe (1980) and Crowe et al. (1998) described these transfer mechanisms of spray drying. Momentum transfer consists mainly of the drag force and gravity force. Nikas et al. (2001)

reported the importance of buoyancy force acting on the particles according to their numerical simulation of flow in a spray dryer. At the droplet–hot air interface, heat is transferred into and moisture is removed from the droplet surface. According to the heat and mass transfer analogy, the external transfer of mass or heat is obtained from the transfer relation Equation 19.160 expressed in terms of the Nusselt number (Nu) for heat transfer and the Sherwood number (Sh) for mass transfer (see Chapter 1) together with a suitable droplet drying model (see Section 19.2.3).

19.4.4.2 Air-Spray Flow Pattern

The transient behavior and complex structure of the two-phase flow within a spray dryer has been investigated for many systems. If a swirl vane is mounted at the air inlet, the swirl vane angle affects the air-spray flow pattern, as reported by Oakley (1997), Oakley et al. (1988), Stafford et al. (1997), Kieviet and Kerchof (1995), and Southwell and Langrish (2000, 2001). The common pattern of air flows during spray operation with no swirl induced (or 0° swirl vane angle) exhibits fast flowing central core surrounded by a large recirculation zone (Kröger, 2001). As the inlet swirl increases, the large recirculation zone near the wall becomes less stable. From approximately 25° swirl vane angle and on, a precessing-vortex-core (PVC) begins to form in the core region and at swirl vane angle above 30°, the near-wall recirculation zone is less visible and finally disappears. At the higher swirl vane degree and with atomizer turned off, a central recirculation zone forms, but disappears when the atomizer is turned on. The central recirculation zone is undesirable as the dried particles are pushed back to heat-intensive regions, which may cause thermal degradation of products. Southwell and Langrish (2000, 2001) reported the formation of PVC, disappearance of near-wall large recirculation zone and the tendency that central recirculation might form at the axial distance further from the measurement point at 45° swirl vane angle. Figure 19.107 illustrates the effect on the airflow pattern of swirl by using vane-wheel atomizer.

Southwell and Langrish (2001) reported the spray patterns at various swirl vane angles. The spray cone region could be clearly identified and only small spray fluctuation could be observed at 0° swirl vane angle. As the swirl vane angle increased, the spray cone region was less visible and more transient. The width of the spray cone also increased when increasing the swirl vane angle. At 45°, the spray was torn apart and dispersed toward the wall within 0.2 m of the atomizer. The value of 25° has been found as the optimum swirl vane angle; good spray air mixing without excessive spreading of spray cloud and wall deposition is achieved. At this swirl angle, the spray cone did not spread as widely or interact with the inlet air as violently as at higher swirl vane angles, but adequate mixing was observed in the main body of dryer. Straatma et al. (1999) reported a computational fluid dynamics (CFD) study of two different cases. In the first case, simulation of an existing spray dryer with a rotary-wheel atomizer is performed. At the actual rotary speeds, reversal of the main airflow circulation occurred and a shortcut of hot air from inlet to outlet could be predicted from calculation (also observed in experiments). In the second case study, an industrial spray dryer equipped with one central and several noncentral air inlet channels with nozzle atomizers is simulated. The powder deposition in the conical section was serious, since the particle hit the cone when it was still wet and sticky. Larger, noncentral air inlets at a larger distance from the center solved this problem. This illustrates the importance of airflow pattern in a spray dryer on the drying process.

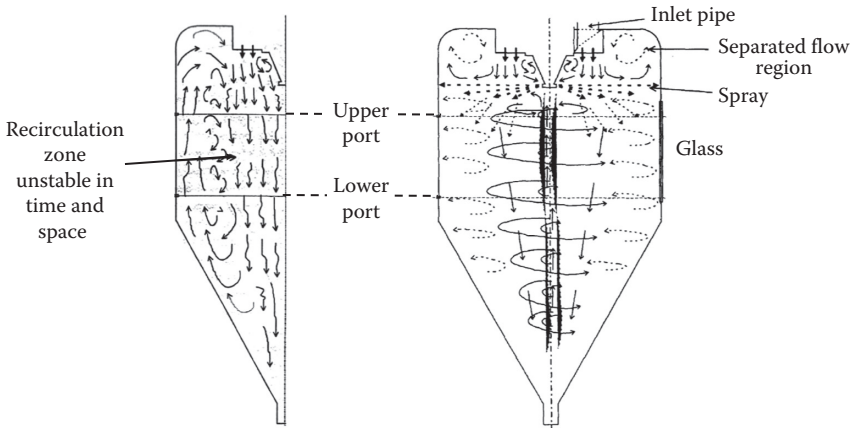


Figure 19.107

Spray dryer flow field. (Adapted from Southwell, D.B. and Langrish, T.A.G., *Dry. Technol.*, 18(3), 661, 2000.)

Mezhericher et al. (2012) argued that a proper formulation of the droplet drying kinetics and realistic 3D flow modeling are crucial for accurate numerical representation of the actual spray dryer performance. Therefore, in their study, a novel 3D CFD model of multiscale multiphase transport phenomena in a steady-state spray-drying process is proposed for predicting more realistic particles paths, residence times, temperatures, and moisture contents. A comprehensive formulation (or deterministic model) of two-stage droplet drying kinetics is employed to describe internal and external transport phenomena, as illustrated in Figure 19.108a. The continuous phase of drying air is treated by an Eulerian approach, and a standard k–ε turbulence model is applied. The trajectories of spray droplets/particles and their essential parameters are calculated using a discrete phase model (DPM) in a Lagrangian moving reference frame by taking into account the drag force, the added mass force, the pressure gradient force, and the gravitational force. The model has been validated on different levels, for example, of drying kinetics of single droplet/wet particle, airflow patterns, and 3D drying of wet particles in a spray dryer. Three-dimensional simulations of silica slurry drying have been carried out based on a cylinder-on-cone short form pilot-scale spray dryer with a cocurrent flow of drying air and spray droplets. The preheated air was supplied without swirling into the drying chamber through a central round inlet of the flat horizontal ceiling at an angle of 35° with respect to the vertical axis. The results of 3D steady-state predictions of particle trajectories colored by moisture contents, particle surface temperatures, and particle morphological states are shown in Figure 19.108b through d, respectively. The 3D calculations predict asymmetric particle flow in the spray chamber: a particle descending motion

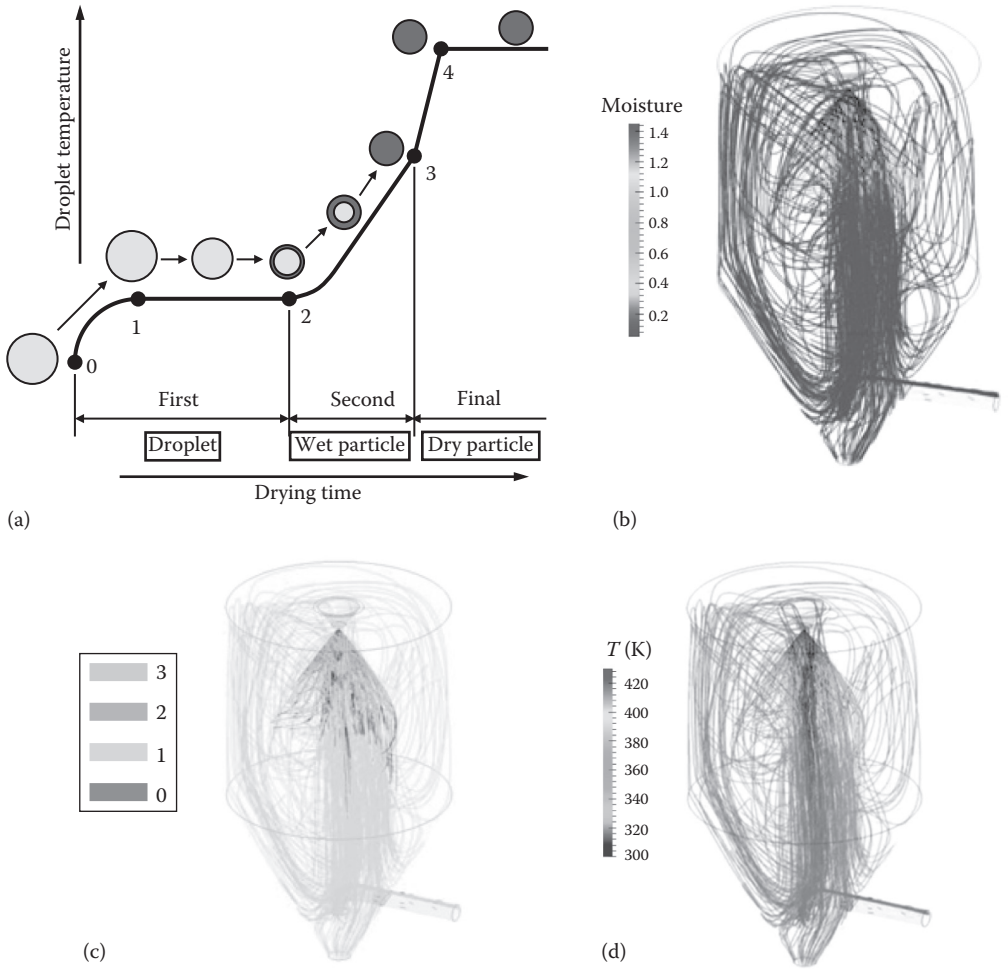


Figure 19.108

(a) Schematic illustration of two-stage drying kinetics with temperature curve and morphological states of the droplet; simulation: (b) particle trajectories colored by particle moisture content; (c) particle trajectories colored by particle law index. Here, 0 indicates initial heating, 1 indicates the first drying stage, 2 indicates the second drying stage, and 3 indicates the final particle sensible heating; (d) particle trajectories colored by particle temperature. (Adapted from Mezhericher, M. et al., *Dry. Technol.*, 30, 1256, 2012.)

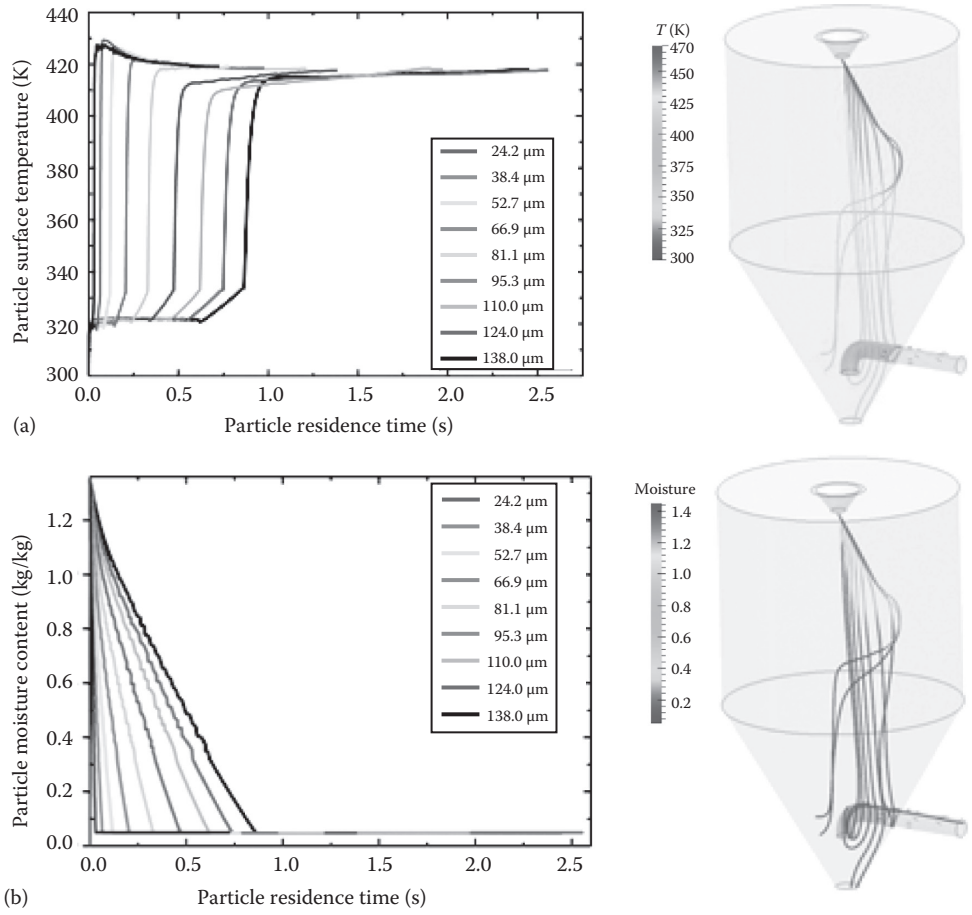


Figure 19.109

Drying kinetics of droplets: (a) particle surface temperatures; (b) particle moisture contents, droplet initial diameters as indicated. (Adapted from Mezhericher, M. et al., *Dry. Technol.*, 30, 1256, 2012.)

in the central core and subsequent upward particle transport with recirculation that occurs mainly in the chamber-half opposite the air outlet pipe, and that all particles that hit the chamber walls are completely dry. For the droplet drying kinetics, Figure 19.109 shows the calculated particle surface temperatures and average moisture contents evolving in time and in the chamber space, which indicates that larger droplets have longer PRTs and correspondingly longer first and second drying stages.

19.4.4.3 Effect of Turbulence Level at Air Inlet on Evaporation Rate

Zbicinski et al. (1996) investigated the effect of turbulence level on heat and mass transfer during atomization in an experimental air tunnel. Turbulence promoters increased turbulence level of the airflow in the tunnel to 17%. A comparative analysis of results obtained for heat and mass transfer for natural turbulence and for enhanced turbulence showed that increasing turbulence of a drying agent can cause 20%–25% increase of drying efficiency. Southwell et al. (1999) studied the experimental results of Zbicinski et al. (1996) using CFD. The simulations consistently predicted an increase in the amount of evaporation resulting from enhanced inlet turbulence. The simulation predicted improvements of 5%–11%, which were significantly less than the measured value. Enhancing inlet turbulence appeared to increase evaporation by improving both spray dispersion and the exchange of air between the spray envelope and the surrounding hot and relatively dry air.

19.4.4.4 Particle Residence Time Distribution

For some heat-sensitive materials, PRT distribution in a spray dryer is an important parameter. The effect of the airflow pattern (at different swirl vane angles) on PRT was discussed by Southwell and Langrish (2001). Kieviet and Kerchof (1995) measured PRT distributions by means of pulse tracer analysis. They showed that the distribution plot contains a very long tail. Wide ranges of residence time

have been reported and suggested that the PRT distribution did not depend on the time consumed as airborne particle but also depended largely on the time a particle may slide down the cylindrical and conical section of the dryer wall.

19.4.4.5 Particle Collision and Agglomeration

Particle–particle collision is a significant phenomenon in spray processes. In the spray-drying process, especially for hygroscopic materials, droplet collision and agglomeration is desirable (e.g., milk, coffee, and detergent) to attain attractive product features (e.g., reduction of fine particles). Droplets collision effects depend on the droplet surface condition, which, depending on the droplet drying stage in spray drying, is not always a homogeneous liquid surface as (1) surface tension dominated, *std* (liquid surface), (2) viscous dominated, *vd* (solid/liquid mixture surface), and (3) dry particle, d_p (solid surface).

19.4.4.6 Agglomeration Model

Details on droplet/droplet collision modeling have been given in Section 19.2.1. Within spray drying, Ho and Sommerfeld (2002) developed a stochastic Lagrangian agglomeration model for dry-dry (d_p) particles. The interparticle collision model of Sommerfeld (2001) has been used. In addition, the collision efficiency due to the geometrical size difference (i.e., small particle hit the larger collector particle), as a function of Stokes number and agglomeration efficiency of dry-dry particle determined by the sticking potential due to van der Waals force, is taken into account. A critical velocity u_{cr} is calculated from energy balance according to the method coined by Hiller (1981). The formation of agglomerate takes place when

$$u_{rel} \cdot \cos\psi \leq u_{cr} \tag{19.194}$$

In the case of solid/liquid dispersion, Blei and Sommerfeld (2003) introduced a stochastic Lagrangian agglomeration model for the spray-drying process. The simulation model developed by Sommerfeld (1995, 2001) is used. Collision of particles with different material properties such as moisture content, density, and surface property (*std*, *vd* or d_p) are taken into account. The mathematical analysis is based on the assumptions of a fully plastic collision, nondeforming spherical droplet during collision and Newtonian fluid. The derivation of the model allows a droplet of higher viscosity to penetrate into a droplet of lower viscosity. Criteria and postcollision properties of different modes of collision pair are derived.

19.4.4.7 Industrial Practice of Agglomeration Processes in Spray Dryer

The processes and unit operations for agglomeration in spray dryer have been described by Louey and Refstrup (2001). According to their classification, the collision-agglomeration process is a forced-primary agglomeration, which is currently operated by using multiple pressure nozzles and fine return particle atomizer (fine particle fractions after separation from the product are mixed into the atomization zone). The relationship between fine return-liquid collision distance from atomizer and agglomerate structure has been discussed. If the collision between fine-return particles and atomized liquid occurs close to the liquid atomizer, the fine-return particle may penetrate into the liquid droplet, producing an "onion" structure of agglomeration, which has high bulk density and low dispersibility. At an optimum distance of collision, the fine return sticks onto the liquid droplet, producing a "compact grape" structure with good dispersibility and sufficient mechanical strength.

A numerical simulation tool of spray dryer flow conditions and process design including agglomeration in industrial scale food spray dryer is being developed as described by Verdurmen et al. (2003, 2004). Here, a computer simulation–based design tool is built, using an Euler–Lagrange approach with appropriate elementary models for drying, collision, coalescence, and agglomeration of the dispersed phase, as outlined in Figure 19.110. This design tool establishes relations among the configuration of the drying installation (geometry, nozzle selection), process conditions, product composition, and final powder properties.

19.4.4.8 Particle-Wall Deposition

Particle-wall deposition can lead to downtime cleaning, spoiled product, and potential fire hazards. The rate of deposition on the wall is thus the interesting parameter. Chen et al. (1993) investigated particle-wall deposition in an industrial spray dryer. Although the effects of operating parameters on wall deposition were not report quantitatively, they suggested the modification of the near-wall airflow and inlet air-temperature distribution could reduce wall deposition significantly. They also suggested that wall insulation could reduce wall deposition. It has been concluded that the effect of insulation was

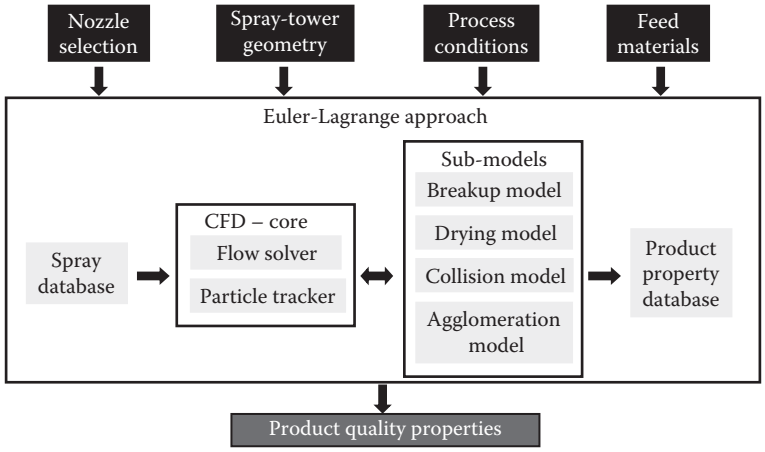


Figure 19.110

General structure of the CFD model for spray-drying process.

to increase the temperature close to the wall, thus preventing both vapor condensation and particles becoming too moist. On the other hand, Brennen et al. (1971) found that when the wall was too hot, more deposition was observed. So, low inlet air temperatures (<180°C) have been used for spray drying of sticky materials to keep the wall cool (Bhandari et al., 1992, 1993).

Ozmen and Langrish (2002) investigated the wall deposition of milk powder in a spray dryer. They measured the wall deposition in terms of wall deposition flux. The effect of inlet air swirl angle, air and chamber temperature and particle moisture content, wall material, and spray duration time on wall deposition flux was investigated. Increasing the angle of swirl from 0° to 30° increased the wall deposition flux by 30% although this increases air-spray mixing and evaporation rate. For temperature effects, if the temperature and moisture plot of a particle is above the sticky-point curve in a sticky point diagram (Hennigs et al., 2001), the wall deposition flux significantly increased (Figure 19.111). They concluded that the sticky point curve appeared to be the better indicator of the tendency for wall deposition flux. With respect to wall insulation, they reported significantly higher deposition flux with insulation compared to noninsulation. The investigation of the adhesion-cohesion process on the measuring plates showed that particle–particle cohesion (which led to agglomerate form) was the controlling process of wall deposition, so the near-wall particle dispersion is important. In this work, particle-wall adhesion had negligible effects on the wall deposition. The measuring surfaces were either nonstick food-grade material, adhesive tape, or stainless steel.

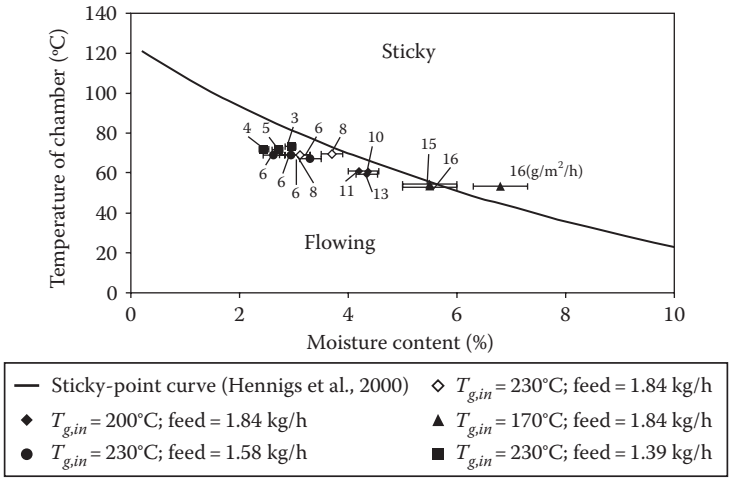


Figure 19.111

Operating condition and corresponding wall deposition fluxes on the sticky-point diagram for skim milk powder. (Adapted from Ozman et al., 2002.)

19.4.5 Spray Painting and Coating

Application of paints by spray processes provides protection and/or decoration of surfaces. Also, controlling of surface properties like roughness, friction control, fire protection, biological barriers, isolation, and so on are typically achieved by (spray) coating applications. Achieving specific surface quality and process yield (minimization of overspray) are the main aims of spray painting and coating processes. Typical yield of industrial spray painting processes sometimes is only about 70%.

In spray painting and coating applications, either pressure atomizers (here often called airless atomizer), twin-fluid atomizers (pneumatic atomizer), or rotary atomizers are used. Because of flexibility and easy application, pneumatic atomizers are most common in spray painting applications. Their disadvantage is the high overspray loss. Airless atomization is typically operated at 100–200 bar pressure and is used when higher throughput is to be achieved. Typical coating qualities are lower than those of pneumatic atomizers. For painting of large surface areas in combination with high-quality demand on optical coating properties (e.g., in automotive industry), so-called high-rotation atomizers (HR) are used. For increasing yield in paint applications, electrocharging of the droplets is used to decrease the overspray. Electrostatic fields in spray painting are also used to assist coating of back and hidden sides of substrates (Svejda, 2003). The different atomization principles result in different spray characteristics. Drop sizes and drop size/velocity correlations vary. Differences between overspray characteristics of a pneumatic atomizer and an HR atomizer are illustrated in Figure 19.112 (Goldschmidt and Streitberger, 2002). The drop size spectrum in pneumatic atomization typically is broader than in rotary atomization, because in pneumatic atomizer (at high gas velocities) the smaller particles are especially deflected by aerodynamic effects around the specimen to be coated. Here, in the spectrum of deposited particles, the smaller drop size fractions are missing (Figure 19.112a). By application of electrostatic forces, the overspray amount is reduced and the yield is increased. In rotary atomization, the larger particles preferably will not be deposited on the surface (even when assisted by an additional airflow). Therefore, in this case, the deposited drop size spectrum shows some missing larger droplets. When the charge of the particles is increased (higher voltage), the overspray amount is decreased (Figure 19.112b).

19.4.5.1 High-Rotation Atomization

For rotary atomization of paints, either disk- or cone-shaped atomizer-geometries are used. Typically, the disintegration mode of rotary atomization for paint applications is the lamella-mode (Goldschmidt and Streitberger, 2002). For increase of yield, in HR atomization, additional gas flow (called steering air flow) and/or electrostatic charging of the droplets are used (ESTA-HR: electrostatic-assisted high-rotation atomization). An HR atomizer consists of a bell and a drive (air drive). Depending on paint material and mass flow rate, HR atomizers are operated at 15,000–60,000 rpm. The bell diameter is typically about 50 mm with variations in geometry and bell edge surfaces. Charging of the paint material is achieved either by contact charging where the atomizer bell is connected to high voltage (typically 50–120 kV) or by ionization charging, where air ions are deposited on the droplet surface that result from outer free electrodes (see Figure 19.113). Contact charging is used for electrically nonconduction paints (e.g., paints based on organic solvents), while ionization charging is used for electrically conducting materials (e.g., in powder paint applications). The overall yields of ESTA-HR processes are in the order of 85%–90% (Svejda, 2003).

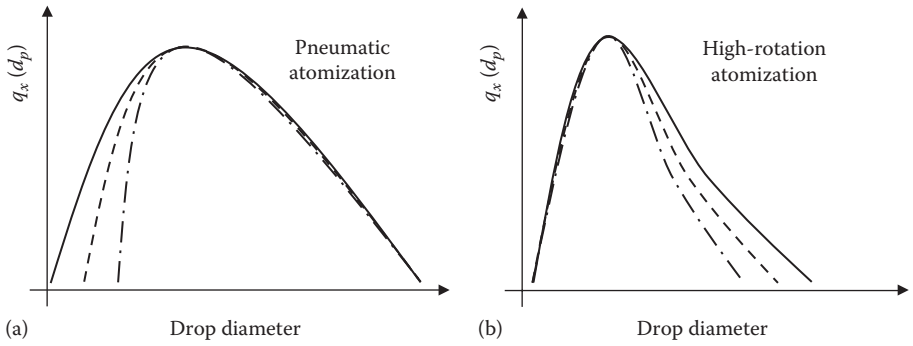


Figure 19.112

Overspray characteristic in coating process by means of pneumatic (a) and rotary (b) atomizer. (Adapted from Goldschmidt, A. and Streitberger, H.J., *BASF-Handbuch Lackiertechnik*, Vincentz Verlag, Hannover, Germany, 2002.)

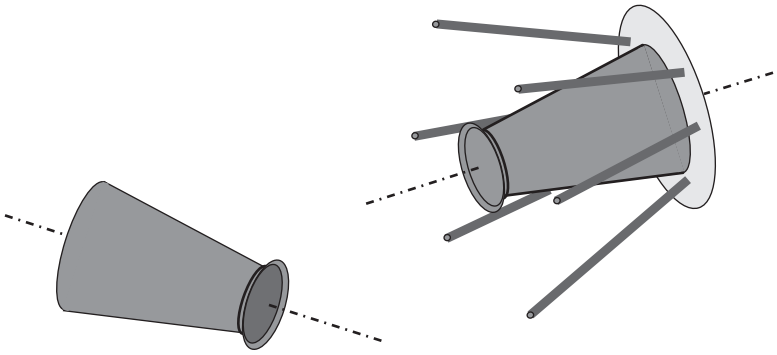


Figure 19.113

Droplet charging in electrostatic assisted coating applications.

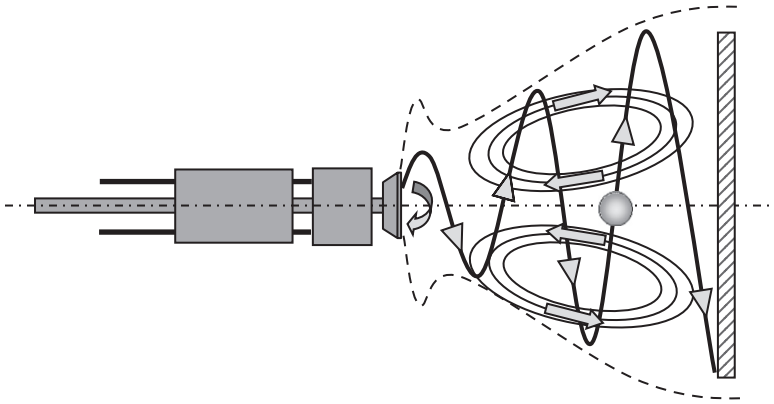


Figure 19.114

Droplet trajectories in ESTA-HR spray painting process. (From Scholz, T., Experimentelle Untersuchungen zur Mehrphasenströmung im Sprühkegel eines elktrostatisch unterstützten Hochrotationszerstäubers, Dissertation, Universität Bremen, VDI-Verlag, Düsseldorf, Germany, 1998. With permission.)

The spray geometry during ESTA-HR process is characterized by the interaction of aerodynamic, inertia, and electrostatic forces onto the droplets (Böttner et al., 1998, Böttner, 2002), resulting in deflection of the droplets toward the substrate in combination with the fragmentation process of the atomizer. Here, after fragmentation, the droplets are first centrifuged radially outward from the rotary atomizer. Steering air in the direction perpendicular to the substrate plus electrostatic forces onto the droplet deflect the droplets in the direction toward the surface. A model of the resulting droplet trajectories and airflow pattern is shown in Figure 19.114 (Scholz, 1998). A hollow cone spray geometry results, leading to a paint deposition characteristic that has a local minimum in the spray center and an off-center maximum (Svejda, 2003). The complex flow structure in the spray has been investigated experimentally (Scholz, 1998) and by numerical simulation (Domnick et al., 1997, 2003, 2005, 2006, 2009, Olivas and Marty, 2002). The gas flow field as a vector plot of the steering airflow of a rotating bell (45,000 rpm) obtained by simulation (Domnick et al., 2006) is illustrated in Figure 19.115. The velocity close to the bell edge is about 30 m/s. A large vortex can be seen located approximately three bell diameters downstream of the bell edge. In the center of this vortex, a recirculation region can be observed, transporting small paint droplets back to the bell.

In Domnick et al. (2009), the dynamic meshing approach has been chosen to calculate the unsteady grid between moving atomizer and fixed target. The calculation domain has basically been divided into a static zone (fixed target), a moving zone (moving atomizer), and a dynamic zone outside the major spray cone. Regarding the main purpose of these calculations, that is, the local thickness of the paint film on the target, the dynamic calculations are in agreement with experimental results. Local differences even on complex targets are typically less than 2 µm. The resulting dynamic deposition film thickness on a stationary flat target in this painting process is shown in Figure 19.116a comparing simulation and experiment. The hollow cone structure of the spray is reflected in the compaction pattern as a maximum in the radial distribution. The resulting dynamic deposition film thickness on a blended plate in this painting process is shown in Figure 19.116b, comparing simulation and experiment.



Figure 19.115

Simulated gas flow field in ESTA-HR spray painting process. (Adapted from Domnick, J. et al., *Part. Part. Syst. Charact.*, 23, 408, 2006. With permission.)

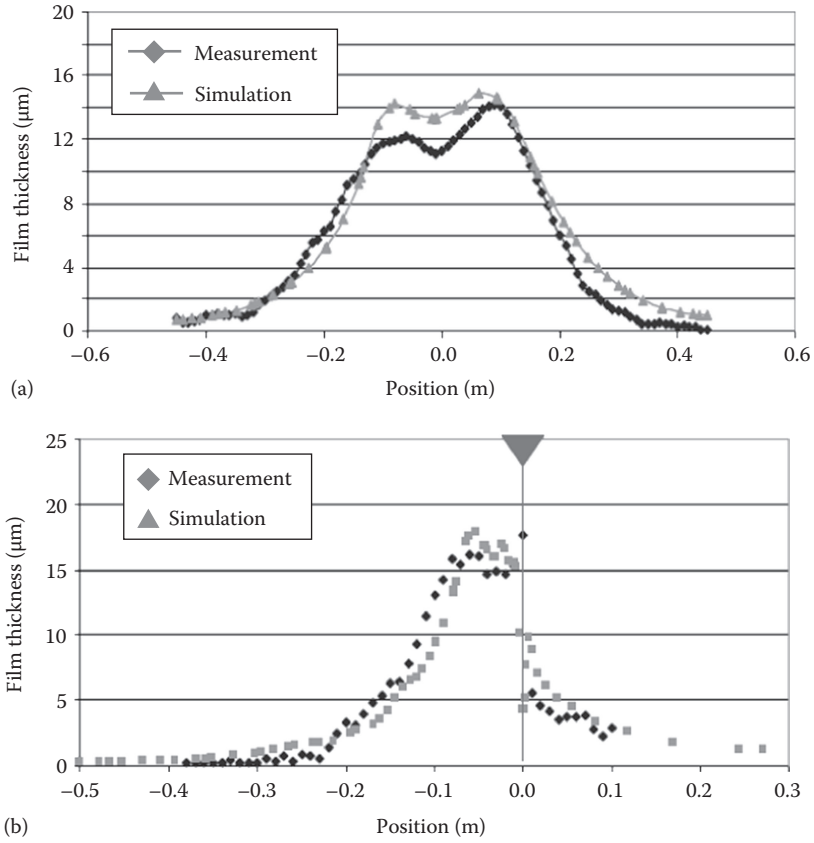


Figure 19.116

Derived dynamic coating thickness within electrostatic spray painting process with high-speed rotary atomizer: (a) on a flat plate; (b) on a blended plate. (Adapted from Domnick, J. et al., Unsteady simulation of the painting process with high speed rotary bells, in *Proceedings of International Conference on Liquid Atomization Spray Systems ICLASS 2009*, Vail, CO, 2009.)

References

Aalburg, C., van Leer, B., and Faeth, G.M., Deformation and drag properties of round drops subjected to shock-wave disturbances, *AIAA—J.*, 41(12), 2371–2378, 2003.

Aamir, M.A. and Watkins, A.P., Dense propane spray analysis with a modified collision model, CD-Rom, in *Proceedings of ILASS—Europe 99*, Toulouse, France, July 5–7, 1999.

Abdalrahman, K.H.M., Sabariman, I., and Specht, E., Influence of salt mixture on the heat transfer during spray cooling of hot metals, *Int. J. Heat Mass Transfer*, 78, 76–83, 2014.

Achelis, L., Drall-Druck-Gas-Zerstäubung von Metallschmelzen, Dissertation, Universität Bremen, Shaker-Verlag, Aachen, Germany, 2009.

Achelis, L., Meierhofer, F., Hodapp, M., Buss, L., Noriler, D., Meier, H.F., and Fritsching, U., Novel atomization process for large scale nanoparticle production by flame spray pyrolysis, in *ASME Proceedings of Multiphase Flow with Heat/Mass Transfer in Process Technology*, Chicago, Illinois, USA, August 3–7, 2014.

Achelis, L., Sulatycki, K., Uhlenwinkel, V., and Mädler, L., Spray angle and particle size in the pressure gas atomization of Tin and Tin-Copper alloys, in *Proceedings of PM 2010, Powder Metallurgy World Congress*, Florence, Italy, October 10–14, 2010.

Achelis, L. and Uhlenwinkel, V., Characterisation of metal powders generated by a pressure-gas-atomizer, *Mater. Sci. Eng. A*, 477, 15–20, 2008.

Agbaglah, G., Delaux, S., Fuster, D., Hoepffner, J., Josserand, C., Popinet, S., Ray, P., Scardovelli, R., and Zaleski, S., Parallel simulation of multiphase flows using octree adaptivity and the volume-of-fluid method, *Comptes Rendus Mecanique*, *High Perform. Comput.*, 339(2–3), 194–207, 2011.

Ahmadi, M. and Sellens, R.W., A simplified maximum-entropy-based drop size distribution, *Atom. Sprays*, 3, 292–310, 1993.

Alam, U., Experimental study of local heat transfer during quenching of metals by spray and multiple jets, PhD thesis, Otto von Guericke University of Magdeburg, Magdeburg, Germany, 2011.

Alam, U., Krol, J., Specht, E., and Schmidt, J., Enhancement and local regulation of metal quenching using atomized sprays, *J. ASTM Int.*, 5(10), 1–10, 2008.

Amsden, A.A., O'Rourke, P.J., and Butler, T.D., KIVA-II: A computer program for chemically reactive flows with sprays, Los Alamos National Laboratory, Report LA-11560-MS, NASA STI, Hampton, VA, 1989.

Anderson, I.E. and Figliola, R.S., Observations of gas atomization process dynamics, in P.U. Gummeson and D.A. Gustafson (Eds.), *Modern Developments in Powder Metallurgy*, Vol. 20, Metal Powder Industries Federation, Princeton, N.J., 1988, pp. 205–223.

Anderson, I.E. and Terpstra, R.L., Progress toward gas atomization processing with increased uniformity and control, *Mater. Sci. Eng. A*, 326(1), 101–109, 2002.

Annavarapu, S. and Doherty, R.D., Inhibited coarsening of solid–liquid microstructures in spray casting at high volume fractions of solid, *Acta Metall. Mater.*, 43(8), 3207–3230, 1995.

Anno, J.N., *The Mechanics of Liquid Jets*, Lexington Books, Lexington, MA, 1977.

Antipas, G., Lekakou, C., and Tsakiropoulos, P., The break-up of melt streams by high pressure gases in spray forming, in *Proceedings of the Second International Conference on Spray Forming (ICSF-2), Swansea,* UK, September 13–15, 1993, pp. 15–24.

Antipas, G.S.E., Review of gas atomisation and spray forming phenomenology, *Powder Metall.*, 56(4), 317–330, 2013.

Armster, S.Q., Delplanque, J.P., Rein, M., and Lavernia, E.J., Thermo-fluid mechanisms controlling droplet based materials processes, *Int. Mater. Rev.*, 47(6), 265–301, 2002.

Ashgriz, N., Numerical techniques for simulating the atomization process, in N. Ashgriz (Eds.), *Handbook of Atomization and Sprays*, Springer-Verlag, New York, 2011.

Ashgriz, N. and Poo, J.Y., Coalescence and separation in binary collision of liquid drops, *J. Fluid Mech.*, 221, 183–204, 1990.

Avvaru, B., Patil, M.N., Gogate, P.R., and Pandit, A.B., Ultrasonic atomization: Effect of liquid phase properties, *Ultrasonics*, 44, 146–158, 2006.

Badami, M., Bevilacqua, V., Millo, F., Chiodi, M., and Bargende, M., GDI swirl injector spray simulation: Combined phenomenological-CFD approach, SAE paper, 3005, SAE International, Warrendale, PA, 2004.

Bahlawane, N., Systematic microstructural investigation of alumina deposited by liquid fuel combustion chemical vapor deposition, *Surf. Coat. Technol.*, 200(12–13), 4097–4103, 2006.

Ballester, J. and Dopazo, C., Discharge coefficient and spray angle measurements for small pressure-swirl nozzles, *Atom. Sprays*, 4(3), 351–367, 1994.
Bartz, F.O., Guildenbecher, D.R., Schmehl, R., Koch, R., Bauer, H.J., and Sojka, P.E., Model comparison for single droplet fragmentation under varying accelerations, in *Proceedings of ILASS-Europe 2011*, Estoril, Portugal, September 5–7, 2011.
Bartz, F.O., Schmehl, R., Koch, R., and Bauer, H.J., An extension of dynamic droplet deformation models to secondary atomization, in *Proceedings of ILASS—Europe 2010*, Brno, Czech Republic, September 6–8, 2010.
Bauckhage, K., Das Zerstäuben metallischer Schmelzen, *Chem. Ing. Techn.*, 64(4), 322–332, 1992.
Bauckhage, K., Stand der Technik beim Sprühkompktieren von Bolzen, *Härterei-Techn. Mitteil.*, 52(5), 319–331, 1997.
Bauckhage, K., Anderson, O., and Schreckenberg, P., Production of fine powders by ultrasonic standing wave atomization, *Powder Technology*, 86(1), 77–86, 1996.
Bauckhage, K., Use of the phase-doppler-anemometry for the analysis and the control of the spray forming process, in *Proceedings of PM²TEC'98*, Las Vegas, NV, May 31–June 4, 1998.
Bauckhage, K., Fundamentals of melt atomization, spray forming and deposition, in *Proceedings of the International Conference on Liquid Atomization and Spray Systems ICLASS 2003*, Sorrento, Italy, 2003.
Bauckhage, K., Bergmann, D., Fritsching, U., Lohner, H., Schreckenberg, P., and Uhlenwinkel, V., Das Scaling-Down-Problem bei der Zweistoffzerstäubung von Metallschmelzen, *Chem. Ing. Techn.*, 73(4), 304–313, 2001.
Bauckhage, K., Bergmann, D., and Tillwick, J., Die Massen- und Enthalpiebilanzierung des Sprühkegels als Kopplung für die Modellvorstellung des Materialaufbaus in der Mix-Schicht, in *Koll. SFB 372*, Vol. 4, University of Bremen, Bremen, Germany, 1999, pp. 139–170.
Bauckhage, K. and Fritsching, U., Production of metal powders by gas atomization, in K.P. Cooper, I.E. Anderson, S.D. Ridder, and F.S. Biancanello (Eds.), *Liquid Metal Atomization: Fundamentals and Practice*, TMS, Warrendale, PA, 2000, pp. 23–36.
Bauman, S.D., A spray model for an adaptive mesh refinement code, PhD thesis, Madison University, Wiconsin, WI, 2001.
Bayvel, L. and Orzechowski, Z., *Liquid Atomization*, Taylor & Francis Publishers, Washington, DC, 1993.
Beale, J.C. and Reitz, R.D., Modeling spray atomization with the Kelvin-Helmholtz/Rayleigh-Taylor hybrid model, *Atom. Sprays*, 9, 623–650, 1999.
Bellan, J., Perspectives on large eddy simulations for sprays: Issues and solutions, *Atom. Sprays*, 10, 409–425, 2000.
Berg, M., Zum Aufprall, zur Ausbreitung und Zerteilung von Schmelzetropfen aus reinen Metallen, Dissertation, Universität Bremen, Bremen, Germany, 1999.
Berg, M. and Ulrich, J., Experimental based detection of the splash limits for the normal and oblique impact of molten metal particles on different substrates, *J. Mater. Synth. Proc.*, 5(1), 45–49, 1997.
Bergmann, D., Modellierung des Sprühkompaktierprozesses für Kupfer- und Stahlwerkstoffe, Dissertation, Universität Bremen, Bremen, Germany, 2000.
Bergmann, D., Fritsching, U., and Bauckhage, K., Averaging thermal conditions in molten metal sprays, in B. Mishra (Ed.), *Proceedings of TMS—Annual Meeting, EPD Congress*, San Diego, CA, February 28–March 4, 1999.
Bergmann, D., Fritsching, U., and Bauckhage, K., A mathematical model for cooling and rapid solidification of molten metal droplets, *Int. J. Therm. Sci.*, 39, 53–62, 2000.
Bergmann, D., Fritsching, U., and Bauckhage, K., Simulation of molten metal droplet sprays, *Comp. Fluid Dynam.—J.*, 9, 203–211, 2001a.
Bergmann, D., Fritsching, U., and Bauckhage, K., Thermische simulation des Sprühkompaktierprozesses, *Härterei-Techn. Mitteil.*, 56(2), 110–119, 2001b.
Bergmann, D., Fritsching, U., and Crowe, C.T., Multiphase flows in the spray forming process, in *Proceedings of the Second International Conference on Multiphase Flow*, Kyoto, Japan, Vol. 1, April 3–7, 1995, pp. SP1–SP8.
Bergström, C., Fuchs, L., and Holmborn, J., large eddy simulation of spray injected in a strong turbulent cross flow, in *CD-Rom Proceedings of ILASS-Europe 99*, Toulouse, France, July 5–7, 1999.
Bhandari, B.R., Dumoulin, E.D., Richard, H.M.J., Noleau, I., and Lebert, A.M., Flavor encapsulation by spray drying: Application to Citral and Linalyl Acetate, *J. Food Sci.*, 57(1), 217–221, 1992.
Bhandari, B.R., Senoussi, A., Dumoulin, E.D., and Lebert, A., Spray drying of Concentrated fruit juices, *Dry. Technol.*, 11(5), 1081–1092, 1993.

Bianchi, G.M., Minelli, F., Scardovelli, R., and Zaleski, S., 3D large scale simulation of the high-speed liquid jet atomization, SAE paper, 2007-01-0244, 2007.
Blei, S. and Sommerfeld, M., Lagrangian modelling of agglomeration during spray drying process, in *Ninth International Conference on Liquid Atomization and Spray Systems* (*ICLASS 2003*), Sorrento, Italy, 2003.
Blokkeel, G., Borghi, R., and Barbeau, B., A 3d Eulerian model to improve the primary breakup of atomizing jet, SAE paper, 2003-01-0005, 2003.
Bolle, L. and Moureau, J.C., Spray cooling of hot surfaces, *Multiphase Sci. Technol.*, 1, 1–97, 1982.
Böttner, C.U., *Über den Einfluss der elektrostatischen Feldkraft auf turbulente Zweiphasenströmungen*, Diss. Univ. Halle-Wittenberg, 2002.
Böttner, C.U., Kohnen, G., and Sommerfeld, M., Numerical calculations of the interaction between fluid dynamics and electrostatics applied to the powder painting process, in *Proceedings of ILASS-Europe '98*, Manchester, U.K., 1998.
Bracco, F.V., Chehroudi, B., Chen, S.H., and Onuma, Y., On the intact core of full cone sprays, *SAE Trans.*, 94, Paper 850126, 1985.
Brackbill, J.U., Kothe, D.B., and Zemach, C., A continuum method for modelling surface tension, *J. Comp. Phys.*, 100, 335–354, 1992.
Bradley, D., On the atomization of liquids by high-velocity gases, Part 1, *J. Phys. D Appl. Phys.*, 6, 1724–1736, 1973a.
Bradley, D., On the atomization of liquids by high-velocity gases, Part 2, J. *Phys. D Appl. Phys.*, 6, 2267–2272, 1973b.
Bradley, S.G. and Stow, C.D., Collision between liquid drops, *Philos. Trans. R. Soc. Lond. Ser. A*, 287, 635–675, 1978.
Brauer, H., *Grundlagen der Einphasen- und Mehrphasenströmungen*, Sauerländer Verlag, Frankfurt, Germany, 1971.
Brenn, G., Concentration fields in evaporating droplets, *Int. J. Heat Mass Transfer*, 48, 395–402, 2005.
Brenn, G., Droplet collision, in N. Ashgriz (Ed.), *Handbook of Atomization and Sprays*, Springer-Verlag, New York, 2011.
Brenn, G. and Kolobaric, V., Satellite droplet formation by unstable binary drop collisions, *Phys. Fluids*, 18, 087101, 1–18, 2006.
Brenn, G., Valkovska, D., and Danov, K.D., The formation of satellite droplets by unstable binary drop collisions, *Phys. Fluids*, 13(9), 2463–2477, 2001b.
Brenn, G., Wiedemann, T., Rensink, D., Kastner, O., and Yarin, A.L., Modeling and experimental investigation of the morphology of spray dryed particles, *Chem. Eng. Technol.*, 24(11), 1113–1116, 2001a.
Brennen, J.G., Herrera, J., and Jowitt, R., A study of some other factors affecting the spray drying of concentrated orange juice on a laboratory scale, *J. Food Technol.*, 6, 295–307, 1971.
Brimacombe, J.K., Agarwal, P.K., Baptista, L.A., Hibbins, S., and Prabhakar, B., Spray cooling in the continuous casting of steel, in *Proceedings of 63rd National Open Hearth and Basic Oxygen Steel Conference*, Washington, DC, 1980, pp. 235–252.
Brodkey, R.S., *The Phenomena of Fluid Motions*, Addison-Wesley Press, Boston, 1967.
Broll, P., *Erfassung der Lamellenparameter an Hohlkegeldüsen*, Diss. Univ. Dortmund, Shaker-Verlag, Aachen, Germany, 2006.
Bruin, S., Velocity distributions in a liquid film flowing over a rotating conical surface, *Chem. Eng. Sci.*, 24(11), 1647–1654, 1969.
Buchholz, M., Uhlenwinkel, V., von Freyberg, A., and Bauckhage, K., Specific enthalpy measurement in molten metal spray, *Mater. Sci. Eng. A*, 326(1), 165–175, 2002.
Buckner, H.N. and Sojka, P.E., Effervescent atomization of high-viscosity fluids: Part I: Newtonian liquids, *Atom. Sprays*, 1, 239–252, 1991.
Bürger, M., Schwalbe, W., Kim, D.S., Unger, H., Hohmann, H., and Schins, H., Two-phase description of hydrodynamic fragmentation processes within thermal detonation waves, *J. Heat Transfer*, 106, 728–734, 1984.
Bürger, M., von Berg, E., Cho, S.H., and Schatz, A., Fragmentation processes in gas and water atomization plants for process optimization purposes, Part 1: Discussion of the main fragmentation processes, *Powder Metall. Int.*, 21(6), 10–15, 1989.
Bürger, M., von Berg, E., Cho, S.H., and Schatz, A., Analysis of fragmentation processes in gas and water atomization plants for process optimization purposes, Part 2: Modelling of growth and stripping of capillary waves in parallel shear flow-the basic fragmentation mechanism, *Powder Metall. Int.*, 24(6), 32–38, 1992.

Bussmann, M., Aziz, S.D., and Chandra, S., Photographs and simulations of molten metal droplets landing on a solid surface, *J. Heat Transfer*, 122, 422, 2000.
Campanile, F. and Azzopardi, B.J., Atomisation of very viscous liquids, in *Proceedings of International Conference on Liquid Atomization and Spray Systems ICLASS 2003*, Sorrento, Italy, 2003.
Cao, X.K., Sun, Z.G., Li, W.F., Liu, H.F., and Yu, Z.H., A new breakup regime for liquid drops identified in a continuous and uniform air jet flow, *Phys. Fluid*, 19(5), 057103, 2007.
Cava, R., Uhlenwinkel, V., Ellendt, N., Santos, R.C.M., Kiminami, C.S., and Bolfarini, C., Spray forming of iron based $Fe_{43.2}Co_{28.8}B_{19.2}Si_{4.8}Nb_4$ glass forming alloy, in *Proceedings of SDMA 2013—Fifth International Conference on Spray Deposition and Melt Atomization*, Bremen, Germany, September 23–25, 2013.
Charojrochkul, S., Choy, K.L., and Steele, B.C.H., Cathode/electrolyte systems for solid oxide fuel cells fabricated using flame assisted vapour deposition technique, *Solid State Ionics*, 121, 107–113, 1999.
Chavez, H. and Obermeier, F., Modelling the effect of modulations of the injection velocity on the structure of liquid jets, in *Proceedings of SPRAY 2002*, Freiburg, Germany, 2002.
Chawla, J.M., Flüssigkeitsinhalt in Rohren für Flüssigkeits/Gas-Gemische bei der Zweiphasenströmung, *Chem. Ing. Techn.*, 5+6, 328–330, 1969.
Chawla, J.M., Atomization of liquids employing the low sonic velocity in liquid/gas mixtures, in *Proceedings of ICLASS 1985*, London, U.K., July 8–10, 1985.
Chawla, J.M. and von Böckh, P., Kritische Massenstromdichte von Fl¨ussigkeits/Gas-Gemischen, *Chem. Ing. Techn.*, 43(20), 1106–1108, 1971.
Chen, X.D., Lake, R., and Jebson, S., Study of milk powder deposition on a large industrial dryer, *Food Bioprod. Process.: Trans. Inst. Chem. Eng., C*, 71(3), 180–186, 1993.
Chen, S.K. and Lefebvre, A.H., Discharge coefficients for plain-orifice effervescent atomizers, *Atom. Sprays*, 4, 275–290, 1994.
Chen, X.D. and Lin, S.X.Q., Air drying of milk droplet under constant and time-dependent conditions, *AIChE J.*, 51(6), 1790–1799, 2005.
Chen, X.D. and Putranto, A., *Modelling Drying Processes: A Reaction Engineering Approach*, Cambridge University Press, New York, 2013.
Chen, X.D. and Xie, G.Z., Fingerprints of the drying behaviour of particulate or thin layer food materials established using a reaction engineering model, *Trans. IChemE*, 75(C), 213–222, 1997.
Chesnel, J., Menard, T., Reveillon, J., and Demoulin, F.X., Subgrid analysis of liquid jet atomization, *Atom. Sprays*, 21(1), 41–67, 2011a.
Chesnel, J., Reveillon, J., Menard, T., and Demoulin, F.X., Large eddy simulation of liquid jet atomization, *Atom. Sprays*, 21(9), 711–736, 2011b.
Chin, J.S. and Lefebvre, A.H., Flow patterns in internal-mixing, twin-fluid atomizers, *Atom. Sprays*, 3, 463–475, 1993.
Choi, K.J. and Kang, B.S., Fluid mechanics and heat transfer in sprays, in *ASME FED*, 78, HTD, Vol. 270, New Orleans, LA, November 28–December 3, 1993, pp. 161–165.
Choi, K.J. and Yao, S.C., Mechanisms of film boiling heat transfer of normally impacting spray, *Int. J. Heat Mass Transfer*, 30(2), 311–318, 1987.
Chou, W.-H. and Faeth, G.M., Temporal Properties of secondary drop breakup in the bag breakup regime, *Int. J. Multiphase Flow*, 24, 889–912, 1998.
Chou, W.-H., Hsiang, L.-P., and Faeth, G.M., Temporal properties of drop breakup in the shear breakup regime, *Int. J. Multiphase Flow*, 23(4), 651–670, 1997.
Chryssakis, C. and Assanis, D.N., A unified fuel spray breakup model for internal combustion engine applications, *Atom. Sprays*, 18, 1–52, 2008.
Churchill, S.W. and Usagi, R., A General expression for the correlation of rates of transfer and other phenomena, *AIChE Journal*, 18, 1121–1128, 1972.
Clift, R., Grace, J.R., and Weber, M.E., *Bubbles, Drops and Particles*, Academic Press, San Diego, CA, 1978.
Conelly, S., Coombs, J.S., and Medwell, J.O., Flow characteristics of metal particles in atomised sprays, *Metal Powder Rep.*, 41, 9, 1986.
Cooper, D. and Yule, A.J., Waves on the air core/liquid interface of a pressure swirl atomizer, in *Proceedings of ILASS-Europe 2001*, Zurich, Switzerland, September 2–6, 2001.
Corbinelli, G., Befrui, B., and Reckers, W., Large eddy simulation and optical studies of the primary break-up of a thin planar-sheet liquid jet, *SAE Int. J. Fuels Lubr.*, 3(1), 266-276, 2010, doi:10.4271/2010-01-0622.
Cousin, J. and Dumouchel, C., Effect of viscosity on the linear instability of a liquid sheet, *Atom. Sprays*, 6, 563–576, 1996.
Cousin, J. and Dumouchel, C., Theoretical determination of spray drop size distribution, in *Proceedings of ICLASS-'97*, Seoul, Korea, August 1997, Part 1: Description of the Procedure, pp. 788–795, Part 2: Applications, pp. 796–803.

Cousin, J., Yoon, S.J., and Dumouchel, C., Coupling of the classical linear theory and the maximum entropy formalism for the prediction of drop size distributions in sprays, application to pressure swirl atomizers, *Atom. Sprays*, 6(5), 601–613, 1996.
Crowe, C.T., Modelling spray-air contact in spray drying systems, *Adv. Dry.*, 1(3), 63–99, 1980.
Crowe, C.T., Sharma, M.P., and Stock, D.E., The particle-source-in-cell method for gas droplet flow, *J. Fluids Eng.*, 99, 325–332, 1977.
Crowe, C.T., Sommerfeld, M., and Tsuji, Y., *Multiphase Flows with Drops and Particles*, CRC Press, Boca Raton, FL, 1998.
Cui, C., Schulz, A., and Uhlenwinkel, V., Co-spray forming of gradient deposits from two sprays of different tool steels using scanning gas atomizers, *Steel Res. Int.*, 84(11), 1075–84, 2013.
Cui, C., Schulz, A., Uhlenwinkel, V., Zobel, F., and Zoch, H.W., Spray forming of stainless steel matrix composites with injection of hard particulates, *Materialwiss. Werkstofftech.*, 41(7), 524–531, 2010.
Czisch, C. and Fritsching, U., Atomizer design for viscous-melt atomization, *Mater. Sci. Eng. A*, 477, 21–25, 2008a.
Czisch, C. and Fritsching, U., Flow-adapted design option for free-fall atomizers, *Atom. Sprays*, 18, 511–522, 2008b.
Czisch, C., Lohner, H., Fritsching, U., and Bauckhage, K., Atomization of highly viscous melts, in *Proceedings of Spray Deposition and Melt Atomization SDMA 2003*, Bremen, Germany, 2003.
Dai, Z. and Faeth, G.M., Temporal properties of secondary drop breakup in the multimode breakup regime, *Int. J. Multiphase Flow*, 27(2), 217–236, 2001.
Davies, J.T., Drop sizes of emulsion related to turbulent energy dissipation rates, *CES*, 40(5), 839–842, 1985.
de Villiers, E., Gosman, A.D., and Weller, H.G., Large eddy simulation of primary diesel spray atomization, SAE Technical Paper, Paper#2004-01-0100, 1–16, 2004, doi:10.4271/2004-01-0100.
Dec, J.E., A conceptual model of DI diesel combustion based on laser-sheet imaging, SAE paper 970873, 1997.
Delplanque, J.P. and Sirignano, W.A., Boundary-layer stripping effects on droplet transcritical convective vaporization, *Atom. Sprays*, 4(3), 325–349, 1994.
Delshad Khatibi, P. and Henein, H., The robustness of the two-colour assumption in pyrometry of solidifying AISI D2 alloy droplets, *Materialwiss. Werkstofftech.*, 45(8), 736–743, 2014.
Delshad Khatibi, P., Ilbagi, A., Beinker, D., and Henein, H., In-situ characterization of droplets during free fall in the drop tube-impulse system, *J. Phys. Conf. Ser.*, 327, 012014, 2011.
Deng, S., Pingali, K.C., and Rockstraw, D.A., Synthesis of Ru–Ni core–shell nanoparticles for potential sensor applications, *IEEE Sens. J.*, 8(6), 730–734, 2008.
Desjardins, O., Detailed numerical investigation of turbulent atomization of liquid jets, in *Proceedings of International Conference on Liquid Atomization and Spray Systems ICLASS 2009*, Vail, CO, 2009.
Desjardins, O., McCaslin, J.O., Owkes, M., and Brady, P., Direct numerical and large-eddy simulation of primary atomization in complex geometries, *Atom. Sprays*, 23(11), 1001–1048, 2013.
Desjardins, O., Moureau, V., and Pitsch, H., An accurate conservative level set/ghost fluid method for simulating turbulent atomization, *J. Comput. Phys.*, 227, 8395–8416, 2008.
Dielewicz, L.G., von Berg, E., and Lampe, M., Computation of transsonic two-phase flow in liquid metal jet atomizers, in *CD-Rom Proceedings of ILASS-Europe 99*, Toulouse, France, July 5–7, 1999.
Djuric, Z. and Grant, P.S., Two dimensional simulation of liquid metal spray deposition onto a complex surface II: Splashing and redeposition, *Model. Simul. Mater. Sci. Eng.*, 9, 111–127, 2001.
Djuric, Z., Newberry, P., and Grant, P.S., Two dimensional simulation of liquid metal spray deposition onto a complex surface, *Model. Simul. Mater. Sci. Eng.*, 7, 553–571, 1999.
Dobre, M. and Bolle, L., Theoretical prediction of ultrasonic spray characteristics using the maximum entropy formalism, in A.J. Yule (Ed.), *Proceedings of ILASS-Europe '98*, Manchester, U.K., July 6–8, 1998, pp. 7–12.
Doherty, R., Cai, C., and Warner Kohler, L.K., Modeling and microstructure development in spray forming, *Int. J. Powder Metall.*, 33(3), 50–60, 1997.
Dolinsky, A.A., High temperature spray drying, *Dry. Technol.*, 19(5), 785–806, 2001.
Dombrowski, N. and Fraser, R.P., A photographic investigation into the disintergration of liquid Sheets, *Philos. Trans. R. Soc. Lond., Ser. A*, 247(924), 101–130, 1954.
Dombrowski, N. and Johns, W.R., The aerodynamic instability and disintegration of viscous liquid sheets, *Chem. Eng. Sci.*, 18, 203–214, 1963.
Domnick, J., Raimann, J., Wolf, G., Berlemont, A., and Cabot, M.-S., On-line process control in melt spraying using phase-doppler anemometry, in *Proceedings of ICLASS-'97*, Seoul, Korea, August 18–22, 1997.
Domnick, J., Scheibe, A., and Ye, Q., The electrostatic spray painting process with High-Speed rotary bell atomizers: Influences of operating conditions and target geometries, in *Proceedings of International Conference on Liquid Atomization Spray Systems ICLASS 2003*, Sorrento, Italy, 2003.

Domnick, J., Scheibe, A., and Ye, Q., The simulation of the electrostatic spray painting process with high-speed rotary bell atomizers. Part I: Direct charging, *Part. Part. Syst. Charact.*, 22, 141–150, 2005.
Domnick, J., Scheibe, A., and Ye, Q., The simulation of the electrostatic spray painting process with high-speed rotary bell atomizers. Part II: External charging, *Part. Part. Syst. Charact.*, 23, 408–416, 2006.
Domnick, J., Scheibe, A., and Ye, Q., Unsteady simulation of the painting process with high speed rotary bells, in *Proceedings of International Conference on Liquid Atomization Spray Systems ICLASS 2009*, Vail, CO, 2009.
Donjat, D., Estivalezes, J.L., Michau, M., and Lavergne, G., Phenomenological study of the pressure swirl atomizer internal flow, in *Proceedings of International Conference on Liquid Atomization Spray Systems ICLASS 2003*, Sorrento, Italy, 2003.
Dubrovsky, V.V., Podvysotsky, A.M., and Shraiber, A.A., Particle interaction in three-phase polydispersed flows., *Int. J. Multiphase Flow*, 18(3), 337–352, 1992.
Duda, J.L. and Vrentas, J.S., Fluid mechanics of laminar liquid jets, *Chem. Eng. Sci.*, 22, 855–873, 1967.
Dumouchel, C., Problemes lies a la d ún pulverizateur mecanique-hydrodynamique de chambre et instabilite de nappe, PhD thesis, University Rouen, France, 1989.
Dunkley, J.J., Liquid metal atomization—A suitable case for investigation, in A.J. Yule (Ed.), *Proceedings of ILASS-Europe '98*, Manchester, U.K., July 6–8, 1998, pp. P1–P6.
Dunkley, J.J. and Telford, B., Control of satellite particles in gas atomization, in *Proceedings of World Congress on Powder Metallurgy and Particulate Materials PM²TEC 2002*, Orlando, FL, 2002.
Edwards, C.F. and Marx, K.D., Multipoint statistical structure of the ideal spray, Part I: Fundamental concepts and the realization density, *Atom. Sprays*, 5, 435–455, 1995a.
Edwards, C.F. and Marx, K.D., Multipoint statistical structure of the ideal spray, Part II: Evaluating steadiness using the interparticle time distribution, *Atom. Sprays*, 5, 457–505, 1995b.
Ellendt, N., Uhlenwinkel, V., Ahmetovic, A., Boddez, L., and Henein, H., Quality of Sn-Ag-powders production by drop-on-demand technique, in *Proceedings of PM 2008*, Washington, DC, June 8–12, 2008.
Elperin, T. and Krasovitov, B., Evaporation of liquid droplets containing small solid particles, *Int. J. Heat Mass Transfer*, 38(12), 2259–2267, 1995.
Eslamian, M., Ahmed, M., and Ashgriz, N., Modeling of nanoparticle formation during spray pyrolysis, *Nanotechnology*, 17, 1674–1685, 2006.
Eslamian, M., Ahmed, M., and Ashgriz, N., Modeling of solution droplet evaporation and particle evolution in droplet-to-particle spray methods, *Dry. Technol.*, 27, 3–13, 2009.
Eslamian, M. and Ashgriz, N., Effect of atomization method on the morphology of spray generated particles, *ASME J. Eng. Mater. Technol.*, 129(1), 130–142, 2007.
Eslamian, M. and Ashgriz, N., Swirl, T-jet and vibrating-mesh atomizers, in N. Ashgriz (Ed.), *Handbook of Atomization and Sprays*, Springer-Verlag, New York, 2011.
Eslamian, M., Rak, J., Ashgriz, N., Preparation of aluminum/silicon carbide metal matrix composites using centrifugal atomization, *Powder Technol.*, 184, 11–20, 2008.
Espina, P.I., Numerical simulation of atomization gas flow, in *Koll. SFB 372*, Vol. 4, University of Bremen, Bremen, Germany, 1999, pp. 127–138.
Espina, P.I. and Piomelli, U., Numerical simulation of the gas flow in gas metal atomizers, in *Proceedings of 1998 ASME-FED*, Washington, DC, FEDSM98-4901, 1998a.
Espina, P.I. and Piomelli, U., Study of the gas jet in a close-coupled gas metal atomizer, in *36th AIAA Aerospace Sciences Meeting and Exhibit,* Reno, NV, U.S.A.*, 1998b,* Paper 98-0959.
Faeth, G.M., Structure and atomization properties of dense turbulent sprays, in *23rd Symposium on Combustion*, The Combustion Institute, Pittsburgh, PA, 1990, pp. 1345–1352.
Faeth, G.M., Dynamics of secondary drop breakup—A rate controlling process in dense sprays, in *Proceedings of ILASS-Europe 2002*, Zaragoza, Spain, September 9–11, 2002.
Faeth, G.M., Hsiang, L.P., and Wu, P.K., Structure and breakup properties of spray, *Int. J. Multiphase Flow*, 21(Suppl.), 99–127, 1995.
Faragó, Z. and Chigier, N., Morphological classification of disintegration of round liquid jets in a coaxial air stream, *Atom. Sprays*, 2, 137–153, 1992.
Ferrari, G., Meerdink, G., and Walstra, P., Drying kinetics for a single droplet of skimmed milk, *J. Food Eng.*, 10, 215–230, 1989.
Focke, C. and Bothe, D., Computational analysis of binary collisions of shear thinning droplets, *J. Non-Newtonian Fluid Mech.*, 166, 799–810, 2011.
Focke, C. and Bothe, D., Direct numerical simulation of binary off-center collisions of shear thinning droplets at high Weber numbers, *Phys. Fluids*, 24, 073105, 1–18, 2012.
Fraser, R.P. and Eisenklam, P., Research into the performance of atomizers of liquids, *Imp. Colloid Chem. Eng. Soc. J.*, 7, 52–68, 1953.
Fraser, R.P., Eisenklam, P., Dombrowski, N., and Hasson, D., Drop formation from rapidly moving liquid sheets, *AICheE J.*, 8, 672–680, 1962.

Fritsching, U., Modelling the spray cone behaviour in the metal spray forming process: Momentum and thermal coupling in two-phase flow, *Phoenics J. Comp. Fluid Dyn.*, 8(1), 68–90, 1995.
Fritsching, U., *Spraysimulation—Modellierung und numerische Simulation von verfahrenstechnischen Prozessen am Beispiel des Sprühkompaktierens von Metallen*, Shaker Verlag, Aachen, Germany, 2001.
Fritsching, U., *Spray Simulation: Modeling and Numerical Simulation of Sprayforming Metals*, Cambridge University Press, Cambridge, U.K., 2004.
Fritsching, U. and Bauckhage, K., Die Bewegung von Tropfen im Sprühkegel einer Ein- und einer Zweistoffdüse, *Chem. Ing. Techn.*, 59(9), 744–745, 1987.
Fritsching, U. and Bauckhage, K., Investigations on the atomization of molten metals: The coaxial jet and the gas flow in the nozzle near field, *Phoenics J. Comp. Fluid Dyn.*, 5(1), 81–98, 1992.
Fritsching, U. and Bauckhage, K., Zum Impuls- und Wärmetransport bei der Zerstäubung und anschließenden Kompaktierung von Schmelzen, *Chem. Ing. Techn.*, 66(3), 380–382, 1994.
Fritsching, U. and Bauckhage, K., Sprayforming of metals, *Ullmann's Encyclopedia of Industrial Chemistry*, 6th edn., 1999 Electronic Release, Wiley VCH, Weinheim, Germany, 1999.
Fritsching, U. and Gao, S., Droplet-particle collisions in intersecting melt sprays, *Atom. Sprays*, 20(1), 31–40, 2010.
Fritsching, U. and Uhlenwinkel, V., Hybrid gas atomization for powder production, in K. Kondoh (Ed.), *Powder Metallurgy*, InTech Publisher, Rijeka, Croatia, 2012, pp. 99–124.
Fritsching, U., Zhang, H., and Bauckhage, K., Thermal histories of atomized and compacted metals, in *Proceedings of Powder Metallurgy World Congress PM-93*, Kyoto, Japan, July 12–15, 1993.
Fritsching, U., Zhang, H., and Bauckhage, K., Numerical simulation of temperature distribution and solidification behaviour during spray forming, *Steel Res.*, 65(7), 273–278, 1994a.
Fritsching, U., Zhang, H., and Bauckhage, K., Numerical results of temperature distribution and solidification behaviour during spray forming, *Steel Res.*, 65(8), 322–325, 1994b.
Frohn, A. and Roth, N., *Dynamics of Droplets*, Springer Verlag, Berlin, Germany, 2000.
Fuster, D., Bague, A., Boeck, T., Le Moyne, L., Leboissetier, A., Popinet, S., Ray, P., Scardovelli, R., and Zaleski, S., Simulation of primary atomization with an octree adaptive mesh refinement and VOF method, *Int. J. Multiphase Flow*, 35(6), 550–565, 2009.
Fyhr, C. and Kemp, I.C., Comparison of different drying kinetics models for single particles, *Dry. Technol.*, 16(7), 1339–1369, 1998.
Gao, S. and Fritsching, U., Study of binary in-flight melt droplet collisions, *Materialwiss. Werkstofftech.*, 41(7), 547–554, 2010.
Garcia-Oliver, J.M., Pastor, J.M., Pandal, A., Trask, N., Baldwin, E., and Schmidt, D.P., Diesel spray CFD simulations based on the Σ-Υ Eulerian atomization model, *Atom. Sprays*, 23(1), 71–95, 2013.
Gelfand, B.E., Droplet breakup phenomena in flows with velocity lag, *Prog. Energy Combust. Sci.*, 22, 201–265, 1996.
Gelfand, B.E., Gubin, S.A., Kogarko, S.M., and Kormar, S.P., Viscous drop destruction peculiarities in shock waves, *J. Eng. Phys.* (The Faraday Press cover-to-cover transl. of *Inzhenerno-fizicheskii zhurnal*), 25(3), 467–471, 1973.
Georjon, T.L. and Reitz, R.D., A drop-shattering collision model for multidimensional spray computations, *Atom. Sprays*, 9, 231–254, 1999.
Gerking, L., Powder from metal and ceramic melts by laminar streams at supersonic speed, *Powder Metall. Int.*, 25(2), 59–65, 1993.
Giffen, E. and Muraszew, A., *The Atomization of Liquid Fuels*, John Wiley & Sons, New York, 1953.
Girin, A.G., Drop deformation and acceleration: The effects of inertia in fragmentation, *Atom. Sprays*, 24(4), 349–366, 2014.
Gjesing, R., Hattel, J., and Fritsching, U., Coupled atomization and spray modelling in the spray forming process using OpenFOAM, *Eng. Appl. Comput. Fluid Mech.*, 3(4), 471–486, 2009.
Glaser, H.W., *Das Zerstäubung von Suspensionen mit Ein- und Zweistoffdüsen*, VDI-Verlag, Düsseldorf, Germany, 1989.
Goldschmidt, A. and Streitberger, H.J., *BASF-Handbuch Lackiertechnik*, Vincentz Verlag, Hannover, Germany, 2002.
Gopala, V.R. and van Wachem, B.G.M., Volume of fluid methods for immiscible-fluid and free-surface flows, *Chem. Eng. J.*, 141, 204–221, 2008.
Gorokhovski, M. and Herrmann, M., Modeling primary atomization, *Annu. Rev. Fluid Mech.*, 40, 343–366, 2008.
Gotaas, C., Havelka, P., Jokobson, H.A., Svendsen, H.F., Hase, M., Roth, N., and Weigand, B., Effect of viscosity on droplet-droplet collision outcome: Experimental study and numerical comparison, *Phys. Fluids*, 19 (102105), 1–11, 2007.
Gramlich, S., Mescher, A., Piesche, M., and Walzel, P., Modeling and numerical simulation of the gas-induced breakup of liquid threads stretched by gravity, *Chem. Eng. Technol.*, 34(6), 921–926, 2011.

Gramlich, S. and Piesche, M., Numerical and experimental investigations on the breakup of particle laden liquid jets in the centrifugal field, *Chem. Eng. Sci.*, 84, 408–416, 2012.
Grant, P.S., Spray forming, *Progr. Mater. Sci.*, 39, 497–545, 1995.
Grant, P.S., Cantor, B., and Katgerman, L., Modelling of droplet dynamic and thermal histories during spray forming-I. Individual droplet behaviour, *Acta Metall. Mater.*, 41(11), 3097–3108, 1993a.
Grant, P.S., Cantor, B., and Katgerman, L., Modelling of droplet dynamic and thermal histories during spray forming-II. Effect of process parameters, *Acta Metall. Mater.*, 41(11), 3109–3118, 1993b.
Grant, R.P. and Middleman, S., Newtonian jet stability, *AIChE J.*, 12(4), 669–678, 1966.
Grass, R.N. and Stark, W.J., Flame synthesis of calcium-, strontium-, barium fluoride nanoparticles and sodium chloride, *Chem. Commun.*, 2005, 1767–1769, 2005.
Grohmann, O., Meyer, C., Schulz, A., Uhlenwinkel, V., and Heinzel, C., Hot forming tool generated via co-spray forming of composite material, in *Proceedings of SDMA 2013—Fifth International Conference on Spray Deposition and Melt Atomization*, Bremen, Germany, September 23–25, 2013.
Gröhn, A.J., Pratsinis, S.E., Sanchez-Ferrer, A., Mezzenga, R., and Wegner, K., Scale-up of nanoparticle synthesis by flame spray pyrolysis: The high-temperature particle residence time, *Ind. Eng. Chem. Res.*, 53, 10734–10742, 2014.
Grosshans, H., Szasz, R.Z., and Fuchs, L., Development of an efficient statistical volumes of fluid-Lagrangian particle tracking coupling method, *Int. J. Numer. Meth. Fluids*, 74, 898–918, 2014.
Grossmann, H.K., Grieb, T., Meierhofer, F., Hodapp, M.J., Noriler, D., Gröhn, A., Meier, H.F., Fritsching, U., Wegner, K., and Mädler, L., Nanoscale mixing during double-flame spray synthesis of heterostructured nanoparticles," *J. Nanopart. Res.*, 17(4), 1–16, 2015.
Gueyffier, D., Li, J., Nadim, A., Scardovelli, R., and Zaleski, S., Volume-of-fluid interface tracking with smoothed surface stress methods for three dimensional flows, *J. Comput. Phys.*, 152, 423–456, 1999.
Guildenbecher, D.R., Lopez-Rivera, C., and Sojka, P.E., Secondary atomization, *Exp. Fluids*, 46(3), 371–402, 2009.
Gutierrez-Miravete, M., Lavernia, E.J., Trapaga, G.M., and Szekely, J., A mathematical model of the liquid dynamic compaction process. Part 2: Formation of the deposit, *Int. J. Rapid Solidif.*, 4, 125–150, 1988.
Haenlein, A., Disintegration of a liquid jet, NACA TN 659, 1932.
Hagerty, W.W. and Shea, J.F., A study of the stability of plane fluid sheets, *J. Appl. Mech.*, 22, 509–514, 1955.
Halada, K., Suga, H., and Muramatsu, Y., Atomizing parameters for centrifugal atomization of metal, in *Proceedings of the International Conference of Powder Metallurgy: PM into the 1990's*, Vol. 1, The Institute of Metals, London, U.K., July 2–6, 1990, 193–199.
Halder, M.R., Dash, S.K., and Som, S.K., Initiation of air core in a simplex nozzle and the effects of operating and geometrical parameters on its shape and size, *Exp. Therm. Fluid Sci.*, 26, 871–878, 2002.
Hammer, E.A., Johansen, G.A., Dyakowski, T., Roberts, E.P.L., Cullivan, J.C., Williams, R.A., Hassan Y.A., and Claiborn, C.S., Advanced experimental techniques, in Clayton T. Crowe (Ed.), *Multiphase Flow Handbook*, 14-1–14-125, CRC Press Taylor & Francis Group, Boca Raton, FL, 2006.
Handscomb, C.S., Kraft, M., and Bayly, A.E., A new model for the drying of droplets containing suspended solids after shell formation, *Chem. Eng. Sci.*, 64(2), 228–246, 2009a.
Handscomb, C.S., Kraft, M., and Bayly, A.E., A new model for the drying of droplets containing suspended solids, *Chem. Eng. Sci.*, 64(4), 628–637, 2009b.
Hansmann, S., Einfluss von Stoff- und Betriebsparametern auf die Zerstäubung hochvoskoser Flüssigkeiten im Ultraschall-Stehwellenfeld, Dissertation, Universität Bremen, Bremen, Germany, 1996.
Hardalupas, Y. and Horender, S., Phase doppler anemometer for measurements of deterministic spray unsteadiness, *Part. Part. Syst. Charact.*, 18, 205–215, 2001.
Hardalupas, Y., Tsai, R.-E., and Whitelaw, J.H., Unsteady breakup of liquid jets in coaxial airblast atomisers, in *Proceedings of ICLASS-'97*, Seoul, Korea, August 18–22, 1997, pp. 326–333.
Hartmann, D., Theoretische Untersuchungen zur Tropfenbildung bei Dispergierprozessen, Dissertation, Martin-Luther-Universität Halle, Halle, Germany, 1993.
Hattel, J.H., Pryds, N., Thorborg, J., and Ottosen, P., A quasi-stationary numerical model of atomized metal droplets, Part I: Model formulation, *Model. Simul. Mater. Sci. Eng.*, 7(3), 413–430, 1999.
Hattel, J.H., Pryds, N.H., Pedersen, T.B., and Pedersen, A.S., Numerical modelling of the spray forming process: The effect of process parameters on the deposited material, in *Proceedings of SDMA 2000*, Bremen, Germany, 2000, pp. 803–812.
Hecht, N., Bouali, Z., Menard, T., Reveillon, J., and Demoulin, F.X., Coupled modeling impact of liquid interface and dispersed sprays, in *Proceedings of ILASS-Europe 2013*, Chania, Greece, September 1–4, 2013.
Heck, U., Zur Zerstäubung in Freifalldüsen, PhD thesis, Universität Bremen, Bremen, Germany, 1998.
Heck, U., Fritsching, U., and Bauckhage, K., Gas-flow effects on twin-fluid atomization of liquid metals, *Atom. Sprays*, 10(1), 25–46, 2000.
Heinlein, J. and Fritsching U., Droplet clustering in sprays, *Exp. Fluids*, 40, 464–472, 2006.

Hembram, K., Sivaprakasam, D., Rao, T.N., and Wegner, K., Large-scale manufacure of ZnO nanorods by flame spray pyrolysis, *J. Nanopart. Res.*, 15, 1461, 2013.
Henein, H., Single fluid atomization through the application of impulses to a melt, *Mater. Sci. Eng. A*, 326(1), 92–100, 2002.
Hennigs, C., Kockel, T.K., and Langrish, T.A.G., New measurements of the sticky behavior of skim milk powder, *Dry. Technol.*, 19(3&4), 471–484, 2001.
Herrmann, M., A balanced force refined level set grid method for two-phase flows on unstructured flow solver grids, *J. Comput. Phys.*, 227(4), 2674–2706, 2008.
Herrmann, M., A parallel Eulerian interface tracking/Lagrangian point particle multi-scale coupling procedure, *J. Comput. Phys.*, 229, 745–759, 2010.
Heukelbach, K. and Tropea, C., Influence of the inner flowfield of flat fan pressure atomizers on the disintegration of the liquid sheet, in *Proceedings of Institute Liquid Atomization and Spray System ILASS-Europe AGM 2001*, Zurich, Switzerland, 2001.
Heywood, J.B., *Internal Combustion Engine Fundamentals*, McGraw-Hill, New York, 1998.
Hiller, R.B., Der Einfluß von Partikelstoßund Partikelhaftung auf die Abscheidung in Faserfiltern, Dissertation, Univerität Karlsruhe, VDI-Verlag GMBH, Düsseldorf, Germany, 1981.
Hinze, J.O. and Milborn, H., Atomization of liquids by means of a rotating cup, *J. Appl. Mech.*, 17, 145–153, 1950.
Hirt, C.W. and Nichols, B.D., Volume of fluid (VOF) method for the dynamics of free boundaries, *J. Comput. Phys.*, 39, 201–225, 1981.
Hirth, J.P., Nucleation, undercooling and homogeneous structures in rapidly solidified powders, *Metall. Trans. A*, 9A(3), 401–404, 1978.
Ho, C.A. and Sommerfeld, M., Modelling of micro-particle agglomeration in turbulent flows, *Chem. Eng. Sci.*, 57, 3073–3084, 2002.
Hohmann, S., Strahlausbreitung und Tropfenverdunstung bei der dieselmotorischen Direkteinspritzung, Dissertation, RWTH Aachen, Shaker Verlag, Aachen, Germany, 1999.
Høj, M., Pham, D.K., Brorson, M., Maedler, L., Jensen, A.D., and Grunwaldt, J.D., Two-nozzle flame spray pyrolysis (FSP) synthesis of $CoMo/Al_2O_3$ hydrotreating catalysts, *Catal. Lett.*, 143(5), 386–394, 2013.
Hong, J.M., Shinar, T., Kang, M., and Fedkiw, R., On boundary condition capturing for multiphase interfaces, *J. Sci. Comput.*, 31, 99–125, 2007.
Hopfinger, E.J., Liquid jet instability and the breakup process in liquid–liquid agitated atomization in a coaxial gas stream, *J. Therm. Eng. Jpn*, 16(4), 313–319, 1998.
Horvay, M., Theoretische und experimentelle Untersuchung über den Einfluß des inneren Strömungsfeldes auf die Zerstäubungseigenschaften von Drall-Druckzerstäubungsdüsen, Dissertation, Universität Karlsruhe, Karlsruhe, Germany, 1985.
Hou, X., Hu, Y., Jiang, H., Huo, J., Li, Y., and Li, C., In situ Au-catalyzed fabrication of branch-type SnO_2 nanowires by a continuous gas-phase route for dye-sensitized solar cells, *J. Mater. Chem. A*, 1, 13814–13820, 2013.
Hsiang, L.P. and Faeth, G.M., Near-limit drop deformation and secondary breakup, *Int. J. Multiphase Flow*, 18(5), 635–652, 1992.
Hsiang, L.P. and Faeth, G.M., Drop properties after secondary breakup, *Int. J. Multiphase Flow*, 19(5), 721–735, 1993.
Hsiang, L.P. and Faeth, G.M., Drop deformation and breakup due to shock wave and steady disturbances, *Int. J. Multiphase Flow*, 21(4), 545–560, 1995.
Huang, Y., Zheng, Z., Ai, Z., Zhang, L., Fan, X., and Zou, Z., Core-shell microspherical $Ti1\text{-}xZrxO_2$ solid solution photocatalysts directly from ultrasonic spray pyrolysis, *J. Phys. Chem. B*, 110, 19323–19328, 2006.
Huppmann, W.J. and Dalal, K., *Metallographic Atlas of Powder Metallurgy*, Schmid, Freiburg, Germany, 1986.
Hwang, S.S., Liu, Z., and Reitz, R.D., Breakup mechanisms and drag coefficients of high-speed vaporizing liquid drops, *Atom. Sprays*, 6(3), 353–376, 1996.
Isenschmid, T., Charaktersisierung von Mehrstoffdüsen für Suspensionen, Dissertation, ETH-Zürich, Zürich, Switzerland, 1992.
Issa, R.J., Multiphase spray cooling technology in industry, in K. Jayanthakumaran (Ed.), *Advanced Technologies*, InTech Publisher, Rijeka, Croatia, 2009, pp. 341–356.
Jayanthi, G.V., Zhang, S.C., and Messing, G.L., Modeling of solid particle formation during solution aerosol thermolysis, *Aerosol Sci. Technol.*, 19, 478–490, 1993.
Jedelsky, J., Some aspects of effervescent atomization: Experimental study, Short version of Habilitation thesis, Brno University of Technology, Brno, Czech Republic, 2013.
Jedelsky, J. and Jicha, M., Unsteadiness in effervescent sprays: A new evaluation method and the influence of operational conditions, *Atom. Sprays*, 18, 49–83, 2008.
Jeffrey, H., On the formation of water waves by wind, *Proc. R. Soc. A*, 107, 189, 1924.

Jeschar, R., Specht, E., and Köhler, C., Heat transfer during cooling of heated metallic objects with evaporating liquids, in H. Tensi et al. (Eds.), *Theory and Technology of Quenching*, Springer Verlag, Berlin, Germany, 1992, pp. 73–92.
Jicha, M., Jedelsky, J., Otahal, J., and Slama, J., Influence of some geometric parameters on the characteristics of effervescent atomization, in *Proceedings of ILASS-Europe*, Zaragoza, Spain, 2002.
Jones, A.R., Factors affecting the performance of large swirl pressure jet atomizers, CEGB Report R/M/N1054, Marchwood, Southampton, U.K., 1982.
Jordan, N., Auswirkungen der Prozeßparameter und der Prozeßführung auf die Eigenschaften sprühkompaktierter Kupferbasis-Werkstoffe, Dissertation, Universität Bremen, Shaker Verlag, Aachen, Germany, 2003.
Joseph, D.D., Belanger, J., and Beavers, G.S., Breakup of a liquid drop suddenly exposed to a high-speed airstream, *Int. J. Multiphase Flow*, 25(6–7), 1263–1304, 1999.
Jossen, R., Pratsinis, S.E., Stark, W.J., and Maedler, L., Criteria for flame-spray synthesis of hollow, shell-like, or inhomogeneous oxides, *J. Am. Ceram. Soc.*, 88(6), 1388–1393, 2005.
Jung, D.S., Lee, H.M., Kang, Y.C., and Park, S.B., Air-stable silver-coated copper particles of sub-micrometer size, *J. Colloid Interface Sci.*, 364, 574–581, 2011.
Kamplade, J., Mack, T., Küsters, A., and Walzel, P., Breakup of initially non-axisymmetric threads under the influence of cross-wind flow, CD-Rom, in *Proceedings of ILASS-Europe 2014*, Bremen, Germany, September 8–10, 2014.
Kamplade, J., Musemic, E., and Walzel, P., Investigation on pressure swirl nozzles with Coanda deflection outlets, in *Proceedings of ILASS-Europe 2013*, Chania, Greece, September 1–4, 2013.
Kang, M., Fedkiw, R., and Liu, X.D., A boundary condition capturing method for multiphase incompressible flow, *J. Sci. Comput.*, 15, 323–360, 2000.
Karlsson, J.A.J., Modeling auto-ignition, flame propagation and combustion in non-stationary turbulent sprays, PhD thesis, Chalmers University, Gothenburg, Sweden, 1995.
Karthikeyan, J., Berndt, C.C., Tikkanen, J., Wang, J.Y., King, A.H., and Herman, H., Nanomaterial powders and deposits prepared by flame spray processing of liquid precursors, *Nanostruct. Mater.*, 8, 61–74, 1997.
Kemmler, J.A., Pokhrel, S., Maedler, L., Weimar, U., and Barsan, N., Flame spray pyrolysis for sensing at the nanoscale, *Nanotechnology*, 24, 442001, 2013.
Kieviet, F. and Kerchof, P.J., Measurement of particle residence time distributions in spray dryer, *Dry. Technol.*, 13(5–7), 1241–1248, 1995.
Kim, J.Y. and Lee, S.Y., Dependence of spraying performance on the internal flow pattern in effervescent atomizers, *Atom. Sprays*, 11, 735–756, 2001.
Kim, S., Kim, D., and Yoon, D.Y., Liquid film thickness measurement for swirl injector, *J. Kor. Soc. Propuls. Eng.*, 10, 70–77, 2006.
Kim, S.S., An experimental study of droplet response to weak shock waves, PhD thesis, Rutgers University, New Brunswick, NJ, 1977.
King, L., On the acoustic radiation pressure on spheres, *Proc. R. Soc. Lond.*, 147A, 212–239, 1934.
Klar, E. and Fesko, J.W., *Powder Metallurgy Metals Handbook*, Vol. 7, American Society for Metals, Materials Park, OH, 1984.
Klein, M., Sadiki, A., and Janicka, J., Influence of the inflow conditions on the direct numerical simulation of primary breakup of liquid jets, in *ILASS-Europe 2001*, Zürich, Switzerland, 2001, pp. 475–480.
Klein, M., Sadiki, A., and Janicka, J., Untersuchung des Primärzerfalls eines Flüssigkeitsfilms: Vergleich direkte numerische Simulation, Experiment und lineare Theorie, *Spray 2002*, Freiberger Forschungshefte A 870 Verfahrenstechnik, TU-Bergakademie Freiberg, 2002, pp. 63–72.
Kolev, N.I., *Thermal and Mechanical Interactions of Multiphase Dynamics*, Vol. 2, Springer, Berlin, Germany, 2002.
Kong, S.C., Han, Z., and Reitz, R.D., The development and application of a Diesel ignition and combustion model, SAE paper, 950278, 1995.
Kramer, C., 1997, Die Kompaktierungsrate beim Sprühkompaktieren von Gauß-förmigen Deposits, Dissertation, Universität Bremen, Bremen, Germany.
Krauss, M., Bergmann, D., and Fritsching, U., In-situ particle temperature, velocity and size measurements in the spray forming process, *Mater. Sci. Eng. A*, 326(1), 154–164, 2002.
Kröger, B., Einfluß der Luftverteilerströmung auf die Ausbreitung der dispersen Phase in einem Sprühtrocknerturm, Dissertation, Universität Bremen, Bremen, Germany, 2001.
Krzeczkowski, S.A., Measurement of liquid droplet disintegration mechanisms, *Int. J. Multiphase Flow*, 6, 227–239, 1980.
Kurt, O., Fritsching, U., and Schulte, G., Binary collisions of droplets with fluid and suspension particles, in *Proceedings of ILASS-Europe 2007*, Mugla, Turkey, September 10–13, 2007.
Kurt, O., Fritsching, U., and Schulte, G., Secondary droplet formation during binary suspension droplet collisions, in *Proceedings of ILASS-Europe 2008*, Como Lake, Italy, September 8–10, 2008.

Kurt, O., Mulhem, B., Fritsching, U., and Schulte, G., Zerstäubung von Suspensionen mittels eines Rotationszerstäubers, in *Spray 2002*, Freiberg, Germany, November 21–22, 2002.
Kuschel, M., Experimentelle Untersuchung und Modellierung des Viskositätseinflusses auf binäre Tropfenkollisionen, Diss., Martin-Luther-Universität Halle-Wittenberg, Halle, Germany, 2013.
Kuschel, M. and Sommerfeld, M., Investigation of droplet collisions for solutions with different solids content, *Exp. Fluids*, 54, 1440, 1–17, 2013.
Kwakkel, M., Breugem, W.P., and Boersma, B.J., Extension of a CLSVOF method for droplet-laden flows with a coalescence/breakup model, *J. Comput. Phys.*, 253, 166–188, 2013.
Lafaurie, B., Mantel, T., and Zaleski, S., Direct Navier-Stokes simulations of the near-nozzle region, in A.J. Yule (Ed.), *Proceedings of ILASS-Europe '98* Manchester, U.K., July 6–8, 1998, pp. 54–59.
Lafaurie, B., Nardonne, C., Scardovelli, R., Zaleski, S., and Zanetti, G., Modeling merging and fragmentation in multiphase flows with SURFER, *J. Comput. Phys.*, 113, 134–147, 1994.
Lagutkin, S., Achelis, L., Sheikhaliev, S., Uhlenwinkel, V., and Srivastava, V., Atomization process for metal powder, *Mater. Sci. Eng. A*, 383, 1–6, 2004.
Lampa, A. and Fritsching, U., Large Eddy Simulation of the spray formation in confinements, *Int. J. Heat Fluid Flow*, 43, 26–34, 2013.
Lampe, K., Experimentelle Untersuchung und Modellierung der Mehrphasenströmung im düsennahen Bereich einer Öl-Brenner-Düse, Dissertation, Universität Bremen, Bremen, Germany, 1994.
Landwehr, F., Feggeler, D., Walzel, P., Weichert, F., Schröter, N., and Müller, H., A fibre sensor based frequency analysis of surface waves at hollow cone nozzles, *Exp. Fluids*, 40, 523–532, 2006.
Landwehr, F., Schmidt, D., and Walzel, P., Messung und Berechnung des kritischen Druckverhältnisses an Zweistoff-Düsen, in *Proceedings of Spray'99*, Bremen, Germany, October 5 and 6, 1999.
Lane, W.R., Shatter of drops in streams of air, *Ind. Eng. Chem.*, 43, 1312–1317, 1951.
Lang, R., Diameter of droplets from ultrasound waves, *J. Acoust. Soc. Am.*, 34, 6–8, 1962.
Langrish, T.A.G. and Kockel, T.K., The assessment of a characteristic drying curve for milk powder for use in computational fluid dynamics, *Chem. Eng. J.*, 84(1), 69–74, 2001.
Lasheras, J.C. and Hopfinger, E.J., Liquid jet instability and atomization in a coaxial gas stream, *Annu. Rev. Fluid. Mech.*, 32, 275–308, 2000.
Lavernia, E.J., Spray atomization and deposition of metal matrix composites, in *Koll. SFB 372*, Vol. 1 Universität Bremen, Bremen, Germany, 1996, pp. 63–122.
Lavernia, E.J., Gutierrez, E.M., Szekely, J., and Grant, N.J., A mathematical model of the liquid dynamic compaction process. Part 1: Heat flow in gas atomization, *Int. J. Rapid Solidif.*, 4, 89–124, 1988.
Lavernia, E.J. and Wu, Y., *Spray Atomization and Deposition*, John Wiley & Sons, Chichester, U.K., 1996.
Lawley, A., *Atomization-The Production of Metal Powders*, Metal Powder Industries Federation, Princeton, NJ, 1992.
Lawley, A., Melt atomization & spray deposition-Quo vadis, in *Proceedings of SDMA 2000*, Bremen, Germany, 2000, pp. 3–16.
Lawley, A., Mathur, P, Apelian, D., and Meystel, A., Sprayforming: Process fundamentals and control, *Powder Metall.*, 33, 109–111, 1990.
Leatham, A.G. and Lawley, A., The Osprey process: Principles and applications, *Int. J. Powder Metall.*, 29(4), 321–329, 1993.
Lebas, R., Blokkeel, G., Beau, P.A., and Demoulin, F.X., Coupling vaporization model with the Eulerian–Lagrangian Spray Atomization (ELSA) model in Diesel engine conditions, SAE papers, 2005-01-0213, 2005.
Lebas, R., Menard, T., Beau, P.A., Berlemont, A., and Demoulin, F.X., Numerical simulation of primary break-up and atomization: DNS and modelling study, *Int. J. Multiphase Flow*, 35, 247–260, 2009.
Lee, C.H. and Reitz, R.D., An experimental study of the effect of gas density on the distortion and breakup mechanism of drops in high speed gas stream, *Int. J. Multiphase Flow*, 26(2), 229–244, 2000.
Lee, E. and Ahn, S., Solidification progress and heat transfer analysis of gas atomized alloy droplets during spray forming, *Acta Metall. Mater.*, 42(9), 3231–3243, 1994.
Lee, S.H. and Ryan, H.S., Development of a new model and heat transfer analysis of impinging Diesel sprays on a wall, *Atom. Sprays*, 11(1), 85–106, 2001.
Lefebvre, A.H., Airblast atomization, *Prog. Energy Combust. Sci.*, 6(3), 233–261, 1980.
Lefebvre, A.H., *Gas Turbine Combustion*, Hemisphere, Washington, DC, 1983.
Lefebvre, A.H., *Atomization and Sprays*, Hemisphere Publishing Corporation, New York, 1989.

Leung, J.C. and Epstein, M., A generalized correlation for two-phase nonflashing homogenous choked flow, *J. Heat Transfer*, 112, 528–530, 1990.
Levi, C.G. and Mehrabian, R., Heat flow during rapid solidification of undercooled metal droplets, *Metall. Trans. A Phys. Metall. Mater. Sci.*, 13A, 221–234, 1982.
Levich, V.G., Physicochemical Hydrodynamics, Prentice Hall, NJ, 1962.
Li, D., Teoh, W.Y., Woodward, R.C., Cashion, J.D., Selomulya, C., and Amal, R., Evolution of morphology and magnetic properties in silica/maghemite nanocomposites, *J. Phys. Chem. C*, 113, 12040–12047, 2009.
Li, X., Mechanism of atomization of a liquid jet, *Atom. Sprays*, 5, 89–105, 1995.
Li, X. and Tankin, R.S., Droplet size distribution: A derivation of Nukyama-Tanasawa type distribution function, *Combust. Sci. Technol.*, 56, 65, 1987.
Li, X.G., Modeling and simulation of the gas-atomization process of metal melts for metal-matrix-composite production, Dissertation, Universität Bremen, Shaker-Verlag, Aachen, Germany, 2014.
Li, X.G. and Fritsching, U., Numerical investigation of binary droplet collisions in all relevant collision regimes, *J. Comput. Multiphase Flows*, 3(4), 207–224, 2011.
Li, X.G. and Fritsching, U., Modeling and simulation of pressure-gas-atomization process for metal powder production, CD-Rom, in *Proceedings of ILASS-Europe 2014*, Bremen, Germany, September 8–10, 2014a.
Li, X.G. and Fritsching, U., Multiscale modeling and simulation in spray processing of composite particles, in *Proceedings of Second International Symposium on Multiscale Multiphase Process Engineering*, Hamburg, Germany, September 24–27, 2014b.
Li, X.G. and Fritsching, U., Numerical investigation of solid particle penetration into liquid droplet, *Materialwiss. Werkstofftech.*, 45(8), 666–682, 2014c.
Li, X.G., Heisterüber, L., Achelis, L., Uhlenwinkel, V., and Fritsching, U., Spray process modeling in metal-matrix-composite powder production, *Atom. Sprays*, 21(11), 933–948, 2011.
Libera, M., Olsen, G.B., and van der Sande, J.B., Heterogeneous nucleation of solidification in atomized liquid metal droplets, *Mater. Sci. Eng. A*, 132, 107–118, 1991.
Lichtarowicz, A., Duggins, R.K., and Markland, E., 1965, Discharge Coefficients for Incompressible Non-vavitating Flow through Long Orifices, *J. Mech. Eng. Sci.*, **7**, 2, 210–219.
Lierke, E.G., Leung, E.W., and Luhmann, D., Atomization by ultrasound, in *Third International College*, *AIP Conference Proceedings*, Monterey, CA, Vol. 197, 1988, p. 71.
Ling, Y. and Zaleski, S., Numerical investigation of spray formation and evolution in gas-assisted atomization, CD-Rom, in *Proceedings of ILASS-Europe 2014*, Bremen, Germany, September 8–10, 2014.
Liu, A.B., Mather, D., and Reitz, R.D., Modeling the effects of drop drag and breakup on fuel sprays, SAE paper, 930072, 1993.
Liu, A.B. and Reitz, R.D., Mechanisms of air-assisted liquid atomization, *Atom. Sprays*, 3(1), 55–75, 1993.
Liu, H., Numerical modelling of gas atomization in spray forming process, in *Proceedings of 1997 TMS Annual Meeting*, Orlando, FL, February 9–13, 1997.
Liu, H., Spray forming, in K.O. Yu (Ed.), *Modelling and Simulation for Casting and Solidification: Theory and Applications*, Marcel Dekker Inc., New York, 2000a.
Liu, H., *Science and Engineering of Droplets: Fundamentals and Applications*, William Andrew Publication, Norwich, NY, 2000b.
Liu, H., Lavernia, E.J., and Rangel, R.H., Numerical investigation of micropore formation during substrate impact of molten droplets in plasma spray processes, *Atom. Sprays*, 4, 369–384, 1994.
Liu, M., Duan, Y., Zhang, T., and Xu, Y., Evaluation of unsteadiness in effervescent spray by analysis of droplet arrival statistics—The influence of fluids properties and atomizer internal design, *Exp. Therm. Fluid Sci.*, 35, 190–198, 2011.
Liu, Y., Liu, Z., Guo, S., Du, Y., Huang, B., Huang, J., Chen S., and Liu F., Amorphous and nanocrystalline $Al_{82}Ni_{10}Y_8$ alloy powder prepared by gas atomization, *Intermetallics*, 13, 393–398, 2005.
Liu, Y., Minagawa, K., and Kakisawa, H., Hybrid atomization process and mode diagram, SFB 372 Kolloquium series, Vol. 6, Bremen, Germany, 2002.
Liu, Y., Rauch, W., Zha, S.W., and Liu, M.L., Fabrication of $Sm_{0.5}Sr_{0.5}CoO_3{-}\delta{-}Sm_{0.1}Ce_{0.9}O_2{-}\delta$ cathodes for solid oxide fuel cells using combustion CVD, *Solid State Ionics*, 166, 3–4, 261–268, 2004.
Liu, Z. and Reitz, R.D., An analysis of the distortion and breakup mechanisms of high speed liquid drops, *Int. J. Multiphase Flow*, 23(4), 631–650, 1997.
Löffler-Mang, M., Düsenströmung, Tropfenentstehung und Tropfenausbreitung bei rücklaufgeregelten Drall-Druckzerstäubern, Dissertation, Universität Karlsruhe, Karlsruhe, Germany, 1992.

Lohmann, M., Herstellung von Partikeln durch elektrostatische Zerstäubung von Flüssigmetallen in gasförmiger Umgebung, Diss., University of Duisburg, Germany, 2000.
Lohner, H., Zerstäuben von Mineralscmelzen mit Heißgas, Dissertation, Universität Bremen, VDI-Verlag, Düsseldorf, Germany, 2003.
Lohner, H., Czisch, C., and Fritsching, U., Impact of gas nozzle arrangement on the flow field of a twin fluid atomizer with external mixing, in *Proceedings of International Conference on Liquid Atomization and Spray Systems ICLASS 2003*, Sorrento, Italy, 2003.
Lohner, H., Czisch, C., Schreckenberg, P., Fritsching, U., and Bauckhage, K., Atomization of viscous melts, *Atom. Sprays*, 15, 169–180, 2005.
Lörcher, M., Zerstäuben von zweiphasigen Gemischen aus Flüssigkeiten und Gasen, VDI Fortschritt Ber., Reihe 3, 764, VDI Verlag, Düsseldorf, Germany, 2003.
Lörcher, M., Schmidt, F., and Mewes, D., Flow field and phase distribution inside effervescent atomizers, in *CD-ROM Proceedings of Ninth International Conference on Liquid Atomization and Spray System ICLASS 2003*, Sorrento, Italy, 2003.
Louey, A.F. and Refstrup, E., Recent advances in agglomeration during Spray drying, in *Sixth World Congress of Chemical Engineering*, Melbourne, Victoria, Australia, 2001.
Low, T.B. and List, R., Collision, coalescence and breakup of raindrops, *J. Atmos. Sci.*, 39, 1591–1618, 1982.
Lozano, A., Call, C.J., and Dopazo, C., An experimental and numerical study of the atomization of a planar liquid sheet, in *Proceedings of ICLASS-94*, Rouen, France, 1994.
Lubanska, H., Correlation of spray ring data for gas atomization of liquid droplets, *J. Metals*, 2, 45–49, 1970.
Lund, M.T., Sojka, P.E., Lefebvre, A.H., and Gosselin, P.G., Effervescent atomization at low mass flow rates. Part 1: The influence of surface tension, *Atom. Sprays*, 3, 77–89, 1993.
Luong, J.T.K. and Sojka, P.E., Unsteadiness in effervescent sprays, *Atom. Sprays*, 9, 87–109, 1999.
Mackay, G.D. and Mason, S.G., The gravity approach and coalescence of fluid drops at liquid interfaces, *Can. J. Chem. Eng.*, 41, 203–212, 1963.
Maedler, L., Liquid-fed aerosol reactors for one-step synthesis of nano-structured particles, *KONA*, 22, 107–120, 2004.
Maedler, L., Kammler, H.K., Mueller, R., and Pratsinis, S.E., Controlled synthesis of nanostructured particles by flame spray pyrolysis, *J. Aerosol. Sci.*, 33(2), 369–389, 2002.
Maedler, L., Roessler, A., Pratsinis, S.E., Sahm, T., Gurlo, A., Barsan, N., and Weimar, U., Direct formation of highly porous gas-sensing films by in situ thermophoretic deposition of flame-made Pt/SnO_2 nanoparticles, *Sens. Actuator B—Chem.*, 114(1), 283–295, 2006.
Magnussen, B.F. and Hjertaeger, B.H., On mathematical modeling of turbulent combustion with special emphasis on soot formation and combustion, in *16th International Symposium on Combustion*, 16(1), The Combustion Institute, Pittsburgh, PA, December, 1977, pp. 719–729.
Malot, H. and Dumouchel, C., Volume-based spray drop size distribution: Derivation of a generalized gamma distribution from the application of the maximum entropy formalism, in *CD-Rom Proceedings of ILASS-Europe 99*, Toulouse, France, July 5–7, 1999.
Mansour, A. and Chigier, N., Effect of turbulence on the stability of liquid jets and the resulting droplet size distributions, *Atom. Sprays*, 4, 583–604, 1994.
Markus, S. and Fritsching, U., Discrete breakup modeling for melt sprays, *Int. J. Powder Metall.*, 42(4), 23–32, 2006.
Markus, S. and Fritsching, U., Spray forming with multiple atomization, in *Proceedings of SDMA 2003*, Bremen, Germany, 2003a.
Markus, S. and Fritsching, U., Modelling secondary break-up of melts in sprays, in *Proceedings of International Conference on Liquid Atomization and Spray Systems, ICLASS 2003*, Sorrento, Italy, 2003b.
Markus, S., Fritsching, U., and Bauckhage, K., Jet break up of liquid metals, *Mater. Sci. Eng. A*, 326, 122–133, 2000.
Marx, K.D., Edwards, C.F., and Chin, W.K., Limitations of the ideal Phase-Doppler system: Extension to spatially and temporally inhomogeneous particle flows, *Atom. Sprays*, 4, 1–40, 1994.
Masters, K., *Spray Drying Handbook*, 5th edn., Longman Scientific & Technical, Essex, England, 1991.
Masters, K., *Spray Drying in Practice*, Spray DryConsult Int. ApS, Charlottenlund, Denmark, 2002.
Mathur, P., Annavarapu, S., Apelian, D., and Lawley, A., Process control, modeling and applications of spray casting, *J. Metals*, 10, 23–28, 1989a.

Mathur, P., Annavarapu, S., Apelian, D., and Lawley, A., Spray casting: An integral model for process understanding and control, *Mater. Sci. Eng. A*, 142(2), 261–276, 1991.
Mathur, P., Apelian, D., and Lawley, A., Analysis of the spray deposition process, *Acta Metall.*, 37(2), 429–443, 1989b.
Matsumoto, S., Saito, K., and Takashima, Y., *Bull. Tokyo Inst. Technol.*, 116, 85, 1973.
Mayer, W., Zur koaxialen Flüssigkeitszerstäubung im Hinblick auf die Treibstoffaufbereitung in Raketentriebwerken, Dissertation Universität Erlangen, Erlangen, Germany, 1993.
Mehring, C. and Sirignano, W.A., Capillary stability of modulated swirling liquid sheets, *Atom. Sprays*, 14, 397–436, 2004.
Meierhofer, F., Hodapp, M., Achelis, L., Buss, L., Noriler, D., Meier, H.F., and Fritsching, U., Investigation of atomization concepts for large-scale flame spray pyrolysis (FSP), *Materialwiss. Werkstofftech.*, 45(8), 765–778, 2014.
Menard, T., Tanguy, S., and Berlemont, A., Coupling level Set/VOF/ghost fluid methods: Validation and application to 3D simulation of the primary break-up of a liquid jet, *Int. J. Multiphase Flow*, 33(5), 510–524, 2007.
Menchaca-Rocha, A., Huidobro, F., Martinez-Davalos, A., Michaelian, K., Perez, A., Rodriguez, V., and Carjan, N., Coalescence and fragmentation of colliding mercury drops, *J. Fluid Mech.*, 346, 291–318, 1997.
Meng, W.W., Wan, R.W.D., Arun, S.M., Meor, Z.M.T., Wu, Z.H., and Siti, M.T., Comparative study of droplet drying models for CFD modelling, *Chem. Eng. Res. Design*, 86, 1038–1048, 2008.
Mescher, A., Kamplade, J., and Walzel, P., Spray drying of particles with narrow PSD by LAMROT atomizer and optimized gas distributor, in *Proceedings of ILASS-Europe 2013*, Chania, Greece, September 1–4, 2013.
Mescher, A., Möller, A., Dirks, M., and Walzel, P., Gravity affected break-up of laminar threads at low gas-relative-velocities, *Chem. Eng. Sci.*, 69, 181–192, 2012.
Messing, G.L., Zhang, S.C., and Jayanthi, G.V., Ceramic powders synthesis by spray pyrolysis, *J. Am. Ceram. Soc.*, 76, 2707–2726, 1993.
Meyer, C., Uhlenwinkel, V., Ristau, R., Jahn, P., Müller, H., Krug, P., and Trojahn, W., Thermal simulation of multilayer composites generated by spray forming, in *Proceedings of SDMA 2009—Fourth International Conference on Spray Deposition and Melt Atomization*, Bremen, Germany, September 7–9, 2009.
Meyer, O., Fritsching, U., and Bauckhage, K., Numerical investigation of alternative process conditions for influencing the thermal history of spray deposited billets, *Int. J. Therm. Sci.*, 42, 153–168, 2003a.
Meyer, O., Schneider, A., Uhlenwinkel, V., and Fritsching, U., Convective Heat Transfer from a billet due to an oblique impinging circular jet within the spray forming process, *Int. J. Therm. Sci.*, 42(6), 561–569, 2003b.
Mezhericher, M., Levy, A., and Borde, I., Heat and mass transfer of single droplet/wet particle drying, *Chem. Eng. Sci.*, 63(1), 12–23, 2008b.
Mezhericher, M., Levy, A., and Borde, I., Modelling of particle breakage during drying, *Chem. Eng. Process.: Process Intensif.*, 47(8), 1404–1411, 2008a.
Mezhericher, M., Levy, A., and Borde, I., Theoretical drying model of single droplets containing insoluble or dissolved solids, *Dry. Technol.*, 25(6), 1025–1032, 2007.
Mezhericher, M., Levy, A., and Borde, I., Theoretical models of single droplet drying kinetics: A review, *Dry. Technol.*, 28, 278–293, 2010.
Mezhericher, M., Levy, A., and Borde, I., Three-dimensional spray-drying model based on comprehensive formulation of drying kinetics, *Dry. Technol.*, 30, 1256–1273, 2012.
Michelson, D., *Electrostatic Atomization*, Adam Hilgier, Bristol, New York, 1990.
Middleman, S., *Modeling Axisymmetric Flows, Dynamics of Films, Jets, and Drops*, Academic Press, San Diego, CA, 1999.
Miki-Yoshida, M., Collins-Martínez, V., Amezega-Madrid, P., and Aguilar-Elguezabal, A., Thin films of photocatalytic TiO_2 and ZnO deposited inside a tubing by spray pyrolysis, *Thin Solid Films*, 419, 60–64, 2002.
Miles, J.W., On the generation of surface waves by shear flows, Part 1, *J. Fluid Mech.*, 3, 185–204, 1957.
Miles, J.W., On the generation of surface waves by shear flows, Part 2, *J. Fluid Mech.*, 6, 568–582, 1958.
Miles, J.W., On the generation of surface waves by shear flows, Part 3, *J. Fluid Mech.*, 7, 469–478, 1960.
Miles, J.W., On the generation of surface waves by shear flows, Part 4, *J. Fluid Mech.*, 13, 433–448, 1961.

Minagawa, K., Kakisawa, H., Osawa, Y., Takamori, S., and Halada K., Production of fine spherical lead-free solder powders by hybrid atomization, *Sci. Technol. Adv. Mater.*, 6, 325–329, 2005.

Minnermann, M., Grossmann, H.K., Pokhrel, S., Thiel, K., Hagelin-Weaver, H., Baeumer, M., and Maedler, L., Double flame spray pyrolysis as a novel technique to synthesize alumina-supported cobalt Fischer-Tropsch catalysts, *Catal. Today*, 214, 90–99, 2013.

Moon, S., Abo-Serie, E., and Bae, C., Liquid film thickness inside the high pressure swirl injectors: Real scale measurement and evaluation of analytical equations, *Exp. Therm. Fluid Sci.*, 34(2), 113–121, 2010.

Mudawar, I. and Deiters, T.A., A universal approach to predicting temperature response of metallic parts to spray quenching, *Int. J. Heat Mass Transfer*, 37(3), 347–362, 1994.

Mudawar, I. and Valentine, W.S., Determination of the local quench curve for spray-cooled metallic surfaces, *ASM J. Heat Treat.*, 7, 107–112, 1989.

Mueller, R., Jossen, R., Pratsinis, S.E., Watson, M., and Akhtar, M.K., Zirconia nanoparticles made in spray flames at high production rates, *J. Am. Ceram. Soc.*, 87(2), 197–202, 2004.

Mujumdar, A.S., *Handbook of Industrial Drying*, 4th edn., CRC Press, Boca Raton, FL, 2014.

Mulhem, B., Bauckhage, K., Fritsching, U., and Schulte, G., Beugungsspektrometrie in Sprays von Suspensionen: Modellexperimente und differenzierte Interpretation der Ergebnisse, in *GALA*, Rostock, Germany, September 10–12, 2002.

Mulhem, B., Fritsching, U., Schulte, G., and Bauckhage, K., Characterisation of twin-fluid atomization for suspensions, in *International Conference on Liquid Atomization and Spray Systems ICLASS*, Sorrento, Italy, July 12–18, 2003a.

Mulhem, B., Fritsching, U., Schulte, G., and Bauckhage, K., Effect of solid particle characteristics on suspension atomization, *Atom. Sprays*, 13, 321–343, 2003b.

Mulhem, B., Khoja, G., Fritsching, U., and Schulte, G., Break-up of hollow cone and flat suspension lamellae of pressure atomizers, in *Proceedings of ICLASS 2006*, Kyoto, Japan, August 27–September 1, 2006a.

Mulhem, B., Schulte, G., and Fritsching, U., Solid–liquid separation in suspension atomization, *Chem. Eng. Sci.*, 61, 2582–2589, 2006b.

Müller, H.R. and Jeschar, R., Wärmeübergang bei der Spritzwasserkühlung von Nichteisenmetallen, *Metallkunde*, 74, 257–264, 1983.

Muoio, N.G., Crowe, C.T., Fritsching, U., and Bergmann, D., Modelling metal droplet sprays in spray forming, in *ASME FED*, Vol. 223, 1995, pp. 111–115.

Musemic, E., Gaspar, M., Weichert, F., Müller, H., and Walzel, P., Experimental examination of the liquid sheet disintegration process using combined photography and fibre based measuring techniques, in *Proceedings of ILASS-Europe 2010*, Brno, Czech Republic, September 6–8, 2010.

Mwakikunga, B.W., Progress in ultrasonic spray pyrolysis for condensed matter sciences developed from ultrasonic nebulization theories since Michael Faraday, *Crit. Rev. Solid State Mater. Sci.*, 39, 46–80, 2014.

Nasr, G.G., Yule, A.J., and Bendig, L., *Industrial Sprays and Atomization: Design, Analysis and Applications*, Springer-Verlag, Heidelberg, Germany, 2002.

Naue, G. and Bärwolf, G., *Transportprozesse in Fluiden*, Deutscher Verlag für Grundstoffindustrie, Leipzig, Germany, 1992.

Nichols, B.D., Hirt, C.W., and Hothkiss, R.S., SOLA-VOF: A solution algorithm for transient fluid flow with multiple free boundaries, Los Alamos Report, LA-8355, 1980.

Nigmatulin, R.I., *Dynamics of Multiphase Media*, English edn., Vols. 1+2, Rev Sub edition, CRC Press, London, 1990.

Nikas, K., Bouris D., Gehrman, D., Steinbeck, M., and Bergeles, G., Optimisation of spray dryer via CFD, *SPAY DRYING'01*, Dortmund, October 8–10, 2001.

Nikolaev, V.S., Vachagin, K.D., and Barychev, Y.N., *Int. Chem. Eng.*, 7, 595, 1967.

Nikolopoulos, N., Nikas, K.S., and Bergeles, G., A numerical investigation of central binary collision of droplets, *Comput. Fluids*, 38, 1191–1202, 2009a.

Nikolopoulos, N., Theodorakakos, A., and Bergeles, G., Off-centre binary collision of droplets: A numerical investigation, *Int. J. Heat Mass Transfer*, 52, 4160–4174, 2009b.

Ning, W., Reitz, R., Diwakar, R., and Lippert, A., An Eulerian-Lagrangian spray and atomization model with improved turbulence modeling, *Atom. Sprays*, 19, 727–739, 2009.

Nobari, M.R.H., Jan, Y.-J., and Tryggvason, G., Head-on collision of drops-a numerical investigation, *Phys. Fluids*, 8, 29–42, 1996.

Nobari, M.R.H. and Tryggvason, G., Numerical simulations of three-dimensional drop collisions, *AIAA J.*, 34, 750–755, 1996.

Nonnenmacher, S. and Piesche, M., Design of hollow cone pressure swirl nozzle to atomize Newtonian fluids, *Chem. Eng. Sci.*, 55, 4339–4348, 2000.
Nordin, N., Complex chemistry modeling of diesel spray combustion, PhD thesis, Chalmers University of Technology, Goteborg, Sweden, 2001.
Noriler, D., Rosebrock, C., Mädler, L., Meier, H.F., and Fritsching, U., Influence of atomization and spray parameters on the flame spray process for nanoparticle production, *Atom. Sprays*, 24(6), 495–524, 2014.
Nourgaliev, R.R. and Theofanous, T.G., High-fidelity interface tracking in compressible flows: Unlimited anchored adaptive level set, *J. Comput. Phys.*, 224, 836–866, 2007.
Nukiyama, S. and Tanasawa, Y., Experiments on the atomization of liquids in an airstream, *Trans. Soc. Mech. Eng. Japan*, 5, 68–75, 1939.
Nunez, L.A., Lobel, T., and Palma, R., Atomizers for molten metals: Macroscopic phenomena and engineering aspects, *Atom. Sprays*, 9(6), 581–600, 1999.
O'Rourke, P.J., Collective drop effects on vaporizing liquid sprays, PhD thesis, Los Alamos National Laboratory, Los Alamos, NM, 1981.
O'Rourke, P.J. and Amsden, A.A., The TAB method for numerical calculation of spray droplet breakup, Los Alamos National Laboratory Report, LA-UR-87-2105, 1987.
Oakley, D.E., Produce uniform particles by spray drying, *Chem. Eng. Progress*, 12, 48–54, 1997.
Oakley, D.E., Bahu, R.E., and Reay, D., The aerodynamics of co-current spray dryers, in *Proceeding of IDS'88*, Versailles, France, 1988.
Ochowiak, M., Broniarz-Press, L., and Rozanski, J., The discharge coefficient of effervescent atomizers, *Exp. Therm. Fluid Sci.*, 34, 1316–23, 2010.
Ohnesorge, W., Formation of drops by nozzles and the breakup of liquid jets, *Z. Angew. Math. Mech.*, 16, 355–358, 1936.
Olguin, H. and Gutheil, E., Derivation and evaluation of a multi-regime spray flamelet model, in *CD-Rom, Proceedings of ILASS-Europe 2014*, Bremen, Germany, September 8–10, 2014.
Olivas, P. and Marty, P., Numerical study of the Coanda effect in a rotating spray paint atomizer, *Atom. Sprays*, 12, 5+6, 2002.
Orme, M., Experiments on droplet collision, bounce coalescence and disruption, *Progr. Energy Combust. Sci.*, 23, 65–79, 1997.
Osher, S. and Fedkiw, R., *Level Set Methods and Dynamic Implicit Surfaces*, Applied Mathematical Sciences, Vol. 153, Springer, New York, 2002.
Osher, S. and Sethian, J.A., Fronts propagating with curvature-dependent speed: Algorithms based on Hamilton-Jacobi formulations, *J. Comput. Phys.*, 79, 12–49, 1988.
Oshinowo, T. and Charles, M.E., Vertical two-phase flow, part 1: Flow pattern correlations, *Canad. J. Chem. Eng.*, 52, 25–35, 1974.
Osmar, L., Vincent, S., Estivalezes, J.L., Menard, T., Aniszewski, W., and Caltagirone, J.P., VOF multi-scale modeling of phase inversion and liquid atomization, in *Proceedings of ILASS-Europe 2013*, Chania, Greece, September 1–4, 2013.
Osterle, B. and Petijean, A., Simulation of particle-to-particle interaction in gas–solid flows, *Int. J. Multiphase Flow*, 9(19), 199–211, 1993.
Ottosen, P., Numerical simulation of spray forming, PhD thesis, Technical University of Denmark, Lyngby, Denmark, 1993.
Ozmen, L. and Langrish, T.A.G., Experiment investigation of the wall deposition of milk powder in spray dryer, Paper#363, in *Proceedings of Ninth APCChE Congress and CHEMECA*, Christchurch, New Zealand, 2002.
Pan, Y. and Suga, K., Numerical simulation of binary liquid droplet collision, *Phys. Fluids*, 17, 082105, 2005.
Panchagnula, M.V., Sojky, P.E., and Bajaj, A.K., The non-linear breakup of annular liquid sheets, in A.J. Yule (Ed.), *Proceedings of ILASS-Europe '98*, Manchester, U.K., July 6–8, 1998, pp. 36–41.
Parthasarathy, R.N., Linear spatial stability analysis of slurry sheets subjected to gas flow, *Atom. Sprays*, 9, 519, 1999.
Patel, K.C. and Chen, X.D., Prediction of spray-dried product quality using two simple drying kinetics models, *J. Food Process Eng.*, 28(6), 567–594, 2005.
Patel, K.C., Chen, X.D., and Lin, S.X.Q., A composite reaction engineering approach to drying of aqueous droplets containing sucrose, maltodextrin (DE6) and their mixtures, *AIChE J.*, 55(1), 217–231, 2009.
Patterson, M.A., Modeling the effects of fuel injection characteristics on diesel combustion and emissions, PhD thesis, University of Wisconsin-Madison, Madison, WI, 1997.

Patterson, M.A. and Reitz, R.D., Modeling the effects of fuel spray characteristics on diesel engine combustion and emissions, SAE paper, 980131, 1998.
Payne, R.D., Matteson, M.A., and Moran, A.L., Application of neural networks in spray forming technology, *Int. J. Powder Metall.*, 29(4), 345–351, 1993.
Payne, R.D., Rebis, A.L., and Moran, A.L., Spray forming quality predictions via neural networks, *J. Mater. Eng. Perf.*, 2(5), 693–702, 1996.
Pedersen, T.B., Spray forming—A new integrated numerical model, PhD thesis, Technical University of Denmark, Lyngby, Denmark, 2003.
Pedersen, T.P., Hattel, J.H., Pryds, N.H., Pedersen, A.S., Buchholz, M., and Uhlenwinkel, V., A new integrated numerical model for spray atomization and deposition: Comparison between numerical results and experiments, in *Proceedings of SDMA 2000*, Bremen, Germany, 2000, pp. 813–824.
Pham, D.K., Hornig, N., Fritsching, U., and Maedler, L., Highly porous film synthesis by single-step direct aerosol deposition, *Earozoru Kenkyu*, 25(2), 140–148, 2010.
Pilch, M. and Erdman, C.A., Use of breakup time data and velocity history data to predict the maximum size of stable fragments for acceleration-induced breakup of a liquid drop, *Int. J. Multiphase Flow*, 13, 741–757, 1987.
Pingali, K.C., Deng, S., and Rockstraw, D.A., Direct synthesis of Ru-Ni core-and-shell nanoparticles by spray-pyrolysis: Effects of temperature and precursor constituent ratio, *Powder Technol.*, 183, 282–289, 2008.
Pischke, P., Modeling of collisional transport processes in spray dynamics, Diss. RWTH Aachen University, Aachen, Germany, 2014.
Pischke, P., Cordes, D., and Kneer, R., A collision algorithm for anisotropic disperse flows based on ellipsoidal parcel representations, *Int. J. Multiphase Flow*, 38, 1–16, 2012a.
Pischke, P., Cordes, D., and Kneer, R., The velocity decomposition method for second-order accuracy in stochastic parcel simulations. *Int. J. Multiphase Flow*, 47, 160–170, 2012b.
Planchette, C., Lorenceau, E., and Brenn, G., The onset of fragmentation in binary liquid drop collisions, *J. Fluid Mech.*, 702, 5–25, 2012.
Platzer, E. and Sommerfeld, M., Modelling of turbulent atomisation with an Euler/Euler approach including the drop size prediction, in *Proceedings of International Conference on Liquid Atomization Spray Systems ICLASS 2003*, Sorrento, Italy, 2003.
Podvysotsky, A.M. and Shraiber, A.A., Coalescence and breakup of drops in two-phase flows, *Int. J. Multiphase Flow*, 10, 195–209, 1994.
Prabhakaran, V.S., Sivakumar, D., Oommen, C., and Tharakan, T.J., Effect of temperature on atomization in gas centered coaxial injection systems, 2009. http://web.nmsu.edu/~sashi/iisc.pdf, date of access: 2013-06-20.
Pratsinis, S.E., Flame aerosol synthesis of ceramic powders, *Prog. Energy Combust. Sci.*, 24, 197–219, 1998.
Prud'homme, R. and Ordonneau, G., The maximum entropy method applied to liquid jet atomization, in *CD-Rom, Proceedings of ILASS-Europe 99*, Toulouse, France, July 5–7, 1999.
Pryds, N., Hattel, J.H., and Thorborg, J., A quasi-stationary numerical model of atomized metal droplets, II: Prediction and assessment, *J. Model. Simul. Mater. Sci. Eng.*, 7, 431–446, 1999.
Puschmann, F., Experimentelle Untersuchung der Spraykühlung zur Qualitätsverbesserung durch definierte Einstellung des Wärmeübergangs, Dissertation, University of Magdeburg, Magdeburg, Germany, 2003.
Puschmann, F., Specht, E., and Schmidt, J., Measurement of spray cooling heat transfer using an infrared-technique in combination with the Phase-Doppler technique and a patternator, *Int. J. Heat Technol.*, 19, 51–56, 2001.
Qian, J. and Law, C.K., Regimes of coalescence and separation in droplet collision, *J. Fluid Mech.*, 331, 59–80, 1997.
Rai, G., Lavernia, E.J., and Grant, N.J., Factors influencing the powder size and distribution in ultrasonic gas atomization, *J. Metals*, 37(8), 22–26, 1985.
Rajan, R. and Pandit, A.B., Correlations to predict the droplet size in ultrasonic atomization, *Ultrasonics*, 39, 235–255, 2001.
Rajathurai, A.M., Untersuchungen zur Dispergierung und Desagglomeration von submikronen Partikelensemblen, Disseration, Universität-Gesamthochschule-Duisburg, Essen, Germany, 1990.
Raju, K., Ojha, S.N., and Harsha, A.P., Spray forming of aluminium alloys and its composites: An overview, *J. Mater. Sci.*, 43(8), 2509–2521, 2008.

Ramos, J.I., *Internal Combustion Engine Modeling*, Hemisphere Publishing Corporation, New York, 1989.
Rangel, R.H. and Sirignano, W.A., The linear and nonlinear shear stability of a fluid sheet, *Phys. Fluids*, A3, 10, 2392–2400, 1991.
Ranz, W.E. and Marshall, W.R., Evaporation from drops-I and II, *Chem. Eng. Prog.*, 48, 141–173, 1952.
Rao, K.P. and Mehrotra, S.P., Effect of process variables on atomization of metals and alloys, in H. Hausner et al. (Eds.), *Modern Developments in Powder Metallurgy*, Vol. 12, Metal Powder Industries Federation, Princeton, NJ, 1980, pp. 113–130.
Rayleigh, L., On the Stability of Jets, *Proc. Lond. Math. Soc.*, 10, 4–13, 1878.
Rein, M., The transitional regime between coalescing and splashing drops, *J. Fluid Mech.*, 306, 145–165, 1996.
Reipschläger, O., Desintegrationsprozesse im Ultraschallfeld: Modellbildung, Simulation, Experiment, PhD dissertation, Uni Paderborn, Paderborn, Germany, 2002.
Reipschläger, O., Bothe, D., Monien, B., Prüss, J., Wiegand, B., and Warnecke, H.-J., Modelling and simulation of the disintegration process in ultrasonic standing wave atomizers, in *Proceedings of 18th Annual Conference on Liquid Atomization and Spray Systems ILASS Europe*, Zaragoza, Spain, 2002.
Reitz, R.D., Effect of drop breakup on fuel sprays, SAE paper, 860469, 1986.
Reitz, R.D., Mechanisms of breakup of round liquid jets, PhD thesis, Princeton University, Princeton, NJ, 1978.
Reitz, R.D., Modeling atomization processes in high-pressure vaporizing sprays, *Atom. Spray Technol.*, 3, 309–337, 1987.
Reitz, R.D. and Bracco, F.V., On the dependence of spray angle and other spray parameters on nozzle design and operating conditions, SAE paper, 790494, 1979.
Reitz, R.D. and Bracco, F.V., Mechanism of atomization of a liquid jet, *Phys. Fluids*, 25(10), 1730–1742, 1982.
Reitz, R.D. and Diwakar, R., Structure of high pressure fuel sprays, SAE paper, 870598, 1987.
Richter, H.J., Separated two-phase flow model, application to critical two-phase flow, *Int. J. Multiphase Flow*, 9(5), 511–530, 1983.
Richter, T. and Glaser, H.W., Auslegung von Hohlkegel-Druckdüsen, *Chem. Ing. Tech.*, 59(4), 332–334, 1987.
Rivas, J.R.R., Pimenta, A.P., and Rivas, G.A.R., Development of a mathematical model and 3D numerical simulation of the internal flow in a conical swirl atomizer, *Atom. Sprays*, 24(2), 97–114, 2014.
Rizk, N.K. and Lefebvre, A.H., Internal flow characteristics of simplex swirl atomizers, *J. Prop. Power*, 1(3), 193–199, 1985.
Roach, S.J., Henein, H., and Owens, D.C., A new technique to measure dynamically the surface tension, viscosity and density of molten metals, *Light Metals*, 4, 1285–1291, 2001.
Rüger, M., Hohmann, S., Sommerfeld, M., and Kohnen, G., Euler/Lagrange calculations of turbulent spray: The effect of droplet collisions and coalescence, *Atom. Sprays*, 10(1), 47–82, 2000.
Sadhal, S.S., Ayyaswamy, P.S., and Chung, J.N., *Transport Phenomena with Drops and Bubbles*, Mechanical Engineering Series, Springer Verlag, New York, 1997.
Sahle-Demessie, E., Gonzalez, M., Wang, Z.M., and Biswas, P., Synthesizing alcohols and ketones by photo-induced catalytic partial oxidation of hydrocarbons in TiO_2 film reactors prepared by three different methods, *Ind. Eng. Chem. Res.*, 38, 3276–3284, 1999.
Sahm, T., Rong, W.H., Barsan, N., Maedler, L., Friedlander, S.K., and Weimar, U., Formation of multi-layer films for gas sensing by in situ thermophoretic deposition of nanoparticles from aerosol phase, *J. Mater. Res.*, 22(4), 850–857, 2007.
Samenfink, W., Hallmann, M., Elsäßer, A., and Wittig, S., Secondary breakup of liquid droplets: Experimental investigation for a numerical description, in *Proceedings of ICLASS-94*, Rouen, France, 1994, pp. 156–163.
Scardovelli, R. and Zaleski, S., Direct numerical simulation of free-surface and interfacial flow, *Annu. Rev. Fluid Mech.*, 31, 567–603, 1999.
Schimmoeller, B., Schulz, H., Pratsinis, S.E., Bareiss, A., Reitzmann, A., and Kraushaar-Czarnetzki, B., Ceramic foams directly-coated with flame-made V_2O_5/TiO_2 for synthesis of phthalic anhydride, *J. Catal.*, 243(1), 82–92, 2006.
Schmehl, R., CFD analysis of fuel atomization, secondary droplet breakup and spray dispersion in the premix duct of a LPP combustor, in *Proceedings of Eighth International Conference on Liquid Atomization and Spray Systems ICLASS*, Passadena, CA, July 2000.
Schmehl, R., Advanced modeling of droplet deformation and breakup for CFD analysis of mixture preparation, in *Proceedings of ILASS-Europe 2002*, Zaragoza, Spain, September 9–11, 2002.

Schmehl, R., Modeling droplet breakup in complex two-phase flows, in *Proceedings of Ninth International Conference on Liquid Atomization and Spray Systems ICLASS 2003*, Sorrento, Italy, July 13–17, 2003.
Schmehl, R., Tropfendeformation und Nachzerfall bei der technischen Gemischaufbereitung, PhD thesis, Universität Karlsruhe, Karlsruhe, Germany, 2004.
Schmelz, F. and Walzel, P., Breakup of liquid droplets in accelerated gas flows, *Atom. Sprays*, 13(6), 357–372, 2003.
Schmidt, D.P., Nouar, I., Senecal, P.K., Rutland, C.J., Martin, J.K., and Reitz, R.D., Pressure-swirl atomization in the near field, SAE paper, 0496, 1999.
Schmidt, D.P. and Rutland, C.J., Reducing grid dependency in droplet collision modeling, *J. Eng. Gas Turbines Power*, 126, 227–233, 2004.
Schmidt, D.P., and Rutland, C.J., A new droplet collision algorithm, *J. Comput. Phys.*, 164, 62–80, 2000.
Schneider, A., Sprühkompaktieren mit Injektion von Feststoffpartikeln, Dissertation, Universität Bremen, VDI-Verlag, Düsseldorf, Germany, 2005.
Schneider, A., Uhlenwinkel, V., and Bauckhage, K., Zum Ausfließen von Metallschmelzen, in *Koll. SFB 372*, Vol. 5, Bremen, Germany, 2001, pp. 69–96.
Schneider, S. and Walzel, P., Zerfall von Flüssigkeiten bei Dehnung im Schwerefeld, in P. Walzel and D. Schmidt (Eds.), *Proceedings of SPRAY 98*, Essen, Germany, October 13–14, 1998.
Scholz, T., Experimentelle Untersuchungen zur Mehrphasenströmung im Sprühkegel eines elktrostatisch unterstützten Hochrotationszerstäubers, Dissertation, Universität Bremen, VDI-Verlag, Düsseldorf, Germany, 1998.
Schröder, T., Tropfenbildung an Gerinneströmungen im Schwere- und Zentrifugalfeld, Fortschr. Ber. VDI Reihe 3: Verfahrenstechnik, Nr. 503, VDI-Verlag, Düsseldorf, Germany, 1997.
Schröder, J., Günther, A., Wirth, K.E., Schuchmann, H.P., and Gaukel, V., Effervescent atomization of polyvinylpyrrolidone solutions: Influence of liquid properties and atomizer geometry on liquid breakup and spray characteristics, *Atom. Spray*, 23(1), 1–23, 2013.
Schröder, T. and Walzel, P., Design of laminar operating rotary atomizers under consideration of the detachment geometry, *Chem. Eng. Technol.*, 21(4), 349–354, 1998.
Schuch, G. and Löffler, F., Über die Abscheidewahrscheinlichkeit von Feststoffpartikeln an Tropfen in einer Gasströmung durch Trägheitseffekte, *Verfahrenstechnik*, 12(5), 302–306, 1978.
Schulte, G., *Zweidimensionale Verteilunen von Partikeleigenschaften*, Shaker Verlag, Aachen, Germany, 1995.
Schulz, H., Maedler, L., Strobel, R., Jossen, R., Pratsinis, S.E., and Johannessen, T., Independent control of metal cluster and ceramic particle characteristics during one-step synthesis of Pt/TiO_2, *J. Mater. Res.*, 20(9), 2568–2577, 2005.
Schulz, H., Stark, W.J., Maciejewski, M., Pratsinis, S.E., and Baiker, A., Flame-made nanocrystalline ceria/zirconia doped with alumina or silica: Structural properties and enhanced oxygen exchange capacity, *J. Mater. Chem.*, 13, 2979–2984, 2003.
Schütz, S., Breitling, M., and Piesche, M., Lamellenzerstäubung von Suspension mit strukturviskosen Stoffeigenschaften, *Chem. Ing. Techn.*, 75, 559–564, 2003.
Sellens, R.W., Prediction of the drop size and velocity distribution in a spray based on the maximum entropy formalism, *Part. Part. Syst. Charact.*, 6, 17–23, 1989.
Sellens, R.W. and Brzustowski, T.A., A prediction of the drop size distribution in a spray from first principles, *Atom. Spray Technol.*, 1, 85, 1985.
Senecal, P.K., Schmidt, D.P., Nouar, I., Rutland, C.J., Reitz, R.D., and Corradini, M.L., Modeling high-speed viscous liquid sheet atomization, *Int. J. Multiphase Flow*, 25(6–7), 1073–1097, 1999.
Sethian, J.A., A fast marching level set method for monotonically advancing fronts, *Proc. Natl. Acad. Sci. USA*, 93, 1591–1595, 1996.
Seydel, P., Blomer, J., and Bertling, J., Modelling particle formation at spray drying using population balance, *Dry. Technol.*, 24, 137–146, 2006.
Shepard, T.G., Bubble size effect on effervescent atomization, PhD thesis, University of Minnesota, Minneapolis, MN, 2011.
Shimizu, S., Hiroaoka, Y., and Nishiyaman, T., Instantaneous photographic observation of abrasive water suspension jets, influence of abrasive particle on jet structure, *JSME Int. J.*, 45, 4, 2002.
Shinjo, J. and Umemura, A., Simulation of liquid jet primary breakup: Dynamics of ligament and droplet formation, *Int. J. Multiphase Flow*, 36, 513–532, 2010.
Shirley, C.T. and Vu, T., Atomization of coal-water slurry using twin-fluid jet atomizer, *Fuel*, 66, 1596–1602, 1987.

Shokoohi, F. and Elrod, H.G., Numerical investigation of the disintegration of liquid jets, *J. Comput. Phys.*, 71, 324–342, 1987.
Simpkins, P.G. and Bales, E.L., Water-drop response to sudden accelerations, *J. Fluid Mech.*, 55, 629–639, 1972.
Sirignano, W.A., *Fluid Dynamics and Transport of Droplets and Sprays*, Cambridge University Press, New York, 1999.
Sivakumar, D. and Kulkarni, V., Regimes of spray formation in gas-centered swirl coaxial atomizers, *Exp. Fluids*, 51(3), 587–596, 2011.
Sizov, A.M., *Dispersion of Melts by Supersonic Gas Jets*, Metallurgija Verlag, Moskau, 1991 (in Russian).
Smagorinsky, J., General experiments with the primitives equations, *Mon. Weather Rev.*, 63, 99–164, 1963.
Sommerfeld, M., The importance of inter-particle collisions in horizontal gas–solid channel flows, in D.E. Stock, M.W. Reeks, Y. Tsuji, E.E. Michaelides, and M. Gautams (Eds.), *ASME Fluids Engineering Conference*, Hilton Head, SC, FED, Vol. 288, 1995, pp. 333–345.
Sommerfeld, M., *Modellierung und numerische Berechnung von partikelbeladenen turbulenten Strömungen mit Hilfe des Euler/Lagrange Verfahrens*, Verlag Shaker, Aachen, Germany, 1996.
Sommerfeld, M., Validation of a stochastic Lagrangian modelling approach for inter-particle collisions in homogeneous isotropic turbulence, *Int. J. Multiphase Flow*, 27, 1829–1858, 2001.
Sommerfeld, M., Kohnen, G., and Rüger, M., Some open question and inconsistencies of Lagrangian particle dispersion models, in *Proceedings of the Ninth Symposium on Turbulent Shear Flows*, Kyoto, Japan, 1993, Paper 15-1.
Sommerfeld, M. and Zivkovic, G., Resent advances in the numerical simulation of pneumatic conveying through pipe systems, in Hirch et al. (Eds.), *Computational Methods in Applied Science First European Computational Fluid Dynamics*, Brussels, Belgium, 1992, pp. 201–212.
Son, S.Y. and Kihm, K.D., Effect of coal particle size on coal-water slurry (CWS) atomization, *Atom. Sprays*, 8, 503–519, 1998.
Southwell, D.B. and Langrish, T.A.G., Observation of flow pattern in a spray dryer, *Dry. Technol.*, 18(3), 661–685, 2000.
Southwell, D.B. and Langrish, T.A.G., The effect of swirl on flow stability in spray dryers, *Trans. IChemE*, 79, Part A, 2001.
Southwell, D.B., Langrish, T.A.G., and Fletcher, D.F., Process intensification in spray dryers by turbulence enhancement, *Trans. IChemE*, 77, Part A, 1999.
Sovani, S.D., Sojka, P.E., and Lefebvre, A.H., Effervescent atomization, *Prog. Energy Combust. Sci.*, 27, 483–521, 2001.
Spalding, D.B., Mixing and chemical reaction in steady confined turbulent flames, in *13th International Symposium on Combustion*, The Combustion Institute, Pittsburgh, PA, 1971, pp. 649–657.
Spicher, U. (Hrsg.), *Direkteinsprizung im Ottomotor III*, Expert Verlag, Renningen, Germany, 2001.
Spielbauer, T.M. and Aidun, C.K., The cause and effects of perforations in a liquid sheet from a splash-plate nozzle, *Atom. Sprays*, 4(4), 405–436, 1994.
Srivastava, V.C., Ellendt, N., Meyer, C., and Uhlenwinkel, V., Synthesis of bulk amorphous und nano-crystalline materials by spray forming, in *Proceedings of SDMA 2013—Fifth International Conference on Spray Deposition and Melt Atomization*, Bremen, Germany, September 23–25, 2013.
Srivastava, V.C., Surreddi, K.B., Scudino, S., Schowalter, M., Uhlenwinkel, V., Schulz, A., Eckert, J., Rosenauer, A., and Zoch, H.W., Novel microstructural characteristics and properties of spray formed Al-RE-TM based alloys, in *Proceedings of SDMA 2009—Fourth International Conference on Spray Deposition and Melt Atomization*, Bremen, Germany, September 7–9, 2009.
Stafford, R.A., Fauroux, O., and Glass, D.H., Flow visualization and instantaneous velocity measurements of spraydryer gas and spray flows using particle image velocimetry, *Dry. Technol.*, 15(6–8), 1661–1671, 1997.
Stark, W.J., Maedler, L., Maciejewski, M., Pratsinis, S.E., and Baiker, A., Flame synthesis of nanocrystalline ceria–zirconia: Effect of carrier liquid, *Chem. Commun.*, 2003, 588–589, 2003.
Sterling, A.M. and Schleicher, C.A., The instability of capillary jets, *J. Fluid Mech.*, 68, 477–495, 1975.
Stewart, I., Massingham, J.D., and Hagers, J.J., Heat transfer coefficient effects on spray cooling, in *1995 AISE Annual Convention and Iron & Stell Exposition*, Pittsburgh, PA, 1995.
Stopic, S., Friedrich, B., Schroeder, M., and Weirich, T.E., Synthesis of TiO_2 core/RuO_2 shell particles using multistep ultrasonic spray pyrolysis, *Mater. Res. Bull.*, 48, 3633–3635, 2013.
Stopic, S., Schroeder, M., Hellmann, A., and Friedrich, B., Process design of ultrasonic spray pyrolysis synthesis of Ru/TiO_2, in *Proceedings of ILASS-Europe 2010*, Brno, Czech Republic, September 6–8, 2010.

Straatma, J., van Houwelingen, G., Steenburgen, A.E., and de Jong, P., Spray drying of food products: 1. Simulation model, *J. Food Eng.*, 42, 67–72, 1999.
Straatma, J., van Houwelingen, G., van Meulman, A.P., and Steenburgen, A.E., DRYSPEC2: A computer model of a two-stage dryer, *J. Soc. Dairy Technol.*, 44, 107–111, 1991.
Strauss, J.T., Hotter gas increases atomization efficiency, *Metal Powder Rep.*, 11, 24–28, 1997.
Strauss, J.T. and Dunkley, J.J., An experimental and empirical study of close-coupled gas atomization, in *Proceedings of PM-World Congress 2000*, Kyoto, Japan, 2000.
Strobel, R., Baiker, A., and Pratsinis, S.E., Aerosol flame synthesis of catalysts, *Adv. Powder Technol.*, 17(5), 457–480, 2006a.
Strobel, R., Maedler, L., Piacentini, M., Maciejewski, M., Baiker, A., and Pratsinis, S.E., Two-nozzle flame synthesis of $Pt/Ba/Al_2O_3$ for NO_x storage, *Chem. Mater.*, 18(10), 2532–2537, 2006b.
Strobel, R. and Pratsinis, S.E., Flame aerosol synthesis of smart nanostructured materials, *J. Mater. Chem.*, 17, 4743–4756, 2007.
Strobel, R. and Pratsinis, S.E., Effect of solvent composition on oxide morphology during flame spray pyrolysis of metal nitrates, *Phys. Chem. Chem. Phys.*, 13, 9246–9252, 2011.
Su, Y.H. and Tsao, C.Y.A., Modeling of solidification of molten metal droplet during atomization, *Met. Mater. Trans. B*, 28B, 1249–1255, 1997.
Sussman, M., Fatemi, E., Smereka, P., and Osher, S., An improved level set method for incompressible two-phase, *Comput. Fluids*, 27, 663–680, 1998.
Sussman, M. and Puckett, E.G., A coupled level set and volume-of-fluid method for computing 3D and axi-symmetric incompressible two-phase flows, *J. Comput. Phys.*, 162, 301–337, 2000.
Suyari, M. and Lefebvre, A.H., Film thickness measurements in a simplex swirl atomizer, *J. Prop. Power*, 2(6), 528–533, 1986.
Svejda, P., *Prozesse und Applikationsverfahren in der industriellen Lackiertechnik*, Vincentz Verlag, Hannover, Germany, 2003.
Takatori, K., Tani, T., Watanabe, N., and Kamiya, N., Preparation and characterization of nano-structured ceramic powders synthesized by emulsion combustion method, *J. Nanopart. Res.*, 1, 197–204, 1999.
Tanasawa, Y., Miyasaka, Y., and Umehara, M., Effect of shape of rotating discs and cups on liquid atomization, in *International Conference On Liquid Atomization Spray Systems ICLASS*, Tokyo, Japan, 1978.
Tanasawa, Y. and Toyoda, S., On the atomization of a liquid jet issuing from a cylindrical nozzle, *Technol. Rep. Tohoky Univ.*, Japan, 19(2), 135, 1955.
Tanguy, S. and Berlemont, A., Application of a level set method for simulation of droplet collisions, *Int. J. Multiphase Flow*, 31, 1015–1035, 2005.
Tani, T., Takatori, K., and Watanabe, N., Characteristics and sintering behavior of barium titanate powder synthesized by emulsion combustion method, *J. Ceram. Soc. Jpn.*, 109(12), 981–985, 2001.
Tani, T., Takatori, K., Watanabe, N., and Kamiya, N., Metal oxide powder synthesis by the "emulsion combustion" method, *J. Mater. Res.*, 13(5), 1099–1102, 1998.
Tani, T., Watanabe, N., Takatori, K., and Pratsinis, S.E., Morphology of oxide particles made by the emulsion combustion method, *J. Am. Ceram. Soc.*, 86(6), 898–904, 2003.
Tanner, F.X., Development and validation of a cascade atomization and drop breakup model for high-velocity dense sprays, *Atom. Sprays*, 14(3), 211–242, 2004.
Tanner, F.X., Liquid jet atomization and droplet breakup modeling of non-evaporating diesel fuel sprays, SAE paper, 970050, 1997.
Tao, F., Numerical modeling of soot and NOx formation in non-stationary diesel sprays with complex chemistry, PhD thesis, Chalmers University of Technology, Göteborg, Sweden, 2003.
Tao, F. and Chomiak, J., Numerical investigation of reaction zone structure and flame liftoff of DI Diesel sprays with complex chemistry, SAE paper, 2002-01-1114, 2002.
Taylor, G.I., Generation of ripples by wind blowing over a viscous liquid, *Collected Works of G.I. Taylor*, Vol. 3, 1949.
Taylor, G.I., The dynamics of thin sheets of fluid, *Proc. R. Soc.*, A 253, 289, 1959.
Taylor, G.I., The shape and acceleration of a drop in a high speed air stream, Technical report, in G.K. Batchelor (Ed.), *Scientific Papers of G. I. Taylor*, Cambridge University Press, Cambridge, 1963.
Teoh, W.Y., Amal, R., and Maedler, L., Flame spray pyrolysis: An enabling technology for nanoparticles design fabrication, *Nanoscale*, 2, 1324–1347, 2010.
Teoh, W.Y., Maedler, L., Beydoun, D., Pratsinis, S.E., and Amal, R., Direct (one-step) synthesis of TiO_2 and Pt/TiO_2 nanoparticles for photocatalytic mineralisation of sucrose, *Chem. Eng. Sci.*, 60(21), 5852–5861, 2005.

Thomas, G.O., The aerodynamic Breakup of Ligaments, *Atom. Sprays*, 13, 117–129, 2003.
Tian, X.S., Zhao, H., Liu, H.F., Li, W.F., and Xu, J.L., Three-dimensional large Eddy simulation of round liquid jet primary breakup in coaxial gas flow using the VOF Method, *Fuel Process. Technol.*, 131, 396–402, 2015.
Ting, J., Peretti, M.W., and Eisen, W.B., The effect of deep aspiration on gas-atomized powder yield, *Mater. Sci. Eng. A*, 326(1), 110–121, 2002.
Tomar, G., Fuster, D., Zaleski, S., and Popinet, S., Multiscale simulations of primary atomization, *Comput. Fluids*, 39, 1864–1874, 2010.
Trapaga, G., Matthys, E.F., Valencia, J.J., and Szekely, J., Fluid flow, heat transfer and solidification of molten metal droplets impinging on substrates—Comparison of numerical and experimental results, *Metall. Trans. B Process Metall.*, 23 B, 701–718, 1992.
Tratnig, A., Eigenschaften von Sprays aus Drall-Druck-Zerstäubern, PhD thesis, Graz University of Technology, Graz, Austria, 2009.
Triebnigg, H., *Der Einblase- und Einspritzvorgang bei Dieselmotoren*, Vienna, Austria, 1929.
Tsao, C.Y.A. and Grant, N.J., Modeling of the liquid dynamic compaction spray process, *Int. J. Powder Metall.*, 30(3), 323–333, 1994.
Tschöke, H., and Leyh, B. (Eds.), *Diesel- und Benzindirekteinspritzung II*, Expert Verlag, Renningen, Germany, 2003.
Tseng, L.K., Wu, P.K., and Faeth, G.M., Dispersed-phase structure of pressurize-atomized sprays at various gas densities, *J. Prop. Power*, 8, 1157–1166, 1992.
Tsunemoto, H., Ishitani, H., Montajir, R.M.D., Hayashi, T., and Kitayama, N., Cylinder to cylinder deviations in fuel spray and exhaust emissions at idling in high pressure DI diesel engines, in *Fifth International Symposium Diagnostics and Modeling Internal Combustion Engines*, Nagoja, Japan, 2001.
Turnbull, D., Formation of crystal nuclei in liquid metals, *J. Appl. Phys.*, 21, 1022–1028, 1950.
Uhlenwinkel, V., Zum Ausbreitungsverhalten der Partikeln bei der Sprühkompaktierung von Metallen, Dissertation, Universität Bremen, Bremen, Germany, 1992.
Uhlenwinkel, V., Achelis, L., Lagutkin, S., and Sheikhaliev, S., Verfahren und Vorrichtung zum Herstellen von Metallpulvern und Keramischen Pulvern, Patent DE 10237213.6, 2002.
Uhlenwinkel, V., Fritsching, U., Bauckhage K., and Urlau, U., Strömungsuntersuchungen im Düsennahbereich einer Zweistoffdüse-Modelluntersuchungen für die Zerstäubung von Metallschmelzen, *Chem. Ing. Techn.*, 62(3), 228–229, 1990.
Ünal, A., Effect of processing variables on particle size in gas atomization of rapidly solidified aluminium powders, *Mater. Sci. Technol.*, 3, 1029–1039, 1987.
Ünal, A., Flow separation and liquid rundown in a gas—Atomization process, *Metall. Trans.*, 20B, 613–622, 1989.
Vallet, A., Burluka, A.A., and Borghi, R., Development of a Eulerian model for the "Atomization" of a liquid jet, *Atom. Sprays*, 11(6), 619–642, 2001.
van der Pijl, S.P., Segal, A., and Vuik, C., A mass-conserving level-set method for modelling of multi-phase flows, *Int. J. Numer. Methods Fluids*, 47, 339–361, 2005.
van der Sande, E. and Smith, J.M., Jet breakup and air entrainment by low-velocity turbulent jets, *Chem. Eng. Sci.*, 31(3), 219–224, 1976.
van Wachem, B.G.M. and Schouten, J.C., Experimental validation of 3-d Lagrangian VOF model: Bubble shape and rise velocity, *AIChE J.*, 48(12), 2744–2753, 2002.
Verdurmen, R.E.M., Menn, P., Ritzert, J., Blei, S., Nhumaio, G.C.S., Sonne Sørensen, T., Gunsing, M. et al., Simulation of agglomeration in spray drying installations; the EDECAD project, *Dry. Technol.*, 22(6), 1403–1461, 2004.
Verdurmen, R.E.M., Verschueren, M., Straatma, J., and Gunsing, M., Simulation of agglomeration in spray drying; the EDECAD project, in *Ninth International Conference on Liquid Atomization and Spray Systems* (*ICLASS 2003*), Sorrento, Italy, 2003.
Viskanta, R. and Incropera, F.P., Quenching with liquid jet impingement, in I. Tanasawa and N. Lior (Eds), *Heat and Mass Transfer in Materials Processing*, Hemisphere Publishing Corporation, New York, 1992, pp. 455–476.
Voller, V.R., Swaminathan, C.R., and Thomas, B.G., General source-based methods for solidification phase change, *Num. Heat Transfer*, Part B, 19, 175–189, 1991.
von Berg, E., Bürger, M., Cho, S.H., and Schatz, A., Analysis of atomization of a liquid jet taking into account effects of the near surface boundary layer, in *Proceedings of 11th ILASS-Europe Conference*, Nürnberg, Bavaria, March 21–23, 1995.

Walzel, P., Zerteilgrenze beim Tropfenaufprall, *Chem. Ing. Techn.*, 52, 338–339, 1980a.
Walzel, P., Turbulenter Zerfall von Flüssigkeitsstrahlen aus der Sicht der Ähnlichkeitstheorie, *Chem. Ing. Techn.*, 52(6), 525–526, 1980b.
Walzel, P., Auslegung von Einstoff-Druckdüsen, *Chem. Ing. Techn.*, 54(4), 313–328, 1982.
Walzel, P., Zerstäuben von Flüssigkeiten. *Chem. Ing. Techn.*, 62(12), 983–994, 1990.
Walzel, P., Liquid atomization, *Int. Chem. Eng.*, 33(1), 46–60, 1993.
Walzel, P., Spraying and atomizing of liquids, *Ullmann's Encyclopedia of Industrial Chemistry*, 6th edn., 1999 Electronic Release, Wiley VCH, Weinheim, Germany, 1999.
Walzel, P., Spraying and atomizing of liquids, *Ullmann's Encyclopedia of Industrial Chemistry*, Vol. 34, Wiley VCH, Weinheim, Germany, 2012, pp. 79–98.
Walzel, P. and Musemic, E., Zerstäubung mit Einstoffdruckdüsen, Kapitel L4.4 im *VDI-Wärmeatlas*, 11. Auflage, VDI Verlag, Düsseldorf, Germany, 2013.
Walzel, P., Schmelz, F., and Schneider, S., Herstellen monodisperser Tropfen mit pneumatischen Ziehdüsen, *Chem. Ing. Techn.*, 73(12), 1599–1602, 2001.
Wan, Y.P., Pitsch, H., and Peters, N., Simulation of autoignition delay and location of fuel sprays under diesel-engine relevant conditions, SAE-paper, 971590, 1997.
Wang, G.X. and Matthys, E.F., Modelling of heat transfer and solidification during splat cooling: Effect of splat thickness and splat/substrate thermal contact, *Int. J. Rapid Solidif.*, 6, 141–174, 1991.
Wang, G.X. and Matthys, E.F., Numerical modelling of phase change and heat transfer during rapid solidification processes: Use of control volume integral with element subdivision, *Int. J. Heat Mass Transfer*, 35, 141–153, 1992.
Wardle, K.E. and Weller, H.G., Hybrid multiphase CFD solver for coupled dispersed/segregated flows in liquid–liquid extraction, *Int. J. Chem. Eng.*, 2013, 1–13, 2013.
Warnatz, J., Mass, U., and Dibble, R.W., *Combustion, Physical and Chemical Fundamentals, Modeling and Simulation, Experiments, Pollutant Formation*, Springer-Verlag, Berlin, Germany, 1996.
Watkinson, D., Hughes, R., Sims, G., Yule, A., and Zhou, C., Gas atomization of polymeric materials, in *Proceedings of Liquid Atomization and Spray Systems ILASS-Europe*, Zurich, Switzerland, 2001.
Weber, C., Zum Zerfall eines Flüssigkeitsstrahles, *Z. Angew. Math. Mech.*, 11, 138–145, 1931.
Weller, H.G., A new approach to VOF-based interface capturing methods for incompressible and compressible flow, Technical Report, OpenCFD Ltd, Bracknell, UK, 2008.
Wendelstorf, J., Spitzer, K.H., and Wendelstorf, R., Spray water cooling heat transfer at high temperatures and liquid mass fluxes, *Int. J. Heat Mass Transfer*, 51, 4902–4910, 2008a.
Wendelstorf, R., Spitzer, K.H., and Wendelstorf, J., Effect of oxide layers on spray water cooling heat transfer at high surface temperatures, *Int. J. Heat Mass Transfer*, 51, 4892–4901, 2008b.
Whitlow, J.D. and Lefebvre, A.H., Effervescent atomizer operation and spray characteristics, *Atom. Sprays*, 3, 137–155, 1993.
Wille, R. and Fernholz, H., Report on the first European Mechanics colloquium on the coanda effect, *J. Fluid Mech.*, 23, 801–819, 1965.
Williams, A.W., *Combustion of Liquid Fuel Sprays*, Butterworths & Co. Publishers, London, U.K., 1990.
Woodruff, D.P., *The Solid–Liquid Interface*, Cambridge University Press, Cambridge, U.K., 1973.
Wozniak, G., *Zerstäubungstechnik: Prinzipien, Verfahren, Geräte*, Springer-Verlag, Berlin, Germany, 2003.
Wruck, N., *Transientes Sieden von Tropfen beim Wandprall*, ShakerVerlag, Aachen, Germany, 1999.
Wu, Y. and Lavernia, E.J., Interaction mechanisms between ceramic particles and atomized metallic droplets, *Metall. Trans. A*, 23(10), 2923–2937, 1992.
Xiao, F., Dianat, M., and McGuirk, J.J., Large Eddy simulation of single droplet and liquid jet primary breakup using a coupled level set/volume of fluid, *Atom. Sprays*, 24(4), 281–302, 2014.
Yang, S.Y. and Kim, S.G., Characterization of silver and silver/nickel composite particles prepared by spray pyrolysis, *Powder Technol.*, 146(3), 185–192, 2004.
Yearling, P.R. and Gould, R.D., Convective heat and mass transfer from single evaporating water, methanol and ethanol droplets, in *ASME FED*, Vol. 223, San Francisco, CA, November 12–17, 1995, pp. 33–38.
Yule, A.J. and Dunkley, J.J., *Atomization of Melts*, Clarendon Press, Oxford, U.K., 1994.
Zaleski, S. and Boeck, T., Direct numerical simulation of high speed jet atomization, in *Proceedings of ICLASS-2003*, Sorrento, Italy, 2003.
Zaleski, S. and Li, J., Direct simulation of spray formation, in *Proceedings of ICLASS-'97*, Seoul, Korea, August 1997, pp. 812–819.

Zaleski, S., Li, J., Succi, S., Scardovelli, R., and Zanetti, G., Direct numerical simulation of flows with interfaces, in *Proceedings of Second International Conference on Multiphase Flow*, Kyoto, Japan, April 1995.
Zbicinski, I. and Li, X., Conditions for accurate CFD modelling of spray-drying process, *Dry. Technol.*, 24(9), 1109–1114, 2006.
Zbicinski, I., Grad, J., and Strumillo, C., Effect of turbulence on heat and mass transfer in the atomization zone, *Dry. Technol.*, 14(2), 231–244, 1996.
Zeoli, N. and Gu, S., Numerical modelling of droplet break-up for gas atomisation, *Comput. Mater. Sci.*, 38, 282–292, 2006.
Zhang, P. and Law, C.K., An analysis of head-on droplet collision with large deformation in gaseous medium, *Phys. Fluids*, 23 (042102), 1–22, 2011.
Zhao, H., Liu, H.F., Li, W.F., and Xu, J.L., Morphological classification of low viscosity drop bag breakup in a continuous air jet stream, *Phys. Fluids*, 22(11), 114103, 2010.
Zhao, Y.Y., Dowson, A.L., and Jacobs, M.H., Modelling of liquid flow after a hydraulic jump on a rotating disc prior to centrifugal atomization, *Modell. Simul. Mater. Sci. Eng.*, 8(1), 55–65, 2000.
Zhu, C., Numerical investigation on the instability and the primary breakup of inelastic non-Newtonian liquid jets, Diss. Univ. Stuttgart, Verlag Dr. Hut, München, Germany, 2014.
Zhu, C., Ertl, M., and Weigand, B., Numerical investigation on the primary breakup of an inelastic non-Newtonian liquid jet with inflow turbulence, *Phys. Fluids*, 25(8), 083102, 2013.
Ziesenis, J., Weiterentwicklung der PDA-Meßtechnik zur on-line Prozeßkontrolle beim Sprühkompaktieren, Dissertation, Universität Bremen, Bremen, Germany, 2003.


Taylor & Francis
Taylor & Francis Group
http://taylorandfrancis.com

20

Aerosols

Yannis Drossinos and Christos Housiadas

20.1 Introduction
20.2 General Dynamic Equation
20.3 Particle Collision Processes
20.4 Gas-to-Particle Conversion
20.5 Single Particle Motion: Deposition Mechanisms
20.6 Convective Transport and Deposition

20.1 Introduction

An aerosol is a dispersion of small solid or liquid particles suspended in a gas, usually air. The term aerosol refers to both the particles and the suspending gas. Aerosol particle sizes range from 0.001 μm (0.001 μm = 10^{-9} m = 1 nm = 10 Å) to 100 μm (10^{-4} m); hence, the particle sizes of interest span several orders of magnitude, ranging from almost macroscopic dimensions down to near-molecular sizes. An aerosol is a two-phase system with a gas phase and a dispersed phase, called particulate phase, which may be solid or liquid. In aerosols, the particulate phase is very dilute. Particles represent a very small fraction, less than 0.0001%, of the total aerosol mass or volume. The two phases are one-way coupled: the hydrodynamics of the gas phase influences the behavior of the particulate phase, while the particulate phase exerts negligible influence on the hydrodynamics of the gas phase.

The technical term aerosol has a much broader meaning than the popular term aerosol, which refers to the spray of droplets released from a spray can. The technical term applies to a large variety of systems, such as clouds, dust, fog, fume, haze, smog, smoke, and sprays, and it may even include airborne biological material like viruses, pollen, bacteria, fungi, etc. Particle size is the most important parameter characterizing an aerosol. In modern aerosol literature, particle size is specified by the particle diameter, d_p, most commonly expressed in micrometers and occasionally in nanometers. Based on their size, aerosol particles can be classified into a number of categories that, however, are not rigorously defined and are usually application specific. If the aerosol particles are not spherical, a characteristic size may be identified as described in Section 20.3 or Chapter 1. In ambient aerosols, for instance, the classification of Whitby (1978) is often used: particles are divided into two main fractions: the *coarse* fraction ($d_p > 2\,\mu m$) and the *fine* fraction ($d_p < 2\,\mu m$). The fine fraction is further subdivided into the *nucleation* mode ($d_p < 0.1\,\mu m$) and the *accumulation* mode ($0.1 < d_p < 2\,\mu m$). Yet, this classification is not standard. Several aerosol scientists consider the diameter of 1 μm as the division line between coarse and fine fractions. To characterize a generic aerosol particle with $d_p < 0.1\,\mu m$, the term *ultrafine particle* is frequently employed. In the atmospheric aerosol literature, the nucleation mode is restricted to particles of sizes $d_p < 0.01\,\mu m$, whereas particles in the size range $0.01 < d_p < 0.1\,\mu m$ are considered to be in the *Aitken mode*. Nowadays, there is an increasing interest in *nanoparticle* applications. Pui and Chen (1997) recommended the convention $d_p < 50\,nm$ to define "nanometer particles," but occasionally, particles smaller than 100 nm (0.1 μm) are also considered nanoparticles.

The recent interest in studies of aerosols stems from the realization that they can be "desirable" or "undesirable." Undesirable aerosol particles are those that induce adverse effects on human health and contribute to air pollution, whereas desirable aerosols are those used in industrial production of high-technology materials like novel functional nanomaterials, ceramic powders, superconducting materials, and optical fibers. Aerosols, also, influence the earth's climate via their effect on the global energy balance. The aerosol direct effect refers to the scattering of solar radiation back into space by some aerosols and to the absorption of solar radiation by other aerosol types. The first indirect effect, also called cloud albedo effect, refers to the interference of atmospheric aerosols in warm, ice and mixed-phase cloud formation processes by increasing droplet and ice particle concentrations: such processes modify the cloud albedo and thereby radiation reflection and cloud lifetimes.

In this chapter, elements of aerosol dynamics and physics will be summarized and critically reviewed. Space limitations do not allow us to cover a number of important topics in aerosol physics, including experimental techniques, aerosol optical properties, nanoparticle formation, and synthesis (for a review, see, e.g., Kruis et al., 1998); particle resuspension and bouncing (for reviews, see, e.g., Ziskind et al., 1995, Henry and Minier, 2014); and respiratory deposition and modeling of inhalation dosimetry (for a brief summary, see, e.g., Housiadas and Lazaridis, 2010).

20.2 General Dynamic Equation

The primary quantity of interest in aerosol flows is the particle size distribution and its variation in space and time. The size distribution is in general a multivariate distribution function that depends on position $\mathbf{r}$, time t, and on variables that describe the particle morphology and chemical composition. If the particle morphology is neglected and particles are assumed to be spherical, a single-species particle is solely specified by its volume $v = \pi d_p^3/6$. Here, the choice of particle volume as an independent variable is preferred to particle diameter (radius), because particle volume is conserved during coagulation. The single-component, continuous particle size distribution for spherical particles is denoted by $n(v; \mathbf{r}, t)$, where $n(v; \mathbf{r}, t)dv$ is the number of particles per unit volume (number density) for particles with volumes within the range v and $v + dv$ located within a fluid volume centered at $\mathbf{r}$ (between $\mathbf{r}$ and $\mathbf{r} + \delta\mathbf{r}$) and time t. Its discrete version $n_k(\mathbf{r}, t)$ gives the number of particles per unit volume for particles with k-subunits (sometimes referred to as k-molecules or k-mers) at time t and location $\mathbf{r}$. It should be noted that with these definitions the continuous size distribution has dimensions of number of particles per volume squared, whereas the discrete size distribution has dimensions of number of particles per volume.

Particle morphology, and in general the description of nonspherical particles, requires the introduction of additional variables (shape descriptors) to account for particle shape. For example, Koh and Friedlander (1990) introduced surface area as a second independent variable to account for aggregate sintering, whereas Kostoglou and Konstandopoulos (2001) used the fractal dimension of colliding particles as additional variables in their analysis of agglomerate structure and coagulation. If the chemical composition of the aerosol particles is important, then an extended multispecies (multicomponent) size distribution function is required. In this chapter, we will concentrate on aerosol flows of spherical, single-species particles, although we discuss extensively power-law agglomerates in Section 20.3.2: further remarks on particle shape, chemical composition, and agglomerate structure will be made in the appropriate sections. The generalized l-species distribution function is discussed in, for example, Williams and Loyalka (1991).

The size distribution of an aerosol within a volume element may change due to processes that occur within it, processes referred to as *internal* processes, and due to processes that transport particles across the volume boundaries, the *external* processes. Figure 20.1 depicts a schematic diagram of aerosol processes that occur within an elemental volume. Internal processes include coagulation, agglomeration, fragmentation, and gas-to-particle conversion, a term that refers collectively to particle condensation or evaporation and nucleation, homogeneous or heterogeneous. Coagulation and agglomeration modify the size distribution without changing the mass concentration, whereas gas-to-particle conversion modifies the aerosol mass concentration. External processes include transport across the boundaries due to gas flow, diffusion, particle motion induced by temperature, concentration, or other gradients in the gas, gravitational and other external forces. All the processes that modify the size distribution are described by a population balance equation that is known as the *general dynamic equation* (GDE), which will be presented in detail in the following sections. The solution of this nonlinear, integro-differential equation for different initial and boundary conditions provides a complete description of the size distribution for arbitrary geometries and gas flows.

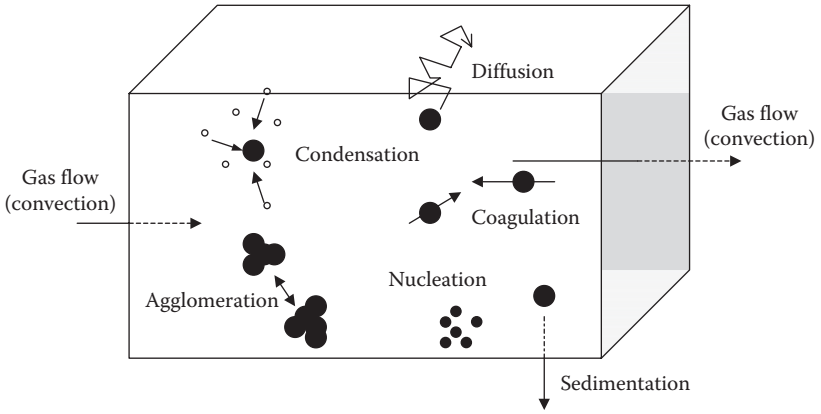


Figure 20.1

Schematic representation of aerosol processes (internal and external) within an elemental volume.

20.2.1 Internal Processes

Smoluchowski (1916) presented the first treatment of the effect of particle coagulation on the discrete particle size distribution. Although his derivation referred to hydrosols (a liquid colloidal suspension), the derivation and the final equation are equally applicable to aerosols. He considered a physical situation without spatial dependencies and without particle gains or losses, where particle coagulation occurred due to Brownian motion and motion induced by a laminar shear. Under the assumption that all particles are spherical, he showed that the dynamic equation for the discrete size spectrum $n_k(t)$ is

$$\frac{dn_k}{dt} = \frac{1}{2}\sum_{i+j=k} K(v_i, v_j) n_i n_j - n_k \sum_{i=1}^{\infty} K(v_i, v_k) n_i \tag{20.1}$$

where $K(v_i,v_j)$, expressed in dimensions of volume per unit time, is the collision frequency function between particles of volume v_i (i-mers) and v_j (j-mers). The first term on the right-hand side (RHS) of Equation 20.1 is the rate (per unit volume) at which k-mers are formed from the collision of i-mers with (k−i)-mers; the factor 1/2 avoids overcounting. The second term is the rate at which k-mers are removed by collisions with other particles that convert them to different size particles. If the collision frequency function is independent of particle size and equal to K, and the aerosol is initially monodisperse with a initial particle volume v_0, the equation for the discrete-size distribution may be solved analytically to give

$$n_k(t) = \frac{N_\infty(0)}{(1+(t/\tau))^{k+1}}\left(\frac{t}{\tau}\right)^{k-1} \tag{20.2}$$

where $N_\infty(0)$ is the total number of particles per unit volume at $t = 0$ and the characteristic time scale is $\tau = 2/[KN_\infty(0)]$. The total number concentration, $N_\infty = \sum_{i=1}^{\infty} n_i$, and the monomer concentration n_1 are found to decrease monotonically in time, whereas the average volume $v_{ave} = N_\infty(0)v_0/N_\infty(t)$ increases linearly with time.

The inclusion of the other internal process, gas-to-particle conversion, by the addition of evaporative fluxes generalizes the Smoluchowski equation. Accordingly, the time-dependent equation for the discrete size distribution within an elemental volume fixed in space and in the absence of sources or sinks becomes (Seinfeld and Pandis, 1998, Friedlander, 2000)

$$\frac{dn_k}{dt} = \frac{1}{2}\sum_{i+j=k} K(v_i, v_j) n_i n_j - n_k \sum_{i=1}^{\infty} K(v_i, v_k) n_i + \alpha_{k+1} s_{k+1} n_{k+1} - \alpha_k s_k n_k \tag{20.3}$$

As before, the first two terms on the RHS are coagulation terms. The last two are the evaporative rates (per unit volume) under the assumption that evaporation occurs via single-molecule events. The evaporative flux from a k-mer is α_k, and the effective area for evaporation is the k-mer surface area s_k. Equation 20.3 includes

condensation and evaporation terms that appear in a kinetic treatment of homogeneous nucleation. This is seen by rewriting the coagulation terms as a group of terms that describe collisions between larger particles ($i, j \neq 1$) and terms that describe single-molecule collision with other particles, for example, terms like $K(v_1,v_{k-1})n_1n_{k-1}$. These single-molecule collision terms added to the evaporative fluxes give the particle current associated to homogeneous nucleation, see Equation 20.84.

For particle volumes much larger than the molecular volume, it is convenient to replace the discrete distribution $n_k(t)$ by the continuous distribution $n(v;t)$. Then, the population balance equation expressed in a compact form becomes

$$\frac{\partial n(v;t)}{\partial t} = \left.\frac{\partial n}{\partial t}\right|_{\text{g-p}} + \left.\frac{\partial n}{\partial t}\right|_{\text{coag}} \tag{20.4}$$

The gas-to-particle conversion term, denoted as the g-p term, is occasionally rewritten in terms of the gradient of a particle current in a form suggestive of motion in particle-volume space. This formulation, according to which the current consists of two terms, renders the incorporation of condensation or evaporation and nucleation in the GDE easier (Friedlander, 2000). One term is proportional to a concentration gradient, and thus, it is interpreted as cluster diffusion with a spatially dependent diffusion coefficient. This diffusion term, which is proportional to $\partial n/\partial v$, and leads to a spread in particle space of an initially monodisperse distribution, is important for homogeneous nucleation. The other term represents cluster transport, or migration, under the influence of an external force. For the growth of large particles, the diffusion term is not significant since the concentration gradient is small, and the migration dominates. Thus, it is customary to model the gas-to-particle conversion term as follows (Seinfeld and Pandis, 1998):

$$\left.\frac{\partial n}{\partial t}\right|_{\text{g-p}} = J_{\text{nuc}}\delta(v - v^\star) - \frac{\partial}{\partial v}\left(n\frac{dv}{dt}\right) \tag{20.5}$$

where the first term J_{nuc} is the particle current due to homogeneously nucleated particles of critical size $v^\star$ (J_{nuc} is the nucleation rate per unit volume, see, e.g., Equation 20.95) and the second term $n\,dv/dt$ is the condensation current with the growth law dv/dt (see, e.g., Equation 20.135). The delta function is the Dirac delta function.

The second term on the RHS of Equation 20.4 is the coagulation term, here written for a continuous size distribution:

$$\left.\frac{\partial n}{\partial t}\right|_{\text{coag}} = \frac{1}{2}\int_0^v d\tilde{v}K(\tilde{v},v-\tilde{v})n(\tilde{v})n(v-\tilde{v}) - n(v)\int_0^\infty d\tilde{v}K(v,\tilde{v})n(\tilde{v}) \tag{20.6}$$

As before, the first term in the RHS of Equation 20.6 denotes the formation of particles of size v from the collision of particles $v-\tilde{v}$ and $\tilde{v}$, and the second the loss of particles of size v through collisions with other particles. Note that the lower limit in the coagulation integrals has been set to 0 instead of the size of the smallest stable (critical) cluster $v^\star$. This approximation renders the evaluation of the integrals easier. It does not cause significant problems, since the initial distribution may be taken to be zero up to the critical size and particles smaller than the critical size are not generated in time. Equation 20.6 is reminiscent of the gain–loss master equation of stochastic theory since $n(v;\mathbf{r},t)$ is a probability distribution function. However, its nonlinearity, which arises from particle collisions, gives it remarkable properties, which do not apply to the linear master equation. In fact, the nonlinearity and gain–loss nature of GDE render it similar to the molecular Boltzmann equation.

20.2.2 External Processes

In the presence of a gas flow, the GDE for a continuous size distribution becomes (Friedlander, 2000)

$$\frac{\partial n}{\partial t} + \nabla\cdot(n\mathbf{v}_p) = \left.\frac{\partial n}{\partial t}\right|_{\text{g-p}} + \left.\frac{\partial n}{\partial t}\right|_{\text{coag}} \tag{20.7}$$

where $\mathbf{v}_p$ is the average particle velocity and $n(v;\mathbf{r},t)dv$ the number density of particles with particle volume in the range v to $v + dv$. The particle flux density $\mathbf{J}_p = n\mathbf{v}_p$ depends on the gas flow velocity and external body forces. The LHS of Equation 20.7 describes changes in the particle size distribution due to external processes, and the RHS changes due to internal processes.

In the aerosol physics literature, it is frequently assumed that transport mechanisms act independently of each other, an assumption that usually leads to fairly good results. The average particle velocity, as obtained from the sum of the various fluxes, becomes

$$\mathbf{v}_p = \mathbf{u} - \mathfrak{D}\nabla \ln n + \mathbf{v}^{\text{ext}} \tag{20.8}$$

where

$\mathbf{u}$ is the carrier gas velocity

$\mathfrak{D}$ is the Brownian diffusion coefficient (see Equation 20.165)

$\mathbf{v}^{\text{ext}}$ is the sum of all other transport velocities, for example, thermophoretic, diffusiophoretic, photophoretic, or other velocities induced by external forces (gravitational, electrostatic)

Each of these terms will be discussed in the appropriate section. The relation of $\mathbf{v}^{\text{ext}}$ to the associated external force is given by Equation 20.167. The GDE, then, takes the form

$$\frac{\partial n(v;\mathbf{r},t)}{\partial t} + \nabla\cdot(n\mathbf{u}) = \nabla\cdot\mathfrak{D}\nabla n + \left.\frac{\partial n}{\partial t}\right|_{\text{g-p}} + \left.\frac{\partial n}{\partial t}\right|_{\text{coag}} - \nabla\cdot(n\mathbf{v}^{\text{ext}}) \tag{20.9}$$

If the coagulation and gas-to-particle conversion terms are neglected, and in the absence of external forces, Equation 20.9 becomes the usual convective diffusion equation

$$\frac{\partial n}{\partial t} + \nabla\cdot(n\mathbf{u}) = \nabla\cdot\mathfrak{D}\nabla n \tag{20.10}$$

whose solutions for different geometries in laminar flow are discussed in Section 20.6.1. Inspection of Equation 20.8 shows that the effect of particle inertia has been neglected. Thus, an assumption inherent in the usual convective diffusion equation is the neglect of inertial particle transport (and, of course, of all internal processes) and the absence of external forces. The effect of particle inertia, and its incorporation in the convective diffusion equation, is described in the following paragraphs, whereas the effect of external forces in Sections 20.5 and 20.6.

Inertial transport is best described in terms of a Lagrangian description, where the particle equations of motions are solved, and not in terms of the Eulerian description implicit in the usual formulation of the population balance equation, Equation 20.7, where processes in a fixed elemental volume are analyzed. However, the determination of important quantities, for example, the local particle concentration field (Slater and Young, 2001) or the mean interphase momentum transfer (Garg et al., 2009), is particularly difficult to obtain. A large number of particle trajectories have to be calculated to minimize statistical error, this renders the Lagrangian approach computationally inefficient. The control of the numerical error associated with Lagrangian simulations becomes more important for highly nonuniform spatial distributions of particles since the number of simulated particles in a grid cell decreases. Accordingly, the statistical error, which is inversely proportional to the square root of the number of particles per cell, increases. Recent advances in numerical implementations of the Lagrangian method have addressed this issue by introducing improved error estimators to obtain numerically convergent simulations (Garg et al., 2009). In addition, if Brownian particle diffusion is of importance, the number of simulated particle trajectories further increases to minimize the noise that arises from the stochastic particle motion. The proper incorporation of inertial transport in the Eulerian description of Equation 20.7 requires an approach similar to that presented in the two-fluid modeling sections of this handbook that are presented in Chapter 2, and the solution of the coupled two-fluid equations for mass, momentum, and energy conservation (Reeks, 1991). The simultaneous description of inertial and diffusional transport is an active area of current research; only a brief summary will be presented herein. In particular, developments to decouple the mass conservation equation from the momentum equation by performing a low Stokes number (the ratio of a particle time scale to a fluid time scale, Equation 20.169) expansion of the (average) particle velocity will be summarized.

In a two-fluid approach to aerosol transport, the average particle velocity $\mathbf{v}_p$ is obtained from the average particle momentum equation, as is common in multifluid modeling approaches to multiphase flows and described elsewhere in this book. If the aerosol particles are considered as a dispersed continuum within another continuous phase, the average momentum equation for the particulate phase may be formally written as (Fernández de la Mora and Rosner, 1982, Konstandopoulos, 1990)

$$\frac{\partial \mathbf{v}_p}{\partial t} + (\mathbf{v}_p \cdot \nabla)\mathbf{v}_p = \beta_V(\mathbf{u} - \mathbf{v}_p) + \frac{1}{mn}\nabla \cdot \ddot{\Pi}_p + \beta_V \sum_i \mathbf{v}_i^{\text{ext}} \tag{20.11}$$

where the Stokes drag has been used, $\ddot{\Pi}_p$ is the particle stress tensor, m is the particle mass within an elemental volume (mn is the local particle concentration), and the external forces per unit particle mass have been expressed in terms of β_V, the inverse particle relaxation time, $\beta_V = 1/\tau_V$ where τ_V is the particle relaxation time, see Equation 20.166 and the discussion following Equation 20.20. In the limit of small particle relaxation times ($\beta_V \to \infty$), a diffusive description of the particle flux becomes appropriate (as discussed in other chapters in this book). Different choices for the particle stress tensor lead to different forms of the GDE and the corresponding convective diffusion equations.

Ramshaw (1979) proposed a phenomenological theory of the motion of Brownian particles in a flowing, nonisothermal, incompressible fluid that leads to a modification of the particle velocity given in Equation 20.8. The derivation clarifies the assumptions and approximations inherent in the usual convective diffusion equation, or, equivalently those related to the linear addition of the various particle currents, as in Equation 20.8. The theory relies on neglecting the particle viscous stresses and assuming that the dispersed (particulate) phase behaves as an ideal gas. The approximation is summarized by $\ddot{\Pi}_p = -\ddot{\mathbf{I}}p_p$, where $\ddot{\mathbf{I}}$ is the identity tensor and p_p is the particle partial pressure (this approximation was examined in Ramshaw (1981)). The approximate expression for the particle stress tensor coupled to the assumption that the particle phase behaves as an ideal gas

$$p_p(\mathbf{r},t) = k_B n(\mathbf{r},t)T(\mathbf{r},t) \tag{20.12}$$

with k_B the Boltzmann constant leads to the following expression for the particle flux:

$$\mathrm{J}_p = n\mathbf{u} - \mathfrak{D}\nabla n - \mathfrak{D}_{\text{th}}\nabla \ln T \tag{20.13}$$

The corresponding transport coefficients are the Brownian diffusion coefficient $\mathfrak{D}$ (see Equation 20.165) and the thermal diffusion coefficient $\mathfrak{D}_{\text{th}}$, which expressed in terms of the Schmidt number Sc_p (see Equation 20.164) and the thermophoretic coefficient K_{th} (see Equations 20.173 and 20.176) becomes

$$\mathfrak{D}_{\text{th}} = n\mathfrak{D}(1 + K_{\text{th}}Sc_p) \tag{20.14}$$

As discussed in Section 20.5.2, and shown in Table 20.1, the particle Schmidt number is much greater than unity. Therefore, for typical aerosol particles (limit of large Sc_p), the thermophoretic term dominates the expression for the thermal diffusion coefficient. Hence, in the limit of large particle Schmidt numbers, the last term of Equation 20.13 becomes $-nK_{\text{th}}\nu_g\nabla \ln T$, and represents the particle mass flux associated with thermophoresis.

Forced diffusion and pressure diffusion are absent in Equation 20.13 because external forces (e.g., gravitational or electromagnetic) and imposed pressure gradients (e.g., centrifugation) were neglected. Their contribution to the total mass flux is discussed in Ramshaw (1979). If these contributions are neglected, the total flux relative to the carrier fluid becomes the sum of concentration and thermal diffusion.

A comparison of Equation 20.13, which was derived in the small particle limit, with Equation 20.11 shows that the inertial acceleration term (LHS of Equation 20.11) has been neglected in the small-particle limit. Fernández de la Mora and Rosner (1982) considered explicitly the effect of inertia on Brownian diffusional transport in isothermal aerosol flows under steady-state conditions. Following arguments similar to those summarized earlier (Ramshaw, 1979), in particular the approximate expression for the particle

Table 20.1 Aerosol Particle Parameters: Spherical Particles of Standard Density (1000 kg/m^3) in Air at 101 kPa (1 atm) and 293 K (20°C)

Particle Diameter d_p (μm)	Slip Correction C_c	Settling Velocity V_s (m/s)	Diffusion Coefficient $\mathfrak{D}$ (m^2/s)	Schmidt Number Sc_p	Relaxation Time τ_V (s)
0.001	224.3	6.75×10^{-9}	5.32×10^{-6}	2.83	6.89×10^{-10}
0.002	112.5	1.35×10^{-8}	1.33×10^{-6}	1.13×10^{1}	1.38×10^{-9}
0.005	45.34	3.41×10^{-8}	2.15×10^{-7}	7.00×10^{1}	3.48×10^{-9}
0.01	22.98	6.92×10^{-8}	5.45×10^{-8}	2.76×10^{2}	7.05×10^{-9}
0.02	11.80	1.42×10^{-7}	1.40×10^{-8}	1.07×10^{3}	1.45×10^{-8}
0.05	5.120	3.85×10^{-7}	2.43×10^{-9}	6.19×10^{3}	3.93×10^{-8}
0.1	2.928	8.82×10^{-7}	6.94×10^{-10}	2.17×10^{4}	8.99×10^{-8}
0.2	1.878	2.26×10^{-6}	2.23×10^{-10}	6.74×10^{4}	2.31×10^{-7}
0.5	1.316	9.91×10^{-6}	6.24×10^{-11}	2.41×10^{5}	1.01×10^{-6}
1.0	1.155	3.48×10^{-5}	2.74×10^{-11}	5.49×10^{5}	3.54×10^{-6}
2.0	1.077	1.30×10^{-4}	1.28×10^{-11}	1.18×10^{6}	1.32×10^{-5}
5.0	1.031	7.76×10^{-4}	4.89×10^{-12}	3.08×10^{6}	7.91×10^{-5}
10.0	1.015	3.06×10^{-3}	2.41×10^{-12}	6.24×10^{6}	3.12×10^{-4}
20.0	1.008	1.21×10^{-2}	1.19×10^{-12}	1.26×10^{7}	1.24×10^{-3}
50.0	1.003	7.55×10^{-2}	4.76×10^{-13}	3.16×10^{7}	7.70×10^{-3}
100.0	1.002	2.49×10^{-1}	2.37×10^{-13}	6.35×10^{7}	3.07×10^{-2}

stress tensor, they obtained a first-order correction to the particle velocity field due to particle inertia. They performed a low Stokes number expansion, Equation 20.169, (a low τ_V expansion) of the average momentum equation to obtain

$$\mathbf{v}_p = \mathbf{u} - \mathfrak{D}\nabla \ln n - \tau_V(\mathbf{u}\cdot\nabla)\mathbf{u} + O(\tau_V^2) \tag{20.15}$$

This relation shows that the particle velocity field of inertial particles is compressible even for an incompressible carrier gas flow and in the absence of diffusion. Equation 20.15 leads to the generalized form of Equation 20.9 (in the absence of external forces)

$$\frac{\partial n}{\partial t} + \nabla\cdot(n\mathbf{u}) - \tau_V\nabla\cdot[n(\mathbf{u}\cdot\nabla)\mathbf{u}] = \nabla\mathfrak{D}\nabla n + \left.\frac{\partial n}{\partial t}\right|_{\text{g-p}} + \left.\frac{\partial n}{\partial t}\right|_{\text{coag}} \tag{20.16}$$

that incorporates effects due to particle inertia to first-order in the particle relaxation time in an Eulerian description. The coupled calculation of diffusion and inertia in an Eulerian description is important, because these two mechanisms act in unison in many aerosol processes, for example, filtration and sampling. This Eulerian approach offers significant advantages over two-fluid models that do not decouple the mass and momentum conservation equations of the dispersed phase. Since the particle momentum equation is solved perturbatively, the particle velocity is expressed solely in terms of the fluid velocity and its spatial derivatives (in steady state, to leading order). It can be used for small particle diameters where the particle equations of motion in a Lagrangian approach become numerically stiff. Finally, it is more accurate than passive tracer models, since it takes into account simultaneously diffusive and inertial particle transport. A detailed examination of the boundary conditions associated with a similar Eulerian description, referred to as the drift flux approach, may be found in Longest and Oldham (2008).

The validity of the particle velocity approximation of Equation 20.15 for various particle relaxation times was tested by Pilou et al. (2011). They examined inertial deposition of aerosol particles in a 90° laminar bend of circular cross section in the absence of internal aerosol processes. Comparison of predictions of the Eulerian model with available experimental data was very good for both low and high Dean-number flows (De = 38 and 419) where the flow Dean number is $De = Re(R_t/R_b)^{1/2}$ where Re is the fluid Reynolds number, R_t is the tube radius, and R_b is the bend radius. Predicted deposition sites, namely, spatial deposition profiles, were also in good agreement with experimental observations. These comparisons suggest that the approximation used for the inertial term, though based on a low-particle relaxation time expansion, provides a reasonable approximation to the particle velocity even at larger τ_V.

The GDE in turbulent flow has not received the attention it deserves although in many cases encountered in practice, for example, in atmospheric dispersion, the underlying flow is turbulent. This case will not be discussed here, but the interested reader is referred to Friedlander (2000), where the full GDE for turbulent flow is presented. It suffices to mention that the starting point of the derivation is the Reynolds assumption. Specifically, if nucleation is neglected, the fluid velocity, the size distribution, and the growth law are each written as the sum of a mean plus a fluctuating component. As a result of time averaging, several new terms appear in the GDE, including a fluctuating growth term and contributions to coagulation from the fluctuating concentrations.

20.2.3 Moment Equations

The GDE may be appropriately integrated to obtain differential equations for moments of the particle size distribution. The moments of the size distribution are defined as

$$M_j(\mathbf{r},t)=\int_0^\infty dv v^j n(v;\mathbf{r},t) \tag{20.17}$$

where we have extended the lower limit to zero, an approximation valid for very small molecular or detection volumes. The zeroth moment of the distribution is of particular interest since it gives the total number concentration $N(\mathbf{r}, t)$,

$$N(\mathbf{r},t)=\int_0^\infty dv n(v;\mathbf{r},t) \tag{20.18}$$

Moment equations may be obtained by performing moment averages of the GDE, for example, of Equation 20.7 or 20.9. For spherical particles, the moments may also be defined in terms of particle diameters

$$M_j(\mathbf{r},t)=\int_0^\infty d(d_p) d_p^j n(d_p;\mathbf{r},t) \tag{20.19}$$

The most important moments are the total number concentration, $N(\mathbf{r}, t) = M_0$, the average particle diameter, $\overline{d}_p = M_1(\mathbf{r}, t)/M_0(\mathbf{r}, t)$, the average surface area per particle, $\overline{S} = \pi M_2(\mathbf{r}, t)/M_0(\mathbf{r}, t)$, and the average volume per particle, $\overline{V} = \pi M_3(\mathbf{r}, t)/[6M_0(\mathbf{r}, t)]$. If the particle density is independent of size, the third moment is proportional to the mass concentration of the particulate phase.

20.2.4 Numerical Methods

Most numerical techniques developed to solve the GDE neglect spatial inhomogeneities by assuming that the aerosol is spatially well mixed. Hence, the numerical methods concentrate on the numerical solution of Equation 20.3 or, more often, its continuous version, Equation 20.4 coupled with Equations 20.5 and 20.6. The numerical solution of the GDE is usually implemented in multidimensional aerosol flow simulations, often in combination with CFD calculations, for a range of applications, for example, in nuclear safety or nanoparticle synthesis applications. Since the evaluation of the particle size distribution is at the core of aerosol-physics calculations, the numerical methods are usually categorized in terms of the functional representation of the size distribution. They may be divided into discrete methods, methods of moments, and sectional (group) methods (Seigneur et al., 1986). These methods may be combined: for example, sectional methods have been combined with discrete methods to optimize the description of the distribution at small particle sizes (Wu and Flagan, 1988).

An early family of the methods of moments are the so-called modal methods (Whitby and McMurry, 1997). The modal methods lead to the numerical solution of moment equations; they are appropriate when the characteristic shape of the size distribution remains unaltered during the simulation period. The GDE is appropriately integrated to obtain integro-differential equations for the moments of the particle size distribution. These coupled, due to the coagulation kernel and the growth law, equations are usually decoupled by postulating a functional form for the unknown distribution function. The usual choices for the distribution

function are lognormal (see, e.g., Pratsinis, 1998), gamma, or multimodal lognormal (see, e.g., Wilck and Stratmann, 1997 and Chapter 1 of this Handbook). In the case of the lognormal distribution, the independent variables reduce to the total particle number, the geometric standard deviation, and the geometric mean. Thus, in modal methods, the solution of the GDE is converted to the numerical solution of a small number of differential equations for these moments, keeping the computational cost at acceptable levels, even for spatially multidimensional problems. Due to their low computational cost, modal methods have been incorporated within CFD calculations for multidimensional aerosol-dynamics simulations (Wilck and Stratmann 1997, Schwade and Roth, 2003, Brown et al., 2006). A significant drawback of modal methods, inherent in the *a priori* assumption for the size distribution shape, is that they do not allow an accurate simulation of the evolution of arbitrary particle size distributions.

The fundamental problem with moment methods is the closure of the evolution-of-moments equations. An important development that avoids the assumption of a distribution function is the quadrature method of moments (QMOM) proposed by McGraw and coworkers (McGraw, 1997, McGraw and Wright, 2003). McGraw (1997) addressed the closure problem by introducing a quadrature-based closure technique, a technique that is applicable to arbitrary growth laws and coagulation kernels. In essence, this method replaces the exact closure by an approximate, but less restrictive, closure. The QMOM method has also been combined and used successfully with CFD calculations (Rosner and Pyykönen, 2002, Marchisio et al., 2003).

In the sectional method (Sugutin and Fuchs, 1970, Gelbard et al., 1980, Raes and Janssens, 1986, Jokiniemi et al., 1994, Hounslow et al., 1988, Park and Rogak, 2004), the particle size spectrum is discretized into a number of size sections (particle-size bins or classes). The GDE is then solved for each section. This method does not require *a priori* assumptions of the functional form of the size distribution: thus, no limitations on the shape of the aerosol size distribution are posed. When a fixed particle-size grid is used, the simulation of nucleation and coagulation is straightforward; however, handling of particle condensational growth is rather troublesome due to numerical diffusion (Zhang et al., 1999). A large number of size sections are needed to cope with condensational growth, which, especially in multidimensional problems, may increase computational costs, rendering the solution impractical (Pyykönen and Jokiniemi, 2000). Alternatively, in the moving grid method (Gelbard, 1990), the bins are allowed to move along the particle-size axis to allow for condensation, thus eliminating numerical diffusion. In the moving grid method, however, the implementation of nucleation and coagulation is not as straightforward as in the fixed grid method because situations may occur where there are no sections at the particle-size of interest, for example, at the size of nucleating particles. The use of a moving particle-size grid raises serious difficulties when simulating particle transport in a multidimensional Eulerian transport framework. To conjoin the advantages of fixed particle-size grid in simulating nucleation, coagulation, and transport with the advantages of a moving grid in solving condensation, methods based on a hybrid (fixed and moving) grid have been developed. In these methods, condensation is accurately solved by allowing particles to grow to their actual size, which is calculated by numerical integration of the growth law. In the moving center method (Jacobson, 1997), particles are then transferred between adjacent sections of the fixed grid, according to their actual size. A new characteristic size is calculated for each section of the fixed grid from the conservation of new and existing particle number and volume. In other hybrid grid methods, the size distribution itself is calculated on the moving grid and then remapped on the fixed grid using high-order polynomial interpolation techniques (e.g., cubic spline) to reduce numerical diffusion (Lurmann et al., 1997, Mitsakou et al., 2005). The latter method was further improved by Mitrakos et al. (2007), who used the cumulative size distribution to ensure conservation of the number of particle during condensation (Yamamoto, 2004). The method was incorporated into a multidimensional transport model through an operator splitting technique. It has been used to simulate aerosol flows involving nucleation, condensation, and coagulation laminar flows (Mitrakos et al., 2008, Kissane et al., 2009).

The Monte Carlo (MC) method, a powerful numerical technique for the evaluation of multidimensional integrals, has been used to solve population balance equations: for example, Kostoglou and Konstandopoulos (2001) used it to study the evolution of fractal aggregates. Coagulation of nonspherical particles has also been studied with a sectional method (Jeong and Choi, 2001).

20.3 Particle Collision Processes

Aerosol particles suspended in a fluid collide with each other due to the following causes: (1) their relative motion, including the motion induced by Brownian diffusion; (2) fluid inhomogeneities (as those generated by turbulence or shear); and (3) motion caused external forces (gravitational, electrostatic, etc.). Concentration

or temperature gradients in the gas phase also induce relative motion, but these effects are considered secondary. Recently, however, thermophoretically dominated coagulation of particles of large thermal conductivity has been shown to modify significantly their size distribution for large local temperature gradients (Rosner and Arias-Zugasti, 2011). When the particles collide, they may agglomerate, namely the colliding primary particles retain their identity and shape, or coagulate, that is, the colliding particles fuse together and lose their identity.

We describe only the most commonly used coagulation kernels, neglecting those less frequently used, for example, the acoustic (or ultrasonic) coagulation kernel. Furthermore, we will not discuss agglomerate fragmentation, a process of significant theoretical and industrial interest; see, for example, Sonntag and Russel (1987), Eggersdorfer et al. (2010), and Vanni and Gastaldi (2010).

The behavior of a moving particle in a gas depends on exchange processes that occur on its surface: particle-to-particle mass-transfer determines their collision behavior, whereas momentum exchange between a particle and the gas determines its friction coefficient. The rates of momentum transfer between gas molecules and a particle are specified by the relative magnitude of the carrier-gas mean free path λ_g to a characteristic particle length scale L. Their ratio, referred to as the gas Knudsen number, $Kn_g = \lambda_g/L$, is the natural parameter to characterize the relative degree of rarefaction of a gas. For spherical particles, the characteristic length scale is the particle radius ($L = a_p$).

In the very small Knudsen number limit, $Kn_g < 0.001$, the fluid behaves as a continuum, characterized by the absence of fluid velocity slip on the particle surface. The drag force may be calculated from (numerical or analytical) solutions of the Navier–Stokes equations with the no-slip velocity boundary condition on the particle surface. In the slip-flow regime, $0.001 < Kn_g < 0.25$, a flow, distinct from the bulk flow, develops around the particle, leading to a velocity slip between the fluid velocity at the surface of the particle and the fluid velocity on the side of the fluid closest to the surface. The flow-velocity field may be calculated from the Navier–Stokes equations with appropriate boundary conditions to simulate the velocity slip. The fluid flow is considered to be transitional when the characteristic particle size is comparable to the gas mean free path, $0.25 < Kn_g < 10$. In the free molecular limit $Kn_g > 10$, gas molecules do not interact with each other close to the particle surface, their velocity distribution being unaffected by the presence of the particle. Exchange processes between gas molecules and the particle may be calculated from kinetic theory. Momentum-transfer processes for colloidal particles dispersed in a liquid are in the continuum regime, $L > \lambda_g$, while for spherical aerosol particles, they may lie in any momentum-transfer regime as the air mean free path is $\lambda_{\text{air}} \sim 66\,\text{nm}$ (under usual atmospheric conditions) and the particle radius may vary from a few nanometers to microns.

The dimensionless number appropriate to describe the relative motion of two colliding particles due to thermal fluctuations (in the absence of an external flow or body forces) may be identified by considering the diffusive motion of a spherical particles colliding with another stationary particle. The Langevin equation that describes the Brownian motion of a spherical particle of radius a_p in the continuum regime is

$$m_p \frac{d\boldsymbol{v}}{dt} = -f\boldsymbol{v} + \boldsymbol{W}(t); \quad \langle \boldsymbol{W}(t) \rangle = 0; \quad \langle \boldsymbol{W}(t)\boldsymbol{W}(t') \rangle = 6fk_BT\delta(t-t'), \tag{20.20}$$

where

$\boldsymbol{W}(t)$ is a noise term that models the effect of collisions between the particle and molecules of the surrounding quiescent gas

$f = \beta_v m_p$ is the friction coefficient with β_v the friction coefficient per unit mass

The random force is assumed to be Gaussian, of zero mean, and white (delta correlated in time). The angular brackets denote an ensemble average over realizations of the random force. Two characteristic time scales may be identified: the inertial particle relaxation time $\tau_V = 1/\beta_v = m_p/(6\pi\mu_g a_p) = 2\rho_p a_p^2/(9\mu_g)$, see, also, Equation 20.166, and the diffusive time scale $\tau_D = a_p^2/\mathfrak{D} = 6\pi\mu_g a_p^3/(k_BT)$, see also Equation 20.165 (Subramanian and Brady, 2004, Lukassen and Oberlack, 2014). By appropriately scaling Equation 20.20, a number of dimensionless numbers may be identified. One is the ratio of the two characteristic time scales. Another is the ratio of the particle velocity mean persistence length, the particle mean free path $\lambda_p = v_{\text{th}}\tau_v = (k_BT/m_p)^{1/2}\tau_V$ herein defined in terms of v_{th} the one-dimensional root mean square particle speed, to the particle radius. Finally, a characteristic temperature may also be defined $T^\star = m_p a_p^2/(k_B\tau_v^2)$ that divided by the system

temperature provides another dimensionless number (Isella and Drossinos, 2010). It is easy to show that these three dimensionless numbers are related. The following particular combination is referred to as the diffusive Knudsen number (Loyalka, 1976, Dahneke, 1983, Rogak and Flagan, 1992, Gopalakrishnan and Hogan, 2011, Thajudeen et al., 2012)

$$Kn_D = \frac{\lambda_p}{a_p} = \left(\frac{\tau_V}{\tau_D}\right)^{1/2} = \left(\frac{T^\star}{T}\right)^{1/2} = \frac{(k_B T m_p)^{1/2}}{6\pi\mu_g a_p^2}. \tag{20.21}$$

The diffusive Knudsen number, which is the ratio of the particle velocity mean persistence length to the particle collision length scale, is the appropriate dimensionless number to describe mass-transfer processes. Therefore, the analysis of collision processes is characterized by the two dimensionless numbers, Kn_g (momentum transfer) and Kn_D (particle–particle mass transfer), each one defining different regimes (continuum, transition, free molecular) for mass or momentum transfer.

For structures more complex than spheres, the identification of the characteristic length scale to be used in the two Knudsen numbers, Kn_g (mobility length) and Kn_D (collision length), is not straightforward. In Section 20.3.1, we consider spherical particles, for which the characteristic scale L is the particle radius and the appropriate momentum-transfer Knudsen number $Kn_g = \lambda_g/a_p$. The increase of L as coagulation progresses with time will not be addressed. In Section 20.3.2, we consider irregularly shaped particles and the associated characteristic length scales. For concreteness, we shall analyze power-law aggregates composed of touching (one-point contact), nonoverlapping (no necking), identical, spherical particles (monomers) that satisfy a scaling law. We shall retain the word coagulation for collision processes that lead to coagulation of colliding spheres, whereas the word agglomeration shall refer to noncoalescing collision processes.

20.3.1 Coagulation: Spherical Particles

For a discrete particle spectrum, the collision frequency function, or collision kernel, $K(i, j)$ which has dimensions of volume per unit time, is defined as follows:

$$N_{ij} = K(i,j) n_i n_j, \tag{20.22}$$

where N_{ij} is the number of particle collision occurring per unit time per unit volume between particles of volumes v_i and v_j, (denoted by the indices i and j) and concentrations n_i, n_j. The collision kernel depends on particle and fluid properties, the mechanisms that force the particles to collide, and the regime of mass/momentum transfer. The particle concentrations in Equation 20.22 are local, instantaneous values: in the aerosol literature, these local values are frequently approximated by average values (well-mixed aerosol assumption), thereby introducing an error that is difficult to quantify. The effect of spatial inhomogeneities on Brownian coagulation kinetics has been addressed by Kasper (1984).

The kernels presented in this section refer to aerosol particles that are perfect, rigid spheres undergoing instantaneous collisions that also yield spheres. The kernels do not include the effect of the modification of the local fluid flow as the particles approach each other (no hydrodynamic interactions). Since these local flows are expected to decrease the collision efficiency, due to increased resistance as the particles move closer, the kernels provide an upper bound to the collision efficiency. Alam (1987) proposed an analytical expression for the effect of the fluid based on the concept that the fluid resists being squeezed out from the region between the approaching particles.

For two colliding entities, the (two-particle) diffusive Knudsen number has to be redefined appropriately. The characteristic length scale associated with the collision cross section (collision radius) becomes the sum of the radii of the colliding spherical particles, the mass is replaced by the reduced mass, $\mu_{ij} = m_i m_j/(m_i + m_j)$, and the length scale associated with the particle relaxation time becomes the "reduced" radius $a_{ij} = a_i a_j/(a_i + a_j)$ (twice the harmonic mean), to obtain

$$Kn_D(i,j) = \frac{(k_B T \mu_{ij})^{1/2}}{6\pi\mu_g a_{ij}} \frac{1}{(a_i + a_j)}. \tag{20.23}$$

20.3.1.1 Brownian Coagulation

The most extensively studied, both experimentally and theoretically, coagulation process is coagulation due to Brownian motion. This process, initially studied by Smoluchowski (1916) and occasionally referred to as thermal coagulation, is important for particles smaller than 1 μm. The collision frequency function in the continuum (mass transfer) regime is

$$K_B^c(i,j) = 4\pi(a_i + a_j)(\mathfrak{D}_i + \mathfrak{D}_j) = \frac{2k_BT}{3\mu_g}\left[\frac{C_c(Kn_g, v_i)}{v_i^{1/3}} + \frac{C_c(Kn_g, v_j)}{v_j^{1/3}}\right]\left(v_i^{1/3} + v_j^{1/3}\right), \tag{20.24}$$

where a_i and a_j are the radii of the colliding particles. The second equality arises from the expression for the Brownian diffusion coefficient, Equation 20.165, that incorporates the slip correction factor $C_c(Kn_g)$, Equations 20.57 and 20.149. The derivation of the Brownian kernel is based on the calculation of the diffusional flux toward a sphere, assuming that the particle diffusion coefficients do not change as the particles approach each other. In the free molecular regime, the collision frequency function is obtained from the kinetic theory of gases, assuming that particle collisions are collision of rigid elastic spheres (Friedlander, 2000)

$$K_B^{FM}(i,j) = \left(\frac{3}{4\pi}\right)^{1/6}\left(\frac{6k_BT}{\rho_p}\right)^{1/2}\left(v_i^{-1} + v_j^{-1}\right)^{1/2}\left(v_i^{1/3} + v_j^{1/3}\right)^2, \tag{20.25}$$

where ρ_p is the particle mass density. The free molecular collision frequency function expressed in terms of the reduced particle mass becomes

$$K_{ij}^{FM}(i,j) = \left(\frac{8\pi k_BT}{\mu_{ij}}\right)^{1/2}(a_i + a_j)^2, \tag{20.26}$$

an expression that manifestly shows the dependence of the collision kernel on the collision cross section. Fuchs (1964) proposed an interpolation formula for the collision frequency function of spherical particles, valid over the entire particle mass-transfer regime:

$$K_B(i,j) = 4\pi(a_i + a_j)(\mathfrak{D}_i + \mathfrak{D}_j)\left[\frac{a_i + a_j}{a_i + a_j + \left(g_i^2 + g_j^2\right)^{1/2}} + \frac{4(\mathfrak{D}_i + \mathfrak{D}_j)}{(a_i + a_j)\left(\bar{c}_i^2 + \bar{c}_j^2\right)^{1/2}}\right]^{-1}, \tag{20.27}$$

where the mean particle velocity is $\bar{c}_i = (8k_BT/\pi m_i)^{1/2}$ with $m_i = \rho_p v_i$ as the particle mass, and g_i is the so-called Fuch's length

$$g_i = \frac{1}{3d_i l_i}\left[(d_i + l_i)^3 - \left(d_i^2 + l_i^2\right)^{3/2}\right] - d_i, \tag{20.28}$$

with $l_i = 8\mathfrak{D}_i/(\pi\bar{c}_i) = (8/\pi)^{1/2}\lambda_p(i)$, a slightly different definition of the particle mean free path. The particle diffusion coefficients in Equation 20.27 are obtained from the Stokes–Einstein expression, but they often include the Cunningham factor to provide an additional correction for the transition from the slip to the continuum regime (see Section 20.3.1.2, Equation 20.165 and subsequent discussion). The interpolation formula was derived under the assumption that every collision results in coagulation. Fuchs (1964) also discusses the effects of relaxing this assumption in terms of the collision efficiency, the fraction of collisions that result in coagulation.

The two limiting cases of the collision kernel, continuum and free molecular with respect to Kn_D, may be expressed compactly in terms of the (two-particle) diffusive Knudsen number. Since it has dimensions of volume per unit time, it may be rendered dimensionless by the scaling

$$\tilde{K}_B(i,j) = K_B(i,j)\frac{\mu_{ij}}{6\pi\mu_g a_{ij}}\frac{1}{(a_i + a_j)^3}, \tag{20.29}$$

where the second factor on the RHS is the characteristic time scale and the third is related to the collision length scale. The limiting forms of the dimensionless collision kernel become

$$\tilde{K}_B^c(i,j) = 4\pi Kn_D^2(i,j) \quad \text{as } Kn_D(i,j) \to 0, \tag{20.30}$$

$$\tilde{K}_B^{FM}(i,j) = (8\pi)^{1/2} Kn_D(i,j) \quad \text{as } Kn_D(i,j) \to \infty. \tag{20.31}$$

Various authors have proposed Brownian collision kernels valid over the entire particle mass-transfer regime; for example, Veshchunov (2010), who, using a careful analysis of the diffusive motion of colliding particles, proposed a kernel obtained via a six-parameter fit. We present the collision kernel proposed by Gopalakrishnan and Hogan (2011)

$$\tilde{K}_B(i,j) = \frac{4\pi Kn_D^2(i,j) + C_1 Kn_D^3(i,j) + \sqrt{8\pi} C_2 Kn_D^4(i,j)}{1 + C_3 Kn_D(i,j) + C_4 Kn_D^2(i,j) + C_2 Kn_D^3(i,j)}, \tag{20.32}$$

where $C_1 = 25.836$, $C_2 = 11.211$, $C_3 = 3.502$, and $C_4 = 7.211$. The constants were determined from a least-squares regression for transition-regime diffusive Knudsen numbers ($0.05 < Kn_D < 2.0$). The transition-regime collision kernel has the expected low and high Kn_D limits, continuum, as in Equation 20.30, and free molecular, as in Equation 20.31. The same reference compares literature expressions for various dimensionless collision kernels, all expressed in terms of the diffusive Knudsen number. Brownian agglomeration is also discussed in Williams and Loyalka (1991) and Friedlander (2000).

20.3.1.2 Brownian Coagulation in an External Force Field

The collision kernel is modified when the colliding particles exert a force on each other. For spherical particles interacting via a conservative force field, $\mathbf{F} = -\nabla\Phi$ where Φ is the interaction potential, the steady-state coagulation flow of particles (number of collisions per unit time per unit volume) is modified by a correction factor W as follows:

$$N_{ij} = \frac{1}{W} K_B(i,j) n_i n_j. \tag{20.33}$$

The correction factor is related to the interaction potential. Analysis of the diffusional flux toward a spherical particle leads to

$$W = \frac{1}{2}(d_i + d_j) \int_{0.5(d_i+d_j)}^{\infty} \frac{dx}{x^2} \exp\left[\frac{\Phi(x)}{k_B T}\right]. \tag{20.34}$$

Thus, for an attractive interaction potential (Φ negative), the collision frequency increases, whereas for a repulsive potential, the collision frequency decreases.

We consider two applications of Equation 20.34: van der Waals forces, which are always present, and Coulomb forces between charged particles. The van der Waals interaction potential between two spheres of different radii is a complicated function of the separation distance and particle radii, and it depends on Hamaker's constant A (see, e.g., Israellachvili, 1992). For two spheres of equal radius a_p separated by a distance r (distance between the centers of the spheres), the interaction potential simplifies to

$$\Phi = -\frac{A}{6}\left[2\left(\frac{a_p}{r}\right)^2 + \frac{2a_p^2}{r^2 - 4a_p^2} + \ln\left(1 - \frac{4a_p^2}{r^2}\right)\right]. \tag{20.35}$$

For electrically charged particles, neglecting induction forces, the Coulomb potential between two particles of radii a_i and a_j leads to a correction factor that may be calculated analytically to give

$$W = \frac{1}{y}(e^y - 1), \tag{20.36}$$

where the dimensionless parameter y is

$$y = \frac{z_i z_j e^2}{\varepsilon k_B T (a_i + a_j)}, \tag{20.37}$$

ε is the dielectric constant of the medium, and z_i is the number of charges on particle i. Thus, for uncharged particles, the correction factor vanishes, whereas for unipolar particles, the correction factor is positive and greater than unity, resulting in collision rates lower than for uncharged particles. The opposite applies to bipolar particles. The introduction of an additional interaction potential requires that an additional term be incorporated in the definition of the diffusive Knudsen number (Gopalakrishnan and Hogan, 2012).

20.3.1.3 Coagulation due to Laminar Shear

Particles in a laminar shear collide due to their relative motion induced by the gas flow spatial inhomogeneity, and thus, they may coagulate. Smoluchowski (1916) showed that in a uniform shear flow with a velocity gradient $\gamma = du/dy$, in the absence of Brownian motion, the collision frequency function becomes

$$K_{LS}(i,j) = \frac{\gamma}{6}(d_i + d_j)^3, \tag{20.38}$$

As argued earlier, this expression is approximate in that the approaching, interacting particles influence the fluid flow and the fluid streamlines about the particle are deflected around it. This effect has not been taken into account in Equation 20.38, but it may be considered by integrating the associated equations of motion in the presence of the shear, or of other inhomogeneities or of external forces, in a Lagrangian description of the particle motion.

20.3.1.4 Gravitational Coagulation

In a polydiperse aerosol in a gravitational field, heavier particles move faster than lighter ones, catching up with them and eventually colliding. This process is significant in the atmosphere where falling raindrops may scavenge aerosol particles. The coagulation kernel becomes the product of the effective target area times the relative particle velocity to give

$$K_G(i,j) = \frac{\pi}{4}(d_i + d_j)^2 \left| V_{s,i} - V_{s,j} \right|, \tag{20.39}$$

where the settling velocities are denoted by $V_{s,i}$, and are given explicitly by Equation 20.155. For spherical particles of the same material density ρ_p, the coagulation kernel may be expressed in terms of particle volume

$$K_G(i,j) = \frac{\rho_p g}{6\mu_g}\left(\frac{3}{4\pi}\right)^{1/3}\left(v_i^{2/3} + v_j^{2/3}\right)\left| v_i^{2/3} C_c(Kn_g, v_i) - v_j^{2/3} C_c(Kn_g, v_j) \right|, \tag{20.40}$$

where $C_c(Kn_g, v_i)$, the Cunningham factor, accounts for corrections in the slip regime (see Equation 20.149). The standard derivation (see, e.g., Williams and Loyalka, 1991) neglects interparticle forces that may lead to particles not colliding even though they would have done so in a purely geometrical calculation. Gravitational coagulation may be neglected for submicrometer particles, but it becomes significant for particle diameters larger than a few micrometers.

20.3.1.5 Turbulent Coagulation

Particles in a turbulent flow may collide due to inertial effects (inertial effects in turbulent flow are described in Section 20.6.3) and due to instantaneous fluid-flow inhomogeneities, that is, local velocity gradients. The first mechanism is due to the large (material) density differences between the fluid and the particle, whereas the second is always present. Saffman and Turner (1956) analyzed both mechanisms. Particles distributed uniformly

in a turbulent fluid collide as a result of small-scale shear flows over distances smaller than the Kolmogorov microscale. Thus, the analysis also requires that particle concentrations be relatively high so that the distance between colliding particles is less than the Kolmogorov microscale. As such, turbulent shear coagulation is similar to coagulation induced by laminar shear. Dimensional analysis arguments lead to the following result for the coagulation kernel due to turbulent shear

$$K_{TS}(i,j) = \frac{1.3}{8}\left(\frac{\varepsilon_d}{\nu}\right)^{1/2}(d_i + d_j)^3, \tag{20.41}$$

where ε_d is the energy dissipation rate per unit mass of the fluid. Note the similar functional dependence of the turbulent coagulation kernel and the laminar shear kernel (Equation 20.38) on particle diameter and on the local shear rate (which in isotropic turbulent flow has been related to the energy dissipation rate and the fluid kinematic viscosity).

Levich (1962) presented an alternative derivation of the turbulent coagulation kernel using concepts of classical diffusion. In the limit of dominant Brownian motion over turbulent motion, the expression he derived reproduces the classic Brownian coagulation kernel (Equation 20.24), whereas in the other limit, it reproduces the Saffman and Turner result except that the numerical prefactor 1.3 (actually the prefactor in Equation 20.41 is $(8\pi/16)^{1/2}$) becomes 5.65.

Saffman and Turner (1956) also considered coagulation due to inertial effects. They used the particle equations of motion to describe the relative particle motion and statistical arguments for isotropic turbulent flow in the high Reynolds number limit to obtain the collision frequency kernel

$$K_{TI}(i,j) = \frac{5.7}{4}(d_i + d_j)^2\left|\frac{1}{\beta_{V,i}} - \frac{1}{\beta_{V,j}}\right|\frac{\varepsilon_d^{3/4}}{\nu^{1/4}}, \tag{20.42}$$

where $\pi(d_i + d_j)^2/4$ is the collision cross section. Williams and Loyalka (1991) summarize results for the coagulation kernels in turbulent flow. They, also, present a generalized theory of turbulent coagulation that incorporates in a single formula the combined effects of Brownian diffusion, turbulent diffusion, and turbulent inertial motion. Their generalized result reproduces the formulae summarized herein (sometimes with slightly different numerical prefactors, e.g., the numerical prefactor 5.7 of Equation 20.42 becomes 6.2), and it provides an approximate expression for the combined effect of Brownian diffusion and gravitational settling. Such derivations are important to estimate inaccuracies inherent in linear (or quadratic) additions of coagulation kernels (see Section 20.3.1.6).

Theoretical developments (Reeks, 2005) suggest that the turbulent agglomeration kernels summarized in Equations 20.41 and 20.42 neglect the effect of coherent turbulent structures. Since these effects have been shown to have a nonnegligible effect on single particle motion in such flows, it has been argued that they might influence significantly coagulation in turbulent flows.

20.3.1.6 Kernel Addition

Some of the mechanisms responsible for coagulation may act simultaneously, for example, Brownian and gravitational coagulation, or gravitational and turbulent. A linear addition of Brownian with turbulent or gravitational kernels is frequently made, since particle coagulation may occur in regimes where one of them is significant and the others are not. This is not the case for the gravitational and turbulent kernels that have similar functional forms, and they may be of the same order of magnitude. An alternative, and more frequently used, approximation based on the work of Saffman and Turner (1956) is to add them quadratically as follows:

$$K_{\text{total}}(i,j) = K_B(i,j) + \left[K_G^2(i,j) + K_{TS}^2(i,j) + K_{TI}^2(i,j)\right]^{1/2}. \tag{20.43}$$

The precise nature of this approximation, or the magnitude of the error introduced in Equation 20.43, is not quantitative at the moment. Williams and Loyalka (1991) discuss a number of cases where two coagulation mechanisms act simultaneously (e.g., Brownian and shear coagulation), and they provide analytical expressions for the combined kernels.

20.3.2 Agglomeration: Power-Law Aggregates

The results presented in the previous section assumed that colliding spherical particles coagulate upon collision. Experiments and numerical simulation show that in some cases the colliding particles form agglomerates composed of smaller, primary particles. Particles that retain their identity upon collision are emitted during combustion in diesel engines, coal combustion in power plants, and commercial production of fine particles, among other processes. The size of the primary particles, the constituents of the agglomerate, ranges from nanometers to approximately 0.1 μm, and the resulting agglomerate structures vary from 0.1 μm to several micrometers. For simplicity, it is frequently assumed that the primary particles are monodisperse even though it is known that primary combustion particles are almost always polydisperse. The importance and influence of a polydispersed primary-particle size distribution on the dynamics of agglomerates is the topic of active current research (Eggersdorfer and Pratsinis, 2012, Eggersdorfer et al., 2012).

We will not distinguish between agglomerates and aggregates, even though the term aggregate (sometimes referred to as cluster) will be preferred. Their usual definitions are as follows (Kulkarni et al., 2011): An agglomerate is a loosely linked group of primary particles often held together by van der Waals forces or surface tension. Agglomerates are usually formed in the gas phase by particle collisions driven by Brownian motion or external forces or flow fields. An aggregate consists of strongly bound primary particles, often generated through coalescence and sintering at high temperatures. Strong necking between the primary particles makes the aggregate difficult to break apart, often rendering the identification of primary particles difficult. Finally, flocculates are also composed of loosely bound primary particles, held together by electrostatic forces. They break up easily in a shear flow.

20.3.2.1 Morphology

Forrest and Witten (1979), in their analysis of agglomeration of ultrafine smoke particles, were the first to suggest that the resulting agglomerates are power-law objects that obey the scaling law (over a finite size range):

$$N = k_f \left(\frac{R_g}{a_1} \right)^{d_f}, \tag{20.44}$$

where

N is the number of primary particles that form the agglomerate
d_f is the fractal (or Hausdorff) dimension
k_f is the fractal prefactor (also referred to as lacunarity (Lapuerta et al., 2010) or structure factor (Gmachowski, 1996))
R_g is the radius of gyration
a_1 is the radius of the primary particles

The fractal dimension provides a quantitative measure of the degree to which a structure fills physical space beyond its topological dimension: a compact three-dimensional structure has $d_f = 3$, whereas a line $d_f = 1$. The fractal prefactor, a parameter whose importance is increasingly being appreciated (Wu and Friedlander, 1993, Gmachowski, 1996, Sorensen and Roberts, 1997), is an essential ingredient of a complete description of power-law aggregates, as suggested by the scaling law. The radius of gyration is a geometric measure of the spatial mass distribution about the aggregate center of mass. For N identical, spherical monomers, it may be calculated via

$$R_g^2 = \frac{1}{N} \sum_{i=1}^{N} (\boldsymbol{r}_i - \boldsymbol{R}_{CM})^2 + c_1^2, \tag{20.45}$$

where $\boldsymbol{r}_i$ is the position of the ith monomer's center, and the aggregate center of mass is $\boldsymbol{R}_{CM} = 1/N \sum_{i=1}^{N} \boldsymbol{r}_i$. The additional term c_1^2 is frequently added to ensure that the scaling law remain valid even as the number of monomers tends to unity: otherwise, Equation 20.45 evaluates to zero for a monomer. It may be chosen to be the monomer radius (Filippov, 2000) or, preferably, the radius of gyration of a single 3d sphere, $c_1 = a_1\sqrt{3/5}$ (Sorensen and Roberts, 1997). Of course, for large N, the choice of the additional additive term is irrelevant.

Equation 20.44 suggests a complex and intricate interdependence of N, d_f, and k_f. Analyses of computer-generated, *in silico* synthetic, aggregates suggest that the prefactor is an indicator of local structure. It is an indicator of an aggregate's small-scale morphology, as determined, for example, from the probability distribution of the angles formed by three adjacent monomers (Melas et al., 2014a). Alternatively, it is a descriptor of packing of the primary particles, as initially proposed by Wu and Friedlander (1993). The fractal dimension is an indicator of the overall aggregate shape (large-scale aggregate morphology). A complementary indicator of large-scale structure is the cluster shape anisotropy, a measure of cluster stinginess (Heinson et al., 2010). For fixed fractal dimension, the mean shape anisotropy provides a good descriptor of aggregate morphology at large scales. The aggregate shape anisotropy is the ratio of two principal radii of gyration, obtained from the diagonalization of the aggregate inertial tensor, $R_g^2 = (R_{g,1}^2 + R_{g,2}^2 + R_{g,3}^2)/2$ with $R_{g,1} \geq R_{g,2} \geq R_{g,3}$. It is defined by $A_{13} = R_{g,1}^2 / R_{g,3}^2$.

Hence, a precise description of an aggregate is provided by the ordered pair (d_f, k_f). The simplest realization of a power-law aggregate is a straight chain, characterized by $(d_f = 1, k_f = \sqrt{3})$.

The fractal-like scaling law Equation 20.44 is valid in a statistical sense, in that aggregate properties become self-similar after an ensemble average over many aggregate realizations. Moreover, since the aggregates have a finite extent, they are never exactly self-similar: they exhibit self-similarity over a finite range of scales. For that reason, these power-law aggregates are referred to as fractal-like or quasi-fractal aggregates, and the scaling law as fractal-like. Note that the scaling law relation is independent of whether the aggregate has a real scale-invariant (self-similar) morphology.

The fractal dimension of an aggregate depends on the agglomeration mechanism: computer simulations have been used extensively to study the fractal dimension of aggregates formed via particle–cluster or cluster–cluster agglomeration in two and three dimensions, the agglomeration mechanisms being diffusive, reaction-limited, or ballistic. For example, three-dimensional simulations of ballistic-limited cluster–cluster growth predict $d_f = 1.80$, and particle–cluster growth gives $d_f = 2.50$ (see, e.g., Table 1.6 in Colbeck, 1998). The most studied aggregates are those generated via diffusion-limited cluster aggregation (DLCA) or reaction-limited cluster aggregation (RLCA). For both groups, the agglomeration mechanism is particle diffusion, the difference arising from the cluster–monomer sticking probability: it is unity for DLCA clusters and approximately 0.001 for RLCA clusters. The most frequently used scaling-law parameters are $(d_f = 1.8, k_f = 1.3)$ for DLCA and (2.05, 0.94) for RLCA clusters.

An alternative, more precise, description of aggregate morphology is provided by the two-point, orientationally averaged monomer–monomer correlation function $g(r)$. It gives the probability (per unit volume) of finding a monomer at distance r from an arbitrarily chosen monomer (Heinson et al., 2012). Note that the pair correlation function, defined with respect to an arbitrarily chosen monomer, is distinct from the radial (mass) distribution function $\rho(r)$, which gives the aggregate (mass) distribution with respect to its center of mass. An analytic expression for $g(r)$ is highly desirable as structural and dynamical aggregate properties may be expressed in terms of it. The expected functional form is

$$g(r) = \frac{A}{a_1^{d_f}} r^{d_f - 3} h\left(\frac{r}{\xi}\right), \tag{20.46}$$

where A is a dimensionless constant. The pair correlation function is normalized to (for large N)

$$N = 4\pi \int_0^\infty dr r^2 g(r), \tag{20.47}$$

and the radius of gyration is $R_g^2 = \langle r^2 \rangle$ where the average is taken with respect to $g(r)$. The algebraic decay arises from the scaling behavior, and the cut-off function $h(r/\xi)$ models the diffuse cluster interface. The correlation length ξ is a measure of interface roughness. The cutoff function is usually taken to be a stretched (or compressed if $\gamma > 1$) exponential,

$$h\left(\frac{r}{\xi}\right) = \exp\left[-\left(\frac{r}{\xi}\right)^\gamma\right], \tag{20.48}$$

the exponent γ at most weakly dependent on the agglomeration mechanism. Values suggested are γ = 2.02 (Heinson et al., 2012) or 2.20 (Lattuada et al., 2003) for DLCA, and 2.16 for RLCA aggregates (Lattuada et al., 2003). The most accurate expression, so far, for $g(r)$ was proposed by Lattuada et al. (2003) who appreciated the importance of small-scale structure by identifying specific functional forms at the first and second shells ($r = 2R_1$ and $2R_1 < r < 4R_1$). The suggested functional form was based on the analysis of synthetic aggregates.

Naumann (2003) considered the morphology of aggregates in the limit of a sharp interface ($\gamma \to \infty$). He introduced the geometric radius R_{geo} to describe the spatial extent of an aggregate: it is defined as the radius of the largest sphere encompassing the aggregate centered at its center of mass (the radius of the smallest convex envelope). For a sharp cluster interface, the radial mass distribution function $\rho(r)$, which gives the probability that a monomer be found at a given distance from the cluster center of mass, decays algebraically with distance $\rho(r) \sim r^{d_f - 3}$ (no exponential cutoff). The geometric radius is related to the radius of gyration by

$$\frac{R_g}{a_1} = \left[\frac{\int_0^{R_{geo}} dr r^4 \rho(r)}{\int_0^{R_{geo}} dr r^2 \rho(r)} \right]^{1/2} = \left(\frac{d_f}{d_f + 2} \right)^{1/2} \frac{R_{geo}}{a_1}, \tag{20.49}$$

and the fractal prefactor becomes

$$k_f = \frac{1}{f} \left(\frac{d_f}{d_f + 2} \right)^{-d_f/2}, \tag{20.50}$$

with f the filling factor, a factor introduced to ensure that monomer packing does not exceed the densest packing arrangement of hard spheres $\eta_{packing} = \pi/(3\sqrt{2}) \approx 0.7405$. An important feature of Equation 20.50 is that it imposes limits on the fractal prefactor as the volume filling factor is constrained by $\eta_{packing}$. The suggested one-to-one correspondence between the fractal dimension and the prefactor, however, is only approximate, as the more accurate analytical work of Heinson et al. (2012) and the morphological analyses of synthetic clusters (Melas et al., 2014a) show. Heinson et al. (2012) suggested that the dimensionless constant A, under the assumption that Equation 20.46 hold at all distances, may be expressed as

$$A = \frac{\phi d_f}{4\pi}, \tag{20.51}$$

with ϕ the packing fraction. The packing fraction was defined by generalizing its three-dimensional definition via $N(r) = \phi (r/a_1)^{d_f}$. Since the radius of gyration is (for large N)

$$R_g^2 = \langle r^2 \rangle = \frac{2\pi}{N} \int_0^{\infty} dr r^4 g(r), \tag{20.52}$$

the prefactor may be expressed as follows:

$$k_f = \left[\frac{2\Gamma(d_f/\gamma)}{2\Gamma((d_f + 2)/\gamma)} \right]^{d_f/2} \frac{\phi d_f \Gamma(d_f/\gamma)}{\gamma}. \tag{20.53}$$

The prefactor, thus, is a complex function of the fractal dimension, the stretching exponent, and monomer packing.

If the aggregate surface is approximately treated as sharp, the scaling law Equation 20.44 may be generalized to

$$N = k_L \left(\frac{L}{a_1} \right)^{d_L}, \tag{20.54}$$

where L is a characteristic length scale and k_L, d_L generalized prefactor and fractal dimension (respectively). The characteristic length scale is an appropriately chosen measure of an aggregate's spatial extent. As is apparent from the generalized scaling law, and already noted by Wu and Friedlander (1993), the generalized prefactor, a measure of average monomer packing, is not well defined because it depends on the choice of L. The arbitrariness in selecting a characteristic length scale arises from the absence of a well-defined interface of orientationally averaged fractal-like aggregates.

Both geometric and dynamic length scales have been chosen for L. A commonly used geometric length scale, in addition to the radius of gyration, is the outer radius, defined as half the maximum distance between any two monomers. It is easily determined from transmission electron microscopy (TEM) images. Its main shortcoming is that a sphere of radius R_{out} centered at the middle of the maximum distance (between monomers) does not necessarily enclose all monomers: only a sphere of radius $2R_{\text{out}}$ centered at an arbitrary monomer ensures that all monomers are enclosed. The geometric radius may also be chosen to be the characteristic length: the corresponding prefactor is related to the volume filling factor $k_{\text{geo}} = 1/f$ (Naumann, 2003). Occasionally, the equivalent volume radius R_{eq}, the radius of a sphere that has the same volume as the aggregate, is used. Simulations suggest that when a geometric length scale is used in the generalized scaling law, the fractal exponent does not change, remaining d_f (Melas et al., 2014a), whereas the prefactor becomes a function of the chosen measure of monomer packing.

20.3.2.2 Dynamics

The continuum-regime Brownian collision kernel suggests that the collision kernel depends on two processes: momentum transfer between particle and gas molecules, specified by Kn_g, which depends on a particle characteristic length scale, and particle-to-particle mass transfer, specified by Kn_D, which depends on the collision radius. We address each process and the associated Knudsen number separately. We remark that there is an important difference between the determination of the collision kernel via the Smoluchowski equation and numerical simulations: in the latter, the fractal dimension of the aggregate is directly obtained from the simulation (see, e.g., Isella and Drossinos, 2010), whereas in the former, the fractal dimension is an input. We also note that Kostoglou and Konstandopoulos (2001) presented an alternative description of the effect of aggregate morphology on the agglomeration rate. They considered a generalized coagulation term in the GDE for the continuous size distribution that depends on two descriptors: aggregate size (as is the case for spherical particles) and fractal dimension.

For concreteness, we concentrate on power-law aggregates composed of N touching (single-point contact), nonoverlapping spherical monomers. The friction coefficient $f_N(Kn_g)$ of an aggregate composed of N monomers over the entire (momentum-transfer) transition regime is usually expressed in terms of the empirical relation:

$$f_N(Kn_g) \equiv \frac{f_N(0)}{C_c(N, Kn_g)}, \tag{20.55}$$

where

$f_N(0)$ is the aggregate friction coefficient in the continuum regime

$C_c(N,Kn_g)$ is the N-monomer slip correction factor, also known as the Cunningham correction factor (Friedlander, 2000)

The slip correction factor $C_c(N,Kn_g)$ is unity in the continuum regime, increasing as the Knudsen increases, leading to a decreasing friction coefficient, see also Equation 20.149.

The slip correction factor of a sphere in the continuum and slip flow regimes may be calculated analytically (Ivchenko et al., 2007):

$$C_c(1, Kn_g) = \frac{f_1(0)}{f_1(Kn_g)} = \frac{1 + 3c_m Kn_g}{1 + 2c_m Kn_g}, \tag{20.56}$$

where c_m is the isothermal slip velocity coefficient. For planar surfaces in the absence of temperature gradients parallel to the surface, an approximate expression is $c_m = 5\pi(2 - \alpha_\tau)/(16\alpha_\tau)$, where α_τ is the momentum accommodation coefficient. It is the fraction of diffusely reflected molecules, or equivalently, the fraction of tangential momentum of incident molecules transmitted to the surface by all molecules. It varies from zero

for specular reflection on the particle's surface to one for perfect accommodation (diffuse reflection). The accommodation coefficient depends on the particle chemical composition, rendering the slip factor material dependent. The slip factor may be calculated across the entire momentum-transfer transition regime via the empirical Knudsen–Weber formula (Friedlander, 2000):

$$C_c(1, Kn_g) = 1 + Kn_g\left[a + b\exp\left(-\frac{c}{Kn_g}\right)\right]. \tag{20.57}$$

The experimentally determined parameters (a, b, c) depend on the material composition of the particle, where a is a function of particle surface roughness (Allen and Raabe, 1985). Their relation to the accommodation coefficient α_τ may be derived by comparing the free molecular limit of the slip correction factor of a sphere to kinetic theory results. Specifically, the friction coefficient of a spherical particle in the continuum regime is given by the (creeping flow, small particle Reynolds number) Stokes expression

$$f_1^c(Kn_g = 0) = 6\pi\mu_g a_1, \tag{20.58}$$

whereas in the free molecular limit it becomes (Friedlander, 2000)

$$f_1^{FM}(Kn_g \to \infty) = \frac{8}{3}a_p^2\rho_g\left(\frac{2\pi k_B T}{m_g}\right)^{1/2}\left(1 + \frac{\pi\alpha_\tau}{8}\right). \tag{20.59}$$

The free molecular limit may be expressed more intuitively via the kinetic theory expression for the molecular viscosity

$$\frac{\mu_g}{\lambda_g} = \phi_{KT}\rho_g\bar{c} = \phi_{KT}\rho_g\left(\frac{8k_B T}{\pi m_g}\right)^{1/2}, \tag{20.60}$$

where

ϕ_{KT} is a dimensionless constant

$\bar{c}$ the mean velocity of gas molecules, see also the discussion following Equation 20.27

Use of Equation 20.60 in the free molecular friction coefficient yields

$$f_1^{FM} = \frac{4}{3\phi_{KT}}\frac{\mu_g}{\lambda_g}\left(1 + \frac{\pi\alpha_\tau}{8}\right)A_p(1), \tag{20.61}$$

where $A_p(1) = \pi a_1^2$ is the collision cross section (projected area) of a sphere. Since in free-molecular limit of the Knudsen–Weber expression, Equation 20.57 gives $C_c(1, Kn_g) \to Kn_g(a + b)$, the friction coefficient may also be expressed as

$$f_1^{FM} = \frac{6}{a+b}\frac{\mu_g}{\lambda_g}A_p(1). \tag{20.62}$$

Comparison of Equations 20.61 and 20.62 leads to

$$\alpha_\tau = \frac{4}{\pi}\left(\frac{9\phi_{KT}}{a+b} - 2\right), \tag{20.63}$$

suggesting that the sum $a + b$ is related to the nature of gas–molecule interactions. Equation 20.63 provides a relationship between the accommodation coefficient and two parameters of the slip factor, parametrized by ϕ_{KT}. A frequently used value for ϕ_{KT} is 0.5, whereas more recent calculations suggest $\phi_{KT} = 5\pi/32 \approx 0.491$

(Ivchenko et al., 2007). The most accurate slip-factor constants are considered to be (a = 1.142, b = 0.558, c = 0.999) (Allen and Raabe, 1985), corresponding to a fraction of diffuse reflections $\alpha_\tau = 0.763$ (Cheng et al., 1988). The fraction of diffuse reflections has also been taken to be $\alpha_\tau = 0.93$, a choice that coupled to $\phi_{KT} = 0.5$ leads to the constants proposed by Millikan, (1.234, 0.414, 0.876), or $\alpha_\tau = 0.84$, which leads to (1.257, 0.4, 0.876). Irrespective of the difference in the slip-flow parameters, the calculated slip correction factors are practically identical.

The analysis of the limiting forms of the friction coefficient of a sphere leads to the important observation that it depends linearly on the particle radius in the continuum regime and quadratically in the free molecular regime (or to the orientationally averaged projected area). These dependencies remain valid even for nonspherical objects under the condition that appropriately length scales are chosen.

The slip correction factor of a N-aggregate $C_c(N,Kn_g)$ is difficult to calculate for nonspherical structures. Instead, their mobility is usually analyzed via *virtual* spherical particles that have desired properties. Two such spheres are commonly used: the equivalent mobility sphere (see, e.g., Rogak and Flagan, 1992), of equivalent mobility radius a_m, and the adjusted sphere (Dahneke, 1973), of radius a_{adj}. In addition, the equivalent hydrodynamic sphere (Filippov, 2000), of radius a_h, is occasionally used to describe aggregate mobility in near-continuum flows. The mapping of the aggregate to a virtual sphere allows the use of the single-sphere slip factor $C_c(1, Kn_g)$ in the corresponding form of Equation 20.55.

In the transition regime, the friction coefficient expressed in terms of the hydrodynamic radius is

$$f_N(Kn_g) \equiv 6\pi\mu_g a_h(Kn_g) = \frac{6\pi\mu_g a_h(0)}{C_c(N,Kn_g)}, \tag{20.64}$$

where the functional dependence of Stokes friction coefficient was used, $f_N(0) = 6\pi\mu_g a_h(0)$, with $a_h(Kn_g)$ as the hydrodynamic radius. Equation 20.64 defines the hydrodynamic radius as the radius of a sphere that has the same average mobility (the same friction and diffusion coefficients) in the *continuum* regime as the aggregate at a given Knudsen number. Its defining equation may be considered a generalization of the Stokes relation over the entire transition regime, or equivalently, a dimensionless friction coefficient.

The mobility radius $a_m(Kn_g)$, the proper hydrodynamic radius of an aggregate, is the radius of a sphere that has the same average mobility under the *same* flow conditions. The friction coefficient becomes

$$f_N(Kn_g) \equiv \frac{6\pi\mu_g a_m(Kn_g)}{C_c(1,Kn_m)}, \tag{20.65}$$

where the mobility Knudsen number is defined with respect to the only particle length scale associated with the fictitious sphere, $Kn_m \equiv \lambda_g/a_m = Kn_g a_1/a_m$. In the continuum regime, the aggregate hydrodynamic and mobility radii are equal, $a_h(0) = a_m(0)$, and for a sphere, they equal the sphere radius.

Dahneke (1973) introduced the adjusted-sphere method to calculate the friction coefficient of nonspherical objects over the entire momentum-transfer regime. The adjusted-sphere radius a_{adj} is defined as the radius of a sphere that has the same *slip* factor as the aggregate over the entire transition regime. This characteristic length is assumed to be constant, independent of the Knudsen number (i.e., independent of the flow regime as specified by the gas mean free path λ_g), in contrast to the mobility radius. The associated adjusted-sphere Knudsen number $Kn_{\text{adj}} \equiv \lambda_g/a_{\text{adj}} = Kn_g a_1/a_{\text{adj}}$ varies with Kn_g. The friction coefficient becomes

$$f_N(Kn_g) \equiv \frac{f_N(0)}{C_c(1,Kn_{\text{adj}})}. \tag{20.66}$$

According to numerous authors (e.g., Dahneke, 1973, Rogak and Flagan, 1992, Zhang et al., 2012), it is the Knudsen number that is appropriate to describe aggregate mobility in the transition regime. There is considerable evidence, both numerical and experimental, of the validity of the adjusted-sphere method in the transition regime, and it has been used in numerical simulations and analyses of experiments (Cheng et al., 1988, Rogak et al., 1991, Thajudeen et al., 2012). More recently, Zhang et al. (2012) using direct simulation MC calculated the friction coefficient of power-law aggregates over the entire momentum-transfer regime. They found excellent agreement of their results with the friction coefficients calculated via the adjusted-sphere method.

The adjusted-sphere method provides a very useful, and successful, computational method to determine the friction coefficient of irregularly shaped particles. Since a_{adj} is posited to be independent of the fluid Knudsen number, it is sufficient to calculate it once and use it for all Knudsen numbers. Nevertheless, the physical interpretation of the adjusted sphere is not transparent (it may be viewed as a constant auxiliary length introduced to calculate an aggregate's drag), nor can it be measured directly, as the equivalent mobility radius.

The adjusted-sphere radius is determined by requiring that the slip factor of the adjusted sphere have the correct continuum and free molecular limits. The free molecular limit (defined as $Kn_m \to \lambda_g/a_m(\infty)$, with $a_m(\infty)$ as the mobility radius in the free molecular regime) of

$$\frac{a_m(0)}{C_c(1, Kn_{\text{adj}})} = \frac{a_m(Kn_g)}{C_c(1, Kn_m)}, \tag{20.67}$$

an expression, which may be derived from the defining equation of the mobility and adjusted-sphere radii, leads to

$$Kn_{\text{adj}} = Kn_g \frac{a_1 a_m(0)}{a_m^2(\infty)} \quad \text{with } \frac{a_{\text{adj}}}{a_1} = \frac{a_m^2(\infty)}{a_1 a_m(0)}. \tag{20.68}$$

Rogak and Flagan (1992), in their study of agglomeration of fractal-like aggregates, were the first (to our knowledge) to present Equation 20.68. They referred to the adjusted-sphere method as an interpolation method between the continuum and transition regimes. Zhang et al. (2012) used dimensional arguments to obtain it.

Equation 20.68 shows that the adjusted-sphere radius may be calculated solely from the continuum $a_m(0)$ and free molecular $a_m(\infty)$ mobility radii. Numerous authors have suggested that in the continuum regime, the momentum-transfer mobility radius $a_m(0)$ may be reliably approximated by the mass-transfer radius. Hubbard and Douglas (1993) argued that the scalar friction coefficient of an arbitrarily shaped Brownian particle may be calculated from the solution of the Laplace equation. They showed that the angular average (corresponding to a physical orientational average due to Brownian motion) of the Oseen tensor leads to the free-space Green's function for the Laplace operator. Similarly, Isella and Drossinos (2011) proposed the collision rate method to calculate the mass-transfer radius in the continuum regime via a heuristic argument based on the calculation of the collision rate of virtual Brownian particles with straight chains. They concluded that the solution of the Laplace equation gives the continuum-regime mass-transfer radius. Comparison of their results with previous calculations confirmed that the mobility (momentum-transfer) radius is approximately equal to the mass-transfer radius. Gopalakrishnan et al. (2011) used the Langevin equation for point mass particles, an alternative way to solve the diffusion equation, to calculate the mass-transfer radius, referring to it as the Smoluchowski radius. Melas et al. (2014b, 2015) extended the collision rate method to slip flow, thus providing additional support that the approximate equality of the momentum and mass-transfer radii is valid in the transition regime. Of course, particle–particle hydrodynamic interactions are neglected in this treatment.

In the continuum regime, Melas et al. (2014a), by studying synthetic aggregates generated by a tunable cluster–cluster agglomeration mechanism (Filippov et al., 2001), proposed an empirical fit that relates aggregate morphological properties to the mass-transfer radius (taken to be equal to the mobility radius):

$$\frac{a_m(0)}{a_1} = 0.248(2 - N^{-1/3})\frac{R_g}{a_1} + 0.69N^{0.415}. \tag{20.69}$$

The empirical fit was based on synthetic-cluster calculations, where the clusters were characterized by ([1.5, 2.1], [1,1.6]). The particularity and usefulness of Equation 20.69 is that the continuum mobility radius may be estimated from the fractal dimension and prefactor in the particular combination that defines the radius of gyration R_g, and from the number of monomers, and the monomer radius a_1. This contrasts to most empirical fits available in the literature (see, e.g., Sorensen, 2011) where the continuum mobility radius is expressed in terms of aggregate statistical properties like d_f and k_f. Equation 20.69 shows that the mobility radius may be estimated for a single cluster if the monomer positions are known (either from measurements or simulations) since the independent variables do not depend on ensemble-averaged properties.

The mobility radius of bead-composed structures in the continuum regime is often estimated via the Kirkwood–Riseman formula (Kirkwood and Riseman, 1948), an expression developed in their pioneering analysis of the translational diffusion coefficient of flexible macromolecules. The Kirkwood–Riseman expression is also a geometric expression, in that it depends only on the position $\boldsymbol{r}_i$ of the monomers in the aggregate:

$$\frac{Na_1}{a_m(0)} = 1 + \frac{1}{N}\sum_{j=1}^{N}\sum_{m=1,m\neq j}^{N}\frac{a_1}{|\mathbf{r}_j - \mathbf{r}_m|}. \tag{20.70}$$

A comparison of predictions of Equation 20.69 with those of Kirkwood–Riseman shows that the latter provides a very good approximation to the mobility radius of both open and compact structures, the difference increasing as the number of monomers decreases (as expected since it is a large N expression). Thajudeen et al. (2012) proposed a slightly different, six-parameter, expression for the Smoluchowski (mass-transfer) radius of limited region of validity.

In the free molecular regime, experiments and gas-molecular scattering calculations suggest that the friction coefficient of power-law aggregates is proportional to their orientationally averaged projected area (Sorensen, 2011, Larriba and Hogan, 2013). The mobility radius of an aggregate was found to be proportional to the square root of its projected area, rendering the mobility radius and the mass-transfer radius in the free molecular regime approximately equal. Therefore, $a_m^2(\infty) = A_p(N)/\pi$ where $A_p(N)$ is the projected area of a N monomer aggregate. The adjusted-sphere radius may be re-expressed as

$$\frac{a_{\text{adj}}}{a_1} = \frac{A_p(N)}{\pi a_1 a_m(0)} = \frac{a_m^2(\infty)}{a_1 a_m(0)}. \tag{20.71}$$

MC sampling has been used to estimate the orientationally averaged projected area it; see, for example, Mackowski (2006). We present the empirical fit proposed by Melas et al. (2014b), an expression derived for aggregates composed of N = [10,60] monomers with ([1.5, 2.1], [1.0, 1.6]),

$$\frac{A_p(N)}{A_p(1)} = \frac{a_m^2(\infty)}{a_1^2} = 1.172N^{0.704}\left(\frac{R_g}{a_1}\right)^{2(-0.146N^{-1/3}+0.192)}, \tag{20.72}$$

where $A_p(1) = \pi a_1^2$ is the projected area of a sphere. The orientationally averaged projected area of a N-monomer straight chain may be approximately calculated via

$$A_p(N) = NA_p(1) - (N-1)A_{\cap}, \tag{20.73}$$

where the monomer–monomer overlap is $A_{\cap} \simeq 0.47a_1^2$.

The expressions for the continuum-regime mobility radius and the orientationally averaged projected area may be combined to obtain an expression for the adjusted-sphere radius of power-law aggregates (accurate to within less than 1%):

$$\frac{a_{\text{adj}}}{a_1} = -0.052(2 + N^{-1/3})\frac{R_g}{a_1} + 1.15N^{0.42}\ \text{(power-law aggregates)}. \tag{20.74}$$

A similar equation for straight chains valid in the entire momentum-transfer regime is

$$\frac{a_{\text{adj}}}{a_1} = -0.14\left(\frac{R_{\text{eq}}}{a_1}\right)^2 + 1.54\frac{R_{\text{eq}}}{a_1} - 0.41\ \text{(straight chains)}, \tag{20.75}$$

where $R_{\text{eq}}/a_1 = N^{1/3}$ is the radius of the equivalent volume sphere.

Equations 20.74 and 20.75 show, as initially postulated by Dahneke (1973) and discussed extensively by Thajudeen et al. (2012), that the adjusted-sphere radius becomes a geometric descriptor of an aggregate: it depends solely on the morphology of the aggregate. For an aggregate, it depends on the radius of gyration, the number of monomers, and the monomer radius, all geometric quantities. For a straight chain, it depends on the number of monomers and the monomer radius.

Given the adjusted-sphere radius, it is easy to calculate the friction coefficient of fractal-like aggregates via the defining equation of the adjusted-sphere radius and the expression for the single-sphere slip correction factor. It is instructive to reconsider the limiting behavior of Equation 20.66. We obtain, in the continuum limit Kn_g, $Kn_{\text{adj}} \to 0$,

$$f_N^c = 6\pi\mu_g a_m(0)\,, \tag{20.76}$$

and in the free molecular limit (Kn_g, $Kn_{\text{adj}} \to \infty$)

$$f_N^{FM} = \frac{6}{a+b}\frac{\mu_g}{\lambda_g}\pi a_m^2(\infty) = \frac{4}{3\phi_{KT}}\frac{\mu_g}{\lambda_g}\left(1+\frac{\pi\alpha_\tau}{8}\right)A_p(N) \approx 2.67\frac{\mu_g}{\lambda_g}\xi A_p(N), \tag{20.77}$$

where the last expression, proposed by Zhang et al. (2012), was evaluated for $\alpha_\tau = 0.91$ (leading to $\xi \approx 1.36$), $\phi_{KT} = 0.5$. The similarities to Equations 20.58 and 20.61 are remarkable.

It has been argued that the scaling law remains valid even when the characteristic length scale is chosen to be the mobility radius. The fractal-like scaling law may be written as

$$N = k_m\left[\frac{R_m(Kn_g)}{a_1}\right]^{d_m}, \tag{20.78}$$

where d_m is the mass-mobility exponent. The scaling law expressed in terms of the mobility equivalent radius is very frequently used in the interpretation of experimental measurements since many instruments, for example, differential mobility analyzer (DMA), measure (electrical) mobility. Even though the fractal dimension does not depend on the choice of the geometric length scale, it changes when the mobility radius is used. Analyses of experimental measurements on some combustion aerosol yielded $d_m \approx 2.1$–2.4, values that correspond to $d_f \approx 1.8$, indicative of DLCA aggregates (Sorensen, 2011). A slight dependence of both (d_m, k_m) on Kn_g has been reported (Melas et al., 2014b).

The previously derived quantities for a single aggregate may be appropriately redefined to obtain a generalized dimensionless collision kernel for nonspherical objects. According to Thajudeen et al. (2012), the dimensionless collision kernel becomes

$$\tilde{K}_B(i,j) = K_B(i,j)\frac{\mu_{ij}}{f(i,j)}\frac{1}{a_{\text{adj}}^2(i,j)}\frac{1}{a_m^{(i,j)}(0)}, \tag{20.79}$$

and the corresponding diffusive Knudsen number

$$Kn_D(i,j) = \frac{(k_B T\mu_{ij})^{1/2}}{f(i,j)}\frac{1}{a_{\text{adj}}(i,j)}, \quad a_{\text{adj}}(i,j) = \frac{A_p(i,j)}{\pi a_m^{(i,j)}(0)}, \tag{20.80}$$

where

$f(i,j) = f_i(Kn_g)f_j(Kn_g)/[f_i(Kn_g) + f_j(Kn_g)]$ is the reduced friction coefficient

$a_{\text{adj}}(i,j)$, $a_m^{(i,j)}(0)$, and $A_p(i,j)$ are determined from combined properties of the two colliding entities.

The functional form of the dimensionless Brownian collision kernel Equation 20.32 remains identical as long as it is appropriately rendered dimensionless and the right diffusive Knudsen number is used. The reader may consult their work for approximate expressions for the necessary two-particle correlations.

It is instructive to compare the expressions for the friction coefficient and the collision radius of power-law aggregates, and the ensuing collision kernel, to a frequently used collision kernel based on a generalization of the Smoluchowski kernel. An expression for the continuum regime kernel for large aggregates $N > 1000$ for which the diffusion coefficient approaches the Stokes–Einstein value, Equation 20.165, is (Friedlander, 2000)

$$K_B^c(i,j) = \frac{2k_BT}{3\mu_g}\left(v_i^{-1/d_f} + v_j^{-1/d_f}\right)\left(v_i^{1/d_f} + v_j^{1/d_f}\right). \tag{20.81}$$

For $d_f = 3$, Equation 20.81 reduces to the Brownian coagulation kernel for spherical particles, Equation 20.24 without the slip correction. The free molecular kernel is taken to be

$$K_B^{FM}(i,j) = \left(\frac{6k_BT}{\rho_p}\right)^{1/2}\left(\frac{3}{4\pi}\right)^{\lambda} a_1^{2-6/d_f}\left(v_i^{-1} + v_j^{-1}\right)^{1/2}\left(v_i^{1/d_f} + v_j^{1/d_f}\right)^2, \tag{20.82}$$

with

$$\lambda = \frac{2}{d_f} - \frac{1}{2}. \tag{20.83}$$

For coalescing spheres ($d_f = 3$), Equation 20.82 reduces to the kernel for Brownian coagulation of spherical particles, Equation 20.25. The region of validity is considered to be $d_f \geq 2$. Both kernels were derived under the assumption that the fractal prefactor is unity, an assumption that if removed would modify the overall constant. More importantly, the collision radius in both regimes was considered to be the radius of gyration. The mobility radius in the continuum regime $a_m(0)$ was also taken to be the radius of gyration, and it was assumed that in the free molecular regime, the two colliding particles behaved as spheres (to calculate the friction coefficient) whose radius is the radius of gyration. Furthermore, it was assumed that the colliding aggregates have the same fractal dimension.

20.4 Gas-to-Particle Conversion

Gas-phase physical or chemical processes may generate a supersaturated ($p_{\text{vap}}(T) > p_{\text{sat}}(T)$, and hence, metastable) vapor state that relaxes to equilibrium either via the generation of new particles (homogeneous nucleation) or via growth of already existing particles (condensation or heterogeneous nucleation). Physical processes that lead to a supersaturated state include cooling at a surface, adiabatic expansion or mixing, turbulent mixing, whereas condensable vapor species may be generated by gas-phase chemical reactions.

20.4.1 Nucleation

A metastable vapor phase state relaxes to equilibrium via homogeneous nucleation in the absence of aerosol particles. Homogeneous nucleation is important in numerous fields: in the atmosphere, for example, ice nucleation in supercooled water droplets is the main mechanism for the formation of cirrus clouds in the upper troposphere, whereas nanoparticle formation in engine emissions occurs via homogeneous nucleation. Herein, we concentrate on the transition from the gas phase (supercooled vapor) to a condensed phase by the formation of liquid droplets: the opposite process, bubble nucleation in superheated liquids. Similarities and differences between these two processes will be briefly mentioned.

Nucleation is a physical process that refers to the appearance of a new phase during a first-order phase transition: it is a thermally activated process that occurs via large-amplitude, localized fluctuations that may be viewed as "droplets" of the new, stable phase. Being an activated process, new particle formation requires the surmounting of a nucleation barrier. At given thermodynamic conditions (e.g., constant temperature), the new condensed phase is stable with respect to the vapor phase (its chemical potential is lower), but there is a free energy cost associated with the creation of the interface between the two phases. The competition between the free energy gain due to the creation of the stable phase and the free energy loss due to the creation of an interface creates the nucleation barrier. Whereas a metastable state decays via nucleation, an unstable state decays via a process that does not involve barrier crossing and which is called spinodal decomposition. Spinodal decomposition, not addressed herein, occurs via the growth of small-amplitude, long-wavelength fluctuations.

Space limitations do not allow us to cover some important nucleation topics including experimental measurements of nucleation rates (see, e.g., the review Heist and He 1994), computer simulations, rigorous definitions of physically consistent clusters, ion-induced nucleation, and Ostwald ripening.

20.4.1.1 Classical Nucleation Theory

The original work of Becker and Döring (1935) on isothermal nucleation and subsequently refined by Zeldovich (1942) forms what is now referred to as classical nucleation theory (CNT). These authors argued that nucleation is an activated process and that the rate should depend exponentially on the reversible work of cluster formation. For an early review of homogeneous nucleation, cf. Feder et al. (1966), whereas for more recent presentations and reviews of CNT, cf. Laaksonen et al. (1995) and Debenedetti (1996).

A complete theory of nucleation considers the dynamics of growth of the stable clusters (also referred to as embryos, droplets, or nuclei) of the new phase. For nonassociated vapors and low cluster concentrations, clusters grow or shrink by the addition or removal of a single molecule. Thus, the rate per unit volume (expressed in number of clusters per unit volume and unit time) at which the number concentration of i-molecule clusters changes is

$$J(i) = f_{i-1}s_{i-1}\beta_{i-1} - f_i s_i \alpha_i \tag{20.84}$$

where

f_i is the nonequilibrium number concentration of i-molecule clusters
s_i is the respective surface area
β_i is the forward (condensation) flux per unit time and area at which an i-cluster gains a molecule
α_i is the backward (evaporation) flux at which the cluster loses a molecule

The following assumptions are usually made:

- The forward and backward fluxes are independent of cluster size, and they do not depend on whether the system is in equilibrium.
- An equilibrium concentration of clusters is established in the bulk metastable state. This assumption converts a kinetic problem into a thermodynamic one by defining an equilibrium cluster distribution that obeys usual Boltzmann statistics. Microscopic reversibility, then, relates n_i, the equilibrium i-cluster concentration, to n_{i-1}

$$\beta s_{i-1} n_{i-1} = \alpha s_i n_i \tag{20.85}$$

  Thus, the assumption of an equilibrium distribution allows the determination of the evaporation flux α, a quantity that is difficult to evaluate, in terms of the condensation flux β, a quantity that may be easily calculated from, for example, kinetic theory of gases. The difficulty to calculate α is thus transformed to the calculation of the equilibrium droplet concentration, or, equivalently, to the study of the energetics of embryo formation. For the equilibrium, unsaturated system the evaporation flux may be calculated from the Kelvin relation (see Equation 20.89).
- A steady-state, i-independent, current (nucleation rate per unit volume) J is established.

Frenkel (1955) argued that the equilibrium cluster distribution takes the form

$$n_i = n_1 \exp\left(-\frac{\Delta G_i}{k_B T}\right) \tag{20.86}$$

where the free energy of an i-cluster is ΔG_i. The proportionality constant is taken to be the total number density of the bulk metastable state n_1 (i.e., the monomer number density, which is frequently denoted as the vapor number density n_{vap}), since it was assumed that there is no free energy change associated with the formation of a single-molecule cluster. The free energy of formation of an i-cluster is calculated by invoking the capillarity approximation, which is the fundamental assumption of CNT. Accordingly, the cluster free energy is determined by treating the cluster as an incompressible macroscopic spherical droplet with

macroscopic (bulk and surface) properties. A perfectly sharp interface is assumed to obtain a droplet free energy that depends on a volume and a surface term

$$\Delta G_i = -\frac{4\pi}{3} a_p^3 n_{\text{liq}} k_B T \ln S + 4\pi a_p^2 \sigma = -i k_B T \ln S + (36\pi)^{1/3} v_{\text{liq}}^{2/3} \sigma i^{2/3} \tag{20.87}$$

where the number of molecules in the droplet is $i = 4\pi a_p^3 n_{\text{liq}}/3$, n_{liq} is the bulk liquid number density, $S = p_{\text{vap}}/p_{\text{sat}}$ is the saturation ratio with p_{vap} the vapor pressure and p_{sat} the saturation pressure (over a flat surface), v_{liq} is the molecular volume in the liquid phase, $v_{\text{liq}} = 1/n_{\text{liq}}$, and σ is the macroscopic surface tension. The liquid number density is related to the liquid material density via $n_{\text{liq}} = \rho_l N_A/\mathfrak{M}$: a similar expression holds for the vapor number density. For a stable vapor phase (saturation ratio less than unity), the droplet free energy is a monotonically increasing function of the droplet radius. For $S > 1$ (metastable vapor phase), the volume term becomes negative. The competition between the negative volume contribution and the positive surface energy term generates a free energy maximum at the critical radius $a_p^\star$

$$a_p^\star = \frac{2\sigma v_{\text{liq}}}{k_B T \ln S} \tag{20.88}$$

Equation 20.88 determines the equilibrium radius of a droplet as a function of the saturation ratio. If rearranged and the saturation ratio is interpreted as the ratio of the vapor pressure at the surface of a spherical droplet p_{drop} to the saturation pressure far from the droplet p_{sat}, then

$$p_{\text{drop}}(a_p) = p_{\text{sat}} \exp\left(\frac{2\sigma v_{\text{liq}}}{k_B T a_p}\right) \tag{20.89}$$

Equation 20.89, known as the Kelvin equation, is a fundamental equation in the thermodynamics of aerosols, because it relates the vapor pressure of a droplet to the (saturation) vapor pressure above a planar interface of the bulk material p_{sat}. It shows that the vapor pressure above a droplet is higher than the vapor pressure above a flat surface, an effect that becomes significant for $d_p < 0.1\,\mu\text{m}$.

The nucleation current is obtained from Equation 20.84 by approximating it according to the previously summarized CNT assumptions. The equilibrium cluster distribution of Equation 20.86 is used. The current, then, is related to the sum of cluster equilibrium distributions times their respective surface areas, summed up to an arbitrarily large cluster size (see, e.g., Debenedetti, 1996). The discrete sum may be replaced by an integral and the clusters free energy of formation is expanded to second-order (an excellent approximation because the integrand is sharply peaked about the critical cluster) to give

$$J = j_{i^*} Z n_{i^*} \tag{20.90}$$

where

the first term j_{i^*} is the rate of arrival of single molecules to the critical droplet
the second factor Z is the so-called Zeldovich nonequilibrium factor
the last term n_{i*} is the equilibrium number concentration of critical nuclei

The rate of arrival of monomers is the product of the forward flux constant β (also known as the impingement rate per unit area), which is the single-molecule growth rate calculated from the kinetic theory of gases (with a unity accommodation coefficient), and the critical droplet surface area:

$$j_{i^*} = 4\pi\left(a_p^\star\right)^2 \beta = 4\pi\left(a_p^\star\right)^2 \frac{p_{\text{vap}}}{(2\pi m_{\text{mol}} k_B T)^{1/2}} \tag{20.91}$$

where $m_{\text{mol}} = \mathfrak{M}/N_A$ is the molecular mass of an impinging molecule. The Zeldovich nonequilibrium factor arises from number fluctuations in the critical cluster

$$Z = \frac{v_{\text{liq}} \sigma^{1/2}}{2\pi\left(a_p^\star\right)^2 (k_B T)^{1/2}} \tag{20.92}$$

The third term $n_{i^\star}$ is the equilibrium number concentration of critical nuclei, which is obtained from Equation 20.86 evaluated at the critical cluster. For completeness, note that the critical droplet-free energy expressed in terms of the critical radius is

$$\Delta G^\star = \frac{4\pi}{3}\left(a_p^\star\right)^2 \sigma \tag{20.93}$$

whereas the number of molecules in the critical cluster is

$$i^\star = \frac{32\pi v_{\text{liq}}^2 \sigma^3}{3(k_B T \ln S)^3} \tag{20.94}$$

Hence, the CNT expression for the nucleation rate per unit volume becomes

$$J_{\text{CNT}} = J_0^{\text{CNT}} \exp\left(-\frac{\Delta G^\star}{k_B T}\right) = \nu_{\text{liq}} n_{\text{vap}}^2 \left(\frac{2\sigma}{\pi m_{\text{mol}}}\right)^{1/2} \exp\left[-\frac{16\pi}{3}\frac{\sigma^3 v_{\text{liq}}^2}{(k_B T)^3 (\ln S)^2}\right] \tag{20.95}$$

where the number density in the vapor phase has been used, $n_{\text{vap}} = p_{\text{vap}}/(k_B T)$. The classical prefactor is often expressed in terms of n_{liq}, the bulk liquid number density,

$$J_0^{\text{CNT}} = \frac{n_{\text{vap}}^2}{n_{\text{liq}}}\left(\frac{2\sigma}{\pi m_{\text{mol}}}\right)^{1/2} \tag{20.96}$$

Note that the CNT expression is occasionally divided by the saturation ratio (Seinfeld and Pandis, 1998), a correction that arises from a different treatment of nucleation kinetics (see the following text for a discussion on consistency issues of CNT).

CNT is one of the most frequently used nucleation theories due to its simplicity and the availability of the required molecular data. Even though its predictions are not very accurate (usually they are accurate to 5–10 orders of magnitude), it provides a qualitative understanding of nucleation. It gives, however, reasonable results for the critical saturation ratio $S_c(T)$, the saturation ratio at which the nucleation rate is $J_{\text{nuc}}[S_c(T)] = 1\,\text{cm}^{-3}\,\text{s}^{-1}$. Two important conclusions can be drawn from comparisons of CNT predictions with experimental data (see Figure 20.2):

1. The isothermal dependence of the nucleation rate on the saturation ratio is well predicted. Theoretical predictions and experimental measurements of the slopes of ln J_{nuc} versus ln S are in reasonable agreement.
2. The temperature dependence of the rate is in considerable disagreement with experimental values: CNT consistently under predicts experimental rates at low temperature, whereas it may overpredict at high temperatures.

The CNT gas-to-liquid nucleation rate differs from the rate frequently used in bubble nucleation, as derived by Blander and Katz (1975), in the preexponential kinetic factor by a factor of $(n_{\text{liq}}/n_{\text{vap}})^2$. This difference stems from the calculation of the concentration of elementary vacancies in the liquid; for the gas-to-liquid transition, this concentration is identified to the monomer concentration, the concentration of the metastable vapor, see Equation 20.86. For bubble nucleation, the calculation of the concentration of elementary vacancies is not as straightforward. Nevertheless, both droplet and bubble nucleation rates are predicted to have an Arrhenius dependence on the critical cluster-free energy, a dependence that dominates the rate calculation.

The main limitation of CNT is the use of macroscopic (bulk and surface) thermodynamic properties to describe the critical droplet. It assumes a sharp interface, thereby neglecting the curvature dependence of the surface tension. The capillarity approximation, moreover, does not distinguish between metastability and instability, that is, it does not predict the existence of a spinodal curve along which the free energy

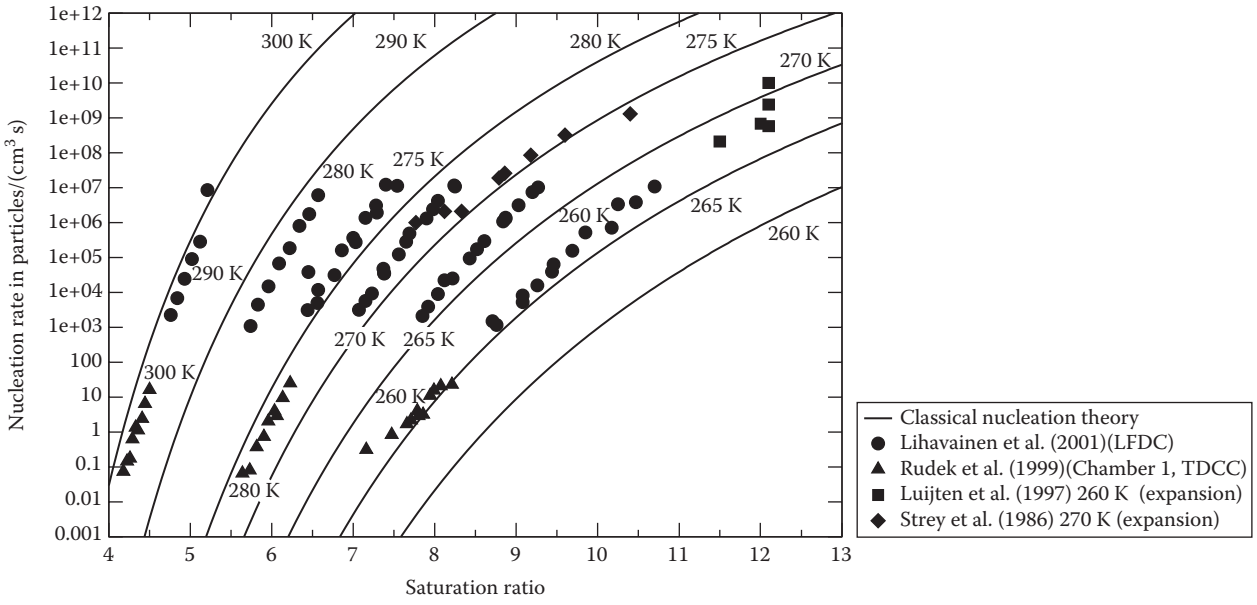


Figure 20.2

Experimental measurements of *n*-pentanol nucleation rates and CNT predictions. LFDC refers to laminar flow diffusion chamber (*n*-pentanol in helium), TDCC to thermal diffusion cloud chamber (*n*-pentanol in helium), and expansion either to pulse-expansion wave tube (Luijten et al. (1997), *n*-pentanol in helium) or to two-piston expansion chamber (Strey et al. (1986), *n*-pentanol in argon).

barrier vanishes and the decay process changes from nucleation to spinodal decomposition. Another important limitation of the classical derivation is the requirement that an equilibrium cluster distribution be established in the metastable state, allowing the use of microscopic reversibility to calculate the evaporative flux α, and thus leading to an equilibrium cluster distribution of the form shown in Equation 20.86.

The preexponential factor in Equation 20.86 is established by requiring that there is no free energy cost for the formation of a single-molecule cluster, $\Delta G_1 = 0$. However, the free energy change in the capillarity approximation does not vanish for $i = 1$, rendering CNT internally inconsistent (limiting inconsistency). The internally consistent classical nucleation theory (ICCT) (Girshick and Chiu, 1990) removes this inconsistency by requiring that $\Delta G_i = 0$ for monomers. As a result, the classical rate is multiplied by c/S, where c is a constant. It should be noted, however, that the physical basis of this correction is questionable, as is the requirement that the capillarity approximation be valid for monomers.

In addition, the CNT cluster distribution Equation 20.86 violates the law of mass action. Courtney (1961) suggested an equilibrium cluster distribution that satisfies the law of mass action, a modification that leads to the previously mentioned division of the CNT rate by the saturation ratio. Numerous other attempts have been made to make the classical theory internally consistent and to satisfy mass action (for a critical review, see Wilemski, 1995). However, all these attempts require consistency in CNT instead of a critical re-evaluation of the underlying assumptions of the theory.

CNT calculates the free energy of formation for a stationary droplet, thereby neglecting the effect of translational fluctuations on the cluster free energy and the nucleation rate. The effect of translational invariance on the rate (i.e., that the droplet may appear anywhere within the system volume) is not taken into consideration by CNT. Lothe and Pound (1962) proposed one of the most intriguing corrections to CNT: they argued that the translational and rotational degrees of freedom of a nucleating droplet are not properly accounted for in CNT. The additional terms they suggested increased theoretical predictions by 10^{18}. The so-called translation-rotation paradox resulted in a long-standing controversy.

Reiss and coworkers (see, e.g., Reiss and Kegel, 1996) emphasized the important relation between a proper counting of translational degrees of freedom and the mixing entropy in mesoscopic, continuum descriptions of nucleation phenomena. Recently, Reiss et al. (1997) suggested that the volume scale required to enumerate states for the calculation of the mixing entropy is the variance of volume fluctuations: a nucleating droplet may be identified as a physical object up to its volume fluctuations. Ford (1997), who used a detailed analysis of the statistical mechanics of molecular clusters, and Barrett (1997) suggested that the scaling

volume in the classical expression should be the molecular volume in the liquid phase. Instead, CNT implicitly assumes that the scaling volume is the molecular volume in the metastable vapor phase. Even though these attempts to resolve the paradox stem from different considerations and they are theoretically sound, they have not managed to improve significantly in comparison with experiments, even though in some cases improved temperature dependence was noted.

Drossinos and Kevrekidis (2003) presented a field-theoretic derivation of a correction to the nucleation rate that arises from the contribution of the translational degrees of freedom of a nucleating droplet (viewed as the translational eigenfunctions of the droplet) to the rate. They argued that the proposed correction is consistent with CNT. Their derivation provides a heuristic justification of the capillarity approximation starting from microscopic, molecular considerations. They concluded that the droplet free energy is modified by an additive mixing-entropy term. The additional contribution, which contains a logarithmic correction to the surface energy term, defines a scaling volume that depends on the range of the coarse-grained, attractive intermolecular interaction potential.

A number of phenomenological modifications of CNT are based on removing the assumption of a sharp interface. Dillman and Meier (1991) extended the work of Tolman on the dependence of the surface tension on the droplet radius through the so-called Tolman length and proposed

$$\sigma = \sigma_\infty \left(1 + c_1 i^{-1/3} + c_2 i^{-2/3}\right) \tag{20.97}$$

where

σ_∞ is the planar surface tension
i is the number of molecules in the i-cluster
c_1, c_2 are constants

Initial predictions greatly improved comparison with experiments, but Laaksonen et al. (1994) pointed out an inconsistency in the Dillman and Meier theory, which when corrected rendered theoretical predictions worse.

Gránásy, in a series of papers (see, e.g., Gránásy, 1997), developed the so-called diffuse interface theory where the finite interface thickness is taken into consideration. A new length scale is introduced to characterize the interface thickness, which can be calculated in terms of measurable quantities, as opposed to the determination of Tolman's length. The resulting model predicts reasonably well nucleation rates for nonane and toluene, but fails for more polar substances.

Ruckenstein and coworkers (see, e.g., Nowakowski and Ruckenstein, 1991) took a different approach by developing a kinetic theory of nucleation, thereby avoiding the equilibrium assumption of CNT. The theory is based on the calculation of the evaporation rate α_i at which a single molecule leaves an i-cluster. Their approach is based on a diffusion equation in energy space. The theory predicts nucleation rates higher than CNT, with more pronounced effects at high supersaturation ratios.

CNT refers to isothermal nucleation where latent heat release is neglected. Barrett (1994) considered nonisothermal nucleation by incorporating energy fluctuations of the critical cluster, but his results did not significantly improve agreement with experiments. Lazaridis and Drossinos (1997) reached a similar conclusion for binary nucleation.

20.4.1.2 Numerical Simulations

In addition to analytical studies of the nucleation process, computer simulations provide additional, difficult to obtain via analytical theories, information. Whereas most analytical theories require various approximations, molecular simulations provide a powerful tool to investigate the nucleation process at the microscopic level. Numerical simulations may be divided into two classes: *Monte Carlo* (MC) and *molecular dynamics* (MD) methods (Kalikmanov, 2013).

In MD simulations, the Newtonian equations of motion for a systems of interacting particles (be they, atoms, ions, molecules, or even spherical nanoparticles (Isella and Drossinos, 2010)) are numerically integrated in time. Time averages of quantities of interest (pressure, velocity, configurational or kinetic energy, etc.) are calculated, and, following the ergodic hypothesis, they are taken to be equal to ensemble averages. In MC methods, physical time is not present: simulations are not performed in physical space but in configurational space. As such, the results of MC simulations are ensemble averaged. MC movements are so constructed that the approach to the equilibrium state is relatively fast, rendering them a powerful tool to simulate systems

with high activation barriers; for such systems, MD simulations would require considerable (often prohibitive) computational times. The two approaches provide complementary information at the molecular level: MD simulations provide insights on the kinetics of the nucleation process, whereas MC methods on the thermodynamics of the process.

A noteworthy contribution to the calculation of the nucleation rate via MC simulations was made by Wedekind et al. (2007). They developed a method to analyze molecular and Brownian dynamics simulations of activated process based on the concept of mean first-passage time (MFPT). The method allows a precise determination of the rate at which an activation barrier is crossed, as well as the location of the transition state (critical cluster for nucleation processes). They analyzed the behavior of the MFPT $\tau(x_0;a,b)$ defined (in one dimension, with x the reaction coordinate) as the average elapsed time until the system, starting at x_0, leaves a prescribed domain $[a, b]$ for the first time. Whereas the MFPT is usually analyzed in terms of the reaction coordinate x_0 Wedekind et al. (2007) considered its behavior as a function of the end point b. This provides information on the average time the system takes to reach b for the first time; in particular, $\tau(b = x^*)$ is the average time needed to reach for the first time the transition state x^*, that is, the top of the activation barrier. They showed, by solving the appropriate Fokker–Planck equation by the steepest descent method, that for high activation barriers, the MFPT in the vicinity of the transition state (critical cluster) may be expressed as

$$\tau(b) = \frac{\tau_J}{2}\{1 + \mathrm{erf}[(b - x^*)c]\}, \tag{20.98}$$

where erf is the error function, $\mathrm{erf}(x) = 2/\sqrt{\pi}\int_0^x dx e^{-x^2}$, c is the local curvature at the top of the barrier and

$$\tau_J = \frac{1}{JV}. \tag{20.99}$$

Thus, the transition rate becomes the inverse of τ_J. For the case of nucleation processes, the (steady-state) nucleation rate (nucleated clusters/s) is $I = VJ = \tau_J^{-1}$ with V the system volume. By evaluating the MFPT from simulations of an activated process, and subsequent fitting of the results to Equation 20.98, many important parameters of the activated process may be obtained: the barrier crossing rate (nucleation rate $I = JV$), the location of the transition state (critical cluster) in the appropriate reaction coordinate, and the curvature at the top of the barrier. The method was applied successfully in a simulation of condensation of Lenard-Jones argon vapor.

20.4.1.3 Density Functional Theory

Density functional theory (DFT) is an alternative approach to phenomenological corrections to CNT. It is intermediate between the capillarity approximation and a purely microscopic theory, as the more rigorous attempts by Reiss and coworkers (Reiss et al., 1990, Senger et al., 1999) or modern computer simulations (Weakliem and Reiss, 1994, ten Wolde et al., 1996). The main idea of DFT as used in nucleation theory is to treat a nucleating droplet within a metastable vapor phase as an inhomogeneous fluid. Then, as is usually done in density functional theories, a free energy functional that depends on the nonuniform average density profile is postulated. The spatially inhomogeneous average density profile $\rho(\mathbf{r})$ is obtained by extremizing the free energy functional. In the grand canonical ensemble, where the number of molecules fluctuates, the critical nucleus is unstable with respect to growth or shrinkage. Equivalently, the matrix of second-order derivatives of the free energy functional with respect to the density has one negative eigenvalue corresponding to droplet growth or decay; the other nonzero eigenvalues are positive. The critical nucleus, thus, is a saddle point of the free energy functional that separates the metastable and stable phases. By introducing a spatially nonuniform density profile, DFT incorporates curvature effects on the surface tension. It can also be shown that it predicts the existence of a spinodal curve.

Cahn and Hilliard (1958, 1959), in their study of spinodal decomposition of a binary fluid, presented the first use of DFT in descriptions of phase transitions. They used a square-gradient approximation of the free energy functional, since during spinodal decomposition, average density changes are small in comparison to atomic dimensions. Oxtoby and coworkers pioneered the use of DFT in vapor-to-liquid nucleation. They extended the van der Waals theory of interfaces, also used by Cahn and Hilliard, by using liquid-state perturbation theory to obtain the Helmholtz free energy of the inhomogeneous fluid.

Oxtoby and Evans (1988) decomposed the Helmoltz free energy into a local, hard-sphere repulsive part and a nonlocal part that depends on the nonlocal attractive part of the interaction potential. The decomposition is based on liquid-state perturbation theory according to which equilibrium fluid properties may be related to a hard-sphere reference fluid with known equilibrium properties; the attractive intermolecular forces are then treated as a perturbation. The highly accurate Carnahan–Starling equation of state was used to determine the properties of the hard-sphere fluid. The grand canonical potential $\Omega[\rho]$ of the inhomogeneous system was accordingly written as

$$\Omega[\rho(\mathbf{r})] = \int d\mathbf{r} f_h[\rho(\mathbf{r})] - \mu \int d\mathbf{r}\rho(\mathbf{r}) + \frac{1}{2}\int\int d\mathbf{r}d\mathbf{r}'\rho(\mathbf{r})\rho(\mathbf{r}')V_{\text{att}}(|\mathbf{r}-\mathbf{r}'|) \tag{20.100}$$

where

$f_h(\rho)$ is the Helmoltz free energy density of a uniform hard sphere fluid of density ρ
μ is the chemical potential of the metastable vapor
$V_{\text{att}}(\mathbf{r})$ is the long-range attractive part of the intermolecular interaction potential

The attractive part has been modeled by, for example, the attractive Yukawa potential or the Lennard–Jones potential decomposed according to the Weeks–Chandler–Andersen perturbation theory. The critical nucleus profile is obtained by extremizing Equation 20.100 with respect to density variations. This procedure amounts to setting the functional derivative of the grand canonical potential to zero, $\delta\Omega(\rho)/\delta\rho(\mathbf{r}) = 0$. The resulting equation, known as the Euler–Lagrange equation, is

$$\mu_h[\rho(\mathbf{r})] = \mu - \int d\mathbf{r}'\rho(\mathbf{r}')V_{\text{att}}(|\mathbf{r}-\mathbf{r}'|) \tag{20.101}$$

with μ_h as the chemical potential of the hard-sphere reference fluid

$$\mu_h = \left.\frac{df_h(\rho)}{d\rho}\right|_T \tag{20.102}$$

Equation 20.101 has to be solved iteratively with the boundary condition that the density far away from the droplet becomes the metastable vapor density. As mentioned earlier, the nonuniform density profile is not a minimum but a saddle point of $\Omega[\rho]$, rendering the iteration process unstable. Oxtoby and Evans (1988) and Zeng and Oxtoby (1991a) suggested an iterative numerical procedure to calculate the saddle point configuration. It consists of an initial guess for the density profile that is substituted on the RHS of Equation 20.101 to obtain the hard-sphere chemical potential at each point, which in turn yields a new density profile and the iterative procedure continues. For a judicious initial guess, the iteration initially converges, allowing the determination of the critical nucleus density profile, but eventually, it diverges away from the saddle point. Once the density profile has been calculated, the nucleation barrier associated with the creation of the critical nucleus is obtained, $\Delta\Omega^*_{\text{DFT}} = \Omega(\rho_{\text{drop}}) - \Omega(\rho_{\text{vap}})$. Most DFT calculations proceed by determining the nucleation rate using $\Delta\Omega^*$ as calculated from DFT, and retaining the classical preexponential factor, $J_{\text{DFT}} = J_0^{\text{CNT}} \exp\left(-\Delta\Omega^*_{\text{DFT}}/k_BT\right)$.

Oxtoby and Evans (1988) noted significant nonclassical effects in that the DFT-calculated liquid density at the center of the droplet was found to differ significantly from either the liquid-state density or the coexistence density at the same chemical potential. Moreover, the nucleation barrier was found to be smaller than the barrier predicted by CNT, and it was found to vanish at the spinodal. A sensitive dependence of the nucleation barrier height (and, thus, of the nucleation rate) on the range of the attractive potential was observed.

DFT is a powerful technique for rigorous calculations of the free energy barrier to nucleation. It has been used extensively in bubble nucleation in superheated liquids, liquid nucleation in dipolar fluids, binary nucleation of liquids and bubbles, phase transitions in micropores, crystallization, and many other systems (for a recent review of the multiple uses of DFT, see Oxtoby, 2002). The studies of bubble nucleation (keeping as previously mentioned the CNT kinetic prefactor) showed that deviations from CNT are more dramatic than those calculated for droplet nucleation. Recently, a time-dependent DFT theory of fluids (Marini Bettolo Marconi and Tarazona, 1999) has been developed.

The calculation of the kinetic prefactor J_0 has received much less attention. Langer and Turski (1973) calculated it for a system close to the critical point using a hydrodynamic model, but their numerical results were not significantly different from those of CNT. Talanquer and Oxtoby (1994) using a dynamical DFT of gas–liquid nucleation concluded that the correction to the preexponential factor due to cluster translation is relatively small. Barrett (1997) used mean-field DFT to calculate the effect of cluster translation on the kinetic prefactor. He showed that the compensation for translational motion leads to a significant increase in the rate, an amount approximately equal to the ratio of liquid to vapor densities. Drossinos et al. (2001) combined DFT with field theoretic methods to calculate the effect of the droplet's translational eigenfunctions on the nucleation-rate prefactor by deriving an expression for their functional form (see, also, the discussion following Equation 20.108).

20.4.1.4 Nucleation Theorems

The derivation of nucleation theorems constitutes a significant recent development in nucleation theory. The first nucleation theorem was proposed by Kashchiev (1982) and later extended by Oxtoby and Kashchiev (1994), Ford (1997), and Bowles et al. (2001). It relates the derivative of the work of formation of the critical droplet with respect to the chemical potential in the metastable phase to the number of molecules in the nucleus

$$\left.\frac{\partial \Delta G^*}{\partial \mu}\right|_{V,T} = -(i^* - \bar{i}) \tag{20.103}$$

where

i^* is the total number of molecules within the volume occupied by the droplet

$\bar{i}$ is the number of molecules that would have occupied the same volume in the uniform metastable phase

Their difference gives the excess number of molecules in the critical droplet over those present in the same volume in the metastable vapor. For most cases of interest, the metastable vapor is dilute, and hence, the term $\bar{i}$ is neglected. The initial derivation required that the cluster surface energy be independent of the chemical potential. Oxtoby and Kashchiev (1994) generalized it to multicomponent nucleation, showing that it is a much more general result. Bowles et al. (2001) extended the nucleation theorem and concluded that it is more valid than the initial derivation had suggested.

The importance of the nucleation theorem becomes apparent when it is rewritten in a form that relates experimental quantities. The Arrhenius form of the nucleation rate

$$J_{\text{nuc}} = J_0 \exp\left(-\frac{\Delta G^*}{k_B T}\right) \tag{20.104}$$

combined with the nucleation theorem yields

$$i^* = \left.\frac{\partial k_B T \ln J_{\text{nuc}}}{\partial \mu}\right|_{V,T} - \left.\frac{\partial k_B T \ln J_0}{\partial \mu}\right|_{V,T} \tag{20.105}$$

Since the kinetic prefactor J_0 is weakly dependent on the chemical potential of the metastable phase, the correction to i^* is expected to be in the range from 0 to 1. Ford (1997) using a combination of statistical mechanics and population cluster dynamics showed that Equation 20.105 becomes

$$\left.\frac{\partial \ln J_{\text{nuc}}}{\partial \ln S}\right|_{V,T} = 1 + i^* \tag{20.106}$$

Typical values for i^* are 30–50 molecules. Thus, $i^* + 1 \approx i^*$, allowing the replacement of the RHS of Equation 20.106 by i^*, a form that is occasionally reported in the literature. Note that since the chemical potential derivative is taken at constant temperature, it has been replaced by a derivative with respect to $k_B T \ln S$. The nucleation theorem in the form of Equation 20.106 is extremely useful in the analysis of experimental results and computer simulations because the number of molecules in a critical cluster may be determined from the slopes of the logarithm of isothermal nucleation rates versus $\ln S$.

It is worth noting that CNT does not satisfy the first nucleation theorem, a violation that according to Ford (1997) stems from the neglect of translational corrections. As mentioned earlier, Section 20.4.1.1, in the capillarity approximation, the droplet-free energy is calculated for a droplet fixed within the system volume, thereby neglecting the mixing entropy associated with translational fluctuations of the cluster. Oxtoby and Kashchiev (1994) as well as Ford (1997), note that ICCT satisfies the nucleation theorem, but the agreement is considered fortuitous, since ICCT does not satisfy the second nucleation theorem.

Ford (1997) presented a second nucleation theorem that concerns the temperature dependence of the nucleation rate at constant supersaturation. In a sense, the second theorem is conjugate to the first. It is usually written as

$$\left.\frac{\partial \ln J_{\text{nuc}}}{\partial T}\right|_{\ln S} = \frac{1}{k_B T^2}\left[L_p - k_B T + E_x(i^*)\right] \tag{20.107}$$

where

L_p is the latent heat per molecule

$E_x(i^*)$ is the excess internal energy of the critical nucleus

Another recent development parallel to the use of nucleation theorems in the study of nucleation phenomena is the use of scaling relations for molecular properties of the critical cluster and the nucleation rate. McGraw and Laaksonen (1996) derived scaling relations for the number of molecules in the critical cluster and the nucleation barrier height. They argued that these scaling relationships constrain functional dependencies of departures from CNT. Thus, they may help in the construction of consistent phenomenological models. These scaling relations were later extended to bubble nucleation (Shen and Debenedetti, 2001).

20.4.1.5 Multicomponent Nucleation

Multicomponent nucleation is an important mechanism for new particle formation since it occurs even in mixtures of unsaturated vapors, as opposed to the unary (single-component) nucleation discussed earlier where supersaturation is required. Multicomponent nucleation is important in the atmosphere where various condensable species, for example, sulfuric acid and water, occur at relatively low concentrations. Langer (1969) proposed a general expression for the decay rate of a metastable state that can be used to calculate multicomponent nucleation rates. Under some general conditions, he showed that the nucleation rate I_{nuc} (not its density J_{nuc}) may be written as

$$I_{\text{nuc}} = \frac{\kappa}{2\pi} V J_{\text{tran}} \Omega' \exp\left(-\frac{\Delta\Omega^*}{k_B T}\right) \tag{20.108}$$

where, as before, $\Delta\Omega^*$ is the nucleation barrier (in the grand canonical ensemble) and κ, the so-called dynamical prefactor, is related to the initial growth rate of a droplet slightly greater than the critical size. The other terms constitute what is called the statistical prefactor: V is the system volume, Ω' is a generalization of the Zeldovich factor that contains contributions of Gaussian fluctuations about the uniform metastable and the spatially nonuniform droplet density profiles (see Equation 20.92 for the Zeldovich factor in unary nucleation, a correction that arises from number fluctuations in the critical cluster). The generalized Zeldovich factor may be viewed as a leading-order fluctuations correction to the droplet free energy. The prime in Ω' denotes that fluctuations corresponding to the translational eigenmodes of the droplet have been excluded. These fluctuations are treated separately to obtain the term VJ_{tran}, where J_{tran} is the Jacobian for the change of variables to the collective co-ordinates associated with the droplet's translational eigenfunctions. The complete expression is reported in Langer and Turski (1973), whereas an alternative formal expression that relates the nucleation rate to the imaginary part of the true system free energy is reported by Langer (1967, 1974). One of the main difficulties in using Equation 20.108 is the evaluation of the statistical prefactor.

The formal procedure introduced by Langer (1969) to solve multidimensional Fokker–Planck equations that arise in nucleation problems, also used to obtain the nucleation rate Equation 20.108, has proven to be useful and versatile. It has been used to calculate the effect of energy fluctuations on the nucleation rate (Barrett, 1994, Lazaridis and Drossinos, 1997), to calculate the contribution of translational fluctuations to the rate (Drossinos et al., 2001), and to calculate nucleation rates in ternary systems (Lazaridis, 2001).

Trinkaus (1983) presented a slightly different expression for the nucleation rate in multicomponent systems. His result, which does not consider the contribution of the droplet translational eigenmodes, is

$$J_{\text{nuc}} = \frac{|\kappa|/\pi}{\sqrt{-\det(\ddot{D}/\pi)}} n_{\text{tot}} \exp\left(-\frac{\Delta G^\star}{k_B T}\right) \tag{20.109}$$

where

$n_{\text{tot}} \exp(-\Delta G^\star/k_B T)$ is the number density of critical clusters

$\ddot{D}$ is the matrix of second-order derivatives of the droplet-free energy with respect to the number of molecules n_i of each species evaluated at the saddle point,

$$D_{ij} = \frac{1}{2k_B T} \frac{\partial \Delta G}{\partial n_i \partial n_j}\bigg|_\star \quad (i,j = 1,\ldots,m) \tag{20.110}$$

m being the number of species. The factor κ is the negative eigenvalue of the product of a growth tensor, a multicomponent generalization of Equation 20.91, times $\ddot{D}$. Note that the determinant of $\ddot{D}$ is negative since the critical nucleus corresponds to a saddle point in number-composition space (see the discussion on DFT in Section 20.4.1.3). This expression has been used to calculate binary nucleation rates in the sulfuric acid–water system (Noppel et al., 2002) and in ternary nucleation of sulfuric acid–ammonia–water (Napari et al., 2002).

For the specific case of two-component nucleation, Reiss (1950) presented the first rigorous binary nucleation theory. He argued that the nucleation rate should be calculated at the saddle point in droplet-composition space by following a steepest descent path. Stauffer (1976) noted that the steepest-descent path resulted in an inconsistent evaluation of the steady-state nucleation rate; instead, he proposed a self-consistent method. Stauffer's result is the most frequently used expression to calculate binary nucleation rates. More recently, Kevrekidis et al. (1999) used the method introduced by Langer (1969) to obtain the rate. Their result is formally identical to Stauffer's result, but much easier to evaluate. Accordingly, the binary nucleation rate for nonassociated vapors is

$$J_{\text{nuc}} = \frac{n_{\text{vap}} \exp\left(-\Delta G^\star/k_B T\right)}{2\left(D_{12}^2 - D_{11}D_{22}\right)^{1/2}} \left[D_{11}R_{11} + D_{22}R_{22} - \sqrt{(D_{11}R_{11} - D_{22}R_{22})^2 + 4D_{12}^2 R_{11}R_{22}}\right] \tag{20.111}$$

where

$n_{\text{vap}} = n_{\text{vap},1} + n_{\text{vap},2}$ is the total number density of condensable vapors

R is the droplet growth tensor

As in unary nucleation, the growth matrix (which is diagonal for nonassociated vapors) is expressed as the product of the droplet surface area and the impingement rate of a molecule of species i, $R_{ij} = \delta_{ij}\beta_i 4\pi(a_p^\star)^2$, with δ_{ij} as the Kronecker symbol (see Equation 20.91 for the corresponding expression for unary nucleation). The impingement rate (per unit area) β_i may be calculated as summarized in the CNT analysis of the condensation flux, Equation 20.91, to give $\beta_i = p_i/(2\pi m_{\text{mol},i} k_B T)^{1/2}$ where p_i is the partial vapor pressure of species i.

Similar to unary nucleation, the free energy barrier in the capillarity approximation (cf. Equation 20.93) is expressed as

$$\Delta G^\star = \frac{4\pi}{3}\left(a_p^\star\right)^2 \sigma \tag{20.112}$$

where

$a_p^\star$, the radius of the (spherical) critical droplet

σ, the droplet surface tension, are functions of the composition of the droplet

According to the revised classical theory, which distinguishes between surface and interior droplet compositions as if the droplet were macroscopic (Wilemski, 1984, 1987), the Gibbs–Thomson equation can be

solved for the critical radius and composition. Accordingly, the bulk composition x of the critical cluster, in particular, the mole fraction of component 2 in the bulk of the droplet ($x = n_2/(n_1 + n_2)$ with n_i as the number of moles of species i in the bulk interior), is found by solving

$$\nu_{\text{sol},1}\Delta\mu_2 = \nu_{\text{sol},2}\Delta\mu_1 \tag{20.113}$$

where

$\nu_{\text{sol},i}$ is the partial molecular volume in the solution droplet of species i (i = 1,2)
$\Delta\mu_i = \mu_i^{\text{liq}} - \mu_i^{\text{vap}} = -k_B T \ln S_i$ the chemical potential difference

The critical radius is

$$a_p^\star = \frac{-2\sigma\bar{\nu}_{\text{sol}}}{(1-x)\Delta\mu_1 + x\Delta\mu_2} \tag{20.114}$$

where the molecular volume of the solution $\bar{\nu}_{\text{sol}} = (1-x)\nu_{\text{sol},1} + x\nu_{\text{sol},2}$ has been expressed in terms of the partial molecular volumes in the liquid–solution droplet.

An alternative approach to binary nucleation was taken by Zeng and Oxtoby (1991b), who developed a DFT for gas–liquid nucleation in binary fluids.

20.4.1.6 Heterogeneous Nucleation

In the presence of a solid substrate, for example, an aerosol particle, the surface provides an interface upon which the new phase may nucleate. The surface limits the extent of penetration in the metastable region; thus, heterogeneous nucleation upon insoluble particles takes place at lower saturation ratios than homogeneous nucleation. The Kelvin equation, Equation 20.89, still governs whether a nucleated cluster will grow or shrink. In the atmosphere, where saturation ratios are low, most nucleation is heterogeneous on already existing particles, for example, on cloud condensation nuclei.

As in the case of homogeneous nucleation, the heterogeneous nucleation rate (nucleated clusters/s) depends on the free energy of formation of the heterogeneously nucleated cluster $\Delta G_{\text{het}}^\star$ through the Arrhenius form

$$I_{\text{het}} = I_{\text{het}}^0 \exp\left(-\frac{\Delta G_{\text{het}}^\star}{k_B T}\right), \tag{20.115}$$

where I_{het}^0 is a kinetic prefactor, and the superscript star refers to quantities evaluated at the critical cluster. Note the difference between the heterogeneous nucleation rate I_{het} discussed in this section and the homogeneous nucleation rate per unit volume (nucleation current) J discussed earlier. The free energy of formation of a heterogeneously nucleated cluster is at most equal to the free energy of formation of a homogeneously nucleated droplet, $\Delta G_{\text{hom}}^\star$. The modification of the free energy of formation due to a preexisting surface is expressed through a multiplicative factor f_g

$$\Delta G_{\text{het}}^\star = f_g(\cos\theta)\Delta G_{\text{hom}}^\star. \tag{20.116}$$

The factor f_g arises from geometric considerations: it is a function of the contact angle θ between the nucleating cluster and the surface. The contact angle varies from 0 (perfect wetting) to 180° (no surface effect), whereas the geometric factor varies from 0 to 1. For water nucleation, the solid is considered hydrophobic or hydrophilic, depending on whether the contact angle is greater or less than 90°. At bulk (mechanical) equilibrium, the contact angle is given by Young's equation (Seinfeld and Pandis, 1998)

$$m \equiv \cos(\theta) = \frac{\sigma_{vl} - \sigma_{sl}}{\sigma_{vl}}, \tag{20.117}$$

where σ_{ij} are the surface tensions between the various phases: vapor (v), liquid (l), and solid (s).

The geometric factor for a nucleated cluster that forms a liquid cap onto the surface of a seed particle of radius R_p is (Fletcher, 1958)

$$f_g(\cos\theta)=\frac{1}{2}\left[1+\left(\frac{1-X\cos\theta}{g}\right)^3+X^3\left(2-3\left(\frac{X-\cos\theta}{g}\right)+\left(\frac{X-\cos\theta}{g}\right)^3\right)+3X^2\cos\theta\left(\frac{X-\cos\theta}{g}-1\right)\right], \quad (20.118)$$

with

$$X=\frac{R_p}{a_p^\star}, \quad g=\sqrt{1+X^2-2X\cos\theta}. \quad (20.119)$$

As before $a_p^\star$ is the critical radius of the nucleated cluster. A contact angle of 180° indicates no affinity of the condensing vapor for the particle, the vapor nucleates homogeneously: $f_g(\theta=\pi)=1$. At smaller contact angles, the seed reduces the free energy activation barrier [$f_g(\theta<\pi)<1$]. The higher the affinity of the vapor for the particle, the smaller the contact angle is (smaller f_g) and the smaller the free energy barrier. In the limit of a zero contact angle (perfect wetting), the cluster forms a film onto the surface of the particle seed. For perfect wetting, there is no activation barrier for particle growth [$f_g(\theta=0)=0$] if the size of the particle is larger than the critical cluster size $a_p^\star$. However, if the particle radius is smaller than the critical cluster size, nucleation becomes again an activated process. Specifically, the geometric prefactor for perfect wetting ($\theta=0$) reduces to (Giechaskiel et al., 2011)

$$f_g=\begin{cases}0, & \text{for } X>1\,(R_p\geq a_p^\star)\\ (1-X)^2(1+2X), & \text{for } X\leq 1\,(R_p\leq a_p^\star)\end{cases} \quad (20.120)$$

In the limit of a flat surface, $R_p\to\infty$ the geometric factor evaluates to

$$f(m)=\frac{1}{4}(2+m)(1-m)^2. \quad (20.121)$$

Inherent in the derivations that lead to the previous equations are the assumptions that the effect of the line tension along the interface between the liquid cap and the seed particle is neglected, and that the surface tension is independent of cluster curvature. These assumptions, in conjunction with the use of macroscopic quantities (as required by CNT), render the contact angle the macroscopic contact angle θ_∞. Their removal leads to additional terms in the activation free energy barrier. We shall consider only the terms that arise from the line tension, neglecting the curvature dependence of the surface tension (in the spirit of CNT).

Fletcher's (1958) initial analysis did not consider the line tension τ formed at the circumference of the cluster cap where the three phases (particle seed, vapor, and cluster) coexist. Inclusion of line-tension effects modifies the critical cluster free energy of formation and contact angle (Lazaridis, 1993)

$$\Delta G_{\text{het}}^\star=f_g(\cos\theta)\Delta G_{\text{hom}}^\star-\frac{2\tau\pi R_p(1-\cos\varphi)}{\tan\varphi}+2\pi R_p\tau\sin\varphi, \quad (20.122)$$

with the associated change of the contact angle

$$\cos\theta=\cos\theta_\infty-\frac{\tau}{\sigma_{gl,\text{planar}}R_p\tan\varphi}, \quad (20.123)$$

where φ is the angle formed between the circumference of the cap and the center of the particle seed. In the limit of negligible line tension, the contact angle does not depend on the particle size, becoming equal to the macroscopic contact angle.

Geometric considerations show that φ is related to the contact angle through (Mamakos et al., 2013)

$$\tan\varphi = \frac{a_p^\star \sqrt{1-\cos^2\theta}}{R_p - a_p^\star \cos\theta}. \tag{20.124}$$

Equations 20.123 and 20.124 allow the calculation of the microscopic contact angle and, therefore, the calculation of the free energy of formation of the critical cluster. The critical radius is independent of the line tension (Lazaridis, 1993). Typical values of the line tension are in the range $[10^{-12}–10^{10}]$ Nt, as determined by studies of the shape of sessile droplets on solid surfaces near the contact line. The line tension can be either positive of negative. Note, however, that measurement of the line tension is notoriously difficult due to its extreme smallness (see also, Hienola et al., 2007).

As in the case of homogeneous nucleation, the nucleation rate is primarily determined by the free energy barrier. It is, thus, sufficient to calculate the kinetic prefactor to an accuracy of one or two orders of magnitude. Following the approach used in homogeneous nucleation, the prefactor may be written as the product of three terms (see also, Equation 20.90):

$$I_{\text{het}}^0 = R_{\text{grow}}^{\text{het}} Z_{\text{het}} \text{F}\,, \tag{20.125}$$

the cluster growth rate $R_{\text{grow}}^{\text{het}}$, the Zeldovich nonequilibrium factor Z_{het}, and a quantity F that, for homogeneous nucleation, is the product of a number concentration and the system volume. The critical cluster growth rate is obtained by considering growth by collisions with single-vapor molecules, neglecting growth by surface diffusion, and assuming that the exposed surface area of the critical cluster is approximately the surface area of the vapor–liquid interface: under these conditions, it equals j_{i^*} defined in Equation 20.91. The Zeldovich nonequilibrium factor Z_{het} arises from number fluctuations in the critical cluster that may cause it to shrink. It is frequently approximated by the homogeneous nucleation factor (Equation 20.92).

The evaluation of F is not as straightforward as in homogeneous nucleation. A frequently used approximation is $F = N_{\text{ads}} A_{\text{ads}}$, where N_{ads} is the total number of molecules adsorbed per unit particle area and A_{ads} is the available surface area for adsorption per particle (Hamill et al., 1982); thus, F becomes the number of adsorbed molecules per particle. The surface concentration of adsorbed molecules is $N_{\text{ads}} = \beta_{\text{ads}} \tau_{\text{ads}}$ where β_{ads} is the collision rate of vapor molecules per unit particle surface and τ is the average time an adsorbed vapor molecule remains on the particle surface (Lazaridis et al., 1991, Wagner et al., 2003, Winkler et al., 2008). A frequently used approximation is $\beta_{\text{ads}} = \beta$, defined in Equation 20.91. The residence time of an adsorbed molecule on the surface is taken to be $\tau_{\text{ads}} = \tau_{\text{ads},0} \exp(E_{\text{lat}}/R_g T)$, where E_{lat} is the heat of adsorption, taken to be the latent heat of condensation. The characteristic time scale $\tau_{\text{ads},0}$ is approximately the inverse vibrational frequency of two harmonically bound molecules $\tau_{\text{ads},0} = 2\pi m_\mu^{1/2} (d^2 V/dr^2)^{-1/2}$, where V is the intermolecular interaction potential and m_μ is the reduced mass. As an example, we present characteristic values for *n*-butanol, the condensing fluid in condensation particle counters, particle counters that detect and count aerosol particles through heterogeneous nucleation on *n*-butanol and subsequent condensational growth. The *n*-butanol Lennard–Jones potential with $\varepsilon/k_B = 593.06$ K and $\sigma_{LJ} = 5.645$ Å leads to $\tau_{\text{ads},0} = 1.29 \times 10^{-12}$ s (Giechaskiel et al., 2011), a value of the same order of magnitude as previously reported for *n*-propanol (Wagner et al., 2003).

Hamill et al. (1982) suggested that the available surface area for adsorption per particle be taken the surface area, a choice that gives the maximum nucleation rate $A_{\text{ads}} = 4\pi R_p^2$. This approximation allows the formation of multiple clusters per particle. Accordingly, the heterogeneous nucleation rate becomes (see, also, Winkler et al., 2008)

$$I_{\text{het}} \equiv I_{\text{het}}^0 \exp\left(-\frac{\Delta G_{\text{het}}^\star}{k_B T}\right) = 4\pi R_p^2 R_{\text{grow}}^{\text{het}} Z N_{\text{ads}} \exp\left(-\frac{\Delta G_{\text{het}}^\star}{k_B T}\right). \tag{20.126}$$

Due to the Arrhenius dependence of the nucleation rate on the free energy of formation of the critical cluster, its accurate determination is more important than a precise calculation of the kinetic prefactor. Fletcher (1958) suggested that the constant value $I_{\text{het}}^0 \approx 4\pi R_p^2 10^{25}$ (particle diameter expressed in cm) would provide a reasonable approximation for most cases.

Heterogeneous nucleation is intimately related to particle activation, a process where by a stable aerosol particle starts to grow rapidly by condensational growth. Particle activation determines the stability of atmospheric aerosol particles and it specifies whether seed particles will grow to become cloud condensation nuclei (Pruppacher and Klett, 1997). Moreover, particle activation determines the counting efficiency of particle instruments like the condensation particle counter, where submicron particles grow to optically measurable supermicron sizes.

The mechanism that determines whether and how a particle activates depends on the relative chemical composition and affinity of the condensing vapor for the pre-existing seed particle. For particles insoluble in the condensing vapor, a heterogeneous nucleated cluster forms on the surface of the seed, with subsequent rapid condensational growth of the condensed phase (determined by the Kelvin equation). The rate of particle activation is specified by the heterogeneous nucleation rate, a process that is usually activated, as discussed. If the seed particle and the condensing vapor are identical, the seed particle grows immediately via condensational growth if the condition for the Kelvin equation is satisfied. If the particle is a solution droplet (or it consists of an insoluble core covered by a soluble coating), or it is soluble in the vapor, then Köhler theory, discussed in Section 20.4.1.7, determines whether seed particle will activate (Seinfeld and Pandis, 1998). These observations become quantitative via the activation probability $P_d(t)$.

Let the number concentration of inactivated particles of diameter d_p be $N_d(t)$. In the presence of a condensable vapor, it changes as (Kalikmanov, 2013, Mamakos et al., 2013)

$$\frac{dN_d(t)}{dt} = -k_{\text{act}} N_d(t), \tag{20.127}$$

where k_{act} is the activation rate constant (nucleated clusters/s) that depends on the chemical composition of the seed particles and on properties of the vapor. The activation probability $P_d(t)$ is the ratio of the concentration of activated particles to their initial concentration $N_{d,in}$,

$$P_d(t) = \frac{N_{d,in} - N_d(t)}{N_{d,in}} = 1 - \exp(-k_{\text{act}} t)\cdot \tag{20.128}$$

The activation probability gives the probability that at least one seed particle would activate to growth during time t. For large number of events, it gives the ratio of activated seed particle to their initial number (at constant volume): for this reason, it is also called nucleation probability, the quantity measured in heterogeneous nucleation experiments (Wagner et al., 2003). The onset condition for heterogeneous nucleation is usually taken to occur at $P_d = 0.5$. Irrespective of the activation mechanism, particles are considered to be activated once their activation probability is greater or equal to 0.5.

The activation rate constant may be calculated by thermodynamic arguments, as in Kelvin and Köhler theories discussed in Section 20.4.1.7, or by kinetic arguments, as in heterogeneous nucleation theories (Giechaskiel et al., 2011). According to thermodynamic theories, that activation rate constant is

$$k_{\text{act}} = \begin{cases} 0 & \text{for } S < S_c \\ \infty & \text{for } S > S_c \end{cases}, \tag{20.129}$$

where the saturation ratio of the ambient vapor S is the ratio of the vapor pressure at the surface of a droplet to its saturation pressure over a planar interface. The critical saturation ratio S_c is given either by Kelvin theory, or Köhler theory and its variants, or multilayer adsorption theory. Thermodynamic theories are not stochastic, since particles are either all activated ($k_{\text{act}} = \infty$, $P_d = 1$) or not activated ($k_{\text{act}} = 0$, $P_d = 0$): the activation probability is independent of the characteristic time.

For kinetic theories, the activation rate constant is the heterogeneous nucleation rate, $k_{\text{act}} = I_{\text{het}}$. Since activation is considered to occur when the activation probability is $P_d \geq 0.5$, the critical activation rate constant is $k_{\text{act},c} = \ln(2)/t = 7\,\text{s}^{-1}$ for $t = 0.1$ s: activation occurs for $k_{\text{act}} \geq k_{\text{act},c}$. Thus, the time t in Equation 20.128 is relevant only for kinetic theories: it is, approximately, the time associated with heterogeneous nucleation of the supersaturated vapor. The nucleation time scale has been chosen from a few milliseconds to 1000 s (Lazaridis et al., 1992, Kulmala et al., 2001, Wagner et al., 2003). An alternative way to determine the activation probability without introducing a characteristic time is to specify a nucleation threshold: Porstendörfer et al. (1985) suggested $k_{\text{act},c} = I_{\text{het}}^{\text{threshold}} = 10^2\,\text{s}^{-1}$.

20.4.1.7 Thermodynamics of Aqueous Droplets

According to the Kelvin relation, Equation 20.89, a pure solvent droplet is in unstable equilibrium: a small perturbation in the form of an infinitesimal droplet radius change would cause the droplet to shrink or grow. However, a solution droplet may be stabilized due to solute vapor-pressure lowering.

For the specific case of an ideal, dilute water solution containing a fixed amount of solute, the vapor pressure of the solution droplet is (Rogers and Yau, 1989)

$$\ln\left[\frac{p_1(d_p)}{p_{\text{sat},1}}\right] = \frac{4\sigma_1\overline{v}_1}{R_u T d_p} - \frac{6n_2\overline{v}_1}{\pi d_p^3} \tag{20.130}$$

where the subscript 1 refers to water (the solvent) and 2 to the solute, and $p_{\text{sat},1}$ is the pure water vapor pressure above a planar, water surface (i.e., a pure-solvent surface). The number of moles of solute is denoted by n_2, and $\overline{v}_1$ is the molar volume of water in the solution. For a dilute solution, the molar volume of water may be taken to be the molar volume of pure water, $\overline{v}_1 \approx \mathfrak{M}_1/\rho_1$. Similarly, to a good approximation, the solution surface tension may be taken to be independent of concentration and equal to the water surface tension.

Equation 20.130, referred to as the Koehler equation or curve, is the fundamental equation of the thermodynamics of aqueous droplets. It combines the two primary effects that determine the vapor pressure above a liquid droplet: the Kelvin effect that increases the pressure and the solute effect that decreases it. Since the two effects have different dependencies on the droplet diameter (and different signs), the curvature (Kelvin) effect behaves as d_p^{-1} and the solute effect as d_p^{-3}, a critical droplet diameter exists. For small droplets, the solute effect dominates, whereas for large droplets, the dominant effect is the Kelvin effect. Stability arguments show that droplets in the ascending part of the Koehler curve (d_p less than the critical droplet diameter) are in stable equilibrium with their environment, whereas those in the descending part (d_p greater that the critical droplet) are in unstable equilibrium. Hence, the Koehler equation gives the wet droplet diameter as a function of saturation ratio. It is frequently used to determine the stability of atmospheric particles.

The saturation ratio S_c of a particle at the critical diameter, obtained by evaluating Equation 20.130 at the critical droplet diameter, is an important particle property. If the ambient saturation ratio S is lower than S_c, droplets of diameter less than the critical droplet diameter are in stable equilibrium, whereas larger droplets are in unstable equilibrium (since the Kelvin effect dominates). If $S > S_c$, no stable equilibrium particle size exists: droplets will grow indefinitely as long as the inequality $S > S_c$ holds. Atmospheric particles for which $S_c < S$ are said to be activated, and they start growing rapidly, becoming cloud or fog droplets (Seinfeld and Pandis, 1998), as discussed in Section 20.4.1.6, Equation 20.129.

20.4.2 Growth

In the presence of supersaturation ($p_{\text{vap}} > p_{\text{sat}}$), preexisting aerosol particles or newly generated particles (via homogeneous nucleation) grow. Condensation or evaporation is driven by the pressure difference between the ambient vapor pressure and the vapor pressure at the surface of the particle: the direction of net vapor flux (evaporation or condensation) depends on their relative magnitude. Since latent heat is released or absorbed at the particle surface during these processes, the treatment of particle growth or shrinkage requires considerations of heat and mass transfer between the particle and the ambient gas mixture. Isothermal conditions prevail when the heat of vaporization may be neglected; otherwise, heat and mass transfer should be considered simultaneously.

Clement (1985) presented a general treatment of heat and mass transfer and their coupling in vapor–gas mixtures. He argued that in addition to the Lewis number, the ratio of the rate of heat transport by conduction to the rate of mass transport by diffusion, another dimensionless number, the surface condensation number, is useful in heat- and mass-transfer processes. The condensation number is defined as the ratio of the conductive heat current to the latent heat carried by the mass current at the surface. The importance of the Lewis number in nucleation experiments has been discussed by, among others, Housiadas et al. (2002).

Chemical reactions may also lead to particle growth. Growth laws, that is, laws that express the rate of change in particle size as a function of particle size and chemicophysical properties of the aerosol system, may be transport or reaction limited. If growth is limited by gas-phase transport, the growth law is transport limited; otherwise, it may be surface-reaction or volume-reaction controlled. Moreover, if growth depends on surface reactions and the reaction rate is fast with respect to transport, the growth law is still determined by gas-phase transport. Surface reactions will lead to growth if the reaction products accumulate at the surface. When the surface reaction is slow, it is frequently assumed that the gas phase concentration of the reacting

species near the surface is the same as the bulk concentration far away from the particle. Volume reaction–controlled growth refers to growth that depends on the conversion of a dissolved species to a condensed phase species. Reaction-controlled growth will be only briefly mentioned herein.

For simplicity, only diffusional growth, primarily in the continuum regime, will be considered in this section: other smaller additional fluxes due to Stefan flow, thermal diffusion, and the Dufour effect are discussed in Kulmala and Vesala (1991).

20.4.2.1 Single-Particle Growth

Isothermal, steady-state growth rates of a single spherical particle in a stagnant gas are presented. Diffusional processes toward a moving particle are discussed in Hindy and Brock (1970). In the continuum regime, the vapor condensation rate (expressed in molecules per second) toward a spherical particle of the same composition is calculated from the steady-state diffusion equation ($\nabla^2 n = 0$ around a sphere) to be

$$J = \frac{2\pi d_p \mathfrak{D}}{k_B T}(p_\infty - p_{\text{sur}}) \tag{20.131}$$

where

$p_\infty = p(T_\infty)$ is the ambient vapor pressure
p_{sur} is the vapor pressure at the surface of the particle

For $p_\infty > p_{\text{sur}}$, the droplet grows, whereas for $p_\infty < p_{\text{sur}}$, the droplet shrinks. The diffusional flow toward a spherical particle and the associated temperature change were first derived by Maxwell (1890) in an article in Encyclopedia Britannica on the theory of the wet-bulb thermometer. The theory of steady-state growth of a spherical particle in the continuum regime is known as Maxwell theory.

In the molecular regime, the net condensation rate (molecules per second) is obtained from kinetic theory to be

$$J = \frac{\alpha\pi d_p^2}{(2\pi m_{\text{mol}} k_B T)^{1/2}}(p_\infty - p_{\text{sur}}) \tag{20.132}$$

where α is the accommodation coefficient or sticking probability ($0 \le \alpha \le 1$). It gives the fraction of incident molecules that are adsorbed. A value of unity means that once a vapor molecule hits the surface, the probability of sticking is unity. The accommodation coefficient may depend on whether evaporation or condensation is considered and its value is determined experimentally.

The calculation of the steady-state flow of vapor molecules toward a spherical droplet in the transition regime requires the solution of the Boltzmann equation. In the absence of a general solution, a number of approximations based on the so-called flux-matching techniques (introduced by Fuchs, 1964) have been proposed. These techniques require matching of the continuum expression with the kinetic at a given distance from the particle surface. For an extensive presentation of the various interpolation formulae, see, for example, Seinfeld and Pandis (1998). The most frequently used interpolation formula was proposed by Fuchs and Sutugin (1971):

$$f_{FS}(\lambda_g, d_p) = \frac{1 + 2\lambda_g/d_p}{1 + 3.42\lambda_g/d_p + 5.33(\lambda_g/d_p)^2} \tag{20.133}$$

where λ_g is the mean free path of the vapor species (see Equation 20.150). Thus, the vapor condensation rate becomes

$$J = \frac{2\pi d_p \mathfrak{D}}{k_B T} f_{FS}(\lambda_g, d_p)(p_\infty - p_{\text{sur}}) \tag{20.134}$$

Equation 20.134 is approximate in that it reproduces the continuum expression, but in the free molecular regime, it gives the kinetic expression multiplied by approximately 1.2 (for $\alpha = 1$).

The previous expressions may be converted into transport-limited growth laws by performing a mass balance on the growing or evaporating particle. Since the rate of change of the number of molecules in a particle equals the total rate of condensing or evaporating molecules,

$$\frac{dv}{dt} = \frac{2\pi \mathfrak{D} d_p v_{\text{liq}}}{k_B T} f_{FS}(\lambda_g, d_p)(p_\infty - p_{\text{sur}}) \tag{20.135}$$

where v_{liq} is the molecular volume of the condensing species ($v_{\text{liq}} = 1/n_{\text{liq}}$ when expressed in terms of the condensed-phase number density). In Equation 20.135, the accommodation coefficient has been set to unity. Growth laws are frequently used for the rate of change of particle radii,

$$\dot{a}_p = \frac{\mathfrak{D} v_{\text{liq}}}{a_p k_B T} f_{FS}(\lambda_g, d_p)\left(p_\infty - p_{\text{sur}}\right) \tag{20.136}$$

For surface reaction growth, if the surface reaction rate is slow compared to transport, the concentration of the reacting species at the particle surface is taken approximately equal to the concentration far away from the particle. The growth law becomes

$$\frac{dv}{dt} = \frac{\alpha \pi d_p^2 v_{\text{liq}}}{(2\pi m_{\text{mol}} k_B T)^{1/2}} p_\infty \tag{20.137}$$

where α, the fraction of effective collisions, is usually much less than unity. A summary of limiting growth laws for gas-to-particle conversion is presented in Friedlander (2000).

Equation 20.135 or 20.136 may be used to calculate the change of mass of a particle if the appropriate expression for the vapor pressure at the particle surface is used. As argued in Section 20.4.1.7, cf. Equation 20.130, the vapor pressure above a droplet depends on the curvature and, for a solution droplet, on the amount of solute present. For small liquid droplets, the exponential terms are usually expanded to obtain (the notation is explained in the discussion following Equation 20.130)

$$\frac{p_{\text{sur}}(T)}{p_{\text{sat}}(T)} = 1 + \frac{4\sigma_1 \bar{v}_1}{R_u T d_p} - \frac{6 n_2 \bar{v}_1}{\pi d_p^3} \tag{20.138}$$

As mass transfer continues, the particle temperature changes due to latent heat release or absorption. The growth rate is then obtained by solving the coupled equations for heat and mass transfer. In the continuum regime, the particle temperature is determined from the steady-state heat conduction equation. Mason (1971) introduced an analytical approximation to the two coupled equations for the rate of growth of a droplet by condensation (see, also, Rogers and Yau, 1989). He proposed

$$\dot{a}_p = \frac{1}{a_p}\left(\frac{S-1}{f_{\text{mass}} + f_{\text{heat}}}\right) \tag{20.139}$$

where $S = p_\infty / p_{\text{sat}}(T_\infty)$ is the ambient saturation ratio. The term f_{mass} represents the contribution associated to vapor diffusion, and thus, it is related to the continuum growth law presented in Equation 20.136

$$f_{\text{mass}} = \frac{k_B T_\infty}{v_{\text{liq}} \mathfrak{D} p_{\text{sat}}(T_\infty)} \tag{20.140}$$

The term f_{heat} is the contribution to the growth rate due to heat conduction

$$f_{\text{heat}} = \left(\frac{L_{\text{mol}}}{k_B T_\infty} - 1\right)\frac{L_{\text{mol}}}{v_{\text{liq}} T_\infty k_g} \tag{20.141}$$

where

L_{mol} is the latent heat per molecule (= $L\mathfrak{M}/N_A$ if expressed in terms of the latent heat per unit mass)

k_g is the thermal conductivity of the gas (e.g., air)

The temperature T_∞ is the temperature far away from the droplet surface. Equation 20.139 is known as Mason's equation. As before, solution and curvature effects may be incorporated into Mason's equation by modifying the droplet's equilibrium surface pressure according to Equation 20.130, namely by replacing the term $S - 1$ in the numerator of Equation 20.139 by

$$S - 1 - \frac{4\sigma_1 \bar{v}_1}{R_u T_\infty d_p} + \frac{6 n_2 \bar{v}_1}{\pi d_p^3} \tag{20.142}$$

Pruppacher and Klett (1997) present modifications of Mason's equation that account for noncontinuum effects in the transition regime. Their results are expressed in terms of a modified diffusion coefficient $\mathfrak{D}'$ and thermal conductivity k_g' that should be used in Equations 20.140 and 20.141. Seinfeld and Pandis (1998) proposed simplified expressions for $\mathfrak{D}'$ and k_g' for the case of air–water vapor system. The modified diffusion coefficient is

$$\mathfrak{D}' = \frac{\mathfrak{D}}{1 + (2\mathfrak{D}/\alpha_c d_p)(2\pi \mathfrak{M}_1 / R_u T)^{1/2}} \tag{20.143}$$

where α_c is the condensation coefficient (mass accommodation coefficient). The modified form of the thermal conductivity is

$$k_g' = \frac{k_g}{1 + (2k_g/\alpha_T d_p \rho_a \hat{c}_p)(2\pi \mathfrak{M}_a / R_u T_a)^{1/2}} \tag{20.144}$$

where

α_T is the thermal accommodation coefficient (frequently assumed equal to the mass accommodation coefficient)

ρ_a, $\hat{c}_p$ are the density and specific heat of humid air, respectively

Barrett and Clement (1988) used the generalized equations for heat and mass transfer in vapor–gas mixtures (Clement, 1985) to study growth rates for liquid droplets. They obtained, in addition to expressions for growth in the molecular regime and the transition regime, an expression for the droplet growth rate in the continuum regime that generalizes Mason's equation. They argued that for water droplets, the most important uncertainty is the choice of the molecular sticking probability.

20.4.2.2 Population of Droplets

A polydisperse aerosol is characterized by its size distribution, whose change in time and space is described by the GDE. Since condensation and evaporation are aerosol processes that occur much faster than coagulation, changes induced by them may be calculated separately without solving the full dynamic equation. In general, the GDE must be solved numerically: inclusion of a growth term in sectional methods leads to numerical diffusion, a problem that has stimulated the development of a number of different numerical schemes (summarized in Section 20.2.4). Alternatively, approximate analytical techniques have been developed. The GDE in the absence of coagulation, homogeneous nucleation, and external processes takes the form (expressed here in terms of the particle radius)

$$\frac{\partial n(a_p;t)}{\partial t} + \frac{\partial}{\partial a_p}[n(a_p;t)\dot{a}_p] = 0 \tag{20.145}$$

In Equation 20.145, the particle current, introduced in Section 20.2.1, see Equation 20.5, has been approximated by the migration term only, $n\dot{a}_p$, because homogeneous nucleation has been neglected. Inclusion of the homogeneous nucleation term would replace the zero on the RHS of Equation 20.145 by the nucleation rate $J_{\text{nuc}}\delta(a_p - a_p^\star)$, where $\delta(a)$ is the Dirac delta function. Equation 20.145 is occasionally referred to as the condensation equation.

The condensation equation can be solved analytically for constant gas-phase supersaturation, unity accommodation coefficient, and in the continuum regime. Under these approximations, the growth law is inversely proportional to the particle radius, $\dot{a}_p = A/a_p$, with A as a constant easily determined from

Equation 20.136. After a suitable transformation, Equation 20.145 may be solved via the method of characteristics. Along the characteristic, the solution is

$$d_p^2(t) = d_{p0}^2 + 2At \tag{20.146}$$

where d_{p0} is the initial ($t = 0$) diameter. Initially, $2At \ll d_{p0}^2$ and, thus, particles do not grow perceptively. In fact, smaller particles grow much faster than larger particles. In the long-time limit, the growth term $2At$ dominates so that condensation tends to shrink the size distribution, and the distribution tends to become more and more monodisperse.

The total condensation rate, defined as the change of aerosol mass due to condensation or evaporation, is related to a single droplet growth rate by considering the third moment of the GDE to obtain (Clement, 1985)

$$\frac{dm}{dt} = 4\pi\rho_l \int da_p n(a_p;t) a_p^2 \dot{a}_p \tag{20.147}$$

The previous equation is obtained by differentiating the third moment of the number distribution, see Section 20.2.3, and substituting Equation 20.145.

20.5 Single Particle Motion: Deposition Mechanisms

In this section, we focus on the mechanisms determining the motion of a single, spherical aerosol particle suspended in a fluid. Aspects of the dynamics of nonspherical, power-law aggregates were covered in Section 20.3.2.2. The fluid itself may be stagnant or in motion. In the latter case, in particular in accelerating fluid motion, the effects associated with the particle's own inertia become manifest. The mechanisms driving particle motion can be collectively called deposition mechanisms because their result is to make particles migrate from the suspending fluid to a surface and deposit there. Clearly, the same mechanisms are also responsible for transferring particles across boundaries within the flow. Therefore, the mechanisms discussed in this section correspond to the external processes in the GDE discussed in Section 20.2.2, with the exception of convection. Convective transport of particles will be addressed separately in Section 20.6.

In most cases, the flow around a moving aerosol particle is in the Stokes regime, $Re_p \ll 1$, where Re_p is the particle Reynolds number, $Re_p = d_p U/\nu_g$. The only point that merits further discussion here is related to noncontinuum flow effects in aerosol systems. In the aerosol literature, the Knudsen number (discussed extensively in Section 20.3, and specifically in 20.3.2 where variants of Equation 20.148 appropriate for nonspherical agglomerates are presented) is defined in terms of particle radius, $Kn_g = \lambda_g/a_p$, rather than particle diameter. For small particles, there is a departure from the continuum flow regime and a corresponding decrease in the Stokes drag force. This effect is taken into account by introducing a correction factor as follows:

$$F_D(Kn_g) = \frac{3\pi\mu U d_p}{C_c(Kn_g)} \tag{20.148}$$

The correction factor C_c, known as Cunningham correction factor or slip correction factor, is given by (Allen and Raabe, 1985)

$$C_c(Kn_g) = 1 + Kn_g\left[1.142 + 0.558\exp\left(-\frac{0.999}{Kn_g}\right)\right] \tag{20.149}$$

This correction factor for spherical particles and other expressions for it are given by Michaelides (2014). For nonspherical, power-law agglomerates, it is discussed in Section 20.3.2, where variants of Equation 20.148 appropriate for nonspherical objects are presented. To evaluate Equation 20.149, knowledge of the gas mean free path λ_g is required. The mean free path according to the kinetic theory of gases is, see, also, Equation 20.60,

$$\lambda_g = \frac{1}{\sqrt{2} n_g \pi d_M^2} \tag{20.150}$$

where
n_g is the number concentration of gas molecules
d_M is the collision diameter of a molecule

For air at 101 kPa (1 atm) and 293 K (20°C), the mean free path is $\lambda_{ref} = 0.0664\,\mu m$, while for air under other conditions, the following formula can be used (Willeke, 1976):

$$\lambda_g = \lambda_{ref}\left(\frac{101}{p}\right)\left(\frac{T}{293}\right)\left(\frac{1+110/293}{1+110/T}\right) \tag{20.151}$$

where
p is in kPa
T in K

For other gases, accurate determination of the mean free path from kinetic theory, Equation 20.150, is difficult. One may resort to the theory that relates the mean free path to gas macroscopic properties, like viscosity. A good approximate formula is (see also Equation 20.60)

$$\lambda_g = \frac{\mu_g}{p}\left(\frac{\pi R_u T}{2\mathfrak{M}}\right)^{1/2} \tag{20.152}$$

Table 20.1 gives values for the slip correction factor at different particle diameters. For a 1 μm particle at standard conditions in air, the slip correction is of the order of 15% and it increases sharply as size decreases. On the other hand, slip effects can be considered negligible for particles with $d_p > 10\,\mu m$.

20.5.1 Gravitational Settling

The terminal velocity of a spherical particle due to gravitational settling can be obtained by equating the drag force (Newton's resistance) on the particle, F_D, which in the general form is written as (Hinds, 1999):

$$F_D = C_D\frac{\pi}{8}\rho_g d_p^2 V_s^2, \tag{20.153}$$

to the force of gravity, $F_G = \pi\rho_p d_p^3 g/6$. Thus,

$$V_s = \left(\frac{4\rho_p d_p g}{3\rho_g C_D}\right)^{1/2}, \tag{20.154}$$

Equation 20.154 holds for any particle size; it gives the terminal settling velocity, if the appropriate drag coefficient, C_D, is used. Buoyancy effects are neglected in Equation 20.154, a largely legitimate assumption, since in most practical cases, $\rho_p \gg \rho_g$.

For Stokes flow, which is the usual case for most aerosols, the drag coefficient is equal to $C_D = 24/Re_p$ as explained in more detail in Chapter 1. Thus, Equation 20.154 becomes

$$V_s = \frac{\rho_p d_p^2 g C_C(Kn_g)}{18\mu_g} \quad \text{for } Re_p < 1. \tag{20.155}$$

Slip correction has been taken into account; hence, the aforementioned expression can be used for any particle size. The Stokes regime strictly holds for $Re_p < 0.1$; however, Equation 20.155 is a good approximation over the extended range $0.1 < Re_p < 1$ (Vincent, 1995, Hinds, 1999). For $10^3 < Re_p < 3 \times 10^5$, the drag coefficient is constant and approximately equal to $C_D = 0.44$; as shown in Chapter 1, the terminal settling velocity becomes

$$V_s = 1.74\left(\frac{\rho_p}{\rho_g} d_p g\right)^{1/2} \quad \text{for } 10^3 < Re_p < 3\times 10^5. \tag{20.156}$$

In the intermediate region, that is, for $1 < Re_p < 10^3$, the drag coefficient depends on the particle Reynolds number, Re_p, thus on V_s itself; therefore, the particle terminal settling velocity has to be calculated iteratively. Methods to calculate V_s at higher particle Reynolds numbers are given by Hinds (1999). In particular, if Equation 20.154 is rearranged and both sides are multiplied by Re_p^2, then

$$C_D Re_p^2 = \frac{4 d_p^3 \rho_p \rho_g g}{3 \mu_g}. \tag{20.157}$$

The RHS of Equation 20.157 does not contain the unknown terminal settling velocity; thus, the quantity $C_D Re_p^2$ can be calculated. If, in addition, the Schiller and Nauman correlation for the drag coefficient in the intermediate region is used, the resulting system of equations gives the particle Reynolds number and, consequently, the terminal settling velocity V_s as a unique function of Re_p.

A quantity related to the terminal settling velocity (not necessarily restricted to gravitational settling) and frequently used in aerosols is the *particle mechanical mobility*, B, in m/N/s. It is defined as the ratio of the terminal velocity to the steady-state force that produces it. In the Stokes regime,

$$B = \frac{C_c(Kn_g)}{3\pi \mu_g d_p} \tag{20.158}$$

Thus, the terminal velocity a particle acquires is the applied force times its mechanical mobility; see also Equation 20.148.

For nonspherical particles, a correction is introduced in Equation 20.154, called the dynamic shape factor χ, when the diameter d_p is replaced by the *equivalent volume diameter*, d_e. The equivalent volume diameter, already mentioned in Section 20.3.2.1, is the diameter of a sphere that has the volume of the particle. With these conventions, Equation 20.154 becomes

$$V_s = \frac{\rho_p d_e^2 g C_c(Kn_g)}{18 \mu_g \chi} \quad \text{for } Re_p < 0.1 \tag{20.159}$$

The slip correction factor for an irregularly shaped particle is difficult to determine with accuracy (see, however, the analysis for power-law aggregates, Section 20.3.1.2). It is occasionally approximated by $a_p = d_e/2$ or by $a_p = R_g$, where the radius of gyration was defined in Equation 20.45, in Equation 20.149. Except for certain streamlined shapes, the dynamic shape factor is greater than 1.0. Colbeck (1998) and Hinds (1999) present tables of the dynamic shape factor for various particle shapes, whereas calculated shape factors for straight chains may be found by Isella and Drossinos (2011) and for fractal-like aggregates by Melas et al. (2014a,b).

A diameter used to characterize nonspherical particles is the *Stokes diameter* d_S. This is the diameter of a sphere of the same density and same settling velocity as the particle. Usually, the Stokes diameter is defined in terms of the bulk material density of the particle, ρ_b, to avoid the problem of specifying the true density that may be affected by porosity or agglomerated structure. From Equation 20.159, it follows

$$d_S = d_e \left(\frac{\rho_p}{\rho_b \chi} \right)^{1/2} \left(\frac{C_c(d_e)}{C_c(d_S)} \right)^{1/2} \tag{20.160}$$

Obviously, for a spherical particle of uniform density $d_S = d_p$. Since the Cunningham slip correction factor depends itself on diameter, an iterative procedure is required to achieve consistency between the Stokes diameter and the respective slip correction factor. For particles with $d_e > 1\,\mu$m, the slip correction is small anyway, and the ratio $C_c(d_e)/C_c(d_S)$ becomes approximately one. On the other hand, for particles with $d_e < 1\,\mu$m and shape factor close to unity, the difference between d_e and d_S is such that the influence of the ratio $C_c(d_e)/C_c(d_S)$ is not very large. Therefore, very often Equation 20.160 simplifies to

$$d_S = d_e \left(\frac{\rho_p}{\rho_b \chi} \right)^{1/2} \tag{20.161}$$

Another characteristic diameter, extensively used in aerosol science and technology, is the *aerodynamic diameter* d_a. This is the diameter of a spherical particle of density $\rho_0 = 1000\,\text{kg/m}^3$ that settles with the same terminal velocity as the particle. The aerodynamic diameter is given by

$$d_a = d_e\left(\frac{\rho_p}{\rho_0\chi}\right)^{1/2}\left(\frac{C_c(d_e)}{C_c(d_a)}\right)^{1/2} = d_S\left(\frac{\rho_b}{\rho_0}\right)^{1/2}\left(\frac{C_c(d_S)}{C_c(d_a)}\right)^{1/2} \tag{20.162}$$

and, in the same way as in Equation 20.160, the calculation requires an iterative procedure. As before, there are many practical cases in which the effect of ratios of slip factors is not very large, (namely, for large particles with $d_e > 1\,\mu\text{m}$, or small particles of smooth shape and density close to ρ_0), and Equation 20.162 is approximately written as

$$d_a = d_e\left(\frac{\rho_p}{\rho_0\chi}\right)^{1/2} = d_S\left(\frac{\rho_b}{\rho_0}\right)^{1/2} \tag{20.163}$$

The aerodynamic diameter and, to a lesser extent, the Stokes diameter are essential parameters; both are used to characterize aerosol behavior irrespective of particle geometry and material. For example, the aerodynamic diameter is used to characterize filtration or respiratory deposition. Several instruments, such as impactors and elutriators, measure aerodynamic diameter.

20.5.2 Diffusion

Aerosol particles exhibit a random motion called Brownian motion as a consequence of their continuous bombardment by the molecules of the surrounding gas. Equation 20.20 is the stochastic Langevin equation that describes the Brownian motion of a particle in a quiescent fluid. The macroscopic effect of Brownian motion is the net transfer of particles from regions of high to low concentration, a process known as diffusion. Diffusion of aerosol particles due to Brownian motion is described by the well-known (macroscopic) Fick's law in terms of number of particles diffused, namely, $\mathbf{J}_p = -\mathfrak{D}\nabla n_p$, where $\mathbf{J}_p$ is the number flux vector (particles/m^2 s), n_p is the number particle concentration (particles/m^3), and $\mathfrak{D}$ is a diffusion coefficient (m^2/s).

The diffusion coefficient depends strongly on particle size, with smaller particles diffusing much more efficiently than larger particles. Table 20.1 gives values of the diffusion coefficient in air for particles of various sizes. The effect of particle size is strong: under the same concentration gradient, the diffusive mass flux of a 0.01 μm particle is about 20,000 times larger than that of a 10 μm particle. A related dimensionless number is the particle Schmidt number defined as in molecular mass transfer

$$Sc_p = \frac{\nu_g}{\mathfrak{D}} \tag{20.164}$$

where ν_g is the kinematic viscosity of the suspending gas. Values of the particle Schmidt number are provided in Table 20.1. Generally, the diffusion coefficient of aerosol particles is orders of magnitude smaller than the diffusion coefficient of molecular diffusion in gases, and comparable in magnitude to diffusion coefficients observed in molecular diffusion in liquids. Accordingly, the particle Schmidt number is generally very large, $Sc_p \gg 1$. Hence, as a rule, the concentration boundary layer of aerosol particles is much thinner than the viscous or thermal boundary layers over a surface.

The particle diffusion coefficient is

$$\mathfrak{D} = \frac{k_B T_g C_c(Kn_g)}{3\pi\mu_g d_p} \tag{20.165}$$

which, without the slip correction factor $C_c(Kn_g)$, cf. Equation 20.149, is known as the Stokes–Einstein equation. Note that the diffusion coefficient depends on particle diameter and gas properties (temperature and viscosity), but not on particle physical properties (e.g., density).

A quantity used to characterize the strength of Brownian diffusion is $x^2_{\text{rms}} = \langle[x(t+\Delta t) - x(t)]^2\rangle$, the root-mean-square net displacement of a diffusing particle over a time interval Δt. This displacement is related

to the diffusion coefficient through the expression $x_{\text{rms}} = \sqrt{2\mathfrak{D}\Delta t}$. The ratio $x_{\text{rms}}/V_s\Delta t$, where $V_s\Delta t$ represents the displacement due to gravitational settling, is an indicator of the importance of diffusion. For spherical particles of standard density in air, this ratio is of order one for $d_p \sim 1\,\mu\text{m}$, whereas it is of order 10^3 for $d_p \approx 0.01\,\mu\text{m}$ and of order 10^{-3} for $d_p \approx 10\,\mu\text{m}$. It follows that Brownian diffusion is an important transport mechanism only for small particles of the submicrometer range. Instead, for particles greater than 1 μm in diameter, gravitational settling and inertial effects outweigh diffusional transport. In turbulent flows, particles diffuse due to eddies, an important mechanism that is extensively discussed in Chapter 2.

20.5.3 Inertial Effects: Impaction

In an accelerating flow field, particles are not able to follow perfectly the fluid motion due to their own mass. In straight-line accelerating (decelerating) motion, aerosol particles lag behind (ahead) the Lagrangian "fluid particles." In curvilinear motion, for example, in a flow around a body surface, particle trajectories deviate from the fluid streamlines and may impinge on the surface. This mechanism, known as *impaction*, is a major deposition mechanism of great practical importance in inertial size classifiers (e.g., cascade impactors), aerosol sampling, filtering, gas-cleaning equipment, respiratory deposition, and generally, in all processes involving particle collection. Such inertial effects become increasingly important with increasing particle size. As a rule of thumb, inertial effects become important for particles with diameter ≥1 μm.

The extent to which the motion of an aerosol particle adjusts to or deviates from the motion of the fluid is described by three interrelated characteristic parameters: the *relaxation time* τ_V, the *stop distance* S_L, and the Stokes number *St*. These parameters are defined for the case of Stokesian particles (strictly for $Re_p < 0.1$, but to a good approximation also for $0.1 < Re_p < 1$).

The particle relaxation time, or velocity response time, is a time scale characterizing the adjustment of particle velocity to a changing fluid velocity. It is calculated by considering the time required by the particle to reach its terminal settling velocity when released with zero initial velocity in a quiescent fluid. The relaxation time is given by, see also the discussion following Equation 20.20, the following equation:

$$\tau_V = \frac{\rho_p d_e^2 C_c(Kn_g)}{18\mu_g \chi} \tag{20.166}$$

Therefore, by Equation 20.159, it can be regarded as the settling velocity of a particle on which a unit gravitational acceleration acts, namely, $V_s = \tau_V g$. This permits one to derive the following useful expression for the calculation of the terminal velocity *U* of an aerosol particle subjected to a constant force *F*:

$$U = \tau_V \frac{F}{m_p} \tag{20.167}$$

Values of particle relaxation times as function of particle size for particles in air at standard conditions are given in Table 20.1. It is important to realize that particle relaxation time, and generally inertial effects and impaction, does not depend on the properties of the particle only, but on the properties of the combined particle–fluid system. The dependence on fluid properties is clearly attested by Equation 20.166, which involves the viscosity of the gas as well as the mean-free path of the gas through the slip correction.

Stop distance is a length scale that characterizes the persistence of a particle to continue its original motion in a changing flow field before it equilibrates again with the fluid motion. The stop distance is simply the initial velocity times the relaxation time

$$S_L = U_0 \tau_V \tag{20.168}$$

This expression is obtained by considering the distance a particle travels in still fluid before it comes to rest, following injection with initial velocity U_0 and in the absence of any external force.

The Stokes number, introduced in Chapter 1, is a dimensionless number defined as the ratio of the stop distance to a characteristic length of the flow, or equivalently, as the product of a characteristic velocity times the relaxation time divided by a characteristic length

$$St = \frac{S_L}{L} = \frac{U_0 \tau_V}{L} = \frac{\rho_p d_e^2 C_c(Kn_g) U_0}{18\mu_g \chi L} \tag{20.169}$$

The Stokes number is an important similarity parameter used to scale particle trajectories, and hence impaction deposition, in particle–flow systems that are geometrically and hydrodynamically similar. Also, it is a widely used practical criterion to determine the responsiveness of aerosol particles to changes of fluid velocity, thereby predicting if impaction will take place. For $St \ll 1$, the particles follow closely the fluid motion and do not impact on surfaces, whereas for $St \gg 1$, the particles escape the flow and may deposit by impaction.

It should be noted that all the definitions assume the validity of Stokes law for the drag force throughout the entire period of motion of the particle. Occasionally, for large particles and high initial velocities, particle motion may be found outside the Stokes regime. Some results on impaction deposition of non-Stokesian particles are given in Section 20.6.2.2.

An important case of inertial transport arises in turbulent flow, originating from the inability of high-inertia particles to follow the fluid turbulent eddies. Inertial deposition due to turbulence is commonly referred to as *turbulent impaction*, *eddy impaction*, or, even, *turbophoresis* (Reeks, 1983), the latter referring to the tendency of inertial particles to acquire a drift velocity in the direction of decreasing turbulence intensity; it is presented in Section 20.6.3.

20.5.4 Motion in an Electric Field

A charged particle placed in an electric field of strength E is subjected to an electrostatic force $F_E = neE$ where n is the number of elementary units of charge on the particle and e the charge of an electron ($e = 1.609 \times 10^{-19}$ C). Large particles frequently acquire multiple charges ($n > 1$), but the probability of charging decreases with decreasing particle size. For small particles, usually $n = 1$. Aerosol particles can readily acquire charge through a variety of processes, such as thermionic emission (e.g., in a flame), diffusion charging (attachment of diffusing ions to particles), field charging (collision of particles with ions in a strong electric field, e.g., a corona discharge), or static electrification (e.g., spray electrification). Radioactive aerosols become self-charged by emitting α or β particles, and they may acquire very high charge during radioactive decay.

Electrostatic forces may give rise to appreciable particle drifts due to the high mobility of aerosol particles. The terminal velocity, referred to as *electrical drift velocity*, can be obtained for the case of a Stokesian spherical particle with the help of Equation 20.167 as follows:

$$V_E = \frac{neEC_c(Kn_g)}{3\pi\mu_g d_p} = neEB \tag{20.170}$$

This expression is the basic formula used to analyze electrical migration of aerosol particles. It is also customary to use the so-called *electrical mobility* of the particle, Z, which is the particle velocity in a field of unit intensity, namely

$$Z = \frac{neC_c(Kn_g)}{3\pi\mu_g d_p} \tag{20.171}$$

The electrical mobility is related to the mechanical mobility by

$$Z = neB = qB \tag{20.172}$$

where q is the charge of the particle. In terms of the electrical mobility, the particle velocity in an electrical field is simply written as $V_E = ZE$.

The electrical properties of aerosols find wide application in air cleaning equipment (electrostatic precipitators), in electrodynamic levitation techniques (electrodynamic balances), and in measurements of particle size distribution (or generally in size classification) with electrical mobility analyzers. For information on electrical measurements techniques, the reader is referred to the reviews by Flagan (1998, 2001) and Davis (2001).

20.5.5 Phoretic Effects

Besides gravitational and electrostatic forces, aerosol particles may be subjected to a variety of forces arising from other external fields. Such forces, negligible for macroscopic objects, may influence significantly the motion of small aerosol particles because of their high mobility. The induced motion is generally coined after the name of the causal agent and the conjunctive "phoresis," which in Greek means "being carried by."

Accordingly, a particle may move by *thermophoresis* (motion induced by a temperature gradient in the carrier gas), *diffusiophoresis* (induced by the concentration gradient of a vapor diffusing through the carrier gas), *photophoresis* (induced by a light beam), *radiation pressure* (induced by an incident electromagnetic radiation), and *sonarphoresis* or *acoustic pressure* (induced by acoustic waves). The following description is limited to the two most common phoretic effects: thermophoresis and diffusiophoresis.

20.5.5.1 Thermophoresis

It has been known for long (since the nineteenth century) that a hot body placed in a dusty gas creates a dust-free zone around it. Indeed, aerosol particles suspended in a nonisothermal gas tend to migrate from the hotter to the colder regions. This movement is called *thermophoresis*: it arises from the asymmetric bombardment exerted on a particle by the gas molecules in the presence of a temperature gradient in the gas. The momentum received on the "hotter side" of the particle is more than that on the "colder side," and the macroscopic result is net transport in the direction of decreasing temperature.

The thermophoretic velocity can, thus, be expressed as a function of the local temperature gradient as follows:

$$\mathbf{v}_{\text{th}} = -K_{\text{th}} \frac{\nu_g}{T} \nabla T \tag{20.173}$$

and, from Equation 20.167, the thermophoretic force is written as $\mathbf{F}_{\text{th}} = \mathbf{v}_{\text{th}} m_p / \tau_v$. In Equation 20.173 K_{th} is a dimensionless parameter, the thermophoretic coefficient, that depends on properties of both the gas and the particle. Theoretical expressions for K_{th} have been rigorously derived only in the limits of continuum flow ($Kn_g = \lambda_g / a_p \ll 1$), the so-called Epstein expression (Fuchs, 1964),

$$K_{\text{th}}^{\text{Epstein}} = \frac{3}{2} \frac{k_g / k_p}{(1 + 2k_g / k_p)} \quad (\text{for } Kn_g \to 0) \tag{20.174}$$

or in the limit of free molecular flow ($Kn_g \gg 1$), the so-called Waldmann expression (Fuchs, 1964),

$$K_{\text{th}}^{\text{Waldmann}} = \frac{3}{4(1 + \pi/8)} \quad (\text{for } Kn_g \to \infty) \tag{20.175}$$

Talbot et al. (1980) proposed a fitting formula over the entire momentum-transfer regime, range $0 \le Kn_g \le \infty$, which agrees to within 20% or better with most of the available experimental data. The fitting formula was obtained by introducing an improved value for the numerical factor in the theoretical expression of Brock (1962), who had suggested an expression for the thermophoretic force valid in the slip-flow regime. The Brock–Talbot expression is

$$K_{\text{th}} = 2C_s \frac{C_c(Kn_g)(k_g / k_p + 2C_t \lambda_g / d_p)}{(1 + 6C_m \lambda_g / d_p)(1 + 2k_g / k_p + 4C_t \lambda_g / d_p)} \tag{20.176}$$

In this equation,

k_g / k_p is the ratio of gas-to-particle thermal conductivity
$C_c(Kn_g)$ is the Cunningham correction factor, cf. Equation 20.149

The order-unity constants C_s, C_t, C_m arise from noncontinuum effects at the particle interface: they are associated with the temperature and velocity boundary conditions (jump conditions) at the particle–gas interface. The recommended values are $C_s = 1.17$ (thermal creep coefficient), $C_t = 2.18$ (temperature jump coefficient), and $C_m = 1.14$ (velocity jump coefficient). Young (2011) revisited theoretical analyses and experimental measurements to suggest an interpolation formula that provides improved comparison with experimental data and is more consonant with theoretical developments than the Brock–Talbot expression. Nevertheless, the Brock–Talbot expression remains the most commonly used formula.

Figure 20.3 shows the thermophoretic coefficient K_{th} as a function of the Knudsen number Kn_g and is parametrized by k_g / k_p. As can be seen, K_{th} typically has values around 0.5 and becomes a constant for very small particles in the free molecular regime. For large particles, it depends both on particle size and on the gas-to-particle thermal conductivity ratio. This dependence is due to the nonnegligible temperature gradient established within a particle of appreciable size, which affects locally the temperature gradient of the gas.

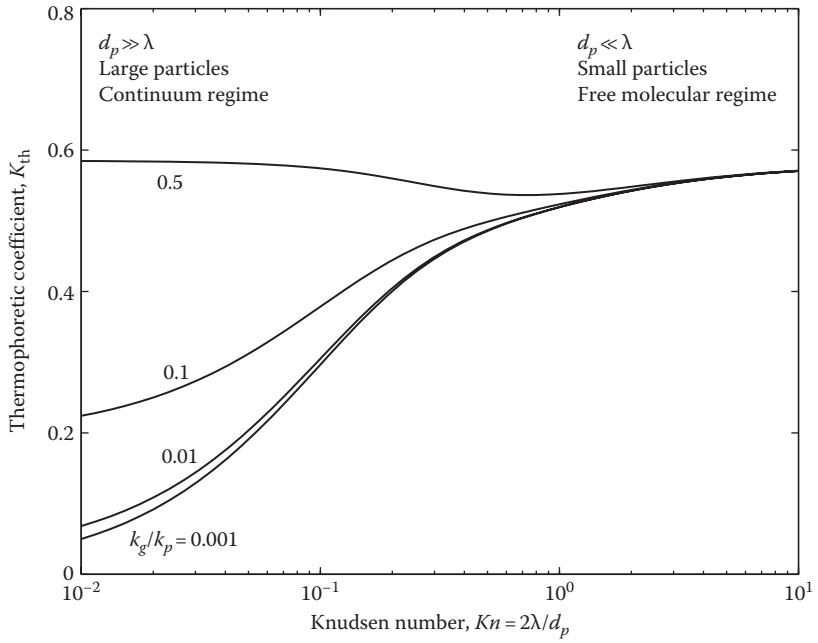


Figure 20.3

Thermophoretic coefficient K_{th} as a function of Knudsen number, $Kn_g = \lambda_g/a_p$, for various gas-to-particle thermal conductivity ratios k_g/k_p.

More details on the thermophoretic motion of particles may be found in Chapter 1 and its relationship to the Brownian motion in Michaelides (2015).

20.5.5.2 Diffusiophoresis and Entrainment by Stefan Flow

Particles suspended in a nonequilibrium binary gas mixture, where two gases interdiffuse, experience unequal momentum transfers by collisions with the molecules of one gas diffusing in one direction and the molecules of the other diffusing in the opposite direction. A net force develops on the particle in the direction of diffusion of the heavier gas molecule. The resulting motion, which is driven by the prevailing concentration gradient, is called *diffusiophoresis*. The diffusiophoretic motion of particles should not be confused with the diffusion of particles: the former is driven by the concentration gradient of a diffusing gas, whereas the latter is driven by the concentration gradient of the particles themselves.

This process, that is, diffusion of two noncondensable gases into each other, is not very usual in aerosol flows. Instead, most practical cases are concerned with diffusion of a condensable vapor through a background gas (e.g., evaporation or condensation of water droplets in air, or wall condensation of steam in nitrogen–steam or air–steam mixtures in nuclear safety experiments). Under such circumstances, a secondary convective flow is established within the gas, known as *Stefan flow*, which arises from a subtle mass balance between the diffusive flows of the gas and the vapor. The direction of Stefan flow is always away from an evaporating surface or toward a condensing surface. Therefore, the motion of the particle is determined by the combined action of Stefan flow and diffusiophoresis. The latter still takes place due, as described earlier, to diffusion of vapor and counterdiffusion of gas. For the combined motion due to diffusiophoresis and Stefan flow, Waldmann and Schmitt (1966) provided the following theoretical expression for the particle drift velocity:

$$V_p = -\frac{\sqrt{\mathfrak{M}_1}}{\psi_1\sqrt{\mathfrak{M}_1} + \psi_2\sqrt{\mathfrak{M}_2}}\frac{\mathfrak{D}_{12}}{\psi_2}\nabla\psi_1 \tag{20.177}$$

where

$\mathfrak{M}_1, \mathfrak{M}_2$ are the molecular weights of the condensable vapor and the background gas
ψ_1, ψ_2 are the molar fraction of the vapor and the gas
$\mathfrak{D}_{12}$ is the binary gas diffusion coefficient

Note that the velocities derived from Equation 20.177 are independent of particle size. The predictions of Equation 20.177 are in very good agreement with the experimental data of Goldsmith and May (1966) that were obtained with small nichrome particles ($0.02 \le d_p \le 0.2\,\mu m$) in diffusing water vapor in air and helium. The use of Equation 20.177 for larger particles requires caution. The measurements of Goldsmith and May (1966) for the case of water vapor in air can be correlated within ±5% as

$$V_p = -1.9\times10^{-4}\,(\mathrm{cm^2/s/mb})\frac{dp_1}{dx} \tag{20.178}$$

where dp_1/dx is the gradient of the partial pressure of the condensable vapor. If Equation 20.177 is evaluated for water vapor diffusing in air at standard conditions, a numerical expression identical to Equation 20.178 is recovered (note that $(1/\psi_2)d\psi_1/dx$ can be written as $(1/p_2)dp_1/dx$ where p_2 is the partial pressure of the gas). Therefore, Equation 20.178 has the appealing property of being both an empirical and a theoretical formula suitable for the calculation of the particle drift velocity due to combined diffusiophoresis and Stefan flow in water vapor–air systems.

20.6 Convective Transport and Deposition

The behavior of aerosol particles as they are transported in a flowing fluid is of fundamental importance in predicting rates of deposition onto surfaces in a great variety of applications, including gas-cleaning equipment, aerosol filtration, aerosol instrumentation and measurements, nuclear safety relevant experiments, respiratory deposition, etc. For submicrometer particles, and in the absence of external force fields, Brownian or turbulent diffusion is the basic mechanism that drives deposition. For particles larger than about 1 μm, deposition is primarily due to inertial impaction and gravitational settling.

A basic quantity characterizing convective transport of an aerosol is the *penetration ratio*, or *penetration fraction*, defined as the fraction of the inflowing particles that exit the flow system. It can be written as

$$f_p = \frac{C_{\mathrm{out}}}{C_0} \tag{20.179}$$

where C_{out} and C_0 are the particle concentrations (either mass or number) at the outlet and inlet, respectively. Alternatively, a *removal efficiency*, or *collection efficiency,* can be defined as the fraction of the inflowing particles that is lost by deposition. The removal efficiency is simply related to penetration fraction by

$$n_R = 1 - f_p \tag{20.180}$$

Another quantity widely employed to characterize deposition in convective aerosol flows is *deposition velocity* is defined as

$$V_d = \frac{G_p}{C_{\mathrm{av}}} \tag{20.181}$$

where

G_p is the particle mass flux to the wall

C_{av} is the average particle concentration above the surface

The latter is taken equal to the average concentration over the cross section of the conduit, or, in external flow systems, equal to the concentration in the undisturbed stream. The usual boundary condition employed at the wall is that deposited particles are totally absorbed there; thus, a zero particle concentration is imposed, $C_w = 0$. Then, Equation 20.181 can be rewritten as $G_p = V_d(C_{\mathrm{av}} - C_w)$. As such, the deposition velocity should be interpreted as a mass-transfer coefficient of the process, and not as the velocity with which particles arrive at the surface (as its name might imply).

In closed ducts, flow can be generally considered hydrodynamically fully developed. The particle Schmidt number is large and as a result, velocity profiles develop much more rapidly than particle concentration profiles. Chen and Comparin (1976) demonstrated that the effects of a developing velocity become negligible when $Sc_p \ge 10$, a condition usually satisfied for particles with $d_p > 0.002\,\mu m$.

Next, the most relevant cases of convective transport/deposition are addressed. First, cases of convection combined with a single additional transport mechanism (e.g., diffusion, inertial transport, gravitational settling, and thermophoresis) are reviewed. The section concludes by addressing one important case in which all deposition mechanisms act in combination: filtration.

20.6.1 Convective Diffusion from Laminar Flow in Ducts

20.6.1.1 Circular Tube

The analytical solution for the fundamental case of convective diffusion of small particles suspended in laminar flow inside a circular tube, cf. Equation 20.10, was derived by Gormley and Kennedy (1949). The Gormley and Kennedy solution is a classic result in the aerosol literature and, as such, it is reproduced here

$$f_p = 1 - 6.46\Delta^{2/3} + 4.8\Delta + 1.124\Delta^{4/3} + \cdots \quad \text{for } \Delta < 0.0312$$

$$f_p = 0.8191\exp(-14.628\Delta) + 0.0975\exp(-89.2\Delta) + 0.0325\exp(-228\Delta) + \cdots \quad \text{for } \Delta > 0.0312 \tag{20.182}$$

where Δ is the dimensionless parameter

$$\Delta = \frac{\mathfrak{D}L}{D^2U} = \frac{\pi}{4}\frac{\mathfrak{D}L}{\dot{V}} \tag{20.183}$$

with L as the length of the tube and U as the mean velocity through the tube. The parameter Δ corresponds to the standard dimensionless length $L/D\,Re\,Sc_p$ commonly used in the mass-transfer literature. However, in the aerosol literature, it has become customary to use the expression of Equation 20.183 that manifestly shows that deposition depends (for a given aerosol) on the flowrate and the length of the tube and not on the tube diameter. Hence, the same deposition result is obtained by passing the same flow through a single long tube or by cutting it into a large number of parallel short tubes. This principle has found wide application in the design of *diffusion batteries*, apparatuses relying on convective diffusional losses in laminar flow to determine the diffusion coefficient and thus particle size. It can also be used to analyze convective diffusion inside a *tube bundle* (Housiadas et al., 1998).

Ingham (1975) derived a single asymptotic expression for the penetration fraction that is valid for both large and small values of Δ:

$$f_p = 0.819\exp(-14.63\Delta) + 0.0976\exp(-89.2\Delta) + 0.0325\exp(-228\Delta) + 0.0509\exp(-125.9\Delta^{2/3}) \tag{20.184}$$

Equation 20.184 is accurate to better than 0.5% for all values of Δ as compared to more accurate solutions.

In the same spirit, Alonso et al. (2010) presented an approximate analytical expression for the two-dimensional fully developed particle concentration profile. In the fully developed region ($\Delta \geq 0.05$), the overall particle concentration profile continues to decay, whereas the radial profile retains a constant shape. They suggested

$$f_p(L,r) = 1.477\exp(-14.636\Delta)\left[1 - \frac{1}{11}(18r^2 - 9r^4 + 2r^6)\right] \quad \text{for } \Delta > 0.05 \tag{20.185}$$

where r was rendered dimensionless by scaling it on the tube radius, $r = 1$ being the wall. The initial condition was uniform particle concentration at the tube entrance.

An expression similar to Equation 20.184 for plug flow (uniform velocity) is (Ingham, 1975)

$$f_p = \frac{4}{\alpha_1^2}\exp(-4\alpha_1^2\Delta) + \frac{4}{\alpha_2^2}\exp(-4\alpha_2^2\Delta) + \frac{4}{\alpha_3^2}\exp(-4\alpha_3^2\Delta) + \left\{1 - 4\left(\frac{1}{\alpha_1^2} + \frac{1}{\alpha_2^2} + \frac{1}{\alpha_3^2}\right)\right\} \exp\left[-\frac{8\Delta^{1/2}}{\sqrt{\pi}\left[1 - 4\left(1/\alpha_1^2 + 1/\alpha_2^2 + 1/\alpha_3^2\right)\right]}\right] \tag{20.186}$$

where α_1, α_2, α_3 are the first three zeros of the Bessel function J_0, which, to an accuracy of four decimal points, are $\alpha_1 = 2.4048$, $\alpha_2 = 5.5201$, $\alpha_3 = 8.6537$. As before, Equation 20.186 is valid for all dimensionless lengths Δ to an accuracy of better than 0.5%. Expression (20.186) in combination with Equation 20.184 permits the calculation of the envelop values of f_p for the case of a hydrodynamically developing flow at the entrance of a tube.

20.6.1.2 Nonuniform Inlet Concentration

In practical situations, the distribution of aerosol mass at the inlet of the tube may deviate from uniformity. Consider, for example, the case of an aerosol flow through a circular tube with nonuniform inlet concentration, whose profile is described as a function of the dimensionless radial co-ordinate $r^\star = r/R$ by a polynomial of degree K

$$C_0 \sim a_0 + a_1 r^\star + a_2 (r^\star)^2 + a_3 (r^\star)^3 + \cdots + a_K (r^\star)^K \tag{20.187}$$

The penetration ratio can be calculated with the help of the series solution of the convective diffusion equation and methods proposed by Housiadas et al. (1999, 2000):

$$f_p = -8 \sum_{n=1}^{\infty} \frac{I_n \exp(-2\lambda_n^2 \Delta)}{\lambda_n \Lambda_n} \tag{20.188}$$

In this expression, the constants I_n are determined by

$$I_n = a_0 (E_1^n - E_3^n) + a_1 (E_2^n - E_4^n) + \cdots + a_K (E_{K+1}^n - E_{K+3}^n) \tag{20.189}$$

whereas the coefficients E_j^n are calculated from the recurrence relation

$$E_j^n = \frac{R_n}{\lambda_n^2} + \frac{(j-3)^2}{\lambda_n^2} E_{j-4}^n + E_{j-2}^n, \quad j = 4,5, \ldots, K+3 \tag{20.190}$$

Table 20.2 gives the eigenvalues λ_n and constants Λ_n, R_n, E_0^n, E_1^n, E_2^n, E_3^n required in the numerical evaluation of the solution up to order $n = 5$. By using five terms, the series solution (20.188) converges to the correct result with an accuracy of better than 1% for all dimensionless lengths $\Delta > 4 \times 10^{-4}$ (better than 2% for all dimensionless lengths $\Delta > 5 \times 10^{-5}$, i.e., for all practical values of Δ).

20.6.1.3 Ducts of Other Geometry

Flat *rectangular geometry* is generally considered the most efficient geometry for the collection of submicrometer particles. Accurate solutions have been derived for particle penetration through a rectangular channel of long side W and short side H with $W \gg H$ (Tan and Thomas, 1972, Bowen et al., 1976):

$$f_p = 1 - 1.526\Delta^{2/3} + 0.15\Delta + 0.0342\Delta^{4/3} \quad \text{for } \Delta \le 0.05 \tag{20.191}$$

Table 20.2 Eigenvalues and Related Constants for the Numerical Evaluation of the Series Solution Equation 20.188

	λ_n	R_n	Λ_n	E_0^n	E_1^n	E_2^n	E_3^n
1	2.7044	−1.0143	−0.5009	0.5782	0.1968	0.0979	0.0581
2	6.6790	1.3492	0.3715	0.0512	−0.0830	−0.0707	−0.0527
3	10.6734	−1.5723	−0.3183	0.1518	0.0526	0.0449	0.0388
4	14.6711	1.7460	0.2865	0.0256	−0.0385	−0.0347	−0.0304
5	18.6699	−1.8909	−0.2645	0.0864	0.0303	0.0275	0.0249

Source: Data from Housiadas, C. et al., *Int. J. Heat Mass Transfer*, 42, 3013, 1999; Housiadas, C. et al., *J. Aerosol Sci.*, 31, 959, 2000.

Table 20.3 First Eigenvalues and Coefficients for Different R_1/R_2 Ratios of a Circular-Tube Annulus

R_1/R_2	0.05	0.1	0.25	0.5	0.75	0.9	0.95
λ_1	3.493	3.6102	3.7641	3.8507	3.8776	3.8828	3.8833
λ_2	7.906	8.0870	8.3141	8.4356	8.4728	8.4798	8.4805
λ_3	12.31	12.557	12.866	13.033	13.083	13.093	13.094
K_1	0.879	0.889	0.9004	0.9076	0.9098	0.9103	0.91034
K_2	0.036	0.026	0.0118	0.0033	0.0006	0.00007	0.00002
K_3	0.044	0.046	0.050	0.052	0.053	0.05312	0.05314

Source: Adapted from Kerouanton, D. et al., *J. Aerosol Sci.*, 27, 345, 1996.

$$f_p = 0.9104\exp(-2.8278\Delta) + 0.0531\exp(-32.147\Delta) + 0.01528\exp(-93.475\Delta) + 0.00681\exp(-186.805\Delta) \quad \text{for } \Delta > 0.05 \tag{20.192}$$

Here, the definition of the dimensionless parameter Δ is $\Delta = 8\mathfrak{D}L/3UH^2 = 8\mathfrak{D}LW/3\dot{V}H$. Hinds (1999) suggests a simplified form of these expressions by neglecting the last term in Equation 20.191 and the two last terms in Equation 20.192. With these simplifications, the calculated penetration fractions agree within 1% with more accurate predictions over the whole range of values of Δ.

The case of a *circular-tube annular* cross section was treated by Kerouanton et al. (1996) who presented the solution as an infinite series:

$$f_p = \sum_{n=1}^{\infty} K_n \exp\left(-2\lambda_n^2 \Delta\right) \tag{20.193}$$

with $\Delta = \mathfrak{D}L/4U(R_2 - R_1)^2 = (\pi/4)(\mathfrak{D}L/\dot{V})$, where R_2 and R_1 are the outer and inner radii of the annulus, respectively. Table 20.3 provides the first three eigenvalues λ_n and coefficients for different R_1/R_2 ratios, as reported in Kerouanton et al. (1996). The use of three terms in the series enables an accurate evaluation of the solution for $\Delta > 0.005$.

20.6.2 External Flows

Here, the collection of particles by objects placed in an unconfined aerosol flow is considered. There are a great variety of practical cases involving external aerosol flow, for example, particle capture by fibers in a filter, build-up of deposits on the outer surfaces of heat exchanger tube bundles, icing of air-plane wings, particle scavenging by falling raindrops, and deposition from the atmosphere on roughness elements of the surface.

In flows around bodies, the particle removal (collection) efficiency n_R is defined as the ratio of the particles collected by the body to the particles geometrically incident on the body, as shown in the schematic diagram of Figure 20.4.

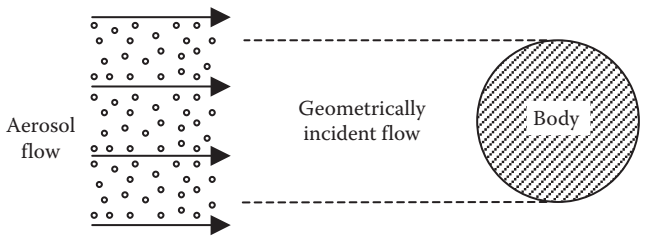


Figure 20.4

Schematic for particle collection efficiency in an external aerosol flow around a body.

20.6.2.1 Deposition at Low Stokes Numbers (St ≪ 1)

This case generally refers to particles with $d_p < 1\,\mu m$ for which the basic deposition mechanism is diffusion and, sometimes, direct *interception*. The latter arises from the finite physical size of the particle, which results in capture when the particle trajectory, although not directed to the surface, passes by within a distance of one particle radius. Interception is characterized by the dimensionless parameter

$$R = \frac{a_p}{L} \tag{20.194}$$

where

a_p is the radius of particle

L is a characteristic dimension of the body

For macroscopic bodies $R \ll 1$ and interception can be ignored, or, equivalently, particles can be taken as point particles. Instead, interception may be important in deposition onto very fine objects like filter fibers, or for particles small in terms of Stokes diameter but of elongated form like asbestos or mineral fibers.

If interception can be ignored, the problem of aerosol deposition becomes formally identical to the problem of convective heat transfer in an external flow, for which extensive amount of information is available in standard books. For combined diffusion and interception, Friedlander (2000) gives a detailed analysis for an aerosol flow around a cylinder placed with its axis normal to the flow.

For $Re < 1$ (e.g., around a filter fiber), the analysis leads to the functional relationship

$$n_R R\, Re\, Sc_p = \frac{\pi V_{d,\text{mean}} d_p}{\mathfrak{D}} = f(\Pi) \quad \text{for } Re < 1 \tag{20.195}$$

where $V_{d,\text{mean}}$ is the mean deposition velocity (taken over the whole circumference of the cylinder). In Equation 20.195, Π is a dimensionless group dependent on the interception parameter, the Reynolds number, and the particle Schmidt number:

$$\Pi = R(A\, Re\, Sc_p)^{1/3} \tag{20.196}$$

where $A = (4 - 2\ln Re)^{-1}$. The function f in Equation 20.195 cannot be analytically determined, but the dependence of n_R on particle size can be shown to exhibit a characteristic U-shape variation, that is, it passes through a minimum. First, n_R decreases with increasing particle size because diffusion decreases with increasing particle size until a size is reached where the interception parameter R becomes nonnegligible, and interception becomes effective, reversing the decreasing trend. An analytical solution can be obtained for the deposition velocity at the forward stagnation point, $V_{d,0}$, which reads

$$V_{d,0} = \frac{(2\mathfrak{D}/d_p)\exp(-AR^3\, Re\, Sc_p/3)}{\displaystyle\int_1^\infty \exp(-AR^3\, Re\, Sc_p\, z/3)dz} \tag{20.197}$$

Although this result applies only at the region of the forward stagnation point, the deposition is greatest there and it reflects the dependence on Re and Sc_p over the entire cylinder.

The case $Re \gg 1$ (e.g., around macroscopic objects) was analyzed by Fernández de la Mora and Friedlander (1982). Based on this analysis, approximate expressions were provided by Parnas and Friedlander (1984) for cylinders and spheres. For cylinders,

$$n_R = 1.88 Re^{-1/2} Sc_p^{-2/3} + 0.8 R^2 Re^{1/2} \quad \text{for } 10^2 < Re < 10^4 \tag{20.198}$$

and for spheres,

$$n_R = 2.40 Re^{-1/2} Sc_P^{-2/3} + 1.10 R^2 Re^{1/2} \quad \text{for } 10^2 < Re < 10^4 \tag{20.199}$$

20.6.2.2 Deposition at High Stokes Numbers ($St \gg 1$)

This case is mainly concerned with particles greater than 1 μm in diameter. Such particles are primarily deposited by inertial impaction. The removal efficiency n_R is usually called *impaction efficiency* in this case. Figure 20.5 shows the removal efficiency by impaction on a single sphere, a single cylinder placed normal to the flow, and an airfoil placed with zero angle of attack. The data are taken from Golovin and Putnam (1962) who surveyed experimental and theoretical results on inertial impaction on single elements for bodies of various shapes. They are presented in terms of removal (impaction) efficiency as a function of Stokes number. In Figure 20.5, the Stokes number does not include the Cunningham correction factor (cf. Equation 20.169), because as such, it was employed in the original data. This exclusion is not a serious limitation, because for supermicrometer particles, slip correction is anyway close to unity (see Table 20.1). The parameter Φ_p shown in Figure 20.5 is $\Phi_p = Re_p^2/St$ and it accounts for deviations from the Stokes regime. For $\Phi_p = 0$, particle motion obeys Stokes law. The results with $\Phi_p = 2000$ correspond to non-Stokesian particle behavior.

20.6.3 Turbulent Pipe Flow

Numerous experimental and theoretical studies have investigated particulate deposition in turbulent flows. Figure 20.6 summarizes the most important experimental measurements on deposition in turbulent pipe flow in terms of the (dimensionless) deposition velocity as a function of (dimensionless) particle relaxation time. The dimensionless particle relaxation time is defined by $\tau_V^\star \equiv \tau_V (u^\star)^2/\nu_g$ where $u^\star$ is the friction velocity, and the dimensionless deposition velocity is $V_d^\star \equiv V_d/u^\star$, with V_d the deposition velocity, see also Equation 20.181. As seen, for $\tau_V^\star < 0.3$, deposition is due almost exclusively to gradient diffusion, whereas for $\tau_V^\star > 0.3$, inertial effects assume importance, resulting in a spectacular increase of deposition rates with particle size. The main principles of inertial deposition were discussed in Section 20.5.3.

The experimental measurements shown in Figure 20.6 may be broadly interpreted as follows. Deposition of low-inertia particles, $\tau_V^\star < 1$, is governed mainly by Brownian and turbulent diffusion. The principal deposition mechanism of moderate-inertia particles, $1 \le \tau_V^\star \le 100$, is turbulent migration (turbophoresis), namely, the mechanism by which particles acquire a drift velocity that moves them from high to low turbulence regions in the fluid. For these particles, and for a range of $\tau_v^\star$, the lift force can exert noticeable influence on their deposition, provided the particle/fluid density ratio is not high. Moreover, for the smaller particles in that size range, preferential accumulation of particles close to the wall occurs: particles are driven close to the wall by turbophoresis, but they do not have enough inertia, to reach the wall. Particle accumulation close to the wall is most prominent at $\tau_v^\star \sim 10$. High-inertia particles ($\tau_V^\star > 100$) are

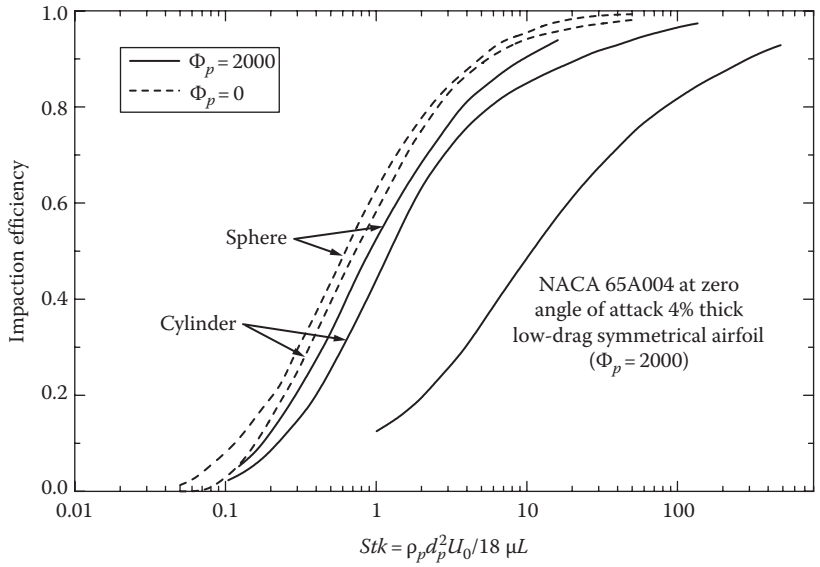


Figure 20.5

Impaction efficiency as a function of Stokes number, for a number of different target shapes. For the cylinder and the sphere L = diameter; for the airfoil L = thickness (maximum distance between upper and lower surfaces of the cross section).

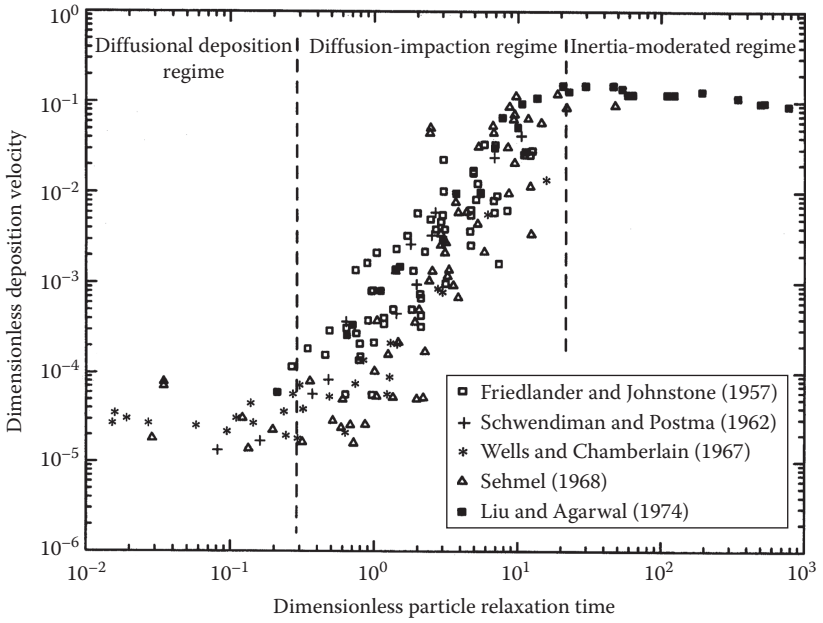


Figure 20.6

Particle deposition from fully developed turbulent pipe flow: a summary of experimental data. (From Young, J. and Leeming, A., *J. Fluid Mech.*, 340, 129, 1997. With permission from Cambridge University Press.)

weakly involved in the turbulent motion of the carrier fluid, their deposition being governed by the characteristics of near-wall turbulence and to a larger extent by the Reynolds number of the fluid. For high-inertia particle, gravity exerts considerable influence on their deposition. The theoretical investigation of particle interactions with turbulence is a vast area of intensive research. The subject is more extensively discussed in Chapter 2. In the following, the discussion is limited to providing practical means for the calculation of particulate deposition in turbulent flow.

For fully developed turbulent flow in a circular pipe of length L, the deposition velocity V_d may be considered as nonvarying along the tube, and the penetration fraction can be expressed as

$$f_p = \exp\left(-\frac{4V_d L}{UD}\right) \tag{20.200}$$

This expression results from a simple mass balance along the tube, and it enables the calculation of penetration through knowledge of the deposition velocity.

For deposition in the diffusional regime, the expression for deposition velocity proposed by Wells and Chamberlain (1967) can be used

$$\frac{V_d}{u^\star} = 0.2 Sc_p^{-2/3} Re^{-1/8} \tag{20.201}$$

This correlation applies for particles with $\tau_V^\star < 0.3$. In most cases, this condition is satisfied for particles with diameter $d_p < 1\,\mu\text{m}$. For deposition in the impaction regime ($\tau_V^\star > 0.3$, or roughly, for sizes $d_p > 1\,\mu\text{m}$), the theory of Friedlander and Johnstone (1957) is frequently used. The theory, known as the "free-flight" model or "stop-distance" model, assumes that particles diffuse with an eddy diffusion coefficient equal to that of the fluid up to one stop-distance of the wall, where they dispose sufficient inertia to escape the flow and reach the wall by flying freely through the quiescent viscous sublayer. The model presents the shortcoming of requiring injection "free-flight" velocities too high in comparison to the fluid radial root mean square velocities encountered close to the surface. Nevertheless, the model finds wide application because it is based

on correct physical arguments and it has proved very successful in reproducing experimental results. The deposition velocity is calculated as follows:

$$\frac{V_d}{U} = \frac{f/2}{1+\sqrt{f/2}\left(\left(1525/S_L^{*2}\right)-50.6\right)} \qquad \text{for } S_L^* < 5$$

$$\frac{V_d}{U} = \frac{f/2}{1+\sqrt{f/2}\left\{5\ln\left[5.04/\left(S_L^*/5-0.959\right)\right]-13.73\right\}} \qquad \text{for } 5 \le S_L^* \le 30 \tag{20.202}$$

$$\frac{V_d}{U} = \frac{f}{2} \qquad \text{for } 30 < S_L^*$$

where S_L^*, the dimensionless stop-distance, is calculated from Equation 20.168 using as injection velocity $0.9u^*$ (which approximates the experimentally determined mean square radial fluctuating velocity) to obtain

$$S_L^* = \frac{\rho_g d_p^2 \rho_p U^2 f/2}{18\mu_g^2} \tag{20.203}$$

It is sometimes useful to express the deposition velocity as a function of particle relaxation time. In the region $\tau_V^* > 0.3$, the experimental results of Figure 20.6 can be simply described by

$$\frac{V_d}{u^*} = \min[6\times10^{-4}\tau_V^{*2}, 0.1] \tag{20.204}$$

This correlation follows very closely the data of Liu and Agarwal (1974), the most frequently quoted experimental results among those summarized in Figure 20.6.

20.6.4 Convective-Gravitational Deposition in Ducts

The case of gravitational deposition from laminar flow in a circular tube is analyzed by Fuchs (1964), Pich (1972), and Heyder and Gebhart (1977). The penetration fraction is

$$f_p = 1-\frac{2}{\pi}\left[2\Phi\sqrt{1-\Phi^{2/3}} - \Phi^{1/3}\sqrt{1-\Phi^{2/3}} + \arcsin(\Phi^{1/3})\right] \tag{20.205}$$

$$\Phi = \frac{3LV_s}{4UD}\cos\theta \tag{20.206}$$

for

$$\frac{V_s \sin\theta}{U} \ll 1 \tag{20.207}$$

with θ as the inclination angle to the horizontal. The criterion expressed by Equation 20.207 requires the streamwise component of the particle settling velocity to be small in comparison to the fluid velocity.

For gravitational deposition from turbulent flow inside a circular tube, Fuchs (1964) provides the following approximation:

$$f_p = \exp\left(-\frac{16\Phi}{3\pi}\right) \tag{20.208}$$

with parameter Φ defined as in Equation 20.206. In general, for the same value of Φ, Equation 20.208 yields higher penetration fractions than Equation 20.205. However, the difference is significant only for $\Phi > 0.3$. Instead, for, $\Phi < 0.3$ the penetration through the tube is essentially the same for both laminar and turbulent flow conditions.

20.6.5 Convective Thermophoretic Deposition in Ducts

Thermophoretic deposition in tube flow has been studied extensively, as it is important in numerous practical applications, such as nuclear safety, gas cleaning, heat exchangers corrosion, microcontamination, and nanoparticle production. Convective deposition of particles in a fluid flow can be calculated in a Lagrangian or Eulerian framework (see relevant discussion in Section 20.2.2). Accurate thermophoretic deposition calculations have been performed by Lagrangian particle tracking in terms of stochastic Langevin equations (Dehbi, 2009). In an Eulerian approach, thermophoretic deposition arises from an additional drift velocity in the average particle velocity, see Equations 20.8 and 20.13; the thermophoretic velocity is calculated by Equation 20.173. In both approaches, the required carrier fluid velocity and temperature fields are provided by multidimensional CFD calculation, except for simple cases, for example, laminar flow in simple geometries, for which analytical solutions exist. In many practical applications, average quantities are needed: for example, in large nuclear safety codes. In such cases, one-dimensional approximations (bulk-averaged over the tube cross section) are used. Recent investigations suggest that the simplified 1D approach provides an accurate description of thermophoretic deposition in laminar flow (Housiadas and Drossinos, 2005, Muñoz-Bueno et al., 2005). In turbulent conditions, the approach appears adequate for small gas-to-wall temperature differences, but for elevated temperature differences, a multidimensional description may provide more accurate predictions (Housiadas and Drossinos, 2005).

An important quantity, of interest in practical applications, is the removal efficiency n_R, Equation 20.180. Several correlations have been proposed for n_R, obtained either from empirical fits or analytically. Housiadas and Drossinos (2005) solved analytically the one-dimensional heat and mass-transfer problem. They derived a universal formula for the convective thermophoretic removal efficiency, valid for laminar and turbulent flow and for any PrK_{th},

$$n_R = 1 - f_p = 1 - \exp\left[-4 Pr\, K_{\text{th}} \int_0^{x^+} d\xi^+ \frac{\theta_m(\xi^+) Nu(\xi^+)}{\theta_m(\xi^+) + \theta^\star} \right]. \tag{20.209}$$

The variables that appear in the previous equation are as follows: K_{th} is the thermophoretic coefficient, see Equation 20.176, x^+ is the dimensionless axial co-ordinate, θ_m is the dimensionless mean fluid temperature, and $\theta^\star$ is a characteristic dimensionless temperature. The dimensionless quantities are

$$x^+ = \frac{x}{2R\, Re\, Pr}; \quad \theta_m = \frac{T_m - T_w}{T_0 - T_w}; \quad \theta^\star = \frac{T_w}{T_0 - T_w}, \tag{20.210}$$

with x the axial coordinate, R the tube radius, T_m and T_0 the mean and inlet fluid temperatures, respectively, and T_w the temperature of wall.

Equation 20.209 was derived for the general case of a Nusselt number (Nu), varying with the distance from the tube inlet due to thermal development effects. If the Nusselt number is taken to be constant, it simplifies to

$$n_R = 1 - \left[\frac{\theta^\star + \exp(-2Nu\, x / R\, Re\, Pr)}{1 + \theta^\star} \right]^{Pr\, K_{th}}. \tag{20.211}$$

In laminar tube flow, the Nusselt number depends on the distance from the tube inlet due to the appreciable size of the thermal entrance zone. In carrying out the numerical evaluation of Equation 20.209, the empirical fits provided by Shah and London are recommended to specify the function $Nu(x^+)$ (Housiadas and Drossinos, 2005). In a turbulent flow, the thermal entrance zone is usually very short and the Nusselt number may be approximated by a constant. For such flows, Equation 20.211 is recommended, along

with the Gnielinski expression for Nu, in conjunction with Churchill's expression for the friction factor (Housiadas and Drossinos, 2005).

In the limit $x \to \infty$, that is, for tubes longer than the thermal entrance length (fully developed regime established), Equation 20.209 becomes

$$n_{R,\infty} = 1 - f_{p,\infty} = 1 - \left(\frac{\theta^*}{1+\theta^*} \right)^{PrK_{th}} = 1 - \left(\frac{T_w}{T_0} \right)^{PrK_{th}}. \tag{20.212}$$

This equation is a practical, universal expression, valid for convective thermophoretic deposition in both laminar and turbulent flows. It shows that in a long tube the total thermophoretic deposition efficiency is a function of only two parameters: the characteristic dimensionless temperature θ^* (or equivalently the ratio of the temperature of the wall to the initial fluid temperature) and the product PrK_{th}. It is valid as long as the one-dimensional description is accurate. This is the case for laminar flow, provided appropriate dimensionless scaling is selected. For turbulent flow, it was found to provide sufficient accuracy in practical applications with moderate gas-to-wall temperature differences (Housiadas and Drossinos, 2005).

20.6.6 Deposition in Filters

Filters are the most commonly used means to collect aerosol particles for sampling or air cleaning purposes. There are several types of filters, but the two most important types are *fibrous filters* and *porous membrane filters*. Fibrous filters consist of mats of individual fibers (e.g., cellulose fibers or glass fibers) that are arranged normal to the flow. Porous membrane filters consist of films (usually a polymeric material) of a porous structure that lets the air to flow through under pressure. The structure of a fibrous filter is characterized by a high void fraction, or porosity, that is, the space between fibers is large relative to their diameter. Typically, porosities in fibrous filters range from 70% to greater than 99%, with fibers having diameters between less than 1 and 100 μm. Porosities in porous membrane filters are typically between 50% and 90%, and the pore sizes are 0.01–10 μm. Despite the differences in structure, both fibrous filtering and porous membrane filtering rely on the same collection mechanisms. The filtering characteristics of a porous membrane filter are equivalent to those of a fibrous filter having fibers with a diameter that is slightly less than the actual pore size. The choice of a given type is mostly based on postsampling criteria rather than collection characteristics.

It is important to realize that an aerosol filter does not work like a sieve, where particles smaller than the holes pass and larger particles are collected, but rather as a trap that collects all sizes. The "holes" in fibrous filters are much larger than particles, but the latter are very efficiently collected by the fibers as they flow through the "holes" by the combined action of various deposition mechanisms, namely, diffusion, interception, inertial impaction, gravitational settling, and, sometimes, electrostatic deposition.

Single fiber efficiency can be analyzed using the same principles discussed in Section 20.6.2. The overall collection efficiency of a filter can be shown to depend on the collection efficiency of a single fiber and the volume fraction of fibers. The collection efficiency of a filter as function of particle size is shown in Figure 20.7. The trend is characteristic in aerosol filtering: large particles deposit very efficiently due to impaction and, eventually, gravitational sedimentation; small particles deposit efficiently as well, as they undergo significant Brownian diffusion due to their high diffusion coefficient. In between, there is a size range where retention drops because particles are too large to diffuse effectively and too small to exhibit significant inertial effects. In this size range, the transition from diffusion to interception takes place and the characteristic U-shaped variation with size is obtained, as discussed in Section 20.6.2.1. As Figure 20.7 shows aerosol filtration exhibits a somehow counterintuitive behavior: the difficulty is not in collecting ultrafine particles from a flow, but particles of intermediate sizes. The particle size corresponding to the minimum efficiency point is called the *most penetrating particle size*. As shown in Figure 20.7, this size also depends on the velocity at the face of the filter. Depending on the filter and velocity, the minimum efficiency is usually in the range 0.05–0.5 μm, but it is generally taken to be approximately at $d_p = 0.3\,\mu m$. This is the basis for the standard DOP test method, where DOP (dioctyl phthalate) particles of 0.3 μm in diameter are used to characterize the collection efficiency of high-efficiency particulate air (HEPA) filters.

Aerosol filtration is a vast domain. Other important issues in aerosol filtration are pressure drop, loading and clogging, selection criteria, etc. For detailed information, the reader may refer to Davies (1973) and Brown (1993).

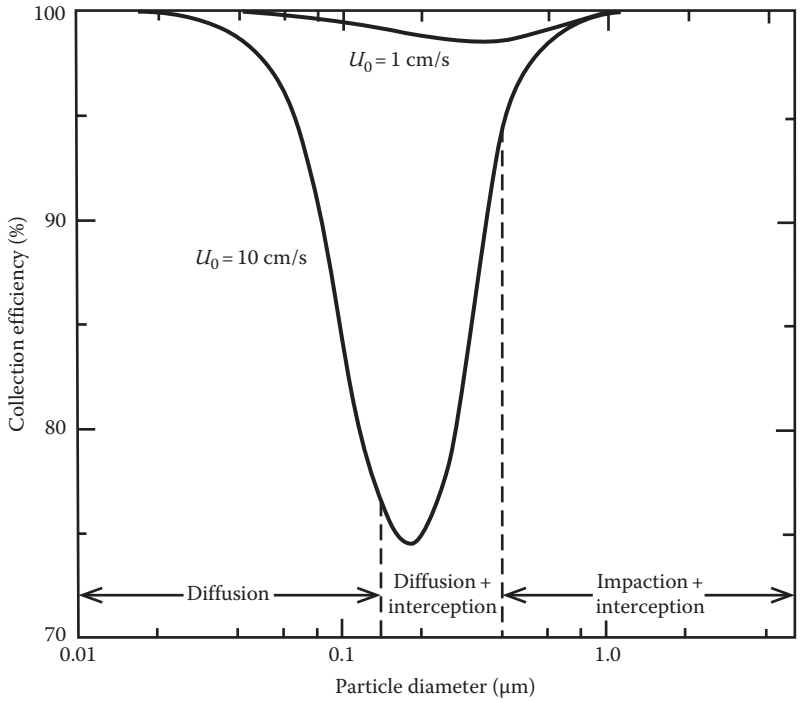


Figure 20.7

Filter collection efficiency versus particle size for face velocities of 0.01 and 0.1 m/s; the filter thickness is 1 mm and the fiber diameter 2 μm. (From Hinds, W.C.: *Aerosol Technology: Properties, Behavior, and Measurement of Airborne Particles,* 2nd edn. 1999. Copyright Wiley-VCH Verlag GmbH & Co. KGaA. Reproduced with permission.)

References

Alam, M.K., The effect of van der Waals and viscous forces on aerosol coagulation, *Aerosol Sci. Technol.*, 6, 41, 1987.

Allen, M.D. and Raabe, O.G., Slip correction measurements of spherical solid aerosol particles in an improved Millikan apparatus, *Aerosol Sci. Technol.*, 4, 269–286, 1985.

Alonso, M., Alguacil, F.J., and Huang, C.-H., Analytical approximation to the fully developed concentration profile of diffusive aerosol particles in laminar flow in a circular tube, *J. Aerosol Sci.*, 41, 413–417, 2010.

Barrett, J., Equilibrium and steady-state distributions of vapour clusters in nucleation theory, *J. Phys. A Math. Gen.*, 27, 5053, 1994.

Barrett, J., Cluster translation and growth in density functional theories of homogeneous nucleation, *J. Chem. Phys.*, 107, 7989, 1997.

Barrett, J.C. and Clement, C.F., Growth rates for liquid drops, *J. Aerosol Sci.*, 19, 223, 1988.

Becker, R. and Döring, W., Kinetische Behandlung der Keimbildung Übersättigten Dampfen, *Ann. Phys.* (Leipzig) 24, 719, 1935.

Blander, M. and Katz, J.L., Bubble nucleation in liquids, *AIChE J.* 21, 833.

Bowen, B.D., Levine, S., and Epstein, N., Fine particle deposition in laminar flow through parallel-plate and cylindrical channels, *J. Colloid Interface Sci.*, 54, 375, 1976.

Bowles, R.K., Reguera, D., Djikaev, Y., and Reiss, H., A theorem for inhomogeneous systems: The generalization of the nucleation theorem, *J. Chem. Phys.*, 115, 1853, 2001.

Brock, J.R., On the theory of thermal forces acting on aerosol particles, *J. Colloid Sci.*, 17, 768, 1962.

Brown, D.P., Kauppinen, E.I., Jokiniemi, J.K., Rubin, S.G., and Biswas, P., A method of moments based CFD model for polydisperse aerosol flows with strong interphase mass and heat transfer, *Comput. Fluids*, 35, 762, 2006.

Brown, R.C., *Air Filtration, An Integrated Approach to the Theory and Applications of Fibrous Filters*, Pergamon Press, Oxford, U.K., 1993.

Cahn, J.W. and Hilliard, J.E., Free energy of a nonuniform system. I. Interfacial free energy, *J. Chem. Phys.*, 28, 258, 1958.
Cahn, J.W. and Hilliard, J.E., Free energy of a nonuniform system. III. Nucleation in a two-component incompressible fluid, *J. Chem. Phys.*, 31, 688, 1959.
Chen, R.Y. and Comparin, R.A., Deposition of aerosols in the entrance of a tube, *J. Aerosol Sci.*, 7, 335, 1976.
Cheng, Y.S., Allen, M.D., Gallegos, D.P., Yeh, H.C., and Peterson, K., Drag force and slip correction of aggregate aerosols, *Aerosol Sci. Technol.*, 8, 199–214, 1988.
Clement, C.F., Aerosol formation from heat and mass transfer in vapour–gas mixtures, *Proc. R. Soc. Lond. A*, 398, 307, 1985.
Colbeck, I., Introduction to aerosol science, in I. Colbeck (Ed.), *Physical and Chemical Properties of Aerosols*, Blackie Academic & Professional (Chapman & Hall), London, U.K., 1998.
Courtney, W.G., Remarks on homogeneous nucleation, *J. Chem. Phys.*, 35, 2249, 1961.
Dahneke, B.E., Slip correction factors for nonspherical bodies—III: The form of the general law, *Aerosol Sci.*, 4, 163–170, 1973.
Dahneke, B.E., Simple kinetic theory of Brownian diffusion in vapors and aerosols, in R.E. Meyer (Ed.), *Theory of Dispersed Multiphase Flows*, Academic Press, New York, 1983, pp. 97–133.
Davies, C.N., *Air Filtration*, Academic Press, London, U.K., 1973.
Davis, E.J., Electrodynamic levitation of particles, in P.A. Baron and K. Willeke (Eds.), *Aerosol Measurement: Principles, Techniques, and Applications*, John Wiley & Sons, Inc., New York, 2001.
Debenedetti, P.G., *Metastable Liquids: Concepts and Principles*, Princeton University Press, Princeton, NJ, 1996.
Dehbi, A., A stochastic Langevin model of turbulent particle dispersion in the presence of thermophoresis, *Int. J. Multiphase Flow*, 35, 219–226, 2009.
Dillman, A. and Meier, G.E.A., A refined droplet approach to the problem of homogeneous nucleation from the vapor phase, *J. Chem. Phys.*, 94, 3872, 1991.
Drossinos, Y. and Kevrekidis, P.G., Classical nucleation theory revisited, *Phys. Rev. E*, 67, 026127, 2003.
Drossinos, Y., Kevrekidis, P.G., and Georgopoulos, P.G., Translational invariance in nucleation theories: Theoretical formulation, *Phys. Rev. E*, 63, 036123, 2001.
Eggersdorfer, M.L., Gröhn, Sorensen, C.M., McMurry, P.H., and Pratsinis, S.E., Mass-mobility characterization of flame-made ZrO_2 aerosols: Primary particle diameter and extent of agglomeration, *J. Colloid Interface Sci.*, 387, 12–23, 2012.
Eggersdorfer, M.L., Kadau, D., Herrmann, H.J., and Pratsinis, S.E., Fragmentation and restructuring of soft-agglomerates under shear, *J. Colloid Interface Sci.*, 342, 261–268, 2010.
Eggersdorfer, M.L. and Pratsinis, S.E., The structure of agglomerates consisting of polydisperse particles, *Aerosol Sci. Technol.*, 46, 347–353, 2012.
Feder, J., Russell, K.C., Lothe, J., and Pound, G.M., Homogeneous nucleation and growth of droplets in vapours, *Adv. Phys.*, 15, 111, 1966.
Fernández de la Mora, J. and Friedlander, S.K., Aerosol and gas deposition to fully rough surfaces: Filtration model for blade-shaped elements, *Int. J. Heat Mass Transfer*, 25, 1725, 1982.
Fernández de la Mora, J. and Rosner, D.E., Effects of inertia on the diffusional deposition of small particles to spheres and cylinders at low Reynolds numbers, *J. Fluid Mech.*, 125, 379, 1982.
Filippov, A.V., Drag and torque on clusters of N arbitrary spheres at low Reynolds number, *J. Colloid Interface Sci.*, 229, 184–195, 2000.
Filippov, A.V., Zurita, M., and Rosner, D.E., Fractal-like aggregates: Relation between morphology and physical properties, *J. Colloid Interface Sci.*, 229, 261–273, 2001.
Flagan, R.C., History of electrical aerosol measurements, *Aerosol Sci. Technol.*, 28, 301, 1998.
Flagan, R.C., Electrical techniques, in P.A. Baron and K. Willeke (Eds.), *Aerosol Measurement: Principles, Techniques, and Applications*, John Wiley & Sons, Inc., New York, 2001.
Fletcher, N.H., Size effect in heterogeneous nucleation, *J. Chem. Phys.*, 29, 572–576, 1958.
Ford, I., Nucleation theorems, the statistical mechanics of molecular clusters, and a revision of classical nucleation theory, *Phys. Rev. E*, 56, 5615, 1997.
Forrest, S.R. and Witten, T.A., Long-range correlations in smoke-particle aggregates, *J. Phys. A*, 12, L109–L117, 1979.
Frenkel, J., *Kinetic Theory of Liquids*, Dover, New York, chap. 7, 1955.
Friedlander, S.K., *Smoke, Dust, and Haze: Fundamentals of Aerosol Dynamics*, 2nd edn., Oxford University Press, New York, 2000.

Friedlander, S.K. and Johnstone, H.F., Deposition of suspended particles from turbulent gas streams, *Ind. Eng. Chem.*, 49, 1151, 1957.
Fuchs, N.A., *The Mechanics of Aerosols*, Dover Publication Inc., New York, 1964.
Fuchs, N.A. and Sutugin, A.G., High dispersed aerosols, in G.M. Hindy and J.R. Brock (Eds.), *Topics in Current Aerosol Research*, Vol. II, Pergamon, Oxford, U.K., 1971.
Garg, R., Narayanan, C., and Subramaniam, S., A numerically convergent Lagrangian-Eulerian simulation method for dispersed two-phase flows, *Int. J. Multiphase Flow*, 35, 376, 2009.
Gelbard, F., Modeling multicomponent aerosol particle growth by vapor condensation, *Aerosol Sci. Technol.*, 12, 399, 1990.
Gelbard, F., Tambour, Y., and Seinfeld, J., Sectional representations for simulating aerosol dynamics, *J. Colloid Interface Sci.*, 76, 541, 1980.
Giechaskiel, B., Wang, X., Gilliland, D., and Drossinos, Y., The effect of particle chemical composition on the activation probability in n-butanol condensation particle counters, *J. Aerosol Sci.*, 42, 20–37, 2011.
Girshick, S.L. and Chiu, C.-P., Kinetic nucleation theory: A new expression for the rate of homogeneous nucleation from and ideal supersaturated vapor, *J. Chem. Phys.*, 93, 1273, 1990.
Gmachowski, L., Hydrodynamics of aggregated media, *J. Colloid Interface Sci.*, 178, 80–86, 1996.
Goldsmith, P. and May, F.G., Diffusiophoresis and thermophoresis in water vapour systems, in C.N. Davies (Ed.), *Aerosol Science*, Academic Press, New York, 1966.
Golovin, M.N. and Putnam, A.A., Inertial impaction on single elements, *Ind. Eng. Chem. Fundam.*, 1, 264, 1962.
Gopalakrishnan, R. and Hogan Jr., C.J., Determination of the transition regime collision kernel from mean first passage times, *Aerosol Sci. Technol.*, 45, 1499–1509, 2011.
Gopalakrishnan, R. and Hogan Jr., C.J., Coulomb-induced collisions in aerosols and dusty plasmas, *Phys. Rev. E*, 85, 026410, 2012.
Gopalakrishnan, R., Thajudeen, T., and Hogan Jr., C.J., Collision limited reaction rates for arbitrarily shaped particles across the entire diffusive Knudsen number range, *J. Chem. Phys.*, 135, 054302, 2011.
Gormley, P.G. and Kennedy, M., Diffusion from a stream flowing through a cylindrical tube, *Proc. R. Irish Acad.*, 52, 163, 1949.
Gránásy, L., Nucleation and spinodal decomposition, *Solid State Phenom.*, 56, 67, 1997.
Hamill, P., Turco, R.P., Kiang, C.S., Toon, O.B., and Whitten, R.C., An analysis of various nucleation mechanisms for sulfate particles in the stratosphere, *J. Aerosol Sci.*, 13, 561–585, 1982.
Heinson, W.R., Sorensen, C.M., and Chakrabarti, A., Does shape anisotropy control the fractal dimension in Diffusion-Limited Cluster-Cluster aggregation?, *Aerosol Sci. Technol.,* 44, i, 2010.
Heinson, W.R., Sorensen, C.M., and Chakrabarti, A., A three parameter description of the structure of diffusion limited cluster fractal aggregates, *J. Colloid Interfac Sci.,* 375, 65, 2012.
Heist, R.H. and He, H., Review of vapor to liquid homogeneous nucleation experiments from 1968 to 1992, *J. Phys. Chem. Ref. Data*, 23, 781, 1994.
Henry, C. and Minier, J.-P., Progress in particle resuspension from rough surfaces by turbulent flows, *Prog. Energy Combust. Sci.*, 45, 1–53, 2014.
Heyder, J. and Gebhart, J., Gravitational deposition of particles from laminar aerosol flow through inclined circular tubes, *J. Aerosol Sci.*, 8, 289, 1977.
Hienola, A.I., Winkler, P.M., Wagner, P.E., Vehkamäki, H., Lauri, A., Napari, I., and Kulmala, M., Estimation of line tension and contact angle from heterogeneous nucleation experimental data, *J. Chem. Phys.*, 126, 094705, 2007.
Hinds, W.C., *Aerosol Technology: Properties, Behavior, and Measurement of Airborne Particles*, 2nd edn., John Wiley & Sons, Inc., New York, 1999.
Hindy, G.M. and Brock, J.R., *The Dynamics of Aerocolloidal Systems*, Pergamon Press, Oxford, U.K., 1970.
Hounslow, M.J., Ryall, R.L., and Marshall, V.R., A discretised population balance for nucleation, growth and aggregation, *AIChE J.*, 34, 1821, 1988.
Housiadas, C. and Drossinos, Y., Thermophoretic deposition in tube flow, *Aerosol Sci. Technol.*, 39, 304, 2005.
Housiadas, C., Ezquerra Larrodé, F., and Drossinos, Y., Numerical evaluation of the Graetz series, *Int. J. Heat Mass Transfer*, 42, 3013, 1999.
Housiadas, C., Ezquerra Larrodé, F., and Drossinos, Y., Convective diffusion in a tube with non-uniform inlet conditions, *J. Aerosol Sci.*, 31, 959, 2000.
Housiadas, C. and Lazaridis, M., Inhalation Dosimetry Modelling, in M. Lazaridis and I. Colbeck (Eds.), Human Exposure to Pollutants via dermal Adsorption and Inhalation, Springer, Dordrecht, the Netherlands, 2010.

Housiadas, C., Papanicolaou, E., and Drossinos, Y., Combined heat and mass transfer in laminar-flow diffusion nucleation chambers, *J. Aerosol Sci*., 33, 797, 2002.
Housiadas, C., Schrader, K.H., and Drossinos, Y., Dehumidification of air flow through cooling at subfreezing temperatures, *Int. J. Heat Mass Transfer*, 41, 1821, 1998.
Hubbard, J.B. and Douglas, J.F., Hydrodynamic friction of arbitrarily shaped Brownian particles, *Phys. Rev. E*, 47, R2983–R2986, 1993.
Ingham, D.B., Diffusion of aerosols from a stream flowing through a cylindrical tube, *J. Aerosol Sci*., 6, 125, 1975.
Isella, L. and Drossinos, Y., Langevin agglomeration of nanoparticles interacting via a central potential, *Phys. Rev. E*, 82, 011404, 2010.
Isella, L. and Drossinos, Y., On the friction coefficient of straight-chain aggregates, *J. Colloid Interface Sci*., 356, 505–512, 2011.
Israellachvili, J., *Intermolecular and Surface Forces*, 2nd edn., Academic Press, London, U.K., 1992.
Ivchenko, I.N., Loyalka, S.K., and Tompson, R.V., *Analytical Methods for Problems of Molecular Transport*, Springer, Dordrecht, the Netherlands, 2007.
Jacobson, M.Z., Development and application of a new air pollution modeling system—II. Aerosol module structure and design, *Atmos. Environ*., 31, 131, 1997.
Jeong, J.I. and Choi, M., A sectional method for the analyses of growth of polydisperse non-spherical particle undergoing coagulation and coalescence, *J. Aerosol Sci*., 32, 565, 2001.
Jokiniemi, J., Lazaridis, M., Lehtinen, K., and Kauppinen, E., Numerical simulation of vapour-aerosol dynamics in combustion processes, *J. Aerosol Sci*., 25, 429, 1994.
Kalikmanov, V.I., *Nucleation Theory*, Springer, Heidelberg, Germany, 2013.
Kashchiev, D., On the relation between nucleation work, nucleus size, and nucleation rate, *J. Chem. Phys*., 76, 5098, 1982.
Kasper, G., On the coagulation rate of aerosols with spatially inhomogeneous particle concentrations, *J. Colloid Interface Sci*., 102, 560, 1984.
Kerouanton, D., Tymen, G., and Boulaud, D., Small particle diffusion penetration of an annular duct compared to other geometries, *J. Aerosol Sci*., 27, 345, 1996.
Kevrekidis, P.G., Lazaridis, M., Drossinos, Y., and Georgopoulos, P.G., A unified kinetic approach to binary nucleation, *J. Chem. Phys*., 111, 8010, 1999.
Kirkwood, J.K. and Riseman, J., The intrinsic viscosities and diffusion constants of flexible macromolecules in solution, *J. Chem. Phys*., 16, 565–573, 1948.
Kissane, M.P., Mitrakos, D., Housiadas, C., and Sabroux, J.C., Investigation of thermo-catalytic decomposition of metal-iodide aerosols due to passage through hydrogen recombiners, *Nucl. Eng. Des*., 239, 3003, 2009.
Koh, W. and Friedlander, S.K., The effect of particle coalescence on the surface area of coagulating aerosols, *J. Colloid Interface Sci*., 140, 419, 1990.
Konstandopoulos, A.G., Deposition of inhaled aerosol particles in a generation of the tracheobronchial tree, *J. Aerosol Sci*., 21, 983, 1990.
Kostoglou, M. and Konstandopoulos, A.G., Evolution of aggregate size and fractal dimension during Brownian coagulation, *J. Aerosol Sci*., 32, 1399, 2001.
Kruis, F.E., Fissan, H., and Peled, A., Synthesis of nanoparticles in the gas phase for electronic, optical and magnetic applications—A review, *J. Aerosol Sci*., 29, 511, 1998.
Kulkarni, P., Baron, P.A., and Willeke, K., Introduction to Aerosol Characterization, in P. Kulkarni, P.A. Baron and K. Willeke (Eds.), *Aerosol Measurement: Principles, Techniques, and Applications,* 3rd Ed., John Wiley & Sons, NJ, 2011.
Kulmala, M., Lauri, A., Vehkamäki, H., Laaksonen, A., Petersen, D., and Wagner, P.E., Strange predictions by binary heterogeneous nucleation theory compared with a quantitative experiment, *J. Phys. Chem. B*, 105, 11800, 2001.
Kulmala, M. and Vesala, T., Condensation in the continuum regime, *J. Aerosol Sci*., 22, 337, 1991.
Laaksonen, A., Ford, I., and Kulmala, M., Revised parametrization of the Dillmann-Meier theory of homogeneous nucleation, *Phys. Rev. E*, 49, 5517, 1994.
Laaksonen, A., Talanquer, V., and Oxtoby, D.W., Nucleation: Measurements, theory, and atmospheric applications, *Annu. Rev. Phys. Chem*., 46, 489, 1995.
Langer, J.S., Theory of the condensation point, *Ann. Phys.* (*NY*), 41, 108, 1967.
Langer, J.S., Statistical theory of the decay of metastable states, *Ann. Phys.* (*NY*), 54, 258, 1969.

Langer, J.S., Metastable states, *Physica*, 73, 61, 1974.
Langer, J.S. and Turski, L.A., Hydrodynamic model of the condensation of a vapor near its critical point, *Phys. Rev. A*, 8, 3230, 1973.
Lapuerta, M., Martos, F.J., and Martín-González, G., Geometrical determination of the lacunarity of agglomerates with integer fractal dimension, *J. Colloid Interface Sci*., 346, 23–31, 2010.
Larriba, C. and Hogan Jr., J.C., Free molecular collision cross section calculation methods for nanoparticles and complex ions with energy accommodation, *J. Comp. Phys*., 251, 344–363, 2013.
Lattuada, M., Wu, H., and Morbidelli, M., Hydrodynamic radius of fractal clusters, *J. Colloid Interface Sci*., 268, 96–105, 2003.
Lazaridis, M., The effects of surface diffusion and line tension on the mechanism of heterogeneous nucleation, *J. Colloid Interface Sci*., 155, 386–391, 1993.
Lazaridis, M., New particle formation of ternary droplets in the atmosphere—A steady-state nucleation kinetics approach, *Atmos. Environ*., 35, 599, 2001.
Lazaridis, M. and Drossinos, Y., Energy fluctuations in steady-state binary nucleation, *J. Phys. A: Math. Gen*., 30, 3847, 1997.
Lazaridis, M., Kulmala, M., and Gorbunov, B., Binary heterogeneous nucleation at a non-uniform surface, *J. Aerosol Sci*., 23, 457–466, 1992.
Lazaridis, M., Kulmala, M., and Laaksonen, A., Binary heterogeneous nucleation of a water-sulfuric acid system: The effect of hydrate interaction, *J. Aerosol Sci*., 22, 823–830, 1991.
Levich, V.G., *Physicochemical Hydrodynamics*, Prentice Hall, Englewood Cliffs, NJ, 1962.
Lihavainen, H., Viisanen, Y., and Kulmala, M., Homogeneous nucleation of n-pentanol in a laminar flow diffusion chamber, *J. Chem. Phys*., 114, 10031, 2001.
Liu, B.Y.H. and Agarwal, J.K., Experimental observation of aerosol deposition in turbulent flow, *J. Aerosol Sci*., 5, 145, 1974.
Longest, P.W. and Oldham, M.J., Numerical and experimental deposition of fine respiratory aerosols: Development of a two-phase drift flux model with near-wall velocity corrections, *J. Aerosol Sci*., 39, 48–70, 2008.
Lothe, J. and Pound, G.M., Reconsiderations of nucleation theory, *J. Chem. Phys*., 36, 2080, 1962.
Loyalka, S.K., Brownian coagulation of aerosol, *J. Colloid Interface Sci*., 57, 578–579, 1976.
Luijten, C.C.M., Baas, O.D.E., and van Dongen, M.E.H., Homogeneous nucleation rates for n-pentanol from expansion wave tube experiments, *J. Chem. Phys*., 106, 4152, 1997.
Lukassen, L.J. and Oberlack, M., Colored-noise Fokker-Planck equation for the shear-induced self-diffusion process of non-Brownian particles, *Phys. Rev. E*, 89, 052145, 2014.
Lurmann, F.W., Wexler, A.S., Pandis, S.N., Musarra, S., Kumar, N., and Seinfeld, J.H., Modelling urban and regional aerosols—II. Application to California's south coast air basin, *Atmos. Environ*., 31, 2695, 1997.
Mackowski, D.W., Monte Carlo simulation of hydrodynamic drag and thermophoresis of fractal aggregates of spheres in the free-molecule flow regime, *J. Aerosol Sci*., 37, 242–259, 2006.
Mamakos, A., Giechaskiel, B., and Drossinos, Y., Experimental and theoretical investigations of the effect of the calibration aerosol material on the counting efficiencies of TSI 3790 Condensation Particle Counter, *Aerosol Sci. Technol*., 47, 11–21, 2013.
Marchisio, D.L., Vigil, R.D., and Fox, R.O., Implementation of the quadrature method of moments in CFD codes for aggregation-breakage problems, *Chem. Eng. Sci*., 58, 3337, 2003.
Marini Bettolo Marconi, U., and Tarazona, P., Dynamic density functional theory of fluids, *J. Chem. Phys*., 110, 8032, 1999.
Mason, B.J., *The Physics of Clouds*, Clarendon Press, Oxford, U.K., 1971.
Maxwell, J.C., Diffusion, in W.D. Niven (Ed.), *The Scientific Papers of James Clerk Maxwell*, Vol. II, Dover Publications Inc., p. 625, 1965.
McGraw, R., Description of aerosol dynamics by the quadrature method of moments, *Aerosol Sci. Technol*., 27, 255, 1997.
McGraw, R. and Laaksonen, A., Scaling properties of the critical nucleus in classical and molecular-based theories of vapor–liquid nucleation, *Phys. Rev. Lett*., 76, 2754, 1996.
McGraw, R. and Wright, D.L., Chemically resolved aerosol dynamics for internal mixtures by the quadrature method of moments, *J. Aerosol Sci*., 34, 189, 2003.
Melas, A.D., Isella, L., Konstandopoulos, A.G., and Drossinos, Y., Morphology and mobility of synthetic colloidal aggregates, *J. Colloid Interface Sci*., 417, 27–36, 2014a.

Melas, A.D., Isella, L., Konstandopoulos, A.G., and Drossinos, Y., Friction coefficient and mobility radius of fractal-like aggregates in the transition regime, *Aerosol Sci. Technol*., 48, 1320–1331, 2014b.
Melas, A.D., Isella, L., Konstandopoulos, A.G., and Drossinos, Y., A methodology to calculate the friction coefficient in the transition regime: Application to straight chains, *J. Aerosol Sci*., 82, 40–50, 2015.
Michaelides, E.E., *Nanofluidics—Thermodynamic and Transport Properties*, Springer, New York, 2014.
Michaelides, E.E., Brownian movement and thermophoresis of nanoparticles in liquids, *Int. J. Heat Mass Transfer*, 81, 179–187, 2015.
Mitrakos, D., Hinis, E., and Housiadas, C., Sectional modeling of aerosol dynamics in multi-dimensional flows, *Aerosol Sci. Technol*., 41, 1076, 2007.
Mitrakos, D., Jokiniemi, J., Backman, U., and Housiadas, C., Aerosol flow in a tube furnace reactor of gas-phase synthesised silver nanoparticles, *J. Nanoparticle Res*., 10, 745, 2008.
Mitsakou, C., Helmis, C., and Housiadas, C., Eulerian modelling of lung deposition with sectional representation of aerosol dynamics, *J. Aerosol Sci*., 36, 75, 2005.
Muñoz-Bueno, R., Hontañón, E., and Rucandio, M.I., Deposition of fine aerosols in laminar tube flow at high temperature with large gas-to-wall temperature gradients, *J. Aerosol Sci*., 36, 495, 2005.
Napari, I., Noppel, M., Vehkämaki, H., and Kulmala, M., An improved model for ternary nucleation of sulfuric acid-ammonia-water, *J. Chem. Phys*., 116, 4221, 2002.
Naumann, K.-H., COSIMA—A computer program simulating the dynamics of fractal aerosols, *J. Aerosol Sci*., 34, 1371–1397, 2003.
Noppel, M., Vehkämaki, H., and Kulmala, M., An improved model for hydrate formation in sulfuric acid-water nucleation, *J. Chem. Phys*., 116, 218, 2002.
Nowakowski, B., and Ruckenstein, E., A kinetic approach to the theory of nucleation in gases, *J. Chem. Phys*., 94, 1397, 1991.
Oxtoby, D., Density functional methods in the statistical mechanics of materials, *Ann. Rev. Mater. Res*., 32, 39, 2002.
Oxtoby, D. and Evans, R., Nonclassical nucleation theory for the gas–liquid transition, *J. Chem. Phys*., 89, 7521, 1988.
Oxtoby, D.W. and Kashchiev, D., A general relation between the nucleation work and the size of the nucleus in multicomponent nucleation, *J. Chem. Phys*., 100, 7665, 1994.
Park, S.H. and Rogak, S.N., A novel fixed-sectional model for the formation and growth of aerosol agglomerates, *J. Aerosol Sci*., 35, 1385, 2004.
Parnas, R. and Friedlander, S.K., Particle deposition by diffusion and interception from boundary-layer flows, *Aerosol Sci. Technol*., 3, 3, 1984.
Pich, J., Theory of gravitational deposition of particles from laminar flows in channels, *J. Aerosol Sci*., 3, 351, 1972.
Pilou, M., Tsangaris, S., Neofytou, P., Housiadas, C., and Drossinos, Y., Inertial particle deposition in a 90-degree laminal-flow bend: An Eulerian fluid-particle approach, *Aerosol Sci. Technol*., 45, 1376, 2011.
Porstendörfer, J., Scheibel, H.G., Pohl, F.G., Preining, O., Reischl, G., and Wagner, P.E., Heterogeneous nucleation of water vapor on monodispersed Ag and NaCl particles with diameters between 6 and 18 nm, *Aerosol Sci. Technol*., 4, 65–79, 1985.
Pratsinis, S.E., Simultaneous nucleation, condensation, and coagulation in aerosol reactors, *J. Colloid Interface Sci*., 124, 416, 1998.
Pruppacher, H.R. and Klett, J.D., *Microphysics of Clouds and Precipitation*, 2nd edn., Kluwer Academic Publishers, Dordrecht, the Netherlands, 1997.
Pui, D.Y.H. and Chen, D.-R., Nanometer particles: A new frontier for multidisciplinary research, *J. Aerosol Sci*., 28, 539, 1997.
Pyykönen, J. and Jokiniemi, J., Computational fluid based sectional aerosol modelling schemes, *J. Aerosol Sci*., 31, 531, 2000.
Ramshaw, J.D., Brownian motion in a flowing fluid, *Phys. Fluids*, 22, 1595, 1979.
Ramshaw, J.D., Brownian motion in a flowing fluid revisited, *Phys. Fluids*, 24, 1210, 1981.
Raes, F. and Janssens, A., Ion-induced aerosol formation in a H_2O–H_2SO_4 system—II. Numerical calculations and conclusions, *J. Aerosol Sci*., 17, 715, 1986.
Reeks, M.W., The transport of discrete particles in inhomogeneous turbulence, *J. Aerosol Sci*., 14, 729, 1983.
Reeks, M.W., On a kinetic equation for the transport of particles in turbulent flows, *Phys. Fluids A*, 3, 446, 1991.

Reeks, M.W., On model equations for particle dispersion in inhomogeneous turbulence, *Int. J. Multiphase Flow*, 31, 93–114, 2005.
Reiss, H., The kinetics of phase transitions in binary systems, *J. Chem. Phys*., 18, 840, 1950.
Reiss, H. and Kegel, W.K., Replacement free energy and the 1/S factor in nucleation theory as a consequence of mixing entropy, *J. Phys. Chem*., 100, 10428, 1996.
Reiss, H., Kegel, W.K., and Katz, J.L., Resolution of the problems of replacement free energy, 1/S, and internal consistency in nucleation theory by consideration of the length scale for mixing entropy, *Phys. Rev. Lett*., 78, 4506, 1997.
Reiss, H., Tabazadeh, A., and Talbot, J., Molecular theory of vapor phase nucleation: The physically consistent cluster, *J. Chem. Phys*., 92, 1266, 1990.
Rogak, S.N., Baltensperger, U., and Flagan, R.C., Measurement of mass transfer to agglomerate aerosol, *Aerosol Sci. Technol*., 14, 447–458, 1991.
Rogak, S.N. and Flagan, R.C., Coagulation of aerosol agglomerates in the transition regime, *J. Colloid Interface Sci*., 151, 203–224, 1992.
Rogers, R.R. and Yau, M.K., *A Short Course in Cloud Physics*, 3rd edn., Pergamon Press, Oxford, U.K., 1989.
Rosner, D.E. and Arias-Zugasti, M., Thermophoretically dominated aerosol coagulation, *Phys. Rev. Lett*., 106, 015502, 2011.
Rosner, D.E. and Pyykönen, J.J., Bivariate moment simulation of coagulating and sintering nanoparticles in flames, *AIChE J*., 48, 476, 2002.
Rudek, M.M., Katz, J.L., Vidensky, I.V., Ždímal, V., and Smolík, J., Homogeneous nucleation rates of n-pentanol measured in an upward thermal diffusion cloud chamber, *J. Chem. Phys*., 111, 3623, 1999.
Saffman, P. and Turner, J., On the collision of drops in turbulent clouds, *J. Fluid Mech*., 1, 16, 1956.
Schwade, B. and Roth, P., Simulation of nano-particle formation in a wall-heated aerosol reactor including coalescence, *J. Aerosol Sci.,* 24, 339, 2003.
Schwendiman, L.C. and Postma, A.K., Turbulent deposition in sampling tubes, Tech. Inf. Div. Rep. TID-7628, Book 1 (USAEC), 1962.
Sehmel, G.A., Aerosol deposition from turbulent airstreams in vertical conduits, Batelle Northwest Laboratory, Richland, WA, Report BNWL-578, 1968.
Seigneur, C., Hudischewskyj, A.B., Seinfeld, J.H., Whitby, K.T., Whitby, E.R., Brock, J.R., and Barnes, H.M., Simulation of aerosol dynamics—A comparative review of mathematical models, *Aerosol Sci. Technol*., 5, 205, 1986.
Seinfeld, J.H. and Pandis, S.N., *Atmospheric Chemistry and Physics: From Air Pollution to Climate Change*, John Wiley & Sons, New York, 1998.
Senger, B., Schaaf, P., Corti, D.S., Bowles, R., Voegel, J.-C., and Reiss, H., A molecular theory of the homogeneous nucleation rate. I. Formulation and fundamental issues, *J. Chem. Phys*., 110, 6421, 1999.
Shen, V.K. and Debenedetti, P.G., Density-functional study of homogeneous bubble nucleation in the stretched Lennard-Jones fluid, *J. Chem. Phys*., 114, 4149, 2001.
Slater, S. and Young, J., The calculation of inertial particle transport in dilute gas-particle flows, *Int. J. Multiphase Flow*, 27, 61, 2001.
Smoluchowski, M., Drei Vortrage uber Diffusion, Brownsche Molekularbewegung und Koagulation von Kolloidteilchen, *Physik Zeits*., 17, 557, 1916.
Sonntag, R.C. and Russel, W.B., Structure and breakup of flocs subjected to fluid stresses, *J. Colloid Interface Sci*., 115, 378–389, 1987.
Sorensen, C.M., The mobility of fractal aggregates: A review, *Aerosol Sci. Technol*., 45, 755–769, 2011.
Sorensen, C.M. and Roberts, G.C., The prefactor of fractal aggregates, *J. Colloid Interface Sci*., 186, 447–452, 1997.
Stauffer, D., Kinetic theory of two-component ("hetero-molecular") nucleation and condensation, *J. Aerosol Sci*., 7, 319, 1976.
Strey, R., Wagner, P.E., and Schmeling, T., Homogeneous nucleation rates for n-alcohol vapors measured in a two-piston expansion chamber, *J. Chem. Phys*., 84, 2325, 1986.
Subramanian, G. and Brady, J.F., Multiple scales analysis of the Fokker-Planck equation for simple shear flow, *Physica A*, 334, 343–384, 2004.
Sugutin, A. and Fuchs, N., Formation of condensation aerosols under rapidly changing environmental conditions, *J. Aerosol Sci*., 1, 287, 1970.

Talanquer, V. and Oxtoby, D.W., Dynamical density functional theory of gas–liquid nucleation, *J. Chem. Phys*., 100, 5190, 1994.
Talbot, L., Cheng, R.K., Schefer, R.W., and Willis, D.R., Thermophoresis of particles in a heated boundary layer, *J. Fluid Mech*., 101, 737, 1980.
Tan, C.W. and Thomas, J.W., Aerosol penetration through a parallel-plate diffusion battery, *J. Aerosol Sci*., 3, 39, 1972.
ten Wolde, P.R., Ruiz-Montero, M.J., and Frenkel, D., Numerical calculation of the rate of crystal nucleation in a Lennard-Jones system at moderate undercooling, *J. Chem. Phys*., 104, 9932, 1996.
Thajudeen, T., Gopalakrishnan, R., and Hogan Jr., C.J., The collision rate of nonspherical particles and aggregates for all diffusive Knudsen numbers, *Aerosol Sci. Technol*., 46, 1174–1186, 2012.
Trinkaus, H., Theory of the nucleation of multicomponent precipitates, *Phys. Rev. B*, 27, 7372, 1983.
Vanni, M. and Gastaldi, A., Hydrodynamic forces and critical stresses in low-density aggregates under shear flow, *Langmuir*, 27, 12822–12833, 2010.
Veshchunov, M.S., A new approach to Brownian coagulation theory, *J. Aerosol Sci*., 41, 895–910, 2010.
Vincent, J.H., *Aerosol Science for Industrial Hygienists*, 1st edn., Elsevier Science Inc., New York, 1995.
Wagner, P.E., Kaller, D., Vrtala, A., Lauri, A., Kulmala, M., and Laaksonen, A., Nucleation probability in binary heterogeneous nucleation of water-n-propanol vapor mixtures on insoluble and soluble particles, *Phys. Rev. E*, 67, 021605, 2003.
Waldmann, L. and Schmitt, K.H., Thermophoresis and diffusiophoresis of aerosols, in C.N. Davies (Ed.), *Aerosol Science*, Academic Press, New York, 1966.
Weakliem, C.L. and Reiss, H., Toward a molecular theory of vapor phase nucleation. IV. Rate theory using the modified liquid drop model, *J. Chem. Phys*., 101, 2398, 1994.
Wedekind, J., Strey, R., and Reguera, D., New method to analyze simulations of activated processes, *J. Chem. Phys*., 126, 134103, 2007.
Wells, A.C. and Chamberlain, A.C., Transport of small particles to vertical surfaces, *Br. J. Appl. Phys*., 18, 1793, 1967.
Wilck, M. and Stratmann, F., A 2-D multicomponent modal aerosol model and its application to laminar flow reactors, *J. Aerosol Sci*., 28, 959, 1997.
Wilemski, G., Composition of the critical nucleus in multicomponent vapor nucleation, *J. Chem. Phys*., 80, 1370, 1984.
Wilemski, G., Revised classical binary nucleation theory for aqueous alcohol and acetone vapors, *J. Phys. Chem*., 91, 2492, 1987.
Wilemski, G., The Kelvin equation and self-consistent nucleation theory, *J. Chem. Phys*., 103, 1119, 1995.
Willeke, K., Temperature dependence of particle slip in a gaseous medium, *J. Aerosol Sci*., 7, 381, 1976.
Winkler, P.M., Steiner, G., Vrtala, A., Vehkamäki, H., Noppel, M., Lehtinen, K.E.J., Reischl, G.P., Wagner, P.E., and Kulmala, M., Heterogeneous nucleation experiments bridging the scale from molecular ion clusters to nanoparticles, *Science*, 319, 1374–1377, 2008.
Whitby, E.R. and McMurry, P.H., Modal aerosol dynamics modeling, *Aerosol Sci. Technol*., 27, 673, 1997.
Whitby, K.T., The physical characteristics of sulfur aerosols, *Atmos. Environ*., 12, 135, 1978.
Williams, M.W. and Loyalka, S.K., *Aerosol Theory and Practice*, Pergamon Press, Oxford, U.K., 1991.
Wu, J.J. and Flagan, R.C., A discrete-sectional solution to the aerosol dynamic equation, *J. Colloid Interface Sci*., 123, 339, 1988.
Wu, M.K. and Friedlander, S.K., Note on the power law equation for fractal-like aerosol agglomerates, *J. Colloid Interface Sci*., 159, 246–248, 1993.
Yamamoto, M., A solver for aerosol condensation equation semi-Lagrangian scheme with correction exactly conserving total particle number, *Aerosol Sci. Technol*., 38, 1033, 2004.
Young, J. and Leeming, A., A theory of particle deposition in turbulent pipe flow, *J. Fluid Mech.,* 340, 129, 1997.
Young, J.B., Thermophoresis of a spherical particle: Reassessment, clarification, and new analysis, *Aerosol Sci. Technol*., 45, 927–948, 2011.
Zeldovich, Ya.B., On the theory of new phase formation: Cavitation, *J. Exp. Theor. Phys*., 12, 525, 1942. (Translated in *Selected works of Yakov Borisovich Zeldovich. Volume 1. Chemical physics and hydrodynamics*, J.P. Ostriker, G.I. Barenblatt, and R.A. Sunayev (Eds.), Princeton University Press, Princeton, NJ, 1992, p. 120.)

Zeng, X.C. and Oxtoby, D.W., Gas–liquid nucleation in Lennard-Jones fluids, *J. Chem. Phys.*, 94, 4472, 1991a.
Zeng, X.C. and Oxtoby, D.W., Binary homogeneous nucleation theory for the gas-liquid transition: A non-classical approach, *J. Chem. Phys.*, 95, 5940, 1991b.
Zhang, C., Thajudeen, T., Larriba, C., Schwartzentruber, T.E., Hogan Jr., C.J., Determination of the scalar friction Factor for nonspherical particles and aggregates across the entire Knudsen number range by Direct Simulation Monte Carlo (DSMC), *Aerosol Sci. Technol.*, 46, 1065–1078, 2012.
Zhang, Y., Seigneur, C., Seinfeld, J.H., Jacobson, M.Z., and Binkowski, F.S., Simulation of aerosol dynamics: A comparative review of algorithms used in air quality models, *Aerosol Sci. Technol.*, 31, 487, 1999.
Ziskind, G., Fichman, M., and Gutfinger, C., Resuspension of particulates from surfaces to turbulent flows-Review and analysis, *J. Aerosol Sci.*, 26, 613, 1995.

21

Dispersed Flow in Non-Newtonian Fluids

Raj P. Chhabra

21.1 Introduction
21.2 Newtonian and Non-Newtonian Fluids
21.3 Rigid Nondeformable Particles
21.4 Fluid Spheres
21.5 Other Effects
21.6 Concluding Remarks and Future Directions

21.1 Introduction

The preceding chapters have been concerned with the flow situations when the individual phases on their own are Newtonian fluids and the complexities of the flow stemmed either from the multiphase nature of the fluid (Chapters 3 through 5, 10, 11) or due to phase change (Chapters 8 and 9) or from the turbulent nature of the flow itself (Chapter 12), etc. Undoubtedly, most low-molecular-weight fluids like organic and inorganic liquids, or solutions of inorganic salts, gases, molten metals, and salts, all exhibit what is known as the Newtonian fluid behavior. Their behavior in simple shear is described by a single parameter, namely, the shear or dynamic or simply viscosity of the fluid, which is a function of the temperature and pressure for each substance. For most gases, the viscosity increases with both increasing temperature and pressure, whereas for a liquid, its viscosity decreases with temperature and it increases with pressure. Ever since the development of the Navier–Stokes equations more than 150 years ago, significant advances have occurred in various aspects of the mechanics of Newtonian fluids, as can be gauged from the state-of-the-art chapters included in this book.

In contrast, most structured fluids like solutions of high-molecular-weight (>5000 or so) natural (gums and resins) and synthetic polymers and their melts, slurries, pastes, suspensions, foams, emulsions, and surfactant-laden worm-like micellar solutions, for instance, do not conform to the Newtonian postulate and are accordingly known variously as "non-Newtonian," "rheologically complex," or "nonlinear" fluids. It is difficult to imagine modern life without such materials. Think of the range of processed foodstuffs we consume every day, personal- and health-care products used routinely, cleaning aids and polishing waxes, etc., all of which fill the aisles of modern supermarkets, for instance.

All modern technologies, including modern transportation (in terms of smart materials of construction or advanced fuels), entertainment industry (films, DVDs), medicine, environment, energy generation and conservation, etc., all exploit non-Newtonian characteristics in one form or the other at some stage during the course of their manufacture or application. The extraction of oil from rocks via polymer flooding, the soft gels used to make optical lenses, and the next generation of aviation fuels, all hinge on successfully imparting the desirable rheological characteristics to achieve the satisfactory product quality. Indeed, so widespread is the non-Newtonian fluid behavior that it would be no exaggeration to say that the Newtonian fluid behavior is more of an exception rather than the rule! Consequently, over the past 50–75 years or so, this branch of fluid mechanics has begun to receive systematic attention, albeit it is still in its embryonic stage (Boger and Walters, 1992, Tanner and Walters, 1998, Denn, 2004). Undoubtedly, significant advances

have been made in some simple geometries like flow in ducts of circular and noncircular cross sections (Lawal and Mujumdar, 1987, Chhabra, 1999), porous media flows (Chhabra, 1993, 2006, Chhabra et al., 2001), batch mixing vessels (Chhabra, 2003, Paul et al., 2004, Chhabra and Richardson, 2008), etc. In contrast, the corresponding body of knowledge on external flows such as that over a rigid or fluid (bubble or drop) sphere is rather limited. This chapter is concerned with the momentum and heat transfer characteristics of a single rigid (spherical and nonspherical) particle and a fluid sphere (bubble, drop) in different types of confined and unconfined non-Newtonian fluids. The corresponding behavior in a Newtonian fluid is used as the reference line to draw qualitative inferences regarding the influence of non-Newtonian rheology, and therefore, frequent reference will be made to the pertinent sections of Chapter 1. We begin with the definitions and classification of the different types of non-Newtonian characteristics in the next section.

21.2 Newtonian and Non-Newtonian Fluids

One may classify the behavior of a given fluid in many ways including as being compressible or incompressible, single phase or multiple phase or depending upon its response to the applied stress, as is done here. Thus, for instance, when a shear stress ($\vec{\tau}_{yx}$) is applied to a thin layer of a fluid confined in the narrow gap in between two parallel plates by applying a tangential force to the top plate while keeping the bottom plate stationary, eventually, a linear velocity profile is established (i.e., the constant shear rate, $\dot{\vec{\gamma}}_{yx}$) as shown schematically in Figure 21.1. The response of a Newtonian fluid is characterized by a linear relationship between $\vec{\tau}_{yx}$ and $\dot{\vec{\gamma}}_{yx}$ as

$$\vec{\tau}_{yx} = \mu \dot{\vec{\gamma}}_{yx} \tag{21.1}$$

In Equation 21.1, μ is the viscosity or dynamic viscosity of the fluid, which has a constant value (independent of $\vec{\tau}_{yx}$ and $\dot{\vec{\gamma}}_{yx}$) for a given substance and is a function of temperature and pressure only. Most low-molecular-weight substances like gases, organic liquids, inorganic salts and their solutions, molten metals, and electrolytes exhibit Newtonian fluid behavior and are accordingly known as Newtonian fluids. With further assumption of incompressibility (applicable throughout this chapter), such a fluid will obviously satisfy the familiar Navier–Stokes equations written in their generalized three-dimensional form, for example, see Bird et al. (2002).

In contrast, a substance that, in simple shear, does not conform to Equation 21.1 is called a non-Newtonian fluid. It is customary to further categorize non-Newtonian fluid behavior into three broad types as follows:

21.2.1 Time-Independent Fluid Behavior

In simple one-dimensional shear, such as that shown in Figure 21.1, the current value of the shear stress at a point in such a fluid is determined only by the corresponding value of the rate of shear and vice versa. The steady shear behavior of this type of fluids is thus described by a relation of the form

$$\vec{\tau}_{yx} = f(\dot{\vec{\gamma}}_{yx}) \tag{21.2}$$

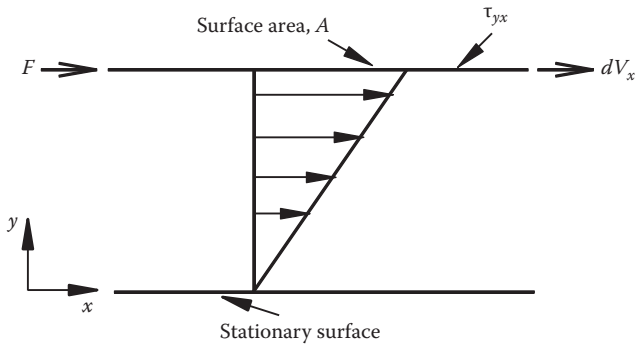


Figure 21.1

Schematic representation of unidirectional shearing flow.

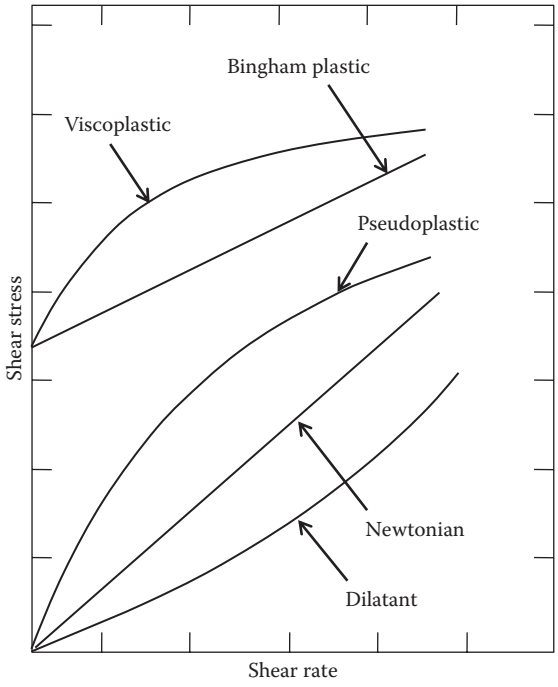


Figure 21.2

Qualitative flow curves for time-independent fluid behavior.

or, its inverse form

$$\vec{\dot{\gamma}}_{yx} = f^{-1}(\vec{\tau}_{yx}) \tag{21.3}$$

Of course, Equation 21.1 is a limiting subset of this family of fluids. Depending upon the nature of the function in Equation 21.2 or 21.3, three distinct types of fluid behaviors can be identified:

1. Shear-thinning or pseudoplastic
2. Shear-thickening or dilatant
3. Viscoplastic with and without shear-thinning

Figure 21.2 shows schematically these three types of fluid characteristics including the limiting case of Newtonian fluid behavior. Each of these will now be treated in some detail.

21.2.1.1 Shear-Thinning (or Pseudoplastic) Fluids

This is possibly the commonest type of time-independent non-Newtonian fluid characteristics encountered in industrial practice. In a simple shear test, it is characterized by an apparent viscosity, μ, defined as $\left|\vec{\tau}_{yx}\right| / \left|\vec{\dot{\gamma}}_{yx}\right|$, which progressively decreases with the increasing shear rate. Most polymeric solutions exhibit Newtonian plateau (constant viscosity) at very high and very low shear rates, that is, the apparent viscosity approaches a constant value of μ_∞ (infinite shear value) and μ_0 (zero shear value), as can be seen in Figure 21.3 for a polymer solution. This figure also illustrates the fact that often several instruments are required to span such a wide range of shear rate or shear stress. Obviously, the infinite shear limiting value, μ_∞, is not observed for polymer melts, or emulsions, or foams, etc. (Bird et al., 1987). While it is difficult to provide generalizations, the onset of shear-thinning behavior is influenced by factors such as concentration, molecular weight, structure (linear, branched, etc.) of the polymer, type of solvent, temperature, etc. Generally, the lower the concentration and/or the molecular weight of the polymer, the higher is the shear rate required to induce shear-thinning behavior in a system (Larson, 1998).

Over the years, many mathematical forms of the functional relationship depicted by Equation 21.2 or 21.3 have been proposed in the literature, for example, see Chhabra and Richardson (2008), Ibarz-Ribas and Barbosa-Canovas (2003). A representative selection of the widely used viscosity models is included here.

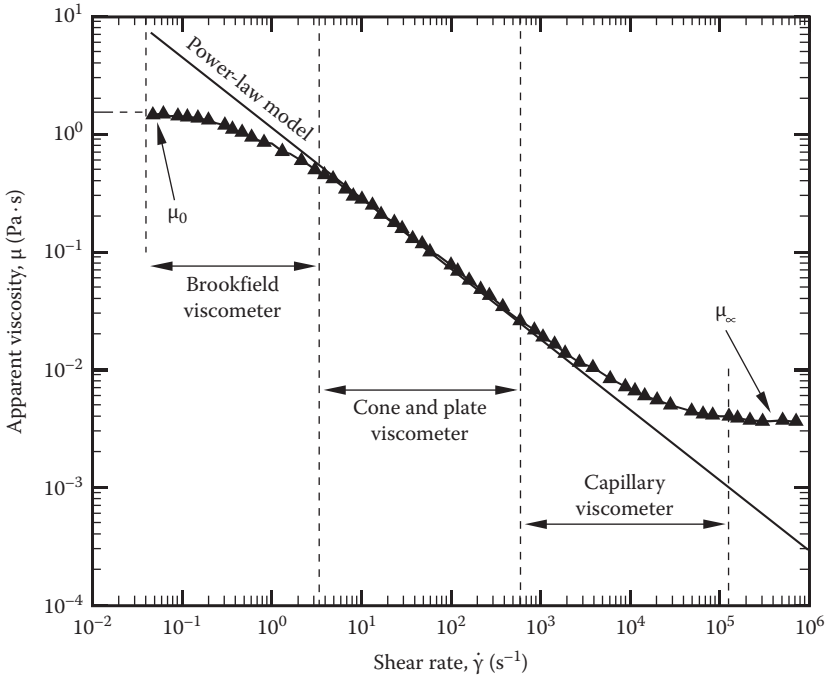


Figure 21.3

Demonstration of zero shear and infinite shear viscosities for a shear-thinning polymer solution. (From Boger, D.V., *Nature*, 265, 126, 1977.)

21.2.1.1.1 Power-Law Model Generally, the relationship between the shear stress ($\vec{\tau}_{yx}$) and shear rate ($\vec{\dot{\gamma}}_{yx}$) for a shear-thinning material can be approximated by a linear dependence on log-log scales, which follows the power law:

$$\left|\vec{\tau}_{yx}\right| = m\left(\left|\vec{\dot{\gamma}}_{yx}\right|\right)^{n} \tag{21.4}$$

Or alternately, it can be written in terms of the apparent viscosity, μ, as

$$\mu = \frac{\left|\vec{\tau}_{yx}\right|}{\left|\vec{\dot{\gamma}}_{yx}\right|} = m\left(\left|\vec{\dot{\gamma}}_{yx}\right|\right)^{n-1} \tag{21.5}$$

For, $n < 1$, Equation 21.5 predicts $\left(\left|d\mu / d\dot{\gamma}_{yx}\right|\right) < 0$, that is, decreasing viscosity with the increasing shear rate. Therefore, the values of the power-law index, n, smaller than unity correspond to shear-thinning behavior. Many polymeric solutions and melts exhibit the value of power-law index, n, in the range of ~0.3 to ~0.7. Still smaller values of power-law index (n = ~ 0.1–0.2) are obtained with fine particle aqueous slurries like china clay, bentonite, coal, etc. (Chhabra and Richardson, 2008). Thus, in contrast to the Newtonian fluids whose flow behavior is characterized by the value of a single parameter, namely, viscosity, a power-law fluid necessitates at least two parameters, m and n for defining its viscosity behavior. However, while Equation 21.4 or 21.5 affords the simplest mathematical representation of the shear-thinning fluid behavior, it predicts unrealistically $\mu_0 = \infty$ and $\mu_\infty = 0$ in the limits of $\left|\vec{\dot{\gamma}}_{yx}\right| \to 0$ and $\left|\vec{\dot{\gamma}}_{yx}\right| \to \infty$ respectively, as can be seen in Figure 21.3. Also, the constant values of m and n are valid generally only over a narrow range of shear stress or shear rate values (e.g., see, Figure 21.4) and, hence, one needs to know *a priori* the expected range of shear rate in a given application (Barnes et al., 1989, Chhabra and Richardson, 2008, Schramm, 2014). In spite of these limitations, this is possibly the most widely (and also most maligned!) used viscosity model in the realm of non-Newtonian engineering fluid mechanics.

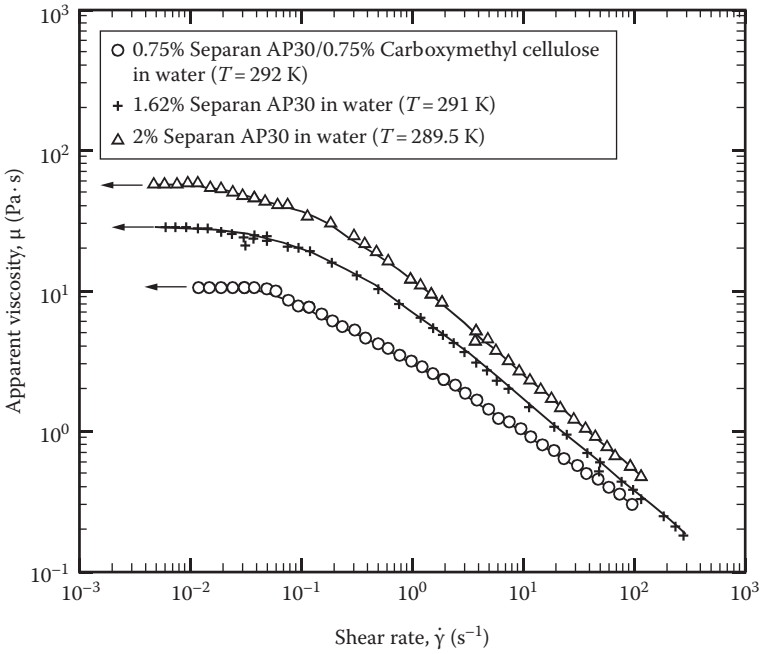


Figure 21.4

Representative apparent viscosity plots for three pseudoplastic (shear-thinning) polymer solutions. (From Chhabra, R.P. and Richardson, J.F., *Non-Newtonian Flow and Applied Rheology*, 2nd edn., Butterworth-Heinemann, Oxford, U.K., 2008.)

21.2.1.1.2 Cross Model Most of the aforementioned deficiencies of the power-law model are rectified by another popular empirical model known as the Cross model (Cross, 1965), written in simple shear as

$$\frac{\mu-\mu_\infty}{\mu_0-\mu_\infty}=\left[1+m\left(\left|\dot{\vec{\gamma}}_{yx}\right|\right)^n\right]^{-1} \tag{21.6}$$

This model also predicts shear-thinning behavior for $n < 1$. Unlike Equation 21.4 or 21.5, it includes the limiting values of μ_0 and μ_∞ under appropriate conditions. However, this improvement has been achieved at the expense of four disposable parameters, namely, μ_0, μ_∞, m, and n as opposed to only two parameters (m, n) present in the simple power-law model, Equation 21.5.

21.2.1.1.3 Carreau Viscosity Equation Based on molecular ideas, Carreau (1972) independently put forward the following viscosity equation, which is similar to Equation 21.6:

$$\frac{\mu-\mu_\infty}{\mu_0-\mu_\infty}=\left[1+\left(t_0\left|\dot{\vec{\gamma}}\right|\right)^2\right]^{-1/2(n-1)/2} \tag{21.7}$$

This is also a four constant viscosity model and it does span the entire range of shear rates including the zero-shear and infinite-shear viscosities.

21.2.1.2 Shear-Thickening (or Dilatant) Fluids

These materials are similar to shear-thinning fluids except for the fact that their apparent viscosity increases with the increasing shear rate. Initially, Reynolds (e.g., see Barnes, 1989, Goddard and Bashir, 1990) observed this behavior in concentrated suspensions and explained it by the dilation or expansion of such a suspension under shear. At low shear rates, the voidage of such a system remains fixed and the volume of liquid available is sufficient to completely fill the interparticle volume. Under such conditions, the motion of particles past each other is lubricated by the fluid present in the system. However, at high shear rates, the system dilates, resulting in an increase in the void volume. In turn, the available liquid is no longer sufficient to fill the

interstitial void volume to lubricate the particle motion. Naturally, due to solid–solid friction, the resulting shear stress shows a stronger dependence on the shear rate than that in Newtonian fluids ($n = 1$). This type of behavior is frequently seen in sand dunes, titanium-di-oxide in water suspensions, aqueous start and corn flour dispersions, etc. This subclass of time-independent fluids has evoked very little interest (Barnes, 1989, Mewis and Wagner, 2012), though now it is receiving increasing attention in the context of pasty materials encountered in a broad spectrum of processing applications. From an engineering perspective, it is customary to approximate the simple shear data for such fluids also using the power-law model, Equation 21.4, with the flow behavior index taking on values greater than unity, that is, $n > 1$. Some of the polymer solutions used as thickening agents in food and pharmaceutical products exhibit values of the power-law index, n, in the range 1.2–1.6 (Barnes, 1989). It is not uncommon for such a substance to exhibit shear-thinning behavior at low shear rates and shear-thickening characteristics at high shear rates.

21.2.1.3 Viscoplastic Fluids

This type of fluid behavior is characterized by the existence of a threshold stress (also known as the yield stress or the apparent yield stress, $\vec{\tau}_0$), which must be overcome for such a substance to shear like a fluid (see Figure 21.2). For stress levels below the fluid yield stress $\left(|\vec{\tau}_0|\right)$, it deforms like an elastic solid. Furthermore, for $|\vec{\tau}_{yx}| > |\vec{\tau}_0|$, such a material may exhibit a constant shear viscosity (Bingham fluid) or shear-thinning behavior (Herschel–Bulkley fluid). This type of dual behavior is generally explained by postulating the presence of three-dimensional structures of sufficient rigidity, which can resist deformation for $|\vec{\tau}_{yx}| < |\vec{\tau}_0|$ by offering very high values of the apparent viscosity, that is, yield stress. On the other hand, for $|\vec{\tau}_{yx}| > |\vec{\tau}_0|$, the structure breaks down, at least partially, and the substance behaves like a viscous fluid. There are three widely used viscosity models for viscoplastic behavior and these are presented here (Bird et al., 1983).

21.2.1.3.1 Bingham Model

$$\vec{\tau}_{yx} - \vec{\tau}_0^B = \mu_B \vec{\dot{\gamma}}_{yx} \quad \text{for } |\vec{\tau}_{yx}| > |\vec{\tau}_0^B| \tag{21.8}$$

$$\vec{\dot{\gamma}}_{yx} = 0 \quad \text{for } |\vec{\tau}_{yx}| < |\vec{\tau}_0^B| \tag{21.9}$$

Once the applied stress exceeds the magnitude of the fluid yield stress, a Bingham fluid exhibits Newtonian flow behavior with a constant shear viscosity, μ_B. However, strictly speaking, this model also predicts shear-thinning behavior because the apparent viscosity of the fluid, $\mu = \mu_B + \left(\vec{\tau}_0^B / |\vec{\dot{\gamma}}_{yx}|\right)$, decreases with the increasing shear rate.

21.2.1.3.2 Herschel–Bulkley Model

This replaces the constant μ_B by a power-law viscosity as

$$\vec{\tau}_{yx} - \vec{\tau}_0^H = m\left(|\vec{\dot{\gamma}}_{yx}|\right)^n \quad \text{for } |\vec{\tau}_{yx}| > |\vec{\tau}_0^H| \tag{21.10}$$

$$\vec{\dot{\gamma}}_{yx} = 0 \quad \text{for } |\vec{\tau}_{yx}| < |\vec{\tau}_0^H| \tag{21.11}$$

This model is used when the flow curve is nonlinear above the fluid yield stress (see Figure 21.2).

21.2.1.3.3 Casson Model

This model has its origins in modeling the rheological behavior of blood, but subsequently, it has been successfully employed for other dispersed systems also. In simple shear, it is written as follows:

$$\left(|\vec{\tau}_{yx}|\right)^{0.5} - \left(|\vec{\tau}_0^C|\right)^{0.5} = \left(\mu_C |\vec{\dot{\gamma}}_{yx}|\right)^{0.5} \quad \text{for } |\vec{\tau}_{yx}| > |\vec{\tau}_0^C| \tag{21.12}$$

$$\vec{\dot{\gamma}}_{yx} = 0 \quad \text{for } |\vec{\tau}_{yx}| < |\vec{\tau}_0^c| \tag{21.13}$$

Typical examples of the structured fluids displaying yield stress include blood, fire fighting and shaving foams, tomato sauce, cosmetics, cleaning waxes, drilling muds, etc. (Barnes, 1999, Mewis and Wagner, 2012).

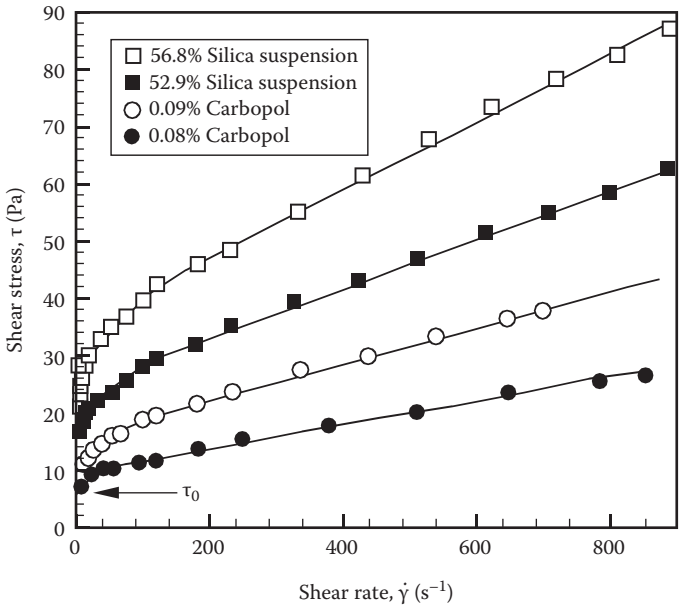


Figure 21.5

Typical experimental data for two polymer solutions and two silica suspensions exhibiting viscoplastic behavior.

Figure 21.5 shows steady shear data for two concentrated silica suspensions and two polymer solutions exhibiting viscoplastic behavior.

Before leaving this subsection, it is appropriate to mention here that it has long been (and continues to be) a matter of debate whether a true yield stress in liquid-like systems exists or not (Barnes and Walters, 1985, Barnes, 1999). Many researchers view the yield stress in terms of a transition from solid-like to fluid-like behavior, the so-called biviscous fluid approach (O' Donovan and Tanner, 1984, Glowinski and Wachs, 2011). Naturally, whether a true yield stress exists or not seems to be closely related to the time scale of observation. Notwithstanding these difficulties, the notion of an apparent yield stress is of practical utility in the context of engineering applications, especially in the formulation and manufacture of food-, pharmaceuticals, and health-care–related products (Laba, 1993).

21.2.2 Time-Dependent Fluid Behavior

Many substances encountered in health-care, food-, and personal-care product sectors (Laba, 1993, Ibarz-Ribas and Barbosa-Canovas, 2003) exhibit rheological characteristics, which cannot be adequately approximated by simple mathematical expressions presented in Section 21.2.1. This difficulty stems primarily from the fact that, in simple shear, their apparent viscosity is not only a function of the shear stress $\left(\vec{\tau}_{yx}\right)$ or shear rate $\left(\vec{\dot{\gamma}}_{yx}\right)$, but it shows additional dependence on the kinematic history, duration of shearing, etc. For instance, when materials such as cement paste, waxy crude oils, hand lotions and creams, etc. are sheared at a constant shear rate following a long period of rest, their viscosities may decrease as the internal structures present in such a substance are progressively broken down. As the number of linkages available for breaking down decreases, the rate of change of viscosity with time approaches zero. Conversely, as the structure breaks down, the rate at which these linkages can re-form increases; thereby, a state of dynamic equilibrium is reached when the rates of building-up and of breakdown are balanced. This can directly be compared with the dynamics of a first-order reversible chemical reaction. Such behavior is known as thixotropy, and these systems are accordingly known as thixotropic materials. On the other hand, the opposite type of behavior has been observed in a few systems in which the application of shear promotes building-up of internal structures and, hence, the apparent viscosity of such a substance increases with the duration of shearing. This behavior is called antithixotropy or rheopexy and such fluids are known as rheopectic (Barnes et al., 1989, Barnes, 1997).

It stands to reason that when the shear rate is steadily increased from a zero value to a maximum value and then decreased at the same rate, this class of materials will exhibit hysteresis phenomenon, as shown schematically in Figure 21.6. Note that the arrows indicating the increasing and decreasing shear rates are opposite to each other for a thixotropic and for a rheopectic material. The area enclosed by these loops is a

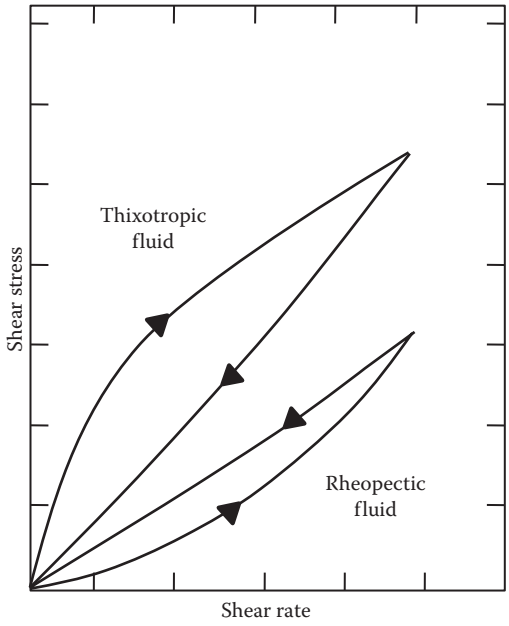


Figure 21.6

Qualitative shear stress–shear rate behavior for thixotropic and rheopectic materials.

crude measure of the severity of time-dependent behavior. This will be zero for a time-independent material described in Section 21.2.1. On the other hand, larger is the area enclosed by the loop, stronger is the time-dependent behavior. Figure 21.7 shows the experimental data for a cement paste exhibiting thixotropic behavior.

The mathematical equations required to describe the rheological behavior of time-dependent materials tend to be far more complex than that presented in the preceding section. While this chapter is not concerned with thixotropic and rheopectic fluids, interested readers are referred to the excellent review article

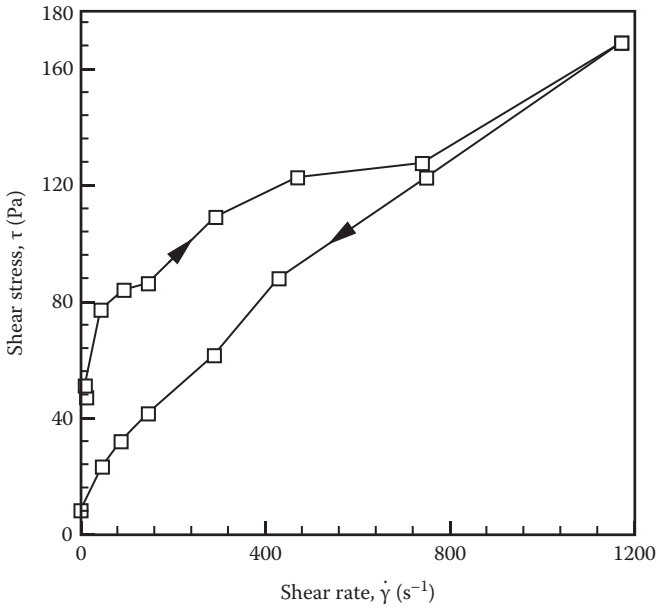


Figure 21.7

Thixotropic behavior of a cement paste. (Data from Struble, L.J. and Ji, X., Rheology, in Ramachandran, V.S. and Beaudoin, J.J., Eds., *Handbook of Analytical Techniques in Concrete Science and Technology*, William Andrew Inc., New York, 2001, Chapter 9.)

of Barnes (1997) and a recent book on this subject (Mewis and Wagner, 2012) for a detailed treatment of time-dependent behavior.

21.2.3 Viscoelastic Fluid Behavior

It is customary to categorize a given substance either as an elastic solid or as a viscous fluid. At one extreme is the Newtonian fluid behavior characterized by a constant shear viscosity, Equation 21.1; the other extreme is the so-called Hookean elastic behavior, which is characterized by the linear relationship between the applied stress and strain, the constant of proportionality being the familiar Young's modulus. From another vantage point, the energy expended in deforming a fluid element at a constant rate is completely lost when the stress is removed. Such a substance thus shows no recovery or has no memory of its virgin state. On the other hand, an ideal elastic solid will exhibit complete recovery and it has a perfect memory. Many materials of industrial relevance show a blend of both viscous and elastic effects under appropriate conditions. In the absence of thixotropic and rheopectic effects, such a material is called elasticoviscous (more solid-like) or viscoelastic (more fluid-like). Therefore, perfectly elastic deformation and viscous flow represent the two limiting cases of viscoelastic behavior. In some materials, only these limits are easily observed. For instance, the viscosity of ice and the elasticity of water may generally go unnoticed! Most polymeric systems exhibit viscoelastic characteristics. In simple shear, a viscoelastic substance exhibits normal stress difference effects, which are in stark contrast to the case of equal normal stresses in Newtonian fluids. Thus, in addition to the shear stress, one also requires the normal stress difference as functions of the applied shear rate to characterize viscoelasticity. Similarly, viscoelastic fluids deviate from Newtonian fluids and time-independent fluids even more dramatically when subject to small amplitude oscillatory shear and extensional deformation (Bird et al., 1987, Macosko, 1994, Larson, 1998). For instance, it is common for a viscoelastic fluid to exhibit shear-thinning viscosity in simple shear and strain hardening in extensional flow.

The corresponding constitutive relations connecting the stress tensor to the rate of strain tensor for a viscoelastic material are invariably in the form of integral and differential equations and a detailed discussion is neither required here nor is possible. Excellent treatises are, however, available on this subject (Bird et al., 1987, Carreau et al., 1997, Larson, 1998). Suffice it to add here that the so-called Deborah number, *De*, is often introduced to ascertain the importance of elastic effects in a given flow situation. In its general form, it is defined as

$$De = \frac{\lambda_f}{\lambda_p} \tag{21.14}$$

where

λ_f is a characteristic time of the fluid
λ_p is the representative process time

In a crude sense, λ_f is a measure of the fluid's memory span. Thus, if $\lambda_p \gg \lambda_f$, the stresses developed in the fluid due to the flow have sufficient time to relax and, hence, no elastic effects are expected. On the other hand, for the case of $\lambda_p \ll \lambda_f$, a fluid element is subjected to rapidly changing kinematic environment such that the fluid element does not have sufficient time to respond to it. Clearly, in this case, viscoelastic effects will manifest. Broadly, vanishingly small values of $De \to 0$ correspond to a viscous response (no memory and recovery) and large values $De \to \infty$ relate to an elastic response (perfect memory and recovery). It is thus not uncommon for the same substance to behave like a viscous fluid in one setting and like an elastic solid in another situation (Bird et al., 1987, Carreau et al., 1997, Tanner, 2000). A great deal of confusion exists, however, in the literature regarding the definitions and evaluation of λ_f and λ_p (Bird et al., 1987). Notwithstanding the gross oversimplification entailed in assigning a single (constant) value to the fluid characteristic time, λ_f, it is sometimes extracted purely from viscosity data (Bird, 1965) or first normal stress difference or small amplitude oscillatory shear results. All of these are probably some measures of the fluid viscoelasticity, but such varied approaches make cross-comparisons impossible. Similarly, the characteristic process time, λ_p, is a "crude" measure of the residence time of the fluid. The following illustrative example further elucidates these ideas. Let us consider a polymer solution with a characteristic time of 10 ms, that is, $\lambda_f = 10$ ms. A small and light sphere of 1 mm diameter settles in it at a terminal velocity of 1 mm/s. Thus, the characteristic process time can be taken as the time required to fall through a distance equal to one diameter, that is, λ_p = diameter/velocity = 1 s. The resulting value of the Deborah number, *De*, is thus, $De = 10 \times 10^{-3}/1 = 0.01$. In contrast, a sphere made of heavy metal but of the same diameter (1 mm) will settle

faster, say, with a velocity of 20 mm/s. In this case, the value of the Deborah number is $De = (10 \times 10^{-3})/(1/20)$, that is, $De = 0.2$, which is much larger than the previous value of 0.01. This thought experiment suggests that the viscoelastic effects are likely to be stronger for the second (heavy) sphere than that for the first (light) sphere. Naturally, the estimated values of De are dependent on the methods of evaluation of λ_f and λ_p; the qualitative inference will, however, not be influenced by such rescaling of the Deborah number.

Before concluding this section, it is worthwhile to reiterate here that in order to solve a transport phenomena problem, one must combine the constitutive relationship with the momentum and energy equations. Therefore, considerable intuition is required in choosing an appropriate fluid model to keep the level of complexity of the resulting partial differential equations at a tractable level. This section is concluded by reiterating that the primary focus in this chapter is on the momentum and heat transfer characteristics of an isolated rigid and fluid sphere in power-law, and Bingham and Herschel–Bulkley fluid models with and without wall effects. This is followed by the prediction of drag and Nusselt number behavior of axisymmetric spheroidal and hemispherical particles and nonspherical particles in power-law and viscoplastic fluids. In view of the limited and inconclusive nature of the corresponding body of knowledge concerning the role of fluid viscoelasticity in these systems, this aspect is discussed only briefly and qualitatively. However, we begin with the case of a single rigid sphere undergoing steady translation in different types of non-Newtonian fluids.

21.3 Rigid Nondeformable Particles

While a detailed discussion of the interactions between particles and moving fluids in a range of settings is presented in Section 1.4, Chapter 1, when the continuous phase exhibits the standard Newtonian fluid behavior, the corresponding information for non-Newtonian fluids is presented in this section. Current interest in such problems stems from both fundamental and pragmatic considerations. From a theoretical standpoint, the flow over a sphere has been used as a model configuration to understand the nature of underlying physical processes to characterize their momentum and convective heat/mass transport aspects. In addition, this simple configuration, which is free from geometric singularities, has also been used to benchmark the efficacy of numerical solution methodologies as well as to test the applicability of the rheological equations of state whose parameters (like $m, n,$ or τ_o^B, μ_B, etc.) are evaluated in well-defined viscometric flows, whereas the flow over a sphere is nonviscometric. In view of the long history of this flow configuration, significant research effort has been expended in obtaining the non-Newtonian equivalent of the Stokes solution. Unfortunately, the answer to this seemingly simple question depends upon the choice of the rheological model (or simply the viscosity model). In view of the nonlinear nature of the viscosity models (such as those discussed in Section 21.2), this aspect adds enormously to the level of difficulty in obtaining solutions to the momentum equations even when the nonlinear inertial effects are neglected altogether (Chhabra, 2006). In addition to its fundamental significance, there are numerous industrial settings where the settling velocity of a sphere in such fluids is frequently needed in process design calculations. For instance, depending upon the application, sometimes, it is necessary to keep particles from settling under the influence of gravity to meet the product specifications (such as in fruit yogurts, health and personal care products and cleaning aids). Similarly, there are occasions when it is desired to effect liquid–solid separation using gravity settling ponds or hydrocyclones or in the dewatering of slurries, etc. In either event, reliable values of the settling velocity of a sphere of the known size and density in a liquid of given density and rheology (values of $m, n,$ or τ_o^B, μ_B, etc.) are thus required. This information is conveniently expressed using the common dimensionless parameters like drag coefficient, Reynolds number, Nusselt number, and the additional dimensionless groups, depending upon the choice of a specific viscosity model. Consequently, over the past 50–60 years, significant advances have occurred in developing reliable expressions for predicting the settling velocity and the rate of heat transfer from a sphere in different types of non-Newtonian fluids. We begin with the case of a rigid sphere undergoing steady translation in unconfined power-law fluids.

21.3.1 Sphere in Power-Law Fluids

Naturally, any attempt to parallel the Stokes analysis must begin with the continuity and Cauchy's momentum equations, which can be written in their compact forms for incompressible flow as follows:
Continuity equation

$$\vec{\nabla} \cdot \vec{u} = 0 \tag{21.15}$$

Momentum equation

$$\rho_f \frac{D\vec{u}}{Dt} = -\vec{\nabla} p + \vec{\nabla} \cdot \vec{\vec{\tau}} + \rho_f \vec{g} \tag{21.16}$$

When the constitutive relation for a Newtonian fluid is substituted in Equation 21.16, it reduces to Equation 1.87 in Chapter 1.

One must, therefore, substitute for the extra stress tensor term $\vec{\vec{\tau}}$ using the tensorial form of the power-law constitutive equation (similar to Equation 21.4). Detailed equations are available, for example, in Adachi et al. (1973); our main focus here is on the presentation and discussion of the results, which have accrued during the past 50–60 years.

Dimensional considerations of the case of a steady flow of power-law fluid with a uniform velocity of u_0 past a sphere of radius a suggest that the drag force on the sphere in the creeping (Stokes) regime is given as follows:

$$F_D = 6\pi a u_0 m \left(\frac{u_0}{a}\right)^{n-1} \cdot X(n) \tag{21.17}$$

In Equation 21.17, $X(n)$ is called the drag correction factor, which accounts for the influence of power-law viscosity on the Stokes drag. Clearly, in the limit of the Newtonian fluid behavior, that is, $n = 1$, no correction is required, that is, $X(n) = 1$ and as expected Equation 21.17 reduces to the familiar Stokes drag formula. It is customary to introduce a dimensionless drag coefficient C_D, defined by Equation 1.96, to rewrite Equation 21.17 as follows:

$$C_D = \frac{24}{Re_{PL}} X(n) \tag{21.18}$$

where the modified definition of the Reynolds number for power-law fluids is given by

$$Re_{PL} = \frac{\rho_f (2a)^n (u_0)^{2-n}}{m} \tag{21.19}$$

In the creeping flow limit ($Re_{PL} \to 0$), the earliest estimates of the drag correction factor $X(n)$ are due to Tomita (1959), who employed the velocity variational principle to get an approximate upper bound on the drag correction factor $X(n)$. Indeed, the first full numerical solution of the momentum equations for power-law fluids was attempted by Crochet et al. (1984), which showed the approximate nature of Tomita's results. Table 21.1 presents the currently available best estimates of the value of $X(n)$ (Song et al., 2009).

Table 21.1 Values of $X(n)$ for a Rigid Sphere

n	$X(n)$
0.1	1.343
0.2	1.434
0.3	1.485
0.4	1.497
0.5	1.42
0.6	1.381
0.7	1.316
0.8	1.258
0.9	1.141
1	1.00

The numerical values of $X(n)$ summarized in Table 21.1 are reasonably well approximated by the following expression:

$$X(n) = \left(\sqrt{6}\right)^{n-1} \left(\frac{3}{n^2 + n + 1}\right)^{n+1} \tag{21.20}$$

The values of $X(n) > 1$ endorse the fact that the drag on a sphere in shear-thinning power-law fluids in the creeping flow regime is augmented over and above the Stokes value in Newtonian fluids. However, the value of $X(n)$ is seen to go through a maximum at about $n \sim 0.4–0.5$. The creeping flow regime generally persists up to about $Re_{PL} \simeq 0.1$ or so.

The next generation of studies in this field have elucidated the role of inertial effects by considering the Reynolds number up to about $Re_{PL} = 500$ (Graham and Jones, 1994, Tripathi et al., 1994, Dhole et al., 2006a, Song et al., 2009). Most of these studies have focused on the prediction of drag coefficient, albeit scant results are also available on the wake characteristics (e.g., angle of separation and wake length). The available information is so sparse that it is not yet possible to develop a predictive expression for drag in the finite Reynolds number range. Table 21.2 tabulates the currently available results for the steady translation of a sphere in power-law fluids beyond the creeping flow regime.

It is worthwhile to make a few observations here about the results summarized in Table 21.2. Firstly, the currently available numerical predictions are restricted to the maximum value of the Reynolds number, $Re_{PL} = 500$. Such predictions become progressively less precise with the decreasing value of the power-law index and/or with the increasing value of the Reynolds number (Chhabra, 2006, Song et al., 2009) owing to the numerical difficulties. On the other hand, reasonable experimental results are available for the drag on a sphere up to about $Re_{PL} \sim 1000–1200$ (Shah et al., 2007) and these are consistent (within ±25% or so)

Table 21.2 Drag on a Sphere in Power-Law Fluids at Finite Reynolds Numbers

Value of n	Re_{PL}	C_D	Source
0.5	5	7.35	Song et al. (2009)
	10	3.937	Song et al. (2009)
	20	2.053	Dhole et al. (2006a)
	50	1.128	Song et al. (2009)
	100	0.685	Dhole et al. (2006a)
	200	0.482	Dhole et al. (2006a)
	500	0.314	Dhole et al. (2006a)
0.6	5	7.306	Song et al. (2009)
	10	4.015	Song et al. (2009)
	20	2.197	Dhole et al. (2006a)
	50	1.219	Song et al. (2009)
	100	0.787	Song et al. (2009)
	200	0.534	Dhole et al. (2006a)
	500	0.356	Dhole et al. (2006a)
0.8	5	7.23	Song et al. (2009)
	10	4.18	Song et al. (2009)
	20	2.47	Dhole et al. (2006a)
	50	1.402	Song et al. (2009)
	100	0.938	Song et al. (2009)
	200	0.639	Dhole et al. (2006a)
	500	0.395	Dhole et al. (2006a)
1	5	7.143	Song et al. (2009)
	10	4.311	Song et al. (2009)
	20	2.692	Dhole et al. (2006a)
	50	1.577	Song et al. (2009)
	100	1.089	Song et al. (2009)
	200	0.744	Dhole et al. (2006a)
	500	0.486	Dhole et al. (2006a)

with the numerical predictions. These results are thus nowhere near as extensive or coherent as the standard Newtonian drag curve for the estimation of drag on a sphere in unconfined Newtonian fluids. Secondly, the inertial effects rapidly increase with the increasing Reynolds number and therefore, the power-law index (n) exerts only a weak influence on the value of drag at high Reynolds numbers. Therefore, many authors have argued that for $Re_{PL} > \sim 50$ or so, one can use the standard Newtonian drag curve for estimating the hydrodynamic drag (or the free falling velocity) of a sphere in power-law fluids with an error band of $\pm 25\%$ (Chhabra, 2006).

At the next level, no results are available on the delineation of flow regimes like transition from the axisymmetric to unsteady nonaxisymmetric, or even regarding the onset of flow separation from the surface of the sphere. The available results seem to suggest faster spatial decay of the velocity field in shear-thinning fluids ($n < 1$) than that in Newtonian fluids under otherwise identical conditions. This implies that one can employ shorter flow domains (both in experimental and numerical studies) to approach the unconfined flow approximation (Missirlis et al., 2001, Chhabra, 2006, Song et al., 2009). The angle of separation (θ_s) is only weakly dependent on the power-law index and, similar to Newtonian fluids, it shows a rather strong dependence on the Reynolds number. Thus, for instance, $\theta_s \simeq 139°–140°$ at $Re_{PL} = 50$ over the range $1 \geq n \geq 0.5$, which drops to $\theta_s \simeq 123°–126°$ at $Re_{PL} = 100$, that is, it moves forward on the surface of the sphere toward the front stagnation point. On the other hand, the wake length shows a positive dependence on the Reynolds number, which is modulated by the value of the power-law index. For instance, in Newtonian fluids ($n = 1$), the wake length more than doubles as the Reynolds number is increased from $Re_{PL} = 50$ to $Re_{PL} = 100$. In contrast, the corresponding change is three-fold in a highly shear-thinning fluid, $n = 0.5$ over the identical interval of Reynolds number values (Dhole et al., 2006a, Song et al., 2009). Unfortunately, in view of the paucity of the available data, it is not yet possible to put forward definitive predictive expressions for drag, θ_s, wake length, etc. which can rival the well-established state-of-the-art equations for Newtonian fluids, for example, see Clift et al. (1978) and Michaelides (2006).

21.3.1.1 Heat Transfer

Whenever there exists a temperature gradient between a sphere and the ambient fluid, heat transfer occurs from the regions of high temperature to that of low temperature. Depending upon the kinematic (fluid flow) conditions, heat transfer can occur in three possible regimes. In the absence of the externally imposed fluid flow and buoyancy effects, heat transfer occurs solely by conduction. In this extreme case, the viscosity characteristics of the ambient medium are irrelevant and the Nusselt number, $Nu = hd/k$, has a constant value given as $Nu = 2$, which applies for both Newtonian and non-Newtonian fluids. On the other hand, when fluid motion occurs, it is customary to discern three distinct heat transfer regimes: forced convection, free convection, and mixed convection. Dimensional considerations as applied to the thermal energy equation and the boundary conditions suggest that the Nusselt number is expected to be a function of the Reynolds number and Prandtl number or combinations thereof (such as Peclet number) for a given geometrical configuration and type of boundary conditions in the forced convection regime. In the free or natural convection regime, the fluid motion is caused solely by the temperature-dependent density and in this case, the overall heat transfer between a quiescent fluid medium and the submerged sphere is determined by the Grashof number (Gr) and the Prandtl number (Pr) or the combinations thereof, the most common being Rayleigh number ($Ra = Gr \cdot Pr$). In the mixed-convection regime, that is, when both forced- and free-convection effects are present, it is customary to use the familiar Richardson number, $Ri = Gr/Re^2$, to ascertain the relative importance of the two contributions. Naturally, the two limiting conditions of $Ri \to 0$ and $Ri \to \infty$ correspond to the pure forced- and free-convection regimes, respectively. On the other hand, the value of the Richardson number of order one denotes the condition when both the forced- and buoyancy-induced effects are comparable. Furthermore, depending upon the direction of the imposed flow with respect to that of the gravity vector, three distinct mixed flow regimes are identified, namely, aiding-, opposing-, and cross-buoyancy. As the name suggests, both flows are "additive" in a sense (both being in the same direction) in the case of the aiding-buoyancy regime. In the opposing-buoyancy case, the two are oriented in the opposite directions, and finally, the two flows are perpendicular to each other in the cross-buoyancy mixed-convection regime, as shown schematically in Figure 21.8. Broadly, the aiding-buoyancy configuration stabilizes the flow and augments heat transfer by strengthening the flow, and the opposing- and cross-buoyancy configurations destabilize the flow by inducing asymmetry in the flow and/or by accelerating the onset of vortex shedding regime, which directly impinges on the scaling of the Nusselt number with the pertinent variables. In the ensuing sections, heat transfer from a sphere in power-law fluids in the three regimes is discussed in some detail.

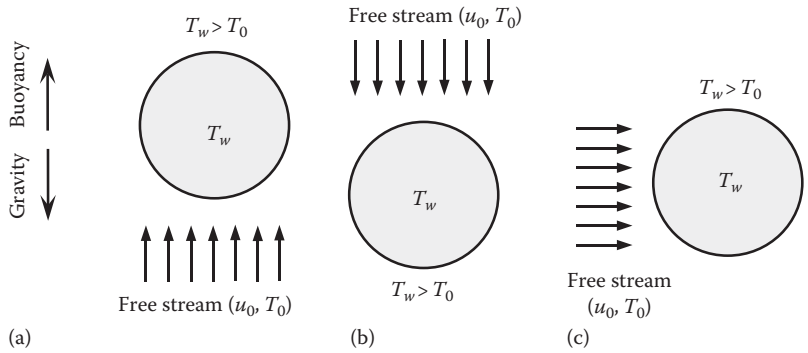


Figure 21.8

Schematics of different mixed-convection regimes: (a) aiding-buoyancy, (b) opposing-buoyancy, and (c) cross-buoyancy.

21.3.1.2 Forced Convection Regime

In the creeping flow limit, many authors (Acharya et al., 1976, Kawase and Ulbrecht, 1981) have employed the high Prandtl (or Schmidt for mass transfer) number thin boundary layer approximation initially introduced by Lochiel and Calderbank (1964) to delineate the role of power-law index (n) on heat/mass transfer. This approach yields a correction factor, $X_m(n)$, in the creeping flow limit for heat/mass transfer akin to $X(n)$ in Equation 21.18 for drag as follows:

$$X_m(n) = 0.866\left[\frac{3}{2} - \frac{9n(n-1)}{2n+1}\right]^{1/3} \tag{21.21}$$

Equation 21.21 predicts varying levels of enhancement in heat/mass transfer on account of shear-thinning behavior ($n < 1$), which is consistent with the available scant experimental results (Chhabra, 2006). The assumption of high Peclet number was relaxed by Westerberg and Finlayson (1990), who solved the field equations in the creeping flow regime from an isothermal sphere in Nylon-6 melt. However, their results are restricted to a specific material and it is thus not possible to develop generalized expressions based on their results.

In the other limit of high Reynolds number ($Re_{PL} \to \infty$), the early studies in this field are invariably based on the boundary layer flow approximation, pioneered by Acrivos et al. (1960) and subsequently by many others including Bizzell and Slattery (1962). Naturally, this analysis yields the general scaling of the Nusselt number as follows:

$$Nu = A(n)Re_{PL}^{(n+2)/3(n+1)}Pr^{1/3} \tag{21.22}$$

where $A(n)$ is a function of the power-law flow behavior index (n). Its value depends on the shape of the particles. Suffice it to add here that the available experimental results are not inconsistent with the functional dependence represented by Equation 21.22. Naturally, such boundary layer results are valid in the limit of $Re_{PL} \to \infty$ and/or $Pr \to \infty$ wherein the boundary layers are really very thin, one can also neglect the curvature effects in the case of a sphere or a cylinder. This approach, however, does not take into account the wake phenomenon encountered at finite Reynolds numbers. In this case, the boundary layer predictions do a good job up to the point of flow detachment from the surface of the sphere.

It is not known *a priori* up to what values of the Reynolds and/or Prandtl numbers the boundary layer approximation is correct. These critical values are expected to be functions of the power-law index. Under otherwise identical conditions, the boundary layer thickness is smaller in shear-thinning fluids ($n < 1$) than that in Newtonian fluids and of course, the reverse is true for shear-thickening fluids ($n > 1$). Finally, for Newtonian fluids, that is, $n = 1$, Equation 21.22 reduces to the well-known scaling of $Nu \sim Re^{1/2}Pr^{1/3}$. In contrast, the dependence of the Nusselt number on the Reynolds number in shear-thinning fluids is seen to be stronger than $Nu \sim Re^{1/2}$.

One must resort to the numerical solution of the complete momentum and energy equations to patch up the intermediate region in between the creeping flow and boundary layer approximation regions. As noted in Section 1.4.4, for Newtonian fluids, the heat transfer from a sphere in power-law fluids is influenced by a

large number of parameters. In the limiting case of an unconfined sphere and for a specific thermal boundary conditions (constant temperature or constant heat flux on the surface of the sphere), with constant thermophysical properties (thermal conductivity, thermal heat capacity, density, rheological constants) and in the absence of viscous dissipation effects (small Brinkman number), the scaling arguments suggest the average Nusselt number (Nu) to be a function of the Reynolds number, Prandtl number, and power-law index, that is,

$$Nu = f\left(Re_{PL}, Pr, n\right) \tag{21.23}$$

This functional dependence has been established by Dhole et al. (2006b) over the following ranges of conditions: $5 \leq Re_{PL} \leq 200$; $1 \leq Pr \leq 400$ (maximum Peclet number ≤ 2000) and $0.5 \leq n \leq 2$. For an isothermal sphere, Equation 21.23 is of the form:

$$Nu = 0.922 + Re_{PL}^{1/n+2} Pr^{1/3} + 0.1 Re_{PL}^{2/3} Pr^{1/3} \tag{21.24}$$

The corresponding expression for an isoheat flux (dissipating heat at a constant flux) sphere is given by

$$Nu = 1 + Re_{PL}^{1/n+2} Pr^{1/3} + 0.158 Re_{PL}^{2/3} Pr^{1/3} \tag{21.25}$$

Both of these equations predict the value of the average Nusselt number with an uncertainty of about ~10%. Subsequently, some of these results have been corroborated independently by Song et al. (2010) and others (Nirmalkar et al., 2013b). These numerical predictions are in line with the limited experimental heat and mass transfer data for spheres in power-law media (Chhabra, 2006).

21.3.1.2.1 Free Convection Regime In this case, the momentum and energy equations are coupled via the buoyancy force even in the case of Newtonian fluids even if all the thermophysical properties other than the fluid density are constant and viscous dissipation effects are neglected. This coupling is accentuated in the case of power-law fluids by the nonlinearity of the power-law constitutive equation. Early analyses pioneered by Acrivos (1960) and subsequently by Stewart (1971) are based on the approximate boundary layer equations, which are valid in the limit of $Gr \to \infty$ and/or $Pr \to \infty$. Undoubtedly, such attempts have led to the correct scaling relationship between the Nusselt number, on one hand, and the Grashof number, Prandtl number, and power-law index, on the other. In essence, the Nusselt number is given by

$$Nu \simeq c(n) \cdot \Omega \tag{21.26}$$

where $\Omega = Gr^{1/2(n+1)} Pr^{n/3n+1}$.

In Equation 21.26, the value of $c(n)$ ranges from 0.9 for $n = 0.1$ to 1.4 for $n = 1.5$ and Acrivos (1960) himself advocated the use of a single value of $c(n) = 1.1$, which compares rather favorably with the experimental value of 1.122 (Liew and Adelman, 1975). However, subsequent experimental data by Amato and Tien (1976) and Lee and Donatelli (1989), which span wider ranges of experimental conditions, correlate much better with the following equation rather than with Equation 21.26:

$$Nu = \Omega \quad \text{for } \Omega > 10 \tag{21.27}$$

$$Nu = 2\Omega^{0.68} \quad \text{for } \Omega < 10 \tag{21.28}$$

In Equation 21.27, the value of $c = 1$ is remarkably close to the value of 1.1 proposed by Acrivos (1960). This seems to suggest that the boundary layer approximation is good for $\Omega > 10$. One must, however, solve the complete field equations for the intermediate values of the Grashof and Prandtl numbers corresponding to the regime characterized by $\Omega < 10$, as has been done in a recent numerical study (Prhashanna and Chhabra, 2010). Indeed, while their numerical results for $\Omega > 10$ are in perfect agreement with Equation 21.27, these deviate only slightly from Equation 21.28, in so far that the exponent of Ω is found to be 0.72 as opposed to 0.68. Such a close correspondence between experiments (represented by Equations 21.27 and 21.28) and the numerical results (Prhashanna and Chhabra, 2010) lends credibility to both the experiments

of Amato and Tien (1976) as well as to the approximate boundary layer flow predictions of Acrivos (1960) under appropriate conditions. Lastly, an examination of the definition of Ω reveals that while for $n = 1$, it coincides with the familiar scaling of $Nu \sim Ra^{1/4}$; the dependence of the Nusselt number on Grashof and Prandtl numbers is modulated by the value of the power-law index, n. For instance, for $n = 0.5$, the composite parameter Ω is given by $Gr^{1/3}Pr^{1/5}$, that is, stronger dependence on Gr and weaker dependence on Pr with reference to that in Newtonian fluids.

21.3.1.2.2 Mixed-Convection Regime Only limited results are available on the laminar mixed-convection heat transfer from a sphere even in Newtonian fluids (mainly air): for example, see Acrivos (1966), Chen and Mucoglu (1977, 1978), who extended the boundary layer flow approximation in both aiding- and opposing-buoyancy configurations for both an isothermal and isoflux sphere. A good review of these as well as of the other pertinent theoretical and numerical studies can be found in Kotouč et al. (2008, 2009). Also Nirmalkar and Chhabra (2013) have thoroughly reviewed the corresponding studies in both Newtonian and power-law media. Only three studies are available on mixed convection from a sphere in power-law fluids. Both Wang and Kleinstreuer (1988) and Meissner et al. (1994) have exploited the boundary-layer flow equations for the aiding-buoyancy configuration and highlighted the positive influence of the Richardson number on skin friction and Nusselt number. As noted earlier, naturally these predictions are applicable in the limit of large values of the Grashof and Prandtl numbers and do not account for wake effects. These results have been complemented by a recent numerical study (Nirmalkar and Chhabra, 2013). Over the range of conditions as $0 \le Ri \le 2$, $0.2 \le n \le 2$, $1 \le Re_{PL} \le 100$ and $1 \le Pr \le 100$ in the aiding-buoyancy configuration, the average Nusselt number values for an isothermal sphere are well correlated by the following equation:

$$Nu = 0.88 Pe^{\star 1/3}\, \Delta^{0.74} \tag{21.29}$$

where the modified Peclet number, $Pe^{\star}$, is defined as

$$Pe^{\star} = Re^{\star} \cdot Pr^{\star} \tag{21.30}$$

with,

$$Re^{\star} = Re_{PL}\left(1 + \sqrt{Ri}\right)^{2-n} \tag{21.31}$$

$$Pr^{\star} = Pr\left(1 + \sqrt{Ri}\right)^{n-1} \tag{21.32}$$

and

$$\Delta = \left(\frac{3n+1}{4n}\right) \tag{21.33}$$

The preceding definitions of $Pe^{\star}$, $Re^{\star}$, and $Pr^{\star}$ include the forced convection limit ($Ri = 0$) as well as the Newtonian fluid limit ($n = 1$). Also, since $\Delta > 1$ for shear-thinning fluids ($n < 1$), its inclusion in Equation 21.29 implies that the shear-thinning fluid behavior enhances the rate of heat transfer over and above that in Newtonian fluids at fixed values of the Reynolds, Prandtl, and Richardson numbers.

No such results are available for a sphere in power-law fluids for the other mixed-convection regimes, that is, opposing- or cross-buoyancy configurations. Nor is there any information available about the conditions for transition from one flow regime to another, that is, laminar/turbulent, steady/time-dependent, etc.

This section is concluded by noting that irrespective of the mode of convection, free, forced, or mixed, it is possible to augment the rate of heat transfer in shear-thinning fluids ($n < 1$) with reference to that in Newtonian fluids at fixed values of the influencing parameters. However, the degree of enhancement is strongly dependent on the value of the Reynolds and Prandtl numbers in the forced-convection; of the Grashof and Prandtl numbers in the free-convection; and of Reynolds, Richardson, and Prandtl numbers in the mixed-convection regimes. This can lead to significant energy savings in chemical and allied process engineering applications.

21.3.1.3 Wall Effects

The confining walls are known to exert an extra retardation force on a freely falling sphere, thereby slowing down its descent in a quiescent fluid. This retardation effect stems from the upward flow of the fluid displaced by a falling sphere. The narrower the annular gap between the particle and the wall, the stronger is the upward flow, thereby augmenting the relative velocity between the fluid and the particle. Even at the detailed level, velocity and pressure (and hence the temperature) fields are altered with reference to that for an unconfined sphere. Such changes, in turn, manifest at the macroscopic level by enhancing the values of the corresponding drag, and Nusselt and Sherwood numbers for a sphere. The most common configuration studied for this purpose is to understand the wall effects on a sphere situated at the axis of a tube, though some studies are also available for eccentric positioning of a particle in a tube filled with Newtonian fluids (Suresh and Kannan, 2013) and/or in vessels of noncircular cross section (Chhabra, 2002, 2006). The available literature on this topic in Newtonian fluids has been reviewed in Section 1.4.3.10 in this book and in other sources, for example, see Chhabra (2002, 2006).

The practical motivation for such studies really comes from the use of falling ball viscometer, chromatographic columns, electrophoresis in slurries, blood flow in arteries, etc. In this section, consideration is given to the analogous studies in power-law fluids. Firstly, owing to the nonlinearity of the power-law and other non-Newtonian viscosity models, analytical results, which can rival the celebrated results of Faxen (1923) or of Haberman and Sayre (1958) in the creeping regime of Newtonian media, are theoretically not possible for power-law fluids. Therefore, one must seek numerical solutions to the governing equations. It is customary to introduce a wall factor, f_w, to quantify the extent of wall effects. From an experimental view point, the wall factor, f_w, is defined simply as the ratio of the terminal falling velocity (u_m) in a confined medium to that in an unconfined medium (u_∞), for a given sphere–liquid–tube combination as

$$f_w = \frac{u_m}{u_\infty} \tag{21.34}$$

Naturally, the wall factor, f_w, ranges from zero (sphere diameter equal to tube diameter) to unity (when tube diameter $\to \infty$). The experimental determination of the wall correction factor thus necessitates measuring the settling velocity of a sphere in tubes of different (at least three) diameters (D) and extrapolating these results to $1/D \to 0$ and the intercept on the ordinate corresponds to the unconfined settling velocity u_∞ for a given sphere–fluid combination. Dimensional considerations of the case of a sphere settling at the axis of a cylindrical tube filled with a power-law fluid suggest the wall correction factor to be governed by three dimensionless parameters, namely, Reynolds number (Re_{PLm}), power-law index (n), and sphere-to-tube diameter ratio, $\Xi (= d/D)$, that is,

$$f_w = f\left(Re_{PLm}, \Xi, n\right) \tag{21.35}$$

In the creeping flow regime for Newtonian fluids, k_{wall} defined by Equation 1.160 is equal to the reciprocal of the wall factor introduced here, that is, $k_{wall} = f_w^{-1}$. However, this relationship is more involved than this for non-Newtonian fluids and/or beyond the creeping flow regime (Clift et al., 1978, Chhabra, 2002, Michaelides, 2006). By analogy with the trends seen in Newtonian fluids (Uhlherr and Chhabra, 1995, Chhabra, 2002), the wall factor, f_w, is independent of the Reynolds number (Re_{PLm}) in the both creeping ($Re_{PLm} \to 0$) and fully inertial ($Re_{PLm} \to \infty$) regimes in power-law fluids (Chhabra, 2006), that is, these two limiting values can be written as

$$Re_{PLm} \to 0; \quad f_{wo} = f_1\left(\Xi\right) \tag{21.36}$$

$$Re_{PLm} \to \infty; \quad f_{w\infty} = f_2\left(\Xi\right) \tag{21.37}$$

Between these two limits, the wall factor is a function of both Ξ and Re_{PLm}. It is, however, somewhat surprising that the presently available experimental results do not point to any influence of the power-law index, n, at least over the range $n \geq 0.5$ on the value of f_w. On the other hand, irrespective of the value of the power-law index, the wall effects are less severe in power-law fluids than that in Newtonian fluids, as can be

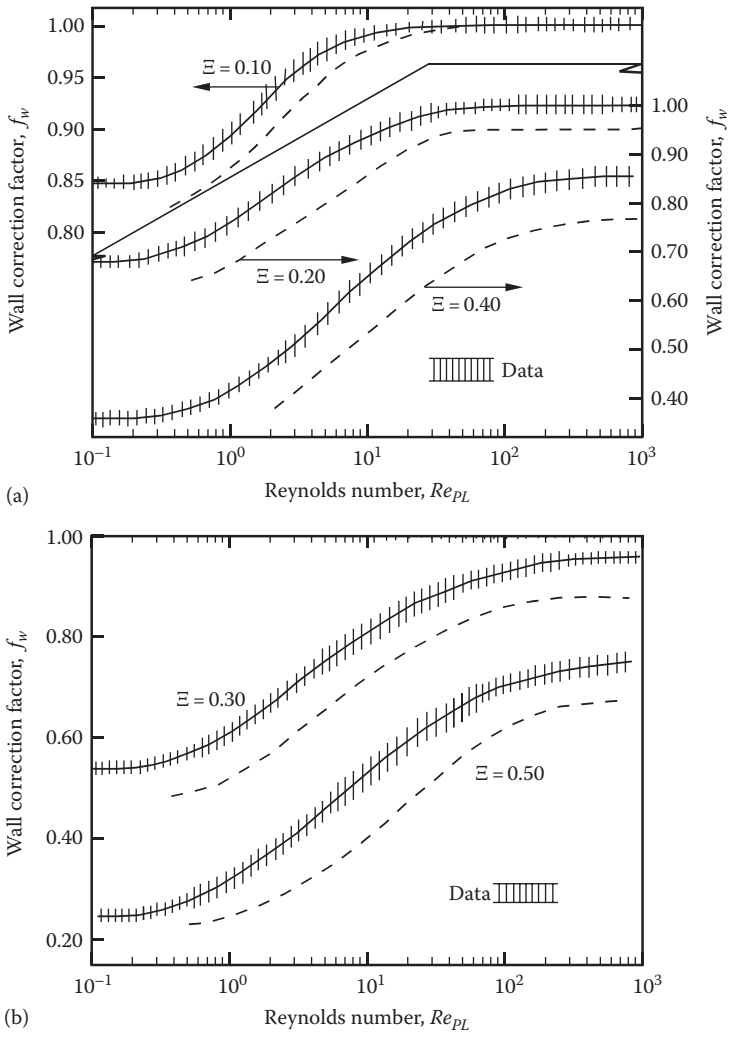


Figure 21.9

Wall correction factor as a function of the Reynolds number and diameter ratio for spheres falling in power-law liquids. The prediction of Equation 21.40 is shown as solid line; the corresponding Newtonian results are shown as broken lines. (Data from Chhabra, R.P. et al., Wall effect for sphere motion in inelastic non-Newtonian fluids, in *Proceedings of the Sixth Australasian Hydraulics Fluid Mechanical Conference*, Adelaide, South Australia, Australia, 1977, pp. 435–438.)

seen in Figure 21.9. Most of the literature results ($\Xi \leq 0.5$; $n \geq 0.5$ and $Re_{PLm} \leq 1000-1200$) are reasonably well approximated by the following set of equations:

$$f_{wo} = 1 - 1.6\Xi \tag{21.38}$$

$$f_{w\infty} = 1 - 3\Xi^{3.5} \tag{21.39}$$

$$\frac{(1/f_w) - (1/f_{w\infty})}{(1/f_{wo}) - (1/f_{w\infty})} = \left(1 + 1.3Re_{PLm}^2\right)^{-0.33} \tag{21.40}$$

Equations 21.38 through 21.40 are based on experimental data spanning $10^{-2} \leq Re_{PLm} \leq 10^3$; $\Xi \leq 0.5$ and $0.53 \leq n \leq 0.95$ (Chhabra et al., 1977, Chhabra and Uhlherr, 1980, Chhabra, 2002, 2006). Subsequently, these equations have been shown to correlate the other literature data also within about ±8% (Chhabra, 2006).

Numerical predictions of wall effects in the creeping flow regime (Missirlis et al., 2001) and up to $Re_{PLm} \simeq 100$ and $\Xi \leq 0.5$ (Song et al., 2009) are not inconsistent with the predictions of Equations 21.38 through 21.40 in overall terms. However, the experimental results and numerical simulations do differ in a significant manner. Both numerical studies (Missirlis et al., 2001, Song et al., 2009) predict a reasonably strong influence of the power-law index on wall effects, especially in the creeping flow regime, but the available experimental results do not reveal such a dependence.

The effect of eccentric positioning of the sphere in a tube has been studied by Suresh and Kannan (2013) and that of a fully developed profile in a tube has been investigated by Song et al. (2011, 2012). The eccentricity further augments the drag force of a sphere by varying amounts depending upon the value of Ξ and the degree of eccentricity, though the effect is less dramatic in power-law fluids than that in Newtonian fluids. Similarly, scant experimental results are also available on wall effects for the steady translation of a sphere at the axis of a duct of square cross section (Balaramakrishna and Chhabra, 1992) and for scores of shapes of nonspherical particles (including cylinders, cones, needles, prisms, rectangles, etc.) in circular tubes (Chhabra, 1995, 1996). In this case, the wall effect is strongly influenced by the orientation of the settling particle. The wall correction factor shows a linear dependence on Ξ, though the slope of such a dependence is seen to vary strongly with the shape of the particle. Also, in this case, d is replaced by the equal volume sphere diameter, d_V.

So far, the consideration has been given to the role of confinement in the settling velocity (or drag force) of a sphere in power-law fluids. Owing to the intimate connection between the velocity and temperature fields prevailing in the close proximity of a heated sphere, the confining walls also influence the resulting values of the Nusselt (or for mass transfer the Sherwood) number for a sphere. This effect is explained by the sharpening of the temperature gradient on the surface of the sphere, which directly influences the value of the Nusselt number for an isothermal sphere. There has not been much activity on this aspect even in Newtonian fluids (Clift et al., 1978, Michaelides, 2006). This is because the wall effects do not influence the rates of heat and mass transfer to the same extent as the hydrodynamic drag force. Owing to the large values of the Prandtl and Schmidt numbers, the temperature and concentration boundary layers are thin and the confining walls seldom influence their thickness. Thus, Song et al. (2010, 2012) studied the wall effects on forced convection heat transfer in power-law fluids from an isothermal sphere mounted on the axis of a cylindrical tube with adiabatic walls. They considered two situations. In the first instance, the configuration was equivalent to a sphere falling in quiescent fluid medium at the axis of the tube. Their numerical study encompassed the range of conditions as follows: $0.2 \leq n \leq 1$; $\Xi \leq 0.5$; $5 \leq Re_{PL} \leq 100$ and $1 \leq Pr \leq 100$. In this case, the enhancement in heat transfer on account of the fluid shear-thinning behavior is found to be maximum for an unconfined sphere and the relative enhancement decreases with the increasing blockage, that is, the value of Ξ. This counterintuitive trend stems from two factors: the boundary layers are known to be thinner in shear-thinning fluids than that in Newtonian fluids under otherwise identical conditions. Conversely, it stands to reason that the confining walls modify the boundary layers in Newtonian fluids much more strongly than that in power-law fluids. The second factor, which contributes to this trend, is the fact that the shear rate varies from one point to another on the surface of the sphere. This is of no consequence for a Newtonian fluid whose viscosity is independent of shear rate. In the case of power-law fluids, however, this can lead to wide ranging values of the fluid viscosity depending upon the value of the power-law index (n) and hence, the increase in heat transfer is reduced for a confined sphere. These trends were further corroborated by their follow-up study (Song et al., 2012), which explored the effect of the fully developed profile in a tube on the forced convection heat transfer from a sphere. These predictions are in line with the few experimental results available in the literature; for example, see Song et al. (2009, 2010, 2011, 2012) for limited comparisons between numerical predictions and experimental data.

In summary, one may conclude that the wall effects influence the drag significantly more than the corresponding heat and mass transfer of a sphere, at least in the axisymmetric flow regime.

21.3.2 Sphere in Viscoplastic Fluids

As noted in Section 21.2.1.3, a viscoplastic fluid exhibits dual characteristics. Such a substance in unsheared state has the capacity to support the weight of an embedded particle for a long time. Conversely, a sphere of given size and density may or may not settle in a quiescent viscoplastic fluid depending upon its weight *vis-a-vis* the fluid yield stress. Indeed, this property is routinely exploited in the formulation and manufacture of a range of food-, health-care, and personal-care products of multiphase nature that keep particles from settling under the influence of gravity. Owing to the nonviscometric nature of the flow field produced around a sphere, it is obvious that flow domain is spanned by the simultaneous coexistence of yielded or fluid-like and unyielded

or solid-like regions. This complexity not only adds to the difficulty of numerical solutions, but it also directly impinges on the resulting values of the drag and Nusselt number. It must be noted that the sole mechanism for heat transfer is conduction in unyielded solid-like subdomains and convection is limited to yielded fluid-like regions. In steady-state situations, conduction may be the overall rate-determining step for heat transfer. Therefore, the mixing/homogenization, heating/cooling of such substances is rather difficult. In this section, the current state of the art is reviewed. In particular, consideration is given to the following aspects: static equilibrium (whether a sphere will settle or not), yield surfaces delineating the fluid-like and solid-like domains, drag behavior, heat transfer, and wall effects for a sphere undergoing steady translation in viscoplastic media.

21.3.2.1 Static Equilibrium

Most of the relevant experimental results in this field have been summarized by Chhabra (2006) and are based on the instances where the motive force is the buoyant weight of the sphere. It is customary to introduce a new dimensionless group indicative of the ratio of the fluid yield stress and the motive force for pushing the sphere as follows:

$$Y = \frac{\tau_0}{gd(\rho_s - \rho_f)} \tag{21.41}$$

Thus, large values of Y (yield stress force > buoyant weight) would correspond to the particle not settling and small values of Y would favor sphere motion. It is obvious that the delineation of this transition in experiments is far from being objective and straightforward. For instance, many researchers (e.g., see Uhlherr, 1986, Schurz, 1990) have simply equated the vertical component of the force due to the yield stress to the buoyant weight of the sphere, thereby arriving at a value of $Y = 0.212$. This argument is open to criticism that the stress (tangential and normal) distribution over the surface of the sphere is not known *a priori* and the shear stress everywhere may not be the fluid yield stress. Notwithstanding this intrinsic difficulty, it is still convenient to explain the available results in terms of the dimensionless parameter, Y. Currently available experimental and numerical values of Y range from about 0.04 to 0.212, that is, a fivefold variation. The numerical predictions (Beris et al., 1985, Beaulne and Mitsoulis, 1997, Blackery and Mitsoulis, 1997) as well as the experimental observations (Jossic and Magnin, 2001, Merkak et al., 2006, Tabuteau et al., 2007a,b) result in the critical value of Y in the range 0.04–0.08. These are considered to be more reliable than the oft-quoted higher value of $Y \sim 0.2$ or so. However, such diverse values of the parameter, Y, seem to suggest inherently different response of such a material whether the motion/no motion condition is approached from above or below. Sometime this effect is also explained in terms of the "static" and "dynamic" yield stress.

21.3.2.2 Yield Surfaces

As noted earlier, depending upon the magnitude of the local stress tensor at a point in the fluid *vis-a-vis* the value of the fluid yield stress, the material may or may not yield. These regions are separated by the so-called yield surfaces. There has not been much experimental activity in this field except the flow visualization studies reported by Atapattu et al. (1990, 1995); representative results are shown in Figure 21.10 in the limit of the creeping flow regime. It is not feasible to achieve truly unconfined flow conditions in experiments, corresponding numerical predictions for a range of values of Ξ and Bn are shown for Herschel–Bulkley model fluids (Beaulne and Mitsoulis, 1997). Broadly, the fluid-like cavity encapsulating the sphere is seen to extend up to about 1.5–2 times the sphere diameter in lateral and axial directions under most conditions. Figure 21.11 shows the effect of Reynolds number on yielded surfaces based on the numerical studies of Nirmalkar et al. (2013a,b). At this juncture, one can remark that the fluid inertia (increasing Reynolds number) tends to expand the yielded regions, whereas this tendency is countered by the increasing Bingham number. For a given Reynolds number, there must exist a limiting Bingham number wherein the yield surfaces attain a limiting morphology corresponding to the fully plastic flow limit. Also, the small blobs of unyielded material adhering at the front and rear stagnation points predicted by the numerical studies have not been observed in the visualization studies of Atapattu et al. (1990, 1995) very likely because of the rather crude resolution scale of the photographic technique employed in this study.

21.3.2.3 Drag Behavior

From a theoretical standpoint, the main difficulty stems from the fact that the yield surfaces are not known *a priori* and therefore, one does not know the flow domain completely. Also, the inherently discontinuous form of the viscosity models, Equations 21.8 through 21.13, does not allow them to be incorporated

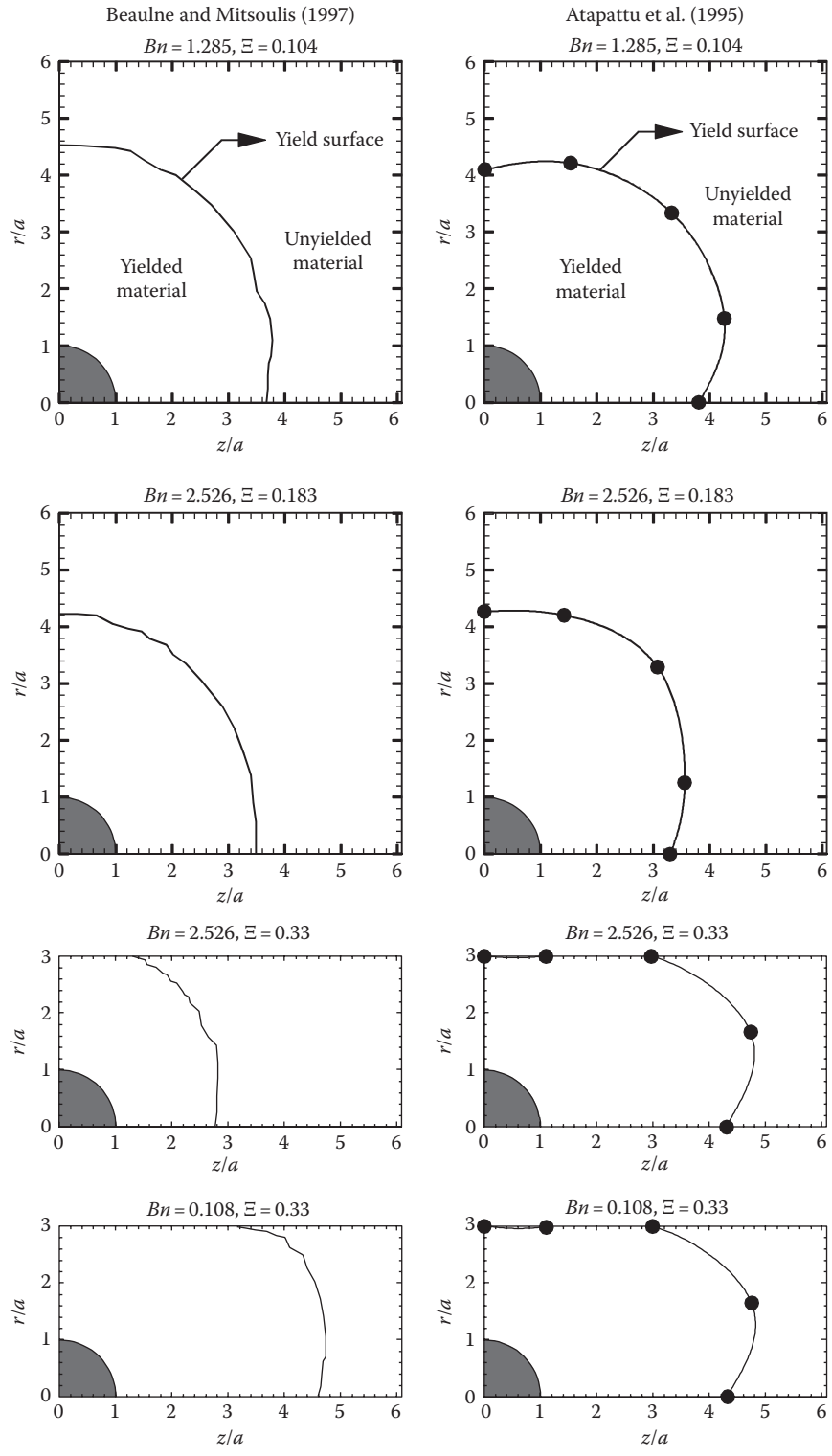


Figure 21.10

Yield surfaces predicted by the numerical results of Beaulne and Mitsoulis (1997) and experimental results of Atapattu et al. (1995) for the creeping motion of a sphere in confined Herschel–Bulkley fluids. Flow is in upward direction.

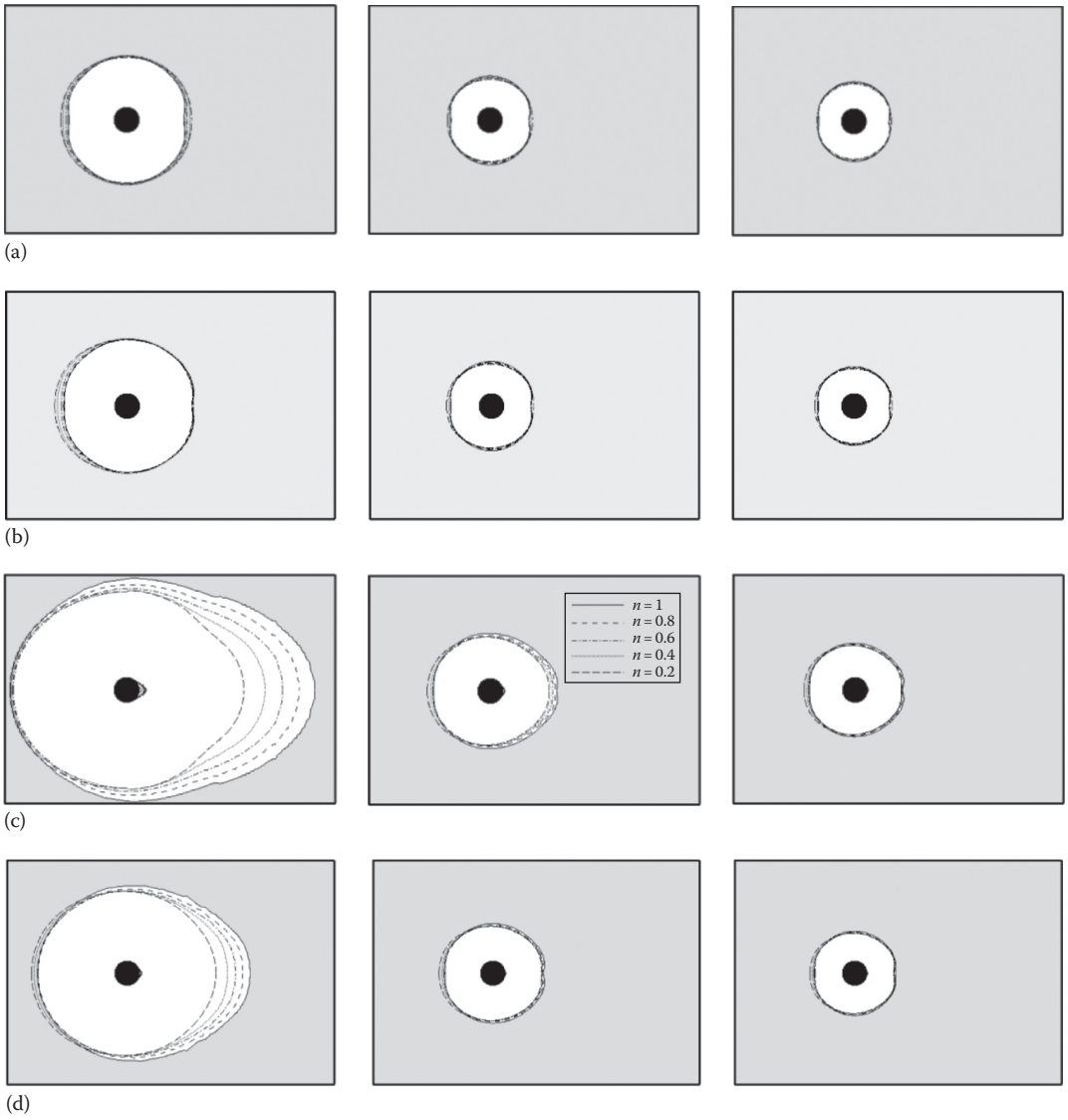


Figure 21.11

Effect of Reynolds number, Bingham number, and power-law index on the structure of yield surfaces for a sphere (Nirmalkar and Chhabra, 2013a,b). Flow is from left to right. Shaded parts denote the unyielded regions.

directly into any numerical solution scheme. One way is to solve for the appropriate momentum equations in both the solid and fluid regions in a trial and error fashion, because the yield surfaces are not known *a priori*. This is very cumbersome. A few regularization schemes have evolved, which convert the abrupt transition from the solid-like to fluid-like behavior into a gradual one (Glowinski and Wachs, 2011). Three such schemes due to Bercovier and Engleman (1980), O' Donovan and Tanner (1984), and Papanastasiou (1987) have gained wide acceptance in the literature and are introduced briefly here.

It is useful to rewrite Equations 21.8 and 21.9 in terms of the apparent viscosity, which brings out the inherent difficulty in its direct implementation in a numerical scheme. In terms of a dimensionless viscosity, Equations 21.8 and 21.9 becomes

$$\mu^{\star} = 1 + \frac{Bn}{\left|\vec{\vec{\dot{\gamma}}}\right|} \quad \text{for } \left|\vec{\vec{\tau}}\right| > Bn \tag{21.42}$$

$$\mu^{\star} = \infty \quad \text{for } \left|\vec{\vec{\tau}}\right| \leq Bn \tag{21.43}$$

Equation 21.43 shows the fluid viscosity to be unbounded for the stress levels below the fluid yield stress. Thus, Papanastasiou (1987) regularized this discontinuity using an exponential function as

$$\mu^{\star} = 1 + Bn\left(\frac{1-\exp\left(-M\left|\dot{\overline{\overline{\gamma}}}\right|\right)}{\left|\dot{\overline{\overline{\gamma}}}\right|}\right) \tag{21.44}$$

where M is the sole regularization parameter. In the limit of $M \to 0$, Equation 21.44 reduces to the Newtonian fluid behavior and for large values of $M \to \infty$, Equation 21.44 reproduces the true Bingham plastic model, that is, Equations 21.8 and 21.9. Thus, large values of M are required to adequately approximate the Bingham behavior, as shown schematically in Figure 21.12. The second regularization scheme, the so-called biviscous model, simply replaces the unbounded viscosity, Equation 21.43, by the so-called yielding viscosity (μ_y) which is several orders of magnitudes larger than the Bingham plastic viscosity (μ_B). This scheme is shown schematically in Figure 21.13, where the increasing values of (μ_y/μ_B) approach the true Bingham behavior. In this framework, Equations 21.42 and 21.43 are written as

$$\mu^{\star} = 1 + Bn\left[1-\left(\frac{1}{\mu_y/\mu_B}\right)\right]\frac{1}{\left|\dot{\overline{\overline{\gamma}}}\right|} \quad \text{for } \left|\overline{\overline{\tau}}\right| > Bn \tag{21.45}$$

$$\mu^{\star} = \frac{\mu_y}{\mu_B} \quad \text{for } \left|\overline{\overline{\tau}}\right| \le Bn \tag{21.46}$$

Clearly, at the limit of $\mu_y \to \infty$, Equations 21.45 and 21.46 coincide with Equations 21.42 and 21.43, respectively. Hence, as large values of μ_y as possible must be used in numerical simulations to obtain reliable results.

In the third approach (Bercovier and Engleman, 1980), the discontinuity is tamed by introducing a small magnitude of the rate of strain tensor into Equation 21.42 as

$$\mu^{\star} = 1 + \frac{Bn}{\left|\dot{\overline{\overline{\gamma}}}\right| + \delta} \tag{21.47}$$

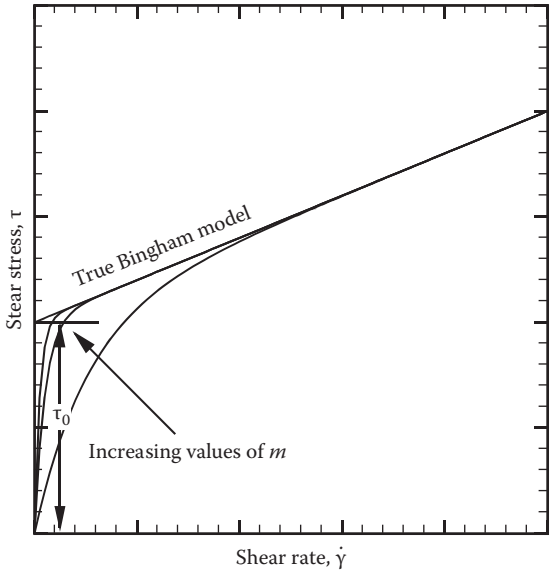


Figure 21.12

Typical shear stress versus shear rate plot for Papanastasiou's regularization approximation, Equation 21.44.

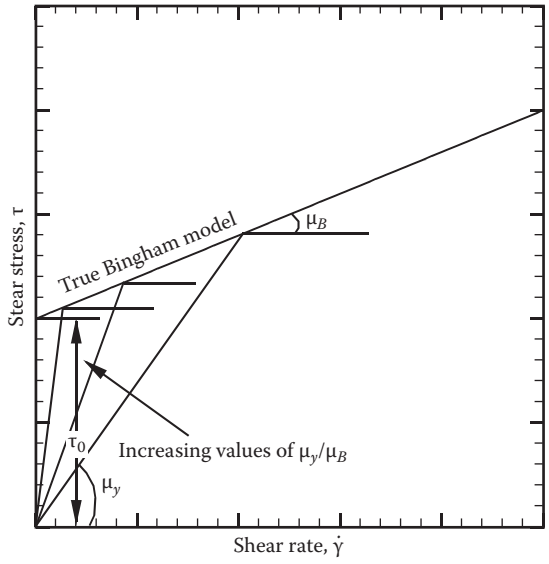


Figure 21.13

Typical shear stress versus shear rate plot for biviscous regularization approximation, Equations 21.45 and 21.46.

In this case, δ denotes the relatively small values of the strain rate in unyielded subdomains when $\left|\dot{\dot{\gamma}}\right| = 0$ and in this case, δ = 0 corresponds to the true Bingham fluid behavior and hence, δ is assigned values as small as 10^{-8} in numerical studies to minimize the numerical artifacts.

Detailed descriptions concerning the relative merits and demerits of the preceding three schemes as well as the other procedures available in the literature can be found in numerous references (Liu et al., 2002, Frigaard and Nouar, 2005, Glowinski and Wachs, 2011, Balmforth et al., 2014, for instance). All these approaches have been successfully employed within the context of the calculation of drag on a sphere and a cylinder in yield stress fluids with and without shear-thinning behavior.

Early attempts at the prediction of drag on a sphere are based on the application of the velocity and stress variational principles (Yoshioka et al., 1971). These results are valid only in the creeping (zero Reynolds number) regime and are based on *a priori* assumption concerning the shape and location of the yield surfaces; that is, an approximate solution to the momentum equations is sought in the yielded region only. Beris et al. (1985) were seemingly the first to seek the numerical solution of the complete momentum equations for the creeping flow of Bingham plastic fluids over an unconfined sphere. Subsequently, the drag values have also been reported by Blackery and Mitsoulis (1997) and Deglo de Besses et al. (2004) with wall effects. For an unconfined sphere in the creeping flow regime, the numerical results of Blackery and Mitsoulis (1997) and of Beris et al. (1985) can be consolidated via the relationship:

$$C_D = \frac{24}{Re_B}\left(1 + 2.93Bn^{0.83}\right) \tag{21.48}$$

In the limit of the fully plastic flow ($Bn \to \infty$), Blackery and Mitsoulis (1997) reported the limiting value of drag coefficient as

$$C_{D\infty} = \frac{28.08Bn}{Re_B} \tag{21.49}$$

This limit was observed for $Bn \to 1000$ and this is in line with the early experiments of Valentik and Whitmore (1965) and Pazwash and Robertson (1975), as detailed in Chhabra (2006).

While the limited analogous results of Beaulne and Mitsoulis (1997) for Herschel–Bulkley fluid model, Equations 21.10 and 21.11, were found to be in fair agreement with the experimental drag data of Atapattu et al. (1995), the effect of fluid slippage on the sphere surface was examined by Deglo de Besses et al. (2004). They concluded that, as expected, the wall slip lowers the drag on the sphere. The effect of inertia up to

Reynolds number values of 100 on the drag of an isolated sphere has been studied numerically only recently (Nirmalkar et al., 2013a,b). These results can be reasonably well approximated by the following expressions:

$$C_D = \frac{28.63}{Re^+}\left(1 + 0.19\left(Re^+\right)^{0.33}\right) \tag{21.50}$$

$$C_{DP} = \frac{21.84}{Re^+}\left(1 + 0.04\left(Re^+\right)^{0.77}\right) \tag{21.51}$$

The modified Reynolds number Re^+ incorporates the influence of the Bingham number, Bn, as follows:

$$Re^+ = \frac{Re_B}{1 + Bn} \tag{21.52}$$

From another vantage point, Equation 21.52 is equivalent to using $(\mu_B + \tau_0 d/u_0)$ as the characteristic viscosity scale as opposed to the Bingham plastic viscosity μ_B, which does not account for the fluid yield stress. This idea was initially postulated by Ansley and Smith (1965) and has since been used extensively by numerous workers including Atapattu et al. (1995) for a sphere, Nirmalkar and Chhabra (2014) for a cylinder, etc.

It must be noted that the numerical predictions of drag, given by Equation 21.50, are within 10% or so of the available limited experimental results (Nirmalkar et al., 2013a,b). Also, the pressure forces seem to make up almost 75% of the total drag even at small values of Re^+, which is in stark contrast to the 1/3 contribution in Newtonian fluids. Finally, similar results for Herschel–Bulkley model fluids are also available, but these are very limited in terms of the range of parameters (Nirmalkar et al., 2013b).

21.3.2.4 Heat Transfer

In this section, we follow the same structure as that used in Section 21.3.1.2 in the context of heat transfer from a sphere in power-law fluids. At the outset, it needs to be recognized that additional complexities arise in the case of heat transfer from a sphere in viscoplastic fluids due to their dual nature, that is, blend of fluid-like and solid-like characteristics. Notwithstanding the fact that difficulties are encountered in numerical solutions of the momentum and energy equations, it stands to reason that heat transfer in such systems tends to be problematic in view of the role of conduction, howsoever small it may be in a given situation. This problem becomes even more acute in the free convection regime wherein the buoyancy-induced flow is generally very weak and, in an extreme case, it is unable to overcome the yield stress effects (Vikhansky, 2009, 2010). This section presents an overview of the limited body of knowledge available in this field and begins with the case of forced convection, followed by the free- and mixed-convection regimes.

21.3.2.4.1 Forced Convection Regime There have been essentially only three numerical studies dealing with the forced convection heat transfer from an isothermal sphere (at a higher temperature than the ambient fluid medium) in unconfined Bingham plastic and Herschel–Bulkley model fluids (Nirmalkar et al., 2013a,b) and from an isothermal sphere confined in a cylindrical tube filled with a Bingham plastic medium (Das et al., 2015). In each case, the fluid properties have been assumed to be temperature independent and viscous dissipation effects in the energy equation have been neglected.

For an unconfined isothermal sphere, scaling arguments suggest the average Nusselt number, Nu, to be a function of the Reynolds number (Re_B), Bingham number (Bn), and Prandtl number (Pr) for Bingham plastic fluids, whereas it shows additional dependence on the power-law index (n) in the case of Herschel–Bulkley model fluids together with the modified definitions of the Reynolds number (Re_{HB}), Prandtl number (Pr_{HB}), and Bingham number (Bn_{HB}) or also known as the Oldroyd number (Od). Broadly, for fixed values of the Bingham number and/or of n, the average Nusselt number bears a positive relationship with the Reynolds and Prandtl numbers. This is attributed to the progressive thinning of the thermal boundary layer within the framework of the classical boundary layer theory for simple fluids. On the other hand, for fixed values of the Reynolds and Prandtl numbers, the fluid yielding is limited to a very thin layer close to the submerged sphere. This may increase or decrease the temperature gradient on the surface of the sphere, because the temperature within the unyielded part adjusts itself to maintain the steady-state rate of heat transfer. Under the same conditions and since the boundary layers are known to be thinner in shear-thinning fluids ($n < 1$) than

Table 21.3 Values of $A_o(n)$ in Equation 21.54

		% Error	
n	$A_o(n)$	Average	Maximum
0.2	13.35	11.50	26.03
0.3	10.22	12.27	28.01
0.4	7.870	12.55	28.45
0.5	6.070	12.95	27.50
0.6	4.701	12.97	28.98
0.7	3.977	12.88	28.94
0.8	3.122	13.50	26.92
0.9	2.452	13.97	35.60
1	2.290	15.76	40.54

that in Newtonian fluids, the Nusselt number is correlated positively with the increasing degree of shear-thinning, that is, with decreasing values of power-law index (n). With these considerations, Nirmalkar et al. (2013a) were able to consolidate their numerical values of the average Nusselt number for an unconfined isothermal sphere in Bingham plastic fluids as follows:

$$Nu \simeq 2.29\left(Re^{+} \cdot Pr^{+}\right)^{1/3} \quad \text{for } 10^{-4} \le Re^{+} \le 100 \tag{21.53}$$

where Re^{+} is defined by Equation 21.52 and $Pr^{+} = Pr(1 + Bn)$. Equation 21.53 spans the range: $1 \le Re_B \le 100$; $1 \le Pr \le 100$ and $Bn \le 10^4$. The resulting average and maximum errors are of the order of 15% and 30%, respectively; most of the large error data points relate to $Pr \sim 1$, which is of no great interest in the context of Bingham plastic fluids. Subsequently, this work was extended to Herschel–Bulkley model fluids (Nirmalkar et al., 2013b) over the range $1 \le Re_{HB} \le 100$; $1 \le Pr_{HB} \le 100$; $0.2 \le n \le 1$ and $10^{-3} \le Bn_{HB} \le 10$ and the resulting correlation is of the form

$$Nu \sim A_o(n)\left(Re^{+} \cdot Pr^{+}\right)^{1/3} \tag{21.54}$$

The values of $A_o(n)$ are summarized in Table 21.3, where the increasing values of $A_o(n)$ with the decreasing values of n elucidate varying levels of enhancement in heat transfer in shear-thinning fluids. The modified definitions of Re_{HB}, Pr_{HB} and Bn_{HB} are given as follows:

$$Re_{HB} = Re_{PL}; \quad Pr_{HB} = \frac{Cm}{k}\left(\frac{u_0}{d}\right)^{n-1}$$

$$Bn_{HB} = \frac{\tau_0}{m(V_0/d)^n}; \quad Re^{+} = \frac{Re_{HB}}{1 + Bn_{HB}}$$

$$Pr^{+} = Pr_{HB}\left(1 + Bn_{HB}\right) \tag{21.55}$$

The uncertainty associated with Equation 21.54 is comparable to that of Equation 21.53. The scaling of $Nu \sim Pe^{1/3}$ observed at low Reynolds numbers/high Prandtl numbers in Newtonian fluids is seen to apply here up to as high Reynolds numbers as 100. This is simply due to the creeping flow-like character imparted by the fluid yield stress.

21.3.2.4.2 Free Convection Regime There has not been much research activity on free convection heat transfer in yield stress fluids from a sphere. In a recent numerical study, Nirmalkar et al. (2014b) presented extensive results on the detailed kinematics of laminar free convection from an isothermal sphere submerged in a Bingham plastic medium in the range: $10^2 \le Ra \le 10^6$; $10 \le Pr \le 100$ and $0 \le Bn \le 10^4$. They employed the exponential and biviscous regularization forms of the Bingham constitutive equation to solve the coupled momentum and energy equations. Figure 21.14 elucidates the combined effects of the Bingham number,

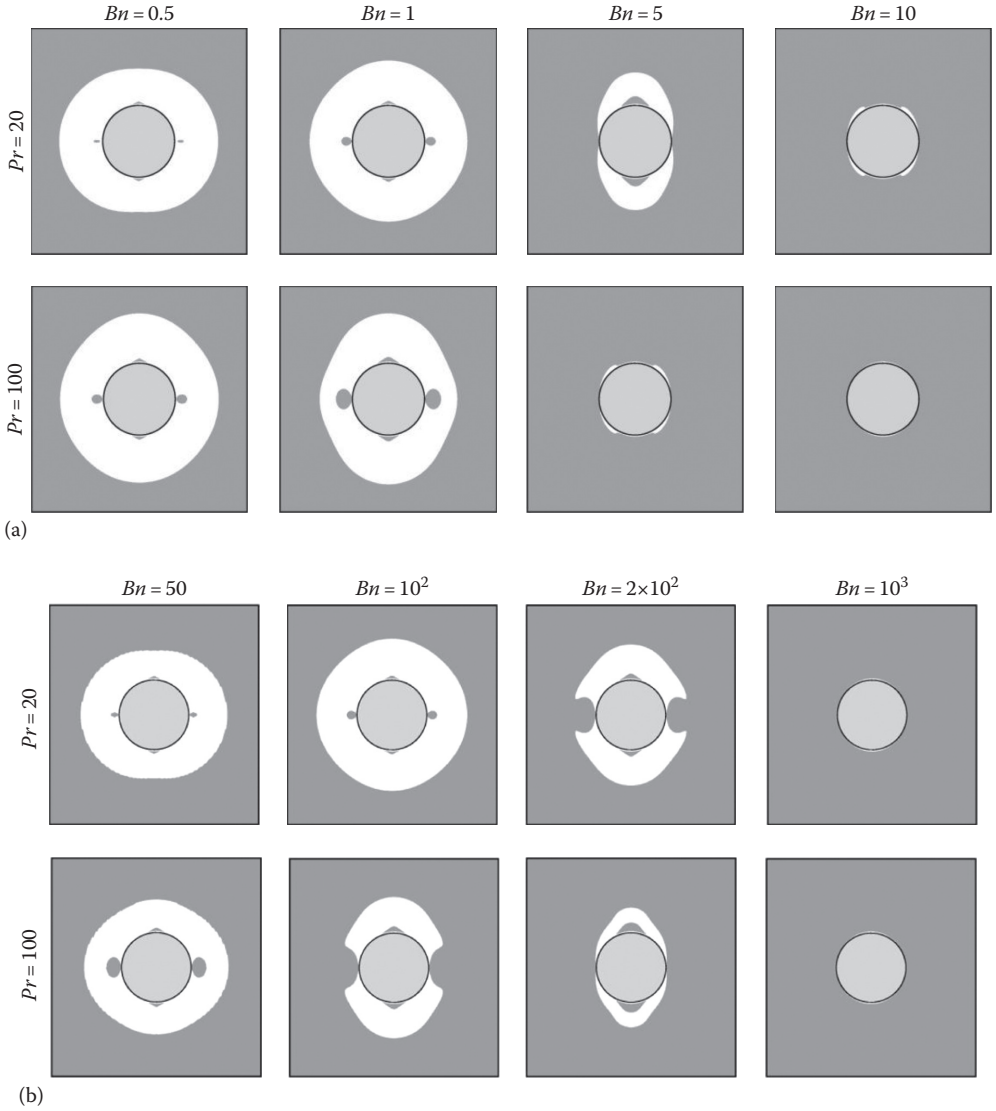


Figure 21.14

Effect of the Bingham number and Prandtl number on the structure of yielded surfaces for a sphere in free-convection regime at (a) $Ra = 10^2$ and (b) $Ra = 10^6$. Shaded parts denote the unyielded regions. (Results are taken from Nirmalkar, N. et al., *Ind. Eng. Chem. Res.*, 53, 17818, 2014b.)

Prandtl number, and Rayleigh number on the morphology of the yielded and unyielded regions around the sphere. The limiting condition of fully plastic limit is seen to approach in all cases. Indeed, for a given value of the Rayleigh number, there exists a limiting Bingham number, Bn_{max}, beyond which no fluid yielding occurs. Naturally, higher the Rayleigh number, the larger is the limiting value of the Bingham number is, that is, Bn_{max}. For instance, for $Ra \leq \sim 1000$, the limiting Bingham number is almost equal to zero. Based on their numerical results, Nirmalkar et al. (2014b) put forward the following expression linking the limiting Bingham number, Bn_{max}, with the other relevant parameters:

$$Bn_{max} = 0.215 + 0.06Ra^{0.65}Pr^{-0.47} \quad \text{for } 10^2 \leq Ra \leq 10^4 \tag{21.56}$$

$$Bn_{max} = 1.04\left(\frac{Ra}{Pr}\right)^{0.35} \quad \text{for } 10^4 < Ra \leq 10^6 \tag{21.57}$$

Conversely, for given values of Ra and Pr, for Bingham number values exceeding the value of Bn_{max}, given by Equations 21.56 and 21.57, the heat transfer occurs solely by conduction and the corresponding Nusselt number is given by the familiar limit: $Nu = 2$. At the other extreme of $Bn \to 0$, the Nusselt number should

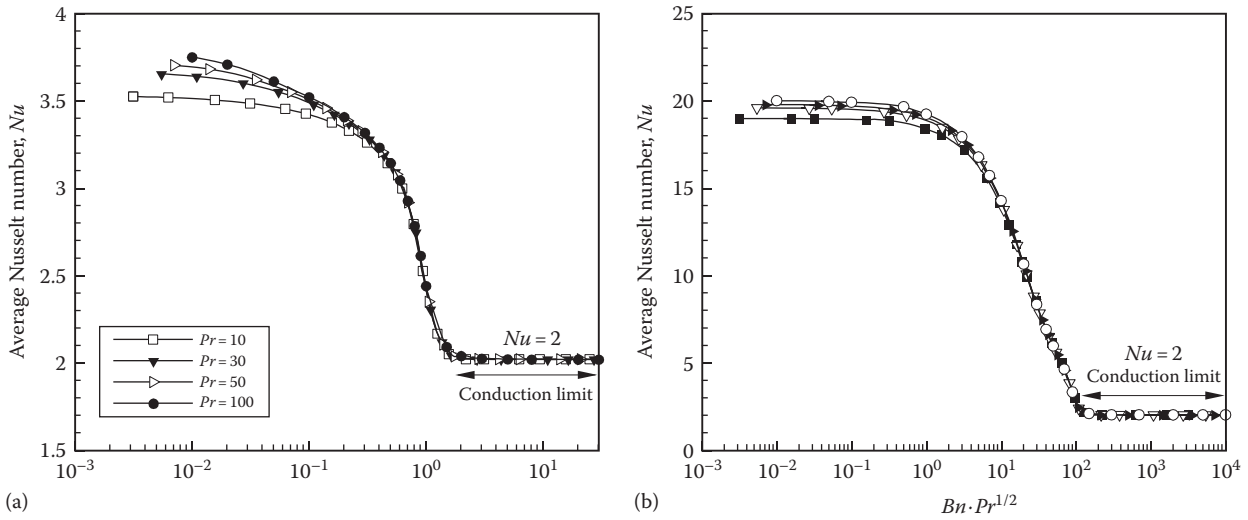


Figure 21.15

Dependence of the average Nusselt number on composite parameter $Bn \cdot Pr^{1/2}$ for: (a) $Ra = 10^2$ and (b) $Ra = 10^6$.

approach the well-known Newtonian limit. Thus, the Nusselt number for a sphere in Bingham plastic fluids progressively decreases from its maximum value in Newtonian fluids ($Bn = 0$) to the conduction limit of $Nu = 2$ with the increasing value of the Bingham number. This behavior is clearly seen in Figure 21.15, wherein the average Nusselt number is plotted against the mixed dimensionless group of $Bn \cdot \sqrt{Pr}$. This group denotes the ratio of the yield stress forces to the buoyancy effects. Except for a minor Prandtl number effect seen at small Bingham numbers (~ close to the Newtonian fluid behavior), the composite parameter $Bn \cdot \sqrt{Pr}$ does collapse the results for different Prandtl numbers to a single curve. Bearing in mind the foregoing factors, Nirmalkar et al. (2014b) have developed the following expressions for the *a priori* estimation of the value of the average Nusselt number in a new application:

$$Nu = 2 \quad \text{for } Bn \geq Bn_{\max} \tag{21.58}$$

$$Nu = 2 + \frac{0.55 Ra^{1/4} \left(1 - \dfrac{Bn}{Bn_{\max}}\right)^{4.66}}{\left(1 + Bn\right)^{0.178}} \quad \text{for } Bn < Bn_{\max} \tag{21.59}$$

The corresponding value of $Bn_{\max}$ is obtained from Equations 21.56 and 21.57 in a new application.

21.3.2.4.3 Mixed-Convection Regime Only Nirmalkar et al. (2014a) have studied the case of buoyancy-assisted mixed-convection heat transfer in Bingham plastic media from an isothermal sphere. Within the framework of the exponential and biviscous regularization schemes, they sought numerical solutions to the coupled momentum and energy equations over the range of conditions as: $0 \leq Ri \leq 2$; $0.1 \leq Re_B \leq 100$, $10 \leq Pr \leq 100$, and, $Bn \leq 10$. As expected, the morphology of the yielded and unyielded regions is found to be a sum of those in the forced and free convection regimes, as can be seen in Figure 21.16, with the limiting behavior being reached at $Bn = 10$ for the strongest flow corresponding to $Re = 100$ and/or $Ri = 2$. A detailed examination of the results suggests the contribution of the free convection to be maximum in Newtonian fluids, that is, $Bn = 0$ and it progressively diminishes with the increasing Bingham number. Following the method of redefining the Reynolds and Prandtl numbers in Section 21.3.1.2 to incorporate the effect of Richardson number, we renormalize the Reynolds and Prandtl numbers to account for the buoyancy induced flow as

$$Re^{\star} = Re_B \left(1 + \sqrt{Ri}\right) \tag{21.60}$$

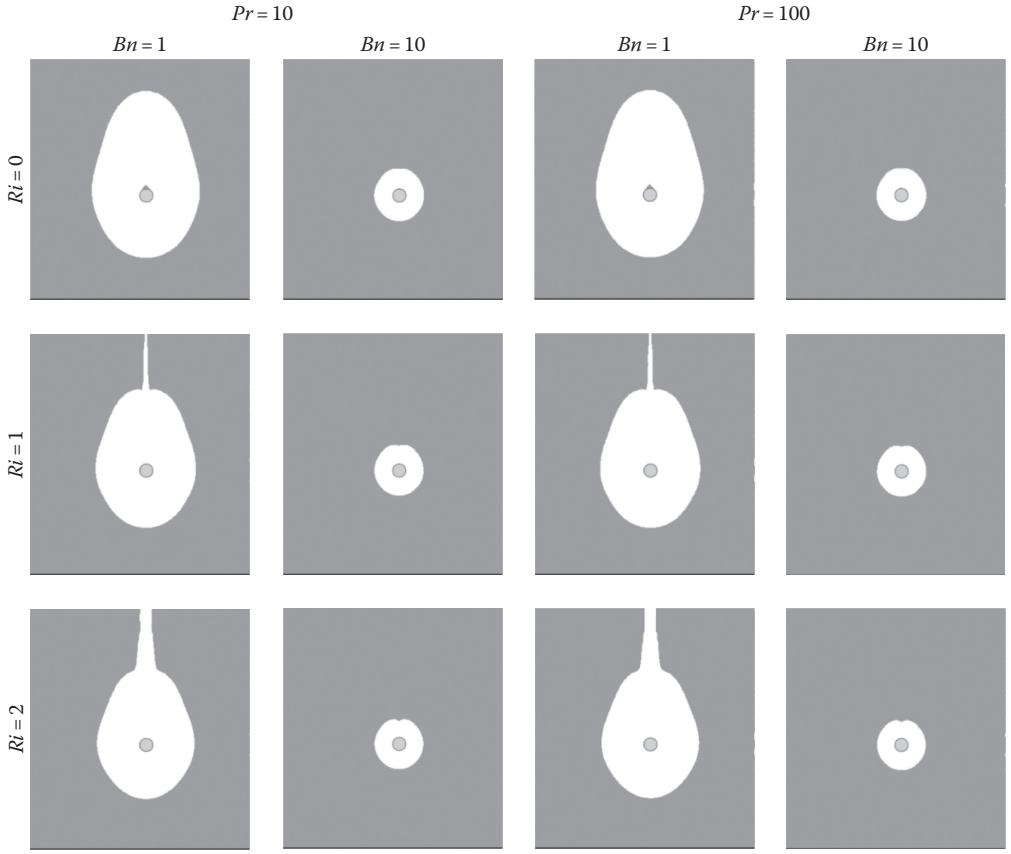


Figure 21.16

Combined effects of the Richardson number, Prandtl number, and Bingham number on the structure of yielded/unyielded regions for aiding-buoyancy, mixed-convection heat transfer from a sphere at Re = 100 (Nirmalkar et al., 2014a). Forced flow is in upward direction. Shaded parts denote the unyielded regions.

$$Bn^{\star} = \frac{Bn}{\left(1+\sqrt{Ri}\right)} \tag{21.61}$$

Naturally, this is tantamount to simply adding the forced convection and buoyancy-induced flow currents. These definitions can be further modified to incorporate the effect of Bingham number as

$$Re_{\text{mod}} = \frac{Re^{\star}}{\left(1+Bn^{\star}\right)} \tag{21.62}$$

$$Pr^{+} = Pr\left(1+Bn^{\star}\right) \tag{21.63}$$

One can, thus, postulate the average Nusselt number for a sphere in the mixed convection to be a function of Re_{mod} and Pr^{+}. Based on their numerical results, Nirmalkar et al. (2014a) developed the following predictive expression:

$$Nu = 1.25\left(Re_{mod}\cdot Pr^{+}\right)^{1/3} \tag{21.64}$$

Equation 21.64 incorporates the known limiting cases of Newtonian fluids (Bn = 0) or pure forced convection (Ri = 0). It predicts the average Nusselt number with an average error of 10%.

21.3.2.5 Wall Effects

In addition to the complications described in Section 21.3.1.3 due to the confinement, the situation gets accentuated further in the context of the translation of a sphere in viscoplastic fluids. This stems from the fact that the fluid yielding is restricted to a region, which at most extends up to three-to-four times the sphere radius, especially in the lateral direction. Thus, if such a yielded region does not reach the physical wall, the sphere does not see the confining boundary and there should be no extra retardation experienced by the settling sphere. This conjecture is borne out by the preliminary experimental results of Atapattu et al. (1986, 1990).

The first detailed systematic numerical study on wall effects on a sphere undergoing steady translation axially in a tube filled with Bingham plastic media is due to Blackery and Mitsoulis (1997). This is, however, restricted to the creeping regime only, as is their subsequent and less extensive study of wall effects in Herschel–Bulkley model fluids (Beaulne and Mitsoulis, 1997). In particular, Blackery and Mitsoulis (1997) outlined expressions for the hydrodynamic drag force of a sphere as the function of blockage ratio, Ξ, ($\Xi \leq 0.5$) and Bingham number ($Bn \leq 1000$) of the following form:

$$X = X_N + a_1(Bn)^{a_2} \tag{21.65}$$

where

X is defined as $(C_D Re_B/24)$

X_N is its value in Newtonian fluids

Thus, the factor X accounts for both effects, that is, blockage and Bingham number and accordingly, X_N is the value of X at $Bn = 0$ (i.e., in a Newtonian fluid). One can also show that $X_N = (1/f_w) = k_{wall}$ where k_{wall} is given by Equation 1.160. These values, along with that of a_1 and a_2, are summarized in Table 21.4.

In a recent work, Das et al. (2015) extended these results to finite Reynolds numbers ($Re_B \leq 100$) to elucidate the effect of blockage on the drag and heat transfer of a sphere. Using the definitions of the modified Reynolds number, Re^+ (Equation 21.52), they put forward the following expressions for calculating the drag coefficient:

$$C_D = \frac{24}{Re^+}\left(1 + 0.32\left(Re^+\right)^{0.31}\right)(1+\Xi)^{2.8} \quad \text{for } Bn \leq 1 \tag{21.66}$$

$$C_D = \frac{24}{Re^+}\left(1 + 0.75\left(Re^+\right)^{0.19}\right)(1+\Xi)^{0.05} \quad \text{for } 1 < Bn \leq 100 \tag{21.67}$$

The smaller exponent of the $(1 + \Xi)$ term in the second equation testifies to the diminishing importance of blockage with the increasing Bingham number. This is very likely due to the fact that fluid-like yielded region shrinks with the increasing Bingham number and these regions terminate well before reaching the physical wall, as can be seen in Figure 21.17. The limited results of Yu and Wachs (2007) for $\Xi = 0.25$ are in line with these equations. Similarly, Das et al. (2015) collapsed their heat transfer data ($1 \leq Pr \leq 100$) using the modified definitions of the Reynolds and Prandtl numbers as

$$Nu = 1.76\left(Re^+ \cdot Pr^+\right)^{1/3} \quad \text{for } Bn \leq 1 \tag{21.68}$$

Table 21.4 Values of Constants in Equation 21.65

Ξ	X_N	a_1	a_2
0	1	2.93	0.83
0.02	1.05	2.59	0.86
0.1	1.26	2.33	0.88
0.125	1.35	2.28	0.89
0.25	1.98	1.92	0.92
0.5	5.94	1.63	0.95

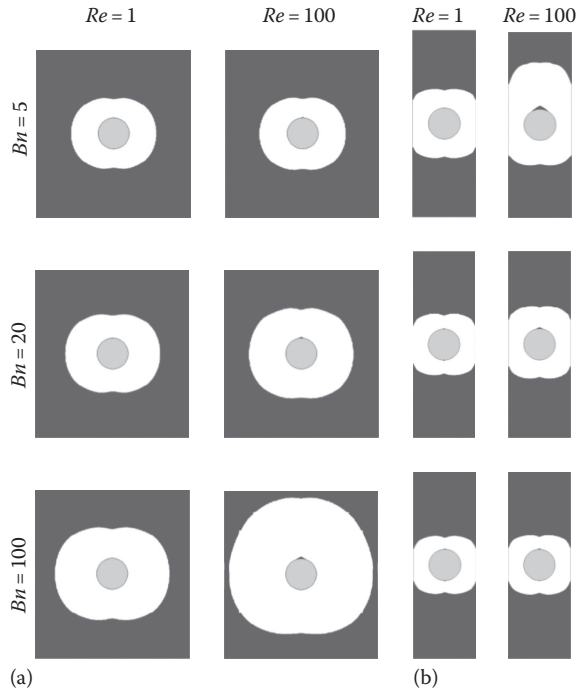


Figure 21.17

Morphology of yielded/unyielded regions for a sphere confined in Bingham plastic fluids from Das et al. (2015): (a) Ξ = 0.2 and (b) Ξ = 0.5. Flow is in upward direction. Shaded parts denote the unyielded regions.

and

$$Nu = 2.11\left(Re^{+} \cdot Pr^{+}\right)^{1/3} \quad \text{for } 1 < Bn \leq 100 \tag{21.69}$$

Though these global correlations incorporate the effect of Ξ implicitly, the resulting deviations can be as high as 40%. Equations 21.68 and 21.69 can be written in terms of a constant a_0 as

$$Nu = a_0\left(Re^{+} \cdot Pr^{+}\right)^{1/3} \tag{21.70}$$

Now a_0 becomes a function of Ξ, as summarized in Table 21.5. Though the maximum error is still of the order of 30%, Equation 21.70 does offer some improvement over the global correlations given by Equations 21.68 and 21.69.

Before concluding this subsection, and notwithstanding the scarcity of results in this field, it appears that the Nusselt number scales as $Pe^{1/3}$ with a suitably modified definition of the Peclet number and the effect of the blockage on drag only shows up if the yielded regions intersect with the physical boundary. Also, the heat transfer is influenced less by wall effects compared to the corresponding hydrodynamic drag on a sphere.

21.3.3 Nonspherical Particles

It is known that most solid particles encountered in real life process engineering applications are nonspherical, regular- and/or irregular-shaped particles. In view of the fact that each nonspherical particle is unique, the developments in this field have not only been rather slow, but these also lack universal appeal, as noted in Section 1.4.3.7. Also, it needs to be recognized here that the shape of a particle exerts much more influence on the drag of a single particle than that in the case of an assemblage of particles such as that encountered in concentrated suspensions and slurries, fixed- and fluidized bed systems, porous media, etc. In the latter case, the interparticle interactions far outweigh the effect of particle shape (Chhabra, 2006). In contrast to the unique case of a sphere, at least three attributes are required to account for the effect of shape

Table 21.5 Value of a_0 in Equation 21.70

		% Error		
Ξ	a_0	Mean	Maximum	Range of *Bn*
0	1.73	12.3	29.3	$Bn \leq 1$
0.1	1.74	12.6	29.4	
0.2	1.73	11.4	28.2	
0.3	1.72	7.6	21.4	
0.4	1.73	4.5	11.6	
0.5	1.89	3.6	9.6	
0	2.17	9.1	22.2	$1<Bn \leq 100$
0.1	2.16	9.1	21.2	
0.2	2.14	8.1	22.9	
0.3	2.07	7.5	23.7	
0.4	2.00	6.5	25.6	
0.5	2.13	6.5	22	

on the drag of a *regular*-shaped object. Firstly, a measure of its size is needed. The most common approach is to employ the so-called equal volume sphere diameter, d_V, defined by Equation 1.146. Second, some measure of the particle shape is needed. Several possible measures of this aspect are available in the literature; for example, see the extensive reviews by Kasper (1982), Hoerner (1965), Clift et al. (1978), Michaelides (2006), and Loth (2008), among others. The simplest and possibly also the most widely used parameter is the so-called sphericity, ψ, defined by Equation 1.147. It is simply the ratio of the surface area of the equal volume sphere to that of the actual particle and therefore, the sphericity is always smaller than unity for nonspherical particles. The fact that the surface area of irregular particles cannot be readily calculated or measured immediately reveals the deficiency of this approach. Besides, both these measures are static in nature and do not account for the actual orientation of the particle during its settling. For instance, for a cylinder of given diameter and length, both d_V and ψ have fixed values, yet it is a common experience that the terminal settling velocity (or hydrodynamic drag) of such a cylinder is strongly influenced by its orientation. Therefore, a parameter, which adequately quantifies this aspect, is also required. There is no simple scheme available to account for the orientation in the calculation of the drag of a nonspherical particle. One approach, which has gained some acceptance in the literature, is by characterizing the orientation of a settling particle by defining a circle of diameter, d_N, whose area is equal to the projected area of the particle (Ganser, 1993, Rajitha et al., 2006). It is worthwhile to add here that even the use of these three measures, namely, d_V, ψ, and d_N, is not entirely foolproof because a cone settling with its apex pointing upward or downward will exhibit different drag characteristics, whereas the values of d_V, ψ, and d_N are identical in these two configurations! A thorough review of the corresponding body of knowledge for Newtonian fluids can be found in Chhabra et al. (1999) and Concha (2014).

21.3.3.1 Power-Law Fluids

Currently available methodologies for treating the drag behavior of nonspherical particles in both Newtonian and power-law fluids fall into two distinct categories. The first approach is aimed at developing drag expressions for a fixed shape and orientation via the numerical solutions of the field equations and/or tow tank experiments, as reviewed by Chhabra (2006). Within the context of power-law fluids, numerical drag values are available only for prolates and oblates (Tripathi et al., 1994, Tripathi and Chhabra, 1995), hemispheres (Sasmal et al., 2013), and long cylinders of circular, elliptical, square, triangular, and semicircular cross sections (e.g., see, Chhabra, 2011). We limit our discussion only to spheroids and hemispheres. Sasmal et al. (2013) solved the momentum equations describing the steady axisymmetric flow over a hemisphere (with its curved surface oriented upstream) and put forward the following expression for the drag coefficient:

$$C_D = \frac{28}{Re_{PL}}\left(1 + 0.064nRe_{PL}^{-0.205n+1.02}\right) \tag{21.71}$$

Over the range of conditions as $1 \leq Re_{PL} \leq 150$ and $0.1 \leq n \leq 1$, Equation 21.71 approximates their numerical data with an average error of ~10%. The diameter of the hemisphere is used as the linear dimension in the definition of Re_{PL}. Sasmal et al. (2013) validated their numerics by using the experimental drag data for hemispheres falling in Newtonian media (Wang et al., 2009). In contrast, the analogous results of Tripathi et al. (1994) and Tripathi and Chhabra (1995) for spheroids are available only in tabular form over the range of conditions of $0.01 \leq Re_{PL} \leq 100$; $0.4 \leq n \leq 1.8$ and aspect ratios of 0.2, 0.5, 1, 2, 5. Broadly, for a given shape, the drag was enhanced over and above its Newtonian value on account of the shear-thinning behavior ($n < 1$). This effect diminishes with the increasing Reynolds number, due to the growing importance of inertial effects. However, the shape of the spheroid exerted significant influence on the drag force. Some of these predictions have been corroborated by the independent numerical studies of Reddy and Kishore (2014) who also reported scant results on wall effects ($0.2 \leq \Xi \leq 0.5$) for particle aspect ratio in the range 0.5–2.5.

It is worthwhile to add here that this family of studies and expressions developed therefrom work well for a specific shape and/or orientation, but extrapolations to other shapes and orientations are clearly not justified. Also, it is unlikely that the numerical results will ever become available for all possible shapes or orientations or flow conditions (laminar, turbulent flow, etc.). Therefore, such numerical studies must be supplemented by experimental results, which are required not only for the purpose of validation of the numerical predictions but also to encompass the range of Reynolds numbers, which is beyond the reach of the numerical solutions, at least as of now.

The second approach to the prediction of drag on nonspherical particles in power-law fluids hinges on the use of the conventional Reynolds number – drag coefficient coordinates together with a set of parameters capturing the deviation from spherical shape, that is, ψ and d_N, etc. to account for the shape and orientation of the particle. The scant results on the drag of scores of shapes including cylinders, cones, prisms, cubes, thin disks and plates, rectangles, oblates, and prolates in power-law fluids have been reviewed by Rajitha et al. (2006) and Chhabra (2006). Based on the available experimental and numerical results, Rajitha et al. (2006) developed the following drag expression for both spherical and nonspherical rigid particles:

$$C_D = C_{Do} + \chi C_{D_\infty} C_{Do}^{2A_o} B_o \left\{ \frac{6X(n)b_o}{6X(n)b_o + C_{Do}} \right\}^{A_o} + C_{D_\infty} \left\{ \frac{6X(n)b_o}{6X(n)b_o + 128C_{Do}} \right\}^{11/12} \tag{21.72}$$

In Equation 21.72, C_{Do} and C_{D_∞} are the values of the drag coefficient in the Stokesian and Newtonian regimes, respectively. The effects of shape and orientation are embodied in the single parameter χ, which is defined as

$$\chi = \frac{4}{\psi}\left(\frac{d_V}{d_N}\right)^2 \tag{21.73}$$

In physical terms, it denotes the ratio of the surface area of the particle to its projected area. Clearly, for a sphere, $\chi = 4$, and this is the minimum value of this parameter. The function $X(n)$ is given by Equation 21.20; the other constants appearing in Equation 21.72 are given as follows:

$$b_o = \exp\{3(C - \ln 6)\} \tag{21.74}$$

$$B_o = \left(\frac{3-C}{6C}\right)\exp\left[3\left\{\frac{3-C}{6C}\right\}\ln 3\right] \tag{21.75}$$

$$A_o = \frac{11\sqrt{6}}{48}\left[1 - \exp\left\{\left(\frac{3-C}{2C}\right)^2 \ln\frac{\sqrt{6}-1}{\sqrt{6}}\right\}\right] \tag{21.76}$$

$$C = \left[6^{(1-n)/2} \cdot X(n)\right]^{1/n+1} \tag{21.77}$$

Regarding the value of C_{D_∞} in Newtonian fluids, the widely accepted values of the limiting drag coefficient C_{D_∞} are 0.44 for a sphere and very close to 1 for an infinitely long cylinder oriented transverse to the flow. However, neither experimental nor numerical results are available to extract the corresponding values for power-law fluids for either of these shapes. On the other hand, it is readily acknowledged that the role of non-Newtonian viscosity weakens with the increasing Reynolds number. Thus, in the absence of any definitive information, Rajitha et al. (2006) suggested the use of the same value of C_{D_∞} as that in Newtonian fluids, that is, $C_{D_\infty} = 0.44$ for a sphere in power-law fluids, at least as a first approximation. The efficacy of Equation 21.72 was tested against an extensive data set spanning wide ranges of conditions as $0.33 \leq \psi \leq 1$ and $10^{-6} \leq Re_{PL} \leq 400$ by Rajitha et al. (2006) and subsequently by Agarwal and Chhabra (2007) for scores of particles of regular shape.

21.3.3.1.1 Heat Transfer Numerical results for forced convection heat transfer in power-law fluids from isothermal spheroids have been reported by Reddy and Kishore (2014), Srinivas and Ramesh (2014) and Sreenivasulu et al. (2014). Though both Sreenivasulu et al. (2014) and Reddy and Kishore (2014) have put forward correlations for the average Nusselt number, these are considered too tentative to be included here. Sasmal et al. (2013) analyzed the forced convection heat transfer from a hemisphere in power-law fluids and they correlated their heat transfer data as follows:

For an isothermal hemisphere:

$$Nu = 1.80\left(Re_{PL} \cdot Pr_{PL}\right)^{1/3}\left(\frac{3n+1}{4n}\right)^{0.21} \tag{21.78}$$

For an isoflux hemisphere:

$$Nu = 1.85\left(Re_{PL} \cdot Pr_{PL}\right)^{1/3}\left(\frac{3n+1}{4n}\right)^{0.24} \tag{21.79}$$

The mean uncertainty in using these equations is in the range 13%–14% over the following ranges of conditions as follows: $1 \leq Re_{PL} \leq 150$; $0.1 \leq n \leq 1$ and $0.72 \leq Pr_{PL} \leq 100$. Given the complexities of the system, this is considered accurate.

21.3.3.2 Bingham Plastic Fluids

Limited information is available about the drag and heat transfer aspects for spheroids and hemispheres in viscoplastic fluids. As noted earlier, the key distinguishing feature of the external flows of such fluids is the simultaneous coexistence of fluid-like and solid-like regions in the flow domain, as noted in Section 21.3.2.2 in the context of the steady translation of a sphere. The forced flow over a spheroid has been studied numerically by Gupta and Chhabra (2014). Using the axis perpendicular to the flow as the characteristic linear dimension in the definitions for the definitions of the Reynolds number, Bingham number, and Nusselt number, they put forward the following expression for drag coefficient:

$$C_D = \frac{24}{Re^+}\left(1 + b_o\left(Re^+\right)^{c_o}\right) \tag{21.80}$$

where the modified Re^+ is still given by Equation 21.48. The resulting values of b_o and c_o are summarized in Table 21.6.

Equation 21.80 consolidates the numerical values of drag coefficient with a mean deviation of about 12% over the range of conditions as: $1 \leq Re_B \leq 100$, $0 \leq Bn \leq 100$, and $0.2 \leq e \leq 5$. They also studied the corresponding forced convection heat transfer problem for an isothermal spheroid for Prandtl number values ranging from 1 to 100 and developed the following expression for the surface average Nusselt number:

$$Nu = a_o\left(Re^+ \cdot Pr^+\right)^{1/3} \tag{21.81}$$

Table 21.6 Values of b_o and c_o in Equation 21.80

Aspect Ratio, e	b_o	c_o
0.2	0.34	0.26
0.5	0.42	0.19
1	0.60	0.13
2	1.04	0.09
5	2.4	0.06

Table 21.7 Value of a_o in Equation 21.81

e	$Re^+ < 0.5$	$Re^+ \geq 0.5$
0.2	2.55	2.20
0.5	2.47	2.25
1	2.18	2.02
2	1.75	1.66
5	1.27	1.20

where

$$Pr^+ = Pr\left(1 + Bn\right).$$

Because of the large number of dimensionless parameters, a single value of the fitted constant a_o could not be obtained to fit the entire data set with acceptable levels of accuracy. Therefore, Gupta and Chhabra (2014) divided the data into two regions as $Re^+ < 0.5$ and $Re^+ \geq 0.5$. The resulting values of a_o are reported in Table 21.7.

The mean deviation associated with Equation 21.81 is ~7% at low Reynolds numbers and/or large Bingham numbers ($Re^+ < 0.5$) and ~14% at high Reynolds numbers and/or low Bingham numbers ($Re^+ \geq 0.5$).

The case of buoyancy assisted mixed convection from a hemisphere in Bingham plastic fluids in the steady axisymmetric regime with the curved surface of the hemisphere oriented in the upstream direction has been studied recently by Nalluri et al. (2015). They have discussed in detail the interplay between the forced- and buoyancy-induced flow and the corresponding kinematics of the flow in terms of the yielded and unyielded regions, and temperature profiles. Their values of the mean Nusselt number shows the following dependence on the pertinent dimensionless groups:

$$Nu = 2.255 + 0.91\left(Re_{mod}\right)^{0.32}\left(Pr^+\right)^{0.42} \tag{21.82}$$

The constant term of 2.255 denotes the conduction limit for this configuration, which is reached for large values of the Bingham number ($\rightarrow \infty$). This is equivalent to $Re_{mod} \rightarrow 0$. The modified Prandtl number is given as $Pr^+ = Pr(1 + Bn^*)$, whereas the modified Reynolds number, Re_{mod}, incorporates the effects of both the fluid yield stress and of the buoyancy-induced flow as

$$Re_{mod} = \frac{Re_B\left(1 + \sqrt{Ri}\right)}{\left(1 + Bn^*\right)} \tag{21.83}$$

where

$$Bn^* = \frac{Bn}{1 + \sqrt{Ri}} \tag{21.84}$$

Equation 21.82 is applicable in the range: $1 \leq Re_B \leq 100$; $1 \leq Pr \leq 100$; $0 \leq Bn \leq 100$ and $0 \leq Ri \leq 10$. The analogous case of forced convection heat transfer from a hemisphere (constant wall temperature and constant heat flux condition) with its curved surface facing upward or downward in Bingham plastic fluids has recently been investigated (Patel et al., 2015). In addition, similar results are also available for two-dimensional cylinders of circular (Bose et al., 2015) and elliptical (Patel and Chhabra, 2016) cross sections.

This section is concluded by noting that scant experimental results are available on the drag behavior of thin plates and disks, cones, cylinders, etc. in viscoplastic fluids and these have been reviewed extensively by Chhabra (2006) and more recently by Ahonguio et al. (2015). Earlier works (Valentik and Whitmore, 1965, Pazwash and Robertson, 1975, etc.) are based on inadequate rheological characterization of the test media used, whereas the major thrust of some of the recent studies is on extracting the value of the fluid yield stress from the velocity-force data in the limit of diminishing velocities. Overall, this field remains relatively less explored as compared to its Newtonian and power-law fluids counterparts.

21.3.4 Effect of Viscoelasticity

Ever since the seminal paper of Leslie and Tanner (1961) dealing with the slow translation of a sphere in Oldroyd model fluids, much has been written about the effect of fluid viscoelasticity on the detailed kinematics and macroscopic parameters like drag and Nusselt number for a sphere, albeit the bulk of the information deals with the fluid mechanical aspects. This problem occupied the center stage for both the experimentalists as well as numerical researchers for well over 10 years; for example, see Walters and Tanner (1992), McKinley (2002) and Chhabra (2006) for state-of-the-art reviews. On the other hand, under appropriate kinematic and rheological conditions, viscoelasticity gives rise to a myriad of intriguing phenomena including: "negative wake"; bouncing and oscillations of sphere; "velocity overshoot"; "stress-induced migration"; "drag reduction or enhancement", etc. Some of these effects have been explained by the currently available numerical and phenomenological considerations, albeit the emerging picture is neither as cohesive nor as conclusive as that available for Newtonian fluids (Chapter 1), or in time-independent viscous fluids (earlier sections in this chapter). Much of the literature (numerical) examines the influence of fluid elasticity on the drag of a sphere in the absence of shear-thinning viscosity, which predicts no or little reduction (~5%–10%) from the Stokes value at low Weissenberg numbers and beyond a critical value of the Weissenberg number, drag augmentation may occur. In contrast, experimental results in model elastic fluids exhibit drag reduction of the order of 25% or drag enhancement of up to 200% with reference to the Stokes value. Similarly, many workers have performed terminal velocity measurements in test fluids exhibiting both viscoelasticity as well as shear-dependent viscosity. Overall, one may say that the drag on a sphere is determined primarily by the viscosity behavior of the fluid, though fluid elasticity seems to modify the detailed flow field, especially in the rear of the sphere. Similarly, limited available studies seem to suggest that both the blockage effects on drag and the rate of heat transfer are suppressed in viscoelastic fluids (Chhabra, 2006). Interested readers should refer to the state-of-the-art reviews and the references therein for further details (Walters and Tanner, 1992, Mckinley, 2002, Chhabra, 2006).

21.4 Fluid Spheres

Additional difficulties arise while studying the rise or fall of bubbles and drops (fluid particles) due to their deformability even in Newtonian fluids, as noted in Section 1.4.3.8, both from experimental and theoretical standpoints, especially in the case of drops made up of a liquid of finite viscosity. In this case, the momentum equations for both inner (dispersed) and outer (continuous) phase must be solved simultaneously. These equations are coupled via the boundary conditions at the interface, that is, continuity of velocity vector and stress tensor. Thus, the momentum is transmitted across the interface, thereby setting up circulation inside the drop also. The case of a bubble can be seen as the limiting behavior of a fluid sphere when the ratio of the viscosity of the dispersed phase to that of the continuous phase, λ, is vanishingly small, that is, $\lambda \to 0$. At the other extreme is the case of a rigid sphere, which is characterized by large values of $\lambda \to \infty$, as seen in Section 1.4.3.8. While it is not possible to provide generalizations, but typically $\lambda \leq 0.01$ offers a good approximation for bubbles and $\lambda \geq 100-500$ corresponds to the case of a rigid sphere in many situations as far as the calculation of the hydrodynamic drag (terminal rise or fall velocity) is concerned. When the motion occurs under the influence of gravity, depending upon the relative magnitudes of viscous, inertial, and interfacial tension forces, fluid spheres (particularly bubbles) exhibit a variety of axisymmetric shapes up to moderate Reynolds numbers, which transit to three-dimensional shapes at still higher Reynolds numbers, as described in detail by Clift et al. (1978), Crowe et al. (1998), and Michaelides (2006) in the context of Newtonian fluids. Therefore, in a given situation, the shape of a fluid particle is continuously evolving and must be calculated at each stage by employing the normal stress balance at the interface to infer the local radius of curvature. Finally, depending upon the nature and concentration of the surface-active contaminants, a part or the whole of the interface may be immobilized. Under such conditions, a part of the surface of the fluid particle exhibits a mobile interface, while the remaining portion behaves like a rigid particle.

The role of the aforementioned factors gets accentuated when either the dispersed or continuous or both phases exhibit non-Newtonian characteristics. It is, therefore, not at all surprising that not only the progress in the field of bubble and drop phenomena in non-Newtonian fluids has been rather slow, but the current body of information is also nowhere near as extensive or definitive as that in Newtonian media; for example, see Chapter 1 or the excellent treaties of Clift et al. (1978), Sirignano (1999), Zapryanov and Tabakova (1999), and Michaelides (2006). We begin our discussion with the case of a bubble in power-law and yield stress fluids in the next section.

21.4.1 Bubbles ($\lambda \to 0$)

Much of the developments in this field are based on *a priori* assumption of the spherical shape of the bubble. In the creeping region, the early developments are based either on the application of a regular perturbation approach (Hirose and Moo-Young, 1969, Bhavaraju et al., 1978, Kawase and Ulbrecht, 1981) or on the application of stress and velocity variational principles (Nakano and Tien, 1968, Mohan, 1974, Gummalam and Chhabra, 1987). All these predictions pertain to a clean (free from impurities) and spherical bubble in an infinite sea of power-law or Bingham plastic fluid in the Stokes regime. By analogy with the case of a rigid sphere, Equation 21.18, the most celebrated result of Hirose and Moo-Young (1969) for a bubble is given by

$$X(n) = (2)^n (3)^{\frac{n-3}{2}} \left\{ \frac{13 + 4n - 8n^2}{(2n+1)(n+2)} \right\} \tag{21.85}$$

Naturally, in the limit of Newtonian fluid behavior, that is, $n = 1$, Equation 21.85 predicts the value of the drag correction factor $X(n) = 2/3$, which when combined with Equation 21.18 yields the expected result of $C_D = 16/Re$ for a spherical bubble in a clean Newtonian fluid in the creeping regime. In view of the approximations inherent in the analysis leading to Equation 21.85, it is expected to hold only for mildly non-Newtonian fluid behavior, that is, the value of power-law index (n) not too far away from its value of $n = 1$ corresponding to the Newtonian fluid behavior.

There has not been much numerical activity at finite Reynolds numbers for the predictions of drag on a rising bubble in power-law fluids except for the work of Dhole et al. (2007a). However, many investigators (Nakano and Tien, 1967, 1970, Ohta et al., 2003, 2005 2006, Kishore et al., 2007a) have solved the governing equations for a drop from which one can recover the case of a spherical bubble by setting $\lambda = 0$. These predictions are found to be broadly in agreement with the available scant experimental results. Thus, for instance, Dhole et al. (2007a) correlated their numerical drag data for spherical bubbles in clean power-law fluids as

$$C_D = \frac{16}{Re_{PL}} \left(1 + 0.27 Re_{PL}^{\frac{1.41n}{0.335n+3.76}} \right) \tag{21.86}$$

Equation 21.86 encompasses the range of conditions as follows: $0.5 \leq n \leq 2$ and $5 \leq Re_{PL} \leq 500$. These results are also in line with the other numerical predictions. The most severe weakness of such results is the assumption of the fixed spherical shape of the bubbles even at as high Reynolds number as 500, which is at odds with the variety of bubble shapes observed experimentally (Chhabra, 2006).

Even less is known about the rising bubbles in viscoplastic fluids. An early and very approximate perturbation result due to Bhavaraju et al. (1978) predicts an increase in drag coefficient in the creeping flow regime for a spherical bubble as

$$X = \frac{C_D \cdot Re_B}{24} = 1 + 1.61 Bn \tag{21.87}$$

Naturally, this analysis assumes *a priori* that the motive force exceeds the value of the force due to the yield stress of the fluid. Equation 21.87 strictly applies in the limit of $Bn \to 0$.

The issue of the critical conditions, whether a bubble of certain size in a yield-stress fluid will ascend or not, has been investigated by Stein and Buggisch (2000), Dubash and Frigaard (2004, 2007), Singh and Denn (2008), and Tsamopoulos et al. (2008). Stein and Buggisch (2000) studied the effect of pulsation in order to mobilize the entrapped bubbles in a Bingham fluid. Both their analysis and experimental results

revealed that the larger bubbles ascended faster than the smaller ones at similar pressure amplitudes. The other studies listed have attempted to obtain the limiting value of Y, defined by Equation 21.41, thereby denoting the motion/no motion transition under the effect of gravity and in the limit of creeping flow regime. Unlike in the case of a solid sphere, the shape of a freely rising bubble is influenced in an interactive fashion by a large number of variables (density, viscosity, surface tension, size), which, in turn, determines the rise velocity that influences the drag and hence the shape (Terasaka and Tsuge, 2001). For highly deformed bubbles with long tails or bullet shaped (Sikorski et al., 2009), further confusion results as some workers use an equal volume bubble diameter, while others have advocated the use of the maximum diameter normal to the direction of flow, etc. Naturally, the conversion from one to another form is not possible without making additional assumptions regarding the shape of the bubble. In the limit of small Bond number (large surface tension), the most reliable estimate of Y appears to be ~0.0715, above which the bubble will remain suspended (Tsamopoulos et al., 2008). On the other hand, using the notion of strain minimization and stress maximization, Dubash and Frigaard (2004) obtained a value of $Y \geq$ ~0.29, which turns out to be a sufficient but not necessary condition for a bubble to move or not in a Bingham plastic fluid. For a two-dimensional circular bubble, Singh and Denn (2008) reported a value of $Y \sim 0.0835$, which is slightly larger than the corresponding value for a solid cylinder of $Y_G \sim 0.06$. Using a slightly different definition of $Y_m (\equiv \pi\tau_0 d_{\max}^2 / 2\rho_f g V_b)$, Sikorski et al. (2009) reported that the bubble motion is possible only for $Y_m \leq 0.53$. While limited results are available on the shape and drag of a bubble as functions of the Bond number, Archimedes number for Bingham fluids (Tsamopoulos et al., 2008) and for Herschel–Bulkley fluids (Dimakopoulos et al., 2013), no predictive correlations have yet been developed, which can be used in a new application.

In contrast to the preceding numerical/analytical studies on bubble motion in power-law and yield stress fluids, there exists an equally extensive experimental body of knowledge, which has been reviewed in Chhabra (2006). Indeed, a great variety of intriguing effects including velocity jump, first reported by Astarita and Apuzzo (1965), negative wake (Hassager, 1979, Bisgaard and Hassager, 1982, Bisgaard, 1983) and a wide variety of shapes (Dekee and Chhabra, 1988, Dekee et al., 1990), etc. have been documented in the literature associated with the motion of bubbles in non-Newtonian fluids. Still diverse shapes of bubbles are encountered in yield-stress fluids (Vasil'chenko and Potapov, 1996, Sikorski et al., 2009). Naturally, all of these effects influence in varying proportions of measure the rise velocity, shape, and drag of a bubble, but some of these phenomena have not yet been explained completely. This coupled with the poor reproducibility of experimental results in this field have led to numerous inconsistencies and conflicting trends in the literature.

Based on the use of the so-called horizontal bubble diameter, $d_{\max}$, (in the calculation of the projected area normal to the flow), Dewsbury et al. (1999) put forward the following correlation for drag on bubbles in inelastic power-law fluids:

$$C_D = \frac{16}{Re_{PL}}\left(1 + 0.173 Re_{PL}^{0.66}\right) + \frac{0.413}{1 + 16300 Re_{PL}^{-1.09}} \tag{21.88}$$

Equation 21.88 encompasses the range of power-law index, $0.16 \leq n \leq 1$ and of the bubble Reynolds number, $Re_{PL} \leq$ ~1000.

21.4.1.1 Mass Transfer

The corresponding problem of mass transfer from a spherical bubble rising in power-law fluids has been studied for the simplest case of a fixed size spherical bubble with negligible mass transfer resistance inside the bubble. In the limiting case of the creeping flow and high Schmidt number (thin boundary layer approximation), the shear-thinning fluid behavior enhances the rate of gas–liquid mass transfer that is consistent with the limited experimental results on single bubbles available in the literature (Barnett et al., 1966, Moo-Young et al., 1970). In the large Peclet number limit, the Sherwood number for a bubble is given by the following expression (Hirose and Moo-Young, 1969):

$$Sh = 0.65 Pe^{1/2} \left\{ \frac{-4n^2 + 6n + 1}{2n + 1} \right\}^{1/2} \tag{21.89}$$

The corresponding expression for mass transfer from a bubble in Bingham plastic fluids is given as follows (Bhavaraju et al., 1978):

$$Sh = 0.65 Pe^{1/2} \left(1 + 0.25 Bn\right)^{1/2} \tag{21.90}$$

Equation 21.90 is valid in the limit of $Bn \to 0$.

At finite Reynolds numbers, over the range of narrow conditions $5 \leq Re_{PL} \leq 100$, $1 \leq Sc \leq 1000$, and $0.7 \leq n \leq 2$, Dhole et al. (2007b) reported only a weak influence of the power-law behavior and one could safely use the corresponding correlations available for Newtonian continuous phase without incurring errors greater than 10%.

21.4.2 Drops

Unlike in the case of a gas bubble ($\lambda = 0$) and a rigid sphere ($\lambda \to \infty$), the internal and external flow fields are coupled via the interfacial conditions for a fluid sphere (of a liquid of finite viscosity) undergoing steady translation in another immiscible liquid medium. Two situations are possible in this case: liquid sphere settling in a liquid continuous medium and a liquid sphere falling in air. The former is relevant to the production of emulsions and polymer blends, the latter is pertinent to the production of aerial sprays. In either event, reliable knowledge of the hydrodynamic force experienced by the fluid sphere is required in numerous process engineering applications. In the absence of surface-active agents and for spherical particles, the drag force gradually increases as the value of λ is progressively increased from $\lambda = 0$ (bubble) to $\lambda \to \infty$ (solid sphere) at the same value of the Reynolds number, as seen in Chapter 1. This trend is also seen for a Newtonian fluid sphere undergoing a steady translation in a quiescent power-law medium. The early approximate results based on the velocity and stress variational principles for a variety of ambient media including power-law (Mohan, 1974), Ellis model (Mohan and Venkateswarlu, 1974), and Carreau viscosity model (Chhabra and Dhingra, 1986, Jarzebski and Malinowski, 1987) confirm this expectation in the creeping flow regime. In this case, the so-called drag correction factor, $X(n)$, is not only a function of the power-law index for power-law fluids and of the additional non-Newtonian parameters depending upon the choice of a specific viscosity model (Chhabra, 2006) but also of the viscosity ratio, λ, which itself needs to be modified to account for the shear-dependent viscosity of the continuous or the dispersed or of both phases. It is thus not possible to develop an analytical expression for drag force even in the limit $Re \to 0$, which can rival the celebrated result of Hadamard and Rybczynski, Equation 1.96 in Section 1.3.4.1 for a Newtonian ambient fluid. For a fixed value of λ, the hydrodynamic drag is augmented with the decreasing value of the power-law index, that is, the increasing extent of shear-thinning behavior. However, the degree of augmentation itself increases with the increasing value of λ, that is, as one transits from a gaseous sphere to a solid sphere.

The effect of finite Reynolds numbers on a Newtonian droplet settling in quiescent power-law media has been studied less extensively (Nakano and Tien, 1970, Kishore et al., 2007a). Kishore et al. (2007a) numerically solved the inner and outer flow field equations for a fluid sphere ($0.1 \leq \lambda \leq 50$) undergoing steady translation in a power-law fluid ($0.6 \leq n \leq 1.6$) over a wide range of Reynolds number (of the continuous phase) as $5 \leq Re_{PL} \leq 500$ with the implicit assumption of small values of the Bond number, that is, large surface tension effects, which ensure the shape to be spherical over the range of Reynolds number of interest. While they reported a variety of results on surface viscosity and vorticity, their drag results can be consolidated by the following expression over the aforementioned ranges of conditions of λ, Re_{PL} and n:

$$C_D = \left(\frac{2^{n+1}}{\lambda + 1.85}\right)\left[1.55\lambda\left\{\frac{6.063}{Re_{PL}^{1.36}} + \frac{1}{Re_{PL}^{0.38}}\right\} + \frac{6.2}{Re_{PL}^{0.78}}\right] \tag{21.91}$$

The average error associated with the use of Equation 21.91 is of the order of 13%, which, in view of the large number of influencing parameters (λ, Re_{PL}, n), is considered to be acceptable. In a subsequent study (Kishore et al., 2007b), they also studied convective mass transfer from a Newtonian fluid sphere (with negligible internal resistance) in power-law fluids and put forward the following expression for the average Sherwood number, Sh:

$$Sh = \left\{\frac{1.19(n+1)}{1.7n + 1.5}\right\} Re_{PL}^{0.53} Sc^{0.42} \lambda^{-0.14} + \left(\frac{n+1}{1.5n}\right)\left(Re_{PL} \cdot Sc\right)^{-0.15} \lambda^{0.25} \tag{21.92}$$

This equation extends over the same range of conditions as Equation 21.91 together with $1 \leq Sc \leq 1000$. With the increasing value of λ, the value of Sherwood number progressively decreases as one transits from a shear free bubble ($\lambda = 0$) to a rigid sphere ($\lambda \to \infty$). In the limit of $n \to 1$, the predictions of Equations 21.91 and 21.92 are consistent with the corresponding results in Newtonian fluids; for example, see Feng and Michaelides (2001a,b) and Juncu (1999).

In contrast, there has been very little activity in seeking solutions of the fluid equations describing the steady translation of a Newtonian fluid sphere in fluids with yield stress (Bingham plastics or Herschel-Bulkley fluids). Thus, for instance, Potapov et al. (2006) have examined shapes of single droplets and interactions between a pair of drops settling at the axis of a cylindrical tube filled with Herschel–Bulkley fluids. They found that, depending upon the values of the Capillary number and Bingham number, a single fluid sphere exhibits a long transient region before reaching a quasisteady settling velocity. There exists a critical Bingham number up to which a fluid sphere remains suspended (without moving) in the medium due to the overwhelming yield stress effects. On the other hand, two drops arranged in series seem to undergo shape changes, depending upon the value of the Capillary number, and the two may merge and/or retain their identity, depending upon the initial separation between the two and/or the extent of the yielded region created by the leading drop in its rear, as also confirmed by subsequent experiments (Holenberg et al., 2011). Subsequently, Lavrenteva et al. (2009) have experimentally examined the wall effects on a single fluid sphere falling in a tube. Consistent with the previous observations for the solid sphere, a falling drop "sees" the wall only when the fluid-like yielded region extends up to the solid boundary. Interactions between two and three droplets in various geometric configurations falling simultaneous in Bingham plastic fluids have also been studied numerically by Singh and Denn (2008).

21.4.3 Effect of Viscoelasticity

While it is known that the viscoelasticity of the continuous phase influences the shapes and deformation of both bubbles and drops in a significant way and their coalescence behavior at detailed and gross levels (Chhabra, 2006), little definitive information is available on the prediction of engineering parameters, like drag coefficient and Sherwood number in viscoelastic fluids. It is widely believed that mass transfer deteriorates in viscoelastic liquids with reference to that in Newtonian and purely inelastic liquids. The currently available information is really too scant and/or tentative that it is not yet possible to develop reliable prediction methods for these engineering parameters in a new application.

21.4.4 Wall Effects

It is useful to recall that in the case of a rigid sphere, the effect of confining walls on drag and heat transfer can be assessed in an unambiguous fashion because the particle shape remains fixed. The corresponding situation with bubbles and drops is more complex due to their tendency for deformation, which may be accentuated with the increasing extent of blockage. Thus, the confining boundaries exert varying levels of influence both on the settling (or rising) velocity of a fluid particle as well as on the shape that itself determines the velocity. Most studies in this field pertain to the conditions when the walls have very little influence on the shape *per se*. In Newtonian liquids, this is the case when $\Xi \leq \sim 0.6$ or so (Clift et al., 1978). While there is a reasonable body of numerical results available on wall effects on fluid spheres in Newtonian liquids filled in cylindrical tubes (Hartholt et al., 1994, Higdon and Muldowney, 1995, Wham et al., 1997, Krishna et al., 1999, etc.) spanning up to moderate Reynolds numbers, only Chhabra and Bangun (1997) have reported some experimental results on Newtonian droplets settling in power-law solutions ($0.52 \leq n \leq 0.87$) and up to about $\Xi \leq \sim 0.45$ but limited to the Stokes regime only. However, as the maximum value of λ in their experiments was only about ~0.07, their fluid spheres behaved more like gas bubbles rather than droplets. Under these conditions, the terminal settling velocity has a linear dependence on Ξ, and this is slightly weaker than that predicted by the available numerical results. A subsequent experimental study concerning wall effects on rising bubbles in power-law fluids suggests the wall effects to be less severe in these systems than that in Newtonian liquids (Dziubinski et al., 2001).

21.5 Other Effects

The discussion so far has been confined to the simplest class of the problems, namely, the steady translation of an isolated rigid or fluid sphere in confined and unconfined media mainly in power-law and Bingham plastic fluids. Analogous results based on the use of other viscosity models like Carreau, Ellis,

and Sutterby, etc. are qualitatively similar and have been compiled by Chhabra (2006). Undoubtedly, this body of knowledge provides a solid foundation to build upon and explore more complex and realistic flows, including interactions between multiple rigid and fluid particles. The former are relevant to the development of constitutive equations for suspensions and/or to model the flow in porous structures. A rational understanding of similar interactions in swarms of bubbles/drops is germane to develop models for coalescence in chemical reactors, multiphase flow in pipes, such as that covered here in Chapter 4 when the liquid phase is Newtonian. The corresponding discussion for the simultaneous flow of a gas and non-Newtonian liquid in pipes can be found in Chhabra and Richardson (2008). Additional effects have been observed depending upon the flow field a sphere is subjected to, for example, shearing and elongational. This gives rise to the migration of rigid particles away or toward the solid wall, depending upon whether the fluid is viscoelastic or not and/or the fluid inertia. This body of literature has been reviewed by Leal (1980) and more recently (but tersely) by Chhabra (2006). Scant results are also available on the transient settling of a sphere in power-law fluids, which enable the estimation of the time/distance required to reach the terminal fall condition (Bagchi and Chhabra, 1991). The influence of dispersed phase rheology on the hydrodynamic behavior of a single drop and their swarms undergoing steady translation in another immiscible non-Newtonian phase has been studied by Tripathi and Chhabra (1992) and Kishore et al. (2008).

21.6 Concluding Remarks and Future Directions

Based on the foregoing detailed discussion, the state of the art of non-Newtonian multiphase flow systems can be summarized as:

1. For the case of steady translation of a rigid sphere in power-law model fluids, adequate information is now available on the hydrodynamic drag exerted on the sphere. Based on a combination of numerical predictions and experimental results, the drag curve akin to the standard drag curve for Newtonian fluids is now available up to about the Reynolds number values of 1,000. As expected, the role of power-law index progressively diminishes with the increasing Reynolds number. In the Stokes regime, the drag is augmented by up to ~40% in power-law fluids under appropriate conditions.

   The effect of confining walls is seen to be qualitatively similar to that for Newtonian fluids except that the wall effects are less severe in shear-thinning fluids due to the rapid spatial decay of the velocity field. This suggests that one can employ shorter domains (both in computations and experiments) than that required for Newtonian fluids otherwise under identical conditions. However, very little is known about the wake phenomena (length and volume, angle of separation, etc.), flow regimes, and transition from one regime to another. Limited results available on heat transfer from a sphere in power-law fluids encompassing forced-, free-, and aiding-buoyancy mixed-convection regimes suggest varying levels of enhancement in Nusselt number over and above that in Newtonian fluids. Suffice it to add here that the numerical predictions and experimental results are mutually consistent, at least qualitatively.
2. The analogous body of knowledge for the steady translation of a sphere in yield stress fluids is less extensive than that in power-law fluids. While it is possible to make reasonable estimates of the hydrodynamic drag on a sphere, much confusion exists concerning the conditions under which a sphere will move or not in such fluids.

   Heat transfer results show a positive influence of the both Reynolds and Prandtl numbers but that of the Bingham (yield stress) number is modulated by the regime of heat transfer, that is, forced, free, or mixed convection. For instance, the Nusselt number gradually decreases from its maximum value in Newtonian fluids to the conduction limit with the increasing Bingham number in the free-convection regime. This is in stark contrast to the positive influence of the Bingham number on the average Nusselt number in the forced-convection regime.
3. Only a few numerical results for axisymmetric nonspherical shapes like hemisphere, spheroids, and circular disks are available for power-law and Bingham plastic fluids. An extensive database has accrued over the years based on experimental drag results for cylinders, cones, prisms, disks, and cubes in power-law fluids. This has led to the development of a predictive empirical correlation for drag on nonspherical rigid particles in power-law fluids, which permits *a priori*

estimation of drag on a regular shaped nonspherical particle settling in power-law fluids with a precision of ±25%.

4. For the case of fluid spheres, the available literature deals only with the most elementary situation of a spherical fluid particle and that too mainly in the absence of surface tension effects. It is accurate to say that the currently available information is more of exploratory nature. The predictive formulae lack universal applicability and these certainly must not be extrapolated beyond the range of their validity.

This chapter is concluded by making two pertinent observations: firstly, the current body of information for the types of model flows considered here is nowhere near as extensive or coherent as that described in this book in the context of Newtonian media. Secondly, considerable scope exists for both numerics and experiments in this little-known branch of non-Newtonian fluid mechanics to explore, discover, and model various aspects of the dispersed flows encountered in a range of industrial applications.

Nomenclature

$A(n)$	function of power-law index, n, Equation 21.22 (dimensionless)
$A_o(n)$	function of power-law index, n, Equation 21.54 (dimensionless)
a	sphere radius (m)
Bn	Bingham number ($\tau_0^B d/\mu_B u_0$) (dimensionless)
Bn_{HB}	Bingham or Oldroyd number $\left[=\left(\tau_0^H/m\right)\left(d/u_0\right)^n\right]$ (dimensionless)
$Bn_{\max}$	maximum value of Bingham number (dimensionless)
C_D	drag coefficient = ($8F_D/\pi d^2\rho_f u_0^2$) (dimensionless)
C_p	thermal heat capacity of fluid (J/kg K)
$c(n)$	function of power-law index, n, Equation 21.26 (dimensionless)
D	tube diameter (m)
De	Deborah number (dimensionless), Equation 21.14
D_m	molecular diffusivity (m^2/s)
d	sphere diameter (m)
d_N	diameter of a circle with equivalent projected area (m)
d_V	equal volume sphere diameter (m)
e	aspect ratio of a spheroid (dimensionless)
F_D	hydrodynamic drag (N)
f_w	wall correction factor (dimensionless), Equation 21.34
f_{wo}	value of f_w in the Stokes regime (dimensionless)
$f_{w\infty}$	value of f_w in the limit of infinite Reynolds number (dimensionless)
Gr	Grashof number (dimensionless)
$\vec{g}$	acceleration due to gravity (m/s^2)
h	convective heat transfer coefficient ($W/m^2 \cdot K$)
h_m	convective mass transfer coefficient (m/s)
k	thermal conductivity of fluid (W/m K)
M	regularization parameter, Equation 21.44 (dimensionless)
m	power-law consistency coefficient ($Pa \cdot s^n$)
n	power-law index (dimensionless)
Nu	Nusselt number = (hd/k) (dimensionless)
Pe	Peclet number ($=Re \cdot Pr$) (dimensionless)
$Pe^\star$	modified Peclet number ($=Re^\star \cdot Pr^\star$) (dimensionless)
Pr	Prandtl number ($=C_p\mu/k$) (dimensionless)
$Pr^\star$	modified Prandtl number, Equation 21.32 (dimensionless)
Pr^+	modified Prandtl number, Equation 21.55 (dimensionless)
Pr_{PL}	Prandtl number for a power-law fluid $\left[=\left(C_p/mk\right)\left(d/u_0\right)^{n-1}\right]$ (dimensionless)
p	pressure (Pa)
Ra	Rayleigh number ($=Gr \cdot Pr$) (dimensionless)
Re_B	Bingham Reynolds number ($=\rho_f u_0 d/\mu_B$) (dimensionless)
Re_{PL}	power-law Reynolds number for ($\rho_f u_0^{2-n} d^n/m$) (dimensionless)
$Re^\star$	modified Reynolds number, Equation 21.31 (dimensionless)

Re^+ modified Reynolds number, Equation 21.52 (dimensionless)
Re_{mod} modified Reynolds number, Equation 21.62 (dimensionless)
Sc Schmidt number (dimensionless)
Sh Sherwood number ($=h_m d/D_m$) (dimensionless)
t_0 rheological constant, Equation 21.7 (s)
$\vec{u}$ velocity vector (m/s)
u_0 free stream or terminal settling velocity (m/s)
u_m measured velocity of a sphere in a confined fluid (m/s)
u_∞ terminal settling velocity in an unconfined fluid (m/s)
X drag correction factor, Equation 21.65 (dimensionless)
X_N drag correction due to wall effects in Newtonian fluids, Equation 21.65 (dimensionless)
$X(n)$ drag correction factor in power-law fluids, Equation 21.17 (dimensionless)
$X_m(n)$ mass transfer correction factor in power-law fluids (dimensionless)
Y dimensionless parameter, Equation 21.41 (dimensionless)

Greek Alphabets

$\vec{\vec{\dot{\gamma}}}$ rate of strain tensor (s^{-1})
$\dot{\vec{\gamma}}_{yx}$ xy component of $\vec{\vec{\dot{\gamma}}}$ (s^{-1})
δ regularization parameter, Equation 21.47 (s^{-1})
θ_s angle of separation (degree)
Δ function, Equation 21.33 (dimensionless)
λ ratio of viscosity of dispersed phase to continuous phase (dimensionless)
λ_f fluid characteristic time (s)
λ_p process characteristic time (s)
μ Newtonian or apparent viscosity (Pa · s)
μ_B Bingham plastic viscosity (Pa · s)
μ_C Casson fluid viscosity (Pa · s)
μ_y yielding viscosity (Pa · s)
μ_0 zero-shear viscosity (Pa · s)
μ_∞ infinite-shear viscosity (Pa · s)
Ξ diameter ratio (d/D) (dimensionless)
ρ_f fluid density (kg/m^3)
ρ_s density of sphere (kg/m^3)
$\vec{\vec{\tau}}$ extra stress tensor (Pa)
$\vec{\tau}_{yx}$ xy component of $\vec{\vec{\tau}}$ (Pa)
$\vec{\tau}_0$ yield stress (Pa)
$\vec{\tau}_0^B$ Bingham yield stress (Pa)
$\vec{\tau}_0^C$ Casson yield stress (Pa)
$\vec{\tau}_0^H$ Herschel–Bulkley yield stress (Pa)
ψ sphericity (dimensionless)

References

Acharya, A., Mashelkar, R.A., and Ulbrecht, J., Flow of inelastic and viscoelastic fluids past a sphere, *Rheol. Acta*, 15, 454–470, 1976.

Acrivos, A., A theoretical analysis of laminar natural convection heat transfer to non-Newtonian fluids, *AIChE J.*, 6, 584–590, 1960.

Acrivos, A., On the combined effect of forced and free convection heat transfer in laminar boundary layer flows, *Chem. Eng. Sci.*, 21, 343–352, 1966.

Acrivos, A., Shah, M.J., and Petersen, E.E., Momentum and heat transfer in laminar boundary layer flows of non-Newtonian fluids past external surfaces, *AIChE J.*, 6, 312–317, 1960.

Adachi, K., Yoshioka, N., and Yamamoto, K., On non-Newtonian flow past a sphere, *Chem. Eng. Sci.*, 28, 2033–2043, 1973.

Agarwal, N., and Chhabra, R.P., Settling velocity of cubes in Newtonian and power-law fluids, *Powder Technology*, 178, 17–21, 2007.
Ahonguio, F., Jossic, L., and Magnin, A., Motion and stability of cones in a yield stress fluid, *AIChE J.*, 61, 709–717, 2015.
Amato, W.S., and Tien, C., Free convection heat transfer from isothermal spheres in polymer solutions, *Int. J. Heat Mass Transfer*, 19, 1257–1266, 1976.
Ansley, R.W., and Smith, T.N., Motion of spherical particles in a Bingham plastic, *AlChE J.*, 13, 1193–1196, 1965.
Astarita, G., and Apuzzo, G., Motion of gas bubbles in non-Newtonian liquids, *AIChE J.*, 11, 815–820, 1965.
Atapattu, D.D., Chhabra, R.P., Tiu, C., and Uhlherr, P.H.T., The effect of cylindrical boundaries for spheres falling in fluids having a yield stress, in *Proceedings of the Ninth Australasian Fluid Mechanics Conference*, Auckland, New Zealand, 1986, pp. 584–587.
Atapattu, D.D., Chhabra, R.P., and Uhlherr, P.H.T., Wall effect for spheres falling at small Reynolds number in a viscoplastic medium, *J. Non-Newt. Fluid Mech.*, 38, 31–42, 1990.
Atapattu, D.D., Chhabra, R.P., and Uhlherr, P.H.T., Creeping sphere motion in Herschel-Bulkley fluids: Flow field and drag, *J. Non-Newt. Fluid Mech.*, 59, 245–265, 1995.
Bagchi, A., and Chhabra, R.P., Accelerating motion of spherical particles in power-law type non-Newtonian fluids, *Powder Technol.*, 68, 85–90, 1991.
Balaramakrishna, P.V., and Chhabra, R.P., Sedimentation of a sphere along the axis of a long square duct filled with non-Newtonian Liquids, *Can. J. Chem. Eng.*, 70, 803–807, 1992.
Balmforth, N.J., Frigaard, I.A., and Ovarlez, G., Yielding to stress: Recent developments in viscoplastic fluid mechanics, *Ann. Rev. Fluid Mech.*, 46, 121–146, 2014.
Barnes, H.A., Shear-thickening ("dilatancy") in suspensions of non-aggregating solid particles dispersed in Newtonian fluids, *J. Rheol.*, 33, 329–366, 1989.
Barnes, H.A., Thixotropy—A review, *J. Non-Newt. Fluid Mech.*, 70, 1–33, 1997.
Barnes, H.A., The yield stress—A review or 'παντα ρει'—everything flows? *J. Non-Newt. Fluid Mech.*, 81, 133–178, 1999.
Barnes, H.A., Hutton, J.F., and Walters, K., *An Introduction to Rheology*, Elsevier, Amsterdam, The Netherlands, 1989.
Barnes, H.A., and Walters, K., The yield stress myth? *Rheol. Acta*, 24, 323–326, 1985.
Barnett, S.M., Humphery, A.E., and Litt, M., Bubble motion and mass transfer in non-Newtonian fluids, *AIChE J.*, 12, 253–259, 1966.
Beaulne, M., and Mitsoulis, E., Creeping motion of a sphere in tubes filled with Herschel–Bulkley fluids, *J. Non-Newt. Fluid Mech.*, 72, 55–71, 1997.
Bercovier, M., and Engleman, M., A finite-element method for incompressible non-Newtonian flows, *J. Comput. Phys.*, 36, 313–326, 1980.
Beris, A.N., Tsamopoulos, J.A., Armstrong, R.C., and Brown, R.A., Creeping motion of a sphere through a Bingham plastic, *J. Fluid Mech.*, 158, 219–244, 1985.
Bhavaraju, S.M., Mashelkar, R.A., and Blanch, H.W., Bubble motion and mass transfer in non-Newtonian fluids, *AIChE J.*, 24, 1063–1070, 1978.
Bird, R.B., Experimental tests of generalized Newtonian fluid models containing a zero shear viscosity and a characteristic time, *Can. J. Chem. Eng.*, 43, 161–168, 1965.
Bird, R.B., Armstrong, R.C., and Hassager, O., *Dynamics of Polymeric Liquids: Fluid Dynamics*, 2nd edn., Wiley, New York, Vol. 1, 1987.
Bird, R.B., Dai, G.C., and Yarusso, B.J., The rheology and flow of viscoplastic materials, *Rev. Chem. Eng.*, 1, 1–70, 1983.
Bird, R.B., Stewart, W.E., and Lightfoot, E.N., *Transport Phenomena*, 2nd edn., Wiley, New York, 2002.
Bisgaard, C., Velocity fields around spheres and bubbles investigated by laser Doppler anemometry, *J. Non-Newt. Fluid Mech.*, 12, 283–302, 1983.
Bisgaard, C., and Hassager, O., An experimental investigation of velocity fields around spheres and bubbles moving in non-Newtonian liquids, *Rheol. Acta*, 21, 537–539, 1982.
Bizzell, G.D., and Slattery, J.C., Non-Newtonian boundary-layer flow, *Chem. Eng. Sci.*, 17, 777–782, 1962.
Blackery, J., and Mitsoulis, E., Creeping motion of a sphere in tubes filled with a Bingham plastic material, *J. Non-Newt. Fluid Mech.*, 70, 59–77, 1997.
Boger, D.V., Demonstration of upper and lower Newtonian fluid behaviour in a pseudoplastic fluid, *Nature*, 265, 126–128, 1977.
Boger, D.V., and Walters, K., *Rheological Phenomena in Focus*, Elsevier, Amsterdam, The Netherlands, 1992.

Bose, A., Nirmalkar, N., and Chhabra, R.P., Effect of aiding-buoyancy on mixed-convection from a heated cylinder in Bingham plastic fluids, *J. Non-Newt. Fluid Mech*., 220, 3–21, 2015.
Carreau, P.J., Dekee, D., and Chhabra, R.P., *Rheology of Polymeric Systems: Principles and Applications,* Hanser, New York, 1997.
Carreau, P.J., Rheological equations from molecular network theories, *Trans. Soc. Rheol*., 16, 99–127, 1972.
Chen, T.S., and Mucoglu, A., Analysis of mixed forced and free convection about a sphere, *Int. J. Heat Mass Transfer*, 20, 867–875, 1977.
Chen, T.S., and Mucoglu, A., Mixed convection about a sphere with uniform surface heat flux, *J. Heat Transfer*, 100, 542–544, 1978.
Chhabra, R.P., Fluid flow, heat and mass transfer in non-Newtonian fluids: Multiphase systems, *Adv. Heat Transfer*, 23, 187–278, 1993.
Chhabra, R.P., Wall effects on free settling velocity of non-spherical particles in viscous media in cylindrical tubes, *Powder Technol*., 85, 83–90, 1995.
Chhabra, R.P., Wall effects on terminal velocity of non-spherical particles in non-Newtonian polymer solutions, *Powder Technol*., 88, 39–44, 1996.
Chhabra, R.P., Heat and mass transfer in rheologically complex systems, in D. Siginer, D. DeKee, and R.P. Chhabra (Eds.), *Advances in Flow and Rheology of Non-Newtonian Fluids*, Elsevier, Amsterdam, the Netherlands, 1999, chap. 39.
Chhabra, R.P., Wall effects on spheres falling axially in cylindrical tubes, in D. DeKee and R.P. Chhabra (Eds.), *Transport Processes in Bubbles, Drops and Particles*, 2nd edn., Taylor & Francis, New York, 2002, Chapter 13.
Chhabra, R.P., Fluid mechanics and heat transfer with non-Newtonian liquids in mechanically agitated vessels, *Adv. Heat Transfer*, 37, 77–178, 2003.
Chhabra, R.P., *Bubbles, Drops and Particles in Non-Newtonian Fluids*, 2nd edn., CRC Press, Boca Raton, FL, 2006.
Chhabra, R.P., Fluid flow and heat transfer from circular and non-circular cylinders submerged in non-Newtonian liquids, *Adv. Heat Transfer*, 43, 289–417, 2011.
Chhabra, R.P., Agarwal, L., and Sinha, N.K., Drag on non-spherical particles: An evaluation of available methods, *Powder Technol*., 101, 288–297, 1999.
Chhabra, R.P., and Bangun, J., Wall effects on terminal velocity of small drops in Newtonian and non-Newtonian Fluids, *Can. J. Chem. Eng.*, 75, 817–822, 1997.
Chhabra, R.P., Comiti, J., and Machac, I., Flow of non-Newtonian fluids in fixed and fluidized beds: A review, *Chem. Eng. Sci*., 56, 1–27, 2001.
Chhabra, R.P., and Dhingra, S.C., Creeping motion of a Carreau fluid past a Newtonian fluid sphere, *Can. J. Chem. Eng*., 64, 897–905, 1986 Also see *ibid*, 66, 176, 1988.
Chhabra, R.P., and Richardson, J.F., *Non-Newtonian Flow and Applied Rheology*, 2nd edn., Butterworth-Heinemann, Oxford, U.K., 2008.
Chhabra, R.P., Tiu, C., and Uhlherr, P.H.T., Wall effect for sphere motion in inelastic non-Newtonian fluids, in *Proceedings of the Sixth Australasian Hydraulics Fluid Mechanics Conference*, Adelaide, South Australia, Australia, 1977, pp. 435–438.
Chhabra, R.P., and Uhlherr, P.H.T., Wall effect for high Reynolds number motion of spheres in shear-thinning fluids, *Chem. Eng. Commun*., 5, 115–123, 1980.
Clift, R., Grace, J.R., and Weber, M.E., *Bubbles, Drops and Particles*, Academic Press, New York, 1978.
Concha, F.A., *Solid-Liquid Separation in the Mining Industry*, Springer, Berlin, Germany, 2014.
Crochet, M.J., Davies, A.R., and Walters, K., *Numerical Simulation of Non-Newtonian Flow*, Elsevier, Amsterdam, the Netherlands, 1984, chap. 9.
Cross, M.M., Rheology of non-Newtonian fluids: A new flow equation for pseudoplastic systems, *J. Colloid Sci*., 20, 417–437, 1965.
Crowe, C., Sommerfeld, M., and Tsuji, Y., *Multiphase Flows with Droplets and Bubbles*, CRC Press, Boca Raton, FL, 1998.
Das, P.K., Gupta, A.K., Nirmalkar, N., and Chhabra, R.P., Effect of confinement on forced convection from a heated sphere in Bingham plastic fluids, *Korea-Aust. Rheol. J*., 27, 75–94, 2015.
Deglo De Besses, B., Magnin, A., and Jay, P., Sphere drag in a viscoplastic fluid, *AIChE J.*, 50, 2627–2629, 2004.
DeKee, D., and Chhabra, R.P., A photographic study of shapes of bubbles and coalescence in non-Newtonian polymer solutions, *Rheol. Acta*, 27, 656–660, 1988.

DeKee, D., Chhabra, R.P., and Dajan, A., Motion and coalescence of gas bubbles in non-Newtonian polymer solutions, *J. Non-Newt. Fluid Mech*., 37, 1–18, 1990.
Denn, M.M., Fifty years of non-Newtonian fluid mechanics, *AIChE J*., 50, 2335–2345, 2004.
Dewsbury, K.H., Karamanev, D.G., and Margaritis, A., Hydrodynamic characteristics of free rise of light solid particles and gas bubbles in non-Newtonian liquids, *Chem. Eng. Sci*., 54, 4825–4830, 1999.
Dhole, S.D., Chhabra, R.P., and Eswaran, V., Flow of power law fluids past a sphere at intermediate Reynolds numbers, *Ind. Eng. Chem. Res*.,45, 4773–4781, 2006a.
Dhole, S.D., Chhabra, R.P., and Eswaran, V., Forced convection heat transfer from a sphere to non-Newtonian power law fluids, *AIChE J*., 52, 3658–3667, 2006b.
Dhole, S.D., Chhabra, R.P., and Eswaran, V., Drag of a spherical bubble rising in power law fluids at intermediate Reynolds numbers, *Ind. Eng. Chem. Res*., 46, 939–946, 2007a.
Dhole, S.D., Chhabra, R.P., and Eswaran, V., Mass transfer from a spherical bubble rising in power-law fluids at intermediate Reynolds numbers, *Int. Commun. Heat Mass Transfer*, 34, 971–978, 2007b.
Dimakopoulos, Y., Pavlidis, M., and Tsamopoulos, J., Steady bubble rise in Herschel-Bulkley fluids and comparison of predictions via the Augmented Lagrangian Method with those via the Papanastasiou model, *J. Non-Newt. Fluid Mech*., 200, 34–51, 2013.
Dubash, N., and Frigaard, I., Conditions for static bubbles in viscoplastic fluids, *Phys. Fluids*, 16, 4319–4330, 2004.
Dubash, N., and Frigaard, I.A., Propagation and stopping of air bubbles in carbopol solutions, *J. Non-Newt. Fluid Mech*., 142, 123–134, 2007.
Dziubinski, M., Orczykowska, M., Kiljanski, T., and Budzynski, P., Wall effects for bubbles flow in Newtonian and non-Newtonian liquids, *Inzynieria Chemiczna I Proceswa*, 22, 403, 2001.
Faxen, H., Die bewegung einer starren kugel langs der achse eines mit zaher flussigkeit gefullten rohres, *Ask. Mat. Arstron. Fys*., 17, 1–27, 1923.
Feng, Z.-G., and Michaelides, E.E., Drag coefficients of viscous spheres at intermediate and high Reynolds numbers, *ASME J. Fluids Eng*., 123, 841–849, 2001a.
Feng, Z.-G., and Michaelides, E.E., Heat and mass transfer coefficients of viscous spheres, *Int. J. Heat Mass Transfer*, 44, 4445–4454, 2001b.
Frigaard, I.A., and Nouar, C., On the usage of viscosity regularisation methods for visco-plastic fluid flow computation, *J. Non-Newt. Fluid Mech*., 127, 1–26, 2005.
Ganser, G.H., A rational approach to drag prediction of spherical and non-spherical particles, *Powder Technol*., 77, 143–152, 1993.
Glowinski, R., and Wachs, A., On the numerical simulation of viscoplastic fluid flow, in R. Glowinski and J. Xu (Eds.), *Handbook of Numerical Analysis*, Elsevier/North-Holland, Amsterdam, The Netherlands, 2011, pp. 483–717.
Goddard, J.D., and Bashir, Y.M., On Reynolds dilatancy, in D. DeKee and P.N. Kaloni (Eds.), *Recent Developments in Structured Continua*, Longman, London, U.K., 1990, chap. 2.
Graham, D.I., and Jones, T.E.R., Settling and transport of spherical particles in power-law fluids at finite Reynolds number, *J. Non-Newt. Fluid Mech*., 54, 465–488, 1994.
Gummalam, S., and Chhabra, R.P., Rising velocity of a swarm of spherical bubbles in a power law non-Newtonian liquid, *Can. J. Chem. Eng*., 65, 1004–1008, 1987.
Gupta, A.K., and Chhabra, R.P., Spheroids in viscoplastic fluids: Drag and heat transfer, *Ind. Eng. Chem. Res*., 53, 18943–18965, 2014.
Haberman, W.L., and Sayre, R.M., Motion of rigid and fluid spheres in stationary and moving liquids inside cylindrical tubes, David Taylor Model Basin Report, No. 1143, Department of Navy, Washington, DC, 1958.
Hartholt, G.P., Hoffmann, A.C., Janssen, L.P.B.M., Hoogstraten, H.W., and Moes, J.H., Finite element calculations of flow past a spherical bubble rising on the axis of a cylindrical tube, *ZAMP*, 45, 733–745, 1994.
Hassager, O., Negative wake behind bubbles in non-Newtonian liquids, *Nature*, 279, 402–403, 1979.
Higdon, J.J.L., and Muldowney, G.P., Resistance functions for spherical particles, droplets and bubbles in cylindrical tubes, *J. Fluid Mech*., 298, 193–210, 1995.
Hirose, T., and Moo-Young, M., Bubble drag and mass transfer in non-Newtonian fluids: Creeping flow with power-law fluids, *Can. J. Chem. Eng*., 47, 265–267, 1969.
Hoerner, S.F., *Fluid Dynamic Drag*, Hoerner Fluid Dynamics, Bricktown, NJ, 1965.
Holenberg, Y., Lavtenteva, O.M., and Nir, A., Interaction of viscous drops in a yield stress material, *Rheol. Acta*, 50, 375–387, 2011.

Ibarz-Ribas, A., and Barbosa-Cánovas, G.V., *Unit Operations in Food Engineering*, CRC Press, Boca Raton, FL, 2003.
Jarzebski, A.B., and Malinowski, J.J., Drag and mass transfer in a creeping flow of a Carreau fluid over drops or bubbles, *Can. J. Chem. Eng.*, 65, 680–684, 1987.
Jossic, L., and Magnin, A., Drag and stability of objects in a yield stress fluid, *AIChE J.*, 47, 2666–2672, 2001.
Juncu, G., A numerical study of steady viscous flow past a fluid sphere, *Int. J. Heat Fluid Flow*, 20, 414–421, 1999.
Kasper, G., Dynamics and measurement of smokes I: Size characterization of non-spherical particles, *Aerosol Sci. Technol.*, 1, 187–199, 1982.
Kawase, Y., and Ulbrecht, J.J., Newtonian fluid sphere with rigid or mobile interface in a shear-thinning liquid: Drag and mass transfer, *Chem. Eng. Commun.*, 8, 213–231, 1981.
Kawase, Y., and Ulbrecht, J.J., Approximate solutions for power-law fluid flow past a particle at low Reynolds numbers, *J. Non-Newt. Fluid Mech.*, 21, 167–177, 1986.
Kishore, N., Chhabra, R.P., and Eswaran, V., Drag on a single fluid sphere translating in power-law liquids at moderate Reynolds numbers, *Chem. Eng. Sci.*, 62, 2422–2434, 2007a.
Kishore, N., Chhabra, R.P., and Eswaran, V., Mass transfer from a single fluid sphere to power-law liquids at moderate Reynolds numbers, *Chem. Eng. Sci.*, 62, 6040–6053, 2007b.
Kishore, N., Chhabra, R.P., and Eswaran, V., Effect of dispersed phase rheology on the drag of single and of ensembles of fluid spheres at moderate Reynolds numbers, *Chem. Eng. J.*, 141, 387–392, 2008.
Kotouč, M., Bouchet, G., and Dušek, J., Loss of axisymmetry in the mixed convection, assisting flow past a heated sphere, *Int. J. Heat Mass Transfer*, 51, 2686–2700, 2008.
Kotouč, M., Bouchet, G., and Dušek, J., Drag and flow reversal in mixed convection past a heated sphere, *Phys. Fluids*, 21, 054104, 2009.
Krishna, R., Urseanu, M.I., van Baten, J.M., and Ellenberger, J., Wall effects on the rise of single bubbles in liquids, *Int. Commun. Heat Mass Transfer*, 26, 781–790, 1999.
Laba, D., *Rheological Properties of Cosmetics and Toileteries*, Marcel-Dekker, New York, 1993.
Larson, R.G., *The Structure and Rheology of Complex Fluids*, Oxford University Press, New York, 1998.
Lavrenteva, O.M., Holenberg, Y., and Nir, A., Motion of viscous drops in tubes filled with yield stress fluids, *Chem. Eng. Sci.*, 64, 4772–4786, 2009.
Lawal, A., and Mujumdar, A.S., Laminar duct flow and heat transfer to purely viscous non-Newtonian fluids, in R.A. Mashelkar, A.S. Mujumdar, and M.R. Kamal (Eds.), *Transport Phenomena in Polymeric Systems-1*, Wiley, Delhi, India, 1987, pp. 352–444.
Leal, L.G., Particle motions in a viscous fluid, *Ann. Rev. Fluid Mech.*, 12, 435–476, 1980.
Lee, T.-L., and Donatelli, A.A., Mass transfer by natural convection from a solid sphere to power law fluids, *Ind. Eng. Chem. Res.*, 28, 105–107, 1989.
Leslie, F.M., and Tanner, R.I., The slow flow of a viscoelastic liquid past a sphere, *Quart. J. Mech. Appl. Maths*, 14, 36–48, 1961.
Liew, K.S., and Adelman, M., Laminar natural heat transfer from an isothermal sphere to non-Newtonian fluids, *Can. J. Chem. Eng.*, 53, 494–499, 1975.
Liu, B.T., Muller, S.J., and Denn, M.M., Convergence of a regularization method for creeping flow of a Bingham material about a rigid sphere, *J. Non-Newt. Fluid Mech.*, 102, 179–191, 2002.
Lochiel, A.C., and Calderbank, P.H., Mass transfer in the continuous phase around axisymmetric bodies of revolution, *Chem. Eng. Sci.*, 19, 471–484, 1964.
Loth, E., Drag on non-spherical solid particles of regular and irregular shape, *Powder Technol.*, 182, 342–353, 2008.
Macosko, C.W., *Rheology: Principles, Measurements and Applications*, VCH, Munich, Germany, 1994.
McKinley, G.H., Steady and transient motion of spherical particles in viscoelastic liquids, in D. Dekee and R.P. Chhabra (Eds.), *Transport Processes in Bubbles, Drops and Particles*, Taylor & Francis, New York, 2002, pp. 338–375.
Meissner, D.L., Jeng, D.R., and De Witt, K.J., Mixed convection to power-law fluids from two-dimensional or axisymmetric bodies, *Int. J. Heat Mass Transfer*, 37, 1475–1485, 1994.
Merkak, O., Jossic, L., and Magnin, A., Spheres and interactions between spheres moving at very low velocities in a yield stress fluid, *J. Non-Newt. Fluid Mech.*, 133, 99–108, 2006.
Mewis, J., and Wagner, N.J., *Colloidal Suspension Rheology*, Cambridge University Press, New York, 2012.
Michaelides, E.E., *Particles, Bubbles & Drops: Their Motion, Heat and Mass Transfer*, World Scientific, Singapore, 2006.

Missirlis, K.A., Assimacopoulos, D., Mitsoulis, E., and Chhabra, R.P., Wall effects for motion of spheres in power-law fluids, *J. Non-Newt. Fluid Mech*., 96, 459–471, 2001.
Mohan, V., Creeping flow of a power law fluid over a Newtonian fluid sphere, *AIChE J*., 20, 180–182, 1974.
Mohan, V., and Venkateswarlu, D., Lower bound on the drag offered to a Newtonian fluid sphere placed in a flowing Ellis fluid, *J. Chem. Eng. Jpn*., 7, 243–247, 1974.
Moo-Young, M., Hirose, T., and Ali, S., Rheological effects on liquid phase mass transfer in two phase dispersions: Results for creeping flow, in *Proceedings of the Fifth International Congress on Rheology*, Kyoto, Japan, 1970, p. 233.
Nakano, Y., and Tien, C., Approximate solutions of viscous incompressible flow around fluid spheres at intermediate Reynolds numbers, *Can. J. Chem. Eng*., 45, 135–140, 1967.
Nakano, Y., and Tien, C., Creeping flow of power-law fluid over a Newtonian fluid sphere, *AIChE J*., 14, 145–151, 1968.
Nakano, Y., and Tien, C., Viscous incompressible non-Newtonian flow around a fluid sphere at intermediate Reynolds numbers, *AIChE J*., 16, 569–574, 1970.
Nalluri, S.V., Patel, S.A., and Chhabra, R.P., Mixed convection from a hemisphere in Bingham plastic fluids, *Int. J. Heat Mass Transfer*, 84, 304–318, 2015.
Nirmalkar, N., Bose, A., and Chhabra, R.P., Mixed convection from a heated sphere in Bingham plastic fluids, *Numer. Heat Transfer*, Part A, 66, 1048–1075, 2014a.
Nirmalkar, N., and Chhabra, R.P., Mixed convection from a heated sphere in power-law fluids, *Chem. Eng. Sci*., 89, 49–71, 2013 See *ibid*, 140, 359–360, 2016.
Nirmalkar, N., and Chhabra, R.P., Momentum and heat transfer from a heated circular cylinder in Bingham plastic fluids, *Int. J. Heat Mass Transfer*, 70, 564–577, 2014.
Nirmalkar, N., Chhabra, R.P., and Poole, R.J., Numerical predictions of momentum and heat transfer characteristics from a heated sphere in yield stress fluids, *Ind. Eng. Chem. Res*., 52, 6848–6861, 2013a.
Nirmalkar, N., Chhabra, R.P., and Poole, R.J., Effect of shear-thinning behaviour on heat transfer from a heated sphere in yield-stress fluids, *Ind. Eng. Chem. Res*., 52, 13490–13504, 2013b.
Nirmalkar, N., Gupta, A.K., and Chhabra, R.P., Natural convection from a heated sphere in Bingham plastic fluids, *Ind. Eng. Chem. Res*., 53, 17818–17832, 2014b.
O'Donovan, E.J., and Tanner, R.I., Numerical study of the Bingham squeeze film problem, *J. Non-Newt. Fluid Mech*., 15, 75–83, 1984.
Ohta, M., Iwasaki, E., Obata, E., and Yoshida, Y., A numerical study of the motion of a spherical drop rising in shear-thinning fluid systems, *J. Non-Newt. Fluid Mech*., 116, 95–111, 2003.
Ohta, M., Iwasaki, E., Obata, E., and Yoshida, Y., Dynamic processes in a deformed drop rising through shear-thinning fluids, *J. Non-Newt. Fluid Mech*., 132, 100–107, 2005.
Ohta, M., Yoshida, Y., and Sussman, M., Three-dimensional computations of the motion of a Newtonian drop rising through immiscible quiescent shear-thinning liquids, *J. Chem. Eng. Jpn*., 39, 394–400, 2006.
Patel, O.P., Patel, S.A., Raja, A.H., and Chhabra, R.P., Forced convection heat transfer from a hemisphere in Bingham plastic fluids: Effects of orientation and thermal boundary condition, *Journal of Energy, Heat and Mass Transfer*, 37, 27–56, 2015.
Papanastasiou, T.C., Flow of materials with yield, *J. Rheol*., 31, 385–404, 1987.
Patel, S.A., and Chhabra, R.P., Laminar free convection in Bingham plastic fluids from a heated elliptical cylinder, *J. Thermophys. Heat Transfer*, 30, 153–168, 2016.
Paul, E.L., Atiemo-Obeng, V.A., and Kresta, S.M., *Handbook of Industrial Mixing: Science and Practice*, Wiley, New York, 2004.
Pazwash, H., and Robertson, J.M., Forces on bodies in Bingham fluids, *J. Hydraulic Res*., 13, 35–55, 1975.
Potapov, A., Spivak, R., Lavrenteva, O.M., and Nir, A., Motion and deformation of drops in Bingham fluid, *Ind. Eng. Chem. Res*., 45, 6985–6995, 2006.
Prhashanna A., and Chhabra, R.P., Free Convection in Power-law Fluids from a Heated Sphere, *Chem. Eng. Sci*., 65, 6190–6205, 2010.
Rajitha, P., Chhabra, R.P., Sabiri, N.E., and Comiti, J., Drag on non-spherical particles in power law non-Newtonian media, *Int. J. Mineral Process*., 78, 110–121, 2006.
Reddy, C.R., and Kishore N., Momentum and heat transfer phenomena of confined spheroid particles in power-law liquids, *Ind. Eng. Chem. Res*., 53, 989–998, 2014.
Sasmal, C., Shyam, R., and Chhabra, R.P., Laminar flow of power-law fluids past a hemisphere: Momentum and forced convection heat transfer characteristics, *Int. J. Heat Mass Transfer*, 63, 51–64, 2013.

Schramm, L.L., *Emulsions, Foams, Suspensions and Aerosols: Microscience and Applications*, 2nd edn., Wiley-VCH, Weinheim, Germany, 2014.
Schurz, J., The yield stress—An empirical reality, *Rheol. Acta*, 29, 170–171, 1990.
Shah, S.N., El Fadili, Y., and Chhabra, R.P., New model for single spherical particle settling velocity in power law (visco-inelastic) fluids, *Int. J. Multiphase Flow*, 33, 51–66, 2007.
Sikorski, D., Tabuteau, H., and de Bruyn, J.R., Motion and shape of bubbles rising through a yield stress fluid, *J. Non-Newt. Fluid Mech*., 159, 10–16, 2009.
Singh, J.P., and Denn, M.M., Interacting two-dimensional bubbles and droplets in a yield-stress fluid, *Phys. Fluids,* 20, 040901, 2008.
Sirignano, W.A., *Fluid Dynamics and Transport of Droplets and Sprays*, Cambridge University Press, New York, 1999.
Song, D., Gupta, R.K., and Chhabra, R.P., Wall effects on a sphere falling in power-law fluids in cylindrical tubes, *Ind. Eng. Chem. Res*., 48, 5845–5856, 2009.
Song, D., Gupta, R.K., and Chhabra, R.P., Effect of blockage on heat transfer from a sphere in power-law fluids, *Ind. Eng. Chem. Res*., 49, 3849–3861, 2010.
Song, D., Gupta, R.K., and Chhabra, R.P., Drag on a sphere in Poiseuille flow of shear-thinning power-law fluids, *Ind. Eng. Chem. Res*., 50, 13105–13115, 2011.
Song, D., Gupta, R.K., and Chhabra, R.P., Heat transfer to a sphere in tube flow of power-law liquids, *Int. J. Heat Mass Transfer*, 55, 2110–2121, 2012.
Sreenivasulu, B., Srinivas, B., and Ramesh, K.V., Forced convection heat transfer from a spheroid to a power-law fluid, *Int. J. Heat Mass Transfer*, 70, 71–80, 2014.
Srinivas, B., and Ramesh, K.V., Numerical analysis of heat transfer from a spheroidal shaped body to a power law fluid at finite Reynolds number, *CFD Lett*., 6, 1–14, 2014.
Stein, S., and Buggisch, H., Rise of pulsating bubbles in fluids with a yield stress, *J. Appl. Math. Mech*., 80, 827–834, 2000.
Stewart, W.E., Asymptotic calculation of free convection in laminar three-dimensional systems, *Int. J. Heat Mass Transfer*, 14, 1013–1031, 1971.
Struble, L.J., and Ji, X., Rheology, in V.S. Ramachandran and J.J. Beaudoin (Eds.), *Handbook of Analytical Techniques in Concrete Science and Technology*, William Andrew Inc., New York, 2001, chap. 9.
Suresh, K., and Kannan, A., Effect of particle blockage and eccentric in location on the non-Newtonian fluid hydrodynamic around a sphere, *Ind. Eng. Chem. Res.,* 51, 14867–14883, 2013.
Tabuteau, H., Coussot, P., and de Bruyn, J.R., Drag force on a sphere in steady motion through a yield-stress fluid, *J. Rheol*., 51, 125–137, 2007a.
Tabuteau, H., Oppong, F.K., de Bruyn, J.R., and Coussot, P., Drag on a sphere moving through an aging system, *Europhys. Lett*., 78, 68007-1–68007-5, 2007b.
Tanner, R.I., *Engineering Rheology*, 2nd edn., Oxford University Press, Oxford, U.K., 2000.
Tanner, R.I., and Walters, K., *Rheology: An Historical Perspective*, Elsevier, Amsterdam, the Netherlands, 1998.
Terasaka, K., and Tsuge, H., Bubble formation in a nozzle submerged in viscous liquids having yield stress, *Chem. Eng. Sci*., 56, 3237–3245, 2001.
Tomita, Y., On the fundamental formula of non-Newtonian flow, *Bull. JSME*, 2, 469–474, 1959.
Tripathi, A., and Chhabra R.P., Slow motion of a power-law liquid drop in another immiscible power-law liquid, *Arch. Appl. Mech*., 62, 495–504, 1992.
Tripathi, A., and Chhabra R.P., Drag on spheroidal particles in dilatant fluids, *AIChE J*., 41, 728–731, 1995.
Tripathi, A., Chhabra, R.P., and Sundararajan, T., Power law fluid flow over spheroidal particles, *Ind. Eng. Chem. Res*., 33, 403–410, 1994.
Tsamopoulos, J., Dimakopoulos, Y., Chatzidai, N., Karapetsas, G., and Pavlidis, M., Steady bubble rise and deformation in Newtonian and viscoplastic fluids and conditions for bubble entrapment, *J. Fluid Mech*., 601, 123–164, 2008.
Uhlherr, P.H.T., A novel method for measuring yield stress in static fluids, in *Proceedings of the Fourth National Conerence on Rheology*, Adelaide, South Australia, Australia, 1986, pp. 231–236.
Uhlherr, P.H.T., and Chhabra, R.P., Wall effect for the fall of spheres in cylindrical tubes at high Reynolds number, *Can. J. Chem. Eng.*, 73, 918–923, 1995.
Valentik, L., and Whitmore, R.L., The terminal velocity of spheres in Bingham plastics, *Br. J. Appl. Phys*., 16, 1197–1203, 1965.

Vasil'chenko, S.V., and Potapov, A.G., Gas bubble dynamics in a viscoelastic-plastic medium, *Heat Transfer Res.*, 27, 4–8, 1996.
Vikhansky, A., Thermal convection of a viscoplastic liquid with high Rayleigh and Bingham numbers, *Phys. Fluids*, 21, 103103, 2009.
Vikhansky, A., On the onset of natural convection of Bingham liquid in rectangular enclosures, *J. Non-Newt. Fluid Mech.*, 165, 1713–1716, 2010.
Walters, K., and Tanner, R.I., The motion of a sphere through an elastic liquid, in R.P. Chhabra and D. DeKee (Eds.), *Transport Processes in Bubbles, Drops and Particles*, Hemisphere, New York, 1992, chap. 3.
Wang, J., Qi, H., and You, C., Experimental study of sedimentation characteristics of spheroidal particles, *Particuology*, 7, 264–268, 2009.
Wang, T.-Y., and Kleinstreuer, C., Local skin friction and heat transfer in combined free-forced convection from a cylinder or sphere to a power law fluid, *Int. J. Heat Fluid Flow*, 9, 182–187, 1988.
Westerberg, K.W., and Finlayson, B.A., Heat transfer to spheres from a polymer melt, *Num. Heat Transfer*, Part A, 17, 329–348, 1990.
Wham, R.M., Basaran, O.A., and Byers, C.H., Wall effects on flow past fluid spheres at finite Reynolds number: Wake structure and drag correlations, *Chem. Eng. Sci.*, 52, 3345–3367, 1997.
Yoshioka, N., Adachi, K., and Ishimura, H., On creeping flow of a viscoplastic fluid past a sphere, *Kagaku Kogaku*, 10, 1144–1152, 1971.
Yu, Z., and Wachs, A., A fictitious domain method for dynamic simulation of particle sedimentation in Bingham fluids, *J. Non-Newt. Fluid Mech.*, 145, 78–91, 2007.
Zapryanov, Z., and Tabakova, S., *Dynamics of Bubbles, Drops and Rigid Particles*, Kluwer, Dordrecht, the Netherlands, 1999.

Index

A

Acoustic cavitation, 780–781
Acoustic streaming model, 658–664
Acoustic turbulence microbubbles, 762–763
Active nuclei, 776
Aerodynamic breakup
  axisymmetric shape of drop, 813
  bag breakup, 812–813
  catastrophic breakup, 812–813
  droplet deformation, 813–814
  empirical correlation, 815
  Reynolds number, 812
  shear breakup, 812–813
  SMD, 814
  stretching/thinning breakup, 812–813
  temporal behavior of drop, 813
  total breakup time, 815
  Weber number, 812
Aerodynamic diameter, 1297
Aerosols
  coagulation and agglomeration, 1252
  convective transport/deposition
    convective diffusion, 1303–1305
    external flows, 1257, 1305–1307
    filters, 1311–1312
    gravitational deposition, 1309–1310
    penetration ratio/fraction, 1302
    thermophoretic deposition, 1310–1311
    turbulent pipe flow, 1307–1309
  external processes
    average particle velocity, 1255
    Brownian diffusion coefficient, 1256–1257
    forced diffusion, 1256
    gas flow, 1254–1255
    inertial transport, 1255
    particle relaxation time, 1257
    pressure diffusion, 1256
    turbulent flow, 1258
    two-fluid approach, 1256
  gas-to-particle conversion
    chemical reaction, 1290–1291
    condensation/evaporation, 1290
    nucleation, 1275–1290
    population of droplets, 1293–1294
    single-particle growth, 1291–1293
  internal processes, 1252–1254
  moment equation, 1258
  numerical methods, 1258–1259
  particle collision
    agglomeration, 1266–1275
    Brownian coagulation, 1262–1264
    causes, 1259
    collision frequency function, 1261
    collision kernel, 1261
    gravitational coagulation, 1264
    Kernel addition, 1265
    Knudsen number, 1260–1261
    laminar shear, 1264
    Langevin equation, 1260
    turbulent coagulation, 1264–1265
  single particle motion
    Cunningham correction factor, 1294
    diffusion, 1297–1298
    diffusiophoresis, 1301–1302
    electric field, 1299
    gravitational settling, 1295–1297
    inertial effects, 1257, 1298–1299
    mean free path, 1294–1295
    slip correction factor, 1257, 1295
    thermophoresis, 1300–1301
  size distribution, 1252
Agglomeration
  adjusted-sphere method, 1271–1272, 1274
  averaged monomer-monomer correlation function, 1267
  collision kernel, 1269
  continuum regime kernel, 1275
  cutoff function, 1267–1268
  fractal dimension, 1266–1267
  free molecular limit, 1272–1273
  friction coefficient, 1269
  gas-molecular scattering, 1273
  hydrodynamic radius, 1271
  Kirkwood-Riseman formula, 1273

mass-transfer radius, 1272
mobility radius, 1271, 1273
packing fraction, 1268
power-law objects, 1266
scaling law, 1267–1269, 1274
sharp interface, 1268
size of, 1266
slip correction factor, 1269–1271
Stokes expression, 1270
Air filters
efficiency, 865
electrostatic fibrous filter, 869
experimental time dependency of performance
of air filter with liquid particles, 866–867
of air filter with solid particles, 866–867
morphology of captured particles
on fiber by inertia and interception effect, 866, 869
general morphologies, 866, 869
time change, 866, 868
time dependency of solid particles, 866, 868
penetration of HEPA filter, 869–870
single fiber collection efficiency
at different charging state, 865–866
by diffusion and interception, 865
by inertia and interception effect, 865
total efficiency, 866–867
types, 866
Airflow and particle deposition
abnormality, 891
anatomy, human airway system, 887–890
CFD models
dispersion of microparticles, 923–927
micro-and nanoparticle deposition, 908–913, 915–919
micro-and nanoparticle transport, 908–913
regional particle depositions, 918–923
septal deviation effect, 913–915
total and regional fiber deposition, 927–930
computational methodology, 899–900
Eulerian and Lagrangian approaches, 890
experimental studies, 892–893
fibrous particle transport and deposition, 897
governing equations
mass diffusion of nanoparticles, 904
microparticle transport equation, 900–902
motion of ellipsoidal fibers, 904–908
stochastic fluctuation velocity models, 902–903
nasal upper airway, 894
oral upper airway, 893
particle shape, 892
realistic 3-D models, 891
surrounding effects, 896–897
targeted deposition, 897–898
tracheobronchial airways, 893
turbulence effects, 895–896
unsteady breathing, 898
upper respiratory system, 892
virtual surgery, 894–895
Air movers
classification, 374–375
fans, 379–380
rotary lobe blowers, 380–381
screw compressors, 381
selection, 398
Annular flow, 290
CHF, 591–593
closed-form solutions, 340
entrainment mechanisms, 338–340
in horizontal tube, 613–614
microgravity two-phase flows, 546–547
SFM, 324
transitions, 299–300
triangular relationship
assumptions, 340
flowchart, 343
interfacial friction factors, 342–343
liquid entrainment fraction, 344–345
liquid film thickness, 345
smooth gas–liquid interface, 342
two-phase frictional multiplier, 341–342
two-phase pressure drop, 344–345
in vertical tube, 614–615
Antifreeze protein/glycoprotein, 951–952
Apparent rough surface (ARS) model, 330–331, 334–335
Archie's equation, 691–692
Arrhenius form, 517
Atomization
applications, 1091–1092
CAB model, 1148
characterization, 1098
continuous jet length, 1121–1122
DNS, 1132–1137
droplet breakup mechanism, 1142–1145
droplet deformation model, 1149–1152
efficiency, 1097–1098
electrostatic atomizer, 1096
ELSA model, 1141–1142
empirical drop size correlation, 1161–1162
energy demand, 1094, 1098
ETAB model, 1147–1148
gas flow, 1108–1115
glass/slags, 1155–1159
gravity-stretched laminar threads, 1131–1132
highly viscous liquids, 1152–1155
ICM, 1138–1141
large-wavelength area, 1124
LES, 1137–1138
liquid flow, 1099–1108
LISA model, 1129–1130
LPT, 1138–1141
MEF, 1160–1161
melts, 1154–1155, 1164–1165
monosized droplet generation, 1095–1096
pneumatic atomizer, 1094–1095
polymer melts, 1155
prefilming hybrid atomizer, 1096–1097
pressure atomizer, 1094, 1117–1119
principles, 1093
processes, 1091–1093
regime, 1116
rotary atomizer, 1095, 1119–1121
semiempirical breakup models, 1145–1146

single-fluid atomization, 1115–1117
size parameters, 1098–1099
small-wavelength area, 1124–1129
solid/liquid suspensions, 1158–1160
specific energy input, 1097
spherical drop, 1122–1123
surface-tension forces, 1122
surface wave, 1123
suspension atomization, 1162–1164
TAB model, 1146–1147
tundish reactions, 1154–1155
twin-fluid atomizer, 1117
ultrasonic atomizer, 1095–1096
viscous forces, 1123
wave/KH breakup model, 1148–1149
Atwood number, 455–456

B

Back-coupling effect, 485
Bag breakup, 812–813
Bag filters
collection mechanism
grade efficiency, 874
shape of bag filter element, 873–874
time change, different filtration velocities, 874–875
methods of dislodging the dust particles, 876
pressure drop, 875
Barrier-type dust collectors, 832
Barrier-type separators, 873
Base fluids, *see* Nanofluids
Basset force, 487, 736–737
Bayesian Smoothing Spline Analysis of Variance (BSS-ANOVA) models, 282
Bhatnagar-Gross-Krook model, (BGK), 132
Binary drop collisions
bouncing, 817
coalescence, 817–818
critical impact factor, 817
hydrocarbon droplets, 817
reflexive separation, 817–818
schematic representation, 816
stretching separation, 817–818
Bingham plastics model, 412–413, 415–416, 1326
Biological systems
airflow and particle deposition, 887–931
biomimetics and bioinspiration, 948–952
blood flow, 937–946
Biomimetics and bioinspiration
capillary flow, 949
combination of surfaces, different hydrophobicity, 950–951
ice growth inhibitors, 951–952
skin separation, 949
stressors, 948–949
superhydrophobic surfaces, 949–950
Black oil simulator equations, 722–725
Blake critical radius, 777
Blood flow
apparent viscosity and Fåhræus–Lindqvist effect, 937–938
blood cells modeling, 938–939
as dispersed multiphase flows, 937
numerical method
BEM, 939
full Eulerian formulation, 939–941
IB method, 939
shear-induced deformation problem, 941
suspension of RBC and platelets in capillary tube, 941–944
time history, deformation parameter, 941
platelet adhesion, 944–946
Boundary condition, powder and granular flow, 642–643
Boundary element method (BEM), 939
Boundary layer ejection model, 589
Boussinesq–Basset equation, 25, 37
Box counting methods, 735
Breakdown Thoma number, 787
Brown field workflow, 725
Bubble cloud dynamics
computational conditions, 769–770
frequency response
high pressure amplitude cases, 770–772
low pressure amplitude cases, 770, 772
spherical bubble
assumptions, 767–768
damping effects, 767
geometry, 766, 768
governing equations, 769
mass and momentum conservation equations, 766
natural frequencies, 767
radius, 767
Bubble dynamics
bubble cloud, 766–772
bubble nucleation, 564
deformation and fragmentation, collapse
amplitude, 763
boundary integral method, 765
cavitation, 764–765
instability, 763–764
jet and counterjet development, 764
departure diameter, 565–566
departure frequency, 566
growth period, 564–565
single spherical
direct numerical simulation, 753–759
nonlinear behavior and acoustic turbulence, 762–763
reduced-order modeling, 759–762
Bubble layer model, 589–590
Buckley–Leverett theory, 718–719
Butt cleats, 687–688, 696

C

Capillary breakup, 815–816
Capillary pressure
and capillary radius, 702–704
and height of interface, 704–705
measurement, 706–707
Carrier phase equations of motion
convective heat transfer, 482
definition, 481
diffusion model, 482

for dilute flow, 481
ideal gas, 482
Navier–Stokes equations, 481
turbulence, 482–483
volume-averaged force, 481
volume fraction, 482
Carrier phase turbulence, 482–484
Cartesian grid cut-cell technique, 260–262
Casson model, 412, 417
Catastrophic breakup, 812–813
Cavitation
acoustic, 780–781
Alpheus heterochaelis, 788
aquasonolysis, 788
in biomedical applications, 787–788
collapse
acoustic emission, 777
attenuation phase, 779
fragile alloys, 780
Gilmore equation, 777
incubation period, 779
MDPR, 778
nearing solid boundary, 778
timescale, 777
ultimate resilience, 778
desinence, 775
developed, 775
erosion, 778–779
in hydraulic machinery
breakdown Thoma number, 787
critical Thoma number, 787
inception Thoma number, 787
injector nozzles and fuel pumps, 787
marine propellers, 787–788
pump performance curves, 787
Sigma Thoma number, 786
hydrodynamic, 781
inception, 774–775
intensity, 778
nuclei and bubble growth
active nuclei, 776
bubble radius, 776
equivalent critical liquid pressure, 776
heterogeneous nucleation, 775
homogeneous nucleation, 775
measurement methods, 777
quasi-static equilibrium, 775
Rayleigh–Plesset equation, 775
partial/attached, 774
sheet, 781–784
shot-less peening, 788
sonochemistry, 788
susceptibility meters, 777
vortex, 784–786
Cellular model, 524
Centrifugal separation, dry cyclones
blow-down effect
blow-down and blowup ratios, 840
fluid velocity distributions, 841
fractional separation efficiency, 841–842
particle trajectories, 841–842
centrifugal acceleration, 837
classification theory, 837–838
cut size control, free-vortex-type classifier
calculated fluid velocity vectors, 843–844
cyclone with movable inlet guide plate, 843
fractional separation efficiency, 843, 845
inlet guide plate effect, 843
particle trajectories, 843–844
numerical calculations
direct-method approach, 838
fluid velocity distribution, 838–839
fractional separation efficiency, 839–840
k-ε turbulence model, 838–839
particle trajectories, 839–840
Stokes number, 839
pressure drop estimation method
estimation equations, 846–847
inlet systems and configurations for cyclone separator, 845–846
multicyclone structure, 847–848
partial separation efficiency curves, 847–848
Circulating fluidized bed (CFB)
average density, 1005
correlations, 1005, 1011–1013
energy equation, 1010–1011
membrane tube wall, 1004–1005
radiative and convective heat transfer, 1007–1010
suspension densities, 1004
temperature, 1006–1007
thermal boundary layer, 1005–1006
vertical heat-transfer surface, 1005–1006
wing walls, 1004
Circulating fluidized bed combustors (CFBCs), 1041–1043
Classical nucleation theory (CNT)
assumptions, 1276
bubble nucleation, 1278
critical droplet-free energy, 1278
diffuse interface theory, 1280
entropy, 1279–1280
equilibrium cluster distribution, 1276–1277
experimental data, 1278
free energy, 1280
isothermal nucleation, 1280
macroscopic thermodynamic properties, 1278–1279
monomers, 1277
numerical simulations, 1280–1281
preexponential factor, 1279
rate per unit volume, 1276
second-order approximation, 1277
translation-rotation paradox, 1279
Zeldovich nonequilibrium factor, 1277
Clausius–Clapeyron equation, 522, 563
Coal capillary pressure, 704
Coal compressibility, 689
Coal directional permeability, 700
Coalescence, 817–818
Coal permeability, 696–697
Coal porosity
face and butt cleats, 687–688
mineral filled face and butt cleats, 687–688

natural fractures, 687
phyteral porosity, 687, 689
Coal relative permeability, 708–710
coal-gas-water relative permeabilities, 709
gas-water relative permeabilities, 709
mobile water, 708
principal methods, 709
seam-gas-water relative permeabilities, 709–710
Coanda effect, 1113–1115
Cohesion effect, 673–675
Collection efficiency, 1302
Collisional stress model, 638–639
Collision models
Grad's theory, 181–183
interparticle collision time, 183
particle-fluid-correlated, 181
Column collapse, 643
Composite stress model, 640
Compressibility, porosity, 689–690
Compressible dense particle flows, 492–493
Compressible dilute particle flows
carrier phase equations of motion, 481–484
dispersed phase equations of motion, 484–487
drag coefficient, 477–480
gas-particle interaction, 492
Mach and Reynolds number effects, 476–477
nonspherical effects, 480–481
response times, 473–475
shock-particle interaction, 487–491
Compressible flows
averaging techniques
Favre averaging, 457–458
mixture properties, 458–459
time averaging, 456
volume averaging, 457
dispersed phase flows, 471–495
multicomponent and multiphase continua, 456
equation of state, 470–471
Eulerian approach, 459–468
jump relations, 470–472
Lagrangian approach, 459
shock interaction, material interfaces, 468–469
shocked continua interfaces, 495–508
single component, 456
Computational fluid dynamics (CFD) models, human upper airway systems
dispersion of microparticles
CRW model, DRW model and mean track, 925–926
deposition patterns for breathing rates of 30, 45, and 60 L/min, 925, 927
deposition patterns for breathing rates of 45 L/min, 925–926
velocity magnitude contours and turbulence intensity, 923–925
micro-and nanoparticle deposition, 915–919
micro-and nanoparticle transport and deposition
coronal and sagittal cross sections, 908
IP, defined, 909
predicted deposition efficiency *vs.* IP, 909–911
spatial deposition patterns, 911–912
3-D model, nasal upper airway, 908–909
microparticles transport and deposition, 912–913
regional particle depositions
for breathing rate of 7 L/min, 923
computational domain, 918, 920
deposition fractions comparison, 922–923
distribution pattern of 2 μm particles, 921–922
mannequin, facial features, 918, 920
path lines of inhaled air colored with velocity magnitude, 920–921
3-D airway model to mannequin, 920
total deposition fractions, 920–921
septal deviation effect, 913–915
total and regional fiber deposition
equivalent aerodynamic diameters, 927–928
fiber model *vs.* HL model, 929–930
spatial distribution of deposition pattern, 929–930
unit density *vs.* impaction parameter, 928–929
variation of total DF *vs.* IP, 928
Concurrent versioning system (CVS), 242
Condensation
circular tube, 612
definition, 605
direct contact condensation
on drops, 624–625
on liquid films, 625
on liquid jets, 625
on liquid sheets, 625
enhanced condensation, 626–630
on flat surfaces
dropwise condensation, 608–609
film condensation, 609–612
heterogeneous nucleation, 607–608
homogeneous nucleation, 605–607
horizontal tubes
annular flow, 612–614
stratified annular flow, 612–613
in microchannels, 623
in minichannels, 623
noncondensable gases effects, 623–624
on plain tube, 623
stress ratio, 613
superheating effects, 624
vertical tube
annular flow, 614–615
flow regimes, 612
laminar film condensation, 616–620
turbulent film theory, 620–622
Contact angle, 702
Contact line region heat transfer, 567
Contact model effect, 646–647
Continuity equation, reservoir flow model, 721–722
Continuous phase
dispersed-phase reference frame, 88–89
mixed-fluid volume, 87
momentum, 87–88
Continuous random walk (CRW) models
dispersion of microparticles, 925–926
stochastic fluctuation velocity models, 903
turbulence effects, 895–896
Continuous size distribution, 11–13
Convective boiling, 1077–1078

Convective diffusion
circular-tube annular, 1303–1305
nonuniform inlet concentration, 1304
rectangular geometry, 1304–1305
Convective flow boiling, 559
Conventional spray pyrolysis (CSP) process, 1192–1193
Corey shape factor, 8
Creeping flow, 25–26
Critical heat flux (CHF), 1078–1079
flow boiling
in annular flow, 591–593
correlations, 591
enhancement, 594–595
in low-quality saturated flow boiling, 590
in subcooled flow boiling, 589–590
nucleate boiling
balance of forces, 571–572
contact angle, 571
cutback phenomenon, 571–572
definition, 560, 571
equivalent *K* factor, 573
vs. HTC, 575
roughness effect, 575
Critical Thoma number, 787
Crossing trajectory effects, 736
Cross model, 1325
Cunningham correction factor, 1294
Cutback phenomenon, 571–572

D

Darcy's law, 710
extension from one dimension to three dimensions, 699–700
friction factors, 365
in gravitational field, 699
permeability, porous medium, 692–693
for radial flow of gas, 694–695
for radial flow of liquid, 694
relative permeability, 710
Decaying isotropic turbulence, 742
Dense phase conveying
classification of, 375
control of
and diagnostics strategy, 403–404
flow diagram, 401–403
operating window, 401–403
description, 372
discontinuous dense phase, 376
extrusion flow, 376
phase diagram, 367–369
plug/slug flow
force balance, 398–399
momentum balance, 399
overall system pressure drop calculation, 399, 401
stationary layer, 399
velocity estimation, 399–400
two-phase flow, 376
Dense suspension upflow (DSU), 962–963, 978
Density functional theory (DFT), 1281–1283
Density method, porosity, 687
Depth-averaged shallow flow model, 643–644
Deterministic reservoir forecasting, 725
Diesel injection (DI), 1190–1192
Diffusiophoresis, 1301–1302
Dilute phase conveying
closed-loop systems, 373–374
control of, 401–402
description, 372
designing steps
air mover selection, 398
conveying requirements and performance criterion, 394
feeder selection, 397
gas-solid separator selection, 397
initial pipe diameter selection, 397
material properties, 394
overall pressure drop and gas flow rate requirement calculation, 386–393
pipe diameter, recheck selection, 397
suitable line layout identification, 396–397
system type/conveying mode selection, 394–396
feeder type/air-solids' mixing device, 374
open-loop systems, 373
phase diagram, 365–367
pressure drop
acceleration (gas-solids), 382–383
in bends, 385–386
blower piping and feed section, 382
in gas-solid separator/filter receiver, 386
overall calculation, 386–393
in straight sections, 383–385
in vertical section, 385
pressure type, 372–374
Direct contact condensation
on drops, 624–625
on liquid films, 625
on liquid jets, 625
on liquid sheets, 625
Direct fuel injection (DI), 1189–1192
Directional permeability, porous media
coal directional permeability, 700
Darcy's law, gravitational field, 699
extension of Darcy's law to three dimensions, 699–700
Direct numerical simulation (DNS), 463, 895
bubbly flows
air-assisted breakup, 103
channel flow, 102
close-up, 100, 102
drafting, kissing, and tumbling, 99–100
front-tracking method, 100
interface topology, 100
laminar and turbulent flows, 100
large-scale simulation, 100–101
Navier–Stokes equations, 101
periodic domains, 99
droplet collisions, 1169–1170
finite Reynolds number flows, 97–99
fragmentation process, 1132–1133
heat transfer, 103–104
liquid sheets, 1127
LS method, 1134

primary atomization, 1134–1137
simple flows, 96–97
single-fluid formulation, 1133–1134
single-phase turbulent flows, 103
two-fluid model, 96
two-phase turbulent combustion, 531–533
VOF method, 1134
Discontinuous dense phase conveying, 376
Discrepancy function,280– 281
Discrete element method (DEM), particle-based simulations
bulk properties estimation, 646
contact model effect, 646–647
parameters, 644–646
Discrete random walk (DRW) model
dispersion of microparticles, 925–926
stochastic fluctuation velocity models, 902–903
turbulence effects, 895–896
Discrete size distribution, 10–12
Dispersed phase
continuum equations
Boltzmann collision integral, 180
collision models, 181–183
gas-solid turbulent flows, 178–179
inelastic collision, 179
Eulerian approach
continuum assumption, 85–87
equations of motion, 84
Lagrangian approach
numerical interpolation, 82–84
particle equation of motion, 79–81
Dispersed phase equations of motion
back-coupling effect, 485
governing equations, 484
inviscid-unsteady force, 485–487
pressure-gradient force, 485
quasi-steady force, 485
viscous-unsteady force, 487
Dispersed phase flows
compressible dense particle flows, 492–493
compressible dilute particle flows
carrier phase equations of motion, 481–484
dispersed phase equations of motion, 484–487
drag coefficient, 477–480
gas-particle interaction, 492
Mach and Reynolds number effects, 476–477
nonspherical effects, 480–481
response times, 473–475
shock-particle interaction, 487–491
dilute and dense flows, 473
dusty gas flows, jump relations, 493–495
Eulerian frame, 471
Lagrangian tracking, 471
phase coupling, 473
volume averaging method, 472
Distributed-force technique, 92–93
d^2-law, 517
Double circle model, 331–332, 335–336
Drift flux model (DFM)
correction factors, 311
distribution parameter, 307–308
general form, 307
graphical representation, 308
ID model, 308
Laplace number, 311
slug flow regime, 309
two-phase friction factor, 310
for vertical upward bubbly flow, 308–309
void fraction correlation, 309–310
Drift velocity, 54
Droplet breakup
aerodynamic breakup, 811–815
capillary effects, 811
causes, 810
deformation, 810–811
relative rim velocity, 810
Reynolds number, 810
in viscous flow, 815–816
Drop-wall impact
influencing parameters, 818
onto dry substrate
average threshold Weber number, 822
corona splash, 821–822
partial/complete rebound, 822
prompt splash, 821
receding breakup, 822
splashing threshold, 822
onto partially wettable substrate, 821
onto wetted wall
bubble entrainment, 823
corona splash, 822
critical *K*-number, 823
prompt splash, 822
splash threshold, 823
stick regime, 822
theoretical modeling, 823–824
wetting, dry surface
dynamic contact angle, 819–820
Hoffman–Voinov–Tanner law, 819
static advancing, 819
static contact angle, 819, 821
static receding, 819
Young's relation, 819
Dropwise condensation
on flat surfaces, 608–609
nanostructured surfaces, 628–629
surface promoters, 628
Drug delivery devices, 891
Durand's correlation, 426–427
Dust collection
of high-resistivity particles
applied voltage and corona current, 855–856
collection efficiency of various kinds of coal, 855, 857
collection efficiency *vs.* moisture content, 859, 861
collection efficiency *vs.* 2Na + K, 859–860
corona current density influence, 855
corona power and collection efficiency, 855, 857
gas temperature influence, 858
low-temperature operation influence, 859
Na, K, Ca and S content influence, 859–860
temperature influence, 855–856
of low-resistivity particles, 854–855

Dust removal equipment
barrier-type dust collectors, 832
classification, 832–833
collection efficiency, 833
flow-through-type dust collectors, 832
gas velocity *vs.* initial capital cost, 833
general features, 832
obstacle-through-type dust collectors, 832
Dynasen piezoelectric probes, 497, 499

E

Eddy impaction, 1298–1299
Effective permeability, 707–708
Effective pore space, 686
Effective porosity, 686–687
Electrical drift velocity, 1299
Electrical mobility, 1299
Electric field-enhanced condensation, 630
Electrostatic precipitator (ESP)
collection conditions
dust collection of high-resistivity particles, 855–861
dust collection of low-resistivity particles, 854–855
dust resistivity, 852–853
space between collection electrodes, 853
collection efficiency, 851–852
electric mobility, 850–851
general features, 832
particle charging
AC charging, 850
charged ions and particle diameter, 849–850
DC charging, 850
diffusion, 849
field, 849
pulse charging, 850
principles, 848–850
Ellipsoidal fibers, equations of motion, 904–907
Emulator function, 281
End pinching, 815–816
Enhanced condensation
dropwise condensation, 628–629
electric field-enhanced condensation, 630
fin spacing, 626
heat transfer enhancements, 626
of tube
bundle effect, 628
3D complex surfaces, 627
2D low fin surfaces, 626–627
Enhanced convection, 567
Eulerian approach
basic equations, 460
continuous phase
dispersed-phase reference frame, 88–89
mixed-fluid volume, 87
momentum, 87–88
dispersed phase
continuum assumption, 85–87
equations of motion, 84
mechanical and thermal equilibrium
five-equation model, 461
four-equation model, 461
response times, 460
resultant equations, 460–461
turbulence, 461–465
mechanical and thermal nonequilibrium
acoustic impedance, 468
characteristic length scale, 468
compaction equation, 467
conservation equations, 466–467
density, 468–469
material velocity, 468–469
pressure, 467–469
seven-equation model, 465
shock velocity, 468–469
timescale, 468
velocity relaxation coefficient, 467
volume fraction gradients, 467
Eulerian–Lagrangian spray atomization (ELSA) model, 1141–1142
Euler–Lagrange methods
angular velocity, 204
conveying pipe configuration, 206–208
drag coefficient, 204
elementary processes, 205
flow structure
air velocity streamlines, 221, 2221
gas-phase fluctuation velocity, 225–226
normalized fluctuating velocities, 225
particle-induced vortices, 220
secondary flow intensity, 219, 221–222
slip velocity, 226
interparticle collisions, 213–214
mass loading, 218–219
particle phase, 201
particle response time, 208
particle size
mean flow deflection, 217
nondimensional segregation parameter, 215–216
normalized particle concentration, 214–215
particle concentration, 214–217
pipe diameter, 214
radial displacement, 216
pipe bend, erosion
CFD-based erosion models, 231
configuration, 235
cutting and deformation, 231
erosion ratio, 231
experimental pipe configuration, 231–232
friction coefficient, 232
gradual refinement, 232
interparticle collisions, 235–237
mechanisms, 230
Oka model, 230–231
parameters, 233
particle mass loading, 239
particle-wall impact angle, 237
penetration rate map, 232–233
penetration ratio, 231, 239
predictive equation, 230
restitution model, 232, 235
shielding effect, 238
trigonometric functions, 230

validation, 231
wall collisions, 237
wall material and wall surface structure, 230
pneumatic conveying systems, 200–201
pressure drop analysis
calculations, 226
interparticle collisions, 228
particle-wall collisions, 225–226
pipe elements, 228
ripple structure, 229
RANS, 201
slip-rotation lift force, 204–205
slip-shear force, 204
Stokes number, 208
two-way coupling procedure, 205–206
validation, 209
wall roughness effects, 209–213
Evaporation, definition, 559
External boundary force (EBF) method, 112–114
External flow boiling, 559
External group combustion, 527

F

Face cleats, 687–688, 696
Falling-film evaporation, 559
Fanning's friction factors, 365
Favre averaging, 457–458
Faxén theorem, 485
Fibrous filters, 1311–1312
Film condensation, 609–612
laminar film, 609–611
turbulent film, 611–612
Fischer–Tropsch (F-T) process, 1035–1036, 1044
Flame-assisted spray pyrolysis (FASP), 1194
Flame spray pyrolysis (FSP), 1194–1196
Flat surface model, *see* Taitel and Dukler (1976) model
Flow boiling
applications, 559, 577
augmentation, 594
of binary mixtures, 586–588
CHF, 589–593
in circular tube, 577–578
in compact heat exchangers, 593–594
convective flow boiling, 559
definition, 559
external flow boiling, 559
flow boiling map, 586
flow patterns, 579–580
fully developed boiling, 578
heat flux, 578
NVG, 578
ONB, 578–579
partial boiling region, 578
saturated flow boiling heat transfer
asymptotic model, 583
convective boiling-dominant region, 583
correlation, 583
fluid-surface parameter, 583–585
friction factor, 584
Froude number multiplier, 584
Kandlikar (1990) correlation, 584–585
nucleate boiling-dominant region, 583
single-phase all-liquid heat transfer coefficient, 584
subcooled flow boiling heat transfer, 580–583
Flow regimes
dilute pneumatic conveying, 963
DSU, 962–963
minimum fluidization, 957–961
minimum slugging velocity, 961–962
superficial gas velocity, 957–958, 961
transport velocity, 962
turbulent fluidization, 962
upward gas flow, 957, 959
Flow-through-type dust collectors, 832
Flow-through-type separators, 834–836
Fluid catalytic cracking (FCC)
advantages, 1033
crude oil cracking, 1031
disadvantages, 1033
fixed/moving-bed operation, 1031–1032
hot catalys, 1032–1033
in North America, 1034
petroleum refining, 1031
QC reactor, 1034–1035
RFCC, 1034
solid catalyst, 1031
Fluidized bed combustion (FBC)
advantages, 1040–1041
CFBC, 1041–1043
coal particles, 1040
nitrogen monoxide, 1041
PFBC, 1043
SFBC, 1041–1043
volatiles and properties, 1040–1041
Fluidized bed reactor
bubble-free fluidization, 964
bubbling fluidization
entrainment, 970–972
freely bubbling bed without tubes, 965–966
gas mixing, 968–969
gas-solid contacting, 969–970
solids mixing and motion, 960, 966–969
throughflow, 964
tubes and baffles, 966
classification, 1030–1031
coking, 1038–1040
equipment design and operation, 956, 983–984
fast fluidization
axisymmetric flow, 976
configuration, 975
DSU, 978
saturation carrying capacity, 977
solids holdup profiles, 976
solids velocity, 977–978
time-mean voidage, 977
FCC
advantages, 1033
crude oil cracking, 1031
disadvantages, 1033
fixed/moving-bed operation, 1031–1032

hot catalys, 1032–1033
in North America, 1034
petroleum refining, 1031
QC reactor, 1034–1035
RFCC, 1034
solid catalyst, 1031
features, 1036
flow regimes
dilute pneumatic conveying, 963
DSU, 962–963
minimum fluidization, 957–961
minimum slugging velocity, 961–962
superficial gas velocity, 957–958, 961
transport velocity, 962
turbulent fluidization, 962
upward gas flow, 957, 959
F-T process, 1035–1036
gas/liquid velocity, 1029
gas-solid reactions
biomass, 1045–1047
calcination, 1047–1048
coal gasification, 1043–1044
coal utilization, 1039
drying, 1048–1050
FBC, 1040–1043
heat exchangers, 1049–1051
incineration of wastes, 1044–1045
particle coating, 1051–1052
powder coating, 1052–1053
roasting, 1047
gas-solid systems, 1030
GLSFB, 1054
grain particles, 1029
heat and mass transfer
active fuel particles, 1016–1019
CFB, 1004–1013
correlations, 995, 999–1000
dense bed, 1019–1020
heat-transfer coefficient, 994–995
laboratory-scale experiments, 1012–1013
maximum heat transfer, 995–999
mechanism, 1000–1001
models, 1001–1004
Nusselt number, 1013–1014
particle beds, 1015–1016
Sherwood number, 1013–1014
single-phase flow, 1014–1015
LSFBs, 1053–1054
particulate/homogeneous fluidization, 963–964
productions, 1036–1037
properties, 955–957, 1030
slugging, 972–973
spouted bed, 1053
geometry, 978–979
maximum spouting, 980
minimum spouting velocity, 980–981
particle weight-minus-buoyancy, 979–980
thermal cracking, 1037–1038
three-phase fluidization, 981–983
turbulent fluidization
axial and radial voidage variation, 973–974
chemical reaction, 974
entrainment, 975
gas and solids mixing, 974
mass transfer, 974
types, 1029
Fluid-solid flow
pneumatic conveying systems, 357–407
slurry flows, 407–449
Fluid spheres
bubbles, 1357–1359
drops, 1359–1360
momentum, 1356
viscoelasticity, 1360
wall effects, 1360
Fokker–Planck differential equation, 536
Forced boiling, 1077–1078
Formation resistivity factor, 691
Fractal dimension
conditions, 10
Koch curve, 8–9
particle aggregates, 9
porosity, 10
self-similar patterns, 9
Fractional efficiency, 830–831
Fractional flow, immiscible fluids, 715–719
Free energy model, 123
Free shear flows, 746
Frictional stress model, 639–640
Furutsu–Novikov (FN) method, 149

G

Gaseous combustion, 516–517
Gas expansion method, porosity, 687
Gas-liquid-solid fluidized beds (GLSFB), 1054
Gas–liquid two-phase flow
actual phase velocity, 288
flow maps
for downward inclined two-phase flow, 293–294
facts and limitations, 295
for horizontal flow, 290–292
pressure drop variation, 293–294
transition boundaries, 295
for upward pipe inclinations, 292–293
for vertical upward flow, 292
flow patterns
annular flow, 290, 337–345
bubbly flow, 289
intermittent flow, 290
slug flow, 289
stratified flow, 290, 328–337
flow quality, 288
gas volumetric flow fraction, 288
nonboiling two-phase heat transfer
Reynolds analogy, 347, 349–350
two-phase heat transfer model, 346–349
one-component flow, 287
phase superficial velocity, 288
pressure drop
accelerational pressure drop, 312
fluid properties effect, 316–317
frictional component, 312

hydrostatic/gravitational component, 312
phase flow rates effect, 312, 314–316
pipe diameter effect, 315–316
pipe orientation effect, 312–314
pressure gradient minimum phenomenon, 318–320
surface roughness effect, 317
two-phase pressure drop modeling, 320–328
slip ratio, 288
superficial Reynolds number, 288
transitions
between annular and nonannular flows, 299–300
between bubbly and slug flows, 295–296
between stratified and nonstratified flows, 297–299
two-component flow, 287
two-phase mixture velocity, 288
void fraction
definition, 288
DFM, 307–311
phase flow rate effect, 302–304
pipe diameter effect, 304–305
pipe orientation effect, 301–303
separated flow model, 305–307
Gas-solid reactions
biomass, 1045–1047
calcination, 1047–1048
coal gasification, 1043–1044
coal utilization, 1039
drying, 1048–1050
FBC, 1040–1043
heat exchangers, 1049–1051
incineration of wastes, 1044–1045
particle coating, 1051–1052
powder coating, 1052–1053
roasting, 1047
Gas-to-particle conversion
chemical reaction, 1290–1291
condensation/evaporation, 1290
nucleation, 1275–1290
population of droplets, 1293–1294
single-particle growth, 1291–1293
Gaussian vortex, 784
Generalized Bingham model, 413
Generalized Langevin method (GLM)
constitutive relations
algebraic model, 163–164
eddy viscosity model, 164
fluid-particle velocity correlation, 162–163
LHS, 162
transport equations, 162
simple shear and rotational flows, 155–157
Geostatistics, 698–699
Gillies–Shook correlation, 429
Global reaction mechanism, 517
Godunov scheme, 465
Grade efficiency, 830–831
Grad's theory, 181–183
Granular flow, *see* Powder and granular flow
Granular leidenfrost effect, 671–673
Gravitational collectors, 836
Gravitational effects, 736
Green field workflow, 725
Gridded interface method (GIM), 93–94
Group of drops
interactive combustion, 527–530
interactive evaporation, 524–526

H

Hadamard–Rybczynski analysis, 26
Haider and Levenspiel (HL) model, 907–908
Heat transfer
blowing effects, 61–62
creeping/Stokes flow, 54–56
flow turbulence, 60
IBM, 134–135
nonspherical particles, 1354
Peclet number, 54
Prandtl number, 54
radiation effects, 64–65
Reynolds number effects
interfacial velocity slip, 58–59
solid spheres, 56–57
temperature difference, 58–59
viscous spheres, 57–58
rotational motion, 59–60
transient effects, 62–64
viscoplastic fluids
forced convection regime, 1345–1346
free convection regime, 1346–1348
mixed-convection regime, 1348–1349
Herschel–Bulkley model, 413, 416, 1326
Heterogeneous nucleation, 607–608, 775
Heterogeneous slurry flows
with moving bed, 409–410
settling slurries, 424–439
solids' concentration profiles, 409
with stationary bed, 409–410
Hoffman–Voinov–Tanner law, 819
Homogeneous gas-solid flows, 742–744
Homogeneous nucleation, 605–607, 775
Homogeneous slurry flows
of nonsettling slurries
Newtonian slurries, 411
non-Newtonian slurries, 412–413
pressure loss, pipe fittings, 424
pressure loss, straight circular pipe, 414–423
rheological property, 411
particle distributions, 409
principle of continuum mechanics, 409
solids' concentration profiles, 409
Hopper flow, 643
Hydraulic conductivity, 694
Hydraulic conveying, 358
Hydraulic radius, 690
Hydrodynamic bubble cavitation, 781
Hysteresis, 706, 819–820

I

Imbibition method, porosity, 687
Immersed boundary method (IBM), 939
bilinear interpolation, 129

body force density, 127
drag and heat transfer rate
drag coefficient, 138–139
Nusselt Number, 140
Prandtl number, 138
temperature contours, 141
vortex structures, 139–140
elastic fibers and fluid, 128
fluid-particle interface, 128
fluid velocity, 129
fractional step method, 129
heat transfer, 134–135
implementation, 128
Newtonian framework, 126
particle-particle and particle-wall interactions, 130
hybrid lubrication force scheme, 138
repulsive force scheme, 137–138
soft-sphere scheme, 136–137
particle surface, 130
Proteus code, 127
RDPM, 141–142
rigid body motion, 129
3D isothermal flows
Boltzmann equation, 131
boundary nodes, 130
Cauchy theorem and Gauss integral, 132
differential equations, 133
Eulerian grid spacing, 131
force density, 132
LBM, 132
linear momentum, 133
rigid body motion, 134
rotation matrix, 133
spherical particle, 130, 133–134
spreading function, 131
surface force, 131
torque, 133
translational and rotational velocities, 133
two-relaxation-times, 134
Immersed interface method (IIM), 94–95
Immiscible displacement
Buckley–Leverett theory, 718–719
frontal advance in fracture, 720–721
nonwetting phase and wetting phase, 717
Welge's method, 719–720
Immiscible fluids
fractional flow, 715–717
interface in cylindrical capillary, 703
Inception Thoma number, 787
Inclined flow, 643
Inertial dust collectors, 863–864
Interface capturing method (ICM)
coupling procedure, 1138–1139
droplet size, 1139
Eulerian–Lagrangian approach, 1140
swirling conical liquid sheet, 1140–1141
turbulent liquid jet, 1139
Interfacial tension (IFT), 700–701, 711–714
Internal group combustion, 529
Internal mixing twin-fluid atomizer, 1105–1108
Interstitial velocity, 693
IP model, 909
Isolated drop
combustion
convective flow, 522
empirical relations, 523–524
heptane drop, temporal variations, 523
Lewis number, 521
one-state envelope flame, 523
one-state vaporization, 523
quasi-steadiness assumption, 522
saturated drop surface, 522
Sherwood number, 522
spherical drop, species profiles, 521–522
two-state envelope flame vaporization, 523
two-state wake flame vaporization, 523
evaporation
computational domain, 519–520
coordinate system, 519–520
of deformed drop, 520
dimensionless mass flux, 520
energy balance, 519
finite element simulations, 519
gas-phase energy conservation, 518
gas-phase mass conservation, 518
Lewis number, 518
mass flow rate, 519
normalized mass flux variations, 520
saturation temperature, 518
spherical harmonics, 519
steep temperature gradient, 518–519
Isolated pore space, 686

K

Kapila's model, 465–466
Kelvin–Helmholtz (KH) breakup model, 1148–1149
Kinetic method (KM)
constitutive relations
advection–diffusion equation, 158–159
coefficients, 158
identities, 158
kinetic stresses, 161
particle-carrier velocity covariances, 159–161
MFIX, 264
nonreactive gas-particle flows, 148–151
simple shear and rotational flows, 154–155
Klinkenberg effect, 695–696
Koch curve, 8–9
Kolmogorov timescale, 729
k–ω-based turbulence model, 895–896

L

Lagrangian approach, 457
numerical interpolation, 82–84
particle equation of motion, 79–81
Lagrangian history direct interaction (LHDI) method, 148, 150
Lagrangian particle tracking (LPT) approach
coupling procedure, 1138–1139
droplet size, 1139
Eulerian–Lagrangian approach, 1140

swirling conical liquid sheet, 1140–1141
turbulent liquid jet, 1139
Lagrangian velocity autocorrelation, 732
Laminar film condensation
coordinate system, 616
liquid layer, 616–617
vapor system, 617–620
Laminar flows
Newtonian slurries, 415
non-Newtonian slurries
Bingham plastics model, 415–416
Casson model, 417
Herschel–Bulkley model/generalized Bingham model, 416
numerical integration method, 417
power-law model, 415
pipeline pressure loss, 414
shear stress, 414
volume flow rate, 414
Large eddy simulation/filtered mass density function (LES/FMDF) model
atomization, 1137–1138
block diagram, 534
chemical kinetics model, 536
drop response time, 537
filtered gas dynamics equations, 534
FMDF equations, 534–535
Fokker–Planck differential equation, 537
high-speed turbulent spray, 538
Lagrangian equations, 536
Spalding mass transfer number, 538
symmetric heat and mass transfer equations, 537
turbulence, compressible flows, 463
Laser Doppler velocimetry (LDV), 499–500
Lattice Boltzmann method (LBM), 66–67
Boltzmann equation, 108
conservation of momentum, 108
deformable fibers
flexible fiber model, 119–120
linear shear flow, 120
relative shear viscosity, 121
deformable particles and capsules
finite element method, 116–117
spectrin-link method, 117–119
equilibrium density distribution, 109
fluid-solid interaction
EBF, 112–114
linear shear flow, 114–116
SBB, 109–112
liquid-gas flow
free energy model, 123
front tracking, 124–125
mean field theory model, 124
R-K model, 122
S-C model, 122–123
particle velocity, 108
Level set (LS) method, 1134
Lewis number, 521
Limiting particle trajectory, 835
Liquid flow blockage model, 590
Liquid-fuel spray group combustion, 527–528
Liquid instability sheet atomization (LISA) model, 1129–1130
Liquid-phase particle separation
cut size control
classification performance, 880–881
cross section of cyclone with guide plate, 880–881
experimental apparatus, 879–880
hydrocyclones
characteristics, 877
fractional separation efficiency and corrected one, 877, 879
normal operating conditions, 877
standard cyclone and flow pattern, 877–878
tangential liquid velocity distribution, 877–878
tangential velocity, 877
inlet slurry temperature effect, 880–882
wet separation, 877
Liquid-solid flows, 746–747
Liquid-solid fluidized beds (LSFBs), 1053–1054
Liquid sublayer dryout model, 590
Lithium niobate (LN) probe
cloud pressure, 501
current, time history, 500
engineering diagram, 499
height, 501–502
quasi-static failure stress, 499
sensitivity, 499
voltage, 501–502
vs. x-ray measurements, 501–502
Log-normal distribution, 15
Louver-type dust collector, 863–864

M

Mach and Reynolds number effects, 476–477
Mainwaring and Reed classification, bulk solids
deaeration factor, 361–364
permeability factor, 360–361
Marker-and-cell (MAC) method, 96–97
Mass transfer
chemical reactions, 23–24
fluid spheres, 1357–1359
thermodynamic equilibrium
Clausius–Clapeyron equation, 20
diffusion coefficient, 22
droplet diameter, 22
Fick's law, 22
internal pressure, 20
Kelvin number, 21
mass conservation equation, 21
mole fraction, 21
partial pressure, 19–20
phase transition, 20
pressure and temperature fields, 19
Ranz–Marshall relation, 22
saturation relation, 20
Sherwood number, 22
sublimation and evaporation, 21
vapor pressure, 19
velocity, 21
Maxey–Riley–Gatignol (MRG) equation, 487
Maximum entropy formalism (MEF), 1160–1161

Mean depth of penetration rate (MDPR), 778
Mean field theory model, 124
Mercury injection method, porosity, 687
Mesoscopic Eulerian formalism (MEF), 189
Mesoscopic Eulerian particle velocity fields (MEPVF), 186–189
Metal-matrix-composite (MMC) particles
  ceramic particles, 1202
  generation of, 1203–1204
  macroscale, 1204–1205
  mesoscale, 1206–1207
  microscale, 1206–1207
  particle incorporation efficiency, 1207–1208
Metzner–Reed method, 423
MFIX
  accessing, 262–263
  Cartesian grid cut-cell technique, 260–262
  conductive heat flux, 253
  conservation
    of internal energy, 251–252
    of mass, 244
    of momentum, 245
  continuous integration, 243
  CVS database, 242
  development, 243
  filtered models, 258–260
  gas-phase stress tensor, 247–248
  gas-solid heat transfer, 252–253
  gas-solid momentum transfer, 245–247
  high-fidelity gasifier simulations, 265–266
  history, 242–243
  initial and boundary conditions, 253–254
  kinetic theory, 264
  Lagrangian solid model, 242
  NETL, 242
  numerical method, 254–255
  point sources, 258
  pyroclastic flows, 268–269
  solid-phase stress tensor, 243
    formulation, 248
    plastic regime, 248–249
    viscous regime, 249–251
  spouted-bed nuclear fuel coater, 267–268
  stiff chemistry solver, 256–257
  subgrid cylinder array model, 264–265
  using, 262–263
  variable solid density, 257–258
  wood gasification, 266–267
Microbubbles, 762–763
Microgravity two-phase flows
  annular flow, 546–547
  applications of, 545–546
  bubbly flow, 546–547
  flow pattern map, 548
  flow pattern transitions, 547–548
  gas–liquid pressure drop
    dimensional analysis model, 550
    empirical methods, 549
    homogeneous model, 549–550
    Lockhart–Martinelli correlation, 550
    momentum equations, 549
  heat transfer, 551–554
  interfacial waves, 554
  slug flow, 546–547
  transitional flow, 546–547
  void fraction, 551
  wave shape, 554–555
Microlayer evaporation, 567
Mie–Grüneisen equation, 470
Minimum fluidization velocity
  large particles, 956, 961
  vs. particle diameter, 956, 960
  pressure drop, 957–958
  small particles, 961
  time-mean pressure, 958
  transition, 958–960
Mixed-fluid approach, 89–90
Mobility, relative permeability, 710–711
Mohr–Coulomb model, 639
Molecular dynamics (MD) method, 1280–1281
Momentum transfer
  blowing effects, 34–35
  boundary effects
    Bohlin expression, 49
    cylindrical boundary, 49
    dispersed flows, 51
    Faxen's expression, 49
    flow inertia, 49
    migration velocity, 50
    Stokes drag coefficient, 52
    suspended and settled particles, 51
    2D drops, 51
    wall correction factor, 49–50
  characteristic velocity, 24
  compressibility and rarefaction effects, 35–37
  deformable bubbles and drops, 43–45
  deformable particle, 41–43
  dimensionless expression, 24
  flow turbulence, 33–34
  hydrodynamic force, 24, 47–48, 52
  irregular particle, 41–43
  lift effects and transverse forces
    conditions, 46
    evaporation/sublimation, 48–49
    growing/receding bubbles and drops, 47
    lift coefficient, 47
    magnitude, 47
    Magnus force, 46–47
    rotation parameter, 46
    suspended particles, 48
  mass conservation equation, 24
  Oseen equations, 24
  Reynolds number effects
    interfacial velocity slip, 32–33
    solid spheres, 27–29
    viscous spheres, 29–32
  Stokes/creeping flow, 25–26
  thermophoresis and turbophoresis, 52–54
  transient flow effects
    creeping flow, 37–39
    hydrodynamic force, 40
    semiempirical equations, 40–41

Monte Carlo (MC), 1280–1281
Multicomponent and multiphase continua, 456
  equation of state, 470–471
  Eulerian approach, 459–468
  jump relations, 470–472
  Lagrangian approach, 459
  shock interaction, material interfaces, 468–469
Multiphase flow
  concentration effects
    Brinkman screening length, 67
    bubbles, 67–68
    dilute, 65–66
    drag coefficient, 66–67
    finite element methods, 66–67
    fluidization systems, 66
    hydrodynamic force, 67
    LBM, 66–67
    mass coefficient, 68
    porous particles, 68–69
    viscous fluid, 68
  Corey shape factor, 8
  dimensionless numbers, 6–7
  dispersed phase, 1
  equivalent diameter, 7–8
  fractal dimension, 8–10
  gas-liquid flows, 1
  gas-particle flows, 1–2
  heat transfer
    blowing effects, 61–62
    creeping/Stokes flow, 54–56
    flow turbulence, 60
    Peclet number, 54
    Prandtl number, 54
    radiation effects, 64–65
    Reynolds number effects, 56–59
    rotational motion, 59–60
    transient effects, 62–64
  liquid-solid flows, 2
  mass transfer
    chemical reactions, 23–24
    thermodynamic equilibrium, 19–22
  momentum transfer
    blowing effects, 34–35
    boundary effects, 49–52
    characteristic velocity, 24
    compressibility and rarefaction effects, 35–37
    deformable bubbles and drops, 43–45
    deformable particle, 41–43
    dimensionless expression, 24
    flow turbulence, 33–34
    hydrodynamic force, 24
    irregular particle, 41–43
    lift effects and transverse forces, 46–49
    mass conservation equation, 24
    Oseen equations, 24
    Reynolds number effects, 27–33
    Stokes/creeping flow, 25–26
    thermophoresis and turbophoresis, 52–54
    transient flow effects, 37–41
  phase velocity, 4
  quality, concentration, and loading, 4
  response times, 4–6
  separated flow, 1
  size distributions
    continuous distribution, 11–13
    discrete distribution, 10–12
    log-hyperbolic distribution, 17–18
    log-normal distribution, 15
    mean, 14
    median, 15
    mode, 14
    Nukiyama–Tanasawa distribution, 17
    Rosin–Rammler distribution, 16–17
    sauter mean diameter, 14
    square-root normal distribution, 16
    upper-limit log-normal distribution, 16
    variance, 14
  superficial velocity, 4
  three-phase flows, 2
  transport coefficients, 18
  volume fraction and densities, 3–4

N

Nanofluids
  boiling
    CHF, 1078–1079
    convective/forced boiling, 1077–1078
    pool boiling, 1077
  effective diffusivity
    analysis, 1080–1081
    experimental studies, 1081–1082
    mass transfer equation, 1080
    molecular diffusivity, 1082
    NMR/permeable membrane, 1082–1083
    process of, 1079–1080
  effective viscosity
    alumina-water nanofluids, 1062–1063
    analytical studies, 1061–1062
    correlation function, 1063–1064
    diameter, 1064
    fluid viscosity, 1062
    intrinsic viscosity, 1063
    non-Newtonian fluids, 1064–1067
    temperatures and shear rates, 1063
  heat transfer characteristics, 1059
  heat transfer coefficients, 1075–1076
  mass transfer characteristics, 1059
  metallic and oxide nanofluid, 1059–1060
  natural convection, 1076
  specific heat capacity, 1083–1084
  thermal conductivity
    analytical expressions, 1068–1069
    Brownian movement, 1072–1073
    electric charges, 1072
    experimental studies, 1067–1068
    heat transfer mechanism, 1074
    interfacial solid layer, 1072
    parameters, 1074
    particle conductivity, 1069–1070
    particle distribution and aggregation, 1073–1074
    particle orientation, 1070–1072
    particle shape, 1070

pH, 1072
preparation, 1074
ratio of, 1059–1060
surfactants, 1074
transient motion, 1073
transport properties, 1060–1061
Nanoparticles, mass diffusion, 904
National Energy Technology Laboratory (NETL), 242
Navier–Stokes equations, 481
Near-wall bubble crowding model, 590
Necking breakup, 815–816
Negative slip model, 664–665
Net vapor generation (NVG), 578
Newitt correlation, 432
Newtonian fluid, 1060
NMR, 1072, 1082–1083
Nonboiling two-phase flow, *see* Two-component two-phase flow
Nonlinear oscillations, microbubble, 762
Nonlinear Taylor analogy breakup (NLTAB) model, 1149–1150
Non-Newtonian fluids
CNT, 1066–1067
fluid-solid suspensions, 1064–1065
fluid spheres
bubbles, 1357–1359
drops, 1359–1360
momentum, 1356
viscoelasticity, 1360
wall effects, 1360
linear velocity profile, 1322
local shear, 1064, 1066
nonspherical particles
Bingham plastic fluids, 1354–1356
equal volume sphere diameter, 1352
power-law fluids, 1352–1354
regular-shaped object, 1351–1352
sphericity, 1352
power-law fluids
continuity equation, 1330
drag coefficient, 1331
drag correction factor, 1331
drag force, 1331
forced convection regime, 1334–1336
heat transfer, 1333–1334
momentum equation, 1331
nonspherical particles, 1352–1354
Reynolds number, 1331–1333
wall effects, 1337–1339
preparation and treatment, 1066
shear thinning, 1065
time-dependent fluid behavior, 1327–1329
time-independent fluid behavior
qualitative flow curves, 1323
shear stress and shear rate, 1322
shear-thickening, 1325–1326
shear-thinning, 1323–1325
unidirectional shearing flow, 1322
viscoplastic fluids, 1326–1327
viscoelastic fluid behavior, 1329–1330
viscoelasticity effect, 1356
viscoplastic fluids
drag behavior, 1340–1345
heat transfer, 1345–1349
static equilibrium, 1340
wall effects, 1350–1351
yield surfaces, 1340–1342
weak gel structures, 1065–1066
Nonsettling slurries
pressure loss, pipe fittings, 424
pressure loss, straight circular pipe
friction factor, 414
laminar flows, 414–417
laminar–turbulent transition, 422–423
turbulent flows, 417–422
rheological models
Newtonian slurries, 411
non-Newtonian slurries, 412–413
property, 411
Nonspherical particles
Bingham plastic fluids, 1354–1356
equal volume sphere diameter, 1352
power-law fluids, 1352–1354
regular-shaped object, 1351–1352
sphericity, 1352
Nucleate boiling
bubble dynamics, 564–566
contact angles q, 568
C_{sf} and n values, 567–568
dimensional analysis, 568
fluid-surface effect, 567
fully developed nucleate boiling, 560
heat transfer mechanisms, 566–567
with mixtures, 569–571
numerical approach, 567
Nusselt number, 569
ONB, 560–564
reduced pressures p/p_{cr}, 568
Nucleation
aqueous droplets, 1290
CNT
assumptions, 1276
bubble nucleation, 1278
critical droplet-free energy, 1278
diffuse interface theory, 1280
entropy, 1279–1280
equilibrium cluster distribution, 1276–1277
experimental data, 1278
free energy, 1280
isothermal nucleation, 1280
macroscopic thermodynamic properties, 1278–1279
monomers, 1277
numerical simulations, 1280–1281
preexponential factor, 1279
rate per unit volume, 1276
second-order approximation, 1277
translation-rotation paradox, 1279
Zeldovich nonequilibrium factor, 1277
DFT, 1281–1283
first-order phase transition, 1275
heterogeneous, 1286–1289

homogeneous, 1275
multicomponent, 1284–1286
theorems, 1283–1284
Nukiyama–Tanasawa distribution, 17
Numerical integration method, 417
Numerical simulation, single bubble dynamics
boundary conditions at gas–liquid interface
for energy conservation, 757
for mass conservation, 756
for momentum conservation, 756
bubble motion and mist formation, 758–760
governing equations
gas phase, 754–755
liquid phase, 755–756
pressure and temperature distribution, 757–758
single-phase and multiphase flows, 753
thermal diffusion effect, bubble motion
computational conditions, 757–758
helium bubble, 759
mean temperature, 757–758
pressure, bubble center, 757–758
properties of internal gas, 759
time histories, bubble radius, 757–758

O

Obstacle-through-type dust collectors, 832
Obstacle-type separators
collection efficiency, 862
schematic representation, 861
single body collection efficiency, 862
single collecting obstacles, 862–863
One-component two-phase flow, 287
Onion skin model, 522
Onset of nucleate boiling (ONB)
flow boiling, 578–579
nucleate boiling
Clausius–Clapeyron equation, 563
critical radius, 564
definition, 560
liquid temperature profile, 563
metastable liquid and vapor conditions, 561
vapor bubble growth, 562
Optical shadowgraphy, 501–503
Oseen equations, 24
Overall separation efficiency, 830–831

P

Partial/attached cavitation, 774
Partial separation efficiency, 830–831
Particle dispersion, 732–733
Particle momentum number, 747–748
Particle motion and distribution, 731–732
Particle–particle interaction
cohesive force
adhesion, 801
electrostatic force, 802–803
force due to liquid bridge, 802
Van der Waals forces, 803–804
hard sphere model, 796–797
particles colliding, 794–795
soft sphere model
Coulomb-type friction law, 799
damping coefficients, 800–801
damping vibration, 796–797
normal force, 798
particle with several contact forces, 799
stiffness, 800
tangential force, 798–799
two particles contacting, 797–798
Particle residence time (PRT) distribution, 1220–1221
Particle separation methods and systems
air filters, 864–870
bag filters, 873–876
barrier-type separators, 873
centrifugal separation, dry cyclones, 837–848
classification, 831–832
electrostatic precipitators, 848–861
flow-through-type separators, 833–836
grade efficiency, 830–831
gravitational collectors, 836
inertial dust collectors, 863–864
liquid-phase particle separation (hydrocyclone), 877–882
obstacle-type separators, 861–863
scrubbers, 870–873
separation efficiency, 829–831
Particle source in cell (PSIC) method, 532
Particle velocity vectors, 79–80
Particle–wall interaction
momentum and energy exchange at walls
compression and recovery periods, 806
difference in angular momentum, 805
particle colliding with wall, 805
pre-and postcollisional velocities, 807
three-dimensional particle-wall collision, 806–807
nonspherical particles and rough walls
contact point between particle and wall, 808
irregular bouncing, 807–808
particle collision with rough wall, 808
regular bouncing, 807–808
wall roughness model, 808–809
Penetration fraction, 1302
Penetration ratio, 1302
Permeability, porous medium
averaging techniques, 698
coal permeability, 696–697
Darcy's law, 692–693
directional, 699–700
distribution, 698
hydraulic conductivity, 694
interstitial velocity, 693
Klinkenberg effect, 695–696
measurements, 695–696
for radial flow of gas, 694–695
for radial flow of liquid, 694
relative, 708–715
superficial velocity, 693
Phase Doppler interferometry, 528
Pneumatic atomizer, 1094–1095, 1100–1101
Pneumatic conveying systems
air movers
classification, 374–375
fans, 379–380

rotary lobe blowers, 380–381
screw compressors, 381
application, 357
bulk solids
conveying characteristics, affecting properties, 359
Geldart/Dixon classification, 360–361
Jones and Mills classification, 364
Mainwaring and Reed classification, 360–364
Pan classification, 364–365
pilot-scale tests, 365
choking velocity, 371–372
components, 357
dense phase conveying
classification of, 375
description, 372
discontinuous dense phase, 376
extrusion flow, 376
phase diagram, 367–369
two-phase flow, 376
design errors
component selection, 404
conveying line layout, 403–404
conveying velocity selection, 402–403
dense phase conveying lines, 405
dual-purpose systems limitations, 405
elbows and bends usage, 403–404
gas leakage, 404
multiple source and multiple destination systems, 404
dilute phase conveying
closed-loop systems, 373–374
description, 372
designing steps, 393–398
feeder type/air-solids' mixing device, 374
open-loop systems, 373
phase diagram, 365–367
pressure drop calculation, 382–393
pressure type, 372–374
disadvantages, 357
feeders
blow tanks, 378–379
material suitability, 377
operating range, 377
rotary airlock/feeder, 378
flow patterns
for coarse granular materials, 359–360
for fine powders, 359
for gas and solid particles, 358
gas-solid separation devices, 382
performance measurement, 405
saltation velocity, 367–371
start-up, 406
stepping pneumatic conveying lines, 398
troubleshooting basics, 405–406
wear, 406–407
Zenz plot, 365–366
Point force approach, 91–92
Pool boiling, 1077
applications, 559
boiling curve, 559–560
definition, 559
enhancement
classification, 573
microstructures, 574
patterned surface, 574
reentrant cavity, 573
film boiling region, 560–561, 575–577
natural convection, 560
nucleate boiling
bubble dynamics, 564–566
CHF, 560, 571–575
contact angles q, 568
C_{sf} and n values, 567–568
dimensional analysis, 568
fluid-surface effect, 567
fully developed nucleate boiling, 560
heat transfer mechanisms, 566–567
with mixtures, 569–571
numerical approach, 567
Nusselt number, 569
ONB, 560–564
reduced pressures p/p_{cr}, 568
orientation effect, 569–570
saturated pool boiling, 560
subcooling, 569
transition boiling region, 560, 575–577
Porous medium
fractional flow, two immiscible fluids, 715–717
geostatistics, 698–699
immiscible displacement
Buckley–Leverett theory, 718–719
frontal advance in fracture, 720–721
nonwetting phase and wetting phase, 717
Welge's method, 719–720
permeability, 692–715
porosity
Archie's equation, 691–692
bulk volume of block, 685–686
coal porosity, 687–689
compressibility, 689–690
density method, 687
distribution, 697
effective porosity, 686–687
formation resistivity factor, 691
gas expansion method, 687
hydraulic radius, 690
imbibition method, 687
mercury injection method, 687
pore volume, 686
probability, 697
saturation and fluid volume, 691
specific surface, 690
tortuosity, 690
reservoir flow model
black oil simulator equations, 722–725
continuity equation, 721–722
workflows, 725
rock–fluid interaction
capillary pressure and capillary radius, 702–704
capillary pressure and height of interface, 704–705
capillary pressure measurement, 706–707

coal capillary pressure, 704
surface tension and interfacial tension, 700–701
wettability, 702
Porous membrane filters, 1311–1312
Powder and granular flow
boundary condition, 642–643
collisional stress model, 638–639
composite stress model, 640
depth-averaged shallow flow model, 643–644
frictional stress model, 639–640
particle-based simulations, 644–647
phenomenological model, rheology law, 640–642
segregation phenomenon and cohesion effect, 673–675
vertical vibration bed
dynamics and flow physics, 648–657
problem, 647–648
theoretical modeling, 657–673
Power-Law fluids
continuity equation, 1330
drag coefficient, 1331
drag correction factor, 1331
drag force, 1331
forced convection regime
correction factor, 1334
free convection regime, 1335–1336
isoheat flux sphere, 1335
mixed-convection regime, 1336
Nusselt number, 1334–1335
heat transfer, 1333–1334
momentum equation, 1331
nonspherical particles, 1352–1354
Reynolds number, 1331–1333
wall effects, 1337–1339
Power-Law model, 413, 1324–1325
Pressure atomizer, 1094, 1099–1100
Pressure gradient effects, 736–737
Pressure swirl atomizer
air core, 1101–1102
atomizer constant, 1103
discharge coefficient, 1103
discharge velocity, 1104–1105
film thickness, 1103–1104
spray angle, 1104
Pressure type dilute phase conveying system
characteristics, 373–374
positive pressure/push system, 372–373
push-pull system, 371
vacuum/pull system, 371
Pressurized fluidized bed combustor (PFBC), 1043
Probabilistic reservoir forecasting, 725
Probability density function (Pdf)
aerodynamic force, 147
analytic forms, 192–194
collision kernel predictions, 194
constitutive relations
GLM, 160–164
kinetic model, 158–161
continuum equations, 157–158
definition, 144
density-weighted particle velocity, 152
diffusion equation, 152
energy conservation, 147
evaporating/condensing particle, 146
Gaussian, 152
inertial particles, 147–148
kinetic method, 145
momentum conservation, 147
nonreactive gas-particle flows
kinetic model, 148–151
SDM, 151–152
particle equations of motion, 146
particle pair mixing and dispersion
binary collision rates, 175
dispersed phase continuum equations, 178–183
equation and solutions, 189–194
local fluid motion, 175
particle collision kernel, 176
particle-fluid velocity correlation, 176–178
RUM and caustics, 194–198
particle segregation and demixing, 184–186
phase space dimension, 145–146
RUM and MEPVF, 186–189
simple shear and rotational flows
GLM, 155–157
kinetic model, 154–155
spherical droplet, 146
turbulent boundary layers
continuum theory, 166
diffuse reflection, 170
gravitational force, 167
Hermite polynomials, 167–168
interface and wall bc's, 168
particle deposition, 171–172
particle impact and rebound velocities, 166–167
particle resuspension, 172–175
peaks, 169
specular reflection, 168–169
transport and deposition, 170–171
universal form, 167
uniform flows, 153–154

Q

Quantity of interest (QoI), 278, 283
Quick contact (QC) reactor, 1034–1035

R

Radial distribution function (RDF), 735–736
Random-uncorrelated motion (RUM), 186–189
Rankine–Hugoniot jump conditions, 470
Ranz–Marshall relation, 22
Rapid granular flow, 638
Rayleigh–Taylor (RT) instabilities, 462
Rectified diffusion, 780
Reduced-order modeling, single bubble
compressibility effect in liquid phase, 760–761
thermal phenomena effect in gas phase, 761–762
Relative conductivity, 1059–1060
Relative mobility, 710–711
Relative permeability
coal relative permeability, 708–710
correlations, 715

Darcy's law, 710
effective permeability, 707–708
interfacial tension effect, 711–713
mobility and relative mobility, 710–711
viscosity ratio effect, 713–714
wettability effect, 711
Removal efficiency, 1302
Reservoir flow model
black oil simulator equations, 722–725
continuity equation, 721–722
workflows, 725
Residue fluid catalytic cracking (RFCC), 1034
Resolved discrete particle model (RDPM), 141–142
Resolved-surface approach, 93–95
Reversed convection and roll doubling
container shape effect, 656–657
overall dynamics, 657
phenomenon and mechanism, 650–653
surface pattern and base arch, 653–656
Reynolds averaged Navier–Stokes (RANS) model, 463, 531, 895, 1137–1138
Rheology law, phenomenological model, 640–642
Richtmyer–Meshkov (RM) instability model, 462, 505–508
Rock–fluid interaction
capillary pressure
and capillary radius, 702–704
and height of interface, 704–705
measurement, 706–707
coal capillary pressure, 704
surface tension and interfacial tension, 700–701
wettability, 702
Rosin–Rammler distribution, 16–17
Rotary atomizer, 1105
Rotating drum flow, 643
Rothman and Keller model, 122

S

Saltation velocity
correlation selection guidelines, 370
of fine powders, 369–370
Matsumoto correlation, 369–371
nondimensional representation, 367
power-law index, 369
Rizk correlation, 370–371
solids loading *vs.* Froude number, 367–368
Saurel's model, 467–468
Sauter mean diameter (SMD), 14, 814
Scrubbers
performance, 870–871
Rem vs. collector diameter, 872–873
Reynolds number, 872
separation efficiency, 871
Stokes number, 872
types, 870–871
Secondary flow intensity (SFI), 221, 222–223
Segregation phenomenon and cohesion effect, 673–675
Separated flow model (SFM)
adiabatic and evaporating flow conditions, 325–326
annular flow, 324
conditional equations, 326
frictional component, 324–325
interfacial slippage, 323
refrigerants, 327
single-phase Darcy friction factor, 327
single-phase friction factors, 325
two-phase frictional multiplier, 325–326
two-phase mixture density, 323–324
volume fraction, 324
Separation efficiency, 829–831
for laminar flow, 834–835
for turbulent flow, 835–836
Settling slurries, heterogeneous flow
horizontal pipe flows
combined homogeneous–heterogeneous flows, 438
critical velocity, 425–430
pressure loss, 430–438
transitional velocities, 424–425
inclined slurry pipe flows, 439
vertical pipe flows, 438–439
Shan and Chen model, 122–123
Shear breakup, 812–813
Sheet cavitation
complex bubble-boundary layer interactions, 782–783
on 2D NACA009 hydrofoil, 781–782
partial cavities, 783–784
partial cavity and supercavity, 782
σ-α space, 782
Strouhal number (*St*), 783
Sherwood number, 522
Shocked continua interfaces
amplitude variations, 495
defect volume, 496
Dynasen piezoelectric probes, 497, 499
HE physics and diagnostics package, 497–498
high explosive-and gun-driven ejecta experiments, 497–498
LDV, 499–500
lithium niobate probe
cloud pressure, 501
current, time history, 500
engineering diagram, 499
height, 500–502
quasi-static failure stress, 499
sensitivity, 499
voltage, 501–502
vs. x-ray measurements, 501–503
mass measurements, 496
mass-velocity distributions, 497
optical shadowgraphy, 503–505
preshocked and postshocked geometries, 495–496
Richtmyer–Meshkov instability model, 505–508
shock wave, 495
surface roughness, 496
Shock-particle interaction
direct numerical simulation, 489
Faxén theorem, 487
length scale, 487–488
MRG equation, 487
particle deformation, 489–491
point-particle model, 489

standard quasi-steady drag model, 489
viscous-unsteady kernels, 488
volume and surface averages, 488
Simple shear flow, 643
Single drop combustion, 527
Single-phase gaseous combustion, 516–518
Sisko model, 413
Slurry flows
apparent viscosity, 408
design procedure, 439–441
flow velocity, 407
heterogeneous flow
with moving bed, 409–410
settling slurries, 424–439
solids' concentration profiles, 409
with stationary bed, 409–410
homogeneous flow
of nonsettling slurries, 411–424
particle distributions, 409
principle of continuum mechanics, 409
solids' concentration profiles, 409
intermediate regimes, 409
mass fraction, 407–408
measurement techniques
flow rate, 446–449
particle size, 449
pressure, 449
slurry viscosity, 443–444
solids' concentration, 443–446
in pipe, 410
predictive model limitations, 441–442
slurry density, 408
transient pipe flow behavior, 442
volume fraction, 407
Soft-sphere contact model
bulk properties estimation, 646
contact model effect, 646–647
parameters, 644–646
Solid spheres, 27–29
Sonoluminescence, 781
Spalding mass transfer number, 536
Spalding number, 517
Spatial averaging, 455
Specific surface, porous medium, 691
Spectrin-link (SL) method, 117–119
Spontaneous drop spreading, 819–820
Spray atomization, 813
Spray drying
agglomeration model, 1221–1222
air-spray flow pattern, 1218–1220
configuration, 1216–1217
particle-gas interaction, 1217–1218
particle-wall deposition, 1221–1222
PRT distribution, 1220–1221
turbulence level, 1220
Spray forming
advantages, 1208–1209
deposition efficiency, 1214–1216
particle transport, 1211–1214
principle of, 1208–1209
twin-fluid atomization, 1209–1211
Spray pyrolysis (SP)
CSP, 1192–1193
FASP, 1194
flame-made powder, 1198, 1200
FSP, 1194–1196
impermeable crust, 1192–1193
particle characteristics, 1197–1199
particle formation mechanism, 1193
USP, 1195–1197
VAFS, 1194
Spray system
atomization
CAB model, 1148
characterization, 1098
continuous jet length, 1121–1122
DNS, 1132–1137
droplet breakup mechanism, 1142–1145
droplet deformation model, 1149–1152
efficiency, 1097–1098
electrostatic atomizer, 1096
ELSA model, 1141–1142
empirical drop size correlation, 1161–1162
energy demand, 1094, 1098
ETAB model, 1147–1148
gas flow, 1108–1115
glass/slags, 1155–1159
gravity-stretched laminar threads, 1131–1132
highly viscous liquids, 1152–1155
ICM, 1138–1141
large-wavelength area, 1124
LES, 1137–1138
liquid flow, 1099–1108
LISA model, 1129–1130
LPT, 1138–1141
MEF, 1160–1161
melts, 1154–1155, 1164–1165
monosized droplet generation, 1095–1096
pneumatic atomizer, 1094–1095
polymer melts, 1155
prefilming hybrid atomizer, 1096–1097
pressure atomizer, 1094
pressure swirl atomizer, 1117–1119
principles, 1093
processes, 1091–1093
rotary atomizer, 1095, 1119–1121
semiempirical breakup models, 1145–1146
single-fluid atomization, 1115–1117
size parameters, 1098–1099
small-wavelength area, 1124–1129
solid/liquid suspensions, 1158–1160
specific energy input, 1097
spherical drop, 1122–1123
surface-tension forces, 1122
surface wave, 1123
suspension atomization, 1162–1164
TAB model, 1146–1147
tundish reactions, 1154–1155
twin-fluid atomizer, 1117
ultrasonic atomizer, 1095–1096
viscous forces, 1123
wave/KH breakup model, 1148–1149

dental amalgams, 1198
fuel injection, 1189–1192
MMC particles, 1202–1208
particle shapes, 1199–1201
spray behavior
clustering of droplets, 1173–1175
coalescence, 1166
collisions, 1166–1169
DNSs, 1169–1170
drying mechanism, 1181–1183
environment interaction, 1179–1180
features, 1165
individual droplet behavior, 1175–1177
numerical models, 1171–1173
particle relaxation time, 1165–1166
single droplet drying, 1183–1185
solidification, 1185–1186
spray cone spreading, 1178–1179
transfer mechanisms, 1179–1181
spray-drying, 1216–1222
spray forming, 1208–1216
spray impact
drop impingement, 1186
spray quenching, 1186–1188
spray painting and coating, 1223–1225
spray pyrolysis, 1192–1198
surface morphology and microstructure, 1199, 1201
thermal losses, 1201–1202
two-phase flow field, 1202–1203
Spray transport, 809–810
Square-nosed slugging, 972–973
Square-root normal distribution, 16
Stability function method, 423
Standard bounce-back (SBB) method, 109–112
Stationary (bubbling) fluidized bed combustors (SFBCs), 1041–1043
Stefan flow, 524–526
Stepping pneumatic conveying lines, 396
Stokes flow, 25–26
Stokes load, 747
Stokes number *(St)*, 474, 729
Stratified flow, 290
ARS model, 330–331, 334–335
double circle model, 331–332, 335–336
geometry considerations, 329
Taitel and Dukler (1976) model, 329–330, 333–334
transitions, 297–299
Streamwise normal stress, 745
Streamwise turbulence intensity, 744–745
Stretching separation, 817–818
Stretching/thinning breakup, 812–813
Superficial velocity, 693
Surface tension, 700–701
Surrogate model, 280

T

Taitel and Dukler (1976) model, 327–328, 331–332
Temporal averaging, 456
Thermophoresis, 52–54, 1300–1301
Thin-film evaporation, 559
Thoma number, 786–787
Three-phase fluidized beds, 1054
Time-dependent fluid behavior, 1327–1329
Time-independent fluid behavior
qualitative flow curves, 1323
shear stress and shear rate, 1322
shear-thickening, 1325–1326
shear-thinning
apparent viscosity, 1323
Carreau viscosity equation, 1325
Cross model, 1325
polymer solution, 1323–1324
Power-Law model, 1324–1325
unidirectional shearing flow, 1322
viscoplastic fluids
Bingham model, 1326
Casson model, 1326–1327
fluid yield stress, 1326
Herschel-Bulkley model, 1326
Tip streaming, 815–816
Tortuosity, 690
Transient conduction, 566–567
Transport coefficients, 18–19
Transport disengaging height (TDH), 970–972
Turbophoresis, 52–54, 1298–1299
Turbophoretic velocity, 733
Turbulence, compressible flows
for binary fluid mixture, 464
density-specific volume covariance, 464
DNS, 463
Godunov scheme, 465
heavy gas (SF_6) curtain, 462
length scale, 464
LES, 463
mixing zone thickness, 465–466
pressure strain models, 464
RANS approach, 463
Reynolds stresses, 463, 465–466
RM instabilities, 462
RT instabilities, 462
turbulent diffusion process, 463
velocity profile, 465–466
yield strength, 464
Turbulence effects, human airway system, 895–896
Turbulence interactions
added mass, 736–737
Basset force, 736–737
coupling forces and heat transfer, 737–738
gravitational effects, 736
particle dispersion, 732–733
particle motion and distribution, 731–732
preferential concentration
box counting methods, 735
correlation dimension, 736
divergence of particle velocity, 734
homogeneous turbulence, 735
particle-laden flow in forced air jet, 734
Poisson distribution, 735
RDF, 735–736
turbulent wall-bounded flows, 734

pressure gradient, 736–737
turbulence attenuation and augmentation
carrier-phase mean velocity, 740
extra dissipation of turbulence, 741
force field, 741
Navier–Stokes equations, 741
randomly positioned laminar wakes, 740
transport equation, TKE, 741
turbulence modulation
definition, 738
free shear flows, 746
homogeneous gas-solid flows, 742–744
liquid-solid flows, 746–747
parameterization, 747–748
TKE, 738–739
wall-bounded gas-solid flows, 744–746
Turbulent film theory, 620–622
Turbulent flows, 1258
Bingham plastic slurries models, 421–422
Herschel–Bulkley models/generalized Bingham slurries, 421
Newtonian slurries, 417–418
non-Newtonian slurries, 418
power-law slurries, 420
Wilson and Thomas model, 418–420
Turbulent fluidization
axial and radial voidage variation, 973–974
chemical reaction, 974
entrainment, 975
gas and solids mixing, 974
mass transfer, 974
Turbulent impaction, 1298–1299
Turbulent kinetic energy (TKE), 730, 738–747
Turbulent pipe flow, 1307–1309
Turian's correlations, 429
Turian–Yuan correlation, 434–435
Two-component two-phase flow, 287
Two-fluid model (TFM); *see also* MFIX
accessing, 262–263
Cartesian grid cut-cell technique, 260–262
conductive heat flux, 253
conservation
of internal energy, 251–252
of mass, 244
of momentum, 245
continuous integration, 243
CVS database, 242
development, 243
filtered models, 258–260
gas-phase stress tensor, 247–248
gas-solid heat transfer, 252–253
gas-solid momentum transfer, 245–247
high-fidelity gasifier simulations, 265–266
history, 242–243
initial and boundary conditions, 253–254
kinetic theory, 264
Lagrangian solid model, 242
NETL, 242
numerical method, 254–255
point sources, 258
pyroclastic flows, 268–269
solid-phase stress tensor, 248–249
formulation, 248
plastic regime, 248–249
viscous regime, 249–251
spouted-bed nuclear fuel coater, 268–269
stiff chemistry solver, 256–257
subgrid cylinder array model, 264–265
using, 262–263
variable solid density, 257–258
wood gasification, 266–267
Two-layer model, 435–438
Two-phase pressure drop modeling
homogeneous flow model, 321–323
SFM
adiabatic and evaporating flow conditions, 325–326
annular flow, 324
conditional equations, 326
frictional component, 324–325
interfacial slippage, 323
refrigerants, 327
single-phase Darcy friction factor, 327
single-phase friction factors, 325
two-phase frictional multiplier, 325–326
two-phase mixture density, 323–324
volume fraction, 324
two-phase friction factor models, 327–328
Two-phase theory of fluidization, 965
Two-phase turbulent combustion
dense regime, 532
dilute spray regime, 532
Eulerian–Eulerian approach, 530
Eulerian–Lagrangian approach, 531
Lagrangian–Lagrangian approach, 531
LES/FMDF model, 533–539
reacting flows modeling, 532–533

U

Ultimate resilience (UR), 778
Ultrasonic cavitation, 780–781
Ultrasonic spray pyrolysis (USP), 1195–1197
Ultrasonic standing wave atomizer (USWA), 1108
Uncertainty quantification
Bayesian calibration, 280–282
calibration process, 283
CFD, 275
hierarchical validation, 282–283
prediction, 278–280, 283–284
verification and validation, 276
Upper-limit log-normal distribution, 16
Upward convection roll
acoustic streaming model, 658–664
negative slip model, 664–665

V

Van Kampen (VK) operator, 150–151
Vapor-fed aerosol flame synthesis (VAFS), 1194
Variable solid density model, 257–258
Verification and validation (V&V), 276
Vertical vibration bed, granular flow
depth profile, 657–658

dynamics and flow physics
reversed convection and roll doubling, 650–657
transition from bouncing bed to convection roll, 648–650
granular leidenfrost effect, 671–673
problem, 647–648
surface pattern via stability analysis, 665–671
upward convection roll
acoustic streaming model, 658–664
negative slip model, 664–665
Vibrating bed flow, 643
Vibratory cavitation, 780–781
Viscoelastic fluid behavior, 1329–1330
Viscoelasticity effect, 1356
Viscoplastic fluids
drag behavior
Bingham plastic model, 1343
biviscous regularization, 1343–1344
dimensionless viscosity, 1342
drag coefficient, 1344
exponential function, 1343
Herschel–Bulkley fluid model, 1344
a priori assumption, 1344
Reynolds number, 1345
solid and fluid regions, 1340, 1342
strain tensor, 1343
heat transfer
forced convection regime, 1345–1346
free convection regime, 1346–1348
mixed-convection regime, 1348–1349
static equilibrium, 1340
wall effects, 1350–1351
yield surfaces, 1340–1342
Viscosity ratio effect, 713–714
Viscous spheres
Bond number, 32
correction functions, 32
drag coefficients, 29, 31
heat transfer, 57–58
streamlines and vorticity, 29–30
Volume-of-fluid (VOF) method, 97, 99, 1134
Vortex cavitation, 784–786

W

Wall-bounded gas-solid flows, 744–746
Wave breakup model, 1148–1149
Weakly separated approach, 90–91
Welge's method, 719–720
Wettability, 702, 711
Wilson's nomogram, 427–428
Wood gasification, 266–267
Wood model, 458

Y

Yield power-law, 413
Young–Laplace equation, 701, 703

Z

Zaichik's model, 197–198
Zandi–Govatos correlation, 428–429
Zenz plot, 363–364